



PROCEEDINGS OF THE SIXTEENTH INTERNATIONAL SYMPOSIUM ON ARTIFICIAL LIFE AND ROBOTICS

(AROB 16th '11)

Jan.27–29, 2011

B-Con Plaza, Beppu, Oita, JAPAN

Editors: Masanori Sugisaka and Hiroshi Tanaka

Publisher: ALife Robotics Co., Ltd.

Publication Date: Jan. 15, 2011

ISBN 978-4-9902880-5-1

Proceedings of the Sixteenth International Symposium on

ARTIFICIAL LIFE AND ROBOTICS

(AROB 16th '11)

January 27- 29, 2011
B-Con Plaza, Beppu, Oita, Japan

Editors: Masanori Sugisaka and Hiroshi Tanaka



AROB 17th '12



Plenary Speakers

We will upload it to our website as soon as it has been decided.

General Chair

Masanori Sugisaka

Program Chair

Hiroshi Tanaka

Vice Chairs

John L. Casti
Yingmin Jia
Ju-Jang Lee
Henrik Hautop Lund
Hiroshi Tanaka

Workshop Chair

Jang-Myung Lee

Advisory Committee Chair

Fumio Harashima

Assistant General Chair

Takao Ito

**ALife ROB
Robotics**



SICE

ICROS



The Seventeenth International Symposium on Artificial Life and Robotics

2nd CALL FOR PAPERS

January 19-21, 2012

B-Con Plaza, Beppu, Oita - JAPAN

History

The AROB was founded in 1996 under the support of Science and International Affairs Bureau, Ministry of Education, Culture, Sports, Science and Technology, Japanese Government. Since then, the symposium organized by the AROB has been held every year at B-Con Plaza, Beppu, Japan except AROB 5th '00 (Oita) and AROB 6th '01 (Tokyo). The seventeenth symposium will be held on January 19–21, 2012, at B-Con

Objective

This symposium will bring together researchers to discuss development of new technologies concerning *artificial life and robotics* based on computer simulations and hardware designs of state-of-the-art technologies, and to share findings on how advancements in artificial life and robotics technologies that relate to artificial intelligence, virtual reality, and computer science are creating the basis for exciting new research and applications in various fields listed in the following Topics.

Topics of interest include, but are not limited

- | | | |
|-------------------------------------|------------------------------------|----------------------------|
| • Artificial brain research | • Artificial intelligence | • Artificial life |
| • Artificial living | • Artificial mind research | • Bioinformatics |
| • Bipedal robot | • Brain science | • Chaos |
| • Cognitive science | • Complexity | • Computer graphics |
| • Control techniques | • Data mining | • DNA computing |
| • Evolutionary computations | • Fuzzy control | • Genetic algorithms |
| • Human-machine cooperative systems | • Human-welfare robotics | • Image processing |
| • Intelligent control & modeling | • Learning | • Management of technology |
| • Medical surgical robot | • Micromachines | • Mobile vehicles |
| • Molecular biology | • Multi-agent systems | • Nano-biology |
| • Nano-robotics | • Neurocomputing technologies | • Neural networks |
| • Pattern recognition | • and its application for hardware | • Quantum computing |
| • Robotics | • Soccer robot | • Virtual reality |
| • Visualization | | |

and also workshop, tutorial, and robotics exhibition will be held at the same time during the symposium (AROB 17th '12). The workshop committee and robotics exhibition committee members will be announced soon.

Important Dates

- | | |
|-----------------------------|---|
| • September 1, 2011 | Abstract submission date |
| • September 15, 2011 | Notification of acceptance |
| • October 1, 2011 | Author's kit except final camera-ready papers |
| • October 15, 2011 | Final camera-ready papers submission date |

Conference Language

- **English**

Publication

Accepted papers will be published in the Proceedings of the AROB. Extended versions of the selected papers will be published in the international journal : **ARTIFICIAL LIFE AND ROBOTICS** and in the special issue on special topics of **Artificial Life and Robotics**, Applied Mathematics and Computation

All correspondence related to the symposium should be addressed to:

AROB Secretariat

ALife Robotics Corporation Ltd.

1068-1 Oaza Oshino, Oita, 870-1121, JAPAN

Tel / Fax: +81-97-594-0181 Email: arobsecr@isarob.org

Organized By

International Organizing Committee of International Symposium on Artificial Life and Robotics (AROB)

AROB 17th 2012

Co-Operated by

The Society of Instrument and Control Engineers (SICE, Japan)
The Robotics Society of Japan (RSJ, Japan)
The Institute of Electrical Engineers of Japan (IEEJ, Japan)
The Institute of Systems, Control and Information Engineers (ISCIE)
The Institute of Electronics, Information and Communication Engineers (IEICE)

IEEE Japan Council (IEEE Robotics and Automation Society Japan Chapter)
Japan Robot Association (JARA)
Institute of Control, Robotics and Systems (ICROS, Korea)
Chinese Association for Artificial Intelligence (CAAI, P. R. China)

General Chair

- M. Sugisaka (Nippon Bunri University and ALife Robotics Co., Ltd., Japan)

Vice-Chairs

- J. L. Casti (International Institute for Applied Systems Analysis, Austria)
- Y. Jia (Beihang University, P. R. China)
- J. J. Lee (KAIST, Korea)
- H. H. Lund (Technical University of Denmark, Denmark)
- H. Tanaka (Tokyo Medical & Dental University, Japan)

Advisory Committee Chair

- F. Harashima (Tokyo Metropolitan University, Japan)

Advisory Committee

- B. Eisenstein (Drexel University, Former IEEE President, USA)
- R. Fischl (Drexel University, USA)
- T. Fukuda (Nagoya University, Japan)
- F. Harashima (Tokyo Metropolitan University, Japan)
- P. Kalata (Drexel University, USA)

Program Chair

- H. Tanaka (Tokyo Medical & Dental University, Japan)

Workshop Chair

- J. M. Lee (KAIST(Pusan National University), Korea)

Assistant General Chair

- T. Ito (Ube National College of Technology, Japan)

International Organizing Committee

- H. Abbass (University of New South Wales, Australia)
- K. Aihara (The University of Tokyo, Japan)
- C. Barrett (Los Alamos National Laboratory, USA)
- M. Bedau (Reed College, USA)
- M. Eaton (University of Limerick, Ireland)
- J. M. Epstein (The Brookings Institution, USA)
- A. Grzech (Wroclaw University of Technology, Poland)
- H. Hashimoto (The University of Tokyo, Japan)
- D. J. G. James (Coventry University, UK)
- K. Kyuma (Mitsubishi Electric Corporation, Japan)

- M. H. Lee (Pusan National University, Korea)
- M. Nakamura (Research Institute of Systems Control, Japan)
- M. Oswald (Vienna University of Technology, Austria)
- S. Rasmussen (University of Southern Denmark, Denmark)
- T. S. Ray (University of Oklahoma, USA)
- K. Shimohara (Doshisha University, Japan)
- C. Taylor (University of California-Los Angeles, USA)
- J. Wang (Beijing Jiaotong University, P. R. China)
- C. Zhang (Tsinghua University, P. R. China)

International Program Committee

- T. Arita (Nagoya University, Japan)
- R. Belew (University of California-San Diego, USA)
- S.-M. Chen (National Taiwan University of Science and Technology, Taiwan)
- Y. I. Cho (The University of Suwon, Korea)
- M. Chow (North Carolina State University, USA)
- Y. Y. Fan (University of California-Davis, USA)
- T. Fuchida (Kagoshima University, Japan)
- H. Hamdan (SUPELEC, France)
- S. H. Han (Kyungnam University, Korea)
- N. Homma (Tohoku University, Japan)
- Y. Ishida (Toyohashi University of Technology, Japan)
- S. Ishikawa (Kyushu Institute of Technology, Japan)
- T. Iwamoto (Mitsubishi Electric Corporation, Advanced Technology R&D Center, Japan)
- J. Johnson (The Open University, UK)
- H. Kinjo (University of the Ryukyus, Japan)
- M. Kono (University of Miyazaki, Japan)
- K. Kurashige (Muran Institute Technology, Japan)
- H. H. Lee (Waseda University, Japan)
- J. M. Lee (Pusan National University, Korea)
- K. J. Mackin (Tokyo University of Information Sciences, Japan)
- K. Merrick (University of New South Wales and ADFA, Australia)
- C. Mi (University of Michigan-Dearborn, USA)
- J. Murata (Kyushu University, Japan)
- K. Nakano (The University of Electro-Communications, Japan)

- K. Naitoh (Waseda University, Japan)
- W. Nistico (University of Dortmund, Germany)
- N. Okada (Kyushu University, Japan)
- S. Omatu (Osaka Institute of Technology, Japan)
- H. Oogai (Waseda University, Japan)
- L. Pagliarini (Technical University of Denmark, Denmark)
- R. Pfeifer (University of Zurich-Irchel, Switzerland)
- M. Rozailan (TATI University College, Malaysia)
- S. Sagara (Kyushu Institute of Technology, Japan)
- P. Sapaty (National Academy of Sciences of Ukraine, Ukraine)
- J. Y. Sim (Kangnam University, Korea)
- M. Svinin (Kyushu University, Japan)
- K. Sugawara (Tohoku Gakuin University, Japan)
- H. Suzuki (The University of Tokyo, Japan)
- I. Tanev (Doshisha University, Japan)
- T. Tsuji (Hiroshima University, Japan)
- H. Umeo (Osaka Electro-Communication University, Japan)
- K. Uosaki (Fukui University of Technology, Japan)
- K. Watanabe (Okayama University, Japan)
- H. Yanagimoto (Osaka Prefecture University, Japan)
- I. Yoshihara (University of Miyazaki, Japan)
- M. Yokota (Fukuoka Institute of Technology, Japan)
- Y. Yu (Kagoshima University, Japan)
- T. Zhang (Tsinghua University, P. R. China)

Local Arrangement Committee

- F. Dai (Tianjin University of Science & Technology, P. R. China)
- Z. Ibrahim (TATI University College, Malaysia)
- M. Rizon (King Saud University, Saudi Arabia)
- S. Sagara (Kyushu Institute of Technology, Japan)

- M. Sugisaka (ALife Robotics Co., Ltd, Japan) (Chair)
- J. Wang (Beijing Jiaotong University, P. R. China)
- H. Zhao (Shanghai Institute of Technology, P. R. China)

Artificial Life and Robotics

We invite you to publish your paper

in this journal full of inventive scientific findings and state-of-the art technologies.

Two types of papers from the world are

- I . Recommended papers presented at **the International Symposium on Artificial Life and Robotics (ISAROB)**,
- II . Contributed papers

Contribution fee :

4 pages or Under	¥19,950 / page (¥19,000 + 5 % consumption tax: only in Japan)
Extra page charge	¥16,800 / page (¥16,000 + 5% consumption tax: only in Japan)

(Pages are counted on single-line basis as they appear in the journal.)

Shipping Cost:

domestic	¥700 / delivery
overseas	¥3,000 / delivery

We deliver every corresponding author (or sponsor) one copy of journal in which his/her paper is included. We would like to thank authors for their support in the form of contribution fee payable before publication, which funds the production of this journal contracted by Springer Japan.

Order:

1. Price for co-authors

¥ 5,250 (¥5,000 + 5 % consumption tax: only in Japan) **per copy**
(for every co-author)

If necessary, please order extra copies for co-authors to the Journal Office.

2. Subscription fee

¥ 21,000 (¥20,000 + 5 % consumption tax: only in Japan) **per year**,

3. Purchase price for single issue

¥ 8,400 (¥8,000 + 5 % consumption tax: only in Japan) **per issue**.

AROB Journal Office : joffice@isarob.org

Artificial Life and Robotics

Our Review System

For contributed papers,

1. Duration:

Two months is our target time of the whole review process, however, we are trying our best to make it as short as possible.

2. Review results:

Every contributed paper will be reviewed by three assigned reviewers with score ranging from 1 (highest mark) to 4 (lowest mark);

1. publish with no revision,
2. publish with minor revisions,
3. possibly publish with revision and re-review,
4. reject.

Review results, a total score of the three evaluation scores, would be read as;

- | | | |
|---------------|---|---|
| 3 or 4 | : | accepted and to be published as it is, |
| 4, 5, or 6 | : | accepted and to be published after minor revisions, |
| 7, 8, or 9 | : | acceptable but subject to rewriting and re-review, |
| 10, 11, or 12 | : | rejected |

For recommended papers,

The recommended papers are ones that the chair of each session reads before, during, and after the symposium that year and recommends to AROB Journal Office using the same evaluation score above. Therefore, the quality of recommended papers is apparent at the time of recommendation.

We express our heartfelt gratitude to chairs and reviewers of ISAROB for their support and sincere voluntary work without which this journal never exists.

*AROB Journal Office : joffice@isarob.org
Artificial Life and Robotics*

We invite you to advertise your company

in this international journal financed by **ISAROB (International Symposium on Artificial Life and Robotics)** and produced by a renowned publisher, Springer Japan.

Merits:

- **Connectivity with ambitious academic circles in the rapidly-advancing fields,**
- **Expanded publicity through toll electronic circulation by Springer-Japan,**
- **Reasonable advertising fee** (1 page = ¥ 90,000, 2 pages = ¥ 150,000)
(Fee+ 5 % consumption tax: only in Japan)

*Please contact AROB Journal Office at ALife Robotics Corporation Ltd.
joffice@isarob.org tel/fax: +81-97-594- 0181*

Intelligent Mobile Robot



Fig.1: Full
Version
(Taro-1 and
Taro-2)



Fig.2: Simplified
Version (Taro-A)

Fig.1 Full Version(Taro-1(right),Taro-2(left) and Simplified Vesion

Full Version

Features:

1. Recognizes lines and moves on or along the line
2. Recognizes the shape of objects
3. Can be controlled by voice (more than 20 sentences)
4. Recognizes human faces (approx. 10 people)
5. Can be controlled by the Internet and mobile phone (remote control)

Price: ¥4,000,000 (\$48,000)

Simplified Version (Taro-A)

Size and weight of robot is half of those shown in Fig.1

Functions of full version 1.~4. are equipped with:

- Fundamental software based on Windows and Linux, is provided
- The robot is most suitable for R & D (Masters and Doctorate courses)

Price (Only hardware from ¥1,000,000 (\$12,000)) with fundamental software

Specs. and style can be changed

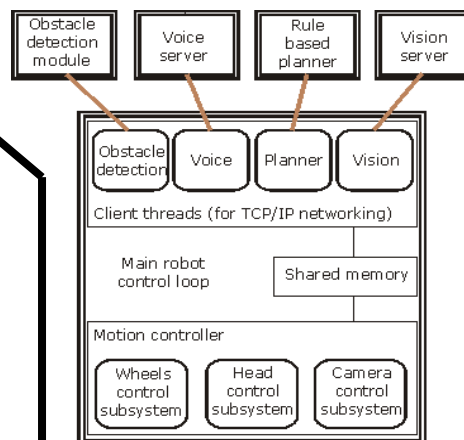


Fig.2 System block diagram

Those unit belongs to Australian Defense Force Academy (ADFA)(Australia), KAIST (South Korea), TATiUC (Malaysia), others.

1068-1 Oaza Oshino, Oita, Japan 870-1121
Tel: +81-97-567-3088 Fax:+81-97-594-0181
URL:alife-robotics.co.jp E-mail ms@alife-robotics.co.jp

Main Specification of Taro-A



ALife Robotics
Corporation Ltd.

- **Weight: 28kg**
- **Height: 60 cm (from the floor:65cm), Width: 28cm, Depth: 40cm**
- **Robot behaviors can be controlled by voice or remote control**
- **Behaviors of the Simplified Version of the Intelligent Mobile Robot:**
 1. **The robot can understand human voice commands and can reply in a robot voice . In addition, the robot can provide various information humans.**
 2. **A human asks the robot. "What is this?" and shows an object to the robot. The robot answers verbally. (Pattern recognition and understanding)**
 3. **The robot can carry various things (Foods, Letters, Newspapers, Other heavy materials (approximately 25-30kg). The robot can turn around accurately to a specified degree.**
 4. **The robot can climb a sloop of 15-30 degrees.**
 5. **The robot can teach a child by answering questions from the child in pleasant playing conditions as a private teacher.**
 6. **The robot can teach English, Japanese, Chinese, and any other languages to humans.**

- **Size and weight : ½ of Full version of Intelligent Mobile Robot "Taro"**

- **We provide fundamental software for robot by Window or Linux**

- **Most suitable for research and development on mobile robot**

- **Most suitable for human being's partner**

Price JPY 1,000,000 (\$12,000)

(*) Design and specification will be decided in consultation with customer

1068-1 Oaza Oshino, Oita, Japan 870-1121
Tel: +81-97-567-3088 Fax:+81-97-594-0181
URL:alife-robotics.co.jp E-mail ms@alife-robotics.co.jp



ALife Robotics
Corporation Ltd.



This unit belongs to Electro-Communication University, Tokyo, Japan

Sales Record (From 2009)

1. ADFA, Australia
2. Electro-Communication Univ., Japan
3. KAIST, Korea
4. TATiUC, Malaysia
5. Others

1068-1 Oaza Oshino, Oita, Japan 870-1121
Tel: +81-97-567-3088 Fax: +81-97-594-0181
URL: alife-robotics.co.jp E-mail ms@alife-robotics.co.jp

Main Specification of Fish Robot



ALife Robotics
Corporation Ltd.

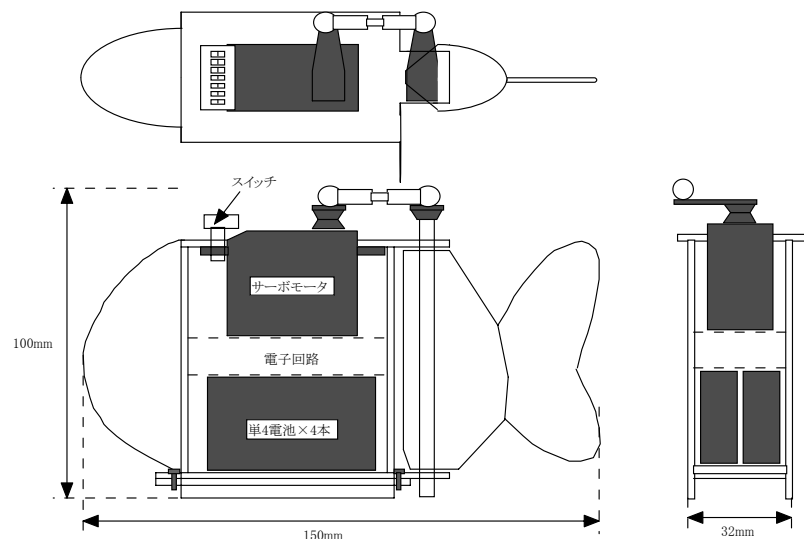


Fig.1 Fish Robot (Sizes)



Fig.2 Picture of Fish Robot

Table 1 Functions of Fish Robot

Switch No.	Functions	Comments
1	Power: ON,OFF	
2	Right Turn	
3	Left Turn	
4	Change of Speed	LOW, HIGH Mode
5	Change of Swing Angle of Caudal Fin	4 positions
6		
7	Random Mode	

Price (¥15,000≈\$181)

Included:

1. Hardware and Fundamental Software
2. PIC Writer
3. Text Book for Learning Control Techniques Based on PIC

OPTIONS:

C-MOS Camera, Remote Control Unit, Dorsal, Pectoral, Ventral Fins can be installed

1068-1 Oaza Oshino, Oita, Japan 870-1121
Tel: +81-97-567-3088 Fax: +81-97-594-0181
URL: alife-robotics.co.jp E-mail ms@alife-robotics.co.jp

**THE SIXTEENTH INTERNATIONAL SYMPOSIUM
ON
ARTIFICIAL LIFE AND ROBOTICS
(AROB 16th '11)**

ORGANIZED BY

International Organizing Committee of International Symposium on Artificial Life and Robotics (AROB)
(ALife Robotics Corporation Ltd. and Nippon Bunri University (NBU), Japan)

SPONSORED BY

Mitsubishi Electric Corporation Advanced Technology R&D Center
Oita Gas Co., Ltd.
ME System Co., Ltd.
SANWA SHURUI Co., Ltd.

CO-OPERATED BY

The Society of Instrument and Control Engineers (SICE, Japan)
The Robotics Society of Japan (RSJ, Japan)
The Institute of Electrical Engineers of Japan (IEEJ, Japan)
The Institute of Systems, Control and Information Engineers (ISCIE)
The Institute of Electronics, Information and Communication Engineers (IEICE)
IEEE Japan Council (IEEE Robotics and Automation Society Japan Chapter)
Japan Robot Association (JARA)
Institute of Control, Robotics and Systems (ICROS, Korea)
Chinese Association for Artificial Intelligence (CAAI, P. R. China)

SUPPORTED BY

Kyushu Bureau of Economy, Trade and Industry, Ministry of Economy, Trade and Industry
OITA PREFECTURE
Oita City
BEPPU CITY
The oita chamber of commerce and industry
Oita Joint Industrial Association
Kyodo News
Jiji Press
Oita Godo Shimbunsha
The Asahi shimbun
The Mainichi Newspaper Co., Ltd.
The Yomiuri Shimbun, Seibu
The Nishinippon Shimbun
THE NIKKAN KOGYO SHIMBUN, LTD
Japan Broadcasting Corporation Oita Station
Oita Broadcasting System
Television Oita System Corporation
Oita Asahi Broadcasting co., ltd.

GENERAL CHAIRMAN

M. Sugisaka (Nippon Bunri University and Alife Robotics Co., Ltd., Japan)

VICE-CHAIRMAN

J. L. Casti (International Institute for Applied Systems Analysis, Austria)

Y. Jia (Beihang University, P. R. China)

J. J. Lee (KAIST, Korea)

H. H. Lund (Technical University of Denmark, Denmark)

H. Tanaka (Tokyo Medical & Dental University, Japan)

ADVISORY COMMITTEE CHAIRMAN

F. Harashima (Tokyo Metropolitan University, Japan)

PROGRAM CHAIRMAN

H. Tanaka (Tokyo Medical & Dental University, Japan)

ASSISTANT GENERAL CHAIRMAN

T. Ito (Ube National College of Technology, Japan)

ADVISORY COMMITTEE

B. Eisenstein (Drexel University, Former IEEE President, USA)

R. Fischl (Drexel University, USA)

T. Fukuda (Nagoya University, Japan)

F. Harashima (Tokyo Metropolitan University, Japan)

P. Kalata (Drexel University, USA)

M. Kam (Drexel University, IEEE President, USA)

H. Kimura (RIKEN, Japan)

P. Oh (Drexel University, USA)

M. Tomizuka (University of California-Berkeley, USA)

Y. G. Zhang (Academia Sinica, P. R. China)

INTERNATIONAL ORGANIZING COMMITTEE

H. Abbass (University of New South Wales, Australia)

K. Aihara (The University of Tokyo, Japan)

C. Barrett (Los Alamos National Laboratory, USA)

M. Bedau (Reed College, USA)

M. Eaton (University of Limerick, Ireland)

J. M. Epstein (The Brookings Institution, USA)

A. Grzech (Wroclaw University of Technology, Poland)

H. Hashimoto (The University of Tokyo, Japan)

D. J. G. James (Coventry University, UK)

K. Kyuma (Mitsubishi Electric Corporation, Japan)
M. H. Lee (Pusan National University, Korea)
M. Nakamura (Research Institute of Systems Control, Japan)
M. Oswald (Vienna University of Technology, Austria)
S. Rasmussen (University of Southern Denmark, Denmark)
T. S. Ray (University of Oklahoma, USA)
K. Shimohara (Doshisha University, Japan)
C. Taylor (University of California-Los Angeles, USA)
J. Wang (Beijing Jiaotong University, P. R. China)
C. Zhang (Tsinghua University, P. R. China)

INTERNATIONAL PROGRAM COMMITTEE

T. Arita (Nagoya University, Japan)
R. Belew (University of California-San Diego, USA)
S.-M. Chen (National Taiwan University of Science and Technology, Taiwan)
Y. I. Cho (The University of Suwon, Korea)
M. Chow (North Carolina State University, USA)
Y. Y. Fan (University of California-Davis, USA)
T. Fuchida (Kagoshima University, Japan)
H. Hamdan (SUPELEC, France)
S. H. Han (Kyungnam University, Korea)
N. Homma (Tohoku University, Japan)
Y. Ishida (Toyohashi University of Technology, Japan)
S. Ishikawa (Kyushu Institute of Technology, Japan)
T. Iwamoto (Mitsubishi Electric Corporation, Advanced Technology R&D Center, Japan)
J. Johnson (The Open University, UK)
H. Kinjo (University of Ryukyus, Japan)
M. Kono (University of Miyazaki, Japan)
K. Kurashige (Muroran Institute of Technology, Japan)
H. H. Lee (Waseda University, Japan)
J. M. Lee (Pusan National University, Korea)
K. J. Mackin (Tokyo University of Information Sciences, Japan)
K. Merrick (University of New South Wales and ADFA, Australia)
C. Mi (University of Michigan-Dearborn, USA)
J. Murata (Kyushu University, Japan)
K. Nakano (The University of Electro-Communications, Japan)
K. Naitoh (Waseda University, Japan)
W. Nistico (University of Dortmund, Germany)
N. Okada (Kyushu University, Japan)
S. Omatu (Osaka Institute of Technology, Japan)
H. Oogai (Waseda University, Japan)
L. Pagliarini (Technical University of Denmark, Denmark)
R. Pfeifer (University of Zurich-Irchel, Switzerland)
M. Rozalian (TATi University College, Malaysia)
S. Sagara (Kyushu Institute of Technology, Japan)
P. Sapaty (National Academy of Sciences of Ukraine, Ukraine)
J. Y. Sim (Kangnam University, Korea)
M. Svinin (Kyushu University, Japan)
K. Sugawara (Tohoku Gakuin University, Japan)
H. Suzuki (The University of Tokyo, Japan)
I. Tanev (Doshisha University, Japan)
T. Tsuji (Hiroshima University, Japan)

H. Umeo (Osaka Electro-Communication University, Japan)
K. Uosaki (Fukui University of Technology, Japan)
K. Watanabe (Okayama University, Japan)
H. Yanagimoto (Osaka Prefecture University, Japan)
I. Yoshihara (University of Miyazaki, Japan)
M. Yokota (Fukuoka Institute of Technology, Japan)
Y. Yu (Kagoshima University, Japan)
T. Zhang (Tsinghua University, P. R. China)

LOCAL ARRANGEMENT COMMITTEE

F. Dai (Tianjin University of Science & Technology, P. R. China)
Z. Ibrahim (TATi University College, Malaysia)
M. Rizon (King Saud University, Saudi Arabia)
S. Sagara (Kyushu Institute of Technology, Japan)
M. Sugisaka (Alife Robotics Co., Ltd., Japan) (Chair)
J. Wang (Beijing Jiaotong University, P. R. China)
H. Zhao (Shanghai Institute of Technology, P. R. China)

HISTORY

The AROB was founded in 1996 under the support of Science and International Affairs Bureau, Ministry of Education, Culture, Sports, Science and Technology, Japanese Government. Since then, the symposium organized by the AROB has been held every year at B-Con Plaza, Beppu, Japan except AROB 5th '00 (Oita) and AROB 6th '01 (Tokyo). The sixteenth symposium will be held on January 27–29, 2011, at B-Con Plaza, Beppu, Japan.

OBJECTIVE

This symposium will bring together researchers to discuss development of new technologies concerning *artificial life and robotics* based on computer simulations and hardware designs of state-of-the-art technologies, and to share findings on how advancements in artificial life and robotics technologies that relate to artificial intelligence, virtual reality, and computer science are creating the basis for exciting new research and applications in various fields listed in the following Topics.

GENERAL SESSION TOPICS

Artificial intelligence
Chaos & Complexity
Data mining
Human-machine cooperative systems
& Human-welfare robotics
Mobile vehicles
Pattern recognition & Visualization Poster
Robotics

Artificial life
Control techniques
Evolutionary computations
Image processing
Learning
Neural networks
session

ORGANIZED SESSION TOPICS

Advanced technologies
& Management skills
Bio-inspired theory and application
Biomimetic machines and robots
Control and automata
Data mining

Embracing complexity in
natural intelligence
Human agent interaction
toward social modification
Intuitive human-system interaction
Medical science and complex system
Special environment navigation
and localization
System sensing and control

Advanced vehicle control
AI-based systems
for human awareness promotion
Computer vision and sound analysis
Control and its application
Dynamical information processing
in the brain
Embracing complexity in
sensor system organization
Intelligent control
Intelligent systems
Learning control and robotics
Robotics and pattern recognition
Structural change detection
for ongoing time series

COPYRIGHTS

Accepted papers will be published in the proceeding of AROB and some of high quality papers in the proceeding will be requested to re-submit their papers for the consideration of publication in an international journal ARTIFICIAL LIFE AND ROBOTICS. All correspondence related to the symposium should be addressed to AROB Secretariat.

AROB Secretariat
ALife Robotics Corporation Ltd.
1068-1 Oaza Oshino, Oita, 870-1121, JAPAN
TEL/FAX: +81-97-594-0181
E-MAIL: arobsecr@isarob.org
Home Page: <http://isarob.org/>

ADDRESS



Takayuki Hirai
Nippon Bunri University
President



Takayuki Hirai
Nippon Bunri University
President

It is a great pleasure for me to welcome you all to the Sixteenth International Symposium on Artificial Life and Robotics. I have deep respect and great admiration for the many people who attend this event every year and contribute to the development of technology on Artificial Life and Robotics.

Everyone's activities on the Organizing Committee of International Symposium on Artificial Life and Robotics are outstanding. Especially, our colleague, General Chairman Professor Sugisaka, has made a large contribution.

In the universities of Japan, Artificial Robotics has been gaining great interest by researchers and will develop as one of the leading research fields, which will support future society. However, while many industries of Artificial Robotics have arrived and developed, it is said that there is still a great demand for engineers engaged in those industries.

It is our role to teach the young of the future the technology of Artificial Life Robotics which has been advanced and developed by all of you working internationally, and send talented people to society. To take this role, the research achievements of you attending this International Symposium are very valuable.

It's my heartfelt hope that this International Symposium will be successful and all of you will have a great time here in Beppu.

MESSAGES



Fumio Harashima
Advisory Committee Chairman
(Professor, Tokyo
Metropolitan University)

Fumio Harashima
Advisory Committee Chairman of AROB

The science and technology (S&T) on Artificial Life and Robotics was born in 1996, and it's been providing human being with happiness. This S & T is not only important but also necessary for people living in the world to maintain high quality of life. Research is heart and desire of human being and the S&T is going toward clarifying tool to achieve our objective.

I would like to congratulate researchers who work in the fields on Artificial Life and Robotics.



Masanori Sugisaka
General Chairman
(Professor, Nippon Bunri
University and President,
ALife Robotics Corporation,
Ltd., Japan)

Masanori Sugisaka
General Chairman of AROB

It is my great pleasure to invite you all to the Sixteenth International Symposium on Artificial Life and Robotics (AROB 16th '11).

The symposium from the first (1996) to the Fourteenth (2009) were organized by Oita University, Nippon Bunri University (NBU), and ALife Robotics Corporation Ltd. under the sponsorship of the Science and Technology Policy Bureau, the Ministry of Education, Science, Sports, and Culture (Monbusho), presently, the Ministry of Education, Culture, Sports, Science, and Technology (Monkasho), Japanese Government, Japan Society for the Promotion of Science (JSPS), The Commemorative Organization for the Japan World Exposition ('70), Air Force Office of Scientific Research, Asian Office of Aerospace Research and Development (AFOSR/AOARD), USA. I would like to express my sincere thanks to not only Monkasho, JSPS, the Commemorative Organization for the Japan World Exposition ('70), AFOSR/AOARD but also Japanese companies (Mitsubishi Electric Corporation, Advanced Technology R&D Center, Oita Gas Co., Ltd., ME System Co. LTD, and Sanwa Shurui Co., LTD. for their repeated supports.

This symposium is organized by International Organizing Committee of AROB and is co-operated by the Santa Fe Institute (USA), RSJ, IEEEJ, ICASE (Now ICROS) (Korea), CAAI (P. R. China), ISCIE, IEICE, IEEE Robotics and Automation Society Japan Chapter, JARA, and SICE.

The AROB symposium is growing up by absorbing many new knowledge and technologies into it. The new technologies presented in this symposium bring happiness to human society.

I hope that this symposium will facilitate the establishment of an international research Institute of Artificial Life and Robotics in future.

Welcome and enjoy your stay in Beppu.



Takao Ito
Assistant General Chairman
(Professor, Ube National
College of Technology)

Takao Ito
Assistant General Chairman of AROB

Given the intense competition in the field of artificial life and robotics, the effective coordination and efficient maintenance of information exchange take on increased importance. The AROB international conference provides us a unique opportunity to enjoy the discussions of all new issues, and to share experiences related to the advanced technologies. I am pleased to put together this excellent program that represents submissions from many countries around the world.

I hope that you will enjoy this conference and enjoy Beppu, Oita and the culture richness it has to offer.



Hiroshi Tanaka
Program Chairman
and
Vice chairman
(Professor, Tokyo Medical
and Dental University)

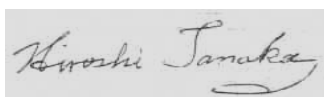
Hiroshi Tanaka
Program Chairman and Vice chairman
of AROB

On behalf of the program committee, it is my great pleasure and honor to invite you all to the Fifteenth International Symposium on Artificial Life and Robotics (AROB 15th 2011). This symposium is made possible owing to the cooperation of Nippon Bunri University and Santa Fe Institute. We are also debt to Japanese academic associations such as SICE, RSJ, and several private companies. I would like to express my sincere thanks to all of those who make this symposium possible.

As is needless to say, the Alife or biologically-inspired Robotics approach now attracts wide interests as a new paradigm of science and engineering. Taking an example in the field of bioscience, the accomplishment of HGP (Human Genome Project) and subsequent post-genomic comprehensive "Omics data" such as transcriptome, proteome and metabolome, bring about vast amount of bio-information. However, as a plenty of omics data becomes available, it becomes sincerely recognized that the framework by which these omics data can be understood to make a whole picture of life is critically necessary. Thus, in the post-genomic era, biologically-inspired systems approach like Alife is expected to give one of new alternative ideas to integrate this vast amount of bio-data.

This example shows the Alife approach is very promising and may exert a wide influence on the effort to develop a new paradigm for next generation of life science. We hope this symposium becomes a forum for exchange of the ideas of the attendants from various fields, including the life science field, who are interested in the future possibility of biologically-inspired computation and systems approach.

I am looking forward to meeting you in Beppu, Oita.

A handwritten signature in cursive script that reads "Hiroshi Tanaka".



Ju-Jang Lee
Vice Chairman
(Professor, KAIST)

A handwritten signature in black ink, appearing to read 'J. Lee'.

Ju-Jang Lee
Vice Chairman of AROB

The Sixteenth International Symposium on Artificial Life and Robotics (AROB) will be held in Beppu, Oita, Japan from Jan. 27th to 29th, 2011. This year's Symposium will be held amidst the high expectation of the increasingly important role of the new interdisciplinary paradigm of science and engineering represented by the field of artificial life and robotics that continuously attracts wide interests among scientists, researchers, and engineers around the globe.

Since the time of the very first AROB meeting in 1996, each year, distinguished researchers and technologists from around the world are looking forward to attending and meeting at AROB. AROB is becoming the annual excellent forum that represents a unique opportunity for the academic and industrial communities to meet and assess the latest developments in this fast growing artificial life and robotics field. AROB enables them to address new challenges, share solutions, discuss research directions for the future, exchange views and ideas, view the results of applied research, present and discuss the latest development of new technologies and relevant applications.

In addition, AROB offers the opportunity of hearing the opinions of well known leading experts in the field through the keynote sessions, provides the bases for regional and international collaborative research, and enables to foresee the future evolution of new scientific paradigms and theories contributed by the field of artificial life and robotics and associated research area. The twenty-first century will become the century of artificial life and intelligent machines in support of humankind and AROB is contributing through wide technical topics of interest that support this direction.

It is a great for me as the Vice Chairman of the 16th AROB 2011 to welcome everyone to this important event. Also, I would like to extend my special thanks to all authors and speakers for contributing their research works, the participants, and the organizing team of the 16th AROB.

Looking forward to meeting you at the 16th AROB in Beppu-Oita and wishing you all the best.



John Casti
Vice Chairman
(Professor, International
Institute for Applied
Systems Analysis, Vienna,
Austria)

A handwritten signature in black ink, appearing to read 'John L. Casti'.

John L. Casti
Vice Chairman of AROB

It is my great privilege to invite you all to the Sixteenth International Symposium on Artificial Life and Robotics (AROB 16th '11). As always at the AROB, the program contains a wide variety of contributions to the developing areas of computer simulation of human processes, robotics, and general systems modeling. We are grateful to all the contributors for their hard work in preparing their presentations, and look forward to the cutting-edge research that will be described.

I hope that fruitful discussions and exchange of ideas between researchers during symposium will yield new technological innovations for contributing to a better life for humans in the coming decades. This is truly a challenging period to be alive, and the AROB 16th conference holds the promise of offering solutions to some of our most pressing global human problems.



Henrik Hautop Lund
Vice Chairman
(Professor, Center for
Playware, Technical
University of Denmark)

Henrik Hautop Lund
Vice-Chairman of AROB

I am much honored to invite you to the Sixteenth International Symposium on Artificial Life and Robotics (AROB 16th '11). The international symposium has been held each year since 1996, initially organized by Oita University and now being organized by Nippon Bunri University.

The symposium attracts an impressive range of researchers from all continents, who all share the vision of merging research based upon artificial life and robotics. The symposium is visionary in merging these two, science and engineering disciplines, and has become the most important forum for research into merging artificial life and robotics.

The research in artificial life and robotics is very important since it both brings us insight into ourselves as human beings and natural systems, and brings us new engineering solutions that may influence our lives. It is my hope that you will use this insight and opportunity to develop systems that help humankind in socially responsible ways.

I would like to take this opportunity to thank the general chairman of AROB, Prof. Masanori Sugisaka, for being so visionary 16 years ago to engage in creating and organizing this important annual event for our research community. It takes a lot of courage to be the first to create a novel interdisciplinary research field such as the one that comes from the merge between artificial life and robotics. Prof. Sugisaka has shown how being courageous enough to engage in the adventurous activities of merging two fields may lead to very fruitful research and to the lively research community that you are now part of with your participation in this international symposium.

I would also take this opportunity to thank Springer-Verlag for supporting this research community, and remind all participants of the Springer-Verlag Artificial Life and Robotics Journal. Hopefully, we will see numerous, high quality contributions to the journal as the outcome of this symposium and the research collaboration that may entail the symposium. Indeed, it is my hope that you will all engage in open and fruitful scientific discussions with your colleague researchers during the symposium, and that these discussions may open up for future research collaborations in order to bring new insight into artificial life and robotics to the community.

Yingmin Jia
Vice-Chairman of AROB



Yingmin Jia
Vice-Chairman of AROB
(Professor, Beihang
University, P.R.China)

The 16th International Symposium on Artificial Life and Robotics (AROB) will be held in Beppu, Oita, Japan from Jan. 27th to 29th, 2011. As a vice-chairman, I am honored and privileged to invite you all to this fruitful 3-day event.

In 1996, the first Symposium was created and organized by Prof. Masanori Sugisaka, the general chairman of AROB. Since then, the symposium attracts an impressive range of researchers from all continents, and distinguished achievements have been obtained that shows his foresight in merging two disciplines of artificial life and robotics. Moreover, it is gratifying to see that there are more and more young colleagues, researchers and engineers from the universities, research institutions and industries interested in the field. I believe there is a rapid and better development in the near future.

Looking forward to meeting you at the 16th AROB in Beppu, Oita and wishing you enjoy your stay in Japan.

Plenary talker:



**Professor
Jun Ho Oh**

PT1 : Development Outline of Humanoid Robot: HUBO II

Jun Ho Oh

Professor of Mechanical Engineering, KAIST
Director of Humanoid Robot Research Center (Hubo Lab)

The full size humanoid robot with height of around 1.5 m is quite different from the toy size small ones in many aspects. It should have very stable and well designed structure with little uncertainties. It must be strong enough to move its body weight but not so heavy to minimize the torques to drive the body parts. All the electrical parts and sensors must be compact to be fit in the enclosure of the body. We designed such kind of parts including force/torque sensors, inertia sensors and all the driver circuits, internal decentralized control architecture and hardware. Another important task is design walk algorithm. Walking algorithm is composed with two parts: off-line gait pattern design and real time stabilization control. Gait pattern design is to find a periodic function for each joint of leg such that humanoid robot is to walk with desired velocity keeping certain level of stability. We suggested a simple function connected with cubic spline and sine functions with minimal number of parameters. This approach simplifies the parameter adjustment procedure. Play back of gait pattern found from the former process, however, does not guarantee the robot walks in real practice since there are number of uncertainties involved in real situation. The uncertainties include ground inclination, friction, un-modeled vibration of the body. The stabilization algorithm should deal with such kind of problems. Hubo's walk algorithm has 8 levels of hierarchical control architecture to cope with the general circumstances in walking environment. The general issues including mentioned above will be presented.

Education:

- In 1977, B.S. degree in Mechanical Engineering from Yonsie University, Korea
- In 1979, M.S. degree in Mechanical Engineering from Yonsie University, Korea
- In 1985, Ph.D. in Mechanical Engineering, University of California, Berkeley, USA

Professional Training and Employment:

- | | |
|------------------|--|
| - 1985 – present | Professor of Mechanical Engineering, KAIST |
| - 2010 – present | Distinguished Professor at KAIST |
| - 1997 – 1998 | Visiting Professor, University of Texas, Austin, USA |
| - 2010 | Member of National Academy of Engineering of Korea |

PT2 : Robotics:From Manufacturing to Intelligent Machine

Tzyh Jong Tarn



**Professor
Tzyh Jong Tarn**

This presentation describes the evolution from tele-robotics to interactive robotics and to intelligent machines due to the silicon revolution. The impacts of this transformation to the manufacturing culture as well as the automated manufacturing research facility are outlined. Finally the current trends in robotics research and new applications to intelligent life are described.

Education:

- 1959, B.S. degree in Chemical Engineering, National Cheng Kung University, Tainan, Taiwan, China
- 1965, M.E. degree in Chemical Engineering, Stevens Institute of Technology, Hoboken, USA
- 1968, D. Sc. Degree in Control Engineering, Washington University, St. Louis, USA

Professional Training and Employment:

- 1968-1969 Postdoctoral Fellow, Washington University, St. Louis, USA
- 1969-1972 Assistant Professor, Washington University, St. Louis, USA
- 1972-1977 Associate Professor, Washington University, St. Louis, USA
- 1 977- Professor, Washington University, St. Louis, USA
- 2003-2006 Chair Professor in Quantum Control, Tsinghua University, Beijing, China
- 2 006- Director, Center for Quantum Information Science and Technology, Tsinghua University, Beijing, China
- 2009-2010 Distinguished Visiting Chair Professor, National Cheng Kung University, Tainan, Taiwan, China



**PT3 : Rescue Robot Systems
- From Snake-like Robots to Human Interface -**

Fumitoshi Matsuno

**Professor
Fumitoshi Matsuno**

(Kyoto University, Japan)

Intelligent rescue systems with information and communications technologies (ICT) and robotics technology (RT) have been proposed to mitigate disaster damages, especially in Japan after the 1995 Hanshin-Awaji Earthquake. In particular, it has been stressed the importance of developing robots for search and rescue tasks, which can actually work in a real disaster site. In USA the September 11, 2001 terrorist attack on New York City and Washington, DC, the hijacked plane crash in Pennsylvania, and the Anthrax attack that immediately followed instantly changed people attitude about safety and security in their personal lives. Public safety and security problems are not limited to Japan and the United States, since every country has experienced man-made and natural disasters in the past. Solutions will depend up on new, unconventional approaches to search and rescue. Robotics, information and communications technologies, devices and system integration can play an important role in providing technology that can contribute to Safety, Security and Rescue activities. In this talk, I would like to explain my motivation to start the development of rescue robot systems for the disaster response and discuss necessary technologies that can accomplish search and rescue missions. I also introduce developed rescue robots for the information correction and teleoperation human interface.

Education:

- In 1981, B.E. degree in Instrumentation Engineering from Nagoya Institute of Technology, Japan
- In 1983, Master Degree from Dept of Control Engineering at Osaka University Japan
- In 1986, Doctor Degree from Dept of Control Engineering at Osaka University, Japan

Professional Training and Employment:

- 1986 – 1991 Research Associate, Osaka University
- 1991 – 1996 Associate Professor, Kobe University
- 1996 – 2003 Associate Professor, Tokyo Institute of Technology
- 2003 – 2009 Professor, University of Electro-Communications, Tokyo
- 2009 – Professor, Dept of Mechanical Engineering and Science, Kyoto University

Invited talker:



**Associate Professor
Michita Imai**

IT1 : Human-Robot Interaction and Social Relation

Michita Imai
(Keio University, Japan)

This talk presents the factor of designing an anthropomorphic agent such as a communication robot and an embodied communicative agent. Communication is a cooperative phenomenon between participants. People involved in a communication speak and hear actively during the conversation. However, it is difficult to engage them in the communication with a robot because they seldom actively consider the communicative intention of the robot. This talk explains the importance of social relationship between a human and a robot for engaging people in the communication. In particular, we consider how the relation makes them consider the intention of the robot. Also, I show what factors of the robot design elicit the social relation.

Education:

- In 1994, M.S. degree in Computer Science from Department of Computer Science, Keio University, Japan
- In 2002, Ph.D.(Eng.) in Computer Science from Department of Computer Science, Keio University, Japan

Professional Training and Employment:

- 1994-1997, Researcher, Human-Interface Laboratories, Nippon Telephone Telegram (NTT), Japan
- 1997-2002, Researcher, ATR Media Integration and Communications Research Laboratories, Japan
- 2002-2003, Assistant Professor, Department of Information and Computer Science, Keio University, Japan
- 2002-2006, Researcher, JST Prest "Interaction and Intelligence"
- 2003-2005, Lecturer, Department of Information and Computer Science, Keio University, Japan
- 2005-present, Associate Professor, Department of Information and Computer Science, Keio University, Japan



IT2 : Micro Nano Robotics

Tatsuo ARAI
(Osaka University, Japan)

Manipulation, sensing, actuation, and automation in micro nano scale have various applications and contributions in biotechnology, pharmacy, medicine as well as in industries. Micro hands are **Prof. Tatsuo ARAI** manipulate micro and nano order size objects dexterously. Micro channels fabricated on a chip, called micro TAS or lab on chip, can provide various operations and processes for cells and tissues. Those activities include elaborating machining, assembly, fabrication and integration with MEMS technique as well as robotics and mechatronics. The talk will cover mainly two topics, micro manipulation system with dexterous hand and desktop bio plant, along with their background and the state of the art in Japan.

Tatsuo ARAI was born in 1952 in Tokyo. He received B.S., M.S., and PhD degrees from the University of Tokyo in 1975, 1977, and 1986 respectively. He joined the Mechanical Engineering Laboratory, AIST, MITI (now METI) in 1977, and was engaged in research and development of new arm design and control, mobile robot, teleoperation, and micro robotics. He stayed at MIT as a visiting scientist in 1986-1987. He was an adjunct lecturer at Chiba University in 1986-1996, and a visiting professor at the Science University of Tokyo in 1996-1997. He moved to Osaka University in 1997 and since then he has been a Full Professor at the Department of Systems Innovation, Graduate School of Engineering Science. His current research topics are mechanism design including parallel mechanisms, legged working robot, micro robotics for bio applications, humanoid robot, haptic interface, and network robotics. He has published more than 300 journal and conference papers on robotics and automation, 6 books, and has 37 patents including foreign 8. The publication list is on http://www-arailab.sys.es.osaka-u.ac.jp/publication/e_index.html

He is a member of IEEE, International Association of Automation and Robotics in Construction (IAARC), Robotic Society of Japan (RSJ), Society of Instrumentation and Control Engineers, Japan Society of Mechanical Engineers (JSME), and other societies. He is currently an Editor-in-Chief of Journal of Robotics and Mechatronics. He served as a Vice President of IAARC, a chair of Robotics and Mechatronics Division of JSME, a Director of RSJ, a chair of the Technical Advisory Committee of the Destruction of Abandoned Chemical Weapon of the Cabinet Office. He has been organizing and chairing many research committees, conferences, and symposia for IEEE, IAARC, RSJ, SICE, and JSME.



**Associate Professor
Mamiko Sakata**

IT3 : Quantifying Dance Movement *Waza* in *Nihon-Buyo*

Mamiko SAKATA
(Doshisha University, Japan)

Dance is an intangible cultural asset. It is passed on from one person to another through oral instruction, and so are the *waza*, the skills and techniques. involved in dance. Many traditional dances in Japan, however, are 'endangered species' due to the shortage of practitioners. We are attempting to create digital archives to record and store the body motions of *buyo* using digital technologies, such as motion capture. We are endeavoring to solve this serious issue of losing an important tradition. In my talk, I would like to present part of our scientific analysis of the *waza* in *Nihon-buyo*, which have been passed down, sometimes in silent, tacit manners.

Education:

- 1999: M.S. degree in Cultural Studies and Human Sciences from Kobe University, Kobe, Japan
- 2002: Ph.D. in Cultural Studies and Human Sciences from Kobe University, Kobe, Japan

Professional Training and Employment:

- 1999-2001: Researcher, ATR Media Integration & Communications Research Laboratories, Japan
- 2002-2005: Lecturer, Department of Nursery, Fukushima College, Japan
- 2005-2008: Lecturer, Faculty of Culture and Information Science, Doshisha University, Japan
- 2008-present: Associate Professor, Faculty of Culture and Information Science, Doshisha University, Japan



**Professor
Henrik Hautop Lund**

IT4 Social playware for mediating tele-play interaction over distance

Henrik Hautop Lund and Tumi Thorsteinsson
(Technical University of Denmark, Denmark)

We suggest that novel playware technology can function as a mediator for playful social interaction over distance, where people are separated by physical distance but feel the presence of each other mediated through the interaction with the playware technology. In order to investigate such social playware, we developed the Playware Soccer game and tested this with more than 1,000 users during the FIFA World Cup 2010 in South Africa. The test was conducted in townships, orphanages for HIV/AIDS children, markets, FIFA fan parks, etc. along with simultaneous tests with similar set-ups in Europe and Asia. With the social playware, players would compete against each other simultaneously in the three continents, Africa, Europe and Asia, and feel the presence of the competitors on the other continents expressed through the playware. The playware game is set up to motivate players to engage in training of technical soccer skills by receiving immediate feedback and offering challenges to players of all skills on the soccer playing on a modular interactive wall composed of modular interactive tiles that respond with coloured light, sound and scores on the players performance. This paper outlines the concept of social playware and physical-virtual teleplay, and exemplifies this with the playware soccer game.

Education:

- M.Sc. degree in Computer Science from University of Aarhus, Denmark
- Ph.D. degree in Computer Systems Engineering from University of Southern Denmark

Professional Training and Employment:

- 1992-1993 and 1994-1995, Research Assistant, the National Research Council, Rome
- 1996-1997, Research Associate (Post Doctor), Department of Artificial Intelligence, Edinburgh, UK
- 1997-2000, Head of LEGO Lab
- 1998-2000, Research Associate, Department of Computer Science, University of Aarhus, Denmark
- 2000-2008, Full Professor, the Maersk Mc-Kinney Moeller Institute, University of Southern Denmark
- 2003-2007, Member of the Danish Research Council
- 2008-present, Full Professor, the Center for Playware, Technical University of Denmark



**Professor
Luigi Pagliarini**

IT5 An Educational Tool for Interactive Parallel and Distributed Processing

Luigi Pagliarini^{1,2} and Henrik Hautop Lund¹
(¹Technical University of Denmark, Denmark)
(²Academy of Fine Arts of Bari, Via Gobetti, Italy)

In this paper we try to describe how the Modular Interactive Tiles System (MITS) can be a valuable tool for introducing students to interactive parallel and distributed processing programming, by forcing and challenging programmers in designing interactive parallel and distributed systems. Indeed, MITS seems to bring a series of goals into the education, such as parallel programming, distributedness, communication protocols, master dependency, software behavioural models, adaptive interactivity, feedback, connectivity, topology, island modeling, user and multi-user interaction, which can hardly be found in other tools. We introduce the system of modular interactive tiles as a tool for easy, fast, and flexible hands-on exploration of these issues, and through examples show how to implement interactive parallel and distributed processing with different software behavioural models such as open loop, randomness based, rule based, user interaction based, AI and ALife based software.

Education:

- Master Degree in Experimental Neuropsychology

Professional Training and Employment:

An Artist, Art Curator, Psychologist, Multimedia and Software Designer, and a worldwide known as a theoretician and expert in (mainly Artistic) Robotics, A.I. and Artificial Life.

- Professor, Theories of Perception and Psychology of Shape and of Computer Art, the Academy of Fine Arts of Bari, Italy
- Associate Professor, Center for Playware, Technical University of Denmark
- Founder and Director, the Pescara Electronic Artists Meeting
- President, the Cultural Association Artificialia
- Art Director, Ecoteca
- Founder of RoboCup Junior and Member of its International Committee

TIME TABLE (1/27)

		Room A	Room B	Room C	Room D
1/26	13:00				
(Wed)	17:00	Registration (Registration Desk)			
		Welcome Party (at Hotel Shiragiku)			
1/27	8:00	Registration (Registration Desk)			
(Thu)	9:10	OS 1 (5) Chair M. Uchida will end at 10:25	OS 18 (4) Chair K. J. Mackin	OS 2 (4) Chair H. Tanaka	GS 4 (4) Chair S. Nakayama
	10:10	Coffee Break			
	10:30	Opening Ceremony (Room G) Chair J. M. Lee			
	10:55	Plenary Talk (Room G) PT1 J. H. Oh Chair Y. G. Zhang			
	11:45	Lunch			
	12:40	IT1 M. Imai IT2 T. Arai Chair M. Nakamura	GS 10 (7) Chair H. Yamamoto	GS 21 (7) Chair B. Fu	PS 1 (8) Chair J. J. Lee will end at 14:40
	14:25	Coffee Break			
	14:45	OS 5 (5) Chair S. Sagara	GS 16 (5) Chair K. Ikeda	OS 24 (4) Chair M. Imai will end at 15:45	OS 17 (5) Chair K. Naitoh
	16:00				
	16:05	OS 3 (5) Chair M. Yokomichi	OS 4 (5) Chair Y. M. Jia	GS 3 (5) Chair D. E. Kim	GS 19 (6) Chair A. Nakamura will end at 17:35
	17:20				

GS: General Session OS: Organized Session PS: Poster Session PT: Plenary Talk IT: Invited Talk

GS1 Artificial intelligence	GS20 Robotics IV	OS14 Dynamical information processing in the brain
GS2 Artificial life I	GS21 Robotics V	OS15 Bio-inspired theory and application
GS3 Artificial life II	PS1 Poster Session	OS16 Biomimetic machines and robots
GS4 Chaos & Complexity	OS1 System sensing and control I	OS17 Medical science and complex system
GS5 Control techniques	OS2 System sensing and control II	OS18 Data mining
GS6 Data mining	OS3 Control and its application	OS19 Embracing complexity in natural intelligence
GS7 Evolutionary computations	OS4 Intelligent Control	OS20 Embracing complexity in sensor system organization
GS8 Human-machine cooperative systems & Human-welfare robotics I	OS5 Advanced vehicle control	OS21 Learning control and robotics
GS9 Human-machine cooperative systems & Human-welfare robotics II	OS6 AI-based systems for human awareness promotion	OS22 Robotics and pattern recognition
GS10 Image processing I	OS7 Advanced technologies & Management skills	OS23 Intelligent systems II
GS11 Image processing II	OS8 Structural change detection for ongoing time series	OS24 Human agent interaction toward social modification
GS12 Learning	OS9 Computer vision and sound analysis	
GS13 Mobile vehicles	OS10 Intelligent systems I	
GS14 Neural networks I	OS11 Control and automata	
GS15 Neural networks II	OS12 Special environment navigation and localization	
GS16 Pattern recognition & Visualization	OS13 Intuitive human-system interaction	
GS17 Robotics I		
GS18 Robotics II		
GS19 Robotics III		

TIME TABLE (1/28)

		Room A	Room B	Room C	Room D
1/28	8:00	Registration (Registration Desk)			
(Fri)	8:40	GS 5 (5) Chair J. Murata	OS 8 (5) Chair T. Hattori	OS 13 (5) Chair M. Yokota	GS 15 (5) Chair N. Kamiura
	9:55	Coffee Break			
	10:15	Plenary Talk (Room G) PT2 T. J. Tarn Chair J. J. Lee			
	11:05	OS 7 (5) Chair T. Ito	GS 8 (4) Chair T. Fuchida will end at 12:05	GS 9 (4) Chair N. Okada will end at 12:05	OS 12 (5) Chair J. M. Lee
	12:20	Lunch			
	13:15	OS10 (6) Chair K. L. Su	GS 2 (6) Chair T. Arita	OS 9 (6) Chair Y. Yoshitomi	GS 17 (5) Chair D. W. Lee will end at 14:30
	14:45	Plenary Talk (Room G) PT3 F. Matsuno Chair H. H. Lund			
	14:50	Coffee Break			
	15:40	OS11 (6) Chair K. H. Hsia	GS 7 (6) Chair P. S. Sapaty	GS 18 (5) Chair E. Inohira will end at 17:15	GS 13 (6) Chair F. Dai
	16:00	AROB Award Ceremony (Chair K. Naito) Banquet – Hotel Shiragiku (Chair Y. I. Cho)..... Address Y. G. Zhang / Y. Ishida/ T. Arita J. M. Lee / K. L. Su / L. Pagliarini			
	17:30				
	18:30				
	21:00				

GS: General Session OS: Organized Session PS: Poster Session PT: Plenary Talk IT: Invited Talk

GS1 Artificial intelligence

GS2 Artificial life I

GS3 Artificial life II

GS4 Chaos & Complexity

GS5 Control techniques

GS6 Data mining

GS7 Evolutionary computations

GS8 Human-machine cooperative systems

& Human-welfare robotics I

GS9 Human-machine cooperative systems

& Human-welfare robotics II

GS10 Image processing I

GS11 Image processing II

GS12 Learning

GS13 Mobile vehicles

GS14 Neural networks I

GS15 Neural networks II

GS16 Pattern recognition & Visualization

GS17 Robotics I

GS18 Robotics II

GS19 Robotics III

GS20 Robotics IV

GS21 Robotics V

PS1 Poster Session

OS1 System sensing and control I

OS2 System sensing and control II

OS3 Control and its application

OS4 Intelligent Control

OS5 Advanced vehicle control

OS6 AI-based systems for human

awareness promotion

OS7 Advanced technologies

& Management skills

OS8 Structural change detection for

ongoing time series

OS9 Computer vision and sound analysis

OS10 Intelligent systems I

OS11 Control and automata

OS12 Special environment navigation

and localization

OS13 Intuitive human-system

interaction

OS14 Dynamical information

processing in the brain

OS15 Bio-inspired theory

and application

OS16 Biomimetic machines

and robots

OS17 Medical science

and complex system

OS18 Data mining

OS19 Embracing complexity in

natural intelligence

OS20 Embracing complexity in

sensor system organization

OS21 Learning control

and robotics

OS22 Robotics and

pattern recognition

OS23 Intelligent systems II

OS24 Human agent interaction

toward social modification

TIME TABLE (1/29)

		Room C	Room D	Room E	Room F
1/29	8:00	Registration (Registration Desk)			
(Sat)	8:40	OS 14 (5) Chair H. Suzuki will end at 09:55	GS 6 (5) Chair J. S. Shieh will end at 09:55	GS 14 (5) Chair T. Yamada will end at 09:55	OS 19 (6) Chair Y. Ishida
	10:10	Coffee Break			
	10:30	OS 6 (7) Chair K. Hashimoto	GS 11 (5) Chair J. Wang will end at 11:45	OS 15 (7) Chair M. Yasunaga	OS 16 (7) Chair K. Watanabe
	12:15	Lunch			
	13:10	OS 20 (6) Chair Y. Ishida	OS 21 (6) Chair H. H. Lee	GS 12 (7) Chair Y. G. Zhang will end at 14:55	IT 3 M. Sakata IT 4 H. Lund IT 5 L. Pagliarini Chair Y. I. Cho will end at 14:55
	14:40	Coffee Break			
	15:00	OS 22 (7) Chair C. Zhang	OS 23 (6) Chair M. K. Habib will end at 16:30	GS 20 (4) Chair N. Uchiyama will end at 16:00	GS 1 (4) Chair T. Nakashima will end at 16:00
	16:45	Farewell Party (Room F)			
	17:00				
	18:00				

GS: General Session OS: Organized Session PS: Poster Session PT: Plenary Talk IT: Invited Talk

GS1 Artificial intelligence
GS2 Artificial life I
GS3 Artificial life II
GS4 Chaos & Complexity
GS5 Control techniques
GS6 Data mining
GS7 Evolutionary computations
GS8 Human-machine cooperative systems
& Human-welfare robotics I
GS9 Human-machine cooperative systems
& Human-welfare robotics II
GS10 Image processing I
GS11 Image processing II
GS12 Learning
GS13 Mobile vehicles
GS14 Neural networks I
GS15 Neural networks II
GS16 Pattern recognition & Visualization
GS17 Robotics I
GS18 Robotics II
GS19 Robotics III

GS20 Robotics IV
GS21 Robotics V
PS1 Poster Session
OS1 System sensing and control I
OS2 System sensing and control II
OS3 Control and its application
OS4 Intelligent Control
OS5 Advanced vehicle control
OS6 AI-based systems for human
awareness promotion
OS7 Advanced technologies
& Management skills
OS8 Structural change detection for
ongoing time series
OS9 Computer vision and sound analysis
OS10 Intelligent systems I
OS11 Control and automata
OS12 Special environment navigation
and localization
OS13 Intuitive human-system
interaction

OS14 Dynamical information
processing in the brain
OS15 Bio-inspired theory
and application
OS16 Biomimetic machines
and robots
OS17 Medical science
and complex system
OS18 Data mining
OS19 Embracing complexity in
natural intelligence
OS20 Embracing complexity in
sensor system organization
OS21 Learning control
and robotics
OS22 Robotics and
pattern recognition
OS23 Intelligent systems II
OS24 Human agent interaction
toward social modification

TECHNICAL PAPER INDEX

January 27 (Thursday)

Room G

10:55~11:45 Plenary Talk

Chair Y. G. Zhang (Academia Sinica, China)

PT1 *Development Outline of Humanoid Robot: HUBO II*
J. H. Oh (KAIST, Korea)

Room A

12:40~14:25 Invited Talks

Chair M. Nakamura (Research Institute of Systems Control, Japan)

IT1 *Human-Robot Interaction and Social Relation*
M. Imai (Keio University, Japan)

IT2 *Micro Nano Robotics*
T. Arai (Osaka University, Japan)

January 28 (Friday)

Room G

10:15~11:05 Plenary Talk

Chair J. J. Lee (KAIST, Korea)

PT2 *Data-driven two degree-of-freedom control for a micropump and microneedle integrated device for diabetes care*
Ruoting Yang (Washington University, USA)
Mingjun Zhang (University of Tennessee, USA)
T. J. Tarn (Washington University, USA)

14:50~15:40 Plenary Talk

Chair H. H. Lund (Technical University of Denmark, Denmark)

PT3 *Rescue Robot Systems - From Snake-like Robots to Human Interface -*
F. Matsuno (Kyoto University, Japan)

January 29 (Saturday)

Room F

13:10~14:55 Invited Talks

Chair Y. I. Cho (Suwon University, Korea)

IT3 *Quantifying "Waza" in Nihon-Buyo Dance Movements*
M. Sakata (Doshisha University, Japan)

IT4 *Social playware for mediating tele-play interaction over distance*
H. H. Lund, T. Thorsteinsson (Technical University of Denmark, Denmark)

IT5 *An Educational Tool for Interactive Parallel and Distributed Processing*
L. Pagliarini (Technical University of Denmark, Denmark / Academy of Fine Arts of Bari, Italy)
H. H. Lund (Technical University of Denmark, Denmark)

January 27 (Thursday)

8:00~Registration

Room A

9:10~10:25 OS1 【System sensing and control I】

Chair: M. Uchida (The University of Electro-Communications, Japan)

Co-Chair: T. Mizuno (Tokyo Polytechnic University, Japan)

OS1-1 *Analysis of speech signal based on frequency distribution and intonation*

Naoya Ohta, Akio Nozawa (Meisei University, Japan)

OS1-2 *Color influences on human being evaluated with nasal skin temperature*

Tota Mizuno, Naoki Nakategawa, Yuichiro Kume (Tokyo Polytechnic University, Japan)

OS1-3 *Air speed control of airship-type fish robot*

Kunihiko Sato, Masafumi Uchida (The University of Electro-Communications, Japan)

OS1-4 *Regulated plus and minus power supply using approximate 2DOF robust digital control*

Atsushi Saitoh, Yusuke Tsuruhori, Yoshihiro Ohta, Kohji Higuchi, Kazushi Nakano (The University of Electro-Communications, Japan)

OS1-5 *Angle-based neuro-fuzzy navigation for autonomous mobile robots*

Shu Hosokawa, Joji Kato, Kazushi Nakano, Kazunori Sakurama (The University of Electro-Communications, Japan)

14:45~16:00 OS5 【Advanced vehicle control】

Chair: S. Sagara (Kyushu Institute of Technology, Japan)

Co-Chair: M. Oya (Kyushu Institute of Technology, Japan)

OS5-1 *Robust active suspension control of vehicles with measurement noises*

Katsuhiro Okumura (Fukuoka Industrial Technology Center, Japan)

Hideki Wada (Shin-Nippon Nondestructive Inspection, Japan)

Yuichiro Taira (National Fisheries University, Japan)

Masahiro Oya (Kyushu Institute of Technology, Japan)

OS5-2 *A method to improve stability of adaptive steering driver-vehicle systems*

Shingo Tamaru, Jinxin Zhuo, Qiang Wang, Masahiro Oya (Kyushu Institute of Technology, Japan)

OS5-3 *Robust controller for underwater vehicle-manipulator systems including thruster dynamics*

Yuichiro Taira (National Fisheries University, Japan)

Junpei Sugino (Kyushu Institute of Technology, Japan)

Natsuki Takagi (Miyakonojo National College of Technology, Japan)

Masahiro Oya (Kyushu Institute of Technology, Japan)

OS5-4 *Digital adaptive control of a winged rocket applicable to abort flight*

Tomoaki Shimozaawa, Shinichi Sagara (Kyushu Institute of Technology, Japan)

OS5-5 *A master-slave control system for semi-autonomous underwater vehicle manipulator system*
Kana Kawano, Tomoaki Shimozawa, Shinichi Sagara (Kyushu Institute of Technology, Japan)

16:05~17:20 OS3 【Control and its application】

Chair: M. Yokomichi (University of Miyazaki, Japan)

Co-Chair: N. Takahashi (University of Miyazaki, Japan)

OS3-1 *Observer-based guaranteed cost control*
Erwin Susanto, Mitsuaki Ishitobi, Sadaaki Kunitatsu (Kumamoto University, Japan)

OS3-2 *Observer based control of a manipulator system with structured uncertainty*
Chikara Aikawa, Nobuya Takahashi, Osamu Sato, Michio Kono (University of Miyazaki, Japan)

OS3-3 *Analysis of manipulator in consideration of collision between link and object*
Asaji Sato (Miyakonojo National College of Technology, Japan)
Osamu Sato, Nobuya Takahashi, Masahiro Yokomichi (University of Miyazaki, Japan)

OS3-4 *Motion control of 2 DOF orthogonal robots with adaptive control*
Kazuma Funahashi, Feifei Zhang, Masanori Ito (Tokyo University of Marine Science and Technology, Japan)

OS3-5 *Development of 6-DOF force feedback system for rehabilitation of wrist paralysis*
Yasunobu Hitaka (Kitakyushu National College of Technology, Japan)
Yoshito Tanaka (Fukuoka Institute of Technology, Japan)
Yutaka Tanaka (Hosei University, Japan)
Tomonori Kato (Fukuoka Institute of Technology, Japan)

Room B

9:10~10:10 OS18 【Data mining】

Chair: K. J. Mackin (Tokyo University of Information Sciences, Japan)

Co-Chair: T. Yamaguchi (Tokyo University of Information Sciences, Japan)

OS18-1 *Two-level time-series clustering for satellite data analysis*
Ayahiko Niimi, Takehiro Yamaguchi, Osamu Konishi (Future University Hakodate, Japan)

OS18-2 *PSP practice support system using defect types based on phenomenon*
Daisuke Yamaguchi (Toin University of Yokohama, Japan)
Ayahiko Niimi (Future University Hakodate, Japan)
Fumiyo Katayama, Muneo Takahashi (Toin University of Yokohama, Japan)

OS18-3 *Development and evaluation of satellite image data analysis infrastructure*
Akihiro Nakamura, Jong Geol Park, Kotaro Matsushita, Kenneth J. Mackin, Eiji Nunohiro (Tokyo University of Information Sciences, Japan)

OS18-4 *Application of neural network swarm optimization for paddy field classification from remote sensing data*
Kazuma Mori, Takashi Yamaguchi, Jong Geol Park, Kenneth J. Mackin (Tokyo University of Information Sciences, Japan)

12:40~14:25 GS10 【Image processing I】
Chair: H. Yamamoto (Gifu University, Japan)

GS10-1 *Anomalous situations detection based on confluence*

Tatsuya Gibo, Shigeki Aoki, Takao Miyamoto, Motoi Iwata, Akira Shiozaki (Osaka Prefecture University, Japan)

GS10-2 *Automatic segmentation of liver region from non-contrast and contrast CT images employing tree-structural image transformations*

Masafumi Komatsu, , Guangxu Li, Hyoungseop Kim, Joo Kooi Tan, Seiji Ishikawa (Kyushu Institute of Technology, Japan)

Akiyoshi Yamamoto (Kyushu Institute of Technology and Kyoaikai Tobata Kyoritsu Hospital, Japan)

GS10-3 *Obstacle detection using a moving camera*

Shao Hua Qian, Joo Kooi Tan, Seiji Ishikawa, Takashi Morie (Kyushu Institute of Technology, Japan)

GS10-4 *Hardware implementation of a census-based stereo matching using FPGA*

Jiho Chang, Sung-Min Choi, Eul-Gyoon Lim, Jae-il Cho (Electronics and Telecommunication Research Institute, Korea)

GS10-5 *Hand detection using Adaboost*

Jae-chan Jeong (Electronics and Telecommunication Research Institute and University of Science and Technology, Korea)

Seung-min-Choi (Electronics and Telecommunication Research Institute, Korea)

Ho-chul Shin (Electronics and Telecommunication Research Institute and University of Science and Technology, Korea)

Jae-il Cho (Electronics and Telecommunication Research Institute, Korea)

GS10-6 *Improvement of early recognition of gesture patterns based on Self-Organizing Map*

Atsushi Shimada, Manabu Kawashima, Rin-ichiro Taniguchi (Kyushu University, Japan)

GS10-7 *Detection of a bicycle and its driving directions using HOG Feature*

Heewook Jung, Joo Kooi Tan, Hyeongseop Kim, Seiji Ishikawa (Kyushu Institute of technology, Japan)

14:45~16:00 GS16 【Pattern recognition & Visualization】
Chair: K. Ikeda (Nara Institute of Science and Technology, Japan)

GS16-1 *Parts layout decision of cell production assembly line using generic algorithm system and virtual system*

Hidehiko Yamamoto, Tomokazu Watanabe, Takayoshi Yamada (Gifu University, Japan)

Masahiro Nakamura (LEXER RESEARCH Inc., Japan)

Rafat Hessen Elsayed Elshaer (Zagazig University, Egypt)

GS16-2 *Parallelizing fuzzy rule generation using GPGPU*

Takesuke Uenishi, Tomoharu Nakashima, Noriyuki Fujimoto (Osaka Prefecture University, Japan)

GS16-3 *Interactive musical editing system to support human errors and offer personal preferences for an automatic piano*

- *A method for searching for similar phrases using DP matching* -

Kenichi Koga, Kentaro Minowa, Eiji Hayashi (Kyusyu Institute of Technology, Japan)

GS16-4 *Subsurface imaging for anti-personal mine detection by Bayesian super-resolution with Smooth-gap prior*

Satoshi Kozawa, Takashi Takenouchi, Kazushi Ikeda (Nara Institute of Science and Technology, Japan)

GS16-5 *Construction of a sense of force feedback and vision for micro-objects:*

Development the Haptic Device's controlling

J.Noda, E.Hayashi (Kyushu Institute of Technology, Japan)

16:05~17:20 OS4 【Intelligent Control】

Chair: Y-M. Jia (Beihang University, China)

Co-Chair: C. Jia (Beihang University, China)

OS4-1 *Feedback stabilization of linear systems with distributed input time-delay by backstepping method*

Chaohua Jia (Beijing University, China)

OS4-2 *Discrete-time iterative learning control for relative degree systems: a 2-D approach*

Deyuan Meng, Yingmin Jia (Beihang University, China)

OS4-3 *Distributed robust consensus control of uncertain multi-agent systems*

Yang Liu, Yingmin Jia (Beihang University, China)

OS4-4 *Switching synchronization in a heterogeneous agent network*

Lei Wang, Yang Liu, Qi-ye Zhang (Beihang University, China)

OS4-5 *Model matching adaptive control of time delay systems with unknown relative degree*

Haixia Su, Yingmin Jia (Beihang University, China)

Room C

9:10~10:10 OS2 【System sensing and control II】

Chair: H. Tanaka (Kogakuin University, Japan)

Co-Chair: A. Nozawa (Meisei University, Japan)

OS2-1 *Quantitative evaluation of body-sway caused by tactile apparent movement*

Kennichi Mogi, Masafumi Uchida (The University of Electro-Communications, Japan)

OS2-2 *A visual-taste interference model and the EEG measurement*

Hisaya Tanaka, Yuichi Sato (Kogakuin University, Japan)

OS2-3 *Dynamic analysis of dorsal thermal image*

Akio Nozawa, Yuya Takei (Meisei University, Japan)

OS2-4 *Feature extraction of human face image for preference database*

Yu Tachikawa, Akio Nozawa (Meisei University, Japan)

12:40~14:25 GS21 【Robotics V】

Chair: B.Fu (Sahngai Jiao Tong University, China)

GS21-1 *Designing practical omni-directional mobile module in the robot hardware platform for common use*

Moosung Choi, Sulhee Lee, Byungkyu Ahn, EunCheul Shin, Kwangyoong Yang, Hongseuk Kim
(Korea Institute of Industrial Technology, Republic of Korea)

GS21-2 *New acoustic positioning system for under water robot using multiple frequencies*

Xiu Jing Gao, Feifei Zhang, Masanori Ito (Tokyo University of Marine Science and Technology, Japan)

GS21-3 *Development of under water use humanoid robot*

Yunyi Li, Eturo Shimizu, Masanori Ito (Tokyo University of Marine Science and Technology, Japan)

GS21-4 *Linear estimation method for position and heading with RDOA measurements*

G. H. Choi (Yonsei University, Korea)
H. S. Cheon (Changwon National University, Korea)
J. B. Park (Yonsei University, Korea)
T. S. Yoon (Changwon National University, Korea)

GS21-5 *Omnidirectional state-changing gripper for various objects*

Kenjiro Tadakuma (Osaka University, Japan)
Riichiro Tadakuma (Yamagata University, Japan)
Hiroki Tanaka, Takuto Fukuda, Mitsuru Higashimori, Makoto Kaneko (Osaka University, Japan)

GS21-6 *Object co-occurrence graph for object search in 3D environment*

Puwanan Chumtong, Yasushi Mae, Kenichi Ohara, Tomohito Takubo, Tatsuo Arai (Osaka University, Japan)

GS21-7 *Study on the wall climbing robot driven by the caterpillar tracks*

Jiwu Wang, Yisong Wang, Weijie Gao (Beijing Jiaotong University, China)
Sugisaka Masanori (Nippon Bunri University, Japan)

14:45~15:45 OS24 【Human agent interaction toward social modification】

Chair: M. Imai (Keio University, Japan)

Co-Chair: H. Osawa (Japan Science and Technology Agency and Keio University, Japan)

OS24-1 *Social modification using implementation of partial agency toward objects*

Hiroataka Osawa (Japan Science and Technology Agency, Japan)
Seiji Yamada (National Institute of Informatics, Japan)

OS24-2 *Inducement of attention to agent through averting gaze from the other*

Manami Suzuki, Yugo Takeuchi (Shizuoka University, Japan)

OS24-3 *Behaviors for getting conscious responses*

Toshihiro Osumi, Masato Noda (Keio University, Japan)
Hirotaka Osawa (Japan Science and Technology Agency, Japan)
Yuki Kuwayama (Keio University, Japan)
Kazuhiko Shinozawa (ATR, Japan)
Michita Imai (Keio University, Japan)

OS24-4 *Cross-modal effects between gestures and words in human robot interaction*

Takamasa Iio (Advanced Telecommunications Research Institute International and Doshisha University, Japan)
Masahiro Shiomi, Kazuhiko Shinozawa, Takaaki Akimoto (Advanced Telecommunications Research Institute International, Japan)
Katsunori Shimohara (Doshisha University, Japan)
Norihiro Hagita (Advanced Telecommunications Research Institute International, Japan)

16:05~17:20 GS3 【Artificial life II】

Chair: D. E. Kim (Yonsei University, Korea)

GS3-1 *Demand level investigation for future domestic system*

Shuki Inoue, Eiji Mimura (R&D Center The Kansai Electric Power Co., Inc., Japan)
Shingo Aoki, Hiroshi Tsuji (Osaka Prefecture University, Japan)

GS3-2 *Visualizing language evolution as an emergent phenomenon based on biological evolution and learning*

Tsubasa Azumagakito, Reiji Suzuki, Takaya Arita (Nagoya University)

GS3-3 *Self-organizing stability of food web that emerges from the evolution of restrictions on speciation*

Hirofumi Ochiai, Reiji Suzuki, Takaya Arita (Nagoya University, Japan)

GS3-4 *Modeling electrosensory system of weakly electric fish*

Miyoung Sim, DaeEun Kim (Yonsei University, South Korea)

GS3-5 *Simultaneous cognitive origin of life and information*

Koji Ohnishi (Niigata University, Japan)

Room D

9:10~10:10 GS4 【Chaos & Complexity】

Chair: S. Nakayama (Kagoshima University, Japan)

GS4-1 *Study on discrete adiabatic quantum computation in 3-SAT problems*

Mohamed El-fiky, Satoshi Ono, Shigeru Nakayama (Kagoshima University, Japan)

GS4-2 *Fault-tolerant image filter design using particle swarm optimization*

Zhiguo Bao, Fangfang Wang, Xiaoming Zhao, Takahiro Watanabe (Waseda University, Japan)

GS4-3 *(p,q)-Duffing oscillators and nonlinear energy harvesting (**withdrawal**)*

Tokuzo Shimada, Takanobu Moriya, Hisakazu Uchiyama (Meiji University, Japan)

GS4-4 *A most simple, alternative non-computer-aided proof of the Four-Color Theorem*

Koji Ohnishi (Niigata University, Japan)

12:40~14:40 PS1 【Poster session】

Chair: J. J. Lee (KAIST, Korea)

PS1-1 *Authentication of the reconstructed image from Computer Generated Hologram:
To use the digital watermark*

Norihiro Fujii, Ken-ichi Tanaka (Meiji University, Japan)

PS1-2 *An aerial handwritten character recognition based on motion direction and ratio of
stroke length*

Y. Nishida (Fukui University of Technology, Japan)

K. Ogura, H. Miura, N. Matsuda, H. Taki (Wakayama University, Japan)

N. Abe (Kyushu Institute of Technology, Japan)

PS1-3 *Gamer robot for the rock-paper-scissors game by hand motion recognition*

Ho Seok Ahn, Dong-wook Lee, Hogil Lee (Korea Institute of Industrial Technology, Republic of Korea)

PS1-4 *Analysis method of tooth meshing condition and motion of gears*

Edzrol Niza Mohamad, Masaharu Komori, Hiroaki Murakami, Aizoh Kubo (Kyoto University, Japan)

PS1-5 *Research for an adaptive user's intent-detection method for the use in rehabilitation robots*

Jun-Young Jung, Duk-Yeon Lee, DongWoon Choi, In-Hun Jang, Ho-Gil Lee, HyunSub Park,
Dong-Wook Lee (University of Science and Technology and Korea Institute of Industrial Technology,
Republic of Korea)

PS1-6 *Development of touch sensor system of silicone-type artificial skin for an interactive
android robot*

Duk-Yeon Lee, Dong-Wook Lee, Dongwoon Che, Hyun-Sub Park, Ho-Gil Lee, Jun-Young Jung
(Korea Institute of Industrial Technology, Republic of Korea)

PS1-7 *Remote control and conversation system between human and android robot via internet*

Dong-Wook Lee, Dongwoon Che, Jun-Young Joung, Hoseok Ahn, Hyunsub Park, Ho-Gil Lee
(Korea Institute of Industrial Technology, Republic of Korea)

PS1-8 *The optimal method of searching the effective combination of dither matrix*

Tsuneyasu Kato, Ken-ichi Tanaka (Meiji University, Japan)

14:45~16:00 OS17 【Medical science and complex system】

Chair: K. Naitoh (Waseda University, Japan)

Co-Chair: T. Matsuo (Kanagawa Institute of Technology, Japan)

OS17-1 *The inevitability of the bio-molecules: five nitrogenous bases and twenty amino acids*

K.Hashimoto, H.Inoue, K.Naitoh (Waseda University, Japan)

OS17-2 *Engine for brain development: Similarity between engine and brain*

H. Kawanobe, K. Naitoh (Waseda University, Japan)

OS17-3 *Spatial surface wave spread network from Ambient Noise correlation*

Z. Zheng, K. Yamasaki, T. Fujiwara, N. Sakurai, K. Yoshizawa (Tokyo University of Information
Science, Japan)

OS17-4 *Effect of hot summer against environment which was induced by extra economical demand via Japanese Ecological Footprint*

K. Yamasaki, T. Fujiwara, N. Sakurai, K. Yoshizawa, Z. Zheng (Tokyo University of Information Sciences, Japan)

OS17-5 *Blood flow velocity waveforms in the middle cerebral artery at rest and during exercise*

T. Matsuo, S. Watanabe, M. Sorimachi, M. Kanda, Y. Ohta (Kanagawa Institute of Technology, Japan)

T. Takahashi (Asahikawa Medical College, Japan)

16:05~17:35 GS19 【Robotics III】

Chair: A. Nakamura (National Institute of Advanced Science and Technology, Japan)

GS19-1 *Design of the transmitting device for motion control of robots*

Masaharu Komori, Jungchul Kang, Fumi Takeoka, Yukihiro Kimura (Kyoto University, Japan)

GS19-2 *Construction and basic performance tests of underwater monitoring network*

Chunhu Liu, Bin Fu, Han Zhang, Lian Lian (Shanghai Jiao tong University, China)

GS19-3 *On the use of human instruction for improving the behavior of RoboCup soccer agents*

Yosuke Nakamura, Tomoharu Nakashima (Osaka Prefecture University, Japan)

GS19-4 *Development of an autonomous-drive personal robot*

“An environment recognition system using image processing and an LRS”

Yasushi Kibe, Hideki Ishimaru, Eiji Hayashi (Kyushu Institute of Technology, Japan)

GS19-5 *Design of robotic behavior that imitates animal consciousness*

—Emotion expression of robotic arm based on eyeball movement —

Koichiro Kurogi, Kei Ueyama, Eiji Hayashi (Kyushu Institute of Technology, Japan)

GS19-6 *Development and experimental study of a novel pruning robot*

S. Ueki (Toyota Colleges of Technology, Japan)

H. Kawasaki (Gifu University, Japan)

Y. Ishigure (Marutomi Seikou Co., Ltd., Japan)

K. Koganemaru (Gifu University, Japan)

Y. Mori (Hashima karyuu kougyou Ltd., Japan)

January 28 (Friday)

8:00~ Registration

Room A

8:40~9:55 GS5 【Control techniques】

Chair: J. Murata (Kyushu University, Japan)

GS5-1 *Autonomous decentralized control scheme for large scale and dense wireless sensor networks with multiple sinks*

Masahito Maki, Akihide Utani, Hisao Yamamoto (Tokyo City University, Japan)

GS5-2 *Advanced adaptive communication protocol for ubiquitous sensor networks*
Shuichi Osawa, Akihide Utani, Hisao Yamamoto (Tokyo City University, Japan)

GS5-3 *Lateral control of unmanned vehicle using PD controller*
Young Chul Cha (Pusan National University, Korea)
Jong Il Bae (Pukyung National University, Korea)
Kil Soo Lee, Dong Seok Lee, Yun Ja Lee, Man Hyung Lee (Pusan National University, Korea)

GS5-4 *A control method with pheromone information for transport system*
Yoshitaka Imoto, Yasutaka Tsuji, Eiji Kondo (Kyushu University, Japan)

GS5-5 *Implementation of real-time distributed control for discrete event robotic manufacturing systems using Petri nets*
Gen'ichi Yasuda (Nagasaki Institute of Applied Science, Japan)

11:05~12:20 OS7 【Advanced technologies & Management skills】

Chair: T. Ito (Ube National College of Technology, Japan)

Co-Chair: Y. Uchida (Ube National College of Technology, Japan)

OS7-1 *An analysis of firm's capacity in Mazda's Keiretsu*
R. Takida, T. Ito, S. Matsuno (Ube National College of Technology, Japan)
K. Voges (University of Canterbury, New Zealand)
Y. Ishida (Toyohashi University of Technology, Japan)
M. Sakamoto (University of Miyazaki, Japan)

OS7-2 *An analysis of structure importance in Mazda's Keiretsu*
S. Tagawa, R. Takida, T. Ito (Ube National College of Technology, Japan)
R. Mehta (New Jersey Institute of Technology, USA)
H. Hasama (Fukuoka Institute of Technology, Japan)
M. Sakamoto (University of Miyazaki, Japan)

OS7-3 *A centrality analysis between transactions and cross shareholdings in Mazda's Keiretsu*
E. Niki, R. Takida, T. Ito (Ube National College of Technology, Japan)
R. Mehta (New Jersey Institute of Technology, USA)
L. P. NG (Hoecheong Industries (Holding) Co., Ltd, China)
M. Sakamoto (University of Miyazaki, Japan)

OS7-4 *Bottom-up pyramid cellular acceptors with four-dimensional layers*
Yasuo Uchida, Takao Ito (Ube National College of Technology, Japan)
Makoto Sakamoto, Takashi Ide, Kazuyuki Uchida, Ryoju Katamune,
Hiroshi Furutani, Michio Kono, Satoshi Ikeda (University of Miyazaki, Japan)
Tsunehiro Yoshinaga (Tokuyama College of Technology, Japan)

OS7-5 *Cooperating systems of four-dimensional finite automata*
Yasuo Uchida, Takao Ito (Ube National College of Technology, Japan)
Makoto Sakamoto, Kazuyuki Uchida, Takashi Ide, Ryoju Katamune,
Hiroshi Furutani, Michio Kono (University of Miyazaki, Japan)
Tsunehiro Yoshinaga (Tokuyama College of Technology, Japan)

13:15~14:45 OS10 【Intelligent systems I】

Chair: K-L. Su (National Yunlin University of Science and Technology, Taiwan)

Co-Chair: J-H. Tzou (National Formosa University, Taiwan)

OS10-1 *The study of path error for an Omnidirectional Home Care Mobile Robot*

Jie-Tong Zou (National Formosa University, Taiwan)

Feng-Chun Chiang (WuFeng Institute of Technology, Taiwan)

OS10-2 *A* searching algorithm applying in Chinese chess game*

Cheng-Yun Chung (National Yunlin University of Science and Technology, Taiwan)

Te-Yi Hsu (Industrial Technology Research Institute, Taiwan)

Jyh-Hwa Tzou (National Formosa University, Taiwan)

Kuo-Lan Su (National Yunlin University of Science and Technology, Taiwan)

OS10-3 *Multi-robot based intelligent security system*

Yi-Lin Liao, Kuo-Lan Su (National Yunlin University of Science and Technology, Taiwan)

OS10-4 *Implementation of an auction algorithm based multiple tasks allocation using mobile robots*

Kuo-Lan Su, Jr-Hung Guo (National Yunlin University of Science and Technology, Taiwan)

Chun-Chieh Wang (Chienkuo Technology University, Taiwan)

Cheng-Yun Chung (National Yunlin University of Science and Technology, Taiwan)

OS10-5 *Fuzzy programming for mixed-integer optimization problems*

Yung-Chin Lin (National Yunlin University of Science and Technology, Taiwan)

Yung-Chien Lin (WuFeng University, Taiwan)

Kuo-Lan Su (National Yunlin University of Science and Technology, Taiwan)

Wei-Cheng Lin (I-Shou University, Taiwan)

Tsing-Hua Chen (WuFeng University, Taiwan)

OS10-6 *Develop a vision based auto-recharging system for mobile robots*

Ting-Li Chien (Wu-Feng University, Taiwan)

16:00~17:30 OS1 1 【Control and automata】

Chair: K-H. Hsia (Far East University, Taiwan)

Co-Chair: K-L. Su (National Yunlin University of Science and Technology, Taiwan)

OS11-1 *Super-twisting second order sliding mode control for a synchronous reluctance motor*

Huann-Keng Chiang, Wen-Bin Lin, Chang-Yi Chang (National Yunlin University of Science and Technology, Taiwan)

Chien-An Chen (Automotive Research and Testing Center, Taiwan)

OS11-2 *Shape recognition applied in a semi-autonomous weapon robot*

Chun-Chieh Wang, Chyun-Luen Lin (Chienkuo Technology University, Taiwan)

Kuo-Lan Su (National Yunlin University of Science and Technology, Taiwan)

OS11-3 *Camera position estimation and feature extraction from incomplete image of landmark*

Kuo-Hsien Hsia (Far East University, Taiwan)

Shao-Fan Lien (National Yunlin University of Science and Technology, Taiwan)

Juhng-Perng Su (National Yunlin University of Science and Technology and Overseas Chinese University, Taiwan)

OS11-4 *A novel variable structure theory applied in design for wheeled mobile robots*
Chun-Chieh Wang (Chienkuo Technology University, Taiwan)

OS11-5 *Parameter identification of Lorenz system using RBF neural networks with time-varying learning algorithm*
Chia-Nan Ko, Yu-Yi Fu, Cheng-Ming Lee, Guan-Yu Liu (Nan-Kai University of Technology, Taiwan)

OS11-6 *Motion planning of a landmine detection robot*
Kuo-Lan Su (National Yunlin University of Science and Technology, Taiwan)
Hsu-Shan Su, Sheng-Wen Shiao, Jr-Hung Guo (Yunlin University of Science and Technology, Taiwan)

Room B

8:40~9:55 OS8 [Structural change detection for ongoing time series]

Chair: T. Hattori (Kagawa University, Japan)

Co-Chair: H. Kawano (NTT Advanced Technology, Japan)

OS8-1 *DP method for structural change detection as optimal stopping*
---- verification and extension ---
Tetsuo Hattori, Katsunori Takeda (Kagawa University, Japan)
Hiromichi Kawano (NTT Advanced Technology, Japan)
Tetsuya Izumi (Micro Technica Co., Ltd., Japan)

OS8-2 *Change detection experimentation for multiple regression using ESPRT*
---- one variation is periodic function ---
Katsunori Takeda, Tetsuo Hattori (Kagawa University, Japan)
Hiromichi Kawano (NTT Advanced Technology, Japan)
Tetsuya Izumi (Micro Technica Co., Ltd., Japan)

OS8-3 *Continuous change point detection for time series images using ESPRT*
Katsunori Takeda, Tetsuo Hattori (Kagawa University, Japan)
Hiromichi Kawano (NTT Advanced Technology, Japan)
Tetsuya Izumi (Micro Technica Co., Ltd., Japan)
Shinichi Masuda (C Micro Co., Ltd., Japan)

OS8-4 *DP method for structural change detection as optimal stopping*
---- experimentation in multiple regression model ---
Hiromichi Kawano (NTT Advanced Technology, Japan)
Tetsuo Hattori, Katsunori Takeda (Kagawa University, Japan)
Tetsuya Izumi (Micro Technica Co., Ltd., Japan)

OS8-5 *Comparison of change detection methods for ongoing time series data*
---- extended SPRT, Chow Test, extended DP ----
Hiromichi Kawano (NTT Advanced Technology, Japan)
Tetsuo Hattori, Katsunori Takeda (Kagawa University, Japan)
Tetsuya Izumi (Micro Technica Co., Ltd., Japan)

11:05~12:05 GS8

【Human-machine cooperative systems & Human-welfare robotics I】

Chair: T. Fuchida (Kagoshima University, Japan)

GS8-1 *EMG control of a pneumatic 5-fingered hand using a Petri net*

Osamu Fukuda, Jonghwan Kim (National Institute of Advanced Industrial Science and Technology, Japan)

Isao Nakai, Yasunori Ichikawa (SQUSE Inc., Japan)

GS8-2 *Haptic warning method on steering behavior for urgent lane change situation*

Jae-Woo Sim, Chi-Hoon Shin (University of Science and Technology, Korea)

Young Woo Kim (Electronics and Telecommunication Research institute, Korea)

GS8-3 *Depth calculation by using Face detection ASIC*

Seung Min Choi (Electronics and Telecommunications Research Institute, Korea)

Jae-chan Jeong (University of Science and Technology, Korea)

Jaeil Cho (Electronics and Telecommunications Research Institute, Korea)

GS8-4 *An experimental study on interactive reinforcement learning*

Tomoharu Nakashima, Yosuke Nakamura, Takesuke Uenishi, Yosuke Narimoto (Osaka Prefecture University, Japan)

13:15~14:45 GS2 【Artificial life I】

Chair: T. Arita (Nagoya University, Japan)

GS2-1 *Improved artificial bee colony algorithm for large-scale optimization problems*

Ryuta Gocho, Akihide Utani, Hisao Yamamoto (Tokyo City University, Japan)

GS2-2 *Simulation of self-reproduction phenomenon of cells in two-dimensional hybrid-cellular automata model*

Takeshi Ishida (Nippon Institute of Technology, Japan)

GS2-3 *A physics modeling of butterfly's flight control by GA and ANN and its over-evolution problem*

R. Ooe, I. Suzuki, M. Yamamoto, M. Furukawa (Hokkaido University, Japan)

GS2-4 *Emergence of behavior intelligence on artificial creature in different virtual fluid environments*

Keita Nakamura, Ikuo Suzuki, Masahito Yamamoto, Masashi Furukawa (Hokkaido University, Japan)

GS2-5 *Behavior emergence of virtual creature living in complex environments*

Kenji Iwadate, Ikuo Suzuki, Masahito Yamamoto, Masashi Furukawa (Hokkaido University, Japan)

GS2-6 *Three-dimensional morphogenesis by cell division and death in viscoelastic amorphous computing*

Eisuke Arai, Fumiaki Tanaka, Masami Hagiya (University of Tokyo, Japan)

16:00~17:30 GS7 【Evolutionary computations】

Chair: P. Sapaty (National Academy of Sciences, Ukraine)

GS7-1 *A study on efficient query dissemination in distributed sensor networks*

- *Forwarding power adjustment of each sensor node using particle swarm optimization* -

Junya Nagashima, Akihide Utani, Hisao Yamamoto (Tokyo City University, Japan)

GS7-2 *Evaluation of a competitive particle swarm optimizer in multimodal functions with complexity*

Yu Taguchi, Hidehiro Nakano, Akihide Utani, Arata Miyauchi, Hisao Yamamoto (Tokyo City University, Japan)

GS7-3 *An effective allocation method of ZigBee sensor nodes using a discrete particle swarm optimizer*

Ryota Saito, Hidehiro Nakano, Akihide Utani, Arata Miyauchi, Hisao Yamamoto (Tokyo City University, Japan)

GS7-4 *An implementation of probabilistic model-building coevolutionary algorithm*

Takahiro Otani, Takaya Arita (Nagoya University, Japan)

GS7-5 *Modeling and solution for optimization problems with incomplete information*

-- *A general framework and an application to cruising taxi problems* --

Makoto Ohara, Hisashi Tamaki (Kobe University, Japan)

GS7-6 *Prime number generation using memetic programming*

Emad Mabrouk (Kyoto University, Japan)

Julio César Hernández Castro (University of Portsmouth, UK)

Masao Fukushima (Kyoto University, Japan)

Room C

8:40~9:55 OS13 【Intuitive human-system interaction】

Chair: M. Yokota (Fukuoka Institute of Technology, Japan)

Co-Chair: T. Oka (Nihon University, Japan)

OS13-1 *A High-speed 3D image Measurement Method*

Ke Sun, Yundi Yao, Cunwei Lu (Fukuoka Institute of Technology, Japan)

OS13-2 *3-D face recognition method based on optimum 3-D image measurement technology*

Hiroya Kamitomo, Yao Xu, Cunwei Lu (Fukuoka Institute of Technology, Japan)

OS13-3 *User study of a life-supporting humanoid directed in a multimodal language*

T. Oka (Nihon University, Japan)

T. Abe (Nihon Computer Kaihatsu Co. Ltd, Japan)

K. Sugita, M. Yokota (Fukuoka Institute of Technology, Japan)

OS13-4 *A multimodal language to communicate with life supporting robots through a touch screen and a speech interface*

T. Oka, H. Matsumoto, R. Kibayashi (Nihon University, Japan)

- OS13-5 *Some consideration on user interface switching functions for the weaker at IT*
Shinichi Inenaga, Kaoru Sugita (Fukuoka institute of technology, Japan)
Tetsushi Oka (Nihon University, Japan)
Masao Yokota (Fukuoka institute of technology, Japan)

11:05~12:05 GS9

【Human-machine cooperative systems & Human-welfare robotics II】

Chair: N. Okada (Kyushu University, Japan)

- GS9-1 *Crutch gait pattern for robotic orthosis by the feature extraction*
In Hun Jang, Jun-Young Jung, Duk-Yeon Lee, DongWook Lee, Ho-Gil Lee, HyunSub Park
(Korea Institute of Industrial Technology, Republic of Korea)
- GS9-2 *Design of personal support system in telephone correspondence using smart phone*
Hiroyuki Nishiyama, Fumio Mizoguchi (Tokyo University of Science, Japan)
- GS9-3 *Advanced networking and robotics for societal engagement and support of elders*
Peter Sapaty (National Academy of Sciences, Ukraine)
Masanori Sugisaka (Nippon Bunri University, Japan)
- GS9-4 *Construction of the muscle fatigue evaluation model based on accuracy of power*
Akihiro Suzuki, Norihiko Kato, Yoshihiko Nomura, Hirokazu Matsui (Mie University, Japan)

13:15~14:45 OS9 【Computer vision and sound analysis】

Chair: Y. Yoshitomi (Kyoto Prefectural University, Japan)

Co-Chair: M. Tabuse (Kyoto Prefectural University, Japan)

- OS9-1 *Outdoor autonomous navigation using SURF features*
M. Tabuse, T. Kitaoka (Kyoto Prefectural University, Japan)
D. Nakai (Kyoto Prefectural Subaru High School, Japan)
- OS9-2 *Facial expression recognition of a speaker using front-view face judgment, vowel judgment and thermal image processing*
T. Fujimura (Works Applications Co. Ltd, Japan)
Y. Yoshitomi, T. Asada, M. Tabuse (Kyoto Prefectural University, Japan)
- OS9-3 *Facial expression recognition of a speaker using vowel judgment and thermal image processing*
Y. Yoshitomi, T. Asada (Kyoto Prefectural University, Japan)
K. Shimada (Nova System Co., Ltd., Japan)
M. Tabuse (Kyoto Prefectural University, Japan)
- OS9-4 *A human-machine cooperative system for generating sign language animation using thermal image processing, fuzzy algorithm, and simulated annealing*
T. Asada, Y. Yoshitomi (Kyoto Prefectural University, Japan)
- OS9-5 *Music recommendation system using the time-series discrete wavelet transform and the fastICA*
K. Horiike (Taka Dance Fashion Co., Ltd., Japan)
Y. Yoshitomi (Kyoto Prefectural University, Japan)
T. Tokuyama (Shofu Inc., Japan)
M. Tabuse (Kyoto Prefectural University, Japan)

OS9-6 *Music recommendation system aimed at improving recognition ability*
H. Konishi, Y. Yoshitomi (Kyoto Prefectural University, Japan)

16:00~17:30 GS18 【Robotics II】

Chair: E. Inohira (Kyushu Institute of Technology, Japan)

GS18-1 *DEA various method used Restricted Multiplier DEA*
Shingo Aoki, Ryota Gejima, Tomoharu Nakashima (Osaka Prefecture University, Japan)

GS18-2 *Efficient distributed ontology management scheme for inference in surveillance networks*
Soomi Yang (The University of Suwon, Korea)

GS18-3 *Recovery technique from classified errors in adjustment tasks of domestic appliances*
Akira Nakamura, Yoshihiro Kawai (National Institute of Advanced Industrial Science and Technology, Japan)

GS18-4 *A visual debugger for developing RoboCup soccer 3D agent*
Yosuke Nakamura, Tomoharu Nakashima (Osaka Prefecture University, Japan)

GS18-5 *Development of pulse control type MEMS micro robot with hardware neural network*
Kazuto Okazaki, Tatsuya Ogiwara, Dongshin Yang, Kentaro Sakata, Ken Saito, Yoshifumi Sekine, Fumio Uchikoba (Nihon University, Japan)

Room D

8:40~9:55 GS15 【Neural networks II】

Chair: N. Kamiura (University of Hyogo, Japan)

GS15-1 *Medical image diagnosis of lung cancer by revised GMDH-type neural network using various kinds of neurons*
Tadashi Kondo, Junji Ueno (The University of Tokushima, Japan)

GS15-2 *Neural Network application using GPGPU*
Yuta Tsuchida, Michifumi Yoshioka (Osaka Prefecture University, Japan)

GS15-3 *Evaluation of an optimal design method for multilayer perceptron by using the Design of Experiments*
E. Inohira, H. Yokoi (Kyushu Institute of Technology, Japan)

GS15-4 *A learning method for dynamic Bayesian network structures using a multi-objective particle swarm optimizer*
Kousuke Shibata, Hidehiro Nakano, Arata Miyauchi (Tokyo City University, Japan)

GS15-5 *Remarks on folding behavior of mapping capability of neural network direct controller for many-to-one plant*
Takayuki Yamada (Ibaraki University, Japan)

11:05~12:20 OS12 【Special environment navigation and localization】

Chair: J. M. Lee (Pusan National University, South Korea)

- OS12-1 *Optimal posture control of two wheeled inverted pendulum robot on a slanted surface*
Youngkuk Kwon, Joonbae Son, Jaeoh Lee, Jongho Han, Jangmyung Lee (Pusan National University, Korea)
- OS12-2 *Efficient CAN-based network for marine engine state monitoring system*
Junseok Lee, Yoseop Hwang, Jaehan Jo, Jangmyung Lee (Pusan National University, Korea)
- OS12-3 *Localization Algorithm using Virtual Label for a Mobile Robot in Indoor and Outdoor Environment*
Kiho Yu, Mincheol Lee, Junghun Heo, Youngeun Moon (Pusan National University, South Korea)
- OS12-4 *Potential field method applied on the navigation of multiple mobile robots with limited ultrasonic sensing*
Chiyen Kim, Mincheol Lee, Junyoung Beak, Chibeom Noh (Pusan National University, South Korea)
- OS12-5 *Adaptive tuning of a Kalman filter using Fuzzy logic for attitude reference system*
Taerim Kim, Joocheol Do, Eunkook Jung, Gyeongdong Baek, Sungshin Kim (Pusan National University, South Korea)

13:15~14:30 GS17 【Robotics I】

Chair: D. W. Lee (Korea Institute of Industrial Technology, Korea)

- GS17-1 *Trajectory control of biomimetic robots for demonstrating human arm movements*
T. Kashima, M. Iwaseya (Tomakomai National College of Technology, Japan)
- GS17-2 *A study on reinforcement learning scheme in cooperative network-systems of sensor nodes and mobile robots*
Koichi Hirayama, Akihito Utani, Hisao Yamamoto (Tokyo City University, Japan)
- GS17-3 *Towards the automation of cashew shelling operation*
Son Doan Tran (Ho Chi Minh University of Technology, Vietnam)
Naoki Uchiyama, Suguru Kirita, Norifumi Yamanaka (Toyohashi University of Technology, Japan)
Phat Minh Ho (Ho Chi Minh University of Technology, Vietnam)
- GS17-4 *Research on the velocity variation method for precise motion transmission*
Masaharu Komori, Jungchul Kang, Yukihiko Kimura, Fumi Takeoka (Kyoto University, Japan)
- GS17-5 *Towards the enhancement of biped locomotion and control techniques - walking pattern classification*
Basak Yuksel (Mitsubishi Electric Corporation, Advanced Technology R&D Center, Japan and Middle East Technical University, Turkey)
Kemal Leblebicioğlu (Middle East Technical University, Turkey)

16:00~17:30 GS13 【Mobile vehicles】

Chair: F. Dai (Tianjin University of Science & Technology, China)

GS13-1 *Geometrical analysis and design of motion transmitting element for mobile vehicles*
Masaharu Komori, Fumi Takeoka, Jungchul Kang, Yukihiro Kimura (Kyoto University, Japan)

GS13-2 *Underwater unknown acoustic source localization based on Sound Propagation Loss: theory analysis and simulation results*
Han Zhang, Bin Fu, Chunhu Liu, Lian Lian (Shanghai Jiao tong University, China)

GS13-3 *Position recognition system of autonomous vehicle via Kalman filtering*
Dong Jin Kim (Pusan National University, Korea)
Jong Il Bae (Pukyung National University, Korea.)
Kil Soo Lee, Dong Seok Lee, Yun Ja Lee, Man Hyung Lee (Pusan National University, Korea)

GS13-4 *Dynamic modeling, stability and energy efficiency analysis of crab walking of a six-legged robot (**withdrawal**)*
Shibendu Shekhar Roy (National Institutes of Technology, India)
Dilip Kumar Pratihar (Indian Institutes of Technology, India)

GS13-5 *Motion analysis of towed vehicle on survey system for deep sea*
Kohei Oshima, Etsuro Shimizu, Masanori Ito, Sadanobu Omichi (Tokyo University of Marine Science and Technology Japan)

GS13-6 *Path planning of an autonomous mobile robot considering region with velocity constraint in real environment*
Tae Hyon Kim (Kyoto University, Japan)
Kiyohiro Goto (The University of Electro-Communications, Japan)
Hiroki Igarashi, Kazuyuki Kon, Noritaka Sato, Fumitoshi Matsuno (Kyoto University, Japan)

January 29 (Saturday)

8:00~ Registration

Room C

8:40~9:55 OS14 【Dynamical information processing in the brain】

Chair: H. Suzuki (The University of Tokyo, Japan)

Co-Chair: T. Kohno (The University of Tokyo, Japan)

OS14-1 *Signal transmission in multilayer asynchronous neural networks*
Wataru Kobayashi, Makito Oku, Kazuyuki Aihara (The University of Tokyo, Japan)

OS14-2 *A two-variable silicon neuron circuit based on Izhikevich model*
Nobuyuki Mizoguchi, Yuji Nagamatsu, Kazuyuki Aihara, Takashi Kohno (The University of Tokyo, Japan)

OS14-3 *A three-variable silicon neuron circuit*
Yohei Nakamura, Kazuyuki Aihara, Takashi Kohno (University of Tokyo, Japan)

OS14-4 *Theory of mind in a microscopic pedestrian simulation model*
Ryo Adachi, Kazuyuki Aihara (The University of Tokyo, Japan)

OS14-5 *A neural network model for categorical effects in color memory*
Chihiro Imai (University of Tokyo, Japan)
Satohiro Tajima (Japan Broadcasting Corporation, Japan)
Kazuyuki Aihara, Hideyuki Suzuki (University of Tokyo, Japan)

10:30~12:15 OS6 【AI-based systems for human awareness promotion】

Chair: K Hashimoto (Osaka Prefecture University, Japan)

Co-Chair: K. Takeuchi (Osaka Electro-Communication University, Japan)

OS6-1 *A Survey of AI-based systems for human awareness promotion in meta-cognition*
Kiyota Hashimoto, Kazuhisa Seta, Hiroshi Tsuji (Osaka Prefecture University, Japan)
Kazuhiro Takeuchi (Osaka Electro-Communication University, Japan)

OS6-2 *A multilingual problem-based learning environment for awareness promotion*
Ryusuke Taguchi, Katsuko T. Nakahira (Nagaoka University of Technology, Japan)
Hideyuki Kanematsu (Suzuka National College for Technology, Japan)
Yoshimi Fukumura (Nagaoka University of Technology, Japan)

OS6-3 *An effective visualization of style inconsistencies for interactive text editing*
Kazuki Shimamura, Kazuhiro Takeuchi (Osaka Electro-Communication University, Japan)
Kiyota Hashimoto (Osaka Prefecture University, Japan)

OS6-4 *An intelligent meta-learning support system through presentation*
Kazuhisa Seta (Osaka Prefecture University, Japan)

OS6-5 *A task ontology construction for presentation skills*
Kiyota Hashimoto (Osaka Prefecture University, Japan)
Kazuhiro Takeuchi (Osaka Electro-Communication University, Japan)

OS6-6 *Country domain governance: An analysis by datetermining of country domains*
Katsuko T. Nakahira, Hiroyuki Namba, Minehiro Takeshita, Shigeaki Kodama, Yoshiki Mikami
(Nagaoka University of Technology, Japan)

OS6-7 *Extraction and comparison of tourism information on the web*
Xiaobin Wu, Sachio Hirokawa, Chengjiu Yin, Tetsuya Nakatoh, Yoshiyuki Tabata (Kyushu
University, Japan)

13:10~14:40 OS20 【Embracing complexity in sensor system organization】

Chair: Y. Ishida (Toyohashi University of Technology, Japan)

Co-Chair: Y. Watanabe (Nagoya City University, Japan)

K. Harada (Toyohashi University of Technology, Japan)

OS20-1 *Performance evaluation of immunity-based statistical en-route filtering in wireless sensor networks*
Yuji Watanabe (Nagoya City University, Japan)

OS20-2 *Improvement of immunity-based diagnosis for a motherboard*

Haruki Shida, Takeshi Okamoto (Kanagawa Institute of Technology, Japan)

Yoshiteru Ishida (Toyohashi University of Technology, Japan)

OS20-3 *Visualization of keystroke data and its interpretation*

T. Samura, K. Tani (Akashi National College of Technology, Japan)

Y. Ishida (Toyohashi University of Technology, Japan)

OS20-4 *Extraction of learning point by visualization of skill*

Shihoko Kamisato, Yukihiro Mori, Nobuhiro Yamashiro, Kentaro Noguchi (Okinawa National College of technology, Japan)

Yoshiteru Ishida (Toyohashi University of Technology, Japan)

OS20-5 *Prediction of electron flux environment at geosynchronous orbit using neural network technique*

Kentarou Kitamura, Yusuke Nakamura (Tokuyama College of Technology, Japan)

Masahiro Tokumitsu, Yoshiteru Ishida (Toyohashi University of Technology, Japan)

Shinichi Watari (National Institute of Information and Communications Technology, Japan)

OS20-6 *A diagrammatic classification in a combinatorial problem: The case of a Stable Marriage Problem*

Tatsuya Hayashi, Yoshikazu Hata, Yoshiteru Ishida (Toyohashi University of Technology, Japan)

15:00~16:45 OS22 【Robotics and pattern recognition】

Chair: C. Zhang (Tsinghua University, China)

Co-Chair: T. Zhang (Tsinghua University, China)

OS22-1 *Application of the genetic algorithm on face recognition*

Fengzhi Dai (Tianjin University of Science and Technology, China)

Liqiang Shang (Vestas Wind Technology (China) Co., Ltd, China)

Naoki Kushida (Oshima National College of Maritime Technology, Japan)

Masanori Sugisaka (Nippon Bunri University, ALife Robotics Co., Ltd, Japan)

OS22-2 *Study on the disturbance rejection of Virtual Slope Walking by Stepper-2D Robot*

Mingguo Zhao (State Key Laboratory of Robotics and System (HIT) and Tsinghua University, China)

HaoDong, Naiyao Zhang (State Key Laboratory of Robotics and System (HIT), China)

OS22-3 *A new method for mobile robots to avoid collision with moving obstacles*

Yi Zhu, Tao Zhang, Jingyan Song (Tsinghua University, China)

Masatoshi Nakamura (Saga University, Japan)

OS22-4 *Some thought for the Mckibben muscle robots*

Huailin Zhao (Shanghai Institute of Technology, China)

Xiaoqing Jia (Shanghai Maritime University, China)

Masanori Sugisaka (Nippon Bunri University, Japan)

OS22-5 *Vehicle 3D estimation based on time series images and prior knowledge*

Haoyin Zhou, Tao Zhang, Changshui Zhang, Peng He (Tsinghua University, China)

OS22-6 *Automatic drawing of correct topographical distribution of EEG rhythms based on unified suitable reference selection*

Bei Wang, Xingyu Wang (East China University of Science and Technology, China)
Akio Ikeda (Kyoto University, Japan)
Takashi Nagamine (Sapporo Medical University, Japan)
Hiroshi Shibasaki (Takeda General Hospital Research, Japan)
Masatoshi Nakamura (Saga University, Japan)

OS22-7 *Research on surface crack detection based on laser scanning and image processing techniques*
Guangming Cai, Jiwu Wang, Mingcheng E, Wenliang Guo (Beijing Jiaotong University, China)
Sugisaka Masanori (Nippon Bunri University, Japan)

Room D

8:40~9:55 GS6 【Data mining】

Chair: J. S. Shieh (Yuan Ze University, Taiwan)

GS6-1 *Development of motion analysis system using acceleration sensors for tennis and its evaluations*
Takaya Maeda, Kenichirou Fuji, Hiroki Tamura, Koichi Tanno (University of Miyazaki, Japan)

GS6-2 *Discriminate approach for data selection in data envelopment analysis*
Akio Naito, Shingo Aoki (Osaka Prefecture University, Japan)

GS6-3 *Proposal of recommender system simulator based on small-world model*
Ryosuke Saga, Kouki Okamoto (Kanagawa Institute of Technology, Japan)
Hiroshi Tsuji (Osaka Prefecture University, Japan)
Kazunori Matsumoto (Kanagawa Institute of Technology, Japan)

GS6-4 *Construction and analysis of purchase factor model by using creativity method*
Kodai Kitami, Ryosuke Saga, Kazunori Matsumoto (Kanagawa Institute of Technology, Japan)

GS6-5 *Developing a monitoring psychological stress Index system via photoplethysmography*
Jiann-Shing Shieh¹, Yu-Ren Chiou (Yuan Ze University, Taiwan)
Shou-Zen Fan (National Taiwan University, Taiwan)

10:30~11:45 GS1 1 【Image processing II】

Chair: J. Wang (Beijing Jiaotong University, China)

GS11-1 *Simple analog-digital circuit for motion detection and its application to target tracking system*
Takuya Yamamoto, Kimihiro Nishio (Tsuyama National College of Technology, Japan)

GS11-2 *Analog motion detection circuit using CCD camera based on the biological vision system and its application to mobile robot*
Yasuyuki Kondo, Takumi Yamasaki, Kimihiro Nishio (Tsuyama National College of Technology, Japan)
Toshinori Furukawa (Kurashiki University of Science and the Arts, Japan)

GS11-3 *Real-time visual target tracking for Augmented Reality (**withdrawal**)*
Donghoon Lee (University of Science and Technology, Korea)
Inhun Jang, Hyunsub Park, Moonhong Baeg (Korea Institute of Industrial Technology, Korea)

GS11-4 *Detecting human flows on a road different from main flows*
Mison Park, Joo Kooi Tan, Yuuki Nakashima, Hyongseop Kim, Seiji Ishikawa
(Kyushu Institute of Technology, Japan)

GS11-5 *Study on the height measurement based on the image processing technique*
Jiwu Wang, Weijie Gao, Yisong Wang (Beijing Jiaotong University, China)
Masanori Sugisaka (Nippon Bunri University, Japan)

13:10~14:40 OS21 【Learning control and robotics】

Chair: H. H. Lee (Waseda University, Japan)

Co-Chair: H. Ogai (Waseda University, Japan)

OS21-1 *A neuro PID control of power generation using low temperature gap*
Kun-Young Han, Hee-Jae Park, Hee-Hyol Lee (Waseda University, Japan)

OS21-2 *An efficient identification scheme for nonlinear polynomial NARX model*
Yu Cheng, Miao Yu, Lan Wang, Jinglu Hu (Waseda University, Japan)

OS21-3 *Traffic signal control of multi-forked road*
ChengYou Cui, Mizuki Takamura, Hee-Hyol Lee (Waseda University, Japan)

OS21-4 *Control design methods for platooning in robot car*
Ryo Takaki, Xin Zhao, Harutoshi Ogai (Waseda University, Japan)

OS21-5 *Building of reverse logistics model in reusable recovery and optimization considering transportation, inventory, and backorder costs*
Jeong-Eun Lee, Hee-Hyol Lee (Waseda University, Japan)

OS21-6 *Advanced pipe inspection robot using rotating probe and image processing*
Ryuta Oyabu, Kentarou Nishijima, Zhicheng Wang, Harutoshi Ogai (Waseda University, Japan)
Bishakh Bhattacharya (Indian Institute of Technology, India)

15:00~16:30 OS23 【Intelligent systems II】

Chair: M. K. Habib (The American University in Cairo, Egypt)

Co-Chair: Y. I. Cho (University of Suwon, Korea)

OS23-1 *Intelligent speech recognition filtering*
Yong Im Cho (University of Suwon, Korea)

OS23-2 *Multi robotic system and the development of cooperative navigation behaviors for humanitarian demining*
Maki K. Habib (The American University in Cairo, Egypt)

OS23-3 *Development of Flexible Surgical Manipulator for Natural Orifice Transluminal Endoscopic Surgery*
Jungwook Suh, Hoseok Song, Kiyoun Kim, Jungju Lee (Korea Advanced Institute of Science and Technology, Republic of Korea)

OS23-4 *Swing-up and LQR stabilization of rotary inverted pendulum*
Minho Park, Yeoun-Jae Kim, Ju-Jang Lee (Korea Advanced Institute of Science and Technology, Republic of Korea)

OS23-5 *Intelligent information retrieval system*

Young Im Cho (University of Suwon, Korea)

OS23-6 *A study on real-time face verification and tracking with segmented common vector*

Dongkyu Ryu, Minho Park, Ju-Jang Lee (Korea Advanced Institute of Science and Technology, Republic of Korea)

Room E

8:40~9:55 GS14 【Neural networks I】

Chair: T. Yamada (Ibaraki University, Japan)

GS14-1 *A study of SVM using the combination with online learning method and*

Midpoint-Validation Method

Shingo Yamashita, Takeshi Yoshimatsu, Hiroki Tamura, Koichi Tanno (University of Miyazaki, Japan)

GS14-2 *Video object segmentation using color-component-selectable learning for self-organizing maps*

Shin-ya Umata, Naotake Kamiura, Ayumu Saitoh, Teijiro Isokawa, Nobuyuki Matsui (University of Hyogo, Japan)

GS14-3 *Properties of localized oscillatory excitation on the non-linear oscillatory field*

Ryota Miyata, Koji Kurata (University of the Ryukyus, Japan)

GS14-4 *Multiple Granger causality tests for network structure estimation from time-series data*

Hikaru Harima (Kyoto University, Japan)

Shigeyuki Oba (Kyoto University and Japan Science and Technology Agency, Japan)

Shin Ishii (Kyoto University, Japan)

GS14-5 *A simulation study of visual perceptual learning with attentional signals*

Satoshi Naito, Naoto Yukinawa (Kyoto University, Japan)

Shin Ishii (Kyoto University and RIKEN, Computational Science Research Program, Japan)

10:30~12:15 OS15 【Bio-inspired theory and application】

Chair: M. Yasunaga (University of Tsukuba, Japan)

Co-Chair: K. Yamamori (University of Miyazaki, Japan)

OS15-1 *Study of computational performance of Genetic Algorithm for 3-Satisfiability problem*

QingLian Ma, Yu-an Zhang, Makoto Sakamoto, Hiroshi Furutani (University of Miyazaki)

OS15-2 *An adaptive resolution hybrid binary-real coded genetic algorithm*

Omar Abdul-Rahman, Masaharu Munetomo, Kiyoshi Akama (Hokkaido University, Japan)

OS15-3 *Neural network with exponential output neuron for estimation of physiological activities from protein expression levels*

Kazuhiro Kondo, Kunihito Yamamori, Ikuo Yoshihara (University of Miyazaki, Japan)

OS15-4 *Asynchronous migration for parallel genetic programming on computer cluster with multi-core processors*

Shingo Kurose, Kunihiro Yamamori, Masaru Aikawa, Ikuo Yoshihara (University of Miyazaki, Japan)

OS15-5 *Classification of species by information entropy and visualization by self-organizing map*

Kentaro Nishimuta, Ikuo Yoshihara, Kunihiro Yamamori (University of Miyazaki, Japan)
Moritoshi Yasunaga (University of Tsukuba, Japan)

OS15-6 *Digital-signal-waveform improvement on VLSI packaging including inductances*

H. Shimada, S. Akita, M. Ishiguro, N. Aibe (University of Tsukuba, Japan)
I. Yoshihara (University of Miyazaki, Japan)
M. Yasunaga (University of Tsukuba, Japan)

OS15-7 *Digital-signal improvement-method using Pareto optimization*

S. Akita, H. Shimada, M. Ishiguro, N. Aibe, M. Yasunaga (University of Tsukuba, Japan)
I. Yoshihara (University of Miyazaki, Japan)

13:10~14:55 GS12 【Learning】

Chair: Y. G. Zhang (Academia Sinica, China)

GS12-1 *Reinforcement learning with the mechanism of short-term depression for learning rate*

S. Kubota (Yamagata University, Japan)

GS12-2 *A method for finding multiple subgoals for reinforcement learning*

Fuminori Ogihara, Junichi Murata (Kyushu University, Japan)

GS12-3 *Temporal difference approach in linearly-solvable Markov decision problems*

M. A. P. Burdellis, K. Ikeda (Nara Institute of Science and Technology, Japan)

GS12-4 *Mutual learning of multi consciousness agent including the ego for autonomous vehicle*

Atsunori Mori, Hirokazu Mastui (Mie University, Japan)

GS12-5 *Reinforced learning by using a learned results of a different form robot*

Nobuo Shibata, Hirokazu Matsui (Mie University, Japan)

GS12-6 *The acquisition of sociality by using Q-learning in a multi-agent environment*

Yasuo Nagayuki (Otemae University, Japan)

GS12-7 *Effect of interaction between rules on rule dynamics in multi-group minority game*

Takashi Sato (Okinawa National College of Technology, Japan)

15:00~16:00 GS20 【Robotics IV】

Chair: N. Uchiyama (Toyohashi University of Technology, Japan)

GS20-1 *Design of the android robot head for stage performances*

Dongwoon Choi, Dong Wook Lee, Duk Yeon Lee, Jun Young Jung, Hogil Lee (Korea Institute of Industrial Technology, Korea)

GS20-2 *Implementation of IMU using wavelet transform and variable IIR filter*

Woojin Seo, Bongsu Cho (Pusan National University, Korea)

Jaehong Lee (Hyosung Industrial Machinery, Korea)

Kwang Ryul Baek (Pusan National University, Korea)

GS20-3 *Development of crawler type rescue robot with slide mechanism*

Go Hirano (Kinki University, Japan)

Seiji Furuno (Kitakyushu National College of Technology, Japan)

GS20-4 *Proposal of intelligence module type robot that can exchange it in seamless*

Shunta Takahashi, Kohei Miyata, Yuhki Kitazono, Lifeng Zhang, Seiichi Serikawa (Kyushu Institute of Technology, Japan)

Room F

8:40~10:10 OS19 【Embracing complexity in natural intelligence】

Chair: Y. Ishida (Toyohashi University of Technology, Japan)

Co-Chair: T. Okamoto (Kanagawa Institute of Technology, Japan)

K. Harada (Toyohashi University of Technology, Japan)

OS19-1 *A systemic payoff in a self-repairing network*

Masahiro Tokumitsu, Yoshiteru Ishida (Toyohashi University of Technology, Japan)

OS19-2 *Effects of a membrane formation in Spatial Prisoner's Dilemma*

Yuji Katsumata, Yoshiteru Ishida (Toyohashi University of Technology, Japan)

OS19-3 *Extracting probabilistic cellular automata rules from spatio-temporal patterns and analyzing features of these rules*

Takuya Ueda, Yoshiteru Ishida (Toyohashi University of Technology, Japan)

OS19-4 *Emergence of observable rules in a spatial game system*

K. Harada, Y. Ishida (Toyohashi University of Technology, Japan)

OS19-5 *An artificial intelligent membrane for detect network intrusion*

Takeshi Okamoto (Kanagawa Institute of Technology, Japan)

OS19-6 *A dynamic Houjin (square) and a symmetric Houjin*

Yuki Tsuzuki, Yoshiteru Ishida (Toyohashi University of Technology, Japan)

10:30~12:15 OS16 【Biomimetic machines and robots】

Chair: K. Watanabe (Okayama University, Japan)

Co-Chair: K. Izumi (Saga University, Japan)

OS16-1 *Basic position/force control of single-axis arm designed with an ultrasonic motor*

Keisuke Ogiwara, Fusaomi Nagata (Tokyo University of Science, Japan)

Keigo Watanabe (Okayama University, Japan)

OS16-2 *Cooperative swarm control for multiple mobile robots using only information from PSD sensors*

Takahiro Yamashiro, Fusaomi Nagata (Tokyo University of Science, Japan)

Keigo Watanabe (Okayama University, Japan)

OS16-3 *Control of movement on stairs for a cleaning robot*

Takahisa Kakudou, Keigo Watanabe, Isaku Nagai (Okayama University, Japan)

OS16-4 *Jumping rhythm generator by CPG for a multi-legged robot*

Masaaki Ikeda, Kiyotaka Izumi (Saga University, Japan)
Keigo Watanabe (Okayama University, Japan)

OS16-5 *A bearing-only localization solved by an unscented Rauch-Tung-Striebel smoothing*

Saifudin bin Razali, Keigo Watanabe, Shoichi Maeyama (Okayama University, Japan)

OS16-6 *Trajectory tracking control for nonholonomic mobile robots by an image-based approach*

Tatsuya Kato, Keigo Watanabe, Shoichi Maeyama (Okayama University, Japan)

OS16-7 *A nonholonomic control method for stabilization an X4-AUV*

Zainah Md. Zain, Keigo Watanabe (Okayama University, Japan)
Kiyotaka Izumi (Saga University, Japan)
Isaku Nagai (Okayama University, Japan)

15:00~16:00 GS1 【Artificial intelligence】

Chair: T. Nakashima (Osaka Prefecture University, Japan)

GS1-1 *Adaptive co-construction of state and action spaces in reinforcement learning*

Masato Nagayoshi (Niigata College of Nursing, Japan)
Hajime Murao, Hisashi Tamaki (Kobe University, Japan)

GS1-2 *Autonomous acquisition of cooperative behavior based on a theory of mind using parallel Genetic Network Programming*

Kenichi Minoya, Takaya Arita (Nagoya University, Japan)
Takashi Omori (Tamagawa University, Japan)

GS1-3 *A comparison of learning performance in two-dimensional Q-learning by the difference of Q-values alignment*

Kathy Thi Aung, Takayasu Fuchida (Kagoshima University, Japan)

GS1-4 *Robot path planning in unknown environment based on ant colony algorithm*

Cu Xuan Tien, Young Sik Hong (Dongguk University, South Korea)

Development Outline of the HUBO2

Jun Ho Oh

Humanoid robot research center, Korea advanced institute of science and technology



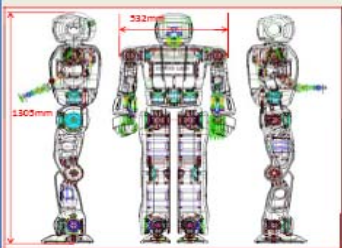
Development Outline of the HUBO2

Prof. Jun Ho Oh
Humanoid Robot Research Center,
Korea Advanced Institute of Science and Technology

HUBO Lab
KAIST

Mechanical Design – Body design

- High stiffness with light weight
- Over all weight is about 41kg including exterior case
- Avoid cantilever like structure
- 40 DOF



HUBO Lab
KAIST


Mechanical Design – Body design

Part		DOF	
		HUBO	HUBO2
Upper body	Head	4	3
	Shoulder	$3 \times 2 = 6$	$3 \times 2 = 6$
	Elbow	$1 \times 2 = 2$	$1 \times 2 = 2$
	Wrist	$3 \times 2 = 6$	$3 \times 2 = 6$
	Hand	$5 \times 2 = 10$	$5 \times 2 = 10$
Lower body	Torso	1	1
	Hip	$3 \times 2 = 6$	$3 \times 2 = 6$
	Knee	$1 \times 2 = 2$	$1 \times 2 = 2$
	Ankle	$2 \times 2 = 4$	$2 \times 2 = 4$
Total DOF		41	40
Total Weight (Kg)		65	45

HUBO Lab
KAIST

Mechanical Design – Body design

- High stiffness with light weight design
- Expected weight(include exterior case): 41kg
- 30% weight reduction compare to the HUBO



HUBO Lab
KAIST

Mechanical Design – Body design

Part		Weight (Kg)
Mechanical Parts	Frame	11.000
	Harmonic Drive	7.937
	Motor	7.421
	Case	5.500
Electrical Parts	Controller (Motor + Sensor)	3.439
	Battery	2.896
	PC (2EA)	1.420
	Wire	1.500
Total		41.113

HUBO Lab
KAIST

Mechanical Design – Light weight arm


- Light weight arm design
- Actuators are located to upper arm closely to reduce rotational momentum
- 1 rotational and 2 linear motors for wrist mechanism
- Simple structure
- It is possible to move up and down with 3Hz frequency.

DOF	Length	Weight	Momentum
Shoulder : 3	375.5 mm	HUBO : 3.0 kg	HUBO : 0.113 kgm ²
Elbow : 1		HUBO2 : 1.46 kg	HUBO2 : 0.045 kgm ²
Wrist : 3		56% reduced	

HUBO Lab
KAIST


Mechanical Design – Light weight arm

- It is possible to move up and down with 3Hz frequency.
- 7 DOF



HUBO Lab
KAIST

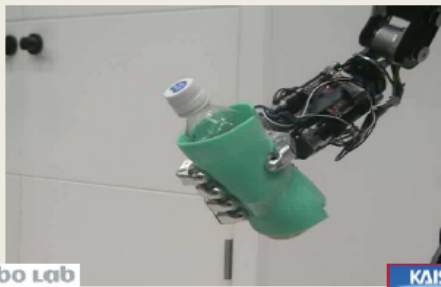
Mechanical Design – Light weight arm



HUBO Lab
KAIST

Mechanical Design – Adaptive hand

★ Various wrist movements



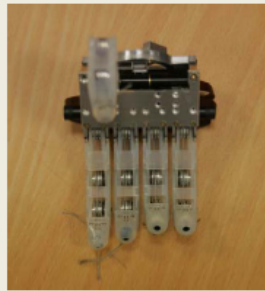
HUBO Lab
Humanoid Robot Research Center

KAIST

Mechanical Design – Adaptive hand

★ Functional hand mechanism design

- ★ 1 motor /finger
- ★ Tendon drive system
- ★ Shape adaptive grasping
- ★ Compact size

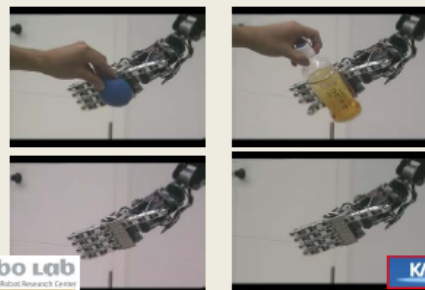


HUBO Lab
Humanoid Robot Research Center

KAIST

Mechanical Design – Adaptive hand

★ Various hand movements

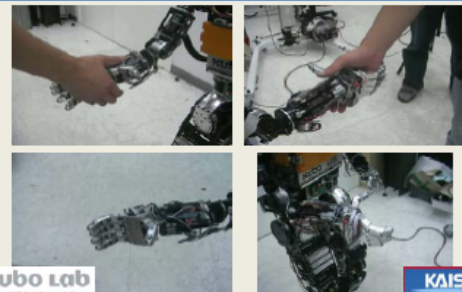


HUBO Lab
Humanoid Robot Research Center

KAIST

Mechanical Design – Adaptive hand

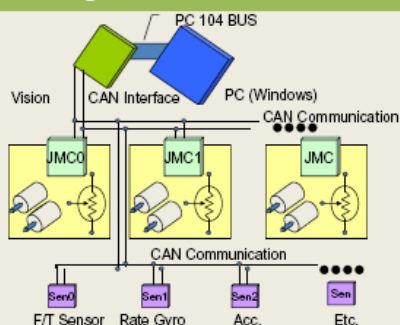
★ Handshake movements



HUBO Lab
Humanoid Robot Research Center

KAIST

System Integration



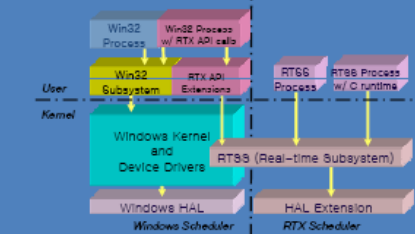
HUBO Lab
Humanoid Robot Research Center

KAIST

System Integration

★ Real-time control in Windows environment:

: we have used RTX HAL Extension software to realize real-time control



HUBO Lab
Humanoid Robot Research Center

KAIST

Electrical Design – BLDC motor controller

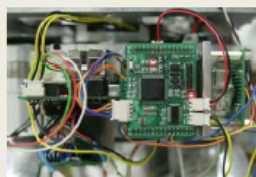
★ High power 2ch BLDC motor controller

- ★ 90mm × 95mm size 2ch 48V BLDC motor controller
- ★ TI DSP 320F2811 (150MHz CPU Clock)
- ★ 2ch encoder input, CAN communication interface, GPIO and ADC
- ★ Direct or indirect current measurement (for torque control)
 - ★ Direct current measurement using ADC
 - ★ Indirect current measurement using observer
- ★ Controller and motor protection using over current block function
- ★ CAN ID setting using DIP switch
- ★ It has the function that automatically return to the initial position using limit sensor.

HUBO Lab
Humanoid Robot Research Center

KAIST

Electrical Design – Sensors



- ★ IMU(Inertia Measurement Unit)
- ★ 3 Gyro + 2 Inclinator
- ★ 10Hz Bandwidth



- ★ 3-axis force-torque sensor
- ★ Maximum load: 1000N
- ★ Maximum moment: 30 Nm

HUBO Lab
Humanoid Robot Research Center

KAIST

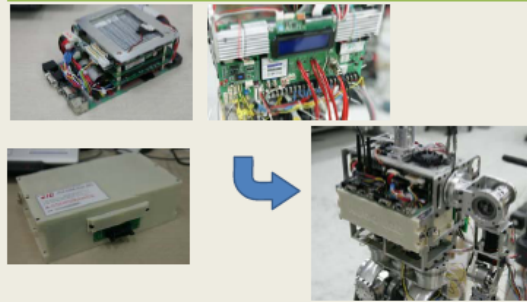
Electrical Design – Other electrical parts

- ★ PC module
 - ★ PC-104 type Intel 1GHz CPU
 - ★ 2ch CAN, Wireless lan, sound port, USB and so on
- ★ Power distribution module
 - ★ Selectable external power or internal battery
 - ★ 48V to 48V, 12V and 5V
- ★ Battery module
 - ★ Lithium-Ion Polymer
 - ★ 48 Volt – 8 Ampere

HUBO Lab
Humanoid Robot Research Center

KAIST

Electrical Design – Other electrical parts



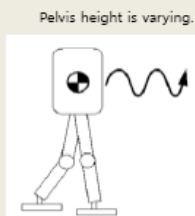
HUBO Lab
Humanoid Robot Research Center

KAIST

Stretched Leg Walking Algorithm – Motivation

Stretched leg Walking

- Advantage
 - Similar to human walking
 - Reduction of load on actuator
 - Efficient walking in a point of view (energy, speed)
- Disadvantage
 - Singularity problem to solve inverse kinematics
 - Large landing impact.



HUBO Lab
Humanoid Robot Research Center

KAIST

Stretched Leg Walking Algorithm – Experiment



Stretched leg walking realize **HIGH SPEED WALKING**.

HUBO Lab
Humanoid Robot Research Center

KAIST

Stretched Leg Walking Algorithm – Experiment

Energy consumption per each step.

Step Length	Bent knee walking (E1)	Stretched leg walking (E2)	E2/E1
200mm	74 (J) 2.04 (A)	61.4 (J) 1.60 (A)	83 %
300mm	146.9 (J) 3.66 (A)	83.4 (J) 2.15 (A)	56 %

Stretched leg walking is more **EFFICIENT** than bent knee walking.

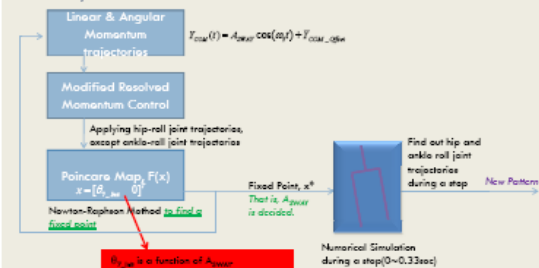
HUBO Lab
Humanoid Robot Research Center

KAIST

Running algorithm

Running Pattern Generation

3) Y-directional Pattern Generation in the Frontal Plane

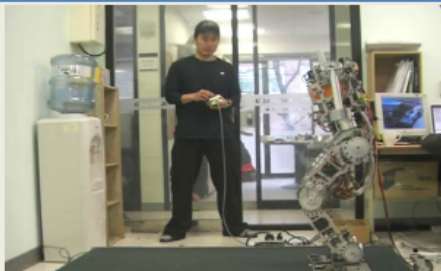


HUBO Lab
Humanoid Robot Research Center

KAIST

Running algorithm – 3D running

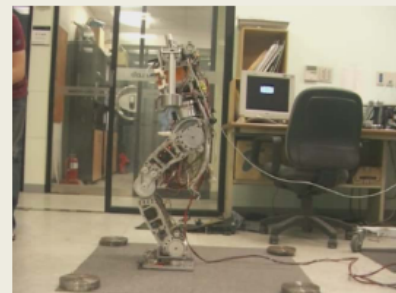
- ★ Velocity : 3 km/h
- ★ Flying time : 0.05sec



HUBO Lab
Humanoid Robot Research Center

KAIST

Running algorithm – Stabilization



HUBO Lab
Humanoid Robot Research Center

KAIST

Data-driven Two Degree-of-Freedom Control for a Micropump and Microneedle Integrated Device for Diabetes Care

Ruoting Yang*, Mingjun Zhang**, and Tzyh-Jong Tarn*

* Department of Electrical and Systems Engineering, Washington University, St. Louis, MO, 63130, USA

e-mail: ryang@wustl.edu, tarn@ese.wustl.edu.

**Department of Mechanical, Aerospace and Biomedical Engineering, University of Tennessee, Knoxville, TN, USA.

email: mjzhang@utk.edu.

Abstract: This paper presents a dynamic model for a micropump and microneedle integrated system for diabetes care. A novel data-driven two degree-of-freedom control mechanism is proposed for regulating blood glucose concentration to shorten regulating time while maintaining the stability of the system in the presence of model uncertainties and unexpected disturbances. Exact feedforward linearization, gain scheduling, and data-driven planning technique are applied to improve regulation performance as well as robustness. Simulation results indicate that the proposed control has great potential in drug delivery problems.

1 Introduction

Diabetes mellitus is a disease in which the patient has difficulty regulating blood glucose. Diabetes may affect the functioning of many physiological systems, causing everything from retinopathy and circulatory problems, to nephropathy and heart disease. While diabetes can be treated with insulin, the dosage of insulin must be strictly regulated - excess insulin can cause hypoglycemia, whereas insufficient insulin can cause hyperglycemia.

Fig. 1 shows a schematic drawing of a insulin infusion microdevice consisting of a piezoelectric micropump, multiple silicon microneedles, an insulin reservoir, a membrane, wireless telemetry, and a remote control component. This control system regulates blood glucose levels by driving the piezoelectric micropump based on glucose sensor measurements. Very generally, sensor readings are passed via wireless telemetry to the controller, which then drives the micropump, causing the release of insulin from the reservoir, through the microneedles into the patient's bloodstream.

The challenges of controller design mainly come from three areas. First, these systems usually have serious nonlinearities, which are poorly estimated by the corresponding linearized systems. Second, the output measurements often have large model uncertainties, disturbances, and slow sampling rates. Third, in the event of an accidental insulin overdose, there is no way to retrieve the insulin to avoid hypoglycemia.

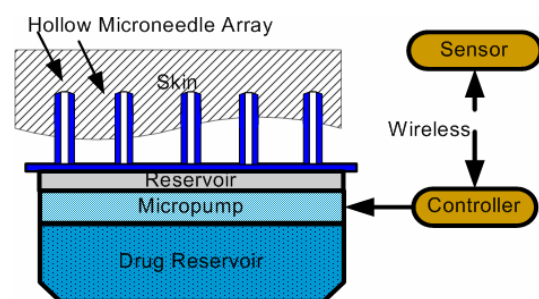


Fig. 1 A schematic drawing of a micropump and microneedle integrated for controlled insulin delivery

Recently, advanced control mechanisms have been applied for glucose control, including PID [1, 2], model predictive control [3, 4], and robust control [5], among others [6]. However, the regulating time that draws the blood glucose concentration from a high level to the basal level is still too long for all these methods. In this paper, we propose a new data-driven feedback and feedforward integrated 2DOF (Two Degree-Of-Freedom) control mechanism to shorten regulating time while maintaining the stability of the system in the presence of model uncertainties and unexpected disturbances. As shown in Fig. 2, the 2DOF control method contains two parts: (1) the feedforward control provides the nominal control to rapidly drive the system towards the desired goal; (2) the feedback control stabilizes the system. It has been proven that the 2DOF controller performs better than controllers that only use feedback under reasonable model uncertainty[7]. The 2DOF control mechanism is said to be time-based if the reference trajectory is given by a time-driven planner. In contrast, a data-driven 2DOF control mechanism

utilizes a data-driven planner to generate the reference trajectory.

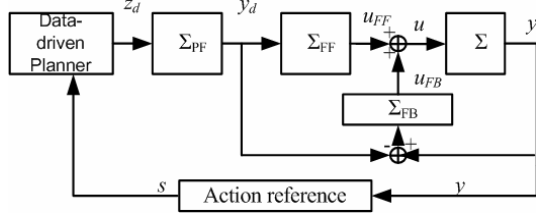


Fig. 2 The schematic of data-driven 2DOF method. Σ_{FF} is the feedforward controller, Σ_{FB} is the feedback controller, and Σ_{PF} is the coordinate transformation between the flat output reference z_d and the output y_d . The data-driven planner is driven by an action reference s generated by the output measurement, instead of driven by time.

The data-driven 2DOF control uses exact feedforward linearization and gain scheduling methods, instead of exact feedback linearization, to improve robustness to model uncertainties, while has the same regulation performance. In addition, we use a data-driven planning technique, which can further improve robustness towards model uncertainties and unexpected disturbances in comparison to the other 2DOF controls. While the data-driven planner aids in robustness, it is also advantageous compared to other planning approaches because it does not need to replan and regenerate the reference trajectory at every sampling time instant [8]. Since the action reference parameter is calculated nearly at the same rate as the feedback control, the planning process is adjusted rapidly, which enables the planner to handle unexpected disturbances within one control execution sampling time.

This paper is organized as follows. Dynamics modeling of the microdevice is introduced in Section II. The data-driven 2DOF control mechanism is discussed in Section III-V. Computer simulation is conducted in Section VI. Conclusions and future work are discussed in the final section.

2 Dynamics modeling

2.1 The micropump

The piezoelectric diaphragm displacement pump can be modeled as follows [9],

$$\Delta Vol = \frac{3a^4(5+2\mu)(1-\mu)d_{13}V_0}{4h^2(3+2\mu)}, \quad (1)$$

where ΔVol is the volume change and V_0 is the voltage applied to the lead zirconate titanate film with piezoelectric coefficient $d_{13} = 3 \times 10^{-10} m/N$ and Poisson's ratio $\mu = 0.3$. The thickness and the radius of the membrane are h and a , respectively.

Papers [10] and [11], demonstrated that the flow rate increases linearly at low actuating frequencies. When the actuating frequency exceeds a critical value, though, the flow rate does not increase and may even decrease sharply. As a result of this electro-mechanical-fluid coupling, the membrane deflects in an undesirable way at high frequencies[12].

If a voltage signal with changing polarity drives the micropump, then the flow rate can be approximated as a linear function with respect to the voltage and the actuating frequency at low frequencies.

$$Q_{pump}(V_0, f) = 2f\Delta Vol = A_d f V_0, \quad (2)$$

where $A_d = 6a^4(5+2\mu)(1-\mu)d_{13}/4h^2(3+2\mu)$ is a constant coefficient.

If, for example, $V_0 = 1.5 V$, $a = 100 \mu m$ and $h = 10 \mu m$ then according to equation (1), we will have $\Delta Vol = 3.675 \times 10^{-3} \mu l$. Assuming that the micropump is driven at 100 Hz, equation (2) gives the pumping speed as 0.735 $\mu l/s$.

2.2 Microneedle

Microneedles are attractive for medical applications in that they are able to provide painless drug transport pathways while at the same time largely reducing the risk of infection at injection site.

The volume flow rate of a microneedle can be expressed as

$$Q_{needle} = \Delta P / R, \quad (3)$$

where ΔP is the pressure drop across the channel, and R is the channel resistance for a circular channel, where

$$R = 8\mu L / \pi r^4, \quad (4)$$

In equation (4), μ is the fluid viscosity, while L and r are the channel length and radius, respectively. We choose a straight microneedle with 100/30 μm outside/inside diameter.

Because the total resistance of a microneedle array is often smaller than the sum of the individual channel

resistances, a high needle density increases the volume flow rate as follows,

$$Q_{\text{needle}} = \Delta P / k_d R, \quad (5)$$

where k_d is the discount coefficient.

The microneedle array is not sufficiently large to allow free flow, but it is large enough not to cause significant resistance. Ma *et al.* [13] showed that for microneedles, the flow rate is nearly linear to the actuating frequency at low frequencies. As a result, it is reasonable to assume that the microneedle array does not impede the flow from the micropump.

2.3 Microsensor

One of the major glucose sensors is the amperometric sensor, which determines the solution concentration by measuring the current generated during a chemical reaction. The amperometric sensor can be modeled as follows [14]:

$$\dot{I}_{\text{sig}} = -c_2 I_{\text{sig}} + c_1 G + OS, \quad (6)$$

$$G_S = CF(I_{\text{sig}} - OS), \quad (7)$$

where G_S and G are the sensor and blood glucose level, respectively. I_{sig} is the sensor signal, CF is the calibration factor and OS is the offset current. The sensor sensitivity is characterized by the ratio of c_1 and c_2 ,

The sensor glucose model can be rewritten as

$$\begin{aligned} \dot{G}_S &= -c_2 G_S + c_1 CF \cdot G + CF(1 - c_2)OS \\ &= -\theta_1 G_S + \theta_2 G + OF, \end{aligned} \quad (8)$$

where $\theta_1 = c_2$, $\theta_2 = c_1 CF$, and $OF = CF(1 - c_2)OS$.

2.4 Glucose-insulin Kinetics

Shimoda's three-compartment model [15] can be used to describe the kinetics of either regular insulin or a monomeric insulin analog supplied as a continuous subcutaneous infusion.

$$\dot{Q}_1 = -kQ_1 + u \quad (9)$$

$$\dot{Q}_2 = -(p + o)Q_2 + kQ_1 \quad (10)$$

$$\dot{I} = -k_e(I - i_b) + pQ_2 / V_i \quad (11)$$

Here Q_1 and Q_2 stand for the insulin masses at the injection site and the intermediate site, respectively. I is the plasma insulin concentration with the basal value i_b . u is the subcutaneous insulin infusion rate. k and p are the transition rate constants, and o and k_e are degradation decay rates. The parameter V_i stands for the plasma distribution volume.

The minimal model [16] has been widely accepted as the fundamental model to describe insulin-glucose interactions:

$$\dot{G} = -XG + P_1(G_b - G) + GI \quad (12)$$

$$\dot{X} = -P_2X + P_3(I - I_b), \quad (13)$$

where G is the plasma glucose level (with basal value G_b), X is the interstitial insulin concentration, GI is the intravenous glucose uptake, P_1 is a coefficient for glucose effectiveness, and P_3 / P_2 is a measure of insulin sensitivity [16].

Combining all subsystems and letting $x_1 = S - OF / \theta_1$, $x_2 = G - G_b$, $x_3 = X$, $x_4 = I - I_b$, $x_5 = Q_2$, $x_6 = Q_1$, and $\theta_3 = p / V_i$, we have the following sixth-order nonlinear model. The meaning of the parameters are summarized in the Table I.

$$\begin{aligned} \dot{x}_1 &= -\theta_1 x_1 + \theta_2 x_2 \\ \dot{x}_2 &= -(x_2 + G_b)x_3 - P_1 x_2 + GI \\ \dot{x}_3 &= -P_2 x_3 + P_3 x_4 \\ \dot{x}_4 &= \theta_3 x_5 - k_e x_4 \\ \dot{x}_5 &= kx_6 - (p + o)x_5 \\ \dot{x}_6 &= -kx_6 + u \\ y &= x_1, \end{aligned} \quad (14)$$

subject to $0 \leq u(t) \leq 10 \text{ U/h}$ and $y(t) \geq 75 \text{ mg/dL}$.

The input $u = CV_0$ is a linear function of the applied voltage V_0 according to the arguments presented in subsections A and B. In order to simplify the presentation, let us assume $C = 1$.

TABLE 1: Physical variables in the dynamic models

Symbol	Description
$x_1(\text{mg/dL})$	sensor measured plasma glucose level
$x_2(\text{mg/dL})$	plasma glucose level
$x_3(\text{min}^{-1})$	interstitial insulin
$x_4(\text{mU/L})$	plasma insulin level
$x_5(\text{mU/Kg})$	insulin mass at intermediate site
$x_6(\text{mU/Kg})$	insulin mass at the injection site
$P_1(\text{min}^{-1})$	glucose effectiveness
$P_3/ P_2(\text{L/ mU})$	insulin sensitivity
$V_i(\text{L/Kg})$	plasma distribution volume
$u(\text{mU/Kg/min})$	insulin infusion rate
$G_b(\text{mg/dL})$	basal plasma glucose level
$i_b(\text{mU/L})$	basal plasma insulin level
OF	calibration factor
OS	offset current
c_1 / c_2	sensor sensitivity

Consider a class of nonlinear systems

$$\dot{x} = f(x, u) \quad (15)$$

$$y = h(x) \quad (16)$$

with state $x \in R^n$, input $u \in R^m$ and output $y \in R^m$. In equations (15)-(16), we assume that the vector field $f(x, u)$ and the function $h(x)$ are smooth.

The glucose control problem is to regulate the blood glucose concentration from a high level to the basal level. Exact feedback linearization based nonlinear controls [17] can have good performance, however, these methods are sensitive to model uncertainties and disturbances, which is a big issue in glucose control problem. As a result, we will apply exact feedforward linearization technique based on differential flatness, which is more robust to the feedback linearization[18]. The feedforward linearization problem is to design a control u_d to track a smooth reference trajectory connecting two stationary setpoints (u_d^0, x_d^0, y_d^0) and (u_d^T, x_d^T, y_d^T) within a finite time interval $t \in [0, T]$. The control and state variables satisfy the following relationships

$$(u_d^0, x_d^0) : f(x_d^0, u_d^0) = 0, y_d^0 = h(x_d^0), \quad (17)$$

$$(u_d^T, x_d^T) : f(x_d^T, u_d^T) = 0, y_d^T = h(x_d^T). \quad (18)$$

2.5 Differential flatness

Definition [19, 20]: A system is said to be differentially flat if there exists a set of m differentially independent variables, $z = [z_1, \dots, z_m]^T$ such that

$$z = \mathcal{C}(x, u, \dot{u}, \dots, u^{(\beta)}), \quad (19)$$

$$x = \mathcal{A}(z, \dot{z}, \dots, z^{(\alpha)}), \text{ and} \quad (20)$$

$$u = \mathcal{B}(z, \dot{z}, \dots, z^{(\alpha+1)}), \quad (21)$$

where \mathcal{A} , \mathcal{B} , and \mathcal{C} are smooth functions of their arguments at least in an open subset of $R^{n+m(\beta+1)}$, $R^{m(\alpha+1)}$, and $R^{m(\alpha+2)}$, respectively. A vector z which satisfies the above equations is called a flat output, and then the output vector can be written with respect to the flat output,

$$y = h(x) = h(\mathcal{A}(z, \dot{z}, \dots, z^{(\alpha)})). \quad (22)$$

All flat systems can be transformed into a normal form

$$\begin{aligned} \dot{\xi}_1 &= \xi_2 \\ &\vdots \\ \dot{\xi}_{r_i-1} &= \xi_{r_i} \\ \dot{\xi}_{k_i} &= \alpha_i(\xi, u, \dot{u}, \dots, u^{(\sigma_i)}), \text{ for } i = 1, \dots, m \end{aligned} \quad (23)$$

via the Brunovsky state [21]:

$$\xi = (\xi_1^1, \xi_2^1, \dots, \xi_{r_1}^1, \xi_1^2, \xi_2^2, \dots, \xi_{r_2}^2, \dots, \xi_1^m, \dots, \xi_{r_m}^m)^T, \quad (24)$$

where $\sum_{i=1}^m r_i = n$.

By Delaleau and Rudolph [21], for the set of algebraic equations

$$\alpha_i(\xi, u, \dot{u}, \dots, u^{(\sigma_i)}) = v_i \quad (25)$$

there always exists a solution

$$u = \Theta(\xi, v, \dot{v}, \dots, v^{(\sigma)}), \quad (26)$$

where $v = [v_1, \dots, v_m]^T$ and $\sigma = \max(\sigma_i)$.

For example, consider a MIMO system

$$\dot{x}_1 = x_2 + u_1 \quad (27)$$

$$\dot{x}_2 = x_3 + x_1 u_1 \quad (28)$$

$$\dot{x}_3 = x_2 + u_2. \quad (29)$$

Set the Brunovsky state: $\xi = (x_1, x_2, \dot{x}_2)$. Then the MIMO system can be transformed into

$$\dot{\xi}_1^1 = \xi_2^1 + u_1 \quad (30)$$

$$\dot{\xi}_2^2 = \xi_2^1 + \xi_2^1 u_1 + u_1^2 + \xi_2^1 \dot{u}_1 + u_2. \quad (31)$$

As a result,

$$u_1 = \xi_1^1 - \xi_2^1 \quad (32)$$

$$u_2 = \xi_2^2 - \xi_1^1 (\xi_1^1 - \xi_2^1) - \xi_1^1 (\xi_1^1 - \xi_2^1). \quad (33)$$

In fact, differential flatness is equivalent to dynamic feedback linearization on an open and dense set using a class of invertible dynamic feedbacks [20]. For SISO systems, a differentially flat system is equivalent to a static feedback linearizable system [22]. Fliess *et al.* [20] has proved that a flat system is controllable.

Hagenmeyer and Delaleau [18] showed that if the desired trajectory is in close proximity to the initial condition x_0 , i.e.,

$$\|x_0 - \mathcal{A}(z_d, \dot{z}_d, \dots, z_d^{(\alpha)})\| < \delta, \quad (34)$$

then after applying the exact feedforward linearization control

$$u = \Theta(\xi_d, v_d, \dot{v}_d, \dots, v_d^{(\sigma)}), \quad (35)$$

the MIMO nonlinear system (23) is equivalent to the Brunovsky normal form (Proposition 1, [18]).

$$\begin{aligned} \dot{\xi}_{r_i-1}^j &= \xi_{r_i}^j \\ \dot{\xi}_{r_i}^j &= \xi_{dr_i}^j \end{aligned} \quad (36)$$

2.6 Two degree-of-freedom Control

As shown in Fig. 2, the 2DOF controllers contain two components: feedforward control providing nominal input, and feedback control ensuring stability. The addition of feedforward controllers can improve the tracking performance when compared with the use of feedback controllers alone under acceptable model uncertainties, and thereby, significantly shorten the regulating time. However, model-based feedforward controllers alone cannot resist large model

uncertainties[23], feedback controllers have been employed in conjunction with feedforward to reduce uncertainty-caused errors, such as sliding mode control [24], backstepping control[25], and PID control [18]. In this paper, we propose a 2DOF controller described as follows:

$$u = \Theta(\xi_d, v_d, \dot{v}_d, \dots, v_d^{(\sigma)}) + K(\xi)(\xi - \xi_d), \quad (37)$$

where $K(\xi)$ is a scheduled gain. The gain scheduling control is designed to compensate unknown model uncertainties and avoid singularity problem, which often occur when using linearization techniques [26, 27]. Several gain scheduling methods[8] can be chosen dependent on the system requirements. These include hard switching, linear interpolation, and switching with hysteresis.

The 2DOF method improves the robustness of the conventional feedback linearization[17], which is very sensitive to model uncertainties. The feedback linearization technique exactly cancels nonlinearities via state feedback, while the 2DOF control method uses exact feedforward linearization (35), which is known to be more robust than feedback linearization in terms of model uncertainties[18].

In the next section, a data-driven planning technique will be presented to further improve robustness towards both model uncertainties and unexpected disturbances.

3 Data-driven Planner

The 2DOF control can have better tracking performance than the use of feedback control alone in the presence of acceptable model uncertainties.[7] In reality, model uncertainties and unexpected disturbances can be large and result in substantial deviation of the output trajectory from the predefined planning trajectory. The time-driven 2DOF control often deteriorates this deviation, since the time-driven planner cannot stop, but instead continues to give offline-computed values as time evolves. This fact will lead to poor performance, and even instability. The data-driven planner, however, refers to the current output and the planning trajectories 'stop' and 'wait' the system recovered from the disturbances. As a result, the data-driven 2DOF controller will not deteriorate the substantial deviation created by the model uncertainties or disturbances.

As shown in equation (17)-(18), we need plan a sufficiently smooth reference trajectory connecting an

initial setpoint and a terminal setpoint in the time interval T , and then use this trajectory to develop a exact feedforward linearization control (35). The sufficiently smooth reference trajectory (Fig. 3 the dotted curve) can be constructed using a polynomial series [28] as follows,

$$y_d(t) = y_0 + (y_T - y_0) \sum_{j=r+1}^{2r+1} a_j (t/T)^j, t \in [0, T], \quad (38)$$

where r is the relative degree [17] of the nonlinear system (15)-(16), and

$$a_j = \frac{(-1)^{j-(r+1)}(2r+1)!}{j \cdot r!(j-(r+1))!(2r+1-j)!}, j = r+1, \dots, 2r+1. \quad (39)$$

Alternatively, we can use an exponential function (Fig. 3 the solid curve),

$$y = (y_0 - y_T)(t/b + 1)e^{-t/b} + y_T, \quad (40)$$

where $b = T/10$.

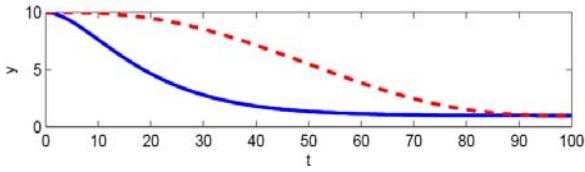


Fig. 3 Polynomial planner (dotted) v.s. Exponential planner (solid). In this illustration, we choose $T = 100$, $y_0 = 10$ and $y_T = 0$.

These reference trajectories $y_d(t)$ are sufficiently smooth, yet steep. As shown in Fig. 4(a), if an unexpected disturbance is applied over a short time period Δt , the output error $y(t) - y_d(t)$ grows sharply, as does the state error $e = x - x_d$. According to [18] and equation (34), the feedforward control u_d will fail to translate the nonlinear system into a normal form. This problem occurs because the time-driven planning trajectory refers to the reference trajectory at time instant t , i.e., $y_d(t)$. As a result, the time-driven feedforward control can have poor tracking performance, which may even lead to instability.

The data-driven planner [29, 30] is a closed-loop planner (Fig. 2) driven by an action reference, s , which is a non-time scalar factor generated by measurement data. As shown in Fig. 4(b), a simplified data-driven reference trajectory refers to the reference trajectory in

the output level, i.e., $y_d(y)$. The output error is zero and the corresponding state error is much smaller than the state error generated when using time-driven planning. As a result, the feedforward controller can guarantee good tracking performance. Theorem 1 gives a sufficient condition for stability of the data-driven control approach. Very generally, this theorem implies that the stability of data-driven control is at least the same as the stability of the time-driven control.

Moreover, in contrast to other planning approaches [8], the data-driven planner need not replan and regenerate a reference trajectory at every sampling time instant. In fact, the action reference parameter is calculated nearly at the same rate as the feedback control, meaning that the planning process is adjusted rapidly, enabling the planner to handle unexpected disturbances within one control execution sampling time.

Theorem 1 [30]: If the nonlinear system (15)-(16) is asymptotically stable with a time-driven controller $u(t)$, and the event s is monotonically increasing (or non-decreasing) with time t , i.e.,

$$ds/dt > 0 \quad (\text{or } ds/dt \geq 0), \quad (41)$$

Then this system is asymptotically stable (or stable) under the data-driven controller $u(s)$.

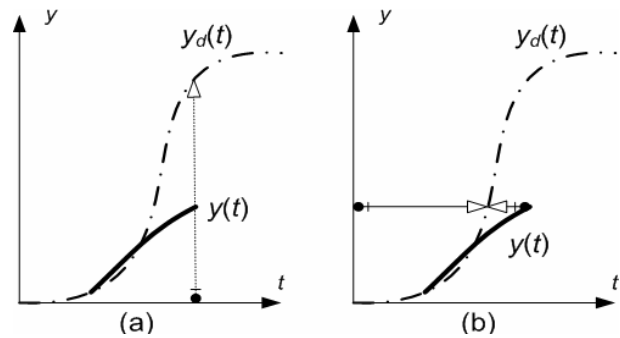


Fig. 4 Time-driven versus data-driven planning trajectory. A time-driven planning trajectory refers to the time instant t , while a data-driven planning trajectory refers to the output level y .

The data-driven planner develops a relationship between the output y and its derivatives \dot{y}, \ddot{y}, \dots , and $y^{(r)}$. The exponential reference trajectory is easier to analyze than the polynomial trajectory, although y_T can only be approximately reached in time T . Given the output y , the time t can be calculated from equation

(40) directly.

$$t/b + 1 = W, \quad (42)$$

where $W = W(-1, (y_T - y)/(y_0 - y_T)e)$ is the -1 branch of the Lambert W function, which is the solution of the function $(y_T - y)/(y_0 - y_T)e = We^W$. From these equations, the first order derivative $\dot{y}(t)$ is

$$\dot{y}(t) = (y_0 - y_T)(W + 1)e^{W+1}/b. \quad (43)$$

If the output monotonically decreases with t , the event S is defined as

$$S = y_0 - y; S_0 = 0, \quad (44)$$

Thus, the derivatives of y can be written as functions of S ,

$$\dot{y}(S) = (y_0 - y_T)(W(S) + 1)e^{W(S)+1}/b, \quad (45)$$

$$y^{(i)}(S) = -(y^{(i-2)}(S) + 2by^{(i-1)}(S))/b^2, i > 2, \quad (46)$$

$$\ddot{y}(S) = -[y(S) - y_T + 2b\dot{y}(S)]/b^2, \quad (47)$$

where $W(S) = W(-1, [y_T - y(S)]/(y_0 - y_T)e)$.

Keeping in mind that the output $y(t)$ may suddenly increase because of a short unexpected disturbance, we examine the effect of this disturbance on the event S . In order to keep the monotonically nonincreasing condition required for Theorem 1, as shown in Fig. 5, the event S first increases as y decreases, but then stops evolving after y reaches a valley y_c . S resumes evolution again only after y returns to the level of y_c .

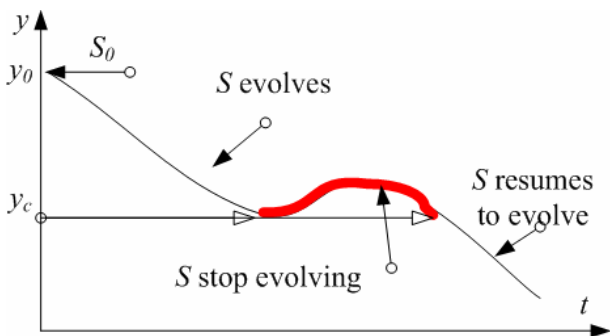


Fig. 5 The event S stops growing until y is recovered from the disturbance.

4 Control Application

In this section, we will construct flatness-based feedforward control for the insulin delivery system (14). The output is $z = x_1$, so the states can be described as functions of $z, \dots, z^{(n)}$

$$x_1 = z,$$

$$x_2 = (\tau \dot{z} + z)/\rho,$$

$$x_3 = -(\dot{x}_2 + P_1(x_2 - G_b))/x_2,$$

$$x_4 = (\dot{x}_3 + P_2x_3 + P_3i_b)/P_3,$$

$$x_5 = (\dot{x}_4 + k_e(x_4 - i_b))/V_i/p,$$

$$x_6 = (\dot{x}_5 + (p + o)x_5)/k.$$

In this case, the input also is a function of $z, \dot{z}, \dots, z^{(n-1)}$, since

$$u = \dot{x}_6 + kx_6 \quad (48)$$

Hence, the system (14) is differentially flat.

The 2DOF controller can be written as

$$u = \Theta(\xi_d) + K(z)PD(e), \quad (49)$$

where $K(z)$ is a hard-switching scheduled gain, and the state $\xi_d = [z_d, \dot{z}_d, \dots, z_d^{(n-1)}]$. The PD controller is

$$PD(e) = K_p(z - z_d) + K_d(\dot{z} - \dot{z}_d). \quad (50)$$

The feedforward control $u_d = \Theta(\xi_d)$ can be computed as

$$\bar{x}_2 = (\xi_d + \theta_1 \dot{\xi}_d)/\theta_2,$$

$$D = -1/(\bar{x}_{21} + G_b),$$

$$\bar{x}_{31} = [\bar{x}_{22} + P_1\bar{x}_{21}]D,$$

$$\bar{x}_{32} = [\bar{x}_{23} + (P_1 + \bar{x}_{31})\bar{x}_{22}]D,$$

$$\bar{x}_{33} = [\bar{x}_{24} + (P_1 + \bar{x}_{31})\bar{x}_{23} + 2\bar{x}_{32}\bar{x}_{22}]D,$$

$$\bar{x}_{34} = [\bar{x}_{25} + (P_1 + \bar{x}_{31})\bar{x}_{24} + 3\bar{x}_{32}\bar{x}_{23} + 3\bar{x}_{33}\bar{x}_{22}]D,$$

$$\bar{x}_{35} = [\bar{x}_{26} + (P_1 + \bar{x}_{31})\bar{x}_{25} + 4\bar{x}_{32}\bar{x}_{24} + 6\bar{x}_{33}\bar{x}_{23} + 4\bar{x}_{34}\bar{x}_{22}]D,$$

$$\bar{x}_4 = (\bar{x}_3 + P_2\bar{x}_3)/P_3,$$

$$\bar{x}_5 = (\bar{x}_4 + k_e\bar{x}_4)/\theta_3,$$

$$\bar{x}_6 = (\bar{x}_5 + (p + o)\bar{x}_5)/k,$$

$$\Theta(\xi_d) = \bar{x}_{62} + k\bar{x}_{61}.$$

(51)

5 Simulation Results

To demonstrate the effectiveness and robustness of the data-driven 2DOF control algorithm, we test different cases by computer simulation using Matlab and Simulink. The system parameters are set as Table II.

Table 2: System Parameters Used In The Simulation

Parameters	Value	Parameters	Value
P_1	0.003082	k_e	0.267
P_2	0.02093	θ_1	0.33
P_3	0.00001282	θ_2	0.33
G_b	85	i_b	0
o	0.0125	P	0.25
k	0.25	V_i	0.21

5.1 Test of robustness

First of all, the robustness of the data-driven 2DOF control method is tested by a couple of cases.

Case 1: Various initial glucose input

Initial glucose inputs range from 5 to 40 mg/min at 6 - 11 min and the BGL(blood glucose level) is sampled every 5 min. When the data-driven 2DOF control is applied, the BGL converges to the basal level in 80 - 130 min, and remains above the minimal level. The magnitude of the insulin infusion rate grows as the initial glucose input increases. The maximum insulin infusion reaches 7 U/h, which is under the constraints.

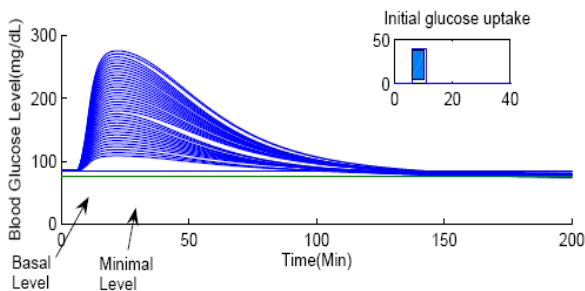


Fig. 6 The data-driven 2DOF control approach is tested by various initial glucose input, the BGL converges to the basal level in 80 - 130 min, and remains above the minimal level.

Case 2: Various sampling interval

Two glucose inputs 40 and 3 mg/min are administered at 6 - 11 min and 17 - 26 min, respectively. The BGL is

sampled from 5 to 20 min. The BGL converges to the basal level in 130 - 160 min. Clearly, the proposed method can control blood glucose levels even for a 20 min sampling interval, which would cause poor performance in most feedback-based controllers. The feedforward linearization technique in the 2DOF control largely reduces the dependence of the real-time feedback, leading to the sampling robustness observed in our simulations.

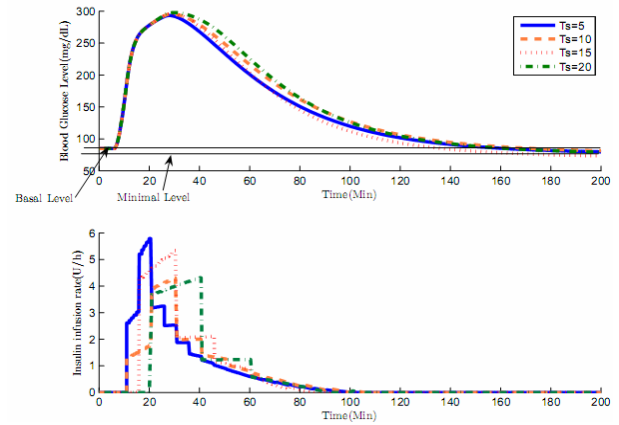


Fig. 7 The BGL is sampled from 5 min to 20 min. The BGL converges to the basal level in between 130 min and 160 min.

Case 3: model uncertainties

Two glucose inputs 40 and 3 mg/min are administered at 6 - 11 min and 17 - 26 min, respectively. The BGL is sampled every 5 min. The system (14) with model uncertainties can be written as

$$\dot{x} = f(x, u) + \delta f(x, 0), \quad (52)$$

where $\delta f(x, 0)$ implies that model uncertainties are proportional to vector field $f(x, 0)$, and $\delta > 0$ is a constant coefficient. For δ values of 0.5, 1, and 1.5, the BGL still converges under the same controller parameters. The larger model uncertainty leads to a longer convergence time; however, one can always adjust the gains of the PD controller (50) to achieve desired performance.

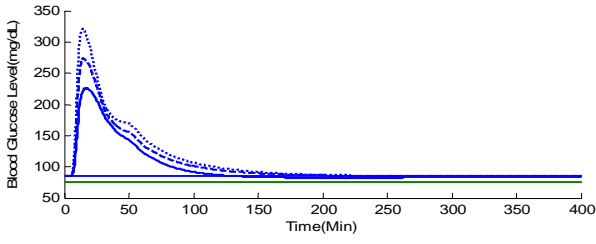


Fig. 8 The BGL converges to the basal level subject to model uncertainties. The model uncertainties are assumed to be 0.5 (solid), 1(dashed) and 1.5(dotted) times of the proposed model.

5.2 Comparing to other control algorithms

1) Time-driven approach

With a 10 mg/min initial glucose, a disturbance of 1 mg/min glucose is applied over the time period from 36 - 47 min. The data-driven approach converges to the basal level at 130 min, while the time-driven approach requires 200 min - a significant, and biologically costly delay relative to the data-driven approach.

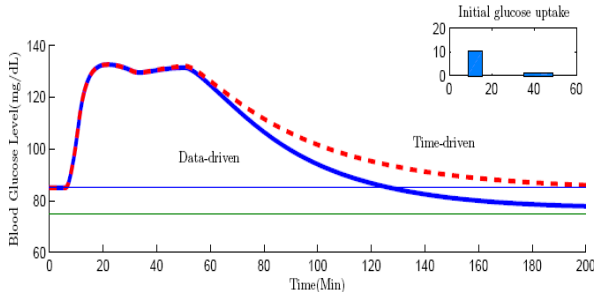


Fig. 9 In the event of disturbance, the time-driven control converges to the basal level at 200 min, while the data-driven control converges at 130 min.

2) MPC approach

The MPC (Model Predictive Control)[3, 31] is the most extensively applied control mechanism in industrial processing besides PID control. The Linear MPC approach first applies local Jacobian linearization, then uses a finite-horizon optimal control as follows,

$$\begin{aligned} & \sum_{i=1}^p (y(k+i|k) - r(k+i))^T Q (y(k+i|k) - r(k+i)) \\ & + \sum_{i=1}^m u(k+i-1)^T R u(k+i-1) \end{aligned} \quad (86)$$

Two glucose inputs 40 and 3 mg/min are administered at 6 - 11 min and 17 - 26 min, respectively. Using the MPC approach with a 5 min sampling interval, the BGL

converges to the basal level at 170 min, while the data-driven 2DOF control stabilizes the BGL at 140 min.

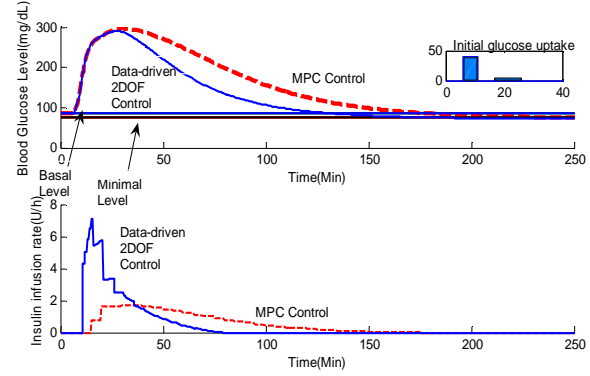


Fig. 10 BGL converges to the basal level at 170 min by MPC approach, while BGL converges at 130 min by the data-driven 2DOF control approach.

3) PD control

Two glucose inputs 20 and 3 mg/min are administered at 6 - 11 min and 17 - 26 min, respectively. Using the classical PD approach with a 5 min sampling interval, the BGL converges to the basal level at 160 min. When the first initial glucose input changes to 40 mg/min, however, the BGL significantly undershoots the minimal allowable glucose level, which may be dangerous to the patient. For both 20 mg/min and 40 mg/min, though, the data-driven 2DOF control approach makes the BGL converge at 140 min while at the same time remaining will within the safety range.

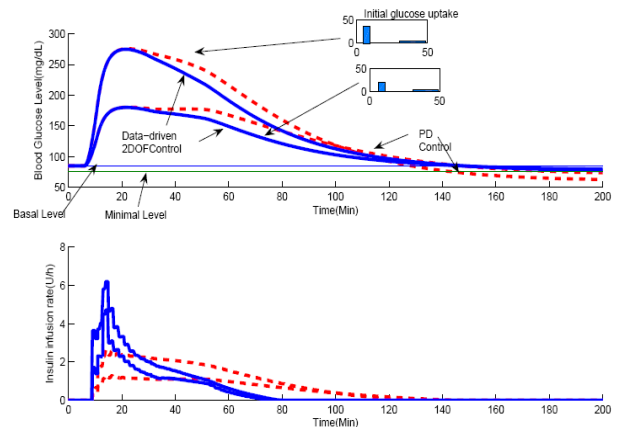


Fig. 11 Using the data-driven 2DOF control approach, the BGL converges at 140 min and above the minimal level in both cases, while the BGL goes underneath the minimal level using the classical PD control approach.

4) Backstepping control with Extended Kalman Filter
Yang *et al.* [6] proposed a backstepping control algorithm for the glucose control problem. Two glucose inputs 20 and 3 mg/min are administered at 6 - 11 min and 17 - 26 min, respectively. When we apply the classical backstepping control approach with a 5 min sampling interval and given full state information, we find that the BGL converges to the basal level at 150 min, which is comparable with our proposed approach. However, when EKF (Extended Kalman Filter) [32] is applied to estimate the states, the BGL goes underneath the minimal allowable level.

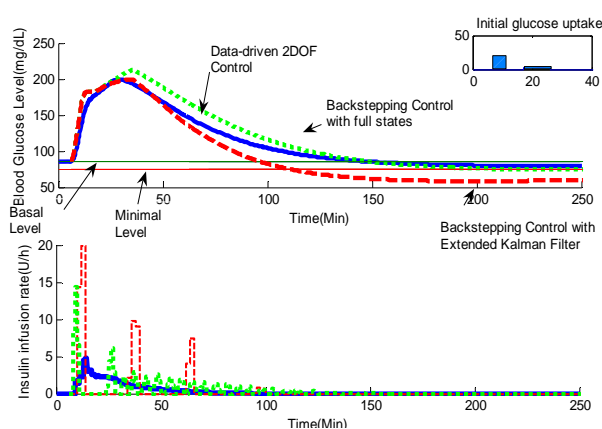


Fig. 12 Using the backstepping control approach with full states information, the BGL converges to the basal level at 150 min, similar to the data-driven approach. However, when EKF is used to estimate the states, the BGL goes underneath the minimal level.

6 Conclusions

A new data-driven 2DOF control mechanism for controlling a micropump and microneedle integrated device is presented in this paper. Compared with several feedback techniques in literature, this approach demonstrates much shorter regulating time for glucose control. In addition, this method also resists more model uncertainties and unexpected disturbances than other 2DOF controls, while has the same regulation performance. This work focuses on theoretical breakthrough and validation by computer simulation. Laboratory experiments will be implemented in future work.

ACKNOWLEDGMENT

This material is based upon work supported by the

National Science Foundation under Grant No. 0328378. The authors are grateful to the Associate Editor and to the anonymous reviewers for their valuable criticisms and suggestions, and to Dr. Sharon Bewick for many useful suggestions.

REFERENCES

- [1] G. M. Steil, K. Rebrin, J. Mastrototaro, B. Bernaba, and M. F. Saad: 'Determination of Plasma Glucose During Rapid Glucose Excursions with a Subcutaneous Glucose Sensor,' *Diabetes Technology & Therapeutics*, 2003, 5, pp. 27-31
- [2] G. Marchetti, M. Barolo, L. Jovanovic, H. Zisser, and D. E. Seborg: 'An Improved PID Switching Control Strategy for Type 1 Diabetes,' *IEEE Transactions on Biomedical Engineering*, 2008, 55, pp. 857-865
- [3] R. Hovorka, V. Canonico, L. J. Chassin, U. Haueter, M. Massi-Benedetti, M. O. Federici, T. R. Pieber, H. C. Schaller, L. Schaupp, T. Vering, and M. EWilinska: 'Nonlinear model predictive control of glucose concentration in subjects with type 1 diabetes,' *Physiol. Meas.*, 2004, 25 pp. 905-920
- [4] S. M. Lynch and B. W. Bequette: 'Model predictive control of blood glucose in type I diabetes using subcutaneous glucose measurements,' *Proc. American Control Conference*, 2002, pp. 4039-4043
- [5] F. Chee, A. V. Savkin, T. L. Fernando, and S. Nahavandi: 'Optimal H_{∞} Insulin Injection Control for blood glucose regulation in Diabetic patients,' *IEEE Transactions on Biomedical Engineering*, 2005, 52, pp. 1625 - 1631
- [6] R. Yang, M. Zhang, and T. J. Tarn, 'Control Mechanisms for Life Science Automation,' in *Life Science Automation: Fundamentals and Applications*, M. Zhang, B. Nelson, and R. A. Felder, Eds.: Artech House Publishers, 2007.
- [7] S. Devasia: 'Should model-based inverse inputs be used as feedforward under plant uncertainty?,' *IEEE Trans. on Automatic Control*, 2002, 47, pp. 1865-1871
- [8] M. van Nieuwstadt: 'Trajectory Generation for Nonlinear Control Systems,' California Institute of Technology, 1996.
- [9] D. L. Polla, A. G. Erdman, W. P. Robbins, D. T. Markus, J. Diaz-Diaz, R. Rizq, Y. Nam, H. T. Brickner, A. Wang, and P. Krulvitch: 'Microdevices in Medicine,' *Annual Review of Biomedical Engineering*, 2000, 2, pp. 551-576
- [10] N. T. Nguyen and X. Huang: 'Miniature valveless pumps based on printed circuit board technique,' *Sensors Actuators A* 2001, 88 pp. 104-11
- [11] T. Gerlach and H. Wurmus: 'Working principle and performance of the dynamic micropump,' *Sensors Actuators A* 1995, 50, pp. 135-40
- [12] B. Fan, G. Song, and F. Hussain: 'Simulation of a piezoelectrically actuated valveless micropump,' *Smart Mater. Struct.*, 2005, 14, pp. 400-405
- [13] S. A. Ramsey, J. J. Smith, D. Orrell, M. Marelli, T. W. Petersen, P. de Atauri, H. Bolouri, and J. D. Aitchison: 'Dual feedback loops in the GAL regulon suppress cellular heterogeneity in yeast,' *Nature Genetics*, 2006, 38, pp. 1082-1087
- [14] G. M. Steil, A. E. Panteleon, and K. Rebrin: 'Closed-loop insulin delivery - the path to physiological glucose control,' *Advanced Drug Delivery Reviews*, 2004, 56, pp. 125-144
- [15] S. Shimoda, K. Nishida, M. Sakakida, Y. Konno, K. Ichinose, M. Uehara, T. Nowak, and M. Shichiri: 'Closed-loop subcutaneous insulin infusion algorithm with a short-acting insulin analog for long-term clinical application of a wearable artificial endocrine pancreas,' *Frontiers Medical Biological engineering*, 1997, 8, pp. 197-211
- [16] R. N. Bergman, L. S. Phillips, and C. Cobelli: 'Physiologic evaluation of factors controlling glucose tolerance in man,' *Journal of Clinical Investigation*, 1981, 68, pp. 1456-1467
- [17] A. Isidori: *Nonlinear Control Systems* (Springer, New York 1989)

- [18] V. Hagenmeyer and E. Delaleau: 'Exact feedforward linearization based on differential flatness,' *International J. Control*, 2003, 76, pp. 537-556
- [19] M. Fliess, J. Levine, P. Martin, and P. Rouchon: 'Flatness and defect of nonlinear systems: introductory theory and examples,' *International J. Control*, 1995, 61, pp. 1327-1361
- [20] M. Fliess, J. Levine, P. Martin, and P. Rouchon: 'A Lie-Backlund approach to equivalence and flatness of nonlinear systems,' *IEEE Trans. on Automatic Control*, 1999, 44, pp. 922-937
- [21] E. Delaleau and J. Rudolph: 'Control of flat systems by quasi-static feedback of generalized states,' *International Journal of Control*, 1998, 71, pp. 745-765
- [22] M. van Nieuwstadt, M. Rathinam, and R. M. Murray: 'Differential Flatness and Absolute Equivalence of Nonlinear Control Systems,' *J. Control and Optimization*, 1998, 36, pp. 1225-1239
- [23] Y. Zhao and S. Jayasuriya: 'Feedforward controllers and tracking accuracy in the presence of plant uncertainties,' *Proc. American Control Conference, 1994*, 1994, pp. 360-364 vol.1
- [24] H. Sira-Ramirez, "Sliding mode control of the PPR mobile robot with a flexible join," in *Nonlinear Control in the Year 2000*. vol. 259 London: Springer, 2000, pp. 421-442.
- [25] P. Martin, R. M. Murray, and P. Rouchon, "Flat systems, equivalence and feedback," in *Advances in the Control of Nonlinear Systems*. vol. 264 London: Springer, 2000, pp. 5-32.
- [26] R. Yang, M. Zhang, and T. J. Tarn: 'Dynamic Modeling and Control of a Micro-needle Integrated Piezoelectric Micro-pump for Diabetes Care,' *Proc. IEEE Conference on Nanotechnology*, Cincinnati, USA, 2006
- [27] F. Doyle III, J. Harting, C. Dorski, and N. Peppas: 'Control and modeling of drug delivery devices for the treatment of diabetes,' *Proc. American Control Conf*, Seattle, WA, 1995, pp. 776-780
- [28] A. Piazzzi and A. Visioli: 'Optimal Inversion-Based Control for the Set-Point Regulation of Nonminimum-Phase Uncertain Scalar,' *IEEE Transactions On Automatic Control*, 2001, 46, pp. 1654-1659
- [29] T. J. Tarn, N. Xi, and A. K. Bejczy: 'Path-Based Approach to Integrated Planning and Control for Robotic System,' *Automatica*, 1996, 32,
- [30] N. Xi and T. J. Tarn: 'Stability analysis of non-time referenced internet - based telerobotic systems,' *Robotics and Autonomous Systems*, 2000, 32, pp. 173-178
- [31] R. S. Parker, F. J. Doyle III, and N. A. Peppas: 'A model-based algorithm for blood glucose control in type I diabetic patients,' *IEEE Transactions on Biomedical Engineering* 1999, 46, pp. 148-157
- [32] M. Boutayeb and D. Aubry: 'A strong tracking extended Kalman observer for nonlinear discrete-time systems,' *IEEE Transactions on Automatic Control*, 1999, 44, pp. 1550-1556

Rescue robot systems -From snake-like robots to human interface-

Fumitoshi Matsuno

Kyoto University, Yoshida Honmachi, Sakyo-ku, Kyoto 606-8510, Japan
(Tel : 81-75-753-5232; Fax : 81-75-753-4862)
(matsuno@mi.kyoto-u.ac.jp)

Abstract: Intelligent rescue systems with high information and robot technology have been expected to mitigate disaster damages, especially in Japan after the 1995 Hanshin Awaji Earthquake and in USA after the September 11, 2001 terrorist attack on New York City. Public safety and security problems are not limited to Japan and the United States, since every country has experienced man-made and natural disasters in the past. This paper introduces a developed grouped rescue robot systems with high-functionality multiple mobile robots and robust/scalable information infrastructure for searching tasks in disaster scenario.

Keywords: search and rescue, safety and security, RT and ICT,

I. Introduction

Intelligent rescue systems with information and communications technologies (ICT) and robotics technology (RT) have been proposed to mitigate disaster damages, especially in Japan after the 1995 Hanshin-Awaji Earthquake. In particular, it has been stressed the importance of developing robots for search and rescue tasks, which can actually work in a real disaster site. In USA the September 11, 2001 terrorist attack on New York City and Washington, DC, the hijacked plane crash in Pennsylvania, and the Anthrax attack that immediately followed instantly changed people attitude about safety and security in their personal lives. Public safety and security problems are not limited to Japan and the United States, since every country has experienced man-made and natural disasters in the past. Solutions will depend upon new, unconventional approaches to search and rescue. Robotics, information and communications technologies, devices and system integration can play an important role in providing technology that can contribute to Safety, Security and Rescue activities.

II. DDT project of rescue robot systems

Japan, which suffered Hanshin Awaji Earthquake, has drawn on the lessons of that experience to alleviate the damage caused by disasters in major urban areas. It is well known that rescue in 3 hours is desirable, and that the survival rate becomes drastically low after 72 hours. We should search and rescue victims from debris within this 'golden 72 hours' [1].

A lot of rescue robots have been developed in Japan. From 2002 to 2007 "Special Project for Earthquake Disaster Mitigation in Urban Areas" (DDT Project) launched by Ministry of Education, Culture, Sports, Science and Technology, Japan [2]. In DDT project we have 4 mission units (MU) to accomplish our objective as follows with considering disaster scenario (Fig. 1).



Fig. 1 Overall concept in disaster scenario

1. Information Infrastructure System Mission Unit

Main systems in this MU are RF ID tags and Micro servers. Tasks of this group is global information collection (> 10 km) using ad hoc networks, micro servers, RF ID tags, home facilities, etc. and development of communication protocols, data structures, etc. for data integration.

2. Aerial Robot System Mission Unit

Main systems in this MU are helicopters, airships, balloons. Tasks of this group are global surveillance (< some km) for information collection at the initial state of incidents and local surveillance from sky (< 200 m) for victim search and support of ground vehicles as the second deployment. Fig. 2 and 3 show an autonomous

helicopter (Prof. H. Nakanishi, Kyoto Univ.) and a balloon for information gathering (Prof. M. Onosato, Hokkaido Univ.), respectively.



Fig. 2 Autonomous helicopter (Prof. H. Nakanishi)



Fig. 3 Info-balloon (Prof. M. Onosato)

3. In-Rubble Robot System Mission Unit

Main systems in this MU are serpentine robots, crawler-type robots, and sensor balls. Tasks of this group are local information collection in the rubble pile (< 30 m) for victim search and environmental check. Serpentine snake-like robots KOHGA (Prof. F. Matsuno, Kyoto Univ.) and SORYU (Prof. S. Hirose, Tokyo Institute of Technology) are shown in Fig. 4 and Fig. 5, respectively.



Fig. 4 KOHGA (Prof. F. Matsuno)



Fig. 5 SORYU (Prof. S. Hirose)

4. On-Rubble Robot System Mission Unit

Main robots in this MU are crawler type, wheeled, and jumping robots. Tasks of this group are local surveillance on the rubble pile (< 50 m) for victim search and environmental check. Fig. 6, 7 and 8 show a wheel type robot FUMA (Prof. F. Matsuno, Kyoto Univ.), a two-tracks robot with an arm HELIOS (Prof. S. Hirose, Tokyo Institute of Technology) and a four-tracks robot with an arm KOHGA3 (Prof. F. Matsuno, Kyoto Univ.), respectively.



Fig. 6 FUMA
(Prof. F. Matsuno)



Fig. 7 HELIOS
(Prof. S. Hirose)



Fig. 8 KOHGA 3 (Prof. F. Matsuno)

These rescue robot systems have some sensor, for example a camera and a laser range finder (LRF). An operator controls a robot using a user interface based on the transmitted information from the remote site. Their abilities are restricted by communication performance in a practical environment.

III. Development and Integration of New Grouped Rescue Robots System

When size of a disaster area is very large and fast information gathering is required, robotic system has to use multiple robots to acquire information. Another requirement is online data processing to use collected information to subsequent rescuer operation. To address these issues, the project [3] in our group founded by NEDO from 2006 to 2008 focuses on the following:

- I. A high-functionality multiple mobile robot system.
- II. A robust and scalable information infrastructure, which includes network and GIS data system.

III. An efficient user interface and control system to operate robots and to manage lots of information.

To design above systems, we also focused following issues:

ADAPTABILITY: There are no "same-situation and same-environments" in a disaster target area, and a situation will change fast in the disaster. The system has to have adaptability by a configuration and capabilities to adapt to changing environments.

SCALABILITY: To deploy robots, the communication infrastructure is also extensible physically. Note: only robots can address to the disaster area, robots have to have network building function by itself.

USABILITY: The human resource is one of the highest cost components of the system. The system has to have efficient/usable interface to operate. For example, simultaneous multiple robots operation support, semi-auto operation support and information presentation interface that only shows necessary information to operators, for each situation.

According to the above mentioned sub-themes and issues, we newly developed four elements: mobile robot platforms, ad-hoc wireless network called Robohoc network, user interface to control multiple robots and GIS data server

1. Mobile robot platforms

We have developed two types of mobile robot platforms which achieve 1.0[m/sec] driving on a flat plane, and have high mobility and high ability. One is a pioneer type robot as shown in Fig. 9 (a), and the other is a surveyor type robot as shown in Fig. 9 (b). The



(a) Pioneer robot

(b) Surveyor robot

Fig. 9 Developed Robot system (Prof. F. Matsuno)

function and role of each type are below.

At first of a given mission, pioneer type robots expand the wireless network area by deploying wireless network ad-hoc nodes. The robot can eliminate

lightweight obstacles and open doors by using a mounted manipulator. To construct a wireless infrastructure, the pioneer type robot is mainly teleoperated from a remote safe place by an operator.

Next of the mission, a number of surveyor type robots semi-autonomously search a target building under the information infrastructure that was already constructed by the pioneer type robots, and gather information of damaged building and victims.

Each robot has a network camera, a fish-eye camera, a LRF, an attitude sensor, IR sensors, rotary encoders for motors which drive tracks, and potentiometer to measure angles of multifunctional and flipper arms. To control developed mobile robot platforms, following methods are implemented.

M1. Full manual control method with virtual bumper: A robot is controlled by sending commands related to translational velocity and rotational velocity directly with joystick device. Function of the virtual bumper stops the movement of the controlled robot when an obstacle is detected within the pre-defined area around the robot by LRF and IR sensors.

M2. Line trajectory trace method: An operator points a sub-goal location of the robot on an environment map generated by a LRF, then the robot is controlled to follow the line created by connecting the current and sub-goal points with a certain velocity until the robot reaches the goal point.

M3. Right/Left hand wall following full-autonomous control method: In this mode, a robot autonomously cruises in the building along right/left wall with keeping a certain distance from the wall without operator's commands.

M4 Direction oriented semi-autonomous control method: In this mode, an operator commands desired moving direction of a robot. The robot runs to the direction according to compass data with avoiding obstacles.

2. GUI for controlling multiple robots

Developed user interface is shown in Fig. 10. GUI enables to control multiple robots by one operator. For selecting a control method of a robot, the operator clicks a control button at the upper side of GUI (1 in Fig. 10). To select destination of command for a robot, an operator selects a target robot in a panel located at the bottom of the GUI. Outside of the selected robot panel is colored. For each robot, the selected control method is indicated in the robot panel (2 in Fig. 10). The robot

panel displays 3D CG model of each robot and shows arm position, velocity and attitude of each robot, laser range finder data around robot and on/off status of the virtual bumper (3 in Fig. 10). The robot panel also displays the state of network communication for the robot (4 in Fig. 10). The robots have two or three cameras, and images from them are displayed at the upper left side of GUI. To select which camera image to be displayed, a camera selecting button is located at the right side of the camera image (5 in Fig. 10). Note that an operator can select only one camera, in order not to affect a heavy load to Robohoc network. Quality of camera image (frame rate and compressing rate) also can be selected by a slider bar (6 in Fig. 10). Moreover, the operator can choose a sending method of image data. In first method a raw jpeg image is send directly. In the other method a jpeg image is divided into small reconfigurable images and divided images are sent.

3. Communication system

To operate multiple robots simultaneously in the



Fig. 10 GUI (Prof. F. Matsuno)

disaster area, a sort of full-wireless network system is required. Moreover, it should be robust to withstand environment changes and dynamic extension by robots themselves. We proposed a network system which has the characteristics in our previous paper [4], and called it as "Robohoc network".

There are lots of previous studies about the networking for the robotic system and/or the sensor network system. However, the most important issue for the network for the disaster situation is the adaptability to the environment rather than the performance (throughput, number of nodes, etc.). This adaptability also relates to the network bandwidth management because both of the network throughput and latency are variable parameters. The system has to change the total usage of its network to follow such changes.

Followings are the requirements for the communication system from the system design's point of view

- R1.** Use wireless communication technology to communicate with multiple moving robots simultaneously and to collect information from lots of sensors which are deployed by robots in the target area.
- R2.** To communicate with moving robots and static sensors.
- R3.** To supply enough bandwidth to sent a video stream from a robot.
- R4.** To show the up-to-date status of the network itself to other system.
- R5.** To be physically extensible by robots alone without human help.

We developed not only the software and protocols for Robohoc network, but also the prototype of Robohoc nodes to construct the wireless ad-hoc network for our field trials (Fig. 11).

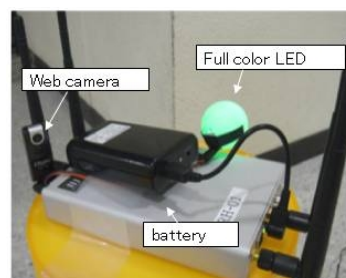


Fig. 11 Robohoc node (Dr. Y. Uo)

It is necessary to communicate information such as commands to robots and sensor data to an operator including video images stably with considering not to break down all network performance. Constructed Robohoc network is a kind of wireless ad-hoc network, so it has a limitation of throughput. To manage the bandwidth of Robohoc network, communication data is classified into four categories according to two attributes, data size and responsiveness, as shown in Fig. 12. This bandwidth management mechanism is based on time sharing of communication resource, namely not all

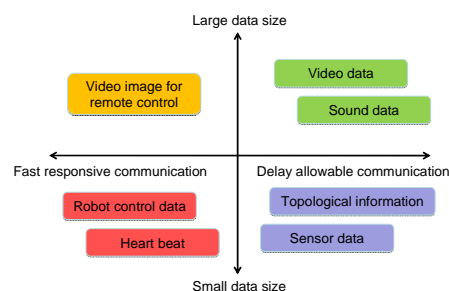


Fig. 12 Categories of communication data
(Dr. Y. Uo)

data have to be sent in real time and there are delayable data.

4. GIS server

We categorized roles of GIS as two spheres, spatial temporal database management sphere and operation support sphere. In spatial temporal database management sphere GIS has to deal with following four types information;

I1. Base map information: In most of public building or underground space base map data exists. In this mission we assume that rescue team can get base map data before rescue activity. If different accuracy sets of data are provide, the highest accuracy data have to be selected.

I2. Information collected by grouped rescue robots: Trajectories of mobile robots to check their behavior, time series sensor information for robots themselves, environmental information to get from various sensors mounted on the mobile robots to check damage condition of the target space, and locations of access points for Robohoc network placed by the pioneer robots to manage Robohoc network condition must be stored.

I4. Robohoc network condition: Radio field intensity, correspondence of access points, and transmission path must be stored.

I5. Resources of mobile robots and access points for Robohoc network: Remaining amount of battery of each robot and access point, HDD of each robot, equipped access points of each pioneer type robot must be stored.

In operation support sphere we have two functions as follows;

F1. Function for making support information for robot operators: Calibration of initial point of robots, input of changed objects from base map information, and alert of no-operation areas caused by ground/communication condition are assumed.

F2. Function for operation support for information administrators: Access point location planning, removing location errors from environment map information generated by LRF data, input no-operation and search areas are assumed.

In order to realize the requirements for GIS it is effective to use a temporal GIS as a database management system. In this case we select our original temporal GIS "DiMSIS" which have been developed since immediately after Great Hanshin-Awaji

Earthquake as a common spatial temporal database management system for disaster risk management [5]. Fig. 13 shows a screenshot of viewer of GIS.

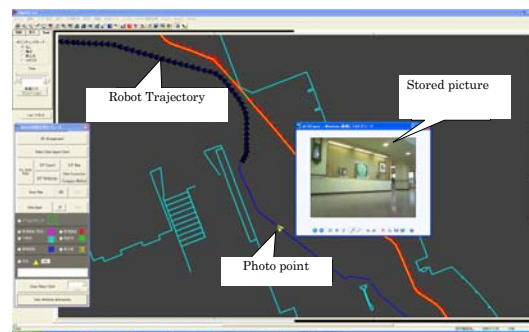


Fig. 13 Screenshot of viewer of GIS
(Prof. M. Hatayama)

5. System Integration

Constructed system structure is shown in Fig. 14.

The system consists of an operator PC, a GIS server and a FE (Front End) server in the operator station, Robohoc network and robots. The GUI on the operator PC is an application for controlling grouped robots remotely, and displaying instantaneous data sending from robots. GIS server is a database server handling global position data such as position of robots, rescue teams and victims in the disaster site. FE server is an application to connect user interface, GIS server and robots. Robohoc network ensures communications between the operator station and robots. To use Robohoc network, the operator station system robots equip a special network controller. To connect with this special network controller, the operator station and robots are connecting each other without paying attention to the Robohoc network like normal wireless LAN network.

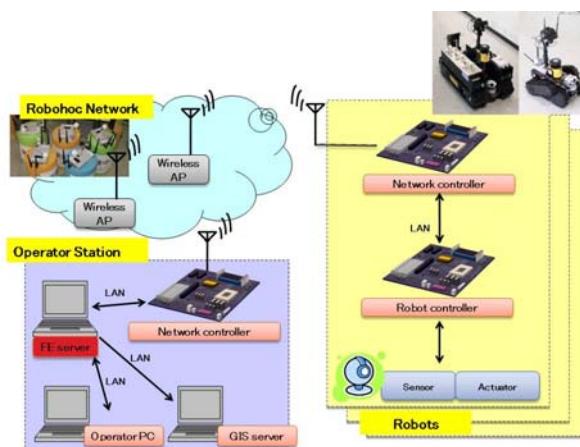


Fig. 14 Constructed system structure
(Dr. T. Kamegawa)

IV. DEMONSTRATIVE EXPERIMENTS AND TRAININGS

We carried out the demonstrative trainings to test developed robot system as shown in Fig. 15. This event was held as a special event for SICE International Conference on Instrumentation, Control and Information Technology 2008 (SICE Annual Conference 2008) in Tokyo on 21st August, 2008. In this training, two incumbent fire fighters controlled 4 robots manually, and Robohoc network was not utilized.

As a mission scenario, the pioneer type robot was controlled to put Rohoboc nodes on an environment, and then the surveyor type robots were controlled to investigate in a building. As a result, they could accomplish to find (dummy) victims through video images from the surveyor type robots.



Fig. 15 Demonstrative training by fire fighters

After a while, we carried out another demonstrative experiment for rescue activities using fully developed grouped robot systems as shown in Fig. 16.



Fig. 16 Demonstrative training by using Robohoc network

In the demonstrative experiments, the system was handled by three people, a commander for all system, a robot operator and an information operator, and 5 robots were controlled. In this demonstrative experiments, the size of target area is 57[m]x32 [m] that is larger than previous demonstrative trainings, and 8 Robohoc nodes were previously set in the building. It is assumed that a part of the map of the building were available for GIS data server. Fig. 17 shows an application of a network status monitoring viewer that indicates connection of

wireless network to neighborhood nodes and which robot connects to which node.

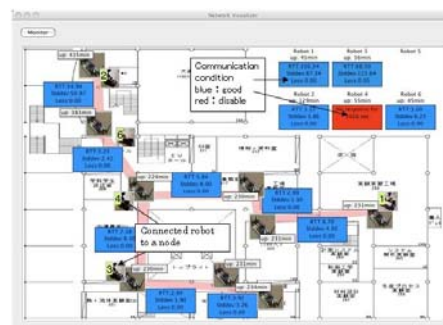


Fig. 17 Network status monitoring viewer (Dr. Y. Uo)

At first, the pioneer type robot was manually controlled to put Rohoboc nodes on an environment. Then the surveyor type robots were manually and automatically controlled to investigate in a building. When the robot operator found something to update to GIS data server, the information operator inputs the data to GIS. The information operator sometime fixes a robot trajectory drawn in a global map. When the robot entered new area, it means there is no previous map, the information operator creates a new map according to LRF information. Finally, operators could accomplish to find (dummy) all victims in the floor through video images from the surveyor type robots.

V. CONCLUSION

In this paper, the developed grouped rescue robots system for searching in damaged buildings is described. The system is consisted of four elements, mobile robot platforms, user interface, ad-hoc wireless network and GIS server. The system was integrated so as to complement the element's limitations each other.

REFERENCES

- [1] Matsuno F (2004), Rescue Robots and Systems in Japan, Proc. IEEE Int. Conf. on Robotics and Biomimetics (Special Invited Talk)
- [2] Tadokoro S (2010), Rescue Robotics: DDT Project on Robots and Systems for Urban Search and Rescue, Springer.
- [3] Matsuno F (2008), NEDO Rescue Robot System Project, Interactive Organized Session, Proc. SICE Annual Conference.
- [4] Fujita S, Shima K, Uo Y, Esaki H (2009), A Decentralized VPN Service over Generalized Mobile Ad-hoc Networks, IEICE Trans. Information Systems, E92-D, 10.
- [5] Kakumoto S, Hatayama M, Kameda H, Taniguchi T, (2009), Development of disaster management spatial information system (DiMSIS), Proc. GIS'97, 595-598.

Human-Robot Interaction and Social Relation

Michita Imai (Dept. of Computer and Information Science, Keio University)

This paper presents the factor of designing an anthropomorphic agent such as a communication robot and an embodied communicative agent. Communication is a cooperative phenomenon between participants. People involved in a communication speak and hear actively during the conversation. However, it is difficult to engage them in the communication with a robot because they seldom actively consider the communicative intention of the robot. The paper explains the importance of social relationship between a human and a robot for engaging people in the communication. In particular, we consider how the relation makes them consider the intention of the robot. Also, I show what factors of the robot design elicit the social relation.

1 Introduction

Researches related to HRI (Human-Robot Interaction) investigate how to design a robot which has a anthropomorphic character, behaves autonomously, communicates with people. And they consider what application the robot achieves. In spite of progress of many researches, few systems use the merit of HRI. An agent which makes people anthropomorphize itself is used at ATM or MS Office. However, it gives their functions just something extra. However, there are a lot of researchers in the field of HRI. This means that they consider intuitively that there are valuable things in the interaction between people and a robot. The paper explains what are the key factors for applying HRI technology to an interactive system.

2 Key Factors at HRI research

Key factors at HRI research depend on a type of a used robot. There are two types of robots; one has a anthropomorphic figure and the other does not. This paper focuses on the robot which has an anthropomorphic figure because HRI researches are related to the aspect of communications. In particular, researches about non-verbal expressions such as gestures and gaze movements are important for HRI field.

I write four main factors which are important in designing a robot as a interactive system.

i. Characteristic of being anthropomorphized

A human-like figure enhances the tendency of anthropomorphizing a robot. The robots which have a human-like figure are intended to utilize the characteristic. The human-like figure makes the robot communicate with people easily using verbal and non-verbal expressions.

ii. Capability of sharing environments with people

The words "sharing environments" do not indicate simply that the robot exists in the same place with a person. Those mean "cognitive sharing" (it is called Joint attention in developmental psychology [3]) that the robot pays its attention to the same thing/event as people and that it makes people consider that both of them look at it together. The design of the robot's behaviors is crucial to establish joint attention [1] [5]. The robot intentionally turns its gaze toward a target, makes eye contact with a person, and points at it with its hand at an appropriate timing. A research reported that the ability of establishing joint attention in a real world is higher than CG character on a PC screen [6]. The robot is more advantageous than the other devices in terms of sharing environmental information. For example, it can explain items at an exhibition or a route to a place by using verbal and non-verbal expressions. Moreover, since the body of the robot exists physically in our environment, the robot's expressions can be seen by people around the robot. The embodied expressions give information to them even though they are not a primary person in the communication.

iii. Establishing relation with people

The relation between people and a robot is significant for natural communication between them. People understand what the other said by inferring his/her communicative intention. However, they do not make the inference for an anonymous person. Since the inference is an active mental function, people make the inference for someone related to them. They seldom infer the communicative intention of the others who do not have relation with them. Although the relation exists between friends, family, colleague, and so on, it is not necessarily a formal one. People do not understand actively what the other says when they do not even have a casual relation. The study [4] found that the existence of the relation between a experimental participant and a robot have effect on whether he/she can understand the robot's utterance. The physical existence of the robot gives it the advantage when it establishes the relation with people.

iv. Constraints coming from existence

Since a robot has a physical body, it occupies our living environment. However, the physical body improves the abilities of sharing environments and establishing relations. CG character can also make the relations by preparing a context which engages a person in the interaction. However, it is difficult for CG character to communicate with people passing by. The CG character's abilities of attracting people is weaker than the robot's. The HRI research should employ the effect of the physical existence positively. For example, station staffs can manage the flow of crowded people in rush hour by just standing. Although nowadays robots do not have such a existence like a station staff, the HRI researches like an android science[2] will reveal what is an important factor to manage people.

3 Reconsider HRI research

The question related to HRI researches is that we need a robot as the interface of an interactive system. This section discusses the issue.

Is a robot needed to just achieve a communication with people? ?

Dose a robot need an anthropomorphic figure?

Is the anthropomorphic figure important to refer to information in a real world?

We do not need a robot if a system just gives us information. On the other hand, we must discuss the role of communications in human-society to conclude the question.

Humans do a lot of activities by communicating with the others: establishing a relation with others, empathizing with them, behaving considering them, and sharing an experience with them. The important matter among them is to behave considering the others. If a human and a robot behave considering the other's mind each other, not only the robot takes account of the human, but also he/she considers the robot when doing something. The bidirectional consideration makes them share their experience. The sharing the experience differentiates the robot from a simple computer which just gives anyone the same cold information. There is possibility that the robot can give each individual different information reflecting a shared experience between them.

We should reconsider the robot as the interface of an interactive system after succeeding in developing a robot which can interact with people based on shared experiences.

References

- [1] M. Imai, T. Ono, and H. Ishiguro. Physical relation and expression: Joint attention for human-robot interaction. *IEEE Transactions on Industrial Electronics (ITIED 6)*, 50(4):636–643, 2003.
- [2] H. Ishiguro and T. Minato. Development of androids for studying on human-robot interaction. In *Proceedings of 36th International Symposium on Robotics, TH3H1*, 2005.
- [3] C. Moore and P. J. Dunham. *Joint Attention: Its Origins and Role in Development*. Lawrence Erlbaum Associates, Inc., 1985.
- [4] T. Ono and M. Imai. Reading a robot's mind: A model of utterance understanding based on the theory of mind mechanism. In *Proceedings of AAAI-2000*, pages 142–148, 2000.
- [5] O. Sugiyama, T. Kanda, M. Imai, H. Ishiguro, and N. Hagita. Three-layered draw-attention model for humanoid robots with gestures and verbal cues. In *Proc. of 2005 IEEE/RSJ Intl. Conf. on Intelligent Robots and Systems (IROS 2005)*, pages 2140–2145, 2005.
- [6] K. Shinozawa, F. Naya, J. Yamato, and K. Kogure. Differences in effect of robot and screen agent recommendation on human decisionmaking. *International Journal of Human-Computer Studies*, 62(2):109–123, 2005.

Micro Nano Robotics

Tatsuo Arai

Micro nano robotics, Tatsuo arai, Osaka University, Japan

MICRO NANO ROBOTICS, Tatsuo ARAI, OSAKA University

Micro Nano Robotics

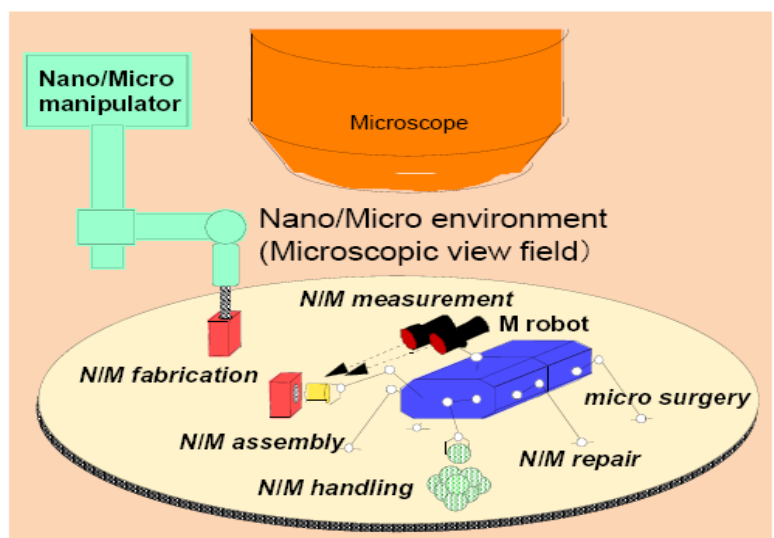
Tatsuo ARAI
OSAKA University

16th International Symposium on Artificial Life and Robotics, Oita, JAPAN, January 28, 2011

MICRO NANO ROBOTICS, Tatsuo ARAI, OSAKA University

What is Micro Nano Robotics?

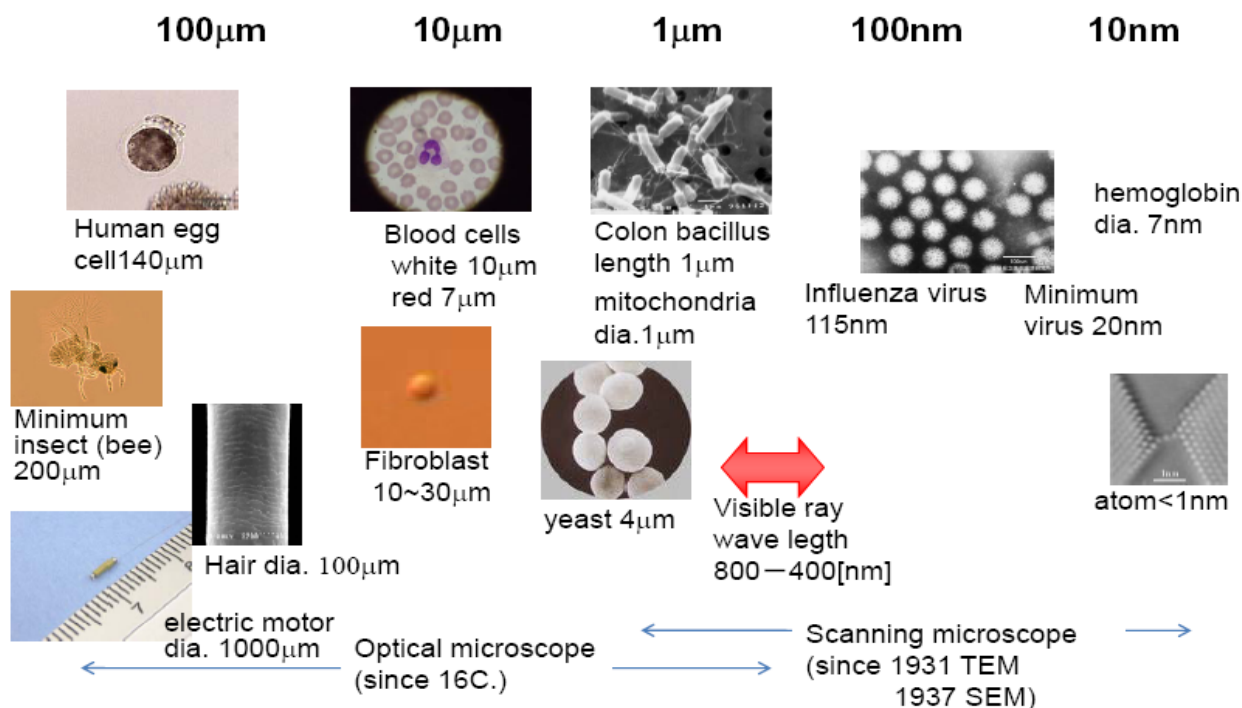
***Fabrication, mechanization,
automation, and
system integration,
targeting 1milli(10^{-3}) – 1nano
(10^{-9}) scale in size and force.
1mm - 1nm
1mN - 1nN(pN)***



16th International Symposium on Artificial Life and Robotics, Oita, JAPAN, January 28, 2011

MICRO NANO ROBOTICS, Tatsuo ARAI, OSAKA University

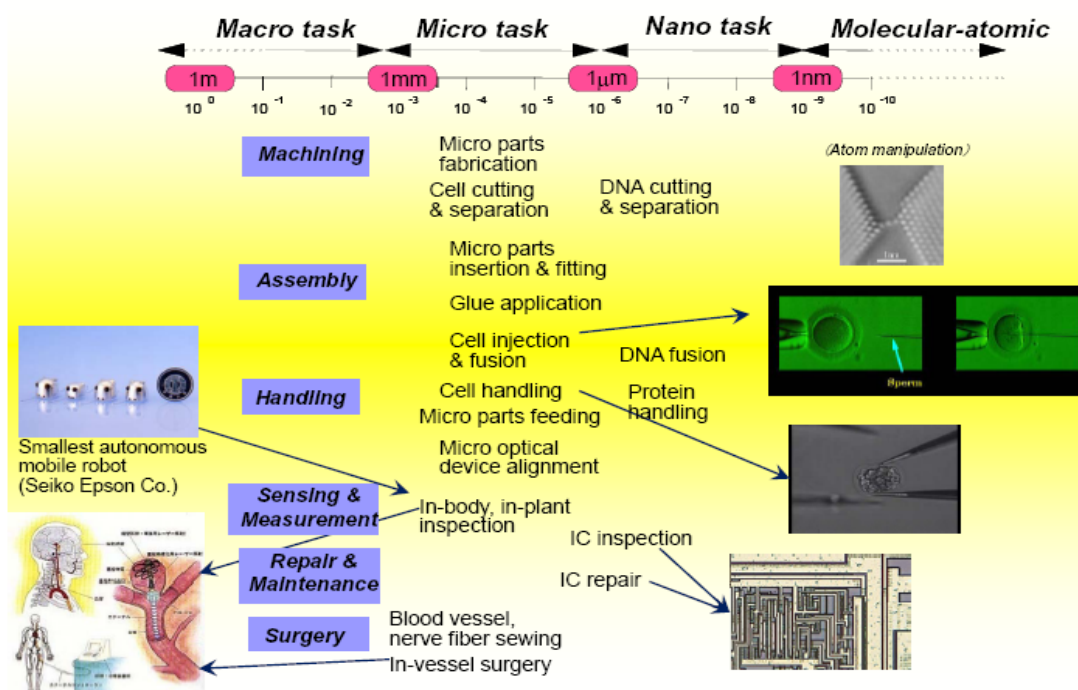
Micro Nano Scales



16th International Symposium on Artificial Life and Robotics, Oita, JAPAN, January 28, 2011

MICRO NANO ROBOTICS, Tatsuo ARAI, OSAKA University

Micro/Nano Tasks



16th International Symposium on Artificial Life and Robotics, Oita, JAPAN, January 28, 2011

Physical property in M/N environment

Scale effect:

- surface/volume comes to larger.
- friction, viscosity, surface force, electrostatic force appear dominantly.

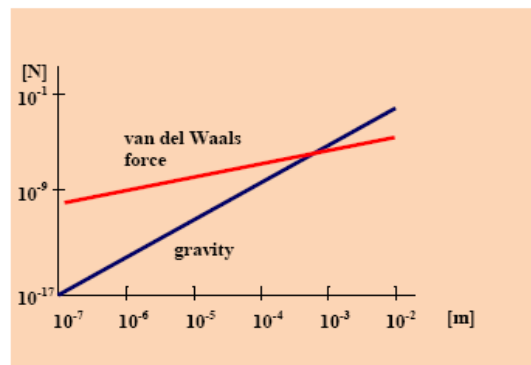
Ex.) $1\mu\text{m}^3$ copper

-gravity: 8.7×10^{-2} pN

-van del Waals force: 2.1×10 pN

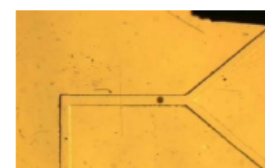
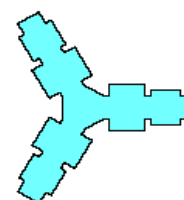
- Higher resonance frequency.
- Smaller heat capacity.
- Smaller Reynolds number.

$$Re = \frac{UL}{(\mu/\rho)} \quad (U : \text{velocity}, L : \text{distance}, \mu : \text{viscosity}, \rho : \text{density})$$



Advantages and disadvantages

- Micro objects will stick to everything.
➔ Manipulation problem.
- Much friction in rubbing motions.
➔ No rotational motion, no revolute joint.
- Inertia has no effect in under-liquid propelling.
- High speed in motion, heat response.
- Low energy consumption.
- Small Reynolds number.
➔ Stable laminar flow in micro channel.



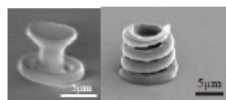
MICRO NANO ROBOTICS, Tatsuo ARAI, OSAKA University

Current micro nano robotics

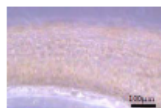
MEMS & Nano-Technology



ECL actuator
(Ritsumeikan Univ)



Micro-stereo-lithography
(Yokohama Univ)

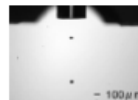


Micro-bio actuator using
cardiomyocyte (TUAT)

Micro-gripper using
photo-sensitive ionic
gel (Yokohama Univ)



M/N Fluid System



Micro-injection using
ink-jet tech (TUAT)



3D MMT cell loader
(Tohoku Univ)

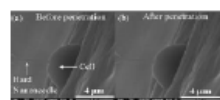


3x3 micro-array
(Ritsumeikan Univ)

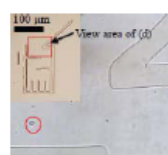


Micro liquid
dispenser (OIT)

M/N Manipulation System



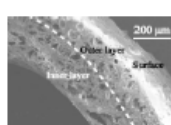
Stiffness measurement of
single cell (Nagoya Univ)



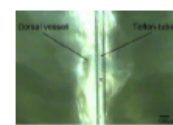
On-chip cell observation &
manipulation (Tohoku Univ)



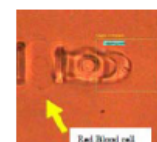
M/NBio System



Multi-layered scaffold
for vascular
regeneration (Nagoya
Univ)



Tube-type
micro-pump
using insect
vessel (TUAT)



Single cell force
detectable optically
driven gripper
(Nagoya Univ)

16th International Symposium on Artificial Life and Robotics, Oita, JAPAN, January 28, 2011

MICRO NANO ROBOTICS, Tatsuo ARAI, OSAKA University

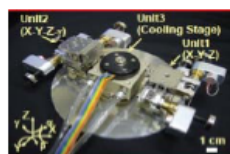
M/N robotics in bio applications

Sensing and manipulations for single cell are current major issues!

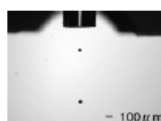
ACTUATION & MECHANISM



Micro manipulation
system (Osaka
Univ)



Nano manipulation
system (Nagoya
Univ)



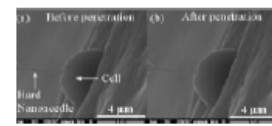
Micro-injection using
ink-jet tech (TUAT)



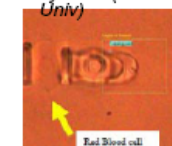
Bio printer (Toyama U)



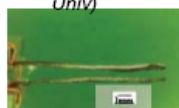
Stiffness measurement of
single cell (Osaka Univ)



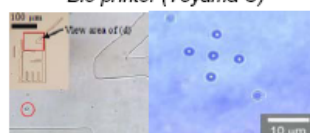
Stiffness measurement of
single cell (Nagoya Univ)



Single cell force
detectable optically
driven gripper
(Nagoya Univ)



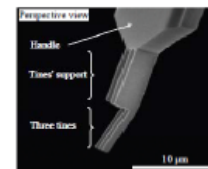
Micro-gripper using
photo-sensitive ionic
gel (Yokohama Univ)



On-chip cell observation &
manipulation (Tohoku Univ)



Force measurement for
cell sheet adhesion
(UAT)



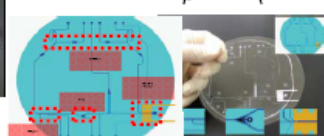
Nano force sensor for
single cell adhesion
(Nagoya Univ)



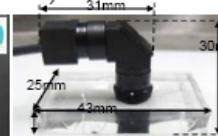
3D MMT cell loader
(Tohoku Univ)



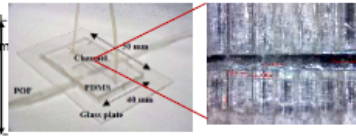
3x3 micro-array
for sorting
(Ritsumeikan
Univ)



Desktop bio plant for
cloning
(BRAIN Consortium05-09)



On-chip microscope
(Osaka Univ)

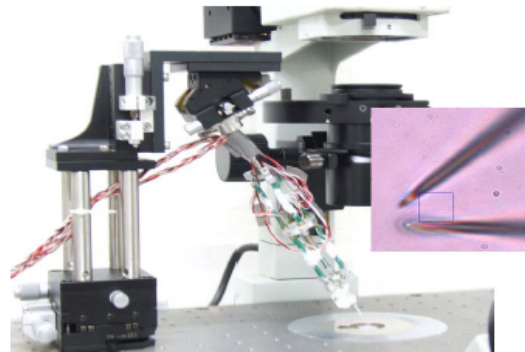


In-micro channel flowing cell
detection sensor (Osaka
Univ.)

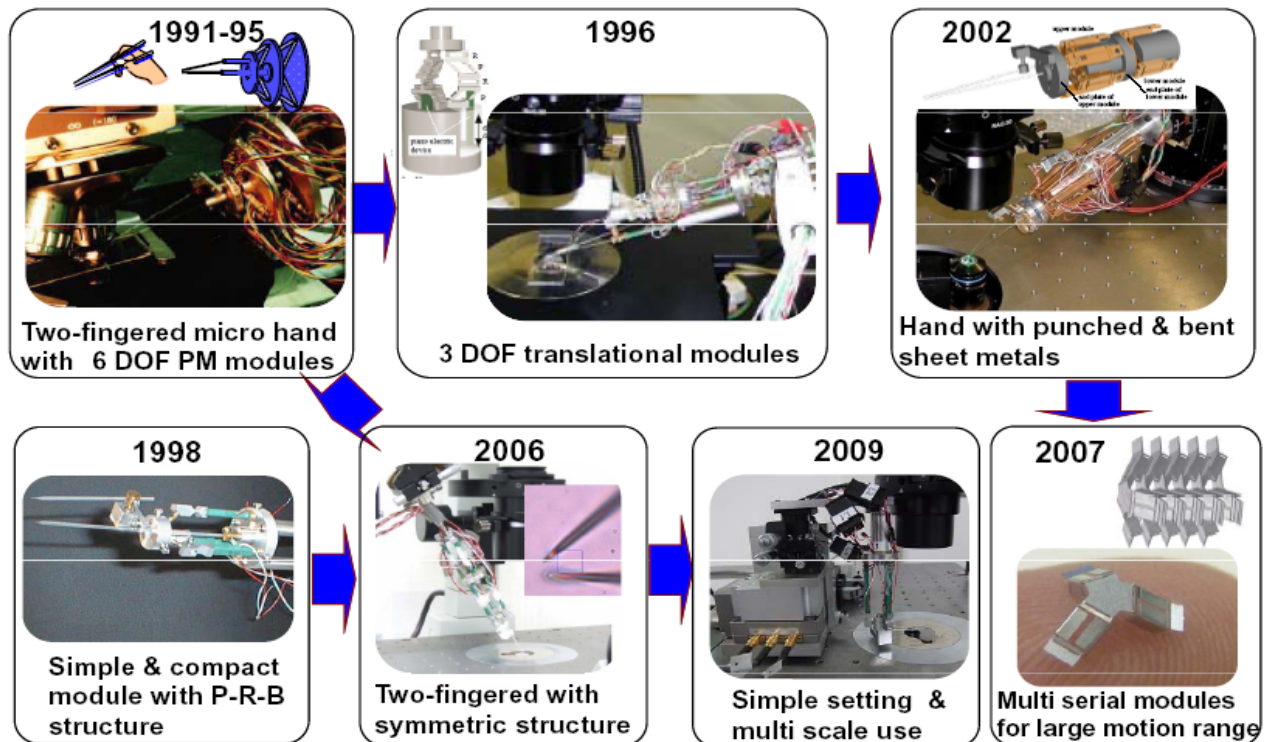
16th International Symposium on Artificial Life and Robotics, Oita, JAPAN, January 28, 2011

Topic 1: Dexterous micro manipulation

1. Motivations
2. Designing and prototyping two-finger hand
3. Sensors and controls
4. Demonstrations



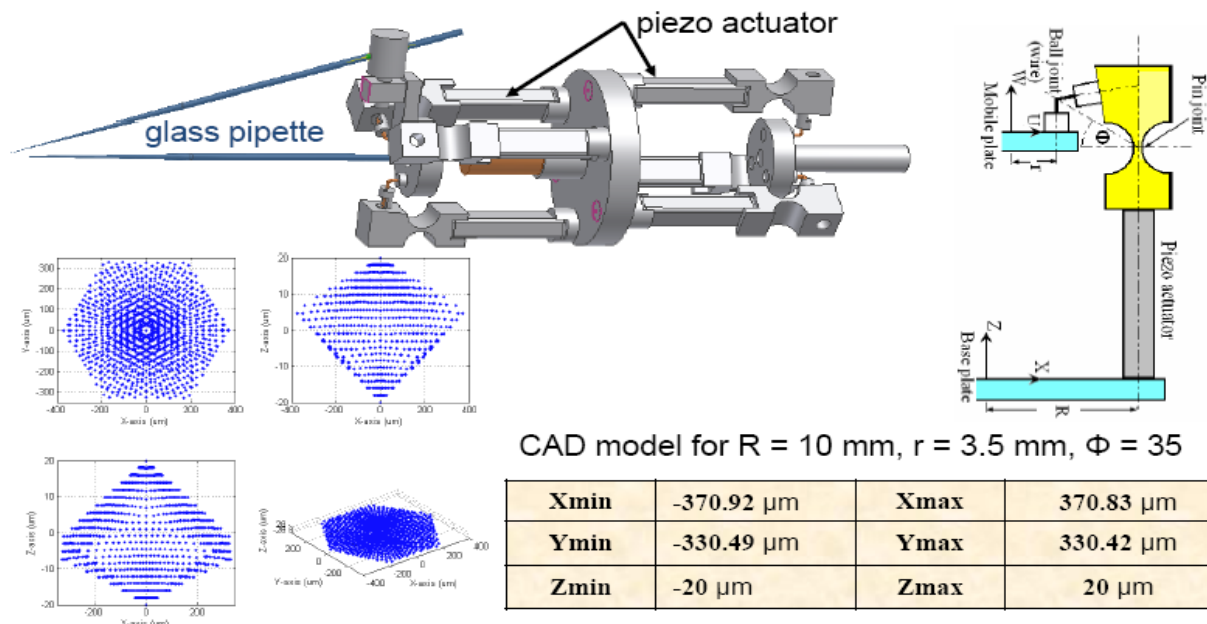
Our micro hand developments in 20 years



MICRO NANO ROBOTICS, Tatsuo ARAI, OSAKA University

2006 Model

Symmetric and straight configurations aiming at compactness and large workspace.

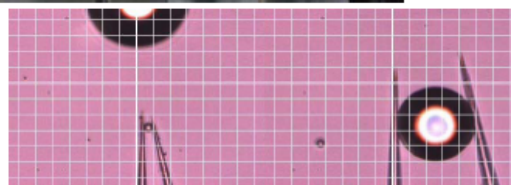
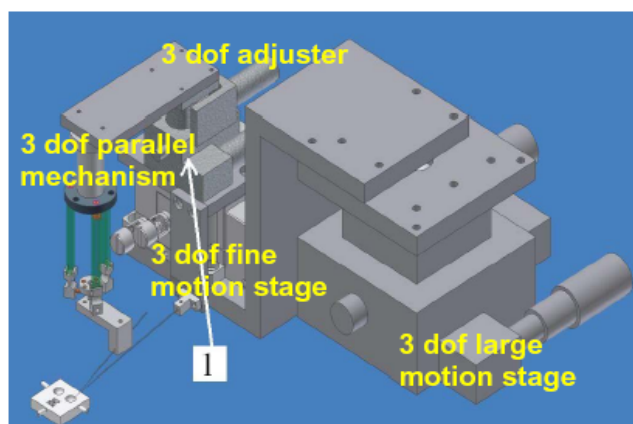


16th International Symposium on Artificial Life and Robotics, Oita, JAPAN, January 28, 2011

MICRO NANO ROBOTICS, Tatsuo ARAI, OSAKA University

2009 Model

Combination of large, fine motion stages, adjuster and parallel mechanism yields multi-scalability and simple set up procedure, and is capable of manipulating 100 μm & 20 μm in the same scene.



10 μm and 100 μm objects can be manipulated in the same scene.

16th International Symposium on Artificial Life and Robotics, Oita, JAPAN, January 28, 2011

Micro manipulation system

Two-fingered micro hand



Sensing devices

- Optical microscope
- All in focus imaging ▶
- AFM cantilever ▶
- Fine force sensor ▶

Other tools & devices

- User interfaces including Omni-Device joystick ▶
- Micro drop dispenser & micro gluing ▶
- 6DOF fine motion stage



Low level control

- Tele-operation ▶
- Force control ▶
- Auto focusing ▶
- All in focusing ▶
- 3D auto tracking ▶
- Auto calibration ▶
- Auto capturing ▶

High level control

- Task understanding
- Skill application
- Task planning

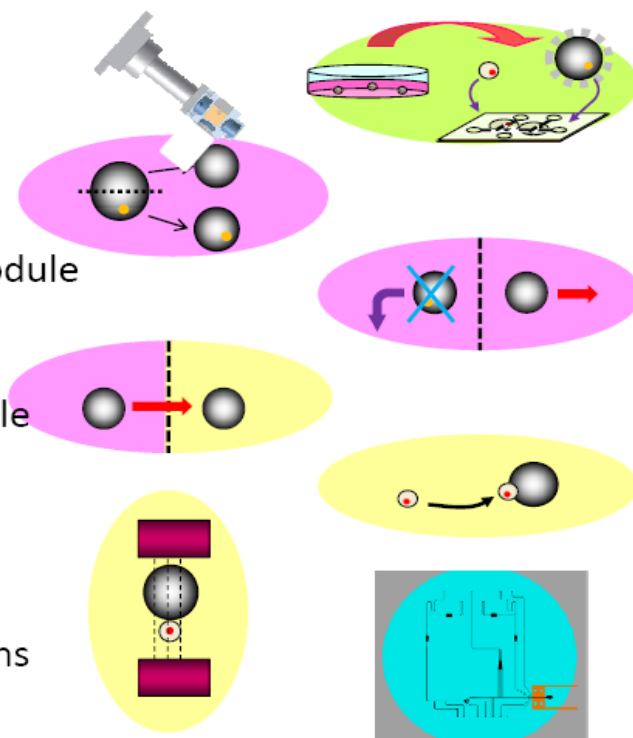
Achieved applications

- Assembling micro structures
- Extracting nucleus in cloning
- Stiffness measurement of yeast & human blood cell

16th International Symposium on Artificial Life and Robotics, Oita, JAPAN, January 28, 2011

Topic2: Automated Cell Manipulation and Cloning

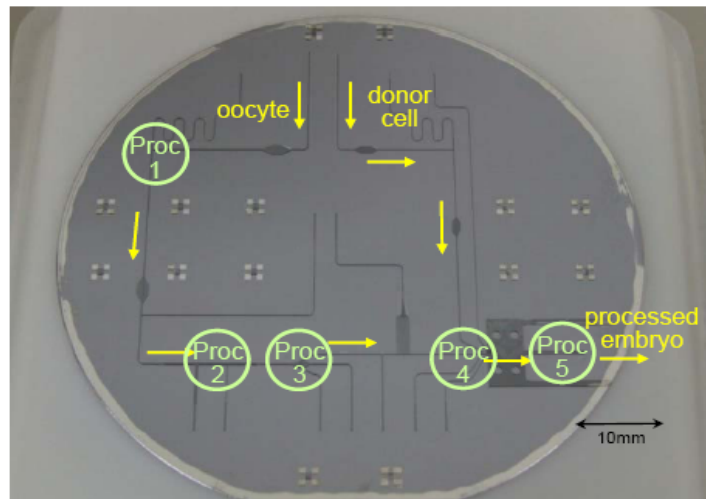
- Background
- Objectives
- Developed devices
 - micro vision sensors
 - cell supply & loading module
 - cutting module
 - separation module
 - solution replacing module
 - coupling module
 - fusion module
- All-in-one chip
- Cultivation & embryological evaluations
- summary



16th International Symposium on Artificial Life and Robotics, Oita, JAPAN, January 28, 2011

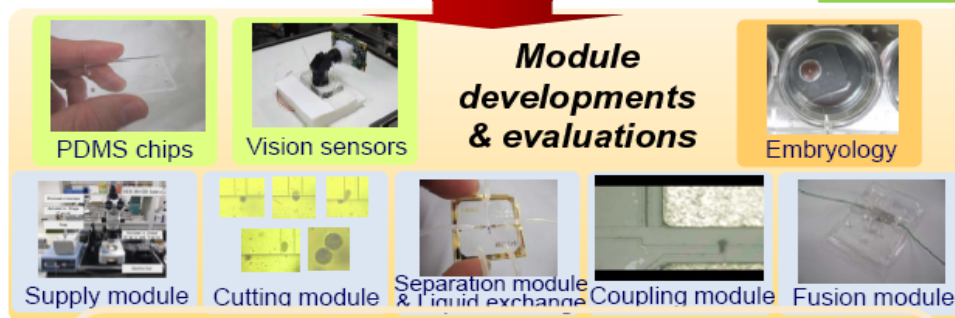
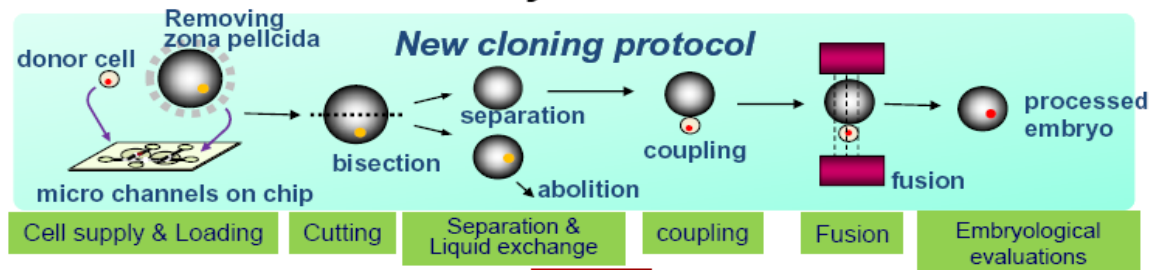
Learning from factory

- Cells may be conveyed in micro channels.
- Every process is achieved in channels.
- Automation may be achieved similarly to factory assembly line system.



Micro channels and process devices are fabricated on PDMS chip.

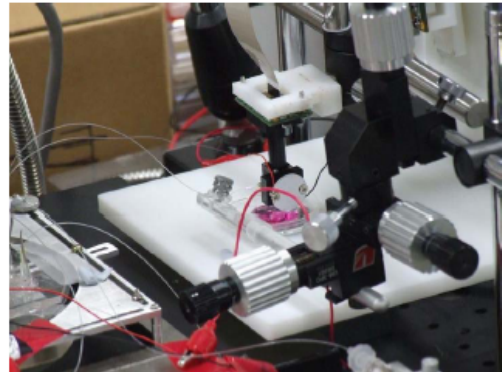
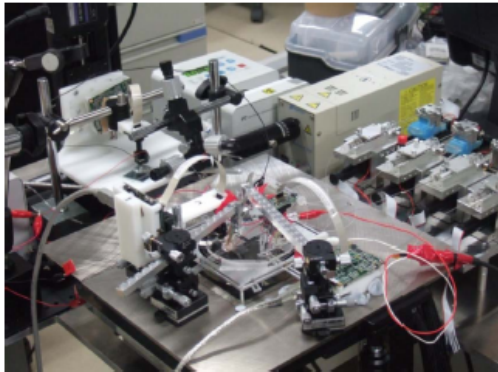
Objectives



Target specification:

- total processing time of 100 cells/3h(tentative).
- total success rate of 30% more.

Desktop bio-plant system for cloning



The system includes fabricated one-chip device, various sensors, pumps. The experiments verifies cloning capability using bovine oocyte and fibroblast.

Quantifying “Waza” in *Nihon-Buyo* Dance Movements

Mamiko Sakata

*Faculty of Culture and Information Science, Doshisha University
1-3 Tatara Miyakodani, Kyotanabe City, 610-0394 Japan
(Tel : 81-774-65-7703; Fax : 81-774-65-7703)
(msakata@mail.doshisha.ac.jp)*

Abstract: Dance is an intangible cultural asset. It is passed on from one person to another through oral instruction, and so are the *waza*, the skills and techniques, involved in dance. Many traditional dances in Japan, however, are ‘endangered species’ due to the shortage of practitioners. We are attempting to create digital archives to record and store the body motions of *buyo* using digital technologies, such as motion capture. We are endeavoring to solve this serious issue of losing an important tradition. In this paper, I would like to present part of our scientific analysis of the *waza* in *Nihon-buyo*, which have been passed down, sometimes in silent, tacit manners.

Keywords: Japanese traditional dance, *Nihon-buyo*, Motion Capture

I. INTRODUCTION

Dance is an intangible cultural asset. It is passed on from one person to another through oral instruction, and so are the *waza*, the skills and techniques, involved in dance. Many traditional dances in Japan, however, are ‘endangered species’ due to the shortage of practitioners. We are attempting to create digital archives to record and store the body motions of *buyo* using digital technologies, such as motion capture. We are endeavoring to solve this serious issue of losing an important tradition. In this paper, I would like to present part of our scientific analysis of the *waza* in *Nihon-buyo*, which have been passed down, sometimes in silent, tacit manners.

The purpose of this research is to examine how the performers of *Nihon-buyo* differentiate the basic motions when performing different dance roles and how their proficiency levels affect the differentiation. We plan to achieve our goal by analyzing their motions and evaluating the impressions generated.

II. THE DESCRIPTION OF THE WORK

This research examines “*Musume-Dojoji*” and “*Tenaraiko*,” both key titles in *Nihon-buyo*. “*Musume-Dojoji*,” which premiered in 1753, portrays an adolescent girl who is in love with a mountain priest. “*Tenaraiko*,” which premiered in 1792, portrays a precocious downtown girl who is on her way back home from a temple school called *Terakoya*. “*Tenaraiko*” is a play that was made about forty years after “*Musume-Dojoji*,” and a passage from this earlier play is used in

“*Tenaraiko*.” The girl in “*Musume-Dojoji*” dances with her heart filled with love, and this same passage is used in “*Tenaraiko*” when the young town girl dances in a precocious manner. The lyrics and the dance motions are the same in both plays. However, while the amorous attention of an adolescent girl has to be portrayed in the former, almost a childlike innocence of a precious girl has to be portrayed in the latter.

III. ABSTRACTION IN MOTIONS

This research examines the aforementioned common portions of the dances from “*Musume-Dojoji*” and “*Tenaraiko*,” namely, the three basic motions of *Nihon-buyo*: *Okuri*, *Osuberi* and *Mitsukubi*.

Okuri is about the motion of walking. Although it is a simple walking motion, the performer in “*Musume-Dojoji*” is required to walk with her toes turned inward and slide on the floor, while her knees and pelvic region are relaxed *Musume-Dojoji*. On the other hand, in “*Tenaraiko*,” the performer is required to walk lightly with short steps while pressing the legs and knees together.

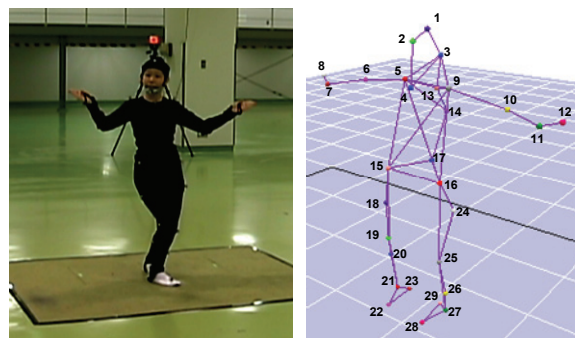


Fig.1. Positions of markers

IV. MOCAP AND THE METHOD

We used an optical motion capture system to measure the body motions from the aforementioned dance. In our research, we placed 29 markers on the dancer's body, and her movements were measured with 10 cameras(See Fig.1.). The acquired data can be observed as a time series of 3 dimensional coordinate values (x, y, z) of each marker in a frame (60 fps).

1. The Experiment: Performers

The performers selected for our motion analysis were three women who have studied *Nihon-buyo*. Their experience varies. Performer A with *Nihon-buyo* training and experience of less than a year, Performer B, 17 years, and Performer C, 15 years. We asked them to dance each play five times. After taking the measurements, we asked the performers what dance strategies they used in their renditions.

2. Feature Values for Body Motion

In order to understand the intensity of the features of each dance motion, its physical features were extracted from the perspective of time, space and dynamics, which are the components of a movement.

Result of Okuri movement analysis

From the simple walking motion of *Okuri*, 16 physical features were obtained: the velocity and the acceleration of the vertex of the head, right shoulder, right elbow, right fist, lower back, right knee and right toes, the angle of the knee and the height of the lower back. We then conducted a principal component analysis using a total of 32 variable quantities, which were the mean values and the standard variations. We extracted 5 principal components with the eigenvalues of 1 or greater, with an accumulated contribution rate of 84.5%. We interpreted PC1 to be the variable quantity showing “the speed of motion,” PC2 “the motion of hand,” PC3 “the strength of the lower body,” PC4 “the strength of the elbow” and PC5 as the “the strength of the feet.”

The PC1 and PC2 scores were plotted on the x-axis and the y-axis respectively, and all trials were plotted on the x-y graph, as in Fig. 2. PC1 is the axis showing the speed of motion. In this Fig., the speed increases as the score shifts toward the right side of the graph and decreases as it shifts toward the left. PC2 is the axis showing the motion of the hand. In the same Figure, the hand is moving more quickly as the score nears the top

of the graph, while the movement is slower when the score approaches the bottom.

Fig. 2 shows that these measurable variables were largely divided into three groups according to each performer. Comparing the performers, it was found that performers B and C, with higher proficiency levels, moved more quickly than performer A, a dance beginner. All performers danced “*Musume-Dojoji*” and

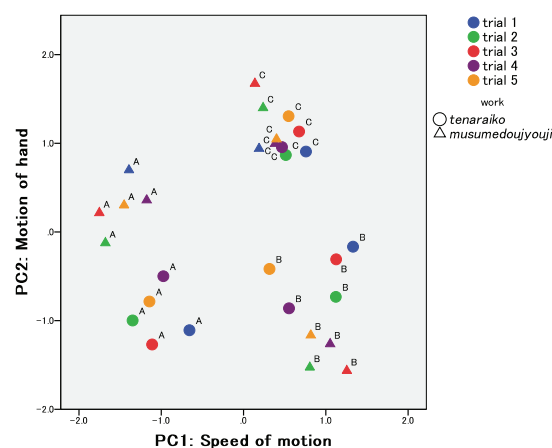


Fig.2. Plot of PCA score of *Okuri*

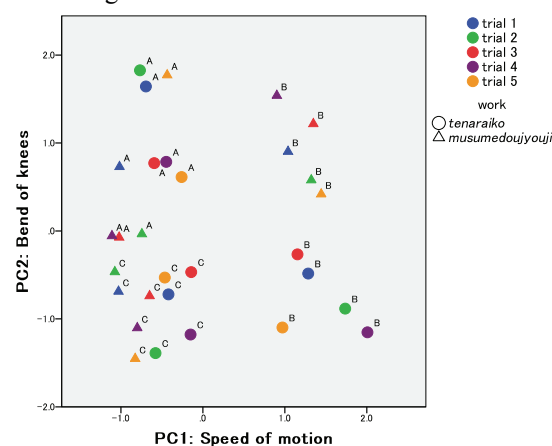


Fig.3. Plot of PCA score of *Osuberi*

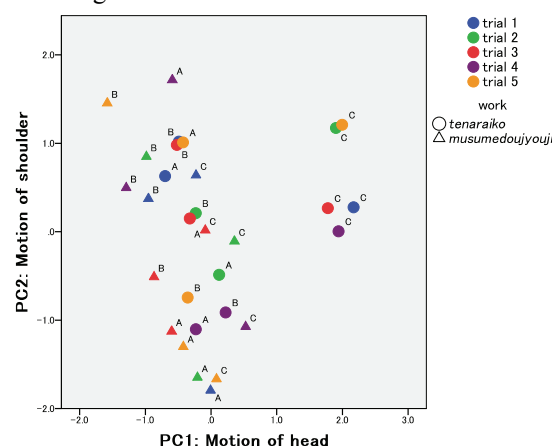


Fig.4. Plot of PCA score of *Mitsukubi*

“*Tenaraiko*” differently; however, the ways they differentiated their dances varied considerably from performer to performer.

Result of *Osuberi* movement analysis

From the soft curvilinear motion of *Osuberi*, we obtained 12 physical features: the velocity and acceleration of the vertex of the head, right shoulder, right elbow, right fist, lower back, right knee and the toes of the right foot, the angle of the right knee and the height of the lower back. Again, we conducted a principal component analysis using a total of 24 variable quantities, which were the mean values and the standard variations. As a result, 5 principal components with eigenvalues of 1 or greater were extracted (the accumulated contribution rate was 85.3%). We named PC1 as “the speed of motion,” PC2 as “the bend of the knees,” PC3 as “the strength of the body’s center,” PC4 as “the strength of the area below the neck” and PC5 as “the strength of the feet.”

We plotted the PC1 and PC2 scores on the x-axis and y-axis respectively; all trials were plotted on the x-y graph. The result is shown in Fig. 3. PC1 is the axis showing the speed of motion. In Fig. 3, the speed increases toward the right side of the graph and it decreases toward the left. PC2 is the axis showing the bend of the knees. In the Fig., the knee is stretched more as it nears the top of the graph, but the knee is more bent towards the bottom, with the lower back in an increasingly lower position.

As Fig. 3 shows, quantitative measurements of the *Osuberi* motion showed similarity with *Okuri*, i.e., the results were divided into three groups according to the performer. It was also found that performers B and C, with higher proficiency levels, differentiated the dances for each play. Performer A, however, was not able to differentiate them quite as well.

Result of *Mitsukubi*

Mitsukubi mainly involves the motions of the head and the shoulders, so we only calculated 4 kinds of physical features, i.e., the speed and the acceleration of the vertex of the head and the shoulders. By conducting a principal component analysis using a total of 8 variable quantities, which were the mean values and the standard variations, 2 principal components with eigenvalues of 1 or greater were extracted, with an accumulated contribution rate of 80.2%. PC1 was named “the motion of the head” and PC2 “the motion of the neck.”

We plotted the PC1 and PC2 scores on the x-axis and y-axis respectively, plotting 35 trials on the x-y graph. This is shown in Fig. 4, and the variables plotted by each performer are shown in Fig. 5. PC1 is the axis showing the motion of the head. In these figures, the head moves more quickly toward the right side of the graph and more slowly when plotted toward the left. PC2 is the axis showing the motion of the shoulders. The figures show that the shoulders move more quickly and strongly when plotted near the top of the graph and more slowly and weakly when plotted near the bottom.

Unlike *Okuri* and *Osuberi*, the quantified variables of *Mitsukubi* did not divide into groups according to the performer. Notably, only the motions of performer C in “*Tenaraiko*” were very different. Regardless of the proficiency level, PC2 (the motion of the shoulder) was not stable, suggesting that the performers paid less attention to their shoulders than to their heads.

V. PSYCHOLOGICAL EXPERIMENTS

In order to examine the type of impression perceived from the body movement of the two plays, we conducted a psychological rating experiment using stick figure animation (see Fig. 1) of the motion capture data. Twenty-four observers (7 men and 17 women) participated in this experiment. The mean and the standard deviation of age among the 24 observers were 21.7 and 0.98 respectively. They had no experience in dance performances of any kind and no particular knowledge about dancing and traditional Japanese culture. The animation was projected on a 50-inch display with no sound. The stick figure animation and muted audio were used to force the viewers to focus on the impression expressed by the body movements alone, discarding other factors such as facial expressions, costumes, music, etc.

After each movement was shown, the viewers were asked to answer the questions on the response sheets. In this rating, we employed the Semantic Differential questionnaire. In the SD questionnaire, 10 image-word pairs were used for rating the movements. We selected 10 word pairs which were thought more suitable for the evaluation of human body motions, based on the list presented by Osgood [2]. The viewers rated the impression of the movement by placing checks in each word pair scale on a sheet.

The rating was done in 5 ranks from 1 to 5. Rank 1 was assigned to the left-side word of each word pair and

5 for the right side. Using this rating, we obtained a numerical value representing an impression for each of the body motions from each subject.

We then conducted a principal component analysis, PCA, based on a correlation matrix, to the mean value of the rating value and obtained the principal component matrix. Two significant principal components were extracted, which were PC1—PC2. We used the word pairs ‘natural – unnatural,’ ‘experienced – inexperienced,’ ‘like – dislike,’ etc., which are often used to represent refinement. Hence, it was interpreted that PC1 was a variable that related to the “refinement” of the motion. Similarly, PC2 was related to the “activity,” as indicated by words such as ‘large motion – small motion,’ ‘adult-like – childlike,’ ‘bright – dark’ and ‘happy – sad.’

We can conclude that the characteristics of the dance motions in “*Musume-Dojoji*” and “*Tenaraiko*” are based on two aspects - “refinement” and “activity.”

Fig. 5 is a plot of the principal component scores of each motion datum. Since the x-axis (PC1) represents the degree of refinement, the performance is more refined toward the right side of the graph and less refined toward the left. The y-axis (PC2) represents activity. There is more activity toward the top of the graph and less activity as the plots near the bottom of the graph.

By looking at each motion, it was found that *Okuri* motions were more active for every performer in “*Tenaraiko*” but more refined in “*Musume-Dojoji*.” Considering that “*Tenaraiko*” is the dance of a child and “*Musume-Dojoji*” the dance of an adolescent girl, the psychological intentions of the performers seem to have been understood well by the audience. As for the *Osuberi* motion, the degrees of “refinement” and “activity” were higher for “*Musume-Dojoji*.” As for the

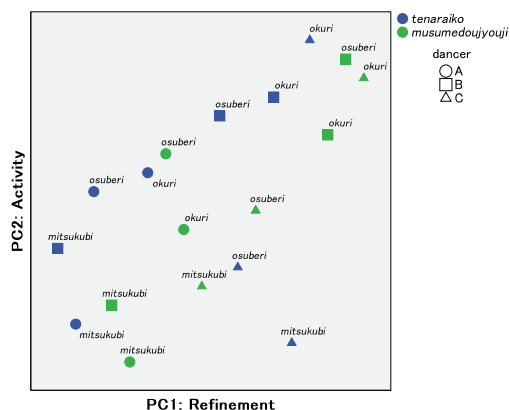


Fig.5. Plot of PCA score of the psychological rating

Mitsukubi motion, the audience received different impressions from different performers.

As a result of the evaluation experiment, it was revealed that even the audience lacking any knowledge of *Nihon-buyo* understood, to some extent, the differences in the roles played in the stories. There was also a tendency for the audience to perceive the “different characters” of the performers rather than the “difference in choreography” of their dances. That is to say, it was revealed that the audience was seeing the motions of each performer, or the difference in personal characteristics, rather than the difference in the dance’s choreography.

VI. FUTURE POSSIBILITIES

We can get information concerning the personality of the subject when we observe his or her body motion. We may get various impressions from body motions. This means that the human body motions convey emotion and personality of the person. Personality might be the involuntary and continuous expression of emotions, which are peculiar to the individual.

The results of this paper could be applied to producing a robot or CG character animation with personalities. Until now, many attempts have been made to add or enhance emotional expression of robots using linguistic communication, some simple body motions, e.g. nodding, and facial expressions. Also, changing the design or shape of robots might be a simple way of providing a robot with personalities. However, we could not find much research on giving robots personalities with body motions.

We think changing the personalities of a robot by changing its own body motions, and changing the expression of the affects of the robot through body motions are very promising areas for further investigation.

REFERENCES

- [1] Hachimura K(2006), Digital Archiving of Dancing, Review of the National Center for Digitization 8: 5
- [2] Osgood, C. E. et al.(1957), The measurement of meaning, U. of Illinois Press

Social playware for mediating tele-play interaction over distance

Henrik Hautop Lund Tumi Thorsteinsson

Center for Playware, Technical University of Denmark, Building 325, 2800 Kgs. Lyngby, Denmark

hhl@playware.dtu.dk

www.playware.dk

Abstract

We suggest that novel playware technology can function as a mediator for playful social interaction over distance, where people are separated by physical distance but feel the presence of each other mediated through the interaction with the playware technology. In order to investigate such social playware, we developed the Playware Soccer game and tested this with more than 1,000 users during the FIFA World Cup 2010 in South Africa. The test was conducted in townships, orphanages for HIV/AIDS children, markets, FIFA fan parks, etc. along with simultaneous tests with similar set-ups in Europe and Asia. With the social playware, players would compete against each other simultaneously in the three continents, Africa, Europe and Asia, and feel the presence of the competitors on the other continents expressed through the playware. The playware game is set up to motivate players to engage in training of technical soccer skills by receiving immediate feedback and offering challenges to players of all skills on the soccer playing on a modular interactive wall composed of modular interactive tiles that respond with coloured light, sound and scores on the players performance. This paper outlines the concept of social playware and physical-virtual teleplay, and exemplifies this with the playware soccer game.

Social Playware

Playware is defined as intelligent hardware and software that creates play and playful experiences for users of all ages [1]. In this paper, we suggest that novel playware technology can function as a mediator for playful social interaction over distance, where people are separated by physical distance but feel the presence of each other mediated through the interaction with the playware technology. Often, human-machine interaction is viewed as a 1-to-1 interaction between an individual human being and the technological artefact, and a lot of research within the fields of human-robot interaction, social intelligent robotics, and human-computer interaction has put focus on the individual relationship and interaction with the technology (e.g. [2, 3]). In many cases, the

creation of playful technology, e.g. robotic toys and interactive playgrounds, has taken its inspiration from such human-machine interaction research. Based on this, the research community has also gained knowledge on how the individual interacts and plays with such playware products (e.g. [4, 5]).

In our point of view, it is important to expand the playware research to focus on the social interaction, so that the starting point for the research and development becomes the *social interaction* mediated by the technology rather than the individual interaction mediated by the technology. We can define social playware as follows: *social playware is playware which aims at creating playful social interaction between several users.*

Such playful social interaction can, for instance, be play between children in a kindergarten mediated by an interactive playground, multiplayer games with a physical game platform like Nintendo Wii, and interaction of a team of elderly performing games for health e.g. with Dance Dance Revolution, i.e. in all cases a free activity that the users engage in for the pleasure of play and social interaction in itself. Hence, this is in accordance with the definition of play, which can be defined as "*Play is actions which we undertake and participate in with the purpose to create a reality-sphere within which we are free and independently can create and regulate moods (physical and mental states of tension) which provides us with specific, wanted experiences (of delight), socially and individually*" [6]. The definition underlines that play is submitted to free will, and that human beings play because we want to play. At the same time it underlines that we, in the act of playing, manage our lives at our own choice, as we create the special form of lived life outside the "regular" life where (lust for) life and happiness as the essence of play rules. By building on this play definition, the definition of social playware simply focuses on the human desire to engage in social interactions and to live as a social being. It can therefore also be argued that social playware is included by playware. Indeed, we view social playware as a sub-discipline of playware, which however allow the research community to direct focus on the social interaction mediated by playware, and thereby provide

further understanding on how to create social interactions that are playful and which the users engage in for the pleasure of the social interaction.

We will exemplify the social playware in this work with physical-virtual *teleplay*, which allow users to engage in social interaction over distance mediated by the playware technology. In such a case, we can view the playware technology to mediate a playful tele-presence between people interacting with each their playware tool through which they sense the presence of the other people (in essence, presence removes the impression of mediation from a mediated experience). Examples of teleplay and social playware are seen in the form of massively multiplayer online games (MMOG), which are multiplayer video games which are capable of supporting hundreds or thousands of players playing together simultaneously over the Internet. However, such games do not allow for extensive physical and natural interactions (other than e.g. pressing keyboard and speaking). Some physical interaction is promoted with some multiplayer online games, e.g. in the Japanese and Korean arcade halls, in the form of interaction with game cards (e.g. soccer cards). For a more natural and physical interaction, tele-presence has been studied intensively e.g. by Ishiguro with the studies of humanlike presence using tele-operated androids [7, 8]. Such studies have promoted a humanlike technology to study presence, and some large videoconferencing set-ups have allowed for a soccer teleplay [9]. We, on the other hand, have made a first step with a much simpler, yet playful technology for mediating social interaction (in the line of the simple, yet effective FeelLight technology for mediating social interaction by Suzuki and Hashimoto [10]). Hence, we will study tele-presence without a large and bulky infrastructure, and without any anthropomorphic expression, but a simple expression of simple light patterns, sound, and score. In the specific example, we made social playware connecting players in Asia, Africa, and Europe in a soccer game on a playware technology in the form of modular interactive tiles.

Playware Soccer

During the FIFA World Cup 2010, we ran a RoboSoccer World Cup in Asia, Europe and Africa, amongst other places in townships, orphanages for HIV/AIDS children, markets, etc. in South Africa. As an example of playware, the game is set up to motivate players to engage in training of technical soccer skills by receiving immediate feedback and challenge players at different levels on the soccer playing on a modular interactive wall composed of modular interactive tiles that respond with coloured light, sound and scores on the players

performance. The soccer game was developed together with professional soccer players Laudrup and Høgh for promoting playful soccer skills. For the test conducted during the World Cup tournament, the soccer wall was composed of 3*4 modular interactive tiles. It is a distributed system as each tiles has its own processor, battery and communication to neighbouring tiles. The distributed nature of the system aimed at allowing the system to be easily set up and taken down within minutes anywhere and by anyone. Indeed, the flexibility obtained with a modular and distributed processing system should provide the opportunity to bring the new playware technology out to any township, market, and village in Africa and on other continents since there was no demand for any physical infrastructure whatsoever.

Often, other technological systems for physical interaction are characterised by being based on a centralised processing system making the systems fixed sized (and sometimes large and bulky), and/or they are characterised by the demand for some kind of infrastructure, e.g. electricity, access to screen/projector, or similar. Examples include Lightspace, Makoto, Sportswall and even DanceDance Revolution with more participants, which needs to have a centralised control station. This makes it somewhat difficult to apply the traditional technology for any user anywhere, since in many places of the World, the necessary infrastructure is not readily available to allow such technology to be applied. This is, for instance, the case many places in Africa, and even in a comparably developed country like South Africa, where the FIFA World Cup 2010 was held, there are townships with no electricity (Fig. 1).



Fig. 1. Playware soccer in the township Atteridgeville, South Africa, during FIFA World Cup 2010.

If, on the other hand, we take as point of departure for our technology design that no infrastructure is available, it will lead to technology that is free from infrastructure demands and which thereby possibly can be applied and used anywhere. It gives the possibility to bring technology to anybody anywhere, and thereby help in

contextualising both technology development and education in developing countries. The advantages of such technology outcome may not be limited to the developing part of the World, but the freedom from infrastructure requirements may also have important impact on the distribution and use of technological solutions in the developed part of the World (e.g. for home care in the private homes of elderly). Even in a private garden or a football training field in the developed World, the necessary infrastructure such as electricity outlets or computer monitors may not necessarily be available. Therefore, it is interesting to research the flexibility of the modular playware for allowing the technology to be set up and used anywhere within minutes.

Hence, the playware soccer game was developed with the modular interactive tiles system [11], which is an example of modular playware [12]. The system is composed of a number of modular interactive tiles which can attach to each other to form the overall system. Each modular interactive tile has a quadratic shape measuring 300mm*300mm*33mm. It includes an ATmega 1280 as the main processor in each tile, and each tile can communicate with infra-red (IR) to its four neighbouring tiles. Each side of a tile is made as a jigsaw puzzle pattern (see Fig. 2) to provide opportunities for the tiles to attach to each other. A force sensitive resistor (FSR) is mounted as a sensor on the center of a raised platform underneath the cover. This allows analogue measurement on the force exerted on the top of the cover.

On the PCB, a 2 axis accelerometer (5G) is mounted, e.g. to detect horizontal or vertical placement of the tile. Eight RGB light emitting diodes (LED SMD 1206) are mounted with equal spacing in between each other on a circle on the PCB, so they can light up underneath the transparent satinice circle.



Fig. 2. Assembly of the modular interactive tiles as a jigsaw puzzle.

The modular interactive tiles are individually battery powered and rechargeable. There is a Li-Io polymer battery (rechargeable battery) on top of the PCB. A fully charged modular interactive tile can run continuously for

approximately 30 hours and takes 3 hours to recharge. On the PCB, there are connectors to mount an XBee radio communication chip. Hence, there are two types of tiles, those with a radio communication chip (master tiles) and those without (slave tiles). The master tile may communicate with a game selector box (game card reader) and initiates the games on the built platform. Every platform has to have at least one master tile if communication is needed e.g. to game selector box or a PC.

With this specification, a system composed of modular interactive tiles is a fully distributed system, where each tile contains processing (ATmega 1280), own energy source (Li-Io polymer battery), sensors (FSR sensor and 2-axis accelerometer), effectors (8 colour LEDs), and communication (IR transceivers, and possibly XBee radio chip). In this respect, each tile is self-contained and can run autonomously. The overall behavior of the system composed of such individual tiles is however a result of the assembly and coordination of all the tiles.

Connectivity

In order to develop teleplay for social interaction it is important that the physical interactive platforms can communicate with each other, locally and globally, so that the social interaction can be mediated through the playware.

Local connection

For creating local communication between physically separated groups of modular interactive tiles, and between a group of tiles and a PC, we used the XBee with the ZigBee radio communication protocol. In each group of tiles, there is one tile (master tile) with the XBee radio communication chip. This tile can collect and send information. The information can thereby be communicated between two "islands" of tiles, i.e. between the master in one island and the master in another island. For communication to and from a host computer, we designed an XBee USB dongle to be connected to the host computer, which then can communicate with the master tile using the same protocol.

Global connection

With the local communication allowing easy communication between tiles and a host computer, e.g. a laptop/netbook, we were able to relay the global communication over laptops connected to the internet, e.g. laptops with 3G wireless connection, so that the teleplay could happen on platforms that communicate to each other over the Internet. A Java program was

designed to run on the laptop, which was connected to the tiles with the XBee. The Java program kept track of the hits on the tiles, played feedback sounds, showed the time and score of the game at run-time, and kept the total score of each game. At the end of each game, the program sent information to a web-site that saved it together with a username, password and location on a highscore list which was updated immediately. The highscore list updates would be visible on internet connected computers at different locations, anywhere globally, at run time.

With the design of both local and global connectivity, it is possible to create both local and global physical interactive games. The local connectivity was used to create feedback from a local host computer in the form of time and score displayed on a monitor, and sound from a loudspeaker connected to the host computer. The global connectivity was used to allow feedback in the form of run-time score updates in competition between users playing the same physically interactive game in different parts of the World, i.e. allowing for social interaction over distance.

Soccer Game

The game content was crucial to ensure training of soccer skills in a playful manner, so we collaborated with professional soccer players Laudrup and Høgh, in order to create an appropriate game utilizing just 3*4 tiles. In the soccer game, a specific number of tiles light up in different colours. Each of them counts down with their eight LEDs. The player has to hit the tile before the LEDs are all turned off, and gets points for how many LEDs are turned on at hit time, and points are multiplied by a factor for how high the tile is positioned (row 1, 2, or 3). Also, at random time, one of the tiles will have its LEDs making a fast spinning pattern, indicating that if the tile is hit, a bonus round will be initiated, during which the player can gain extra points when hitting the tiles that are lit up.

Preliminary testing with a number of adult players showed that the soccer game could be set to an appropriate difficulty level that was both easy enough to play for all the test persons and difficulty enough that all would be challenged to obtain higher score. This difficulty level was set experimentally by investigating the time needed for people to kick the ball and hit a tile, so as to set the LED countdown time to an appropriate level (the time used from all 8 LEDs were turned on, until all LEDs were turned off, and the light would jump to another tile).

Layered Multi-Modal Feedback

For increasing the motivation to play the game, we designed a multi-modal immediate feedback, so that the player would not only receive immediate feedback directly from the tiles in terms of the changing coloured light, but we also added sound feedback and graphical feedback in terms of time and score via a host computer, to enhance the system as social playware. When a player would hit a lit tile, the light would turn off on that tile and jump to another tile, a sound would be played from a loudspeaker, and the increase in score would be shown on a monitor. And when the game ended, the position on the high score list would be shown on a monitor.

It is noteworthy, that the game design was made so that the game can run as an interesting game even without these additional feedback modalities. Both the additional immediate (sound, score, time) and delayed (local highscore list and global highscore list) feedback modalities can be added as layers on top of the basic game that runs on the modular interactive tiles only (see Fig. 3). Hence, with this layered design of feedback modalities, it is possible to (i) run the game as a simple game with only the lowest level of feedback (coloured light) on the modular interactive tiles, (ii) run it with higher levels of feedback (sound, score, time) by adding a laptop PC, or (iii) run it also with the highest level of feedback (global highscore list) by adding an internet connection. This third option (iii) was used for the teleplay experiments to create the soccer game as a social playware.

Layer	Platform	Type
5	Internet	Global highscore list
4	PC monitor	Local highscore list
3	PC monitor	Time & Score
2	PC loudspeaker	Sound
1	Tiles	Light

Fig. 3. The layered multi-modal feedback design for the playware soccer game.

The layered structure in designing feedback modalities may resemble the layered design in much behavior-based robotic engineering [13]. For instance, the original subsumption architecture by R. Brooks [14] defines that behaviors can be designed to run in parallel on top of each other, starting from the design of the simplest behaviors. Once the simplest behavior is designed, implemented and debugged, this behavior can run by itself, and a behavior can be designed, implemented and debugged to run in parallel on top of the simple behavior. So forth continues the design with layers of behavior on

top of the previous ones that all run in parallel, and the lower levels continue to function as originally designed. The design of multi-modal feedback, which we propose here, works with the same principle. First, a simple feedback is designed which can run by itself, and then new layers of feedback can be added on top to run in parallel. In the present case of the soccer game, the simplest feedback is designed to be the change of light on the modular interactive tiles when a tile is hit. Once this feedback modality was designed, implemented and debugged, on top of this, we designed, implemented and debugged the sound modality, which would run in parallel with the light feedback. Then, on top of this, we designed, implemented and debugged the time and score feedback from a monitor. On top of this, we added the local highscore list feedback. And on top of this, we designed, implemented and debugged the global highscore list.

As with the original subsumption architecture where different behavior modules can run on different time scales, also with this layered multi-modal feedback design, the different layers may run on different time scales, with the lower levels executing with the fastest feedback time cycle and the highest levels the slowest feedback time cycle. The lower level behaviors / feedback modalities need to give a very fast response for the system to work, whereas the higher level behaviors / feedback modalities can give response once in a while.

The advantage of this layered multi-modal feedback design is that it is possible to create simple layers of feedback, that can run by themselves and work at their own right, and then add new layers to run in parallel on top of the previously designed layers, and when the user is executing the system, it is possible to add/remove layers (feedback modalities) from the top. Essentially, this can even be done at run-time, adding and removing new feedback modalities, since the lower levels will keep running and working whatever is added on top of them. This gives a high flexibility of the system for both the designer and the user of the system.

Tests

In order to explore social playware and the potential of such social playware mediating social interaction, we needed to test broad ranges of cultural differences in users and environments. Therefore, we tested the system simultaneously in Denmark (Europe), South Africa (Africa), and Japan (Asia) during the FIFA World Cup 2010. For instance, in Asia the system was tested in highly metropolitan areas, such as in Shibuya, Tokyo, whereas in South Africa we tested in a variety of places, including an orphanage, numerous townships, a public

market, a village, an official FIFA Fan Park, a science discovery centre, a university, a fan bar, a public park in Soweto, etc. This variety of places was selected in order to ensure the broadest possible test in terms of variation on the environment, the social status, the age group, the educational level, the technology interest, and the soccer interest of the users. Indeed, users were from 3 years old to 80 years old (see Fig. 4), they were from orphanages with children from families with HIV/AIDS to adult soccer fans from high income areas, and they were ranging from people with no education to people with university degree.

The system was designed for flexibility with the modular interactive tiles and the layered multi-modal feedback design, which together aimed at creating a system that could be set up and used by anybody anywhere within minutes. The modular interactive tiles can be viewed to provide hardware building blocks, and the layered multi-modal feedback design to provide feedback building blocks, and simple construction with these building blocks should give a high degree of flexibility for the designer and the user to create various set-ups and interaction possibilities in an easy manner.



Fig. 4. An older man playing the playware soccer at a taxi rank in Randburg, South Africa.

In total, the system was tested with more than 1,000 users during the FIFA World Cup 2010. The distributed nature of the system (each tile with its own processor, battery and communication to neighbouring tiles) allowed the system to be easily set up and taken down. Indeed, the flexibility obtained with a modular and distributed processing system gave the opportunity to bring the new playware technology out to any township, market, and village in Africa since there was no demand for any physical infrastructure whatsoever. It proved possible to set up the system in a very fast manner on the grounds in townships such as Soweto and Atteridgeville, in public parks in Soweto, markets and bus station in Randburg, and in remote villages such as Phokeng. At some places, the system was run with only part of the layered multi-

modal feedback, and in other places it was run with all layers active. The layered multi-modal feedback allowed a set-up with e.g. just layer 1 or just layer 1-4 in some places, and in other places to run the full system with layer 1-5 (including global high score list via internet connection, see Fig. 5). Therefore the system proved flexible to make fit to the time available, the local use and the aim of the game at a particular place with a particular set of users.

Rank	Name	Game	Event	Country	Points	Time	Date
1	H125	Street Soccer	FMSouthAfrica	SOUTH AFRICA	512	00	23/02/10
2	A151	Street Soccer	Cup Olimpia	SOUTH AFRICA	454	00	19/02/10
3	A157	Street Soccer	Cup Olimpia	AFRICA	416	00	19/02/10
4	Denny	Street Soccer	Japan South Africa	SOUTH AFRICA	404	00	26/02/10
5	K154	Street Soccer	Japan South Africa	JAPAN	364	00	26/02/10
6	H118	Street Soccer	FMSouthAfrica	SOUTH AFRICA	348	00	23/02/10
7	H110	Street Soccer	FMSouthAfrica	SOUTH AFRICA	348	00	23/02/10
8	H206	Street Soccer	FMSouthAfrica	SOUTH AFRICA	328	00	23/02/10
9	A166	Street Soccer	Cup Olimpia	SOUTH AFRICA	326	00	19/02/10
10	T115	Street Soccer	Cup Olimpia	GERMANY	321	00	19/02/10

Fig. 5. The global highscore list on the internet (www.playwaresoccer.com).

When running the system with all five layers and in different locations at the same time, the system became a social playware which mediated social interaction over distance. Most often, social interaction would happen around the single set-up e.g. in a township or a market with lots of people gathering around the playware soccer set-up cheering, helping, and interacting socially around the playware and the individual player (e.g. see Fig. 1). So it was evident from the test observations that even with the playware soccer set-up utilizing only the lower layers of feedback modality, it became a social playware. However, this was reinforced to a large degree when the game was set up with all five layers and run in parallel at different locations, e.g. simultaneously in the small village of Phokeng in South Africa and in Shibuya in the center of Tokyo in Japan. In such cases, the players were observed to engage in a competition over distance: in one location (on one continent) they would see the scores of players in the other location (on another continent) playing with the playware soccer. The players would experience the high score list change minute after minute depending on the score at their own location and the score at the other location (visualized and continuously updated on the monitor next to the playware soccer set-up). In all cases, players engaged immediately in trying to get higher scores than in the other location, and cheering and shouts related to the scores of the remote location on the other continent allowed us to

observe the emotional engagement and social bonding both locally around the game, player and audience, and also between the remote competitors who were invisible and unknown to each other.

Discussion and Conclusion

As a test of social playware, during the FIFA World Cup 2010, we ran a RoboSoccer World Cup in Asia, Europe and Africa, most notably in townships, orphanages for HIV/AIDS children, markets, etc. in South Africa. We linked the events together with a novel kind of physical-virtual live competition, which can be termed teleplay, and which as a social playware mediated social interaction. The teleplay took place between people in these African environments and metropolitan fans in larger cities in the developed World, e.g. in Tokyo, thereby trying to create a social bond and feeling between the fans world-wide during the World Cup through the physical-virtual teleplay. The social bonding was mediated through the physical football game between players on different continents who at the same time, through the teleplay with social playware, can compete directly and physically between the continents.

The flexibility of the modular interactive tiles and the layered multi-modal feedback design, allowed the creation of a system that could be set up and used by anybody anywhere within minutes, and it was therefore possible to test the system with more than 1,000 users during the FIFA World Cup 2010. Videos of some tests are available at: www.playwaresoccer.com

In general, the advantages of the proposed modular, social playware can be summarized to a flexible set-up, independence on context, runtime feedback, competition as a motivation factor, framing of the game (World Cup soccer where one country wants to beat another country), audience friendly game through sounds and score which can be followed by the audience, and where the audience can take on roles and feel as a part of the game (cheering, collect balls, make indications on bonus rounds, etc.). Hence, the layered multi-modal feedback in the playware set-up can mediate both local social interaction and global social interaction. The disadvantages of the set-up as proposed here are that this is not in-game presence (the tele-presence is not immediate but delayed), it is a single-player game, physical differences may mean that players are not competing on equal footing (e.g. the physical status of the opponent on the other continent is unknown to the player). Another disadvantage of the presented study is that we only have “event-based” observations and no long-term observations. We will elaborate further on these issues and on social playware in general in future work.

Acknowledgement

The work was performed with the help of colleagues at the Center for Playware, Technical University of Denmark and Danish School of Education (AU). Baldur Bjarnason, Niels Sandmann, Jacob Nielsen, Steffen Andersen and Bjarke Pedersen made highly valuable contributions to the development and Stine Ejsing-Duun to the concept discussions. Also thanks to local organizers including A. Smith, Meraka Institute, B. Windram, Junior Engineers for Africa, Royal Danish Embassy in Tokyo, Brian Laudrup, Lars Høgh.

References

- [1] H. H. Lund, T. Klitbo, and C. Jessen. Playware Technology for Physically Activating Play, *Artificial Life and Robotics Journal*, 9:4, 165-174, 2005
- [2] C. Breazeal. Designing Sociable Robots. MIT Press, Cambridge MA, 2002.
- [3] T. Fong, I. Nourbakhsh, and K. Dautenhahn, "A survey of socially interactive robots," *Robotics and Autonomous Systems*, vol. 42, no. 3-4, pp. 143-166, 2003.
- [4] A. Billard. "Robota: clever toy and educational tool." *Robotics and Autonomous Systems* 42: 259-269, 2003.
- [5] M. Resnick, F. Martin, R. Berg, R. Borovoy, V. Colella, K. Kramer, B. Silverman "Digital manipulatives: new toys to think with." In: *Proceedings of the CHI'98 conference on human factors in computing systems*, Los Angeles, California, April 1998, pp 281-287
- [6] C. Jessen, and H. H. Lund "On play forces, play dynamics and playware". Unpublished manuscript.
- [7] H. Ishiguro "Android science: Conscious and subconscious recognition," *Connect. Sci.*, vol. 18, no. 4, pp. 319-332, 2006.
- [8] D. Sakamoto, T. Kanda, T. Ono, H. Ishiguro, and N. Hagita, "Android as a telecommunication medium with human like presence," in *Proc.2nd ACM/IEEE Int. Conf. Human-Robot Interact.*, 2007.
- [9] F. Mueller, A. Agamanolis, R. Picard "Exertion Interfaces: Sports over a Distance for Social Bonding and Fun", In *Proceedings of CHI 2003*, ACM, 5:1, 561-568, 2003.
- [10] K. Suzuki and S. Hashimoto. "FeelLight: A Communication Device for Distant Nonverbal Exchange", *Proceedings of ETP'04*, New York, USA, ACM, 2004.
- [11] H. H. Lund. "Modular Robotics for Playful Physiotherapy," in *Proceedings of IEEE International Conference on Rehabilitation Robotics*, IEEE Press, 2009, 571-575.
- [12] H. H. Lund, and P. Marti. "Designing Modular Robotic Playware." In *18th IEEE International Symposium on Robot and Human Interactive Communication (Ro-Man 2009)*, IEEE Press, 2009, 115-121.
- [13] R. C. Arkin. *Behavior Based Robotics*, MIT Press, Cambridge MA, 1998.
- [14] R. A. Brooks. "A robust layered control system for a mobile robot." *IEEE Journal of Robotics and Automation*, 2(1), 1986, 14-23.

An Educational Tool for Interactive Parallel and Distributed Processing

Luigi Pagliarini^{1,2} Henrik Hautop Lund¹

¹ Centre for Playware, Technical University of Denmark, 2800 Kgs. Lyngby, Denmark

² Academy of Fine Arts of Bari, Via Gobetti, 8. 70125 Bari, Italy

luigi@artificialia.com hhl@playware.dtu.dk
www.playware.dk

Abstract

In this paper we try to describe how the Modular Interactive Tiles System (MITS) can be a valuable tool for introducing students to interactive parallel and distributed processing programming. This is done by providing an educational hands-on tool that allows a change of representation of the abstract problems related to designing interactive parallel and distributed systems. Indeed, MITS seems to bring a series of goals into the education, such as parallel programming, distributedness, communication protocols, master dependency, software behavioral models, adaptive interactivity, feedback, connectivity, topology, island modeling, user and multi-user interaction, which can hardly be found in other tools. Finally, we introduce the system of modular interactive tiles as a tool for easy, fast, and flexible hands-on exploration of these issues, and through examples show how to implement interactive parallel and distributed processing with different software behavioural models such as open loop, randomness based, rule based, user interaction based, AI and ALife based software.

Introduction

Parallel and distributed processing has been an important subject within computer science and artificial intelligence for decades, and is one of the major focus points in most computer science curricula and theoretical educational textbooks. It is normally viewed as an important subject to teach computer science and engineering students, since numerous applications and systems are based on the principle of parallel and distributed processing, including the Internet, cloud computing, parallel computers, multi-agent systems, swarm intelligence, etc. There are numerous important issues related to parallel and distributed processing that a student has to learn about. Within *algorithmics*, it is important to learn to what extend parallelism can improve efficiency and what kind of algorithms can exploit parallelism. This leads, for instance, to a demand for knowing about hierarchical and functional decomposition of problems. An educational

tool for this kind of algorithmics learning should allow students to learn about when to utilise shared variables (e.g. in the master) and distributed variables, when to use a scheduler (in the master), how to use semaphores for critical sections, and for instance allow students to confront the mutual exclusive problem [1]. Also, general computer science learning about *operating systems* demands learning about distributed systems, and the issues related to topology, communication, event based control, prevention of deadlocks, data transfer, etc. (e.g. [2]). Obviously, learning about *artificial intelligence* also demands learning about distributed systems for learning about artificial neural networks, evolutionary computation, multi-agent systems, swarm intelligence, etc., including also learning of *artificial life* and *robotics* (e.g. multi-robot systems).

A number of these computer science themes can appear quite abstract to the engineering and computer science student. There is clearly a need to have an educational tool that allows the students to confront these themes in a very concrete manner. We suggest that the best way to learn about these abstract issues is through direct *hands-on problem solving*, following the pedagogical principles of Piaget [3] known as constructionism [4, 5, 6] and guided constructionism in the computer science literature [7]. We combine this with an approach of trying to contextualise IT training for students by allowing them to work with building blocks [8]. Numerous experiments have shown that the hands-on, problem-solving, constructionism approach allow the learner to confront abstract, cognitive problem solving in a simpler manner through the physical representation. The feature that different representations (e.g. physical representation) can cause dramatically different cognitive behaviour is referred to as "representational determinism" [9]. In fact, Zhang and Norman [10] propose a theoretical framework in which internal representations and external representations form a "distributed representational space" that represents the abstract structures and properties of the task in "abstract task space" (p. 90). They developed this framework to support rigorous and

formal analysis of distributed cognitive tasks and to assist their investigations of "representational effects [in which] different isomorphic representations of a common formal structure can cause dramatically different cognitive behaviours" (p. 88). "External representation are defined as the knowledge of the structure in the environment, as physical symbols, objects, or dimensions (e.g., written symbols, beads of abacuses, dimensions of a graph, etc.), and as external rules, constraints, or relations embedded in physical configurations (e.g., spatial relations of written digits, visual and spatial layout of diagrams, physical constraints in abacuses, etc.)" (p. 180) [9].

For the distributed processing education, we suggest using *interactive* parallel and distributed processing that allows the student to easily represent, interact with and create their own parallel and distributed processing system in a physical manner. Here, we will divide the work into some of the sub-problems that the students will have to confront and learn about through practical implementations. These sub-problems include distributedness, master dependency, software behavioural models, adaptive interactivity, feedback, connectivity, topology, island modeling, and user interaction.

Indeed, designing software for *interactive parallel and distributed systems* means moving away from the traditional routes and to face another way of developing algorithms. This other programming paradigm demands the programmer to get into a new "state of mind", which is a most difficult thing to do. It is therefore important to have a clear idea of the concepts and definitions underlying this paradigm of interactive parallel and distributed processing:

Interactivity

For interactivity, here we intend a physical and tangible interaction. The physical parallel and distributed system enables the experience of physically manipulating objects and the material representations of information. The technology embeds physical, conceptual and cultural constraints. The mapping between the physical affordances of the objects with the digital components (different kinds of output and feedback) is a design and technological challenge, since the physical properties of the objects serve as both representations and controls for their digital counterparts [11]. Here, we make the digital information directly manipulatable, perceptible and accessible through our senses by physically embodying it.

While playing with the system, the user can take advantage of the distinct perceptual qualities of the system and this makes the interaction tangible, lightweight, natural and engaging. Interacting with a physical parallel and distributed system may mean jumping over, pushing, assembling, touching physical

objects and experiment a dialogue with the system in a very direct and non-mediated way, and hence it is viewed as highly suitable e.g. for student training. Undeniably, this allows for a direct hands-on experience and learning.

Parallel and Distributed

A computational process is called distributed [12] when a single computational atom is on one side autonomous and on the other insufficient to determine the desired outcome. Therefore a computational process will be called distributed when two or more computers – communicating through any possible network - will contribute to accomplish the very same task by sharing different roles in a computational problem or process.

Besides that, whenever considering a *distributed (computational) process*, it is necessary to define the level of parallel vs. serial computational flow that the system should perform, as well as to define the "computational group" characteristics. The Parallel computing is a form of computation in which many calculations are carried out simultaneously, operating on the principle that large problems can often be divided into smaller ones, which are then solved concurrently ("in parallel"). There are several different forms of parallel computing: bit-level, instruction level, data, and task parallelism. Since the modular interactive tiles system is mostly dedicated to the task parallelism problem it tends to run distributed processes in, at least, three different ways: *Fully-Distributed*, *Semi-Distributed* or *Centralized*.

Modular Interactive Tiles System

Under an educational point of view what is really needed, as well as would be a real additional value, is a tool that allows for investigating and understanding parallel and distributed processing meanwhile stressing the user and/or multi-user interactivity component. One possibility is the Modular Interactive Tiles System (MITS) may provide novel programmers with such a tool and approach, since the system is based on robotic modules with certain properties: Each robotic module has a physical expression and is able to process and communicate with its surrounding environment. The communication with the surrounding environment is through communication to neighbouring robotic modules and/or through sensing or actuation. A modular robot is constructed from many robotic modules.

The MITS approach inherits the behaviour-based robotics methods [13] and exploits it with the belief that behaviour-based systems can include not only the coordination of primitive behaviours in terms of control units, but also include coordination of primitive behaviours in terms of physical control units. We,

therefore, imagine a physical module being a primitive behaviour. Thereby, the physical organisation of primitive behaviours will (together with the interaction with the environment) decide the overall behaviour of the system. Hence, in a similar way to the control of robot behaviours by the coordination of primitive behaviours, we can imagine the overall behaviour of a robotic artefact to emerge from the coordination of a number of physical robotic modules that each represents a primitive behaviour, eventually opened to single/multi user-interaction.

The modular interactive tiles can attach to each other to form the overall system. The tiles are designed to be flexible and in a motivating way to provide immediate feedback based on the users' physical interaction, since following design principles for modular playware [14].



Fig. 1. Modular tiles used for feet or hands interaction.

Each modular interactive tile has a quadratic shape measuring 300mm*300mm*33mm – see Fig. 1. It is moulded in polyurethane. In the center, there is a quadratic dent of width 200mm which has a raised circular platform of diameter 63mm in the centre. The dent can contain the printed circuit board (PCB) and the electronic components mounted on the PCB, including an ATmega 1280 as the main processor in each tile. At the center of each of the four sides of the quadratic shape, there is a small tube of 16mm diameter through which infra-red (IR) signals can be emitted and received (from neighboring tiles). On the back of a tile there are four small magnets. The magnets on the back provide opportunity for a tile to be mounted on a magnetic surface (e.g. wall). Each side of a tile is made as a jigsaw puzzle pattern to provide opportunities for the tiles to attach to each other. The jigsaw puzzle pattern ensure that when two tiles are put together they will become aligned, which is important for ensuring that the tubes on the two tiles for IR communication are aligned. On one side of the tile, there is also a small hole for a charging plug (used for connecting a battery charger), including an on/off switch.

There is a small groove on the top of the wall of the quadratic dent, so a cover can be mounted on top of the dent. The cover is made from two transparent satinice plates on top of each other, with a sticker in between as visual cover for the PCB.

A force sensitive resistor (FSR) is mounted as a sensor on the center of the raised platform underneath the cover. This allows analogue measurement on the force exerted on the top of the cover.

On the PCB, a 2 axis accelerometer (5G) is mounted, e.g. to detect horizontal or vertical placement of the tile. Eight RGB light emitting diodes (LED SMD 1206) are mounted with equal spacing in between each other on a circle on the PCB, so they can light up underneath the transparent satinice circle.

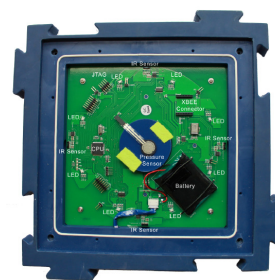


Fig. 2. PCB and components of a modular interactive tile.

The modular interactive tiles are individually battery powered and rechargeable. There is a Li-Io polymer battery (rechargeable battery) on top of the PCB. A fully charged modular interactive tile can run continuously for approximately 30 hours and takes 3 hours to recharge. The battery status of each of the individual tiles can be seen when switching on each tile and is indicated by white lights. When all eight lights appear the battery is fully charged and when only one white light is lit, the tile needs to be recharged. This is done by turning of the tiles and plugging the intelligent charger into the DC plug next to the on/off switch to recharge each tile.

On the PCB, there are connectors to mount an XBee radio communication add-on PCB, including the MaxStream XBee radio communication chip. Hence, there are two types of tiles, those with a radio communication chip (*master tiles*) and those without (*slave tiles*). The master tile may communicate with the game selector box and initiates the games on the built platform. Every platform has to have at least one master tile if communication is needed e.g. to game selector box or a PC.



Fig. 3. Assembly of the modular interactive tiles as a simple jigsaw puzzle.

With these specifications, a system composed of modular interactive tiles is a fully distributed system, where each tile contains processing (ATmega 1280), own energy source (Li-Io polymer battery), sensors (FSR sensor and 2-axis accelerometer), effectors (8 colour LEDs), and communication (IR transceivers, and possibly XBee radio chip). In this respect, each tile is self-contained and can run autonomously. The overall behavior of the system composed of such individual tiles is however a result of the assembly and coordination of all the tiles.

The modular interactive tiles can easily be set up on the floor or wall within one minute. The modular interactive tiles can simply attach to each other as a jigsaw puzzle, and there are no wires. The modular interactive tiles can register whether they are placed horizontally or vertically, and by themselves make the software games behave accordingly.



Fig. 4. Physical interaction with the modular interactive tiles placed on the ground.

Also, the modular interactive tiles can be put together in groups (i.e.: tiles islands), and the groups of tiles may communicate with each other wireless (radio). For instance, a game may be running distributed on a group of tiles on the floor and a group of tiles on the wall, demanding the user to interact physically with both the floor and the wall.

Theoretical Aspects of Interactive Parallel and Distributed Processing

Interactive parallel and distributed systems programming demands the student programmer to shape specific abilities, and we believe that the MITS can simplify this learning process. We will present a number of the interactive parallel and distributed sub-problems that a student needs to learn about, and we believe MITS provides an open tool for facing all the aspects of programming both low and high level programming or front and back end representation.

Classical parallel and distributed processes subtasks

Coding parallel and distributed processes stress programming and understanding of different levels, such as: physical level (i.e.: bit transmission); data link level (i.e.: packages, transmission errors and recovery);

network level (i.e.: addresses and packages destination); transport level (i.e.: messages exchanges between clients and master/s); session level (i.e.: defining and implementing sessions in terms of priorities and process-to-process communication); representation level (i.e.: working on data-format differences); application level (i.e.: the end-user interaction and feedback); and to understand and implement solutions for robustness (i.e.: errors diagnosis and recovery); reconfiguration (i.e.: modules assembling); unreliable communication (i.e.: data loss, duplication and corruption); parallelism and concurrency (i.e.: language non-deterministic side-effects); fixed and expanding parallelism (i.e.: modifying the number of involved processors).

It is also essential when teaching information distribution to work on problems such as system connection (i.e.: total vs. partial connection); token-passing (i.e.: how to share and act on critical information); deadlock prevention (i.e.: wait-die, wound-wait, etc.); memory sharing (i.e.: how to locate the physical memory of the distributed system); topology (i.e.: ordinary and complex topology algorithms, initial vs. run-time topology building, etc.); processes transfer (i.e.: distributing the work-load, speeding up calculation, hardware and software specialization amongst the system modules); centralized vs. hierarchy vs. distributed approaches (i.e.: leaded or unleaded information flow); and run-time adaptation (i.e.: adapting the system re/actions on-the-fly).

Besides all of the above “classical” sub-problems of computer science, our platform forces the educational session to face other aspects that software designers should deal with when learning parallel and distributed processing. Such sub-tasks include local and global connectivity, hardware multifaceted topologies, interactivity and adaptive interactivity, and multimodal feedback.

Connectivity

To materialize a proper interactive parallel and distributed platform, the modular interactive tiles system has to implement both a *local connection* system - through which the hardware cells communicate to the neighbourhood and propagate such information from side to side - and a *global connection* device - through which to connect with neighbour platforms and any external tool.

Hardware Multifaceted Topologies

Since the modular interactive tiles system implies the use of run-time de/attachable modules, the emphasis on hardware/software topology is quite strong and it demands a big effort to comprehend the programming

and dealing with such structures. In our model we were able to identify three specific subtypes of topologies:

1. *Regular*, that is a one-block (i.e. any given group of hardware cells attached in a contiguous way and sharing a single master cell) platform with modules attached in a squared or rectangular shape;
2. *Irregular*, which is a one-block platform, which can be arranged in any desired shape. Nevertheless hardware cells have to be continuous (i.e. the assembling does not reveals discontinuity and there is not any isolated cell or group of cells);
3. *Islands Configurations*, that is a platform made with two or more one-blocks (i.e. as defined above in point 1, and 2). It makes no difference whether master cells communicate amongst each others, through an external device, or do not communicate at all.

Interactivity

Implementing software for modular interactive tiles implies designing, or at least dealing with a quite relevant interactive scenario, since in most cases the use of the software itself relies on the users' physical and continuous action. The software designer will have to deal with completely different requirements accordingly to single-user or multi-user targeted software. Often, the software designer will also have to hypothesize a large variety of behavioural situations, even including situations (according to our personal experience) where a single-user platform will be used by many users, or a multi-user software will be run by a single user.

Adaptive Interactivity

The way we approach interaction in such a modular and distributed model leads beyond the classic idea of human-machine interaction (HMI), and is of fundamental importance since it prospects and applies - under both physical and cognitive circumstances - user adaptation and user adaptivity. First of all, our model being architecturally reconfigurable - eventually run-time reconfigurable - represents by itself the essence of adaptation. In addition, being focused on users' physical action, such a system can be easily tailored to users' activity, either in real time or in the long run. To reach such a goal, modular interactive tiles can be programmed using many different strategies that also depend on the quality and quantity of feedback the software designer is willing to exchange with the users. (Feedback and multimodal feedback will be introduced in the next paragraph). Indeed, in more than one case we showed [15, 16] that using modular interactive tiles we could detect some of the users' characteristics, and therefore adapt the software execution to those. Last but not the least, in further tests it has been shown that by capturing the users' provisory attitude and adapting the software

execution to that it is possible, in some cases, to eventually modify the users' behaviour itself [16].

Multimodal Feedback

When talking about HMI we kind of committed ourselves to the "how you give is more important of what you give" motto. Therefore, in recent years we pushed our research towards software and tools that can both give and get feedbacks from the user(s).

When developing software for modular interactive tiles we constantly try to provide the user with an *immediate feedback* (e.g. LED, experience report) as well a *delayed* or *long term feedback* (e.g. adaptivity, documentation software). For the immediate feedback from modular interactive tiles we use light (LED) configuration or colours. In addition to that, anytime there is a need for a stronger or a more complex or long-run "signal", we interface the modular interactive tiles with external devices in a layered mode, where each layer of feedback can be added/removed freely on top of each other. This is what we call Layered Multi-modal Feedback [17]. The external devices we use can be "passive" as vision oriented feedback (e.g. screen, projector, etc.), sound oriented feedback (e.g. loud speakers, buzzers, etc.), or "active" such as computational devices that through an external communication (e.g. radio and internet) run an analysis or link the user action to specific databases.

In conclusion, to manage and teach the many features of parallel and distributed programming we need to run on a system, which is robust, reliable and easily reconfigurable. This is where we believe that the MITS can express a certain degree of efficiency, besides of being ideal in shifting the level of representation from the very abstract representation to an empirical representation. Therefore, in the following paragraph we provide examples, which attempt to show how one can access the above-described aspects in a fast, comprehensible and easily generalizable way.

Implementations Examples

As a first step the teacher/tutor should introduce students to the hardware platform (Figures 2, 3, and 4) and ask the class to implement all the needed protocols for obtaining a robust, efficient and reliable parallel and distributed system. This would require and encourage students to face the basic algorithms and protocols that the subtasks of parallel and distributed systems need (e.g.: physical level, data link level, network level, transport level, session level, representation level, etc.).

Once such a start-up system is obtained (from the students work or from the pre-made system), a second step could be, for example, testing the system by working on problems such as application, robustness,

communication, system connection, token-passing, deadlock prevention, parallelism, reconfiguration, memory sharing, topology, and process transferring. The MITS model is ideal for implementing all of the above challenges since the hardware components are minimalistic and the distributed system complexity can be developed and tested in a quick and easy manner (Figure 5).

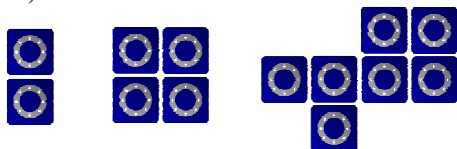


Fig. 5. Examples of different topologies

Once students have reached this new level of competencies, the tutor can drive their attention to a higher level of representation and ask them to implement end-user interaction based applications, such as in the following examples.

Games Examples.

Once a specific topology is chosen, the software engineering student can implement and run a large variety of tasks (here we start by considering examples to apply to a *semi-distributed, single user application* on a *regular topology* platform).

Open Loop and Randomness based software.

The simplest case, a naïve one, could be the following Easy Game (Figure 6).

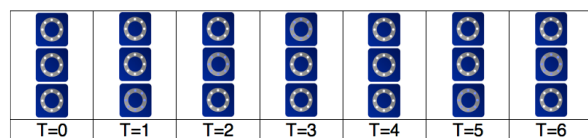


Fig 6. Easy Game, a sequence of 7 states

In Easy Game the light is “passed” from one module to either an adjacent or a distant one (i.e. with a predefined open loop algorithm or randomness based one). In both the above cases the software cycling is endless and we need to introduce the *interactivity level* (e.g. the game finishes when the user hit the lighted tile) to stop it, and by doing so transforming the two into very young children games. When the user press a tile, then the dynamics somehow stops and the tiles freeze in a particular pattern, until the user presses the lighted tile again, and the light shift sequence will start again.

Rule(s) based software.

One step further is a rule-based software characterized by the fact that pattern sequence - which can either be

predefined or random based – is governed by a specific rule or set of rules. The simplest case we can think of is the one where, given any machine state and configuration (e.g. two tiles) those states which are ON turns OFF and those states which are OFF turns ON. Of course, we can design a much more complex setting but, essentially, this is the logic that is used in rule based software.

On the other hand, when introducing the interaction element in rule based software we obtain a more dynamic scenario denoted by the fact that the rules and users are coactive and contribute step by step to the system state. Such a situation can be clearly observed in the *American Football* game (Figure 7).

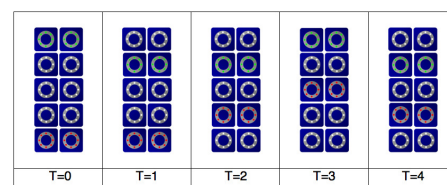


Fig. 7. American Football, a sequence of 5 states

This is one-against-one game where, given a, say, 5 (width) per 2 (height) cluster of modular interactive tiles, such interactive software is made so that at the beginning of the game the platform extremes appear activated (i.e. light on) and of two different colours (i.e. blue in one extreme and red in the other extreme). By squeezing the tiles, the user “pushes” the color/activation forward in the row (i.e. switches off the squeezed tile and switches on the adjacent one towards the opponent). The user who first pushes its color to the opposite extreme of the game platform wins the game.

User-interaction based software.

The user-interaction based program is, per se, an interactive software conception in which the user directly contributes to the next machine state (i.e. tiles color or activation). Such a software model is quite similar to the interactive version of the rule based software – since the user itself cannot determine the machine states if not aided by some underlying algorithm. It only differs from that in terms of strain used on increasing the user role and contribution to the next machine state, and the attempt to reduce the rule component. A good example could be the *Final Countdown* game (Figure 8). In the *Final Countdown* the tiles platform can vary both in aspect and size, since the game components behave all in the very same way. It consists of a number of tiles that, when the game is initiated, all of the tiles are fully lighted (i.e. any color would do). After initialization and with a given interval (e.g. one second) they all start to “fade-out” switching OFF one of their 8 light bulbs after the other in a clockwise sequence. If one of them gets completely

OFF the game is over. To restore a single tile to the initial state, the user has to squeeze it. The wider is the platform the more important becomes the strategy users bring into play to keep the game alive.

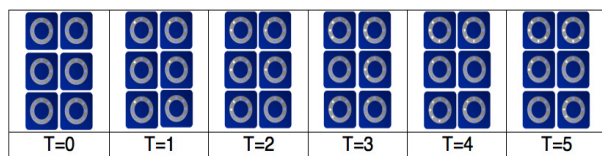


Fig. 8. *Final Countdown*, a sequence of 6 states

A.I. and ALife based software.

The A.I. and ALife based software are, again, a complication of what we defined as rule based systems. Essentially they rely on the same principles, both for the autonomous and the interactive version, although the quality of the computational experience is much higher in terms of software behavioral equality/variety, un/predictability, and etc. Further, since modular interactive tiles tend to resemble pixel-made structures it seems to easily incorporate a consistent number of classical and modern A.I. paradigms. A good example is the Cellular Automata (i.e. CA), a discrete model used in computability theory and many different fields, which consists of a regular grid of cells, each one with a finite number of possible states (e.g. ON, OFF), that can change their state accordingly with their neighborhood activation states [18]. We, first, implemented one of the most famous CA algorithms, the *Conway's Game of Life* on modular interactive tiles and, after that, added the interactive aspect.

Conclusion

We developed the concept of *interactive* parallel and distributed processing in order to put focus on the physical interaction with parallel and distributed system, and to highlight the many challenges that the student programmers might face in understanding and designing interactive parallel and distributed systems.

It is our belief that a system like the modular interactive tiles is a tool for easy, fast, and flexible learning and exploration of these challenges, e.g. as shown with the examples of how to implement interactive parallel and distributed processing with different software behavioral models such as open loop, randomness based, rule based, user interaction based, AI and ALife based software.

Indeed, MITS provides an educational hands-on tool that allows a change of representation of the abstract problems related to designing interactive parallel and distributed systems, so that students can learn about classical and modern aspects of parallel and distributed systems.

Acknowledgements

The authors wish to thank the Centre for Playware colleagues for discussions of the concept and implementations.

References

- [1] Harel, D. *Algorithmics*, Addison-Wesley, 1987
- [2] Silberschatz, A., Peterson, J., Galvin, P. *Operating System Concepts*, Addison-Wesley, 1991
- [3] Piaget, J. and Inhelder, B. *La psychologie de L'enfant*. Paris, P.U.F, 1966.
- [4] Papert, S. *Mindstorms: Children, Computers, and Powerful Ideas*. Basic Books, New York, 1980.
- [5] Papert, S. *Constructionism: A New Opportunity for Elementary Science Education. A proposal to the National Science Foundation*, 1986.
- [6] Martin, F. "Ideal and Real Systems: A Study of Notions of Control in Undergraduates Who Design Robots". In Y. Kafai and M. Resnick (Eds.), *Constructionism in Practice: Rethinking the Roles of Technology in Learning*, MIT Press, MA, 1994.
- [7] Lund, H. H. "Robot Soccer in Education". *Advanced Robotics Journal*, 13:8, 737-752, 1999.
- [8] Lund, H. H., and Sutinen, E. "Contextualised ICT4D: a Bottom-Up Approach", *Proceedings of 10th International Conference on Applied Computer Science*, WSEAS, Japan, 2010.
- [9] Zhang, J. The Nature of external Representations in Problem Solving. *Cognitive Science* 21:2, 179-217, 1997.
- [10] Zhang, J., Norman, D.A. Representations in Distributed Cognitive Tasks. *Cognitive Science* 18: 87-122, 1994.
- [11] Ishii, H. Ullmer, B. *Tangible Bits: Towards Seamless Interfaces between People, Bits and Atoms*. In *Proceedings of CHI: Human Factors in Computing Systems*. pp. 234-41, 1997.
- [12] Rumelhart, D., McClelland, J., et al., 1986, *Parallel Distributed Processing*, vol. I, Cambridge, Mass.: MIT Press.
- [13] Brooks, R. "A robust layered control system for a mobile robot". *IEEE Journal of Robotics and Automation*, 2(1):14-23, 1986.
- [14] Lund, H. H. and Marti, P. "Designing modular robotic playware," the IEEE Int. Workshop Robots Human Interactive Commun Toyama, Japan. Sep. 27-Oct. 2., IEEE Press, 2009.
- [15] Hammer, F. Derakhshan, A., Hammer, F., and Lund, H. H. "Adapting Playgrounds for Children's Play Using Ambient Playware". In *Proceedings of IEEE Intelligent Robots and Systems (IROS'06)*, IEEE Press, Hong Kong, 2006.
- [16] Thorsteinsson, T. and Lund, H. H. "Adaptive Modular Playware". (in press).
- [17] Lund, H. H. and Thorsteinsson, T. "Social Playware for mediating tele-play interaction over distance" to appear in *Proceedings of 16th International Symposium on Artificial Life and Robotics, ISAROB*, Japan, Jan. 2011.
- [18] Neumann, J. v. "The general and logical theory of automata," in L.A. Jeffress, ed., *Cerebral Mechanisms in Behavior – The Hixon Symposium*, John Wiley & Sons, New York, 1951, pp. 1-31.

Analysis of speech signal based on frequency distribution and intonation

Naoya OHTA and Akio NOZAWA

Meisei University, 2-1-1 Hodokubo, Hino, Tokyo, JAPAN
(Tel : +81-02-591-5895; Fax : +81-42-591-5895)
(akio@ee.meisei-u.ac.jp)

Abstract: In this study, the atmosphere as a communication mode of human was defined by time information of speech. The objective of this study was the development of quantitative measurement technique of the atmosphere as KANSEI in a group. The communication mode of the group was indexed by using a time frequency distribution analysis on conversation voice. In particular, a speech duration time was focused. And the correlation between the time series of the speech duration time and a communication modality was evaluated. Consequently, the difference of the communication mode between man and woman was seen in the speech duration time. And a difference of the characteristics of speech was found in the duration time and the frequency.

Keywords: atmosphere, communication, speech duration time, frequency

I. INTRODUCTION

The atmosphere of field was unexpressed explicitly in language of emotional relationship in situation of interpersonal relationship and social group, power relationship, and interest. Atmosphere was idiomatic phrase of Japanese which indicating many elements of relationship without expression. Awakening atmosphere is implicit. This ability is called social intelligence by psychology [1]. Reading atmosphere is cognition of communication mode. In particular, subtlety in communication is technique which learned in interpersonal psychology. That is, the skill of human relations is not innate target in interpersonal psychology.

In recent years, student evaluation system has been introduced into many schools [2]. The objective of the system is to find the problem of the class in order to refine the class. However, the questionnaire was written by the student whose grade was in the hands of teachers [3]. The evaluation by those students may tend to be rather high. Thus, the evaluation doesn't have much value for the objective. The introduction of the system in school is seen as just the evidence of an enthusiasm for refining the class. That is, an alibi. A basis of the evaluation has variety. The relationship between the effect of learning and the satisfaction for the class doesn't always has a correlation. Sometimes, they could have an inverse relationship. Because teachers tend to have the priority to the satisfaction of students and ignore the effect of learning. This is like putting the cart before the horse. The student evaluation system has the

aspects of understandability, an effect of learning, an ambition and an attitude of teacher, which are evaluated by students. Because of these factors, objective evaluation of the class becomes increasingly important. The activity of the class was evaluated as atmosphere. Understanding of refining of student evaluation system is considered become one of indicators.

In recent years, the various applications that was introduced the sound recognition technology was developed[4]. Speech dialogue system as target to information guidance was practical use. Many of those speech dialogue is remain handle only language information contained in speech. Therefore, uniform response is shown against any opponent. Dialogue between humans is and non speech information obtained from ears and eyes. There are also non-verbal information contained in speech. They are born deep interaction by use together. That is similar about recognition of communication mode including atmosphere. Factor to form an atmosphere was interpersonal relationship and emotional relationship and power relationship and interests relationship. Atmosphere is difficult captured properly by machine. In addition, atmosphere is difficult captured properly by human with no prior knowledge. But human is can catch sensuously an atmosphere. Because it is interpret atmosphere as communication mode of group based at nonverbal information of facial expression, tone, gesture not only explicit language information in content. Interpret of nonverbal information by machine is studied extensively by area of human-machine system.

Table1. Stats of speech duration time

object	Freq/times	Total/s	Avg/s	Max/s	volume
news(M)	130.82	190.96	1.47	5.03	131.08
news(F)	152.14	195.41	1.34	4.70	98.45
Intr(F-M)	246.00	177.79	0.76	5.79	64.33
Intr(F-F)	235.13	174.66	0.80	6.01	66.79

Study example as object for communication mode of group is little. In addition interpret of verbal information concerning communication mode is become premise to interpretation of context whole of communication. Therefore complexity isn't avoided. This study, atmosphere as communication mode of between humans was defined by time information of speech. Purpose of this study is develop quantitative measurement technique of atmosphere as sensitivity of group. As result of this study is improvement of student evaluation system. Quantitative evaluation of the atmosphere is considered become one of evaluation indicator concerning communication mode as group. In addition, by communication mode visualization and quantify is function as one of indicator grasp familiarity density in talks. This is brings the efficiency of information transmission. This study was focused in relationship of speech duration time and speech frequency. This study is analysis of speech signal based on frequency distribution and intonation.

II. EXPERIMENT METHODOLOGY

In this study, conversation sound was used as analysis object. Recorded audio signal at PC was analyzed as digital data. Audio signal was converted by PCM method to A/D. Audio signal was recorded in file at WAVE form. sampling frequency was 22.050kHz. Recorded file was quantized at 16bit. In addition, the number of channels was one (monaural). Speech sound of record object was not included acoustic of sound effect except speech. The conversation to become object is idealized the speech of professionals trained concerning speech. But securement of subjects was difficult. So, audio source sample was acquired equivalent audio source from internet. Audio source sample is read sound of male announcer in radio news (News(M)) of internet delivery. And, read sound of female announcer in radio news (News(F)) of internet delivery. And, interview from female to male (Intr(F-M)) in internet delivery program. And, interview from female to female (Intr(F-F))in internet delivery program.

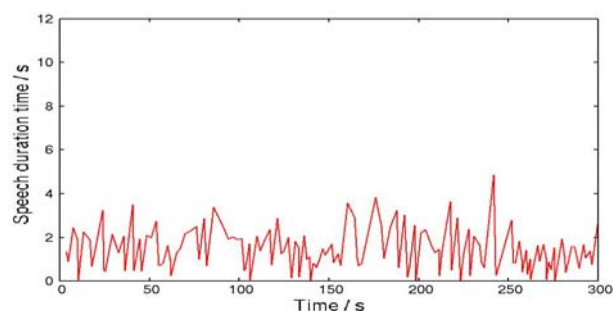


Fig.1. time series of speech duration time (News(M))

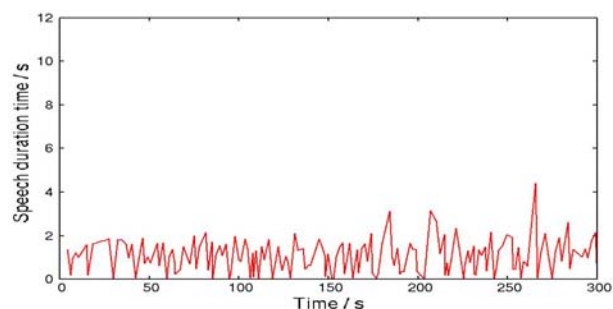


Fig.2. time series of speech duration time (News(F))

III. ANALYSIS PROCEDURE

Audio Source sample used at analysis was News(M) of 10kinds. And News(F) of 7 kinds. And Intr(F-M) of 6 kinds. And Intr(F-F) of 8 kinds. Audio source sample of news recitation is 17kinds in total. Audio source sample of interview is 14 kinds in total. Absolute value processing was administered for recorded voice signal. And get at envelope of peak value. Speech duration time and the corresponding speech time was recorded at time series. Voice signal per one sound source was 300 seconds. 10 seconds of first is silence part for environmental noise level evaluation. Extract of speech is performed as standard of environmental noise level. Threshold was about 3 times of the average environmental noise level. And tried visualization of communication mode by conversation sound analysis. This study was focused in speech duration time. The conversation breaks were detected as standards silence part of constant time. This study conversation break was regarded silence part more than 0.2 second.

IV. RESULT AND DISCUSSION

Table.1 is result of the stats concerning speech duration time. Fig.1 is result of time series of speech duration time (News(M)). Fig.2 is result of time series of speech duration time (News(F)). Fig.3 is result of time series of speech duration time (Intr(F-M)). Fig.4 is

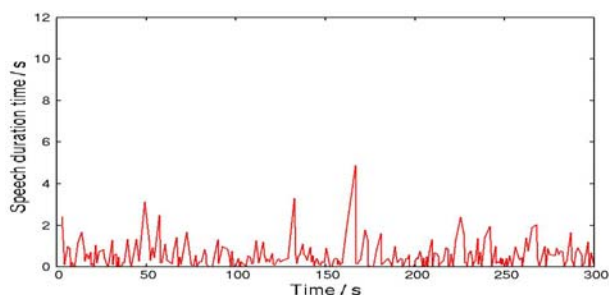


Fig.3. time series of speech duration time(Intr(F-M))

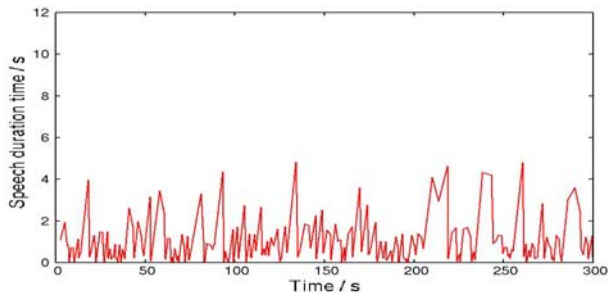


Fig.4. time series of speech duration time(Intr(F-M))

result of time series of speech duration time (Intr(F-F)).

Fig.5, 6 is result of Time frequency distribution of speech of news recitation and interview. Fig.7, 8, 9, 10 is result of each frequency analysis. From result of table 1, number of speech of men of the news recitation is 130.82 times. Number of speech of female of the news recitation is 152.14 times. Number of speech of female is lot of than men. Summation of time series of speech duration time is 190.96 second by news recitation of male. Summation of time series of speech duration time is 195.41 second by news recitation of female. Average of speech duration time is 1.47 second by news recitation of male. Average of speech duration time is 1.34 second by news recitation of female. Maximum of speech duration time is 5.03 second by news recitation of male. Maximum of speech duration time is 4.70 second by news recitation of female. Average of volume of speech duration time is 131.08 db by news recitation of male. Average of volume of speech duration time is 98.45 db by news recitation of female. Female is seen tend extension of speech duration time than men. For result of male of news recitation of time series of fig.1, amplitude is seen fit into within constant. In addition, male of news recitation of fig.1 is bigger than amplitude female. For result of female of news recitation of time series of fig.2, amplitude is seen fit into within constant. Amplitude of female of fig.2 is seen to smaller than amplitude of male of fig.1 Summation of speech duration time concerning news recitation wasn't seen both male and female significant difference. Both

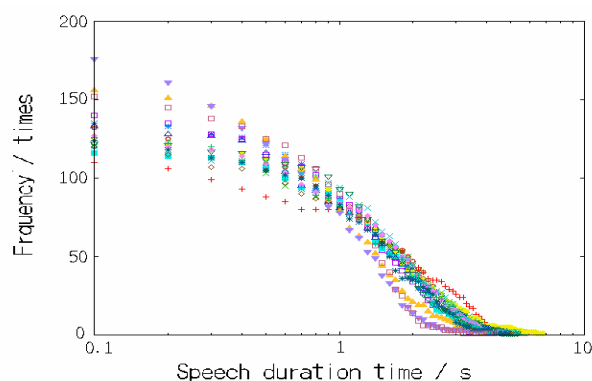


Fig.5. Time frequency distribution of speech of news recitation

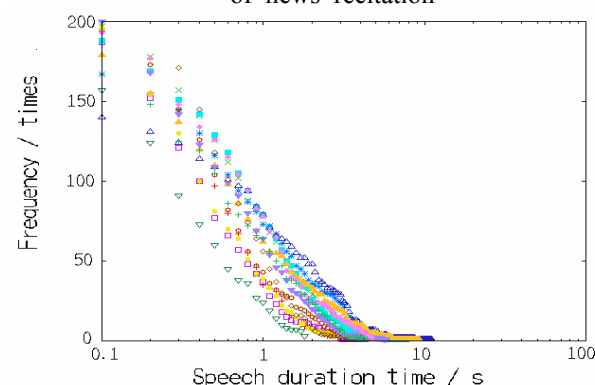


Fig.6. Time frequency distribution of speech of interview

difference of news recitation is showing at distribute of speech duration time. This report, news contents is not control. Therefore, difference between male and female in distribute of speech duration time is cannot disaffirmance possible of factor of contents. Result of news recitation of both male and female is seen constant amplitude within the range. Speech of news recitation is spoken by constant rhythm easy to hear. So, amplitude is considered become constant. Number of speech of interview of female for male is 5.79 times. Number of speech of interview of female for female is 6.01 times. Summation of time series of speech duration time of interview of female for male is 177.79 second. Summation of time series of speech duration time of interview of female for female is 174.66 second. Average of speech duration time of interview of female for male is 0.76 second. Average of speech duration time of interview of female for female is 0.80 second. Max of speech duration time of interview of female for male is 5.79 second. Max of speech duration time of interview of female for female is 6.01 second. Average of volume of speech duration time of interview of female for male is 64.33 db. Average of volume of speech duration time of interview of female for female is 66.79 db. Number of speech and max time of

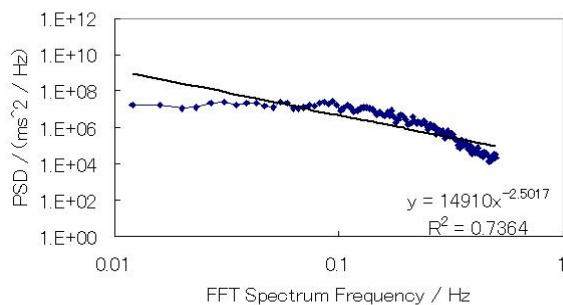


Fig.7. frequency analysis (News(M))

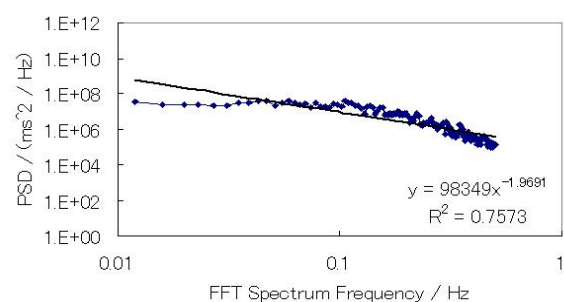


Fig.9. frequency analysis (Intr(F-M))

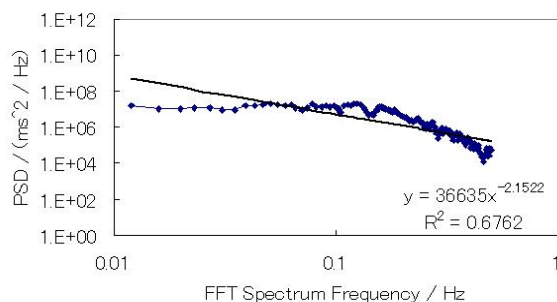


Fig.8. frequency analysis (News(F))

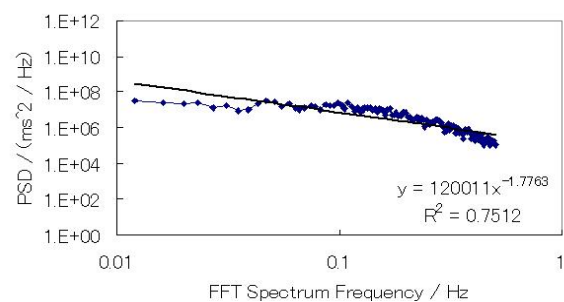


Fig.10. frequency analysis (Intr(F-F))

interview is greater than the news recitation. But summation and average of speech duration time is smaller than the news recitation. Principal speech of conversation of interview is 2 man. And conversation of interview is accrual communication. And conversation is hard to break. And speech duration time is inferred extending. Accretion of principal speech is not bring accretion of speech time. Information concerning speech duration time as per the communication mode is indicating difference arise. From result of time frequency distribution of fig.5, 6, speech of short time is increased frequency of occurrence. Conversely long speech of duration time is low frequency of occurrence. Time frequency distribution of speech is inferred take on fractal structure. From result of frequency analysis of fig.7, 8, 9, 10, power spectrum density is inverse proportion f of frequency. And this is become relationship in $1/f$ fluctuation.

V. CONCLUSION

In this study, focusing at non-verbal part of speech. Object is to visualize communication mode from implicit called atmosphere. Conversation sound as analysis target was applied time frequency distribution. In particular, focused at speech duration time. And evaluate is concerning of time series of the speech duration time and the communication mode. As result, difference of speech mode concerning to sex was

acknowledged. In addition, speech frequency and speech duration time was ascertained possible indicate a fractal structure. Fractal dimension of news recitation of speech as analysis target is constant. News recitation is thinking became constant fractal dimension by spoke trained announcer. Fractal dimension in interview is multiplicity. Therefore Fractal dimension in interview is considered possible to be one of the indicators to capture the communication mode.

REFERENCES

- [1]John D. Mayey, Peter Salovey, David R.Caruso : "Emotional Intelligence : Thaeory, Finding and Implications," Psychological Inquiry, Vol15, No3, pp.197-205(2004)
- [2]Yumiko M, Kensaku S, Toshio O, Akihumi J, Akiko I, The Enforcement and the Tabulation of the Class Evaluation Questionnaire(in Japanese). Tokyo Management College, Vol.17, pp.47-58(2009)
- [3]Yoshiaki H, Anonymous course evaluation and final evaluation of each class registered (in Japanese). International financial and administrative Vol.23, pp.47-58(2009)
- [4]Yosuke A, Kiyoshi S, Atsushi K, A Study for a Scalability Evaluation Model of Spoken Dialogue System(in Japanese), Information Processing Society of Japan, Vol. 46, No.9, pp.2269-2278(2005)

Color Influences on Human Being Evaluated with Nasal Skin Temperature

Tota MIZUNO, Naoki NAKATEGAWA and Yuichiro KUME

*Tokyo Polytechnic University, 1583 Iiyama, Atsugi, Kanagawa 243-0297 Japan
(Tel : +81-46-242-9508; Fax : +81-46-242-9508)
(mizuno@mega.t-kougei.ac.jp)*

Abstract: Since colors affect human conditions physiologically and mentally, various studies about the color influences have been conducted. Most of the studies have been focused on psychological aspects. In this study, we investigate the color influences physiologically by use of infrared thermography. With this technique, subjects wear no devices, and objective values are expected to be obtained to evaluate the color influences. Nasal skin temperatures were measured by infrared thermography under yellow, red and blue illuminations. As a result, significant temperature change was observed under red illumination.

Keywords: color, nasal skin temperature, visual analog scale, infrared thermography

I. INTRODUCTION

Since colors affect human conditions physiologically and mentally, various studies about the color influences have been conducted [1,2]. For an example, long wavelength lights, such as red or yellow, excite human beings. These colors raise the awakening level or the grip strength. On the contrary, the short wavelength lights, such as blue or green, are the sedation colors. While a number of studies have been supporting these points, a lot of negative data have also been reported. The conclusion has not been clarified yet [3].

In our previous studies, mental work-loads (MWL) have been examined with physiological and psychological measurements under arithmetic calculation tasks.

It was shown that changes of nasal skin temperature are remarkable as a physiological index [4,5]. In generally, nervous systems about brain waves or the heartbeats respond quickly to change the tasks, but this reaction does not continue for long period. Living bodies tend to be adapted to tasks quickly. On the other hand, the nasal skin temperature changes more slowly along with the task. In nasal skin, there are many arteriovenous anastomoses (AVAs) which are sympathetic nervous systems. Nasal skin temperature changes slowly with increase and decrease of the bloodstream with the antagonism of a sympathetic and the parasympathetic nerve. This reaction continues for long period to stimulations which affect an autonomic nervous system. From this viewpoint, nasal skin temperature is more suitable for the evaluation for a long period for mental stimulations about MWL [4,5].

Nasal skin temperature can be measured by infrared thermography, which is featured with non-contact. When physiological and mental influences by color stimulation are measured, the non-contact device has an advantage that the subjects do not wear any sensors. Previous color influence studies have been conducted with brain wave or heartbeat measurements [1]. No studies about nasal skin temperature to evaluate color influences have been reported.

In this study, we investigated the color influences psychologically and physiologically by use of infrared thermography. The purpose of this study is to clarify nasal temperature changes in terms of color illuminations, and the relationship between psychological evaluation and nasal temperature.

II. EXPERIMENT

The relationship of physiological and psychological indices was investigated, when environmental color (red, blue, yellow) was changed.

1. An evaluation index

Visual Analogue Scale (VAS) was used as a psychological index, while nasal skin temperature was used as a physiological index. Figure 1 shows an example of VAS. Subjective senses and feelings can be measured by marking a position on 10cm long scale characterized by a pair of opposite words or phrases at the both ends. This method is featured with little individual differences in the understanding of the description, and shorter time to perform measurements. In this study, seven pairs of words for VASs were employed.

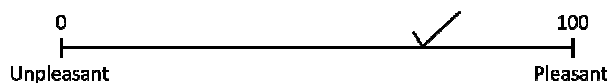


Fig.1. Visual Analogue Scale

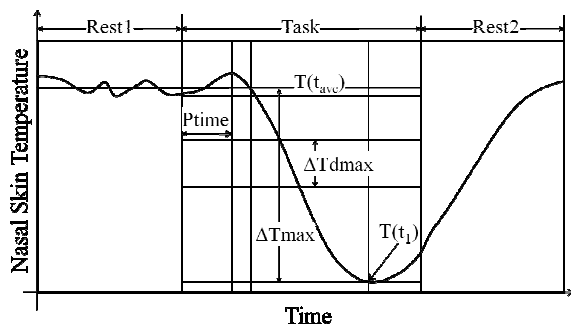


Fig.2. Nasal skin temperature

There were “Unpleasant-Pleasant”, “Distracted-Concentrate”, “Unhappy-Happy”, “Fatigue-Vigor”, “Cold-Hot”, “Dark-Light” and “Sleepy-Awake”. For the evaluation, we used the VAS value differences between before and after color illuminations.

Figure 2 shows a change of nasal skin temperature. As the physiological index, we used temperature differences between forehead and nasal skin. Nasal skin temperatures are well affected by the activities of autonomous nerves. In addition, forehead skin temperatures are little affected by the activities of autonomous nerves. Skin temperatures are affected by ambient conditions. The ambient influences can be reduced by subtracting forehead skin temperature from nasal skin temperature. Therefore, relationship of sympathetic system and the parasympathetic system can be measured indirectly with time changes of temperature differences between forehead and nasal skins. (Afterward, difference of forehead and nasal skin temperature is called NST.)

In previous studies, the time change of NST were employed for various evaluations [4-8]. As an example, a time changes of NST is shown in Figure 2. In this experiment, NST is denoted by $T(t)$, and t is the time after starting color illumination.

P_{time} is the time when NST reaches the maximum between starting color illumination and the time when NST is less than NST average in Rest1. P_{time} is the time which is from starting color stimulation to appearance of physiological human changes. We defined maximum temperature displacement by ΔT_{max} ($\Delta T_{max} = T(t_{ave}) - T(t_1)$). This ΔT_{max} is a total variation which is influence by the color illumination. In addition, we defined the maximum of the greatest temperature decrease by ΔT_{dmax} . ($\Delta T_{dmax} = \max (T(t) - T(t+60s))$).

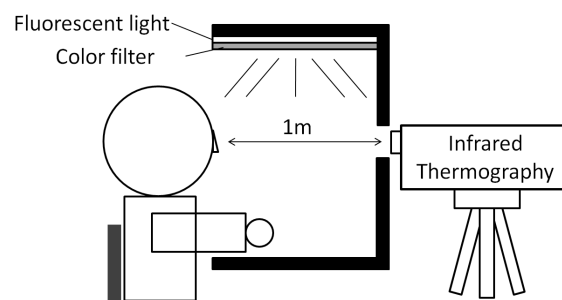


Fig.3. Experimental environment

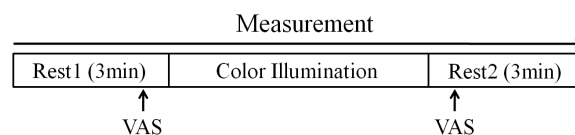


Fig.4. Experimental protocol

This ΔT_{dmax} is the maximum value which is affected by the color illumination for minutes. In this experiment, we used these P_{time} , ΔT_{max} and ΔT_{dmax} as evaluation measures. In addition, NST data were statistically analyses to study individual differences. NSTs were normalized as follows: Dispersion=1 and Average=0.

2. Experiment method

The experimental system is shown in Figure 3. A subject sat in front of a gray booth. In this booth, ambient colors were changed by LEE Filters (Dfilter (yellow (104), red (166) and blue (161))) and fluorescent lamps (Toshiba (FLD6500)) on the ceiling of the booth. Horizontal illuminations of all colors were $500 \pm 10\%$ (lx) in the booth. Infrared thermography device (NEC/Avio TVS-200EX) was placed at 1m horizontal distance from nose of the subject. The thermal image size was 320×240 [pixel], and the temperature resolving power was 0.08 degree centigrade. Skin emissivity was 0.98, and sampling period was 1sec.

Figure 4 shows the experimental protocol. A subject took rest (REST1) for three minutes, sitting and opening the eyes. After this rest, color illumination started and continued for five minutes. After color illumination, another rest (REST2) for three minutes was taken in the booth. The booth inside was illuminated by white light during the rests. VAS was carried out under the color illumination in first and last one minute. This protocol was performed with each color three times. The subjects were normal male adults aged from 21 to 24. This experiment was based on Helsinki Declaration (1964) for ethical consideration.

Table.1. Results of VAS (VAS Value (SD))

VAS	Yellow	Red	Blue
Unpleasant-Pleasant	0.4(1.1)	-0.1(1.4)	0.1(2.0)
Distracted-Concentrate	-0.1(1.5)	-1.1(1.6)	0.7(1.5)
Unhappy-Happy	0.1(1.3)	-0.4(1.3)	0.7(1.4)
Fatigue- Vigor	0.5(2.0)	-0.7(1.0)	0.1(1.7)
Cold-Hot	0.4(1.9)	0.5(1.8)	0.0(1.1)
Dark-Light	0.5(1.6)	-0.2(2.0)	0.2(2.3)
Sleepy-Awake	-0.1(1.8)	-1.5(2.7)	0.9(1.5)

3. Result and Discussion

Table 1 shows averages and standard deviations of VAS values of all subjects. Most of the VAS values were positive under blue and yellow illuminations, and 6 of the 7 VAS values were negative under red illumination. An analysis of variance and multiple comparisons (Bonferroni method) were performed statistically to test significant difference in each item of VAS values by the colors. In two VAS values of “Distracted-Concentrate” and “Sleepy-Awake”, there was a significant differences were shown in red and blue ($p<0.05$). From this result, it is understood that colors affect human conditions mentally. In particular, Red affects the VAS values of negative side among the three colors.

Figure 5-7 show average of NSTs of all subjects. The NSTs were maintained or increased for Ptime after starting color illuminations, and decreased after Ptime. Each NST was slightly different in the change by a color. The NST changed after starting each color illumination. The t-tests of statistical analysis were performed between temperatures of the starting and temperatures of the ending at the tasks under all color illuminations. As a result, in the both temperatures, there was a significant difference ($p<0.001$). From this viewpoint, it was shown that color illuminations affect human conditions physiologically.

Table 2 shows averages and standard deviations of Ptime, ΔT_{max} and ΔT_{dmax} . Red was the most effective color physiologically, since Ptime was short, ΔT_{max} and ΔT_{dmax} for red were the biggest of three colors. Although, NSTs of several subjects obviously were affected for color illuminations, the statistical significant differences were not observed between NST and colors. It is thought that there were no significant difference for state of subjects about the physical condition, mental condition and the taste color illuminations.

Table 3 shows the results of correlations between

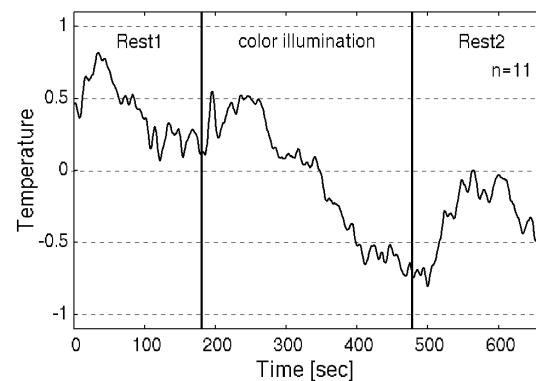


Fig.5. NST in yellow illumination

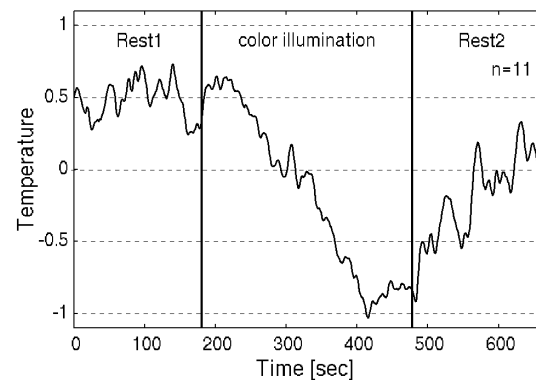


Fig.6. NST in red illumination

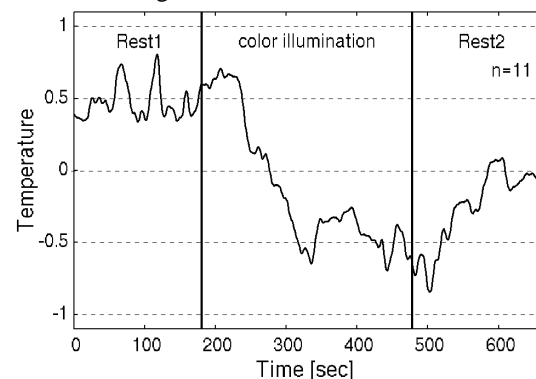


Fig.7. NST in blue illumination

Table.2. Results of Ptime, ΔT_{max} , ΔT_{dmax}

Colors	Yellow	Red	Blue
Ptime (s) (SD)	104.2(84.0)	76.1(62.8)	82.5(103.4)
ΔT_{max} (SD)	1.8(1.1)	2.4(0.8)	2.0(1.1)
ΔT_{dmax} (SD)	1.2(0.5)	1.5(0.7)	1.1(0.3)

VAS value and NSTs (Ptime, ΔT_{max} , ΔT_{dmax}). There were intermediate and strong correlations (four VAS values for yellow, eleven VAS values for red and six VAS values for blue). As a result, red is most influential color physiologically and psychologically. Particularly, high correlation coefficient 0.82 was observed between “Unpleasant-Pleasant” and ΔT_{max} for red. From this viewpoint, the NST decreases when red illumination is felt unpleasant.

Table.3. VAS vs NST(Ptime, ΔT_{max} and ΔT_{dmax})

Colors	Yellow			Red			Blue		
VAS	Ptime	ΔT_{max}	ΔT_{dmax}	Ptime	ΔT_{max}	ΔT_{dmax}	Ptime	ΔT_{max}	ΔT_{dmax}
Unpleasant-Pleasant	0.26	-0.50	0.25	0.14	0.82	0.52	-0.29	-0.44	-0.16
Distracted-Concentrate	-0.02	-0.35	-0.33	-0.66	-0.02	-0.16	0.15	-0.41	-0.23
Unhappy-Happy	0.34	-0.18	0.38	-0.41	0.32	-0.06	-0.03	-0.48	-0.39
Fatigue- Vigor	0.25	-0.72	-0.24	-0.68	-0.54	-0.51	-0.44	-0.32	0.01
Cold-Hot	0.27	-0.33	0.25	-0.07	-0.59	0.03	-0.49	0.00	0.38
Dark-Light	0.34	-0.76	-0.17	0.04	-0.11	0.48	-0.35	0.01	-0.07
Sleepy-Awake	0.21	-0.74	-0.19	-0.70	0.00	-0.50	0.41	-0.14	-0.23

However, there were correlations between “Unpleasant-Pleasant” and ΔT_{max} in yellow and blue illuminations. On the contrary, positive correlations were shown in red. This result cannot be explained by the conventional hypothesis that NST decreases with unpleasant feeling.

This result can be explained as follows: NST decreases “fast” down with unpleasant feeling. Red is the most influential physiologically and psychologically at three colors and there was a negative intermediate correlation between “Unpleasant-Pleasant” and ΔT_{dmax} of red.

In previous studies, the stimulations by tasks or loads to subjects were calculation problem [4,5], metal scratch noise [7] and driving task[8]. The reaction of NST for these stimulations decreased fast immediately after starting the stimulation. However, NST decreased after Ptime in this experiment. In comparison between the results of previous studies and this experiment, the color illumination might be less influential to human conditions physiologically and mentally than the stimulations previously used.

III. CONCLUSION

In this study, we investigated the color influences physiologically by use of nasal skin temperature measured by infrared thermography under yellow, red and blue illuminations. As a result, it was suggested that the mental and physical conditions are affected by the colors difference. Significant temperature change was observed under red illumination.

It is necessary to examine color influences mental and physiological with more subjects, more the VAS items and more color illuminations.

In order to clarify the relationship between NST and human mental/physiological conditions, further studies are required. It is expected to develop a novel system by

infrared thermography to measure human mental/physiological conditions.

REFERENCES

- [1] H.kubo, Y.Inoue, The Influence of Lighting by Used Chromatic Light on Physiological and Psychological Responses, Illum, Engng, Onst, Jpn, Vol.92, No.9, pp.645-649, 2008
- [2] Y.Kaku, K.Momose, M.Saito, Physiological effects and psychological effects of color light, Color Science Association of Japan, Vol.31 SUPPLEMENT, pp20-21, 2007
- [3] T.Oyama, M.Saito, An introduction to Color Theory: “Kansei” and the Psychology of Color, University of Tokyo Press, 2009
- [4] K.Hioki, A.Nozaawa, T.Mizuno, and H.Ide, Physiological Evaluation of Mental Workload in Time Pressure, T.IEEJ Trans.EIS, 127(7), pp.1000-1006, 2007.
- [5] T.Mizuno, S.Nomura, A.Nozaawa, H.Asano and H.Ide, Evaluation of the Effect of Intermittent Mental Work-Load by Nasal Skin Temperature, IEICE, J93-D(4), 535-543, 2010.
- [6] Advanced Industrial Science and Technology - Institute for Human Science and Biomedical Engineering, Handbook of Human measurement, Asakura publisher, 2003.
- [7] H.Zenju, A.Nozaawa, H.Tanaka, H.Ide, Estimation of Unpleasant and Pleasant States by Nasal Thermogram, IEEJ Trans. EIS, Vol.124, No.1, pp.213-214 (2004)
- [8] R.Sakamoto, A.Nozaawa, H.Tanaka, T.Mizuno, and H.Ide, Evaluation of the Driver’s Temporary Arousal Level by Facial Skin Thermogram –Effect of Surrounding Temperature and Wind on the Thermogram-, IEEJ Trans.EIS, 126(7), 804-809, 2006.

Air speed control of airship-type fish robot

Kunihiko Sato* and Masafumi Uchida**

*The Graduate School of the University of Electro-Communications

**The Department of Electronic Engineering, The University of Electro-Communications

1-5-1, Chofugaoka, Chofu, Tokyo, Japan

(Tel: +81-42-443-5173; Fax: +81-42-443-5173)

(Email: sato@zidane.ee.uec.ac.jp)

Abstract: This paper deals with progress in the motion performance and control of a Balloon Fish Robot (BFR). The BFR is a fish-type airship robot that derives its propulsion from vibrations of two joints. The BFR is moved in three-dimensional space by an actuator. We consider the thrust of the BFR and measured it with a force sensor. The purpose of this research is to construct an equation of motion for the BFR and to control its air speed.

Keywords: Airship Robot, Fish Robot

I. INTRODUCTION

Recently, there has been progress in research on airship robots that float in the air. An airship robot has the advantage of being able to move in three dimensions without being influenced by obstacles on the ground and without disturbing people's work. Moreover, because an airship uses a gas that is lighter than air to obtain buoyancy, the energy necessary for floatage is less than that of other types of flying robots, such as airplane and helicopter robots. Airship robots have been studied for applications in disaster relief and indoor patrol and surveillance systems [1].

On the other hand, there have been advances in research on the movement of fish, which have superior propulsive performance in water. There has been some work on applying fish-type underwater robots to offshore surveying and underwater surveys of natural resources [2][3]. In addition, a robot that employs the propulsion principle of aquatic organisms in the air, not water, has been developed. An example is the manta-type flying robot (Air Ray) developed by FESTO Co. developed.

We developed an airship robot based on a fish's propulsion principle, called the Balloon Fish Robot (BFR). The purpose of our research is to construct an equation of motion for the BFR and to control its air speed.

II. Structure and equation of motion of BFR

1. Structure of the BFR

Fig. 1 shows the structure of the BFR, and Fig. 2 shows a photograph of the BFR. The BFR is composed

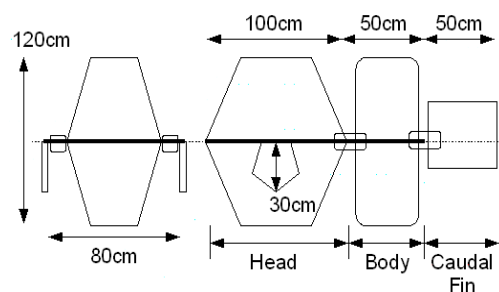


Fig.1. Structure of the BFR



Fig.2. Appearance of the BFR

of three parts: the head, the body, and the caudal fin. The head and the body are formed of aluminum film balloons filled with helium, giving the BFR a buoyancy of about 300 grams.

The BFR has two joints. One is a servo motor-driven joint between the head and the body, and the other is a spring joint between the body and the caudal fin. The servo motor moves symmetrically by various angles and at various frequencies and the BFR vibrates smoothly to obtain thrust. This movement is generally referred to as a fish's wriggling motion [4].

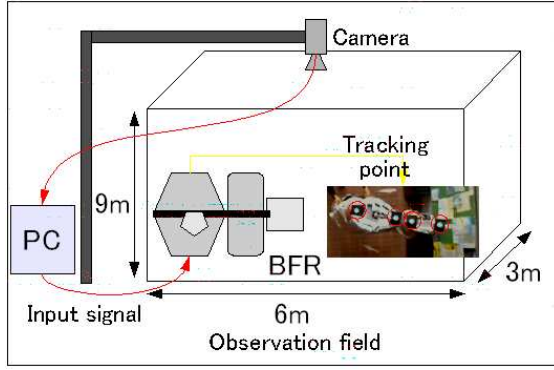


Fig.3. Real machine experimental system

2. Equation of motion of the BFR

Zhang constructed an equation of motion for an airship under the following three conditions [5]:

1. The airship is a rigid body.
2. There is no rotary motion about the three axes.
3. There is no air flow.

The propulsion direction of the BFR is taken as the x axis, the horizontal direction is taken as the y axis, and the vertical direction is taken as the z axis. Since we deal with propulsion of the BFR, it is assumed that there is no movement along the z axis. Because the wriggling motion is a symmetric motion, the y-axis components of the thrust cancel each other out. The x-axis component of the thrust determines the propulsion of the BFR. The equation of motion in the x-axis:

$$m \frac{d^2}{dt^2} x = -\frac{1}{2} \rho C S \frac{d}{dt} x + F \cos \theta, (1)$$

where m is the mass of the BFR, F is thrust, θ is the angle of the wriggling motion, ρ is the density of air, C is the air resistance coefficient, and S is the projected area of the BFR. The thrust F is measured to construct the equation of motion of the BFR.

III. MEASUREMENT SYSTEM

We focused on the thrust of the BFR and measured it with a force sensor. We considered two parameters of the BFR's wriggling motion: the oscillation angle and the oscillation frequency. To determine the equation of motion, we measured the thrust. In addition, the actual robot movements were measured, and the results were compared with those of the thrust measurement experiment. The thrust is corrected because there is a

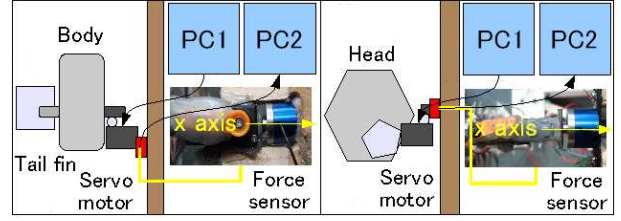


Fig.4. Thrust measurement system

difference in the position of the rotation axis in the real machine and the thrust measurement experiment.

1. Real machine measurements

We measured the propulsion of the BFR experimentally using an actual robot. Fig. 3 shows the real machine measurement system. Four tracking points were set on the BFR, and images were captured as the BFR advanced. The movement of the BFR was measured as two-dimensional coordinates.

2. Thrust measurement

In this study, the thrust of the BFR was measured with a force sensor. Fig. 4 shows the thrust measurement system. The force sensor, the body, and the caudal fin of the BFR were fixed to a wood post (prop), and the force generated by the wriggling motion was measured with the force sensor. Similarly, the movement of the head, which vibrates along with the wriggling motion, was also measured.

3. Thrust correction

There is a difference in the position of the rotation axis in the real machine and in the thrust measurement experiment, as illustrated in Fig. 5. In the thrust measurement experiment, the rotation axis determines the position of the servo motor. In this case, the length of the BFR that contributes to propulsion is the entire length of the BFR. The length of the head is defined as L_1 , and the length of the body is defined as L_2 .

The rotation axis moves in the actual machine, as shown in Fig. 5. Therefore, the length of the BFR that contributes to propulsion is shorter in both the head and the body. There is a difference in the thrust produced in the real machine and the thrust measurement experiment. In this case, the length of the head that contributes to propulsion is defined as nL_1 , and that of the body is defined as mL_2 ($0 < n < 1$, $0 < m < 1$). The numerical values of n and m are the coordinates of the rotation axis in the head and the body where the wriggling motion of the BFR occurs. The two points are the points that exist between two tracking points of the head and the body in the real machine experiment, where the distance moved is minimized.

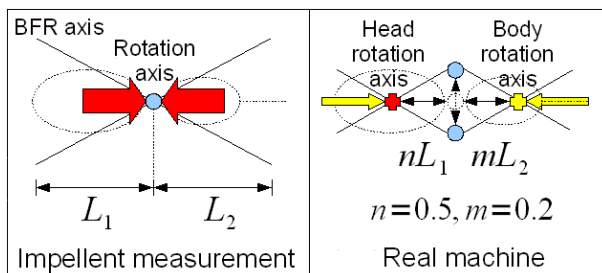


Fig.5. Difference of rotation axis

The numerical values of n and m were calculated from the results of the real machine experiment. The values of n and m were varied from 0.1 to 0.9 in steps of 0.1, and the values that minimized the distance moved were identified. The numerical results are illustrated in Fig. 6. From the results, we defined $n = 0.5$ and $m = 0.2$. Therefore, in the real machine, the length of the head that contributes to propulsion is $0.5L_1$, and that of the body is $0.8L_2$.

In short, because the thrust produced is different in the real machine and the thrust measurement experiment, it is necessary to correct the thrust with the values of n and m .

First, the thrust of the head is corrected. Because $n = 0.5$, the rotation axis of the head is at the center of the head. A positive thrust and a negative thrust cancel each other out in the wriggling motion in one cycle. Therefore, the thrust that the head generates is 0.

Next, the thrust that the body generates is corrected. The thrust is proportional to the volume of air pushed out behind by the wriggling motion. In this case, where $m = 0.2$, the length of the body that contributes to propulsion is $0.8L_2$, and a body length of $0.2L_2$ generates a negative thrust. As a result, the thrust that the body and the caudal fin generate is corrected by a factor of 0.6. In addition, the angle of the wriggling motion is 45 degree, but because the rotation axis and the head move, the angle of the wriggling motion becomes smaller than 45 degree. From the measurement results, the angle of the head was 15 degree, and the angle of the body was 30 degree during the wriggling motion. Therefore, the oscillation angle of the body is assumed to be 30 degree in the thrust measurement experiment.

IV. EXPERIMENT

1. Real machine experiment

Images of the BFR during propulsion were captured with a camera. The wriggling motion of the BFR is oscillating movement having an oscillation angle and

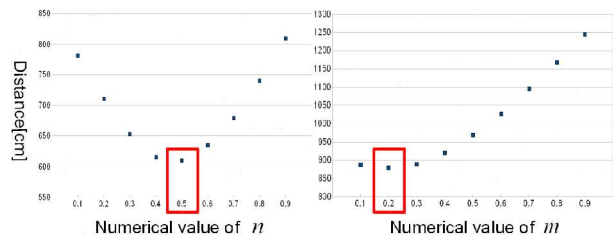


Fig.6. Numerical values of n and m

oscillation speed. In a preliminary study, we found that the velocity of the BFR was highest when the oscillation angle was 45 degrees and increased as the oscillation speed increased. Therefore, we set the following experimental conditions: the oscillation angle was 45 degree, the oscillation frequency was 0.5 Hz, which was the maximum speed of the servo motor, the measurement time was 15 s, and the sampling frequency was 30 fps.

2. Thrust measurement experiment

The thrust of the BFR was measured with the force sensor. We set the experimental conditions according to the thrust correction. The oscillation angle was 30 degree, the oscillation frequency was 0.5 Hz, the measurement time was 15 s, and the sampling frequency was 1024 Hz.

V. RESULTS

The velocity of the BFR was calculated from the results of the real machine experiment and the thrust measurement experiment.

The distance moved by the tracking points on the BFR was measured from the results of the real machine experiment, and the velocity of the BFR was calculated every 0.3 s.

The results of the thrust measurement experiment were substituted into the equation of motion of the BFR, and the velocity of the BFR was calculated. Fig. 7 shows the numerical results. In Fig. 7, the horizontal axis corresponds to time and the vertical axis corresponds to the velocity of the BFR. In the thrust measurement experiment, the velocity of the BFR was calculated using the thrust values before correction and after correction. The bottom graph shows the difference between the results of the real machine experiment and those after thrust correction. In Fig. 7, because the thrust was corrected, the calculated value become close to the velocity of the real machine. As a result, it was possible to construct an equation of motion closer to that of the real machine by considering the movement of the real machine. The maximum velocity of the BFR was about 0.6 m/s for the real machine and the equation of motion,

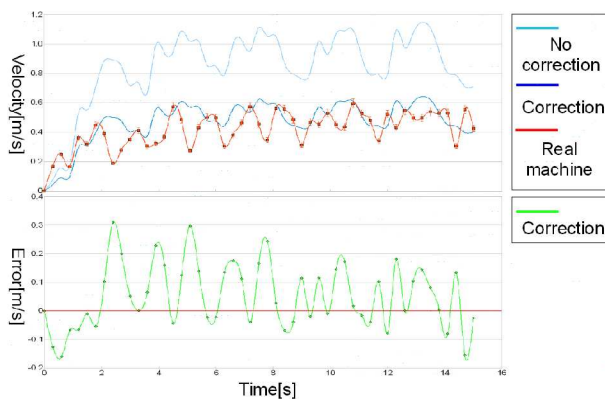


Fig.7. Velocity of the BFR

showing good agreement. However, even after the thrust had been corrected, it was confirmed that the difference in velocity compared with the real machine was about 0.3 m/s at most. Therefore, there must be force that was not taken into account in constructing the equation of motion.

VI. DISCUSSION

There was a difference between the results observed with the real machine and those obtained with the equation of motion. In Fig. 7, the velocity periodically decreases in the calculation results for the real machine.

The cause of this is thought to be the change in the projected area. In this study, the projected area of the BFR was assumed to be constant in calculating the velocity. In practice, however, the projected area changes over time because the head of the BFR moves during the wriggling motion. The reason why the velocity of the real machine decreases is that the projected area increases periodically.

Similarly, it is also necessary to consider the force that the pectoral fins generate during the wriggling motion.

In this research, the velocity of the BFR was calculated for one pattern of wriggling motion; in future, it will be necessary to calculate the velocity for other wriggling motions.

VII. CONCLUSION

The aims of this study were to measure the thrust of the BFR and to construct an equation of motion. We measured the thrust with a force sensor and constructed the equation of motion by comparing the results with those for real machine movement. As a result, it was possible to construct an equation of motion closer to that

of the real machine by considering the movement of the real machine.

VIII. FUTURE TASKS

Tasks to be implemented in future work include considering the change in the projected area, conducting experiments using other wriggle motion patterns, repeating the motion experiments for a BFR with pectoral fins, constructing an equation of motion, and controlling the air speed.

ACKNOWLEDGMENTS

A part of this study was supported by the HAYAO NAKAYAMA Foundation for Science & Technology and Culture and a Grant-in-Aid for Scientific Research (Basis Research (C), Assignment Number: 21500511).

REFERENCES

- [1] Kazuhiro Hosoi, Masanori Sugimoto, "An Autonomous Security System Using Multi-Flying Robots," The 18th Annual Conference of the Japanese Society for Artificial Intelligence, 2C1-04, 2004.
- [2] Junzhi Yu, Lizhong Liu, Long Wang, Min Tan, De Xu, "Turning Control of a Multilink Biomimetic Robotic Fish," IEEE TRANSACTIONS ON ROBOTICS, Vol. 24, No. 1, pp. 201-206, February 2008.
- [3] Junzhi Yu, Long Wang, Min Tan, "Geometric Optimization of Relative Link Length for Biomimetic Robotic Fish," IEEE TRANSACTIONS ON ROBOTICS, Vol. 23, No. 2, pp. 382-386, APRIL 2007.
- [4] Motomu Nakashima, Kyosuke Ono "Dynamics of Two-Joint Dolphinlike Propulsion Mechanism (1st Report, Analytical Model and Analysis Method)," The Japan Society of Mechanical Engineers, 62-600(B), pp. 3044-3051, 1996.
- [5] H. Zhang, J. P. Ostrowski, "Visual Servoing with Dynamics: Control of an Unmanned Blimp," Proc. IEEE Int. Conf. Robotics and Automation, pp. 618-623, 1999.

Regulated Plus and Minus Power Supply Using Approximate 2DOF Robust Digital Control

Atsushi Saitoh¹, Yusuke Tsuruhori², Yoshihiro Ohta³, Kohji Higuchi⁴, Kazushi Nakano⁵

^{1,2,3,4,5}The University of Electro-Communications,

1-5-1 Chofu-ga-oka, Chofu, Tokyo 182-8585, Japan

email:saitoh@francis.ee.uec.ac.jp, tsuruhori@francis.ee.uec.ac.jp, ohta@francis.ee.uec.ac.jp,

higuchi@ee.uec.ac.jp, nakano@ee.uec.ac.jp

Abstract—A plus and minus switching power supplies are needed for many applications, for example audio power supply. Since the output voltage changes of such power amplifiers which are loads are large, the power supply voltage are changed largely. Usually, in order to suppress the change, a capacitor with large capacity is used at the output end. If the capacities are made small, the power supplies can be compacted. In this paper, it is shown that the capacities can be made small using a robust digital control using an approximate 2DOF. The derived controller is actually implemented on a DSP. It is demonstrated from experiments that the power supplies can be compacted by the robust controller.

I. INTRODUCTION

The DC-DC converter is used for a switching power supply of an plus and minus power amplifier for many applications, for example an audio amplifier. This power supply is needed to be compacted. In usual power supply, in order to suppress an output voltage change for load change and input voltage change, a capacitor with large capacity is used for the output end. It can be considered that that the capacity is made small as one means of a compact the audio power amplifier. The authors proposed the method of designing a approximate 2-degree-of-freedom (2DOF) controller of DC-DC converter[1] as a robust digital controller. The digital controller makes the control bandwidth wider, and at the same time makes the change of the output voltage very small at sudden changes of load and the input voltage. This robust digital controller was applied to control one side power supply[2]. In this paper, it is shown that the output voltage change of the both sides plus and minus power supply can fully be suppressed and the power supply can be compacted by the capacitor with small capacity using this type robust digital control. The robust digital controller is actually implemented on a DSP. It is demonstrated from experiments that the capacity can be made small by the robust controller.

II. PLUS AND MINUS POWER SUPPLY

The configuration of the audio power supply is shown in Fig. 1. The part except for the controller is a controlled

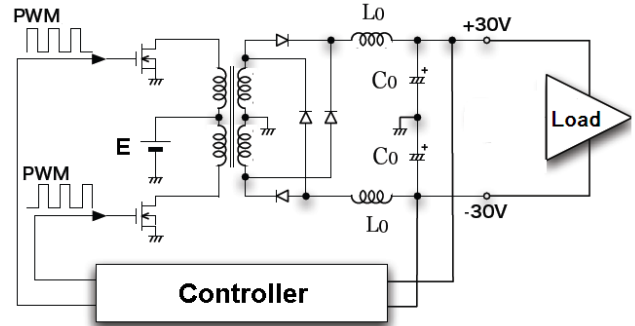


Fig. 1. Plus and Minus power supply

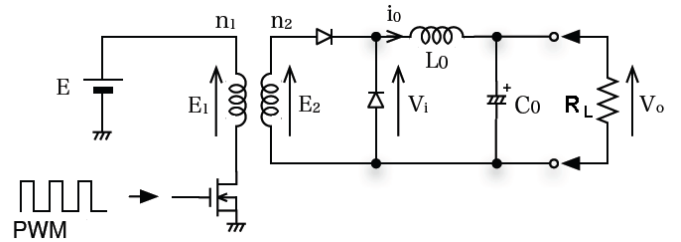


Fig. 2. Plus side model of power supply

object. The triangular wave carrier is adopted for the PWM switching signal. The switching frequency is set at 100[KHz] and E is 14.5[V], $n_1 : n_2 = 4 : 13$. The LC circuit is a filter for removing carrier and switching noises. C_0 is 1000[μ F] and L_0 is 70[μ H]. In Fig.1, a plus side and a minus side are symmetrical, and the plus side model is shown in Fig. 2. The state equation of Fig. 2 is derived. If the frequency of control signal u is smaller enough than that of the carrier, the state equation of the DC-DC converter at a resistive load in Fig.1 except for the controller in DSP can be expressed from the state equalizing method as follows :

$$\begin{cases} \dot{x} = A_c x + B_c u \\ y = C x \end{cases} \quad (1)$$

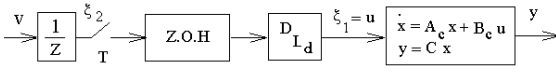


Fig. 3. Controlled object with input dead time $L_d (\leq T)$

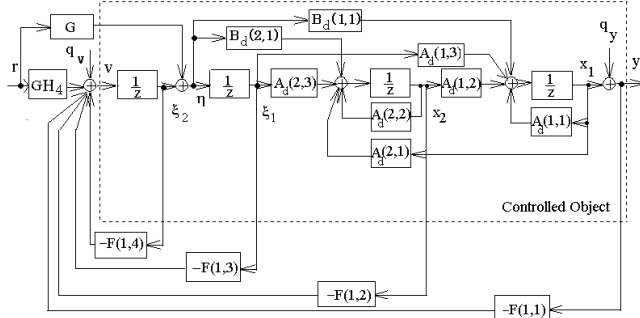


Fig. 4. Equivalent disturbances due to load variations (parameter variations) and model matching system with state feedback

where

$$x = \begin{bmatrix} e_o \\ i \end{bmatrix} \quad A_c = \begin{bmatrix} -\frac{1}{C_0 R_L} & \frac{1}{C_0} \\ -\frac{1}{L_0} & -\frac{R_0}{L_0} \end{bmatrix} \quad B_c = \begin{bmatrix} 0 \\ \frac{K_p}{L_0} \end{bmatrix}$$

$$C = \begin{bmatrix} 1 & 0 \end{bmatrix} \quad u = e_i \quad y = e_o \quad K_p = \frac{V_i N_2}{C_m N_1}$$

R_0 is the total resistance of coil and ON resistance of FET, etc., and the value is $0.015[\Omega]$. When realizing a digital controller by a DSP, a delay time exists between the starting time of the sampling operation and the outputting time of the control signal due to the calculation and AD/DA conversion times. This delay time is considered to be equivalent to the input dead time which exists in the controlled object as shown in Fig. 3. Then the state equation of the system in Fig.3 is expressed as follows :

$$\begin{cases} x_{dw}(k+1) = A_{dw}x_{dw}(k) + B_{dw}v(k) \\ y(k) = C_{dw}x_{dw}(k) \end{cases} \quad (2)$$

where

$$x_{dw}(k) = \begin{bmatrix} x_d(k) \\ \xi_2(k) \end{bmatrix} \quad x_d(k) = \begin{bmatrix} x(k) \\ \xi_1(k) \end{bmatrix}$$

$$A_{dw} = \begin{bmatrix} A_d & B_d \\ 0 & 0 \end{bmatrix} \quad B_{dw}(k) = \begin{bmatrix} 0 \\ 1 \end{bmatrix}$$

$$A_d = \begin{bmatrix} e^{A_c T} & e^{A_c(T-L_d)} \int_0^{L_d} e^{A_c \tau} B_c d\tau \\ 0 & 0 \end{bmatrix}$$

$$B_d = \begin{bmatrix} \int_0^{T-L_d} e^{A_c \tau} B_c d\tau \\ 1 \end{bmatrix}$$

$$C_{dw} = \begin{bmatrix} C_d & 0 \end{bmatrix} \quad C_d = \begin{bmatrix} C & 0 \end{bmatrix} \quad \xi_1(k) = u(k)$$

It can be considered that the input voltage E and the load change by change of the amplitude of a voice signal etc. is parameter changes for the controlled object.

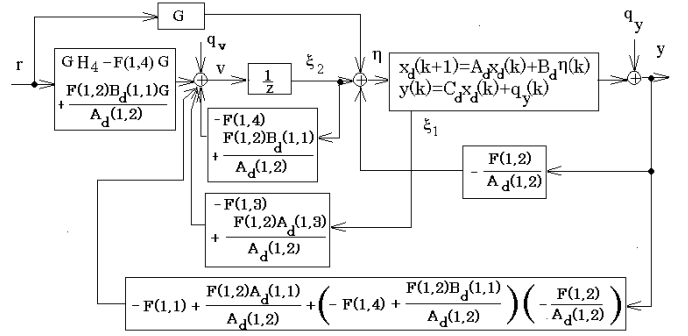


Fig. 5. Model matching system using only voltage (output) feedback

These parameter changes can be considered to be equivalent disturbances q_u and q_y inputted into the controlled object from the exterior as shown in Fig. 4. If the transfer functions between the equivalent disturbances and the output voltage can be made small, it will become the control system hardly influenced of the input voltage change and the load changes. Therefore, if the controller is designed so that this transfer function may become small, the compact audio power supply will be attained even if the capacity C_0 is small.

III. ROBUST DIGITAL CONTROLLER

A. Configuration of control system

First, the transfer function between the reference input r and the output y is specified as follows :

$$W_{ry}(z) = \frac{(1+H_1)(1+H_2)(1+H_3)(z-n_1)(z-n_2)(z+H_4)}{(1-n_1)(1-n_2)(z+H_1)(z+H_2)(z+H_3)(z+H_4)} \quad (3)$$

where, n_1 and n_2 are the zeros for the discrete-time control object (2). It shall be specified that the relation of H_1 and H_2, H_3 becomes $|H_1| \gg |Re(H_2)|, |H_1| \gg |Re(H_3)|$. Then $W_{ry}(z)$ can be approximated to the following first-order model:

$$W_{ry}(z) \approx W_m(z) = \frac{1+H_1}{z+H_1} \quad (4)$$

This target characteristics $W_{ry}(z) \approx W_m(z)$ is specified so that the bandwidth of the audio power supply becomes as wide as possible.

Applying a state feedback

$$\begin{aligned} v &= -Fx^* + GH_4 r \\ x^* &= [y \quad x_2 \quad \xi_1 \quad \xi_2]^T \end{aligned} \quad (5)$$

and feedforward

$$\xi_1(k+1) = Gr \quad (6)$$

to the discrete-time controlled object as shown in Fig. 4, we decide $F = [F(1,1) \ F(1,2) \ F(1,3) \ F(1,4)]$ and G so

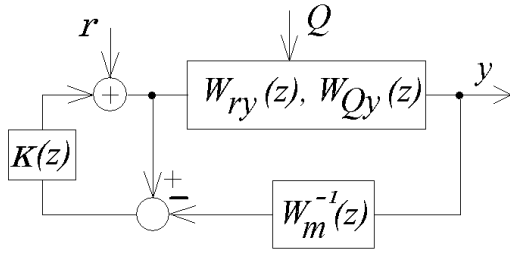


Fig. 6. System reconstituted with inverse system and filter

that $W_{ry}(z)$ becomes eq.(3). The current feedback is used in Fig. 4. This is transformed to voltage and control input feedbacks without changing the pulse transfer function between $r - y$ by an equivalent conversion. The following relation is obtained from Fig. 4:

$$\begin{aligned} -F(1,2)x_2(k) &= -\frac{F(1,2)}{A_d(1,2)}(x_1(k+1) \\ -A_d(1,1)x_1(k) &- A_d(1,3)\xi_1 - B_d(1,1)\eta) \end{aligned} \quad (7)$$

If the current feedback is transformed equivalently using the right-hand side of this equation, the control system with only voltage feedback as shown in Fig. 5 will be obtained. The transfer function $W_{Qy}(z)$ between this equivalent disturbance $Q = [q_v \ q_y]^T$ and y of the system in Fig. 5 is defined as

$$W_{Qy}(z) = \begin{bmatrix} W_{qv}(z) & W_{qy}(z) \end{bmatrix} \quad (8)$$

The system added the inverse system and the filter to the system of Fig.5 is constituted as shown in Fig. 6. In Fig. 6, the transfer function $K(z)$ becomes

$$K(z) = \frac{k_z}{z-1+k_z} \quad (9)$$

The transfer functions between $r - y$ and $Q - y$ of the system in Fig. 6 are given by

$$y = \frac{1+H_1}{z+H_1} \frac{z-1+k_z}{z-1+k_z W_s(z)} W_s(z) r \quad (10)$$

$$y = \frac{z-1}{z-1+k_z} \frac{z-1+k_z}{z-1+k_z W_s(z)} W_{Qy}(z) Q \quad (11)$$

where

$$W_s(z) = \frac{(1-H_2)(1+H_3)(z-n_1)(z-n_2)}{(z-H_2)(z+H_3)(1-n_1)(1-n_2)} \quad (12)$$

Here, if $W_s(z) \approx 1$, then Eqs.(9) and (10) become, respectively,

$$y \approx \frac{1+H_1}{z+H_1} r \quad (13)$$

$$y \approx \frac{z-1}{z-1+k_z} W_{Qy}(z) Q \quad (14)$$

From eqs.(12) and (13), it turns out that the characteristics from r to y can be specified with H_1 , and the characteristics from Q to y can be independently specified with k_z . That is, the system in Fig. 6 is an approximate 2DOF, and its sensitivity against disturbance becomes lower with the increase of k_z .

If an equivalent conversion of the controller in Fig. 6 is carried out, the approximate 2DOF digital integral-type control systems will be obtained as shown in **Fig.6**. In Fig. 7, the parameters of the controller are as follows :

$$\begin{aligned} k_1 &= F(1,1 + F(1,2)FF(1,1) + ((-F(1,4) \\ &- F(1,2)FF(1,4))(-F(1,2)/FF(1,2))) \\ &+ (GH_4 + GF_z)(k_z/(1+H_2)) \\ k_2 &= F(1,2)/FF(1,2) + G(k_z/(1+H_2)) \\ k_3 &= F(1,3) + F(1,2)(FF(1,3)) \quad k_4 = -F_z \\ k_{i1} &= Gk_z \quad k_{i2} = (GH_4 + GF_z)k_z \\ k_{r1} &= G \quad k_{r2} = GH_4 + GF_z \end{aligned} \quad (15)$$

where

$$\begin{aligned} FF(1,1) &= -A_d(1,1)/A_d(1,2) \\ FF(1,2) &= A_d(1,2) \\ FF(1,3) &= -A_d(1,3)/A_d(1,2) \\ FF(1,4) &= -B_d(1,1)/A_d(1,2) \\ F_z &= -F(1,4) - F(1,2)FF(1,4) \end{aligned}$$

In the audio amplifier power supply, since a plus side and a minus side is symmetrical, the controller which controls only the plus side is designed. A model for the controlled object of the plus side becomes as shown in Fig. 2. The robust control system to this controlled object becomes as shown in Fig. 7. This system is an approximate 2DOF system and can specify independently the characteristics between the reference value and the controlled output, and the characteristics between the disturbance and the controlled output. If the parameter of the controller is set up so that the transfer function between the disturbance and the controlled output may become small, the control system will become low sensitivity very much. Therefore, even if the capacity is small, the large load changes can be suppressed. The same controller of Fig. 7 is applied to the minus side of Fig. 1. The averaged control input is switched to the plus side and minus side.

IV. EXPERIMENTAL STUDIES

The sampling period T are set at $10[\mu s]$ and the input dead time L_d is about $0.999T[\mu s]$. The nominal value of R_L is $4[\Omega]$. We design a control system so that all the specifications are satisfied. First of all, in order to satisfy the specification on the rising time of startup transient response, H_1, H_2, H_3 and H_4 are specified as

$$H_1 = -0.9 \quad H_2 = 0.1 + 0.1i \quad H_3 = 0.1 - 0.1i$$

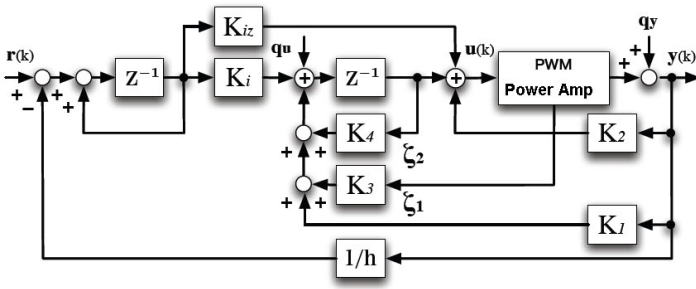


Fig. 7. Approximate 2DOF robust digital control system

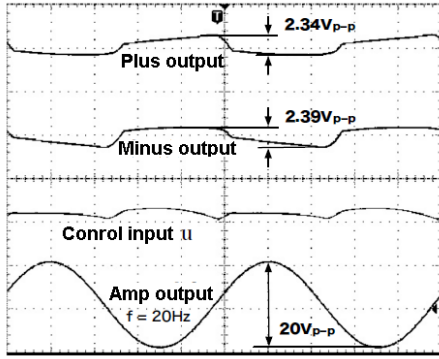


Fig. 8. Experimental results by the approximate 2DOF robust digital control at $C_0 = 1000[\mu F]$

$$H_4 = -0.999 \quad k_z = 0.15 \quad (16)$$

Then the parameters of controller become

$$\begin{aligned} k_1 &= 14.063 \quad k_2 = -11.605 \quad k_3 = -0.022209 \\ k_4 &= -0.20448 \quad k_i = -1.3752 \quad k_{iz} = 1.1427 \end{aligned} \quad (17)$$

We used the DSP(TI TMS320LF2808). Fig. 8 and Fig. 9 show the output voltage changes by the approximate 2DOF robust control at $C_0 = 1000[\mu]$ and $C_0 = 220[\mu]$, respectively. From these results, it turns out that output voltage change hardly changes even if capacity be-

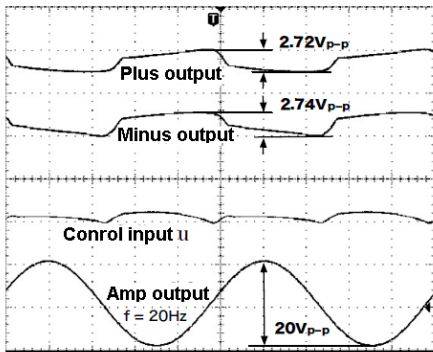


Fig. 9. Experimental results by the approximate 2DOF robust digital control at $C_0 = 220[\mu F]$

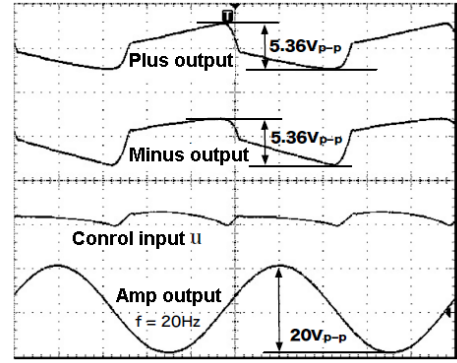


Fig. 10. Experimental results by PI control at $C_0 = 1000[\mu F]$

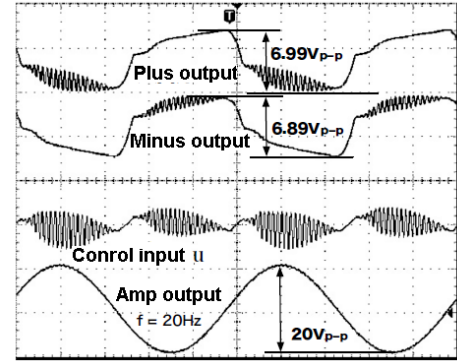


Fig. 11. Experimental results by PI control at $C_0 = 220[\mu F]$

comes very small. Fig. 10 and Fig. 11 show the output voltage changes by PI control at $C_0 = 1000[\mu]$ and $C_0 = 1000[\mu]$, respectively. It turns out that the output voltage changes are very large compared with the robust control. Moreover, the output voltage changes are oscillating at $C_0 = 220[\mu]$. These results show that the robust control by approximate 2DOF is effective in compact audio power supply.

V. CONCLUSION

In this paper, the robust digital control was performed by DSP. Consequently, even if it made capacity small, it was shown that output voltage changes of the both sides of the plus and minus power supply can be suppressed almost like the time when capacities are large. A future subject is designing the robust digital controller which can make the value of output voltage change smaller.

REFERENCES

- [1] K. Higuchi, K. Nakano, K. Araki and F. Chino, "NEW ROBUST CONTROL OF PWM POWER AMPLIFIER," IFAC 15th Triennial World Congress(CD-ROM), 2002.
- [2] T. Kanai, K. Higuchi, K. Nakano, T. Kajikawa, A. Shimizu, O. Yoshizawa, "Compact Size of Audio Power Supply using Robust Control," SICE 7th Annual Conference on Control Systems, pp.62-1-2, March, 2007.

Angle-based neuro-fuzzy navigation for autonomous mobile robots

Shu Hosokawa, Joji Kato, Kazushi Nakano, Kazunori Sakurama

Dept. of Electronic Eng., The University of Electro-Communications, Japan

(Tel : 81-42-443-5190; Fax : 81-42-443-5183)

(hosokawa@francis.ee.uec.ac.jp)

Abstract: This paper presents a neuro-fuzzy navigation method for mobile robots based on local sensors mounted on the robot. This method is not sensitive to sensor noise, and is able to automatically adjust the internal parameters given by the teacher signal. However, most of previous studies dealt with two-wheel driven robots have focused on the acceleration control of their wheels. For this reason, it is difficult to generate teacher signals for robots with many actuators such as omnidirectional mobile robots. In this paper, we propose a method of neuro-fuzzy navigation based on control of rotation speed of the robots. We demonstrate the validity of our proposed method through simulations and experiments.

Keywords: Omnidirectional mobile robot, Neuro fuzzy, Robot navigation, Local sensor

I. Introduction

Recently, the autonomous mobile robots working in dangerous environments such as disaster sites have been studied. These robots cannot get information about their operating environments in advance. For this reason, these robots require navigation methods to a target point based on information from local sensors mounted on the robots.

There are some methods based on the fuzzy inference techniques using local sensors on the robots to navigate to a target point [1][2]. Those methods can reduce the effect of observation noises from local sensors, but adjustments of the parameters by experts are necessary. Automatic parameter turning methods which incorporate neural network structures into fuzzy inference systems have been proposed in [3][4]. These controllers are able to adjust the parameters automatically by giving desired moving patterns. However, most of previous studies deal with the two wheel robots considering the acceleration of the motors as input. But when applying these methods to more complex systems (for example: snake-like robots, omnidirectional mobile robots and so on), the complexity makes it difficult to generate teacher signals.

In this paper, we propose a method using the rotation speeds of the robots as the input for the robot. By using the rotation speed instead of the acceleration of each actuator, we can generate the teacher signals for the controller. The validity of the proposed method is demonstrated through simulations and experiments.

II. Omnidirectional mobile robot

Figure 1 shows an omnidirectional mobile robot in this study, where θ is the angle between y-axis and a wheel, V_x is the velocity at the front direction of the

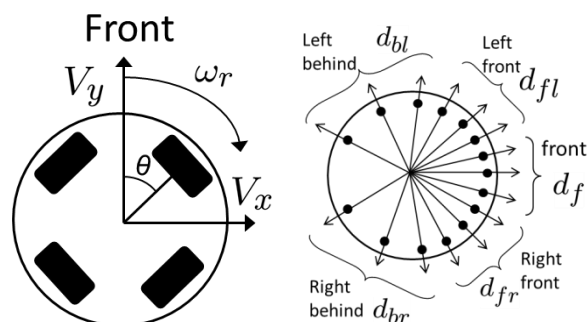


Figure 1 Omnidirectional mobile robot

Figure 2 Obstacle sensor placements

robot, V_y is the velocity at the lateral direction of the robot, and ω_r is the velocity of the rotation of the robot. In this study, the rotation speed of each wheel is controlled by a suitable controller (for example: PID), and is assumed to accurately rotate according to the reference value. The following equation shows the relationship between the moving velocity of the robot and the velocity of each wheel:

$$\begin{bmatrix} w_1 \\ w_2 \\ w_3 \\ w_4 \end{bmatrix} = \frac{1}{R_w} \begin{bmatrix} \sin(\theta) & -\cos(\theta) & R \\ \sin(\theta) & \cos(\theta) & R \\ -\sin(\theta) & \cos(\theta) & R \\ -\sin(\theta) & -\cos(\theta) & R \end{bmatrix} \begin{bmatrix} V_x \\ V_y \\ \omega_r \end{bmatrix} \quad (1)$$

where R is the radius of the robot, and R_w is the radius of the wheel. In this study, we design a controller using two pieces of information; the distance between the obstacle and the robots, the angle of the target point from the front direction of the robot.

Figure 2 shows the arrangement of fifty obstacle detection sensors mounted on the robot. Those sensors are divided into five groups of three adjacent sensors {right behind, right front, front, left front, left behind}. The output value of each sensor group is selected to take a smallest value in the groups. The angle of the target direction is given from the front of the robot. In this paper, we assume a constant velocity at the lateral direction for simplicity.

III. Angle-based neuro-fuzzy navigation

This section, explains the proposed method of angle-based neuro-fuzzy controller. At first, we explain the controller structures and how to adjust the parameters of the fuzzy membership functions.

1. Controller structure

Figure 3 shows the structure of the proposed angle-based neuro-fuzzy controller. This controller consists of a five-layer neural network. The first layer receives the target direction and distance information from the obstacle sensors. The second layer converts an input value to a fuzzy grade using the fuzzy inference logic. Membership functions of the target direction consist of five fuzzy sets {right behind, right front, front, left front, left behind}, in the form of triangular type functions:

$$p_{ij} = \begin{cases} 1 - \frac{2|u_i - m_{ij}|}{\sigma_{ij}}, & m_{ij} - \frac{\sigma_{ij}}{2} < u_i < m_{ij} + \frac{\sigma_{ij}}{2} \\ 0.001, & \text{otherwise} \end{cases} \quad (2)$$

where i is a input number, j is a fuzzy set number, p_{ij} is the fuzzy grade, m_{ij} is the center value of the membership function, u_i is the input value, σ_{ij} is the width of the membership function. Otherwise, the membership function of the obstacle sensor consists of two fuzzy sets to determine the distance from the obstacle. A Z-type function in (3) is adopted as the membership function that represents the distance between the robot and the obstacle:

$$p_{ij} = \begin{cases} 0.001, & u_i \geq m_{ij} + \frac{\sigma_u}{2} \\ 1, & u_i < m_{ij} \\ 1 - \frac{2|u_i - m_{ij}|}{\sigma_{ij}}, & \text{otherwise} \end{cases} \quad (3)$$

while, a S-type function in (4) is adopted as the membership function that represents the closeness between the robot and the obstacles.

$$p_{ij} = \begin{cases} 0.001, & u_i \leq m_{ij} - \frac{\sigma_u}{2} \\ 1, & u_i > m_{ij} \\ 1 - \frac{2|u_i - m_{ij}|}{\sigma_{ij}}, & \text{otherwise} \end{cases} \quad (4)$$

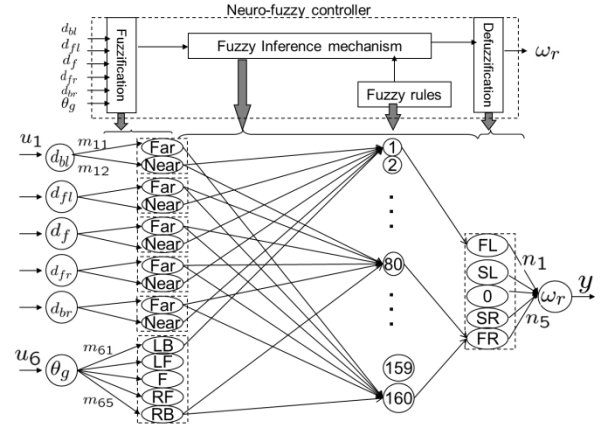


Figure 3 Angle-based neuro-fuzzy controller

The third layer represents the fuzzy controller based on the if-then rules, which has the connection with the second layer as the antecedent, and the connection with the fourth layer as the consequent. As for the if-then rule, there are 160 rules from five fuzzy sets of the target direction and two fuzzy sets of five groups of obstacle sensors. The fourth layer represents the output linguistic grades. The fifth layer is the output of the controller, which gives the center of gravity defuzzification of fuzzy sets of the four layers. The center of gravity is calculated using the lowest grade in the antecedent of each fuzzy rule:

$$y = \frac{\sum_{k=1}^{160} v_k q_k}{\sum_{k=1}^{160} q_k} \quad (5)$$

$$q_k = \min\{p_1 k_1, p_2 k_2, p_3 k_3, p_4 k_4, p_5 k_5, p_6 k_6\} \quad (6)$$

where y is the output value of the rotation value, k is the number of fuzzy rule sets, v_k is the center value of the fuzzy membership function, and q_k is the fitness of the k -th fuzzy rules.

2. Learning algorithm

We explain a parameter adjustment law adopted by our proposed method to use teacher signals. The proposed method has the parameters; the center value of fuzzy membership function and the width of fuzzy membership function. In this study, we update only the center values of fuzzy membership functions.

Adjustment of the parameters is performed by using the evaluation function described by the following equation:

$$E = \frac{1}{2} (y - \hat{y})^2 \quad (7)$$

where E is the error, \hat{y} is the teacher signal. This evaluation is based on the least mean square method. \mathbf{Z} as the median to be updated, the update formula is expressed as

$$\mathbf{Z}(t+1) = \mathbf{Z}(t) - \varepsilon \frac{\partial E}{\partial \mathbf{Z}} \quad (8)$$

where ε is the learning rate, $\mathbf{Z}(t)$ is the parameter vector at the update number t . Each parameter is updated by the following equation:

$$m_{ij}(t+1) = m_{ij}(t) - \varepsilon \frac{\partial E}{\partial m_{ij}} \quad (9)$$

$$n_s(t+1) = n_s(t) - \varepsilon \frac{\partial E}{\partial n_s} \quad (10)$$

where, if $q_k = p_{ij}$ and $p_{ij} \neq \text{const}$,

$$\begin{aligned} \frac{\partial E}{\partial m_{ij}} = & -2 \left\{ (y - \hat{y}) \frac{v_k \sum_{k=1}^{160} q_k - \sum_{k=1}^{160} v_k q_k}{(\sum_{k=1}^{160} q_k)^2} \right\} \\ & \times \frac{\text{sign}(u_i - m_{ij})}{\sigma_{ij}} \end{aligned}$$

otherwise

$$\frac{\partial E}{\partial m_{ij}} = 0$$

And also, if $v_k = n_s$,

$$\frac{\partial E}{\partial n_s} = (y - \hat{y}) \frac{q_k}{\sum_{k=1}^{160} q_k}$$

otherwise

$$\frac{\partial E}{\partial n_s} = 0$$

Teacher signals are used in expressions to produce more updates from the history of the human-robot operation. The teacher signals has the three types of parameters; the angle of the target point from the front direction of the robot, the distance from the obstacles were measured by the local sensor mounted on the robot, and the velocity of the rotation of the robot were controlled by a human. Parameter adjustment is repeated until the error falls below the set value δ ($0 < \delta$).

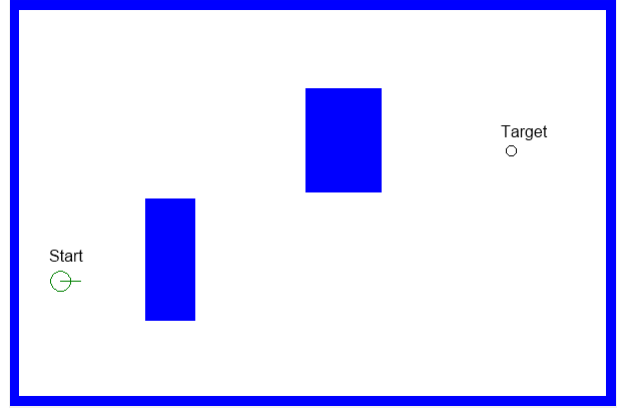


Figure 4 Training environment

Table 1 Simulation parameters

Robot radius	10 cm
Working space	405 cm × 605 cm
Measuring range of the obstacle sensor	0 cm ~ 100 cm
Translation velocity	20 cm/s
Control cycle	200 ms

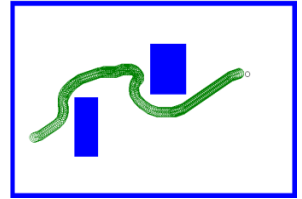
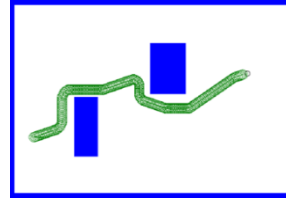


Figure 5 Trajectory for training data

Figure 6 Trajectory after parameter adjustment

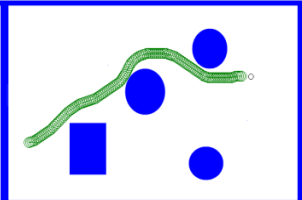
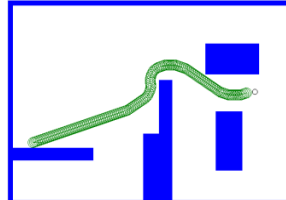
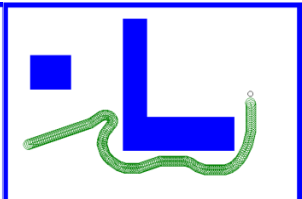
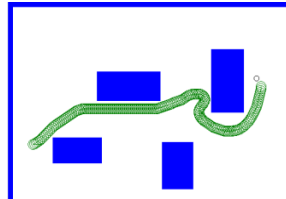


Figure 5 Results in various environments

IV. Simulation and experimental results

This section shows simulation and experiment results of our proposed method. First, we explain how to generate the teacher signal in the training environment, and adjust the parameters of fuzzy membership functions. Next, we show some different environments. Finally, we demonstrate the results of the actual robot.

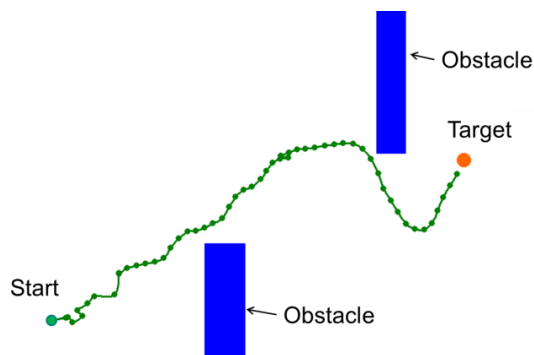


Figure 6 Actual results

Figure 4 shows the environment in the simulation. Table 1 is the list of the parameters used in these simulations. The simulation purpose is to move a robot to a goal position on the left side of each environment from the start at the right side without colliding against obstacles.

Figure 5 shows the trajectory of the robot operated by a human teacher. Figure 6 shows the trajectories of the robot after the parameter adjustment based on the teacher. By adjusting the parameters of fuzzy membership functions, we can see that the robot reaches the target without colliding against obstacles.

Next, we show the result in some different environments with pre-adjusted parameters in the previous environment. The starting position and the target point are the same as the previous environment. Figure 7 shows the results in the four simulation environments in different shapes, where the numbers of obstacles are different. We can see that the robot reach the target in all the environments without re-adjusting the parameters.

Finally, we apply our proposed method to the actual robot. We prepare a simulated environment created by the teacher signals shown in Figure 5. The parameters of membership functions are obtained by the simulation. Figure 8 shows the trajectory obtained by the actual robot. We can see that the actual robot reach the target without colliding with obstacles.

VI. Conclusion

In this study, we proposed an angle-based neuro-fuzzy navigation method. We control the rotation speed of robots instead of the acceleration of each motor. Thus, a controller structure was too compact to simplify the generation of teaching signals even when applying the robot to a complex structure. We showed the validity of

our proposed method through simulations and experiments.

REFERENCES

- [1] Eugenio Aguirre and Antonio Gonzalez (2003), A fuzzy perceptual model for ultrasound sensors applied to intelligent navigation for mobile robots. *Applied Intelligence* 19, 171-187
- [2] S.M.Raguraman, D.Tamilselvi and N. Shivvakumar (2009), Mobile robot navigation using fuzzy logic controller. *International conference on control , automation, communication and energy conservation*
- [3] Kai-Tai-Song and Liang-Hwang Sheen (2000), Heuristic fuzzy-neuro network and its application to reactive navigation of a mobile robot. *Fuzzy Set and Systems* 110, 331-1340
- [4] Anmin Zhu and Simon X. Yang (2007), Neurofuzzy-based approach to mobile robot navigation in unknown environments. *IEEE trans. on Systems, Man, and Cybernetic – Part C: Applications and Review* 37(4), 610-621

Quantitative Evaluation of Body-sway Caused by Tactile Apparent Movement

Kennichi Mogi* and Masafumi Uchida**

*The Graduate School of Electro-Communications, The University of Electro-Communications
**The Graduate School of Informatics and Engineering, The University of Electro-Communication
1-5-1, Chofugaoka, Chofu, Tokyo, Japans
(Tel : 81-42-443-5173; Fax : 81-42-443-5173)
(mogi@zidane.ee.uec.ac.jp)

Abstract: The recognition of tactile apparent movement is normally a subjective sense. However, when applying tactile apparent movement to an engineering system, quantitative evaluation is necessary. In a previous study, we examined the body-sway caused by tactile apparent movement under fixed experimental conditions; however, the body-sway characteristics were not fully investigated. In this study, we investigated the body-sway caused by tactile apparent movement under fixed experimental conditions. We focused on biological information and body-sway, and compared cases where the apparent motion was recognized and not recognized. Our findings will help to improve the performance of systems that use tactile apparent movement.

Keywords: Tactile Apparent Movement, Body-sway, EMG,

I. INTRODUCTION

The tactile sense of our skin is one sense that is being investigated for sensory substitution because the possibility of losing the tactile sense is lower than the possibility of losing sight, hearing, and other senses due to congenital or acquired causes. Sensory substitution means substituting a remaining sense for a lost sense. For example, a tactile display can transmit information using the tactile sense instead of the visual sense.

Apparent movement is a sensory illusion mainly studied and reported in the field of vision. However, it is known that apparent movement also appears in the tactile sense. When two stimuli appear one after another with an appropriate time lag, we sense movement of the stimulus; that is to say, we sense that one stimulus moves to the other stimulus.

The frequency characteristics of tactile apparent movement have been investigated [1]–[3]. Ueda *et al.* proposed a tactile display that combined tactile apparent movement and phantom sensation [7],[8]. Park *et al.* designed a person identification authentication system based on a tactile stimulus using a tactile display [9]. When applying tactile apparent movement to a tactile display in which stimulation elements are arrayed, the number of stimulation elements increases as a result of increasing transinformation [10],[11]. By applying apparent movement to tactile displays, it should be possible to realize smaller displays.

The recognition of apparent movement is normally a subjective sense. On the other hand, when applying tactile apparent movement to an engineering system, quantitative evaluation is necessary. In many previous studies, however, evaluation of the recognition of apparent movement was based on statistical techniques, and quantitative evaluation was difficult.

In our previous study, we reported the body-sway of an upper limb caused by tactile apparent movement under fixed experimental conditions [4]–[6]. If quantitative evaluation of the body-sway becomes possible, we will be able to evaluate the tactile apparent movement. The characteristics of the body-sway were analyzed using an averaged electromyography (EMG) waveform when apparent movement was recognized based on frequency analysis. In that study, however, the body-sway was not fully evaluated quantitatively.

In this study, we focused on the frequency characteristics of body-sway and investigated the body-sway caused by tactile apparent movement.

II. MEASUREMENTS

Fig. 1 shows the measurement system used in our study. It consists of two PCs and five components: (1) an EMG measurement system, (2) a three-axis acceleration sensor, (3) a tracking system, (4) a stabilometer, and (5) a vibrotactile stimulation presentation system.

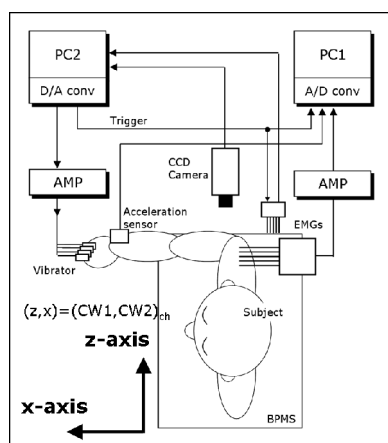


Fig. 1. Measurement system.

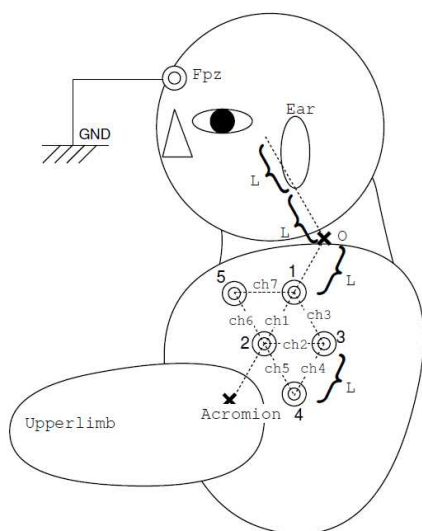


Fig. 2. Arrangement of 5 electrodes and body earth.

The sampling frequencies were different in each system. In detail, biological information and three-axis acceleration were acquired via the same A/D converter, whose sampling frequency was 2000 Hz. The tracking system's sampling frequency was 60 Hz, and the stabilometer's sampling frequency was 80 Hz. PC1 was synchronized with PC2 via a synchronization signal that PC2 generated.

The number and positions of the EMG measurement channels were defined as shown in Fig. 2. The number of EMG channels was 7. The sampling conditions are shown in Table 1.

The tracking system consisted of a CCD camera (Library Corp.: GE60). Positions of tracking markers are shown in Fig. 3. The tracking points were the upper limb, shoulder, body, and below the ear lobe. Tracking results were recorded on PC2 as coordinate data (X, Y). The three-axis acceleration sensor was worn on the right wrist.

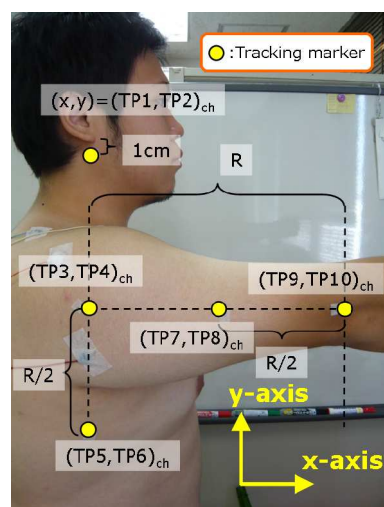


Fig. 3. Arrangement of 5 tracking markers.

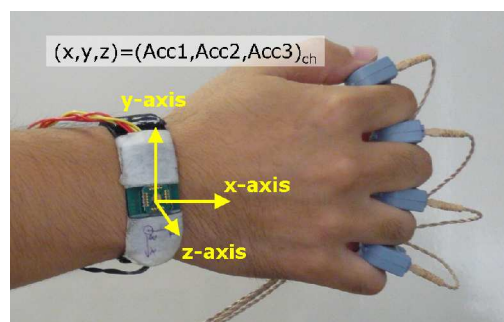


Fig. 4. Arrangement of four vibrators and accelerometer.

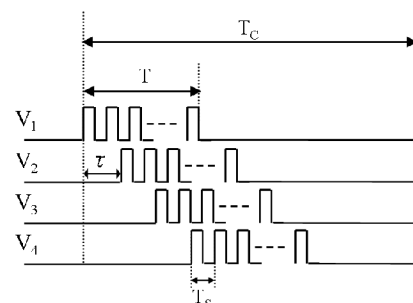


Fig. 5. Drive waveform of vibrator.

A stabilometer (Nitta Corp.: BPMS) measured the subject's center of gravity while standing still. The posture on the stabilometer was based on stabilometry defined by the Japan Society for Equilibrium Research.

The vibrotactile stimulation presentation system consisted of four vibrators (Audiological Engineering Corp.: Skin Stimulator). The subject held four vibrators (SS1, SS2, SS3 and SS4) as shown in Fig. 4. The vibrators were driven by the drive waveform shown in Fig. 5. The drive waveform had four parameters, T , T_s , T_c , and τ . In this study, tactile apparent movement was generated by adjusting only the parameter τ . The other parameters, T , T_s , and T_c ,

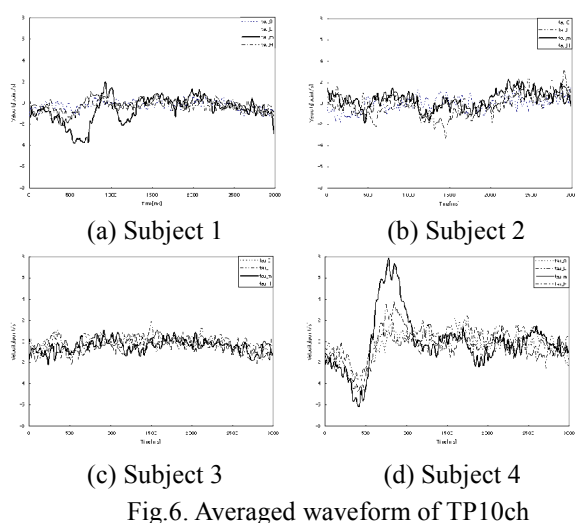


Fig.6. Averaged waveform of TP10ch

were fixed at $T = 100$ ms, $T_S = 4$ ms, and $T_C = 3000$ ms. One trial was assumed to consist of driving vibrators SS1 to SS4 in sequence. One set consisted of 30 trials, and ten sets in total were performed.

The value of parameter τ when the subject felt the apparent movement the most is τ_m . The values of parameter τ representing the difference threshold for the apparent movement are τ_L and τ_H . They were measured by employing an adjustment method used in psychophysics measurements. In this study, vibrotactile stimulations each composed of τ_0 , τ_L , τ_m , and τ_H were presented to the subject. The body-sway caused by the tactile apparent movement was evaluated by comparing and examining the subject's reaction at this time. The parameters τ_0 , τ_L , and τ_H do not cause any apparent movement while τ_m causes tactile apparent movement. Here, the relation of the τ parameters is $\tau_0 < \tau_L < \tau_m < \tau_H$. One of the τ parameters was selected randomly in each trial, and a vibrotactile stimulation was presented to the subject using that parameter. In the measurement, the subject stood on the stabilometer, with their eyes closed, wearing noise canceling headphones and holding their dominant arm horizontally.

III. ANALYSIS

The body-sway caused by apparent movement reported in the previous study caused the upper limb to move in the direction in which the stimulation image was moved when the subject recognized an apparent movement. In the present experiment, the subject held his or her upper limb horizontally. If body-sway is caused, it is expected that the arm would center on the shoulder and shake periodically. Therefore, we focused on the frequency of the measurement data. When periodic shaking appears

upon recognizing apparent movement, a significant difference should be observable in

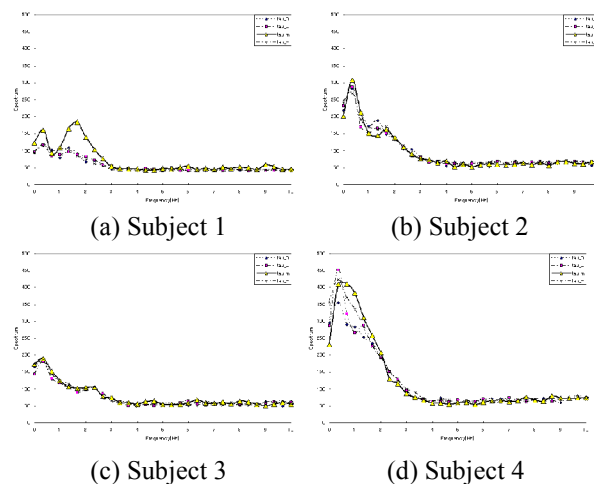


Fig.7. Averaged spectrum of TP10ch

the spectrum at a specific frequency compared with the case where the apparent movement is not recognized.

As preprocessing, the EMG was filtered from 20 Hz to 500 Hz and subjected to envelope processing, the acceleration value was filtered from 0 Hz to 45 Hz, and the velocity of the tracking points and the center of gravity were analyzed using the finite difference method. Then, the preprocessing data for 3000 ms (for center of gravity only: 2500 ms) from the beginning of the stimulation was averaged. The frequency spectrum was calculated from the preprocessing data, averaged over all trials for every τ . The spectral intensity of each frequency was compared to examine the difference between recognized and non-recognized apparent motion, and a statistically significant difference was found.

IV. RESULTS

Table 1 shows the results of psychophysics measurements. The parameter τ that each subject selected was different, indicating that the recognition of tactile apparent movement is subjective.

Table 1. Results of the psychophysics measurement.

	τ_L [ms]	τ_m [ms]	τ_H [ms]
Subject 1	20	70	120
Subject 2	10	70	120
Subject 3	30	70	110
Subject 4	10	80	160

As one example of the result, Fig. 6 shows the average waveform of the preprocessing data for the tracking point 10ch (TP10ch, Fig. 3). It is thought that TP10ch

contains a lot of information about the body-sway because TP10ch is an element in the same direction as the direction in which the stimulation image is moved. From Fig. 6, subject 1 and subject 4 exhibited periodic shaking. This result suggests the possibility of the body-sway having periodicity. Fig. 7 shows the averaged spectrum of TP10ch. From 0 Hz to 10 Hz, the difference in spectral intensities by a factor of 2 or more between the recognized and non-recognized apparent motions for subjects 1 and 4 was statistically significant ($P < 0.01$, t-test). From the above result, it is possible that the body-sway has periodicity because both subjects showed a significant difference at a specific frequency. Here, the channel on which the frequency with a significant difference existed was extracted from all channels, and the results are shown in Tables 2–4. Table 2 shows the result of comparing τ_m with τ_0 , Table 3 shows the result of comparing τ_m with τ_L , and Table 4 shows the result of comparing τ_m with τ_H . From the results, besides TP10ch, other channels are expected to show a periodic response. However, these are not reactions common to all subjects.

Table 2. Extracted channels for τ_m vs. τ_0

Subject	TP	CW	EMG	Acc
1	ch3,ch4 ch7,ch8 ch9,ch10	ch1	ch1, ch2	ch1, ch2
2	ch6	---	---	---
3	ch7	---	ch6, ch7	ch1
4	ch5, ch8 ch10	---	ch1	ch1

Table 3. Extracted channels for τ_m vs. τ_L

	TP	CW	EMG	Acc
1	ch3,ch4	---	ch6	---
2	ch3,ch9	ch1,ch2	---	ch2
3	ch8	---	ch6,ch7	---
4	ch3,ch5	---	ch2,ch5	---

Table 4. Extracted channels for τ_m vs. τ_H

	TP	CW	EMG	Acc
1	ch9	---	ch2	---
2	ch5,ch6 ch7	ch1,ch2	ch2,ch5	---
3	---	---	---	ch1
4	ch6	---	ch7	---

This is thought to be due to the fixed parameter T in the presented stimulation, because the parameter T is an important parameter causing apparent movement. Therefore, it will be necessary to conduct an experiment that considers the influence of parameter T in the future.

V. CONCLUSION

In this study, we investigated the body-sway caused by tactile apparent movement. Focusing on the frequency characteristics of the body-sway, we tried to evaluate the body-sway quantitatively. The results show the possibility that periodic shaking occurred when apparent movement was recognized. In future work, the T parameter of the presented stimulation will be examined, and quantitative evaluation of the body-sway caused by tactile apparent movement will be attempted.

REFERENCES

- [1] J.H. Kirman: "Tactile apparent movement: The effects of interstimulus onset interval and stimulus duration", *Perception & Psychophysics*, Vol. 15, pp. 1-6 (1974).
- [2] J.H. Kirman: "Tactile apparent movement: The effects of number of stimulators", *Journal of Experimental Psychology*, Vol. 103, pp. 1175-1180 (1974).
- [3] J.H. Kirman: "Tactile apparent movement: The effects of shape and type of motion", *Perception & Psychophysics*, Vol. 34, No. 1, pp. 96-102 (1983).
- [4] K. Kawahara, Y.-I. Park, and M. Uchida: "Characteristic Extraction of EMG with Recognition of Tactile Apparent Movement", *IEEJ Trans. SM*, Vol. 129, No.6, pp. 187-188 (2009) (in Japanese).
- [5] Y.-I. Park and M. Uchida: "Analysis of Surface EMG with Apparent Movement of Tactile sense", *Proc. of the SICE Annual Conference 2009*, 2C12-6 (2009).
- [6] Y.-I. Park and M. Uchida: "Swing Analysis of Body-parts Motion Accompanied by Apparent Movement", *The International Symposium on Artificial Life and Robotics 2010 (AROB 15th)*, OS1-4 (2010).
- [7] S. Ueda, M. Uchida, A. Nozawa, and H. Ide: "A Tactile Display Used Phantom Sensation with Apparent Movement Together", *IEEJ Trans. FM*, Vol. 127, No. 6, pp. 227-284 (2007) (in Japanese).
- [8] Y.-I. Park and M. Uchida: "A Tactile Display by Using Phantom Sensation with an Apparent Movement based on Electro-stimulation", *Proc. of the International Conference on Electrical Engineering (ICEE)*, CD-ROM, P-131 (2008).
- [9] Y.-I. Park and M. Uchida: "System of personal identification by using tactile stimuli", *Artificial Life and Robotics*, Vol. 13, No. 1, pp. 209-213 (2008).
- [10] C. Domenici and D. Derossi: "A stress-component-selective tactile sensor array", *Sensors and Actuators*, Vol. 13, pp. 97-100 (1992).
- [11] B.L. Gray and R.S. Fearing: "A surface-micromachined micro-tactile sensor array", *IEEE Int. Conf Rob. and Auto.*, Vol. 1, pp. 1-6 (1996).

A visual-taste interference model and the EEG measurement

Hisaya Tanaka and Yuichi Sato

*Department of Information Design, Kogakuin University
1-24-2, Nishi-shinjuku, Shinjuku-ku, Tokyo, 163-8677, Japan
(Tel : 81-3-3340-0890; Fax : 81-3-3348-3486)
(hisaya@cc.kogakuin.ac.jp, j206051@ns.kogakuin.ac.jp)*

Abstract: Taste cognition is interfered by visual information; however the mechanism has not been clarified. We assumed the interference model in the process of taste and visual information. The model was tested with frequency analysis on EEG and the button response time. The tasks were matched/miss-matched between taste and visual information of orange or apple juice. There were changes in α waves that originated in visual processing of a juice package and changes in β waves that originated in taste processing. There was the possibility with the parallel processing mechanism in the visual-taste interference.

Keywords: taste cognition, visual information, interference, EEG

I. Introduction

There are studies using facial expressions [1] or skin temperature on the nasal area [2] as a method to give an objective evaluation on taste. There are also various papers that handled taste and the brain [3] [4]. However, those papers that handled the brain and taste have not reached an objective evaluation of products. In this paper, therefore, a method to give an objective evaluation on taste as well as products presented was reviewed based on the relationship between taste and the brain. Spontaneous brain waves were measured in order to develop the taste processing model in this paper, by focusing on integrated processing of vision and taste. The taste processing model was designed to measure the interaction of visual information and taste, including whether information obtained from people's eyes influences taste cognition, or only taste influences taste cognition.

II. Interference between taste and vision

1. Proposal of taste processing model

The process to reach taste cognition in interdependence between vision and taste was proposed as the "taste processing model" in this experiment. Information received from two sensory organs, i.e., eyes for vision and the tongue for taste, is communicated to the nerve center. Images entered through eyes are recognized in the vision area, the information is sent to the temporal association cortex, and the images seen are interpreted as meaningful. Taste entered from the tongue transmits from the receptor called the taste buds

on the tongue onto sensory nerve fibers, and the five-taste (sweet, salty, delicious, bitter and sour) information is taken over to the taste area in the brain. These two kinds of information in the above are integrated in the brain and the integrated information is related to memory, leading to taste cognition (Fig.1).

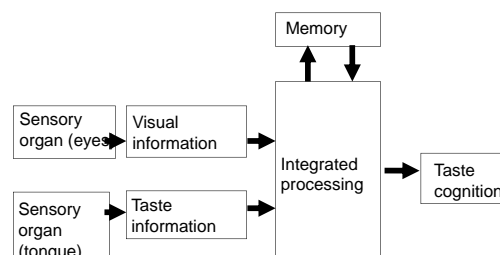


Fig.1. Proposed taste processing model

2. Verification of hypotheses with brain waves

The following three hypotheses are considered based on the taste processing model. If responses of spontaneous brain waves are successfully obtained in accordance with these hypotheses, it will be useful to support development of the taste processing model. Spontaneous brain waves can be divided into three bands including α waves (8-13Hz), β waves (14-30Hz) and θ waves (4-7Hz). α waves appear when eyes are closed, when relaxed or not nervous, or when brain activities are calm. β waves appear when stress is accepted or during calculation. θ waves appear in the course from awakening to onset of sleep. It is also known that α waves decrease when visual information is given, in comparison with the time at rest [4]. In addition to the above, we considered that the volume of

thoughts occurring in the brain when taste is given (difficulty in relating short-term memory from vision or long-term memory to taste) was involved in the increase/decrease of α waves and β waves in this paper. If these three hypotheses are verified with experiments, the taste processing model will be successfully developed. Hypotheses at this time were prepared based on brain waves including α , β and θ waves when taste information of water was given.

III. EXPERIMENTS

1. Experiment method

Subjects were four healthy males (age: 21-22). The experiment was conducted in a lab which was not a shielded room, and lights were turned off during the experiment, i.e., the condition of a dark room. First of all, subjects sat on chairs, the experimenter presented a table with the names of six samples (water, apple, orange, strawberry, banana and pear) to ensure taste cognition, and indicated one of them would be put into the mouth. The subjects were instructed to identify which sample was put into the mouth. They were to push down the switch at hand immediately after they knew what sample it was (considered that taste was recognized). The reason for pushing down the button is that the time from completion to integrate vision with taste until taste cognition as shown in Fig.1 is considered to be interrelated with the time until pushing down the button by the subjects. Therefore, after explaining about the experiment, we asked them to avoid movements except pushing down the button or teeth grinding during the experiment. After full explanation, subjects were instructed to put on an electrode cap to measure brain waves. They were also asked to hold the hose ($\phi 5 \times 7$ mm) connected to the One Shot Measure 30ml (Sentec D-19002BK) in the mouth using the lips, to enable input of a fixed amount. (The hose was not sticking to the face, and the sample was not visible.) Since the photo of the package is shown before giving the sample (taste stimulation) in this experiment, the task is in the order of visual stimulation and taste stimulation. Eyes were opened when visual stimulation was given, and closed when it ended. Visual stimulation was given for five seconds, and another five seconds were provided for the time to close the eyes. Then, input of taste began. The sample was input without notifying the subject of the timing of input. The timeline of the experiment is indicated in Fig.2.

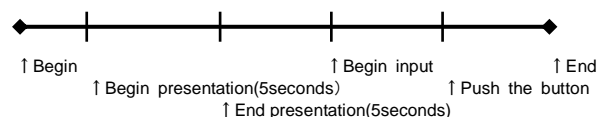


Fig.2: Timetable for the experiment

Table 1 includes Tasks 1 to 11. Enough time was maintained between task and task in the experiment, and the oral cavity was rinsed with water after and immediately before taste stimulation. To avoid the same sample to be input in a row, Tasks 1 to 5 and Tasks 6 to 11 in the experiment were conducted at least with one-week interval.

Table 1: Tasks in the experiment

Task No.	1	2	3	4	5	6	7	8	9	10	11
Visual presentation	O	A	x	x	x	O	A	O	A	O	A
Experiment samples	x	x	W	O	A	O	A	A	O	W	W

In regards to symbols in Table 1, O represents orange juice, A represents apple juice and x represents no stimulation. Orange juice and apple juice used in the experiment was "Tropicana 100% Orange Juice" and "Tropicana 100% Apple Juice." Packages for these two kinds of juice were photographed with a digital camera for presentation. With the response time like in Tasks 3, 4 and 5 as the reference where only the sample was given, Tasks 8, 9, 10 and 11 were considered to take longer for integrated processing when the subjects respond, leading to a long button response time. On the other hand, the button response time was considered to be shorter for tasks which seem to take less time for integrated processing.

2. Measurement method

Neurofax EEG1100 (Nihon Kohden) was used to measure brain waves, and FOCUS (Nihon Kohden) was used for analysis. 31 exploring electrodes in accordance with the International 10-20 method are arranged on the electrode cap (Electro Cap) (refer to Fig.3). Unipolar induction was used for measurement with both earlobes (A1 and A2) as reference electrodes. Experiments were completed within 60 minutes after the electrode cap was worn (Fig.3). In regards to brain waves extracted, the band with α waves was at 8-13Hz, β waves at 14-30Hz and θ waves at 4-7Hz. The intervals to analyze brain waves included from the beginning of visual stimulation presentation to the completion of visual stimulation presentation, and from

the beginning of taste stimulation presentation to button pushing by a subject. The FFT was applied to these intervals and the content of brain waves in all channels were averaged to obtain the content rate for these three bands.

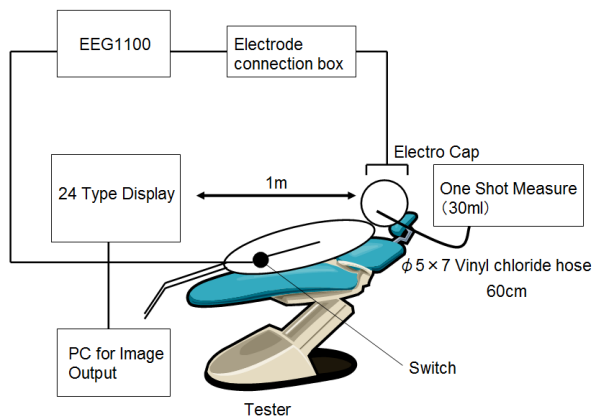


Fig.3: Measurement system

IV. RESULTS

1. Hypothesis 1: Taste and electroencephalographic response

Tasks with taste presentation only are compared. For Hypothesis 1, it was considered in the cases of samples with and without taste that α waves decrease and β waves increase because the burden of taste integration increases for the sample with taste, as a result of the load from the work to relate to long-term memory. As a result of experiment, the content rate of α waves tended to decrease and the content rate of β waves tended to increase for samples with taste in comparison with samples without taste, when Tasks 3 and 4 as well as Tasks 3 and 5 were compared, and the content rate of θ waves decreased. This is because the volume of thoughts increased more for the process to screen orange or apple out of the given hints (water, apple, orange, strawberry, banana and pear) than the case of water. Significant difference was not recognized in Student's t-test (significance level=0.05; two-sided test) of brain waves for either Tasks 3 and 4 or Tasks 3 and 5. Based on the above, the tendency of the hypothesis was observed but statistically significant differences were not recognized (Fig.4).

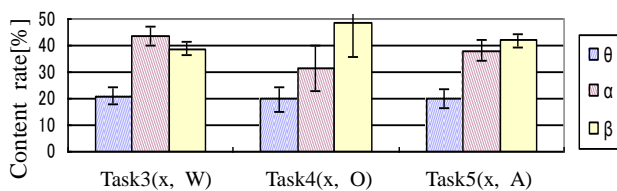


Fig.4: Taste and electroencephalographic response (average \pm standard deviation)

2. Hypothesis 2: Presence of visual presentation and electroencephalographic response

Next, tasks with taste information only are compared with tasks where the same visual and taste information are presented such as visual information of apple and taste information of apple (Tasks 6 and 7). For Hypothesis 2, the volume of thoughts decreases upon taste cognition, since integrated processing of vision and taste goes easier with tasks with visual information. Thus, we considered that α waves increase and β waves decrease in comparison with brain waves when only taste is presented. As a result of the experiment, the content rate for α waves and β waves decreased when Tasks 4 and 6 were compared, and increased when Tasks 5 and 7 were compared. θ waves have a tendency to increase when vision is presented rather than presenting taste only. A significant difference was not recognized in Student's t-test (significance level=0.05; two-sided test) for Tasks 4 and 6 as well as Tasks 5 and 7. Based on the above results, it is assumed that in the case of Tasks 4 and 6, α waves decreased and β waves increased as a result of relating to long-term memory, and in the case of Tasks 5 and 7, α waves increased and β waves decreased as a result of relating to short-term memory (Fig.5).

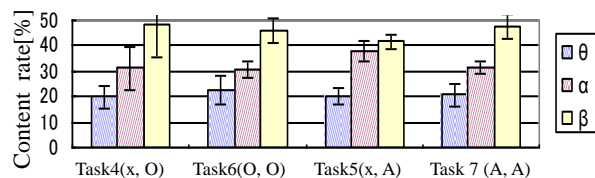


Fig.5: Presence of visual presentation and electroencephalographic response (average \pm standard deviation)

3. Hypothesis 3: Electroencephalographic response to match/mismatch of taste and visual presentations

Next, tasks where the same vision and taste are presented are compared with tasks where different vision and taste are presented (Tasks 8 and 9). For Hypothesis 3, we considered the case where taste information does not match vision information given, e.g., visual information of apple and taste information of orange. In this case, integrated processing becomes extremely difficult and the volume of thoughts increases; therefore we considered that α waves decrease and β waves increase compared with the case where the same visual and taste information is given. First of all, the content rate of α waves decreased, the content rate of β waves increased and θ waves also increased in the case of Task 8 (A, O) compared with Task 7 (O, O). On the other hand, the content rate of α waves and β waves decreased and θ waves increased in the case of Task 9 (O, A) compared with Task 6 (A, A). Significant difference was not recognized in Student's t-test (significance level=0.05; two-sided test) of brain waves for Tasks 7 and 8 as well as Tasks 6 and 9. It is considered that α waves decreased with short-term memory in regards to the mismatch (Fig.6).

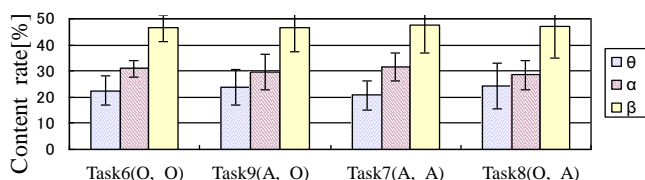


Fig.6: Electroencephalographic response (average \pm standard deviation) in match/mismatch of taste and visual presentations

V. DISCUSSIONS

Based on the results of experiments at this time, visual information as well as specific work in integrated processing is added to the taste processing model (Fig.1).

The model under Hypotheses 1 was indicated in the taste-vision processing model in Fig.7. The decrease of α waves and increase of β waves can be explained with the increase in the volume of thoughts at the time of screening taste. Based on this, the model was restructured.

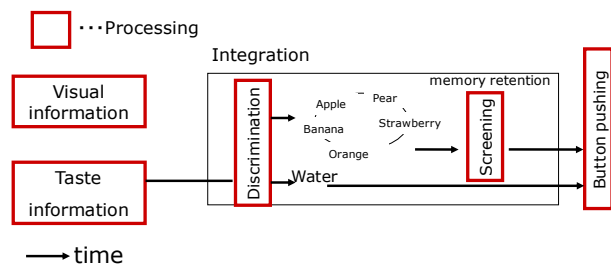


Fig.7: Restructured taste-vision processing model (in the case of Hypothesis 1)

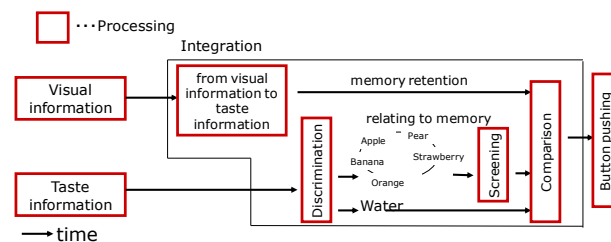


Fig.8: Restructured taste-vision processing model (in the cases of Hypotheses 2 and 3)

The model under Hypotheses 2 and 3 was indicated in Fig.8. Increase/decrease of α waves and β waves was considered to change depending on long-term memory and short-term memory used to relate to memory when the same taste information as visual information is given. On the other hand, when taste information different from visual information is given, α waves decreased while β waves did not increase, by relating to long-term memory without using short-term memory; therefore the model was restructured.

VI. CONCLUSION

We measured spontaneous brain waves for the taste processing model. In these experiments, a tendency of α wave decrease and β wave increase was observed for tasks with taste information only in comparison with tasks where taste information of water only was presented under “4.1 Taste and electroencephalographic response.” Based on these results, the vision-taste processing model was developed. It is possible to explain from this model that integrated processing is conducted in the interaction of vision and taste. We hope to carry out statistical review by increasing the number of subjects as well as the number of trials in the future.

We had assumed that β waves of brain waves covered at this time increase/decrease as a result of relating taste to memory; however a significant difference was not recognized in any task. We will confirm whether or not a significant difference is recognized by calculating brain waves with the content rate. Higher brain activities might not be occurring when taste is obtained if there is no difference in β waves; therefore review is desired. In this paper, a model was developed by focusing on vision and taste and conducting experiments. It is needless to say that when an object is tasted, not only vision and taste but also smell is an important sense, and we plan to review the influence of smell on the brain in our future studies.

REFERENCES

- [1] Masamitsu Okumura, Kunihiro Kato, Kazuhiko Yamamoto: "Study on Change of Facial Expression with Taste Stimulation," The Institute of Image Information and Television Engineers Technical Report 32(35), 53-56, 2008/8
- [2] Toru Furuichi, Aoki Nozawa, Hideo Ide: "Comparison between Amount of Gustatory Sense and Nasal Skin Temperature," IEICE Technical Report MBE2006-50, 2006/09
- [3] Kiyota H, Morita K, Murayama N, "Evoked Potential to Gustatory Stimuli in Man," TECHNICAL REPORT OF IEICE MBE98-120, 1999/01
- [4] Hiroaki Uematsu, Kentaro Hirata, Hiroaki Morino, Sanae Takasaki, Yasuo Morodomi, Michiaki Mito: Analysis of Emotional Response to Visual Stimulation with β Wave Mapping," IEICE Technical Research Report MBE, ME and Bio Cybernetics, 103(637), 65-70, 2004/01
- [5] Yuichi Sato, Hisaya Tanaka: Measurement of Spontaneous Brain Waves to Develop Taste Processing Model," The Institute of Electrical Engineers of Japan Research Report 2009/12

Dynamic analysis of dorsal thermal image

Akio Nozawa and Yuya Takei

*School of Science and Engineering, Meisei University, Tokyo, Japan
(Tel: +81-42-591-5895; Fax: +81-42-591-5895)
(Email akio@ee.meisei-u.ac.jp)*

Abstract: A dynamic analysis was subjected to thermal images of dorsal of the foot in this study. A psychophysiological effect of a facial massage by aesthetician was evaluated. First, psychophysiological effects of facial massage were assessed on proprietary stress test. Physiological indices measured were alpha-wave power spectrum, dorsal skin temperature variations and high frequency component of heart rate variability. STAI, POMS (Brief Form) and amount of sensory awareness was administered to evaluate for psychological status. The aspects of the amount of sensory awareness were comfortable, awakening and effect of massage. Secondary, we assessed stress response on thermal image of dorsal of foot. Thermal image of dorsal of foot was measured by infrared thermography device.

Keywords: Thermal image, Peripheral skin temperature, Dynamic analysis, Comfort evaluation, Physiology measurement, Stress test

I. INTRODUCTION

Comfort evaluation has been performed by sensory evaluation method or physiology index. Sensory evaluation method has been widely used to quantitatively evaluate the tendency of preference and feeling of the user [1-5]. Though the sensory evaluation method is easy-to-use, possible issues regarding examinee's individual variability on interpretation of evaluation words have been indicated; a temper of examinee affects the evaluation [6-8]. And unconscious mental stress isn't able to evaluate. Physiological index is provided by bioinstrumentation, which is measured by person. Physiological index is changed by physiology condition and mind condition. Physiology index is able to evaluate serial quantitative and objective in comfort evaluation. However, corporeity on electrode measurement such as electroencephalogram (EEG) and electrocardiogram (ECG) may give physical and mental stress. Noncontact and unconfined and noninvasive measurement can be measured by infrared thermography device. Measurement with infrared thermography device will be projected to reduce physical and mental stress. Peripheral of body is nasal, hand, foot and such. Peripheral skin temperature (PST) is regulated by the sympathetic nervous system. We have evaluated psychophysiological condition such as mental stress evaluation and comfort evaluation by peripheral skin temperature. Peripheral skin temperature was measured by infrared thermography device. In this

study a dynamic analysis was subjected to thermal images of dorsal of the foot. A psychophysiological effect of a facial massage by aesthetician was evaluated. First, psychophysiological effects of facial massage were assessed on proprietary stress test. Physiological indices measured were alpha-wave power spectrum, dorsal skin temperature variations and high frequency component of heart rate variability. STAI, POMS (Brief Form) and amount of sensory awareness was administered to evaluate for psychological status. The aspects of the amount of sensory awareness were comfortable, awakening and effect of massage. Secondary, we assessed stress response on thermal image of dorsal of foot. Thermal image of dorsal of foot was measured by infrared thermography device

II. EXPERIMENTAL

Experimental equipment set-up and electrode arrangement for scalp EEG are shown in figure 1. Experiments were executed in a measurement room. An infrared thermography system (TVS-200EX, AVIONICS) was installed 1 m in front of subject. Thermograms of dorsal of foot were created with 1-s sampling periods. Image resolution of thermograms was 320×240 pixels, and room temperature was set at 26±1.0 degrees Celsius. Infrared emissivity of skin is $\epsilon=0.98$. The subject was in a seated position in a resting state. EEG was recorded at a sampling frequency of 200 Hz using a biological amplifier/sampler (5102 EEG HEAD BOX, NF Electronic Instruments) and digital

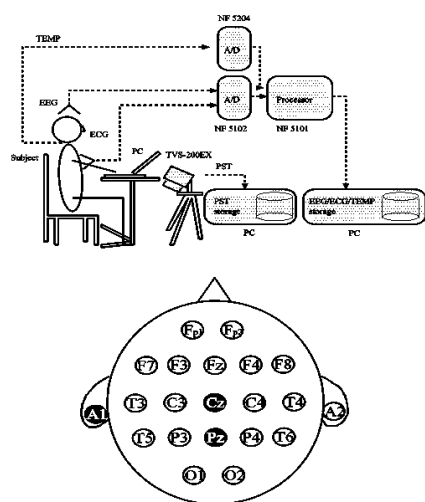


Fig.1. The measurement system and electrode arrangement for EEG.

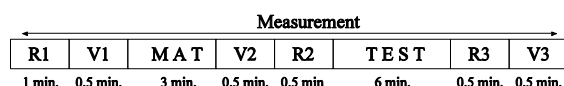


Fig.2. Protocol of the experiment.

signal processor unit (5101 PROCESSOR BOX, NF Electronic Instruments). Electrodes used for scalp EEG was Pz, based on the international 10-20 method, and a reference electrode was A1. Electrodes used for ECG were put on the superior margin of the sternum and the cardiac apex, based on modified Lead NASA, in order to reduce the artifacts of EMG from the ECG. A common electrode for both EEG and the ECG was put on Cz. An auditory stimulus of scratch sound was reproduced by PC as a control stimulus. The protocol of the experiment is shown in figure 2. Subjects were nineteen 18- to 23-year-old healthy women. Subjects were well-informed about the experiments and the objective of this study before participation for experiments. The experiment was performed once per a subject. The measurement was not begun until the subject had been in the room for at least 15 minutes in order to habituate to the room temperature. The measurement consisted of eye-closed resting periods (period R1, R2 and R3), eye-opened evaluation periods for evaluation of sensory awareness (period V1, V2 and V3), eye-opened period under the controlled stimulation of the mental work task (MAT) and eye-opened period under the facial massage operation (period TEST).

The power spectra time series were calculated as follows. The power spectrum time series of the EEG

Table.1. Overall evaluation results of indices in facial massage.

Indices	Interpretation	Significance
α -wave	Brain activity	n.s.
PST	Sympathetic acceleration	n.s.
HF	Parasympathetic acceleration	P**
POMS	Depressive moods	N+
STAI	Trait anxiety	P+
VAS #1	Comfortable	P**
VAS #2	Arousal	N+

lead from Pz was calculated every 5 s by FFT using 1024 data points at a sampling frequency of 200 Hz. The α -waves were defined as the frequency components of the EEG in the frequency range from 8 Hz to 13 Hz. The power of α -wave was created as the sum of the frequency components in the frequency range.

The PST time series was calculated as follows. Thermal images of the right first toe region of the foot were extracted from the thermogram of dorsal of foot time series. PST time series were created as a cascade of spatial average temperature for pixels in the interested area of each thermal image.

HF time series was calculated as follows. A source R-wave interval time series was extracted from ECG time series by using threshold processing. Temporally equidistant R-wave intervals (HRV) were derived by resampling process in frequency of 20 Hz after cubic spline interpolation. The power spectrum time series of HRV was calculated every 1 s by fast Fourier transformation (FFT) using 512 data points at a sampling frequency of 20 Hz. Finally, HF time series was created as a summation of discrete frequency components in power spectrum time series of HRV, in which the frequency range of HF was 0.15 Hz to 0.4 Hz.

POMS-short form, which had been shortened and translated into Japanese, was administered. The POMS-short form comprised of 30 questions about the current mood state. These 30 questions were classified in 6 sub-scales: T-A ('tension and anxiety'), D ('depression and dejection'), A-H ('anger and hostility'), V ('vigor'), F ('fatigue'), and C ('confusion'). The subjects selected the raw score from one of five values (0, 1, 2, 3 and 4, where 0 = no such mood state and 4 = extreme mood state). These raw scores in each sub-scale were then added to generate each sub-scale score.

The STAI is a 20-item scale that measures acute level of anxiety. The subjects selected the raw score from one of four values (1, 2, 3, and 4, where 1 = not at all and 4 = very much). A summary score is obtained by adding the weight of each item. The STAI scores indicate an increase in response to situational stress and a decline under relaxing conditions. In this study, STAI-JYZ, which regards Japanese cultural factors better, was used. The STAI-JYZ exhibits acceptable internal consistency and test-retest reliability. The aspects of the amount of sensory awareness were comfortable, awakening and effect of massage. Each data was expressed as 'means \pm standard error (SE)'. Wilcoxon signed-rank test was performed to evaluate them.

III. RESULTS AND DISCUSSION

1. Psychophysiological effects of facial massage

Table.1 shows the result of the statistical test representing the psychophysiological effect of the facial massage. "P" means positive response for the interpretation of each index, and "N" means negative response. Each physiological index was normalized by period R2. R2 was a baseline for the statistical test and was compared with period R3 by the test. α -wave ratio was 0.067 ± 0.054 which indicates that a brain activity had been maintained by having performed a facial massage. PST ratio was 0.631 ± 0.490 which represented that had no significant changes in the massage. It is considered that this is because of rather large standard error between subjects. HF ratio was 1.406 ± 0.094 and increased remarkably after the massage ($p < 0.01$). This shows that the parasympathetic activity was enhanced by the facial massage. POMS score was compared in each scale before and after experiment. Most scores, which indicate negative feeling, tended to decline after the experiment. Especially, T-A ('tension and anxiety') significantly declined from 42.68 ± 1.747 to 39.58 ± 1.294 ($p < 0.05$), A-H ('anger and hostility') dropped 38.05 ± 0.609 to 37.16 ± 0.158 ($p < 0.1$), and also F ('fatigue') was decreased 40.47 ± 1.035 to 37.32 ± 0.769 ($p < 0.05$). Similarly, the score for anxiety in the STAI significantly declined from 43.79 ± 1.829 to 40.32 ± 2.013 following the massage ($p < 0.1$). Amount of sensory awareness was compared before and after TEST. 'Comfortable' gathered from 0.503 ± 0.015 to 0.621 ± 0.029 ($p < 0.01$). 'Awakening' declined from 0.563 ± 0.033 to 0.517 ± 0.045 ($p < 0.1$). The 'Anxiety' in the STAI and negative moods in POMS were

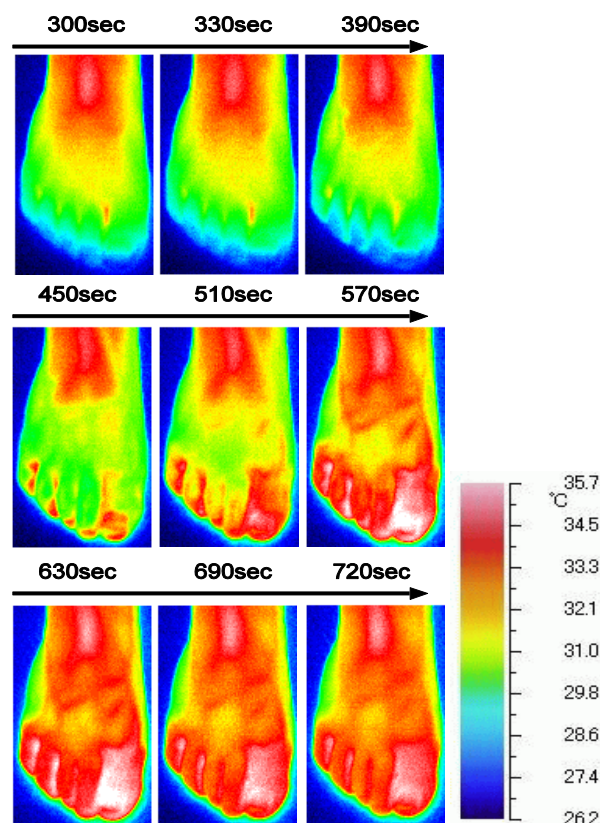


Fig.3. Thermal image of dorsal of right foot

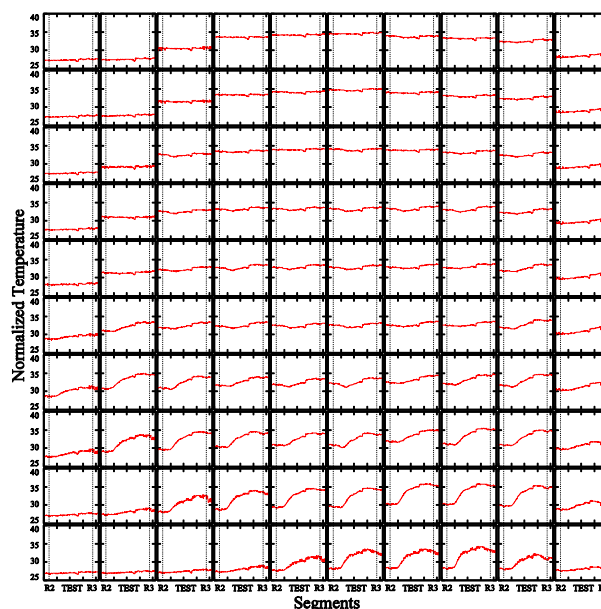


Fig.4. A temperature change in each area.

significantly decreased following the massage. These results suggested that the facial massage had strong effects on stress alleviation or psychological relaxation.

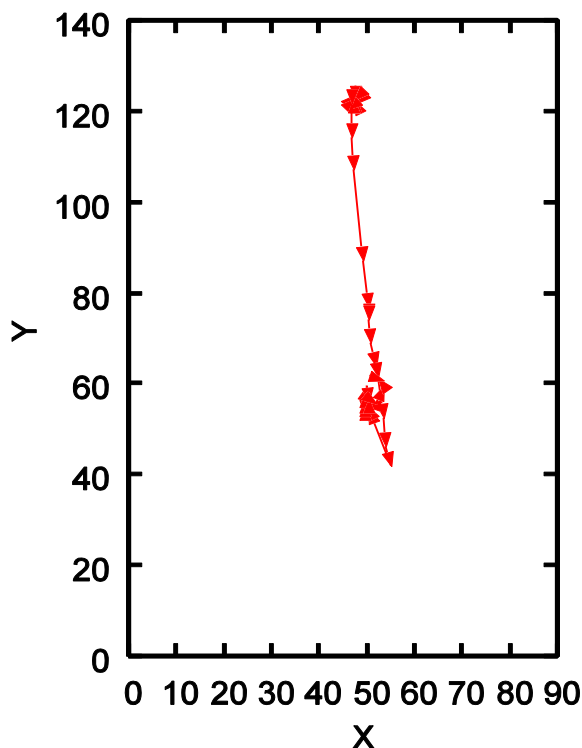


Fig.5. A trail of the center of gravity of the interested area in PST.

2. Dynamic analysis of dorsal thermal image

Thermal image of the measured dorsum of the right foot is shown in Fig.3. Images were recorded at 300 s, 330 s, 390 s, 450 s, 510 s, 570 s, 630 s, 690 s, 690 s and 720 s each. The ankle, which is not peripheral part, had small variations in temperature, while the temperature in tiptoe changed rather large. These variations in temperature were analyzed in detail. Thermal images of the dorsum of the right foot were divided into squared areas of 9 x 14 pixels each. Fig.4 shows time evolution of variations in temperature of each divided area. Large variations in temperature were shown in the areas of tiptoe, while there were a small temperature changes in the areas of ankle. It was indicated that the variations in temperature were different in parts. However, similar changes in temperature were seen generally. And the time in which has greatest value in temperature of each area was different. Fig.5 indicates a trail of the center of gravity of focused area of a certain temperature in range from period R2 to period R3. The range in temperature was defined as follows. Highest temperature was tracked in each area from period R2 to period R3. The maximum and the minimum values were collected from the tracked highest temperatures of each area. Then, the range in temperature was defined as rank in the top 20%

from the maximum to the minimum. In the trail, a center of gravity was in the part of the ankle at the beginning. The ankle has little variations in temperature which is shown in figure 3. And the temperature of the ankle tends to be high. The center of gravity of the interested area moved towards a tiptoe in the middle of period TEST.

IV. CONCLUSION

In this study, an activity of the autonomic nervous system was evaluated by dynamic analysis in peripheral skin temperature which shows activity of the autonomic nervous systems. Peripheral skin temperature in the dorsal of the foot was measured by infrared thermography. A facial massage was used to promote comfort. The rise of peripheral skin temperature by the inhibition of the sympathetic nerve activity was found in the area of tiptoe. Variations in temperature were greatest in the area of tiptoe. A similar change in temperature was seen in the area except the ankle.

V. REFERENCES

- [1] Parente, M. E., Gambaro, A. and Ares, G.: Sensory Characterization of Emollients. *J. Sens. Stud.* 23(2): 149-161, 2008
- [2] Stern, P., Valentova, H. and Pokorny, J.: Relations between Rheological and Sensory Characteristics of Cosmetic Emulsions. *Seifen-oele-Fette-Wachse* 123(7): 445-448, 1997
- [3] Tanaka, Y. and Sukigara, S.: Evaluation of "Shittoi" Characteristic for Fabrics. *J. Text. Eng.* 54(3): 75-81, 2008
- [4] Senoo, M., Takemoto, Y. and Jingu, H.: Change in Affections by Continuous Use of Skincare Cosmetics. *KANSEI Eng. Int.* 3(3/4): 31-36, 2002
- [5] Armanini, L. and Aucar, B.: Tactile Evaluations of Cosmetic Ingredients. *Seifen-Oele-Fette-Wachse* 118(20): 1247-1254, 1992
- [6] Kusakari, K., Yoshida, M., Matsuzaki, F., Yanaki, T., Fukui, H. and Date, M.: valuation of postapplication rheological changes in cosmetics using a novel measuring device: Relationship to sensory evaluation. *J. Cosmet. Sci.* 54(4): 321-333, 2003
- [7] Dykes, P. J.: What are meters measuring? *Int. J. Cosmet. Sci.* 24(4): 241-245, 2002
- [8] Wang, S., Kislalioglu, M. S. and Breuer, M.: The effect of rheological properties of experimental moisturizing creams/lotions on their efficacy and perceptual attributes. *Int. J. Cosmet. Sci.* 21(3): 167-188, 1999

Feature extraction of human face image for preference database

Yu Tachikawa and Akio Nozawa
Graduate School of Meisei University
(Tel: 81-42-591-5895; Fax: 81-42-591-5895)
(you@biel.ee.meisei-u.ac.jp)

Abstract: In this study, aimed for a preference judgment for the face image of the person by the single trial ERP. Cognitive task imposed on subjects with human faces. At the time of the image presentation of the key push it down, and impose a problem the time response time (RT).200ms to 400ms after image presentation time of peak positive potentials appear focused ± 100 ms. Calculated from the maximum amplitude ± 100 ms latency and area of potential. P300 is analyzed to extract frequency components, 1.28 seconds for ERP 2-3Hz amplitude spectra obtained.1 Analyzed EEG frequency components appear to recognize the human face image and asked the potential spectrum. Spectral correlation potential in the area and potential. Correlated with latency and RT. Single-trial ERP waveforms were extracted correctly.

Keywords: ERP, P300, preference, face image, feature extraction.

I. INTRODUCTION

When a human being runs a social life, ability to read the will of another person, and to take the appropriate behavior is very important as towards other people communicative competence. Emotional intelligence EQ is famous in recent year[1]. "KANSEI" is socialized in the same way of frequent occurrence for "Human being serious consideration" and "KANSEI society". Communication is transmission of "KANSEI". If "KANSEI information" has gotten across to machine, It should have gone of smooth communication between person and person. Preference is one of the factors of human action. KANSEI information communication technology is expected of used to human preference. It will be the application as quite new communications tool. Event Related Potential (ERP) is caused cerebral evoked potential reaction of the mental work of the subjects [2]. Preference is involved with attention and a cognitive level. There have been various investigations of preference to the event [3]. ERP was evaluated sensitivity information about the preference. However, face images were not evaluated. That was aimed at estimating the correlation of the face image as preference because quantity of characteristic of the face image was extracted.

II. EXPEROMENTAL

Experimental equipment setup and electrode arrangement for scalp EEG are shown in figure1. Experiments were executed in a measurement booth divided with partition walls of 1.8m in height. An

infrared thermograph system (TVS-200EX, AVIONICS) was installed 0.7m in front of subject. Facial skin thermograms were created with 1s sampling periods. Image resolution of thermograms was 320×240 pixels, and room temperature was set at 26 ± 1.0 degrees Celsius. a seated position in a resting. An electrode headpiece (Pasteless Electrode Helmet, Brain Function Laboratory) and set of headphones were placed on the subject. EEG was recorded at a sampling frequency of 200 Hz using a biological plifier/sampler (5102 EEG HEAD BOX, NF Electronic Instruments) and digital signal processor unit (5101 PROCESSOR BOX, NF Electronic Instruments). Electrodes used for scalp for scalp EEG were Pz, based on the international 10-20 method, and a reference electrode was A1. Electrodes used for ECG were put on the superior margin of the sternum and cardiac apex based on a modified Lead NASA in order to reduce artifacts of EEG from ECG. A common ground electrode for both EEG and ECG was put on Cz. EEG was recorded at a sampling frequency of 200 Hz using a biological amplifier/sampler (5102 EEG Head Box, NF Electronic Instruments) and digital signal processor unit (5101 Processor Box, NF Electronic Instruments).The protocol for the experiment is shown in figure2. Subject was 22 year-old healthy men. Subject was well informed about the experiments and the objective of this study before participation experiments. The day of experiment could be before or after the day scheduled. The measurement was not begun until the subject had been in the room for at least 15 minutes to habituate to the room temperature. In this study, subjects performed discrimination task of the face images. The subject carried out a discrimination

task to distinguish images shown every 0.5 second in the measurement. The images consist of the faces of the man and woman. The target image is told to a subject before the measurement. The target image was displayed on the display of the PC. Subjects was instructed to push the key as quickly as possible. Response time (RT) was defined as the time of pushing down the key on presenting stimulation. The presentation frequency of a target image and the non-target image follows (Non-target) : (Target) = 1:1. In addition, subjects carried out POMS (short form) and STAI-JYZ and VAS (pleasant - unpleasant) before and after the measurement pleasant. After an experiment, preference of each image was measured by VAS. The measurement was not begun until the subject had been in the room for at least 15 minutes to habituate to the room temperature. The experiment was conducted during the day except with in 2 hours after eating, a was limited to be conducted once daily for each subject. And an oral explanation about experiment contents, purpose and investigation object were given by a document, and the subjects confirmed an agreement for the experiment cooperation by a signature. The ERP is the reaction that is caused when a percept. A component of ERP called P300 is related to the cognition of stimulus. P300 can represent reaction corresponding to the discrimination of the stimulus quantitatively. The ERP is expressed definitely so that discrimination of the stimulation is performed easily. ingredient called P300 wave related to the recognition develops, and ERP are shown in figure 3. An areal voltage and latency of the ERP were focused to evaluated quantity of the preference for the face image. In this study, P300 was defined as 300ms the positive peak potential in range of 300 ± 100 ms. It was reported that P300 and preference have positive correlation. Positive areal potential in range of ± 100 ms of the latency of the peak was calculated. Areal voltage and latency of the peak are assumed from the time when showed the positive peak of ± 100 ms. Preference for the stimulation of the subjects have been assessed with areal voltage and latency of the peak. Calculated from the maximum amplitude ± 100 ms latency and area of potential. Areal Voltage and Amplitude spectrum are shown are shown in figure 4. P300 is analyzed to extract frequency components, 1.28 seconds for ERP 1-7Hz amplitude spectra obtained. ERP is reaction of induced by mental work to impose on task of subject.

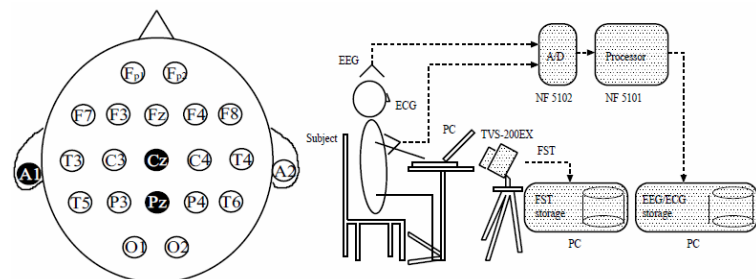


Fig.1. Measurement system and EEG electrode arrangement

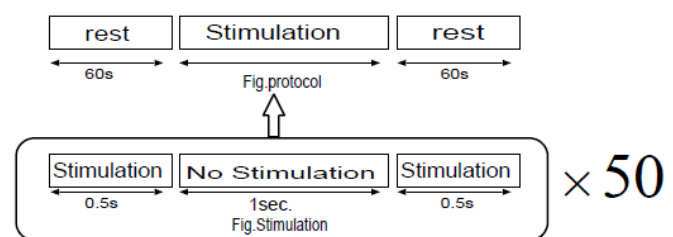


Fig.2. Experiment protocol

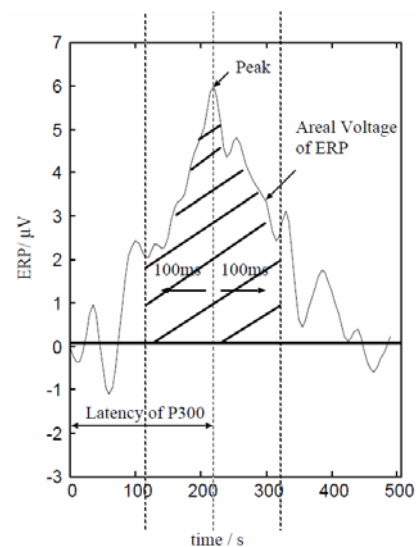


Fig.3. Latency and Areal Voltage of P300

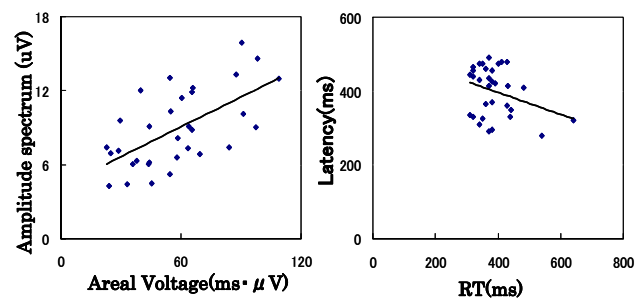


Fig.4. Areal Voltage and Amplitude spectrum

An ingredient called P300 wave related to the recognition develops, and ERP for the discrimination problem by the sight stimulation can arrest reaction corresponding to the discrimination of the stimulation quantitatively. ERP is developing that a difference of the stimulation is big. In this study, preference of subject was measured based on the areal voltage and latency of ERP. Furthermore, P300 was extracted by frequency analysis. Characteristic of an ERP pattern provided from target stimulation, expression of the positive electric potential is accepted as of 300ms by the stimulation presentation and is called P300 wave generally. Analysis of the ERP, evaluation are usually made by extracting the amplitude of P300, an area, quantity of characteristic such as the top latency. The ingredient related to discrimination should be included during the response button exercise start time to push it down from the time of the sensory receptor excitement by the presentation stimulation. In addition, the evoked potential should develop for positive electric potential because P300 wave affects it in one way or another for cognitive process. It is quantity of characteristic of the ERP to reflect these two businesses and refers to this parameter. Method of evaluating on brain waves is reading of P300 of top latency of positive electric potential 250ms-500ms interval. About ERP and the connection of the preference, the amplitude value and an amplitude spectrum and correlation of the preference of P300 were reported [4]. Imitated this in this study, attention to ± 50 ms of the top latency of the positive electric potential of the single trial ERP wave pattern, an amplitude spectrum is demanded of 1-7Hz from the time when the positive greatest amplitude for the amplitude value and the ERP of 1.28 second time of P300 in the section of ± 50 ms was showed. The amplitude value and an amplitude spectrum were assumed on evaluation value. Preference for stimulation of the subject was evaluated. The amplitude value, amplitude spectrum, RT and latency relations is shown in figure 3. Than a precedent study, the preference has relation to an electric potential area of the amplitude value of P300 for latency. Than a precedent study, the preference has relation to an electric potential area of the amplitude value of P300 for latency. Even this study imitates, the preference as latency and an electric potential area of P300 were estimated. An expression as a lineament was extracted. The extraction method of the expression compares eyebrows width and the width of

the mouth with a standard value for a standard price at the interval of the eyes of right and left. The correlation of the psychology index was estimated as the numerical value extracted

III. RESULTS AND DISCUSSION

An electric potential area when the face image of the man a target assumed and an amplitude spectrum and RT and correlation of the latency are shown in figure 5. Equilateral correlation ($r=0.406, n=50, *p < 0.05$) was accepted between an electric potential area and amplitude spectra in the case of a man a target. It is supposed that an electric potential area and extraction of amplitude spectrum P300 wave based for top latency were made from P300 wave between 250-500ms. As a result, an electric potential area and an amplitude spectrum for an index were used when correlation of the preference was judged. Because the electric potential area was based for top latency, latency was used for an evaluation index of the preference equally. Latency and preference on correlation when the face image was made of the man a target are shown in figure 6. Negative correlation ($r=-0.271, n=50, *p < 0.05$) was accepted between a target liking it in the case of a man with latency. When a subject discriminated the image of the woman from it, as for meaningful correlation having come out to the face image of the man than a woman, it is thought that taste did not show a remarkable difference because an object is the opposite sex. A target used it for an index of the image extraction as a result of above more because the taste in case of the man was based on ERP. Eyebrows width and the width of the mouth and the ratio of the interval of both eyes are shown in figure 7. Eyebrows width and the ratio and the taste of the interval of eyes did not have the correlation. The width of the mouth and the ratio and the taste of the interval of eyes did not have the correlation. The graph was divided which was into top and bottom 15 items of the polarity of the preference valuated are shown in figure 8. Correlation ($r=0.418, n=15, *p$) equilateral between the width of the mouth of the image which taste was reflected on weakly and the ratio with the interval of eyes and taste (> 0.05) was accepted. If the width of the mouth was wide, for the face image of the man, it followed that it was favorable for the image. As for the width of the mouth being wide, the subject takes the expression of the person as "a smile". Therefore it

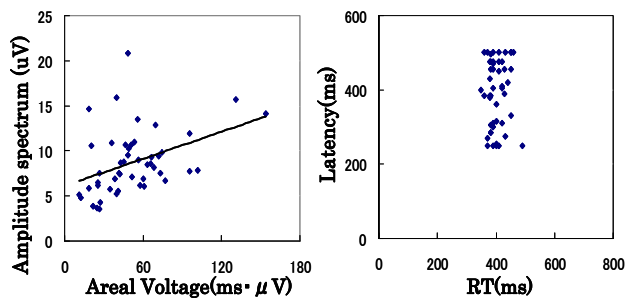


Fig.5. Areal Voltage and Amplitude spectrum

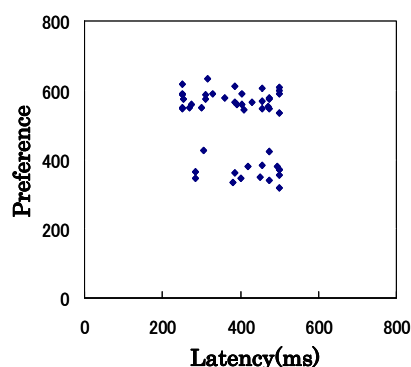


Fig.6. Latency and Preference

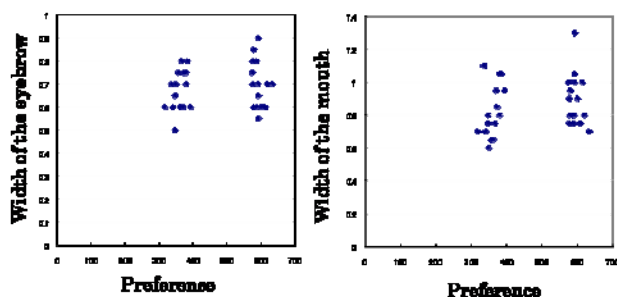


Fig.7. Preference and Width of the eye brow and mouth

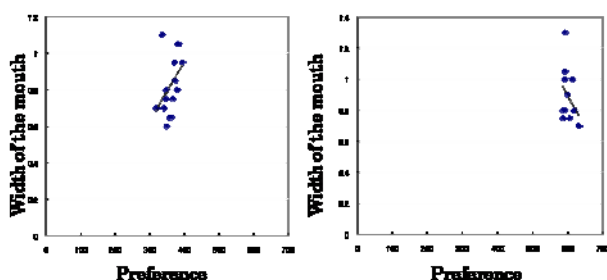


Fig.8. Preference and Width of the eye brow and mouth

followed that a subject had a favorable impression from an image.

VI. CONCLUSION

In this study, the preference for the face of the subject was evaluated. Brain waves and the correlation of the psychology index were accepted when used ERP. An expression was extracted for quantity of characteristic of the image. width of the mouth was used for quantity of characteristic of the expression. As a result, correlation was accepted by area and the taste of the width of the mouth.

REFERENCES

- [1] John D. Mayer, Peter Salovey, David R. Caruso : "Emotional Intelligence : Theory, Finding, and Implications," Psychological Inquiry, Vol15, No3, p.197- 215(2004)
- [2] Y. Nageishi and Shimokochi: "Endogenous components of Event Related Potentials (ERP) and principal-component analysis," Clinical brain waves, Vol.26, No.10, pp.623- 628(1984)
- [3] Mariko FUNADA, Miki SHIBUKAWA, Satoki P. NINOMIYA: "Objective Measurement of Event Related Potentials 'Changes,' Ergonomics, Vol38, pp.538- 539(2002)
- [4] Kazuya TANOUE, Nobuki MURAYAMA, Tomohiko IGASAKI, Ryuji ESHIGE, and Yukari NOGUCHI: "Examination of stimulus methods and frequency analysis for Communication by using EEG" Science Citation Index. MBE, Society for Medical and Biological Engineering 2004(1), 83-86, 2005-01-30

Observer-based Guaranteed Cost Control

Erwin Susanto¹, Mitsuaki Ishitobi² and Sadaaki Kunimatsu³

^{1,2,3}*Department of Mechanical Systems Engineering*

Kumamoto University, Kumamoto 860-8555

Tel: +81-96-342-3866

E-mail: ¹095d9213@st.kumamoto-u.ac.jp, ²mishi@kumamoto-u.ac.jp, ³kunimatu@mech.kumamoto-u.ac.jp

Abstract: This paper presents a design scheme of a minimal order observer-based guaranteed cost controller for uncertain linear systems. The perturbations are assumed to be described by structural uncertainties. An iterative linear matrix inequality (ILMI) approach is used to design the observer-based controller since the problems contain inverse relations. We modify the algorithm of Matsunaga et al by optimizing a sufficiently large initial guaranteed cost. This method can be implemented by LMI control toolbox of Matlab. Finally, a numerical example is given to illustrate the effectiveness of the proposed method.

Keywords: robust control, guaranteed cost control, minimal order observer

I. INTRODUCTION

Considerable attention to the problem in robust stability analysis and robust stabilization of uncertain systems has been attracting many authors for several last decades. One approach to this problem is the guaranteed cost control method which not only achieves the stability of the uncertain system but also guarantees an adequate level of performance via linear matrix inequality (LMI) techniques (Lien [2], Won and Park [3]).

Although the controller is usually constructed by using state variables, it may not be possible to measure all the states of the system in many cases. The observer-based control is probably well suited and better than the state control feedback in such situations.

Since inverse relations among variables appear, this paper concerns a design method of a minimal order observer-based guaranteed cost controller via an iterative linear matrix inequality (ILMI) technique under an assumption that the statistical properties of the initial state variables are known.

II. PROBLEM STATEMENT

Consider a continuous-time uncertain system

$$\begin{aligned}\dot{\mathbf{x}}(t) &= (A + \Delta A(t))\mathbf{x}(t) + (B + \Delta B(t))\mathbf{u}(t) \quad (1) \\ \mathbf{y}(t) &= C\mathbf{x}(t) \quad (2)\end{aligned}$$

where $\mathbf{x}(t) \in \mathbb{R}^n$ is the state vector, $\mathbf{u}(t) \in \mathbb{R}^r$ is the control input vector, $\mathbf{y}(t) \in \mathbb{R}^m$ is the measured output vector, A , B , C are known constant real-valued matrices with appropriate dimensions, and C is restricted to the form of $C = [O \ I_m]$. Matrices $\Delta A(t)$ and $\Delta B(t)$ denote real-valued matrix functions representing parameter uncertainties. It is assumed that

$$\Delta A(t) = D_A F_A(t) E_A, \quad \Delta B(t) = D_B F_B(t) E_B \quad (3)$$

with

$$F_A^T(t) F_A(t) \leq I, \quad F_B^T(t) F_B(t) \leq I$$

where D_A , D_B , E_A , E_B are constant real-valued known matrices with appropriate dimensions, and $F_A(t)$ and $F_B(t)$ are real time-varying unknown continuous and deterministic matrices.

We further assume that the initial state variable $\mathbf{x}(0)$ is unknown, but their mean and covariance are known

$$E[\mathbf{x}(0)] = \mathbf{m}_0 \quad (4)$$

$$E[(\mathbf{x}(0) - \mathbf{m}_0)(\mathbf{x}(0) - \mathbf{m}_0)^T] = \Sigma_0 > O \quad (5)$$

where $E[\cdot]$ denotes the expected value operator.

The problem considered here is to design a minimal order observer

$$\dot{\mathbf{z}}(t) = D\mathbf{z}(t) + E\mathbf{y}(t) + F\mathbf{u}(t) \quad (6)$$

$$\hat{\mathbf{x}}(t) = P\mathbf{z}(t) + W\mathbf{y}(t) \quad (7)$$

and a controller

$$\mathbf{u}(t) = K\hat{\mathbf{x}}(t) \quad (8)$$

with

$$D = A_{11} + LA_{21}, \quad PT + WC = I_n,$$

$$F = TB, \quad TA - DT = EC, \quad A = \begin{bmatrix} A_{11} & A_{12} \\ A_{21} & A_{22} \end{bmatrix},$$

$$P = [I_{n-m} \ \mathbf{0}]^T, \quad T = [I_{n-m} \ L]$$

so as to achieve an upper bound on the following quadratic performance index

$$E[J] = E \int_0^\infty (\mathbf{x}^T(t)Q\mathbf{x}(t) + \mathbf{u}^T(t)R\mathbf{u}(t))dt \quad (9)$$

associated with the uncertain system (1) and (2) where Q and R are given symmetric positive-definite matrices.

III. MAIN RESULTS

In this section, a sufficient condition is established for the existence of a minimal order observer-based guaranteed cost controller for the uncertain system (1) and (2). Here, it is assumed that the feedback gain matrix is

$$K = -R^{-1}B^T S_1 \quad (10)$$

where S_1 is a symmetric positive-definite matrix.

The main result of this study is given by Theorem 1.

Theorem 1. If the following matrix inequalities optimization problem; $\min \{\gamma_0 + \gamma_1 + \gamma_2 + \gamma_3 + \gamma_4\}$ subject to

$$\begin{bmatrix} \Lambda_0 & XE_A^T & XE_A^T & X^T \\ E_A X & -\zeta I & 0 & 0 \\ E_A X & 0 & -\theta I & 0 \\ X & 0 & 0 & -Q^{-1} \end{bmatrix} < 0 \quad (11)$$

$$\begin{bmatrix} \bar{\Lambda}_0 & G_1^T & G_1^T & G_2^T & G_3^T & G_3^T & G_4^T \\ G_1 & -\delta I & 0 & 0 & 0 & 0 & 0 \\ G_1 & 0 & -\mu I & 0 & 0 & 0 & 0 \\ G_2 & 0 & 0 & -\theta_{inv} I & 0 & 0 & 0 \\ G_3 & 0 & 0 & 0 & -\nu_{inv} I & 0 & 0 \\ G_3 & 0 & 0 & 0 & 0 & -\mu_{inv} I & 0 \\ G_4 & 0 & 0 & 0 & 0 & 0 & -R \end{bmatrix} < 0 \quad (12)$$

$$\sum_{k=1}^n e_{nk}^T \Theta_0 e_{nk} < \gamma_0, \quad \sum_{k=1}^m e_{mk}^T \Theta_1 e_{mk} < \gamma_1$$

$$\sum_{k=1}^m e_{mk}^T \Theta_2 e_{mk} < \gamma_2, \quad \sum_{k=1}^m e_{mk}^T \Theta_3 e_{mk} < \gamma_3 \quad (13)$$

$$\begin{bmatrix} -\gamma_4 & v_1^T Y^T & v_2^T Y^T & \dots & v_m^T Y^T \\ Y v_1 & -S_2 & & & \vdots \\ Y v_2 & & \ddots & & \vdots \\ \vdots & & & \ddots & \vdots \\ Y v_m & \dots & \dots & \dots & -S_2 \end{bmatrix} < 0 \quad (14)$$

where

$$\begin{aligned} \Lambda_0 &= AX + XA^T - BR^{-1}B^T + \zeta D_A D_A^T + \epsilon D_B D_B^T \\ &\quad + \epsilon_{inv} BR^{-1}E_B^T E_B R^{-1}B^T + \delta D_B D_B^T \\ &\quad + \nu_{inv} BR^{-1}E_B^T E_B R^{-1}B^T \\ \bar{\Lambda}_0 &= S_2 A_{11} + A_{11}^T S_2 + Y A_{21} + A_{21}^T Y^T \\ Y &= S_2 L, \quad Z = [S_2 \quad Y], \\ G_1 &= E_B R^{-1}B^T S_1 P, \quad G_2 = D_A^T Z^T \\ G_3 &= D_B^T Z^T, \quad G_4 = B^T S_1 P \\ \Theta_0 &= \frac{1}{2}(S_1(\Sigma_0 + m_0 m_0^T) + (\Sigma_0 + m_0 m_0^T)^T S_1) \\ \Theta_1 &= \frac{1}{2}(S_2 \Sigma_{11} + \Sigma_{11} S_2), \quad \Theta_2 = \frac{1}{2}(Y \Sigma_{21} + \Sigma_{21}^T Y^T) \end{aligned}$$

$$\Theta_3 = \frac{1}{2}(Y^T \Sigma_{12} + \Sigma_{12}^T Y), \quad \Sigma_{22}^{1/2} = [v_1, v_2, \dots, v_m]$$

$$\Sigma_0 = \begin{bmatrix} \Sigma_{11} & \Sigma_{12} \\ \Sigma_{21} & \Sigma_{22} \end{bmatrix}, \quad e_{ik} = [\mathbf{0}_{k-1}^T \quad 1 \quad \mathbf{0}_{i-k}^T]^T$$

has a solution $S_1 > 0, S_2 > 0, X > 0, Y, Z, \zeta > 0, \delta > 0, \epsilon > 0, \epsilon_{inv} > 0, \theta > 0, \theta_{inv} > 0, \mu > 0, \mu_{inv} > 0, \nu_{inv} > 0, \gamma_0, \gamma_1, \gamma_2, \gamma_3, \gamma_4$ which satisfy the relation $\epsilon^{-1} = \epsilon_{inv}, \theta^{-1} = \theta_{inv}, \mu^{-1} = \mu_{inv}$ and $S_1^{-1} = X$, then the minimal order observer-based control law (6)-(8) with (10) is a guaranteed cost controller which gives the minimum expected value of the guaranteed cost

$$E[J^*] = E[\mathbf{x}^T(0)S_1 \mathbf{x}(0) + \boldsymbol{\xi}^T(0)S_2 \boldsymbol{\xi}(0)] \quad (15)$$

where $\boldsymbol{\xi}(t) = \mathbf{z}(t) - T\mathbf{x}(t)$ is the estimated error of the minimal order observer.

Remark 1: Since (11) and (12) have a constraint of the relationship of the inverse, ILMI approach is introduced to solve (Ghaoui et al [4], Cao et al [5]).

Before giving a proof of Theorem 1, a key lemma is introduced (Mahmoud and Zribi [6]).

Lemma 1. Let D and E be matrices of appropriate dimensions, and F be a matrix function satisfying $F^T F \leq I$. Then for any positive scalar α , the following inequality holds

$$DFE + E^T F^T E^T \leq \alpha D D^T + \alpha^{-1} E^T E. \quad (16)$$

Proof of Theorem 1.

Equations (1) and (6)-(8) yield the closed-loop system

$$\begin{aligned} \dot{\mathbf{x}}(t) &= \Phi_1 \Phi_2 \mathbf{x}(t) \\ \dot{\boldsymbol{\xi}}(t) &= \Phi_3 \Phi_4 \boldsymbol{\xi}(t) \end{aligned} \quad (17)$$

where

$$\begin{aligned} \Phi_1 &= A + \Delta A(t) + (B + \Delta B(t))K \\ \Phi_2 &= (B + \Delta B(t))KP \\ \Phi_3 &= -T\Delta A(t) - T\Delta B(t)K \\ \Phi_4 &= D - T\Delta B(t)KP \end{aligned}$$

Define a candidate of Lyapunov function as

$$V(t) = \mathbf{x}^T(t)S_1 \mathbf{x}(t) + \boldsymbol{\xi}^T(t)S_2 \boldsymbol{\xi}(t) \quad (18)$$

then, the time derivative of (18) along to (17) is calculated as

$$\dot{V}(t) = \mathbf{w}^T(t)\Omega \mathbf{w}(t) - (\mathbf{x}^T(t)Q\mathbf{x}(t) + \mathbf{u}^T(t)Ru(t)) \quad (19)$$

where

$$\mathbf{w}(t) = \begin{bmatrix} \mathbf{x}(t) \\ \boldsymbol{\xi}(t) \end{bmatrix}, \quad \Omega = \begin{bmatrix} \Lambda_1 & \Lambda_2 \\ \Lambda_2^T & \Lambda_3 \end{bmatrix}$$

$$\begin{aligned} \Lambda_1 &= S_1(A + \Delta A(t)) + (A + \Delta A(t))^T S_1 \\ &\quad - S_1 B R^{-1} B^T S_1 + Q - 2S_1 \Delta B(t) R^{-1} B^T S_1 \\ \Lambda_2 &= -S_1 \Delta B(t) R^{-1} B^T S_1 P - \Delta A^T(t) T^T S_2 \\ &\quad + S_1 B R^{-1} \Delta B^T(t) T^T S_2 \\ \Lambda_3 &= S_2 D + D^T S_2 + P^T S_1 B R^{-1} B^T S_1 P \\ &\quad + 2S_2 T \Delta B(t) R^{-1} B^T S_1 P \end{aligned}$$

Under the condition

$$\Omega < 0 \quad (20)$$

equation (19) leads to

$$\dot{V}(t) < -(\mathbf{x}^T(t)Q\mathbf{x}(t) + \mathbf{u}^T(t)R\mathbf{u}(t)) < 0 \quad (21)$$

for any $\mathbf{x}(t) \neq \mathbf{0}$ and the closed-loop system is asymptotically stable.

Applying lemma 1., pre- and post-multiplying by $\text{diag}(S_1^{-1}, I)$ on both sides, denoting $X = S_1^{-1}$, $Y = S_2L$, $\epsilon_{inv} = \epsilon^{-1}$, $\theta_{inv} = \theta^{-1}$, $\mu_{inv} = \mu^{-1}$, $\nu_{inv} = \nu^{-1}$, and using Schur Complement lead to (11) and (12).

Then, integrating (21) from 0 to T and as T tends to the infinity yields

$$\begin{aligned} J &= \int_0^\infty (\mathbf{x}^T(t)Q\mathbf{x}(t) + \mathbf{u}^T(t)R\mathbf{u}(t))dt \\ &< \mathbf{x}^T(0)S_1\mathbf{x}(0) + \boldsymbol{\xi}^T(0)S_2\boldsymbol{\xi}(0) = J^* \end{aligned} \quad (22)$$

where J^* denotes the guaranteed cost. Here, we consider the optimal expected value of the guaranteed cost. It is calculated as

$$E[J^*] = \text{tr}S_1E[\mathbf{x}(0)\mathbf{x}^T(0)] + \text{tr}S_2E[\boldsymbol{\xi}(0)\boldsymbol{\xi}^T(0)] \quad (23)$$

A relation between mean and covariance of $\mathbf{x}(0)$ is given by

$$\Sigma_0 = E[\mathbf{x}(0)\mathbf{x}^T(0)] - \mathbf{m}_0\mathbf{m}_0^T \quad (24)$$

Substituting (24) into (23) yields

$$\begin{aligned} E[J^*] &= \text{tr}S_1(\Sigma_0 + \mathbf{m}_0\mathbf{m}_0^T) \\ &+ \text{tr}S_2E[(\mathbf{z}(0) - T\mathbf{x}(0))(\mathbf{z}(0) - T\mathbf{x}(0))^T] \end{aligned} \quad (25)$$

Here, it is readily seen that

$$\begin{aligned} &E[(\mathbf{z}(0) - T\mathbf{x}(0))(\mathbf{z}(0) - T\mathbf{x}(0))^T] \\ &= T\Sigma_0T^T + (\mathbf{z}(0) - T\mathbf{m}_0)(\mathbf{z}(0) - T\mathbf{m}_0)^T \end{aligned} \quad (26)$$

Hence, (25) leads to

$$\begin{aligned} E[J^*] &= \text{tr}S_1(\Sigma_0 + \mathbf{m}_0\mathbf{m}_0^T) + \text{tr}S_2(T\Sigma_0T^T \\ &+ (\mathbf{z}(0) - T\mathbf{m}_0)(\mathbf{z}(0) - T\mathbf{m}_0)^T) \end{aligned} \quad (27)$$

Here, it can be assumed that an initial value of a minimal order observer $\mathbf{z}(0)$ satisfies the following equation without loss of generality.

$$\mathbf{z}(0) - T\mathbf{m}_0 = \mathbf{0} \quad (28)$$

Substituting (28) into (27) yields

$$\begin{aligned} E[J^*] &= \text{tr}S_1(\Sigma_0 + \mathbf{m}_0\mathbf{m}_0^T) \\ &+ \text{tr}S_2(\Sigma_{11} + L\Sigma_{21} + \Sigma_{12}L^T + L\Sigma_{22}L^T) \end{aligned} \quad (29)$$

where

$$\Sigma_0 = \begin{bmatrix} \Sigma_{11} & \Sigma_{12} \\ \Sigma_{21} & \Sigma_{22} \end{bmatrix}$$

Here, we consider positive scalars $\gamma_0, \gamma_1, \gamma_2, \gamma_3, \gamma_4$ satisfying the following inequalities

$$\text{tr}S_1(\Sigma_0 + \mathbf{m}_0\mathbf{m}_0^T) < \gamma_0 \quad (30)$$

$$\text{tr}S_2\Sigma_{11} < \gamma_1 \quad (31)$$

$$\text{tr}S_2L\Sigma_{21} < \gamma_2 \quad (32)$$

$$\text{tr}S_2\Sigma_{12}L^T < \gamma_3 \quad (33)$$

$$\text{tr}S_2L\Sigma_{22}L^T < \gamma_4 \quad (34)$$

Minimizing $\gamma_0 + \gamma_1 + \gamma_2 + \gamma_3 + \gamma_4$ results in giving $\min E[J^*]$. By recalling $\text{tr}(AB) = \text{tr}(BA)$, (30)-(33) lead to (13). Next, by denoting $\Sigma_{22}^{1/2} = [\mathbf{v}_1, \mathbf{v}_2, \dots, \mathbf{v}_m]$, (34) is calculated as

$$\begin{aligned} &\text{tr}S_2L\Sigma_{22}L^T \\ &= \mathbf{v}_1^TY^TS_2^{-1}Y\mathbf{v}_1 + \mathbf{v}_2^TY^TS_2^{-1}Y\mathbf{v}_2 \\ &+ \dots + \mathbf{v}_m^TY^TS_2^{-1}Y\mathbf{v}_m \\ &= [\mathbf{v}_1^TY^T \mathbf{v}_1^TY^T \dots \mathbf{v}_m^TY^T] S_2^{-1} \begin{bmatrix} Y\mathbf{v}_1 \\ Y\mathbf{v}_2 \\ \vdots \\ Y\mathbf{v}_m \end{bmatrix} < \gamma_4 \end{aligned} \quad (35)$$

Further, Schur complement derives (14) from (35).
Q.E.D.

It is noted that the inequalities (11) and (12) cannot be solved directly by LMI because they contain the scalars $\epsilon, \epsilon_{inv}, \theta, \theta_{inv}, \mu, \mu_{inv}$, and two matrices S_1, X which satisfy the relation $S_1^{-1} = X$, $\epsilon^{-1} = \epsilon_{inv}$, $\theta^{-1} = \theta_{inv}$, $\mu^{-1} = \mu_{inv}$. There are a number of algorithms available in literature, and we apply the cone complementarity linearization approach (Ghaoui et al [4]) to propose the algorithm as follows.

Step 0: Set k_{max}, γ_{min} and κ .

Step 1: Choose a sufficiently large initial γ such that there exists a feasible solution to LMI conditions

$$\begin{aligned} &\begin{bmatrix} S_1 & I \\ I & X \end{bmatrix} > 0, \gamma_0 + \gamma_1 + \gamma_2 + \gamma_3 + \gamma_4 < \gamma, \\ &\epsilon\epsilon_{inv} > 1, \theta\theta_{inv} > 1, \mu\mu_{inv} > 1, \\ &\text{inequalities (11)-(14)} \end{aligned}$$

Step 2.1 : Set $\bar{\gamma} = \gamma, k = 0, i = 1$, set $S_1(k) = S_1, X(k) = X, \epsilon(k) = \epsilon, \epsilon_{inv}(k) = \epsilon_{inv}, \theta(k) = \theta, \theta_{inv}(k) = \theta_{inv}, \mu(k) = \mu, \mu_{inv}(k) = \mu_{inv}$.

Step 2.2 : Solve the following LMI problem

$$\begin{aligned} t_k = &\text{Minimize}(\text{tr}[S_1(k)X + X(k)S_1]) + \\ &\epsilon(k)\epsilon_{inv} + \epsilon\epsilon_{inv}(k) + \theta(k)\theta_{inv} + \theta\theta_{inv}(k) + \end{aligned}$$

$\mu(k)\mu_{inv} + \mu\mu_{inv}(k)$
subject to

$$\begin{aligned} \begin{bmatrix} S_1 & I \\ I & X \end{bmatrix} &> 0, \quad \gamma_0 + \gamma_1 + \gamma_2 + \gamma_3 + \gamma_4 < \gamma, \\ \epsilon\epsilon_{inv} &> 1, \quad \theta\theta_{inv} > 1, \quad \mu\mu_{inv} > 1, \\ \text{inequalities (11)-(14)} \end{aligned}$$

Step 3.1 : If $k < k_{max}$ and $t_k > 2n + 6 + \kappa$ then set $k = k + 1$ and go to 2.2.

Step 3.2 : If $k \leq k_{max}$, $t_k \leq 2n + 6 + \kappa$, LMI conditions are satisfied, and $\gamma(0.5)^i > \gamma_{min}$ then $\bar{\gamma} = \bar{\gamma} - \gamma(0.5)^i$. Else if $\gamma(0.5)^i \leq \gamma_{min}$ then exit and $\bar{\gamma}$ is an optimal value.

Step 3.3 : If $k < k_{max}$, $t_k \leq 2n + 6 + \kappa$, LMI conditions are not satisfied, $i \neq 1$ and $\gamma(0.5)^i > \gamma_{min}$ then $\bar{\gamma} = \bar{\gamma} + \gamma(0.5)^i$. Else if $\gamma(0.5)^i \leq \gamma_{min}$ then exit and $\bar{\gamma}$ is an optimal value. Else if $i = 1$ then exit and no optimal solution is obtained.

Step 3.4 : If $k = k_{max}$, $t_k > 2n + 6 + \kappa$, $i \neq 1$ and $\gamma(0.5)^i > \gamma_{min}$ then $\bar{\gamma} = \bar{\gamma} + \gamma(0.5)^i$. Else if $\gamma(0.5)^i \leq \gamma_{min}$ then exit and $\bar{\gamma}$ is an optimal value. Else if $i = 1$ then exit and no optimal solution is obtained.

Step 4 : Set $i = i + 1$ and return to 3.1.

This algorithm allows the optimal value $\bar{\gamma}$ can be reached faster than that of Matsunaga et al [1] because the correction is not fixed but depending on iteration i .

IV. AN ILLUSTRATIVE EXAMPLE

Consider a system with

$$A = \begin{bmatrix} -3 & 0 & -2 & 0 \\ 0 & -2 & 0 & -1 \\ 1 & 0 & 0 & 0 \\ 0 & 1 & 0 & 0 \end{bmatrix}, \quad B = \begin{bmatrix} 3 \\ 2 \\ -6 \\ 1 \end{bmatrix},$$

$$C = [O_2 \ I_2], \quad m_0 = 0_4, \quad \Sigma_0 = I_4, \quad R = 9,$$

$$Q = \text{diag}(7, 15, 1, 3), \quad D_A = \begin{bmatrix} 0.1I_2 & O_2 \\ O_2 & O_2 \end{bmatrix},$$

$$E_A = \begin{bmatrix} 0.3I_2 & 0.3I_2 \\ O_2 & O_2 \end{bmatrix}, \quad D_B = \text{diag}(0.3, 0.1, 0.3, 0.1),$$

$$E_B = [1 \ -1 \ 1 \ -1]^T.$$

Applying Theorem 1, with $k_{max}=200$, $\gamma_{min}=0.0001$, $\kappa=0.000001$ and initial $\gamma=100$, we obtain a solution

$$L = \begin{bmatrix} -0.1844 & -0.0440 \\ -0.0074 & -0.2493 \end{bmatrix},$$

$$K = [-0.3837 \ -0.4460 \ 0.5278 \ -0.4720],$$

$$\bar{\gamma} = E[J^*] = 16.8893.$$

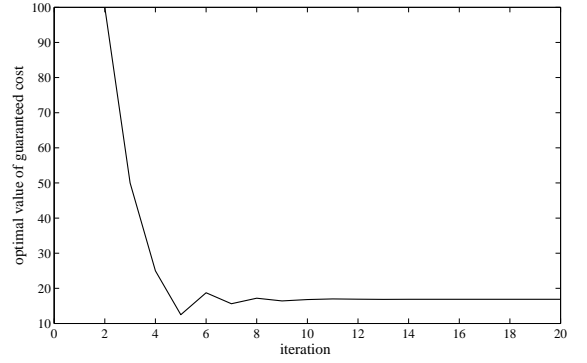


Fig. 1: Trajectory of optimal guaranteed cost γ .

V. CONCLUSION

A guaranteed cost observer-based control problem concerned on a minimal order observer has been discussed. A sufficient condition for the existence of state feedback guaranteed cost controllers is derived on the basis of the ILMI approach to solve inverse relation. A numerical example is given to illustrate the proposed method.

References

- [1] D. Matsunaga, M. Ishitobi and S. Kunitatsu (2009), An ILMI approach to guaranteed cost controllers with a minimal order observer. Proc. of ICROS-SICE International Joint Conference 2009:583–588.
- [2] C. H. Lien (2004), Robust observer-based control of systems with state perturbations via LMI approach. IEEE Trans. on Automatic Control Vol.49(8):1365–1370.
- [3] S. Won and J. H. Park (1999), Design of observer-based controller for perturbed time-delay systems. JSME International Journal C Vol.42(1):129–132.
- [4] L. E. Ghaoui, F. Oustry and M. AitRami (1997), A cone complementarity linearization algorithm for static output-feedback and related problems. IEEE Trans. on Automatic Control Vol.42(8):1171–1176.
- [5] Y. Cao, J. Lam and Y. Sun (1998), Static output feedback stabilization: an ILMI approach. Automatica Vol.34(12):1641–1645.
- [6] M. S. Mahmoud and M. Zribi (2003), Guaranteed cost observer-based control of uncertain time-lag systems. Computers and Electrical Engineering Vol.29(1):193–212.

Observer based control of a manipulator system with structured uncertainty

Chikara AIKAWA, Nobuya TAKAHASHI, Osamu SATO and Michio KONO

Faculty of Engineering, University of Miyazaki
1-1 Gakuenkibanadai-Nishi, Miyazaki, 889-2192, JAPAN
Tel & Fax : +81-985-58-7419
E-mail : ntaka@cs.miyazaki-u.ac.jp

Abstract : In this paper, we show an uncertain model of a two link RR manipulator with uncertainties in the two rotation angles of each joint, and show the extended system with uncertainty also in an output matrix. For this system, we apply a guaranteed cost control method based on a linear upper bound. Parameter tuning of γ_i in the linear upper bound is effective to design a feedback gain which have appropriate characteristics. In the numerical simulation, we show an advantage that the state observer is effective to reduce the influence of signal noise in state vector.

Keywords : Uncertain system, Guaranteed cost control, Observer based control

1 Introduction

The guaranteed cost control (GCC) is one of an effective approach to design a robust control system. This method is an extended version of the linear quadratic regulator (LQR) that is one of the efficient method for designing control system, and it is stated as an essential concept in the modern control theorem. However, LQR method is formulated as nominal form, thus, it is weak for the effect of the disturbance which is caused by the uncertainty of the system model, secular distortion, signal noise, and so on. The system performance is degraded by these disturbance effects.

For such a problem, under the assumption that an uncertain parameter variation is in an admissible closed set, the GCC method guarantees the upper bound of the performance index variation [1]. Takahashi et al. extended the GCC method to the case with uncertainty in an output matrix [2], and they proposed the modeling method for the uncertain inverted pendulum car system which include uncertainty in a pendulum angle and apply the guaranteed cost control method [3]. In this paper, we will propose a method of the GCC to the system with structured uncertainties in input, state and also output matrix. And show the effectiveness of the parameter tuning in the upper bound. At last, we will apply the state observer to consider the influence of disturbance.

2 Formulation of the GCC problem

In this section, we will show the GCC problem with parameter variation in state, input and also output matrix.

Let us consider the following uncertain system.

$$\begin{cases} \dot{\mathbf{x}}(t) &= A(\xi)\mathbf{x}(t) + B(\zeta)\mathbf{u}(t) \\ \mathbf{y}(t) &= C(\psi)\mathbf{x}(t) \end{cases} \quad (1)$$

where, state, output and input vector are $\mathbf{x} \in \mathbb{R}^n$, $\mathbf{y} \in \mathbb{R}^m$ and $\mathbf{u} \in \mathbb{R}^l$, respectively. Uncertain state matrix $A(\xi) \in \mathbb{R}^{n \times n}$, input matrix $B(\zeta) \in \mathbb{R}^{n \times l}$, and output matrix $C(\psi) \in \mathbb{R}^{m \times n}$ are defined as

$$A(\xi) = A_0 + \sum_{i=1}^p \xi_i A_i, \quad |\xi_i| \leq 1 \quad (2)$$

$$B(\zeta) = B_0 + \sum_{j=1}^q \zeta_j B_j, \quad |\zeta_j| \leq 1 \quad (3)$$

$$C(\psi) = C_0 + \sum_{k=1}^r \psi_k C_k, \quad |\psi_k| \leq 1 \quad (4)$$

where, A_0, B_0 and C_0 represent the system structure that could be included in the linear system model. We call these matrices as nominal element. A_i, B_j and C_k represent the uncertain system structure that could not be included in the linear system model. We call these matrices as uncertainties. Where p, q and r are numbers of the corresponding uncertainties, ξ_i, ζ_j and ψ_k are indeterminate scalar parameters which represent the scale of uncertainties and included a bounded closed set. These parameters are used to normalize the structures of uncertainties.

Here we consider the GCC problem for the system of eq. (1) which has uncertainty in an output matrix. The performance index function consists of the quadratic forms of

the input vector $\mathbf{u}(t)$ and the output vector $\mathbf{y}(t)$.

$$J(\mathbf{y}, \mathbf{u}, \xi, \zeta, \psi) = \int_0^\infty \{\mathbf{y}^T(t)Q\mathbf{y}(t) + \mathbf{u}^T(t)R\mathbf{u}(t)\} dt \quad (5)$$

where $Q \in \mathbb{R}^{m \times m} \geq 0$ and $R \in \mathbb{R}^{l \times l} > 0$ are weighting matrices of input and output vector, respectively. In virtue of the uncertain structure (2), (3) and (4), the linear upper bound becomes:

$$U_L(A(\xi), B(\zeta), C(\psi), P, Q, R) = \sum_{i=1}^p (\gamma_i^{-1}P + \gamma_i A_i^T P A_i) + P R_s P + Q_s \quad (6)$$

where

$$R_s = \sum_{j=1}^q (B_j R^{-1} B_0^T + B_0 R^{-1} B_j^T) \quad (7)$$

$$Q_s = \sum_{k=1}^r (C_0^T Q C_k + C_k^T Q C_0 + C_k^T Q C_k) \quad (8)$$

By applying this upper bound, we have stochastic algebraic Riccati equation (SARE) based on the linear upper bound:

$$(A_0 + \gamma I)^T P + P(A_0 + \gamma I) + C_0^T Q C_0 + Q_s - P(R_n - R_s)P + \sum_{i=1}^p \gamma_i A_i^T P A_i = O \quad (9)$$

where $\gamma = 1/2 \sum_{i=1}^p \gamma_i^{-1}$, $R_n = B_0 R^{-1} B_0^T$. Feedback gain is obtained as:

$$F = -R^{-1} B_0^T P$$

3 Skeletal form of the uncertain model

From the past research [4], we have a dynamics of uncertain LTI system of a two link RR manipulator. The link 1 is connected to the base with a rotation joint 1 and the link 2 is connected to another end point of the link 1 with a rotation joint 2. Each joints and arms have physical parameters illustrated in table 1.

Table 1 : Parameters of the Manipulator

Parameters	Meaning [unit]
θ_i	Angle of the joint [rad]
m_i	Mass of the arm [kg]
I_i	Inertia moment of the arm [kg · m ²]
l_i	Length of the arm [m]
l_{Gi}	Distance from the joint to the center of gravity of the arm [m]
g	Gravity [m/s ²]
τ_i	Input torque to the joint [N · m]

Let us define a state vector $\mathbf{x}(t)$ and an input vector $\mathbf{u}(t)$ are

$$\mathbf{x}(t) = \begin{bmatrix} \theta_1(t) \\ \dot{\theta}_1(t) \\ \theta_2(t) \\ \dot{\theta}_2(t) \end{bmatrix}, \mathbf{u}(t) = \begin{bmatrix} u_1(t) \\ u_2(t) \end{bmatrix}$$

An input matrix $A(\xi)$ and an output matrix $B(\zeta)$ are obtained as following:

$$A(\xi) = \begin{bmatrix} 0 & 1 & 0 & 0 \\ \bar{h}_{11}/h_D & 0 & \bar{h}_{12}/h_D & 0 \\ 0 & 0 & 0 & 1 \\ \bar{h}_{21}/h_D & 0 & \bar{h}_{22}/h_D & 0 \end{bmatrix}$$

$$B(\zeta) = \begin{bmatrix} 0 & 0 \\ h_{22}/h_D & -h_{12}/h_D \\ 0 & 0 \\ -h_{12}/h_D & h_{22}/h_D \end{bmatrix}$$

where

$$h_D = h_{11}h_{22} - h_{12}^2$$

$$\bar{h}_{11} = \Delta c_1 g (h_{22}(m_1 l_{G1} + m_2 l_1) + \Delta c_2 m_2 l_{G2}(h_{22} - h_{12}))$$

$$\bar{h}_{12} = \Delta c_1 \Delta c_2 m_2 g l_{G2}(h_{22} - h_{12})$$

$$\bar{h}_{21} = \Delta c_1 (-h_{12} g (m_1 l_{G1} + m_2 l_1) + \Delta c_2 m_2 g l_{G2}(h_{11} - h_{12}))$$

$$\bar{h}_{22} = \Delta c_1 \Delta c_2 m_2 g l_{G2}(h_{11} - h_{12})$$

h_{11} , h_{12} and h_{22} are given as follows:

$$h_{11} = I_1 + m_1 l_{G1}^2 + I_2 + m_2 (l_1^2 + l_{G2}^2 + 2\Delta c_2 l_1 l_{G2})$$

$$h_{12} = I_2 + m_2 (l_{G2}^2 + \Delta c_2 l_1 l_{G2})$$

$$h_{22} = I_2 + m_2 l_{G2}^2$$

From $A(\xi)$ and $B(\zeta)$, we can obtain deterministic elements A_0 and B_0 as $(\Delta\theta_1, \Delta\theta_2) = (0, 0)$. A_1 and B_1 are obtained in the condition of $(\Delta\theta_1, \Delta\theta_2) = (max_1, 0)$ and A_2 and B_2 are obtained in the condition of $(\Delta\theta_1, \Delta\theta_2) = (0, max_2)$. Where max_i is a maximum uncertainty of the rotational angle in the joint i .

4 State observer

In this section, we consider the application of an identical state observer to the uncertain system (1). $\hat{\mathbf{x}}(t)$ is the state of the observer (estimation of the plant state), $\mathbf{y}(t)$ is output from the plant, and $\mathbf{u}(t)$ is the input from the controller to the plant, respectively.

$$\dot{\hat{\mathbf{x}}}(t) = (A - KC)\hat{\mathbf{x}}(t) + G\mathbf{y}(t) + H\mathbf{u}(t)$$

where, K is observer gain.

5 Numerical example

5.1 Uncertain system

In this section, we will show the numerical example. Here we consider that the joint 2 is passive, thus the input matrix $B(\zeta)$ becomes

$$B(\zeta) = \begin{bmatrix} 0 \\ h_{22}/h_D \\ 0 \\ -h_{12}/h_D \end{bmatrix}$$

The values of the physical parameters are illustrated as in table 2.

Table 2: Parameters			
Parameter	Value	Parameter	Value
m_1	1	m_2	1
I_1	0.03	I_2	0.03
l_1	0.3	l_2	0.3
l_{G1}	0.15	l_{G2}	0.15
g	9.8		

For the above parameters, we have uncertain system as follows:

$$A_0 = \begin{bmatrix} 0.0000 & 1.0000 & 0.0000 & 0.0000 \\ 30.3093 & 0.0000 & -12.1237 & 0.0000 \\ 0.0000 & 0.0000 & 0.0000 & 1.0000 \\ -28.2887 & 0.0000 & 50.5155 & 0.0000 \end{bmatrix}$$

$$B_0 = \begin{bmatrix} 0.0000 \\ 9.6220 \\ 0.0000 \\ -17.8694 \end{bmatrix}$$

For the disturbance $\Delta\theta_1 = \Delta\theta_2 = 0.08$, uncertain system becomes:

$$A_1 = \begin{bmatrix} 0.0000 & 0.0000 & 0.0000 & 0.0000 \\ -0.0969 & 0.0000 & 0.0388 & 0.0000 \\ 0.0000 & 0.0000 & 0.0000 & 0.0000 \\ 0.0905 & 0.0000 & -0.1616 & 0.0000 \end{bmatrix}$$

$$A_2 = \begin{bmatrix} 0.0000 & 0.0000 & 0.0000 & 0.0000 \\ 0.0056 & 0.0000 & 0.1059 & 0.0000 \\ 0.0000 & 0.0000 & 0.0000 & 0.0000 \\ -0.0168 & 0.0000 & -0.3192 & 0.0000 \end{bmatrix}$$

$$B_1 = \begin{bmatrix} 0.0000 \\ 0.0000 \\ 0.0000 \\ 0.0000 \end{bmatrix}, \quad B_2 = \begin{bmatrix} 0.0000 \\ -0.0228 \\ 0.0000 \\ 0.0686 \end{bmatrix}$$

5.2 Parameter Tuning γ_i of the linear upper bound

In this paper, we use the linear upper bound for the SARE. In the past research [2], we had shown that the effective of

the parameter tuning of γ_i in the linear upper bound to design a system which have an appropriate characteristic of closed loop system, in the case of the system have only one uncertainty. Here we show the result with two uncertainties of A_i where $p = 2$.

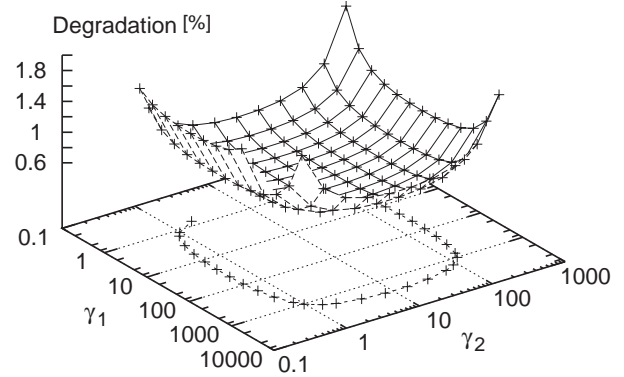


Figure 1 : Degradation of the Performance Index

At first, we solve the SARE on the any point of γ_1 and γ_2 in $0.1 \leq \gamma_i \leq 10000$ ($i = 1, 2$), and calculate the performance index as $J_{LQR} = x_0^T P_{LQR} x_0$ and $J_{GCC} = x_0^T P_{GCC} x_0$. The weighting matrices are $Q = \text{diag}(1, 1)$ and $R = 1$. From these results, we examine the ratio of the degradation of the performance index. This result is illustrated in the figure 1 by double logarithm 3D-chart, which x - and y -axis are logarithmic and z -axis is plotted with a linear scale. In figure 1, the surface illustrates the degradation ratio of the performance index between GCC and LQR. The contour line on the z -plane denotes a line of J_{LQR} and J_{GCC} are equal. The minimum value takes $J_{GCC}/J_{LQR} = 0.6568$ at a point $(\gamma_1, \gamma_2) = (46.8750, 15.6250)$. This point is surrounded by the square contour line that the corner is round. Inside of this square, the GCC method provides a good result. But in the outside region, a reversed result is provided.

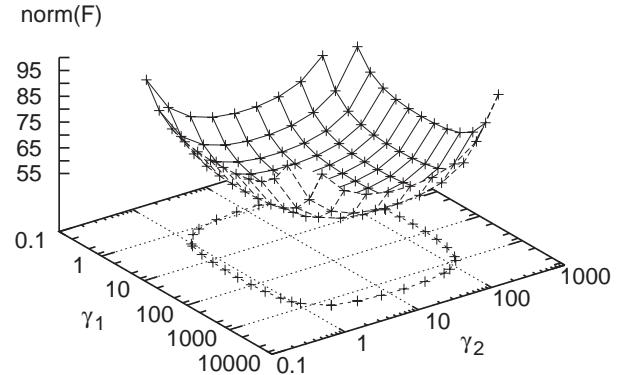


Figure 2 : Norm of F_{GCC}

Next, we will show the comparison of the norm of feedback gain in the same region. In figure 2, the contour line on the z -plane denotes a results of the LQR method that $F_{LQR} = 68.8696$. The minimum value of the norm of feedback gain is $\text{norm}(F_{GCC}) = 55.2322$ on the same

minimum point of figure 1. These results have a similar tendency.

5.3 Numerical solution of SRAE

Here we show and compare the results of GCC and LQR. The following results is the solution of the SARE (Proposed method) on the minimum point (γ_1, γ_2) .

$$P_{GCC} = \begin{bmatrix} 214.9665 & 54.3720 & 163.5782 & 31.4218 \\ 54.3720 & 13.7897 & 41.6448 & 7.9989 \\ 163.5782 & 41.6448 & 128.8797 & 24.5399 \\ 31.4218 & 7.9989 & 24.5399 & 4.6930 \end{bmatrix}$$

Feedback gain is

$$F_{GCC} = [-38.3216 \quad -10.2522 \quad -37.8073 \quad -6.8958]$$

Eigenvalues of the closed loop system are:

$$(-7.8958 \pm 2.3148i, -4.3929 \pm 0.5460i)$$

The LQR result (Ordinary method) is follows.

$$P_{LQR} = \begin{bmatrix} 309.6216 & 80.0140 & 250.8530 & 45.7467 \\ 80.0140 & 20.8360 & 65.4442 & 11.9295 \\ 250.8530 & 65.4442 & 210.2729 & 37.8890 \\ 45.7467 & 11.9295 & 37.8890 & 6.9139 \end{bmatrix}$$

Feedback gain is

$$F_{LQR} = [-47.5721 \quad -12.6897 \quad -47.3509 \quad -8.7623]$$

Eigenvalues of the closed loop system are:

$$(-23.0041 \quad -4.3278 \pm 0.7210i \quad -2.8177)$$

5.4 Comparison of the numerical simulation

Here we will show the numerical simulation of uncertain systems. Now, we compare the performance index function value of eq. (5) with the difference of system composition i) with/without observer, ii) with/without disturbance. The simulation is calculated by Euler's method with step time is 0.01, time interval (0, 30) with an initial state value is $x(0) = [1 \ 0 \ 1 \ 0]^T$ and initial observer state value is $\hat{z}(0) = [0.1 \ 0 \ 0.1 \ 0]^T$. The disturbance is added in the state vector $(x_2, x_4) = (\theta_1, \dot{\theta}_2)$ as a signal noise of uniformly random number between $(-0.08, 0.08)$ on every step time.

Table 3: Comparison of the degradation

	No Noise	with Noise	Degradation [%]
LQR1	1108.2367	1214.8047	1.0962
GCC1	1203.4899	1317.1795	1.0945
LQR2	1916.9598	2621.1953	1.3674
GCC2	2866.6822	3257.1295	1.1362

In table1, LQR1 and GCC1 are the result without observer. LQR2 and GCC2 are the result with observer. It express the GCC have high performance value index but have more robustness than the LQR method. In the case with observer, this tendency becomes more remarkable.

6 Conclusion

For the system which has two uncertainties, we showed the advantage of the state observer for the influence of disturbance and parameter tuning of linear upper bound.

References

- [1] S. Chang and T. Peng (1972), Adaptive Guaranteed Cost Control of System with Uncertain Parameters, IEEE Transactions on AC, 17(4):474-473
- [2] N. Takahashi, M. Kono and O. Sato (2009), Guaranteed Cost Control of the Uncertain System with Parameter Variations in an Output Matrix, Proceedings of the 1st Japan-Korea Joint Symposium on Dynamics & Control, 139-142
- [3] N. Takahashi, O. Sato and M. Kono (2009), Robust Control Method for the Inverted Pendulum System with Structured Uncertainty Caused by Measurement Error, Artificial Life and Robotics 14
- [4] J. Hara, N. Takahashi, J. Kato, O. Sato and M. Kono (2010), A study of Guaranteed Cost Control of the Manipulator with Passive Revolute Joint, Proceedings of the 15th International Symposium on Artificial Life and Robotics, 910-913
- [5] S. Yamamoto, Q. Shen and H. Kimura (1993), Quadratic Stabilization for a class of Uncertain Linear Systems and its Application to a Magnetic Levitation system, Transactions of the Society of Instrument and Control Engineers, 29:334-339
- [6] N. Takahashi, M. Kono, K. Hiranuma and O. Sato (2000), Generalization of Guaranteed Cost Control, Transactions of the Japan Society of Mechanical Engineers (Series C), 66(645):1531-1536 (Japanese)
- [7] M. Kono, N. Takahashi, O. Sato and A. Sato (2002), Generalization of Guaranteed Cost Control - Extension to the case with Cross Terms, Proceedings of the SICE Annual Conference 2002, 542-545
- [8] A. Sato, O. Sato, N. Takahashi and M. Kono (2008), A Study of Manipulator with Passive Revolute Joint, Artificial Life and Robotics, 13:31-35

Analysis of Manipulator in Consideration of Collision between Link and Object

Asaji SATO¹, Osamu SATO², Nobuya TAKAHASHI² and Masahiro YOKOMICHI²

¹Dept. of Mechanical Engineering, Miyakonojo National college of Technology, Miyakonojo 885-8567, Japan.

²Dept. of Computer Science and Systems Engineering, Faculty of Engineering, University of Miyazaki, Miyazaki 889-219, Japan.

Abstract: In this paper, equations of motion of a manipulator are derived in consideration of characteristics of driving source. Considering the collision between the link and object, and considering the active motion to absorb kinetic energy of the object, trajectories for saving energy are calculated by iterative dynamic programming. And, the dynamic characteristics of manipulator controlled based on the trajectory for saving energy are analyzed theoretically and investigated experimentally.

Keywords: Manipulator, Trajectory, Dynamic Programming, DC Motor, Minimum Energy .

1 Introduction

For the purpose of enlarging the work space about carriage work, it is necessary for studying about the throwing motion and catching motion of the manipulator. In a previous report [1], a casting manipulator is introduced, and it has large work space compared with its simple mechanism. But, the consideration of energy consumption is not enough. And, evaluation of robotic mechanisms subjected to impact load are investigated [2]. But, energy consumption is not considered.

In previous report by the authors [3][4], trajectories for saving energy about the throwing motion of manipulator, were easily calculated by iterative dynamic programming. And, dynamic characteristics of the system were analyzed.

In this paper, equations of motion of a manipulator are derived in consideration of the characteristics of DC servomotors, and a performance criterion for saving energy is defined in consideration of energy consumption of the driving source. When the manipulator is operated in a vertical plane, the system is highly non-linear due to gravity, and an analytical solution can not be found. Then, a numerical approach is necessary. Considering the collision between the link and object, and considering the active motion to absorb the kinetic energy of the object, the trajectories for energy saving are calculated by iterative dynamic programming. The dynamic characteristics of manipulator controlled based on above mentioned trajectory are analyzed theoretically and investigated experimentally.

2 Modeling of manipulator

The dynamic equations of the manipulator with

two degrees of freedom as shown in Figure 1, which is able to move in a vertical plane, are as follows.

$$\begin{bmatrix} A_{11} & A_{12} \\ A_{21} & A_{22} \end{bmatrix} \begin{bmatrix} \ddot{\theta}_1 \\ \ddot{\theta}_2 \end{bmatrix} = \begin{bmatrix} A_{13} \\ A_{23} \end{bmatrix} \quad (1)$$

where

$$A_{11} = a_1, \quad A_{12} = a_3 \cos(\theta_1 - \theta_2), \quad A_{21} = A_{12}, \quad A_{22} = a_2$$

$$A_{13} = \tau_1 - a_3 \dot{\theta}_2^2 \sin(\theta_1 - \theta_2) - a_4 \cos \theta_1 - Fl_1 \cos \theta_1$$

$$A_{23} = \tau_2 + a_3 \dot{\theta}_1^2 \sin(\theta_1 - \theta_2) - a_5 \cos \theta_2 - Fl_c$$

$$a_1 = m_1 l_{g1}^2 + I_{G1} + m_2 l_1^2, \quad a_2 = I_{G2} + m_2 l_{g2}^2$$

$$a_3 = m_2 l_1 l_{g2}, \quad a_4 = (m_1 l_{g1} + m_2 l_1)g, \quad a_5 = m_2 g l_{g2}$$

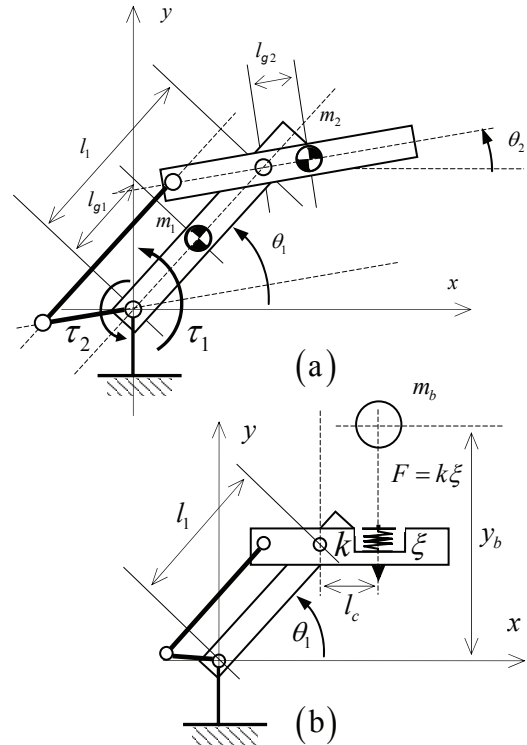


Fig.1 Mechanism of manipulator

The kinetic energy of the mechanism and object is

$$K = \frac{1}{2} a_1 \dot{\theta}_1^2 + \frac{1}{2} a_2 \dot{\theta}_2^2 + a_3 \dot{\theta}_1 \dot{\theta}_2 \cos(\theta_1 - \theta_2) + \frac{1}{2} m_b \dot{y}_b^2, \quad (2)$$

and potential energy is

$$U = a_4 \sin \theta_1 + a_5 \sin \theta_2 + \frac{1}{2} k \xi^2 + m_b g y_b. \quad (3)$$

(ξ ; displacement of spring)

And, absorbed energy by motor is

$$E_{ab} = - \int \tau_1 \cdot \dot{\theta}_1 dt - \int \tau_2 \cdot \dot{\theta}_2 dt. \quad (4)$$

The applied voltage of the servomotor is

$$e_j = b_{1j} \dot{\theta}_j + b_{2j} \ddot{\theta}_j + b_{3j} \tau_j + b_{3j} \tau_{fj} \text{sign}(\dot{\theta}_j) \quad (5)$$

where

$$b_{1j} = k_{vj} + (R_{aj} / k_{tj}) D_{mj}, \quad b_{2j} = (R_{aj} / k_{tj}) I_m, \quad b_{3j} = R_{aj} / k_{tj},$$

i_{aj} : electric current of the armature,
 R_{aj} : resistance of armature,
 I_m : moment of inertia of armature,
 D_{mj} : coefficient of viscous damping.

Then, the electric current is

$$i_{aj} = (e_j - k_{vj} \dot{\theta}_j) / R_{aj}. \quad (6)$$

And, the consumed energy is

$$E = \sum_{j=1}^2 \int (e_j \cdot i_{aj}) dt. \quad (7)$$

3 Simulation of the manipulator

We shall take the parameters of the system as shown in Table 1.

Figure 2 shows a flow chart for iterative dynamic programming method. In frame (A), the trajectory for saving energy is searched by dynamic programming [3]. In frame (B), the searching region is shifted to minimize the consumed energy, and width of the region is changed smaller.

Figure 3 shows the trajectory for searching, and initial trajectory for searching is expressed as

$$\theta_j = \theta_{ij} + \frac{(\theta_{fj} - \theta_{ij})}{2} \left\{ 1 - \cos \left(\frac{\pi}{t_f} t \right) \right\}. \quad (8)$$

Figure 4 shows the motion of an object to fall free. Initial height is $y_b = 0.15$ (m), and velocity is $\dot{y}_b = 0$. When $t = 0.128$ (s), the object contacts with the link. And then, $y'_b = 0.069$ (m) and $\dot{y}_b = -1.25$ (m/s). Under the condition that $\theta_{i1} = 0.1$ and $\theta_{f1} = 0.05$ (rad), optimal trajectory is calculated by IDP method. The performance criterion is

$$E' = \sum_{j=1}^2 \int (e_j \cdot i_{aj}) dt + C_1 \int |F| \cdot dt + C_2 |y_b - y'_b|. \quad (9)$$

In Figure 4, the solid line shows the motion of object whose kinetic energy is absorbed by the motor.

Table 1 Parameters of the manipulator

Parameter	Value	Parameter	Value
l_1 (m)	0.10	I_{G1} (kgm ²)	1.7×10^{-5}
l_c (m)	0.01	I_{G2} (kgm ²)	1.7×10^{-5}
l_{g1} (m)	0.05	k (N/m)	500
l_{g2} (m)	0.01	k_{t1} (Nm/A)	0.046
m_1 (kg)	0.02	k_{v1} (Vs/rad)	0.046
m_2 (kg)	0.02	D_{m1} (Nms/rad)	7.9×10^{-5}
m_b (kg)	0.02	τ_{f1} (Nm)	0.0013
r_b (m)	0.01	R_{a1} (Ω)	3.5

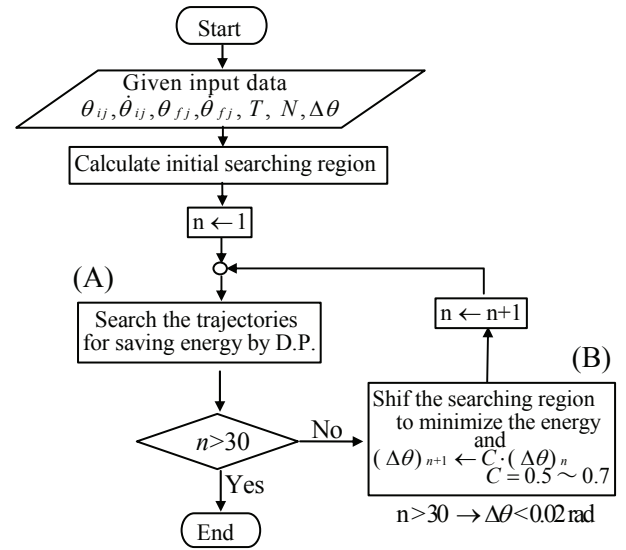


Fig.2 Flow chart for simulation

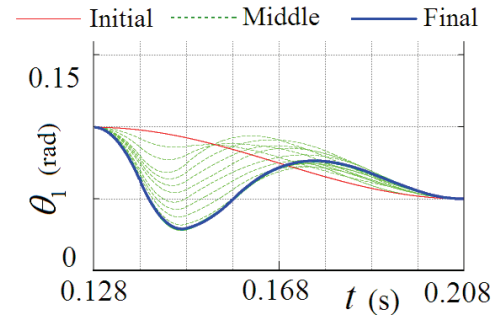


Fig.3 Trajectory for searching

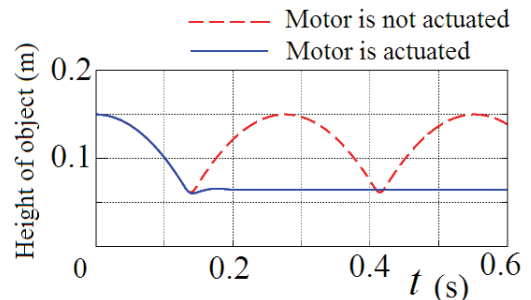


Fig.4 Motion of object to fall free

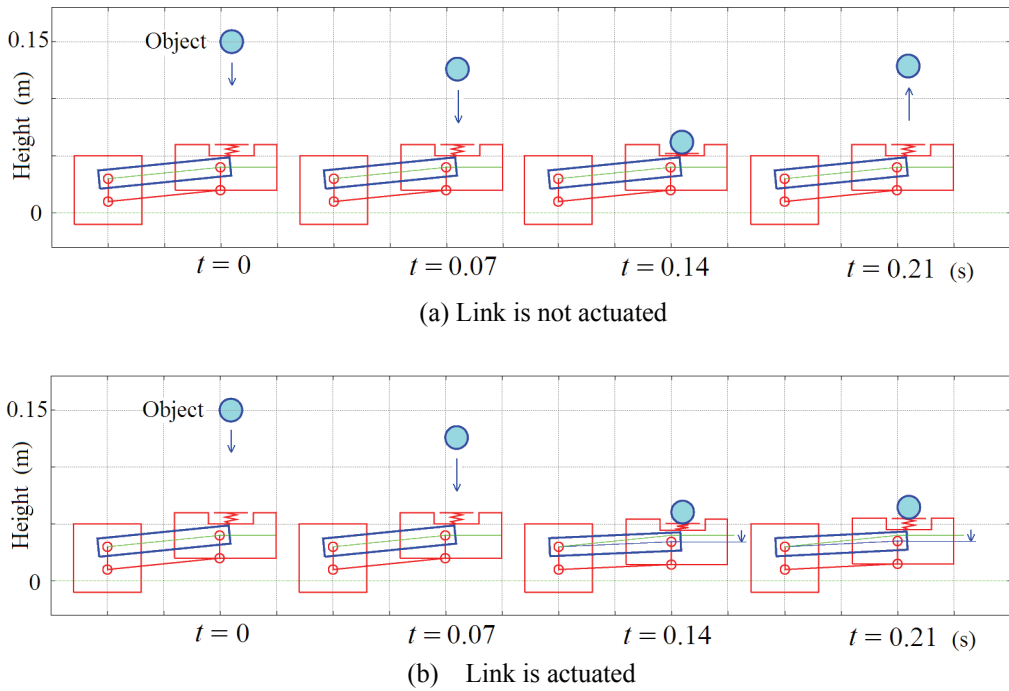


Fig.5 Motion of the object and the mechanism

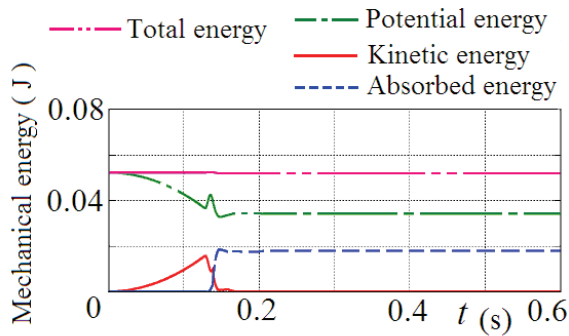


Fig.6 Mechanical energy

Figure 5 shows the motion of the object and the mechanism. In Figure (b), link 1 is actuated, and kinetic energy of the object is absorbed. And, the response about conservation of mechanical energy are shown in Fig.6.

5 Experimental results

In this section, the results of fundamental experiment are shown to examine the effectiveness of modeling for the simulations.

Figure 7 shows an experimental apparatus. Slide board is tilted ($\pi/3$) measured from the level surface. And, two Laser displacement meters are installed for measuring the passing time of the object.

The parameter of the link 1 and the motor are shown in Table 1, and the motor (rated 24 V, 60W) are on the frame, and sampling time of the control is 0.002 s. The feedback gain for angular displacement is 50 V/rad, and the feedback gain for angular velocity is 0.5 Vs/rad.

Figure 8 (a) and (b) show experimental results about motion of the link and object. In Figure (a), the link is fixed at initial position, and the object bounds high. In Figure (b), the link is actuated along the trajectory calculated by IDP method, and the object bounds low.

Figure 9 show are experimental results about the response of the link and motor. About the angular

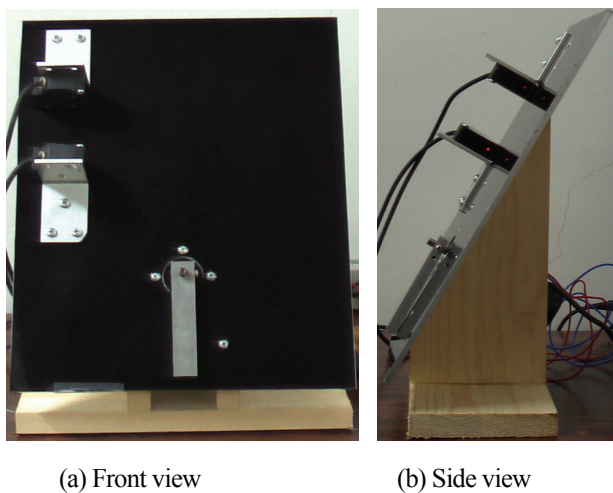


Fig.7 Experimental apparatus

displacement and angular velocity, experimental results (blue line) are similar to the theoretical results (red line).

From these results, it is considered that modeling for simulation is effective.

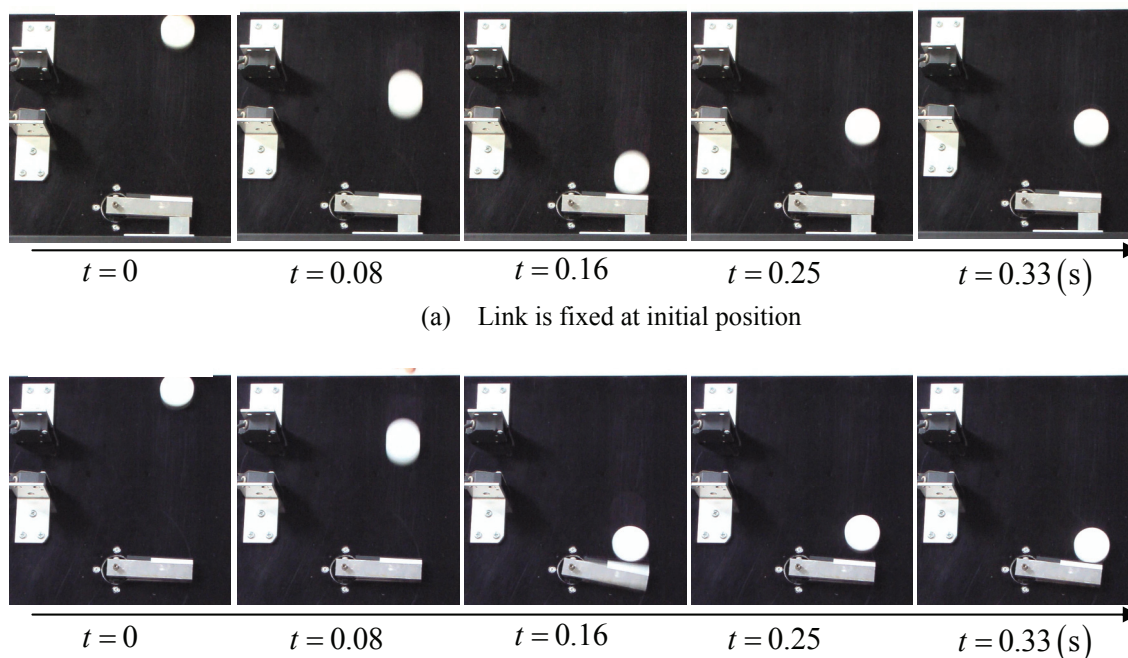
6 Conclusions

The results obtained in this paper are summarized as follows.

- (1) It is considered that the active motion to absorb the kinetic energy of object is possible by analyzing the relative motion about the collision between the link and object.
- (2) From experimental results, it is considered that modeling for simulation is effective.

References

- [1] H.Arisumi, K.Yokoi, T.Kotoku et al (2002), Casting manipulation (Experiments of swing and gripper throwing control), International Journal of JSME, Vol.45, No.1 C, 267-274.
- [2] H.Tachiya, K.Urano et al (1996), Characteristics evaluation and comparisons of robotic mechanisms (2nd report, Evaluation of robotic mechanisms subjected to impact load, Journal of JSME (in Japanese), Vol.62 No.598, 2395-2402.
- [3] A.Sato, O.Sato, N.Takahashi and M.Kono (2006), Trajectory for saving energy of direct-drive manipulator in throwing motion, Artif Life Robotics, 11:61-66
- [4] A.Sato, O.Sato, N.Takahashi and M.Kono (2008), A study of manipulator with passive revolute joint, Artif Life Robotics, 13: 31-35



(a) Link is fixed at initial position
(b) Link is actuated along the trajectory calculated by IDP method
Fig.8 Experimental results (motion about the link and object)

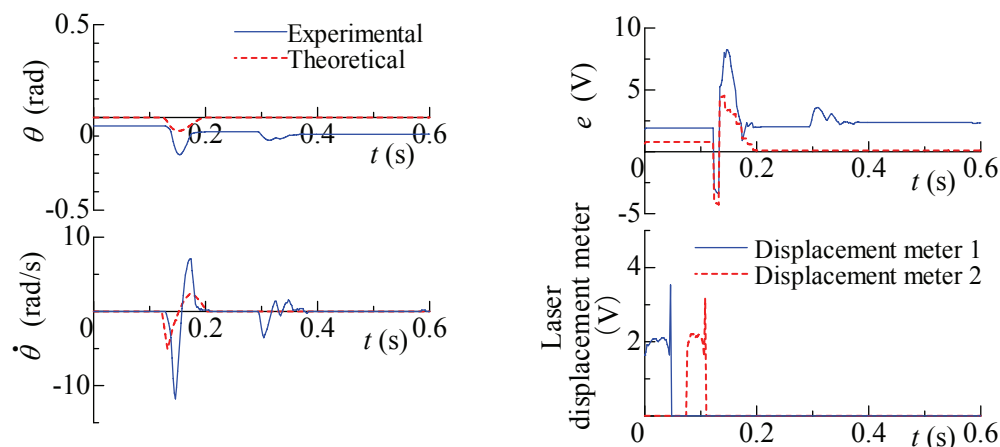


Fig.9 Experimental results (response of link and motor)

Motion Control of 2 DOF Orthogonal robots with Adaptive Control

Kazuma.Funahashi, Feifei.Zhang and Masanori.Ito

Tokyo University of Marine Science and Technology,
2-1-6 Echujima, Koto-ku, Tokyo 135-8533, JAPAN
(Tel : 81-3-5245-7422; Fax : 81-3-5245-7422)

Abstract: This study considers motion control of 2 DOF orthogonal robot that is crossed two industrial linear robots with adaptive control under the various load condition. We constructed experimental facility with putting 0.5m length linear robot on a 1m length linear robot and confirmed performance under various conditions with applying adaptive control of fast sampling and control interval. The results show a prescribed control performance can be satisfied. Therefore, adaptive control can be expected as a useful control method for industrial, high-speed positioning robot.

Keywords: linear robot, motion control, adaptive control

I. INTRODUCTION

The adaptive control that can reflect the change of characteristics of the control targets was thought as an effective control method for modern control system. However it requires many and complex calculation in the control for real time estimating of the target model and adjusting control signal, then control interval becomes rather large. It is a weak point of adaptive control. So, main current of the control theory moves to the robust control. On the contrary, the conventional PID control is used in industrial fields because of the easiness and high speed. However, needs to high productivity or accuracy in production system require high level of automatic control system which can comply with a change of characteristics of target or environmental condition in those days instead of conventional PID control.

In the fields of industrial robot, it becomes more evident, so we treated the motion control that can satisfy the predetermined condition under the change of load for linear transfer robot with applying adaptive control of high performance of computer.

which the weak point is thought to be improved with the

Saying concretely, we constructed experimental system with crossly putting 0.5m length linear robot on a 1m length linear robot, and moved both robots at the same time with predetermined pattern under the change of carrying weight with adaptive control. Through those experimental researches, we confirmed the effectiveness of adaptive control.

II. EXPERIMENTAL SYSTEM

Figure 1 shows the configuration of experimental system. Each linear robot is composed of servomotor with resolver, ball screw, carrying table, motor driver and controller. The carrying load is set on the carrying table of upper robot. In this system, we used a personal computer as the controller and control program is designed with using Simulink toolbox of MATLAB by Mathworks. Here, the torque control signal is calculated with adaptive control algorithm based on the position signal with resolver and output to motor through driver.

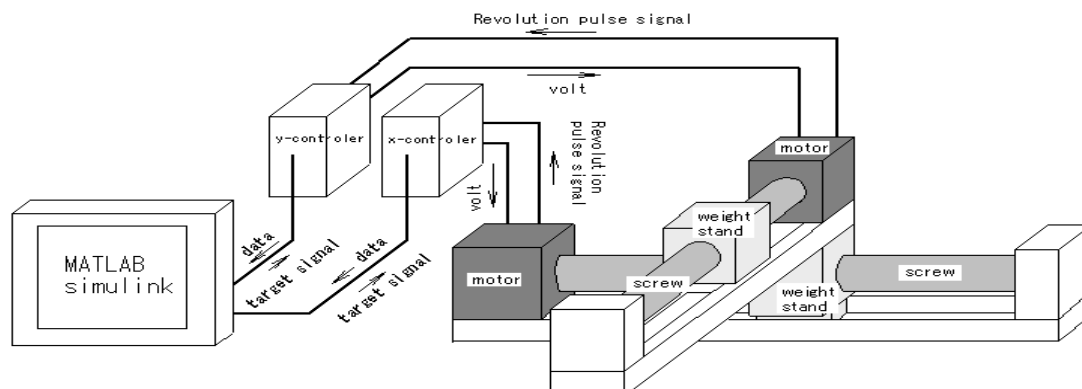


Fig.1 Experimental system

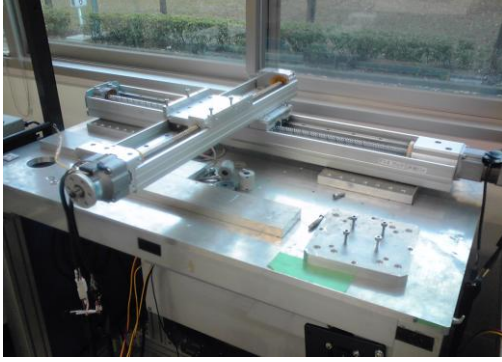


Fig.2 Photo of Experimental system

The specifications of main components are shown in Table 1.

Table 1 Specifications of main components

<u>Lower Linear Robot</u>	
Stroke	:1000mm
Max. Carrying Load	: 30kg
Carrier	: Ball Screw(Lead: 20mm/rev.)
Power Source	: AC SERVO MOTOR (Output; 200W, Max. Rpm; 3000, Max. Torque;0.64Nm)
Reduction Gear Ratio	: 1/3
Position Sensor	: Resolver (Resolution; 16384 pulse/rotation)
<u>Upper Linear Robot</u>	
Stroke	: 500mm
Max. Carrying Load	: 10kg
Carrier	:Ball Screw(Lead: 20mm/rev.)
Power Source	:AC SERVO MOTOR (Output; 200W, Max. Rpm; 3000, Max. Torque;0.64Nm)
Reduction Gear Ratio	: 1/3
Position Sensor	: Resolver (Resolution; 16384plase/rotation)

III. CONTROL DESIGN

The control problem of precise positioning robot is to make the angle of the motor accurately follow to the target signal. It is well known in PID control, that the control system contains a PI speed control loop, and a P position control loop. In this study, we use adaptive control instead of PI control for the speed control loop, as shown in Fig. 2, the purpose of which is to absorb the response speed change caused the load change .

The RLS method (recessive minimum mean square method) is used as the model identification, and the model order is assumed 2 in consideration of the complexity and rapidity of response of the system. Some referred expression is as follows.

Model :

$$y(k) = a_1 y(k-1) + a_2 y(k-2) + b_1 u(k-1) + b_2 u(k-2) \quad (1)$$

$$= \theta^T(k) \varphi(k)$$

Where, $y()$ and $u()$ indicate plant output and control input, respectively, and

$$\theta = [a_1 \quad a_2 \quad b_1 \quad b_2]^T$$

$$\varphi = [y(k-1) \quad y(k-2) \quad u(k-1) \quad u(k-2)]^T$$

The parameter vector $\theta(k)$ is calculated repeatedly as follows.

$$\theta(k) = \theta(k-1) + \frac{P(k-1)\varphi(k)}{1 + \varphi^T(k)P(k-1)\varphi(k)} \varepsilon(k) \quad (3)$$

$$P(k) = P(k-1) - \frac{P(k-1)\varphi(k)\varphi^T(k)P(k-1)}{1 + \varphi^T(k)P(k-1)\varphi(k)} \quad (4)$$

$$\varepsilon(k) = y(k) - \varphi^T(k)\theta(k) \quad (5)$$

,with the following initial conditions.

$$\theta = [1 \quad 1 \quad 1 \quad 1]^T \quad (6)$$

$$P = I$$

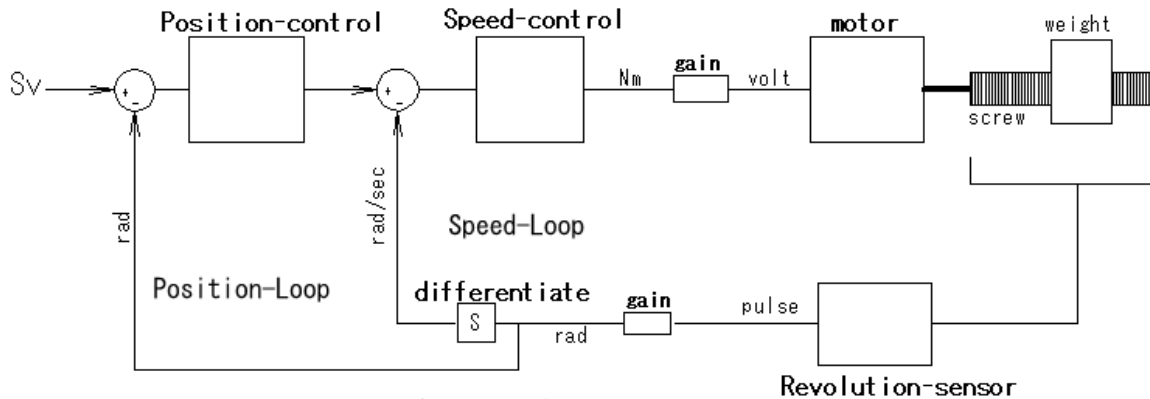


Fig.3 Control system

Lastly, the expression of the control input is as follows.

$$u(k) = \frac{u_m(k) - b_2 u(k-1) - a_1 y(k) - a_2 y(k-1)}{b_1} \quad (7)$$

IV. RESULTS AND EVALUATION

Here we show the results of experiments and make evaluation for them.

In the following figures, we only referred to the results of motion on lower robot when both robots were moved in the experiment. The sampling rate of those experiments was 0.001 second.

Figure 4 and Figure 5 show the results of the motion following to sine wave under the load of 0kg and 5kg. Here, continuous line is set value, and dash line and dot line are responses for 0kg and 5kg loads, respectively.

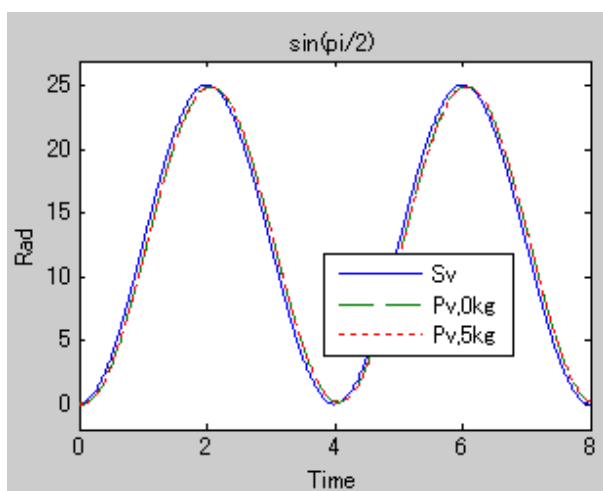


Fig.4 Response to $4\pi\sin(\pi/2 \cdot t)$

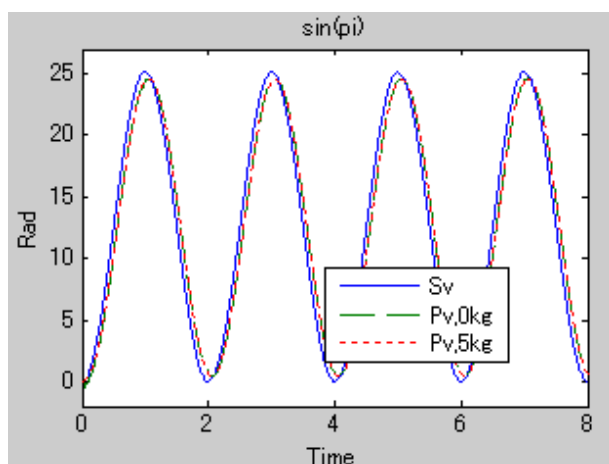


Fig.5 Response to $4\pi\sin(\pi \cdot t)$

Figure 6 shows the results of the motion following to linear patterns of different speed, one is 94rad/8sec (300mm/8sec) and the other is 47rad/8sec (150mm/8sec).

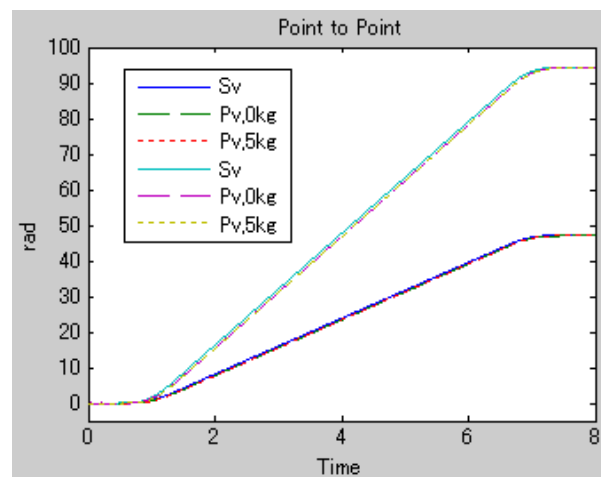


Fig.6 Comparison of linear motion
(Moved distance: 150mm and 300mm)

Figure 7 and Figure 8 show the starting and stopping process to the order of moving 150mm/ 8sec for evaluation. We tried this test for the case of 300mm (94 radian of total rotation). The result is omitted here because they are nearly equal to the results of 150mm (47 radian).

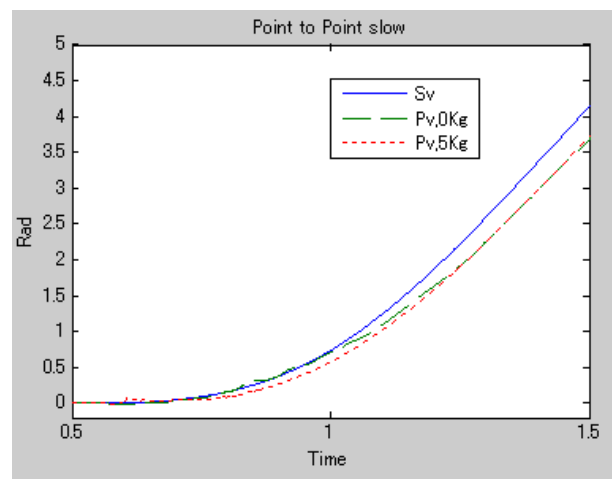
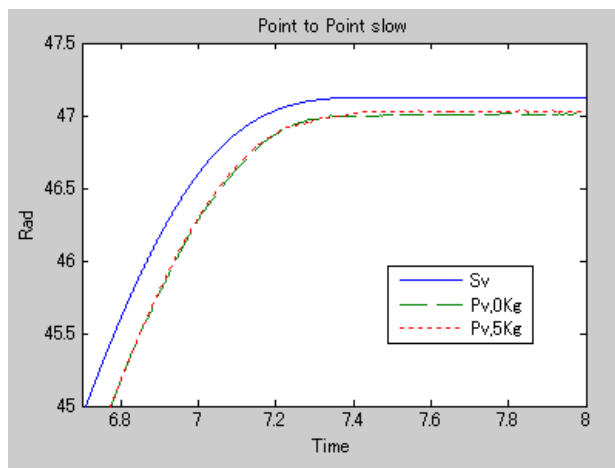


Fig.7 Detail at starting of 150 mm movement



• Fig.8 Detail at stopping of 150 mm movement

In those results, the dash line and dot line in each figure show almost same responses. This means that the difference of load does not influence to the results. Especially, the difference of stopping position between the carrying weight of 0kg and 5kg is very small (from Fig.8, it is 0.03mm). We think this is the allowable margin of error because it is the level of machinery error. All these merits obviously come from adaptive control.

Figure 7 shows a small shaking of response at just after starting. This is allowable, because it is an initial and usual process of adaptive control, and shows that control system has started learning for targets, and disappears immediately.

On the other hand, it is seen that the delay of response becomes remarkable depending on a frequency of input signal. In this case, the delay is connecting to control error directly. Also, the positioning error at stopping point (see, Fig.8) is about 0.3mm, this is larger than the demanded accuracy (0.04mm).

We think these problems are depending on the structure of control system, because the position control loop use the conventional P control. How to control both speed and position of high speeded robot with adaptive control is our next subject.

V. CONCLUSION

This study shows that the performance of transfer system with linear robot can be improved with adaptive control. We can ensure the desired performance to the linear robot under specified range of load condition. The weak point of adaptive control that is not so fast is improved to the level of robot motion control with computer performance. Of course, the study was

accomplished in a laboratory and having big difference to actual industrial use. Decreasing the level of error, optimization of initial parameter for adaptive control, or simplifying the algorithm and speed up of calculation for small computer are the subjects for actual use.

Now we are continuing study for the level-up of accuracy with improving position and speed control, especially optimizing the initial value of θ , and the speed-up of calculation with combining speed and position control and/or decreasing the degree of referring model.

REFERENCE

- [1] System Identification for Control, Shuuichi Adachi, Tokyo Denki Univ.
- [2] Theory & Practice of Adaptive Control Systems, I. D. Landau and M. Tomizuka, OHM Co., Ltd.

Development of 6-DOF Force Feedback System for Rehabilitation of Wrist Paralysis

Yasunobu HITAKA*, Yoshito TANAKA**, Yutaka TANAKA*** and Tomonori KATO **

* *Kitakyushu National College of Technology*

Tel : +81-93-964-7244

Email hitaka@kct.ac.jp

** *Hosei University*

*** *Fukuoka Institute of Technology*

Abstract: The increasing number of paralyzed persons and a shortage of the physical therapist is becoming an increasing problem, focusing attention on rehabilitation support. Noting the increase in wrist paralysis, we are developing corresponding rehabilitation support. Our basic approach centers on force feedback system based on the parallel 6-degree-of-freedom (DOF) Stewart platform. In this paper, we focus on the generation of a desired force which is a resultant force of the six cylinder forces of the parallel mechanism. Also we focus on drawing a 3D computer graphic (CG) model which shows harmonic movement with the parallel mechanism in virtual space. It is the feedback information for wrist rehabilitation. In this paper, we show that the experimental results of the desired force generation and the 3D-CG model moves harmonically with the parallel mechanism assigned distance place via the Local Area Network.

Keywords: Stewart type parallel mechanism, six degree of freedom,

I. INTRODUCTION

For the cases of persons afflicted with paralysis increasing, due to adult disease, traffic accidents and aging, the shortage of physical therapists is a growing problem requiring rehabilitation support. In our focus on wrist paralysis, we considered rehabilitation support, requiring multiple degrees of freedom (DOF) and compactness, taking into account the parallel Stewart platform, which generates 6-DOF force and provides high power and rigidity ^[1]. It applies 6-DOF force to wrist of a patient through a gripper on the platform for rehabilitation therapy instead of the physical therapist.

In our past research, we developed a prototype of the parallel Stewart platform with six pneumatic air cylinder actuators and achieved the thrust control of individual pneumatic cylinder by a pulse width modulator (PWM) control ^[2]. The goal of our research is that one physical therapist can treat multiple patients at the same time by remote controlling the parallel mechanisms. To achieve the purpose, it is necessary that the parallel mechanism can output the desired force on the platform gripper. It is also necessary that the physical therapist can see the situation of rehabilitation treatment.

This paper focuses on controlling force act on the platform gripper. It is a resultant force of six pneumatic cylinder forces. Thus, to generate a desired force on the platform gripper, the component forces generated by

individual cylinders must be calculated. They are calculated by solving six simultaneous equations representing static force relationships.

This paper also focuses on drawing a 3D computer graphic (CG) model showing synchronized movement with the parallel mechanism in virtual space. It is the feedback information for wrist rehabilitation. The therapist can recognize the situation of treatment at a distant place on real time by viewing the movement of the 3D-CG model. The model is drawn from the 6-DOF attitude information. It is calculated by solving direct kinematics of the parallel mechanism with data on cylinder length. From the calculation result, the PC draws a similar parallel mechanism which shows the synchronized movement with the real one in a virtual workspace displayed.

The desired force generation and 3D-CG model drawing can be achieved for the parallel mechanism assigned a distance place via LAN by using the TCP/IP connection.

This paper is organized as follows: Section 2 introduces the system configuration. Section 3 focuses on controlling force act on the platform gripper and gives the results of force control experiments. Section 4 focuses on drawing a 3D-CG model of the parallel mechanism and shows that the 3D-CG model moves harmonically with the parallel mechanism assigned distance place via the Local Area Network. Section 5 is conclusions.

II. SYSTEM CONFIGURATION

Figure 1 shows the force feedback configuration we propose, which consists of a pneumatic parallel mechanism and two personal computers (PC). The one is for the physical therapist and the other is for a patient. The parallel mechanism is connected with the patient side PC through I/O board. These PCs communicate with each other by TCP/IP via LAN. When a desired force which will act on the platform gripper is input at the therapist side PC, six cylinder forces corresponding to the desired force are calculated by solving six simultaneous equations representing static force relationships. The calculated cylinder forces are sent to the patient side PC and translated into PWM signals and sent to twelve solenoid valves mounted the parallel mechanism. Each cylinder has two valves and one is used for pushing the cylinder and the other is for pulling. The force resulting from six cylinders should be equivalent to the desired force.

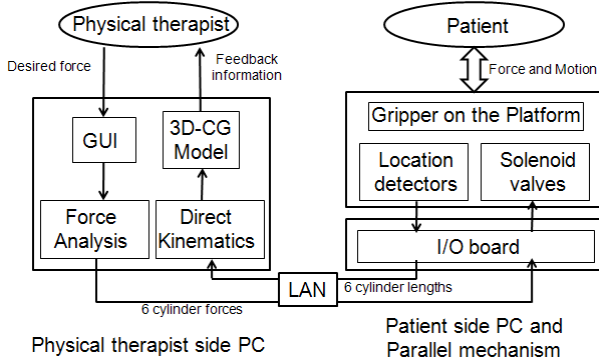


Fig1. Force feedback configuration

When the parallel mechanism is moved, the patient side PC detects the six cylinders length by the six location detectors, each of which is mounted on the cylinder. The patient's PC sends the cylinder length data to the physical therapist side PC. The therapist side PC calculates the parallel mechanism attitude by solving the direct kinematic equations with the cylinder data. From calculation results, the therapist side PC draws a 3D-CG model of the parallel mechanism. It shows the movement synchronized with the real parallel mechanism in a virtual work space displayed. The CG model in virtual space is drawn using OpenGL.

By this way, the physical therapist can see the situation of rehabilitation treatment in detail even if he isn't around the patient. Moreover, if multiple parallel mechanisms are prepared, it is expected that one

physical therapist can treat multiple patients at the same time by sending rehabilitation commands to the individual parallel mechanisms of the patients.

III. FORCE GENERATION

To generate a desired force on the gripper, cylinders must generate the component forces of output by the six equations representing the relationship of static force act on the gripper, shown in Figure 2.

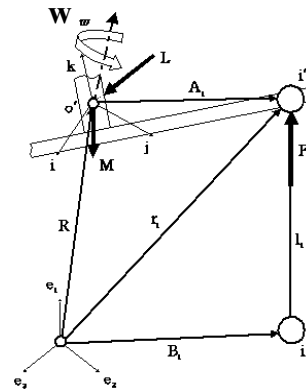


Fig2. Analytical model of parallel mechanism

These are i -th cylinder force F_i ($i = 1, \dots, 6$), desired output force L , desired moment w and force of gravity M . These force vectors have coordinates (F_{ix}, F_{iy}, F_{iz}) , (L_x, L_y, L_z) , (w_x, w_y, w_z) and $(0, 0, -mg)$ for the fixed frame, m is platform mass and g is gravity acceleration.

The static force relationship for translational movement is as follows:

$$\sum_{i=1}^6 F_i + L + M = 0. \quad (1)$$

For rotational movement, the relationship is as follows:

$$\sum_{i=1}^6 (r_i \times F_i) + (R \times L) + (R \times M) + w = 0. \quad (2)$$

Eq.(1) and Eq.(2) are the six simultaneous equations for cylinder force F_i , and solving them by using following relationship

$$(F_{ix}, F_{iy}, F_{iz}) = \frac{F_i}{\sqrt{l_{ix}^2 + l_{iy}^2 + l_{iz}^2}} (l_{ix}, l_{iy}, l_{iz}),$$

the component forces F_i of the desired output L and desired moment w are obtained. When a desired force is input at the physical therapist's PC, F_i are calculated by above analysis, sent to the patient's PC. At

patient's PC, they are translated into PWM signals to control the solenoid valves [2].

The force control experiments are conducted and results are presented. Figure 3 shows the overall view of force control experiments for the pneumatic parallel mechanism.

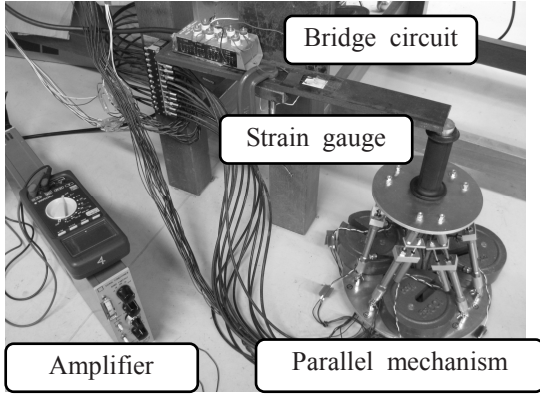


Fig.3: Parallel mechanism experiments



Fig4. Force controller interface

Figure 4 is the interface of the force input on the physical therapist' PC. Inputting components of a desired force along x, y and z direction, corresponding duty rates for the twelve solenoid valves are calculated and sent to the I/O board. Also, these values are displayed on the interface.

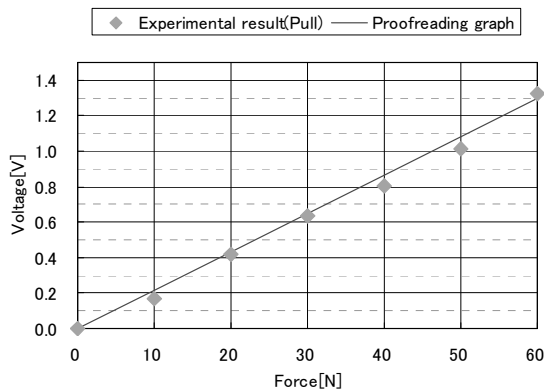


Fig.5: Experimental results (z direction (+))

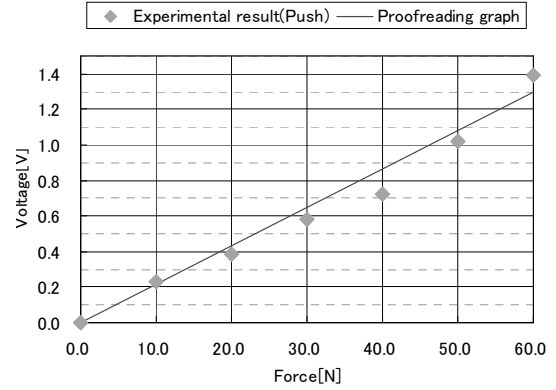


Fig.6: Experimental results (z direction (-))

Figure 5 shows the results for plus direction and Fig. 6 for minus direction. Initial positioning is adjusted as neutral position (cylinder expansion and contraction: 15mm) and supply pressure is 0.15Mpa. For both directions, measurement and proofreading results coincide well confirming that arbitrary force is generated in the z direction.

IV. 3D-CG DRAWING BASED ON DIRECT KINEMATICS

To draw a 3D-CG model showing the movement synchronized with the parallel mechanism, it is necessary 6-DOF attitude information of the platform. The parallel mechanism has six location detectors detecting each cylinder length. Thus, by solving the direct kinematics of the parallel mechanism with data on cylinder length, 6-DOF attitude can be obtained.

Figure 3 is i-th cylinder vector diagram. \mathbf{o} is the origin of the fixed frame, \mathbf{o}' is the origin of the motion frame assigned at the centroid of the platform. It shows a relationship as follows:

$$\mathbf{l}_i = \mathbf{A}_{im}T + \mathbf{R} - \mathbf{B}_i \quad (3)$$

Where, \mathbf{l}_i is a cylinder vector, \mathbf{R} is a position vector of centroid of the platform, and \mathbf{B}_i is a position vector of lower attachment point and there vectors are with respect to the fixed frame. $\mathbf{A}_{im}T$ denotes upper attachment point with respect to the motion frame and the coordinate transform matrix T is

$$T = \begin{bmatrix} \cos \theta \cos \psi & \cos \theta \sin \psi & -\sin \theta \\ \sin \phi \sin \theta \cos \psi - \cos \phi \sin \psi & \sin \phi \sin \theta \sin \psi + \cos \phi \cos \psi & \sin \phi \cos \theta \\ \cos \phi \sin \theta \cos \psi - \sin \phi \sin \psi & \cos \phi \sin \theta \sin \psi - \sin \phi \cos \psi & \cos \phi \cos \theta \end{bmatrix}$$

, where, ϕ , θ , and φ are “roll”, “pitch”, and “yaw” angles of the platform with respect to the motion frame.

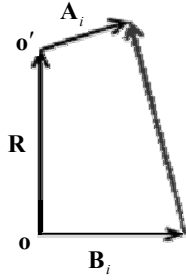


Fig3. Vector diagram for i-th cylinder

Here, let l_{if} be the measured value of i-th cylinder vector and α be the vector of the platform attitude and define a function $f(\alpha)$ as follows:

$$\begin{aligned} f(\alpha) &= (f_1(\alpha), f_2(\alpha), f_3(\alpha), f_4(\alpha), f_5(\alpha), f_6(\alpha)) \\ f_i(\alpha) &= A_{im} A_{im}^T + R R^T + B_i B_i^T \\ &\quad + 2 R T^T A_{im}^T - 2 \psi B_i T^T A_{im}^T - 2 R B_i^T - l_{if}^2 = 0 \\ \alpha &= (x, y, z, \phi, \theta, \psi)^T \quad i = 1, \dots, 6 \end{aligned} \quad (4)$$

Equation (4) is a couple of nonlinear 6 dimensional equations and it is difficult to derive the solution α by any analytical ways. Thus, by using the Newton-Raphton method which is one of a numerical method, approximate solution of α is derived.

Let $\alpha^{(n)}$ be an approximate solution which is in the n times iterations and applied the Newton-Raphton method to the Eq. (4), following equation is obtained.

$$M(\alpha^{(n+1)} - \alpha^{(n)}) = -f(\alpha^{(n)}) \quad (5)$$

Where, M is a matrix of the partial differentiation of $f(\alpha^{(n)})$.

By solving Eq. (5) iteratively, approximate solution of α can be derived.

By this way, PC of the force feedback system calculates the 6 DOF attitude of the platform. From the result, it draws the 3D-CG model of the parallel mechanism.

Figure 7 is set of the still images of the 3D-CG model and the parallel mechanism. These pictures are clips of the experiment of the synchronized movement.

In this figure, the parallel mechanism is moved by hand. It is shown that the 3D-CG model moves synchronized with the parallel mechanism.

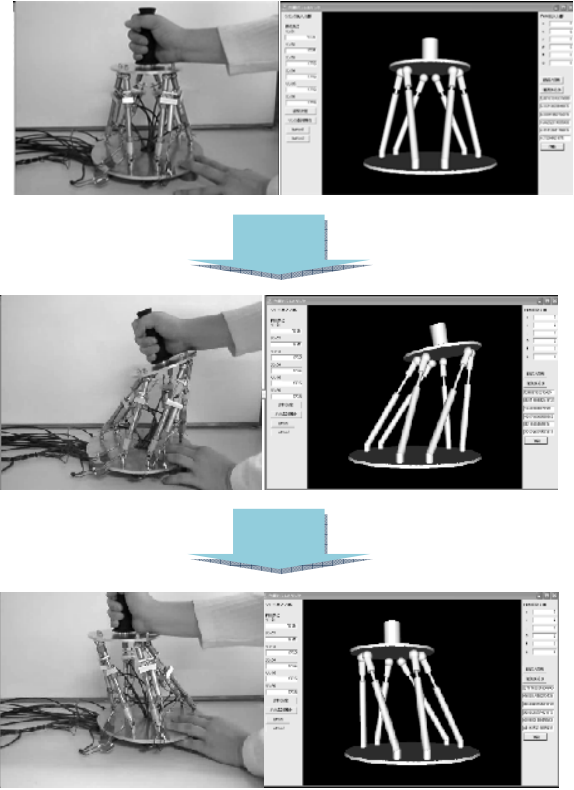


Fig7. Experiments of harmonic movement

VI. CONCLUSION

In this paper, for the development of the force feedback system applied to the wrist rehabilitation support system, generating desired force act on the platform gripper was detailed. Also, drawing a 3D-CG model showing the movement synchronized with the parallel mechanism in virtual space was detailed. These can be achieved for the parallel mechanism assigned a distance place via LAN by using the TCP/IP connection.

In projected works, we plan to measure force for other direction, to display detail information on the 3D-CG model, like force value, vector image of force, etc.

References

- [1] Stewart, D., A Platform with 6 degrees of freedom, Proc. Inst. Mech. Eng., Vol.180, Part I, No.15, pp.371-386, 1965-66.
- [2] Hitaka, Y., Tanaka, Y., Tanaka, Y., Ishii, J., Development of 6DOF Force Feedback System with Pneumatic Parallel Mechanism, Proceedings of the 15th International Symposium on Artificial Life and Robotics in Beppu, Japan(2010).

Feedback Stabilization of Linear Systems with Distributed Input Time-delay by Backstepping Method

Chaohua Jia^{1,2}

¹*School of Mathematics and Systems Science, Beijing University of Aeronautics and Astronautics;*

²*LMIB of the Ministry of Education, Beijing 100191, P. R. China
(jiach@buaa.edu.cn)*

Abstract: The stabilization problem of a linear time-invariant system with lumped and distributed delays in the control will be investigated by the backstepping method. A transformation is introduced firstly to reduce the system with distributed input delay into a system with lumped input delay. The transformation kernel can be expressed explicitly through solving a Cauchy problem of ODEs. Then the backstepping arguments presented by Krstic and Smyshlyaev in [1] can be applied to work out a feedback control for the original system, where the key point is to model the lumped delay by a first-order hyperbolic partial differential equation.

Keywords: time-delay systems, distributed delay, backstepping method, reduction transformation.

I. INTRODUCTION

In many engineering systems, the variation of the system state depends on past states. Such a character is called time-delay. Time-delay systems are also known as systems with aftereffect or dead-time, hereditary systems, which have attracted the attention of many researchers because of their importance and widespread occurrence. They are special infinite dimensional systems, and researches indicate that the time delays lead to some complexity. On one hand, the time delays may deteriorate the control performance or even cause the instability of a dynamic system. On the other hand, several studies have shown that voluntary introduction of delays can also benefit the control.

The stabilization for time-delay systems is a topic of great importance and has received increasing attention [2], [3], [4], [5]. Smith-predictor is well-known for designing linear feedback controllers for systems with delay. However, this method is confined to stable plants because it implies pole-zero cancellations. Moreover, Smith predictor is sensitive to parameter errors. The model reduction method is another important approach to deal with the systems with input delays, where the so-called Artstein model reduction is often involved. Briefly speaking, the model reduction is a transformation through which one can simplify a dynamic system with input delay into an equivalent delay-free system. Considering the following linear system with lumped input delay,

$$\dot{x}(t) = Ax(t) + B_0 u(t) + B_1 u(t - \tau), \quad (1)$$

introduce the new variable $y(t)$ defined by

$$y(t) = x(t) + e^{-A\tau} \int_{t-\tau}^t e^{A(t-s)} B_1 u(s) ds. \quad (2)$$

Then (1) is reduced to a delay-free system

$$\dot{y}(t) = Ay(t) + (B_0 + e^{-A\tau} B_1) u(t).$$

It is straightforward to compute a state feedback control $u(t) = Ky(t)$, provided that $(A, B_0 + e^{-A\tau} B_1)$ is stabilizable. Thus the system (1) can be stabilized by the control law

$$u(t) = Kx(t) + e^{-A\tau} \int_{t-\tau}^t e^{A(t-s)} B_1 u(s) ds. \quad (3)$$

Kwon and Pearson were the first who clearly put forward the reduction transformation (2) for a system with lumped input delay [4]. In [4], the authors applied the receding horizon method to the stabilization of linear time-invariant systems with lumped input delay. It was shown how the receding horizon control suggested the reduction transformation (2). Afterwards, Artstein established the general abstract theory of the reduction method in [2]. According to this theory, one can transform general linear time-varying systems into delay-free systems. It has been shown by many researches that the reduction provides a strong tool for manipulating systems with delays in the controls, even for linear systems with time-varying lumped input delay [2].

It has also been pointed out in [5] that any lumped time-delay $U(t) = u(t - \tau)$ can be represented by a classical transport equation:

$$\begin{cases} \tau \frac{\partial}{\partial t} v(x, t) + \frac{\partial}{\partial x} v(x, t) = 0, & x \in [0, 1], \\ v(0, t) = u(t), & v(1, t) = U(t). \end{cases}$$

In other words, we can use a first-order hyperbolic partial differential equation to model the lumped delay. A problem of boundary feedback stabilization of first-order hyperbolic partial differential equations was considered in [1], where the authors applied the backstepping

method to design controllers. As an example of the applications, the authors studied the stabilization of a linear time-invariant system with lumped input delay by combining the backstepping design for hyperbolic PDEs with the backstepping design for linear ODEs.

Motivated by the researches mentioned above, we will investigate the stabilization problem of a linear time-invariant system with lumped and distributed delays in the control by the backstepping method. We first transform the linear system with distributed input delay into a system with lumped input delay, where the transformation kernel is determined by a Cauchy problem of ODEs. This transformation kernel can be expressed explicitly. Then the procedure presented in [1] can be applied in our circumstance. Concretely, we model the lumped delay by a first-order hyperbolic partial differential equation, and replace the resulting system in the first step by an ODE-PDE cascade. After introducing a backstepping transformation, we obtain the target system whose origin is exponentially stable. Thus we can work out the corresponding feedback control law for the original system.

The rest of this paper is organized as follows. In section 2, the linear time-invariant system with lumped and distributed delay under consideration is given. The feedback stabilization control law is deduced in detail based on an integral transformation and the backstepping method, and the main result is presented. The conclusion and some remarks are given in Section 3.

II. Design of feedback controllers and main results

We now consider the following linear time-invariant system,

$$\dot{X}(t) = AX(t) + B_1 u(t) + B_2 u(t - \tau) + \int_0^\tau D(s) u(t - s) ds, \quad (4)$$

where $X(\cdot) \in \mathbb{R}^n$ denotes the state vector, and $u(\cdot) \in \mathbb{R}^m$ is the vector of control input. The constant matrices $A \in \mathbb{R}^{n \times n}$ and $B_1, B_2 \in \mathbb{R}^{n \times m}$ are known. The lumped delay appears in the term $B_2 u(t - \tau)$, while the distributed delay is represented by the integral term $\int_0^\tau D(s) u(t - s) ds$. The known function $D(\cdot) : [0, \tau] \rightarrow \mathbb{R}^{n \times m}$ is assumed to be continuous, and the positive constant τ denotes the known time delay.

It is to be noticed that $X(t)$ is only the state of lumped portion of the delay system. The complete state of the system (4) at time t is $\{X(t); u(s), t - \tau \leq s < t\}$. Then the initial conditions are assumed to be

$$X(0) = X_0, \quad u(t) = u_0(t), \quad \forall t \in [-\tau, 0].$$

In order to design a feedback controller which stabilize the system (4), we take the following procedure.

Firstly, inspired by the reduction method in [2], [4], we introduce an integral transformation as follows,

$$W(t) = X(t) + \int_{t-\tau}^t P(t-s) u(s) ds, \quad (5)$$

where the transformation kernel matrix $P(\cdot) : [0, \tau] \rightarrow \mathbb{R}^{n \times m}$ is to be determined later. Now one can calculate easily that

$$\begin{aligned} \dot{W}(t) = & \int_0^\tau (\dot{P}(s) - AP(s) + D(s)) u(t-s) ds \\ & + (B_1 + P(0)) u(t) + (B_2 - P(\tau)) u(t - \tau) \\ & + AW(t) \end{aligned}$$

Choosing such a transformation kernel matrix $P(\cdot)$ that

$$\begin{cases} \dot{P}(s) - AP(s) + D(s) = 0, & s \in [0, \tau], \\ P(0) = -B_1, \end{cases} \quad (6)$$

we then get that

$$\dot{W}(t) = AW(t) + (B_2 - P(\tau)) u(t - \tau). \quad (7)$$

Obviously, the solution of the Cauchy problem (6) reads

$$P(s) = -e^{As} B_1 - \int_0^s e^{A(s-\xi)} D(\xi) d\xi, \quad \forall s \in [0, \tau],$$

which combined with (7) yields

$$\begin{aligned} \dot{W}(t) = & B_2 + e^{A\tau} B_1 + \int_0^\tau e^{A(\tau-s)} D(s) ds \quad u(t - \tau) \\ & + AW(t). \end{aligned} \quad (8)$$

Hence the integral transformation (5) is

$$\begin{aligned} W(t) = & X(t) - \int_{t-\tau}^t e^{A(t-s)} B_1 u(s) ds \\ & - \int_{t-\tau}^t \int_0^{t-s} e^{A(t-s-\xi)} D(\xi) u(s) d\xi ds. \end{aligned} \quad (9)$$

For the sake of simplicity, we define the matrix B as

$$B = B_2 + e^{A\tau} B_1 + \int_0^\tau e^{A(\tau-s)} D(s) ds, \quad (10)$$

which depends on the constant time delay τ . We then get the following linear system with lumped time-delay,

$$\dot{W}(t) = AW(t) + Bu(t - \tau). \quad (11)$$

In one word, we have reduced the system (4) with distributed input delay into the system (11) with only the lumped input delay through the transformation (9).

Secondly, we can go a step further to rewrite the system (11) as

$$\begin{cases} \dot{W}(t) = AW(t) + Bv(0, t), \\ v_t(x, t) = v_x(x, t), \quad x \in (0, \tau), \\ v(\tau, t) = u(t), \end{cases} \quad (12)$$

where $v(0, t) = u(t - \tau)$ just gives the input in (11). In the sequel, we discuss under the hypothesis: *there exists such a matrix K that $(A + BK)$ is Hurwitz*. It has been proven in [1] that the origin of the following system is exponentially stable ,

$$\begin{cases} \dot{W}(t) = (A + BK)W(t) + B\phi(0, t), \\ \phi_t(x, t) = \phi_x(x, t), \\ \phi(\tau, t) = 0. \end{cases} \quad (13)$$

Aiming to transform the system (12) into the target

system (13), introduce the so-called backstepping transformation,

$$\phi(x, t) = v(x, t) - \int_0^x k(x, \theta) v(\theta, t) d\theta - Q(x)^T W(t). \quad (14)$$

The integral kernel $k(x, \theta)$ and $Q(x)$ is determined by the following system,

$$\begin{cases} k_x(x, t) + k_t(x, t) = 0, & k(x, 0) = Q(x)^T B, \\ Q'(x) = A^T Q(x), & Q(0) = K^T. \end{cases} \quad (15)$$

Please refer to [1] for the details. It is not difficult to obtain that

$$k(x, t) = K e^{A(x-t)} B, \quad Q(x) = (K e^{Ax})^T.$$

Thus the backstepping transformation (14) reads

$$\begin{aligned} \phi(x, t) = & -K \int_0^x e^{A(x-\theta)} B v(\theta, t) d\theta + e^{Ax} W(t) \\ & + v(x, t) \end{aligned} \quad (16)$$

Noting $u(t) = v(\tau, t)$ in (12) and $\phi(\tau, t) = 0$ in (13), we then set $x = \tau$ in (16) to get

$$u(t) = K e^{A\tau} W(t) + \int_{t-\tau}^t e^{A(t-s)} B u(s) ds. \quad (17)$$

Hence we actually obtain the feedback control for the original system (4),

$$\begin{aligned} u(t) = & K \int_{t-\tau}^t \int_{t-s}^\tau e^{A(t+\tau-s-\xi)} D(\xi) u(s) d\xi ds \\ & + K e^{A\tau} X(t) + \int_{t-\tau}^t e^{A(t-s)} B_2 u(s) ds \end{aligned} \quad (18)$$

Now we are ready to state the main result on the stabilization for the system (4).

Theorem 1: Let K be such a matrix that $A + B_2 K + e^{A\tau} B_1 K + \int_0^\tau e^{A(\tau-s)} D(s) K ds$ is Hurwitz. The linear time-invariant system (4) with distributed input delay can be stabilized by the feedback control $u(t)$ given in (18).

Proof We would like to prove that

$$\exists c_1, c_2 > 0, \quad \text{s. t.} \quad |X(t)| + \int_{t-\tau}^t |u(s)| ds \leq c_1 e^{-c_2 t}. \quad (19)$$

In the sequel, c_1, c_2 stand for generic positive constants, whose values may change from line to line. In view of the form of $u(t)$ given in (17), let $u(t) = KZ(t)$ with

$$Z(t) = e^{A\tau} W(t) + \int_{t-\tau}^t e^{A(t-s)} B u(s) ds. \quad (20)$$

It is easy to check that $Z(t)$ satisfies

$$\dot{Z}(t) = (A + BK)Z(t).$$

By the assumption on K , it is known that

$$|Z(t)| \leq c_1 e^{-c_2 t}$$

for some positive constants c_1, c_2 . So we can conclude after some simple calculations that

$$\int_{t-\tau}^t |u(s)| ds \leq c_1 e^{-c_2 t}.$$

Naturally, $|W(t)|$ decays exponentially in view of (20),

which together with (9) implies $|X(t)| \leq c_1 e^{-c_2 t}$. This completes the proof.

III. CONCLUSIONS

In this paper, we present a feedback stabilization control law for linear time-invariant systems with lumped and distributed input delay. The system under consideration in this paper is a general model for linear time-invariant systems with delay in the control input. The result obtained in this paper can cover the stabilization result for linear systems with lumped input delay only in [4].

In fact, the system (4) degenerates to the system (1) if $D(\cdot) \equiv 0$. And the feedback control $u(t)$ given in (18) now reads

$$u(t) = K e^{A\tau} X(t) + \int_{t-\tau}^t e^{A(t-s)} B_2 u(s) ds, \quad (21)$$

which seems to differ by a factor $e^{A\tau}$ from (3) derived in [4]. If examining (20), we then find out that (20) is a new transformation which reduce the time-delayed system (11) into the delay-free system

$$\dot{Z}(t) = AZ(t) + Bu(t).$$

This transformation differs also by a factor $e^{A\tau}$ from the reduction transformation (2), which coincides with the difference between (21) and (3). This relation was discovered too in [7] through discussing the relations between continuous reduction transformation and discrete one.

IV. ACKNOWLEDGMENTS

This work was supported by the National Natural Science Foundation of China (Grant No. 10626002).

REFERENCES

- [1] M. Krstic and A. Smyshlyaev, "Backstepping boundary control for first-order hyperbolic PDEs and application to systems with actuator and sensor delays," *Sys. Control Lett.*, Vol. 57(9), pp. 750-758, 2008.
- [2] Z. Artstein, "Linear systems with delayed controls: a reduction," *IEEE Trans. on Automat. Contr.*, Vol. 27(4), pp. 869-879, 1982.
- [3] K. Gu and S.-I. Niculescu, "Survey on recent results in the stability and control of time-delay systems," *Transactions of ASME*, Vol. 125, pp. 158-165, 2003.
- [4] W. H. Kwon and A. E. Pearson, "Feedback stabilization of linear systems with delayed control," *IEEE Trans. on Automat. Contr.*, Vol. 25(2), pp. 266-269, 1980.
- [5] J. Richard, "Time-delay systems: an overview of some recent advances and open problems," *Automatica*, Vol. 39(10), pp. 1667-1694, 2003.
- [6] S.-I. Niculescu, *Delay Effects on Stability: A Robust Control Approach*, Springer-Verlag, Heidelberg, Germany, 2001.
- [7] B. Liu, M. Haraguchi and H. Hu, "A new reduction-based LQ control for dynamic systems with a slowly time-varying delay," *Acta Mech. Sin.*, Vol. 25(4), pp. 529-537, 2009.

Discrete-Time Iterative Learning Control for Relative Degree Systems: A 2-D Approach

Deyuan Meng and Yingmin Jia

*The Seventh Research Division and the Department of Systems and Control,
Beihang University (BUAA), Beijing 100191, China
(E-mail: dymeng23@126.com, ymjia@buaa.edu.cn)*

Abstract: This paper is devoted to the two-dimensional (2-D) design problem that arises from discrete-time iterative learning control (ILC). For linear time-invariant (LTI) systems with well-defined relative degree, a unified ILC algorithm is considered which provides wider freedom for the updating law formation. It demonstrates that an appropriately defined variable, together with the tracking error, can be employed to establish the Roesser systems based 2-D description of the ILC process. This enables both asymptotic stability and monotonic convergence of the relative degree ILC systems to be achieved. In particular, conditions for the monotonic convergence are described in terms of linear matrix inequalities (LMIs), which directly give formulas for the updating law design.

Keywords: Discrete-time iterative learning control; relative degree; monotonic convergence; linear matrix inequality.

I. INTRODUCTION

Iterative learning control (ILC) is known as an effect technique for systems operating repetitively over a fixed time interval. The key feature of ILC is a fundamentally two-dimensional (2-D) process [1], with evolution in two independent directions. In order to take into account the entire dynamics of an ILC, the 2-D analysis approach is found to be a good alternative which can be implemented based on the Roesser's type 2-D systems (see, e.g., [2]-[7]). Hence, the well-developed theory of 2-D systems can be employed to deal with the ILC design. However, the existing 2-D analysis approach is only applicable to the ILC design for such systems with relative degree that is not more than one. This is because it is difficult to establish the 2-D model description of ILC systems with higher-order relative degree. In fact, the system relative degree plays a significant role not only in the ILC design but also in the ILC convergence analysis [8]. Moreover, the area of monotonically convergent ILC design has seen relatively little activity when it comes to addressing systems with higher-order relative degree.

In this paper, the 2-D design approach is investigated for discrete-time ILC with relative degree. It shows that the 2-D Roesser systems can be established to describe the entire dynamics involved in ILC with well-defined system relative degree. Based on the 2-D system theory, a convergence analysis of ILC can be directly presented, and a necessary and sufficient condition can be provided, which is dependent only upon the first non-zero Markov parameter matrix. Moreover, after giving the relationship between two sequential iteration tracking errors from the 2-D Roesser systems, the monotonic convergence of ILC can be obtained by applying the bounded real lemma [9]. In this case, it shows that the monotonically convergent

ILC can be designed through the linear matrix inequality (LMI) technique, and formulas can be presented for the control law design. Finally, a simulation test is proposed to illustrate that the 2-D approach can be used to address monotonically convergent ILC with relative degree.

Notations: I and 0 denote the identity matrix and the zero matrix with required dimensions, respectively; $M > 0$ (respectively, $M < 0$) denotes a symmetric positive (respectively, negative) definite matrix; an asterisk (\star) denotes a term that is induced by symmetry. Matrices, if their dimensions are not explicitly stated, are assumed to be compatible for algebraic operations. For a given vector $x_k(t)$, let q be a shift operator such that $q : x_k(t) \rightarrow qx_k(t) = x_k(t+1)$, and Δ be a difference operator such that $\Delta : x_k(t) \rightarrow \Delta x_k(t) = x_{k+1}(t) - x_k(t)$.

II. ILC SYSTEM DESCRIPTION

Consider the system over $t \in \{0, 1, \dots, T-1\}$ (short for $t \in [0, T-1]$) and $k \in \mathbb{Z}_+$:

$$\begin{aligned} x_k(t+1) &= Ax_k(t) + Bu_k(t) \\ y_k(t) &= Cx_k(t), \quad x_k(0) = x_0, \quad \forall k \end{aligned} \quad (1)$$

where $x_k(t) \in \mathbb{R}^n$ is the state, $u_k(t) \in \mathbb{R}^m$ is the input, $y_k(t) \in \mathbb{R}^l$ is the output, and (A, B, C) is the constant system matrix pair of appropriate dimensions.

It is assumed that system (1) has a relative degree of $r \geq 1$ which is defined as follows.

- *Relative Degree:* The relative degree r of system (1) is an integer which can be characterized by the following conditions:

- 1) $CA^iB = 0$ for all $i < r-1$;
- 2) $CA^{r-1}B \neq 0$ and is of full-row rank.

To deal with the relative degree r , the ILC considered

in this paper uses an updating law given by

$$u_{k+1}(t) = u_k(t) + \sum_{i=0}^r K_i q^i e_k(t) \quad (2)$$

where $e_k(t) = y_d(t) - y_k(t)$ is the tracking error, and K_i , $i = 0, 1, \dots, r$, is an $m \times l$ gain matrix to be designed. The trajectory $y_d(t)$ is the desired output to be tracked over $[r, T + r]$.

The objective of this paper is to address convergence and design problems of the ILC system (1) and (2) by developing a 2-D approach under the Roesser systems framework. To this end, we assume that the initial reset condition is satisfied, i.e., $q^i y_k(0) = q^i y_d(0)$ and, without loss of generality, $q^i y_k(0) = q^i y_d(0) = 0$ is considered, where $i = 0, \dots, r-1$.

III. MAIN RESULTS

A. 2-D System Representation

First of all, the 2-D Roesser systems based approach will be developed for ILC with a system relative degree $r \geq 1$. To this end, let us denote

$$\left\{ \begin{array}{l} \eta_{1k}(t) = A^r q^{-r} \Delta x_k(t) \\ \eta_{2k}(t) = \sum_{j=0}^{r-1} \sum_{i=0}^j A^j B K_i q^{-(j-i)-1} e_k(t) \\ \eta_{3k}(t) = \sum_{j=0}^{r-1} \sum_{i=j+1}^r A^j B K_i q^{i-j-1} e_k(t) \\ \eta_{4k}(t) = \sum_{j=0}^{r-1} A^r B K_j q^{-r+j} e_k(t) \\ \eta_{5k}(t) = \sum_{j=0}^{r-2} \sum_{i=j}^{r-2} A^{i+1} B K_{i-j} q^{-j-1} e_k(t) \end{array} \right. \quad (3)$$

where $\sum_{j=i}^{i-1} (\cdot)_j \triangleq 0$, $\forall i$. Particularly, $\eta_{5k}(t) = 0$ always holds when $r = 1$. For the variables of (3), some properties are given as follows.

Lemma 1: Consider $\eta_{ik}(t)$ defined in (3), where $i = 2, 3, 4$, and 5. Then

a) $\eta_{2k}(t)$ can be rewritten as

$$\eta_{2k}(t) = \sum_{j=0}^{r-1} \sum_{i=j}^{r-1} A^i B K_{i-j} q^{-j-1} e_k(t). \quad (4)$$

b) $\eta_{3k}(t)$ can be such that

$$C \eta_{3k}(t) = C A^{r-1} B K_r e_k(t). \quad (5)$$

c) $\eta_{4k}(t)$ and $\eta_{5k}(t)$ satisfy

$$\eta_{4k}(t) + \eta_{5k}(t) = A \eta_{2k}(t). \quad (6)$$

Proof: The proof can be immediately derived with some algebraic operation and, thus, is omitted here. ■

Now with Lemma 1, let us consider the 2-D representation of ILC systems. The use of $e_k(t) = y_d(t) - y_k(t)$

and $y_k(t) = C x_k(t)$ leads to

$$\begin{aligned} e_{k+1}(t) &= \Delta e_k(t) + e_k(t) \\ &= \Delta [y_d(t) - y_k(t)] + e_k(t) \\ &= -\Delta y_k(t) + e_k(t) \\ &= -C \Delta x_k(t) + e_k(t). \end{aligned} \quad (7)$$

where $\Delta x_k(t)$, by using the first equation of system (1), satisfies

$$\begin{aligned} q \Delta x_k(t) &= \Delta q x_k(t) \\ &= \Delta x_k(t+1) \\ &= \Delta [A x_k(t) + B u_k(t)] \\ &= A \Delta x_k(t) + B \Delta u_k(t). \end{aligned} \quad (8)$$

Since $\Delta x_k(0) = 0$, the use of (8) can yield

$$\Delta x_k(t) = A q^{-1} \Delta x_k(t) + B q^{-1} \Delta u_k(t). \quad (9)$$

Following the same steps repetitively, it can be developed further from (9) that

$$\begin{aligned} \Delta x_k(t) &= A^r q^{-r} \Delta x_k(t) + \sum_{j=0}^{r-1} A^j B q^{-j-1} \Delta u_k(t) \\ &= \eta_{1k}(t) + \sum_{j=0}^{r-1} A^j B q^{-j-1} \Delta u_k(t). \end{aligned} \quad (10)$$

The ILC law of (2) can be rewritten as

$$\Delta u_k(t) = \sum_{i=0}^r K_i q^i e_k(t). \quad (11)$$

Then insert (11) into (10) to get

$$\begin{aligned} \Delta x_k(t) &= \eta_{1k}(t) + \sum_{j=0}^{r-1} A^j B q^{-j-1} \sum_{i=0}^r K_i q^i e_k(t) \\ &= \eta_{1k}(t) + \sum_{j=0}^{r-1} \sum_{i=0}^r A^j B K_i q^{i-j-1} e_k(t) \\ &= \eta_{1k}(t) + \sum_{j=0}^{r-1} \sum_{i=0}^j A^j B K_i q^{-(j-i)-1} e_k(t) \\ &\quad + \sum_{j=0}^{r-1} \sum_{i=j+1}^r A^j B K_i q^{i-j-1} e_k(t) \\ &= \eta_{1k}(t) + \eta_{2k}(t) + \eta_{3k}(t). \end{aligned} \quad (12)$$

In view of (5) and by inserting (12) into (7), it follows immediately that

$$\begin{aligned} e_{k+1}(t) &= -C [\eta_{1k}(t) + \eta_{2k}(t)] - C \eta_{3k}(t) + e_k(t) \\ &= -C \xi_k(t) + (I - C A^{r-1} B K_r) e_k(t) \end{aligned} \quad (13)$$

where

$$\xi_k(t) = \eta_{1k}(t) + \eta_{2k}(t). \quad (14)$$

From (13), it is obvious that an iterative equation about the tracking error is obtained, which can reflect the ILC system dynamics along the iteration axis k . With this fact, $\xi_k(t)$ will be further discussed in order to disclose the time-domain dynamics involved in the ILC system (1) and (2).

To describe the ILC system dynamics along the time

axis t , next let us consider $\xi_k(t+1) = q\xi_k(t)$. Towards this end, compute $q\eta_{1k}(t)$ and then insert (8) and (11) to obtain

$$\begin{aligned} q\eta_{1k}(t) &= q[A^r q^{-r} \Delta x_k(t)] \\ &= A^r q^{-r} q \Delta x_k(t) \\ &= A^{r+1} q^{-r} \Delta x_k(t) + A^r B q^{-r} \Delta u_k(t) \\ &= A\eta_{1k}(t) + A^r B q^{-r} \sum_{j=0}^r K_j q^j e_k(t) \\ &= A\eta_{1k}(t) + \sum_{j=0}^{r-1} A^r B K_j q^{-r+j} e_k(t) + A^r B K_r e_k(t) \\ &= A\eta_{1k}(t) + \eta_{4k}(t) + A^r B K_r e_k(t). \end{aligned} \quad (15)$$

And with (4), $q\eta_{2k}(t)$ is computed by

$$\begin{aligned} q\eta_{2k}(t) &= q \sum_{j=0}^{r-1} \sum_{i=j}^{r-1} A^i B K_{i-j} q^{-j-1} e_k(t) \\ &= \sum_{j=1}^{r-1} \sum_{i=j}^{r-1} A^i B K_{i-j} q^{-j} e_k(t) + \sum_{i=0}^{r-1} A^i B K_i e_k(t) \\ &= \sum_{j=0}^{r-2} \sum_{i=j}^{r-2} A^{i+1} B K_{i-j} q^{-j-1} e_k(t) + \sum_{i=0}^{r-1} A^i B K_i e_k(t) \\ &= \eta_{5k}(t) + \sum_{i=0}^{r-1} A^i B K_i e_k(t). \end{aligned} \quad (16)$$

Use (6), (15) and (16) to obtain

$$\begin{aligned} q\xi_k(t) &= q\eta_{1k}(t) + q\eta_{2k}(t) \\ &= A\eta_{1k}(t) + \eta_{4k}(t) + \eta_{5k}(t) + \sum_{i=0}^r A^i B K_i e_k(t) \\ &= A[\eta_{1k}(t) + \eta_{2k}(t)] + \sum_{i=0}^r A^i B K_i e_k(t) \\ &= A\xi_k(t) + \sum_{i=0}^r A^i B K_i e_k(t). \end{aligned} \quad (17)$$

Thus, based on (13) and (17), the following 2-D Roesser model can be established:

$$\begin{bmatrix} \xi_k(t+1) \\ e_{k+1}(t) \end{bmatrix} = \begin{bmatrix} A & \sum_{i=0}^r A^i B K_i \\ -C & I - CA^{r-1} B K_r \end{bmatrix} \begin{bmatrix} \xi_k(t) \\ e_k(t) \end{bmatrix} \quad (18)$$

which clearly describes the two independent dynamics involved in the ILC system (1) and (2), as claimed in [2]-[4], [6]. For the 2-D model of (18), the use of (3) and (14) yields

$$\begin{aligned} \xi_k(t) &= A^r q^{-r} \Delta x_k(t) + \sum_{j=0}^{r-1} \sum_{i=0}^j A^j B K_i q^{-(j-i)-1} e_k(t) \\ &= A^r \Delta x_k(t-r) + \sum_{j=0}^{r-1} \sum_{i=0}^j A^j B K_i e_k(t - (j-i) - 1). \end{aligned}$$

Note that $\Delta x_k(0) = 0$ holds, and $q^i y_k(0) = q^i y_d(0)$ implies $y_k(i) = y_d(i)$, i.e., $e_k(i) = 0$, for $i = 0, 1, \dots, r-1$. Hence, it is obvious that $\xi_k(r) = 0$ holds for $k \in \mathbb{Z}_+$.

Consequently, the boundary conditions for (18) are:

$$\xi_k(r) = 0 \text{ for } k \in \mathbb{Z}_+ \text{ and finite } e_0(t) \text{ for } t \in [r, T+r]. \quad (19)$$

Remark 1: From (18), it is clear that Roesser models can be developed with $\xi_k(t)$ and $e_k(t)$ to describe the 2-D processes resulting from the ILC system (1) and (2). This implies that a general 2-D framework is established for ILC systems with relative degree. For the particular case where $r = 1$, it can be easily shown that the 2-D Roesser system (18) provides an alternative approach to describe the ILC systems that have been considered in, e.g., [2]-[4].

B. Convergence Analysis of ILC

With the development of 2-D system representation, both asymptotic stability and monotonic convergence can be considered for ILC systems with relative degree. First, the following result is given for the asymptotic stability of ILC.

Proposition 1: Consider the ILC system (1) and (2) of the general relative degree $r \geq 1$. Then the tracking error $e_k(t)$ converges asymptotically to zero as $k \rightarrow \infty$ if and only if the matrix $I - CA^{r-1}BK_r$ is stable, i.e., the spectral radius fulfills $\rho(I - CA^{r-1}BK_r) < 1$.

Proof: With the 2-D system theory applied to (18) and (19), the proof is immediate. For more details, see [3] and [4]. ■

Remark 2: From Proposition 1, it is obvious that the asymptotic stability of ILC depends only upon the first non-zero Markov parameter matrix $CA^{r-1}B$, regardless of the system relative degree r .

Next, the following result is presented for the monotonic convergence of ILC.

Proposition 2: Consider the ILC system (1) and (2) of the general relative degree $r \geq 1$. Then the tracking error $e_k(t)$ converges monotonically to zero when $k \rightarrow \infty$ in the sense of the \mathcal{L}_2 -norm if there exist scalars $\varepsilon_1 > 0$, $\varepsilon_2 > 0$ and matrices $Q > 0$, X_i , $i = 0, \dots, r$, that satisfy the following LMIs

$$\varepsilon_1 \leq \varepsilon_2 \quad (20)$$

$$\begin{bmatrix} -Q & (\star) & (\star) & (\star) \\ QA^T & -Q & (\star) & (\star) \\ \sum_{i=0}^r X_i^T B^T A^i & 0 & -\varepsilon_1 I & (\star) \\ 0 & CQ & \varepsilon_2 I + CA^{r-1} B X_r & -\varepsilon_1 I \end{bmatrix} < 0. \quad (21)$$

If the LMIs of (20) and (21) are feasible, then the gain matrices are given by

$$K_i = -\varepsilon_2^{-1} X_i, \quad i = 0, \dots, r. \quad (22)$$

Proof: With the bounded real lemma (see, e.g., [9]) applied, the proof can be proved based on the use of (18) and in the same way as in the proof of [8, Theorem 3] and, thus, is omitted here. ■

Remark 3: Proposition 2 implies that although the asymptotic stability of the updating law (2) depends only on the selection of K_r , its other learning gains can help

to achieve the monotonic convergence of ILC to ensure good performance.

IV. NUMERICAL EXAMPLE

In this example, system (1) is considered with matrices given by:

$$A = \begin{bmatrix} 0 & 1 & 0 & 0 & 0 & 0 \\ 0 & 0 & 1 & 0 & 0 & 0 \\ 0 & 0 & 0 & 1 & 0 & 0 \\ 0 & 0 & 0 & 0 & 1 & 0 \\ 0 & 0 & 0 & 0 & 0 & 1 \\ -0.0043 & 0.0004 & 0.12 & 0.149 & -0.71 & -1.7 \end{bmatrix}$$

$$B = \begin{bmatrix} 0 & 0 & 0 \\ 0 & 0 & 0 \\ 1 & 0 & 0 \\ 0 & 1 & 0 \\ 0 & 0 & 1 \\ 0 & 0 & 0 \end{bmatrix}$$

$$C = \begin{bmatrix} 0 & 1 & 0 & 0 & 0 & 0 \\ 0 & 0 & 0 & 0 & 0 & 1 \end{bmatrix}.$$

Clearly, it is easy to show that $CB = 0$ and CAB has full-row rank, resulting in system (1) with a relative degree of $r = 2$.

To perform the simulation, the zero initial control input $u_0(t) = 0$ is used, and the following desired trajectory is considered:

$$y_d(t) = \begin{bmatrix} y_{d1}(t) \\ y_{d2}(t) \end{bmatrix} = \begin{bmatrix} 20 - 20\cos(0.02\pi t) \\ 6 \cdot 10^{-10}t^5 - 1.5 \cdot 10^{-7}t^4 + 10^{-5}t^3 \end{bmatrix}$$

where $t \in [0, 100]$. Accordingly, $y_k(t) = [y_{1k}(t), y_{2k}(t)]^T$ is denoted for the sake of notations. Then solve LMIs (20) and (21) with $r = 2$ to derive

$$K_0 = \begin{bmatrix} 0.0434 & 0.1665 \\ -0.0119 & 2.4293 \\ 0.0078 & -1.0000 \end{bmatrix}$$

$$K_1 = \begin{bmatrix} 0.2855 & -0.2664 \\ -0.0354 & 1.1861 \\ -0.0007 & -2.4293 \end{bmatrix}$$

$$K_2 = \begin{bmatrix} 0.5883 & -0.0000 \\ -0.3300 & 0.2664 \\ 0.0309 & -1.3525 \end{bmatrix}.$$

Now using such gain matrices, we perform the ILC system (1) and (2), and show the test results in Figs. 1 and 2. Fig. 1 shows the evolution of tracking errors $\|y_{d1}(t) - y_{1k}(t)\|_2$ and $\|y_{d2}(t) - y_{2k}(t)\|_2$ with respect to the iteration number k , and Fig. 2 shows the time evolution of the reference trajectory $y_d(t)$ and actual output $y_k(t)$ for $k = 1, 3, 5$. From Figs. 1 and 2, it is clear that the ILC process converges monotonically. It illustrates that the proposed 2-D approach can effectively address the design of ILC with system relative degree.

V. CONCLUSIONS

In this paper, the 2-D design approach to discrete-time ILC with relative degree has been discussed. It has been

shown that the asymptotic stability of ILC is dependent only upon the first non-zero Markov parameter matrix. Moreover, sufficient conditions have been provided in terms of LMIs to guarantee the monotonic convergence of ILC and give formulas for the updating law design. For ILC designed through solving LMIs, its effectiveness has been verified finally through simulation test.

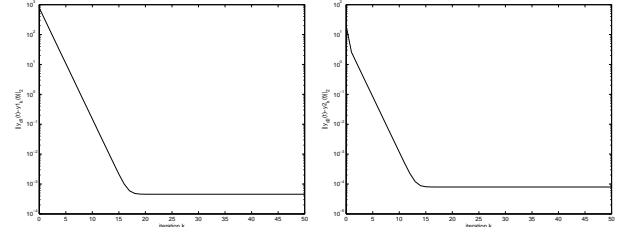


Fig.1. Left: The error between $y_{d1}(t)$ and $y_{1k}(t)$.
Right: The error between $y_{d2}(t)$ and $y_{2k}(t)$.

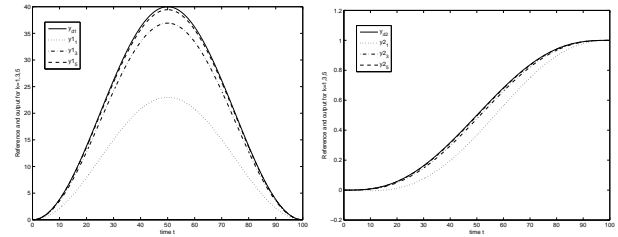


Fig.2. Left: $y_{d1}(t)$ and $y_{1k}(t)$ for $k = 1, 3, 5$.
Right: $y_{d2}(t)$ and $y_{2k}(t)$ for $k = 1, 3, 5$.

ACKNOWLEDGMENTS

This work was supported by the NSFC (60727002, 60774003, 60921001, 90916024), the MOE (20030006003), the COSTIND (A2120061303), and the National 973 Program (2005CB321902).

REFERENCES

- [1] Ahn H.-S., Chen Y., and Moore K. L. (2007), Iterative learning control: Brief survey and categorization. IEEE Transactions on Systems, Man, and Cybernetics-Part C: Applications and Reviews 37(6): 1099–1121
- [2] Geng Z., Carroll R., and Xie J. (1990), Two-dimensional model and algorithm analysis for a class of iterative learning control systems. International Journal of Control 52(4): 833–862
- [3] Kurek J. E. and Zaremba M. B. (1993), Iterative learning control synthesis based on 2-D system theory. IEEE Transactions on Automatic Control 38(1): 121–125
- [4] Saab S. S. (1995), A discrete-time learning control algorithm for a class of linear time-invariant systems. IEEE Transactions on Automatic Control 40(6): 1138–1142
- [5] Li X.-D., Chow T. W. S., and Ho J. K. L. (2005), 2-D system theory based iterative learning control for linear continuous systems with time delays. IEEE Transactions on Circuits and Systems-I: Regular Papers 52(7): 1421–1430
- [6] Meng D., Jia Y., Du J., et al (2009), Robust discrete-time iterative learning control for nonlinear systems with varying initial state shifts. IEEE Transactions on Automatic Control 54(11): 2626–2631
- [7] Meng D., Jia Y., Du J., et al (2009), Robust design of a class of time-delay iterative learning control systems with initial shifts. IEEE Transactions on Circuits and Systems-I: Regular Papers 56(8): 1744–1757
- [8] Meng D. and Jia Y. (2010), Effects of initial input on stochastic discrete-time iterative learning control systems. Proceedings of the Chinese Control Conference 2193–2200
- [9] Hsiung K.-L. and Lee L. (1999), Lyapunov inequality and bounded real lemma for discrete-time descriptor systems. IEEE Proceedings-Control Theory and Applications 146(4): 327–331

Distributed Robust Consensus Control of Uncertain Multi-Agent Systems

Yang Liu and Yingmin Jia

*The Seventh Research Division and the Department of Systems and Control,
Beihang University (BUAA), Beijing 100191, China*

(E-mail: ylbuaa@163.com, ymjia@buaa.edu.cn)

Abstract: This paper is devoted to the robust consensus control of multi-agent systems with model parameter uncertainties and external disturbances for networks with switching topology. In particular, a sufficient condition for the consensus performance with a given H_∞ disturbance attenuation level is established for the multi-agent system governed by general linear differential equations, and meanwhile the unknown feedback matrix of the proposed distributed state feedback protocol is determined. The condition is given in terms of linear matrix inequalities (LMIs) and can be easily verified. A numerical example is included to validate the theoretical results.

Keywords: Consensus, Robust H_∞ control, Multi-agent systems, External disturbances, Model uncertainties

I. INTRODUCTION

Recently, some researchers have studied the consensus problem of multi-agent systems with various external disturbances and random communication noises [1]-[6]. However, unavoidable model and parameter uncertainties in the agents' dynamics have not been considered in the existing literature. This motivates us to investigate the consensus problem for multi-agent systems with both model uncertainties and external disturbances.

In this paper, we study the consensus control for networks of multiple agents modeled by general high-dimensional linear differential equations with both model uncertainties and external disturbances, and propose a distributed protocol with an undetermined state feedback matrix. In order to use the existing robust H_∞ theory of linear systems, a controlled output is defined to reformulate the consensus control problem as a robust H_∞ control problem, and a series of model transformations are conducted to convert the original singular closed-loop system to be an equivalent stabilized reduced-order one. Then, sufficient conditions in terms of LMIs are derived to ensure the consensus performance with a given H_∞ index for the disturbed multi-agent system without and with model uncertainties respectively, and the feedback matrix of the proposed protocol is determined accordingly.

II. PROBLEM REFORMULATION AND PROTOCOL DESIGN

A. Problem statement and preliminaries

Consider a multi-agent system consisting of n identical agents with the i th one modeled by

$$\dot{x}_i(t) = Ax_i(t) + B_1\omega_i(t) + B_2u_i(t), \quad (1)$$

where $x_i(t) \in \mathbb{R}^m$ is the state, $u_i(t) \in \mathbb{R}^{m_2}$ is the control input or protocol, and $\omega_i(t) \in \mathbb{R}^{m_1}$ is the external dis-

turbance that belongs to $\mathcal{L}_2[0, \infty)$, the space of square-integrable vector functions over $[0, \infty)$. If system matrices A , B_1 , B_2 are uncertain, they are assumed to take the following forms:

$$A = A_0 + \Delta A(t), B_1 = B_{10} + \Delta B_1(t), B_2 = B_{20} + \Delta B_2(t), \quad (2)$$

where A_0 , B_{10} , B_{20} are constant matrices, and $\Delta A(t)$, $\Delta B_1(t)$, $\Delta B_2(t)$ are time-varying uncertain matrices satisfying

$$[\Delta A(t) \ \Delta B_1(t) \ \Delta B_2(t)] = E\Sigma(t)[F_1 \ F_2 \ F_3]. \quad (3)$$

In (3), E and F_i ($i = 1, 2, 3$) are constant matrices of appropriate dimensions, and $\Sigma(t)$ is an unknown time-varying matrix that satisfies $\Sigma^T(t)\Sigma(t) \leq I$. It is also assumed that (A_0, B_{20}) is stabilized. A protocol $u_i(t)$ is said to asymptotically solve the consensus problem, if and only if the states of agents satisfy

$$\lim_{t \rightarrow \infty} [x_i(t) - x_j(t)] = \mathbf{0}, \quad \forall i, j \in \{1, \dots, n\} \triangleq \mathcal{N}.$$

Undirected graphs are used to model the interaction topologies among agents. Let $\mathcal{G} = (\mathcal{V}, \mathcal{E}, \mathcal{A})$ be an undirected weighted graph of order n with the set of nodes $\mathcal{V} = \{v_1, \dots, v_n\}$, the set of undirected edges $\mathcal{E} \subseteq \mathcal{V} \times \mathcal{V}$, and a symmetric adjacency matrix $\mathcal{A} = [a_{ij}]$ with weighting factors $a_{ij} \geq 0$. It is stipulated that the adjacency elements associated with edges are positive, i.e., (v_i, v_j) or $(v_j, v_i) \in \mathcal{E}$ if and only if $a_{ij} = a_{ji} > 0$. In graph \mathcal{G} , node v_i represents the i th agent, and edge (v_i, v_j) represents that information is exchanged between agents i and j . Then the set of neighbors of v_i is denoted by $\mathcal{N}_i = \{v_j \in \mathcal{V} : (v_i, v_j) \in \mathcal{E}\}$. The Laplacian of a weighted graph \mathcal{G} is defined as $L = \mathcal{D} - \mathcal{A}$, where diagonal matrix $\mathcal{D} = \text{diag}\{d_1, \dots, d_n\}$ is named the degree matrix of \mathcal{G} , whose diagonal elements are $d_i = \sum_{j=1}^n a_{ij}$. To describe the variable topologies, a piecewise-constant switching signal function $\sigma(t) :$

$[0, \infty) \mapsto \{1, \dots, M\} \triangleq \mathcal{M}$ is defined, where $M \in \mathbb{Z}^+$ denotes the total number of all possible undirected interaction graphs. The interaction graph at time instant t is denoted by $\mathcal{G}_{\sigma(t)}$, and the corresponding Laplacian is $L_{\sigma(t)}$. In this paper, the switching graphs $\mathcal{G}_{\sigma(t)}$ are assumed to be always connected for all $\sigma(t) \in \mathcal{M}$.

B. Problem reformulation

Define controlled output functions

$$z_i(t) = x_i(t) - \frac{1}{n} \sum_{j=1}^n x_j(t), \quad i = 1, \dots, n \quad (4)$$

to reformulate the consensus control problem of multi-agent system (1) as the following H_∞ control problem:

$$\begin{aligned} \dot{x}(t) &= (I_n \otimes A)x(t) + (I_n \otimes B_1)\omega(t) + (I_n \otimes B_2)u(t) \\ z(t) &= (L_c \otimes I_m)x(t), \end{aligned} \quad (5)$$

where $x(t) = [x_1^T(t) \dots x_n^T(t)]^T \in \mathbb{R}^{mn}$, $\omega(t) = [\omega_1^T(t) \dots \omega_n^T(t)]^T \in \mathbb{R}^{m_1n}$, $u(t) = [u_1^T(t) \dots u_n^T(t)]^T \in \mathbb{R}^{m_2n}$, $z(t) = [z_1^T(t) \dots z_n^T(t)]^T \in \mathbb{R}^{mn}$, and $L_c = [L_{cij}] \in \mathbb{R}^{n \times n}$ is defined by

$$L_{cij} = \begin{cases} \frac{n-1}{n}, & i = j \\ -\frac{1}{n}, & i \neq j \end{cases}.$$

Therefore, the objective is to design a distributed protocol $u_i(t)$ ($i \in \mathcal{N}$) such that

$$\|T_{z\omega}(s)\|_\infty = \sup_{v \in \mathbb{R}} \bar{\sigma}(T_{z\omega}(jv)) = \sup_{\omega \neq 0(t) \in \mathcal{L}_2[0, \infty)} \frac{\|z(t)\|_2}{\|\omega(t)\|_2} < \gamma$$

holds, where $\gamma > 0$ is a given H_∞ performance index.

C. Protocol design and model transformation

Using the neighbors' local information, the distributed protocol of agent i is designed as

$$u_i(t) = K \sum_{j \in \mathcal{N}_i(t)} a_{ij}(t) [x_i(t) - x_j(t)], \quad (6)$$

where $\mathcal{N}_i(t)$ is the neighbor set of agent i at time instant t , $a_{ij}(t)$ are adjacency elements of the interaction graph $\mathcal{G}_{\sigma(t)}$, and $K \in \mathbb{R}^{m_2 \times m}$ is an undetermined feedback matrix. Substituting protocol (6) into the system (5) results in the following closed-loop system

$$\begin{aligned} \dot{x}(t) &= (I_n \otimes A + L_{\sigma(t)} \otimes B_2 K)x(t) + (I_n \otimes B_1)\omega(t) \\ z(t) &= (L_c \otimes I_m)x(t), \end{aligned} \quad (7)$$

where $L_{\sigma(t)}$ is the Laplacian matrix of graph $\mathcal{G}_{\sigma(t)}$.

Note that the symmetric matrix $L_{\sigma(t)}$ has a zero eigenvalue. Thus, the state matrix of system (7) can not be robust stable if A_0 is unstable. In order to apply the H_∞ theory, we first convert the system (7) to be an equivalent reduced-order one that is completely stabilized, by a series of model transformations. This will be presented in the following.

By Lemmas 1 and 5 of [4], there exists an orthogonal matrix $U \in \mathbb{R}^{n \times n}$ such that

$$U^T L_c U = \begin{bmatrix} I_{n-1} & 0 \\ 0 & 0 \end{bmatrix} \triangleq \bar{L}_c, \quad U^T L_{\sigma(t)} U = \begin{bmatrix} L_{1\sigma(t)} & 0 \\ 0 & 0 \end{bmatrix} \triangleq \bar{L}_{\sigma(t)}, \quad (8)$$

and $L_{1\sigma(t)}$ is positive definite since the graph $\mathcal{G}_{\sigma(t)}$ is connected. For the convenience of discussion, denote $U = [U_1 \ U_2]$ with $U_2 = \frac{1}{\sqrt{n}}$ being its last column. Let

$$\begin{aligned} \hat{x}(t) &= (U^T \otimes I_m) \bar{x}(t) = \begin{bmatrix} (U_1^T \otimes I_m) \bar{x}(t) \\ (U_2^T \otimes I_m) \bar{x}(t) \end{bmatrix} \triangleq \begin{bmatrix} \hat{x}^1(t) \\ \hat{x}^2(t) \end{bmatrix} \\ \hat{\omega}(t) &= (U^T \otimes I_{m_1}) \omega(t) = \begin{bmatrix} (U_1^T \otimes I_{m_1}) \omega(t) \\ (U_2^T \otimes I_{m_1}) \omega(t) \end{bmatrix} \triangleq \begin{bmatrix} \hat{\omega}^1(t) \\ \hat{\omega}^2(t) \end{bmatrix} \\ \hat{z}(t) &= (U^T \otimes I_m) z(t) = \begin{bmatrix} (U_1^T \otimes I_m) z(t) \\ (U_2^T \otimes I_m) z(t) \end{bmatrix} \triangleq \begin{bmatrix} \hat{z}^1(t) \\ \hat{z}^2(t) \end{bmatrix}, \end{aligned} \quad (9)$$

where

$$\bar{x}(t) = x(t) - \frac{1}{n} \otimes \left(\sum_{j=1}^n x_j(t) \right). \quad (10)$$

From (7)-(10), we have

$$\begin{aligned} \dot{\hat{x}}(t) &= (\bar{L}_c \otimes A + \bar{L}_c \bar{L}_{\sigma(t)} \otimes B_2 K) \hat{x}(t) + (\bar{L}_c \otimes B_1) \hat{\omega}(t) \\ \hat{z}(t) &= (\bar{L}_c \otimes I_m) \hat{x}(t) \end{aligned} \quad (11)$$

that can be divided into the following two independent subsystems:

$$\begin{aligned} \dot{\hat{x}}^1(t) &= (I_{n-1} \otimes A + L_{1\sigma(t)} \otimes B_2 K) \hat{x}^1(t) + (I_{n-1} \otimes B_1) \hat{\omega}^1(t) \\ &\triangleq H_{\sigma(t)} \hat{x}^1(t) + G \hat{\omega}^1(t) \\ \hat{z}^1(t) &= \hat{x}^1(t) \end{aligned} \quad (12)$$

and $\hat{x}^2(t) = \mathbf{0}$, $\hat{z}^2(t) = \mathbf{0}$. Then by the definition of H_∞ norm, it can be proved that $\|T_{z\omega}(s)\|_\infty = \|T_{\hat{z}\hat{\omega}}(s)\|_\infty = \|T_{\hat{z}^1\hat{\omega}^1}(s)\|_\infty$. In addition, the state matrix $I_{n-1} \otimes A + L_{1\sigma(t)} \otimes B_2 K$ can be robust stable by designing an appropriate matrix K , since (A_0, B_{20}) is assumed to be stabilized and matrix $L_{1\sigma(t)}$ is positive definite. Therefore, we can analyze the H_∞ performance of the stabilized reduced-order system (12) instead of (11). To summarize, the consensus performance of the closed-loop multi-agent system (7) is achieved with H_∞ disturbance attenuation index γ , if the system (12) is asymptotically stable and satisfies the H_∞ level γ .

III. CONDITIONS FOR ROBUST H_∞ CONSENSUS

In this section, the robust H_∞ performance of switched system (12) is analyzed, and sufficient conditions are derived to ensure the desired consensus performance of multi-agent system (1) under the protocol (6). First, we consider the multi-agent system (1) by neglecting matrix uncertainties in (2), i.e., matrices A , B_1 , B_2 are known constants. Denote $\lambda_{\sigma(t)i}$ as the i th real positive eigenvalue of matrix $L_{\sigma(t)}$, $i = 1, \dots, n-1$. Let $\sigma_*(t)i_*$ and $\sigma^*(t)i^*$ be the subscripts associated with the minimum and the maximum nonzero eigenvalues of all Laplacian matrices $L_{\sigma(t)}$, respectively.

The following lemma is derived from Lemma 3.2 of [5] and Schur Complement Formula:

Lemma 1: For a given index $\gamma > 0$, the switched system (12) is asymptotically stable and satisfies $\|T_{\hat{z}^1\hat{\omega}^1}(s)\|_\infty < \gamma$, if there exists a positive definite matrix

$P \in \mathbb{R}^{(n-1)m \times (n-1)m}$ such that

$$H_{\sigma(t)}^T P + P H_{\sigma(t)} + \gamma^{-2} P G G^T P + I < 0 \quad (13)$$

holds for $\forall \sigma(t) \in \mathcal{M}$.

Theorem 1: Under protocol (6), the multi-agent system (1) achieves consensus with a given H_∞ disturbance attenuation index γ , if there exist $P \in \mathbb{R}^{m \times m} > 0$ and $Q \in \mathbb{R}^{m_2 \times m}$ such that the linear matrix inequality (LMI)

$$\begin{bmatrix} P A^T + A P + \lambda_{\sigma(t)i} Q^T B_2^T + \lambda_{\sigma(t)i} B_2 Q + \gamma^{-2} B_1 B_1^T & P \\ P & -I \end{bmatrix} < 0 \quad (14)$$

is satisfied for $\sigma(t)i = \sigma_*(t)i_*$ and $\sigma^*(t)i^*$. If the above two LMIs are feasible, then the feedback matrix of the consensus protocol is $K = QP^{-1}$.

Proof: By Lemma 1, the system (12) is asymptotically stable and satisfies $\|T_{z_1 \omega_1}(s)\|_\infty < \gamma$, if there exists a positive definite matrix $P \in \mathbb{R}^{(n-1)m \times (n-1)m}$ satisfying (13). Particularly, take $P = I_{n-1} \otimes X$ with $X \in \mathbb{R}^{m \times m} > 0$.

Since $L_{1\sigma(t)}$ is positive definite, there exists an orthogonal matrix $U_{1\sigma(t)}$ such that $U_{1\sigma(t)}^T L_{1\sigma(t)} U_{1\sigma(t)} = \text{diag}\{\lambda_{\sigma(t)1}, \dots, \lambda_{\sigma(t)(n-1)}\}$. Let $\bar{U}_{1\sigma(t)} = U_{1\sigma(t)} \otimes I_m$. According to the proof of Theorem 3.3 in [5], pre- and post-multiplying the matrix inequality (13) with $\bar{U}_{1\sigma(t)}^T$ and $\bar{U}_{1\sigma(t)}$, respectively, can yield a group of matrix inequalities

$$X A + A^T X + \lambda_{\sigma(t)i} X B_2 K + \lambda_{\sigma(t)i} K^T B_2^T X + \gamma^{-2} X B_1 B_1^T X + I < 0 \quad (15)$$

$\sigma(t) = 1, \dots, M$, $i = 1, \dots, n-1$, which are equivalent to (13). Due to Schur Complement Formula, inequality (15) is also equivalent to

$$\begin{bmatrix} (A + \lambda_{\sigma(t)i} B_2 K)^T X + X(A + \lambda_{\sigma(t)i} B_2 K) + \gamma^{-2} X B_1 B_1^T X & I \\ I & -I \end{bmatrix} < 0. \quad (16)$$

Then pre- and post-multiplying the inequality (16) with $\text{diag}\{X^{-1}, I\}$ yields (14) with $P = X^{-1}$ and $Q = KP$. To summarize, the multi-agent system (1) achieves consensus with a given H_∞ disturbance attenuation index γ , if the LMI (14) holds for $\forall \sigma(t)i$.

Due to the convex property of LMIs, if (14) holds when $\lambda_{\sigma(t)i}$ takes its extreme values $\lambda_{\sigma_*(t)i_*}$ and $\lambda_{\sigma^*(t)i^*}$, then the LMI (14) holds for $\forall \sigma(t)i$, and the desired consensus performance is guaranteed. Further, if the above condition is satisfied, then from $Q = KP$, it is obtained that the feedback matrix of the proposed consensus protocol is $K = QP^{-1}$. \square

Based on the previous development, the consensus condition is now given for the multi-agent system (1) with model uncertainties (2). To achieve this, we adopt the following lemma.

Lemma 2 [7]: Given symmetric matrices $X, Y, Z \in \mathbb{R}^{n \times n}$ satisfying $X \geq 0$, $Y < 0$, $Z \geq 0$, if for any nonzero vector $\zeta \in \mathbb{R}^n$, $(\zeta^T Y \zeta)^2 - 4 \zeta^T X \zeta \zeta^T Z \zeta > 0$ holds, then there exists a scalar $\lambda > 0$ such that $\lambda^2 X + \lambda Y + Z < 0$.

Theorem 2: Under protocol (6), the multi-agent system (1) with model uncertainties (2) can achieve

consensus with a given H_∞ disturbance attenuation index γ , if for a scalar $\lambda > 0$, there exist $P \in \mathbb{R}^{m \times m} > 0$ and $Q \in \mathbb{R}^{m_2 \times m}$ such that the LMI

$$\begin{bmatrix} \Psi_{\sigma(t)i} & B_{10} & P & \frac{1}{\lambda}(F_1 P + \lambda_{\sigma(t)i} F_3 Q)^T \\ B_{10}^T & -\gamma^{-2} I & 0 & \frac{1}{\lambda} F_2^T \\ P & 0 & -I & 0 \\ \frac{1}{\lambda}(F_1 P + \lambda_{\sigma(t)i} F_3 Q) & \frac{1}{\lambda} F_2 & 0 & -I \end{bmatrix} < 0$$

$$\Psi_{\sigma(t)i} = P A_0^T + A_0 P + \lambda_{\sigma(t)i} Q^T B_{20}^T + \lambda_{\sigma(t)i} B_{20} Q + \lambda^2 E E^T \quad (17)$$

is satisfied for $\sigma(t)i = \sigma_*(t)i_*$ and $\sigma^*(t)i^*$. If the above two LMIs are feasible, then the feedback matrix of the consensus protocol is $K = QP^{-1}$.

Proof: Due to Schur Complement Formula, the matrix inequality (14) in Theorem 1 is equivalent to

$$\Xi_{\sigma(t)i} = \begin{bmatrix} P A^T + A P + \lambda_{\sigma(t)i} Q^T B_2^T + \lambda_{\sigma(t)i} B_2 Q & B_1 & P \\ B_1^T & -\gamma^2 I & 0 \\ P & 0 & -I \end{bmatrix} < 0.$$

By the definition of negative definite matrices, $\Xi_{\sigma(t)i} < 0$ if and only if $\xi^T \Xi_{\sigma(t)i} \xi < 0$ holds for any nonzero vector ξ . Hence, to ensure the desired robust H_∞ consensus performance, we only need to find conditions for $\xi^T \Xi_{\sigma(t)i} \xi < 0$ in the presence of uncertainties (2).

From (2) and (3), it is obtained that $\Xi_{\sigma(t)i} = \Gamma_{\sigma(t)i} + \Delta \Gamma_{\sigma(t)i}$, where

$$\Gamma_{\sigma(t)i} = \begin{bmatrix} P A_0^T + A_0 P + \lambda_{\sigma(t)i} Q^T B_{20}^T + \lambda_{\sigma(t)i} B_{20} Q & B_{10} & P \\ B_{10}^T & -\gamma^2 I & 0 \\ P & 0 & -I \end{bmatrix}$$

$$\Delta \Gamma_{\sigma(t)i} = \begin{bmatrix} \Delta \Gamma_{11} & E \Sigma(t) F_2 & 0 \\ F_2^T \Sigma(t)^T E^T & 0 & 0 \\ 0 & 0 & 0 \end{bmatrix}$$

with $\Delta \Gamma_{11} = P F_1^T \Sigma(t)^T E^T + E \Sigma(t) F_1 P + \lambda_{\sigma(t)i} Q^T F_3^T \Sigma(t)^T E^T + \lambda_{\sigma(t)i} E \Sigma(t) F_3 Q$. That is, model uncertainties are decoupled from the determined constant system matrices. Let $\xi = [\xi_1^T \xi_2^T \xi_3^T]^T$ be a nonzero vector. The inequality $\xi^T \Xi_{\sigma(t)i} \xi < 0$ holds if and only if

$$\begin{aligned} & \xi^T \Xi_{\sigma(t)i} \xi \\ &= \xi^T \Gamma_{\sigma(t)i} \xi + 2 \xi_1^T E \Sigma(t) [(F_1 P + \lambda_{\sigma(t)i} F_3 Q) \xi_1 + F_2 \xi_2] < 0 \end{aligned} \quad (18)$$

is satisfied for any $\Sigma^T(t) \Sigma(t) \leq I$. Actually, if one takes

$$\Sigma(t) = \frac{(E^T \xi_1) [(F_1 P + \lambda_{\sigma(t)i} F_3 Q) \xi_1 + F_2 \xi_2]^T}{\|E^T \xi_1\|_2 \|(F_1 P + \lambda_{\sigma(t)i} F_3 Q) \xi_1 + F_2 \xi_2\|_2}, \quad (19)$$

then $\xi^T \Xi_{\sigma(t)i} \xi$ reaches its maximum value. Therefore, (18) holds for any $\Sigma(t)$ satisfying $\Sigma^T(t) \Sigma(t) \leq I$ if and only if it holds when $\Sigma(t)$ is taken as (19). Instituting (19) into (18) leads to

$$\xi^T \Gamma_{\sigma(t)i} \xi + 2 \sqrt{\xi^T X \xi} \sqrt{\xi^T Z_{\sigma(t)i} \xi} < 0, \quad (20)$$

where

$$X = \begin{bmatrix} E E^T & 0 & 0 \\ 0 & 0 & 0 \\ 0 & 0 & 0 \end{bmatrix} \geq 0$$

$$Z_{\sigma(t)i} = \begin{bmatrix} Z_{11} & (F_1 P + \lambda_{\sigma(t)i} F_3 Q)^T F_2 & 0 \\ F_2^T (F_1 P + \lambda_{\sigma(t)i} F_3 Q) & F_2^T F_2 & 0 \\ 0 & 0 & 0 \end{bmatrix} \geq 0$$

$$Z_{11} = (F_1 P + \lambda_{\sigma(t)i} F_3 Q)^T (F_1 P + \lambda_{\sigma(t)i} F_3 Q). \quad (21)$$

Obviously, (20) is satisfied if and only if $\Gamma_{\sigma(t)i} < 0$ and

$$(\xi^T \Gamma_{\sigma(t)i} \xi)^2 - 4 \xi^T X \xi \xi^T Z_{\sigma(t)i} \xi > 0. \quad (22)$$

Using Lemma 2, we obtain that (22) holds if and only if there exists a scalar $\lambda > 0$ satisfying $\Gamma_{\sigma(t)i} + \lambda^2 X + \lambda^{-2} Z_{\sigma(t)i} < 0$. Inserting (21) into the above inequality results in

$$\Gamma_{\sigma(t)i} + S^T S < 0, \quad (23)$$

$$S = \begin{bmatrix} \lambda E^T & 0 & 0 \\ \lambda^{-1} (F_1 P + \lambda_{\sigma(t)i} F_3 Q) & \lambda^{-1} F_2 & 0 \end{bmatrix}.$$

According to Schur Complement Formula, the matrix inequality (23) becomes

$$\begin{bmatrix} \Gamma_{\sigma(t)i} & S^T \\ S & -I \end{bmatrix} < 0,$$

which is further equivalent to (17). Combining with Theorem 1, we know that if for a scalar $\lambda > 0$, there exist $P > 0$ and Q such that the LMI (17) holds for $\sigma(t)i = \sigma_*(t)i_*$ and $\sigma^*(t)i^*$, then the multi-agent system (1) with model uncertainties (2) achieves consensus with H_∞ index γ . Further, if the two LMIs are feasible, then $K = QP^{-1}$ is obtained. \square

IV. SIMULATION RESULTS

Consider a network of four agents, and the matrices in (2) and (3) are given by

$$A_0 = \begin{bmatrix} 0 & -1 \\ 2 & 1 \end{bmatrix}, B_{10} = \begin{bmatrix} 0 \\ 1 \end{bmatrix}, B_{20} = \begin{bmatrix} 1 & 0 \\ 0 & 2 \end{bmatrix},$$

$$E = \begin{bmatrix} 0 & 0 \\ 0.8 & 0.8 \end{bmatrix}, \Sigma(t) = \begin{bmatrix} \sin(10t) & 0 \\ 0 & 0 \end{bmatrix},$$

$$F_1 = \begin{bmatrix} 1.2 & 0 \\ 0 & 1.2 \end{bmatrix}, F_2 = \begin{bmatrix} 0.5 \\ 0.5 \end{bmatrix}, F_3 = \begin{bmatrix} 0.8 & 0 \\ 0 & 0.8 \end{bmatrix}.$$

The external disturbance is assumed to be band-limited white noise. The H_∞ performance index is chosen as $\gamma = 1$. For simplicity, the interaction graphs are constrained to be within the set shown in Fig. 1, whose nonzero weighting factors are all 1.

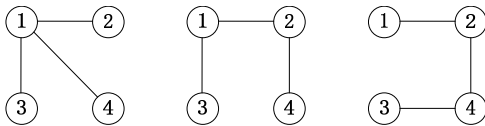


Fig. 1. Undirected interaction graphs.

Fig. 2 depicts the state trajectories of four agents $x_i(t) = [x_{i,1}(t) \ x_{i,2}(t)]^T$ under the proposed protocol (6). Fig. 3 gives the energy relationship between the controlled output $z(t)$ and the external disturbance $\omega(t)$. Obviously, the consensus is achieved with H_∞ disturbance attenuation index 1.

V. CONCLUSIONS

This paper has addressed the consensus control problem for switching networks of autonomous agents with both model uncertainties and external disturbances by robust H_∞ theory. Time delays arising in the information exchange among agents are not considered in this paper, and this will be a topic of future research.

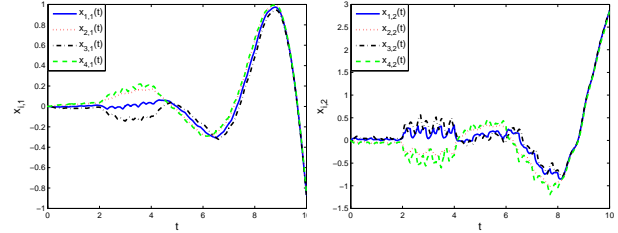


Fig. 2. Left: The first element of states. Right: The second element of states.

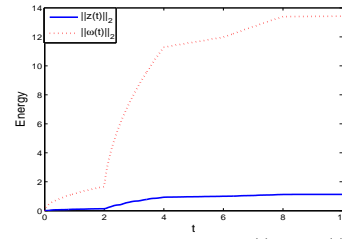


Fig. 3. Energy trajectories of $z(t)$ and $\omega(t)$.

ACKNOWLEDGMENTS

This work was supported by the Fundamental Research Funds for the Central Universities, the NSFC (60727002, 60774003, 60921001, 90916024), the MOE (20030006003), the COSTIND (A2120061303), the National 973 Program (2005CB321902).

REFERENCES

- [1] Xiao L., Boyd S. and Kim S. (2007), Distributed average consensus with least-mean-square deviation. *Journal of Parallel and Distributed Computing* 67(1): 33–46
- [2] Li T. and Zhang J. (2009), Mean square average-consensus under measurement noises and fixed topologies: Necessary and sufficient conditions. *Automatica* 45(8): 1929–1936
- [3] Li Z., Duan Z. and Huang L. (2009), H_∞ control of networked multi-agent systems. *Journal of Systems Science and Complexity* 22: 35–48
- [4] Lin P., Jia Y. and Li L. (2008), Distributed robust H_∞ consensus control in directed networks of agents with time-delay. *Systems and Control Letters* 57: 643–653
- [5] Liu Y. and Jia Y. (2010), H_∞ consensus control of multi-agent systems with switching topology: A dynamic output feedback protocol. *International Journal of Control* 83(3): 527–537
- [6] Liu Y. and Jia Y. (2010), Consensus problem of high-order multi-agent systems with external disturbances: An H_∞ analysis approach. *International Journal of Robust and Nonlinear Control* 20(14): 1579–1593
- [7] Jia Y. (2007), Robust H_∞ Control (in Chinese). Beijing: Science Press

Switching synchronization in a heterogeneous agent network

Lei Wang, Yang Liu and Qi-ye Zhang

*Laboratory of Mathematics, Information and Behavior of the Ministry of Education, Department of Systems and Control, Beihang University, Beijing 100191, P.R.China.
(Tel:010-82317934)*

Abstract: Motivated by the fact that many real-world networks exhibit a mixture feature of time-invariant and time-varying topologies, we propose a heterogeneous agent network as a simple representation. The presented network consists of two types of nodes: fixed agents and mobile agents, where the connections between fixed agents are constant, while the mobile agents, abstracted as random walkers in plane, interact with the neighboring agents. Under the assumption of fast-switching constraint, we further explore synchronized behavior in the heterogeneous network. The theoretical and numerical results show that the mobile agent density determines synchronization of the considered heterogeneous network. In particular, compared with the network constructed by the fixed agents, synchronizability is enhanced and a global synchronization appears by introducing a proper mobile agent density.

Keywords: Synchronization, switching topology, mobile agent networks.

I. INTRODUCTION

Synchronization in large-scale networks of coupled chaotic oscillators has been intensively investigated in recent years. It has been demonstrated that two or more chaotic oscillators can synchronize by mutual couplings among them, thus a particular interest in this concern is how the network topology influences the propensity of the coupled individuals to synchronize [1-2]. The master stability function (MSF) approach relates the stability of the fully synchronized state to the spectral properties of the underlying topological structure, and further provides a framework of analyzing the stability of synchronous state of large populations of identical oscillators [3]. Synchronizability of such a network is then explored based on the notions of MSF and synchronized region.

So far, most investigations have been established on static networks, partially because of a successful performance of the MSF approach in dealing with synchronization problems of static networks. Having examined a variety of network topologies in reality, the classical static network is very restrictive and only reflects a few practical situations. Then the case of connections which do evolve in time is more realistic to depict complex networks, and various synchronization results have been deduced for complex networks with switching topology [4-7]. Of particular interest is synchronization of a set of mobile agents. The mobile agent network, indeed, can be used to explore many problems such as clock synchronization in mobile robots [8], swarming animals or the appearance of synchronized bulk oscillations [9], consensus problem in multi-agent systems [10] and so on.

None of two cases above mentioned, i.e. static network model and mobile agent network model, however,

also seems to be an adequate description of many relevant phenomena. For instance, in social networks, lobby groups go about inducing voters whose attitudes are already interacted by a fixed relationship to elect a candidate or to give up an initial view, where the lobbies can be depicted by mobile agents, and static topology seems to be more suitable to characterize interactions between voters [11]; in communication systems, a mobile wireless network attaches the physical network by clock synchronization so that data is transmitted and processed [12]; and in volleyball, the libero as a mobile agent influences the whole team cohesion, while other players share relatively fixed connections. Roughly speaking, there are two types of nodes in all systems above mentioned, and the network corresponding to the system can be decomposed into a (relative) static subnetwork and a switching subnetwork due to the heterogeneity of nodes. Then there appears a question: Is synchronization of the heterogeneous network easier to achieve or not under the existence of mobile agents. There is no doubt, lobbies in social networks, mobile wireless sensors, or volleyball libero player, seem to work as the role of pinned nodes — guiding their neighbor nodes towards the desired objective — in synchronizing a complex network of coupled systems through pinning. This paper is an attempt to explore synchronized behavior based on a heterogeneous agent network model. In this paper, we present a heterogeneous agent network model to characterize a mixture feature of real-world network. Under fast-switching constraints, we investigate the synchronization problem of the heterogeneous agent network. Particularly, we focus on the effect of mobile agents to synchronization of the static network, which provides an insight into regulatory mechanisms and design of complex systems.

II. A HETEROGENEOUS AGENT NETWORK MODEL

Generally, a complex network consisting of l linearly and diffusively coupled nodes is described by

$$\dot{\mathbf{x}}_i = \mathbf{f}(\mathbf{x}_i) - \sigma \sum_{j=1}^l G_{ij}^s H \mathbf{x}_j, \quad i = 1, 2, \dots, l, \quad (1)$$

where $\mathbf{x}_i = (x_{i1}, x_{i2}, \dots, x_{in})^T \in \mathbb{R}^n$ is the state vector of node i , $\mathbf{f}(\cdot) : \mathbb{R}^n \rightarrow \mathbb{R}^n$ is a smooth vector-valued function, governing the dynamics of each isolated node, $\sigma > 0$ is the overall coupling strength, $H \in \mathbb{R}^{n \times n}$ is the inner linking matrix, and the coupling matrix $G^s = (G_{ij}^s) \in \mathbb{R}^{l \times l}$ is a zero-row sum matrix, describing network topology. If network (1) is connected in the sense of having no isolated clusters and edges signify the bidirectional ability, then G^s is symmetric and all its eigenvalues are ranked as $0 = \mu_1 < \mu_2 \leq \dots \leq \mu_l$, where eigenratio $R^s = \mu_l / \mu_2$ is used to measure network synchronizability.

To obtain a heterogeneous agent network, we first assign the l nodes in network (1) to be fixed agents. For simplicity, we denote by \mathcal{N}_l the set of fixed agents, and all agents in \mathcal{N}_l are uniformly distributed in a two-dimensional space of size L with periodic boundary conditions. Moreover, we introduce m mobile agents to the plane, each of which is considered as a random walker whose position and orientation are updated according to

$$\begin{cases} \mathbf{y}_i(t + \Delta t) = \mathbf{y}_i(t) + \mathbf{v}_i(t) \Delta t, \\ \theta_i(t + \Delta t) = \eta_i(t + \Delta t), \end{cases} \quad (2)$$

where $i \in \mathcal{N}_m$, \mathcal{N}_m is the set of mobile agents, $\mathbf{y}_i(t)$ is the position of agent i in the plane at time t , $\eta_i(t)$, $i \in \mathcal{N}_m$ are independent random variables chosen at each time unit with uniform probability from the interval $[-\pi, \pi]$, $\mathbf{v}_i(t)$ is the velocity of agent i , and Δt is the time unit. In the following, assume that the time unit is sufficiently small so that fast-switching synchronization is guaranteed. Similar to Ref.[5], each agent of the heterogeneous network is associated with a chaotic oscillator whose state variable is characterized by $\mathbf{x}_i \in \mathbb{R}^n$. Then agent i evolves according to $\dot{\mathbf{x}}_i = \mathbf{f}(\mathbf{x}_i)$. Without lack of generality, we consider the case of Rössler oscillators, where the state dynamics of each agent is given by $\dot{x}_{i1} = -(x_{i2} + x_{i3})$, $\dot{x}_{i2} = x_{i1} + ax_{i2}$, $\dot{x}_{i3} = b + x_{i3}(x_{i1} - c)$ with $\mathbf{x}_i = (x_{i1}, x_{i2}, x_{i3})^T$, and $a = 0.2$, $b = 0.2$, $c = 7$.

It is obvious that, the heterogeneous agent network of order N can be conveniently described by graph $\mathcal{G} = \{\mathcal{N}, \mathcal{E}\}$, where $\mathcal{N} = \mathcal{N}_l \cup \mathcal{N}_m$ is the node set (representing N agents) and $\mathcal{E} \subset \mathcal{N} \times \mathcal{N}$ is the edge set of the graph, which is defined as: Each mobile agent, $i \in \mathcal{N}_m$, interacts at a given time with only those agents located within a neighborhood of an interaction radius according to the rule of moving neighborhood network. In detail, agents i and j are said to be adjacent if and only if

$$|\mathbf{y}_i(t) - \mathbf{y}_j(t)| < r, \quad \forall i \in \mathcal{N}_m, j \in \mathcal{N} \quad (3)$$

at time t , where r is a parameter that defines the size of a neighborhood, $|\cdot|$ refers to an induced norm. For any two fixed agents, denoted by $i, j \in \mathcal{N}_l$, the connection between them is a constant, i.e., $G_{ij} = G_{ij}^s$. In other words, the constant matrix G^s describes the topology of network $\mathcal{G}_l = \{\mathcal{N}_l, \mathcal{E}\}$. Hence, we construct a heterogeneous agent network by combining fixed and mobile agents, chaotic oscillators and their dynamical laws, where the heterogeneous couplings include the time-invariant connections between nodes in \mathcal{N}_l and the switching connections due to the moving of agents.

Based on above assumptions, the heterogeneous network can be mathematically formulated as:

$$\dot{\mathbf{x}}_i = \mathbf{f}(\mathbf{x}_i) - \sigma \sum_{j=1}^N G_{ij}(t) H \mathbf{x}_j, \quad i \in \mathcal{N}, \quad (4)$$

where the entries of the coupling matrix $G(t) = (G_{ij}(t)) \in \mathbb{R}^{N \times N}$ are as follows: for non-diagonal entries, $G_{ij}(t) = G_{ij}^s$ if $i, j \in \mathcal{N}_l$, and $G_{ij}(t) = G_{ji}(t) = -1$ if agent $i \in \mathcal{N}_m$ or agent $j \in \mathcal{N}_m$ are adjacent at time t ; and the diagonal entries satisfy $G_{ii}(t) = -\sum_{j=1, j \neq i}^N G_{ij}(t)$. Thus there exists a completely synchronized state in network (4), i.e., $\mathbf{x}_1(t) = \mathbf{x}_2(t) = \dots = \mathbf{x}_N(t) = \mathbf{s}(t)$, which is a solution of an isolated node $\dot{\mathbf{s}} = \mathbf{f}(\mathbf{s})$.

III. ANALYSIS OF SWITCHING SYNCHRONIZATION

This section investigates the synchronized behavior of the heterogeneous network under the constraint of fast-switching. As shown in Ref.[4], Stilwell et al. consider a switching network topology of coupled chaotic oscillators and provide a fast-switching synchronization criterion. Following this result, we will show that synchronization of network (4) can be also assessed by a particular static network.

We first give an average of $G(t)$ for network (4). Consider an infinite sequence of contiguous time intervals $[t_k, t_{k+1})$, $k = 0, 1, \dots$, with $t_0 = 0$ and $t_{k+1} - t_k = \Delta t$. It is easy to see that $G(t)$ is a constant matrix for any $t \in [t_k, t_{k+1})$ and $k = 0, 1, \dots$. For simplicity, let G^k be the constant coupling matrix at k -th interval $[t_k, t_{k+1})$, then we derive the average of coupling matrix $G(t)$ satisfying

$$\bar{G} = \sum_{i=1}^o p_i G^i, \quad (5)$$

where p_i is the probability that topological configuration i occurs, o is the number of possible configurations.

Recalling the evolution of network (4), we learn that the connections between any fixed agents are time-invariant, i.e., $\bar{G}_{ij} = G_{ij}(t) = G_{ij}^s$, $\forall i, j \in \mathcal{N}_l$. And for other cases, $\bar{G}_{ij} = \sum_{i=1}^m p_i G_{ij}^i$, $i \in \mathcal{N}_m$ or $j \in \mathcal{N}_m$. Therefore, we write down the non-diagonal entries of \bar{G} for network (4):

$$\bar{G}_{ij} = \begin{cases} G_{ij}^s, & \text{if } i, j \in \mathcal{N}_l \\ -p, & \text{otherwise} \end{cases} \quad (6)$$

where $p = \pi r^2 / L^2$ is the probability that two agents are neighbors, I_l is an $l \times l$ identity matrix. By elementary transformation, we calculate the N eigenvalues of the average Laplacian \bar{G} as

$$\lambda_i = \left\{ 0, \mu_j + mp, \underbrace{pN, \dots, pN}_m, j = 2, \dots, l \right\}. \quad (7)$$

Note that \bar{G} is a symmetric constant matrix, then synchronization of switching network (4) can be investigated by the network reading

$$\dot{\mathbf{x}}_i = \mathbf{f}(\mathbf{x}_i) - \sigma \sum_{j=1}^N \bar{G}_{ij} H \mathbf{x}_j. \quad (8)$$

Let \mathbf{e}_i be the variation on the i -th node and $\mathbf{e} = (\mathbf{e}_1^T, \mathbf{e}_2^T, \dots, \mathbf{e}_N^T)^T$ be the collection of variations. Then linearizing network (8) at $\mathbf{x}_i = \mathbf{s}$ yields $\dot{\mathbf{e}} = [I_N \otimes \mathbf{J}_f(\mathbf{s}) - \sigma \bar{G} \otimes H] \mathbf{e}$, where \mathbf{J}_f is the Jacobian of the function \mathbf{f} evaluated at $\mathbf{s}(t)$, and \otimes stands for the Kronecker product. It is easy to verify that the linear stability of the synchronized state $\mathbf{s}(t)$ for network (8) can be studied by diagonalizing the variational equations of network (8) into N blocks of the form

$$\dot{\xi}_i = (\mathbf{J}_f - \sigma \lambda_i H) \xi_i, \quad i = 1, \dots, N, \quad (9)$$

where $\xi_i = (U \otimes I_n) \mathbf{e}_i \in \mathbb{R}^n$, $U \in \mathbb{R}^{N \times N}$ is a unitary matrix such that $U^T \bar{G} U = \text{diag}(\lambda_1, \dots, \lambda_N)$. Furthermore, the synchronized state $\mathbf{s}(t)$ is stable if the Lyapunov exponents for the N blocks are negative i.e., $\Gamma(\sigma \mu_i) < 0$ for $i = 2, \dots, N$. For the coupled Rössler oscillator with $H = \text{diag}(1, 0, 0)$, there is a single interval (γ_1, γ_2) , in which the largest Lyapunov exponent is negative, where γ_1 and γ_2 are constant. Therefore, synchronization of network (4) can be guaranteed by

$$\frac{\gamma_1}{\sigma} < \lambda_2 < \lambda_N < \frac{\gamma_2}{\sigma}, \quad (10)$$

where λ_2 and λ_N are the second smallest and largest eigenvalues of matrix \bar{G} , respectively. Based on Eq.(7) and Eq.(10), we thus derive the synchronization condition for the heterogeneous network.

IV. DISCUSSIONS AND NUMERICAL SIMULATIONS

The existence of mobile agents affects the eigenvalues of \bar{G} , which further plays an important role in synchronizing network (4). It is noted that Eq.(10) is fulfilled for some values of σ when the eigenratio R satisfies the following inequality $R \equiv \frac{\lambda_N}{\lambda_2} < \frac{\gamma_2}{\gamma_1}$. We then characterize, similarly to the definition in static network, the synchronizability of network (4) with R .

Compared with the static network (1), the heterogeneous network (4) shows a better synchronizability if $R < R^s$. By solving this inequality, we derive $\rho_m > \rho_m^c$, where ρ_m^c is a critical value of ρ_m satisfying

$$\rho_m^c = \frac{R^s}{R^s - 1} \cdot \max\left\{0, \frac{\mu_2}{\kappa \rho_l} - 1, \frac{1}{R^s} - \frac{\mu_2}{\kappa \rho_l}\right\}, \quad (11)$$

$\rho_l = l/L^2$ is the fixed agent density and $\rho_m = m/L^2$ is the mobile agent density. Namely, a smaller ρ_m probably means the heterogeneous network (4) is harder to achieve synchronization from the point of view of the interval width in Eq.(10), while synchronization is probably easier to realize by assigning a larger mobile agent density.

Though a larger mobile agent density ρ_m means a better synchronizability of network (4), it is likely to lead to the largest eigenvalue of \bar{G} over the upper bound in Eq.(10). And synchronization is lost with a large mobile agent density for a particular heterogeneous network. According to Eq.(10), an upper bound of ρ_m is given by

$$\rho_m < \rho_m^u = \frac{\gamma_2}{\sigma \kappa} - \max\left\{\rho_l, \frac{\mu_l}{\kappa}\right\}. \quad (12)$$

An obvious result is that, no matter what value of ρ_m is, the heterogeneous network (4) is not synchronizable about synchronized state in the condition of $\mu_l > \gamma_2/\sigma$, where the expression $\mu_l > \gamma_2/\sigma$ implies a nonsynchronized motion of static network (1). It is not difficult to see the existence of mobile agents fails to synchronize the considered heterogeneous network. As a result, we favor the introduction of mobile agents for those static networks (1) whose eigencoupling $\sigma \mu_l$ is located in the negative region of the MSF. In the following, we always assume that $\sigma \mu_l < \gamma_2$ holds.

Similarly, we derive a lower bound of mobile agent density from Eq.(10), i.e.,

$$\rho_m > \rho_m^l = \frac{\gamma_1}{\sigma \kappa} - \min\left\{\rho_l, \frac{\mu_2}{\kappa}\right\}. \quad (13)$$

To validate our theoretical findings, we consider the static network G^s to be the case of a Barabási-Albert (BA) network [13], where the parameters of BA model are given by $m_0 = m = 3$, and the degree distribution follows a power law. Fig.1 reports a numerical simulation, where synchronization error $\delta x(t) = (\sum_{i=2}^N \|\mathbf{x}_i - \mathbf{x}_1\|)/N$. As explained in Fig.1, the considered network achieves synchronization again when $\rho_m > 0.2$. Also notice that a synchronized motion disappears as $\rho_m > 0.5$ due to the bounded synchronization region.

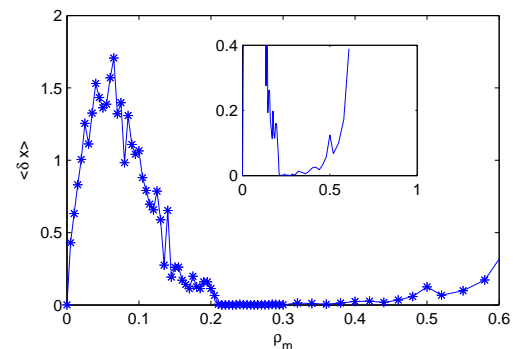


Fig.1. Synchronization index $\langle \delta x \rangle$ vs mobile agent density ρ_m .

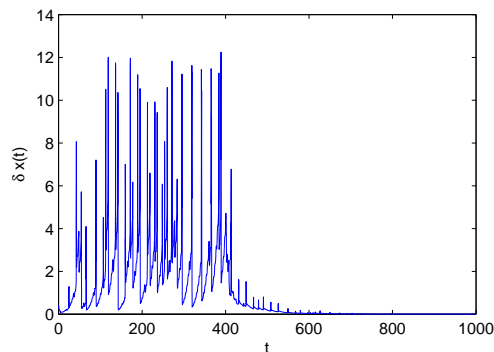


Fig.2. Synchronization index $\langle \delta x \rangle$ vs mobile agent density ρ_m .

Under the other case $\sigma\mu_2 < \gamma_1$, it has been shown by MSF that static network (1) cannot synchronize. However, synchronization can be easily realized by introducing some, even only one mobile agent to network (1) according to Eq.(13). A numerical example is given in Fig.2 to validate the analytical result, where μ_2 is assigned to be zero. It is obvious that \mathcal{G}_l is an unconnected graph, then a global synchronization of static network (1) cannot be accessed due to isolated clusters in \mathcal{G}_l . We observe from Fig.2 that adding several mobile agents (in simulations, five mobile agents are introduced to network at $t = 400s$) can guarantee network synchronization. The role of mobile agents works as a bridge which creates connections among different isolated clusters.

From above discussions, there does exist a bounded region of mobile agent density: synchronization of network (4) is ensured if and only if $\rho_m \in (\rho_m^l, \rho_m^u)$. For a particular static network (1) with given G^s and ρ_m , a too large or a too small mobile agent density will prevent heterogeneous network (4) from achieving synchronization.

V. CONCLUSIONS

In this paper, we propose a heterogeneous agent network to capture a mixture feature of time-invariant and time-varying topologies existing in many real-world complex network. The heterogeneous network consists of a certain number of mobile agents and fixed agents, each of which is equipped with a chaotic oscillator in a planar space. In particular, the connections between fixed agents are assigned to be time-invariant, and the mobile agents, abstracted as random walkers, interact with the neighboring agents. Then the heterogeneous agent network can be simply regarded as a mixture of a static subnetwork and a switching subnetwork. Under the constraint of fast-switching, we theoretically and numerically show that synchronization of the heterogeneous network depends on the mobile agent density, the fixed agent density and the spectrum of time-invariant subnetwork. For a given heterogeneous network, synchronization motion can be established if mobile agent density of the network lies in an bounded interval, in

which its two end-points are determined by the fixed agent density and the static topology. It is worth noting that, compared with the static network, synchronizability can be enhanced when a proper density of mobile agents is introduced to the heterogeneous network. All these results may provide some insights for the future theoretical investigations and practical engineering designs.

VI. ACKNOWLEDGMENTS

This work is supported by the Fundamental Research Funds for the Central Universities, the National Natural Science Foundation of China No. 61004106.

REFERENCES

- [1] S. Boccaletti, V. Latora, Y. Moreno, M. Chavez and D.-U. Hwang, "Complex networks: Structure and dynamics," *Phys. Rep.*, Vol. 424, pp. 175-308, 2006.
- [2] A. Arenas, A. Díaz-Guilera, J. Kurths, Y. Moreno and C. S. Zhou, "Synchronization in complex networks," *Phys. Rep.*, Vol. 469, pp. 93-153, 2008.
- [3] L. M. Pecora and T. L. Carroll, "Master stability functions for synchronized coupled systems," *Phys. Rev. Lett.* Vol. 80, pp. 2109, 1998.
- [4] D. J. Stilwell, E. M. Bollt and D. G. Roberson, "Sufficient conditions for fast switching synchronization in time varying network topologies," *SIAM J. Appl. Dyn. Syst.*, Vol. 5, pp. 140-156, 2006.
- [5] M. Frasca, A. Buscarino, A. Rizzo, L. Fortuna, and S. Boccaletti, "Synchronization of moving chaotic agents," *Phys. Rev. Lett.*, Vol. 100, pp. 044102, 2008.
- [6] J. Zhao, D. J. Hill, T. Liu, "Synchronization of complex dynamical networks with switching topology: a switched system point of view," *Automatica*, Vol. 45, pp. 2502-2511, 2009.
- [7] L. Wang, H. Shi, Y. X. Sun, "Power adaptation for a mobile agent network," *Europhys. Lett.*, Vol. 90, pp. 1001, 2010.
- [8] A. Buscarino, L. Fortuna, M. Frasca, and A. Rizzo, "Dynamical Network Interactions In. Distributed Control Of Robots," *Chaos*, Vol. 16, pp. 015116, 2006.
- [9] S. DanóS, P. G. Sórensen, and F. Hynne, "Sustained oscillations in living cells," *Nature*, Vol. 402, pp. 320-322, 1999.
- [10] Y. Hong, L. Gao, D. Cheng, and J. Hu, "Lyapunov-based approach to multiagent systems with switching jointly connected interconnection," *IEEE Trans. on Automatic Control*, Vol. 52, pp. 943-948, 2007.
- [11] F. Amblard and G. Deffuant, "The role of network topology on extremism propagation with the relative agreement opinion dynamics," *Physica A*, Vol. 343, pp. 725-738, 2004.
- [12] H. Karl, and A. Willig, *Protocols and Architectures for Wireless Sensor Networks* John Wiley & Sons, Inc, New York, 2005.
- [13] Barabási A L, and Albert R, "Emergence of scaling in random networks," *Science*, Vol. 286, pp. 509-512, 1999.

Model Matching Adaptive Control of Time Delay Systems with Unknown Relative Degree

Haixia Su and Yingmin Jia

*The Seventh Research Division and the Department of Systems and Control, Beihang University (BUAA),
Beijing 100191, China*

*(Tel : +86-10-82317661; Fax : +86-10-82316100)
(haixsu@yahoo.cn, ymjia@buaa.edu.cn)*

Abstract: This paper considers the adaptive control problem of time delay systems with unknown relative degree based on model matching technique. For single-input single-output (SISO) systems, the only known knowledge of the relative degree is the upper bound of it. An adaptive control scheme is designed so that all signals in the close-loop systems are bounded and the tracking error can converge to zero. A simulation example is included to illustrate the proposed adaptive control scheme.

Keywords: Model matching control; adaptive control; time delay; unknown relative degree

I. INTRODUCTION

Time delay exists in many industrial control systems such as chemical process systems, hydraulically actuated systems and combustion systems. Researches have paid much attention to the control of time delay systems since last century. Stability analysis and controller design for delay systems are more difficult than delay-free systems. Many methods have been proposed to deal with time delay systems. The known smith predictor proposed in [1] could cancel the time delay from the characteristic equation of the closed-loop systems. The finite spectrum assignment method in [6] could assign the eigenvalues of the closed-loop plant at arbitrary prescribed place of the complex plane. However, the two methods are difficult to be applied to adaptive control.

Model matching technique can be easily used to adaptive control scheme design. This technique is to design a controller so that the transfer function of the closed-loop plant coincides exactly with the transfer function of the reference model. Controller design for linear systems based on model matching technique can be found in the book [5]. This method was used to controller design for SISO delay systems in [2]. Then the result was extended to adaptive control in [3]. For multivariable delay systems, a general solution of model

matching control of multiple-output-delay systems was given in [4]. However, only unknown parameter uncertainty was considered in [3-4]. In this paper, we will consider the adaptive control of time delay systems with unknown relative degree.

A strict assumption is that the relative degree is exactly known in the adaptive control literature. This assumption was relaxed in [7] for plants with relative degree n^* satisfying $1 \leq n^* \leq 3$. A new model reference adaptive control (MRAC) scheme was proposed in [8]. Where the control required only the known upper bound of the relative degree, this result was obtained at the expense of additional complexity in the control and adaptive laws. However, to the best of our knowledge, there is few results about time delay systems with unknown relative degree yet. In this paper, a class of SISO delay systems with unknown relative degree is considered. An adaptive control scheme is designed using the model matching technique.

This paper is organized as follows. Section 2 is problem statement. In section 3, an adaptive control scheme is designed for SISO delay systems and the stability analysis is completed. A simulation example is given in section 4 to illustrate the designed scheme. The last section is a conclusion of this paper.

II. PROBLEM STATEMENT

Consider the SISO linear time-invariant time delay systems

$$y(s) = \frac{gr(s)}{p(s)} e^{-Ls} u(s) \quad (1)$$

This work was supported by the NSFC (60727002, 60774003, 60921001, 90916024), the MOD (20030006 003), the COSTIND (A2120061303), the National 973 program (2005CB321902).

Where $y(t)$ and $u(t)$ are the output and the input, respectively. g is the gain, L is the known time delay. $r(s)$ and $p(s)$ are monic polynomials with degree m and n respectively, denote $\partial[r(s)] = m$, $\partial[p(s)] = n$, where

m and n are unknown constants. The following assumptions are made for the plant (1).

Assumption 1: $r(s)$ is a Hurwitz polynomial.

Assumption 2: The upper bound \bar{n} of the unknown degree n of $p(s)$ is known, i.e. $n \leq \bar{n}$.

Assumption 3: The relative degree n^* satisfies $1 \leq n_l^* \leq n^* \leq n_u^*$, where n_l^* and n_u^* are known constants.

The reference model is chosen to be

$$y_d(s) = \frac{g_d r_d(s)}{p_d(s)} e^{-Ls} v(s) \quad (2)$$

Where $p_d(s)$ is a stable polynomial, its degree is \bar{n} , the relative degree of the reference model satisfies $\partial[p_d(s)] - \partial[r_d(s)] \geq n_l^*$. The reference input $v(t)$ is a uniform bounded piecewise continuous signal. The objective is to design an adaptive control scheme so that all signals in the closed-loop systems are bounded and the plant output tracks the reference model output as close as possible for any given reference input.

III. ADAPTIVE CONTROL DESIGN

First, we design the model matching controller structure for the systems (1). The controller design procedure is different from that the known relative degree case.

Choose monic stable polynomials $r^*(s)$ and $p^*(s)$, $\partial[p^*(s)] = \bar{n}$, $\partial[r^*(s)] = \bar{n} - n_l^*$. Then the reference model can be rewritten as

$$y_d(s) = \frac{r^*(s)}{p^*(s)} e^{-Ls} \frac{g_d r_d(s) p^*(s)}{p_d(s) r^*(s)} v \quad (3)$$

Denote

$$\bar{v} = \frac{g_d r_d(s) p^*(s)}{p_d(s) r^*(s)} v \quad (4)$$

Obviously, \bar{v} is a realizable dynamical input signal.

When both $r^*(s)$ and $p(s)$ have single or distinct roots, write

$$\frac{r^*(s)p(s) - gr(s)p^*(s)}{r^*(s)p(s)} = \sum_{i=1}^{\bar{n}-n_l^*+n} \frac{\beta_i}{s-z_i} + 1 - \bar{g} \quad (5)$$

where z_i are roots of $r^*(s)$ for $k=1, 2, \dots, \bar{n}-n_l^*$ and roots of $p(s)$ for $k=\bar{n}-n_l^*+1, \dots, \bar{n}-n_l^*+n$, respectively. Obviously, we have

$$\bar{g} = \begin{cases} g & n^* = n_l^* \\ 0 & n_l^* < n^* \leq n_u^* \end{cases} \quad (6)$$

Define the polynomial $\phi(s)$ satisfying the equation

$$\frac{r^*(s)p(s) - \phi(s)}{r^*(s)p(s)} = \sum_{i=1}^{\bar{n}-n_l^*+n} \frac{\beta_i e^{z_i L}}{s-z_i} + 1 - \bar{g} \quad (7)$$

Remark 1: In order to employ the precompensator in (7)

$$\frac{r^*(s)p(s) - gr(s)p^*(s)}{r^*(s)p(s)} \quad (8)$$

should satisfy

$$\partial[r^*(s)] + \partial[p(s)] \geq \partial[r(s)] + \partial[p^*(s)] \quad (9)$$

i.e.

$$\begin{aligned} \partial[r^*(s)] &\geq \partial[p^*(s)] - \partial[p(s)] + \partial[r(s)] \\ &\geq \bar{n} - n^* \\ &\geq \bar{n} - n_l^* \end{aligned} \quad (10)$$

Therefore, the monic stable polynomial $r^*(s)$ should be chosen as $\partial[r^*(s)] \geq \bar{n} - n_l^*$. In this paper, we choose $\partial[r^*(s)] = \bar{n} - n_l^*$.

Define a polynomial equation by

$$k(s)p(s) + gh(s)r(s) = \bar{g}r^*(s)p(s) - \phi(s) \quad (11)$$

where $k(s)$ and $h(s)$ are unknown polynomials.

Theorem 1. There are solutions $k(s)$ and $h(s)$ for the polynomial equation (11) with degrees $\partial[k(s)] \leq \bar{n} - n_l^* - 1$ and $\partial[h(s)] \leq \bar{n} - 1$.

Proof. From the equation (7), $\bar{g}r^*(s)p(s) - \phi(s)$ is of degree at most $\bar{n} - n_l^* + n - 1$. It is known that there are unique polynomial solutions $k(s)$ and $h(s)$. $k(s)$ of degree at most $\bar{n} - n_l^* - 1$, polynomial $h(s)$ of degree at most $n - 1$. However, the degree n of $p(s)$ is not known, the only knowledge of it is $n \leq \bar{n}$. Therefore, $h(s)$ is of degree at most $\bar{n} - 1$. The proof is completed.

Using the equations (5) and (7), we have the following integral

$$\begin{aligned} &\int_{-L}^0 \sum_{i=1}^{\bar{n}-n_l^*+n} \beta_i e^{-\sigma z_i} u(s) e^{\sigma s} d\sigma \\ &= \sum_{i=1}^{\bar{n}-n_l^*+n} \frac{\beta_i}{s-z_i} u(s) - \sum_{i=1}^{\bar{n}-n_l^*+n} \frac{\beta_i e^{Lz_i}}{s-z_i} u(s) e^{-Ls} \\ &= -\frac{gr(s)p^*(s)}{r^*(s)p(s)} u(s) + \bar{g}u(s) + \frac{\phi(s)}{r^*(s)p(s)} u(s) e^{-Ls} \\ &\quad - \bar{g}u(s) e^{-Ls} \end{aligned} \quad (2)$$

Using the equation (11), the above equation (12) can be rewritten as

$$\int_{-L}^0 \sum_{i=1}^{\bar{n}-n_l^*+n} \beta_i e^{-\sigma z_i} u(s) e^{\sigma s} d\sigma$$

$$= -\frac{gr(s)p^*(s)}{r^*(s)p(s)}u(s) - \frac{k(s)}{r^*(s)}u(s)e^{-Ls} - \frac{h(s)}{r^*(s)}y(s) + \bar{g}u(s) \quad (13)$$

Another delay compensator is needed to design the controller. Choose any monic stable polynomial $\bar{r}(s)$ with degree $\partial[\bar{r}(s)] = \partial[r^*(s)] = \bar{n} - n_l^*$, then we have

$$-\frac{g\bar{r}(s)}{r^*(s)} = -g + \sum_{i=1}^{\bar{n}-n_l^*} \frac{\bar{\beta}_i}{s-z_i} \quad (14)$$

Define the polynomial $\bar{\phi}(s)$ by

$$-\frac{\bar{\phi}(s)}{r^*(s)} = -g + \sum_{i=1}^{\bar{n}-n_l^*} \frac{\bar{\beta}_i e^{z_i L}}{s-z_i} \quad (15)$$

Using the equations (14) and (15), we can obtain another integral

$$\begin{aligned} & \int_{-L}^0 \sum_{i=1}^{\bar{n}-n_l^*} \bar{\beta}_i e^{-\sigma z_i} u(s) e^{\sigma s} d\sigma \\ &= -\frac{g\bar{r}(s)}{r^*(s)}u(s) + gu(s) + \frac{\bar{\phi}(s)}{r^*(s)}u(s)e^{-Ls} - gu(s)e^{-Ls} \end{aligned} \quad (16)$$

Combining the two integrals in the equation (13) and (16) yields

$$\begin{aligned} & \int_{-L}^0 \sum_{i=1}^{\bar{n}-n_l^*+n} \beta_i e^{-\sigma z_i} u(s) e^{\sigma s} d\sigma + \int_{-L}^0 \sum_{i=1}^{\bar{n}-n_l^*} \bar{\beta}_i e^{-\sigma z_i} u(s) e^{\sigma s} d\sigma \\ &= -\frac{gr(s)p^*(s)}{r^*(s)p(s)}u(s) - \frac{k(s)}{r^*(s)}u(s)e^{-Ls} \\ & - \frac{h(s)}{r^*(s)}y(s) - \frac{g\bar{r}(s)}{r^*(s)}u(s) + \frac{\bar{\phi}(s)}{r^*(s)}u(s)e^{-Ls} \\ & + \bar{g}u(s) + gu(s) - gu(s)e^{-Ls} \end{aligned} \quad (17)$$

Therefore, we can choose the controller u as

$$\begin{aligned} u(s) &= \frac{1}{g} \left\{ \frac{k(s)}{r^*(s)}u(s)e^{-Ls} + \frac{h(s)}{r^*(s)}y(s) + \frac{g\bar{r}(s)}{r^*(s)}u(s) \right. \\ & - \frac{\bar{\phi}(s)}{r^*(s)}u(s)e^{-Ls} + \int_{-L}^0 \sum_{i=1}^{\bar{n}-n_l^*+n} \beta_i e^{-\sigma z_i} u(s) e^{\sigma s} d\sigma \\ & \left. + \int_{-L}^0 \sum_{i=1}^{\bar{n}-n_l^*} \bar{\beta}_i e^{-\sigma z_i} u(s) e^{\sigma s} d\sigma - \bar{g}u(s) \right. \\ & \left. + gu(s)e^{-Ls} + \bar{v}(s) \right\} \end{aligned} \quad (18)$$

Substituting the controller in the equation (18) into the equation (17), we can obtain

$$\frac{gr(s)p^*(s)}{r^*(s)p(s)}u(s) = \bar{v} \quad (19)$$

It is noting that the polynomials $p^*(s)$ and $r^*(s)$ are chosen to be stable polynomials. Therefore, the above equation (19) can be further rewritten as

$$\frac{gr(s)}{p(s)}e^{-Ls}u(s) = \frac{r^*(s)}{p^*(s)}e^{-Ls}\bar{v} \quad (20)$$

The system output is equal to the reference model output. Therefore, the controller in (18) is the desired controller. In time domain, the controller can be rewritten as

$$\begin{aligned} u(t) &= \frac{1}{g} \left\{ \frac{k(p)}{r^*(p)}u(t-L) + \frac{h(p)}{r^*(p)}y(t) + \frac{g\bar{r}(p)}{r^*(p)}u(t) \right. \\ & - \frac{\bar{\phi}(p)}{r^*(p)}u(t-L) + \int_{-L}^0 \sum_{i=1}^{\bar{n}-n_l^*+n} \beta_i e^{-\sigma z_i} u(t+\sigma) d\sigma \\ & \left. + \int_{-L}^0 \sum_{i=1}^{\bar{n}-n_l^*} \bar{\beta}_i e^{-\sigma z_i} u(t+\sigma) d\sigma - \bar{g}u(t) \right. \\ & \left. + gu(t-L) + \bar{v}(t) \right\} \end{aligned} \quad (21)$$

where p is the differential operator in time domain.

Because $\partial[\bar{\phi}(s)] \leq \bar{n} - n_l^*$, $\partial[k(s)] \leq \bar{n} - n_l^* - 1$, and

$\partial[h(s)] \leq \bar{n} - 1$. Thus, they can be written as

$$\begin{aligned} \bar{\phi}(s) &= q_{\bar{n}-n_l^*} s^{\bar{n}-n_l^*} + q_{\bar{n}-n_l^*-1} s^{\bar{n}-n_l^*-1} + \dots + q_0, \\ k(s) &= k_{\bar{n}-n_l^*-1} s^{\bar{n}-n_l^*-1} + k_{\bar{n}-n_l^*-2} s^{\bar{n}-n_l^*-2} + \dots + k_0, \end{aligned} \quad (22)$$

$$h(s) = h_{\bar{n}-1} s^{\bar{n}-1} + h_{\bar{n}-2} s^{\bar{n}-2} + \dots + h_0$$

respectively, where the coefficients of the polynomials are unknown constants. Define parameter vector

$$\begin{aligned} \theta &= \frac{1}{g} [k_{\bar{n}-n_l^*-1}, \dots, k_0, \dots, h_{\bar{n}-1}, \dots, h_0, \\ & q_{\bar{n}-n_l^*}, \dots, q_0, \bar{g}, g, 1]^T, \end{aligned} \quad (23)$$

$$\lambda = \sum_{i=1}^{\bar{n}-n_l^*+n} \beta_i e^{-\sigma z_i} + \sum_{i=1}^{\bar{n}-n_l^*} \bar{\beta}_i e^{-\sigma z_i}$$

and the signal vector

$$\begin{aligned} \omega(t) &= \left[\frac{p^{\bar{n}-n_l^*-1}}{r^*(p)}u(t-L), \dots, \frac{1}{r^*(p)}u(t-L), \frac{p^{\bar{n}-1}}{r^*(p)}y(t), \dots, \right. \\ & \frac{1}{r^*(p)}y(t), -\frac{p^{\bar{n}-n_l^*}}{r^*(p)}u(t-L), \dots, -\frac{1}{r^*(p)}u(t-L), \\ & \left. -u(t), \frac{\bar{r}(p)}{r^*(p)}u(t) + u(t-L), \bar{v}(t) \right]^T \end{aligned} \quad (24)$$

Then the controller (22) can be represented as

$$u(t) = \hat{\theta}^T(t)\omega(t) + \int_{-L}^0 \hat{\lambda}(t, \sigma)u(t+\sigma) d\sigma \quad (25)$$

where $\hat{\theta}(t), \hat{\lambda}(t, \sigma)$ are the estimates of the real parameters $\theta, \lambda(\sigma)$, respectively. Define the tracking error by

$$e(t) = y(t) - y_d(t) \quad (26)$$

Theorem 2. The tracking error can be represented by the following equation

$$\begin{aligned} e(t) &= g \frac{r^*(p)}{p^*(p)} q^{-L} \left\{ \tilde{\theta}^T(t)\omega(t) \right. \\ & \left. + \int_{-L}^0 \tilde{\lambda}(t, \sigma)u(t+\sigma) d\sigma \right\} \end{aligned} \quad (27)$$

where $\tilde{\theta}(t) = \hat{\theta}(t) - \theta$, $\tilde{\lambda}(t, \sigma) = \hat{\lambda}(t, \sigma) - \lambda(\sigma)$. q^{-L} denotes a time delay operator, $q^{-L}u(t) = u(t-L)$.

In order to design the adaptive law of the controller parameters, define a signal by

$$\eta = \left\{ \tilde{\theta}^T(t) \bar{\omega}(t) + \int_{-L}^0 \tilde{\lambda}(t, \sigma) \bar{u}(t + \sigma) d\sigma \right\} - \frac{r^*(p)}{p^*(p)} q^{-L} \left\{ \tilde{\theta}^T(t) \omega(t) + \int_{-L}^0 \tilde{\lambda}(t, \sigma) u(t + \sigma) d\sigma \right\} \quad (28)$$

where

$$\bar{\omega}(t) = \frac{r^*(p)}{p^*(p)} \omega(t-L), \quad \bar{u}(t) = \frac{r^*(p)}{p^*(p)} u(t-L) \quad (29)$$

The augmented error is defined by

$$\begin{aligned} \varepsilon(t) &= e(t) + \hat{g}(t) \eta(t) \\ &= g \left\{ \tilde{\theta}^T(t) \bar{\omega}(t) + \int_{-L}^0 \tilde{\lambda}(t, \sigma) \bar{u}(t + \sigma) d\sigma \right\} + \tilde{g}(t) \eta(t) \end{aligned} \quad (30)$$

Define a signal by

$$\Omega(t) = [\bar{\omega}(t), \sup_{-L \leq \sigma \leq 0} \bar{u}(t + \sigma), \eta(t)]^T \quad (31)$$

Choose the following adaptive law

$$\begin{aligned} \dot{\hat{g}}(t) &= -\alpha \frac{\eta(t)}{1 + \|\Omega(t)\|^2}, \\ \dot{\hat{\theta}}(t) &= -\beta \frac{\bar{\omega}(t)}{1 + \|\Omega(t)\|^2}, \\ \dot{\hat{\lambda}}(t, \sigma) &= -\gamma \frac{\bar{u}(t + \sigma)}{1 + \|\Omega(t)\|^2}, \quad -L \leq \sigma \leq 0, \end{aligned} \quad (32)$$

where α, β, γ are positive constant parameters to be chosen.

Theorem 3: The adaptive control scheme consists of the controller (25) and the adaptive law (32) designed for the plant (1), it can guarantee that all signals in the closed-loop plant are bounded and the tracking error converges to zero.

Proof. Without loss of generality, g is assumed to be positive. Consider a Lyapunov function

$$V(t) = \frac{1}{2\alpha} \tilde{g}^2(t) + \frac{g}{2\beta} \tilde{\theta}^T(t) \tilde{\theta}(t) + \frac{g}{2\gamma} \int_{-L}^0 \tilde{\lambda}^2(t, \sigma) d\sigma \quad (33)$$

The proof procedure is similar to the proof of the theorem 7 in [5]. Therefore, it is not detailed here.

IV. SIMULATION EXAMPLE

Consider a SISO time delay system in the form of (1), the known knowledge is $\bar{n} = 5$, $n_i^* = 1$, and $n_u^* = 3$. The reference model is chosen to be

$$t_d(s) = \frac{1}{s^5 + 9s^4 + 31s^3 + 51s^2 + 40s + 12} e^{-3s} \quad (34)$$

Choose the monic stable polynomials

$$\begin{aligned} p^*(s) &= s^5 + 10s^4 + 38s^3 + 68s^2 + 57s + 18, \\ r^*(s) &= s^4 + 10s^3 + 35s^2 + 50s + 24, \\ \bar{r}(s) &= s^4 + 3.6s^3 + 3.85s^2 + 1.35s + 0.1 \end{aligned} \quad (35)$$

When the plant model is

$$y(s) = \frac{2(s^2 + 4.5s + 2)}{s^4 + 8.5s^3 + 21.5s^2 + 21.5s + 7.5} e^{-3s} u(s) \quad (36)$$

When the reference input is the unit step signal, use the adaptive control scheme designed in this paper and the parameters $\alpha = \beta = \gamma = 2$, the simulation result is given in Figure 1. Figure 1 shows that the tracking error converges to zero. The designed adaptive control scheme achieves the control objective.

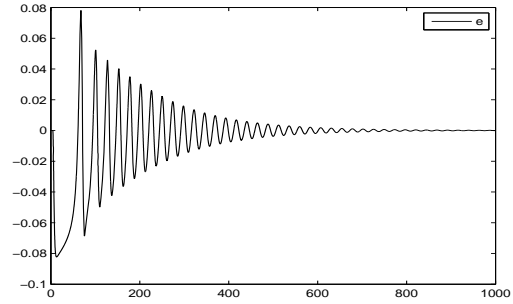


Figure 1. Tracking error of the system.

V. CONCLUSION

This paper design adaptive control schemes for delay systems with unknown relative degree. The schemes are obtained at the expense of updating more parameters than the case of known relative degree.

REFERENCES

- [1] Smith O (1957), Closer control of loops with dead time. Chemical Engineering Progress 53(5): 217-219
- [2] Ichikawa K (1985), Frequency-domain pole assignment and exact model matching for delay systems. International Journal of Control 41(4): 1015-1024
- [3] Ichikawa K (1986), Adaptive control of delay system. International Journal of Control 43(6): 1653-1659
- [4] Jia YM (2009), General solution to diagonal model matching control of multiple-output-delay systems and its applications in adaptive scheme. Progress in Natural Science 19: 79-90
- [5] Ichikawa K (1985), Control system design based on exact model matching techniques. Lecture Notes in Control and Information Sciences, Berlin: Springer.
- [6] Manitius AZ, Olbrot AW (1979), Finite spectrum assignment problem for systems with delays. IEEE Transactions on Automatic Control, 24:541-553.
- [7] Morse AS (1987), A 4(n+1)-dimensional model reference adaptive stabilizer for any relative degree one or two, minimum phase system of dimension n or less, Automatica 23(1): 123-125.
- [8] Tao G, Ioannou PA (1993), Model reference adaptive control for plants with unknown relative degree, IEEE Transactions on Automatic Control, 38, (6): 976-982.

Robust Active Suspension Control of Vehicles with Measurement Noises

Katsuhiko Okumura, Hideki Wada, Yuichiro Taira and Masahiro Oya

*Fukuoka Industrial Technology Center, 3-6-1 Norimatsu, Yahatanishi-ku, Kitakyushu-shi, Fukuoka, Japan
(Tel: +81-93-691-0260; Fax: +81-93-691-0252) (E-mail: kokumura@fitc.pref.fukuoka.jp)*

*Shin-Nippon Nondestructive Inspection Co., Japan, 4-10-13, Ibori, Kokurakita-ku, Kitakyushu-shi, Fukuoka, Japan
National Fisheries University, 2-7-1, Nagatahonmachi, Shimonoseki-shi, Yamaguchi, Japan
Kyushu Institute of Technology, 1-1 Sensui-cho, Tobata-ku, Kitakyushu-shi, Fukuoka, Japan*

Abstract: In this paper, we propose a robust ride comfort control scheme for vehicles without using measurements of tire deflections. To realize good ride comfort without using measurements of the tire deflections, we propose using an estimator for the acceleration of the road disturbance, the derivative of the suspension strokes and the derivatives of the displacements from the road disturbance to the vehicle body. Using the estimates, we can design a combined ideal vehicle. Then, a tracking controller is designed so that the real vehicle can track the motion of the combined ideal vehicle. Moreover, by carrying out numerical simulations, the influence of measurement disturbances on control performance will be investigated. As a result, it is shown that the proposed ride comfort control scheme is effective even in the presence of measurement disturbances.

Keywords: Vehicle, Ride comfort, Active suspension, Estimator, Robust Tracking Control, Ideal Model

I. INTRODUCTION

Recently, in order to achieve good ride comfort and good handling qualities, a large number of control schemes using active suspensions have been proposed in [1]-[4]. In conventional schemes [1]-[4], the active suspensions are controlled so that the suspension strokes lie within an admitted range and the handling quality does not become worse. As a result, the ride comfort will be best at only one specified location on the vehicle body. In cases when the specified location has to be moved, too much time is needed to redesign an active suspension controller. To struggle with this problem, the authors have proposed some active suspension control schemes [5]-[7]. In vehicle systems using controllers proposed in [5]-[7], the following good properties exist: (1) The ride comfort at a specified location will be best. (2) The best location can be easily moved by setting only one design parameter without redesigning the suspension controller. However, in the proposed schemes [5]-[7], it is assumed that the tire deflections can be measured. Since road surfaces are uneven, and using noncontact sensors such as laser position sensors, it is difficult to measure the tire deflections with high accuracy.

To overcome this problem, the authors have proposed a ride comfort control scheme without using the measurements of tire deflections [8],[9]. To realize good ride comfort without using measurements of the tire deflections, the signals are measured such as the vertical acceleration on the vehicle body, the displacement and the velocity of the suspension stroke, the vertical acceleration of the unsprung mass and the force added to the vehicle body. In addition, we propose using an estimator for the acceleration of the road disturbance and the deriva-

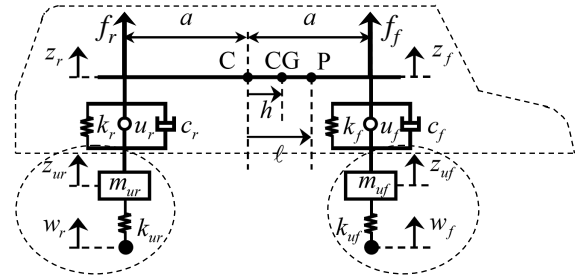


Fig. 1. Two wheels model.

tives of the displacements from the road disturbances to the vehicle body. In the papers [8],[9], however, the influence of measurement disturbances on control performance has not been considered. Moreover, it is assumed that the derivative of the suspension strokes can be rigorously measured.

In this paper, we propose an estimator for the acceleration of the road disturbance, the derivative of the suspension strokes and the derivatives of the displacements from the road disturbances to the vehicle body. A robust active suspension controller with the estimated signals is proposed. Moreover, carrying out numerical simulations, the influence of measurement disturbances on control performance is investigated. As a result, it is shown that the proposed ride comfort controller is very effective even in the presence of measurement disturbances.

II. VEHICLE MODEL

The two wheels model is shown in Fig. 1. The explanation for parameters is shown in Table 1. It is assumed that the pitching angle is small, and then, the dynamic

equation of vehicles is given as follows.

$$\left. \begin{aligned} \ddot{\mathbf{x}}_z(t) &= \mathbf{d}(t) - \mathbf{H}^{-1} \ddot{\mathbf{w}}(t) \\ \ddot{\mathbf{x}}_u(t) &= \mathbf{K}_u \mathbf{x}_u(t) - \mathbf{M}_u^{-1} \mathbf{f}(t) - \ddot{\mathbf{w}}(t) \\ \mathbf{x}_z(t) &= \mathbf{H}^{-1} [z_f(t) \quad w_f(t), z_r(t) \quad w_r(t)]^T \\ \mathbf{x}_u(t) &= [z_{uf}(t) \quad w_f(t), z_{ur}(t) \quad w_r(t)]^T \\ \mathbf{d}(t) &= \mathbf{M}^{-1} \mathbf{H}^T \mathbf{f}(t) \\ \mathbf{f}(t) &= [f_f(t), f_r(t)]^T \\ &= \mathbf{C} \dot{\mathbf{x}}_s(t) - \mathbf{K} \mathbf{x}_s(t) + \mathbf{u}(t) \end{aligned} \right\} (1)$$

$$\left. \begin{aligned} \mathbf{x}_s(t) &= \mathbf{H} \mathbf{x}_z(t) \quad \mathbf{x}_u(t) \\ \mathbf{u}(t) &= [u_f(t), u_r(t)]^T, \quad \mathbf{w}(t) = [w_f(t), w_r(t)]^T \\ \mathbf{M} &= (\mathbf{T}_h^T)^{-1} \text{diag}[m, i_c] \mathbf{T}_h^{-1} \\ \mathbf{M}_u &= \text{diag}[m_{uf}, m_{ur}], \mathbf{K} = \text{diag}[k_f, k_r] \\ \mathbf{C} &= \text{diag}[c_f, c_r], \mathbf{K}_u = \mathbf{M}_u^{-1} \text{diag}[k_{uf}, k_{ur}] \\ \mathbf{T}_h &= \mathbf{I}_2 \quad D\mathbf{h}, \mathbf{H} = \begin{bmatrix} 1 & a \\ 1 & a \end{bmatrix}, \mathbf{D} = \begin{bmatrix} 0 & 1 \\ 0 & 0 \end{bmatrix} \end{aligned} \right\} (2)$$

The control objective is to develop an active suspension controller so that the ride comfort at a specified location becomes best. In general, humans feel uncomfortable in the vertical oscillation with the frequency about 1 Hz. Therefore, to achieve the control objective, we develop a controller so that the vertical acceleration can be reduced to a small value at any specified location ℓ on the vehicle body. To meet the objective, the following assumptions are made for actual vehicles.

- A1 The accelerations $\ddot{z}_f(t)$, $\ddot{z}_r(t)$, $\ddot{z}_{uf}(t)$ and $\ddot{z}_{ur}(t)$ are measured.
- A2 The force $\mathbf{f}(t) = [f_f(t), f_r(t)]^T$ added to the sprung mass are measured.
- A3 Suspension displacement $\mathbf{x}_s(t)$ is measured.
- A4 Vehicle parameters are known except for the length a , the front and the rear tire stiffness k_{uf} , k_{ur} and the tire mass m_{uf} , m_{ur} .
- A5 The second and third derivation of the road disturbance $\mathbf{w}(t)$ are bounded.

III. ACTIVE SUSPENSION CONTROLLER

Fig. 2 shows the configuration of the vehicle active suspension system proposed in [7]. The combined ideal model shown in Fig. 2 has good properties. Namely, 1) The ride comfort at a specified location becomes best, 2) The best location can be easily moved by setting only one design parameter without redesigning the combined ideal vehicle. If the real vehicle can track the motion of the designed combined ideal vehicle, the control objective can be achieved. The active suspension control system in Fig. 2 is designed so that the real vehicle can track the motion of the combined ideal vehicle. To achieve the control objective, the signals of road disturbance $\ddot{\mathbf{w}}(t)$ and state variables $\mathbf{x}_z(t)$, $\dot{\mathbf{x}}_z(t)$, $\mathbf{x}_u(t)$, $\dot{\mathbf{x}}_u(t)$ $\mathbf{d}(t)$ are required in the controller proposed in [7].

According to the assumption A1, it can be seen that the following signals are available.

$$\left. \begin{aligned} \ddot{\mathbf{x}}_s(t) &= [\ddot{z}_f(t), \ddot{z}_r(t)]^T \quad [\ddot{z}_{uf}(t), \ddot{z}_{ur}(t)]^T \\ \mathbf{H} \mathbf{d}(t) &= [\ddot{z}_f(t), \ddot{z}_r(t)]^T \end{aligned} \right\} (3)$$

Table 1 Notation of vehicle model.

C, CG	center and center of gravity of vehicle body
z_{cg}, θ	vertical displacement at CG and pitching
z_f, z_r	vertical displacement of vehicle body at positions on front and rear wheel axle
z_{uf}, z_{ur}	vertical displacement of front and rear unsprung mass
w_f, w_r	vertical displacement of road disturbance added to front and rear wheel
v	longitudinal velocity of vehicle
m, i_c	sprung mass and moment of inertia of vehicle body
a	half of vehicle body length
h, ℓ	distances from C to CG and from C to P
m_{uf}, m_{ur}	front and rear unsprung mass
k_f, k_r	front and rear suspension stiffness
c_f, c_r	front and rear suspension damping rate
k_{uf}, k_{ur}	front and rear tire spring stiffness
f_f, f_r	front and rear force added to sprung mass
u_f, u_r	front and rear active suspension control force

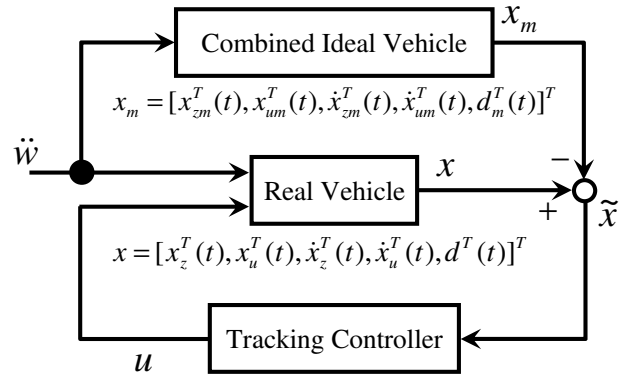


Fig. 2 Configuration of active suspension control system.

Moreover, it is easy from (1), (2) to ascertain that the following signals are also available.

$$\left. \begin{aligned} \mathbf{p}_1(t) &= \mathbf{K}_u^{-1} \left(\ddot{\mathbf{x}}_s(t) - (\mathbf{H} \mathbf{d}(t) + \mathbf{M}_u^{-1} \mathbf{f}(t)) \right) \\ &= \mathbf{x}_u(t) \\ \mathbf{p}_2(t) &= \mathbf{x}_s(t) + \mathbf{p}_1(t) = \mathbf{H} \mathbf{x}_z(t) \end{aligned} \right\} (4)$$

If an estimator for $\dot{\mathbf{x}}_s(t)$ and $\dot{\mathbf{x}}_z(t)$ are developed, then, the signal $\dot{\mathbf{x}}_u(t)$ becomes also available. Therefore, we will develop an estimator for $\dot{\mathbf{x}}_s(t)$, $\dot{\mathbf{x}}_z(t)$ and $\ddot{\mathbf{w}}(t)$. Consider the new state $\boldsymbol{\eta}(t) = [\boldsymbol{\eta}_1(t)^T, \boldsymbol{\eta}_2(t)^T, \boldsymbol{\eta}_3(t)^T]^T = [\dot{\mathbf{x}}_s(t)^T, \mathbf{H} \dot{\mathbf{x}}_z(t)^T, \ddot{\mathbf{w}}(t)^T]^T$. Then, the estimator for the state $\boldsymbol{\eta}(t)$ is proposed as

$$\left. \begin{aligned} \hat{\boldsymbol{\eta}}_1(t) &= \alpha \mathbf{x}_s(t) + \boldsymbol{\zeta}_1(t), \\ \dot{\boldsymbol{\zeta}}_1(t) &= \ddot{\mathbf{x}}_s(t) - \alpha \hat{\boldsymbol{\eta}}_1(t), \\ \boldsymbol{\zeta}_1(0) &= \alpha(\mathbf{p}_2(0) - \mathbf{p}_1(0)) \end{aligned} \right\} (5)$$

$$\left. \begin{aligned} \hat{\boldsymbol{\eta}}_2(t) &= 2\alpha \mathbf{p}_2(t) + \boldsymbol{\zeta}_2(t), \\ \dot{\boldsymbol{\zeta}}_2(t) &= 2\alpha \hat{\boldsymbol{\eta}}_2(t) + \mathbf{H} \mathbf{d}(t) - \boldsymbol{\eta}_3(t), \\ \boldsymbol{\zeta}_2(0) &= 2\alpha \mathbf{p}_2(0) \end{aligned} \right\} (6)$$

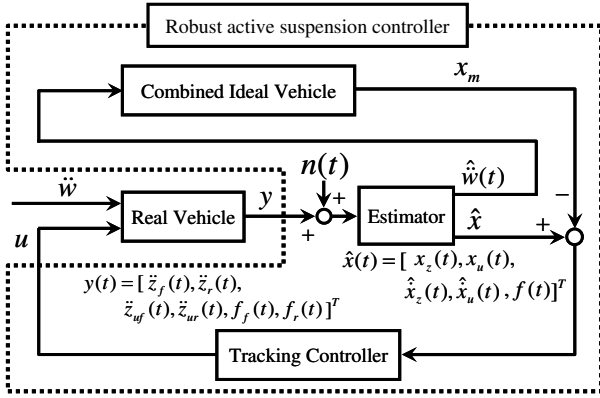


Fig. 3 Configuration of active suspension control system using proposed estimator.

$$\left. \begin{aligned} \hat{\eta}_3(t) &= 3\alpha^2 p_2(t) + \zeta_3(t), \\ \dot{\zeta}_3(t) &= 3\alpha^2 \hat{\eta}_2(t), \\ \zeta_3(0) &= 3\alpha^2 p_2(0) \end{aligned} \right\} \quad (7)$$

where $\hat{\eta}_i, i = 1, 2, 3$ are estimated signals for $\eta_i, i = 1, 2, 3$, and α is a positive design parameter introduced to improve performance of the proposed estimator. Differentiating the first equation in (5)(6)(7), we obtain the following equation.

$$\left. \begin{aligned} \dot{\hat{\eta}}_1(t) &= \alpha \tilde{\eta}_1(t) + \ddot{x}_s(t) \\ \dot{\hat{\eta}}_2(t) &= 2\alpha \tilde{\eta}_2(t) + H d(t) \\ \dot{\hat{\eta}}_3(t) &= 3\alpha^2 \tilde{\eta}_2(t) \end{aligned} \right\} \quad \hat{\eta}_3(t) \quad (8)$$

$$\dot{\tilde{\eta}}(t) = \begin{bmatrix} \alpha & O_2 & O_2 \\ O_2 & 2\alpha & I_2 \\ O_2 & 3\alpha^2 & O_2 \end{bmatrix} \tilde{\eta}(t) + \begin{bmatrix} 0 \\ 0 \\ 1 \end{bmatrix} \ddot{w}(t) \quad (9)$$

Where $\tilde{\eta} = \eta - \hat{\eta}$ and $\tilde{\eta}_i = \eta_i - \hat{\eta}_i, i = 1, 2, 3$. It is assumed that the proposed controller starts in the situation where the oscillation of the vehicle body dose not occur. According to the assumption A5, for the proposed estimator(5)(6)(7), the following theorem holds.

Theorem 1: For estimation $\tilde{\eta}_1(t), \tilde{\eta}_2(t), \tilde{\eta}_3(t)$, there exist bounded positive constants $\bar{\rho}_{Ei}, i = 1, 2$ independent of the design parameter α such that

$$\left. \begin{aligned} \|\tilde{\eta}_1(t)\|^2 &= 0 \\ \|\tilde{\eta}_2(t)\|^2 &\leq \bar{\rho}_{E1} \alpha^{-4} \\ \|\tilde{\eta}_3(t)\|^2 &\leq \bar{\rho}_{E2} \alpha^{-2} \end{aligned} \right\}. \quad (10)$$

It can be concluded from the theorem 1 that the estimated errors decrease as the design parameter α increases. In case when the design parameter α is set to be large enough, we can obtain the signals $H\dot{x}_z(t)$ and $\dot{x}_s(t)$ with enough accuracy. Then, the signal $\dot{x}_u(t) = H\dot{x}_z(t) - \dot{x}_s(t)$ becomes also available. Namely, from (3), (4) and theorem 1, it can be concluded that the all required signals are available. Configuration of the active suspension control system using the proposed estimator is shown in Fig. 3.

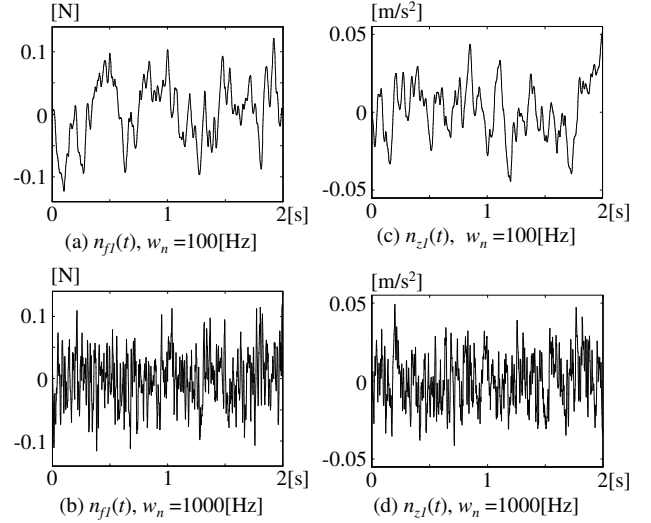


Fig. 4 Disturbance $n_{f1}(t), n_{z1}(t)$ added to measurements $f_f, \ddot{x}_z(t)$.

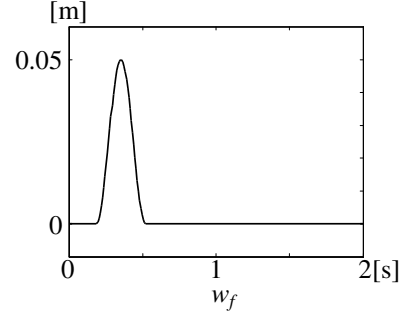


Fig. 5. Road disturbance $w_f(t)$.

IV. NUMERICAL SIMULATION RESULTS

To investigate the influences of measurement disturbances, numerical simulations are carrying out. The frequencies of measurement disturbances are set as 100[Hz] and 1000[Hz]. The measurement disturbance $n_{f1}(t)$ added to a signal of force sensor $f_f(t)$ are shown in Figs. 4 (a), (b), and the measurement disturbance $n_{z1}(t)$ added to a signal of acceleration sensor ($c^T \ddot{x}_z(t)$, $c = [1, 0]^T$) are shown in Figs. 4 (c), (d). The maximum values of measurement disturbances of force sensors and acceleration sensors are set as 0.12[N] and 0.05[m/s²], respectively. For the other sensors, similar measurement disturbances are added. The values of vehicle parameters are shown in Table 2. The design parameter α for the proposed estimator is set as $\alpha = 2000$. The design parameters for the tracking controller shown in Fig. 2 are set as a large value so that the tracking error between the actual vehicle and the ideal vehicle model can become small. And the vehicle velocity is set as $v = 100 - 1000/3600$ [m/s]. Road disturbance $w_f(t) = w_r(t - L)$, $L = 2a/v$ is shown in Fig. 5.

Fig. 6 shows the responses of the vertical acceleration of the controlled vehicle shown in Fig. 3 at the specified location $l = 1.0(l_p = 0.7)$. The thin line shows the responses of the acceleration of the controlled vehicle without measurement disturbances. The thick lines show

Table 2 Nominal values of parameters.

m	781	kg	i_c	990	kgm ²
h	0.04	m	a	1.38	m
k_f	27160	N/m	k_r	29420	N/m
c_f	4000	Ns/m	c_r	2500	Ns/m
m_{uf}	69	kg	m_{ur}	96	kg
k_{uf}	229000	N/m	k_{ur}	255000	N/m

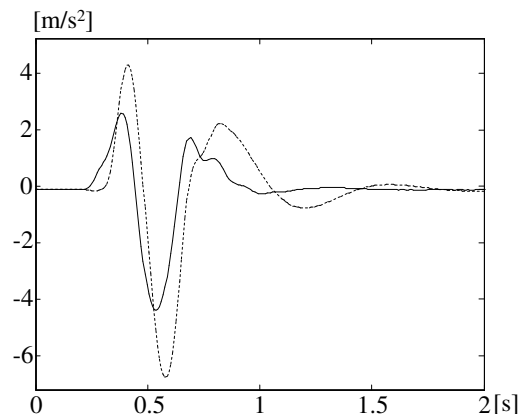
the responses of the controlled vehicle with measurement disturbances, and the dashed lines show the responses of the passive vehicle. It is seen from Fig. 6 that the acceleration responses do not vary even in the presence of the measurement disturbances.

V. CONCLUSION

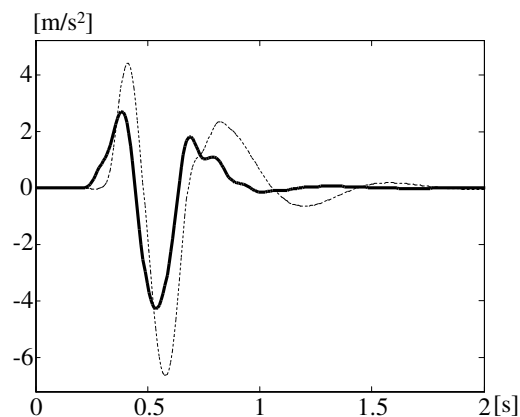
We have proposed the active suspension control scheme in which tire deflections are not required. The proposed suspension controller has a good property that the location where the ride comfort becomes best can be easily moved by setting only one design parameter l_p . It has been shown by carrying out numerical simulations that in the closed loop system using the proposed ride comfort control scheme, the influence of measurement disturbances is analyzed by using numerical simulations. As a result, it is shown that the proposed ride comfort control scheme is very effective even in the presence of measurement disturbances.

REFERENCES

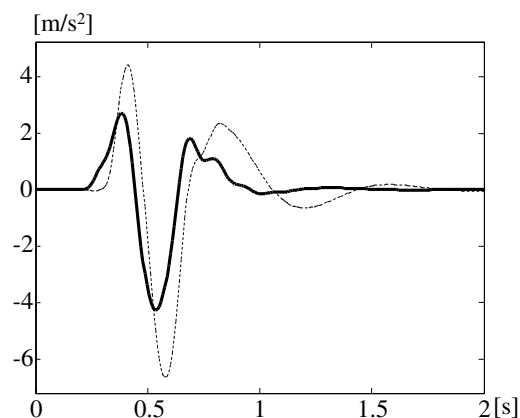
- [1] Hrovat, D., Survey of Advanced Suspension Developments and Related Optimal Control Application, *Automatica*, Vol.33-10, pp.1781-1817, (1997).
- [2] Y. Zhang, and A.G. Alleyne, A New Approach to Half-Car Active Suspension Control, *Proc. of the American Control Conference*, pp. 3762-3767, (2003).
- [3] Thompson, A.G., and Davis, B.R., RMS Values of Force, Stroke and Tire Deflection in a Half-Car Model with Preview Controlled Active Suspension, *Vehicle System Dynamics*, Vol.39-3, pp.245-253, (2003).
- [4] J.-S. Lin and C.-J. Huang, Nonlinear backstepping active suspension design applied to a half-car model, *Vehicle System Dynamics*, Vol. 42, No. 6, pp. 373-393, (2004).
- [5] M. Oya, H. Harada, Y. Araki, An Active Suspension Controller Achieving the Best Ride Comfort at Any Specified Location on A Vehicle, *Journal of System Design and Dynamics*, pp.245-256, (2007).
- [6] H. Okuda, Y. Tsuchida, M. Oya, Q. Wang, and K. Okumura, Robust Active Suspension Controller Achieving Good Ride Comfort, *Proc. of SICE Annual Conference 2007*, September 17-20, Kagawa, Japan, pp. 1305-1310, (2007).
- [7] M. Oya, Y. Tsuchida, Q. Wang, Y. Taira, Adaptive Active Suspension Controller Achieving the Best Ride Comfort at Any Specified Location on Vehicles with Parameter Uncertainties, *International Journal of Advanced Mechatronic Systems*, Vol. 1, No. 2, pp. 125-136, (2008).
- [8] Katsuhiro Okumura, Masahiro Oya, Masashi Nagae, Hidetaka Ota and Hideki Wada, Active Suspension Control Scheme for vehicles without Measurements of Tire Deflection, *Proc. of the 8th IEEE International Symposium on Computational Intelligence in Robotics and Automation*, Daejeon, Korea, December 15-18, pp. 153-158, (2009)
- [9] Katsuhiro Okumura, Masahiro Oya and Hideki Wada, Robust Ride Comfort Control of vehicles without Measurements of Tire Deflection, *Artificial Life and Robotics*, Volume 15, Number 2, pp. 133-137, (2010)



(a) $\ddot{z}_l(t)$
 $l = -1.0 (l_p = -0.7)$



(b) $\ddot{z}_l(t)$
 $l = -1.0 (l_p = -0.7), w_n = 100[\text{Hz}]$



(c) $\ddot{z}_l(t)$
 $l = -1.0 (l_p = -0.7), w_n = 1000[\text{Hz}]$

Fig. 6 Responses of the vertical acceleration of the vehicle at the specified location $l = -1.0 (l_p = -0.7)$

A Method to Improve Stability of Adaptive Steering Driver-Vehicle Systems

Shingo Tamaru, Jinxin Zhuo, Qiang Wang, Masahiro Oya

1-1 Sensui-cho, Tobata-ku, Kitakyusyu-shi, Fukuoka, Japan

(Tel : 093-884-3103)

(Email: i344209s@tobata.isc.kyutech.ac.jp)

Abstract: We have developed an adaptive steering controller achieving good tracking performance. However, we have designed an ideal vehicle model in disregard of the variations of the driver properties. For the variations of the driver properties, if an adequate ideal vehicle model can be designed, the better handling stability of the adaptive driver-combined-vehicle systems can be realized. In this paper, we propose a scheme to design an ideal vehicle model adequate for the variations of the driver properties. Finally, it is shown by carrying out numerical simulations that the designed ideal vehicle model is very effective.

Keywords: Steering Control, Adaptive Control, Model Following Control

I. INTRODUCTION

To improve handling stability of combined vehicles, the three states, the combination angle, the lateral velocity and yaw rate of tractor, must be controlled with three independent control inputs. Recently, the researches of steer-by-wire, are conducted actively^[1]. Using the technology of steer-by-wire, the three steering angles such as the steering angle of the trailer, the front and rear steering angle of the tractor can be used as the independent control inputs possibly. Based on the notion, control schemes have been proposed^[2,3] in which three independent steering control inputs are used. However, these proposed controllers require all accurate knowledge of combined vehicle parameter.

To straggle with the problem stated above, the authors have proposed robust steering control schemes^[4,5]. In the schemes, an ideal vehicle model is designed, and then, the steering controller is developed so that the actual vehicle tracks the ideal vehicle model even if the large parameter variation occurs in the vehicle dynamics. In the proposed schemes, however, an ideal vehicle model is designed in disregard of the variations of the driver properties. Therefore, the authors have proposed a design scheme for ideal vehicle models^[6,7] adequate for the variations of the deriver properties. In the scheme, several ideal vehicle models are designed against the variation of the driver properties and the ideal vehicle model has to be changed according to the variation. For this reason, the scheme proposed in [6,7] require accurate information of the variation of the driver properties. In addition, there exists the problem that the construction of controller becomes too complex.

In this paper, we propose a new design scheme for an ideal vehicle model. A design method based on a cost function is proposed and only one ideal vehicle model is

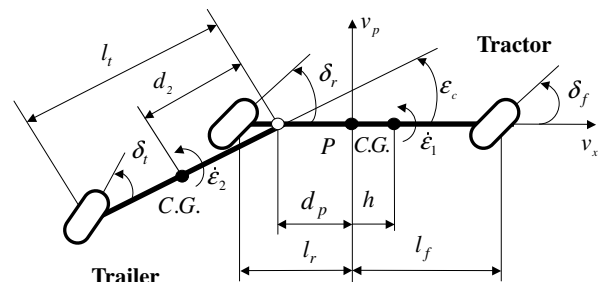


Fig.1 Tractor-semitrailer model

designed. In the designed ideal vehicle model, the rough information of the variation of the driver properties is only required. Carrying out numerical simulations, for the variation of the driver properties, it is shown that the adaptive steering controller using the proposed ideal vehicle model has good effectiveness.

II. INTRODUCTION

In this paper, a simplified bicycle model of tractor-semitrailers shown in Figure 1 is used to design an adaptive steering controller. In Figure 1, the point C.G. is the center of gravity, and the point P is the reference point. Definitions for parameters of combined vehicles are shown in Table 1.

The following assumptions are made to develop a controller for the combined vehicles shown in Fig.1.

- A1 Lateral velocity of tractor $v_p(t)$, yaw rate of tractor $\gamma_1(t)$, combination yaw rate $\dot{\epsilon}_c(t)$ and combination angle $\epsilon_c(t)$ can be measured.
- A2 The length d_p, l_f, l_r and the length of trailer l_t are known. The other parameters include uncertainties.
- A3 Longitudinal velocity v_x is a bounded constant and available.

The dynamic equation of combined vehicle can be described as follows.

Table 1 Notation of tractor-semitrailer model

v_x	longitudinal velocity of tractor
v_p, v_c	lateral velocity of tractor at P and C.G
$\varepsilon_1, \varepsilon_2$	yaw angles of tractor and trailer
ε_c	combination angle
γ_1	yaw rate of tractor
$\delta_f, \delta_r, \delta_t$	steering angles
m_1, m_2	mass of the tractor and trailer
J_{z1}, J_{z2}	tractor's moment of inertia and trailer's moment of inertia
l_f, l_r	distances from P to front and rear wheel axle of tractor
l_t	length of trailer
d_p, d_2	distances from the connector to P and C.G
h	distance from P to C.G
c_f, c_r, c_t	cornering stiffness

$$\dot{z}(t) = A_z z(t) + B_z(u(t) - b\varepsilon_c(t)) \quad (1)$$

$$\left. \begin{aligned} z(t) &= H_p^T [v_p(t) \quad \gamma_1(t) \quad \dot{\varepsilon}_c(t)]^T, u(t)^T = [\delta_f(t) \quad \delta_r(t) \quad \delta_t(t)] \\ A_z &= -v_x D_z - v_x^{-1} B_z, B_z = QK, b^T = [0 \quad 0 \quad 1] \\ Q &= H_p^T (T^T M_c T)^{-1} H_p, K = \text{diag}[c_f \quad c_r \quad c_t] \end{aligned} \right\} \quad (2)$$

$$\left. \begin{aligned} M_c &= \begin{bmatrix} m_1 + m_2 & -m_2 d_3 & m_2 d_2 \\ -m_2 d_3 & J_{z3} + m_2 d_3^2 & -J_{z2} - m_2 d_2 d_3 \\ m_2 d_2 & -J_{z2} - m_2 d_2 d_3 & J_{z2} + m_2 d_2^2 \end{bmatrix} \\ D_z &= H_p^T \begin{bmatrix} 0 & 1 & 0 \\ 0 & 0 & 0 \\ 0 & 0 & 0 \end{bmatrix} (H_p^T)^{-1}, T = \begin{bmatrix} 1 & h & 0 \\ 0 & 1 & 0 \\ 0 & 0 & 1 \end{bmatrix} \\ H_p^T &= \begin{bmatrix} 1 & 1 & 1 \\ l_f & -l_r & -(d_p + l_t) \\ 0 & 0 & l_t \end{bmatrix} \end{aligned} \right\} \quad (3)$$

Where $d_1 = d_p + h, d_3 = d_1 + d_2$ and $J_{z3} = J_{z1} + J_{z2}$. M_c is a positive definite matrix.

The nominal values of combined vehicle are shown in Table 2.

III. IDEAL VEHICLE MODEL

1. Driver Model

In this paper, a linear preview driver model [8] is employed to describe the properties of drivers. In Fig.2, the solid lines represent the state of the combined vehicles, and the dashed lines represent the ideal state of the combined vehicles tracking the target lane. $y_r(t)$ is the lateral distance between P and the target lane, $\varepsilon_r(t) = \varepsilon_1(t) - \varepsilon_d(t)$ is the relative yaw angle between the vehicle and the target lane. $\varepsilon_d(t)$ is the yaw angle of the ideal state, $\rho(t)$ is the curvature of target lane. The predicted deviation $\tilde{y}_r(t)$ is defined by

$$\tilde{y}_r(t) = y_r(t) + T_p \dot{y}_r(t) \quad (4)$$

where T_p is the preview time constant, v_x is the longitudinal velocity of the combined vehicles.

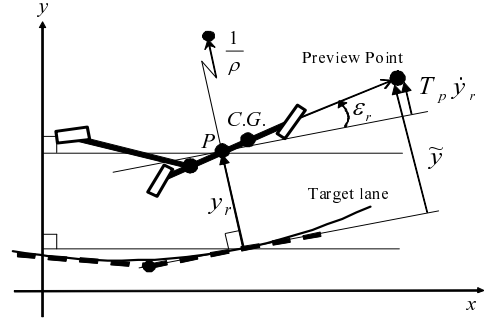


Fig.2 Driver-Vehicle-System

Therefore, the equation of the driver steering angle $\delta_c(t)$ is given by

$$T_s \ddot{\delta}_c(t) + \dot{\delta}_c(t) = -g_p \dot{\tilde{y}}_r(t) - g_i \tilde{y}_r(t) \quad (5)$$

where T_s is a steering time constant and denotes the reaction time delay of drives and mechanical systems, g_p, g_i is the steering gain. In this paper, we add an integrator to the driver model of [8] so that $y_r(t)$ can converge to zero when the curvature of target lane is not zero.

2. The Form of Ideal Vehicle Model

In the following explanation, s is Laplace variable, the symbols $\mathcal{L}, \mathcal{L}^{-1}$ denote Laplace transform and inverse Laplace transform.

Based on the proposed ideal vehicle model proposed in [5], the form of ideal vehicle modes is proposed as

$$\left. \begin{aligned} v_{pd}(t) &= \mathcal{L}^{-1} \left[\frac{g_v \omega_n^2 s}{A_M(s)} \mathcal{L}[v_x \delta_c(t)] \right] \\ \gamma_{ld}(t) &= \mathcal{L}^{-1} \left[\frac{g_\gamma \omega_n^2 (\eta s + 1)}{A_M(s)} \mathcal{L}[v_x \delta_c(t)] \right] \\ A_M(s) &= s^2 + 2\omega_n \zeta s + \omega_n^2 \\ g_v &= \bar{g}_v \frac{\bar{g}_p s + \bar{g}_i}{\hat{g}_p s + \hat{g}_i} \frac{\bar{T}_p s + 1}{\hat{T}_p s + 1}, g_\gamma = \bar{g}_\gamma (v_x) \frac{\bar{g}_p s + \bar{g}_i}{\hat{g}_p s + \hat{g}_i} \frac{\bar{T}_p s + 1}{\hat{T}_p s + 1} \end{aligned} \right\} \quad (6)$$

$$\mathcal{L}[\varepsilon_{cd}(t)] = \frac{\omega_n^2}{A_M(s)} \mathcal{L}[\delta_{ci}(t)], \varepsilon_{ci}(t) = \frac{2d_p v_x \gamma_{ld}(t)}{v_x^2 - (d_p \gamma_{ld}(t))^2} \quad (7)$$

where $\omega_n, \zeta, \eta, \bar{g}_v, \bar{g}_\gamma(v_x), \bar{g}_p, \bar{g}_i, \bar{T}_p$ are positive design parameters to be determined later. $v_{pd}(t)$ is the ideal lateral velocity of the tractor, $\gamma_{ld}(t)$ is the ideal combination yaw angle, and $\varepsilon_{cd}(t)$ is the ideal combination yaw angle. In (6), $\hat{g}_p, \hat{g}_i, \hat{T}_p$ are the estimated values of the steering gains g_p, g_i and the preview time constant T_p . In the case of a constant driver steering angle, the desired lateral velocity $v_{pd}(t)$ of the tractor converges to zero and the desired yaw rate $\gamma_{ld}(t)$ of the tractor tends to a constant value $\lim_{t \rightarrow \infty} \gamma_{ld}(t) = \bar{\gamma}_{ld}$. Then, the tractor becomes tangent to the circular lane with the radius $v_x / \bar{\gamma}_{ld}$ and travels.

In the actual combined vehicles using the adaptive steering controller, the property of the actual vehicles becomes as same as that of the ideal vehicle model. In this case, the following property can be obtained.

Table 2 Nominal values of parameters

m_1	1060	kg	J_{z1}	1507	kgm ²
l_f	1.13	m	l_r	1.34	m
d_p	2.27	m	h	0	m
d_2	2.26	m			
c_f	29700	N/rad	c_r	41460	N/rad
m_2	436	kg	J_{z2}	805	kgm ²
l_t	2.48	m	c_t	100000	N/rad

$$\left. \begin{aligned} Y_r(s) &= \frac{-s(T_s+1)A_M(s)v_x^2}{s^3(T_s+1)A_M(s)+C(s)v_x\omega_n^2B_M(s)}\rho(s) \\ &+ \frac{s^2(T_s+1)A_M(s)+D(s)T_p v_x\omega_n^2B_M(s)}{s^3(T_s+1)A_M(s)+C(s)v_x\omega_n^2B_M(s)}Y_r(0) \\ B_M(s) &= \bar{g}_v s^2 + v_x \bar{g}_\gamma \eta s + v_x \bar{g}_\gamma \\ C(s) &= (\bar{g}_p s + \bar{g}_i)(\bar{T}_p s + 1) \frac{\bar{g}_p s + \bar{g}_i}{\hat{g}_p s + \hat{g}_i} \frac{T_p s + 1}{\hat{T}_p s + 1} \\ D(s) &= (\bar{g}_p s + \bar{g}_i) \frac{\bar{g}_p s + \bar{g}_i}{\hat{g}_p s + \hat{g}_i} \frac{\bar{T}_p s + 1}{\hat{T}_p s + 1} \end{aligned} \right\} (8)$$

From (8), it can be seen easily that if the estimated values $\hat{g}_p, \hat{g}_i, \hat{T}_p$ are almost equal to the parameters g_p, g_i, T_p of actual vehicle, the variation of the property shown in (8) becomes small.

3. Determination of Design Parameters

In the passive combined vehicles, the nominal values of vehicle parameters (see Table 2) are used. In the following explanation, the determination method of design parameters $\omega_n, \zeta, \eta, \bar{g}_v, \bar{g}_\gamma(v_x), \bar{g}_p, \bar{g}_i, \bar{T}_p$ is shown.

Step 1 In order that oscillation cannot occur in the desired trajectories of a ideal vehicle model, ζ is set as $\zeta = 1$.

Step 2 Using the average values of the driver parameters, the driver parameters g_p, g_i, T_p are set as $g_p = 0.008, g_i = 0.0012, T_p = 2.2$. In addition, it is assumed that $g_p = \bar{g}_p = \hat{g}_p, g_i = \bar{g}_i = \hat{g}_i, T_p = \bar{T}_p = \hat{T}_p$.

Step 3 For a constant longitudinal velocity v_x , we can obtain the yaw rate gain as $\bar{g}_\gamma(v_x) = \frac{3.06 \times 10^2}{7.59 \times 10^2 + 2.24 \times v_x(t)^2}$. In order to make it easy for the ideal vehicle model to drive a corner, the design parameter $\bar{g}_\gamma(v_x)$ is determined as

$$\bar{g}_\gamma(v_x) = \frac{1.8 \times 3.06 \times 10^2}{7.59 \times 10^2 + 2.24 \times v_x(t)^2} \quad (9)$$

Step 4 To design a vehicle model with good handling stability, an evaluation function is introduced by using the trail and error approach.

$$J = \int_0^T (2y_r(t)^2 + 2y_{rr}(t)^2 + 4\ddot{y}_r(t)^2 + 4\ddot{\epsilon}_c(t)^2) dt + 3 \max \ddot{y}_r(t) + 3 \max \ddot{\epsilon}_c(t) \quad (10)$$

Where T is the simulation time. Based on the evaluation function, the remaining design parameters $\bar{g}_v, \eta, \omega_n$ are determined so that the following conditions can be satisfied.

(a) The imaginary part of the eigenvalues of $B_M(s)$ is minimized preferably.

(b) The evaluation function is minimized preferably in lane change and cornering maneuver.

Step 5 If the designed ideal vehicle model does not have good handling stability, we return to Step 3~4.

As result, $\bar{g}_v, \eta, \omega_n$ are set as $\bar{g}_v = 0.25, \eta = 0.39, \omega_n = 5.4$. In the following part, using numerical simulations, the property of designed the ideal vehicle model is shown. In the lane change maneuver, the curvature of target lane is $\rho(t) = 0[m]$. The initial value of $y_r(t)$ is set as $y_r(0) = -3.0[m]$. In the cornering maneuver, the curvature of target lane is $\rho(t) = 1/500[m]$. The initial value of $y_r(t)$ is set as $y_r(0) = -1.0[m]$. Until now, from many research results, the value of T_s is obtained as $0.05 \sim 0.4[s]$. For this reason, in the following numerical simulations, we check controlled performance in $0.05 \leq T_s \leq 0.4[s]$.

At first, the effectiveness of the proposed ideal vehicle model is shown in the lane change maneuver. In the case of varying v_x and T_s , the variation of J is shown in Figure 3. Fig.3 (a) shows the values of J for the passive combined vehicle, Fig.3 (b) shows the values of J for the adaptive steering driver vehicle system using the proposed ideal vehicle model. Hereafter, it is called the adaptive vehicle simply. In Fig.3, in case where J exceeds 80, the values of J are shown as 80. As shown Fig.3 (a), there exists a region in which J exceed 80. In the region, the handling performance of the passive vehicle becomes unstable. However, as shown in Fig.3 (b), for the adaptive vehicle, the values of J are less than 70 and good handling performance can be achieved.

Next, the effectiveness of the proposed ideal vehicle model is shown in the cornering maneuver. In the case of varying v_x and T_s , the variation of J is shown in Figure 4. Fig.4 (a) shows the values of J for the passive combined vehicle, Fig.4 (b) shows the values of J for the adaptive vehicle. In Fig.4, in case where J exceeds 35, the values of J are shown as 35. As shown Fig.4 (a), there exists a region in which J exceeds 35. In the region, the handling performance of the passive vehicle becomes unstable. However, as shown in Fig.4 (b), for the adaptive vehicle, the values of J are less than 21 and good handling performance can be achieved.

Moreover, we show the effectiveness of the proposed ideal vehicle in the presence of the estimated errors in $\hat{g}_p, \hat{g}_i, \hat{T}_p$. In case where the values of g_p / \hat{g}_p and g_i / \hat{g}_i are not equal to one, we can obtain the similar graphs to Fig.3 (b) and Fig.4 (b). For each values of g_p / \hat{g}_p and g_i / \hat{g}_i , the maximum value of Fig.3 (b) is plotted in Fig.5 (a) and the maximum value of Fig.4 (b) is plotted in Fig.5 (b). Similarly, for each values of T_p / \hat{T}_p , the maximum values of Fig.3 (b), Fig.4 (b) are plotted in Fig.6.

As shown in Fig.5, in the region of $0.6 \leq g_p / \hat{g}_p \leq 1.4$ and $0.8 \leq g_i / \hat{g}_i \leq 1.6$, the values of J became less than 75 in the lane change maneuver and

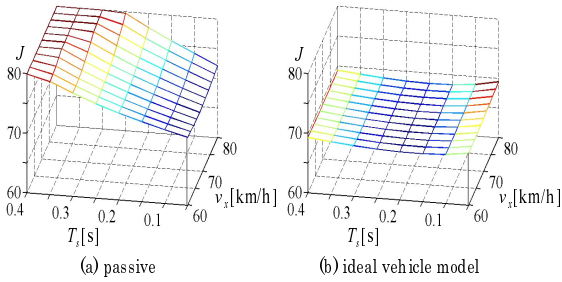


Fig.3 Variation of J for various T_s and v_x (lane change)

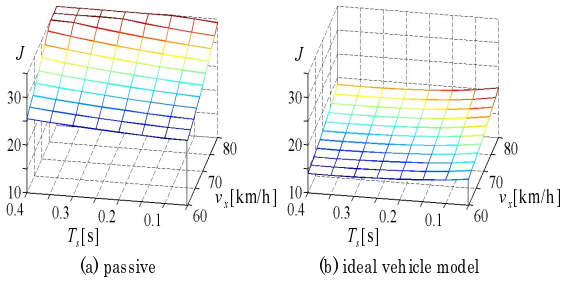


Fig.4 Variation of J for various T_s and v_x (cornering)

the values of J became less than 30 in the cornering maneuver. As shown in Fig.6, in the region of $0.7 \leq T_p / \hat{T}_p \leq 1.3$, the values of J became less than 75 in the lane change maneuver and the values of J became less than 25 in the cornering maneuver. From the facts, it can be concluded that the proposed ideal vehicle model is very effective when the estimated values of the driver parameters are within the regions $0.6 \leq g_p / \hat{g}_p \leq 1.4, 0.8 \leq g_i / \hat{g}_i \leq 1.6$ and $0.7 \leq T_p / \hat{T}_p \leq 1.3$. Namely, it can be seen that accurate values of the driver parameters are not required.

IV. CONCLUSION

In this paper, we propose a design method to design not several ideal vehicle models but only one ideal vehicle model against variations of the driver properties. Carrying out numerical simulations, it is shown that the handling performance in the adaptive driver vehicle system is far better than that of passive combined vehicle. Moreover, it is also shown that in the design scheme of an ideal vehicle model, rough information of the driver properties are only required to maintain good handling performance.

REFERENCES

- (1) P. Pisu, A. Serrani, S. You, and L. Jalics, Adaptive Threshold Based Diagnostics for Steer-by-wire Systems, Trans. ASME. Journal of Dynamic Systems, Measurement, and Control, vol.128, (2006), pp.428-435.
- (2) B.A. Jujnovich, A.M.C. Odhams, R.L. Roebuck and D. Cebon, Active Rear Steering Control of a Tractor-Semitrailer, Proceedings of International Symposium on Advanced Vehicle Control, Aachen,

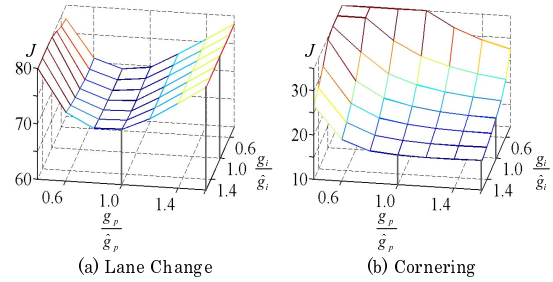


Fig.5 Variation maximum value of J for various g_p and g_i

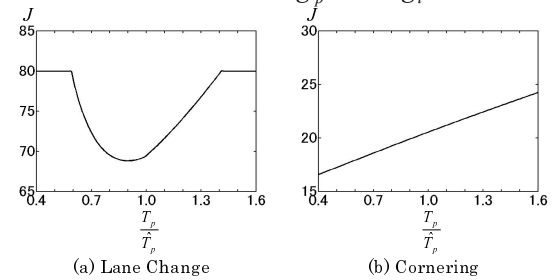


Fig.6 Variation maximum value of J for various T_p

- 1996, pp.395-408.
- (3) R. Hayama, S. Maeda, S. Kawahara, S. Nakano and H. Kumamoto, Bilateral Control of Human Machine Interface for Steer-By-Wire System, Proceedings of International Symposium on Advanced Vehicle Control, Kobe, 2008, pp.752-757.
- (4) Qiang Wang, Masahiro Oya, and Toshihiro Kobayashi, Robust Integral Control to Improve Stability of Tractor-Semitrailer Combination Vehicles, Proc. 2005 International Symposium on Advanced Control of Industrial Processes, Seoul, Korea, (2005), pp. 121-126.
- (5) Q. Wang, M. Oya, N. Takagi, Y. Taira and H. Ota, Adaptive Steering Controller to Improve Handling Stability for Driver-Combined-Vehicle System, Proc. of the 8th IEEE International Symposium on Computational Intelligence in Robotics and Automation, Daejeon, Korea, December 15-18, (2009), pp.409-414.
- (6) Qiang Wang, Masahiro Oya, Natsuki Takagi, On Design of Ideal Vehicle Models in Adaptive Steering Driver-Vehicle Systems, Proc. of the Second International Conference of Modeling Identification and Control, Okayama, Japan, July 17-19, pp.203-208, 2010.
- (7) Qiang Wang, Singo Tamaru, Hideki Wada, Masahiro Oya, One Design Method for Ideal Vehicle Models In Adaptive Driver-Combined Vehicle Systems, Proc. of the SICE Annual Conference 2010, Taipei, Taiwan, August 18-21, pp.156-161, 2010.
- (8) J. Ishio, H. Ichikawa, Y. Kano, M. Abe, Vehicle-handling quality evaluation through model-based driver steering behaviour, Vehicle System Dynamics, vol.46, 2008, pp.549-560.

Robust Controller for Underwater Vehicle-Manipulator Systems Including Thruster Dynamics

Yuichiro Taira*, Junpei Sugino†, Natsuki Takagi‡, and Masahiro Oya†

*Dept. of Ocean Mechanical Engineering, National Fisheries University, Shimonoseki 759-6595, Japan
(taira@fish-u.ac.jp)

†Dept. of Mechanical and Control Engineering, Kyushu Institute of Technology, Kitakyushu 804-8550, Japan
(oya@cmtl.kyutech.ac.jp)

‡Dept. of Mechanical Engineering, Miyakonojo National College of Technology, Miyakonojo 885-8567, Japan
(takagi@cc.miyakonojo-nct.ac.jp)

Abstract: This paper deals with a control scheme for underwater vehicle-manipulator systems with the dynamics of thrusters in the presence of uncertainties in system parameters. We have developed an adaptive controller that overcomes thruster nonlinearities, which cause an uncontrollable system. However, the structure of the adaptive controller is very complex due to the regressors of dynamic system models and parameter estimators. In this paper we develop a robust controller whose structure is much simpler than that of the adaptive controller.

Keywords: Underwater vehicle-manipulator system, thruster dynamics, robust control.

I. INTRODUCTION

An autonomous underwater vehicle with manipulators, referred to as underwater vehicle-manipulator system (UVMS), is expected to play an important role in ocean development [1]. Adaptive or robust control schemes for UVMSs have recently been developed in the presence of not only hydrodynamic forces acting on the UVMS and the dynamic coupling between the vehicle and the manipulator but also uncertainties in system parameters [1–5]. In a general type of UVMS, the vehicle is propelled by marine thrusters, whereas the manipulator is driven by electrical motors. Despite such a different actuator system, the existing control schemes in [1–5] were designed based on the dynamic system models without the thruster dynamics to obtain a simply-structured controller. In each control scheme, furthermore, a high gain control system is constructed in order to achieve good control performance. However, the vehicle propelled by marine thrusters generally has a considerably slower time response than the manipulator driven by electrical motors [4], and hence the high gains may excite the ignored thruster dynamics, which degrades control performance and may even cause instability.

In order to overcome the problem, the authors have developed an adaptive controller for UVMSs with the thruster dynamics [6]. Since the slow thruster dynamics was taken into consideration in the development of controller, control performance can be improved by the adaptive controller with high gains. However, the structure of the adaptive controller is very complex, compared with that of a normal robust controller, due to the regressors of the dynamic system models and the parameter estimators. In this paper we develop a robust controller whose structure is much simpler than that of the adaptive controller proposed in [6].

II. UVMS MODEL

Consider an underwater vehicle equipped with a Dm link manipulator with revolute joints. Without loss of generality, we assume that $Dm = Dp + Do$, where Dp and Do are the numbers of translational and rotational dimensions, respectively. As in [1, 2], the mathematical model without the thruster dynam-

ics is expressed as

$$M(\phi)\ddot{x}(t) + f(\phi, u) = J(\phi)^{-T} \begin{bmatrix} \bar{R}(\phi)\bar{f}_b(t) \\ \tau_m(t) \end{bmatrix} \quad (1)$$

$$\left. \begin{aligned} M(\phi) &= J(\phi)^{-T} \bar{M}(\phi) J(\phi)^{-1} \in R^{Dn \times Dn} \\ f(\cdot) &= J(\phi)^{-T} [\bar{f}(\phi, u) \\ &\quad - \bar{M}(\phi) J(\phi)^{-1} \dot{J}(\phi, u) u(t)] \in R^{Dn} \end{aligned} \right\} \quad (2)$$

where the explanation of the main symbols is shown in Table 1. Most of the controllers reported in the literature of UVMS control are designed for the model (1) without the dynamics of $\bar{f}_b(t)$. In our controller design, the following dynamic model for thrusters is used [7]:

$$\left. \begin{aligned} \bar{f}_b(t) &= \bar{K} D(v) v(t) \\ \dot{v}(t) &= -\frac{1}{2} A D(v) v(t) + \frac{1}{2} B \tau_b(t) \end{aligned} \right\} \quad (3)$$

$$D(v) = \text{diag}\{|v_1|, \dots, |v_{Dm}|\} \in R^{Dm \times Dm} \quad (4)$$

Table 1. Symbols in the models (1) to (4)

Da	Number of dimension $Dp + 2Do$
Dn	Number of dimension $2(Dp + Do) = 2Dm$
$x(t)$	Signal composed of vehicle's and manipulator end-effector's positions and orientations ($\in R^{Dn}$)
$\phi(t)$	Signal composed of vehicle's orientation and manipulator's joint angles ($\in R^{Da}$)
$u(t)$	Signal composed of vehicle's translational velocity and $\dot{\phi}(t)$ ($\in R^{Dn}$)
$\bar{f}_b(t)$	Thrust forces produced by thruster's propellers ($\in R^{Dm}$)
$\tau_m(t)$	Joint torques of manipulator ($\in R^{Dm}$)
$J(\phi)$	Jacobian matrix in the equation $\dot{x}(t) = J(\phi)u(t)$ ($\in R^{Dn \times Dn}$)
$\bar{R}(\phi)$	Transformation matrix from $\bar{f}_b(t)$ to force and torque concerning inertial coordinate system ($\in R^{Dm \times Dm}$)
$\bar{M}(\phi)$	Inertia matrix ($\in R^{Dn \times Dn}$)
$\bar{f}(\cdot)$	Signal composed of centrifugal, Coriolis, gravitational and buoyant forces, fluid drag and bounded disturbances ($\in R^{Dn}$)
$v(t)$	Shaft velocities of thruster's propellers ($\in R^{Dm}$)
$\tau_b(t)$	Shaft torques of thruster's propellers ($\in R^{Dm}$)
A, B, \bar{K}	Diagonal matrices composed of thruster's system parameters ($\in R^{Dm \times Dm}$)

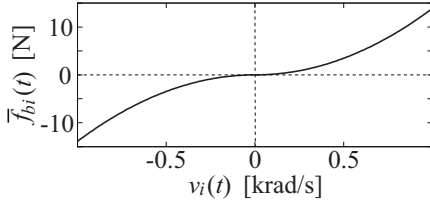


Fig. 1. Nonlinearity in thruster dynamics

where the explanation of the main symbols is shown in Table 1, and $v_i(t)$ is the i th element of $v(t)$. Fig. 1, where $\bar{f}_{bi}(t)$ is the i th element of $\bar{f}_b(t)$, shows the schematic representation of the first equation of (3). As shown in Fig. 1, the thruster model (3) has the dead-zone-like nonlinearity that $\bar{f}_{bi}(t) = 0$ and $d\bar{f}_{bi}(t)/dt = 0$ when $v_i(t) = 0$.

In this paper, the backstepping control technology is used to develop a robust controller. To this end, the state $v(t)$ has to be replaced by the new one $z(t) = D(v)v(t) \in R^{Dm}$. Combining (1) and (3), and rewriting the signal $D(v)v(t)$ as $z(t)$, we obtain the new representation

$$\left. \begin{aligned} M(\phi)\ddot{x}(t) + f(\phi, u) &= J(\phi)^{-T} R(\phi) K \begin{bmatrix} z(t) \\ \tau_m(t) \end{bmatrix} \\ \dot{z}(t) &= -AD(v)z(t) + BD(v)\tau_b(t) \end{aligned} \right\} \quad (5)$$

$$R(\phi) = \begin{bmatrix} \bar{R}(\phi) & 0 \\ 0 & I_m \end{bmatrix}, \quad K = \begin{bmatrix} \bar{K} & 0 \\ 0 & I_m \end{bmatrix} \in R^{Dn \times Dn} \quad (6)$$

where $I_m \in R^{Dm \times Dm}$ is an identity matrix.

The model (5) has the following properties useful for our controller development [1, 7]:

P1) The diagonal elements of A , B and \bar{K} are positive constants, and there exists a positive constant c_B such that $c_B \|\bar{y}\|^2 \leq \bar{y}^T B \bar{y}$ for any $\bar{y} \in R^{Dm}$.

P2) Each of $J(\phi)$ and $R(\phi)$ is composed of the kinematic parameters (e.g., length) and the functions of $\phi(t)$. In addition, if each of $J(\phi)$ and $R(\phi)$ has a full rank, then there exists a positive constant c_{RKJ} such that $c_{RKJ} \|\bar{x}\|^2 \leq \bar{x}^T J(\phi)^{-T} R(\phi) K R(\phi)^T J(\phi)^{-1} \bar{x}$ for any $\bar{x} \in R^{Dn}$.

P3) If $J(\phi)$ has a full rank, then $M(\phi)$ is symmetric and positive definite, and there exists a positive constant c_{M1} such that $\|M(\phi)\| \leq c_{M1}$.

III. CONTROLLER DESIGN

The control objective is to develop a controller so that all signals in the closed loop system are bounded and the state $x(t)$ tracks the desired trajectory $x_r(t)$ under the condition that the dynamic and hydrodynamic parameters (e.g., mass and a drag coefficient) are unknown constants.

In order to meet the objective, we make the following assumptions about the model (5) and the reference model (i.e., the desired trajectory $x_r(t)$):

A1) The signals $\phi(t)$, $x(t)$, $u(t)$ and $v(t)$ are available.

A2) The kinematic parameters in (5) are known constants.

A3) Each of the matrices $J(\phi)$ and $R(\phi)$ in (5) has a full rank.

A4) The desired trajectory $x_r(t)$ and the derivatives $\dot{x}_r(t)$ and $\ddot{x}_r(t)$ exist and are bounded.

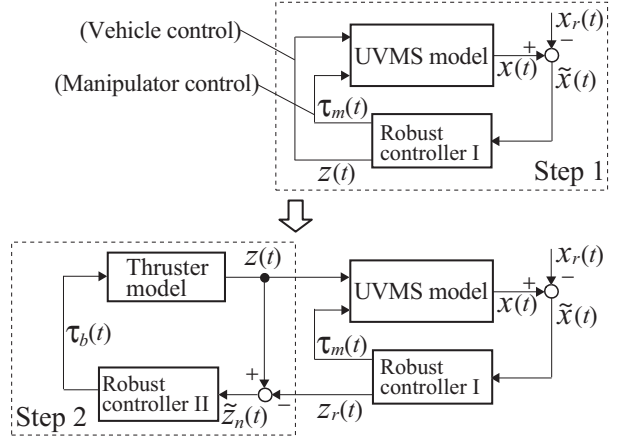


Fig. 2. Controller design procedure

It follows from the property P2 and the assumptions A1 and A2 that $J(\phi)$ and $R(\phi)$ are known matrices, and hence $\dot{x}(t)$ is available by using the equation $\dot{x}(t) = J(\phi)u(t)$.

In the following subsections we develop a controller that achieves the control objective by using a two-step backstepping procedure, as shown in Fig. 2. The first step is the design of a robust controller with the inputs $z(t)$ and $\tau_m(t)$, called robust controller I in this paper. The second step is the design of a robust controller with the input $\tau_b(t)$, called robust controller II in this paper. In this step we first replace $z(t)$ determined in the first step by the desired trajectory $z_r(t)$, and then design the control input $\tau_b(t)$ for the second equation of (5) so that $z(t)$ tracks $z_r(t)$.

1. Robust Controller I

According to the design procedure shown in Fig. 2, we make the following assumption in the design of robust controller I:

A5) The control inputs are $z(t)$ for vehicle control and $\tau_m(t)$ for manipulator control.

In order to achieve the aforementioned control objective, we use the tracking errors

$$\tilde{s}(t) = \dot{\tilde{x}}(t) + \alpha \tilde{x}(t), \quad \tilde{x}(t) = x(t) - x_r(t) \quad (7)$$

where $\alpha > 0$ is a design parameter. Using the first equations of (5) and (7), we have the error models

$$\left. \begin{aligned} M(\phi)\dot{\tilde{s}}(t) &= J(\phi)^{-T} R(\phi) K \begin{bmatrix} z(t) \\ \tau_m(t) \end{bmatrix} - \frac{1}{2} \dot{M}(\cdot) \tilde{s}(t) \\ &\quad + f_x(t) - \tilde{x}(t) \\ \dot{\tilde{x}}(t) &= -\alpha \tilde{x}(t) + \tilde{s}(t) \end{aligned} \right\} \quad (8)$$

$$\left. \begin{aligned} f_x(t) &= -f(\cdot) + M(\phi)[\alpha \dot{\tilde{x}}(t) - \ddot{x}_r(t)] \\ &\quad + \frac{1}{2} \dot{M}(\cdot) \tilde{s}(t) + \tilde{x}(t) \in R^{Dn} \end{aligned} \right\} \quad (9)$$

and $f_x(t)$ has the following property useful for our controller development:

P4) There exists a positive constant c_x such that

$$\|f_x(t)\| \leq c_x \omega_x(t) \quad (10)$$

$$\omega_x(t) = 1 + \alpha + \alpha^2 + (1 + \alpha^2) \|\tilde{x}(t)\|^2 + \|u(t)\|^2 \in R. \quad (11)$$

The robust control law for the error models (8) subject to the assumptions A1 to A5 is given by

$$\begin{bmatrix} z(t) \\ \tau_m(t) \end{bmatrix} = -\mu_x(t)R(\phi)^T J(\phi)^{-1} \tilde{s}(t) \quad (12)$$

$$\mu_x(t) = \alpha + \beta_x \epsilon^2 + \beta_x \omega_x(t)^2 \in R \quad (13)$$

where $\beta_x, \epsilon > 0$ are design parameters. It is shown that the robust controller (12) guarantees an ultimate boundedness of the tracking error $\tilde{x}(t)$.

2. Robust Controller II

According to the design procedure shown in Fig. 2, we make the following assumption instead of the assumption A5 in the design of robust controller II:

A6) The control inputs are $\tau_b(t)$ for vehicle control and $\tau_m(t)$ for manipulator control.

As shown in Fig. 2, we first replace the input $z(t)$ in (12) by the desired trajectory $z_r(t)$, i.e.,

$$\begin{bmatrix} z_r(t) \\ \tau_m(t) \end{bmatrix} = -\mu_x(t)R(\phi)^T J(\phi)^{-1} \tilde{s}(t) \quad (14)$$

and then design robust controller II by using the tracking error of $z(t)$. When we choose the error as the normal one $\tilde{z}_n(t) = z(t) - z_r(t)$, then the error model is written as $\dot{\tilde{z}}_n(t) = -AD(v)z(t) - \dot{z}_r(t) + BD(v)\tau_b(t)$. This model has a situation where the system is uncontrollable due to lack of the rank of $BD(v)$ when some of $v_i(t)$ equal zero. This situation is caused by the thruster nonlinearities shown in Fig. 1. In order to avoid the situation, we propose the following error instead of the normal one $\tilde{z}_n(t)$:

$$\tilde{z}(t) = z(t) - z_r(t) + 2\epsilon l(v) \quad (15)$$

$$\left. \begin{aligned} l(v) &= \{I_m - E(v)\} \bar{v}(v) \in R^{Dm} \\ E(v) &= \text{diag} \{e^{-|v_1|}, \dots, e^{-|v_{Dm}|}\} \in R^{Dm \times Dm} \\ \bar{v}(v) &= [\text{sgn}(v_1), \dots, \text{sgn}(v_{Dm})]^T \in R^{Dm} \end{aligned} \right\} \quad (16)$$

It should be noted that the signal $l(v)$ is bounded for all $v(t)$. As a result of adding the term $l(v)$, the error model of $\tilde{z}(t)$ is expressed as

$$\dot{\tilde{z}}(t) = BL(v)\tau_b(t) - \bar{I}^T K R(\phi)^T J(\phi)^{-1} \tilde{s}(t) + f_z(t) \quad (17)$$

$$\left. \begin{aligned} L(v) &= D(v) + \epsilon E(v) \in R^{Dm \times Dm} \\ \bar{I} &= \begin{bmatrix} I_m \\ 0 \end{bmatrix} \in R^{Dn \times Dm} \\ f_z(t) &= -AL(v)z(t) + \bar{I}^T K R(\phi)^T J(\phi)^{-1} \tilde{s}(t) \\ &\quad - \dot{z}_r(t) \in R^{Dm} \end{aligned} \right\} \quad (18)$$

and $f_z(t)$ has the following property useful for our controller development:

P5) There exists a positive constant c_z such that

$$\|f_z(t)\| \leq c_z \omega_z(t) \quad (19)$$

$$\left. \begin{aligned} \omega_z(t) &= w_{z2}(t) + w_{z3}(t) \|\tilde{s}(t)\| \in R \\ w_{z1}(t) &= 1 + \|u(t)\|^2 + \|z(t)\| + \|\tau_m(t)\| \\ w_{z2}(t) &= [w_{z1}(t) + \alpha \|\dot{\tilde{x}}(t)\|] \mu_x(t) + \|L(v)z(t)\| \\ w_{z3}(t) &= 1 + (1 + \alpha^2) \beta_x \omega_x(t) \|\tilde{x}(t)\| \|\dot{\tilde{x}}(t)\| \\ &\quad + [\mu_x(t) + \beta_x \omega_x(t) w_{z1}(t)] \|u(t)\|. \end{aligned} \right\} \quad (20)$$

It is noteworthy that the coefficient matrix $BL(v)$ of the input $\tau_b(t)$ in the error model (17) has a full rank for all $v(t)$, and hence the error model is controllable in spite of the thruster nonlinearities.

The robust control law for the error model (17) subject to the assumptions A1 to A4 and A6 is given by

$$\tau_b(t) = -\mu_z(t)L(v)^{-1} \tilde{z}(t) \quad (21)$$

$$\mu_z(t) = \alpha + \beta_z \omega_z(t)^2 \in R \quad (22)$$

where $\beta_z > 0$ is a design parameter.

In addition to the error $\tilde{z}(t)$, we use the errors $\tilde{s}(t)$ and $\tilde{x}(t)$, introduced for the design of robust controller I, to guarantee the stability of the overall closed loop system. The error models (8) concerning $\tilde{s}(t)$ and $\tilde{x}(t)$ need to be modified because $z(t)$ in the input (12) for robust controller I is replaced by $z_r(t)$. Using (15), we rewrite (8) as

$$\left. \begin{aligned} M(\phi) \dot{\tilde{s}}(t) &= J(\phi)^{-T} R(\phi) K \begin{bmatrix} z_r(t) \\ \tau_m(t) \end{bmatrix} - \frac{1}{2} \dot{M}(\cdot) \tilde{s}(t) \\ &\quad + J(\phi)^{-T} R(\phi) K \bar{I} \tilde{z}(t) + f_x(t) - \tilde{x}(t) \\ &\quad - 2\epsilon J(\phi)^{-T} R(\phi) K \bar{I} l(v) \\ \dot{\tilde{x}}(t) &= -\alpha \tilde{x}(t) + \tilde{s}(t) \end{aligned} \right\} \quad (23)$$

For robust controller I and II, the following theorem holds:

Theorem 1 Consider the robust controller (14) and (21) for the error models (17) and (23) subject to the assumptions A1 to A4 and A6. This controller guarantees that the signals $x(t)$, $\dot{x}(t)$, $u(t)$, $v(t)$, $z(t)$, $z_r(t)$, $\tau_m(t)$ and $\tau_b(t)$ in the closed loop system are bounded, and that the tracking error $\tilde{x}(t)$ satisfies the inequality

$$\|\tilde{x}(t)\|^2 \leq \rho_1 e^{-\gamma \alpha t} + \frac{\rho_2}{\alpha \beta} \quad (24)$$

where ρ_1 and ρ_2 are positive constants, $\beta = \min\{\beta_x, \beta_z\}$, and $\gamma = \min\{2c_{RKJ}/c_{M1}, 2, 2c_B\}$.

The inequality (24) in Theorem 1 means that an ultimate bound of $\tilde{x}(t)$ can be arbitrarily reduced by increasing the design parameters α , β_x and β_z . It should be noted that a high gain controller can be constructed for the model (5), since the slow thruster dynamics is taken into consideration in the design of controller.

Proof: We first choose the positive definite function

$$V(t) = \frac{1}{2} [\tilde{s}(t)^T M(\phi) \tilde{s}(t) + \tilde{x}(t)^T \tilde{x}(t) + \tilde{z}(t)^T \tilde{z}(t)] \quad (25)$$

and then the time derivative of $V(t)$ along the solutions of (17) and (23) is given by

$$\dot{V}(t) \leq -\gamma \alpha V(t) + \frac{\gamma \rho_2}{2 \beta} \quad (26)$$

In the derivation of (26), we use the control law (14) and (21), the inequalities in the properties P1 to P3 and the inequalities

$$\left. \begin{aligned} -\beta_x \omega_x(t)^2 \tilde{s}(t)^T H(\phi) \tilde{s}(t) + \tilde{s}(t)^T f_x(t) &\leq \frac{\rho_3}{2 \beta_x} \\ -\beta_x \epsilon^2 \tilde{s}(t)^T H(\phi) \tilde{s}(t) \\ &\quad - 2\epsilon \tilde{s}(t)^T J(\phi)^{-T} R(\phi) K \bar{I} l(v) \leq \frac{\rho_4}{2 \beta_x} \\ -\beta_z \omega_z(t)^2 \tilde{z}(t)^T B \tilde{z}(t) + \tilde{z}(t)^T f_z(t) &\leq \frac{\rho_5}{2 \beta_z} \end{aligned} \right\} \quad (27)$$

$$H(\phi) = J(\phi)^{-T} R(\phi) K R(\phi)^T J(\phi)^{-1} \in R^{Dn \times Dn} \quad (28)$$

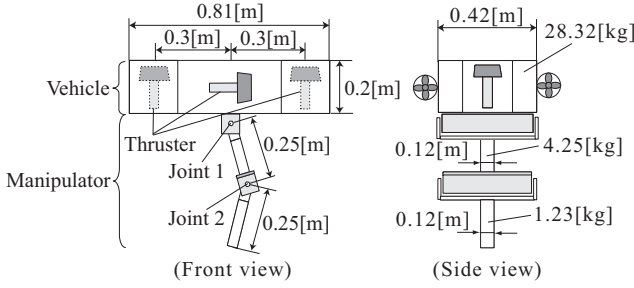


Fig. 3. UVMS for numerical simulation

where ρ_3, ρ_4 and ρ_5 are positive constants. From Lemma 3.2.4 in [8], (26) can be rewritten as

$$V(t) \leq e^{-\gamma\alpha t} V(0) + \frac{\rho_2}{2\alpha\beta}. \quad (29)$$

It follows from (29) that $\tilde{s}(t), \tilde{x}(t), \tilde{z}(t) \in L^\infty$. Using (7), (11), (13) to (16), (20) to (22), the assumption A4 and the inequalities in APPENDIX, we can easily prove that $x(t), \dot{x}(t), u(t), v(t), z(t), z_r(t), \tau_m(t)$ and $\tau_b(t) \in L^\infty$. Moreover, we can directly derive the inequality (24) from (29), and the proof is complete.

IV. SIMULATION EXAMPLE

In order to confirm the usefulness of our robust controller (14) and (21), we performed numerical simulation. Typical simulation results are presented in this paper. The UVMS simulated here was an underwater vehicle with a two-link manipulator, as shown in Fig. 3. The values of these system parameters were the same as those used in the reference [6]. In this figure, only the values of the main parameters are shown. Except for α , the controller design parameters were chosen as $\beta_x = 0.003, \beta_z = 0.001, \epsilon = 1$. Each of the desired trajectories of the vehicle's position and the manipulator end-effector's position is set up along a straight path. Each of the velocities is given by a filtered trapezoidal function. On the other hand, the desired trajectory of the vehicle's orientation is selected to remain at the initial value.

Fig. 4 shows the simulation result for $\alpha = 10$. It can be seen from this figure that $x(t)$ (the vehicle's position and orientation) and the manipulator end-effector's position tracks the desired trajectory $x_r(t)$ in spite of the nonlinearities of thruster dynamics and the uncertainties of system parameters.

The simulation where α is selected as various values was carried out. In this paper, the tracking errors for $\alpha = 8, 9, 10$ are shown in Fig. 5. As shown in Fig. 5, the control performance is improved by increasing the design parameter α .

V. CONCLUSION

In this paper we developed a robust controller for underwater vehicle-manipulator systems with thruster dynamics. In the controller development we presented a new tracking error model that overcomes uncontrollability caused by the thruster dynamics. It is, furthermore, shown that all signals in the closed loop system are bounded, and that an ultimate bound of the tracking error can be reduced by increasing controller's design parameters.

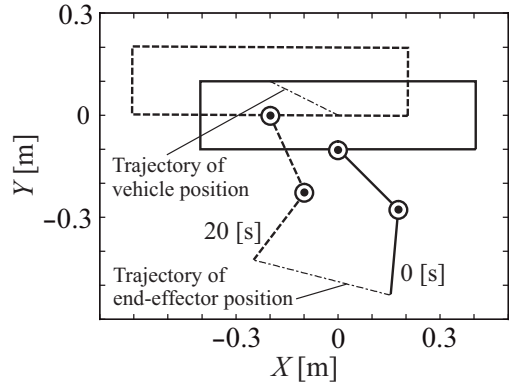


Fig. 4. Robot motion for $\alpha = 10$

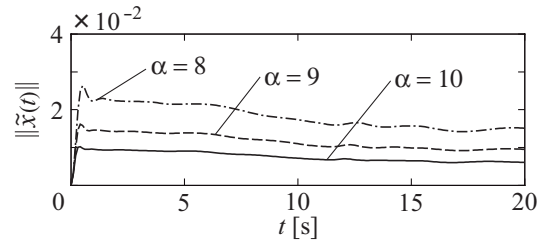


Fig. 5. Tracking error \tilde{x} for $\alpha = 8, 9, 10$

APPENDIX

Inequalities: The following inequalities, where c_* is a positive constant, are used for the design of controller in this paper:

- (i) $\|J(\phi)\| \leq c_{J1}, \|\dot{J}(\cdot)\| \leq c_{J2}\|u(t)\|, \|R(\phi)K\| \leq c_{RK}, \|R(\phi)\| \leq c_{R1}, \|\dot{R}(\cdot)\| \leq c_{R2}\|u(t)\|, \|\dot{u}(t)\| \leq c_u w_{z1}(t)$
- (ii) $\|\dot{M}(\cdot)\| \leq c_{M2}\|u(t)\|, \|M(\phi)^{-1}\| \leq c_{M3}, \|f(\cdot)\| \leq c_f(1 + \|u(t)\|^2), \|J(\phi)^{-1}\| \leq c_{J3}$ (if $J(\phi)$ has a full rank)

REFERENCES

- [1] Antonelli G (2003), Underwater robots: motion and force control of vehicle-manipulator systems. Springer-Verlag
- [2] Fossen TI (1991), Adaptive macro-micro control of nonlinear underwater robotic systems. Proc Int Conf Advanced Robotics, pp 1569-1572
- [3] Sarkar N, Yuh J, Podder TK (1999), Adaptive control of underwater vehicle-manipulator systems subject to joint limits. Proc IEEE/RSJ Int Conf Intelligent Robots and Systems, pp 142-147
- [4] Canudas de Wit C, Diaz EO, Perrier M (2000), Nonlinear control of an underwater vehicle/manipulator with composite dynamics. IEEE Trans Control Systems Technology 8(6): 948-960
- [5] Yatoh T, Sagara S, Tamura M (2008), Digital type disturbance compensation control of a floating underwater robot with 2 link manipulator. Artificial Life and Robotics 13(1): 377-381
- [6] Taira Y, Oya M, Sagara S (2010), An adaptive controller for underwater vehicle-manipulator systems including thruster dynamics. Proc Int Conf Modelling, Identification and Control, pp 185-190
- [7] Yoerger DR, Cooke JG, Slotine JJE (1990), The influence of thruster dynamics on underwater vehicle behavior and their incorporation into control system design. IEEE J Oceanic Engineering 15(3): 167-178
- [8] Ioannou PA, Sun J (1996), Robust adaptive control. Prentice Hall, p 75

Digital Adaptive Control of a Winged Rocket Applicable to Abort Flight

Tomoaki Shimozawa Shinichi Sagara

Department of Control Engineering, Kyushu Institute of Technology
Tobata, Kitakyushu 804-8550, Japan
E-mail: sagara@cntl.kyutech.ac.jp

Abstract: Since reusable launch vehicles (RLVs) have wide range flight conditions, the values of parameters of the dynamic equation are not constant. Then some adaptive control methods for the RLVs have been proposed and digital control systems are suited for digital computers. However, the control performance decreases when the nonlinearity strengthens though a linear adaptive control has an excellent performance when the nonlinearity of the controlled system can be disregarded. In this paper, we apply a digital adaptive feedback linearization control method with time-scale separation to a winged rocket in the abort flight. The simulation results show the effectiveness of the control systems.

Keywords: Adaptive Control, Flight Control

Nomenclature

$\delta_a, \delta_e, \delta_r$	=aileron, elevator and rudder deflection angles
p, q, r	=rotational rates
α, β	=angle of attack, sideslip angle
ϕ, θ	=bank angle, pitch angle
L_*, M_*, N_*	=aerodynamic rolling, pitching and yawing moments
I_{ij}	=moment/product of inertia
V_{TAS}	=true airspeed

1 Introduction

In late years space development is performed lively all over the world, and the research of space transportation systems to enable them is performed. Especially, Reusable Launch Vehicles (RLVs) are expected for the space transportation systems because the RLVs are the low-cost and highly reliable transport system instead of the conventional disposable rockets.

Since the RLVs have wide range flight conditions to the space from the ground, the values of parameters of the dynamic equation of the RLVs are not constant. Therefore, gain scheduling control method [1] that is linearized at a series of design points to be decided by the velocity and the altitude of the RLV and whose parameters of the controller are switched for the change of flight conditions has been applied for the RLVs. However, the gain scheduling control method has drawbacks for the RLVs. First, when the air traffic window expands, the number of required gains to be designed and the schedule becomes very

large to guarantee control performance above a certain level in all flight conditions. Second, since the gain scheduling control method can only correspondence to the known change; the control performance of the method becomes worse for the unpredictable change in the flight condition such as the abort flight.

For the change of the flight conditions, adaptive control methods using approximated linear dynamic equation of the RLVs have been researched [2]– [5]. However, the control performance decreases when the nonlinearity strengthens though a linear adaptive control has an excellent performance when the nonlinearity of the controlled system can be disregarded. Then, the feedback linearization method for deleting the nonlinear term by the state feedback for the nonlinear equation of motion of the RLV have been researched [6]. In addition, the method for dividing time-scale by a fast motion and a slow motion is researched for the simplification of the structure of the control system [7]. However, an internal aerodynamic parameter is fixed in their control methods.

In this paper, we apply a digital adaptive feedback linearization control method with time-scale separation to a winged rocket [8] in the abort flight, and the simulations are done to validate the effectiveness of the control systems in wide range flight conditions. The simulation results show that the control system has a good control performance.

2 Model of winged rocket

Fig. 1 shows an outline of a winged rocket [8] and the parameters are shown in Table 1. It has two elevons and two rudders as aerodynamic control surfaces. Since the configuration of the winged rocket

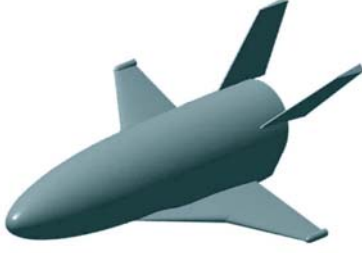


Fig. 1 Winged Rocket

Table 1 Winged rocket parameters

	Parameter
Body length	2.5[m]
Mass	241[kg]
Body outer diameter	0.57[m]
Wing area	1.05 [m ²]
Wing span	1.8[m]
Mean aerodynamic chord	0.67[m]
Position of center of gravity	65[%]

shown in Fig. 1 is similar for general airplanes, the nonlinear equation of fast states motion is expressed as follows [9]:

$$\dot{\mathbf{x}}(t) = \mathbf{A}(\mathbf{x})\mathbf{x}(t) + \mathbf{B}(\mathbf{x})\mathbf{u}(t) + \mathbf{C}(\mathbf{x})\mathbf{w}(t) \quad (1)$$

where

$$\mathbf{x}(t) = [p \ q \ r]^T, \quad \mathbf{u}(t) = [\delta_{ac} \ \delta_{ec} \ \delta_{rc}]^T,$$

$$\mathbf{w}(t) = [pq \ qr \ rp \ r^2 - p^2 \ \alpha \ \beta]^T,$$

$$\mathbf{A}(\mathbf{x}) = \mathbf{I}_d \begin{bmatrix} L_p & 0 & L_r \\ 0 & M_q & 0 \\ N_p & 0 & N_r \end{bmatrix},$$

$$\mathbf{B}(\mathbf{x}) = \mathbf{I}_d \begin{bmatrix} L_{\delta_a} & 0 & L_{\delta_r} \\ 0 & M_{\delta_e} & 0 \\ N_{\delta_a} & 0 & N_{\delta_r} \end{bmatrix},$$

$$\mathbf{C}(\mathbf{x}) = \mathbf{I}_d$$

$$\cdot \begin{bmatrix} I_{xz} & I_{yy} - I_{zz} & 0 & 0 & 0 & L_\beta \\ 0 & 0 & I_{zz} - I_{xx} & -I_{xz} & M_\alpha & 0 \\ I_{xx} - I_{yy} & -I_{zz} & 0 & 0 & 0 & N_\beta \end{bmatrix}$$

and \mathbf{I}_d is inertia matrix. When $\dot{\mathbf{x}}$ is discretized for forward difference by sampling period T , Eq. (1) is expressed as follows:

$$\begin{aligned} \mathbf{x}(k+1) &= (\mathbf{I} + T\mathbf{A}(\mathbf{x}))\mathbf{x}(k) \\ &\quad + T\mathbf{B}(\mathbf{x})\mathbf{u}(k) + T\mathbf{C}(\mathbf{x})\mathbf{w}(k) \\ &= \mathbf{A}_T(\mathbf{x})\mathbf{x}(k) + \mathbf{B}_T(\mathbf{x})\mathbf{u}(k) + \mathbf{C}_T(\mathbf{x})\mathbf{w}(k) \end{aligned} \quad (2)$$

where, \mathbf{I} is identity matrix.

On the other hand, nonlinear equation of slow states motion is expressed as follows [9]:

$$\dot{\mathbf{y}}(t) = \mathbf{D}(\mathbf{y})\mathbf{x}(t) + \mathbf{E}\mathbf{h}(t) + \mathbf{g}(t) \quad (3)$$

where,

$$\mathbf{y}(t) = [\alpha \ \beta \ \phi]^T$$

$$\mathbf{h}(t) = \left[\frac{\sin \alpha}{V_{TAS} \cos \beta} \quad \frac{\cos \alpha}{V_{TAS} \cos \beta} \quad \frac{1}{V_{TAS}} \right]^T$$

$$\mathbf{D}(\mathbf{y}) = \begin{bmatrix} -\cos \alpha \tan \beta & 1 & -\sin \alpha \tan \beta \\ \sin \alpha & 0 & -\cos \alpha \\ 1 & \sin \phi \tan \theta & \cos \phi \tan \theta \end{bmatrix},$$

$$\mathbf{E} = \begin{bmatrix} -\frac{X}{m} & \frac{Z}{m} & 0 \\ 0 & 0 & \frac{Y}{m} \\ 0 & 0 & 0 \end{bmatrix},$$

and $\mathbf{g}(t)$ is the vector consisting of the gravitational forces. Similar for fast states motion, $\dot{\mathbf{y}}$ is discretized for forward difference by sampling period T , Eq. (3) is expressed as follows:

$$\mathbf{y}(k+1) = \mathbf{y}(k) + \mathbf{D}_T(\mathbf{y})\mathbf{x}(k) + \mathbf{E}_T\mathbf{h}(k) + T\mathbf{g}(k). \quad (4)$$

3 Control system

The design method in this paper is a digital adaptive feedback linearization control method with time-scale separation. To derive the input \mathbf{u} to control the output \mathbf{y} , this method is separated into two time-scales. In the fast time-scale, control surface deflection command $\mathbf{u} = [\delta_{ac} \ \delta_{ec} \ \delta_{rc}]^T$ is derived from rotational rate command $\mathbf{x}_c = [p_c \ q_c \ r_c]^T$. In the slow time scale, rotational rate command \mathbf{x}_c is derived from output command $\mathbf{y}_c = [\alpha_c \ \beta_c \ \phi_c]^T$.

3.1 Inner loop for the fast states

Here, control input to Eq. (2) is defined as

$$\begin{aligned} \mathbf{u}(k) &= \mathbf{B}_T^{-1} \{ \mathbf{x}_d(k+1) - \mathbf{A}_T(\mathbf{x})\mathbf{x}(k) - \mathbf{C}_T(\mathbf{x})\mathbf{w}(k) \\ &\quad - \mathbf{A}(\mathbf{x}_d(k) - \mathbf{x}(k)) \} \end{aligned} \quad (5)$$

where, $\mathbf{A} = \text{diag}\{\lambda_i\}$ ($i = p, q, r$) is the gain matrix and \mathbf{x}_d is the output of the reference model. From Eqs. (2) and (5), the output error $\mathbf{e}_f(k) = \mathbf{x}_d(k) - \mathbf{x}(k)$ is

$$\mathbf{e}_f(k+1) = \mathbf{A}\mathbf{e}_f(k). \quad (6)$$

And if λ_i is selected to satisfy $0 < \lambda_i < 1$, the output error $\mathbf{e}_f(k)$ tends to zero as k tends to infinity. In a case of unknown parameters, we introduce the matrices $\hat{\mathbf{A}}_T(\mathbf{x})$, $\hat{\mathbf{B}}_T(\mathbf{x})$ and $\hat{\mathbf{C}}_T(\mathbf{x})$ whose coefficients are estimated values of the coefficients in $\mathbf{A}_T(\mathbf{x})$, $\mathbf{B}_T(\mathbf{x})$ and $\mathbf{C}_T(\mathbf{x})$, respectively. The coefficients in $\hat{\mathbf{A}}_T(\mathbf{x})$, $\hat{\mathbf{B}}_T(\mathbf{x})$ and $\hat{\mathbf{C}}_T(\mathbf{x})$ are estimated by using adaptive algorithms [11].

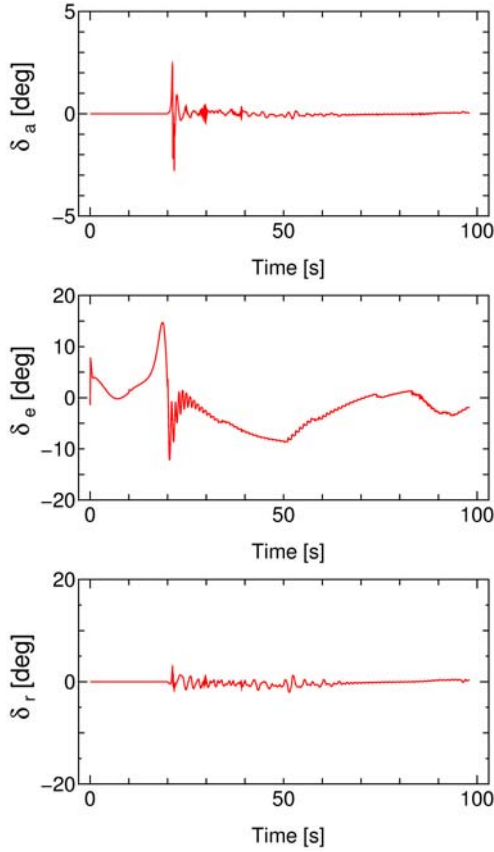


Fig. 2 Input

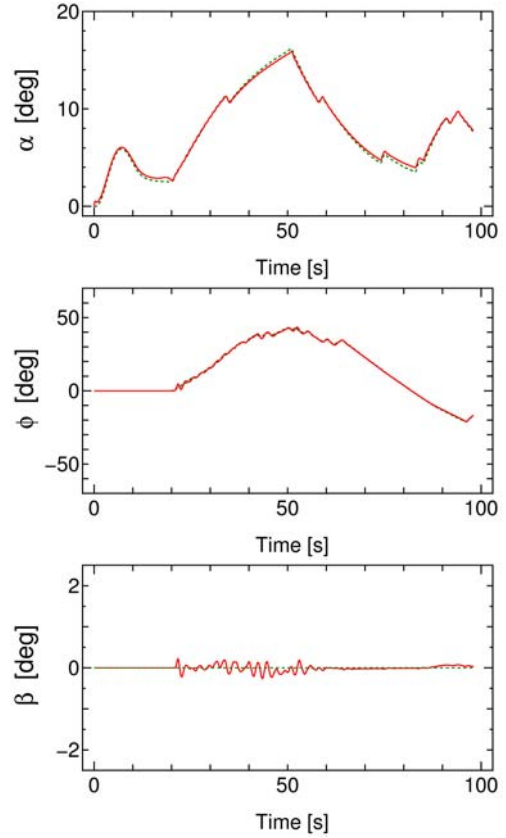


Fig. 3 Output

3.2 Outer loop for the slow states

From Eq. 4, the rotational rate command is obtained by following equations:

$$\mathbf{x}_c(k) = \mathbf{D}_T^{-1} \{ \mathbf{y}_d(k+1) - \mathbf{y}(k) - \mathbf{E}_T(\mathbf{y})\mathbf{h}(k) - \mathbf{T}g(k) - \mathbf{P}(\mathbf{y}_d(k) - \mathbf{y}(k)) \} \quad (7)$$

where, $\mathbf{P} = \text{diag}\{p_i\}$ ($i = \alpha, \beta, \phi$) is gain matrix and \mathbf{y}_d is output of the reference model. From Eq. 3 and 7, output error $\mathbf{e}_s(k) = \mathbf{y}_d(k) - \mathbf{y}(k)$ is

$$\mathbf{e}_s(k+1) = \mathbf{P}\mathbf{e}_s(k). \quad (8)$$

And if p_i is selected to satisfy $0 < p_i < 1$, the output error $\mathbf{e}_s(k)$ tends to zero as k tends to infinity.

In this paper, unknown parameters in Eq. 7 uses the fixed values obtained from the wind tunnel examination result.

4 Numerical simulation

To validate the adaptive control system described, computer simulations for a 6-DOF nonlinear winged rocket model [10] considering the atmospheric fluctuation are performed. simulation condition is follows. When the winged rocket is climbing, a trouble is happened at about 4000[m] in altitude. Then

the winged rocket changes the thrust power from 3000[N] into 0[N] for changing the route. That is an abort flight. At the start of the simulation, the altitude of the winged rocket is 3200[m], downrange is 3000[m], crossrange is 0[m], the velocity is 80[m/s] and the pitch angle is 70[deg]. At the target point, downrange and crossrange are 0[m], and altitude is 200[m]. The aerodynamic coefficient of the winged rocket uses the value obtained from the wind tunnel examination result. The actuators of elevons is used that the attenuation coefficient $\zeta = 0.7$ and the natural frequency $\omega_n = 72[\text{rad/s}]$. The sampling period of the control system is $T = 0.01[\text{s}]$. The gain of fast states are $\lambda_p = 0.95$, $\lambda_q = 0.90$ and $\lambda_r = 0.90$. The gain of slow states are $p_\alpha = 0.90$, $p_\beta = 0.92$ and $p_\phi = 0.95$. A constant trace algorithm [11] is utilized for parameter estimation.

Figs. 2 and 3 show the input and the output, respectively. In Fig. 3, the dotted lines show the output of the reference model. From Fig. 2, we can see that the input commands to the actuators is almost smooth. And from Fig. 3, it can be seen that the angle of attack and the bank angle follow to the reference output well, and the side-slip angle is suppressed to 0.5[deg] or less. Next, Fig. 4 is flight trajectory. From Fig. 4, we can see that the winged

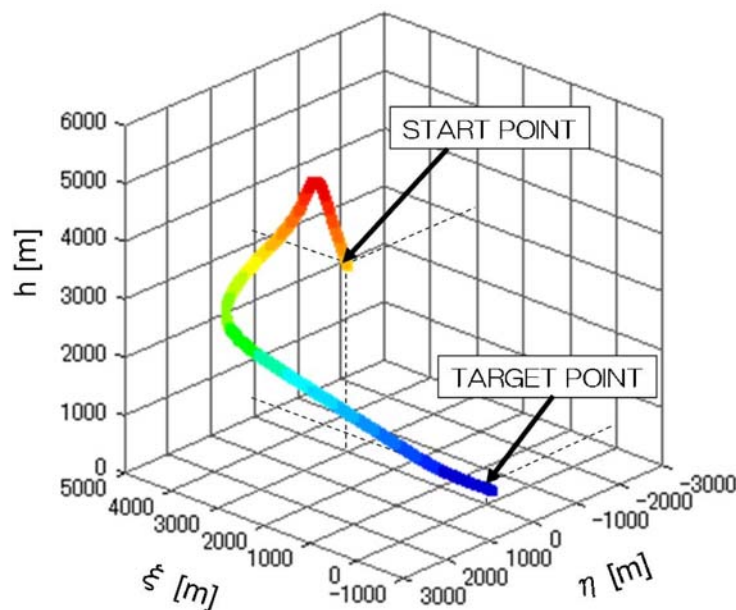


Fig. 4 Trajectory

rocket arrives at the neighborhood the target point.

From the simulation result, it can be confirmed that the applied control method is effective for the flight control of the winged rocket.

5 Conclusion

In this paper, we apply a digital adaptive feedback linearization control method with time-scale separation to a winged rocket in the abort flight. From the numerical simulation, we showed that the control system of the winged rocket has a good control performance.

References

- [1] T. Tsukamoto, H. Suzuki, T. Ninomiya, "Guidance and Control Law Design for High Speed Flight Demonstration Phase II", *JAXA Research and Development Report*, JAXA-RR-04-006, 2004 (in Japanese).
- [2] Eric N. Johnson, Anthony J. Calise, "Limited Authority Adaptive Flight Control for Reusable Launch Vehicles", *Journal of Guidance, Control, and Dynamics*, vol. 26, no. 6, pp. 906-913, 2003.
- [3] M. Morimoto, K. Uchiyama, Y. Shimada, A. Abe, "Adaptive Attitude Control with Reduced Number of Estimated Parameters for Automatic Landing System", *International Conference on Control, Automation and Systems 2007*, pp. 2865-2870, 2007.
- [4] J. Brinker. and K. Wise, "Reconfigurable Flight Control for a Tailless Advanced Fighter Aircraft", *Proceedings of AIAA Guidance, Navigation and Control Conference*, pp. 75-87, 1998.
- [5] Eric N. Johnson, Anthony J. Calise, "Pseudo-Control Hedging: A New Method for Adaptive Control", *Advances in Navigation Guidance and Control Technology Workshop*, November, 1-2, 2000.
- [6] Eric N. Johnson, Anthony J. Calise, "A Six Degree of Freedom Adaptive Flight Control Architecture for Trajectory Following", *Proceedings of the AIAA Guidance, Navigation, and Control Conference*, 2002.
- [7] P. K. Menon, V. R. Iragavarapu, and E. J. Ohlmeyer, "Nonlinear Missile Autopilot Design Using Time-Scale Separation", *AIAA paper*, 97-3765-CP, pp. 1791-1803, 1997.
- [8] K. Yonemoto, T. Shidooka, K. Okuda, "Development and Flight Test of Winged Rocket", *The 27th International Symposium on Space Technology and Science*, 2009.
- [9] B. Etkin, L. D. Reid, *Dynamics of Flight: Stability and Control*, New York: John Wiley & Sons, Inc, 1996.
- [10] HIMES Research Group, "Conceptual Design of HIMES (Winged Test Rocket)", *Institute of Space and Astronautical Science, Ministry of Education*, March 19, 1987 (in Japanese).
- [11] G. C. Goodwin, R. H. Middleton, *Digital Control and Estimation*, Prentice-Hall International, p. 379, 1990.

A Master-Slave Control System for Semi-Autonomous Underwater Vehicle-Manipulator System

Kana Kawano Tomoaki Shimozawa Shinichi Sagara

Department of Control Engineering, Kyushu Institute of Technology
Tobata, Kitakyushu 804-8550, Japan
E-mail:sagara@cntl.kyutech.ac.jp

Abstract: Underwater Vehicle-Manipulator Systems (UVMS) are expected to make important roles in ocean exploration. It is considered that UVMSs will be operated by automatic and manual control. We have proposed an automatic control method. In this paper, we propose a master-slave system for UVMS. The effectiveness of the proposed master-slave control systems is demonstrated by using a floating underwater robot with 2-link manipulator.

Keywords: Underwater Robot, Manipulator, Master-Slave Control System

1 Introduction

Underwater robots are expected to make important roles in ocean exploration and many studies on Underwater Vehicle-Manipulator Systems (UVMS) are performed in recent years [1–5]. However there are only a few experimental studies. We have proposed digital Resolved Acceleration Control (RAC) methods for UVMS [6,7] and the effectiveness of the RAC methods has been demonstrated by using a floating underwater robot with vertical planar 2-link manipulator.

Here, underwater robots having small size manipulators have been used in real situations. Since the robots are operated by manual control, it is considered that UVMSs will be operated by automatic and manual control.

In this paper, we propose a master-slave control system for UVMS. The master-slave control system is consisting of the master controllers of the vehicle and the manipulator, and UVMS equipped with the RAC. Our proposed master controller of the vehicle can manipulate only one hand. The effectiveness of the proposed master-slave control systems is demonstrated by using a floating underwater robot with 2-link manipulator.

2 Configuration of Master-Slave Control System

2.1 UVMS

The underwater robot used in this paper is shown in Fig. 1. The robot has a robot base (vehicle) and a 2-link manipulator. By six thrusters equipped in the robot base, three-dimensional movement is possible.

Our proposed Resolved Acceleration Control (RAC) method [6] is applied to the control system



	Base	Link 1	Link 2
Mass [kg]	23.05	4.65	4.65
Volume [$\times 10^{-3}$ m ³]	25.95	3.3	3.1
Moment of inertia [kgm ²]	1.67	0.075	0.075
Link length (x axis) [m]	0.870	0.35	0.28
Link length (y axis) [m]	0.640	-	-
Link length (z axis) [m]	0.335	-	-
Link diameter [m]	-	0.13	0.13
Added mass(x) [kg]	34.05	0.35	0.35
Added mass(y) [kg]	24.48	3.31	3.31
Added mass(z) [kg]	60.43	3.31	3.31
Added moment of inertia [kgm ²]	1.28	0.06	0.06
Drag coefficient(x)	1.2	0	0
Drag coefficient(y)	1.2	1.0	1.0
Drag coefficient(z)	1.2	1.0	1.0

Fig. 1 2 link underwater robot

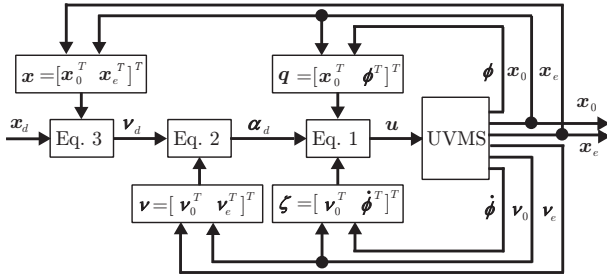


Fig. 2 Configuration of RAC system

of the robot. The RAC method is consisting of the following equations of motion of the robot, desired acceleration and desired velocity:

$$\mathbf{u} = \mathbf{M}(\mathbf{q})\alpha_d + \mathbf{N}(\mathbf{q}, \zeta)\zeta + \mathbf{f} \quad (1)$$

$$\alpha_d(k) = \frac{1}{T}\mathbf{W}(k)^\# \{\nu_d(k+1) - \nu_d(k) + \mathbf{A}\mathbf{e}_\nu(k) + T\mathbf{f}(k)\} \quad (2)$$

$$\nu_d(k) = \frac{\mathbf{S}_{0e}}{T}\{\mathbf{x}_d(k) - \mathbf{x}_d(k-1) + \mathbf{T}\mathbf{e}_x(k-1)\} \quad (3)$$

where for Eq. (1) $\mathbf{q} = [\mathbf{x}_0^T, \phi^T]^T$ and $\zeta = [\dot{\mathbf{x}}_0^T, \dot{\phi}^T]^T$, \mathbf{x}_0 is the position and attitude vector of robot base, ϕ is the relative joint angle vector, \mathbf{v}_0 is the linear and angular vector of robot base, \mathbf{M} is the inertia matrix including the added mass and inertia, $\mathbf{N}(\mathbf{q}, \zeta)\zeta$ is the vector of Coriolis and centrifugal forces, \mathbf{f} is the vector consisting of the drag, gravitational and buoyant forces and moments, $\mathbf{u} = [\mathbf{f}_0^T, \tau_0^T, \tau_m^T]^T$, \mathbf{f}_0 and τ_0 are the force and torque vectors of vehicle, τ_m is the joint torque vector of manipulator. For Eqs. (2) and (3) $\mathbf{e}_\nu(k) = \nu_d(k) - \nu(k)$ and $\mathbf{e}_x(k) = \mathbf{x}_d(k) - \mathbf{x}(k)$, T is a sampling period, \mathbf{S}_{0e} is the transformation matrix, and $\mathbf{W}^\#$ is the pseudoinverse of \mathbf{W} , i.e. $\mathbf{W}^\# = \mathbf{W}^T(\mathbf{W}\mathbf{W}^T)^{-1}$, \mathbf{x}_d is the desired value of $\mathbf{x} = [\mathbf{x}_0^T, \mathbf{x}_e^T]^T$, $\mathbf{A} = \text{diag}\{\lambda_i\}$ and $\mathbf{T} = \text{diag}\{\gamma_i\}$ ($i = 1, \dots, 12$) are the velocity and the position feedback gain matrices.

Fig. 2 shows the configuration of the RAC system.

2.2 Master controller

Fig. 3 shows our developing operating device consisting of base and manipulator operation parts.

The base operating device can perform the operation of 3-DOF position and 3-DOF attitude with having grasped a rectangular solid in the center of the hemisphere with one hand. At first the roll, pitch and yaw of the rectangular solid which is inclined to the arbitrary direction of the rotational motion is measured by three servo actuators which were arranged so that an axis is perpendicular at the center of rectangular solid. The posture of the rectangular

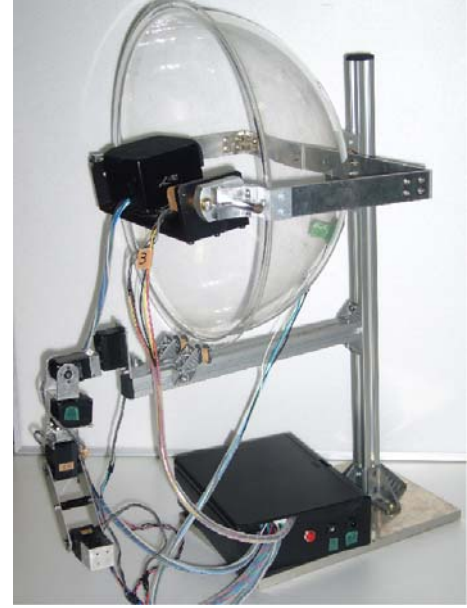


Fig. 3 Master Controller

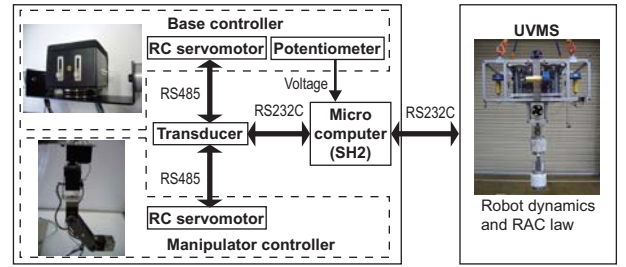


Fig. 4 Configuration of master-slave system

solid can reduce the burden of the manipulator because it is maintained when the operator separated a hand by using the servo actuator. Next, the operator can perform the translational motion by three potentiometer equipped the rectangular solid. It can come true by handling it as translational speed in proportion to displacement (a potential difference) from the center of a lever of the potentiometer.

On the other hand, servo actuators are equipped to each joint of the manipulator operation device. The servo actuators are used for the keeping the posture of the manipulator and the obtaining the joint angles.

The configuration of the master-slave control system is shown in Fig. 4. Using the three potentiometers and three servo actuators the desired translational speed and attitude of the robot base are transmitted to the robot base through a microcomputer. In the similar manner, using the two servo actuators the desired joint angles are transmitted to the manipulator. The transmission rate between the microcomputer and the robot is 115200[bps].

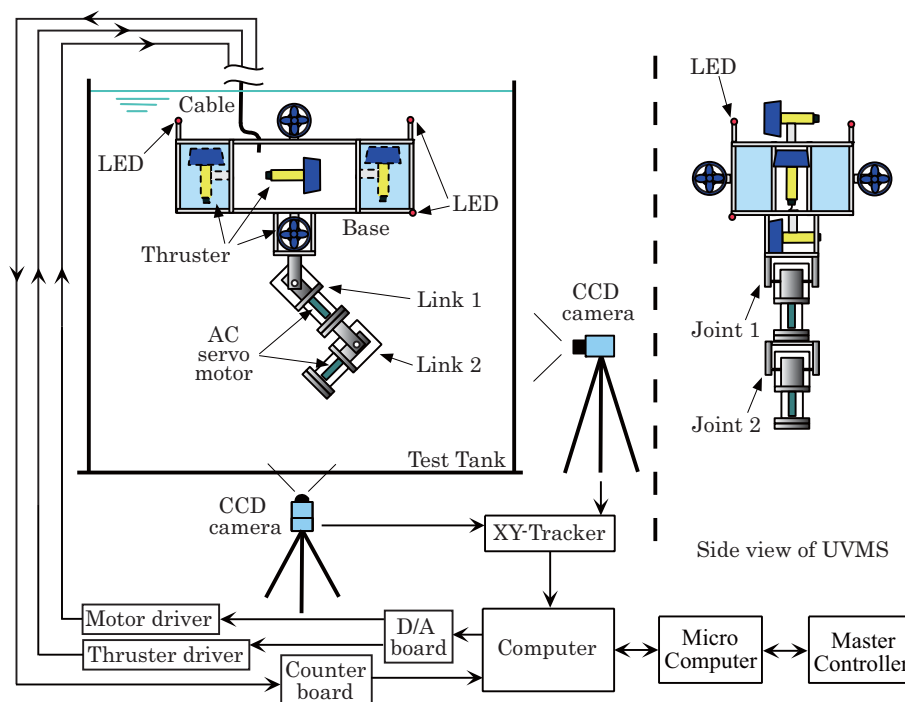


Fig. 5 Configuration of experimental system

3 Experiments

In this section, experiments are done to verify the effectiveness of the master-slave control system for UVMS using the experimental system shown in Fig. 5

Fig. 6 shows an experimental result in the case of the rotational motion. From this figure, we can see that the robot base can follow the posture of the operating device. Especially, it can be seen that the robot base can keep the position and posture in spite of the movement of the manipulator from Fig. 6(b).

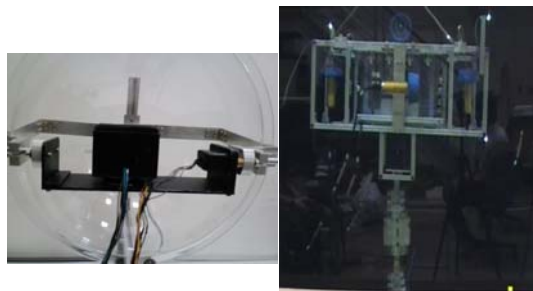
Fig. 7 shows an experimental result in the case of the translational motion. The pictures of Fig. 7(a) and (b) were taken from the front of the water tank, and the picture of Fig. 7(c) was taken from the side of the water tank. In this operation, robot base can be operated by using three potentiometers of the base operating device shown in Fig. 8.

4 Conclusion

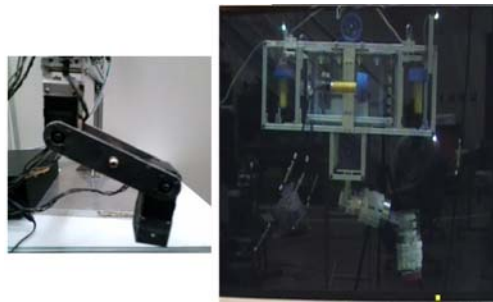
In this paper, we proposed a master-slave control system for UVMS. Our proposed master controller of the vehicle can manipulate only one hand. The effectiveness of the proposed master-slave control systems was demonstrated by using a floating underwater robot with 2-link manipulator.

References

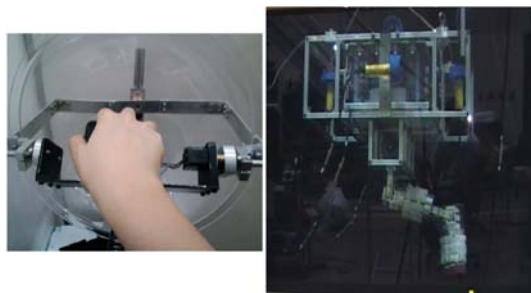
- [1] H. Maheshi *et al.*, "A Coordinated Control of an Underwater Vehicle and Robotic Manipulator", *J. Robotic Systems*, Vol. 8, No. 3, pp. 339 – 370, 1991.
- [2] T. W. McLain *et al.*, "Experiments in the Coordinated Control of an Underwater Arm/Vehicle System", *Autonomous Robots 3*, Kluwer Academic Publishers, pp. 213 – 232, 1996.
- [3] G. Antonelli *et al.*, "Tracking Control for Underwater Vehicle-Manipulator Systems with Velocity Estimation", *IEEE J. Oceanic Eng.*, Vol. 25, No. 3, pp. 399 – 413, 2000.
- [4] N. Sarkar and T. K. Podder, "Coordinated Motion Planning and Control of Autonomous Underwater Vehicle-Manipulator Systems Subject to Drag Optimization", *IEEE J. Oceanic Eng.*, Vol. 26, No. 2, pp. 228 – 239, 2001.
- [5] G. Antonelli, *Underwater Robotics*, Springer, pp. 1194–1206, 2003.
- [6] S. Sagara *et al.*, "Digital RAC for Underwater Vehicle-Manipulator Systems Considering Singular Configuration", *J. Artificial Life and Robotics*, Vol. 10, No. 2, pp. 106 – 111, 2006.
- [7] S. Sagara *et al.*, "Digital RAC with a Disturbance Observer for Underwater Vehicle-Manipulator Systems", *J. Artificial Life and Robotics*, Vol. 15, No. 3, pp. 270 – 274, 2010.



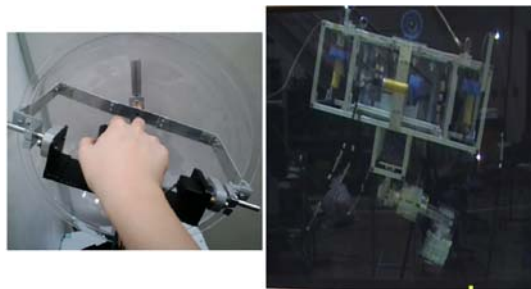
(a) initial posture



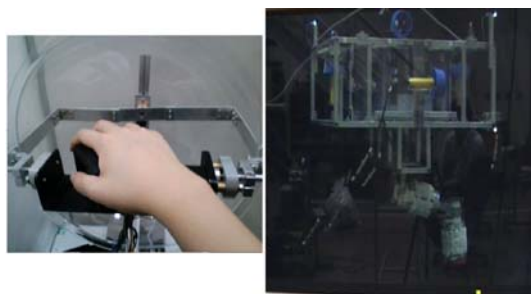
(b) operation of manipulator



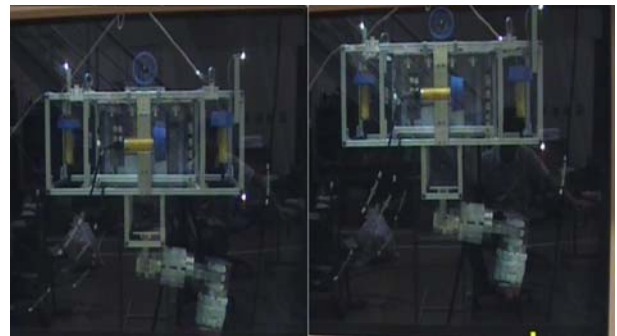
(c) operation of base (roll)



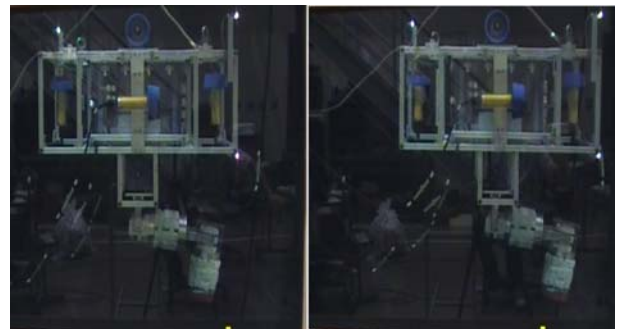
(d) operation of base (pitch)



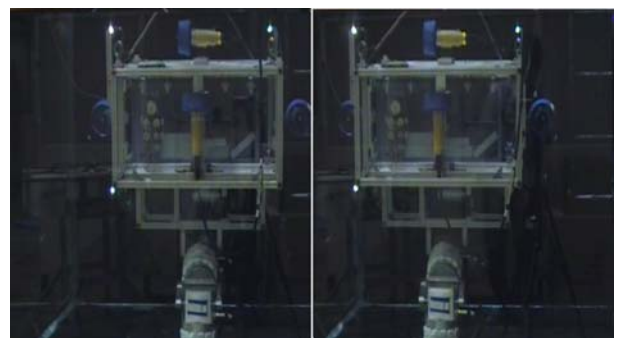
(e) operation of base (yaw)
Fig. 6 Rotational motion



(a) vertical direction



(b) horizontal direction



(c) seesaw direction

Fig. 7 Translational motion

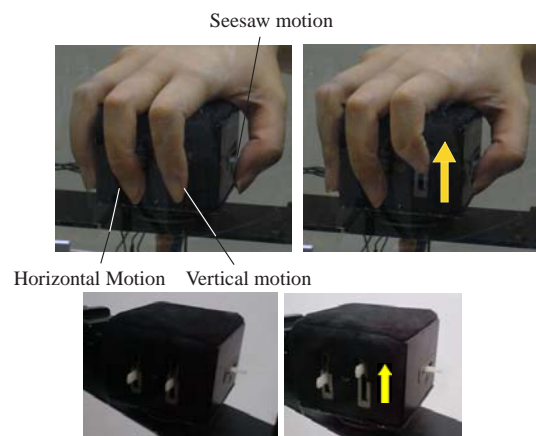


Fig. 8 Operation for translational motion

Survey of AI-Based Systems for Human Awareness Promotion in Meta-Cognition

Kiyota Hashimoto*, Kazuhisa Seta*, Hiroshi Tsuji*, and Kazuhiro Takeuchi**

Osaka Prefecture Univ.: 1-1, Gakuen-cho, Naka-ku, Sakai, 599-8531, Japan*
*Osaka Electro-Communication Univ**., 18-8, Hatsu-machi, Neyagawa, 572-8530, Japan*
(Tel : 81-72-252-1161; Fax : 81-72-254-9944)
(hash@lc.osakafu-u.ac.jp)

Abstract: More and more AI-based systems are being developed and used for human awareness promotion. Human awareness promotion is important in various fields like those of learning and problem-solving where participants are expected to be aware of the changing contextual information of themselves and the environments around them to perform better. For a better computational supports of such promotions, AI-based approaches with particular reference to the mechanism of human meta-cognition seem to be plausible. In this paper, as an introduction to the session dedicated to this issue, we give a short survey on the definition of awareness and key factors of AI-based approaches to human awareness promotion.

Keywords: AI-based system, human awareness, awareness promotion, meta-cognition

I. INTRODUCTION

When we do something, we do not only do the task but perform a variety of mental activities related to the task. One of the most important performances among them is awareness. We humans are always aware of, and sometimes miss, something that may be related to the task we are doing. Then what and how are we aware of, and how can computational supports promote and facilitate human awareness?

In this paper, we will review the concept of human awareness and some key factors of AI-based applications for human awareness promotion.

II. AWARENESS AND METACOGNITION

Although we too often take human awareness for granted, the nature and characteristics of human awareness is not apparently obvious. In fact, researchers have discussed human awareness differently from different perspectives.

Most broadly, awareness is the mental state or ability of a person to perceive, to feel, or to be conscious of anything, from events that are happening, to the situation around him, to the conditions of himself. In this sense, awareness may not imply understanding what it is and what it means. From the viewpoint of computational support of the awareness, however, it is usually assumed that awareness implies understanding.

More specifically, awareness may be classified into several kinds: situational awareness, workspace awareness, knowledge awareness and self-awareness,

though not limited to these.

Gutwin and Greenberg [1], for example, discuss human awareness as a situational one with which humans are aware of situational changes related to the task they are doing. They identified the following four basic characteristics of human awareness, as distinct from other kinds of knowing, according to [2],[3],[4].

1. Awareness is knowledge about the state of some environment, a setting bounded in time and space. For example, the environment might be the airspace that an air traffic controller is responsible for, and their knowledge might include aircraft headings, altitudes, and separation, and whether these factors imply a safe or unsafe situation.
2. Environments change over time, so awareness is knowledge that must be maintained and kept up-to-date. Environments may change at different rates, but in all cases a person must continually gather new information and update what they already know.
3. People interact with the environment, and the maintenance of awareness is accomplished through this interaction. People gather information from the environment through sensory perception, and actively explore their surroundings based on the information that they pick up.
4. Awareness is almost always part of some other activity. That is, maintaining awareness is rarely the primary goal of the activity: the goal is to complete some task in the environment. For

example, the air traffic controller's task is to move aircraft through a region efficiently and safely, and although awareness may affect success, it is not the primary intent. ([1] pp.8-9)

Here, importantly, Gutwin and Greenberg clearly state that awareness is something related to the surrounding environment during the course of performing a task. Then they distinguish situational awareness from workspace awareness. Workspace awareness, they argue, is "the up-to-the-moment understanding of another person's interaction with the shared workspace ([1] p.10)," according to [2]. Note that their concept of workspace awareness is solely related to the people in the workspace and how they interact with it.

On the other hand, Ogata, Matsuura, and Yano focus on knowledge awareness in their seminal works [5]-[10]. They follow the definition of awareness by Dourish and Bellottie [11]: "understanding of the activities of others, which provides a context for your own activity," and define knowledge awareness as awareness of the use of knowledge. Knowledge awareness, they argue, "gives each learner information about other learners' activities in a shared knowledge space." [10]

Both Gutwin and Greenberg and Ogata et al. focus on the possibility of computational support for a successful group dynamics and the sharing of knowledge in the group. Thus computational systems to support awareness along these lines, including many studies on computer-supported collaborative learning/work (CSCL/CSCW), are inevitably designed to facilitate awareness of others' activities.

However, awareness can also be viewed as a mental activity of a single individual. In this context, awareness is captured as the monitoring of object-level in the metacognitive process, as shown in Fig. 1, and as the discovery of something useful for the task and/or the development of metacognitive ability. From this viewpoint, not only the awareness of what a learner is doing and the environment around him but also the awareness of his own mental state and process is focused.

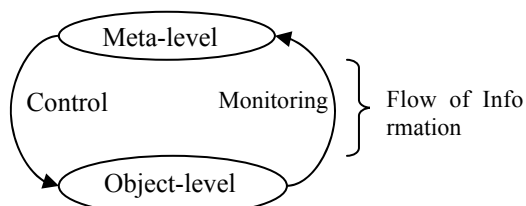


Fig. 1 Theoretical Model of the Mechanism of Metacognitive Process (Nelson and Narens 1990)

This concept of awareness is heavily related to the concept of self-regulated learning [13],[14]. According to the idea of self-regulated learning, learning is considered to be guided by metacognition, cognition in learning processes, and motivation, as shown in Fig. 2.

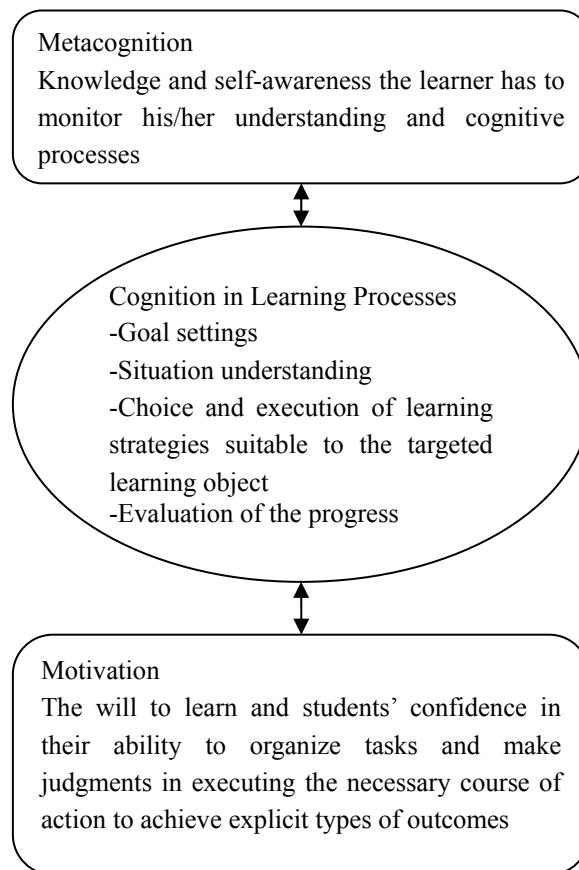


Fig. 2 Simple model of self-regulated learning

Here, what learners are supposed to learn is what a better learning is, as well as the learning objects. Thus, computational systems to support awareness along this line focus on facilitating or promoting awareness of self-condition compared to the desirable condition. There are numerous attempts along this line, including [15],[16],[17],[18].

Before leaving this section, note that these two different lines do not contradict each other. Rather, self-awareness can be boosted with the help of awareness of the others around him. Thus, the latter often focus on the cooperative or collaborative efforts in the group for a better self-awareness.

III. KEYS TO HUMAN AWARENESS PROMOTION

For promoting human awareness, whether it be

shared awareness in a group or self-awareness, there seem to be some key factors that must be considered: personalization or adaptivity, inferential model, effective information extraction, and explicitization or manifestation, though not limited to these. All these factors are expected to be supported effectively by AI-based systems.

1. Personalization or adaptivity

Naturally, humans differ from one another, not only in their preferences, characteristics, and socio-cultural backgrounds but also in their maturity and ability. Thus, any computational support system for promoting awareness has to adapt to individual learners in order to bridge the gap among different types of learners. In order to achieve this kind of adaptivity, the presentation of the domain knowledge and/or the learner's learning condition should be tailored in complexity and granularity according to his changing profiles. Formerly, this was achieved by preparing different profile-corresponding templates the choice of which was done by the learner himself. However, as expected, dependence on the learner's choice do not always reflect the actual condition of the learner and the more detailed, the harder the choice will. This naturally requires the system to be driven by an inferential modeling in order to be intelligent enough.

2. Data-driven inferential model

If voluntary choices of preferences, conditions, and others, are not informed of by the learner himself, computational support systems have to obtain relevant information otherwise. For example, most web-based learner support systems make use of various records of user actions as well as conscious inputs by the users. All these data, however, speak nothing by themselves. A rather detailed mental/learning process model is needed. The model to be adopted may vary among systems, but due to the large number of possible complex combinations of the acquired data, more than a simple matching method will be needed, and AI-based methods have been utilized. In particular, more and more studies are pursuing the utilization of ontology as a descriptive engine for inferential reasoning. As for mental models in detail, see [19]-[25], for example.

3. Effective information extraction and mining

Modern computational support system for awareness promotion naturally have to deal with a great quantity of data both on learning objects and learner monitoring.

Thus it has to be investigated what a better, effective way is to extract or mine the relevant, useful information, and to present it to learners.

4. Explicitization or manifestation

As we can walk without being consciously aware of inner muscle movements, we often do something without being aware of our relevant mental processes. However, the concept of self-regulated learning assumes that the more conscious, the better.. Sharing knowledge requires each to be conscious of what they know. Thus awareness, be it shared in the group or noticed by a single individual, involve the process of making the unknown or the hidden explicit to cognition. So computational support systems for awareness promotion has to do with effective explicitization of unknown or hidden information by persuading learners to turn their eyes to them.

VI. CONCLUDING REMARKS

This paper attempted a short, fragmental survey of awareness promotion, roughly consisting of review of the concept of awareness and key factors related to awareness promotion. To see more instances of computational support systems for awareness promotion, [26],[27] are a good starting point, together with the proceedings of annual ICWL, CSCWD, ICCE, and other related conferences and workshops.

REFERENCES

- [1] Gutwin, C. and S. Greenberg (1999) A Framework of awareness for small groups in shared-workplace groupware, Technical Report 99-1, Dept. of Computer Science, Univ. of Saskatchewan, Canada.Mourlas, C., N.
- [2] Adams, M., Y. Tenney, and R. Pew (1995) Situation awareness and the cognitive management of complex systems, *Human Factor*, 37(1), 85-104.
- [3] Endsley, M. (1995) Toward a theory of situation awareness in dynamic systems, *Human Factors*, 37(1), 32-64.
- [4] Norman, D. (1993) *Things that make us smart*, Reading, MA: Addison-Wesley.
- [5] Matsuura, N. T. Hidaka, K. Okada, and Y. Matsushita, (1995) VENUS: An informal communication environment supporting interest awareness, *Trans. Information Processing Society of Japan*, 36-6, 1322-1341.
- [6] Ogata, H. K. Matsuura, and Y. Yano (1996) Knowledge awareness: bridging between shared

- knowledge space and collaboration in Sharlok, *Proc. of Educational Telecommunications '96*, 232-237.
- [7] Ogata, H., K. Matsuura, and Y. Yano (1997) Awareness filtering: toward efficient collaborative learning, *Proc. of Artificial Intelligence in Education*, 207-214.
- [8] Ogata, H. and Y. Yano (1998) Knowledge awareness: bridging learners in a collaborative learning environment, *International Journal of Educational Telecommunications*, AACE, 4-2/3, 219-236.
- [9] Ogata, H., K. Imai, K. Matsuura, and Y. Yano (1999) Knowledge awareness map for open-ended and collaborative learning on World Wide Web, *Proc. of ICCE '99*, Vol.1, 319-326.
- [10] Ogata, H., Matsuura, K. and Yano, Y. (2003) Supporting Awareness in a CSCL Environment, *International Journal of Cognitive Processing* Vol.2-3, 1-15.
- [11] Dourish, P. and V. Bellotti (1992) Awareness and coordination in shared workspaces, *Proc. of Computer Supported Cooperative Work '92*, 107-114.
- [12] Nelson, T.O. and L. Narens (1990) Metamemory: A theoretical framework and new findings, *The Psychology of Learning and Motivation*, 26: 125-173.
- [13] Zimmerman, B. J. and Martinez-Pons, M. (1990) Student differences in self-regulated learning: Relating grade, sex, and giftedness to self-efficacy and strategy use, *Journal of Educational Psychology*, 82, 51-59.
- [14] Zimmerman, B. J., & Risemberg, R. (1997). Self-regulatory dimensions of academic learning and motivation. In G. D. Phye (Ed.), *Handbook of academic learning: Construction of knowledge*, pp. 105-125, New York: Academic Press.
- [15] Seta, K., K. Tachibana and M. Umano (2003) Basic consideration on reflection in problem-solving oriented learning, *Proc. of ICCE 03*, 160-168.
- [16] Seta, K., K. Tachibana, M. Umano and M. Ikeda (2005) Human Factor Modeling for Development of Learning Systems Facilitating Meta-Cognition, in C.-K. Looi, D. Jonassen, M. Ikeda (Eds): *Towards Sustainable and Scalable Educational Innovations Informed by the Learning Sciences, Frontiers in Artificial Intelligence and Applications*, Vol. 133, pp. 396-403, IOS Press
- [17] Seta, K. and M. Ikeda (2008) Conceptualizations for Designing a Learning System to Facilitate Metacognitive Learning, *Proc. of World Conference on Educational Multimedia, Hypermedia & Telecommunication*, 2134-2143.
- [18] Nakagawa, Y., H. Tsuji, K. Seta and K. Hashimoto (2010) Prototype of Collaborative Communication Portfolio for Better Awareness through Self-Reviews, *Proc. of International Symposium on Aware Computing*, 220-226.
- [19] Dunlosky, J. and J. Metcalfe (2009) *Metacognition*, Los Angeles: Sage.
- [20] Flavell, J. H. (1979) Metacognition and cognitive monitoring: a new area of cognitive-developmental inquiry, *American Psychologist* 34, 906-911.
- [21] Fox, E. and M. Riconscente (2008) Metacognition and self-regulation in James, Piaget, and Vygotsky, *Educational Psychological Review* 20, pp.373-389.
- [22] Hacker, D.J. and J. Dunlosky (eds.) (2009) *Handbook of Metacognition in Education*, New York: Routledge.
- [23] Hacker, D.J., J. Dunlosky, and A.C. Grasser (eds.) (1998) *Metacognition in Educational Theory and Practice*, New Jersey: Lawrence Elbaum Associates.
- [24] Perfect, T.J. and B.L. Schwartz (eds.) (2002) *Applied Metacognition*, Cambridge: Cambridge Univ. Pr.
- [25] Nonaka, I. and H. Takeuchi (1995) *The knowledge creating company. How Japanese companies create the dynamics of innovation*, New York: Oxford University Press.
- [26] Pahl, C. (2008) *Architecture Solutions for E-learning Systems*, Idea Group Reference.
- [27] Tsianos, and P. Germanakos (2009) *Cognitive and Emotional Processes in Web-Based Education: Integrating Human Factors and Personalization*, Hershey, NY: Information Science Reference

A Multilingual Problem-Based Learning Environment for Awareness Promotion

R. Taguchi, Katsuko T. Nakahira, H. Kanematsu*, and Y. Fukumura

Nagaoka University of Technology *Suzuka Technical College

(Tel : 81-258-47-9847)

(s095146@stn.nagaokaut.ac.jp)

Abstract: Traditionally, Problem Based Learning (PBL) has attracted attention as a method for training in engineering design skills. However, PBL is constrained in that students have to gather in one location, so cooperation between several institutions is difficult. Constructing a multilingual PBL environment in a virtual space on the Web (*Second Life*) is one solution to this problem. In this paper, a summary is provided of one such multilingual PBL that has been constructed.

Keywords: Less than 6 words.

I. INTRODUCTION

Traditionally, Problem Based Learning (PBL) has attracted attention as a method for training in engineering design skills. PBL is a learning process by which learners communicate with each other about a certain issue and discuss methods of solution. It is often employed in fields such as medicine and engineering where importance is placed on solving technical problems on site. However, when carrying out PBL, the learners need to gather in one location and work together, making cooperation between widely scattered institutions difficult. Furthermore, due to the globalization of recent years, the nationalities of students are becoming diverse and the language barrier this causes is also a problem.

Use of a virtual space connected to via a network and equipped with multilingual functionality is one answer to this problem. By using it, students are not restricted by location and, as well as being able to communicate synchronously and remotely with other users, it is possible to promote constructive PBL amongst students of diverse nationalities. Also, by providing materials that exploit the characteristic features of the virtual space, the effectiveness of learning can be further enhanced. There are many reported cases, such, for example, as teaching materials which enable visualisation of a miniaturised world, or learning through Virtual Reality (VR) (XXX[1]); medical teaching materials using 3D computer graphics (XXX[2]); or, by adding simulation functionality in addition to these, a system which can provide insight

into the variations in the various parameters and the relationships between phenomena. Using a virtual space can provide learners with experiences not possible in traditional e-learning or face-to-face lessons, making it possible to promote new discoveries by the learners.

For this paper, we investigated the requirements for multilingual PBL in a virtual space and implemented them.

II. DEVELOPPING MULTILINGUAL PBL SUPPORT SYSTEM

An overview of the multilingual PBL support environment and a configuration diagram of the multilingual PBL support system constructed are shown in Figures 1. In this paper, *Second Life (SL)* [4] was used as the virtual space. *SL* is a virtual space operated by the US company, Linden Lab. As well as being able to freely construct environments such as classrooms within the region possessed, by using the dedicated language, Linden Script (LSL), functionality such as HTTP communication with an external server can be implemented. The multilingual PBL support system used mainly this mechanism to implement various features. PHP+PostgreSQL and Ajax were used for system development. The multilingual PBL support system is composed of a client that the students operate and a university server that is able to connect to Lang, the Language Grid(LanG)[5] server that is required for the multilingual functionality provided within *SL*. Also, the SOAP protocol was used to communicate between the university server and the LanG server. In the section below, the multilingual communication functionality,



Figure 1 System View of Second Life

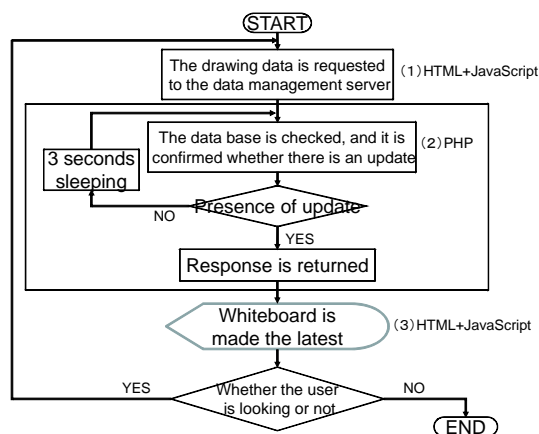


Figure 3. Flowchart for whiteboard update

whiteboard system and learner monitoring functionality are explained.

1. Improving Multilingual Communication Function

The most difficult point in multilingual communication is the language used when communicating. Usually, in international conferences and the like, English is used as a common language to communicate; however this can be a high hurdle, particularly for students carrying out multilingual communication for the first time. Machine translation is provided within *SL* as a HUD [6]; however, as translation is supported only between Japanese and English, it cannot be used to interact with users whose mother tongue is a language besides these two. For this paper, the text-based multilingual communication functionality developed by Yoshino and Ikenobu [7] was used so that this language barrier did not inhibit lively discussion. This is achieved by connecting the chat feature implemented in *SL* with LanG. LanG is the

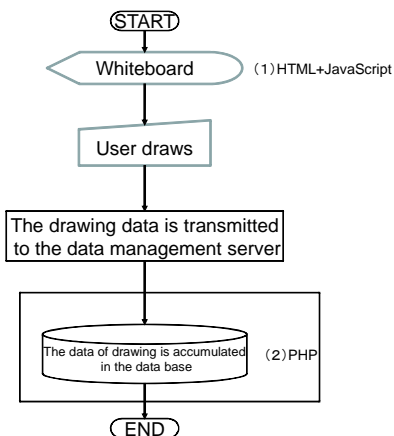


Figure 2. Flowchart of writing on whiteboard

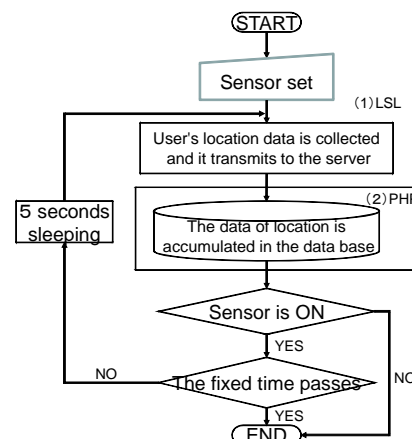


Figure 4. Process for gathering recorded learner behaviour

service infrastructure enabling sharing of translation services and dictionaries over the internet. Currently, English, Japanese, Chinese, Korean, etc., are supported, but, by adding dictionaries, support of other languages is possible. For this paper, only Japanese, Chinese and Korean are used, but in the future, 11 languages will be provided in LanG starting with Malay, which is handled in the dictionary for engineering training at this university, and this will enable contributions to be made to engineering education.

2. Common White Board

Even with the multilingual communication functionality included, it is perfectly conceivable that students are not able to develop the discussion in the way they expected. In that kind of case, using diagrams to supplement text broadens the possibilities for students to communicate their ideas in greater depth. Consequently, a shared whiteboard was implemented, on which the students could freely write. As part of



Figure 5. Learner monitoring screen

understanding student behaviour, the shared whiteboard saves the drawing history, and a feature enabling browsing on an administrator Web page was implemented. Further, from this record of drawings, instructors should be able to comprehend more precisely such things as the content of the discussion and the students' levels of understanding. The processing flow of the shared whiteboard from drawing to recording is as shown in Figures 2 and 3.

Figure 2 shows the processing that occurs when a user writes something down on the whiteboard and the data written down is sent to the server and registered in the table that records the state of the whiteboard in the database. In addition, Figure 3 shows the processing when the whiteboard is checked for updates and updated to the latest state when someone has written something down. The whiteboard continues to function as long as the user displays it, but it is devised so as not to return a response until it has been updated, thus easing the communication load. Through these features, the students are able to share the same whiteboard, and are also able to keep the recorded drawings. This whiteboard is not only viewable from within SL, but also from a web browser.

3. Learner Monitoring Function

In PBL where the students are the main actors, when student evaluation is carried out, understanding the students' conversations and behaviour during the lesson is particularly important. Remarks by the students during the lesson are recorded, if able to be monitored, and the level of student contribution to the discussion can be understood. If information about the students' positions and directions in the metaverse can be recorded, it can be used to identify such things as the level of interest students have towards their studies, and which students did not take part in any discussion. Therefore, in order to achieve this, learner monitoring

functionality was implemented that records and enables browsing of learners' behaviour.

After the user chat and behavioural records are collected using LSL within the metaverse, they are sent to the university server after passing through the SL server and are stored in the database. The flowchart for this functionality is shown in Figure 4.

Monitoring is not always ongoing: information gathering begins when the instructor turns on the sensor switch in the virtual space. If the switch is turned off or a set amount of time passes, there is a mechanism to halt information gathering.

It is possible to browse the gathered information on an administrator Web page. Figure 5 shows the administrator Web interface which enables browsing of the students' position information and the most recent conversations.

It is possible to browse the students' positional information and the most recent conversations at the time and date indicated by the upper timer. As well as being able to operate the timer manually using a button, it is also possible to advance it or move it backwards automatically. Also, the position information alone or the conversation information alone can be browsed. In addition, the whiteboard drawing history can also be displayed. This functionality is implemented in Ajax, and a request is sent to the server when the timer is operated, and information is acquired at the indicated time and date.

III. THE RELATION OF LEARNER MONITORING AND MULTILINGUAL PBL SUPPORT SYSTEM

Based on the above elements, it was possible to carry out PBL practice in the metaverse. Here we consider the relationship between the activities of learners that were acquired from the metaverse and the awareness triggered in the instructors.

The state of the individual learners in the metaverse classroom can be confirmed through 3 steps: confirmation of spatial participation status by checking the learner's avatar's position, confirmation of the status of the student's avatar's utterances, and confirmation of the content of the student's avatar's utterances. This confirmation is also carried out in the real world, but in the real world it is not possible to confirm down to the detailed content of the utterances. On the teacher's side, by using the learners, it is possible to provide guidance

to stimulate utterances from learners' avatars that have been unable to contribute to group chat.

Next, the content of the group debate within the metaverse classroom can be confirmed, right down to the quality of conversation, by carrying out a bibliometric analysis of the chat between students in real time (Nakahira et. al., [8]).

Furthermore, in a PBL among people who are multilingual, i.e., possess diverse values, remarks about a given problem can also be expected to differ from those in a discussion involving only people of identical backgrounds. As stated by Kido[9], to carry out intercultural collaboration, besides language issues it is necessary to understand the differences and similarities due to differences in ways of thinking and values. Conversely, through learners' experiencing differences in values and ways of thinking, it is possible to obtain an extraordinary chance, even if it is just in the metaverse. It is conceivable that intellectual stimulation coming from the extraordinary will be a trigger to open new perspectives not only for the learners but also for the instructors.

However, from the educational point of view, there are limits to the intercultural collaboration possible with simple conversations alone. In particular, thinking about the elements of intercultural collaboration incorporated into the training of engineers, what is required is not only an understanding of the other party's culture, but also an understanding of the differences between one's own and the other party's way of thinking and values, and to develop the communicative ability to overcome differences and cooperate to accomplish a project. In that sense, in setting the scene, just setting up simple conversations is not sufficient. As with PBL, it is important that students be given some kind of problem by which they can gain experience in the process of working together to solve problems.

IV. CONCLUSION

For this paper, a multilingual PBL learning environment was set up and implemented in the metaverse, and an environment was provided to make records of various learning activities. Chiefly, 1) a classroom was constructed to acquire records of learning activities in the metaverse, and 2) improvements in multilingual communication

functionality, construction of a shared whiteboard, and a learner monitoring system were developed as a support system to carry out livelier multilingual PBL. In addition to providing the above environment, by enabling the PBL to take place in the metaverse, there was mutual understanding of differences in ways of thinking and values, and it was possible to foster communication ability to overcome differences and cooperate together to accomplish a project.

REFERENCES

- [1] Kimihiko Shirato, Hitoshi Sasaki, and Makoto Takeya,(1998), The Distance Education System using Virtual Reality Technology(in Japanese), the Technical Report of IEICE, ET 98(144):73-78.
- [2] Masayuki Kawamoto et. al.(1995), Application of 3D Computer-Graphics to Dental Education: Part. 1 Development of the Trial Teaching Aids for Bevel Preparation of Metal Inlay Cavity(in Japanese), Journal of Japanese Association for Dental Education, 11(1):101-107.
- [3] Satoru Fujii, Toru Watanabe, Sanshiro Sakai, and Tadanori Mizuno(2003), A System for Learning Ecology having local materials database constructed with XML(in Japanese), Technical Report of IPSJ, 2003(52):25-30.
- [4] <http://jp.secondlife.com/>
- [5] <http://langrid.nict.go.jp/jp/>
- [6] <http://experience.co.jp/gallery/index.html>
- [7] T. Yoshino and K. Ikenobu(2008), Multilingual Chat Communication Experiment on 3D Online Virtual Space(in Japanese), The Special Interest Group Notes of Information Processing Society of Japan 2008(91):125-130
- [8] Katsuko T. Nakahira, Rodrigo N. R., Ryosuke Taguchi, Hideyuki Kanematsu, and Yoshimi Fukumura,(2010), Design of a Multilinguistic Problem Based Learning learning Environment in the Metaverse, the Proceedings of ISAC2010, in press.
- [9] T. Kido(1999), Information Sharing for Diversity Collaboration(in Japanese), The Special Interest Group Notes of Information Processing Society of Japan, 47:25-30.

An effective visualization of style inconsistencies for interactive text editing

Kazuki Shimamura

Department of Engineering Informatics,
Osaka Electro-Communication University
18-8, Hatsu-cho, Neyagawa,
572-8530, Japan

Email: shimason.1988@takelab.jp

Kazuhiro Takeuchi

Department of Engineering Informatics,
Osaka Electro-Communication University
18-8, Hatsu-cho, Neyagawa,
572-8530, Japan

Email: kazuh@takelab.jp

Kiyota Hashimoto

School of Humanities
and Social Sciences,
Osaka Prefecture University
1-1, Gakuen-cho, Naka-ku, Sakai,
599-8531, Japan
Email: hash@lc.osakafu-u.ac.jp

Abstract : Any authors, particularly learners, have much difficulty choosing the proper style for their particular writing and detecting style inconsistencies. We propose a new system that allows users to revise documents through human-system interaction. Although many systems for text writing have been proposed, most of the works focused mainly on automated techniques that detect human errors in texts. In contrast to those works, our study focuses on the visualization of multi-level style inconsistencies in texts to promote authors' awareness. In order to evaluate and visualize the differences in styles, we propose a model to compute the style similarity between a part and some genres. The similarity function that we propose is based on a model in which sentences are regarded as sequences of functional expressions. Applying the function, we develop a tryout system that shows which parts are inconsistent with the other parts from various viewpoints. Through interactions between users and the system, the user can repeat revising the text until the text maintains consistencies in various levels. Much has to be done towards a practically effective system, but our system helps to point out undesirable text should be conscious of stylistic differences in writing text.

Keywords : writing support, style consistency, corpora-based approach, awareness promoting visualization

I. INTRODUCTION

We can easily distinguish a newspaper article and a newspaper editorial, or a textbook for graduate students and one for undergraduate or high school students, not just in terms of their contents but in terms of their style, though few of us can always make clear our criteria for this kind of distinction. How to narrate, or style, is highly related to the targeted audience and the author's communicative purpose of the text, and stylistic consistency is required in a text, though deliberate inconsistencies bring extra literary effects. [1]

Several studies have tackled with style; particularly it has been pointed out that basic stylistic consistency is held by the restrictive use of functional expressions particularly in the case of Japanese and other languages that have a rich variety of stylistic grammar forms. For example, the following pair has the same meaning ('This is a book' in English) but differs in the style:

- Kore-wa hon-desu.
- Kore-wa hon-da.

Both 'desu' and 'da' are auxiliary copular verbs and the difference is up to politeness, which in turn should be determined according to the targeted audience and the author's communicative purpose. So the mixed use of 'desu' and 'wa' causes undesirable stylistic inconsistency and thus should be avoided. Particularly for languages like Japanese, which has a rich set of style-sensitive functional expressions, the mere detection of the misuses of such functional expressions is useful to some degree for style consistency.

II. Environment for Text Editing

Stylistic consistency does not only depend on the inner consistency in the text, but also on the appropriate choice of style for the textual purpose. In other words, the targeted audience and the author's communicative purpose determine the desirable style; then the author, with his/her limited reading experiences, attempts to keep stylistic consistency: i.e., he or she tries to use as many appropriate stylistic features as possible and tries not to use inappropriate stylistic features. As a fundamental dimension of the features, it is necessary for him/her to be aware of the following two viewpoints.

- intra-sentential consistency
- passage-level consistency

For dealing with the first consistency in computer systems, many previous works have been developed. And now some of the modules that detect errors (and inconsistencies) of sentences are provided through WEB-API services in the Internet. The followings are an example of the list which we can use through of the such WEB-APIs. These kinds of the features, which detects sentence-level consistencies such as spelling errors and simple syntactic errors, have been implemented in some word processors such as *Microsoft Word*.

- a) Spelling errors
- b) Inappropriate use of Synonyms
- c) Inappropriate use of Kanji-characters
- d) Inconsistency of Proper Nouns

- e) Inconsistency of Okurigana
- f) Use of Double Negations
- g) Use of Redundant Expressions
- h) Inappropriate use of Abbreviations

On the other hand, some discussions still remain concerning visualization of the inconsistency from the second viewpoint (passage-level consistency). With this in mind, we have been investigated on the visualization of passage-level inconsistency based on a set of textual corpora that consists of two or more subgenres and extract stylistic features of each subgenre. These sets roughly correspond to our reading experiences but the larger size is naturally expected to contribute to a better detection of stylistic features.

For the first approximation, let us consider that stylistic features of a subgenre are based on the use of preferable expressions for the subgenre and the lack of undesirable expressions for it. The definition of 'expression' may vary, but it should be noted here that a large number of words, including misspelled ones.

A scatter diagram between these two subgenres is shown in Fig.1, where samples of atomic expressions are distributed on the corresponding two axis. The determination of the proper (range of) n is a heuristic issue, and we first adopt the range of n as two to four, mainly because most of the Japanese words consist of one or two characters. To conduct the first experiment, we used a dumped file of Japanese Wikipedia[2] and a sample of 2ch BBS (<http://www.2ch.net/>) as sample contrastive data set, the sizes of which are shown in Table 1.

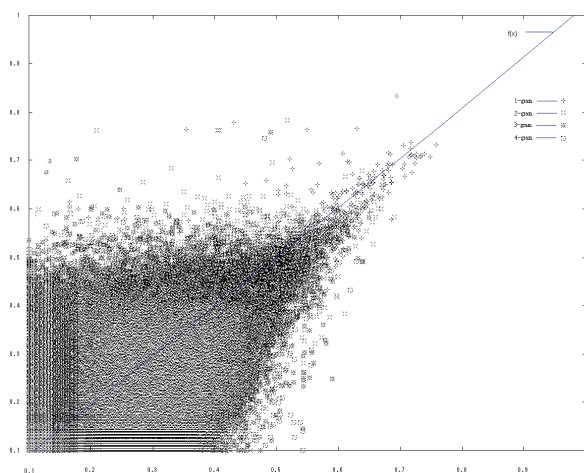


Fig.1. Scatter Diagram of 2- to 4-gram expression

Table1 Data SET

Data	Number of characters
Wikipedia	161,223,892
2ch	108,031,243

The frequency of each atomic expression in Wikipedia and 2ch classifies them roughly into three classes: (a)

atomic expressions frequently used in Wikipedia but not frequently used in 2ch, (b) atomic expression frequently used in both data, and (c) atomic expressions not frequently used in Wikipedia but frequently used in 2ch. This classification means that the class (b) consists of rather neutral atomic expressions, whose use may well not characterize a text as either of the two, while the class (a) and (c) are to be considered to be stylistic features for Wikipedia and 2ch, respectively.

With these classes representing the resemblance of a given text T with the model set of texts of the targeted genre, we have been able to visualize the textual characteristics on this aspect[3]. Suppose that the function $freq(a, X)$ is the frequency of occurrence of atomic expression a in the corpus X . For computing the stylistic similarity of a to the style of Wikipedia, we compare $freq(a, Wikipedia)$ and $freq(a, Y)$, in which Y is another corpus (for example, corpus of BBS articles).

This stylistic similarity of atomic expressions whose the size is three or four characters shown in Fig.1, is too short to represent the passage-level consistency. For the problem, we have to extend the function $freq(a, X)$ to a function $freq(w, X)$ for computing the appearances of desirable expressions for the targeted subgenre X , where w is a function that returns the set of expressions included from certain span in the text. With this function, we compute the style similarity of any span in the text to a certain subgenre.

III. Inconsistency Analysis Based on Templates

As we have summarized in Section II, there are expressions which are successfully used in identifying the genre of a text. Those n -grams are often parts of content words and perhaps they would be better to find frequently occurring words. Content words are defined as the words which are not functional expressions. In contrast with them, functional expressions are those that have little lexical meaning or have ambiguous meaning. For example, dictionaries always define the specific meanings of content words, but only describe the general usages of function words. Instead of the complexities to describe the meaning of function words, these words serve to express grammatical structure of a sentence or clause and specify the attitude or mood of the writer. In order to extend a simple consistency analysis based on content words to adopt more various degree of consistency, we adopt a method based on occurrence of function words.

One of the problems when we examine the occurrence of functional expressions is that the use of them strongly depends on the own style of the writers. If we adopt a corpus in which sentences are corrected from a free Internet forum to which a lot of writers can freely post their articles, the use of functional expressions must quite vary. In other words, it is difficult to collect a large corpus in which the use of functional expressions is expected to be consistent.

In order to overcome the problem of the shortage, we

prepare templates that are sequence patterns of the functional expressions. We extract these templates from students' essays that we assigned them to write the essays referring to some Wikipedia articles. The purpose of this setting is that the students will use their familiar functional expressions even if they refer to the articles (Wikipedia articles) in which the consistency of the use of functional expressions is maintained.

The process to extract templates is conducted based on comparison between the sentences which the student writes and their corresponding sentences in the Wikipedia articles. The measures for the comparison is computed based on how many content words are common between the sentences. For example, each pair of sentences in (s1) and (s2) is compared because of more than half content words are commonly used between them.

(s1)(Wikipedia)テキストをデータ構造に変換する。

(Student)テキストにデータ構造は変換されます。

(Template) ○に ○は変換されます。

(s2)(Wikipedia)北米は家庭に約2台のパソコンがある。

(Student)北米は家庭の パソコンがあります。

(Template) ○は ○の ○があります。

As a result of comparing process between them, the words which are anything other than the functional expressions in (s1) and (s2) are replaced with meta word '○', and we obtain a ordered sequence of functional expressions like {'に','は'変換されます'} and {'は','の','が'あります'}. In this paper, we refer to the sequences as "templates." Because each template mainly shows a kind of features of the syntactic structure of the sentence, the occurrences of infrequent content words in the sentence are ignored with the computations which adopt the templates.

By using the collection of these templates, we extend the function appropriately, which we have mentioned in Section II. For the purpose of evaluating the passage-level consistency, the first argument w in the function $freq(w, X)$ to be extended. In our proposal, our algorithm to evaluate the consistencies from the viewpoint of the passage-level processes sentence by sentence. This evaluation is conducted by the algorithm shown in Fig.2.

Regarding a target text as the set of sentences like $\{s_1, s_2, \dots, s_n\}$, each sentence is evaluated whether it holds the expected style by applying the function $freq(w, X)$, where X is the corpus in which texts are assumed to be written in the expected style. Note that the algorithm needs one or more corpora to compare the style similarities of the target sentences to the various styles. As outputs of the algorithm, either of three characters {'+', '*', '-'} is to output for each unit by the *print* command. This output does not need to be displayed directly, it means that we have to devise an effective way to promote users' awareness of the inconsistency in

the text.

```
{s1,s2,...,sn}.each do |w|
  y = freq(x, Wikipeda) - freq(w, 2ch)
  if y > 0 then
    print "+"
  else if y < 0 then
    print "-"
  else
    print "*"
  endif
end
```

Fig.2. Algorithm for Evaluating Passage-Level Consistency

IV. Proposal for Interactive Editing

Systems for interactive text editing are designed to allow one to use pre- and post-processing of subparts of the text when he/she is inputting or editing it. A system we propose here has the following features:

- detecting the errors in the inputted phrases and suggest the exact parts to correct
- visualizing the multi-level consistencies (from intra-sentential and passage-level viewpoints)

We designed our system to be run on the server computer and to be used through web browsers. In the internet, some of the useful modules which analyze some errors of intra-sentential inconsistencies are available for such kind of text processing services which are used from Web browsers. The algorithm that we described in Section III is implemented as a module like them and our system is developed combining these various modules.

Interactive input systems are familiar with Japanese people because these systems have been developed to help to input Japanese characters. Intelligent interactive text editing is also investigated as applications of the machine translation. For example, some works focus on interactive text pre-editing to improve the output quality of machine translation[3][4], in which the user can input or edit the source-language sentence interactively referring to the obtained sentence by translating it. Like the works, in which the users edit his/her writing text according to the messages from the system, our system provides an interface that allows the user to check his/her writing text from two viewpoints (passage-level consistency and intra-sentence consistency).

Fig.3 shows the screenshot of our interface, in which there are two big input boxes on the upper side of the page and under these boxes there are two areas for interactive editing to the inputted text.

An original text is inputted in the left hand side of the big input boxes and then the user pushes the check button to edit the inputted text. The box on the right hand side displays the log for the editing history.

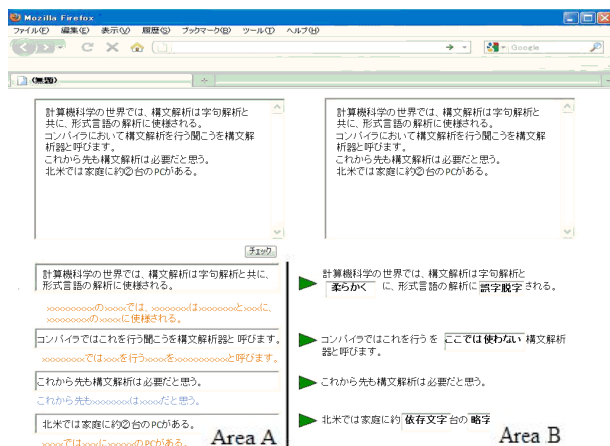


Fig.3. Screenshot of Our System

The interactive edit area is divided into the two areas as shown in Fig. 4 and Fig. 5.

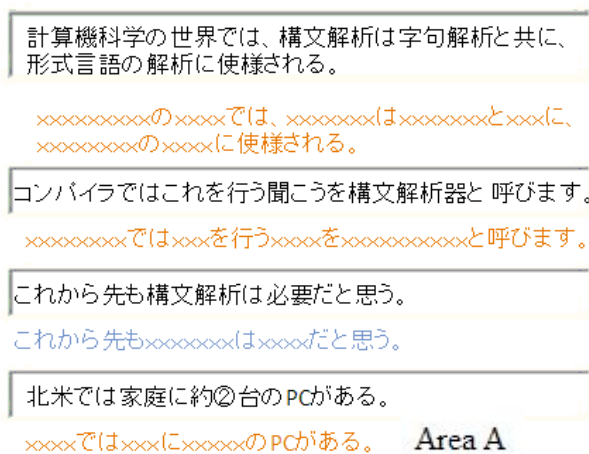


Fig.4.Area A

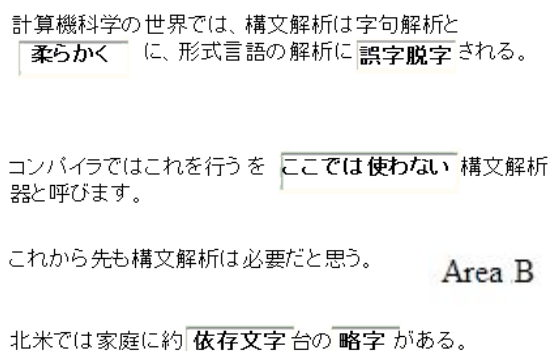


Fig.5.Area B

We designed that each sentence is displayed with the information of its style in the edit area A. Under each sentence box, the template which the sentence contains is colored with the color which represents the style similarity for user to check the consistency from the passage-level viewpoint. The computation of the style similarity follows the algorithm described in Section III.

On the other hand, the user can concentrate on correcting the intra-sentential errors in the edit area B. In the edit area, some parts of the sentences are replaced to the input boxes, to which the system promote the users' awareness of errors and mistakes that are detected from intra-sentential viewpoint to correct them. For each box, the reason why the corresponding part should be correct is also informed.

In this way, the user can be aware of the changes of the consistencies in the passage-level as soon as he/she revises the errors in area B. On the other hand, he/she rewrites a whole sentence in the edit area A to hold the passage-level consistency of the context, the system interactively evaluate the intra-sentential consistencies of the corresponding parts.

V. CONCLUSION

In this paper, we proposed a system for interactive text editing that allows one to check the multi-level consistencies in his/her writing text. In the system, we used the sequences of functional expressions to compute one of the consistencies from the passage-level viewpoint. In order to promote awareness on the multi-level consistencies of the writing text, we combined it with some algorithms that previous works proposed. Much has to be done towards a practically effective tool, but any advanced tool to help to detect undesirable expression should be conscious of stylistic differences among subgenres and our proposed methods are fundamentally effective.

ACKNOWLEDGMENT

This work was partly supported by KAKENHI (21500113).

REFERENCES

- [1] Schiffrin, D., D. Tannen, and H.E. Hamilton (2001) *The Handbook of Discourse Analysis*, Blackwell
- [2] Japanese Wikipedia dumped file.
<http://download.wikimedia.org/jawiki/20071013/jawiki-20071013-pages-articles.xml.bz2>
- [3] K. Hashimoto, K. Takeuchi, H. Ando (2010) A Corpora-based detection of stylistic inconsistencies of text in the targeted subgenre, AROB15, pp.110-113
- [4] K. Uchimoto, N. Hayashida, T. Ishida and H. Isahara (2005) Automatic Rating of Machine Translatability, In Proceedings of 10th Machine Translation Summit, pp. 235-242
- [5] N. Hayashida, T. Ishida (2005) Performance Prediction of Supporting Self-Initiated Repair by Translation Agents (in Japanese) The transactions of the IEICE. D-I J88-D-I(9), pp.1459-1466

An Intelligent Meta-Learning Support System Through Presentation

Kazuhisa Seta

*Graduate School of Science, Osaka Prefecture University
1-1, Gakuen-cho, Naka-ku, Sakai, Osaka, 599-8531, Japan
(Tel : 81-72-254-9691; Fax : 81-72-254-9691)
(seta@mi.s.osakafu-u.ac.jp)*

Abstract: As described in this paper, we propose a presentation-based meta-learning scheme. Firstly, we present support functions that we embed into the system. Secondly, we conduct experiments to verify the meaningfulness of our learning scheme, which suggests the system can stimulate learners' reflection on their learning processes. Furthermore, it can stimulate learners' meta-learning communications. Results show that users tightened their criteria to evaluate their own learning processes and understanding states. It is useful for learners to facilitate change in their learning processes.

Keywords: meta-learning, meta-learning communication, presentation-based learning

I. INTRODUCTION

Research into computer-supported systems to enhance meta-cognitive skill is investigated by many researchers [2, 3, 4, 5]. Results show, particularly in the educational psychology field, that an emphasis on meta-cognition must accompany domain-specific instruction in each of the disciplines, but not generic instruction in a general context, because the type of monitoring that is required will vary [1]. In a history course, for example, a student might be asking herself in an internal self-conversation, "who wrote this document, and how does that knowledge affect the interpretation of events," whereas in a physics course, the student might be monitoring her understanding of the underlying physical principle at work [1].

Our research goal is the enhancement of meta-learning through stimulation of learners' reflections on their own learning processes. To achieve this goal, we assign a task to make a presentation material on a specific pre-learned topic for other learners whose academic abilities are similar to those of the learner.

Collaborative learners with no regulation, however, might stray in undesired directions: in the case of our presentation-based learning, for instance, they tend to discuss illustrations of the slides, the impact of the presentation, and so on.

We therefore propose a support system that facilitates meta-learning communication by providing learners with viewpoints to discuss their learning methods.

II. Embedding Support Functions to Facilitate Meta-learning Communication

In our research, we developed a presentation-based meta-learning scheme whereby learners can specifically examine learning on their own learning processes. Learners in our learning scheme perform learning by following three steps.

- i. Learning specific domain contents through self-study or attending lectures until they think they have understood them
- ii. Making comprehensive presentation materials to teach other learners who have the same academic level
- iii. Collaborative learning using presentation materials

In the following, we explain support functions embedded into the system at (ii) and (iii) phases to facilitate meta-learning, although phase (i) is beyond our support.

1. Intention Structure Reflecting Learning Contexts

To encourage meaningful meta-communication among learning partners, each learner must (A) become aware of performing meta-learning and (B) share individual learning contexts. In our learning system, providing a representation to describe their intention of the presentation, intention structures and guidance function according to them play roles of enhancing their awareness at the presentation design phase.

At the presentation design phase, we make learners construct intention structures to be aware of learning skill acquisition. Giving appropriate instructions

according to learners' learning contexts is significant to facilitate their learning skill acquisition processes.

In our task setting of making truly comprehensive presentation materials for use by those who have the same academic level with the presenter, we adopt an assumption that intention structures of presentation reflect learners' learning contexts in their learning.

In the intention structure (Fig. 1. (iii)), each node represents an educational goal and terms to represent them are provided from the system to represent the learners' educational goals.

2. Guidance Function to Enhance Meta-Cognitive Awareness

Guidance information to facilitate the learner's reflection on personal learning processes is provided when the learner intends to move to the subsequent collaborative learning phase. It represents queries on domain-specific learning activity based on the learner's intention structure. The teacher giving a presentation subjects also constructs an intention structures and indicates required learning (teaching) activities on them that should be embedded into learners' intention structures. The system cannot understand the contents of learners' presentation written in natural language. However, it can process intention structures by referring learning skill ontology. Therefore, if learners did not embed them, then the system provides queries by referring domain-specific learning skill ontology and the teacher's intention structure as follows:

- (1) "Do the following learning activities need to be included in your presentation to achieve the

learning goal "make the learners understand DP using Abstract Factory pattern as an example?" Choose "embed into presentation" by right-mouse clicking if you think you need to do so.

- (2) "Do you have sufficient understanding of these teaching activities? Check the items you had already understood."

- ☐ Make the learner understand the meaningfulness of the fact that each DP has its own name.
- ☐ Make the learner understand the advantages of object-oriented programming by combining its general theories with concrete examples in the Design Patterns.
- ☐ ... (Required learning activities defined in learning skill ontology are listed)

The learner is required to examine the importance of each learning activity for constructing comprehensive presentation materials: the learner judges whether the learner's presentation is valid or not and whether each learning activity should be included in the learner's presentation. This guidance is a stimulation to facilitate the learner's reflection on personal learning processes.

The fact that the learner did not embed listed learning activities is interpreted as follows: (a) the learner has no learning activities as domain-specific learning operators in his own consciousness, (therefore the learner cannot perform them) or (b) the learner does not understand the importance of the learning activities even if they have and they had performed their learning processes. The learner's checking activity in query (2) is interpreted as a declaration of whether the learner has them as learning operators.

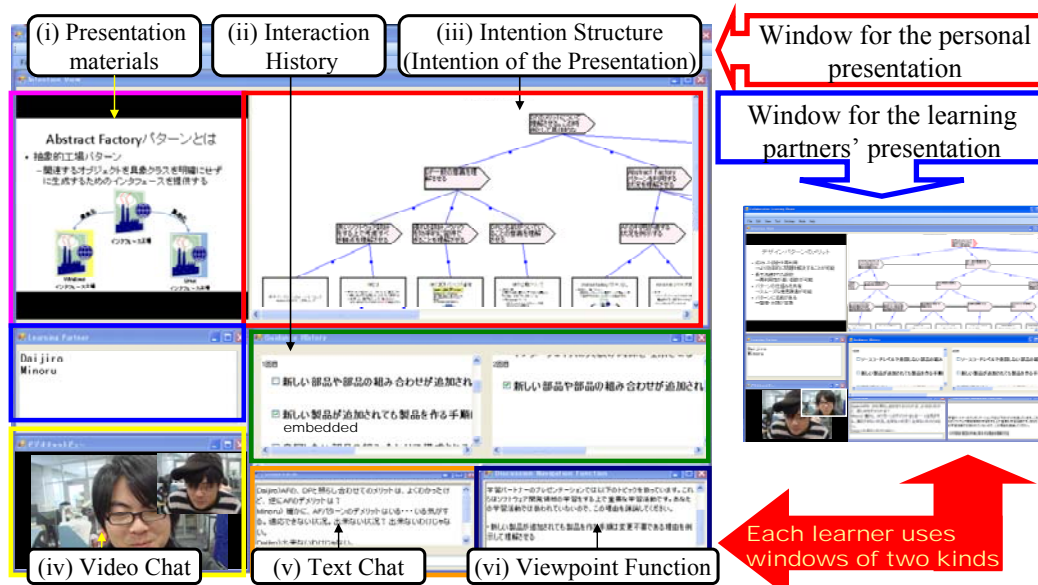


Figure 1. CSCL Environment to Facilitate Meta-Learning Communication.

For (a), the learner must perform the learning activities spontaneously or must be taught from the learning partners at the collaborative learning phase. For (b), the learner must encourage internal self-conversation to consider the importance of each learning activity.

The guidance function plays a role of building a foundation to encourage meta-learning communications among learning partners by stimulating their awareness in meta-learning before starting collaborative learning.

3. Viewpoint Function to Stimulate Meaningful Learning Communications

Figure 1 portrays a screen image at the collaborative learning phase. The window comprises six panes: the presentation pane (Fig. 1 (i)), interaction history pane (Fig. 1 (ii)), intention structure pane (Fig. 1 (iii)), video chatting pane (Fig. 1 (iv)), text chatting pane (Fig. 1 (v)) and discussion viewpoint pane (Fig. 1 (vi)). The system is implemented in Visual Basic and Java, functioning cooperatively with Power Point (Microsoft Corp.).

The system in the collaborative learning phase provides support of two kinds to facilitate learners' learning skill acquisitions (acquiring learning operators and tightening evaluation criteria) as follows.

- (1) Support to share learning (teaching) contexts of learning partners by referring to presentation materials with intention structures.
- (2) Facilitate meaningful discussions to encourage their reflections on their own learning processes by providing discussion viewpoints.

As described in this paper, we particularly examine the topics on the viewpoint function.

Thinking processes related to one's own learning processes are quite tacit. Therefore it is not easy to externalize and to discuss learners' thinking processes (while teaching processes reflecting their learning processes are externalized as intention structure). Ordinary learners with no support tend to discuss the appearance of illustrations, animations, and so on.

To eliminate the problem, our system provides viewpoints to discuss their teaching and learning methods based on the interaction history between the learner and the system at the presentation design phase. As shown in Fig. 1 (vi), the system provides each learner with respective viewpoints to discuss as follows: "You judged the learning activity "Make the learner understand the significance of the fact that an interface specifies the name of each method by taking an

example." as important. It is an important learning activity in the software development domain and you embedded it into your presentation. On the other hand, your learning partner judged it as not important. Explain why you think this learning activity is important."

Collaborative learners can discuss their domain-specific teaching methods by referring to the viewpoints for meta-learning communication.

III. Experimentation

We conducted an experiment to verify the meaningfulness of our learning scheme and usefulness of support functions embedded into the system. We specifically examine the issues of whether the system can encourage meta-learning communications. The outline of the experimentation is described below.

- ✓ **Subjects:** 16 graduate students participated. They had completed software engineering (UML) and object-oriented (Java) programming courses when they were undergraduate students. They were divided into two groups at random: eight students were in the experimental group (ExpG) using the system; eight were in the control group (CtlG).
- ✓ **Presentation topic:** Make presentation materials explaining the merits of building design patterns by taking the abstract factory pattern as an example.
- ✓ **Flow of the experiments:** Continuous 7 days lecture (90 min lecture each day) without weekend:

Table 1 presents results of questionnaires after their collaborative learning. Questionnaire items 1 is related to the usefulness of the presentation-based learning scheme and 2-3 are related to learning effects from the viewpoint of meta-learning.

Regarding item 1, participants in both ExpG and CtlG gave quite high marks, which suggests the presentation based meta-learning stimulates learners' reflection on their learning processes.

It is expected that learners will execute better learning processes using the acquired domain-specific learning activities and tightened evaluation criteria if the learners' meta-learning processes are performed successfully. Items 2-6 inquired the about learners' consciousness of them. Both groups gave high marks to each item. However, CtlG gave higher marks than ExpG for the acquisition of domain-specific learning activities (items 3 and 5), whereas ExpG gave higher marks than

Table 1. Results of Questionnaire after the Collaborative Learning Phase

Questionnaire Items		ExpG		CtlG	
		Mean	SD	Mean	SD
1	Do you think the collaborative learning after making your presentation materials enhanced your reflection on your own learning processes?	4.375	0.267	4.375	1.982
2	Do you think collaborative learning changed your criteria to evaluate your understanding of DP?	2.875	1.553	3.375	1.982
3	Do you think you could acquire learning methods using collaborative learning?	3.375	0.839	3.625	1.41
4	Do you think your learning processes for other DPs will change after performing this presentation-based learning?	3.75	1.071	3.5	1.428
5	Do you think you could acquire learning methods by performing this presentation-based learning?	3.625	0.553	4.125	0.982
6	Do you think your consciousness of learning will change by performing this presentation-based learning?	4.1	0.238	3.875	0.982

CtlG for items related to the consciousness of changes of their own future learning processes (items 4 and 6). Those responses seem to be mutually contradictory. However, they are not so by the following interpretation: learners in ExpG had tightened their learning criteria to evaluate their learning processes and understanding states; thereby, they also strictly evaluated their meta-learning processes. The results of the average time ratio of meta-learning communication support this. However, the fact that participants in ExpG gave low marks related to item 2 suggests that they were unable to perform all meta-learning processes by themselves even though they were able to understand the importance of meta-learning. They might be conscious of the functions. Actually, we do not embed the functions that support performance of learning activities acquired by meta-learning processes even when the system triggers learning activities. On the other hand, participants in CtlG spent less time for meta-learning communications, suggesting that the learners' evaluation criteria had not been tightened through their communications. Consequently, their evaluation results for these items were more tolerant.

IV. CONCLUDING REMARKS

As described in this paper, we present discussion of a presentation-based meta-learning scheme. We introduced our presentation based meta-learning scheme. Then, we conducted an experiment to verify the meaningfulness of our learning scheme and usefulness of support functions embedded into the system, which suggests that the system was able to stimulate learners' reflection on their learning processes. It stimulates learners' meta-learning communications. Consequently, they tightened their criteria to evaluate their own

learning processes and understanding states. It is meaningful for the learner to change their learning processes. We also evaluated their learning outcomes of domain dependent knowledge: it suggests participants in ExpG could get higher mark than ones in CtlG. We will carefully address the issues of this in future works.

REFERENCES

- [1] Bransford, J., Brown, A., & Cocking, R. (2000). Brain, Mind, Experience, and School, In *How People Learn*. Washington, DC: National Academy Press.
- [2] Flavell, J. H. (1976). Metacognitive aspects of problem solving, In L. Resnick (Ed): *The Nature of Intelligence*. (pp. 231-235) Hillsdale, NJ: Lawrence Erlbaum Associates.
- [3] Kayashima, M., Inaba, A., & Mizoguchi, R. (2005). What Do You Mean by to Help Learning of Metacognition?, *Proc. 12th Artificial Intelligence in Education (AIED2005)*, pp. 346-353, Amsterdam, The Netherlands.
- [4] Maeno, H., Seta, K., & Ikeda, M. (2010). Development of Meta-Learning Support System based on Model based Approach. *Proc. 10th IASTED International Conference on Artificial Intelligence and Applications (AIA2010)*, (pp.442-449).
- [5] Noguchi, D., Seta, K., Fujiwara, M. and Ikeda, M. (2010): Presentation Based Learning Support System to Facilitate Meta-Learning Communications, *Proc. of 18th International Conference on Computers in Education (ICCE)*, (to appear),

A Task Ontology Construction for Presentation Skills

Kiyota Hashimoto* and Kazuhiro Takeuchi**

Osaka Prefecture Univ.: 1-1, Gakuen-cho, Naka-ku, Sakai, 599-8531, Japan*
*Osaka Electro-Communication Univ**., 18-8, Hatsu-machi, Neyagawa, 572-8530, Japan*
(Tel : 81-72-252-1161; Fax : 81-72-254-9944)
(hash@lc.osakafu-u.ac.jp)

Abstract: Presentation is an integrated art of communication in which both linguistic and paralinguistic skills are employed, and deliberate preparation is necessary. We're developing a comprehensive learner support system for to help learn presentation skills. This paper reports our development of task ontology for presentation skills as one of the foundational components of our system. It consists of three sub-ontologies: presentation strategy ontology, rhetorical structure ontology, and lexical ontology. They are used for background inferences and evaluations of learners' presentations. With a prototypical application of them shows the employment of task ontologies is effective for intelligent learning support systems.

Keywords: Task ontology, Presentation strategy, Rhetorical Structure Theory, rhetorical structure ontology, learner's presentation

I. INTRODUCTION

It is more and more important for any one of us to make a good presentation, particularly that in English, in various situations. Oral presentation is one of the most sophisticated communicative activities; deliberately designed to be presented to specific audience with slides to deliver information and attempt to make a persuasion. Not only the linguistic organization but also the paralinguistic effects like body language and eye contact are utilized, and the presenter should have a deep understanding not only of what he or she delivers but of how the audience will react. Most of the people who have to make presentations have some difficulties preparing and making them, and computational learning support is desirable. From this viewpoint, we are developing a comprehensive online learning support system for presentation [1], and are constructing a multimedia learner corpus of learners' presentations [2]. The former contains Presentation Organizer which can be used to construct oral manuscripts and corresponding slides simultaneously, and the latter contains orally spoken texts and slides to be annotated. Both require a fine-grained way of describing and representing the text organization, or rhetorical structure of presentation. Thus, we have designed and constructed a couple of ontologies related to presentations. In this paper, we report two of them, Presentation Strategy Ontology and Rhetorical Structure Ontology.

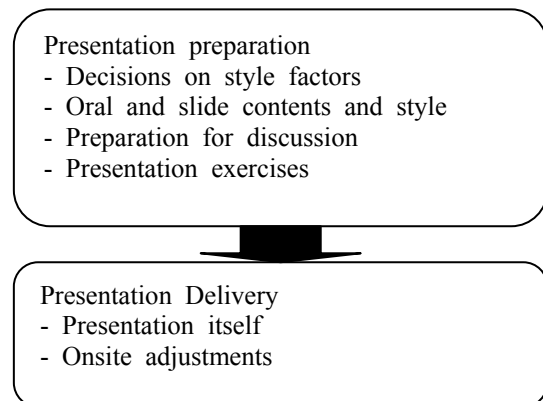


Fig.1 Presentation process

II. PRESENTATION STRATEGY ONTOLOGY

The process of preparing and delivering a presentation is roughly done in a way as shown in Fig. 1. As this simple process tells, the success or failure of a presentation is mostly decided by the preparation phase. Thus, any talk ontology for presentation has to focus on the preparation phase.

Presentation, whether it is oral or written, is delivered for a particular communicative purpose, which is to determine what and how to be delivered—content and style. A communicative purpose can be analyzed into different aspects. Let us call these aspects style factors. As each style factor affects what and how to be delivered, they have to be deliberately considered. Numerous books on presentation preparation emphasize the consideration of style factors, though each calls style factors differently, and we classify them as in Table 1.

Factors	Examples
Topical (Genre)	inorganic chemistry English literature ... (Note that the topical factor can be very much specific.)
Media	newspaper textbook oral presentation ...
Targeted reader/ audience	laypeople professionals ...
Purpose	persuasion explanation ...
Intention	formal informal or friendly ...
Time	the length of presentation

Table 1 Style Factors

With the decisions on style factors, oral and slide contents are to be made not only on what to be delivered but also how to deliver it. Preparation for discussion is also affected. In other words, all the other aspects of presentation preparation and delivery are decided along the line of the choices of the appropriate style factors for the presentation. Particularly, all the linguistic style elements (See Fig.2) which manifest the choices are heavily affected. Note that the logical organization in Fig.2 is more concerned with the other ontology, Rhetorical Structure Ontology, which we will discuss in the next section.

With these consideration in mind, we have devised a prototype of Presentation Strategy Ontology as in Fig. 3

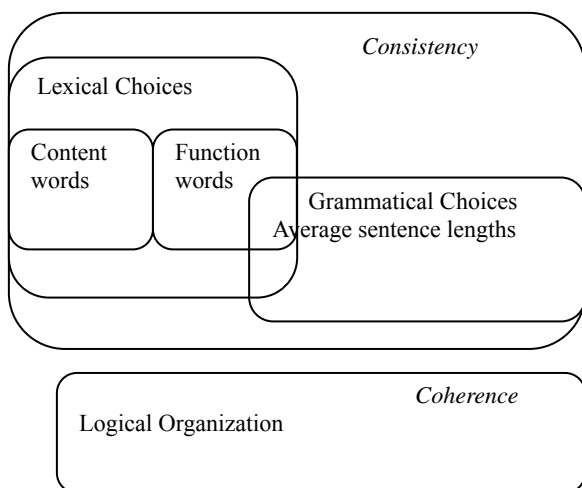


Fig.2 Linguistic Style Elements

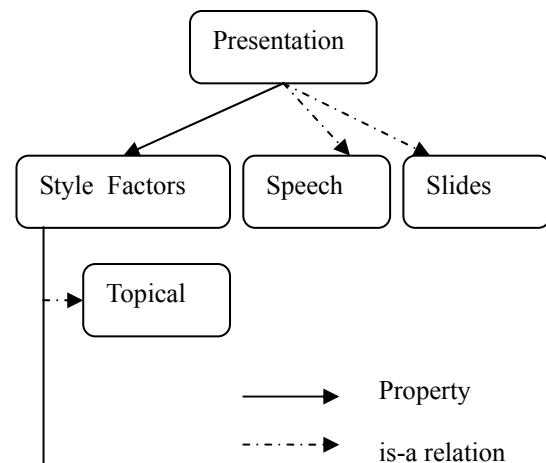


Fig.3 Brief Overview of Presentation Strategy Ontology

III. RHETORICAL STRUCTURE ONTOLOGY

1. Rhetorical Structure Theory and Ontology

Rhetorical structure has long been investigated in literature and linguistics, and computational linguists have pursued the possibility of applying it to natural language generation and automatic summarization in particular [3]. A number of theories and frameworks have been proposed [4], of which Rhetorical Structure Theory, originally proposed by Mann and Thompson [5],[6],[7], is the most popular.

In the RST framework, the discourse structure of a text is considered to be coherent and thus capable of being represented as a single-rooted tree with a set of directed graphs. Each directed graph is labeled for its rhetorical relation. Originally 23 relations were proposed [8], but the exact number proposed varies among researchers.

Various types of domain ontology have been investigated in order to make structured knowledge machine-readable, and instances of rhetorical structure ontology have also been proposed [8]-[11]. In particular, Rahal et al.[11] share a similar perspective with us in that their system is intended for supporting collaborative writing. None of them, however, can deal with presentations successfully.

2. Reconsideration of RST

A. EDU

As shown in the previous section, RST is basically clause-based: its EDU is assumed to be clausal. A number of researchers have repeatedly reinvestigated the validity of this approach both from theoretical and

practical perspectives, but nearly all of them still assume clause as EDU [3],[4],[8]. However, Kibble pointed out, in investigating a small corpus of pharmaceutical leaflets, that at least a nominalized noun phrase, particularly a gerundive one, plays the same role as a clause[12], and a given relation between two conceptual units can be embodied in several different ways. So we define the EDU as a “semantically” clausal segment. “Semantically” clausal segment means a segment in which a subject-predicate relation is contained, whether explicitly or implicitly.

B. Surface or Deep?: Potential Textual Inconsistencies and Imperfections

Rhetorical structure deals with the detailed organization of the content to be written or told. In that sense, a given rhetorical structure is assumed to represent the deep structure of the content, on the naïve assumption that the deep structure is properly mapped onto the surface structure, the text. This cannot be assumed, however, in the case of learner’s presentations. Thus, in order to reveal textual inconsistencies and imperfections, it is important to annotate a rhetorical structure mainly based on surface logical cues.

C. Supra-textual Cues

One of the biggest differences between written texts and oral presentations is the existence of interactions between the text itself and the outer world. A presenter frequently gives instructions to the audience to draw their attention to some part of the slide, such as “Look

at the graph.” This type of instruction is to be considered supra-textual in that it points out some element outside the orally spoken content, but it still has its nucleus adjacent to it, since such instructions are naturally give in elaborating an EDU. So supra-textual cues are to be incorporated into rhetorical relations.

D. Revised RST for representing the rhetorical structure of presentation

Based on the discussions in the previous sections, we defined our revised RST as shown in Table 2.

3 Rhetorical Structure Ontology for Presentation

Our revised RST discussed above has to be formalized for machine-readability, and one of the plausible implementations is to make a rhetorical ontology. We are now implementing a prototypical rhetorical ontology for presentations, PRESONTO, using OWL 2.0. A key feature is to annotate rhetorical structures of the oral part and the slide part of a presentation in the same way. The underlying assumption is that a span, maximally of a slide, necessarily corresponds to a span of oral speech, and this correspondence guarantees the correspondence between oral speech and slides. Furthermore, it is possible, with this correspondence, even non-verbal elements like graphs and pictures to be properly annotated in the same way. PRESONTO is still prototypical, but its overview is shown in Fig. 4.

EDU: Semantically clausal segments

A rhetorical relation is primarily based on the surface structure and is assigned 0 or 1 according to the logical validity.

The Set of Rhetorical Relations for our purpose

Name	Description (* in the Name indicates that the item is newly introduced here)	Order of N&S
Background	Satellite provides background information to the nucleus	S before N
Contrast	Applies to two nuclei that contrast each other	
Elaboration	Satellite elaborates the information in the nucleus	N before S
*Elaborative	Satellite exemplifies the information in the nucleus	N before S
Example		
Enablement	Information in the satellite enables the audience to perform the action in the nucleus	N before S N before S
Evidence	Satellite provides evidence to the statement in the nucleus	
Justify	Satellite justifies the nucleus	
Motivation	Satellite motivates the reader to perform the action in the nucleus	
List	Listed nuclei	S before N
Sequence	Multiple nuclei that follow each other in sequence	
Solutionhood	Satellite is the problem; Nucleus provides the solution.	N before S
Summary	Short summary or paraphrase of the previous span	
*Supra-textual Cue	Cue for an action on the part of the audience.	
*Orphaned	Any other orphaned nucleus, to be connected to the nearest dominating nucleus	

Table 2 Our Revised RST

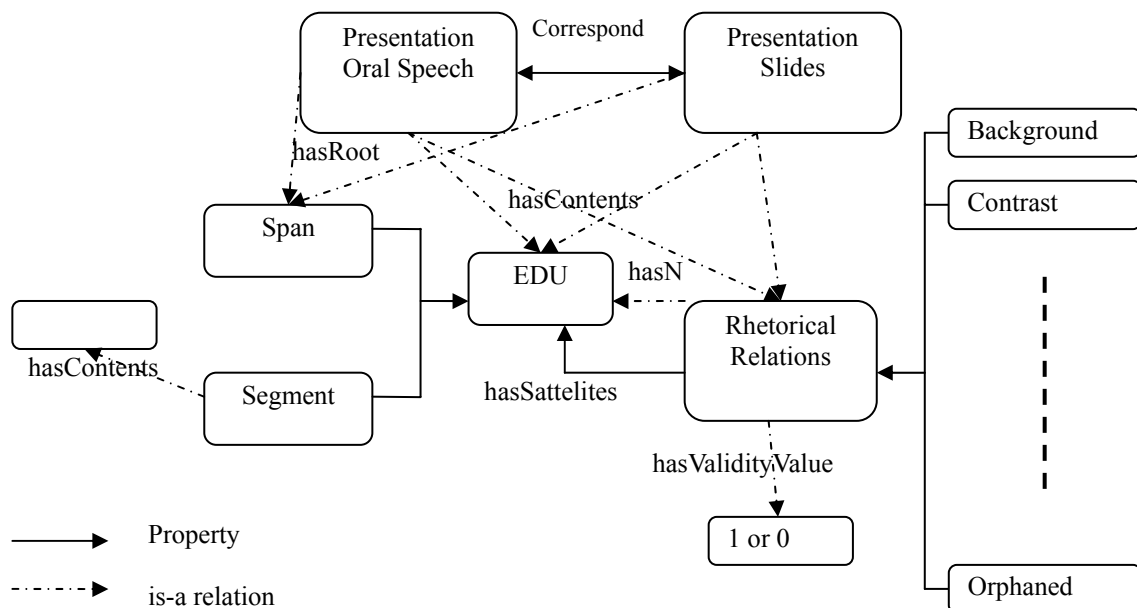


Fig.4 Overview of PRESONTO, a Rhetorical Ontology for Presentations

VI. CONCLUSION

In this paper, we reported our ontologies for presentation description. They are expected to serve both as a descriptive tool and as a hinting tool to support learners' preparation of presentations. We are currently refining our related modules of learner support system for presentation to utilize these ontologies.

ACKNOWLEDGMENT

This study is supported by KAKENHI (22520576).

REFERENCES

- [1] Hashimoto, K. and K. Takeuchi (2010) Prototypical Development of Awareness Promoting Learning Support System of Basic Presentation, *Proceedings of ISAC 2010*.
- [2] Hashimoto, K. and K. Takeuchi (2010) Multimedia Learner Corpus of Foreigner's Basic Presentation in English with Evaluations, *Proc. of International Conference of Educational and Information Technology 2010*, Volume 2, 469-473.
- [3] Forsbom, E. (2005) Rhetorical Structure Theory in Natural Language Generation, (<http://stp.lingfil.uu.se/~evafo/gslt/nlg/assignment.pdf>)
- [4] Groza, T.; Handschuh, S.; Clark, T.; Buckingham Shum, S. and de Waard, A. (2009). A Short Survey of Discourse Representation Models, *Proc. of 8th International Semantic Web Conference, Workshop on Semantic Web Applications in Scientific Discourse. Lecture Notes in Computer Science*, Springer Verlag: Berlin, (available from <http://ceur-ws.org/Vol-523Groza.pdf>)
- [5] Mann, W.C. and S.A. Thompson (1987) Rhetorical Structure Theory: A Theory of Text Organization, ISI/RS-87-190.
- [6] Mann, W.C. and S.A. Thompson (1988) Rhetorical Structure Theory: Toward a Functional Theory of Text Organization, *Text* 8(3), 241-281.
- [7] Taboada, M. and W.C. Mann (2006b) Applications of Rhetorical Structure Theory, *Discourse Studies* 8(4), 567-588.
- [8] Nicholas, N. (1994) *Problems in the Application of Rhetorical Structure Theory to Text Generation*, Unpublished M.Eng. Sc. Thesis, University of Melbourne.
- [9] Harris, R. and C. DiMarco (2009) Constructing a Rhetorical Figuration Ontology, *Proc. of Symposium on Persuasive Technology and Digital Behaviour Intervention, Convention of the Society for the Study of Artificial Intelligence and Simulation of Behaviour (AISB)*, April 2009, Edinburgh, Scotland.
- [10] Pinto, H.S., S. Staab, and C. Tempich (2004) DILIGENT: Towards a fine-grained methodology for Distributed, Loosely-controlled and evolvInG Engineering of oNTologies, *Proc. of ECAI 2004*, 393-398.
- [11] Rahhal, C., et al. (2007) *OntoReST: A RST-based Ontology for Maintaining Semantic Consistency in Collaborative Writing*, Rapport de recherche n 6384.
- [12] Rodger Kibble (1999) Nominalisation and rhetorical structure, *Proc. of ESSLLI Formal Grammar 1999*, pp.49-60.

Country Domain Governance: An analysis by Datamining of Country Domains

Katsuko T. Nakahira, Hiroyuki Namba, Minehiro Takeshita, Shigeaki Kodama, and Yoshiki Mikami

Nagaoka University of Technology, Nagaoka, Japan
(Tel : +81-258-47-9847)
(Email katsuko@vos.nagaokaut.ac.jp)

Abstract: Along with the expansion of opportunities to use the internet, the system of managing it has become a serious problem. Even from the global perspective, questions concerning internet governance have been raised at various places, starting with the WSIS (World Summit on the Information Society). However, the main discussion has been from the viewpoint of administrators and service providers, placing emphasis on ensuring safety and equal opportunities of use, while the discussion from the user's point of view is limited. This is thought to be due to the acquisition of statistical data which the discussion is based on being largely derived from statistics related to the physical means of communication, and to the difficulty of comprehending all user activity in the internet space. In this paper, in response to the challenge of internet governance, we propose the country domain governance index. This is an index for comprehensive discussion of governance of internet resources from the point of view of both administrators and users by carrying out data mining by region by merging various pieces of Web information obtained from results of observations in the Language Observatory with various statistical data.

Keywords: Less than 6 words.

I. INTRODUCTION

Along with the progress of the IT revolution that started with the use of the internet, it has been pointed out since the 1990s that a gap in enjoyment of the benefits continues to exist between countries[1]. This gap is termed the "digital divide," but the digital divide is classified into several layers according to the object of research. For example, in [2] the difference in the "place" in which the IT technology is used is identified. Among these, in particular, the digital divide between countries caused by economic disparities and various other gaps, starting with the language barrier (education gap), are addressed, and the need for the elimination of the digital divide is discussed. However, these are all based on statistical values related to the physical means of communication, and do not afford a view of the big picture of the overall disparity.

Mikami et. al. established the Language Observatory (LOP)[3] with the purpose of carrying out observations of the digital divide between languages on the internet. LOP combines Web crawling technology and a language identification engine[4] to retrieve up to 10⁹ multi-lingual Web pages, and automatically retrieve data included in a Web page such as URL information, tags, the main body, and Web server response time. By

combining the results of these observations and existing statistical data, it is possible to obtain a large amount of information such as the number of Web pages per capita and the number of Web pages by language, the ratio of native language pages, the degree of mixing-up of character codes, and basic research concerning the infrastructure. Some of the results have been published by Nakahira and Mikami[5], but this does not extend to the interpretation of the results obtained nor to the development of an index to systematically handle them. In this paper, we consider country domain governance based on a distribution/growth chart of outdegree, which is one of the data mined LOP observation results, and on an investigation of numbers of links.

II. COUNTRY DOMAIN GOVERNANCE

Country domain governance (CDG) indicates appropriate governance of a country code domain, but in this paper, it indicates in particular the domain administration policy. The creation of an index is required for investigating CDG. We set up what serves as a CDG index as in Table 1. By carrying out general mining of widely available statistical data and Web crawling data gathered in LOP, these indices can be shown for the first time.

Table 1. CDG Index

Level		Title	Index
System	Accessible/ Affordable	Accessible and Affordable	Relative Price of DN's to Monthly Income/the Global average price, Number of DN's (published) per Population/ GDP, Ratio of Servers Located Outside of the jurisdiction
	Linguistic Diversity	IDN service	Availability of IDN Service in local language, Number of Active IDNs
	Secure and Trusted	Security, Stability, and Resiliency	Ratio of DN's whose Registrant is Anonymous, ...(other)
Content	Accessible/ Affordable	Openness of Network	Ratio of the number of total outgoing links to the number of Outgoing links to news Media
	Linguistic Diversity	Local language use	Number of Local language pages per population, Ratio of total pages to pages written in Local Languages, Linguistic Diversity measured by Lieberman Index/Entropy
	Secure and Trusted	Trustable content	Availability of Dispute Resolution Process, ...(other)

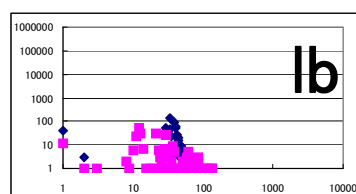
III. WEB LINK ANALYSIS AND OUTDEGREE GROWTH CHART

On the other hand, for an investigation carried out of the usual Web space, outdegree distribution is used. Outdegree distribution plots the number of Web pages taking each outdegree value on the vertical axis against the outdegree value on the horizontal axis. The outdegree distribution follows a power law as indicated originally by Broder et. al.[7],but in cases where there are a lot of automatic Web page creation such as with shopping sites, which are coming to form the mainstream these days, or CMS, an outdegree distribution is shown in the form of a power law with a δ function superimposed, because things with particular outdegree values are distributed in greater numbers

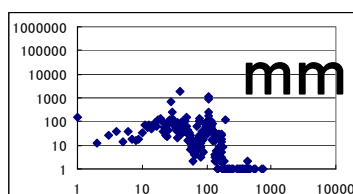
(Fukuda, [8]).

If this property is used, the state of the Web space that produced the outdegree distribution can be determined simply by looking at the outdegree distribution. Namely, if the outdegree distribution looks like white noise then the Web space is undeveloped, and if it is a power series, the Web space is developing with mutual links. However, with the increase in automatically created sites, as more in-depth services are being provided in the Web space with the formation of portal sites, shopping sites and the like, the Web can be said to be in the mature stage.

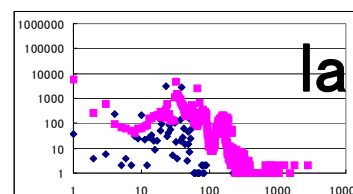
These kind of properties are ascertained and the outdegree distribution is produced for each country code top level domain (ccTLD), and the distribution indicated for each state of the Web space is the



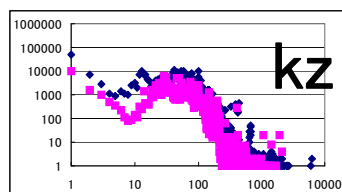
(a) Type 0: low growth



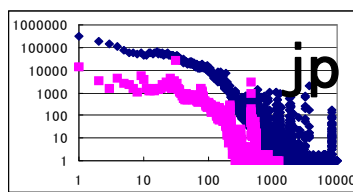
(b) Type I: domestic growth only



(c) Type II:
major offshore growth



(d) Type III(a): balanced growth



(e) Type III(b) : beyond maturity

Figure 1. Example of an outdegree maturity diagram. The horizontal axis represents the number of links, and the vertical axis the number of pages which have that many links. Black squares represent domestic s
ervers, and white squares the offshore servers.

outdegree growth chart. An example is shown in Figure 1. We have roughly divided them into 5 grades from type 0 to type III(b).

VI. EXAMPLE OF OBSERVED CDG INDEX

Next, we show several actually observed Web space examples based on the CDG Index.

1. Openness of Network

Openness of the network is determined by verifying whether or not the environment allows users within the domain to freely view content outside the domain. Care

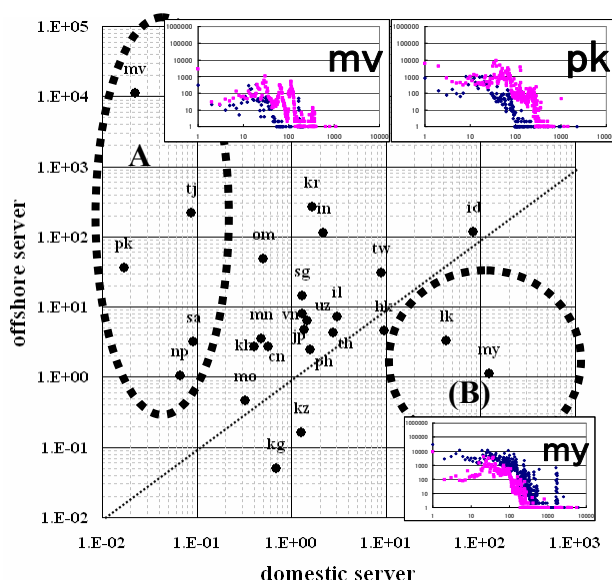


Figure 2. Ratio of the number of total outgoing links to the number of Outgoing links to news media and outdegree diagrams.

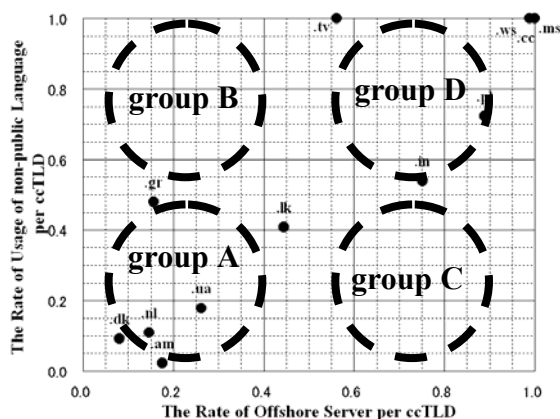


Figure 3. Estimated actual usage of ccTLD

must be taken over the fact that the guarantee of openness is roughly divided into (1) access restrictions due to censorship, and so on, and (2) social barriers to implementation, for example undeveloped infrastructure. Case (1) is connected to the restriction of the user's free use of the internet, and case (2) is seen as an infrastructure development problem, in advance of domain management problems. Whichever the case, investigation of the openness of the network can be analysed through investigating the number of Web pages belonging to the relevant ccTLD, and the link structure.

Several results of this are shown. In Figure 2, the number of links to the global news media (GNM) site of each ccTLD to which Web pages belong are graphed according to the physical location of the Web server on which the Web page resides. In producing this data, the UbiCrawler[6] that LOP uses was run in December, 2009 on approximately 2.3×10^7 Web pages used in 42 countries across Asia.

In Figure 2, the average number of links to the GNM per server from Web pages on domestic servers on the horizontal axis, are plotted against equivalent data for offshore servers on the vertical axis. Therefore, the point at the top left of chart A indicates that the links to the GNM are concentrated on offshore servers, and the point at the bottom right of B indicates that the links to the GNM are concentrated on domestic hosts. The 4 countries fj, np, pk, mv illustrate these possibilities for A, and the 2 countries lk and my for B. The outdegree distribution corresponding to these ccTLDs is also shown in Figure 2.

2. Relationship between Indicators

With the CDG Maturity Index, it is also possible to integrate each of the indicators and analyse them.

An example of this is shown in Figure 3. Figure 3 indicates the percentage of overseas installation of Web servers in each ccTLD and the percentage of non-official language usage in the regions belonging to the ccTLD. This corresponds to visualisation in an identical space of the index and indicated "percentage of servers located outside of the jurisdiction" in Accessibility and Affordable, and the index and indicated "ratio of total pages to pages written in local languages" in Local Language Use.

Figure 3 divides the whole region into 4 groups and gives each group a meaning. In group A, the domestic

infrastructure is basically stable, and a country is envisaged in which installation of a Web server is also possible if desired. For this reason, the ratio for overseas installation of Web servers is low, and also, as it is easy to make use of the internet in the mother tongue, usage of Web pages in the official language or mother tongue is common. In group B, although the domestic infrastructure is stable, for some reason such as users being restricted to overseas or to a minority living in that country, usage of Web pages in a language besides the official language or mother tongue is common. Group C represents cases where the domestic infrastructure is too unstable to be able to set up a Web server within the country, or where the domain for a local server is too expensive to purchase. Even in this kind of country, if mobile communication is developed, Web pages can be placed on overseas servers, and it is conceivable that Web pages in the country's official language or mother tongue could be used. Group D represents countries that do not even consider web page usage within the country, but want to profit by selling domains, or where a minority is able to obtain the country's ccTLD and make use of it.

Through these considerations, by looking in detail at the relationship between indicators, we believe that we can more precisely understand the reality of the digital divide using the CDG Maturity Index.

V. ANALYSIS TOOL FOR CDG

Through the analysis carried out so far, by using the CDG index, we have shown that we have approached more closely the realities of the management policy for each ccTLD and the realities of the digital divide.

However, to gather the data on which these analyses are based, appropriate analysis tools are required. Accordingly, we have added modules to and carried out preparation for the stable operation of the analysis tool (iGalaxy) currently developed by Arai et. al. [9]. iGalaxy consists mainly of an information input part (including crawling data), an information management part (CDG Index analysis), and an output part, and in one crawl it is possible to gather roughly 10^7 - 10^8 Web pages (approximately 10GB of crawling data). If these data were, for example, gathered every quarter, the data size would be so huge as to require a database with special data striping. We have implemented this using pgpool-II[10].

VI. CONCLUSION

In this paper, the CDG index is proposed as an observation index by which to home in on the reality of country domain governance. This allows indexing of the reality of the digital divide in a form that is closer to the conditions of use to be undergone, along with carrying out data mining by region in a form in which the various pieces of Web information obtained from the Language Observatory observation results are merged with the various statistical data. Several observation examples of this have been provided here. In the future, we plan to continue observation of Web space based on this index.

REFERENCES

- [1] Ohashi Ikuo, Toward the construction of a global information society: international trends and issues surrounding the digital divide, and creation of intellectual property 2009(3):6-36.
- [2] NTT C&C Foundation, the Digital Divide (in Japanese), NTT Foundation book: 2002.
- [3] Y. Mikami et. al., The Language Observatory Project: Proceedings of the 14th International World Wide Web Conference 2005 :990-991
- [4] S. T. Nandasara et. al., An Analysis of Asian Language Web Pages: The International Journal on Advances in ICT for Emerging Regions 2008 01 (01) : 12 - 23
- [5] K. T. Nakahira and Y. Mikami, Measuring Language Diversity in Cyberspace: International Conference on Linguistic and Cultural Diversity in Cyberspace, Yakutsk, Russia, July 2-4, 2008.
- [6] Boldi, P. et. al., UbiCrawler: a scalable full Distributed web crawler: Software-Practice & Experience, 34(8):711-726.
- [7] Broder, A. et. al., Graph Structure in the Web, Computer Networks: The International Journal of Computer and Telecommunications Networking Archive 33: 1-6
- [8] Kensuke Fukuda (2004), Analysis of Statistical Properties of WWW (in Japanese), IPSJ SIG Technical Report, 2004(136): 17-22.
- [9] Y. Arai et. al., A survey on language distribution on the internet : The 8th Proceedings of Forum on Information Technology 2008-4:529-532.
- [10] <http://pgpool.projects.postgresql.org/>

Extraction and Comparison of Tourism Information on the Web

Xiaobin Wu¹⁾, Sachio Hirokawa²⁾, Chengjiu Yin²⁾, Tetsuya Nakatoh²⁾, Yoshiyuki Tabata²⁾

¹⁾Graduate School of Information Science and Electrical Engineering,

²⁾Research Institute for Information Technology, Kyushu University
Hakozaki 6101, Fukuoka,
8128581, JAPAN

2ie10056y@s.kyushu-u.ac.jp, {hirokawa,yin,nakatoh,tabata}@cc.kyushu-u.ac.jp

Abstract: The number of tourists to Japan from foreign countries is drastically increased in recent years. However, there is a scene where the traveler is made uneasy by differences between the word, the custom and the culture in traveling abroad. We are aiming at the construction the horizontal search engine intended for tourism information in the Kyushu region as a test case of a special vertical search engine. As the first step for the research, we extracted 312 events from a public tourism portal site and compared the ranking of each event in the site with that in the general search engine. We confirmed a weak correlation of the ranking. Moreover, we found that the big difference of rankings for the events with strong regionality. The number of tourists to Japan from foreign countries is drastically increased in recent years. However, there is a scene where the traveler is made uneasy by differences between the word, the custom and the culture in traveling abroad. We are aiming at the construction the horizontal search engine intended for tourism information in the Kyushu region as a test case of a special vertical search engine. As the first step for these the research, we extracted 312 events from a public tourism portal site and compared the ranking of each event in the site with that in the general search engine. We analyzed the correlation of the rankings and confirmed a weak correlation. In addition, it was also confirmed that there was a large gap for the events with strong regionality.

Keywords: Search engine, information extraction, rank correlation coefficient, data collection, area tourism

I. INTRODUCTION

According to the development of the Internet, many information came to exist on WWW. By using a general search engine, we can get Web pages which contain the keywords we send to the search engine as query. However, it is not easy to reach the information unless we know appropriate keywords. Even if we know some of suitable keywords, the target pages, we are searching for, might be buried under the major pages displayed with higher ranked position of the search results.

One of the reasons of this problem is in that the coverage of general search engine is too wide and too general for particular purpose. We are studying the search engine focused on specific fields and objects on WWW. By limiting the search targets, we can expect to realize a search engine excellent in precision and recall for the targets. The present paper focuses on the tourism information on WWW, and compares the feature of information found in a tourism portal site and in a general search engine.

The number of foreign tourists visiting Japan are increasing continuously in recent years. Thanks to the simplification of the visa to the well-to-do population of China, more and more Chinese tourists are expected to come to Japan. However, there are many scenes where a traveler feels uneasy by the difference in

language, in a custom, or in culture. Of course, guide books have been used as helpful tools. Information on the Internet is much useful and reliable with respect to newest and up-to-date tourism information. This paper chooses touristic event information in Kyushu area in Japan, as the target of the analysis.

We collected the tourism information from the portal site of "Kyushu Tourism Promotion Organization." We analyzed the ranking of each event in the portal and the ranking of that in the general search engine Google. To evaluate the ranking, we used the estimated number of Web pages that match the name of the events which we send as a query.



Fig.1. The information of Welcomekyushu

II. Collection of Tourism Event Information

The event information on the Kyushu area was chosen as tourism information dealt with by this

research. We prepare the list of events as follows. Firstly, we obtained the 906 information from the "event list of Kyushu and Okinawa" in the web site of the "Kyushu Tourism Promotion Organization", which we refer as "welcomekyushu" in the sequel of the present paper. This list contains not only the names of event but also the names of food, such as "colander tofu", and the names of places, such as "alpine rose park". We removed these non-event names and compiled 316 event names. Some of the events are held every year with the name of the year, such as "X festival 2009" and "X festival 2010". The list of 312 events was obtained by removing these duplication. Some of the list is shown in Table 1.

Table 1. 20 Events of Event Name list of Kyushu

十五夜ソラヨイ, 鏡山スカイスポーツフェスティバル, 串木野浜競馬, 「小城」ホテルの里ウオーク, とす弥生まつり, べっふ鶴見岳一気登山大会, 宮崎神宮大祭, 美山窯元祭り, 小倉祇園太鼓, 四十九所神社「やぶさめ祭り」, 白地楽, 幸若舞, うすき竹宵, 筑前いづか雛のまつり, 牛深ハイヤ祭り, 武雄の荒踊り, 門司みなと祭, 鹿児島カップ火山めぐりヨットレース, 南大隅町ねじめドラゴンボートフェスティバル, 山鹿灯籠浪漫・百華百彩
--

Next, in order to compare the amount of information which exists in the general Web page on WWW, and the amount of information which exists in a tourism special site, the number of the search results with the event names was obtained. Google was chosen as a general search engine and the Kyushu Tourism Promotion Organization was chosen as a tourism special site. First, each event name was searched with Google and the

number of the obtained search results was made into the amount of information on a general Web page. Next, the search range of Google was limited to www.welcomekyushu.jp using the "site:" operator. The number of the search results obtained from welcomekyushu was made into the amount of information of a tourism special site. The number of the information in a general Web page was from 29 to 241,000,000 by the event name. by the event name, The number of the information on a tourism special site was from 2 to 603 similarly. Fig. 2 plotted the number of search results in descending order of it.

III. Analysis by Rank Correlation

1. Kendall tau rank correlation coefficient

We compared event information with Kendall tau rank correlation coefficient [1]. A computational procedure consists of four following Steps. The paper title text is 15 point bold font in Times New Roman.

Step 1. The number of measured value is set to n about two variables X and Y . That is, there are measured values of X_k and Y_k ($k = 1 \dots n$).

Step 2. Ranking is attached to an ascending order at Variable X and Variable Y . When there is equal order, average of the ranks is given. They are arranged in an ascending order about Variable X .

Step 3. The number of the equal order in Variable X and Variable Y is set to n_x and n_y . The size of equal order is set to t_i and t_j ($i = 1, 2, \dots, n_x; j = 1, 2, \dots, n_y$). Then, T_x and T_y can be found as follows.

$$T_x = \sum_{i=1}^{n_x} \frac{t_i(t_i - 1)}{2} \quad T_y = \sum_{j=1}^{n_y} \frac{t_j(t_j - 1)}{2}$$

Step 4. Number in the case of being $Y_i < Y_j$ about Y_i ($i = 1, \dots, n-1$) and Y_j ($j = i+1, i+2, \dots, n$) is set to P_i . Number in the case of being $Y_i > Y_j$ about Y_i and Y_j is set to Q_i . $\sum P_i$ is the number of times whose direction of the ranking of two variables corresponds. $\sum Q_i$ is the number of times whose direction of the ranking of two variables corresponds with an opposite direction. At this time, a rank correlation coefficient is calculated for by the following formula.

$$r_k = \frac{\sum_{i=1}^n P_i - \sum_{i=1}^n Q_i}{\sqrt{\frac{n(n-1)}{2} - T_x} \sqrt{\frac{n(n-1)}{2} - T_y}}$$

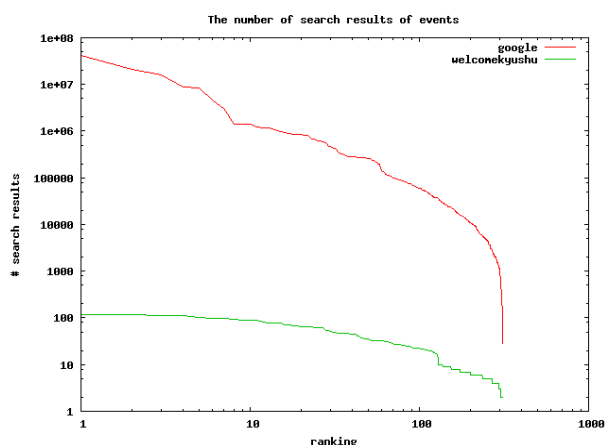


Fig.2. The Number of Search Results of Each Event

2. Examination

To compare the ranking of each event from 312 events, in the portal site "welcomekyushu" and with that in general search engine, we used the estimated number of Web pages that contain the name of the event. The obtained rank correlation coefficient was 0.20744. The correlation coefficient is not so strong to confirm a clear correlation. However, the p-value we obtained is 4.616×10^{-8} , which is less than the required significance level 5% ($\alpha = 0.05$). Thus, we can reject the null hypothesis at the given level of significance. Eventually, we see that the correlation is true.

IV. Events with Ranking Gaps

In Fig.3, each point represents to an event, where the x-axis is the ranking of the event in Google, and the y-axis is the ranking of the event in welcomekyushu.

There is a large gap between the ranking by Google and by welcomekyushu, when an event is displayed in distance from the line A, which represents the strong correlation. By analyzing those events, we observed the following four facts.

1) The points in Domain X support the correlation of the two rankings. The more points are in X, the higher is the correlation coefficient. We can find out weak correlation from Fig. 3.

2) The points in Domain Y have a high ranking in Google, and a low ranking in welcomekyushu. The names of these events seems to appear anywhere all over Japan. "Ohito Kabuki" and "Amazake Festival"(Fig.2) are samples of such names.

3) The points in Domain Z have a low ranking in Google, and a high ranking in Welcomekyushu. Those events are peculiar to Kyushu area. Many event titles

contained a name of a place. "Hosenji firefly festival" and the "Sakurajima enjoying -the-evening-cool tour ship" (Fig.3) are samples of these names.

4) The area Y contains more events than that of Z. The region Z displays the regional strength of the site.

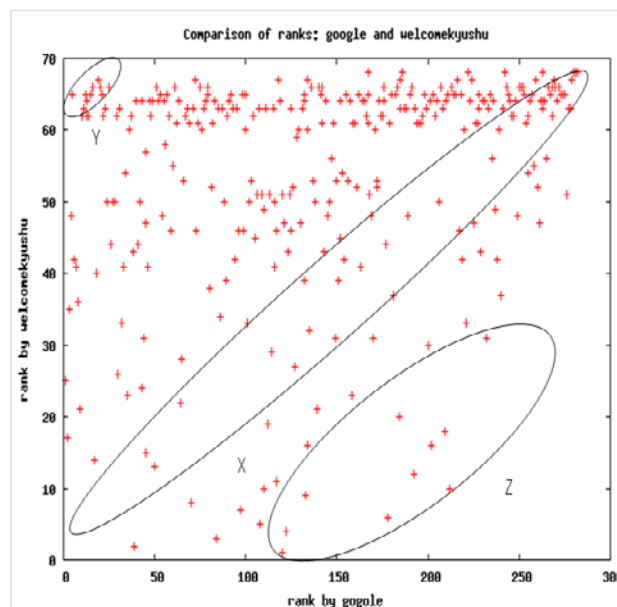


Fig.3 Ranking of Events

We compared the ranking of the number of the search results for each event name, in order to confirm the difference between the amount of information in a general Web page, and the amount of information of a tourism special site. Table 2 shows the list of events with high ranking with Google search engine. Table 3 shows the list of events with high ranking in welcomekyushu. From these two tables, we can say that regional events are much easier to find by welcomekyushu than by Google.

Table 2. 10 Events with High Ranking in Google, Low Ranking in WelcomeKyushu

Ranking	$Rk-Rg^*$	Rg^*	Rg	Rk	G	K	Event
1	63.79	1.21	5	65	8710000	5	竹ん芸
2	62.42	4.58	19	67	858000	3	おしろい祭
3	62.14	3.86	16	66	935000	4	みそ五郎まつり
4	62.11	2.89	12	65	1240000	5	甘酒まつり
5	61.38	3.62	15	65	965000	5	鮎市
6	61.18	4.82	20	66	836000	4	八天神社例大祭
7	60.87	3.13	13	64	1180000	6	大人歌舞伎
8	60.35	2.65	11	63	1400000	7	出の山ホテル恋まつり
9	59.97	6.03	25	66	625000	4	サン・サン・さんわフェスティバル
10	59.94	5.06	21	65	819000	5	くも合戦

Table 3. 10 Events with High Ranking in WelcomeKyushu, Low Ranking in Google

Ranking	Rg^*-Rk	Rg^*	Rg	Rk	G	K	Event
303	23.07	32.07	133	9	25700	93	皿山まつり
304	24.37	44.37	184	20	10200	65	早岐茶市
305	24.94	55.94	232	31	3970	47	長串山つつじまつり
306	25.42	29.42	122	4	32700	112	薩摩のひなまつり
307	27.94	28.94	120	1	36300	603	山鹿温泉祭
308	32.40	50.40	209	18	6100	67	仙酔峡つつじ祭り
309	32.71	48.71	202	16	6790	72	筑後吉井おひなさまめぐり
310	34.30	46.30	192	12	8980	83	宝泉寺ホテル祭り
311	36.92	42.92	178	6	10900	101	桜島納涼観光船
312	41.12	51.12	212	10	5950	90	人吉球磨は、ひなまつり

Each item shown in Table 2 and Table 3 is described as below

Rg^* : normalization ranking of Google search results

Rk : ranking of Welcomekyushu search results

K : number of Welcomekyushu search results

Rg : ranking of Google search results

G : number of Google search Results

V. Related Work

The tourism industry is one of the industries that suffered big influence of internet. Sightseeing information was unavailable only in a special travel agent before. Now, everyone can easily obtain it thanks to the internet. We can find sightseeing information on Web in (a) tourism portal sites, (b) general web pages, and (c) blog sites.

There are several systems and researches intended for each targets. [2] proposes a recommendation and a clustering system and shows their effectiveness for tourism portals.[6]proposes a natural language interface for tourism search engine. [5] analyses the patterns in HTML documents that characterize the occurrences of NEs(Named Entity), such as the name of the location and the name of the touristic events. [3] studies the clue words that can be used to extract tourism related NES. [4] reports the characteristic keywords that distinguish tourism blogs from other general blogs. We are aiming at the construction of the vertical search engine for tourism information. The difference of the characteristic of (a) and (b) was examined in the present paper.

VI. CONCLUSION

This paper analyzed tourism information available on a public tourism portal site that covers 7 prefectures in Kyushu area. 312 events were extracted from the site and were used to compare the portal site with a general search engine. We analyzed the correlation of the rankings of each event in the portal site and in the general search engine. It turned out that there exists a weak correlation between the rankings. It is also confirmed that there is a large gap for the events with strong regionality, which indicates a characteristic of the portal site. One of the lessons we learned is the usefulness of the lists of names, such as the names of

events, locations, shrines and souvenirs. We used 312 events for comparison of portal and general search engine. We extracted them from the lists in the portal site. Therefore, the development of the technique of the list discovery is an important problem. It is also necessary to devise a method to identify the same events with different names. As the next step of the research, we are considering to analyze other regional portal sites to compare with each other.

REFERENCES

- [1] H. Abdi, Kendall rank correlation, In N.J. Salkind (Ed.): Encyclopedia of Measurement and Statistics. Thousand Oaks (CA): Sage,2007.
- [2] S. Esparcia, V. Sanchez-Anguix, E. Argente, A. Garcia-Fornes, V. Julian, Integrating Information Extraction Agents into a Tourism Recommender System, Proc. HAIS2010, Springer LNAI 6077, pp.193-200, 2010.
- [3] Q. Hao, R. Cai, Ch.Wang, R. Xiao, J.-M. Yang, Y. Pang, L. Zhang, Equip Tourist with Knowledge Mined from Travelogues, Proc. WWW2010, pp.401-410, 2010.
- [4] A. Ishino, H. Nanba, H. Gaguma, T.Ozaki, D. Kobayashi, T. Takezawa, Automatic Compilation of Travel Information from Automatically Identified Travel Blogs(in Japanese), IEICE Tech Report, WI2-2009, pp.19-23, 2009.
- [5] I. Kinjo, A. Ohuchi, Web data analysis for Hokkaido tourism information (in Japanese) IEICE Tech. Report, DE2001-07,pp.99-104,2001.
- [6] J. M. Ruiz-Martinez, D. Castellanos-Nieves, R. Valencia-Garcia, J. T. Fernandez-Brieis, F. Garcia-Sanchez, P. J. Vivancos-Vincente, J. S. Castejon-Garrido, J. B. Camon, R. Martinez-Bejar, Accessing Touristic Knowledge Bases through a Natural Language Interface, Proc. PKAW2008, Springer LNAI 5465, pp.147-160, 2009.

An Analysis of Firm's Capacity in Mazda's Keiretsu

R. Takida¹, T. Ito¹, S. Matsuno¹, K. Voges², Y. Ishida³, and M. Sakamoto⁴

*1 Dept. of Business Administration, Ube National College of Technology, Yamaguchi, Japan
(Tel : 81-836-35-7115; Fax : 81-836-35-7115)*

(ito@ube-k.ac.jp, matsuno@ube-k.ac.jp)

*2 Dept. of Management, University of Canterbury, New Zealand
(Tel : 64-3364-2987; Fax : -)*

(kevin.voges@canterbury.ac.nz)

*3 Dept. of Knowledge-Based Information Engineering, Toyohashi University of Technology, Japan
(Tel : 81-532-44-6872; Fax : -)*

(ishida@utk.tut.ac.jp)

*4 Dept. of Computer Science and Systems Engineering, University of Miyazaki, Japan
(Tel : 81-985-58-7392; Fax : 81-985-58-7392)*

(sakamoto@cs.miyazaki-u.ac.jp)

Abstract: Capacity is defined as the power resulting from the specific position in network organizations in this paper. Thus, it becomes one of the important issues to measure firm's capacity. In this paper, we review the relevant studies of network organizations, and focus our study on Yokokai, the Mazda's Keiretsu. We propose a new approach to calculate firm's capacity. The capacity is divided into two categories, take-in capacity and take-out capacity in this paper. The relationship between the two capacities is called capacity difference. The relationship between capacity difference and corporate performance has been analyzed in order to discover the determinants of corporate performance in network organizations. Therefore, this paper provides a new perspective to find the determinants of the successful corporate management.

Keywords: capacity, capacity difference, corporate performance, Keiretsu

I. INTRODUCTION

As a special type of corporate group, Keiretsu is one of the well known organization forms widely today. It is an important factor for successful Japanese companies because Keiretsu is considered as the sources of the Kaizen and technical innovations. Many studies about the Keiretsu research have been published recently. In this paper, we propose a new structural index, capacity, in order to discover the rational relationship between capacity and corporate performance. The main contributions of this paper are: 1) the new quantitative concept of capacity is proposed; 2) the validity of capacity is proved; 3) rational relationship between capacity and corporate performance is analyzed. Therefore, this paper provides a new perspective to find the determinants of the corporate performance.

This paper is organized as follows. In Section 2, we briefly review some relevant researches of quantitative approaches of Keiretsu. Section 3 introduces the capacity model. Section 4 shows the results, and discusses the implications of the results. Finally in Section 5 we conclude by a summary of this paper.

II. BACKGROUND

Relationship is one of the important factors in structural analysis. Most researchers use strong tie and/or weak tie to describe the different strength of the relationship.

However, quantitative approaches are needed to discover the determinants of corporate performance. Dyer H. J. analyzed the relationship among firms based on distances between their locations and the frequency of face-to-face communication among engineers in the automobile industry [1].

High correlation relationship between degree and corporate performance has been found [2]. Inter-organizational relationships in the Keiretsu have been analyzed with quantitative analysis tools such as CONCOR and other statistical methods [3]. Moreover, Fukuoka et al. reported a new finding in relationships between firms in the Keiretsu of Nissan from the viewpoints of transaction and cross shareholdings [4]. Recently T. Ito begins to apply graph theory to network organization analysis, and clarifies some characteristics such as centrality, size of network [5-7]. Like other indices, such as centrality and density, capacity is also

one of the important indices of the analysis of the corporate performance. To the best of our knowledge and investigation, no study has examined capacity from an organizational network vantage point; therefore this study attempts to shed light on one of the most advanced quantitative analysis using data gathered from Mazda's Yokokai Keiretsu.

III. METHOD

Basically Capacity means power pertaining to, or resulting from, the possession of strength, wealth. It shows one kind of possible powers of being or of doing. In this paper, capacity is defined as the power resulting from the specific position in network organizations.

1. Outline of the capacity model

Generally a graph consists of a set of nodes and a set of arcs. Two nodes are connected if a path between these two nodes. Path is one of the important concepts in graph theory. According to graph theory, a path is a sequence of nodes such that the nodes and the arc are adjacent. A walk is a sequence of nodes and arcs such that the nodes and arcs are adjacent. The difference between path and walk is that a path is a walk that does not include any node twice, except that its first node might be the same as its last. For digraphs, walks can travel arcs only in the direction of the arrows.

The length of walk is formed by a sequence of the number of arcs such that any two successive arcs in the sequence share a node. Basically the node's capacity is determined by the length of walk and the number of walks.

Suppose $S(r)_{ij}$ is the summation of the length of walks from node p_i to p_j when the length of the walk equals to r .

$$S(r)_{ij} = A + A^2 + A^3 + \dots + A^r \quad (1)$$

A is a normalized adjacent matrix. The reachable matrix, denoted by A^r , refers to the fact that node p_i can reach node p_j through the number of steps r . For instance, A^2 means that node p_i can reach node p_j through 2 steps. The element of matrix A is the number of the walks between node p_i and p_j .

The strength of the walk should be considered as the inverse of the length of the walk. In other words, the strength will be weaker if the length of walk is longer.

Then the value of capacity of nodes can be expressed as follows.

$$C(r)_{ij} = \sum_{i=1}^r \left(\frac{A}{L} \right)^i \quad (2)$$

where

- C capacity from node p_i to p_j
- A the number of walks in a given graph
- L parameter of the length from node p_i to p_j
- r length of the walk from node p_i to p_j

Then the terminal capacity of the row will be calculated as follows.

$$C(p_i, r) = C(r)_{i1} + C(r)_{i2} + C(r)_{i3} + \dots + C(r)_{in} \quad (3)$$

When the r equals to infinite, the total capacity of C is calculated as follows.

$$C = C(\infty) = \left(I - \left(\frac{A}{\eta} \right) \right)^{-1} - I \quad (4)$$

The summation of row in matrix C means take-out capacity, and the summation of column means take-in capacity.

In real society, the node generally means the individual and/or firm, and the arc means the relationship. In transaction network, walk can be explained as one power to begin transaction with other companies. Therefore, the volume of walk could be explained as firm's capacity in network organization. In transaction matrix take-out capacity means the capacity of firm i that sell its parts to all other firms, and take-in capacity means the capacity of firm j that purchases parts from all other firms.

2. Data collection

In order to measure all firms' capacity in Yokokai, transaction data in the Yokokai keiretsu have been collected from our interviews and the publications of the Japan Auto Parts Industries Association and Automotive Parts Publishing Company [8].

In 2004, 177 parts suppliers are included in Yokokai. 72 parts suppliers and Mazda have reciprocal transactional relationships, and 105 parts suppliers are singletons. A singleton is an isolate company whose in-degree and out-degree are both 0. In Yokokai's case,

singleton means the firm which has no relationship with other firms.

The transactional relationships among the companies were identified through graph modeling. A tie shows the percentage of the transaction between each pair of firms. We collected directed and weighted data to measure the capacity of each firm.

IV. RESULTS AND DISCUSSIONS

We developed a computer program and calculated the capacity of each firm in Yokokai. The result of the capacity of transactions is shown in Fig. 1.

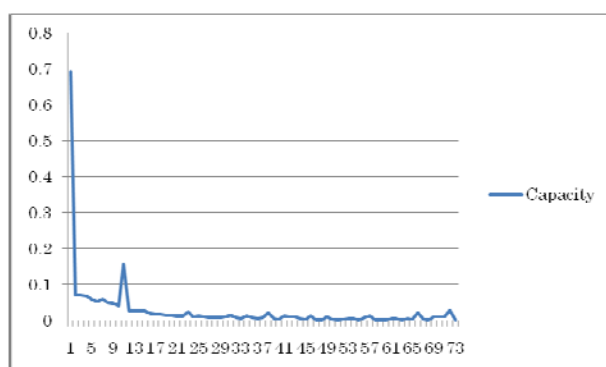


Fig. 1 Yokokai's capacity in 2004

As mentioned above, the capacity can be divided into two categories, take-in capacity and take-out capacity. The difference between those two capacities means the difference between the purchase capacity and sell capacity. It is called capacity difference. The firm has unbalanced issue if the absolute value of the capacity difference is high.

In order to discover the rational relationship between capacity and corporate performance, we collected the data of corporate performance including sales and profit from Mazda in fiscal years of 2004 and 2005, and calculated correlation coefficient between the capacity and corporate performance. Car maker Mazda is excluded because this paper focused on the study of parts suppliers. The result is shown as Table 1.

Table 1 shows us that a high correlation between capacity difference and corporate performance. Therefore, basically it is effective to improve corporate performance if the parts supplier to find the way to cut down the capacity difference.

In order to compare with Mazda's results, we collected transactional data from Nissan group. The correlation coefficient between capacity difference and sales and profit is 0.44 ($p=0.01$) and 0.39 ($p=0.02$)

respectively in 2004, and 0.52 ($p=0.00$) and 0.49 ($p=0.02$) respectively in 2005. Therefore, it is clear that certain correlation between capacity difference and corporate performance exists.

Table 1 Matrix of correlation coefficient between capacity difference and corporate Performance

	2004			2005		
Sales	1			1		
	-			-		
	33			37		
Profit	0.64**	1		0.53**	1	
	0	-		0.00	-	
	31	31		31	31	
Capacity Difference	0.44**	0.88**	1	0.69**	0.42*	1
	0.1	0	-	0	0.2	-
	33	31	42	37	31	53

The scatter diagram between capacity difference and sales can be illustrated as Fig. 2.

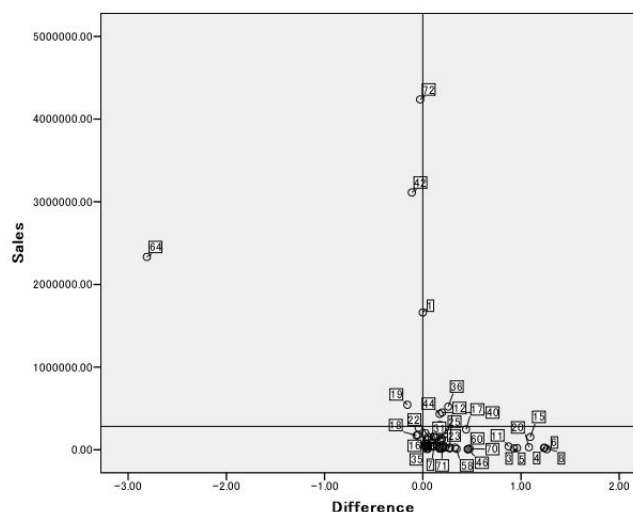


Fig. 2 Scatter diagram of capacity difference and sales

The selling power is larger than its purchase power if its capacity difference is larger than zero. Therefore, these firms have good management skills if the value of sales of these firms is high; otherwise the management skills of these firms, such as No. 6; Sumino Kogyo Co. Ltd., and No. 4; Keylex, should be improved. No. 64 is Denso. Its capacity difference is -2.83, but its sales are high. It means Denso's selling power is less than its buying power because Denso is one of the main subsidiaries in Toyota's group. Denso purchases parts in Mazda's keiretsu and sells them in Toyota's group. This

is the reason why Denso has negative value of capacity difference but high sales.

The scatter diagram of take-out and sales, take-in and sales can be drawn as Fig. 3 and 4 respectively.

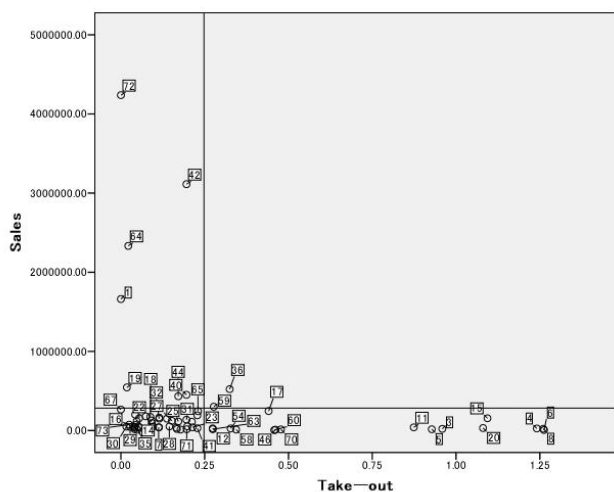


Fig. 3 Scatter diagram of take-out capacity and sales

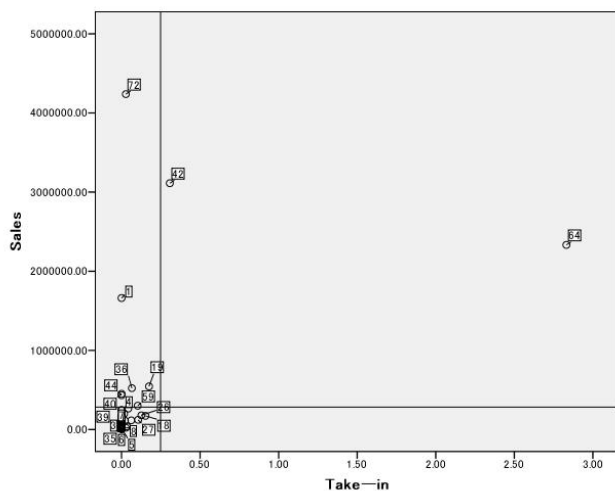


Fig. 4 Scatter diagram of take-in capacity and sales

In Fig. 3, No. 6 is Sumino Kogyo Co. Ltd., No.8 is Japan Climate Systems Corporation, and No. 4 is Keylex. They have high value of take-out capacity. It means that these firms have strong power to sell their parts in Mazda's keiretsu. But their sales are low. Therefore, the selling policy of these firms' should be adjusted.

In Fig. 4, No. 64 is Denso. Denso has an extremely high value of take-in capacity. It means that Denso purchases parts in this group, and maintains its good corporate performance because Denso has strong selling power in its own market.

V. CONCLUSION AND FUTURE WORKS

In this paper, the new approach of capacity analysis is proposed, and its validity is proved. We discovered the rational relationship between capacity and corporate performance using the example of Mazda's Keiretsu. However, much more works should be done to build up rational relationship with other parts suppliers. For instance, two indices are helpful to find the unbalance issue in corporate management. One is the difference between capacity difference and other corporate performance, such as capitals and stock prices, and other is the difference between capacity difference and centrality. Furthermore, the relationship between capacity and density should be done in the near future.

Acknowledgment: This research was partially supported by the Ministry of Education, Culture, Sports, Science, and Technology, Grant-in-Aid for Exploratory Research, 21510171, 2009.

REFERENCES

- [1]Dyer H. J. (1996) "Specialized Supplier Networks as a Source of Competitive Advantage: Evidence from the Auto Industry", *Strategic Management Journal*, Vol. 17, 271-291
- [2]Ito T. (2004) Quantitative analysis of the firm's relationship in the Keiretsu of Toyota group, Proceedings of the 2004 Information Resources Management Association, International Conference on Innovations Through Information Technology, pp.1078-1079, May 23-26, 2004, New Orleans USA
- [3]Lincoln R. L. and Gerlach M.L. (2004) *Japan's Network Economy Structure, Persistence, and Change*, Cambridge University Press
- [4]Fukuoka S., Ito T., Passerini K. and Sakamoto M. (2006) An Analysis between Transaction and Cross Shareholdings in the Keiretsu of Nissan, *Managing Information in the Digital Economy Issues & Solutions*, 163-169, IBIMA International Conference, Bonn Germany
- [5] T. Ito, K. Passerini, M. Sakamoto (2008) Structure Analysis of Keiretsu of Toyota, *Encyclopedia of Networked and Virtual Organizations*, pp.1542-1548, Idea Group Publishing
- [6]T. Ito, C. Medlin, K. Passerini, M. Sakamoto (2009) Influence Trust and Trade in the Keiretsu of Toyota: A Centrality Analysis, *Trust, Globalisation and Market Expansion*, Chapter 8, pp.101-118, Nova Science
- [7]Ito T., Matsuno S., Xia Z., Sakamoto M., and Rajiv Mehta (2010) An Analysis of Interactive Influence in Mazda's Yokokai Keiretsu, *Artificial Life and Robotics*, Volume 15, Number 3, 249-252, Springer Japan
- [8]JAPIA&APPC (2005) *Japanese Automotive Parts Industry*, Automotive Parts Publishing Company, (Japanese Edition)

An analysis of structure importance in Mazda's Keiretsu

S. Tagawa¹, R. Takida¹, T. Ito¹, R. Mehta², H. Hasama³, and M. Sakamoto⁴

*1 Dept. of Business Administration, Ube National College of Technology, Yamaguchi, Japan
(Tel : 81-836-35-7115; Fax : 81-836-35-7115)*

(niki@ube-k.ac.jp, ito@ube-k.ac.jp)

*2 School of Management, New Jersey Institute of Technology, USA
(Tel : 1-973-596-6419; Fax : 1-973-596-3074)*

(Mehta@njit.edu)

*3 Dept. of System Management, Fukuoka Institute of Technology, Japan
(fit-doctor_mas@kmd.biglobe.ne.jp)*

*4 Dept. of Computer Science and Systems Engineering, University of Miyazaki, Japan
(Tel : 81-985-58-7392; Fax : 81-985-58-7392)
(sakamoto@cs.miyazaki-u.ac.jp)*

Abstract: Centrality is one of the effective indices to measure organizational structure. Freeman once proposed a set of centrality indices including degree, closeness, and betweenness. However, Ito discussed the implications of centrality, and found that differences exist even when the centrality is same. In this paper, the authors collected the data of transactions and cross shareholdings from Mazda's Keiretsu Yokokai, and calculated the structural importance based on the new method, so-called SNW model. Furthermore, the authors discussed the implication based on the results of correlation coefficient between the SNW results and corporate performance such as sales and profits. This paper provides a new perspective to discover the structural importance of the network organizations.

Keywords: degree, betweenness, closeness, transaction, cross shareholdings, Keiretsu

I. INTRODUCTION

According to the conventional organization theories, corporate organizations can be basically categorized into at least three types. The first one is line organizations, the second is line-and-staff organizations, and the third is functional organizations. Other types such as matrix organizations and project-team organizations have been developed recently. As a new type of successful organizations, Davidow and Malone suggested a new idea of virtual organization in the beginning of 1900's [1]. Another typical successful organization is considered as the Keiretsu in Japan [2]. The authors reviewed the previous research and completed a comparative study of the virtual organizations and Keiretsu theoretically. The authors found many common characteristics between them. One is that they both can be defined as a network organization with mutual transactions and shared information. The common issue in these different organizations is how to discover the effective structure. Centrality is one of the effective indices to measure organizational structure.

The main contributions of this paper are: 1) the new quantitative analysis, so-called SNW model, is discussed; 2) centrality index of all firms including in Mazda's group Yokokai are calculated; 3) correlation

coefficient between the new findings of the results of the SNW and corporate performance such as sales and profits are analyzed. Therefore, this paper provides a new perspective to discover the structural importance of the network organization.

This paper is organized as follows. In Section 2, the relevant literature of organizational structure is reviewed briefly. In section 3, the authors introduced some basic concepts, and explained the SNW model. Section 4 shows the measurement results, and discusses the implications of the new findings. Finally in Section 5 we conclude by a summary of this paper.

II. BACKGROUND

Most of the research of network organizations can be characterized by qualitative approach and quantitative approach. One of the most important issues in this field is to discover what kind of relationship is the most effective for corporate management in the IT age today. To determine the relationship in the network organizations, many different models have been developed. A classic but typical method is called Freeman model proposed by Freeman in 1979 [3]. It includes a set of centrality index to calculate the network organizations from the viewpoint of degree, closeness and betweenness. Many new measurements

have been discovered on the basis of Freeman model later. For instance, Tyler et al. proposed a new method applying a betweenness algorithm to identify community within a network [4]. For calculating the relationship of cross shareholdings between firms in the Keiretsu of Toyota, as a revised Freeman model, Ito introduced directed and valued connection lines into Freeman model, and developed new computer program to calculate the centrality index using the data of Toyota's Keiretsu. Strong correlation among out-degree, betweenness and corporate performance has been found [5]. Centrality index is a useful tool for the structure analysis of the network organizations. The structure analysis could be carried out from many different viewpoints, such as position, size in any network organizations. It is obvious that importance analysis of each firm would be one of the most important steps for the structure analysis.

II. METHOD

Freeman proposed centrality of each node from three viewpoints of degree, betweenness and closeness [3]. Degree index is calculated as follows.

1 Degree

Freeman defines a degree of node p_k is the number of node connect with it directly. Therefore, Freeman calculated it with the measurement developed by Nieminen [6]. The centrality index of degree of node k can be defined in the following way.

$$C_D(p_k) = \sum_{i=1}^n a(p_i, p_k) \quad \dots\dots (1)$$

where

$a(p_i, p_k)=1$ if and only if p_i and p_k connected by a line
 $a(p_i, p_k)=0$ otherwise

The number of nodes adjacent to a given node in a symmetric network is the degree of that node. For asymmetric network the in-degree of a node p_k is the number of ties received by p_k and the out-degree is the number of ties initiated from p_k .

The degree means the proportion of other nodes that are adjacent to p_k and is viewed as important index of its potential communication activity.

2 The SNW analysis

In order to discuss the implication of the Freeman model, following example was given [7].

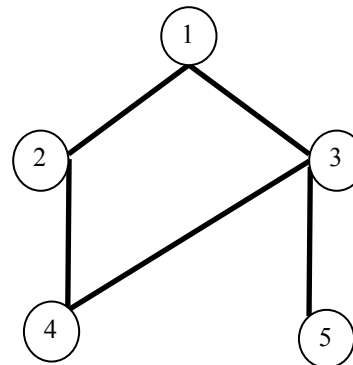


Figure 1 A 5-Node Network

According to Freeman model, the degree index of node 1, 2 and 4 are 2. It is obvious that their structural importance is quite different. The degree index of the entire network is 0.417. But the degree index of the sub-network excluded node 1, 2 and 4 are 0.33, 1 and 0.33 respectively. Node 2 and 3 are more important because the degree index of sub-network excluded node 3 is less than the degree of the entire network.

Therefore, a third method called the SNW model is proposed in 2005 [7]. The SNW model is expressed as follows.

$$I_D(p_k) = C_D - C_D(p_k) \quad \dots\dots (2)$$

where

$$C_D = \frac{\sum_{i=1}^n [\max C_D(p_i) - C_D(p_i)]}{n^2 - 3n + 2}$$

Node k is called strengthening node if the centrality index of sub-network excluded node k is less than that of the entire network. In this case, $I_D(p_k)$ is larger than zero. The opposite is called weakening node when $I_D(p_k)$ is less than zero. Node k is called neutral node if the centrality index excluded sub-network of node k is equivalent to that of the entire network. In this case, $I_D(p_k)$ is equivalent to zero.

III. MEASUREMENT

To avoid conceptual confusions, some important concepts of network organization are given as below.

1 Keiretsu and network

The definition of network organization means a group of nodes, such as persons or firms, having certain relationships among themselves under the condition of having common purpose and willingness to participate. In accordance with this definition, Keiretsu could be interpreted as one kind of network organization in management science.

A graph consists of a set of points and a set of lines connecting pairs of point. The point, which composes a network, is called node, and the line, which connects any two nodes directly, is called an edge in graph theory. A graph is a model with an undirected dichotomous relation. In other words, a tie is present or absent between each pair of nodes. The data consists of valued and directed connections in which the strength or intensity of each tie is recorded. Therefore, a graph could be considered as one specific type of network organizations. In network organization, generally the firm should be the node, and the edge should be the different types of relationships such as transactional relationship and friend relationship.

2 Data collection

Data of transactions and cross shareholdings in the Keiretsu of Mazda are collected from the publications and investigation by interviews [8].

The process of data-collection can be expressed as follows.

Step1: Determine the boundary of the network;

Step2: Collect the data of transactions and cross shareholdings; basically the data is percent value of the transactions or stock holdings between two firms. And input the data into a matrix table.

Step3: Remove singletons in the matrix table.

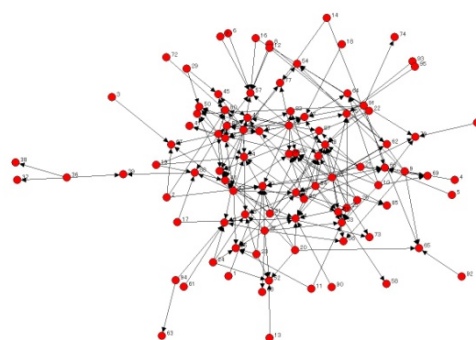
The data of each cell in the matrix means transactional relationship which the firm in column accepts auto-components from other suppliers in row of the transactions network, or capital relationships which the firm in row invests in stocks to other firms in column in the network of cross shareholdings.

The authors removed the singleton in Keiretsu of Mazda. Singleton means that the node has no any relation with other nodes. They are isolated in the network. The total number of the firms which hold capital relationship with each other in the network of

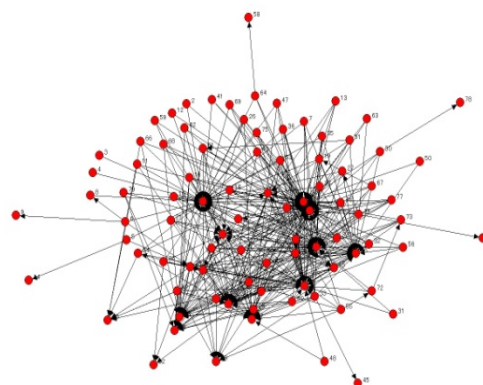
cross shareholdings is 230. It includes 177 parts suppliers, 11 carmakers, 42 banks and financial institutions. The total number of the firms in the network of transactions is 188, including 177 parts suppliers and 11 carmakers.

The numbers of singletons in the networks of transactions and cross shareholdings are 99 and 135 respectively. Therefore, there are 11 car makers and 77 parts suppliers which have reciprocal transaction relationships, 87 companies including Mazda, 51 suppliers and 35 banks and financial institutions have reciprocal capital relationship in Yokokai.

The network of transactions and cross shareholdings of Mazda can be illustrated as Figure 2.



Network of transactions



Network of cross shareholdings

Figure 2 Network of transactions and Cross shareholdings of Mazda in 2004

IV. RESULTS AND DISCUSSIONS

It is difficult to determine which firm is more important in Figure 2. To calculate the importance of each firm, two methods mentioned above are applied in this paper.

The results of the first method can be expressed in Table 1.

Table1 Selected part of degree of each firm in Yokokai

No	out-degree(T)	in-degree(T)	out-degree(C)	in-degree(C)
1	0	0	3	0
2	0	0	9.4	0
3	0	0	5.4	0
4	0	0	2.6	0
5	0	0	3.5	0
6	0	0	1.9	0
7	0	0	1.9	0
8	0	0	6.2	0
9	0	0	23.7	0
10	0	0	24.8	0
11	0	0	13.2	0
12	0	0	6.9	0
13	0	0	3.1	0
14	0	0	10.8	0
15	0	0	3.8	0
16	0	0	8	0
17	0	0	4.4	0
18	0	0	3.4	0
19	0	0	4.8	0
20	0	0	17.9	0
21	0	0	13.7	0
22	0	0	6.8	0
23	0	0	12.5	0
24	0	0	16	0
25	0	0	16.5	0
26	0	0	13	0
27	0	0	46.1	0
28	0	0	59.4	0
29	0	0	7.4	0
30	0	0	31.5	0
31	0	0	19.5	0
32	0	0	40.7	0
33	0	0	86.4	0
34	0	0	107.1	0
35	0	0	52.4	0
36	0	901.13	143.3	0
37	66	0	0	0
38	70	0	0	0
39	90.6	0	0	35
40	66.8	0	0	75
41	89	0	0	0
42	48.9	0	0	0
43	92	2	0	66.6
44	0	2	0	0
45	84	0	0	0
46	76.5	0	0	0
47	40	0	0	0
48	81.3	0	0	0
49	0	4.9	0	0
50	66.6	0	0	31.3

In Table 1, (T) and (C) means transaction and cross share holding respectively. Generally the firm which has high value of out-degree and in-degree of cross shareholdings, and the firm which has high value of out-degree and in-degree of transactions is an important hypothesis in the network organization.

In order to identify the rational relationship between degree and corporate performance, the authors calculated the correlation coefficient among degree and sales, profits. It can be illustrated as Figure 3.

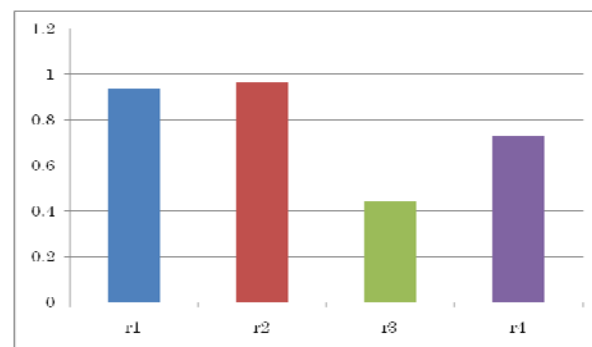


Figure 3 Correlation coefficients between degree and corporate performance

In Figure 3, r1 and r2 means correlation coefficient between profits and in-degree (T), profit and out-degree (C) respectively. And r3 and r4 is correlation coefficient between sales and in-degree (T) and sales and out-degree (C) respectively. All of them are significant. Basically the suppliers which have high value of out-degree (C) have strong control power for other suppliers. And the suppliers which have high value of in-degree (T) should have specific skills of production and manufacturing. From this result, higher degree, stronger sales and profit is hold. Unfortunately, not only the value of all correlation coefficients between corporate performance and degree out-degree (T) and in-degree (C) are very low, but also they are not significant. Therefore, the authors calculated the structural importance using the SNW model. The results are shown in Table 2.

The authors calculated the correlation coefficient between the SNW and sales, profits. Not only the value of the results between the SNW and sales are very low, but also all of them are not significant. The results of the SNW and profit can be illustrated as Figure 4.

In Figure 4, r5 and r6 means correlation coefficient between out-degree (T) of the SNW and profit, and between in-degree (C) and profit respectively. All of them are significant. High value of out-degree means strong selling power. Therefore, stronger selling power, more profit is hold. The suppliers which accept investment higher should be considered as they are under control of the investment companies. Therefore, the prices of the orders comes from investment companies may be very low. This is the considerable reason to explain why correlation coefficient of r6 is negative.

Table 2 Structural importance of each firm in Yokokai
based on the SNW analysis

No	Out-degree(T)	In-degree(T)	Out-degree(C)	In-degree(C)
	Criterion=0.54	Criterion=9.85	Criterion=2.99	Criterion=0.87
1	-	-	W	W
2	-	-	W	W
3	-	-	W	W
4	-	-	W	W
5	-	-	W	W
6	-	-	W	W
7	-	-	W	W
8	-	-	W	W
9	-	-	W	W
10	-	-	W	W
11	-	-	W	W
12	-	-	W	W
13	-	-	W	W
14	-	-	W	W
15	-	-	W	W
16	-	-	W	W
17	-	-	W	W
18	-	-	W	W
19	-	-	W	W
20	-	-	W	W
21	-	-	W	W
22	-	-	W	W
23	-	-	W	W
24	-	-	W	W
25	-	-	W	W
26	-	-	W	W
27	-	-	W	W
28	-	-	W	W
29	-	-	W	S
30	-	-	W	W
31	-	-	W	W
32	-	-	W	W
33	-	-	W	W
34	-	-	W	W
35	-	-	W	W
36	W	S	W	W
37	W	S	-	-
38	W	S	-	-
39	W	S	W	W
40	W	S	W	W
41	W	S	-	-
42	W	W	-	-
43	W	S	W	W
44	S	W	-	-
45	W	W	-	-
46	W	S	-	-
47	W	S	-	-
48	W	W	-	-
49	S	W	-	-
50	W	W	S	W

IV. CONCLUSION AND FUTURE WORKS

The authors calculated the degree, one of the centrality indices, and the structural importance using the SNW model. In order to identify the determinants of corporate performance, correlation coefficients between degree and sales and between degree and profit, between the results of the SNW and sales and profit have been measured. Degree and the SNW are both very effective. And it is shown that these two methods are practical for the empirical study in this paper.

Needless to say, some problems are still left. For instance, the data collected is only one fiscal year in this

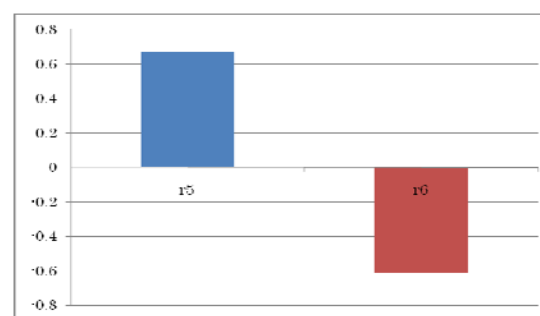


Figure 4 Correlation coefficients between the SNW and Profit

paper. Much more data are required for further analysis. Correlation coefficient between sales and the results of the SNW model is also needed to be analyzed more. Moreover, the SNW is only applied into degree, more analysis applying into other centrality indices such as closeness and between need to be done in the near future.

Acknowledgment: This research was partially supported by the Ministry of Education, Culture, Sports, Science, and Technology, Grant-in-Aid for Exploratory Research, 21510171, 2009.

REFERENCES

- [1] Davidow, W. H. and Malone, M. S. (1992). The Virtual Corporation, Harper Collins Publishers Inc.
- [2] Imai, K. (1989). Firm's group, In Imai K. and Komiya R. (ed.) Japanese Firm, Tokyo University Publication (Japanese Edition).
- [3] Freeman, L. C. (1978/1979). Centrality in Social networks Conceptual clarification, Social Networks 1.
- [4] Tyler J. R., Wilkinson D. M., and Huberman B. A. (2003) Email as spectroscopy: Automated discovery of community structure within organizations, in Proceedings of the International Conference on Communities and Technology. (Netherlands), Kluwer Academic Publishers.
- [5] Ito, T. (2004). Quantitative Analysis of a Firm's Relationship in the Keiretsu of Toyota group, Innovations Through Information Technology, IRMA 2004 International Conference, New Orleans, USA, 1078-1079.
- [6] Nieminen J. (1974) On centrality in a graph, Scandinavian Journal of Psychology 15, 1974, pp.322-336.
- [7] Ito, T. and Sakamoto, M. (2005) Importance Analysis of Each Firm in the Keiretsu of Toyota. Managing Modern Organizations with Information Technology, IRMA 2005 International Conference, pp.930-933.
- [8] JAPIA and APPC (2004) Japanese Automotive Parts Industry, Automotive Parts Publishing Company, (Japanese Edition).

A centrality analysis between transactions and cross shareholdings in Mazda's Keiretsu

E. Niki¹, R. Takida¹, T. Ito¹, R. Mehta², L. P. NG³, and M. Sakamoto⁴

*1 Dept. of Business Administration, Ube National College of Technology, Yamaguchi, Japan
(Tel : 81-836-35-7115; Fax : 81-836-35-7115)*

(niki@ube-k.ac.jp, ito@ube-k.ac.jp)

*2 School of Management, New Jersey Institute of Technology, USA
(Tel : 1-973-596-6419; Fax : 1-973-596-3074)*

(Mehta@njit.edu)

*3 Hoecheong Industries (Holding) Co., Ltd, China
(Tel : 86-595-2208-5151; Fax : 86-595-2208-5188)*

(hcgroupp@hoecheong.com)

*4 Dept. of Computer Science and Systems Engineering, University of Miyazaki, Japan
(Tel : 81-985-58-7392; Fax : 81-985-58-7392)*

(sakamoto@cs.miyazaki-u.ac.jp)

Abstract: Firm's relationship is one of the important issues in the field of corporate management. The authors review network literature related with the automotive industry, and focus their study on the firm's relationship in the Keiretsu of Mazda, Yokokai, in this paper. The authors collected the data of transactions, cross shareholdings, and sales from all firms in Yokokai, and calculated the centrality index based on graph theory in order to discover the rational relationship between transactions and sales and between cross shareholdings and sales. Generally centrality index are calculated based upon degree, betweenness and closeness indicators. Certain correlation between transactions and sales, and between cross shareholdings and sales have been found. Implications of these findings are discussed. This paper provides a new perspective to find the determinants of the successful corporate management.

Keywords: degree, betweenness, closeness, transaction, cross shareholdings, the Keiretsu

I. INTRODUCTION

Firm's relationship is one of the important issues in the field of corporate management. The Keiretsu, as one special type of group companies is known broadly today. One of the Keiretsu's characteristics is cross shareholdings. The purpose of cross shareholdings can be expressed as follows [1].

The first is to secure long-term strong stockholders for stabilization of corporate governance under the regulation of financial policy. The second is to acquire the latent profits of stock-holding brought by rising of stock prices as a buffer to stabilize corporate performance. And the third is to realize the high productivity by attempting stabilization of the so-called reciprocal business transactions.

However, only a few empirical studies to prove the correlations between transactions and cross shareholdings have been reported until now [2, 3]. And further research is required in this area to improve corporate management relationships and priorities. Therefore, it is necessary to measure the quantitative relationships among the firms, and verify the correlation between transactions and cross shareholdings. This

research focuses on the firm's relationship in the keiretsu of Mazda.

The main contributions of this paper are: 1) To uncover the correlation between transactions and sales, and between cross shareholdings and sales, measures of graph theory such as centrality index, including degree and betweenness are measured using computer software called Ucinet. 2) Certain correlation between transactions and cross shareholdings, and between transactions and sales has been found. All of these new findings have been discussed.

This paper is organized as follows. In Section 2, we introduce some basic concepts and explain the centrality model including degree, closeness and betweenness. Section 3 shows the measurement results, and discusses the implications of the new findings. Finally in Section 4 we conclude by a summary of this paper.

II. METHOD

A graph consists of a set of points and a set of lines connecting pairs of point. The point, which composes a network, is called node, and the line, which connects any two nodes directly, is called an edge in graph theory.

The shortest path linking a given pair of nodes is called geodesic. A graph is a model with an undirected dichotomous relation. In other words, a tie is present or absent between each pair of nodes. The data consists of valued and directed relationship in which the strength or intensity of each tie is recorded. The authors collected directed and valued data to compute the centrality of each firm.

1. Outline of the centrality model

Freeman proposed centrality of each node from three viewpoints of degree, betweenness and closeness [4].

1.1 Degree

Freeman defines a degree of node p_k is the number of node connect with it directly. Therefore, Freeman calculated it using the measurement developed by Nieminen [5]. The centrality index of degree of node k can be defined in the following way.

$$C_D(p_k) = \sum_{i=1}^n a(p_i, p_k) \quad \dots\dots (1)$$

where

$a(p_i, p_k)=1$ if and only if p_i and p_k connected by a line
 $a(p_i, p_k)=0$ otherwise

The number of nodes adjacent to a given node in a symmetric network is the degree of that actor. For asymmetric network the in-degree of a node p_k is the number of ties received by p_k and the out-degree is the number of ties initiated from p_k .

The degree means the proportion of other nodes that are adjacent to p_k and is viewed as important index of its potential communication activity.

1.2 Betweenness

The index of betweenness is calculated as a probability that node p_k falls on a randomly selected geodesic linking p_i and p_j . Freeman defines the centrality index of betweenness of node k as follows [6].

$$C_B(p_k) = \frac{\sum_{i=1}^n \sum_{j=1}^n g_{ij}(p_k)}{g_{ij}} = \sum_{i=1}^n \sum_{j=1}^n b_{ij}(p_k) \quad \dots\dots (2)$$

where

$i \neq j \neq k$;

$g_{ij}(p_k)$: The number of geodesics linking p_i and p_j that contains p_k

g_{ij} : The geodesics linking p_i and p_j

Betweenness is useful as an index of the potential of the node for control of communication, and it is also useful as an index of network structure.

1.3 Closeness

The third is an index of closeness that is a distance from p_k to all other node linking with p_k directly or indirectly. It expresses the distance conditions from a node p_k to other nodes in a network. Closeness index may be useful when measures based upon independence or efficiency is desired.

Closeness index is excluded because all nodes in the networks of transactions and cross shareholdings are not connected with each other. Therefore the distance among firms is infinite. It could not be calculated technically.

2. Data collection

Data of transactions and cross shareholdings in the Keiretsu of Mazda has been collected from the publications and investigation by interviews [8].

The process of data-collection can be expressed as follows.

Step 1: Determine the boundary of the network;

Step 2: Collect the data of transactions and cross shareholdings. Basically the data is a percent value of the transactions or stock holdings between two firms. And input the data into a matrix table.

Step 3: Remove singletons in the matrix table.

The data of each cell in the matrix means transactional relationship which the firm in column accepts auto-components from other suppliers in row of the network of transactions, or capital relationships which the firm in row invests in stocks to other firms in column of the network of cross shareholdings.

The total number of the firms which hold capital relationship with each other in the network of cross shareholdings is 230. It includes 177 firms, 42 financial institutions, and 11 carmakers. The total number of the firms in the network of transactions is 188, including 177 firms and 11 carmakers.

Part of them is isolated in the network. It means that these companies have no any relation with other companies. They are called singletons. All of the singletons are removed from the networks of transactions and cross shareholdings because no essential difference exists between the entire network and the entire network excluded singletons. The network of transactions and cross shareholdings of Mazda can be illustrated as Figure 1.

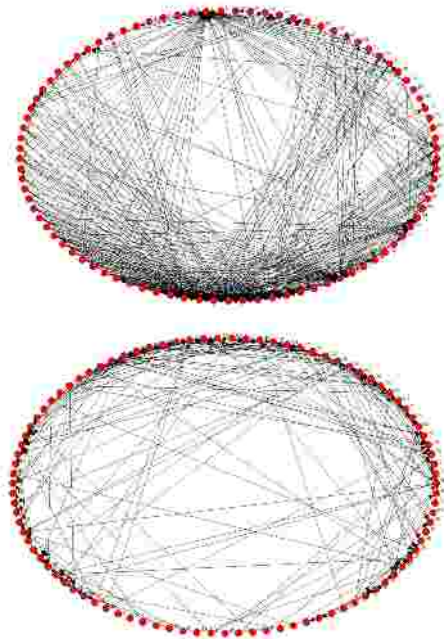


Figure 1 Network of transactions (upper) and cross shareholdings (lower) of Mazda in 2004

In Figure 1, a dot represents a company and an edge means a relation of transactions or cross shareholdings. 89 companies and 95 companies are included in the networks of transactions and cross shareholdings respectively.

III. MEASUREMENT AND ANALYSIS

The authors calculated the centrality including degree and betweenness of each firm in the networks of transactions and cross shareholdings of Mazda. The top ten of each centrality index in 2004 are summarized in Table 1.

It means the volume of the firm's purchasing power is big if the value of in-degree is high. If the value of out-degree is high, it means the firm has strong selling power in its network. And if the firm has high value of betweenness, it means the firm purchases and sells its parts simultaneously.

In Table 1, only Hitachi has high values of in-degree, out-degree, and betweenness. It means Hitachi plays an important role in Yokokai because it has extremely power of centrality.

The second finding is that part of the firms such as Denso and Calsonic Kansei Corp. are included in in-degree and betweenness both. It means that certain correlation between in-degree and betweenness exists in the transaction network.

Table 1 Top ten of the centrality index in the transactions network of Mazda in 2004

(1) Top ten of in-degree

No#	Name of firms	In-degree
1	Mazda Motor Corporation	901.13
70	Denso Corp.	205.24
25	Jatco Ltd.	54.74
44	Hitachi, Ltd.	22.14
58	Aisin AI, Ltd.	15.3
20	Calsonic Kansei Corp.	12.7
52	Mitsubishi Electric Corporation	11.54
19	Kayaba Industry Co., Ltd.	11.11
27	Stanley Electric Co., Ltd.	9.2
22	Kuramon Co., Ltd.	8.8

(2) Top Ten of Out-degree

No#	Name of firms	Out-degree
46	The Furukawa electric Co., Ltd.	100
28	Takata Corporation	99.99
44	Hitachi, Ltd.	99.96
43	Piolax, Inc.	99.96
29	Tokyo Roki co., Ltd.	95.04
61	Imasen Electric industrial Co., Ltd.	92.6
8	Japan Climate Systems Corporation	92
34	Nisshinbo Industries, Inc.	91.63
71	Tokai Rika Co., Ltd.	91.3
4	Keylex Corporation.	90.6

(3) Top Ten of Betweenness

No#	Name of firms	Betweenness
70	Denso Corp.	35.5
38	Japan Brake Industrial Co., Ltd.	28
20	Calsonic Kansei Corp.	11
65	Hikari Seiko Co., Ltd.	8
44	Hitachi, Ltd.	6
73	Toyota Gosei Co., Ltd.	6
72	Toyo Tire & Rubber Co., Ltd.	4
61	Imasen Electric industrial Co., Ltd.	2.5
57	Aisan Industry Co., Ltd Hiroshima Sales	2
19	Kayaba Industry Co., Ltd.	2

The third finding is that part of the firms are selling their parts in the network of transactions because the top ten firms in the group of in-degree is quite different with the top ten firms in the group of out-degree.

In order to discover the relationship mentioned above, the relationship between in-degree, out-degree, betweenness and sales is required. The results are shown in Table 2.

Form Table 2, we can get three new findings as follows.

The first is that the correlation coefficient between out-degree and in-degree is -0.499 ($p=0.01$). It means the more the firms sell, the less the firms purchase. In other words, it means most of the parts sold out in the network are produced out of this group. The second is that certain correlation between transactions and cross

Table 1 The correlation coefficient of centrality between network of transaction and cross shareholdings[#]

	Out-degree (T)	In-degree (T)	Betweenness (T)	Out-degree (C)	In-degree (C)	Betweenness (C)	Sales
Out-degree (T)	1						
	–						
	89						
In-degree (T)	-.499**	1					
	0	–					
	89	89					
Betweenness (T)	0.127	0.026	1				
	0.237	0.811	–				
	89	89	89				
Out-degree (C)	-.354**	.723**	0.226	1			
	0.006	0	0.086	–			
	59	59	59	95			
In-degree (C)	.542**	-.380**	0.116	-.218*	1		
	0	0.003	0.383	0.034	–		
	59	59	59	95	95		
Betweenness (C)	0.03	–0.015	.414**	.243*	0.1	1	
	0.82	0.907	0.001	0.018	0.337	–	
	59	59	59	95	95	95	
Sales	–0.19	.441**	.392**	.727**	–0.11	.770**	1
	0.12	0	0.001	0	0.453	0	–
	68	68	68	49	49	49	68

C means cross shareholdings network and T means transactions network. These data means correlation ratio/probability/number of sample. **p<0.01 (two-sided); *p<0.05 (two-sided)

shareholdings among out-degree, in-degree and betweenness are significant. Especially the correlation coefficient between out-degree (C) and in-degree (T) reach 0.723(p=0.01). It means the more investment on other suppliers the stronger purchasing power they have. And from the fact that correlation coefficient between in-degree (C) and out-degree (T), we can say the more investment the firms accept the stronger selling power the firms hold. The third is that almost of the centrality indices have strong impacts on sales, one of the important indices of corporate performance.

One of the interest issues is that the correlation coefficient between out-degree (T) and sales, between in-degree (C) and sales are not significant. The main reason is considered as most of the parts are not purchased by the firms in Mazda's group.

IV. CONCLUSION AND FUTURE WORKS

The authors calculated the centrality of network index of Yokokai, and find strong correlation between transactions and cross shareholdings. To discover the effective network structure, more research such as capacity analysis and comparative research of different networks such as Toyota and Honda are required in the near future.

Acknowledgment: This research was partially supported by the Ministry of Education, Culture, Sports, Science, and Technology, Grant-in-Aid for Exploratory Research, 21510171, 2009.

REFERENCES

- [1] Tsuru K. (1994) A system of Market Economy in Japan, Kodansha Ltd (Japanese Edition).
- [2] Ito T and Sakamoto M. (2005) Importance analysis of each firm in the Keiretsu of Toyota, Managing Modern Organizations with Information Technology, IRMA 2005 International Conference pp.930-933, San Diego, USA.
- [3] Fukuoka S, Ito T, Passerini K. and Sakamoto M. (2006) An Analysis between Transaction and Cross Shareholdings in the Keiretsu of Nissan, IBIMA International conference on Managing Information in the Digital Economy: Issues & Solutions, pp. 163-169, Bonn Germany.
- [4] Freeman L.C. (1979) Centrality in Social networks Conceptual clarification, Social Networks 1, 1979, pp.215-239.
- [5] Nieminen J. (1974) On centrality in a graph, Scandinavian Journal of Psychology 15, 1974, pp.322-336.
- [7] Freeman, L. C. (1977) A set of Measure of Centrality Based on betweenness, Sociometry, 40, 1977, pp.35-41.
- [8] JAPIA and APPC (2004) Japanese Automotive Parts Industry, Automotive Parts Publishing Company, (Japanese Edition).

Bottom-Up Pyramid Cellular Acceptors with Four-Dimensional Layers

Yasuo UCHIDA¹, Takao ITO¹, Makoto SAKAMOTO², Takashi IDE², Kazuyuki UCHIDA²,
Ryoju KATAMUNE², Hiroshi FURUTANI², Michio KONO², Satoshi IKEDA², and Tsunehiro YOSHINAGA³

¹ Ube National College of Technology ² University of Miyazaki ³ Tokuyama College of Technology

Abstract

In 1967, M.Blum and C.Hewitt first proposed two-dimensional automata as a computational model of two-dimensional pattern processing. Since then, many researchers in this field have been investigating many properties of two- or three-dimensional automata. In 1997, C.R.Dyer and A.Rosenfeld introduced an acceptor on a two-dimensional pattern (or tape), called the *pyramid cellular acceptor*, and demonstrated that many useful recognition tasks are executed by pyramid cellular acceptors in time proportional to the logarithm of the diameter of the input. They also introduced a *bottom-up pyramid cellular acceptor* which is a restricted version of the pyramid cellular acceptor, and proposed some interesting open problems about bottom-up pyramid cellular acceptors. On the other hand, we think that the study of four-dimensional automata has been meaningful as the computational model of four-dimensional information processing such as computer animation, moving picture processing, and so forth[9]. In this paper, we investigate about bottom-up pyramid cellular acceptors with four-dimensional layers, and show their some accepting powers.

Key Words : cellular automaton, diameter, finite automaton, four-dimension, pattern recognition.

1 Introduction

M.Blum and C.Hewitt first proposed two-dimensional automata as a computational model of two-dimensional pattern processing, and investigated their pattern recognition abilities [1]. Since then, many researchers in this field have been investigating a lot of properties about automata on a two- or three-dimensional tape. In [2], C.R.Dyer and A.Rosenfeld introduced an acceptor on a two-dimensional pattern (or tape), called the *pyramid cellular acceptor*, and demonstrated that many useful recognition tasks are executed by the pyramid cellular acceptors in time proportional to logarithm of the diameter of the input. They also introduced a *bottom-up pyramid cellular acceptor*, which is a restricted version of the pyramid cellular acceptor, and proposed some interesting open problems about it.

On the other hand, the question of whether processing four-dimensional digital patterns is much difficult than two- or three-dimensional ones is of great interest from the theoretical and practical standpoints. Thus, the study of four-dimensional automata as the computational model of four-dimensional pattern processing has been meaningful. From this point of view, we are interested in four-dimensional automata.

In this paper, we study about bottom-up pyramid cellular acceptors with four-dimensional layers, and deal with the following problems (which is one of the open problems) : Does the class of sets accepted by deterministic bottom-up pyramid cellular acceptors with four-dimensional layers include the class of sets accepted by deterministic *four-dimensional finite automata* [3-7]? This paper shows that the class of sets accepted by four-dimensional finite automata is incomparable with the class of sets accepted by deterministic bottom-up pyramid cellular acceptors which operate in time of order lower than the *diameter* of the input.

2 Definition

Let Σ be a finite set of symbols. A *three-dimensional tape* over Σ is a four-dimensional rectangular array of elements of Σ . The set of all the four-dimensional tapes over Σ is denoted by $\Sigma^{(4)}$. Given a tape $x \in \Sigma^{(4)}$, for each j ($1 \leq j \leq 4$), we let $l_j(x)$ be the length of x along the j th axis. The set of all $x \in \Sigma^{(4)}$ with $l_1(x) = n_1, l_2(x) = n_2, l_3(x) = n_3$, and $l_4(x) = n_4$ is denoted by $\Sigma^{(n_1, n_2, n_3, n_4)}$. When $1 \leq i_j \leq l_j(x)$ for each j ($1 \leq j \leq 4$), let $x(i_1, i_2, i_3, i_4)$ denote the symbol in x with coordinates (i_1, i_2, i_3, i_4) . Furthermore, we define $x[(i_1, i_2, i_3, i_4), (i_1', i_2', i_3', i_4')]$, when $i \leq i_j \leq i_j' \leq l_j(x)$ for each integer j ($1 \leq j \leq 4$), as the four-dimensional input tape y satisfying the following (i) and (ii) : (i) for each j ($1 \leq j \leq 4$), $l_j(y) = i_j' - i_j + 1$; (ii) for each r_1, r_2, r_3, r_4 ($1 \leq r_1 \leq l_1(y), 1 \leq r_2 \leq l_2(y), 1 \leq r_3 \leq l_3(y), 1 \leq r_4 \leq l_4(y)$), $y(r_1, r_2, r_3, r_4) = x(r_1 + i_1 - 1, r_2 + i_2 - 1, r_3 + i_3 - 1, r_4 + i_4 - 1)$.

For each $x \in \Sigma^{(n_1, n_2, n_3, n_4)}$ and for each $1 \leq i_1 \leq n_1, 1 \leq i_2 \leq n_2, 1 \leq i_3 \leq n_3, 1 \leq i_4 \leq n_4$, $x[(i_1, 1, 1, i_4), (i_1, n_2, n_3, i_4)]$, $x[(1, i_2, 1, i_4), (n_1, i_2, n_3, i_4)]$, $x[(1, 1, i_3, i_4), (n_1, n_2, i_3, i_4)]$, $x[(i_1, 1, i_3, i_4), (i_1, n_2, i_3, i_4)]$, and $x[(1, i_2, i_3, i_4), (n_1, i_2, i_3, i_4)]$ are called

the i_1 th (2-3) plane of each x , the i_2 th (1-3) plane of each x , the i_3 th (1-2) plane of each x , the i_1 th row on the i_3 th (1-2) plane of each x , and the i_2 th column on the i_3 th (1-2) plane of each x .

We next give some basic concepts about bottom-up pyramid cellular acceptors with four-dimensional layers [7]. A *bottom-up pyramid cellular acceptor with four-dimensional layers* (3-UPCA) is a pyramidal stack of four-dimensional arrays of cells in which the bottom four-dimensional layer has size $2^n \times 2^n \times 2^n \times 2^n$ ($n \geq 0$), the next lowest $2^{n-1} \times 2^{n-1} \times 2^{n-1} \times 2^{n-1}$, and so forth, the $(n+1)$ st four-dimensional layer consisting of a single cell, called the *root*. Each cell is defined as an identical finite-state machine, $M = (Q_N, Q_T, \delta, A)$, where Q_N is a nonempty, finite set of states, $Q_T \subseteq Q_N$ is a finite set of *input states*, $A \subseteq Q_N$ is the set of *accepting states*, and $\delta : Q_N^{17} \rightarrow Q_N$ is the *state transition function*, mapping the current states of M and its sixteen son cells in a $2 \times 2 \times 2 \times 2$ block on the four-dimensional layer below into M 's next state. Let c be some cell on the $(i+1)$ st four-dimensional layer, and let c (UNWP), c (UNWF), c (USWP), c (USWF), c (USEP), c (USEF), c (UNEP), c (UNEF), c (DNWP), c (DNWF), c (DSWP), c (DSWF), c (DSEP), c (DSEF), c (DNEP), and c (DNEF) be sixteen son cells (on the i th four-dimensional layer) of c , where c (UNWF) is c 's upper northwest son in the most future direction, c (DNWP) is c 's lower northwest son in the most past direction, etc. For example, if the coordinates of c on the $(i+1)$ st layer is $(1, 1, 1, 1)$ ($(2^n, 2^n, 2^n, 2^n)$), the coordinates of sixteen son cells of c on the i th layer c (UNWP), c (UNWF), c (USWP), c (USWF), c (USEP), c (USEF), c (UNEP), c (UNEF), c (DNWP), c (DNWF), c (DSWP), c (DSWF), c (DSEP), c (DSEF), c (DNEP), and c (DNEF) are $(1, 1, 1, 1)$, $(1, 1, 1, 2)$, $(1, 2, 1, 1)$, $(1, 2, 1, 2)$, $(1, 2, 2, 1)$, $(1, 2, 2, 2)$, $(1, 1, 2, 1)$, $(1, 1, 2, 2)$, $(2, 1, 1, 1)$, $(2, 1, 1, 2)$, $(2, 2, 1, 1)$, $(2, 2, 1, 2)$, $(2, 2, 2, 1)$, $(2, 2, 2, 2)$, $(2, 1, 2, 1)$, $(2, 1, 2, 2)$, $((2^n - 1, 2^n - 1, 2^n - 1, 2^n - 1)$, $(2^n - 1, 2^n - 1, 2^n - 1, 2^n)$, $(2^n - 1, 2^n, 2^n - 1, 2^n - 1)$, $(2^n - 1, 2^n, 2^n - 1, 2^n)$, $(2^n - 1, 2^n, 2^n, 2^n - 1)$, $(2^n - 1, 2^n, 2^n, 2^n)$, $(2^n, 2^n - 1, 2^n - 1, 2^n - 1)$, $(2^n, 2^n - 1, 2^n - 1, 2^n)$, $(2^n, 2^n - 1, 2^n, 2^n - 1)$, $(2^n, 2^n - 1, 2^n, 2^n)$, $(2^n, 2^n, 2^n - 1, 2^n - 1)$, $(2^n, 2^n, 2^n - 1, 2^n)$, $(2^n, 2^n, 2^n, 2^n - 1)$, $(2^n, 2^n, 2^n, 2^n)$, $(2^n, 2^n - 1, 2^n, 2^n - 1)$, $(2^n, 2^n - 1, 2^n, 2^n)$), respectively. Then $q_c(t+1) = \delta(q_c(t), q_{c(\text{UNWP})}(t), q_{c(\text{UNWF})}(t), q_{c(\text{USWP})}(t), q_{c(\text{USWF})}(t), q_{c(\text{USEP})}(t), q_{c(\text{USEF})}(t), q_{c(\text{UNEP})}(t), q_{c(\text{UNEF})}(t), q_{c(\text{DNWP})}(t), q_{c(\text{DNWF})}(t), q_{c(\text{DSWP})}(t), q_{c(\text{DSWF})}(t), q_{c(\text{DSEP})}(t), q_{c(\text{DSEF})}(t), q_{c(\text{DNEP})}(t), q_{c(\text{DNEF})}(t))$, where for example $q_c(t)$ means the state of c at time t . At time $t = 0$, the input tape $x \in Q_T^{(4)}$ [$l_1(x) = l_2(x) = l_3(x) = l_4(x) = 2^n$, $n \geq 0$] is stored as the initial states of the bottom four-dimensional layer, henceforth called the *base*, in such a

way that $x(i_1, i_2, i_3, i_4)$ is stored at the cell of the i_1 th row and the i_2 th column on the i_3 th plane of the i_4 th four-dimensional rectangular array, and the other cells are initialized to a *quiescent state* q_s ($\in Q_N - Q_T - A$). As usual, we let $\delta(q_s, q_s, q_s, q_s, q_s, q_s, q_s, q_s, q_s, q_s, q_s, q_s, q_s, q_s, q_s, q_s, q_s) = q_s$. The input is *accepted* if and only if the root cell ever enters an accepting state. This 4-UPCA is called *deterministic*. A *nondeterministic bottom-up pyramid cellular acceptor* is defined as a 4-UPCA using $\delta : Q_N^{17} \rightarrow 2^{Q_N}$ instead of the state transition function of the deterministic 4-UPCA. Below, we denote a deterministic 4-UPCA by 4-DUPCA, and a nondeterministic 4-UPCA by 4-NUPCA. A 4-DUPCA (or 4-NUPCA) operates in time $T(n)$ if for every four-dimensional tape of size $2^n \times 2^n \times 2^n \times 2^n$ ($n \geq 0$) it accepts the four-dimensional tape, then there is an accepting computation which uses no more than time $T(n)$. By 4-DUPCA($T(n)$) [4-NUPCA($T(n)$)] we denote a $T(n)$ time-bounded 4-DUPCA [4-NUPCA] which operates in time $T(n)$.

We next introduce a four-dimensional finite automaton [8]. A *four-dimensional finite automaton* (4-FA) is a four-dimensional Turing machine with no workspace. A 4-FA M has a read-only four-dimensional tape with boundary symbols $\#$'s, finite control, and an input head. The input head can move in eight direction – east, west, south, north, up, down, future, or past – unless it falls off the input tape. Formally, M is defined by the 5-tuple $M = (K, \Sigma \cup \{\#\}, \delta, q_0, F)$, where K is a finite set of *states*, Σ is a finite set of *input symbols*, $\#$ is the *boundary symbol* (not in Σ), $\delta : K \times (\Sigma \cup \{\#\}) \rightarrow 2^{K \times \{E, W, S, N, U, D, F, P, H\}}$ is the *state transition function*, where E, W, S, N, U, D, F, P , and H represent the move directions of the input head – east, west, south, north, up, down, future, past, and no move, respectively, $q_0 \in K$ is the *initial state*, and $F \subseteq K$ is the set of *accepting states*. The action of M is similar to that of the one-dimensional (or two-dimensional) finite automaton [4], except that the input head of M can move in eight directions. That is, when an input tape $x \in \Sigma^{(4)}$ with boundary symbols is presented to M , M starts in its initial state q_0 with the input head on $x(1, 1, 1, 1)$, and determines the next state of the finite control and the move direction of the input head, depending on the present state of the finite control and the symbol read by the input head. We say that M *accepts* the tape x if it eventually enters an accepting state. We denote a deterministic 4-FA [nondeterministic 4-FA] by 4-DFA [4-NFA].

We let each sidelength of each input tape of three automata, throughout this paper, be equivalent. We denote the set of all four-dimensional tapes accepted by M by $T(M)$. Define \mathcal{L} [4-DUPCA] = $\{T \mid T(M) \text{ is accepted by some 4-DUPCA } M\}$. \mathcal{L} [4-NUPCA], \mathcal{L} [4-DFA], etc. are defined similarly.

Finally, we give definition of *diameter*. Given a

subset S of a tape $x \in \Sigma^{(4)}$, we can define its *extent* in a given direction θ as the length of its projection on a plane in that direction. Here the length of a projection is the distance between its farthest apart nonzero values. Thus the extent of S is the distance between a pair of parallel planes perpendicular to θ that just bracket S . The *diameter* of S is defined as its extent in any direction.

3 Results

In this section, we show that the class of sets accepted by 4-DFA's is incomparable with the class of sets accepted by 4-DUPCA's which operate in time of order lower than the diameter of the input. It has often been noticed that we can easily get several properties of four-dimensional automata by directly applying the results of one- or two-dimensional case, if each sidelength of each four-dimensional input tape of these automata is not equivalent. So we let each sidelength of each input tape, throughout this paper, be equivalent in order to increase the theoretical interest.

Lemma 3.1. *Let $T_1 = \{x \in \{0,1\}^{(4)} \mid \exists n (n \geq 1) [\ell_1(x) = \ell_2(x) = \ell_3(x) = \ell_4(x) = 2^n] \text{ and } x(2^{n-1}, 2^{n-1}, 2^{n-1}, 2^{n-1}) = 1\}$. Then,*
(1) $T_1(x) \notin \mathcal{L}[4\text{-DFA}]$, and
(2) $T_1(x) \in \mathcal{L}[4\text{-DUPCA}(n)]$.

Proof : The Proof of (1) is similar to that of Theorem 3 in [7]. On the other hand, by using the same technique as in the proof of Lemma 1 in [6], we can get Part (2) of the lemma. \square

Lemma 3.2. *Let $T_2 = \{x \in \{0,1\}^{(4)} \mid \exists n (n \geq 1) [\ell_1(x) = \ell_2(x) = \ell_3(x) = \ell_4(x) = 2^n] \text{ and } x[(1,1,1,1), (2^n, 2^n, 2^n, 1)] = x[(1,1,1,2^n), (2^n, 2^n, 2^n, 2^n)]\}$. Let $T(n)$ be a time function such that $\lim_{n \rightarrow \infty} [T(n)/2^{2n}] = 0$. Then,*
(1) $T_2 \in \mathcal{L}[4\text{-DFA}]$, and
(2) $T_2 \notin \mathcal{L}[4\text{-DUPCA}(T(n))]$.

Proof : It is obvious that there is a 4-DFA accepting T_2 , and so (1) of the lemma holds. Below, we prove (2). Suppose that there is a 4-DUPCA B which accepts T_2 and operates in time $T(n)$, and that each cell of B has k states. For each $n \geq 2$, let

$W(n) = \{x \in \{0,1\}^{(4)} \mid \ell_1(x) = \ell_2(x) = \ell_3(x) = \ell_4(x) = 2^n\}$, and

$$\begin{aligned} W'(n) &= \{x \in \{0,1\}^{(4)} \mid \ell_1(x) = \ell_2(x) = \ell_3(x) = \ell_4(x) \\ &= 2^{n-1} \\ &\& x[(1,1,1,1), (2^{n-1}, 2^{n-1}, 2^{n-1}, 1)] \in \{0,1\}^{(4)} \\ &\& x[(1,1,1,2), (2^{n-1}, 2^{n-1}, 2^{n-1}, 2^{n-1})] \in \{0\}^{(4)}\}. \end{aligned}$$

We consider the cases when the tapes in $W(n)$ are presented to B . Let c be the cell which is situated at the first row, the first column, the first plane, and the first three-dimensional rectangular array in the n th layer (i.e., the layer just below the root cell). (Note that there are eight cells in the n th layer.) For each x in $W(n)$ such that $x[(1,1,1,1), (2^{n-1}, 2^{n-1}, 2^{n-1}, 2^{n-1})] \in W'(n)$, and for each $r \geq 1$, let $q_r(x)$ be the state of c at time r when x is presented to B . Then the following proposition must hold.

Proposition 3.1. *Let x, y be two different tapes in $W(n)$ such that both $x[(1,1,1,1), (2^{n-1}, 2^{n-1}, 2^{n-1}, 2^{n-1})]$ and $y[(1,1,1,1), (2^{n-1}, 2^{n-1}, 2^{n-1}, 2^{n-1})]$ are in $W'(n)$ and $x4[(1,1,1,1), (2^{n-1}, 2^{n-1}, 2^{n-1}, 2^{n-1})] \neq y[(1,1,1,1), (2^{n-1}, 2^{n-1}, 2^{n-1}, 2^{n-1})]$. Then, $(q_1(x), q_2(x), \dots, q_{T(n)}(x)) = (q_1(y), q_2(y), \dots, q_{T(n)}(y))$.*

[Proof : For suppose that $(q_1(x), q_2(x), \dots, q_{T(n)}(x)) = (q_1(y), q_2(y), \dots, q_{T(n)}(y))$. We consider two tapes z, z' in $W(n)$ such that

- (i) $z[(1,1,1,1), (2^{n-1}, 2^{n-1}, 2^{n-1}, 2^{n-1})] = x[(1,1,1,1), (2^{n-1}, 2^{n-1}, 2^{n-1}, 2^{n-1})]$ and $z'[(1,1,1,1), (2^{n-1}, 2^{n-1}, 2^{n-1}, 2^{n-1})] = y[(1,1,1,1), (2^{n-1}, 2^{n-1}, 2^{n-1}, 2^{n-1})]$,
- (ii) the part of z except for $z[(1,1,1,1), (2^{n-1}, 2^{n-1}, 2^{n-1}, 2^{n-1})]$ is identical with the part z' except for $z'[(1,1,1,1), (2^{n-1}, 2^{n-1}, 2^{n-1}, 2^{n-1})]$,

and

- (iii) $z[(1,1,1,1), (2^n, 2^n, 2^n, 1)] = z[(1,1,1,2^n), (2^n, 2^n, 2^n, 2^n)]$.

By assumption, the root cell of B enters the same states until time $T(n)$, for the tapes z and z' . Since B operate in time $T(n)$ and z is in T_2 , it follows that z' is also accepted by B . This contradicts the fact that z' is not in T_2 . \square

Let $t(n)$ be the number of different sequences of states which c enters until time $T(n)$. Clearly, $t(n) \leq k^{T(n)}$. On the other hand (for any set S , let $|S|$ denote the number of elements of S), $|W'(n)| = 2^{2^{3(n-1)}}$. Since $\lim_{n \rightarrow \infty} T(n)/2^{2n} = 0$ (by assumption of the lemma), it follows that $|W'(n)| > t(n)$ for large n . Therefore, it follows that for large n there must exist two different tapes x, y in $W(n)$ such that

- (i) both $x[(1,1,1,1), (2^{n-1}, 2^{n-1}, 2^{n-1}, 2^{n-1})]$ and $y[(1,1,1,1), (2^{n-1}, 2^{n-1}, 2^{n-1}, 2^{n-1})]$ are in $W'(n)$,
- (ii) $x[(1,1,1,1), (2^{n-1}, 2^{n-1}, 2^{n-1}, 2^{n-1})] \neq y[(1,1,1,1), (2^{n-1}, 2^{n-1}, 2^{n-1}, 2^{n-1})]$, and

$$\begin{aligned} \text{(iii)} \quad & (q_1(x), q_2(x), \dots, q_{T(n)}(x)) \\ & = (q_1(y), q_2(y), \dots, q_{T(n)}(y)). \end{aligned}$$

This contradicts the above Proposition 3.1, and thus the Part (2) of the lemma holds. \square

From Lemmas 3.1 and 3.2, we can get the following theorem.

Theorem 3.1. *Let $T(n)$ be a time function such that $\lim_{n \rightarrow \infty} [T(n)/2^{2n}] = 0$ and $T(n) \geq n (n \geq 1)$. Then $\mathcal{L}[4\text{-DFA}]$ is incomparable with $\mathcal{L}[4\text{-DUPCA}(T(n))]$.*

Corollary 3.1. *$\mathcal{L}[4\text{-DFA}]$ is incomparable with $\mathcal{L}[4\text{-DUPCA}(n)]$, which is the class of sets accepted by 4-DUPCA's operating in real time.*

Corollary 3.2. *$\mathcal{L}[4\text{-DFA}]$ is incomparable with $\mathcal{L}[4\text{-NUPCA}(n)]$.*

4 Conclusion

In this paper, we investigated the accepting powers of bottom-up pyramid cellular acceptors with four-dimensional layers, and showed that the class of sets accepted by 4-DFA's is incomparable with the class of sets accepted by 4-DUPCA's which operate in time of order lower than the diameter of the input. It is still unknown whether the class of sets accepted by 4-DUPCA's includes the class of sets accepted by 4-DFA's.

References

- [1] M.Blum and C.Hewitt, Automata on a two-dimensional tape, in *IEEE Symposium on Switching and Automata Theory*, pp.155-160, 1967.
- [2] C.R.Dyer and A.Rosenfeld, Cellular pyramids for image analysis, *Technical Report TR-544, Computer Science Center, University of Maryland*, 1977.
- [3] K.Inoue, and A.Nakamura, Some properties of two-dimensional on-line tessellation acceptors, *Information Sciences*, Vol.13, pp.95-121, 1977.
- [4] K.Inoue, I.Takanami, and A.Nakamura, A note on two-dimensional finite automata, *Information Processing Letters*, Vol.7, No.1, p.49, 1978.
- [5] K.Inoue and I.Takanami, Remarks on two-dimensional finite automata with multiplication and bottom-up pyramid acceptors, *Technical Report IECE of Japan*, No.AL77-61, 1978.
- [6] K.Inoue and I.Takanami, A note on bottom-up pyramid acceptors, *Information Processing Letters* Vol.8, No.1, pp.34-37, 1979.
- [7] M.Sakamoto, S.Nogami, K.Inoue, and M.Kono, A relationships between the accepting powers of three-dimensional finite automata and time-bounded bottom-up pyramid cellular acceptors with three-dimensional layers, *Trans. of SCI(Japan)*, Vol.17, No.10, pp.451-458, 2004.
- [8] H.Taniguchi, K.Inoue, and I.Takanami, A note on three-dimensional finite automata, *Information Sciences*, Vol.26, pp.65-85, 1982.
- [9] Y.Uchida, T.Ito, H.Okabe, M.Sakamoto, H.Furutani, and M.Kono, Four-dimensional multi-inkdot finite automata, *WSEAS Trans. on Computers*, Issue 9, Vol.7, pp.1437 - 1446, 2008.

Cooperating Systems of Four-Dimensional Finite Automata

Yasuo UCHIDA¹, Takao ITO¹, Makoto SAKAMOTO², Kazuyuki UCHIDA², Takashi IDE²,
Ryoju KATAMUNE², Hiroshi FURUTANI², Michio KONO² and Tsunehiro YOSHINAGA³

¹ Ube National College of Technology ² University of Miyazaki ³ Tokuyama College of Technology

Abstract

M. Blum and C. Hewitt first proposed two-dimensional automata as a computational model of two-dimensional pattern processing, and investigated their pattern recognition abilities in 1967. Since then, a lot of researchers in this field have been investigating many properties about automata on a two- or three-dimensional tape. On the other hand, the question of whether processing four-dimensional digital patterns is much more difficult than two- or three-dimensional ones is of great interest from the theoretical and practical standpoints. Thus, the study of four-dimensional automata as a computational model of four-dimensional pattern processing has been meaningful. This paper introduces a cooperating system of four-dimensional finite automata as one model of four-dimensional automata. A cooperating system of four-dimensional finite automata consists of a finite number of four-dimensional finite automata and a four-dimensional input tape where these finite automata work independently (in parallel). Those finite automata whose input heads scan the same cell of the input tape can communicate with each other, that is, every finite automaton is allowed to know the internal states of other finite automata on the same cell it is scanning at the moment. In this paper, we mainly investigate several accepting powers of a cooperating system of seven-way four-dimensional finite automata. The seven-way four-dimensional finite automaton is a four-dimensional finite automaton whose input head can move east, west, south, north, up, down, or in the future, but not in the past on a four-dimensional input tape.

Key Words : computational complexity, cooperating system, finite automaton, four-dimension, multihead.

1 Introduction

A cooperating system of four-dimensional finite automata (CS-4-FA) [2-4,8] consists of a finite number of four-dimensional finite automata and a four-dimensional input tape where these finite automata work independently (in parallel). Those finite automata whose input heads scan the same cell of the input tape can communicate with each other, that is, every finite automaton is allowed to know the internal states of other finite automata on the same cell it is scanning at the moment.

In this paper, we propose a cooperating system of seven-

way four-dimensional finite automata (CS-SV4-FA) which is a restricted version of CS-4-FA's, and mainly investigate its several properties as four-dimensional language acceptors. The seven-way four-dimensional finite automaton [7] is a four-dimensional finite automaton [1] whose input head can move east, west, south, north, up, down, or in the future, but not in the past. The paper has six sections in addition to this Introduction. Section 2 contains some definitions and notions. Section 3 investigates a relationship between seven-way four-dimensional simple multihead finite automata (SV4-SPMHFA's) and CS-SV4-FA's. It is shown that SV4-SPMHFA's and CS-SV4-FA's are equivalent in accepting power if each sidelength of each four-dimensional input tape of these automata is equivalent. Section 4 investigates the difference between the accepting powers of CS-SV4-FA's and CS-4-FA's, and shows that CS-SV4-FA's are less powerful than CS-4-FA's. Section 5 investigates the difference between the accepting powers of deterministic and nondeterministic CS-SV4-FA's, and shows that deterministic CS-SV4-FA's are less powerful than nondeterministic CS-SV4-FA's. Section 6 concludes by giving some open problems. In this paper, we let each sidelength of each input tape of these automata be equivalent in order to increase the theoretical interest.

2 Preliminaries

Definition 2.1. Let Σ be a finite set of symbols. A *four-dimensional tape* over Σ is a four-dimensional rectangular array of elements of Σ . The set of all four-dimensional tapes over Σ is denoted by $\Sigma^{(4)}$. Given a tape $x \in \Sigma^{(4)}$, for each integer j ($1 \leq j \leq 4$), we let $l_j(x)$ be the length of x along the j th axis. The set of all $x \in \Sigma^{(4)}$ with $l_1(x) = n_1, l_2(x) = n_2, l_3(x) = n_3$, and $l_4(x) = n_4$ is denoted by $\Sigma^{(n_1, n_2, n_3, n_4)}$. When $1 \leq i_j \leq l_j(x)$ for each j ($1 \leq j \leq 4$), let $x(i_1, i_2, i_3, i_4)$ denote the symbol in x with coordinates (i_1, i_2, i_3, i_4) . Furthermore, we define

$$x[(i_1, i_2, i_3, i_4), (i'_1, i'_2, i'_3, i'_4)],$$

when $1 \leq i_j \leq i'_j \leq l_j(x)$ for each integer j ($1 \leq j \leq 4$), as the four-dimensional input tape y satisfying the following conditions:

- (i) for each j ($1 \leq j \leq 4$), $l_j(y) = i'_j - i_j + 1$;

- (ii) for each $r_1, r_2, r_3, r_4 (1 \leq r_1 \leq l_1(y), 1 \leq r_2 \leq l_2(y), 1 \leq r_3 \leq l_3(y), 1 \leq r_4 \leq l_4(y)), y(r_1, r_2, r_3, r_4) = x(r_1 + i_1 - 1, r_2 + i_2 - 1, r_3 + i_3 - 1, r_4 + i_4 - 1)$.
(We call $x[(i_1, i_2, i_3, i_4), (i'_1, i'_2, i'_3, i'_4)]$ the $[(i_1, i_2, i_3, i_4), (i'_1, i'_2, i'_3, i'_4)]$ -segment of x .)

We recall a *seven-way four-dimensional simple k -head finite automaton* (SV4-SP k -HFA)[5,6]. An SV4-SP k -HFA M is a finite automaton with k read-only input heads operating on a four-dimensional input tape surrounded by boundary symbols \sharp 's. The only one head (called the '*reading*' head) of M is capable of distinguishing the symbols in the input alphabet, and the other heads (called '*counting*' heads) of M can only detect whether they are on the boundary symbols or a symbol in the input alphabet. When an input tape x is presented to M , M determines the next state of the finite control, the next move direction (east, west, south, north, up, down, future, past or no move) of each input head, depending on the present state of the finite control, the symbol read by the reading head, and on whether or not the symbol read by each counting head is boundary symbol. We say that M *accepts* x if M , when started in its initial state with all its input heads on $x(1, 1, 1, 1)$, eventually halts in an accepting state with all its heads on the bottom boundary symbols of x . As usual, we define nondeterministic and deterministic SV4-SP k -HFA's.

A *seven-way four-dimensional sensing simple k -head finite automaton* (SV4-SNSP k -HFA) is the same device as a SV4-SP k -HFA except that the former can detect coincidence of the input heads.

We denote a deterministic (nondeterministic) SV4-SP k -HFA by SV4-SP k -HDFA (SV4-SP k -HNFA), and denote a deterministic (nondeterministic) SV4-SNSP k -HFA by SV4-SNSP k -HDFA (SV4-SNSP k -HNFA).

We now give formal definition of a *cooperating system of k four-dimensional deterministic finite automata* (CS-4-DFA(k)) as an acceptor.

Definition 2.2. A CS-4-DFA(k) is a k -tuple $M = (FA_1, FA_2, \dots, FA_k)$, $k \geq 1$, such that for each $1 \leq i \leq k$,

$$FA_i = (\sum, Q_i, X_i, \delta_i, q_0 i, F_i, \phi, \sharp),$$

where

1. \sum is a finite set of *input symbols*.
2. Q_i is a finite set of *states*.
3. $X_i = (Q_1 \cup \{\phi\}) \times \dots \times (Q_{i-1} \cup \{\phi\}) \times (Q_{i+1} \cup \{\phi\}) \times \dots \times (Q_k \cup \{\phi\})$, where ' ϕ ' is a special state not in $(Q_1 \cup Q_2 \cup \dots \cup Q_k)$.
4. $\delta_i : (\sum \cup \{\sharp\}) \times X_i \times Q_i \rightarrow Q_i \times \text{east} (= (0, +1, 0, 0)), \text{west} (= (0, -1, 0, 0)), \text{south} (= (+1, 0, 0, 0)), \text{north} (= (-1, 0, 0, 0)), \text{up} (= (0, 0, -1, 0)), \text{down} (= (0, 0, +1, 0)), \text{future} (= (0, 0, 0, +1)), \text{past} (= (0, 0, 0, -1)), \text{no move} (= (0, 0, 0, 0))$ is the *next move function*, where ' \sharp ' is the *boundary symbol* not in \sum .

5. $q_0 i \in Q_i$ is the *initial state* of FA_i .

6. $F_i \subseteq Q_i$ is the set of *accepting states* of FA_i .

Every automaton of M independently (in parallel) works step by step on the same four-dimensional tape x over \sum surrounded by boundary symbols \sharp 's. Each step is assumed to require exactly one time for its completion. For each $i (1 \leq i \leq k)$, let q_i be the state of FA_i at time ' t '. Then each FA_i , enters the next state ' p_i ' at time ' $t + 1$ ' according to the function

$$\delta_i(x(\alpha, \beta, \gamma, \rho), (q'_1, \dots, q'_{i-1}, q'_{i+1}, \dots, q'_k), q_i) = (p_i, (d_1, d_2, d_3, d_4)),$$

where $x(\alpha, \beta, \gamma, \rho)$ is the symbol read by the input head of FA_i at time ' t ' and for each $j \in \{1, \dots, i-1, i+1, \dots, k\}$,

$$q'_j = \begin{cases} q_j \in Q_j & \text{if the input heads of } FA_i \text{ and } FA_j, \\ & \text{are on the same input position at} \\ & \text{the moment 't';} \\ \phi & \text{otherwise,} \end{cases}$$

and moves 1st input head to $x(\alpha + d_1, \beta + d_2, \gamma + d_3, \rho + d_4)$ at time ' $t + 1$ '. We assume that the input head of FA_i never falls off the tape beyond boundary symbols.

When an input tape $x \in \sum^{(4)}$ is presented to M , we say that M *accepts* the tape x if each automaton of M , when started in its initial state with its input head on $x(1, 1, 1, 1)$, eventually enters an accepting state with its input head on one of the bottom boundary symbols.

We next introduce a *cooperating system of k seven-way four-dimensional deterministic finite automata* (CS-SV4-DFA(k)), with which we are mainly concerned in this paper.

Definition 2.3. A CS-SV4-DFA(k) is a CS-4-DFA(k) $M = (FA_1, FA_2, \dots, FA_k)$ such that the input head of each FA_i can only move east, west, south, north, up, down, or in the future, but not in the past.

To give the formal definition of a *cooperating system of k four-dimensional nondeterministic finite automata* (CS-4-NFA(k)) and a *cooperating system of k seven-way four-dimensional nondeterministic finite automata* (CS-SV4-NFA(k)) is left to the reader. For each $X \in \{\text{SV4-SP}k\text{-HDFA}, \text{SV4-SP}k\text{-HNFA}, \text{SV4-SNSP}k\text{-HDFA}, \text{SV4-SNSP}k\text{-HNFA}, \text{CS-4-DFA}(k), \text{CS-4-NFA}(k), \text{CS-SV4-DFA}(k), \text{CS-SV4-NFA}(k)\}$, by X^c we denote an X which each sidelength of each input tape is equivalent; by $\mathcal{L}[X](\mathcal{L}[X^c])$ we denote the class of sets of input tapes accepted by X 's (X^c 's). We will focus our attention on the acceptors which each sidelength of each input tape is equivalent.

3 Relationship between SV4-SPMHFA's and CS-SV4-FA's

In this section, we establish a relation between the accepting powers of seven-way four-dimensional simple multihead finite automata and cooperating systems of seven-way four-dimensional finite automata over input tapes which each sidelength is equivalent. This result will be used in the latter sections.

Lemma 3.1. For any $k \geq 1$ and $X \in \{N, D\}$,

$$\mathcal{L}[\text{SV4-SNSP}k\text{-HXFA}^c] \subseteq \mathcal{L}[\text{CS-SV4-XFA}(2k)^c]$$

Proof. Let M be an $\text{SV4-SNSP}k\text{-HFA}^c$. We will construct a $\text{CS-SV4-XFA}(2k)^c$ M' to simulate M . M' acts as follows:

1. M' simulates the moves of the reading head of M and all the east, west, south, north up, or down moves of counting heads of M by using its $(k+1)$ finite automata.
2. M' simulates all the moves in the future direction of counting heads of M by making the down moves of input heads of its other $(k-1)$ finite automata.
3. During the simulation, if M moves its reading head in the future direction, then M' makes all of input heads of finite automata of M' move in the future direction so that all the automata of M' can keep their input heads on the same three-dimensional rectangular array and can communicate with each other in that three-dimensional rectangular array.

It is easy to see that M' can simulate M . \square

Lemma 3.2. For any $k \geq 1$ and any $X \in \{N, D\}$,

$$\mathcal{L}[\text{CS-SV4-XFA}(k)^c] \subseteq \mathcal{L}[\text{SV4-SNSP}(2k^2 - k + 1)\text{-HXFA}^c].$$

Proof. Let $M = (\text{FA}_1, \text{FA}_2, \dots, \text{FA}_k)$ be a $\text{CS-SV4-XFA}(k)^c$. We will construct an $\text{SV4-SNSP}(2k^2 - k + 1)\text{-HXFA}^c$ M' to simulate M . Let R denote the reading head of M' , and $h_1, h_2, \dots, h_{2k^2-k}$ denote the $2k^2 - k$ counting heads of M' . M' acts as follows:

1. M' stores the internal states of $\text{FA}_1, \text{FA}_2, \dots, \text{FA}_k$ in its finite control.
2. For each three-dimensional rectangular array of the input tape:
 - (a) M' simulates the east, west, south, north, up, or down moves of input heads of $\text{FA}_1, \text{FA}_2, \dots, \text{FA}_k$ by using R and h_1, h_2, \dots, h_k .
 - (b) M' stores in its finite control the internal state of each FA_i , $1 \leq i \leq k$, when the input head of FA_i leaves the three-dimensional rectangular array and the order, (d_1, d_2, \dots, d_k) , in which

the input heads of $\text{FA}_1, \text{FA}_2, \dots, \text{FA}_k$ leave the plane subsequently (i.e., FA_{d_1} firstly moves its input head in the future direction from the three-dimensional rectangular array. FA_{d_2} secondly moves its input head in the future direction from the three-dimensional rectangular array, and so on.), and M' keeps the position where the input head of each FA_i , $1 \leq i \leq k$, leaves the three-dimensional rectangular array by the positions of h_1, h_2, \dots, h_k .

- (c) Furthermore, for each i ($1 \leq i \leq k-1$), the interval between the times at which FA_{d_i} and $\text{FA}_{d_{i+1}}$ move their input heads in the future direction from the three-dimensional rectangular array is stored by a counter with $O(n^{6k})$ space bound, which can be realized by using $h_{(2i-1)k-1}, h_{(2i-1)k-2}, \dots, h_{(2i-1)k}$, where n is the number of rows (or columns or planes or three-dimensional rectangular array) of the input tape.

Note that M works in $O(n^{6k})$ time, that is, if an input tape with n rows (or columns or planes) is accepted by M , then it can be accepted by M in $O(n^{6k})$ time. Thus, it is easy to verify that M' can simulate M . \square

From [5], it follows that $\cup_{1 \leq k < \infty} \mathcal{L}[\text{SV4-SP}k\text{-HXFA}^c] = \cup_{1 \leq k < \infty} \mathcal{L}[\text{SV4-SNSP}k\text{-HXFA}^c]$ for any $X \in \{N, D\}$. Combining this result with Lemmas 3.1 and 3.2, we have the following theorem.

Theorem 3.1. $\cup_{1 \leq k < \infty} \mathcal{L}[\text{SV4-SP}k\text{-HXFA}^c] = \cup_{1 \leq k < \infty} \mathcal{L}[\text{CS-SV4-XFA}(k)^c]$ for any $X \in \{N, D\}$.

Corollary 3.1. For any $k \geq 1$, there is no $\text{CS-SV4-NFA}(k)$ that accepts the set of connected patterns.

Remark 3.1. It is easy to see that for each $k \leq 1$, (1) four-dimensional sensing simple k head finite automata [5] are simulated by cooperating systems of $(k+1)$ four-dimensional finite automata, and (2) cooperating systems of k four-dimensional finite automata are simulated by four-dimensional sensing simple $(k+1)$ head finite automata.

Remark 3.2. It is shown in [9] that (one-dimensional) one-way simple multihead finite automata and cooperating systems of (one-dimensional) one-way deterministic finite automata are incomparable in accepting power. From this fact, it follows that SV4-SPMHFA 's and CS-SV4-DFA 's are incomparable in accepting power if the input tapes are restricted to those x such that $l_4(x) > l_1(x) = l_2(x) = l_3(x)$. We can also show that SV4-SPMHFA 's are more powerful than CS-SV4-DFA 's if the input tapes are restricted to those x such that $l_4(x) < l_1(x) = l_2(x) = l_3(x)$.

4 Seven-way versus Eight-Way

In this section, we investigate the difference between the accepting powers of CS-4-DFA(k)^c's [CS-4-NFA(k)^c's] and CS-SV4-DFA(k)^c's [CS-SV4-NFA(k)^c's].

Theorem 4.1. For each $X \in \{N, D\}$, $\mathcal{L}[\text{CS-4-DFA}(1)^c] - \cup_{1 \leq k < \infty} \mathcal{L}[\text{CS-SV4-XFA}(k)^c] \neq \emptyset$.

Proof. Let $T_1 = \{x \in \{0, 1\}^{(4)} | (\exists m \geq 2)[l_1(x) = l_2(x) = l_3(x) = l_4(x) = m \ \& \ x[(1, 1, 1, 1), (m, m, m, 1)] = x[(1, 1, 1, 2), (m, m, m, 2)]]\}$. Clearly, $T_1 \in \mathcal{L}[\text{CS-4-DFA}(1)^c]$. From [5], it is easy to see that T_1 is not in $\cup_{1 \leq k < \infty} \mathcal{L}[\text{SV4-SPk-HNFA}^c]$. From this fact and Theorem 3.1, the theorem follows. \square

From Theorem 4.1, we can get the following corollary.

Corollary 4.1. For each $k \geq 1$ and $X \in \{N, D\}$, (1) $\mathcal{L}[\text{CS-SV4-XFA}(k)^c] \subsetneq \mathcal{L}[\text{CS-4-XFA}(k)^c]$, and (2) $\cup_{1 \leq k < \infty} \mathcal{L}[\text{CS-SV4-XFA}(k)^c] \subsetneq \cup_{1 \leq k < \infty} \mathcal{L}[\text{CS-4-XFA}(k)^c]$.

5 Nondeterminism versus Determinism

In this section, we investigate the difference between the accepting powers of CS-SV4-NFA(k)^c's and CS-SV4-DFA(k)^c's.

Theorem 4.2. $\mathcal{L}[\text{CS-SV4-NFA}(1)^c] - \cup_{1 \leq k < \infty} \mathcal{L}[\text{CS-SV4-DFA}(k)^c] \neq \emptyset$.

Proof. Let $T_2 = \{x \in \{0, 1\}^{(4)} | (\exists m \geq 2)[l_1(x) = l_2(x) = l_3(x) = l_4(x) = m] \ \& \ \exists i, \exists j (1 \leq i \leq m, 1 \leq j \leq m, 1 \leq k \leq m)[x(i, j, k, 1) = x(i, j, k, 2) = 1]\}$. Clearly, $T_2 \in \mathcal{L}[\text{CS-SV4-NFA}(1)^c]$. From [5], it is easy to see that T_2 is not in $\cup_{1 \leq k < \infty} \mathcal{L}[\text{SV4-SPk-HDFA}^c]$. From this fact and Theorem 3.1, the theorem follows. \square

From Theorem 4.2, we get the following corollary.

Corollary 4.2. For each $k \geq 1$, (1) $\mathcal{L}[\text{CS-SV4-DFA}(k)^c] \subsetneq \mathcal{L}[\text{CS-SV4-NFA}(k)^c]$, and (2) $\cup_{1 \leq k < \infty} \mathcal{L}[\text{CS-SV4-DFA}(k)^c] \subsetneq \cup_{1 \leq k < \infty} \mathcal{L}[\text{CS-SV4-NFA}(k)^c]$.

6 Conclusion

We conclude this paper by giving several open problems except the open problem stated in the previous section.

In this paper, we introduced a cooperating system of four-dimensional finite automata, and investigated several basic accepting powers. We conclude this paper by giving an open problem as follows.

For each $k \geq 2$,

$$\mathcal{L}[\text{CS-4-DFA}(k)^c] \subsetneq \mathcal{L}[\text{CS-4-NFA}(k)^c] ?$$

References

- [1] M.Blum and C.Hewitt, Automata on a two-dimensional tape, in *IEEE Symp. Switching Automata Theory*, pp.155-160, 1967.
- [2] M.Blum and K.Kozen, On the power of the compass, in *Processings of the 19th Annual Simp. on Foundations of Computer Science*, 1987.
- [3] M.Blum and W.J.Sakoda, On the capability of finite automata in 2 and 3 dimensional space, in *Processings of the 18th Annual Simp. on Foundations of Computer Science* pp.147-161, 1977.
- [4] A.Hemmerling, Normed two-plane trapes for finite system of cooperating compass automata, in *EIK* 23(8/9), pp.453-470, 1978.
- [5] K.Inoue, I.Takanami, and H.Taniguchi, Three-way two-dimensional simple multihead finite automata – hierarchical properties (in Japanese), *IECE Jan. Trans.(D)*, pp.65-72, 1979.
- [6] K.Inoue, I.Takanami, and H.Taniguchi, Three-way two-dimensional simple multihead finite automata – closure properties (in Japanese), *IECE Jan. Trans.(D)*, pp.273-280, 1979.
- [7] M.Sakamoto, Three-dimensional alternating Turing machines, *Ph.D.Thesis, Yamaguchi University*, 1999.
- [8] M.sakamoto, S.Okatani, K.Kajisa, M.Fukuda, T.Matsukawa, A.Taniue, T.Ito, H.Furutani, and M.Kono, Hierarchies based on the number of cooperating systems of three-dimensional finite automata, *International Journal of AROB*, Vol.4, No.3, pp.425-428, 2009.
- [9] Y.Wang, K.Inoue, and I.Takanami, Some properties of cooperating systems of one-way finite automata (in Japanese), *IECE Jan. Trans.(D-I)* No.7, pp.391-399, 1992.

DP method for Structural Change Detection as Optimal Stopping

--- Verification and Extension ---

*Tetsuo Hattori, *Katsunori Takeda, **Hiromichi Kawano, *** Tetsuya Izumi

*Graduate School of Engineering, Kagawa University / 2217-20 Hayashi, Takamatsu City, Kagawa 761-0396, Japan

** NTT Advanced Technology / Musashino-shi Nakamachi 19-18, Tokyo 180-0006, Japan

*** Micro Technica Co., Ltd./ Yamagami BLD. 3-12-2 Higashi-ikebukuro, Toshima-ku, Tokyo 170-0013, Japan
(Tel : 81087-864-2221; Fax : 81-087-864-2262)
(hattori@eng.kagawa-u.ac.jp)

Abstract: Previously, we have formulated the structural change detection method in time series as an Optimal Stopping Problem with an action cost, using the concept of DP (Dynamic Programming). Then we have proved a theorem that the solution satisfies an inequality. In this paper, we verify the solution by numerical computation and gives the extension of the method by clarifying the notions of estimated structural change point and detection time point that the structure has changed so far.

Keywords: time series, structural change, optimal stopping problem

I. INTRODUCTION

For ongoing time series analysis, three stages are considered: prediction model construction, structural change detection (and/or disparity detection between the model and observing data), and renewal of prediction model. Especially in the second stage, it is important to detect the change point as quickly and also correctly as possible, in order to renew the accurate prediction model as soon as possible after the detection.

As the structural change detection, or change point detection (CPD), some methods have been proposed [1]-[4]. The standard well known method is Chow Test that is used in econometrics [2]. It does a statistical test by setting the hypothesis that the change has occurred at time t for all of data obtained so far.

Previously, we have formulated the structural change detection method in time series as an Optimal Stopping Problem with an action cost, using the concept of DP (Dynamic Programming) [5],[6]. Moreover, we have shown a theorem [6]. This paper presents the verification of the theorem and shows the extension.

II. OPTIMAL STOPPING DP METHOD

1. Formulation ([5],[6])

According to the previously presented description ([5],[6]), we formulate the DP method for the change point detection problem (CPD), using an evaluation function that sums up the cost involved by prediction error and action cost to be taken after the change detection.

For example, a prediction expression is given in the following equation as a function of time t , where y_t , β_1 , β_0 , ε mean the function value, two constant coefficients, and error term, respectively.

$$y_t = \beta_1 \cdot t + \beta_0 + \varepsilon \quad (1)$$

The error term ε is given as a random variable of the normal distribution of variance σ^2 and average of 0, i.e., $\varepsilon \sim N(0, \sigma^2)$. For a time series data based on the equation (1), we think of two situations: one is the situation that the observed data goes out from the tolerance zone that means missing the range of $\pm 2\sigma$ from the predicted value. And, another is the situation that the observed data goes in the zone. We call the former situation “failing” (or “Out”) and the latter “hitting” (or “In”). We assume that the structure changes when the failing occurs for continuing N times.

The evaluation function is given by (2) as the sum of two kinds of cost: the damage caused by the failing (i.e., failing loss) and action cost to be taken after the change detection.

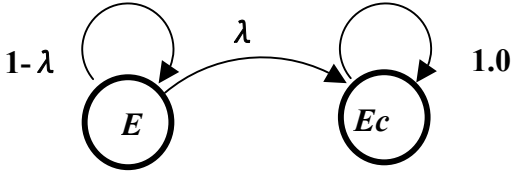
$$\text{Total_cost} = \text{cost}(A) + \text{cost}(n) \quad (2)$$

where $\text{cost}(n)$ is the sum of the loss by continuing n times failing before the structural change detection, and $\text{cost}(A)$ denotes the cost involved by the action after the change detection. Then we have to find the number of N that minimizes the expectation value of Total_cost, assuming that the structural change occurs randomly.

2. Structural change model ([5],[6])

We can assume that the structural change is Poisson occurrence of average λ , and that, once the change has occurred during the observing period, the structure does

not go back to the previous one. The reason why we set such a model is that we focus on the detection of the first structural change in the sequential processing (or sequential test). The concept of the structural change model is shown in Fig. 1.



Ec : State that the structural change occurred.
E : State that the structure is unchanged.
λ : Probability of the structural change occurrence.
(Poisson Process.)

Fig.1. Structural change model.

Moreover, we introduce a more detailed model. Let R be the probability of the failing when the structure is unchanged. Let R_c be the probability of the failing when the structure change occurred. We consider that R_c is greater than R , i.e., $R_c > R$. The detailed model for the State Ec and E are illustrated as similar probabilistic finite state automats in Fig.2 and Fig.3, respectively.

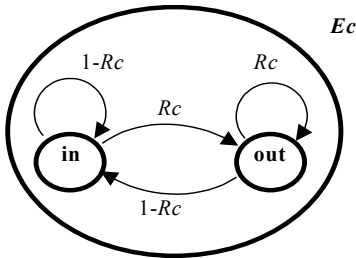


Fig.2. Internal model of the State E .

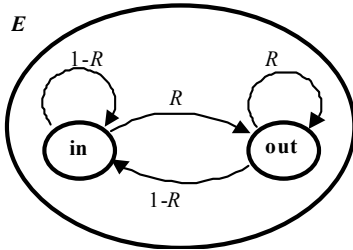


Fig.3. Internal model of the State Ec .

3. Definition ([5],[6])

Let the $\text{cost}(n)$ be $a \cdot n$ as a linear function for n , where a is the loss caused by the failing in one time. And for simplicity, let T and A denote the Total_cost and

cost (A), respectively. Then, the evaluation function in (2) is denoted as the following equation (3).

$$T = A + a \cdot n \quad (3)$$

We recursively define a function $ET(n, N)$ to obtain the optimum number of times n that minimizes the expectation value of the evaluation function of Equation (3), using the concept of DP (Dynamic Programming). Let N be the optimum number. Let the function $EC(n, N)$ be the expectation value of the evaluation function at the time when the failing has occurred in continuing n times, where n is less than or equal to N , i.e., $0 \leq n \leq N$.

Thus the function is recursively defined as follows.

$$(\text{if } n = N) \quad ET(n, N) = A + a \cdot N \quad (4)$$

$$(\text{if } n < N) \quad ET(n, N) = P(\bar{S}_{n+1} | S^n) \cdot a \cdot n + (1 - P(\bar{S}_{n+1} | S^n)) ET(n+1, N) \quad (5)$$

where S^n means the state of failing in continuing n times, \bar{S}_{n+1} the state of hitting at the $(n+1)$ th observed data, and $P(\bar{S}_{n+1} | S^n)$ means the conditional probability that the state \bar{S}_{n+1} occurs after the state S^n .

The first term in the right-hand side (RHS) of the equation (4) indicates the expectation value of the evaluation function at the time when hitting happens at the $(n+1)$ th data after the continuing n times failing. The second term in the RHS of the equation (5) indicates the expectation value of the evaluation function for the time when failing happens at the $(n+1)$ th data after continuing n times failing.

Then, from the definition of the function $ET(n, N)$, the goal is to find the N that minimizes $ET(0, N)$, because the N is the same as n that minimizes the expectation value of the evaluation function of (4).

4. Minimization of the evaluation function

The analytical solution N that minimizes $EC(0, N)$ can be deduced. The strict proof needs many pages, then we show numerical solution.

The function $ET(0, N)$ is defined by recursive expressions (4) and (5), then $ET(0, N)$ can be computed by recursively. In the process of this computation, $P(\bar{S}_{n+1} | S^n)$ can be calculated as follows.

Let E_{cn} be the event that the structural change occurs once during the period of observation in continuing n times. Let $P(E_{cn} | S^n)$ be the conditional probability that the E_{cn} happens under the condition

that failing has already occurred for continuing n times. Based on the model in Fig.1-3,

$$P(\bar{S}_{n+1} | S^n) = (1-R)(1-P(E_{cn} | S^n)) + (1-R_c)P(E_{cn} | S^n) \quad (6)$$

Subsequently, we show the Lemma 1 and Lemma 2.

Lemma 1: Let E_{cn} be the event that the structural change occurs once during the period of observation in continuing n times. Let $P(E_{cn} | S^n)$ be the conditional probability that the E_{cn} happens under the condition that failing ("Out") occurs in continuing n times. $P(E_{cn} | S^n)$ is an increase function for n .

Proof: Let E be the event that there is no structural change. According to the Bayes' theorem, we have

$$\begin{aligned} P(E_{cn} | S^n) &= \frac{P(S^n | E_{cn})P(E_{cn})}{P(S^n | E_{cn})P(E_{cn}) + P(S^n | E)P(E)} \\ &= \frac{\sum_{i=0}^{n-1} (1-\lambda)^i R^i \lambda R_c^{n-i}}{\sum_{i=0}^{n-1} (1-\lambda)^i R^i \lambda R_c^{n-i} + (1-\lambda)^n R^n} \\ &= \frac{1}{1 + \frac{(1-\lambda)^n R^n}{\sum_{i=0}^{n-1} (1-\lambda)^i R^i \lambda R_c^{n-i}}} = \frac{1}{1 + D(n)} \end{aligned} \quad (7)$$

where $D(n) = \frac{(1-\lambda)^n R^n}{\sum_{i=0}^{n-1} (1-\lambda)^i R^i \lambda R_c^{n-i}}$.

The $D(n)$ is also expressed as follows.

$$D(n) = \frac{(1-\lambda)^n \left(\frac{R}{R_c}\right)^n}{\lambda \sum_{i=0}^{n-1} (1-\lambda)^i \left(\frac{R}{R_c}\right)^i} = \frac{X^n}{\lambda \sum_{i=0}^{n-1} X^i} \quad (8)$$

where $X = (1-\lambda) \frac{R}{R_c}$.

Since $0 \leq \lambda < 1$, $0 < 1-\lambda \leq 1$, and $R_c > R$, then $0 < X < 1$. So, the $D(n)$ becomes a monotonous decrease for n . Therefore, the probability $P(E_{cn} | S^n)$ is a monotonous increase function. This means that, if the number of the failing times n increases, the probability that the structural change has occurred increases. This meets our intuition clearly.

Lemma 2: The conditional probability $P(\bar{S}_{n+1} | S^n)$ is a decrease function for n .

Proof: Notice the equation (6).

$$P(\bar{S}_{n+1} | S^n) = (1-R)(1-P(E_{cn} | S^n)) + (1-R_c)P(E_{cn} | S^n)$$

The first term in the RHS of (6) shows the probability that the hitting ("In") occurs for the $(n+1)$ -th time observed data when the structure is unchanged. The second term shows the probability that the hitting occurs for the $(n+1)$ -th time observed data when the structure changed.

From the equation (6), we have

$$P(\bar{S}_{n+1} | S^n) = 1 - R + P(E_{cn} | S^n)(R - R_c) \quad (9)$$

By the aforementioned Lemma 1, $P(E_{cn} | S^n)$ is an increase function, and $R < R_c$, therefore, $P(\bar{S}_{n+1} | S^n)$ is a decrease function for n .

Remark: Lemma 2 indicates that, if the number of times of continuous failing increases, the probability of the fitting for the next observed data after those continuous failing decreases. This is intuitively clear, because, by Lemma 1, the probability of the structural change increases if the number of times of the continuous failing increases.

By using the above Lemma 1 and 2, and the reduction to absurdity, the following theorem holds [6], that gives the n that minimizes the expectation value $ET(0, N)$.

Theorem [6].

The N that minimizes $ET(0, N)$ is given as the largest number n that satisfies the following Inequality (10).

$$a < (A + a) \cdot P(\bar{S}_n | S^{n-1}) \quad (10)$$

where the number $N+1$ can also be the optimum one that minimizes $ET(0, N)$, i.e., $ET(0, N) = ET(0, N+1)$, only if

$$a = (A + a) \cdot P(\bar{S}_{N+1} | S^N)$$

III. VERIFICATION AND EXTENSION

1. Verification of the Theorem by numerical computation

By numerical computation, we evaluate the $ET(0, N)$ and the Inequality(10) under the same conditions. Fig.4 (a) shows that the relation between the expectation $ET(0, N)$ and N , and Fig.4(b) shows the value $a - (A + a) \cdot P(\bar{S}_{N+1} | S^N)$. We can easily verify that the number 3 minimize $ET(0, N)$, and at the same time, is the largest number satisfying Inequality (10). Fig.5 also shows that the relation between the expectation $ET(0, N)$ and N by varying the A/a and fixed λ . It implies that as

the action cost A is greater, the N that minimizes $ET(0,N)$ becomes greater.

2. Extension of the change point notion

We separate the notion of CPD into two that one is the time point when the change has been detected so far at the observing time and another is the estimated change point just the time when the change has occurred.

Then we define that, if the aforementioned detected change point is t_c , then estimated change point exits within a section $[t_c-N, t_c]$. We have also verified by experimentation for ongoing real time series data, that the extended definition works very well.

IV. CONCLUSION

We have verified and shown by numerical computation, that the Theorem surely holds. And we also have proposed the extended notion of change point detection. We consider that the optimal stopping DP method and the extension will be promising.

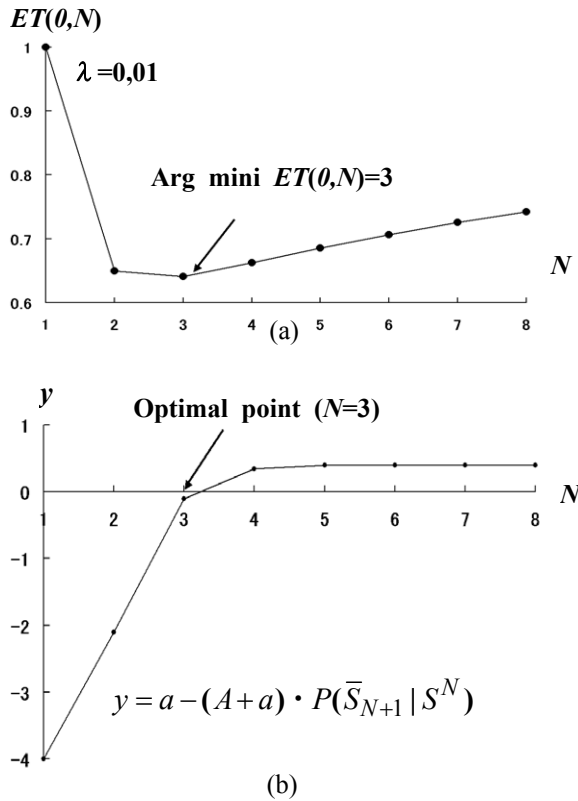


Fig.4. Evaluation of the expectation $ET(0,N)$ and Inequality $a < (A+a) \cdot P(\bar{S}_n | S^{n-1})$ appeared in the Theorem [6].

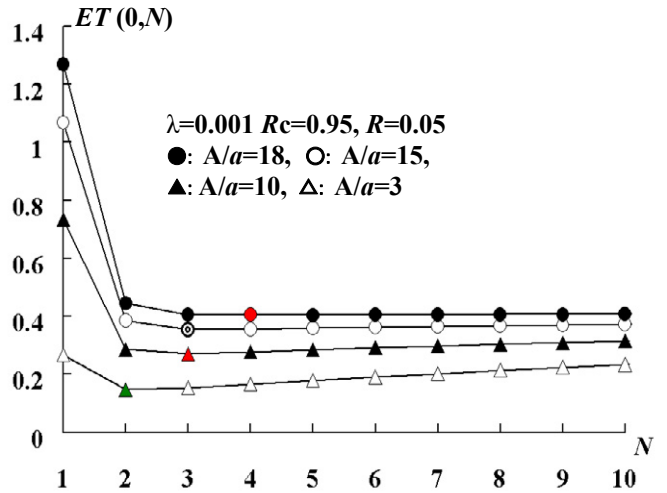


Fig.5. Relation between the expectation $ET(0,N)$ and N with R_c and λ fixed and varying $A/a(18, 15, 10, 3)$. Optimal N is 4,3,3,2, respectively, depending the order of the above ratio of A/a .

REFERENCES

- [1] R.Jana and S.Dey (2000), Change detection in Teletraffic Models, IEEE Trans. Signal Processing, vol.48, No.3, pp.846-853.
- [2] Chow,G.C. (1960), Tests of Equality Between Sets of Coefficients in Two Linear Regressions, Econometrica, Vol.28, No.3, pp.591-605.
- [3] S.MacDougall, A.K. Nandi and R.Chapman (1998), Multisolution and hybrid Bayesian algorithms for automatic detection of change points, Proc. of IEEE Visual Image Signal Processing, vol.145, No.4, pp.280-286.
- [4]E.S.Page (1954), Continuous inspection schemes, Biometrika, Vol.41, pp.100-115.
- [5] Tetsuo Hattori, Katsunori Takeda, Izumi Tetsuya, Hiromichi Kawano (2010): "Early Structural Change Detection as an Optimal Stopping Problem (I) --- Formulation Using Dynamic Programming with Action Cost ----", Proc. of the 15th International Symposium on Artificial Life and Robotics (AROB15th'10), ISBN 978-4-9902880-4-4, pp.763-766.
- [6] Hiromichi Kawano, Tetsuo Hattori, Katsunori Takeda, Izumi Tetsuya (2010): "Early Structural Change Detection as an Optimal Stopping Problem (II) --- Solution Theorem and its Proof Using Reduction to Absurdity ----", Proc. of the 15th International Symposium on Artificial Life and Robotics (AROB15th'10), ISBN 978-4-9902880-4-4, pp.767-772.

Change Detection Experimentation for Multiple Regression Using ESPRT

--- One Variation is Periodic Function ---

*Katsunori Takeda, *Tetsuo Hattori, **Hiromichi Kawano, ***Tetsuya Izumi

*Graduate School of Engineering, Kagawa University / 2217-20 Hayashi, Takamatsu City, Kagawa 761-0396, Japan

**NTT Advanced Technology/ Musashino-shi Nakamachi 19-18, Tokyo 180-0006, Japan

***Micro Technica Co., Ltd. / Yamagami BLD. 3-12-2 Higashi-ikebukuro, Toshima-ku, Tokyo 170-0013, Japan

(Tel : 81-87-864-2221; Fax : 81-87-864-2262)

(hattori@eng.kagawa-u.ac.jp)

Abstract: Previously, we have proposed the application of sequential probability ratio test (SPRT) to the structural change detection of ongoing time series data. Moreover, we have also proposed the extended method of SPRT (ESPRT). In this paper, we show experimental results by the Extended SPRT (ESPRT) and Chow Test when applying to time series data that are generated by a multiple regression model in the case where one explanatory variation is periodic function (sine function). And we clarify the effectiveness of the ESPRT, in the sense of ability of early and correct change detection and computational complexity.

Keywords: Time series, multiple linear regression, ESPRT (Extended Sequential Probability Ratio Test), Chow Test

I. INTRODUCTION

Generally, we have three stages in predicting ongoing time series data ([1], [2]). First, we have to find a prediction model that adequately represents the characteristics of the early time series data. Second, we have to detect the structural change of the time series data, as quickly and correctly as possible, when the estimated prediction model does not meet the data any more ([3],[4]). Third, we have to reconstruct the next prediction model as soon as possible after the change detection.

For the second problem, we have already proposed an application of SPRT (sequential probability ratio test) that has been mainly used in the field of quality control [5], [6]. And we have presented the experimental results in comparison with Chow Test that is well-known standard method for such structural change detection of time series data ([6], [7]).

However, the experimentation has been done using single regression model and has shown that the SPRT is more effective than Chow Test. Since multiple regression models are more generally used for time series data analysis than single regression one, we have examined by experimentation if the SPRT surpasses Chow Test as well for the case of multiple regression model data [8]. Moreover in the literature [8], we have shown the extended SPRT (ESPRT) aiming at more accurate estimation of the change point.

II. ESPRT AND CHOW TEST

1. SPRT ([8])

The sequential probability ratio test (SPRT) is used for testing a null hypothesis H_0 (e.g. the quality is under pre-specified limit 1%) against hypothesis H_1 (e.g. the quality is over pre-specified limit 1%). And it is defined as follows:

Let Z_1, Z_2, \dots, Z_i be respectively observed time series data at each stage of successive events, the probability ratio λ_i is computed as follows.

$$\lambda_i = \frac{P(Z_1 | H_1) \cdot P(Z_2 | H_1) \cdots P(Z_i | H_1)}{P(Z_1 | H_0) \cdot P(Z_2 | H_0) \cdots P(Z_i | H_0)} \quad (1)$$

where $P(Z | H_0)$ denotes the distribution of Z if H_0 is true, and similarly, $P(Z | H_1)$ denotes the distribution of Z if H_1 is true.

Two positive constants C_1 and C_2 ($C_1 < C_2$) are chosen. If $C_1 < \lambda_i < C_2$, the experiment is continued by taking an additional observation. If $C_2 < \lambda_i$, the process is terminated with the rejection of H_0 (acceptance of H_1). If $\lambda_i < C_1$, then terminate this process with the acceptance of H_0 .

$$C_1 = \frac{\beta}{1 - \alpha}, \quad C_2 = \frac{1 - \beta}{\alpha} \quad (2)$$

where α means type I error (reject a true null hypothesis), and β means type II error (accept a null hypothesis as true one when it is actually false).

2. Procedure of SPRT ([8])

The concrete procedure of structural change detection is as follows (see Fig. 1):

Step1: Make a prediction expression and set the tolerance band (a) (e.g. $a=2\sigma_s$) that means permissible error margin between the predicted data and the observed one. (σ_s denotes a standard deviation in learning sample data at early stage.)

Step2: Set up the null hypothesis H_0 and alternative hypothesis H_1 .

H_0 : Change has not occurred yet.

H_1 : Change has occurred.

Set the values α, β and compute C_1 and C_2 , according to Equation (2). Initialize $i = 0$, $\lambda_0 = 1$.

Step3: Incrementing i ($i = i+1$), observe the following data y_i . Evaluate the error $|\varepsilon_i|$ between the data y_i and the predicted value from the aforementioned prediction expression.

Step4: Judge as to whether the data y_i goes in the tolerance band or not, i.e., the ε_i is less than (or equal to) the permissible error margin or not. If it is Yes, then set $\lambda_i = 1$ and return to Step3. Otherwise, advance to Step5.

Step5: Calculate the probability ratio λ_i , using the following Equation (3) that is equivalent to Equation (1).

$$\lambda_i = \lambda_{i-1} \frac{P(\varepsilon_i | H_1)}{P(\varepsilon_i | H_0)} \quad (3)$$

where, if the data y_i goes in the tolerance band, $(P(\varepsilon_i | H_0), P(\varepsilon_i | H_1)) = (\theta_0, \theta_1)$, otherwise, $(P(\varepsilon_i | H_0), P(\varepsilon_i | H_1)) = ((1-\theta_0), (1-\theta_1))$.

Step6: Execution of testing.

(i) If the ratio λ_i is greater than C_2 ($= (1-\beta)/\alpha$), dismiss the null hypothesis H_0 , and adopt the alternative hypothesis H_1 , and then End.

(ii) Otherwise, if the ratio λ_i is less than C_1 ($= \beta/(1-\alpha)$), adopt the null hypothesis H_0 , and dismiss the alternative hypothesis H_1 , and then set $\lambda_i = 1$ and return to Step3.

(iii) Otherwise (in the case where $C_1 \leq \lambda_i \leq C_2$), advance to Step7.

Step7: Observe the following data y_i incrementing i . Evaluate the error $|\varepsilon_i|$ and judge whether the data y_i goes in the tolerance band, or not. Then, return to Step5 (calculation of the ratio λ_i).

Here, we call **Case a-c** for each combination of (θ_0, θ_1) , respectively, as follows:

Case a ($\theta_0=0.1, \theta_1=0.9$),

Case b ($\theta_0=0.2, \theta_1=0.8$),

Case c ($\theta_0=0.3, \theta_1=0.7$).

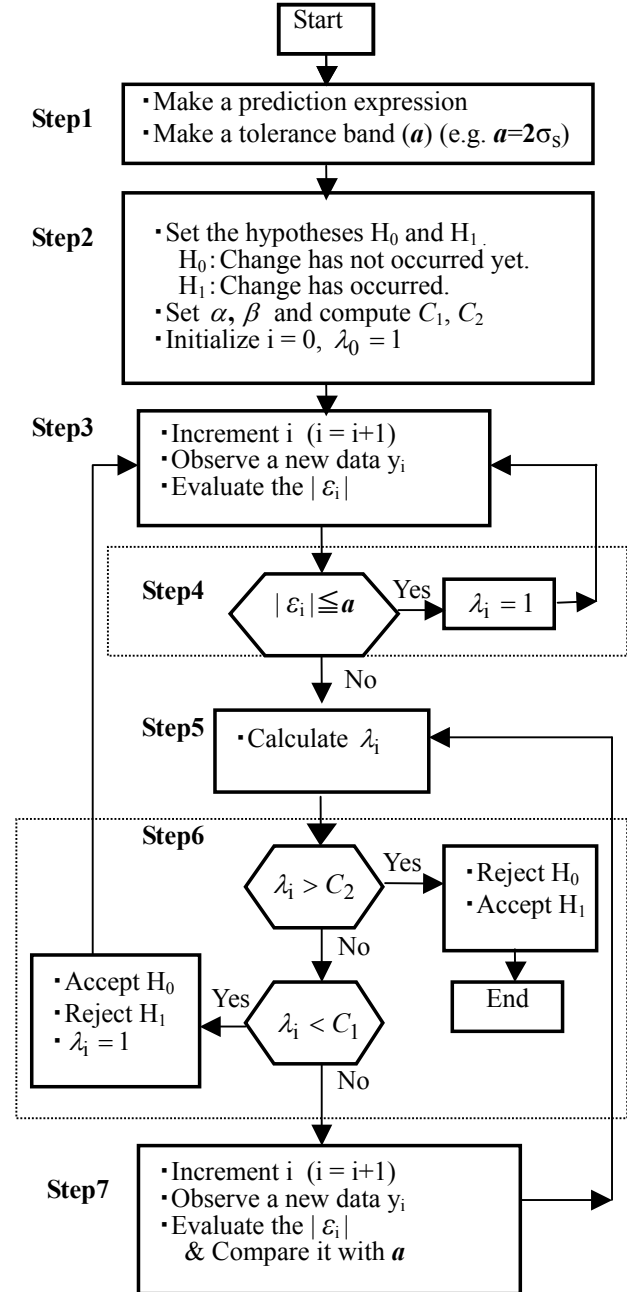


Fig.1. SPRT structural change detection [8].

3. Extended SPRT ([8])

The SPRT detects a change point at the time when the probabilistic ratio λ_i is greater than C_2 ($= (1-\beta)/\alpha$). Then, the detected change point equals to the terminated time point and its detection tends to be delayed from true

change point. So, as an extension of SPRT, we define the estimated change point that exists in the intersection $[tc-M, tc]$, where tc means the aforementioned detected change point and M is the number of times when the observed data continuously goes of tolerance zone until the ratio $\lambda_i > C_2$. The number M can be obtained from the equation (4).

$$\left(\frac{\theta_1}{\theta_0}\right)^M > C_2 \left(\frac{1-\beta}{\alpha}\right) \quad (4)$$

Then we have the following equation using Gauss notation. So, the value of M depends on the parameters (see Table 1). That is, $M=2$ (Case **a**), $M=3$ (Case **b**), $M=4$ (Case **c**).

$$M = \left\lceil \log_{\frac{\theta_1}{\theta_0}} \frac{1-\beta}{\alpha} \right\rceil \quad (5)$$

Table 1. Parameter values in SPRT and M .

α	β	θ_0	θ_1	M
0.05	0.05	0.1	0.9	2
		0.2	0.8	3
		0.3	0.7	4

4. Chow Test ([6]-[8])

The well known Chow Test checks if there are significant differences or not, among residuals for three Regression Lines, where regression Line 1 obtained from the data before a change point tc , Line 2 from the data after tc , and Line 3 from the whole data so far, by setting up the change point hypothesis at each point in the whole data (Fig.2).

III. EXPERIMENTATION

Generally, in the experimentation for the case of time series data based on multiple linear regression model, the data is supposed to be generated by the following equations.

$$y = a_{11}x_1 + a_{12}x_2 + b + \varepsilon \quad (t \leq t_c^*) \quad (6)$$

$$y = a_{21}x_1 + a_{22}x_2 + b + \varepsilon \quad (t_c^* \leq t) \quad (7)$$

where $\varepsilon \sim N(0, \sigma^2)$, i.e., the error ε is subject to the Normal Distribution with the average 0 and the variation σ^2 , and tc^* means the change point. In addition, we have set $tc^*=70$.

Setting the coefficients of equation (6) and (7) as shown in the Table 2, we examine the case where

$$x_1 = t, x_2 = \sin\left(\frac{1}{8}\pi t\right) \quad (8)$$

Table 2. Parameters for generating time series data.

Equation (6) ($t=1,2,\dots,69$)	Equation (7) ($t=70,71,\dots,100$)	σ
$y = x_1 + 20x_2 + 5 + \varepsilon$	$y = x_1 + 10x_2 + 5 + \varepsilon$	5

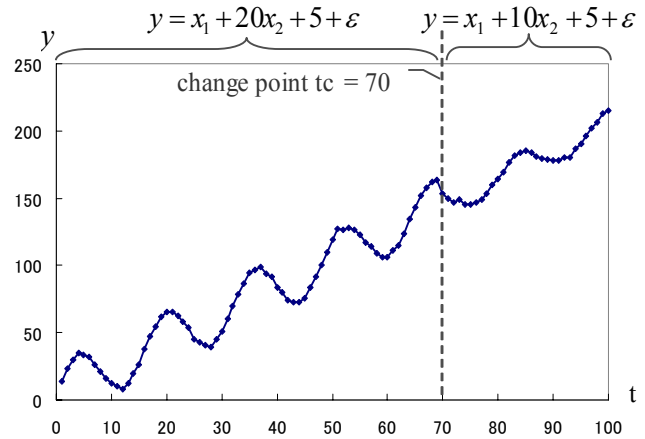


Fig.2. Example of the time series data generated by equations (6) and (7), where x_1 and x_2 are time functions such as $x_1=t$, and $x_2=\sin(\pi t/8)$. (The true change point $tc=70$.)

Fig.2 shows the example of the time series data according to the equations in Table 2. Fig.3 illustrates results in Chow Test and SPRT, where horizontal axis shows observing time t (detection operation has started from $t=41$). The vertical axis shows the detected change point tc , whose value is the average of experimentation results for 200 sets of generated time series data.

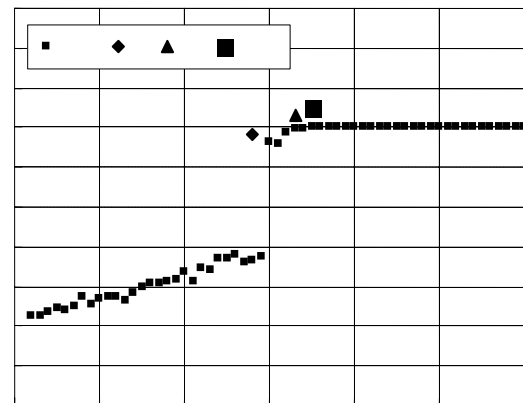


Fig.3. Resultant relation between detected change point tc and time point t , where CT means Chow Test and a-c corresponds to each of Cases a-c, respectively.

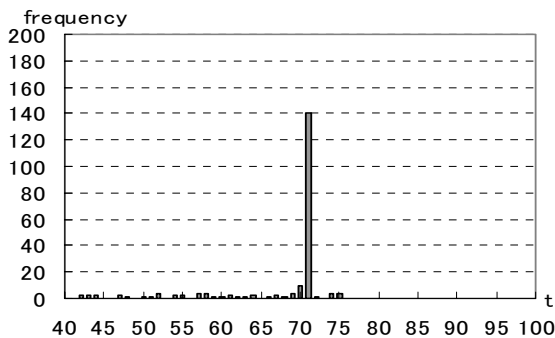


Fig.4. Frequency of the detected change point t_c by SPRT in the Case a.

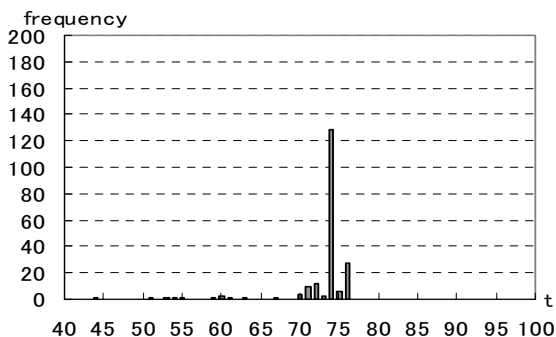


Fig.5. Frequency of the detected change point t_c by SPRT in the Case b.

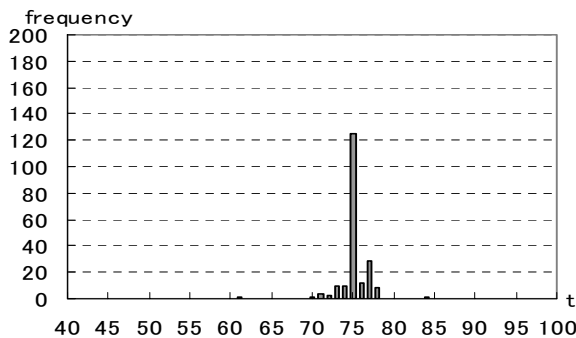


Fig.6. Frequency of the detected change point t_c by SPRT in the Case c.

Fig.3 shows that Chow Test outputs the change point at the time when every data is observed after $t=40$. This means that Chow Test tends to make false detection before the true change point. And, the time when Chow Test works well is long enough after the true change point. Comparing with Chow Test, the SPRT works better depending on the Cases **a**, **b**, **c**. In order to interpret the results as ones by ESPRT, we only have to consider $[t_c - M, t_c]$, where $M=2, 3, 4$ corresponding to

Case a, b, c, respectively. From Fig.4-6, we can see that the ESPRT works better than SPRT and Chow Test.

IV. CONCLUSION

We have experimented the structural change point detection by SPRT, ESPRT, and Chow Test for ongoing time series data generated by multiple linear regression model, where two variations are time functions and the one of two variation is periodic. From the results, we consider that ESPRT works more effective than SPRT and Chow Test in the sense of early detection, accuracy, and computational cost.

REFERENCES

- [1] C.G.E.P.Box and G.M.Jenkins (1976), Time Series Analysis: Forecasting and Control, Prentice Hall.
- [2] Peter J. Brockwell and Richard A. Davis (2003), Introduction to Time Series and Forecasting, Springer; 2nd edition.
- [3] C.Han, P.k.Willet and D.A.Abraham (1999), Some methods to evaluate the performance of Page's test as used to detect transient signals, IEEE Trans. Signal processing, Vol.47, No.8, pp.2112-2127.
- [4] S.D.Blostein (1991), Quickest detection of a time-varying change in distribution, IEEE Trans. Information Theory, Vol.37, No.4, pp.1116-1122.
- [5] A. Wald (1947), Sequential Analysis, John Wiley & Sons.
- [6] Hiromichi Kawano, Tetsuo Hattori, Ken Nishimatsu (2008), Structural Change Point Detection Method of Time Series Using Sequential Probability Ratio Test—Comparison with Chow Test in the ability of early detection — (in Japanese), IEEJ Trans. EIS, Vol.128, No.4, pp.583-592.
- [7] Chow, G. C. (1960), Tests of Equality Between Sets of Coefficients in Two Linear Regressions, Econometrica, Vol.28, No.3, pp.591-605.
- [8] Katsunori Takeda, Tetsuo Hattori, Izumi Tetsuya, Hiromichi Kawano (2010), Extended SPRT for Structural Change Detection of Time Series Based on Multiple Regression Mode, Proceedings of the 15th International Symposium on Artificial Life and Robotics (AROB 15th '10), pp.755-758, ISBN: 978-4-9902880-4-4, Oita, Japan, Feb..

Continuous Change Point Detection for Time Series Images Using ESPRT

*Katsunori Takeda, *Tetsuo Hattori, **Hiromichi Kawano, ***Tetsuya Izumi, ****Shinichi Masuda

**Graduate School of Engineering, Kagawa University / 2217-20 Hayashi, Takamatsu City, Kagawa 761-0396, Japan*

***NTT Advanced Technology, / Musashino-shi Nakamachi 19-18, Tokyo 180-0006, Japan*

****Micro Technica Co., Ltd., / Yamagami BLD. 3-12-2 Higashi-ikebukuro, Toshima-ku, Tokyo 170-0013, Japan*

*****C Micro Co., Ltd., 269-1 Hayashi-Cho, Takamatsu City, Kagawa 761-0396, Japan*

(Tel : 81-87-864-2221; Fax : 81-87-864-2262, hattori@eng.kagawa-u.ac.jp)

Abstract: In order to continuously detect the change point in ongoing time series data, we propose a method using extended sequential probability ratio test (ESPRT). That is, it is a repetition of three stages, where the first stage is prediction model construction, and change point detection as the second stage, and reconstruction of prediction model as the third stage. In this paper, we show experimental results by applying the method to time series data of image storage, where the images are transmitted as compressed data (i.e. JPEG file) from remote monitoring camera systems.

Keywords: Continuous change detection, monitoring camera system, time series images, extended sequential probability ratio test (ESPRT), security

I. INTRODUCTION

Today, monitoring camera systems are widely used in the society [1]. However, because there is a channel capacity limit in the public communication line, remote monitoring systems ordinarily use compressed data (e.g. JPEG file) to send scene images if there happens something abnormal or something changed. For this reason, the camera system is required to become smart enough to judge by itself as to whether something abnormal has occurred or not.

On the other hand, if something moves in the scene image, the quantity of the compressed image tends to be different from the steady situation so far. Based on the characteristics, in our previous paper, we have proposed a method for the change detection using applying the Sequential Probability Ratio Test (SPRT) ([2], [3]) to the scene images of time series [6]. Moreover, in the literature, we have experimented with the real time series images from a monitoring camera and have compared the SPRT the method with the well-known Chow Test [4].

However, we have just only presented the results of first change detection. In fact, we need to continuously deal with the change detection from the time series images, and so that we have to use the Extended SPRT (ESPRT), in order to know the change time point correctly and reconstruct the next prediction model [5].

In this paper, we show the experimental results of continuous change detection from real time series images, and discuss the performance of the method.

II. SPRT AND CHANGE DETECTION

For the change detection problem, we propose an application of Sequential Probability Ratio Test (SPRT) that has been mainly used in the field of quality control.

1. SPRT ([2],[3])

The SPRT is used for testing a null hypothesis H_0 (e.g. the quality is under pre-specified limit 1%) against hypothesis H_1 (e.g. the quality is over pre-specified limit 1%). In addition, it is defined as follows.

At each stage of successive events Z_1, Z_2, \dots, Z_i that are respectively corresponding to observed time series data, the probability ratio λ_i is computed.

$$\lambda_i = \frac{P(Z_1 | H_1) \cdot P(Z_2 | H_1) \cdots P(Z_i | H_1)}{P(Z_1 | H_0) \cdot P(Z_2 | H_0) \cdots P(Z_i | H_0)} \quad (1)$$

where $P(Z | H_0)$ denotes the distribution of Z when H_0 is true and $P(Z | H_1)$ denotes the distribution of Z when H_1 is true.

Two positive constants C_1 and C_2 ($C_1 < C_2$) are chosen. If $C_1 < \lambda_i < C_2$, the experiment is continued by taking an additional observation. If $C_2 < \lambda_i$, the process is terminated with the rejection of H_0 (acceptance of H_1). If $\lambda_i < C_1$, the process is terminated with the acceptance of H_0 .

$$C_1 = \frac{\beta}{1 - \alpha} \quad C_2 = \frac{1 - \beta}{\alpha} \quad (2)$$

where α means type I error (reject a true null hypothesis), and β means type II error (accept a null hypothesis as true one when it is actually false).

2. Procedure

The concrete procedure of structural change detection is as follows.

Step1: Make a prediction expression and set the tolerance band (a) (e.g. $a=2\sigma_s$) that means permissible error margin between the predicted data and the observed one (where σ_s means the standard deviation).

Step2: Set up the null hypothesis H_0 and alternative hypothesis H_1 .

H_0 : Change has not occurred yet.

H_1 : Change has occurred.

Set the values α, β and compute C_1 and C_2 , according to Equation (2). Initialize $i = 0$, $\lambda_0 = 1$.

Remark: The statement of the null hypothesis H_0 , "Change has not occurred yet.", means in statistical sense. It means that the generation probability for the data to go out from the tolerance band is less than (or equal to) θ_0 (for instance, 1%). Similarly, the statement of the alternative hypothesis H_1 , "Change has occurred." means that the generation probability for the data to go out from the tolerance band is greater than (or equal to) θ_1 (for instance, 99%). Additionally, we suppose that θ_1 is considerably greater than θ_0 .

Step3: Incrementing i ($i = i+1$), observe the following data y_i . Evaluate the error $|\varepsilon_i|$ between the data y_i and the predicted value from the aforementioned prediction expression.

Step4: Judge as to whether the data y_i goes in the tolerance band or not, i.e., the ε_i is less than (or equal to) the permissible error margin or not. If it is Yes, then set $\lambda_i = 1$ and return to Step3. Otherwise, advance to Step5.

Step5: Calculate the probability ratio λ_i , using the following Equation (3) that is equivalent to Equation (1)

$$\lambda_i = \lambda_{i-1} \frac{P(\varepsilon_i | H_1)}{P(\varepsilon_i | H_0)} \quad (3)$$

where, if the data y_i goes in the tolerance band,

$P(\varepsilon_i | H_0) = \theta_0$ and $P(\varepsilon_i | H_1) = \theta_1$, otherwise,

$P(\varepsilon_i | H_0) = (1 - \theta_0)$ and $P(\varepsilon_i | H_1) = (1 - \theta_1)$.

Step6: Execution of testing.

- (i) If the ratio λ_i is greater than C_2 ($= (1 - \beta) / \alpha$), dismiss the null hypothesis H_0 , and adopt the alternative hypothesis H_1 , and then End.

- (ii) Otherwise, if the ratio λ_i is less than C_1 ($= \beta / (1 - \alpha)$), adopt the null hypothesis H_0 , and dismiss the alternative hypothesis H_1 , and then set $\lambda_i = 1$ and return to Step3.

- (iii) Otherwise (in the case where $C_1 \leq \lambda_i \leq C_2$), advance to Step7.

Step7: Observe the following data y_i incrementing i . Evaluate the error $|\varepsilon_i|$ and judge whether the data y_i goes in the tolerance band, or not. Then, return to Step5 (calculation of the ratio λ_i).

3. Extended SPRT [5]

We extend the definition of detected change point by SPRT. As such extension, we adopt the number $tc-M$ where tc is ordinary aforementioned change point and M is the number of times when the observed data continuously goes of tolerance zone until the ratio $\lambda_i > C_2$. The number M can be obtained from the equation below.

$$\left(\frac{\theta_1}{\theta_0} \right)^M > C_2 \left(= \frac{1 - \beta}{\alpha} \right) \quad (4)$$

Then we have the following equation using Gauss notation. The value of M depends on the parameters (see Table 1).

$$M = \left\lceil \log_{\frac{\theta_1}{\theta_0}} \frac{1 - \beta}{\alpha} \right\rceil \quad (5)$$

From some experimental results, we have found that, if we adopt the interval $[tc-M+1, tc]$ as the existing range of true change point, the hitting (or correct estimation) percentage will considerably increase.

Table 1. Parameter values in SPRT and M .

α	β	θ_0	θ_1	M
0.05	0.05	0.1	0.9	2
		0.2	0.8	3
		0.3	0.7	4

III. CONTINUOUS CHANGE DETECTION FOR IMAGE SEQUENCE

In order to continuously detect the structural change of the scene images from a monitoring camera, we apply the ESPRT method to the time series of compressed image data (JPEG file) quantity (Kbyte).

Fig.1 and Fig.2 show two kinds of images when a person has moved into and out of the scene at high speed and low speed, respectively. Fig.3 and Fig.4 show two graphs on time series data of JPEG file volumes, corresponding to Fig.1 and Fig.2, respectively.

We assume that there are four change points in the both of the two kinds of time series images. The first change point is the time when some person appears in the scene image, and the second is when he stops walking, the third when he begins to move again, and the fourth when he moves out of scene.

The results of change detection by SPRT and Chow Test are shown in the graphs in Fig.5 and Fig.6, respectively, where the SPRT detects change points in the case of condition 1 ($\theta_0=0.9$, $\theta_1=0.1$). The number of sample points for learning and analysis is five, where those samples are used for deciding prediction model (regression line) in both cases.

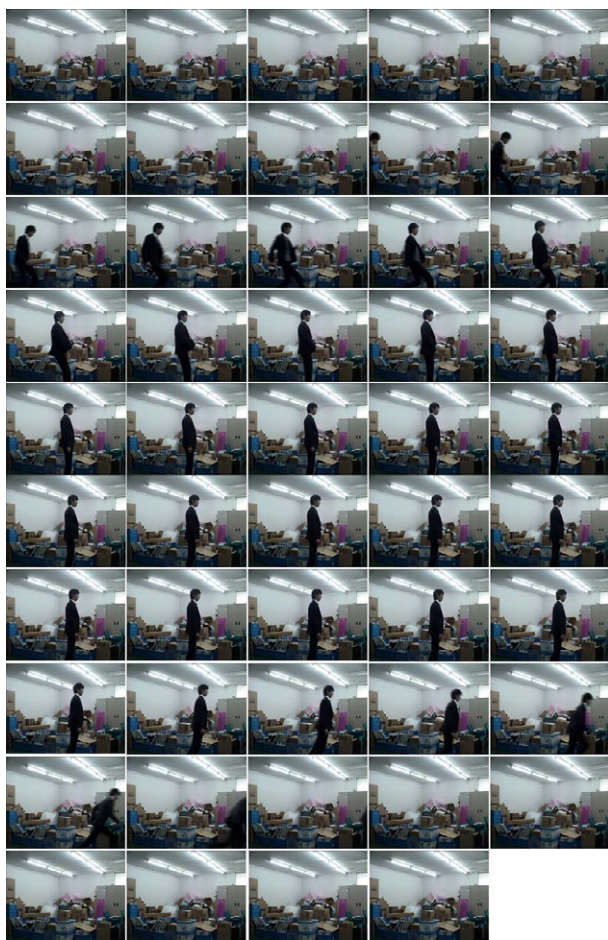


Fig.1. Example of time series images where someone moves in, stops walking, moves again, and moves out at high speed what we call “Fast-In Fast-Out Case”. (Time is counted from the upper left to the lower right.)

If SPRT detects the change at t_c , the ESPRT estimates the true point as t_c-1 under the condition 1. Then after the first detection, next five points from t_c-1 to t_c+3 will be used as learning samples for reconstructing the next prediction model.

The experimental results show that ESPRT method continuously detects the change point better than Chow Test in the two kinds of time series images.

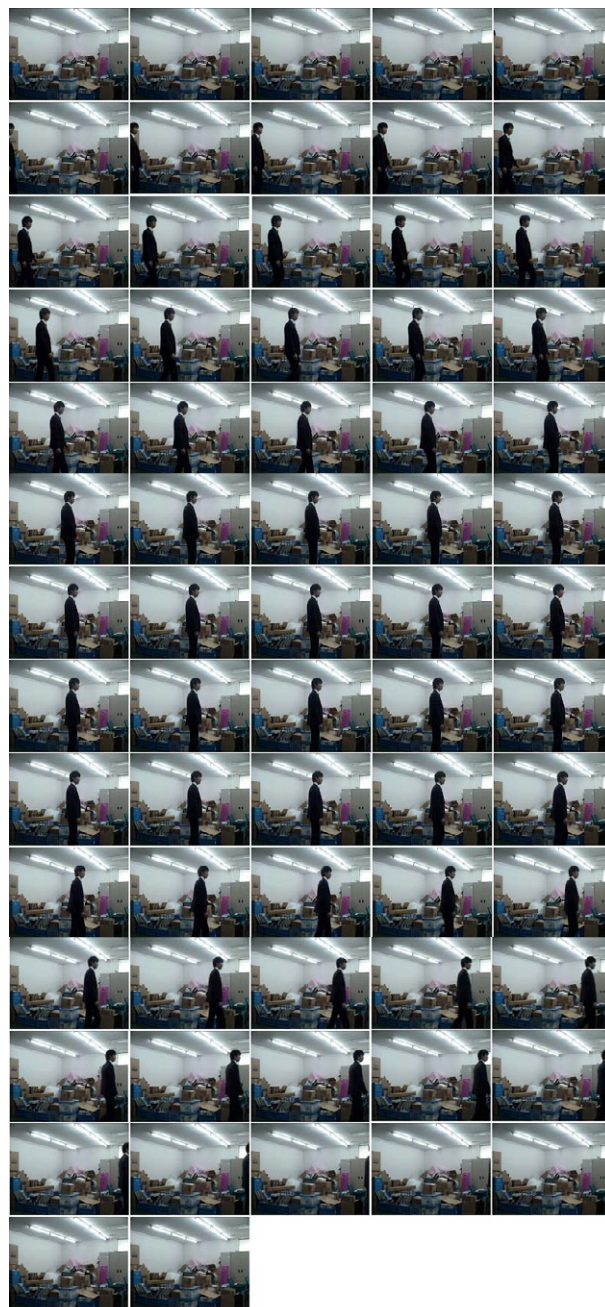


Fig.2. Example of time series images where someone moves in, stops walking, moves again, and moves out at low speed what we call “Slow-In Slow-Out Case”. (Time is counted from the upper left to the lower right.)

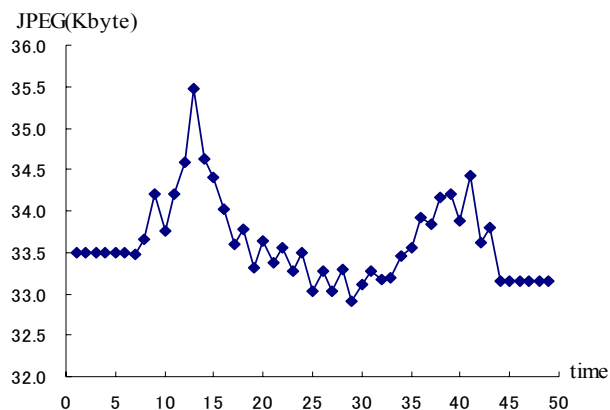


Fig.3. Time series data of JPEG file volumes in Fig.1 (Fast-In Fast-Out Case).

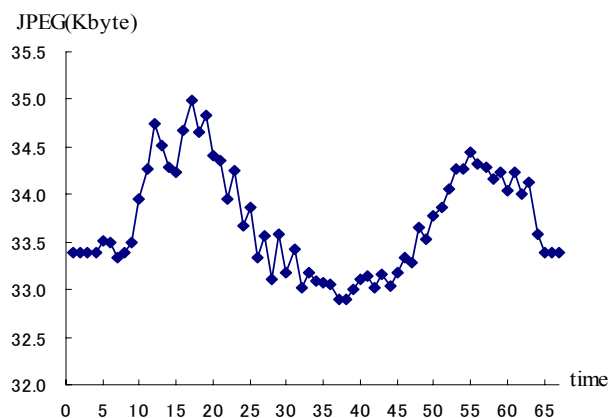


Fig.4. Time series data of JPEG file volumes in Fig.2 (Slow-In Slow-Out Case).

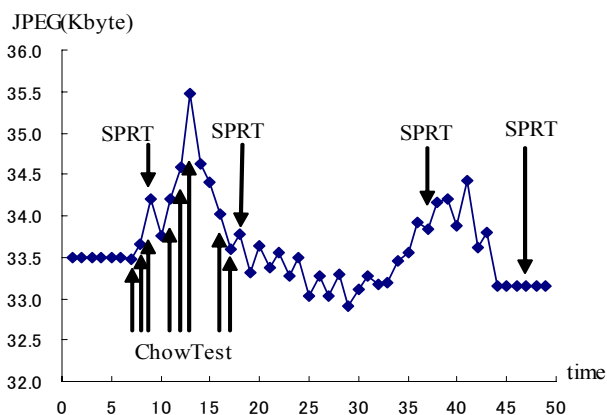


Fig.5. Change detection results by SPRT and Chow Test for the time series data in Fig.3 (Fast-In Fast-Out Case).

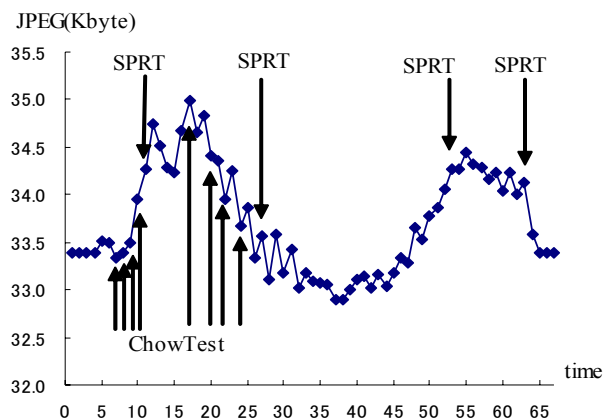


Fig.6. Change detection results by SPRT and Chow Test for the time series data in Fig.4 (Slow-In Slow-Out Case).

IV. CONCLUSION

This paper has proposed the ESPRT method for continuous change detection and have shown its effectiveness by experimental results that the method has detected the four change points in two kinds of time series data, more correctly than Chow Test.

REFERENCES

- [1] Shinichi Masuda, Tetsuo Hattori (2007), Development of a Wireless Remote Monitoring System Utilizing Multiple Wireless Sensors (in Japanese), IEEJ Trans. IA, Vol.127, No.6, pp.610-617.
- [2] A. Wald (1947), Sequential Analysis, John Wiley & Sons.
- [3] Hiromichi Kawano, Tetsuo Hattori, Ken Nishimatsu (2008), Structural Change Point Detection Method of Time Series Using Sequential Probability Ratio Test—Comparison with Chow Test in the ability of early detection— (in Japanese), IEEJ Trans. EIS, Vol.128, No.4, pp.583-592.
- [4] Chow, G.C. (1960), Tests of Equality Between Sets of Coefficients in Two Linear Regressions, Econometrica, Vol.28, No.3, pp.591-605.
- [5] Katsunori Takeda, Tetsuo Hattori, Izumi Tetsuya, Hiromichi Kawano (2010): "Extended SPRT for Structural Change Detection of Time Series Based on Multiple Regression Model", Proceedings of the 15th International Symposium on Artificial Life and Robotics (AROB15th'10), ISBN 978-4-902880-4-4, pp.755-758.
- [6] Katsunori Takeda, Tetsuo Hattori, Izumi Tetsuya, Hiromichi Kawano, Shinichi Masuda (2010): "Application of SPRT to Image Data Sequence for Remote Monitoring System", Proceedings of the 15th International Symposium on Artificial Life and Robotics (AROB 15th'10), ISBN 978-4-9902880-4-4, pp.759-762.

DP method for Structural Change Detection as Optimal Stopping ---- Experimentation in Multiple Regression Model ---

***Hiromichi Kawano, **Tetsuo Hattori, **Katsunori Takeda, ***Tetsuya Izumi**

(*Musashino-shi Nakamachi 19-18, Tokyo 180-0006, Japan

NTT Advanced Technology,

**2217-20 Hayashi-Cho, Takamatsu City, Kagawa 761-0396, Japan

Graduate School of Engineering, Kagawa University,

***Yamagami BLD. 3-12-2 Higashi-ikebukuro, Toshima-ku, Tokyo 170-0013, Japan

Micro Technica Co., Ltd.)

Abstract: If a model begins to fail to prediction of the time series, we have to detect such a structural change (i.e., disparity between the prediction model and the data) quickly and correctly, and to renew the prediction model after the change detection as soon as possible. In this paper, we formulate the structural change detection of time series as an optimal stopping problem, using Dynamic Programming (DP). Moreover, we present experimental results of the change point detection in multiple regression modeled time series data, comparing with SPRT and Chow Test.

Keywords: Time series analysis, Dynamic Programming, sequential probability ratio test (SPRT), Chow Test

I. INTRODUCTION

Structural change detection for ongoing time series data as early and correctly as possible is a very important problem in a practical sense, especially in the field of quality control and management of something that depends on time. For example, early degradation detection of the quality in communication system, manufactures from production lines in a factory, and etc., are such kind of serious problems [1].

We have already proposed an application of Sequential Probabilistic Ratio Test (SPRT). Moreover, we have proposed a Dynamic Programming (DP) method for the case where we have not only to detect the change point, but also to take into account an action cost after the detection. And we have presented the effectiveness of the two methods in comparison with the well-known Chow Test. Our experimentation has been done just by using single regression model [2]. However, multiple regression models are more generally used for time series data analysis than single regression one. And also, the theory of Chow Test is based on the general multiple linear regression itself.

In this paper, we examine how the DP method, SPRT and Chow Test work for the change detection of multiple regression model based data, by experimentation.

II. DP method, SPRT and Chow Test

1. DP method and SPRT

For simplicity, we explain the detection methods using a linear single regression model as shown in Fig.1. The concrete procedure of structural change detection is as follows (see an example of time series data in Fig.1).

Step1: Make a prediction expression and set the tolerance band (a) (e.g. $a=2\sigma$) that means permissible error margin between the predicted data and the observed one.

2.DP method model ([2])

Step2 : While monitoring the coming data, if the data comes into a specified tolerance zone, then we call the situation “in”, or “hitting”, otherwise “out” or “failing”. Based on this monitoring, we can judge that the structure of the time series data has changed, if the failing occurs by continuing N times. This specified tolerance is defined as, e.g., 2σ of the distribution error as shown in the Fig.1.

We assume that the structural change is Poisson occurrence of average, and that, once the change has occurred during the observing period, the structure does not go back to the previous one (Fig.2). The reason why we set such a model is that we focus on the detection of the first structural change in the sequential processing.

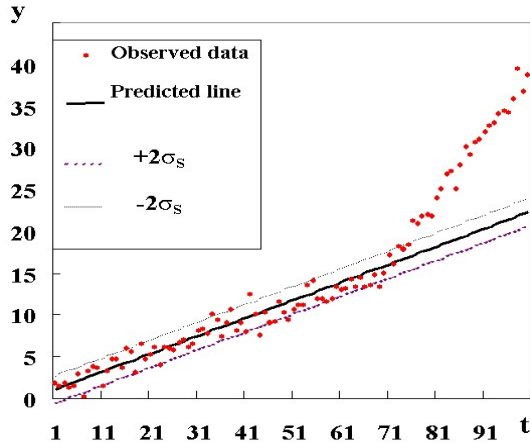
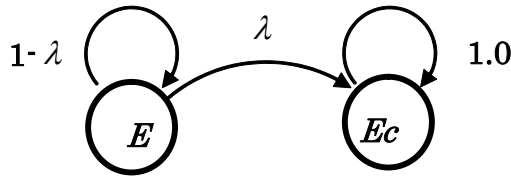
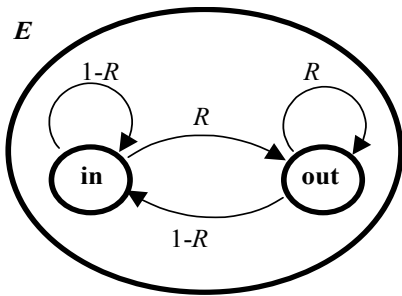


Fig.1. Example of time series data where the change point $t_c^* = 70$.

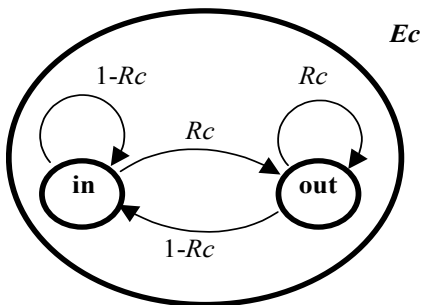


Ec : State that the structural change occurred.
E : State that the structure is unchanged.
 λ : Probability of the structural change occurrence.
(Poisson Process.)

(a) Structural change model



(b) Internal model of the State E.



(c) Internal model of the State Ec.

Fig.2. Structural change model of time series data.

3. Definition of cost function

Let the cost (n) be $a \cdot n$ as a linear function for n , where " a " is the loss caused by the failing in one time. And for simplicity, let T and A denote the Total cost and Action cost. The Action cost means the cost when some action has been taken at the time of structural change detection. Then, the evaluation function is denoted as follows..

$$T = A + a \cdot n$$

We recursively define a function $ET(n, N)$ to obtain the optimum number of times n that minimizes the expectation value of the evaluation function of T , using the concept of DP. Let N be the optimum number. Let the function $ET(n, N)$ be the expectation value of the Total cost at the time when the failing has occurred in continuing n times, where n is less than or equal to N , i.e., $0 \leq n \leq N$.

Then, the function is recursively given as in the following.

$$(n = N) \quad ET(n, N) = A + a \cdot N \quad (1)$$

$$(n < N) \quad ET(n, N) = P(\bar{S}_{n+1} | S^n) \cdot a \cdot n + (1 - P(\bar{S}_{n+1} | S^n)) \cdot ET(n+1, N) \quad (2)$$

where S^n is the state of failing in continuing n times, \bar{S}_{n+1} is the state of hitting for the $(n+1)$ th time observed data, and $P(\bar{S}_{n+1} | S^n)$ is the conditional probability that the state \bar{S}_{n+1} occurs after the state S^n occurred. Then, from the definition of the function $ET(n, N)$, the goal is to find the N that minimizes $ET(0, N)$, because the N is the same as n that minimizes the expectation value (Eq.(2)).

4. Optimal solution

For the aforementioned $ET(0, N)$, the following theorem holds, and gives the n that minimizes the expectation value of the evaluation function of Eq. (2).

Theorem ([2]).

The N that minimizes $ET(0, N)$ is given as the largest number n that satisfies the following Inequality (3).

$$a < (A + a) \cdot P(\bar{S}_n | S^{n-1}) \quad (3)$$

5. Procedure of SPRT ([3])

The concrete procedure of structural change detection is as follows (see Fig.1).

Step2: Set up the null hypothesis H_0 and alternative hypothesis H_1 . H_0 means change has not occurred yet.

H_1 means Change has occurred. Set the values α , β

and compute $C_1 (= \beta / (1 - \alpha))$ and $C_2 (= (1 - \beta) / \alpha)$.

Initialize $i = 0$, $\lambda_0 = 1$.

Step3: Incrementing i ($i = i+1$), observe the following data y_i . Evaluate the error $|\varepsilon_i|$ between the data y_i and the predicted value from the aforementioned prediction expression.

Step4: Judge as to whether the data y_i goes in the tolerance band or not, i.e., the ε_i is less than (or equal to) the permissible error margin or not. If it is Yes, then set $\lambda_i = 1$ and return to Step3. Otherwise, advance to Step5.

Step5: Calculate the probability ratio λ_i , using the following Equation (4).

$$\lambda_i = \lambda_{i-1} \frac{P(\varepsilon_i | H_1)}{P(\varepsilon_i | H_0)} \quad (4)$$

where, if the data y_i goes in the tolerance band, $P(\varepsilon_i | H_0) = \theta_0$ and $P(\varepsilon_i | H_1) = \theta_1$, otherwise, $P(\varepsilon_i | H_0) = (1-\theta_0)$ and $P(\varepsilon_i | H_1) = (1-\theta_1)$.

Step6: Execution of testing.

- (i) If the ratio λ_i is greater than C_2 , dismiss the null hypothesis H_0 , and adopt the alternative hypothesis H_1 , and then End.
- (ii) Otherwise, if the ratio λ_i is less than C_1 , adopt the null hypothesis H_0 , and dismiss the alternative hypothesis H_1 , and then set $\lambda_i = 1$ and return to Step3.
- (iii) Otherwise (in the case where $C_1 \leq \lambda_i \leq C_2$), advance to Step7.

Step7: Observe the following data y_i incrementing i . Evaluate the error $|\varepsilon_i|$ and judge whether the data y_i goes in the tolerance band, or not. Then, return to Step5 (calculation of the ratio λ_i).

6. Chow Test ([3])

The well known Chow Test checks the significant differences among residuals of three Regression Lines, where regression Line 1 obtained from the data before a change point t_c , Line 2 from the data after t_c , and Line 3 from the whole data so far, by setting up hypothesis of change point at each point in the whole data.

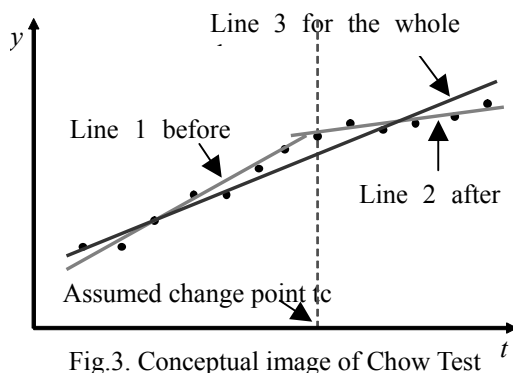


Fig.3. Conceptual image of Chow Test

III. Experimentation

In our experimentation, time series data is generated by the following equations.

$$y = a_{11}x_1 + a_{12}x_2 + b + \varepsilon \quad (t \leq t_c^*) \quad (5)$$

$$y = a_{21}x_1 + a_{22}x_2 + b + \varepsilon \quad (t_c^* \leq t) \quad (6)$$

where $\varepsilon \sim N(0, \sigma^2)$, i.e., the error ε is subject to the Normal Distribution with the average 0 and the variation σ^2 , and t_c^* means the change point. In addition, we have set $t_c^* = 70$.

We have experimented with DP method and Chow Test for the artificial data based on the above equations (5) and (6).

1. Experimental conditions

- (i) Tolerant error: $\pm 2\sigma$ of the distribution on error ε .
- (ii) The concrete values of parameters are shown in Table 1. (Fig.4 shows an example of the graph of generated time series data by the above equations.).
- (iii) Repetition times for making sets of data: $M=100$.
- (iv) Parameters setting for detection:
 - (a) SPRT: parameters are shown in Table 2
 - (b) DP method: $\lambda = 0.01$, $A/a = 10, 20$.
 - (c) Chow Test: significance level ($\alpha=0.05$) for testing.

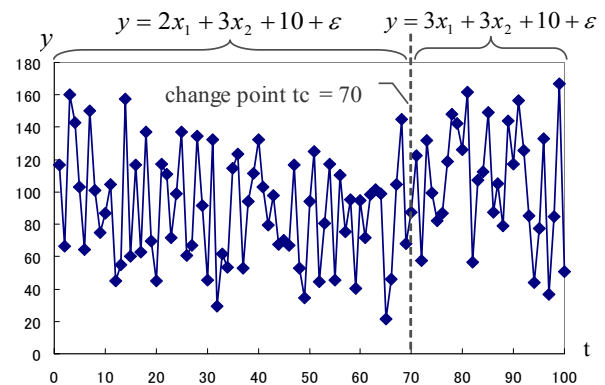


Fig.4. Example of time series data in Data 1.
(True change point: $t=70$.)

Table 1. Equations for generating time series

Data No.	equation (time $t=1,2,\dots,69$)	equation (time $t=70,71,\dots,100$)	σ
1	$y = 2x_1 + 3x_2 + 10$	$y = 3x_1 + 3x_2 + 10$	5
2		$y = 2.5x_1 + 3x_2 + 10$	5
3		$y = 2.5x_1 + 3x_2 + 10$	1

Table 2. Parameter values in SPRT

Case	Data No.	α	β	θ_0	θ_1
1-a	1	0.05	0.05	0.1	0.9
1-b				0.2	0.8
1-c				0.3	0.7
2-a	2	0.05	0.05	0.1	0.9
2-b				0.2	0.8
2-c				0.3	0.7
3-a	3	0.05	0.05	0.1	0.9
3-b				0.2	0.8
3-c				0.3	0.7

2. Results

The results are illustrated in Fig.5, where horizontal axis shows observation time t (observation is started after $t=40$) and vertical axis shows the time when the change point was detected. Those results are based on the average value of 100 times computation. It is expected that the change point will be detected around the time at $t=70$.

We have verified that the two methods (SPRT and OS method) meet our intuition very well as follows.

(i) The graph of Chow test takes continuous value for time t . This means that Chow test detects change at every time when data is observed.

(ii) From Fig.5-Fig.7, even after the enough time passes, Chow test cannot detect change point properly.

(iii) Both of SPRT and DP method can detect a change point more suitably than Chow Test.

(iv) Both of SPRT and DP method have a tendency to detect a change point early when the σ is small. This is because, when the σ becomes smaller, the probability that exceeds the tolerant interval (2σ) becomes larger, i.e., the “failing” easily occurs.

IV. CONCLUSION

We have made a comparison between both of SPRT and DP method and Chow Test using multiple regression modeled time series data. We have found that SPRT and DP method can detect the change point very well for the real time ongoing data. Although the DP method depends on the ratio A/a (A : Action cost, a : loss cost), we can expect that it works well in a practical sense. As further study, we investigate the relation between the parameters of SPRT and OS method.

REFERENCES

- [1] J.Chen and A.K.Gupta (2000), Parametric Statistical Analysis, Birkhauser.
- [2] Hiromichi Kawano, Tetsuo Hattori, Ken Nishimatsu (2004), "Structural Change Detection in Time Series

Based on DP with Action Cost", Proc. of the 2004 IEEE IRI, pp.402-407.

[3] Katsunori Takeda, Tetsuo Hattori, Izumi Tetsuya, Hiromichi Kawano (2010), Extended SPRT for Structural Change Detection of Time Series Based on Multiple Regression Mode, Proc. of AROB15th'10, pp.755-758.

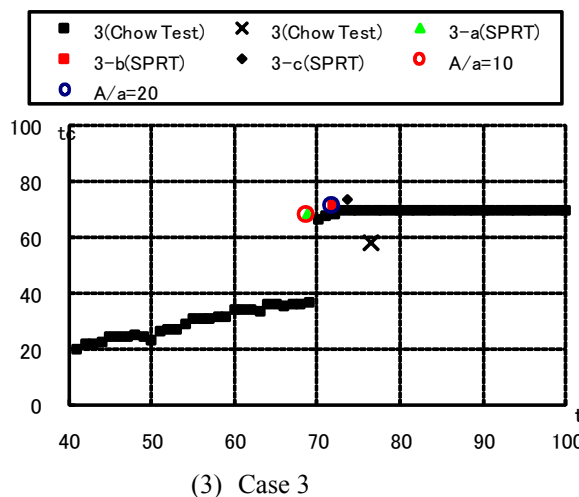
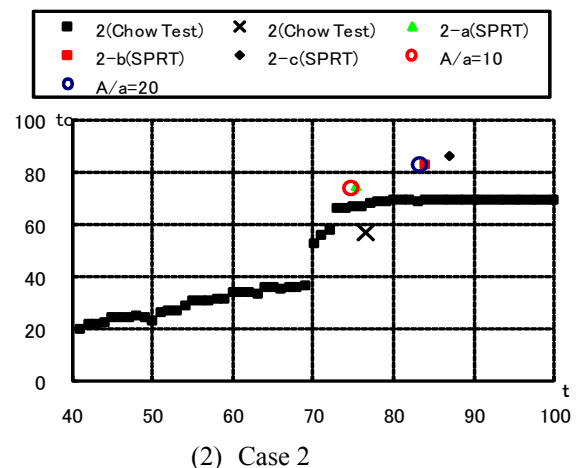
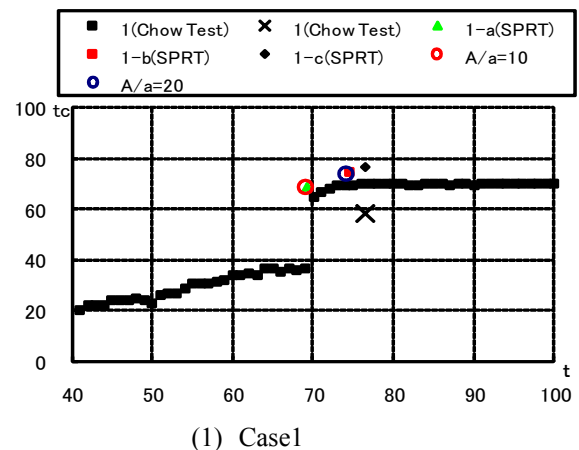


Fig.5. Relation between the observing time t and detected change point t_c .

Comparison of Change Detection Methods for Ongoing Time Series Data

---- Extended SPRT, Chow Test, Extended DP ----

*Hiromichi Kawano, **Tetsuo Hattori, **Katsunori Takeda, ***Tetsuya Izumi

(* NTT Advanced Technology/ Musashino-shi Nakamachi 19-18, Tokyo, Japan

**Kagawa University/ 2217-20 Hayashi-Cho, Takamatsu City, Kagawa, Japan

*** Micro Technica Co., Ltd./ Yamagami BLD. 3-12-2 Higashi-ikebukuro, Toshima-ku, Japan)

(hattori@eng.kagawa-u.ac.jp)

Abstract: For change point detection of time series data, we have already proposed an application of Sequential Probabilistic Ratio Test (SPRT). In addition, we have proposed a Dynamic Programming (DP) method as well, for the case where we have not only to detect the change point, but also to take into account an action cost after the detection. In this paper, we show the effectiveness and differences of the two extended methods (ESPRT and EDP) in comparison with the well-known Chow Test, by experimental results.

Keywords: Time series analysis, Dynamic Programming, sequential probability ratio test (SPRT), Chow Test

I. INTRODUCTION

Change point detection (CPD) problem in time series is to identify whether the generation structure of monitoring data has changed at some time point by some reason, or not. We consider that the problem is very important and that it can be applied to a wide range of application fields. [1].

We have already proposed an application of Sequential Probabilistic Ratio Test (SPRT) and a Dynamic Programming (DP) method for the case where we have not only to detect the change point, but also to take into account an action cost after the detection. And we have presented the effectiveness of the two methods in comparison with the well-known Chow Test by using multiple regression model [2]. We extend the definition of the structural change point in the SPRT method (ESPRT), and show the improvement of the change detection accuracy [2]. In this paper, we extend the definition of the structural change point in the DP method (EDP) and we show the effectiveness and differences of the two extended methods (ESPRT and EDP) in comparison with the well-known Chow Test, by experimental results.

II. DP method, SPRT and Chow Test

1. DP method and SPRT

For simplicity, we explain the detection methods using a linear single regression model as shown in Fig.1.

2. DP method model ([3])

The concrete procedure of structural change detection is as follows (see an example of time series data in Fig.1).

Step1: Make a prediction expression and set the tolerance band (a) (e.g. $a=2\sigma$) that means permissible error margin between the predicted data and the observed one.

Step2 : While monitoring the coming data, if the data comes into a specified tolerance zone, then we call the situation “in”, or “hitting”, otherwise “out” or “failing”. Based on this monitoring, we can judge that the structure of the time series data has changed, if the failing occurs by continuing N times. This specified tolerance is defined as, e.g., 2σ of the distribution error as shown in the Fig.1.

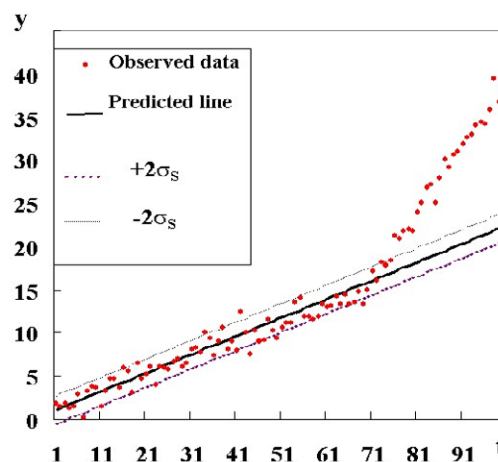


Fig.1. Example of time series data where the change point $t_c^* = 70$.

3. Cost function and optimal solution

Let the cost (n) be $a \cdot n$ as a linear function for n , where " a " is the loss caused by the failing in one time. And for simplicity, let T and A denote the Total cost and Action cost. The Action cost means the cost when some action has been taken at the time of structural change detection. Then, the evaluation function is denoted as follows.

$$T = A + a \cdot n \quad (1)$$

We recursively define a function $ET(n, N)$ to obtain the optimum number of times n that minimizes the expectation value of the evaluation function of T , using the concept of DP. Let N be the optimum number. Let the function $ET(n, N)$ be the expectation value of the Total cost at the time when the failing has occurred in continuing n times, where n is less than or equal to N , i.e., $0 \leq n \leq N$. Then, the function is recursively given as in the following.

$$(n = N) \quad ET(n, N) = A + a \cdot N \quad (2)$$

$$(n < N) \quad ET(n, N) = P(\bar{S}_{n+1} | S^n) \cdot a \cdot n \\ + (1 - P(\bar{S}_{n+1} | S^n)) \cdot ET(n+1, N) \quad (3)$$

where S^n is the state of failing in continuing n times, \bar{S}_{n+1} is the state of hitting for the $(n+1)$ th time observed data, and $P(\bar{S}_{n+1} | S^n)$ is the conditional probability that the state \bar{S}_{n+1} occurs after the state S^n occurred.

For the aforementioned $ET(0, N)$, the following theorem holds, and gives the n that minimizes the expectation value of the evaluation function of Eq. (1).

Theorem ([3]).

The N that minimizes $ET(0, N)$ is given as the largest number n that satisfies the following Inequality (4).

$$a < (A + a) \cdot P(\bar{S}_n | S^{n-1}) \quad (4)$$

4. Procedure of SPRT ([2])

The concrete procedure of structural change detection is as follows (see an example of time series data in Fig.1).

Step2: Set up the null hypothesis H_0 and alternative hypothesis H_1 . H_0 means change has not occurred yet. H_1 means Change has occurred. Set the values α , β and compute $C1 (= \beta/(1-\alpha))$ and $C2 (= (1-\beta)/\alpha)$. Initialize $i = 0$, $\lambda_0 = 1$.

Step3: Incrementing i ($i = i+1$), observe the following data y_i . Evaluate the error $|\varepsilon_i|$ between the data y_i and the predicted value from the aforementioned prediction

expression.

Step4: Judge as to whether the data y_i goes in the tolerance band or not, i.e., the ε_i is less than (or equal to) the permissible error margin or not. If it is Yes, then set $\lambda_i = 1$ and return to Step3. Otherwise, advance to Step5.

Step5: Calculate the probability ratio λ_i , using the following Equation (5).

$$\lambda_i = \lambda_{i-1} \frac{P(\varepsilon_i | H_1)}{P(\varepsilon_i | H_0)} \quad (5)$$

where, if the data y_i goes in the tolerance band,

$P(\varepsilon_i | H_0) = \theta_0$ and $P(\varepsilon_i | H_1) = \theta_1$, otherwise,

$P(\varepsilon_i | H_0) = (1-\theta_0)$ and $P(\varepsilon_i | H_1) = (1-\theta_1)$.

Step6: Execution of testing.

(i) If the ratio λ_i is greater than C_2 , dismiss the null hypothesis H_0 , and adopt the alternative hypothesis H_1 , and then End.

(ii) Otherwise, if the ratio λ_i is less than C_1 , adopt the null hypothesis H_0 , and dismiss the alternative hypothesis H_1 , and then set $\lambda_i = 1$ and return to Step3.

(iii) Otherwise (in the case where $C_1 \leq \lambda_i \leq C_2$), advance to Step7.

Step7: Observe the following data y_i incrementing i .

Evaluate the error $|\varepsilon_i|$ and judge whether the data y_i goes in the tolerance band, or not. Then, return to Step5 (calculation of the ratio λ_i).

5. Chow Test ([2])

The well known Chow Test checks the significant differences among residuals of three Regression Lines, where regression Line 1 obtained from the data before a change point t_c , Line 2 from the data after t_c , and Line 3 from the whole data so far, by setting up hypothesis of change point at each point in the whole data.

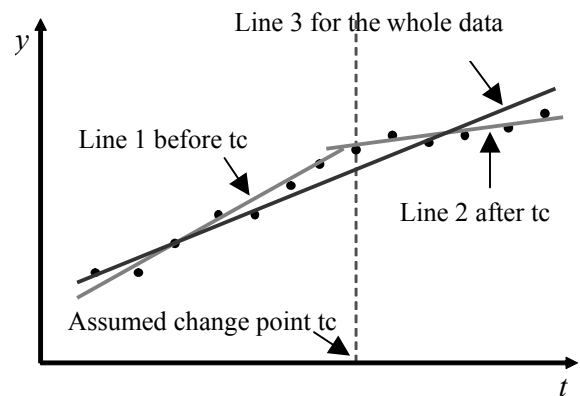


Fig.2. Conceptual image of Chow Test

III. Extended DP and SPRT

1. Extended DP

The DP detects a change point at the time when the expectation value of the evaluation function of Eq. (1) is minimized. Then, the detected change point equals to the terminated time point and its detection tends to be delayed from true change point. Thus in this section, we extend the definition of detected change point by DP method. As such extension, we adopt the number $tc-M$ where tc is ordinary aforementioned change point and M is the number of times when the observed data continuously goes of tolerance zone until the n that minimize the expectation value. M is given by using the posterior probability $P(E_{cn}|S_n)$. According to the Bayes' theorem, the posterior probability $P(E_{cn}|S_n)$ is given by the following (6).

$$P(E_{cn}|S_n) = \frac{P(S_n \cap E_{cn})}{P(S_n \cap E_{cn}) \cup P(S_n \cap E^n)}$$

$$= \frac{\sum_{i=0}^{n-1} (1-\lambda)^i R^i \lambda R_c^{n-i}}{\sum_{i=0}^{n-1} (1-\lambda)^i R^i \lambda R_c^{n-i} + (1-\lambda)^n R^n}$$

$$= \frac{1}{1 + \frac{(1-\lambda)^n R^n}{\sum_{i=0}^{n-1} (1-\lambda)^i R^i \lambda R_c^{n-i}}} = \frac{1}{1 + D(n)} \quad (6)$$

$$\text{where } D(n) = \frac{(1-\lambda)^n R^n}{\sum_{i=0}^{n-1} (1-\lambda)^i R^i \lambda R_c^{n-i}}$$

and λ means the probability of the structural change occurrence and R is the probability of the failing when the structure is unchanged, R_c is the probability of the failing when the structural change occurred.

2. Extended SPRT([2])

The SPRT detects a change point at the time when the probabilistic ratio λ_i is greater than $C_2 (= (1-\beta)/\alpha)$. Then we adopt the number $tc-M$ where tc is ordinary aforementioned change point and M is the number of times when the observed data continuously goes of tolerance zone until the ratio $\lambda_i > C_2$. The number M can be obtained from the equation (7).

$$\left(\frac{\theta_1}{\theta_0} \right)^M > C_2 \left(= \frac{1-\beta}{\alpha} \right) \quad (7)$$

Then we have the equation (7) using Gauss notation. So, the value of M depends on the parameters (Table 2). That is, $M=2$ (case a), $M=3$ (case b), $M=4$ (case c).

$$M = \left\lceil \log_{\frac{\theta_1}{\theta_0}} \frac{1-\beta}{\alpha} \right\rceil$$

IV. Experimentation

In our experimentation, time series data is generated by the following equations.

$$y = a_{11}x_1 + a_{12}x_2 + b + \varepsilon \quad (t \leq t_c^*) \quad (8)$$

$$y = a_{21}x_1 + a_{22}x_2 + b + \varepsilon \quad (t_c^* \leq t) \quad (9)$$

where $\varepsilon \sim N(0, \sigma^2)$, i.e., the error ε is subject to the Normal Distribution with the average 0 and the variation σ^2 , and tc^* means the change point. In addition, we have set $tc^*=70$.

Table 1 Equations for generating time series

Data No.	equation (time $t=1,2,\dots,69$)	equation (time $t=70,71,\dots,100$)	σ
1	$y = 2x_1 + 3x_2 + 10$	$y = 3x_1 + 3x_2 + 10$	5
2		$y = 2.5x_1 + 3x_2 + 10$	5
3		$y = 2.5x_1 + 3x_2 + 10$	1

Table 2 Parameter values in SPRT

Case	Data No.	α	β	θ_0	θ_1
1-a	1	0.05	0.05	0.1	0.9
1-b				0.2	0.8
1-c				0.3	0.7
2-a	2	0.05	0.05	0.1	0.9
2-b				0.2	0.8
2-c				0.3	0.7
3-a	3	0.05	0.05	0.1	0.9
3-b				0.2	0.8
3-c				0.3	0.7

We have experimented with DP method and Chow Test for the artificial data based on the above equations (8) and (9).

1. Experimental conditions

- Tolerant error: $\pm 2\sigma$ of the distribution on error ε .
- The concrete values of parameters are shown in Table 1. (Fig.4 shows an example of the graph of generated time series data by the above equations.).
- Repetition times for making sets of data: $M=100$.
- Parameters setting for detection:
 - SPRT: parameters are shown in Table 2
 - DP method: $\lambda = 0.01$, $A/a = 10, 20$.
 - Chow Test: significance level ($\alpha=0.05$) for testing.

Table 3. Change detection point.

Data No.	method	SPRT			DP		ChowTest
	conditions	$\theta_0=0.1, \theta_1=0.9$	$\theta_0=0.2, \theta_1=0.8$	$\theta_0=0.3, \theta_1=0.7$	A/a=10	A/a=20	
1	Average	69.25	74.50	76.54	68.95	74.14	76.50
	Standard deviation	6.35	4.73	4.97	6.54	4.04	16.02
2	Average	75.39	83.84	86.88	74.59	83.30	76.60
	Standard deviation	11.70	9.22	7.98	11.51	8.71	16.16
3	Average	68.85	71.88	73.53	68.61	71.73	76.50
	Standard deviation	6.02	1.90	1.70	6.27	1.78	16.02

Table 4. Estimated change point.

Data No.	method	SPRT			DP		ChowTest
	conditions	$\theta_0=0.1, \theta_1=0.9$	$\theta_0=0.2, \theta_1=0.8$	$\theta_0=0.3, \theta_1=0.7$	A/a=10	A/a=20	
1	Average	67.62	69.25	69.01	67.95	72.14	58.21
	Standard deviation	6.09	2.42	2.35	6.54	4.04	20.38
2	Average	73.39	77.93	77.35	73.71	81.24	57.09
	Standard deviation	21.24	9.42	8.46	11.42	8.72	20.95
3	Average	67.58	69.21	68.94	67.61	69.37	58.35
	Standard deviation	6.05	2.35	2.29	6.27	5.36	20.38

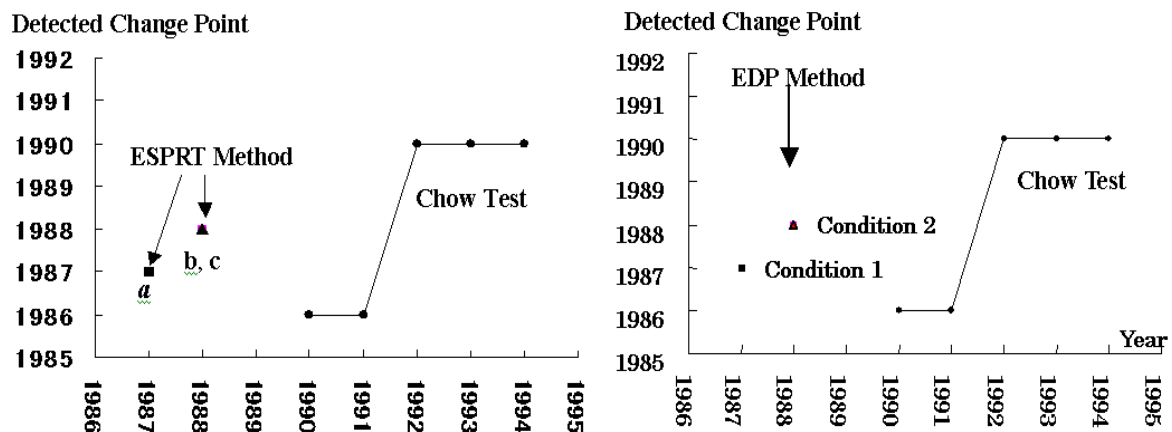


Fig.3.Results for Power supply time series.

2. Results for artificial data

The results are shown in Table 3(Change detection point) and Table 4(estimated change point using ESPRT and EDP). Those results are based on the average value and standard deviation of 100 times computation. It is expected that the change point will be detected around the time at $t=70$.

Applying the extended definition, we obtain the improvement of the change detection accuracy

3. Results for real data

Results for the time series data of power generation quantity in Japan are shown in Fig.3. In 1986 (Condition 1 denotes $A/a=10$, Condition 2 denotes $A/a=20$). The “oil shock” happened in the worldwide and oil prices suddenly rose. We can see that Chow Test correctly detects the change point of 1986, at 1990 and 1991. Until then, it detects no change point. But after 1991, it outputs 1990 as change point. Both of ESPRT and EDP can estimate change point.

IV. CONCLUSION

We have made a comparison between both of ESPRT and EDP method and Chow Test using multiple regression modeled time series data and real data. We have found that ESPRT and EDP method works very well. As further study, we investigate the relation between the parameters of ESPRT and EDP method.

REFERENCES

- [1] J.Chen and A.K.Gupta (2000), Parametric Statistical Analysis, Birkhauser.
- [2] Katsunori Takeda, Tetsuo Hattori, Izumi Tetsuya, Hiromichi Kawano (2010), Extended SPRT for Structural Change Detection of Time Series Based on Multiple Regression Mode, Proc. of AROB 15th '10, pp.755-758.
- [3] Hiromichi Kawano, Tetsuo Hattori, Ken Nishimatsu (2004), "Structural Change Detection in Time Series Based on DP with Action Cost", Proc. of the 2004 IEEE Intern'l Conf. on IRI, pp.402-407.

Outdoor Autonomous Navigation Using SURF Features

M. Tabuse¹, T. Kitaoka² and D. Nakai³

¹*Graduate School of Life and Environmental Science, Kyoto Prefectural University
1-5 Hangi-Cho Shimogamo, Sakyo-ku, Kyoto 606-8522, JAPAN
tabuse@kpu.ac.jp*

²*Department of Informatics and Environmental Science, Kyoto Prefectural University
1-5 Hangi-Cho Shimogamo, Sakyo-ku, Kyoto 606-8522, JAPAN*

³*Kyoto Prefectural Subaru High School
120 Mukaijima-Nishi-joke, Fushimi-ku, Kyoto 612-8156, JAPAN*

Abstract: In this paper, we propose SURF feature based approach for outdoor autonomous navigation. In this approach, we capture environmental images by using omni-directional camera and extract features of these images by using SURF. We treat these features as landmarks and estimate robot self-location and direction of motion. SURF features are invariant under scale change and rotation and robust under image noise, change in light condition and change viewpoint. Therefore, SURF features are appropriate ones for robot self-location estimation and navigation.

Keywords: Mobile robot navigation, SURF feature, Robot self-location, Omni-directional camera

I. INTRODUCTION

Recently, autonomous mobile robots are actively researched. In order to work in the same environment as people, the mobile robot must possess the ability to move everywhere. The most basic function for the mobile robot is to be able to move to the destination autonomously. Therefore, the robot must estimate self-location and direction to the destination.

Many methods of autonomous navigation are proposed. Odometry is used in many mobile robots. However, it has the cumulative error in the movement. It is unsuitable to measure the movement of long distance. Therefore, odometry is used with other sensors, e.g., GPS, visual sensor, laser range finder, gyroscope, etc. GPS is a system that measures the position on the earth by using the space satellite. However, near a high building the position is not always measured accurately by GPS. Another navigation method is view based approach. In view based approach, many images are memorized and self-location estimation is performed by template matching. In general, image data is very large amount of information and calculating cost of template matching is large.

In this paper, we propose SURF feature [1] based approach. In this approach, we capture environmental images by using omni-directional camera and extract features of these images by using SURF. We treat these features as landmarks and estimate robot self-location and direction of motion. SURF features are invariant

under scale change and rotation and robust under image noise, change in light condition and change view point. Furthermore, SURF calculation is several times faster than SIFT [2][3]. Therefore, SURF features are appropriate ones for robot self-location estimation and navigation, because a mobile robot moves around and environmental images are captured from different positions and directions.

II. SYSTEM OVERVIEW

In our research, mobile robot navigation method consists of two mode; teaching mode and navigation mode. Fig.1 shows the flowchart of our method. In the teaching mode, the operator navigates the robot to a destination. The robot memorizes a sequence of environment using an omni-directional camera. In the navigation mode, the robot captures omni-directional environmental image, calculates SURF features in this image. Then the robot compares these features with SURF features of memorized images and estimates self-location and direction of movement.

III. Self-Location Estimation

Firstly, we extract feature points in captured image and in memorized images using SURF. Then we find feature points in each memorized images matching to feature points in capture image. We estimate that a memorized image which has maximum number of matching feature points is neighbor of capture image.

Diagram of self-location estimation is shown in Fig.2. At a starting of navigation, robot doesn't know where it is. Hence, we find matching feature points in all memorized images and estimate self-location. After estimating the self-location, we find matching feature points in the image of self-location estimation and next 3 images.

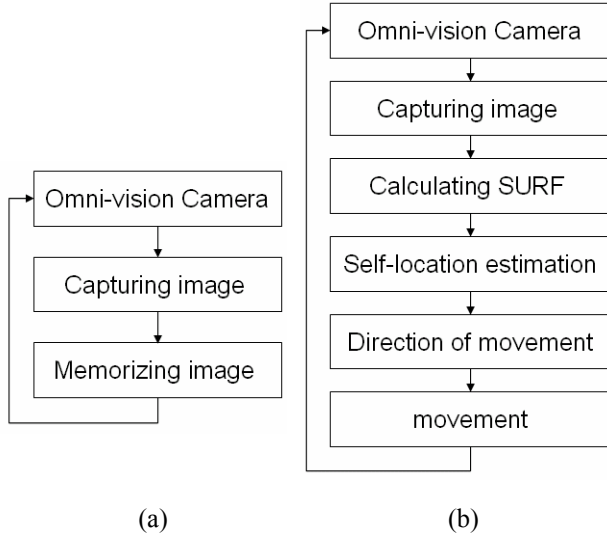


Fig.1. Flowchart of our method. (a) teaching mode. (b) navigation mode.

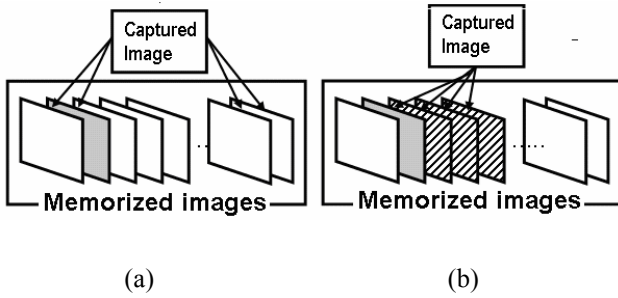


Fig.2. Diagram of self-location estimation. (a) At first time, full searching. (b) After estimating the self-location, searching the image of self-location estimation and next 3 images.

IV. Movement of Mobile Robot

In order to determine movement of mobile robot, we calculate angles of feature points in the neighbor memorized image used in self-location estimation to matching feature points in the next memorized image, and angles of feature points in capture image to matching feature point in the neighbor memorized image. Fig.3 shows feature points in an image and the matching feature points in the next image denoted by circles and movement of feature points denoted by lines. We divide omni-directional image in 4 regions, shown

in Fig.4. In each region, we calculate average angle, (front angle θ_F , back angle θ_B , left angle θ_L , right angle θ_R), respectively. In the case of going forward shown in Fig.3 (a), θ_L and θ_R are large and similar angles. But, θ_F and θ_B are small. On the other hand, in the case of rotation shown in Fig.3 (b), θ_F , θ_B , θ_L and θ_R are similar. Therefore, we define movement angle Θ_M and rotation angle Θ_R as follows:

$$\Theta_M = \frac{\theta_R - \theta_L}{2}, \quad (1)$$

$$\Theta_R = \frac{\theta_F + \theta_B}{2}. \quad (2)$$

We determine movement of mobile robot using the movement angle Θ_M and the rotation angle Θ_R of the neighbor memorized image and the next memorized image and correct the direction of mobile robot using the rotation angle of the capture image and the neighbor image. For more detail, see the next section.

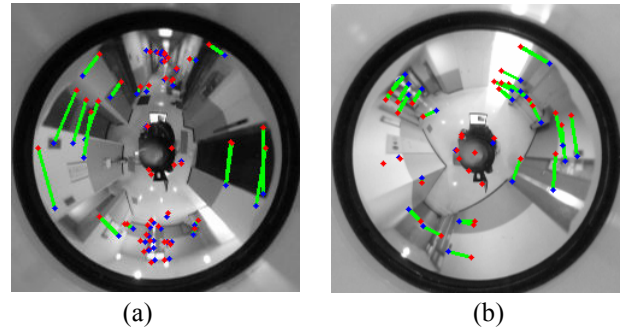


Fig. 3. Movement of feature points. (a) going forward. (b) turning left.

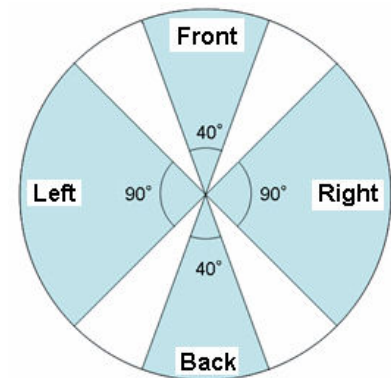


Fig. 4. 4 regions of omni-directional image.

V. Control System

In our experiments, we use an electric wheelchair as a mobile robot. The wheelchair is controlled by joystick controller. The joystick controller has two axes of movement and outputs 2 channel voltages (V_0, V_1). When we move the joystick forward (back), the joystick controller outputs $V_0 = 0$ [V] and $V_1 = 1.85$ [V] ($V_0 = 3.7$ [V] and $V_1 = 1.85$ [V]) and the wheelchair goes forward (back) at maximum speed, respectively. When we move the joystick left (right), the joystick controller outputs $V_0 = 1.85$ [V] and $V_1 = 0$ [V] ($V_0 = 1.85$ [V] and $V_1 = 3.7$ [V]) and the wheelchair turns left (right) at maximum speed, respectively.

Controlling the wheelchair by PC, we setup AD/DA converter in PC. We modify the wire lines connecting from the joystick controller to wheelchair main controller, so that 2 channel outputs of the joystick controller and of PC are switched with a switch (Fig. 5).

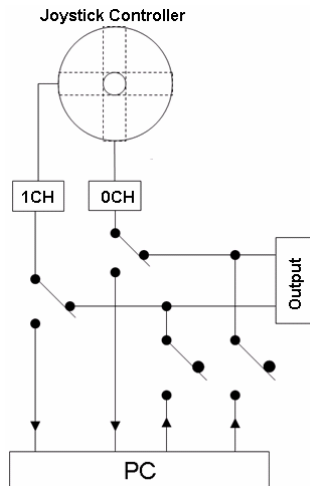


Fig. 5. Control system.

Fig. 6 shows 2 channel outputs while the wheelchair is moved by the joystick controller. In the area 1, two channel outputs (0CH, 1CH) are ($V_0 = 1.85$ [V], $V_1 = 1.85$ [V]) and wheelchair is stopped state. In the area 2, two channel outputs are ($V_0 = 0$ [V], $V_1 = 1.85$ [V]) and wheelchair goes forward at maximum speed. In the area 3, two channel outputs are ($V_0 = 0.25$ [V], $V_1 = 3$ [V]) and wheelchair goes forward while turning right. In the area 4, two channel outputs are ($V_0 = 1.85$ [V], $V_1 = 0$ [V]) and wheelchair turns left.

Therefore, we define 2 channel outputs (V_0, V_1) as follows:

$$V_0 = f(1.85 - \alpha \Theta_M), \quad (3)$$

$$V_1 = f(1.85 + \beta(\Theta_R + \Delta\Theta_R)), \quad (4)$$

where Θ_M , Θ_R and $\Delta\Theta_R$ denote movement angle and rotation angle of feature points in the neighbor memorized image and the next memorized image, and rotation angles of feature points of capture image and the neighbor memorized image, respectively. $\alpha = 0.78$, $\beta = 0.1552$, determined by experiment, and

$$f(x) = \begin{cases} 0.0 & (x < 0.0) \\ x & (0.0 \leq x \leq 3.7) \\ 3.7 & (x > 3.7) \end{cases}$$

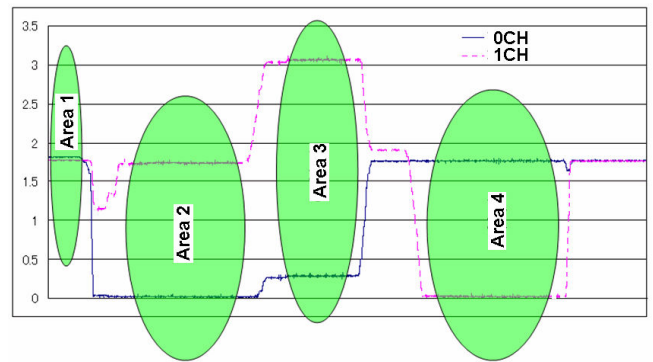


Fig. 6. 2 channel outputs.

VI. EXPERIMENT

1. Mobile Robot

A mobile robot is an electric wheelchair (SUZUKI MC2000). Omni-directional camera is setup at 150cm in height (Fig.7).

Hardware and software of our mobile robot are as follows:

Electric wheelchair : SUZUKI MC2000

Omni-directional camera :

Camera : SONY DCR-HC 88

Omni-directional mirror : Vstone VS-C42N-TR

Note PC : Dell Latitude E6400

(CPU : Core2Duo 2.66GHz, Memory : 2GB

OS : Windows XP)

AD/DA converter : CONTEC AD12-8(PM)

C++ Compiler : Microsoft Visual C++ 6.0

Computer Vision Library : OpenCV 1.1pre



Fig. 7. Mobile robot

2. Teaching mode

In the teaching mode we control the wheelchair using the joystick controller and teach a navigation course. The course is about 150 m outdoor course on the campus of Kyoto Prefectural University, where the wheelchair goes straight from the entrance of the library to the corner, turns to the right and goes straight to the next corner, turns on the left and goes straight to the destination (Fig.8). We memorize 282 omni-directional images in this course.



Fig.8. Navigation course.

3. Navigation mode

In the navigation mode, the mobile robot is moved near the starting point and navigates to the destination autonomously. Fig. 9 shows several captured images in the navigation mode. Trajectories in the teaching and the navigation mode are shown in Fig. 10. The mobile robot navigates along the teaching course adjusting direction of motion. Maximum error of navigation trajectories is 3.3 m. Maximum speed is 4.5 km/h and average speed is 2.9 km/h.

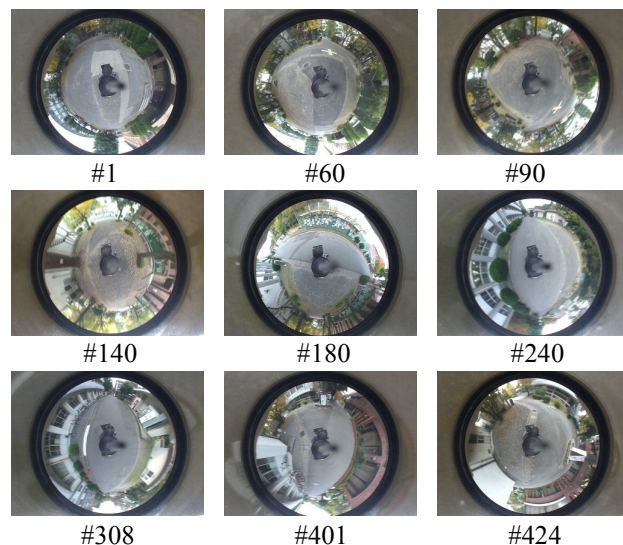


Fig. 9. Capture images in the navigation mode.

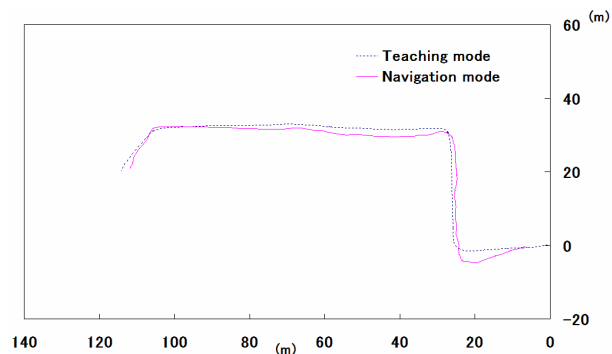


Fig.10. Trajectories in teaching mode and navigation mode.

VII. CONCLUSION

In this paper we present mobile robot navigation using SURF features. The processing time of SURF is several times shorter than that of SIFT. Therefore, the navigation speed of the mobile robot becomes near the person walking speed.

REFERENCES

- [1] H. Bay, A. Ess, T. Tuytelaars, L. van Gool, Speeded-up Robust Features (SURF), Computer Vision and Image Understanding (CVIU), Vol. 110, No.3, 2008, pp. 346-359.
- [2] D. G. Lowe, Object recognition from local scale-invariant features, Proc. of IEEE International Conference on Computer Vision (ICCV), 1999, pp.1150-1157.
- [3] D. G. Lowe, Distinctive image features from scale-invariant keypoints, Proc. of International Journal of Computer Vision (IJCV), Vol. 60, No. 2, 2004, pp. 91-110.

Facial Expression Recognition of a Speaker Using Front-view Face Judgment, Vowel Judgment, and Thermal Image Processing

T. Fujimura¹, Y. Yoshitomi², T. Asada², and M. Tabuse²

¹*Works Applications Co. Ltd., 1-12-32 Akasaka, Minato-ku, Tokyo 107-6019, Japan,*

²*Graduate School of Life and Environmental Sciences Kyoto Prefectural University,
1-5 Nakaragi-cho, Shimogamo, Sakyo-ku, Kyoto 606-8522, Japan,
E-mail: yoshitomi@kpu.ac.jp*

Abstract: For facial expression recognition, we previously selected three images: (i) just before speaking, and speaking (ii) the first vowel and (iii) the last vowel in an utterance. In this study, as a pre-processing module, we added a judgment function to discriminate a front-view face for facial expression recognition. A frame of the front-view face in a dynamic image is selected by estimating the face direction. The judgment function measures four feature parameters using thermal image processing and selects the thermal images that have all the values of the feature parameters within limited ranges decided on the basis of training thermal images of front-view faces. As an initial investigation, we adopted the utterance of the Japanese name “Taro,” which is semantically neutral. The mean judgment accuracy of the front-view face was 99.3% for six subjects who changed their face direction freely. Using the proposed method, the facial expressions of six subjects were discriminable with 87.7% accuracy when he or she exhibited one of the intentional facial expressions of “angry,” “happy,” “neutral,” “sad,” and “surprised.” We expect the proposed method to be applicable for recognizing facial expressions in daily conversation.

Keywords: Facial expression recognition, Front-view face judgment, Speech recognition, Vowel judgment, Thermal image processing

I. INTRODUCTION

To better integrate robots into our society, a robot should be able to interact in a friendly manner with humans. The goal of our research is to develop a robot that can perceive human feelings and mental states.

The first stage is to develop a method for integrating the information of human expression. The basic information for integration is the visible ray (VR) image, thermal image, and voice. In this first stage, an automatic, real-time, interactive system is not necessary. It will be very difficult to equip a robot with a computer which can process the information inputted to it with the efficiency of the human brain. Therefore, we chose to enable the robot to use a type of information, such as thermal imaging, that the human brain cannot process. Thermal imaging is a good example because it is impossible for a human to perceive heat via the naked eye.

The second stage is to develop an automatic, real-time, interactive system that has the information integration of human expression as a processing characteristic. The third stage is to develop a robot that has a function developed from the synthesis of the first and second stages for use in our daily lives.

The present investigation investigates the first stage of development, in which a robot can visually detect

human feelings or inner mental states. Although recognizing facial expressions has received considerable attention in the field of computer vision research, the mechanism of recognition still falls far short of human capability, especially from the viewpoint of robustness under widely varying lighting conditions. One of the reasons is that the nuances of shade, reflection, and local darkness influence the accuracy of facial expression recognition through the inevitable change of gray levels.

To avoid this problem and to develop a robust method for facial expression recognition applicable under widely varied lighting conditions, we did not use a VR image, as would be expected. Instead, we used an image produced by infrared rays (IR), which describe the thermal distribution of the face [1]–[9]. Although a human cannot detect IR, it is possible for a robot to process the information of the thermal images created by IR. Therefore, as a new mode of robot vision, thermal image processing is a practical method that is viable under natural conditions.

The timing of recognizing facial expressions is also important for a robot because the processing might be time-consuming. In a previous report, we adopted an utterance as the key to expressing human feelings or mental states because humans tend to say something when expressing a feeling [5]–[9].

Our reported method [5]–[9] is applicable only to a front-view face. However, in daily conversations, we often change our face direction, and therefore we need to select a frame of the front-view face in a dynamic image. In this paper, we propose a pre-processing module that has a judgment function to discriminate a front-view face. Using the module, a frame of the front-view face in a dynamic image is selected by estimating the face direction. Consequently, by using the proposed function for choosing the front-view face, facial expressions are discriminable even when a person changes his or her face direction freely.

II. IMAGE ACQUISITION

The principle behind thermal image generation is the Stefan–Boltzmann law, expressed as $W = \varepsilon \sigma T^4$, where ε is emissivity, σ is the Stefan–Boltzmann constant ($=5.6705 \times 10^{-12} \text{ W/cm}^2\text{K}^4$), and T is the temperature (K). For human skin, ε is estimated as 0.98 to 0.99 [10], [11]. In this study, the approximate value of 1 was used as ε for human skin because the value of ε for almost all substances is lower than that of human skin [10]. Consequently, the human face region is easily extracted from an image by using the value of 1 for ε when a range of skin temperatures is selected to produce a thermal image [1]–[9], [12]. Fig. 1 shows examples of face images of a male, obtained by VR and IR. We can obtain a thermal image of the face without light, even at night. In principle, the temperature measurement by IR does not depend on skin color [11], darkness, or lighting condition, and so the face region and its characteristics are easily extracted from a thermal image.

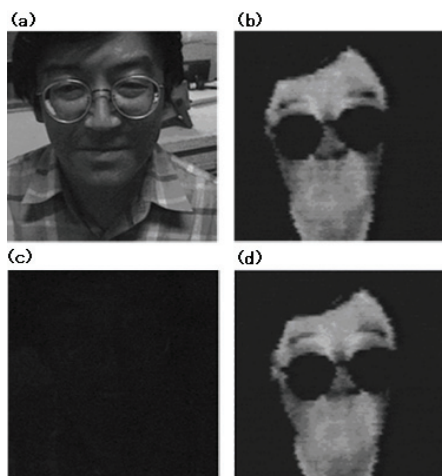


Fig. 1. Examples of a face image at night:
(a) VR with lighting, (b) IR with lighting, (c) VR without lighting, (d) IR without lighting [3]

III. PROPOSED METHOD

In this study, as a pre-processing module, we add a judgment function [12] of a front-view face to our reported method for facial expression recognition.

Fig. 2 illustrates the flow chart of our method. We have two modules in our system. The first is a module for speech recognition and dynamic image analysis, and the second is a module for learning and recognition. In the module for learning and recognition, we embed the module for front-view face judgment. The procedure including the proposed pre-processing module for front-view face judgment is explained in the following.

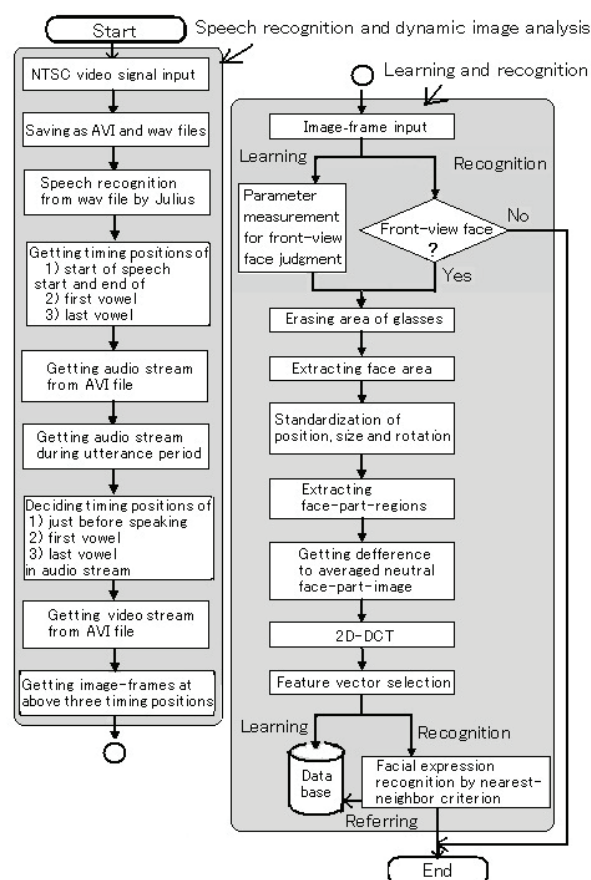


Fig. 2. Flow chart of our method

1. Front-view Face Judgment

We define the face rotation around the X , Y , and Z axes, as demonstrated in Fig. 3. The training data is calculated from the images of a front-view face. After normalizing the horizontal Feret's diameter of the segmented face image, the centerline of the face region in the limited region is drawn as the first standard line. Each pixel point in the centerline has the same number of pixels on both the left and the right sides of the point. Then, a straight line as the second standard line is drawn

from the upper to the lower edgepoints of the centerline. The two standard lines are used to estimate the deviation from the front-view face. To evaluate the face direction, we use four feature parameters (*nod*, *up*, *rotate*, *lean*), explained below.

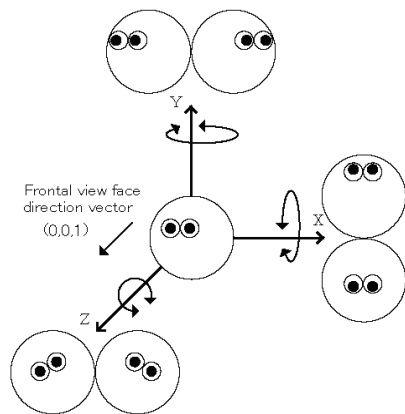


Fig. 3. The three-dimensional coordinate system

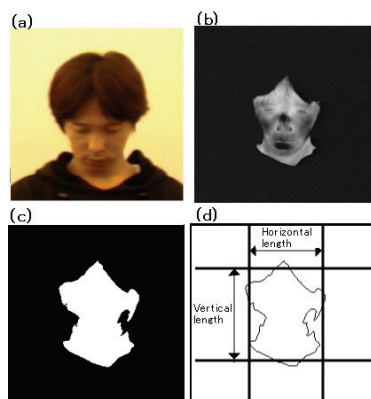


Fig. 4. Downward rotation; (a) visible image, (b) thermal image, (c) binary image, (d) schematic diagram for the parameter *nod*

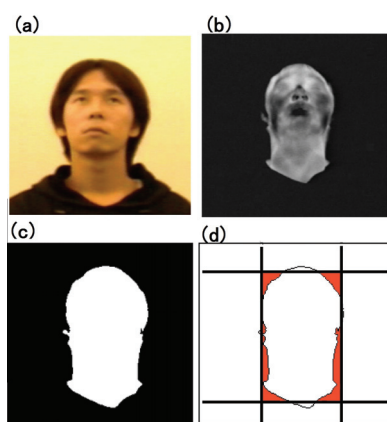


Fig. 5. Upward rotation; (a) visible image, (b) thermal image, (c) binary image, (d) schematic diagram for the parameter *up*

A. Parameter *nod*

The feature parameter *nod* is the value of the vertical Feret's diameter divided by the horizontal Feret's diameter on the segmented face image. This parameter is used to evaluate the downward rotation around the X axis (Fig. 4). Here, to eliminate the influence of the hair style and the throat region on the segmented face image as much as possible, the area having horizontal pixels less than an experimentally decided threshold is ignored in the measurement of the vertical Feret's diameter on the segmented face image, and the area having vertical pixels less than another experimentally decided threshold is also ignored in the measurement of the horizontal Feret's diameter on the segmented face image (Fig. 4). When a subject looks downward, the feature parameter *nod* tends to be smaller than that of the front-view face of the subject.

B. Parameter *up*

The feature parameter *up* is the area ratio of the region having a gray level of "0" in the rectangle defined by the straight lines determined by the measurements of the horizontal and vertical Feret's diameters to the rectangular area on the segmented face image. This parameter is used to evaluate the upward rotation around the X axis (Fig. 5). When a subject looks upward, the feature parameter *up* tends to be smaller than that of the front-view face of the subject.

C. Parameter *rotate*

The feature parameter *rotate* is the area of the region surrounded by the first and the second standard lines, on which are explained in the first paragraph in Section III-1 ("Front-view Face Judgment"). This parameter is used to evaluate the rotation around the Y axis (Fig. 6). Here, to eliminate the influence of the hair style and the throat region on the segmented face image as much as possible, the top and bottom of both the first and second standard lines are set inside the face region by each constant pixel, which is also decided experimentally (Fig. 6). The feature parameter *rotate* tends to increase when the rotation from the front-view face around the Y axis increases.

D. Parameter *lean*

The feature parameter *lean*, which is the angle between the second standard straight line and the horizontal line, is used to estimate the rotation around the Z axis. The value of *lean* is never greater than 90 degrees. The rotation is estimated to be small when the deviation of the value of *lean* from 90 degrees is small.

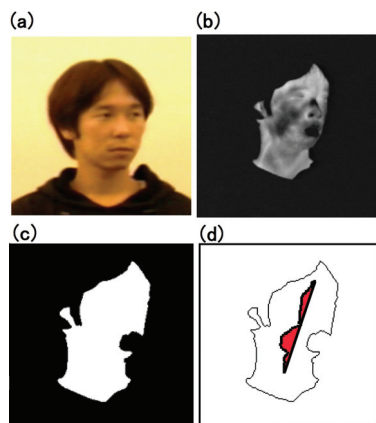


Fig. 6. Images expressing the face rotation around the Y axis; (a) visible image, (b) thermal image, (c) binary image, (d) schematic diagram for the parameter *rotate*

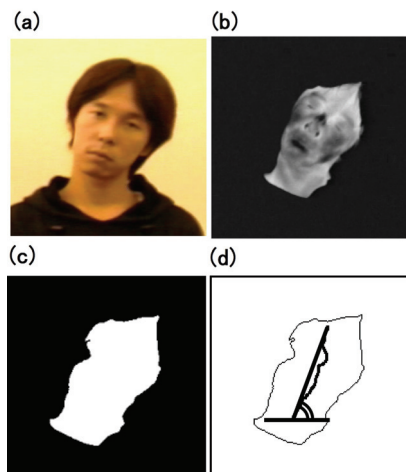


Fig. 7. Images expressing face rotation around the Z axis; (a) visible image, (b) thermal image, (c) binary image, (d) schematic diagram for the parameter *lean*

2. Speech Recognition and Dynamic Image Analysis

We use a speech recognition system named Julius [14] to obtain the timing positions of the start of speech, and the first and last vowels in a WAV file [8], [9]. Fig. 8 shows an example of the waveform of the Japanese name “Taro”; the timing position of the start of speech and the timing ranges of the first vowel (/a/) and the last vowel (/o/) were decided by Julius. By using the timing position of the start of speech and the timing ranges of the first and last vowels obtained from the WAV file, three image frames are extracted from an AVI file at the three timing positions. As the timing position just before speaking, we use the timing position of 84 ms before the start of speech, as determined in our previously reported study [7]. As the timing position of the first vowel, we

use the position where the absolute value of the amplitude of the wave form is the maximum while speaking the vowel. For the timing position of the last vowel, we apply the same procedure used for the first vowel.

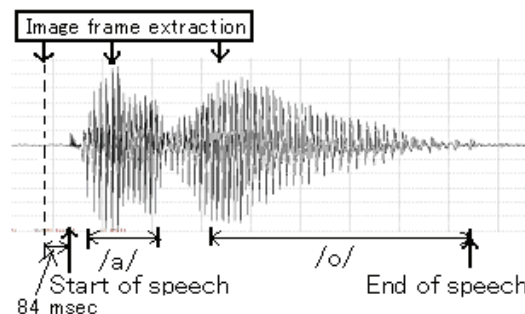


Fig. 8. Speech waveform of “Taro” and timing positions for image frame extraction [8]

3. Learning and Recognition

For the static images obtained from the extracted image frames, the process of erasing the area of the glasses, extracting the face area, and standardizing the position, size, and rotation of the face are performed according to the method described in our previously reported study [7]. In the next step, we generate difference images between the averaged neutral face image and the target face image in the extracted face areas in order to perform a 2D discrete cosine transform (2D-DCT). The feature vector is generated from the 2D-DCT coefficients according to a heuristic rule [6], [7].

As stated above, we use the speech recognition system named Julius. Julius sometimes makes a mistake in recognizing the first and/or last vowel(s). For example, /a/ for the first vowel might be misrecognized as /i/. For the training data, we correct the misrecognition. However, a correction cannot be made on the test data. The facial expression is recognized by the nearest-neighbor criterion in the feature vector space by using the training data just before speaking and just speaking the phonemes of the first and last vowels.

IV. EXPERIMENTS

1. Condition

The thermal image produced by the thermal video system (Nippon Avionics TVS-700) and the sound captured from an Electret condenser microphone (Sony ECM-23F5), amplified by a mixer (Audio-Technica AT-PMX5P), were transformed into a digital signal by an A/D converter (Thomson Canopus ADVC-300) and

input into a computer (DELL Optiplex 760, CPU: Intel Core 2 Duo E7400 2.80 GHz, main memory: 2.0 GB, and OS: Windows XP (Microsoft) with an IEEE1394 interface board (I-O Data Device 1394-PCI3/DV6). We used Visual C++ 6.0 (Microsoft) as the programming language. To generate a thermal image, we applied the condition that the thermal image had 256 gray levels for the range 5 to 12.9 K. Accordingly, one gray level corresponded to 1.95×10^{-2} to 5.04×10^{-2} K. The temperature range for generating a thermal image was decided for each subject in order to easily extract the face area on the image. We saved the visual and audio information in the computer as a Type 2 DV-AVI file, in which the frame had a spatial resolution of 720×480 pixels and 8-bit gray levels and the sound was saved in a PCM format of a stereo type, 48 kHz, and 16-bit levels.

Six subjects exhibited in alphabetic order each of the intentional facial expressions of “angry,” “happy,” “neutral,” “sad,” and “surprised,” while speaking the semantically neutral utterance “Taro.” Fig. 9 shows examples of the thermal image of each subject. Subjects A and B were males with glasses. Subjects C and D were females without glasses. Subject E was a male without glasses. Subject F was a male with a cap. Fig. 10 shows examples of the images of subject A.

In the experiment, all subjects kept intentionally front-view faces in the AVI files saved as the training data, and they freely changed their face direction in the AVI files saved as the test data. We obtained the feature parameter ranges for judging the front-view face with the use of the training data and the proposed method mentioned in Section III-1 (“Front-view Face Judgment”). The range was calculated as $a_i - \sigma_i < x_i < a_i + \sigma_i$ for the *nod*, *up*, and *rotate* parameters of subject A, and $a_i - 2\sigma_i < x_i < a_i + 2\sigma_i$ for the *lean* parameter of subject A and all feature parameters of other subjects, where x_1, x_2, x_3, x_4 were *nod*, *up*, *rotate*, and *lean*, and a_1, a_2, a_3, a_4 were their mean values and $\sigma_1, \sigma_2, \sigma_3, \sigma_4$ were their standard deviation values, respectively. In the case of subject A, the difference of *nod*, *up*, and *rotate* between the front-view and the non-front-view faces was relatively small, and so the feature parameter ranges for judging the front-view face were set to be narrower than those of the other subjects. We assembled twenty samples as training data and ten or less samples as test data, in which all facial expressions of all subjects were judged as front-view faces by the proposed method. The number of test data was decided as a result of the front-view face judgment. From one sample, we obtained

three images at the timing positions of just before speaking and just speaking the phonemes of the first and last vowels. We had the training data of only /a/ for the first vowel and only /o/ for the last vowel. If Julius misrecognized the vowel of the test sample, the corresponding image was not used for facial expression recognition. We had four cases on misrecognition for vowel(s); (1) no misrecognition for the first and last vowels, (2) misrecognition only for the first vowel, (3) misrecognition only for the last vowel, (4) misrecognition for both of the first and last vowels. We prepared feature vectors of the training data in each of the four cases.

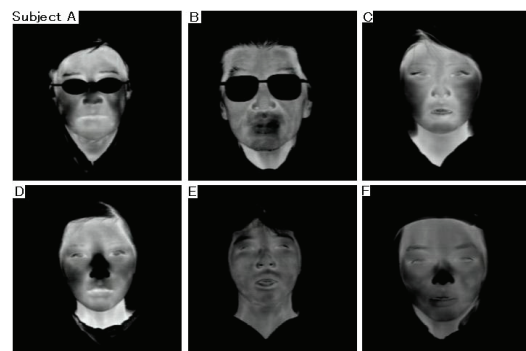


Fig. 9. Examples of thermal images having a neutral facial expression just before speaking

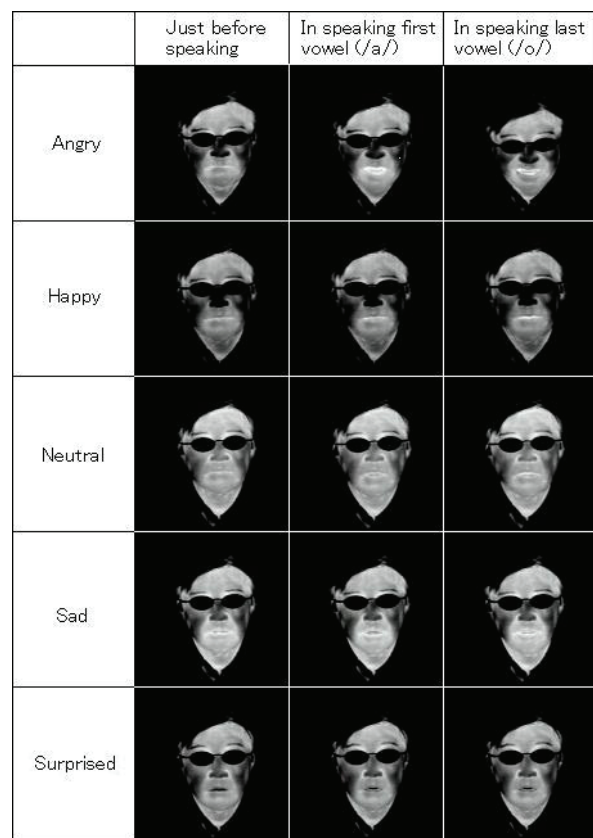


Fig. 10. Examples of thermal images of subject A having each facial expression in speaking

2. Results and Discussion

The mean value of the front-view face judgment accuracy for all subjects was 99.3%. The mean value of the recognition accuracy of vowels decided by Julius for all subjects was 93.6% for the first vowel (/a/) and 88.0% for the last vowel (/o/). Table 1 shows the facial expression recognition accuracy for all subjects. The mean recognition accuracy was 87.7%. The mean recognition accuracy for each subject was 88% for Subject A, 90% for Subject B, 88% for Subject C, 82% for Subject D, 84% for Subject E, and 94% for Subject F. We have applied the present method to a speaker of any utterance to prepare the training data for all combinations of the first and last vowels [15]. We expect the proposed method to be applicable for recognizing facial expressions in daily conversation.

Table 1. Recognition accuracy for all subjects

		Input facial expression				
		Angry	Happy	Neutral	Sad	Surprised
Output	Angry	90	1.7		10	3.3
	Happy	3.3	93.3			1.7
	Neutral			80	3.3	1.7
	Sad	5		5	86.7	5
	Surprised	1.7	5	15		88.3

V. CONCLUSION

We developed a method for facial expression recognition for a speaker by using thermal image processing and a speech recognition system. In this paper, we propose a pre-processing module that has a judgment function for discriminating the front-view face. Using the module, a frame of the front-view face in a dynamic image is selected by estimating the face direction. The mean judgment accuracy of the front-view face was 99.3% for six subjects, who changed their face direction freely. Using the proposed method, five kinds of facial expressions of six subjects were discriminable with 87.7% accuracy when the subject changed his or her face direction freely.

Acknowledgment

We would like to thank all the subjects who cooperated with us in the experiments. This work was supported by KAKENHI(22300077).

REFERENCES

[1] Yoshitomi Y, Kimura S, Hira E, and Tomita S (1996), Facial expression recognition using infrared

rays image processing. Proc. of the Annual Convention IPS Japan, 2:339-340

[2] Yoshitomi Y, Kimura S, Hira E, and Tomita S (1997), Facial expression recognition using thermal image processing. IPSJ SIG Notes, CVIM103-3:17-24

[3] Yoshitomi Y, Miyawaki N, Tomita S, and Kimura S (1997), Facial expression recognition using thermal image processing and neural network. Proc. of 6th IEEE Int. Workshop on Robot and Human Communication 380-385

[4] Sugimoto Y, Yoshitomi Y, and Tomita S (2000), A method for detecting transitions of emotional states using a thermal face image based on a synthesis of facial expressions. J. Robotics and Autonomous Systems 31:147-160

[5] Yoshitomi Y, Kim SIII, Kawano T, and Kitazoe T (2000), Effect of sensor fusion for recognition of emotional states using voice, face image and thermal image of face. Proc. of 6th IEEE Int. Workshop on Robot and Human Interactive Communication 178-183

[6] Ikezoe F, Ko R, Tanijiri T, and Yoshitomi Y (2004), Facial expression recognition for speaker using thermal image processing (in Japanese). Trans. Human Interface Society 6(1):19-27

[7] Nakano M, Ikezoe F, Tabuse M, and Yoshitomi Y (2009), A study on the efficient facial expression using thermal face image in speaking and the influence of individual variations on its performance (in Japanese). J. IEIJ 38(2):156-163

[8] Koda Y, Yoshitomi Y, Nakano M, and Tabuse M (2009), Facial expression recognition for a speaker of a phoneme of vowel using thermal image processing and a speech recognition system. Proc. of 18th IEEE Int. Symp. on Robot and Human Interactive Communication 955-960

[9] Yoshitomi Y (2010), Facial expression recognition for speaker using thermal image processing and speech recognition system. Proc. of 10th WSEAS Int. Conf. on Applied Computer Science 182-186

[10] Kuno H (1994), Infrared rays engineering (in Japanese). Tokyo, IEICE 22

[11] Kuno H (1994), Infrared rays engineering (in Japanese). Tokyo, IEICE 45

[12] Yoshitomi Y, Tsuchiya A, and Tomita S (1998), Face recognition using dynamic thermal image processing. Proc. of 7th IEEE Int. Workshop on Robot and Human Communication 443-448

[13] Yamazaki S, Kamakura H, Tanijiri T, and Yoshitomi Y (2004), Three-dimensional CG expression of face rotation using fuzzy algorithm and thermal face image (in Japanese). Trans. Human Interface Society, 6(3):321-331

[14] <http://julius.sourceforge.jp/>

[15] Yoshitomi Y, Asada T, Shimada K, and Tabuse M (2011), Facial expression recognition of a speaker using vowel judgment and thermal image processing. Proc. of 16th Int. Symp. on Artificial Life and Robotics in press

Facial Expression Recognition of a Speaker Using Vowel Judgment and Thermal Image Processing

Y. Yoshitomi¹, T. Asada¹, K. Shimada², and M. Tabuse¹

¹*Graduate School of Life and Environmental Sciences Kyoto Prefectural University,
1-5 Nakaragi-cho, Shimogamo, Sakyo-ku, Kyoto 606-8522, Japan,
E-mail: yoshitomi@kpu.ac.jp, t_asada@mei.kpu.ac.jp, tabuse@kpu.ac.jp*

²*Nova System Co., Ltd., 3-3-3 Nakanoshima, Kita-ku, Osaka 530-0005, Japan*

Abstract: We previously developed a method for the facial expression recognition of a speaker. For facial expression recognition, we previously selected three images: (i) just before speaking, and speaking (ii) the first vowel and (iii) the last vowel in an utterance. By using the speech recognition system named Julius, thermal static images are saved at the timing positions of just before speaking, and just speaking the phonemes of the first and last vowels. To implement our method, three subjects, who spoke 25 Japanese first names providing all combinations of the first and last vowels, were used to prepare first the training data and then the test data. Julius sometimes makes a mistake in recognizing the first and/or last vowel(s). For example, /a/ for the first vowel is sometimes misrecognized as /i/. In the training data, we correct this misrecognition. However, the correction cannot be performed in the test data. In the implementation of our method, the facial expressions of three subjects were discriminable with the mean accuracy of 80.1% when the subjects exhibited one of the intentional facial expressions of “angry,” “happy,” “neutral,” “sad,” and “surprised,” and the mean accuracy of the speech recognition of vowels by Julius was 71.0%.

Keywords: Facial expression recognition, Speech recognition, Vowel judgment, Thermal image processing

I. INTRODUCTION

To better integrate robots into our society, a robot should be able to interact in a friendly manner with humans. The goal of this research is to develop a robot that can perceive human feelings and mental states. For example, a robot could encourage a person who looks sad, advise an individual to stop working and rest when he or she looks tired, or take care of an elderly person.

The present investigation concerns the first stage of the development of a robot that has the ability to detect visually human feeling or inner mental states. Although the mechanism for recognizing facial expressions has received considerable attention in the field of computer vision research [1]–[6], at the present stage, it still falls far short of human capability, especially from the viewpoint of robustness under widely varying lighting conditions. One of the reasons for this is that nuances of shade, reflection, and local darkness influence the accuracy of facial expression recognition through the inevitable change of gray levels.

To develop a robust method for facial expression recognition applicable under widely varied lighting conditions, we do not use a visible ray (VR) image. Instead, we used an image produced by infrared rays

(IR), which show the thermal distribution of the face [7]–[16]. Although a human cannot detect IR, it is possible for a robot to process the information in the thermal images created by IR. Therefore, as a new mode of robot vision, thermal image processing is a practical method that is viable under natural conditions.

In addition, the timing of recognizing facial expressions is important for a robot because the processing can be time-consuming. We adopted an utterance as the key to expressing human feelings or mental states because humans tend to say something to express feeling [11]–[16].

In this paper, we briefly introduce our method [14] for the facial expression recognition of a speaker. For facial expression recognition, we select three images: (i) just before speaking, and speaking (ii) the first vowel and (iii) the last vowel in an utterance. A frame of the front-view face in a dynamic image is selected by estimating the face direction [16]. To apply our method [14], three subjects, who spoke 25 Japanese first names providing all combinations of the first and last vowels, were used to prepare first the training data and then the test data.

II. IMAGE ACQUISITION

The principle behind thermal image generation is the Stefan-Boltzmann law, expressed as $W = \varepsilon \sigma T^4$, where ε is emissivity, σ is the Stefan-Boltzmann constant ($=5.6705 \times 10^{-12} \text{ W/cm}^2\text{K}^4$), and T is the temperature (K). For human skin, ε is estimated as 0.98 to 0.99 [17], [18]. In this study, the approximate value of 1 was used as ε for human skin because the value of ε for almost all substances is lower than that of human skin [17]. Consequently, the human face region is easily extracted from an image by using the value of 1 for ε when a range of skin temperatures is selected to produce a thermal image [7]–[16], [19]. Fig. 1 shows examples of face images obtained by VR and IR of a male. Thermal images of a face can be obtained without light, that is, even at night. In principle, the temperature measurement by IR does not depend on skin color [18], darkness, or lighting condition, and so the face region and its characteristics are easily extracted from a thermal image.

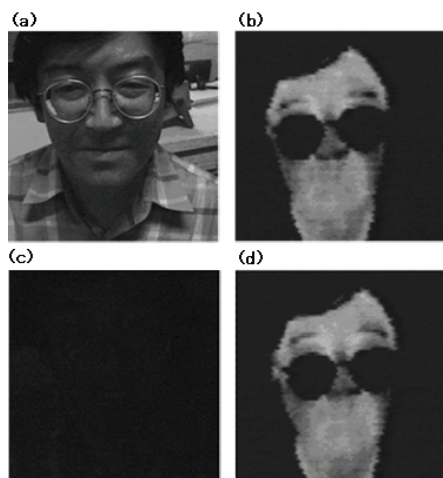


Fig. 1. Examples of a face image at night: (a) VR with lighting, (b) IR with lighting, (c) VR without lighting, (d) IR without lighting [9]

III. PROPOSED METHOD

As a pre-processing module, we added a judgment function [19] of a front-view face to our method [14] for facial expression recognition [16]. Therefore, we can choose a front-view face as the target for recognizing facial expressions in daily conversation.

Fig. 2 illustrates the flow chart of our method. We have two modules in our system. The first is a module for speech recognition and dynamic image analysis, and the second is a module for learning and recognition. In

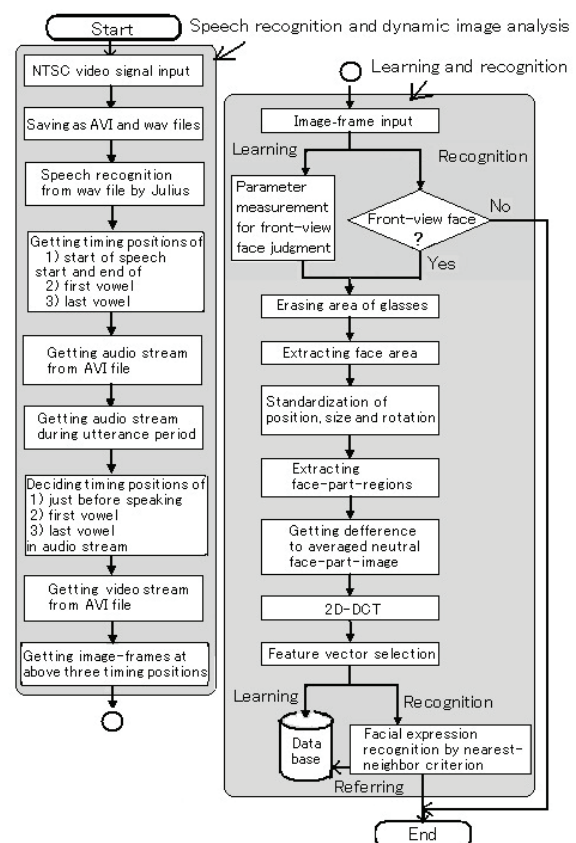


Fig. 2. Flow chart of our method [16]

the module for learning and recognition, we embedded the module for front-view face judgment. The procedure, except the pre-processing module for front-view face judgment [16], is explained in the following.

1. Speech Recognition and Dynamic Image Analysis

We use a speech recognition system named Julius [20] to save the timing positions of the start of speech, and the first and last vowels in a WAV file [14]–[16]. Fig. 3 shows an example of the waveform of the Japanese first name “Taro”; the timing position of the start of speech and the timing ranges of the first vowel (/a/) and the last vowel (/o/) were decided by Julius. By using these three timing positions obtained from the WAV file, three thermal image frames are extracted from an AVI file. As the timing position just before speaking, we use 84 ms before the start of speech, as determined in our previously reported study [13]. As the timing position of the first vowel, we use the position where the absolute value of the amplitude of the waveform is the maximum while speaking the vowel. For the timing position of the last vowel, we apply the same procedure used for the first vowel.

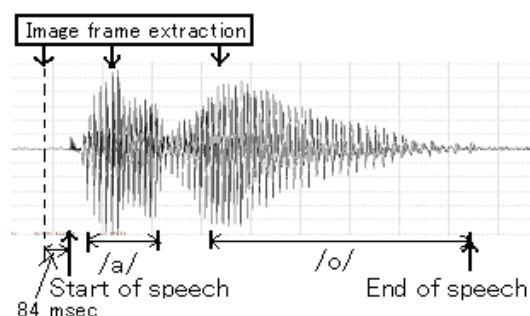


Fig. 3. Speech waveform of “Taro” and timing positions for image frame extraction [14]

2. Learning and Recognition

For the static thermal images obtained from the extracted image frames, the process of erasing the area of the glasses, extracting the face area, and standardizing the position, size, and rotation of the face are performed according to the method described in our previously reported study [13]. Fig. 4 shows the blocks for extracting the face areas in a thermal image having 720×480 pixels. In the next step, we generate difference images between the averaged neutral face image and the target face image in the extracted face areas in order to perform a 2D discrete cosine transform (2D-DCT). The feature vector is generated from the 2D-DCT coefficients according to a heuristic rule [12], [13].

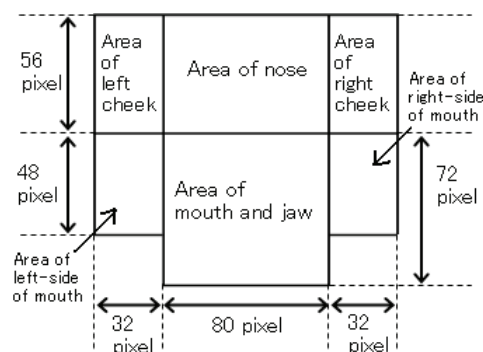


Fig. 4. Blocks for extracting face areas in the thermal image [14]

As stated above, we use the speech recognition system named Julius, which sometimes makes a mistake in recognizing the first and/or last vowel(s). For example, /a/ for the first vowel is sometimes misrecognized as /i/. For the training data, we correct the misrecognition. However, a correction cannot be made on the test data. For example, when Julius correctly judges the first vowel at the utterance of “Taro” but misjudges the last vowel as /a/, the training data in speaking “Ayaka” are used for recognition instead of those for speaking “Taro.” The facial

expression is recognized by the nearest-neighbor criterion in the feature vector space by using the training data just before speaking and while speaking the phonemes of the first and last vowels.

IV. EXPERIMENTS

1. Condition

The thermal image produced by the thermal video system (Nippon Avionics TVS-700) and the sound captured from an Electret condenser microphone (Sony ECM-23F5), amplified by a mixer (Audio-Technica AT-PMX5P), were transformed into a digital signal by an A/D converter (Thomson Canopus ADVC-300) and input into a computer (DELL Optiplex GX620, CPU: Pentium IV 3.4 GHz, main memory: 2.0 GB, and OS: Windows XP (Microsoft)) with an IEEE1394 interface board (I-O Data Device 1394-PCI3/DV6). We used Visual C++ 6.0 (Microsoft) as the programming language. To generate a thermal image, we applied the condition that the thermal image had 256 gray levels for the detected temperature range. This range was decided independently for each subject in order to best extract the face area. We saved the visual and audio information in the computer as a Type 2 DV-AVI file, in which a frame had a spatial resolution of 720×480 pixels and 8-bit gray levels, and the sound was saved in a PCM format of stereo type, 48 kHz, and 16-bit levels.

All subjects exhibited in alphabetic order each of the intentional facial expressions of “angry,” “happy,” “neutral,” “sad,” and “surprised,” while speaking the semantically neutral utterance of each of the Japanese first names listed in Table 1. Fig. 5 shows examples of the thermal image of each subject. There were three subjects. Subject A was a male without glasses. Subject B was a male with glasses. Subject C was a female without glasses. Fig. 6 shows examples of the images of Subject A.

Table 1. Japanese first names used in the experiment

		First vowel				
		a	i	u	e	o
Last vowel	a	ayaka	shinnya	tsubasa	keita	tomoya
	i	kazuki	hikari	yuki	megumi	koji
	u	takeru	shigeru	fuyu	megu	noboru
	e	kaede	misae	yusuke	keisuke	kozue
	o	taro	hiroko	yuto	keiko	tomoko

In the experiment, all subjects kept intentionally front-view faces in the AVI files saved as both the training and test data. Accordingly, the pre-processing

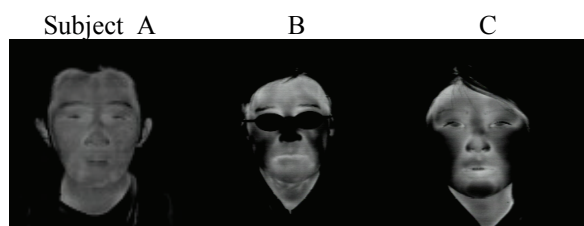


Fig. 5. Examples of thermal images having a neutral facial expression just before speaking “Ayaka”

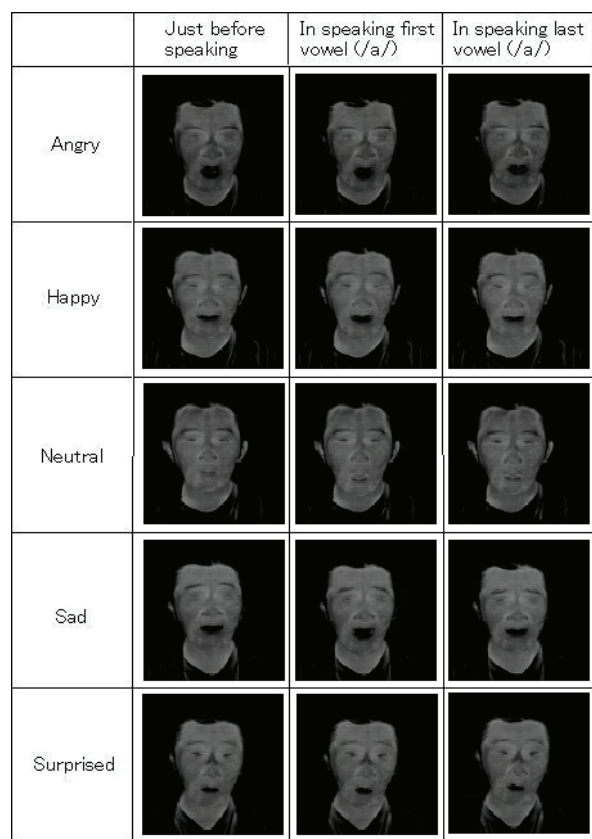


Fig. 6. Examples of thermal images of Subject A having each facial expression in speaking “Ayaka”

module for judging the front-view face [16] was not used in the experiment. We assembled 20 samples as training data and 10 samples as test data. From one sample, we obtained three images at the timing positions of just before speaking and just speaking the phonemes of the first and last vowels. We obtained training data for all combinations of vowel type of the first and last vowels.

2. Results and Discussion

The mean value of the recognition accuracy for the first vowels and last vowels of all subjects was 71.0%. The mean value of the recognition accuracy for the first vowels and last vowels was 84% for Subject A, 70% for Subject B, and 59% for Subject C. Table 2 shows the recognition accuracy for the first and last vowels of

Table 2. Accuracy (%) of speech recognition for Subject A

First-last vowel	Angry	Happy	Neutral	Sad	Surprised	Mean
a-a	56	70	80	90	0	59
a-i	90	100	100	90	90	94
a-u	80	40	100	100	80	80
a-e	20	20	30	70	100	48
a-o	100	80	100	100	100	96
i-a	100	100	100	100	70	94
i-i	90	90	100	100	80	92
i-u	90	90	90	100	90	92
i-e	40	90	100	88	0	64
i-o	100	100	90	60	100	90
u-a	90	100	50	100	40	76
u-i	90	100	40	10	100	68
u-u	100	100	90	100	100	98
u-e	100	100	100	100	100	100
u-o	100	100	90	100	100	98
e-a	63	50	60	40	0	43
e-i	100	100	100	100	100	100
e-u	40	60	100	100	90	78
e-e	22	90	80	90	50	66
e-o	90	100	100	100	100	98
o-a	100	90	100	100	50	88
o-i	100	100	100	100	100	100
o-u	100	100	100	100	70	94
o-e	90	100	100	100	80	94
o-o	100	100	100	100	100	100
Mean	82	87	88	90	76	84

Table 3. Accuracy (%) of facial expression recognition

Subject A		Input facial expression				
		Angry	Happy	Neutral	Sad	Surprised
Output	Angry	90.8	0.4	0.0	4.8	3.6
	Happy	2.8	94.8	2.4	4.4	8.0
	Neutral	0.0	0.0	94	0.0	0.0
	Sad	3.2	3.2	0.8	79.2	15.2
	Surprised	1.6	1.6	2.8	11.6	73.2

Subject B		Input facial expression				
		Angry	Happy	Neutral	Sad	Surprised
Output	Angry	64.1	5.2	5.2	6.7	9.4
	Happy	10.8	77.6	0.8	6.9	12.6
	Neutral	0.0	3.6	83.6	0.4	0.0
	Sad	7.2	7.6	2.0	78	10.9
	Surprised	17.9	6	8.4	8	67.3

Subject C		Input facial expression				
		Angry	Happy	Neutral	Sad	Surprised
Output	Angry	78.8	4.4	7.2	5.2	0.8
	Happy	2.4	77.1	3.6	2.4	0.0
	Neutral	10.8	2.0	71.9	3.2	2.0
	Sad	2.8	11.3	12.9	78.8	5.2
	Surprised	5.2	5.2	4.4	10.4	92

Table 4. Accuracy (%) of facial expression recognition of Subject A

First-last vowel	Angry	Happy	Neutral	Sad	Surprised	Mean
a-a	100	100	100	100	0	80.0
a-i	100	100	70	100	90	92.0
a-u	90	100	100	100	90	96.0
a-e	100	100	100	100	100	100.0
a-o	100	100	100	60	90	90.0
i-a	60	80	100	60	60	72.0
i-i	100	100	70	100	100	94.0
i-u	100	100	100	100	40	88.0
i-e	90	100	100	90	90	94.0
i-o	90	100	90	90	100	94.0
u-a	90	100	60	40	70	72.0
u-i	100	100	100	0	100	80.0
u-u	100	100	90	90	100	96.0
u-e	100	100	100	100	100	100.0
u-o	100	100	90	100	90	96.0
e-a	100	80	100	50	10	68.0
e-i	80	100	100	70	100	90.0
e-u	100	80	100	90	100	94.0
e-e	100	90	80	80	0	70.0
e-o	10	100	100	50	30	58.0
o-a	100	60	100	100	10	74.0
o-i	100	90	100	90	100	96.0
o-u	100	100	100	30	90	84.0
o-e	90	100	100	90	90	94.0
o-o	70	90	100	100	80	88.0
Mean	90.8	94.8	94.0	79.2	73.2	86.4

Subject A. Table 3 shows the facial expression recognition accuracy as mean values over all combinations of first and last vowels. The mean recognition accuracy of the facial expressions of all subjects was 80.1%. The mean recognition accuracy of the facial expressions was 86.4% for Subject A, 74.1% for Subject B, and 79.7% for Subject C. Tables 4 to 6 show all the values of the recognition accuracy of the facial expressions of each subject. We have not yet found a relationship between the recognition accuracy of vowels and the recognition accuracy of facial expressions. As a continuation of our work, we will apply our method for facial expression recognition by using other subjects.

V. CONCLUSION

We previously developed a method for facial expression recognition for a speaker by using thermal

Table 5. Accuracy (%) of facial expression recognition of Subject B

First-last vowel	Angry	Happy	Neutral	Sad	Surprised	Mean
a-a	10	70	10	90	90	54.0
a-i	50	50	100	40	44	56.8
a-u	80	90	100	89	89	89.6
a-e	22	100	100	78	80	76.0
a-o	30	100	100	60	50	68.0
i-a	100	30	90	70	80	74.0
i-i	40	80	100	90	10	64.0
i-u	70	100	100	100	100	94.0
i-e	90	100	90	90	78	89.6
i-o	60	100	100	90	80	86.0
u-a	60	10	70	90	30	52.0
u-i	0	90	90	40	70	58.0
u-u	100	40	40	90	70	68.0
u-e	100	100	100	83	100	96.6
u-o	80	40	100	80	90	78.0
e-a	90	90	90	90	90	90.0
e-i	90	90	100	90	0	74.0
e-u	10	80	100	90	20	60.0
e-e	100	100	10	100	70	76.0
e-o	90	100	100	100	80	94.0
o-a	50	90	100	70	90	80.0
o-i	50	60	100	10	50	54.0
o-u	50	80	100	80	80	78.0
o-e	80	90	0	100	70	68.0
o-o	100	60	100	40	70	74.0
Mean	64.1	77.6	83.6	78.0	67.2	74.1

image processing and a speech recognition system. To implement our method, three subjects spoke 25 Japanese first names, which provided all combinations of the first and last vowels. These subjects were used to prepare first the training data and then the test data for all combinations of the first and last vowels. The mean accuracy of the recognition of vowels by Julius was 71.0% for all subjects. Using our method, the facial expressions of three subjects were discriminable with 80.1% accuracy when he or she exhibited one of the intentional facial expressions of “angry,” “happy,” “neutral,” “sad,” and “surprised.” We expect our method to be applicable for recognizing facial expressions in daily conversation.

Acknowledgment

We would like to thank all the subjects who cooperated with us in the experiments. This work was supported by KAKENHI (22300077).

Table 6. Accuracy (%) of facial expression recognition of Subject C

First-last vowel	Angry	Happy	Neutral	Sad	Surprised	Mean
a-a	100	67	30	40	80	63.4
a-i	80	50	100	30	60	64.0
a-u	70	100	80	70	100	84.0
a-e	60	70	10	60	60	52.0
a-o	100	50	78	60	100	77.6
i-a	80	100	100	100	90	94.0
i-i	80	100	100	60	90	86.0
i-u	40	70	90	60	60	64.0
i-e	70	40	70	30	100	62.0
i-o	60	80	90	80	90	80.0
u-a	80	100	90	90	90	90.0
u-i	90	10	50	90	100	68.0
u-u	60	90	90	100	100	88.0
u-e	80	100	100	80	100	92.0
u-o	90	10	10	90	100	60.0
e-a	100	100	70	80	100	90.0
e-i	90	100	100	100	100	98.0
e-u	100	80	40	60	100	76.0
e-e	90	100	100	100	100	98.0
e-o	90	100	30	100	100	84.0
o-a	40	80	80	100	100	80.0
o-i	90	60	80	90	80	80.0
o-u	70	90	20	100	100	76.0
o-e	90	100	100	100	100	98.0
o-o	70	80	90	100	100	88.0
Mean	78.8	77.1	71.9	78.8	92.0	79.7

REFERENCES

- [1] Yuille AL, Cohen DS, and Hallinan PW (1989), Feature extraction from faces using deformable templates. Proc. of IEEE Conf. on Computer Vision and Pattern Recognition 104-109
- [2] Harashima H, Choi CS, and Takebe T (1989), 3-D model-based synthesis of facial expressions and shape deformation (in Japanese). Human Interface 4:157-166
- [3] Mase K (1990), An application of optical flow – extraction of facial expression. IAPR Workshop on Machine Vision and Application 195-198
- [4] Mase K (1991), Recognition of facial expression from optical flow. Trans. IEICE E74(10):3474-3483
- [5] Matsuno K, Lee C, and Tsuji S (1994), Recognition of facial expressions using potential net and KL expansion (in Japanese). Trans. IEICE J77-D-II(8):1591-1600
- [6] Kobayashi H and Hara F (1994), Analysis of neural network recognition characteristics of 6 basic facial expressions. Proc. of 3rd IEEE Int. Workshop on Robot and Human Communication 222-227
- [7] Yoshitomi Y, Kimura S, Hira E, and Tomita S (1996), Facial expression recognition using infrared rays image processing. Proc. of the Annual Convention IPS Japan, 2:339-340
- [8] Yoshitomi Y, Kimura S, Hira E, and Tomita S (1997), Facial expression recognition using thermal image processing. IPSJ SIG Notes, CVIM103-3:17-24
- [9] Yoshitomi Y, Miyawaki N, Tomita S, and Kimura S (1997), Facial expression recognition using thermal image processing and neural network. Proc. of 6th IEEE Int. Workshop on Robot and Human Communication 380-385
- [10] Sugimoto Y, Yoshitomi Y, and Tomita S (2000), A method for detecting transitions of emotional states using a thermal face image based on a synthesis of facial expressions. J. Robotics and Autonomous Systems 31:147-160
- [11] Yoshitomi Y, Kim SIII, Kawano T, and Kitazoe T (2000), Effect of sensor fusion for recognition of emotional states using voice, face image and thermal image of face. Proc. of 6th IEEE Int. Workshop on Robot and Human Interactive Communication 178-183
- [12] Ikezoe F, Ko R, Tanijiri T, and Yoshitomi Y (2004), Facial expression recognition for speaker using thermal image processing (in Japanese). Trans. Human Interface Society 6(1):19-27
- [13] Nakano M, Ikezoe F, Tabuse M, and Yoshitomi Y (2009), A study on the efficient facial expression using thermal face image in speaking and the influence of individual variations on its performance (in Japanese). J. IEIJ 38(2):156-163
- [14] Koda Y, Yoshitomi Y, Nakano M, and Tabuse M (2009), Facial expression recognition for a speaker of a phoneme of vowel using thermal image processing and a speech recognition system. Proc. of 18th IEEE Int. Symp. on Robot and Human Interactive Communication 955-960
- [15] Yoshitomi Y (2010), Facial expression recognition for speaker using thermal image processing and speech recognition system. Proc. of 10th WSEAS Int. Conf. on Applied Computer Science 182-186
- [16] Fujimura T, Yoshitomi Y, Asada T, and Tabuse M (2011), Facial expression recognition of a speaker using front-view face judgment, vowel judgment, and thermal image processing. Proc. of 16th Int. Symp. on Artificial Life and Robotics in press
- [17] Kuno H (1994), Infrared rays engineering (in Japanese). Tokyo, IEICE 22
- [18] Kuno H (1994), Infrared rays engineering (in Japanese). Tokyo, IEICE 45
- [19] Yoshitomi Y, Tsuchiya A, and Tomita S (1998), Face recognition using dynamic thermal image processing. Proc. of 7th IEEE Int. Workshop on Robot and Human Communication 443-448
- [20] <http://julius.sourceforge.jp/>

A Human-machine Cooperative System for Generating Sign Language Animation Using Thermal Image Processing, Fuzzy Algorithm, and Simulated Annealing

T. Asada and Y. Yoshitomi

*Div. of Environmental Sciences, Graduate School of Life and Environmental Sciences, Kyoto Prefectural University
1-5 Nakaragi-cho, Shimogamo, Sakyo-ku, Kyoto 606-8522, Japan
E-mail: t_asada@mei.kpu.ac.jp, yoshitomi@kpu.ac.jp*

Abstract: We propose a method for sign language animation by skin region detection applied to a thermal infrared image. In a system incorporating the proposed method, a 3D CG model corresponding to a person's characteristic posture while using sign language is generated automatically by pattern recognition of the thermal image, and then a person's hand in the CG model is set. The hand part is made manually beforehand. If necessary, the model can be replaced manually by a more appropriate model corresponding to training key frames and/or the same generated model can be refined manually. In our experiments, three hearing-impaired people, experienced in using sign language, recognized the Japanese sign language gestures of 70 words expressed as animation with 94.3% accuracy. We further improved the system by correcting the position and the direction of the hand of the automatically generated model through the use of a fuzzy algorithm and simulated annealing.

Keywords: Japanese Sign Language, Thermal Image Processing, Computer Graphics, Model Fitting, Fuzzy Algorithm, Simulated Annealing.

I. INTRODUCTION

Sign languages enable hearing-impaired people to communicate with each other. However, it is inconvenient for communication with non-hearing-impaired people because there are not enough sign language interpreters. Therefore, there is a strong need for an automatic sign language translation system. In addition to a sign language recognition function, an animation function is necessary for such a system. Several systems for sign language animation have been studied [1-4]. For animations expressing personality and/or emotion appropriately, conventional systems need many extra manual operations. To lower the workload of sign language systems, one of the most promising approaches is to improve the animation automatically acquired from dynamic images of real motion, with only the refinement performed manually. We previously proposed a method for expressing a sign language gestures as computer graphics (CG) animation that uses a human thermal infrared image taken without placing special restrictions on the person providing the image [5].

In this study, we evaluated a system implementing our method [5] for generating sign language animation from a dynamic image of a hearing-impaired person by measuring the recognition accuracy of other hearing-impaired people. Then, we further improved the system by correcting the position and the direction of the hand

of the automatically generated model through the use of a fuzzy algorithm and simulated annealing.

II. PROPOSED METHOD

The flowchart for generating sign language animation from an input dynamic image is shown in Fig. 1. In the next sections, important elements in the total procedure are described.

1. Thermal image generation

The thermal image is produced by a thermal video system (NEC Avio Infrared Technologies Co., Ltd., Neo Thermo TVS-700), then transformed into a digital signal by an A/D converter (Thomson Canopus ADVC-300), and input into a computer with an IEEE1394 interface board (IO Data Device 1394-PCI3/DV6). Then, the image for each signed word is recorded as an AVI file on a PC. The images that are input into the computer have a spatial resolution of 720×480 pixels and 256 possible gray levels.

2. Selection of key frames from training images

After erasing the noise on each image frame in the AVI file, the sum of the differences of the gray levels of all pixels between the present frame and the previous frame is calculated. On the assumption that the characteristic postures in sign language gestures correspond to frames showing slower movement, a frame having a small gray level difference from the previous frame is considered to be a candidate of

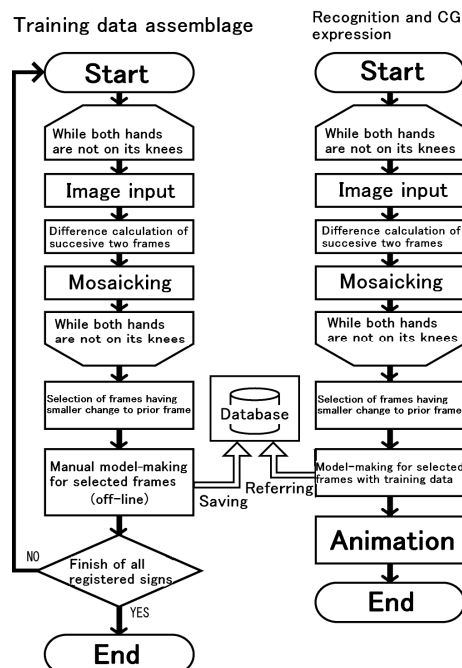


Fig. 1. Flowchart for generating sign language animation

a suitable frame (hereafter called a key frame) for making a 3D CG model. That is, the sum of the differences of the gray levels for the previous frame is used for picking out several key frames. As the selection criterion, we first select the top β % frames of the inverse value of the sum. However, similar successive frames can be selected. To select the key frames, we remove all frames except the first and last frames (when three or more successive frames are selected) with the same value of β for the inverse value of the sum of the gray level differences (Fig. 2). We use 25, 50, and 75 as the values of β . All frames selected with each of these three values for a sign are designated as key frames. The feature vector used for pattern recognition is made from the mosaic image after smoothing.

3. CG model generation for thermal images

The CG model has a hierarchical structure of 34 joints (Figs. 3 and 4) and is described with rotation angles for the corresponding joints. The 3D CG model corresponding to each key frame for a sign is made manually (Fig. 5). We store the feature vectors of the key frames and the corresponding 3D CG models as training data.

4. Animation

To animate a sign, key frames are selected according to the process mentioned in Section II-2, followed by

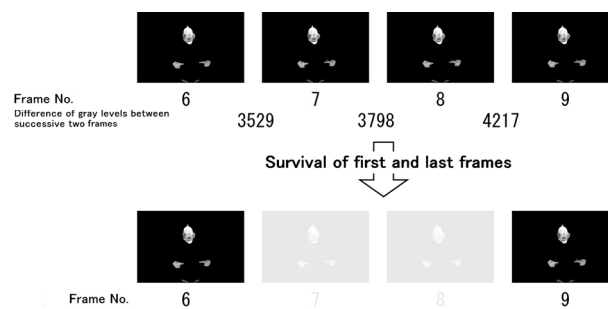


Fig. 2. Selection of key frames from candidates [5]

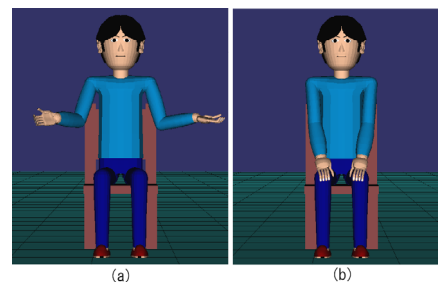


Fig. 3. Human model (a), standard posture (b) [5]

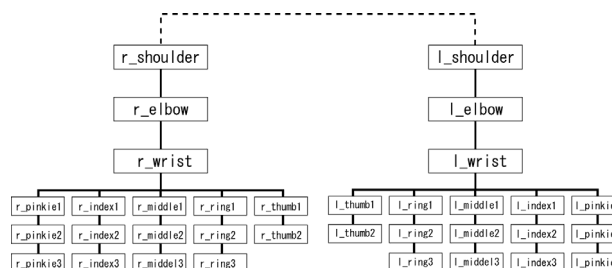


Fig. 4. Structure of the human model [5]

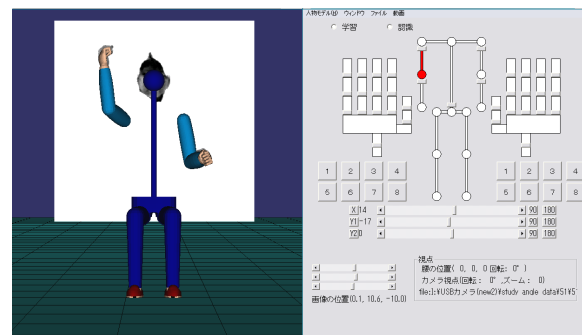


Fig. 5. Manual model fitting [5]

recognition using the “nearest neighbor” criterion for the feature vectors in the training data. When the user judges that the CG model corresponding to the key frame acquired from the input dynamic thermal image is not appropriate, the model can be replaced manually by a more appropriate model corresponding to the one made for the training key frames (Fig. 6) and/or the same model can be refined manually. We assume that we know the meaning of each sign for making the animation. The hands in all CG models are replaced by those made manually as training data. Then, the animation is generated with the CG models

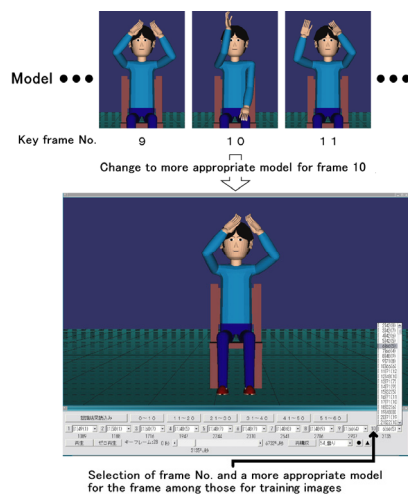


Fig. 6. Modification of model for key frame [5]

corresponding to the key frames by smoothing each rotation angle around the axis for each joint according to the appropriate time sequence.

III. EXPERIMENTS AND DISCUSSION

1. Conditions

In the experiments, a personal computer, Dell Dimension 8300 (CPU: Pentium IV 3.2 GHz, main memory: 2.0 GB, OS: Windows XP), was used, and Microsoft Visual C++ 6.0 was used for programming. The temperature range for detection was 302.3 to 306.7 K.

First, 70 signs were selected for the training data and for investigating the performance of our system according to the following necessary sign conditions: a noun that includes a large motion observable by the listener or the camera and does not include a meaning movement of the head, a movement in the direction of the listener or the camera, the crossing of hands, or the need for an initial pose. With the thermal video system for obtaining the thermal images and a CCD camera for obtaining the visible images, 70 signs by subject A, who was hearing-impaired and knew Japanese sign language, were recorded twice as an AVI file for each word. The first sign for the word was used to make the training data, and the second sign for the word was used for recognition and animation generation. In our experiments, the sign language was Japanese.

2. Results

For the evaluation of our system, the training image expressing the same meaning as that used for recognition was not used. Therefore, 69 signs which did not involve the sign having the same meaning as that for

recognition were used to make the training images and test each sign. Three subjects (B, C, and D), who were hearing-impaired and knew Japanese sign language, evaluated the sign language animation produced by our system. The three subjects wrote down the meaning of each sign and rated it according to one of the following three categories—Level 1: instantly understandable, Level 2: understandable through checking the sign language gesture expressed by the visible ray image for training, Level 3: not understandable (no answer). The animations were produced under two conditions—Condition 1: with neither the modification nor the manual refinement of the models, Condition 2: with both the modification (Fig. 6) and the manual refinement of the models. Table 1 shows the correct answer rates at each level. As shown in Table 2, some misunderstandings occurred because subjects B and C did not often check the sign language gestures expressed by the visible ray image for training. The modification of the models, an example of which is shown in Fig. 6, and the manual refinement of the models improved the animation, especially at Level 2, as shown in Table 1. The average correct answer ratio of subjects B, C, and D, except for the misunderstandings caused by their lack of referring to the sign language gesture expressed by the visible ray image for training, was 51.3% and 94.3% under Conditions 1 and 2, respectively. The time required was approximately 20 minutes to make an animation for the sign language gesture using the training image, whereas it took approximately 25 seconds and 15 minutes to make an animation for the sign language gesture using the test image under Conditions 1 and 2, respectively.

Table 1. Number of correct answers at each level

		Level 1	Level 2	Total
Subject B	Condition 1	27/37 (73.0%)	3/7 (42.9%)	30/70 (42.9%)
	Condition 2	52/57 (91.2%)	6/6 (100%)	58/70 (82.9%)
Subject C	Condition 1	24/33 (72.7%)	10/26 (38.5%)	34/70 (48.6%)
	Condition 2	51/59 (86.4%)	8/10 (80.0%)	59/70 (84.3%)
Subject D	Condition 1	22/26 (84.6%)	15/18 (83.3%)	37/70 (52.9%)
	Condition 2	54/55 (98.2%)	10/13 (76.9%)	64/70 (91.4%)

Table 2. Number of misunderstandings

	Number of incorrect answers	Reference shortage			Poor CG		
		Level 1	Level 2	Level 3	Level 1	Level 2	Level 3
Subject B	12	2	0	6	3	0	1
Subject C	11	6	1	0	2	1	1
Subject D	6	0	2	1	1	1	1

3. Estimation of the position errors in CG space

The accuracy rate under Condition 2 was much higher than that under Condition 1, whereas the workload to generate an animation under Condition 2 was larger than that under Condition 1. To find some strategies for improving the accuracy rate under Condition 1, the position errors in several sign languages gestures using only the movement of one hand (the right hand) were evaluated in CG space. We investigated the causes of the poor animation under Condition 1 when Condition 2 provided a correctly understandable animation but Condition 1 did not. To find the cause of the position errors, we attached markers to the hand. We compared each position of the markers attached on a subject's hand in physical space with the corresponding position on the model in CG space. For simplicity, we selected animations in which only the right hand moved while performing the sign language gesture.

A. Inspection Method

We used the motion capture system named Radish (Library) for measuring the position of the markers attached on the subject. We attached 15 markers each on subject A and the model in CG space (Fig. 7). Then the model was manually refined to fit the human posture. The markers on the model were set as accurately as possible on the positions in CG space so that they had the same positions as those of subject A in physical space.

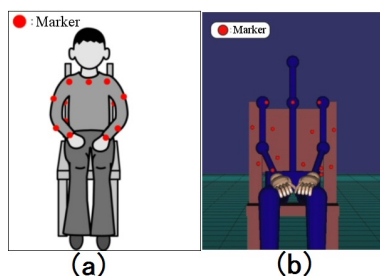


Fig. 7. (a) Subject with attached markers, and (b) model with attached markers

B. Results

Fig. 8 shows the position errors of the markers attached to the model in CG space. When an animation under Condition 1 was correctly understood, the position errors were, on the whole, smaller than those in the case of misunderstanding the animation. However, even when the position error was small, the animation was sometimes misunderstood. This phenomenon was primarily caused by the unwanted movement of the other hand (left hand). However, another phenomenon

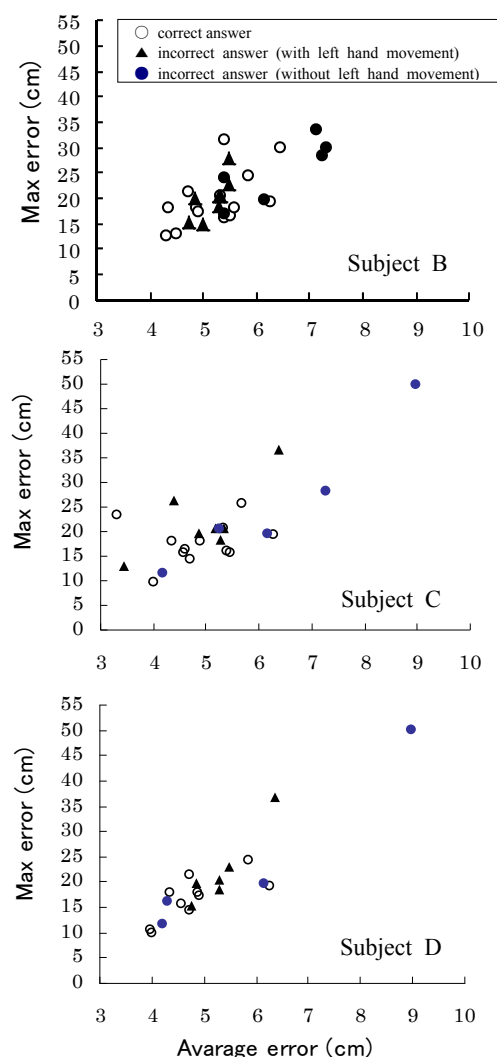


Fig. 8. Position errors of markers on subjects B, C, and D

causing the poor animation was found, as discussed in Section III-4.

4. Discussion

The sign language animation for “Meiji Era” generated under Condition 1 was compared with that generated under Condition 2. Though the difference between the animations generated under Conditions 1 and 2 was relatively small with regard to the hand orbit, the rotation of the elbow under Condition 1 was remarkably different from that under Condition 2 at time instances important for recognizing the animation (Fig. 9). In the case of the sign language animation for “younger brother”, the same phenomenon was observed (Fig. 10). Therefore, we thought that a technique to correct the direction of the arm including the elbow was necessary. We used the angular information and the vector expressing the hand direction for the key frame

selected in the training images to produce a fuzzy system to improve the hand orientation. When fitting a model, as described in Section II-3, the hand direction and the center of gravity coordinates of the three markers (A, B, and C) in the 3D CG model corresponding to the key frame for the training image were recorded. A hand direction is expressed as the vector from marker A to marker B (hereinafter called vector B) and the vector from marker A to marker C (hereinafter called vector C) (Fig. 11).

Using cluster analysis, 487 key frames for the training images of sign language gestures in which only one hand moved were investigated. For this analysis, Ward's method was applied to 18 elements composed of the angles of the shoulder, elbow and wrist, vector B, vector C, the center of gravity coordinates of markers A, B, and C. The number of groups divided by the cluster analysis was used as the number of rules of the fuzzy algorithm. This value was experimentally decided as 24.

The fuzzy rules are described in (1). The fuzzy algorithm is described in (2) to (5).

$$\left. \begin{array}{l} \text{IF } x_1 \text{ is } A_{i1} \text{ and } x_2 \text{ is } A_{i2} \\ \text{and } x_3 \text{ is } A_{i3} \text{ and } x_4 \text{ is } A_{i4} \\ \text{and } x_5 \text{ is } A_{i5} \text{ and } x_6 \text{ is } A_{i6} \\ \text{and } x_7 \text{ is } A_{i7} \text{ and } x_8 \text{ is } A_{i8} \\ \text{and } x_9 \text{ is } A_{i9} \\ \text{THEN } y_1 \text{ is } B_{i1} \text{ and } y_2 \text{ is } B_{i2} \\ \text{and } y_3 \text{ is } B_{i3} \text{ and } y_4 \text{ is } B_{i4} \\ \text{and } y_5 \text{ is } B_{i5} \text{ and } y_6 \text{ is } B_{i6} \\ \text{and } y_7 \text{ is } B_{i7} \text{ and } y_8 \text{ is } B_{i8} \\ \text{and } y_9 \text{ is } B_{i9} \end{array} \right\} \quad (1)$$

$$(i = 1, 2, \dots, 24)$$

$$\mu_{B_{ij}}^*(y_j) = w_i \mu_{B_{ij}}(y_j) \quad (2)$$

$$(i = 1, 2, \dots, 24, j = 1, 2, \dots, 9)$$

$$w_i = \min_j \mu_{A_{ij}}(x_i^*) \quad (3)$$

$$(i = 1, 2, \dots, 24, j = 1, 2, \dots, 9)$$

$$B_j^0 = \bigcup_{i=1}^{24} B_{ij}^* \quad (j = 1, 2, \dots, 9) \quad (4)$$

$$y_j^* = \frac{\int \mu_{B_j^0}(y_j) y_j dy_j}{\int \mu_{B_j^0}(y_j) dy_j} \quad (j = 1, 2, \dots, 9) \quad (5)$$

where x_1, x_2, \dots, x_9 denote the parameters of the antecedent; y_1, y_2, \dots, y_9 denote the parameters of the consequent; $A_{i1}, A_{i2}, \dots, A_{i9}, B_{i1}, B_{i2}, \dots, B_{i9}$ denote the corresponding fuzzy labels; w_i denotes the fitness value of the i th rule to the input of $x_1^*, x_2^*, \dots, x_9^*$;

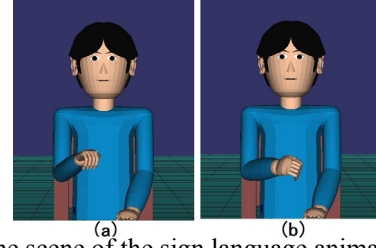


Fig. 9. One scene of the sign language animation for the Meiji Era under (a) Condition 1, (b) Condition 2

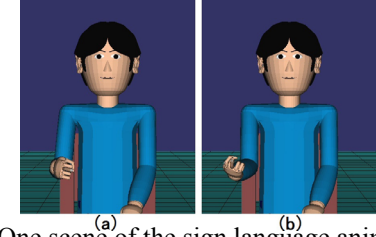


Fig. 10. One scene of the sign language animation for “younger brother” under (a) Condition 1, (b) Condition 2

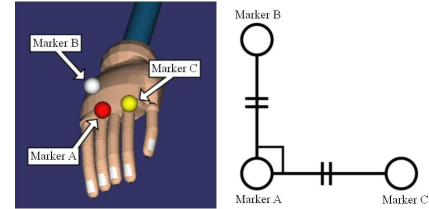


Fig. 11. Hand model with attached markers

and y_i^* denotes the output for y_i . In this study, the coordinates of the center of gravity for markers A, B, and C attached on the model were assigned for (x_1, x_2, x_3) ; the elements of vectors B and C were assigned for (x_4, x_5, x_6) and (x_7, x_8, x_9) , respectively; and the rotation angles on the shoulder, the elbow, and the wrist in the model were assigned for y_1, y_2, \dots, y_9 , respectively. Each norm of vectors B and C had the value of 1. Fig. 12 shows a schematic diagram of the membership functions used for both the antecedent and the consequent, where C_i denotes a fuzzy label of the antecedent or consequent, for example, A_{11} , whereas Z corresponds to a variable of the antecedent or consequent, for example, x_1 . Each membership function had a pentagonal shape and a value of 1 at the corresponding measured mean value and a value of 0.5 at the corresponding measured minimum and maximum values. We used a fuzzy

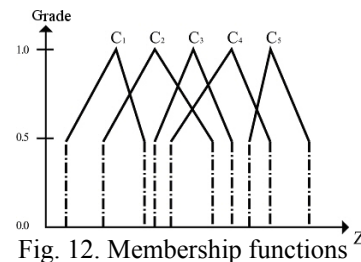


Fig. 12. Membership functions Z

algorithm having 24 rules, 9 antecedent valuables, and 9 consequent variables. The rotation angles of the shoulder, elbow, and wrist are inferred using this fuzzy algorithm.

Next, we propose a method to improve the rotation angle set to the joint of the elbow by decreasing the difference of the hand direction for the test image to that for the training image, and the difference of the center of gravity coordinates of markers A, B, and C of the models before and after using the fuzzy algorithm. The rotation angle of the elbow joint was acquired by simulated annealing (SA). The amount of the modification in the rotation angle of each rotation axis of the elbow joint is $n_q (q=1,2,3)$. The value of a uniform random number generated with the value of $-T$ to T is $n_q(T)$. We used the experimentally decided (6), shown below, as the cooling schedule.

$$T(s) = \frac{T_0}{\log\left(2.0 + \frac{s}{20.0}\right)}, \quad (6)$$

where T_0 is the initial temperature and s is the number of steps of the iteration operation. As initial values for (6), the angles of the model obtained from the recognition result were used. The total error to be reduced is defined as the sum of the errors in the hand direction to that for the training image, and the error in the center of gravity of the three markers attached on the hand with respect to that obtained from the recognition result. When the total error obtained at an iteration step is smaller than the minimum value obtained before the step, the rotation angles of each rotation axis of the elbow joint are updated to those at that step. The iteration operation is terminated at a previously decided step. Condition 3 denotes the condition for the sign language animation generated under Condition 1 followed by improvement using the fuzzy algorithm and SA. The sign language animations generated under Condition 3 are more natural than those under Condition 1 (Figs. 13 and 14).

IV. CONCLUSION

We developed an enhanced system for generating sign language animation using skin region detection on a thermal infrared image. In this system, a 3D CG model corresponding to a characteristic posture used in sign language is generated automatically by pattern recognition of the thermal image, whereas the human hand in the CG model is created manually. In experiments, three people experienced in using sign language recognized with good accuracy the Japanese sign language gestures of 70 words expressed as animations. Then, using the fuzzy algorithm and

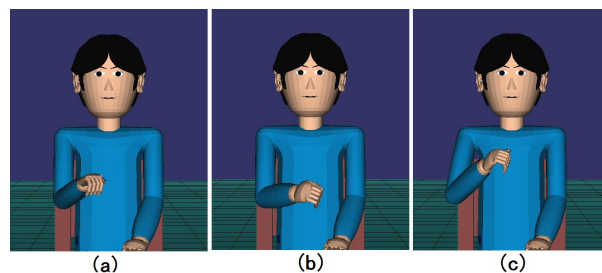


Fig. 13. One scene of the animation of “Meiji Era”; (a) Condition 1, (b) Condition 2, and (c) Condition 3

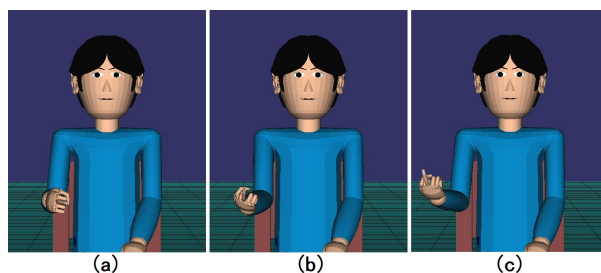


Fig. 14. One scene of the animation of “younger brother”; (a) Condition 1, (b) Condition 2, and (c) Condition 3

simulated annealing, we improved the system to correct the position and the direction of the hand of the automatically generated model.

Acknowledgment

We would like to thank all the subjects who cooperated with us in the experiments.

REFERENCES

- [1] Sagawa H, Sakou H, Oohira E, et al (1994), Sign-Language Recognition Method Using Compressed Continuous DP Matching (in Japanese). IEICE Trans. Inf. & Syst 77(4):753-763
- [2] Watanabe K, Iwai Y, Yagi Y, et al (1998), Manual Alphabet Recognition by Using Colored Gloves (in Japanese). IEICE Trans. Inf. & Syst 80(10):2713-2722
- [3] Igi S, Watanabe R, and Lu S (2001), Synthesis and Editing Tool for Japanese Sign Language Animation (in Japanese). IEICE Trans 84 (6):987-995
- [4] Kurokawa T (2004), Representation of sign animation for Japanese-into-Japanese sign language translation (in Japanese). Proc. of 32nd Symp. of visualization 24(1):273-276
- [5] Asada T, Yoshitomi Y and Hayashi R (2008), A Human-machine Cooperative System for Generating Sign Language Animation Using Thermal Image. Journal of Artificial Life and Robotics 13:36-40

Music Recommendation System Using the Time-series Discrete Wavelet Transform and the FastICA

K. Horiike¹, Y. Yoshitomi², T. Tokuyama³ and M. Tabuse²

1: Taka Dance Fashion Co., Ltd., 1-13 Ikutamamae-machi, Tennouji-ku, Osaka 543-0072, Japan

2: Graduate School of Life and Environmental Sciences, Kyoto Prefectural University,
1-5 Nakaragi-cho, Shimogamo, Sakyo-ku, Kyoto 606-8522, Japan,

E-mail: yoshitomi@kpu.ac.jp

3: Shofu Inc., 11 Kamitakamatsu-cho, Fukuine, Higashiyama-ku, Kyoto 605-0983, Japan

Abstract: We previously proposed a content-based music recommendation system that uses several strategies for music recommendation. Each strategy, based on the user's music evaluation history up to the present time, is composed of a feature vector and a decision rule for music recommendation. Vocal signals are an important factor in music recommendation. Therefore, we use FastICA to separate vocal components from music. In an experiment to evaluate the proposed system, 10 users rated 100 music files in a music database. Of these 100 music files, 49 contained vocal components. For all 100 music files, the mean recommendation accuracy by the proposed system was 67.2%, and the mean recommendation accuracy of random recommendation was 32.1%. For songs containing vocal signals, the mean recommendation accuracy by the proposed system was 45.3% with FastICA and 35.8% without FastICA.

Keywords: Content-based music recommendation, Vocal characteristics, Independent component analysis, FastICA.

I. INTRODUCTION

Currently, many computer users enjoy a large number of music files stored on their computer or using the Internet. The increasing amounts of available audio data require the development of a music recommendation system. There are two kinds of music recommendation systems: content-based recommendation and collaborative filtering. We previously proposed a content-based music recommendation system [1].

In this study, in our music recommendation system, we add the time series of Mel-frequency cepstral coefficients (MFCCs) [2], [3] as the feature parameters. Moreover, because vocal signals are an important factor in a listener's musical tastes, we add a module using FastICA [4] for separating vocal signals from music.

II. FEATURE PARAMETERS

In the content-based music recommendation system, we use three kinds of feature parameters for characterizing music: time series of wavelet transform coefficients, time series based on MFCCs, and rhythmic content [5]. We explain these feature parameters in the following subsections.

1. Wavelet transform coefficients

Original audio data $s_k^{(0)}$, where k denotes the element number in the data, are used as the level-0 wavelet decomposition coefficient sequence. The

$s_k^{(0)}$ data are decomposed into the multi-resolution representation (MRR) and the coarsest approximation by repeatedly applying the discrete wavelet transform (DWT). The wavelet decomposition coefficient sequence $s_k^{(j)}$ at level j is decomposed into two wavelet decomposition coefficient sequences at level $j+1$, as shown below in (1) and (2):

$$s_k^{(j+1)} = \sum_n \overline{p_{n-2k}} s_n^{(j)}, \quad (1)$$

$$w_k^{(j+1)} = \sum_n \overline{q_{n-2k}} s_n^{(j)}, \quad (2)$$

where p_k and q_k denote the scaling and wavelet sequences, respectively, and $w_k^{(j+1)}$ denotes the development coefficient at level $j+1$. The development coefficients at level J are obtained by using (1) and (2) iteratively from $j=0$ to $j=J-1$.

In the present study, we use Daubechies wavelet for the DWT. As a result, we obtain the following relation between p_k and q_k :

$$q_k = (-1)^k p_{1-k}. \quad (3)$$

It is known that the histogram of the wavelet coefficients of each domain of MRR sequences has a distribution centered at approximately 0 when the DWT is performed on audio data [6]. We use the time series of wavelet coefficients of each domain of the MRR sequences as elements of the feature vector.

2. MFCCs

MFCCs are obtained for each frame of a sound signal by using reported techniques [3]. The following are used as elements of the feature vector: the time-

series of the mean values and the standard deviations of 12-dimensional MFCCs, the logarithmic power of 12-dimensional MFCCs, the 12-dimensional MFCC difference between frames, and the 12-dimensional MFCC logarithmic power difference between frames.

3. Rhythm content

Rhythmic content feature parameters are obtained by using reported techniques [5]. A set of feature parameters based on a beat histogram are calculated. These are as follows:

- $A0, A1$: the relative amplitude (divided by the sum of the amplitudes) of the first and second histogram peaks, respectively [5];
- RA : the ratio of the amplitude of the second peak divided by the amplitude of the first peak [5];
- $P1, P2$: the period of the first and second peaks, respectively, in beats per minute (bpm) [5];
- $SUM1, SUM2, SUM3$: sum of beat strength in the histogram in the range of 40–90, 90–140, 140–250 bpm, respectively.

Each of the three kinds of feature parameters, which are a : [$SUM1$], b : [$A0, A1, SUM1, SUM2, SUM3$], c : [$A0, A1, P1, P2, RA, SUM1, SUM2, SUM3$], is used as a feature parameter in the proposed system described in Section IV.

III. FastICA

Independent component analysis (ICA) [7], which is a statistical and computational technique for separating hidden factors in a signal, is a promising technique for separating vocal signals from songs [8]. In this study, we use FastICA [4], for performing ICA.

IV. PROPOSED SYSTEM

To explain the decision rules for music recommendation, we describe a set of music indices as $M = \{m | 1, \dots, N_M\}$, an evaluation by a user as a score s ($1 \leq s \leq 5$), where 1, 2, 3, 4, and 5 mean “dislike,” “slightly dislike,” “neutral,” “slightly favorite,” and “favorite,” respectively, and a set of evaluated music indices as $M_s = \{m_s | 1, \dots, N_{Ms}\}$.

1. Elements of decision rules for the recommendation

A. Decision rules using one kind of feature parameter

After principal component analysis (PCA) on the feature vectors obtained from unevaluated music m' file and the number N_{Ms} of evaluated music files of a

user, the principal components up to the l th component are selected under the condition that the accumulated contribution ratio first exceeds 80% at the l th component. The score s for music m^* file having the maximum value of similarity to music m' file among the number N_{Ms} of evaluated music files is assigned to the score of music m' file. The similarity is calculated as the inverse value of the Euclidean distance in the l -dimensional feature vector space obtained by the above PCA. When the assigned score is 4 or 5 (“slightly favorite” or “favorite”), the unevaluated music m' file is recommended for the user.

B. Decision rules using two or three kinds of feature vectors

Table 1 shows the decision rules for music recommendation using two or three kinds of feature parameters.

Table 1. Decision rules for music recommendation using two or three kinds of feature parameters

A	Score (1 kind of feature parameters) = 4 or 5 Score (another) = 3~5
B	Score (1 kind of feature parameters) = 4 or 5 Similarity order (another) : within top 50 %
C	Score (1 kind of feature parameters) = 4 or 5 Similarity (another) : average or higher than average

When using 3 kinds of feature parameters, “another” is replaced by “other two”, and then naming replacement ($A \Rightarrow D, B \Rightarrow E, C \Rightarrow F$) is performed.

2. Recommendation system

The system finds a suitable strategy for music recommendation for each user among 74 combinations of decision rule and feature parameter(s), as shown in Table 2, based on the user’s music evaluation history up to the present time. Assuming that we have evaluated $K-1$ music files, one unevaluated music m file is judged recommendable or not recommendable according to the following two criteria.

Criterion 1:

One music m^{**} file among $K-1$ evaluated music files is considered an unevaluated music file, and each strategy of the 74 combinations of decision rule and feature parameter(s) is used to judge whether music m^{**} file is recommendable by using $K-2$ evaluated music files as training samples. Then, each recommendation is checked using the score of music m^{**} file to determine whether each judgment is correct. The recommendation accuracy for each strategy is obtained by selecting one music m^{**} file in order among $K-1$ evaluated music files. The recommendation strategy having the best accuracy among

Table 2. Strategies for music recommendation in our system.

Strategy no.	Decision rule	Feature vector	
		Main	Other(s)
1	Using only one kinds of feature parameter(s)	Wavelet	
2		MFCC	
3		Rhythm a	
4		Rhythm b	
5		Rhythm c	
6	A	Wavelet	MFCC
7			Rhythm a
8			Rhythm b
9			Rhythm c
10		MFCC	Wavelet
11			Rhythm a
12			Rhythm b
13			Rhythm c
14		Rhythm a	Wavelet
15		Rhythm b	
16		Rhythm c	
17		Rhythm a	MFCC
18		Rhythm b	
19		Rhythm c	
20~33	B	(Same as those described at No.6~19)	
34~47	C	(Same as those described at No.6~19)	
48	D	Wavelet	MFCC, Rhythm a
49			MFCC, Rhythm b
50			MFCC, Rhythm c
51		MFCC	Wavelet, Rhythm a
52			Wavelet, Rhythm b
53			Wavelet, Rhythm c
54		Rhythm a	Wavelet, MFCC
55		Rhythm b	
56		Rhythm c	
57~65	E	(Same as those described at No.48~56)	
66~74	F	(Same as those described at No.48~56)	

all strategies is used to judge whether each unevaluated music m file is recommendable by using $K-1$ music files as training samples.

Criterion 2:

When an unevaluated music m file is judged to be recommendable under criterion 1 and the main feature vector having the second highest similarity to the feature vector obtained from the unevaluated music m file is obtained from the music file having a score of 4 or 5, the unevaluated music m file is judged to be recommendable.

V. PERFORMANCE EVALUATION

1. Conditions

Fig. 1 shows the flowchart for the evaluation of the system. K was set as 100 in using 100 music files in the database, while it was set as 49 in using the 49 music files with vocal.

We used 100 music files in the real world computing (RWC) music database, which is available for research [9]. To evaluate the performance of the proposed system, all music files in the database were assigned scores s ($1 \leq s \leq 5$) by 10 users. Of the 100 music files, 49 with vocal signals were used to evaluate FastICA as a pre-processing module. The feature parameters from wavelet transform coefficients and those from rhythmic content were calculated under the conditions described in our previous reported paper [1]. To calculate the feature parameters from MFCCs, a sound signal of 10 to 65 seconds from the beginning of a music signal was used. The sound signal was obtained under the following conditions: window length 30 ms, shift pitch 10 ms, Hanning window used as the window function, and 24 filter banks. The sound signal was equally divided into five signals as the time-series. In this experiment, a sound signal of 55 seconds was divided into five sound signals of 11 seconds, and 52

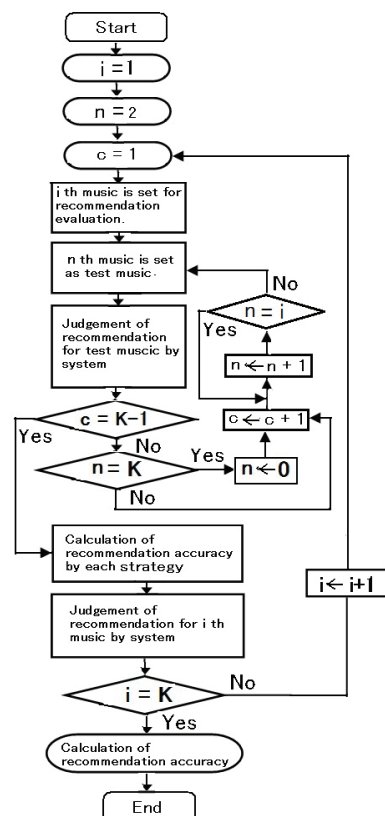


Fig. 1. Flowchart for evaluation of the system

feature parameters were obtained for a sound signal of 11 seconds according to the method described in Section II-2. As a result, we obtained a 260-dimensional feature vector from the sound signal of 55 seconds.

2. Results and discussions

Table 3 shows the recommendation accuracy for 100 music files. The recommendation accuracy of criterion 2 was almost always better than that of criterion 1. The mean recommendation accuracy by the proposed system (criterion 2) was 67.2%, while that of random recommendation was 32.1%. For songs containing vocal signals, the mean recommendation accuracy by the proposed system with FastICA was 45.3%, but that without FastICA was 35.8% under only criterion 1 (Fig. 2). These results confirm that FastICA improves the recommendation accuracy of songs with vocal signals.

Table 3. Recommendation accuracy for 100 music files

User No.	Criterion 1		Criterion 2	
	Recommendation accuracy	Difference to random recommendation	Recommendation accuracy	Difference to random recommendation
1	55.6	15.6	83.3	43.3
2	40.0	11.0	28.6	-0.4
3	66.7	32.7	100.0	66.0
4	59.1	17.1	60.0	18.0
5	44.4	15.4	30.8	0.8
6	50.0	23.0	60.0	33.0
7	84.6	50.6	100.0	66.0
8	68.8	33.8	71.4	36.4
9	35.5	-4.5	37.5	-2.5
10	57.1	47.1	100.0	90.0
Mean	56.2	24.2	67.2	35.1

(%)

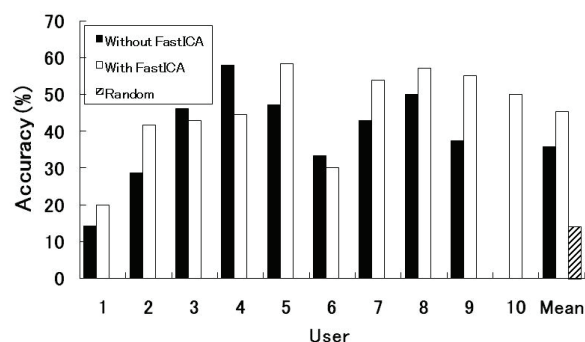


Fig. 2. Effect of FastICA on recommendation accuracy

VI. CONCLUSION

We propose a content-based music recommendation system with several possible strategies. Each strategy is

composed of a feature vector and a decision rule for music recommendation. The strategy for each user is based on the user's music evaluation history up to the present time. Since vocal signals are an important factor of a listener's musical tastes, we use FastICA as a pre-processing module to separate vocal signals from songs. In the experiment, 100 music files in the RWC database were used for estimating the performance of the proposed system. The mean recommendation accuracy by the proposed system was 67.2%, and the mean accuracy of random recommendation was 32.1%. For 49 songs containing vocal signals, FastICA improved the mean accuracy of music recommendation.

Acknowledgment

We would like to thank all the participants who cooperated with us in the experiments.

REFERENCES

- [1] Tanaka M and Yoshitomi Y (2008), A music recommendation system based on user preferences using the discrete wavelet transform (in Japanese). Proc. of the 7th annual convention of forum on information technology. 2:245-248
- [2] Davis S and Mermelstein P (1980), Experiments in syllable-based recognition of continuous speech. IEEE Trans. Acoust., Speech Signal Processing. 28:357-366
- [3] Shikano K, Itou K, Kawahara T, Takeda K, and Yamamoto M (2001), Speech recognition system. Ohmsha (in Japanese)
- [4] Hyvärinen A (1999), Fast and robust fixed-point algorithms for independent component analysis. IEEE Trans. on Neural Networks. 10(3):626-634
- [5] Tzanetakis G and Cook P (2002), Musical genre classification of audio signals. IEEE trans. speech audio process. 10(5):293-302
- [6] Murata S, Yoshitomi Y and Ishii H (2007), Optimization of embedding position in an audio watermarking method using wavelet transform (in Japanese). Abstracts of autumn research presentation forums of ORSJ 210-211
- [7] Hyvärinen A and Oja E (2000), Independent component analysis: algorithms and applications. Neural Networks. 13(4-5):411-430
- [8] Feng Y, Zhuang Y and Pan Y (2002), Popular song retrieval based on singing matching. PCM '02 Proc. of the Third IEEE Pacific Rim Conference on Multimedia: Advances in Multimedia Information Processing. 639-646
- [9] Goto M, Hashiguchi H, Nishimura T, and Oka R (2004), RWC music database: database of copyright-cleared musical pieces and instrument sounds for research purposes (in Japanese). Trans. of IPSJ. 45(3):728-738

Music Recommendation System Aimed at Improving Recognition Ability

H. Konishi¹ and Y. Yoshitomi²

1: Department of Environmental Information, Kyoto Prefectural University,
1-5 Nakaragi-cho, Shimogamo, Sakyo-ku, Kyoto 606-8522, Japan,

2: Graduate School of Life and Environmental Sciences, Kyoto Prefectural University,
1-5 Nakaragi-cho, Shimogamo, Sakyo-ku, Kyoto 606-8522, Japan,

E-mail: yoshitomi@kpu.ac.jp

Abstract: Recently, music therapy has been used for improving the recognition ability of people. Music therapy may be more effective when the favorite music of each person is adopted. We propose a music recommendation method that fuses content-based music recommendation and collaborative filtering. For characterizing the music in our content-based music recommendation system, we use three kinds of feature parameters for characterizing music: time series of wavelet transform coefficients, time series based on Mel-frequency cepstral coefficients, and parameters characterizing the rhythmic content. Several strategies for music recommendation are prepared. Each strategy is composed of a feature vector and a decision rule. The system can determine a good strategy for music recommendation for each user by not only exploiting the user's music evaluation history up to the present time but also the music evaluations by other users. In the experiments, 12 users rated 52 songs coming from a textbook database of songs for elementary schools. The number of recommended songs by the proposed method was 6.75 per user, and the number by collaborative filtering was 5.17 per user. The recommendation accuracy of the proposed method was 81.8%, and that of collaborative filtering was 74.1%.

Keywords: Recognition ability, Music therapy, and Music recommendation.

I. INTRODUCTION

In Japan, the average age of the population has been increasing, and this trend is expected to continue. Recently, music therapy has been used for improving the recognition ability of people, particularly older people. Music therapy may be more effective when the favorite music of each person is adopted. To the best of our knowledge, no research reports exist on the technology of music recommendation aimed at improving recognition ability. In the present study, we propose a music recommendation method that combines content-based music recommendation [1] and collaborative filtering to improve recognition ability. We evaluate the proposed method with children's songs, which tend to be familiar to older people.

II. FEATURE PARAMETERS

In the content-based music recommendation system, we use three kinds of feature parameters for characterizing music: time series of wavelet transform coefficients, time series based on Mel-frequency cepstral coefficients (MFCCs) [2], [3], and parameters describing the rhythmic content [4]. These parameters are described in the following subsections.

1. Wavelet transform coefficients

Original audio data $s_k^{(0)}$, where k denotes the element number in the data, are used as the level-0 wavelet decomposition coefficient sequence. The $s_k^{(0)}$ data are decomposed into the multi-resolution representation (MRR) and the coarsest approximation by repeatedly applying the discrete wavelet transform (DWT). The wavelet decomposition coefficient sequence $s_k^{(j)}$ at level j is decomposed into two wavelet decomposition coefficient sequences at level $j+1$, as shown below in (1) and (2):

$$s_k^{(j+1)} = \sum_n \overline{p_{n-2k}} s_n^{(j)}, \quad (1)$$

$$w_k^{(j+1)} = \sum_n \overline{q_{n-2k}} s_n^{(j)}, \quad (2)$$

where p_k and q_k denote the scaling and wavelet sequences, respectively, and $w_k^{(j+1)}$ denotes the development coefficient at level $j+1$. The development coefficients at level J are obtained by using (1) and (2) iteratively from $j=0$ to $j=J-1$.

In the present study, we use Daubechies wavelet for the DWT. As a result, we obtain the following relation between p_k and q_k :

$$q_k = (-1)^k p_{1-k}. \quad (3)$$

It is known that the histogram of the wavelet coefficients of each domain of MRR sequences has a distribution centered at approximately 0 when the DWT is performed on music [5]. We found out that the

standard deviation of the wavelet coefficients of each domain of the MRR sequences of music changed in its time series. In addition, the change depended on the music. Therefore, we use the time series of the wavelet coefficients of each domain of the MRR sequences as elements of the feature vector.

2. MFCC features

MFCCs are obtained for each frame of a sound signal by the conventional method [3]. The following are used as elements of the feature vector: the time series of the mean values and the standard deviations of 12-dimensional MFCCs, the logarithmic power of 12-dimensional MFCCs, the 12-dimensional MFCC difference between frames, and the 12-dimensional MFCC logarithmic power difference between frames.

3. Rhythm content features

Rhythmic content feature parameters are obtained by using the techniques described in Ref. [4]. A set of feature parameters based on a beat histogram are calculated. These are as follows:

- $A0, A1$: the relative amplitude (divided by the sum of the amplitudes) of the first and second histogram peaks, respectively [4];
- RA : the ratio of the amplitude of the second peak divided by the amplitude of the first peak [4];
- $P1, P2$: the period of the first and second peaks, respectively, in beats per minute [4];
- $SUM1, SUM2, SUM3$: the sum of beat strength in the histogram in the range of 40–90, 90–140, and 140–250, respectively, in beats per minute.

Each of the three kinds of feature parameters, which are a : [$SUM1$], b : [$A0, A1, SUM1, SUM2, SUM3$], c : [$A0, A1, P1, P2, RA, SUM1, SUM2, SUM3$], is used as a feature parameter in the method described in Section III.

III. CONTENT-BASED METHOD

To explain some of the methods for music recommendation, we describe a set of music indices as $M = \{m | 1, \dots, N_M\}$, an evaluation by a user as a score $s (1 \leq s \leq 5)$, where 1, 2, 3, 4, and 5 mean “dislike,” “slightly dislike,” “neutral,” “slightly favorite,” and “favorite,” respectively, and a set of evaluated music indices as $M_s = \{m_s | 1, \dots, N_{Ms}\}$.

1. Methods using one kind of feature parameter

After principal component analysis (PCA) on the feature vectors obtained from unevaluated music m'

file and the number N_{Ms} of evaluated music files of a user, the principal components up to the l th component are selected under the condition that the accumulated contribution ratio first exceeds 80% at the l th component. The score s for music m^* file having the maximum value of similarity to music m' file among the number N_{Ms} of evaluated music files is assigned to the score of music m' file. The similarity is calculated as the inverse value of the Euclid distance in the l dimensional feature vector space obtained by the above PCA. When the assigned score is 4 or 5 (“slightly favorite” or “favorite”), the unevaluated music m' file is recommended for the user.

2. Methods using two or three kinds of feature vectors

Table 1 shows the conditions for music recommendation by methods using two or three kinds of feature parameters.

Table 1. Conditions for music recommendation by methods using two or three kinds of feature parameters

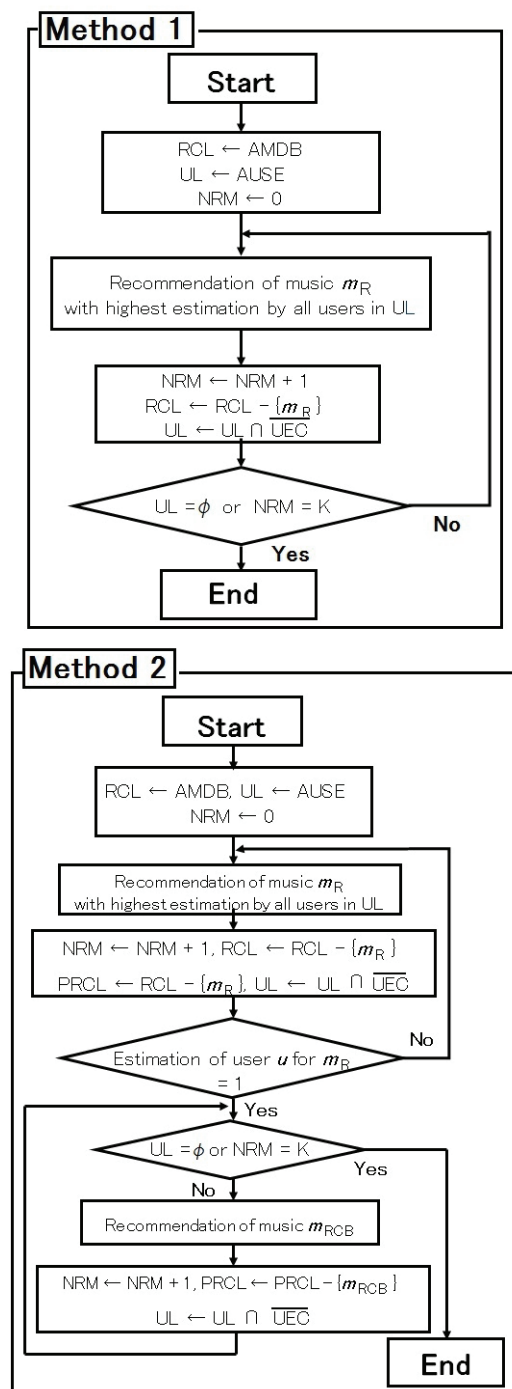
Method A	Score (1 kind of feature parameters) = 4 or 5 Score (another) = 3~5
B	Score (1 kind of feature parameters) = 4 or 5 Similarity order (another) : within top 50 %
C	Score (1 kind of feature parameters) = 4 or 5 Similarity (another) : average or higher than average

When using 3 kinds of feature parameters, ‘another’ is replaced by ‘other two’, and then naming replacement ($A \Rightarrow D, B \Rightarrow E, C \Rightarrow F$) is performed.

IV. PROPOSED METHOD

Fig. 1 shows two music recommendation methods. Method 1 is collaborative filtering only and it is used for comparison with Method 2, which is our proposed method that combines the content-based method and collaborative filtering. Our system recommends music stored in a database to user u , as described in Fig. 1.

In the flowchart of Method 2 described in Fig. 1, the estimation of user u for music m_R is set as 1 when the score of user u for music m_R is 4 or 5 (“slightly favorite” or “favorite”), and it is set as 0 when the score is 1 to 3 (“dislike,” “slightly dislike,” or “neutral”). Moreover, m_{RCB} is decided for user u by using the most suitable recommendation method and feature parameter(s) selected among 74 combinations [1], [6] of method and feature parameter(s) by our previously reported method [1], in which we used the content-based recommendation method described in



Abbreviations ;

AMDB : set of all music in data base

RCL : set of music in recommendation candidate list

AUSE : set of all users with subjective estimation

UL : set of user in reference user list

NRM : number of recommended music

UEC : set of user(s) who estimate(s) recommended music m_R contrary to user u

PRCL : set of music in recommendation candidate list made of music having 3.5 or higher than 3.5 of average score by users in UL

m_{RCB} : music having the most similarity to the currently recommended music having score of 4 or 5 by user u among music in PRCL

Section III and the feature parameter(s) described in Section II. In selecting the most suitable recommendation method and feature parameter(s) in Method 2, we use the scores of user u for music that has already been recommended for and evaluated by user u and the scores of other users in a reference user list (UL) for music not yet recommended for user u .

V. PERFORMANCE EVALUATION

1. Conditions

Because older people tend to prefer children's songs [7], we selected a CD described as an anthology of good older songs enjoyed by older people with dementia [8], and then we selected 52 songs on the CD that were also included in a music textbook database for elementary schools [9]. For evaluating the music recommendation methods, all 52 of selected songs in the database were assigned scores s ($1 \leq s \leq 5$) by 12 users (teens: 1, twenties: 6, fifties: 5). Using the same conditions as used in our previous research [1], the feature parameters were obtained by the method described in Section II. We used 10 as the value of K in Fig. 1. For evaluating the two music recommendation methods described in Section IV, we chose each of the 12 users as user u and put the remaining users in the reference user list UL described in Fig. 1. Then, we obtained the result of the music recommendation for each user for each method described in Section IV.

2. Results and discussions

Table 2 shows the process of the music recommendation process for user 8. As shown in Table 2, Method 2 tended to recommend more music and have a higher accuracy of music recommendation than did Method 1. Fig. 2 shows the performance of the two methods. The number of recommended songs by the proposed method (Method 2) was 6.75 per user, whereas that of collaborative filtering (Method 1) was 5.17 per user. The recommendation accuracy of the proposed method was 81.8%, whereas that of collaborative filtering was 74.1%. For both the recommendation accuracy and the number of recommended songs, the proposed method was better than collaborative filtering. In both methods, the recommendation process was terminated at the rate of 5/6, when the number of users staying in the UL became zero. Accordingly, an increase in the number of users in UL might contribute to an increased number of recommended songs.

Fig. 1. Flow chart of music recommendation methods

Table 2. Music recommendation process for user 8

[Method 1]

Order	Recommended music No.	Acceptance	User No. in UL
1	52	○	1,2,3,4,5,6,7,9,10,11,12
2	41	○	1, 3,4,5,6,7,9,10,11,12
3	50	○	1, 3,4,5, 7,9,10, 12
4	21	○	1, 3, 5, 7,9, 12
5	37	×	9
6	49	×	none

[Method 2]

Order	Recommended music No.	Acceptance	User No. in UL
1	52	○	1,2,3,4,5,6,7,9,10,11,12
2	16	○	1,2,3,4,5, 7,9, 12
3	3	○	1, 3,4,5, 7,9
4	26	○	1, 3,4,5, 7,9
5	21	○	1, 3, 5, 7,9
6	5	○	1, 5, 7
7	17	○	1, 7
8	4	○	1
9	13	×	none

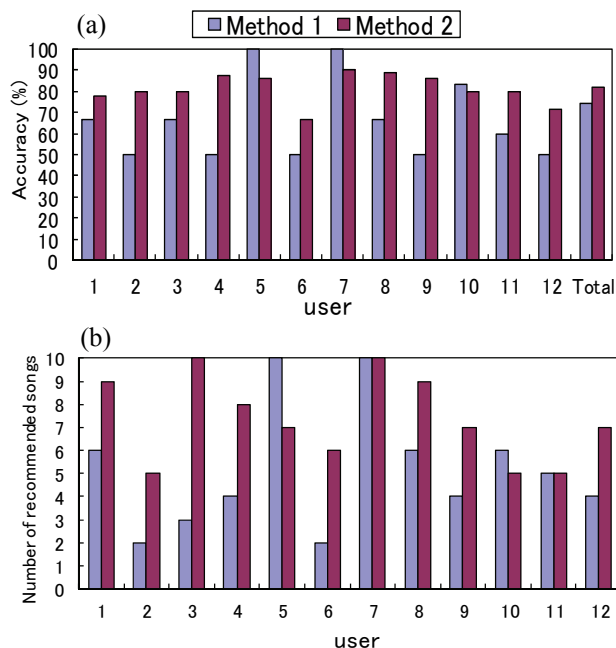


Fig. 2. Performance of music recommendation methods;
(a) recommendation accuracy,
(b) number of recommended songs

VI. CONCLUSION

We propose a music recommendation method combining our previously reported method based on music features and collaborative filtering. We showed that the proposed method is more effective for music recommendation than using only collaborative filtering when used on a music database composed of children's songs. In future work, we will increase the number of users who evaluate the music in the database and apply the proposed method to people who are much older and/or have a cognitive impairment.

Acknowledgments

We would like to thank Associate Professor M. Tabuse of Kyoto Prefectural University for his valuable advice and support on this research. We would also like to thank all the participants who cooperated with us in the experiments.

REFERENCES

- [1] Tokuyama T, Yoshitomi Y, Tanaka M and Tabuse M (2009), A study on music recommendation system using the time-series discrete wavelet transform (in Japanese). Proc. of the 8th annual convention of forum on information technology. 2:325-328
- [2] Davis S and Mermelstein P (1980), Experiments in syllable-based recognition of continuous speech. IEEE Trans. Acoust., Speech Signal Processing. 28:357-366
- [3] Shikano K, Itou K, Kawahara T, Takeda K, and Yamamoto M (2001), Speech recognition system. Ohmsha (in Japanese)
- [4] Tzanetakis G and Cook P (2002), Musical genre classification of audio signals. IEEE trans. speech audio process. 10(5):293-302
- [5] Murata S, Yoshitomi Y and Ishii H (2007), Optimization of embedding position in an audio watermarking method using wavelet transform (in Japanese). Abstracts of autumn research presentation forums of ORSJ 210-211
- [6] Horiike K, Yoshitomi Y, Tokuyama T, and Tabuse M (2011), Music recommendation system using the time-series discrete wavelet transform and the FastICA. Proc. of 16th Int. Symposium on Artificial Life and Robotics. in press
- [7] Takahashi T (1997), Research report on songs familiar to people advanced in years (in Japanese) Journal of Japanese music therapy associate 15(1):68-75
- [8] Akahoshi T (2009), Good old anthology enjoyable for people advanced in years and troubled with dementia. Kirara shobo (in Japanese)
- [9] Music textbook database for elementary school by Kanagawa prefectural education center (in Japanese); http://kjd.edu-ctr.pref.kanagawa.jp/daizai_music/

The study of path error for an Omnidirectional Home Care Mobile Robot

Jie-Tong Zou¹ and Feng-Chun Chiang²

¹. Department of Aeronautical Engineering, National Formosa University, Taiwan
(scott@nfu.edu.tw)

². Institute of Opto-Mechatronics and Materials, WuFeng Institute of Technology, Taiwan
(q053751519@yahoo.com.tw)

Abstract:

The first objective of this research is to develop an Omnidirectional Home Care Mobile Robot. The PC-based controller can control the mobile robot platform. This service mobile robot is equipped with "Indoor positioning system" and obstacle avoidance system. The indoor positioning system is used for rapid and precise positioning and guidance of the mobile robot. The obstacle avoidance system can detect static and dynamic obstacles.

In order to understand the stability of three wheeled omni-directional mobile robot, we make some experiments to measure the rectangular and circular path error of the proposed mobile robot in this research. From the experiment results, the path error is smaller with the guidance of the localization system. The mobile robot can return to the starting point. The localization system can successfully maintain the robot heading angle along a circular path.

Keywords: Home care; intelligent mobile robot; omni-directional; localization system; heading angle.

I. INTRODUCTION

Nowadays, intelligent robots were successfully fielded in hospitals [1], museums [2], and office buildings/department stores [3], where they perform cleaning services, deliver, educate, or entertain [4]. Robots have also been developed for guiding blind people, as well as robotic aids for the elderly.

Rapid progress of standard of living and health care resulted in the increase of aging population. More and more elderly people do not receive good care from their family or caregivers. Maybe the intelligent service robots can assist people in their daily living activities. Robotics aids for the elderly have been developed, but many of these robotics aids are mechanical aids. [5] [6] [7]. The intelligent service robot can assist elderly people with many tasks, such as remembering to take medicine or measure blood pressure on time.

A service mobile robot for taking care of elderly people was developed in our laboratory [8]. This service mobile robot is equipped with "Indoor positioning system". Five reflective infrared sensors are placed around the robot for obstacle avoidance.

On the aid of an internet remote control system, remote family member can control the robot and talk to the elderly. This intelligent robot also can deliver the medicine or remind to measure the blood pressure or blood sugar on time. We hope this intelligent robot can be a housekeeper or family guard to protect our elderly people or our family. The functions of the proposed robot are illustrated as follows:

1. Deliver medicine or food on time
2. Remind to measure and record the blood pressure or blood sugar of the elderly on time
3. Remind the elderly to do something important
4. Assist the elderly to stand or walk
5. Send a short message automatically under emergency condition

6. With the remote control system, remote family member can control the robot and talk to the elderly.

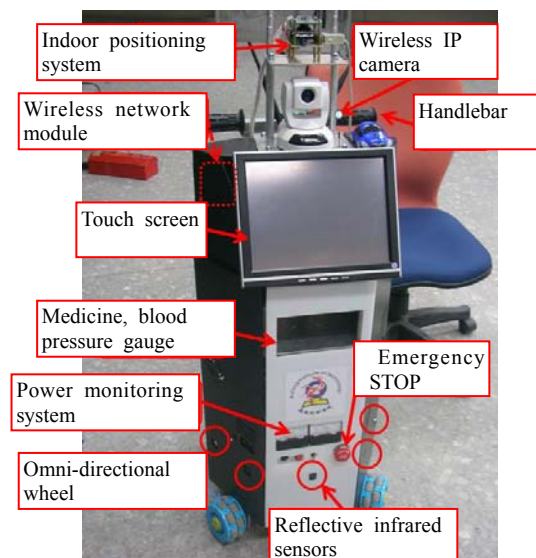


Fig.1. The proposed Omnidirectional Home Care Mobile Robot.

The proposed service mobile robot for taking care of elderly people is shown in Fig. 1. Hardware structure of the proposed mobile robot is shown in Fig. 2. A PC based controller was used to control three DC servo motors. The indoor positioning system was used for rapid and precise positioning and guidance of the mobile robot. Five reflective infrared sensors are connected to an I/O card for sensor data acquisition. The GSM modem can send a short message automatically under emergency condition. The live image of the wireless IP camera on the robot can be transferred to the remote client user.

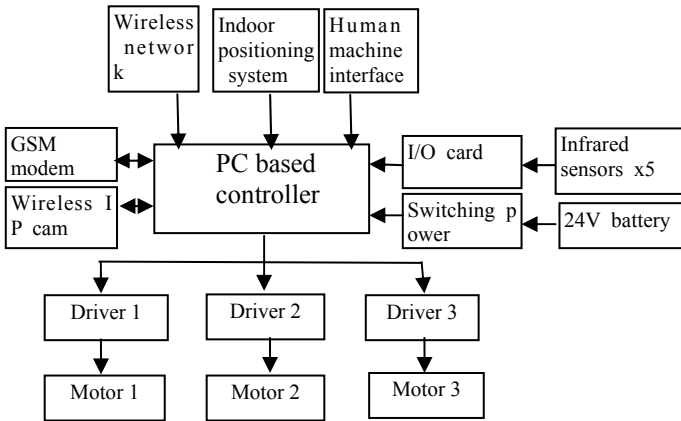


Fig.2. Hardware structure of the Omnidirectional Home Care Mobile Robot.

II. The Omni-directional Robot Platform

The proposed omnidirectional home care mobile robot is shown in Fig. 2. Many wheeled mobile robots are equipped with two differential driving wheels. Since these robots possess 2 degrees-of-freedom (DOFs), they can rotate about any point, but cannot perform holonomic motion including sideways motion[9]. To increase the mobility of this service robot, three omnidirectional wheels driven by three DC servo motors are assembled on the robot platform (see Fig. 1). The omnidirectional mobile robots can move in an arbitrary direction without changing the direction of the wheels.

The three-wheeled omni-directional mobile robots are capable of achieving 3 DOF motions by driving 3 independent actuators [10] [11], but they may have stability problem due to the triangular contact area with the ground, especially when traveling on a ramp with the high center of gravity owing to the payload they carry.

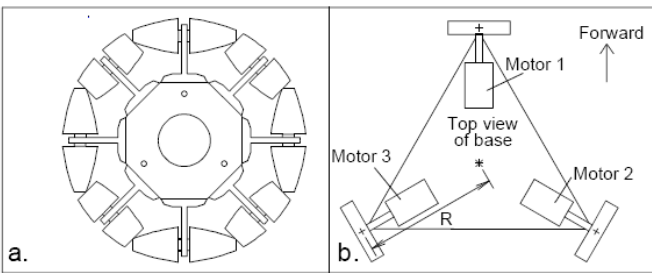


Fig.3. (a) Structure of Omni-directional wheel; (b) Motor layout of Robot platform

Fig. 3(a) is structures of the omni-directional wheel, Fig. 3(b) is the motor layout of the robot platform. The relationship of motor speed and robot moving speed is shown as:

$$\begin{aligned} V_1 &= \omega_1 r = V_x + \omega_p R \\ V_2 &= \omega_2 r = -0.5V_x + 0.867V_y + \omega_p R \\ V_3 &= \omega_3 r = -0.5V_x - 0.867V_y + \omega_p R \end{aligned} \quad (1)$$

Where:

V_i =Velocity of wheel i
 ω_i =rotation speed of motor i
 ω_p = rotation speed of robot

r =radius of wheel

R =distance from wheel to center of the platform

III. Indoor Localization System



Fig. 4. Indoor localization system (Hagisonic co.)

As shown in Fig. 4, Indoor localization system [12], which used IR passive landmark technology, was used in the proposed service mobile robot. The localization sensor module (see Fig. 5) can analyze infrared ray image reflected from a passive landmark with characteristic ID. The output of position and heading angle of a mobile robot is given with very precise resolution and high speed. The position repetition accuracy is less than 2cm; the heading angle accuracy is 1 degree.



Fig. 5. localization sensor module (Hagisonic co.)

IV. Experimental Results

In order to understand the stability of three wheeled omni-directional mobile robot, an experiment for the straight line path error had been discussed [8]. From these experimental results, when the robot moves faster or farther, the straight line error will increase. We make some experiments to measure several different paths error of the proposed mobile robot in this research.

1. Rectangular path error test for the omni-directional robot platform.

In this experiment, the proposed mobile robot will move along a rectangular path with or without the guidance of the indoor localization system. As shown in Fig. 6, the mobile robot moves along a rectangular path (a→b→c→d→a) without the guidance of the localization system. The localization system is only used to record the real path in this experiment.

In Fig. 6, solid line represents the ideal rectangular path, dot lines (■:Test1, ▲:Test2) are the real paths of the mobile robot without the guidance of the localization system. The vertical paths (path b→c and d→a) have larger path error. Finally, the mobile robot cannot return to the starting point "a".

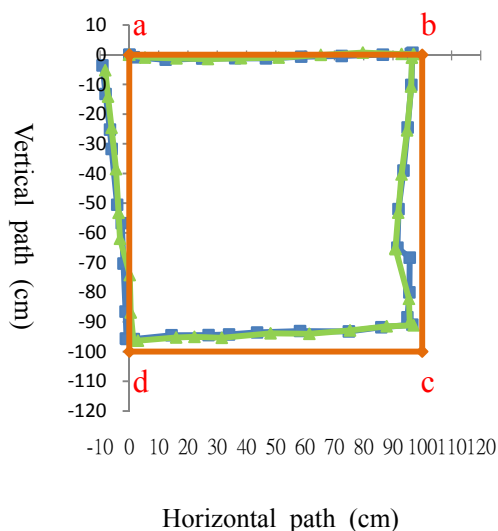


Fig. 6 Rectangular path error without the guidance of the localization system.

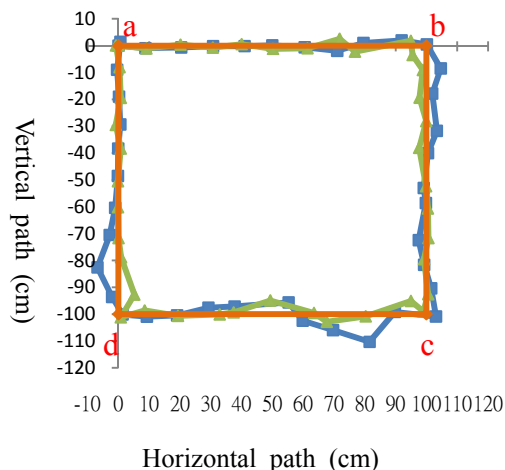


Fig. 7 Rectangular path error with the guidance of the localization system.

As shown in Fig. 7, the mobile robot moves along a rectangular path (a→b→c→d→a) with the guidance of the localization system. In Fig. 7, solid line represents the ideal rectangular path, dot lines (■:Test1, ▲:Test2) are the real paths of the mobile robot with the guidance of the localization system. With the guidance of the localization system, the mobile robot can pass through the corner points a, b, c, d. The rectangular path error in Fig.7 is smaller than that in Fig. 6. The maximum path error is under 10 cm in Fig.7. Finally, the mobile robot can return to the starting point “a”. The rectangular path is closed at point “a”.

2. Circular path error test for the omni-directional robot platform.

The omni-directional mobile robot can move in an arbitrary direction without changing the direction of the wheels. In this experiment, the proposed mobile robot will move along a circular path with or without the guidance of the indoor localization system. As shown in

Fig. 8, the mobile robot moves along a circular path without the guidance of the localization system. The robot heading angle is 90° (upwards) during this test. The localization system is only used to record the real path in this experiment.

The circular path without the guidance of the localization system is shown in Fig. 9. The shape of the real path is similar to a circle, but the starting point and the end point cannot overlap. The heading angle error with different circular angle (θ) of the robot is shown in Fig. 10. The maximum heading angle error is about 8° .

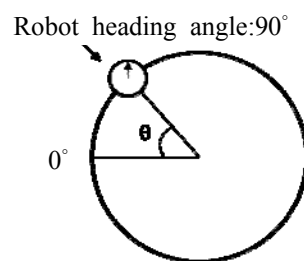


Fig. 8 Circular angle (θ) of the robot

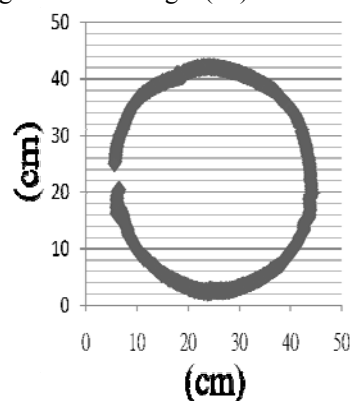


Fig. 9 Circular path without the guidance of the localization system.

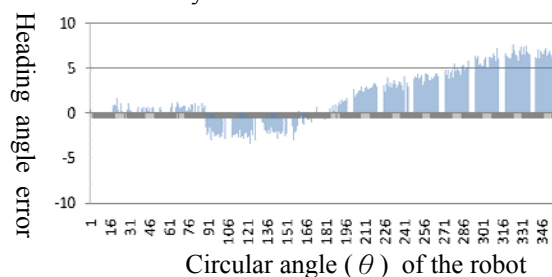


Fig. 10 Heading angle error with different circular angle (θ) of the robot

The circular path with the guidance of the localization system is shown in Fig. 11. The shape of this path is more similar to a circle; the starting point and the end point are overlapped. The heading angle error with different circular angle (θ) of the robot is shown in Fig. 12. The maximum heading angle error is about $\pm 1^\circ$. From this experiment result, the localization system can successfully maintain the robot heading angle along a circular path.

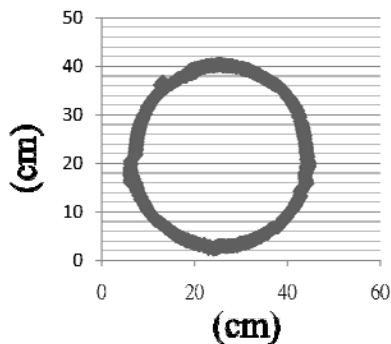


Fig. 11 Circular path with the guidance of the localization system.

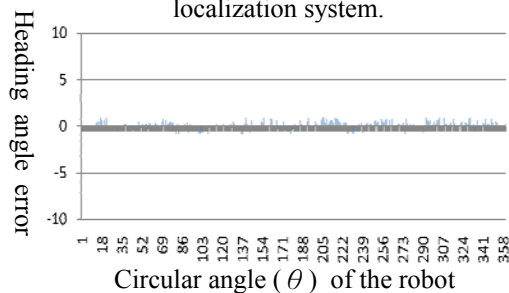


Fig. 12 Heading angle error with different circular angle (θ) of the robot

V. CONCLUSION

The objective of this research is to develop a service mobile robot for taking care of elderly people. This service mobile robot is equipped with "Indoor positioning system". The indoor positioning system is used for rapid and precise positioning and guidance of the mobile robot. Five reflective infrared sensors are placed around the robot for obstacle avoidance.

In order to understand the stability of three wheeled omni-directional mobile robot, we make some experiments to measure the rectangular and circular path error of the proposed mobile robot in this research.

Firstly, the mobile robot moves along a rectangular path without the guidance of the localization system. The experimental paths have larger path error. Finally, the mobile robot cannot return to the starting point.

With the guidance of the localization system, the mobile robot can pass through the corner points. The rectangular path error is smaller than that without the guidance of the localization system. The mobile robot can return to the starting point. The rectangular path is closed at point "a".

Secondly, the proposed mobile robot can move along a circular path with or without the guidance of the indoor localization system. The circular path without the guidance of the localization system cannot be closed. The maximum heading angle error is about 8° .

The circular path with the guidance of the localization system is more similar to a circle; the starting point and the end point are overlapped. The maximum heading angle error is about $\pm 1^\circ$. From

this experiment result, the localization system can successfully maintain the robot heading angle along a circular path.

REFERENCES

- [1] King, S., and Weiman, C, "Helpmate autonomous mobile robot navigation system", Proceedings of the SPIE Conference on Mobile Robots, Vol. 2352, pp.190-198, 1990.
- [2] Burgard, W.; Cremers, A.; Fox, D.; Hähnel, D.; Lakemeyer, G.; Schulz, D.; Steiner, W.; and Thrun, S. "Experiences with an interactive museum tour-guide robot", Artificial Intelligence, 1999.
- [3] Endres, H.; Feiten, W.; and Lawitzky, G., "Field test of a navigation system: Autonomous cleaning in supermarkets.", Proceedings of the 1998 IEEE International Conference on Robotics & Automation (ICRA 98), 1998.
- [4] Schraft, R., and Schmierer, G., "Serviceroboter", Springer verlag. In German, 1998.
- [5] Song, W.-K.; Lee, H.-Y.; Kim, J.-S.; Yoon, Y.-S.; and Bien, Z. Kares, "Intelligent rehabilitation robotic system for the disabled and the elderly. Proceedings of the 20th Inter. Conf. of the IEEE Engineering in Medicine and Biology Society, Vol. 5, pp. 2682-2685, 1998.
- [6] Dario, P.; Laschi, C.; and Guglielmelli, E., "Design and experiments on a personal robotic assistant.", Advanced Robotics 13(2), pp.153-69, 1999.
- [7] Takahashi, Y.; Kikuchi, Y.; T. Ibaraki; and Ogawa, S., "Robotic food feeder.", Proceedings of the 38th International Conference of SICE, pp. 979-982, 1999.
- [8] Jie-Tong Zou, Kuo L. Su and Feng-Chun Chiang, "The development of the Omnidirectional Home Care Mobile Robot", The Fifteenth International Symposium on Artificial Life and Robotics (AROB 15th '10), B-Con Plaza, Beppu, Oita, Japan, Feb. 4- 6, 2010.
- [9] Jae-Bok Song and Kyung-Seok Byun, "Design and Control of an Omnidirectional Mobile Robot with Steerable Omnidirectional Wheels", Mobile Robots, Moving Intelligence, pp. 576, 2006.
- [10] Carlisle, B. "An Omnidirectional Mobile Robot", Development in Robotics, Kempston, pp.79-87, 1983.
- [11] Pin, F. & Killough, S., "A New Family of Omnidirectional and Holonomic Wheeled Platforms for Mobile Robot", IEEE Transactions on Robotics and Automation, Vol. 15, No. 6, pp. 978-989, 1999.
- [12] <http://www.hagisonic.com/>

A* Searching Algorithm Applying in Chinese Chess Game

Cheng-Yun Chung¹, Te-Yi Hsu², Jyh-Hwa Tzou³, Kuo-Lan Su⁴,

1. *graduate school Engineering Science and technology, National Yunlin University of Science & Technology*

2. *Industrial Technology Research Institute, Taiwan*

3. *Department of Aeronautical Engineering, National Formosa University, Taiwan*

4. *Department of Electrical Engineering, National Yunlin University of Science & Technology, Taiwan*

E-mail: g9610808@yuntech.edu.tw, teyihsu@itri.org.tw, scott@nfu.edu.tw, sukl@yuntech.edu.tw

Abstract: The article presented A* searching algorithm based to be applied in path planning of Chinese chess game, and used multiple mobile robots to present the scenario. The mobile robot has the shape of cylinder and its diameter, height and weight is 8cm, 15cm and 1.5kg. The controller of the mobile robot is MCS-51 chip. We play the Chinese chess game using multiple mobile robots according to the evaluation algorithm of Chinese chess game, and calculate the displacement by the encoder. The A* searching algorithm can solve shortest path problem of mobile robots from the start point to the target point on the chess board. The simulated results can found the shortest motion path for mobile robots (chesses) moving to target points from start points in a collision-free environment. Finally, we implement the simulated results on the Chinese chess board using mobile robots. Users can play the Chinese chess game using the supervised computer via wireless RF interface. The scenario of the Chinese chess game feedback to the user interface using image system.

Keywords: A* searching algorithm, Chinese chess game, mobile robot, wireless RF interface

I. INTRODUCTION

Chinese chess [1] game is one of the most popular games. A two-player game with a complexity level is similar to Western chess. In the recent years, the Chinese chess game has gradually attracted many researches' attention. The most researchers of the fields is belong to computer science, expert knowledge and artificial intelligent. Chinese chess game is not only the most old-line chess game in the world, but also more complex than other chess game. There are many evolutionary algorithms to be proposed. Darwen and Yao proposed the co-evolutionary algorithm to solve problems where an object measure to guide the search process is extremely difficult to device [2]. Yong proposed multiagent systems to share the rewards and penalties of successes and failures [3].

The application of co-evolutionary models to learn Chinese chess strategies, and uses alpha-beta search algorithm, quiescence search and move ordering [4]. Wang use adaptive genetic algorithm (AGA) to solve the problem of computer Chinese chess [5]. Lee and Liu take such an approach to develop a software framework for rapidly online chess games [6]. Zhou and Zhang present the iterative sort search techniques based on percentage evaluation and integrate percentage evaluation and iterative sort into problem of Chinese chess computer game [7]. Su and Shiao develop smart mobile robot using microchip, and program the trajectories for multiple mobile robot system [8]. The article used the evolutionary method to build up the rules of the Chinese chess game. In some condition, the mobiles robot (chess) must avoided the other chess moving to the next position. We used A* searching algorithm to program the short motion path on the Chinese chess game. A* heuristic function are introduced to improve local

searching ability and to estimate the forgotten value [9]. We use A* searching algorithm to program motion paths for multiple mobile robots in the article.

The paper is organized as follows: Section II describes the system structure of the multiple robot based Chinese chess game system, and describes the structure of the mobile robot. Section III explains the evaluation method of the Chinese chess game using multiple mobile robots, and described A* searching algorithm for path planning of mobile robots from the start point moving to the target point. The experimental results are implemented in section IV. Section V presents brief concluding comments.

II. SYSTEM ARCHITECTURE

The system architecture of the multiple robot based Chinese chess game system is shown in Fig 1. The system contains a supervised computer, an image system, a wireless RF interface, a remote supervised computer, a color CCD and thirty-two mobile robots. There are two algorithms (evaluation algorithm and A* searching algorithm) to be implemented in the supervised computer. The Chinese chesses (Mobile robots) are classified red side and black side. There are sixteen chesses in each side. The supervised computer can control mobile robots to present the motion trajectory of the mobile robots, and receives the status of the mobile robot via wireless RF interface. The signals contain the ID code, orientation and displacement of mobile robots. The supervised computer can transmit the ID code and command to the mobile robot. The mobile robot moves the next point according to the command, and transmits the ending code to the supervised computer via wireless RF interface. The Chinese chess system can transmit the real-time image to the supervised

computer via image system. Users can play the Chinese chess game with others on the supervised computer using mouse, or play the game on the remote supervised computer via wireless Internet.

The mobile robot has the shape of cylinder, and it's equipped with a microchip (MCS-51) as the main controller, two DC servomotors and driver devices, some sensor circuits, a voice module, three Li batteries, a wireless RF interface and some reflect IR sensors. Meanwhile, the mobile robot has four wheels to provide the capability of autonomous mobility. The structure of the mobile robot is shown in Fig. 2.

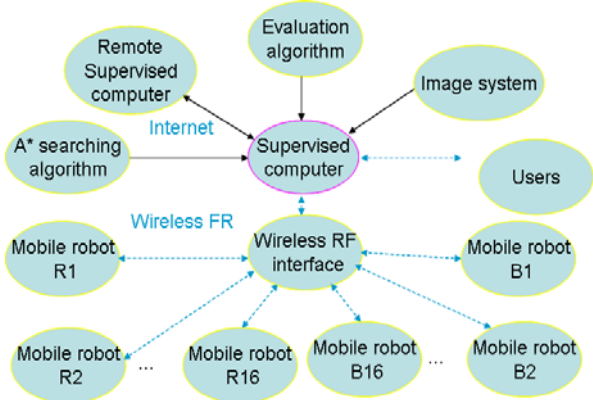


Fig. 1 The architecture of the Chinese chess system

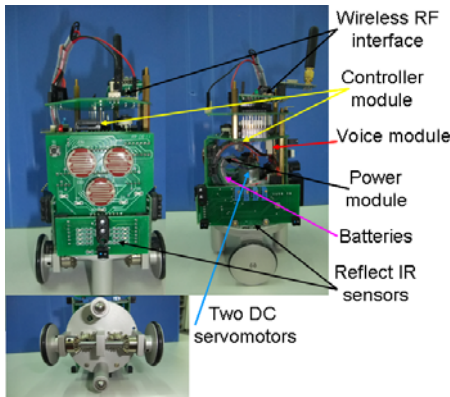


Fig. 2. The structure of the mobile robot

The controller of the mobile robot can acquire the detection signal from sensors through I/O pins, and receives the command via wireless RF interface, and transmits the detection results to the supervised computer via wireless RF interface. The switch input can turn on the power of the mobile robot, and selects power input to be Li batteries or adapter. The encoder of the servomotor can calculate the moving distance. We can set the pulse number for per revolution to be P , and the mobile robot move pulse number from the encoder to be B . We can calculate the displacement D of the mobile robot using the equation.

$$D = 4.25 \times \pi \frac{B}{P} \quad (1)$$

The diameter of the wheel is 4.25 cm. The chess board is grid platform to be shown in Fig. 3. The arrangement of the chess board is 11 grids on the horizontal direction (X axis), and is 12 grids on the vertical direction (Y axis). The distance is 30cm between the center of corridor on the X axis and Y axis of the

chess board, and the width of the corridor is 12cm. The mobile robot uses IR sensors to detect obstacles, and decides the cross points of the chess board.

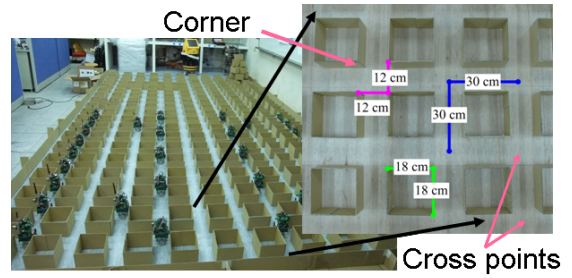


Fig. 3 The chess board of the Chinese chess game

III. ALGORITHM ANALYZE

The evaluation algorithm of the Chinese chess game is defined by the attribution of the chesses. The definition of the board is shown in Fig. 4. Then we define the initial position all chess pieces. Such as the position of "red king" is (5,1), and "black king" is (5,10)...etc. We plot the possible motion trajectory using black line for the chesses on the board. Then we define the evaluation algorithm, and move the chess piece to the target point. Such as the chess piece "black horse" can move to the position (1,8), (3,8) or (4,9). But the chess piece can't move to the position (4,9) according to the rules of the Chinese chess game. The chess "black horse" has an obstacle (black elephant) on the right side.

We define the start positions of the chesses to be (x, y) , and define the movement rules of the chesses as following. n is movement displacement on the x axis, and m is movement displacement on the y axis. n and m must be plus integrate. The rules of the Chinese chesses are listed in the reference [10].

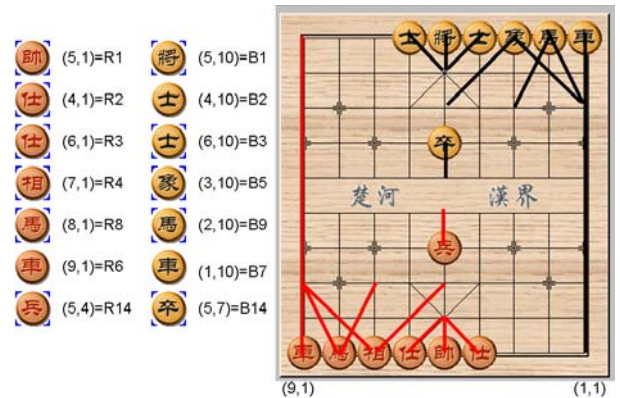


Fig. 4 The definition of the Chinese chesses

A* searching algorithm is proposed by Hart in 1968, and solve the shortest path problem of multiple nodes travel system. The formula of A* searching algorithm is following

$$f(n) = g(n) + h(n) \quad (2)$$

The core part of an intelligent searching algorithm is the definition of a proper heuristic function $f(n)$. $g(n)$ is the exact cost at sample time n from start point to the target point. $h(n)$ is an estimate of the minimum cost from the start point to the target point. In this study, n is reschedules as n' to

generate an approximate minimum cost schedule for the next point.
The equation (2) can be rewritten as follows:

$$f(n) = g(n) + h(n') \quad (3)$$

We make an example to explain algorithm. Such as a mobile robot move to the target point “T” from the start point “S”. The position of the start point is (2,6), and the target position is (2,9). We set some obstacle on the platform. The white rectangle is unknown obstacle. The black rectangle (obstacle) is detected by the mobile robot using A* searching algorithm. We construct two labels (Open list and Close list) in the right side of Fig. 5. The neighbour points of the start point fill in the “Open list”. The “Close list” fills the start point and evaluation points. We construct label on the first searching result to be shown in Fig. 5. We calculate the values of $f(n)$, $g(n)$ and $h(n)$ function, and use the proposed method to compare the values of the function. We select the minimum value of the function $f(n)$ to be stored in “Close list”. We can find the target point on the final searching result to be shown in Fig. 5, and we can decide a shortest path to control the mobile robot moving to the target point.

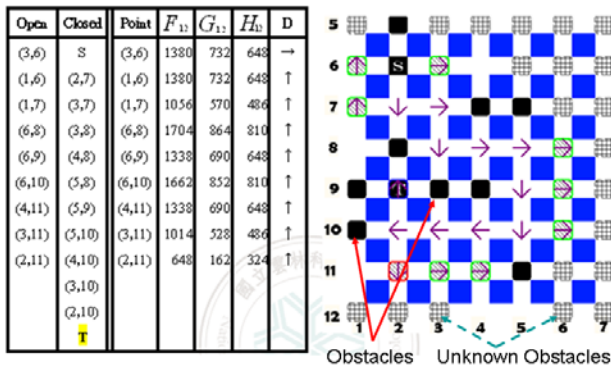


Fig.5 The final searching result

The total distance of the shortest path C_{st} can be calculated as

$$C_{st} = \sum_{n=1}^m G_n(m=t-1) = 2043 \quad (4)$$

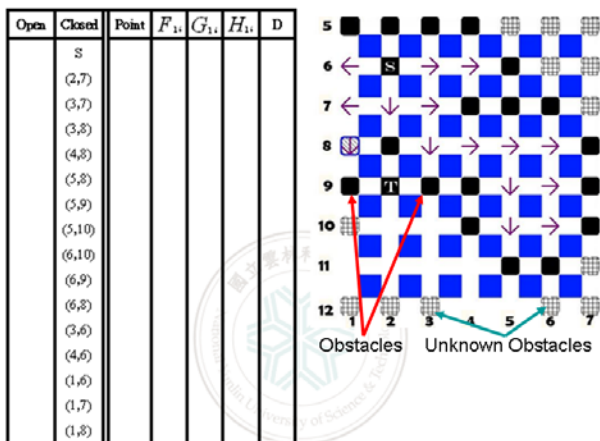


Fig. 6 The final searching result

In the other condition, we rebuild the positions of the obstacles on the platform to be shown in Fig. 6. The mobile robot

can't find the path C_{st} moving to the target position using the proposed method. The total distance C_{st} as

$$C_{st} = \infty \quad (5)$$

IV. EXPERIMENTAL RESULTS

We implement some experimental results on the multiple mobile robots based Chinese chess game system. The first experimental scenario is “red elephant”. The user moves the chess “red elephant” using the mouse to be shown in Fig. 7 (a). The start position of the “red elephant” chess is (3,1). The supervised computer orders the command to the mobile robot “red elephant”. The chess piece moves forward two grids, and turn left angle to be $\pi/4$. Then the mobile robot moves two grids to the next position (5,3), and turn right angle $\pi/4$ to face the black side and stop. The user interface of the Chinese chess game system uses multiple mobile robots to be shown in Fig. 7(a). The mobile robot can calculate the displacement via encoder, and speak the movement status of the mobile robot using voice module, too. The experimental scenarios use the mobile robot to execute the motion path of the chess “red elephant” to be shown in Fig. 7 (b)-(e). There is not obstacle on the motion path of the chess. We don't the shortest path using A* searching algorithm.

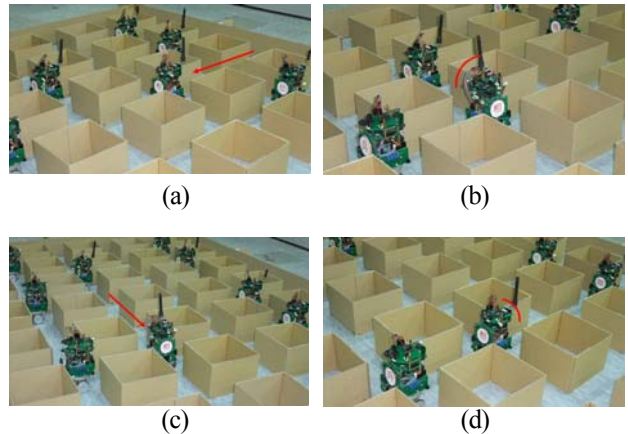
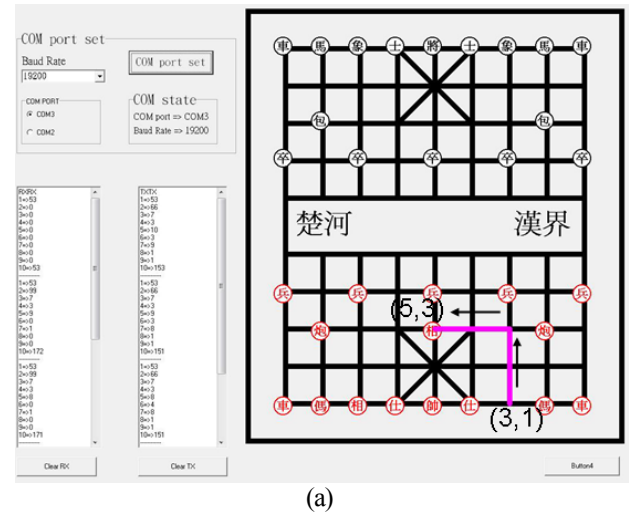
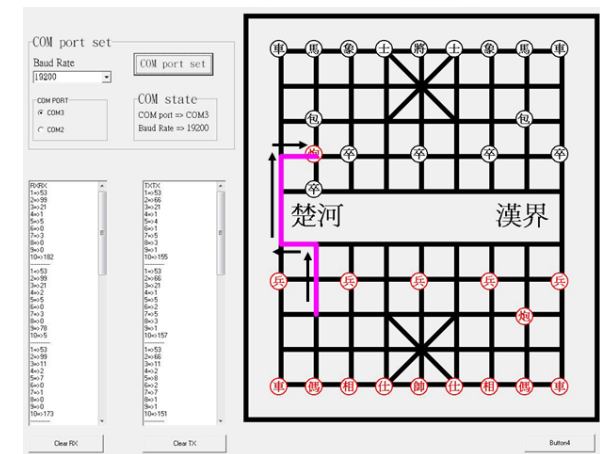


Fig. 7 The experimental result for “red elephant”

The second experimental scenario is “red cannon”. The user moves the chess piece “red cannon” using the mouse to be shown in Fig. 8 (a). The start position of the “red cannon” chess is (8,3),

and the target point is (8,7). The motion path of the mobile robot (red cannon) has obstacle (chess). The supervised computer reconstructs all possible paths using A* searching algorithm for red cannon step by step. Finally, we can find out the shortest path to avoid the obstacle (chess). The path can displays on the interface using red line. The supervised computer controls the mobile robot moving to the target point from the start point using the shortest path to avoid the obstacle. The experiment result is shown in Fig. 8 (a). The supervised computer calculates the cost $f(n)$ to be listed on the left side of the Fig. 8 (a).

The supervised computer orders the command to the mobile robot "red cannon". The chess piece moves forward two grids, and turn left angle to be $\pi/4$. Then the mobile robot moves one grid to, and turn right angle $\pi/4$. Then the mobile robot moves two grids, and turn right angle $\pi/4$. Finally the mobile robot moves one grid to the next position (8,7), and turn left angle $\pi/4$ to face the black side and stop. Finally, the experiment scenarios are shown in Fig. 8(b)-(e).



(a)



(b)



(c)



(d)



(e)

Fig. 8 The experimental result with obstacle

V. CONCLUSION

We have presented a Chinese chess game system using multiple mobile robots. The system contains a supervised computer, a wireless RF interface, a remote supervised computer, an image system and thirty-two mobile robots (chesses). The mobile robot has the shape of cylinder and its diameter, height and weight is 8cm, 15cm and 1.5kg, and executes the chess attribute using two interfaces. One is wireless RF interface, and the other is voice interface. We develop the user interface on the supervised

computer for the Chinese chess game system. The supervised computer can control mobile robots using evaluation algorithm according to the rule of Chinese chess game, and receive the status of mobile robots via wireless RF interface. The chess (mobile robot) has obstacle on the motion path, and uses A* searching algorithm to program the shortest path moving to the target point. In future, we want to develop the artificial intelligent rule to decide which side (red or black) to be a winner.

ACKNOWLEDGMENT

This work was supported by the National Science Council of Taiwan, R. O. C. under Grand NSC 99- 2221- E-224-060.

REFERENCE

1. S. J. Yen, J. C. Chen, T. N. Yang and S. C. Hsu (2004) Computer Chinese Chess, ICGA Journal, Vol.27, No. 1, pp.3-18
2. P. Darwen and X. Yao (2002) Coevolution in Iterated Prisoner's Dilemma with Intermediate Levels of Cooperation: Application to Missile Defense, International Journal of Computational Intelligence Applications, Vol. 2, No. 1, pp.83-107
3. C. H. Yong and R. Miikkulainen (2001) Cooperative Coevolution of Multi-agent Systems, University of Texas, Austin, USA, Tech. Rep. AI01-287
4. C. S. Ong, H. Y. Quek, K. C. Tan and A. Tay (2007) Discovering Chinese Chess Strategies Through Coevolutionary Approaches, IEEE Symposium on Computational Intelligence and Games, pp.360-367
5. J. Wang, Y. H. Luo, D. N. Qiu and X. H. Xu (2005) Adaptive Genetic Algorithm's Implement on Evaluation Function in Computer Chinese Chess, Proceeding of ISCIT, pp.1206-1209
6. W. P. Lee, L. J. Liu and J. A. Chiou (2006) A Component-Based Framework to Rapidly Prototype Online Chess Game for Home Entertainment, IEEE International Conference on System, Man and Cybernetics, pp.4011-4016
7. W. Zhou, J. L. Zhang and Y. Z. Wang (2008) The Iterative Sort Search Techniques Based on Percentage Evaluation, Chinese Control and Decision Conference, pp.5263-5266
8. K. L. Su, S. V. Shiao, J. H. Guo and C. W. Shiao (2009) Mobile Robot Based Onlin Chinese Chess Game, The Fourth International Conference on Innovative Computing, Information and Control, pp.63
9. Y. Saber and T. Senjyu (2007) Memory-bounded ant colony optimization with dynamic programming and A* local search for generator planning, IEEE Trans. on Power System, Vol.22, No. 4, pp.1965-1973
10. S. H. Chia, K. L. Su, C. C. Wang and S. V. Shiao (2010) Multiple Robot System Applying in Chinese Chess Game, The Innovative Computing, Information and Control – Express Letters (ICIC-EL), Vol. 4, No. 5(B), pp.2027-2032

Multi-robot Based Intelligent Security System

Yi-Lin Liao¹, Kuo-Lan Su²

1. graduate school Engineering Science and technology, National Yunlin University of Science & Technology

2. Department of Electrical Engineering, National Yunlin University of Science & Technology, Taiwan

E-mail: g9910801@yuntech.edu.tw, sukl@yuntech.edu.tw

Abstract: The article develops a multiple security modules based intelligent security system that has multiple communication interfaces to be applied in home automation. The interfaces of the intelligent security system contain wire RS485, wireless RF and Internet. The detection modules of the system have active security modules and passive security modules. The passive security modules contain wire security modules and wireless security modules. The control unit of all security modules is HOLTEK microchip. Each security module has two variety interfaces. They use voice module to alarm users for event condition, and transmit the real-time event signals to the supervised computer via wire RS485 or wireless RF interface. If the event occurrence, the supervised computer calculates the belief values using Dempster-Shafter evidence theory according to the passive wire and wireless security modules. The belief value is over the threshold. The supervised computer controls the mobile robot moving to the event location, and receives the signal from the mobile robot via wireless RF interface, and recognizes the final decision output using Dempster-Shafter evidence theory, and displays detection and decision output values on the monitor of the user interface. Finally, we present some experimental results using wire passive security modules, wireless passive security modules and active security modules on the fire detection and gas leakage detection using the platform of the intelligent security system.

Keywords: home automation, wire RS485, wireless RF, Internet, HOLTEK microchip, Dempster-Shafter evidence theory

I. INTRODUCTION

Intelligent buildings and home can provide safety, convenience and welfare for human living in the 21st century, and control and manage resource with minimum life-time costs. An intelligent building system (IBS) is the integration of various systems. They contain security system, building heating, ventilating and air-conditioning (HVAC) technologies, computer system, tele-communication and Internet. The most important role of the intelligent building is security system. In generally, the security system contains supervised system, active security modules, passive security modules and appliance control modules, and uses redundant and complementally information fusion algorithms to enhance system reliability and certainty of intelligent building, and construct the safety network using multiple level protection.

In the past literatures, many experts research in the security system. Wang and So [1] presented the history of development of building automation system (BAS). The structure of features of a modern BAS was introduced and future trends of BAS are discussed. Azegami and Fujiyoshi [2] described a systematic approach to intelligent building design. Kujuro and Yasuda [3] discussed the systems evolution in intelligent building. The quality of building services can be enhanced by updated information processing and communications functions of building automation systems. Finley *et al.* [4] presented a survey of intelligent building and reviews issues such as system perspective, subsystem services, and multi-tenant building. Chung and Fu expect to set up the standard of appliances and communication protocols, and propose a complete system architecture with integrate control kernel to construct an intelligent building system [5].

In recent years, mobile robots have been widely applied in the security system as the active security modules. Recently more and more research takes interest in the field especially intelligent service robot. There are some successful examples, ASIMO, KHR, QRIO, WABIAN-2R and AIBO. In our lab, we have been designed a fighting mobile robot (ISLR-I) [6] and a module based mobile robot [7]. The research field of mobile robot includes many directions, such as motion planning, vision system, self-location, speech recognition, supervised and remote supervised communication and environment detection. Yoichi Shimosasa *et al.* developed autonomous guard robot [8, 9] which integrate the security and service system, the robot can guide visitors in daytime and patrol at the night.

The paper is organized as follows: section II describes the system structure of the multiple mobile robots based intelligent security system for intelligent home. The functions of the mobile robot are described in Section III. The section IV presents the Dempster-Shafter evidence theory to be applied in the intelligent security system. Section V presents the experimental results of the system on the fire detection and gas leakage detection. The brief concluding comments are described in Section VI.

II. SYSTEM ARCHITECTURE

The system architecture of the multiple robots based intelligent security system is shown in Fig 1. The system contains three levels. There is passive detection level, active detection level and system supervised level [10]. We develop the user interface using Visual Basic language for the security system. The system supervised

level receives detection signals via wire RS485 or wireless RF interface, and control the multiple mobile robots moving to the event location via wireless RF interface.

In the architecture, there are many security detection modules and appliance control modules in the system. They are independent and autonomous, and can work concurrently. Each module of the security system can transmits the measurement values, parameter values and decision results to the active security modules and the supervised computer via wireless RF interface. The active security and passive security modules can speech Chinese on real-time event status using voice module. Users can reset the critical values of these modules from the user interface of the supervised computer.

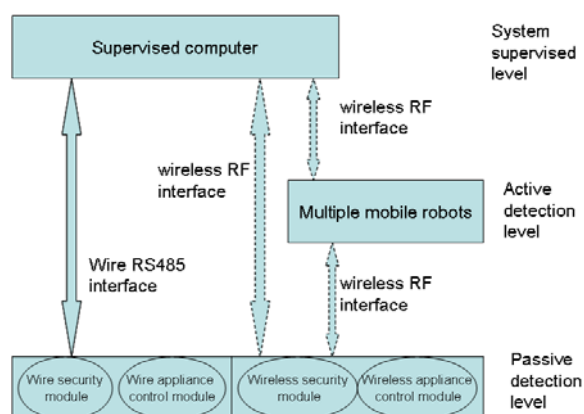


Fig. 1 The system architecture



Fig. 2 The platform of the security system

The controller of the security modules is HOLTEK microchip. These modules of the passive detection module are classified three types. There are wire security modules, wireless security modules and wire/wireless appliance control modules. The active detection level may be some remove platforms. The main device of the security system is mobile robots. We arrange an ID code in each module, and identify the module function by the ID code. The experimental platform of the multiple mobile robots based security system is shown in Fig. 2. The platform has three floors, and contains three rooms for each floor. The supervised computer controls the elevator to carry the mobile robots moving to the event location via wireless RF interface. The mobile robot communicates with the elevator via wireless RF interface, and controls the status of the elevator. Each room contains more than one wire security module, one wireless security module and one appliance control module. We arrange the same detection function security modules with wire or wireless interface on the same location enhance the detection precision using Dempster-shafter's

evidence theory.

The user interface of the intelligent security system is shown in Fig. 3. The user interface contains two parts. The right side is fire detection function. The other side is gas detection function. The upper part of each side displays the image from the camera. The bottom can displays the detection and decision results from three security modules (wire/wireless security modules and mobile robot), and controls the direction of the camera using mouse. We use the green label to present no event status of the security modules, and use red label to present event status for fire or gas leakage event.

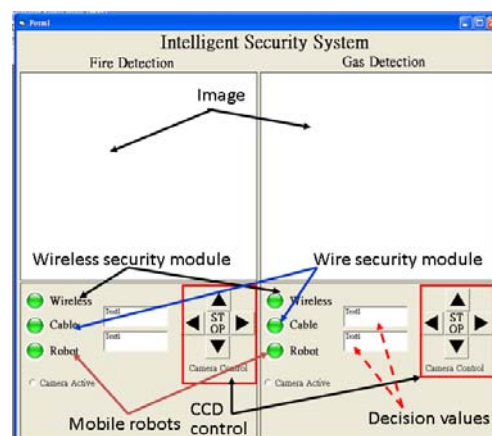


Fig. 3. The structure of the mobile robot

III. MOBILE ROBOT

The mobile robot has the shape of cylinder, and it's equipped with a HOLTEK microchip as the main controller, two DC servomotors and driver devices, one compass module, obstacle detection devices, security modules (fire detection device or gas detection module), a voice module, three Li batteries and a wireless RF interface. Meanwhile, the mobile robot has four wheels to provide the capability of autonomous mobility. The mobile robot can carries variety sensors (fire or gas) moving on the platform of the security system. The structure and the hardware devices of the mobile robot are shown in Fig. 4.

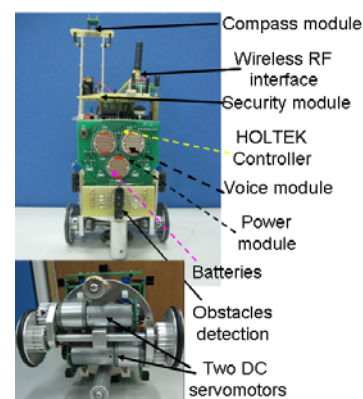


Fig. 4. The structure of the mobile robot

The controller of the mobile robot can acquires the detection signal from sensors using I/O pins, and receives the command from the supervised computer via wireless RF interface, and transmits the detection signals to the supervised computer via

wireless RF interface. The detection signals are fire event or gas leakage signal. The switch input can turn on the power of the mobile robot, and selects power input to be Li batteries or adapter. The encoder of the servomotor can calculates the moving distance. We can set the pulse numbers of per revolution to be P on the wheel of the mobile robot, and the mobile robot move pulse numbers to be B . We can calculate the displacement D of the mobile robot using the equation

$$D = 4.25 \times \pi \frac{B}{P} \quad (1)$$

The diameter of the wheel is 4.25 cm. The compass module can transmits the measurement values (x and y) of two axes (X axis and Y axis) to the controller of the mobile robot. It can calculate the orientation angle θ using Eq. (2). The supervised computer can controls the direction of the mobile robot using the compass module.

$$\theta = \tan^{-1}(-y/x) \quad (2)$$

IV. ALGORITHM ANALYZE

The development of evidence theory began in the 1960s when Dempster [11,12] developed the mathematical foundations of a two-value uncertainty mapping, upper and lower uncertainty measures, between two space. The system is satisfied the assumption with two value output on event detection. A result of this work is dempster's rule of combination, which operates on belief or mass functions as Baye's rule dose on probability functions. Shafer [13], a student of Dempster, has extended the development of belief functions and is the major proponent of evidence theory.

A brief overview of the Dempster-shafter's evidence theory is provided as follows. Let θ represents the set of hypotheses H_n , called the frame of discernment. The knowledge about the problem induces a basic belief assignment which allows to define a belief function m from 2^θ to $[0,1]$ such as [14]:

$$m(\Phi) = 0 \quad (3)$$

$$\sum_{H_n \subseteq \theta} m(H_n) = 1 \quad (4)$$

Subsets H_n of θ such that $m(H_n) > 0$ are called focal elements of m . From this basic belief assignment m , the credulity $Bel(H_n)$ and plausibility $Pl(H_n)$ can be computed using the equations:

$$Bel(H_n) = \sum_{A \subseteq H_n} m(A) \quad (5)$$

$$Pl(H_n) = \sum_{H_n \cap A \neq \phi} m(A) \quad (6)$$

The value $Bel(A)$ quantifies the strength of the belief that event A occurs. These functions (m , Bel and Pl) are derived from the concept of lower and upper bounds for a set of

compatible probability distributions. In addition, Dempster-Shafer's theory allows the fusion of several sources using the Dempster's combination operator. It is defined like the orthogonal sum (commutative and associative) following the equation:

$$m(H_n) = m_1(H_n) \oplus \dots \oplus m_M(H_n) \quad (7)$$

For two sources S_i and S_j , the aggregation of evidence for a hypothesis $H_n \subseteq \theta$ can be written:

$$m(H_n) = \frac{1}{K} \sum_{A \cap B = H_n} m_i(A) \cdot m_j(B) \quad (8)$$

where K is defined by:

$$K = 1 - \sum_{A \cap B = \phi} m_i(A) \cdot m_j(B) \quad (9)$$

The normalization coefficient K evaluates the conflict between two sources. An additional aspect of the Dempster-Shafer's theory concerns the attenuation of the basic belief assignment m_j by a coefficient α_j for a source S_j . For all $H_n \subseteq \theta$, the attenuated belief function can be written as:

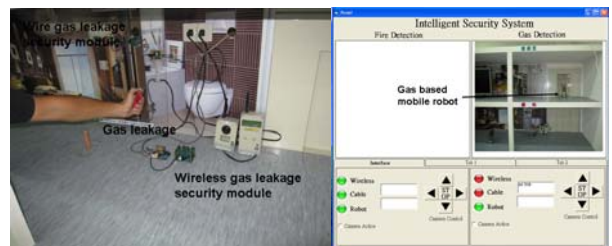
$$m_{(\alpha,j)}(H_n) = \alpha_j \cdot m_j(H_n) \quad (10)$$

$$m_{(\alpha,j)}(\theta) = 1 - \alpha_j + \alpha_j \cdot m_j(\theta) \quad (11)$$

V. EXPERIMENTAL RESULTS

In the intelligent security system, we use wire and wireless gas security modules and gas based mobile robot to detect the gas leakage on the platform. We use one lighter to provide gas on the gas leakage detection modules. The modules can transmit the detection results to the supervised computer via wire RS485 and wireless RF interface. The label of the gas security modules displays red. The experimental results are shown in Fig. 5 (a). The belief value is 0.8522 over the threshold value using Dempster-Shafer evidence theory. The experimental results are shown in Fig. 5 (b).

The supervised computer controls the mobile robot with gas detection sensor moving to the event location. The mobile robot detects the gas leakage event, and transmits the event signal to the supervised computer. The experimental result is shown in Fig. 5(c). The supervised computer receives the event signal to calculate the belief value using Dempster-shafter evidence theory to be shown in Fig. 5 (d). The value is over the threshold value, and alarm the event to users.



(a)

(b)

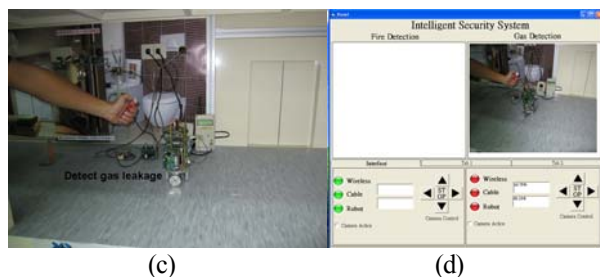


Fig. 5 The experimental result for gas leakage detection

Then we use wire and wireless fire security modules and fire based mobile robot to detect the fire source on the platform, too. The modules detect fire event, and transmit the detection results to the supervised computer via wire RS485 and wireless RF interface. The label of the fire security modules displays red. The experimental results are shown in Fig. 6 (a). The belief value is 0.8522 over the threshold value, and the experimental result is shown in Fig. 6 (b). The supervised computer controls the fire based mobile robot moving to the event location, and transmits the event signal to the supervised computer. The experimental result is shown in Fig. 6 (c). The supervised computer receives the event signal to calculate the belief value using Dempster-shafter evidence theory to be shown in Fig. 6 (d).

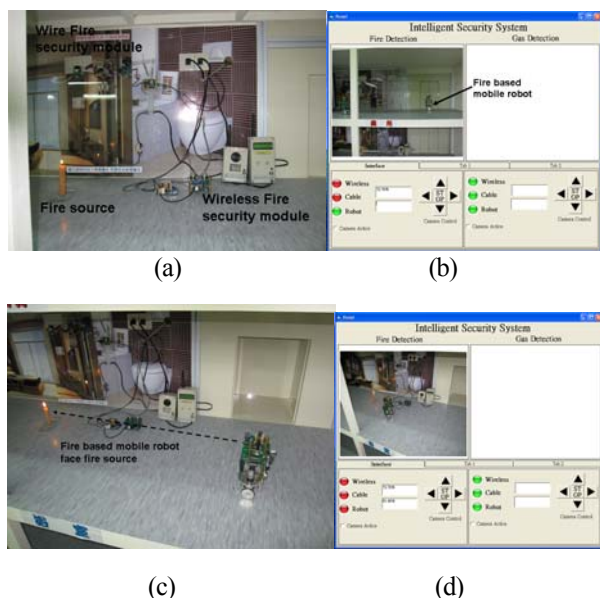


Fig. 6. The experimental result for fire source detection

VI. CONCLUSION

We have presented a multiple mobile robots based intelligent security system that has multiple interfaces to be applied in intelligent home. The controller of the security modules and active modules (mobile robots) is HOLTEK microchip. We use Dempster-Shafter evidence theory to enhance the detection results using passive and active security modules. The security detection modules and the mobile robots can transmit real-time event signals to the supervised computer via wire RS485 or wireless RF interface. In the paper, we use fire and gas leakage events to implement the function of the multiple mobile robots based security system for intelligent home. The experimental results are very nice to double check the event occurrence on the system. In

the future, we want to increase intelligent security detection modules, and use multisensory fusion algorithm to enhance the precision of the security system, and develop remote supervised system to connect with the security system via Internet. The security decreases the false alarm condition for the event detection.

ACKNOWLEDGMENT

This work was supported by the project "Development of a module based education robot" under Ministry of Education of Taiwan. (99-A010-5).

REFERENCES

- [1] C. W. Wang and A. T. P. So (1997), Building Automation In The Century, The 4-th International Conference on Advance on Advances in Power System Control, Operation Management, APCOM-97, Hong Kong, , pp.819-824.
- [2] M. Azegami and H. Fujixoshi (1993), A systematic Approach to Intelligent Building Design, IEEE Communications Magazine, pp.46-48.
- [3] A. Kujuro and H. Yasuda (1993), Systems Evolution in Intelligent Building, IEEE Communication Magazine, pp.22-26.
- [4] M. R. Finley, Jr. A. Karajura *et al.* (1991), Survey of Intelligent Building Concepts, IEEE Communication Magazine, pp.18-20.
- [5] W. Y. Chung, L. C. Fu *et al.* (2001), A Flexible, Hierarchical and Distributed Control Kernel Architecture for Rapid Resource Integration of Intelligent System, IEEE International Conference on Robotics Automation, Seoul, Korea, pp.1981-1987.
- [6] K. L. Su (2006), Automatic Fire Detection System Using Adaptive Fusion Algorithm for Fire Fighting Robot, IEEE International Conference on System, Man and Cybernetics (SMC 2006), Grand Hotel, Taipei, Taiwan, pp966-971.
- [7] S. H. Chia, K. L. Su *et al* (2010), Multiple Robot System Applying in Chinese Chess Game, The Innovative Computing, Information and Control – Express Letters (ICIC-EL), Vol. 4, No. 5(B), pp.2027-2032.
- [8] Y. Shimosasa, J. Kanemoto *et al* (2010), Some Results of The Test Operation of a Security Service System With Autonomous Guard Robot, IEEE International Conference on Industrial Electronic, Control, and Instrumentation, pp.405-409.
- [9] Y. Shimosasa, J. Kanemoto *et al* (1999), Security Service System Using Autonomous Mobile Robot, IEEE International Conference on System, Man, and Cybernetics, pp.825-829.
- [10] S. H. Chia, K. L. Su (2010), Multi-level Multi-sensor Based Security System for Intelligent Home, International Symposium on Artificial Life and Robotics (AROB 15th), Beppu, Japan, Feb. 4-6, pp.379-382.
- [11] A. P. Dempster (1967), Upper and Lower Probabilities Induced by a Multivalued Mapping, Ann Math Statistics, Vol38.
- [12] A. P. Dempster (1968), Ageneralization of Bayesian Inference, J. Royal Statistical Soc, Series B, Vol30.
- [13] G. A. Shafer (1967), Mathematical Theory of Evidence, Princeton university Press, Princeton, NJ.
- [14] E. Lefevre and O Colot (1999), A Classification Method Based On the Dempster-Shafer's theory and information criteria, ISIF , pp.1179-7786.

Implementation of an Auction Algorithm Based Multiple Tasks Allocation Using Mobile Robots

Kuo-Lan Su¹, Jr-Hung Guo², Chun-Chieh Wang³ and Cheng-Yun Chung²

1. *Department of Electrical Engineering, National Yunlin University of Science & Technology, Taiwan*
2. *graduate school Engineering Science and technology, National Yunlin University of Science & Technology*
3. *Department of Electronic Engineering Chienkuo Technology University, Taiwan*
E-mail: sukl@yuntech.edu.tw, g9710801@yuntech.edu.tw, jasonccw@ctu.edu.tw

Abstract: The article uses the ant colony system (ACS) and auction algorithms to solve the path planning and task allocation problems of multiple mobile robots such that the robots can move from different start points to reach to different task points in a collision-free space. Ant colony optimization (ACO) is a new evolution algorithm that is proposed by Dorigo M., and solves some task allocation and target searching problems. The utilization of the auction algorithm improve the efficiency of the tasks allocation. The article uses three performance functions to compare the cost on the motion displacement and waiting time for mobile robots. In this manner, a near optimal assignment of multiple task points according to a team objective can be obtained using the proposed algorithms. The simulated results present that Ant colony optimization and auction algorithm find the optimization motion path for multiple mobile robots moving to task points from start points in a collision-free environment.

Keywords: ant colony system. auction algorithm. path planning. Task allocation. multiple mobile robots.

I. Introduction

There have been a growing interest in multi-robot coordination research in recent years. Multi-robot cooperation is fundamental and significant in the robotic research fields. With the increasing number of robots in one task team efficiency important and energy consumption reduction research become more important in robots coordination. Compared to single robot, multiple mobile robots can operate to faster task completion, higher quality solutions, as well as increased robustness ability to compensate robot failure [1]. The path planning and task allocation problems of the multiple mobile robots are important research issues. Its task is to find collision-free paths from different start points moving to the different target points in an known or unknown environment with obstacles according to a reasonable algorithm.

Motion control and path planning of the wheel based mobile robots is a currently active area of robot research field. The motion control of multiple mobile robots for path tracking [2], navigation [3,4], wall following [5], task allocation [6] and path planning [7] has been proposed [8]. How to cooperate effectively with multiple robot is a challenge. To overcome the challenge, many cooperation algorithms have been proposed which mainly include behavior-based approach [9], auction algorithm [10], ant colony optimization (ACO) algorithm [11], threshold-based approach [12], particle swarm optimization algorithm (PSO) [13], etc. Especially, ant colony optimization and auction algorithm have received significant attention to be growing in popularity [1], and have been implemented in the article.

Ant Colony Optimization (ACO) is a new computational paradigm to solve the path planning of the task allocation problems in Swarm Intelligent. Ant colony algorithm is proposed by Italian scholars Dorigo M., and simulates the routing behavior

of natural ant and the algorithm is a kind of random optimization approach. It solves some difficult problems in the optimization path planning of the mobile robot system using the ability of optimization in the process of ant colony searching food. The algorithm has the following advantages; such as good robustness, distributed computing and easy combined with other methods. Ant colony algorithm can combine auction algorithm easily to reinforce its performance [14]. Jones and Dias developed a coordination mechanism which was applied by pickup teams in the treasure hunt field [15]. Kishimoto and Sturevant use auction algorithm as solution to multiple robots coordination in routing problem in terms of computational complexity [16]. Michael and Kumar et al have implemented to assign dynamically tasks to multiple agents using distributed solution in formation control scenario [17]. Nanjanath and Gini present auction based method for multirobot dynamic coordination to visited different locations in the map [18].

The article is organized as follows: Section II describes the ant colony algorithm and auction algorithm for the mobile robot system, and propose three performance functions to compare the cost of finishing task allocation. Section III presents the experimental results on the target research in the known environment using the multiple mobile robots system. Section IV presents brief concluding remarks.

II. Searching algorithm

The ant system algorithm was developed by Marco Dorigo and his colleagues in the 1990s. Ants move in random orientation from the start point. Pheromones are deposited on the ground from the tail as they move around. The ants would choose motion paths based on the amount of pheromones intensity on all possible

motion paths from the start point moving to the target point. Subsequent ants are more likely to choose a shorter path with greater pheromone trail intensity. The ant decides the motion path according to transition probability, $p_{i,j}^k$. The transition probability is influenced by the pheromone of the ant:

$$p_{i,j}^k = \frac{(\tau_{i,j})^\alpha (\eta_{i,j})^\beta}{\sum_{l \in N_i^k} (\tau_{i,l})^\alpha (\eta_{i,l})^\beta}, \text{ if } j \in N_i^k \quad (1)$$

$$= 0 \quad \text{if } j \notin N_i^k$$

The left side of the Eq. (1) represents the transition probability in which ant k will traverse from point i to point j . The numerator on the right side of the equation consists of a product of two terms, $(\tau_{i,j})^\alpha$ represents the intensity of the pheromone trail between points i and j with a corresponding weight value of α . On the other hand, $(\eta_{i,j})^\beta$ represents the heuristic information between points i and j with corresponding weight value of β . $\eta_{i,j} = 1/d_{i,j}$, while $d_{i,j}$ is the distance between points i and j . N_i^k is point i 's feasible neighbourhood at the ant k . The denominator on the right side of the equation is a summation of the products of the pheromone intensity and heuristic information for all possible moving paths [19].

The pheromone value evaporates on all paths by a constant factor, and adds pheromone on the paths. Pheromone evaporation is implemented by Eq. (2). The parameter $\rho (0 < \rho \leq 1)$ is used to avoid unlimited accumulation of the pheromone. Where $\Delta \tau_{i,j}^k$ is the amount of pheromone for the ant k depositing on the motion paths it has visited? It is defined as follows:

$$\tau_{i,j} = (1 - \rho)\tau_{i,j} + \sum_{k=1}^m \Delta \tau_{i,j}^k, \forall (i, j) \in L \quad (2)$$

$$\Delta \tau_{i,j}^k = \begin{cases} 1/C^k, & \text{if path}(i, j) \text{ belongs to } T^k; \\ 0, & \text{otherwise;} \end{cases} \quad (3)$$

Where C^k , the length of the tour T^k that is build by the ant k moving to the target point successfully, and is computed as the sum of the lengths of the paths belonging to T^k , or $\Delta \tau_{i,j}^k = 0$.

Auction algorithm solves the tasks allocation problem using a fleet of mobile robots, and is classified single-item auctions and combinatorial auctions. The single-item auction parallel contains single-item auction and sequential single-item auction. We use sequential single-item auction in the paper, and assign the mobile robots moving to the formation position using ant colony algorithm. A formal definition of the auction algorithm is given a number of tasks t_1, t_2, \dots, t_m , and subtasks are, $T = \{T_1, T_2, \dots, T_N\}$. A subtask T_i is a set that contains some tasks that is bided and completed by the robot R_i . Then how to decide the optimal allocation methods between robots and subtasks so that the pattern formation task is achieved efficiently? A fleet of robot set is defined $R = \{R_1, R_2, \dots, R_N\}$. A function $TD(R_i, t_j)$ that specifies the cost of executing task t_j by the robot R_i , and find the assignment that allocation one task per robot to minimize the global cost defined as $\sum_{i=1}^N TD(R_i, t_j)$, where task

j is assigned to the robot i .

$TD(R_i, T_i)$ specifies the cost of executing subtasks T_i by the robot R_i . $TW(R_i, T_i)$ is defined the waiting time cost of the robot R_i to execute subtasks T_i . We have three performance function to compare the efficiently for the team robots executing tasks allocation. There have MINSUM, MINMAX and MINAVE functions. The MINSUM function is the displacement summation of the total paths for team robots executing all subtasks to be minimized. The MINMAX function is the maximum displacement of the robot R_i that has been finished the subtask to be minimized. The MINAVE function is the average cost of the waiting time for all robots to be minimized. These functions can be represented as follows:

$$MINSUM : \min_T \sum_{i=1}^N TD(R_i, T_i) \quad (4)$$

$$MINMAX : \min_T \max_i TD(R_i, T_i) \quad (5)$$

$$MINAVE : \min_T \frac{1}{m} \sum_{i=1}^N TW(R_i, T_i) \quad (6)$$

III. Experimental results

We implement the simulation results on the known map of Yunlin University of Science & Technology Electrical Engineering Department in order to verify the effectiveness of the ant colony algorithm and auction algorithm using the multiple mobile robots. The map is shown in Fig.1, and contains 64 nodes (black rectangles). The mobile robot can moves on the path between node and node. We use four ants (mobile robots) to search the twelve different task points from different start points. We compare the cost of the performance functions (MINSUM, MINMAX and MINAVE) to find target points. In the map, we use black point to represent the mobile robot (R_1, R_2, R_3 and R_4), and the black rectangle represent the task points. The motion paths of four mobile robots are presented by variety color lines. The mobile robots are the same speed in the simulation experiment, and waiting time is proportion to the displacement of mobile robots.

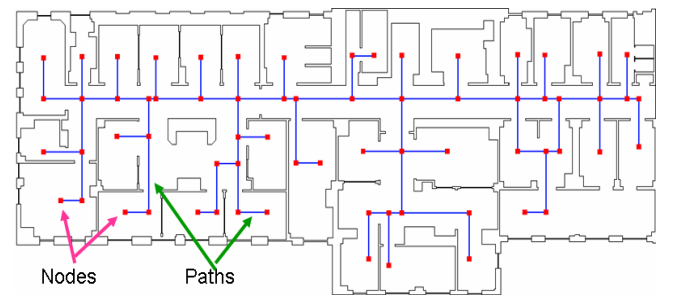


Fig. 1 The map of task allocation for four mobile robots

In the simulation results, we use four mobile robots assign twelve task points from different start points, and use three performance functions to compare the cost. We can list the cost of the performance functions in Table 1, Table 2 and Table 3. We can see the total displacement of the MINSUN function to be

minimum, and has long waiting time to be shown in Table 1. The time of each mobile robot moves to each node to be listed in Table 4. We can see the cost of MINSUM to be equal to the total time of Table 4 (R_2). The value is 58.2.

Table 1. The cost of MINSUM

	MINSUM	MINAVE
R_1	19	36
R_2	58.2	175
R_3	8	8
R_4	27	40.5
Cost	112.2	259.5

Table 2. The cost of MINMAX

	MINMAX	MINAVE
R_1	37	91
R_2	35.2	68.6
R_3	23.5	49.5
R_4	32	54
Cost	127.7	263.1

Table 3. The cost of MINAVE

	MINSUM	MINAVE
R_1	19	36
R_2	35.2	68.6
R_3	20	28
R_4	42	87.5
Cost	116.2	220.1

Table 4. The time of each node for MINSUM

R_1				R_2				R_3				R_4			
Start Node	End Node	Node time	Total Time	Start Node	End Node	Node time	Total Time	Start Node	End Node	Node time	Total Time	Start Node	End Node	Node time	Total Time
2	6	4	4	65	66	4	4	18	22	2	2	30	31	4	4
6	10	3	7	66	63	2.2	6.2	22	21	4	6	31	32	0.5	4.5
10	13	3	10	63	62	4	10.2	21	26	2	8	32	33	5	9.5
13	14	3	13	62	63	4	14.2					33	32	5	14.5
14	15	6	19	63	60	4	18.2					32	31	0.5	15
				60	61	4	22.2					31	24	5	20
				61	58	1	23.2					24	20	3	23
				58	54	2.8	26					20	19	4	2
				54	53	4	30								
				53	49	5.2	35.2								
				49	44	5	40.2								
				44	45	4	44.2								
				45	37	4	48.2								
				37	45	4	52.2								
				45	46	5	57.2								
				46	41	1	58.2								

Table 5. The time of each node for MINMAX

R_1				R_2				R_3				R_4			
Start Node	End Node	Node time	Total Time	Start Node	End Node	Node time	Total Time	Start Node	End Node	Node time	Total Time	Start Node	End Node	Node time	Total Time
2	6	4	4	65	66	4	4	18	22	2	2	30	31	4	4
6	10	3	7	66	63	2.2	6.2	22	21	4	6	31	32	0.5	4.5
10	13	3	10	63	62	4	10.2	21	26	2	8	32	36	5	9.5
13	14	3	13	62	63	4	14.2	26	25	2	10	36	44	4.5	14
14	15	6	19	63	60	4	18.2	25	24	3	13	44	45	4	18
15	14	6	25	60	61	4	22.2	24	31	5	18	45	37	4	22
14	13	3	28	61	58	1	23.2	31	32	0.5	18.5	37	45	4	26
13	17	1	29	58	54	2.8	26	32	33	5	23.5	45	46	5	31
17	20	4	33	54	53	4	30					46	41	1	32
20	19	4	37	53	49	5.2	35.2								

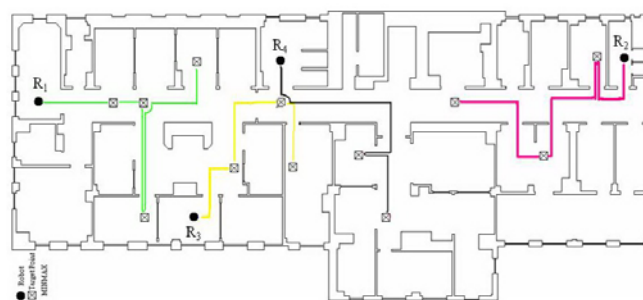
In the Table 2, we can see the four mobile robots that have been finished the tasks allocation to be faster. The time of each mobile robot moves to each node to be listed in Table 5. We can see the cost of MINSUM to be equal to the total time of Table 2 (R_1). The value is 37. The MINAVE value is long time, too. The time of each mobile robot moves to each node to be listed in Table 6. We can see the cost of MINSUM to be equal to the total time of Table 3 (R_3). The value is 20.

Table 6. The time of each node for MINAVE

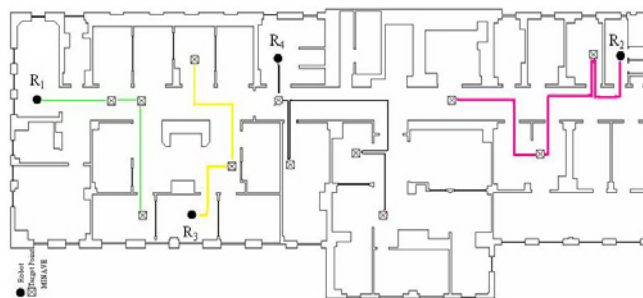
R_1				R_2				R_3				R_4			
Start Node	End Node	Node time	Total Time	Start Node	End Node	Node time	Total Time	Start Node	End Node	Node time	Total Time	Start Node	End Node	Node time	Total Time
2	6	4	4	65	66	4	4	18	22	2	2	30	31	4	4
6	10	3	7	66	63	2.2	6.2	22	21	4	6	31	32	0.5	4.5
10	13	3	10	63	62	4	10.2	21	26	2	8	32	33	5	9.5
13	14	3	13	62	63	4	14.2	26	25	2	10	33	32	5	14.5
14	15	6	19	63	60	4	18.2	25	24	3	13	32	36	5	19.5
				60	61	4	22.2	24	20	3	16	36	44	4.5	24
				61	58	1	23.2	20	19	4	20	44	45	4	28
				58	54	2.8	26					45	37	4	32
				54	53	4	30					37	45	4	36
				53	49	5.2	35.2					45	46	5	41
												46	41	1	42



(a) The motion paths of MINSUM function



(b) The motion paths of MINMAX function



(c) The motion paths of MINAVE function

Fig. 2 The experiment results of task allocation

Finally, we make the minimum of the waiting time of four mobile robots to allocate twelve task points, and the average value of MINAVE function is minimum to be shown in Table 3. In the three cases, the motion paths of four mobile robots according to the variety performance functions to be shown in Fig. 2. We can see the displacement of the mobile robot R_2 is bigger than the others to be shown in Fig 2 (a). We reduce the displacement of the robot R_2 , and allocate some task to the others using the MINMAX function to be shown in Fig. 2 (b). Fig. 2 (c) is the motion paths of four mobile robots on the MINAVE function.

IV. Conclusion

The article presents the path planning and task allocation problems of mobile robots using ant colony algorithm and auction algorithm. It solves the shorter paths of the mobile robots to allocate all task points. We have been implemented variety performance functions to compare the cost for finishing task allocation, and implement the simulation results using the proposed algorithms on the known map. In future, we want to implement the different task allocation using a fleet of robots, and use mobile robots to present the scenario on the platform.

ACKNOWLEDGEMENT

This work was supported by National Science Council of Taiwan, (NSC 99- 2221- E-224-060).

REFERENCE

1. T. Song, X. Yan, A. Liang and K. Chen (2009) A distributed bidirectional auction algorithm for multirobot coordination, The International Conference on Research Challenges in Computer Science, pp.145-148
2. P. Rusu, E. M. Petriu, T. E. Whalen, A. Cornell and H. J. W. Spoelder (2003) Behavior-based neuron-fuzzy controller for mobile robot navigation, IEEE Trans. Instrum. Meas., Vol. 52, No. 4, pp. 1335-1340
3. A. Chatterjee, K. Pulasinghe, K. Watanabe and K. Izumi (2005) A practical swarm-optimized fuzzy-neural network for voice-controlled robot systems, IEEE Trans. Ind. Electron., Vol.52, No. 6, pp. 1478-1489
4. M. J. Er and C. Deng (2004) Online tuning of fuzzy inference system using dynamic fuzzy Q-learning, IEEE Trans. Syst. Man. Cybern. B, Cybern., Vol.34, No. 3, pp.1478-1489
5. A. K. Kulatunga, D. k. Liu and G. Dissanayake (2006) Ant colony optimization based simultaneous task allocation and path planning of autonomous vehicles, IEEE Conference on Cybernetics and Intelligent System, pp. 1-6
6. S Liu, L. Mao and J. Yu (2006) Path planning based on ant colony algorithm and distributed local navigation for multi-robot systems, IEEE International Conference on Mechatronics and Automation, pp.1733-1738
7. C. F. Juang and C. H. Hsu: Reinforcement ant optimized fuzzy controller for mobile-robot wall-following control, IEEE Transactions on Industrial Electronics, Vol. 56, No. 10, pp.3931-3940, 2009.
8. K. Sugihara and J. Smith (1997) Genetic algorithm for adaptive motion planning of an autonomous mobile robot, IEEE International Symposium on Computational Intelligence in Robotics and Automation, Monterey, CA; pp. 138-146
9. F. Tang and L. E. Parker (2005) ASyMTRe: automated synthesis of multirobot task solution through software reconfiguration, IEEE International Conference on Robotics and Automation, Barcelona, Spain, pp.1501-1508
10. M. J. Mataric, G. S. Sukhatme and H. Ostergaarde (2003) Multi-robot task allocation in uncertain environments, Autonomous Robots, Vol.14, No.2-3, pp.255-263
11. P. Tarasewich and P. R. McMullen (2002) Swarm intelligence: power in numbers, Communication of ACM, Vol.45, No.8, pp.62-67
12. N. Kalra and A. Martinoli (2006) A comparative study of market-based and threshold-based multirobot task allocation, EPFL, Lausanne, Switzerland, Tech. Rep. SWIS-IPI, February
13. J. Kennedy and R. C. Eberhart (1995) Particle swarm optimization, IEEE International Conference on Neural Networks, Perth. Australia, pp. IV: 1942-1948
14. Y. Cen, C. Song, N. Xie and L. Wang (2008) Path planning method for mobile robot based on ant colony optimization algorithm, IEEE Conference on Industrial Electronics and Applications, pp. 298-301
15. E. G. Jones, B. Browning and M. B. Dias (2006) Dynamically formed heterogeneous robot teams performing tightly-coordination, IEEE Conference on Robotics and Automation, Orlando, Florida, pp.570-575
16. A. Kishimoto and N. Sturtevant (2008) Optimized algorithms for multi-agent routing, The 7th International Conference on Autonomous Agents and Multiagent System, L. Padgham, Parkes, D. C., J. Muller, S. Parsons(eds), pp.1585-1588
17. N. Michael, M. M. Zavlanos, V. Kumar and G. J. Pappas (2008) Distributed multi-robot task assignment and formation control, The IEEE Conference on Robotics and Automation, Pasadena, C. A., pp.128-133
18. M. Nanjanath and M. Gini (2006) Auction for task allocation to robot: The 9th International Conference on Intelligent Autonomous System, Tokyo, pp.550-557
19. Y. Z. Cong and S. G. Ponnambalam (2009) Mobile robot path planning using ant colony optimization, IEEE International Conference on Advanced Intelligent Mechatronics, pp. 851-856

Fuzzy Programming for Mixed-Integer Optimization Problems

Yung-Chin Lin^a, Yung-Chien Lin^b, Kuo-Lan Su^a, Wei-Cheng Lin^c, Tsing-Hua Chen^b

^aDepartment of Electrical Engineering, National Yunlin University of Science & Technology, Yunlin, Taiwan

^bDepartment of Electrical Engineering, WuFeng University, Chiayi, Taiwan

^cDepartment of Electrical Engineering, I-Shou University, Kaohsiung, Taiwan

e-mail: {yclin@wfu.edu.tw; chien-lin@wfu.edu.tw; sukl@yuntech.edu.tw; byron@isu.edu.tw; thchen@wfu.edu.tw}

Abstract: Mixed-integer optimization problems belong to NP-hard combinatorial problems. Therefore, they are difficult to search for the global optimal solutions. The mixed-integer optimization problems are always described by precise mathematical programming models. However, many practical mixed-integer optimization problems inherit more or less imprecise nature. Under this circumstance, if we take into account the flexibility of constraints and the fuzziness of objectives, the original mixed-integer optimization problems can be formulated as fuzzy mixed-integer optimization problems. Mixed-integer differential evolution (MIHDE) is an evolutionary search algorithm, and has been successfully applied to many complex mixed-integer optimization problems. In this paper, a fuzzy mixed-integer mathematical programming model is developed to formulate the fuzzy mixed-integer optimization problem. And then the MIHDE is introduced to solve this fuzzy mixed-integer programming problem. Finally, the illustrative example shows that satisfactory results can be obtained by the proposed method. This demonstrates that the MIHDE can effectively handle the fuzzy mixed-integer optimization problems.

Keywords: fuzzy programming, mixed-integer optimization, evolutionary algorithm.

I. Introduction

Many real-world optimization problems involve integer or discrete design variables in addition to continuous design variables. This kind of problems is called mixed-integer optimization problems. Mixed-integer optimization problems belong to NP-hard combinatorial problems, therefore they are difficult to search for the global optimal solutions. On the other hand, the mixed-integer optimization problems are always described by precise mathematical programming models. However, many practical mixed-integer optimization problems inherit more or less imprecise nature. Under this circumstance, if we take into account the flexibility of constraints and the fuzziness of objectives, the original mixed-integer optimization problems can be formulated as fuzzy mixed-integer optimization problems.

In the fuzzy mixed-integer optimization problems, the constraints and objectives are defined by fuzzy sets and denoted as “fuzzy constraints” and “fuzzy goals” [1]. Combined with fuzzy constraints, fuzzy goals and fuzzy decision, a fuzzy mixed-integer optimization problem can be transformed into a mixed-integer optimization problem. Therefore, one can use a mixed-integer optimization approach to solve such a mixed-integer optimization problem.

Evolutionary algorithms (EAs) [2, 3] are powerful search algorithms based on the mechanism of natural selection. Unlike conventional search approaches, they simultaneously consider many points in the search space so as to increase the chance of global convergence. Recently, EAs have exhibited promising results for solving complex problems such as highly

nonlinear, non-differentiable and multi-modal optimization problems [4]. Mixed-integer differential evolution (MIHDE) [5] is an evolutionary algorithm. A mixed coding is introduced in MIHDE to implement the evolutionary process of continuous and integer variables. The MIHDE has been successfully applied to many complex mixed-integer optimization problems [5-8].

In this paper, a fuzzy mixed-integer programming model is developed to formulate the fuzzy mixed-integer optimization problem. The MIHDE is introduced to solve this fuzzy mixed-integer programming problem. Finally, the illustrative example show that satisfactory results can be obtained by the proposed method. This demonstrates that the MIHDE can effectively handle the fuzzy mixed-integer optimization problems.

II. Fuzzy Mixed-Integer Mathematical Programming

If we soften the rigid requirements of a mixed-integer optimization problem, the mixed-integer optimization problem can be stated by a fuzzy mixed-integer programming model as follows:

$$\min_{\mathbf{x}, \mathbf{y}} f(\mathbf{x}, \mathbf{y}) \quad (1)$$

$$\text{subject to } g_j(\mathbf{x}, \mathbf{y}) \lesssim 0, j = 1, \dots, m_i \quad (2)$$

where \mathbf{x} represents an n_c -dimensional vector of continuous variables, \mathbf{y} is a n_i -dimensional vector of integer variables, and the symbol “ \lesssim ” respectively denote the softened or fuzzy versions of constraints $g_j(\mathbf{x}, \mathbf{y})$. It means that the minimized objective function can be further improved with properly softened constraints.

The fuzzy goal and fuzzy constraints can be quantified by the membership functions. Here a linear membership function such as triangular function is employed. The membership functions are represented by $\mu_f(\mathbf{x}, \mathbf{y})$ and $\mu_{g_j}(\mathbf{x}, \mathbf{y})$ as defined by equations (3) and (4).

$$\mu_f(\mathbf{x}, \mathbf{y}) = \begin{cases} 0 & \text{if } f(\mathbf{x}, \mathbf{y}) \leq f^0 \\ \frac{f^1 - f(\mathbf{x}, \mathbf{y})}{f^1 - f^0} & \text{if } f^0 < f(\mathbf{x}, \mathbf{y}) < f^1 \\ 1 & \text{if } f(\mathbf{x}, \mathbf{y}) \geq f^1 \end{cases} \quad (3)$$

$$\mu_{g_j}(\mathbf{x}, \mathbf{y}) = \begin{cases} 0 & \text{if } g_j(\mathbf{x}, \mathbf{y}) \geq g_j^0 \\ \frac{g_j^0 - g_j(\mathbf{x}, \mathbf{y})}{g_j^0 - g_j^1} & \text{if } g_j^1 < g_j(\mathbf{x}, \mathbf{y}) < g_j^0 \\ 1 & \text{if } g_j(\mathbf{x}, \mathbf{y}) \leq g_j^1 \end{cases} \quad (4)$$

where f^0 and g_j^0 are respectively denote the values of f and g_j such that the grades of the membership functions $\mu_f(\mathbf{x}, \mathbf{y})$ and $\mu_{g_j}(\mathbf{x}, \mathbf{y})$ are 0, and f^1 and g_j^1 represent the values of f and g_j such that the grades of the membership function $\mu_f(\mathbf{x}, \mathbf{y})$ and $\mu_{g_j}(\mathbf{x}, \mathbf{y})$ are 1.

The fuzzy decision $\mu_D(\mathbf{x}, \mathbf{y})$ is expressed as

$$\mu_D(\mathbf{x}, \mathbf{y}) = \{\mu_f(\mathbf{x}, \mathbf{y})\} \cap \left\{ \bigcap_{j=1}^{m_i} \mu_{g_j}(\mathbf{x}, \mathbf{y}) \right\} \quad (5)$$

If we follow the fuzzy decision of Bellman and Zadeh [9], the optimal solution $(\mathbf{x}^*, \mathbf{y}^*)$ of fuzzy decision $\mu_D(\mathbf{x}, \mathbf{y})$ can be selected by maximizing the smallest membership function such that

$$\mu_D(\mathbf{x}^*, \mathbf{y}^*) = \max \min \{\mu_f(\mathbf{x}, \mathbf{y}), \mu_{g_1}(\mathbf{x}, \mathbf{y}), \dots, \mu_{g_{m_i}}(\mathbf{x}, \mathbf{y})\} \quad (6)$$

By introducing the auxiliary variable λ , the max-min problem can be transformed into the following mixed-integer nonlinear programming (MINLP) problem:

$$\text{maximize } \lambda \quad (7)$$

$$\text{subject to } \lambda \leq \mu_f(\mathbf{x}, \mathbf{y}) \quad (8)$$

$$\lambda \leq \mu_{g_j}(\mathbf{x}, \mathbf{y}), \quad j = 1, \dots, m_i \quad (9)$$

In order to solve this MINLP problem effectively, the MIHDE algorithm is applied to solve this problem and find the maximizing decision. The details of MIHDE are described in the following section.

III. Mixed-Integer Hybrid Differential Evolution

Let us consider a general MINLP problem as follows:

$$\min_{\mathbf{x}, \mathbf{y}} f(\mathbf{x}, \mathbf{y}) \quad (10)$$

$$\mathbf{x}^L \leq \mathbf{x} \leq \mathbf{x}^U$$

$$\mathbf{y}^L \leq \mathbf{y} \leq \mathbf{y}^U$$

where \mathbf{x} represents an n_C -dimensional vector of real-valued variables, \mathbf{y} is an n_I -dimensional vector of integer-valued variables, and $(\mathbf{x}^L, \mathbf{y}^L)$ and $(\mathbf{x}^U, \mathbf{y}^U)$ are the lower and upper bounds of the corresponding decision vectors.

The procedure of MIHDE includes the following 5 steps.

1) Representation and Initialization

MIHDE uses N_p decision vectors $\{\mathbf{z}_i^G\} = \{(\mathbf{x}^G, \mathbf{y}^G)_i\}$, $i = 1, \dots, N_p$ to denote a population of N_p individuals in the G -th generation. The decision vector (chromosome), $(\mathbf{x}, \mathbf{y})_i$, is represented as $(x_{1i}, \dots, x_{ji}, \dots, x_{n_C i}, y_{1i}, \dots, y_{ji}, \dots, y_{n_I i})$. The decision variables (genes), x_{ji} and y_{ji} , are directly coded as real-valued and integer-valued numbers. The initialization process generates N_p decision vectors $(\mathbf{x}, \mathbf{y})_i$ randomly, and should try to cover the entire search space uniformly as in the form:

$$(\mathbf{x}^0, \mathbf{y}^0)_i = (\mathbf{x}^L, \mathbf{y}^L) + \lfloor \rho_i \{(\mathbf{x}^U, \mathbf{y}^U) - (\mathbf{x}^L, \mathbf{y}^L)\} \rfloor, \quad i = 1, \dots, N_p \quad (11)$$

where $\rho_i = \text{Diag}(\rho_{i,1}, \rho_{i,2}, \dots, \rho_{i,n_C+n_I})$ is a diagonal matrix, the diagonal elements $(\rho_{i,1}, \rho_{i,2}, \dots, \rho_{i,n_C+n_I})$ are random numbers in the range $[0,1]$, the other elements are zero, and the rounding operator $\lfloor \mathbf{a} = \rho_i(\mathbf{x}^U - \mathbf{x}^L), \mathbf{b} = \rho_i(\mathbf{y}^U - \mathbf{y}^L) \rfloor$ in (11) is defined as $(\mathbf{a}, \text{INT}[\mathbf{b}])$ in which the operator $\text{INT}[\mathbf{b}]$ is expressed as the nearest integer-valued vector to the real-valued vector \mathbf{b} .

2) Mutation

The i -th mutant individual $(\mathbf{u}^G, \mathbf{v}^G)_i$ is obtained by the difference for two random individuals as expressed in the form

$$\begin{aligned} (\mathbf{u}^G, \mathbf{v}^G)_i &= (\mathbf{x}^G, \mathbf{y}^G)_p + \lfloor \rho_m \{(\mathbf{x}^G, \mathbf{y}^G)_k - (\mathbf{x}^G, \mathbf{y}^G)_l\} \rfloor \\ &= (\mathbf{x}^G, \mathbf{y}^G)_p + (\rho_m(\mathbf{x}_k^G - \mathbf{x}_l^G), \text{INT}[\rho_m(\mathbf{y}_k^G - \mathbf{y}_l^G)]) \end{aligned} \quad (12)$$

where random indices $k, l \in 1, \dots, N_p$ are mutually different. The operator $\text{INT}[\mathbf{b} = \rho_m(\mathbf{y}_k^G - \mathbf{y}_l^G)]$ in (12) is to find the nearest integer vector to the real vector \mathbf{b} . The mutation factor ρ_m is a real random number between zero and one. This factor is used to control the search step among the direction of the differential variation $(\mathbf{x}^G, \mathbf{y}^G)_k - (\mathbf{x}^G, \mathbf{y}^G)_l$.

3) Crossover

In crossover operation, each gene of the i -th individual is reproduced from the mutant vector $(\mathbf{u}^G, \mathbf{v}^G)_i = (u_{1i}^G, u_{2i}^G, \dots, u_{n_C i}^G, v_{1i}^G, v_{2i}^G, \dots, v_{n_I i}^G)$ and the

current individual $(\mathbf{x}^G, \mathbf{y}^G)_i = (x_{1i}^G, x_{2i}^G, \dots, x_{n_{ci}}^G, y_{1i}^G, y_{2i}^G, \dots, y_{n_{ti}}^G)$ as follows:

$$u_{li}^{G+1} = \begin{cases} x_{li}^G, & \text{if a random number} > \rho_c \\ u_{li}^G, & \text{otherwise;} l=1, \dots, n_c, i=1, \dots, N_p \end{cases} \quad (13)$$

$$v_{li}^{G+1} = \begin{cases} y_{li}^G, & \text{if a random number} > \rho_c \\ v_{li}^G, & \text{otherwise;} l=1, \dots, n_t, i=1, \dots, N_p \end{cases} \quad (14)$$

where the crossover factor $\rho_c \in [0,1]$ is a constant and the value can be specified by the user.

4) Evaluation and Selection

The operation includes two evaluation phases. The first phase is performed to produce the new population in the next generation as (15). The second phase is used to obtain the best individual as (16).

$$(\mathbf{x}^{G+1}, \mathbf{y}^{G+1})_i = \operatorname{argmin}\{f((\mathbf{x}^G, \mathbf{y}^G)_i), f((\mathbf{u}^{G+1}, \mathbf{v}^{G+1})_i)\} \\ i=1, \dots, N_p \quad (15)$$

$$(\mathbf{x}^{G+1}, \mathbf{y}^{G+1})_b = \operatorname{argmin}\{f((\mathbf{x}^{G+1}, \mathbf{y}^{G+1})_i), i=1, \dots, N_p\} \quad (16)$$

where $(\mathbf{x}^{G+1}, \mathbf{y}^{G+1})_b$ is the best individual with the smallest objective function value.

5) Migration

In order to increase the exploration of the search space, a migration operation is introduced to generate a diversified population. Based on the best individual $(\mathbf{x}^{G+1}, \mathbf{y}^{G+1})_b = (x_{1b}^{G+1}, x_{2b}^{G+1}, \dots, x_{n_{cb}}^{G+1}, y_{1b}^{G+1}, y_{2b}^{G+1}, \dots, y_{n_{tb}}^{G+1})$, the j -th gene of the i -th individual can be diversified by the following equations:

$$x_{ji}^{G+1} = \begin{cases} x_{jb}^{G+1} + \rho_1(x_j^L - x_{jb}^{G+1}), & \text{if a random number} < \frac{x_{jb}^{G+1} - x_j^L}{x_j^U - x_j^L} \\ x_{jb}^{G+1} + \rho_1(x_j^U - x_{jb}^{G+1}), & \text{otherwise;} j=1, \dots, n_c, i=1, \dots, N_p \end{cases} \quad (17)$$

$$y_{ji}^{G+1} = \begin{cases} y_{jb}^{G+1} + \operatorname{INT}[\rho_2(y_j^L - y_{jb}^{G+1})], & \text{if a random number} < \frac{y_{jb}^{G+1} - y_j^L}{y_j^U - y_j^L} \\ y_{jb}^{G+1} + \operatorname{INT}[\rho_2(y_j^U - y_{jb}^{G+1})], & \text{otherwise;} j=1, \dots, n_t, i=1, \dots, N_p \end{cases} \quad (18)$$

where ρ_1 and ρ_2 are the random numbers in the range $[0,1]$.

The migration operation in MIHDE is performed only if a measure for the population diversity is not satisfied, that is when most of individuals have clustered together, the migration has to be actuated to make some improvements. In this study, we propose a measure called the population diversity degree η to check whether the migration operation should be performed. In order to define the measure, we first introduce the following gene diversity index for each real-valued gene x_{ji}^{G+1} and for each integer-valued gene y_{ki}^{G+1} ,

$$dx_{ji} = \begin{cases} 0, & \text{if } \left| \frac{x_{ji}^{G+1} - x_{jb}^{G+1}}{x_{jb}^{G+1}} \right| < \varepsilon_2; j=1, \dots, n_c, i=1, \dots, N_p, i \neq b \\ 1, & \text{otherwise} \end{cases} \quad (19)$$

$$dy_{ji} = \begin{cases} 0, & \text{if } y_{ji}^{G+1} = y_{jb}^{G+1}; j=1, \dots, n_t, i=1, \dots, N_p, i \neq b \\ 1, & \text{otherwise} \end{cases} \quad (20)$$

where dx_{ji} and dy_{ji} are the gene diversity indices and $\varepsilon_2 \in [0,1]$ is a tolerance for real-valued gene provided by the user. According to (19) and (20), we assign the j -th gene diversity index for the i -th individual to zero if this gene clusters to the best gene. We now define the population diversity degree η as a ratio of total diversified genes in the population. From (19) and (20) we have the population diversity degree as

$$\eta = \left\{ \sum_{i=1}^{N_p} \left[\sum_{j=1}^{n_c} dx_{ji} + \sum_{j=1}^{n_t} dy_{ji} \right] \right\} / \{(n_c + n_t)(N_p - 1)\} \quad (21)$$

From equation (19), (20) and (21), the value of η is in the range $[0,1]$. Consequently, we can set a tolerance for population diversity, $\varepsilon_1 \in [0,1]$, to assess whether the migration should be actuated. If η is smaller than ε_1 , then MIHDE performs the migration to generate a new population to escape a local solution. Contrary, if η is not less than ε_1 , then MIHDE suspends the migration operation to keep a constant search direction to a target solution.

IV. Computational Example

Consider a design problem of pressure vessel, as presented by Sandgren [10], is shown in Figure 1.

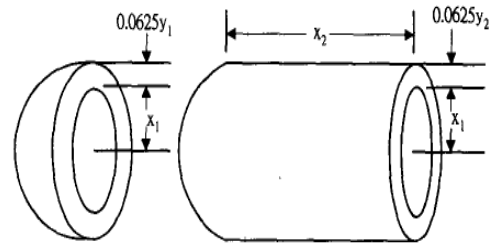


Figure 1. Pressure Vessel design.

The design variables are the dimensions required for the specifications of the vessel, i.e.

$$(\mathbf{x}, \mathbf{y}) = (x_1, x_2, y_1, y_2).$$

The objective function is the combined costs of material, forming and welding of the pressure vessel. The constraints are set in accordance with the respective ASME codes. The mixed-integer optimization problem is expressed as:

$$\begin{aligned} \min_{\mathbf{x}, \mathbf{y}} f(\mathbf{x}, \mathbf{y}) = & 0.6224(0.0625y_1)x_1x_2 + 1.7781(0.0625y_2)x_1^2 \\ & + 3.1611(0.0625y_1)^2x_2 + 19.84(0.0625y_1)^2x_1 \end{aligned} \quad (22)$$

$$\begin{aligned} \text{subject to } g_1(\mathbf{x}, \mathbf{y}) = & 0.0193x_1 - 0.0625y_1 \leq 0 \\ g_2(\mathbf{x}, \mathbf{y}) = & 0.00954x_1 - 0.0625y_2 \leq 0 \\ g_3(\mathbf{x}, \mathbf{y}) = & 750 \times 1728 - \pi x_1^2x_2 - \frac{4}{3}\pi x_1^3 \leq 0 \\ g_4(\mathbf{x}, \mathbf{y}) = & x_2 - 240 \leq 0 \\ & 10.0 \leq x_1 \leq 100.0 \\ & 10.0 \leq x_2 \leq 240.0 \\ & 10 \leq y_1 \leq 32 \\ & 10 \leq y_2 \leq 32 \end{aligned}$$

Using the MIHDE algorithm to solve this mixed-integer optimization problem, the obtained optimal solution is $(\mathbf{x}^*, \mathbf{y}^*) = (x_1^*, x_2^*, y_1^*, y_2^*) = (38.8754, 221.4069, 12, 10)$, $f(\mathbf{x}^*, \mathbf{y}^*) = 6521.3198$

Instead of giving the crisp values for this mixed-integer optimization problem, the fuzzy goal and the fuzzy constraints are described in Table 1.

Table 1. Fuzzy goal and fuzzy constraints.

	$\mu_f = 0$ or $\mu_{g_j} = 0$	$\mu_f = 1$ or $\mu_{g_j} = 1$
$f(\mathbf{x}, \mathbf{y})$	$f^0 = 6200.0$	$f^1 = 6500.0$
$g_1(\mathbf{x}, \mathbf{y})$	$g_1^0 = 5.0$	$g_1^1 = -5.0$
$g_2(\mathbf{x}, \mathbf{y})$	$g_2^0 = 5.0$	$g_2^1 = -5.0$
$g_3(\mathbf{x}, \mathbf{y})$	$g_3^0 = 5.0$	$g_3^1 = -5.0$
$g_4(\mathbf{x}, \mathbf{y})$	$g_4^0 = 5.0$	$g_4^1 = -5.0$

For this fuzzy mixed-integer optimization problem, the obtained optimal solution by MIHDE is $(\mathbf{x}^*, \mathbf{y}^*) = (x_1^*, x_2^*, y_1^*, y_2^*) = (40.6027, 196.1014, 12, 10)$, $f(\mathbf{x}^*, \mathbf{y}^*) = 6350.6731$, $\lambda = 4.9664$

From computational result, the cost of pressure vessel can be decreased through the fuzzy programming for the original mixed-integer optimization problem. This implied that the cost function can be further improved if the constraints are softened to a more favorable degree.

V. Conclusions

In this paper, a fuzzy mixed-integer mathematical programming model is developed to formulate the fuzzy mixed-integer optimization problem. And then the MIHDE is introduced to solve this fuzzy mixed-integer programming problem. Finally, the illustrative example shows that satisfactory results can be obtained by the proposed method. This demonstrates that the MIHDE can effectively handle the fuzzy mixed-integer optimization problems.

References

- [1] H. J. Zimmermann, "Application of fuzzy sets theory to mathematical programming," *Information Science*, vol. 36, pp. 29-58, 1985.
- [2] Z. Michalewicz, "Genetic Algorithm + Data Structure = Evolution Programs," Springer-Verlag, 1994.
- [3] T. Back, D. Fogel, and Z. Michalewicz, *Handbook of Evolutionary Computation*. New York: Oxford Univ. Press, 1997.
- [4] Z. Michalewicz, Z. and M. Schoenauer, "Evolutionary Algorithms for Constrained Parameter Optimization Problems," *Evolutionary Computation*, vol. 4, no. 1, pp. 1-32, 1996.
- [5] Y. C. Lin, K. S. Hwang, and F. S. Wang, "A mixed-coding scheme of evolutionary algorithms to solve mixed-integer nonlinear programming problems," *Computers & Mathematics with applications*, vol. 47, pp. 1295-1307, 2004.
- [6] Y. C. Lin, K. S. Hwang, and F. S. Wang, "Co-evolutionary hybrid differential evolution for mixed-integer optimization problems," *Engineering Optimization*, vol. 33, no. 6, pp. 663-682, 2001.
- [7] Y. C. Lin, K. S. Hwang, and F. S. Wang, "An evolutionary Lagrange method for mixed-integer constrained optimization problems," *Engineering Optimization*, vol. 35, no. 3, pp. 267-284, 2003.
- [8] Y. C. Lin, Y. C. Lin, and K. L. Su, "Production planning based on evolutionary mixed-integer nonlinear programming," *ICIC Express Letters*, vol. 4, no. 5(B), pp. 1881-1886, 2010.
- [9] R. E. Bellman and L. A. Zadeh, "Decision making in a fuzzy environment," *Management Science*, vol. 17, pp. 141-164, 1970.
- [10] E. Sandgren, "Nonlinear integer and discrete programming in mechanical design," *ASME J. Mechanical Design*, vol. 112, pp. 223-229, 1990.

Develop a Vision Based Auto-recharging System for Mobile Robots

Ting-Li Chien

Department of Electronic Engineering, Wu-Feng University, Taiwan
cdl@mail.wfu.edu.tw

Abstract: The article develops a vision based auto-recharging system that guides the mobile robot moving to the docking station. The system contains a docking station and a mobile robot. The docking station contains a docking structure, a control device, a charger and a safety detection device and a wireless RF interface. The mobile robot contains a power detection module (voltage and current), an auto-switch, a wireless RF interface, a controller and a camera. The controller of the power detection module is Holtek chip. The docking structure is designed with one active degree of freedom and two passive degrees of freedom. In image processing, the mobile robot uses a webcam to capture the real-time image. The image signal transmits to the controller of the mobile robot via USB interface. We use Otsu algorithm to recognize the distance and orientation of the docking station from the mobile robot. In the experiment results, the proposed method can guided the mobile robot moving to the docking station.

Keywords: auto-recharging system. mobile robot. docking station. degrees of freedom. USB interface. Otsu algorithm

I. INTRODUCTION

Mobile robots have been widely applied in many fields with passing year. Such as factory automation, dangerous environment detection, office automation, hospital, entertainment, space exploration, farm automation, military, education, learning and security system and so on. The mobile robot has been working in long time, and the power of the mobile robot is weakness, and moves to the docking station autonomously before under control.

In the past literature, many researches have been proposed power detection methods. Levi was one of the first to comment upon the characteristics of CMOS technology which make it special amenable to I_{DD} Testing [1]. Malaiya used I_{DD} testing and estimating the effects of increased integration on measurement resolution [2]. Frenzel proposed the likelihood ration test method applying on power-supply current diagnosis of VLSI circuits [3]. Horning *et al* reported on numerous experiments where current measurements have forecast reliability problems in devices which had previously passed conventional test procedures [4]. Maly *et al.* proposed a build-in current sensor which provides a pass/fail signal when the current exceeds a set threshold [5]. In image processing, many techniques have been proposed. Weszka *et al.* use the valley sharpening method to restrict the histogram on the pixels with large absolute value [6]. Watanabe used the different histogram method to select the threshold at gray level with the maximal amount of difference [7].

The article is organized as follows: Section II describes the system structure of the auto-recharging

system for the mobile robot, and explains the functions of the power detection module and the power measurement and prediction algorithms. Section III presents hardware structure and docking processing of the station. The section IV explains the image processing method to find out the docking station. Section V presents the experiment results of the auto-recharging processing for the mobile robot moving to the station using the proposed method. Section VI presents brief concluding remarks.

II. SYSTEM ARCHITECHTURE

The hardware structure of the auto-recharging system is classified two parts: one is designed in docking station. The other is designed in the mobile robot. The relation is shown in Fig. 1. In the docking station, there are a limit switch, a landmark, a safety detection device, a wireless RF interface and a charger. The landmark can guide the mobile robot moving to the docking station using vision system. The safety detection device contains safety switch and power detection module. The limit switch can detect the mobile robot touching the station or not. The wireless RF interface can communicate with the mobile robot via RS232 interface, and transmits the status of the recharging processing between the docking station and the mobile robot.

The power of the mobile robot is weakness on the free space. The camera can find out black bars of the docking station using the proposed method. The mobile robot decides the direction from the docking station according to the relation position of the two black bars.

The wireless RF interface can communicate with the docking station, and transmits and receives the real-time signal. The power detection module can measure current and voltage values of the auto-recharging processing, and transmits to the controller of the mobile robot via RS232 interface. The prototype of the power detection module is shown in Fig. 2. The IR sensor can decide the mobile robot touching the docking station, and transmits the signal to the controller of the mobile robot. The mobile robot opens the auto-switch, and touches with the connective pins of the docking station.

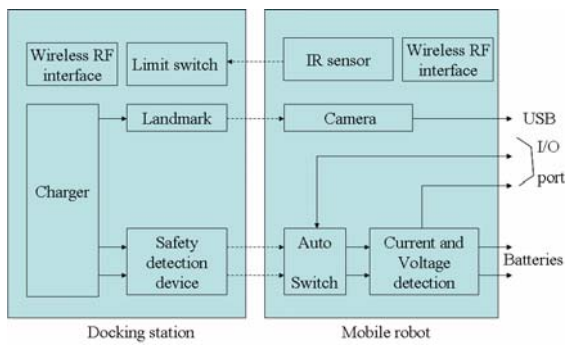


Fig. 1. The auto-recharging system

The mobile robot has the shape of cylinder and its diameter, height, and weight are 40 cm, 70 cm, and 25 kg, respectively. It has four wheels to provide the capability of autonomous mobility [8]. The mobile robot contains six systems, including structure, motion and driver system, software development and supervised system, detection system, auto-recharging system and camera.

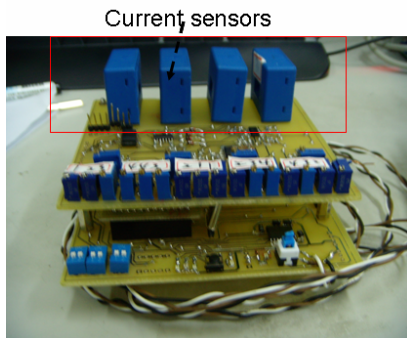


Fig. 2. The power detection module

In the power detection module, we use four current sensors to measure the current variety of the mobile robot and charging current, and use two multisensor fusion methods (redundant management method and a statistical prediction method) to detect current and voltage signals status. We can get an exact measured value for power detection [9]. Then we want to predict the residual power of the mobile robot. First we must fit

the curve from the power detection value of the mobile robot. Next the user can set the critical value of the power. The main controller of the mobile robot can calculate the extrapolation value from the critical value, and can calculate the residual working time for the mobile robot.

We fit a second-order polynomial regression

$$y = a_0 + a_1x + a_2x^2 + e \quad (1)$$

The sum of the squares of the error is

$$S_r = \sum_{i=1}^n (y_i - a_0 - a_1x_i - a_2x_i^2)^2 \quad (2)$$

To generate the least squares fit, we take the derivative of Equation (2) with respect to each of the unknown coefficient of the polynomial, and we can get

$$\begin{aligned} na_0 + (\sum x_i)a_1 + (\sum x_i^2)a_2 &= \sum y_i \\ (\sum x_i)a_0 + (\sum x_i^2)a_1 + (\sum x_i^3)a_2 &= \sum x_i y_i \\ (\sum x_i^2)a_0 + (\sum x_i^3)a_1 + (\sum x_i^4)a_2 &= \sum x_i^2 y_i \end{aligned} \quad (3)$$

Finally we can calculate a_0 , a_1 , and a_2 from Equation (3). Then we set the power critical value to be P_s and

$$a_2x^2 + a_1x + a_0 = P_s \quad (4)$$

We can calculate the x value (the unit is second) from Equation (4). The sample time of the power detection module is 1 second.

III. Docking station

The docking station is shown in Fig. 3, and provides two connective points to provide charging current to the mobile robot. The docking station is designed with two passive DOF (Degree Of Freedom) and one active DOF. It can rotate in the Z-axis and use compression spring to move for various docking condition. The weight of the docking station is almost 6 kg, and its length, and height, and width are 70cm, 50cm and 80cm, respectively. The station extends 15 cm to touch the mobile robot providing a 30° entry window. The connective docking mechanism is mounted on the back of the mobile robot.

The mobile robot docking mechanism is shown in left side of the Fig. 3 (c). The recharging adapters are at the inside of the holes. Each hole is shaped as a cone in order to help the docking smoothly. Since both the connection pins and adapters are rigid, the docking

station is designed for providing compliance for reasonable robot docking angle and offset. When the mobile robot is approaching to the docking station with offset and docking angle, the guiding stick mounted on the docking station functions to guide the recharging pins for inserting into the adapters. We plot two black bars on the front of the docking station to be shown in Fig. 4. The mobile robot recognizes the position of the docking station according to the two black bars using vision system.

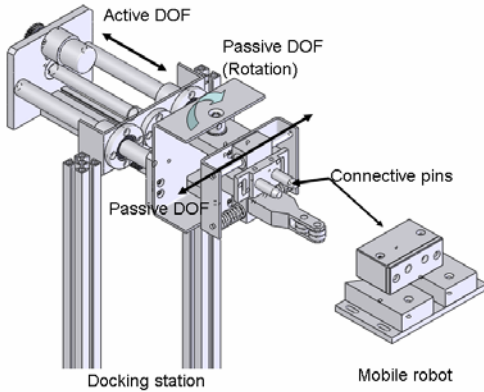


Fig. 3. The structure of the docking station

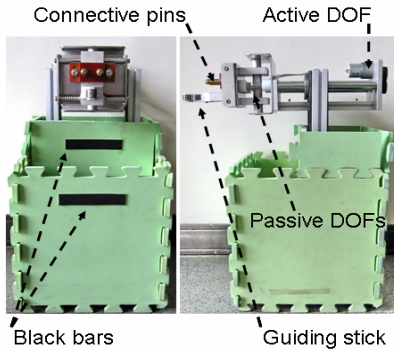


Fig. 4. The docking station

IV. Algorithms analysis

We use Otsu algorithm to recognize the landmark of the station docking. In image reorganization, we define the pixels of a given picture be represented in L in gray levels $[1, 2, \dots, L]$. The number of pixels at level i is denoted by n_i , and the total number of pixels is $N = n_1 + n_2 + \dots + n_L$. In order to simplify the discussion, we can rewrite the gray level histogram to be normalized and regarded as a probability distribution:

$$p_i = n_i / N, \quad p_i \geq 0, \quad \sum_{i=1}^L p_i = 1 \quad (5)$$

Now suppose that we dichotomize the pixels into two classes C_0 and C_1 (back ground and objects) by a threshold at level k ; C_0 denotes pixels with levels

$[1, 2, \dots, k]$, and C_1 denotes pixels with levels $[k+1, k+2, \dots, L]$. Then the probabilities of class occurrence and the class mean levels, respectively, are given by

$$\omega_0 = \Pr(C_0) = \sum_{i=1}^k p_i = \omega(k) \quad (6)$$

$$\omega_1 = \Pr(C_1) = \sum_{i=k+1}^L p_i = 1 - \omega(k) \quad (7)$$

$$\omega(k) = \sum_{i=1}^k p_i, \quad \mu(k) = \sum_{i=1}^k i p_i, \quad \mu_G = \mu(L) = \sum_{i=1}^L i p_i \quad (8)$$

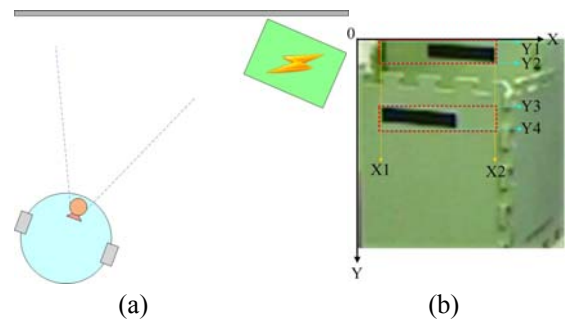
Then the optimal threshold k^* can be funded to maximize η [10,11].

$$\eta(k) = \sigma_B^2(k) / \sigma_G^2, \quad \sigma_B^2(k) = \frac{[\mu_G \omega(k) - \mu(k)]^2}{\omega(k)[1 - \omega(k)]} \quad (9)$$

$$\sigma_B^2(k^*) = \max_{1 \leq k \leq L} \sigma_B^2(k) \quad (10)$$

V. Experimental results

We make an experiment to implement the auto-recharging processing using the Otsu algorithm for the robot moving to the docking station. The power of the mobile robot is under the critical power. The mobile robot searches the docking station using camera to be shown in Fig. 5. The mobile robot finds out the landmark of the station using camera. Then it moves closed to the docking station using the proposed algorithm to decide the direction of the mobile robot. The experiment result is shown in Fig. 5(a). The original gray-level picture of the station is shown in Fig 5(b). We focus on the landmark, and set two points (X_1 and X_2) on column projection, and set four points (Y_1 , Y_2 , Y_3 and Y_4) on row projection. We use Otsu algorithm to process the picture from the camera, and calculate the results of the threshold, and plot the row projection image and the column projection image to be shown in Fig. 5(c) and (d). The mobile robot can calculates the direction and distance from the docking station.



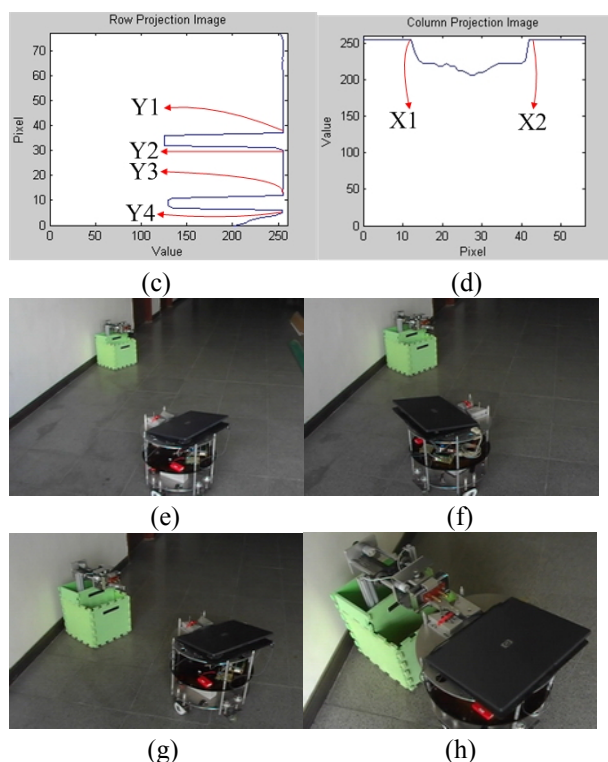


Fig. 5. The experiment result of auto-docking for the mobile robot

The mobile robot moves to the front of the docking station to be shown in Fig. 5(e), and turn left to face the station. Then it moves the station, and modifies the direction according to the position of landmark. The experiment scenario is shown in Fig 5(f). The mobile robot moves to the docking station, and touch the limit switch. The docking station transmits RF signal to the mobile robot. The mobile robot must stop, and prepares to execute the charging processing. The experimental results are shown in Fig. 5 (g) and (h). We make some tests on variety direction of the robot moving the docking station to determine the performance using the proposed method, 100 experimental results were performed, and show a 99% successful rate for the docking processing.

VI. CONCLUSION

We have developed a vision based auto-recharging system that had been integrated in the mobile robo. The system contains a docking station and a mobile robot. We can get an exact measured value for power detection, and calculate the residual working time using second-order polynomial regression. We use Otsu algorithm to recognize the two black bars of the docking station, if the mobile robot locates on the front of the docking

station. The proposed algorithm can guides the mobile robot moving to the docking station. In future, we want to implement the auto-recharging processing and path planning on the multiple docking stations for mobile robots.

REFERENCES

- [1] M. W. Levi: (1981), CMOS is most testable, Proceedings of International Test Conference, pp.217-220.
- [2] Y. K. Malaiya and S. Y. H. Su, (1982), A new fault model and testing technique for CMOS devices, Proceedings of International Test Conference, pp.25-34
- [3] J. F. Frenzel, (1994), Power-Supply Current Diagnosis of VLSI Circuits, IEEE Transaction on reliability Vol. 43, No.1, pp.30-38.
- [4] L. K. Horning *et al.*, (1987), Measurements of quiescent power supply current for CMOS ICs in production testing, Proceedings of International Test Conference, pp.300-309.
- [5] W. Maly and P. Nigh, (1988), Build-in current testing- Feasibility study, Proceedings of International Conference on Computer-Aided Design, pp.340-343.
- [6] J. S. Weszka, R. N. Naget and A. Rosenfeld, (1974), A threshold selection technique, IEEE Transaction on Computer, Vol. C-23, pp. 1322-1326.
- [7] S. Watanabe and CYBEST Group: An automated apparatus for cancer prescreening: CYBEST, Comp. Graph., Image Process., Vol.3, 1974, pp.350-358.
- [8] K. L. Su, T. L. Chien and J. H. Guo (2005), Decelop a Seft-diagnosis Function Auto-recharging Device for Mobile Robot, IEEE International Workshop on Safety, Security, and Rescue Robot, pp.1-6.
- [9] K. L. Su, Jyh H. Tzou and Chien C. Liu (2007), Development of a Multisensor-Based Residual Power Prediction System for Mobile Robots, IEEE Workshop on Advanced Robotics and its Social Impacts 2007 (ARSO '07), Hsinchu, Taiwan, December 9-11, pp.114-119
- [10] K. Fukunage, (1972), Introduction to statistical pattern recognition, New York, Academic, pp.260-267.
- [11] N. Otsu, (1979), A threshold selection method from gray-level histograms, IEEE International Conference on System, Man, and Cybernetics, Vol.9, No. 1, pp.62-66.

Super-Twisting Second Order Sliding Mode Control for a Synchronous Reluctance Motor

Huann-Keng Chiang¹, Wen-Bin Lin², Chang-Yi Chang¹, and Chien-An Chen³

¹ Department of Electrical Engineering, National Yunlin University of Science & Technology, Taiwan, R.O.C.

² Graduate School of Engineering Science & Technology, National Yunlin University of Science & Technology, Taiwan, R.O.C.

³ Electronic Vehicle and System Verification Group R & D Division, Automotive Research and Testing Center, Taiwan, R.O.C.

Fax : +886-5-5312065

E-mail: chianghk@yuntech.edu.tw

Abstract: This paper presents design and implementation of a super-twisting second order sliding mode controller (SOSMC) for a synchronous reluctance motor. The second order sliding mode control is an effective tool for the control of uncertain nonlinear systems since it overcomes the main drawbacks of the classical sliding mode control, i.e., the large control effort and the chattering phenomenon. Its real implementation implies simple control laws and assures an improvement of the sliding accuracy with respect to conventional sliding mode control. This paper proposes a novel scheme that based on the technique of super-twisting second order sliding mode control. First, the SOSMC is derived by mathematics. Finally, the performance of the proposed method is verified by simulation and experiment. The proposed SOSMC shows the robustness for the motor parameters variation and the improvement of chattering phenomenon.

Keywords: Super-Twisting Algorithm, Second Order Sliding Modes, Synchronous Reluctance Motor, Chattering Phenomenon.

I. INTRODUCTION

Fast accurate dynamic response is of primary importance in control systems. The motor control system with the high robustness is an important issue in research. Synchronous reluctance motor (SynRM) have a mechanically simple and robust structure. They can be used in high speed and high temperature environments. The rotor circuit of the SynRM is open circuit such that the flux linkage of SynRM is directly proportional to the stator currents. The torque of SynRM can be controlled by adjusting the stator currents. Therefore, there has been renewed interest in SynRM [1-4].

Sliding mode control (SMC) has attracted increasing attention in recent years because it is an effective and robust technology for parameter variation and external disturbance rejection. It has been applied to robot and motor control [3,5-7]. Sliding mode control (SMC) is a robust control for nonlinear systems. However, sliding mode is a mode of motions on the discontinuity set of a discontinuous dynamic system. Hence, reducing the chattering is very important for SMC. The second-order sliding mode technique has the same properties of robustness to uncertainties of model and external disturbances. Second-order SMC (SOSMC) [8] improves the chattering phenomenon. Due to few literatures about SOSMC in SynRM control application, therefore, it has valuable on research in SynRM control application for SOSMC.

Different from the conventional first order SMC, the SOSMC is belonging to the region of higher-order sliding mode (HOSM). Levant [8] had discussed the theory of HOSM. HOSM control have been applied to

motor, FEM fuel cells and automatic docking [9-12].

There is no paper adopting super-twisting SOSMC in SynRM speed control so far. Therefore, this paper proposes a novel scheme that based on the technique of super-twisting SOSMC. Finally, the performance of the proposed method is verified by simulations.

II. MODELING OF THE SYNRM

The d-q equivalent voltage equations of ideal SynRM model with a synchronously rotating rotor reference frame are shown in Fig. 1:

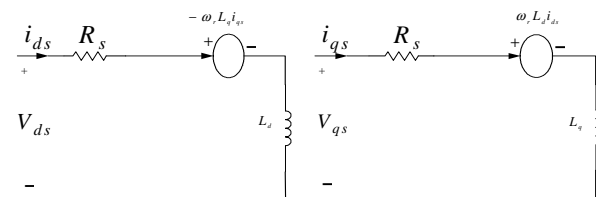


Fig.1. The d-q axis equivalent-circuit of SynRM

$$V_{ds} = R_s i_{ds} + L_d \frac{di_{ds}}{dt} - \omega_r L_q i_{qs} \quad (1)$$

$$V_{qs} = R_s i_{qs} + L_q \frac{di_{qs}}{dt} + \omega_r L_d i_{ds} \quad (2)$$

The corresponding electromagnetic torque T_e is:

$$T_e = \frac{3}{4} P_{ole} (L_d - L_q) i_{ds} i_{qs} \quad (3)$$

The corresponding motor dynamic equation is:

$$T_e - T_L = J_m \frac{d\omega_r}{dt} + B_m \omega_r \quad (4)$$

where V_{ds} and V_{qs} are direct and quadrature axis terminal voltages, respectively; i_{ds} and i_{qs} are,

respectively, direct axis and quadrature axis terminal currents or the torque producing current; L_d and L_q are the direct and quadrature axis magnetizing inductances, respectively; R_s is the stator resistance; and ω_r is the speed of the rotor. P_{ole} , T_L , J_m , and B_m are the poles, the torque load, the inertia moment of the rotor, and the viscous friction coefficient, respectively. In this paper, the maximum torque control (MTC) strategy [3,4] is adopted. The torque current commands are shown in equation (5) and (6) [3]:

$$i_{ds}^* = \sqrt{\frac{|T_e|}{\frac{3}{8}P_{ole}(L_d - L_q)}} \cos\left(\frac{\pi}{4}\right) \quad (5)$$

$$i_{qs}^* = \text{sgn}(T_e) \sqrt{\frac{|T_e|}{\frac{3}{8}P_{ole}(L_d - L_q)}} \sin\left(\frac{\pi}{4}\right) \quad (6)$$

III. INTEGRAL VARIABLE STRUCTURE SLIDING MODE CONTROLLER

We can rewrite the equation (4) as

$$\begin{aligned} \frac{d\omega_r}{dt} &= \left(-\frac{B_m}{J_m}\right)\omega_r + \frac{1}{J}(T_e - T_L) \\ &= a\omega_r + b(T_e - T_L) \\ &= (a_0 + \Delta a)\omega_r + (b_0 + \Delta b)(T_e - T_L) \\ &= a_0\omega_r + b_0(u(t) + f) \end{aligned} \quad (7)$$

where

$$a \equiv -\frac{B_m}{J_m} = a_0 + \Delta a$$

$$b \equiv \frac{1}{J} = b_0 + \Delta b$$

$$u \equiv T_e$$

$$f \equiv \frac{1}{b_0}(\Delta a\omega_r + \Delta b u(t) - bT_L)$$

$$J_m \equiv J_0 + \Delta J$$

$$B_m \equiv B_0 + \Delta B$$

The subscript index “o” indicates the nominal system value; “Δ” represents uncertainty, and f represents the lumped uncertainties.

Define the velocity error as $e(t) = \omega_r^* - \omega_r$, where ω_r^* is the velocity command. The velocity error differential equation of SynRM can be expressed as equation (8):

$$\frac{de(t)}{dt} = \dot{\omega}_r^* - a_0\omega_r - b_0[u(t) + f] \quad (8)$$

Let

$$S = e(t) + c \int_{-\infty}^t e(\tau) d\tau, \quad c > 0 \quad (9)$$

The input control $u(t)$ (the electromagnetic torque T_e)

of (8) can be defined as equation (10):

$$u(t) = u_{eq}(t) + u_n(t) \quad (10)$$

where $u_{eq}(t)$ is used to control the overall behavior of the system and $u_n(t)$ is used to suppress parameter uncertainties and to reject disturbances. By making mathematical calculation, we get the overall control $u(t)$ as equation (10) [3]:

$$u(t) = \frac{1}{b_0}[\dot{\omega}_r^* - a_0\omega_r + ce(t)] + \left(K + \frac{\eta}{b_0}\right) \text{sgn}(S) \quad (11)$$

where $|f| \leq K$.

IV. SUPER-TWISTING SECOND-ORDER SLIDING MODE CONTROLLER

In conventional sliding mode control design, the control target is let the system state move into sliding surfaces $S = 0$. But a second-order sliding mode controller aims for $S = \dot{S} = 0$. The system states converge to zero intersection of S and \dot{S} in state space.

Super-twisting method mainly develops relative one order system for reducing chattering phenomenon [7]. The state trajectory of S and \dot{S} phase plane is shown in Fig.2. It twists together and approaches in state space. Finally, it converges to the origin of phase plane.

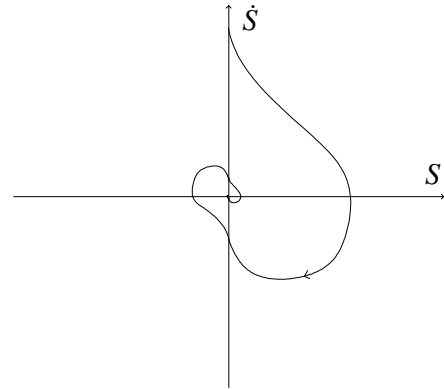


Fig.2. The phase plane trajectory of Super-twisting

Consider sliding variable dynamics given by a system with a relative degree two:

$$\dot{y}_1(t) = \varphi_{ST}(y_1, t) + \gamma_{ST}(y_1, t)u_{ST}(t) \quad (12)$$

where $y_1(t)$ means the sliding variable S , in which φ_{ST} and γ_{ST} are uncertain functions with the upper and lower bounds of equation (13), and $u_{ST}(t)$ is the scalar control input.

$$\begin{cases} |\varphi_{ST}| \leq \Phi_{ST} \\ 0 < \Gamma_{mST} \leq \gamma_{ST} \leq \Gamma_{MST} \end{cases} \quad (13)$$

The control $u_{ST}(t)$ can be given as a sum of two components as shown in equation (14) [6,7]:

$$u_{ST}(t) = u_1(t) + u_2(t) \quad (14)$$

where

$$\dot{u}_1(t) = \begin{cases} -u_{ST}, & \text{if } |u_{ST}| > U \\ -W \operatorname{sgn}(y_1), & \text{if } |u_{ST}| \leq U \end{cases} \quad (15)$$

$$u_2(t) = \begin{cases} -\lambda |S_0|^\rho \operatorname{sgn}(y_1), & \text{if } |y_1| > S_0 \\ -\lambda |y_1|^\rho \operatorname{sgn}(y_1), & \text{if } |y_1| \leq S_0 \end{cases} \quad (16)$$

where U is control value boundary, and S_0 is a boundary layer around the sliding surface S .

We define state variable as shown in equation (17):

$$\begin{cases} x_1(t) = \int_{-\infty}^t x_2(\tau) d\tau \\ x_2(t) = e(t) = \omega_r^* - \omega_r \end{cases} \quad (17)$$

We define sliding function y_1 as

$$y_1 = x_2 + cx_1 \quad (18)$$

Then, the system equation can be expressed as

$$\dot{y}_1 = \dot{\omega}_r^* + \left(-\frac{B_m}{J_m} + c \right) x_2 + \frac{1}{J_m} T_L + \frac{B_m}{J_m} \omega_r^* + u_{ST}(t) \quad (19)$$

where

$$\begin{cases} \varphi(\cdot) = \dot{\omega}_r^* + \left(-\frac{B_m}{J_m} + c \right) x_2 + \frac{1}{J_m} T_L + \frac{B_m}{J_m} \omega_r^* \\ \gamma(\cdot) = 1 \\ u_{ST}(t) = -\frac{1}{J_m} T_e \end{cases} \quad (20)$$

According to equation (20), the practical controllable signal T_e of SynRM is a continuous controllable signal. Different from the discontinuous controllable signal of conventional SMC, it can improve the chattering problem in SOSMC of SynRM apparently.

V. SIMULATION RESULTS

A block diagram of the experimental SynRM drive and the super-twisting second-order sliding mode controller speed control block diagram of the SynRM servo drive are shown in Fig. 3. The proposed controller was applied to a 0.37 kw three-phase SynRM whose nominal parameters and proposed controller parameters are shown in Table 1. The detail specifics of SynRM are shown in Appendix 2.

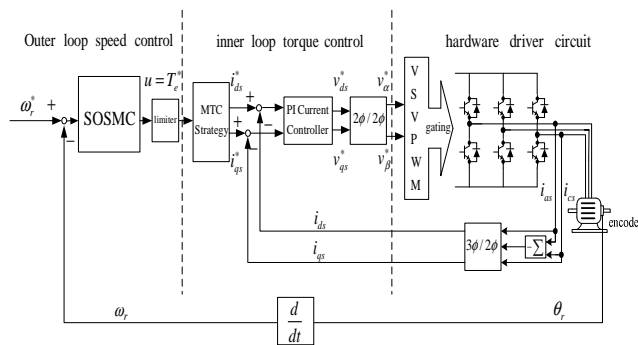


Fig.3. Super-Twisting SOSMC speed control block diagram of SynRM servo drive

Table 1. Parameters of SynRM (0.37kW)

$R_s = 4.2 \Omega$	$P_{ole} = 2$
$L_{ds} = 0.328$ ($f = 60 \text{ Hz}$)	$L_{qs} = 0.181 \text{ H}$ ($f = 60 \text{ Hz}$)
$J_m = 0.00076 \text{ Kg-m}^2$	$B_m = 0.00012 \text{ Nt-m/rad/sec}$

In Fig.4, the simulation velocity response of the SMC due to $\omega_r^* = 600$ rev/min without machine load in the nominal motor inertia and friction coefficient condition is depicted. In Fig.5, the simulation velocity response of the SOSMC due to $\omega_r^* = 600$ rev/min without machine load in the nominal motor inertia and friction coefficient condition is depicted. The velocity response of SOSMC is smoother than the convention SMC. In Fig.6, the simulation velocity response of the SOSMC due to $\omega_r^* = 600$ rev/min under an 0.3 Nt-m machine load at the beginning and an 0.9 Nt-m machine load at 3seconds is added for the 2 times nominal case of the motor inertia and friction coefficient condition is presented. Hence, the SOSMC is a robust controller and improve the chattering phenomenon when the system has external disturbances and parameter variations.

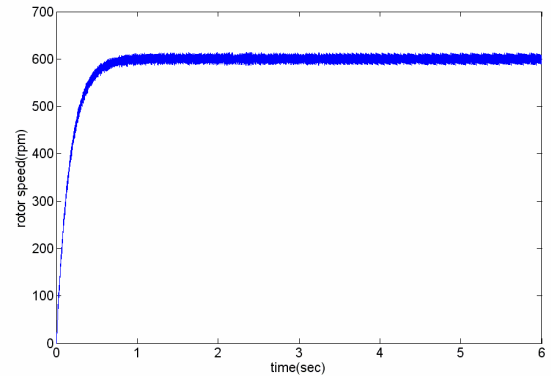


Fig.4. Simulation velocity response of the SMC due to $\omega_r^* = 600$ rev/min without machine load in the nominal motor inertia and friction coefficient condition

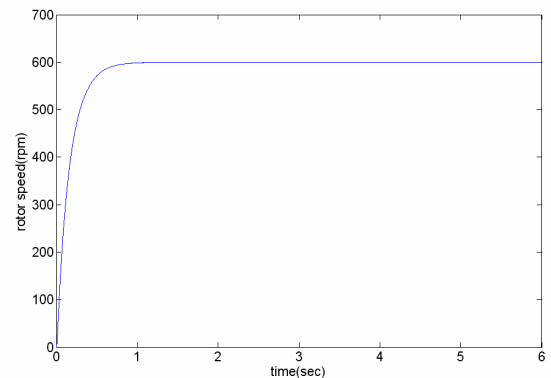


Fig.5. Simulation velocity response of the super-twisting SOSMC due to $\omega_r^* = 600$ rev/min without machine load in the nominal motor inertia and friction coefficient condition

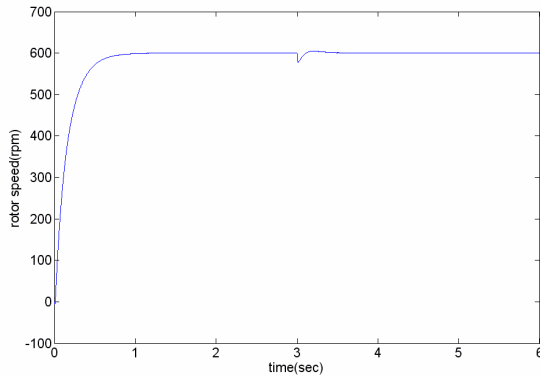


Fig.6. Simulation velocity response of the super-twisting SOSMC due to $\omega_r^* = 600$ rev/min under a 0.3 Nt-m machine load at the beginning and a 0.9Nt-m machine load at 3 seconds in the 2 times nominal case of the motor inertia and friction coefficient condition

VI. CONCLUSION

In this paper, a super-twisting second-order sliding mode (SOSMC) speed control design for robust stabilization and disturbance rejection of SynRM drive. The simulation results show good performance of SOSMC under uncertain load subject to variatons in inertia and system frction. Also with SOSMC, there is no need for acceleration feedback. An experimental setup has been prepared to assess the performace of the proposed controller. Employing the experiments, this controller provides a fast and good response for the parameter variations and external disturbances. Apart from the robustness feature, the proposed second-order SMC laws have the advantage of being continuous, thus eliminating the chattering effect apparently and being more acceptable in application.

ACKNOWLEDGMENT

This work is supported by the National Science Council in Taiwan, Republic of China, through grant NSC99-2221-E-224-072.

APPENDIX

Table 2. Rated parameters of SynRM

Specifics	Value
Rated voltage	230/400 V
Rated current	4.7/2.7 V
Rated speed	3600 rpm
Rated power	0.37 kW
Power factor	0.37
Insulation class	F
Waterproof and dust-proof class	IP 20

REFERENCES

[1] Bianchi N., Bolognani S., Bon D., and Pre M. D. (2009), Rotor flux-barrier design for torque ripple reduction in synchronous reluctance and PM-assisted synchronous reluctance motors. IEEE Transactions on Industry Applications 45(3):921-928

[2] Kim W. H., Kim K. S., Kim S. J., Kang D. W., Go S. C., Chun Y. D., and Lee J. (2009), Optimal PM design of PMA-SynRM for wide constant-power operation and torque ripple reduction. IEEE Transactions on Magnetics 45(10):4660-4663

[3] Chen C. A., Lin W. B., and Chiang H. K. (2009), Design and implementation sliding mode controller based on radial basis function neural network for synchronous reluctance motor. ICIEA 2009, 4th IEEE Conference on Industrial Electronics and Applications: 281-286.

[4] Betz R. E., Lagerquist R., Miller T. J. E., and Middleton R. H. (1993), Control of synchronous reluctance machines. IEEE Transactions on Industry Applications 29(6):1110-1122

[5] Shyu K. K., and Lai C. K. (2002), Incremental motion control of synchronous reluctance motor via multisegment sliding mode control method. IEEE Transactions on Control Systems Technology 10(2): 169-176

[6] Huang Y. S., and Sung C. C. (2010), Implementation of sliding mode controller for linear synchronous motors based on direct thrust control theory. IET Proceedings on Control Theory & Applications 4(3):326-338

[7] Bartolini G., Ferrara A., Levant F., and Usai E. (1999), Variable Structure Systems, Sliding Mode and Nonlinear Control. Springer-Verlag

[8] Levant A. (1993), Sliding order and sliding accuracy in sliding mode control. International Journal of Control Automation and Systems 58(6):1247-1263

[9] Rashed M., Goh K. B., Dunnigan M. W., MacConnell P. F. A., Stronach A. F., and Williams B. W. (2005), Sensorless second-order sliding-mode speed control of a voltage-fed induction-motor drive using nonlinear state feedback., IEE Proceedings on Electric Power Applications 152(5):1127-1136

[10] Kunusch C., Puleston P. F., Mayosky M. A., and Riera J. (2009), Sliding mode strategy for PEM fuel cells stacks breathing control using a super-twisting algorithm. IEEE Transactions on Control Systems Technology 17(1):167-174

[11] Tournes C., and Shtessel Y. (2007), Automatic docking using second order sliding mode control. 2007 American Control Conference:3455-3460

[12] Mohamadian M., Pedram M. M., and Ashrafzadeh F. (2004), Digital second order sliding mode control for a synchronous reluctance motor. 2004 IEEE Industry Applications Conference:1899-1902

Shape Recognition Applied in a Semi-Autonomous Weapon Robot

Chun-Chieh Wang¹, Chyun-Luen Lin², Kuo-Lan Su³

¹*Department of Electronic Engineering, Chienkuo Technology University
No. 1, Chieh Shou N. Rd., Changhua City, Taiwan
(Tel : 886-4-7111111ext3350; Fax : 886-4-7111139)
(Email address: jasonccw@ctu.edu.tw)*

²*Department of Electronic Engineering, Chienkuo Technology University
No. 1, Chieh Shou N. Rd., Changhua City, Taiwan
(Tel : 886-4-7111111ext3350; Fax : 886-4-7111139)
(Email address: a829327@yahoo.com.tw)*

³*Department of Electrical Engineering, National Yunlin University of Science & Technology,
No. 123, Section 3, University Road, Douliu, Yunlin, Taiwan
(Tel : 886-5-5342601ext4249; Fax : 886-5-5312065)
(Email address: sukl@yuntech.edu.tw)*

Abstract: A weapon robot with semi-autonomous shooting is implemented in this paper. The principal aim is the application of a shape recognition method so that the MP5K electric BB gun can shoot semi-autonomously. In addition, we designed a human-machine interface surveillance system via the LabVIEW graphical programming environment, such that the supervisor can control the weapon robot by a keyboard or a specially adapted mouse. In order to accomplish all these achievements, there have been major additions and overhauls in both system software codes and system circuit board developments. The experimental results have shown the practicality of the shape recognition, the 89C51 microcontroller, the LabVIEW graphical programming environment, and ZigBee wireless technology applied to weapon robots.

Keywords: LabVIEW, ZigBee, Semi-autonomous shooting, Shape recognition, POB-Basic system.

I. INTRODUCTION

There are times when a rescue team is unable to enter the scene of an accident owing to various problems that might endanger the lives of the rescuers. In order to overcome these possible obstacles, researchers have built several robots that can enter such dangerous sites instead of the rescuers. However, as regards HMI-guided control, few researchers have used the LabVIEW platform to experiment with tracked robots. In 2001, Priya Olden et al. [1] presented an open-loop motor speed control with LabVIEW [1]. In 2006, Prasanna Ballal et al. [2] proposed a LabVIEW-based test-bed with off-the-shelf components for research into mobile sensor networks.

Therefore, we extended previous research [3–7] to implement a weapon robot. The principal aim is the application of a shape recognition method so that the MP5K electric BB gun can shoot semi-autonomously. In addition, we designed a human-machine interface surveillance system via the LabVIEW graphical programming environment, such that the supervisor can control the weapon robot by a keyboard or a specially adapted mouse.

In order to accomplish all these achievements, there have been major additions and overhauls in both system software codes and system circuit board developments. To illustrate the effectiveness of the design, we planned an urban fight as the scenario in which the robot could use all its functions. The experimental results validate

the practicality of the shape recognition, the 89C51 microcontroller, the LabVIEW graphical programming environment, and the ZigBee wireless technology applied to weapon robots.

II. SELF-MADE WEAPON ROBOT

2.1 Mechanism of the Robot

Figure 1 shows an overview of the platform of the weapon robot. Figure 2 shows the right-hand side view. The structure has two active wheels and one small assistant wheel. The specifications of the robotic platform are (1) length 41 cm, (2) width 31 cm, and (3) height 20 cm. The home-made weapon robot is shown in Fig.3. We put an MP5K electric BB gun on the platform of the robot, and set one camera behind the gun sights. The specifications of the weapon robot are (1) length 52 cm, (2) width 31 cm, and (3) height 43 cm.

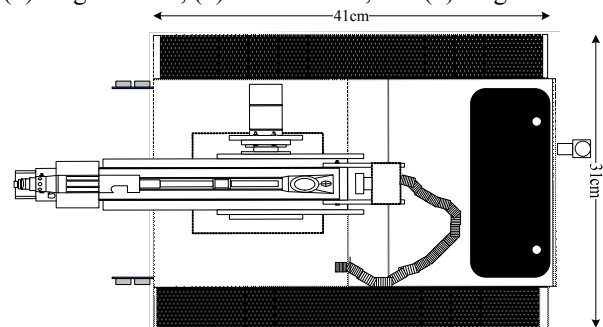


Fig.1. Vertical view of the platform

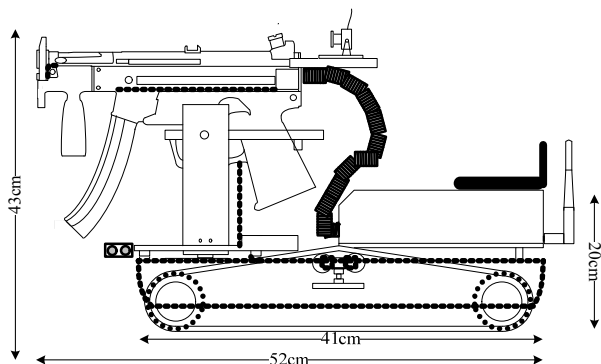


Fig.2. Right side view of the platform



Fig.3. Weapon robot

2.2 Wireless Network Camera and Router

In this paper, an AXIS 207MW wireless network camera, as shown in Fig.4, is applied to take a scene. Figure 5 shows the D-LINK DIR-615 router.



Fig.4. AXIS 207MW wireless network camera



Fig.5. D-LINK DIR-615 router

III. LabVIEW [4]

The Laboratory Virtual Instrument Engineering Workbench (LabVIEW) is an easy-to-use graphical development environment which allows users to rapidly develop applications for experiment, measurement and

control. A complete system can be constructed very fast with hardware modules for data accomplishment, image processing, motion domination, or communication available from National Instruments (NI). Each application created in LabVIEW is referred to as a virtual instrument (VI). A VI consists of a user interface front panel and a block diagram. A VI can also be called from another VI, called a sub-VI. The standard LabVIEW package comes with various VIs in the form of libraries and drivers to permit rapid program development.

Here, we use LabVIEW graphical programming to design a human machine interface surveillance system. From the transmission of RS-232 and ZigBee modules, a command will be delivered to the controller and placed on the weapon robot so that the vehicle will arrive at assigned place. The LabVIEW front panel is shown in Fig.6. There are eight function-blocks in this figure. Block 1 is the safety push-button. If we put the button, all of the functions can't be fulfilled. Block 2 displays a keyboard/genius mouse switch device. We can choose the keyboard or the mouse to control the robot. Moreover, we can set the RS232 I/O port and baud rate by Block 3 and Block 4, respectively. Block 5 displays the character string when the keyboard is pressed. The ASCII code is shown in Block 6. Block 7 indicates the frame of controlling the order through the mouse. Block 8 displays the scene, taken by the wireless network camera.

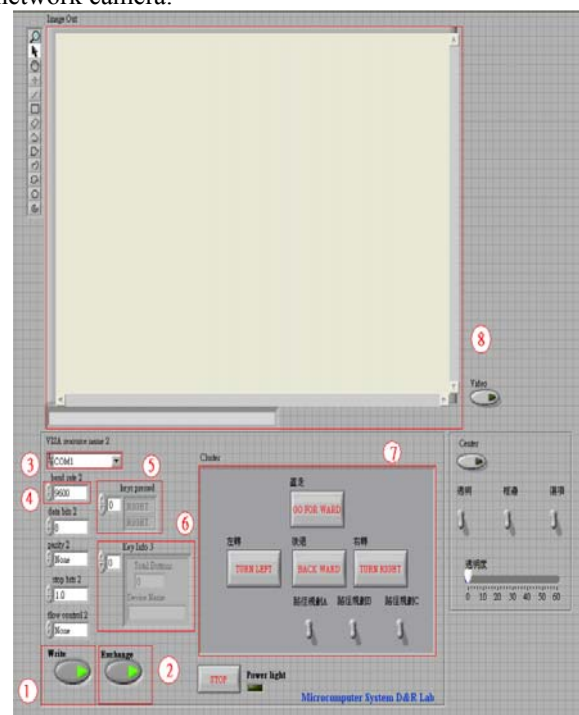


Fig.6. LabVIEW front panel

IV. ZIGBEE TRANSPARENT-P2P MODE

ZigBee is an intelligent digital protocol, operating at three frequencies, with the commonest one being at 2.4

GHz. At this operating frequency, data rates up to 250 kbit/s are claimed. This is a relatively low bandwidth compared to other protocols such as Bluetooth. In addition, the features of ZigBee contain the robustness and simplicity of IEEE 802.15.4 standard, the versatility of the ZigBee compliance platform, low consumption and cost, and the standard-based short-range wireless networking.

Here, ZigBee is developed for point-to-point transmission and area positioning. IP-Link 2220H, as shown in Fig.7, provides a host of AT commands to allow easy configuration of the key attributes of an IP-Link 2220 module. Users can use any terminal emulation utility or UART communication library on a particular host platform to issue these AT commands to IP-Link 2220. Figure 8 shows the transparent point-to-point mode. The signal can be transmitted by connecting RS-232 series port and ZigBee transmitter so that it can be received. In addition, a tag (placed on the robot) transmits a continuous signal so that the node (placed on the scenario setting space), which is closest to the robot, can receive the signal and display it on the monitor. Then, the supervisor will know the present position of the robot.



Fig.7. IP-Link2220H



Fig.8. Transparent P2P Mode

V. POB-BASIC SYSTEM AND SHAPE RECOGNITION

In general, a black/white LCD screen uses one bit to color a pixel and the screen displays 8 pixels with a byte, as shown in Fig.9. In addition, the buffer uses 8192 bits (the POB-LCD screen is 128 pixels by 64 pixels) of memory on POB-EYE module. The challenge of this buffer is to have a ratio of “1 bit = 1 pixel”. The operations on bits are processor-intensive. The advantage of this “1 bit = 1 pixel” ratio is that it does not use much memory. In fact, we need to apply a mask in order to change a bit value in memory. Moreover, this mask will be different whether the bit is set to 0 or to 1. Thus this computation can be relatively time consuming

because it must be done 8129 times. That is why using the technique “1 bit = 1 pixel” will need less memory space. Another way of drawing a pixel on the screen is to consider that 1 byte draws 1 pixel. In that case they will be no delay or mask when switching on or off a pixel. Nevertheless, such a technique will take 8 times more memory than the previous one. However, for shape recognition, we have to transfer 2-D array into 1-D array, as shown in Fig.10, such that the externals (length, width, and height) of the figure will be stored in the POB-EYE memory.

	0	1	2	3
0	0	1	2	3
1	4	5	6	7
2	8	9	10	11
3	12	13	14	15
4	16	17	18	19

Fig.9. 2-D Array

0	1	2	3	4	5	6	7	8	9	10	11	12	13	14	15	16	17	18	19
---	---	---	---	---	---	---	---	---	---	----	----	----	----	----	----	----	----	----	----

Fig.10. 1-D Array

Figure 11 and Figure 12 display the hardware of POB-EYE and the main electronic board of POB-EYE, respectively.

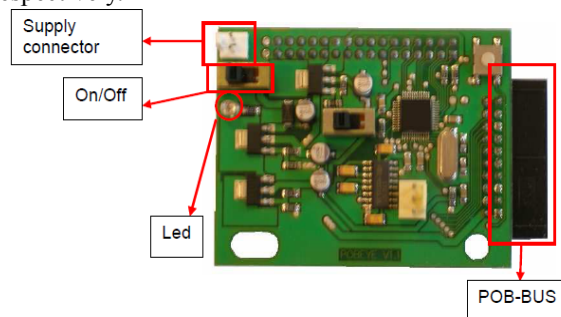


Fig.11. Hardware of POB-EYE

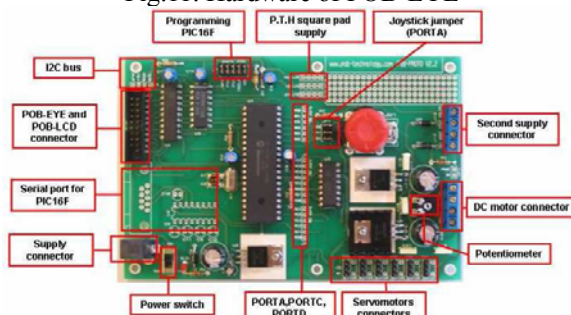


Fig.12. Main electronic board of POB-EYE

The graphics resources can be displayed using the library supplied with the POB-compiler tools. The graphic functions allow us to manage the transparency of the images and to carry out the superposition of images on the LCD screen. Images are displayed using

the “DrawBitmap” function, as shown in Fig.13. This function uses a number to display the desired image. For more clarity in our code, POB-Bitmap generates in “.h” a series of “#define” from the image’s name. The call to “DrawBitmap” can be becomes (if the name of the file is cross.bmp): DrawBitmap(X, Y, 1, Tableau) → DrawBitmap(X, Y, IDB_CROSS, Tableau).

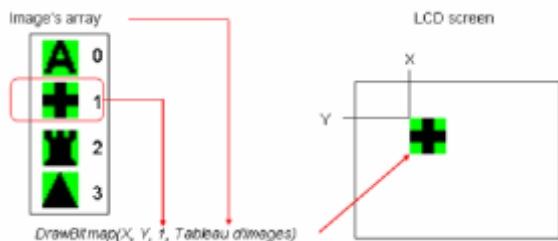


Fig.13. POB-Pattern

VI. EXPERIMENTAL RESULTS

Figure 14 shows the target. The MP5K electric BB gun can shoot the target semi-autonomously via shape recognition techniques.

For the scenario setting and the experimental test, we planned the indoor orientation diagram, as shown in Fig.15. The robotic weapon will look for the objects (balloons), aim at them, and shoot them. Moreover, it can pass along a difficult route and look for that route. Then the tracking vehicle can move toward the objects and shoot them again.

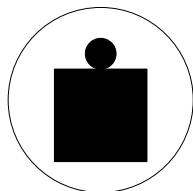


Fig.14. Mark



Fig.15. Indoor orientation diagram

VII. CONCLUSION

A weapon robot with semi-autonomous shooting has been implemented. A shape recognition method was applied to design a controller so that the MP5K electric BB gun can shoot semi-autonomously. We also designed a human-machine interface surveillance system via the LabVIEW graphical programming environment so that the supervisor could control the weapon robot by either a keyboard or a specially adapted mouse. The experimental results validate the practicality of the shape recognition, the 89C51 microcontroller, the LabVIEW graphical programming environment, and ZigBee wireless technology applied to weapon robots.

REFERENCES

- [1] Olden P., Robinson K., Tanner K., Wilson R., and Basher A.M.H. (2001), Open-loop motor speed control with LabVIEW, Proceedings of 2001 IEEE Southeast Conference, 259-262.
- [2] Ballal P., Giordano V., Dang P., Gorthi S., Mireles J., and Lewis F. (2006), A LabVIEW based test-bed with off-the-shelf components for research in mobile sensor networks, Proceedings of the 2006 IEEE International Symposium on Intelligent Control, 112-118.
- [3] C.C. Wang, K.H. Hsia, K.L. Su, Y.C. Hsieh, and C.L. Lin (2010), Application of a Remote Image Surveillance System in a Robotic Weapon, International Journal of Artificial Life and Robotics, vol. 15, pp.284-290.
- [4] C.C. Wang, C.L. Lin, K.H. Hsia, and Y.C. Hsieh (2010), Obstacle Avoidance and Wireless Network Surveillance of a Weapon Robot, 2010 International Symposium on Computer, Communication, Control and Automation, May 5-7, Tainan, Taiwan, pp.261-264.
- [5] C.C. Wang, K.L. Su and, C.T. Shen (2009), Implementation of a Tour Guide Robot via Shape Recognition and Path Planning, Proceedings of The Fourth International Conference on Innovative Computing, Information and Control (ICICIC 2009), Dec. 7-9, Kaohsiung City, Taiwan.
- [6] C.C. Wang, C.L. Lin, and, K.L. Su (2009), Shape Recognition for an Entertainment Robot with a five-axle Arm, Proceedings of 2009 CACS International Automatic Control Conference, Nov. 27-29, NTUT, Taipei, Taiwan, pp.377-380.
- [7] C.C. Wang, K.L. Su, K.H. Hsia, Y.C. Hsieh, C.L. Lin (2009), Implementation of a Robotic Weapon via an AVR Microcontroller, The 17th National Conference on Fuzzy Theory and Its Applications, NUK, Kaohsiung, Taiwan, Dec. 18-19, pp.681-686.

Camera Position Estimation and Feature Extraction from Incomplete Image of Landmark

Kuo-Hsien Hsia¹, Shao-Fan Lien² and Juhng-Perng Su³

¹*Department of Management Information System, Far East University
No. 49, Chung Hua Rd., Hsin-Shih, Tainan County 74448, Taiwan, R.O.C.
(Tel : 886-6-597-9566#5862; Fax : 886-6-597-7010)
(E-mail: khhsia@cc.feu.edu.tw)*

²*Graduate School of Engineering Science & Technology (Doctoral Program)
National Yunlin University of Science & Technology
No. 123, University Road, Section 3, Douliou, Yunlin 64002, Taiwan, R.O.C.
(E-mail: g9510801@yuntech.edu.tw)*

³*Department of Electrical Engineering, National Yunlin University of Science & Technology
No. 123, University Road, Section 3, Douliou, Yunlin 64002, Taiwan, R.O.C.*

³*Department of Information Technology, Overseas Chinese University
No. 100, Ciao Kwang Rd., Taichung 40721, Taiwan, R.O.C.
(E-mail: sujp@yuntech.edu.tw)*

Abstract: On the autonomous unmanned helicopter landing problem, the position of the unmanned helicopter relative to the landmark is very important. A camera carried on the unmanned helicopter could capture the image of the landmark. In the earlier researches, the camera position could be estimated by the extracted features of the landmark image. However, it is necessary that the landmark image should be complete or with slight deficiency in order for the estimation process. In this paper, the innovated method is designed for camera position estimation from single image with incomplete landmark. An ANFIS is utilized for constructing the mapping relation between the features of complete and incomplete landmark image. It will be verified that it is possible to estimate the camera position from a landmark image with defects more than half via the proposed method.

Keywords: Camera position estimation, Incomplete landmark image, Feature extraction, ANFIS.

I. INTRODUCTION

Unmanned helicopters are very useful vehicles for aerial photography or investigation in hazardous locations. The research of autonomous unmanned helicopter control has been ongoing for several years. GPS (Global Positioning System) is the most commonly used sensor for position control of unmanned helicopters. Unfortunately, GPS error can range up to 6 meters [1]. Greater accuracy can be achieved by incorporating image-guided methods in conjunction with a GPS system.

In earlier researches, image servo control systems for a small scale autonomous unmanned helicopter are discussed in [2] and [3]. In these two references, two marks are used for assisting unmanned helicopter positioning. However, in practice when an unmanned helicopter is landing, the landmark constitutes a single reference on the ground. Consequently, image-guided methods are proposed for locating the landmark [4] and estimating the position information [5-6].

Image-guided methods are usually employed to guide an unmanned helicopter on close approach to a target. The distance between the vehicle and target is usually smaller than the range of GPS error while the

vehicle is landing. Fig. 1 shows the situation concerned in [5-6] that an unmanned helicopter is approaching the landmark. The position of an unmanned helicopter can be described by θ and R . The θ and R can be estimated from the captured landmark image with the method proposed in [6].

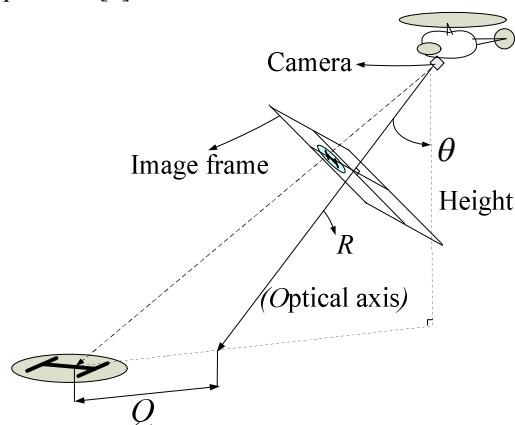


Fig.1. Situation of an unmanned helicopter approaching a landmark

In [5], it is necessary that the captured landmark image must be complete. Since the helicopter may yaw due to the effect of wind or the image size of the landmark may be larger than the image available to the

camera this restriction has to be overcome. The case in which more than half the landmark image is available, called “Case 1”, has been discussed in [6].

In this paper, we will focus on the case in which more than half of the landmark image is defective, called “Case 2”. This scenario presents serious problems for extracting useful features. A feature extraction method is developed for extracting the features from the incomplete image of landmark in which more than half of the landmark image is defective. We use ANFIS to capture and estimate the useful features from an incomplete landmark image.

Simulation results verify that under some conditions it is possible to estimate the camera position from a landmark image in which less than half the total image is available.

II. MAPPING RELATIONS AND CAMERA POSITION ESTIMATING METHOD

1. Projective geometry of landmark image

The five quantities, as defined in (1-5), obtained via geometric projection [7] are the projection of the features of the landmark image. We defined (6) for estimating the camera position [5].

$$k = (\tan(\gamma + \sigma) - \tan \gamma) * \bar{R} \quad (1)$$

$$h = (\tan(\gamma + \sigma + \omega) - \tan(\gamma + \sigma)) * \bar{R} \quad (2)$$

$$\bar{Q} = \tan(\gamma + \sigma) * \bar{R} \quad (3)$$

$$d = \sqrt{(\tan \lambda * \bar{R})^2 + (\tan \delta * \bar{R})^2} \quad (4)$$

$$\bar{r} = \frac{r \times \sqrt{(\bar{S})^2 + (\bar{R})^2}}{\sqrt{(\cos \theta \times \bar{R} + T)^2 - (\sin \theta * \bar{R})^2}} \quad (5)$$

$$\begin{cases} \text{Ratio}_{\text{project}} = h/k \\ \text{Ratio}_{\text{height}} = \bar{r}/d \\ \text{Ratio}_{\text{angle}} = h/\bar{r} \\ \text{Ratio}_{\text{position}} = k/\bar{Q} \end{cases} \quad (6)$$

We further consider the cases of incomplete landmark images, specifically, the case of the landmark image in which more than half of the image is available [6]. The four quantities: k , \bar{r} , x , and y , related to the completed landmark image, are selected for estimating the approximate h . The estimated h is called \hat{h} . Here k and \bar{r} have been derived from (1) and (2), respectively.

Consider the case in which more than half the landmark image is defective, as shown in Fig.2. The five quantities: I_1 , I_2 , I_3 , I_4 and I_5 which are related to the complete landmark image are selected for estimating the approximate h and k , called \hat{h} and \hat{k} , respectively.

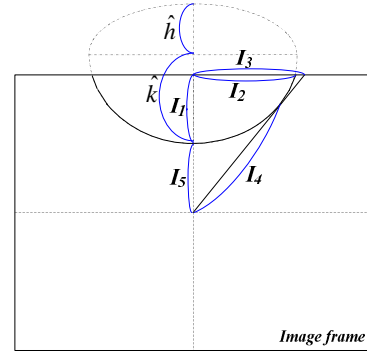


Fig.2. Incomplete landmark image and features

The projective relation between the landmark and camera position is shown in Fig. 3. Definitions of θ_α , θ_β and θ_e are provided as

$$\begin{cases} \theta_\alpha = \tan^{-1}\left(\frac{f+b+e+r}{h}\right) - \tan^{-1}\left(\frac{f+b+e}{h}\right) \\ \theta_\beta = \tan^{-1}\left(\frac{f+b+e}{h}\right) - \tan^{-1}\left(\frac{f+b+e-r}{h}\right) \\ \theta_e = \tan^{-1}\left(\frac{f+b+e}{h}\right) - \tan^{-1}\left(\frac{f+b}{h}\right) \end{cases} \quad (7)$$

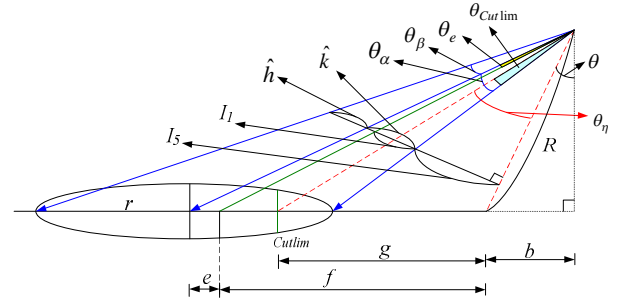


Fig.3. Projective geometry of landmark features

Fig. 4 illustrates the projective relations of features I_2 , I_3 and I_4 . From Fig.3 and Fig.4, the derivations of \hat{h} , \hat{k} , I_1 , I_2 , I_3 , I_4 and I_5 can be obtained as shown in (8-13) and the estimated \hat{h} and \hat{k} in (14).

$$I_5 = \tan[\eta + (\theta_\beta - \theta_e)]R \quad (8)$$

$$I_1 = (\tan \eta)R - I_5 \quad (9)$$

$$I_2 = \frac{\sqrt{(r^2 - e^2)}\sqrt{(I_1 - I_5)^2 + R^2}}{\sqrt{H^2 + (b+f)^2}} \quad (10)$$

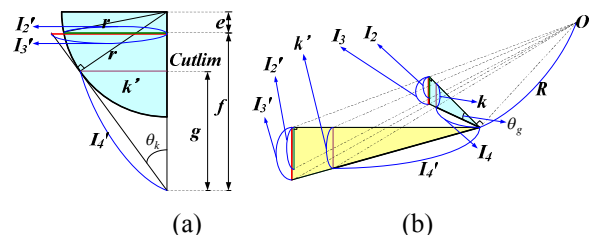


Fig.4. (a) Top view of the landmark features
(b) Projections of the landmark features

$$I_3 = \frac{[f \cdot \tan(\theta_k)] \sqrt{(I_1 - I_5)^2 + R^2}}{\sqrt{H^2 + (b + f)^2}} \quad (11)$$

$$I_4 = \frac{\tan(\eta + \theta_e - \theta_\beta + \theta_{cut\ lim}) R}{\tan^{-1} \left[\frac{I_3}{I_1 + I_5} \right]} \quad (12)$$

$$\theta_g = \tan^{-1} \left(\frac{g + b}{h} \right) - \theta - (\eta + \theta_e - \theta_\beta) \quad (13)$$

$$\begin{cases} \hat{k} = \tan(\eta + \theta_\beta) R - I_5 \\ \hat{h} = \tan(\eta + \theta_e + \theta_\alpha) R - I_1 - I_5 \end{cases} \quad (14)$$

Obviously, from Fig. 2, I_4 is an important quantity for estimating \hat{h} and \hat{k} . Therefore the restriction of this method is that the tangent I_4 must be available, i.e., $I_1 + I_5$ has to be less than $Cutlim$ defined by

$$Cutlim = \sqrt{r^2 - s^2} \quad (15)$$

where $s = (\sin \theta_k) \sqrt{(f + e)^2 - r^2}$.

2. Camera position estimation method

The proposed method is illustrated in Fig.5. There are two major parts in this method. The first part is “*Landmark image detection algorithm*”. The algorithm is designed for computing the landmark image and detecting:

1. Is the landmark image complete?
2. Is more than half of the image defective?
3. Is the landmark image beyond sensor range?

The basic rectangle is employed not only for executing efficient detection but also for fast computation of the features.

The second part is “*Image feature based camera position estimation method*”. The incomplete landmark image features database could be constructed by (1-15). The ANFIS is employed for recognizing the mapping relations between the image features and the camera positions. Furthermore, the camera positions can be estimated quickly via the established mapping model.

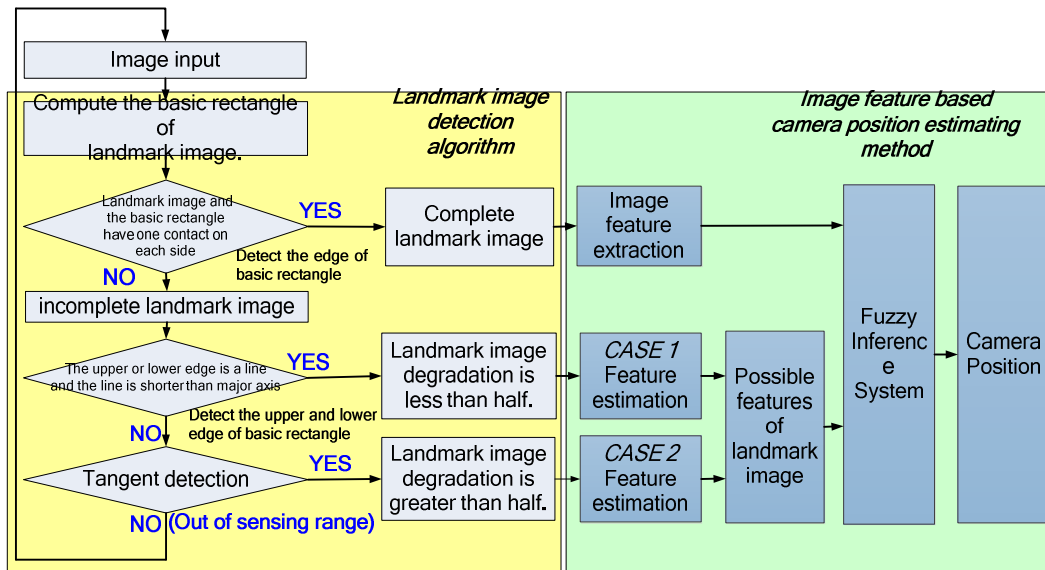


Fig.5. Flow chart of camera position estimation method

3. ANFIS training

The model for “Case 1” has been established and confirmed in [6]. We only discuss “Case 2” in this paper. Two ANFIS are provided for estimating the \hat{h} , and \hat{k} . In addition, the database is established by (7-15), and the network is illustrated in Fig. 6.

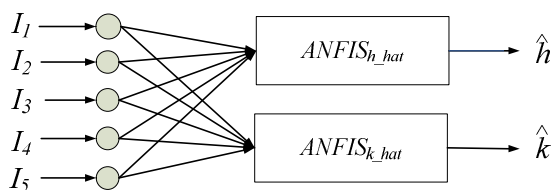


Fig.6. Illustration of \hat{h} and \hat{k} computation with dual ANFIS

III. SIMULATION RESULTS

In this section, we will demonstrate the estimation results of the \hat{h} and \hat{k} from the incomplete landmark features I_1 , I_2 , I_3 , I_4 and I_5 via ANFIS. The simulation is based on the following qualities:

1. The image size of the camera is 320×240 pixels.
2. The diameter of the circular landmark is 3 cm.
3. The range of R is 20 ~ 300 cm.
4. The range of θ is 0 ~ 62 degrees.

The estimation results of features \hat{h} and \hat{k} are illustrated in Table 1. There are 10 sets of data utilized for testing the ANFIS training results. In Table 1 the

RMSE of \hat{h} and \hat{k} are 0.000615 and 0.000471, respectively. The \hat{h} and \hat{k} are utilized to approximate the complete landmark image features. Table 2 illustrates the estimation results of camera position with the features \hat{h} and \hat{k} . The RMSE of the θ , R and Q are 0.45868, 0.506617 and 0.240798, respectively.

IV. CONCLUSION

In this paper, a scenario in which more than half of a landmark image is defective has been analyzed. The method for estimating the approximate features of incomplete landmark images is provided. From simulation results, it is clear that the approximate features can be very closely estimated via the known quantities. Moreover, we have shown that the approximate features can be used for camera position estimation. The inherent camera position estimation error range is acceptable for practical applications. The method proposed in this paper is a functional tool for camera position estimation.

REFERENCES

[1] GPS 18 Technical Specifications (2005), Revision D, Garmin International, USA.

- [2] Mori R, Hirata K and Kinoshita T (2007), Vision-Based Guidance Control of a Small-Scale Unmanned Helicopter, International Conference on Intelligent Robots and Systems, 2648-2653.
[3] Mori R, Kubo T and Kinoshita T (2006), Vision-Based Hovering Control of a Small-Scale Unmanned Helicopter, SICE-ICASE International Joint Conference, 1274-1278.
[4] Wang CC, Lien SF and Hsia KH et al (2009), Image-Guided Searching for Landmark, Artificial Life and Robotics, 14(1):95-100.
[5] Lien SF, Hsia KH and Su JP (2010), Image-Guided Height Estimation for Unmanned Helicopter Landing, ICIC Express Letters, 4(6B):2299-2304.
[6] Hsia KH, Lien SF and Su JP (2010), Camera Position Estimation by ANFIS from Incomplete Landmark Image, Conference on Fuzzy Theory and Its Applications, Accepted.
[7] Hartley R and Zisserman A (2003), Multiple View Geometry in Computer Vision, Cambridge University Press.

Acknowledgement

This research was supported by the National Science Council, Taiwan, R.O.C., under Grant No. NSC99-2221-E-269-020.

Table 1. The estimation results of features \hat{h} and \hat{k}

No.	θ	R (cm)	k	\hat{k}	Error of feature k	h	\hat{h}	Error of feature h
1	32°	31	1.58891	1.58823	0.00068	1.70474	1.70463	0.00011
2	21°	44	2.87088	2.87023	0.00065	2.73393	2.73451	-0.00058
3	42°	78	2.06710	2.06790	-0.00080	1.96832	1.96786	0.00046
4	53°	113	0.16088	0.16187	-0.00099	0.15886	0.15934	-0.00048
5	19°	157	1.78014	1.78001	0.00013	1.76272	1.76347	-0.00075
6	60°	163	0.77189	0.77171	0.00018	0.74055	0.73976	0.00079
7	10°	173	2.78694	2.78656	0.00038	2.77071	2.77091	-0.00020
8	35°	201	0.92258	0.92308	-0.00050	0.91298	0.91274	0.00024
9	13°	240	3.22209	3.22278	-0.00069	3.22209	3.22176	0.00033
10	29°	289	2.92995	2.92951	0.00044	2.91630	2.91611	0.00019

Table 2. The estimation results of camera position with the features \hat{h} and \hat{k}

No.	θ	R (cm)	Q (cm)	Error of estimated θ	Error of estimated R	Error of estimated Q
1	32°	31	10	-0.619	0.421	-0.174
2	21°	44	23	-0.354	-0.572	0.243
3	42°	78	189	0.475	-0.435	0.314
4	53°	113	78	-0.487	-0.376	-0.197
5	19°	157	63	0.221	0.636	0.231
6	60°	163	284	-0.334	0.551	0.299
7	10°	173	174	-0.531	-0.417	-0.143
8	35°	201	124	0.437	0.623	0.354
9	13°	240	254	-0.634	-0.581	-0.208
10	29°	289	365	-0.312	0.352	0.146

A Novel Variable Structure Theory Applied in Design for Wheeled Mobile Robots

Chun-Chieh Wang

*Department of Electronic Engineering, Chienkuo Technology University
No. 1, Chieh Shou N. Rd., Changhua City, Taiwan
(Tel : 886-4-7111111ext3350; Fax : 886-4-7111139)
(Email address: jasonccw@ctu.edu.tw)*

Abstract: This paper is concerned with the control of wheeled mobile robots (WMRs) using a modified variable structure theory. Firstly, we introduce the dynamic characteristic of a WMR. Secondly, the conventional variable structure control is reviewed. To remarkably improve the transient response during the reaching phase, a modified variable structure control is proposed. The validity of the proposed variable structure theory is verified by means of a simulation testing on a homemade wheeled mobile vehicle. The simulation results validate the superiority and practicality of the modified variable structure for WMRs.

Keywords: Variable Structure theory, Sliding mode control, Wheeled mobile robot.

I. INTRODUCTION

Mobile robots have a wide background of application, and motion control of WMRs has found considerable attentions over the last decades. The path-tracking control problem of WMRs has received sustained attention [1][2][14]. However, the above researches are mainly based on kinematic models of nonholonomic mobile robots. Moreover, the velocity commands must be converted into the actual control input for vehicles. Hence, dynamic models of systems should be considered. Recently, several authors also consider the dynamic model of the WMR [7][13].

Variable structure control was initiated in Russia by many researchers, like Barbashin [3], Utkin [10], Emel'yanov [8]. The control scheme has successfully been applied to many engineering problems including automatic flight control, chemical processes, helicopter stability augmentation systems, electric motors, robots, etc. Variable structure control law is deliberately changed according to some defined rules which depend on the state of the system. The scheme has been mainly considered for continuous-time systems in the form of sliding mode control.

Sliding mode control is known to be very robust against parameter variations and external disturbances and has been widely accepted as an efficient method for tracking control of uncertain nonlinear systems. It has been shown to be able to achieve 'perfect' performance in principle in the presence of parameter uncertainties, bounded external disturbance, etc [6]. However, in order to account for the presence of parameter uncertainties and bounded disturbances, a discontinuous switching function is inevitably incorporated into the control law to achieve so-called sliding condition [11]. Due to imperfect switching in practice it will raise the issue of chattering, which is usually undesirable. To suppress

chattering, a continuous approximation of the discontinuous sliding control is usually employed in the literature. Though, the chattering can be made negligible if the width of the boundary layer is chosen large enough, the guaranteed tracking precision will deteriorate if the available control bandwidth is limited. To reach a better compromise between small chattering and good tracking precision in the presence of parameter uncertainties, various compensation strategies have been proposed. For example, integral sliding control [4], [5], [9], sliding control with time-varying boundary layers [5] etc., were presented. Alternatively, applying so-called reaching law approach, Gao et al. [12] proposed sliding controllers such that the trajectories are forced to approach the sliding surface faster when they are far away from the sliding surface. This approach seems to be an efficient method capable of increasing the approaching speed to the sliding surface; however, the behavior of the system dynamics, governed by the transformed first-order equation, can only be predicted through the measurement of the generalized error; hence the transient response during the reaching phase may not be remarkably improved.

In this paper, it is concerned with the control of a WMR using a modified variable structure theory in the boundary layer. Then we will review the conventional variable structure control scheme and present the modified variable structure control theory. The effectiveness of the newly developed control scheme will be demonstrated through the control of the WMR. We'll show that the transient response during the reaching phase has been remarkably improved by the proposed control.

II. HOME-MADE WMR

The home-made WMR is shown in Fig.1. It consists of a vehicle with two driving wheels mounted on the same axis and a free front wheel. The motion and orientation are achieved by independent actuators. Hence in the WMR model, we assume the coordinates of the

mass center of the WMR is located in the middle of the hind driving wheel.



Fig.1. Home-made WMR

© Dynamic Equations of a WMR

The 2-D figure of a WMR is shown in Fig. 2. Fig. 3 shows 2-D of the car motion. The dynamic equations are described as follows,

$$\begin{bmatrix} \dot{x} \\ \dot{y} \\ \dot{\theta} \end{bmatrix} = \begin{bmatrix} \cos \theta & 0 \\ \sin \theta & 0 \\ 0 & 1 \end{bmatrix} \begin{bmatrix} v_l \\ v_r \end{bmatrix} \quad (1)$$

where v_l is the linear velocity and v_r is the angle velocity.

Let (x_r, y_r, θ_r) be the reference coordinate, $(x_e, y_e, \theta_e) = (x_r - x, y_r - y, \theta_r - \theta)$ be the coordinate errors and $\dot{y} \cos \theta - \dot{x} \sin \theta = 0$ be the non-holonomic constraint. By mathematical processing, we have the error equations

$$\begin{aligned} \dot{e}_1 &= -v_l + e_2 v_r + v_l^R \cos e_3 \\ \dot{e}_2 &= -e_1 v_r + v_l^R \sin e_3 \\ \dot{e}_3 &= -v_r + v_r^R \end{aligned} \quad (2)$$

where v_l^R is the reference linearly velocity and v_r^R is the reference angle velocity. If e_1 and e_3 converge to zero, the e_2 will also converge to zero. So we concern the stability of the error equations.

$$\begin{aligned} \dot{e}_1 &= v_l^R \cos e_3 + e_2 v_r - v_l \\ \dot{e}_3 &= v_r^R - v_r \end{aligned} \quad (3)$$

The object is to design v_l and v_r such that $e_1 = e_3 = 0$.

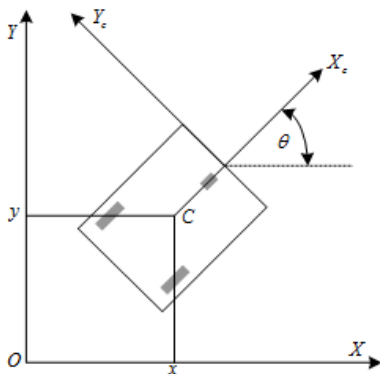


Fig.2. 2-D of a wheeled mobile

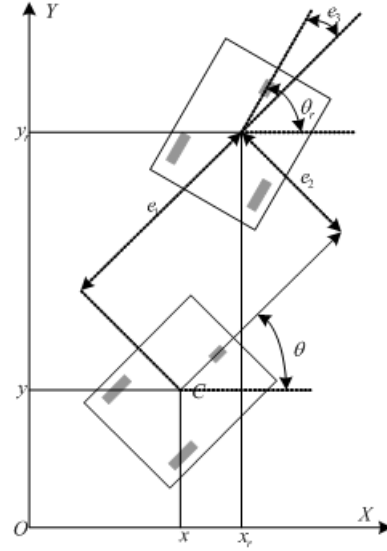


Fig.3. 2-D of the car motion

III. CONVENTIONAL VARIABLE STRUCTURE CONTROL

Consider the double integrator given by

$$\ddot{y}(t) = u(t) \quad (4)$$

Let the feedback control law be

$$u(t) = -ky(t) \quad (5)$$

where k is a strictly positive scalar. We have

$$\ddot{y} = -k\dot{y}y \quad (6)$$

Integrating this expression gives the following relationship between velocity and position

$$\dot{y}^2 + ky^2 = c \quad (7)$$

where c is a strictly positive and constant value.

Since y and \dot{y} remain bounded for all time, the closed-loop systems are stable. For asymptotic stability, the control law of the form given in (5) is not appropriate. Consider instead the control law

$$u(t) = \begin{cases} -k_1 y(t), & \text{if } y\dot{y} < 0 \\ -k_2 y(t), & \text{otherwise} \end{cases} \quad (8)$$

where $0 < k_1 < 1 < k_2$. Then the phase portrait must spiral in towards the origin and an asymptotically stable motion result. Next, consider a second-order system

$$\begin{aligned} \dot{x}_1 &= x_2 \\ \dot{x}_2 &= 2x_2 - x_1 + u \end{aligned} \quad (9)$$

with

$$u = \begin{cases} -4x_1, & \text{if } s(x_1, x_2) > 0 \\ 4x_1, & \text{if } s(x_1, x_2) < 0 \end{cases} \quad (10)$$

where the switching function is defined by

$$\begin{aligned} s(x_1, x_2) &= x_1 \sigma \\ \sigma &= 0.5x_1 + x_2 \end{aligned} \quad (11)$$

The system structure varies along the switching lines: $x_1 = 0$ and $\sigma = 0$. Figure 4 shows the phase portrait of the subsystem under $u = -4x_1$. Similarly, Figure

5 shows the phase portrait of the subsystem under $u = 4x_1$. Evidently, both subsystems are unstable. However, the origin can be made asymptotically stable by the switching law, as shown in Fig. 6. Note that the phase portrait under variable structure control consists of a reaching mode during which trajectories starting off $s = 0$ move toward it and reach it in finite time, followed by a sliding mode ($\sigma = 0.5x_1 = \dot{x}_1 = 0$) during which the motion will be confined to $s = 0$. During the sliding mode, trajectory dynamics are of a lower order than the original mode. The sliding mode is a trajectory that is not inherent in either one of the two subsystems.

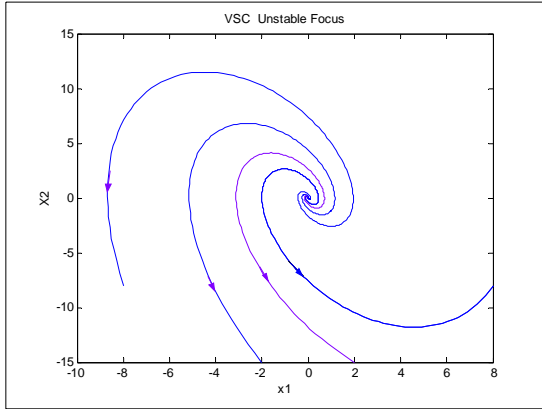


Fig.4. Phase portrait of an unstable focus

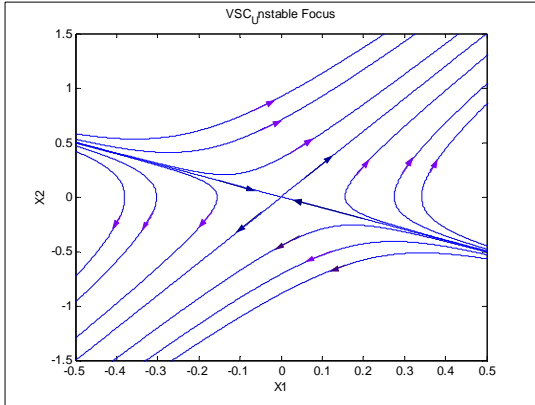


Fig.5. Phase portrait of an unstable saddle

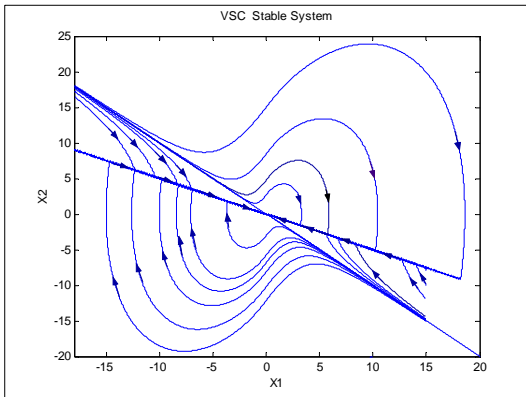


Fig.6. Phase portrait of the VSC stable system

IV. MODIFIED VARIABLE STRUCTURE CONTROL

Consider a simple n^{th} -order SISO nonlinear system

$$y^{(n)} = f(t, y, \dots, y^{(n-1)}) + g(t, y, \dots, y^{(n-1)})u \quad (12)$$

Assume that $f = \hat{f} + \Delta f$, where \hat{f} is the known part and Δf is the uncertain part, which includes the internal noise bounded in $|\Delta f| \leq F$. The object is to find a sliding control u such that the output y of (12) will approximately track a desired signal, y_d which is assumed to be n^{th} -order continuously differentiable and all of its derivatives are uniformly bounded. Given the tracking error

$$e(t) = y(t) - y_d(t) \quad (13)$$

For any $q > 0$, define the following transformation

$$s(t) = \left(\frac{d}{dt} + q \right)^{n-1} e(t) \quad (14)$$

Then

$$\dot{s} = \hat{f} + \hat{w} + u \quad (15)$$

where

$$\hat{w} = \sum_{k=1}^{n-1} \binom{n-1}{k-1} e^{(k)} \lambda^{n-k} - y_d^{(n)} \quad (16)$$

An n^{th} -order tracking problem can be transformed into an equivalent 1st-order stabilization problem. It is easy to show that the control law

$$u = \frac{1}{g} (\hat{u} + u_f) \quad (17)$$

with

$$\begin{cases} \hat{u} = -\hat{f} - \hat{w} \\ u_f = -\Gamma \text{sat}\left(\frac{s}{\Phi}\right) \end{cases} \quad (18)$$

will result in a closed-loop system satisfying the reaching condition:

$$s\dot{s} \leq -\eta|s|, \quad \forall |s| \geq \Phi, \quad (19)$$

Provided $\Gamma \geq F + \eta$, for some $\eta > 0$.

This controller ensures that starting from any initial state the error trajectory will reach the boundary layer, $|s| \leq \Phi$ in finite time.

V. SIMULATION RESULTS

To illustrate the performance of the above, the WMR is considered, given as the section II. According to the notations given above, we assume initial values are chosen as $(x_0, y_0, \theta_0) = (3, 1, \pi)$ and expected values are $(x_r, y_r, \theta_r) = (0, 0, \pi/4)$. By setting the parameters as $\Phi_y = 1$, $\lambda_y = 7$, $\Phi_a = 15$, and $\lambda_a = 25$.

Figure 7 and figure 8 indicate the tracking errors via a CVSC and MVSC, respectively.

VI. CONCLUSION

We have presented a modified variable structure control scheme in this paper for a WMR. Not only the conventional variable structure control has exhibited good responses but also the proposed control law has shown to be capable of improving the transient response as well as the steady state response. Simulation results showed good responses to any initial conditions.

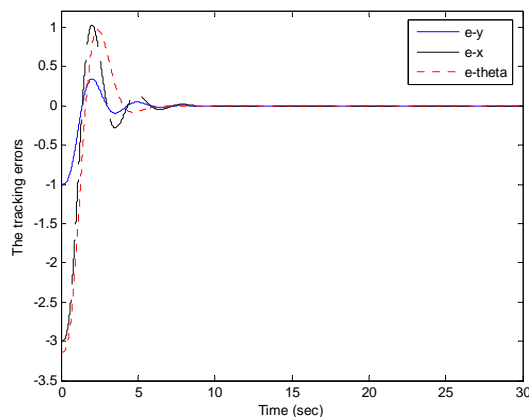


Fig. 7. Tracking errors via CVSC

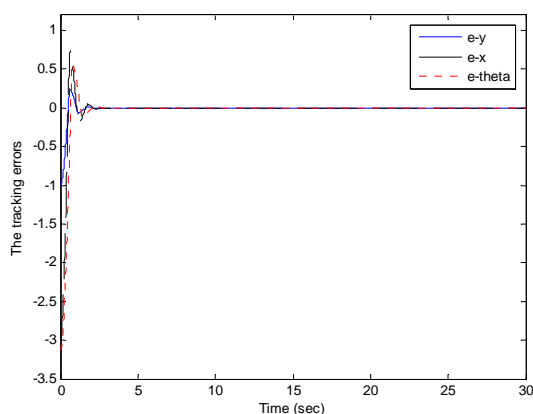


Fig. 8. Tracking errors via MVSC

REFERENCES

- [1] A.M. Bloach and S. Drakunov (1996), Stabilization and tracking in the nonholonomic integrator via sliding modes, *System & Control Letters*, Vol. 29, No. 2, pp. 91-99.
- [2] D.H. Kim and T.H. Oh (1999), Tracking control of a two-wheeled mobile robot using input-output linearization, *Control Engineer Practice*, Vol. 7, pp. 369-373.
- [3] E.A. Barbashin and E.I. Geraschenko (1965), On speeding up sliding modes in automatic control systems (in Russian), *Differentsialniye Uravneniya*, Vol. 1, pp. 25-32.
- [4] I.C. Baik, K.H. Kim, H.S. Kim, G.W. Moon, and M.J. Youn (1996), Robust nonlinear speed control of PM synchronous motor using boundary layer integral sliding control with sliding load torque observer, *IEEE PESC'96 Record*, pp.1242-1247.
- [5] J.H. Lee, J.S. Ko, S.K. Chun, J.J. Lee, and M.J. Youn (1992), Design of continuous sliding mode controller for BLDDM with prescribed tracking performance, *Conference Record, IEEE PESC'92*, pp.770-775.
- [6] J.J. Slotine, E. and W. Li (1991), *Applied Nonlinear Control*, Prentice-Hall: Englewood Cliffs, NJ.
- [7] K.D. Do, Z.P. Jiang, and J. Pan (2004), Simultaneous tracking and stabilization of mobile robots: an adaptive approach, *IEEE Trans. On Automatic Control*, Vol. 49, No. 7, pp.1147-1152.
- [8] S.V. Emelyanov (1985), *Binary control systems*, International Research Institute for Management Sciences, Vol. 1.
- [9] T.L. Chern and Y.C. Wu (1993), Design of brushless DC position servo systems using integral variable structure approach, *IEE Proceedings - Electr. Power Appl.* Vol. 140, pp. 27-34.
- [10] U.I. Utkin (1992), *Sliding Modes in Control and Optimization*, Springer-Verlag.
- [11] V.I. Utkin (1997), Survey paper-variable structure systems with sliding modes, *IEEE Trans. Automat. Contr.* Vol. 22, No. 2, pp. 212-222.
- [12] W. Gao and J.C. Hung (1993), Variable structure control of nonlinear systems: a new approach, *IEEE Trans. on Indust. Elect.* Vol. 40, pp. 45-55.
- [13] Z. Hu, Z. Li, R. Bicker, and C. Marshall (2004), Robust output tracking control of nonholonomic mobile robots via higher order sliding mode, *Nonlinear Studies*, Vol. 11, No. 1, pp.23-35.
- [14] Z.P. Jiang and H. Nijmeijev (1999), A recursive technique for tracking control of nonholonomic system in chained form, *IEEE Trans. On Automatic Control*, Vol. 44, No. 2, pp. 265-279.

Parameter Identification of Lorenz System Using RBF Neural Networks with Time-Varying Learning Algorithm

Chia-Nan Ko¹, Yu-Yi Fu², Cheng-Ming Lee³, and Guan-Yu Liu⁴

^{1,2}*Department of Automation Engineering,*

³*Department of Computer and Communication Engineering,*

⁴*Department of Electronic Engineering,*

^{1,2,3,4}*Nan-Kai University of Technology, Tasotun, Nantou 542, Taiwan*

(E-mail: ¹t105@nku.edu.tw; ²t098@nku.edu.tw; ³t104@nku.edu.tw; ⁴guanyu@nku.edu.tw)

Abstract: A hybrid evolutionary algorithm is proposed to identify parameters for Lorenz chaotic system. In the proposed algorithm, time-varying learning algorithm based on annealing robust concept (ARTVLA) is adopted to optimize a radial basis function neural network (RBFNN) for parameter identification of Lorenz system. In the ARTVLA, the determination of the learning rate would be an important work for the trade-off between stability and speed of convergence. A computationally efficient optimization method, particle swarm optimization (PSO) method, is adopted to simultaneously find a set of promising learning rates and optimal parameters of RBFNNs. The proposed RBFNN (ARTVLA-RBFNN) has good performance for identifying parameters of Lorenz system. Simulation results are illustrated the effectiveness and feasibility of the proposed ARTVLA-RBFNN.

Keywords: Parameter identification, time-varying learning algorithm, particle swarm optimization, Lorenz chaotic system.

I. INTRODUCTION

A chaotic system is a nonlinear deterministic system that has some special features of sensitive dependence on initial conditions and unstable bounded trajectories in the phase space. Due to their characteristics sensitivity to initial conditions, chaotic systems are not easy to identify. Recently, some researchers have endeavored to improve the identification of chaotic systems^[1-3].

Recently, RBFNNs have received considerable applications in various fields, such as function approximation, prediction, recognition, etc^[4,5]. Since RBFNNs have only one hidden layer and have fast convergence speed, they are widely used for nonlinear system identification recently. Besides, the RBFNNs are often referred to as model-free estimators since they can be used to approximate the desired outputs without requiring a mathematical description of how the outputs functionally depend on the inputs^[6,7].

When utilizing RBFNNs, a learning rate serves as an important role in the procedure of training RBFNNs. Generally, the learning rate is selected as a time-invariant constant by trial and error. However, there still exist several problems of unstable or slow convergence. Some researchers have engaged in exploring the learning rate to improve the stability and the speed of convergence^[8,9]. In this article, time-varying learning algorithm (TVLA) is then applied to train the RBFNN (TVLA-RBFNN), in which PSO method^[10] is adopted to find optimal learning rates during learning procedure. A typical system, Lorenz chaotic system, will be given to illustrate the feasibility and efficiency of the proposed TVLA-

RBFNNs for parameter identification of the chaotic system.

II. PROBLEM FORMULATION

Considering the following n -dimensional chaotic system:

$$\dot{\mathbf{X}} = F(\mathbf{X}, \mathbf{X}_0, \mathbf{Q}_0) \quad (1)$$

where $\mathbf{X} \in R^n$ denotes the state vector, \mathbf{X}_0 denotes the initial state, and \mathbf{Q}_0 is a set of original parameters.

When estimating the parameters, suppose the structure of the system is known in advance, and thus the estimated system can be described as follows:

$$\dot{\hat{\mathbf{X}}} = F(\mathbf{X}, \mathbf{X}_0, \mathbf{Q}) \quad (2)$$

where $\hat{\mathbf{X}} \in R^n$ denotes the state vector, and \mathbf{Q} is a set of estimated parameters. Therefore, the problem of parameter estimation can be formulated as the following optimization problem:

$$\text{Min } J = \frac{1}{M} \sum_{k=1}^M \|\mathbf{X}_k - \hat{\mathbf{X}}_k\|^2 \quad (3)$$

where M denotes the length of data used for parameter identification, \mathbf{X}_k and $\hat{\mathbf{X}}_k$, denote state vectors of the original and the identified systems at time K , respectively.

Obviously, the parameter identification for chaotic systems is a multi-dimensional continuous optimization problem, where the decision vector is \mathbf{Q} and the optimization goal is to minimize J .

III. ARTVLA-BASED RBFNNs USING PSO

1. Architecture of RBFNNs

In general, the input-output relation of a nonlinear system can be expressed as

$$\mathbf{y}(t+1) = \mathbf{f}(\mathbf{y}(t), \mathbf{y}(t-1), \dots, \mathbf{y}(t-n_y), \mathbf{x}(t), \mathbf{x}(t-1), \dots, \mathbf{x}(t-n_x)) \quad (4)$$

where $\mathbf{x}(t) \in R^m$ is the input vector, $\mathbf{y}(t) \in R^p$ is the output vector, n_x and n_y are the maximal lags in the input and output, respectively, and $\mathbf{f}(t) \in R^p$ denotes the nonlinear relation to be estimated. One can use a neural network to estimate the input-output relation of a nonlinear system.

A radial basis function neural network (RBFNN) consists of three layers, the input layer, the hidden layer, and the output layer. The transformation from the input layer to the hidden layer is nonlinear. The output layer is linear and gives a summation at the output neurons. The structure of an RBFNN is shown in Fig. 1. When the Gaussian function is chosen as the radial basis function, an RBFN can be expressed in the form

$$\hat{y}_j(t+1) = \sum_{i=1}^l G_i w_{ij} = \sum_{i=1}^l w_{ij} \exp\left(-\frac{\|\hat{\mathbf{x}} - \mathbf{m}_i\|^2}{2\sigma_i^2}\right) \quad \text{for } j = 1, 2, \dots, p, \quad (5)$$

where $\hat{\mathbf{x}}(t) \in R^m$ is the input vector, $\hat{y}_j(t+1)$ is the j th output, w_{ij} is the synaptic weight between the i th hidden neuron and the j th output neuron, G_i is the Gaussian function at the i th neuron in the hidden layer, \mathbf{m}_i and σ_i are the center and width of G_i , respectively, and l is the number of the Gaussian functions, which is also equal to the number of hidden layer nodes.

2. PSO-Based ARTVLA

In the training procedure of the proposed RBFNNs, the annealing concept in the cost function of robust back-propagation learning algorithm was adopted to overcome the existing problems in robust back-propagation learning algorithm, such as slow convergence rate and getting into local minimum^[11]. A cost function for the ARTVLA is defined here as

$$J_j(h) = \frac{1}{N} \sum_{k=1}^N \rho[e_j^{(k)}(h); \beta(h)] \quad \text{for } j = 1, 2, \dots, p \quad (6)$$

where

$$e_j^{(k)}(h) = y_j^{(k)} - \hat{y}_j(\mathbf{x}^{(k)}) \quad (7)$$

h is the epoch number, $e_j^{(k)}(h)$ is the error between the j th desired output and the j th output of the RBFNN at epoch h for the k th input-output training data in a nonlinear system, $\beta(h)$ is a deterministic annealing schedule acting like the cut-off point, and $\rho(\cdot)$ is a logistic loss function defined as

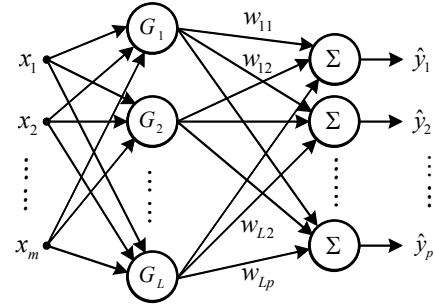


Fig. 1. The structure of an RBFNN.

$$\rho[e_j^{(k)}; \beta] = \frac{\beta}{2} \ln \left[1 + \frac{(e_j^{(k)})^2}{\beta} \right] \quad \text{for } j = 1, 2, \dots, p \quad (8)$$

Based on the gradient-descent kind of learning algorithms, the synaptic weights w_{ij} , the centers \mathbf{m}_i , and the widths σ_i of Gaussian functions are updated as

$$\Delta w_{ij} = -\eta_w \frac{\partial J_j}{\partial w_{ij}} = -\frac{\eta_w}{N} \sum_{k=1}^N \varphi_j(e_j^{(k)}; \beta) \frac{\partial e_j^{(k)}}{\partial w_{ij}} \quad (9)$$

$$\Delta \mathbf{m}_i = -\eta_c \frac{\partial J_j}{\partial \mathbf{m}_i} = -\frac{\eta_c}{N} \sum_{j=1}^p \sum_{k=1}^N \varphi_j(e_j^{(k)}; \beta) \frac{\partial e_j^{(k)}}{\partial \mathbf{m}_i} \quad (10)$$

$$\Delta \sigma_i = -\eta_\sigma \frac{\partial J_j}{\partial \sigma_i} = -\frac{\eta_\sigma}{N} \sum_{j=1}^p \sum_{k=1}^N \varphi_j(e_j^{(k)}; \beta) \frac{\partial e_j^{(k)}}{\partial \sigma_i} \quad (11)$$

$$\varphi_j(e_j^{(k)}; \beta) = \frac{\partial \rho(e_j^{(k)}; \beta)}{\partial e_j^{(k)}} = \frac{e_j^{(k)}}{1 + (e_j^{(k)})^2 / \beta(h)} \quad (12)$$

where η_w , η_c , and η_σ are the learning rates for the synaptic weight w_{ij} , $j = 1, 2, \dots, p$, the center \mathbf{m}_i , and the width σ_i , respectively, $\varphi(\cdot)$ is usually called the influence function.

In (9) to (11), when the learning rates are constant, the work for selecting an appropriate learning rate is tedious; moreover, there exists a tendency to get stuck in a near-optimal solution or to converge slowly. To overcome the stagnation in searching a globally optimal solution, TVLA is proposed to approach the optimal solution closely in this paper. In the TVLA, a nonlinear time-varying evolution concept is adopted over iterations, in which the learning rates η_w , η_c , and η_σ with a high value η_{\max} and nonlinearly decreases to η_{\min} at the maximal number of epochs, respectively. This means that the mathematical expressions are given as shown as

$$\eta_w = \eta_{\min} + \left(1 - \frac{h}{\text{epoch}_{\max}}\right)^{pw} (\eta_{\max} - \eta_{\min}) \quad (13)$$

$$\eta_c = \eta_{\min} + \left(1 - \frac{h}{\text{epoch}_{\max}}\right)^{pc} (\eta_{\max} - \eta_{\min}) \quad (14)$$

$$\eta_\sigma = \eta_{\min} + \left(1 - \frac{h}{\text{epoch}_{\max}}\right)^{ps} (\eta_{\max} - \eta_{\min}) \quad (15)$$

where $epoch_{max}$ is the maximal number of epochs and h is the current number of epochs. In the updated procedure, appropriate functions for the learning rate η_w , η_c , and η_σ can promote the performance of RBFNNs. However, simultaneously determining the optimal combination of pw , pc , and ps is a time-consuming work.

In this paper, the PSO method is adopted to find the optimal combination (pw , pc , ps) of learning rates in (13) to (15) and optimal parameters of RBFNNs for parameter identification of Lorenz system. In the system identification, the goal is to minimize the error between the desired outputs and the trained outputs. Therefore, the root mean squares error ($RMSE$) should be used to define a fitness function. This means that the fitness function will be defined as

$$RMSE = \sqrt{\frac{1}{N} \sum_{k=1}^N (y^{(k)} - \hat{y}^{(k)})^2} \quad (16)$$

where $y^{(k)}$ is the desired output, $\hat{y}^{(k)}$ is the trained output for N sampling data.

IV. SIMULATION RESULTS

The identification scheme of a chaotic system is depicted in Fig. 2, training input-output data are obtained by feeding a signal $x(k)$ to the system and measure its corresponding output $y(k+1)$. Then subject to the same input signal, the objective of identification is to construct an ARTVLA-RBFNN using PSO method, which produces an output $\hat{y}(k+1)$ to approximate $y(k+1)$ as closely as possible.

In this section, Lorenz system is used to verify the feasibility of the proposed ARTVLA-RBFNNs. When applying the proposed algorithm, the population size, the maximal iteration number, and the maximal epoch number are chosen to be 30, 200, and 200, respectively. The variables pw , pc , and ps in learning rate functions (13) to (15) are all chosen as real numbers in the range $[0.1, 5]$. Meanwhile, the values of η_{max} and η_{min} are set as 3.0 and 0.5, respectively.

Two problems are investigated for Lorenz system. First, the impact on efficiency of annealing robust learning algorithms (ARLA) for various learning rates is studied, in which the best learning rate will be determined by trial and error. Secondly, the comparison between the proposed ARTVLA-RBFNN with nonlinear time-varying learning rates and the ARLA-based RBFNN (ARLA-RBFNN) with a fixed learning rate is illustrated. The $RMSE$ (16) of the training data is adopted to evaluate the performance of the RBFNNs.

Example: A typical chaotic system, Lorenz system, is considered as an example described as follows^[2,12].

$$\begin{cases} \dot{x} = q_1(y - x) \\ \dot{y} = q_2x - y - xz \\ \dot{z} = xy - q_3z \end{cases} \quad (17)$$

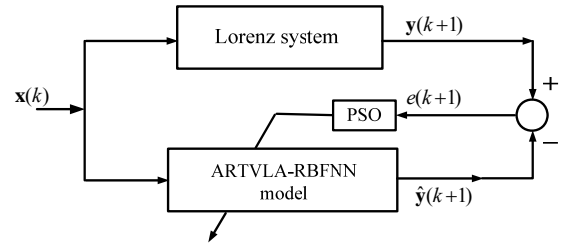


Fig.2. The proposed PSO-based ARTVLA-RBFNN scheme for parameter identification of Lorenz system.

where $q_1 = 1$, $q_2 = 5.46$, $q_3 = 20$ are the original parameters. The initial values of the system are $x(0) = -0.3$, $y(0) = 0.3$, $z(0) = 0.2$.

With the 2000 training data, two annealing robust algorithms are then applied to train the RBFN, respectively.

Problem 1:

In the ARLA-RBFNNs, various learning rates, $0.5 \leq \eta \leq 3.0$, are used to train the RBFNNs. After 200 training epochs, the $RMSE$ values for various learning rates are obtained, respectively. The details of the simulation results are shown in Table 1.

Problem 2:

With the nonlinear learning rates, the ARTVLA is adopted to train the RBFNNs, in which the optimal learning rates are determined by linear time-varying evolution PSO^[13] method. The optimal sets in (13) to (15) are obtained as follows:
 $(pw, pc, ps) = (1.3379, 0.0547, 1.0273)$,
 $(pw, pc, ps) = (4.4722, 0.0309, 3.2897)$, and
 $(pw, pc, ps) = (1.4503, 0.3081, 4.1117)$ for $x(t)$, $y(t)$, and $z(t)$, respectively. Meanwhile, the final values of $RMSE$ with ARTVLA-RBFNNs are found to be 0.02313, 0.02733, and 0.05276 shown in Table 1. Figure 3 shows the values of $RMSE$ for $x(t)$, $y(t)$, and $z(t)$ using the proposed algorithm with optimal learning rates. To show the feasibility of the ARTVLA-RBFNNs, the errors of training data after 200 epochs are illustrated in Fig. 4.

V. CONCLUSIONS

This paper presented PSO-based ARTVLA to train RBFNNs for parameter identification of Lorenz chaotic system. In the proposed ARTVLA-RBFNNs, time-varying learning rates and optimal parameters of RBFNNs are simultaneously determined by PSO method. Then the optimal RBFNNs are adopted to identify the chaotic system. From the simulation results, the effectiveness and the feasibility of the proposed ARTVLA-RBFNNs identifying parameter of Lorenz system has been verified. Meanwhile, the superiority of the proposed ARTVLA-RBFNNs with nonlinear learning rates over the ARLA-RBFNNs with fixed learning rates for parameter identification has been illustrated.

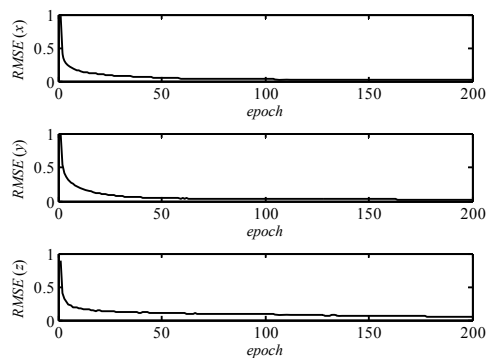


Fig. 3. The values of $RMSE$ after 200 training epochs using ARTVLA-RBFNN with the optimal learning rates.

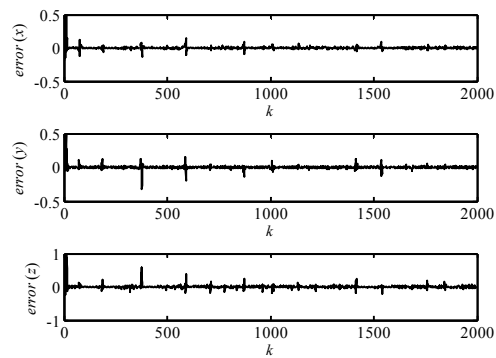


Fig. 4. The plots of $error = y(k) - \hat{y}(k)$ for 2000 training data after 200 training epoch.

Table 1. The values of $RMSE$ (16) for Lorenz chaotic system after 200 training epochs, in which ARLA with various learning rates and ARTVLA with time-varying learning rates are applied to train the RBFNNs.

Learning rates and ARTVLA with time-varying learning rates are applied to train the RDLNNs.										
ARTVLA		ARLA (learning rate η)								
		4.0	3.5	3.0	2.5	2.0	1.5	1.0	0.5	0.2
$x(t)$	0.0231	0.0657	0.0392	0.0356	0.0386	0.0419	0.0389	0.0492	0.0727	0.0925
$y(t)$	0.0273	0.0929	0.0927	0.0584	0.0750	0.0431	0.0393	0.0824	0.1077	0.1560
$z(t)$	0.0528	0.1024	0.1008	0.0945	0.0944	0.0880	0.0623	0.0675	0.0703	0.0976

ACKNOWLEDGMENT

This work was supported in part by the National Science Council, Taiwan, R.O.C., under grant NSC 98-2221-E-252-004.

REFERENCES

- [1] Gu H, Wang HW (2007), Fuzzy prediction of chaotic time series based on singular value decomposition. *Applied Mathematics and Computation* 185:1171-1185
- [2] Pan ST, Lai CC (2008), Identification of chaotic systems by neural network with hybrid learning algorithm. *Chaos, Solitons and Fractals* 37(1): 233-244
- [3] Modares H, Alfi A, Fateh MM (2010), Parameter identification of chaotic dynamic systems through an improved particle swarm optimization. *Expert Systems with Applications* 37:3714-3720
- [4] Chuang CC, Jeng JT, Lin PT (2004), Annealing robust radial basis function networks for function approximation with outliers. *Neurocomputing* 56: 123-139
- [5] Sing JK, Basu DK, Nasipuri M, Kundu M (2007), Face recognition using point symmetry distance-based RBF network. *Applied Soft Computing* 7: 58-70
- [6] Kosko B (1992), *Neural networks and fuzzy systems: a dynamical systems approach to machine intelligence*. Prentice-Hall, NJ
- [7] Fu YY, Wu CJ, Jeng JT, Ko CN (2009), Identification of MIMO systems using radial basis function networks with hybrid learning algorithm. *Applied Mathematics and Computation* 213: 184-196
- [8] Yu W (2004), Nonlinear system identification using discrete-time recurrent neural networks with stable learning algorithms. *Information Science* 158:131-147
- [9] Yoo SJ, Park JB, Choi YH (2007), Indirect adaptive control of nonlinear dynamic systems using self recurrent wavelet neural networks via adaptive learning rates. *Information Science* 177:3074-3098
- [10] Kennedy J, Eberhart R (1995), Particle swarm optimization. In *Proceedings of the IEEE Int Conf on Neural Networks*, pp. 1942-1948
- [11] Chuang CC, Su SF, Hsiao CC (2000), The annealing robust backpropagation (BP) learning algorithm. *IEEE Transactions on Neural Networks* 11(5):1067-1077
- [12] Fu YY, Wu CJ, Jeng JT, Ko CN (2010), ARFNNs with SVR for prediction of chaotic time series with outliers. *Expert Systems with Applications* 37: 4441-4451
- [13] Ratnaweera A, Halgamuge SK, Watson C (2004), Self-organizing hierarchical particle swarm optimizer with time-varying acceleration coefficients. *IEEE Transactions on Evolutionary Computation* 8(3):240-255

Motion Planning of a Landmine Detection Robot

Kuo-Lan Su¹, Hsu-Shan Su², Sheng-Wen Shiao², Jr-Hung Guo²

1. Department of Electrical Engineering, National Yunlin University of Science & Technology, Taiwan

2. graduate school Engineering Science and technology, National Yunlin University of Science & Technology

E-mail: sukl@yuntech.edu.tw, g9610808@yuntech.edu.tw, g9710801@yuntech.edu.tw

Abstract: The article develops a landmine detection system that contains a landmine-detection mobile robot and a following mobile robot. In this system, the landmine-detection mobile robot goes ahead, and uses landmine detector and GPS module to find out landmines, and record the coordinate location, and transmits the landmine's coordinate to the following mobile robot via wireless RF interface. The following mobile robot can record the location and orientation of the landmine detection robot and the landmines on the region. The following robot moves closed to the landmine, and programs the motion path to avoid obstacles automatically. The driver system of the landmine detection mobile robot uses a microprocessor dsPIC 30F4011 as the core, and controls two DC servomotors to program the motion path. The user interface of the landmine detection mobile robot and the following mobile robot uses Borland C++ Builder language to receive the location data. In the experimental results, the landmine mobile robot records the location of the landmines using GPS module, and transmits the location to the following robot via wireless RF interface. The following mobile robot avoids landmines quickly, and enhances the safety to carry peoples or materials cross over the landmine area.

Keywords: mobile robot system, landmine-detection mobile robot, following mobile robot, GPS module, wireless RF interface, dsPIC 30F4011, Borland C++ Builder

I. INTRODUCTION

Landmines are one of the great scourges on the human life. Thousands of people are injured each year by accidental landmine explosions on the known or unknown environment. There are approximately 100 million landmines buried throughout the world in approximately 70 different countries. Current methods can neutralize only about 100000 per year. The procedure for landmine removal varies greatly depending on such factors as: location, terrain, landmine distribution, soil density, age of minefield, covering vegetation and locally available resources [1]. How to develop a safety processing method to detect landmines is a challenge problem.

The currently floating to detect and dispose landmines and explosive ordnance is to commit an unmanned vehicle that equips a detection and disposal system to the suspected terrain. In landmine detection, a huge amount of research has been directed at sensor technology such as: odor sensors, acoustic sensors, electromagnetic induction sensors, electrical impedance sensors, infra-red and microwave, radiometry and radar [2,3].

There are many studies about landmine detection in the literature. Sweeping, detecting and clearing landmines is possible thanks to electromagnetic induction spectroscopy [4]. There are some studies related to a landmine detector assembled on a remote controlled mobile platform or vehicle [5]. There are also landmine detectors with inductive and capacitive [6] RF microcontrollers, as well as GPS-based [7] and GPR-designed ones [8]. A six-legged walking robot was equipped with a metal detector and communicated with a supervisory computer to mark suspected landmine locations using a differential GPS system [9]. Furthermore, rolling machines are also faster and more stable than legged device on landmine detection. [10,11].

The paper is organized as follows: section II describes the system structure of the landmine detection system. The system contains a landmine detection robot and a following robot, and explains functions of the two mobile robots. The section III presents how to program the motion trajectories of the two mobile robots avoiding landmines in the landmine region. Section V presents the experimental results of the landmine detection and avoidance using the proposed method. The brief concluding comments are described in Section VI.

II. SYSTEM ARCHITECTURE

The architecture of the landmine detection system is shown in Fig. 1. There are two mobile robots in the system. One is the landmine detection robot, and the other is the following robot. The controller of the landmine detection robot is personal computer, and drives two DC servomotors through dsPIC 30F4011 chip. The mobile robot can find out locations of the mines in the dangerous region using landmine detector and GPS module, and transmits the locations of the landmines to the following mobile robot using wireless RF module. The following robot programs the trajectory to avoid the landmines, and enhance the safety moving in the landmine region. The driver system of the following robot is similar to the landmine detection robot.

The platform of the landmine detection robot is shown in Fig 2. The mobile robot has the shape of rectangle, and its length, width and weight is 80cm, 50cm and 10kg. The rubber belt was used as a track on the mobile robot, and rolled tightly on the ground using fixed wheel. The mobile robot drives the rubber belt using DC servomotor. The landmine detector is arranged on the front of the mobile robot, and is driven by stepping motor with reduce

gear. The rotation angle range is about 50 degree, and rotates back and forth on a fixed joint. The GPS module is on the side of the landmine detector to record the location of the landmine.

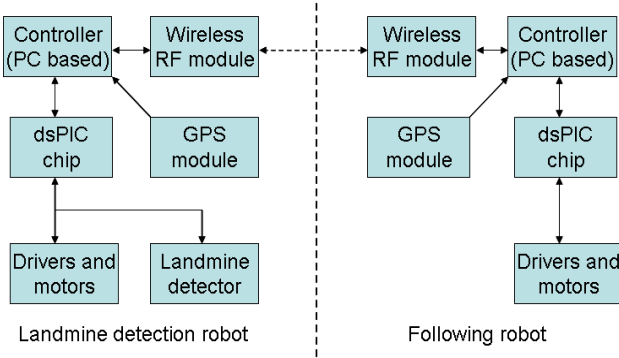


Fig. 1 The system architecture of the landmine detection system

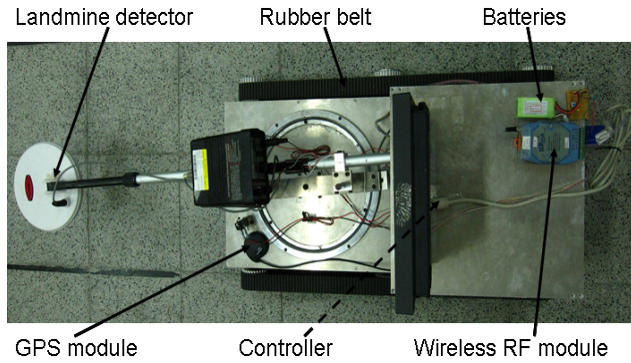


Fig. 2 The platform of the landmine detection robot

The platform of the following robot is shown in Fig 3. The mobile robot has the shape of rectangle, too. Its length, width and weight is 90cm, 71cm and 12kg respectively. The mobile robot is driven by four DC servomotors. Each rubber belt is driven by two DC servomotors to increase loading capability. The controller of the mobile robot is arranged on the front of the mobile robot. The GPS module is on the front of the mobile robot to record the coordinate of the following mobile robot.

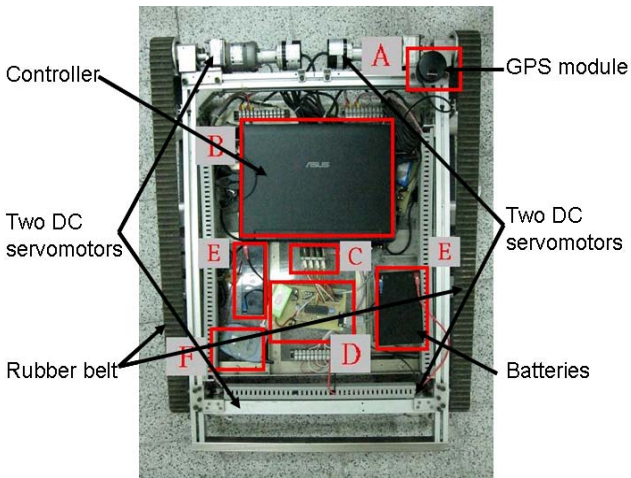


Fig. 3 The platform of the following robot

III. MOTION PLANNING

The GPS is the only fully functional Global Navigation Satellite System (GNSS) [12]. The GPS uses a constellation of

between 24 and 32 Medium Earth Orbit (MEO) Satellites that transmit precise microwave signals to determine current location, time and velocity. These signals travel at the speed of light and the receiver uses the arrival time to measure the distance and position. We use the GPS that is produced by GARMIN Company to determine the coordinate of the robot. GPS takes longitude and latitude values from satellite [13]. We calculate the angle σ and distance d using the great-circle distance formula.

$$\sigma = \arccos(\sin \phi_s \sin \phi_f + \cos \phi_s \cos \phi_f \cos \Delta\lambda) \quad (1)$$

$$d = r\sigma \quad (2)$$

ϕ_s is the start value on latitude. ϕ_f is the final value on latitude. $\Delta\lambda$ is the difference on longitude. d is distance from the start location to the target location. r is radius of the earth.

The landmine detection mobile robot to detect mines using the mine detector moving on the free-space, and transmits locations of the landmines and the landmine detection robot to the following mobile robot. The following robot tracks the landmine detection robot according the coordinate of the landmine robot. The experimental area of the system is 20mX10m. The mobile robot moves forward from the start location to the target location. The mobile robot detects landmines to stop, and transmits the coordinate of the landmine to the following robot via wireless RF interface. The simulation result is shown in Fig. 4. The mobile robot turns right to avoid the landmine, and crosses over the dangerous area to be shown in Fig. 4. Finally, the landmine detection robot moves to the target location, and transmits coordinate of the fixed position from the motion path to the following robot.

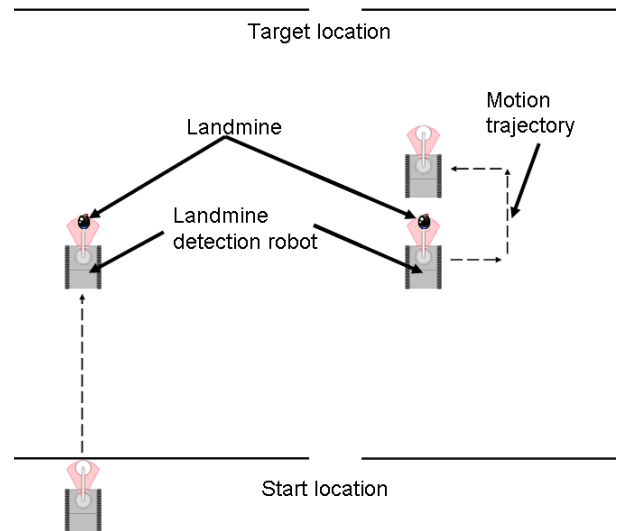


Fig. 4. The motion path of the landmine detection robot

The following mobile robot moves forward according to the trajectory that is built using the fixed coordinate from the landmine detection robot, and receives the landmine location from the landmine detection robot via wireless RF interface. The mobile robot moves ahead the landmine to be 3m, and turns right moving forward 3m to cross over the landmine area. The simulation result

is shown in Fig. 5. Then the mobile robot turns left moving forward about 6m. The mobile robot turns left moving 3m to avoid the landmine. Finally, the mobile robot turns right and moves to the target location. The simulation result is shown in Fig. 5.

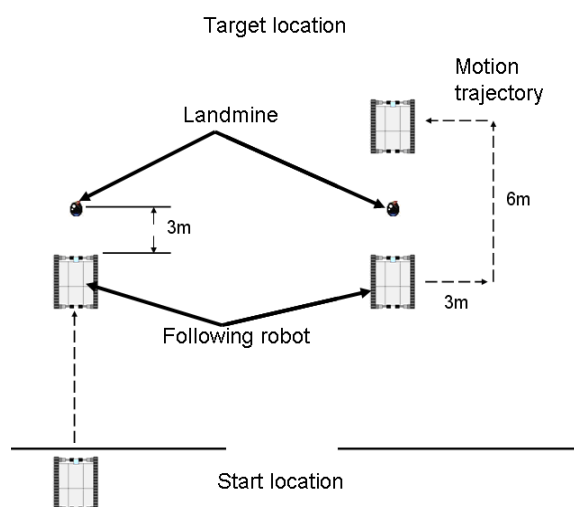
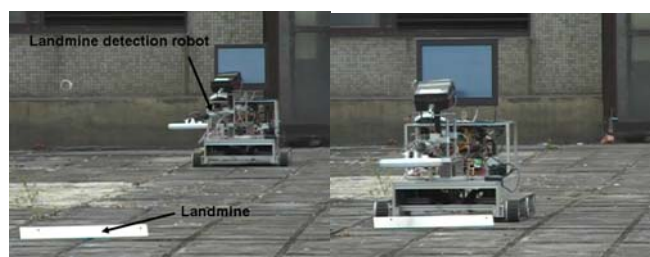


Fig 5. The motion path of the following robot

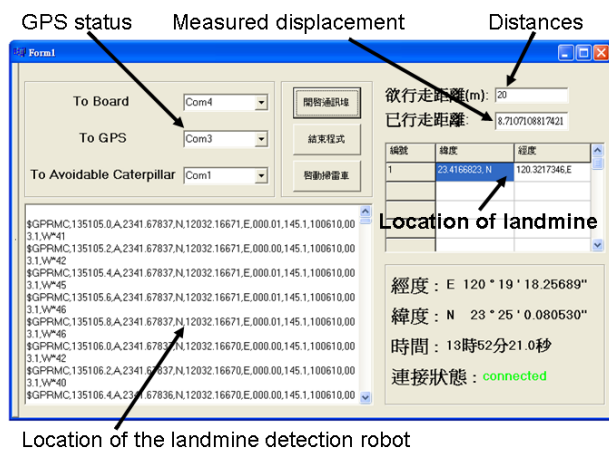
IV. EXPERIMENTAL RESULTS

We implement the experimental scenarios on the four floor of the department of electrical engineering in my school. In the landmine detection, we use a metal bar as the landmine. The landmine detection mobile robot moves forward from the start location. The scenario is shown in Fig. 6 (a). The mobile robot uses the mine detector to detect the coordinate of landmines around the region, and transmits the coordinate of the landmine to the following mobile robot.



(a)

(b)



(c)

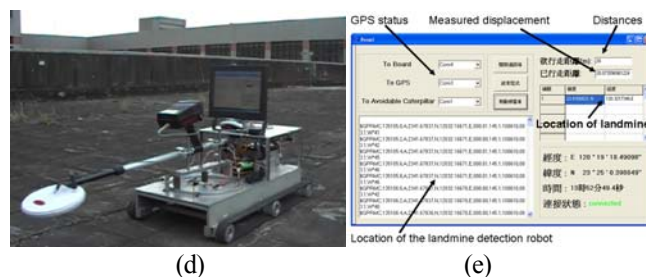


Fig. 6 The experimental result of the landmine detection robot

The mobile robot detects the mine on the motion path, and displays the coordinate of the landmine and the displacement of the landmine detection robot on the user interface. The experimental results are shown in Fig. 6 (b) and (c). Then the mobile robot transmits the coordinate of the landmine to the following robot, and moves to the target location step by step. Finally, the mobile robot stops at the target location. The experimental result is shown in Fig. 6 (d). The measured displacement is calculated from the encoder of two DC servomotors is 20.07m to be shown in Fig. 6 (e). The error displacement is only 7cm on the test.

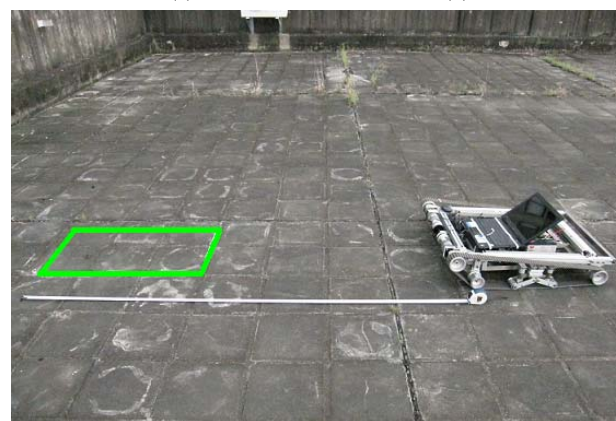
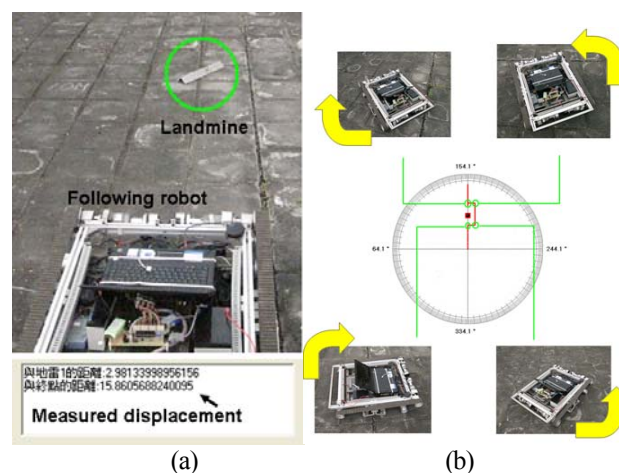


Fig. 7. The experimental result of the following robot

The following robot receives the coordinate of the motion path from the landmine detection robot, and moves forward to target location. The scenario is shown in Fig. 7 (a). The user interface of the following mobile robot can displays the motion displacement and the distance far from the target location. The following robot moves forward closed to the location of the landmine that is

recorded on the memory, and avoids the landmine according to the proposed motion path. The motion processing of the mobile robot is shown in Fig. 7 (b), and displays the orientation to implement the programmed trajectory. Finally, the mobile robot moves to the target position to be shown in Fig. 7 (c). The error displacement is smaller than 1 meter from the start location to the target location.

V. CONCLUSION

We have presented a landmine detection system that contains a landmine-detection mobile robot and a following mobile robot. In this system, the landmine-detection mobile robot goes ahead, and uses landmine detector and GPS module to find out landmines, and record the coordinate location, and transmits the landmine's coordinate to the following mobile robot via wireless RF interface. The following mobile robot can record the location and orientation of the landmine detection robot and the coordinate of the landmines on the region. The following robot moves closed to the landmine, and program the motion path to avoid obstacles automatically. In the future, we want to develop the curve path to avoid landmines on the landmine detection robot and following robot, and program the uniform user interface of the landmine detection system.

ACKNOWLEDGMENT

This work was supported by the project "Development of a module based education robot" under Ministry of Education of Taiwan. (99-A010-5).

REFERENCE

- [1] M. Freese, E. F. Fukushima, S. Hirose and W. Singhose, (2007), Endpoint Vibration Control of a Mobile Mine-Detecting Robotic Manipulator, The American Control Conference, New York, USA, pp.7-12.
- [2] J. P. Trevelyan (1997), Robots and landmines, Industrial Robot, Vol. 24, No. 2, pp.114-125.
- [3] M. Ghaffari, D. Manthena, A. Ghaffari and E. L. Hall, (2004), Mines and human casualties, a robotic approach toward mine clearing, SPIE Intelligent Robots and Computer Vision XXI: Algorithms, Techniques and Active Vision, Vol. 5608.
- [4] I. J. Won, D. A. Keiswetter and T. H. Bell (2001), Electromagnetic induction spectroscopy for clearing landmines, IEEE Trans. Geoscience and Remote Sensing, Vol. 39, No. 4, pp.703-709.
- [5] Y. Baudoin, E. Colon (1998), Humanitarian demining and robotics, Proceedings of the IEEE International Conference on Control Applications, 1-4, September, Trieste, Italy.
- [6] M. E. V. Steenberg, A. Washabaugh and N. Goldfine (2001), Inductive and capacitive sensor arrays for In Situ composition sensors, Aerospace Conference, IEEE Proceedings, Vol. 1, pp. 1/299-309.
- [7] M. Hussain (2005), RF controlled GPS based hovering mine detector, 9th International Multitopic Conference, IEEE INMIC.
- [8] D. J. Daniels and P. Curtis (2003), Minetec, 2nd International Workshop on Advanced GPR, Delft, The Netherlands, 14-16, May.

- [9] P. G. Santos, M. Armada, J. Estremera and M. Jimenez (1999), Walking machines for humanitarian demining, European Journal of Mechanical and Environmental Engineering, Vol. 44, No. 2, pp.91-95.
- [10] P. Debenest, E. F. Fukushima and S. Hirose (2002), Gryphon-I-robot for field applications on uneven terrain, in SICE Annual Conference, Osaka, Japan, pp.397-402.
- [11] D. T. Akeabay, N. Perkins and Z. D. Ma (2004), Predicting the mobility of tracked robotic vehicles, American Society of Mechanical Engineers, Dynamic System and Control Division (Publication) DSC, Vol. 73, No. 1, PART A, pp.233-242.
- [12] Global Positioning System (GPS) Available at: <http://www.wli.us.com/SitePage.aspx?PageID=444>.
- [13] M. T. Qadri and M. Tayyab (2009), Real time defense communicator using video processing, Bluetooth and GPS, International Conference on Signal Processing System, pp.629-632.

Optimal posture control of two wheeled inverted pendulum robot on a slanted surface

Youngkuk Kwon, Joonbae Son, Jaeoh Lee, Jongho Han and Jangmyung Lee

Dept. of Electronics Engineering, Pusan National University, Korea

(Tel : +82-51-510-1696; Fax : +82-51-510-1693)

(kyk1104@pusan.ac.kr, waggish82@pusan.ac.kr, jaeoh2@pusan.ac.kr, gkswhdgh114@pusan.co.kr, jmlee@pusan.ac.kr)

Abstract: Most of the conventional researches are concentrated on the compensation algorithm of the gyroscope signal and posture control on the flat ground. But Segway has been considered as next the generation vehicle, and as its application spread out to the whole of society, its stability and optimal posture on the slanted surface has been discussed worldwide. So, this paper proposes an optimal posture of two wheeled inverted pendulum robot on a slanted surface.

In order to realize posture balance on the slanted surface, tilted weight should be compensated by the proposed algorithm. Dynamic state equation was derived from the system's structure, and an LQR regulator was designed based on the tilted angle obtained from the ultra-sonic sensor. Optimal posture control experiment was iterated as the slanted angles varied. Effectiveness of the proposed algorithms has been verified and demonstrated through simulations and real experiments.

Keywords: Two - Wheel Inverted Pendulum Robot, Optimal Posture Control, ARS (Attitude Reference System).

I. INTRODUCTION

Conventional researches are highly concentrated on the posture control under ideal environment,[1] but posture control for the slanted surface was not studied. According to the social needs of the next generation vehicle, this paper proposes an optimal posture control of the two wheeled inverted pendulum not only on the flat ground but also on the slanted environment. From the experimental results of the proposed algorithm, the difference between the conventional compensation algorithm and proposed algorithm has been presented.

Finally, optimal posture for the climbing movement from the ARS(Attitude Reference System) will be presented. Optimal posture was defined as a stability of the mobile robot during climbing on a slanted surface. This paper consists of five sections including introduction. In Section 2, the modeling of the proposed robot structure and controller design scheme are described, and in Section 3, climbing a slanted surface algorithm will be stated. In Section 4, experimental environment and its results are shown. Conclusions and future research plans are illustrated in Section 5.

II. Modeling of The robot structure and Design of Controller

Dynamics modeling from the proposed structure has been proposed. Fig. 1. illustrates the structure of the

inverted pendulum. And table 1 shows each parameters for the mobile inverted pendulum

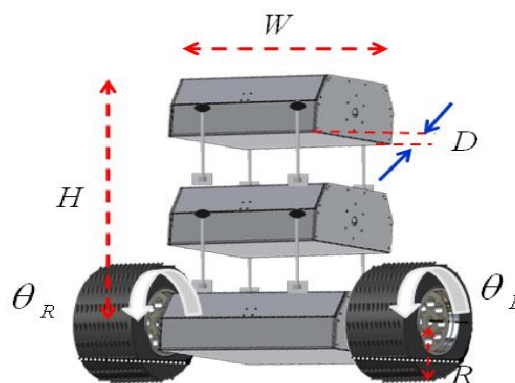


Fig. 1. Two wheeld inverted pendulum.

Table 1. Each parameters for the mobile inverted pendulum

θ	The angle of rotation of wheel from the center
ϕ	A tilted angle of body from the center
β	The angle of rotation of body from rotation of wheel
M_B	The mass of the body
M_W	The mass of the wheel

294

Dynamics for the given system has two kinds of parameters, body angle, and wheel angle. Equation (1) shows the dynamics according to the β, θ

$$\frac{d}{dt}\left(\frac{\partial T}{\partial \beta'}\right) - \left(\frac{\partial T}{\partial \beta}\right) + \left(\frac{\partial U}{\partial \beta}\right) + \left(\frac{\partial D}{\partial \beta'}\right) = \mathcal{Q}_\beta \quad (1)$$

T : Kinetic energy D : Disturbances
U : Potential energy Q : generalized force

D : Disturbances

Q : generalized force

$$T = \frac{1}{2}M_w(S_2' + Z_2') + \frac{1}{2}M_B(S_1' + Z_1') + \frac{1}{2}I_w\theta' + \frac{1}{2}I_B(\theta' - \beta') + \frac{1}{2}I_M\eta^2\beta' \quad (3)$$

$$U = M_W gr + M_B gl \cos(\theta - \beta) \quad (4)$$

$$Q_\beta = u, Q_\theta = 0 \quad (6)$$

$$\begin{bmatrix} (M_B l^2 + I_B + I_M \eta^2) \phi'' \\ + (M_B r l \cos \phi - I_M \eta^2) \theta'' \\ + \mu_s \phi' - \mu_s \theta' - M_B g l \sin \phi + u \end{bmatrix} = 0 \quad (7)$$

System dynamics could be expressed as equation (7), and (8).

From the dynamic analysis for the proposed structure, the linearized dynamic equation could be derived as follow. Non-linear dynamic equation (7) and (8) could be linearized as (9).

Equation (10) shows the generalized state space equations.

Representing the robot structure to the state space equations, then (11) could be attained.

Representing the robot structure to the state space equations, then (11) could be attained.

The LQR controller from the equation (11) was designed by Simulink. Its figure is illustrated in Fig. 2.



During the climbing control of the robot, unexpected disturbance forces are essentially caused by the irregular

contact force which comes from the irregular contact angle between the wheel and the terrain.[2] The disturbances have effects on the optimal posture of the mobile robot to compensate the slanted angle. So, In order to realize posture balance on the slanted surface, tilted weight should be compensated by the proposed algorithm.

Table 2. Robot parameters for the slanted surface

M_w	The mass of the wheel
g	acceleration of gravity
l	Distance from the body center of gravity
s	Moving distance of the mobile robot
f_c	Coefficient of friction with the slop
F	External force to the mobile robot
N	External force to the actuator from the robot body
α	Slope angle

Table 2 describes the robot parameters while climbing a slanted surface. The governing equation for the flat ground for the equilibrium state was derived in equation (12).

$$F = M_w s'' + M_w g \sin \alpha + f_c \cos \alpha - N \quad (12)$$

The governing equation for the slanted ground for the equilibrium state was derived in equation (13).

$$F = (M_w + M_B) s'' + M_B l \phi'' \cos \phi - M_B l \phi^2 \sin \alpha + M_w g \sin \alpha + f_c \cos \alpha s' \quad (13)$$

Assuming that ϕ is a tiny enough value to ignore, we can simplify $\phi = 0$, $\sin \phi = \phi$, $\cos \phi = 1$ (14)

Inserting (14) into (13), then we can attain equation (15) as follows.

$$F - M_w g \sin \alpha = (M_w + M_B) s'' + M_B l \phi'' + f_c s' \quad (15)$$

For the difference between a pre-linearized equation and linearized equation, $M_w g \sin \alpha$ should be compensated a under slated environment.

So, if the ground is tilted to the amount of α , the posture control of the mobile robot on the slanted surface could be realized by compensating amount of $M_w g \sin \alpha$. We can establish a driving command of $M_w g \sin \alpha + \beta$ where β stands for the moving direction's tilted angle.

IV. Experiment

The proposed system consists of a two-wheeled Inverted Pendulum Robot shown in Fig. 7. The body of a mobile robot is designed with two-wheels and motor drive controllers. The controller-related hardware is composed of MCU (Micro Controller Unit, DSP-28335), a gyro sensor, an accelerometer and an ultrasonic sensor

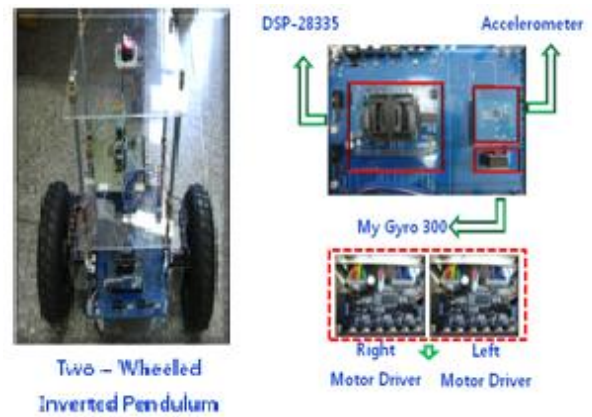


Fig. 3. The configuration of the two-wheeled-inverted robot system

The experiment for driving of the two-wheeled inverted pendulum robot, was conducted on two different environments; when giving a disturbance to the robot on the ground, and when driving on slanted surfaces of $5^\circ, 10^\circ, 15^\circ, 20^\circ, 25^\circ$. In addition, Fig. 4 shown that the slope was slanted using a clinometer.



Fig. 4. The experiment environment for climbing on the slanted surface.

Using an ultrasonic sensor located under the robot, which receives the distance information from the ground, it is possible to expect information of the slope degree between the ultrasonic sensor and the ground.

Below, Table 3 shows the changed slope angle information from the distance obtained by the ultrasonic sensor.[3]

Table 3. conversion of the angle from distance between the ultrasonic sensor and the ground

Angle (Degrees)	Distance (Centimetres)
0 °	10 cm
5 °	8.5 cm
10 °	7.0 cm
15 °	5.5 cm
20 °	4.0 cm
25 °	2.5 cm
30 °	1.0 cm

The result when given disturbance to the robot on the ground is shown in Fig. 5, and the environment like Fig. 4 shows driving test results at Fig. 5 and Fig. 6. , 7.

The current measured angle from the slope randomly gave 5° more; it was made the two-wheeled Inverted Pendulum Robot can be driven on slope. And When the robot completed climbing at the slope, the two-wheeled inverted pendulum robot can be stopped by converging back to the current angle of the slope. Below, the results shows the current slope values of the acceleration sensor, and target values. Sampling Time is the horizontal axis and the vertical axis represents the Slope Angle.

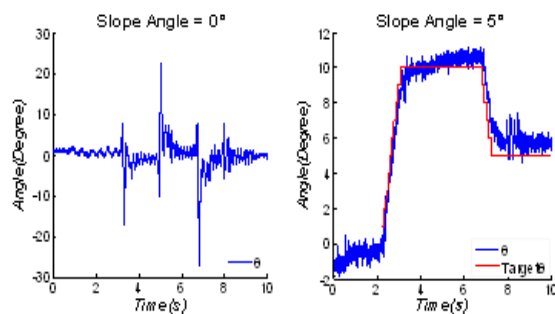


Fig. 5. Driving on an even surface and a 6 degree slope

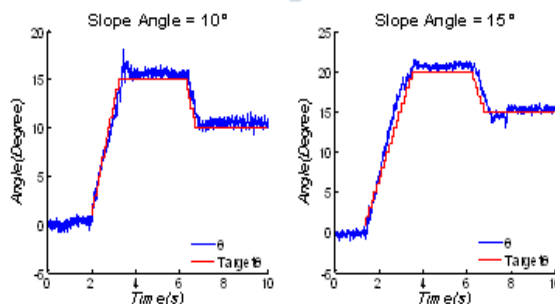


Fig. 6. Driving on a 10 and 15 degree slope

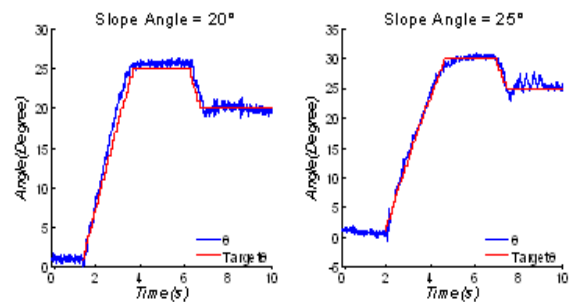


Fig. 7. Driving on a 20 and 25 degree slope

VI. Conclusion

In this paper, when controlling the two-wheel-inverted Pendulum on the slanted environment, we acquired the slope information using the ultrasonic sensor. By varying the operating point of the inverted pendulum and compensating gravity as per the lean of operating point, even the slanted environment, can be controlled for optimal posture. And also, The equation of motion was suggested to satisfy driving speed of the two wheeled robot and slope angle conditions according to the angle of the slope. Therefore, the results of this study will prove useful not only for the mechanism of the two-wheel-inverted Pendulum but also in determining the slope of various other types of wheeled type mobile robot mechanisms.

ACKNOWLEDGEMENT

This research was supported by the MKE(The Ministry of Knowledge Economy), Korea, under the Human resource development program for robotics support program supervised by the NIPA(National IT Industry Promotion Agency). (NIPA-2010-(C7000-1001-0009))

This research was supported by Basic Science Research Program through the National Research Foundation of Korea(NRF) funded by the Ministry of Education, Science and Technology(2010-0024129)

REFERENCES

- [1] H.J Lee and S. Jung, "Gyro sensor drift compensation by Kalman filter to control a mobile inverted pendulum robot system", IEEE ICIT. PP 1026-1031, 2009
- [2] G. Sohl and A Jain, "Wheel-Terrain Contact Modeling in the Roams Planetary Rover Simulation", Proc. Fifth ASME International Conference on Multi body Systems, Nonlinear Dynamics and Control, Long Beach, CA, September 2005.

Efficient CAN-based network for marine engine state monitoring system

Junseok Lee, Yoseop Hwang, Jaehan Jo and Jangmyung Lee

Dept. of Electronics Engineering, Pusan National University, Korea

(Tel : +82-51-510-1696; Fax : +82-51-510-1693)

(sukidda@pusan.ac.kr; mmx001@pusan.ac.kr; jjhan@pusan.ac.kr; jmlee@pusan.ac.kr)

Abstract: This paper presents the marine engine state monitoring system implemented with Controller Area Network. As the marine engine state monitoring system requires various kind of engine information, it consists of a lot of sensor nodes. So, with the features of Controller Area Network which supports huge numbers of message ID, and its message arbitration ability, this paper presents scheduling method for the performance of monitoring system. And its effectiveness and validity have been shown through experiments.

Keywords: CAN(Controller Area Network), Engine State Monitoring System, DPQ(Distributed Precedence Queue)

I. INTRODUCTION

Marine Engine State Monitoring System purposes precise and rapid transmission of engine condition data from various measurement instruments to the engine control room. A failure of engine in sailing ship affects critically to the operating the ship, and may causes enormous financial loss. So, real-time monitoring system for preventing the unpredictable failure and maintaining support of marine engine is needed.

A major advantage in using the CAN technology with respect to the other kinds of field-buses available is the wide choice of very cheap electronic components. The Engine State Monitoring System requires lots of sensor nodes and needs cheaper field-bus solution. Additionally, CAN can simplify the sensor node wiring and prioritize the message transmissions which satisfy an urgent message transmission needed at industrial environment.[1],[2]

But if network is overloaded, data transmission is decreased rapidly due to increasing data transmission collision. If this state is continuous, a network may be groggy and non-transmission condition for a long time. This paper presents a mechanism that can be a fair transmission and can reduce delay time with assignment precedence queue to delayed sensor node.

II. Engine State Monitoring System

State Monitoring can be started with measuring of each part of engine (Fig. 2). Engine State Monitoring System can be divided into three parts. Status measuring sensors which measures temperature, pressure, perception of flowing and various status indication factors are equipped with the CAN Module. And CAN

Module consist of microprocessor and CAN transceiver and transmits data from sensors to the SPU, respectively. And SPU(Signal Processing Unit) collects entire network data and transmits engine condition signal to the ECR(Engine Control Room) via RS-485.

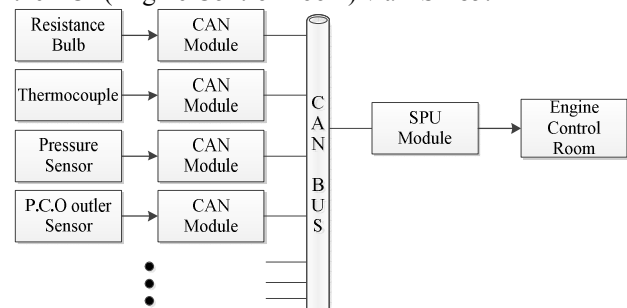


Fig. 1. Engine State Monitoring System Architecture

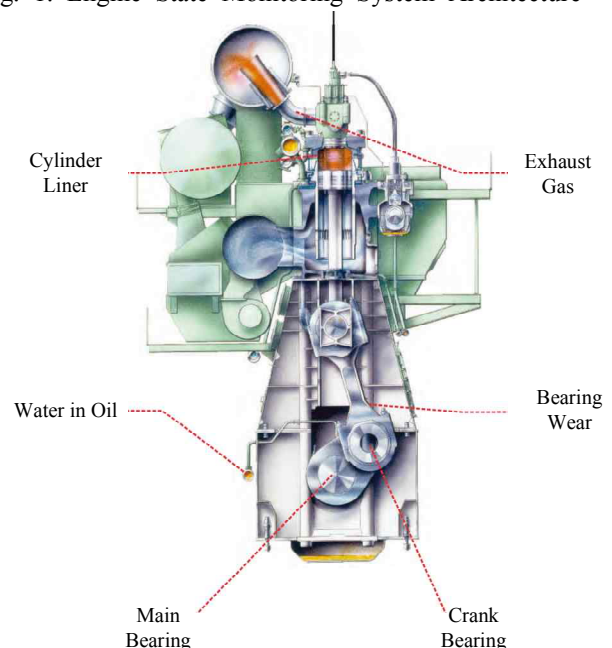


Fig. 2. Marine Engine

III. Controller Area Network Protocol

CAN is based on a CSMA/CS channel access technique, modified to enforce a deterministic resolution of collisions on a network which uses a priority scheme based on the identifiers of exchanged objects. The CAN protocol adopts a layered architecture which is based on the OSI reference model, even though it is not fully OSI compliant. As with other networks conceived for the factory automation environment, it relies on a reduced protocol stack, consisting only of the Physical layer, Data link layer, and Application layer. This paper is focused on the data link layer. In fact most of the features of CAN which concern topics such as the sharing of the bandwidth among the different stations and the access delays they experience depend on the mechanism adopted at this level.[3]

S O F	Arbitration Field	Control Field	Data Field	CRC Field	A C K	E O F
1 bit	11 bit or 29 bit	4 bit	0-8 bytes	15 bit	2 bit	7 bit

Fig. 3. CAN Data Frame format

IV. Distributed Precedence Queue (DPQ)

The CAN implicitly assigns to each object exchanged in the network a priority that corresponds to the identifier of the object itself. Even though this mechanism enforces a deterministic arbitration that is able to resolve any conflict that occurs when several nodes start transmitting at the same time, it is clearly unfair. If many nodes are connected in the network, nodes that are of low priority rank can continuously lose a transmission opportunity. That is, if high priority objects transmit continuously, finally a low priority object can miss an important message which is relatively unimportant compared to that of a high priority object.

Accordingly, a mechanism that uses a relative priority according to the consideration of low priority nodes is necessary although the CAN implicitly assigns a priority. Fair behavior, which for example enforces a round-robin policy among different stations, has to be guaranteed to all the objects exchanged at a given priority level.

In this paper, it is shown that this kind of behavior can be obtained by slightly modifying the frame acceptance filtering function of the LLC sub-layer. In particular, only the significance of the identifier field in the transmitted frame has to be modified in some way. The resulting arbitration mechanism is able to enforce a

round-robin policy among the stations that want to transmit a message on the bus, and provides two levels of priority for the frame transmission services. Little or nothing has to be changed at the MAC level; and in this way it is possible to reuse the same electronics components developed for the implementation of the standard CAN protocol.

1. DPQ basic principle

The basic idea of this CAN fairness control mechanism that is to insert into a global queue all of the nodes that want to transmit over the shared medium. For Node C, of which transmission is continuously delayed, a queue is created to transmit Node C and the other nodes that transmit with C. So, several queues can be partially made in this research, two queue were used.

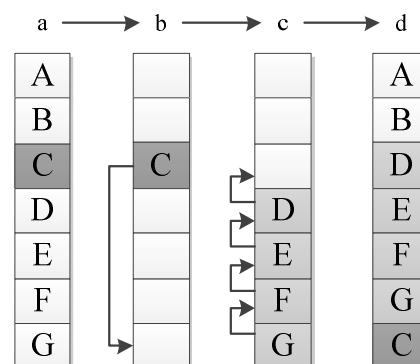


Fig. 4. Generation of a precedence queue in DPQ

This distributed precedence queue protocol provides the opportunity to create precedence queues for all nodes in a network. And, in the case that several precedence queues exist, each precedence queue assigned a priority so that they can be implemented independently.

The DPQ mode ID, which is stored in the 11 bit standard ID field, indicates the precedence queue order of each node. Whenever a node carries out a transmission, it moves to the end of the queue, thus lowering its precedence to the minimum. All of the nodes following the transmitting node advance by one position in the queue, occupying the space that has just been created. Using this round-robin policy, collisions among messages are avoided.

The queue is not stored in some specific location. Instead, it is distributed among all the nodes in the network. Each node is responsible for storing and updating. That is, if the maximum permission delay time is reached, it creates a precedence queue, and then it has to dynamically change priorities to transmit

preferentially with other nodes. And a precedence queue has to be dissolved when is completed an urgent task.[4]

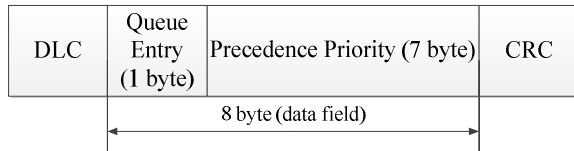


Fig. 5. Structure of a data field for DPQ

We suppose a network that is composed of Nodes A to G as shown in Fig 4. If Node C builds up a queue, the ID that is entered into the data frame queue can transmit and designate to 7 by lower 7 byte. At this time, it will be designated precedence priority to higher byte. Then, each node filters to enter itself into the queue, and it assigns its queue. After Node C transmits a message, it will go to the last position in the queue. And the other nodes will move up one position by order. And the remaining nodes that to be transmitted are designated using the upper 1 byte as shown in Fig 5; their queues will be dissolved or maintained using the upper 1 byte, as shown the Fig 5 after all transmissions are completed.

2. DPQ Implementation Issues

The DPQ mechanism can be implemented without any modifications to the basic format of CAN frames. It uses an identifier field to designate the priority queue. Because the length of the conventional identifier field defined in the CAN standard is too small, the CAN extended format can be adopted.



Fig. 6. Format of the header of extended CAN Frame

The DPQ uses the first 11 bits of the identifier field for its control information, whereas the remaining lower order 18 bits (ID ext.) are used to dynamically store the effective identifier of the an exchanged object (EID).

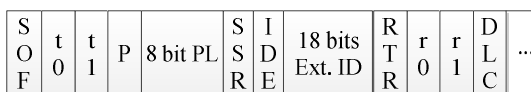


Fig. 7. Format of the header DPQ Frame

The first two bits (t0, t1) must be set at the logical value of zero as shown in Fig 7. Then, the protocol is divided by a standard CAN communication and DPQ mechanism. So, DPQ always has a higher priority than a CAN mechanism, and they can exist in this same space.

The priority bit P specifies whether the frame has to be transmitted as a high priority frame (P=0) or as a low priority frame (P=1). When t1 and P are used, the priority can be assigned a maximum 4 queues.

The next 8 bits represent the precedence level of the frame. Namely, these 8 bits show the transmission queue order. The DPQ, which was used in this research, uses t0, t1, and then distinguishes the standard CAN mechanism, and sets each queue using P, and concludes the precedence in the queue using 8 bits.

V. Experiment and Result

In this paper, we experimented via Engine State Monitoring System which is composed of ten CAN Modules and one SPU to evaluate the effectiveness of the proposed method.

CAN Module uses sensors (Resistance Bulb, Thermocouple, Pressure Sensor...) actually used in marine engine. And it uses data from measuring elements composed as shown in Fig.9. And CAN Module use Microchip's dsPIC30F4012 and SPU uses TI's TMS320F28335.

Fig. 9 shows the monitoring program for PC via LabVIEW to monitor the state of network and data in real-time. Each of vertical fill slides indicate occupied bandwidth of node and gauge indicates shows temperature of measuring element. We set the bitrate of network at 500Kbps considering the length of network installed in the low-speed marine engine.

To verify the effectiveness of DPQ mechanism, we presented transmission result comparing normal CAN transmission with transmission in DPQ mode. For actual monitoring system for the Low-speed engine in large vessel, they use about hundreds of sensor; we set the transmission period at 500us for more possible transmission collisions.

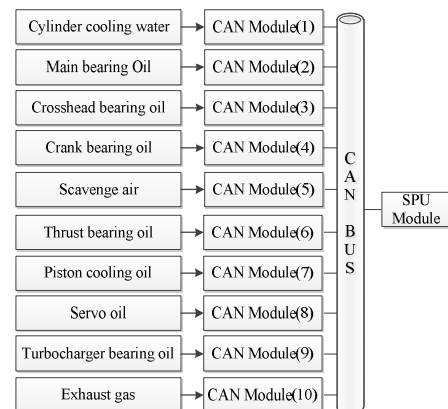


Fig. 8. Experiment System Architecture

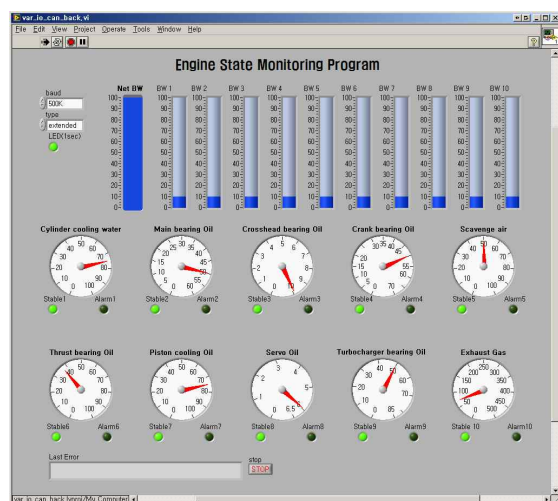


Fig. 9 Engine State Monitoring Program

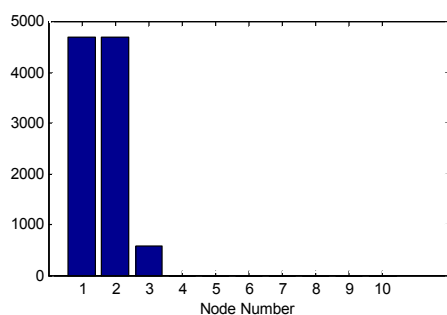


Fig. 10 Received Messages in normal CAN transmission

Fig. 10 shows received message numbers for each sensor nodes when network received 10000 messages. Because of consecutive collision and short transmission period, messages with low-priority are not transmitted while messages with high-priority occupy most of bandwidth.

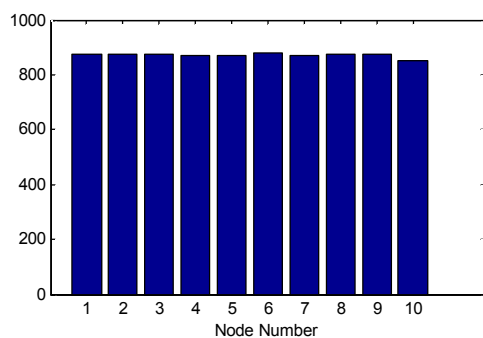


Fig. 11. Received Messages in DPQ mode

Fig. 11 shows result of transmission of DPQ mode in identical condition. It shows evenly distributed received messages.

But data frames derived from the process of making and dissolving the precedence queue, actual state monitoring messages are decreased about 10 percent.

VI. Conclusion

In this paper, we proposed the Marine Engine State Monitoring System using DPQ mechanism to improve fairness in network.

Through these methods, messages with low-priority were ensured to transmit message and delay its time was improved. Features of the Marine engine monitoring system are as follows.

1. CAN communication module is connected to sensor used in actual Marine, is distinguished according to set ID and is designed for adding extra modules easily.

2. SPU (Signal Processing Unit) module for processing total data which transmit in CAN module is able to check Whole engine, bearing state and etc.

3. Whole states of Marine engine is able to be checked through the output values (voltage, current, resistor) of all sensors using the SPU (Signal Processing Unit) module.

4. Conventional communication method as RS232 and RS485 is supported for compatibility with the existing Marine engine system. Therefore, state of Marine is able to be checked in ECR (Engine Control Room).

ACKNOWLEDGEMENT

This research was financially supported by the Ministry of Knowledge Economy (MKE) and Korea Institute for Advancement of Technology (KIAT) through the Research and Development of Regional Industry.

This research was supported by the MKE (The Ministry of Knowledge Economy), Korea, under the Human resource development program for robotics support program supervised by the NIPA (National IT Industry Promotion Agency). (NIPA-2010-(C7000-1001-0009))

REFERENCES

- [1] Bosch, "CAN Specification Version 2.0.", Robert Bosch GmbH. Stuttgart, 1991.
- [2] International Standard Organization, "Road - vehicles Interchange of digital information - Controller area network for high-speed communication", ISO 11898, November 1993.
- [3] G. Cena and A. Valenzano, "An Improved CAN Fieldbus for Industrial Application", IEEE Trans. On Industrial Electronics, Vol. 44, No. 4, Aug, 1997.
- [4] S. Corriganm, Intriduction to the Controller Area Network, TI, Application Report. Texas Instruments, 2002.

Localization Algorithm using Virtual Label for a Mobile Robot in Indoor and Outdoor Environment

Kiho Yu*, Mincheol Lee**, Junghun Heo*, Youngeun Moon*

** The School of Mechanical Engineering, Pusan National University,
#405 RIMT, Pusan National Univ, Jangjeon, kuemjeong, Pusan, south korea 609-735
(Tel : 82-51-510-3081; Fax : 82-51-512-9835)
yukiho1118@pusan.ac.kr*

*** The School of Mechanical Engineering, Pusan National University,
#405 RIMT, Pusan National Univ, Jangjeon, kuemjeong, Pusan, south korea 609-735
(Tel : 82-51-510-2439; Fax : 82-51-512-9835)
mclee@pusan.ac.kr*

Abstract: The scanning laser range sensors provide range data consisting of a set of point-measurements. The laser sensor (URG-04LX) has a distance range of approximately 0.02 to 4 meter and scanning angle range 240 degrees. Usually, such a range image is acquired from one view-point by "moving" the laser beam using rotating mirrors/prisms. The orientation of the laser beam can be easily measured and converted into coordinates of the image. This paper conducts localization using virtual labels with environment distance data gotten from the 2D distance laser sensors. This method puts virtual labels on special feature and points which is on the way of mobile robot path. The current location is calculated by combining the virtual label and the range image of laser range finder.

Keywords: Virtual Label, Laser Range Finder, Encoder, Localization

I. INTRODUCTION

Mobile robots have been applied in various fields such as logistics automation, security, industrial automation and consumer products, and etc. The absolute positioning of mobile robot becomes essential part. The research for the localization problems are focused on robust and minimum error against unknown environment. As advance of mobile robot technologies, localization for mobile robots is widely researched and developed such as a dead reckoning system, an active badge system, an active beacon system and the localization system using a landmark, a RFID and a GPS [1-8].

The dead reckoning system is one of well-known localization method based on measuring the relative position. The dead reckoning system has an advantage of high sampling rate and outstanding accuracy in short interval. However, this system cannot avoid inevitable accumulation of the error because of time integral term with current direction and distance. Especially, cumulative error of the direction angle may cause infinitely large positioning error as time passed [1], [2].

In order to detect the location of people inside building, the active badge system with infrared ray has been researched. However, this system has problems

such as the short communication distance and weakness performance against sunshine [4]. Active beacon system with ultrasonic sensors is known as relatively high accurate performance and low power consumption. However, this method gets influences with an obstacle between a transmitter and a receiver, external temperature, and noise [5].

The localization method using a landmark or a RFID is robust to external environment such as changes in temperature or solar light. However, it has fatal defect in that it can be applied only to limited space where RFID tag or landmark is able to be attached. In addition, it is impossible to use outdoors [3], [4]. In outdoors, GPS (global positioning system) is most powerful localization method to recognize the absolute position. However, it has a limitation area of GPS signal and low position accuracy [6].

In order to solve these problems, this paper proposes the localization method with virtual labels to become robust against space constraints and indoor/outdoor environments. The proposed method is based on virtual labeling techniques. This paper uses a laser range finder and an encoder in indoor environment. And, in outdoor environment, a GPS only is adopted to calculate initial position.

The paper is divided into the following sections: generation of range finder scans (section 2), and localization with virtual label algorithm (section 3). Section 4 shows experiment results of implementation within typical indoor/outdoor scenes. And conclusion and future work are discussed in Section 5.

II. LASER RANGE FINDER SCANNING

This study constructs a mobile robot equipped with a laser range finder as shown in Fig. 1. 2D laser range finder (URG-04LX) made by HOKUYO Co. LTD is used. URG-04LX has 100 ms cycle time and 765 resolutions from 60 mm to 4,095 mm distance value divided by 0.36 degree. Specifications of the laser range finder are listed in Table 1.



Figure 1. Laser range finder & Indoor environment

TABLE I. SPECIFICATIONS OF URG-04LX

	<i>Spec.</i>
Measuring area	60 to 4095 mm , 240°
Accuracy(Repeatability)	60 to 1000 mm : ± 10 mm 1000 to 4095 mm : 70 mm
Angular resolution	Step Angle : 0.36° (360° /1024 steps)
Scanning time	100 ms/scan

Figure 2 shows output data of the laser range finder in indoor environment. This sensor is available to scan 240 degree and 765 distance output data according to distance each cycle at 100ms. In this paper, localization is calculated in 210 degree areas. 600 distance output data are used to build 2D coordinates including the virtual label as shown in Fig. 3. This distance output data is transformed to 2D coordinates by using equation (1) and (2).

$$x_i = D_i(\cos(i \times 0.3515625)) \left(\frac{3.14}{0.5\pi} \right), i = 0, 1, 2, \dots, 600 \quad (1)$$

$$y_i = D_i(\sin(i \times 0.3515625)) \left(\frac{3.14}{0.5\pi} \right), i = 0, 1, 2, \dots, 600 \quad (2)$$

Where, $\theta_i(0.3515625)$ is the angular resolution from 1 point to 600 point and D_i is the distance output data. Figure 3 shows distance conversion of 2D coordinates.

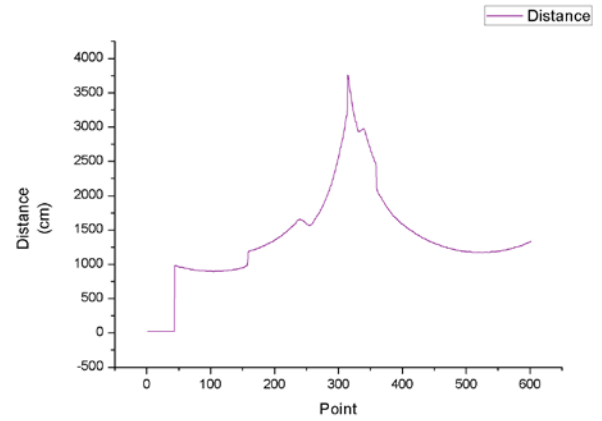


Figure 2. Distance data of a laser range finder

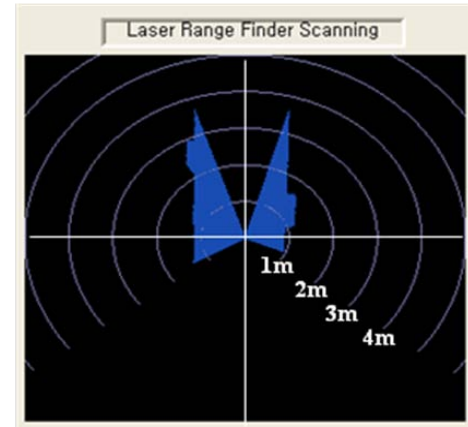


Figure 3. Distance data conversion of 2D coordinates

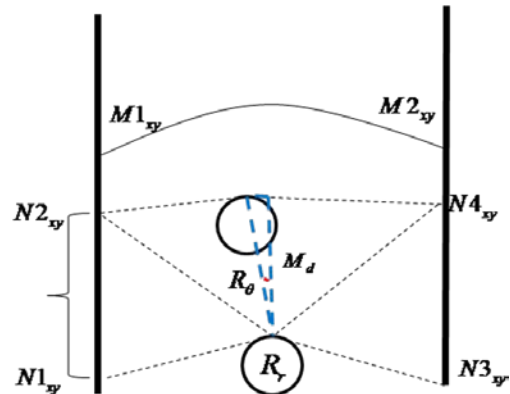


Figure 4. Segmentation area

It is necessary to classify movable area ($Mk_{x,y}$) and non-movable area ($Nk_{x,y}$) in transformed coordinates (x_i, y_i). In Fig. 4, $Nk_{x,y}$ is used to map virtual label and $Mk_{x,y}$ is used to determine mobile robot's path. After determining $Mk_{x,y}$ and $Nk_{x,y}$, the map is generated with considering radius of robot (R_r), moving distance of robot (M_d), and direction of robot (R_θ). As repeating and

accumulating of above proposed process using equation (3), (4), virtual label is named on the map simultaneously.

$$X_{map_j} = Nk_x \quad (3)$$

$$Y_{map_j} = Nk_y \quad (4)$$

By using the proposed virtual label algorithm which is explained in section 3, a map is effectively generated in indoor or outdoor environment. Only for the outdoor circumstance, GPS is used to get initial position additionally.

III. VIRTUAL LABEL ALGORITHM

Before moving the mobile robot, the virtual label should be allocated on the map which can be generated by scanning the current circumstance with laser range finder. The virtual label is not needed to be on real points, lines and space in the circumstance. As the name **'virtual', the label can be generated on virtual structures** which do not exist in real space. Then, the temporary virtual wall is allocated in the left and right of 45 degree space.

The proposed virtual label method is accomplished as following procedure,

- [Step 1] In order to initialize current position of mobile robot, scan the circumstance.
- [Step 2] Label on the map using scanned data, feature points, lines and spaces.
- [Step 3] If feature points, lines and spaces cannot be found, virtual wall and label will be generated on the map as shown in Fig. 5. The virtual walls are built on both sides. And the virtual labels (VLm_x , VLm_y) are attached on 45 degree diagonal position on the virtual walls.
- [Step 4] Let a current robot position localize by using distance (D_n) and angle (R_θ) toward the label.
- [Step 5] Movable domain ($M1_{x,y}$, $M2_{x,y}$) and not movable domain ($N1_{x,y}$, $N2_{x,y}$) have to be added on the map involving the label.
- [Step 6] After moving mobile robot, returned to the Step 1.

The position of mobile robot is acquired by using distance D_n and $VLm_{x,y}$. The current position is calculated by using the following equation (5) and (6).

$$R_x = (VLm_x \pm D_n) \quad (5)$$

$$R_y = (VLm_y) \quad (6)$$

Where, D_n is the distance from mobile robot to virtual label ($VLm_{x,y}$).

Figure 6 is the block diagram of virtual label allocation.

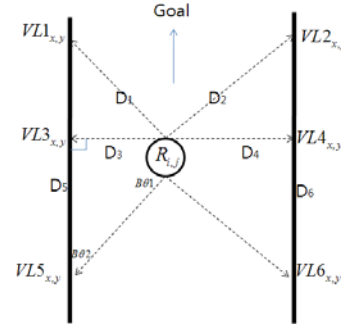


Figure 5. Virtual labeling for indoor environment

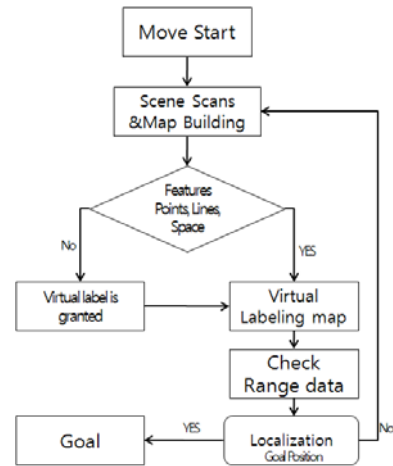


Figure 6. Block diagram of a virtual labeling

IV. EXPERIMENTS

In order to evaluate the localization and map formation of the proposed virtual label algorithm, the moving experiments of mobile robot were carried out in indoor environment showed as Fig. 1 and outdoor environment showed as Fig. 7.

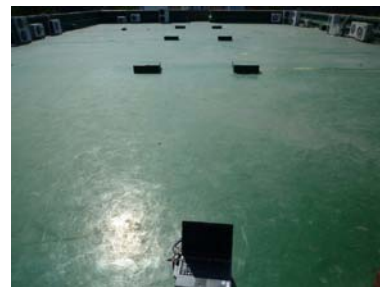


Figure 7. Outdoor environment

Experiment (Indoor)

In indoor environment, the virtual labeling algorithm is applied to generate the map for

localization. The map applied the virtual label algorithm is shown as Fig. 8. The distance between start and goal point is 10 m straight path. The test condition is selected to compare localization effect by using encoder data with localization effect by using the virtual label algorithm in indoor environment. The mobile robot speed is 0.54 m/s. Test result with the virtual label algorithm is shown as Fig. 9.

After 5 times experiments over 5 times, location error of mobile robot was found as about $\pm 2\text{cm}$. In previous study, repetitive error was about $\pm 3\text{cm}$ by using encoder data [3]. However, localization by using encoder data is not much different. Thus, the experiment shows that virtual label algorithm is precise localization method.

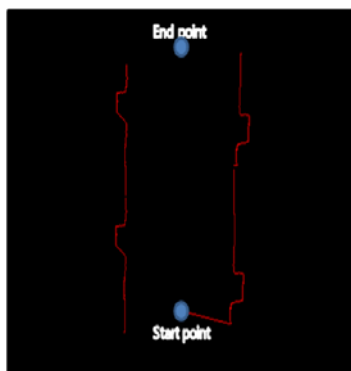


Figure 8. Map building of an indoor environment

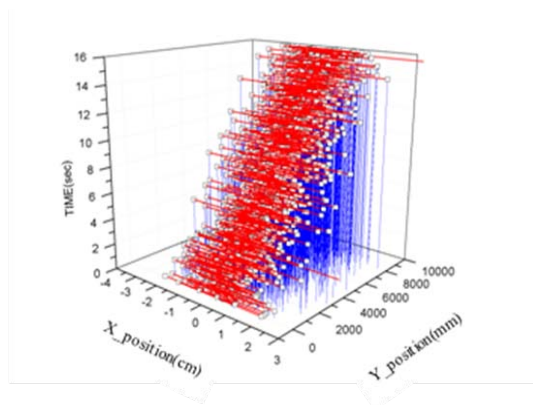


Figure 9. Moving trajectory of mobile robot with the virtual labeling algorithm in indoor

Experiment (outdoor)

In outdoor environment, with mobile robot equipped with a laser range finder and a GPS, the virtual labeling algorithm is applied to generate maps for localization. GPS sensor only is adopted to calculate an initial position. The map obtained by applying the virtual label algorithm is shown in as Fig. 10.

The distance between start and goal point is 17 m straight path. The mobile robot speed is 0.54 m/s. The result of 5 times repetitive driving is shown as Fig. 11.

If there is not the space to make label in the scan data of range finder, label is allocated to virtual wall for localization.

After experiments over 5 times, repetitive error of mobile robot is about $\pm 4\text{cm}$ because of rough road in outdoor. And the repetitive error by only using encoder was about $\pm 10\text{cm}$. Thus, localization with the virtual label algorithm is superior to localization method with the GPS.

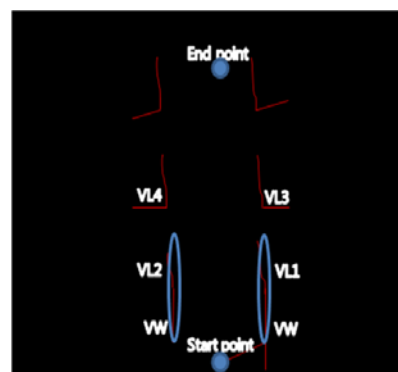


Figure 10. Map building of an outdoor environment

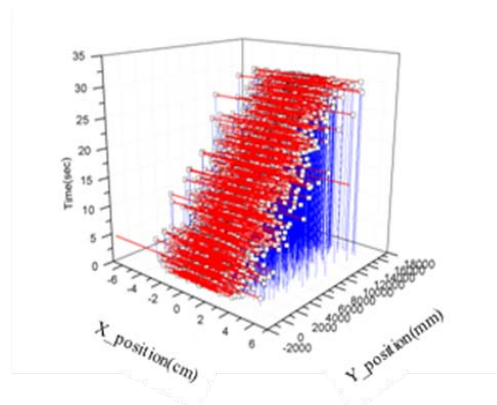


Figure 11. Moving trajectory of mobile robot with the virtual labeling algorithm in outdoor

V. CONCLUSION

In order to localize and build a map in indoor/outdoor environments, this study proposed the localization algorithm with the virtual label algorithm. And this paper carried out experimental test using mobile robot to evaluate the proposed virtual label algorithm. In the experimental test, the proposed virtual label algorithm performed precise localization result that location error of mobile robot is about $\pm 2\text{cm}$ in indoor environment and about $\pm 4\text{cm}$ in outdoor environment. In the future work, it will be improved to have localization maximum error within $\pm 5\text{mm}$ in the various indoor/outdoor environments. In addition, it will be compared with other localization algorithms.

ACKNOWLEDGE

This research was supported by the MKE(The Ministry of Knowledge Economy), Korea, under the Human resource development program for robotics support program supervised by the NIPA(National IT Industry Promotion Agency). (NIPA-2010-(C7000-1001-0009))

REFERENCES

- [1] F. Dellaert(1999), D. Fox, W. Burgard, and S. Thrun., Monte carlo localization for mobile robots, Proceedings of the IEEE International Conference on Robotics and Automation (ICRA)
- [2] P.Buschka(2002) and A. Saffiotti, A Virtual Sensor for Room Detection, Proc. IEEE/RSJ Int. Conf. On Intelligent Robots and Systems EPFL , pp.637-642.
- [3] H. J. Lee(2006) and M. C. Lee, Localization of Mobile Robot Based on Radio Frequency Identification Devices, 2006 SICE-ICASE International Joint Conference, pp.5934-5939.
- [4] J. Borenstein(1996) and L Feng, Measurement and corrections of systematic odometry errors in mobile robots, IEEE Trans. on Robotics and Automation, vol. 12, no. 6, pp.869-880.
- [5] T. Venet(2002), T. Capitaine, M. Hamzaoui and F. Fazzino One active beacon for an indoor absolute localization of a mobile vehicle, IEEE International Conference on Robotics &Automation .Washington, May
- [6] J. Borenstein(1997), H. R. Everett, L. Feng, and D.Wehe, Mobile robot positioning:Sensors and techniques, J. Robot. Syst., vol. 14, Aug., pp.231-249.
- [7] Albert Diosi(2005), Geoffrey Taylor and Lindsay Kleeman, Interactive SLAM using Laser and Advanced Sonar, Proc. IEEE Int. Conf. On Robotics and Automation, pp.1103-1108.
- [8] Yusuke Misono(2007), Yoshitaka Goto, Yuki Tarutoko, Kazuyuki Kobayashi and Kajiro Watanabe, Development of Laser Rangefinder-based SLAM Algorithm for Mobile Robot Navigation, SICE Annual Conf., pp.392-396.

Potential field method applied on the navigation of multiple mobile robots with limited ultrasonic sensing

Chiyen Kim*, Mincheol Lee**, Junyoung Beak*, Chibeom Noh*

* *The School of Mechanical Engineering, Pusan National University,
#405 RIMT, Pusan National Univ, Jangjeon, kuemjeong, Pusan, south korea 609-735
(Tel : 82-51-510-3081; Fax : 82-51-512-9835)*

chiykim@pnu.edu

** *The School of Mechanical Engineering, Pusan National University,
#405 RIMT, Pusan National Univ, Jangjeon, kuemjeong, Pusan, south korea 609-735
(Tel : 82-51-510-2439; Fax : 82-51-512-9835)*

mclee@pusan.ac.kr

Abstract: Multi-robot manipulation can accomplish complex task with simple robot systems comparing with singular mobile robot. In spite of systemic simplicity, multi-robot cause subsidiary problem, group driving. Each mobile robots have to consider not only target and obstacles but also other member robots. Previous researches attempt to solve it by using communication and formation method. As this paper studies to solve the problem in the simplest way, it is proposed the formatted navigation method using simple microrobots equipped with ultrasonic sensor without network communications. The navigation is based on potential field algorithm, and virtual hill concept is applied for the formation. Before the experimental test, this paper shows the simulation test to evaluate proposed method.

Keywords: multiple mobile robots, formation, virtual hill, navigation, platoon, potential field

I. INTRODUCTION

As working as human performance, robot requests several sensors and actuators. However, increasing sensors and actuators occur system complexity problems. Especially as mobile robot basically has to pursue safe and right driving as well as another requested task, the robot can meet serious problem at the several addition of sensors and actuators for the special purpose. For the problem, many researches approach the problem with cooperative manipulation by multi robots [1]. However, in the multi mobile robot system, corporative driving and manipulation occurs new problem. Each mobile robot has to consider not only target and obstacles but also other member robots. To solve it, many researches adopt network communication and machine vision system [2][3]. But, these solutions are still contraposed against system simplicity.

This study researches the solution laying emphasis on the system simplification. The system simplification is acquired by only using economic ultrasonic sensors for the environmental recognition without any other sensors and network devices. For a start, this paper considers only multi mobile robot navigation before researching the manipulation. This challenge can

contribute for reducing operating load for driving and in same time increasing program space for other task.

In this paper, whole robots' driving is proposed based on platoon formatted navigation. The formation is made up by virtual hill method which helps mobile robots make a set-upped distance with other ones. In the proposed method, all mobile robots follow potential ingredient decent direction not only avoiding obstacle but also keeping distance with other member robots.

The previous research done by P. Song, and V. Kumar showed that potential field method is adoptable in multi mobile robot navigation [4]. The study was based on vision system. But, this paper wishes to contribute to make a multi robot navigation method affordable to very simplified system.

In this paper, potential field method is briefly explained and virtual hill method is introduced. The adoptable simple multi mobile robots are modeled for simulation test. And simulation test evaluates the proposed method before experimental test.

II. Potential Field Method

1. Goal Navigation

A variety of effective attraction and repulsion potential fields are summarized in [5], [6]. Let

$r_{ij} = \|r_i - r_j\|$ be the Euclidean distance between robot and the object or the goal, a simple quadratic attractive potential function can be expressed as

$$V_{io}^a = 1 / 2k_{io} r_{io}^2 \quad (1)$$

r_i and r_o are the position vectors of the robot and the object, respectively.

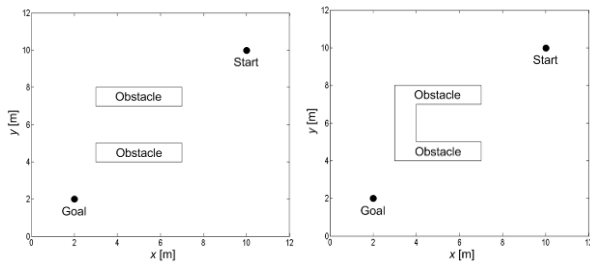
An expression of the repulsive potential is

$$V_{ij}^r = k_{ij} / r_{ij} \quad (2)$$

where $r_{ij} = \|r_i - r_j\|$ is the Euclidean distance between robots i and j . In each control mode, the force vector generated by potential fields and an appropriately designed dissipative function provide the driving force to the robots.

2. Artificial Virtual Hill

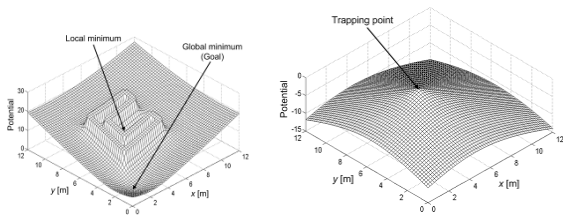
The artificial virtual hill was proposed in previous research to avoid local minimum [7]. In unknown environments, the robot initially does not have any information about the environment, and it has a limited sensing range to detect obstacles. The environment in Fig. 1(a) does not contain a local minimum, so robots may successfully reach the goal using the general potential field approach. In the environment of Fig. 1(b), however, robots may be trapped in a local minimum as Fig. 2(a). In the study, the virtual hill in global potential was proposed as Fig. 2(b). And then final global field become as Fig. 3.



(a) Open aisle

(b) Closed aisle

Fig. 1. Two types of obstacles with aisle shapes



(a) The potential field

(b) virtual hill

Fig. 2. The potential field and virtual hill

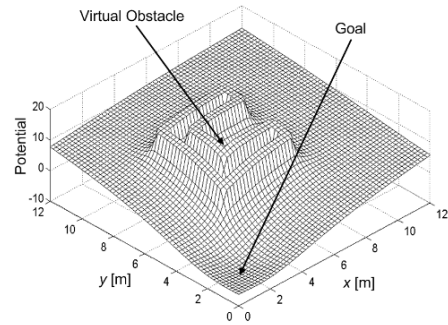


Fig. 3. Global potential with a virtual obstacle

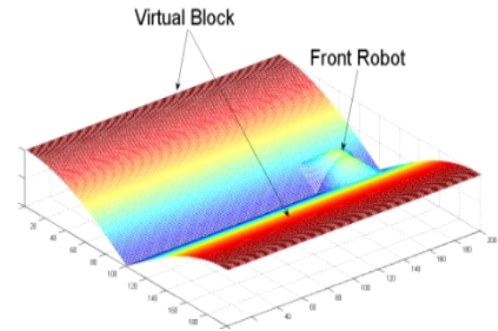


Fig. 4. Virtual hill for one line formation

3. One Line Formation

In this paper, the virtual field is applied to make a formation of multi robots as Fig. 4. Fig 4 is simple one line formation potential field. In the figure, high hill is shown. This hill can keep robot follow front robot. But between robots, there occurs a few repulsive potential energy to keep a few distance between robots. The repulsive hill to make line formation is paralleled with the line made between goal and leader robot. If there are three mobile robots in the field, only one or two of them can recognize the goal point. Although a few member know and pursue the goal, if other members unknowing the goal just drive to make a formation, the all of them can reach the goal by cooperative navigation in the end.

Except all robots do not recognize the goal, there are three cases of states. The one is that only one robot knows the goal. The second case is that two robot recognize the goal and the other doesn't. The third one is that all member find the goal same time.

A. Only one robot recognize goal

The first case is beginning state. If robot find only goal without other member, the robot will approaches the goal only. Remaining robots follows the first moving members.

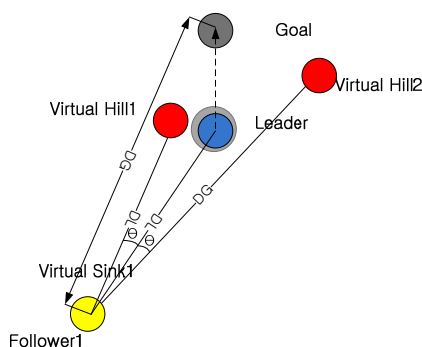


Fig. 5. The Potential field of the first followers

B. Two robot recognize goal

If there are goal and one other robot in the sensor view, the robot compares the distance to goal and other robot. From the result of distance, the shortest distance robot becomes the leader which just pursues the goal. And remaining robot becomes follower.

If the robot becomes follower, then it makes 2 virtual hills as shown in Fig. 5. The first hill is located on the line to goal with the distance to the leader. And the second hill is set on the deposited point to leader with same angle between goal and leader. The distance toward second hill is the same one to goal.

C. Remaining follower

If there are two more robots and goal in the view of robot, the robots distinguish the leader and the front follower by comparing relative distance with goals. If two more robots is shown and goal is not founded in the view of robot, the robot searches the first moving robot who will become the leader. Then by comparing the distance to the leader, the robot decides its order.

The second follower robot set the virtual sink which is temporary goal and two virtual hills as shown in Fig. 6. When the robot decides the lower priority order, the virtual sink is set at the nearest member to leader robot.

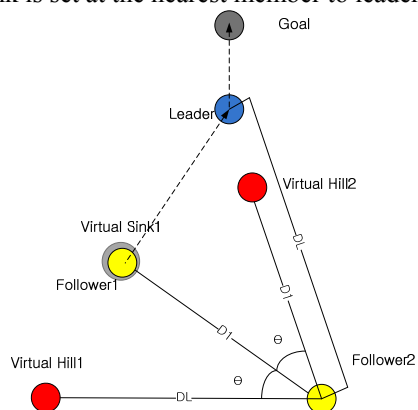


Fig. 6. The Potential field of the second followers

Two virtual hills are set as Fig 6. One is set on the line to leader. The other is set on the opposite site to virtual sink with same angular between the sink and leader. The distance is same as the one to sink. Thus, after making line formation, the relative potential field becomes as Fig. 4.

III. Simulation Test

1. Robot Modeling

The whole study will evaluate the proposed technique using experimental test. This paper does it using simulation test before experimental test. Thus, this chapter describes the simulation model based on experimental system. Fig. 7 shows the concept designs of the robot figure on the stocks. The robot is centralized 2 wheels robot equipped rotatable ultrasonic sensor scanner, 2 IR photodiodes and IR ramp array. The purpose of IR usage is recognition of other robot. But the communication is not implied. The IR sensors are also attached on the ultrasonic sensor scanner to get the direction of the member robots. Fig. 8(a) shows the prototype of ultrasonic sensors scanner. 2 directional sensors is designed to be rotated 90 degree to get the environment distance within 180 degree. Fig. 8(b) is the experimental test result. Table 1 is the designed specification of robot and environment.

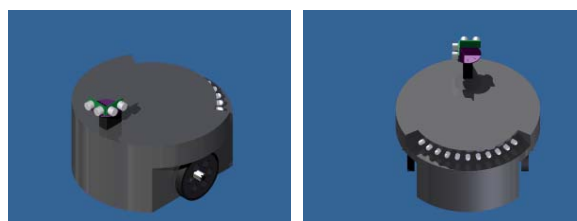
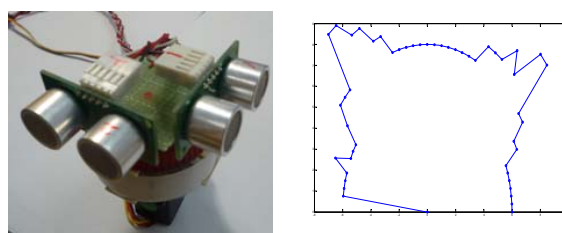


Fig. 7. Concept designs of the experimental robot



(a) Ultrasonic Scanner (b) Experimental test result

Fig. 8. Concept designs of the experimental robot

Table 1. Specification of Multi mobile robot system

Sort	Specification
Robot Size	200(D)150(H)
Field Size	4,000(W) 4,000(L)
The range of Ultrasonic sensor	3,000mm
The degree of Ultrasonic sensor	180 degree
Maximum Velocity of	20mm/sec
Number of Robot in flied	3

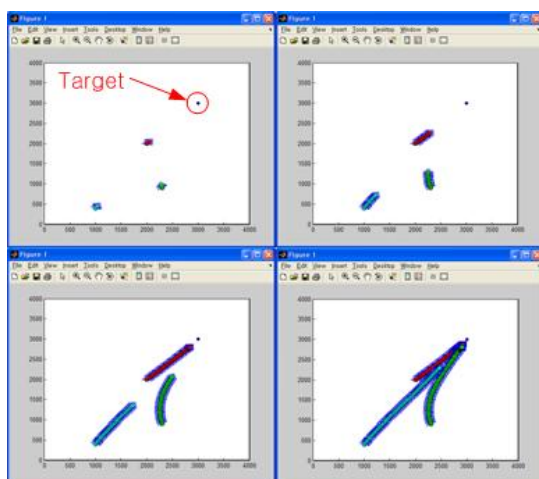


Fig. 9. Simulation test result

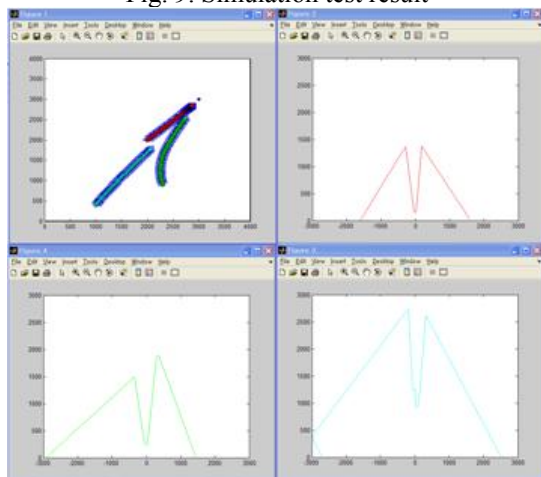


Fig. 10. Sensors monitoring in Simulation test

2. Simulation Test

The proposed formation method using potential virtual hill is evaluated by simulation test. The robots were located in the 4 by 4 meter simulation field arbitrarily. Fig. 9 is the simulation test result showing the progress of formation and navigation. From the repetitious test and various case of initial setting, the result reveals that the proposed algorithm make a line formation and goal arrival in simulation test. Fig. 10 shows the ultrasonic sensor recognition of each robot

during simulation test. From the result, it is known that the robot can approach in the tail of front robot or target goal and find out only front robot and goal in the sensed range result. The whole study will evaluate the proposed technique using experimental test. This paper does it using simulation test before experimental test.

VI. CONCLUSION

This paper studies the multi mobile robot formation and navigation method in the simplest system by only using ultrasonic sensors for environmental recognition. The potential field method is adopted to drive mobile robot. To achieve corporative navigation, this paper proposed line formation method using virtual hilled potential field navigation. The proposed method was evaluated simulation test. In the future, experimental test has to be executed and compared with simulation test

ACKNOWLEDGE

This research was supported by the MKE(The Ministry of Knowledge Economy), Korea, under the Specialized Field Navigation/Localization Technology Research Center support program supervised by the NIPA(National IT Industry Promotion Agency)" (NIPA-2010-(C7000-1001-0004))

REFERENCES

- [1] T. Arai(2002), E. Pagello, L. E. Parker, Editorial: Advance in Multi-Robot Systems. IEEE TRANSACTIONS ON ROBOTICS AND AUTOMATION. Vol. 18. No. 5: 655-661.
- [2] B. MacLennan(1991), Synthetic ethology: An approach to the study of communication, In Proceedings of the 2nd interdisciplinary workshop on synthesis and simulation of living systems. 631-658
- [3] A. Das(2002), R. Fierro, V. Kumar, et al, A vision-based formation control framework. IEEE TRANSACTIONS ON ROBOTICS AND AUTOMATION. Vol. 18. No. 5: 813-825.
- [4] P. Song(2002), and V. Kumar, A Potential Field Based Approach to Multi-Robot Manipulation," ICRA'02, Proceedings:1217-1222
- [5] O. Khatib(1986), Real-time obstacle avoidance for manipulators and mobile robots, International Journal of Robotics Research 5:90-98.
- [6] R. Volpe(1990) and P. Khosla, Manipulator control with superquadricartificial potential functions: Theory and experiments, IEEE Trans. on Syst., Man, and Cyber., 20(6):1423-1436.
- [7] M. K. Park(2001), M. C. Lee, Object Tracking Algorithm for a Mobile Robot using Ultrasonic Sensors, ICCAS'01 , Proceedings:333-336.

Adaptive tuning of a Kalman filter using Fuzzy logic for attitude reference system

Taerim Kim, Joocheol Do, Eunkook Jung, Gyeongdong Baek, and Sungshin Kim

*School of Electrical Engineering, Pusan National University,
Jangjeon-dong, Geumjeong-gu, Busan, 609-735, Republic of Korea
(Tel : 82-51-510-2367; Fax : 82-51-513-0212)
(Email : {rimkt, colorhorse, silverkook, gdbaek, sskim}@pusan.ac.kr)*

Abstract: This paper proposed parameter control method for covariance of Kalman filter using fuzzy logic. Most people use accelerometer and gyro for calculating attitude and Kalman filter for fusion algorithm of two sensors. However, parameter of Kalman filter isn't correctly predicted and attitude reference system (ARS) using Kalman filter which has non-controlled parameter has many errors when it is moved a great variation. For improving this problem, we proposed parameter of Kalman filter tuning method using fuzzy logic and then we compared our ARS module with Crossbow Nav420CA.

Keywords: ARS, Kalman filter, Fuzzy logic, Accelerometer, Gyro, Euler angle.

I. INTRODUCTION

Recently, the development in micro-electro-mechanical system (MEMS) technology has made it possible to make cheap chip like accelerometer and gyro sensors, which have been adopted into many applications but traditionally inertial sensors have been too costly [1-2]. Attitude reference system (ARS) estimates body's roll and pitch. It is widely used in robot, aircraft, ship and so on. Particularly, there is getting popular robot market. Humanoid and military robots have been interesting topics for the past decade. Therefore, inexpensive and high efficient attitude sensor is necessary for an effective attitude control [2].

Most of the ARS is consist of accelerometer and gyro. Accelerometer measures acceleration of the body and gyro measures angular rate of the body. Before time, attitude calculation is possible by simple integration using gyro. However, there is difficult to attitude calculation as using low cost MEMS sensors because of accumulated error of output. Therefore, there is recently study about calibrated method of gyro error using accelerometer. Fusion method of two different sensors uses widely Kalman filter [2-3]. But it has trend that unstable filter by parameter of Kalman filter which is difficult to estimate. We had known through experiment that if variation of accelerometer is large then Kalman filter error is large. Using this fact, this paper proposed calibration method that controls parameter of Kalman filter using fuzzy logic.

II. ATTITUDE DETERMINATION FROM EACH SENSOR

1 Attitude determination from gyro

The roll(ϕ), pitch(θ), yaw(ψ) rate of the body are measured using gyro and accelerometer. We need to consider its body axis system so that we can calculate attitude. Attitude calculation method is divided into quaternion method, cosine matrix method and Euler angle method. Among these methods, we used Euler angle method because it can easily recognize user to attitude of the body. The following equation is direction cosine matrices of each axis [3-4].

$$C_x = \begin{bmatrix} 1 & 0 & 0 \\ 0 & \cos \phi & \sin \phi \\ 0 & -\sin \phi & \cos \phi \end{bmatrix} \quad (1)$$

$$C_y = \begin{bmatrix} \cos \theta & 0 & -\sin \theta \\ 0 & 1 & 0 \\ \sin \theta & 0 & \cos \theta \end{bmatrix} \quad (2)$$

$$C_z = \begin{bmatrix} \cos \psi & \sin \psi & 0 \\ -\sin \psi & \cos \psi & 0 \\ 0 & 0 & 1 \end{bmatrix} \quad (3)$$

The transformation from reference frame to body frame can be represented in Fig. 1. Therefore, the relation between gyro output and Euler angles can be described using (1)-(3) as follows :

$$\begin{bmatrix} \omega_x \\ \omega_y \\ \omega_z \end{bmatrix} = \begin{bmatrix} \dot{\phi} \\ 0 \\ 0 \end{bmatrix} + C_x \begin{bmatrix} 0 \\ \dot{\theta} \\ 0 \end{bmatrix} + C_x C_y \begin{bmatrix} 0 \\ 0 \\ \dot{\psi} \end{bmatrix} \quad (4)$$

where each ω_x , ω_y , ω_z are the gyro outputs in the x , y , z axis. We get next term by applying the Euler angles to gyro output.

$$\begin{bmatrix} \dot{\phi} \\ \dot{\theta} \\ \dot{\psi} \end{bmatrix} = \begin{bmatrix} 1 & \sin \phi \tan \theta & \cos \phi \tan \theta \\ 0 & \cos \phi & -\sin \phi \\ 0 & \sin \phi \sec \theta & \cos \phi \sec \theta \end{bmatrix} \begin{bmatrix} \omega_x \\ \omega_y \\ \omega_z \end{bmatrix} \quad (5)$$

This paper proposed ARS development so that $\dot{\phi}$ and $\dot{\theta}$ is only used.

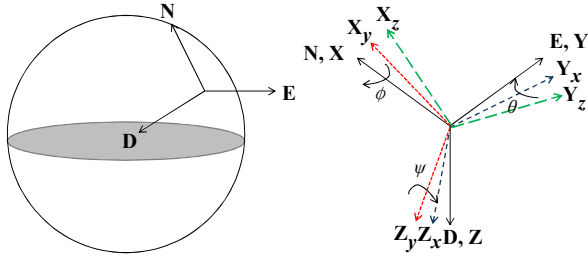


Fig.1. Definition of Euler angle

2. Attitude determination from accelerometer

Accelerometer output is used to obtain roll and pitch. The relational equation expressed accelerometer output equals to add acceleration of body frame and acceleration of gravity[5].

$$f^b = \dot{v}^b + \omega_{nb}^b \times v^b - g^b \approx \begin{bmatrix} g \sin \theta \\ -g \sin \phi \cos \theta \\ -g \cos \phi \cos \theta \end{bmatrix} \quad (6)$$

where f^b is specific force and g^b is the gravity vector in body frame. v is linear velocity component of each axis and it can't be measured without external sensors so that we ignore those terms. Therefore Eq. (6) is reduces to the following as :

$$\theta = \sin^{-1}\left(\frac{f_x}{g}\right), \quad \phi = \sin^{-1}\left(\frac{-f_y}{g \cos \theta}\right) \quad (7)$$

We can calculate roll and pitch using simple equation. Therefore, we can calculate roll and pitch by fusion of gyro and accelerometer.

III. KALMAN FILTER USING FUZZY LOGIC SYTEM

1. Kalman filter

Kalman filter is used for fusion of gyro and accelerometer. Kalman filter is consisted of process model and measurement model.

$$\begin{aligned} x_k &= Ax_{k-1} + Bu_k + w_{k-1} \\ z_k &= Hx_k + v_k \end{aligned} \quad (8)$$

where w_k and v_k represent the process and measurement noise respectively. We are assumed to be independent and with normal probability distributions.

$$\begin{aligned} w_k &\sim N(0, Q) \\ v_k &\sim N(0, R) \end{aligned} \quad (9)$$

where Q is the process noise covariance and R is the measurement noise covariance[6-7].

We used that process model is gyro output and measurement model is calculated attitude of accelerometer as shown in Fig. 2. However, parameter of Kalman filter can't estimate accuracy values. Through experiment, we could know that ARS has large errors when it is greatly changed so we used fuzzy logic for improving performance [8].

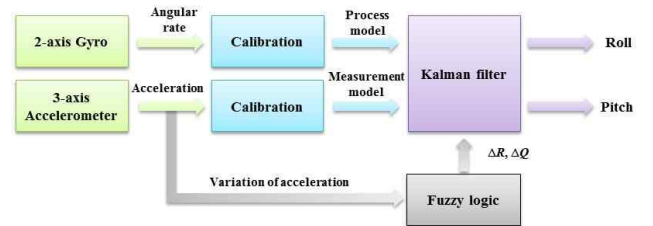


Fig.2. Structure of attitude reference system

2. Fuzzy logic for controlling parameter

We used fuzzy logic for modifying process and measurement noise covariance. Before Kalman filter is used, we have to calculate Fuzzy logic using output of sensors and reflect changed parameter. Input of fuzzy logic is acceleration's variation of x axis and y axis and output is variation of R , Q . We used mamdani method and simple rules. The following two fuzzy rules are used :

Rule1. If $|\Delta a|$ is small then R is increased and Q is decreased.

Rule2. If $|\Delta a|$ is large then R is decreased and Q is increased.

where $|\Delta a|$ is variation of each axis' accelerometer output and absolute value. If variation of acceleration is large then we can't trust output of accelerometer and R must be changed to be increased because sensor movement is supposed to be measured. The membership functions of fuzzy sets are shown in Fig. 3.

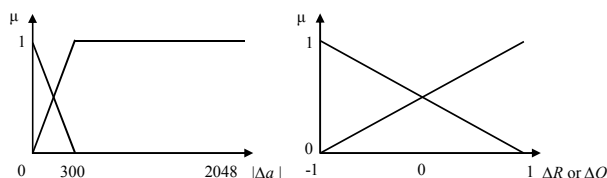


Fig.3. Membership functions

Range of Δa is determined by output range of accelerometer sensor and heuristic method. Output range of using accelerometer is from -1024 to 1024.

IV. EXPERIMENT

The proposed parameter tuning method of Kalman filter using fuzzy logic has been tested and compared with Crossbow Nav420CA. Nav420CA is INS(Inertial Navigation System). It can measure roll, pitch and has high accuracy which is 0.75°rms . We made ARS module and it consists of microprocessor, 3-axis accelerometer and 2-axis gyro. We used LIS3LV02DQ accelerometer and IDG-300 gyro. Microprocessor is used ATmega128. We measured roll and pitch of ARS module and Nav420CA at the same time using the stewart platform in shown as Fig.4.

The results obtained that proposed algorithm is better than Kalman filter in shown as Fig. 5. We confirmed response delay and it is due to response rate of microprocessor and parameter of Kalman filter. To knowing accuracy, we calculated errors based upon a simple root mean squared error (RMSE). Here, we assumed truth model is Nav420CA. When we used only Kalman filter, RMSE is in shown as Table 1. Because of reducing errors, we can tell that proposed algorithm is better than simple Kalman filter.

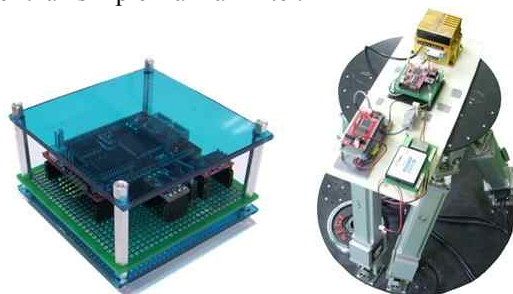


Fig.4. ARS module and experimental environment

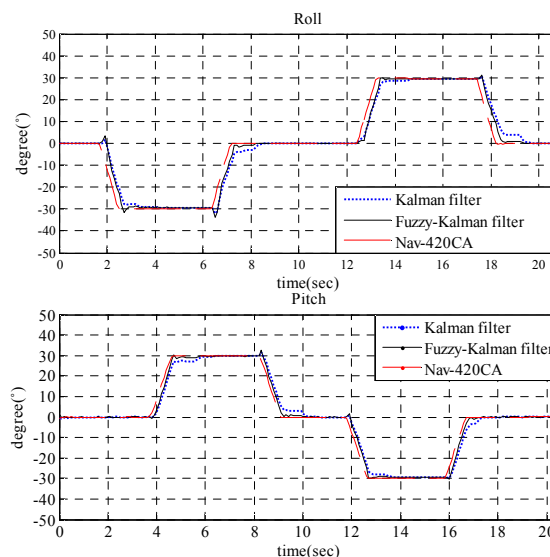


Fig.5. Roll and pitch rotation test result

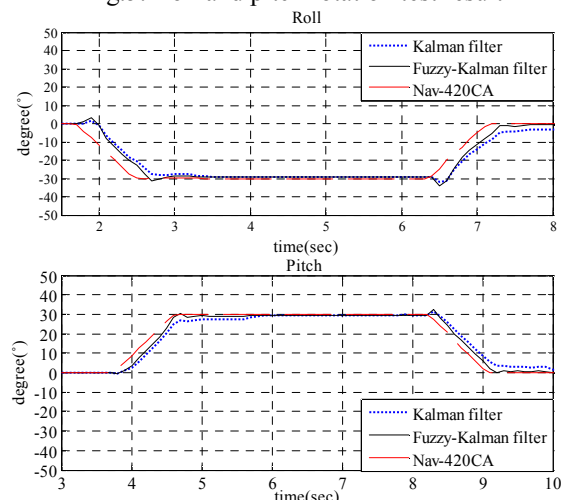


Fig.6. Zoom in roll and pitch rotation test result

Table 1. RMSE of the test result

	Kalman filter		Fuzzy-Kalman filter	
	roll	pitch	roll	pitch
Static	0.20	0.10	0.20	0.03
Dynamic	1.43	1.07	0.72	0.71

V. CONCLUSION

This paper proposed parameter of Kalman filter tuning method using fuzzy logic. In order to attitude calculation, we used gyro calibration by Euler angle method. Fusion of sensors is usually used Kalman filter. We determined process model is output of calibrated gyro and measurement model is calculated attitude of accelerometer. However, result of this algorithm has large errors when it moves greatly. To this problem, we changed parameter of Kalman filter using fuzzy logic. If

ARS module is moved large, then we trust gyro so that Q is decreased and R is increased. We tested to confirm proposed method. We made ARS module using 3-axis accelerometer and 2 axis gyro. The result is reduced errors than simple Kalman filter. We confirmed that proposed algorithm is very simple but it is high performance. If we have a chance, we want to research magnetic sensor. Magnetic sensor is used calculation of yaw. We will add our ARS module to magnetic sensor and then we will be able to make AHRs(Attitude Heading Reference System) module.

Acknowledgment

This research was supported by the MKE(The Ministry of Knowledge Economy), Korea, under the Human resource development program for robotics support program supervised by the NIPA(National IT Industry Promotion Agency). (NIPA-2010-(C7000-1001-0009))

REFERENCES

- [1] Isaac Skog[1], Peter Handel[2](2006), Calibration of a MEMS Inertial Measurement Unit, XVII IMEKO World Congress
- [2] Chul Woo Kang[1], Chan Gook Park[2](2009), Attitude Estimation with Accelerometers and Gyros Using Fuzzy Tuned Kalman filter, Proceedings of the European Control Conference 2009:3713-3718
- [3] Rong Zhu[1], Dong Sun[2], Zhaoying Zhou[3], Dingqu Wang[4](2007), A linear fusion algorithm for attitude determination using low cost MEMS-based sensors, Measurement Volume 40, Issue 3:322-328
- [4] Rong Zhu[1], Zhaoying Zhou[2](2006), Calibration of three-dimensional integrated sensors for improved system accuracy, Sensors and Actuators A 127:340-344
- [5] Sung Kyung Hong(2003), Fuzzy logic based closed-loop strapdown attitude system for unmanned aerial vehicle(UAV), Sensors and Actuators A 107:109-118
- [6] J.Z. Sasiadek [1], Q.Wang [2], M.B.Zeremba[3] (2000), Fuzzy Adaptive Kalman Filter for INS/GPS Data Fusion, Proceedings of the 15th IEEE International Symposium on Intelligent Control:181-186
- [7] Nebot E.[1], Durrant-Whyte H.[2](1999), Initial Calibration and Alignment of Low Cost Inertial Navigation Units for Land Vehicle Applications, Journal of Robotics Systems, Vol.16, No.2:81-92.
- [8] D. Loebis[1], R. Sutton[2], J.Chudley[3], W.Naeem[4](2004), Adaptive tuning of a Kalman filter via fuzzy logic for an intelligent AUV navigation system, Control Engineering Practice 12:1531-1539

A High-speed 3D Image Measurement Method

Ke Sun Yundi Yao and Cunwei Lu

Fukuoka Institute of Technology
(Tel : 81-92-606-3578; Fax : 81-92-606-0726)
(bd08001@bene.fit.ac.jp) and (lu@fit.ac.jp)

Abstract: The intensity modulation projection technique has been in great anticipation of practicability with the popularization of digital camera and projector recently with reason that it may get much more information with single projection pattern through measurement and calculate the high sensitive 3D information. But the technique is premised on the situation that it must get observation pattern image with essential number of stripe and intensity distribution, that is to say, the ideal observation pattern image so as to secure the sensitivity and accuracy of measurement. So, as for the target object without specification on the surface reflectance and distribution of surface color, the measurement would encounter several problems such as deficiency of the volume of information on the observation pattern, uncertainty of the target measurement sensitivity as well as the trouble of measurement manipulation. In order to solve the problems presented above. We propose an image analysis method of intensity correction with synthesis image technique in order to extract the stripes precisely when measuring the 3D shape of an object by using single projection pattern. By using this analysis method, if the surface reflection of the target is simple, 3D shape measurement is realized using only one observation image.

Keywords: 3D Shape Measurement, Optimal, Intensity Modulation, Pattern Projection, Image Synthesis.

I. INTRODUCTION

Three-dimensional (3D) shape measurement has different applications in engineering fields, such as inspection of product quality, face recognition, body surface evaluation, and surgery simulation and navigation in biomedical engineering[1].

At present, popular 3D shape measurement techniques include stereo vision, structured light, moiré method, and the other methods. Depending on the light source and the receiving style, many techniques have been proposed, active systems and passive systems. The stereo vision is based on imaging the scene from two or more points of view and then finding correspondences between the different images in order to triangulate the 3D position. Triangulation is possible if cameras are previously calibrated. The structured light technique generates a full pattern to cover the object so that the surface can be captured as a whole field recording. Therefore, the encoding of the structured pattern becomes important because it determines the local features of the recorded images to be identified in spatial recognition and height evaluation.

When we measure a color object, the color distribution of the object often influences the code word of project pattern; here we use a monochrome projection pattern to avoid the influence from color. In this method, we only do analysis on the intensity of the

observation image, so the combination of monochrome projection and monochrome analysis do not take object color into consideration. Here we use optimal intensity modulation pattern, which is made by a special algorithm. This kind of pattern is easier to do the stripe extraction just because the adjacent stripes have a good maximum intensity difference, which makes the stripe easily to be distinguished[2-3].

In this paper, we propose an analysis method based on the optimal intensity modulation pattern projection technique, in which a structured monochrome projection pattern is projected and a color image of the observation pattern is captured. The paper focuses on the optimal analysis of optimal intensity modulation projection technique by using single projection pattern and the contradistinction against the conventional methods in stripe analysis. The intensity distribution stripes offer an identifiable pattern so that the whole surface pattern image of the object can be obtained to easily analyze surface depth information by triangulation. Not only can we get better detection accuracy and faster computation speed through optimizing the stripe intensity distribution, but also can get better stripe order detection by modulating the intensity differences between adjacent stripes[4-5].

II. ALGORITHM

Figure 1 was a composition of typical 3D shape measurement system. The projection pattern been

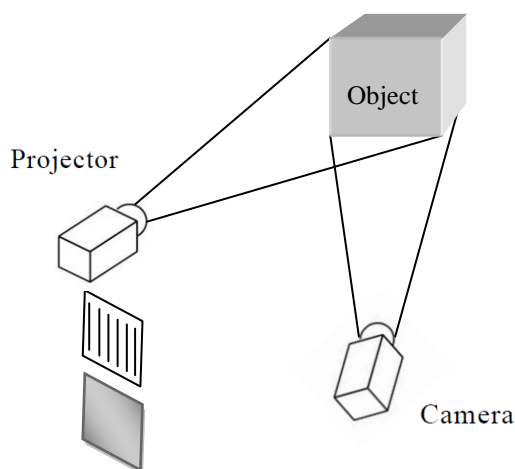


Fig.1. 3D shape measurement of pattern projection system

output by the computer was projected to the measurement object from the projector, camera was used to take a picture of the projected pattern reflected to the measurement object as an observation pattern image, finally, the information stored in the camera was input to the computer. Next, the directions of the stripes of projection pattern were detected from the observation pattern image which had been input, and then 3D shape of the object was restored based on the principle of the triangulation. The following contained processing of each step was stated simply[4].

Step1: Projecting optimal intensity modulation pattern to measurement object.

Step2: Taking a picture of the image and using it as the initial observation pattern image.

Step3 : Doing color analysis of the initial observation image and synthesizing the image for the measurement based on the color channel for the measurement. The color channel that reflection intensity value was stronger than the others was extracted every pixel from input image and used it as the channel for the measurement. The influence caused by other color components and the surface reflectance in the same part of the measurement object were reduced by synthesizing single channel image for calculation with a channel for the measurement of each pixel.

Step4: Extracting measurement object from the image for measurement and deleting the noise with threshold extraction method.

Step5: Confirming the influence of surface reflectance. If there were no influence, Step 6 should be omitted and jumped to step 7 directly.

Step6: Correcting the influence of the surface reflectance of the measurement object from the image for the measurement with the object of detecting stripes address in high accuracy and sharpening stripes pattern for the measurement. In the following Chapter 3, we described the technique and principle.

Step7 : Extracting slit pattern address in the light of a linear relation of each stripes intensity value from the corrected image for measurement because the intensity value of each stripes pattern was decided by majority according to the intensity value of each pixel of each stripes pattern.

Step8 : Calculating the 3D space world coordinates based on the detected stripes address. The calculation of three dimension shape by using the principle of the triangulation was omitted in this thesis.

III. PRINCIPLE AND METHOD

1. Problem of reflectivity reduction

About the optimal intensity modulation pattern projection measurement, it was ideal that the relation between the intensity of the reflection pattern stripes obtained from the input image and a pattern stripes degree were a one-to-one correspondence in order to obtain three dimension shapes with accuracy. However, the measurement object was multiple color distribution, and it was difficult to obtain such an ideal relation when it had reflectivity taken with a versatile digital camera. Generally, the gray projection pattern was projected to the measurement object with a variety of color distribution, information obtained from the reflection pattern image was only brightness, coordinates, and color information on the measurement object decreased and the measurement range confused became narrow[6].

2. Past method of intensity correction

For the projected pattern intensity $P(x, y)$, if pixel intensity $I(i, j)$ in the image was always (1), the correction method of traditional reflectivity should be ideal.

$$P(x, y) : I(i, j) = 1 : 1 \quad (1)$$

Actually, Surface reflection element $O(x, y)$ of the object can be actually contained, and intensity of each pixel in the reflection pattern image that hit the object be shown as follows.

$$I_l(i, j) = P_n(x, y) \times O(x, y) \quad (2)$$

At this time, because the surface reflection element had its influences in (2), stripes degree n of $P_n(x, y)$ cannot be detected. Then, we projected projection pattern with uniform intensity $P_f(x, y)$ to the same measurement scene, the relation of (3) was obtained.

$$I_f(i, j) = P_f(x, y) \times O(x, y) \quad (3)$$

The following relation was obtained from (2) and (3).

$$\frac{I_l(i, j)}{I_f(i, j)} = \frac{P_n(x, y)}{P_f(x, y)} \quad (4)$$

That is to say, the image for the calculation with the projection light stripes intensity distribution and linear correspondence was obtained by the dividing calculation correction. With correction method, steady stripes pattern for measurement could be obtained, but confronting the fact, which meant its difficulty to deal with the moving object, furthermore, it is necessary to use two pieces of observation image, which made the measurement cost time[7].

3. Propose method of intensity correction

Previous method can give us a good result when measuring a stationary object. Typically, this method takes time to send two frames of projection pattern when measuring. In fact, we do not need high precision of the full-light observation image which means not very necessary to do the full-light image capturing. If we can analyze the distribution through some processing algorithm, the original image after gray scale may be not necessary.

In order to realize 3D shape measurement using one image, we propose an optimal image analysis method. Intensity information of no-pattern area is used to recover intensity information pattern area. Color changes of object surface have little effect on the change of reflectivity. So we set a specific filter to do recovery of pattern pixel in this specific domain. We try to use the neighbor pixel intensity of the no-pattern area to fill in the pixel of pattern area, and then let the filter move to the next pixel to do the same work of the correction processing. Under this way, we could obtain the random pixel intensity distribution, this kind of information transference still carry over the no-pattern pixel intensity approximately. We can obtain a synthesis full-light image by using this method, in which there is no pattern area. We use this synthesis image to do

division calculation, and then to avoid the effect of reflectivity of object surface color. At last, pattern image used for measurement which is in linear relation is obtained.

IV. OUTCOME OF AN EXPERIMENT

The experiment was done in the spaciousness environment where the lighting was erased. The experiment system was composed of the liquid crystal projector, the CCD color camera, and the computer, the stripe number of the optimal intensity modulation projection pattern was set to 20.

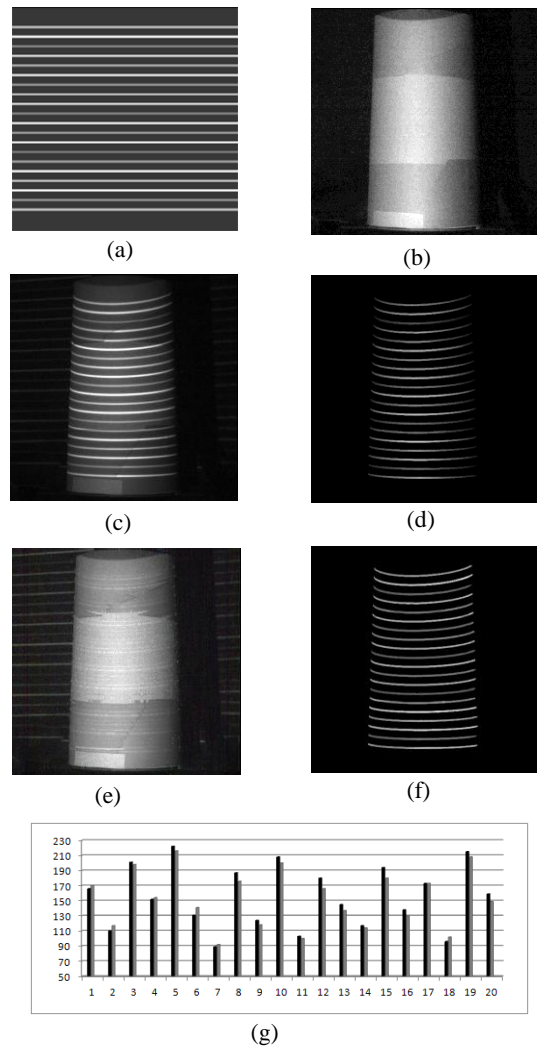


Fig.2 Experiment result: (a) Optimal intensity modulation projection pattern. (b) Column object. (c) Observation pattern image. (d) Extracted pattern image. (e) Synthesis image. (f) Corrected pattern image. (g) Intensity distribution image for comparison.

First of all, 20 stripes (Figure 2(a)) optimal intensity modulation patterns were projected to the column (Figure 2(b)), the reflected pattern, as an observation

pattern image (Figure 2(c)), was taken a photo by camera. And, the observed pattern was extracted, which formed extracted pattern image (Figure 2(d)). Next, the synthesis image (Figure 2(e)) by the technique of propose was generated, Pattern intensity was corrected by the dividing calculation with Figure 2(d) and Figure 2(e), which formed the corrected pattern image (Figure 2(f)). Figure 2(g) is the comparison of the intensity distribution of Figure 2(a) and Figure 2(f), just shown here, it can be seen that the intensity distribution of the corrected image is almost similar with the one of projection pattern image, our method is successfully proved to be done in this kind of correction processing.

V. CONCLUSION

The paper presents a technique of 3D shape measurement by using single projection pattern to do optimal analysis based on convolution theory. The optimal intensity modulation projection pattern is chosen to encode the surface area of the object; and uniform intensity projection pattern formed by program is used to reduce the impact of the colors in stripe region. This method is applied to revise the color distribution of projection pattern stripes by using the background information in 3D projection pattern measurement technique.

The future task is to measure object surface which has complicated texture, and verify the robustness of this technique.

REFERENCES

- [1] S. Inokuchi and K. Satou: 3D Imaging Techniques for Measurement; *Shokodo*, Toukyou(1990).
- [2] G. Cho and C. Lu: 3D Image Measurement for Object with Multiplex Color Information Analysis; *Proceedings of 9th Symposium on Sensing via image Information(SSII 03)*, pp.79-82(2003).
- [3] G. Cho and C. Lu: Practical 3D Measurement System based on Projection Pattern Control Techniques; *IEEJ Trans. EIS*; Vol.127, No.4, pp561-567(2007).
- [4] Cunwei Lu, Limin Xiang and Seiji Inokuchi: Optimization of the Projection Pattern and a Quasi-Optimal Combination Generation Algorithm for 3-D Shape Measurement; *The Institute of Electronics,*

Information and Communication Engineers D-II; Vol.J88-D-II, No.2, pp.325-333, 2005.

[5] Cunwei Lu and Seiji Inokuchi : Intensity - modulated moiré topography; *Applied Optics*; Vol.38, No.19, pp.4019-4029(1999).

[6] C. Lu and G. Cho: 3D Image Measurement by Combination of Monochrome-Projection Color-Analysis and OIMP Technique; *Transactions of The Institute of Systems, Control and Information Engineers*: Vol.17, No.6,pp.233-240(2006)

[7] Cunwei Lu and Limin Xiang: Optimal intensity-modulation projection technique for three-dimensional shape measurement; *Applied Optics*; Vol.42, No.23, pp.4649-4657, 2003.

3-D Face Recognition Method Based on Optimum 3-D Image Measurement Technology

Hiroya Kamitomo, Yao Xu and Cunwei Lu

Fukuoka Institute of Technology, 30-1 Wajirohigashi3-chome, Higashi-ku, Fukuoka

(Tel : 81-92-606-7395)

(bd09001@bene.fit.ac.jp, lu@fit.ac.jp)

Abstract: We propose a 3-D face recognition method using the iterative closest point (ICP) algorithm. So far, the reported 2-D face recognition methods have weak points by source of light, make-up and facial positioning. A using 3-D shape measurement system includes a technique for optimizing the intensity-modulation pattern projection. Therefore, we propose 3-D face recognition system which is robustness in the color change. The face recognition method is possible for facial registrations. This method estimate rotations and translations for different positions and directions. Consequently, experimental results obtained the high accuracy that the rate of face recognition is 96%.

Keywords: 3-D shape measurement, 3-D image, face recognition, iterative closest point, registration

I. INTRODUCTION

The biometrics is the security technology used for access control. The two main types of biometrics are behavioral method and physiological method. The examples of behavioral method are voice, gait and handwriting. This method's problem is influenced by the condition of person. The examples of physiological method are fingerprint, iris and face recognition. This method is more highly accurate than behavioral method. However, fingerprint and iris recognition are difficult to get people's approval. Many people become unpleasant feelings because of measurement. Face recognition is easy to measure biometric information. Therefore, face recognition has a lot of researches. Past face recognition uses the two-dimensional image. The biometric system extracts a feature from the facial image. The first time a feature data is stored. In subsequent uses, the feature data is compared. However, face recognition does not work well under conditions of lighting and make-up. The matching of feature data fails by appearance changes of the facial image. To deal with this problem, the three-dimensional face recognition attracts attention. This technique uses 3-D shape measurement system to capture information about the shape of a face. One advantage of 3-D face recognition is that it is not affected by changes in lighting like other techniques. Popular 3-D recognition algorithm is the matching of z-range images. The z-range image is 2.5-D information. The problem of this information is the changes of facial position with rotation and translation. We proposed the

practicable 3-D image measurement system based on optimal intensity-modulation projection technique. This system is possible to obtain 3-D facial images in high-speed and high-accurate. The registration of 3-D facial image is easy under changes with rotation and translation. We propose technique of recognition using 3-D facial image.

II. 3-D SHAPE MEASUREMENT

The method of triangulation is the radical principle of 3-D shape measurement based on the pattern light projection. The pattern light is projected to the target object from the source of light, and the camera captures images of the appearance from a different angle.

Formula (1) is used to measure a depth distance of target point by the triangulation principle.

$$z = \frac{b}{\tan \alpha + \tan \beta} \quad (1)$$

Here, z is a depth distance of the measurement point; b is a base length (the distance between source of light and the center of lens of camera); α is stripes projection angle; β is an observation angle degree; β is computable by stripes coordinates on the observation image.

When the strength modulation pattern light is used as shown in Fig 1, stripes projection angle could be calculated by a single piece of picture theoretically. However, this pattern is influenced by the surface color of the measurement object and reflection. The intensity value of the projection stripes in the observation image

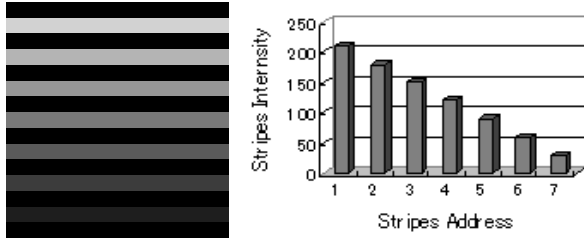


Fig.1. Intensity modulated pattern

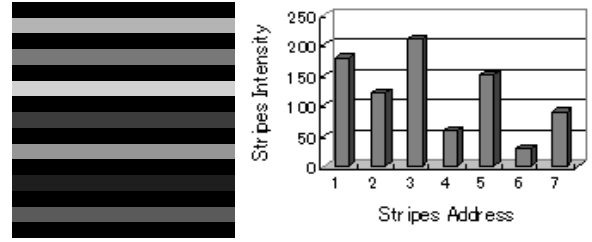
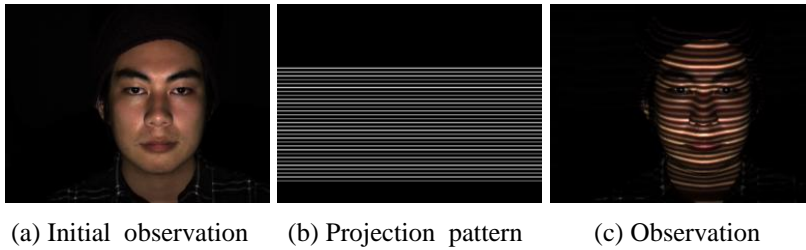


Fig.2. Optimal intensity modulated pattern



(a) Initial observation (b) Projection pattern (c) Observation

Fig. 3. Projection pattern and capture images



Fig. 4. 3DCG of face

changed and the correspondence to the projection angle collapsed. There is an optimum strength combination pattern light projection method to solve such a problem. It is a technique to optimize projection pattern and to seek for regulation of variations in intensity at a maximum about intensity difference of projection between adjacent stripes[1].

In a set of stripes addresses $\{1, 2, \dots, N\}$, when the intensity order of the address $p_i \in \{1, 2, \dots, N\}$, the projection light intensity of the stripes strength order is defined as the following magnitude correlations.

$$I_{\min} \leq I_{p_1} \leq I_{p_2} \leq \dots \leq I_{p_N} \leq I_{\max} \quad (2)$$

Here, I_{p_i} is the projection light intensity of stripe address, I_{\min} and I_{\max} are minimum value and maximum value of the projection light intensity respectively. The function is defined when the projection light intensity difference of the stripes strength distribution combination (I_1, I_2, \dots, I_N) is at the maximum, evaluation function $d(I_1, I_2, \dots, I_N)$ is also at the maximum.

$$d(I_1, I_2, \dots, I_N) = \sum_{i=M+1}^N \sum_{j=1}^M k_j |I_i - I_{i-j}| \quad (3)$$

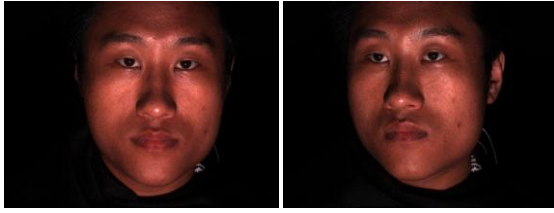
Here, k_j is a weight factor. M is width of the filter on which evaluation function has been set. As the relation of formula (2), when $d(I_1, I_2, \dots, I_N)$ is at the maximum, $d(p_1, p_2, \dots, p_N)$ amounted to the same

thing. Thus, it can be said that $d(p_1, p_2, \dots, p_N)$ seek combination (p_1, p_2, \dots, p_N) at the maximum as its optimum combination. Projection pattern shown in Fig 2 is replaced by the stripes order of projection pattern in Fig 1. We know that the strength difference between adjacent stripes has been increasing as graph. As a result, stripes projection angle should be computable accurately as long as the strength change rule is maintained even if the error margin is included in the detection of stripes projection light intensity.

III. 3-D FACE RECOGNITION

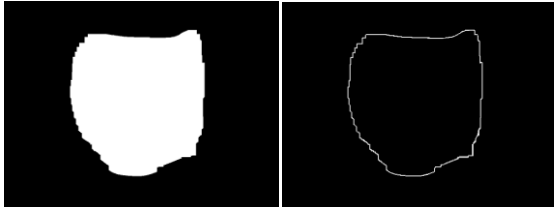
We obtain 3-D facial images by proposed 3-D shape measurement system. A using projection pattern and captured images show in Fig 3 (a) (b) (c). The obtained 3-D image can be displayed as 3DCG (Fig 4). The 3-D face recognition needs registration of 3-D facial images. The registration algorithm is used as an aligning two 3-D shape data. A propose recognition method uses the Iterative Closest Point (ICP) algorithm[2]. We mounted ICP for 3-D face recognition on the system. ICP is comprised of four steps.

1. Selection ; select 3-D point cloud
2. Matching ; detect correspondence point-pairs
3. Rejecting ; reject illegal point-pairs
4. Minimizing ; minimize error between shapes



(a) Model texture (b) Scene texture

Fig. 5. Camera captured images



(a) Measurement-area (b) Boundary-area

Fig. 7. Mask images for rejecting

A concrete steps are shown in the following.

1. Selection

The first time a system obtains the 3-D point cloud from 3-D facial images. 3-D point cloud is comprised of many three-dimensional coordinates. 3-D point cloud in enrollment time is called *Model*, 3-D point cloud in unknown input time is called *Scene*. However, *Model* is measurement data of frontal faces. Images that 3-D measurement system captured are shown in Fig 5. Fig 5 (a) and Fig 5 (b) are texture color images of *Model* and *Scene*. At first, two facial positions are different. 3DCG of *Model* and *Scene* shows in Fig 6.

2. Matching

System finds a point-to-point correspondence between *Model* and *Scene*. The corresponding point of *Scene* is the closest point in *Model*. We usually takes long time of $O(N)$ that search a corresponding point of one query point. Here, N is number of 3-D points in *Model*. We use k-dimensional tree (k-d tree) structure to make the search processing faster[4]. We take time of $O(\log N)$ for searching with k-d tree. This algorithm finds the corresponding points of all 3-D points in *Scene*. The point-to-point pair between *Scene* and *Model* is (p_i, q_i) $i=0,1,2,\dots,M-1$. Here, M is number of 3-D points in *Scene*, p is 3-D point in *Scene*, q is 3-D point in *Model*.

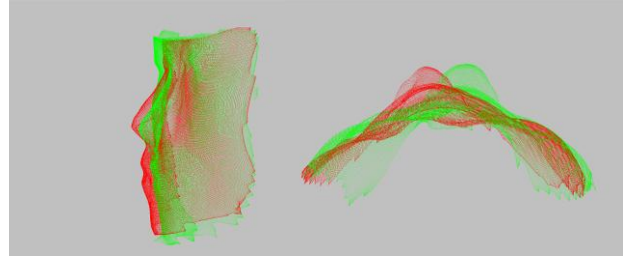
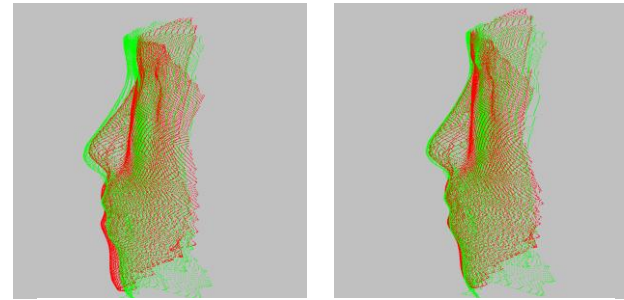


Fig. 6. Initial position of two faces



(a) Before minimizing (b) After minimizing

Fig. 8. Registration of two faces

3. Rejecting

The purpose of this is to eliminate outliers. The corresponding point-to-point pairs include the illegal point-pairs. This method eliminates pairs containing points on mesh boundaries. Mask images used for rejecting are shown in Fig 6. Fig 6 (a) is 3-D measurement-area. Fig 6 (b) is boundary-area. The corresponding pairs are eliminated on boundary-area.

4. Minimizing

The purpose of this is to minimize error of corresponding point-to-point. This method finds the rigid transformation that minimizes a weighted least-squared distance between the pairs of points. The transformation is comprised of rotation and translation.

$$\sum_{i=0}^{M-1} \|q_i - R p_i - t\|^2 \rightarrow \min \quad (4)$$

Here, R is rotation matrix, t is translation vector. t is obtained using center of gravity.

$$t = \bar{q} - R \bar{p} \quad (5)$$

Here, \bar{p} is center of gravity in *Scene*. \bar{q} is center of gravity in *Model*.

$$\begin{aligned} p'_i &= p_i - \bar{p} \\ q'_i &= q_i - \bar{q} \end{aligned} \quad (6)$$

p and q is translated using center of gravity. Formula (4) is changed to formula (7).

$$\sum_{i=0}^{M-1} \|q'_i - R p'_i\|^2 \rightarrow \min \quad (7)$$

Formula (7) and formula (8) are the same meanings.

$$\text{Tr}[R^T N] \rightarrow \max \quad (8)$$

Formul (8) can be solved by the eigen problem of correlation coefficient matrix. R can be calculated out from formula (8). Then t can be found from formula (5) with R . 3-D points in *Scene* are transformed into 3-D points in *Model* using rotation and translation. *Model* and *Scene* shows in Fig 7.

5. Verification

Scene and *Model* are aligned using iteration of four steps. At the last step, we verify identities of 3-D facial images of personal person. The distance of *Model* and *Scene* is distinguished with the threshold. The recognition system accepts *Scene* when the distance is smaller than the threshold. The recognition system rejects *Scene* when the distance is larger than the threshold.

IV. EXPERIMENT AND DISCUSSION

This section describes experiment steps and results. The first time, we measure *Models* of 15 persons. *Model* is 3-D measurement data of frontal face. They move face when measure *Scene*. A number of 3-D measurement data is 105 samples. We recognize all samples by an application using proposed method. We measures rate of misidentification about false rejection rate (FRR) and false acceptance rate (FAR). The threshold is variable parameter in verification step. FAR and FRR shows in Fig 9. The receiver operating characteristic (ROC) plot is a visual characterization of the trade-off between the FAR and the FRR. In this experiment, FAR = 0.038, FRR = 0.047. The rate of false is small when a person moves a face. This method using registration is effective face recognition with moving. The lighting and make-up does not influence this method because without facial color information. However, this method is used for a one to one comparison of a 3-D facial image. The stored template data is individual person's *Model*. This method takes long time when it is used for a one to many comparison. Therefore, 3-D face recognition system using this method is in conjunction with an ID card or username. And, we are necessary to shorten the processing time. It

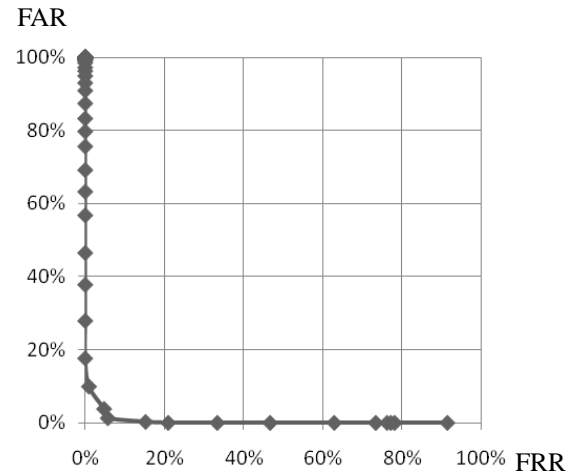


Fig. 9. ROC of 3-D face recognition

is depended on the improvement of hardware and refactoring of software.

V. CONCLUSION

In this paper we proposed a face measurement and face recognition method, our system is possible to measure 3-D facial shape with moving. This recognition method is possible to verify personal persons with make-up and lighting. The 3-D face recognition system aligns 3-D facial images when a person moves a face. This method calculates the distance between two faces. The verification step compares a face to stored face. The rate of false is small when a person moves a face. Serious disadvantage is that our system is less effective if the facial expressions vary. A weakness of registration is the changes of 3-D shape. Therefore, our system now allows only neutral facial expressions. The future work is to deal with facial expressions and facial accessory problem.

REFERENCES

- [1] Lu C (2003), Optimal Intensity-Modulation Projection Technique for Three-Dimensional Shape Measurement. *Applied Optics-IP* 42(23):4649-4657
- [2] Besl P J (1992), A method for registration of 3-D shapes. *IEEE Trans Pattern Analysis and Machine Intelligence* 14(2):239-256
- [3] Horn B K P (1987), Closed-form solution of absolute orientation using unit quaternions. *J. Opt. Soc. Am A* 4:629-642
- [4] Berg M, Kreveld M, Overmars M, Schwarzkopf O (1997), *Computational Geometry Algorithms and Applications*. Springer Verlag

User study of a life-supporting humanoid directed in a multimodal language

T. Oka¹, T. Abe², K. Sugita³, and M. Yokota³

¹ Nihon University, 1-2-1 Izumicho, Narashino, Chiba, 275-8575 JAPAN

² Nihon Computer Kaihatsu Co. Ltd., 6-24-9, Minami-Ooi, Shinagawa-ku, Tokyo, 140-0013, JAPAN

³ Fukuoka Institute of Technology, 3-30-1, Wajiro-higashi, Higashi-ku, Fukuoka, 811-0295, JAPAN

Tel : 81-47-474-9693; Fax : 81-47-474-2669

oka.tetsushi@nihon-u.ac.jp, t-abe@nck-tyo.co.jp, {sugita, yokota}@fit.ac.jp

Abstract: This paper describes a user study of a life-supporting humanoid directed in a multimodal language and discusses the results. Twenty inexperienced users commanded the humanoid in a computer simulated remote home environment in the language by pressing keypad buttons and speaking to the robot. The results show that they comprehended the language well and were able to give commands successfully. They often chose a button press action in place of verbal phrases to specify a direction, speed, length, angle, and/or temperature value, and preferred multimodal commands to spoken commands. However, they did not think that it was very easy to give commands in the language. This paper discusses the results and points out both strong and weak points of the language and robots.

Keywords: Life-supporting robot, multimodal language, user study, humanoid, human-robot interaction

I. INTRODUCTION

It is predicted that in near future life supporting robots will help people in homes, streets, hospitals, offices, etc. In order to design and develop such robots, one should take into account both cost and user friendliness, since such robots must be affordable for people in need and designed for those untrained.

Although menu-based conventional GUIs are cost effective, they are not suited for untrained people and through such interfaces one cannot communicate with robots in a natural manner even if they look like humans. It is understandable that we expect robots to communicate with us just like ourselves. In fact, there are thousands of robots which can speak and understand verbal messages [1]. However, verbal communication is just one aspect of human communication; we use gestures, postures, eye contacts, paralanguage, etc. to convey different kinds of information [2]. Therefore, we can well image that humanoids will communicate with us both verbally and nonverbally. Obviously, such robots will be more user friendly than robots operated through a conventional user interface [3]. Unfortunately, in order to communicate like humans, robots will need many kinds of sophisticated sensors to perceive verbal and nonverbal signals, high-performance computers to disambiguate messages and infer users' intentions [4], and an articulated body which look and move smoothly like a human. For this reason, precise imitation of a human will prevent us from developing affordable user friendly life-supporting robots.

The authors have designed RUNA (Robot Users' Natural Command Language), a multimodal command language [5-8], taking into account both cost effectiveness and natural human-robot communication. In RUNA, one can command an action without ambiguity by specifying its type and parameter values. Several versions of RUNA, which combine spoken

verbal messages and nonverbal messages such as hand gestures, body touch actions, and button press actions have been developed and evaluated with novice users.

A small humanoid that can be directed in an earlier version of RUNA was investigated [5]. Novice users remotely commanded the humanoid in RUNA to explore a room. All the users completed their task with help from a three-page leaflet and most of them conceived a fairly high opinion of the robot and the language, although there were some shortcomings and limitations in the robot. The overall command success rate during the task was about 70 % and the robot reacted to noises due to our poor cheap microphone. Because of the limitation of the onboard computer, the robot had to choose among 80 actions of walking, turning, looking around, and so on; it were able to turn by 30 degrees but not by 40 degrees, so it rejected some grammatical commands in RUNA. It was difficult for novice users to inform the robot one out of five turning angle values by pressing a button for a definite period of time; they had no idea how long they should press it to turn the robot as much as they want, because they were given no instructions or opportunities to practice.

After the study, we developed a simulated humanoid with a more sophisticated command interpreter and eliminated some of the shortcomings found in our first humanoid. The new robot has a larger repertoire of actions, including 540 left turns. We redesigned a set of button press actions to specify action parameter values such as speed, angle, length, temperature values.

This paper presents a user study of the new life-supporting humanoid. All of the twenty users completed their tasks, to explore a remote room and operate an air conditioner, successfully commanding the robot in RUNA. The success rate of each user's commands was over 90 % and several of the problems in the old humanoid were resolved. Most of the users preferred multimodal commands to single modal spoken

commands and often selected a button press action to specify parameter values. However, the users did not think that it was very easy to command the robot in the new version of RUNA. The results shed light on some problems of our multimodal language as well as advantages. Most importantly, it will be easier for novice users to communicate with a life-supporting robot, if they can convey parameter values one by one in nonverbal messages and can always omit some parameter values which are obvious in the context or values which they do not care about. Since there are cases in which it is hard to determine parameter values beforehand, users should be allowed to modify commands at any time.

II. MULTI-MODAL LANGUAGE

In the study presented in this paper, we used a version of the multi-modal language, RUNA [6], which comprises a set of grammar rules and a lexicon for spoken commands, and a set of non-verbal events detected using keypad buttons. The spoken language enables users to command a humanoid in Japanese utterances, completely specifying an action to be executed. Commands in the spoken language can be modified by nonverbal events.

An action command in RUNA consists of an action type such as *walk*, *turn*, *report*, and *lowertemp* (for lowering the temperature setting) and action parameters such as *speed*, *direction*, *angle*, *object* and *temperature*. Table 1 shows examples of action types and commands. The action types are categorized into 24 classes based on the way action parameters are specified in Japanese.

There are more than 300 generative rules for the full version of RUNA. These rules allow Japanese speakers to command robots actions by speech alone. In RUNA, a spoken action command is an imperative utterance including a verb to determine the action type and other words to specify action parameters. There are more than 250 words, categorized into about 100 groups identified by non-terminal symbols.

Table 1 Examples of action commands

Type	Command	English Utterance
<i>walk</i>	<i>walk_s_3steps</i>	Take 3 steps slowly!
<i>turn</i>	<i>turn_f_l_30deg</i>	Turn 30 deg. left quickly!
<i>move</i>	<i>move_m_r_2steps</i>	Move 2 steps right!
<i>look</i>	<i>look_f_l</i>	Look left quickly!
<i>raisetemp</i>	<i>raisetemp_room_2deg</i>	Raise the temperature of the room by 2 degrees!
<i>settemp</i>	<i>settemp_aircon_22deg</i>	Set the air-conditioner temperature around 22 degrees!
<i>query</i>	<i>query_aircon_all</i>	Report the status of the air-conditioner!

In RUNA, non-verbal events modify the meaning of spoken commands. They convey information about parameters of action commands. Table 2 shows examples of non-verbal events; users can use keypad buttons to specify action parameters values instead of

mentioning them. This reduces average number of words in a command and speech recognition errors. One can command a robot saying “turn” and pressing a button simultaneously instead of saying “turn 60 degrees left slowly!” Furthermore, multimodal commands are often more natural than spoken commands: e. g. pointing a glass and saying “pick this up” or saying “lower the temperature” pressing a button.

If a button event has been arrived within a short period of time, a spoken command will be modified as shown in Table 2. The twelve buttons are assigned to specific parameter values (Fig. 1). The direction and speed of a turning action command are determined by the key pressed most recently by the user. A single key press action conveys an angle value (10, 20, 40, 50 or 60 degrees) and a step value (1, 2, 4, 5, or 8 step(s)) depending on the duration, while a multiple key press action conveys values (90 or 180 degrees and 10, 20, and 30 steps). Likewise, the robot will make the preset temperature *two* degrees higher, if a key has been pressed *twice* before a spoken command “raise the room temperature!”

Finally, the repeat button and query button allow users to command robots without speaking. The empty button convey default parameter values, such as 3 steps, 30 degrees, right, normal speed, etc.

Table 2 Button event and action parameters

action type	duration	count	button
<i>sidestep/walk</i> etc.	distance	distance	speed direction
<i>turn</i> etc.	angle	angle	speed direction
<i>look</i> etc.	-	-	speed/target
<i>raise/lowertemp</i>	-	temperature	-

← Left	↑ up	→ right	Fast
← Left		→ right	Moderate
← Left	↓ down	→ right	Slow
empty	query	repeat	Cue

Fig. 1 Key assignment for action parameters

III. USER STUDY METHOD

We conducted a user study of a humanoid which can be commanded in RUNA using a remote interface. Five users who had experienced another version of RUNA and 15 novice users (male and female, aged 13-30 years) commanded the robot to achieve two different tasks: exploring a remote room and operating an air conditioner in the room. Before commanding the robot, the users watched a short demonstration movie for 70 seconds and read an eight-page document illustrating how to give commands in RUNA in diagrams and figures for five minutes. Then, we explained them how to give spoken and multimodal commands showing the

same document. They were allowed to practice commanding the robot for up to 20 minutes.

In order to test their comprehension and competence, we also gave them a comprehension test and asked them to give some extra spoken and multimodal commands precisely as printed in sheets of paper. In addition, they were asked to answer questions about the robot and our multimodal language at the final stage.

IV. RESULTS

Table 3 summarizes the data of each user. Users 1-15 commanded the robot in RUNA for the first time, while users A-E had already contributed to our previous studies. All the users completed their tasks: they answered three questions about the remote room correctly and switched on, changed the temperature setting, and switch off the air conditioner as instructed.

As shown in Tables 4 and 5, they gave many spoken and multimodal commands to move forward and turn the robot to explore the virtual remote home. They often repeated to move the robot forward or turn it to the same direction as if to look how the camera view image on the screen changed. Some users gave repetition commands to do so by pressing the "repeat" button in Fig. 1, but the other users did not. For some types of actions there were more multimodal commands than speech only commands (Table 5). Table 6 shows how the users specified angles and distance values. About 70% of the commands were given within ten seconds after the previous command was completed.

Table 3 Representative data of each user

ID	SR	nc	nw	time	test	Q1	Q2	Q3	Q4
A	100	42	1.0	7:30	8	6	7	M	Y
B	100	48	2.3	9:55	8	4	3	M	N
C	97	33	3.4	11:16	8	4	4	M	Y
D	100	21	2.4	6:07	7	2	3	S	Y
E	100	41	2.5	10:00	10	4	3	M	Y
1	100	36	1.4	8:20	8	6	4	M	N
2	100	31	2.0	12:00	8	4	6	M	Y
3	100	23	2.1	10:37	8	2	3	M	Y
4	100	33	2.0	19:50	10	5	5	M	Y
5	100	38	1.9	9:45	10	5	5	M	Y
6	100	43	1.5	12:10	9	5	4	S	Y
7	100	27	2.1	8:05	10	4	5	M	Y
8	100	26	2.9	8:03	10	4	4	S	Y
9	99	74	1.9	23:06	8	6	7	M	Y
10	98	43	1.8	10:43	9	5	5	M	Y
11	97	31	3.8	11:35	6	6	6	M	Y
12	96	31	4.2	9:20	7	4	4	S	Y
13	96	25	3.7	11:10	7	2	2	S	Y
14	91	23	2.2	13:30	6	4	5	M	Y
15	90	31	2.5	11:46	8	3	5	S	Y
ave	-	35	-	11:20	8.3	4.3	4.5	-	-

SR: Command success rate nc: Number of given commands
nw: average number of words time: task completion time
test: comprehension test result before the tasks (ten questions)
Q1. Did you command the robot in a natural way? (7 pt. scale)
Q2. Was it easy to command the robot? (7 pt. scale)
Q3. Which do you prefer, spoken or multimodal commands?
Q4. Is this robot helpful for you? (Do you want it?)

At the beginning, some of the users consulted the eight-page document, but they did it less frequently at the end. Some users seldom turned the pages or took

time to look at the diagrams.

Table 6 shows that the users were poor at conveying one of five values by the duration of a button press action even after achieving their tasks, while it was straightforward for them to give parameter values by pressing a button twice or three times. The users selected *quick/fast* actions most frequently and there were more multimodal commands to turn the robot to the right than to the left for some reasons (Table 7).

After some practice, most of the users spoke clearly and fluently in most cases. However, they failed to convey action types and/or parameter values by speech for several reasons. Some users hesitated to give commands including many words a few times. Seven users failed to change the temperature setting of the air conditioner using a wordy speech only command, saying "change the temperature setting of the air conditioner to 23 degrees" and failed instead of giving a simpler multimodal command, pressing a button twice and saying "lower the room temperature!" There were also ambiguous and *ungrammatical* commands such as a button press action followed by an utterance "lower it!"

A few users tried to modify or restate a command and failed while the robot was executing an action. Some users used words which are not included in the lexicon of RUNA. Some spoken messages were utterly clear and fluent but misrecognized by the speech recognition system. Finally, Table 8 shows some important comments from users.

Table 4 Modality choice for parameter values

type	value	duration	count	speech	default
turn	0-30 deg.	85	-	8	49
	31-60 deg.	17	-	18	-
	61-180 deg.	-	31	29	-
walk & move forward	0-9 steps	30	-	36	16
	10-50 steps	-	109	34	-
	0-99 cm	-	-	1	-
move forward	1-3 m	-	-	5	-
	"much"	-	-	1	-

Table 5 Number of commands given by users

action type	spoken	multimodal	button	total
walk/forward	56	174	-	230
backward	2	1	-	3
turn	92	147	-	239
sidestep	18	24	-	42
look	12	9	-	21
look around	10	0	-	10
switch on/off	45	-	-	45
query	15	-	11	26
settemp	18	-	-	18
lowertemp	1	4	-	5
repetition	-	-	53	53

Table 6 Success rates of parameter specification

modality	Value	Success rate (%)
duration	0-150[ms]	76.2
	700-1300[ms]	81.0
	1300-2000[ms]	47.6
count	2	100
	4	100

Table 7 Parameter specifications using a button

parameter	value	specifications
speed	fast	251
	moderate	81
	slow	9
direction	left	38
	right	75

Table 8 Users' comments

C1	It was difficult to specify a parameter value by the duration of a button press action.
C2	It was hard to measure the distance from the robot to a target in the camera image.
C3	It was difficult to specify an angle value verbally or nonverbally.
C4	It was difficult to command the robot to move forward and turn.
C5	It was difficult to change the temperature setting.
C6	I wish if I had more time to practice.
C7	I could not speak to the robot fluently.

V. DISCUSSION

The results show that the users understood the language well and mostly succeeded in giving commands during the tasks (Tables 3 and 5). They often chose a button press action and specified direction, speed, and temperature values without difficulty (Tables 5 and 7). They preferred to use buttons and thought that the robot was helpful (Q3 and Q4 in Table 3). Each user spoke only one to four words and well avoided speech recognition errors, slips of the tongue and wordy commands. We presume that it gets easier for users to specify action parameter values using a button and they will choose button press actions more often, since cognitively speaking it is easier to press a button than to generate verbal phrases.

It is obvious that they did not think that the language was a very natural or easy one to communicate with the robot (Q1 and Q2). Surprisingly, this result is worth than the previous study [5]. Although it is difficult to find the good reasons in the data, we can point out some disadvantages of the language which might have caused difficulties for the beginners. First, there are action parameter values, such as angles and walking steps, which are difficult to determine before giving a command (C2 in Table 8); many users chose short turns using a single press and 10-30 step walks using a multiple press possibly because they did not know the right values. They did not know how to turn the robot to a target or how much to move the robot forward to reach a target point. Therefore, robots should allow users to modify parameter values at any time. It would be better if one can send a cue to stop the robot at the right place. Second, they were unable to choose among angle or step values using a single press action (Table 6 and C1 and C3), none the less because they were given some time to practice. Although users may adapt, there should be ways around for beginners. Third, we suspect that it is difficult for beginners to specify two or more values in a single button press action, because in the previous study button press actions specified one or two

values while in this study users had to specify two or three values at once without omission. Therefore, it would be better if one can specify values one by one and leave out parameters which are not important. The language will be more natural if robots can infer users intentions based on the context. In fact, novice users often left out words whenever it was natural in daily communication. In addition, beginners may hesitate or restate commands, so life supporting robots must be able to deal with hesitant or halting spoken commands.

We think that the current version of RUNA is too complicated for novice users and has some defects which make the language a little awkward. The language should cover as many natural verbal commands as possible. We also suspect that the eight page document might have been a little confusing. We should not force users to learn what words and phrases they can say.

The results of our studies show that multimodal commands are advantageous in some ways and preferred by novice users of life supporting robots. We have realized a cost effective humanoid novice users can successfully direct to a position and make operate an air conditioner. The robot will be more user-friendly if one can communicate with it in a simpler, more natural, and flexible language.

ACKNOWLEDGMENT

This work was supported by KAKENHI Grant-in-Aid for Scientific Research (C) (19500171).

REFERENCES

- [1] Prasad R, Saruwatari H, Shikano K (2004) Robots that can hear, understand and talk. *Advanced Robotics* 18-5:533-564
- [2] Knapp ML, Hall JA (2010) *Nonverbal Communication in Human Interaction*. Wadsworth
- [3] Perzanowski D, et. al. (2001) Building a multimodal human-robot interface. *IEEE Intelligent Systems*, 16-1, pp. 16-21
- [4] Jurafsky D, Martin JH (2000) *Speech and Language Processing*. Prentice Hall
- [5] Oka T, Abe T, Shimoji M, Nakamura T, Sugita K, Yokota M (2008) Directing humanoids in a multi-modal command language. *The 17th International Symposium on Robot and Human Interactive Communication*
- [6] Oka T, Abe T, Sugita K, Yokota M (2009) RUNA: a multi-modal command language for home robot users. *Journal on Artificial Life and Robotics* 13-2: 455-459
- [7] Oka T, Abe T, Sugita K, Yokota M (2009) Success rates in a multimodal command language for home robot users. *Journal on Artificial Life and Robotics* 14-2:219-223
- [8] Oka T, Sugita K, Yokota M (2010) Commanding a humanoid to move objects in a multimodal language. *Journal on Artificial Life and Robotics* 15-1:17-20

A multimodal language to communicate with life supporting robots through a touch screen and a speech interface

T. Oka, H. Matsumoto, and R. Kibayashi

College of Industrial Technology, Nihon University, 1-2-1 Izumicho, Narashino, Chiba, 275-8575 JAPAN

Tel : 81-47-474-9693; Fax : 81-47-474-2669

oka.tetsushi@nihon-u.ac.jp

Abstract: This paper proposes a multimodal language to communicate with life supporting robots through a touch screen and a speech interface. The language is designed for untrained users who need support in daily lives from cost effective robots. In this language, the users can combine spoken and pointing messages in an interactive manner in order to convey their intentions to robots. Spoken messages include verb and noun phrases which describe intentions. Pointing messages are given when users finger-touch a camera image, a picture containing a robot body, or a button on a touch screen at hand, which convey a location in their environment, a direction, a body part of the robot, a cue, a reply to a query, or other information to help the robot. This work presents the philosophy and structure of the language.

Keywords: Life-supporting robot, multi-modal language, speech, touch screen, human-robot interaction

I. INTRODUCTION

It is expected that life supporting robots will help people in their daily lives in near future. Such robots must be easy to communicate with those untrained including elderly and disabled, and particularly those people must be able to learn how to communicate with their robot in a short period of time without much effort. On the one hand, although a conventional user interface using pull-down menus and buttons is a cost effective choice, it is difficult to build an easy-to-learn natural interface with life supporting robots that are given many kinds of tasks. Unless users learn many short-cuts, they have to go through a long sequence of choosing among menu items or buttons. On the other hand, it will be a long journey to realize robots that can speak and communicate like humans. Such robots will need sophisticated sensors to collect information and powerful computers to recognize different situations, perceive verbal and nonverbal messages from their counterpart, and disambiguate them based on various knowledge sources[1-3]. Therefore, we predict that it will take decades to develop affordable robots one can convey intentions to in the same way as to humans. Thus, in the near future we will need an *artificial language* for natural communication with robots.

In human face-to-face communications, nonverbal messages play a great role [4]. They can fill in gaps in verbal messages and convey some kind of information more efficiently than explicit words. Since robots are often given physical tasks, nonverbal messages are particularly important for smooth and efficient communication between humans and robots. For this reason, nonverbal and multimodal communications between humans and robots are subject of current research [5-7]. However, there are few arguments on multimodal or nonverbal *languages* between humans and robots.

RUNA [8-12] is the first multimodal language designed for communication between untrained people and cost effective robots. In the language, one can command a robot by combining a spoken message in Japanese and nonverbal message such as a hand gesture, body touch, and button press action. In some recent user studies, novice users were able to successfully command a robot and achieve some tasks without a long training. Many of them preferred multimodal commands to single modal spoken commands. The results of these studies imply that more experienced users would be able to command robots combining verbal and nonverbal messages more efficiently and successfully. In addition, since the language is designed so that one can give a command on a context free basis without ambiguity, one can build a responsive command interpreter at low cost.

Although most of the commands by the novice users were successful, there were some human errors as well as system errors. Many of them failed to give spoken commands with many words which specify a robot action in detail. It looks also difficult for beginners to convey multiple values in a single nonverbal message. For example, those users who commanded a robot simultaneously conveying a speed, direction, and angle in a gesture or button press action thought that it was harder to communicate in the language than the other users. Therefore, the efficiency of RUNA seems to be an obstacle for beginners.

Another problem of the current version of RUNA is that it does not have a means to point at an object or a location. For this reason, users had to direct a robot to a location or an object in an indirect manner using spoken words, buttons and gestures. Direct pointing at locations and objects would make it much easier to convey intentions to life supporting robots.

Based on the advantages and disadvantages of RUNA, this paper discusses a multimodal language in which one can communicate with life supporting robots

through a speech interface and a touch screen, both of which are common and not expensive in recent years. The language allows users to communicate with a robot more slowly and in a more interactive manner than RUNA. Using a touch screen at hand, they can point at a location or an object in a camera image and send cues, pieces of advice and parts of intentions to their robot by tapping on a button. In the following sections, we describe the principles and structures of the language.

II. COMMUNICATION

The multimodal language proposed in this paper will be developed so that untrained novice users should be able to communicate with a life supporting robot without taking much time to learn about the language and their robot. Based on the results of studies of RUNA, we predict that an affordable user friendly life supporting robot will be realized if we develop a good multimodal language. Above all, a touch screen and a speech interface should provide a good means for users of such a robot. For this reason, the language is strategically-designed to utilize such devices. Figure 1 depicts a touch screen showing windows for interactions in the language. The camera image window shows real images from a camera on the robot in real time. Some buttons appear in the button window, which guide users to convey intentions. Users may point at a location or a body part of the robot and use gestures on the screen. The language is designed based on the following *laws*:

1. Users must be able to convey their intentions in an interactive manner.
2. Users must be able to send messages at any time.
3. Users must be allowed to speak in as natural a way as possible.
4. A touch screen must help users as much as possible.
5. Users must be able to point at 3D positions or locations in their environment without difficulty.
6. Users must be able to point body parts of their life supporting robot.
7. Whenever necessary, buttons must appear on the touch screen.
8. Users must be able to use gestures to convey their intentions.
9. The touch screen must display messages to help users and realize smooth communications.
10. Robots must send spoken messages to help users.

III. MULTIMODAL LANGUAGE

A. Semantic Representation

Table 1 exemplifies intensions users can convey to robots in the language. Intensions are identified by their type and parameter values. For instance, an intension to start a robot moving forward slowly is formally represented by a type *move forward* and a speed value *slow*. The robot must identify the type and parameter

value by interpreting verbal and nonverbal messages from the user. In our language, users can leave out optional parameter values if they do not care about them; if one does not care about the speed, one does not need mention it. As seen in Table 1, all the types of intension belong to one of the classes, such as *action*, *cue*, and *advice*.

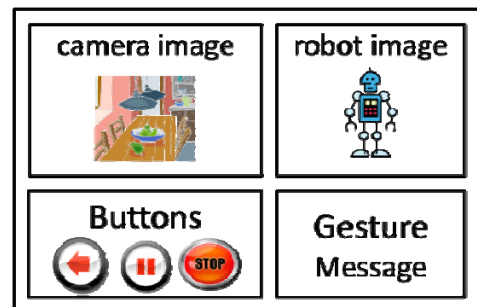


Fig. 1 Touch Screen Windows

Table 1 Intension Representation

Class	Type	Parameters
<i>action</i>	<i>move forward</i>	speed(optional)
	<i>turn/move aside</i>	direction(mandatory) speed(o)
	<i>go to</i>	destination(m) speed(o)
	<i>come to</i>	destination(o) speed(o)
	<i>turn to</i>	target position(m)
	<i>pick up</i>	position(m) size(o) hand(o)
	<i>bring</i>	position(m) size(o) hand(o)
	<i>place</i>	position(m)
	<i>push / pull</i>	position(m) size(o) hand(o)
	<i>look</i>	target position(m)
	<i>grasp</i>	hand(m) size(o) speed(o)
	<i>release</i>	hand(m) speed(o)
	<i>rotate wrist</i>	hand(m) direction(m) speed(o)
	<i>move hand</i>	direction(m) hand (o)
	<i>move object</i>	position(m) destination(m) size(o)
	<i>throw away</i>	position(m) destination(m) type(o) size(o)
	<i>vacuum- clean</i>	room(m) location(o) area(o) mode(o)
	<i>device op</i>	device (m) operation(m) value(m)
	<i>report</i>	content(m)
	<i>sing / dance</i>	genre(o)
<i>cue</i>	<i>start stop</i>	
	<i>pause</i>	
	<i>resume</i>	
	<i>cancel ok</i>	
<i>advice</i>	<i>subgoal</i>	position(m)
	<i>obstacle</i>	position(m)
	<i>landmark</i>	position(m) label(m)
	<i>bail out</i>	direction(o)

B. Interpretation

Since inexperienced users may not be able to express their intensions without effort, our language allows them to send verbal and nonverbal messages that contain partial information. In other words, one can inform a robot of the type and mandatory and optional parameters of their intension bit by bit in separate

messages (Fig. 2). For instance, a spoken message “turn” brings a *left button* and a *right button* on the touch screen to help the user to convey a direction. The robot also sends spoken messages and screen messages to inform the user of what has been received and what information is needed. Unmentioned parameter values are inferred by the robot based on the default values and context. In addition, one can restate a type or parameter value at any time before the robot starts its action.

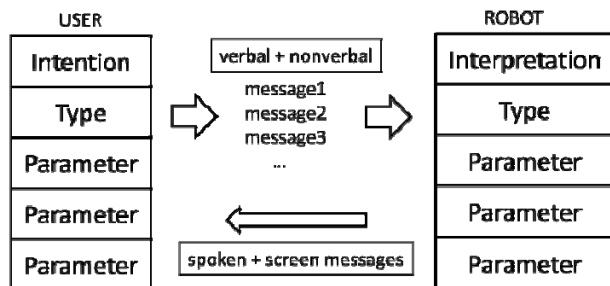


Fig. 2 Communication of Intentions

After conveying a complete intension, namely, the type and mandatory parameter values, one can cue the robot to start by sending a spoken or pointing message. A cancel cue removes received information and stops the current action if being executed. While the robot is executing an action, the user can send a cue, an overriding parameter value, or advice to the robot.

Table 2 Grammar rules

Rule	Description
$S \rightarrow \text{INTENTION}$	intention
$S \rightarrow \text{INTENTION_PARAMS}$	parameters
$S \rightarrow \text{CUE}$	cue
$S \rightarrow \text{ADVICE}$	advice
$\text{INTENTION} \rightarrow \text{IP1 IT11}$	intention type and parameters
$\text{INTENTION_PARAMS} \rightarrow \text{IP1}$	parameters(type1)
$\text{IP1} \rightarrow \text{SPEED SHORTSLIENCE}$	speed + short silence
$\text{IP3} \rightarrow \text{TO_LOCATION}$	location
$\text{TO_LOCATION} \rightarrow \text{HERE TO}$	to here
$\text{TO_LOCATION} \rightarrow \text{KITCHEN}$	the kitchen
$\text{TO_LOCATION} \rightarrow \text{THIS DOOR TO}$	to this door
$\text{IT1} \rightarrow \text{MOVEFORWARD}$	move forward
$\text{CUE} \rightarrow \text{START}$	cue to start action

IV. SPOKEN MESSAGES

A spoken message of our language is a sentence, phrase, or word in Japanese to partially convey an intension that can be represented as in Table 1. A sentence includes a word or phrase denoting an intension type, so one can specify the type and one or more parameter values in a sentence like “turn to the left slowly.” It is also possible to send a single phrase message that contains only a parameter value or type. Thus, a beginner can convey an intension bit by bit slowly. It is also easy to modify parameter values that have been already sent.

The lexicon of the language includes deictic words

such as *kono/kore* (this) and *koko* (here). For example, one may give commands like “place the bottle *here*,” “turn to *this* quickly,” “pick up *this can*,” or “move *this here*.” Although such words certainly do not help robots to determine parameter values, one can command a robot in a natural manner by combining a pointing message and such a word.

Table 2 shows some examples of grammar rules of our new spoken language. The grammar is similar to RUNA’s grammar, but it includes more deictic expressions and less numerical expressions.

V. POINTING MESSAGES

Pointing messages are such messages that are sent through a touch screen. A touch on a camera image conveys a parameter value, e. g. the position of an object or a location in the robot’s view. One can touch a button on the screen to send a cue, a parameter value, or a piece of advice. For instance, a touch on a picture of the robot’s body creates a nonverbal message containing a location or a body part.

A cue can be sent by a touch on a cancel, start, stop, pause, or resume button. Users can send a cancel cue and restart commanding at any time, terminate or interrupt an ongoing action, and resume an interrupted action by touching a button on the screen. After the type of an intension is identified in a spoken message, buttons appear on the screen to allow the user to choose among parameter values. The user can modify parameter values at any time before the action terminates.

VI. 2D GESTURES

Finger gestures on a touch screen can convey contours, trajectories, directions, speeds, lengths, heights, angles, locations, and symbols. First, using gestures on a camera image and deictic expressions in spoken messages, one can inform a robot a safe route to a location, a hand trajectory to an object, the contour and size of an object, a direction, etc. Next, 2D gestures on a robot picture help users to intuitively communicate directions, speeds, lengths, angles, body motions, heights, etc. Moving a finger across the body of the robot with a spoken message “put the cup up” is quite a natural way to command a robot. Finally, symbolic gestures substitute for or emphasize spoken words. We expect that using these gestures users will be able to communicate more naturally.

VII. INTERACTIONS

This section illustrates some example of interactions between a robot and its user.

Interaction A (moving to a location)

U: Turn...
R: Left or right? (Displays buttons)
U: (Touches on the “right button”)
R: OK! (Starts moving and displays new buttons)
U: (Touches on the “slow” button)
R: (Slows down)

U: (Touches on the “stop” button)
R: OK!
U: (Points at the camera image.)
R: (Displays a mark on the point.)
U: Go here!
R: Shall I go here? (Displays a “start” button)
U: (Touches on the “start” button.)
R: OK! (Starts moving and displays buttons.)

Interaction B (moving an object to a location)

U: (Points at an object)
R: (Displays a mark on the object)
U: (Points at a location)
R: (Displays a mark at the point)
U: Move this here!
R: Shall I move this here? (Displays a start button)
...

Interaction C (throwing away a bottle)

U: (Points at a bottle on the floor)
U: Uh, this bottle.
R: This bottle? (Displays a mark)
U: Throw it away!
R: Shall I throw this away? (Displays a “start” button)
...

Interaction D (changing the temperature setting)

U: The, uh, air conditioner...
R: Shall I operate the air conditioner? (Displays buttons)
U: (Touches on the “temperature” button)
R: (Displays the current temperature setting and buttons to change the temperature)
U: (Changes the temperature and cues OK)

VIII. DISCUSSION

In general, direct pointing and speech are among the easiest input methods for most users. Our language allows beginners, who cannot efficiently combine pointing gestures and speech, to convey their intentions slowly and interactively. Using key words and phrases in Japanese, one can inform a robot of the type of an intention without using a keyboard shortcut or selecting among menu items, and then convey parameter values guided by the robot. Experienced users of our language will be able to achieve their goals more quickly by sending spoken and nonverbal messages.

Needless to say, it is difficult to specify locations, objects, and body parts without pointing at or touching them. Spoken commands to life supporting robots tend to be wordy and tongue-twisting [12, 13]. In addition, the use of nonverbal messages instead of verbal messages will often decrease cognitive loads.

IX. SUMMARY AND FUTURE WORK

This paper proposed a multimodal language and a user interface for untrained users of life supporting robots. The language is designed based on experiences

and results of some earlier studies on RUNA, and allows beginners to convey their intentions on a more interactive basis. A touch screen will help them to select among options and interact with a robot in an intuitive manner. At this moment, we are developing a test bed for user studies of the new multimodal language. Our future work include user studies of life supporting robots based on the language, design of a multimodal language integrating speech, 3D gesture, body and screen touch, and other modalities.

ACKNOWLEDGMENT

This work was supported by KAKENHI Grant-in-Aid for Scientific Research (C) (22500179).

REFERENCES

- [1] Prasad R, Saruwatari H, Shikano K (2004) Robots that can hear, understand and talk. *Advanced Robotics* 18-5:533-564
- [2] Jurafsky D, Martin JH (2000) *Speech and Language Processing*. Prentice Hall
- [3] Bos J, Oka T (2007) A spoken language interface with a mobile robot. *Journal of Artificial Life and Robotics* 11-1:42-47
- [4] Knapp ML, Hall JA (2010) *Nonverbal Communication in Human Interaction*. Wadsworth
- [5] Perzanowski D, et. al. (2001) Building a multimodal human-robot interface. *IEEE Intelligent Systems*, 16-1, pp. 16-21
- [6] Iba S, Paredis CJJ, Adams W, Khosla PK (2004) Interactive multi-modal robot programming, *The 9th International Symposium on Experimental Robotics (ISER '04)*, pp. 503-512
- [7] Igarashi T (2008) User Interface for Robots, *Journal of Robotics Society of Japan*, Vol. 28, No. 3, pp.246-248 (in Japanese)
- [8] Oka T, Abe T, Shimoji M, Nakamura T, Sugita K, Yokota M (2008) Directing humanoids in a multi-modal command language. *The 17th International Symposium on Robot and Human Interactive Communication*
- [9] Oka T, Abe T, Sugita K, Yokota M (2009) RUNA: a multi-modal command language for home robot users. *Journal on Artificial Life and Robotics* 13-2: 455-459
- [10] Oka T, Abe T, Sugita K, Yokota M (2009) Success rates in a multimodal command language for home robot users. *Journal on Artificial Life and Robotics* 14-2:219-223
- [11] Oka T, Sugita K, Yokota M (2010) Commanding a humanoid to move objects in a multimodal language. *Journal on Artificial Life and Robotics* 15-1:17-20
- [12] Oka T, Abe T, Sugita K, Yokota M (2011) User study of a life supporting humanoid directed in a multimodal language. *The 16th International Symposium on Artificial Life and Robotics (AROB11)*
- [13] Oka T, Sugita K, Yokota M (2009) Spoken command language to direct a robot cleaner. *FAN2009*

Some Consideration on User Interface Switching Functions for the Weaker at IT

Shinichi Inenaga¹, Kaoru Sugita², Tetsushi Oka³, Masao Yokota²

¹*Graduate School of Fukuoka Institute of Technology, 3-30-1, Wajiro-Higashi, Higashi-ku, Fukuoka, 811-0295, Japan*

²*Fukuoka Institute of Technology, 3-30-1, Wajiro-Higashi, Higashi-ku, Fukuoka, 811-0295, Japan*
Nihon University College of Industrial Technology, 1-2-1 Izumicho, Narashino-shi, Chiba 275-8575 Japan

Tel : 81-92-606-4965; Fax : 81-92-606-4965

¹mgm08004@bene.fit.ac.jp, ²{sugita, yokota}@fit.ac.jp, ³oka.tetsushi@nihon-u.ac.jp

Abstract: We have already proposed a new concept of 'universal multimedia access' intended to narrow the digital divide by providing appropriate multimedia expressions according to users' (mental and physical) abilities, computer facilities and network environments. Previous works, have evaluated some types of multimedia user interfaces according to users' (mental and physical) abilities, computer facilities and network environments. In this paper, we discuss the user interface switching functions.

Keywords: Multimedia, User Interface, Switching Functions.

I. INTRODUCTION

Recently, immense multimedia information has come to be exchanged on the Internet, where 3DCG, video, image, sound, and text are involved in various circumstances with terminal devices, networks and users different in their competences and performances. This fact may easily lead to 'digital divide' so called unless any special support is given to the weaker.

The universal design concept is proposed to support handicapped people in their social activities¹. In the computer science field, the universal web2 has been proposed to evolve this concept. However, this does not support to switch the contents, media and its quality of service (QoS) function to work the devices and network environments in their full performances. On the other hand, many studies about the QoS function proposed to optimize the video quality for priorities on users' requests³. These studies focused on performances of devices and network environments but neither users' abilities nor contents. Of course, there were also several studies on 'universal multimedia access (UMA)' but they could not narrow the digital divide because they concerned 'content switching' only⁴.

Considering this fact, we have already proposed a new concept of UMA and its switching functions⁵ intended to narrow the digital divide by providing appropriate multimedia expressions according to users' (mental and physical) abilities, computer facilities and network environments. In this paper, we redefine these

switching functions and propose a concept of user adaptive interface for UMA.

II. UNIVERSAL MULTIMEDIA ACCESS

The digital divide is caused by the differences in users' personal competences, computer facilities and network environments with such detailed items as follows.

(1) Personal competence: sight ability, hearing ability, handling ability, language ability, computer skill and culture,

(2) Computer facility: processing power, resolution, color quality, sound quality and battery life,

(3) Network environment: bandwidth availability, specification and transfer mode.

Therefore, multimedia information is necessarily accompanied by switching user interface, media and QoS parameters reflecting these differences. Here, we present a new approach to UMA for handicapped people to work their devices and network environments in full performances. Our purpose is exclusively to develop a new mechanism for switching appropriately user interfaces, media and QoS parameters based on such a concept as shown in Fig.1.

III. SWITCHING FUNCTIONS

UMA is to selectively provide three kinds of switching function, namely, user interface switching

(UIS), media switching (MS) and QoS switching (QS). Fig.2 shows these switching functions working as follows:

(SF1) UIS: switch to user interfaces (UI) appropriate for users' competences and display devices,

(SF2) MS: switch to media appropriate for users' competences, performances of terminal devices and networks,

(SF3) QS: control media qualities appropriate for users' competences and terminal devices.

These functions are applied in the ascending order (from SF1 to SF3) at beginning to play multimedia information or in the descending order at playing.

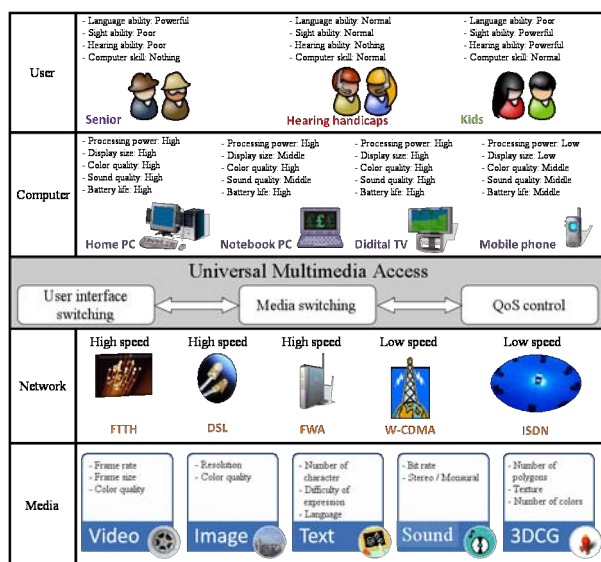


Fig.1. Universal Multimedia Access

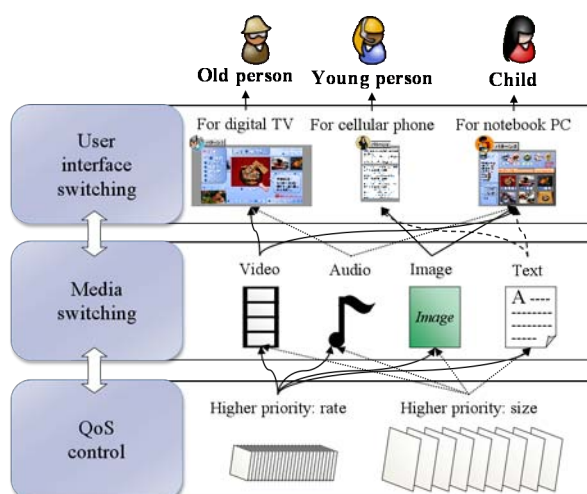


Fig.2. Switching Functions

IV. USER INTERFACE SWITCHING

UIS sets up the following items according to computer skill and computer facilities.

(U1) Writing style appropriate for language ability,

(U2) UI type and annotation option appropriate for computer skill,

(U3) Media size, font size, number of media and number of characters appropriate for display device size.

Additionally, I/O function is reflected by the users' disability.

1. Operations and Media

UI provides for operations and media according to computer skill and computer facilities. Computer skill is graded to select operation as follows.

(G0) No Knowledge about Computer: Unable to operate any computer functions.

(G1) Computer Beginner: Able to startup an application software such as Web browser and play media.

(G2) General Web User: Able to operate general Web pages and select to play a media.

(G3) Internet Expert: Able to use efficiently interactive online applications such as a search engine.

On the other hands, computer facilities are composed by some components and classified to 4 levels (None, Low, Middle, High) to setup media.

2. User Interface

A. Template for User Interface

UI is different at each level depending on computer skills and facilities. Considering such differences, 12 types of UI are expressed in a matrix as shown in Table.1.

Computer beginners are supposed to select Broadcast Operation (BO) so as to play media according to the program without complicated operations. The user can get information just like watching TV because it is not necessary to operate any application software fundamentally. Choice Operation (CO) is intended for general Web users so as to select media only. But it takes user much time to select one from a lot of media. Search Operation (SO) is supposed to support Internet experts by providing a keyword search function.

Low power terminals are supported to play AA and text with only low graphics power and narrow bandwidth of network. Middle power terminals are to

display contents such as combinations of still image and text. High power terminals play video requiring not only high power CPU but also high power Graphic device.

B. Layout of Media

A layout is used to put media on UI and to specify the display region, display size and number of media for resolution of the terminal device and the media. Typical resolutions in terminal devices are shown in Fig.3 and the numbers of available media are affected by these resolutions. These relations enable a layout to specify the display position according to the display size and the number of media. Typical devices can display the number of media as follows:

(Ex.B1) Cellular phone (Resolution: 240 x 320 [pixel])

Character (10.5pt): 374

Image (96 x 120 [pixel]): 6

Video (QCIF: 176 x 144 [pixel]): 1

(Ex.B2) PDA (Resolution: 800 x 600 [pixel])

Character (10.5pt): 2394

Image (96 x 120 [pixel]): 40

Video (QCIF: 176 x 144 [pixel]): 1

(Ex.B3) Notebook computer (Resolution: 1024 x 768 [pixel])

Character (10.5pt): 3942

Image (320 x 240 [pixel]): 9

Video (DV: 720 x 480 [pixel]): 1

(Ex.B4) Desktop computer (Resolution: 1280 x 1024 [pixel])

Character (10.5pt): 6643

Image (320 x 240 [pixel]): 16

Video (720p: 1280 x 720 [pixel]): 1

C. Expression of Media

An expression is to facilitate the options of writing style, Kana-Kanji conversion, alternative media and language in order for better readability.

(Ex. 1) For children (supposed to be lower in language ability): simple Kana text with notes

(Ex. 2) For aged person (supposed to be higher in language ability): replacement of loan words by Japanese traditional words

In addition, cross-media switching, for example text to video conversion, has been provided for better

readability, including such functions as to filter out harmful media contents.

3. Approach to User Interface Switching

In order to introduce UIS, we focused on CO because willing users are supposed to perform this operation driven by necessity. On the other hand, they will not use any operation without CO. From this point of view, CO is applied to UIS switching from a current UI to desired one and controlling types of UI with buttons just like TV remote control.

V. Implementation

Our ideas were implemented as Flash applications running on a web browser as shown in Fig.4. These applications conduct a person the way from the Fukkodaimae station to Fukuoka Institute of Technology providing abovementioned 12 UIs. These UIs can be switched to a desired one using 'software remote controller (SRC)' as shown in Fig.5. SRC is supposed for general Web users and over so as to select a UI with simple button operation because other users would not like complicated operations.

Table 1. User Interface According to User's Operation and Types of Media

Operation	Media			
	AA (Ascii Art)	Text	Image&Text	Video
Broadcast	- No operation - Displaying a AA according to the program	- No operation - Displaying a text according to the program	- No operation - Displaying images and text according to the program	- No operation - Playing a video according to the program
Choice	- Selection - Displaying a AA according to the program	- Selection - Displaying a text according to the program	- Selection - Displaying selected images and text	- Selection - Playing a selected video
Search	- Keyword search - Displaying a AA according to the program	- Keyword search - Displaying a text according to the program	- Keyword search - Playing searched images and text	- Keyword search - Playing a searched video

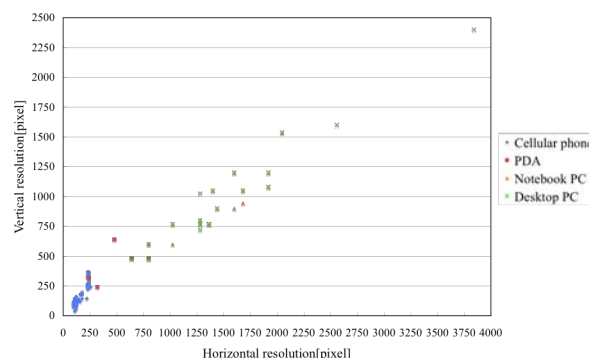


Fig.3. Resolution of Terminal Device

Operation	AA	Text	Image & Text	Video
Broadcast		福工大前駅から福岡工業大学のD棟まで案内		
Choice		福岡工業大学の案内 福工大前駅から福岡工業大学の校門まで案内 福岡工業大学の校門からA棟まで案内 福岡工業大学の校門からB棟まで案内 福岡工業大学の校門からC棟まで案内 福岡工業大学の校門からD棟まで案内		
Search		福岡工業大学の案内 福工大前駅から福岡工業大学の校門まで案内 福岡工業大学の校門からA棟まで案内 福岡工業大学の校門からB棟まで案内 福岡工業大学の校門からC棟まで案内 福岡工業大学の校門からD棟まで案内		

Fig.4. Implemented User Interfaces

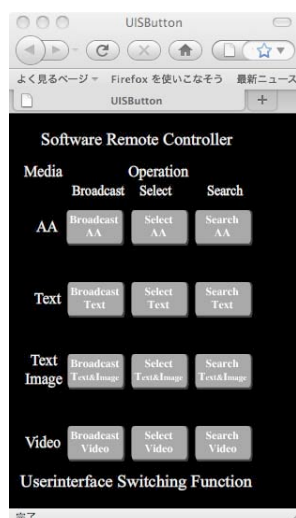


Fig.5. Software Remote Controller

VI. CONCLUSION

In this paper, we discussed the UIS and its UI appropriate for computer skills and facilities. Especially, we introduced SRC into UIS for simple button operation. SRC is simple solution to switch a desired UI employing UIS function. Currently, we are evaluating SRC and its UI. In near future, we will construct some types of contents for evaluating UIS and other switching functions for UMA.

REFERENCES

- [1] Ronald L. Mace, Graeme J. Hardie, and Jaine P. Place (1991), Accessible Environments: Toward Universal Design, The Center for Universal Design, North Carolina State University, USA
- [2] Kazuhiko Yamazaki (2001), Achievement of universal Web (1) (in Japanese). Design study research 48:330-331
- [3] Mohan, R, Smith, J.R and Chung-Sheng Li (1999), Adapting multimedia Internet content universal access, IEEE Multimedia Transactions 1(1):104-114
- [4] Fernando Pereira and Ian Burnett (2003), Universal Multimedia Experience for tomorrow, IEEE Signal Processing Magazine, IEEE 20(2): 63-73
- [5] Y. Maeda, K. Sugita, T. Oka, and M. Yokota (2008), Proposal of a New Concept of Universal Multimedia Access, Proc. 13th International symposium on ARTIFICIAL LIFE AND ROBOTICS (AROB 13th '08), OS7-6.
- [6] Y. Maeda, E. Tsujimura, K. Sugita, T. Oka, and M. Yokota (2009), Some consideration on user adaptive interface for universal multimedia access, Proc. 13th International symposium on ARTIFICIAL LIFE AND ROBOTICS (AROB 14th '09), OS13-5.
- [7] Y. Maeda, K. Sugita, T. Oka, M. Yokota (2009), Evaluation of some user interfaces for universal multimedia access, Proc. the 19th Intelligent System Symposium (FAN2009), F3-3:120-124.

Signal transmission in multilayer asynchronous neural networks

Wataru Kobayashi¹, Makito Oku², Kazuyuki Aihara^{1,2}

¹Graduate School of Engineering, The University of Tokyo, Tokyo 153-8505, Japan

²Graduate School of Information Science and Technology,
The University of Tokyo, Tokyo 153-8505, Japan
(Tel : +81-3-5452-6697; Fax : +81-3-5452-6694)
(Email: kobayashi@sat.t.u-tokyo.ac.jp)

Abstract: It is believed that common input to nearby neurons leads to their synchronous spiking. However, recent studies have shown that recurrent neural networks can generate an asynchronous state characterized by low mean spiking correlations despite substantial amounts of shared input. The asynchronous state is generated by the interaction of excitatory and inhibitory populations, which is called active decorrelation. Here, we investigate the advantage of the active decorrelation on signal transmission in multilayer neural networks. The results of numerical simulations show that the active decorrelation is suitable for transmission of rate code because it can suppress the layer-by-layer growth of correlation.

Keywords: Neural Networks, Asynchronous States, Active Decorrelation.

1 Introduction

It is thought that brains process information by the temporal and spatial patterns of neuronal firing. Previous studies showed that synchronous firing plays functional roles such as binding information. However, a recent experiment [1] has shown that the correlation of neuronal firing in monkey's V1 is extremely low, and a theoretical study[2] has proposed the mechanism that can generate an asynchronous state although neurons share a large amount of input. The asynchronous state is generated by the effect of balanced excitatory and inhibitory populations, which is called active decorrelation. In this study, we investigate the advantage of the active decorrelation for information processing by numerical simulations. We investigate how the active decorrelation improves transmission of rate code in multilayer neural networks.

2 Methods

2.1 Model Description

As mentioned earlier, we consider multilayer neural networks that transmit rate code (see Fig. 1). This network structure corresponds to the hierarchical organization in the real brains. For example, visual information is transmitted through retina, LGN, V1, V2, and so on. Although it is known that brains send top-down signals to process information effectively, here, we do not consider such feedback connections for simplicity.

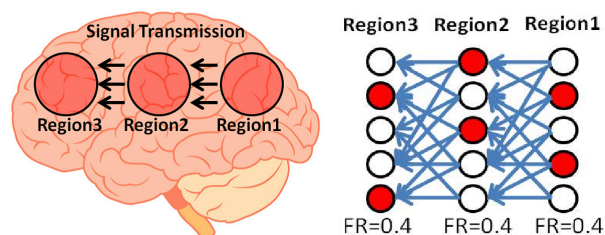


Figure 1: Transmission of rate code in a multilayer network. FR, firing rate.

2.1.1 Neuron Model

Here, we use McCulloch-Pitts model[3], which is the simplest and popular neuron model. The model outputs 1 if the sum of input from other neurons exceeds the threshold θ . If not, it outputs 0. The model's equation can be described as follows:

$$x_i(t+1) = 1[\sum_j w_{ij}x_j(t) - \theta], \quad (1)$$

where w_{ij} is the connection strength from j th neuron to i th one, θ is the threshold, and $1[u]$ is the step function:

$$1[u] = \begin{cases} 1 & (u \geq 0) \\ 0 & (u < 0) \end{cases}. \quad (2)$$

2.1.2 Network

The network architecture of our model is shown in Fig. 2. X is external input consisting of excitatory neurons, E denotes an excitatory population, and I denotes an inhibitory population. The number of neurons in each populations is $N=1000$, and neurons are connected with probability $p=0.2$. The layers correspond to the regions in Fig. 1. The inter-layer connections of the model in Fig. 2 are only from excitatory populations because it is known anatomically that axons of excitatory neurons are longer than those of inhibitory neurons. Axons mean a part of neurons which play a role of connection. Detail of parameter settings are the same to the Renart's study[2].

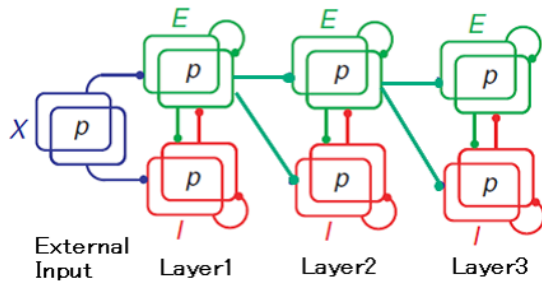


Figure 2: Schematic of the network architecture.

2.2 Evaluation

2.2.1 Rate Code

Rate code is one of the important information representations in brains. In this study, we consider mean firing rate that is the number of firing neurons divided by the population size. So the range is $[0,1]$. In other words, a neuronal population represents one scalar value. Here, we investigate the efficiency of transmission of rate code signals when the active decorrelation works effectively (active decorrelation ON) and when it does not (active decorrelation OFF).

2.2.2 Correlation

We evaluate whether the system is in synchronous states or in asynchronous states by calculating correlation of neuronal activities in each layer. The correlation is calculated as follows:

$$r_{ij} = \frac{\sum_{t=1}^T (\mathbf{E}_i(t) - \bar{\mathbf{E}}_i)(\mathbf{E}_j(t) - \bar{\mathbf{E}}_j)}{\sqrt{\sum_{t=1}^T (\mathbf{E}_i(t) - \bar{\mathbf{E}}_i)^2} \sqrt{\sum_{t=1}^T (\mathbf{E}_j(t) - \bar{\mathbf{E}}_j)^2}}, \quad (3)$$

where r_{ij} is the correlation between i th neuron and j th neuron, \mathbf{E} is the time series of neuronal activities represented by 1 (firing) and 0 (rest). $\bar{\mathbf{E}}_i$ means the time average of

$\mathbf{E}_i(t)$. We consider the average of r_{ij} over all the pairs in a population as the correlation of the population.

2.2.3 Time Response

Vreeswijk et al.[4] mentioned that the response time of the population rates is shorter than the time constant of single neurons in the balanced state. Here, we check the phenomenon by changing the firing rate of external input m_X according to a sine curve and measuring the lag of the peaks of population rates between layers.

3 Simulation Results

3.1 Transmission of Rate Code

The response against sine input is shown in Fig. 3. Each line means each layer's firing rate. The active decorrelation is ON in Fig. 3 (A) and OFF in Fig. 3 (B). We change the parameter τ , which is the relative time constant of inhibitory neurons against excitatory ones, to switch between active decorrelation ON and OFF. τ is set to 1 in Fig. 3 (A) and 2 in Fig. 3 (B). The system transmits rate code clearly when the active decorrelation is ON.

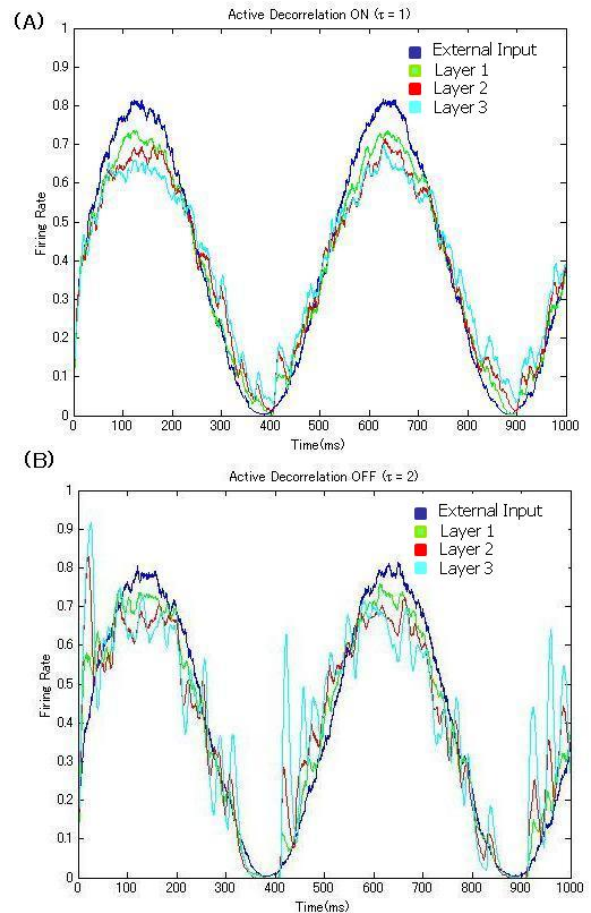


Figure 3: Time series of the firing rate of each excitatory population in response to a sinusoidal input.

The correlation and raster plots are shown in Fig. 4 where external input m_X is fixed to 0.1 to check whether the active decorrelation creates an asynchronous state. The blue dots in Fig. 4 represent neuronal firing. Vertical stripes mean synchronous firing of neurons. You can see that layer 3 is in a highly synchronous state when the active decorrelation is OFF. The active decorrelation suppresses the layer-by-layer growth of correlations, and it is suitable for transmission of rate code.

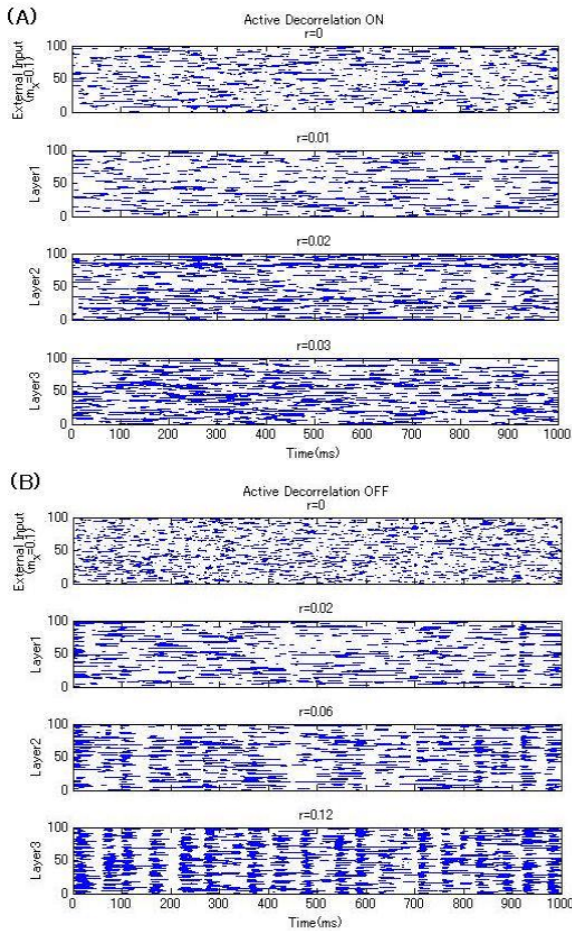


Figure 4: Raster plots and the correlations of neuronal firing in multilayer networks.

By carefully checking Fig. 3 and Fig. 4, you can find some features. In Fig. 3(A), the rough profile of the sine curve is transmitted well but the correct values are not. For example, the peaks of the firing rates are about 0.8 in external input, 0.7 in layer 1, 0.65 in layer 2 and 0.60 in layer 3. It is thought that the values of the firing rates decay because of the deviation from linearity in the input-output relationship, as shown in Fig. 5.

The intersection is about 0.5 in Fig. 5. It is the equilibrium point because signals converge to the intersection when they are transmitted through layers repeatedly. It is easy to check if the intersection is stable or not. We denote the value of the intersection as a and the response curve of layer 1 as f . Here, a is about 0.5, and f is the red line

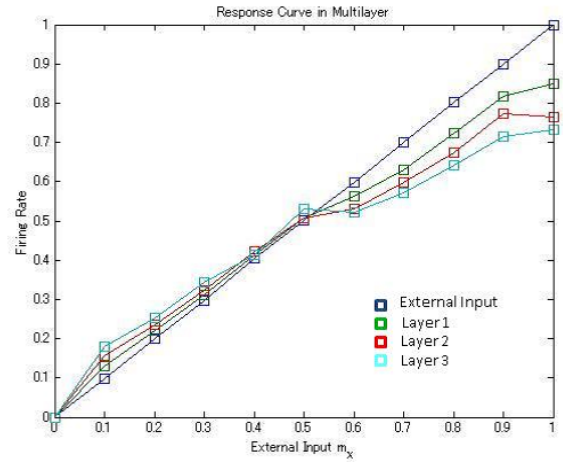


Figure 5: Firing rates in excitatory populations against external input. The active decorrelation is ON.

in Fig. 5. If $f'(a) > 1$, a is an unstable fixed point, and the firing rate converges to 0 or 1 depending on the initial condition. If $f'(a) < 1$, a is a stable fixed point, and the firing rate converges to a . For the above reason, the only perfect linear system can transmit rate code in infinite layers, and such a perfect one can not exist. So what we can do for good transmission of rate code is to make the response curve closer to linear one. This problem of response curves between layers has been mentioned by Litvak[5].

In this paper, we have shown two problems to transmit rate code in multilayer networks. One is the layer-by-layer increase of correlation. The other is the nonlinearity in the response curves. We have shown that the former problem can be resolved by the active decorrelation.

3.2 Time Response

We investigate another advantage of the active decorrelation—time response. As the frequency of external

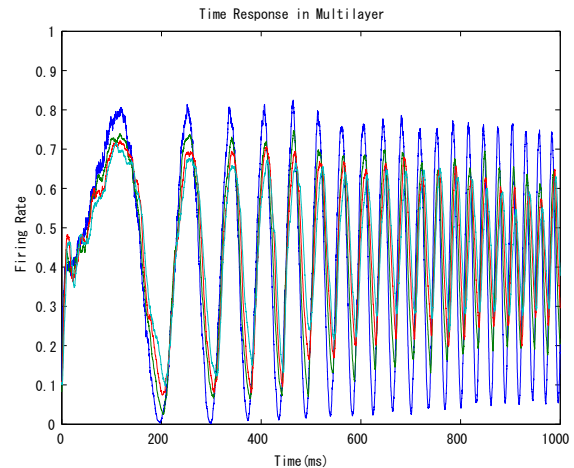


Figure 6: Responses to a sinusoidal input with increasing frequency. The active decorrelation is ON.

input m_X increases in Fig. 6, the time lag becomes apparent. You can see the lag is several milliseconds between successive layers in Fig. 7 which is an enlarged view of Fig. 6. In this model, the time constant of one excitatory neuron is 10 ms, so the populations track the signal changes quickly as compared with the time constant. A previous study[4] has shown theoretically that such a quick tracking occurs in balanced states. The study showed that the lag decreases in proportion to $1/\sqrt{K}$, where K is the number of connections per neuron. We have shown that such a quick tracking also occurs in multilayer networks.

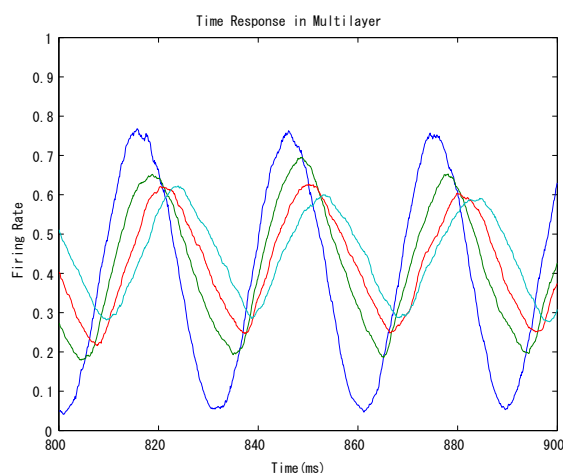


Figure 7: An enlarged view of Fig. 6 in the range from 800 to 900 ms.

3.3 Characteristic Frequency

Another point that we can find from Fig. 3 and Fig. 4 is that a synchronous network has a characteristic frequency. In Fig. 4(B), synchronous firing which is represented as vertical stripes is observed in layer 3, and it seems to be periodic. We set external input to various frequencies in the situation of active decorrelation "OFF" ($\alpha = 2$) to check its periodicity. An interesting phenomenon like sympathetic vibration is observed in Fig. 8. It is not observed against higher frequencies. So we can conclude that the network with the active decorrelation OFF has a characteristic frequency. It can play a role as oscillator in vivo. Further parameter analysis would be required to check whether the phenomenon occurs broadly.

4 Conclusion

We have investigated the advantage of the active decorrelation for transmission of rate code in multilayer neural networks. However, the active decorrelation seems incompatible with other codes such as temporal code. So it can be thought that the brains use both synchronous and asynchronous states depending on the situation and areas of the

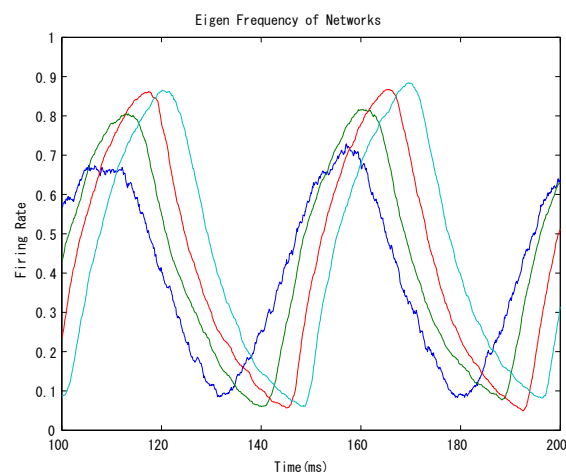


Figure 8: Sympathetic vibration in a synchronous network. The active decorrelation is OFF.

brain. We have also observed the existence of characteristic frequencies in synchronous networks. The networks seem to have a range of resonant frequencies, and it is our future problem to check the generality of the phenomenon.

Acknowledgements

This research is partially supported by the FIRST program, Grant-in-Aid for Scientific Research (A) (20246026) and Grant-in-Aid for JSPS Fellows (21-937) from JSPS.

References

- [1] Alexander S. Ecker, Philipp Berens, Georgios A. Kelliris et al., "Decorrelated neuronal firing in cortical microcircuits", *Science* 327, 584 (2010).
- [2] Alfonso Renart, Jaime de la Rocha, Peter Bartho et al., "The asynchronous state in cortical circuits", *Science* 327, 587 (2010).
- [3] Warren S. McCulloch and Walter Pitts, "A logical calculus of the ideas immanent in nervous activity", *Bulletin of Mathematical Biology* 5(4), 115 (1943).
- [4] C. van Vreeswijk and H. Sompolinsky, "Chaos in neuronal networks with balanced excitatory and inhibitory activity", *Science* 274, 1724 (1996).
- [5] Vladimir Litvak, Haim Sompolinsky, Idan Segev et al., "On the transmission of rate code in long feed-forward networks with excitatory-inhibitory balance", *The Journal of Neuroscience* 23(7), 3006 (2003).

A two-variable silicon neuron circuit based on the Izhikevich model

Nobuyuki Mizoguchi, Yuji Nagamatsu, Kazuyuki Aihara, and Takashi Kohno

*Institute of Industrial Science, The University of Tokyo, 4-6-1 Komaba, Meguro-ku, Tokyo 153-8505, Japan
(mizoguti@sat.t.u-tokyo.ac.jp)*

Abstract: The silicon neuron is an analog electronic circuit that reproduces the dynamics of a neuron. It is a useful element for artificial neural networks that work in real time. Silicon neuron circuits have to be simple and at the same time be able to reproduce rich dynamics in order to reproduce various activities of neural networks with a compact, low-power consumption, and easy-to-configure circuit. We have been developing a silicon neuron circuit based on the Izhikevich model, which has rich dynamics in spite of its simplicity. In our previous works, we proposed a simple and low-power consumption silicon neuron circuit by reconstructing the mathematical structure in the original model using an analog electronic circuit. In this paper, we propose an improved circuit in which all of the MOSFETs are operated in the subthreshold region.

Keywords: Silicon neuron, Izhikevich model, mathematical structure-based method, subthreshold

I Introduction

The dynamics of neurons and that of neural networks have been widely researched. Many mathematical models of neurons have been developed[1, 2, 3] to reconstruct their dynamics and simulations conducted[4, 5, 6] to reproduce various functions of neural networks such as rhythmic movements, associative memory, and pattern recognition. The silicon neuron reproduces the dynamics of a neuron in an electronic circuit. The network of silicon neurons can operate in real time regardless of its size, which is difficult by the simulation using digital computers. In addition, it can be compact if it is implemented into an analog Very Large Scale Integrated circuit (aVLSI). For those reasons, the silicon neuron is expected to be applied for real time systems such as hybrid systems, medical devices, and robots.

Basically, silicon neurons have been developed by two different approaches. The first one is to reproduce only significant neuronal behaviors, which is called the phenomenological method. Silicon neuron circuits designed by this method[7] tend to be simple but can only reproduce a few firing patterns because of its oversimplified dynamics. The second one is to reproduce the neuronal dynamics minutely by solving the ionic conductance models, which is called the conductance based method. Silicon neurons designed by this method[8] can reproduce various firing patterns but their circuitry is complex and large.

Recently, Kohno[9] have proposed another method, the mathematical-structure-based approach, which allows us to design simple circuits with rich dynamics by reproducing the mathematical structure of the original models. By using this method, Nagamatsu[10] proposed a silicon neuron circuit (we call it the previous circuit in this paper) which reproduces the mathematical structure of the Izhikevich model[11]. This silicon neuron circuit reconstructs the dynamics of the original model with a simple circuit whose average power consumption is about 15 nW. However, in

the circuit that implements jump of the state in the original model (we call this circuit reset circuit) the voltage variation is relatively large in comparison to other parts of the circuit operated in subthreshold region. Besides this, the input current that triggers spiking of the silicon neuron needs to be considerably small. It is likely to be difficult to produce.

In this paper, we propose an improved circuit with a new reset circuit in which the voltage swing is about 0.4 V, which is lower than that of the previous circuit by about 2.25 V. In addition, we scaled up the input current by altering a part of the circuit. These modifications are expected to lower the difficulty in aVLSI implementation of this circuit.

II Izhikevich model

The Izhikevich model consists of two-variable differential equations with jump of the state:

$$\frac{dv}{dt} = 0.04v^2 + 5v + 140 - u + I \quad (1)$$

$$\frac{du}{dt} = a(bu - v) \quad (2)$$

$$\text{if } v = 30 \text{ mV then } v \leftarrow c, u \leftarrow u + d \quad (3)$$

where v and u are the membrane potential and an internal variable respectively. This model can reproduce 20 firing patterns that neurons in the cortical area of the brain exhibit, by tuning the four parameters: a , b , c , and d [12]. The parameter a controls the time constant of u , and b represents the slope of the u -nullcline, the line where the derivative of u is zero, which is shown in Fig. 3(a). The parameters a and b control the characteristics of the equilibrium points where the v -nullcline intersects with the u -nullcline. The parameters c and d respectively determine the membrane potential and the increment of u when a jump of the state occurs. These two parameters mainly control the characteristics of

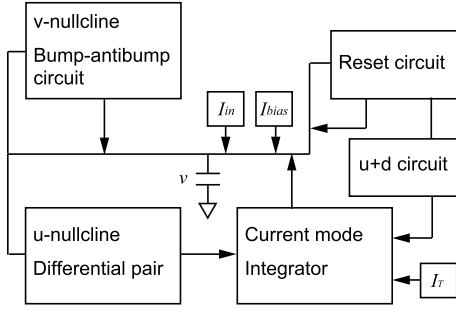


Figure 1: Block diagram of our silicon neuron circuit.

the burst firing.

III Designed circuit

In this section, we show the design of the improved silicon neuron circuit based on the Izhikevich model comparing to the previous one proposed by Nagamatsu[10]. Figure 1 shows the block diagram of our improved circuit.

1 Mathematical-structure-based approach

This circuit is designed by using mathematical-structure-based approach proposed by Kohno[9]. In this method, we reconstruct the mathematical structure in the original model using output characteristic curves of simple analog electronic circuits, which allows us to avoid using complex circuits to directly approximate the equations in the original model.

2 Reproducing v - and u -nullclines

To reconstruct the mathematical structure, we reproduced the v - and the u -nullclines by circuits shown in Fig. 2. In the previous circuit, the v -nullcline was reproduced by two differential pair circuits, but in the improved circuit, a bump-antibump circuit[13] is used because it consumes half as much power as the two differential pairs to get the parabolic output current of the same scale. We have increased the bias voltage to scale up the input current that triggers spiking of the silicon neuron, yet the improved circuit consumes as low power as the previous one. It is because the new reset circuit consumes less power than the previous one by about 9 nW. This cancels the increment of the power consumption of the alternative v -nullcline circuit which is about 7 nW. The u -nullcline is reproduced by the same circuit as the previous one: a differential pair circuit with source degeneration. The characteristic curves of the v -nullcline and the u -nullcline circuits are shown in Fig. 3(b) and their theoretical formulae are described in Eqs. (4) and (5) respectively.

$$I_{out} = I_b \left(1 - \frac{1}{1 + \frac{4}{S} \cosh^2 \frac{\kappa(V_{in} - V_{ud})}{2}} \right) \quad (4)$$

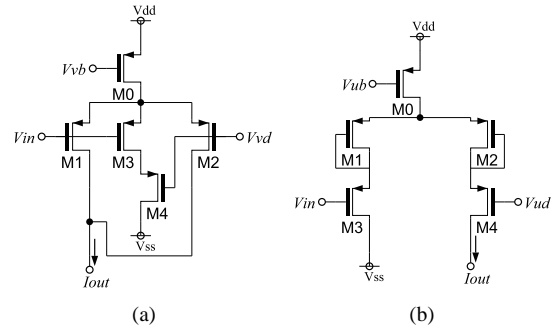


Figure 2: Schematics of the circuits that produce the nullclines. (a) The bump-antibump circuit that produces the v -nullcline. (b) The degenerated differential pair circuit that produces the u -nullcline.

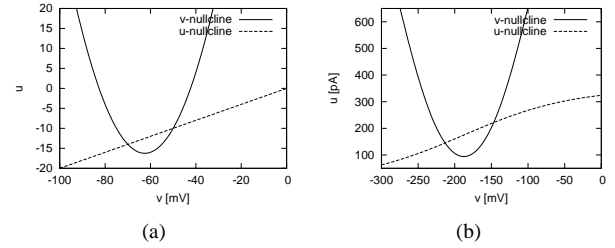


Figure 3: Comparison between the nullclines of the original model and those of our circuit. (a) The v - and the u -nullclines of the original model. (b) Those of our circuit that has the same geometry as the original model even though they don't have exactly the same shape.

$$I_{out} = \frac{I_b}{1 + \exp \frac{-\kappa(V_{in} - V_{ud})}{2U_T}} \quad (5)$$

As shown in Fig. 3(b), the width of the v -nullcline of our circuit is three times as large as that of the original model but it doesn't matter if we scale the membrane potential appropriately. We have to add an amplifier that scales v down to one-third to output the original membrane potential, but there is no need to do so if silicon neurons are interconnected via silicon synapses that reproduce the dynamics of synapses because their circuit can be designed to accept the voltage scale of our silicon neuron circuit. Also, in our circuit the v -nullcline is not exactly parabolic and the u -nullcline not exactly linear but it doesn't matter because it has the same geometrical arrangement as the original one and we can reconstruct the same mathematical structure if we configure the parameters appropriately.

3 Current-mode integrator

A current-mode integrator is used to integrate the equation for the variable u because it is represented by the amount of the current from the capacitance that represents the membrane potential v . Figure 4 shows the current-mode integrator designed to operate in the subthreshold region

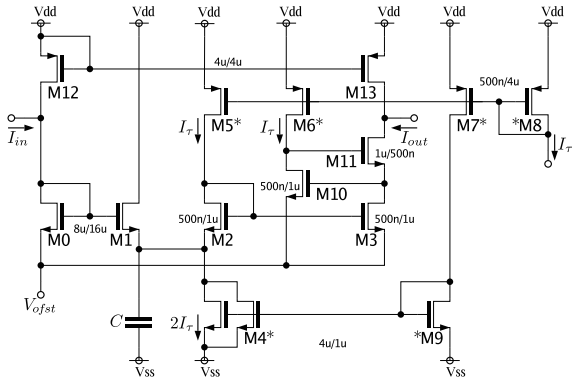


Figure 4: Schematic of the current-mode integrator[14]. I_{out} is temporal integration of $I_{in} - I_{out}$, which represents the variable u . The time constant depends on C and I_τ , which corresponds to the parameter a

and to be suitable for implementation by relatively fine process such as $.35 \mu\text{m}$ [14]. This circuit implements the integration described as follows:

$$\frac{dI_{out}}{dt} = \frac{I_\tau}{CU_T} (I_{in} - I_{out}) \quad (6)$$

where I_{out} is the output current of the integrator that represents u , I_{in} is the input current that comes from the u -nullcline circuit, C is the capacitance in the integrator, U_T is the thermal voltage, and I_τ is the constant current that represents the parameter a .

4 Reset circuit and u+d circuit

In the previous silicon neuron circuit, the output voltage of the reset circuit swings from -1.65V to 1V when it switches v from 30 mV to c , which is relatively large voltage variation in comparison to the other parts of the circuit operated in subthreshold region. This considerably increases the difficulty in layout mask design and potential troubles in its operation. In the improved circuit, we propose a new reset circuit with a circuit that switches u to $u+d$ (we call it $u+d$ circuit) as shown in the Fig. 5. The reset circuit switches the membrane potential v to c when it exceeds 90 mV (30 mV in the original model). In this operation, the output voltage of our reset circuit keeps high, which makes the $u+d$ circuit increase or decrease the variable u by d . The voltage swing of the output voltage is about 0.4 V , which is lower than that of the previous one by about 2.25 V . The parameter c and d can be configured by the bias voltages V_{rvb} and V_{rvd} in Fig. 5(a) and by V_d in Fig. 5(b) respectively.

5 Bias current that controls the position of v -nullcline

We use the bias current I_{bias} to configure the parameter b as in the previous circuit. Current I_{bias} is injected into or taken up from the capacitor that represents the membrane potential v . In the u - v phase plane, it means I_{bias} moves the v -nullcline up or down and this can configure the char-

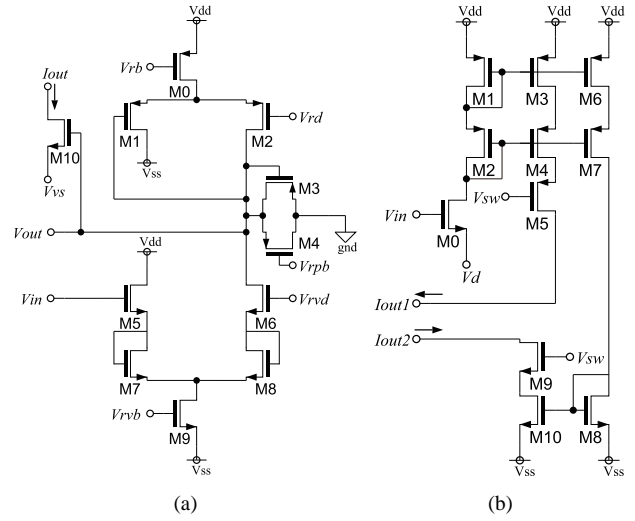


Figure 5: Schematics of the circuits that implement the jumps of the state. (a) The reset circuit that switches v from 90 mV to $c \text{ mV}$. Both V_{in} and I_{out} are connected to the capacitance that represents the membrane potential v . V_{out} becomes high while reset operation. (b) The $u+d$ circuit that increases u by d while the reset circuit is switching the value of v . The input voltage V_{in} is connected to V_{out} of the reset circuit. The bias voltage V_{sw} is the switch that shuts off either I_{out1} that represents the positive d or I_{out2} that represents the negative d .

acteristics of the equilibrium points as the parameter b in the original model (see Fig. 6).

IV Simulation

We validated our silicon neuron circuit by HSpice circuit simulation using TSMC $.35\mu\text{m}$ CMOS mixed signal process PDK. V_{dd} and V_{ss} are 1.65V and -1.65V respectively. The simulation results are shown Fig. 7. We have successfully found the parameter voltages for 17 firing patterns out of 20 that the Izhikevich model produces.

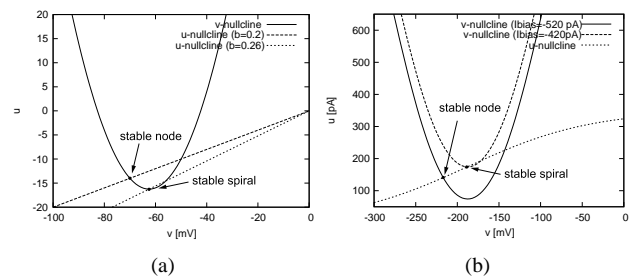


Figure 6: (a) In the original model, the parameter b controls the slope of the u -nullcline. (b) In our circuit, the parameter I_{bias} moves the v -nullcline up and down. The characteristics of the equilibrium points are tuned to be same as in (a).

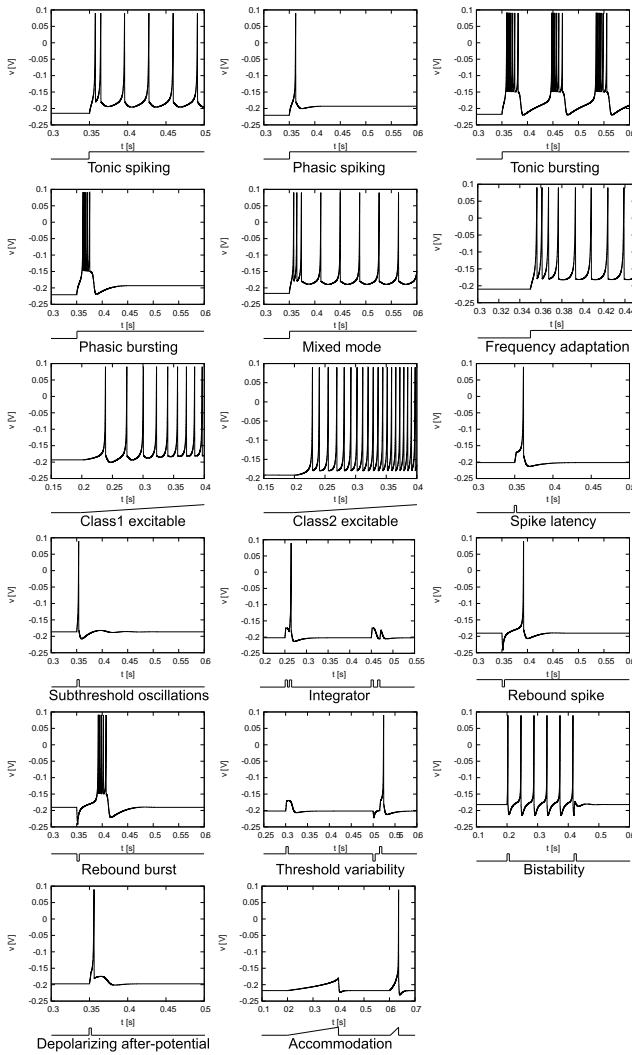


Figure 7: Produced firing patterns.

V Conclusion

We proposed an improved silicon neuron circuit based on the Izhikevich model. The voltage swing of the new reset circuit is about 0.4 V which is smaller than that of the previous circuit by about 2.25 V. In addition, we redesigned the v -nullcline circuit and changed the bias voltages to scale up the input current, yet the improved circuit consumes as low power as the previous one does. These improvements are suitable for aVLSI implementation in which MOSFETs are operated in subthreshold region. We have reproduced 17 firing patterns out of 20 that the Izhikevich model produces.

Acknowledgements

The study was supported by JST PRESTO program and was partially supported by a Grant-in-Aid for Young Scientists (A) 19680015 from the Ministry of Education, Culture, Sports, Science, and Technology, the Japanese Government.

References

- [1] A. L. Hodgkin and A. F. Huxley, "A quantitative description of membrane current and its application to conduction and excitation in nerve," *The Journal of Physiology*, vol. 117, no. 4, pp. 500-544, Aug. 1952.
- [2] C. Morris and H. Lecar, "Voltage oscillations in the Barnacle giant muscle fiber," *Biophysical Journal*, vol. 35, no. 1, pp. 193-213, Jul. 1981.
- [3] J. L. Hindmarsh and R. M. Rose, "A model of neuronal bursting using three coupled first order differential equations," *Proceedings of the Royal Society B*, vol. 221, no. 1222, pp. 87-102, Mar. 1984.
- [4] A. A. V. Hill, J. Lu, M. A. Masino, O.H. Olsen, R.L. Calabrese, "A model of a segmental oscillator in the leech heartbeat neuronal network," *J. Comp. Neurosci.* 10, 281-302, 2001.
- [5] E. M. Izhikevich, "Weakly pulse-coupled oscillators, FM interactions, synchronization, and oscillatory associative memory," *IEEE Transactions on Neural Networks*, 10, pp. 508-526, 1999.
- [6] C. D. Brody, J. J. Hopfield, "Simple networks for spike-timing-based computation, with application to olfactory processing," *Neuron* 37:843-52, 2003.
- [7] G. Indiveri, "A low-power adaptive integrate-and-fire neuron circuit, *Circuits and Systems*," 2003. *ISCAS '03. Proceedings of the 2003 International Symposium*, Vol. 4, pp. 820-823.
- [8] M. F. Simoni, G. S. Cymbalyuk, and M. E. Sorensen, "A Multiconductance Silicon Neuron With Biologically Matched Dynamics," *IEEE Transactions on Biomedical Engineering*, Vol.51, No.2, 2004.
- [9] T. Kohno and K. Aihara, "A Design Method for Analog and Digital Silicon Neurons -Mathematical-Model-Based Method-," *AIP Conference Proceedings*, Vol. 1028, pp. 113-128, 2008.
- [10] Y. Nagamatsu, K. Aihara, and T. Kohno, "An Izhikevich type silicon neuron circuit," *Proceedings of International Symposium on Artificial Life and Robotics 2010, OS4-1*, 6th, Feb., 2010.
- [11] E. M. Izhikevich, "Simple Model of Spiking Neurons," *IEEE Transactions on Neural Networks*, Vol. 14, No. 6, November 2003.
- [12] E. M. Izhikevich, "Which Model to Use for Cortical Spiking Neurons?," *IEEE Transactions on Neural Networks*, Vol. 15, No. 5, September 2004.
- [13] T. Delbruck, "Bump Circuits," Caltech, Pasadena, CA, Tech. Rep. CNS Memo 26, May 1993.
- [14] T. Kohno and K. Aihara, "A simple aVLSI burst silicon neuron circuit," *Proceedings of the 2008 International Symposium on Nonlinear Theory and its Applications*, pp. 556-559, Sep., 2008.

A three-variable silicon neuron circuit

Yohei Nakamura¹, Kazuyuki Aihara¹, Takashi Kohno¹,

¹Institute of Industrial Science,
The University of Tokyo, Tokyo 113-8656, Japan
(Tel : +81-3-5452-6693; Fax : +81-3-5452-6694)
(Email: nakamura@sat.t.u-tokyo.ac.jp)

Abstract: The silicon neuron is a type of artificial neuron implemented with electronic circuit. Previously a design approach based on mathematical structures under neuronal dynamics was proposed. It is based on the mathematical techniques such as phase plane and bifurcation analysis. These methods allow us to implement silicon neuron with smaller circuit area and to strategically adjust the bias parameter voltages without losing variety of output patterns. In this study we demonstrate a mathematical-structure-based silicon neuron, which operates a three-dimensional system. This silicon neuron can generate a firing pattern called square-wave bursting. In this report we show the experimental results of this silicon neuron. We are planning to make pattern generating network using this silicon neuron and silicon synapses.

Keywords: Silicon neuron, MOSFET, Phase plane, Bifurcation analysis

I Introduction

The neuromorphic hardware is an electronic system that mimics functions of nerve systems. Biological studies revealed that nervous systems process information in fundamentally different ways from digital computers. They have good adaptability to their environment and high robustness. To investigate the mechanism of such splendid information processing ability and to reproduce it in artificial systems, many biophysical and theoretical studies have been done about the neuron and the synapse which are the basic component of the nerve system. Silicon neurons have been produced through the efforts to reproduce various properties elucidated by these studies using electronic circuits.

There have been two major types of approaches, one is phenomenological approach and the other is conductance-based one. Phenomenological silicon neurons are based on extremely simplified neuron models such as the leaky integrate-and fire model [1]. They could be implemented by relatively simple and compact circuit because phenomenological neuron models focus on the specific properties of neurons, thus they are suitable for investigating large silicon neural networks. However, they reproduce limited aspects of neuronal dynamics because these models ignore the ionic dynamics in neurons. On the other hand, conductance-based silicon neurons, such as [2] are intended to emulate the dynamics of ionic channels in neurons. They have the ability to generate various firing patterns by adjusting the externally applied parameter voltages to the circuit. However, they have drawbacks of complexity in their circuitry and a number of parameter voltages to be adjusted. These points raise difficulty in circuit implementation and oper-

ation under the presence of device mismatch and noises. Thus it is hard to compose large silicon neural networks of the conductance-based silicon neurons.

In previous studies [3], Kohno proposed a mathematical-structure-based approach to design silicon neurons. Qualitative neuron models, such as the FitzHugh-Nagumo [4] and the Hindmarsh-Rose models [5] can generate various firing patterns with fewer parameters. However, their equations are not suitable for implementation by electronic circuit. In the mathematical-structure-based approach, the equations of the qualitative models are modified so that they can be implemented by electronic circuit effectively while preserving their mathematical structures utilizing phase plane and bifurcation analyses. In this study we present a mathematical-structure-based silicon neuron, which has three dimensional system equations and designed to produce a burst firing pattern called square-wave bursting when all of the three variables are activated.

II System equations of our silicon neuron

The system equations of our silicon neuron contain three variables, v , n and q . Variable v corresponds to the membrane potential of the neuron, n and q are the variables that represent an ionic channel and a negative feedback cur-

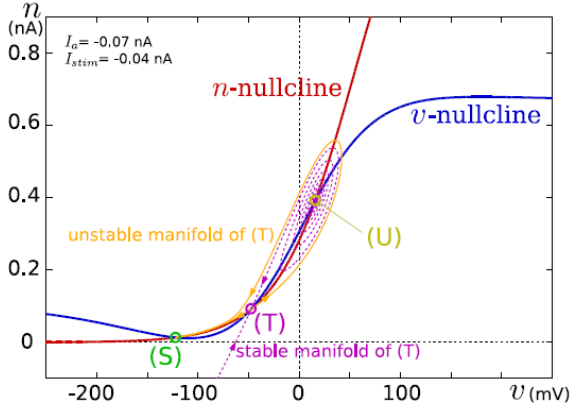


Figure 1: The n - v phase plane of silicon neuron model (simulation). n -nullcline and q -nullcline are respectively the set of $\frac{dn}{dt} = 0$ and $\frac{dq}{dt} = 0$

rents. They are written as follows:

$$C_v \frac{dv}{dt} = f_m(v) - g(v) - n - q + I_a + I_{stim} \quad (1)$$

$$\frac{dn}{dt} = \frac{f_n(v) - n}{T_n} \quad (2)$$

$$\frac{dq}{dt} = \frac{f_q(v) - q}{T_q} \quad (3)$$

where I_a is an ionic current which is independent of the membrane potential. Current I_{stim} is an externally applied stimulus current. Constant C_v is the membrane capacitance. Constant T_n and T_q are the time constants for n and q .

The functions $f_x(v)$ ($x = m, n, q$) and $g(v)$ are the sigmoidal characteristic curves of the differential-pair circuitries, which are expressed in the following forms:

$$f_x(v) = M_x \frac{1}{1 + \exp(-\frac{\kappa}{U_T}(v - \delta_x))} \quad (4)$$

$$g(v) = S \frac{1 - \exp(-\frac{\kappa}{2U_T}(v -))}{1 + \exp(-\frac{\kappa}{2U_T}(v -))} \quad (5)$$

Equations (1) and (2) comprise the basic excitable system, which can reproduce the same mathematical structures as various non-bursting neuron models, such as Hodgkin-Huxley and Morris-Lecar models. Equation (3) comprises the negative feedback system that generates positive current q into the membrane capacitor while the potential v is high, and negative current while v is low, whose mechanism cause the square-wave bursting when the basic excitable system has a kind of bistability. Figure 1 shows the v - n phase plane of the basic excitable system of our silicon neuron. When no stimulus current is applied, the membrane potential stays at the stable equilibrium (S) (resting point). If the stimulus current is small, the system state cannot move over a stable manifold of the saddle point (T)

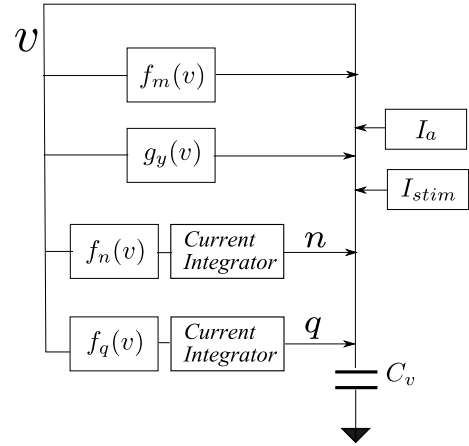


Figure 2: Block diagram of our silicon neuron

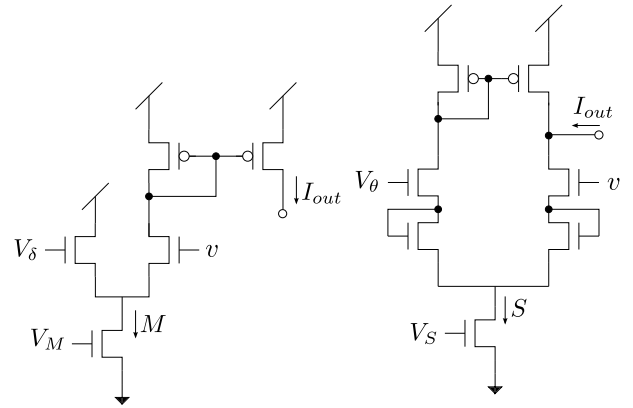


Figure 3: Schematics of $f(v)$ (left) and $g(v)$ (right) generator circuits.

and go back to (S). However, if the stimulus is sufficiently strong, the system state travels around the unstable node (U) and come back to the resting state. In the next section, we present the circuit experiment results of our basic excitable system.

III Circuit of our silicon neuron

In Fig.2 the block diagram of our silicon neuron is shown. It is composed of differential pair (Fig.3), current mirror, and current-mode integrator (Fig.4) circuits. The differential pair circuits make the functional curves of the nullclines, and the current-mode integrator integrates the system equations. Each of function modules generates output current which depends on membrane potential v , and the output currents flow into the membrane capacitor whose voltage represents v through current mirror or current-mode integrator.

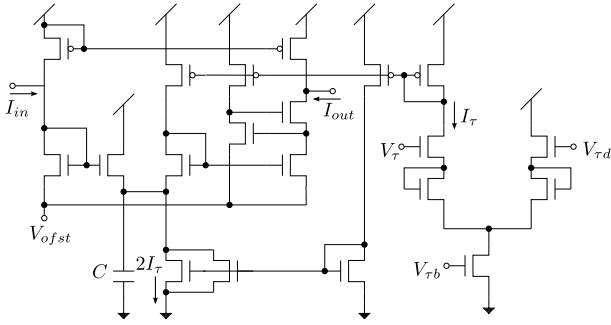


Figure 4: Schematic of the current-mode integrator circuit where MOSFETs are operated in the subthreshold condition. This circuit realize the integration in Eqs. (2) and (3).

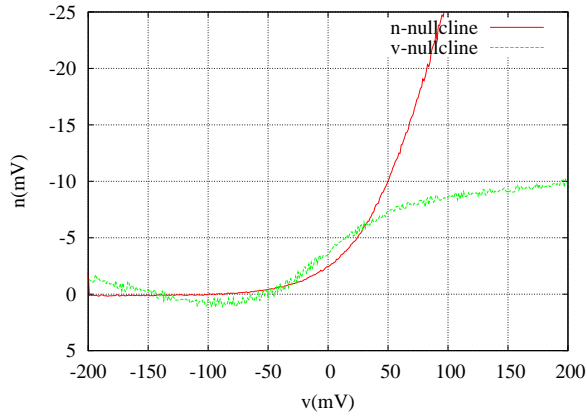


Figure 5: The v - and the n -nullclines drawn by the voltage clamp system implemented in the same chip with silicon neuron.

IV Experimental results

1 Drawing phase plane

Our silicon neuron has the voltage-clamp measurement system inside the same VLSI chip, which can generate the output currents of each functional modules while clamping the membrane potential to a specific voltage. Figure 5 shows the v - n phase plane of our silicon neuron, which was drawn by this system. In the following subsections we present experimental results of the basic excitable system in our silicon neuron circuit. The values of parameter voltages are shown in Table 1.

2 Responses to singlet pulse stimuli

Figure 6 shows the behaviour of the membrane potential v in response to the singlet pulse stimuli. The duration of the input pulse is 1.0 ms and the amplitude $\delta_{I_{stim}}$ is varied from -90 mV to -30 mV. The value of the amplitude is

Table 1: Operating parameter set

Parameters	Values[V]	Parameters	Values [V]
V_{DD}	3.3	V_{δ_n}	0.09
V_{SS}	0	V_{M_n}	0.395
V_{δ_m}	-0.01	$V_{\tau b_n}$	0.243
V_{M_m}	0.31	V_{ofst}	0.39
V_{θ}	-0.13	V_{τ}	0
V_S	0.3	$V_{\tau d}$	0
$V_{\delta_{I_a}}$	0	$V_{\delta_{I_{stim}}}$	0
$V_{S_{I_a}}$	0.35	$V_{S_{I_{stim}}}$	0.35

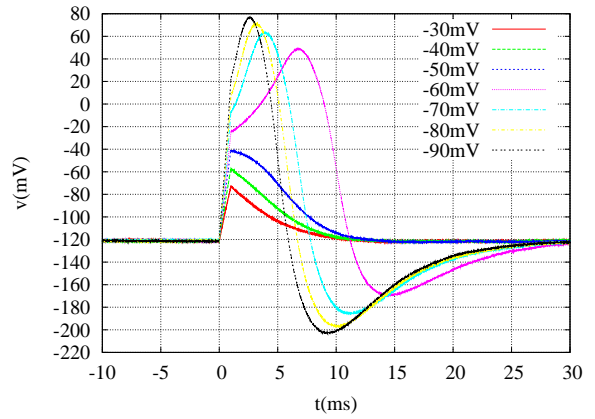


Figure 6: Response of the membrane potential to singlet pulse stimuli. Stimulus is applied to the membrane capacitor through a V - I transmitter circuit in the VLSI chip, which converts negative voltage to positive current. The duration of the stimulus pulse is 1.0 ms, and the strength is varied from -30 mV to -90 mV.

negative voltage because stimulus current is applied via a V - I transmitter circuit that converts negative input voltage into positive current. These results demonstrate that our silicon neuron has the first four out of the five properties of silent neurons described by Zeeman [6]. (1) a stable equilibrium point exists that corresponds to the resting state. (2) and action potential can be generated in response to an external stimulus, and the size of the response is absolutely larger than that of the stimuli. (3) a threshold of the stimulus magnitude exists for the generation of action potential. (Fig.6 shows that the threshold voltage of our silicon neuron exists between -50 mV and -60 mV.) (4) an action potential returns to the resting state more slowly than its rising phase. (5) refractoriness exists after generation of an action potential.

3 Responses to doublet pulse stimuli

Figure 7 shows the responses to the doublet pulse stimuli. The duration of the input pulse is 1.0 ms and their in-

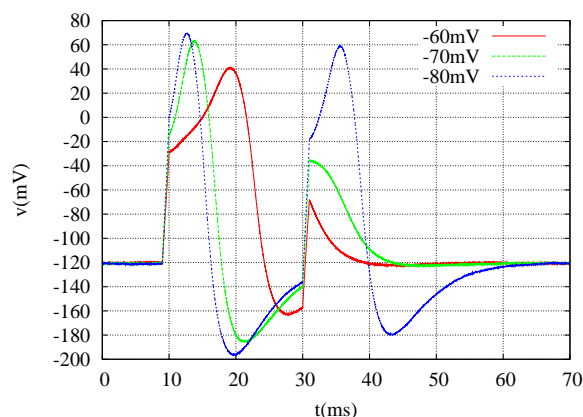


Figure 7: Responses to doublet pulse stimuli. The duration of the input pulse is 1.0 ms and their interval is 20 ms. Both of the pulses have the same amplitude of -60 mV, -70 mV, or -80 mV. This graph shows that the responses to second pulse is smaller than first one's. This result indicates the existence of refractory period after the firing.

interval is 20 ms. Both of the pulses have the same amplitude of -60 mV, -70 mV, or -80 mV. In each amplitude, membrane potential v was less responsive to the second stimulus in comparison to the first one. This indicates the existence of refractory period which is the fifth property in the Zeeman's characterization listed above.

V Square-wave burster mode

When the parameters are selected appropriately, a saddle-loop homoclinic orbit bifurcation emerges in the basic excitable system when q is varied. In this situation, there exists a bistability between a stable limit cycle that represents a tonic firing state and a stable equilibrium that represents a silent state (see Fig.8). When the system state is in the left side of the q -nullcline, $\frac{dq}{dt}$ is positive, thus the state point moves to the right direction generating tonic firing. At the point of the saddle-loop homoclinic orbit bifurcation, the minimum potential of the stable limit cycle reaches to the saddle point and the state point is attracted to the stable node along the unstable manifold of saddle node. Then $\frac{dq}{dt}$ becomes negative, thus the state point moves to the left until jumps to the limit cycle to generate tonic firing again. These are the mechanism of generating square-wave bursting in our silicon neuron.

VI Conclusion

We introduced a mathematical-structure-based silicon neuron circuit with 3 variables and reported the experimental results of its basic excitable system. The mathematical structure which dominates the circuit operation was repre-

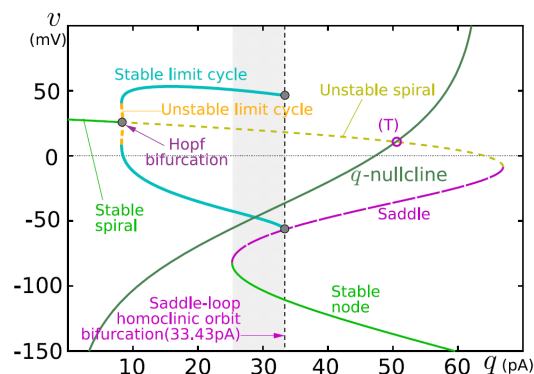


Figure 8: The v - q plane of the system equations of our silicon neuron. At the point of $q = 33.47$ pA, minimum of the stable limit cycle reaches to the saddle point.

sented by the phase plane. We determined the externally applied parameter voltages utilizing the structures in the phase plane. In HSpice circuit simulation, our silicon neuron circuit successfully produced burst firing patterns including square-wave bursting (not shown). We are working on the circuit experiments of the total system in our silicon neuron, which will be presented in our future publications.

Acknowledgements

The study was supported by JST PRESTO program and was partially supported by a Grant-in-Aid for Young Scientists (A) 19680015 from the Ministry of Education, Culture, Sports, Science, and Technology, the Japanese Government.

References

- [1] Indiveri, G., A low-power adaptive integrate-and-fire neuron circuit. Proceedings of the 2003 International Symposium on Circuits and Systems, 2003. ISCAS 03., p.IV-820-IV-823.
- [2] Simoni, M.F. et al., 2004. A multiconductance silicon neuron with biologically matched dynamics. Biomedical Engineering, IEEE Transactions on, 51(2), p.342354.
- [3] Kohno, T. Aihara, K., 2005. A MOSFET-based model of a Class 2 nerve membrane. IEEE transactions on neural networks / a publication of the IEEE Neural Networks Council, 16(3), pp.754-73.
- [4] Fitzhugh, R., 1961. Impulses and Physiological States in Theoretical Models of Nerve Membrane. Biophysical Journal, 1(6), pp.445-466.
- [5] Rose, R.M. Hindmarsh, J.L., 1989. The Assembly of Ionic Currents in a Thalamic Neuron III. The Seven- Dimensional Model. Proceedings of the Royal Society B: Biological Sciences, 237(1288), pp.313-334.
- [6] Zeeman, E.C., 1972. Differential equations for the heart-beat and nerve impulse. In: Toward a Theoretical Biology, Waddington CH (ed) Edinburgh, UK, Int. Union of Biol. Sciences and Edinburgh Univ. Press, vol. 4, p 8

Theory of mind in a microscopic pedestrian simulation model

Ryo Adachi[†], Kazuyuki Aihara^{†,*}

[†]Graduate School of Information Science and Technology,
The University of Tokyo, Tokyo 113-8656, Japan

^{*}Institute of Industrial Science, The University of Tokyo, Tokyo 153-8505, Japan
(Tel: +81-3-5452-6693; Fax : +81-3-5452-6694)
(Email: ryo@sat.t.u-tokyo.ac.jp)

Abstract: In this paper, we propose a microscopic pedestrian simulation model which focuses on pedestrians' anticipatory behavior in collision avoidance. While it is obviously recognized that inferring other pedestrians' behavior is playing a crucial role when they intend to avoid collision, few models seriously tackled with this mental attribution. Our model assumes that each pedestrian has theory of mind, which refers to the capacity to make accurate judgments about beliefs, desires and intentions of other people, and he decides his action based on his current state in cognitive hierarchy. We also present various simulation results to understand how our anticipatory behavior affects pedestrians' behavior as a whole.

Keywords: Pedestrian Simulation, Decision Making, Theory of Mind

I Introduction

A number of researches analyzing microscopic pedestrians' behavior with computer simulations have been conducted after we experienced vast improvement on computational ability. Such microscopic simulation models adopt physical forces [1], cellular automaton models ([2], [3]) or decision making processes [4]. In these papers, authors' cardinal concerns were how accurate their models could simulate realistic pedestrian behavior in our daily lives, which are obviously important from a practical perspective, and they did not pay much attention to collision avoidance behavior although the game theoretic aspects which occur when we face other pedestrians on a road are fundamental to pedestrians' characteristics, thus should be investigated further. Recent relevant papers which treat collision avoidance game theoretically include [5] and [6].

Although adopting game theory to pedestrians' collision avoidance is insightful, classical game theoretic approaches do not immediately tell pedestrians how they should behave in a certain environment. What a pedestrian do to make reasonable decisions in ever changing environment is that he successively infers and makes belief about the movements of other pedestrians and then decides his response based on that belief. Thus it is natural to incorporate the concept of theory of mind [7], which refers to the ability to make accurate guessing about the beliefs, desires and intentions of other people.

In this paper, we model pedestrian behavior with decision making approaches incorporating theory of mind. We also present various simulation results and discuss anticipatory behavior of pedestrians.

II The model

In this section, we first describe the microscopic pedestrian model we have developed and then discuss how we apply the idea of theory of mind to collision avoidance in our model. Our model assumes that pedestrians' transition are fully specified by utilities calculated on each available state. Such assumption and procedure are one of the most common and powerful approaches in past researches of human decision making.

1 Pedestrians' admissible directions and speeds

Due to computational constraints, we need to discretize pedestrians' applicable directions and speeds at a certain moment. We adopt the same model as in [6], which is described in Figure 1, except for some parameter configuration. Here, θ_i^d and θ_i are desired and current direction,

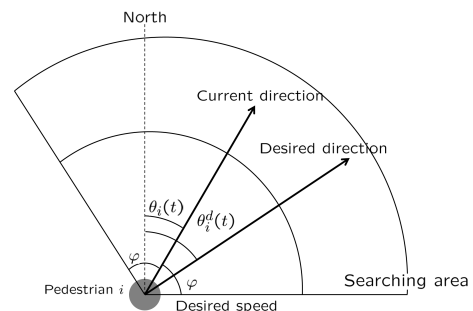


Figure 1: Choice set of pedestrian i

respectively.

At every moment after a certain time called scan interval, pedestrian i decides his new direction within the choice set Θ_i , that are

$$\Theta_i(t) = \{\theta_i(t) | \theta_i(t-1) + \frac{2m-n}{n} \varphi, m = 0, 1, \dots, n\}$$

where φ restricts the admissible change in direction. Also pedestrian i chooses his speed v_i from the choice set V_i , that are

$$V_i = \{v_i | v_i = \frac{k}{l} v_i^d, k = 0, 1, \dots, l\}$$

where v_i^d is the desired speed of pedestrian i .

2 Specifying actual direction and speed

We assume that pedestrian behavior can be divided into two factors, that are goal-directed (GD) behavior and risk-oriented (RO) behavior. GD behavior reflects the fact that pedestrians basically attempt to minimize the time required to reach their goals and RO behavior reflects the fact that pedestrians hate physical contacts with other pedestrians or walls. To represent such behavior, we define the utility of pedestrian i in a simple form as

$$U(s_i(t+1)) = \alpha v_i(t) \cos(\theta_i(t) - \theta_i^d(t)) + \beta f(|s_i(t+1) - s_j(t+1)|) + \gamma f(\text{dist}(s_i(t+1), \text{wall})), \quad (1)$$

where $s_i(t)$ denotes pedestrian i 's position at step t .

In the first term of the equation (1) which represents GD behavior, a pedestrian chooses his direction and speed so as to maximize the distance traveled into his desired direction in anticipatory period. For the function f in the second and the third term, we specify it as

$$f(x) = -e^{-ax}. \quad (2)$$

Applying this f in our utility function, we can ignore interaction between a pedestrian and other pedestrians or walls when their distance is large enough. On the other hand, as the distance becomes smaller, RO behavior to avoid collision becomes dominant and the corresponding value of utility decreases. Also the parameter a should be tuned so that the value of utility be close enough to zero at any distance where pedestrians do not perceive to be uncomfortable due to the existence of other pedestrians or walls.

3 Transition of pedestrians

After every scan interval, pedestrian i moves to another state following the algorithms described below.

- 1) Given the current state $s_i(t)$, pedestrian i calculates the utility for every admissible state $s'_i(t+1)$ after anticipatory period.
- 2) Pedestrian i calculate the probability of moving to an-

other state $s_i(t+1)$ from $s_i(t)$ as

$$p(s_i(t+1)|s_i(t)) = \frac{\exp(\lambda' U(s_i(t+1)))}{\sum_{s'_i(t+1)} \exp(\lambda' U(s'_i(t+1)))}$$

- 3) Pedestrian i moves according to the probability distribution calculated above.

To determine probability of choosing strategies from the value of utility, three forms, exponential (logit), power and normal (probit) have been used in previous researches in decision making. Among these, exponential form which we adopt is considered to be the most preferable experimentally. The parameter λ' controls how likely pedestrian i deviates from the rational choice for unexplained reasons. Also it is known that there is positive correlation between the value of λ' and pedestrian's rationality. We put $\lambda = \lambda'/100$ in what follows.

4 Theory of mind

Theory of mind, namely attribution of mental states, was originally studied in chimpanzees [7] and is now broadly used in researches that investigate our psychological concepts for imputing mental states to others and ourselves. Also there are some recent mathematical models of theory of mind, [8] and [9], from which we gained inspiration for this research.

The concept of theory of mind is considered in pedestrian behavior such that, in a certain environment, a pedestrian makes belief about other pedestrians' future movements and decides his action based on that belief. The utility we mentioned in the last section is calculated with this formed belief.

We model the first- and the second-order type of theory in pedestrian behavior denoted as L1 and L2, respectively as the same manner as in [9]. We assume that pedestrians with type L1 do not represent other pedestrians' behavior, thus do not anticipate others' actions. In contrast, L2 pedestrians are assumed to model other pedestrians' planning processes to predict their future behavior. In practical, a pedestrian with type L1 always chooses his desired direction and speed. Also the utility of a pedestrian with type L2 is calculated assuming that all other pedestrians in his eye sight are having type L1. These L1 and L2 types refer to "going" and "giving way" behavior mentioned in [6].

While we can consider pedestrian types with higher-order contents such as L3, L4, \dots , we only adopt two types L1 and L2 in this paper. We discuss this topic in detail later in concluding remarks. Also for simplicity, we assume that a pedestrian is type L1 with probability p and type L2 with probability $1 - p$. This assumption is natural in congested situations such as intersections, stations or buildings where intermittent changes of environment hinders pedestrians' rational decision makings while it would not apply in cases when interference between only two pedestrians, in other words low density situations, are concerned.

III Simulation

In this section, we present various simulation results for algorithms shown in Section II.

1 Parameter configuration

First of all, let us explain general parameter configuration in our model. Note that we get the parameter values presented below after conducting various simulations.

α and β represent how each pedestrian balances between one's weights on GD and RO behavior. Here the proportion of β to α and γ to β are important, thus we put $\alpha = 1$, $\beta = 2.7 \pm 0.2$ and $\gamma = 1.5$. Someone who is in haste has low value of β and more inclined to GD behavior than to RO behavior, and vice versa. a determines the steepness of the function f in (2) and reflects the distance where a pedestrian begins to feel uneasy due to the existence of other pedestrians or walls and RO behavior starts to hinder GD behavior. We put $a = 2.0$ and $a = 10.0$ in the case of interaction with other pedestrians and walls, respectively. λ reflects pedestrians' rationality as we mentioned earlier and pedestrians become more rational as the value of it increases. Since our aim is to simulate the role of theory of mind in settings that contain intermittent interaction where changing environment makes it difficult for pedestrians to make rational choices, we put $\lambda = 1.0$. Other parameters are basically determined according to [6] and summarized in Table 1.

Table 1: Parameter settings

Scan intervals	0.2 s
Radius of a pedestrian	0.2 m
Searching area	Fan-shape with 5 m radius and $\pm\pi/3$ in range
Desired speed (v_i^d)	1.35 ± 0.2 m/s
Set of directions (φ, n)	$\pi/3, 12$ (every 10°)

Here we present two typical examples in which interaction with other pedestrians are not concerned (Figure 2) or are concerned only within two pedestrians (Figure 3, with a steady pedestrian at [4.0, 1.5] represented by a red circle), only to confirm that above parameter settings work. In both examples, the starting point and the goal are [0, 1.5] and [8.0, 1.5], respectively and we plot trajectories of a hundred pedestrians on the road. Since we defined transition of pedestrians probabilistically and added fluctuation in the value of β and desired speed, we are able to observe trajectories peculiar to each pedestrian.

2 One directional flow

In this section we present simulation results to show how the difference in the value of p affects pedestrian behavior as a whole.

First let us explain the simulation settings. Fifty pedestrians are assigned to walk along the road whose width is

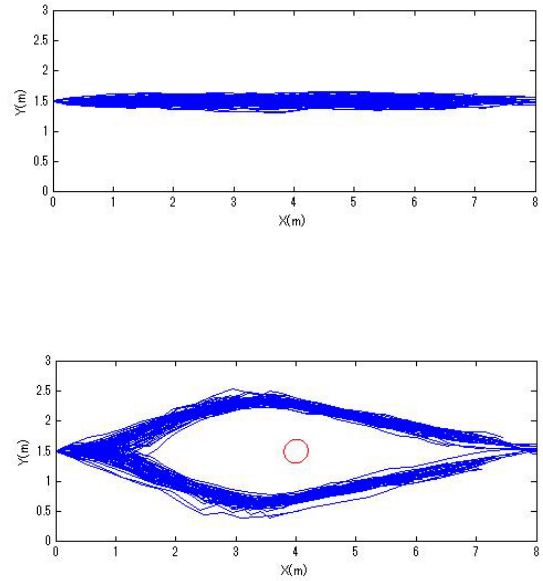


Figure 3: One directional trajectories with an obstacle

5m, starting at [0, 2.5] for fifty seconds. Other parameter configuration is same as that of Table 1. One directional flow simulation we adopt here are simple yet provide profound data about fundamental behavior of pedestrians and used in previous researches. All the data we employ for plots below are averages of the results for five times.

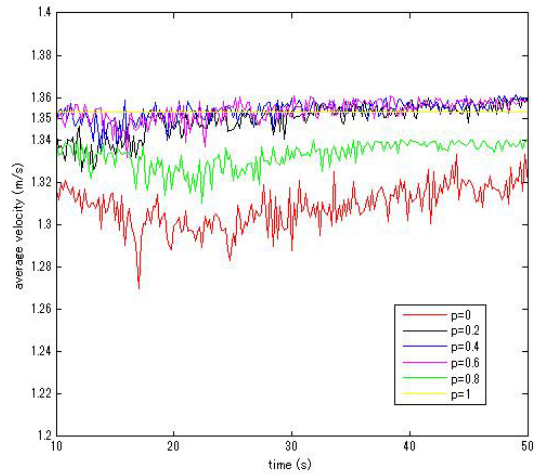


Figure 4: Velocities

We plot velocity of pedestrians after ten seconds in Figure 4 and frequency of collision which is the number of collision divided by the number of nodes among pedestrians in Figure 5 for some values of p . From these figures we see that the value of p close to 0 or 1 are unfavorable for pedestrians. To examine this effect we obtain the average of velocity and frequency of collision for all time steps and plot them in Figure 6. It is implied that the best value of p lies between $p = 0.2$ and $p = 0.5$.

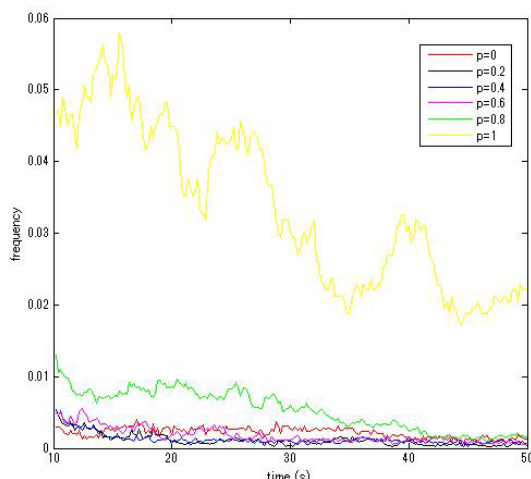


Figure 5: Frequency of collision

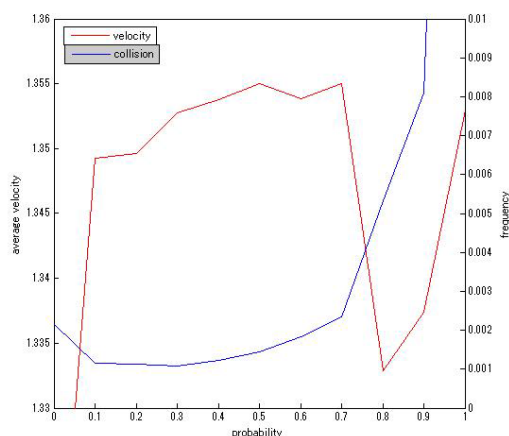


Figure 6: Average of velocity and frequency of collision

IV Concluding remarks

We proposed a microscopic pedestrian simulation model incorporating the concept of theory of mind which we strongly believe is fundamental to pedestrian behavior. We also presented numerical examples for simulated data to show that our model exhibits different behavior due to variation in pedestrians' mental attribution represented by types.

In this paper, we only adopted two types of theory in pedestrians, the first-order and the second-order, although we can consider higher order contents. Such higher-order types would lead to infinite repetition of anticipatory behavior and become unrealistic, while it could be worth considering since we never surely know how pedestrians are capable of using sophisticated strategies. If we take latest perspectives from researches on cognitive hierarchy into account, L3 and probably L4 are worth adopting while contents higher than L5 seem not to be required because such contents are likely to be mapping from states to actions acquired by experience rather than computation in the brain.

Also, although we assumed types in pedestrians are determined probabilistically with p in this paper, exploring a rule that regulates transition in types is valuable since we know by our experience that we choose our types observing the behavior of other pedestrians during a few steps before we make decisions.

These two main interesting topics would be investigated further in our future works.

Acknowledgements

This research is partially supported by the FIRST program from JSPS.

References

- [1] D. Helbing and P. Molnar (1995), "Social force model for pedestrian dynamics", *Physical Review E*, Vol. 51, No. 4, pp. 4282–4286.
- [2] V. J. Blue and J. L. Adler (2000), "Modeling four-directional pedestrian flows", *Transportation Research Record*, No. 1710, pp. 20–27.
- [3] A. Kirchner, H. Klupfel and K. Nishinari et al. (2004), "Discretization effects and the influence of walking speed in cellular automaton models for pedestrian dynamics", *Journal of Statistical Mechanics: Theory and Experiment*, P10011.
- [4] Th. Robin, G. Antonini, M. Bierlaire et al. (2009), "Specification, estimation and validation of a pedestrian walking behavior model", *Transportation Research Part B*, Vol. 43, No. 1, pp. 36–56.
- [5] M. Asano, T. Iryo and M. Kuwahara (2009), "A pedestrian model considering anticipatory behavior for capacity evaluation", in: *Transportation and Traffic Theory 2009*, Springer, New York, pp. 559–581.
- [6] M. Asano, T. Iryo and M. Kuwahara (2010), "Microscopic pedestrian simulation model combined with a tactical model for route choice behavior", *Transportation Research Part C*, Vol. 18, pp. 842–855.
- [7] D. Premack and G. Woodruff (1978), "Does the chimpanzee have theory of mind?", *Behavioral Brain Science*, Vol. 1, pp. 515–526.
- [8] W. Yoshida, R. Dolan and K. Friston (2008), "Game theory of mind", *PLoS Computational Biology*, Vol. 4, No. 12, pp. 1–14.
- [9] C. Baker, N. Goodman and J. Tenenbaum (2008), "Theory-based social goal inference", *Proceedings of the thirtieth annual conference of the cognitive science society*, pp. 1447–1455.

A Neural Network Model for Categorical Effects in Color Memory

Chihiro Imai¹, Satoshi Tajima², Kazuyuki Aihara¹, Hideyuki Suzuki¹

1) The University of Tokyo, 4-6-1 Komaba, Meguro-ku, Tokyo 153-8505, Japan
(Tel: 81-3-5452-6693; Fax: 81-3-5452-6694; Email: chihi@sat.t.u-tokyo.ac.jp)

2) Japan Broadcasting Corporation, Nagano Station, 210-2 Inaba, Nagano-city, Nagano 380-8502, Japan
(Tel: 81-26-291-5230; Fax: 81-26-291-5298; Email: tajima.s-iu@nhk.or.jp)

Abstract: Human color perception is categorical. Previous experimental studies have shown that the color category has profound effects on cortical neural responses, perceptual color discrimination and color memory. However, existing theoretical studies are not enough to provide an inclusive model accounting for those categorical effects in color perception and memory. In this study, we propose a computational model for categorical color processing, where the color memory is represented by a population of color selective neurons in cortex. Our model reproduces the characteristics of color memory reported in the previous experimental studies. Furthermore, it explains the properties of neurons in IT cortex, which change the activity depending on whether the task demands is color categorization or discrimination. This study suggests that perceptual biases found in color processing and task-dependent modulations of neural responses may be explained as a natural consequence of statistically optimal estimation.

Keywords: color memory, categorical color, population coding

I. INTRODUCTION

We perceive millions of colors based on the spectrum of incident light flowing into our eyes. Previous studies show that there are two different ways in how we see colors in spectral space: to look closely or to look as groups. Recognizing very slight differences between colors is called color discrimination. On the other hand, organizing colors within a certain color region into one group is called categorical color perception. Discrimination and categorization are considered as two different functions in color perception.

Psychophysical studies have shown the categorical effects on color discrimination. Hamad (1987) reported that discrimination was better for colors straddling the category boundary than for colors within the same category. Furthermore, considering time factor, color memory is also involved. Perez-Carpinell et al. (1998) showed the mean difference between test color and recalled color increases with the delay time. According to Heider(1972), focal colors (colors at categorical center) are remembered more accurately than non-focal colors.

fMRI and electrophysiological studies suggest that the visual cortical areas subsequent to area V4 play important roles in higher order functions of color vision including categorization and discrimination. Koida et al. (2007) investigated the responses of color-selective neurons in the inferior temporal (IT) cortex of monkeys during making a categorical judgment or a fine discrimination of colors. They found the activity of many IT color-selective neurons differed depending

upon the task. Some IT neurons showed stronger activity in the categorization task or in the discrimination task in response to the same color stimulus.

In spite of these clear evidences that color discrimination, color categorization and color memory are related to each other, there is no inclusive model that account for how our brains fulfill each of these functions depending on the situation. In the present study, we propose a computational model that takes into account the categorical effects in color perception and memory, assuming that color selective neurons in cortex express colors in memory. In particular, our model reproduces neural activities of color-selective neurons in the IT cortex during categorical judgment and discrimination, and the categorical effects in color memory.

II. COLOR PERCEPTION MODEL

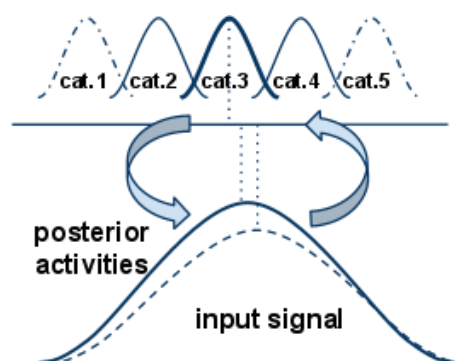


Fig.1. A schematic diagram of the proposed model

Our model explains categorical effects in color perception through the interactions between hue-selective neurons and category-selective neurons. We assume a hue space of one dimension as a color space. The model is summarized in Fig.1.

We assume two groups of color-coding neurons: the first group ('hue-selective neurons') in which the neuronal preferred hue is homogeneously distributed, and the second group ('category-selective neurons') in which the distribution of hue preference is concentrated around some points, which we call 'category center' in this study.

Each hue-selective neuron receives the input signal from earlier processing stages. The strength of the input signal is expressed as a function of the difference between presented hue θ and i th neuron's preferred hue θ_i :

$$\lambda_i(\theta) = f(\theta - \theta_i) = g \cdot e^{k \cos(\theta - \theta_i)} \quad (1)$$

where we used the von-Mises (circular Gaussian) function for the hue selectivity; g is a parameter to control the response gain. When there is no other input to those neurons, we assume that the neuronal spikes are generated with the following Poisson process:

$$P(r_i | \theta) = \frac{(\lambda_i T)^{r_i}}{(r_i T)!} e^{-\lambda_i T} \quad (2)$$

where r_i is the firing rate in one trial; T is the observation duration. The categorical decoding θ_k^c is the hue of k th category center

$$\ln P(\{r_i\} | \theta_k^c) = T \sum_i r_i \ln f(\theta_k^c - \theta_i) + \text{const.} \quad (3)$$

where we used the fact that the summation $\sum_i f(\theta - \theta_i)$ is independent of θ when the neuronal preferred hues are homogeneously distributed. Equation (3) means that the log likelihood of hue category can be calculated as a weighted sum of the hue-selective neurons' activities (the first term) (Jazayeri et al., 2006). In the present model, we hypothesize that the category-selective neurons receive the read-out signals from the hue-selective neurons as follows:

$$a_k^c = \sum_i r_i \ln f(\theta_k^c - \theta_i) \quad (4)$$

By comparing a_k^c for various hue category θ_k^c , we can estimate which category is the most likely to generate the color of visual input. This means that the maximum likelihood estimation of input hue category can be implemented by a winner-take-all process among the category-selective neurons.

Now we consider estimating the hue presented at time $t+1$ based on the knowledge of hue at time t . Given the assumption that the hue presented in future is likely to be generated from the same category as the present

one, the posterior probability is expressed with the Bayes' formula as follows:

$$P(\theta^{t+1} | \{r_i^{t+1}\}) \propto P(\{r_i^{t+1}\} | \theta^{t+1}) P(\theta^{t+1}) \quad (5)$$

We propose that the information of the prior probability distribution $P(\theta_i^{t+1})$ is given by the top-down signal from k -th category-selective neuron to i th hue-selective neuron: $f(\theta_k^c - \theta_i)$. For Poisson-like spike statistics, combining process of two probability distributions is achieved by a simple linear summation of two population activities (Ma et al., 2006). In the present study, we propose that the likelihood and the prior is iteratively recombined through following recurrence formula:

$$\lambda_i(\theta^{t+1}) = \alpha f(\theta^{t+1} - \theta_i) + \beta f(\theta_k^{c,t} - \theta_i) \quad (6)$$

where α and β control the combining ratio. In discrimination task, the parameter β is set to a smaller value than in categorization task. In color memory task, the iteration of Eq. (6) is continued for the length of memory duration. For all of the simulations, $g = 1$, $k = 1$, $T = 1$, $\alpha = 1$, $\beta = 1$, number of category = 2 and number of hue-selective neurons = 2000.

III. RESULTS

1. Categorical effect on Color Memory

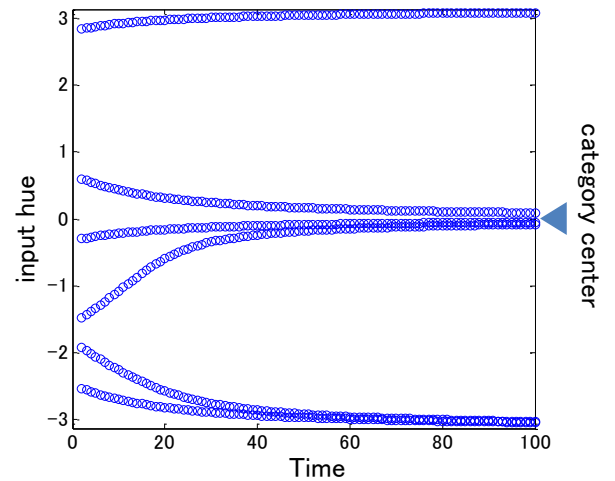


Fig.2. Temporal evolution of the cortical hue representation during the color memory task. We plotted the preferred hue of the neuron that showed the peak activity in the population. The horizontal axis indicates the memory duration. The results for four example initial hues are shown.

Figure 2 shows the temporal evolution of hue values in color memory task. Here, the preferred hue

of hue-selective neuron that showed the maximum magnitudes at each time is plotted. Values at time 0 indicates the input hue presented at the initial point of memory task; Each hue-selective neuron is activated responding to the hue input at first. After time 0, hue selective neurons received only the top-down signals from category-selective neurons, and the input signals were set to zero. When the memory duration evolved, the represented hues approached to the nearest category center.

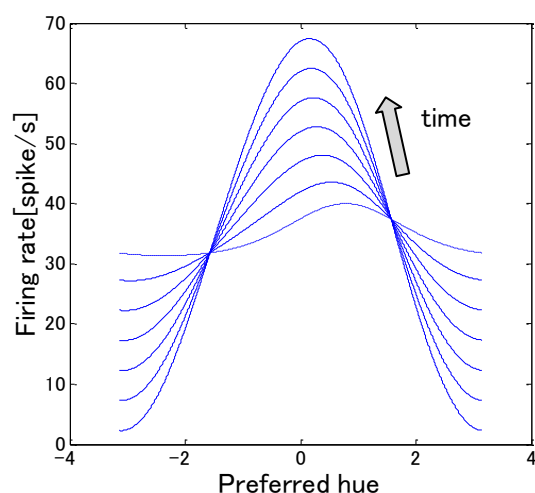


Fig.3 Temporal activity change of hue selective neurons in the color memory task. Horizontal axis denotes the preferred hue of each neuron. Each solid line shows a snapshot of the activities of hue-selective neurons, and dashed line indicates the activity induced by an input signal.

Figure 3 shows the snapshots of the activities of hue-selective neurons, which evolved during the memory task. The peak of the activities distribution of the hue-selective neurons shifts toward the nearest category center. The maximum value of firing rate increases with time.

As it can be considered that the hue centers in the model correspond to the focal colors, these results agree with the characteristics of the results reported by Heider (1972). When input hue is away from each hue center, the model also reproduces the temporal increase in the difference between memory color and initially presented color (Perez-Carpinell et al., 1998).

2. Color categorization and color discrimination

We next investigated how the present model can be related to the response properties of visual neurons in

the different task demands of color categorization and discrimination. We simulated the neuronal responses to 11 sample colors (the horizontal axis in Fig.4) which spread on the axis from red to green. Figure 4 shows the activities of a greenish-preferred neuron. The horizontal axis indicates 11 sample colors. In Fig.4, the activity of a hue-selective neuron is shown. Our model reproduces neural activities of color-selective neurons in the IT cortex during categorical judgment and discrimination (Koida et al. 2007).

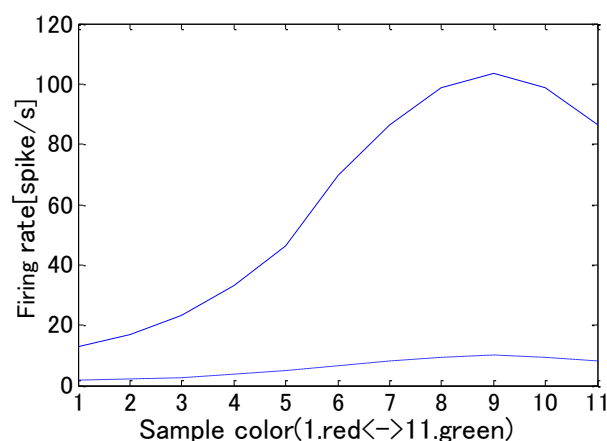


Fig.4 Responses of a hue-selective neuron during categorization (solid line) and discrimination (dashed line).

IV. DISCUSSION

Our model reproduces the characteristics found in the previous experimental studies and provides an inclusive explanation for some of the phenomenon concerning categorical color perception, color discrimination and color memory. From Bayesian viewpoint, the neural response properties in IT cortex can be explained as a natural consequence of statistically optimal estimation. This theoretical framework is possibly applied to similar phenomena found in other cortical area involved in different sensory or feature modalities, such as audition, visual motion or face expression.

We assumed that the main categorical effects are elicited by top-down signals from category selective neurons in the response to the input from hue-selective neurons. In the combining process of input and top-down signals, we applied a simple static linear summation for a purpose of conciseness. Further studies may cover a saturation and adaptation of neuronal responses or weight varying with time.

The present model considers only one-dimensional hue shift with the duration between memory and recall, though shifts of color saturation and lightness are also reported in psychophysical studies of color memory. These factors should be considered in an extension of the current model.

Another topic to be considered is the neurobiological substrate of categorical computation. Although Fig. 4 only depicts the activities of hue-selective neuron, we found that the corresponding category-selective neuron also showed the similar pattern. It can be supposed that the category-preferred neurons in Koida et al. (2007) correspond approximately to the hue-selective neurons in this model, category-preferred neurons also alike.

V. CONCLUSION

We proposed a computational model for higher order mechanisms of color perception. Our model reproduces the characteristics of categorical effects including color memory reported in the previous experimental studies. From the perspective of statistically optimal estimation, this study provides one possible explanation of the relation among categorical color perception, color discrimination and color memory in the higher visual cortex in the brain.

ACKNOWLEDGEMENT

This research is supported in part by the Japan Society for the Promotion of Science (JSPS) through its "Funding Program for World-Leading Innovative R&D on Science and Technology (FIRST Program)."

REFERENCES

- [1] K. Koida & H. Komatsu (2007), "Effects of task demands on the responses of color-selective neurons in the inferior temporal cortex." *Nature Neuroscience*. 10(1) 108-116
- [2] E. R. Heider (1972), "Universals in color naming and memory." *J. Exp. Psychol.* 93, 10-20
- [3] S. Hamad (1987), "Category induction and representation." In S. Hamad (Ed.), *Categorical perception: The Groundwork of Cognition*. 535-565. Cambridge: Cambridge University Press.
- [4] J. Perez-Carpinell, R. Baldoví et al. (1998) "Color Memory Matching: Time Effect and Other Factors." *COLOR research and application*, 23(4) 234-347
- [5] M. Jazayeri & J. A. Movshon (2006) "Optimal representation of sensory information by neural populations." *Nature Neuroscience*, 9(5):690-696.

- [6] W. J. Ma, J. M. Beck et al. (2006) "Bayesian inference with probabilistic population codes." *Nature Neuroscience*, 9:1432-1438

Study of computational performance of Genetic Algorithm for 3-satisfiability problem

QingLian Ma, Yu-an Zhang, Makoto Sakamoto, Hiroshi Furutani
Faculty of Engineering, University of Miyazaki
Miyazaki City 889-2192 Japan

Abstract

In order to improve the computing performance of Genetic Algorithms (GAs), it is important to study the effects of crossover and mutation. In this study, we examine the relations of first hitting time T of optimum solution in population, success probability S , mutation rate p_m and crossover rate p_c by GA experiments, which are carried out on the 3-satisfiability (3-SAT) problem. Here, S is defined as that there is at least one optimum solution in a population at the stationary distribution. We found that, when mutation rate is small, the effects of crossover on T and S are large. S with crossover is larger than that without crossover, and T is smaller than that without crossover. We also observed the relation between T and a/S when mutation rate becomes large, and found that $T = a/S$. When $p_m = 0.02$, $T \approx 1/S$.

1 Introduction

The satisfiability (SAT) problem is a core of a large family of computationally intractable NP-complete problems [1] with relevant practical applications such as automated reasoning, computer-aided design, machine vision, database, robotics, computer network design and so on. Methods to solve the SAT problem play an important role in the fields of efficient computing systems [2].

During the last two decades, several improved algorithms have been developed, and important progress has been achieved. These algorithms have considerably enlarged our capacity of solving large SAT instances. It can be divided into two main classes: complete and incomplete algorithms. The first category includes approaches based on the Davis-Putnam algorithm [3]. Most incomplete algorithms include approaches based on local search [4] and evolutionary algorithms (EAs) [5, 6]. De Jong and Spears (1989) proposed a classical GA for SAT problem, and observed that the GA may not outperform highly tuned

and problem-specific algorithms. Their result was confirmed experimentally by Fleurent and Ferland (1996), who reported poor performance of classical GAs when compared to local search methods. Marchiori designed a rather successful GA-based algorithm for hard 3-SAT problems by combining a native GA with a local search algorithm [7]. GA for SAT employ heuristic information into the fitness function or into the GA operations (selection, crossover, and mutation) [2, 8]. In this paper, we study the computational performance of genetic algorithm on a 3-SAT problem. GA can solve SAT problems. However it usually needs high performance computing. To overcome this problem, we study the mean first hitting time of optimum solution T , success probability S , the mean survival time a and their relations.

2 3-Satisfiability problem

The SAT problem is a task to determine whether there exists an assignment of truth values to a set of Boolean variables that make a conjunctive normal form (CNF) formula to be true [2]. The SAT problem can be formulated as follows: given a set of clauses C_1, C_2, \dots, C_m on the Boolean variables x_1, x_2, \dots, x_n , determine if there is an assignment for the variables such that the formula $C_1 \wedge C_2 \wedge \dots \wedge C_m$ evaluates to true, where \wedge is a logical connector *and*. A clause is a disjunction of literals, e.g., $x_1 \vee \bar{x}_2 \vee x_3$, where a literal is a Boolean variable x or its negation \bar{x} , and \vee is a logical connector *or*. If each C_i contains exactly z distinct literals, then the problem belongs to the z -SAT class [7]. In this paper we consider formulas in conjunctive normal form, and each clause has exactly 3 literals.

We use the following notations, let:

- F be a CNF Boolean formula,
- m be the number of clauses in F ,
- n be the number of variables in F ,
- x_k be the k th variable in F ($1 \leq k \leq n$),

- C_i be the i th clause in F ($1 \leq i \leq m$),
- l be the clause length in C_i ,
- $Q_{i,j}$ be the j th literal in the i th clause in C_i ($1 \leq j \leq l$).

We use bit variable $x_k = 1$ or 0 , corresponding to *true* or *false*, respectively. We count the number of clauses that are fulfilled by the variable assignment. A chromosome is a candidate solution, which is a string of bits having length equal to n .

A common formulation for CNF formulas exists [9]. The fitness function of F is expressed by

$$f(F) = \sum_{i=1}^m C_i, \quad (1)$$

where C_i is denoted as

$C_i = Q_{i,1} \vee Q_{i,2} \vee Q_{i,3}$, $Q_{i,j} = x_k$ or \bar{x}_k ($j = 1, 2, 3$). If all clauses are satisfied, then $f(F) = m$.

In this study a set of benchmark instance was used. Problems in this benchmark are downloaded from the SATLIB-benchmark Problems [10]. The instance provided here is cnf formulae encoded in DIMACS cnf format. We use a uniform random-3-SAT problem, uf20-91, with 20 variables and 91 clauses. Each of clauses is constructed from 3 literals. The input of our program is data file format with 91 rows, 3 columns. We evolve a population of variable assignments until we find an assignment that makes the formula true.

In the following we define some variables for evaluating the GA computing performance. The success probability $S(t)$ is defined as the probability that there is at least one optimum solution at generation t in stationary distribution [11]. S is the time average of $S(t)$ defined by

$$S = \sum_{t=1000}^{3000} S_t. \quad (2)$$

T is defined as the mean first hitting time of the optimum solution in a population. The mean survival time a is the average consecutive generations containing optimum solution in the stationary distribution.

3 Numerical experiments

In this paper, we study the relation between the success probability S and the mean first hitting time T by experiments. We performed numerical calculations of GA with roulette wheel selection on the 3-SAT problem. We carried out the experiments with string length $L = n = 20$, number of clause $m = 91$ and clause length $l = 3$. Crossover was done with the

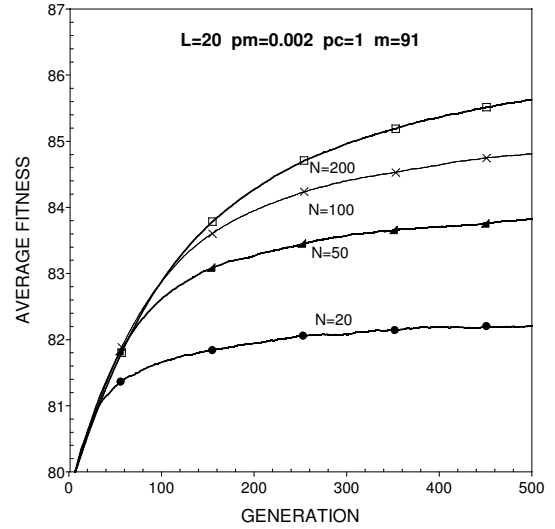


Figure 1: Dependence of average fitness on N . The horizontal axis represents generation.

uniform crossover. The calculations were performed repeatedly, and results were averaged over 10000 runs.

Figure 1 shows the dependence of average fitness on N with $p_c = 1$ and $p_m = 0.002$. By comparing results with $N = 20, 50, 100, 200$, we observe the strong N dependence of average fitness.

Figure 2 shows the dependence of average fitness on p_m with $p_c = 1$ and $N = 200$. By comparing results with $p_m = 0.05, 0.005, 0.0005$, we find strong p_m dependence of average fitness. When mutation becomes strong, the average fitness is low, and converges into a smaller value.

Figure 3 shows N -dependence of success probability S with $p_m = 0.02$. As shown in this figure, the success probability shows little difference between calculations of $p_c = 0$ and $p_c = 1$. The effect of crossover on success probability is small in this case.

Figure 4 shows p_m -dependence of success probability S with population size $N = 50$. The solid line is success probability with crossover rate $p_c = 1$, and the dotted line is success probability with crossover rate $p_c = 0$. We find that the success probability with crossover is larger than that without crossover when mutation rate is small. However, when mutation rate becomes large, the effect of crossover goes to small, and the success probabilities are almost equal.

Figure 5 shows p_m -dependence of the mean first hitting time of optimum solution T with population size $N = 50$. The value of T without crossover is larger than that of with crossover, which means crossover accelerates the speed of evolution in GA. When muta-

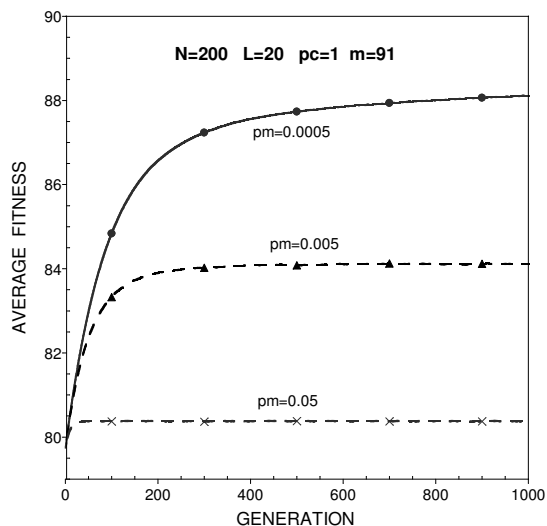


Figure 2: Dependence of average fitness on p_m . The horizontal axis represents generation.

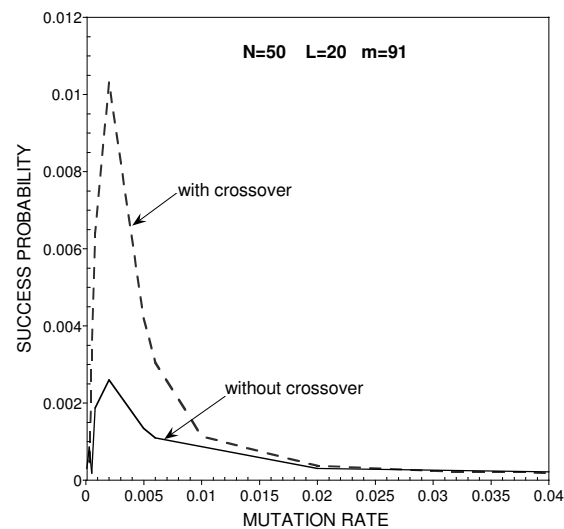


Figure 4: p_m -dependence of success probability S with crossover rates $p_c = 1$ and 0. The horizontal axis represents mutation rate p_m .

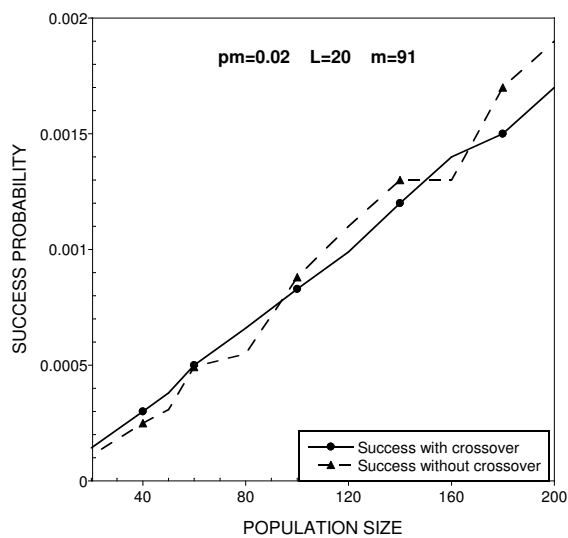


Figure 3: N -dependence of success probability S with crossover rates $p_c = 1$ and 0. The horizontal axis represents population size N .

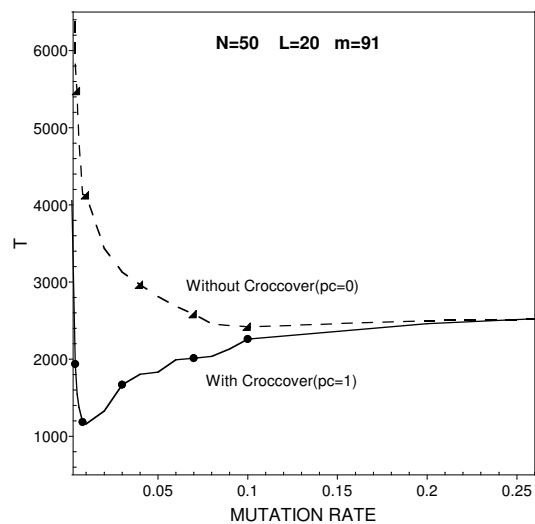


Figure 5: p_m -dependence of T with crossover rates $p_c = 1$ and 0. The horizontal axis represents mutation rate p_m .

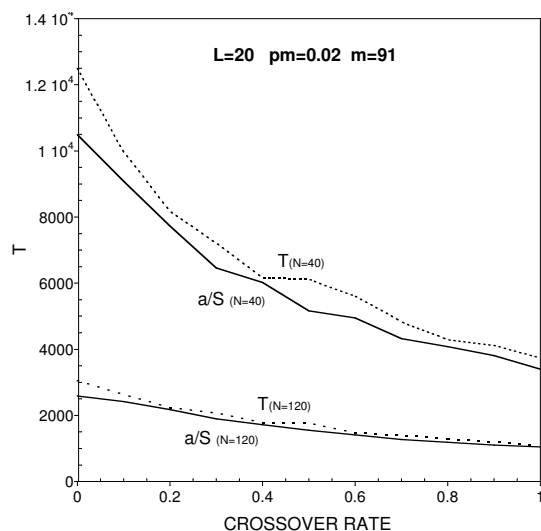


Figure 6: The relation of T and a/S with $N = 40, 120$. The horizontal axis represents crossover rate p_c .

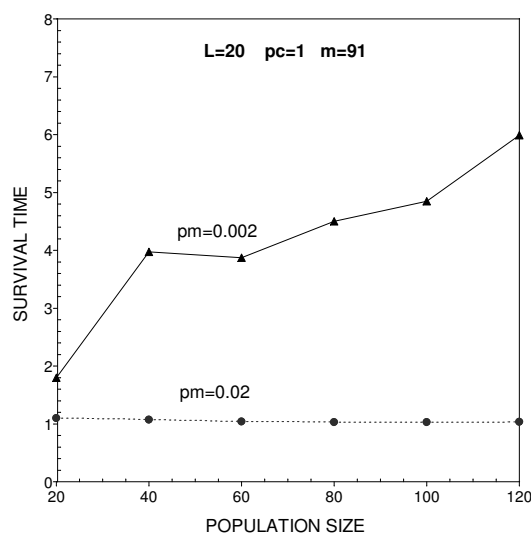


Figure 7: The dependence of a on N with $p_m = 0.02$ and 0.002 . The horizontal axis represents population size N .

tion rate is large, the effect of crossover on T is small.

Figure 6 shows the relation between T and a/S when p_m is 0.02 . a is the mean survival time. From this figure we observe the relation of $T = a/S$. There is strong N dependence of first hitting time of optimum solution T .

Figure 7 shows the dependence of a on N with $p_m = 0.02$ and 0.002 . When $p_m = 0.02$, $a \approx 1$, while $p_m = 0.002$, a is large. Therefore, the conclusion of $T \approx 1/S$ is established if $p_m = 0.02$.

4 Summary

The GA parameters, for example, population size N , string length L , crossover rate p_c and mutation rate p_m , influence the GA performance. In this study of GA on 3-SAT problem, the effects of crossover and mutation are investigated. The results show that :

when mutation rate is small,

- 1) The effects of crossover on S and T are large.
- 2) The success probability S with crossover is larger than that without crossover, which means crossover plays an important role on S .
- 3) The value of T with crossover is smaller than that without crossover, which means crossover accelerates the speed of evolution in GA.

We also observed the relation between T and a/S when mutation rate becomes large, and that $T \approx a/S$. When $p_m = 0.02$, $a \approx 1$ and $T \approx 1/S$.

References

- [1] J. Gu: Randomized and Deterministic Local Search for SAT and Scheduling Problems. *DIMACS Series in Discrete Mathematics and Theoretical Computer Science*, Vol.43, 61-62 (1999).
- [2] J. Gu: Parallel Algorithms for Satisfiability (SAT) Problem. *DIMACS Volume Series in Discrete Mathematics and Theoretical Computer Science*, American Mathematical Society, Vol.22, 105-161 (1995).
- [3] M. Davis, H. Putnam: A Computing Procedure for Quantification Theory. *Journal of the ACM*, Vol.7, Issue 3, 201-215 (1960).
- [4] J. Hansen, B. Jaumard: Algorithms for the maximum satisfiability problem. *Computing*, Vol.44, Issue 4, 279-303 (1990).

- [5] K. De Jong, W. Spears: Using genetic algorithms to solve NP-complete problems. *Proceedings of the Third International Conference on Genetic Algorithms*, 124-132 (1989).
- [6] C. Fleurent, J. Ferland: Object-oriented implementation of heuristic search methods for graph coloring, maximum clique, and satisfiability. *Discrete Mathematics and Theoretical Computer Science*, Vol.26, 619-652(1996).
- [7] E. Marchiori, C. Rossi: A Flipping Genetic Algorithm for Hard 3-SAT Problems. *In Genetic and Evolutionary Computation Conference*, Vol.1, 393-400 (1999).
- [8] J. Gottlieb, E. Marchiori, C. Rossi: Evolutionary Algorithms for the Satisfiability Problem. *Evolutionary Computation*, Vol.10, Issue 1, 35-50 (2002).
- [9] J. Gu: Efficient local search for very large-scale satisfiability problem. *SiGART Bulletin*, Vol.3, Issue 1, 8-12(1992).
- [10] <http://www.cs.ubc.ca/hoos/SATLIB/benchm.html>.
- [11] Y. Zhang, M. Sakamoto, H. Furutani: Effects of Population Size and Mutation Rate on Results of Genetic Algorithm. *Proceedings of Third International Conference on Natural Computation*, Vol.3, 70-75 (2008).

An Adaptive Resolution Hybrid Binary-Real Coded Genetic Algorithm

Omar Abdul-Rahman¹, Masaharu Munetomo² and Kiyoshi Akama²

¹Graduate School of Information Science & Technology, Hokkaido University,

²Information Initiative Center, Hokkaido University, Japan

(Tel : 81-11-706-7890; Fax : 81-11-706-7890)

(omar@ist.hokudai.ac.jp, munetomo@iic.hokudai.ac.jp, akama@iic.hokudai.ac.jp)

Abstract: Which is better to be used in Genetic Algorithms (GAs) binary or floating point coding schemes? In this paper, we try to answer this controversial question by proposing a novel algorithm that shares the computational power between two cooperated versions of GAs, a binary coded GA (bGA) and a real coded GA (rGA). The evolutionary search is primarily led by bGA, which is used to identify promising regions in the search space. While, the rGA is used to increase the quality of the obtained solutions by conduct a detailed search through these regions. The interactions between two versions are organized by a resolution factor that it is increasingly adapted during the evolutionary search. Comparison experiments were conducted over a typical function to proof the feasibility of the algorithm under critical scenarios of increasing problem dimensions and decreasing precision power.

Keywords: Binary coded GA, Real coded GA and Hybridizing.

I. INTRODUCTION

The intersection between Genetic Algorithms (GAs) and artificial intelligence has a long history. From one side, GAs play a central role in many artificial life models. They are currently the most prominent and widely used models of evolution in artificial life systems. In artificial intelligence, GAs have been used both as a tools for solving practical problems and as a scientific models of evolutionary processes. On the other hand, GAs have been successfully applied to solve difficult real world problems related to robotics like path planning, navigation controller optimization and line balancing problem.

In this paper, we try to approach again this long and controversial debate over the real coded and binary coded GAs. For theoretician, binary coded GA is an attractive solution. The theoretical finding of schemata theory supports that enhanced schemata processing is obtained by using alphabet of low cardinality. Binary coded GAs are efficient and the latest developments in the field of GAs research adds much to the robustness, speed and accuracy of such algorithms. However, it is possible to argue that binary coded GAs suffer from several disadvantages when applied to real-world problems involving a large number of real design variables. The direct relationship between the desired precision and the increased binary string length, and the discrepancy between the binary representation space and the actual problem space are good examples of such disadvantages.

On other hand, real coded GAs are preferred by many practitioners. They are on rising usage since the floating point representation is conceptually closest to the real design space, and moreover, the string length reduces to the number of design variables. Real coded GAs are robust, accurate, and efficient. However, it is possible to argue that real coded GAs are still susceptible to premature convergence especially for complex real world problems with a large number of design variables. It is also possible to say that theory of real coded GAs is still far from providing plausible understanding of internal real coded GAs mechanisms, which is a true hinder before the development of advanced techniques in this field.

Therefore, in this paper we propose the adaptive resolution binary-real coded GA (brGA) that combines the advantages of both versions. Under the proposed algorithm, two versions of the same population of solutions are kept, binary coded and real coded populations. They are updated by continuously mapping from one version to another during the evolutionary search. The search is primarily guided by binary coded GA part, which is used to identify promising regions in the search space. While, the real coded GA part is used to increase the quality of the obtained solutions by conduct a detailed search through these regions. The interactions between two parts are organized by a resolution factor that it is increasingly adapted during the evolutionary search. it has a small value at the begin of the search to allow the exploration of the search space by the binary coded GA part, while, its value increases gradually as the search progresses to

allow the exploitation of the search space by real coded GA part.

The remaining part of this paper is organized as follows. Related literature is reviewed in Section II. The proposed algorithm framework and implementation is explained in Section III. Then, experimental results are reported and discussed in Section VI. Finally, we conclude the paper in Section V.

II. LITERATURE REVIEW

Dynamic coding is a sophisticated approach to alter the coarseness of search spaces. An example of such approach is the stochastic genetic algorithm as presented by Krishnakumar et al [1]. In stochastic GAs, the region represented by each point of a binary coded GA is adapted during the optimization process using Evolutionary Strategies (ES). In our work, we adopted a similar concept. However, in contrast to stochastic GAs we employed a real coded GA instead of ES to adapt the region represented by the binary coded GA.

Another example of dynamic coding is the Adaptive Range Genetic Algorithm (ARGAs) as presented by Arakawa and Hagiwara [2]. In ARGAs, mapping rules from binary to real strings is updated during the optimization process according to the population statistics to adapt the population toward promising design regions. However, in our work we depend on a real coded GA that sample from the regions determined by a binary coded GA to adapt the population toward promising region in the search space.

Finally, a different approach is adopted by Barrios et al [3]. in their cooperative binary-real coded GA for designing and training feed-forward artificial neural networks. They employed two interconnected GAs that work parallelly to design and train better neural networks that solves the problem. In our work, we also employed two cooperative GAs, but they interact with each others in an interleaving manner.

III. THE ALGORITHM

The proposed algorithm flowchart is shown in Fig.1, which illustrates the typical optimization cycle. The main components of the algorithm can be described as follows.

1. **Coding schemes:** floating point and binary coding schemes is used to represent two equivalent populations of solutions. These populations are kept updated by continuously

mapping from one version to another during the evolutionary cycle.

2. **Binary coded GA:** the evolutionary cycle is usually led by the binary coded GA. This part is implemented using a binary GA as described by Haupt and Haupt [4]. The main parts of this algorithm are single point crossover operator, one point crossover operator, rank weighting selection scheme.
3. **Population handover:** the population of binary chromosomes that processed by the binary GA is transmitted to the real coded GA and vice versa at specific points of the evolutionary cycle. The process of population handover is controlled by the resolution factor that has an adaptive value that allows the real coded GA to increase the coarseness of the search space. During the process of handover, the best half from the current binary population is directly transmitted to the real coded population, while the other half comes by random sampling within the region determined by the binary population.
4. **Real coded GA;** the role of this version is to adapt the population toward the promising regions of the search space. In this paper, we have implemented this part using Unimodal Normal Distribution (UNDX) as an advanced real crossover operator [5]. Minimal Generation Gap (MGG) is used as a generation-alteration model.

IV. EXPERIMENTAL RESULTS

The proposed algorithm was implemented using MATLAB. Griewangk's function was used to testify the performance of the algorithm. The function is defined as follows.

$$f(x) = \frac{1}{4000} \sum_{i=1}^n x_i^2 - \prod_{i=1}^n \cos\left(\frac{x_i}{\sqrt{i}}\right) + 1 \quad (1)$$

This function has complex structure of numerous local extremum. It has a value of 0 at global optimum.

In the first set of experiments, the performance of the algorithm is testified against increasing problem dimensions. The performance is compared against an ordinary binary GA[4] and UNDX real coded GA[5].

The value of resolution factor was chosen as 2 increases in step of 2. The settings for real and binary coded GA were chosen as recommended in [4] and [5].

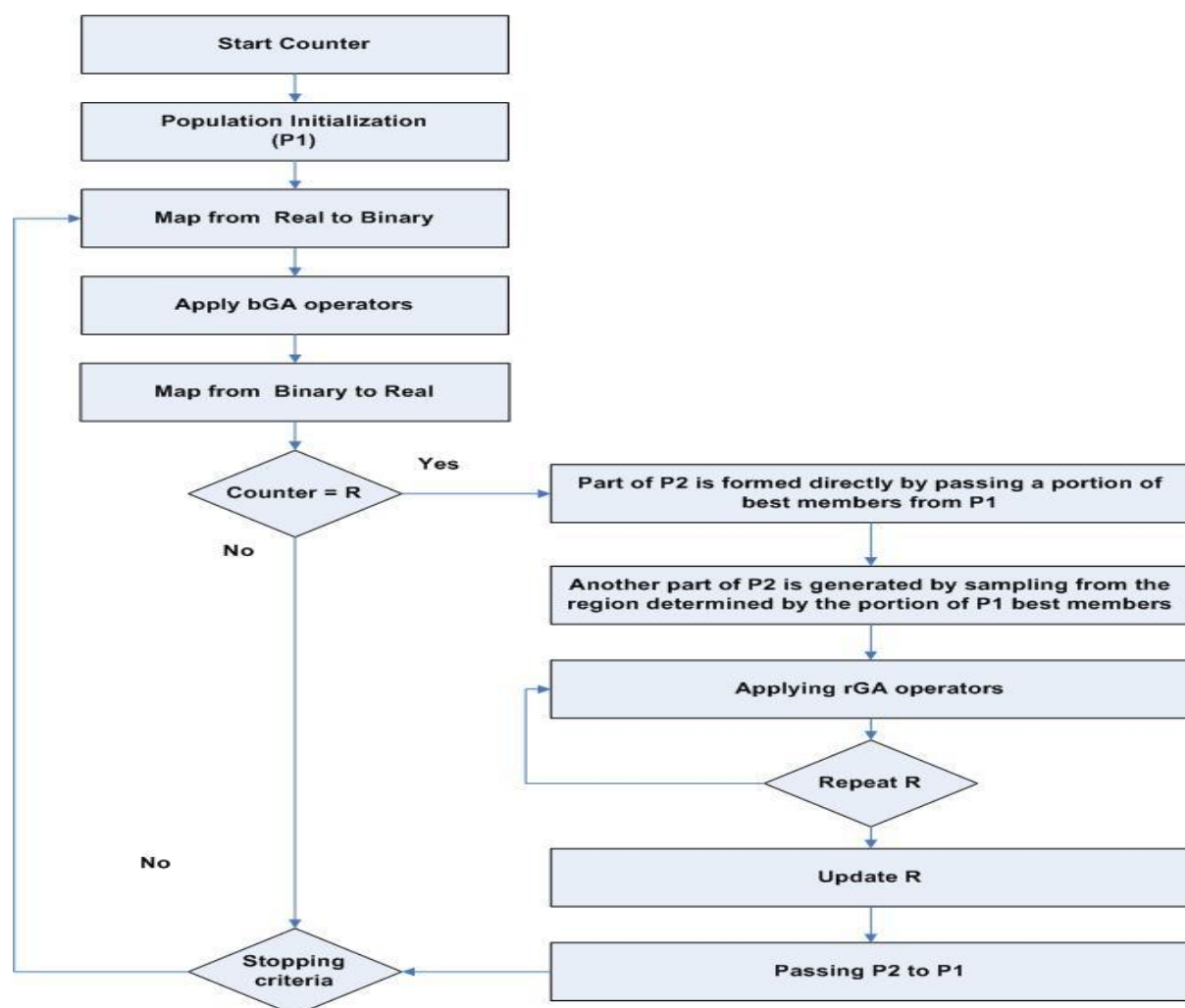


Fig.1. The proposed algorithm flowchart

The results were averaged over 50 experiments. Each run consisted of 990 iterations and a population of 6 members was used. The function is minimized over the range of $5 \leq x \leq -5$. Each parameter is represented by 8 bits.

Experimental results are shown in Table 1. Efficiency rates shown in the table is used to measure quality- computational effort relationship. It is defined according to Hillstrom [6] as follows.

$$\text{Efficiency} = \ln(|f^{(0)} - f^*|/|\hat{f} - f^*|)/T \quad (2)$$

Where $f^{(0)}$, f^* and \hat{f} are the best initial, best known and best final fitness, while, T is the elapsed time in seconds.

By comparing brGA to bGA, it is evident from the table that brGA outperforms in term of performance in all the cases. The difference in performance is clear at higher problem dimensions. In term of efficiency rate, bGA outperforms only in case of 10 dimensions in spite of lower solution quality.

This is due to the fact the implementation of bGA is faster than brGA. However, its efficiency rates degrades drastically to 0 in other cases, while, brGA keeps reasonable efficiency rates. This is due to the fact that the bGA loses the ability to progress the population at higher problem dimensions, which is one of binary coding disadvantages.

On the other hand, by comparing brGA to rGA it is evident that the performance is comparable at lower dimensions (10,50). But, the difference in performance increases at the higher dimensions (100, 120) for the benefit of brGA. So, the hybridizing enhance the performance of rGA at complex situation of high problem dimension. In term of efficiency rates, the results are comparable.

In the second set of experiments, the performance of the algorithm is testified against increasing chromosome length. The same settings as above were used. However, here the dimension is fixed to 2. In addition, only bGA and brGA were testified.

The experimental results are shown in Fig. 2. As expected the performance of bGA is largely depend on chromosome length. By increasing the number of bits, coding precision increases. Which, translated into

Table 1. Performance against increasing problem dimension

Problem Dimension	Binary GA			Real GA			brGA		
	Best	mean	Efficiency	Best	mean	Efficiency	Best	mean	Efficiency
10	0.1391	0.317	4.6125	0.004932	0.011739	3.8532	0.004934	0.012536	3.5739
50	1.0676	1.089	0	0.004305	0.024375	2.6723	0.004655	0.014299	2.2888
100	1.1602	1.188	0	0.61367	0.85668	0.17888	0.28473	0.45065	0.37779
120	1.1885	1.226	0	0.89541	0.98175	0.11178	0.57957	0.7713	0.16254

an enhanced performance. It is clear from Fig. 2 that brGA shows an independent performance against chromosome length. So, the hybriding is useful in decreasing the dependency of its binary part on chromosome length to achieve a better performance. That it is helpful in case of high precision that requires long chromosome representation.

V. CONCLUSION

An adaptive resolution binary-real coded GA is proposed in this paper. It is a framework that integrates the cooperation between rGA and bGA through an adaptive resolution factor to combine the advantages of both versions. Algorithm flowchart is presented, and explained. Then, experimental results over a typical benchmark problem is reported and discussed. It is evident from the results that the proposed algorithm greatly enhanced the performance of the binary GA part against increasing problem dimensions and decreasing chromosome length. On the other hand, the algorithm enhances the performance of rGA in case of higher problem dimension.

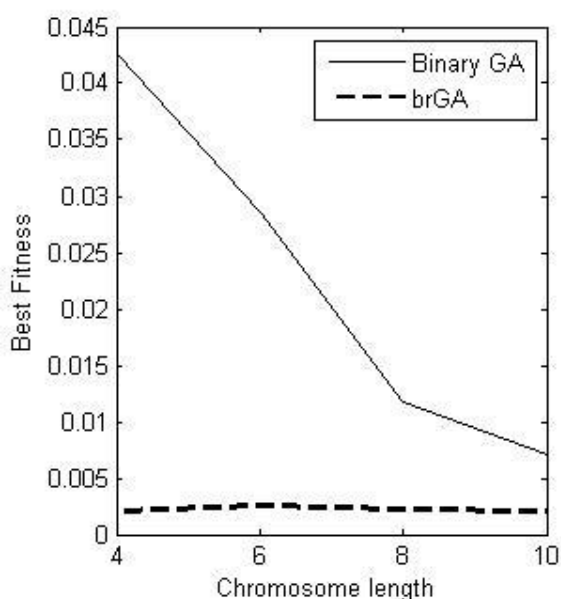


Fig.2. Solution quality versus chromosome length

ACKNOWLEDGMENT

This work is supported by Grant-in-Aid for Scientific Research (C) by MEXT, Japan.

REFERENCES

- [1] Krishnakumar, K., Swaminathan, R., Garg, S. and Narayanaswamy, S., Solving Large Parameter Optimization Problems Using Genetic Algorithms, Proc. of the Guidance, Navigation, and Control Conference, (1995), 449-460.
- [2] Arakawa, M. and Hagiwara, I., Development of Adaptive Real Range (ARRange) Genetic Algorithms, JSME Intl. J., Series C, Vol. 41, No. 4 (1998), 969-977.
- [3] Barrios, D., Carrascal, A., Manrique, D., Ríos, J., Cooperative binary real coded genetic algorithms for generating and adapting artificial neural networks, Neural Computing and Applications 12 (2003), 49-60.
- [4] Haupt, R.L. and Haupt, S.E. Practical Genetic Algorithms. (1998) Wiley, New York.
- [5] Ono, I. and Kobayashi, S., A Real-coded Genetic Algorithm for Function Optimization Using Unimodal Normal Distribution Crossover, Proc. 7th ICGA, 246-253 (1997).
- [6] Hillstom, K. E., A simulation test approach to the evaluation of nonlinear optimization algorithms. ACM Transactions on Mathematical Software, 3(4), 305- 315 (1977).

Neural network with exponential output neuron for estimation of physiological activities from protein expression levels

Kazuhiro KONDO[†] Kunihito YAMAMORI[‡] Ikuo YOSHIHARA[‡]

[†]*Graduate School of Eng., Univ. of Miyazaki*

[‡]*Faculty of Eng., Univ. of Miyazaki*

(Tel : + 81 985 58 7589; Fax : + 81 985 58 7589)

(kondo@taurus.cs.miyazaki-u.ac.jp, {yamamori, yoshiha}@cs.miyazaki-u.ac.jp)

Abstract: Many people expect the third function of foods called as physiological activities that affect our health condition. However, measurement of a physiological activity is troublesome and measurements for all kinds of foods are not impractical. Therefore a system which can easily estimate physiological activities is required. We have proposed a method to estimate physiological activities of foods from protein expression levels using artificial neural networks (ANNs). Estimation of physiological activity using conventional ANN has a problem that physiological activities take positive real number more than 1.0, but dynamic range of ANN is limited from 0.0 to 1.0. So measured physiological activities has to be scaled by dividing the maximum one. But this normalization gives undesirable influence to acceptable error level which is a parameter to terminate training process.

To solve this problem, we employ exponential function as the activation function in output neurons. By using exponential function in output neurons, ANN can directly handle physiological activities as the training signals those are more than 1.0. Experimental results show that our method improves accuracy than conventional ANN with scaled training samples for anti-oxidant activity, anti-inflammation activity and anti-angiogenic activity.

Keywords: physiological activities, protein expression level, exponential activation function, artificial neural network.

I. INTRODUCTION

Foods have three functions; the first is nutrition, the second is taste and the third is biological regulation. The third function of foods attracts attention in recent years because many people expect that the third function of foods will be useful to keep their health and prevent diseases. The third function of foods is measured as physiological activities. However, measurement of physiological activity is troublesome because it needs many sophisticated manual operations, and measurements for all kinds of foods are impossible. Therefore a system which can easily reveal physiological activities is required. For this objective, we have proposed a method to estimate physiological activities from protein expression levels because protein expression levels closely relate to cell condition and some kinds of protein expression levels can be measured at once.

Togo et al. [1] tried to estimate physiological activities by Bayesian classifier. Kamiguchi et al. [2] proposed to estimate physiological activities by multiple regression analysis. But these methods did not achieve

enough estimation accuracy. Tsukuda et al. [3] showed that artificial neural network (ANN) could achieve good estimation accuracy of physiological activities.

Estimation of physiological activities using conventional ANN has a problem. Physiological activities sometimes take positive real number more than 1.0, but dynamic range of a conventional ANN is limited from 0.0 to 1.0. So physiological activities have to be normalized for estimation by conventional ANN. But normalization leads undesirable influence for acceptable error level to terminate training process. To avoid this undesirable influence, we employ exponential function as the activation function in output neuron. By using exponential function in output neuron, ANN can directly handle physiological activities as the training signals those are more than 1.0.

II. ESTIMATION OF PHYSIOLOGICAL ACTIVITIES BY CONVENTIONAL ANN

We use artificial neural network (ANN) [4] for estimation of physiological activity. An ANN has an

input layer, a hidden layer and an output layer. An output of neuron j is calculated by Equation (1),

$$o_j^i = f\left(\sum_k \mathbf{x}^i \mathbf{w}_{jk}\right), \quad (1)$$

where $\mathbf{x}^i (i=0,1,2,\dots,I)$ is the i -th input vector, $\mathbf{w}_{jk} (j=0,1,2,\dots,J, k=0,1,2,\dots,K)$ is a weight vector between the neuron j and the neuron k . $f(x)$ is an activation function. Weight update algorithm of artificial neural network is usually back-propagation algorithm. Back-propagation algorithm minimizes the error between the calculated output o and the desired output y based on the steepest descent method. When the sum of the error define by Equation (2) becomes less than acceptable error level E' , training process is terminated.

$$E = \sum_i \sqrt{(o^i - y^i)^2} \quad (2)$$

where o^i and y^i is the output of ANN and the desired output for the i -th training sample, respectively.

Estimation of physiological activity by conventional ANN has a problem. Physiological activities sometimes take positive real number more than 1.0, but dynamic range of ANN is limited from 0.0 to 1.0. So physiological activities have to be normalized for estimating by conventional ANN. Since dynamic range of physiological activities is usually from 0.0 to 3.0, previous works divide physiological activities by the maximum one. If the acceptable error level to terminate training process is decided based on the original physiological activity, the scaled acceptable error level will become too small to terminate training process. If the acceptable error level is decided based on the scaled physiological activities, and it is large enough to terminate training process, obtained error will become too large because it is multiplied by the maximum value of the physiological activity. Kuno et al. [5] proposed Amplitude Extended Neural Networks to solve this problem. Amplitude Extended Neural Network introduces two parameters k and l into sigmoid function as $y = k/(1 + e^{-lx})$. The parameter k adjusts amplitude of sigmoid function and the parameter l adjusts slope of sigmoid function. Dynamic range of Amplitude Extended Neural Network is extended from 0.0 to k , but we have to decide two parameters for each physiological activity.

III. ANN WITH EXPONENTIAL OUTPUT NEURON

We employ exponential function $f(x) = e^{tx}$ as the activation function in output neuron. Here we introduce a parameter t into exponential function to adjust its slope. By using exponential function as the activation function in output neuron, ANN can directly handle the physiological activity as the training signals those are more than 1.0. Since normalization is unnecessary for proposed ANN, the error does not increase by rescaling. Exponential function is suitable for handling large physiological activities that is difficult to handle by sigmoid function.

Fig. 1 shows a sample of three layer ANNs. The ANN has an input layer, a hidden layer, and an output layer. All neurons of an input layer connects all neurons in hidden layer, and a neuron of hidden layer connects all neurons in output layer. Constitution of our proposed neural network is three layer model and the activation function of the output neuron is exponential function, and that in other layers is sigmoid function.

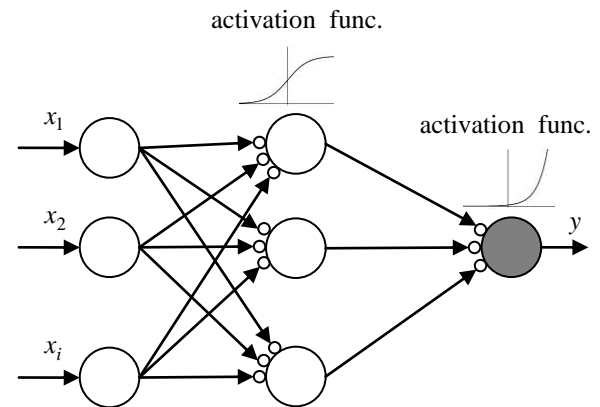


Fig. 1 Neural network with exponential output neuron

We evaluate proposed ANN by preliminary exercises. An artificial data are generated by following equations data1~data4. An input consists of three dimensional vector (a_1, a_2, a_3) , and an output is a scalar y . The elements of input vector is decided at random. The range of the elements in a input vector is 0.0 to 3.0. The x in the following equations is sum of the elements of input vector $x = a_1 + a_2 + a_3$. All x satisfy the condition $0.0 \leq x \leq 5.0$. The output y is normalized by dividing the maximum value for conventional ANN. Table 1 shows ANN parameters for preliminary exercise. We continue the training process until it arrives at the maximum epoch.

- data1: $y = x^2$
- data2: $y = x^2 - 2x + 1$
- data3: $y = x^3$
- data4: $y = 5/(1 + e^{-x})$

Table 2 shows mean square errors between the theoretical y and the output of ANN.

Table 1 ANN parameter for preliminary exercises.

Training rate	0.4
Momentum	0.7
Maximum epoch	20,000
The number of input neurons	3
The number of hidden neurons	2
The number of output neurons	1
Slope of exponential function t	1/256
The number of training sample	400

Table 2 Mean square error of preliminary exercises.

	data1	data2	data3	data4
convetional ANN	0.184	0.204	0.220	0.132
proposed ANN	0.163	0.193	0.134	0.123

Proposed ANN could obtain more accurate approximation model than conventional ANN as shown in Table 2. Mean square error of conventional ANN becomes larger than proposed ANN because the error of conventional ANN becomes large by rescaling. Table 2 also says that proposed ANN is suitable for the model equation approximation like as quadratic or cubic function.

IV. PHYSIOLOGICAL ACTIVITIES ESTIMATION

ANN needs appropriate training samples to make a suitable model. Measured physiological activities and protein expression levels include relatively large noise come from cell condition and measurement environment. We solve this problem by exception of outlier using Smirnov-Grubbs test.

Physiological activities and protein expression levels are measured in multiple times for a constituent of the food, and these are not corresponded each other. It means that we do not construct appropriate training samples consisting of a physiological activity as a training signal and protein expression levels as input signals. We use simple linear regression analysis to correspond a physiology activity and protein expression levels. We make all the available combination between the physiological activities and the protein levels for a

constituent of the food, and apply simple linear regression analysis for these combinations. The combination that has the lowest residual is selected as the adequate training sample.

We use thirty kinds of constituents for three concentrations as training samples. A part of the constituents as shown in Table 3. The constituent is given to HepG2 cells, then protein expression levels and physiological activities are measured, respectively. So a data-set involves $90(=30 \times 3)$ measured values. We measure the expression levels of following proteins; Survivin, HSP70, XIAP, FADD, TXNRD1, HSP90, MxA, tNOX, NQO1, ERK2, p53 and Bcl2.

We compared conventional ANN with proposed ANN for six kinds of physiological activities. These experiments run ten times with the same parameter. Table 4 shows training parameters, and Table 5 shows the number of samples. We evaluate each method by estimation accuracy defined by Equation (3).

$$accuracy = \frac{\text{Number of estimated samples}}{\text{Total number of samples}} \times 100, \quad (3)$$

where the number of estimated samples means that the number of samples they satisfied the error less than 0.2.

Table 3 Samples of constituents and their concentrations

	concentrations(μM)		
LipoicAcid	100	300	1000
EGCG	7	20	50
Genistein	10	20	60
Daizein	25	50	150
Glycitein	10	30	100
Quercetin	5	15	60

Table 4 ANN parameters for estimation experiments

Training rate	0.4
Momentum	0.7
Maximum epoch	20,000
The number of input neurons	13
The number of hidden neurons	6
The number of output neurons	1
Slope of exponential function t	1/256
Acceptable error level	0.2

Table 5 The number of sample

physiological activity	The number of training sample	The number of testing sample
anti-oxidant	627	128
anti-proliferative	642	131
anti-inflammation	637	130
anti-angiogenic	642	131

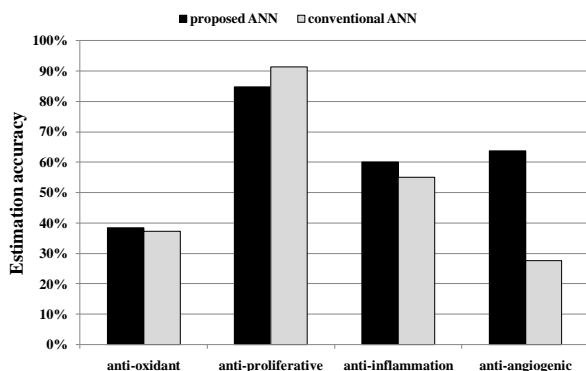


Fig. 2 Results of estimation accuracy

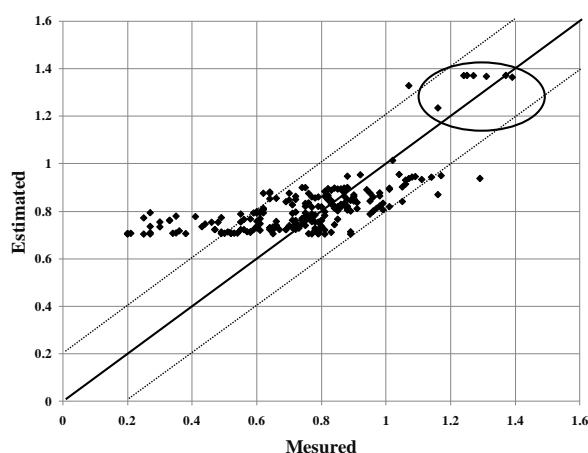


Fig. 3 Scatter diagram for anti-angiogenic activity

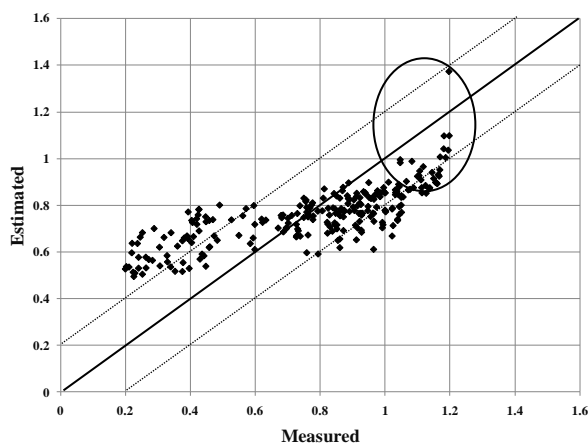


Fig. 4 Scatter diagram for anti-inflammation activity

Fig. 2 shows estimation result of four physiological activities (anti-oxidant, anti-proliferative, anti-inflammation, anti-angiogenic activity) using proposed ANN and conventional ANN. Proposed ANN is more accurate than conventional ANN with normalization for anti-oxidant activity, anti-inflammation activity and anti-angiogenic activity. Fig. 3 and Fig. 4 show estimation results for the anti-angiogenic activity and the anti-inflammation activity by scatter diagram where

the x-axis is measured value and the y-axis is estimated value. In Fig.3 and Fig.4, the dotted-line shows boarder that satisfies ± 0.2 of measured values. Proposed ANN can estimate relatively large physiological activity shown in circles in Fig. 3 and Fig.4.

V. CONCLUSIONS

In this paper, we proposed a neural network with exponential output neuron and applied it to estimate physiological activities from protein expression levels. Experimental results showed that our method achieved more accurate than conventional ANN with normalization for anti-oxidant activity, anti-inflammation activity and anti-angiogenic activity. Furthermore it could realize to directly use measured physiological activities as training samples. However, proposed neural network couldn't follow small physiological activity. It is future subject that estimation by multi-model ANNs to estimate both of large and small physiological activities.

REFERENCES

- [1] Togo S. (2008), Estimating physiological activities of functional foods form protein expression levels using baysian classifier, The Thirteenth International Symposium on artificial Life and Robotics 2008, pp.853-856, OS12-3.
- [2] Kamiguchi M. (2008), Estimation of Physiological Activity Values from Protein Expression Levels with Multiple Regression Analysis, Memoirs of the Faculty of Engineering, University of miyazaki, No.37, pp.269-273.
- [3] Tsukuda S. (2007), Estimation of physiology Activity in Foods with Neural Network from Insufficient Data, Memoirs of the Faculty of Engineering, University of miyazaki, No.36, pp.345-350.
- [4] Sholom WM., Nitin I. (1998), PREDICTIVE DATA MINING., Morgan Kaufmann Publishers, Inc, San Francisco, California.
- [5] Kuno T. (2009), Development of Physiological Activity Estimation System of Foods Using Amplitude Extended Neural Networks, The fourteenth International Symposium on artificial Life and Robotics 2009, pp.853-856.

Asynchronous migration for parallel genetic programming on computer cluster with multi-core processors

Shingo KUROSE¹ Kunihito YAMAMORI² Masaru AIKAWA³ and Ikuo YOSHIHARA²

¹Graduate School of Eng., Univ. of Miyazaki

²Faculty of Eng., Univ. of Miyazaki

³Technical Center, Faculty of Eng., Univ. of Miyazaki

(Tel : 81 985 58 7589; Fax : 81 985 58 7589)

(kurose@taurus.cs.miyazaki-u.ac.jp, {yamamori, yoshiha, aikawa}@cs.miyazaki-u.ac.jp)

Abstract: Island model is a typical implementation model of parallel distributed genetic algorithms, and it is also used in parallel genetic programming. Island model has migration process that exchanges individuals between sub-populations to leave local optimum. However island model requires synchronous process to exchange individuals at the same generation, and synchronous process increases computation time.

This paper proposes a new parallel genetic programming model based on the island model with asynchronous migration. We implement island model using Message Passing Interface (MPI). Fitness calculation which requires the longest computation time is processed in parallel by multi-threading. In addition, proposed method employs a communication thread for migration between computation nodes, and communication thread communicates with another communication thread to exchange individuals at appropriate intervals. The communication and genetic operations can be independently processed on each core. Experimental results show that proposed method with five computation nodes and forty threads can reduce computation time about 17% of serial GP.

Keywords: Genetic programming, MPI, Multi-threading, Island model, Asynchronous migration

I. INTRODUCTION

Genetic Programming (GP) [1,2,3] is one of the evolutionary algorithms for optimization inspired from biological evolution. GP expresses a candidate of solution as a structural individual like a tree. Each individual is evolved by genetic operations such as crossover and mutation, and then only the individuals that have superior fitness remain for next generation. Through these evolutionary processes, GP can make a model automatically. Computation time of GP becomes longer as increasing of the number of individuals and the generations to obtain more accurate solution. So GP is usually implemented in computer cluster. Parallel GP implementation can be classified into two models; master-slave model and island model [2].

This paper proposes a new parallel genetic programming model based on the island model with asynchronous migration. We implement island model using Message Passing Interface (MPI) [3]. Fitness calculation which requires the longest computation time is processed in parallel by multi-threading [4]. In addition, proposed method employs a communication thread for migration between computation nodes to reduce synchronous overhead. We evaluated proposed method on computer cluster.

II. PARALLEL GENETIC PROGRAMMING

1. Island model

Island model [2] is one of the implementation models for parallel distributed genetic algorithms and it is also used for parallel genetic programming. Island model divides a population consisting of individuals into sub-populations, and it assigns a sub-population to a computation node. Individuals in each sub-population

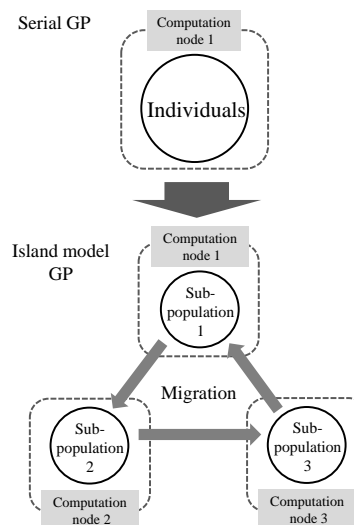


Fig. 1 An example of island model by three computation nodes.

are independently evolved in parallel. The number of individuals in sub-population is reduced, and genetic operations for individuals in each sub-population are processed in parallel, island model can reduce computation time. In usual, island model has migration process, that immigrates individuals from sub-population to another sub-population, to leave local optimum. Figure 1 shows an example of island model by three computation nodes.

2. Synchronous migration

Migration is a process to immigrate individuals from sub-population to another sub-population at every some generations. So the migration on computer cluster requires network communication to exchange individuals. Migrated individuals are chosen by various ways. For example, migrated individual is an elite that has the highest fitness in sub-population. In other way, some individuals are chosen at random. Before migration, computation nodes synchronize their generation because independent evolution leads the difference of computation time for each sub-population. So some sub-populations have to wait their migration until the slowest sub-population has finished their operations.

III. ASYNCHRONOUS MIGRATION FOR PARALLEL GENETIC PROGRAMMING

1. Inter-nodes parallelization and intra-nodes parallelization

Proposed method implements island model using Message Passing Interface (MPI) [3] for inter-nodes parallelization. MPI is a standard library for parallel

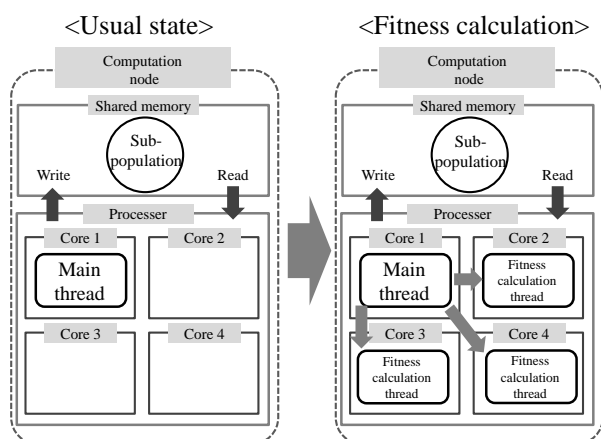


Fig. 2. Intra-nodes parallelization using fitness calculation threads.

programming.

Recent processors equip some processing cores on a die, and they share a main memory. This architecture is suitable for multi-threading [4]. Our method creates threads for fitness calculation, and these threads work in parallel. Shared memory is used to exchange individuals between main thread and fitness calculation threads. Proposed method expects high speed processing by using both inter-nodes parallelization by MPI and intra-nodes parallelization by multi-threading. Figure 2 shows intra-nodes parallelization using fitness calculation threads.

2. Asynchronous migration

Proposed method creates a communication thread to reduce waiting time by synchronization. At first main thread creates individuals at random, and calculates their fitness. Then the main thread of each computation node selects an elite individual and stores it into the transmission buffer. Here, synchronization is executed just for once for reliable migration. Next, the main thread creates a communication thread and it transfer the individual stored in the transmission buffer to the communication thread in the other computation node at appropriate interval. The elite individual is exchanged through the shared memory between the main thread and the communication thread. The communication thread also receives the transferred individual from the other communication thread and stores it into the receiving buffer. The main thread takes the migrated individual from the other sub-population into their own sub-population at appropriate interval when the genetic operations are finished. Figure 3 shows an example of individual exchanging between the main thread and the communication thread. Figure 4 illustrates an example

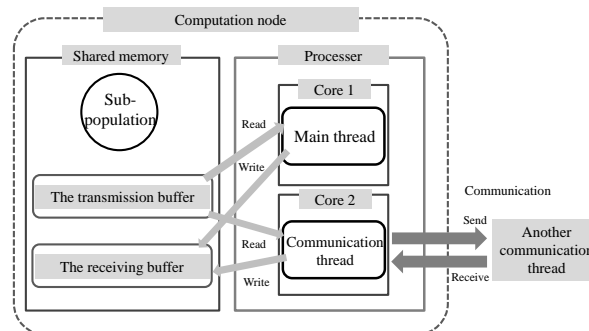


Fig. 3. An example of individuals exchanging between the main thread and the communication thread.

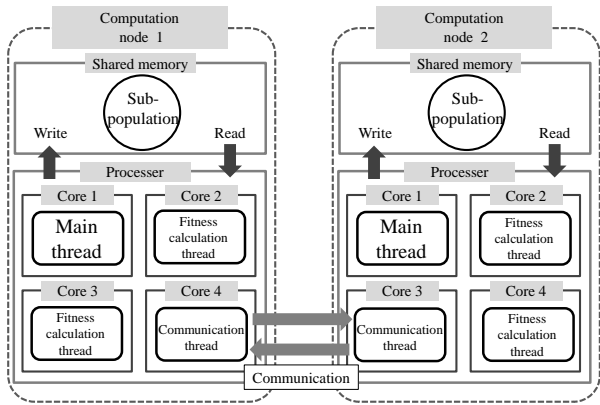


Fig. 4. An example of task allocation for two computation nodes with four processing cores in a processor.

of task allocation for two computation nodes with four processing cores in a processor.

IV. EXPERIMENTAL RESULTS

We evaluate processing time and accuracy of obtained solution on computer cluster. Table 1 shows experimental environments. Computer cluster equips distributed memory, and a multi-core processor has four processing cores, and it equips hyper threading technologies®, so eight threads can work in parallel. We compare with three implementation models of parallel GP. Table 2 shows detail of each model. The iGP is parallel GP using basic island model. The tfGP is the modified iGP using fitness calculation threads. In the tfGP, eight fitness calculation threads are created. The amGP is also the modified iGP using fitness calculation thread and communication thread for asynchronous migration. In the amGP, seven fitness calculation threads and one communication thread are created. We can evaluate the effect of intra-nodes parallelization by

Table. 1. Experimental environments.

CPU	Intel® Xeon E5530 2.40GHz ×2
Core/Thread	4 cores / 8 threads
Memory	8 GB
The number of computation node	12 nodes

Table. 2. Details of each model.

	iGP	tfGP	amGP
Island model	○	○	○
Threaded fitness calculation	×	○	○
Asynchronous migration	×	×	○

Table. 3. Parameters of GP.

Parameters	
The number of generation	1,000
The number of Individual	300
Max depth for Individual	8
The number of Training samples	600
Operator	+, -, *, /, sin, cos, tan, log
Selection	Elitist schemes Roulette selection
Mutation rate	0.1
Migrating individual	Elite
Migration interval	Every 50 generation

comparing the iGP with the tfGP. In addition, we can also evaluate the effect of asynchronous migration by comparing tfGP with amGP. Table 3 shows parameter of GP. Individuals are divided into sub-populations equally. In experimentation, training samples are taken from [5].

Figure 5 shows the computation time with respect to the number of computation nodes. Serial GP takes about 1,000 sec. for 1,000 generations. The iGP with five computation nodes can reduce computation time about 46% of serial GP. However, computation time is increased when more than six computation nodes are used. Figure 6 shows the average number of nodes in an individual for each number of computation nodes. In the iGP, the average number of nodes in an individual increases when the number of computation node is increased. Computation time of fitness calculation is increased by increasing of the number of nodes in an individual. As a result, the computation time for fitness calculation is different among sub-population, and it leads large overhead for synchronous migration. This is the reason of increasing of computation time when more than six computation nodes are used on the iGP and tfGP.

In Figure 5, the tfGP with five computation nodes and forty threads can reduce computation time about 21% of serial GP. Computation time is also increased when more than six processors are used as well as the iGP. It is because that synchronous migration takes large overhead as well as the iGP.

In Figure 5, the amGP with five computation nodes and forty threads can reduce computation time about 17% of serial GP.

Figure 7 shows the average fitness for each number of computation nodes. Fitness of individual s is

calculated by Equation (1).

$$\text{Fitness} = \frac{1}{F}$$

$$F = \frac{1}{n} \sum_{i=1}^n (\hat{y}_i - y_i) \quad (1)$$

In Equation (1), n is the number of training samples, \hat{y}_i and y_i are the desired value and the

output of the model for the i -th training sample, respectively. In Figure 7, the average fitness of amGP increases as well as the iGP and the tfGP when the number of computation node is increased. In Figure 5, computation time of amGP doesn't increase even if more than six processors are used. So, proposed method is effective method when many computation nodes are used to obtain more accurate solution.

V. CONCLUSION

This paper proposed a new parallel genetic programming model based on the island model using asynchronous communication between computation nodes. We implement island model using Message Passing Interface (MPI). Our method creates threads for fitness calculation, and these threads work in parallel. In addition, proposed method employs a communication thread for asynchronous migration between computation nodes. Experimental results showed that fundamental parallel island model with five processors can reduce computation time about 46% of serial GP. Furthermore, our proposed method with five computation nodes and forty threads can reduce computation time about 17% of serial GP. In future, we will improve efficiency of parallelization by investigating the load of each computation node.

REFERENCES

- [1] Numata N, Sugawara K, Yamada S et al. (1999), Time Series Prediction Modeling by Genetic Programming without Inheritance of Model Parameters. Proc. Fourth Int. Sym. Artificial Life and Robotics:500-503
- [2] Eklund SE (2003), Time Series Forecasting using Massively Parallel Genetic Programming. Parallel and Distributed Processing Symposium: 10.1109/IPDS.2003.1213272
- [3] Messom CH and Walker MG (2002), Evolving Cooperative Robotic Behaviour using Distributed Genetic Programming. Control, Automation, Robotics and Vision: 215-219
- [4] Nichols B, Buttler D, Farrell JP (1996), Pthreads Programming (A Nutshell handbook). O'Reilly & Associates Inc (California).
- [5] Kamiguchi M, Yamamori K, Yoshihara I et al. (2009), An Automatic Model Building for Screening Functional Foods with GP. ICROS-SICE International joint Conference 2009:3679-3684

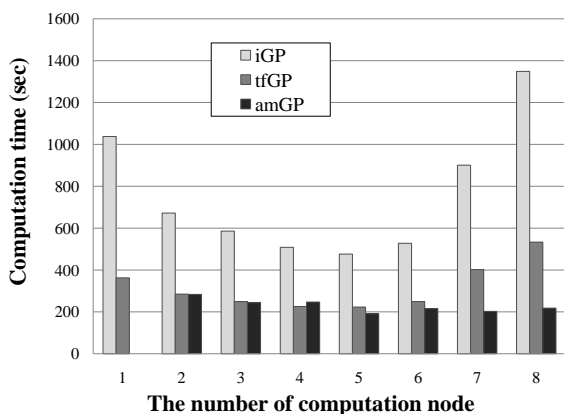


Fig. 5. Computation time with respect to the number of computation nodes.

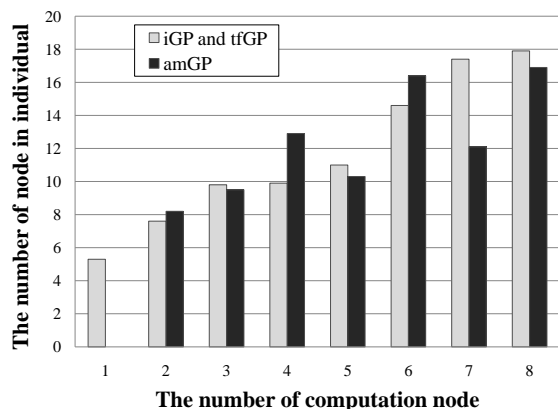


Fig. 6. Average number of nodes in individuals for each number of computation nodes.

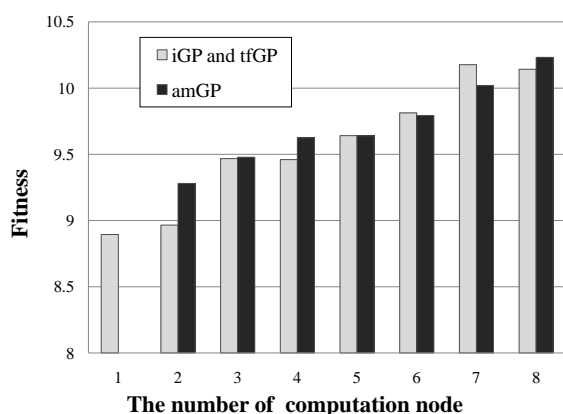


Fig. 7. Average fitness for each number of computation nodes.

Classification of species by information entropy and visualization by self-organizing map

Kentaro NISHIMUTA¹⁾, Ikuo YOSHIHARA¹⁾, Kunihiro YAMAMORI¹⁾, Moritoshi YASUNAGA²⁾

¹⁾1-1, Gakuen Kibanadai-nishi, Miyazaki, 889-2192, Japan, University of Miyazaki

(Tel : +81-985-58-7384; Fax : +81-985-58-7384)

(Email address : { nmuta, yoshiha, yamamori }@taurus.cs.miyazaki-u.ac.jp)

²⁾1-1-1, Tennoudai, Tsukuba, Ibaraki, 305-8573, Japan

Graduate School of Systems and Information, Engineering,

University of Tsukuba

Abstract: Most analysis methods of base sequences are based on the idea of pattern matching, but feature patterns known until today are supposedly a part of all the patterns hidden in base sequences. We develop a novel analyzing method based on disorder of base sequences, for example variance of data, 1/f fluctuation, information entropy and self-information. We try to classify species based on self-information of base sequences. Relations between species are visualized by self-organizing map (SOM). It is probable that neighboring regions of the SOM corresponds to near species. We compare neighboring regions of the SOM with neighboring branches of an evolutionary tree produced by the Clustal-W system.

Keywords: DNA, self-information, information entropy, self-organizing map

I. INTRODUCTION

Evolution degeneration of species must be remained in base sequences, because mutations have been accumulated in them for a long time. Various analysis methods on base sequences are investigated for revealing evolution of living creatures.

Most analysis methods of base sequences are based on pattern matching, but feature patterns known until today are probably a part of iceberg i.e. enormous kinds of patterns are ought to exist. Rule based analysis cannot be applicable to genes of unknown species.

We make up our mind to change the viewpoint of research from strict pattern matching to rough comparison. We propose a novel analyzing method using disorder of base sequences. Though disorder is somewhat vague, various features of species are reflected in disorder.

There exist many candidate methods of analysis concerning to disorder, for example, data compression ratio[1], long range order used in statistical mechanics[2], 1/f fluctuation[3], variance of data[4][5], information entropy[6] etc .

This article employs information entropy, especially self-information as an index of disorder. Self-

information is calculated from appearance rate of codons in sub-sequences cut out from whole the base sequence.

We try to classify species based on self-information of base sequences without using pattern matching, and visualize relations of species by self-organizing map (SOM). One region represents one species.

We validate the method of classification of species and to compare neighboring regions on the SOM with neighboring branches of evolutionary tree produced by the Clustal-W system[7].

II. DISORDER ANALYSIS BY INFORMATION ENTROPY AND SOM

1. Composition of base sequences

Base sequences consist of four kinds of bases; A(Adenine), C (Cytosine), G (Guanine), and T (Thymine).

A sequence of three adjacent bases is called codon. The number of codons is $64=4^3$, because codon is a triplet of 4 kinds of bases.

2. Information entropy

Information entropy of species is assumed to be a measure of characteristic of species.

The complete event system (X, P) is determined by the occurrence probability $P(X_i)$, where X_i is one of 64 codons. $\{X_i\}$ corresponds to AAA, AAG, AAC, ..., TTT.

$$\begin{pmatrix} X \\ P \end{pmatrix} = \begin{pmatrix} \text{AAA} & \text{AAG} & \cdots & \text{TTT} \\ P(\text{AAA}) & P(\text{AAG}) & \cdots & P(\text{TTT}) \end{pmatrix}.$$

Self-information is defined by the probability $P(X_i)$, Self-information has the same number as the codon.

$$I(X_i) = -\log_2 P(X_i) \quad (i = 1, 2, \dots, 64)$$

Information entropy $H(X)$ is an expected value of self-information $I(X)$, i.e. $H(X) = -P(X)\log_2 P(X)$. $H(X)$ derives as follows,

$$H(X_1, X_2, \dots, X_n) = -\sum_{i=1}^{64} P(X_i) \log_2 P(X_i).$$

3. Self-organizing map (SOM)

Self-organizing map (SOM) proposed by Kohonen is an unsupervised-learning neural network which is used for clustering and visualization [8].

The codon of self-information as vector of 64th dimension is used for input of SOM. SOM has two-layer structure. Input layer has nodes the number of which is the same as the number of dimension of the input.

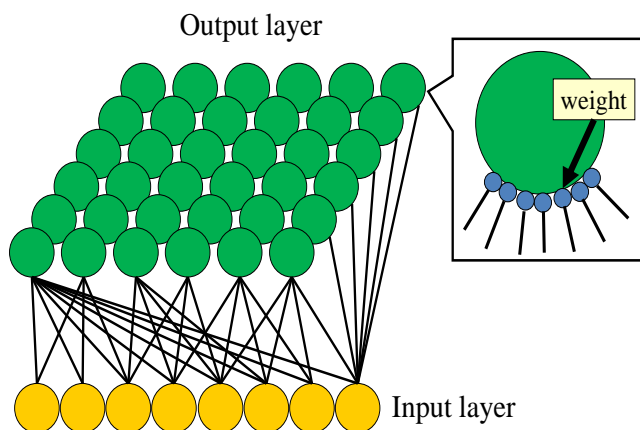


Fig 1 Illustration of input and output layers of SOM

The output layer of SOM is allocated on rectangle lattice(x,y). The size of output layer is arbitrarily decided.

Weights connect input layer and output layer. Weight is strength of connection between input layer and output layer. Two layers unite completely by weight (Fig 1). The relation between the output(O), weight(W) and the input(I) is shown by the following expressions.

$$O(x, y) = \sum_{i=1}^{64} W_i I_i.$$

We use SOM to distinguish species by self-information.

4. Positional information entropy

Sub-sequences are parts of a base sequence cut out with a given length of bases and are information entropy a positional function of the base sequence (Fig 2).

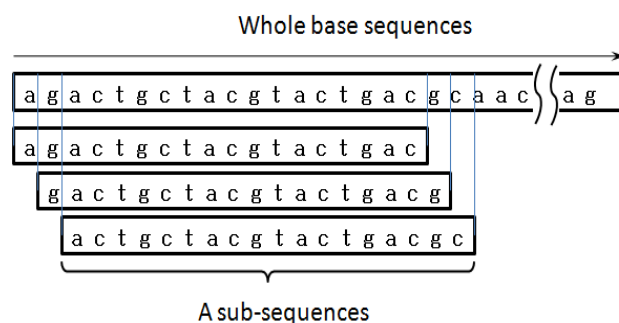


Fig 2 Base representation of the whole base sequence

Self-information of codons is calculated by the appearance probability of codons in sub-sequence (Fig 3).

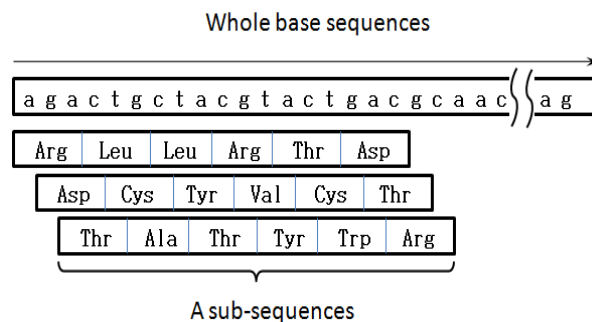


Fig 3 Codon representation of sub-sequences

III. EXPERIMENTS

1. Experimental condition

We validate the proposed method by the following steps.

[Step 1]. Calculation of self-information.

[Step 2]. Visualization by SOM.

[Step 3]. Comparison SOM with evolutionary tree.

Experimental data of base sequences are ribosomal protein genes of 20 species in Table 1, which are taken from the Ribosomal Protein Gene (RPG) Database established by Frontier Science Research Center, University of Miyazaki[9].

The ribosomal proteins used are as follows;

RPL3 RPL4 RPL5 RPL6 RPL7 RPL7A
RPL8 RPL9 RPL10 RPL10A RPL17 RPL23

2. Pre-experiment

First of all, we need to determine experimentally an appropriate length of sub-sequence. We conduct small scale experiments will give us nearly optimal parameters of SOM. 6 kinds of species are used; { A(Hs), B(Mm), H(Ag), I(Ce), J(Mg), and O(Um) } in Table 1.

We change the length of sub-sequence from 64 bases to 2048 bases. Sub-sequence cannot cut out more than 2048 bases, because length of base sequence is different because of species. Parameters of experiments are as follows; map-size is 25×25 , and iteration of learning is 100.

3. Results of pre-experiment

Length of sub-sequence 2048 gives good figure of SOM(Fig 4). Species are separated in 6 regions. Length of sub-sequence is long, species of 6 kinds all separated.

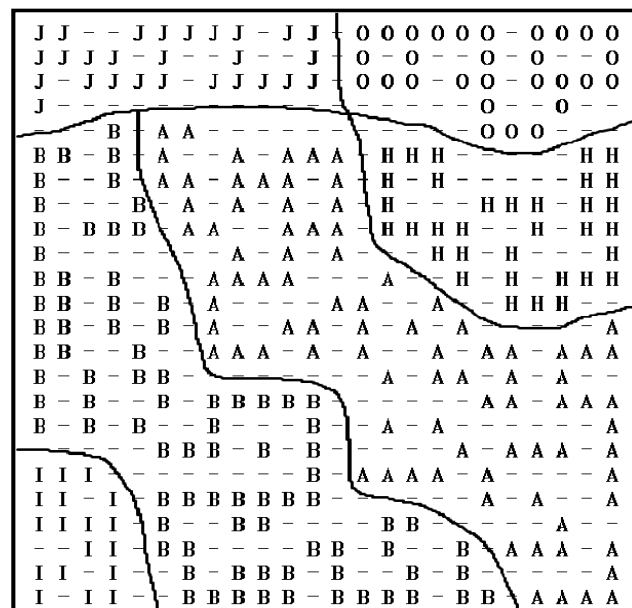


Fig 4 Result of pre-experiment (6 species)

4. Experiment

We validate the proposed method employing data of 20 species. Length of sub-sequences is same for all species i.e.2048 bases. Parameters in experiments are as follows; map-size is 40×40 , and iteration of learning is 100.

5. Results and discussions

Fig 5 (A) is a map produced by SOM and Fig 5 (B) is an evolutionary tree produced by the Clustal-W system. We take a look of parts with same colored mask pattern.

The map of SOM is separated in 21 regions. There are 2 regions of C(Rn). We confirmed to correspond between the neighboring regions of the SOM to the neighboring branches of the evolutionary tree.

Table 1 Correspondence table for experiment

symbol	abbr	species	symbol	abbr	species	symbol	abbr	species	symbol	abbr	species
A	Hs	H.sapiens	F	Dm	D.melanogaster	K	Fg	F.graminearum	P	Ro	R.oryzae
B	Mm	M.musculus	G	Am	A mellifera	L	Yl	Y.lipolytica	Q	Cn	C.neoformans
C	Rn	R.norvegicus	H	Ag	A.gamiae	M	Sc	S.cerevisiae	R	Dd	D.discoideum
D	Fr	F.rubripes	I	Ce	C.elegans	N	Sp	S.pombe	S	At	A.thaliana
E	Ci	C.intestinalis	J	Mg	M.grisea	O	Um	U.maydis	T	Cr	C.reinhardtii

Digital-signal-waveform improvement on VLSI packaging including inductances

Hiroki SHIMADA[†], Shohei AKITA[†], Masami ISHIGURO[†], Noriyuki AIBE[†],
Ikuo YOSHIHARA[‡], and Moritoshi YASUNAGA[†]

[†]Graduate School of Systems and Information Engineering, University of Tsukuba,
1-1-1 Tennodai, Tsukuba-shi, Ibaraki-ken, 305-8573, Japan
(Tel : 81-92-853-5323)

(Email:{shimada@islab, akita@islab, masami@islab, yasunaga, susu@islab}.cs.tsukuba.ac.jp)

[‡] Faculty of Engineering, Miyazaki University,
1-1, Gakuen-kibanadainishi, Miyazaki, Miyazaki, 889-2192, Japan
(Email: yoshiha@cs.miyazaki-u.ac.jp)

Abstract: As digital-signal frequency in PCBs (Printed Circuit Boards) increases, waveform-distortion, or the Signal Integrity (SI) problem is getting serious more and more. The reason why the SI becomes serious is that wires, or traces need to be regard as transmission lines, which are sensitive to electric noises. In order to overcome this problem, we have already proposed a novel methodology called STL (Segmental Transmission Line), and have also shown its effectiveness using computer-simulation and fundamental prototypes. In the STL design however, combinatorial explosion problem occurs as a big problem. To solve this problem, Genetic Algorithms (GA) is used to design STL. In this paper, we newly apply the STL to the bus system that includes inductances, which come from the VLSI packaging. We evaluated the STL on the simulation experiments and the actual experiments using prototypes, and obtained the maximum improvement ratio of 1.53 in the actual experiment.

Keywords: Signal Integrity, Transmission Line, Genetic Algorithms, Inductance, Printed Circuit Board

I. INTRODUCTION

From hundreds of MHz or more, digital signals begin to behave as waves, so that the PCB (Printed Circuit Board) traces must be designed as transmission lines. The transmission line is characterized by the characteristic-impedance Z , which shows the easiness of the signal to transmit. And if some devices or electrical components, which are equivalent to capacitors or inductors, are connected to the transmission line, they become sources of impedance-mismatching, and cause waveform-distortion, or decrease SI (signal integrity) as shown in Fig. 1.

Conventionally, some local-impedance-matching techniques such as SSTL[1] have been used to solve the impedance-mismatching problem. These techniques, however, have not been going well gradually as the frequency increases and approaches to the GHz-region.

In order to overcome this difficulty in the conventional techniques, we have already proposed a novel technique called "Segmental Transmission Line (STL)", and have shown its fundamental effectiveness on some simple transmission models [2][3], where only capacitors are connected. In the high-speed digital-signal transfer, however, not only the capacitances but some inductances, which come from VLSI packages and connectors connected two PCB boards for example, also cause impedance-mismatch and affect the waveform.

In this paper, we apply the STL to the bus system where inductances are also connected to the transmission line as well as the capacitances, and show its effectiveness quantitatively on computer-simulations

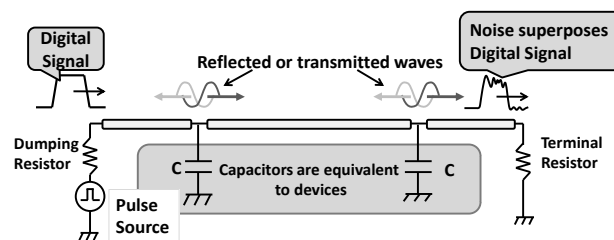


Fig.1 Decline of Signal Integrity

and actual experiments.

II. SEGMENTAL TRANSMISSION LINE

In order to improve SI in PCB traces, we have already proposed a novel transmission called Segmental Transmission Line (STL) [2]. In the STL, a transmission line is divided into multiple segments of individual characteristic-impedance Z_i and segment-length L_i . In the strip-line structure, or micro-strip line structure in the PCB traces, the characteristic impedance Z is a function of the segment-width W , i.e., $Z=f(W)$. Each segment has thus its own width W_i and length L_i individually as design parameters as shown in Fig.2 if the STL is applied to the PCB trace.

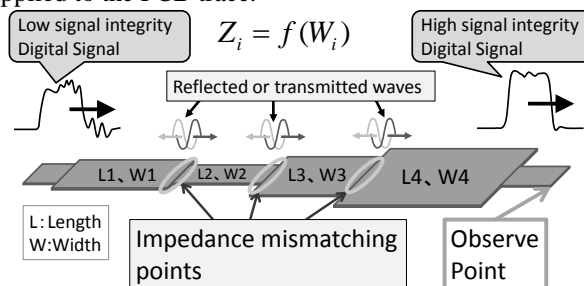


Fig.2 Configuration of Segmental Transmission Line

In the STL, each boundary between adjacent segments causes an impedance-mismatch-point as a matter of course, and reflection waves and transmitted waves occurs at each boundary as a result. In the STL, superposition of the multiple reflection-waves from all boundaries is used to improve the waveform distortion at target points in the transmission line by adjusting W_i and L_i of each segment.

III. GENETIC ALGORITHMS

In the STL, however, there is a troublesome barrier in its design: finding the best combination of all parameters is next to impossible because combinatorial explosion occurs in its search process. Assuming that there are 10 segments, each of which consists of 10 width-candidates and 100 length-candidates, the total number of combinations comes to $(10 \times 100)^{10} = 10^{30}$. This astronomical number prevents us to evaluating all of them in real time. In order to overcome this problem, we apply the genetic algorithms (GA) [4], which is one of optimization algorithms mimicking the biological evolution, to the problem. And more positive reason we use GA is that the STL structure of one dimensional array will be well mapped onto the chromosome structure in GA as shown in Fig.3.

Figure 4 shows the flowchart of the STL-design using GA. Genetic operations are executed repetitively until they reach the finish condition. Difference area between the target and the observed waveforms shown in the figure is used to evaluate the chromosome, that is, the reciprocal of the difference area is used as score, or fitness of the chromosome.

IV. EXPERIMENTAL RESULTS

We use a bus-system shown in Fig.5 to evaluate the STL. This bus-system models a transmission line with a Ball Grid Array (BGA) or a Land Grid Array (LGA) connected with it as shown in Fig. 6. There are bunches of bonding wires inside the BGA or LGA package, and they need to be considered as inductances as the frequency increases.

1. Simulation Experiments

Figure 7 shows a waveform observed at the observing point in Fig. 5. As shown in Fig. 7, the logic-margins decrease to critical ranges; high-level-logic-margin is 0.3V and low-level-logic-margin is 0.32V. To recover the logic margins, STL is thus applied.

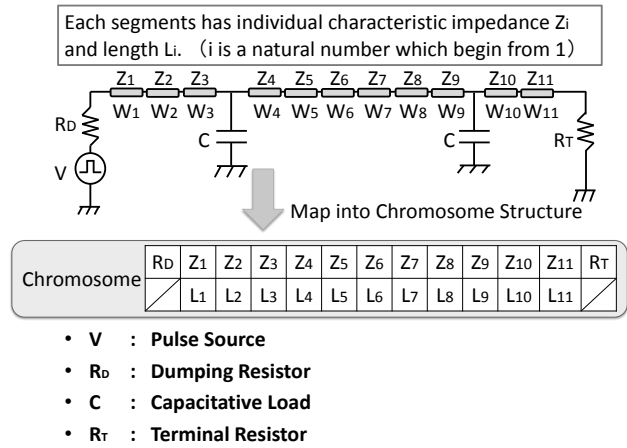


Fig.3 Structure of STL and Chromosome

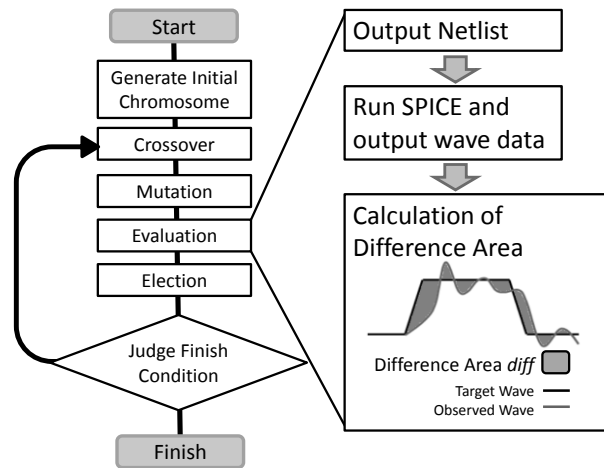


Fig.4 STL-Design Flowchart using GA

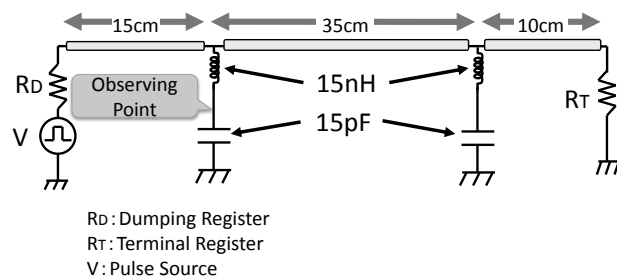


Fig.5 Target Bus-system

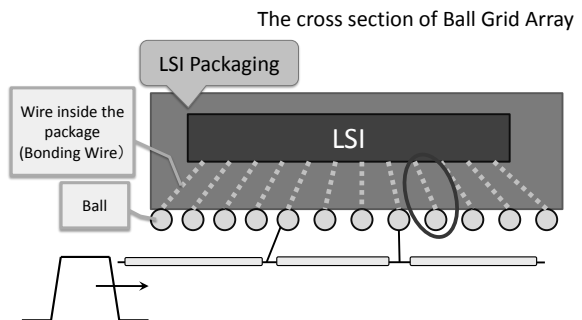


Fig.6 Cross sectional view of Ball Grid Array

Table 1 shows the condition of the STL-Designer using GA, and Fig.8 shows an STL design result for the bus-system including inductances. Figure 9 shows the waveform at the observing point in Fig. 8 in the STL. Both of the high-level-logic-margin and low-level-logic-margin increase to 0.5Vs. Table 2 summarizes the experimental results. High improvement ratios of 1.67 and 1.56 were achieved in high-level-logic-margin and low-level-logic-margin, respectively compared to a conventional transmission line.

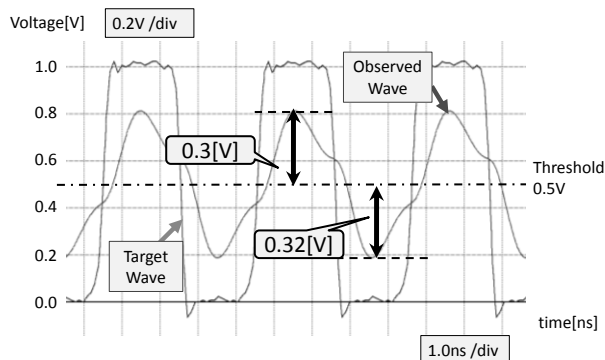


Fig.7 Waveforms of Conventional Transmission Line on Simulations

Table. 1 Conditions of GA

Lengths	15cm,35cm,10cm (Total:60cm)
Fraction of segments	6,7,3
Finish condition	1500 generations

2. Prototype Experiments

We fabricated some PCB prototypes to prove the correctness of the simulation results. Prototype PCB boards are shown in Fig. 10: the upper is a conventional transmission line and the lower is an STL. On the PCBs, chip inductors and chip capacitors are used and soldered as the inductors and capacitors in Figs. 5 and 8.

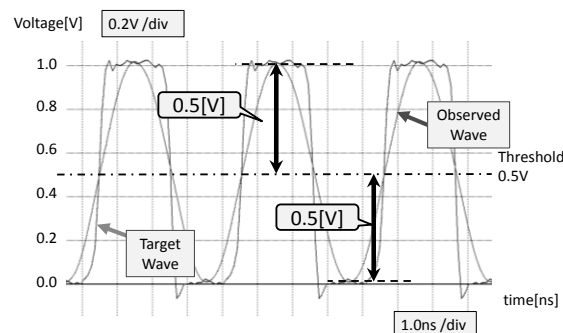


Fig.9 Waveforms of the STL on Simulations

Table. 2 Summary of Simulation Results

	High-level-logic-margin	Low-level-logic-margin
Normal	0.3[V]	0.32[V]
STL	0.5[V]	0.5[V]
Improvement rate	1.67	1.56

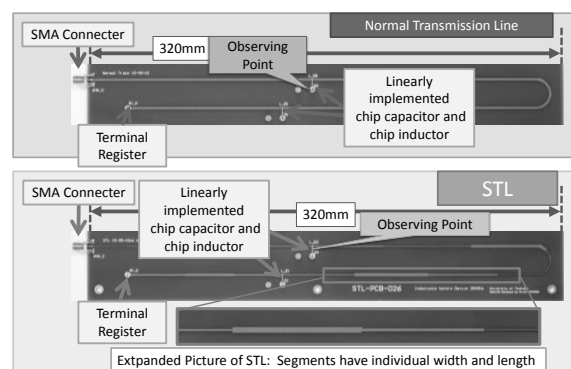


Fig.10 Prototype PCB

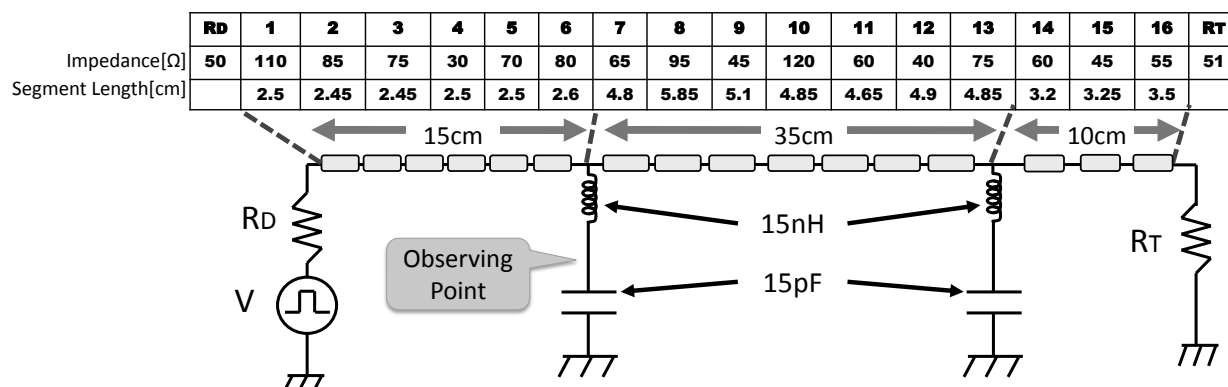


Fig.8 Design Results for STL

Figure 11 shows the measurement environment for the prototype boards. Clock signals are supplied from the pulse generator into the PCBs, and the waveforms are observed using an active probe and a digital sampling oscilloscope.

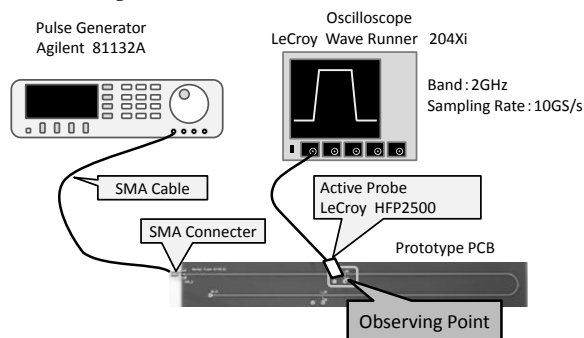


Fig.11 Measurement Environment

Figures 12 and 13 show waveforms in the conventional trace and of the STL, respectively observed with the oscilloscope. Logical margins of 0.34V in high-level and 0.36V in low-level are well improved to 0.52V and 0.5, respectively in the STL.

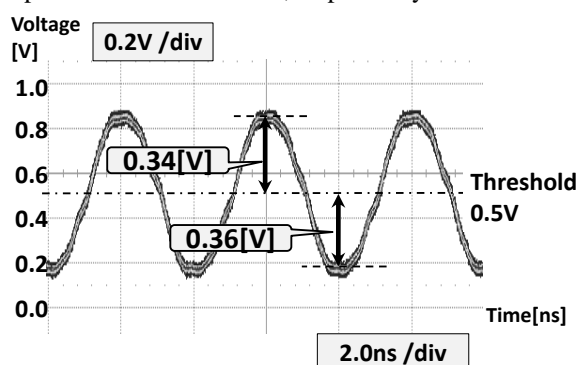


Fig.12 Waveforms observed in Conventional Transmission Line on the Prototype

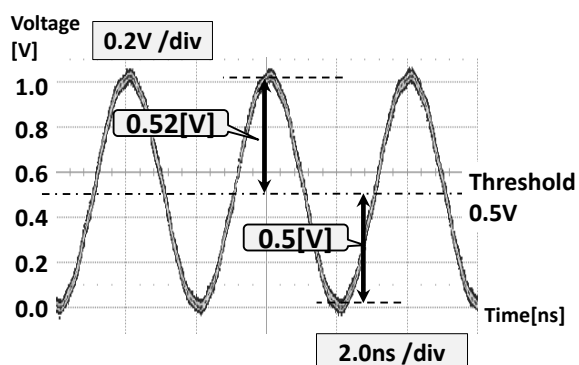


Fig.13 Waveforms observed in STL on the Prototype

Table. 3 Summary of Measurement Results Using Prototype

	High-level-logic-margin	Low-level-logic-margin
Normal	0.34[V]	0.36[V]
STL	0.52[V]	0.5[V]
Improvement rate	1.53	1.39

As the Table. 3 shows, the improvement ratio of high-level-logic-margin is 1.53, and low-level-logic-margin is 1.39. The results indicate that STL is effective to the system which includes inductances directly before the devices.

V. CONCLUSIONS

We newly applied the STL to the bus-system including inductances. The maximum improvement ratio of 1.67 for the distorted waveform in the conventional transmission line was achieved on the computer simulation. We also evaluated the STL using the prototypes, and high improvement ratios of 1.53 and 1.39 were achieved in the high-level-logical-margin, and the low-level-logical-margin, respectively. Those results clearly show that the STL is also effective to the bus-system including inductances as well as capacitances.

Our future works is to make clear the differences between simulation and actual experiments. Furthermore, we will also try to make steeper rising/falling waves in the STL.

REFERENCES

- [1] M.Taguchi, "High-speed, small-amplitude I/O interface circuits for memory bus application", IEICE Trans. Electron., vol.E77-C, no.12, pp.1944-1950, Dec.1994.
- [2] Moritoshi Yasunaga, Ikuo Yoshihara, "The Segmental Transmission Line and Its Design Methodology: Line Trace Ensuring High Signal Integrity in VLSI Mounting Boards", IEICE journal, D-I, J-88-D-I (5), pp.915-929, 2005. In Japanese.
- [3] Yuki Shimauchi, Hiroshi Nakayama, Yoshiki Yamaguchi, Noriyuki Aibe, Ikuo Yoshihara, Moritoshi Yasunaga, "Evaluation of waveform-improvement performance on the segmental transmission line", IEICE technical report 109(317), Design Gaea 2009, pp.63-68, Dec. 2009. In Japanese
- [4] Hiroshi Sato, Isao Ono, Shigenobu Kobayashi, "A New Generation Alternation Model of Genetic Algorithms and Its Assessment", Journal of Japanese Society for Artificial Intelligence Vol.12 No.5, pp.734-744, Sep.1997, In Japanese.

Digital-signal improvement-method using Pareto optimization

Shohei Akita[†], Hiroki Shimada[†], Masami Ishiguro[†], Noriyuki Aibe[†],

Ikuo Yoshihara[‡], Moritoshi Yasunaga[†]

[†] Graduate School of Systems and Information Engineering, University of Tsukuba
Tsukuba Ibaraki 305-8573, JAPAN

E-mail: akita@islab.cs.tsukuba.ac.jp

[‡] Faculty of Engineering, University of Miyazaki
Miyazaki, Miyazaki 889-2192, JAPAN

Abstract Recently, propagating digital signals with low distortion in PCB (printed circuit board) traces is getting difficult more and more as the frequency increases. In order to solve this problem, we have proposed “Segmental Transmission Line (STL)”[†]. In the STL, a transmission line is divided into multiple segments of individual characteristic impedance. The multiple segments are designed to improve the waveform distortion on the transmission line by solving a combinatorial explosion using genetic algorithm. In this paper, we try to improve signal integrity at two points using the STL. In order to achieve the signal integrity improvement at two points, we use the multi-objective GA and pareto-optimal-solutions. We conducted experiments with simulation and an STL prototype using real PCBs. As a result, at two observation points on simulation, logical margins in the STL were improved 3.3 times and 3.0 times simultaneously in their maximum, respectively. And at two observation points in the STL prototype, logical margins were improved 1.7 times and 2.0 times simultaneously, respectively. The result thus indicates that the STL has high ability to improve digital-signal waveform at multiple points simultaneously.

Keywords Signal Integrity, STL, Transmission Line, Genetic Algorithms, Pareto-optimal-solutions

I. Introduction

Signals of GHz frequency, the wavelengths of which are less than 15cm and are shorter than sizes PCBs, are terribly distorted at the impedance mismatching points in the PCB traces.

They have used conventional impedance-matching techniques [1][2] to improve the distorted waveforms usually. These techniques works well up to hundreds MHz, but will not work well at more than GHz.

In order to solve this problem and to ensure the signal integrity we have proposed a novel transmission line called "Segmental Transmission Line (STL)" [3].

In the STL, a transmission line is divided into multiple segments of individual characteristic impedance. In this structure, noises are generated purposely at the segments boundaries to cancel the target noises, which occur due to the impedance mismatching between the transmission line and the devices connected to the transmission line.

In our previous paper, we have already shown effectiveness to GHz-frequency signal at single point using computer simulation and on STL prototype fabricated in real PCBs[4][5]. These STL boards were designed in the MHz-frequency targeting to the GHz-frequency by lengthening the wire (trace) length in proportion to the ration between the MHz and GHz frequencies.

In this paper, we try to improve signal integrity at multiple points using STL and to show its effectiveness using an STL prototype as well as computer simulation.

II. Segmental Transmission Line

The idea of STL is completely different from the

conventional methods such as [1],[2], which aim to decrease noise-emissions.

In the STL, we use counter approach to the conventional ones. Figure 1 shows an overview of STL and its segment-model. And Fig. 2 shows a model of the STL. In the STL, we use noises that are generated purposely at impedance mismatching points to cancel the target noises. To generate these noises purposely, a transmission line is divided into multiple segments which have different impedances and lengths, respectively. Impedance of a segment is function of a segment-width.

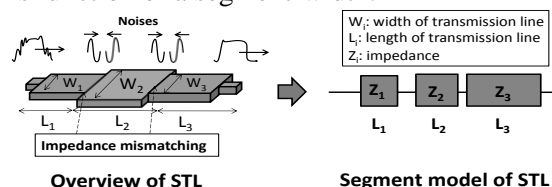


Fig. 1 Outline of STL

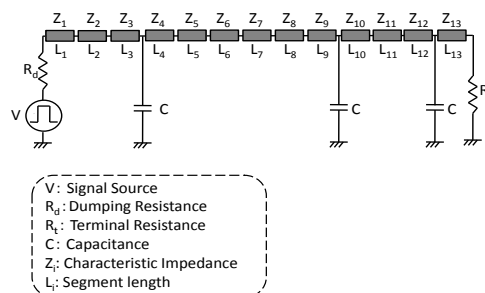


Fig. 2 STL Model

III. STL design methodology using Genetic Algorithms

In the STL, it is necessary to obtain the best, or semi-best impedance and length combination. In the case of complete search of combination, for example, 10 widths and 100 lengths for each of 10 segments results in the combination of $(10 * 100)^{10} = 1.0 * 10^{30}$. It is clearly impossible to calculate all of them, and this difficulty is called combinatorial explosion. In order to overcome this difficulty, we use Genetic Algorithms (GA) [6] to the STL design.

In the GA for the STL design, two kinds of genes are used. One is for the segment-width and the other is for the segment-length. Figure 3 shows the STL design system named STL-Designer, which is composed of a newly developed GA calculation-loop specialized for the STL and the circuit simulator SPICE. Figure 4 shows the gene and chromosome configuration of GA applied to the STL. As shown in the figure, a characteristic impedance and its corresponding length forms a pair of genes in a chromosome.

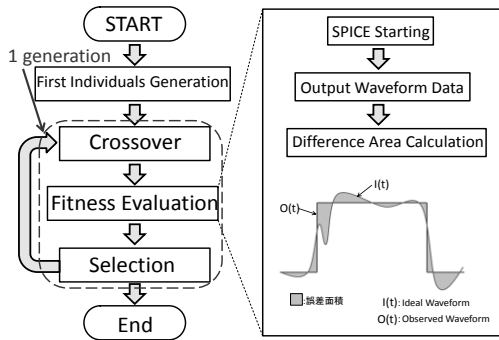


Fig. 3 STL-Designer

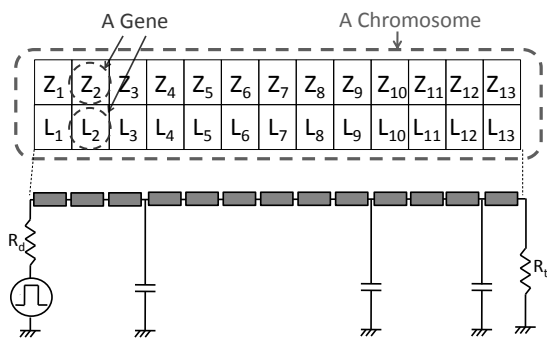


Fig. 4 Gene and Chromosome Constitution

IV. Multi-objective GA and Pareto solutions

To achieve the signal integrity improvement at multiple points, the waveforms at the observation points must be optimized simultaneously. We thus use the multi-objective GA and pareto-optimal-solution [8] to meet the design requirement. Figure 4 shows a chart of the pareto-optimal-solution. Pareto-optimal-solutions is a set of the solutions which cannot be put above the others.

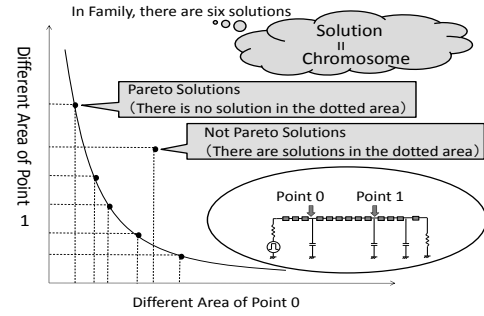


Fig. 5 Pareto optimization solution

V. Signal-Integrity improvement at multiple points on the computer simulation

In the STL design, or in the simulation, we used the circuit simulator ngspice [7] as the SPICE shown in Fig. 3. Figure 6 shows the circuit-diagram of the scale-up STL prototype for 150MHz clock-signal targeted to 1GHz. This model assumes the bus line connecting a CPU with 3 memory modules. The transmission line of 1-m long is divided into 12 segments. Three capacitors of 24pF each represent three device-inputs, e.g., memory modules connected to the transmission line. Point 0 and Point 1 in Fig. 6 are the target or observation points in the STL design. And the solution obtained in the STL is shown in Fig. 7.

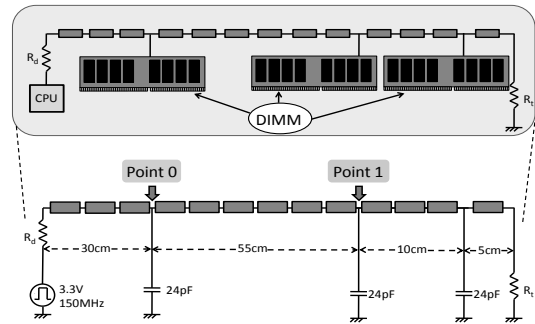


Fig. 6 Circuit-diagram of STL applied to bus system

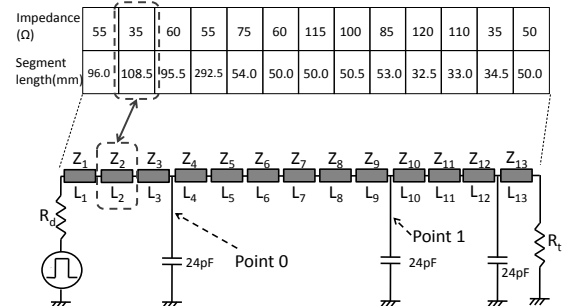


Fig. 7 Solution of GA applied to STL

In Fig. 8, distorted waveforms of red waves in the left column were observed in the conventional transmission line of homogeneous characteristic impedance of 50 ohm at Point 0 and Point1, respectively. The distorted waveforms were well improved in the STL as shown in the red waves in the right column. Blue

waveforms in the figure, which are all the same, are the waveforms observed at Point 0 and Point 1 if no capacitors are connected in the transmission line. The blue waveform was thus used as the target or teacher waveform in the design.

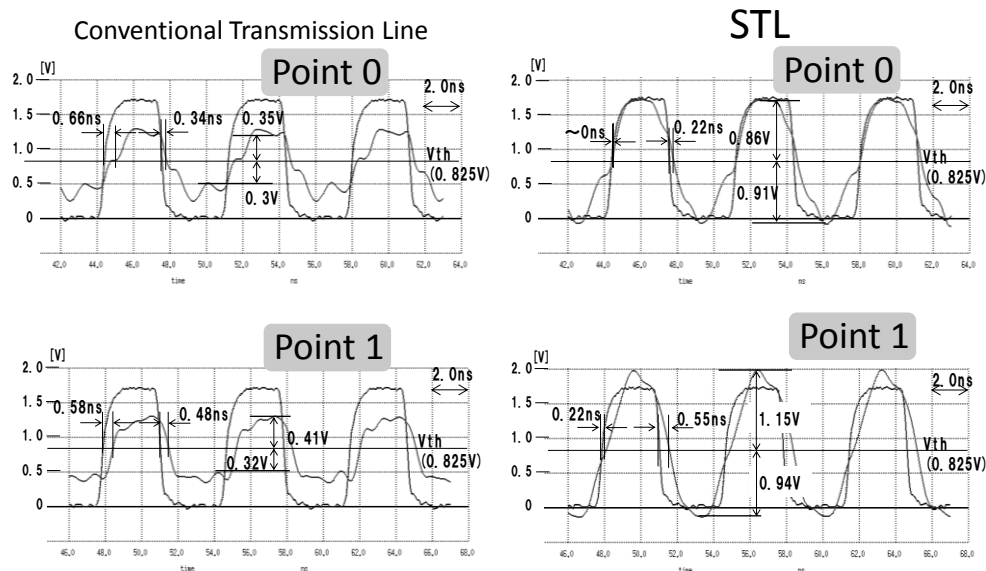


Fig. 8 Comparison of waveforms designed at Point 0

Table. 1 Summary of simulation results

() : Logical Margin Improvement Ratio and
Delay Time Shortening Percentage

		High Logical Margin [V]	Low Logical Margin [V]	Delay Time (Rise) [ns]	Delay Time (Fall) [ns]
Point 0	Conventional Transmission Line	0.35	0.3	0.66	0.34
	STL	0.86 (2.5)	0.91 (3.0)	< 0.1ns (< 0.15)	0.22 (0.65)
Point 1	Conventional Transmission Line	0.41	0.32	0.58	0.48
	STL	1.15 (3.3)	0.94 (3.1)	0.22 (0.38)	0.55 (1.1)

VI. Signal Integrity improvement at multiple points in the STL prototype

Figure 9 shows photographs of the prototypes of conventional transmission line and of STL. Figure 10 shows the measurement environment schematically. Signals from the pulse generator are put into the FPGA, which is used to reshape the waveform, and the outputs from the FPGA are input to the prototype board. The waveforms are observed by the digital storage oscilloscope of 2GHz bandwidth through an active probe.

The waveforms observed by the oscilloscope are shown in Fig. 11, which are corresponding to Fig. 8 (no teacher waveforms in Fig. 8 are shown in Fig. 11). Delay

times are not measured in Fig. 11 due to some restriction in the measurement environment.

Declines in amplitudes in the conventional transmission line, which come from the waveform distortions, are well improved in the STL. The improvement ratios however are not so high as in the design, or simulation in Fig. 8. The results shown in Fig. 11 are also summarized in Tab. 2 as Tab.1.

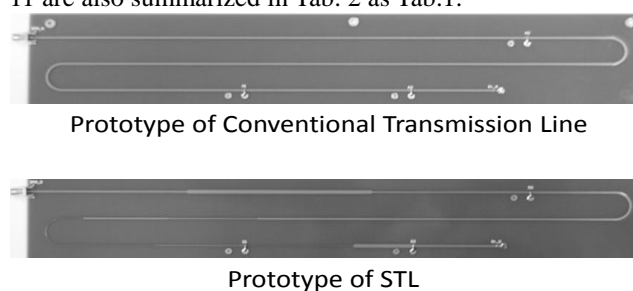


Fig. 9 Photographs of prototypes

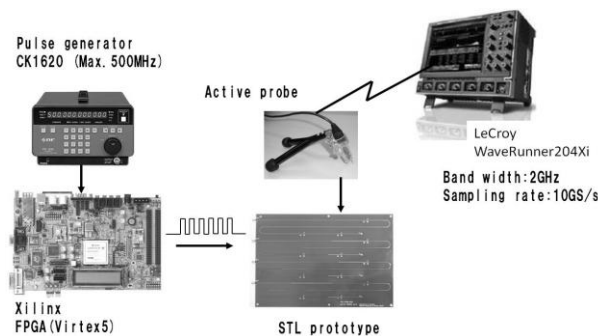


Fig. 10 Measurement environment

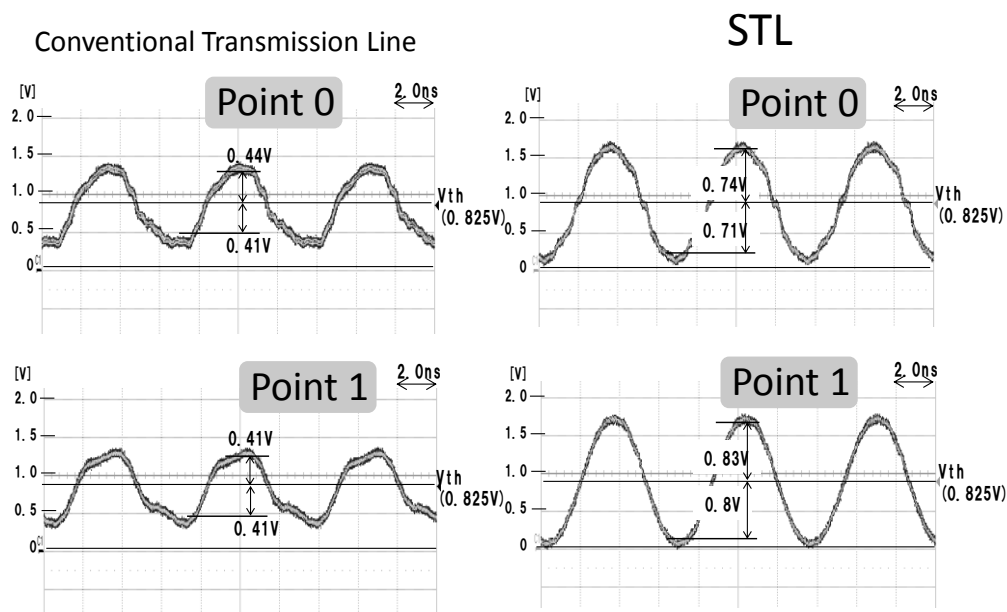


Fig. 11 Comparison of Waveforms measured at Point0 in prototypes)

Table. 2 Summary of measurement results

() : Logical Margin Improvement Ratio and
Delay Time Shortening Percentage

		High Logical Margin[V]	Low Logical Margin[V]
Point 0	Conventional Transmission Line	0.44	0.41
	STL	0.74 (1.7)	0.71 (1.7)
Point 1	Conventional Transmission Line	0.41	0.41
	STL	0.83 (2.0)	0.80 (2.0)

VII. Conclusions and further works

In the simulation experiments, STL showed the maximum improvement ratios of 3.0 and 3.3 at Point 0 and Point 1, respectively in terms of the logical margin. And it also decreased the rise-time delay to less than 15% at Point 0 and the fall-time delay to 38% at Point 1 at Point 1, while the fall-time delay at Point 1 increased 10%.

In the prototype experiments, the STL showed the maximum improvement ratios of 1.7 and 2.0 at Point 0 and Point 1, respectively in terms of the logical margin.

The results clearly indicate that the STL has high ability to improve digital-signal waveform improvement at multiple points simultaneously.

Followings are further works: the fall-delay-time at Point 1 needs to be improved and accuracy of the signal

integrity at two points needs to be improved and increased.

References

- [1] N. Naono, Y. Nakamura: "Details on High-speed Digital System Design", NikkeiBP INC., 2001.
- [2] M. Taguchi, "High-speed, small-amplitude I/O interface circuit for memory bus application", IEICE Trans. Electron., vol.E77-C, no.12, pp.1944-1950, Dec. 1994.
- [3] M. yasunaga, I. Yoshihara "Segmental Transmission Line and Its Design Methodology: Line Trace Ensuring High Signal Integrity in VLSI Mounting Boards", The transactions of Electronics, Information and Communication Engineers. D- I, vol. J88-D-I, no. 5, pp. 915-929, May. 2005
- [4] H. Nakayama, M. Yasunaga, I. Yoshihara et al., "Experimental Verification of Improved Signal Integrity Using the Segmental Transmission Line", The 70th National Convention of Information Processing Society of Japan, 1pp.9-10, tsukuba, Mar. 2008.
- [5] H. Nakayama, I. Yoshihara, M. Yasunaga et al., "A High-Signal-Integrity transmission-Line for High Speed VLSI Packaging: Its proposal and Prototype Evaluation", DA Symposium 2009, pp.187-192.
- [6] M. Mitchell, H. Iba, "An Introduction To Genetic Algorithms", Tokyo Denki University Press, 1997.
- [7] <http://ngspice.sourceforge.net/>
- [8] C. A. Coello. Coello, "A Comprehensive Survey of Evolutionary-Based Multiobjective Optimization Techniques", Knowledge and Information Systems An International Journal vol.1 no.3 pp.269-308 1999

Basic Position/Force Control of Single-Axis Arm Designed with an Ultrasonic Motor

K. Ogiwara and F. Nagata
Tokyo University of Science, Yamaguchi
Sanyo-Onoda, Japan

K. Watanabe
Okayama University
Okayama, Japan

Abstract

Recently, many studies on assist robots are being conducted, in which the development of a unique system is required to support aged persons, physically handicapped persons and/or caretakers. One of the representative systems is called the assist suit and is partly practiced. The assist suit is a mechatronics device which can assist physical human actions. However, the current assist suit has a few problems with respect to cost, size, weight, long-time run and so on. In this article, a fundamental study concerning a compact assist device is conducted. Where the assist device supports is one spot on the body such as a knee, an elbow and a shoulder. First of all, a simple single-axis arm is designed by using an ultrasonic motor which can generate high torque from a low velocity range. Then, a servo system, a torque control system and a passive torque control system are applied and their characteristics are evaluated. Here, the passive torque control includes a stiffness control and a compliance control.

1 Introduction

Recently, many studies on assist robots are being conducted, in which the development of a unique system is required to support aged persons, physically handicapped persons and/or caretakers [1]. One of the representative systems is called the assist suit and is partly practiced. The assist suit is a mechatronics device which can assist physical human actions. However, the current assist suit has a few problems with respect to cost, size, weight, long-time run and so on.

In this article, a fundamental study concerning a compact assist device is conducted [2]. Where the assist device supports is one spot on the body such as a knee, an elbow and a shoulder. First of all, a simple single-axis arm is designed by using an ultrasonic motor which can generate high torque from a low velocity range. Figure 1 shows the experimental setup. Then, a servo system, a joint torque control system and a passive torque control system are applied and their characteristics are evaluated. The passive torque control includes a stiffness control and a compliance control. Finally, a promising application as an assist device is considered. It is assumed that the single-axis

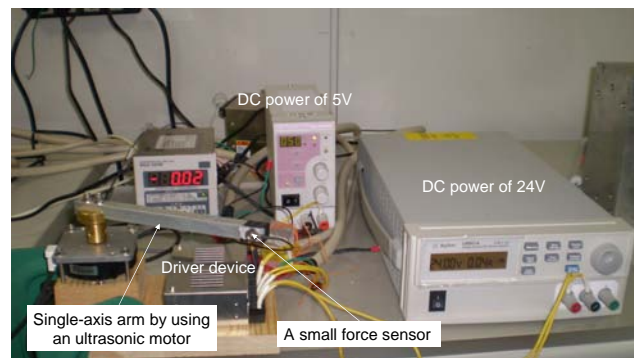


Figure 1: Single-axis arm designed with an ultrasonic motor.

arm is equipped to a damaged joint of a human. The operator can adjust the desired torque, e.g. more stiff or more compliant, while feeling the behavior and the effectiveness of the assist device.

2 A Single-Axis Arm Designed with an Ultrasonic Motor

The ultrasonic motor has two features. One is that it can generate high torque from the low velocity range. The other is that it has a large holding torque when no voltage is given. That is the reason why no brake system is needed and consequently the weight reduction can be realized. Also, the responsiveness of the ultrasonic motor is generally superior to the one of conventional electromagnetic motors, so that the energy consumption can be suppressed. Considering the above points, the simple arm is designed based on an ultrasonic motor. Figure 2 shows the hardware block diagram. The ultrasonic motor used in experiments is the model of USR60-E3T provided by Shinsei Corporation. A DA board(CONTEC DA12-8) is used to control the motor velocity. A digital IO board(CONTEC PIO-48D) is also used to switch the direction of motor rotation, i.e., clockwise or counterclockwise. Further, a counter board(CONTEC CNT32-8M) is incorporated to sense the rotation angle. These cards are connected to the ultrasonic motor via a driver device(Shinsei

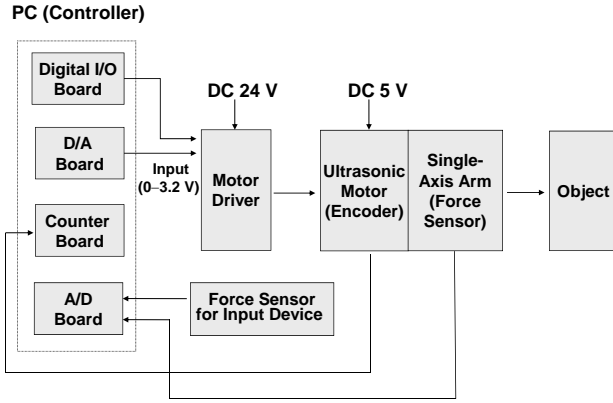


Figure 2: Hardware block diagram of the experimental system.

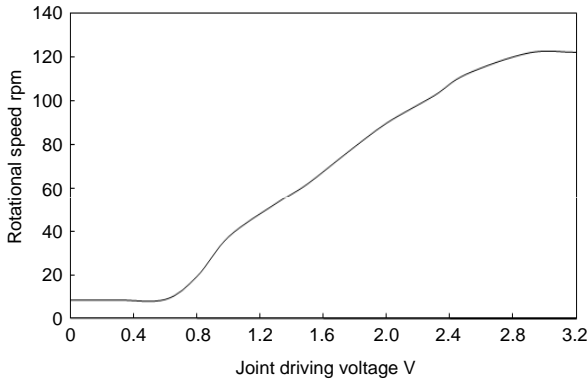


Figure 3: Relation between joint driving torque and rotational speed in steady state.

Corp. D6060 24V). A small force sensor is fixed at the tip of the single-axis arm to estimate the joint torque.

3 Control System

Basic functions were first developed on Microsoft Visual C++ to give the commands such as the direction of rotation and the rotational velocity and to obtain the rotational angle from the encoder. Then, it was measured on how the relation between the voltage and its given time influenced the dynamic response of the motor. Figure 3 shows the characteristics, in which it is confirmed that the velocity tends to be constant under 0.6 V. The dynamic characteristics were used to design a position feedforward controller.

3.1 Basic servo system

The servo system of an ultrasonic motor is easily constructed due to the high holding torque and the responsiveness. Here, a simple proportional control

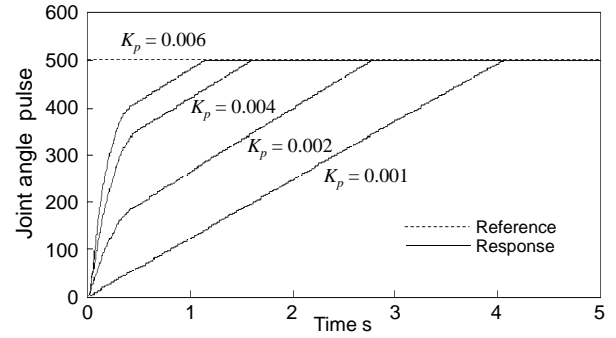


Figure 4: Step responses obtained by using Eq. (1), in which 500 pulses mean π rad.

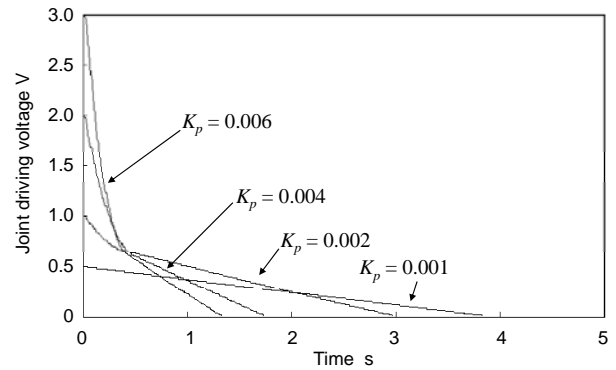


Figure 5: Joint driving voltage calculated from Eq. (1).

has only to be applied as

$$\tau(k) = K_p \{\theta_d - \theta(k)\} \quad (1)$$

where $\tau(k)$ is the joint driving voltage at the discrete time k , K_p is the p -gain; $\theta(k)$ and θ_d are the joint angle and desired one, respectively. In order to conduct high accuracy positioning, when $\theta_d = \theta(k)$ is detected in the sampling loop, the excitation power to the motor has only to be off at the same time. Figure 4 shows examples of step response with several K_p , in which 500 pulses mean π rad. Note that a linear characteristic suddenly appears from a point, for example, in case of $K_p=0.006$. To examine the matter a bit more detail, the relation between the time and the torque obtained by Eq. (1) is measured as shown in Fig. 5. It is observed from Figs. 3, 4 and 5 that the joint velocity tends to show a constant value about 8.5 rpm under the point of 0.6 V. So, in order to cope with the characteristic, Eq. (1) is improved as

$$\tau(k) = K_p \{\theta_d - \theta(k)\} + 0.6 \quad (2)$$

Figure 6 shows the step response when Eq. (2) is employed. As can be seen, a desirable response without an overshoot and delay is observed only by using a p -action. This is the attractive characteristics of the ultrasonic motor used in the experiment.

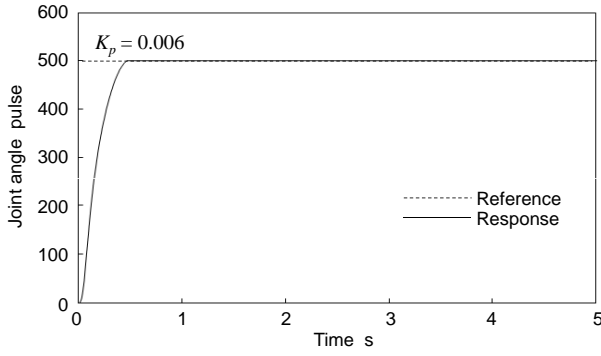


Figure 6: Step responses obtained by using Eq. (2).

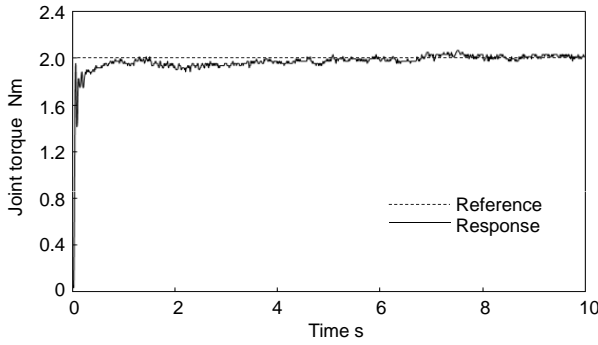


Figure 7: Joint torque control result in using Eq. (3).

3.2 Joint torque control

In the joint torque control mode, the torque acting at the joint is actively controlled by a PI controller written by

$$\tau(k) = K_{fp} \{\tau_d - \tau_s(k)\} + K_{fi} \sum_{n=0}^k \{\tau_d - \tau_s(n)\} + 0.6 \quad (3)$$

where K_{fp} and K_{fi} are the p -gain and i -gain, respectively. τ_d is the desired joint torque, $\tau_s(k)$ is the estimated joint torque which is calculated from the force value sensed by a small force sensor attached to the arm tip. Figure 7 shows a torque control result, in which the response desirably follows the reference 2 Nm by setting K_{fp} , K_{fi} to 3 and 0.001, respectively.

3.3 Passive joint torque control

In the passive joint torque control mode, an external force given to the arm can be absorbed smoothly. Here, a stiffness control and a compliance control are considered. The stiffness control law is given by

$$\tau_s(k) = K_d \{\theta(k) - \theta_d\} \quad (4)$$

where K_d is the desired stiffness [Nm/rad]. Note that in the stiffness control mode, the initial position is set

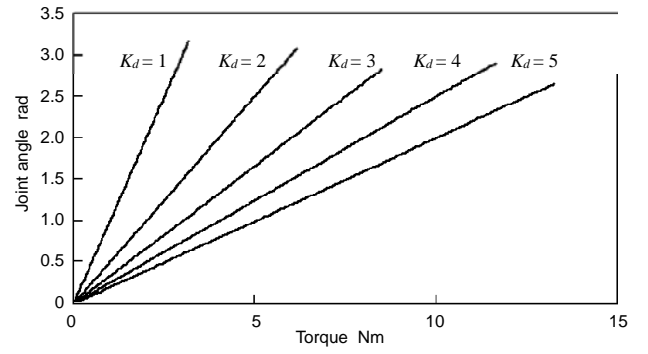


Figure 8: Stiffness control result in using Eq. (4).

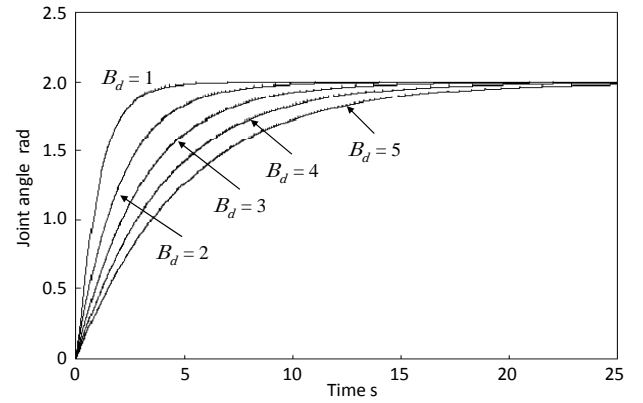


Figure 9: Compliance control result in using Eq. (5).

to the desired position θ_d , and also $\theta(k)$ obtained from Eq. (4) is given to θ_d in Eq. (2). Figure 8 shows an example of the stiffness control result.

Next, the compliance control law is written as

$$\tau_s(k) = B_d \left\{ \dot{\theta}(k) - \dot{\theta}_d \right\} + K_d \{\theta(k) - \theta_d\} \quad (5)$$

where B_d is the desired viscosity [Nm s/rad]. In the compliance control mode, the transient behavior to an equilibrium position can be controlled. Of course, the equilibrium position depends on K_d . If it is assumed that both $\dot{\theta}_d$ and θ_d are 0, and $\tau_s(k) = \tau_{step}(\text{constant})$, then $\theta(k)$ is obtained by

$$\theta(k) = \frac{\tau_{step}}{K_d} (1 - e^{-\frac{K_d}{B_d} \Delta t k}) \quad (6)$$

where Δt is the sampling width. Compliance control can be easily realized by giving $\theta(k)$ obtained from Eq. (6) into θ_d in Eq. (2). Figure 9 shows an example of compliance control result, in which the transient behaviors are changed with B_d . In the experiment, K_d and $\tau_{step}(k)$ are set to 1 and 2, respectively.

4 Example of Application

In this section, a promising application called an assist device is considered. It is assumed that the single-

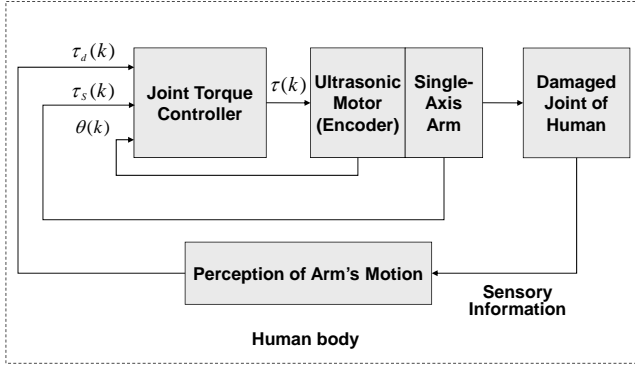


Figure 10: Block diagram of an application called the assist device for assisting a damaged or weakened joint.

axis arm is equipped to a damaged joint of a human. A small and light weight force sensor is used so that the desired torque can be directly given by the fingers of the operator. The operator can adjust the desired torque, e.g. more stiff or more compliant, while feeling the behavior and the effectiveness of the assist device, i.e., the single-axis arm.

The block diagram of the controller is shown in Fig. 10, in which the desired torque $\tau_d(k)$ is manually given by an operator. The control law is derived from Eq. (3) by varying the desired joint torque as

$$\tau(k) = K_{fp} \{ \tau_d(k) - \tau_s(k) \} + K_{fi} \sum_{n=0}^k \{ \tau_d(n) - \tau_s(n) \} + 0.6 \quad (7)$$

$$\tau_d(k) = \alpha f(k) \quad (8)$$

$$\tau_s(k) = LF(k) \quad (9)$$

where $f(k)$ is the small force generated by an operator's fingers, α is the gain which transmits the force to the time-varying desired joint torque. $F(k)$ is the force acting between the arm tip and the object, L is the length of the single-axis arm. In the experiment, $\tau_s(k)$ is regarded as the joint torque.

Figure 11 shows the experimental scene assumed to be the assist device. The control result of $\tau_s(k)$ is shown in Fig. 12, in which the response $\tau_s(k)$ is desirably amplified according to $f(k)$ by giving 1 and 0.15 to α and L , respectively.

5 Conclusions

In this article, a fundamental study concerning a compact assist device is conducted. Where the assist device supports is one spot on the body such as a knee, an elbow and a shoulder. First of all, a simple single-axis arm has been designed by using an ultrasonic motor which can generate high torque from a low velocity range. Then, a servo system, a joint torque control system and a passive torque control system have been applied and their characteristics are evaluated. The passive torque control includes a stiffness

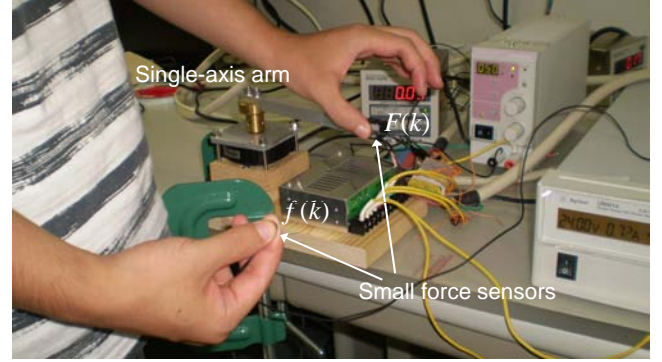


Figure 11: Experimental scene assumed to be the assist device.

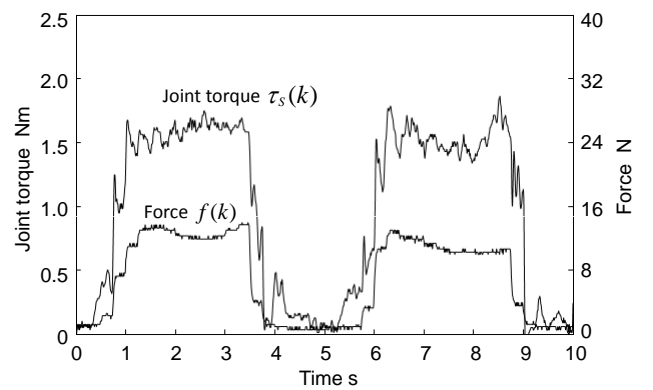


Figure 12: Joint torque manually controlled by an operator. Force is given by the operator's fingers.

control and a compliance control. Finally, a promising application as an assist device has been considered. It is assumed that the single-axis arm is equipped to a damaged joint of a human. The operator can adjust the desired torque, e.g. more stiff or more compliant, while feeling the behavior and the effectiveness of the assist device.

References

- [1] S. Toyama and J. Yonetake, "Development of the Ultrasonic Motor-Powered Assisted Suit System," *Procs. of 2007 IEEE/ICME International Conference on Complex Medical Engineering*, pp. 1361–1366, 2007.
- [2] K. Ogiwara and F. Nagata, "Basic Position/Force Control of a Single-Axis Arm Designed with an Ultrasonic Motor," in *Procs. of the 12th IEEE Hiroshima Section Hiroshima Student Symposium*, (F)–11, 2 pages, 2010 (in Japanese).

Cooperative Swarm Control for Multiple Mobile Robots Using Only Information from PSD Sensors

T. Yamashiro and F. Nagata
Tokyo University of Science, Yamaguchi
Sanyo-Onoda, Japan

K. Watanabe
Okayama University
Okayama, Japan

Abstract

Recently, many studies on swarm robotics are being conducted, in which the aim seems to be the realization of complex task ability by cooperating with each other. Future progression and concrete applications are being expected. The objective of this study is to construct an attractive system by using multiple mobile robots. First of all, multiple mobile robots with six PSD (Position Sensitive Detector) sensors are designed. The PSD sensor is a kind of photo sensors. A control system is considered to realize such a swarm behavior as *Ligia exotica* by using only information of PSD sensors. Experimental results show interesting behaviors of multiple mobile robots such as following, avoidance and schooling. The proposed system was intriguingly demonstrated to high school students in OPEN CAMPUS 2010 held in Tokyo University of Science, Yamaguchi.

1 Introduction

Recently, many studies on swarm robotics are being conducted, in which the aim seems to be the realization of complex task ability by cooperating with each other. It also seems that the research of swarm robotics includes the design of robots, their physical body and their behavior as a controller. Future progression and concrete applications are being expected.

In this study, multiple mobile robots with six PSD (Position Sensitive Detector) sensors are designed [1]. The PSD sensor is a kind of photo sensors. A control system is considered to realize such a swarm behavior as *Ligia exotica* as shown in Fig. 1 by using only information of PSD sensors. A lot of organisms who behave with making a group live in everywhere on the earth. *Ligia exotica* is one of such an organism that swarms at the seashore. Experimental results show interesting behaviors of multiple mobile robots. They are the following behavior, avoidance behavior and schooling behavior. The collective behaviors such as the following, avoidance and schooling emerges from the local interactions among the robots and/or between the robots and the environment.



Figure 1: *Ligia exotica* swarming at seashore.

2 Mobile Robots with PSD Sensors

In experiments, a mobile robot is used as shown in Fig. 2, which is developed based on three wheeled omni-directional mobile robot provided by Tosa Den-shi. In order to real-timely measure the distances to objects, the robot is improved with six PSD sensors. The PSD sensor is mainly composed of an LED, electrical resistance and photodiode, and can calculate the distance through the triangulation technique. In order to cope with the problem of narrow directivity of the PSD sensor, the number of the PSD sensor is increased to six. If possible, PSD sensors more than six are desirable to further reduce the dead angle. Also, each robot has a Bluetooth wireless device to communicate with a PC server.

As for control scheme, self-control mode and server-controlled mode are proposed for the mobile robots. The PC server gives either mode to each robot. When the self-control mode is given, the robots behave based on their own decisions. This will be applied to a simulation of *Ligia exotica* swarming at seaside where they escape around because of the surprise to a sudden surrounding change. In this case, the swarm itself behaves as controlled, however, each individual seems to have only very simple action pattern. That is the reason why several easy action patterns are given to the robots in the self-control mode. However, the software development environment of the mobile robot using a free C language has two restrictions. The one is that the flash ROM of the mobile robot is only 8 kB. The other is that mathematical standard library such as

“exp ()” cannot be compiled. Thus, for example, it is impossible to directly apply the potential field method for path planning.

The server-controlled mode is considered to cope with the poor development environment. In the server-controlled mode, the robots behave according to commands transmitted from the server. All information measured by PSD sensors of each robot are transmitted to the server once, the server can send action commands to the robots totally considering the behavior of the swarm. Of course, the potential field method is available on the server side where the Windows Visual Studio runs. This will be also applied to a simulation experiment of complex swarm intelligence where software developments with comparatively large-scale are required.

Figure 3 shows the coordinate system of this type of mobile robot. ω_i ($i = 1, 2, 3$) is the angular velocity of each wheel. Also, v_i ($i = 1, 2, 3$) is the velocity of each wheel given by

$$v_i = r\omega_i \quad (i = 1, 2, 3) \quad (1)$$

where, r is the radius of the wheel. If the position and orientation vector of the robot, i.e., the origin in the robot coordinate system Σ_R , is given by $[x \ y \ \phi]^T$, then the velocity is represented by $[\dot{x} \ \dot{y} \ \dot{\phi}]^T$. First of all, following equations are obtained from Fig. 3 [2, 3].

$$\dot{x}_r = \frac{1}{2}v_1 - \frac{1}{2}v_2 + v_3 \quad (2)$$

$$\dot{y}_r = \frac{\sqrt{3}}{2}v_1 - \frac{\sqrt{3}}{2}v_2 \quad (3)$$

$$\dot{\phi}_r = \frac{1}{L}v_1 + \frac{1}{L}v_2 + \frac{1}{L}v_3 \quad (4)$$

where L is the distance between the center of the robot and the center of each wheel. Eqs.(2), (3) and (4) lead to

$$\begin{pmatrix} \omega_1 \\ \omega_2 \\ \omega_3 \end{pmatrix} = \frac{1}{r} \begin{pmatrix} \frac{1}{3} & \frac{1}{\sqrt{3}} & \frac{L}{3} \\ \frac{1}{3} & -\frac{1}{\sqrt{3}} & \frac{L}{3} \\ \frac{2}{3} & 0 & \frac{L}{3} \end{pmatrix} \begin{pmatrix} \dot{x}_r \\ \dot{y}_r \\ \dot{\phi}_r \end{pmatrix} \quad (5)$$

By using the relation given by Eq. (5), the robot can be controlled kinematically.

Figure 4 shows the static measurement result of a PSD sensor, which is the relation between the actual distance and the digital value obtained from the PSD sensor. It can be seen that the sensible distance is within the range from 10 cm to 90 cm.

3 Self-Control Mode

In self-control mode, each robot behaves by using only information obtained from six PSD sensors shown in Fig. 5. The robots have three types of self-control modes, which are a following mode, an avoidance mode and a schooling mode. All mobile robots can communicate with a PC server. The PC server switches the mode of each robot individually by sending broadcast commands.

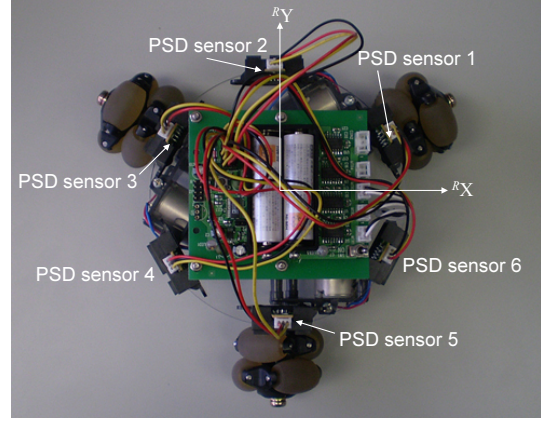


Figure 2: Mobile robot with six PSD sensors.

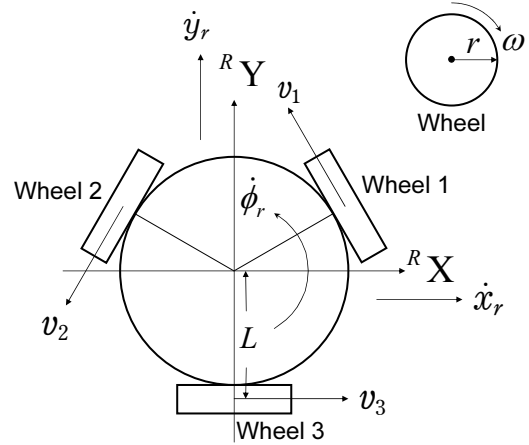


Figure 3: Kinematic model of the mobile robot.

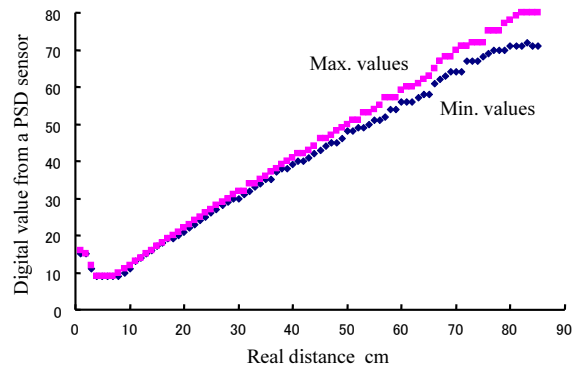


Figure 4: Relation between actual distance and digital value measured from a PSD sensor.

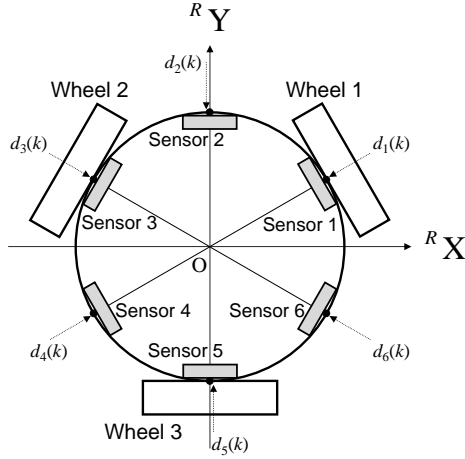


Figure 5: Six PSD sensors equally fixed on a mobile robot.

3.1 Following mode

If the following mode is given, mobile robots try to follow a moving object including other mobile robots in the sensitive region. Six PSD sensors can independently detect distances $d_i(k)$ ($i = 1, \dots, 6$) at the discrete time k . $d_i(k)$ is the value measured by i -th PSD sensor. If the distance to the nearest object is larger than a desired value d_d , the robot tries to shorten the distance by generating the velocity given by

$$\dot{\mathbf{x}}_r = v \frac{\dot{\mathbf{x}}_{ri}}{\|\dot{\mathbf{x}}_{ri}\|} \{d_d - \min_i d_i(k)\} \quad (\forall d_i(k) > d_d) \quad (6)$$

where $\dot{\mathbf{x}}_r = [\dot{x}_r \ \dot{y}_r]^T$ is the translational velocity in Eq. (5), v is the scalar signifying the magnitude of the robot's velocity, $\dot{\mathbf{x}}_{ri} = [\dot{x}_{ri} \ \dot{y}_{ri}]^T$ is the vector signifying the direction as shown in Table 1. d_d is the desired distance to the nearest object.

Table 1: Velocity components to move to the direction of each PSD sensor.

i	1	2	3	4	5	6
\dot{x}_{ri}	$\sqrt{3}$	0	$\sqrt{3}$	$\sqrt{3}$	0	$\sqrt{3}$
\dot{y}_{ri}	1	2	1	1	2	1

3.2 Avoidance mode

If the avoidance mode is given, each mobile robot tries to move away from moving objects including other mobile robots in the sensitive region. When six PSD sensors simultaneously detect shorter distances compared to the restriction d_d , the robot preferentially leaves the nearest object. If the distance to the nearest object is smaller than d_d , the robot tries to expand the space to be d_d by generating the velocity given by

$$\dot{\mathbf{x}}_r = v \frac{\dot{\mathbf{x}}_{ri}}{\|\dot{\mathbf{x}}_{ri}\|} \{d_d - \min_i d_i(k)\} \quad (\exists d_i(k) < d_d) \quad (7)$$

3.3 Schooling mode

If the schooling mode is set to all mobile robots, they try to regularly move along the inner of a circular fence keeping the distance to both the fence and other mobile robots. This mode allows the robots to behave like carps in a Japanese artificial circular pond. For example, when a robot moves counterclockwise along a circular fence, the following control law is basically applied.

$$\dot{\mathbf{x}}_r = v \frac{\dot{\mathbf{x}}_{r2}}{\|\dot{\mathbf{x}}_{r2}\|} \quad (8)$$

In this case, the orientation is simultaneously controlled by

$$\dot{\phi}_r = K_\phi \{d_6(k) - d_1(k)\} \quad (9)$$

where K_ϕ is the gain which can control the orientation of the robot to be parallel to the inner of the circular fence.

3.4 Experiment and discussion

In order to evaluate each behavior, three experiments were conducted.

3.4.1 Following mode

In the following mode, each robot basically stood still and looks around. When an object was detected in the sensing area, the robot tried to follow the object. In order to overcome the problem of blind spot and to skillfully sense a moving object, PSD sensors 1, 2 and 3 shown in Fig. 5 were used. The front of the robot is the direction of sensor 2. The following was conducted to the direction of sensor 2. Note that the sensors 1 and 3 were assistantly used in order not to lose sight of the object. It was observed from the experiments that a robot in following mode could run after other robots.

3.4.2 Avoidance mode

In the avoidance mode, each robot moves around randomly when no object is detected. If a robot detects an object in sensing area, it moves to the reverse direction to the object. Also, when plural objects are detected at a time, the nearest one is regarded as an object and the others are ignored. Desirable and interesting avoidance behaviors were observed from the experiments. Figure 6 shows an experimental scene.

3.4.3 Schooling mode

In the schooling mode, each robot first moved to the front direction to detect a circular fence. After detecting a circular fence, the robots moved around to the counterclockwise direction. Seven mobile robots in schooling mode could move around the fence like carps. In this case, the robots could keep a distance to



Figure 6: Experimental scene of avoidance mode.

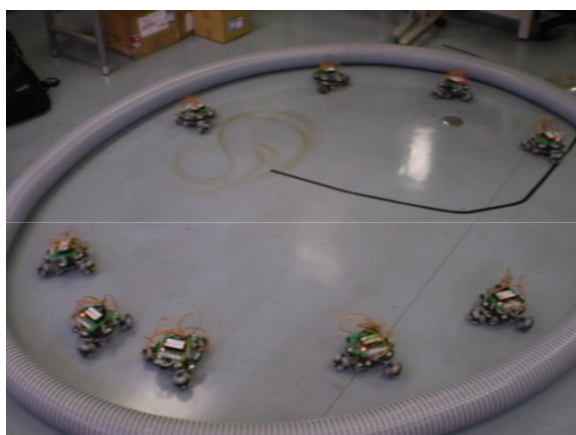


Figure 7: Experimental scene of schooling mode.

the fence by using the two PSD sensors, nos. 1 and 6. Figure 7 shows the experimental scene of the schooling mode, in which nine mobile robots are schooling along the inner of fence.

It has been confirmed from the simple experiments that the actual simulations for following, avoidance and schooling behaviors can be conducted for multiple mobile robots.

4 Conclusions

The objective of this study is to construct an attractive system by using multiple mobile robots. First of all, multiple mobile robots with six PSD (Position Sensitive Detector) sensors have been designed. The PSD sensor is a kind of photo sensors. A control system has been considered to realize such a swarm behavior as *Ligia exotica* by using only the information of PSD sensors. Experimental results have shown interesting behaviors of multiple mobile robots such as following, avoidance and schooling. The proposed system was intriguingly demonstrated to high school students in OPEN CAMPUS 2010 held in Tokyo University of Science, Yamaguchi and was very instructive to the students.

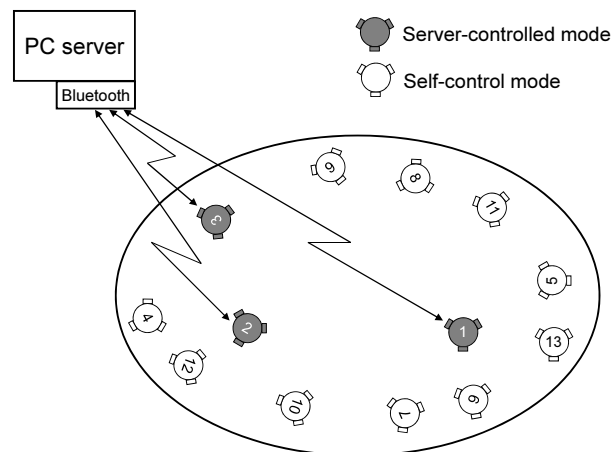


Figure 8: Example of server supervisory mode, in which robots 1, 2 and 3 are set to server-controlled mode, also the others are set to self-control mode by a PC server.

When many multiple mobile robots are used to simulate a swarm or a school, the cost with the increase of the number of robots becomes a serious problem. Therefore, there is an essential demand to construct the system at as low cost as possible. In future work, we plan to consider a server supervisory mode in order that a high level software architecture can be constructed even under the condition of technically and costly poor hardware platform of each mobile robot. In server supervisory mode, all mobile robots can be broadcastly switched self-control mode or server-controlled mode as shown in Fig. 8.

References

- [1] T. Yamashiro and F. Nagata, "Cooperative Control of Schooling for Multiple Mobile Robots by Using only Information from PSD Sensors," in *Procs. of the 12th IEEE Hiroshima Section Hiroshima Student Symposium*, (F)-13, 2 pages, 2010 (in Japanese).
- [2] K. Watanabe, Y. Shiraishi, S. G. Tzafestas, J. Tang and T. Fukuda, "Feedback Control of an Omnidirectional Autonomous Platform for Mobile Service Robots," *Journal of Intelligent & Robotic Systems*, vol. 22, nos. 3/4, pp. 315-330, 1998.
- [3] J. Tang, K. Watanabe, K. Kuribayashi and Y. Shiraishi, "Autonomous Control for an Omnidirectional Mobile Robot with the Orthogonal-Wheel Assembly," *Journal of the Robotics Society of Japan*, vol. 17, no. 1, pp. 51-60, 1999 (in Japanese).

Control of Movement on Stairs for a Cleaning Robot

Takahisa Kakudou, Keigo Watanabe, and Isaku Nagai

Department of Intelligent Mechanical Systems, Graduate School
of Natural Science and Technology, Okayama University
3-1-1 Tsushima-naka, Kita-ku, Okayama, 700-8530, Japan

Tel & Fax: +81-86-251-8064

Email: t.kakudou@usm.sys.okayama-u.ac.jp, {watanabe, in}@sys.okayama-u.ac.jp

Abstract: An autonomous cleaning robot is proposed so as to move on all floors including stairs in a building. In human living environments, it is often the case that the cleaning area is a three-dimensional space such as a high-rise building. However, many of cleaning robots cannot clean and move on stairs, because they are not considered to move on places between floors. The proposed cleaning robot possesses L-shaped legs on the both sides of the body frame of a rectangular solid. The robot climbs down stairs by rotating the body so that the top and bottom sides of it may be reversed using L-shaped legs. In this paper, the mechanism and its control method are described for translational movement on stairs.

Keywords: Cleaning robot, Stairs, Translational movement.

I. INTRODUCTION

Recently, various robots that support and act for the work have been developed to be utilized in various fields. One of such robots is the autonomous cleaning robot [1], [2]. The automation of cleaning by robots reduces labors and saves energy for a cleaning task, so that there is an increasing need for it in large areas such as stations and airports.

In human living environments, it is often the case that the cleaning area is a three-dimensional space such as a high-rise building. However, many of cleaning robots are not considered to move on places between floors. Tajima et al. [3], [4] have developed a robotic system in which the cleaning robot cooperated with the elevator to clean floors in a high-rise building. The cleaning robot was equipped with an optical transmitter to communicate with the elevator. The elevator accepted requests from the robot, opened the door and moved to the designated floor carrying the robot. However, this system did not consider the cleaning of stairs. Also, the several types of vehicle using crawlers, wheels and legs were proposed to move on stairs [5], [6]. However, those vehicles were not assumed to turn and keep posture level on the tread board of stairs during moving on stairs.

The objective of this study is to automate of cleaning in a three-dimensional space to develop a cleaning robot which can move on stairs. A cleaning robot has been already proposed, where its structure was divided into two mechanisms for climbing down stairs and translational movement [7]. The proposed cleaning robot climbed down stairs by rotating the body so that the top and bottom sides of body may be reversed using L-shaped legs which are attached on the both sides of the body frame of a rectangular solid. It was also confirmed that the robot was able to climb down stairs keeping a stable posture through a simulation. In this paper, the mechanism and a control method are further described

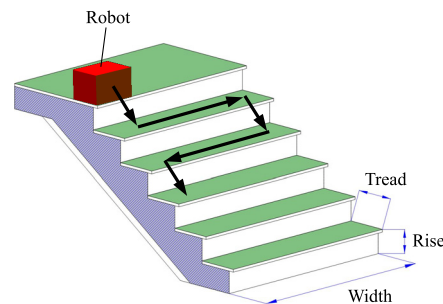


Fig. 1. Outline of stair cleaning by robot

for translational movement on stairs in detail.

II. CONCEPT OF CLEANING ROBOT FOR STAIRS

In this study, stair movement is assumed to climb down stairs. As shown in Fig. 1, whenever the robot moves on step of stairs, it needs to move in the perpendicular direction to a direction of movement. In the followings, several items are considered to design a cleaning robot for stairs:

- The cleaning from the upper floor to the lower floor is efficient for the stairs cleaning.
- The size and shape of the robot are based on the form of stairs for cleaning each step of stairs.
- The simple mechanism of a cleaning robot for stairs is desirable because of control design and weight saving.
- A cleaning area is a flat surface in indoor environment.

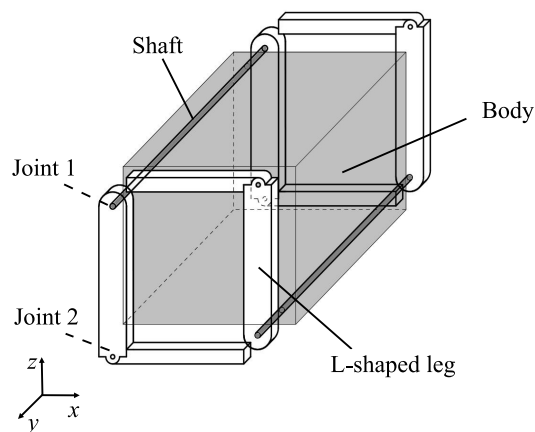
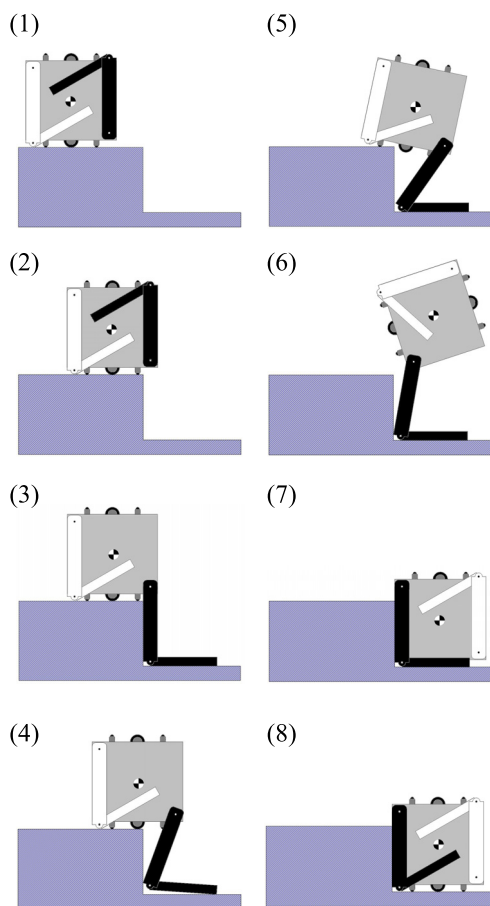


Fig. 2. Mechanism for climbing down stairs



- (1) → (2) : Move to an edge of stairs.
 (2) → (3) : Rotate legs by 180 degrees.
 (3) → (5) : Move the CG of the robot to the support polygon.
 (5) → (7) : Rotate the body keeping the CG of the robot in the support polygon.
 (7) → (8) : Bend legs for translational movement.

Fig. 3. Algorithm of climbing down stairs using L-shaped legs

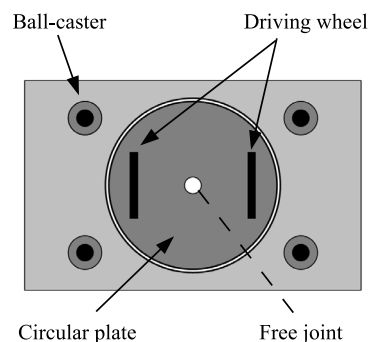


Fig. 4. Mechanism for translational movement

1. Mechanism for Climbing Down Stairs

Fig. 2 shows the proposed robot for climbing down stairs. The robot consists of the body frame of a rectangular solid and four L-shaped legs, where the leg has two degrees-of-freedom. The center of gravity (CG) of the robot is set to the center of the body. The posture of the robot remains in stable, if the CG of the robot is kept within the support polygon. Also it is assumed that this robot does not cause the displacement in y-axis direction for climbing down stairs, because the motion in a pair of L-shaped legs fixed in a shaft is synchronous. Fig. 3 shows the algorithm of stair climbing down stairs. The following is the relation between climbing motions and the number in the figure.

First, the robot moves to the edge of stairs in Fig. 3(1) to Fig. 3(2). The robot is located in the thickness of leg forward from the edge of stairs in Fig. 3(2). Secondly, rotate legs by 180 degrees in Fig. 3(2) to Fig. 3(3). Third, move the CG of the robot within the support polygon using the legs for stability in Fig. 3(3) to Fig. 3(5). The support polygon is to be a convex region surrounded by the sole of leg contacting with floor. Fourth, rotate the body keeping the CG of the robot within the support polygon in Fig. 3(5) to Fig. 3(7). Finally, bend the legs not so as to contact with the floor on the way of translational movement in Fig. 3(7) to Fig. 3(8).

2. Mechanism for Translational Movement

It is assumed that a cleaning robot is used in the indoor environment that is flat such as wooden floor or tile floor. The robot performs translational movement using wheels. The corner of the robot may collide with the wall and the riser of stairs when turning around, because the robot shape is a rectangular solid. Therefore an omni-directional mobility is adopted to move and turn around keeping a posture.

For some of omni-directional mobile mechanisms with wheels, there are mechanisms with omni-wheel, mecanum wheels, etc. Since the robot climbs down stairs by rotating the body so that the upper and lower sides of body may be reversed, two mechanisms for moving are attached to the top and bottom of the robot. To

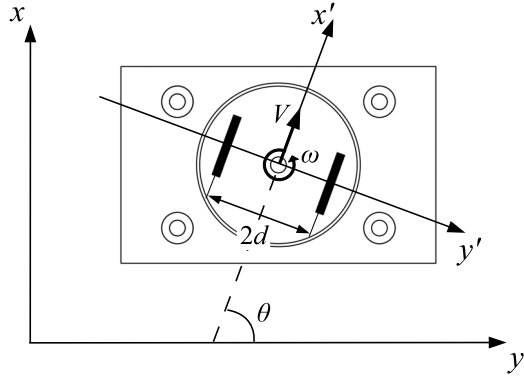


Fig. 5. Kinematic model of two-wheel-drive mechanism

reduce the robot weight, it is desirable to use the fewest possible actuators. Fig. 4 shows the proposed mechanism for translating on stair treads. The mechanism consists of four ball-casters and two driving wheels that are attached on a circular plate with a free joint. This locomotive mechanism is attached to the top and the bottom of the robot body. Also the robot bends legs not so as to contact with the floor during translational movement.

Fig. 5 shows the kinematic model of the mechanism for translational movement. The velocity V and the angular velocity ω of the robot are given by

$$\begin{bmatrix} V \\ \omega \end{bmatrix} = \begin{bmatrix} \frac{r}{2} & \frac{r}{2} \\ \frac{r}{2d} & -\frac{r}{2d} \end{bmatrix} \begin{bmatrix} \dot{\theta}_R \\ \dot{\theta}_L \end{bmatrix} \quad (1)$$

where θ_R and θ_L are the rotational angles for the left and right wheels, r is the wheel radius, $2d$ is the distance between wheels. The kinematic model is given by

$$\begin{bmatrix} \dot{x} \\ \dot{y} \\ \dot{\theta} \end{bmatrix} = \begin{bmatrix} \frac{r}{2} \sin \theta & \frac{r}{2} \sin \theta \\ \frac{r}{2} \cos \theta & \frac{r}{2} \cos \theta \\ \frac{r}{2d} & -\frac{r}{2d} \end{bmatrix} \begin{bmatrix} \dot{\theta}_R \\ \dot{\theta}_L \end{bmatrix} \quad (2)$$

where x and y are the position of the robot, and θ is the turning angle of a circular plate.

III. LOCOMOTION CONTROL

1. Locomotion Process

The locomotion of commonly-marketed cleaning robots is classified into four basic motions [8], [9] as shown in Fig. 6. Parallel motion is a repeated motion combining advance and 90-degree turns. Spiral motion is of moving toward outside on a spiral path. Wall-reflection motion is of changing the direction at random when having an obstacle collision and going straight

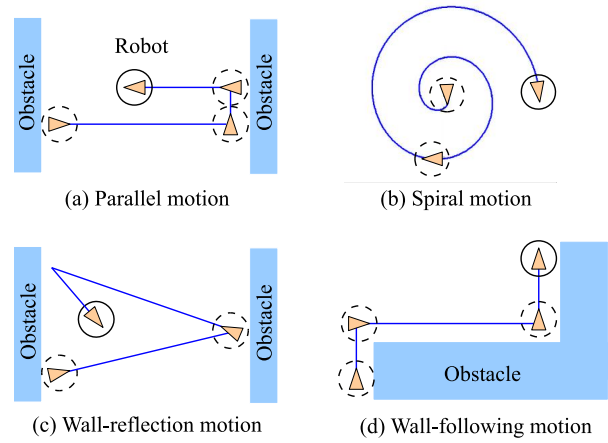


Fig. 6. Basic motion for cleaning robot

ahead. Wall-following motion is of moving along an obstacle when having an obstacle collision.

Spiral motion and wall-reflection motion are unsuitable for the stair cleaning, because one step of stairs is narrow and it takes time to complete the cleaning. On the contrary, parallel motion and wall-following motion are suitable for the stair cleaning, because the shape of step is a rectangular form. In this study, the parallel motion will be adopted.

2. Range sensor

The range sensor is used for the robot to recognize and face stairs. A position sensitive detector (PSD) SHAPE GP2D120 is used as the range sensor. Table 1 shows the electro-optical characteristics of the PSD.

Table 1. Electro-optical characteristics of the PSD

Parameter	Symbol	Value	Unit
Operation supply voltage	V_{cc}	4.5 ~ 5.5	[V]
Average dissipation current	I_{cc}	33	[mA]
Distance measuring range	L	40 ~ 300	[mm]
Measurement period	T	38.3	[ms]
Output terminal voltage	V_o	0.25 ~ 0.55	[V]

The PSD outputs the value that converts a one-way distance to an object into DC voltage. Also, the PSD has less influence on the color of reflective objects and the reflectivity, because it is an optical sensor by applying a triangulation method. In addition, the PSD has less influence on the outside light, because the operational environment is assumed to be indoor in this study.

IV. OPERATIONAL CHECK

An operational check of the robot was conducted with stopping and turning actions in the edge of a step for recognizing stairs.

1. Mobile Robot

Fig. 7 shows the topview of the mobile robot used in experiment. Table 2 shows its specification, where

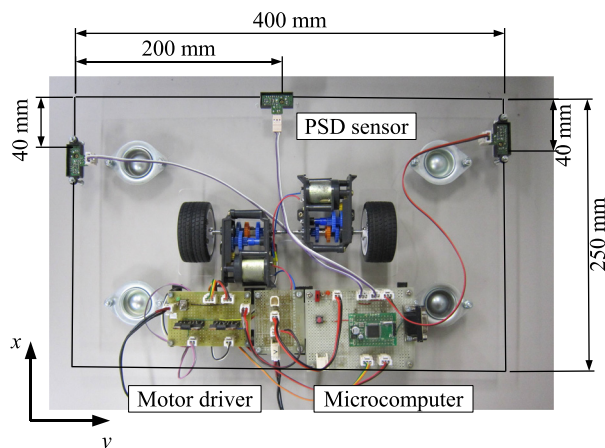


Fig. 7. Topview of mobile robot

Table 2. Specification of mobile robot

Prameter	Value	Unit
Width	400	[mm]
Length	250	[mm]
Vehicle height	20	[mm]
Mobile velocity	15	[cm/s]

the robot consists of two driving wheels and four boll-casters. Three PSDs were attached to the downward. The robot is located in the thickness of leg forward from the edge of stairs with two PSDs attached on both sides of the robot. The thickness of leg is assumed to be 40 mm. The DC voltage is converted from the analog information to the digital information by using an A/D converter of H8/3664 microcomputer, where the resolution of the A/D converter is 10 bits with 5 V. The motor can be controlled in normal and reverse rotation, stop and braking by using a motor driver.

2. Condition

The size of stairs is assumed as follows: the width is 1200 mm, the tread is 270 mm, and the rise is 180 mm. A threshold was defined to recognize stairs with 300 in A/D converted value as shown in Fig. 8. The robot recognized stairs when the threshold was less than or equal to 300.

In stop actions using all PSDs, the robot stops if any one of PSDs reacts. In turning actions using PSDs attached on both sides, if one of PSDs reacts, then the robot turns in the direction so that the other PSDs react.

3. Result and Consideration

As a result, it is confirmed that the robot stopped and turned to recognize stairs using PSDs. However, there was a case that the ball-caster had fallen from stairs before stopping the motor. This problem will be overcome by changing the layout and attached angel of PSDs for securing the distance enough to brake. Also, the robot will be controlled to slow down near the edge of stairs.

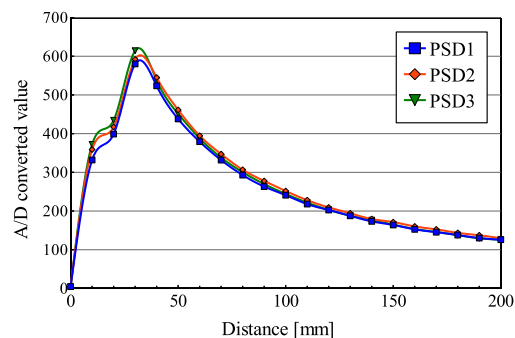


Fig. 8. Relationship between distance to a reflective object and A/D converted value of output voltage

V. CONCLUSION

A cleaning robot to climb down stairs has been developed for cleaning three-dimension space. In particular, a mechanism and a locomotion control method were proposed for the robot to clean and climb down stairs. The operational check of the robot was conducted for recognizing stairs. In the result, it was confirmed that it needs to change the layout of PSDs and control to slow down near the edge of stairs.

As future work, a stair cleaning robot will be developed to solve the above problem, together with making a real robot.

REFERENCES

- [1] Tribelhoron B and Dodds Z (2007), Evaluating the Roomba: A Low-cost, Ubiquitous Platform for Robotics Research and Educations, *Proc. of the IEEE International Conference on Robotics and Automation*, pp. 1393–1399.
- [2] Aoyama H, Tajima S, Yokota K, Ozaki K, and Yamamoto S (1998), Development of Floor Cleaning Robots (in Japanese), *Jour. of the Robotics Society of Japan*, Vol. 16, No. 1, pp. 57–64.
- [3] Tajima S, Aoyama H, Seki T, Ishikawa K, Yokota K, Ozaki K, and Yamamoto S (2004), Development of Robotic Floor Cleaning System for High-Rise Buildings (in Japanese), *Jour. of the Robotics Society of Japan*, Vol. 22, No. 5, pp. 595–602.
- [4] Aoyama H, Ishimura S, Nishihara I, Ishikawa K, Seki J, Wadasako T, Satumi Y, and Adachi Y (2009), The Development of the Cleaning Device of the Office Building Cleaning Robot (in Japanese), *Proc. of the JSME Conference on Robotics and Mechanics*, P1-B14.
- [5] Matsumoto O, Kajita S, Saigo M, and Tani K (1998), Dynamic Trajectory Control of Passing Over Stairs by a Biped Type Leg-wheeled Robot with Nominal Reference of Static Gait (in Japanese), *Jour. of the Robotics Society of Japan*, Vol. 16, No. 6, pp. 868–875.
- [6] Yuan J and Hirose S (2005), Actualization of Safe and Stable Stair Climbing and Three-Dimensional Locomotion for Wheelchair, *Proc. of the IEEE/RSJ International Conference on Intelligent Robots and Systems*, pp. 2391–2396.
- [7] Kakudou T, Nagai I, and Watanabe K (2010), A Cleaning Robot for Stairs and the Simukation of Stair Movement, in *Proc. of the 13th International Conference on Climbing and Walking Robots and the Support Technologies for Moblie Machines*, pp. 1306–1313.
- [8] Katsuki Y, Yamamoto M, and Ikeda T (2008), Motion Primitives and Their Sweeping Efficiency in Sweeping Algorithm (in Japanese), *Proc. of the JSME Conference on Robotics and Mechanics*, 2P1-110.
- [9] Matsumoto K, Ogata H, Torige A, and Matsumura D (2008), Comparison of Simulation Result with Real Sweeping Robot (in Japanese), *Proc. of the JSME Conference on Robotics and Mechanics*, 1A1-D22.

Jumping rhythm generator by CPG for a multi-legged robot

Masaaki Ikeda

Department of Advanced Systems Control Engineering,
Saga University,
1 Honjomachi, Saga 840-8502, Japan
Email : 09539002@edu.cc.saga-u.ac.jp,

Kiyotaka Izumi

Department of Mechanical Engineering,
Saga University,
1 Honjomachi, Saga 840-8502, Japan
FAX: +81-952-28-8587
Email: izumi@me.saga-u.ac.jp

Keigo Watanabe

Department of Intelligent Mechanical Systems,
Okayama University,
1-1-1 Tsushima-naka, Kita-ku,
Okayama-shi 700-8530, Japan
Email: watanabe@sys.okayama-u.ac.jp

Abstract: Three features of a legged robot are listed as the discrete disposition of supported legs, the flexible posture without changing disposition of supported legs, and the obstacle avoidance with a three dimensional behavior. The maximum height of an avoidable obstacle is defined by the leg mechanism of a robot. The capability of obstacle avoidance is improved by a jumping motion. In this paper, we discuss the rhythmic jumping of a multi-legged robot using the central pattern generator (CPG). Authors propose the construction method of CPG for six legged robot, in which each leg has a compressed spring. The effectiveness of the present method is illustrated by some simulations.

Keywords: Legged robot, Jumping robot, Central pattern generator, Robot simulator

I. Introduction

In recent years, working places of robots are expanding from factories to outdoors and homes, etc. Required tasks of mobile robots are rescue operations in dangerous places such as a disaster area and the scene of an accident, and assistance of human at a home. Mobilities on a rough terrain of a robot are demanded to be high. Mobile mechanisms which have high energy efficiency are a wheel type and a crawler type. Those mechanisms are able to travel on the terrain which is secured a continuous contacting surface, however, the mobility of those mechanisms is almost low on the rough terrain which has big bumps. The legged mechanism has a high capability of movement on a rough terrain because of some features which are a discrete disposition of supported legs, the flexible posture without changing the disposition of supported legs, high degree of freedom, etc. Many legged type robots have been developed with several concepts which are biomimetic machines, and improvements of mobile capability and adaptation capability against for any ground conditions.

Moreover, it is listed to one of the features of a legged robot ranging over an obstacle that three-dimensional obstacle avoidance behavior of getting over and mov-

ing is possible. However, the point that the obstacle of the height exceeding the excursion of a leg cannot be overcome as a subject of this feature can be considered. Movement by a jump or flight can be considered to this subject.

It is shown clearly that a living thing controls periodic movement which was autonomously adapted to environment by making feeling feed back to the central pattern generator (CPG) of the neural circuit which exists in a spine. CPG is applied to a legged robot and research which controls an autonomous periodic motion by feeding back the information acquired from the sensor attached to the robot to the mathematical model of CPG to environment like walk behavior is done[1], [2].

In this paper, a jump is adopted as a method of easing restriction of the avoidance operation by the mechanism in the obstacle avoidance of a legged robot, and it thinks of the mobile robot of six leg types which has a jump mechanism. Moreover, CPG generates the desired value for a jump mechanism, and a periodic jump is enabled. The effectiveness of the proposal approach is examined from the result of the simulation using OpenHRP3 which is the distributed component type robot simulator.

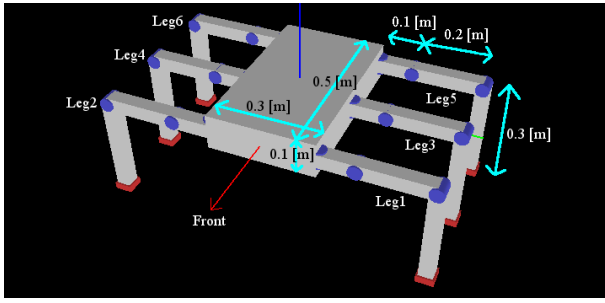


Fig. 1: Jumping six-legged robot

II. Jumping Six-Legged Robot

Although it is in the number of legs of a legged robot variously, in this paper, we adopt a six-legged robot, because this robot can always keep static stability. In order to perform posture maintenance and walk movement, there are three joints in each leg of a robot. It has a mechanism of the direct acting furthermore slid to each leg apical portion as a jump mechanism for leg them. Therefore, as for the jumping-of-flow-control-valve legged robot to examine, since it is an existing six-legged robot, 4 degree of freedom is a robot which has 24 degree of freedom in total at each leg. The target six jumping-of-flow-control-valve robot models, each link length, and the leg number which were used by the kinetics simulator are shown in Fig. 1. The line extended on a robot in Fig. 1 expresses perpendicular above, makes this a z axis, and makes an x-axis the line extended in the direction of this side of a robot. Further Axis, Direction which makes an axis and a right-hand system It is considered as an axis. Moreover, let the field which is in sight to the front with Fig. 1 be a front face of a robot. Saw from the robot, and become an odd number on left-hand side, it is made to turn into even numbers on right-hand side, and the leg number of each leg set the leg number of the front left-hand side leg to Leg1.

The total mass of a robot is 12 kg. The maximum height of the axial direction of the robot in the posture of Fig. 1 is set to 0.35 m. The sliding mechanism for a jump of the leg point is shown in Fig. 2. The sliding mechanism for a jump is slid in +0.05 m and -0.05 m on the basis of the leg point. In addition, the leg used each leg as the same mechanism.

III. Jumping Rhythm Generator

CPG is a kind of a neuron model and generates the periodic signal it is supposed that it is deeply related to the periodical activity of a living thing of the periodic signal.

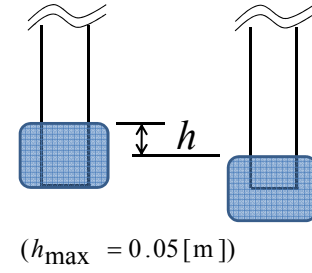


Fig. 2: Slide mechanisms for jump

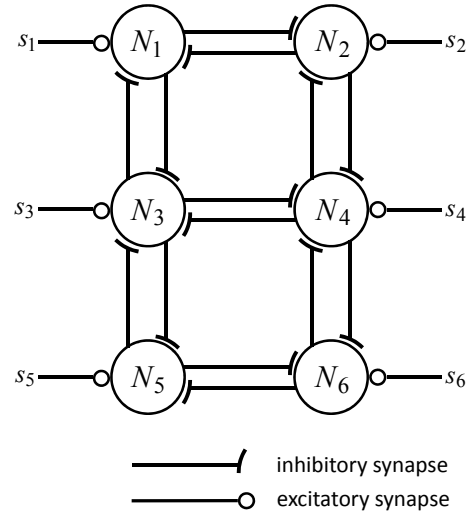


Fig. 3: Network for CPG

When two or more CPG neurons exist, it is known that the phenomenon called drawing in with the passage of time will generate the output cycle signal of each neuron by defining the coupling coefficient between neurons. Although there were some mathematical models proposed so far in CPG, in this paper, Matsuoka oscillator with a comparatively simple relation of a parameter was used[3]. Matsuoka model was following formula.

$$\begin{aligned} T_r \frac{du_i}{dt} + u_i &= - \sum_{j=1}^n a_{ij} y_j + s_i - b f_i \\ y_i &= g(u_i) \quad (g(u_i) \triangleq \max(0, u_i)) \\ T_a \frac{df_i}{dt} + f_i &= y_i \end{aligned} \quad (1)$$

Where, t is time variable, i, j is number of neuron. T_r is rise time constant, u_i is membrane potential of neuron body, a_{ij} (≥ 0 for $i \neq j$ and $= 0$ for $i = j$) is a weight of inhibitory synaptic connection from j -th neuron to the i -th neuron. y_i is a firing rate or output of the neuron, s is an impulse rate of input. b is the parameter that deter-

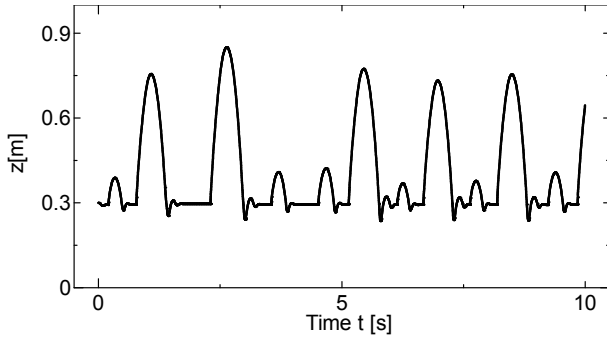


Fig. 4: The vertical position of the robot

mines the steady-state firing rate for a constant input. f is adaptation variable, T_a is adaptation time constant.

The composition of the CPG network by inhibition binding of six neurons used in this paper is shown in Fig. 3. The output value y from each neuron of the constituted CPG network is carried out as a next desired value of the sliding mechanism for a jump of the leg number i as shown in following equation.

$$h_{oi} = -y_i \quad (2)$$

However, it is less than a value with x of the robot center of gravity, and the acceleration of y axial direction, When the acceleration of an axial direction approaches gravitational acceleration enough, it thinks that the shake of a robot was fully settled, and it limits to when the shake of a robot is fully settled, and a CPG output is used as a desired value. The output of the sliding mechanism for a jump is calculated by the following formula using the desired value acquired from CPG.

$$\tau_i = P(h_{oi} - h_i) + D(v_{oi} - \dot{h}_i) \quad (3)$$

Where, i is number of the leg, h_i is the displacement of the slide joint, v_{oi} is objective velocity (Now, $v_{oi} = 0$). P is the proportional gain, D is the differential gain. Thus, the force for a jump is generated with the generated period.

IV. Simulation

1. Setting up of parameters

It is referred to as $T_r = 0.3$, $s_i = 0.25$, $b = 10.5$, $T_a = 0.2$ and each parameter given to the Matsuoka oscillator of CPG used for the simulation is an initial value of the membrane potential u of each neuron. It carried out and the initial value of $u_1 = u_4 = u_5 = 0$, $u_2 = u_3 = u_6 = 0.05$ and a fatigue state f was set to $f_1 = f_4 = f_5 = 0$, $f_2 = f_3 = f_6 = 0.05$. Coupling load of the CPG network

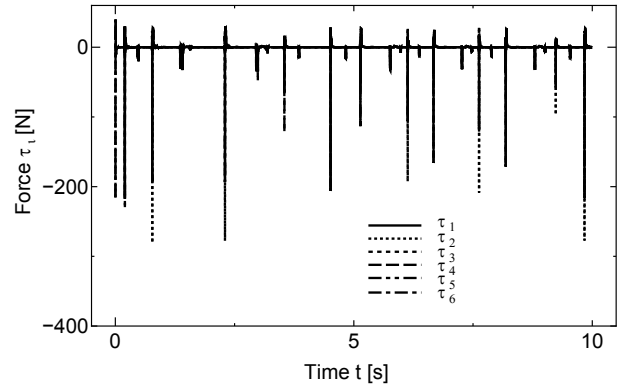


Fig. 5: Driving forces of soles

was set to $a_{12} = a_{13} = 2.5$, $a_{21} = a_{24} = 2.5$, $a_{31} = a_{34} = a_{35} = 2.5$, $a_{42} = a_{43} = a_{46} = 2.5$, $a_{53} = a_{56} = 2.5$ and $a_{64} = a_{65} = 2.5$. The control gain used for the force calculation in the case of a jump was set to $P = 4500$ and $D = 1$.

2. Results

The force outputted to each sliding mechanism is shown in Fig. 5. The orbit of the body of a robot is shown in Fig. 4.

The output of each CPG neuron is shown in Fig. 6. Fig. 6 is put in order by neuron numerical order from the top. By the constituted CPG network, Phases of the first, the fourth and the fifth neurons is same each other. Similarly, outputs of the second, the third and sixth neurons have same phase. Moreover, a phase shift from which the phase angle of such combination obtains the maximum by turns is seen.

The number of times of a jump is because the shake of a robot was not fully settled, so few things are not outputting force compared with the number of times of an output of CPG. Conversely, the force currently outputted calculates the output of CPG when conditions are fulfilled. When the output of Fig. 5 and the orbit of Fig. 4 are measured, it turns out that it has jumped immediately after outputting force. However, it turns out that the height proportional to the output of force has not necessarily come out.

This is because slope of the force outputted since force is outputted when slope of the CPG output of the phase angle of another side is negative when one of the two is 0 among the outputs by two kinds of phase angles also becomes negative. On the contrary, the height to which one output is proportional to force since slope of the force outputted when slope of the CPG output of the phase angle of another side is positive also just becomes by 0 is obtained. When a CPG output is larger, it turns out that

the jump to which it is higher to output force is carried out. Moreover, in order that the direction whose slope of the output of CPG the CPG output of two kinds of phase angles is both positive at the time or more of zero at the time of the output of force may work strongly, it turns out that the height proportional to force is obtained.

V. Conclusions

It is checked that a robot jumps periodically by using the network composed of CPG neurons which are modeling with Matsuoka oscillator. The robot has six legs which are equipped jump mechanism. In the CPG network of this paper, the height of the jump at each time changed unintentionally. This feeds back the force sensor of a robot, and the information on a gyro sensor to CPG, and is expected that a suitable CPG output to which the height of a jump becomes fixed is obtained by presuming time until a posture is stabilized from the flight duration and landing of a robot.

References

- [1] Ijspreet AJ (2008), Central pattern generators for locomotion control in animals and robots: A review. *Neural Networks* 21:642-653
- [2] Liu GL, Habib MK, Watanabe K, Izumi K (2008), Central pattern generators based on Matsuoka oscillators for the locomotion of biped robots. *Artificial Life and Robotics* 12(1-2):264-269
- [3] Matsuoka K (1987), Mechanisms of Frequency and pattern control in the neural rhythm generators. *Biological Cybernetics* 56(5-6):345-353

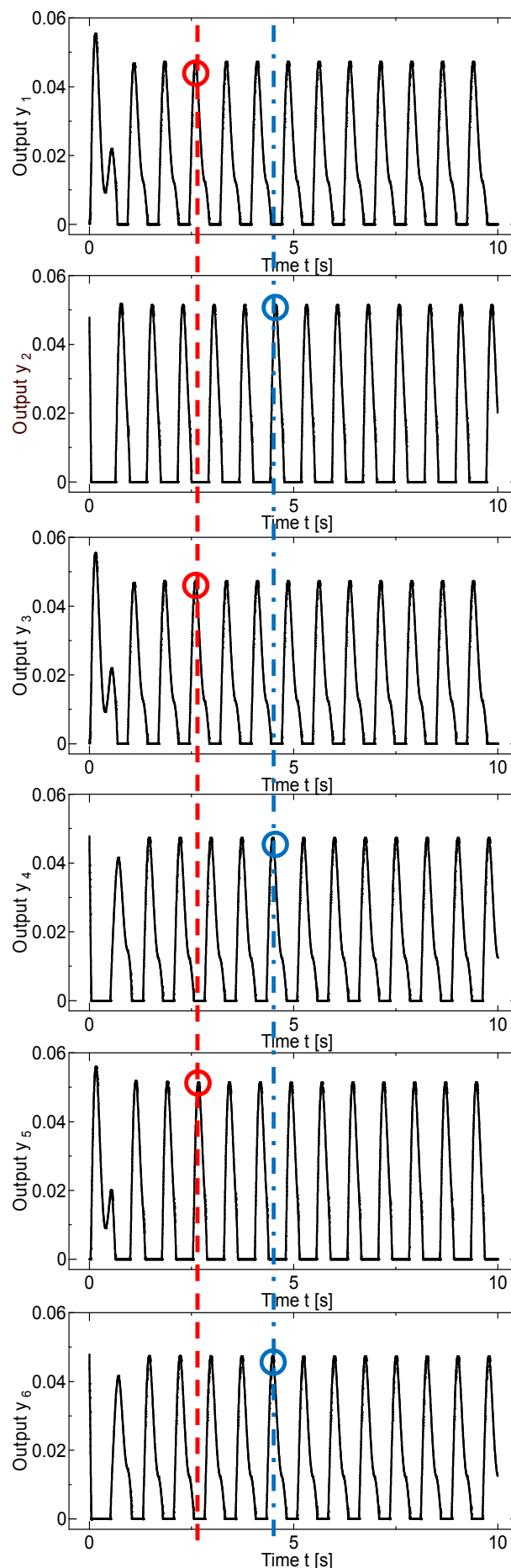


Fig. 6: Outputs of neurons

A Bearing-Only Localization Solved by an Unscented Rauch-Tung-Striebel Smoothing

Saifudin Razali, Keigo Watanabe, and Shoichi Maeyama

Department of Intelligent Mechanical Systems,
Graduate School of Natural Science and Technology, Okayama University,
3-1-1 Tsushima-naka, Kita-ku, Okayama 700-8530, Japan
Tel & Fax: +81-86-251-8064

E-mail: saifudin@usm.sys.okayama-u.ac.jp, {watanabe, maeyama}@sys.okayama-u.ac.jp

Abstract: The unscented Kalman filter (UKF) has become an alternative in nonlinear estimation problems to overcome the limitation of Taylor series linearization used by the extended Kalman filter (EKF). It uses a deterministic sampling approach known as sigma points to propagate nonlinear systems and has been discussed in many literature. However, a nonlinear smoothing problem has received less attention than the filtering problem. Therefore, in this article we examine an unscented smoother based on Rauch-Tung-Striebel form for discrete-time dynamic systems. This smoother has advantages available in unscented transformation over approximation by Taylor expansion as well as its benefit in derivative free. This smoothing technique has been implemented and evaluated through a bearing-only localization problem.

Keywords: Unscented transformation, Rauch-Tung-Striebel smoother, Bearing-only localization problem.

I. INTRODUCTION

The nonlinear filtering problem has been deeply studied and various methods are provided in literature. Among them, the most useful ones are the extended Kalman Filter (EKF), the ensemble Kalman Filter (EnKF), the unscented Kalman Filter (UKF), and the Particle Filter (PF). Historically, the EKF is still the most widely adopted approach to solve the nonlinear estimation problem. It is based on the assumption that nonlinear system dynamics can be accurately modeled by a first-order Taylor series expansion as proved by van der Merwe [1]. The EnKF introduced by Evensen [2] is a reduced rank filter which propagates the states through nonlinearity and updates a relatively small ensemble of samples from which an assumed Gaussian distribution captures the main characteristics in the uncertainty. The PF also uses a sampling approach to estimate the higher-order moments of the posterior probability distribution by propagating and updating a number of particles, but without assuming Gaussian statistics as explained by Arulampalam et al. [3].

The UKF, which is a derivative free alternative to EKF, overcomes the differentiation problem by using a deterministic sampling approach demonstrated by Julier and Uhlmann [4] and Wan and van der Merwe [5]. The state distribution is represented using a minimal set of carefully chosen sample points, called sigma points. This technique is used to linearize a nonlinear function of a random variable through a linear regression between n points drawn from the prior distribution of the random variable. Since we are considering the spread of the random variable during linearization, the technique tends to be more accurate than the Taylor series linearization used in the EKF, particularly in the presence of strong nonlinearities as proved by van der Merwe [1]. The $2n+1$ sigma points, are chosen based on a square-root decom-

position of the prior covariance, where n is the state dimension. These sigma points are propagated through the true nonlinear function, without approximation, and then a weighted mean and covariance is taken. This approach results in approximations that are accurate to the third order Taylor series expansion for Gaussian inputs in all nonlinearities.

However, the nonlinear smoothing problem has received less attention than the filtering problem in the literature. Therefore, in this article we investigate the unscented smoother based on Rauch-Tung-Striebel form [6], [7] for discrete-time dynamic systems studied by Särkkä [8] and Saifudin et al. [9], [10]. This smoother takes a benefit over unscented transformation to the limitation of Taylor approximation as well as its derivative free advantages. To evaluate the performance of this smoother, the algorithm is applied for a bearing-only localization problem. In what follows, note that we will use the abbreviations URTSS for the unscented Rauch-Tung-Striebel smoother.

The structure of this paper is as follows: In section 2 we briefly describe the derivation of unscented Rauch-Tung-Striebel smoother and its summary of an implemented algorithm. A bearing-only localization problem is presented in section 3 as an application example of this algorithm, as well as discussions on the simulation results. The paper is concluded in section 4.

II. UNSCENTED RAUCH-TUNG-STRIEBEL SMOOTHER

Consider a state space model of the form,

$$\begin{aligned} x_k &= F_{k-1}(x_{k-1}, u_{k-1}, w_{k-1}) \\ y_k &= H_k(x_k, v_k) \end{aligned} \quad (1)$$

where $x_k \in \mathbf{R}^n$ is the state, $y_k \in \mathbf{R}^m$ is the measurement at time t_k , u_{k-1} is the control action, $w_{k-1} \sim \mathcal{N}(0, Q_{k-1})$ is the Gaussian process noise, $v_k \sim \mathcal{N}(0, R_k)$ is the Gaussian measurement noise, $F_{k-1}(\cdot)$ is the process model function and $H_k(\cdot)$ is the measurement model function. The time step k runs from 0 to T and at time step 0 there is no measurement, only the prior distribution $x_0 \sim \mathcal{N}(m_0, P_0)$.

The purpose of the smoothing algorithm is to find approximations to the smoothing distributions $p(x_k | y_{1:T})$ for all $k = 1, 2, \dots, T$. The approximations are chosen to be Gaussian:

$$p(x_k | y_{1:T}) \sim \mathcal{N}(x_k | m_k^s, P_k^s). \quad (2)$$

The *optimal smoothing equations* of the model can be written in two options as mentioned by Klaas et al. [11], named as two filter smoother and forward-backward smoother. For the purpose of deriving the Rauch-Tung-Striebel form of smoother, the forward-backward smoothing will be used and it can be written as follows:

$$p(x_k | y_{1:T}) = p(x_k | y_{1:k}) \times \int \frac{p(x_{k+1} | x_k) p(x_{k+1} | y_{1:T})}{p(x_{k+1} | y_{1:k})} dx_{k+1} \quad (3)$$

where $p(x_k | y_{1:k})$ is the filtering distribution of the time step k and $p(x_{k+1} | y_{1:k})$ is the predicted distribution of the time step $k+1$, which can be computed by the prediction step of the optimal filtering. The smoothing recursion is started from last time step $k = T$ and proceeded backwards in time.

From Eq. (3), the Rauch-Tung-Striebel smoother can be derived as shown by Särkkä [8]. Assumed that the (approximate) mean and covariance of the filtering distributions

$$p(x_k | y_{1:k}) \approx \mathcal{N}(x_k | m_k, P_k)$$

for the model in Eq. (1) have been computed by the unscented Kalman filter or a similar method.

Further assume that the smoothing distribution of time step $k+1$ is known and Gaussian

$$p(x_{k+1} | y_{1:T}) \approx \mathcal{N}(x_{k+1} | m_{k+1}^s, P_{k+1}^s).$$

This smoothing algorithm can be summarized as followings steps:

- 1) Form the matrix of sigma points of the augmented random variable $\tilde{x}_k = (x_k^T w_k^T)^T$ such that

$$\tilde{X}_k = [\tilde{m}_k \quad \dots \quad \tilde{m}_k] + \sqrt{c} \begin{bmatrix} 0 & \sqrt{\tilde{P}_k} & -\sqrt{\tilde{P}_k} \end{bmatrix}$$

$$\text{where } \tilde{m}_k = \begin{bmatrix} m_k \\ 0 \end{bmatrix} \text{ and } \tilde{P}_k = \begin{bmatrix} P_k & 0 \\ 0 & Q_k \end{bmatrix}.$$

- 2) Propagate the sigma points through the dynamic model

$$\tilde{X}_{k+1,i}^- = F_k(\tilde{X}_{k,i}^x, \tilde{X}_{k,i}^w), \quad i = 1, \dots, 2n+1$$

where $\tilde{X}_{k,i}^x$ and $\tilde{X}_{k,i}^w$ denote the parts of the augmented sigma point i , which correspond to x_k and w_k , respectively.

- 3) Compute the predicted mean m_{k+1}^- , the predicted covariance P_{k+1}^- and the cross-covariance C_{k+1} :

$$\begin{aligned} m_{k+1}^- &= \sum_i W_{i-1}^{(m)} \tilde{X}_{k+1,i}^- \\ P_{k+1}^- &= \sum_i W_{i-1}^{(c)} \left(\tilde{X}_{k+1,i}^- - m_{k+1}^- \right) \left(\tilde{X}_{k+1,i}^- - m_{k+1}^- \right)^T \\ C_{k+1} &= \sum_i W_{i-1}^{(c)} \left(\tilde{X}_{k+1,i}^x - m_k \right) \left(\tilde{X}_{k+1,i}^- - m_{k+1}^- \right)^T \end{aligned}$$

where the definitions of the weights $W_{i-1}^{(m)}$ and $W_{i-1}^{(c)}$ are the same as in [5].

- 4) Compute the smoother gain D_k , the smoothed mean m_k^s and the covariance P_k^s :

$$\begin{aligned} D_k &= C_{k+1} [P_{k+1}^-]^{-1} \\ m_k^s &= m_k + D_k (m_{k+1}^s - m_{k+1}^-) \\ P_k^s &= P_k + D_k [P_{k+1}^- - P_{k+1}^-] D_k^T \end{aligned}$$

The above procedure is a recursion, which can be used for computing the smoothing distribution of step k from the smoothing distribution of time step $k+1$. Because the smoothing distribution and filtering distribution of the last time step T are the same, we have $m_T^s = m_T$, $P_T^s = P_T$, and thus the recursion can be used for computing the smoothing distributions of all time steps by starting from the last step $k = T$ and proceeding backwards to the initial step $k = 0$.

III. AN EXAMPLE APPLICATION

In this section we consider the problem of bearing only localization as used by Bailey [12].

1. Process and measurement state

The discrete time vehicle state is given by:

$$\mathbf{x}_k = \mathbf{f}(\mathbf{x}_{k-1}, \mathbf{u}_{k-1}, w_{k-1}) \quad (4)$$

where $\mathbf{x}_k = [x_k \ y_k \ \phi_k]^T$ are the vehicle position coordinates and its orientation in time step k , respectively. $\mathbf{u}_{k-1} = [V \ G]^T$ is control action in which V is the vehicle velocity, and G is the vehicle steering angle. w_{k-1} is a zero-mean Gaussian process noise with covariance Q .

This vehicle is equipped with a range and bearing sensor. It can sense an object bounding in ± 30 degree semi-circle with the maximum range of 30 meter. Only bearing measurement data will be used in this example. The measurement equation is as follows:

$$\begin{aligned} z_k &= h(\mathbf{x}_k, \mathbf{f}_i) + v_k \\ &= \left[\tan^{-1} \left(\frac{f_{i,y} - y_k}{f_{i,x} - x_k} \right) - \phi_k \right] + v_k \end{aligned} \quad (5)$$

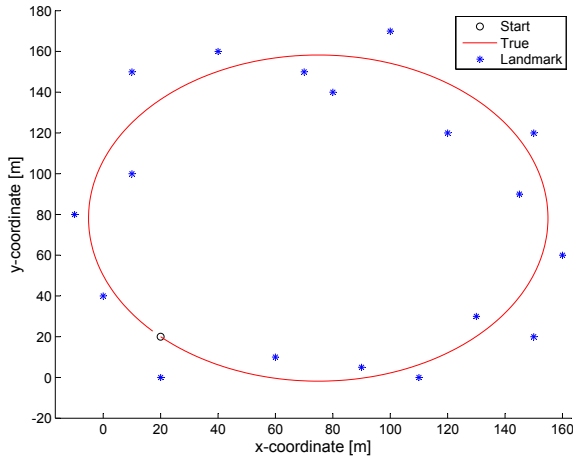


Fig. 1. True trajectory and landmark.

where x_k , y_k and ϕ_k are the vehicle position coordinates and its orientation in time step k , respectively. f_i is a landmark feature available at time when the sensor takes a measurement. This landmark feature is assumed to be static and represented as a Cartesian coordinate system as $(f_{i,x}, f_{i,y})$. v_k is assumed as zero-mean Gaussian white measurement noise with covariance R .

2. Simulation setup

Fig. 1 shows the landmark and true vehicle trajectory setup for this simulation. The vehicle starts at a known location (20 m, 20 m, -0.8 rad) and travels with a nominal speed and a steering angle of 3 m/s and 0.05 rad, respectively. The nominal control values are corrupted with Gaussian noise with standard deviations 0.3 m/s and 0.05 radian, respectively for each 0.5 s sampling interval. The sensor takes bearing measurement and its value is assumed to be corrupted with Gaussian noise with standard deviation 0.09 radian. All simulation parameters and their values are shown in Table 1.

The initial conditions for the filter are set to

$$\begin{aligned}\hat{x}_0 &= x_0 \\ &= \begin{pmatrix} 20 \\ 20 \\ -0.8 \end{pmatrix}\end{aligned}$$

and

$$P_0 = \begin{pmatrix} 10^{-10} & 0 & 0 \\ 0 & 10^{-10} & 0 \\ 0 & 0 & 10^{-10} \end{pmatrix}$$

which basically means that the vehicle initial position and its orientation are known.

3. Result and discussion

Fig. 2 shows the result of both UKF and URTSS. For more reliable result, we calculated the root mean square (rms) error of x -axis, y -axis, ϕ and also its position for every iteration step and they are shown in Figs. 3, 4, 5 and 6 respectively. Figs. 3 and 4 show that the rms errors of the URTSS are always comparable to or lower than

Table 1. Simulation setup

Parameter	Description	Value	Unit
V	Velocity	3	m/s
G	Steering angle	0.05	radian
WB	Wheel-base	4	m
σ_V	Standard deviation of V	0.3	m/s
σ_G	Standard deviation of G	0.05	radian
σ_B	Standard deviation of bearing	0.09	radian

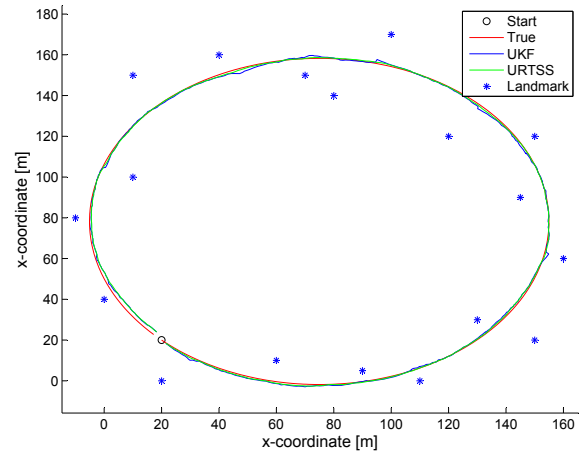


Fig. 2. Estimates by UKF and URTSS.

the error values produced by the UKF. This situation also can be seen in rms vehicle position errors as shown in Fig 6. However, the vehicle orientation rms errors for both methods did not show a significant difference. Furthermore, we took root mean square values for 1000 Monte Carlo runs. The results of filtering and smoothing estimation in x -axis, y -axis, and ϕ are shown in Table 2 and it is proved that the URTSS has a better performance over the UKF.

IV. CONCLUSION

In this paper, an unscented Rauch-Tung-Striebel smoother (URTSS) has been applied to a bearing-only localization problem and its performance has been also evaluated in simulations. It was assumed that the vehicle was equipped with a range and bearing sensor. To compare the performance of both UKF and URTSS, the rms errors were calculated. It was then found the URTSS has a better performance over the UKF.

Table 2. RMS errors

Method	x_{RMSE}	y_{RMSE}	ϕ_{RMSE}
UKF	0.8730	0.8361	0.0941
URTSS	0.7438	0.7367	0.0771

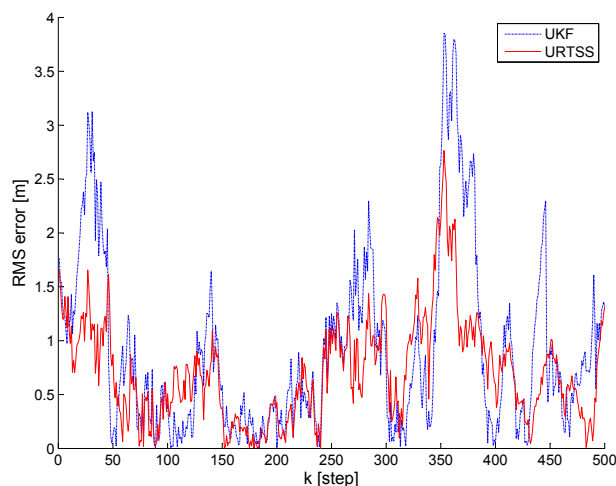


Fig. 3. RMS error of x -axis.

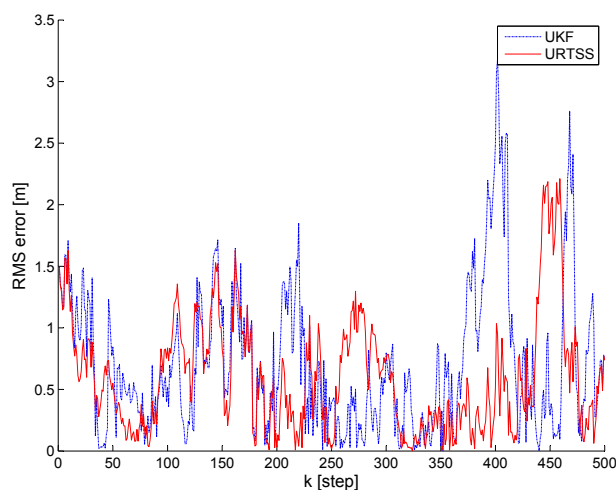


Fig. 4. RMS error of y -axis.

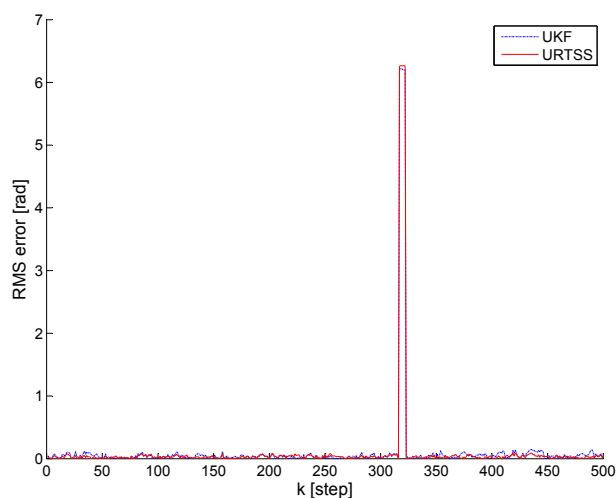


Fig. 5. RMS error of ϕ -axis.

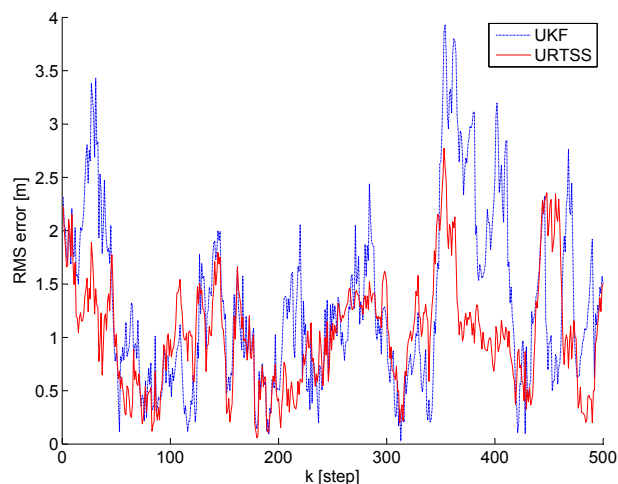


Fig. 6. RMS vehicle position error estimates by UKF and URTSS.

REFERENCES

- [1] van der Merwe R (2004), Sigma point Kalman filter for probabilistic inference in dynamic state-space models. PhD Thesis, Oregon Health & Science University, Portland.
- [2] Evensen G (2003), The ensemble Kalman filter: Theoretical formulation and practical implementation. *Ocean Dynamics*, 53: 343–367.
- [3] Arulampalam MS, Maskell S, Gordon N, and Clapp T (2002), A tutorial on particle filters for online nonlinear/non-Gaussian Bayesian tracking. *IEEE Trans. on Signal Processing*, 50(2): 174–188.
- [4] Julier SJ and Uhlmann JK (2004), Unscented filtering and nonlinear estimation. *Proceedings of the IEEE*, 92(3): 401–422.
- [5] Wan E and van der Merwe R (2004), *The Unscented Kalman Filter*, New York: Wiley.
- [6] Rauch HE, Tung F and Striebel CT (1965), Maximum likelihood estimates of linear dynamic systems. *AIAA Journal* 3(8): 1445–1450.
- [7] Rauch HE (1963), Solutions to linear smoothing problem. *IEEE Trans. on Automatic Control* 8(4): 371–372.
- [8] Särkkä S (2008), Unscented Rauch-Tung-Striebel smoother. *IEEE Trans. on Automatic Control* AC-53(3): 845–849.
- [9] Saifudin R, Watanabe K, Maeyama S and Izumi K (2010), An unscented Rauch-Tung-Striebel smoother for a bearing only tracking problem. *Int. Conf. Control, Automation and Systems* 2010, Gyeonggi-do, Korea.
- [10] Saifudin R, Watanabe K, Maeyama S and Izumi K (2010), An unscented Rauch-Tung-Striebel smoother for a vehicle tracking problem. *Int. Conf. on Soft Computing and Intelligent Systems and Int. Symposium on Advanced Intelligent Systems*, Okayama, Japan.
- [11] Klaas M, Briens M, de Freitas N, Doucet A, Maskell S, and Lang D (2006), Fast particle smoothing: If I had a million particles. *Proceedings of ICML*, 25–29.
- [12] Bailey T (2003), Constrained initialization for bearing only SLAM. *IEEE Int. Conf. on Robotics and Automation* (2): 1966–1977.

Trajectory Tracking Control for Nonholonomic Mobile Robots by an Image-Based Approach

Tatsuya Kato, Keigo Watanabe, and Shoichi Maeyama

Department of Intelligent Mechanical Systems,
Graduate School of Natural Science and Technology, Okayama University,
3-1-1 Tsushima-naka, Kita-ku, Okayama 700-8530, Japan
Tel & Fax: +81-86-251-8064

E-mail: t.kato@usm.sys.okayama-u.ac.jp, {watanabe, maeyama}@sys.okayama-u.ac.jp

Abstract:

The vision-based control that uses cameras for observing a robot environment has been researched widely. Especially, a method called image-based control has high robust properties, because it can control a target on an image plane coordinate without using a robot position. Kurashiki et al. have already studied on an image-based control method that can realize a robust trajectory tracking. Although their objective was to control a nonholonomic mobile robot, the problem setting used there was to be little affected from the nonholonomic constraint. Further more, there were unclear points in deriving a control law. In this paper, such unclear points are explained from an geometric relation and other problem settings, which are clearly affected by a nonholonomic constraint, are proposed.

Keywords: Vision-based control, Image-based control, Trajectory tracking, nonholonomic mobile robot.

I. INTRODUCTION

Unmanned vehicles such as automated driving cars require high robustness against any disturbances for safety. On the other hand, with the popularization of inexpensive cameras, vision-based control has been researched in the domain of robot control. Vision-based control is classified roughly into two methods that are called a “position-based” method and an “image-based” method [1], [2], [3], [4]. In the position-based method, the control errors are calculated from the position and the pose of the camera estimated from captured images. Although the method can control these states directly, the camera calibration is very important to the state estimation. The image-based method does not consider the position of the camera. The control errors are calculated on the coordinate which is attached directly to the captured 2D image. The control input is determined according to the control errors such as the amount of features, the location of the target on the image coordinate and so on. In general, the image-based method is known to be robust not only camera but also robot calibration errors.

The purpose of our research is controlling mobile robots with the image-based method, because it has higher robustness than the position-based method. As the earlier study of the image-based method, Kurashiki [5] developed a system consisting of a nonholonomic robot and a camera so that the robot can track the line drawn on the floor, with controlling the gradient and the intercept of the line on the captured image to their desired values. However, a nonholonomic constraint does not affect its problem setting. Additionally, there is a mistake of the derivation of a control law. In this paper, these two problems are explained and the control law is checked with a simulation experiment. Then, a new problem setting which is influenced by a nonholonomic

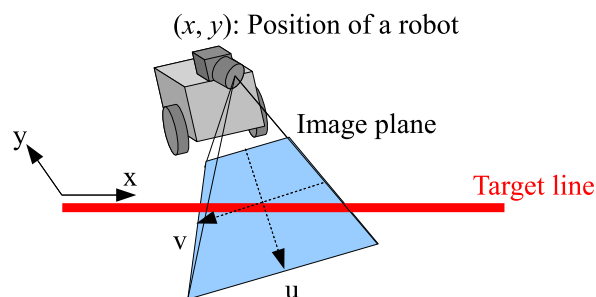


Fig. 1. Definition of coordinates

constraint is described.

II. PROBLEM SETTING

Fig. 1 shows the environment of the trajectory tracking system. A camera is attached on the robot to observe the target line drawn on the floor. The objective of the control is that the robot tracks the target line autonomously based on the captured image.

1. Coordinates

The world coordinate is set such that x-axis is along the target line and y-axis is perpendicular to the x-axis shown in Fig. 1. The v-u coordinate, whose origin corresponds to the center of the captured image plane, is attached on the image plane as shown in Fig. 2. For simplification, the camera is assumed to be equipped at the center of the robot with its downward direction. Thus, the origin of v-u coordinate corresponds to the position of the robot (x, y) on the world coordinate. An anticlockwise rotation is to be positive for the angle between target line and u-axis θ (i. e., θ has a negative value in Fig. 2).

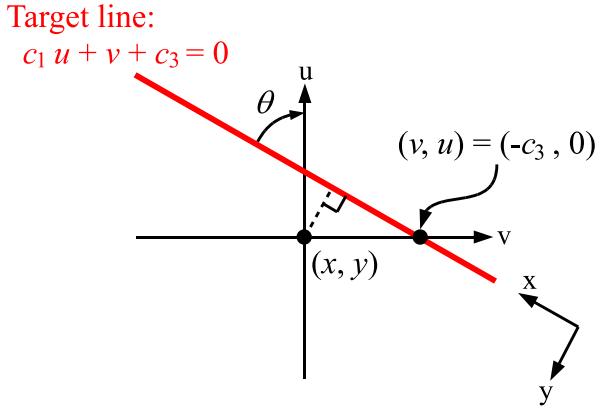


Fig. 2. Coordinate of the image plane

In general, the equation of a straight line on v-u coordinate is denoted as follows:

$$a_1u + a_2v + a_3 = 0 \quad (1)$$

Assuming that this straight line is not parallel to v-axis, a_2 is not 0. Thus, Eq. (1) can be divided by a_2 to obtain Eq. (2),

$$c_1u + v + c_3 = 0, \left(c_1 = \frac{a_1}{a_2}, c_3 = \frac{a_3}{a_2} \right) \quad (2)$$

where c_1 is a factor related to the gradient of the line and c_3 is the reversal sign of v-coordinate value at the intersection of the line and v-axis. Thus, the parameters of the target line are c_1 and c_3 . The relationship between c_1 and θ is written as follows:

$$c_1 = -\tan \theta, \left(-\frac{\pi}{2} < \theta < \frac{\pi}{2} \right) \quad (3)$$

On the other hand, the distance y between the target line and the robot should converge to 0, to track the target line. On the world coordinate, it is just as the y value of the robot position (x, y) . The relationship between c_3 and y is obtained geometrically such as

$$y = -c_3 \cos \theta \cdot \frac{h}{f} \quad (4)$$

where f is a focal length of a camera and h is an altitude of a camera position. Then the above equation is rewritten as follows:

$$c_3 = -\frac{1}{\cos \theta} \cdot \frac{yf}{h} \quad (5)$$

Thus, controlling c_1 and c_3 to zero on the image plane is equivalent to tracking the target line on the world coordinate. The observing equation to obtain c_1 and c_3 from the captured image is written as follows:

$$\begin{bmatrix} c_1 \\ c_3 \end{bmatrix} = \frac{1}{u_2 - u_1} \begin{bmatrix} v_1 - v_2 \\ -u_2v_1 + u_1v_2 \end{bmatrix} \quad (6)$$

where the points of (v_1, u_1) and (v_2, u_2) are arbitrary points on the target line on the captured image. Assuming that the target line is not parallel with v-axis, it follows that $u_2 - u_1 \neq 0$.

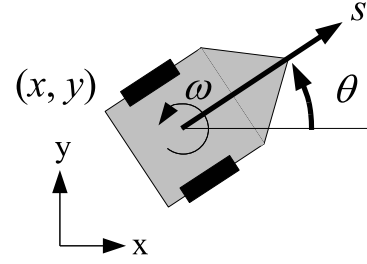


Fig. 3. Robot model

2. Question of Earlier Research

Kurashiki et al. derived the relationship between y and c_3 as follows:

$$y = \sqrt{u_3^2 + v_3^2} \cdot \text{sign}(c_3c_1) \cdot \frac{h}{f} \quad (7)$$

where the point of (v_3, u_3) is the nearest point to the origin of v-u coordinate on the target line. These v_3 and u_3 are calculated by the following equations:

$$v_3 = -\frac{c_3}{c_1^2 + 1} \quad (8)$$

$$u_3 = -\frac{c_1c_3}{c_1^2 + 1} \quad (9)$$

Although Kurashiki et al. said that Eq. (5) was able to be derived with Eqs. (7), (8) and (9), the signum function still remains. Thus, it is necessary to split the case where c_3c_1 is positive or negative, but there is no explanation about it. Additionally, when $c_1 > 0$ and $c_3 < 0$ as shown in Fig. 2, Eq. (7) gives a negative value, though y is positive. Thus, Eq. (7) seems to be a wrong relationship equation. However, note that somehow they derived a right relationship given in Eq. (5).

III. ROBOT MODEL

In this paper, a robot is to be a two-wheel independent driven type shown in Fig. 3. The position of the robot is (x, y) on the world coordinate. The pose of the robot is the angle θ between the direction of forward movement and x-axis. The kinematic model of this robot is denoted by

$$\frac{d}{dt} \begin{bmatrix} x \\ y \\ \theta \end{bmatrix} = \begin{bmatrix} \cos \theta & 0 \\ \sin \theta & 0 \\ 0 & 1 \end{bmatrix} \begin{bmatrix} s \\ \omega \end{bmatrix} \quad (10)$$

where $s = \sqrt{\dot{x}^2 + \dot{y}^2}$ is the translational velocity and $\omega = \dot{\theta}$ is the angular velocity.

IV. CONTROLLER

In this section, a controller is designed based on Liapunov's theory. Since an image-based method is proposed, a control target is not a robot but coefficients of the target line, i. e., parameters c_1 and c_3 on the image plane. The goal of the control is to be the convergence of these values to 0.

To derive a control law, Eqs. (3) and (5) are differentiated with respect to time and they are rearranged to obtain

$$\frac{d}{dt} \begin{bmatrix} c_1 \\ c_3 \end{bmatrix} = \frac{fs}{h} \begin{bmatrix} 0 \\ c_1 \end{bmatrix} - \begin{bmatrix} c_1^2 + 1 \\ c_1 c_3 \end{bmatrix} \omega \quad (11)$$

The next equation is one candidate of a Liapunov function:

$$V = \frac{K_1}{2} c_1^2 + \frac{K_3}{2} c_3^2 \quad (12)$$

where K_1 and K_3 are positive gains. Differentiating it with respect to time gives

$$\frac{dV}{dt} = \frac{fs}{h} K_3 c_1 c_3 - c_1 \{ K_1 (c_1^2 + 1) + K_3 c_3^2 \} \omega \quad (13)$$

Assume that the input value ω is taken as follows:

$$\omega = \{ K_1 (c_1^2 + 1) + K_3 c_3^2 \}^{-1} \left(\frac{fs}{h} K_3 c_3 + K_2 c_1 \right) \quad (14)$$

where K_2 is a positive gain. Then, substituting Eq. (14) into Eq. (13) yields

$$\frac{dV}{dt} = -K_2 c_1^2 \leq 0 \quad (15)$$

Using the Barbalat's lemma [6], it is proved that $\dot{V} \rightarrow 0$ and $c_1 \rightarrow 0$. Also, note that

$$\lim_{t \rightarrow \infty} \dot{c}_1 = - \lim_{t \rightarrow \infty} (K_1 + K_3 c_3^2)^{-1} \frac{fs}{h} K_3 c_3 = 0 \quad (16)$$

Thus, assuming that $s \neq 0$, it is seen that $c_3 \rightarrow 0$, so that the convergence to a desired state is ensured.

V. SIMULATION

A simulation experiment is conducted to test the designed controller. The initial state of a robot is set to $(x, y, \theta) = (0 \text{ [m]}, -0.71 \text{ [m]}, -0.78 \text{ [rad]})$ so as to obtain $(c_1, c_3) = (1, 1)$. The function of a target line is to be $y = 0 \text{ [m]}$. The focal length of a camera is $f = 1 \text{ [m]}$ and its altitude from the floor is $h = 1 \text{ [m]}$. The translational velocity is fixed as $s = 0.5 \text{ [m/s]}$. The control gains are set as $(K_1, K_2, K_3) = (0.1, 3, 10)$.

Fig. 4 shows the experimental result. It is confirmed that controlling c_1 and c_3 to 0 was able to be accomplished by tracking the target line.

VI. CONSIDERATION

Although the mobile robot has nonholonomic characteristics, the problem setting is not affected by such features. In the problem setting explained previously, the robot tracks its target line by controlling only y and θ , without controlling x . Since the states to be controlled are only two, it need not use any crosscut of steering. Therefore, it is necessary to set other problems in which there exist influences due to nonholonomic characteristics.

VII. OTHER PROBLEM SETTINGS

In what follows, two problem settings affected by nonholonomic characteristics are proposed.

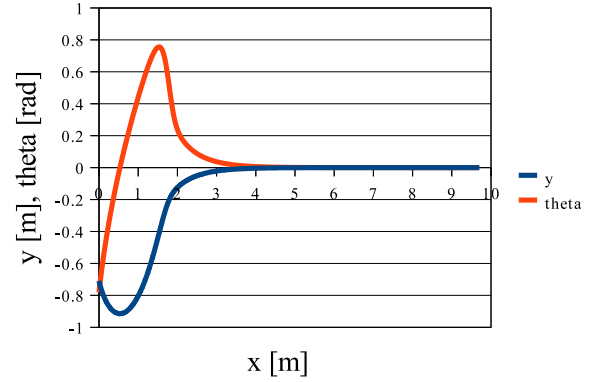


Fig. 4. Simulation result

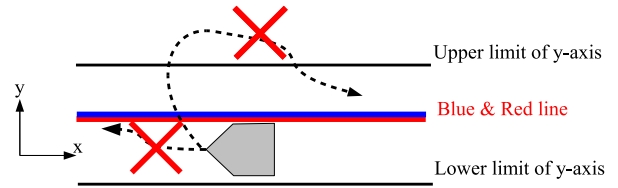


Fig. 5. Situation when the y-axis is given the upper and lower limits

1. Problem Setting 1: Specifying Direction

The target line is to be two colored to specify the robot direction as shown in Fig. 5. Since the problem setting explained previously assumes that the pose of the robot is within $-\pi/2 < \theta < \pi/2$, the robot cannot turn around. When applying any controllers to real robots, specifying the direction of the robot movement is useful for widespread purposes. Additionally, since the controller designed in this paper shows an overshoot shown in Fig. 5, the robot needs to use any crosscut motion by limiting y-axis value.

2. Problem Setting 2: Specifying Endpoint

The controller explained previously makes the robot with nonholonomic features track a target line by ignoring the value of x . This problem setting is given the end point of a target line. The goal of this control is to position the end point to the center of image plane. The forementioned controller cannot accomplish such an objective because the controller ignores x value and the translational velocity is set to be constant. Thus, it needs to set the translational velocity as a variable, instead of setting it as a constant.

VIII. CONCLUSION

In this paper, the paper given in Kurashiki et al. [5] has been questioned and a designed controller has been checked on a simulation experiment. It was confirmed from the simulation experiment that the robot can trace a target line with the designed controller. Two problem settings affected by nonholonomic characteristics were

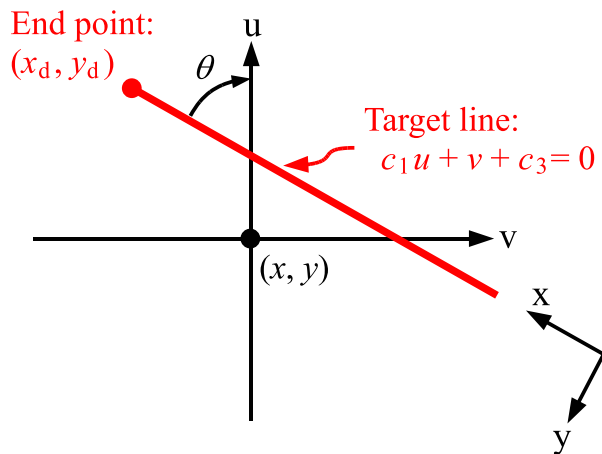


Fig. 6. Situation when the target line has an end point

also proposed to demonstrate the ability of the current image-based control method. In the future, suitable controllers will be designed and checked for the two proposed problems.

REFERENCES

- [1] Hutchinson S, Hager G, and Corke P (1996), A tutorial on visual servo control, *IEEE Trans. on Robotics and Automation*, vol. 12, no. 5, pp. 651–670.
- [2] Chaumette F and Hutchinson S (2006), Visual Servo Control, Part I: Basic Approaches, *IEEE Robotics and Automation Magazine*, vol. 13, no. 4, pp. 82–90.
- [3] Chaumette F and Hutchinson S (2007), Visual Servo Control, Part II: Advanced Approaches, *IEEE Robotics and Automation Magazine*, vol. 14, no. 1, pp. 109–118.
- [4] Malis E (2002), Survey of vision-based control, presented at the *In European Naval Ship Design, Captain Computer IV Forum*, ENSIETA, Brest, France.
- [5] Kurashiki K, Fukao T, and Osuka K (2008), Image-Based Robust Trajectory Tracking Control of a Nonholonomic Mobile Robot (in Japanese), *The 26th Annual Conference of The Robotics*.
- [6] Slotine EJJ and Li W (1991), *Applied Nonlinear Control*, Prentice Hall, pp. 122–126.

A Nonholonomic Control Method for Stabilizing an X4-AUV

Zainah Md. Zain, Keigo Watanabe, Kiyotaka Izumi[†], and Isaku Nagai

Department of Intelligent Mechanical Systems,
Division of Industrial Innovation Sciences,
Graduate School of Natural Science and Technology, Okayama University
3-1-1 Tsushima-naka, Kita-ku, Okayama 700-8530, Japan

Tel & Fax: +81-86-251-8064

E-mail: zainah@usm.sys.okayama-u.ac.jp, {watanabe, in}@sys.okayama-u.ac.jp

[†] Department of Mechanical Engineering,
Graduate School of Science and Engineering, Saga University
1-Honjomachi, Saga 840-8502, Japan

Tel: +81-952-28-8696, Fax: +81-952-28-8587

E-mail: izumi@me.saga-u.ac.jp

Abstract: A nonholonomic control method is considered for stabilizing all attitudes and positions (x , y or z) of an X4-AUV with four thrusters and six degrees-of-freedom (DOF), in which the positions were stabilized according to the Lyapunov stability theory. The derived model is dynamically unstable, so a sequential nonlinear control strategy is implemented for the X4-AUV, composed of translational and rotational subsystems. A controller for the translational subsystem stabilizes one position out of x -, y -, and z -coordinates, whereas controllers for the rotational subsystems generate the desired roll, pitch and yaw angles. Thus, the rotational controllers stabilize all the attitudes of the X4-AUV at a desired (x -, y - or z -) position of the vehicle.

Keywords: AUV, Underactuated control system, Nonholonomic systems.

I. INTRODUCTION

Nowadays control problems of underactuated vehicles motivate the development of new design methodologies in nonlinear control. The control system for such vehicles has fewer number of control inputs than the number of generalized state variables to be controlled. Hence, the dynamical equations of the vehicle exhibit so-called second-order nonholonomic constraints, i.e. non-integrable conditions imposed on the acceleration in one or more DOFs, because the vehicle lacks capability to command instantaneous accelerations in these directions of the configuration space [1]. As pointed in a celebrated paper of Brockett in 1983, such nonholonomic systems cannot be stabilized by usual smooth, time-invariant, and state feedback control algorithms. For the control of underactuated underwater systems, many researches proposed nonlinear feedback control [2], among many others. Nonholonomic property of a mechanical systems can be seen in underactuated systems, even though the connection between nonholonomic control systems and underactuated systems is not completely understood. To control nonholonomic systems, many control approaches have been studied. Kolmanovsky and Clamroch present a vast literature and overview on nonholonomic control in their work [1].

In this paper, we present a model of an underactuated X4-AUV with 6-DOF and four control inputs and propose a control scheme based on Lyapunov approach to stabilize all attitudes and positions of the vehicle. A sequential nonlinear control strategy is implemented for the derived 6-DOF vehicle model, constituted of

translational and rotational subsystems. The controller for the translational subsystem stabilizes the position and the controllers for the rotational subsystems generate the desired roll, pitch and yaw angles.

II. DYNAMICAL MODEL

1. Coordinate System of AUV

In order to describe the underwater vehicle's motion, a special reference frame must be established. There have two coordinate systems: i.e., inertial coordinate system (or fixed coordinate system) and motion coordinate system (or body-fixed coordinate system). The coordinate frame $\{E\}$ is composed of the orthogonal axes $\{E_x, E_y, E_z\}$ and is called as an inertial frame. This frame is commonly placed at a fixed place on Earth. The axes E_x and E_y form a horizontal plane and E_z has the direction of the gravity field. The body fixed frame $\{B\}$ is composed of the orthonormal axes $\{X, Y, Z\}$ and attached to the vehicle. The body axes, two of which coincide with principle axes of inertia of the vehicles, are defined in Fossen [3] as follows:

X is the longitudinal axis (directed from aft to fore)

Y is the transverse axis (directed to starboard)

Z is the normal axis (directed from top to bottom)

Fig. 1 shows the coordinate systems of AUV, which consist of a right-hand inertial frame $\{E\}$ in which the downward vertical direction is to be positive and right-hand body frame $\{B\}$.

Letting $\xi = [x \ y \ z]^T$ denote the mass center of the body in the inertial frame, defining the rotational angles of X -, Y - and Z -axis as $\eta = [\phi \ \theta \ \psi]^T$, the rotational

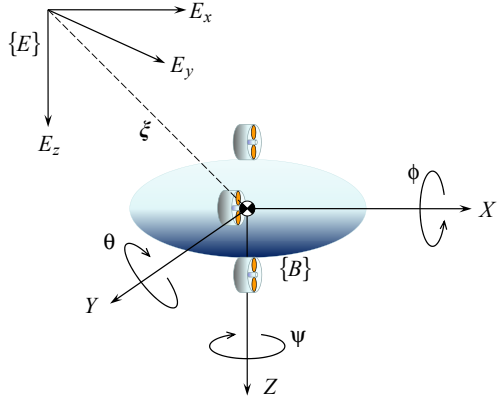


Fig. 1. Coordinate systems of AUV

matrix R from the body frame $\{B\}$ to the inertial frame $\{E\}$ can be reduced to:

$$R = \begin{bmatrix} c\theta c\psi & s\theta c\psi & -s\theta s\psi & c\phi s\theta c\psi + s\phi s\psi \\ c\theta s\psi & s\theta s\psi & -s\theta c\psi & c\phi s\theta s\psi - s\phi c\psi \\ -s\theta & c\theta & 0 & c\phi c\theta \\ 0 & 0 & 0 & s\phi c\theta \end{bmatrix} \quad (1)$$

where $c\alpha$ denotes $\cos \alpha$ and $s\alpha$ is $\sin \alpha$.

2. Derivation of a Dynamical Model

Following a Lagrangian method, this section describes the dynamic model of the X4-AUV with the assumption of balance between buoyancy and gravity. The kinetic energy formula is

$$T = T_{trans} + T_{rot} \quad (2)$$

where T_{trans} and T_{rot} are the translational kinetic energy and the rotational kinetic energy, which are given by

$$T_{trans} = \frac{1}{2} \dot{\xi}^T M \dot{\xi} \quad (3)$$

$$T_{rot} = \frac{1}{2} \dot{\eta}^T J \dot{\eta} \quad (4)$$

in which M is the total mass matrix of the body, and J is the total inertia matrix of the body. From the characteristics of added mass, they can be written as

$$M = \text{diag}(m_1, m_2, m_3) = m_b I + M_f \quad (5)$$

$$J = \text{diag}(I_x, I_y, I_z) = J_b + J_f \quad (6)$$

Here, m_b is a mass of the vehicle, J_b is an inertia matrix of the vehicle and I is a 3×3 identity matrix. Letting ρ denote a density of the fluid and using the formulation of the added mass and inertia [4] under the assumption of $r_1 = 5r$ and $r_2 = r_3 = r$ where r_1, r_2 and r_3 are the lengths of the semi axes of the ellipsoidal vehicle, the added mass matrix M_f and the added inertia matrix J_f are obtained by

$$M_f = \text{diag}(0.394\rho\pi r^3, 5.96\rho\pi r^3, 5.96\rho\pi r^3) \quad (7)$$

$$J_f = \text{diag}(0, 24.2648\rho\pi r^5, 24.2648\rho\pi r^5) \quad (8)$$

From the assumption of the balance between the buoyancy and the gravity, i.e., the potential energy $U = 0$, the Lagrangian can be written as

$$L = T - U \quad (9)$$

$$= T_{trans} + T_{rot} \quad (10)$$

The resultant dynamical model for the X4-AUV is summarized by [5]

$$\begin{aligned} m_1 \ddot{x} &= \cos \theta \cos \psi u_1 \\ m_2 \ddot{y} &= \cos \theta \sin \psi u_1 \\ m_3 \ddot{z} &= -\sin \theta u_1 \\ I_x \ddot{\phi} &= \dot{\theta} \dot{\psi} (I_y - I_z) + u_2 \\ I_y \ddot{\theta} &= \dot{\phi} \dot{\psi} (I_z - I_x) - J_t \dot{\psi} \Omega + l u_3 \\ I_z \ddot{\psi} &= \dot{\phi} \dot{\theta} (I_x - I_y) + J_t \dot{\theta} \Omega + l u_4 \end{aligned} \quad (11)$$

Here, the values of m_1, m_2, m_3, I_x, I_y , and I_z are defined as in (5) and (6). u_1, u_2, u_3, u_4 are the control inputs for the translational (x, y and z -axis) motion, the roll (ϕ -axis) motion, the pitch (θ -axis) motion, and yaw (ψ -axis) motion, respectively. Defining that b is a thrust factor, d is a drag factor, taken from $\tau_{Mi} = d\omega_i^2$, Ω, u_1, u_2, u_3 and u_4 are given by

$$\begin{aligned} \Omega &= (\omega_2 + \omega_4 - \omega_1 - \omega_3) \\ u_1 &= f_1 + f_2 + f_3 + f_4 \\ &= b(\omega_1^2 + \omega_2^2 + \omega_3^2 + \omega_4^2) \\ u_2 &= d(-\omega_2^2 - \omega_4^2 + \omega_1^2 + \omega_3^2) \\ u_3 &= f_1 - f_3 = b(\omega_1^2 - \omega_3^2) \\ u_4 &= f_2 - f_4 = b(\omega_2^2 - \omega_4^2) \end{aligned} \quad (12)$$

III. STABILIZATION CONTROL FOR X4-AUV

The model (11), developed in the previous section, can be rewritten in a state-space form $\dot{X} = f(X, U)$ by introducing $X = (x_1 \dots x_{12})^T \in \mathbb{R}^{12}$ as state vector of the system as follows:

$$\begin{aligned} x_1 &= x \\ x_2 &= \dot{x}_1 = \dot{x} \\ x_3 &= y \\ x_4 &= \dot{x}_3 = \dot{y} \\ x_5 &= z \\ x_6 &= \dot{x}_5 = \dot{z} \\ x_7 &= \phi \\ x_8 &= \dot{x}_7 = \dot{\phi} \\ x_9 &= \theta \\ x_{10} &= \dot{x}_9 = \dot{\theta} \\ x_{11} &= \psi \\ x_{12} &= \dot{x}_{11} = \dot{\psi} \end{aligned} \quad (13)$$

where the inputs $U = (u_1 \dots u_4)^T \in \mathbb{R}^4$.

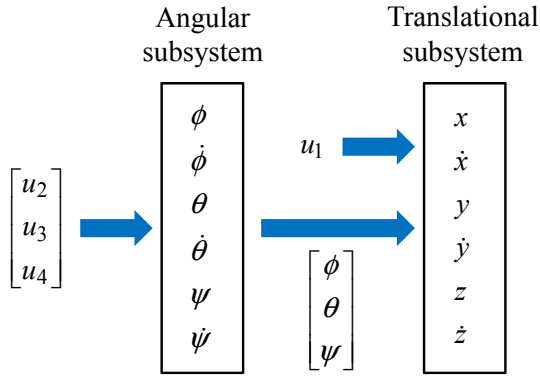


Fig. 2. Connections of rotational and translational subsystems

From (11) and (13) we obtain:

$$f(X, U) = \begin{pmatrix} x_2 \\ (\cos \theta \cos \psi) \frac{1}{m_1} u_1 \\ x_4 \\ (\cos \theta \sin \psi) \frac{1}{m_2} u_1 \\ x_6 \\ (-\sin \theta) \frac{1}{m_3} u_1 \\ x_8 \\ x_{10} x_{12} \left(\frac{I_y - I_z}{I_x} \right) + \frac{1}{I_x} u_2 \\ x_{10} \\ x_8 x_{12} \left(\frac{I_z - I_x}{I_y} \right) - \frac{J_z}{I_y} x_{12} \Omega + \frac{l}{I_y} u_3 \\ x_{12} \\ x_8 x_{10} \left(\frac{I_x - I_y}{I_z} \right) + \frac{J_x}{I_z} x_{10} \Omega + \frac{l}{I_z} u_4 \end{pmatrix} \quad (14)$$

It is interesting to note that in the dynamics of the latter system how the angles and their time derivatives do not depend on the translational components, whereas the translations only depend on the angle. It can ideally imagine the overall system described by (14) as constructed by two subsystems: i.e., the angular rotations and the linear translations (see Fig. 2). The subsystem of the angular rotations has the restriction X_α of X to the last 6 components as state, which is regarded as the roll, pitch, yaw and their time derivatives. The dynamics related to these variables are described by $f_\alpha(X, U)$ corresponding to the last 6 components of the mapping (14). Observe that the mapping $f_\alpha(X, U)$ is a function only of X_α and of $(u_2, u_3, u_4)^T$, and does not depend on the translational components. On the other hand, the translational subsystem (with state X_Δ) consists of the first 6 elements of the state X , which are the x, y, z and their time derivatives, where the dynamics are described by the first 6 rows $f_\Delta(X, U)$ of the mapping (14). The translational subsystem mapping $f_\Delta(X, U)$ is not independent of the angular variables but depends only on the roll, pitch and yaw and not on their time derivatives. Note that these discussions are the same as those for a Quadrotor studied in [6].

1. Rotation Control

Consider first the control for the subsystem of the angular rotations because of its complete independence

from the other subsystem. A stabilization of the X4-AUV angles is considered for $X_\alpha^d = (x_7^d, 0, x_9^d, 0, x_{11}^d, 0)^T$.

Let us consider the Lyapunov function $V(X_\alpha)$ that is positive definite around the desired position X_α^d :

$$V(X_\alpha) = \frac{1}{2}(x_7 - x_7^d)^2 + \frac{1}{2}x_8^2 + \frac{1}{2}(x_9 - x_9^d)^2 + \frac{1}{2}x_{10}^2 + \frac{1}{2}(x_{11} - x_{11}^d)^2 + \frac{1}{2}x_{12}^2 \quad (15)$$

The time derivative of (15), $\dot{V} = (\nabla V)^T f_\alpha$, in the case of X4-AUV ($I_y = I_z$) is drastically reduced to:

$$\dot{V} = x_8(x_7 - x_7^d) + x_{10}(x_9 - x_9^d) + x_{12}(x_{11} - x_{11}^d) + \frac{1}{I_x}x_8u_2 + \frac{l}{I_y}x_{10}u_3 + \frac{l}{I_z}x_{12}u_4 \quad (16)$$

By simply choosing:

$$\begin{aligned} u_2 &= -I_x(x_7 - x_7^d) - k_1x_8 \\ u_3 &= -\frac{I_y}{l}(x_9 - x_9^d) - k_2x_{10} \\ u_4 &= -\frac{I_z}{l}(x_{11} - x_{11}^d) - k_3x_{12} \end{aligned} \quad (17)$$

with k_1, k_2 and k_3 of positive constants, we obtain for (16):

$$\dot{V} = -\frac{1}{I_x}k_1x_8^2 - \frac{l}{I_y}k_2x_{10}^2 - \frac{l}{I_z}k_3x_{12}^2 \quad (18)$$

which is only negative semi-definite. By Lyapunov theorem the simple stability for equilibrium is now ensured. By Lasalle invariance theorem we can ensure also that starting from a level curve of the Lyapunov function defined in (15) where $V(X_\alpha)$ is constant, the state evolution is constrained inside the region bounded by the level curve [6]. This is very useful when trying to avoid particular configuration. It is simply necessary to start with a level curve not containing these points and apply the previous defined control. We can also ensure the asymptotic stability by applying the Lasalle theorem because the maximum invariance set of (angular rotations) subsystem under control (17) contained in the set $S = \{X_\alpha^S \in \mathbb{R}^6 : \dot{V}|_{X_\alpha^S=0}\}$ is restricted only to the equilibrium point [6].

If $V(X_\alpha) > 0$ when $(X_\alpha \neq X_\alpha^d)$ and $\dot{V}(X_\alpha) \leq 0$ ($X_\alpha \neq X_\alpha^d$), the system is asymptotically stable. In the case $\dot{V}(X_\alpha) \equiv 0$, the solution of state equation is given by only $X_\alpha = X_\alpha^d$.

By the latter consideration we can ensure an asymptotical stability starting from a point in a set around the equilibrium. To ensure the global stability, it is sufficient that $\lim_{\|X_\alpha\| \rightarrow \infty} V(X_\alpha) = \infty$, which is our case.

2. Translation Controller

Let us consider the simple task for the X4-AUV to be translated to a particular position $x = x^d, y = y^d$ and $z = z^d$. The dynamics of the x, y and z -position are described by lines 1 and 2, 3 and 4, and 5 and 6 in system (14), i.e.,

x-position:

$$\begin{pmatrix} \dot{x}_1 \\ \dot{x}_2 \end{pmatrix} = \begin{pmatrix} x_2 \\ (\cos x_9 \cos x_{11}) \frac{u_1}{m_1} \end{pmatrix} \quad (19)$$

y-position:

$$\begin{pmatrix} \dot{x}_3 \\ \dot{x}_4 \end{pmatrix} = \begin{pmatrix} x_4 \\ (\cos x_9 \sin x_{11}) \frac{u_1}{m_2} \end{pmatrix} \quad (20)$$

z-position:

$$\begin{pmatrix} \dot{x}_5 \\ \dot{x}_6 \end{pmatrix} = \begin{pmatrix} x_6 \\ (-\sin x_9) \frac{u_1}{m_3} \end{pmatrix} \quad (21)$$

By the previous considerations in the control for the subsystem of the angular rotations, we ensure that starting from an initial condition where $V(X_\alpha) < \pi/2$, the angles and their velocities are constrained in this hypersphere of \mathbb{R}^6 . In this case $\cos x_9 \cos x_{11} \neq 0$, $\cos x_9 \sin x_{11} \neq 0$ and $-\sin x_9 \neq 0$ for all the trajectories of the system under the previous control law. Systems (19), (20) and (21) can be linearized by simply compensating the weighted force by

x-position:

$$u_1 = \frac{m_1 \hat{u}_1}{\cos x_9 \cos x_{11}} \quad (22)$$

y-position:

$$u_1 = \frac{m_2 \hat{u}_2}{\cos x_9 \sin x_{11}} \quad (23)$$

z-position:

$$u_1 = \frac{-m_3 \hat{u}_3}{\sin x_9} \quad (24)$$

where \hat{u}_1 , \hat{u}_2 and \hat{u}_3 are additional terms. By this partial feedback linearization [7], (19), (20) and (21) become

x-position:

$$\begin{pmatrix} \dot{x}_1 \\ \dot{x}_2 \end{pmatrix} = \begin{pmatrix} x_2 \\ \hat{u}_1 \end{pmatrix} \quad (25)$$

or

$$\begin{pmatrix} \dot{e}_1 \\ \dot{e}_2 \end{pmatrix} = \begin{pmatrix} e_2 \\ -\hat{u}_1 \end{pmatrix} \quad (26)$$

y-position:

$$\begin{pmatrix} \dot{x}_3 \\ \dot{x}_4 \end{pmatrix} = \begin{pmatrix} x_4 \\ \hat{u}_2 \end{pmatrix} \quad (27)$$

or

$$\begin{pmatrix} \dot{e}_3 \\ \dot{e}_4 \end{pmatrix} = \begin{pmatrix} e_4 \\ -\hat{u}_2 \end{pmatrix} \quad (28)$$

z-position:

$$\begin{pmatrix} \dot{x}_5 \\ \dot{x}_6 \end{pmatrix} = \begin{pmatrix} x_6 \\ \hat{u}_3 \end{pmatrix} \quad (29)$$

or

$$\begin{pmatrix} \dot{e}_5 \\ \dot{e}_6 \end{pmatrix} = \begin{pmatrix} e_6 \\ -\hat{u}_3 \end{pmatrix} \quad (30)$$

where $e_i \triangleq x_i^d - x_i$, $i = 1, \dots, 6$. Adopting a simple linear state feedback stabilization law $\hat{u}_1 = k_4 e_1 + k_5 e_2$, $\hat{u}_2 = k_6 e_3 + k_7 e_4$ and $\hat{u}_3 = k_8 e_5 + k_9 e_6$ we can stabilize the position by placing the poles of the subsystem in any position in the complex left half plane.

IV. DISCUSSIONS

A nonlinear control strategy is implemented to stabilize the X4-AUV. The position and angles of the X4-AUV are stabilized by using control input u_1 , u_2 , u_3 and u_4 respectively. PD controllers were introduced for controlling each orientation angle such that

$$u_{i+1} = k_{p_i} e_{2i+5} + k_{d_i} \dot{e}_{2i+5}, \quad i = 1, 2, 3 \quad (31)$$

where $k_{p1} \equiv I_x$, $k_{p2} \equiv I_y/l$, $k_{p3} \equiv I_x/l$, $k_{d1} = k_1$, $k_{d2} = k_2$, and $k_{d3} = k_3$.

The angles and their time derivatives of rotational subsystem do not depend on translation components, whereas the translations depend on the angles. Ideally, it can be imagined as two subsystems: the angular rotations and the linear translations. Due to its complete independence from the other subsystem, the angular rotation-related subsystem is tuned first. The rotational control keeps a 3D orientation of the X4-AUV to the desired state and the translational control moves the vehicle to the desired position. The controllers have been implemented on MATLAB and the simulation results for stabilizing the X4-AUV can be found in [8] and [9].

V. CONCLUSION

In this paper, a nonholonomic control method for stabilizing all attitudes and positions (x , y or z) of an underactuated X4-AUV, with four thrusters and 6-DOF has been presented. The controller design was separated into two parts: the rotational and translational dynamics-related controller designs. The stabilization strategy is based on the Lyapunov stability theory. For the future work, an underactuated controller will be constructed by combining such three types of controllers to realize an underactuated control system.

REFERENCES

- [1] Kolmanovsky I and McClamroch NH (1995), Developments in nonholonomic control problems. IEEE Control Systems Magazine, 15(6): 20–36
- [2] Nakamura Y and Savant S (1991), Nonholonomic motion control of an autonomous underwater vehicle. IEEE/RSJ Int. Workshop Intelligent Robots and Systems, 1254–1259
- [3] Fossen TI (1994), Guidance and control of ocean vehicles, John Wiley & Sons Ltd.
- [4] Leonardo NE (1997), Stability of a bottom-heavy underwater vehicle. Automatica, 33(1): 331–346
- [5] Okamura K (2009), Position and attitude control for an autonomous underwater robot using a manifold theory. Master Thesis, Saga University.
- [6] Bouabdallah S, Murrieri P and Siegwart R (2005), Towards autonomous indoor micro VTOL. Autonomous Robots, 18(2): 171–183
- [7] Fantoni I, Lozano R and Spong MW (2000), Energy based control of the pendubot. IEEE Trans. on Automatic Control, 45(4): 725–729
- [8] Zain ZM, Watanabe K, Danjo T, Izumi K and Nagai I (2010), Stabilization control for an X4-AUV. Proc. of the 3rd International Conference on Underwater System Technology: Theory and Applications (USYS '10).
- [9] Zain ZM, Watanabe K, Nagai I and Izumi K (2010), The stabilization control of a position and all attitudes for an X4-AUV. Proc. of the 5th International Conference on Soft Computing and Intelligent Systems and 11th International Symposium on Advanced Intelligent Systems (SCIS & ISIS 2010).

The inevitability of the bio-molecules: five nitrogenous bases and twenty amino acids

K.Hashimoto, H.Inoue and K.Naitoh

*Waseda University, Faculty of Science and Engineering, 3-4-1 Ookubo, Shinjuku, Tokyo, 169-8555 Japan
(Tel : 81-3-5286-3265)
(Email address:k-naito@waseda.jp)*

Abstract: Living beings meta-stable between unstable and neutral-stable conditions use only five types of nitrogenous bases and twenty amino acids selected naturally. The unified momentum theory derived at the triple point of the deterministic Boltzmann equation, the stochastic Langevin equation, and the indeterminacy principle [K. naitoh, Artificial Life Robotics, 2010] reveals the reason why the molecular weights of the twenty types of amino acids show a threefold variation between 240 of cysteine as the maximum and 75 of glycine as the minimum, whereas that of purines and pyrimidines among nitrogenous bases varies by only about 1.5 times, although the variation principle for the energy conservation law cannot do so. Let us take a higher order of the Taylor series for the unified momentum equation describing the deformation motions of biological molecules. Even-numbered terms such as the second and fourth ones show no other quasi-stable size ratios. However, odd-numbered terms result in other quasi-stable ratios. The threefold variation of amino acids will come from the third term of the Taylor series.

Keywords: Asymmetry, Cyto-fluid dynamics

I. INTRODUCTION

Many types of amino acids and bases are possible in the artificial pools of molecules, but living beings meta-stable between unstable and neutral-stable conditions use only five types of nitrogenous bases and twenty amino acids selected naturally. [1-6]

Life can exist only when fully surrounded by water molecules. Thus, the meta-stability of biological molecules such as nitrogenous bases, nucleic acids, amino acids, and proteins in living beings should be analyzed by considering the flows of water molecules.

Our previous model based on traditional fluid dynamics [7-9] has qualitatively revealed the reason why living beings employ only five nitrogenous bases, i.e., two purines of A and G and three pyrimidines of T, C, and U, and also why purines and pyrimidines have a size ratio of about 1.5. However, the model was with some gratuitous assumptions and also analyzed by the first order of accuracy, which led only to qualitative results. Consequently, a qualitative analysis did not reveal the reason why the molecular weights of the twenty types of amino acids show a threefold variation between 240 of cysteine as the maximum and 75 of glycine as the minimum and also why proteins are more various.

In this report, a unified momentum theory is extended from our previous model as a result of statistical mechanics [9] and the theory of adding mass [10]. A higher order of analysis based on the momentum conservation law reveals the size varieties of the five bases and twenty amino acids. The present report reveals several mysteries underlying the bio-molecular systems.

II. CYTO-FLUID DYNAMICS THE ORYBASED ON the γ - ε EQUATION

First, we define a parcel as a flexible spheroid having two long and short radii of $a(t)$ and $b(t)$ dependent on time t and constructed of a bio-molecule such as a base or an amino acid that is surrounded by water molecules. (A parcel consists of a bio-molecule such as nitrogenous base or amino acid, water molecules hydrated with the bio-molecule, and the immerse mass due to adding mass effect while impulsive start and stop of deformations occur [8, 9].)

The parcel size is proportional to that of biological molecules such as nitrogenous base or amino acid.

The parcel becomes a sphere of the radius $r_d (= [ab^2]^{1/3})$ under an equilibrium condition. The deformation rate $\gamma(t)$ is defined as $a(t)/b(t)$, while a sphere without deformation corresponds to $\gamma = 1$.

We assume that the flow field inside the parcel is the potential flow.

We derive a theory for describing the deformation and motions of two connected spheroid parcels having two equilibrium radii of r_{d1} and r_{d2} and two deformation rates of γ_k [$k = 1, 2$], while the size ratio of the two parcels is defined by $\varepsilon = r_{d1}/r_{d2}$. We model the one-dimensional relative motion between the two parcels, nonlinear convections inside the parcels, the interfacial force at the parcel surface due to forces interacting between molecules, and collisions with water molecules

outside the parcels. The interfacial force is evaluated in the form of σ / r^m where m and σ are constants and r is the curvature of parcel surface. [7] Several types of forces such as van der Waals force, coulomb force, and surface tension can be explained by varying m . Here, the relation $m = 1$ implies the surface tension of liquid. The mean density of the parcels is ρ_L .

Moreover, the scale for averaging, i.e., the minimum scale representing the phenomenon, will be smaller than that in continuum mechanics and will be between the atomic scale and the size of the bio-molecule. Thus, this small averaging window applied to the Boltzmann equation [9] leads to a weak indeterminacy of physical quantities such as deformation and density because of molecular discontinuity.

Next, we derive the momentum equation describing the relation between a dimensionless deformation rate $\gamma_k (\equiv a_k / b_k [k = 1, 2])$ of each parcel dependent on dimensionless time $\bar{t}_k = \sqrt{\frac{8\sigma}{\rho_L r_{dk}^{2+m}}} t [k = 1, 2]$ and the size ratio of the two parcels of $\varepsilon = r_{d1} / r_{d2}$. The stochastic governing equation having indeterminacy can be described as

$$\begin{aligned} \frac{d^2}{d\bar{t}_i^2} \gamma_i = & \{ [(-\varepsilon - \varepsilon^4 + \frac{2}{3} \varepsilon E_{0j} \gamma_j^{-1/3}) B_{0i} + \frac{2}{9} \varepsilon^{2+m} E_{0i} \varepsilon \gamma_i^{-4/3}] (\frac{d}{d\bar{t}_i} \gamma_i)^2 \\ & + [\frac{2}{3} \varepsilon^{2+m} E_{0i} \gamma_j^{-1/3} B_{0j} - \frac{2}{9} \varepsilon^{2+m} E_{0i} \gamma_j^{-4/3}] (\frac{d}{d\bar{t}_j} \gamma_j)^2 \\ & + (-\varepsilon - \varepsilon^4 + \frac{2}{3} \varepsilon E_{0j} \gamma_j^{-1/3}) C_{0i} \gamma_i^{\frac{5}{3} - \frac{2}{3}m} + \frac{2}{3} \varepsilon^{2+m} E_{0i} \gamma_j^{-1/3} C_{0j} \gamma_j^{\frac{5}{3} - \frac{2}{3}m} \} / Det \\ & + \delta'_{st} \end{aligned} \quad [for i = 1, 2, j = 1, 2, i \neq j] \quad (1)$$

with

$$\begin{aligned} Det = & -\varepsilon - \varepsilon^4 + \frac{2}{3} \varepsilon^4 E_{0i} \gamma_i^{-1/3} + \frac{2}{3} \varepsilon E_{0j} \gamma_j^{-1/3}, B_{0k} = \frac{1}{3\gamma_k} \frac{\gamma_k^2 - 2}{\gamma_k^2 - 1/2}, \\ C_{0k} = & \frac{3}{8} \frac{2\gamma_k^{2m} - 1/\gamma_k^m - \gamma_k^m}{\gamma_k^2 - 1/2}, \text{ and } E_{0k} = 3 \frac{\gamma_k^{7/3}}{\gamma_k^2 - 1/2} [for k = 1, 2] \end{aligned}$$

where the parameter δ'_{st} denotes random fluctuation.

The long derivation of Eq. (1) is in Ref. 6 confirmed by the referees, although only the stochastic term δ'_{st} is not in Ref. 6.

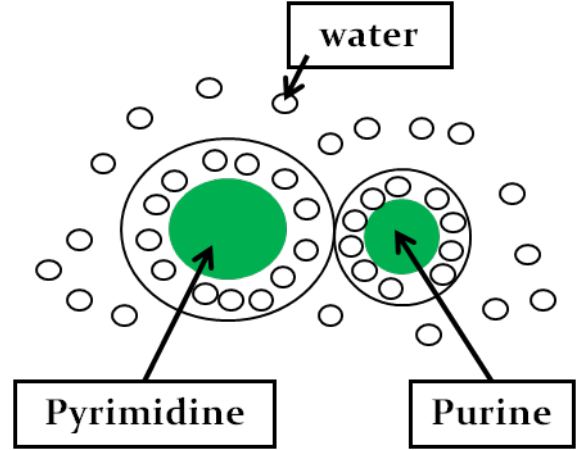


Fig.1. Two parcels connecting

III. FIRST ORDER OF ANALYSIS [6]

We then define the deviation from a sphere as y_i , which is equal to $\gamma_i - 1$. Taking the first order of approximation in the Taylor series leads to

$$\begin{aligned} \frac{d^2}{d\bar{t}_i^2} y_i = & [-\frac{2}{3} (3 - \varepsilon^3 - 2\varepsilon^{2+m}) (\frac{dy_i}{d\bar{t}_i})^2 + 3(3 - \varepsilon^3) m y_i \\ & - 4\varepsilon^{1+m} (\frac{dy_j}{d\bar{t}_j})^2 + 12\varepsilon^{1+m} m y_j] / [3(\varepsilon^3 + 1)] \\ & + \delta'_{st}, \end{aligned} \quad (2)$$

where the parameter δ'_{st} denotes random fluctuation. A symmetric ratio of 1.0 ($\varepsilon = 1$) makes the first term on the right-hand side of the equation zero, while an asymmetric ratio of $\sqrt[3]{3}$ around 1.5 ($\varepsilon^3 = 3$) makes the second term zero. The size ratios of 1.00 and approximately 1.50 can be described by the unified number of the n -th root of n .

We define a system as being quasi-stable when only one term on the right-hand side of the differential equation system governing the phenomenon (Eq. (2)) is zero. Life is relatively quasi-stable because $d^2 y_i / d\bar{t}_i^2$ becomes smaller when the size ratio of connected parcels takes the values of $\varepsilon = 1$ or $\varepsilon^3 = 3$. An important clue for clarifying the inevitability and variety of biological molecules is the concept of quasi-stability (meta-stability) weaker than neutral stability. This is because biological systems are essentially neither neutrally stable nor absolutely stable owing to the potential for a brush with death and also since people can live over 50 years while maintaining the mysterious shape of the body. Thus, a new stability concept between the neutrally stable and unstable conditions is necessary for a meta-stable system of life, i.e., quasi-stability. [6-9]

Free nitrogenous bases in water often seem to be a

column of two identical bases such as adenine-adenine, which are not in a two-dimensional plane. There are multimeric complexes such as that of guanines. Then, it is well known that identical base pairs of $\varepsilon=1$ are often in RNA, while asymmetric base pairs such as the Watson-Crick type of about $\varepsilon^3=3$ are used in DNA. (Fig. 1)

As Eqs. (1) and (2) show a slightly vague solution for the phenomenon, this indeterminacy also implies that variations of molecular sizes are possible in a limited range. This indeterminacy will permit the possibility of sizes around $1: \sqrt[3]{3}$, i.e., two types of base pairs such as A-T and G-C.

IV. HIGHER-ORDER OF ANALYSIS

Higher order of the Taylor series

$$f(y) = f(0) + \frac{f^{(1)}(0)}{1!}y + \frac{f^{(2)}(0)}{2!}y^2 + \frac{f^{(3)}(0)}{3!}y^3 + \dots \quad (3)$$

Can be applied to Eq. (1).

The third order of the Taylor series brings

$$\left\{ \begin{aligned} & a_{31}y_1 + a_{32}y_1^2 + a_{33}y_1y_2 + a_{34}y_1^2y_2 + a_{35}y_1y_2^2 + a_{36}y_1^3 + a_{37}y_1^2y_2 + a_{38}y_1^2y_2^2 + a_{39}y_1^2y_2^2 \\ & + \left(b_{31} + b_{32}y_1 + b_{33}y_2 + b_{34}y_1y_2 + b_{35}y_1^2 + b_{36}y_2^2 \right) \left(\frac{dy_1}{d\tau_1} \right)^2 \\ & + \left(c_{31} + c_{32}y_1 + c_{33}y_1y_2 + c_{34}y_1^2 + c_{35}y_2 + c_{36}y_2^2 \right) \left(\frac{dy_2}{d\tau_2} \right)^2 \end{aligned} \right\} \quad (4)$$

with

$$\begin{aligned} m_3 &= 9(\varepsilon^3 + 1)^3 \square \square a_{31} = -9(\varepsilon^3 - 3)(\varepsilon^2 + 1)^2 \square \square a_{32} = \frac{3}{4}(\varepsilon^3 - 3)(\varepsilon^6 + 34\varepsilon^3 + 33) \square \square \\ a_{33} &= 12\varepsilon^2(3\varepsilon^6 - 8\varepsilon^4 - 2\varepsilon^3 - 8\varepsilon - 5) \square \square a_{34} = -8\varepsilon^2(2\varepsilon^6 + 7\varepsilon^4 + 6\varepsilon^3 - 57\varepsilon - 28) \square \square \\ a_{35} &= \varepsilon^2(-111\varepsilon^6 + 336\varepsilon^4 + 426\varepsilon^3 + 80\varepsilon + 25) \square \square \\ a_{36} &= \frac{1}{2}(\varepsilon^3 - 3)(\varepsilon^6 - 42\varepsilon^3 - 171) \square \square a_{37} = 36\varepsilon^2(\varepsilon^3 + 1)^2 \\ a_{38} &= -3\varepsilon^2(37\varepsilon^6 + 42\varepsilon^3 + 5) \square \square a_{39} = \varepsilon^2(383\varepsilon^6 + 134\varepsilon^3 + 7) \square \square b_{31} = 6(\varepsilon^3 - 1)(\varepsilon^3 + 1)^2 \\ b_{32} &= -2(5\varepsilon^9 + 5\varepsilon^6 - 21\varepsilon^3 - 21) \square \square b_{33} = 32(\varepsilon^6 + \varepsilon^3) \square \square b_{34} = -\frac{32}{3}\varepsilon^3(5\varepsilon^3 + 21) \\ b_{35} &= \frac{8}{3}(5\varepsilon^9 + 9\varepsilon^6 - 27\varepsilon^3 - 63) \square \square b_{36} = -\frac{16}{3}\varepsilon^3(21\varepsilon^3 + 5) \square \square \square \\ \square c_{31} &= -12(\varepsilon^3 + 1)^3 \square \square c_{32} = \frac{4}{3}\varepsilon^2(-9\varepsilon^6 + 6\varepsilon^3 + 15) \square \square \\ c_{33} &= \frac{32}{3}\varepsilon^2(6\varepsilon^6 - 15\varepsilon^3 - 5) \square \square c_{34} = \frac{16}{3}\varepsilon^2(\varepsilon^6 + 3\varepsilon^3 - 14) \square \square \\ c_{35} &= 32\varepsilon^2(2\varepsilon^6 + 3\varepsilon^3 + 1) \square \square c_{36} = -\frac{16}{3}\varepsilon^2(47\varepsilon^6 + 41\varepsilon^3 + 10) \end{aligned}$$

V. QUASI-STABILITY EXTENDED

We can consider only the disturbance for parcell, because the system of two parcels is mathematically symmetric. Then, we get

$$\frac{d^2 y_1}{d\tau_1^2} = \frac{1}{m_2} \left\{ a_{31}y_1 + a_{32}y_1^2 + a_{36}y_1^3 + \left(b_{31} + b_{32}y_1 + b_{35}y_1^2 \right) \left(\frac{dy_1}{d\tau_1} \right)^2 \right\} \quad (5)$$

as the third order of approximation.

The three terms of $a_{31}y_1, a_{32}y_1^2, a_{36}y_1^3$ come from the surface tension, whereas the later terms of $b_{31}, b_{32}y_1, b_{35}y_1^2$ come from convection.

Here, we define

$$a_{31} = 0 \text{ or } b_{31} = 0$$

as the quasistable condition, while

$$a_{32} = 0, a_{36} = 0, b_{32} = 0, \text{ or } b_{35} = 0$$

is semi-quasistable.

Table 1 shows the size ratios of parcels, which bring quasistable and semi-quasistable conditions.

The semi-quasistable ratio of about 1: 3.6 will correspond to a threefold variation between 240 of cysteine as the maximum and 75 of glycine as the minimum, while the other semi-quasistable ones of about 1: 1.27 and 1:1.35 lead to some variations of base pairs such as A-T and G-C.

Table 1. Size ratios of parcels (The third order of approximation type)

Stability	surface tension term	convective term
Quasistable	3:2	1:1
Semi-quasistable	3:2	1.27:1
Semi-quasistable	3:2 3.6:1	1.35:1

VII. CONCLUSION

Higher-order of analysis for the cyto-fluid dynamic theory reveals the size ratios of 1:1 and about 2:3 for nitrogenous bases and also the ratios over 2:3 for amino acids..

REFERENCES

- [1]Miller S.L, (1953) A production of amino acids under possible primitive earth conditions. *Science*, 117: 528-529.
- [2]Oro J and Kimball A.P, (1961) Synthesis of Purines Under Possible Primitive Earth Conditions. I. Adenine from Hydrogen Cyanide, *Arch. Biochem. Biophys.* 94: 217-227.
- [3]Yanagawa H, (1991) How Life Originated. *TBS Britannica*. 1-466.
- [4]Ricardo A and Szostak J.W, (2009) Origin of Life on Earth. *Scientific American*.
- [5]Watson J.D, Hopkins N.H, Roberts J.W, et al. (1987) *Molecular Biology of the Gene*, Fourth edition: The Benjamin/Cummings Publishing Company.
- [6]Naitoh K, (2001) Cyto-fluid Dynamic Theory, *Japan Journal of Industrial and Applied Mathematics*, 18-1: 75-105.
- [7]Naitoh K, (2003) Macroscopic kinetic model on the origins of biological information. *Trans. of JIAM*: 115-137.
- [8]Naitoh K, (2008) Stochastic Determinism underlying Life, *Artificial Life and Robotics*, Springer, 13: 10-17.
- [9]Naitoh K, (2010) Onto-biology: clarifying the spatiotemporal structure, *Artificial Life and Robotics*, Springer, 15: 117-127.
- [10]Lamb H, (1945) *Hydrodynamics*, 6th ed. New York: Dover.

Engine for brain development: Similarity between engine and brain

H. Kawanobe and K. Naitoh

Waseda University, Faculty of Science and Engineering, 3-4-1 Ookubo, Shinjuku, Tokyo, 169-8555 Japan
(Tel : 81-3-5286-3265)
(Email address:k-naito@waseda.jp)

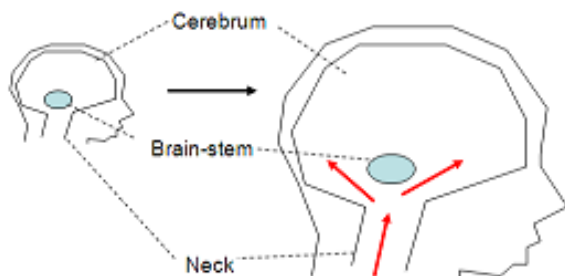
Abstract: Observations of the development of the human brain show the bones of the skull become increasingly larger over the neck, and a lot of soup like fluid for generating brain cells enters the skull from the body. This process is essentially similar to the intake process of an internal combustion engine and also that the soup for generating flexible brain cells can be essentially modeled by using the Navier-Stokes equation. The flow of air during the intake process of a piston engine and fluid flow in the brain, including water as the main component, can be approximated as being incompressible. In this report, we will examine the spatial patterns of convexoconcave of brain and blood vessels in details.

Keywords: Brain shape, Blood vessels, Morphogenesis, Engine, Fluid dynamics

I. CEREBRAL DEVELOPMENT [1]

Observations of the development of the human brain with a high-speed camera reveal that the bones of the skull become increasingly larger over the neck, and a lot of soup-like fluid for generating flexible cells, including nerves and synapses, enters the skull from the body.

(a) Brain volume increasing



(b) Volume increasing during the intake process of a piston engine

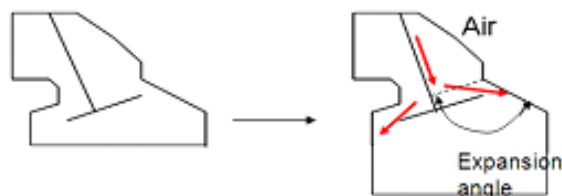


Fig.1 Topological similarity of the brain and an engine[1]

This process is essentially similar to the intake process of an internal combustion engine, because the volume of an engine cylinder, which increases according to the descent of the piston, corresponds geometrically to the development of the skull, and also

because the human neck looks like the intake port that functions as the throat of an engine (Fig.1).

The soup for generating flexible brain cells can be essentially modeled by using the fluid dynamics for flow in an engine. The flow of air during the intake process of a piston engine and fluid flow in the brain, including water as the main component, can be approximated as being incompressible. (The intake process of an engine at low engine speeds is incompressible, although the compression process is strongly compressible with time using the zero-Mach number regime.) [2,3]

II. NAVIER-STOKES EQUATION [1]

We employ the incompressible Navier-Stokes equation [4] as the basic governing equation that describes the flexible dynamic motion of a lot of soup-like fluid for generating brain cells. [1-3] The equation can be written as

$$\frac{\partial u_i}{\partial t} + \sum_j u_j \frac{\partial u_i}{\partial x_j} = -\frac{1}{\rho} \frac{\partial p}{\partial x_i} + \nu \sum_j \frac{\partial^2 u_i}{\partial x_j^2}$$

$$\sum_i \frac{\partial u_i}{\partial x_i} = 0 \quad (1)$$

where u_i , ρ , p , and ν denote the fluid velocity, fluid density, pressure, and kinetic viscosity coefficient, respectively, while x_i ($i=1,2,3$) denotes Cartesian coordinates in three dimensional space. Equation 1 is computed by the finite difference method using a higher order of accuracy. [1, 2, 3] The details of the computational method are given in the references.

III. COMPUTATIONAL RESULTS

Figure 2a shows an image of the human brain obtained with magnetic resonance imaging (MRI) at a horizontal cross section including the two eyes, while Fig.2b is the result of the corresponding computation performed with the Navier-Stokes equation. Red lines in Fig. 2 show that the convexoconcave shapes inside the brain are similar to the flow structure in engine.

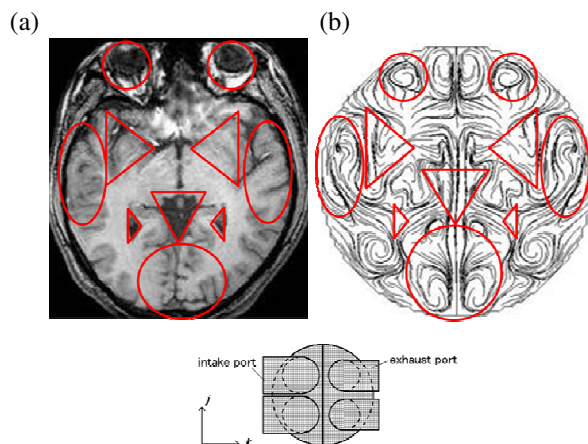


Fig.2 Comparison of brain MRI and engine flow (j-k cross section)
(a) Magnetic resonance imaging (MRI) of brain [5]
(b) Computational result at an engine speed of 1400 rpm

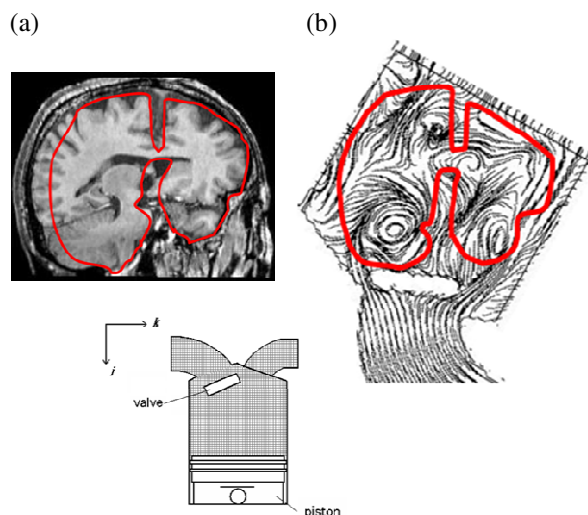


Fig.3 Comparison of brain MRI and engine flow (i-k cross section)
(a) Magnetic resonance imaging (MRI) of brain [5]
(b) Computational result at an engine speed of 1400 rpm

Figure 3a shows an image of the human brain obtained with magnetic resonance imaging (MRI) at a center cross section, while Fig.3b is the result of the corresponding computation performed with the Navier-Stokes equation for engine. Figure 3b is inclined in order to compare with the MRI image and engine flow

field. The convexoconcave shapes inside the brain in Fig.3a are similar to those in Fig.3b.

Figure 4a shows an image of the human brain obtained with magnetic resonance imaging (MRI) at the cross section different from those of Figs. 2 and 3, while Fig.4b shows the vorticity surface computed in the engine. In this figure we can see two spheres representing the eyeballs and a cylinder representing the nose.

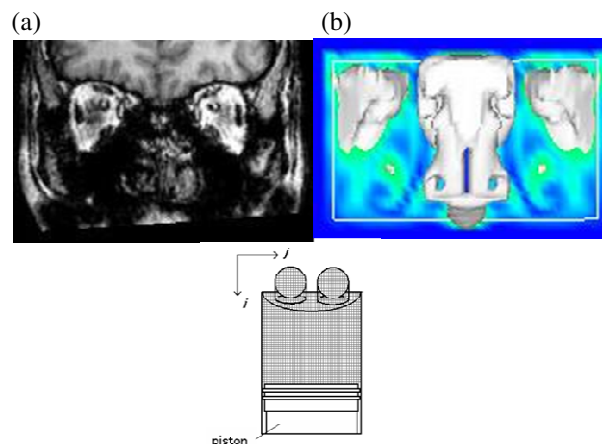


Fig.4 Comparison of brain MRI and vorticity in engine (i-j cross section)
(a) Magnetic resonance imaging (MRI) of brain [5]
(b) Computational result at an engine speed of 1400 rpm

Figure 5 shows the instantaneous stream lines computed at a very low engine speed of 1.4 r.p.m. A comparison with Fig.2 indicates that the flow pattern is independent of the engine speed.

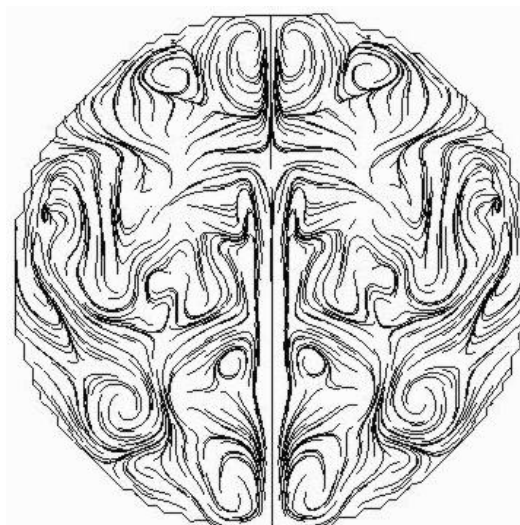


Fig.5 Instantaneous stream lines at a low engine speed of 1.4 r.p.m

Those computations were made at a crank angle of 72° after top dead center (ATDC) in the intake process, because at that point the cylinder volume of the piston engine considered here is about the same as that of the skull. (Fig.3)

Figure 6 shows the categorization of blood vessels in brain. In this figure, red line indicates external carotid artery, green line indicates middle cerebral artery, blue line indicates internal carotid artery, and yellow line indicates vertebral artery. We'll examine these four main blood vessels.

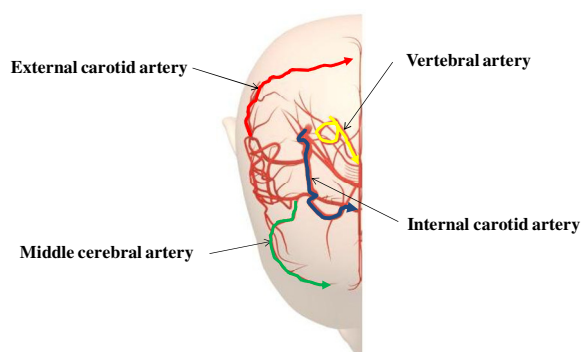


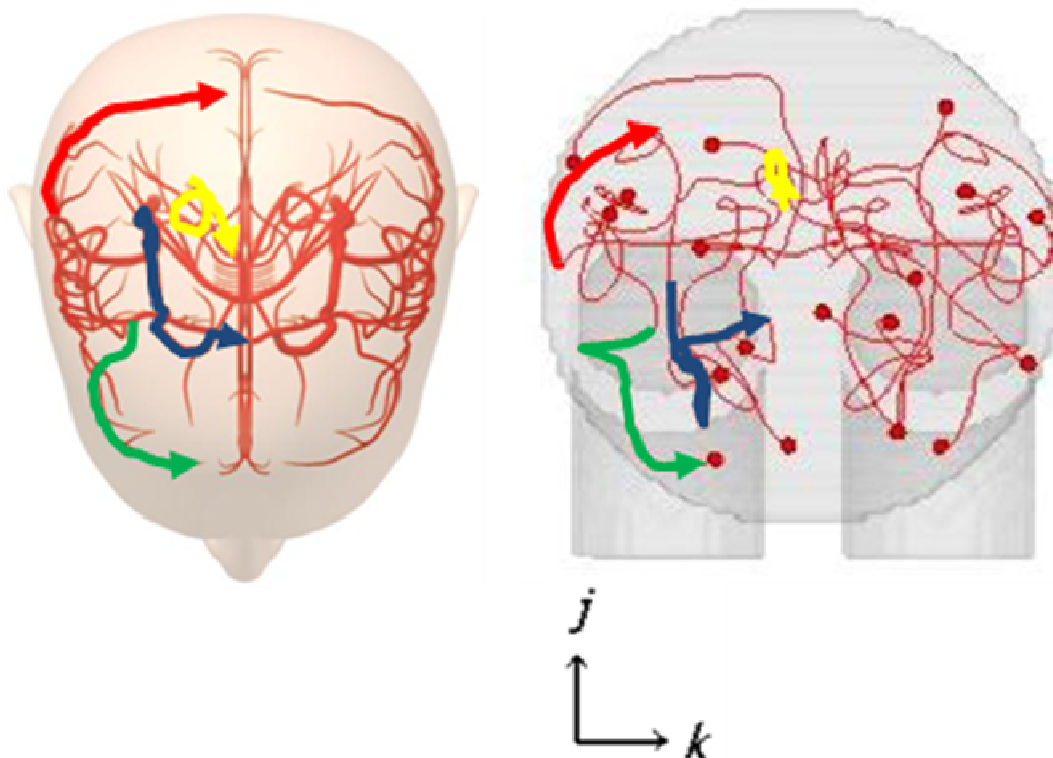
Fig.6 Categorization of blood vessels in brain [6]

Figure 7 shows the blood vessels in brain and the corresponding path lines in engine observed from three different directions. Each blood vessel can be also observed in the path lines for in engine at close positions, while the direction of flows are correct both for blood vessels and path lines in engine.

IV. CONCLUSION

In this paper, we can see the similarity between the convexoconcave forms inside the human brain and the flow structure of engine stream lines. In addition, the vorticity surface represents the eyeballs and nose that corresponds to those in the MRI imaging. Finally, we can conclude there is a similarity between blood vessels in human brain and engine path lines.

Acknowledgments The author sincerely thanks Mr.Keiji Matsuda of the Neuroscience Research Institute, AIST, Tsukuba, Japan, for permission to re-use the MRI images of the brain. Sincere thanks are also due Otsuka Phamaceutical for permission to re-use three dimensional images of blood vessels in brain. And this article is part of the outcome of research performed under Waseda University Grant for special research project (2010B-155).



(a) Blood vessels in brain [6]

(b) Computational result at an engine speed of 1.4r.p.m

Fig.7 Comparison of blood vessels in brain and engine path lines observed from the i direction

REFERENCES

- [1] Naitoh K (2008) Engine for cerebral development. Vol. 13, pp.18-21. J. of Artificial Life and Robotics.
- [2] Naitoh K, Kaneko Y, Iwata K (2004) Cycle-resolved large eddy simulation of an actual 4-valve engine based on a quasi-gridless approach. SAE paper 2004-01-3006
- [3] Naitoh K, Kuwahara K (1992) Large eddy simulation and direct simulation of compressible turbulence and combusting flows in engines based on the BI-SCALES method. Fluid Dyn Res 10:299-325
- [4] Tatsumi T (1998) Fluid dynamics (in Japanese). Baifukan
- [5] <http://riodb.ibase.aist.go.jp/brain/welcome.html> (also in Matsuda K, Oishi T, Higo N (2007) S128, P1-k22 Web-based MRI brain image database system. Neurosci Res 58(suppl 1) (ISSN0618-0102))
- [6] <http://www.otsuka-elibrary.jp/library/support/101/252>

Spatial surface wave spread network from Ambient Noise correlation

Z. Zheng, T. Fujiwara, N. Sakurai, K. Yoshizawa and K. Yamasaki

Tokyo University of Information Science, 265-8501 Japan

(TEL:81-43-236-4652; FAX:81-43-236-4652)

(zhengzy@edu.tuis.ac.jp)

Abstract: We computed the correlations of the ambient noise correlation of 66 stations of F-NET (Broadband Seismic Network JAPAN) that were apart from tens to hundreds kilometers. By stacking cross-correlation functions of ambient noise, we can extract the coherent part of each two stations. Through quantitative analysis of the magnitude of these extracted pluses of ambient noise correlation from any two stations, we construct a network that may reflect the main surface wave spread characters in spatial field.

Keywords: seismic noise, complex network, tomography, correlation function.

I. INTRODUCTION

Campillo and paul Campillo [1] found in 2003 that the stacking cross-correlations function of codas is similar the Green function tensor. Then many researches about the cross-correlations function of seismic waves and network method were carried Bensen et al [3], Shapiro et al [4], Zheng et al [5], Shiraishi et al [6] and Weaver[7]. Recently, some research indicated that these ambient noise correlations may concern with big earthquakes Xu[2]. In our research we analyzed the big area in space and time scale, found that the cross-correlations based on ambient noise may effect by big earthquakes. The big earthquakes have a effect that destroy the stability of cross-correlation in a wide area.

II. DATA AND METHOD

We used the 2003 66 stations of F-net data in 1HZ.

First, the “one-bit” method (3) was used to remove earthquakes and other contaminants from seismic waveform data. We divide the wave of each day of a station into 1440-s-long segments with overlap of 300 s.

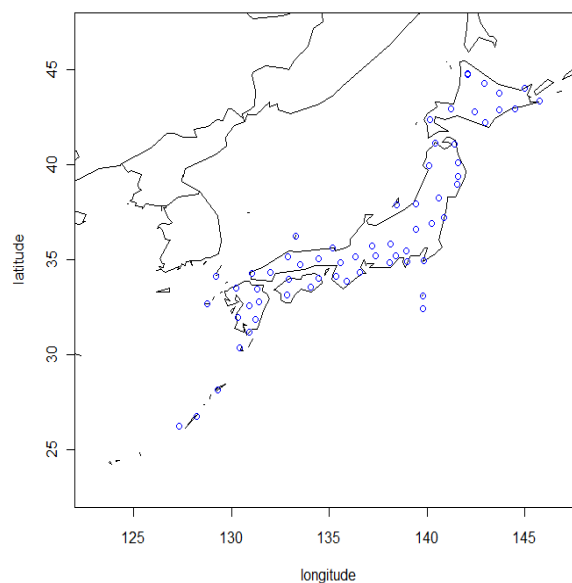


Fig. 1. The F-NET stations that was used in this research. (66 stations)

Then we computed the cross-correlations between these truncated signals, next each pairs' cross-correlations function were stacked to give the signals. The samples were show in Fig. 2. When $SNR > 30$, we may define a link between this two stations. All links construct a network as Fig. 3, her we call this networks is "seismic ambient noise network".

III. RESULTS and DISCUSSION

From Fig. 2 we can found that the correlation function peaks are changed in different day. Tough we don't know the reason of these dynamical changes, in our research we could show that the big earthquake may give some influence to these links. In order to quantitatively show this influence, we sum the links number of "seismic ambient noise network" of each day in 2003, the links numbers graph was show in Fig.4 , from this graph we can found that when each big earthquake (except aftershock) is occurred the links number will go down sharply. The second earthquake in September is an aftershock.

VI. CONCLUSION

In our research, we show the Ambient Noise correlations in the big spatial scale as a network. The network show a very dynamics characters. We checked the total links number in each day of the network.

The result shows that the number would down

precisely when the big earthquake occurred. It indicate one possibility for the earthquake forecast.

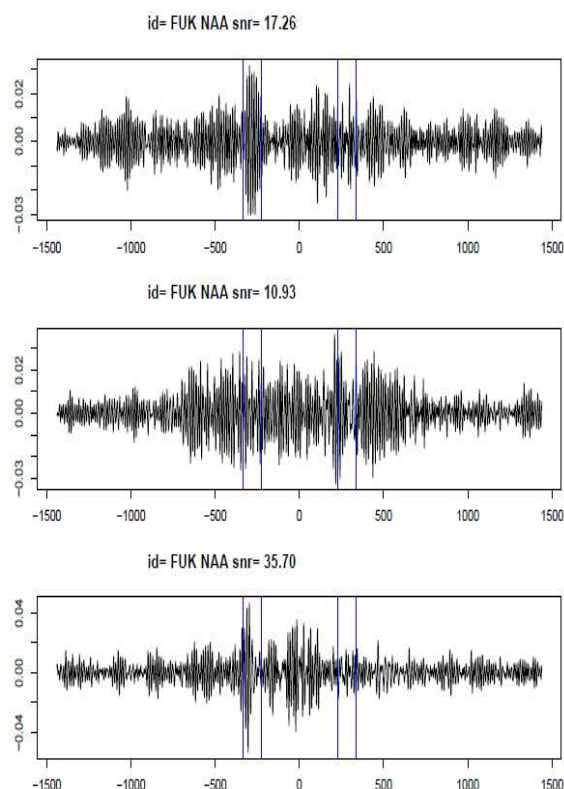


Fig. 2. The sample correlation functions of FUK and NAA stations. Each one indicate one days correlation, this graph shows 3 continues days correlations. The blue vertical lines show the predict maximum and the minimum group arrival times.

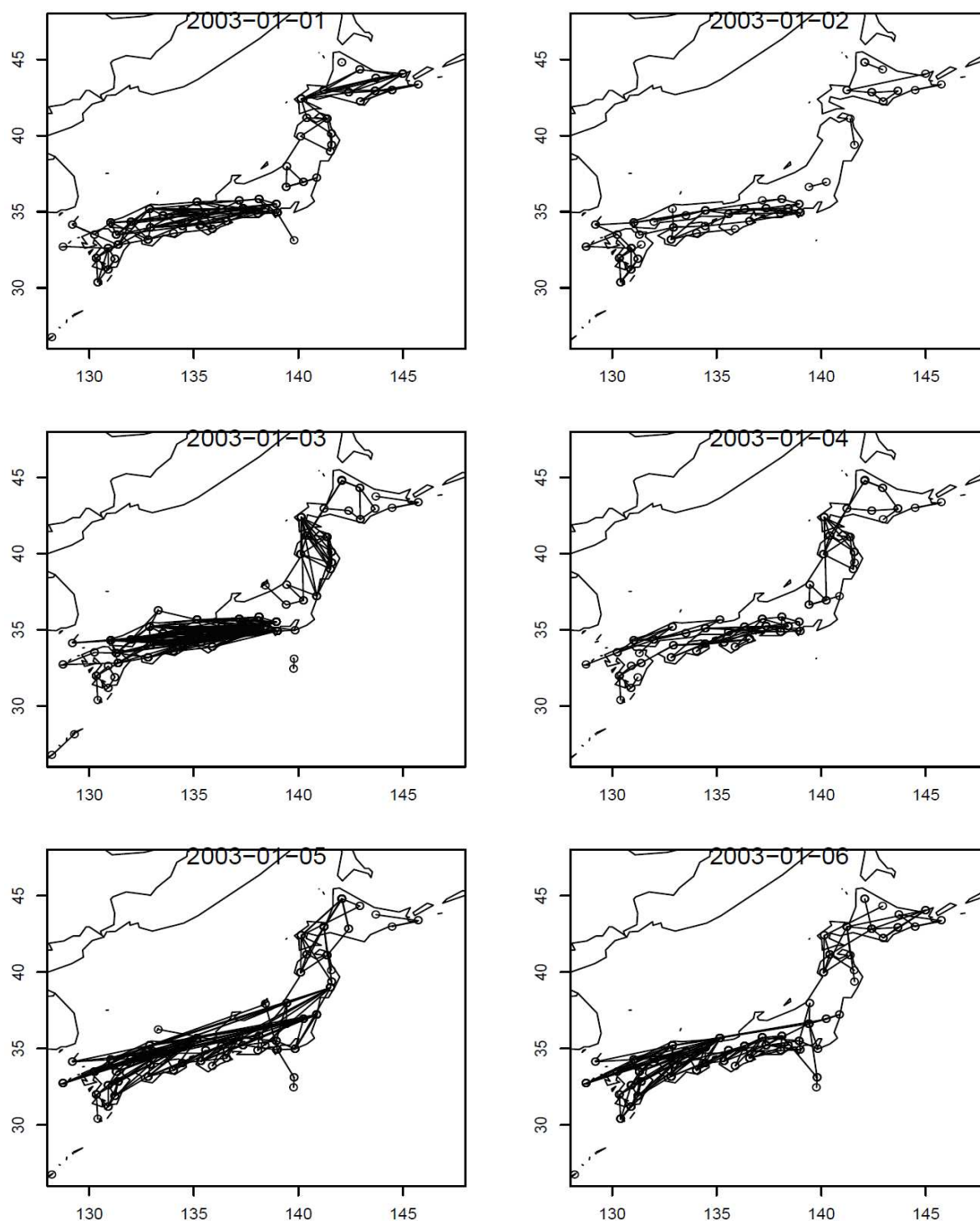


Fig. 3. The example network maps of 6 days in January 2003. The links are changed dynamics.

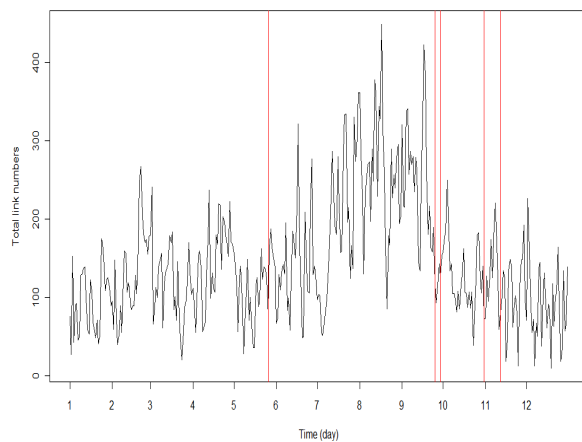


Fig. 4. The total links numbers in each day of 2003.
The red vertical lines indicate the main earthquakes
bigger than magnitude 6.5 in Japan.

Acknowledgment

Thanks for the support of Grant-in-Aid of Research project for the sustainable development of economic and social structure dependent on the environment in eastern Asia.

REFERENCES

- [1] Campillo M and Paul A (2003), Long-Range Correlations in the Diffuse Seismic Coda. *Science* 299: 547-549
- [2] Xu Z and Song X (2009), Temporal changes of surface wave velocity associated with major Sumatra earthquakes from ambient noise correlation. *PNAS* 106: 14207-14212
- [3] Bensen G, Ritzwoller M, Barmin M, et al. (2007), Processing seismic ambient noise data to obtain reliable broad-band surface wave dispersion measurements. *Geophys. J. Int.* 169:1239-1260
- [4] Shapiro N, Campillo M, Stehly L et al. (2005), High-Resolution Surface-Wave Tomography from

Ambient Seismic Noise. *Science* 307: 1615-1618

[5] Zheng S, Sun X, Song X et al. (2008), Surface wave tomography of China from ambient seismic noise correlation. *Geochemistry Geophysics Geosystems* 9

[6] Shiraishi K, Matsuoka T, and Kawanaka T (2008), Review of Seismic Interferometry. *Jour. of Geography* 117:863-869

[7] Weaver R (2005), Information from Seismic Noise. *Science* 307:1568-1567

Effect of Hot Summer against Environment which was induced by Extra Economical Demand via Japanese Ecological Footprint

K. Yamasaki, T. Fujiwara, N. Sakurai, K. Yoshizawa, Z. Zheng

Tokyo University of Information Sciences, 4-1 Onaridai, Wakaba-ku, Chiba, Japan
(Tel&Fax : 81-43-236-4653)
(yamasaki@rsch.tuis.ac.jp)

Abstract: The Ecological Footprint (EF) indicator which had been presented by Wackernagel and Rees in 1990's has attracted larger attention as a numerical assessment value for sustainable development on Earth. In this paper, we analyze the effect of hot summer against environment which was induced by extra demand via Japanese EF based on 47 prefecture's Input-Output table. The electricity sector and the gas & heat supply sector are affected by high temperature within 48 industry sectors in this Input-Output table. The extra demand of the electricity sector increases in the EF through the increase of CO2 emission in the same prefecture and the same sector. The effect of the extra demand loss of the gas & heat supply sector is not strong but is affected opposite direction. The extra demand(demand loss) does not affect other prefectures and other sectors so much.

Keywords: Ecological Footprint, Input-Output table, Induced analysis,

I. INTRODUCTION

We have to pay some money to buy food, clothes and electricity etc. for daily life. Although, the air for breathing is free and we live without being aware of the environmental services such as "regulation of CO2/O2 balance", "greenhouse gas regulation" and "flood control". R. Costanza and his team calculated the main 17 ecosystem services we received in 1997. These values (most of which is outside the market) is estimated US\$33 trillion per year and it's comparable to global world economy of US\$38 trillion per year on purchasing price basis. For sustainable life market price is not enough as the metric and we need more effective numerical value. One of the candidate is EF. The essential part is to convert nation's basic consumption to the nation's virtual area which is necessary to produce it. For example, we consume agricultural products to keep our life, and the consumption is converted to cropland area, and finally our total consumption is compared to bio capacity of the globe.

II. INDUCED ANALYSIS OF EF

EF is represented by total area of six land types, "Cropland", "Forest", "Grazing land", "Fishing ground", "Carbon uptake land" and "Built-up land". Each area is calculated to reproduce our final consumption as necessity area for "the supplies of crop", "the supplies of wood", "the supplies of livestock feed", "the supplies of fish", "absorption of CO2 emission" and "house, factory, road etc.". And it is compared to the real area (bio capacity) on the globe. Actually Japan needs 2.5 times area of Japan to keep our lifestyle, and whole world people need more area than whole area of the

globe.

EF is calculated for an area on the basis of consumption in the area. That is EF of the imported product does not belong to the nation where the product is produced but belongs to the nation where the product is consumed.

$$EF = \sum \frac{1}{y_{N,\alpha}} \varepsilon_{l(\alpha)} \psi_{N,l(\alpha)} \chi_{mi} \chi_{ij} \dots \chi_{k\Omega} C_{\Omega} \quad (1)$$

Here C_{Ω} is the weight of the consumed product Ω of which we want to know the effect, χ_{ij} is the weight of the product i to produce unit weight of product j , $\varepsilon_{l(\alpha)}$ is the equivalence factor of land type $l(\alpha)$ for the product α , $\psi_{N,l(\alpha)}$ is yield factor of nation N and land type $l(\alpha)$, $y_{N,\alpha}$ is the average weight of the product from unit area in the nation N . And the sums are executed in all paths from product Ω to product α through intermediate products i, j, \dots Using the matrix representation, $\{1 + \chi + \chi\chi + \chi\chi\chi + \dots\} = [1 - \chi]^{-1}$, and

$$EF = \lambda [1 - \chi]^{-1} C \quad (2)$$

here λ is diagonal matrix of $\varepsilon_{l(\alpha)} \psi_{N,l(\alpha)} / y_{N,\alpha}$.

But usually it is difficult to know χ_{ij} of all products' pairs $[i, j]$ without double counting. Sometimes we want to measure the effect of consumption toward other sectors or toward other regions, not only on economic effect but also on environmental effect. Input-Output table enables to calculate such influences by induced analysis.

*The equivalence factors and the yield factors are defined by GFN and represent the differences of productivity between different land types and between different nations.

$$\mathbf{EF} = \lambda[\mathbf{I} - \lambda]^{-1} \mathbf{C} + \lambda^{fuel} \mathbf{C}^h \quad (3)$$

In eq.(3), \mathbf{C} is a demand vector of sectors expressed by amount of money, λ is the coefficient matrix and $[\mathbf{I} - \lambda]^{-1}$ is the Leontief Inverse Matrix of the Input-Output table. λ is a kind of induced value added matrix in Input-Output table analysis.

Additional term $\lambda^{fuel} \mathbf{C}$ represents CO2 emission from the direct fuel use of final consumption.

For example, in case of agriculture sector, $y_{N,\alpha}$ is the total amount of agricultural product divided by the total area of the Cropland of the considering region N. $\varepsilon_{l(\alpha)}$ is the equivalence factor of Cropland, $\psi_{N,l(\alpha)}$ is yield factor of the region N and Cropland **.

There is another method to calculate the matrix λ .

GFN calculates nation's EF_l of each land type l every year and these EF_l s represent the area after considering the productivity. If EF_l s were distributed to each sector α (They are called direct **EF**s), λ is able to replace by them. The merit of this method is induced **EF**s are able to compare to other nations' **EF**s through **EF**s calculated by GFN.

III. THE EFFECT OF HOT SUMMER

1. We use "Multi-regional Input-Output table for 47 Prefectures and 48 industry sectors in Japan" in 2000 [1]. First we transform this Chenery-Moses type Input-Output tables of 47 prefectures to a Isard type table[2], which includes 2256x2256 matrix.

Table 1. a part of the Isard type Input-Output table.

		1	2	3	4	5
	million Yen	Hokkaidou_Agriculture	Hokkaidou_Forestry	Hokkaidou_Fishery	Hokkaidou_Mining	Hokkaidou_Food_Drink
1	Hokkaidou_Agriculture	607	30	82	61	1546
2	Hokkaidou_Forestry	111	5	15	11	281
3	Hokkaidou_Fishery	132	6	18	13	335
4	Hokkaidou_Mining	50	2	7	5	127
5	Hokkaidou_Food_Drink	1019	50	138	103	2594
27	Hokkaidou_Electricity	264	13	36	27	671
28	Hokkaidou_Gass	29	1	4	3	74

2. Next we allocate the **EF** calculated by GFN to each sector of each prefecture. **EF**s are allocated in proportion to the total of each sector according to the Table 2. We divide **EF** of Carbon uptake land into two parts in proportion to the total, one is for intermediate industry and the other is for final consumption. Using 3EID table[3], we allocate Carbon uptake land **EF** of intermediate industry in proportion to the total (million yen) of each sector

multiplied by CO2 emission unit requirement(t-CO2/million yen).

Table 2. Land types and corresponding sectors

1	EF of Cropland	Agriculture sectors
2	EF of Forest	Forestry sectors
3	EF of Grazing land	Agriculture sectors
4	EF of Fishing ground	Fishery sectors
5	EF of Carbon uptake land	All sectors
6	EF of Built-up land	Final consumption

3. We use "Monthly Family Budget Survey" calculated by Japanese government[4] to get the extra consumption for the hot summer. We calculate the correlation between temperature and consumption of each 48 sector in July in main cities in Japan. We found that the electricity consumption of 11 years has positive correlation to the temperatures, and that the gas & heat supply consumption has negative correlation.
4. We calculate induced demand using eq.(4) and calculate induced **EF** using eq.(5). The elements of \mathbf{C} are the extra consumption of the electricity sector and the extra loss consumption of the gas & heat supply sector. We calculate the data of the hot summer in July/2010. We also calculate the data of the cold summer July/2003 for comparison. When we use the competitive import type Input-Output table, eq.(3) must be deformed to eq.(5) for separating imported products from domestic products.

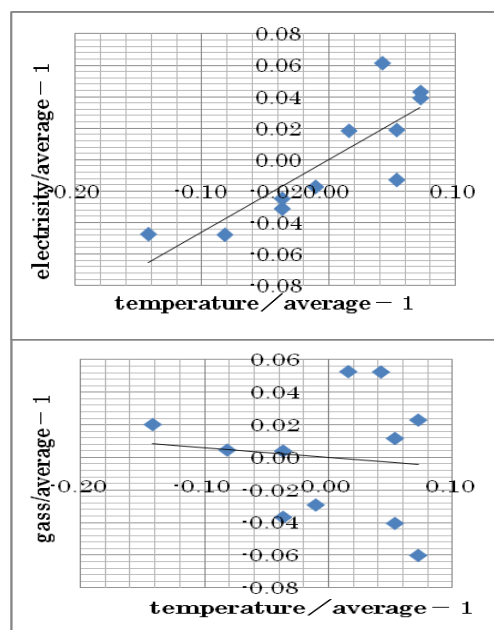


Figure.1. Correlations (consumption and temperature)

**If the region is not a nation, we use $\psi_{N,l(\alpha)}$ of the nation's factor instead.

$$W = [1 - [1 - M]\chi]^{-1} [1 - M]C \quad (4)$$

$$EF = \lambda[1 - [1 - M]\chi]^{-1} [1 - M]C + \lambda^{fuel} C \quad (5)$$

Here **M** is import ratio diagonal matrix whose elements indicate the ratio of imported products in total products.

5. The last term of eq.(5) represents CO2 emission from the direct fuel use of final consumption. Using 3EID table, we calculate the remaining CO2 emission ratios (t-CO2/million yen) in energy sectors and Carbon uptake land **EF** of final consumption is allocated in proportion to the total multiplied by these ratios.

IV. RESULT

Figure.2 shows the effect from extra demand of electricity/gas respectively in 47 prefectures in 2010. Three lines show extra household consumption, induced production and the extra use of the "Carbon uptake land". In July 2010, The hot summer already began in the east part of Japan, but the heavy rainy season still stayed in the west part of Japan. So high demand of electricity is clear in east part of Japan. The high demand does not affect other prefectures' production so much except Fukushima where there is nuclear plant of Tokyo Electric Power Company. The effect from gas consumption is not so clear. Figure.3 shows the effect from extra demand of electricity/gas respectively in 48 sectors. The electricity consumption induces the production of Coke & Petroleum, Finance & insurance and Other business services. But it looks as if production of the electricity does not induce the increase of CO2 emission in other sectors, because the production of the electricity produces carbon dioxide in higher ratio per money than other sectors.

Figure. 4 (Figure. 5) shows the effect from extra(loss) demand of electricity/gas in 47 prefectures(in 48 industry sectors) respectively in cold summer in 2003. The results are almost opposite to the hot summer in 2010.

V. DISCUSSION

The extra demand(demand loss) does not affect other prefectures and other sectors so much. It comes from characteristic of these industries. But the true effect of the hot summer is thought to have spread widely in various industry sectors. Input-output table of 47 prefecture includes only 48 sectors and there is no Input-output table with much sectors in all prefectures level. we have to give up the analysis of the prefectures level and use Input-output table with more sectors to improve the study.

Acknowledgements

The study was supported by research project for a sustainable development of economic and social structure dependent on the environment of the eastern coast of Asia. We thank for not only financial support but also helpful discussion of the project members.

REFERENCES

- [1] Hitomi K. & B. Pongsun(2008), CRIEPI Research Report, No Y07035
- [2] Okamoto N.(2002), Asian Input-output Series, JETRO, No. 61, pp.1-20. (in Japanese)
- [3] 3EID:http://www-cger.nies.go.jp/publication/D031/jpn/index_j.htm
- [4] <http://www.e-stat.go.jp/SG1/estat/OtherList.do?bid=000000330002&cycode=1>
- [5] Simmons C., et al.(2006), WWF One Planet Business Methodology Report V12. <http://old.bestfootforward.com/OPB.html>
- [6] Iha K., Y. Wada (2009), Environmentally Extended Input-Output Analysis (EFIO) for Ecological Footprint and its Application: Japan as a Case Study.
- [7] Yoshizawa K., T. Fujiwara, Z. Zheng , R. Shiba, N. Sakurai, K. Yamasaki(2010), Network Analysis of Japanese Ecological Footprint based on Input-Output Table for the 47 Prefectures in Japan, Proceedings of FOOT PRINT FORUM 2010
- [8] Fujiwara T., K. Yoshizawa, N. Sakurai, K. Yamasaki (2010), The Analysis of Ecological Footprint using Multi-regional Input Output Table for 47 Prefectures in Japan, Proceedings of 38th Annual Meeting of Environmental Systems Research 2010, pp.239-243. (in Japanese)

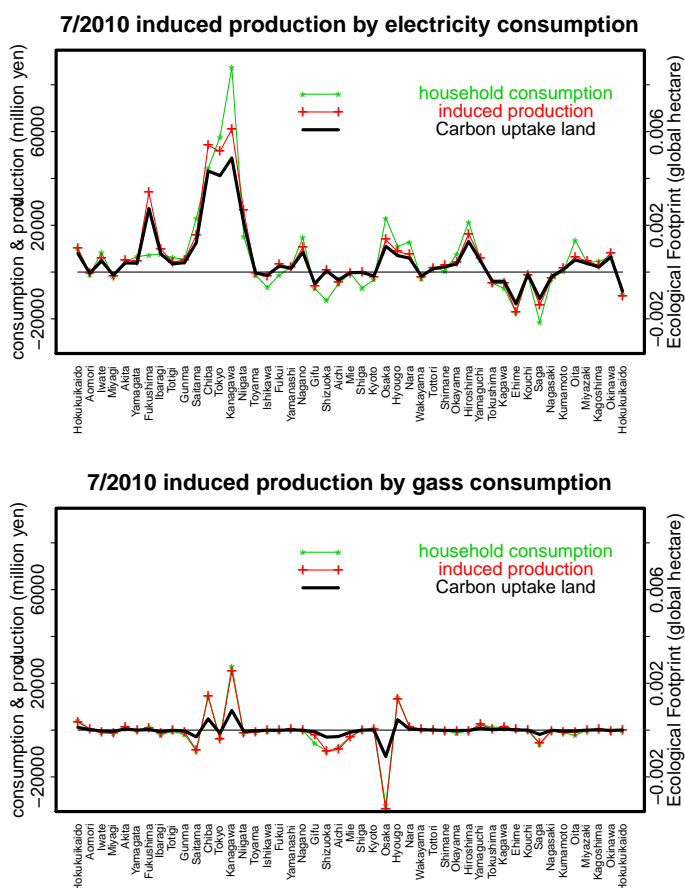


Figure 2

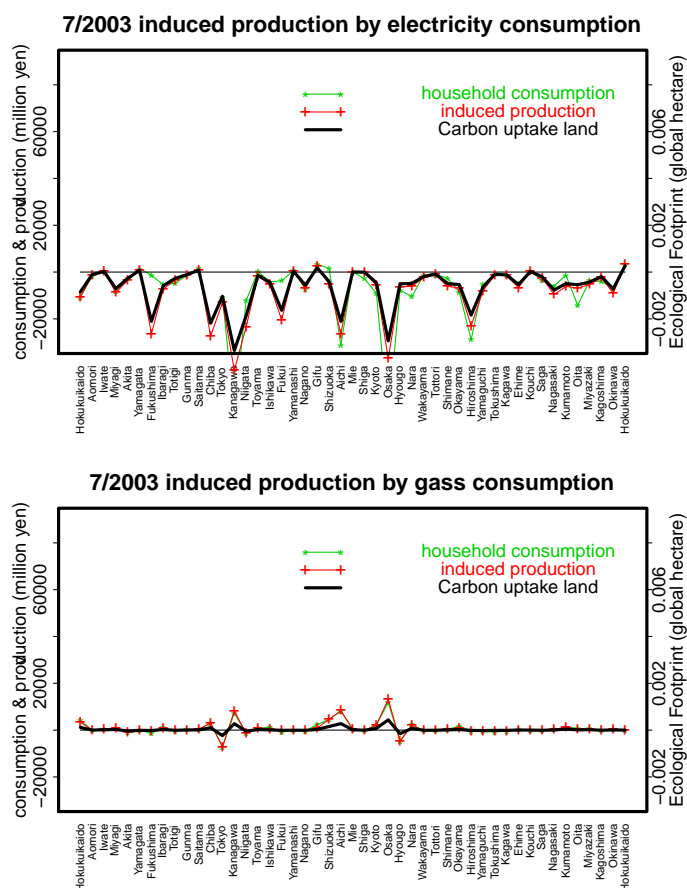


Figure 4

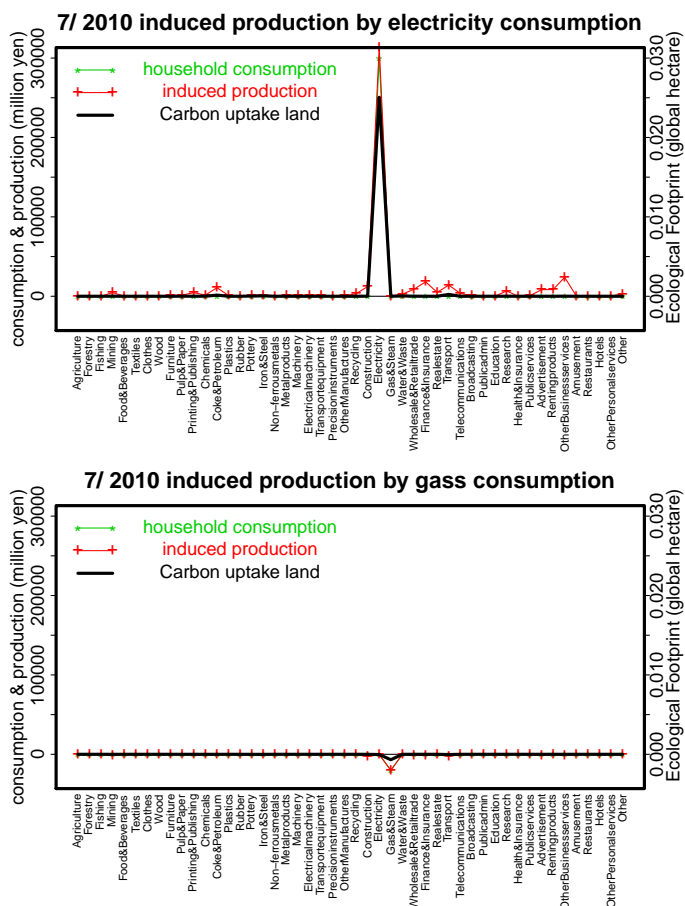


Figure 3

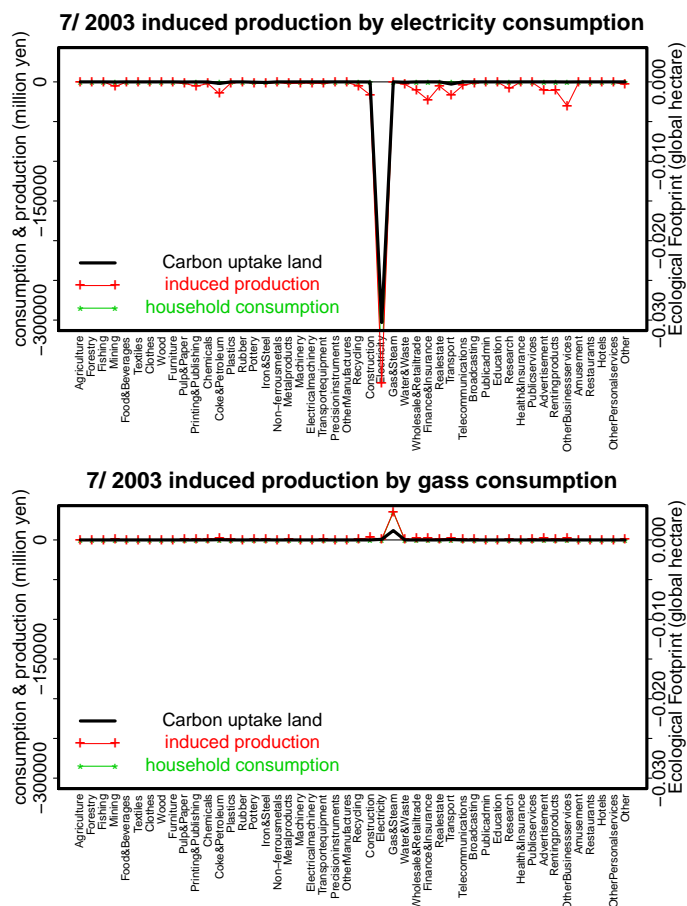


Figure 5

Blood flow velocity waveforms in the middle cerebral artery at rest and during exercise

T. Matsuo, S. Watanabe, M. Sorimachi, M. Kanda, Y. Ohta, and [#]T. Takahashi

Kanagawa Institute of Technology, Shimo-ogino 1030, Atsugi, Kanagawa 243-0292, Japan.

(Tel : 81-46-291-3279; Fax : 81-46-291-3262)

(Email address : matuo@rm.kanagawa-it.ac.jp)

[#]Asahikawa Medical College, Midorigaoka Higashi 2-1-1-I, Asahikawa 078-8510, Japan.

Abstract: The blood flow velocities in the middle cerebral artery were measured under steady-state and incremental cycle exercises using the transcranial Doppler ultrasound velocimeter. The peak-systolic velocity was found to rise markedly under exercise, while the end-diastolic velocity tended to keep a resting value. The fluctuation of velocity and resistance index were calculated in order to evaluate the hemodynamic load on the vessel wall. They also increased markedly under exercise. Such hemodynamic changes in activity might be important in understanding the genesis of vascular diseases as well as physiology of cerebral circulation.

Keywords: Transcranial Doppler, Ultrasound, Middle cerebral artery, Cerebral Circulation, Blood velocity

I. INTRODUCTION

Since the brain tissues are extremely vulnerable in terms of oxygen deficiency, an adequate and continuous supply of oxygenated blood is essential for the function of the brain. The blood flow in the middle cerebral artery (MCA) maintains about 80% of the flow volume arriving at the cerebral hemisphere. Since the blood velocity waveforms are considered to be closely related to the flow disturbances caused by arterial diseases such as stenosis and cerebral aneurysms, blood velocity measurements using transcranial Doppler (TCD) sonography are widely conducted in clinical examination [1][2].

Most of the clinical data of transcranial Doppler have been measured under resting condition. It should, however, be noted that the blood flow would be easily disturbed by daily activity such as work, exercise and posture change, as well as changes in environmental factors such as ambient temperature. In the present study, we measured velocity waveforms in the MCA during cycle exercise in order to understand the dynamics of MCA blood flow caused by physical exercise. Velocity waveforms might contain information concerning the hemodynamic load on the vessel wall such as shear stress and velocity fluctuation which are considered to play an important role of the genesis and development of arterial diseases [2].

II. METHOD

1. Subjects

Six healthy young male and 6 healthy young female volunteers participated in the present study. None of the subjects had any history of cardiovascular,

cerebrovascular, or respiratory disease. All subjects were fully informed about the procedures, risk, and benefits of the study, and written consent was obtained from all subjects before the study. This study was approved by the university institutional board.

2. Experimental design

Each subject was required to keep his body in an upright, seated position on an electromagnetically-braked cycle ergometer during rest and exercise periods. Two kinds of exercises were conducted as follows;

(A) Steady-state exercise;

The work rate was maintained at 100 W for males and at 50 W for females for 15 minutes exercise. During exercise, the subjects pedaled at a constant rate of 60 rpm paced by a metronome. The exercise intensity corresponds to “moderate exercise”.

(B) Incremental exercise;

During 15 minutes exercise, the work rate was increased from 20 to 100 W by a 20 W increment step for males, and from 10 to 50 W by a 10 W step for females. The duration of each step was 3 minutes with keeping a pedaling rate of 60 rpm.

3. Measurement of blood velocity and pressure

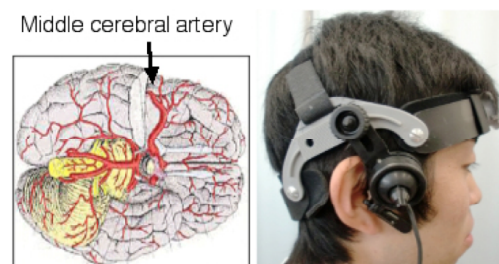


Fig.1 Position for Doppler examination

The blood flow velocity in the right middle cerebral artery was obtained using a 2-MHz pulsed Doppler ultrasound system (Intra-view, Rimed, Israel). Its pulsed probe was located over the temporal bone and the Doppler signal was optimized through a change in the insonation angle. The probe attached to the skull at a fixed angle was held using a headgear with an adjustable positioning system. The blood flow velocity was assessed for 6-10 consecutive cardiac cycle recorded during the last minute before and during exercise. Peak-systolic, end-diastolic, and mean blood flow velocity in MCA were represented by *MCAVs*, *MCAVd*, and *MCAVm*, respectively.

The blood pressure in the brachial artery was sphygmomanometrically measured using a pneumatic arm cuff which was held at heart level. Mean arterial blood pressure (MAP) was calculated as diastolic blood pressure (DBP) plus one-third pulse pressure [3].

III. RESULTS AND DISCUSSION

1. Velocity waveforms

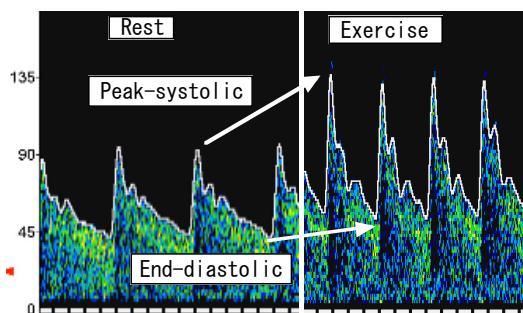


Fig. 2 Measured velocity waveforms in the MCA

In Fig. 2, an example of the obtained velocity waveforms is shown, where the waveform in the exercise is compared with that in the rest. As can be noted in the left panel, the waveform shows substantial variation of flow velocity during one cardiac cycle. The velocity rises sharply at initial systolic phase of heart (peak-systolic velocity), and decreases gradually during diastole. The flow waveform is characterized by a high forward flow at end-diastole, which is as much as half peak-systolic velocity. This feature is characteristic of blood flow in intracranial arteries, and contrasts with the relatively low diastolic flow component in the external carotid artery. This difference is ascribed to the markedly low flow resistance in the cerebral vasculature compared with that in the territory of the external carotid artery [1].

It should be also noted that the peak-systolic velocity (*MCAVs*) markedly increased during exercise, while the end-diastolic velocity (*MCAVd*) showed a trivial change. Accordingly, the difference between *MCAVs* and *MCAVd* was increased.

2. Hemodynamic data during steady-state exercise

Figure 3 shows physiological quantities (blood velocity, blood pressure and heart rate) measured at rest and during steady-state exercise. The measured values given in the graph are average for 12 volunteers (6 females and 6 males). Peak velocity *MCAVs*, systolic blood pressure, and heart rate rise immediately after onset of exercise. On the contrary, the diastolic pressure and end-diastolic velocity *MCAVd* were found to show no statistically significant change during exercise. It is also noted that the heart rate tends to slightly increase during exercise, while *MCAVs* and systolic pressure show slight inclination to decrease.

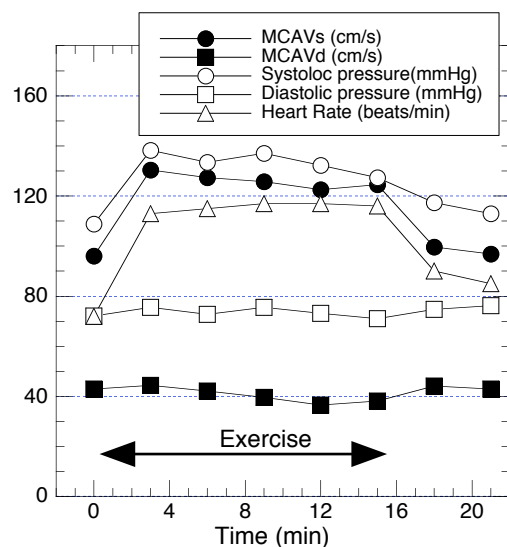


Fig. 3 Physiological quantities measured at rest and during steady-state exercise.

3. Hemodynamic data during incremental exercise

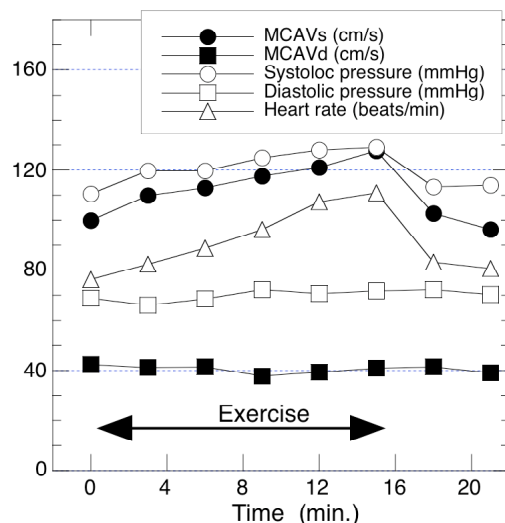


Fig. 4 Physiological quantities measured at rest and during incremental exercise.

The measured physiological quantities under incremental exercise are shown in Fig. 4. The $MCAV_s$ gradually increases as the degree of exercise increases. After 15 minutes, corresponding work rate being 100 W for male and 50 W for female, $MCAV_s$ reaches a value (130 m/s) comparable to that in the steady-state exercise. Also the systolic pressure and heart rate are on the increase. As in the steady-state exercise, both $MCAV_d$ and diastolic pressures show no significant change during exercise.

5. Fluctuation in MCA velocity

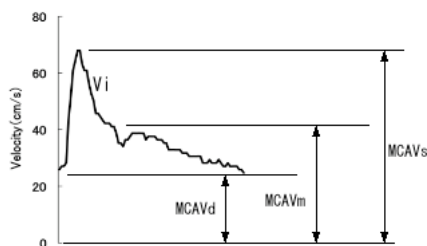


Fig. 5 Indices used in waveform analysis

In order to see the variation in velocity due to exercise, we calculated velocity fluctuation index (VF) for measured velocity waveforms, which is defined as,

$$VF = \sqrt{\frac{\sum_{i=1}^n (V_i - MCAV_m)^2}{n}} \quad \dots\dots(1).$$

Here, V_i : velocity at time t_i , $MCAV_m$: mean velocity averaged over one cardiac cycle, and n : number of measured velocity data for one cardiac cycle. This index is corresponding to the standard deviation in statistics.

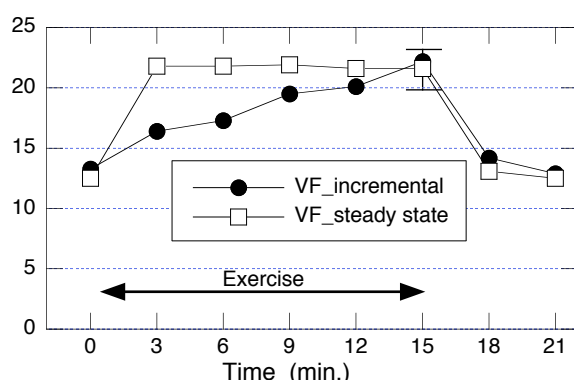


Fig. 6 Velocity fluctuations (VF) of MCA blood flow under incremental and steady-state exercises.

Figure 6 compares VF values calculated for steady-state exercise with those for incremental exercise. Velocity fluctuations in steady-state exercise are well constant during exercise. The VF values under exercise were found to be about 1.8 times larger than those at rest. In the incremental exercise, VF increases as the

exercise intensity increases. Such VF variations as a function of exercise intensity are quite similar to the $MCAV_s$ variations shown in Figs. 2 and 3.

5. Resistance index

Pourcelot [4] introduced the “resistance index” to Doppler sonography as a means to characterize the peripheral resistance in the cerebral circulation. Resistance index (RI) is defined as following equation,

$$RI = \frac{MCAV_s - MCAV_d}{MCAV_s} = 1 - \left(\frac{MCAV_d}{MCAV_s} \right) \quad \dots(2).$$

This index describes the ratio of peak-systolic velocity to the end-diastolic velocity. For the normal common carotid artery, RI is reported to be between 0.55 and 0.75. In arteries that supply high-resistance musculocutaneous beds, RI is known to be greater than 0.75 [4]. The arteries that supply the brain have RI index less than 0.75. A low RI value is also seen post-stenotically in cases where flow resistance is decreased by reactive dilatation of blood vessels [1].

In Figs. 7 and 8, are shown the obtained RI values during exercise, in which results for males and females are indicated individually. Under steady-state exercise shown in Fig. 7, although the variance of the data are considerably large, RI values tend to increase rather gradually from 0.57 to 0.74 in males and from 0.53 to 0.67 in females, compared with the fluctuation index shown in Fig. 6. These values of RI can be well compared with the previous data mentioned above.

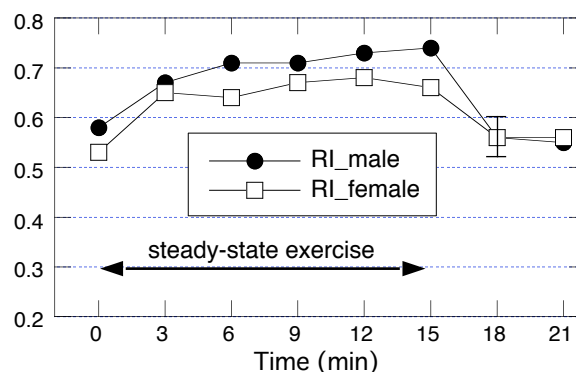


Fig. 7 Resistance index during steady-state exercise

As shown in Fig. 8, in males, the RI values in incremental exercise vary increasingly from 0.57 to 0.69 as increase of exercise intensity. Although an increasing trend is seen also in females, the data points show rather scattering. The reason for the difference between female and male is not clear at present, and sophisticated experiment would be necessary.

The index RI is not only a function of flow resistance but also influenced by vascular compliance. It

is generally known that the velocity waveform changes considerably with aging result from increased resistance due to cerebral atherosclerosis, and decreased compliance of vessel wall [1]. The waveforms of elder subjects were reported to be characterized by high *RI* values and steep decrease of velocity in diastole. The waveform change from rest to exercise shown in Fig. 2 seems to be similar to that due to aging.

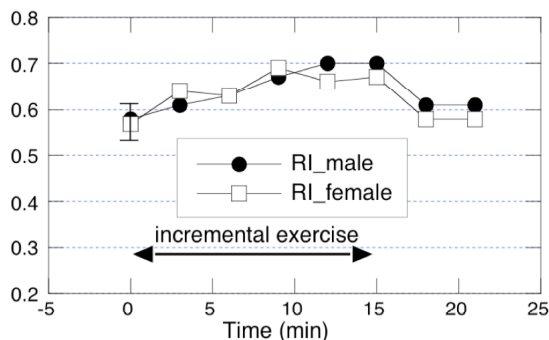


Fig.8 Resistance index during incremental exercise

We also measured velocity waveforms during strong exercise with intensities from 120 to 150 W (data not shown). It was found that above 120 W of exercise intensity, the *MCAVs* values were almost constant, while *MCAVd* values were slightly decreased, resulting in that both velocity fluctuation *VF* and resistance index *RI* were increased.

5. Correlation between hemodynamic variables

Measured hemodynamic variables such as blood velocities, arterial pressures, and heart rate were subjected to correlation analysis each other. Among the results, the relationship between *MCAVs* and systolic blood pressure (*SBP*), and that between *MCAVs* and heart rate *HR* were found to show statistically significant correlation as shown in Figs. 9 and 10. The significant correlation between *MCAVs* and systolic arterial pressure might be supported by the results indicated in Figs. 2 and 3. Although the data are not given here, mean MCA blood velocity *MCAVm* showed significant correlation with mean arterial pressure and heart rate.

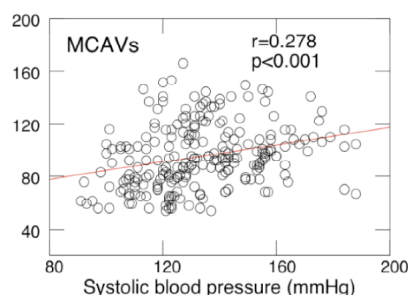


Fig. 9. Correlation between *MCAVs* and systolic arterial pressure

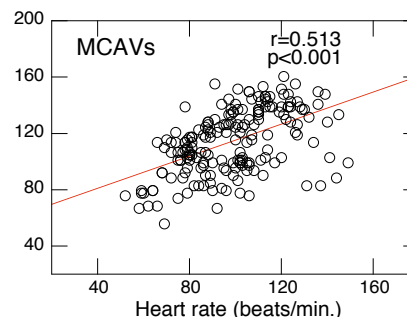


Fig. 10. Correlation between *MCAVs* and heart rate

IV. SUMMARY

The velocity waveforms in the middle cerebral artery in young volunteers were measured under moderate-intensity cycle exercise. The peak systolic velocity *MCAVs* and the end-diastolic velocity *MCAVd* were obtained from measured waveforms. Calculated hemodynamic variables, velocity fluctuation *VF* and resistance index *RI*, showed remarkable increase under exercise. The waveforms in exercise seemed to be similar to those of elder people at rest. A preliminary experiment of high intensity exercise showed nonlinear changes of *MCAVs*, *MCAVd*, *VF* and *RI*, indicating that the influence of exercise on cerebral blood flow is more complicated than thought before. However, the number of volunteers was still limited in the present study and the results are thought to be affected by individual differences in physiological variables. Therefore, further study is required to derive a concrete conclusion. Simultaneous measurements of MCA blood flow waveforms and arterial blood pressure waveforms are under way, since these measurements would provide much information on the regulation of cerebral circulation.

REFERENCES

- [1] G-Michael von Reutern and Hans Joachim von B u e d i n g n (1993), *Ultrasound Diagnosis of Cerebrovascular Disease*, Georg-Thieme Verlag Stuttgart-New York.
- [2] Hennerici M G and Stephen P M (2001), *Cerebrovascular ultrasound: theory, practice and future developments*, Cambridge Univ. Press New York.
- [3] Watanabe S, Matsuo T, Sorimachi M, et al. (2009), Comparison of blood flow velocity in the middle cerebral artery between men and women at rest and during exercise. *Therapeutic Research*, 30(4), 537-544.
- [4] Pourcelot L (1976), *Diagnostic ultrasound for cerebral vascular disease*, in Donald JS, Levi S (eds): *Present and Future of Diagnostic Ultrasound*. Kooiker Rotterdam.

Two-Level Time-Series Clustering for Satellite Data Analysis

Ayahiko Niimi

*Faculty of Systems Information Science
Future University Hakodate
116-2 Kamedanakano-cho, Hakodate-shi,
Hokkaido 041-8655, JAPAN
(niimi@fun.ac.jp)*

Takehiro Yamaguchi

*Graduate School of Systems Information Sciences
Future University Hakodate
116-2 Kamedanakano-cho, Hakodate-shi,
Hokkaido 041-8655, JAPAN
(g2109046@fun.ac.jp)*

Osamu Konishi

*Faculty of Systems Information Science
Future University Hakodate
116-2 Kamedanakano-cho, Hakodate-shi,
Hokkaido 041-8655, JAPAN
(okonishi@fun.ac.jp)*

Abstract: In this paper, we propose a method for finding the frequent occurrence patterns and the frequent occurrence time-series change patterns from the observational data of a weather-monitoring satellite. The observational data of the weather-monitoring satellite are temporal and spatial large-scale data. However, to analyze this large amount of data incurs a high calculation cost. Therefore, we propose parallel computation when the frequent occurrence pattern and the frequent occurrence time-series change pattern are extracted at the Artificial Life and Robotics conference (AROB) 2010. In this paper, we apply the proposed system to Moderate Resolution Imaging Spectroradiometer (MODIS) data and discuss its results.

Keywords: distributed processing, clustering, frequent occurrence pattern extraction, satellite data, data stream

I. INTRODUCTION

In our network society, the development of information processing enables us to collect and utilize massive amounts of data; and data mining has gained attention as a technology to discover new knowledge and patterns. But those data are changing continuous, and new types of large-scale data have emerged. For example, records of financial and distributional transactions, telecommunications records, and network access logs are typical data streams. The term data stream suggests that the temporally changing, massive amounts of data records that are generated, accumulated, and consumed are looked on as flow of data (stream). In the real world, the requirement has been growing to elicit information from those large data streams whenever we need information. At first glance, data mining seems to be effective; but a data stream has the following dynamic properties:

1. massive amounts of data are
2. coming over a high-speed stream,
3. temporally changing, and
4. continue to arrive permanently;

and data mining is intended for static data, not a stream. Therefore, data stream mining technology has been de-

veloped to deal efficiently with large-scale data streams [1, 2, 3, 4, 5, 6, 7].

An example of a data stream for this technology is data from satellites. Satellite data are used for various purposes, such as land-cover classification and forecasts [8] and marine information analysis [9, 10, 11, 12, 13]. However, satellite data treated up to now as static data. Therefore, much computing time was required to analyze a large amount of data. In this paper, we propose a method to solve this problem by using distributed processing.

At the Artificial Life and Robotics conference (AROB) 2010, we propose a method for finding the frequent occurrence patterns and the frequent occurrence time-series change patterns from the observational data of a weather-monitoring satellite [14]. The observational data of the weather-monitoring satellites are temporal and spatial large-scale data. Various uses are possible such as forecasting marine resources by analyzing satellite data. However, there is an issue with respect to the calculation cost to analyze a large amount of data. Thus, we propose to use parallel computation when the frequent occurrence pattern and the frequent occurrence time-series change pattern are extracted in this paper.

Our proposed method is as follows. First, to extract the frequent occurrence pattern from satellite data, the necessary marine information is acquired by using the filter from satellite data. Next, the extracted marine data undergo clustering to merge similar data and are labeled. As a result, similar data are brought together for data with a spatial extension. The labeling data are re-clustered to the data group and re-labeled according to the degree of similarity between labels. As a result, similar data are brought together for data with a time extension. Finally, frequent events are extracted as the frequent occurrence pattern from the labeling data. Moreover, the frequent occurrence of the time-series pattern can be extracted as rules by detecting the change in the labeling data group. However, it takes computing time to analyze long-term data. Therefore, by dividing data and integrating the results, we propose to shorten the computing time by parallel computation of clustering and the frequent occurrence of the time-series pattern rule extraction. As for clustering and the frequent occurrence of the time-series change pattern extraction, parallel computation is possible by dividing data. The shorter computing time can be expected by division degree because each algorithm never influences the parallel calculation. Each algorithm was examined with regard to whether it was possible to make parallel. Because clustering and extracting change patterns can be applied in parallel computing, we constructed the system with clustering of marine information and the extraction of the change pattern.

At AROB 2010, the frequent occurrence pattern and the frequent occurrence of the time-series change pattern of the sea surface temperature are extracted by using the sea surface temperature data, with the weather-monitoring satellite providing verification. In this paper, we use Moderate Resolution Imaging Spectroradiometer (MODIS) data, which includes the sea surface temperature (SST) and the concentration of chlorophyll-a (chl-a) to verify our proposed system and discuss its results.

II. THE PROPOSED METHOD

At AROB 2010, we propose a method for finding the frequent occurrence patterns and the frequent occurrence time-series change patterns from the observational data of a weather-monitoring satellite [14].

Fig. 1 shows a flowchart of the proposed system.

The flow of the algorithm is shown below.

1. First, to extract the frequent occurrence pattern from satellite data, necessary marine information is acquired by using the filter from satellite data.
2. Next, the extracted marine data undergo clustering to merge similar data and are labeled.
3. The labeling data are re-clustered to the data group and re-labeled according to the degree of similarity

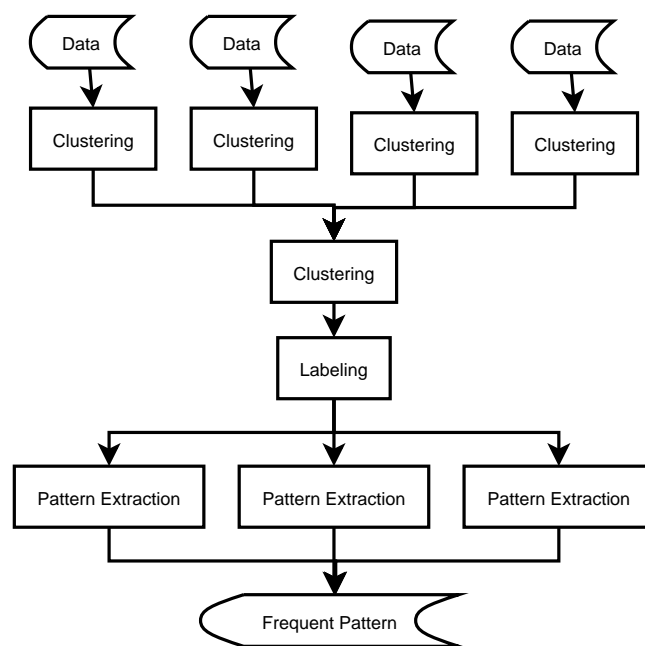


Fig. 1: Flowchart of proposed system

between the labels.

4. Finally, the frequent events are extracted as the frequent occurrence pattern from the data.

In the first clustering, similar data are brought together for data with a spatial extension. In the second clustering, similar data are brought together for data with a time extension. Moreover, the frequent occurrence of the Time-series pattern can be extracted as rules by detecting the change in the labeling data group. However, it takes computing time to analyze long-term data. Therefore, by dividing data and integrating the results, we propose to shorten the computing time by parallel computation of clustering and the frequent occurrence of the time-series pattern rule extraction. As for clustering and the frequent occurrence of the time-series change pattern extraction, parallel computation is possible by dividing data. The shorter computing time can be expected by division degree because each algorithm never influences the parallel calculation. Each algorithm is examined with regard to whether it was possible to make parallel. Because clustering and extracting of change patterns can be applied in parallel computing, we constructed the system with clustering of marine information and the extraction of the change pattern.

III. DETAILS OF SATELLITE DATA

At AROB 2010, we acquire the data of Meteorological Satellite Center as satellite data. We use the observation monthly report of the Meteorological Satellite Cen-

ter for the experiment [15]. The observation monthly report can be obtained on CD-ROM. These CD-ROMs contain the monthly report of observation data derived from Multi-functional Transport Satellite (MTSAT-1R) and the polar orbital meteorological satellite from National Oceanic and Atmospheric Administration (NOAA). For the problem of forecasting the hot spot of marine products using satellite data, the sea surface temperature, the chlorophyll, and the flow of the ocean are often targeted. Because only the sea surface temperature data are included in the observational data, sea surface temperature is used in the experiment. Ten-day mean sea surface temperature consists of grid points arrayed every one degree latitude and longitude covering the area from 50 degrees North to 50 degrees South and 90 degrees East to 170 degrees West. We use data from March 2009 to May 2009 because the regression equation for SST was updated on March 1, 2009.

In this paper, we use MODIS data, which includes Sea Surface Temperature (SST) and the concentration of Chlorophyll-a (Chl-a) to verify our proposed system. MODIS is a key instrument aboard the Terra (Earth Observing System (EOS) AM) and Aqua (EOS PM) satellites. Terra's orbit around the Earth is timed so that it passes from north to south across the equator in the morning, while Aqua passes south to north over the equator in the afternoon. Terra MODIS and Aqua MODIS view the entire Earth's surface every 1 to 2 days, acquiring data in 36 spectral bands, or groups of wavelengths [16, 17, 18, 19]. We use MODIS data from the Academic Frontier Promotion Center of Tokyo University of Information Sciences.

We used the publicly available data of SST and chl-a. The public data contain 30 days composite data, 5 days composite, and daily composite by PNG format, FLAT format, and HDF format. We convert from HDF data to CSV data by HDF utility commands. We use Hakodate-ura data from January 2005 to September 2010.

IV. EXPERIMENTS

In this paper, we try to extract the frequent occurrence pattern and the frequent occurrence of the time-series change pattern using SST data and chl-a with the weather-monitoring satellite for verification.

We use SST and chl-a data from MODIS data. We use linear interpolation with the data at a time before and after the missing value. The input data use nine attributes in which the data of eight neighborhoods are added to the data of a certain point. We already described the data in detail in section III.

We use the InTrigger platform of the information explosion project [20]. InTrigger is a distributed platform for information technology research for the Information Explosion Era. It is a cluster of clusters distributed across

Japan. Weka is used for clustering [21].

The first step clusters data; and the effect of the distributed surrounding is examined. The result is being reasoned now.

V. CONCLUSIONS

We proposed a method for finding the frequent occurrence patterns and the frequent occurrence time-series change patterns from the observational data of a weather-monitoring satellite at AROB 2010. The observational data of the weather-monitoring satellite are temporal and spatial large-scale data. Various uses are possible such as forecasting marine resources by analyzing satellite data. However, there is a problem with respect to calculation cost to analyze a large amount of data. Therefore, we proposed parallel computation when the frequent occurrence pattern and the frequent occurrence time-series change pattern are extracted. In this paper, we applied the proposed system to MODIS data, which includes the sea surface temperature and the concentration of chlorophyll-a to verify our proposed system.

REFERENCES

- [1] Martin H. C. L., Zhang, N., Anil, K. J. (2004), Non-linear Manifold Learning For Data Stream. In Proc. SIAM International Conference for Data Mining, pp.34-44
- [2] Jain, A., Zhang, Z., Chang, E. Y. (2006), Adaptive non-linear clustering in data streams. CIKM '06: Proceedings of the 15th ACM international conference on Information and knowledge management, Arlington, Virginia, USA, pp.122-131
- [3] Graf, H. P., Cosatto, E., Bottou, L., Durdanovic, I., Vapnik, V. (2005), Parallel support vector machines: The cascade svm. In Advances in Neural Information Processing Systems, pp.521-528
- [4] Zhang, Y., Jin, X. (2006), An Automatic Construction and Organization Strategy for Ensemble Learning on Data Streams. SIGMOD Record, Vol.35, No.3, pp.28-33
- [5] Wang, H., Fan, W., Yu, P. S., Han, J. (2003), Mining Concept-Drifting Data Streams Using Ensemble Classifiers. SIGKDD'03, pp.226-235
- [6] Yamaguchi, T., Niimi, A. (2009), Community Graph Sequence with Sequence Data of Network Structured Data. 5th International Workshop on Computational Intelligence & Applications (IW-CIA2009), Hiroshima, Japan, pp.196-201
- [7] Minegishi, T., Ise, M., Niimi, A., Konishi, O. (2009), Extension of Decision Tree Algorithm for

- Stream Data Mining Using Real Data. 5th International Workshop on Computational Intelligence & Applications (IWCIA2009), Hiroshima, Japan, pp.208–212
- [8] Yamaguchi, T., Noguchi, Y., Ichimura, T., Mackin, K.J. (2009), Applying Cluster Ensemble to Adaptive Tree Structured Clustering. 5th International Workshop on Computational Intelligence & Applications (IWCIA2009), Hiroshima, Japan, pp.186–191
- [9] Mustapha, M. A., Saitoh, S. (2008), Observations of sea ice interannual variations and spring bloom occurrences at the Japanese scallop farming area in the Okhotsk Sea using satellite imageries. *Estuarine, Coastal and Shelf Science*, 77, pp.577–588
- [10] Zainuddin, M., Kiyofuji, H., Saitoh, K., Saitoh, S. (2006), Using multi-sensor satellite remote sensing and catch data to detect ocean hot spots for albacore (*Thunnus alalunga*) in the northwestern North Pacific. *Deep-Sea Research II*, 53, pp.419–431
- [11] Iida, T., Saitoh, S. (2007), Temporal and spatial variability of chlorophyll concentrations in the Bering Sea using empirical orthogonal function (EOF) analysis of remote sensing data. *Deep-Sea Research II*, 54, pp.2657–2671
- [12] Radiarta, I. N., Saitoh, S. (2008), Satellite-derived measurements of spatial and temporal chlorophyll-a variability in Funka Bay, southwestern Hokkaido, Japan. *Estuarine, Coastal and Shelf Science*, 79, pp.400–408
- [13] Zainuddin, M., Saitoh, K., Saitoh, S. (2008), Albacore (*Thunnus alalunga*) fishing ground in relation to oceanographic conditions in the western North Pacific Ocean using remotely sensed satellite data. *Fisheries Oceanography*, Vol.17, No.2, pp.61–73
- [14] Niimi, A., Yamaguchi, T., Konishi, O. (2010), Parallel Computing Method of Extraction of Frequent Occurrence Pattern of Sea Surface Temperature from Satellite Data. International Symposium on Artificial Life and Robotics (AROB 15th '10), Beppu, Oita, Japan: 4 pages (in CD-ROM)
- [15] Meteorological Satellite Center Monthly Report, Meteorological Satellite Center.
- [16] MODIS Website, <http://modis.gsfc.nasa.gov/>
- [17] MODIS Near Real Time Data, Japan Aerospace Exploration Agency, http://kuroshio.eorc.jaxa.jp/ADEOS/mod_nrt/
- [18] Earth Observation Research Center (EORC), Japan Aerospace Exploration Agency, <http://www.eorc.jaxa.jp/index.php>
- [19] Academic Frontier Promotion Center of Tokyo University of Information Sciences.
<http://www.frontier.tuis.ac.jp/modis/frontier/index.html>
- [20] InTrigger, <https://www.intrigger.jp/wiki/index.php/InTrigger>
- [21] M. Hall, E. Frank, G. Holmes, B. Pfahringer, P. Reutemann, H. Ian. (2009), The WEKA Data Mining Software. *SIGKDD Explorations*, Volume 11, Issue 1

PSP Practice Support System Using Defect Types based on phenomenon

Daisuke Yamaguchi¹, Ayahiko Niimi², Fumiyo Katayama¹ and Muneo Takahashi¹

1: Toin University of Yokohama, 1614 Kurogane-cho, Aoba-ku, Yokohama, JAPAN
2: Future University-Hakodate, 116-2 Kamedanakano-cho, Hakodate, Hokkaido, JAPAN
yamaguti@intl.toin.ac.jp

Abstract: In this paper, we propose the PSP Practice Support System using Defect Types based on Phenomenon. This system can transmit programming to specific human among many software processes using a Multiagent technology. The system is also synthesized to do parallel and cooperative proposing internally. Applying the proposed method to a personal process-removing task, a flexible programming for quality of software. Software developments depend on information, which is possible to collection of personal process. Agent planning has get use working data on user action and other communication. Therefore collection of all user data is necessary for agent learning. Agent studies the best transmission programming, planning and quality according to the makes planning in the personal process.

Keywords: Multi-Agent System, Personal Software Process, Software Engineering, Artificial Intelligence

I. INTRODUCTION

Software architecture has emerged as an important sub discipline of software engineering [1]. PSP support system is built using this. Moreover, We think that the data inputted can acquire software development process by sorting out using a user action record table [2].

In this paper, the PSP practice support system using Defect Types based on Phenomenon. This PSP practices Support System based on Multiagent Techniques [3]. Generally, software process data is complicated, and when building a support system using such data including some action time, the calculation with expression is difficult in many cases. Then, the PSP systems [2] configuration from a data pattern is effective using the Machine Learning who is excellent in pattern recognition to such a problem.

The system is also synthesized to do parallel and cooperative proposing internally. Applying the proposed method to a personal process-removing task, a flexible programming for quality of software. Software developments depend on information, which is possible to collection of personal process. Agent planning has get use working data on user action and other communication. Therefore collection of all user data is necessary for agent learning. Agent studies the best transmission programming, planning and quality according to the makes planning in the personal process.

II. Intelligent Agents and Multiagent System

Artificial Intelligence (AI) has made great strides in computational problem solving using explicitly represented knowledge extracted from the task. If we continue to use explicitly represented knowledge exclusively for computational problem solving, we may never computationally accomplish a level of problem solving performance equal to humans. From this idea, the paper describes the development of a multiagent system that can be used to support the assessment of design performance in the cellular automata model. Agents represent objects or people with their own behavior, and take the structure of cellular automata lattice.

Intelligent agents and multiagent systems are one of the most important emerging technologies in computer science today [4]. The advent of multiagent systems has brought together many disciplines in an effort to build distributed, intelligent, and robust applications. They have given us a new way to look at distributed systems and provided a path to more robust intelligent applications.

Multiagent systems deal with coordinating intelligent behavior among a collection of autonomous agents. Emphasis is placed on how the agents coordinate their knowledge, goals, skills, and plans jointly to take action or to solve problems. Constructing the multiagent systems is difficult [5,6]. They have all the problems of traditional distributed and concurrent systems plus the

additional difficulties that arise from flexibility requirements and sophisticated interactions.

III. Personal Software Process

The Personal Software Process (PSP) is a self-improvement process that helps you to control, manage, and improve the way you work. It is a structured framework of forms, guidelines, and procedures for developing software [2]. Properly used, the PSP provides the data you need to make and meet commitments, and it makes the routine elements of your job more predictable and efficient.

The PSP's sole purpose is to help you improve your software engineering skills. It is a powerful tool that you can use in many ways. For example, it will help you manage your work, assess your talents, and build your skills. It can help you to make better plans, to precisely track your performance, and to measure the quality of your products. Whether you design programs, develop requirements, write documentation, or maintain existing software, the PSP can help you to do better work.

Rather than using one approach for every job, you need an array of tools and methods and the practiced skills to use them properly. The PSP provides the data and analysis techniques you need to determine which technologies and methods work best for you. PSP write several program using the evolving process shown Figure 1.

The PSP also provides a framework for understanding why you make errors and how best to find, fix, and prevent them. You can determine the quality of your reviews, the defect types you typically miss, and the quality methods that are most effective for you.

After you have practiced the exercises in this book, you will be able to decide what methods to use and when to use them. You will also know how to define, measure, and analyze your own process. Then, as you gain experience, you can enhance your process to take advantage of any newly developed tools and methods.

The PSP is not a magical answer to all of your software engineering problems, but it can help you identify where and how you can improve. However, you must make the improvements yourself. PSP0 and PSP0.1 hierarchy include introduces process discipline and measurement. PSP1 and PSP1.1 hierarchy include introduces estimating and planning. PSP2 and PSP2.1 hierarchy include Introduces quality management and

design. Team Software Process exists over the PSP hierarchies.

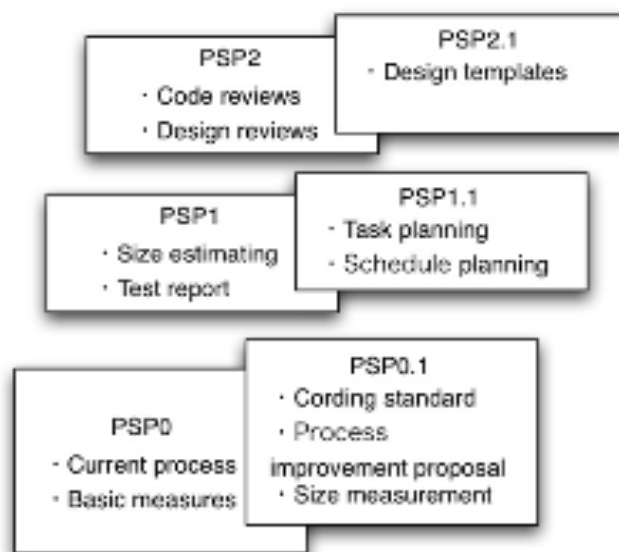


Fig.1. PSP Process Evolution

IV. The PSP Practice support system using Multiagent

In this section, we study combined as it occurs in genetic Techniques into agent learner [2]. We used as a tool for searching wide and complex solution space in Intelligent Agent learns data. Intelligent agent using complex techniques of related research. Multiagent is state in a filed shown Figure 2.

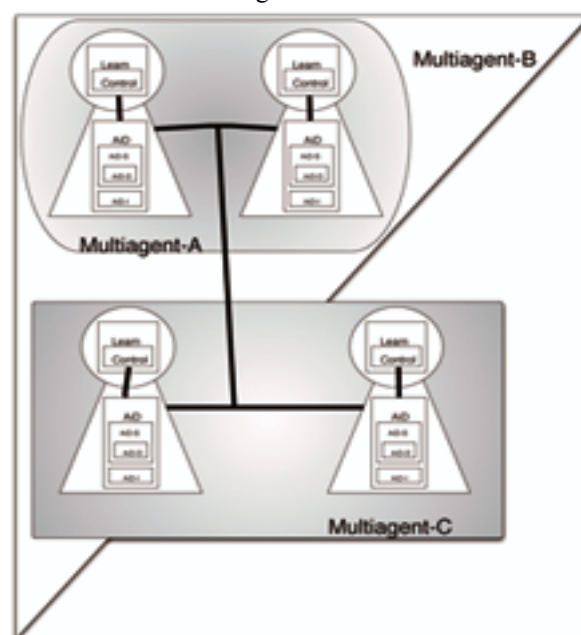


Fig.2. Support System Communication of Multiagent

Figure 2 depicts the Agent Communication Module and shared Information Data. The Agent make filed in order to share information data from Agent communication filed. These fields include other Learner kept in Intelligent Agent shown Figure 3.

Figure shows the Agent between communication modules in other communicate method. In this case, Intelligent Agent supports the PSP time and size measures record to user manipulation data. Intelligent Agent Controller selects Agent Information Data Share (AiD-S) or Agent Information Data Delivery (AiD-D) [3].

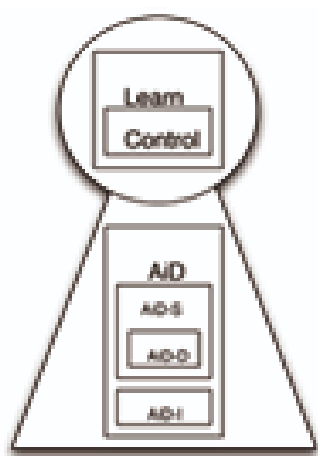


Fig.3. The Configuration of Agent Module

Other Learner support anything AI techniques of input data. Intelligent Agent has made combined these techniques into the Machine Learning. Machine Learning include same function of standard algorithm using user analyses data. These techniques supported by analysis data in time sheet that retrieval of start and end point.

Table 1 shows the PSP record form Time Measures and Size Measures [2].

Table 1. The Sample data scale of Program size categories No.X

	Plan	Results	Accumulation
Base	70	100	+100
Added	5	35	+35
Modified	0	3	+3
Deleted	0	8	+8
New and changed	0	0	0
Re-used	20	40	+40
New Re-used	0	20	+20

Total			
-------	--	--	--

In the PSP, engineers use the time recording log to measure the time spent in each process phase. In this log, they note the time they started working on a task, the time when they stopped the task, and any interruption time. For example, an interruption would be a phone call, a brief break, or someone interrupting to ask a question. By tracking time precisely, engineers track the effort actually spent on the project tasks. Since interruption time is essentially random, ignoring these times would add a large random error into the time data and reduce estimating accuracy.

Since the time it takes to develop a product is largely determined by the size of that product, when using the PSP, engineers first estimate the sizes of the products they plan to develop. Then, when they are done, they measure the sizes of the products they produced. This provides the engineers with the size data they need to make accurate size estimates. However, for these data to be useful, the size measure must correlate with the development time for the product. While a line of code (LOC) is the principal PSP size measure, any size measure can be used that provides a reasonable correlation between development time and product size. It should also permit automated measurement of actual product size.

So, This any measure record to support agent consider with using this Agent Learner expanded of PSP support. A person engaging in a person who experienced PSP and software development for many years is not very worried about a form record-keeping work.

Record keeping is vague, and what is performed of a person pressed by a work still increases. Necessity to perform automatically is important in a soldier, remission of an activity and process assay to record an activity precisely.

Therefore I record all activities, and a support system shares the documentary information, and Intelligent Agent examines to whether be content which documentary information to shows personal characteristic of difference with another person.

V. Improvement of Software Estimate Efficiency Centered Multiagent

In this section, explain improvement of Software Estimate used to Multiagent internal Agent Learner for

Intelligent Agent. Multiagent connects in other Intelligent Agents. Hence, that Intelligent Agent put the Agent Learner on necessary thoughts in Multiagent [7] .

1. Software Estimate Design of Agent Learner

The Software Design Estimate kept in Intelligent Agent. Figure 4 shows the Agent internal Data, PSP database and user logs connection modules in other communication method. In this case, Intelligent Agent supports the PSP time and size (LOC: Line of Code) measures record to user manipulation data. Intelligent Agent used to learning Control on internal database for AiD.

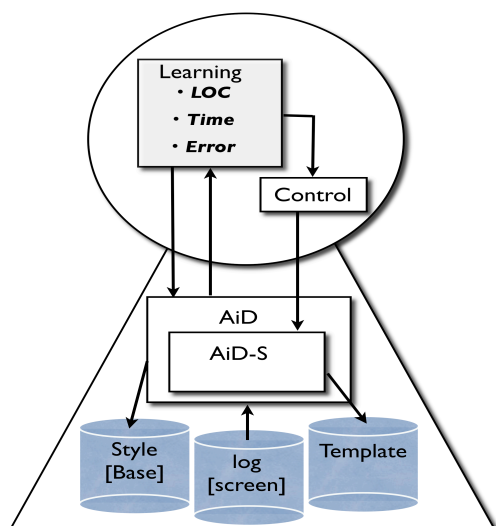


Fig.4. The AiD Data transferred from Agent Learner to action logs

2. The Estimating Probe Method of Agent Software Design

The Probe Method guides user in using historical data to make estimates. With estimated proxy size E , Intelligent Agent can calculate the projected program size P and did total estimate development time. The parameters β_0 and β_1 are used in the following equation to calculate projected added modified size:

$$\text{Projected Added \& Modified size } P = \beta_0 + \beta_1 * E \quad (1)$$

When two sets of data are strongly related, Intelligent Agent can use the linear regression method to represent that relationship. This means that linear regression is often appropriate. The parameters β_0 and β_1 are calculated from user historical data.

VI. CONCLUSION

In this research we were analyses PSP Practice Support System used to phenomenon of working data. We were able to viewpoint different searching user experience data. We create agent learner data in phenomenon data beside with user working analyses and wrote PSP Practice phenomenon error code type.

For future works, we will consider methods quick running of agent learner in data of error type phenomenon and user experience. We try to delete user missing work date filter on experience data. We consider to that delete missing work filter on error type phenomenon error type.

Future versions of PSP Practice Support System User need be conscious of rewrite error type code or fact process from error message of compiler and executor to test pattern data. But, This model will show at the system in a more natural, unscripted scenario, involving multiple parts in addition to other forms of process and error type phenomenon.

REFERENCES

- [1] Paul Clements, Felix Bachmann, Len Bass, David Garlan, James Ivers, Reed Little, Paulo Merson, Robert Nord, Judith Stafford (2010), Documenting Software Architectures SECONDD WDITION, Addison-Wesley
- [2] Watts S. Humphrey (2005), PSP - A Self Improvement Process for Software Engineers, Addison-Wesley
- [3] Daisuke Yamaguchi, Ayahiko Niimi and Muneo Takahashi (2010), Improvement of a Software Estimate Efficiency Centered PSP Practice Support System Using Multiagent Techniques, The Fifteenth International Symposium on Artificial Life and Robotics 2010, pp.857-860
- [4] Weiss, G. (1999), Multiagent Systems, A Modern Approach to Distributed Artificial Intelligence, the MIT Press
- [5] Abul, O., Polat, F., and Alhadjj, R. (2000), Multi-agent Reinforcement Learning Using Function Approximation, IEEE Transaction on systems, man, and cybernetics-part c: application and reviews, Vol. 30, No. 4, pp. 485-497.
- [6] Khosla, R., and Dillon, T. (1997), Engineering Intelligent Hybrid Multi-Agent Systems, Kluwer Academic Publishers
- [7] Carles Sierra, JohnThangarajah, Lin Padgham and Michael Winikoff (2007), Designing Institutional Multi-Agent Systems, AOSE 2006, LNCS 4405, PP.84-103

Development and Evaluation of Satellite Image Data Analysis Infrastructure

Akihiro Nakamura*, Jong Geol Park**, Kotaro Matsushita**

Kenneth J. Mackin**, Eiji Nunohiro**

*: Graduate School of Tokyo University of Information Sciences

** : Tokyo University of Information Sciences

(Tel: 81-43-236-1292; Fax : 81-43-236-1292)

(Email address: nunohiro@rsch.tuis.ac.jp)

Abstract: Tokyo University of Information Sciences (TUIS) receives Moderate Resolution Imaging Spectroradiometer (MODIS) data and provides the processed data to universities and research institutes as part of the academic frontier project. One of the major fields of the research using MODIS data is the analysis on change of environment. We are currently developing applications to analyze the environmental changes. These applications run on our satellite image data analysis system implemented in a parallel distributed system and a database server. When using satellite data, one common problem is the interference of clouds. In order to remove the interference of clouds, the standard solution is to create a composite data of the same regions during a selected time span, and to patch together data not covered by clouds to create a clear image. We introduced a piece processing algorithm, which separates one satellite image data into many small pieces of image data, making it quicker and easier to analyze and process the time-series satellite data. In this research, we implemented the piece processing and composite processing algorithms in order to increase the analysis speed within the satellite image database. We tested the proposed processing and verified the effectiveness for target applications.

Keywords: Satellite image data, MODIS, Composite.

I. INTRODUCTION

The Academic Frontier Project at Tokyo University of Information Sciences (TUIS) is promoting research on “the sustainable development of economic and social structure dependent on the environment in eastern Asia”. As part of this project, TUIS receives and processes Moderate Resolution Imaging Spectroradiometer (MODIS) satellite data, one of the sensors equipped by NASA's Terra and Aqua satellites, to provide to universities and research institutes. One of the major research aims of this project is the analysis on change of environment. For this research, we are developing a satellite image data analysis system to analyze the environmental changes and its effects[1][2][3]. This paper reports on a) an overview of the satellite data analysis system and MODIS data, b) the composite processing algorithm in order to improve the performance and accuracy of the data analysis, and c) the proposed piece processing algorithm to improve the composite processing speed and data utilization efficiency for analytical applications.

II. SATELLITE IMAGE DATA ANALYSIS SYSTEM

1. System Overview

This system works as the main platform of the total satellite image data analysis service, maintains the satellite image data, and implements satellite image data analysis applications. The user can access the system over the network via Web browser or other web applications. Users can request for data analysis, check the results and download satellite image data through the system. The analysis applications currently being developed are 1) search for fire regions in forests and fields, 2) search for similar image data, 3) spatiotemporal analysis of land cover changes of east Asia, 4) creation of east Asian disaster map, 5) Time-series NDVI prediction using auto-regression analysis, and 6) statistical and soft computing analysis for land cover estimation.

Figure 1 shows the system configuration. This system consists of a Web server, distributed computer nodes, and a database server. The user accesses the Web server with a Web browser, following the guidance on the accessed page. The role of the Web server is

accepting requests by web users, execution of specified analysis application at compute nodes, and creating the final Web page of results. The role of the distributed computer nodes are running the analysis applications, and running the piece processing and composite processing algorithm. The role of the database is the management of the original satellite image data and the result data of the composite processing, and piece processing operations.

The satellite image data is extremely large, and direct manipulation of the large data leads to a high load on both the processor and network. In order to improve the throughput and turnaround time of data processing, in the proposed system the computer nodes are configured from high performance servers and multiple PC clusters, implemented as a parallel distributed system. The various analysis applications and piece processing and composite processing operations are run on this distributed computer nodes.

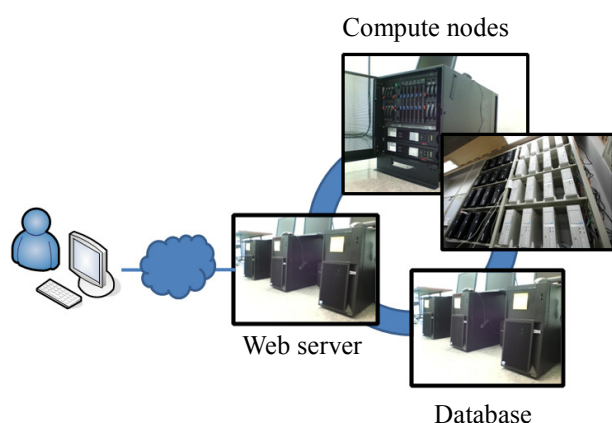


Figure 1 System configuration

2. MODIS

A key instrument aboard Terra (EOS AM) and Aqua (EOS PM), two satellites of the NASA-centered international Earth Observing System project is MODIS (Moderate Resolution Imaging Spectroradiometer). Terra was launched on December 18, 1999, and Aqua was launched on May 4, 2002. MODIS has a viewing swath width of 2,330 km, with a fast orbit covering the entire Earth surface every one to two days. Terra's orbit crosses the equator from north to south in the morning, and aqua passes the equator from north to south in the afternoon. The MODIS detectors measure 36 spectral bands between 0.405 and 14.385 μ m, acquiring the data at three spatial resolutions, 250m, 500m, and 1,000m, depending on the spectral bands.[4]

TUIS receive MODIS data using a tracking antenna. The reception area is between 105 to 180 longitude east and 15 to 65 latitude north. From the received MODIS data, the proposed system uses the standard MODIS products of MOD02, MOD03, and MOD09.

The Level 1A, Level 1B, geolocation and cloud mask products and the Higher-level MODIS land, ocean and atmosphere products are produced by the MODIS Adaptive Processing System.

MOD02 (Level-1B) is Calibrated Geolocation Data Set. The Level 1B data set contains calibrated and geolocated at-aperture radiances for 36 bands generated from MODIS Level 1A sensor counts. The radiances are in W/(m²- μ m-sr). In addition, reflectance may be determined for solar reflective bands (bands 1-19, 26) through knowledge of the solar irradiance.

MOD03 is Geolocation Data Set. The MODIS Geolocation product contains geodetic coordinates, and solar and satellite zenith, and azimuth angle for each 1 km sample. These data are provided as a companion data set to the Level 1B calibrated radiances and the Level 2 data sets to enable further processing.

MODIS Surface Reflectance product (MOD09) is computed from the MODIS Level 1B land bands 1 to 7 at 500m resolution. The product is an estimate of the surface spectral reflectance of each band as it would have been measured at ground level if there were no atmospheric scattering or absorption.

III. COMPOSITE PROCESSING

1. Overview

When analyzing large area satellite data, one common problem is noise caused by cloud interference. In order to remove the interference of clouds, the standard solution is to create a composite data of the same regions during a selected time span, and to patch together data not covered by clouds to create a clear image.

The selected time span for the composite process depends on research objective and region. For example, when analyzing the seasonal variation of vegetation, it is common to use a short 8 day composite. However, when the composite time span is short, there are less data to select from, which leads to a higher possibility of cloud interference remaining in the composite data.

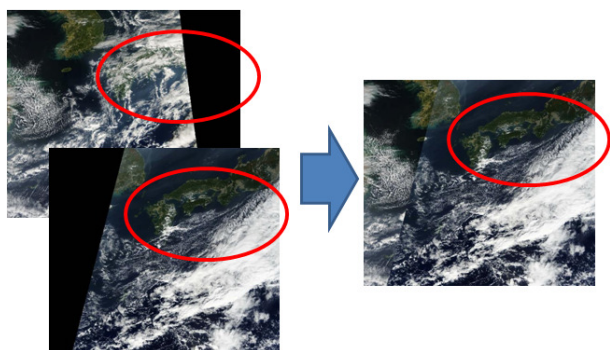


Figure 2 Image of composite processing

2. Effect

Traditionally, it has been the responsibility of the researcher analyzing the satellite data to process the large satellite data and create a composite image for individual research use. Creating a web service to provide systematic composite data processing using large scale computing resource over a parallel distributed configuration, will be valuable for researchers.

IV. PIECE PROCESSING

1. Overview

Satellite image data taken every day from slightly different orbits must be adjusted using some a map projection (e.g. WGS84). For MODIS data, the sensor data (MOD02 or MOD09) are resampled using map coordinate information (MOD03). When a particular map coordinate is out-of-bounds for a given satellite sensor scan, the pixel data for the particular coordinate will be defined an unused parameter value (65000 for MOD02, -10000 for MOD09), as seen in the black area in Figure 3. This leads to large portions of the processed image file being wasted to hold unused data, leading to unnecessary load on the database. Furthermore, analysis applications must process the large image data holding unnecessary data, leading to significant deterioration of calculation time.

2. Effect

In this research, we define “piece processing” as the process of separating a large satellite image data into small squares or “pieces” of equal latitude and longitude sizes.

By piece processing the original large satellite image data, out-of-range data can be eliminated, reducing database size.

Satellite data analysis applications which use the satellite data will also have less data to analyze if out-of-range data is initially removed, leading to improved analysis throughput.

When analyzing satellite data, it is common to focus on specific target areas. For example in the case of Japan, it would be common for researchers to not use all of received MODIS data but limit the region to, for example, northern region (Hokkaido), northeast region (Tohoku), or Central region (Kanto). Piece processing is efficient for selecting limited regions from the total MODIS reception area, making it easier for researchers to select the exact regions necessary, as well as decreasing the analysis computational cost.

The same merit applies to composite data processing. Researchers requiring composite data can request for the exact regions and time span, and with the reduced process area, improve the request turnaround time of on-the-fly composite data processing.

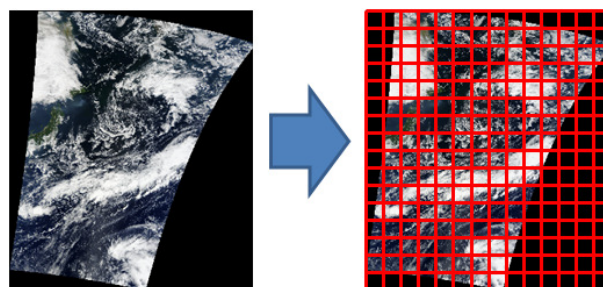


Figure 3 Image of piece processing

V. CONCLUSION

In this paper, a composite processing and piece processing algorithm for effective satellite data handling is proposed. The implemented system is currently under evaluation. It is planned to apply the proposed data preprocess to all of the archived satellite data and open for use by users. For future works, improvement of throughput performance for real-time composite processing will be researched.

ACKNOWLEDGEMENT

This research is supported by the Research project of Tokyo University of Information Sciences for the

sustainable development of economic and social structure dependent on the environment in eastern Asia.

REFERENCES

- [1] Eiji Nunohiro, Jong Geol Park, Kenneth J. Mackin, et al, "Development of satellite data analysis system", Proceedings of the 5th International Conference on Information (2009), pp.143-146
- [2] Eiji Nunohiro, Kei Katayama, Kenneth J. Mackin, et al, "Forest and Field Fire Search System using MODIS Data", Journal of Advanced Computational Intelligence and Intelligent Informatics (JACIII 2007), vol.11 No.8, pp.1043~1048
- [3] Kotaro Matsushita, Kei Katayama, Kenneth J. Mackin, et al, "Development of Satellite Image Searching using Distributed Genetic Algorithm with Normalized Correlation", The twelfth International Symposium on Artificial Life and Robotics, Proceeding Index GS12-7, (AROB 12th, 2007)
- [4] National Aeronautics and Space Administration (NASA), MODIS Web, <http://modis.gsfc.nasa.gov/>

Application of Neural Network Swarm Optimization for Paddy Field Classification from Remote Sensing Data

Kazuma Mori*, Takashi Yamaguchi*, Jong Geol Park** and Kenneth J. Mackin*

* *Department of Information Systems, Tokyo University of Information Sciences,
4-1 Onaridai, Wakaba-ku, Chiba, 265-8501 Japan*

** *Department of Environmental Information, Tokyo University of Information Science,
4-1 Onaridai, Wakaba-ku, Chiba, 265-8501 Japan
(Tel:81-43-236-1329; Fax:81-43-236-1329)
(s07122km@edu.tuis.ac.jp)*

Abstract: Monitoring changes in paddy area is important for economic and environment research since rice is staple food in Asia, and paddy agriculture is a major cropping system in Asia. Recently, remote sensing is used actively to observe the change of paddy area. However, monitoring paddy area by remote sensing is difficult due to the temporal changes of paddy and difference of spatiotemporal characteristics of paddy agriculture between countries or regions. In our previous research using MLP and spatiotemporal satellite sensor data, the proposed classifier yielded 90.8% correct classification rate. In this paper, we proposed a cooperative learning method using PSO as the global search method and MLP as the local search method in order to improve the classification accuracy for practical use.

Keywords: multi-layered perceptron, particle swarm optimization, cooperative learning, classification, remote sensing.

I. INTRODUCTION

Monitoring changes in paddy area is important for economic and environment research since rice is staple food in Asia, and paddy agriculture is thus a major cropping system in Asia. Recently, remote sensing is actively used to observe the change of paddy area. However, monitoring paddy area by remote sensing is difficult due to the temporal changes of paddy and difference of spatiotemporal characteristics of paddy agriculture between countries or regions. To solve this problem, we proposed creating a paddy field classifier by machine learning. Our aim is to automatically create localized classifiers for targeted countries and regions.

In our previous research using multi-layered perceptron (MLP) and spatiotemporal satellite sensor data, the proposed classifier yielded 90.8% correct classification rate [1]. However, it is necessary to further improve accuracy for practical use. One of the known weaknesses of MLP training is the probability of falling into the local optimum causing decline of accuracy. For solving this problem, we proposed a cooperative learning method using particle swarm optimization (PSO) for introducing perturbation to the local search of multiple MLPs in order to improve the accuracy.

In this paper, we applied the proposed artificial neural networks to paddy field classification using moderate resolution sensor data that includes spatiotemporal information. In previous research [2], the teaching signal was either paddy or non-paddy for the input, making it difficult to assess the accuracy of training. On the other hand, promising results for paddy estimation had been reported using paddy area ratio [3].

Thus the teaching signal in this research is modified to using paddy area ratio. Through computer simulation, we investigated the effectiveness of the proposed cooperative learning method and application to paddy field classification using moderate resolution sensor data.

II. METHOD

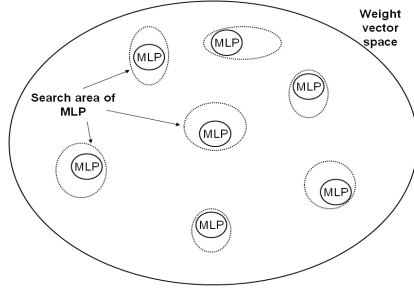
1. Neural Network Swarm Optimization

In this paper, we proposed a cooperative learning method in multiple MLPs. The proposed method repeats local search and global search in order to find a global optimum in a serialized weight vector space of MLP.

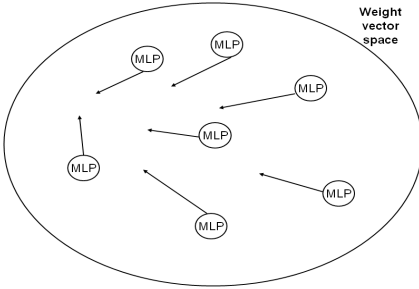
Behavior of the proposed method is shown in Figure 1. First, each MLP (acting as a particle in PSO) searches the neighborhood from its initial position by back-propagation. The search space is a serialized weight vector space of MLP (A in Figure 1). After the back-propagation process, weight values are changed by global search mechanism of PSO (B in Figure 1). The search is repeated from the neighborhood search using the new initial position (updating by the previous PSO search) for each MLP particle (C in Figure 1).

Figure 2 shows a flow chart of the proposed method. Training of MLP is started after the initialization of weight values of each MLP. Training of each MLP is continued to time step τ where τ is a parameter defining the training time step of MLP. Training of PSO is started and continued to time step σ in training process of MLP where σ is a parameter that decide training time step of PSO. Training of MLP and PSO are repeated till the final termination condition is satisfied.

(A) Local search by MLP



(B) Global search by PSO



(C) Local search by MLP again

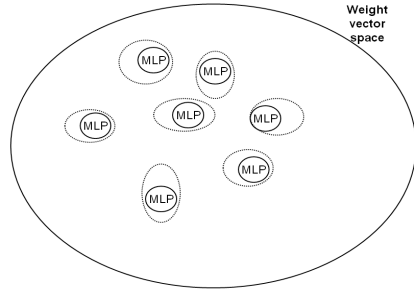


Figure 1. Outline of the proposed method

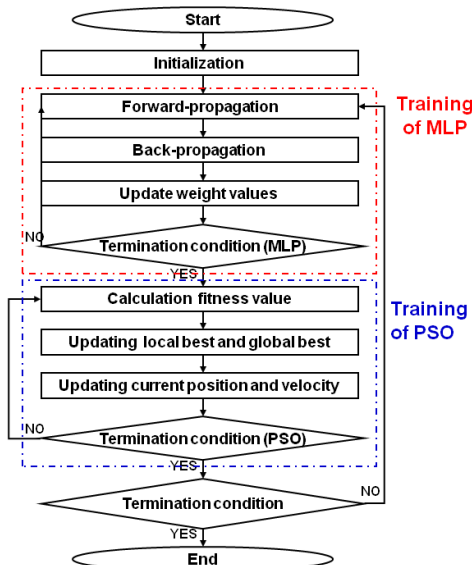


Figure 2. Flow chart of the proposed method

Finally, the MLP classifier with the global best weight values is selected as the final training result.

The detailed algorithm is described below.

2. Multi-Layered Perceptron

MLP is a type of artificial neural network that can approximate complex functions by machine learning [4].

In this research a standard three-layered MLP is used. The structure of three-layered MLP is shown in Figure 3.

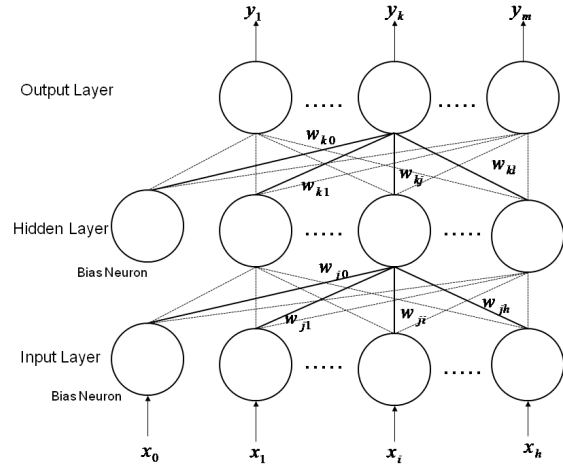


Figure 3. Structure of three-layered MLP

MLP consists of an input layer, a hidden layer, and an output layer. The input layer has h neurons and a bias neuron. The hidden layer has l neurons and a bias neuron. The output layer has m neurons. Each neuron is connected with every neuron in the next layer and each connection has a weight value.

Let $x^d = \{x_1^d, x_2^d, \dots, x_h^d\}$ be the d th input vector and $t^d = \{t_1^d, t_2^d, \dots, t_m^d\}$ be the d th teaching signal vector where $d = 1, 2, \dots, n$ and n is the number of samples in training data set. Let $S = \{s^d\}$ be the training set where $s^d = \{x^d, t^d\}$ for the d th sample.

When input signal x_i is given, the output of j th hidden layer neuron z_j is calculated by x_i and w_{ji} where w_{ji} is the weight value between i th input layer neuron and j th hidden layer neuron by equation (1)

$$z_j = f\left(\sum_{i=0}^h w_{ji} x_i\right) \quad (1)$$

where $i = 0, 1, \dots, h$; $j = 0, 1, \dots, l$; f is the activation function and x_0 is the output of bias neuron in the input layer and always outputs 1.

The output of k th output layer neuron y_k is calculated by z_j and w_{kj} where w_{kj} is the weight value between k th output layer neuron and j th hidden layer neuron by equation (2)

$$y_k = f\left(\sum_{j=0}^l w_{kj} z_j\right) \quad (2)$$

where $k = 1, 2, \dots, m$ and z_0 is the output of bias neuron in the hidden layer and always outputs 1.

For the activation function, a sigmoid function is commonly used. The sigmoid function is defined by equation (3)

$$f(X) = \frac{1}{1 + \exp(-aX)} \quad (3)$$

where a is a user defined parameter.

In the proposed method, back-propagation is used for the training method [4]. Back-propagation is based on a steepest descent method. Updating weight values by back-propagation is shown in equation (4) and equation (5).

Let $\Delta w_{ji}(s)$ be the weight modification of i th input layer neuron and j th hidden layer neuron at time step s , and $\Delta w_{kj}(s)$ be weight modification of k th output layer neuron and j th hidden layer neuron at time step s

$$\Delta w_{ji}(s) = -\lambda \cdot \frac{\partial E}{\partial w_{ji}} + \mu \cdot \Delta w_{ji}(s-1) \quad (4)$$

$$\Delta w_{kj}(s) = -\lambda \cdot \frac{\partial E}{\partial w_{kj}} + \mu \cdot \Delta w_{kj}(s-1) \quad (5)$$

where λ is leaning rate, μ is momentum rate and E is the mean square error.

E is derived by the error between output y_k and teaching signal t_k^d as shown in equation (6)

$$E = \frac{1}{2n} \sum_{d=1}^n \sum_{k=1}^m (t_k^d - y_k^d)^2 \quad (6)$$

where t_k^d is the teaching signal for the output of k th output layer neuron in d th training data and y_k^d is the output of k th output layer neuron in d th training data.

3. Cooperative Learning Method using Particle Swarm Optimization

For the global search method, PSO, a type of population-based search algorithm in evolutionary computation [5], was used in the proposed method. PSO searches for an optimum value in a vector space using multiple particles, similar to other population based search algorithm. For this research, PSO was selected in favor of other population based search methods such as GA, with the expectation that the fast conversion rate of PSO would be advantageous in combination with MLP since the learning in multiple MLPs requires long calculation time.

The particle searches for an optimum by updating current position according to particle velocity. In generation u , updating p th particle velocity \mathbf{v}_p^u and current position \mathbf{r}_p^u is shown as equation (7) and equation (8)

$$\mathbf{v}_p^{u+1} \leftarrow \omega \cdot \mathbf{v}_p^u + \mathbf{u}(0, \phi_1) \otimes (\mathbf{p}\mathbf{l}_p^u - \mathbf{r}_p^u) + \mathbf{u}(0, \phi_2) \otimes (\mathbf{p}\mathbf{l}_{gb}^u - \mathbf{r}_p^u) \quad (7)$$

$$\mathbf{r}_p^{u+1} \leftarrow \mathbf{r}_p^u + \mathbf{v}_p^{u+1} \quad (8)$$

where $p = 1, 2, \dots, q$; q is the number of particles, $\mathbf{p}\mathbf{l}_p^u$ is the position of best fitness for the p th particle (local best) vector in generation u , $\mathbf{p}\mathbf{l}_{gb}^u$ is position of best fitness in all particles (global best) vector in generation

u , \mathbf{u} is a random number vector from 0 to ϕ_1 or ϕ_2 , ω is momentum rate and \otimes is Hadamard product.

Let index set of particle be $P = \{1, 2, \dots, q\}$. In updating local best step, if fitness value of p th particle in generation u is better than fitness value of p th particle local best in generation $u-1$, then $\mathbf{p}\mathbf{l}_p^u$ is set to \mathbf{r}_p^u , else $\mathbf{p}\mathbf{l}_p^u$ is set to $\mathbf{p}\mathbf{l}_p^{u-1}$. In updating global best step, index for $gb \in P$ is update to index that fitness value of local best is best in all particle in generation u .

In addition, search space for PSO is a weight vector space of MLP where the weight vector is serialized weight values in MLP. Thus current position \mathbf{r} is defined as follow in the proposed method.

$$\mathbf{r} = \{w_{10}, \dots, w_{ji}, \dots, w_{lh}, w_{10}, \dots, w_{kj}, \dots, w_{ml}\} \quad (9)$$

The best position in search space is the position where mean square error between the output and the actual answer for each data is smallest. In other words the fitness function of PSO is error function in MLP.

III. EXPERIMENT

1. Application to MODIS Data

In this research, we used MODIS (Moderate Resolution Imaging Spectroradiometer) satellite data collected at Tokyo University of Information Sciences, Japan, for remote sensing data. MODIS data can be widely used for the remote sensing in land, sea and atmosphere research since MODIS data contains 36 bands. In addition, MODIS observes the same area in high frequency because MODIS satellites have a fast orbit compared to high-resolution satellites. Therefore MODIS is effective for monitoring annual cycle of a paddy area.

In this research, spatiotemporal MODIS band 1 (red), band 2 (infra red) and band 6 (short wave infra red) data were used similar to previous research [2].

In previous research [2], input signal consisting of monthly band data from January to December (3 bands x 12 months inputs) was used. The band data of each month was derived from 1-month composite MODIS sensor data of 500m resolution. For the teaching signal, we constructed a land-truth data derived from 1km resolution mesh land-use data from digital national land information provided by the Japanese Ministry of Land, Infrastructure, Transport and Tourism (JMLIT). This value is paddy or non-paddy {1,0}.

In this research, the input signal consists of 4 pixels refraction values of 500m resolution at the corresponding 1km square (4 pixels x 3 bands x 12 months inputs). The value of input is normalized to [0,1]. 4 Neighboring 500m MODIS pixels are merged to a 1km square. The 1km square merged teaching signal is the estimated paddy area ratio. The value of teaching signal is [0,1]. Therefore, it is difficult to approximate for an unknown function in comparison with past research data, and a difference of the capability for classification appeared.

In addition, the answer value of the test data and the output of classifier are divided into paddy or non-paddy by a threshold θ for classification. The threshold θ is defined by equation (10)

$$g(o) = \begin{cases} 1 & \text{if } o > \theta \\ 0 & \text{otherwise} \end{cases} \quad (10)$$

where o is y^b that is the final output in b th test data or t^b is the answer value for the output in b th test data, $b = 1, 2, \dots, c$ and c is the number of samples in test data set.

In this experiment, the parameters were defined as follows. Learning rate of MLP λ is set to 0.1, momentum rate of MLP μ is set to 0.05, input size h is set to 144, hidden size l is set to 144, output size m is set to 1, particle size q is set to 50, momentum rate of PSO ω is set to 0.9, upper limit of random number ϕ_1 and ϕ_2 is set to 2.0, training time step of MLP τ is set to the number of sample $\times 10$, training time step of PSO σ is set to 10, threshold θ is set to 0.4. In addition, the training of proposed method ends when training loop of MLP and PSO are repeated 50 times. The training step and the test step were repeated 10 times, each time changing the initial values and training data and test data, and the average accuracy for the 10 trials were used to evaluate the calcification accuracy.

2. Experiment Result

In this experiment, we evaluated classification accuracy by using the proposed paddy classifier. For evaluating classification accuracy, data set was divided into 2 disjoint subsets, training data set and test data set, by using random sampling from the north region of Chiba, Japan. The number of test data set was 10% of the number of training data set.

Table 1 shows classification accuracy of a) proposed paddy classifier with input signal of 1km square (proposed NNSO), b) previous method with input signal consisting of monthly band data from January to December (previous NNSO), c) and MLP using bagging with input signal of 1km square (MLP-Bagging).

Experiment result showed improved an accuracy of proposed NNSO compared with previous NNSO. In addition, total accuracy of proposed NNSO improved by about 0.3% compared to total accuracy of the MLP-bagging. Notably, as much as 9% improvement over paddy accuracy was seen. In this experiment, the problem is more difficult since the teaching signal is a continuous value. The experimental results showed that the proposed method has better function approximation capability for continuous values.

Table 1. The comparison of classification accuracy in proposed paddy classifier.

	Total	Paddy	Non-Paddy
Proposed NNSO	0.889	0.751	0.946
Previous NNSO	0.867	0.752	0.907
MLP-Bagging	0.886	0.659	0.932

IV. CONCLUSION

In this paper, we proposed applying a cooperative learning method where multiple MLP are used as PSO particles, and weight values of MLP is affected with training of PSO for improving the classifier accuracy.

Experiment result showed the accuracy of proposed NNSO improved in comparison with previous NNSO. However, the dimensions of the weight values were increased. The number of the neuron in the input layer and the hidden layer were fixed in the experiment, and unnecessary weight training may be exists in the process of training. We plan to investigate the structure which can optimize the number of the dimensions automatically.

In addition, the proposed NNSO yields higher accuracy than the MLP-bagging. The proposed method creates a classifier using only 1 MLP with weight values set to the global best, and is advantageous in that the proposed method requires less memory in comparison with commonly used bagging method.

In this research, the classifier output was a binary value of paddy or non-paddy, but the accuracy was improved by using a continuous value of paddy area ration for classifier training. The experiment results showed an advantage of the proposed method in approximation capability. For future works, we plan to investigate the methods to apply the proposed method to estimate paddy area ratio for a given input area.

ACKNOWLEDGMENTS

This research was supported by the Research project of Tokyo University of Information Sciences for the sustainable development of economic and social structure dependent on the environment in eastern Asia.

REFERENCES

- [1] T.Yamaguchi, K.Kishida, E.Nunohiro, J.G.Park, K.J.Mackin, K.Hara, K.Matsushita and I.Harada(2010), Artificial Neural Networks Paddy Field Classifier using Spatiotemporal Remote Sensing Data. Artificial Life and Robotics, vol.15, pp.221-224
- [2] K.Mori, T.Yamaguchi, J.G.Park and K.J. Mackin(2010), Cooperative Learning Artificial Neural Networks using Particle Swarm Optimization for Paddy Field Classification from Remote Sensing Data (in Japanese). Proceedings of the Fuzzy System Symposium, vol.26, pp.642-645
- [3] W.Takeuchi and Y.Yasuoka(2006), Mapping of fractional coverage of paddy fields over China using MODIS 250m data (in Japanese). Journal of The Remote Sensing Society of Japan, vol.26, pp.213-223
- [4] D.E.Rumelhart, G.E.Hinton and R.J.Williams(1986), Learning representations by backpropagating errors. Nature, vol.323, pp.533-536
- [5] R.Poli, J.Kennedy and T.Blackwell(2007), Particle swarm optimization An overview. Swarm Intelligence, vol.1, no.1, pp.33-57, Springer

A Systemic Payoff in a Self-Repairing Network

Masahiro Tokumitsu¹ and Yoshiteru Ishida²

¹*Department of Electrical and Information Engineering,*

²*Department of Computer Science and Engineering,
Toyohashi University of Technology, Tempakucho, Toyohashi, Aichi, 441-8580, Japan
(Tel : +81-53-244-6895; Fax : +81-53-244-6873)
(tokumitsu@sys.cs.tut.ac.jp, ishida@cs.tut.ac.jp)*

Abstract: Cooperation among agents is a crucial problem in autonomous distributed systems composed of selfish agents pursuing their own profits. An earlier study of a self-repairing network revealed that a systemic payoff enabled to make the selfish agents cooperate with other agents. The systemic payoff is a payoff mechanism that sums up not only the agent's own payoff but also neighborhood's payoff. In the systemic payoff, the distance effect between the agents has not been studied yet. This paper considers the systemic payoff that involves the distance effect among the agents. We study the effectiveness of the proposed mechanism for the network performance by computer simulations.

Keywords: Autonomous distributed systems, self-repairing network, selfish agents, kin selection, game theory.

I. INTRODUCTION

Autonomous distributed systems are composed of selfish agents pursuing their own profits. In the autonomous distributed systems, selfish agents need to cooperate with other agents because collective selfish acts of the selfish agents would lead the systems to absorbed states. Studies on selfish routing reported that if agents route their traffic selfishly then the network would show a poor performance [1, 2].

Cooperation is a crucial issue in the autonomous distributed systems. Cooperation mechanisms for preventing the worst performance are investigated in congestion games. The studies [3, 4] introduced the cooperation factor to the agents in which the factor elicits the altruistic behaviors by a tunable parameter.

In evolutionary game theory, several studies for the evolution of cooperation have been investigated by a payoff mechanism and related to the present paper. An earlier [5] investigates effects of a neighborhood size and connectivity in spatial games because spatial structures affect cooperation among individuals.

In the self-repairing network, cooperation is also an important problem in order to maintain the agents [6, 7]. The self-repairing network is a model in which the agents repair other agents mutually [8]. In the self-repairing network, to bring out cooperation among the agents has been studied using spatial strategies and the payoff mechanism.

Earlier studies [7, 8] revealed that the systemic payoff is capable of making the agents cooperate with

other agents in the self-repairing network. Moreover those studies reported that the systemic payoff was similar to kin selection [9]. The systemic payoff sums up not only its own payoff but also the neighborhood's payoff connected. Finally, those studies concluded that the agents with the systemic payoff improved the network performance.

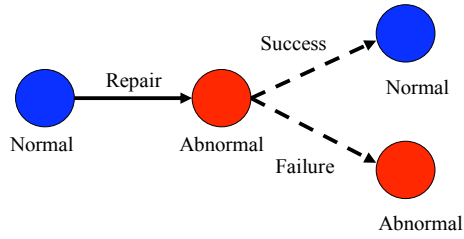
The earlier studies [7, 8] of the self-repairing network have not deeply mentioned a distance effect among the agents in the systemic payoff. In an information network, the agents are connected according to a network structure and distance. This paper considers that a cooperation factor needs to include the distance effect. The earlier studies have not considered the network performance caused by the distance effect of the systemic payoff.

This paper deals with the systemic payoff involving the distance effect between the agents in the self-repairing network. In this assumption, the agents are connected with any distance and connection weight. A connection weight of the systemic payoff represents strength of the relationship among the agents and is different according to the distance among them. We study the performance of the proposed systemic payoff by computer simulations.

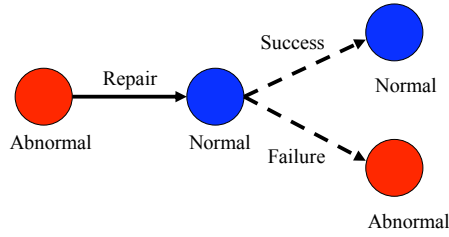
II. MODEL

1. Self-Repairing Network Model

We model the self-repairing network by a Spatial Prisoner's Dilemma [5, 6, 7]. The agents make their decision either repair or not repair. The abnormal agents



(a) Repair by normal agents



(b) Repair by abnormal agents

Fig. 1 Repair scheme of the self-repairing network. The blue and red circles indicate the normal and abnormal agents respectively.

will spread if no agents repair other agents. However, the agents are reluctant to consume their resources. This situation can be modeled by the Spatial Prisoner's Dilemma.

Each agent has binary states: normal or abnormal. We assume that the agents cannot know their own states and the states of other agents. Each agent is placed at each cell in a square lattice network. Basically, interactions of the agents are restricted in eight neighbor agents (Moore neighborhood). The Moore neighborhood of this assumption corresponds to a radius $r = 1$ for the interactions. The agents will repair other agents in the Moore neighborhood. However, the agents are able to communicate for the payoff with the eight neighbors besides the other agents outside of the Moore neighborhood ($r = 1$).

Each agent determines the next action: repair or not repair. The agents determine their action based on the strategies. The agents choose either All-C or All-D strategies. The All-C strategy always repairs other agents, while the All-D does not repair.

Fig. 1 shows a repair scheme of the self-repairing network. The repair success rate is different by the states of the agents. We denote the repair success rate of the normal and abnormal agents by α and β respectively. We assume to simplify the model that the repair by the normal agents is always successful ($\alpha = 1$). The repaired agent becomes normal if the repairing by abnormal agents is successful ($\beta = 0.1$) otherwise the repaired agents become abnormal. We

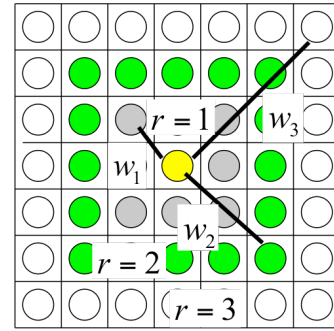


Fig. 2. Simple illustration of the systemic payoff with the distance effect. The agents with the same color are located at the same radius from the central (yellow color) agent.

assume that the normal agents become abnormal by a spontaneous failure. We denote the failure rate by λ .

Each agent has the maximum available resources R_{\max} . The agents consume their resources R_c for every repairing. The agents assign their remained resources as the available resources to their own task. The remained resources of the abnormal agents are always evaluated as empty resources because they do not work well due to their state.

The agents update their strategies to the strategies that earn the highest payoff in the eight neighbors. The strategy update of the agents is done with strategy update cycle S . The agents sum up their payoff by the systemic payoff mechanism in the agent simulations. The strategy update error occurs when the agents update their strategies. The strategy update errors make the agents switch to other strategies. This mechanism contributes to prevent the local minima of the network performance. We denote the rate of the strategy update error by μ .

2. Systemic Payoff

This paper considers the systemic payoff that involves the distance effect of the relationship between the agents. Environmental effects of the neighbor agents reflect to the agents by their payoff. The agents collect information from the weighted payoff of the other agents. The weight of the connection strength between the agents is different according to the distance between them. The payoffs of the agents are weighted with strength of the connection between the agents. The agents will obtain not only local information (neighbor agents) but also global information (outer of the nearest neighbor agents) from the payoff. The systemic payoff allows gathering local and global information from the neighbor agents through their payoff.

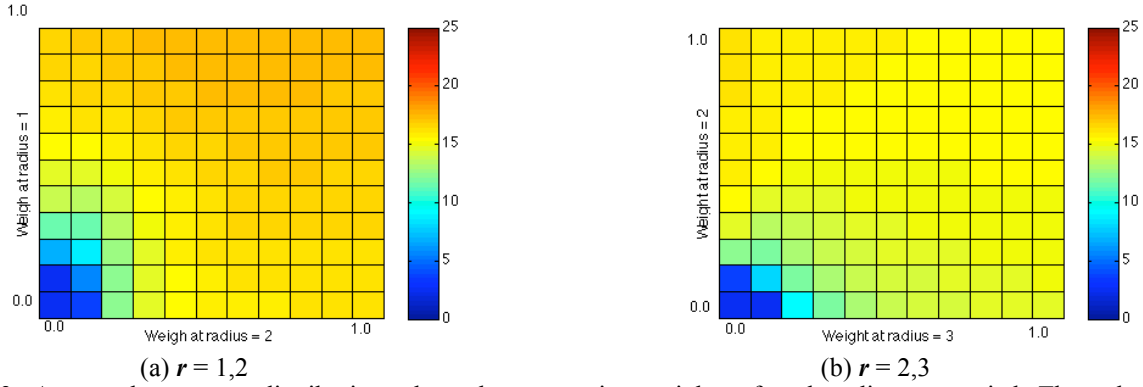


Fig. 3. Averaged resources distribution where the connection weights of each radius are varied. The color bars indicate the averaged resources of each cell for the connection weight pairs.

In the systemic payoff, how much the agents involve the payoff of neighbor agents is a crucial issue because of the neighborhood's payoff affects the decision making of the agents. This paper defines the systemic payoff in the square lattice network (Fig. 2). Let a_{ij} and $R(a_{ij})$ denote the agent and its payoff located at (i, j) in the square lattice network. We denote the connection weight of the systemic payoff from the agent with distance r by w_r . In this paper, we assume that the radius of the systemic payoff for involving the neighborhood's payoff is less equal than five. Let denote the summed payoff of the agent a_{ij} by $R_r(a_{ij})$. Let denote the set of the agents on the radius r from the agent a_{ij} by $A_r(a_{ij})$. Therefore, the total payoff of the agents a_{ij} is expressed as follows:

$$R_r(a_{ij}) = R(a_{ij}) + \sum_r \sum_{a_{xy} \in A_r(a_{ij})} w_r R(a_{xy}) \quad (1)$$

The total payoff of the agents will change by the combination of the connection weights of the systemic payoff. We investigate the relationship between the connection weight of the systemic payoff and the network performance.

III. SIMULATIONS

We obtain the simulation results from computer simulations, and then average the data by the number of the trial counts. The computer simulations use the parameters show in Table. 1. We assume that the agents change their connection weight corresponding to the radius of that agent in the calculation of the systemic payoff.

1. Performance for Connection Weight Pair

For the first simulations, we consider that the agents gather their own payoff from the agents located on the

Table 1. Parameters for computer simulations.

Parameter	Description	Value
T_a	Step	10000
N_t	Number of trial	15
$L \times L$	Number of total agents	10000
$N(0)$	Number of normal agents at initial step	2000
$All - C(0)$	Number of repair agents at initial step	2000
R_{max}	Maximum resources	25
R_c	Repair resources	1
λ	Failure rate	0.01
S	Strategy update cycle	100
μ	Strategy update error rate	0.01
w_r	Connection weight at radius	0.0-1.0

combination of the radiuses. In simulations, we give the agents two pairs of the connection weights corresponding to each radius. Those pairs of the connection weights are $r = 1, 2$ and $r = 2, 3$. We change the connection weight of each radius as simulation parameters from 0.0 to 1.0.

Fig. 3 shows the averaged resources distribution for the fixed radius pairs. The averaged resources are sufficiently kept in both cases where either connection weight is larger than 0.4. Fig.3 (b) shows that the averaged resources drop a little than the case that the payoff interaction is restricted to $r = 1, 2$ (Fig. 3 (a)). The connection weight between the agents should be adjusted strongly, because the weak relationship between them would cause the bad performance.

2. Performance for Single Radius

We evaluate the network performance for the systemic payoff gathering the payoff from the agents on single radius. We change the connection weight w_r for the

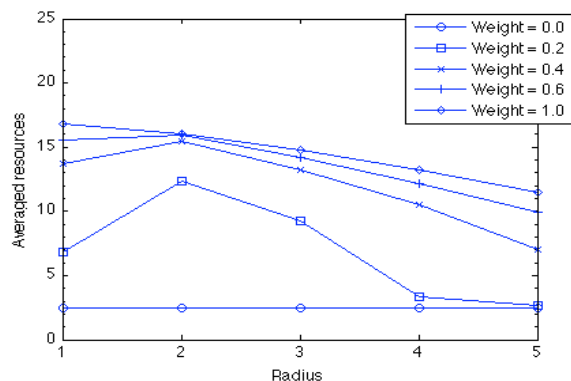


Fig. 4 Averaged resources for the connection weight where the agents obtain from the other agents on single radius.

radius r of the agents. The connection weights excluding the radius r are set to zero.

In Fig. 4, the network performance is worse for all radiuses where the connection weight is less than 0.4. However, the network performance improves as the connection weight grows to the large value. The impact of the connection weight appears when it is set to high, and then the agents choose to the repair action. From these results, the network performance decreases as the distance between the agents becomes longer.

IV. DISCUSSIONS

Agent simulations revealed that the connection weight representing the degree of the relationship between the agents is the dominant parameter for the network performance. From the results, the sufficient large connection weight between the agents can keep the high averaged resources. We think that the strong relationship between the agents in the systemic payoff could support the other agents by repairing because of the sufficient large connection weight could elicit cooperation among the agents.

In computer network, agents interconnect with each other with a distance and structures. It is possible that messages from neighbors to an agent will lose by link failures. In that case, the agents need to determine their decisions based on the neighborhood's payoff. The agent simulations demonstrate that the agents are able to keep the high averaged resources where either connection weight of the pairs is small. These results imply that the systemic payoff involving the distance effect would impact to the decisions of the agents appropriately and have the robustness for the environmental changes.

VI. CONCLUSIONS

We investigated the systemic payoff involving the distance effect that changes the connection weigh according to the distance between the agents. Our simulations showed that the sufficient large connection weight could lead the agents to cooperation, and then network performance improves. Furthermore, the agents can perform well where the agents allow only obtaining local information of the neighbor agents. We consider that the systemic payoff involving the distance effect would support for designing and constructing the autonomous distributed systems.

ACKNOWLEDGEMENT

This work was supported by Global COE Program "Frontiers of Intelligent Sensing," from the ministry of Education, Culture, Sports, Science and Technology.

REFERENCES

- [1] Roughgarden T, Tardos E (2002) How bad is selfish routing? *Journal of the ACM* 49: 236–259.
- [2] Koutsoupias E, Papadimitriou CH (2009) Worst-case equilibria. *Computer Science Review* 3: 65–69.
- [3] Chen PA, Kempe D (2008) Altruism, selfishness, and spite in traffic routing. In: *EC '08: Proceedings of the 9th ACM conference on Electronic commerce*. New York, NY, USA: ACM, pp. 140–149.
- [4] Azad AP, Altman E, Azouzi RE (2009) From altruism to non-cooperation in routing games. In: *Proceedings of Networking and Electronic Commerce Research Conference*.
- [5] Ifiti M, Killingback T, Doebeli M (2004) Effects of neighbourhood size and connectivity on the spatial continuous prisoner's dilemma. *Journal of Theoretical Biology* 231: 97 - 106.
- [6] Oohashi M, Ishida Y (2007) *A Game Theoretic Approach to Regulating Mutual Repairing in a Self-Repairing Network*, Springer, Netherlands, chapter Innovative Algorithms and Techniques in Automation, Industrial Electronics and Telecommunications. pp. 281–286.
- [7] Ishida Y, Tokumitsu M (2008) Asymmetric interactions between cooperators and defectors for controlling self-repairing. *Lecture Notes in Computer Science* 5179: 440–447.
- [8] Ishida Y (2005) A critical phenomenon in a self-repair network by mutual copying. *Lecture Notes in Computer Science* 3682: 86–92.
- [9] Brembs B (2001) *Encyclopedia of Genetics*, Academic Press, chapter Hamilton's Theory. pp. 906–910.

Effects of a membrane formation in Spatial Prisoner's Dilemma

Yuji Katsumata and Yoshiteru Ishida

*Department of Electronic and Information Engineering,
Toyohashi University of Technology,
Tempaku, Toyohashi, Aichi, 441-8580, Japan
(Tel : +81-532-44-6577)
(Email katsumata@sys.cs.tut.ac.jp)*

Abstract: A cooperative relationship has been developed among individuals. However, an altruistic behavior has little advantage against selfish behavior in the sense of rational terms. Each individual chooses a selfish behavior pursuing their own payoff then the altruistic behavior will vanish. Earlier studies proposed the mechanisms based on game theory which explains the problem of the difference between the theoretical prediction and observation. Furthermore, those studies also considered the mechanisms of protecting a cooperators cluster in a spatial prisoner's dilemma involving spatial strategies and a spatial generosity, although did not analyze rigorously effects of the membrane for the cooperators. In this paper, we report the quantitative effect of membrane for protecting the cooperators from the exploitation of the defectors.

Keywords: Spatial Prisoner's Dilemma, Spatial Strategy, cooperation, membrane formation

I. INTRODUCTION

Cooperation is basic components of animals and society. And a cooperative relationship has been developed among individuals. However, an altruistic behavior has little advantage against a selfish behavior in the sense of rational terms. In stead of an altruistic behavior, each individual should choose a selfish behavior pursuing their profit. The mechanisms are proposed by earlier studies for explain the deference between the theoretical consideration and observational results [2, 3]. The some proposed mechanisms are based on the game theory, especially Prisoner's Dilemma model [4-7].

In the model we proposed that is involving spatial strategy and spatial generosity [8], we observed membrane formation as a mechanism for protects cooperators form invasion of defectors [9]. Furthermore, we revealed the condition for constructing membrane. The constructing membrane only depends upon the spatial generosity k [10]. However, we have not analyzed rigorously effects of the membrane on the cooperators.

In this paper, we report the quantitative effect of membrane on protecting the cooperators form the exploitation of the defection.

II. MODEL

1. Prisoner's Dilemma

The Prisoner's dilemma (PD) is a fundamental model of game theory. It played just once by two players have two behavioral options: C (Cooperation), or D (defection). The players decide behavior simultaneously whether to cooperate or to defect. If both players cooperate, both players receive payoff R (reward), whereas if both players defect, both players receive payoff P (punishment). If a player cooperates and an opponent player defects, the cooperator receives payoff S (sucker) and the defector receives payoff T (temptation) where the payoffs must satisfy $T > R > P > S$. If an opponent player chooses behavior whatever cooperation or defection, the other should choose defection, because it is better than choses cooperation. Therefore, the both players always choose defection and receive payoff P lower than that when both choose cooperation.

The Iterated Prisoner's Dilemma (IPD) is temporal expansion model of PD. In IPD, PD is carried out repeatedly. Many strategies have been proposed in IPD. Axelrod reported tit-for-tat (TFT) strategy [1]. In Axelrod's round-robin tournaments, TFT strategy was the best strategy. TFT strategy is consists in playing C in the first round and from then on chose action whatever chosen by other player in the previous round. TFT strategy contains temporal generosity as an element.

2. Spatial Prisoner's Dilemma

Spatial prisoner's dilemma is spatio-temporal version of PD. Our model generalized SPD by introducing spatial strategy. Each player placed at each lattice of the two-dimensional lattice. Each player has an action and a strategy, and receives a score. Spatial strategy determines the next action dependent on the spatial pattern of actions in the neighbors. Each player plays PD with the neighbors, and changes its strategy to the strategy that earns the highest total score among the neighbors. Table 1 is the Payoff Matrix of PD. In our simulations, R, S, T, and P are respectively set to 1, 0, b ($1 < b < 2$, a bias for defectors) and 0 in simulations below following the Nowak-May's simulations.

Table 1. The Payoff Matrix of the Prisoner's Dilemma Game. R, S, T, P are payoff for player 1. ($1 < b < 2$)

		Player 2	
		C	D
Player 1	C	1	0
	D	b	0

Our SPD model is done in the following way with n players.

1. Initial phase: the action and the strategy of each player are determined randomly.
2. Renewal of action: the next action will be determined by player's strategy based on the neighbors' actions and the player's own action.
3. Calculate score: the score for each player is calculated by summing up all the scores received from PD with neighbor players and itself (self-interaction involved to make compare to the Nowak-May model), and the score added to the current player's score.
4. Renewal of strategy: the next strategy will be chosen from the strategy with the highest score among the neighbors including the player itself.

3. Spatial Strategy and spatial generosity

The next action will be determined based on the pattern of neighbor's actions. However, the pattern of neighbor's action is a lot. For simplicity, we restrict ourselves to a "totalistic spatial strategy" that only depends upon the number of D (defection) of the neighbors, not on their positions. To represent a strategy, let l be the number of the D action of the neighbors excluding the player itself. We define k -D strategy that chose action D if $l \geq k$ and C otherwise. This k -D

strategy can be regarded as a spatial version of TFT where k indicates the spatial version of the generosity.

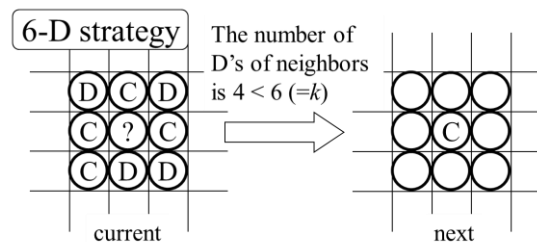


Fig.1. An example of spatial strategy. In this situation, k (spatial generosity) is 6 and neighborhood is Moore neighborhood.

III MEMBRANE FORMATION AND MEMBRANE INDEX

We simulated interaction between All-D (always D) vs. k -D instead of All-D vs. All-C (Nowak-May's simulation). In All-D vs. k -D simulation, we already observed the membrane as a mechanism for protects cooperation from invasion of defectors of All-D. The membrane is composed of only D players of k -D. Fig.2 shows an example of the membrane formation. Although we can understand that the membrane protects cooperators from invasion of defectors intuitively, the effects of the membrane on cooperators have not been investigated mathematically.

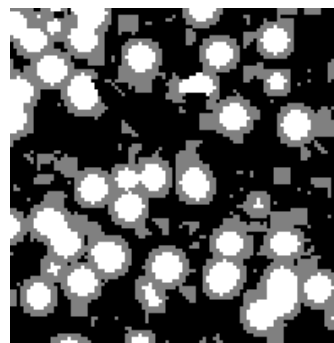


Fig.2. The membrane formation generated by SPD simulation. Black cells indicate All-D players. White and gray cells indicate C and D players of k -D. In this snapshot, k (spatial-generosity) is 6. The C clusters are covered by the membrane (gray color).

This snapshot shows typical membrane.

Therefore we consider a membrane index to investigate quantitative effects of the membrane formation on cooperators. The membrane index means how much membranes protect cooperators from invasion of defectors. The following is definition of the player as a membrane.

1. The player is D player of k -D.
2. The player is playing PD game with C player.

3. The interaction between All-D players and C players is nothing within player's neighborhood.

In other words, we define the membrane in terms of the function protecting cooperators from invasion of the defectors. Fig.3 shows the membrane that satisfied a definition.

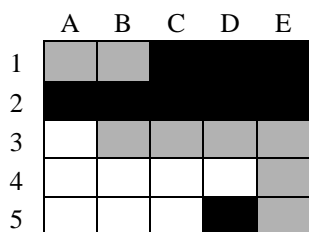


Fig.3. In the Moore neighbors, the center cell (C3 player) is a membrane that satisfied a definition. Black cells indicate All-D players. White and gray cells indicate C and D of k -D. If the immediate left cell of center (B3 player) was white (Cooperator), the center cell did not satisfy a definition of the membrane. Because All-D players and C player (immediate left cell of center cell) will be interaction each other among center cell's neighbors, the 3rd definition of the membrane could not satisfy.

IV SIMULATION

We simulate to investigate quantitative effect of membrane on cooperators with the following parameters list in Table 2.

Table 2. Parameters list for simulations.

Parameter Name	Description	Value
$L \times L$	Size of lattice	500×500
N	Number of players	250,000
T	Number of steps	1000
r	Neighborhood radius	1
b	Bias for defectors of the payoff matrix in Table.1	1.800001

In our simulation, the membrane is formed within certain scope of k [10].

Fig. 4 plots the time evolution of the average score of the C players when the k varies. The 6-D earns highest score among other k -D strategies. We can consider that the cooperators construct a cluster if the score per player is high. Because, if the cooperators have not constructed a cluster, the cooperators would be exploited by defectors, and the average payoff of the C players would become low.

Fig. 5 plots the time evolution of the membrane indexes divided by the number of D of k -D. It means

percentage of the D players of k -D that are effective as a membrane. If the membrane indexes per player are one, all of D players of k -D are action effectively as a membrane.

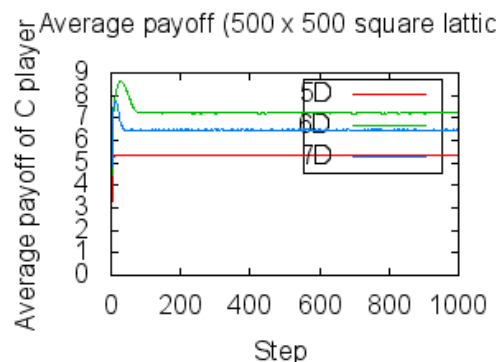


Fig.4. The time evolution of the average payoff of the player C. The 6-D earns highest score among other k -D strategies.

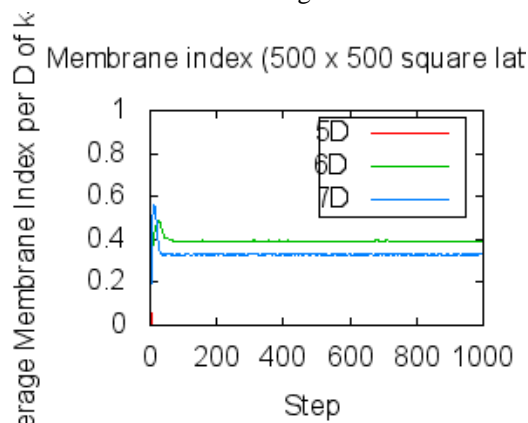


Fig.5. The time evolution of the membrane indexes per D player of k -D.

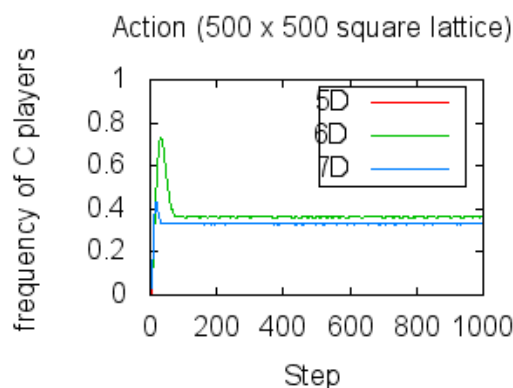


Fig.6 The time evolution of frequency of C players when k varies. The fraction of 6-D is the highest among this three strategies. The fraction of 5-D is the lowest, because the 5-D cluster could not expand although the cluster is protected by the membrane.

Fig.6 plots the time evolution of frequency of C players. In 5-D vs. All-D simulation, the cooperators have been remained in a small amount. In 6-D or 7-D vs. All-D simulations, the cooperators have been remained in a relative large amount.

We calculate coefficient of correlation between average score of C players and membrane indexes per players to investigate effect of the membrane on cooperators.

Table 3 shows the coefficient of correlation between average score of C players and membrane indexes per D players of k -D for each All-D vs. k -D simulation.

Table 3. The coefficient of correlation between average score of C players and membrane indexes per D players of k -D.

k value	Coefficient of correlation
5	-0.7119
6	0.812
7	0.9549

Consequence of calculation of correlation coefficient, we get interesting results. In 5-D vs. All-D simulation, the average score of C players have a negative correlation with the membrane indexes. By contrast, in the simulations of 6-D and 7-D, the average score of C players have a strong positive correlation with the membrane indexes.

We considered that this consequence is related to the conditions the membrane expands. Only 5-D constructs membrane that can not expand among three strategies. Therefore, the amounts of the cooperators do not increase. Thereby a lot of D players of k -D do not satisfy the 2nd condition of the definition that the membrane should interact with cooperators. Hence, although the cooperators construct a cluster and the membrane protects cooperators from defectors, the membrane indexes lower. Because cooperators earn high score by a cluster whereas the membrane indexes lower, the negative correlation occurs.

VI. CONCLUSION

We investigate that membrane formation one of a mechanism for protects cooperation from invasion of defectors. The membrane formation has been reported in SPD, however the quantitative effects have not investigated.

We defined membrane index to investigate the membrane. And we denoted the quantitative effect of membrane on cooperators by membrane index. The

membrane indexes have a strong correlation with the average score of C players when certain scope of k . If the membrane expands, the coefficient of correlation will become positive; otherwise the coefficient of correlation will become negative.

We investigate an effect of membrane on cooperators when Moore neighbors hood. We investigated the simulation in the *Moore* neighborhood; however we need to investigate the simulation in the *Neumann* neighborhood in future to compare both neighborhoods.

ACKNOWLEDGEMENTS

This work was supported in part by Global COE Program "Frontiers of Intelligent Sensing" from the Ministry of Education, Culture, Sports, Science and Technology, Japan.

REFERENCES

- [1] Axelod, R (1984), The Evolution of Cooperation, Basic Books, New York.
- [2] Nowak, M.A. and May, R.M. (1992), Evolutionary games and chaos, *Nature*, vol.359, 826—829
- [3] Nowak, M.A. and May, R.M. (1993), The spatial dilemmas of evolution, *Int. J. Bifurc. Chaos*, vol. 3, 35—78
- [4] Nowak, M.A. (2006), Five Rules for the Evolution of Cooperation, *Science*, vol.314, 1560—1563
- [5] Ohtsuki, H., Hauert, C., Lieberman, E. and Nowak, M.A. (2006) *Nature*, vol.441, 502—505
- [6] Hauert, C. and Doebeli, M. (2004), Spatial structure often inhibits the evolution of cooperation in the spatial Snowdrift game, *Nature*, vol.428, 643—646
- [7] McNamara, J.M., Barta, Z. and Houston A.I. (2004), Variation in behavior promotes cooperation in the Prisoner's Dilemma game, *Nature*, vol.428, 745—748
- [8] Ishida, Y. and Mori, T. (2005), Spatial strategies in a generalized spatial prisoner's dilemma, *J. Artificial Life and Robotics*, vol.9, 139—143
- [9] Ishida, Y. and Katsumata, Y. (2008), A Note on Space-Time Interplay through Generosity in a Membrane Formation with Spatial Prisoner's Dilemma. *KES 2008*, vol.5179, 448—455
- [10] Katsumata, Y. and Ishida, Y. (2008), On a Membrane Formation in a Spatio-Temporally Generalized Prisoners Dilemma, *ACRI 2008*, vol.5191, 60—66

Extracting probabilistic cellular automata rules from spatio-temporal patterns and analyzing features of these rules

Takuya Ueda¹ and Yoshiteru Ishida²

¹Department of Electronic and Information Engineering

²Department of Computer Science and Engineering

Toyohashi University of Technology, Toyohashi, Aichi, Japan 441-8580

Abstract: This research deals with one of the inverse problem. It is estimating rules or strategies of generating spatio-temporal patterns which is generated by natural phenomena or social phenomena. We try to consolidate identifying method and evaluation method to clarify generative mechanism. In this research, mainly, we use probabilistic cellular automata (PCA) to describe generative mechanism. And we restrict spatio-temporal patterns to ASEP patterns. In particular, we discuss conservation of mass in ASEP model from spatio-temporal patterns.

Keywords: Probabilistic Cellular Automata (PCA), Reverse problem, Spatio-temporal patterns, ASEP

1 Introduction

Natural phenomena including physical and biological ones present us inexhaustible amount of spatial patterns: patterns of ice crystal, cloud, coastal railroad, forest fire, leaf arrangement, shells, and butterflies, to name only a few. Social phenomena also generate spatial patterns (e.g. traffic jams). They are a few compared to natural one.

Constructing physical or mathematical models are known as the way of research for understanding the generative mechanisms of these spatial patterns. On the other hand, Richards studied extracting cellular automaton rules directly from experimental data [1]. They dealt with spatial patterns of dendrites formed by NH_4Br . They searched the space of rules which is a set of probabilistic CA (PCA) rules as possible models for spatio-temporal patterns, with a learning algorithm. Ichise proposed a general and theoretical method for identifying a generative mechanism of spatio-temporal patterns in CA frameworks [2]. They restricted rules to one dimensional and straightforward ones. Hence Richards's and Ichise's researches are one of the reverse problems for traditional ones.

In this paper we expand the Ichise's method which can identify generative mechanism of spatio-temporal

patterns to target more complex mechanisms. The previous method targets on spatio-temporal patterns which is generated by one dimensional and straightforward rules of CA. However, we deal with characteristic patterns (e.g. patterns of traffic jams, diffusion of matters and other physical phenomena) which satisfy conservation of mass. In fact, we succeeded to develop a method to discover the conservation of mass from these patterns.

Section 2 states definitions and notations used in this paper. Section 3 represents the method of the generative mechanism identification in the previous study, and its problem. Section 4 expands the previous method for patterns of conservation of mass, and applies to the ASEP model ones.

2 Definitions and Notations

After von Neumann used cellular automata (CA) in his designing self-reproducing automata [3], not only deterministic cellular automata (DCA) (e.g. [4, 5, 6]) but also probabilistic cellular automata (PCA) (e.g. [7]) have been studied extensively. Cellular automaton consists of cells arranged in a d -dimensional lattice where d is a natural number. Each cell is an automaton which has a certain number of states; whose inputs are the state of neighbor cells; and the output is the state of the cell itself. In this paper, we restrict ourselves to the case of binary state: 0 and 1 and one-dimensional lattice with periodic boundary condition where each cell has two neighbor cells: right and left. s_i^t denotes the state of the cell i at the time step t and its state at the next time step defined in equation (1).

$$s_i^{t+1} = f(n_i^t) \quad (1)$$

n_i^t is states of the neighbor cells of the cell i at time step t and defined in equation (2) with neighborhood radius r .

$$n_i^t = (s_{i-r}^t, \dots, s_i^t, \dots, s_{i+r}^t) \quad (2)$$

$f : N \rightarrow S$ is a mapping and called “*transition rule*”. S is the set of state and $N (= S^{2r+1})$ is the set of the neighbor cells state. Where equation (3) represents the graph f^* of f , $l_f (\in f^*)$ is called “*local rule of f* ”. Also, $l \in N \times S$ is called “*local rule*”.

$$f^* = \{l_f | l_f = (n, s), n \in N, s = f(n)\} \quad (3)$$

When each cell changes state stochastically, the probability is described by equation (4).

$$\begin{aligned} &P(s|n) \\ \text{Where,} \\ &\forall n \in N \sum_{s \in S} P(s|n) = 1 \end{aligned} \quad (4)$$

The condition of the cells is expressed by $c \in S^m$ where m is the number of cells and c_t indicates the condition at time step t . Then $C_T = (c_0, c_1, \dots, c_T)$ represents a spatio-temporal pattern with T time steps.

3 Generative Mechanisms Identification

3.1 Deterministic Mechanisms

We consider to identify the transition rule f from a spatio-temporal pattern C_T . Scanning the spatio-temporal pattern C_T gives the local rules $f^* = \{l_f\}$, and we get the transition rule f . For example, the spatio-temporal pattern such as Table 1 is given, we can identify the transition rule of Table 2.

Table 1: An example of spatio-temporal pattern when $m = 5$ and $T = 1$.

c_0	(0, 0, 1, 0, 0)
c_1	(0, 1, 0, 1, 0)

Table 2: The identified deterministic rule from the spatio-temporal pattern of Table 1.

n_i^t	(1, 0, 0)	(0, 1, 0)	(0, 0, 1)	(0, 0, 0)
s_i^{t+1}	0	1	0	1

3.2 Probabilistic Mechanisms

If given C_T is generated by probabilistic rule, we need to estimate probabilistic distribution of local rule from it. Hence we calculate the occurrence ratios of each local rule. For example, Table 3 is a spatio-temporal pattern which is generated by the probabilistic rule and Table 4 is the probabilistic distribution of local rules of it.

Table 3: An example of spatio-temporal pattern when $m = 5$ and $T = 1$.

c_0	(1, 0, 1, 0, 0)
c_1	(1, 0, 0, 1, 0)

Table 4: The identified probabilistic rule from the spatio-temporal pattern of Table 3.

n_i^t	(1, 0, 1)	(1, 0, 0)	(0, 1, 0)	(0, 0, 1)
$P(s_i^{t+1} = 1 n_i^t)$	0	1	0.5	0

4 Conservation of Mass Patterns Identification

4.1 ASEP and its Patterns

ASEP (Asymmetrical Simple Exclusion Process) [8] is known as the traffic jam model which satisfy the conservation of mass. ASEP is also one of PCA. Each car is arranged on the cell and goes forward at each time step with probability p if there is not any car to front (e.g. Figure 1). Each cell has binary state, 1 indicate existing a car and State 0 is not existing.

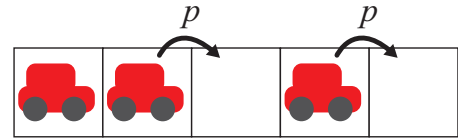


Figure 1: ASEP model. Each cell can be occupied by only single car. Only if there is not a car to front, each car goes forward at each time step with probability p .

Figure 2 shows the spatio-temporal pattern which generated by ASEP. Clumps of black cells indicate that the traffic jams are occurring.

4.2 Problem of Previous Method

The previous method has a problem when the spatio-temporal pattern satisfies the conservation of mass. Because the previous method gives the rule of straightforward CA (such as defined in Section 2). In general, straightforward CA changes states synchronously and cannot generate patterns which satisfy the conservation of mass [9].

Table 5,6 show the rules identified from Figure 2, 3. Figure 2 is different from Figure 3. Figure 2 satisfy the conservation of mass and Figure 3 is not. However, the

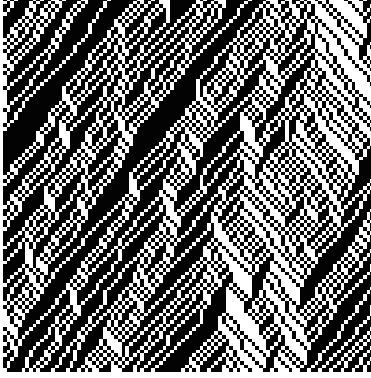


Figure 2: The spatio-temporal pattern which generated by ASEP with $p = 0.8$. The black cells indicate 1 and the white cells are 0. The vertical axis represents time step and the horizontal is space.

rules are remarkably similar. Because the rule of Table 5 lose the conservation of mass. Hence we need expand the previous method in order to solve the problem.

Table 5: The identified probabilistic rule from Figure 2.

n_i^t	(0,1,1)	(0,1,0)	(0,0,1)	(0,0,0)
$P(s_i^{t+1} = 1 n_i^t)$	1.00	0.18	0.00	0.00
n	(1,1,1)	(1,1,0)	(1,0,1)	(1,0,0)
$P(s_i^{t+1} = 1 n_i^t)$	1.00	0.19	0.81	0.80

Table 6: The identified probabilistic rule from Figure 3.

n_i^t	(0,1,1)	(0,1,0)	(0,0,1)	(0,0,0)
$P(s_i^{t+1} = 1 n_i^t)$	1.00	0.18	0.00	0.00
n_i^t	(1,1,1)	(1,1,0)	(1,0,1)	(1,0,0)
$P(s_i^{t+1} = 1 n_i^t)$	1.00	0.19	0.80	0.80

4.3 Identification

In order not to lose the conservation of mass when identifying the transition rule, investigating whether the spatio-temporal pattern satisfies the conservation of mass is necessary. Equation (5) is the necessary and sufficient condition for satisfying the conservation of mass. Equation (5) shows that the sum of variation of mass of cells is 0 at every time step.

$$\sum_{t=0}^{T-2} \sum_{i=0}^{m-1} (s_i^{t+1} - s_i^t) = 0 \quad (5)$$



Figure 3: The spatio-temporal pattern which generated by PCA without the conservation of mass. The black cells indicate 1 and the white cells are 0. The vertical axis represents time step and the horizontal is space.

In addition, the spatio-temporal pattern generated by ASEP (such as Figure 2) also satisfies equation (6) where $*$ is the wild card: 0 or 1 and $l_i^t = (n_i^t, s_i^{t+1})$. When a car goes forward, equation (6) means that other car does not suddenly appear and the car does not either suddenly disappear.

$$\begin{aligned} l_i^t = ((*, 1, 0), 0) &\rightarrow l_{i+1}^t = ((1, 0, *), 1) \\ l_i^t = ((*, 1, 0), 1) &\rightarrow l_{i+1}^t = ((1, 0, *), 0) \end{aligned} \quad (6)$$

We consider a pattern and assume that the pattern satisfies equation (6). Also we assume that the rule of Table 7 identified from the pattern by the previous method. Of course, the rule does not satisfy the conservation of mass. However we can transform the rule to the hierarchical one. The hierarchical rule satisfies the conservation of mass.

Table 8,9 show the hierarchical rule which transformed from the rule of Table 7. In the hierarchical rule, the state of cell is described as $s_i^t = (a_i^t, b_i^t)$.

In the case of ASEP with probability p , the hierarchical rule is represented by equation (7). Where a_i^t indicates whether there is a car on the cell and b_i^t indicates whether a car goes forward. The hierarchical rule consists of the two phase. The first phase is deciding that the car on the cell goes forward with probability p (such as Table 8). The second phase is actually moving the car on the cell to next cell based on the decision of the first phase (such as 9).

$$\begin{aligned} s_i^{t+\frac{1}{2}} &= (a_i^{t+\frac{1}{2}}, b_i^{t+\frac{1}{2}}) \\ b_i^{t+\frac{1}{2}} &= a_i^t(1 - a_{i+1}^t)\sigma_p \\ s_i^t &= (a_i^t, b_i^t) = (a_{i-1}^{t+\frac{1}{2}}, b_{i-1}^{t+\frac{1}{2}}) \end{aligned} \quad (7)$$

$$\begin{aligned} a_i^{t+1} &= (1 - b_{i-1}^{t+\frac{1}{2}})(1 - b_i^{t+\frac{1}{2}})a_i^t \\ &\quad + b_{i-1}^{t+\frac{1}{2}}(1 - b_i^{t+\frac{1}{2}})a_{i-1}^t(1 - a_i^t) \\ \sigma_p &= \begin{cases} 0 & \text{(with probability } 1 - p) \\ 1 & \text{(with probability } p) \end{cases} \end{aligned} \quad (8)$$

Table 7: The straightforward probabilistic rule.

n_i^t	(0,1,1)	(0,1,0)	(0,0,1)	(0,0,0)
$P(s_i^{t+1} = 1 n_i^t)$	p_3	p_2	p_1	p_0
n_i^t	(1,1,1)	(1,1,0)	(1,0,1)	(1,0,0)
$P(s_i^{t+1} = 1 n_i^t)$	p_7	p_6	p_5	p_4

Table 8: The first phase of the transformed hierarchical rule from the rule of Table 7.

n_i^t	(0,1,1)	(0,1,0)	(0,0,1)	(0,0,0)
$P(b_i^{t+\frac{1}{2}} = 1 n_i^t)$	0	p_2	0	0
n_i^t	(1,1,1)	(1,1,0)	(1,0,1)	(1,0,0)
$P(b_i^{t+\frac{1}{2}} = 1 n_i^t)$	0	p_6	0	0

Table 9: The second phase of the transformed hierarchical rule from the rule of Table 7.

		$(a_{i-1}^t, a_i^t, a_{i+1}^t)$			
$(b_{i-1}^{t+\frac{1}{2}}, b_i^{t+\frac{1}{2}})$	$P(a_i^{t+1} n_i^{t+\frac{1}{2}})$	(0,1,1)	(0,1,0)	(0,0,1)	(0,0,0)
	(0,0)	p_3	1	p_1	p_0
	(0,1)	-	0	-	-
	(1,0)	-	-	-	-
	(1,1)	-	-	-	-
		$(a_{i-1}^t, a_i^t, a_{i+1}^t)$			
$(b_{i-1}^{t+\frac{1}{2}}, b_i^{t+\frac{1}{2}})$	$P(a_i^{t+1} n_i^{t+\frac{1}{2}})$	(1,1,1)	(1,1,0)	(1,0,1)	(1,0,0)
	(0,0)	p_7	1	0	0
	(0,1)	-	0	-	-
	(1,0)	-	-	1	1
	(1,1)	-	-	-	-

5 Conclusions

We addressed the problem of previous method. The problem is losing the conservation of mass which is one of the hidden rule in the spatio-temporal pattern when identifying the rule. We solved the problem by expanding the method to identifying the hierarchical rule. The expanded method can investigate the conservation of mass from the spatio-temporal patterns.

Finally, we redefined the ASEP rule as the hierarchical rule.

Acknowledgments

This work was supported in part by Global COE Program “Frontiers of Intelligent Sensing” from the Ministry of Education, Culture, Sports, Science and Technology, Japan.

References

- [1] Richards F, Meyer T, Packard N (1990) Extracting cellular automaton rules directly from experimental data. *Physica D: Nonlinear Phenomena* 45: 189–202.
- [2] Ichise Y, Ishida Y (2008) Reverse engineering spatial patterns in cellular automata. *Artificial Life and Robotics* 13: 172–175.
- [3] Von Neumann J, Burks A, et al. (1966) *Theory of self-reproducing automata*. Univ. of Illinois Press Urbana, IL.
- [4] Wolfram S (1984) Universality and complexity in cellular automata. *Physica D: Nonlinear Phenomena* 10: 1–35.
- [5] Packard N, Wolfram S (1985) Two-dimensional cellular automata. *Journal of Statistical Physics* 38: 901–946.
- [6] Langton C, et al. (1992) *Life at the edge of chaos*. *Artificial life II* 10: 41–91.
- [7] Domany E, Kinzel W (1984) Equivalence of cellular automata to Ising models and directed percolation. *Physical review letters* 53: 311–314.
- [8] Rajewsky N, Santen L, Schadschneider A, Schreckenberg M (1998) The asymmetric exclusion process: Comparison of update procedures. *Journal of statistical physics* 92: 151–194.
- [9] Suzudo T (2004) Spatial pattern formation in asynchronous cellular automata with mass conservation. *Physica A: Statistical Mechanics and its Applications* 343: 185–200.

Emergence of Observable Rules in a Spatial Game System

*Kouji Harada and **Yoshiteru Ishida

***Toyohashi University of Technology

1-1, Tenpaku, Toyohashi-shi, Aichi 441-8585, Japan

(Tel : 81-532-44-6885; Fax : 81-532-44-6873)

{harada, ishida}@cs.tut.ac.jp

Abstract: The present study focuses on player's strategies observed from outside in our original spatial game iterated by players, each of which placed in each lattice site on a two dimensional square lattice. A particularity of the game lies in the point that a player's strategy is not preliminary given, but constructed dynamically in response to a spatial pattern on player's actions. This means the strategy can evolve in time. However simulations bring us unexpected results. Actually all of strategies observed from outside did not evolve and they were fixed in time. This paper enumerates all of the observed strategies in detail and examines their characteristics.

Keywords: Spatial game, Inverse problem, External observer

I. INTRODUCTION

It is very important for many scientific fields ranging from science, medical science to engineering to extrapolate inputs or rules hidden from outside by knowing outputs such as observational results. This kind of problem is called the "inverse problem". Richard et al. [1] try to extract a cellular automaton rule to produce a spatiotemporal pattern of given experimental data by employing the genetic algorithm. Ueda and Ishida [2] deal with one dimensional cellular automata and examine to extrapolate a rule generating given spatiotemporal patterns of cell states. The present study addresses an inverse problem with a spatial game by players placed in a two dimensional square lattice space and discusses whether it is possible to extrapolate player's strategy from spatiotemporal patterns on player's actions. In our model, each player observes actions of its neighborhood players, and builds its own strategy by applying the observed actions for a strategy-building rule and determines its action for the next round game. We suppose an external observer watching a game from outside cannot know what strategy each player applies for determining its action, but can observe actions of all players in each round. Under this setting, the present study discusses a possibility that a player's strategy extrapolated through a global observation by the external observer chimes perfectly with the real player's strategy, and presents a discord case: although each player's strategy actually evolves in each game round, the external observer observes any player obeys a unique steady strategy. This result

suggests that a model which enables to consistently explain the observation results from outside is not always true one.

II. SPATIAL GAME MODEL

Our study considers a spatial game on a two-dimensional square lattice. Each player is placed on each lattice site. To designate each lattice site, a horizontal axis with a suffix j and a vertical one with a suffix i ($i, j=0, 1, \dots, L-1$) are prepared. We let a player to select one of two actions: 0, 1. A symbol, $A_{i,j}^r$ denotes the player (i,j) 's action at the game round r , and a symbol $S_{i,j}^r$ denotes the player (i,j) 's strategy at the game round r . Our model adopts so-called "spatial" strategy. The spatial strategy determines a player's action from the total number of players taking an action "1" in its eight neighborhood players called the *Moore* neighbor.

Figure 1 shows an example of the player (i,j) 's spatial strategy at the round $r+1$. A symbol " k " is the total number of players taking an action "1" in the *Moore* neighbor of (i,j) site. A symbol " A " is the player (i,j) 's action at the round $r+1$. In this example, As k amounts to 5, the strategy determines the player (i,j) 's action at the round $r+1$ becomes 0.

The original of the proposed spatial game [3] lies in that a determination relationship between a strategy and an action is not one-way but mutual way: a strategy determines an action as well as actions determine a strategy. This implies to destroy the original boundary between the strategy and the action. Gunji [4] tries to destroy a boundary between hierarchies on a level of a

coarse graining by introducing an internal observer enabling only local observation.

We introduce a strategy building rule to build a strategy based on a spatial configuration of player's actions. The strategy-building rule defines the correspondence between k and player's action A as follows.

- When k is 0, let an action A to be $A_{i-1, j-1}^r$.
- When k is 1, let an action A to be $A_{i-1, j}^r$.
- When k is 2, let an action A to be $A_{i-1, j+1}^r$.
- When k is 3, let an action A to be $A_{i, j+1}^r$.
- When k is 4, let an action A to be $A_{i+1, j+1}^r$.
- When k is 5, let an action A to be $A_{i+1, j}^r$.
- When k is 6, let an action A to be $A_{i+1, j-1}^r$.
- When k is 7, let an action A to be $A_{i, j-1}^r$.
- When k is 8, let an action A to be $A_{i, j}^r$.

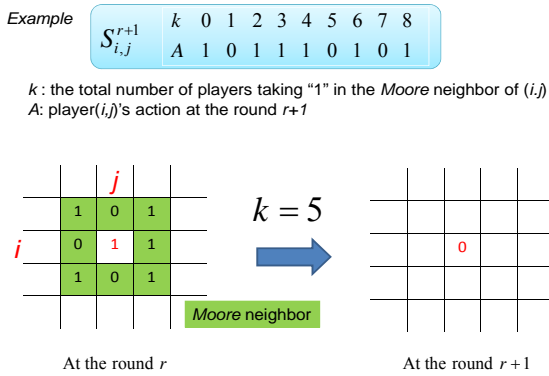


Fig.1. An example of how to build a strategy

Figure 1 shows a process to build the strategy $S_{i,j}^{r+1}$ from a spatial configuration of player (i,j) 's Moore neighbor through the strategy-building rule.

The spatial game proceeds as stated follows. As an initial condition, all players must preliminarily determine their actions. One round game consists of the two steps:

1. Each player estimates the quantity k from player's actions in its Moore neighbor at the previous round, and builds its strategy based on the strategy-building rule.
2. Each player takes the next action corresponding to the quantity k referring to its strategy.

In addition, this study does not interest in relative merits between strategies, thus not consider a scoring process based on a score table representing comparative merits between actions.

III. SIMULATION RESULTS

This study chooses the lattice-size L to be its minimal value: three, hence considers the spatial game on a two dimensional 3×3 square lattice. The number of players is nine. A boundary condition of the square lattice space is periodic.

1. PERIODIC ATTRACTORS

The previous study [3] clarified every observed game becomes periodic. Types of the observed period are period-1 (fixed point), period-3, period-6 and period-9. Some initial bit configurations converge into a periodic game, hence some periodic games are "attractive" in other words, *attractor*. The number of attractors with a certain period: period-1, -3, -6 and -9 is 2, 15, 1 and 2, respectively.

2. EXTERNALLY OBSERVED STRATEGIES

This section shows an odd discrepancy that each player's strategy dynamically evolves in response with change of a bit spatial pattern of its Moore neighbor; however a strategy extrapolated by the external observer is irrelevant with the spatial bit pattern thus steady. This section also mentions that interestingly the external observer sees a player have a memory from its behavior.

PERIOD-3 GAME

Strategies observed from outside in the 3-period games are generally described as a "copy" strategy of memorizing a player's action in the previous round and using its action in the next round. Figure 2 exhibits an example of a strategy observed from outside in a period-3 game, each player memorizes an action in the previous round of a certain player placed in the 'right' side for its own site and the player takes the memorized action in the next round. In the other period-3 game, each player memorizes an action in the previous round of the player placed in not the 'right' but the 'bottom left' for its own site and uses the memorized action. It is interesting that in the period-3 games, the external observer must see any player have one bit memory to memorize one bit action.

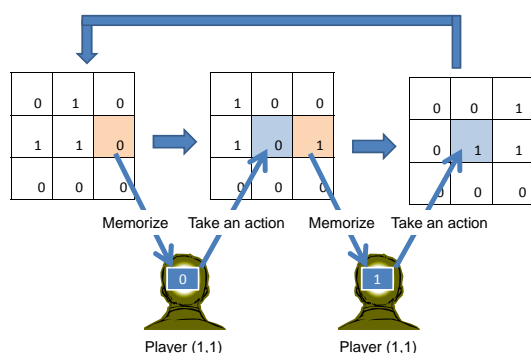


Fig.2. A strategy observed from outside in a period-3 game

PERIOD-6 GAME

A strategy observed from outside in the period-6 game is the same as the one observed in the period-3 game except memorizing a player's action in not the one but two rounds before. Figure 3 exhibits an example of a strategy that each of all players memorizes an action in the two rounds before of the player placed in the right side of each own site, and then takes the memorized action in the next round. In the period-6 game, the external observer must see all players have two bits memory.

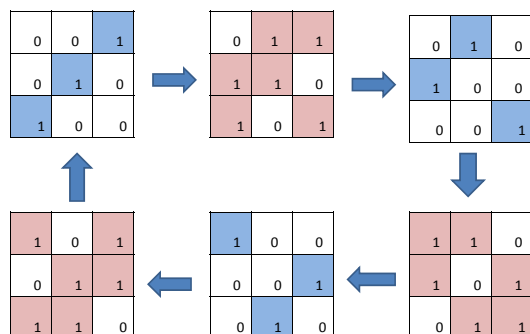


Fig.3. An example of a strategy in the period-6 game

PERIOD-9 GAME

Strategies observed from outside in the period-9 game is the same as those observed in the period-3 and -6 except memorizing a player's action in not the one/two but three rounds before. Figure 4 exhibits an instance of a strategy in a period-9 game that each player memorizes an action in three rounds before of a certain player placed in the just above for each own site, and the player takes the memorized action in the next round. It is interesting that in the 9-period games, the external observer must see any player have three bits memory.

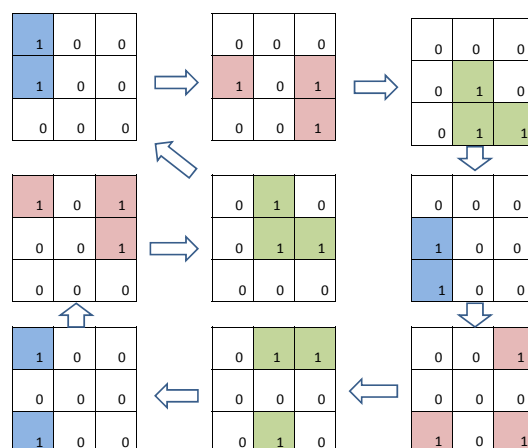


Fig.4. An example of a strategy in a period 9 game

The table 1 sums up all of strategies observed from outside. The strategies are specified by three parameters: P , D and T because all strategies observed in the period " P " games are described as a copy strategy of each player memorizes an action in the " T " round(s) before of a certain player placed in the " D " direction for each own site and then takes the memorized action. The rest of the parameters is N which is a number of different games with a certain strategy.

Table1. All types of strategies observed from outside in every periodic game

P	T	D	N
3	1	Just above	1
		Just below	3
		Top right	2
		Right	4
		Bottom right	2
		Top left	0
		Left	1
		Bottom left	2
6	1	Right	1
9	3	Just above	1
		Left	1

The table.1 suggests that in the period-3 games, a strategy to copy an action of player in the top left position is not observed. It also shows the number of games with a strategy to copy an action of a player in the right side is four, whereas in the case of copying an action of player in the opposite left side, number of games is only one. Like this, in response with the difference of the parameter D , it features that there is imbalance on the number of the observed games. This asymmetric nature is considered due to the asymmetry of the strategy-building rule.

IV. DISCUSSIONS

It seems to be odd that the strategies observed from outside in the proposed game model do not depend on a bit pattern of actions in the *Moore* neighbor although the actual strategy defined in the model depends on it. Figures 2 and 5 shows the same game from outside and inside respectively. The figure 2 exhibits the player (1,1)'s strategy is just a copy strategy irrelevant with a bit pattern of its *Moore* neighbor. On the other hand, Figure 5 exhibits the player (1,1)'s strategy evolves in response with a bit pattern of its *Moore* neighbor. Here we discuss through this example it is possible the situation that externally observed strategies do not evolve but in fact internally defined strategies evolve. Now it supposes the externally observed strategy in Fig. 2 that all the players memorizes an action in the previous round of the player in the just below for their own site and they take their memorized action in the next round. Then a bit pattern at the round $r+1$ of the *Moore* neighbor of a player (i,j) becomes equal with a bit pattern at the r round of the *Moore* neighbor of a player $(i,j+1)$. Following the strategy-building rule, if a pair of bit patterns of the *Moore* neighbor of the two players, (i,j) and $(i,j+1)$ are the same, their strategies are the same:

$$S_{i,j}^{r+1} = S_{i,j+1}^r \quad (1)$$

It would be valid to suppose that at the round r , a bit pattern of the *Moore* neighbor of a player (i,j) does not equal with that of the *Moore* neighbor of a player $(i,j+1)$. Thus,

$$S_{i,j}^r \neq S_{i,j+1}^r \quad (2)$$

Eqs. (1) and (2) lead to

$$S_{i,j}^{r+1} \neq S_{i,j}^r \quad (3)$$

In other words, the strategy of the player (i,j) evolves.

This discussion shows that it is possible that externally observed strategies do not evolve but in fact inner defined strategies evolve.

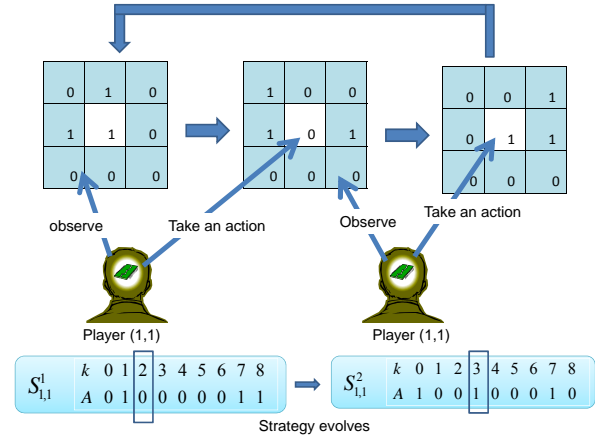


Fig.5 Time evolution of the player (1,1)'s strategy

To solve our inverse problem, what will be needed?

We will need more external observational data on various types of periodic games. However, if we randomly select an initial spatial bit pattern on player's actions and starts the game, it must be hard to observe a certain periodic game with a smaller basin size because a probability of its game being selected becomes lower. For instance, a basin size of the period-6 game in Fig.3 is zero, thus a probability of the game being observed is very low: $6/256$. Here the basin size of a periodic game is defined as the number of initial bit patterns on player's actions which finally transit to its game.

It is necessary to focus on identifying not an individual player's strategy but a "meta"-rule to build an individual strategy: the strategy-building rule. However is it possible to discover not individual rules but a meta-rule which is their origin from the observational data? In the future work, we have to think this issue.

REFERENCES

- [1] Richards F.C., Meyer T.P., and Packard N.H. (1990) Extracting cellular automaton rules directly from experimental data. *Physica D* 45:189-202
- [2] Ueda T and Ishida Y (2009), Reverse Engineering of Spatiotemporal Patterns in Spatial Prisoner's Dilemma. *J. of Artificial Life and Robotics* 14 4:498-501
- [3] Harada K and Ishida Y (2010), A Note on Dynamical Behaviors of a Spatial Game Operated on Intercrossed Rules. *LNAI* 6278:637-644
- [4] Gunji Y.-P (2010) SEIMEI-ICHIGO (in Japanese), SEIDOSYA Press

An Artificial Intelligence Membrane to Detect Network Intrusion

Takeshi Okamoto

Department of Information Network and Communication, Kanagawa Institute of Technology
1030, Shimo-ogino, Atsugi, Kanagawa 243-0292 JAPAN
take4@nw.kanagawa-it.ac.jp

Abstract: We propose an artificial intelligence membrane to detect network intrusion, analogous to a biological membrane that prevents viruses from entering cells. This artificial membrane is designed to monitor incoming packets and to prevent a malicious program code (e.g., a shellcode) from breaking into a stack or heap in a memory. While monitoring incoming TCP packets, the artificial membrane constructs a TCP segment of incoming packets, derives the byte frequency of the TCP segment, from 0 to 255 bytes, as well as the entropy and size of the segment. These features of the segment can be classified by a data mining technique such as a decision tree or neural network. If the data mining method finds a suspicious byte sequence, the sequence is emulated to ensure that it is just a shellcode. If the byte sequence is the shellcode, the sequence is dropped. At the same time, an alert is communicated to the system administrator. Our experiments examined 7 data mining methods for normal and malicious network traffic. The malicious traffic included 114 shellcodes, provided by the Metasploit framework and including 10 types of metamorphic or polymorphic shellcodes. In addition, real network traffic involving shellcodes was examined. We found that a random forest method outperformed all the other data mining methods, with a very high detection accuracy, including a true positive rate of 99.6% and false positive rate of 0.4%.

Keywords: network intrusion detection, malicious software, shellcode, data mining

I. INTRODUCTION

Anti-virus systems protect computers and networks from malicious programs, such as computer viruses and worms, by discriminating between malicious and harmless programs and by removing only the former. Therefore, anti-virus systems can be considered as a computer's immune system.

An innovative method, called a "virus throttle," [1], has been found to slow and halt high-speed worms without affecting normal network traffic. We have previously proposed a "worm filter" to prevent the spread of both slow- and high-speed worms [2]. This worm filter limits the number of unacknowledged requests, rather than the rate of connections to new computers. In addition, we have proposed an immunity-based anomaly detection method to detect worms in network traffic [3].

All of these methods monitor outgoing packets from an internal network; i.e., they detect internal anomalies. Other methods are needed to monitor incoming packets and to detect intrusive attacks. The four types of methods used to detect intrusive attacks include pattern matching [4], heuristic [5], emulation [6], and data mining [7][8] methods. Since pattern matching methods require signatures to detect intrusive attacks, they may miss new attacks due to an absence of signatures. In addition, metamorphic and polymorphic codes can produce so

many patterns that it may be difficult to cover all patterns [9]. Heuristic methods attempt to detect intrusive code sequences such as consecutive NOP sequences (i.e., NOP sleds) and sequences that get a program counter (i.e., getPC). However, some NOP sleds are polymorphic [9],[10], and intrusive attacks may not get the program counter. Emulation methods, which emulate incoming packets as program code, can correctly detect an intrusive program code, but these processes are very slow. Data mining methods use a classifier, such as a decision tree or neural network, to distinguish between benign and malicious traffic using the features of network traffic. Although these methods detect malicious traffic at a high rate, their false positive rates may be high.

We propose here an artificial intelligence membrane to detect network intrusion, analogous to a biological membrane that prevents viruses from entering cells. The artificial membrane was designed to prevent a malicious program code (e.g., a shellcode) from breaking into a stack or heap in memory. Our experiments examined 7 data mining methods for normal and malicious network traffic. The malicious traffic included 114 shellcodes, provided by the Metasploit framework [10], and 10 kinds of metamorphic and polymorphic shellcodes. In addition, real network traffic involving intrusive network attacks was examined.

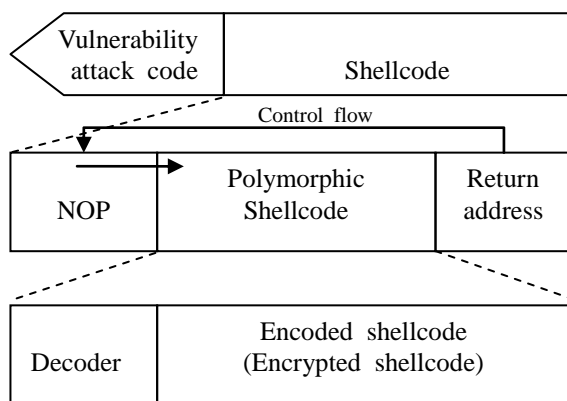


Figure 1. Structure of a polymorphic shellcode. The NOP area contains consecutive NOPs, indicating no operation and control flowing to the shellcode area. The return address area contains the address to which the program counter returns (i.e., the address of the NOP area). If a vulnerability attack is successful, the program counter will jump to the NOP area and enter the shellcode area.

II. Network Intrusion

Most network intrusion attacks are composed of a vulnerability attack and a shellcode execution (Figure 1). The vulnerability attack is used for network intrusion, following which the shellcode is executed. The shellcode is a tiny program code for operating anything on the computer, such as download of malicious software and its execution.

The appearance of a shellcode is often disguised by an encoder (Figure 1). This type of shellcode is called a metamorphic or polymorphic shellcode. In metamorphic shellcodes, a set of instructions is replaced by an equivalent set of different instructions, whereas, in polymorphic shellcodes, a set of instructions is hidden by encryption (Figure 1). These techniques make such shellcodes difficult to detect because the appearance of these shellcodes differ from each other and on each occasion. Although signature-based detection works in some cases, polymorphism will eventually defeat such detection methods [9].

III. AN ARTIFICIAL INTELLIGENCE MEMBRANE TO DETECT NETWORK INTRUSION

To detect shellcodes, we propose an artificial intelligence membrane to detect network intrusions. The membrane plays a role similar to a cell membrane that protects a cell from non-self molecules.

Figure 2 illustrates the algorithm of the artificial intelligence membrane. The artificial membrane monitors incoming TCP packets, and it constructs a TCP segment consisted of incoming packets. It then derives a

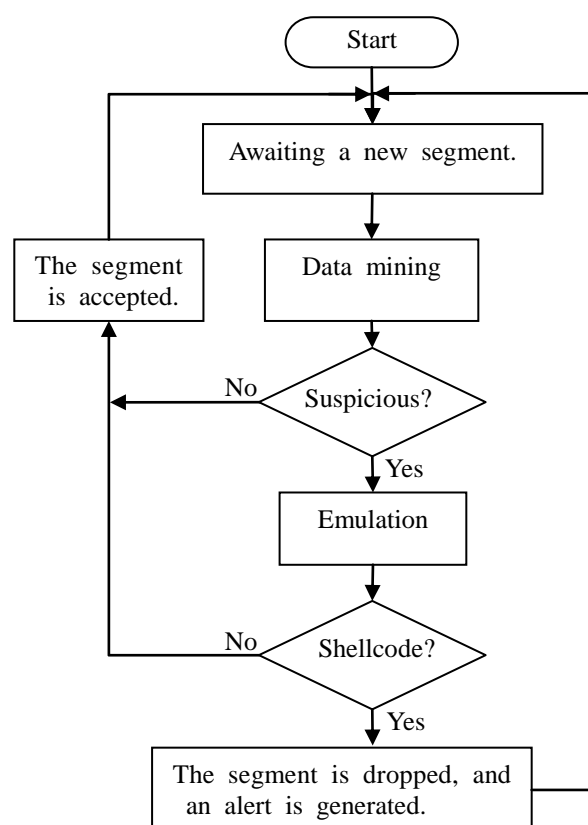


Figure 2. Algorithm of the artificial intelligence membrane. The parameters of the data mining method are trained in advance.

byte frequency of the TCP segment, from 0 to 255 bytes, as well as the entropy and size of the segment. These features of the segment are classified by a data mining method such as a decision tree or a multi-layer perceptron (i.e., a neural network). If the data mining method identifies a suspicious segment, that segment is emulated to ensure that it includes just a shellcode. The emulation plays the role of eliminating false positives. If the segment includes the shellcode, the segment is dropped. At the same time, the system administrator is alerted.

Emulation is performed by “libemu 0.2.0,” a small library offering x86 architecture emulation for shellcode detection [12]. This libemu has been partially modified for brute force detection of a suspicious byte sequence. Thus, the modified libemu can detect all x86 architecture-based shellcodes provided by the Metasploit framework, including all metamorphic and polymorphic shellcodes. Although emulation is very slow, the entire performance of the proposed method is not slow because normal packets are eliminated in advance by the data mining method and most of the packets would not be suspicious.

IV. EVALUATION OF DETECTION ACCURACY

To find the best accuracy of detection of data mining methods, we evaluated accuracy of detection for 7 methods equipped with Wakaito Environment for Knowledge Acquisition (WEKA) [13]: an instance based learner (IBk), decision trees (J48 and random forest), naïve bayes, an inductive rule learner (JRpp), and a support vector machine using sequential minimal optimization (SMO). The algorithm of each data mining method has been described [13]. All parameters of the data mining methods were default settings of WEKA.

Each evaluation has been used for 10-fold cross-validation. The data set was randomly divided into 10 subsets, with 9 subsets used for training and 1 for testing. The process was repeated 10 times for every combination. This methodology can be used to evaluate the robustness of a given approach to detecting shellcodes. Experiments were performed on dual Intel Xeon E5410 2.33GHz processors with 12 GB RAM. The operating system was Debian GNU/Linux Squeeze.

1. Evaluation of simulated traffic

Experimental data consisted of normal http traffic and simulated malicious http traffic. The normal traffic consisted of 544 segments, whereas the malicious traffic was simulated by combining one normal http segment with one shellcode for each of the 114 shellcodes provided by the Metasploit framework, version 3.5.1. Other types of malicious traffic included metamorphic or polymorphic shellcodes encoded by 10 engines: “ADMmutate” [14], “CLET” [10], “alpha mixed,” “alpha upper,” “call4 dword xor,” “context cpuid,” “countdown,” “fnstenv mov,” “jmp call additive,” “shikata ga nai,” with the last 8 engines provided by the Metasploit framework [10].

“CLET” can disguise a shellcode as normal network traffic by padding bytes close to the statistical properties of the normal traffic between the shellcode and the return address sequence (Figure 1). In this experiment, the padding size was 500 bytes. Larger padding results in closer byte frequency between normal and malicious traffic [9], but it also makes it more difficult for the shellcode to control the target computer because the size of the buffer is not always sufficient to intrude into a stack in a memory. Note that only CLET-encoded shellcodes were encoded in advance by the “shikata ga

nai” encoder to remove 0x00 byte codes from the original shellcodes.

In addition, the encoders of “alpha mixed” and “alpha upper” can disguise a shellcode as real traffic by recoding the shellcode in a form that contains bytes matching the statistical properties of real traffic.

The simulated traffic was examined using WEKA. Table 1 shows the accuracy of detection of simulated traffic. The true positive rate (TPR) was defined as the rate at which a suspicious segment was correctly classified as suspicious, whereas the false positive rate (FPR) was the rate at which a normal segment was falsely classified as suspicious. We found that the random forest method outperformed all other data mining methods (Table 1), with a TPR of 99.9% and an FPR of 0%.

Table 2 shows the accuracy of detection of metamorphic and polymorphic shellcodes. The data mining method used in this experiment was a random forest method. All detection accuracies were very high, with all metamorphic and polymorphic shellcodes other than (4) having a TPR of 100% and an FPR of 0%. In addition, the polymorphic shellcodes encoded by CLET had a TPR of 100% and an FPR of 0%, whereas metamorphic shellcodes encoded by “alpha mixed” and “alpha upper” had a $TPR \geq 99.8\%$ and an FPR of 0%, though the statistical properties of these shellcodes were similar to those of normal traffic.

2. Evaluation of real traffic

Experimental data were captured from a high-interactive honeypot on VMware Workstation 6.0.3. The guest operating systems were Microsoft Windows XP Professional, SP1 and SP2. After extracting segment data from the captured data, we examined all the segment data using the modified libemu, finding 1469 normal segments and 976 malicious segments including shellcodes.

To evaluate the performance of the data mining method, we examined all the above segments using the data mining methods of WEKA. Table 3 shows the accuracy of detection and testing time of real traffic. Again, we found that the random forest method outperformed all other data mining methods, with a TPR of 99.6% and an FPR of 0.4%. Eventually, there would be no false positives, because the suspicious segments can be analyzed by emulation.

Table 1 Accuracy of detection of simulated traffic (not all shellcodes were encoded). Each value is a weighted average.

	IBk	J48	Random forest	Multilayer perceptron	JRpp	SMO	Naïve bayes
TPR	99.6%	99.6%	99.9%	99.6%	99%	99.6%	99.3%
FPR	0.7%	0.7%	0%	0.7%	2.7%	1.3%	3.2%

Table 2. Accuracy of detection of simulated traffic for metamorphic and polymorphic shellcodes. Each value is a weighted average. Shellcodes were encoded by the following engines: (1) “ADMmutate,” (2) “CLET,” (3) alpha mixed, (4) alpha upper, (5) call4 dword xor, (6) context cpuid, (7) countdown, (8) fnstenv mov, (9) jmp call additive, and (10) shikata ga nai.

	(1)	(2)	(3)	(4)	(5)	(6)	(7)	(8)	(9)	(10)
TPR	100%	100%	100%	99.8%	100%	100%	100%	100%	100%	100%
FPR	0%	0%	0%	0%	0%	0%	0%	0%	0%	0%

Table 3. Accuracy of detection and testing time of real traffic. Each value is a weighted average.

	IBk	J48	Random forest	Multilayer perceptron	JRpp	SMO	Naïve Bayes
TPR	99.4%	99.3%	99.6%	99%	99.2%	98.9%	98.5%
FPR	0.6%	0.7%	0.4%	0.7%	0.8%	0.8%	1.2%
Time (sec.)	0.66951	0.00054	0.00071	0.20002	0.00049	0.00307	0.02604

V. CONCLUSIONS

We have proposed an artificial intelligence membrane to detect network intrusion. This membrane is analogous to a biological membrane, which prevents viruses from entering cells. Similarly, the artificial membrane prevents shellcodes from breaking into a memory.

Our experiments indicated that the random forest method outperformed all other methods. In addition, all metamorphic and polymorphic shellcodes were detected at a high rate. For real traffic, the TPR was 99.6% and the FPR was 0.4%. This high accuracy of detection is considered due to the training of both normal and malicious traffic data [9].

We are currently planning to implement this artificial intelligence membrane for practical use.

REFERENCES

- [1] Williamson, MM (2002), Throttling viruses: restricting propagation to defeat malicious mobile code. ACSAC Security Conference 2002, 61 – 68
- [2] Okamoto T (2005), A worm filter based on the number of unacknowledged requests. KES'05, LNAI 3682:93 – 99
- [3] Okamoto T, Ishida Y (2006), Towards an immunity-based anomaly detection system for network traffic. KES'06, LNAI 4252: 123 – 130
- [4] Roesch M (1999), Snort: lightweight intrusion detection for networks. LISA'99, 229 – 238
- [5] Pasupulati A, Coit J, Levitt K, Wu SF, Li SH, Kuo JC, Fan KP (2004), Buttercup: on network-based detection of polymorphic buffer overflow vulnerabilities. NOMS, 1:235 – 248
- [6] Polychronakis M, Anagnostakis KG, Markatos EP (2007), Network-level polymorphic shellcode detection using emulation. Journal in Computer Virology 2(4): 257 – 274
- [7] Payer U, Teufl P, Lamberger M (2005), Hybrid engine for polymorphic shellcode detection. LNC S 3548(200):19 – 31
- [8] Masud M, Khan L, Thuraisingham B, Wang X, Liu P, Zhu S (2008), Detecting remote exploits using data mining. IFIP, 285:177 – 189
- [9] Song Y, Locasto ME, Stavrou A, Keromytis AD, Stolfo SJ, On the infeasibility of modeling polymorphic shellcode. Proc. of the 14th ACM CCS'07, 541 – 551
- [10] Metasploit project (2006), <http://www.metasploit.com/>
- [11] Detristan, T, Ulenspiegel, T, Malcom, Y, Underduk, M (2003), Polymorphic shellcode engine using spectrum analysis. Phrack 11(61)
- [12] Baecher P, Koetter M (2007), libemu. <http://libemu.carnivore.it/>
- [13] Witten IH, Frank E (2005), Data mining: Practical machine learning tools and techniques. Morgan Kaufmann, 2nd edition
- [14] K2 (2001), ADMmutate. <http://www.ktwo.ca/ADMmutate-0.8.4.tar.gz>

A Dynamic Houjin (Square) and a Symmetric Houjin

Y. Tsuzuki and Y. Ishida

*Toyohashi University of Technology,
1-1 Hibarigaoka Tenpaku-cho, Toyohashi, Aichi 441-8580, Japan
(Tel.: +81-532-44-6895; Fax: +81-532-44-6895)
(E-mail: ishida@cs.tut.ac.jp)*

Abstract: A Houjin is an n by n square lattice with each cell containing a symbol (such as a number or a letter). Further, these numbers or letters are designed to exhibit symmetry. For example, a magic square is a Houjin where the symmetry embedded is that the numbers in each row, column and a center diagonal have an equal sum. This paper reports a new Houjin: a dynamic Houjin. A dynamic Houjin changes its containing numbers at each time step while satisfying the symmetry as the Houjin (the magic square). The dynamic Houjin has a further symmetry in a time dimension, that is, the sums of the numbers for each cell are identical.

Keywords: Houjin, magic square, Latin square, Euler square, Sudoku.

I. INTRODUCTION

Houjin in Japanese mathematics means a magic square (or *Lo Shu* in Chinese). A Houjin is an n by n square lattice with each cell containing a number where these numbers satisfy a certain constraint: sums in each row, column, and a center diagonal are equal. More general Houjin can have other symmetries.

Several Houjins (squares) have been studied in discrete mathematics, typified by Latin squares and Greco-Latin squares (Euler squares). As several names such as Houjin, Lo Shu, and Squares indicated, they have been extensively studied in world wide ([1-4] in Japan for example) and for a period of historic scale. Greco-Latin squares have been used in the experimental design to make sure all the possible combination of the control factors are involved. As for Latin square, 9x9 two layered latin square are used a puzzle known as Sudoku [5].

On the other hand, cellular automata (CA) have been attracting attention as a potential model for complex systems (e.g., [6]). CA also can be expressed as a square lattice where each cell can take one state among several states. One difference between CA and Houjin is that the former is a dynamical system, while the latter is a static one.

In order to bridge between CA and Houjin, this paper tries a preliminary study to design a dynamic Houjin that changes by a certain rule while satisfying the symmetry of Houjin. Since there is much degree of freedom in a design of the dynamic Houjin, this paper can present an example of the dynamic Houjin based on symmetric Houjins.

Section II briefly states the studies of Houjin focusing on the *spatially* elaborated ones to contrast *temporally* devised ones: the dynamic Houjin. Among spatial Houjins, symmetric Houjins are used to demonstrate the dynamic Houjin. Section III presents the dynamic Houjin, giving an example of the one constructed from 4×4 symmetric Houjin.

II. HOIJIN AS COMPUTATIONAL AND MATHEMATICAL OBJECTS

Houjin have been discussed as a mathematical objects, however, it could be placed as a computational object. For example, Houjin with two numbers in each cell may be related to a matching problem: Stable Marriage Problem (SMP) [7]. An SMP of n men and n women requires two preference matrices: one indicating each man's preference over the set of n women; and another indicating each woman's preference over the set of n men. These two matrices may be combined as a Houjin with two-tuple of numbers (m_{ij}, w_{ij}) where m_{ij} is the preference of man i to woman j and w_{ij} that of woman j to man i in each cell. A Houjin $M = \{ m_{ij} \}$ ($W = \{ w_{ij} \}$) is a half Latin Houjin, since each number appears once and only once in each row (column). When these two Houjins are orthogonal the combined Houjin becomes a Greco-Latin Houjin (Euler Houjin).

1. Recursive Houjin

Recursive Houjin is defined to be a Houjin whose structure is the same one with another row and column added or the one deleted. For example, a *recursive Houjin*, can be generated by the SMP above. When the most popular man and woman, hence they are mutually the first order with each other, are added the resulted

Houjin with two-tuple is the recursive houjin (new row and column is added at the upper left corner).

1/1		
-----	--	--

1/1	2/1
1/2	2/2

1/1	2/1	3/1
1/2	2/2	3/2
1/3	2/3	3/3

Fig.1. Recursive Houjin

Houjin with some specific structure resulted from SMP can be used to study not only SMP (such as the Latin SMP [7]) but also Houjin itself such as the Euler Square.

2. Symmetric Houjin

The numbers in a Houjin can have symmetry. For example, the numbers of a pair of cells in a rotationally symmetric position can be complement. In 4×4 Houjin, for example, a complement numbers are two numbers that sum up to 17 such as 1 and 16; 12 and 5. Fig. 2 shows three examples of 4×4 symmetric Houjin.

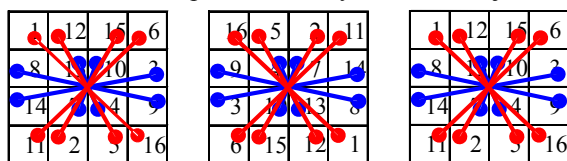


Fig.2. Three examples of 4×4 symmetric Houjin
Complement numbers are connected by the edge.

III. DYNAMIC HOUJIN

Dynamic Houjin can be considered as a special type of three dimensional Houjin whose shapes may not necessarily be cubic and one dimension is a specific type: time. An interesting property of the Dynamic Houjin proposed here satisfies the time sum constant is the specific number; and its partition is realized at each cell. Further, in three dimension Houjin of size N , N^3 distinct numbers appear, although the dynamic Houjin proposed here uses N^2 distinct numbers and the the number set do not change as the time proceeds.

Dynamic Houjin may be placed as a special type of cellular automata where the next state of each cell does not necessarily depend on the states of neighbor cells; rather depend on more global configuration of cell states. Further, it must satisfy the global constraints such as the constant sum for several directions (row, column, center diagonal and pan-diagonal).

Dynamic Houjin is a new type of Houjin that changes as time step proceeds satisfying the two constrains: it must satisfy the constraint of the initial Houjin; and it has a constraint along the time dimension similar to the spatial constraint of the initial Houjin. For example, the dynamic Houjin discussed here satisfies the constraint satisfied by the magic square: the equal sum in row, column, and center diagonal at each step; and at some specific time step the sum of every cell must be identical. We can build an example of 4×4 dynamic Houjin based on 4×4 symmetric Houjin.

When defining dynamic Houjin, an updating rule for generating the next Houjin from the current Houjin is required. A simple updating rule, for this case is exchanging the number in a symmetric position in the square (Fig. 3). Since the numbers in a symmetric position of the symmetric Houjin form a complement of 17, this updating rule defines the dynamic Houjin of the period two. That is, it turns back the original Houjin in two steps; and further the numbers in each cell adds up to 17. We call two Houjins are *complement* when the numbers in one Houjin are complement to the numbers in the same cell in another Houjin.

1	12	15	6
8	13	10	3
14	7	4	9
11	2	5	16

16	5	2	11
9	4	7	14
3	10	13	8
6	15	12	1

$S(0)$ at time=0; $S(1)=S(0)'$ at time=1

Fig.3. A dynamic Houjin with period two.

A dynamic Houjin with the period of 16 can be considered when four operators of exchanging rows and columns are involved (Fig. 4). We denote a Houjin by a number n and its complement by n' and its horizontal (vertical) mirror image nX (nY) (Fig. 5). A Houjin nX is complement to nY . When the initial Houjin is $S(0)$ (Fig. 3 left) and the four operators $R1$, $C1$, $R2$ and $C2$ are applied four times in this order, the trajectory of the dynamic Houjin is shown in Fig. 6. The four operators are depicted by colored arrows.

Note that the Houjin that appears after applying the four operators twice is the Houjin complement to the initial Houjin. That is, the Houjins in a symmetric position in the circle trajectory are complement with each other. Also, a Houjin nX (nY) can be obtained by applying the four operators $R1R2R1R2$ ($C1C2C1C2$) to a Houjin n .

Starting from the same initial Houjin but changing the orders of the application of four operators, several trajectories with distinct symmetric Houjins are obtained (Fig. 7). The trajectory $0-1-9-12-15Y-14X-10X-4'-0'-1'-9'-12'-15X-14Y-10Y-4-0$ is the same trajectory as that shown in Fig. 6. Fig. 7 shows a system of symmetric Houjins, including all possible trajectory when the four operators R_1 , R_2 , C_1 , C_2 are applied in an arbitrary order. It can be observed that this system may be considered a development chart of torus, since a torus (not sphere) will be formed by connecting corresponding Houjins in the boundary.

Another system that includes Houjins nR instead of n exists where nR is the 90 degree clock-wise rotation of the Houjin n . In this system, nR , nXR , nYR , and $n'R$ appear instead of n , nX , nY , and n' , respectively.

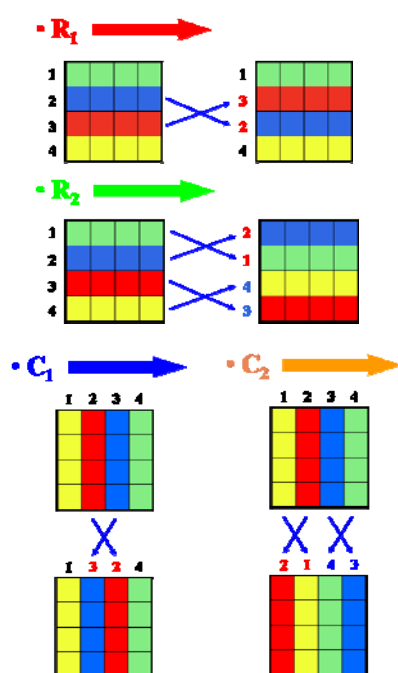


Fig.4. Four operators to change Houjin

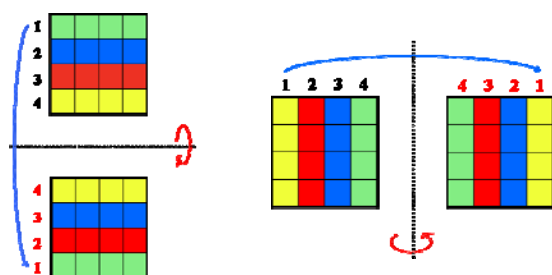


Fig.5. A Houjin n and its horizontal (left) and vertical (right) mirror image nX and nY

VI. DISCUSSIONS

The study of a dynamic Houjin suggested the Houjins themselves would exhibit an external symmetry, although the studies Houjin mainly focused on the internal symmetry embedded in the numbers of a Houjin. For example, the trajectory of the dynamic Houjin (Fig. 6) indicated Houjins in a symmetric position form a complement of Houjin, while in a symmetric Houjin the numbers in a pair of numbers in the cells in a symmetric position form a complement.

Another interesting property of the dynamic Houjin is that the numbers in the same cell add up to 136 which is the sum of all the numbers from 1 to 16 (that is $17 \times 16/2$). However, which numbers (among 1 to 16) appears and how many times in a period depend on the cell, suggesting a possible relation to the partition number.

Further, the dynamic Houjin proposed here is a specific type whose trajectory proceeds with the same set of operators applied repeatedly in a fixed order of operations; and the trajectory of a period is divided into two parts in which Houjins appear in a fixed order in the first half and then the complement Houjins appear in the reversed order in the last half. Various and more general trajectory and the way of change (application of operators) could be found.

VI. CONCLUSION

An attempt to develop new types of Houjin (square) has been made with an emphasis that Houjins would have external symmetry in the relation among Houjins other than the internal symmetry so far studied.

Further, since Houjin is a mathematical object similar to numbers, each Houjin could have a specific character similarly to a specific numbers. Composing new type of Houjin is a design mathematics that is required for education in current Engineering and Science.

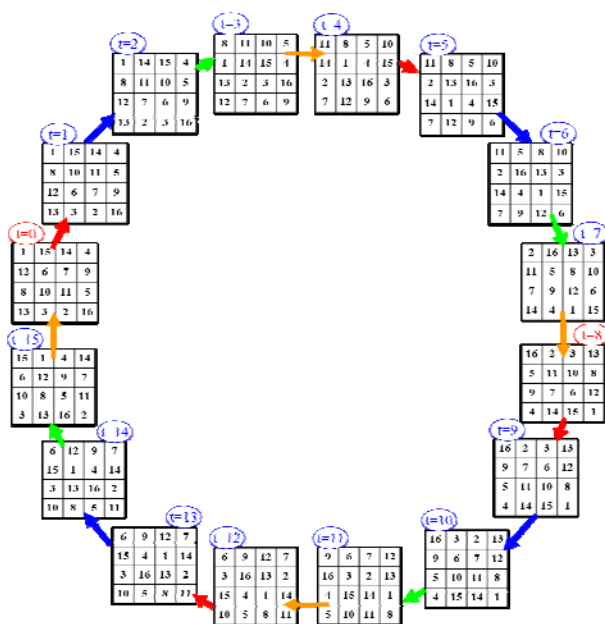


Fig.6. Trajectory of a dynamic Houjin starting from $S(0)$ and four operators $R1$, $C1$, $R2$ and $C2$ are applied in this order.

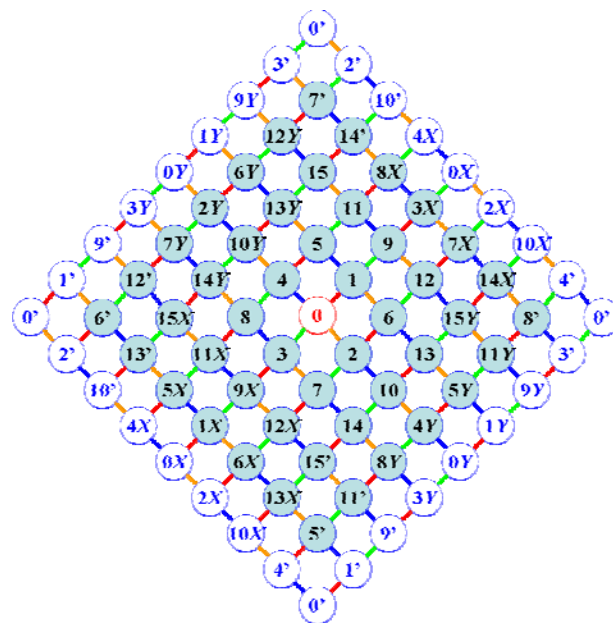


Fig.7. A system of symmetric Houjins, including all possible trajectory when the four operators are applied.

REFERENCES

- [1] Abe G (1994), Unsolved problems on magic squares. *Discrete Mathematics* 127(1-3): 3-13
- [2] Shasha DE (2003), Prime Squares. *SCIENTIFIC AMERICAN* June
- [3] Bell J (2005), An introduction to SDR's and Latin squares. *Morehead Electronic Journal of Applicable Mathematics* Issue 4 — MATH-2005-0
- [4] Ishida Y and Kotovsky K (1995), Symmetry Analysis on Symmetry Cognition on Multi-Level Figures. *Computers & Mathematics with Applications*, 30(7): 93-102
- [5] Delahaye JP (2006), The Science behind Sudoku. *SCIENTIFIC AMERICAN* June 2006
- [6] Wolfram S (2002), *A New Kind of Science*, Wolfram Media, Inc.
- [7] Benjamin AT, Converse C, Krieger HA (1995), How do I marry thee? Let me count the ways, *Discrete Applied Mathematics*

Performance Evaluation of Immunity-based Statistical En-route Filtering in Wireless Sensor Networks

Yuji Watanabe

*Graduate School of Natural Sciences, Nagoya City University,
1 Yamanohata, Mizuho-cho, Mizuho-ku, Nagoya 467-8501 Japan
(Tel : 81-52-872-5037; Fax : 81-52-872-5037)
(yuji@nsc.nagoya-cu.ac.jp)*

Abstract: Statistical en-route filtering (SEF) schemes can detect and eliminate false data injection attack in wireless sensor networks. However, SEF do not address the identification of compromised nodes injecting false reports. In this paper, we propose an immunity-based SEF to identify compromised nodes and achieve the earlier detection of false reports. In the proposed scheme, each node has a list of neighborhood and assigns credibility to each neighbor node. Each node can update the credibility of neighbor node based on success or failure of filtering and communication, and then use the updated credibility as the probability of next communication. Some simulation results show that the immunity-based SEF outperforms the original SEF.

Keywords: wireless sensor networks, statistical en-route filtering, immunity-based approach.

I. INTRODUCTION

In the last decade, wireless sensor networks have paid much attention because of the popularization of sensor nodes that are smaller, cheaper, and more intelligent [1]. In large-sized wireless sensor networks including a lot of sensor nodes, a detected event report can be sent to base station (user) using multi-hop communication where intermediate nodes forward the report. Wireless sensor networks may also be deployed in potentially hostile environment, so that the issue of security must be addressed. Attackers can compromise sensor nodes to inject false data reports of non-existing or bogus events using the compromised nodes. Such an attack is called *false data injection attack* [2]. The attack may cause not only false alarms but also the depletion of the limited energy of the nodes forwarding these reports to the base station.

Several research efforts [2-7] have proposed schemes to overcome such attack. The *statistical en-route filtering* (SEF) scheme [3] can probabilistically filter out false reports en-route in the dense deployment of large sensor networks. In SEF, assuming that the same event can be detected by multiple nodes, forwarding nodes along the way to base station can statistically detect false reports. SEF has achieved the early detection of false data reports with low computation and communication overhead. There are several revised en-route filtering schemes, for example, the dynamic en-route filtering [4], the multipath en-route filtering [5], the ticket-based en-route filtering [6],

and LEDS [7]. However, these schemes do not address the identification of compromised nodes injecting false reports. If the compromised nodes are successfully identified, then neighbor nodes of the compromised nodes can drop false reports at an earlier stage.

For the detection of fault nodes on networks, an *immunity-based diagnostic model* [8] has been proposed inspired by the *Jerne's idiotypic network hypothesis* [9]. In the diagnosis, each node has the capability of testing the neighbor nodes, and being tested by the adjacent others as well. Based on the test outcomes, each node calculates its credibility. However, compromised nodes can not only output bogus test outcomes but also calculate the credibility at random.

In this paper, we propose an immunity-based SEF to identify compromised nodes. In the proposed scheme, each node has a list of neighborhood and assigns credibility to each neighbor node. Each node can not only update the credibility of neighbor node based on success or failure of filtering and communication but also use the updated credibility as the probability of next communication. We carry out some simulations to evaluate the performance of the proposed scheme. Some results show that the immunity-based SEF outperforms the original SEF.

II. SENSOR NETWORK MODEL

Following the previous studies on SEF, we also consider a large sensor network composed of a lot of sensor nodes and a base station which is a data collection center. We further assume that the sensor

nodes are deployed in high density, so that an event (sensing target) can be detected by multiple surrounding nodes. Because it is useless for each of the detecting nodes to send the event report (e.g., the location, the time, and the type of event) to the base station, one of them is elected as the cluster head. The cluster head collects and summarizes all the received event reports, and forward a synthesized report toward the base station. The report potentially traverses a large number of hops.

We assume that the attacker can compromise a node to obtain the security information installed in the node. Once compromised, the node can be used to inject false data reports of bogus events. However, we consider the attacker cannot defeat the base station because the base station has powerful security. Furthermore, this paper does not focus on various other attacks, for instance, false negative attacks and Dos attacks, by the compromised node.

III. STATISTICAL EN-ROUTE FILTERING (SEF) [3]

SEF can probabilistically filter out false reports en-route. SEF exploits collective decision-making by multiple detecting nodes and collective false detection by multiple forwarding nodes. SEF consists of three major components: (1) key assignment and report generation, (2) en-route filtering, and (3) base station verification.

1. Key assignment and report generation

The process of key assignment and report generation is as follows:

- 1) The base station (BS) maintains a global key pool of N secret keys $\{K_i, 0 \leq i \leq N - 1\}$, divided into n non-overlapping partitions. Each partition has m keys. In other words, $N = m \cdot n$.
- 2) Before each sensor node is deployed, it stores randomly chosen k ($k < m$) keys from a randomly selected partition in the key pool.
- 3) When an event appears, multiple surrounding nodes can detect the event. A cluster head (CH) is elected from the detecting nodes to generate the event report.
- 4) Each of the nodes that detected the event generates a keyed message authentication code (MAC) M_i using the event report E and randomly selected K_i , one of its k stored keys. Each detecting node then sends $\{i, M_i\}$, the key index and the MAC, to the CH. K_i is secret while M_i is public.

- 5) The CH collects all the $\{i, M_i\}$ s from the detecting nodes and randomly chooses T MACs from distinct partitions. This set of multiple MACs acts as the proof that the report is legitimate. Then the CH sends the final report attached T key indices and T MACs like $\{E, i_1, M_{i_1}, i_2, M_{i_2}, \dots, i_T, M_{i_T}\}$ toward the BS.

Fig.1 illustrates the example of the key assignment and report generation in SEF. In this figure, the BS has a global key pool of $N = 12$ keys divided into $n = 4$ partitions, each of which has $m = 3$ keys. Each sensor node randomly picks $k = 2$ secret keys from one partition of the key pool. After each detecting node endorses the event report by producing a keyed MAC using one of its stored 2 keys, the CH collects all the MACs from the detecting nodes and attaches randomly selected $T = 3$ MACs, that is, M_2 , M_9 and M_{10} to the event report E .

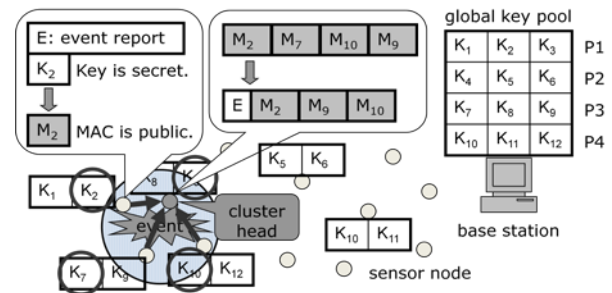


Fig.1. Example of the key assignment and report generation in SEF with 12 keys, 4 partitions, 3 keys in each partition, 2 keys in each node, and 3 MACs attached to event report.

2. En-route filtering

In en-route filtering process, intermediate forwarding nodes verify the correctness of the MACs probabilistically and drop a report with forged MACs en-route. The en-route filtering process is as follows:

- 1) Since a legitimate report carries exactly T MACs produced by T keys of distinct partitions, a report with less than T MACs or more than one MACs in the same partition is dropped.
- 2) Because of the randomized key assignment, each forwarding node has certain probability to possess one of the keys that are used to produce the T MACs. If forwarding node finds out that it has one of the T keys in the report, it reproduces the MAC using its stored key and compares the result with the corresponding MAC attached in the report. If

the attached MAC is different from the reproduced one, the report is dropped.

- 3) When intermediate node does not have any of the T keys, the node forwards the report to the next hop.

The key assignment ensures that each node can produce only *partial* proof for a report. A single compromised node has to forge MACs to assemble a seemingly complete proof in order to forward false reports. In Fig.2, since a malicious node has 2 keys from only partition 1, it needs to forge the other 2 MACs, M_9 and M_{10} . The report with the forged MACs is dropped because the correctness of the MACs can be verified by the intermediate node with K_{10} .

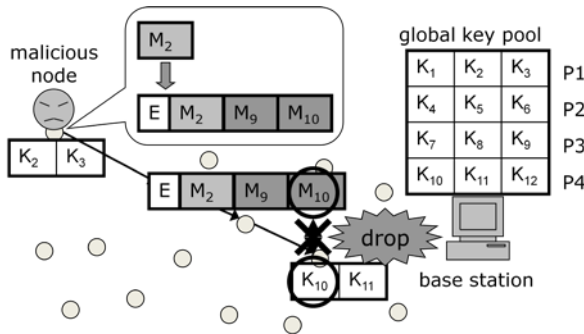


Fig.2. Case that a false report with forged MACs from a malicious node is dropped by the intermediate forwarding node.

3. Base station verification

Due to the statistical nature of the detection mechanism, a few bogus reports with invalid MACs may escape en-route filtering and reach the BS. In base station verification process, the BS further verifies the correctness of each MAC and eliminates false reports that elude en-route filtering.

IV. PROPOSED IMMUNITY-BASED SEF

The original and revised SEFs do not deal with the identification of compromised nodes injecting false reports. Simple trace back is futile if the compromised nodes tell a lie that the false reports are received from the other nodes. To detect fault nodes in networks, the *immunity-based diagnostic model* [8] is a promising approach. In the diagnosis, each node has the capability of testing the neighbor nodes, and being tested by the adjacent others as well. Based on the test outcomes, each node calculates its own credibility. However,

malicious nodes can not only output bogus test outcomes but also calculate the credibility at random.

Therefore, we propose an immunity-based SEF scheme to identify compromised nodes. In the proposed scheme, each node has a list of neighborhood and assigns a state variable $R \in [0, 1]$ indicating *credibility of neighbor* to each neighbor node. Note that each node does not have its own credibility. Node j updates the credibility R_{ji} of the previous neighbor node i sending the event report based on its filtering result and the reply from next neighbor node k as follows:

$$R_{ji}(t+1) = \begin{cases} R_{ji}(t) + \Delta_s & \text{if node } j \text{ receives the reply from next node } k \\ R_{ji}(t) - \Delta_f & \text{if node } j \text{ does not receive the reply from next node } k \\ R_{ji}(t) - \Delta_d & \text{if node } j \text{ drops the report using SEF} \end{cases} \quad (1)$$

The initial value of credibility $R_{ji}(0)$ is 1. If credibility $R_{ji}(t)$ is over 1 (under 0), it is set to 1 (0). The values of the parameters Δ_s , Δ_f and Δ_d should be chosen through mathematical analysis and simulation.

For example, in Fig.3, node i increases the credibility R_{ih} of the previous node h because the reply from next node j can be received. However, node j decreases the credibility R_{ji} of the previous node i because next node k drops the event report using SEF and does not reply to node j . Since node k filters out the report by itself, the credibility R_{kj} of the previous node j also decreases.

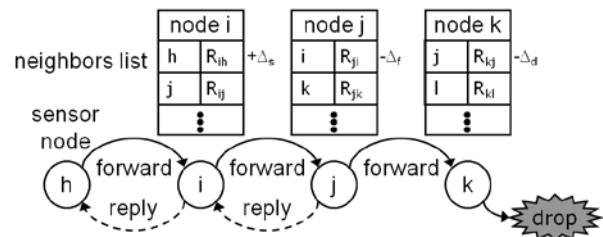


Fig.3. An immunity-based SEF scheme for identifying compromised nodes.

Only the credibility update process cannot achieve the identification of compromised nodes. For instance, in Fig.3, if node h is compromised, false reports are still forwarded toward node k . Therefore each node uses the updated credibility as the probability of next communication. In the same example, node i has

adversely higher probability of receiving the report from compromised node h because of the increase of the credibility R_{ih} . However, since node j has lower probability of receiving the report from node i , node i may fail to communicate with node j at next stage, and then the credibility R_{ih} of the previous node h in the neighbors list of node i decreases. Although the credibility R_{kj} of the previous node j in the neighbors list of node k decreases at first, if node j sends legitimate reports received from the other previous nodes to node k , the credibility R_{kj} can be recovered. By iterating the credibility update and the communication based on the updated credibility, our scheme will be expected to inhibit neighbor nodes of compromised nodes from forwarding false reports.

V. SIMULATION RESULTS

We carry out some simulations to evaluate the performance of the proposed scheme. Simulation conditions are the same as [3]: 340 nodes are uniformly distributed in a field which size is $200 \times 20 \text{ m}^2$. One base station and one event source sit in opposite ends of the field, with about 100 hops in between. The BS has a global key pool of 1000 keys divided into 10 partitions, each of which has 100 keys. Each node has 50 keys, and 5 MACs are attached to event report. The results are averaged over 10 network topologies.

Fig.4 shows the percentage of dropped false reports as a function of the number of forwarding nodes for immunity-based approach ($\Delta_s = \Delta_f = \Delta_d = 0.02$) and SEF, respectively in case that one node is compromised and 1000 bogus reports are sent by the compromised node. Results show that as false reports are forwarded, more and more reports are dropped: about 100% bogus reports are detected within 20 forwarding nodes for both methods. Furthermore, about 65% false reports are dropped by the original SEF within 5 intermediate nodes, while about 73% reports are filtered out by the immunity-based SEF. We confirm that the immunity-based SEF can achieve the earlier detection of false reports than the original SEF.

VI. CONCLUSION

In this paper, we proposed an immunity-based SEF scheme for identifying compromised nodes in wireless sensor networks. Some results show that the immunity-based SEF outperforms the original SEF. In future, the proposed scheme will be additionally combined with other security mechanisms for higher security level.

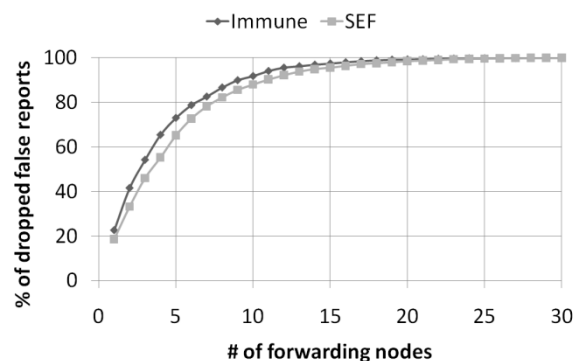


Fig.4. Percentage of dropped false reports as a function of the number of forwarding nodes for immunity-based approach and SEF, respectively.

ACKNOWLEDGEMENTS

This work was partly supported by a Grant-in-Aid for Scientific Research (C) (22500063) from Japan Society for the Promotion of Science.

REFERENCES

- [1] Yick J, Mukherjee B, Ghosal D (2008), Wireless Sensor Network Survey. *Computer Networks* 52: 2292-2330
- [2] Zhu S, Setia S, Jajodia S, Ning P (2004), An Interleaved Hop-by-Hop Authentication Scheme for Filtering of Injected False Data in Sensor Networks. *IEEE Symposium on Security and Privacy*, 259-271
- [3] Ye F, Luo H, Lu S, Zhang L (2005), Statistical En-Route Filtering of Injected False Data in Sensor Networks. *IEEE Journal on Selected Areas in Communications* 23(4):839-850
- [4] Yu Z, Guan Y (2006), A Dynamic En-route Scheme for Filtering False Data Injection in Wireless Sensor Networks. *Proceedings of the 25th IEEE Conference on Computer Communications*, 1-12
- [5] Kim MS, Cho TH (2007), A Multipath En-Route Filtering Method for Dropping Reports in Sensor Networks. *IEICE Transactions on Information and Systems* E90-D(12):2108-2109
- [6] Krauß C, Schneider M, Bayarou K, Eckert C (2007), STEF: A Secure Ticket-Based En-route Filtering Scheme for Wireless Sensor Networks. *2nd IEEE International Conference on Availability, Reliability and Security*, 310-317
- [7] Ren K, Lou W, Zhang Y (2008), LEDS: Providing Location-aware End-to-end Data Security in Wireless Sensor Networks. *IEEE Transactions on Mobile Computing* 7(5):585-598
- [8] Ishida Y (1990), Fully Distributed Diagnosis by PDP Learning Algorithm: Towards Immune Network PDP Model. *Proceedings of International Joint Conference on Neural Networks*, 777-782
- [9] Jerne N (1973), The Immune System. *Scientific American* 229(1):52-60

Improvement of Immunity-Based Diagnosis for a Motherboard

Haruki Shida¹, Takeshi Okamoto¹ and Yoshiteru Ishida²

¹ *Department of Information Network and Communication, Kanagawa Institute of Technology,
1030, Shimo-ogino, Atsugi, Kanagawa 243-0292, Japan*

² *Department of Knowledge-Based Information Engineering, Toyohashi University of Technology,
1-1, Tempaku, Toyohashi, Aichi 441-8580, Japan*

Abstract: We have utilized immunity-based diagnosis to detect abnormal behavior of components on a motherboard. The immunity-based diagnostic model monitors voltages of some components, CPU temperatures, and fan speeds. After simulating the abnormal behaviors of some components on the motherboard, we assessed the ability of the immunity-based diagnostic model to detect these abnormalities. To improve the diagnostic accuracy of the model, which can be decreased by isolated nodes, we used multiple diagnostic networks to connect isolated nodes to a network or other isolated nodes. This simulation showed that the immunity-based diagnostic model containing multiple diagnostic networks was an effective method for detecting abnormal behavior of components on the motherboard.

Keywords: Immunity-based system, fault diagnosis, sensor network, motherboard, immune network

I. INTRODUCTION

The prevalence of technology for cloud computing has increased the demand for data centers that provide such cloud computing. Each server in these data centers must therefore be available for data processing and data transmission. To maintain system availability, it is important to detect abnormalities during their early stages, before system failure.

The simplest way of diagnosing abnormalities consists of evaluating each component individually by comparing the output value of its sensor with a predetermined threshold value. However, it is difficult to identify the abnormal component using this method [1]. Another method of diagnosis uses an immunity-based diagnostic model [2-5], which was derived primarily from the concept of an immune network [6]. In this diagnostic model, mutual tests are performed among nodes and the dynamic propagation of active states. This diagnostic model has been used to diagnose node faults in processing plants [7], to the self-monitoring/self-repairing in distributed intrusion detection systems [3], and to sensor-based diagnostics for automobile engines [4].

We previously applied immunity-based diagnosis to the detection of abnormal behaviors of components on a motherboard [8]. After simulating the abnormal behaviors of some components on the motherboard, we evaluated the ability of this model to diagnose abnormalities of components of motherboard sensors in two experiments. In the first experiment, we found that

the immunity-based diagnostic model outperformed a stand-alone diagnostic model. In the second experiment, which compared a fully-connected network with a correlation-based network for mutually testing the credibility of sensors, we found that the correlation-based network had greater diagnostic accuracy in all test cases. In addition, we utilized a hybrid model, consisting of the stand-alone and immunity-based diagnostic models, to diagnose nodes connected to the network and isolated from the network. We found, however, that the accuracy of hybrid diagnosis for isolated nodes was dependent on the stand-alone diagnostic model. These isolated nodes could decrease the diagnostic accuracy of the hybrid model. In this paper, we sought to improve diagnostic accuracy of multiple diagnostic networks by connecting the isolated nodes with one of the networks.

II. Embedded Sensors on the Motherboard

Since a motherboard has multiple sensors, including voltage, temperature, and fan speed sensors, abnormalities on the motherboard can be detected by monitoring these sensors. We therefore used sensor output values for diagnosis of the motherboard.

We collected sensor output values on a server from July 27 to September 18. The specifications of the server are shown in Table 1. The average air temperature during that period was 25.3 °C, ranging from 20.1°C to 32.8°C. Data were collected using lm_sensors, a hardware health monitoring package for

Linux that allows information to be obtained from temperature, voltage, and fan speed sensors.

Table 1. Server specifications

Motherboard	Supermicro® X7DVL-I
OS	Debian GUN/Linux 5.0
Kernel	2.6.26-2-amd64
Module	lm-sensors version 3.0.2 with libesensors version 3.0.2
CPU	Intel® Xeon E5410 2.33GHz×2
Power supply	Thermaltake Toughpower 700w
Fan	XFan model: RDM8025B×2 Gantle Typhoon D0925C12B2AP×2 ADDA CFX-120S

After collecting the output values from all 29 sensors on the motherboard, we calculated the correlation coefficients of all sensors. We observed correlations involving 5 sensors (Table 2), and we therefore used these 5 sensors for evaluation.

Table 2. Sensors used for evaluation and range of sensor output values

Sensor	Component	Range	Mean	Standard deviation
CPU1	CPU temperature	11.00-48.00(°C)	18.68	4.55
Core2	Core2 temperature	35.00-72.00(°C)	42.79	4.45
VcoreA	CoreA voltage	1.11-1.19(V)	1.121	0.007
Vbat	Internal battery voltage	3.23-3.26(V)	3.237	0.009
Fan5	Fan speed	1012-1044(RPM)	1034	5.021

III. Immunity-Based Diagnostic Model

The immunity-based diagnostic model has the feature of a dynamic network, in which diagnoses are performed by mutually testing nodes (i.e., sensors) and by dynamically propagating their active states. In this paper, the targets of the immunity-based diagnosis are components with a sensor embedded on a motherboard. Each sensor can test linked sensors and can be tested by linked sensors. Each sensor is assigned a state variable R_i indicating its credibility.

The initial value of credibility $R_i(0)$ is 1. The aim of diagnosis is to decrease the credibility of all abnormal sensors. That is, according to this model, if the credibility of a sensor is below a threshold value, that sensor is considered abnormal.

When the value of credibility R_i is between 0 and 1, the model is called a gray model, reflecting the ambiguous nature of credibility. The gray model can be expressed by the equation:

$$\frac{dr_i(t)}{dt} = \sum_j T_{ji}^+ R_j(t) - r_i(t), \quad (1)$$

Where

$$R_i = \frac{1}{1 + \exp(-r_i(t))}, \quad (2)$$

$$T_{ij}^+ = \begin{cases} T_{ij} + T_{ji} - 1, & \text{if one of evaluation from } i \text{ to } j \text{ or } j \text{ to } i \text{ exists,} \\ 0, & \text{if neither evaluation from } i \text{ to } j \text{ nor } j \text{ to } i \text{ exists,} \end{cases} \quad (3)$$

$$T_{ij} = \begin{cases} 1, & \text{if a balance formula between sensors } i \text{ and } j \text{ is satisfied,} \\ -1, & \text{if a balance formula between sensors } i \text{ and } j \text{ is not satisfied,} \\ 0, & \text{if there is no balance formula between sensors } i \text{ and } j. \end{cases} \quad (4)$$

In the right-hand side of Equation (1), the first term is the sum of evaluations from other nodes for node i . The second term is an inhibition term that maintains ambiguous states of credibility. In this model, equilibrium points satisfy the equation $r_i(t) = \sum_j T_{ji}^+ R_j(t)$. Thus R_i monotonically reflects the value of $\sum_j T_{ji}^+ R_j(t)$. If $\sum_j T_{ji}^+ R_j(t)$ is close to 0, then R_i is close to 0.5. The balance formulas were determined by calculating the relationships of the output values of the sensors (Table 3).

Table 3. Balance formulas between sensors

Sensor	Balance formula
CPU1-Core2	$ \text{CPU1-Core2} \leq 26$
CPU1-VCoreA	$ \text{CPU1-VCoreA} \times 25 \leq 20$
CPU1-Vbat	$ \text{CPU1-Vbat} \times 9 \leq 18$
CPU1-Fan5	$ \text{CPU1-Fan5}/34 \leq 18$
Core2-VCoreA	$ \text{Core2-VCoreA} \times 45.5 \leq 28$
Core2-Vbat	$ \text{Core2-Vbat} \times 16 \leq 20$
Core2-Fan5	$ \text{Core2-Fan5}/19 \leq 21$
VCoreA-Vbat	$ \text{VCoreA-Vbat}/2.8 \leq 0.05$
VCoreA-Fan5	$ \text{VCoreA-Fan5}/893 \leq 0.07$
Vbat-Fan5	$ \text{Vbat-Fan5}/316 \leq 0.07$

IV. Evaluation of the immunity-based diagnosis for motherboard sensors

We evaluated the immunity-based diagnostic model for motherboard sensors by a simulation, using the four test cases shown in Table 4.

Test cases 1 and 2 assumed that the speeds of Fan5 were far outside the range shown in Table 2. A significant decrease in Fan speed (test case 1) would therefore cause the CPU temperature to rise, with the overheated CPU causing the server to crash. Conversely, a significant increase in Fan speed (test case 2) would waste power and decrease the life span of the Fan. Therefore, test cases 1 and 2 represent abnormal conditions.

Test cases 3 and 4 assumed that the output values of the sensors were slightly out of the range shown in Table 2. Test case 3 assumed that the speed of Fan5 was

slightly higher than that shown in Table 2, but that Fan5 was not abnormal. Test case 4 assumed that the temperature of CPU1 was slightly higher than that shown in Table 2, but that CPU1 was not abnormal. Temperatures outside the range are not always abnormal, because these temperatures depend on room temperature. Therefore, test cases 3 and 4 represent normal conditions.

Table 4. Test cases

Case	Sensor output value					State
	CPU1	Core2	VcoreA	Vbat	Fan5	
1	70	65	1.12	3.23	200	Abnormal
2	9	35	1.12	3.23	2000	Abnormal
3	14	35	1.12	3.23	1050	Normal
4	50	60	1.12	3.23	1020	Normal

1. Correlation-based network

We previously described the construction of a correlation-based network [8], using the correlation coefficients shown in Figure 1. In the model presented here, we removed a weakly correlated network from a fully-connected network, forming a correlation-based network, because these connections may be unreliable for mutually testing the credibility of their sensors. Table 5 shows the results of correlation-based networks. Each value is a sensor credibility, i.e., R_i of Equation (2).

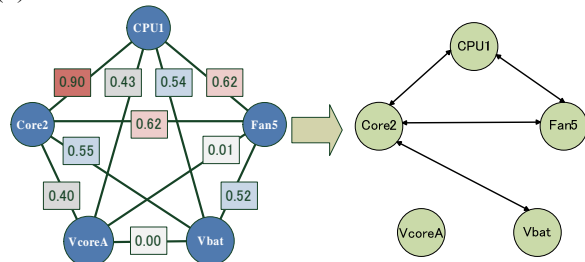


Fig. 1. Correlation-based network

Table 5. Results of a correlation-based network

Test case	Credibility					Decision	Accuracy
	CPU1	Core2	VcoreA	Vbat	Fan5		
1	0.87	0.97	0.50	0.87	0.00	X	O
2	0.87	0.97	0.50	0.87	0.00	X	O
3	0.98	0.99	0.50	0.88	0.98	O	O
4	0.67	0.95	0.50	0.87	0.67	O	O

In Table 5, we assumed that a component on the motherboard was abnormal if its credibility was less than 0.1. A diagnostic decision of “O” indicates an absence of abnormality, whereas a diagnostic decision of “X” indicates an abnormality. An accuracy of “O”

indicates a correct decision, whereas an accuracy of “X” indicates an incorrect decision.

The diagnostic model correctly identified the abnormal Fan5 in test cases 1 and 2, and did not falsely identify abnormalities in test cases 3 and 4. However, this diagnostic model could not correctly diagnose the isolated sensor, because the credibility of the isolated VcoreA sensor was always 0.50.

2. Multiple diagnostic networks

We hypothesized that utilizing multiple diagnostic networks, in which isolated nodes are connected to a network or another isolated node, would approve diagnostic accuracy.

All combinations of the multiple networks used for immunity-based diagnosis are shown in Figure 2. Each evaluation was based on the four test cases shown in Table 4. The diagnostic accuracy of all multiple networks is shown in Table 6.

In Table 6, a diagnostic accuracy of “P” indicates that the diagnostic model could not identify the abnormal component, although it detected multiple abnormalities.

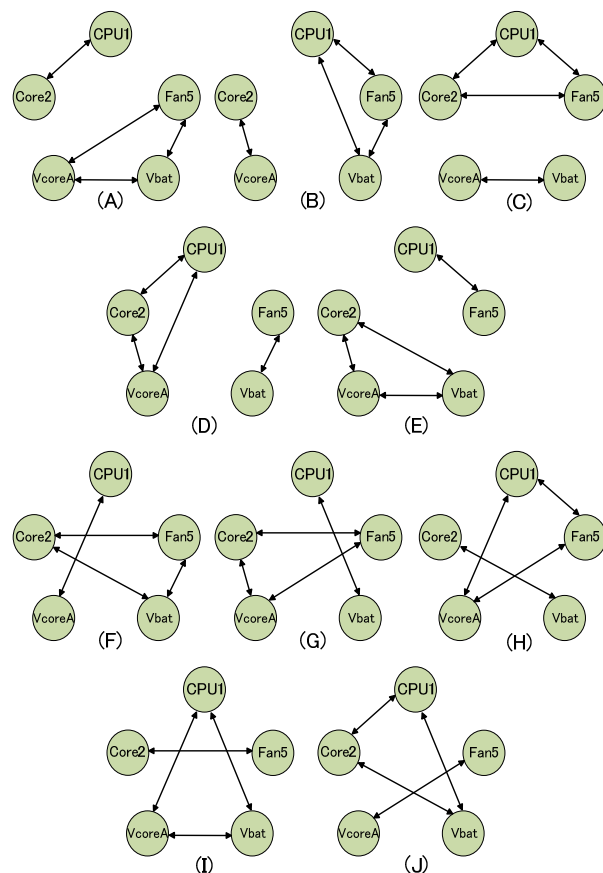


Fig. 2 Multiple diagnostic networks

Table 6. Diagnostic accuracy of multiple networks

Test case	(A)	(B)	(C)	(D)	(E)	(F)	(G)	(H)	(I)	(J)
1	O	X	O	X	X	O	O	X	P	X
2	O	X	O	X	X	O	O	O	X	X
3	O	O	O	O	O	O	O	X	O	O
4	O	X	O	O	O	O	O	O	X	O

We found that diagnostic models (A), (C), (F) and (G) made correct decisions, whereas the other diagnostic models made incorrect decisions.

In test cases 1, 2 and 3, each of the diagnostic networks (A), (C), (F) and (G) consisted of 3 sensors including Fan5. In contrast, the other diagnostic networks either consisted of 2 sensors including Fan5 or were weakly correlated networks. In test case 4, all diagnostic networks other than (B) and (I) showed results similar to those of CPU1.

For example, Table 7 shows the successful results of diagnostic network (C), and Table 8 shows the unsuccessful results of diagnostic network (I).

Table 7. Results of diagnostic model (C)

Test case	Credibility					Decision	Accuracy
	CPU1	Core2	VcoreA	Vbat	Fan5		
1	0.640	0.640	0.659	0.659	0.021	X	O
2	0.640	0.640	0.659	0.659	0.021	X	O
3	0.844	0.844	0.659	0.659	0.844	O	O
4	0.385	0.683	0.659	0.659	0.385	O	O

Table 8. Results of diagnostic model (I)

Test case	Credibility					Decision	Accuracy
	CPU1	Core2	VcoreA	Vbat	Fan5		
1	0.021	0.293	0.640	0.640	0.293	X	P
2	0.385	0.293	0.683	0.385	0.293	O	X
3	0.844	0.659	0.844	0.844	0.659	O	O
4	0.021	0.659	0.640	0.640	0.659	X	X

The diagnostic model in Table 7 misidentified the normal CPU1 in test case 1, and misidentified the abnormal Fan5 in test case 2. These results indicate that an immunity-based diagnostic model could not diagnose sensors on a weakly correlated network consisting of 2 sensors.

In test case 4 of Table 8, the diagnostic network misidentified the normal CPU1 due to a weak correlation network, although CPU1 belongs to the diagnostic network consisting of 3 sensors.

This simulation showed that diagnostic accuracy depends on the size of the network and the correlation between nodes.

V. CONCLUSION

We applied immunity-based diagnosis to the detection of abnormal behaviors of components on a motherboard. We simulated the abnormal behaviors of some components on the motherboard, and we evaluated all the combinations of the diagnostic networks. We showed that diagnostic accuracy depends on the size of the network and the correlation between nodes of the network. In addition, we showed that the immunity-based diagnostic model with multiple diagnostic networks was an effective method for detecting abnormal behavior of components on the motherboard.

In future, we will attempt to determine the relationships among diagnostic network topologies and correlation between nodes, and to improve the accuracy of the diagnostic model.

REFERENCES

- [1] Tanaka T, Kawazu T, Kanda S (2003), Computer-assisted Diagnostic System Applied with ANFIS. Biomedical Fuzzy System Association 5(1):49-54
- [2] Ishida Y (1996), An immune network approach to sensor-based diagnosis by self-organization. Complex Systems Publication 10:73-90
- [3] Watanabe Y, Ishida Y (2003), Immunity-based Approaches for Self-monitoring in Distributed Intrusion Detection System. Knowledge-Based Intelligent Information and Engineering Systems (KES'2003) 2774(2):503-510
- [4] Ishida Y (2006), Designing an Immunity-Based Sensor Network for Sensor-based diagnosis of Automobile Engines. Lecture Notes Computer Science 4252:146-153
- [5] Watanabe Y, Ishida Y (2003), Mutual tests among agents in distributed intrusion detection systems using immunity-based diagnosis. Proc. of AROB 8th '03:682-685
- [6] Jerne N K (1973), The immune system. Scientific American, 229(1):52-60
- [7] Ishida Y (2004), Immunity-Based Systems: A Design Perspective. Springer-Verlag
- [8] Shida H, Okamoto T, Ishida Y (2010), Evaluation of Immunity-Based Diagnosis for a Motherboard. Knowledge-Based Intelligent Information and Engineering Systems (KES'2010) 6278:628-636

Visualization of keystroke data and its interpretation

T. Samura¹, K. Tani¹ and Y. Ishida²

¹*Akashi National College of Technology,
679-3 Nishioka, Uozumi-cho, Akashi, Hyogo 674-8501, Japan
(Tel.: +81-78-946-6079; Fax: +81-78-946-6138)
(E-mail: samura@akashi.ac.jp)*

²*Toyohashi University of Technology,
1-1 Hibarigaoka Tenpaku-cho, Toyohashi, Aichi 441-8580, Japan
(Tel.: +81-532-44-6895; Fax: +81-532-44-6895)
(E-mail: ishida@cs.tut.ac.jp)*

Abstract: Keystroke data from keyboard input is time-series data and follows a fixed pattern. However, it is difficult to intuitively grasp the meaning of the data. In this study, we investigated visualization methods for keystroke data, which is a form of biometric information. We extracted feature indices from the keystroke timing between consonant-vowel letter pairs in Japanese text input and propose three visualization methods: two consonant-vowel doughnut methods, a consonant-vowel matrix method and a keyboard layout method. These patterns of visualization are expected to be useful in analyzing personal characteristics and authenticating users

Keywords: Visualization, Keystroke dynamics, Information security, Man-machine interface.

I. INTRODUCTION

Computers are essential in today's information society, and with the increased frequency of using keyboards, applications that utilize keystroke data are expected to lead to innovations in various fields. Keystroke data is regarded as a form of biometric information from which various personal characteristics can be extracted [1–3]. However, keystroke data is time-series data and difficult to understand intuitively. In this study, we aim to develop methods for visualizing keystroke data in order to extract various personal characteristics.

Prior research on the visualization of keystroke data is limited. Neumann et al. [4] have proposed a method for visualizing input data in order to make signatures and postcard-like art for e-mail and other forms of Internet communication.

In this study, we propose methods for visualizing keystroke data obtained from free typing of Japanese text in order to reveal personal characteristics.

II. Typing Data Collecting System

This section describes the keystroke data collection system[5]. In this study, we used a web-based system

that is able to collect keystroke data from a large number of participants in a single experiment. The system uses typing support software that was familiar to the participants, thereby lowering effects related to unfamiliarity and tension. Figure 1 shows a screenshot of the software interface used in this study.

The document display screen allows participants who are skilled typists to input text while viewing the Japanese text displayed in the upper row. Less skilled typists can type while viewing the Latin alphabet text displayed in the middle row. Latin alphabet text is removed from the screen as it is typed, allowing confirmation of mistyped characters. The top row displays the number of keystrokes, the number of errors, and the amount of time remaining. Because this experiment focuses only on Latin alphabet input keystroke, by design Latin character input is not converted into Japanese kanji characters.

While participants are typing, browser-embedded JavaScript code records character input, key press times, and key release times. Times are recorded using UNIX times (millisecond precision). Recorded data was sent to a server using Ajax.

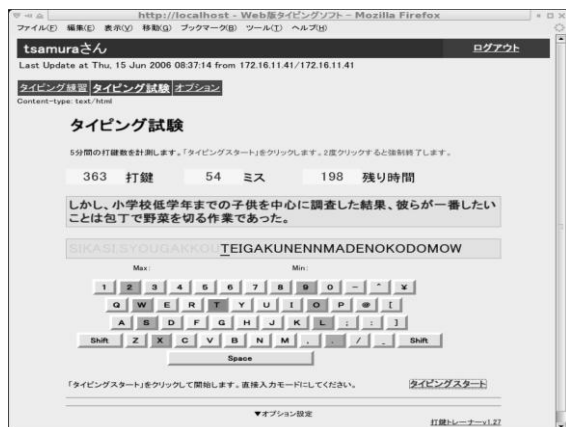


Fig. 1. Screenshot of interface of keystroke data collecting system.

III. CONSONANT-VOWEL DOUGHNUT METHODS

In this section, we propose two consonant-vowel doughnut methods: an absolute transition time method and a relative transition time method, the latter of which is based on the time variance from the average transition time of all participants.

3.1 ABSOLUTE TRANSITION TIME METHOD

The visualization procedure is as follows:

1. Define incoming alphabetic characters as nodes. Exclude the letters "l", "q", "v" and "x", which have a low frequency of occurrence.
2. Arrange the letters in a circular doughnut arrangement, with vowels on the inner circle and consonants on the outer circle. Indicate consonant-vowel letter pairs (hiragana) that appear three times or more using edges.
3. Display the color-coded edges, as indicated in Table 1, on the basis of the transition time T between pressing a key and the next key.

Table 1. Edge colors according to transition time T

Transition Time T [ms]	Color
$T < 70$	Red
$70 < T < 100$	Peach
$100 < T < 130$	Yellow
$130 < T < 160$	Green
$160 < T < 190$	Blue
$190 < T$	Not colored

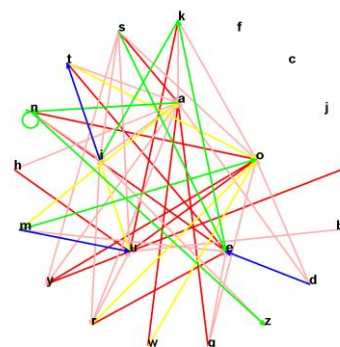


Fig. 2. Visualization pattern based on the absolute transition time method (fast typing)

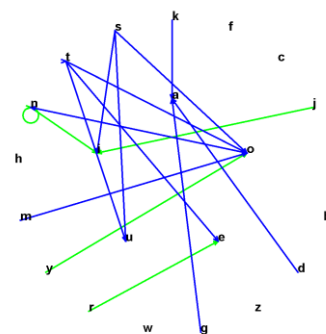


Fig. 3. Visualization pattern based on the absolute transition time method (slow typing)

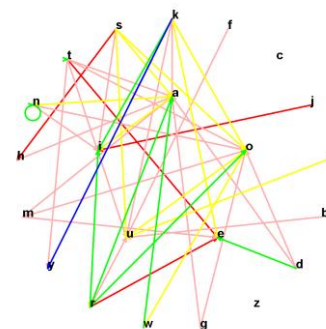


Fig. 4. Visualization pattern based on the absolute transition time method (Hepburn Romanization, "ji" typed quickly)

Figure 2 shows a visualization pattern for a participant who typed Japanese text. It can be seen that the typing speed of this participant was fast, as many edges are colored red and peach. On the other hand, Fig. 3 shows many blue edges, indicating that the typing speed of the participant was slow. In Fig. 4, the edge for "ji" indicates a fast typing speed for this pair, from which we can ascertain that the participant used the Hepburn system of Romanization.

3.2 RELATIVE TRANSITION TIME METHOD

Here, we focus the time variance $\Delta T (=T - \bar{T})$ between targeted transition time T and the average transition time of all participants, \bar{T} . Edges from consonants to vowels are color-coded for only three conditions: fast, average and slow, based on the time variance ΔT . No color is shown for other conditions.

The visualization procedure is as follows:

1. Calculate the average transition time \bar{T} of all participants.
2. Seek the time variance ΔT between transition time T of a participant and the average transition time of all participants, \bar{T} .
3. Draw color-coded edges from consonants to vowels according to Table 2.

Table 2. Edge colors according to time variance ΔT

Time Variance ΔT [ms]	Color
$\Delta T < -60$ (fast)	Green
$-5 < \Delta T < 5$ (average)	Black
$60 < \Delta T$ (slow)	Yellow
Other ($5 \text{ ms} < \Delta T < 60 \text{ ms}$)	Not colored

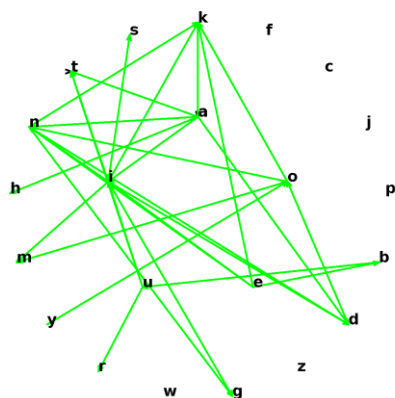


Fig. 5. Visualization pattern based on relative transition time method (fast typing)

Figures 5 and 6 show examples of visualization patterns created using this method. As all edges for the participant in Fig. 5 are colored green, it is indicated that the typing speed of the participant is faster the average. Meanwhile, in Fig. 6, many edges for the participant are colored yellow and black, indicating that the typing speed of the participant is slower than the average. However, only the edge from "y" to "u" is colored green, which shows that the participant has a habit such as typing "y" with the left index finger. In addition, only black edges or no edges at all are seen for typing of "n" to "n" by all participants, indicating that there is no difference in the input time of the transition time among any participants.

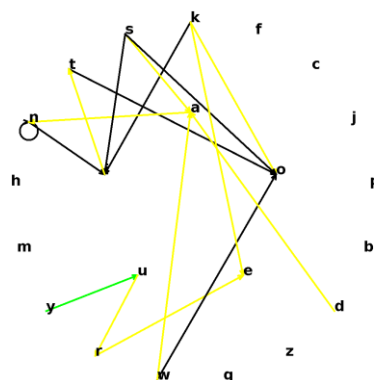


Fig. 6. Visualization pattern based on the relative transition time method (slow typing)

IV. CONSONANT-VOWEL MATRIX METHOD

The visualization procedure is as follows:

1. For hiragana input of consonant-vowel pairs, place consonants of the first letter in columns (vertical) and vowels of the second letter in rows (horizontal). Exclude "c", "f", "j", "l", "p", "q", "v" and "x" because of their low frequency of occurrence.
2. Prepare two keystroke data sets for input by a participant. Obtain variances in the transition time for each single letter. Consonant-vowel letter pairs (hiragana) that appear three times or more are targeted for both data sets. Letters with small time variance are colored dark red and letters with large time variance are colored light red. Thus, the figure is configured to be displayed entirely in dark red if files are input by the same participant, and displayed in white and light red when the files are input by different participants.

Figure 7 shows an image of when a participant typed three different texts. The participant's identity can be confirmed because most of the image is colored dark red. Meanwhile, Fig. 8 shows an image comparing text typed by a different participant. In most cases, typing differs between participants, and thus the image is generally displayed in light red.



Fig. 7. Visualization pattern based on the consonant-vowel matrix method for a certain participant.



Fig. 8. Visualization pattern based on the consonant-vowel matrix method for different participants.

V. Keyboard layout method

The visualization procedure is as follows:

1. Place nodes in the same layout as the QWERTY keyboard.
2. The average time of pressing a letter is displayed as red circles on the nodes, and the transition time is displayed as light blue links. Shorter times are shown in darker colors.

Figure 9 shows a visualization pattern based on this method. For this method, it is verified that a similar network is created even if different texts are typed. In addition, Fig. 9 shows that movements are more active on the right side of the keyboard, which suggests the participant is right-handed.

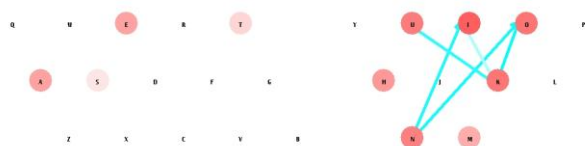


Fig. 9. Visualization pattern based on the keyboard layout method

VI. CONCLUSIONS

In this study, various methods for visualizing keystroke data were proposed, and the results showed that the methods were effective in revealing the characteristics of individuals.

In future work, we plan to study changes in visualization images the typing of English text, programming languages and other documents in addition to Japanese texts. We also plan to investigate typing by non-Japanese participants. In addition, we considered only transition time in this work, and therefore we would like to consider other keystroke times as well.

REFERENCES

- [1] Samura T. & Nishimura H. (2009a), Personal Identification by Keystroke Dynamics in Japanese Free Text Typing. Transactions of the Institute of Systems, Control and Information Engineers (in Japanese). 22(4):145-153
- [2] Samura T. & Nishimura H. (2009b), Keystroke Timing Analysis for Individual Identification in Japanese Free Text Typing, Proceedings of ICROS-SICE International Joint Conference 2009. 3166-3170
- [3] Samura T. & Nishimura H. (2010), A Hybrid Model for Individual Identification Based on Keystroke Data in Japanese Free Text Typing. Transactions of the Society of Instrument and Control Engineers (in press, in Japanese) 46(11)
- [4] Neumann P., Tat A., Zuk T. & Carpendale S. (2007), KeyStrokes: Personalizing Typed Text with Visualization. EuroVis 2007:43-50
- [5] Samura T. (2008), A Web-based Typing Learning System That Supports Japanese Text. Journal of Education in the College of Technology (in Japanese) 31:471-476

Extraction of learning point by visualization of skill

Shihoko Kamisato*, Yukihiro Mori*, Nobuhiro Yamashiro*, Kentaro Noguchi* and Yoshiteru Ishida**

*Information and communication technology
Okinawa national college of technology
Nago 905-2192 Japan

**Department of Knowledge-Based Information Engineering
Toyohashi University of technology.
Toyohashi 441-8580 Japan

(Tel : 81-980-55-4145) *

(Email: kamisato@okinawa-ct.ac.jp, ac104610@edu.okinawa-ct.ac.jp)* (Email: ishida@cs.tut.ac.jp) **

(Email: ac094609@edu.okinawa-ct.ac.jp, knoguchi@okinawa-ct.ac.jp) *

Abstract: Experiments are a valuable tool in reinforcing important concepts in engineering students. In precedence research, we considered the technical skill education imparted during engineering experiments and analyze eye and arm movements of the teachers and students in the experiments. Purpose of this research is improvement of engineering experiment by visualization of skills. We visualized the teaching materials movie of the teacher and student. Furthermore, it made clear a weak point of engineering experiment using principal component analysis and protocol analysis. As a result it was able to make sure of having weak point consciousness with default setting of device and relation of connection of device.

Keywords: visualization, skill, experiments education, learning point, principal component analysis, protocol analysis.

I. INTRODUCTION

Experiments are a valuable tool in reinforcing important concepts in engineering students. Numerous trials for improvement of engineering experiment and training by linking experiment method with lectures are documented in literature [1]-[3]. There are some students who get the knack of experiment, but on the other hand there are many students who cannot get it. A student getting the knack of experiment arranges measuring device simply and understands the operation in a short time. But for most students the arrangement of measuring device is chaotic and moreover they need to get used to its operation. In precedence research, we considered the technical skill education imparted during engineering experiments and analyze eye and arm movements of the teachers and students in the experiments[4]-[6]. As a result the sign parameter was derived. The first was consciousness of experiment time. The second was the operation of experiment device. The third understand of experiment step [7]. Previously these parameters were not take into consideration in experimental education, however our research strongly supports inclusion of these parameter in improvement of educate method.

But a weak point of a student is not clear, and it is not the experiment improvement which considered it.

Purpose of this research is improvement of engineering experiment by visualization of skills. We visualize the teaching materials movie of the teacher and student. Furthermore, it makes clear a weak point of engineering experiment using principal component analysis and protocol analysis.

II. VISUALIZATION OF VIEW TRANSITION

At first we did visualization of a point of student experiment for experiment improvement. The experiment intended for ten students and a teacher. Subject experiments using view camera and records view image. Using this image, it did visualization by showing stationary time and view transition of subject by directed graph. We compare a student with a teacher using the result and make clear the difference. A theme of experiment is electric instrument error measurement. Fig.1 shows the experiment conditions. Node of graph shows stationary time of a gaze point. An edge represents direction and number of times of view transition. It shows view transition graph of a teacher by fig.2. It shows view transition graph of a student by fig.3. As for the teacher, pattern along experiment procedures manual is found. For example, it makes sure with following step, measurement device → power

supply → measurement device → procedures text.
On the other hand, as for the student, pattern is not established. In particular there is much movement to be useless in measurement device node neighborhood. On this account even if stationary time gets longer and compares a teacher, experiment time becomes long. From this thing, a weak point of a student understands that it is concerned with measurement device.

III. EXTRACTION OF WEAK POINTS

In this paper, it makes clear a weak point of a student in measurement experiment and reflects it in improvement.

1. Extraction by principal component analysis

In addition, we searched whether a student was conscious of a weak point. In addition, we searched whether a student was conscious of a weak point. Using questionnaire for experiment, it did self-evaluating about element of experiment such as wiring or operation of device. Table 1 shows abbreviation to use by question item and this report of questionnaire. The experiment of 8 themes was analyzed using principal component analysis.

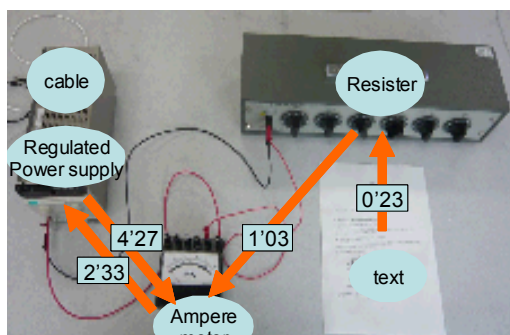
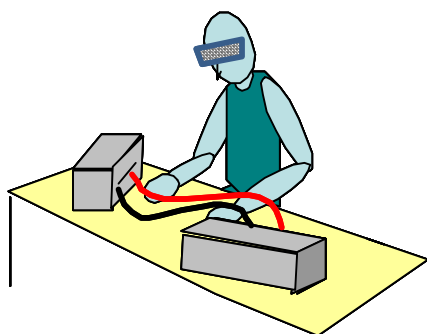


Fig.1 The condition of experiment

Table 1. Question item and symbol

Question	symbol
Experiment time	T
Preparations for lessons of experiment	P
Reconfirmation of text	R
Electric wiring of experiment	W
Operation of device	M
Understanding of principal	U
Understanding of text description	Tx
part	

Figure 4 shows contribution ratio of each principal component. In this research, it paid attention to it to the fourth principal component. In this research, we paid attention to the fourth principal component. Table 2 shows factor loading. The first principal component explains total 43%. In the first principal component, it is the point that electric wiring and operation device are watched by with interest.

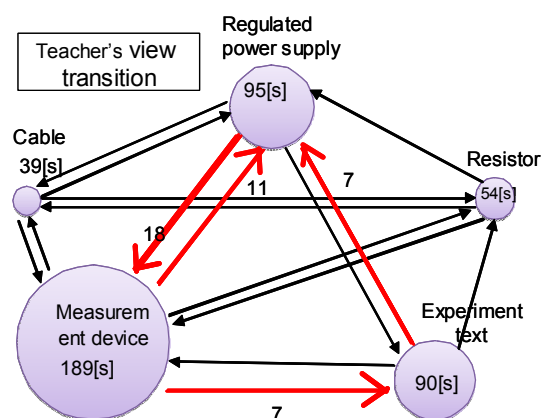


Fig. 2 Transition graph of a teacher

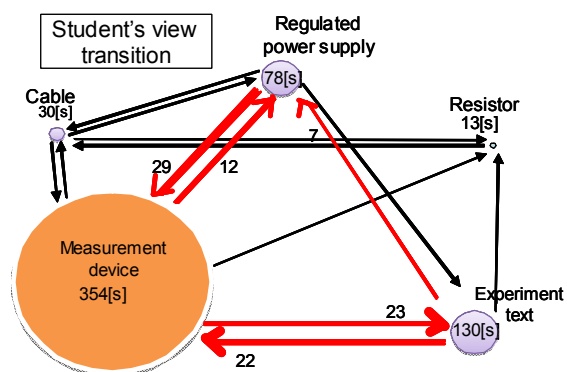


Fig. 3 Transition graph of a student

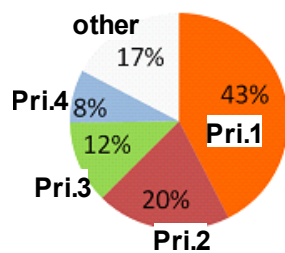


Fig. 4 Contribution ratio of each principal component

Table 2. Factor loading of principal component

Item / principal	Pri.1	Pri.2	Pri.3	Pri.4
Experiment time	-0.09	0.14	-0.09	-0.03
Preparations	-0.13	0.36	-0.39	0.78
Re-verification of text	-0.09	-0.76	-0.34	0.42
Electric wiring	-0.69	-0.31	-0.01	-0.13
Operation of device	-0.64	-0.17	0.06	0.16
Understanding of principal	-0.12	0.17	-0.07	-0.13
Understanding of text description	-0.27	0.81	0.57	-0.23

As a result it shows that there is difference whether a student is weak with it. From this thing, it is suggested by improvement of experiment that we should focus our attention on device operation and electric wiring. It was important that understanding of text was the fourth principal component from the second. It was related with reconfirmation of text. As a result of experiment, there is not good judgment with a little knowledge and experience at once. Therefore we think that device operation, electric wiring and text appear as the element which it is important of experiment.

2. Extraction by protocol analysis

Device operation and electric wiring understood the thing that it was important in improvement from view transition and result of principal component analysis. But concrete weak point and remedy are not clear. However, we cannot make clear a concrete weak points and remedies. Furthermore, detailed analysis becomes necessary. There we use protocol analysis in order to specify weak point in experiment. Protocol is a gesture in an action of subject and record of speech production. Analysis of protocol is used for a problem point in action and detection of the cause. It considers cause with the frequency. By this report, it classed the speech production protocol which it acquired.

Table 3. Job and abbreviation

job	abbreviation
Reads text	TXT
Electric wiring	WC
Device operation	SET
Record	REC
Reading of value	GM / TES

The speech production protocol was classed in action instructions, situation instructions and self speech production. The subject intended for five students of a beginner. It recorded a condition of the experiment which measured each subject. Subject sent own action in experiment on a voice and explained it. The analysis divided it into 22 steps as it was shown experiment to procedures text. Each step paid attention to it by the number of protocol manifestation. It shows abbreviation and job in table 3. It shows association of activity abbreviation and description representing step in table 3. As the situation which represented a weak point of experiment, it examined two situations. One is the situation which self speech production increases. The others are the situation that productive time gets longer. On these points, we take it as a weak point of subject. Fig.5 shows the thing which counted number of self speech production every step. This is average of five subjects. In the job that manifestation of protocol is found, a big thing of value is SET 1, WC1 and TES3. Furthermore, it shows the productive time which each step took by fig.6. This is difference of productive time of a student and a teacher by each step. This calculates average every step.

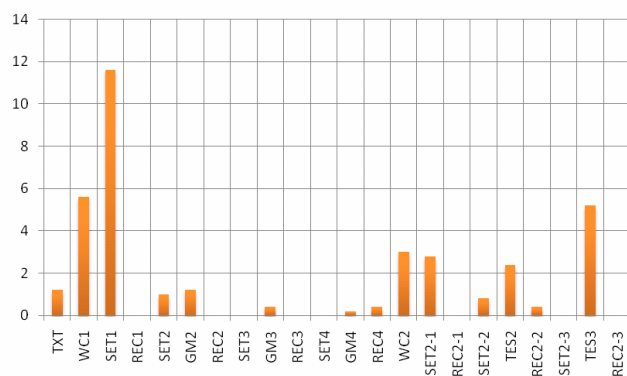


Fig. 5 The number of speech production every step

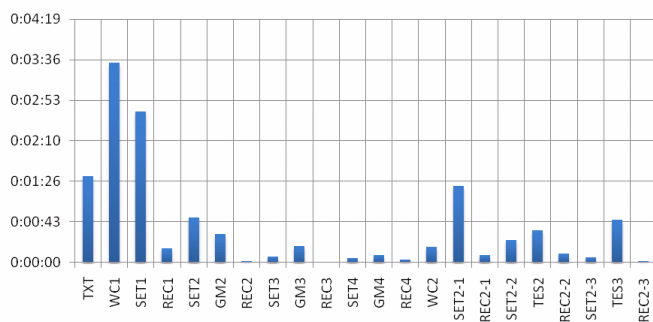


Fig. 6 Difference of productive time of a student and a teacher by each step

Work having difference of time is SET 1 and WC1. As a result it can suppose that the first electric wiring and instrument setup is the job which is a weak point with a lot of subject.

3. Consideration about learning point

We specified a weak point of a student. But it has to look for concrete cause for improvement. We focused our attention on protocol in electric wiring job of subject. At first, as for the confirmed weak point, speech production explaining relation of connection of device is not found. The second draws up circuit with layout completely the same as circuit diagram. The third identifies circuit diagram every one place of electric wiring. In the subject that electric wiring was not a weak point, the speech production which explained relation of connection was found. In addition, the circuit which it drew up was not the same as layout of circuit diagram. As a result they suggest that they use circuit diagram in order to make sure of relation of connection. This inclination was not found in case of weak point electric wiring. To the student who is inexperienced in experiment, it is important that confirmation of device connection. Furthermore, when learning effects rise by supporting it on default setting of device, it is expected.

IV. CONCLUSION

Purpose of this research is improvement of engineering experiment by visualization of skills. We visualized the teaching materials movie of the teacher and student. Furthermore, we identified a weak point of a student using principal component analysis protocol analysis. As a result it was supposed that the first electric wiring was the job which was a weak point with a lot of subject. In particular inclination was found to

the student who was inexperienced in experiment. Necessity to support the weak point by learning before the fact was suggested.

ACKNOWLEDGMENTS

A part of this research was supported by educational cooperation project in Toyohashi University of technology.

REFERENCES

- [1] M. Fuse, M. Suzuki, N. Memoto, T. Michikami and S. Ozawa, "Development of video on demand e-Learning system for general physics," vol. 29, pp. 439-444 Mar. 2006.
- [2] K. Masuda, and S. Chiba, "A method of motivation in the engineering education to third-year students and its effects," vol. 29, pp. 337-342, Mar. 2006.
- [3] K. Kondo, K. Yamamoto, M. Okuno, S. Suzuki and F. Yamada, "Some approaches to improvement of student experiment of department of electrical and electric engineering and results of questionnaires to students on these approaches," vol. 27, pp.341-346, Mar. 2004.
- [4] O. Higa, R. Suzuki, K. Noguchi, S. Kamisato, S. Nozaki, T. Satake and S. Higa, "Relationship of eyes of student and learning level in engineering experiment," Forum on information technology (FIT2006), vol. 5, pp.439-440, Sep. 2006.
- [5] K. Noguchi, S. Kamisato, O. Higa, S. Higa, S. Nozaki, T. Satake, R. Suzuki, "Consideration of effective education technique in engineering experiment," E2-1, Nov. 2006.
- [6] S. Kamisato, K. Noguchi, O. Higa, S. Higa, S. Nozaki, T. Satake, R. Suzuki, "Relationship between operation of device and arm trajectory in engineering experiment," 7th SICE system integration division annual conference (si2006), 1D3-2, Dec. 2006.
- [7] S. Kamisato, K. Noguchi, S. Nozaki, A. Okuda and R. Suzuki "Kaizen of experimental education method focused on evaluation devise operation," 4th IEEE International conference on mechatronics, ThA1-A-1, 2007.
- [8] K. Noguchi, S. Kamisato, and R. Suzuki "Activity of technical skill education based on motion analysis," 39th ASEE/IEEE Frontiers in Education conference (FIE2009), W1E, 2009.

Prediction of Electron Flux Environment at Geosynchronous Orbit using Neural Network Technique

K. Kitamura, Y. Nakamura,

Tokuyama College of Technology, Gakuendai Shunan, Yamaguchi, 745-8181, Japan
(Tel : 81-824-29-6271)
(kitamura@tokuyama.ac.jp)

M. Tokumitsu, Y. Ishida,

Toyohashi University of Technology, Hibarigaoka, Toyohashi, Aichi, 441-8580, Japan
(tokumitsu@sys.cs.tut.ac.jp, ishida@tutkie.tut.ac.jp)

S Watari,

National Institute of Information and Communications Technology, Koganei, Tokyo, 184-8795, Japan
(watari@nict.go.jp)

Abstract: In this study a neural network technique is adopted to a prediction of the electron flux at the geosynchronous orbit using several solar wind data obtained by ACE spacecraft and magnetic variations observed on the ground as input parameters. The parameter tuning for back-propagation learning method is attempted to the feed-forward neural network. As a result, the prediction using the combined data of solar wind and ground magnetic data shows the highest prediction efficiency of 0.61, which is enough to adapt the actual use of the space environment prediction.

Keywords: Neural Network. Spacecraft, Internal charging

I. INTRODUCTION

From 1950's many spacecrafts have been launched into the near earth space and over 300 artificial satellites are operated as the significant infrastructure today. However such satellites are exposed in the severe environment on their orbits. In particular, the orbit in the range from 2 to 7 R_E (Earth Radii) which include the geosynchronous orbit is well known as "Radiation Belt" filled with the high-energy particles. The high-energy ($>10^6$ eV) electrons are thought to be a cause of internal charging which give rise to the serious troubles on the electric circuit onboard the spacecraft.

In order to avoid the significant problems on the satellite systems, it is important to predict the space environment especially for the high-energy particles. The physical element process of the high-energy electrons flux variations has not been understood well though much number of observations have been conducted by many investigators. Thus, it is difficult to predict the electron flux variations by the computer simulation based on the theoretical models, so that some studies of the electron flux predictions using the empirical models based on the statistical analysis were attempted. In the previous observations, it is well known that the electron flux shows the large enhancement during the magnetic storm which is driven

by the disturbance of the solarwind (that is the high-speed plasma stream flowing out from the sun).

Some investigator tried to predict the electron flux variations by the linear prediction filter using the observed space environment data [1][2]. In these studies, the accuracy of the prediction was not enough to adopt the actual operations, though enhancement itself was well reproduced in 24hours-later predictions.

Fukata et al. [3] first attempted the prediction of the electron flux variations using the neural network model. This model well predicted the variation of the electron flux during the disturbance period of the space environment. However, this model was developed by the statistical learning using only disturbed-days data, so that the transition from the quiet days to disturbed days (commencement of the electron flux enhancement) was not reproduced well.

The objective of this study is to establish the prediction system to be applied to an actual space operation. We first attempt the prediction of the high-energy electron flux enhancement by means of the neural network using the much amount of the data obtained by the spacecraft and ground network observations. Then we validate the accuracy of the prediction by using the prediction efficiencies (*PE*) for the various combinations of the input parameters.

II. DATA SET

The electron flux enhancement generally occurs during the magnetic storms which have some precursor variations in the other monitored data.

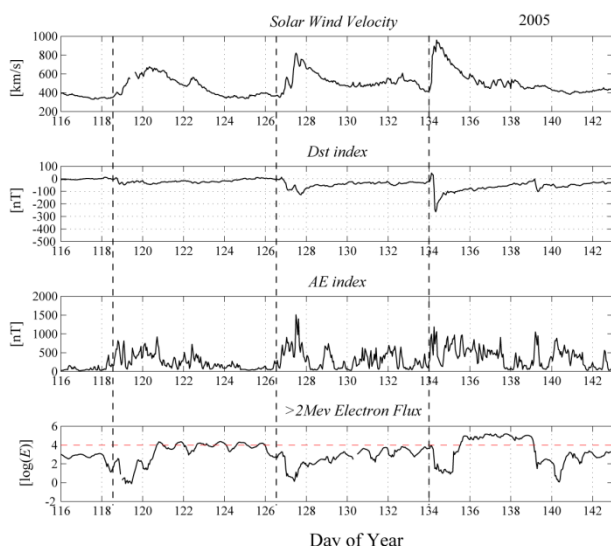


Fig1. Example data of the electron flux enhancement

The bottom panel of Fig.1 shows the electron flux variations for 27 days in 2005. The horizontal axis is Day of year (Jan. 1 = 1 and Dec. 31 = 365). The electron flux increases in 121 and 136 days and exceeds the horizontal dashed line which indicates the alert level for the spacecraft's interference. On the other hand, the obvious precursor could be seen (in the vertical dashed lines), that is, the increasing of the solarwind velocity (top panel) and AE index (third panel) precede the electron flux enhancement by 2 days. The Dst index (second panel) shows the sudden decreasing preceding the electron flux enhancements.

In this study, we use the solarwind data which is observed by Advanced Composition Explorer (ACE) space craft. The dataset of the solarwind consists of the velocity (V_{sw}), north-south component of the magnetic field (B_z) and 3-days integration of epsilon parameter ($\Sigma\epsilon$) (which is calculated from the velocity and magnetic field and is consistent with the electromagnetic poynting flux from solar wind to the earth). The (Auroral Electrojet) AE index is determined from the magnetic field variations observed on the high-latitude ground observatories and is proxy of the Auroral activity due to the solarwind disturbances. The Disturbed field during Storm Time (Dst) index is also determined by the ground magnetic variations. Since the

magnetic observatories used in calculation for the Dst index are not at high latitude but at low latitude, the Dst index is generally utilized for the definitive scale of the magnetic storms (which is major electromagnetic disturbances in the space environment). The high-energy ($>2\text{MeV}$) electron flux (E) at the geosynchronous orbit is observed by the GOES 10 satellite operated by National Oceanic and Atmospheric Administration (NOAA). In the preparation for the analysis, we removed the error data from the hourly data for each observed data in the interval from 1998 to 2006, and got 74376 samples for each hourly data.

III. Neural Network

In this study, since the output data of the model is 24-hours-later prediction, the output data could not physically affect the past data used as the input parameter in actual causality. Thus, we adopted the feed-forward neural network model with the back-propagation leaning method to predict the 24-hours-later electron flux variations. Fig.2 represents the schematic illustration of the network model used in this study. The network consists from arbitrary number of middle layers which also consist from arbitrary number of neurons.

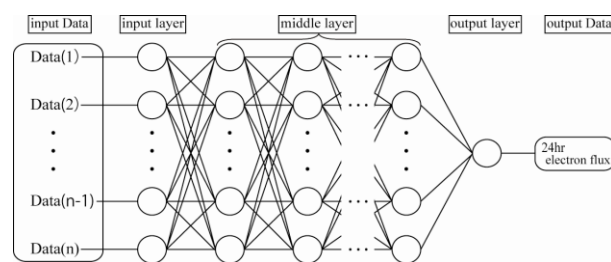


Fig.2 schema of neural network

All the data obtained from 1998 to 2006 were normalized in the range from -1 to 1 to be used as input parameters. In each neuron, input parameters are weighted with an appropriate weight and a sum of the weighted input is send to the transfer function of transient sigmoid. As a result, one output data can be obtained through the reiteration of above mentioned scheme. Then output parameter (O_p) for the input parameters with the arbitrary pattern (p) is compared with the observed 24-hours-later electron flux (T_p)

which is supervised data, and validate the following error function (E).

$$E = \frac{1}{2} \sum_p (O_p - T_p)^2$$

The appropriate weight for each neuron is determined by the steepest descend method to minimize E . In this analysis the reiterating calculation stopped under the condition that the error function E reaches less than 0.01.

IV. Result of the analysis

In the training process, various combinations of input parameters were attempted to evaluate the accuracy of the prediction. In order to quantitatively evaluate the accuracy of the prediction, we calculated the prediction efficiency (PE) which was adopted by NOAA Space Weather Prediction Center (SWPC) [4] as

$$PE = 1 - \frac{MSE}{VAR}$$

$$VAR = \frac{1}{N} \sum_{i=1}^N (x_i - \bar{x}_i)^2$$

$$MSE = \frac{1}{N} \sum_{i=1}^N (f_i - \bar{x}_i)^2$$

where x_i and f_i are observed and predicted values of electron flux, respectively. Thus PE is based on the mean square error which is normalized by variance of the observed values.

We classified the input parameters into three cases, that are, (1) data basically obtained in the space (E , V_{sw} , B_z , $\Sigma\mathcal{E}$, UT), (2) data basically obtained on the ground (E , Dst , AE , UT), (3) combination data obtained both in the space and on the ground (E , V_{sw} , Dst , AE , UT), here UT means Universal Time. For each case, the training was conducted using the data from 1998 to 2006 except 2003. It is known that the solarwind had been much disturbed in 2003 due to the large coronal hole appeared on the surface of Sun, so that we attempted the validation of the prediction to calculation of PE for the predicted electron flux with the observed data in 2003.

We attempted the various combination of the number of middle layers and neurons for above three cases. The result is shown in Fig3. In cases 1 and 2, the relationship between the number of neurons and middle layers are not clear and the maximum PE is less than 0.58. On other hand, in case 3, the dependence of PE on

the number of neurons and middle layers is in the orderly manner. The maximum PE of 0.61 is shown under the condition that number of neurons is more than 6 and number of middle layers is less than 4. This result means that the prediction of the electron flux shows the best performance using the both data observed in the space and on the ground.

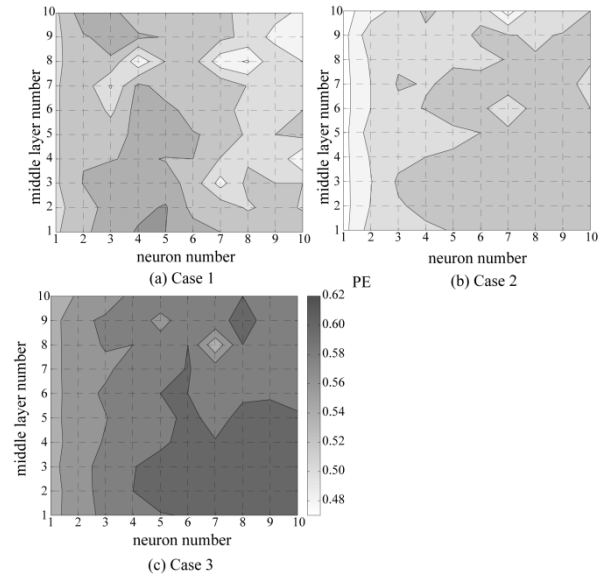


Fig3. Result of the network turning for 3 cases

For the case 3, the comparison between the predicted electron flux and observed electron flux is shown in Fig4. The enhancement of the electron flux is well predicted in entire variations though predicted line (solid line) sometimes shows the over estimation comparing to the observed line (dotted line).

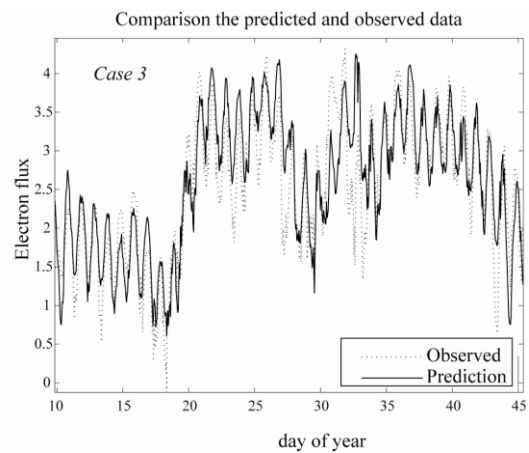


Fig4. Comparison between the predicted and observed variations

The both predicted and observed values for all data in 2003 are shown in the scatter plot of Fig4 to validate the prediction accuracy in more details. The vertical and horizontal axes are the observed and predicted values, respectively. The plots are fairly scattered in the condition that the flux is less than 4, which means the predicted values sometimes deviate from the observed values. In the condition that flux is more than 4, the plots become to concentrate on the dashed line, though the distribution of plots shows the overestimate tendency of ~10%. In terms of the application of the electron flux prediction to the actual space operation, ~10 % of the overestimation could be acceptable to avoid the risk, by contrast the underestimation of the predictions connotes a significant risk for real operations.

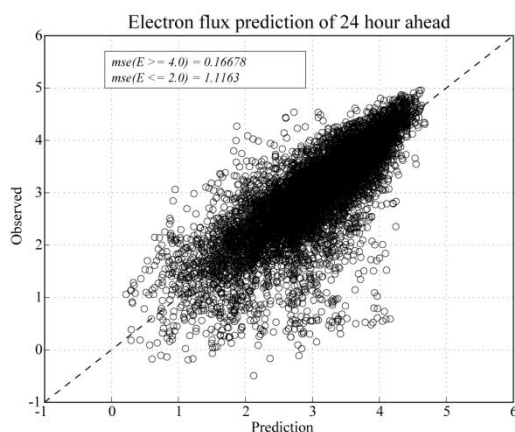


Fig5. Scatter plot of the predicted and observed values

VI. CONCLUSION

In the present study, we attempted the high-energy electron flux variations using the feed-forward neural network with back-propagation learning method. We could summarize the present study as follows. (1) The maximum *PE* shows 0.61 with input parameters obtained both in the space and on the ground. (2) The accuracy of the prediction increases with increasing an amount of the electron flux and tends to be an overestimation of ~10%. These results indicate that the present neural network model could be adopted in the real space environment forecast operation.

ACKNOWLEDGEMENT

The solarwind data obtained by ACE spacecraft and the high-energy electron flux data are provided from National Oceanic and Atmospheric Administration (NOAA). The *Dst* and *AE* indices are provided from World Data Center (WDC) for Geomagnetism, Kyoto.

REFERENCES

- [1] Baker DN, McPherron RL, Cayton TE et al. (1990), Linear prediction filter analysis of relativistic electron properties at 6.6 RE, J. Geophys. Res, 95, 15133-15140
- [2] Koga S, Koshiishi H, Matsumoto H et al. (2006), Prediction of electron flux variations at radiation belt, JAXA-SP-05, P24 (in Japanese)
- [3] Fukata M, Taguchi S, Obara T (2002), Neural network prediction of relativistic electrons at geosynchronous orbit during the storm recovery phase: effects of recurring, Annales Geophysicae, Vol.20, 947-951.
- [4] NOAA/SWPC (2008), Relativistic Electron Forecast Model Documentation, <http://www.swpc.noaa.gov/refm/doc/REFMDoc.html>

A Diagrammatic Classification in a Combinatorial Problem: The Case of a Stable Marriage Problem

T. Hayashi, Y. Hata and Y. Ishida

*Toyohashi University of Technology,
1-1 Hibarigaoka Tenpaku-cho, Toyohashi, Aichi 441-8580, Japan
(Tel.: +81-532-44-6895; Fax: +81-532-44-6895)
(E-mail: ishida@cs.tut.ac.jp)*

Abstract: The Stable Marriage Problem (SMP) is a combinatorial problem to find stable matching between n women and n men given a complete preference list of men over women and vice versa. An instance of SMP can be expressed by a bipartite graph with multiple (weighted) edges. By rearranging the graph, we use a diagram that involves several constraints to visualize several symmetries. By the diagram, all the instances of the size three SMP (three women and three men) are classified. The classification may be supported by the fact that the same class has the same stable matching.

Keywords: Graph equivalence, diagrammatic classification, stable marriage problem, stable matching, decomposition, bipartite graph, stable marriage graph.

I. INTRODUCTION

After the proposal of the matching problem by Gale and Sharpley [1], many matching problems including stable marriage problem (SMP) [2] have been studied extensively. Stable marriage problem is a combinatorial problem to find stable matching between n women and n men given a complete preference list of men over women and vice versa. Stable marriage problem has several variants such as a job assignment problem, roommate problem varying the assumption on the set of members to be matched.

Although the stable marriage problem has too strong assumptions (such as complete list of preference) to be applied to practical problems, symmetries embedded in the problem keep us being attracted. Thus, we tried to visualize the problem by network visualization tool [3]. This paper further focuses the decomposability of the problem by involving diagrams such as a bipartite graph and a stable marriage graph [4, 5].

As a preliminary example, we presented a classification of indecomposable structure of size three (three men by three women) SMP. Decomposition of the problem may be a first thing to do in tackling a complex problem. For SMP, component decomposition [2] and weak (but applicable to the preference matrix) decomposition [6] have been studied. In classifying the size three SMP, we tried to generalize a concept of *mutual infatuation* (a pair of man and woman who rank the partner first). A cycle of first rank relation plays an important role in classifying the SMP.

Section II presents the stable marriage problem and its graphical representation. Section III defines equivalence of instances of SMP through graph homomorphism (equivalence). Section III presents a classification of SMP by diagrams (bipartite graph and marriage graph).

II. STABLE MARRIAGE PROBLEM

The Stable Marriage Problem (SMP) assumes n women and n men each of them has an ordered preference list (or a ranking) without tie to the opposite sex. As in the example shown in Fig. 1, the men m_2 has an ordered preference list (w_3, w_2, w_1) or a ranking (3, 2, 1), which means m_2 likes w_3 best, and he prefers w_3 to w_2, w_2 to w_1 . That is, there is an injection (one to one, but not necessarily onto) mapping from a set of women (men) to an element of permutation group of size n such as shown in the ranking by each person (Fig. 1). We will use a graph that extracts a specific rank (such as the first preference) in classification.

Under the above assumptions, SMP seeks for the complete matching between n women and n men (a bijection from n women to n men), which satisfies stability. The stability requires the concept of blocking pair. Two pairs (m_i, w_p) and (m_j, w_q) are blocked by the pair (m_i, w_q) if m_i prefers w_q to w_p and w_q prefers m_i to m_j . For example, a pair (m_2, w_3) and (m_3, w_2) will be blocked by the pair (m_2, w_2) . A complete matching without being blocked is called *stable matching*.

An instance of SMP can be expressed by a multiple (arcs) bipartite graph in a straightforward way such that an arc of k -th order from m_i to w_j is directed if m_i ranks w_j k -th. Another graphical expression of an instance is the *stable marriage graph* [4,5]. For SMP with size n by n , n^2 nodes of possible pairs (m_i, w_j) are placed in a matrix form. For a row of m_i , an arc from (m_i, w_p) to (m_j, w_q) is placed if m_i prefers w_q to w_p . Fig. 2 shows a stable marriage graph corresponding to the instance shown in Fig. 1. A stable marriage graph can be simplified (as in Fig. 2). In a simplified stable marriage graph, redundant nodes may be abbreviated if it can be derived by a transitivity. For example, if m_1 prefers w_1 to w_2 , and w_2 to w_3 , it follows that m_1 prefers w_1 to w_3 hence the corresponding arc is abbreviated.

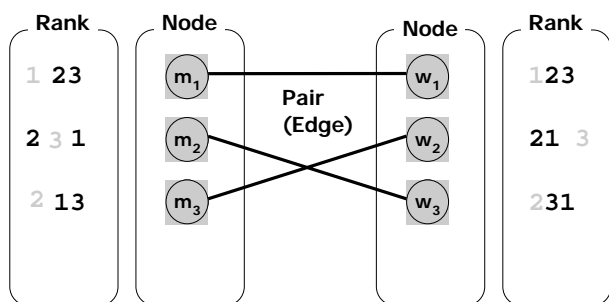


Fig. 1. An illustration of Stable Marriage Problem with size three.

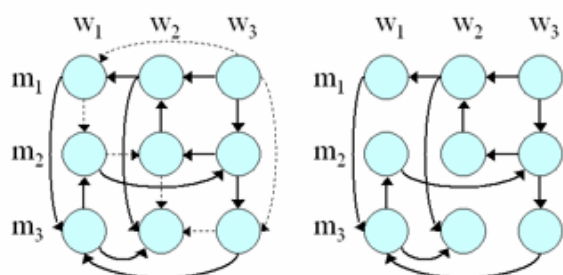


Fig. 2. A stable marriage graph (left) and its simplified one by removing redundant arcs with transitivity (right).

III. EQUIVALENCE OF INSTANCES THROUGH GRAPH

Prime numbers remain to be a mystery not only in discrete mathematics such as Integer Theory but in continuous mathematics such as theory of functions. Prime numbers also plays an important role of an engine for mathematics and other applied mathematics such as cryptography.

Prime numbers are defined on the set of integers by means of factorization with division operation. The

primeness could be defined on other mathematical objects with structures such as instances of Stable Marriage Problem. With expectation of the important role played by “primeness” in the instances of SMP, we study several type of decomposition in instances of SMP, and indecomposable structure of them.

Decomposition of SMP had been traced back to the book by Gusfield and Irving [2], and have been studied [6]. Here, we focus on a decomposability that will be naturally considered by two independence concepts: the concept of extended individual and an independent pair. The extended individual is a set of individuals that can be dealt as if one individual in finding stable matching. The independent stable pair is the two entities that can be paired without affecting any other possible pairs, and hence the pair appears in any stable matching. The decomposition leads to indecomposable structures, yielding a full classification of SMP with size three.

As an example of extended individuals, consider the case of SMP with nationality in members. Half of the members are Japanese and the other half American both in female and male. Assume any woman (man) prefers man (woman) with the same nationality to man (woman) otherwise. Then Japanese women (men) as well as American women (men) can be treated as if they are one woman (man). We use this example also as an example of trivial decomposition of SMP. In fact, this SMP is actually two independent SMPs: one between Japanese women and men and another between American women and men.

As a trivial example of independent pair, woman and man who mutually rank first can be paired without affecting any other pairing. A nontrivial example would be the pair who would turn out to be mutual first rank only after removing the above the trivial independent pair. We call this latter one the independent pair hidden by the former obvious independent pair.

IV. CLASSIFICATION VIA DIAGRAMS

1. Indecomposable Structure by Bipartite Graph

Trivial example of the indecomposable structure in SMP is those with size one (Fig. 3). Obvious example may be the size two (Fig. 4), for we need to eliminate the graph of the size one (otherwise it can be decomposed to two size one SMPs). In the enumeration, we do not distinguish the ones that can be mapped by

the label exchange within the same sex, and exchange the sex with all the members.

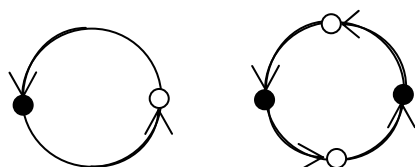


Fig.3. Indecomposable structure of size one (left) and size two (right). Nodes with different color indicate persons with different sex, and arcs indicate the first preference.

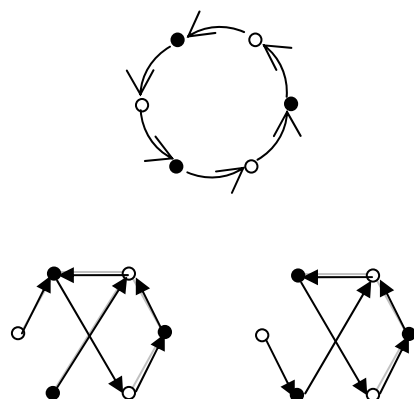


Fig. 4. Indecomposable structure of size three SMP. Arcs of the first preferences are shown. They will be called type 0 (above), 1 (below, left) and 2 (below, right)

2. Indecomposable Structure by Stable Marriage Graph

Stable marriage graph can be reduced by removing nodes dominated by a man optimal node or a woman optimal node, since the pairs corresponding to the nodes dominated do not appear in any stable matching.

By a graph homomorphism of reduced stable marriage graph, all the instances of SMP with size three can be classified to the six classes (Fig. 5). Among them, classes 3, 4, 5 and 6 correspond to indecomposable structure.

We will further classify the SMP with size three by a multiple (arcs) bipartite graph, since several operations are required to obtain the reduced stable marriage graphs, although once obtained they even reveal the structure of stable matching.

Decomposable size 3 SMP	class 1		class 2	
Indecomposable size 3 SMP	class3	class4	class5	class6

Fig.5. Classification of size 3 SMP by a graph homomorphism in the reduced stable marriage graph.

3. Classification of Indecomposable SMP

We will further classify three types based on the bipartite graph of second preference.

Type 0 (Fig. 6) is the simplest, since they can be mapped to class 3, 4, 5, and 6, respectively, by the number of cycles of length two in the bipartite graph of second preference (Fig. 6).

Cycles of 2 nd pref.	Reduced SMP graph

Fig. 6. Indecomposable structures of type 0, size three SMP.

Type 1 (Fig. 7) can be divided into five subtypes, one of which belongs to class 4 (Fig. 5) and the rest to class 3. In the graph, the arcs (of second preference) included in a cycles of length four that appears in the first preference (Fig. 4) but opposite directions are omitted. It can be observed that when the class is

upgraded from class 3 to 4, the arc is added and the number of cycles with length two increases. The graph obtained by adding an arc to the original graph is placed to the right of the original graph.

Type 2 (Fig. 8) are divided into twenty subtypes. Among them, twelve subtypes belong to class 3, seven to class 4, and one to class 5. Again, it can be observed that when the class is upgraded, the arc is added. The number of cycles with length two increases when the class is upgraded from 3 to 4 and 4 to 5, however, it is not true from 3 to 5, although the length 4 cycle with the first preference and second preference mixed appears in the jump from the class 3 to 5.

Indecomposable SMP (size 3 by 3)		
Class 3		Class 4
Arcs of 2 nd preference		

Fig. 7. Indecomposable structures of type 1, size three SMP.

V. SUMMARY

We first classified all the instances of the size three stable marriage problem (SMP) into six classes by the reduced stable marriage graph. Among six classes, four classes correspond to indecomposable structure. Then, we have classified all the instances of indecomposable stable marriage problem with size three into three types based only on the bipartite graph of the first preference. Each type can further be classified to subtypes based on the second preference structure. By mapping these structure to the three classes induced by the reduced stable marriage graph, it is shown that the cycle in a bipartite graph plays a curtail role.

Indecomposable SMP (size 3 by 3)				
Class 3		Class 4		Class5
Arcs of 2 nd preference				

Fig. 8. Indecomposable structures of type 2, size three SMP.

REFERENCES

- [1] Gale D and Shapley LS (1962), College admissions and the stability of marriage, *American Mathematical Monthly*, 69:9-15
- [2] Gusfield D and Irving RW (1989), *The Stable Marriage Problem: Structure and Algorithm*, MIT Press, London
- [3] Morizumi Y, Hayashi T, Ishida Y. (2009) A Network Visualization of Stable Matching in Stable Marriage Problem, *Proc of AROB*
- [4] M. Balinski and G. Ratier, Of stable marriages and graphs, and strategy and polytopes. *SIAM Review* 39 (1997) 575 – 604.
- [5] Nemoto T. (2002) *Handbook of Applied Mathematical Programming*, ASAKURA SYOTEN, 779-830 (in Japanese)
- [6] Veklerov E (1989), On the decomposability of the stable marriage problem. *BIT Numerical Mathematics*, 29(1): 41-46

A Neuro PID control of Power Generation using Low Temperature Gap

Kun-Young Han, Hee-Jae Park, and Hee-Hyol Lee

*The Graduate School of Information, Production and Systems, Waseda University, Kitakyusyu, 808-0135, Japan
2-7 Hibikino, Wakamatsu-ku, Kitakyushu, Fukuoka 808-0135, Japan
(Email address: kyhan@akane.waseda.jp)*

Abstract: Recently, renewable energy is increasingly attractive in solving global problem such as the environmental pollution and energy shortage. Among varieties of renewable energy resource, power generation using low temperature gap has received much attention of researchers. However, this system is difficult to control because each of the components of this system, such as heat exchanger, working fluid and turbine, has a dynamic characteristic or nonlinear factor. In order to overcome this problem, PID controller based on neural network for power generation using low temperature gap is designed to keep the stable speed of the steam turbine in real environment.

Keywords: Power generation, Evaporator, Turbine, PID control, neural network

I. INTRODUCTION

A strong interest in distributed generations using renewable energy such as wind and solar energy have been attracted because the fossil energy will be exhausted in the future and its use causes the environmental issue. Among them, there is some renewable energy that has not yet been used, such as the heat from hot springs or exhaust heat from factories. However, the power generation using these unused renewable energies can only produce a small amount of heat but also have relatively low heat efficiency. Moreover, these heat sources are scattered and their scale are small[1]. Therefore, the suitable control methods must be developed to overcome these problems in that capacity and scale.

On the other hand, the power generation using the low temperature gap used in this paper includes dynamic characteristics and nonlinear factors. Although this system contains these complex factors, most of the control algorithms are based on linear models. The linear models deduced from step responses and impulse responses are desirable, because they can be identified in a straightforward manner. In addition, a goal for most of the applications is to maintain the system at a desired steady state, so a precisely identified linear model is sufficiently accurate in the neighborhood of an operating point. As this point of view, the power generation using low temperature gap based on the approximate linear models are designed in this paper.

PID control is used in process field in generally. Despite PID controllers are applicable to many controlled system, it performs poorly in complex system. Therefore, PID controller cannot be applied directly in

the complex systems. In this paper, an improved neural network, which shows excellent performance for nonlinearity is applied to the power generation using temperature gap. Initial values of a neuro PID controller use the parameters obtained from the linearized model. This paper composed as follows. The power generation system using low temperature gap and each of the components such as an evaporator and a condenser based on heat balance equation, and a turbine element are modeled in Section 2. In the section 3, a traditional PID control is introduced and a neuro PID controller is proposed for the power generation using low temperature.

II. Dynamic modeling of power generation using low temperature gap

The main components of the power system using the low temperature gap with closed cycle are constructed of the heat exchanger (evaporator and condenser), turbine, and pumps. The simple structure of the power generation system using the low temperature gap is shown in Fig.1.

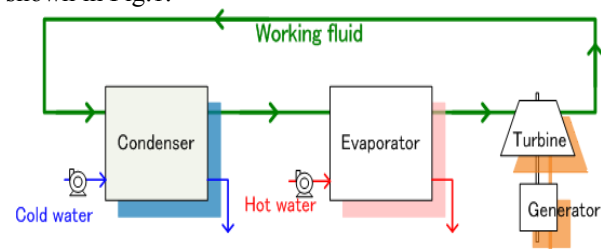


Fig.1. Power generation using the low temperature gap with closed cycle.

2.1 Evaporator model

The evaporator is a shell-and-tube type as shown in Fig.2. The working fluid is a liquid and moves to the

evaporator by a pump. And then the working fluid is boiled and changed to steam in the evaporator by hot water.

Modeling assumption

- 1) Working fluid evaporating pressure is constant in static state.
- 2) Latent heat of working fluid keeps no change.
- 3) Evaporating flow supplies a quantity of heat.

The heat balance equation of hot water, the working fluid, and supply heat are defined as follows [2].

$$\nu_h(\partial \theta_h / \partial x) + (KU / \omega_h)(\theta_h - \theta_s) = 0 \quad (1)$$

$$G_v(h'' - h') = Q \quad (2)$$

$$Q = \int_0^L KU(\theta_h - \theta_s)dx \quad (3)$$

where, ν_h is a speed of a moving fluid of hot water, θ_h is a temperature of hot water, x is a distance, K is a heat transmission coefficient, U is a heating surface area per unit time, ω is heat capacity per unit time and θ_s is a temperature of saturated water vapor.

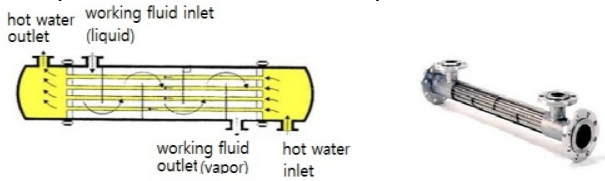


Fig.2. Structure of the evaporator

2.2 Turbine model

The turbine is composed of the steam control valve and a rotor blade. The block diagram of the turbine is shown in Fig.3. The steam is moved from the evaporator to the turbine blade through the steam control valve. It adjusts the flow of steam to the turbine blade. The equations of the turbine systems are given as follows [3]. Mass rate and a control valve of the working fluid steam are defined by Eqs.(4),(5), respectively, and the turbine blade speed is defined by Eq.(6)

$$\mu_T = \frac{\alpha_T \frac{A_1}{A_E}}{M_E [\nu(\alpha_T)]^{1/2}} (P_E - P_T)^{1/2} \quad (4)$$

$$a_1 \frac{dx_1}{dt} = K_3 \left(\frac{\nu}{\nu_{\max}} \right), \quad (0 \leq x_1 \leq 1) \quad (5)$$

$$\frac{d\nu}{dt} = \frac{1}{\tau_T} \left[\frac{P'_E - P'_T}{P'_E - P'_T} \frac{\mu_T}{\nu \mu_T} - (1 - \eta) \frac{\xi(t)}{\nu} - \eta \nu^2 \right] \quad (6)$$

where, α_T is a area of divergence of the valve, A_1/A_E is a cross-sectional area of a pipe leading from the evaporator to the turbine, P_E is a vapor pressure at the evaporator outlet, P_T is a vapor pressure at the turbine outlet, K_3 and a_1 are the gain, ν_{\max} is a maximum speed of the turbine blade, M_E is a constant parameter, τ_T is a system constant, η is a coefficient of loss, ξ is a electric load, and $\overline{P'_E}$, $\overline{P'_T}$, $\overline{\mu_T}$ are desire values.

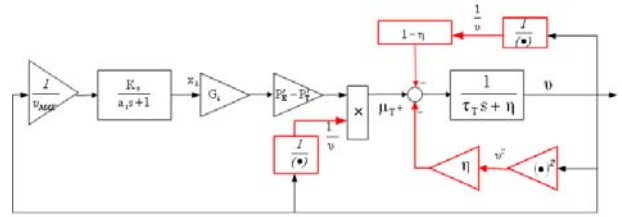


Fig.3. Block diagram of turbine

Linear approximate turbine model

The linear approximate turbine model is obtained by approximating the turbine. Fig.4 shows the linear approximate turbine model, which includes 1st and 2nd order delay elements and dead time element.

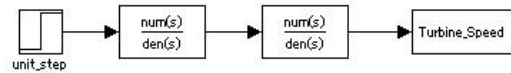


Fig.4. Linear approximate turbine model

2.3 Modeling of power generation system as MIMO system

The evaporator and the condenser are modeled as a multi-input multi-output model(MIMO) illustrated in Fig.5.

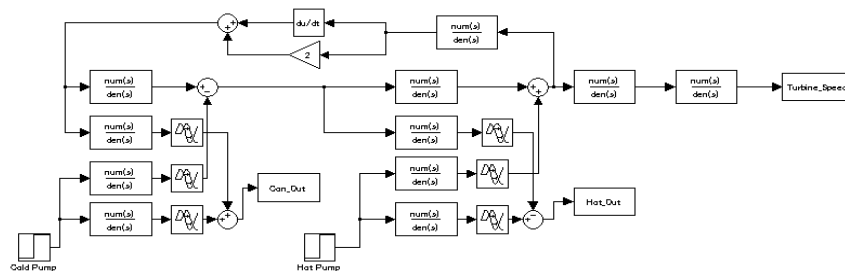


Fig.5. MIMO system for the Power generation

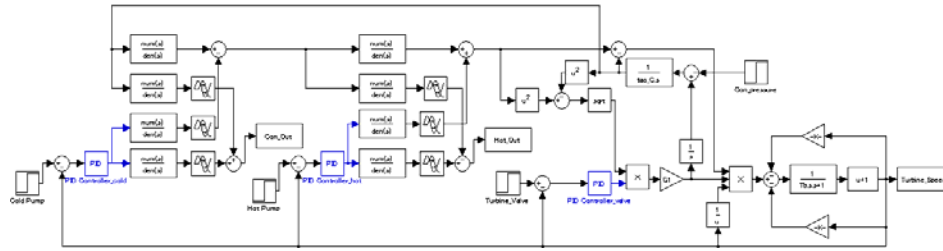


Fig.7. Block diagram of Power generation system with PID controller

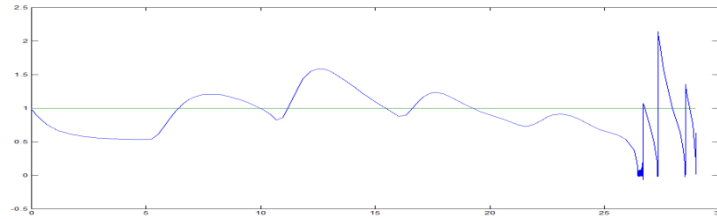


Fig.8. Result of control using PID controller

III. Neuro PID controller

3.1 PID Control

A schematic of a system with a PID controller is shown in Fig.6. The PID controller compares a measured process value y with a reference value r . The difference or error e is then processed to calculate a new process input u . This input will try to adjust the measured process value to the desired value. PID controller is widely used in industrial control systems.

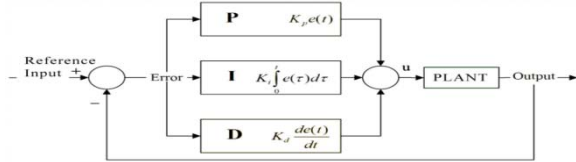


Fig.6. Block diagram of a PID controller

PID algorithm is formed as follow,

$$u(t) = K_p e(t) + K_i \int_0^t e(\tau) d\tau + K_d \frac{d}{dt} e(t) \quad (7)$$

where, K_p is proportional gain, K_i is integral gain, K_d is the differential gain, and $e(t)$ is the error.

3.2 PID tuning

There are several methods for tuning the PID parameters. The parameters are obtained by using the step response method and the ultimate sensitivity method. Fig.7 represents the block diagram of the power generation system with PID controller, and Fig.8 is a result of control using PID control.

3.3 Neuro PID Controller

The PID controller does not lead to good performance. In this paper, PID controller with a neural network is considered, and shown in Fig.9.

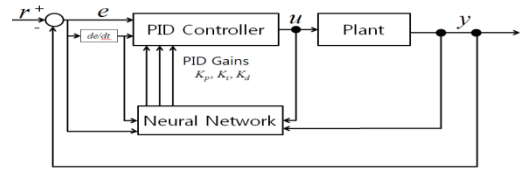


Fig.9. Structure of neuro PID controller

BP network structure

The BP neural network is a multi-layer perception neural network, which consists of three components: input layer, hidden layer, and output layer. The output layer corresponds to the values, which are three adjustable parameters K_p , K_i , and K_d , as shown Fig.9. Therefore, each of parameters can be adjusted by self learning ability of the neural network. And the best values of them can be obtained corresponding to the outputs of BPNN with a certain optimal control law. The PID algorithm is given by Eq.(8).

$$\begin{aligned} u(t) &= u(t-1) + \Delta u(t) \\ \Delta u(t) &= u(t-1) + K_p(t)(e(t) - e(t-1)) + K_i(t)e(t) \\ &\quad + K_d(t)(e(t) - 2e(t-1) + e(t-2)) \\ e(t) &= r(t) - y(t) \end{aligned} \quad (8)$$

where, u is the control value, r is the reference value, and y is the actual output value. On the other hands, the inputs and outputs of the hidden layer in the neural network are given by Eq.(9).

$$\begin{aligned} net_i^2(t) &= \sum_{j=0}^M w_{ij}^{(2)} O_j^{(1)} \\ O_i^{(2)}(t) &= f(net_i^2(t)) \quad (i=1,2,\dots,Q) \\ net_l^{(3)}(t) &= \sum_i^Q w_{li}^{(3)} O_i^{(2)}(t) \\ O_l^{(3)}(t) &= g(net_l^{(3)}(t)) \quad (l=1,2,3) \end{aligned} \quad (9)$$

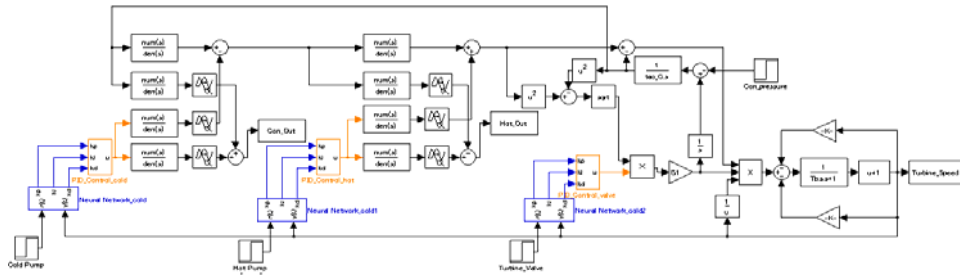


Fig.10. Block diagram of Power generation system with Neuro PID controller

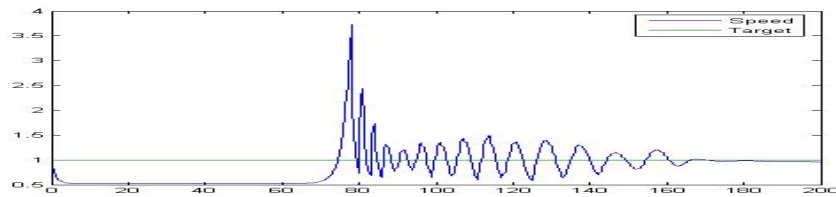


Fig.11. Result of control using Neuro PID controller

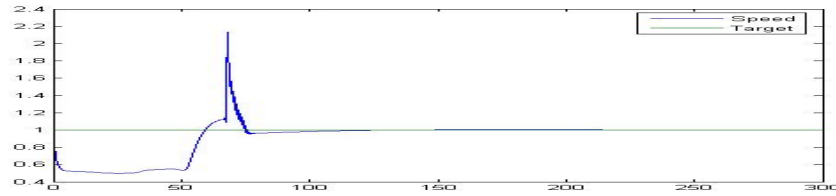


Fig.12. Result of control of Neuro controller using the initial value based on linearized model

where, M and Q are the neuron numbers of the input and hidden layer, respectively, w is the weight, net is the input, and O is the output. The superscript (1), (2) and (3) denote the input, the hidden, and the output layer. f and g are activation functions of the hidden layer and the output layer. Obviously, $O^{(3)}$ is K_p , K_i and K_d . Parameters of K_p , K_i and K_d , which are obtained from the linear approximate model, are used as initial values in this paper. The weights of BPNN are updated according to the gradient-descent algorithm.

$$\Delta w(t) = -\eta [\partial E(t) / \partial w(t)] + \alpha \Delta w(t-1) \quad (10)$$

where, η and α are defined as learning rate and inertia factor, respectively. The inertial item $\alpha \Delta w(t-1)$ is added to accelerate convergence. The manual differentiation method is used to increase the accuracy the value of $\partial E(t) / \partial w(t)$ in Eq.(10). The algorithm of updating the weights for the output layer is given as follows.

$$\Delta w_{li}^{(3)}(t) = \alpha \Delta w_{li}^{(3)}(t-1) + \eta \delta_i^{(3)} O_i^{(2)}(t)$$

$$\delta_i^{(3)} = e(t) \operatorname{sgn}\left(\frac{\partial y(t)}{\partial u(t)}\right) \frac{\partial u(t)}{\partial O_i^{(3)}} \dot{g}(net_i^{(3)}(t)) \quad (l=1,2,3) \quad (11)$$

The process to acquire $\partial E(t) / \partial w(t)$ is complex and fallible especially when the activation functions are complicated or Q is greater than 1. Besides that, according to Eq.(11), the value of the item $\partial y(t) / \partial u(t)$ is substituted by its sign function. That is to say, it is set to be 1 or -1. The impreciseness produced here can be compensated by η . The PID controller with BPNN is applied as shown in Fig.10, and a result of PID control

using BPNN is represented in Fig.11 while K_p , K_i , K_d do not use as initial value. A result of PID control using BPNN is shown in Fig.12 while the initial values of K_p , K_i , and K_d are used based on the linearized model.

V. Conclusion

The power generation system, which consists of the evaporator, the condenser, and the turbine are designed. The conventional PID controller has the advantage of simple structure, good stability, easy to engineering implementation and so on. However, for the complex system such as the power generation system using low temperature gap using the traditional PID control is more difficult to obtain good control performance. This paper combines the BP neural network and PID control. The PID parameters from the linear model are used as initial value in the output layer of BPNN. The neuro controller proposed is successfully implemented.

REFERENCES

- [1] Satomi S, K-Y H, J-S S, et.al (2010) A learning control of unused energy power generation. International symposium on AROB 15th.
- [2] Hashizume T, Kawai S, Machiyama T (1981) Experimental studies on the dynamic characteristics of evaporator in the L.B.M. turbine system. Jpn Soc Mech Eng C 47(421):1161–1168.
- [3] Owens WL (1982) OTEC plant response and control analysis. ASME J Solar Energy Eng 104:208–215.

An Efficient Identification Scheme for Nonlinear Polynomial NARX Model

Yu CHENG, Miao YU, Lan WANG and Jinglu HU

*Graduate School of Information, Production and Systems, Waseda University
Hibikino 2-7, Wakamatsu, Kitakyushu, Fukuoka, 808-0135, Japan
(Tel/Fax : 81-93-692-5271)
(chengyu0930@fuji.waseda.jp)*

Abstract: Nonlinear polynomial NARX model identification often faces the problem of huge pool of candidate terms, which makes the evolutionary optimization based identification algorithm work with low efficiency. This paper proposes an efficient identification scheme with pre-processing to reduce the searching space effectively. Both the input selection and term selection are implemented to truncate the candidate pool with the help of correlation based orthogonal forward selection (COFS) algorithm and simplified orthogonal least square (OLS) algorithm, respectively. Then multi-objective evolutionary algorithm (MOEA) is used to identify the polynomial model in a relative small searching space.

Keywords: nonlinear polynomial model identification, input selection, term selection, efficient

I. INTRODUCTION

Recently, nonlinear polynomial NARX (Nonlinear AutoRegressive with eXogenous inputs) model has attracted much attention because it has shown great potential in the ability of approximating nonlinear input-output relationship. As a kind of effective approach, evolutionary optimization algorithms, such as genetic algorithm (GA) and multi-objective evolutionary algorithm (MOEA) have been commonly used for identification of nonlinear polynomial NARX model. However, it is still considered as a difficult task because the size of candidate terms increase drastically with maximum time delay of input-output data and nonlinearity of polynomial model [1].

So far, some related research has been devoted to complex nonlinear system identification. Ref. [2] claims that a hierarchical encoding technique is introduced to be effective for identifying polynomial models with relatively high-nonlinearity, however, it is just an improvement of GA, and as told by the authors, the process is still time-consuming and easily traps into a local optimum. Moreover, a two-step scheme for polynomial NARX model identification has been proposed in our previous research [3]. It combines heuristic optimization approach with pre-screening process, in which the simplified orthogonal least square (OLS) based term selection method is used to formulate a relative small searching space. However, the selection of input variables is not considered, which has significant influence on the pruning of searching space.

In this paper, an efficient identification scheme is proposed for nonlinear polynomial NARX model with

both input selection and term selection methods [4], which can be seen as pre-processing for evolutionary optimization based searching processing. Firstly, correlation based orthogonal forward search (COFS) algorithm is applied, which makes the orthogonal input variable with maximum correlation coefficient of output select one by one. The final library consisting of all the necessary variables could be determined according to the threshold by the user. Although it is considered somehow not very accurate, it could exclude most of the redundant inputs thus reduce the original candidate pool effectively. Then, term selection will be implemented by using correlation analysis and the simplified OLS algorithm, hence the searching space could be limited within small size. At last, MOEA is used to identify the polynomial model in the reduced space. Simulations are intent to show the effectiveness of the proposed method.

This paper is organized as follows: Section 2 briefly describes the problem to be solved. Section 3 discusses the identification scheme in detail. Section 4 provides numerical simulations to demonstrate effectiveness of the new method, and Section 5 presents the conclusions.

II. STATEMENT OF THE PROBLEM

Consider a single-input-single-output (SISO) nonlinear time-invariant system whose input-output dynamics is described as

$$y(t) = f(x(t)) + e(t) \quad (1)$$

$$x(t) = [x_1(t), x_2(t), \dots, x_n(t)]^T$$

where $x(t)$ is an n -dimensional input vector, y and e denote an output and white noise vector respectively, and $f(\bullet)$ is a nonlinear function.

In the case of nonlinear NARX model, $x(t) = [y(t-1), y(t-2), \dots, y(t-n_y), u(t-1), u(t-2), \dots, u(t-n_u)]$, where y and u are the system input and output. n_u and n_y are unknown maximum delays of input and output.

However, many of the input variables are often redundant and only a subset of them is significant. It is pointed that there are at least two problems induced [5]. First, the model complexity will increase drastically with the number of variables. Second, including irrelevant variables leads to the over-fitting problem, and as a consequence the model may tend to be oversensitive to training data and is likely to exhibit poor generalization properties.

III. IMPLEMENTATION OF EFFICIENT IDENTIFICATION SCHEME

It is found that evolutionary optimization based approaches are very efficient when the size of searching space is not too large. Based on this fact, input selection and term selection method are used as pre-processing for the efficient identification scheme. Then MOEA is applied to determine a set of significant terms to be included in the polynomial model with the help of independent validation data. Readers interested in the details of MOEA based identification may refer to our previous research [3]. In the following, input selection and term selection for pre-processing will be discussed.

1. COFS Based Input Selection

To select significant inputs with big contribution to the output vector from the whole input space, correlation coefficient could be used to evaluate the relationship between each input variable and the output vector and denoted as

$$C(x_i, y) = \left| \frac{\sum_{t=1}^N (x_i(t) - \bar{x}_i)(y(t) - \bar{y})}{\sqrt{\sum_{t=1}^N (x_i(t) - \bar{x}_i)^2 \sum_{t=1}^N (y(t) - \bar{y})^2}} \right|. \quad (2)$$

x_i and y represent input and output variable, N is the length of measurement. The bigger the correlation coefficient is, the more important the input variable is considered.

In order to exclude the influence from other input variables, orthogonal forward search algorithm is used and significant input variables will be selected one by one. At the first step, let

$$l_1 = \arg \max_{1 \leq i \leq n} C(\mathbf{x}_i, \mathbf{y}) \quad (3)$$

where l_1 is the first important input variable selected from the whole library, and the associated orthogonal variable can be chosen as $\mathbf{q}_1 = \mathbf{x}_{l_1}$.

From the second step, every remained input variable is orthogonalized with all the selected inputs, and each correlation coefficient of output will be calculated. Assumed there are already $m-1$ input variables have been selected, the m -th significant input is selected from remaining pool, and orthogonalized with $\mathbf{q}_1, \mathbf{q}_2, \dots, \mathbf{q}_{m-1}$ as below

$$\mathbf{q}_j = \mathbf{x}_j - \frac{\mathbf{x}_j^T \mathbf{q}_1}{\mathbf{q}_1^T \mathbf{q}_1} \mathbf{q}_1 - \dots - \frac{\mathbf{x}_j^T \mathbf{q}_{m-1}}{\mathbf{q}_{m-1}^T \mathbf{q}_{m-1}} \mathbf{q}_{m-1}. \quad (4)$$

Then the orthogonalized input variable which has maximum correlation with the output is chosen as following

$$l_j = \arg \max_{i \in D} C(\mathbf{q}_i, \mathbf{y}) \quad (5)$$

where D is the subset contains all the remained input variables. As the index to reflect the importance of an input variable, ERR is used to represent the contribution of each input to the output vector. The input variables have very little contribution to the output will be ignored. Based on this fact, a threshold is defined which should make sure all the necessary inputs will be included.

2. Term Selection for Identification

Candidate terms formed by all the selected inputs are still too large if system nonlinearity is high. Therefore, term selection is needed to reduce the candidate pool. In this paper, two importance indices are introduced to evaluate the contribution of each term.

A. Importance Index 1

Importance Index 1 $\mathcal{I}_i^{(1)}$ is used to evaluate the correlation of each monomial term to the system output. Let ρ_i denotes the correlation coefficient of monomial term $y_i(t)$ and system output $y(t)$, calculated by

$$\rho_i = \frac{\sum_{t=1}^N (y_i(t) - \bar{y}_i)(y(t) - \bar{y})}{\sqrt{\sum_{t=1}^N (y_i(t) - \bar{y}_i)^2 \sum_{t=1}^N (y(t) - \bar{y})^2}} \quad (6)$$

Therefore, based on the principle of simplicity, Importance Index 1 should be given by

$$\mathcal{I}_i^{(1)} = \frac{|\rho_i|}{e^{O_i}} \quad (7)$$

where O_i is the order of the i -th term.

B. Importance Index 2

Instead of recursive manner of the original OLS method, a simplified OLS algorithm is introduced, in which all the terms are orthogonalized in one time, and the contribution to the output of each orthogonal one is

calculated and denoted as ERR_i [3]. The principal of simplicity is also applied here, and Importance index 2 is given by

$$\mathcal{I}_i^{(2)} = \frac{ERR_i}{e^{o_i}} \quad (8)$$

Although the two importance indices based term selection scheme is not very accurate, it could be used to prune candidate pool efficiently with all the necessary terms included. Therefore, evolutionary optimization for identification can work efficiently with a small searching space.

IV. NUMERICAL SIMULATIONS

To show efficiency of the proposed identification scheme, two experiments are simulated in this section, which are tested with the assumption that the time-delays are unknown thus big values are given.

1. Example Data Sets

In both two examples, 1000 input-output data sets are sampled for training from each model when the systems are excited using random input sequences with amplitude between -1.0 and +1.0.

2. Systems under Study

Example 1: The system is governed by a polynomial model, described by

$$\begin{aligned} y(t) = & -0.5y(t-2) + 0.7u(t-1)y(t-1) \\ & + 0.6u^2(t-2) + 0.2y^3(t-1) \\ & - 0.7u^2(t-2)y(t-2) + e(t). \end{aligned}$$

Example 2: The system is a nonlinear rational model studied by Narendra in 1990

$$y(t) = f[y(t-1), y(t-2), y(t-3), u(t-1), u(t-2)] + e(t)$$

where

$$f[x_1, x_2, x_3, x_4, x_5] = \frac{x_1 x_2 x_3 x_5 (x_3 - 1) + x_4}{1 + x_2^2 + x_3^2}$$

Here, $e \in (0, 0.1)$ is a white Gaussian noise.

3. Parameter Setting

It is assumed that the time delay for Example 1 and 2 are unknown thus initialized by 10 for both inputs and outputs (totally 20 input variables contained), which are considered big enough. However, when it is assumed the maximum order of each case is five, it is found the candidate terms pool is too large for evolutionary algorithms to search directly. Therefore, COFS based input selection and simplified OLS based term selection are implemented, then NSGA-II [6] is applied to extract all the possible polynomial terms. The details of NSGA-II for system identification are from our previous

research [3].

4. Identification Results

In both cases, the thresholds for COFS algorithm are set as 0.9 and 0.98 after normalization in Example 1 and 2, respectively, then all the input variables selected satisfied with the threshold condition are listed in Tab. 1.

Table 1. Input selection for Example 1 and 2

No.	Inputs selected in Example 1	Inputs selected in Example 2
1	$y(t-2)$	$u(t-1)$
2	$y(t-1)$	$y(t-1)$
3	$y(t-3)$	$u(t-2)$
4	$u(t-1)$	$y(t-3)$
5	$u(t-2)$	$y(t-2)$

To make comparison with some other state-of-art input selection methods, subset from Delta Test method [7], linear OLS method [4], and FOS-MOD algorithm [8] are also generated. The minimal subsets include all the real input variables for each method are given in Tab. 2 and Tab. 3.

Table 2. Results comparison for Example 1

Method	Minimal input subsets	size
COFS	$y(t-1), y(t-2), y(t-3), u(t-1), u(t-2)$	5
Delta Test	$y(t-1), y(t-2), y(t-3), y(t-4), u(t-1), u(t-2), u(t-3)$	7
Linear OLS	$y(t-1), y(t-2), y(t-3), y(t-4), y(t-5), y(t-7), u(t-1), u(t-2)$	8
FOS-MOD	$y(t-1), y(t-2), y(t-5), y(t-7), y(t-9), y(t-10), u(t-1), u(t-2), u(t-4), u(t-5), u(t-7), u(t-9), u(t-10)$	13

Table 3. Results comparison for Example 2

Method	Minimal input subsets	size
COFS	$y(t-1), y(t-2), y(t-3), u(t-1), u(t-2)$	5
Delta Test	$y(t-1), y(t-2), y(t-3), u(t-1), u(t-2)$	5
Linear OLS	with all the inputs selected	20
FOS-MOD	with all the inputs selected	20

We can know from the table that COFS method could get the minimal subset to contain all the true input variables with the smallest size. However, linear OLS and FOS-MOD worked not well. In Example 2, with the further insight of the rank list, the inputs $y(t-1)$, $y(t-3)$, $u(t-1)$, $u(t-2)$ ranked top by Linear OLS method, however, the $y(t-2)$ is ranked at the end of the list, therefore, this input variable would be easy to lost in this input selection procedure. What's more, it is

believable that the method FOS-MOD could not deal with this case appropriately because all the important inputs are scattered in the rank list.

Furthermore, the results of term selection are shown in Tab. 4 and Tab. 5.

Table 4. Term selection for Example 1

True model term	Initial rank	Selected rank
$y(t-2)$	2	1
$u^2(t-2)$	39	3
$u(t-1)y(t-1)$	13	5
$u^2(t-2)y(t-2)$	103	10
$y^3(t-1)$	45	13

Table 5. Term selection for Example 2

True model term	Initial rank	Selected rank
$u(t-1)$	5	1
$y^2(t-3)u(t-1)$	87	10
$u(t-1)u(t-3)y(t-2)$	81	15
$u(t-3)y^2(t-1)y(t-3)$	277	261
$y(t-1)y^2(t-3)u(t-2)u(t-3)$	483	308

It can be found that all the true model terms become more significant after the term selection process. The ranking value of each term is improved, and the minimal candidate pool is also reduced from 103 to only 13 to contain all the necessary terms in Example 1, and the similar situation could be found in Example 2, in which, the candidate pool is pruned from 483 to 308. In fact, 300 and 500 terms are selected as the searching space, which is considered big enough to include all the necessary terms.

In the phase of evolutionary optimization based system identification, NSGA-II is applied to identify the model structure. The identified polynomial model for Example 1 is:

$$\begin{aligned}\hat{y}(t) = & -0.4989y(t-2) + 0.6486y(t-1)u(t-1) \\ & + 0.6922u^2(t-2) + 0.1914\hat{y}^3(t-1) \\ & - 0.6545\hat{y}(t-2)u(t-2)^2.\end{aligned}$$

From the final model it is found that although the irrelevant input variable $y(t-3)$ is selected by COFS, it is eliminated and only true inputs are included in the final results.

In Example 2, the identified model could be expressed as:

$$\begin{aligned}y(t) = & 0.9151u(t-1) - 0.2998y^2(t-3)u(t-1) \\ & - 0.4218y(t-2)u(t-1)u(t-3) \\ & - 0.3855y^2(t-1)y(t-3)u(t-3) \\ & + 0.3563y(t-1)y^2(t-3)u(t-2)u(t-3).\end{aligned}$$

To test the obtained polynomial model, a 800 input-

output data is sampled as test data, and the input data is described as

$$u(t) = \begin{cases} \sin(2\pi t / 250) & \text{if } t \leq 500 \\ 0.8\sin(2\pi t / 250) + 0.2\sin(2\pi t / 25) & \text{otherwise.} \end{cases}$$

It's found that the simulation result is as small as 0.1603.

V. CONCLUSIONS

In this paper, our contribution is to introduce an efficient scheme for nonlinear polynomial NARX model identification. In order to make evolutionary optimization based identification worked efficiently, input selection and term selection are implemented to choose the minimal subset with all the necessary terms included. As two examples shown, the proposed COFS algorithm outperforms other input selection methods, and the pre-processed identification could work efficiently with a relative small searching space.

REFERENCES

- [1] L. Ljung, System Identification: Theory for the User, Second Edition, Prentice-Hall PTR, Upper Saddle River, N.J., 1999.
- [2] Z.J. Yang, T. Fujimoto, and K. Kumamaru, A genetic algorithm approach to identification of nonlinear polynomial models, in Proc. of the 12th IFAC Symposium on Identification, Santa Barbara, 2000.
- [3] Y. Cheng, L. Wang and J. Hu, "A Two-step Scheme for Polynomial NARX Model Identification Based on MOEA with Pre-screening Process", IEEJ Trans. on Electrical and Electronic Engineering, Vol.6, No.3, 2011.
- [4] H. L. WEI, S. A. BILLINGS and J. LIU, "Term and Variable Selection or Non-linear System Identification," INT. J. Control, vol. 77, No. 1, pp. 86–110, Jan. 2004.
- [5] K. Z. Mao and S. A. Billings, "Variable Selection in Non-linear Systems Modelling," Mechanical Systems and Signal Processing, vol. 12, no. 2, pp. 351–366, 1999.
- [6] Kalyanmoy Deb, Amrit Pratap, Sameer Agarwal, and T. Meyarivan, "A Fast and Elitist Multi-objective Genetic Algorithm: NSGA-II," IEEE Transaction on Evolutionary Computation, vol. 6, no. 2, pp. 182–197, 2002.
- [7] Emil Eirola, Elia Liitainen, Amaury Lendasse, Francesco Corona and Michel Verleysen, "Using the Delta Test for Variable Selection," Proc. of European Symposium on Artificial Neural Networks, Bruges, Belgium, April, 2008, pp. 25–30.
- [8] H. L. WEI, S. A. BILLINGS "Feature Subset Selection and Ranking for Data Dimensionality Reduction," IEEE Transactions on Pattern Analysis and Machine Intelligence, vol. 29, no. 1, pp. 162–166, Jan. 2007.

Traffic Signal Control of Multi-Forked Road

Chengyou Cui, MizuKi TakaMura, Heehyol Lee

*Graduate School of Information and Systems, Waseda University
2-7 Hibikino, Wakamatsu-ku, Kitakyushu, Fukuoka, 808-0135, Japan
(tel:81-93-692-5164)
(cuichengyou@ruri.waseda.jp)*

Abstract: The traffic jam has become more serious at the multi-forked road intersection, and the conventional pre-timed control is less efficiencies to the congestion problem. In this paper, the new traffic signal control system for multi-forked road is proposed. Firstly, the cellular automaton (CA) model is used to develop a traffic simulator for multi-forked road. Next, the stochastic model of traffic jam is built up. In addition, new traffic signal control algorithm is designed using the optimization technique, Genetic Algorithm (GA). Finally, the effectiveness of the proposed method is shown using the actual traffic data with traffic simulator.

Keywords: Traffic signal control, Multi-Forked, Bayesian Network, Cellular automaton, Urban micro traffic simulator, Genetic algorithm

I. INTRODUCTION

In recent years, the traffic congestion has become serious problem with the exponential grown in vehicles. In the urban area, the road networks are not easy to be extended. In this case, the traffic signal control is considered as an effective way to solve the problem. The traffic signal control can be divided into two classes. One is the offline (pre-timed) control, the other is online (adaptive) control. In the pre-timed traffic signal control, Webster's formula is used to calculate green splits and cycle lengths offline using the historical traffic data of road networks. The pre-timed traffic signal control cannot handle any variation of traffic flows. On the other hand, the adaptive traffic signal control can overcome this limitation and this method can adjust the traffic signals online with changing traffic flows.

The various intelligence techniques such as fuzzy concept, reinforcement learning agents, and neural networks [1-3] are used to implement the adaptive traffic signal control. However, as the limitation of these methods, the green time and/or the cycle length are included as the control target. The signal of the right turn exclusive is not included. And then, the road networks were not concerned multi-forked road intersection. Generally, the traffic signal timing of multi-forked road intersections is more complicated than crossroad intersections or T junction intersection. The inappropriate

traffic signals timing cause the congestion of a part of the roads at multi-forked road intersection.

In this paper, the stochastic forecasting model [4] and Genetic algorithm (GA) is used to design a real time traffic signal control system for multi-forked road. Firstly, the probabilistic distributions of standing vehicles of roads are predicted using the stochastic forecasting model, and then, GA is used to calculate optimal traffic signal to minimize the probability of the traffic jam. An urban micro traffic simulator is developed by using cellular automaton (CA) model. Through the observation of vehicle movements of traffic simulator, the parameters of the GA are determined.

II. URBAN TRAFFIC SIMULATOR

The micro traffic simulator can model the movement of individual vehicles on road network. CA is usually faster than any other traffic micro simulators, the computational requirements are rather low with respect to both storage and computation time, making it possible to simulate large traffic networks on personal computers [5].

The CA traffic movements are based on the SchCh model (highway traffic model) [6]. The rules of the vehicle movements on the road network are shown as follows.

1) Input to cell: according to comparison of a random number (from 0 to 1) with set value, a vehicle will be generated and the direction of travel on the intersection

will be determined.

2) Speed: the vehicle can accelerate up to maximum speed (Maximum speed = move 2 cell; 1cell=7m/1 step [1sec]), when there is no obstacle. According to conditions of the road the speed can be changed randomly by probability.

3) Intersection: when traffic signal is green, the vehicle will be allowed to cross the intersection according to direction of travel, and the direction of the travel on next intersection will be reset.

4) Multi lanes: in multi lanes road, a vehicle can move to parallel lanes. If the direction of travel is right turn, the vehicle moves to the right turn exclusive lane.

By above rules, we can move the vehicles on the road network, and the procedure of the simulator is shown in Fig.1.

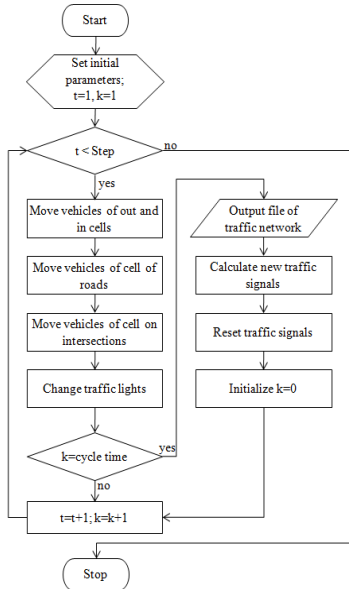


Fig.1. flowchart of simulator

III. STOCHASTIC FORECASTING MODEL

In previously published paper [4] we described a stochastic forecasting model of traffic jam at crossroads. The stochastic forecasting model is used to predict probabilistic distributions of standing vehicles of multi-forked road.

A multi-forked road is considered as an example shown in Fig.2. The random variables of inflows I_k , outflows O_k , standing vehicles S_k on the road 1 have relationship as following:

$$S_k = S_{k-1} + I_k - O_k. \quad (1)$$

And then, a Bayesian network model is built up using this relationship, and the random variables of the inflows and the outflows of each direction, and the standing

vehicles are represented as the nodes.

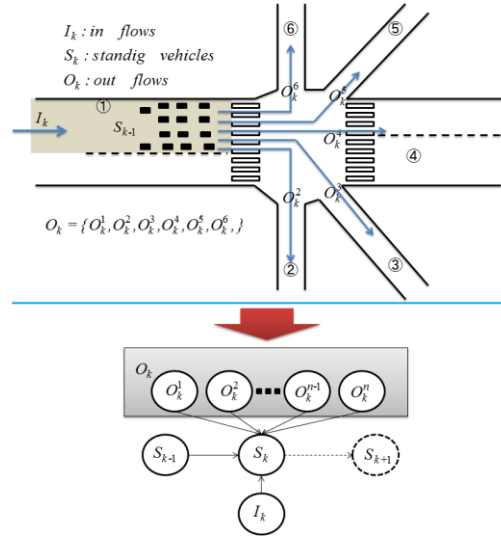


Fig.2. Multi-forked road and BN model

The probabilistic distribution of the standing vehicles at k th cycle is obtained by summing over all values of the other variables as following,

$$P(S_k) = \sum_{S_{k-1}} \sum_{I_k} \sum_{O_k} P(S_k, S_{k-1}, I_k, O_k) \quad (2)$$

$$O_k = \{O_k^1, O_k^2, \dots, O_k^{n-1}, O_k^n\}$$

n : number of the direction

With the chain rule, the joint probabilistic distribution is represented as the product of the conditional probability. And then, according to the d-separation, equation (2) can be represented as

$$P(S_k) = \sum_{S_{k-1}} \sum_{I_k} \sum_{O_k} P(S_{k-1}) \cdot P(I_k) \cdot P(O_k) \quad (3)$$

According to equation (3), the probabilistic distribution of the standing vehicles is predicted. Using this model, the probabilistic distribution of standing vehicles of each road can be predicted.

IV. TRAFFIC SIGNAL CONTROL BY GENETIC ALGORITHM

The objective of the proposed system is to reduce the traffic queue of the congested roads and to maintain the traffic queue of the other roads in a steady range. At first, the stochastic forecasting model is applied to predict the probabilistic distribution of the congested roads. Then, the optimal traffic signal within an adjustable range will be searched according to minimization for the probability of the standing vehicles over a set value S_{max} . (If the standing vehicle is bigger than S_{max} , the road is considered as a traffic jam). In the search process, GA is utilized.

1) Fitness function

For this optimization the fitness function is defined as following;

$$MIN \quad F = \sum_{i=1}^{i=n} w_i \cdot \left(\sum_{S=S_{max}}^{S=\infty} P^i(S_k) \right)$$

$i = \text{number of the roads}$
 $S = \text{number of the standing vehicles}$ (4)
 $S_{max} = \text{set value}$
 $w_i = \text{weight of the function}$

and, the $P^i(S_k)$ can be obtained from equation (2). On the other hand, the probabilistic distribution of the inflows and the outflows will be changed by different traffic signal. According to the characteristics of the traffic flows, an estimating equation is defined as following;

$$P(f_k) = P((f_k / t_{old}) \cdot t_{new})$$

$f_k : \text{the traffic flows of } k\text{-th cycle}$
 $t_{old} : \text{the time of signals of } k\text{-th cycle}$ (5)
 $t_{new} : \text{new time of signals}$

By equation (4) and (5), the fitness value can be calculated.

2) Chromosome encoding

A chromosome is defined as an example shown in Fig.3. In this multi-forked intersection, the traffic signal can be divided into six parts. In the chromosome, each traffic signal is represented using different color, and consisted of some genes. The meaning of each number is time [sec.].

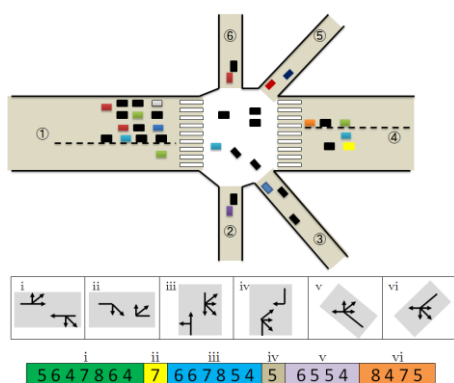


Fig.3. Chromosome encoding

3) Initial population

Chromosomes as an initial population will be generated randomly within adjustable range of the traffic signal.

4) Selection

A truncation and elitism combination is used in this strategy. First, the best chromosome will be cloned to the next generation. The other chromosomes of next generation will be created by crossing 50% of the population.

5) Crossover

Two chromosomes are randomly chosen as a pair of parent chromosome. And then, at four random points, the gene will be interchanged.

6) Mutation

According to a mutation probability, an individual is chosen to be mutated and the changing point will be randomly chosen.

V. SIMULATION

To prove the effectiveness of the proposed system, a simulation was carried out based on the actual data at Fukuoka-city of Japan with the micro traffic simulator. The multi-forked road intersection is shown in Fig.4. In this intersection, the traffic signals of the direction 1 and 4 are same, and direction 2 and 6 are same. Therefore, the congested roads 2, 4 and roads 3, 5 are selected to predict the probabilistic distribution of the standing vehicles, and to optimize the traffic signals using GA.



Fig.4. Multi-forked road intersection

The table 1 presents parameters of the fitness function. The parameters are empirical value by simulation with the simulator. In the GA, the number of generations set to 30; population size set to 31; and the mutation probability is 0.04. During the calculating time of GA, the traffic signal will be updated at every 5cycle (15 minutes).

Table 1. Parameters of fitness function

	Road 2	Road 3	Road 4	Road 5
S_{max}	35	35	110	35
w_i	1	0.7	0.9	0.5

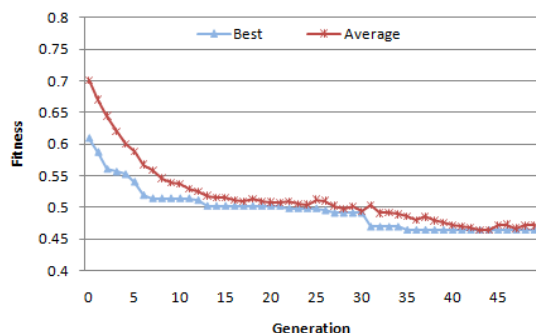


Fig.5 Progress of the fitness function

The progress of the fitness function shows the minimization by the GA illustrated in Fig.5. The traffic signals by the proposed method are shown in Fig.6. The traffic signals of the pre-timed are fixed, but the traffic signals by the new method are updated with the changing traffic flows.

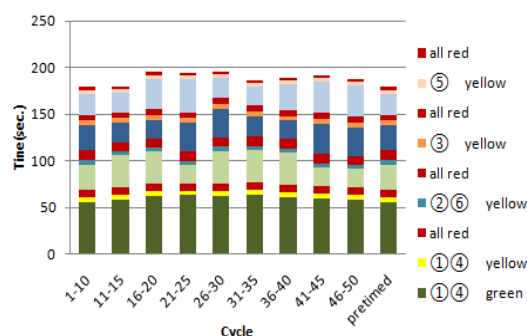


Fig.6 New traffic signals

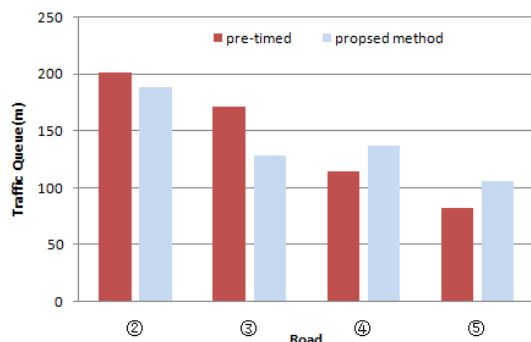


Fig.7 Traffic queue of the roads

Fig.7 represents the traffic queue of the each road. In the congested roads 2 and 3, the traffic queue is reduced by the proposed method. In the road 2 and 3, the average of traffic queue is decreased by 13m and 40 m, respectively. On the other hand, for the road 4 and 5, the traffic queue is maintained in a steady range.

By the proposed method, the average delay time is decreased compare with by the pre-timed, and the results are shown in Fig.8.

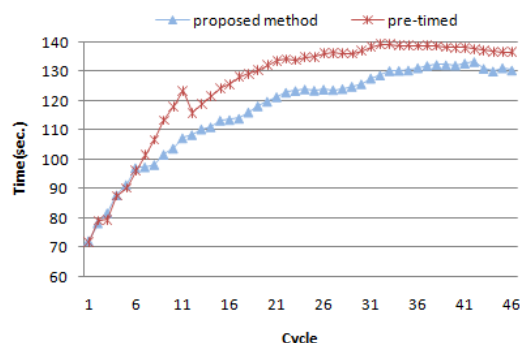


Fig.8 Average delay time of each cycle

The total number of the passing vehicles from the intersection is increased from 8,242[cars] to 8,586[cars].

VI. CONCLUSIONS

In this paper, the optimization of the traffic signal timing by GA and the simulator based on the stochastic forecasting model were proposed. Through the simulation with the multi-forked road intersection of an urban area, the effectiveness of the proposed method is shown.

REFERENCES

- [1]Y.Sazi Murat; Ergun Gedizlioglu(2005)A fuzzy logic multi-phased signal control model for isolated junctions. Transportation Research Part C. 13(1)19-36
- [2]P.G. Balaji; X.German; D.Srinivasan;(2010)Urban traffic signal control using reinforcement learning agents. 4(3): 177-188
- [3]Dipti Srinivasan; Min Chee Choy; Ruey Long Cheu (2006) Neural Networks for Real-Time Traffic Signal Control. IEEE Transactions on intelligent Transportation System.7 (3): 261-272
- [4]CY Cui; JS Shin; HH Lee; (2010)Real-time traffic singl learning control using BPNN based on predictions of the probabilistic distribution of standing vehicles. Artif Life Robotics.15 (1)"59-61
- [5]Javier J.SM; Manuel J.GM; Enrique RR(2010)Traffic Signal Optimization in"La Almozara" District in Saragossa Under Congestion Conditions, Using Genetic Algorithms, Traffic Micro simulation, and Cluster Computing. IEEE Transactions on intelligent Transportation System.11 (1):132-141
- [6]K.Nagel andM.Schreckenberg (1992)A cellular automaton model for freeway traffic. J.Phys. I France.2 (12)2221-2229

Control Design Methods for Platooning in Robot Car

Ryo TAKAKI, Xin ZHAO, Harutoshi OGAI

Waseda University, 2-7 HIBIKINO, WAKAMATSU-KU, KITAKYUSU CITY, FUKUOKA, 808-0135, Japan

(Tel: 81-93-692-5147; Fax: 81-93-692-5147)

(Email address: takaki@akane.waseda.jp, zhaoxin_19870121@yahoo.co.jp)

Abstract: Platooning technology is becoming a future task which suggests as a way of reducing carbon dioxide emissions and realizing safe driving at a high speed velocity. This paper describes a few control methods for vehicle-platooning. The conventional control method improved fuel consumption by shortening the distance between vehicles. By contrast, the method we proposed improves it by controlling the velocity at the time of acceleration gently. The velocity is controlled by generating the desired value of inter-vehicular distance corresponding to the leading vehicle velocity. Another method which is planned to realize a highly efficient arterial traffic distribution system includes reducing aerodynamic drag by minimizing the distance between vehicles to allow drafting. In this paper, the two degrees-of-freedom control system is applied for it. These proposed methods were evaluated by simulation and some experiments.

Keywords: Platooning, control method, two degrees-of-freedom, distance

I. INTRODUCTION

Platooning is considered as one of the innovations in the automotive industry that aim to improve the safety, efficiency, mileage, and time of travel of vehicles while relieving traffic congestion, decreasing pollution and reducing stress for passengers[1]. Also, platooning makes it possible for vehicles to travel together closely and safely. This leads to a reduction in the amount of space used by a number of vehicles on a highway. Thus more vehicles can use the highway without traffic congestion [2].

In our research, we use the equipment of robot car which is a kind of electric cars carrying the laser range sensor and CCD camera. By robot car, we can carry out the research of automation driving and platooning.

In this paper, it designs the model for the robot car platooning system and develops two degrees-of-freedom control system to control the distance of vehicle-platoon.

II. OUTLINE OF PLATOONING SYSTEM

2.1 Modeling of Robot car

In this research, the response characteristic of acceleration from target value to actual value is given by equation (1).

$$G_a(s) = \frac{a(s)}{u_a(s)} = \frac{1}{T_m s + 1} \quad (1)$$

Where, T_m is the time constant of the acceleration response characteristic. The acceleration response characteristic is controlled by model matching control system shown in Fig.1 [3]. This control system consists of model matching compensator, robust compensator and plant. The model matching compensator generates a signal to match the actual response characteristic and ideal response characteristic shown in equation (1). Furthermore, robust compensator generates a signal to reduce the effect of fluctuation of plant characteristic. In this research, we defined the time constant as $T_m=1.0$ in the same way as reference [4].

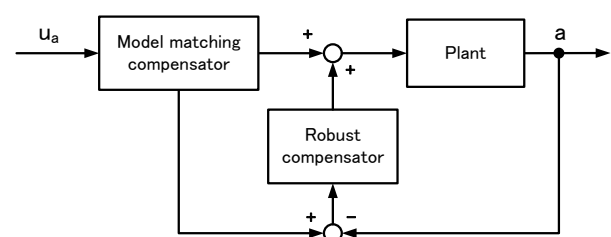


Fig.1. Robust model matching control system

2.2 Constitution of vehicle-platoon

The constitution of platoon is shown in Fig.2. In this research, we deal with three robot cars as a vehicle-platoon. Each robot car detects distance between two cars by radar sensor. The variable's numbers shown in Fig.2 corresponds to each robot car's number. For example, v_2 represents the velocity of robot car 2.

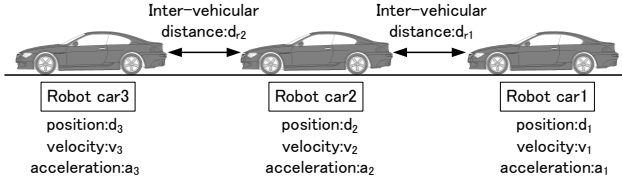


Fig.2. Constitution of platoon

III. DESIGN OF CONTROL SYSTEM

3.1 Object of the system

When the leading car moves quickly, it is necessary to control the velocity of following robot car rapidly for remaining the target inter-vehicular distance. However, the fuel consumption is also increased rapidly. In order to solve this problem, it is necessary to determine the target inter-vehicular distance corresponding to the leading car's driving situation. Moreover, the control system which can regulate the inter-vehicular distance without influencing ride quality is required.

3.2 Constitution of control system

Two degrees-of-freedom control system shown in Fig.3 is designed to attain the design requirements, [6]. The control system consists of controlled object $P(s)$, target inter-vehicular distance generator $G_{ref}(s)$, model matching compensator $G_M(s)$, feed forward compensator $C_{FF}(s)$ and feedback compensator $C_{FB}(s)$. And this kind of control system is carried in each robot car.

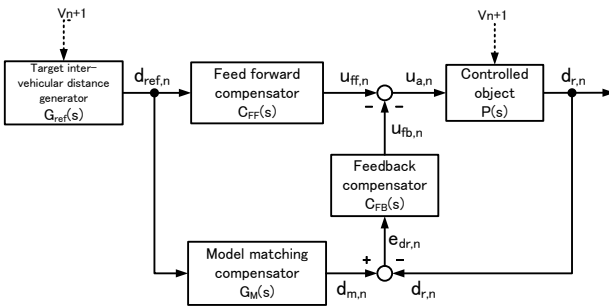


Fig.3. Constitution of control system

3.3 Control objective

The block diagram of the controlled object is shown in Fig.4. The transfer function of the control objective $P(s)$ from target acceleration $u_a(s)$ to actual inter-vehicular distance $d_r(s)$ is given by equation (2).

$$P(s) = \frac{d_{r,n}(s)}{u_{a,n}(s)} = \frac{1}{s} (v_{n+1}(s) - v_n(s))$$

$$= \frac{v_{n+1}(s)}{s} - \frac{u_{a,n}(s)}{T_m s^3 + s^2} \quad (2)$$

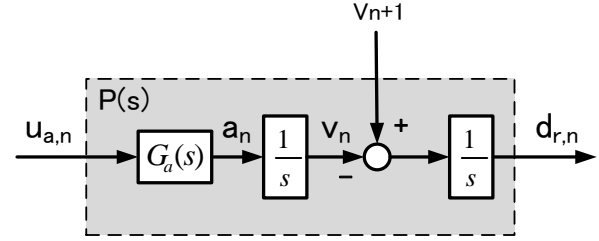


Fig.4. Block diagram of control objective

3.4 Inter-vehicular distance generator of target

Inter-vehicular distance of target $d_{ref,n}(s)$ is calculated by equation (3).

$$d_{ref,n}(s) = d_{ref-v,n}(s) + d_{ref-a,n}(s) \quad (3)$$

Where, $d_{ref-v}(s)$ represents the element of inter-vehicular distance of target correspond to leading car's velocity and $d_{ref-a}(s)$ represents another element of target inter-vehicular distance correspond to the leading car's acceleration. $d_{ref-v}(s)$ and $d_{ref-a}(s)$ are given by equation (4), (5), respectively.

$$d_{ref-v,n}(s) = h v_{n+1}(s) \quad (4)$$

$$d_{ref-a,n}(s) = h \frac{s}{\lambda_{a,n} + s} v_{n+1}(s) \quad (5)$$

Where, h represents inter-vehicular time coefficient and λ_a represents control parameter. Therefore, $d_{ref-v}(s)$ increases as leading car's speed increases. In my research, we defined the inter-vehicular time coefficient as $h=2.0$ in the same way as reference [5]. When leading car moves quickly, $d_{ref-a}(s)$ also increases quickly. Due to long target inter-vehicular distance, it is not necessary for subsequent robot car to accelerate rapidly.

3.5 Model matching compensator

The transfer function of the model matching compensator $G_M(s)$ from inter-vehicular distance of target $d_{ref}(s)$ to inter-vehicular distance response $d_m(s)$ is given by equation (6).

$$G_{M,n}(s) = \frac{d_{m,n}(s)}{d_{ref,n}(s)} = \frac{\omega_n^2}{s^2 + 2\zeta_n \omega_n s + \omega_n^2} F(s) \quad (6)$$

Where, ζ represents attenuation coefficient and ω represents character frequency. $F(s)$ is a filter given by equation (7).

$$F(s) = \frac{1}{T_F s + 1} \quad (7)$$

Where, T_F represents time constant. In this research, time constant is defined as $T_F = 0.1$.

3.6 Feed forward compensator

A block diagram of feed forward control system is shown in Fig.5. In order to match the actual inter-vehicular distance $d_r(s)$ and inter-vehicular distance response $d_m(s)$, it is necessary to equalize the transfer function of feed forward compensator from target inter-vehicular distance $d_{ref}(s)$ to actual inter-vehicular distance $d_r(s)$ and the transfer function of model matching compensator. Therefore, transfer function of feed forward compensator is given by equation (8), (9).

$$\frac{d_{r,n}(s)}{d_{ref,n}(s)} = C_{FF,n}(s)P(s) = G_{M,n}(s) \quad (8)$$

$$C_{FF,n}(s) = \frac{G_{M,n}(s)}{P(s)} \quad (9)$$

Feed forward compensator can control actual inter-vehicular distance $d_r(s)$ similar to inter-vehicular distance response $d_m(s)$. However, due to disturbance and fluctuation of plant characteristic, feedback compensator is also necessary.

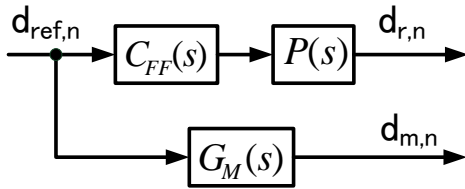


Fig.5. Feedforward control system

3.7 Feedback compensator

A block diagram of feedback control system is shown in Fig.6. This compensator controls transfer characteristic from a disturbance to actual inter-vehicular distance shown in equation (10).

$$\frac{d_{r,n}(s)}{d_{d,n}(s)} = \frac{1}{1 + C_{FB}(s)P(s)} \quad (10)$$

Feedback compensator can control disturbance response without influencing desired value response. In this research, sensitivity function for disturbance is given by equation (11).

$$S(s) = \left(\frac{s}{\lambda_s + s} \right)^3 \quad (11)$$

Where, λ_s represents a parameter of sensitivity function. From equation (10) and (11), transfer function of feedback compensator is calculated as equation (12).

$$C_{FB}(s) = \frac{1 - S(s)}{S(s)P(s)} = \frac{3T_m\lambda_s s^3 + 3\lambda_s(T_m\lambda_s + 1)s^2 + \lambda_s^2(T_m\lambda_s + 3)s + \lambda_s^3}{s} \quad (12)$$

In my research, the parameter of sensitivity function is defined as $\lambda_s = 3.0$.

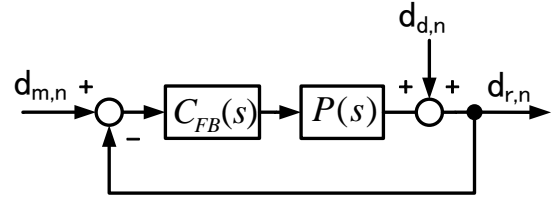


Fig.6. Feedback control system

IV. SIMULATION

4.1 Simulation condition

Initial position of the vehicle-platoon is shown in Fig.7. The vehicle-platoon contains one leading robot car4 and three robot cars 1,2,3 and each initial inter-vehicular distance is 3[m] and each initial velocity is 0[m/s]. The velocity of robot cars1,2,3 are controlled by proposed control system and the velocity of robot car4 is given as Fig.8. Simulation parameters of each Robot car are given by Table.1. Under above conditions, Inter-vehicular distance and velocity of each robot car are simulated.

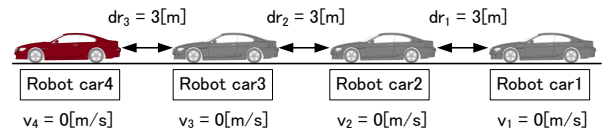


Fig.7. Initial position of Robot car

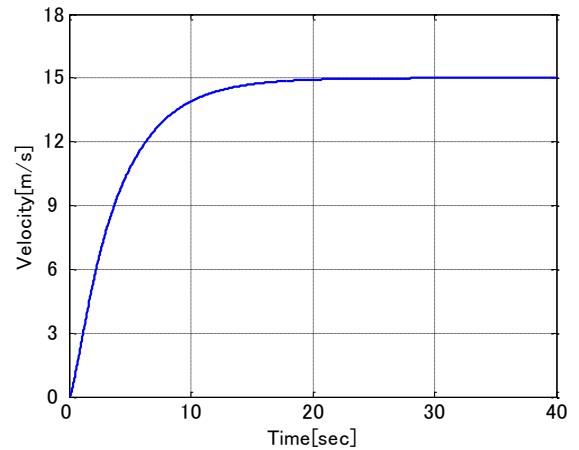


Fig.8. Speed fluctuation of leading-robot car4

Table.1:Simulation parameters

Parameters	Robot car1	Robot car2	Robot car3
λ_a	0.65	0.45	0.25
h	2.0	2.0	2.0
ζ	1.5	1.5	1.5
ω	0.7	0.7	0.7

4.2 Simulation results

The calculated value of robot car's velocity and each inter-vehicular distance is shown in Fig.9(a), Fig.9(b), respectively. From simulation results, it is verified that the velocity of subsequent robot car is controlled more gently than that of leading robot car. This result indicates that the proposed method can prevent subsequent following vehicles from accelerating rapidly. Moreover, Fig.9(b) indicates that actual inter-vehicular distance $d_r(s)$ is controlled accurately to match the inter-vehicular distance response $d_m(s)$.

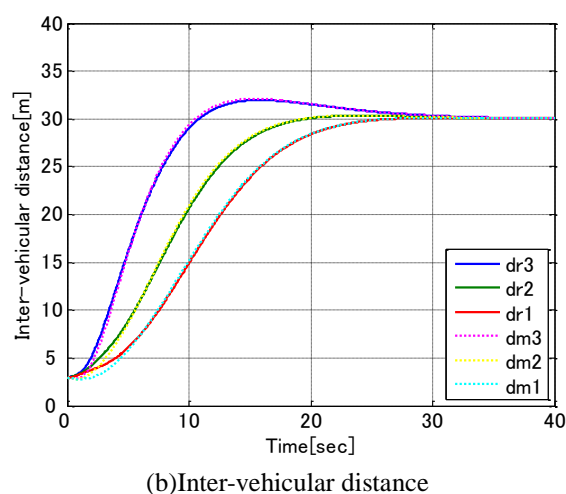
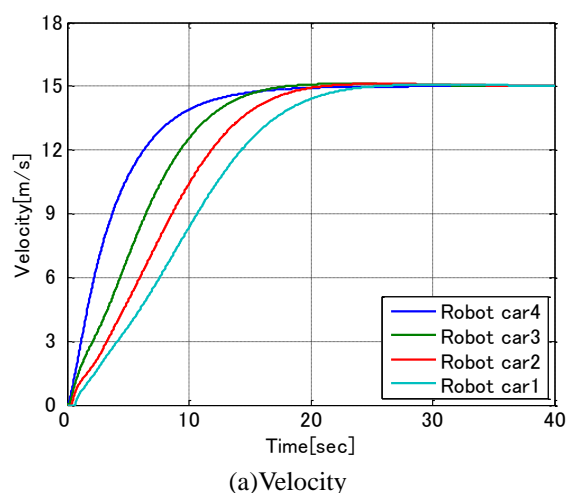


Fig.9. Simulation results

5. CONCLUSION

In our research, it presents a two degrees-of-freedom control system to control the platooning. The system controls the velocity of vehicle-platoon smoothly and keeps the distance of vehicle-platoon accurately.

The future plan is to carry out the simulation of model predictive control and do the comparison. And we will lead the control system into robot car.

REFERENCES

- [1] Using ITS to cut CO2 emissions in half by 2050, "Development of Energy-saving ITS Technologies,"2009.
- [2] Yoshinori YAMAMURA, Yoji SETO and Masao NAGAI, "Study on a String-stable ACC Using Vehicle-to-Vehicle Communication," Japan Society of Mechanical Engineers, No.06-7044.
- [3] Omae M, Fujioka T, Miyake K (1999), Longitudinal Control for Platoon Treated as One Dynamic System (in Japanese). Transactions of the Japan Society of Mechanical Engineers, Vol.65, No.640, pp.126-133.
- [4] Adachi K (2006), Proposal of a target headway distance method and applying this method to a car for adaptive cruise control system (in Japanese). Proceedings of the 15th Transportation and Logistics Division of The Japan Society of Mechanical Engineers, No.6-52, pp.23-28.
- [5] Sugie T, Fujita M (1999), Introduction to Feedback Control (in Japanese). CORONA PUBLISHING.

Building of Reverse Logistics Model in Reusable Recovery and Optimization considering Transportation, Inventory, and Backorder Costs

Jeong-Eun Lee and Hee-Hyol Lee

*The Graduate School of Information, Production and Systems, Waseda University
(Tel : 81-93-692-5017; Fax : 81-93-692-5021)
(leeje@toki.waseda.jp, hlee@waseda.jp)*

Abstract: This paper deals with the building of the reusable reverse logistics model considering the decision of the backorder or the next arrival of goods. The optimization method to minimize the transportation cost and to minimize the volume of the backorder or the next arrival of goods occurred by the Just in Time delivery of the final delivery stage between the manufacturer and the processing center is proposed. Through the optimization algorithms using the priority-based genetic algorithm and the hybrid genetic algorithm, the sub-optimal delivery routes are determined. Based on the case study of a distilling and sale company in Busan, Korea, the new reverse logistics model in reusable recovery of empty bottles is built and the effectiveness of the proposed method is verified.

Keywords: Reusable Recovery, Reverse Logistics, Backorder or Next arrival of Goods

I. INTRODUCTION

For achievement of the resources recycling society and the low carbon society, the reverse logistics which targets the flow from production recovery to reproduction of end of life products has been received attention in the logistics field. During tightening regulation on environment increasingly, the reverse logistics has been magnified by the following reasons: First, economic effect resulted from the cost reduction of raw materials in manufacturing process. Second, the propensity to consume changed to the environment-friendly product. Third, business strategy tried to improve the image of corporate.

However, the reverse logistics is different from the traditional forward logistics where new material or part are produced and sold to customer. In the reverse logistics, it is not only hard to predict the appearing time or amount of arrivals by the used periods or condition of the recovered products, but also the recovery routes are complex as there are lot of recovery centers. Moreover, even though the recovery products are environment-friendly, its market is not large yet because of the stereotype of customers who regard the recovery product as used goods. And the reverse logistics costs more than the traditional forward logistics to construct and operate the system.

There have been lots of researches on the remanufacturing recovery that processing operation is complex and the forms of products are various Jayaraman[1] represented the reverse logistics model of

the Remanufacturing Recovery considering the delivery cost from the returning center to the processing center. And Tang[2] showed the reverse logistics model considering the disassembly process in the processing center. However, they haven't discussed the processing operation to clean and refill the recovered products. On the other hand, researchers[3] extended these models, and represented reverses logistics model of the remanufacturing recovery that the disassembling, cleaning, refilling operations were included in the processing center and the transportation cost from the returning center to the processing center, manufacturing plant is considered. Moreover, they have built the reverse logistics model considering that a reusable part is delivered to the manufacturer and a part to disposal. In additions, they have discussed the reverse logistics model considering the direct route to each processing operation in processing center, recycling center, manufacturing plant or disposal as the condition of recovered product in the returning center. And the remanufacturing reverse logistics model was built considered inventory cost before and behind each processing operation which the recovered product through the returning center.

Therefore, for optimizing the reverse logistics with uncertainty of amount or occurrence time of the recovery product, to build a model is necessary considering not only transportation cost but also the date and the processing of the decision whether waiting for arrival of an end-of-life product with the unclear

amount to the returning center or backordering necessary parts for manufacturing.

In this paper, a reusable reverse logistics model considering the decision of backordering or waiting for the next arrival of goods on the base of the reusable recovery is built. And, the optimization method of the reusable recovery to minimize the transportation cost and the volume of the backorder or next arrival of goods occurred by the just in time delivery of the final delivery stage between the manufacturer and the processing center is described. In addition, this method can be also applied to the remanufacturing recovery and the recycling recovery.

II. BUILDING OF REUSABLE REVERSE LOGISTICS MODEL AND OPTIMIZATION CONSIDERING TRANSPORTATION, INVENTORY, AND BACKORDER COSTS

The reverse logistics model in newly building reusable recovery is considered the Just in Time delivery cost from the processing center to manufacturer included decision whether waiting for arrival of the end-of-life product or backordering necessary parts for manufacturing when the end-of-life product gathering goods to the processing center through the returning center is less than the demand of manufacturer.

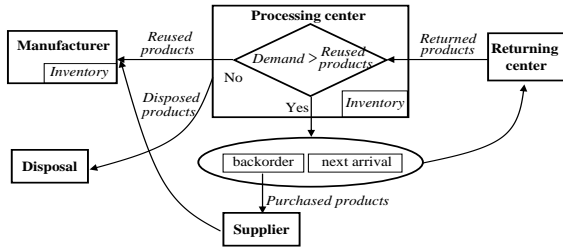


Fig. 1. Reusable reverse logistics model considering backorder or next arrival

Figure 1 describes the model combined the decision factors of the backordering or wait for the next arrival of goods based on the total inventory of the manufacturer in case of the end-of-life product gathering goods to the processing center through the returning center is less than the amount of demand.

Indices

- i : returning center ($i=1, 2, \dots, I$; I : number of returning centers)
- j : processing center ($j=1, 2, \dots, J$; J : number of processing centers)
- t : time period ($t=1, 2, \dots, T$)

Parameters

- a_i : capacity of the returning center i

b_j : capacity of the processing center j

d_K : capacity of the manufacturer K

$r_i(t)$: amount of the end-of-life product recovered to the returning center i

$d_K(t)$: demand of in the manufacturer K

u_K : amount of an upper limit of backorder of the manufacturer K

c_{ij}^1 : unit cost of the transportation from the returning center i to the disassembly center j

c_{jK}^2 : unit cost of the transportation from the processing center j to the manufacturer K

c_{jD}^3 : unit cost of the transportation from the processing center j to the disposal D

c_{SK}^4 : unit cost of the transportation from the supplier S to the manufacturer K

c_j^{op} : unit holding cost of the processing center j

c_j^{H1} : unit inventory cost per period at the processing center j

c_K^{H2} : unit inventory cost per period at the manufacturer k

Decision Variables

$x_{ij}(t)$: amount shipped from the returning center i to the processing center j in the period t

$x_{jK}(t)$: amount shipped from the processing center j to the manufacturer K in the period t

$x_{jD}(t)$: amount shipped from the processing center j to the disposal D in the period t

$x_{KB}(t)$: backorder amount of the manufacturer K at the period t

$y_j^H(t)$: inventory amount at the processing center j in the period t

$z_K^H(t)$: inventory amount at manufacturer K in the period t

$w_K(t)$: Binary variable equals 1 when the safety inventory is secured in manufacturer K and 0 when backorder is necessary

z_j : Binary variable equals 1 when processing center j is hold, otherwise 0.

Objective Function

Minimize the transportation cost, occurred backorder cost or inventory cost by the JIT delivery according to waiting for the next arrival of goods

$$\begin{aligned}
 f &= \alpha_1 f_1 + \alpha_2 f_2 \\
 &= \alpha_1 \sum_{t=1}^T \left[\sum_{j=1}^J c_j^{op} z_j + \sum_{i=1}^I \sum_{j=1}^J c_{ij}^1 x_{ij}(t) + \sum_{j=1}^J c_{jK}^2 x_{jK}(t) \right] \\
 &\quad + \alpha_2 \sum_{t=1}^T \left[c_{SK}^4 x_{KB}(t) + c_K^{H2} z_K^H(t) + \sum_{j=1}^J c_{jD}^3 x_{jD}(t) + \sum_{j=1}^J c_j^{H1} y_j^H(t) \right] \rightarrow \min
 \end{aligned}
 \tag{1}$$

α_1, α_2 : weight

Subject to

The recovered amount of the end-of-life product:

$$\sum_{j=1}^J x_{ij}(t) \leq r_i(t), \quad \forall i, t \quad (2)$$

Capacities of the processing center and manufacturer:

$$\sum_{i=1}^I x_{ij}(t) + y_j^H(t-1) \leq b_j z_j, \quad \forall j, t \quad (3)$$

$$\sum_{j=1}^J x_{jk}(t) + y_k^H(t-1) + x_{KB}(t) \leq e_k, \quad \forall t \quad (4)$$

The amount of the backorder when selecting the backorder:

$$d_k(t) - z_k^H(t-1) - \sum_{j=1}^J x_{jk}(t) = x_{KB}(t), \quad \forall t \quad (5)$$

The inventories of the processing center and manufacturer:

$$y_j^H(t-1) + \sum_{i=1}^I x_{ij}(t) - (x_{jk}(t) + x_{jD}(t)) = y_j^H(t), \quad \forall j, t \quad (6)$$

$$\sum_{j=1}^J x_{jk}(t) + z_k^H(t-1) - d_k(t) = z_k^H(t), \quad \forall t \quad (7)$$

The restriction not to be able to execute waiting of arrival of goods and relapse note at the same time in the processing center:

$$z_k^H(t) \leq u_k w_k(t), \quad \forall t \quad (8)$$

$$x_{KB}(t) \leq u_k (1 - w_k(t)), \quad \forall t \quad (9)$$

Non-negativity of the decision variables:

$$x_{ij}(t), x_{jk}(t), x_{jD}(t), x_{KB}(t) \geq 0, \quad \forall i, j, t \quad (10)$$

Decision variable of the holding determination:

$$z_j \in \{0,1\} \quad \forall j \quad (11)$$

The reverse logistics is formulated as a mixed integer programming problem, and is one of the NP-hard problems. The mixed integer programming problem with comparatively little integer variable is possible to be solved in practicable time using traditional optimization software. But it becomes impossible to be applied for the large-scaled problem in this research since the calculating time or using memory increase geometrically. Therefore, the sub-optimal solution is calculated using GA as the solution of this problem.

III. OPTIMIZATION OF REUSABLE REVERSE LOGISTICS USING GENETIC ALGORITHM

1. Priority based genetic representation

Encoding: The chromosome with length which is totalized by returning center (I) and processing center (J) is generated. The value of each gene represents the priority and an initial value allocated by the priority starts from total of the gene, ($I+J$). Then the priority 1 less than the selected gene randomly is allocated till every gene has the priority value. For example, two chromosomes with the total of returning centers, $I=5$ and total of processing centers, $J=3$, the capacities of the

returning center and the processing center and the transportation cost from the returning center to the processing center are shown in the Figure 2.

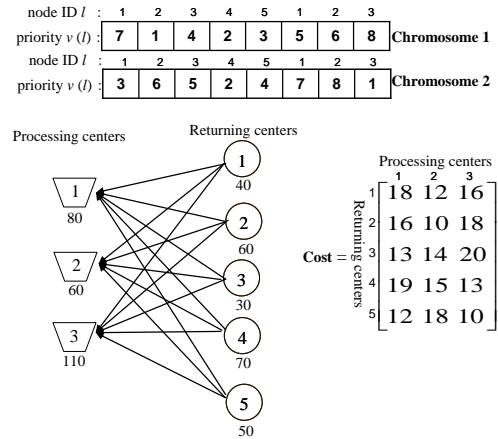


Fig. 2. Example of Representation for Chromosome
Decoding: In case of the first chromosome, the lowest cost of returning center for processing center with the highest priority is the returning center 5. The shipments (50) are decided by the maximum deliveries (50, 110). Moreover, the returning center 4 with the second lowest transportation cost is selected for the processing center 3. The Shipments (60) are decided by the maximum deliveries (70, 60). Since the capacity 110 in the processing center 3 was satisfied, the priority is reset to 0, and the returning center 1 with the second highest priority is selected.

2. Genetic operators

The WMX crossover determines a cutting point randomly and generates an offspring exchanging the right parts of the chromosomes from the cutting point. The exchanged right parts are arranged by each ascending orders. Next, the numbers of genes that become a pair to each other are checked and changed by the relationship. The Swap mutation [4] selects randomly the pairs of the gene exchanged in eight genes and exchanges the selected genes.

3. Optimization by priority-based Genetic Algorithm

Priority-based genetic representation adopted for the chromosome representation is used to show the node of the gene position and the value is used to show the priority of the node.

4. Optimization by hybrid Genetic Algorithm

Besides the function of priGA, hGA improves the searching ability of GA through adjusting the parameter appropriately in each generation using FLC [4] and making a suitable situation by the optimal solution search.

IV. SIMULATION AND RESULTS

1. Numerical example

This paper considers the ten returning centers and the six processing centers, the manufacturer, the disposal and one each supplier. In the Figures 3 and 4, the sub-optimal delivery route and the amount of backorder in period t_1 and t_2 are shown respectively.

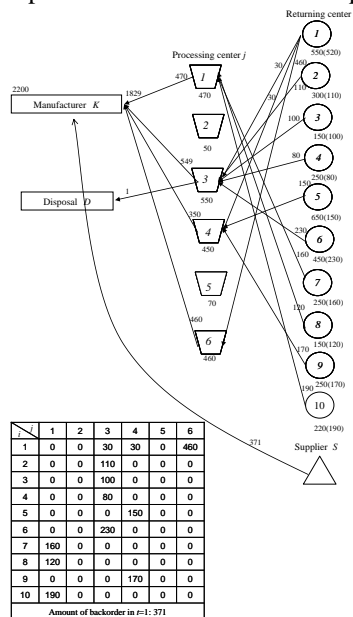


Fig. 3 Sub-optimal delivery routes and amount of backorder of the example at $t=1$

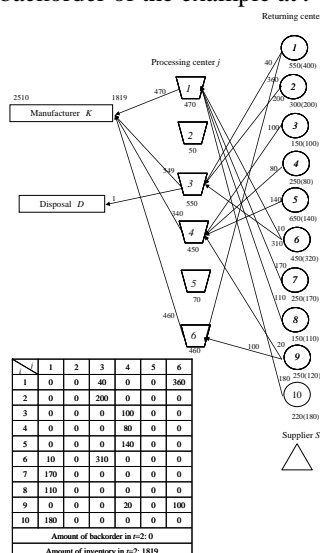


Fig. 4 Sub-optimal delivery routes of the example at $t=2$

This minimum costs 1,290,220 includes the transportation cost of from the returning center to processing center, the holding cost of the processing center, the transportation cost from the processing center to the manufacturer, the inventory cost of the processing center and the manufacturer, the backorder

cost of the supplier and the disposal cost. Neither processing centers 2 and 5 are selected nor is holding cost reduced.

2. Case of Bottle reusable reverse logistics of distilling and Sale Company

The optimization problem of the bottle reusable recovery case with a distilling and sale company in Busan, Korea by the real data was simulated. It set to 20 of the population size, 0.7 of the initial WMX crossover rate, 0.3 of the initial mutation rate, and 5000 of the maximum generation as a simulation condition of the proposed method. The minimum costs of the priGA and hGA are 3,975,048 and 3,963,330 respectively. Figure 5 shows the sub-optimal delivery routes and the selected situation of the returning center. In this sub-optimal delivery routes, the five recovery centers (dotted circle in the Figure 5) are removed because of these high holding cost. The total of variables in this case study is 22435, and it is impossible that the traditional optimization software LINGO calculates the solution in practicable time. However, the priGA and hGA could calculate the solution in the practicable time, 6.42[sec] and 4.45[sec], respectively.

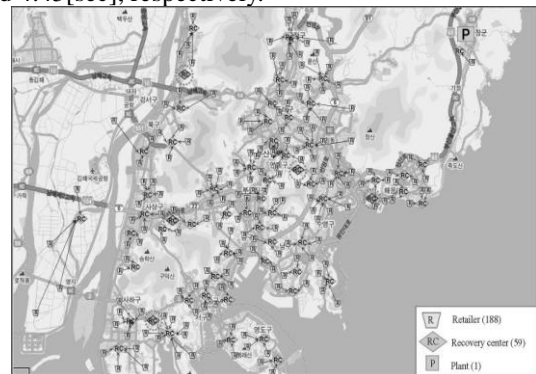


Fig. 5 Sub-optimal delivery routes and selected or unselected recovery centers

REFERENCES

- [1] Jayaraman V., Patterson R. A. and Rolland E. (2003), The design of reverse distribution networks: Models and solution procedures, European Journal of Operational Research, 150:128-149
- [2] Tang O., Grubbstrom R. W. and Zanoni S. (2007), Planned lead time determination in a make-to-order remanufacturing system, Int. J. Production Economics, 108:426-435
- [3] Lee J. E., Gen M. and Rhee K. G. 5 (2008), A Multi-stage Reverse Logistics Networks Problem by using Hybrid Priority-based Genetic Algorithm, IEEJ Trans. on EIS, 128(3): 450-455
- [4] Gen M., Cheng R. and Lin L. (2008), Network Models and Optimization: Multiobjective Genetic Algorithm Approach, Springer, London

Advanced Pipe Inspection Robot using Rotating Probe and Image Processing

Ryuta Oyabu¹, Kentarou Nishijima¹, Zhicheng Wang¹, Harutoshi Ogai¹, Bishakh Bhattacharya²

¹Graduate school of Information, Production and Systems, Waseda University, Japan
(Tel: +81-93-672-5147; Fax: +81-93-672-5147)

(E-mail: ogai@waseda.jp)

²Department of Mechanical engineering, Indian Institute of Technology Kanpur, India

Abstract: Recently many drain pipes used for transportation of water and gas at the plants have become old. These pipes have many defects caused by corrosion and cracking and they cause serious accidents because of leakage, fire and blasts. Therefore, to forestall these accidents, we believe it is important to do drain pipe inspections and maintenance using drain pipe inspection robots.

'Rotating probe' and 'Image processing' are used for the method of inspecting pipe in this research. Then, the development of the Pipe Inspection Robot measures the irregularity and the form of the defect in pipe. Therefore, this robot using the rotating probe of this touch sensor is profitable.

Keywords: Drain pipes, Pipe inspection robot, Rotating probe, Image processing

I. INTRODUCTION

Recently many drain pipes used for transportation of water and gas at the plants have become old. These pipes have many defects caused by corrosion and cracking and they cause serious accidents because of leakage, fire and blasts. Therefore, to forestall these accidents, we believe it is important to do drain pipe inspections and maintenance using drain pipe inspection robots. A lot of pipe inspection robot that uses image processing has been developed up to now. However, whether it is a defect or a pattern might not be understood only from the image processing. Then, the presence of the defect is confirmed with a touch sensor. In this research, the composition of the robot is described, and the image processing, the explanation of the rotating probe, and the outcome of an experiment are described. Subsequently, I describe the future plans.

First of all, the video shooting in pipe is done as a flow of the system of the picture processing. Next, the confirmation and the correction of a center point are done. Finally the developed figure of the video image is made by development of the image and correcting the seam. The recording cameras of the image processing are 300,000 pixels CCD.

Next, the probe (sensor) that enabled the defect detection was developed. The performance experiment of the sensor is installed in the rotational mechanism of 'Mogurinko 250' by 'Ishikawa iron works Ltd'. In separate research, the Indian Institutes of Technology Kanpur has researched a rotating probe using piezo

element for inspecting the inside of pipes with a touch sensor system. It explains the composition and the operation of the probe, and the outcome of an experiment in the made pipe model is shown.

II. ROBOT STRUCTURE

In this research, the robot of 'Mogurinko 250' by 'Ishikawa iron works Ltd' was used. This robot has CCD camera in the front and the rotating probe was installed in the back. Fig.1 shows the appearance diagram.

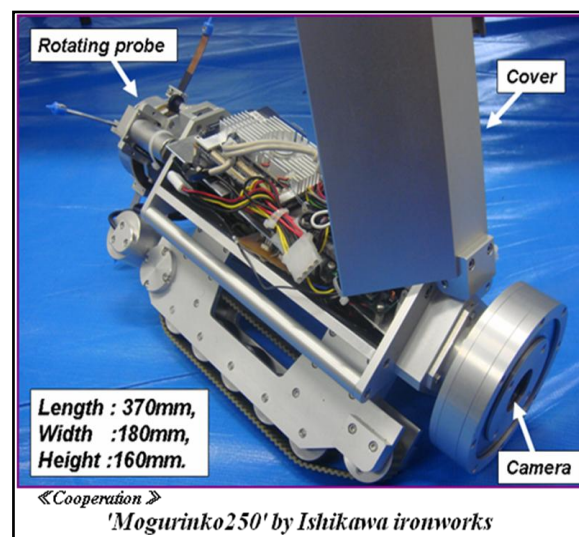


Fig.1 The appearance diagram of robot

This robot can be controlled by wireless radio communication in the inside pipe and can also transmit image information of the inside of the pipe in real time.

Specifications of this inspection robot:

- Size: length 370mm, width 180mm, height 160mm.
- Moving speed: 13.7m/min,
- Driving mode: double motor,
- Electric Power: rechargeable batteries 7.2V.
- Wireless frequency: apply to 2.4/5 GHz and Data transmission by 100 base-T Ethernet.
- USB Camera(300 thousand pixel)

III. IMAGE PROCESSING METHOD

The image processing to be a center point correction of pipe and develop of the image, it is very difficult to recognize the defect based on video in pipe. Then, the image is converted from circular image to zonal image and the inside of pipe is vertically seen. It becomes easy to recognize the defect by processing it like that.

3.1 Center Point Correction

The obtained video doesn't necessarily have the center of the pipe at the center of the image. Accordingly, the center of the pipe is found and it is necessary to process the image centering on the point.

Center point correction method is ' Hough transformation method ' and ' Least squares method '[1]. Fig.2 is the second order polynomial approximation.

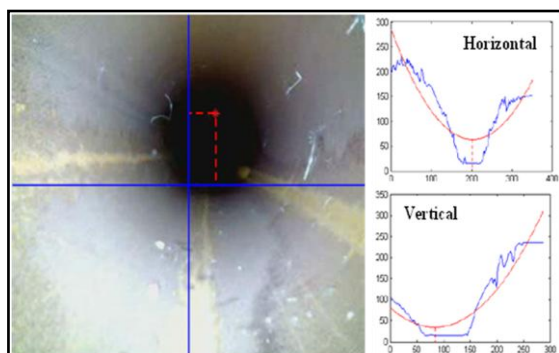


Fig.2 Least-squares method

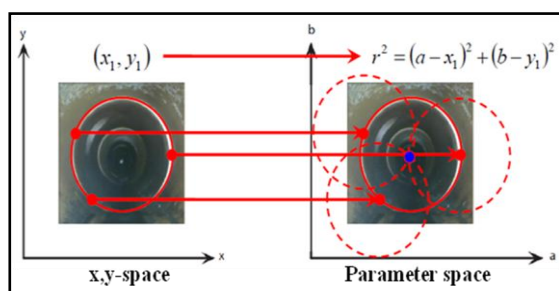


Fig.3 Hough transformation method

3.2 Zonal Image Making

When a center point is found, circular image is developed to the zonal image. The acquired image is taken by perspective. Therefore, the correction is put, and a circular image is converted to a zonal image.

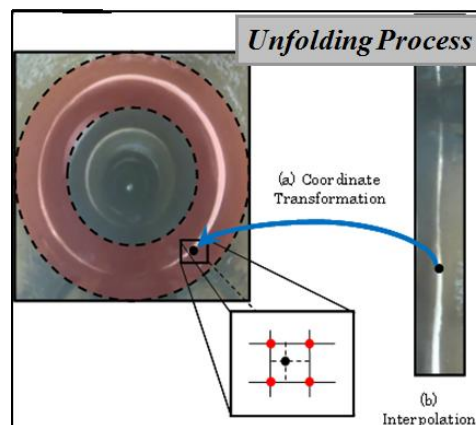


Fig.4 Zonal image making

3.3 Development Image Making

When an arbitrary zonal image is made, a zonal image is continuously made. And, the image of development in pipe is made by joining it.

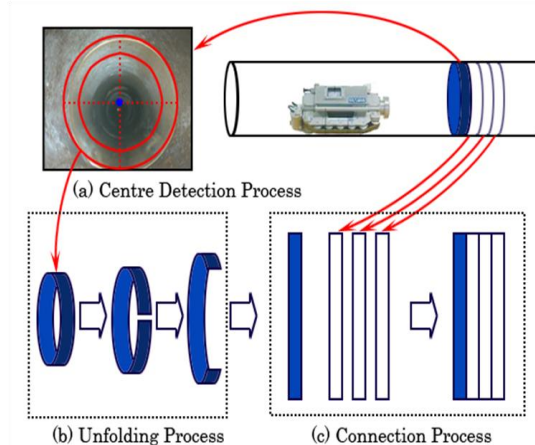


Fig.5 Development Image

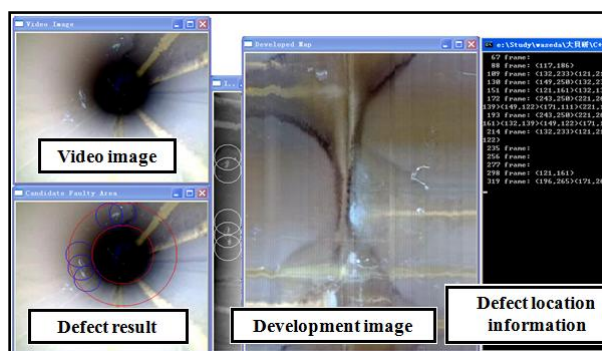


Fig.6 Image processing result

IV. ROTATING PROBE METHOD

4.1 Structure of Rotating Probe

The probe consists of spring steel and piezo film is positioned at the base of the probe. The steel strip can be used as cantilever. To control the cable of the rotating probe, a steel strip was used, as shown in Fig.7

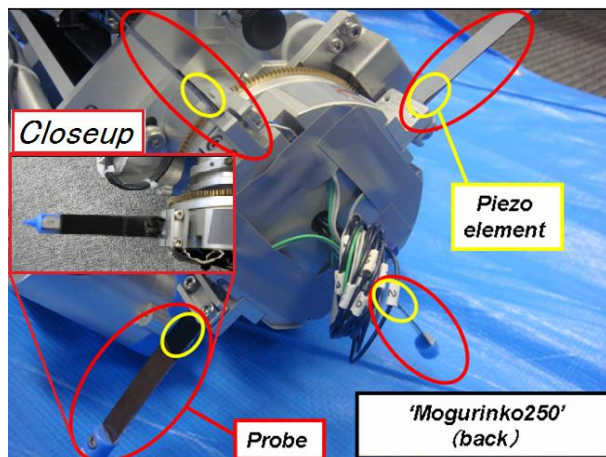


Fig.7 Rotating probe

4.2 Operating Principles of Rotation Probe

When the rotating probe touched the defected area, the piezo film could detect the curve and change of the stress. This stress change of the piezo film can be measured as voltage change. Movement of rotating probe is shown Fig.8.

First, four probes rotate and the probes approach the defect of the inside pipe. (Fig.8-①) Next, the probes start to touch the defect and its detected defect. (Fig.8-②.③) Afterward the probe moves away from the defect. (Fig.8-④)

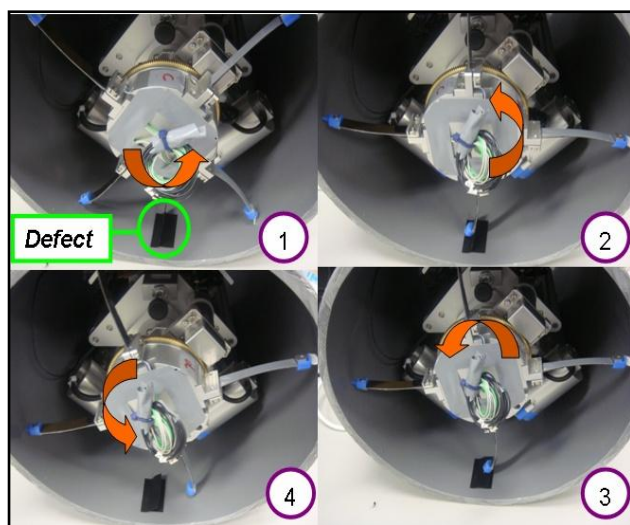


Fig.8 Movement of rotating probe

V. Performance experiment of Probe

This experiment used a resting robot with a rotating probe in a clean vinyl chloride pipe with a 25cm diameter, as shown in Fig.9. The defects were made of slices of eraser.

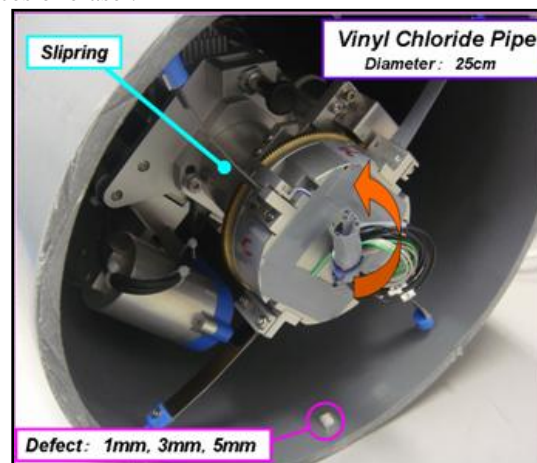


Fig.9 Experiment Conditions

5.1 Data Capture Method

The voltage change happens from bending of the probe. The voltage change is taken into the microcomputer. And, it displays it in CPU of the robot by using serial communications. The sampling period at this time is 0.01 seconds. The microcomputer used H83664tiny microcomputer. Fig.10 shows the appearance diagram of microcomputer.

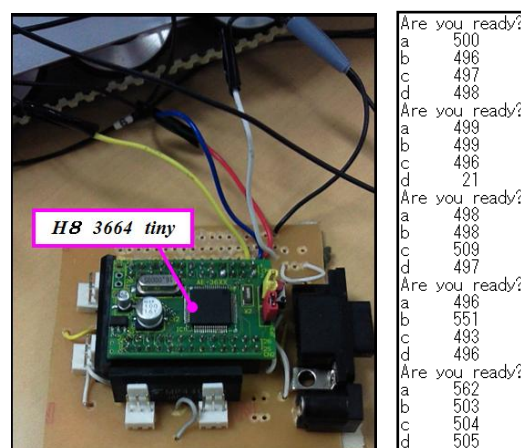


Fig.10 The appearance diagram of microcomputer.

5.2 Experiment Method

The experiment doesn't drive the robot, and operate only the rotation probe. And probe touched to the defect of experimental object. What voltage change happens is measured as a result.

Table.1 shows the experimental condition.

Table.1 Experimental condition.

Experiment 1 (Fundamental feature of Probe)	Defect form : Cube, Cuboid (Height : 10mm , 6mm , 3mm , Width : 10mm)
Experiment 2 (Detection of continuous defect)	Defect form : Five cubes (Height : 10mm , Width : 10mm)
Experiment 3 (Change on defect)	Defect form : Three cuboid (cube) (Height : 10mm , Width : 50mm , 30mm , 10mm)
Experiment 4 (Change according to form)	Defect form : Semicircular (Diameter: 40mm , 30mm , 20mm) Defect form : Equilateral triangle (Sides : 20mm)
Experiment 5 (Damage experiment)	Defect form : Concave type (Width : 10mm , 6mm , 3mm)

5.3 Experimental Environment

Figure of each experimental condition is enumerated as follows.

- Experiment 4

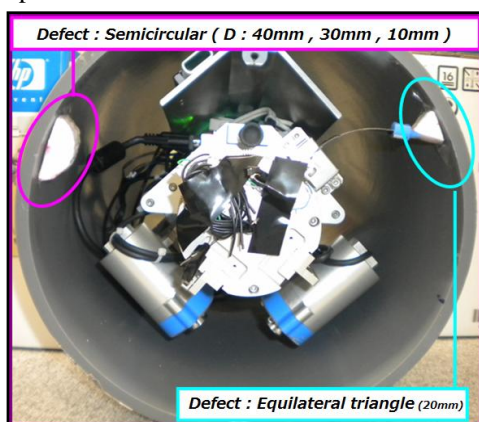


Fig.11 Defect form: Semicircular and Equilateral triangle

- Experiment 5

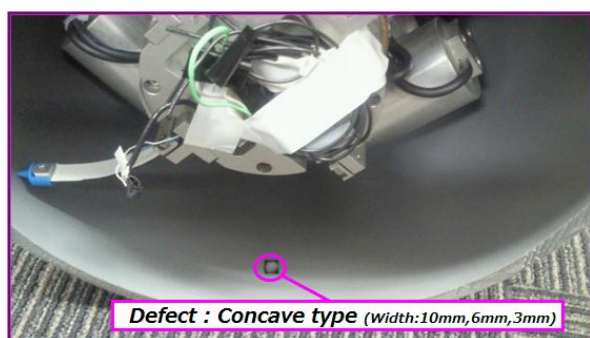


Fig.12 Defect form: Concave type

5.4 Experimental Results

The Table.2 and Table.3 shows the outcome of an experiment.

Table.2 Experimental Results (Size)

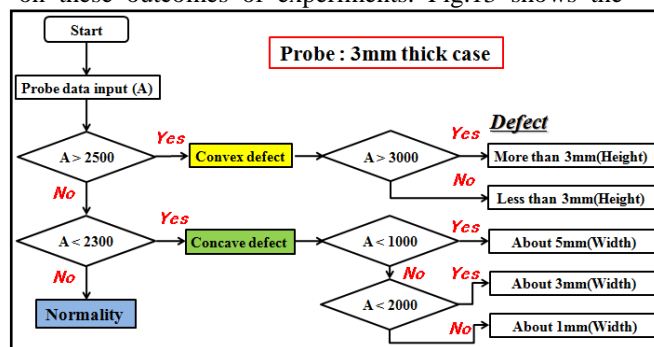
Condition of defect	Voltage [mV]
Defect type : Cube(Height:10mm)	More than 3,000
Defect type :Cube(Height:6mm,3mm)	About 2,700
Defect type : Concave(Width:10mm)	About 900
Defect type : Concave(Width:6mm)	About 1,700
Defect type : Concave(Width:3mm)	About 1,900

Table.3 Experimental Results (Form)

Condition of defect	Voltage change
Defect type : Cuboid (Width:50mm,30mm,10mm)	• Irregularity on defect surface • Width of defect
Defect type : Semicircular (Diameter:40mm,30mm,20mm)	• Smoothly increase, and decreases.
Defect type : Equilateral triangle (Sides:20mm)	• Fixed part and the tip of the probe. (Two times)

VI. AUTOMATIC DEFECT RECOGNITION METHOD

Automatic defect recognition method was made based on these outcomes of experiments. Fig.13 shows the



algorithm of automatic defect recognition method.

Fig.13 Pipe inspection algorithm

VII. CONCLUSION

In this paper, a rotating probe in vinyl chloride pipe was tested, and a new inspection robot system for drain pipe was developed. Moreover, the image was processed, a circular image was developing, and it was possible to make it to a plane image. In the future, these two researches are combined, and the defect diagnostic system with good accuracy will be made. And, it actually experiments in pipe.

ACKNOWLEDGMENTS

We would like to thank ISHIKAWA IRON WORKS, who provides the inspection robot for this research.

REFERENCES

- [1] Zhicheng Wang, Harutoshi Ogai, Shigeyuki Takahiro, "Real-time Generation of Developed View for Sewer Pipe Based on Web Camera Video", The 15th International Symposium on Artificial Life and Robotics 2010, CD-ROM, papers, OS3-4, 2010, Beppu, Japan.
- [2] Kentarou Nishijima, Yixiang Sun, Rupesh Kumar Srivastava, Harutoshi Ogai and Bishakh Bhattacharya, "Advanced Pipe Inspection Robot using Rotating Probe", The 15th International Symposium on Artificial Life and Robotics 2010, CD-ROM, papers, OS3-2, 2010, Beppu, Japan.

Application of the Genetic Algorithm on Face Recognition

Fengzhi DAI¹, Liqiang SHANG², Naoki KUSHIDA³, Masanori SUGISAKA⁴

^{1.} College of Electronic Information and Automation, Tianjin University of Science and Technology, daifz@tust.edu.cn

^{2.} Vestas Wind Technology (China) Co., Ltd, shliq@vestas.com

^{3.} Dept. Electronic Mechanical Engineering, Oshima National College of Maritime Technology, kushida@oshima-k.ac.jp

^{4.} Nippon Bunri University, ALife Robotics Co., Ltd, ms@alife-robotics.co.jp

Abstract: Computer vision and recognition is playing an increasing important role in the modern intelligent control. Object detection is the first and the most important step in object recognition. Traditionally, special objects can be detected and recognized by the template matching method, but the recognition speed has always been a problem. Also for recognition by the neural network, training the data is always time consumption. In this paper, the genetic algorithm-based face recognition system is proposed. The genetic algorithm (GA) has been considered as a robust and global searching method. Here, the chromosomes generated by the GA contain information (parameters) of the image, and we use the genetic operators to obtain the best match between the original image and the face of interest. The parameters are the coordinate (x, y) of the center of the face in the original image, the rate of scale and the angle θ of rotation. Finally, the experimental results and some other considerations are also given.

Keywords: Face detection and recognition, Genetic algorithm, Image processing, Template matching method.

I. INTRODUCTION

Lots of papers and applications are presented on the web, in conference proceedings or journals about the intelligent control. Among them, image processing and recognition occupy a very large percentage [1-3]. The higher the degree of intelligence is, the more important is the image detection and recognition technology.

For an intelligent control system, it is necessary to acquire information about the external world automatically by sensors, in order to recognize its position and the surrounding situation. A camera is one of the most important sensors for computer vision: the intelligent system endeavors to find out what is in an image taken by the camera: traffic signs, obstacles or guidelines, etc.

The reliability and time-response of the object detection and recognition have a major influence on the performance and usability of the whole object recognition system [4]. The template matching method is a practicable and reasonable method for object detection [5], but the recognition speed has always been a problem.

In addition, in order to search for the object of interest in an image, lots of data need to be processed. The genetic algorithm (GA) has been considered to be a robust and global searching method (although it is sometimes said that GA can not be used for finding the global optimization [6]). Here, the chromosomes generated by GA contain information about the image data, and the genetic and evolution operations are used

to obtain the best match to the template [7]: searching for the best match is the goal of this paper.

This thought emerged from the features of GA, and the need to recognize the faces of special people easily and quickly by an intelligent system. The single concept and feature of image processing and the GA will not be introduced here, because there is already extensive literature on these subjects.

In this paper, the encoding and decoding method of the GA and the experimental setting, the experiment and the analysis, and conclusion are addressed sequentially.

II. THEORY AND EXPERIMENT

If we want to find a special person in an image, we first have to detect people in the image, and then recognize which one is the person of interest (sometimes these two steps will be executed simultaneously).

1. Genetic encoding

Since the chromosomes generated by the GA contain information about the image data, the first step is to encode the image data into a binary string to the GA [8].

Some important parameters of GA are given in Table 1, and the search field and region are given in Table 2. Table 2 shows that there are 4 image parameters: the center of a face (x, y) in the original image, the rate of scale of the face, and the rotating angle θ , are encoded into the elements of gene (the meanings of which will be introduced below). Since one parameter uses 8 bits

(1 byte), and there are 4 image parameters, thus one chromosome contains 4 bytes shown in Fig.1.

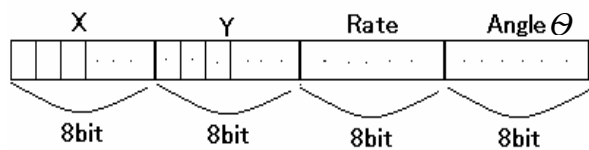


Fig.1. One chromosome contains 4 bytes

Table 1. Setting for the GA parameters

Source	The original and the template images
Generations	Maximum = 300 (the stopping criterion)
Population Size	200
Reproduction (selection)	P_r of the best individuals will be selected to survive. The remained $(1 - P_r)$ will be treated by the genetic operators (crossover and mutation)
Crossover	Offspring are produced from parents by exchanging their genes at the crossover point, the ratio is P_c
Mutation	Produce spontaneous random changes in various chromosomes. The general random change method is used at the rate of P_m

Table 2. Setting for the experiment

Image parameters (field)		
x	8 bits	$(0, \max_x)$
y	8 bits	$(0, \max_y)$
$rate$	8 bits	$(1.0, 3.0)$
Θ	8 bits	$(-35^\circ, 35^\circ)$
GA parameters		
P_r	0.6	
P_c	0.5	
P_m	0.01	

2. Genetic algorithm

The fitness is defined as [9]

$$\text{fitness} = 1.0 - \frac{\sum_{j=0}^{\text{temp_y}} \sum_{i=0}^{\text{temp_x}} |f(x, y, \text{rate}, \theta) - \text{temp}(i, j)|}{(\text{temp_x}) \times (\text{temp_y}) \times 255} \quad (1)$$

In Eq.1, $\text{temp}(i, j)$ is the gray level of the coordinate (i, j) in the template image, the width and height of which are temp_x and temp_y . $f(x, y, \text{rate}, \theta)$ gives the gray level in the original image, the coordinate of which are calculated by translation from (x, y) , and by changing the scale and the rotation angle θ from the template. Since the images have 256 gray levels, in Eq.1,

division by 255 ensures that the resulting fitness is between 0 and 1.

Based on Eq.1, in the program, the fitness is calculated by the following four steps, and Fig.2 gives the figural example.

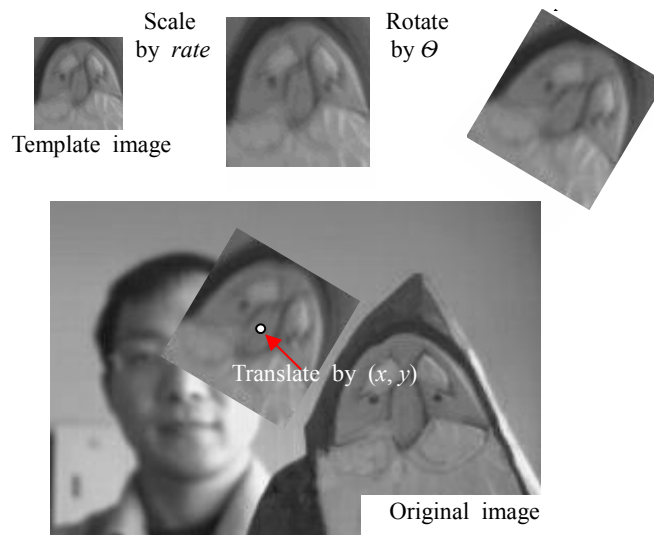


Fig.2. Figural example of calculation by Eq.1

- (1) The coordinate (i, j) in the template is scaled by the value of parameter rate, then we get the result $f(x, y, \text{rate}, \theta) = f(i \times \text{rate}, j \times \text{rate})$;
- (2) The result of step (1) is rotated by the value of parameter θ , thus $f(x, y, \text{rate}, \theta) = f(i \times \text{rate}, j \times \text{rate}, \theta)$;
- (3) The result of step (2) is translated from the coordinate (x, y) in the original image, then the gray level of the pixel $f(x, y, \text{rate}, \theta)$ is gotten;
- (4) All the differences between the gray level of the coordinate (i, j) in the template and that of the calculated $f(x, y, \text{rate}, \theta)$ in the original image are summarized by Eq.1 to calculate the fitness.

If the value of the fitness is larger than the preset threshold, the search process is over and the result is given, otherwise the loop will be continued.

3. Decoding

In order to obtain the true value of the image parameters from the chromosome, decoding is needed. In Eq.2, after decoding from datum of GA, the value of each parameter is standardized. A figural example is given in Fig.3.

$$\text{Value} = \text{MIN} + \frac{\text{MAX} - \text{MIN}}{255} \times (\text{datum from GA}) \quad (2)$$

4. Experiments

The experiment is done by first loading the original and the template images. GA is used to find whether or not there is the object (face) of a template in the original

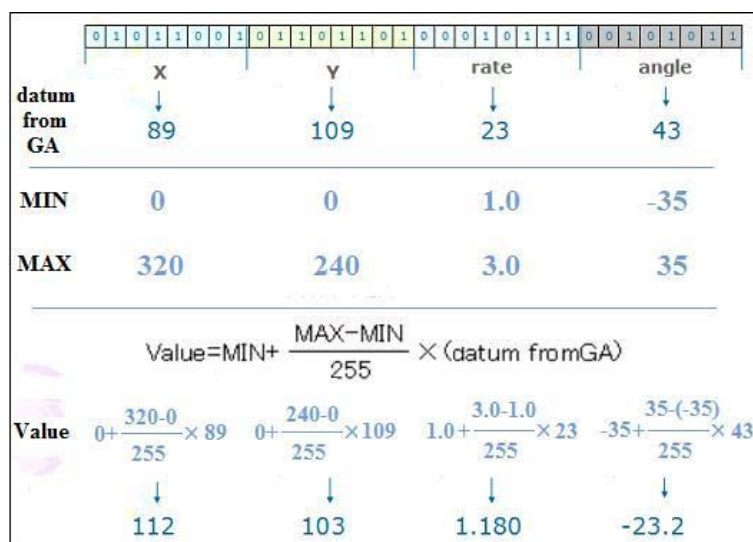


Fig.3. Figural example for decoding

image. If the answer is YES, then in the original image the result gives the coordinate of the center of the face, the rate of scale, and the rotation angle from the template.

Fig.4 and Fig.5 are the template and the original images for the experiment. The values are the width \times height in pixels of the image. In Fig.5, two original images are presented, the sizes of which are the same 320×240 .



30 \times 35

Fig.4. Template for matching (temp_x \times temp_y)

The maximum number of generation is limited to 300, and the threshold of the matching rate is set to 0.85. Thus if within 300 generations the matching rate can reach 0.85, it is said that the template is found in the original image (the template matched the original image by the threshold). The result of the GA-based face recognition is given in Fig.6 and Table 3.

Table 3. Results of searching by GA

	Result for Fig.5a	Result for Fig.5b
Fitness	0.858	0.875
Generation	28	18
(x, y)	(71, 108)	(51, 107)
Rate	2.0039	1.9333
Angle [deg]	12.59	-9.76

III. CONCLUSION

In this paper, the GA-based image (face) recognition method is tested.

The GA starts with an initial set of random solutions called the population. Each individual in the population

is called chromosome, and represents a solution to the problem. By stochastic search techniques based on the mechanism of nature selection and natural genetics, genetic operations (crossover and mutation) and evolution operation (selecting or rejecting) are used to search the best solution [10].

In this paper, the chromosomes generated by the GA contain information about the image, and we use the genetic operators to obtain the best match between the original image and the template. The parameters are the coordinate (x, y) of the center of the object in the original image, the rate of scale, and the rotation angle θ .

In fact, translation, scale and rotation are three main invariant moments in the field of pattern recognition. However, for face recognition, the facial features are difficult to be extracted and calculated by the general pattern recognition theory and method. Even these three main invariant moments will not be invariant because the facial expression is changed in different images.

Thus the recognition only gives the best matching result within an upper predetermined threshold. The result in the paper shows that the recognition is satisfied.

By using the GA-based recognition method, the settings of the search field (in this paper, (x, y, rate, θ) is selected), the determination of the genetic operations, and the selection and the optimization of the fitness function all have a strong effect on the level of recognition of the resultant image.

Based on the results of experiments described here, further work will emphasize (i) optimizing the fields of chromosomes, and (ii) improving the fitness function by adding some terms to it. This work is important and necessary in order to improve the GA-based face recognition system.

Acknowledgment

This work is sponsored in part by the Scientific Research Foundation of Tianjin University of Science and Technology (China) for the Introduced Talented Scholars, No. 20100408.

REFERENCES

- [1] K. Deguchi, I. Takahashi (1999), Image-based simultaneous control of robot and target object motion by direct-image-interpretation, Proc. the 1999 IEEE/RSJ International Conf. of Intelligent Robot and System, vol. 1, 375-380
- [2] H. Takimoto, Tasue Mitsukura, M. Fukumi, et al(2002), A design of face detection system based on the feature extraction method, Proc. of 12th Symp. on

Fuzzy, Artificial Intelligence, Neural Networks and Computational Intelligence, 409-410

[3] F. Dai, T. Kodani, Y. Fujihara (2006), Research on Face Recognition System by Genetic Algorithm, Proc. of the 11th Int. Symp. on Artificial Life and Robotics, CD version, 63-66

[4] M. Sugisaka, X. Fan (2002), Development of a face recognition system for the liferobot, Proc. of the 7th Int. Symp. on Artificial Life and Robotics, vol. 2, 538-541

[5] K. R. Castleman (1998), Digital image processing, Original edition published by Prentice Hall, Inc., a Simon & Schuster Company, Press of Tsinghua University

[6] H. Iba (1994), Foundation of genetic algorithm – solution of mystic GA, Omu Press (in Japanese)

[7] T. Agui, T. Nagao (2000), Introduction to image processing using programming language C, Shoko-do press (in Japanese)

[8] M. Gen, R. Cheng (1997), Genetic algorithms and engineering design, A wiley-Interscience Publication

[9] F. Dai, T. Kodani, Y. Fujihara (2007), Research on a Face Recognition System by the Genetic Algorithm, Journal of Artificial Life and Robotics, Issue: Volume 11, Number 1 / January, 2007, pp. 67-70

[10] F. Dai, T. Adachi, Y. Fujihara, et al (2007), Fundamental Research on Face Recognition by Genetic Algorithm, Proc. of the 12th International Symp. on Artificial Life and Robotics 2007, CD version, pp. 639-642



Fig.5. The original images (size: $max_x, max_y = 320 \times 240$)

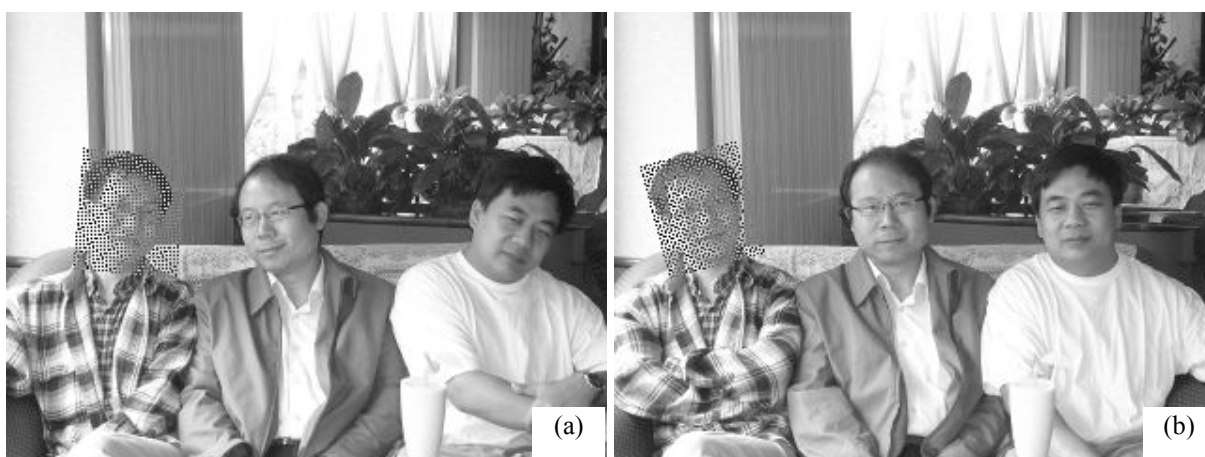


Fig.6. Results of the GA-based recognition

Study on the Disturbance Rejection of Virtual Slope Walking by Stepper-2D Robot

Mingguo Zhao^{1,2}, HaoDong¹ and Naiyao Zhang¹

¹State Key Laboratory of Robotics and System (HIT)

²Department of Automation, Tsinghua University, Beijing 100084, China

(mgzhao@tsinghua.edu.cn, donghao00@mails.tsinghua.edu.cn, zlh@tsinghua.edu.cn)

Abstract: Virtual Slope Walking is a new realization of powered walking based on Passive Dynamic Walking, which is not only effective in generating fast walking, but also achieving advantages on disturbance rejection. Under the open-loop condition without external sensing device, the step-handling walking with maximum step height of 10% leg length is realized on a planar bipedal robot Stepper-2D. This paper theoretically studies the disturbance rejection of Virtual Slope Walking by introducing the ground step perturbation. We theoretically proved that the step perturbation can be transformed to the disturbance of initial system state and successful step handling comes from the system's cyclic stability. The necessary and sufficient condition of recovering from the step perturbation is obtained and confirmed by the experiment on Stepper-2D.

Keywords: Bipedal robot; Virtual Slope Walking; Disturbance Rejection.

I. INTRODUCTION

McGeer [1] demonstrated that a Passive Dynamic Walker can walk down a shadow slope with no control and actuation in the early of 1990. Then the concept of Passive Dynamic Walking has been used as a starting point for designing powered walkers to walk on level ground. Wisse[3], Hobbelen[4] and Collins[5] demonstrated several realizations of powered walking based on kinematic energy complement. Asano [6], Honjo [7] and Harata [8] introduced the parametric excitation for potential energy restoration. In our previous work [9] [10], we proposed Virtual Slope Walking by introducing the leg length modulation and achieved a relative speed of 4.48leg/s on a planar bipedal robot Stepper-2D.

Disturbance rejection, defined as the ability to deal with unexpected disturbances [11], is considered as one of the fundamental performances for bipedal walking. There exists several ways to measure the disturbance rejection for a PDW based walker theoretically, such as Floquet multipliers, Basin of Attraction and the Gait Sensitivity Norm. But the most commonly used experimental measure is the ground step perturbation that a walker can handle without falling. Wisse[12] realized powered walking under a step height of 2% leg length disturbance. Pratt [13] realized powered walking under a step height of 9% leg length. Geng [14] achieved powered walking under a step height of 4% leg length by on-line machine learning and PDW based mechanism designed. We[15][16] have realized a powered walking under a step height of 10% leg length on Stepper-2D based on Virtual Slope Walking.

In this paper, we theoretically study the disturbance rejection of Virtual Slope Walking and present its stabilizing mechanism under. Based on the asymptotic expression of stride function and the fixed point, we theoretically proved that ground step perturbation can be transformed to the disturbance of initial system state and the successful step handling

walking comes from the fixed point's stability. Then the necessary and sufficient condition of recovering from the step perturbation is presented based on the analysis of the relationship between the system state and the minimum initial state in the transition phase, providing the possibility to quantitatively analyze the maximal relative step height.

The remainder of this paper is organized as follows. In Section II, the model of Virtual Slope Walking is presented. In Section III, the ground step disturbance handling is illustrated, and the performance of disturbance rejection is analyzed in Section IV. Section V presents the experimental results and Section VI the conclusion and future work.

II. Model of Virtual Slope Walking

1 Model Description

A cartoon of the Virtual Slope Walking model is shown in Fig. 1. We assumed that the model has two telescopic massless legs and a point mass body at the hip. The stance leg is actuated for extending from r_s to r_e following a smooth leg length trajectory $r(t)$, the swing leg is actuated for shortening from r_e to r_s in one step. The length shorten ratio is then defined as $\beta=r_s/r_e$. Since the swing leg is assumed massless, it can be swung arbitrarily quickly to the position with constant inter-leg angle ϕ_0 before heel strike. The impact of the swing leg with the ground is assumed to be fully inelastic (no slip, no bounce) and instantaneous, which implies that there exists discontinues change in the velocity of the center of mass and unchanged system configuration.

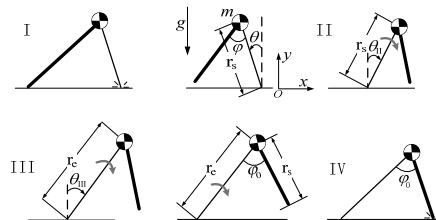


Fig. 1 Model of Virtual Slope Walking

We define a walking step starts when the new stance leg (lighter line) has just made contact with the ground in the upper left picture, namely instant I. The stance leg swings to the position at $\theta=\theta_{II}$ in the upper right picture for the beginning of extension, namely instant II. And the stance leg extension ends at $\theta=\theta_{III}$ in the bottom left picture, namely instant III. The swing leg (heavier line) is shortened and swings to the position with constant inter-leg angle φ_0 just before heel strike in the bottom middle picture, and hits the ground in the bottom right picture, namely instant IV. Then, the stance leg and swing leg exchange subsequently, and the walking cycle repeats continuously.

2 Governing Equations

The governing equations of the system consist of nonlinear differential equations for the swing phase and algebraic equations for the transitions of heel strike.

(1) Swing phase from **I** to **II**: Using *Lagrangian Equations*, the second-order differential equation of motion is given below for the swing phase of the stance leg with the constant length r_s under the dimensionless time variable $\tau = \sqrt{g/r_e} t$

$$\ddot{\theta}(\tau) = \frac{1}{\beta} \sin \theta(\tau) \quad (1)$$

For the simplicity, we will refer to dimensionless time τ as the time variable, henceforward.

(2) Stance leg extension From **II** to **III**: The stance leg acts as an inverted pendulum with variable length $r(\tau)$. Using the *Lagrangian Equations*, the equation of motion can be written as

$$\begin{cases} \ddot{\theta}(\tau) = \frac{r_e}{r(\tau)} \sin \theta(\tau) - \frac{2}{r(\tau)} \dot{r}(\tau) \dot{\theta}(\tau) \\ \ddot{r}(\tau) = r(\tau) \dot{\theta}^2(\tau) - r_e \cos \theta(\tau) + r_e \frac{F}{mg} \end{cases} \quad (2)$$

where F is the force that the leg exert on the center of mass during the stance leg extension.

(3) Swing phase from **III** to **IV**: Similar to the equation in Eq. (1), the equation of motion for the stance leg with the constant length r_e can be written as

$$\ddot{\theta}(\tau) = \sin \theta(\tau) \quad (3)$$

(4) Heelstrike transition from **IV** to **I** of the subsequent step: The heelstrike from step n to the subsequent step $n+1$ occurs when the geometric collision condition

$$\begin{cases} \theta_I(n+1) = -(\varphi_0 - \theta_{IV}(n)) \\ \beta \cos \theta_I(n+1) = \cos \theta_{IV}(n) \end{cases} \quad (4)$$

is met, where the 'I' and 'IV' subscripts denote the instant **I** and **IV** respectively, φ_0 is the constant of the inter-leg angle at heels trike. Eq. (4) also reflects a change of names for the two legs. The swing leg becomes the stance leg, and vice versa.

From the conservation of angular momentum about the swing foot contact point at heel strike, we obtain the following transition equation

$$\omega_I(n+1) = \frac{\cos \varphi_0}{\beta} \omega_{IV}(n) \quad (5)$$

Eq. (1)-(5) construct the dynamic equations of this hybrid system.

3 Stride Function and Fixed Point

The general procedure for the study of this model is based on interpreting a step as a Poincaré map, or, as McGeer termed it, a 'stride function' [1]. Our Poincaré section is at the start of a step, namely instant **I** in Fig. 1. Given the state of the system at instant **I**, the Poincaré map \mathbf{f} determines the state just after the next heelstrike. Note that in the geometric collision condition Eq. (4), the stance leg angle θ_I is constant with inter-leg angle φ_0

$$\theta_I = -\arctan \frac{\beta - \cos \varphi_0}{\sin \varphi_0} \quad (6)$$

So the heels trike transition reduces this problem in 2D state space $\{\theta_I, \omega_I\}$ to a one dimensional map \mathbf{f} , only consisting of angular velocity ω_I . So, while the system has only one independent initial condition, we need to specify ω_I at the start of walking step n to fully determine the subsequent motion at steps $n+1, n+2, \dots$ so that $\omega_I(n+1)$ can be obtained from $\omega_I(n)$ by the Poincaré mapping. We have proved that under the **Equivalent Definition**, The Trajectory Leg Extension (TLE) can be equivalently transformed to the Instantaneous Leg Extension (ILE) [15] in Virtual Slope Walking. Consequently, defining a new variable $q = \omega_I^2$ as the system state, the stride function \mathbf{f} can be analytically obtained under the Instantaneous Leg Extension (ILE) as follows

$$\begin{aligned} \mathbf{f}(q) = & \beta^2 \cos^2 \varphi_0 q \\ & + 2 \cos^2 \varphi_0 [\cos \theta_{II}^* (\frac{1}{\beta^2} - \beta) - \cos \theta_I (\frac{1}{\beta} - \beta)] \end{aligned} \quad (7)$$

where θ_{II}^* is the equivalent extension angle. Since the walking with TLE and its equivalent ILE produces the equivalent cyclic walking motion, ILE can be used as a theoretical tool for the analysis of Virtual Slope Walking without the dependence on numerical simulation.

The fixed point of the stride function is defined as $\mathbf{f}(q^f) = q^f$. From Eq. (7), the fixed point can then be obtained as follows

$$q^f = \frac{2 \cos^2 \varphi_0 [\cos \theta_{II}^* (1 - \beta^3) - \cos \theta_I (\beta - \beta^3)]}{\beta^2 (1 - \cos^2 \varphi_0 \beta^2)} \quad (8)$$

III. Ground Step Disturbance Handling

1. Transition Walking

After entering into the periodic state in Virtual Slope Walking, once the system is perturbed by a single step, there will be a transition phase in the subsequent one or two walking steps. And after that, the system state will approach the fixed point asymptotically the same as the condition of initial state's disturbance in Virtual Slope Walking. We will illustrate such transition walking by introducing the single step-up and step-up-down perturbations in the following section.

2. Single Step-Up Perturbation

We assume that the system is in the periodic state in step $n-2$, and a single step-up perturbation occurs at the end of step $n-1$, just at heel strike. The subsequent transition walking step n is shown in Fig. 2. In the transition phase, there exist the perturbations not only on the system state q , but also on the stance leg angle θ_I and θ_{IV} , which is constant in normal walking, resulting in the variation of the stride function. After the transition phase ends, only disturbance on the system state q exists.

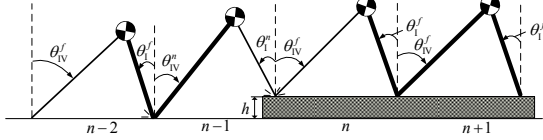


Fig. 2 Transition Walking of the Single Step-Up Perturbation

Let h be the step disturbance height, and $h_r = h/r_e$ be the relative value. Then, the perturbation on the stance leg angle θ_I and θ_{IV} resulted from the step height disturbance in the transition walking step n can be obtained as follows

$$\begin{cases} \theta_{IV}^n + \theta_I^n = \varphi_0 \\ \cos \theta_{IV}^n = \beta \cos \theta_I^n + h_r \end{cases} \quad (9)$$

The system state at the start of step n can be considered as the output of the stride function with perturbed θ_{IV} of step $n-1$. Let θ_I^n and θ_{IV}^n be the constant stance leg angle which is corresponded to the fixed point, then $q(n)$ can be represented as

$$\begin{aligned} q(n) &= \beta^2 \cos^2 \varphi_0 q^f \\ &+ 2 \cos^2 \varphi_0 \left[\cos \theta_{II}^* \left(\frac{1}{\beta^2} - \beta \right) - \left(\frac{1}{\beta^2} \cos \theta_{IV}^n - \beta \cos \theta_I^n \right) \right] \end{aligned} \quad (10)$$

There exists the perturbation on θ_I in transition walking step n (Fig. 2), so $q(n+1)$ can be considered as the output of the stride function with perturbed θ_I of step n

$$\begin{aligned} q(n+1) &= \beta^2 \cos^2 \varphi_0 q(n) \\ &+ 2 \cos^2 \varphi_0 \left[\cos \theta_{II}^* \left(\frac{1}{\beta^2} - \beta \right) - \left(\frac{1}{\beta^2} \cos \theta_{IV}^f - \beta \cos \theta_I^n \right) \right] \end{aligned} \quad (11)$$

θ_I and θ_{IV} returns to the constant value from step $n+1$, then $q(n+2)$ can be represented as

$$\begin{aligned} q(n+2) &= \beta^2 \cos^2 \varphi_0 q(n+1) \\ &+ 2 \cos^2 \varphi_0 \left[\cos \theta_{II}^* \left(\frac{1}{\beta^2} - \beta \right) - \cos \theta_I^f \left(\frac{1}{\beta} - \beta \right) \right] \end{aligned} \quad (12)$$

The transition phase ends after step n , and the system state starts approaching the fixed point asymptotically with the initial state of $q(n+1)$.

It can be concluded from Eq. (10)&(11) that the single step-up perturbation introduces the disturbance on the system state q of step n and transfers such disturbance by the stride function in the subsequent transition phase. It is indicated from Eq. (12) that after the transition phase ends, the step perturbation can be totally transformed to the disturbance of initial system state. So, once the continuous walking condition of the initial state is satisfied, the system state will definitely approach the fixed point in the following walking steps.

3. Single Step-Up-Down Perturbation

We assume that the system is in the periodic state in step $n-2$, and a single step-up-down perturbation occurs at the end of step $n-1$, just at heel strike. The subsequent transition walking steps n and $n+1$ are shown in Fig. 3. The same as the step-up perturbation, in the transition phase, there exist the perturbations not only on the system state q , but also on the stance leg angle θ_I and θ_{IV} , which is constant in normal walking, resulting in the variation of the stride function. After the transition phase ends, only disturbance on the system state q exists.

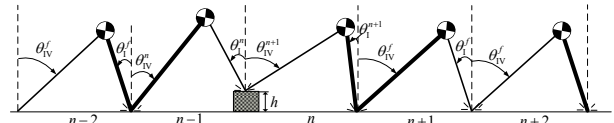


Fig. 3 Transition Walking of the Single Step-Up-Down Perturbation

The perturbation on the stance leg angle θ_I and θ_{IV} resulted from the step height disturbance in the transition walking step n and $n+1$ can be obtained as follows

$$\begin{cases} \theta_{IV}^n + \theta_I^n = \varphi_0 \\ \cos \theta_{IV}^n = \beta \cos \theta_I^n + h_r \end{cases}, \begin{cases} \theta_{IV}^{n+1} + \theta_I^{n+1} = \varphi_0 \\ \cos \theta_{IV}^{n+1} = \beta \cos \theta_I^{n+1} - h_r \end{cases} \quad (13)$$

The system state at the start of step n can be considered as the output of the stride function with perturbed θ_{IV} of step $n-1$. So $q(n)$ can be represented as

$$\begin{aligned} q(n) &= \beta^2 \cos^2 \varphi_0 q^f \\ &+ 2 \cos^2 \varphi_0 \left[\cos \theta_{II}^* \left(\frac{1}{\beta^2} - \beta \right) - \left(\frac{1}{\beta^2} \cos \theta_{IV}^n - \beta \cos \theta_I^f \right) \right] \end{aligned} \quad (14)$$

Both perturbations on θ_I and θ_{IV} exist in transition walking step n (Fig. 5), so $q(n+1)$ can be considered as the output of the stride function with perturbed θ_I of step n and θ_{IV} of step $n+1$

$$\begin{aligned} q(n+1) &= \beta^2 \cos^2 \varphi_0 q(n) \\ &+ 2 \cos^2 \varphi_0 \left[\cos \theta_{II}^* \left(\frac{1}{\beta^2} - \beta \right) - \left(\frac{1}{\beta^2} \cos \theta_{IV}^{n+1} - \beta \cos \theta_I^n \right) \right] \end{aligned} \quad (15)$$

There exists the perturbation on θ_I in transition walking step $n+1$ (Fig. 3), so $q(n+2)$ can be considered as the output of the stride function with perturbed θ_I of step $n+1$

$$\begin{aligned} q(n+2) &= \beta^2 \cos^2 \varphi_0 q(n+1) \\ &+ 2 \cos^2 \varphi_0 \left[\cos \theta_{II}^* \left(\frac{1}{\beta^2} - \beta \right) - \left(\frac{1}{\beta^2} \cos \theta_{IV}^f - \beta \cos \theta_I^{n+1} \right) \right] \end{aligned} \quad (16)$$

θ_I and θ_{IV} returns to the constant value from step $n+2$, then $q(n+3)$ can be represented as

$$\begin{aligned} q(n+3) &= \beta^2 \cos^2 \varphi_0 q(n+2) \\ &+ 2 \cos^2 \varphi_0 \left[\cos \theta_{II}^* \left(\frac{1}{\beta^2} - \beta \right) - \cos \theta_I^f \left(\frac{1}{\beta} - \beta \right) \right] \end{aligned} \quad (17)$$

The transition phase ends after step $n+1$, and the system state starts approaching the fixed point asymptotically with the initial state of $q(n+2)$.

It can be concluded from Eq. (14)-(16) that the single step-up-down perturbation introduces the same disturbance as that of the single step-up perturbation. It

is indicated from Eq. (17) that after the transition phase ends, the step perturbation can be totally transformed to the disturbance of initial system state. The only difference is that the transition phase of single step-up-down perturbation includes one more step than that of single step-up perturbation. So, once the continuous walking condition of the initial state is satisfied, the system state will also definitely approach the fixed point in the following walking steps.

So we can draw the conclusion from the above results that the step height perturbation can be totally transformed to the disturbance of initial system state, and the disturbance rejection problem in Virtual Slope Walking can be transformed to the stabilizing problem of the fixed point if the continuous walking condition is satisfied.

IV Analysis of Disturbance Rejection of Virtual Slope Walking

1. Maximum Relative Step Height

There exists the maximum relative step height h_r^{\max} when $q(n)=q^z(n)$ holds as h_r increases, which describes the performance of disturbance rejection of Virtual Slope Walking. Therefore, h_r^{\max} can be obtained as follows

$$h_r^{\max} = \beta \tan^2 \varphi_0 \cos \theta_1^n$$

$$\begin{cases} \frac{1}{2} \beta^4 q^f + \cos \theta_{II}^* (1 - \beta^3) + \beta^3 \cos \theta_1^f - \frac{\beta}{\cos^2 \varphi_0}, \theta_{II}^* > 0 \\ \frac{1}{2} \beta^4 q^f + \frac{1 - (1 - \beta^3)(1 - \beta^2 \cos^2 \varphi_0) \cos \theta_{II}^*}{\beta^2 \cos^2 \varphi_0} + \beta^3 \cos \theta_1^f, \theta_{II}^* \leq 0 \end{cases} \quad (18)$$

where h_r^{\max} and θ_1^n satisfy

$$\begin{cases} \theta_{IV}^n + \theta_1^n = \varphi_0 \\ \cos \theta_{IV}^n = \beta \cos \theta_1^n + h_r^{\max} \end{cases} \quad (19)$$

It can be concluded from Eq. (18)&(19) that the maximum relative step height h_r^{\max} is determined by the model parameters length shorten ratio β , equivalent extension angle θ_{II}^* and inter-leg angle φ_0 . We will illustrate the influence of model parameters on the disturbance rejection in the following section.

2. Influence of Model Parameters

2.1 Effect of the Length Shorten Ratio β

The maximum relative step height h_r^{\max} is shown as a function of β in Fig.4 with four values of φ_0 . It is indicated from Fig.4 that h_r^{\max} decreases with an increase in β . An increase in β causes a net decrease in the extended leg length, resulting in a decrease in the complementary energy E_c and a decrease in the system kinematic energy which is represented by the system state q . On the other side, an increase in β causes an increase in q_z . Consequently, h_r^{\max} decreases from combined action with the effect of changing in $q(n)$ and $q_z(n)$.

The main conclusion from this graph is that a **decrease in β leads to a greater h_r^{\max} and a larger disturbance rejection in Virtual Slope Walking**. However, β is a

always restricted by the physical parameters of the real robot.

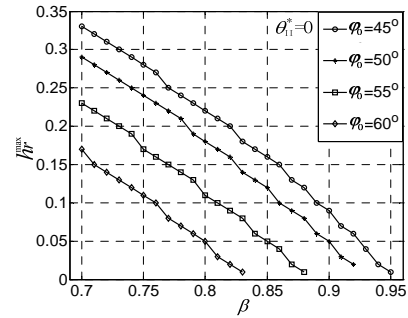


Fig. 4 Trajectory of maximum relative step height h_r^{\max} versus length shorten ratio β

2.2 Effect of the Equivalent Extension Angle θ_{II}^*

The maximum relative step height h_r^{\max} is shown as a function of θ_{II}^* in Fig. 5 with two values of β and φ_0 respectively. Fig. 5 shows a second order relationship between h_r^{\max} and θ_{II}^* . As θ_{II}^* approaching zero from both side, h_r^{\max} increases and reaches a maximum value at $\theta_{II}^* = 0^\circ$. The vertical projection of leg length extension increases as θ_{II}^* approaching zero, and more potential energy is complemented. As a consequence, $q(n)$ and h_r^{\max} increase while $q^z(n)$ stays constant. The vertical projection of leg length extension reaches its maximum at $\theta_{II}^* = 0^\circ$.

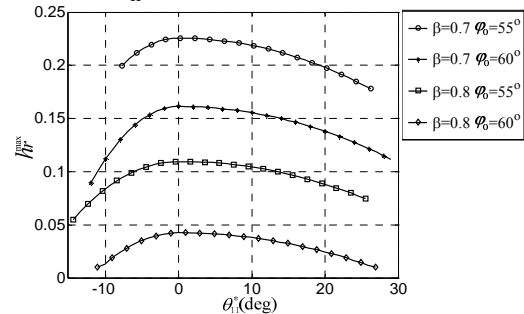


Fig. 5 Trajectory of maximum relative step height h_r^{\max} versus equivalent extension angle θ_{II}^*

It can be concluded from this graph that **extending the stance leg more close to mid-stance will result in a greater h_r^{\max} and a larger disturbance rejection in Virtual Slope Walking**. We can extend this conclusion to the Trajectory Leg Extension (TLE) that the extension phase being close to mid-stance also produces larger disturbance rejection.

2.3 Effect of the Inter-leg Angle φ_0

The maximum relative step height h_r^{\max} is shown as a function of φ_0 in Fig. 6 with four values of β . As shown in Fig. 6, h_r^{\max} decreases with an increase in φ_0 . The dissipation energy E_r increases as φ_0 increases. As a consequence, the system kinematic energy decreases, and $q(n)$ decreases. On the other side, an increase in φ_0 causes an increase in q^z . Consequently, h_r^{\max} decreases from combined action with the effect of changing in $q(n)$ and $q^z(n)$.

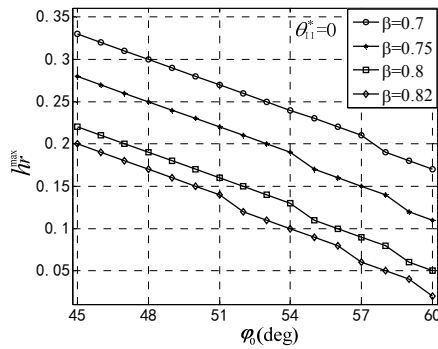


Fig. 6 Trajectory of maximal relative step height h_r^{\max} versus inter-leg angle ϕ_0

So we can conclude from this graph that **a smaller ϕ_0 results in greater h_r^{\max} and a larger disturbance rejection in Virtual Slope Walking.**

2.4 Adjoint Relationship between the Walking Speed and Disturbance Rejection

The walking speed described by the Froude Number F_r is also determined by the model parameters β , θ_{II}^* , and ϕ_0 [16]. Therefore, as the model parameters change, there exists an adjoint relationship between the walking speed and disturbance rejection. The maximum relative step height h_r^{\max} is shown as a function of F_r in Fig. 7.

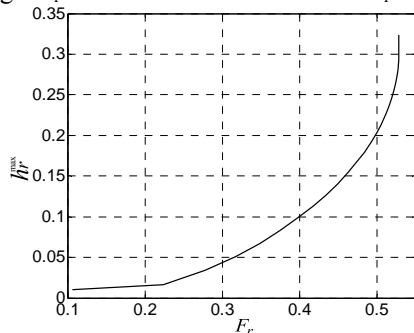


Fig. 7 Trajectory of maximal relative step height h_r^{\max} versus walking speed F_r

It is indicated from Fig. 7 that h_r^{\max} increases with an increase in F_r . Since the effect of model parameters on h_r^{\max} is the same as that on F_r , this conclusion exists distinctly. Such conclusion suggests that achieving fast walking speed always accompanying with large disturbance rejection.

From the above analyze results, it can be concluded that the performance of disturbance rejection in Virtual Slope Walking can be determined by the model parameters β , θ_{II}^* , and ϕ_0 , which will be

confirmed in the following experiment results.

V. Experiment

1. Planar Bipedal Robot Stepper-2D

We use the planar bipedal robot Stepper-2D as a test bed of disturbance rejection in Virtual Slope Walking under single step perturbation. As shown in Fig. 8, Stepper-2D is mounted on a boom to constrain the body motion in the sagittal plane. The boom has three orthogonal DOF and the length is six times more than the height of the robot, so its effect on the robot sagittal movement can be ignored. Stepper-2D's leg length is 250mm and hip mass is 390g.



Fig. 8 Planar Bipedal Robot Stepper-2D with Point Foot.

The leg with the point foot is actuated in the hip and knee joint by digital servo motors. The telescopic leg motion is realized by bending and unbending the knee joint. And the swing leg motion is achieved by hip motor actuation [15]. All digital servo motors are controlled by a computer through serial bus.

2. Experimental Results

Stepper-2D successfully recovers from a maximum single step perturbation of 25mm in height, with a maximum relative step height h_r^{\max} of 10% leg length. The hip and knee joints data from the motor sensors in the real walking experiment. Fig.9&10 presents the image sequences of the walking experiment under a single step-up and step-up-down perturbation of Stepper-2D respectively. The robot reaches the periodic state after several steps. And when the step height is greater than 25mm, it falls backward.

All the videos about the walking experiments including the single step-up and step-up-down could be found on our website
http://v.youku.com/v_show/id_XMjA3ODM5OTcy.html



Fig. 9 Image sequence extracted from video of a single step-up perturbation experiment ($h_r^{\max}=25\text{mm}$)

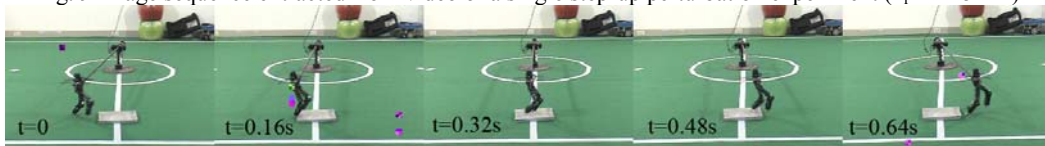


Fig. 10 Image sequence extracted from video of a single step-up-down perturbation experiment ($h_r^{\max}=25\text{mm}$)

The comparison of maximum relative step height of Stepper-2D with other typical dynamic walkers is shown in table 1, suggesting that Stepper-2D achieves an improvement on the disturbance rejection of the previous research.

Table 1 Comparison of maximum relative step height

Type of dynamic walker	Maximum Relative Step Height
Stepper-2D	10%
Flaminge [17]	9%
Runbot [18]	4%
Mike [15]	2%

VI Conclusion and Future Work

In this paper, we analytically study the disturbance rejection of Virtual Slope Walking by introducing the ground step perturbation. We theoretically prove that ground step perturbation can be transformed to the disturbance of initial system state and the successful step handling walking comes from the system's cyclic stability. We then obtain the necessary and sufficient condition of recovering from the step perturbation by analyzing the relationship between the system state and the minimum initial state in the transition phase. Finally, we illustrate the effect of leg length shorten ratio β , equivalent extension angle θ_{II}^* and inter-leg angle ϕ_0 on the maximum relative step height h_r , demonstrating that achieving fast walking speed always accompanying with large disturbance rejection in Virtual Slope Walking. The step handling walking experiment of Stepper-2D verifies the theoretical analysis results and presents an improvement on the disturbance rejection compared with the other current results.

Starting from the step handling walking under the open-loop condition without external sensing device in this paper, we will introduce the sensing data of the step perturbation and study the sensor-based powered walking from the kinematic energy complement viewpoint, aiming at obtaining larger disturbance rejection for Virtual Slope Walking in the future work.

Acknowledgement

This work was supported partially by the National Nature Science Foundation of China (No. 60875065) and Supported by State Key Laboratory of Robotics and System (HIT) (No. SKLRS2010-ZD-01).

REFERENCES

- [1] McGeer, T., 1990a, Passive dynamic walking, *International Journal of Robotics Research*, 9(2), pp. 62-82.
- [2] S. Collins, A. Ruina, R. Tedrake, et al. Efficient Bipedal Passive-Dynamic Walkers. *Science*, 307(5712):1082-1085, 2005.
- [3] M. Wisse. Three additions to passive dynamic walking; actuation, an upper body, and 3d stability, in *Proc., Int. Conf. on Humanoid Robots*. Los Angeles, USA, 2004.
- [4] D.G.E. Hobbelen, M. Wisse. Ankle Actuation for Limit Cycle Walkers. *International Journal of Robotics Research*, 27(6):709-735, 2008.
- [5] Collins, S.H, Ruina, A. A Bipedal Walking Robot with Efficient and Human-Like Gait. In *Proc. IEEE International Conference on Robotics and Automation*, 18-22 April, pp. 1983- 1988, 2005.
- [6] F. Asano, Zhi-Wei Luo. Energy-Efficient and High-Speed Dynamic Biped Locomotion Based on Principle of Parametric Excitation, *IEEE Trans. Robot.*, vol. 24, no. 6, pp. 1289-1301, 2008.
- [7] Toyoyuki Honjo, Zhi-Wei Luo, Akinori Nagano. Parametric excitation of a biped robot as an inverted pendulum," *Proceedings of IEEE/RSJ 2008 International Conference on Intelligent Robots and Systems*, pp. 3408-3413, 2008.
- [8] Yuji Harata, Fumihiko Asano, Kouichi Taji and Yoji Uno. Parametric excitation walking for four-linked bipedal robot, *Proceedings of the 9th International IFAC Symposium on Robot Control (SYROCO)*, pp. 589-594, 2009.
- [9] Mingguo Zhao, Ji Zhang, Hao Dong, Yu Liu, Liguang Li, and Xuemin Su. Humanoid Robot Gait Generation Based on Limit Cycle Stability, In the *proceedings of the RoboCup Symposium, China*, JUL 15-18, 2008.
- [10] Hao Dong, Mingguo Zhao, Ji Zhang, Naiyao Zhang. Hardware design and gait generation of humanoid soccer robot Stepper-3D. *Robotics and Autonomous Systems*, 57:828-838, 2009.
- [11] D. G. E. Hobbelen, M. Wisse. A Disturbance Rejection Measure for Limit Cycle Walkers: The Gait Sensitivity Norm. *IEEE TRANSACTIONS ON ROBOTICS*, VOL. 23, NO. 6, pp.1213-1224, 2007.
- [12] M. Wisse. J. van Frankenhuyzen. Design and construction of mike; a 2d autonomous biped based on passive dynamic walking. *Proc. Conf. Adaptive Motion of Animals and Machines*. Kyoto, Japan: AMAM, 2003.
- [13] Pratt J. Exploiting Inherent Robustness and Natural Dynamics in the Control of Bipedal Walking Robots. PhD Thesis, Massachusetts Institute of Technology, 2000.
- [14] Geng T, Porr B, Wörgötter F. Fast biped walking with a sensor driven neuronal controller and real time online learning. *International Journal of Robotics Research*, vol. 25 no. 3: 243 -259, 2006.
- [15] Hao Dong, Mingguo Zhao, Naiyao Zhang. High Speed and Energy Efficient Biped Locomotion Based on Virtual Slope Walking. *Autonomous Robots*, 2009.
- [16] Mingguo Zhao, Hao Dong, and Naiyao Zhang. The Instantaneous Leg Extension Model of Virtual Slope Walking, In *Proceedings of the IEEE/RSJ International Conference on Intelligent Robots and Systems*, 2009.

A New Method for Mobile Robots to Avoid Collision with Moving Obstacles

Yi Zhu¹, Tao Zhang¹, Jingyan Song¹, Xiaqin Li¹, Masatoshi Nakamura²

¹*Department of Automation, Tsinghua University, Beijing 100084, China*
(Email: taozhang@tsinghua.edu.cn)

²*Research Institute of Systems Control, Saga University, Saga 840-0047, Japan*

Abstract: A new method for mobile robots to avoid collision with moving obstacles is proposed in this paper. It adopts the concept of safe sectors in the vector field histogram (VFH) method but simplifies its description. Moreover, the new method takes the threat of moving obstacles into account when selecting motion direction and a new speed control law that considers more factors is designed. Hence it can better avoid moving obstacles than the VFH method. Simulation results indicate that the new method also shows many advantages over the dynamic potential field (DPF) method which is a representative approach for avoiding moving obstacles. Experiments have further verified its applicability.

Keywords: mobile robots; obstacle avoidance; moving obstacles

I. INTRODUCTION

Obstacle is one of the key issues in many fields. Many methods [1]-[9] have been proposed to indicate the influence of obstacles and solve this problem over the past twenty years. For example, In [2][3], they found recess shape to play an important role in the performance of aerostatic bearings, and found vortex flows in the recess by numerical experiments which cause instabilities and vibrations of the bearing. The elimination of obstacle influence is one of important reasons in this research. This paper mainly studies on the obstacle avoidance of mobile robots. Although there are many methods on this research, most previous works focus on static obstacles and only a few works [6]-[9] address the problem of dealing with moving obstacles.

To deal with moving obstacles, one concept is previously planning a safe path which takes moving obstacles into account to guide the robot [6]. The drawback of this concept is that it assumes the trajectories of moving obstacles are known in advance, which is unrealistic in many scenarios. Another concept is dynamically planning the motion in every control cycle by sensory information [7]-[9]. This concept is more practicable since it can adapt the changing motion of moving obstacles. One representative method based on this concept is the DPF method [7], [8]. In this method, the target generates an attractive force and the threat of all the moving obstacles is represented by a repulsive force. The robot always moves in the direction of their resultant force.

In this paper, we propose a new obstacle avoidance method for mobile robots to deal with moving obstacles. The new method adopts the concept of safe sectors in the VFH method [1] which is a motion planning method mainly for static environments. But the new method simplifies its description to lower the computational and spatial complexity and takes the threat of moving obstacles into account when choosing motion directions. Hence it can better handle moving obstacles than the VFH method. Another improvement of the new method is its speed control law that takes more factors into account than the VFH method. The new method also shows advantages over the DPF method in many aspects, which has been discussed in this paper. The remainder of this paper is arranged as follows: the VFH method is briefly reviewed in Section 2 and the new method is presented in Section 3. Some simulations and experiments are presented in Section 4.

II. THE VFH METHOD

As an efficient obstacle avoidance approach, the VFH method [1] can generate smooth trajectory without oscillations and guide the robot to go through narrow corridors. The VFH method divides all the directions around the robot into some safe sectors that the obstacle density (a value that is proportional to the negative of the distance from the robot to obstacles) in any direction of these sectors is no less than a threshold. The middle directions of such sectors are candidates for motion and the one that has the minimal bias to the target direction is selected as the final motion direction. Nevertheless, the VFH method only takes the distances of obstacles

into account and ignored their velocities. Therefore it's not suitable to be applied in environments containing moving obstacles especially when they move fast.

III. THE PROPOSED METHOD

The new method proposed in this paper adopts the basic concept of safe sectors in the VFH method but improves it in three main aspects. Firstly, the new method directly compares the obstacle distance of one direction with a threshold to judge whether the direction is safe without figuring out a density value based on a grid map that needs updating in every control cycle as the VFH method does since the latter is unnecessary but computational and spatial expensive. Secondly, we design a new speed control law that considers more factors especially the obstacle speed. The third also the key improvement is that in the new method, we take the threat of moving obstacles into account when selecting motion directions. Hence the new method can better deal with moving obstacles. The process for selecting the direction and speed of the robot in the new method is presented below. It can be illustrated by the example shown in Fig.1.

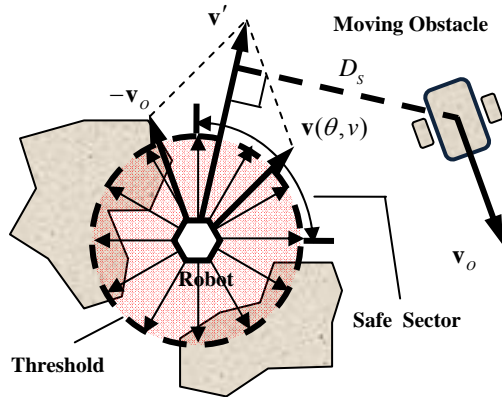


Fig.1. An example that $\theta_0 = 30^\circ$ and $N = 3$

Step 1 (Find all the safe sectors and take their middle directions as candidates for the final motion direction) The new method divides all the directions around the robot into a series of sector units whose width is θ_0 ($\theta_0 = 5^\circ$ in our experiments). Any sector that consists of N ($N = 24$ in our experiments) continuous units whose minimal obstacle distances are all larger than d_s ($d_s = 0.4\text{m}$ in our experiments) is considered as a safe sector. Additionally, there is a special sector whose middle direction is the target direction θ_T and width is $N\theta_0 / 2$. If the minimal obstacle distance in this sector is larger than d_s , it is also considered as a safe sector.

Note that two safe sectors can overlap in part. Only the middle directions of the safe sectors can be selected as the motion direction of the robot. In the example of Fig.1, there is only one safe sector whose middle direction is θ (All the angles in this paper refer to the local coordinates where the original angle equals to the head direction of the robot and anticlockwise direction is positive).

Step 2 (Calculate the corresponding maximum speed of every candidate direction) To keep safe, every candidate direction θ has a corresponding maximum speed that is calculated by

$$v_{\max} = \min_{0 \leq n \leq N} \{v_{\max}^n\} \cdot \cos^2 \left(\min \left\{ \theta, \frac{\pi}{2} \right\} \right)$$

$$v_{\max}^n = \begin{cases} \frac{\sqrt{2\bar{a}(d_n - d_s)}}{\cos|\theta_n - \theta|} & d_n > d_s \\ \frac{v_0 \cdot d_n^2}{d_s^2 \cdot \cos|\theta_n - \theta|} & d_n \leq d_s \end{cases} \quad (1)$$

where d_n and θ_n are the obstacle distance and the direction of the n^{th} sector unit, \bar{a} is the average acceleration of the robot, v_0 is a constant, v_{\max}^n represents the maximum speed limited by the obstacle distance of the n^{th} sector unit based on the requirement that the obstacle distance must be large enough for the process of brake. The item $\cos^2(\dots)$ in (1) is used to slow down the speed when the bias between θ and the current direction of the robot is large, which can shorten the path length generated by turning.

Step 3 (Evaluate the threat from moving obstacles for every candidate direction) We define the threat value $Tht(\theta)$ from a moving obstacle for a candidate direction θ as

$$Tht(\theta) = \begin{cases} \frac{v_o}{\sqrt{2\bar{a}(D_s(\theta, v) - r - r_o)}} & D_s > r + r_o \\ +\infty & D_s \leq r + r_o \end{cases} \quad (2)$$

$$v = \arg \min_{0 \leq v \leq v_{\max}} \left\{ \frac{v_o}{\sqrt{2\bar{a}(D_s(\theta, v) - r - r_o)}} \right\}$$

where r and r_o are the radius of the robot and the obstacle, v_o is the obstacle speed, D_s is the distance from the obstacle to the straight line that passes through the robot's center and parallels the vector \mathbf{v}' which is the relative velocity between the robot and the obstacle if specific θ and its corresponding v are selected as shown in Fig.1. Note that v is the speed that generates the lowest threat value in the speed boundary if specific

θ is chosen. If there are multiple moving obstacles, the final threat value is the maximum $Tht(\theta)$ generated by them.

Step 4 (Select the final motion direction and speed from all the candidates) The final direction is selected by

$$\theta = \arg \min \{ \alpha_1 \cdot |\theta - \theta_T| + \alpha_2 \cdot Tht(\theta) \} \quad (3)$$

where α and α_2 are constants. For soft-landing, the final speed is calculated by $\min \{ v, 0.5 \cdot D_T \}$ where v is the corresponding speed calculated in Step 3, D_T is the distance between the robot and the target.

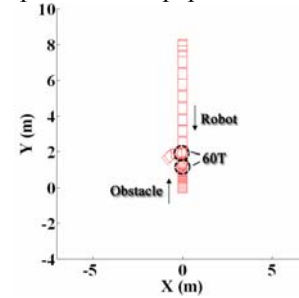
The new method described above shows many advantages over the DPF method for avoiding moving obstacles. In the DPF method, all the effects of moving obstacles are abstracted as a repulsive force. Such a description is simple for implementation. However, as pointed out in [1], it loses detailed information about the obstacle distribution and can lead to a series of problems, e.g., oscillations in the presence of obstacles, difficulties in going through narrow corridors [10]. The VFH method has well solved these problems by introducing safe sectors to describe the distribution of obstacles [1]. The new method proposed in this paper has inherited the concept of safe sectors in the VFH method and therefore it can also avoid the above problems in the DPF method. Furthermore, some works [7] about the DPF method hasn't paid much attention to the speed control law as the method proposed in this paper. Simple linear functions are usually adopted, which will affect their performances. The advantage of the DPF method is that some related works address the problem of how to pursuit a moving target [7], [8], which hasn't been taken into account in this paper.

IV. SIMULATIONS AND EXPERIMENTS

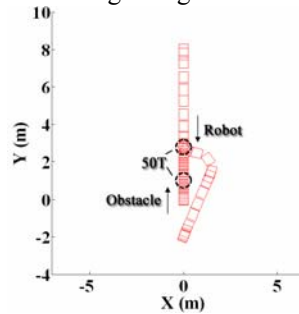
To show the performance of the proposed method, several simulation results are presented below.

For testing the performance of the new method proposed in this paper, we design a scenario that the robot meets an obstacle moving toward it as shown in Fig.2 (In all the simulations in this paper, the start points of the robot and the obstacle are respectively at (0,8) and (0,0); the robot's target is at (0,-2); the dash circle represents the locations of the robot and the obstacle at the time labeled aside). Fig.2(a) shows the result if the robot moves in the direction that has the minimal bias to the target direction from all the middle directions of safe sectors ($d_s = 0.4m$) without taking the obstacle speed

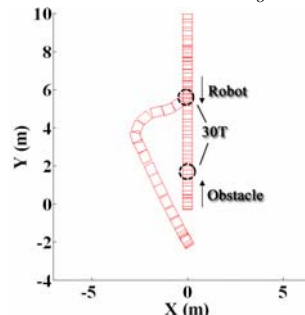
v_o ($v_o = 0.1m/s$) into account, which is the concept of the VFH method. The result is that the robot hits the obstacle at 60T (T is the length of the control cycle). This collision can be avoided if we increase d_s to keep enough distance to the obstacle. However, it will be not safe again if the obstacle increases its speed and a large d_s will make it difficult to go through narrow corridors. As a comparison, navigated by the new method proposed in this paper, the robot smoothly bypasses the same obstacle as shown in Fig.2(b). Moreover, the new method is adaptive when the obstacle increases its speed as shown in Fig.2(c) ($v_o = 0.4m/s$). The simulation results of Fig.2 indicate the importance of taking the obstacle speed into account for obstacles avoidance, which is just the advantage of the method proposed in this paper over the VFH method.



(a) The method ignoring the obstacle speed



(b) The proposed method ($v_o = 0.1m/s$)



(c) The proposed method ($v_o = 0.4m/s$)

Fig.2. Results of simulation 1

The simulations in Fig.3 have compared the new method with the DPF method proposed in [7]. Fig.3(a) is the result of the work in [7] in the same scenario of Fig.2(b). Compared with Fig.2(b), there are oscillations

in the trajectory of Fig.3(a) due to the shake of the potential force shown in Fig.3(b). Such shakes occur frequently when the robot suddenly meets an obstacle and it is an inherent drawback of the DPF method due to its oversimplified description of the obstacle effect. It can be also observed that the trajectory in Fig.3(a) is much longer than the result in Fig.2(b). The proposed method also shows advantages over the work in [7] in many aspects of the speed control. As an example, in the scenario of Fig.3(c) and Fig.3(d) (the robot moves from (0,8) to (0,-2) but its initial direction is opposite to the target), the method proposed in this paper generates shorter path than the work in [7] when turning due to the item $\cos^2(\dots)$ in (1).

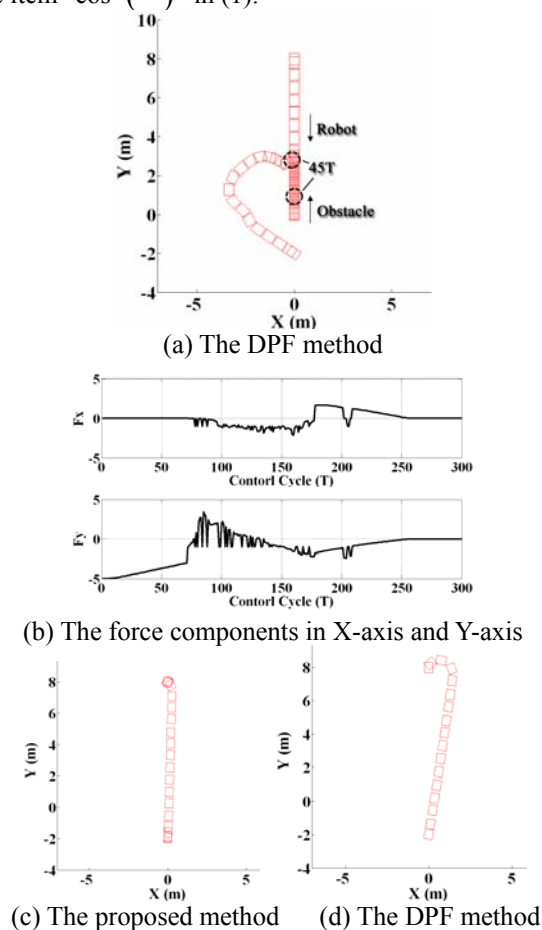


Fig.3. Results of Simulation 2

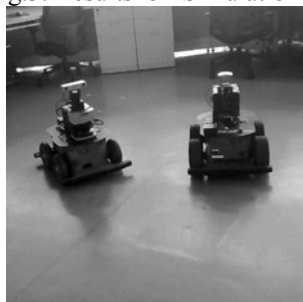


Fig.4. A scenario of experiments on real robots

The proposed method has also been implemented on real Pioneer3-AT robots as shown in Fig.4. Experiment results have further verified its validity and applicability.

V. CONCLUSIONS

A new method for mobile robots to avoid collision with moving obstacles is proposed in this paper. The new method adopts the concept of safe sectors in the VFH method but simplifies its description. Moreover, it takes the threat of moving obstacles into account when selecting motion direction and a new speed control law that considers more factors is designed. Hence it can better deal with moving obstacles than the VFH method. Simulation results show that the new method also performs better than the DPF method in many aspects.

REFERENCES

- [1] Borenstein J, Koren Y (1991), The vector field histogram – fast obstacle avoidance for mobile robots. *IEEE Journal of Robotics and Automation*, 7(3): 278-288.
- [2] Chen X D, He X M (2006), The effect of the recess shape on performance analysis of the gas-lubricated bearing in optical lithography. *Tribology International*, 39(11): 1336-1341.
- [3] He X M, Chen X D (2007), The dynamic analysis of the gas lubricated stage in optical lithography. *International Journal of Advanced Manufacturing Technology*, 32(9-10): 978-984.
- [4] Beaufriere B, Zeghloul S (1995), A mobile robot navigation method using a fuzzy logic approach. *Robotica* 13: 437-448.
- [5] Minguez J, Montano L (2004), Nearness diagram (ND) navigation: collision avoidance in troublesome scenarios. *IEEE Trans Robot Autom* 20(1): 45-59.
- [6] Conn R A, Kam M (1998), Robot motion planning on N-dimensional star worlds among moving obstacles. *IEEE Trans. Robot. Autom* 14(2):320-325.
- [7] Ge S S, Cui Y J (2002), Dynamic motion planning for mobile robots using potential field method. *Autonomous Robots* 13: 207-222.
- [8] Huang L (2009), Velocity planning for a mobile robot to track a moving target - a potential field approach. *Robotics and Autonomous Systems* 57: 55-63.
- [9] Martinez-Gomez L, Fraichard T (2009), Collision avoidance in dynamic environments: an ICS-based solution and its comparative evaluation. *IEEE International Conference on Robotics and Automation*: 100-105.
- [10] Koren Y, Borenstein J (1991), Potential field methods and their inherent limitations for mobile robot navigation. *IEEE International Conference on Robotics and Automation* 2: 1398-1402.

Some Thought for the McKibben Muscle Robots

Huailin Zhao¹ Xiaoqing Jia² Masanori Sugisaka³

¹ School of Electrical & Electronic Engineering, Shanghai Institute of Technology, China

² College of Logistics Engineering, Shanghai Maritime University, China

³ Mec. & Ele. Course, Nippon Bunri University, Japan

Abstract: This paper introduces the background of the research. It summarizes the applications related with robots actuated by McKibben muscles. Based on the robot joint structure, the robots are classified into two types. The paper indicates that the different modeling methods and the control algorithms are needed to the two types of the robots.

Keywords: artificial suit, McKibben muscle, Modeling

1. Introduction

How to simulate the human behave and develop humanoid devices has been a hot spot and a difficulty in the robot field for times. As it is thin and light and soft and similar to the biological muscle, the McKibben muscle has the special advantage for developing humanoid robots when it is used as the actuator to robots. Right just due to its above characteristics, the requirement for its connection to robots is not too high. The connection to robots can simulate the way by which the biological bones and muscles connect with each other in the animal joint. Based on this kind of connection structure and the appropriate control algorithm, the robot can imitate animals much better.

To the robot, in order to complete special tasks, it has to interact with the outer environment. A very important problem is the security, especially when interacting with human such as medical nursing. This means that the robot should keep stable and compliant at the same time when it is carrying out tasks accurately. The traditional robot, consisting of motors or fluid actuators and stiff linkers, is heavy and joint-stiff. So it is not suited to carry out these kinds of tasks, except the very complicated control algorithms are designed. But the McKibben muscle is inherently compliant – just like biological muscles. The robot actuated by it will act easily like animals. It

will easily generate soft touching and relative safe operation. And human will feel the robot more like an animal than a machine.

The world should be welfare. The development of the robot capable of assisting elders, handicappeds, and patients is one of the main directions. Developing the devices capable of helping getting well for patients is one of the main tasks of the modern technology. It's expectant for the McKibben muscle to play an important role in these fields. In some places such as Japan, America, and Europe, the artificial assisted suit made of McKibben muscles has come out. The suit is called as "dressable robot". Besides, the bipedal robot actuated by McKibben muscles has been developed too. These artificial assisted suit or bipedal robot can only realize the main actions. They can't perceive the intention of human actions.

Usually, the McKibben muscle consists of an expandable rubber tube and a fiber weave mask. The outer fiber mask expands when the rubber tube stimulated by the pressured gas, pulls its two ends and shortens the McKibben muscle, just like the biological muscle contracts. The weave mesh changes its length and diameter by changing the incline angle. The pulling force F is linear to the gas pressure P and nonlinear to its length L , which can be calculated by formula (1) in which both b and n are the structure parameters. The maximal contraction ratio is usually less than 30%. Fig.1 shows its structure and the simple operation. It can output enough force and keep definite compliantness, so the robot actuated by McKibben muscles is suited to carry out the "environment friendly" tasks such as nursing handicappeds and snatching at fragile goods and so on.

$$F = Pb^2(3L^2/b^2 - 1)/(4\pi n^2) \quad (1)$$

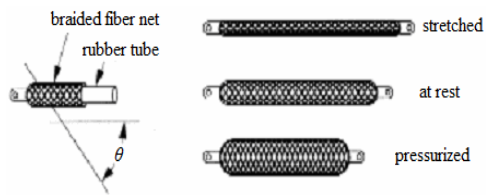


Fig.1 The McKibben muscle

Our project aims at an artificial suit actuated by pieces of McKibben muscles. The artificial suit can put on the human upper body including the two arms. Not only it can act like human arms, but also it can perceive automatically the action intention of the human arms and output the intended actions. But how to configure the McKibben muscles in the artificial suit and how to model and design the control algorithm become the key problems.

2. The applications

There have been many applications about the robots related with our problems. Fig.2 shows the photos of the related robots actuated by McKibben muscles. Fig.2(a) shows a robot which's arms are actuated by McKibben muscles[1]. Fig.2(b) shows a bipedal robot designed by Shadow Robot Company which's legs are actuated by McKibben muscles[2]. Fig.2(c) shows a bipedal robot designed by Oita University which's legs are actuated by McKibben muscles too[2]. But the connection structure is different from that in Fig.2(b). Fig.2(d), Fig.2(e) and Fig.2(f) show the artificial suit actuated by McKibben muscles which are designed by Tokyo University of Science[4]. Fig.2(g) shows an assisted device which can help the patient's ankle.

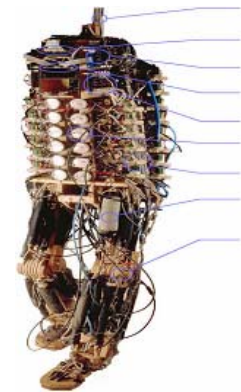


Fig.2(b)



Fig.2(c)



Fig.2(d)

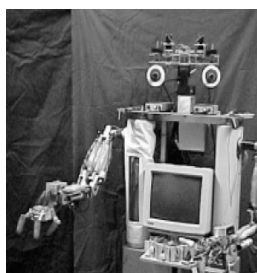


Fig.2(a)



Fig.2(e)



Fig.2(f)



Fig.2(g)

Fig.2 The applications

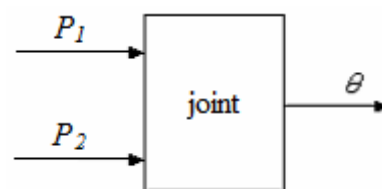


Fig.3(b)

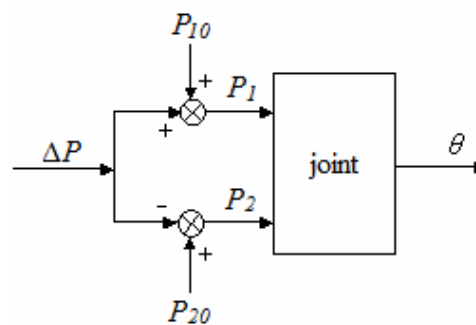


Fig.3(c)

3. The two types of robot joints

To all the different applications, the structure of the robot joint can be classified into two types on whole. One is the “regular” structure with which two McKibben muscles parallel to each other in the same size connect with each other by a pulley, such as Fig.2(a) and Fig.2(b). The other one is the “irregular” structure, such as Fig.2(c), Fig.2(d), Fig.2(e), Fig.2(f) and Fig.2(g). Fig.3(a), Fig.3(b) and Fig.3(c) show that the robot joint with “regular” structure can be analyzed as one-input and one-output system. Fig.3(d), which is the configuration of McKibben muscles in the robot shown in Fig.2(c), can be used to represent the robots with the “irregular” joint structure. Fig.3(e) shows the relationship between the three inputs and the one output. With three Pressure inputs, it can’t be simplified as one-input and one-output system.

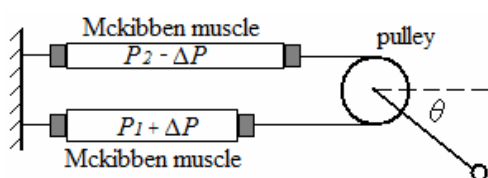


Fig.3(a)

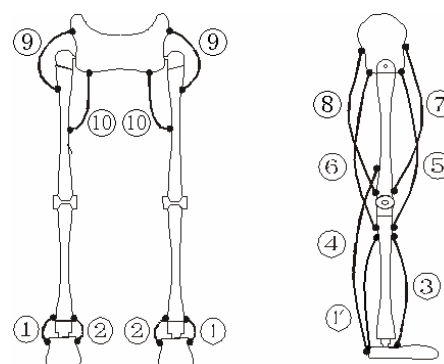


Fig.3(d)

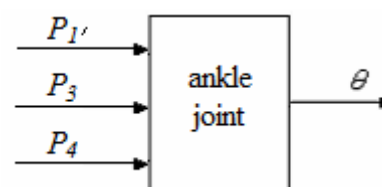


Fig.3(e)

Fig.3 The “regular” structure and the “irregular” structure robot

4. How to model and control the robot

To analyze the robot, the model of it should be established. And to control it, the control algorithm should

be designed. To the “regular” structure robot joint shown in Fig.3(a), the pressures of the two McKibben muscles vary relatively instead of independently. At the initial, the two pressures of the two McKibben muscles are P_{10} and P_{20} respectively. When the joint bends, P_1 increases by ΔP and P_2 decreases by ΔP at the same time. Contrariwise when the joint stretches, P_1 decreases by ΔP and P_2 increases by ΔP at the same time. The change of ΔP leads to the change of both P_1 and P_2 in the opposite direction. In this way the joint angle can be regulated. Therefore the joint system can be considered as a single input (ΔP) and single output (θ) system. At this rate, the system is simplified and the control algorithm for it may be simpler.

But to the “irregular” structure robot, the structure parameters are not “regular”. Different from the “regular” structure joint system, there are more than two McKibben muscles to actuate one robot joint, such as shown in Fig.3(d) and Fig.3(e). The lengths of them are different and they are not parallel to each other. And there is coupling between the neighbor robot joints. So how to model the robot system will be a great challenge.

As to the application shown in Fig.2(g), the robot joint structure can be either “regular” or “irregular”.

With the above application examples, the operation to the McKibben muscles is mainly based on the operation experiences. Few literatures explain their modeling and the related control algorithms.

Anyway, we are going to configure the McKibben muscles in “irregular” structure. And our project aims at the following:

1. Modeling of the artificial suit physically. The key is the configuration of McKibben muscles;
2. Designing the neural network based intelligent control algorithm;
3. Automatic sensing the behaving intention and complete the action rapidly.
4. Realizing the main actions of the human arm.

Based on the literature and the above applications, the elbow joint can bend larger than 100 degrees. The shoulder angle can get to about 90 degree, and so on. Comparing with human[5]. The robot arm joints' rotation angles may be 70-90% of the

human's. One of the main reasons is that the contraction ratio of the McKibben muscle is less than that of the human muscle's[6].

5. Conclusion:

Based on the characteristics of the McKibben muscles and the different applications, it is possible to develop an artificial suit which can realize the main action of the human arm. And most of the related applications configure the McKibben muscles in “irregular” structure. But how to model and control it are the key problems. The achievable angles will be less than the human's. They may be 70-90% of the angles which the human arm joints can realize.

References

- [1] Kazuhiko Kawamura, R.Alan Peters, D.Mitchell Wilkes, W.Anthony Alford, Tamara E.Rogers. ISAC: Foundations in Human-Humanoid Interaction, IEEE Intelligent Systems, Jul.2000, p38-45.
- [2] <http://www.shadow.org.uk>, 2010.11
- [3] Masanori Sugisaka, Kouta Imamura, Kouji Tokuda, Naoki Masuda, A new artificial life body: biologically inspired dynamic bipedal humanoid robots, Artificial life and robotics, Vol.8(1), 2004, p1-4
- [4] Hiroshi Kobayashi, Takamitsu Aida, Takuya Hashimoto, Muscle suit development and factory application, Journal of Automation Technology, Vol.3(6), 2009, p209-213
- [5] R. Nakamura, H. Saito, Fundamental kinesiology, 5th edition, Tokyo, Japan: Ishiyaku Publishers, 2000
- [6] Ching—Ping Chou, Study of human motion control with a physiology based robotic arm and spinal level neural controller:doctor dissertation, Washton Univ., May.1996.

Vehicle 3D Estimation Based on Time Series Images and Prior Knowledge

Haoyin Zhou, Tao Zhang, Changshui Zhang, Peng He

Department of Automation, Tsinghua University, Beijing 100084, China

(Tel: +86-10-62797710, zhouhaoyin@gmail.com)

Abstract: Vehicle 3D estimation is important in intelligent transportation systems. To simplify system structure and improve system accuracy, an algorithm based on one-camera system and prior knowledge is presented. The experimental result shows that the algorithm can achieve satisfied accuracy.

Keywords: prior knowledge, 2D image, 3D estimation, shadow removal

I. INTRODUCTION

In intelligent transportation systems, it is usually to use images captured by video cameras to identification information of vehicles. The most usually method to get vehicle boundary box is to use 2 or more video cameras for 3D estimation. This kind of system considers vehicles as moving objects with no prior knowledge. Hence they usually have low accuracy for 3D estimation. In the method proposed in this paper, we want to take fully use of prior knowledge and estimate 3D information of vehicles based on single video camera.

We get some helpful prior knowledge, including the physical coordinates of 3 or more feature points in the image, physical coordinates of the video camera, the driving direction of vehicles, the range of length and width of a certain kind of vehicle, and the position of light.

The mapping between image coordinates and physical coordinates can be acquired from the physical coordinates of feature points. So vehicle area that is got by motion detection can be projected to physical coordinate. When the vehicle is moving along the street, the length direction of the vehicle can be confirmed. Intuitively, the length of the vehicle can be got by measuring the move area along the driving direction.

However, because of the height and shadow, the vehicle area got by motion detection is not precise. To remove the impact of height information, we can do the measurement in different frames of the same video. In this process, some height information can be got.

Shadow removal is a great problem in CV. If we get the prior information of the position of the light and the average length of this type of vehicle, it is easy to know the approximate location of the shadow. And a suitable

location of the shadow segmentation can be found by calculate variance of a slide window along the length direction. It is the same to estimate the width of a vehicle as the length estimation. In the end, the result of 3D estimation is given.

II. METHOD

1. Motion Detection

Motion Detection is to detect the moving areas in each video frame from the background. When a car is running on the road and a static camera captured the entire scene saved as a piece of video, what we do is to find the moving car area in every video frame. The called “moving area” means that there are one or more moving objects in these labeled moving areas. Effective and efficient motion detection is the basement of tracking of moving objects [1].

Gaussian Background Model has been widely used for robustly modeling complicated backgrounds, especially those with small repetitive movements (such as leaves, bushes, rotating fan, ocean waves, rain). According to Gaussian Background Model, the distribution of each pixel's lightness of a background image meets Gaussian distribution, which means for an image B [2]:

$$I_b(x, y) \sim N(u, \sigma^2) = \frac{1}{\sqrt{2\pi}\sigma} e^{-\frac{(x-\mu)^2}{2\sigma^2}} \quad (\sigma > 0) \quad (1)$$

Thus, each pixel has two parameters which are average u and variance σ^2 . Meanwhile, the background image is changing slowly with time. The parameters of each pixel in the background image should be updated:

$$u(t+1, x, y) = \alpha \cdot u(t, x, y) + (1 - \alpha) \cdot I_{t+1}(x, y) \quad (2)$$

Where $u(t, x, y)$ is point (x, y) 's average in the time t , $I_{t+1}(x, y)$ is the pixel of point (x, y) in $t+1$ frame, and α is the updating speed. The changing of σ^2 is so little to be ignored [3].

According to the model above, we use the first frame without moving to build the background model and update the model with the latest input frame. The moving areas can be got by the current frame subtracting background model. The pixels with high difference belong to moving areas. Then we filtrate the noise in the image by morphologic processing and Gaussian filter. For visual effect, we label background pixel black and object pixel white, producing a binary image. The result shows that the Gaussian background model achieves better performance. Fig. 1(a) is the Gaussian background model. Fig. 1(b) is some frame with a moving object. Fig. 1(c) is got by Fig. 1(b) subtracting background model. Fig. 1(d) is the moving object detected after dilate and erode.

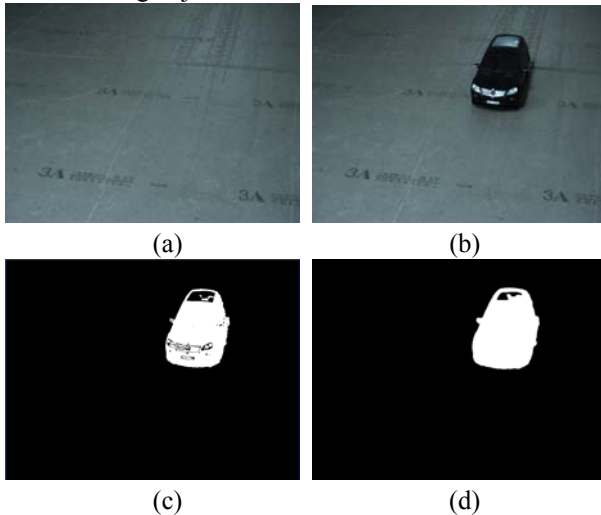


Fig.1 (a) Gaussian background, (b) Frame with vehicle, (c) Subtract result, (d) Dilate & erode

2. Convert to physical coordinate

Image coordinate can be converted to physical coordinate with some necessary prior knowledge. The system geometry is shown below. Here we take the left-bottom point as the origin, and direction of vehicle as y-axis. The z-axis is perpendicular to the ground.

At first, we measure the physical coordinate of the following points: 2 edge points of the view field, which are named $(x1, y1, 0)$ and $(x2, y2, 0)$; point which is in the center of the image $(x4, y4, 0)$; camera optical center points $(x0, y0, z0)$.

If the focus length of the camera is f , the camera imaging plane equation is:

$$\begin{aligned} & (x0 - x4)(x - x0 - \frac{f(x4 - x0)}{\sqrt{x4 - x0)^2 + (y4 - x0)^2 + (h)^2}} \\ & + (y0 - y4)(y - y0 - \frac{f(y4 - y0)}{\sqrt{x4 - x0)^2 + (y4 - x0)^2 + (h)^2}) \\ & + (h)(z - h + \frac{fh}{\sqrt{x4 - x0)^2 + (y4 - x0)^2 + (h)^2}) = 0 \end{aligned} \quad (3)$$

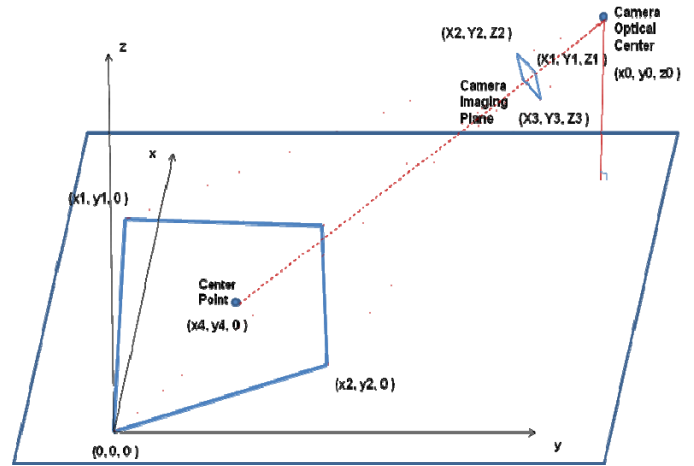


Fig 2 Schematic diagram of the system geometry

The 3 straight line equations that separately get pass the 3 edge points of the view field and camera optical center point are similar, take the line that get pass $(x1, y1, 0)$ and $(x0, y0, z0)$ for example:

$$\begin{cases} x = (x1 - x0)t + x0 \\ y = (y1 - y0)t + y0 \\ z = (z1 - z0)t + z0 \end{cases} \quad (4)$$

With the plane equation and 3 straight line equation, the physical coordinate of the camera imaging plane edge point $(X1, Y1, Z1)$, $(X2, Y2, Z2)$, $(X3, Y3, Z3)$ are got.

If pixel size of the image is 780×560 , the physical coordinate of $(i, 0)$ and $(0, j)$, which is image coordinate, in the camera imaging plane is:

$$\begin{aligned} U1 &= \frac{i}{780}(X2 - X1) + X1 \\ V1 &= \frac{j}{560}(Y2 - Y1) + Y1 \end{aligned} \quad (5)$$

$$\begin{aligned} W1 &= \frac{i}{780}(Z2 - Z1) + Z1 \\ U2 &= \frac{j}{560}(X2 - X1) + X1 \\ V2 &= \frac{j}{560}(Y2 - Y1) + Y1 \\ W2 &= \frac{j}{560}(Z2 - Z1) + Z1 \end{aligned} \quad (6)$$

Physical coordinate and image coordinate are both describing the position of the same point. When $(i, j) = (i, 0) + (0, j)$ in image coordinate, the physical coordinate of (i, j) is

$$\begin{aligned} U &= U1 + U2 \\ V &= V1 + V2 \\ W &= W1 + W2 \end{aligned} \quad (7)$$

The equation of the straight line that get pass the camera optical center and (U, V, W) is:

$$\begin{cases} x = (U - x0)t + x0 \\ y = (V - y0)t + y0 \\ z = (W - z0)t + z0 \end{cases} \quad (8)$$

The intersection of this line and $z=0$ plane is:

$$\begin{aligned} x &= (U - x0) \frac{-z0}{W - z0} + x0 \\ y &= (V - y0) \frac{-z0}{W - z0} + y0 \\ z &= 0 \end{aligned} \quad (9)$$

Here we find the mapping between image pixels to real world point. So the virtual grid can be drawn in images. Every grid is $10\text{cm} \times 10\text{cm}$ in physical world; the sides of grids are separately along the vehicle length and width direction.

3. Shadow Cutting

We use slide window and histogram for shadow cutting. At first, convert the image from RGB space to HSV space, which is more suitable for dividing shadow and vehicle body. Secondly, we create narrow and long window along length direction. And calculate histogram of H component of HSV. Thirdly, compare the difference of histogram of adjacent window, as shown in figure 4, and find some local maximum line. The algorithm of comparison is as follows [4]:

$$\begin{aligned} d(H_1, H_2) &= \frac{\sum_i (H_1'(I) \cdot H_2'(I))}{\sqrt{\sum_i (H_1'(I)^2) \cdot \sum_i (H_2'(I)^2)}} \\ H_k'(I) &= \frac{H_k(I) - 1}{N \cdot \sum_j H_k(J)} \end{aligned} \quad (10)$$

With time-series images, we can find local maximum lines in every image. We can find some stable lines after converted to physical coordinate and fitting,

Here the prior knowledge of statistical average vehicle width can be used, and choose the nearest line as shadow cutting line, Fig. 8 shows the result of shadow cutting.



Fig 3 Virtual grid

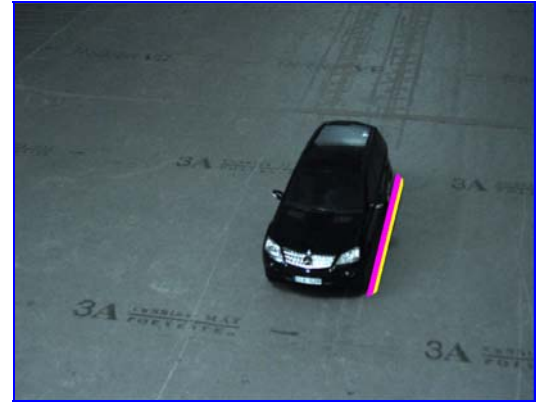


Fig 4 Histogram calculate area

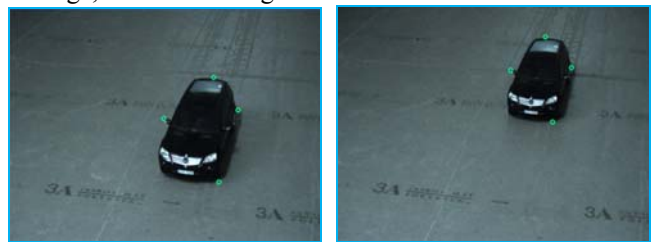


Fig 5 Shadow cutting line

4. Get Real Size

After shadow cutting, we can get the 4 edge point of the vehicle, from which the look length and look width can be got.

The look length of the vehicle can be got in every image, as shown in Fig.7:



(a)

(b)

Fig.6 (a)Edge points, (b)Edge points

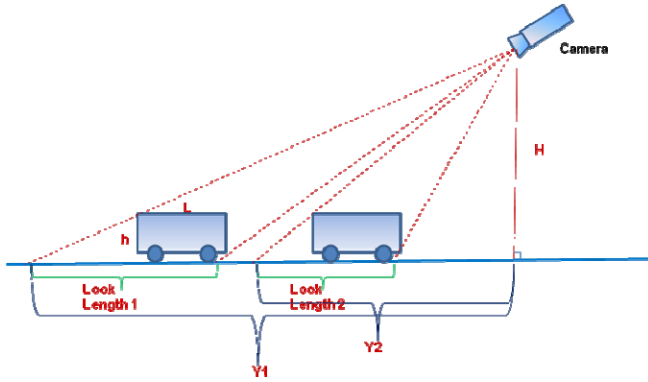


Fig 7 System geometry

With time-series images, a lot of look length can be got by measurement

$$\begin{cases} L + \frac{Y1}{H} h = L1 \\ L + \frac{Y2}{H} h = L2 \\ L + \frac{Y3}{H} h = L3 \\ \dots \end{cases} \quad (11)$$

Define $A = \begin{bmatrix} 1 & Y1/H \\ 1 & Y2/H \\ 1 & Y3/H \\ \dots \end{bmatrix}$, $X = \begin{bmatrix} L \\ h \end{bmatrix}$, $b = \begin{bmatrix} L1 \\ L2 \\ L3 \\ \dots \end{bmatrix}$

To get a least squares solution of the over determined equations, we can calculate the solution of equation:

$$A^T A x = A^T b \quad (12)$$

Because of $Yi \neq Yj (i \neq j)$, the rank of matrix A is 2. So we can get

$$\text{rank}(A^T A) = \text{rank}(A) = 2 \quad (13)$$

Here is the lease square solution:

$$x = (A^T A)^{-1} A^T b \quad (14)$$

III. RESULT

We test our algorithm in 5 different kinds of different vehicles, of which the result is shown in table 1, 2 and 3.

Table 1. 3D estimation result: length

Vehicle type	Real Length	Estimate Length	Length Error
Car	48.00	50.31	-2.31
SUV	46.00	45.35	0.65
Mini-Car	36.00	34.47	1.53
Truck	60.00	58.23	1.77
Bus	72.00	69.78	2.22

Table 2. 3D estimation result: width

Vehicle type	Real Width	Estimate Width	Width Error
Car	20.00	22.03	-2.03
SUV	21.00	21.40	-0.4

Mini-Car	19.00	20.19	-1.19
Truck	35.00	35.49	-0.49
Bus	24.50	25.53	-1.03

Table 3. 3D estimation result: hight

Vehicle type	Real Height	Estimate Height	Height Error
Car	14.00	9.80	4.2
SUV	17.50	16.46	1.04
Mini-Car	14.00	9.64	4.36
Truck	33.00	31.06	1.94
Bus	28.00	26.78	1.22

In table 1, 2 and 3, most estimate error is less than 2 cm, except the height of car and mini-car. That is because the real top point does not influence the look length and look width of the vehicle in images.

IV. CONCLUSION

Vehicle information extraction is being widely studied. This paper comes up with an algorithm for vehicle 3D estimation with prior knowledge. With time series images, 3D information can be extracted from the 2d information in every image.

The shortcoming of the algorithm is that it cannot accurate estimate vehicle information when it changes moving direction.

REFERENCES

- [1] A. J. Lipton, H. Fujiyoshi, and R. S. Patil, "Moving target classification and tracking from real-time video," in Proc. IEEE Workshop Applications of Computer Vision, 1998, pp. 8–14.
- [2] C. Stauffer and W. Grimson, "Adaptive background mixture models for real-time tracking," in Proc. IEEE Conf. Computer Vision and Pattern Recognition, vol. 2, 1999, pp. 246–252.
- [3] H. Z. Sun, T. Feng, and T. N. Tan, "Robust extraction of moving objects from image sequences," in Proc. Asian Conf. Computer Vision, Taiwan, R.O.C., 2000, pp. 961–964.
- [4] M. Kiger, "A shadow handler in a video-based real-time traffic monitoring system," in Proc. IEEE Workshop Applications of Computer Vision, CA, 1992, pp. 11–18.

Automatic Drawing of Correct Topographical Distribution of EEG Rhythms Based on Unified Suitable Reference Selection

Bei Wang¹, Xingyu Wang¹, Akio Ikeda², Takashi Nagamine³, Hiroshi Shibasaki⁴, Masatoshi Nakamura⁵

¹*Key Laboratory of Advanced Control and Optimization for Chemical Processes, College of Information Science and Technology, East China University of Science and Technology, Shanghai 200237, China*

²*Department of Neurology, Kyoto University, Kyoto 606-8501, Japan*

³*Department of System Neuroscience, Sapporo Medical University, Hokkaido 060-8556, Japan*

⁴*Takeda General Hospital, Kyoto 601-1495, Japan*

⁵*Research Institute of Systems Control Institute for Advanced Research and Education, Saga University, Saga 840-0047, Japan*

(Tel: 86-21-64253581; Fax: 86-21-64253386)

(beiwang@ecust.edu.cn)

Abstract: Electroencephalography (EEG) interpretation is important for brain diseases inspection. In this study, an automatic technique was developed to realize the automatic drawing of correct topographical distribution of EEG rhythms, which would be an assistant tool for EEG interpretation. Unified suitable reference electrode was selected automatically to construct the common referential derivation. Topographies were drawn according to the amplitudes of EEG rhythms calculated among the scalp of head. The final result of topographical distribution was helpful to highlight the EEG rhythms of interest for automatic EEG interpretation. The developed technique has application significance for real clinics.

Keywords: Topographical distribution, EEG rhythm, Reference selection, Automatic EEG interpretation

I. INTRODUCTION

The electroencephalogram (EEG) waveforms are generally described by kinds of rhythms according to the frequency, amplitude and shape. The interpretation on the distribution of EEG rhythms had clinical significance for brain diseases inspection, when the normal properties of EEG rhythms were becoming abnormal.

An automatic EEG interpretation system had been applied for real clinics. The relative EEG potential between the recorded electrode position and the reference were analyzed to judge the grade of normality or abnormality of awake EEG records [1] [2]. The EEG waveform under different reference potentials, which was called derivations, could bring different results. When the reference was contaminated by artifacts, the derived EEG waveform would be unsuitable for automatic interpretation. Therefore, the selection of reference was important to obtain correct EEG interpretation result.

In this study, an automatic technique was developed to realize the automatic drawing of correct topographical distribution of EEG rhythms based on unified suitable reference electrode. The ultimate

purpose was to obtain the correct interpretation result for clinical practice. The reference was selected based on an iterative method, to construct the common referential derivation. The obtained EEG waveforms and periodograms under common referential derivation were analyzed. The amplitudes of EEG rhythms were calculated among the scalp of head based on the common referential derivation. Finally, the obtained topographical distributions of EEG rhythms were evaluated comparing with the visual inspection.

II. METHOD

1. Data acquisition and visual inspection

The EEG data of one patient suffered by brain disease was analyzed. The data was recorded at Kyoto University, Japan. According to the International 10-20 System [3], totally 19 channels of EEG waveforms were recorded including Fp1, F3, C3, P3, O1, Fp2, F4, C4, P4, O2, F7, T3, T5, F8, T4, T6, FZ, CZ and PZ which covered the scalp of head. Another 2 channels recorded at left and right ear-lobes of A1 and A2. The recording was done with the time constant of 0.3 s, the high cut filter of 120 Hz and a sensitivity of 0.5 cm/50 μ V. The sampling rate was 200 Hz for all the channels. The long

EEG record was divided into consecutive segments of 5-second long each for analysis.

The recorded data was inspected by a qualified clinician, especially the EEG rhythms distribution. The EEG waveform of test subject was moderately abnormal. There were 'continuous irregular slow wave more on the right posteriorly and can be a localized slow wave in the right midtemporal (T4) to central (C4) region'.

2. Automatic reference selection

An iterative method had been developed to find out the unified suitable reference for EEG interpretation. The flowchart of automatic reference selection was illustrated in Fig. 1.

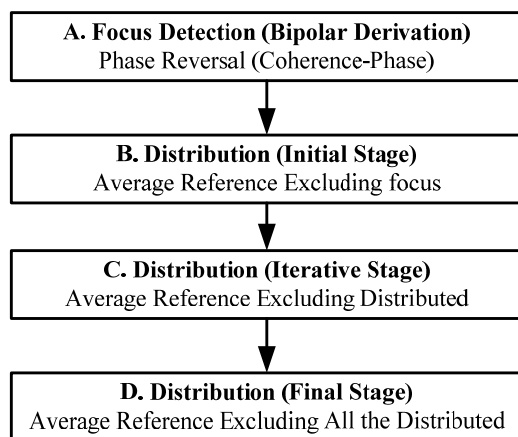


Fig.1. Flowchart of automatic reference selection

There were four main steps. Firstly, the cross-spectrum of bipolar EEG was adopted to detect the focus of EEG rhythm as step A. Under the bipolar derivation, the reference was the neighbor electrode. The cross-spectrum showed the relation of two bipolar EEGs. Parameters of coherence and phase were calculated to analyze phase reversal. The detected phase reversal area corresponded to the focus of EEG rhythm. In step B, C and D, the distribution of amplitude of EEG rhythm was analyzed to detect the distributed area among the scalp of head. Finally, a unified suitable reference was selected excluding all the distributed electrodes. The detail algorithm was described in [4].

3. Topographical distribution of EEG rhythms

A. Referential derivation construction

The 16 channels of EEG waveforms, Fp1, F3, C3, P3, O1, Fp2, F4, C4, P4, O2, F7, T3, T5, F8, T4, and T6 covering left and right hemisphere, were obtained by taking the relative potential of each electrode with the selected unified reference.

B. Distribution of amplitude of EEG rhythm

Fast Fourier Transformation (FFT) was taken for the EEG waveform under the constructed referential derivation. According to the sampling rate, the data length of each 5-second segment was 1000 points. By taking 1024-point FFT, the frequency resolution of peirodogram was 0.2 Hz. The amplitude of EEG rhythm was calculated by

$$A(f) = 4\sqrt{S(f)}, \quad (1)$$

where S was the amount of power within the frequency band of EEG rhythm.

C. EEG rhythm separation

The obtained amplitude value for totally 16 channels indicated the topographical distribution of EEG rhythm among the scalp of head. A band pass filter was utilized to extract the EEG rhythm component from the EEG waveform to evaluate the consistency between the automatic result and visual inspection.

III. RESULTS

1. Unified suitable reference selection

The EEG data of one 5-second segment was analyzed. Based on the original EEG data from EEG recorder, bipolar derivation was constructed. The cross-spectrum of slow wave 0.5-8 Hz was analyzed for both horizontal and vertical directions of bipolar EEG.

The result of cross-spectrum analysis for phase reversal detection was illustrated in Fig. 2. The left side was cross-spectrum, coherence and phase for horizontal bipolar EEG. The right side was the cross-spectrum,

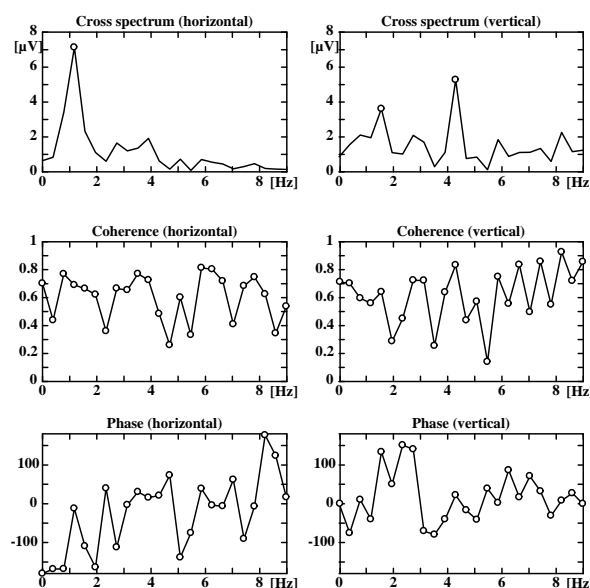


Fig.2. Cross-spectrums of bipolar EEG

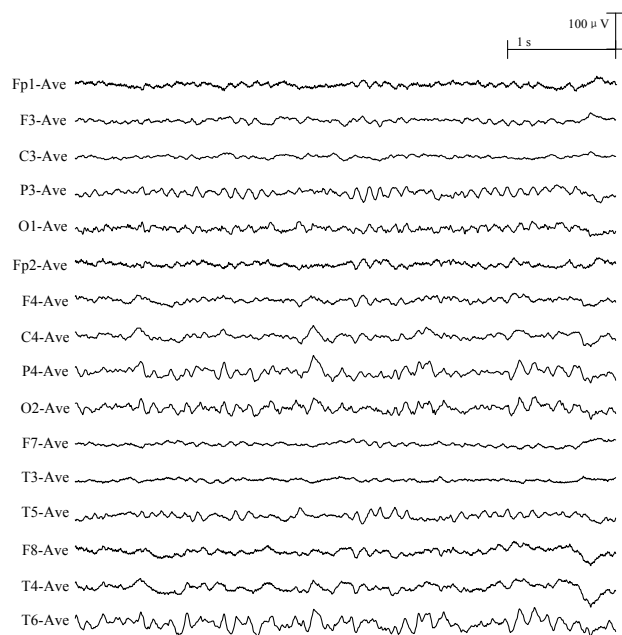


Fig.3. EEG waveforms under referential derivation

coherence and phase for vertical bipolar EEG. For the test subject, T4 was detected automatically as the focus. By using the iterative method, F8, C4, P4, O2 and T6 were detected as the distributed area.

Finally, the automatically selected reference was the average potential of all electrodes excluding T4, F8, C4, P4, O2 and T6. The EEG waveform under the new constructed referential derivation was shown in Fig. 3.

2. Periodograms analysis

The periodogram of the EEG waveform shown in Fig. 2 was obtained by taking 1024-point FFT. The periodograms were illustrated in Fig. 4. For each channel, the power of frequency band from 0.5 to 25 Hz was displayed. The frequency band from 0.5 to 25 Hz covered the main activities of EEG rhythms. The slow wave from 0.5 to 8 Hz was marked by grey color. The scale of each peirodogram was the same and the amount of slow wave can be observed among the scalp of head. The empty circles indicated the automatically detected peaks within the slow wave frequency band. The detected peaks would be utilized for EEG rhythm separation.

3. Topographical distribution of EEG rhythms

According to the peridogram, the amplitude of slow wave from 0.5 to 8Hz was calculated for each channel. The amplitude values were shown as the topographical distribution of EEG rhythm of slow wave. Comparing with other channels, the lager amplitude values can be

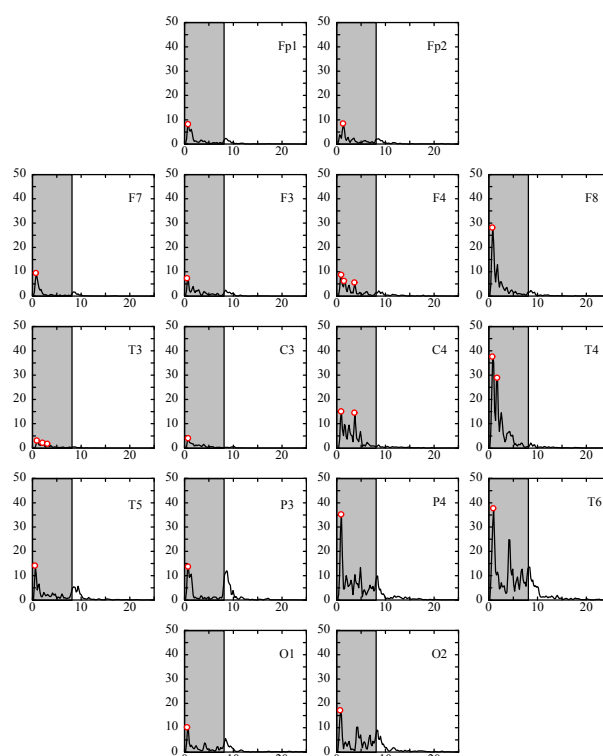


Fig.4. Periodograms.

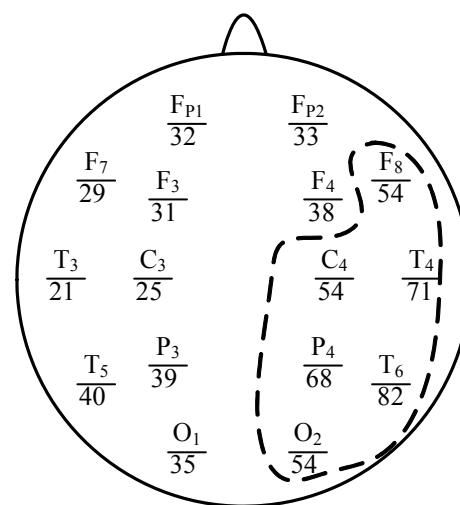


Fig.5. Topographical distribution of EEG rhythm of slow wave among the 16 EEG channels.

observed at the dotted area of focus T4 and distributed F8, C4, P4, O2 and T6 in Fig. 5.

Furthermore, the detected peaks in periodograms showed that the distributed slow wave frequency was lower than 4 Hz. A band pass filter of FFT-IFFT was adopted to separate the frequency activity from 0.5 Hz to 4 Hz out of the EEG waveforms. The separated results were illustrated in Fig. 6. It can be observed that

T4, F8, C4, P4, O2 and T6 had obvious slow wave. The separated results were consistent with the visual inspection.

IV. DISCUSSION

1. Unified suitable reference selection

The visual inspection on EEG interpretation is a critical skill for neurologists. Automatic EEG interpretation had been developed which can bring subjective inspection result as an assistant tool for clinical practice. The reference selection problem was important for both visual inspection and automatic interpretation. When the reference was unproper or contaminated by artifacts, the derived EEG waveform would affect the interpretation result. In this study, we investigated on the reference selection for automatic interpretation. Focus was detected by cross-spectrum of bipolar EEG and distributed area was detected by considering the distribution of EEG rhythm among the scalp. The obtained unified suitable reference can highlight the EEG rhythm of interest and bring correct interpretation result.

2. Topographical distribution of EEG rhythms

According to the selected unified suitable reference, an automatic drawing method for topographical distribution of EEG rhythm was developed. The amplitude of EEG rhythm was calculated for each channel. Band pass filter was adopted to separate EEG rhythm according to the peaks in periodogram. The topographical distribution can be observed based on the amplitude values. The separated waveform can reflect the frequency property of the distributed EEG rhythm. The obtained result highlighted the EEG rhythm of interest and was fit to the visual inspection. For the test subject, the peaks in the periodogram were rather closed. According to the brain diseases, there may be several peak groups in other case. Further proper separation of EEG rhythms would be developed as the future works

V. CONCLUSION

The automatic drawing of topographical distribution of EEG rhythm was investigated. The main method was based on a unified reference selection technique. The obtained automatic result was consistent with visual inspection. The developed technique had clinical application for EEG interpretation.

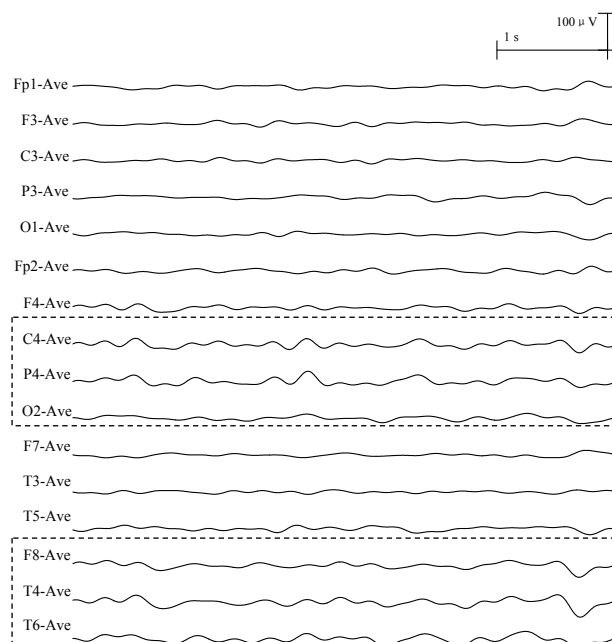


Fig. 6. Separated EEG rhythm from 0.5 to 4 Hz.

ACKNOWLEDGMENTS

The authors are grateful to Dr. Takenao Sugi, Department of Electrical and Electronic Engineering, Saga University, for the technique help on EEG data. This study is supported by Nation Nature Science Foundation of China 60674089, Shanghai Leading Academic Discipline Project B504, and Fundamental Research Funds for the Central Universities WH0914028.

REFERENCES

- [1] Nakamura M, Shibasaki H, Imajoh K, Nishida S, Neshige R, Ikeda A (1992), Automatic EEG interpretation: a new computer-assisted system for the automatic integrative interpretation of awake background EEG. *Electroenceph. Clin. Neurophysiol.* 82: 423-431
- [2] Nakamura M, Sugi S, Ikeda A, Kakigi R, Shibasaki H (1996) Clinical application of automatic integrative interpretation of awake background EEG: quantitative interpretation, report making, and detection of artifacts and reduced vigilance level. *Electroenceph. Clin. Neurophysiol.* 98: 103-112
- [3] Jasper HH (1958), Ten-twenty electrode system of the international federation. *Electroenceph Clin Neurophysiol.* 10:371-375
- [4] Wang B, Wang X, Ikeda A, Nagamine T, Shibasaki H, Sugi T, Nakamura M (2010), Automatic Reference Selection for Quantitative EEG Component Interpretation: Cross Spectrum Analysis Based on Bipolar EEG, *Proceedings of International Conference on Artificial Intelligence and Computational Intelligence*, 79-86, Oct. 23-24 2010, Sanya, China

Research on Surface Crack Detection based on Laser Scanning and Image Processing Techniques

Guangming Cai¹ Jiwu Wang¹ Mingcheng E¹ Wenliang Guo¹

Department of Mechanical and Electrical Engineering, Beijing Jiaotong University, Beijing, China, 100044¹

Sugisaka Masanori²

Nippon Bunri University, Oita, Japan²

(jwwang@bjtu.edu.cn)

Abstract: The traditional Surface crack detection method based on artificial vision, due to low detection efficiency and high labor strength etc., can hardly fit the demand of the actual testing operation. In order to meet this demand, in this paper we propose a new method based on laser scanning and image processing techniques for surface crack detection. The analysis of experimental results has shown the feasibility, accuracy and effectiveness of this method, and detection results were quite satisfied.

Keywords: crack; detection; laser scanning; image processing

I. INTRODUCTION

For engineering structures, products, parts, etc., the crack resulting from various reasons will affect their regular service, durability and security. In many cases, the occurrence of crack is inevitable, and the propagation of crack is usually ongoing. In order to guarantee the safety of life and property, the crack detection is very necessary [1] [2].

The commonly used methods for surface crack detection include manual detection, mechanical detection, optical fiber detection, laser detection, machine vision detection and so on. Among them, the manual detection has many shortcomings, such as low detection efficiency, high labor strength, poor quality and low detection reliability depended on many subjective factors. Mechanical detection is contact detection, and its detection efficiency is low. Both optical fiber detection and laser detection are high precision methods, but their cost is also too high. Although machine vision detection method based on image processing techniques is objective, non-contact, high accuracy and convenient, it also can not meet the demand. That is because images contain many interferences except crack, and there are no common and appropriate methods to eliminate these effects [3].

In this paper we propose a new method based on

laser scanning and image processing techniques for surface crack detection. The main steps of this method are as follows. Firstly, a red laser emitted a laser beam which formulated a straight laser line in the detected surface. Secondly, we used a CCD camera to capture target images from the detected surface. Thirdly, we applied the image processing techniques to judge whether the red laser line in the detection surface is continuous, to identify whether cracks are exist in the images. And the results of experimental have shown that this method can meet the demand of surface crack detection.

II. THE OVIEW

The core idea of this paper is to use machine vision instead of artificial vision for automatic detection of surface crack. Machine vision for crack detection depends on image processing technology [4]. Considering both the disadvantages of image processing technologies and the advantages of laser technology, we use a combination of them to detect surface crack.

The sketch map of the detection method is as follows.

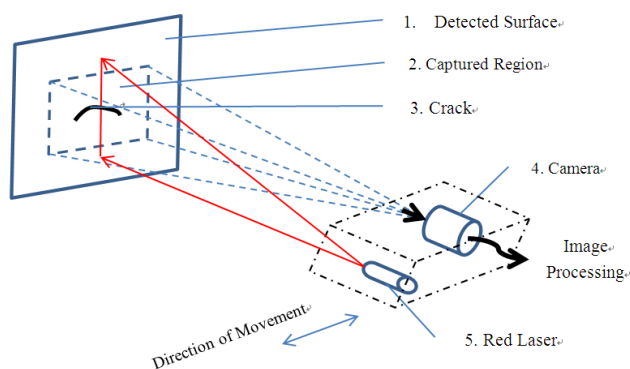


Fig. 1 The sketch map of the detection method

As shown in Fig.1, the 5 is a red laser. It emitted a red laser beam and formulated a straight red laser line in the detected surface (1). And, we used a CCD camera (4) to capture the image from the captured region (2). Then, we saw the CCD camera (4) and the red laser (5) as a whole thing, and let them move together along with the direction of movement. Therefore, we can capture the entire image information of the detected surface. In the end, we applied the image processing techniques to judge whether the red laser line in the detection surface is continuous, to identify whether crack is exist in the images.

III. THE BASIC PRINCIPLE AND EXPERIMENTAL TEST

1. The basic principle of the crack detection method

In addition to crack, the interferences, such as stains, adhesive materials, texture etc., were also contained in the detected surface. Before identifying crack from the interferences, we need to know their differences. And the obvious difference is as follows. When there is a crack in the surface, the material in the crack region is no longer close and a gap will appear in the surface. On the contrary, the interferences usually do not have this feature ^[6].

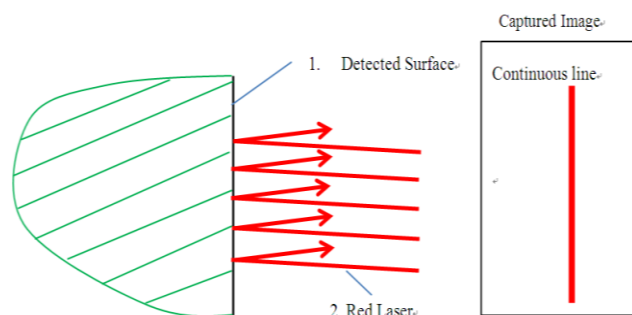


Fig.2 The case without crack and interferences

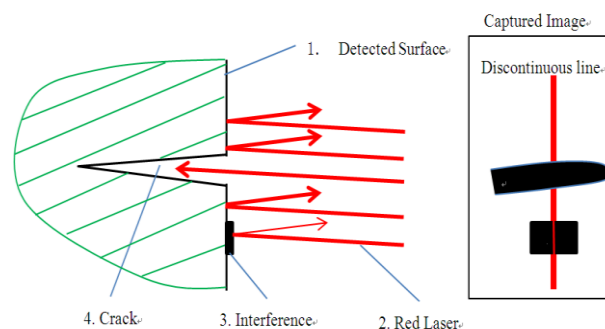


Fig.3 The case with crack and interference

Therefore, we can do the following analysis.

As shown in Fig.2, a red laser beam was emitted to the detected surface and most of it will be reflected back. And in the captured image, we can see a continuous red laser line. As shown in Fig.3, there is a case when surface contains crack and interference. In the crack region, the red-laser beam will through the crack and not be reflected back basically. In the interference region, there were still some of the red laser will be reflected back. Then in the captured image, we can see a red laser line which is discontinuous and uneven thickness.

2. Experiment

To verify the above analysis, we made the following experimental test.

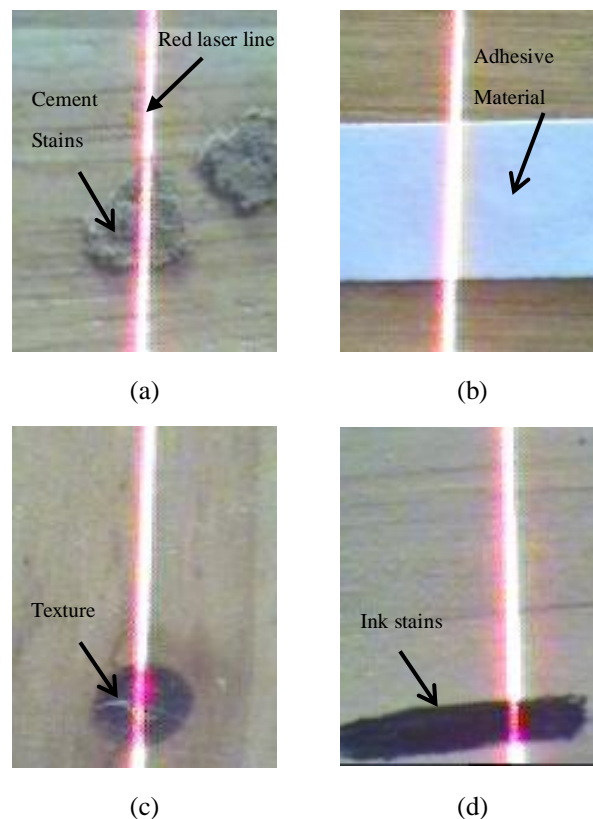


Fig.4. Testing images: containing inferences. (a) Cement stains, (b) Adhesive materials, (c) Texture, (d) Ink stains.

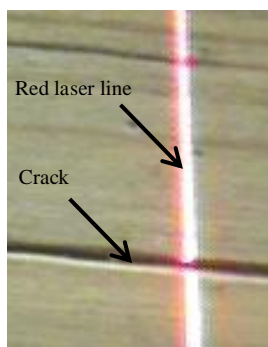


Fig.5. Testing image: containing crack

For the testing images that contain inferences, which is shown in Fig.4, the red laser line is continuous. As shown in Fig.5, the red laser line disconnected obviously in the crack region. According to the above results, we can see that the method for surface crack detection is feasible.

IV. THE IMAGE PROCESSING SYSTEM

In this paper, the surface crack detection method is based on image processing technology. And the image processing system is a core part of the crack detection method. Therefore, image processing system is directly related to the accuracy of the results of image processing.

1. Hardware program

As shown in Fig.6, we designed a hardware program for surface crack detection [5].

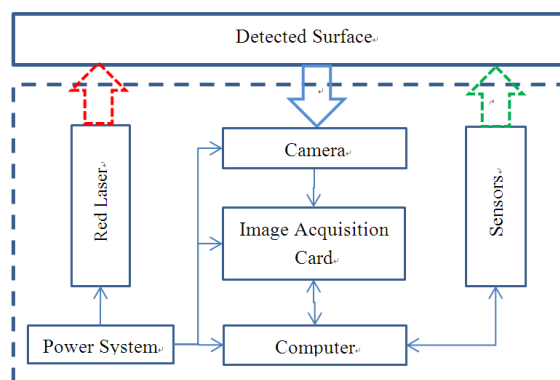


Fig.6 the hardware program

2. Flow chart of crack detection

The image processing flow chart of crack detection is shown as follows [7] [8].

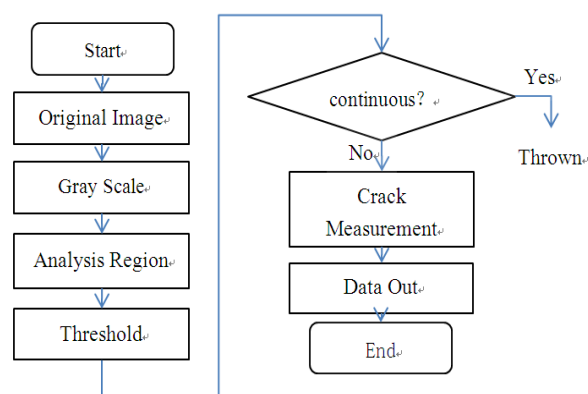


Fig.7. Flow chart of crack detection method.

- A. *Original Image*: Use a CCD camera to capture images.
- B. *Gray Scale*: Make the color image into the gray-scale image, so is suitable for image processing.
- C. *Analysis Region*: According to the least square method, we can get the analysis region (the red laser line region).
- D. *Threshold*: Apply Dual Threshold Method. And the required threshold could be got by calculating the histogram.
- E. *Judge the continuity*: According to the distribution of gray, we can select the analysis region. Then, in the selected region, we can judge the continuity by analysis the ratio of the target gray value.
- F. *Crack Measurement*: Combined with the analysis results of multiple images, we can measure the crack.
- G. *Data Out*: Save data to Access database.

V. THE PROBLEMS

For this crack detection method, we found the following problems by the experimental tests:

- A. *Cannot identify the micro-cracks*: For the micro-crack (its width less than 0.2mm), the intermittent feature of the red laser line in the crack region is unobvious, which is shown in Fig.8. However, by increasing the intensity of laser and the magnification of the camera, we can solve this problem.

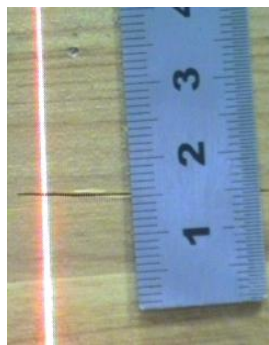


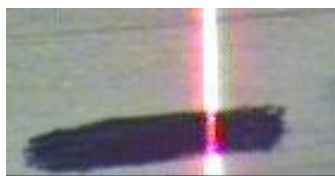
Fig.8. Testing image: containing a micro-crack.

- B. *The impact of a large contrast ratio:* When the color of interferences is much difference from that of background, this method can not rule out the impact of interferences, which is shown in Fig.9.



Fig.9. Testing image: the color of interferences is much difference from that of background.

- C. *The impact of shooting angle of the camera:* Where the shooting angle of the camera is not perpendicular to the detection surface, this method can not rule out the impact of interferences, which is shown in Fig.10.



(a)



(b)

Fig.10. Testing images: containing ink stains. From left to right: the angle between the shooting direction of camera and detection surface is (a)90° , (b)45° .

VI. CONCLUSION

In this paper, we propose a new method based on laser scanning and image processing techniques for surface crack detection. For relying solely on image processing techniques, the crack detection method we have proposed can make up its shortage. The role of laser scanning is equivalent to the function of image filtering. It can effectively filter the interferences except crack form the image. Through experimental tests, we verified the feasibility of this method. However, any method has its shortcomings, this method also exist shortcomings. For example, it is difficult to detect the micro-crack (its width less than 0.2mm); this method has improved the control requirements of movement and detection angle for camera and red laser. The purpose of this paper is to explore new ideas for workers who engaged in the work of crack detection.

REFERENCE

- [1] Ikhlas Abdel-Qader, Osama Abudayyeh, M.ASCE, Michael E. Kelly. "Analysis of Edge-Detection Techniques for Crack Identification in Bridges" [J]. *Journal of Computing in Civil Engineering*, pp. 255-256, October 2003.
- [2] Y. Fujita, Y. Mitani, Y. Hamamoto, "A Method for Crack Detection on a Concrete Structure", *ICPR '06*, Hong Kong, pp.901-904, August 2006.
- [3] Sun Zhaoyun, Chu Yanli, Fan Yao, Dang Le, "Pavement Crack Image Processing System Research based on VC++," *Computer Application and Software*, vol. 26, no. 8, pp. 82-85, August 2009.
- [4] Je-Keun Oh, An-Yong Lee, Se Min Oh, Youngjin Choi, Byung-Ju Yi and Hai Won Yang. "Design and Control of Bridge Inspection Robot System" [J]. *IEEE Computer Society*: 3634-3635.
- [5] Liu Xiaorui, Xie Xiongyao "Rapid Crack Inspection of Tunnel Surface Based on Image Processing," *Chinese Journal of Underground Space and Engineering*, vol. 5, no. 2, pp. 1624-1628, December 2009.
- [6] Fu Hua, Chi Jihui, "Research on Non-destructive Testing of Mold Micro Crack Based on Laser Ultrasonic Surface Wave," *Optoelectronic Technology*, vol. 30, no. 1, pp. 29-32, March 2010.
- [7] Jeong Ho Lee, Jong Min Lee, Hyung Jin Kim and Young Shik Moon. "Machine Vision System for Automatic Inspection of Bridges" [J]. 2008 *Congress on Image and Signal Processing*: 363-366.
- [8] Zou Yiqun, Hou Guicang, Yang Feng. "A Surface Crack Inspection Algorithm based on Digital Image Processing Techniques" [J]. *Control & Automation*, pp. 98-99, April 2004.

Intelligent Speech Recognition Filtering

Young Im Cho

Dept. of Computer Science, Univ. of Suwon, San2-1, Wau-ri, Bongdam-eup, Hwaseong, Gyeonggi-do
(Tel : 82-31-229-8214; Fax : 82-31-229-8281)
(ycho@suwon.ac.kr)

Abstract: In Emergency situation, speech recognition speed is very important. Therefore, in this paper, we propose a fast filtering algorithm. Firstly, FIR filter selectively passes through the frequency range of speech, and secondly, the Wiener filter filters out the extraneous noises. Because of that, the processing time is reduced.

Keywords: FIR filter, Speech recognition, Combination filtering algorithm

I. INTRODUCTION

One of the key factors in the speech recognition is noise[1]. The real situation is quite different from the controlled environment of the speech laboratory. However, the surrounding noises are a particularly difficult problem in the real speech recognition. The difference in the controlled environment and the real environment in speech recognition comes into play in three distinct processes: signal process, feature space process, and model process. Of these three processes, the difference is most evident in the signal process [2].

Here, the noise in the speech data after the signal process is filtered by a novel digital filtering system. A FIR filter is first used to separate the speech region and the noise region, and then a Wiener filter is used to improve the overall speech recognition.

II. Combined Filtering

Generally, the speech recognition system is configured by six stages. In stage 1, voice data are inputted by converting the audio signals into the electrical digital signals. In stage 2, the voice signals are separated from the surrounding noises. In stage 3, useful traits in speech recognition are extracted by using a speech recognition model. In stage 4, a standard speech pattern database is formed by speech recognition training. In stage 5, new voice data are compared to the standard speech pattern database, and the closest match is searched. In the final stage of 6, the matched result is put to use through the user interface.

In the preprocessing (noise elimination) stage of 2, analog audio signals from a CCTV or a sensor are digitized and then fed to the digital filter. The digital filter, which is widely used and proven, selects the passband and filter out the stopband.

This paper is supported by Gyeonggi-do Regional Research Center in Korea (suwon GRRC 2009-B3)

Depending on the presence of feedback processes, the digital filter is divided into IIR(Infinite Impulse Response) and FIR(Finite Impulse Response) filters. The latter is known to be less error-prone. For noise elimination in the subsequent processes, the Wiener and Kalman filters[3] are widely used. In emergency situations that require accurate interpretation of a rather brief voice data, the Wiener filter is usually preferred. The general model-based Wiener filtering process can be expressed as follows:

$$\hat{s}(t) = g(t) * (s(t) + n(t)) \quad (1)$$

Where, $\hat{s}(t)$ is the speech to be recognized, $s(t)$ is the speech data containing noise, $n(t)$ is the noise, and $g(t)$ is the Wiener filter.

In Eq. (1), $\hat{s}(t)$ is being sought. In it, an estimate of $n(t)$ is derived from $s(t)$, and then the approximate value of $\hat{s}(t)$ is obtained by using $n(t)$. In order to achieve a better approximation of $\hat{s}(t)$, the GMM as expressed below in Eq.(2) is used. It expresses mathematically the general characteristic of speech data.

$$P(s) = \sum_k^K p(k) N(s; \mu_k; \sum_k) \quad (2)$$

Based on Eq. (2), the model-based Wiener filter is designed per following steps: In the inputted current frame, the noise region is determined by a statistically-based VAD. In the noise region found, the noise model is renewed to the previous value. In the preprocess-WF block, a temporally noise-free clean speech is estimated using the decision-directed Wiener filter. Using the estimated values from the previous step, the Gaussian post probabilities of the GMM are calculated. In the final WF using the MMSE method, the probabilities are used to estimate the noise-free clean speech. The estimated noise-free speech and the noise model are used to design the final Wiener filter. The current frame

is processed using the Wiener filter designed, and the noise-free clean speech is obtained. Then the above five steps are repeated for the next frame.

For emergency detection, we propose a fast recognition filtering method. The basic concept is to selectively use the audio signal being transmitted from the CCTV's. That is, from the transmitted signal, only the audio energy spectrum that is relevant to the speech is to be selected, digitized, and saved for further analysis. A high-performance FIR Wiener filter can be used to digitally filter out the unwanted portion of the audio signal, prior to actual speech recognition.

As human speech generally falls within 300-3400khz, the FIR filter [4,5] can separate the incoming audio data into passband(the speech region), stopband, and threshold-band. This will greatly reduce the time and improve the performance of a speech recognition system.

The basic mathematical concept of the FIR filter can be expressed as follows:.

$$y[x] = \sum_{k=0}^{N-1} h[k]x[n-k] \quad (3)$$

In Eq.(3), $x[n]$ is the speech information input, $y[n]$ is the output speech information after filtering, $h[k]$ is the finite impulse response characteristic, and N is the filtering step number. As the input information and coefficients are multiplied and summed, the time required for noise filtering is quite long if Eq. (3) is implemented as is. However, the multiplication steps in Eq. (3) can be eliminated if a bit-serial algorithm [6] is applied. The result is expressed in Eq. (4) below:

$$y[x] = \sum_{k=0}^{N-1} \left(\sum_{j=0}^{M-1} h_j[k] \cdot 2^j \right) x[n-k] \quad (4)$$

Here, h_j , N , and M represent the coefficient h 's j th bit, tab number, and coefficient bit number, respectively. The bit-serial algorithm multiplies multiplicand to the multiplier while shifting LSB to MSB and then adds the result to the previous sum. To reduce the total multiplication cycles, the odd and even part of the Eq. (4) can be separated and the result can be written as follows:

$$y[x] = \sum_{k=0}^{N-1} \sum_{j=0}^{M-1} (h_{2j}[k] \cdot 2^{2j} + h_{2j+1}[k] \cdot 2^{2j+1}) x[n-k] \quad (5)$$

Eq. (4) requires a total of multiplication cycles, while Eq. (5) requires a total of multiplication cycles, a factor of 2 increase in the speed.

In this way, utilizing the benefits of the FIR filter, a Wiener filtering that minimizes the noise error by

effectively separating the speech signal and the noise is implemented.

Afterwards, the noise signals are extracted by subtracting the output speech data from the incoming speech data. Then the extracted noise data and the incoming speech data are used in Eq. (1) to design an improved noise filter.

In terms of mathematical expression, the general Wiener filter consists of multiplications and summations of current and past data and filtering coefficients. Thus, it can be designed using the device transfer functions and the mathematical expressions. Within the scope of this research, the physical states, such as operational stability and sensitivity and the safe transmission of data, are assumed to be steady, and the main priority is placed on minimizing the number of devices and increasing the speed of the filter operation.

Finally, the noise elimination Wiener filter is expressed as follows:

$$So(w) = H(w)S(w) \quad (6)$$

In Eq. (6), $s(w)$ is the noise-containing speech signal, $s_0(w)$ is the noise-free speech signal, and $H(w)$ is estimation function of the Wiener filter. An effective way to determine $H(w)$ is a major focus of this research. Accordingly, a mathematical expression for $H(w)$ is proposed as follows:

$$H(w) = \frac{P_s(w)}{P_s(w) + P_d(w)} \quad (7)$$

Here, $P_s(w)$ is the audio spectrum of the original speech signal, and $P_d(w)$ is the audio spectrum of the noise signal. An error is introduced in estimating the audio spectrum of the original speech signal during the filtering process. To reduce the error, a coefficient is introduced as below:

$$H(w) = \left(\frac{P_s(w)}{P_s(w) + \alpha \cdot P_d(w)} \right)^\beta \quad (8)$$

Here, parameters α , β and squaring the averages of the signals are used to reduce the error.

The Wiener filtering processes the noise-containing speech information effectively, but it takes time, so that speech recognition is delayed. To minimize the time delay, the concept expressed in Eq. (8) is applied during the statistically-based VAD process[7] of stage. The resulting process model is expressed in Eq. (9) below. In this model, the speech data and the noise data are considered to be asymmetric. By applying asymmetric window to these two data in designing the Wiener filter,

the time required for noise filtering can be significantly reduced.

$$H(n) = \begin{cases} 0.54 - 0.46 \cos\left(\frac{2\pi n}{P_1}\right), & 0 \leq n \leq n_0 \\ \cos\left(\frac{2\pi(n-n_0)}{P_2}\right), & n_0 \leq n \leq N \end{cases} \quad (9)$$

In Eq. (9), P_1 , P_2 , respectively, represents the period of the left and right portions of the asymmetric window function, n_0 is the location of the maximum value, and N is the total length of the window function.

Based on the noise-free speech signal obtained thus far, a speech recognition database is compiled and used in analysis of emergency situations. In this effort, the phonemic recognition of individual words is initially chosen as the key element of speech recognition, and the database is compiled accordingly.

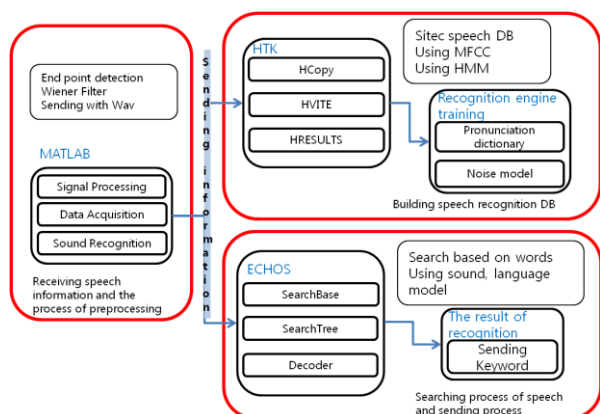


Fig.1. The overview of proposed speech recognition system

Fig. 1 illustrates the overview of the speech recognition system founded on the concepts described in Fig. 1. MATLAB[8] is used for the proposed FIR Wiener filter, and HTK and ECHOS are used for the subsequent processes. The finished speech recognition system basically uses sound models to search key words, and the flat lexicon and lexical tree are used in this word-based speech recognition system. The lexical tree is efficient in the usage of the memory, but is somewhat slow in applying the probability values of the language models and is also somewhat complex in implementing word models. Thus, a duplicate tree algorithm is used. That is, a parallel structure is used in the lexical tree for single-phoneme words.

The speech recognition result obtained by these serious of processes is then sent to the user interface of the system.

IV. Results

To test the speech recognition system developed thus far in this work, speaking word database developed by SITEC is used. The database is recorded in 16kHz/16 bit, and contained the voices of 500 individuals. For comparison to the database, voice data from a microphone or CCTV in 16kHz/16 bit format are used[9].

As discussed in the introduction, it would be unwise to use all the collected voice information in speech recognition, as it will consume too much time and may result in inaccurate analysis. By first extracting the audio frequency region useful for speech recognition by using the FIR filter proposed, the overall processing time can be greatly reduced.

The noise that escapes the initial filtering will then be eliminated by the Wiener filter. By comparing two filtering, it is found that the FIR Wiener filter visibly eliminates the background noise. Also, the effect can be audibly felt by listening to the before and after sounds.

By comparing the noise-free speeches processed through the MATLAB-constructed Wiener filter, to the existing database of key words, a very accurate speech recognition effect was realized.

By filtering out the unnecessary portions of the speech information, such as non-audible frequency regions, environmental noise, and transmission noise from the CCTV's, the level of speech recognition is found to be greatly increased. Also, the word models are found to be very useful in the success of speech recognition and in the reduction of the processing time. That is, the word model that considers the relationships between the words being searched had much more successes.

Using the database complied with noise-free sound data, two-pass bigram and bigram+trigram searches under ECHOS were found to indicate that the word-correlated model was much superior in terms of the recognition success rate and the search time than the simple model that does not consider the relationships between words.

As a result, in case of using model for each words, the speech recognition rate is much faster than without model. In model case, it is about 88.9% in bigram and 90.0% in bigram and trigram combination model of speech recognition rate(%) respectively. However, in without model case, it is about 77.2% in bigram and 80.1% in bigram and trigram combination model of speech recognition rate(%) respectively. Also, the recognition time(sec/sentence) is much faster than without model. It is about 21.0% in bigram and 22.1% in bigram and trigram combination model of speech recognition rate(%) respectively. However, in without model case, it is about 5.4% in bigram and 6.3% in bigram and trigram combination model of speech recognition rate(%) respectively.

It is interesting to note that in HMM the success rate for the standard bigram (left to right) search method is lower by 8% than the trigram search method that searches in the reverse direction and also considers the relationships between different phonemes. Nonetheless, the search time was longer for the latter method.

Lastly, a significant processing time reduction and a fast situation response were realized by selectively processing the audible voice region of the audio signals transmitted from the CCTV.

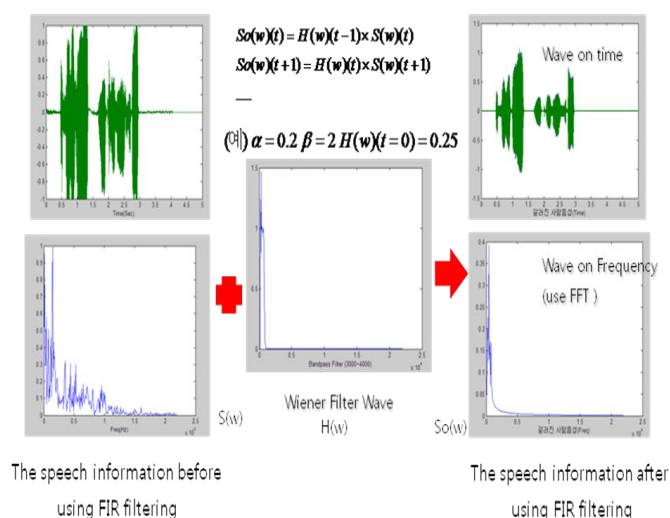


Fig.2 Simulation Result 'Hello'

V. Conclusion

Unlike the controlled environment where a speech recognition system can easily filter out the extraneous noises, it is rather difficult in the real environment where a sensor, such as a CCTV, collects abundant noises from various human, mechanical, and natural sources. The success of speech recognition in the real environment thus depends critically on how well these noises are filtered. Just as important, the processing time for noise filtering needs to be reduced, as time is the most critical element in emergency situations. Thus, effective noise filtering combined with fast processing time is considered to be the essence of speech recognition. Towards these goals, an improved speech recognition system is proposed in this work. The system has the FIR and Wiener filters as the key elements and effectively filters out the extraneous noises and produces clean noise-free speech data in a reasonable time.

One of the problems cited during the work is that the extraneous noise that is present in the audible band of 300-3400khz can still pose some problems even with the proposed FIR filter. As the noise filtering in this

frequency region is not yet completely understood, further research in this front is currently underway.

REFERENCES

- [1] H. Kruegle, "CCTV Surveillance", *Analog and Digital Video Practices and Technology*, Elsevier, pp.227-239, 2007.
- [2] C.-H.Lee, "On Stochastic Feature and Model Compensation Approaches to Robust Speech Recognition", *Speech Communication*, pp.29-47, 1998.
- [3] J.K. Kim, "Min/Max Estimation and Base Estimation for Kalman Filter", *Natural Science Research (Korean)*, vol. 5, pp.21-30, 1995.
- [4] T.K. Ryu, K.H. Park, D.S. Hong, C.O. Kang, "Channel Estimation by Sero-Forcing Method in the Frequency Region," *Kor. J. Telecommunications*, vol.31, no.1, pp.38-47, 2006.
- [5] Y.S. Park, J.H. Jang, "Echo Filtering by Soft Decision in the Frequency Region", *Telecommunications Review (Korean)*, vol.19, no.5, pp.837-844, 2009.
- [6] Robert E.Morley, Jr. Gray E. Christensen, Thomas J. Sullivan, Orly Kamin, "The Design of a Bit-Serial Coprocessor to Perform Multiplication and Division on a Massively Parallel Architecture", in *Proc IEEE, The 2nd Symposium on the Frontiers of Massively Parallel Computation*, Farifax, U.S.A, pp.419-422, 1998
- [7] J.H. Jang, D.K. Kim, N.S. Kim, "A New Statistical Method for Speech Recognition Systems", *Telecommunications Review (Korean)*, vol.15, no.1, pp. 201-209, 2005.
- [8] K.S. Kim, "MATLAB Signal and Image Processing", Ajin Publishing, Korea, pp.213-250, 2007.
- [9] Y.I. Cho and S.S. Jang, "Intelligent Speech Recognition System for CCTV Surveillance", *Kor. J. Intelligent Systems*, vol.19, no.3, pp.415-420, 2009.

Multi Robotic System and the Development of Cooperative Navigation Behaviors for Humanitarian Demining

Maki K. Habib

*The American University in Cairo
New Cairo, Egypt
maki@ieee.org*

Abstract: Multiple robotic systems can accomplish tasks that no single robot achieve, since ultimately a single robot, no matter how capable, is spatially and physically limited. However, achieving cooperative robotics is quite challenging. Many issues must be addressed in order to develop a working cooperative team, such as action selection, coherence, conflict resolution, resources management, coordination, cooperation and communication. In this paper Pemex-BE robot is used to represent the individual robot that makes up a team for multi robotic system dedicated for humanitarian demining. The multi Pemex-BE robots for mine clearance represents an attempt to reduce the gap between the research level and the actual needs on the ground. The technical features and navigation system with obstacle avoidance along with the scenario of multi robotic system is presented.

Keywords: Robotics, Multi robotic systems, Navigation, Sensors, Antipersonnel mines, Humanitarian demining

I. INTRODUCTION

Research on using population of robots for achieving a given task efficiently has mostly been inspired by animal behaviors. There has been increased research interest in systems composed of multiple autonomous mobile robots exhibiting cooperative behavior. The study of multiple-robot systems naturally extends research on single-robot systems. Multiple-robot systems can accomplish tasks that no single robot can accomplish, since ultimately a single robot, no matter how capable, is spatially limited. Achieving cooperative robotics is desirable for a number of reasons [1-4].

1. Many robotic applications are inherently distributed in space, time, or functionality, thus requiring a distributed solution. In addition, tasks may be inherently too complex or impossible for a single robot to accomplish it,
2. It is quite possible that many applications could be solved much more quickly if the mission could be divided across a number of robots operating in parallel by duplicating capabilities across members of the robot team.
3. Building and using several simple robots can be easier, cheaper, flexible, and has the potential of increasing the robustness and reliability of the automated solution through redundancy. It would be much cheaper and more practical in many applications to build a number of less capable robots that can work together at a mission, rather than trying to build one robot which can perform the entire mission with adequate reliability, and
4. The constructive and synthetic approach inherent in cooperative mobile robotics can possibly yield insights into fundamental problems in the social sciences (organization theory, economics, cognitive

psychology), and life sciences (theoretical biology, animal ethology).

Achieving cooperative robotics, however, is quite challenging. Many issues must be addressed in order to develop a working cooperative team, such as action selection, coherence, conflict resolution, resources management, coordination, and communication. Furthermore, these cooperative teams often work in dynamic and unpredictable environments, requiring the robot team members to respond robustly, reliably, and adaptively to: unexpected environmental changes, failures in the inter-robot communication, modifications in the robot team that may occur due to mechanical failure, learning of new skills, the addition or removal of robots from the team by human intervention, or full robot failure etc.

Small, lightweight, and inexpensive robots tend to have better mobility but it might be unavoidably slow [5-7, 9, 10]. Smaller in size and light in weight also means reducing certain capabilities. With the use of a large number of such robots, the good mobility can compensate for the low speed while it is necessary to develop efficient group behaviors to compensate for the reduced capabilities. When designing the multi robotic systems for demining, it is important to decide the type of movement strategy the robots adopt when scanning the minefield, the standard set of behaviors that all individual robot should have and the set of specialized behaviors that are assigned to specific individual robots and the way robots are going to communicate information.

Random collective behaviors with improved algorithms have been proposed to look for mines on beaches [8]. This technique cannot fulfill humanitarian demining requirements, as there is a need to assure that every square inch of the terrain is explored reliably and

as safely and as fast in a minimum amount of time and cost

II. MULTI ROBOTIC SYSTEM SCENARIO FOR HUMANITARIAN DEMINING

The outline of multi robotic system scenario for humanitarian demining using Pemex-BE robot is stated as follows:

- a. The higher level of control is represented by a mobile monitoring station. The monitoring station receives the task description either from human-operator through a multimodal graphical interface, or by using a topographical map, or an aerial picture with precise coordinates. The operator divides the area of the assigned minefield into sectors and allocates a robot for each sector. Then, the monitoring station informs the task and the starting global /reference location of each sector to the relevant robots through radio module. Periodical polling tracks task execution, clarifications, and reported difficulties that might be raised by any of the robots or by the searching mission. The monitoring station helps to resolve any problems by individual robots that are in deadlock situations or robots that require additional resources. In this case the monitoring station and human operator can instruct and extend help to the relevant robot directly to fulfill its needs in finding safe path, resolve the deadlock, emergency help and guide, etc. If this is not possible, the monitoring station reports that to human operator. Human operator interacts with the monitoring station to instruct a specialized robot for emergency to help the robot in question and resolve the deadlock, or give charging service, etc.
- b. Individual robots. Each robot (see Figure 1) initializes itself and performs a self-check to emulate his readiness to achieve a set of possible tasks and informs the monitoring station about its availability and readiness to execute these tasks. Each robot in the multi robot team receives the assigned task from that monitoring station and reports back on its activity and performance update: scanning for mines, marking mines, and communicating with other robots. In addition, each robot tries to get out of a detected deadlock situation by means of its own available knowledge and resources before reporting it to the monitoring station. Mines are marked and possibly exploded using a small charge placed by the robot and triggered after the robot has backed at a safe distance. Each robot has its behavior navigation system with set of standard behaviors available for all robots, and set of specialized behaviors that are dedicated for special tasks and needs (See Figure 2). The principle requirement is that each of the demining robot in the team should operate in a remote control mode or, at least, semi-autonomously. All robots are assumed to have the following capabilities: position encoders, GPS, obstacle

detection sensors, mine sensor, and radio communication. Some of the robots might have extra sensing and physical capabilities depending on the assigned task requirements.



Fig.1. Pemex-BE in different environments

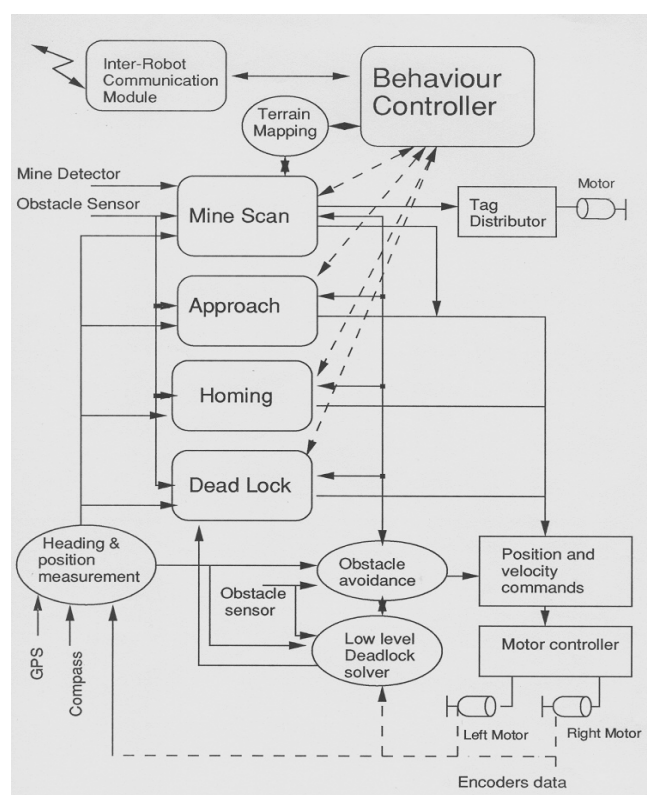


Fig.2. Pemex-BE in different environments

III. IMPLEMENTATION OF THE ADOPTED MULTI ROBOTICS SYSTEM SCENARIO

Pemex-BE robot was used to represent the individual robot that makes up the team for multi robotics system. The mobile monitoring station is considered as a car of suitable size, which can adjust its location as needed to support the demining process and its requirements. In this case, the mobile monitoring station represents the higher level of control. Within this architecture, human-operator stations inside the car interacting with the monitoring station with the possibility to communicate with other land-based sub-operators through radio. The operator describes the task to the monitoring station. The monitoring station

interacts with the assigned operator and takes care of task distribution and allocation for individual robots according to the size of the minefield and the available number of robots. The station supervises the execution and control of tasks, and communicates with robots as individuals, groups or as a whole to follow-up task execution, mapping, and problem solving updates. The skill required by human-operator should be kept to minimum. Figure 3 shows an example for dividing a minefield into three sectors, the mobile monitoring station and some high level behaviors. Efficient distributed robotics architecture must allow robots to be efficiently added to the system or removed from it. Once, a Pemex-BE robot starts to operate; it is in a standby mode while reporting to the monitoring station its readiness in performing a set of tasks according to the associated physical functional capabilities.

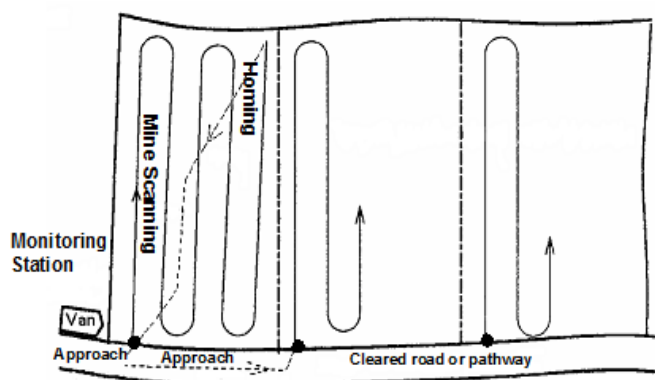


Fig.3. Terrain to be cleared with three robots

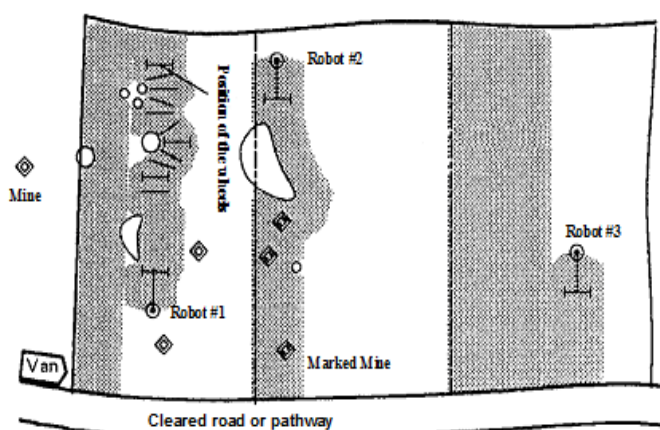


Fig.4. Terrain scanned after certain time by the work of three robots

Each of the dedicated robots for mine search receives the global reference location of an assigned sector along with its width and depth. A digital map of the minefield and the searched area within each of the assigned sectors have to be maintained and continuously updated with the support of a seamless interactive interface between the human operator and the monitoring station from one side and between each

robot and the monitoring station from the other side. Each robot maintains its own version of the map based on its searching activity and shares it with the monitoring station. For the purpose of this work, the operator at the monitoring station is responsible to decide whether the minefield is completely cleared or there are still remaining issues or regions within the assigned sectors that need to further follow-up (see Figure 4). Hence, the operator must have a comprehensive view of the demining process performed by the participating robots that constitute the demining team. Marking a detected mine within an assigned land on a digital map enables immediate and easy interactive interpretation by human operator or the monitoring station. In addition, it helps to decide whether further exploration for that land is needed or not.

During the actual operation of mine searching, an assigned working area for each individual robot can be redefined depending on the circumstances facing the robot and the searching progress, e.g., help can be requested when one robot is discovering more mines or more obstacles within its own assigned area and needs some help from other robots that already finished searching their sectors. Coordination of movements is required if one robot is stuck into a hole or at a corner or lost its detection or mechanism capabilities; in such situation, another robot (either specialized emergency robot for such mission or any of the other individual robots) should pull it back and such a decision is made in consultation through the monitoring station and possibly through human operator too.

The main functional capabilities of the monitoring station can be summarized as:

1. It receives a demining task description through human-friendly graphical user interface using, for example aerial pictures, topological maps, etc.
2. It divides the located mined area into sectors and allocates a robot to each sector. Human has the capability to interfere and do or adjust this job directly.
3. It communicates with the available robots by radio transmission through periodical polling or per demand as needed. This aims to announce a task, track task execution, solve deadlock, manage collaborative action, mapping searched area, re-planning, etc.
4. Tracks all marked mines.
5. It maintains a global and updated digital map of the minefield.
6. It confirms and announces the completion of a demining task.
7. Adding new robots to the team or removing damaged members.

IV. COMMUNICATION MANAGEMENT

In order to enable parallel behaviors and efficient task achievement, follow up progress and update, and to

extend support to any robot in need, a communication management module at each robot and at the mobile monitoring station is considered necessary under the work of this paper for message and information exchanges. Group communication among all robots (inter robots communication) including the monitoring station requires protocols that can operate without central control and handle dynamic topology changes due to the mobility of the robots and the station itself. Multicast is the most important group communication primitive and it is critical in applications where close collaboration of teams is needed. A radio based communication module has been developed and its communication framework consists of communication protocol to establish physical communication link and message protocol to exchange messages corresponding to necessary information. The main functions of the message protocol are negotiation (task assignment, cooperation, etc.), inquiry (look for information, etc.), offer (information, help, etc.), announce and synchronize, deadlock solve, etc.

It is important to remember that even the most sophisticated radio systems are subject to interference, both loss of bandwidth due to RF noise and competition for bandwidth. In addition, when dealing with tasks in real-time, much information has a severely limited useful lifetime which influences how reliability of communication must be addressed. The communication management will be helpful to add new robots to the system and removing damaged ones. When a robot is unreachable through communication by others for varying periods of time, it is considered temporarily to be damaged and the system requires dynamically to do change in the makeup of a robot team.

V. CONCLUSIONS

The multi Pemex-BE robots for mine clearance structure presented in this paper as an attempt to reduce the gap between the research level and the actual needs on the ground. This requires proper understanding of the exact problems at the minefields sites and concludes a design of a low cost, flexible, and light weight mobile robot while considering local resources and constraints.

There is still a need for further analysis to formulate the efficient navigation system for Pemex and its motion. A better sensory combination and fusion techniques are still needed. Better mobility is of high demand. Further analysis is required to develop dynamic behaviors supporting coordination, communication and cooperation capabilities.

REFERENCES

[1] Parker E (1998). Distributed Control of Multi-Robot Teams: Cooperative Baton Passing Task, Proceedings of the 4th International Conference on

Information Systems Analysis and Synthesis (ISAS '98), vol. 3: 89-94.

- [2] Uny Cao Y; Fukunaga A S; Kahng A B (1997). Cooperative Mobile Robotics: Antecedents and Directions, Autonomous Robots, 1997 Kluwer Academic Vol. 4: 1-23.
- [3] Arkin R C; Balch T (1998). Cooperative multiagent robotic systems. In David Kortenkamp, R. Peter Bonasso, and Robin Murphy (Eds), AAAI Press.
- [4] Mataric M J (1990). Navigating with a rat brain: A neurobiologically-inspired model for robot spatial representation. In Proceedings of the First International Conference on Simulation of Adaptive Behavior: From Animals to Animats (SAB'1990). MIT Press: 169 – 175.
- [5] Gage D W (1995). Many-robot MCM Search Systems, Autonomous Vehicles in Mine Countermeasures Symposium, Monterey, CA: 9.56-9.64.
- [6] Loh J; Hengm J; Seet G; Sim S K (1998). "Behavior-based search using small autonomous mobile robot vehicles, Second International Conference on Knowledge-Based Intelligent Electronic Systems, Adelaide, Australia, Vol. 3: 294-301.
- [7] Roumeliotis S I; Pirjanian P; Mataric M J (2000). Ant-inspired navigation in unknown environments, Autonomous Agents 2000, Barcelona, Spain: 25-26.
- [8] Greiner, H.; Sheckman, A.; Chik-yung Won; Elsley, R.; Beith, P.; (1996). Autonomous Legged Underwater Vehicles for Near Land Warfare, Autonomous Vehicles in Mine Countermeasures Symposium, (AUV'96), Monterey: 41 – 48.
- [9] Habib M K (2002). Mine Clearance Techniques and Technologies for Effective Humanitarian Demining, International Journal of Mine Action, Vol.6, No.1, 2002.
- [10] Habib M K (2001). Mine Detection and Sensing Technologies: New Development Potentials in the Context of Humanitarian Demining", 2001 IEEE International Conference of Industrial Electronics, Control and Instrumentation "IECON'2001": 1612-1621.

Development of Flexible Surgical Manipulator for Natural Orifice Transluminal Endoscopic Surgery

Jungwook Suh, Hoseok Song, Kiyoun Kim, and Jungju Lee*

**Dept. of Mechanical Engineering, KAIST, 335 Gwahangno, Yuseong-gu, Daejeon, Republic of Korea
(Tel : 82-42-350-3033; Fax : 82-42-350-3210)
(leejungju@kaist.ac.kr)*

Abstract: Natural Orifice Transluminal Endoscopic Surgery is an advanced and experimental surgical technique performed via natural orifices (mouth, anus, vagina, urethra, etc.). Therefore, unlike other surgery methods such as laparoscopic surgery or single port access surgery, NOTES can avoid remaining external incisions or scars. Surgical manipulator for NOTES should be flexible in order to be inserted into channels of overtube. This paper presents a development of flexible robotic manipulator for NOTES, including design and kinematic analysis. Developed thin manipulator has 4 DOF motion and only 5.0 mm in diameter. And it uses multi-revolute joints that have gradual curve in order to enlarge the workspace and minimize the diameter of manipulator.

Keywords: NOTES (Natural Orifice Transluminal Endoscopic Surgery), MIS, surgical robot

I. INTRODUCTION

Laparoscopic surgery, a kind of MIS which stands for Minimally Invasive Surgery, means a surgical technique performed in the abdomen through some small incisions. These days it is common surgical method in the case of simple abdominal surgery such as cholecystectomy because of advantages like short hospital stay and small scars. However it usually takes longer time to operate laparoscopic surgery than traditional open surgery. Development of laparoscopic instruments helped to make the procedure short and simple, and finally the introduction of medical robot caused a shift of power in the medical surgery. Da Vinci[®], developed by Intuitive Surgical Inc., is the representative medical robot system for the laparoscopic or thoracic surgery. This kind of surgical robot can operate surgery much more dexterously than traditional manual surgery.

The smaller the incisions for surgery are, the bigger the merits of MIS are. Traditional open cholecystectomy needed an incision bigger than 20 cm, while recent laparoscopic operation makes three to five small incisions of only about 10mm. Furthermore, surgeons are trying to minimize the incision for surgery as ever. Therefore they invented two kinds of new experimental surgical methods for abdominal surgery in recent years. One is SPA(Single Port Access) surgery, and the other is NOTES(Natural Orifice Transluminal Endoscopic Surgery). The SPA surgery is performed using single entry port, typically the patient's navel. Though SPA

surgery remains no visible scar after a while, external incision on the patient's skin is still needed. On the other hand, NOTES has significantly different procedure to laparoscopic surgery. The biggest advantage of NOTES is that it makes no incision on patient's skin. Instead, it is performed via natural orifices such as mouth, anus, vagina or urethra, and internal incision on the wall of organ is necessary to approach the surgical site. Patient barely feels pain on the internal incision and can leave the hospital much earlier. Besides, lower anesthesia requirements and avoidance of the potential complications are also big merits of NOTES [1]. Therefore, NOTES can be considered an ideal abdominal surgery from the viewpoint of MIS. However there is an obstacle to carry out this brand-new technique that is absence of proper instruments for NOTES. Unlike SPA surgery, NOTES cannot utilize traditional laparoscopic instruments, because flexible surgical tools should be inserted via bent human orifices [2]. Therefore various surgical instruments for NOTES should be developed so that NOTES can be one of general surgical operations for abdominal surgery. Furthermore, robotic system for NOTES is expected to change the status of NOTES in abdominal surgery as in the case of laparoscopic surgery.

II. DESIGN OF ROBOT ARM

More than two surgical instruments are needed to perform surgical procedures, and they should be exchangeable. Therefore, for the sake of NOTES, two

instruments should be inserted along an overtube with an endoscope as shown in Fig.1. At this moment, there is no commercial NOTES robot system, but some NOTES prototypes, such as EndoSAMURAI (Olympus Corp., Tokyo, Japan) and DDES (Boston Scientific, Natick, MA), are considerable for development [3].

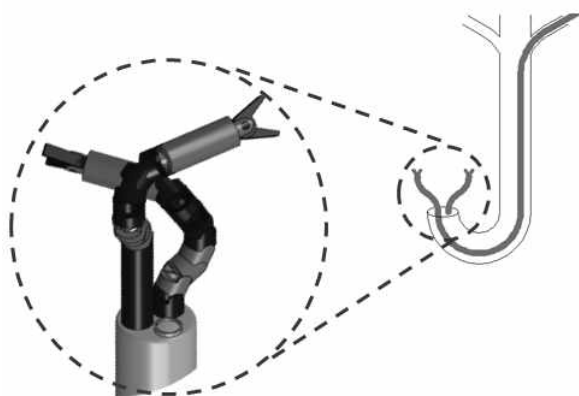


Fig.1. Overview of NOTES robot

The target surgery of this research is transgastric cholecystectomy. The diameter of overtube is limited to 25 mm due to the size of patient's esophagus. Of course, it's obvious that small diameter is good for smooth insertion. In this research, the diameters of overtube and robot arms are determined to 20 mm and 5 mm each. Different from the conventional flexible endoscopic instruments, 2 additional DOF (degrees of freedom) joint can make surgical procedures easy. Thus each robot arm has 4 DOF including translation and axial rotation except grip motion.



Fig.2. Flexible shaft composed of short links



Fig.3. 2 DOF multi-spherical joints driven by 8 wires

Further, flexibility and force are important requirements for robot arm for NOTES. Thin and flexible robot looks nearly impossible to apply heavy radial force on the tip. Therefore, flexible shaft composed of lots of short rigid links are used in order to apply axial and torsional forces effectively. 2 DOF active joint also can be composed of similar links. There are several types of small sized joint mechanism that can be applied to NOTES instruments [4]. Multi-spherical joints design is frequently applied for many researches because of the advantage that it's relatively easy to product small sized joints [5][6]. However this kind of manipulators has a severe problem that they are so weak to external forces that the assembled joints are easily bent. In order to prevent the S-shaped bending by applied external forces, French CNRS fixed lots of actuating wires on each links and actuated them with different speed using pulleys [6]. 5 mm sized Endowrist, laparoscopic instrument for da Vinci[®] system, has similar but advanced mechanism using universal joint at proximal driving part. It helps the system minimize the size of driving part. Notched nylon rod or superelastic NiTi tube can be used for bending joint similarly, and they are good to serve a working channel for gradual bending [7]. Nevertheless, they cannot beat multi-spherical joints because of elasticity and small applicable forces.

Although there is no commercial robotic NOTES system now, lots of researchers are trying to develop NOTES system. Purdue University develops a NOTES robot based on the laparoscopic surgery robot named Laprotek, while Columbia Univ. and Intuitive Surgical, Inc. are developing SPA surgery robot [7][8]. These three systems have elbow-out function in common, because the scope and two arms should be located in small sized overtube head. Therefore the distance between two robot arms is so narrow that it's difficult to secure enough workspace and field of view without elbow-out joints. They are essential for NOTES robot, but wire-driven toggles are sufficient for them. As shown in Fig.4, surgical robot arm consists of tooltip, long flexible shaft and driving part. Three DC motors in the driving part drives the 2 DOF bending joints and the forceps using stainless steel wire ropes. And Fig.5 shows the actual built robot arm combined with the overtube. The overtube serves three working channels for a camera and two arms.

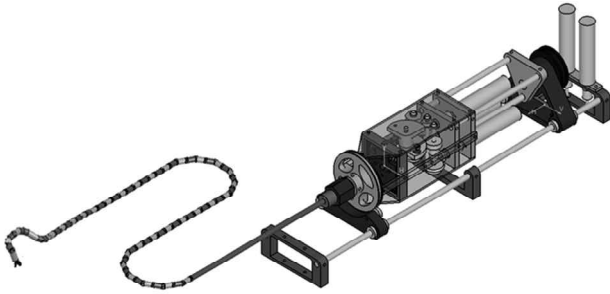


Fig.4. Designed NOTES robot arm



Fig.5. Built robot arm combined with the overtube

III. KINEMATIC ANALYSIS

2 DOF bending section is composed of 4 unit revolute joints. If the number of segmental revolute joints is large enough, this kind of 2 DOF joint can be considered as a long flexible shaft even though it consists of rigid links. Furthermore, it makes a circular arc shaped bending under the assumption of zero gravity and no friction. This bending section is difficult to express using traditional D-H (Denavit-Hartenberg) parameters. It causes some duplicated symbols like θ_3 and θ_4 as shown in Table.1. There are four variables (θ_1 , d_2 , θ_3 , and θ_4) because this manipulator has 4 DOF. And here d_3 is a function of θ_3 as follows.

Link	α_{i-1}	a_{i-1}	d_i	θ_i
1	0	0	0	θ_1
2	0	a_1	d_2	0
2'	0	0	0	θ_4-90°
2''	$-\theta_3/2$	0	0	0
2'''	0	0	d_3	0
2''''	$-\theta_3/2$	0	0	0
4	0	0	0	$90^\circ-\theta_4$
5	0	0	d_4	0

Table.1. Denavit-Hartenberg parameters

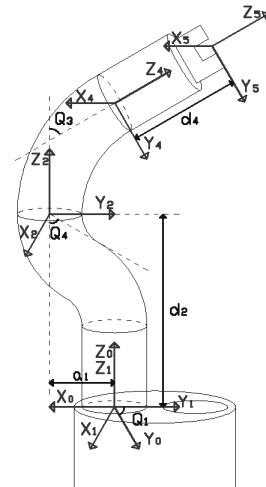


Fig.6. Kinematics of 4 DOF manipulator

$$d_3 = \frac{2L_T}{\theta_3} \sin \frac{\theta_3}{2} \quad (1)$$

L_T is the length of bending section when unfolded, and θ_4 is the angle between x_2 axis and the projected line of bending section on the $x_2 y_2$ plane. As a result, the bending section has 2 DOF motion and it can be expressed as a transformation matrix with two variables, θ_3 and θ_4 , as follows.

$$T_4^2 \approx T_2^2 T_{2'}^{2'} T_{2''}^{2''} T_{2'''}^{2'''} T_4^{2''''} = \begin{bmatrix} c_3 c_4^2 + s_4^2 & (c_3 - 1) c_4 s_4 & s_3 c_4 & \frac{L_T(1 - c_3) c_4}{\theta_3} \\ (c_3 - 1) c_4 s_4 & c_3 s_4^2 + c_4^2 & s_3 s_4 & \frac{L_T(1 - c_3) s_4}{\theta_3} \\ -s_3 c_4 & -s_3 s_4 & c_3 & \frac{L_T s_3}{\theta_3} \\ 0 & 0 & 0 & 1 \end{bmatrix} \quad (2)$$

By the benefit of assumption on the bending section, the overall kinematics also can be expressed with quite simple transformation matrix. (eq.4) and (eq.5) indicate the rotation matrix and the position vector in (eq.3).

$$T_5^0(\theta_1, d_2, \theta_3, \theta_4) \approx T_1^0 T_2^1 T_4^2 T_5^4 = \begin{bmatrix} R_5^0 & P_5^0 \\ 0 & 1 \end{bmatrix} \quad (3)$$

$$R_5^0 = \begin{bmatrix} c_{14} c_3 c_4 + s_{14} s_4 & c_{14} c_3 s_4 - s_{14} c_4 & c_{14} s_3 \\ s_{14} c_3 c_4 - c_{14} s_4 & s_{14} c_3 s_4 + c_{14} c_4 & s_{14} s_3 \\ -s_3 c_4 & -s_3 s_4 & c_3 \end{bmatrix} \quad (4)$$

$$P_5^0 = \begin{bmatrix} c_{14}((1-c_3)\frac{L_T}{\theta_3} + s_3d_4) \\ s_{14}((1-c_3)\frac{L_T}{\theta_3} + s_3d_4) \\ d_2 + c_3d_4 + \frac{s_3L_T}{\theta_3} \end{bmatrix} \quad (5)$$

In spite of the rough assumption, this result does not show a significant error. Besides, the bending amount is meaningless in the NOTES arm because of long and flexible shaft, while the bending direction is quite accurate.

IV. EXPERIMENT

A simple experiment was performed to confirm the linearity between commanded angle and actual measured angle in the bending section. Angles were observed for several cycles of simple bending motion in order to check the repeatability. This experiment was performed with 8 segmented bending section and 400mm long flexible stem in S-shaped experimental working channel whose size is only 70 mm in radius of curvature. The two values of commanded and actual angles would be same on the idealized assumption. Unfortunately, however, the plot shows severe hysteresis. It's impossible to eliminate this phenomenon completely. Nevertheless, it can be improved by minimizing friction and tolerance and slope correction technique [7].

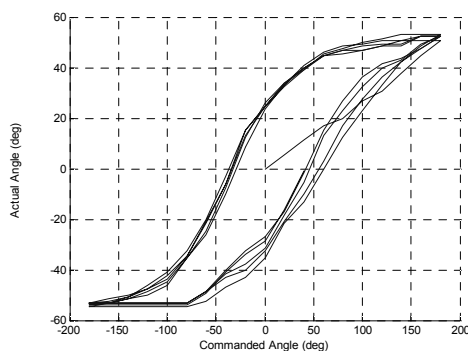


Fig.7. Hysteresis loop for repeated bending motion

V. CONCLUSION

Long, thin and flexible surgical robot suitable for NOTES procedure was developed. Although the diameter is only 5 mm, it serves 4 DOF motion except

grip. It's designed to apply high axial and torsional forces and to have small radius curvature for smooth insertion into bent channel. Even though the result of the repeating experiment was not so good, it showed the possibility of NOTES. In the near future, NOTES is expected to be established as one of the standard procedures for abdominal surgery.

ACKNOWLEDGEMENT

This work was supported by the Korea Science and Engineering Foundation (KOSEF) grant funded by the Korea government (MEST) (No. 2009-0063570)

REFERENCES

- [1] T. H. Baron, "Natural Orifice Transluminal Endoscopic Surgery", *British Journal of Surgery*, Vol. 94, No.1, pp. 1 – 2, 2007
- [2] L. L. Swanstrom, M. Whiteford, and Y. Khajanchee, "Developing Essential Tools to Enable Transgastric Surgery", *Surgical Endoscopy*, Vol. 22, pp. 600 - 604, 2008.
- [3] Sohail N Shaikh and Christopher C Thompson, "Natural orifice transluminal surgery: Flexible platform review", *World Journal of Gastrointestinal Surgery*, Vol.2, No. 6, pp. 210 – 216, 2010
- [4] A. Faraz and S. Payandeh, "Synthesis and Workspace Study of Endoscopic Extenders with Flexible Stem", *Journal of Mechanical Design*, Vol. 119, pp. 412 – 414, September, 1997
- [5] Peter Berkelman and Ji Ma, "A Compact Modular Teleoperated Robotic System for Laparoscopic Surgery", *The International Journal of Robotics Research*, Vol. 28, No. 9, pp. 1198 – 1215, September, 2009
- [6] Frederick Van Meer, Alain Giraud, Daniel Esteve, and Xavier Dollat, "A Disposable Plastic Compact Wrist for Smart Minimally Invasive Surgical Tools", *Proceedings of the 2005 IEEE/RSJ International Conference on Intelligent Robots and Systems*, Alberta, pp. 919–924, 2005.
- [7] Daniel J. Abbott, Chris Becke, Richard I. Rothstein, and William J. Peine, "Design of an Endoluminal Notes Robotic System", *Proceedings of the 2007 IEEE/RSJ International Conference on Intelligent Robots and Systems*, pp. 410 - 416, San Diego, CA, USA, Oct 29 – Nov 2, 2007.
- [8] Jienan Ding, Kai Xu, Roger Goldman, Peter Allen, Dennis Fowler, and Nabil Simaan, "Design, Simulation and Evaluation of Kinematic Alternatives for Insertable Robotic Effectors Platforms in Single Port Access Surgery", *Proceedings of The 2010 IEEE International conference of Robotics and Automation*, pp. 1053 – 1058, Anchorage, Alaska, USA, May 3-8, 2010.

Swing-up and LQR stabilization of rotary inverted pendulum

Minho Park, Yeoun-Jae Kim and Ju-Jang Lee

*Department of Electrical Engineering
Korea Advanced Institute of Science and Technology (KAIST)
Daejeon, Republic of Korea
(Tel : 82-42-350-5432; Fax : 82-42-350-5432)
(cyrano@kaist.ac.kr)*

Abstract: In this paper, we considered swing-up and LQR stabilization of rotary inverted pendulum. A DC motor rotates a rigid arm. At the end of the rigid arm, joint is attached and a pendulum is suspended. Two encoders check the degree of the rigid arm and pendulum every 0.5ms. This paper proposes a modified bang-bang control which swings up a pendulum fast and safe. In order to solve the stabilization problem, this paper used linear quadratic regulator. When the user gives a large disturbance to the pendulum and when the pendulum loses its position, the pendulum quickly recovers to upright position. Experimental results showed that the proposed bang-bang controller and LQR controller can stabilize a rotary inverted pendulum system within 3.0s for any starting point. The system also showed robustness from large disturbance.

Keywords: Inverted pendulum, Swing-up, Linear Quadratic Regulator

I. INTRODUCTION

Inverted pendulum has been a great test bed for decades to deal with the control problems. Inverted pendulum has nonlinear characteristics and are not difficult to analyze systems near the equilibrium point. For these reasons, a lot of researchers used this tool to verify their ideas.

Furuta proposed rotary inverted pendulum which has a direct-drive motor as its actuator source and a pendulum attached to the rotating shaft of the motor [1]. Yoshida proposed an energy-based swing-up control and Åström showed that swinging up a pendulum by energy control is very effective and if acceleration of the pivot is sufficiently large, the pendulum can reach upright position in one swing [2], [3].

In recent years, a lot of control theories have been applied to control inverted pendulum such as fuzzy control [4], adaptive PID control [5], iterative impulsive control [6], neural network control, sliding mode control and other various control methods.

Most papers concentrated on how to swing-up the pendulum and how to stabilize it to upright position. In this paper, we will also deal with situations after the pendulum was stabilized. The user applied large disturbance to a stabilized pendulum which pushed the pendulum to an unstable position. Once the pendulum lost its position, the controller returns it back to stable position quickly. We adjusted the parameters of LQR controller by simulations and experiments.

This paper is organized as follows. In section II, design and kinematics of rotary inverted pendulum by [1] will be introduced. Section III, IV discusses swing-up strategy and LQR controller. Controllers are switched properly by control laws. Experimental results are shown section V. Conclusions are in the last section.

II. ROTARY INVERTED PENDULUM

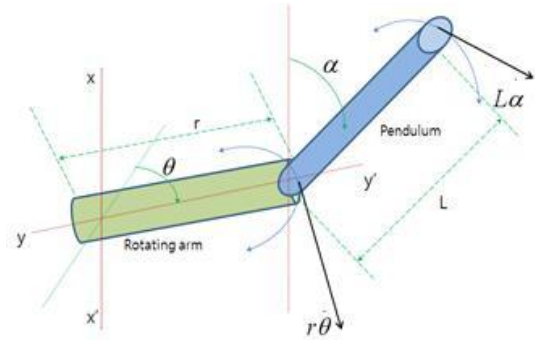


Fig. 1. Sketch of the rotary inverted pendulum

The above figure shows a sketch of the rotary inverted pendulum [1]. To use the Euler-Lagrange dynamic equation,

$$\frac{d}{dt}\left(\frac{\partial L}{\partial \dot{\theta}}\right) - \left(\frac{\partial L}{\partial \theta}\right) = T, \quad \frac{d}{dt}\left(\frac{\partial L}{\partial \dot{\alpha}}\right) - \left(\frac{\partial L}{\partial \alpha}\right) = 0 \quad (1)$$

we need to get the kinetic and potential energy. Assuming that mass of the rotating arm is M and the mass of pendulum is m . The kinetic energy of this system is

$$\begin{aligned} K_{net} &= K_{arm} + K_{pen} \\ K_{arm} &= \frac{1}{2} I \dot{\theta}^2 = \frac{1}{6} M r^2 \dot{\theta}^2 \\ K_{pen} &= \frac{m}{2L} \int_0^L \{ (r\dot{\theta})^2 + (l\dot{\alpha})^2 + 2r\dot{\theta}l\dot{\alpha} \cos \alpha \} dl \\ &= \frac{1}{2} m (r\dot{\theta})^2 + \frac{1}{6} L^2 m \dot{\alpha}^2 + \frac{1}{2} L m r \dot{\theta} \dot{\alpha} \cos \alpha \end{aligned} \quad (2)$$

A rotating arm's potential energy is zero, so the net potential energy of system is

$$P_{net} = P_{pen} = mg \frac{L}{2} \cos \alpha \quad (3)$$

Putting (2) and (3) to Euler-Lagrange equation (1), we can get two equations of motion.

$$\begin{aligned} L &= K_{net} - P_{net} \\ T &= \left(\frac{1}{3} Mr^2 + mr^2 \right) \ddot{\theta} + \frac{1}{2} mL(\ddot{\alpha} \cos \alpha - \dot{\alpha} \sin \alpha) \quad (4) \\ 0 &= \frac{1}{3} mL^2 \ddot{\alpha} + \frac{1}{2} mL \ddot{\theta} \cos \alpha - \frac{1}{2} mgL \sin \alpha \end{aligned}$$

The table below shows a specification of SRV02 with ROTPEN.

Table 1. Specification of inverted pendulum

Parameter	Definition	Value	Units
r	Rotating arm length	20	cm
L	Pendulum length	35	cm
m	Pendulum mass	0.128	kg
M	Rotating arm mass	0.278	kg

III. SWING-UP STRATEGY

Swing-up strategy is giving 90% of maximum torque to the opposite direction of pendulum speed when the pendulum heads near the ground. It is a very simple strategy and it works if motor's torque is enough.

However, if a pendulum being pushed by a user lost its position, it could revolve very fast. If a pendulum's speed is high, then swing-up control laws gives acceleration to the pendulum. When acceleration and speed are increased, LQR controller couldn't hold it anymore. This can makes the pendulum rotates all the time and it may cause malfunction of a motor.

To prevent this problem, we need to modify the control laws. We introduce the weighting factor ω , which decides the working range of swing-up controller. Because encoders give α and θ every 0.005sec, we can get pendulum's speed easily. ω decreases when the pendulum's speed is high and vice versa. A motor operates if α located between $-210 < \alpha < -150$ degrees, and ω changes according to the speed of the pendulum. Output torque is 90% of maximum torque multiplied by ω . By trial and error, if $\dot{\alpha}$ is faster than 900(deg/sec), the pendulum revolves. Therefore we determined ω as follows.

$$\begin{aligned} \omega &= 1 \quad \text{for } |\dot{\alpha}| < 600(\text{deg/sec}) \\ \omega &= 3 - \frac{|\dot{\alpha}|}{900} \quad \text{for } 600 \leq |\dot{\alpha}| (\text{deg/sec}) \end{aligned} \quad (5)$$

Modified control law slowly shuts down the motor when the pendulum's speed is too high. It also operates

the motor in the opposite direction when $\dot{\alpha}$ is extremely high. Overall, this controller is same as the bang-bang controller when $\dot{\alpha}$ is in the normal range.

If you change the working range of swing-up controller, ω should be reconsidered.

IV. LQR STABILIZATION

When the swing-up controller brings the pendulum to the range between -30 degrees and 30 degrees, the LQR controller will operate. We can linearize (4) near the equilibrium point ($\alpha = 0$). For convenience, we set the auxiliary variables as shown in the equations below.

$$\begin{aligned} a_1 &= \frac{1}{3} Mr^2 + mr^2, a_2 = \frac{1}{2} mL, a_3 = \frac{1}{3} mL^2, a_4 = \frac{1}{2} mgL \\ \ddot{\theta} &= \frac{a_2 a_4 - a_3 T}{a_2^2 - a_1 a_3}, \quad \ddot{\alpha} = \frac{a_1 a_4 - a_2 T}{-a_2^2 + a_1 a_3} \end{aligned} \quad (6)$$

By (6), we make the state-space representation:

$$\begin{aligned} \theta &= x_1, \dot{\theta} = x_2, \alpha = x_3, \dot{\alpha} = x_4 \\ \begin{bmatrix} \dot{x}_1 \\ \dot{x}_2 \\ \dot{x}_3 \\ \dot{x}_4 \end{bmatrix} &= \begin{bmatrix} 0 & 1 & 0 & 0 \\ 0 & 0 & \frac{a_2 a_4}{a_2^2 - a_1 a_3} & 0 \\ 0 & 0 & 0 & 1 \\ 0 & 0 & -\frac{a_1 a_4}{a_2^2 - a_1 a_3} & 0 \end{bmatrix} \begin{bmatrix} x_1 \\ x_2 \\ x_3 \\ x_4 \end{bmatrix} + \begin{bmatrix} 0 \\ -\frac{a_3}{a_2^2 - a_1 a_3} \\ 0 \\ \frac{a_2}{a_2^2 - a_1 a_3} \end{bmatrix} T \end{aligned} \quad (7)$$

After digitizing (7) with 2 kHz, the system changes to

$$x(k+1) = \Phi x(k) + \Gamma u(k) \quad (8)$$

The system (7) is unstable but controllable. Therefore by using linear quadratic regulator, we can make it stable. LQR minimize the object function

$$\begin{aligned} J &= \frac{1}{2} \sum_{k=0}^{n-1} [x^T(k) Q_1 x(k) + u^T(k) Q_2 u(k)] \\ &+ \frac{1}{2} x^T(N) Q_0 x(N) \end{aligned} \quad (9)$$

and its control law is

$$\begin{aligned} u(k) &= -K_{\infty} x(k) \\ K_{\infty} &= (Q_2 + \Gamma^T S_{\infty} \Gamma)^{-1} S_{\infty} \Phi \end{aligned} \quad (10)$$

where

$$\begin{aligned} S_{\infty} &= \Phi^T [S_{\infty} - S_{\infty} \Gamma R^{-1} \Gamma^T S_{\infty}] \Phi + Q_1 \\ R &= Q_2 + \Gamma^T S_{\infty} \Gamma \end{aligned} \quad (11)$$

We want to settle α and θ as fast as possible. Q_2 is just 1 and Q_1 is

$$Q_1 = \begin{bmatrix} 10 & 0 & 0 & 0 \\ 0 & 1 & 0 & 0 \\ 0 & 0 & 50 & 0 \\ 0 & 0 & 0 & 1 \end{bmatrix} \quad (12)$$

which emphasize α and θ . After calculate (10) and (11), we can finally get K_∞ .

V. EXPERIMENTAL RESULTS

Controllers discussed in section 3 and 4 are used for these experiments. We used SRV02 with ROTPEN.

1. Swing-up and small disturbance

At the start, the pendulum is located at -180 degree. After the pendulum is stabilized, the user push it to the left and to the right. This changes alpha by almost 20 degrees but not enough to make the pendulum fall down.

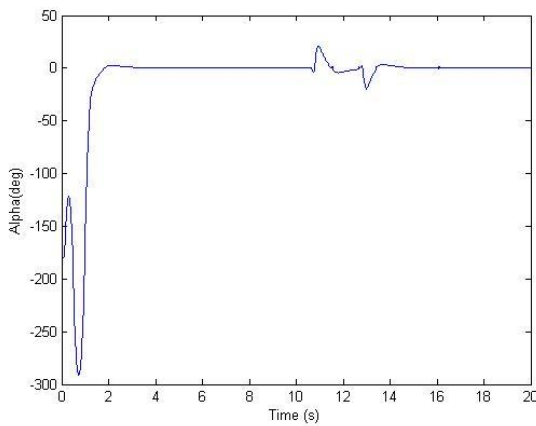


Fig. 2(a). Angle of a pendulum

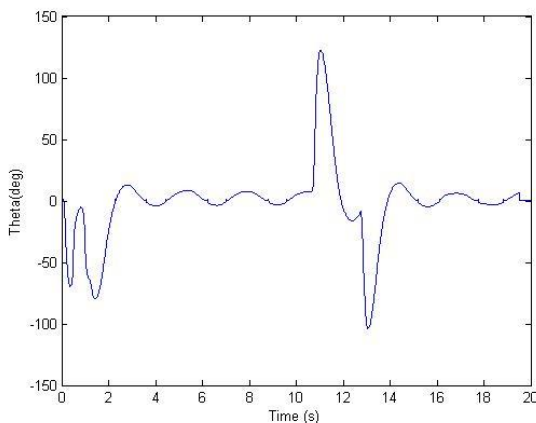


Fig. 2(b). Angle of rotating arm

Fig. 2(a) and Fig. 2(b) show the first experiment result. A pendulum swung to upright position in 2 seconds. Between 10 ~ 14 seconds, the user applied disturbance to the left and right. The pendulum head was moved about 20 degrees and the rotating arm was

moved more than 100 degrees but the controller was able to recover their position quickly. This shows that both controllers work correctly.

2. Large disturbance

This time, the user will apply a large disturbance which can make the pendulum fall down to the bottom. We will show that the controller is still able to move it back to upright position.

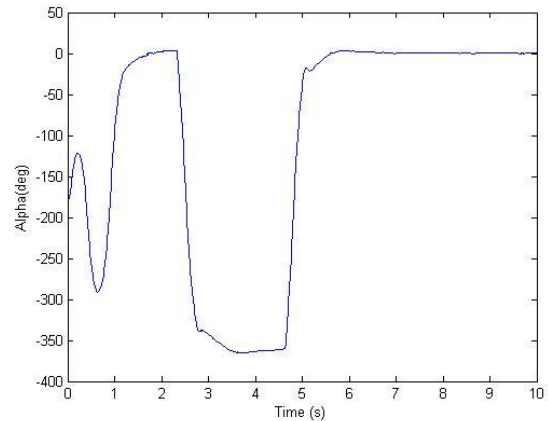


Fig. 3(a). Angle of a pendulum

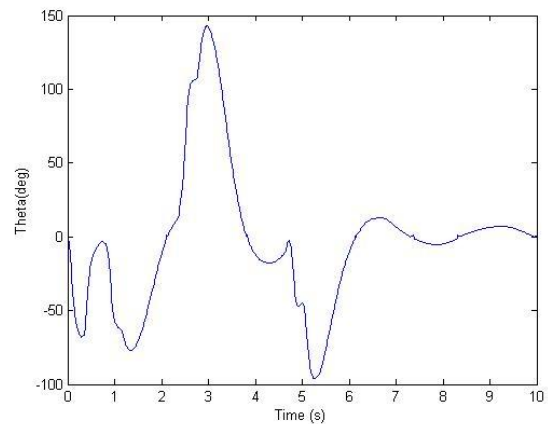


Fig. 3(b). Angle of a rotating arm

Fig. 3(a) and Fig. 3(b) shows the second experiment result. In the figures, 0 and 360 degrees represent same angle. Between 2 and 3 seconds, the pendulum fell down but recovered to the upright position right away. Between 4 and 5 seconds, user applied disturbance to the opposite direction and it still operated.

VI. CONCLUSION

In this paper, the modified bang-bang controller and LQR controller worked successfully. The pendulum showed convergence and achieved robustness from the large disturbance. Swing-up time was less than 3.0s and the whole recovery process worked immediately.

REFERENCES

- [1] K. Furuta, M. Yamakita and S. Kobayashi (1991), Swing Up control of Inverted Pendulum. IECON'91, pp. 2193-2198.
- [2] K. Yoshida (1999), Swing-up control of an inverted pendulum by energy based methods. Proceedings of the American control conference, pp. 4045-4047.
- [3] K. J. Åström, K. Furuta (2000), Swinging up a pendulum by energy control. Automatica, vol. 36, no. 2, pp. 287-295.
- [4] J. Krishen and V.M. Becerra (2006), Efficient fuzzy control of a rotary inverted pendulum based on LQR mapping. IEEE International Symposium on Intelligent Control, pp. 2701-2706.
- [5] T. C. Kuo, Y. J. Huang and B. W. Hong (2009), Adaptive PID with Sliding Mode Control for the Rotary Inverted Pendulum System. Advanced Intelligent Mechatronics, pp. 1804-1809.
- [6] Z. Wang, Y. Chen and N. Fang (2004), Minimum-Time Swing-up of A Rotary Inverted Pendulum by Iterative Impulsive Control. Proceedings of the 2004 American Control Conference, vol. 2, pp. 1335-1340.
- [7] N. Muskinja and B. Tovornik (2006), Swinging up and stabilization of a real inverted pendulum. IEEE Transactions on Industrial Electronics, vol. 53, no. 2, pp. 631-639.

Intelligent Information Retrieval System

Young Im Cho

Dept. of Computer Science, Univ. of Suwon, San2-1, Wau-ri, Bongdam-eup, Hwaseong, Gyeonggi-do
(Tel : 82-31-229-8214; Fax : 82-31-229-8281)
(ycho@suwon.ac.kr)

Abstract: In this paper, we propose a multi agent based information retrieval system in digital library. We propose a new algorithm for each multi agent module in detail. Each module is for personalized information retrieval. In the future, we have to apply to a real situation for proving.

Keywords: Information retrieval, Multi agent system, Agent platform

I. Introduction

Recent developments of the internet and network technologies evoke the technical change of the data processing from conventional centralized and local processing system to the distributed processing system. Many studies have been actively carried out in a distributed processing environment by using agent systems for efficient network management. Multi agent systems promote the efficiency in solving problems by cooperating among agents. Also, each agent independently manages its own tasks by dividing a whole work into smaller units and assigning them to each agent. There are many application areas in the real world, using the multi agent systems. One of these areas is the digital library system. This is a library developed to replace the conventional library, in order to serve information from databases on the web to users according to the development of computers and the related fields.

University of Michigan Digital Library (UMDL) [1, 2] is one of the most famous agent-based digital library systems. Agents in UMDL autonomously use their resources through negotiation among them. Also, the UMDL is very flexible for updating the library system when a new agent needs to be added. As another famous agent-based digital library, Green Stone Digital Library (GSDL) [3] was developed by New Zealand Digital Library project team. The GSDL provides a novel method for organizing information using the open source digital library [4, 5] and making it useful over the internet. McNab et al. [6] improved the open source digital library system by proposing a flexible protocol for communicating between an interface server and a search engine. Their system is suitable for distributed computing environment. Also, Witten et al. [7] improved the functionalities of finding, collecting, and organizing information in the GSDL for the distributed environment.

Even though most conventional digital library systems provide the convenient life to users for searching and managing information, a hot issue has been paid attention

to many researchers. It is that their search results include undesired results because of no information of users' profile. Thus, users have to establish the directories in users' personal computer for developing personalized digital library. In order to solve the problem, the personalized digital library systems have been developed. Bollacker et al. [8] introduced a personalized CiteSeer digital library system which is an automatic paper search system. The system can track and recommend the similar papers whose topics are very relevant, using the content-based relatedness measures [10]. Torres et al. [9] improved the performance of the automatic paper search system by developing the hybrid recommender which is the combination of user-based collaborative filtering method [11] and content-based filtering method [12].

The personalization is done by analyzing the topic of papers. In this case, the papers whose topic is not relevant to the queried keywords request by a user but contents are relevant to them are not recommend. In order to solve the problem, we consider the abstracts in the papers for providing a personalized paper search list according to the user's behavior on the papers and the relevance among keywords in the abstracts.

Also, another problem the multi agent-based digital library systems have is that users themselves should visit all possible search servers one by one. To overcome the problem, we propose a new platform of multi agent digital library system which is mobile search system. Users do not need to visit all possible search servers with the same query by using the new platform. Our system automatically visits to all possible search servers when user requests a query. In this case, the scheduling of visiting the search servers is needed. Also, the negotiation for the results searched from the servers needs to be made for complicated situations such as the duplicated search results from multiple servers. Also, our personalized paper search algorithm builds user's individual relevance network from analyzing the appearance frequencies of keywords in the searched papers. The relevance network is personalized by providing weights to the appearance frequencies of

keywords according to users' behaviors on the searched list, such as "downloading," "opening," and "no-action." Also, we enable interaction among multi agents by developing an artificial negotiation algorithm.

In the experimental section, we demonstrate our method using 100 faculties' search information employed in the University of Suwon. Also, the performance of our method is compared with that of the conventional paper search system by surveying the satisfaction of users for both systems. In addition, we analyze the searching speed of our system to show both the advantage and disadvantage of our mobile-based searching system.

II. Proposed Multi Agent-based Platform for Information Retrieval

A digital library serves a lot of information on-line. The advantages of digital libraries over conventional libraries are user friendly, on-site service, and accessibility. However, in case of not having standardized platform, the search of heterogeneous information from digital libraries may be hard, or impossible in some cases. To solve the problem, we develop a mobile multi agent-based digital library system using DECAF. The 'mobile' means that agents autonomously move a server to a server without user's interference. The mobile multi agent-based digital library system can eliminate unnecessary and duplicate information stored in Internet or DB. Also, existing digital libraries do not have or learn about the user's information. It causes unnecessary or useless information for the user to appear in the searched results. To solve the problem, we propose a mobile multi agent-based personalized digital library system (MAPS). MAPS provide the personalized search list from users' usage history. The overall structure is in Fig.1.

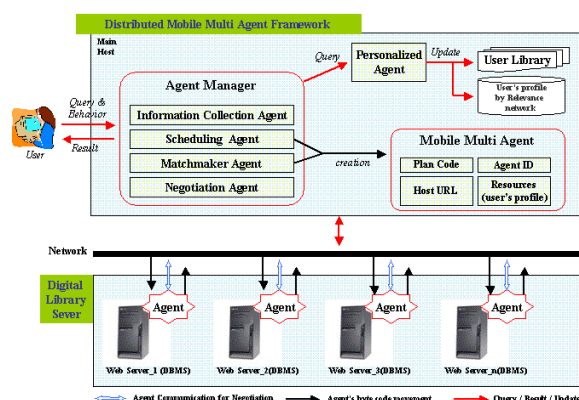


Fig.1 Overall Structure

Once a user requests a query with keywords, Agent Manger (AM) in DMMAF receives the query through the Matchmaker Agent and prepares the user's profile because the search results are obtained by the user's profile. Scheduling Agent determines the order of the agents' visit to the digital library server. The documents are collected from an agent's visit to web servers (DBMS) according to the scheduled order. Digital Library Server (sub host) accepts the agents by defined port, agents approach the DBMS of web servers. During the agent visiting, Negotiation Agent customizes the collection at each web server by eliminating duplicate documents with its previously visited web servers via a network. Each visit is done in company with the Mobile Multi Agent (MMA). The attributes of MMA includes the plan code, agent ID, host URL, and resources (user's profile). The plan code is the agent's task generated by Scheduling Agent. The agent ID is the unique number of each agent, which is generated by Matchmaker Agent. The host URL is the address to return. The resource is the user's profile. Personalization Agent provides the user a personalized search list from the negotiated documents according to the user's profile. Then, Information Collection Agent shows the final searched results to user through the user interface (UI).

DMMAF is a proposed agent framework for distributed environment in this paper. DMMAF has five components such as Agent Manager, Plan Editor, ANS, MMA, Transfer Protocol.

Agent Manager receives a user's query, creates agents, and controls the agents' operations. Matchmaker Agent communicates between Matchmaker Agent and UI. Also, Matchmaker Agent creates agents according to the schedule generated by Scheduling Agent. Scheduling Agent searches the optimal path to visit servers and informs it to the plan editor in DECAF. The plan editor creates the plan codes. Information Collection Agent sends the final searched results to the user through UI. Negotiation Agent removes the duplicated results through KQML communication language among MMAs. Agent Name Server creates the MMA and saves the multi agents' record about creation and deletion information of each MMA. The transfer protocol of the MMA is to encrypt and decrypt the agent byte code, plan code, user profile, and resources. Byte codes which are sent through network are doing the parsing process. MMA visits the host having user keyword and user profile. MMA negotiates with other agents using negotiation algorithm and search the DB.

The proposed negotiation algorithm in Negotiation Agent is explained in detail as seen in Fig. 2.

```

/* improved negotiation algorithm of MMA */
Switch(one of 5 relations) { /* relation_name(sender, receiver) */
case 1: Add_R(Ai_Mi, Aj_Mj)
/* (i≠j), Ai=agent, Mi=method */
while(Aj_Mj is finished)
no-operation (Ai-Mi); break;

```

3

```

case 2: Compensate_R(Ai_Mi, Aj_Mj)
    Ai_Mi and Aj_Mj are operated in real situation
    by call(inference) function;
    Inference() is from user profiles or user information repository;
    break;
case 3: Replace_R(Ai_Mi, Aj_Mj)
    Aj_Mj=Ai_Mi;
    break;
case 4: Contradict_R(Ai_Mi, Aj_Mj)
    Aj_Mj=Aj_Mj;
    break;
case 5: Activate_R(Ai_Mi, Aj_Mj)
    if wait(Aj_Mj) then awake(Aj_Mj) and restart;
    break;
default:
}

```

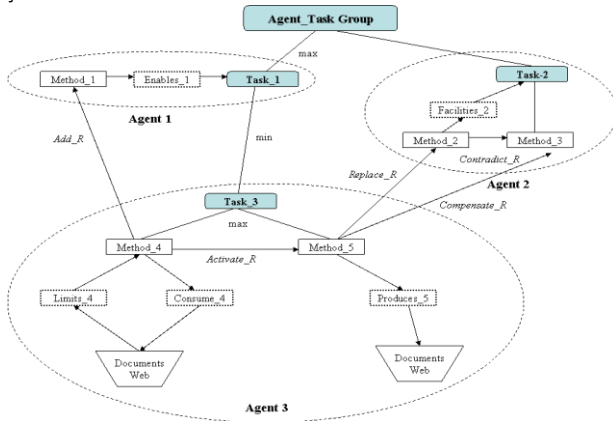


Fig.2 Negotiation method among MMA

Agent_Task Group assigns Task_1, Task_2, and Task_3 to Agent 1, Agent 2, and Agent 3 respectively. The tasks are automatically decomposed into methods, and the agents execute the assigned tasks by the methods. There are five types of relationships among methods. *Add_R* is the add relationship, i.e., adding the result of a method to that of other methods. *Activate_R* is the relationship making the running method keep running continuously. *Compensate_R* is the relationship that compensates the results of methods if needed. *Replace_R* replaces the results of receiving methods with those of sending methods. *Contradict_R* ignores the results of receiving methods. Also, there are lots of relationships between methods and tasks and between methods and resources, such as *Enable*, *Facilitate*, *Produce*, *Consume*, and *Limits*. In the negotiation algorithm, if the agents in the same level take different actions, then *max* operation operates to produce the output of the agents. Otherwise, *min* operation is operated.

Fig. 3 is the flow chart of the negotiation process between two MMAs. Fig. 4 is the schematic of the negotiation mechanism of information exchange between two MMAs by KQML protocol.

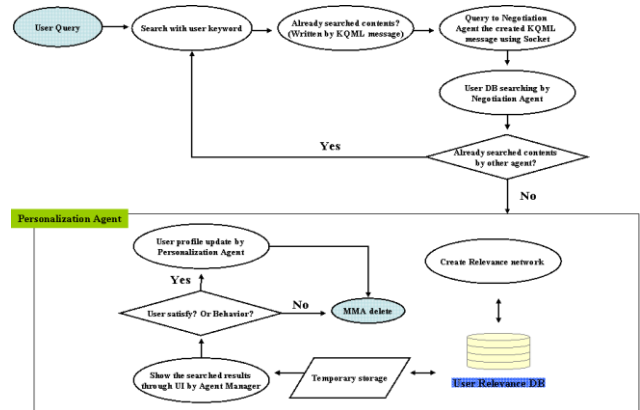


Fig.3 The flowchart of the negotiation process between two MMAs

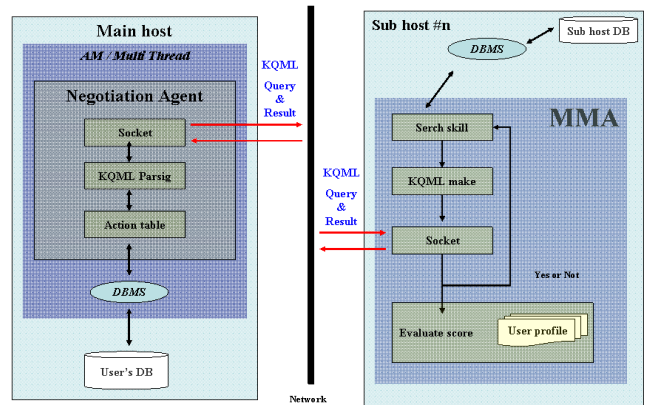


Fig.4 The negotiation mechanism of information exchange between two MMAs by KQML protocol

The information about MMA moving is transferred in byte stream type surrounded by the defined tag of the KQML protocol. The byte stream is parsed according to the defined tag and the clone byte of the byte stream is transferred to the next web server. The detailed algorithm of the moving MMA is the followings.

```

receive( Socket s ) {
    InputStream inputStream = new InputStream();
    inputStream = new InputStream( s.getInputStream() );
    while( ( tempByte = inputStream.read() ) != End ) {
        Parsing()
        if( nextHost == null ) {
            try{
                ByteCode[index++] = (byte)tempByte ;
            } catch( ArrayIndexOutOfBoundsException ) {
                System.out.println("Termination of all host visiting");
                Notify to Agent Manager about Job termination;
            } // end of try
        } else if ( Exist sending socket to next host? ){
            nextHostSocket.write( (byte)tempByte );
        }
    } // end of while
} // end of receive()

```

The algorithm of parsing process is the followings.

```

parsing( InputStream in ) {
  while( ( tempByte = in.read() ) != End ){
    if( Start character of Tag? ){
      inputStream mark();
      Read byte until the Tag length;
      Identification the Tag type;
      if( fail the defined TagSearching ){
        Reset according to marked Stream index;
        Process according to current Tag type;
      } else {
        Branch or activate according to the current Tag and the
        identified next Tag;
      }
    } else if( Ending character of Tag? ){
      if( nTag inTag = false;
        else Process according to current Tag type; }
    } // end of while
  } // end of parsing()
}

```

III. Conclusion

In this paper, we proposed a platform of a mobile-based personalized paper search system. By using our system, users do not need to visit all possible search servers with the same query by using the new platform. Also, our system provides users' personalized search list by building user's individual relevance network from analyzing the appearance frequencies of keywords in the searched papers.

We have to apply this algorithm to the real system in the future for proving of this algorithm.

REFERENCES

- [1] W. P. Birmingham, An Agent-based Architecture for Digital Libraries, D-Lib, July 1995.
- [2] W.P. Birmingham, E.H. Durfee, T. Mullen, "The Distributed Agent Architecture of the University of Michigan Digital Library", AAAI Spring Symposium on Information Gathering from Heterogeneous, Distributed Environments, AAAI Press.
- [3] <http://www.greenstone.org/cgi-bin/library>.
- [4] C. Logoze and D. Fielding, "Defining Collections in Distributed Digital Libraries", D-Lib Magazine, vol. 4 no. 11, 1998, <http://www.dlib.org/dlib/november98/logoze/11logoze.html>.
- [5] C.M. Bowman, P.B. Danzing, U. Manber, and M.F. Schwartz, "Scalable Internet Resource Discovery: Research Problems and Approaches", Communications of the ACM, vol. 37, no. 8, pp. 98-107, 1994.
- [6] R.J. McNab, H. Witten, and S.J. Boddie, "A distributed Digital Library Architecture Incorporating different index styles", Proceedings of IEEE Advances in Digital Libraries, pp. 36-45, 1998.
- [7] H. Witten, R.J. McNab, S.J. Boddie, and D. Bainridge, Greenstone, "A Comprehensive Open-Source Digital Library Software System", Proceedings of Fifth ACM Conference on Digital Libraries, pp. 113-121 2000.
- [8] K.D. Bollacker, S. Lawrence, C.L. Giles, "A System for Automatic Personalized Tracking of Scientific Literature on the Web", Proceedings of ACM Conference on Digital Libraries, pp. 105-113, 1999.
- [9] R. Torres, S.M. McNee, M. Abel, J. A. Konstan, and J. Riedl, "Enhancing Digital Libraries with TechLens", ACM/IEEE-CS Joint Conference on Digital Libraries, pp. 228-236, 2004.
- [10] K. Bollacker, S. Lawrence, and C.L. Giles, "An Autonomous Web Agent for Automatic Retrieval and Identification of Interesting Publications", Proceedings of The Second International Conference on Autonomous Agents, pp. 116-123, 1998.
- [11] W.P. Lee and T.H. Yang, "Personalizing Information Appliances: A Multi-agent Framework for TV Program Recommendations", Expert Systems with Applications, vol. 25, no. 3, pp. 331-341, 2003.
- [12] T. Kamba, K. Bharat, and M.C. Albers, "An Interactive Personalized Newspaper on the Web", Proceedings of International World Wide Web Conference, pp. 159-170, 1995.
- [13] J.R. Graham and K.S. Decker, "Towards Distributed, Environment Centered Agent Framework", Appearing in Intelligent Agents IV, Agent Theories, Architectures, and Languages.
- [14] Lesser, Victor; Horling, Bryan; Klassner, Frank; Raja, Anita; Wagner, Thomas; and Zhang, Shelley. "BIG: An Agent for Resource-Bounded Information Gathering and Decision Making", Artificial Intelligence Journal, Special Issue on Internet Information Agents, vol. 118, no. 1-2, Elsevier Science, pp. 197-244. May 2000.
- [15] John Graham, Victoria Windley, Daniel McHugh, Foster McGeary, David Cleaver, and Keith Decker, "Tools for Developing and Monitoring Agents in Distributed Multi Agent Systems", Workshop on Agents in Industry at the Fourth International Conference on Autonomous Agents, Barcelona, Spain, June, 2000.
- [16] Baeza-Yates, Ribeiro-Neto, Modern Information Retrieval, Addison-Wesley, 1992

A Study on Real-time Face Verification and Tracking with Segmented Common Vector

Dong-kyu Ryu, Min-ho Park and Ju-Jang Lee

*Department of Robotics Program
Korea Advanced Institute of Science and Technology (KAIST)
Daejeon, Republic of Korea
(Tel : 82-42-350-8032; Fax : 82-42-350-5432)
(E-mail: ghostdz@naver.com)*

Abstract: Recently, There has been much interest in automatically face recognition and tracking in many areas such as Intelligent Robotics, Military, Intelligent Transport System (ITS) and Smart device applications. However so far there has not been simultaneously face tracking and verification algorithms, so we propose the method in simultaneously verifying and tracking face which is segmented common vector method and It is theoretically based on discriminative common vector method and Fisher's LDA. The algorithm trains segmented and shift face image to obtain new face vector. The Gram-Schmidt orthogonalization is employed to calculate the orthogonal projection matrix. Our goal can be defined as the identification of individuals and real-time face tracking from video images simultaneously, so we use segmented common vector for two kind of different task at the same time.

Keywords: Discriminative Common Vector, Fisher's LDA, Gram-Schmidt orthogonalization.

I. INTRODUCTION

In computer-vision research area, there has been much demand in verification of human face in video and photo images due to intelligent robotics, military, smart phone and surveillance system. The problem of face verification can be defined as finding the identification of test faces from sample face images which was previously learned, however there are many complex problem in this task. For example, face data has numerous changeable factors such as 3-D pose, hair style, make up, and facial expression. In addition to these can be varied due to lighting, background, and scale changes. Thus there are many researches solving face verification problem as follow.

For face recognition, Harr-like feature and AdaBoost algorithm of Viola and Jones is very famous in face recognition. It is very fast and has high-rate accuracy [1]. In face identification tasks, the verifying face has many hard problems, so it is very important to extract common factors from various data sets for face identification.

To do this, eigen face of Turk and pentland is introduced, and this method uses Principal component analysis (PCA) which is used to find the best set of projection directions in the sample space. From here, the projection directions are called the eigen faces which is vector set having common factors. [2]

After proposed eigen face, several research have been more performed. The Linear Discriminant Analysis (LDA) method is proposed to overcome the limitations of the eigen face method. This method can find projection directions that on one hand maximize the distance between samples of different face and on the other hand minimize the distance between the sample of the alike face [3]. But, in face recognition task, we can't directly calculate projection directions, because dimension of the image samples is very larger than the number of samples which is known as the "small sample size problem"

To solve this problem, Chen proposed the Null space method based on the modified Fisher's LDA [4]. The Null space method is based on the modified Fisher's Linear Discriminant criterion,

$$J_{MFLD}(W_{opt}) = \arg \max_w \frac{|W^T S_B W|}{|W^T S_T W|} \quad (1)$$

For this method, all image samples are first projected onto the null space of S_W and then result in a new within -class scatter that is a zero matrix.

In the special case where $W^T S_W W = 0$ and $W^T S_W W \neq 0$, for all $w \in R^d \setminus \{0\}$, and then a better criterion is given as

$$J(W_{opt}) = \arg \max_{|W^T S_W W|=0} |W^T S_B W| = \arg \max_{|W^T S_W W|=0} |W^T S_T W| \quad (2)$$

The Discriminative Common Vector Method was proposed to extract the common properties of classes in the training set by eliminating the differences of the

samples in each class, it gives more efficient algorithm to find Null space of within-class scatter matrix [5]. In the special case where $W^T S_w W = 0$ and, $W^T S_w W \neq 0$ for all $w \in R^d \setminus \{0\}$, and then a better criterion is given as

$$J(W_{opt}) = \arg \max_{|W^T S_w W|=0} |W^T S_B W| = \arg \max_{|W^T S_w W|=0} |W^T S_T W| \quad (2)$$

To find the optimal projection vectors w in the null space of S_w , we have to project the samples onto the null space of S_w and then obtain the projection vectors by performing PCA.

II. Segmented Common Vector

1. Definition of Segmented Common Vector

We propose the simultaneously face verifying and tracking method which is segmented common vector method. It is theoretically based on discriminative common vector method. However this method presents that several weak classifiers can more easily solve hard problem than one strong classifier such as face tracking problem. So that we have to make several feature vector from each one sample to create various sub classifiers, before the one sample was transferred to only one face feature vector.

2. Algorithm to calculate Segmented Common Vector

A. Span new image sample vector

In this section, we account for process in making segmented common vector in detail.

To make segmented common vectors, in advance we have to make segmented image to span new face vector. The size of segmented image is usually 60~90% than original face size. The size of segmented image is saved as cell size value and it used for face tracking. We should take apart scrap images to be overlapped, because the center of face has many information such as eyes, eyebrows, nose and mouse. The segmented feature extract manner is presented as below.

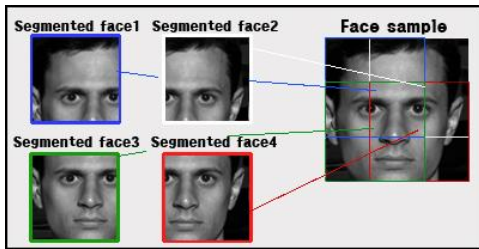


Fig.1 The Manner of Segmenting face image

In this paper, the number of segmented face feature has range from 4 to 9 features

Suppose that we have several people images, each

people becomes each classes, thus the training set is composed of C classes.

To solve real-time tracking problem, new face sample set be generated by using shift-image method.

If we have P samples in each all classes, firstly we should shift face image to 1-3 pixels in order of left, right, top and bottom. This is called shifted sample set, so we can get $N = 5 \times P$ samples. And then we take segmented samples apart this N samples.

- **Definition of sample vectors** $x_{N,S}^C$

Let $x_{m,k}^i$ be a d -dimensional column vector and C be denoted by i -th number of classes, S be denoted by k -th segment set in i -th classes and N is index of m -th sample from k -th segment set in i -th class.

The segmented face vector sets is proposed as sub-class sets which made by segmenting face images from C classes as below.

$$\text{sub class} : x_k^i = \text{span}\{x_{1,k}^i, x_{2,k}^i, \dots, x_{N,k}^i\} \quad (3)$$

$$i\text{-th Class} : x^i \supset x_1^i, x_2^i, \dots, x_S^i$$

So we can have $N \times S$ samples from existing one class and $C \times S$ sub-classes which has N samples, then the number of total samples become $M = N \times S \times C$ in training set. Suppose that $d > M - C$.

In this case, S_w , S_B , and S_T are newly defined as

$$S_w = \sum_{i=1}^C \sum_{k=1}^S \sum_{m=1}^N (x_{m,k}^i - \mu_k^i)(x_{m,k}^i - \mu_k^i)^T, \quad (4)$$

$$S_B = \sum_{i=1}^C \sum_{k=1}^S (\mu_k^i - \mu)(\mu_k^i - \mu)^T, \quad (5)$$

and

$$S_T = \sum_{i=1}^C \sum_{k=1}^S \sum_{m=1}^N (x_{m,k}^i - \mu)(x_{m,k}^i - \mu)^T = S_w + S_B \quad (6)$$

B. Span difference space

To span difference spaces B , we choose any one of the face vectors from the k -th segment sets in i -th class. Difference space is made by subtraction of vector.

$$b_{m,k}^i = x_{m+1,k}^i - x_{1,k}^i, \quad (7)$$

$$(i = 1, \dots, C, k = 1, \dots, S, m = 1, \dots, N-1)$$

The $b_{m,k}^i$ is difference vector from k -th segment in i -th class, so difference space is defined as B_k^i .

The complete difference subspace is represented as below

$$B = B_1^1 + B_2^1 + \dots + B_S^1 + B_1^2 + \dots + B_S^C \\ = \text{span}\{b_{1,1}^1, \dots, b_{N-1,1}^1, b_{1,2}^1, b_{2,2}^1, \dots, b_{N-1,S}^C\} \quad (8)$$

To obtain orthonormal basis vectors $\beta_1, \dots, \beta_{M-C}$, the difference vectors is orthonormalized by using the Gram-Schmidt-orthogonalization procedure.

Its Algorithm is explained as below.

C. Algorithm of learning Segmented Common vector

Step 1: Find the linearly independent vectors $b_{m,k}^i$ that span the difference subspace

$$B = \text{span}\{b_{1,1}^1, \dots, b_{N-1,1}^1, b_{1,2}^1, b_{2,2}^1, \dots, b_{N-1,S}^C\}$$

Step2: Apply the Gram-Schmidt orthogonalization procedure to obtain an orthonormal basis $\beta_1, \dots, \beta_{M-(C \times S)}$ for B

Step 3: Choose any sample from each class and project it onto B to obtain common vectors by using

$$U = [\beta_1 \quad \dots \quad \beta_{M-(C \times S)}], \quad P = UU^T$$

$$x_{k,com}^i = \bar{P}x_{m,k}^i = x_{m,k}^i - Px_{m,k}^i = x_{m,k}^i - UU^T x_{m,k}^i,$$

Step 4: Find the difference vectors that span B_{com}

$$b_{k,com}^i = x_{k+1,com}^i - x_{1,com}^i, \quad i = 1, \dots, C, \quad k = 1, \dots, S$$

Step 5: Apply the Gram-Schmidt orthogonalization to obtain an orthonormal basis $\tilde{\omega}_1, \dots, \tilde{\omega}_{(C \times S)-1}$ for B_{com}

Step 6: The projection matrix $W = [\tilde{\omega}_1, \dots, \tilde{\omega}_{(C \times S)-1}]$

be used to obtain feature vectors in

$$\psi_{m,k}^i = W^T x_{m,k}^i, \quad m = 1, \dots, N, \quad i = 1, \dots, C$$

We call the feature vectors $\psi_{m,k}^i$ segmented common vectors from k-th segmented in i-th class and they are used for classification of segmented face images.

4. Classifier of Segmented Common Vector

For classification, various classification methods can be used. However, in this special case which is real-time tracking, more fast method is needed to reduce calculation time. In this paper, Euclidean distance method is employed for fast classification.

After calculating projection matrix W , the segmented common vectors $\psi_{m,k}^i$ is spanned from samples $x_{m,k}^i$. Also mean of segmented common vector is calculated as below.

$$\text{mean} \psi_k^i = \frac{1}{N} \sum_{m=1}^N \psi_{m,k}^i = \frac{1}{N} \sum_{m=1}^N W^T x_{m,k}^i, \quad (9)$$

$$(i = 1, \dots, C, \quad k = 1, \dots, S, \quad m = 1, \dots, N)$$

Each sub classes of segmented face sets have mean of segmented common vector which is a classifier of this method.

III. EXPERIMENTAL RESULTS

To classify the identification of face, each 10 samples of 7 people is learned by using OPENCV library. The samples is fragmented by 4 pieces and changed as segmented common vectors. The mean shift tracking algorithm [6] is used to track position of face, however segmented common vector is employed to calculate target candidates instead of color histograms which is usually adopted in face tracking. The experiments have been processed with a 3GHz Pentium PC and 2GB of memory under windows. Our implementation of tracker is made from visual studio 2008 environment.

The goal of experiments is to show how well our method tracks the optimal position of face. The tracked face has been changed by position and 3-D pose of face. The face sequence of 1200 frames is shown as below.



Fig.3 The experimental result

The experiment result shows that this method well follow the face of human, and face classification is done as class 1 from 7 classes. The tracker is very tough at various pose and has high precision of position face. The frame rate generally shows speed of algorithm, and, in this experimental, the frame rate of video was 14.5 per seconds. The tracker is very robust at illumination, since proposed method is not based on color feature, so it is also strong point of proposed method. The tracker can efficiently and successfully handle non-rigid and fast moving objects under different background.

IV. CONCLUSION

From experiments, the segmented common vector tracker successfully estimated position of face in complex background and can verify the identification face from several faces which was learned before.

However, the boundary of estimation should be needed for avoiding measurement error about position and size. Since proposed method is not based on color feature, the tracker is very robust at illumination and the tracker can efficiently and successfully handle non-rigid and fast moving objects under similar background. Our implementation of segmented common vector algorithm has proven to be robust to changes in shape, occlusion and color in experiment. However there is limitation of learning peoples, because $d > M$ should be guaranteed in Null-space method.

REFERENCES

- [1] PAUL VIOLA and MICHAEL J. JONES (2004) "Robust Real-Time Face Detection", International Journal of Computer Vision 57(2), 137-154
- [2] M. Turk and A.P. Pentland, (1991) "Eigenfaces for Recognition", J. Cognitive Neuroscience, vol. 3, no. 1, pp. 71-86
- [3] P.N Belhumeur, J.P. Hespanha, and D.J. Kriegman, (1997), "Eigenfaces vs. Fisherfaces: Recognition Using Class Specific Linear Projection", IEEE Trans. Pattern Analysis and Machine Intelligence, vol. 19, no. 7, pp. 711-720
- [4] L.-F. Chen, H.-Y.M. Liao, M.-T. Ko, J.-C. Lin, and G.-J. Yu, (2000) "A New LDA-Based Face Recognition System Which Can Solve the Small Sample Size Problem," Pattern Recognition, vol. 33, pp. 1713-1726
- [5] Hakan Cevikalp, Marian Neamtu, Mitch Wilkes and Atalay Barkana (2005) "Discriminative Common Vectors for Face Recognition". IEEE TPAMI vol.27
- [6] Dorin Comaniciu Visvanathan Ramesh and peter Meer (2000) "Real-Time Tracking of Non-Rigid objects using Mean shift", IEEE CVPR

Social Modification using Implementation of Partial Agency toward Objects

Hiroataka Osawa* and Seiji Yamada**

**JST PRESTO, Honcho 4-1-8, Kawaguchi, Saitama, Japan*

(Tel : 81-48-226-5601; Fax : 81-48-226-5651)

(Email osawa@nii.ac.jp)

***National Institute of Informatics, Hitotsubashi 2-1-2, Chiyoda-ku, Tokyo, Japan*

(Tel : 81-3-4212-2000)

(Email seiji@nii.ac.jp)

Abstract: This paper discusses what kind of partial agency is implementable for objects to bring more suitable agencies toward human agent interaction. Human beings have an ability to inform fellows about our intention, internal states and requirements using verbal talk, gestures, attitudes, timings and other representations. These representations can keep our belief that we are sufficient agents mutually. The robots and virtual agent also mimic these representations, reproduce as if they have an agency, and interact with them. However, their agencies are sometimes too excessive compared to its task. This mismatch leads high cognitive load toward users and brakes interaction consequently. This defect prevents to apply human agent interaction method toward application field. The authors consider that our agency is constructed by multiple features and dividable. If these features are selectable, we can choose more proper design for virtual agents, robots, machineries, daily home appliances according to their traits. The authors categorized these agencies in several group and discusses about what elements achieves these features. The paper also shows what method can extract these features from human being.

Keywords: Anthropomorphization, Human Agent Interaction, Human Robot Interaction, Human Interface

I. INTRODUCTION

Today's human computer interaction field is widely developed by several different background researchers. Various robotics technologies like actuators and sensors gives the researches on informatics field the access method toward real-world. On the other hand, rapid development of computer gives mechanics engineers more sophisticated control method. Ubiquitous, human-robot interaction, interfaces is occupied several researchers. Challenges are tried in several fields.

These studies which related in human computer interaction are conducted by two different policies. One policy is called extension of human's ability. Figure 1-A shows the brief image of this policy. Technologies are accepted as extended third arm and extended machines interfaces. For example, glass type augmented reality (AR) technology gives users more visible information. If someone gets the glass type AR technology, s/he simply gets upgraded eyes. Tele-operation is another kind of extension about our own bodies. If we can manipulate actuators in another location according to our will, these actuators behave as third arms or legs for us.

Another policy places social buffer between users and system and convert several input/output using this buffer (shown in Fig. 1-B). The buffer is called agent [1]. The agent uses several metaphors like internal states, emotions, requirements to inform users. This method is supported by several cognitive science results, the

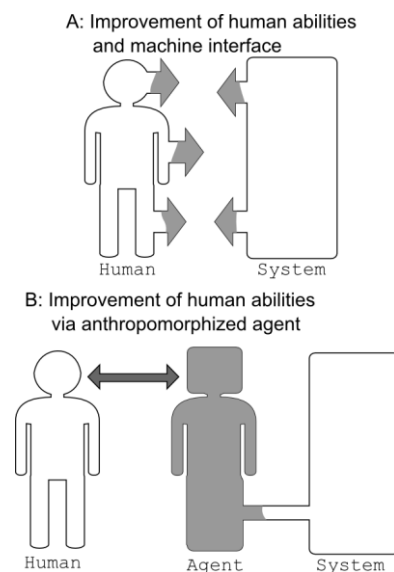


Fig.1. Difference between Extension and Agent Technologies in human computer interaction

background of artificial intelligence and enthusiasm toward lifelike agent. In this paper, we used human agent interaction as covering word of this ideology. We call human agent interaction as HAI. We also call HRI (human robot interaction) as a HAI in the real world.

HAI method has advantages to inform several complex states toward users, especially for implying intentions and internal states by metaphors. For example, several states of video recorder, computers are possible to represent as its emotional states. If the object behaves with sad emotion, it suggests some wrong treatment is ongoing. On the other hand, if the object represents happy emotion, it multiply implies that the transaction is in order. The human-like social stance can bring restrictions toward determination of meanings. Ishida et al showed how conversation system improves quality by using several roles in the conversation.

Our study focuses to extend the application field of human-agent interaction toward more broad area using separation of agency. In this paper, we defines agency as any kind of representations that evocate user's intentional stance described in Dennett's work [2]. If we select and add agency separately according to required task of the system, system's ability will be expand. Figure 2 and 3 show how our approach extends human agent interaction. Figure 2 shows normal human agent interaction method. An agent is placed between the system and a user. It wraps system's input and output using social channels like attitude, emotion, gestures, and joint attentions. In our study, these channels are divided and applied partially according to the task the machineries required. Figure 3 shows the examples of partial agency method. If a machine runs under a location based task like a vacuum shown in Fig.3-A, it uses location related social channels. An attitude can emphasize which direction is informed. This works as a restriction of the representation. Joint attention has more sophisticated role in human-human interaction, but it also works to show a clue of positioned place [3]. On the other hand, emotions and gestures work more in the situation that a machine does not have an actual movement but have complex states like a printing machine shown in Fig.3-B. These social channels can inform several states to a user using metaphors.

This paper is organized as follows. Section 2 refers what kind of studies are conducted psychological field and HAI. Section 3 discusses what kind of problems disturbs the usage of agent toward application field.

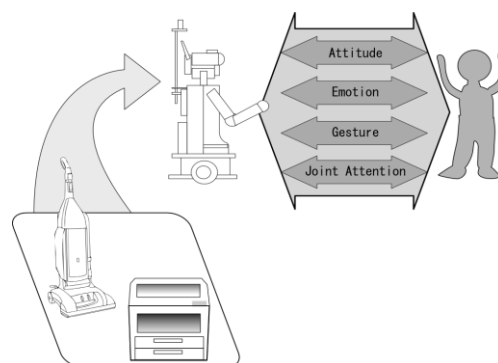


Fig.2. Previous Agent System

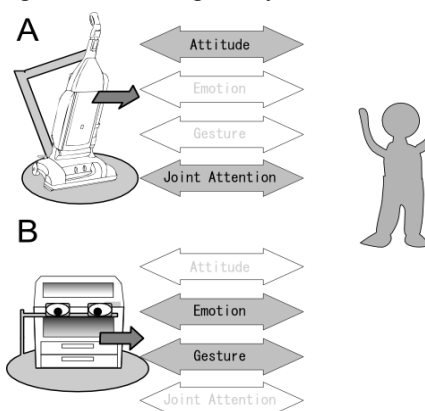


Fig.3. Implementation of Partial Agency

Section 4 shows the detail notion of partial agencies based on section 2 and 3. It also discusses how to extract partial agency from interactions by several implementations. Section 5 concludes our method.

II. STUDIES ABOUT USEFULNESS OF AGENT AND AGENCIES

Psychological studies and human agent studies have been revealed social features like emotions, gestures and attitudes that useful to improve machineries' interactions. We think that these features are important elements to construct agency. In this section, we examine how we have used elements of ourselves.

Emotions are one of the most important parts to evoke agency toward users. Human beings and other animals express emotions. One of the earliest studies about emotion is conducted by Darwin [4]. He compared several animals' expressions and discusses its influences. Paul Ekman categorized human faces with 6 types, happy, sad, angry, fear, disgust and surprise [5]. Robert Levenson organized another model for evaluation [6]. Even if the emotions do not be told just from abstracted appearances, these abstracted models are proposed and commonly used in virtual agent and communication robot. The utilization of emotions is

proposed several times. Rosalind Picard proposed effective computing that uses emotional cues as input and output of the system [7].

Gesture is another good example that is used to realize agencies. It is commonly used to support our conversations [8]. We use some gestures unconsciously, and other gestures intentionally. Mental space studies in psychological field describe how these gestures transfer information from one to another. When we hear spatial information like a feature location, we map the instructed position into our mental space. Psychologists analyzed this situation using blended mental space. The concept of blended mental space is proposed by Fauconnier [9]. Liddell suggests that mental space is also applicable to analyzing gestures [10]. The blended mental space helps to analyze the meaning of users' conversations using the virtual space of each user. For example, if you used the right hand to point a dial on wall and left hand for turning gesture, it is not instructing users to turn a dial in front of them. It instructs the user to blend these two gestures into the same mental space to turn one dial one way.

These human like features are selected from human activities. They have enough ability to make agency toward the object. Several human robot interaction and HAI studies uses these result for the improvement of interaction [1].

III. PROBLEMS BETWEEN HUMAN AGENT INTERACTION AND APPLICATION

Above section shows what kind of basic knowledge about human beings support HAI technologies. However, agent based interaction is sometimes not used in the real application instead of their usefulness. In this section, we discuss about several defects of an agent and HAI studies.

1. Compatibility problems

Agents' various modalities prevent to organize standard knowledge from comparing each study. Rene Descartes noted the importance "to divide each of the difficulties under examination" in his work [11]. This policy is basement of Science. However, HAI and HRI sometimes fails to order this requirement because the results of these studies are strongly related to the agent/robot themselves and difficult to discuss separately. For example, a result based on agent A may not be possible to be applied to another study using agent B, because of their different attributes.

2. Excessive anthropomorphization and agency

The researchers have a trend to hypothesize that anthropomorphism sometimes attracts people. However over-anthropomorphism sometimes distracts people from the interaction. This problem is based on three reasons.

First reason is mismatch of the agency. If the agent expresses the interaction that implies complex agency, the user estimates much more agency from the behavior. Adaptation gap study also noted this problem in the interaction [12].

Second problem is the mismatch of relationship between task and agents. Even if an agent acts is attractive and enough to express the appropriate agency, the mismatch of appearance still harm an interaction. For example, bug type robots are not appropriate for cooking task because it implies dirty image toward users. Robot designer Sonoyama illustrated several mismatch of the design of robots in his book [13].

Last problem is disgust toward anthropomorphization itself. Overwhelming feeling of social connection leads too much cognitive load toward users. Epley et al showed their study that people requires anthropomorphic attitude when they are disconnected by social connections [14]. This result indicates that if one is satisfied for social connection, additional anthropomorphic representation becomes unwanted exaggeration.

IV. HOW TO EXTRACT AGENCIES

In Section 3, we discussed what kind of shortcomings interfere the smooth applying of agency toward interface. To solve above problems, we simply propose the separated evaluation of agency using separated anthropomorphic devices. Each feature for an agency is constructed by each device. Extraction of the agency is achieved by subtraction of the interface from the previous agent equipped full of agencies.

Figure 4 shows what is achieved by our method. Figure 4-A describes the kind of features could be extracted by separation of agency. Each feature has been discussed in previous studies referred on Section 2. Previous HAI studies already researched what kind of agency is useful [1]. However, we can evaluate each feature simultaneously and separately if we divide each agency. As a result, we can evaluate more precise arrangements of agencies according to each user's tendency and attributes (like Fig. 4-B). Our previous study suggested that female users like anthropomorphic

representation more than male participants [15]. If a user does not want too much anthropomorphization, we can decrease features and can adjust most appropriate agency according to the user. Figure 5 shows some implementation according to our method. Figure 5-A shows partial embodiment. Eyes and arms are attached to a vacuum because a vacuum requires precise positioning toward users during cleaning. On the other hand, eyes and arms are removed from Fig. 5-B. Instead of rich appearances, 2 axis motors are implemented to represent to show an attitude because a microwave oven does not require precise positioning.

V. CONCLUSION

We considered that our agency is constructed by multiple features and dividable. If these features are selectable, we can choose more proper design for virtual agents, robots, machineries, daily home appliances according to their traits. We categorized agencies referring previous studies and discussed about what elements are required. We also proposed what method can extract these features from human being using several devices.

ACKNOWLEDGEMENT

This work was supported by JST PRESTO program.

REFERENCES

- [1] Yamada S, Kakusho K, Ono T, Ogawa K, Nakano Y, Komatsu T, Imai M, Osawa H, Komatsu K, Terada K, Kojima H, Nakagawa K, Kiyokawa S, Ueda K, Takeuchi Y (2008), Designing space between human and robot (in Japanese)
- [2] Dennett DC (1987), The Intentional Stance, The MIT Press
- [3] Tomasello M (1995), Joint attention and social cognition. In: C. Moore, & P. Dunham, editors. Joint attention: its origins and role in development, pp. 103–130
- [4] Darwin C (1872), The Expression of the Emotions in Man and Animals, 1872
- [5] Ekman P (1999), Handbook of Cognition and Emotion, John Wiley & Sons, Ltd.
- [6] Levenson RW (1999), The intrapersonal functions of emotion. Cognition and Emotion, 13, 481-504.
- [7] Picard R (1997), Affective Computing, MIT Press
- [8] Morris D (1995), Bodytalk: The Meaning of Human Gestures, Crown
- [9] Fauconnier G (1995), Mental Spaces, MIT Press
- [10] Liddell S (1996), Spatial representations in discourse: comparing spoken and signed language, Lingua 98: pp. 145-167
- [11] Descartes R (1637), Discourse on the Method, <http://www.gutenberg.org/ebooks/59>

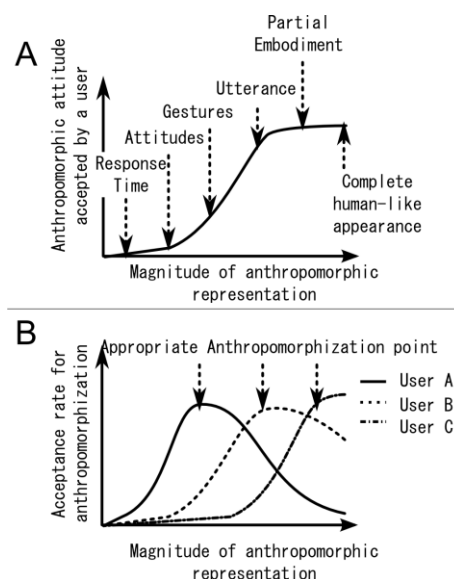


Fig.4. (A) Separated anthropomorphic elements. (B) Appropriate anthropomorphization according to each user.

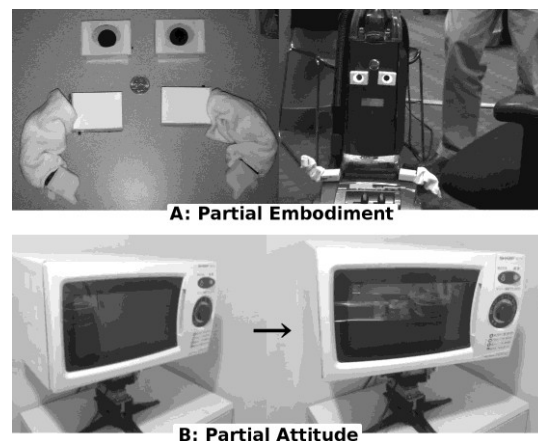


Fig. 5. Partial embodiment and partial attitude

- [12] Komatsu T, Utsunomiya A, Suzuki K, Ueda K, Hiraki K, Oka N (2005), Experiments toward a mutual adaptive speech interface that adopts the cognitive features humans use for communication and induces and exploits users' adaptation, International Journal of Human-Computer Interaction, vol.18 (3), 243-268.
- [13] Sonoyama T (2007), Introduction for Robot Design (in Japanese)
- [14] Epley N, Waytz A, Cacioppo JT (2007), On Seeing Human: A Three-Factor Theory of Anthropomorphism, Psychological Review, 2007, Vol. 114, No. 4, 864-886
- [15] Osawa H, Mukai J, Imai M (2007), Display Robot" - Interaction between Humans and Anthropomorphized Objects, 16th International Symposium on Robot and Human Interactive Communication, Vol.16, pp. 451-456, Jeju, Korea, 2007.8

Inducement of Attention to Agent through Averting Gaze from the Other

M. Suzuki and Y. Takeuchi

*Graduate School of Informatics, Shizuoka University
3-5-1 Hamamatsu, Shizuoka 432-8011, Japan
(Tel: 81-53-478-14551; Fax: 81-53-478-1455)
(gs10029@s.inf.shizuoka.ac.jp / takeuchi@inf.shizuoka.ac.jp)*

Abstract: In the study of social relationship established through mutual gaze, averting one's gaze from another's, which is treated as an act of refusing social relationship, has not been discussed as an act that intends to engage social relationship. Our study treats averting one's gaze from another's as a cue to engage social relationship, and deals with the ambiguity of this act and its effects on social affiliation. In particular, the effects on social affiliation are caused by the difference of contexts in which the act is performed.

Keywords: Eye contact, Gaze, Averting the eyes, Social relationship

I. INTRODUCTION

Intelligent agents such as humanoid/android robots, virtual embodied agents, and conversational systems are becoming more common in daily life, increasing the chances for people to socially interact with them.

Human social interaction centers on concern for other people. In the beginning of the interaction, people perceive another's existence; then, they observe his/her personality or mental state through behavior and/or appearance. Accordingly, the social interaction between human and agent also requires mutual awareness of the other's existence. In general, intelligent agents have an original "body" and appearance different from humans. Therefore, it is sometimes difficult for people to observe and perceive the agent's characteristics or inner condition. This is why the early stage of human-agent interaction is initiated by verbal communication or social roles previously defined by the developer of the agent. These interactions, however, are generally not natural because people do not spontaneously interact with the agent. People merely interact with the agent following given information concerning the agent or a defined social role that people have to play. In short, the human-agent interaction obviously differs from natural human interaction.

The concern for other people is the most important issue between humans in the beginning stage of interaction. Thus, how can we make others perceive our attention to them, and how can we perceive others' attention? The answer to these questions may be that

people gaze at other people to get their attention. In other words, a person who perceives another's gaze can expect that that person is trying to get his/her attention.

Although this human cognition of gaze perception could be a useful and effective means of initiating a social relationship between human and agent, it is difficult to achieve such an interaction. Some reasons for this result from the characteristics of an agent's gaze. In the case of a human gaze, the eyes adjust each angle of vergence to see the object in 3D vision. Accordingly, people can easily perceive another's attention to themselves. In the case of an agent, however, most visual systems do not apply such means to synthesize 3D vision. Therefore, humans cannot perceive an agent's attention even though the agent is focusing on him/her. The second reason is the Mona Lisa effect, which is the visual illusion that the eyes of the portrait follow the viewer from any vantage. The third reason involves characteristic human non-verbal expression. Human mental conditions such as emotion, will, determination, or intention are naturally expressed through facial features or the appearance of the eyes, but these expressions are vague and hard to formulate. Thus, it is difficult to make an agent express its inner conditions by eye movement.

For these reasons, we have to consider how to make people perceive an agent's attention by simple means. An agent's gaze toward a subject does not always succeed in getting its attention, which differs from the case of a human's gaze. People do not perceive attention or concern from the agent even if the agent looks at and

focuses on them. However, a human easily supposes that an agent has something of an embarrassed attitude toward him/her if the agent averts its gaze immediately after making eye contact.

In this paper, we examine whether people perceive attention or concern from an agent when they are refused eye contact. We also discuss natural means of social engagement between human and agent based on the result of a psychological experiment.

II. AVERTING ONE'S GAZE FROM ANOTHER'S

Once two persons look at each other and make eye contact, averting one's gaze from the other's generally indicates a twinge of self-consciousness or embarrassment. Therefore, the person who is refused eye contact normally wonders why the other person averted his/her gaze. In other words, it can be said that this gaze interaction induces one's attention to the other.

Such gaze interaction does not necessarily give an agreeable impression to the person who is refused eye contact by the other. Thus, how do people feel in the case of human-agent interaction? As described in the introduction, an agent gazing toward a subject does not always succeed in getting attention, which differs from the case of a human's gaze. People do not perceive attention or concern from the agent even though the agent looks at and focuses on them. On the other hand, we do not have any idea whether a human perceives attention or concern from an agent when the agent refuses to make eye contact. Also, we have not explored how people feel given such seemingly unsociable interaction.

III. EXPERIMENT

1. Experiment

A. Overview

In this section, the question of whether a human perceives attention or concern from an agent averting eye contact with him/her is explored through a psychological experiment. We aim to demonstrate that a human strongly presumes the agent's intentionality in such an interaction.

In this experiment, the agent, whose eyes move side-to-side in order to express eye contact and averting its gaze from a human subject, appears as a Head-Display (HD); the agent's face and eye movement are projected

onto a dummy head (Fig. 1). The agent's expression and eye movement are designed and controlled through Adobe Flash animation, which the experimenter remotely controls according to the participant's actions.



Fig. 1. Head Display

B. Settings

Three visual stimuli (agent behaviors) are displayed to the participants.

Type 1: Averting. At the start of the experiment the eyes of the agent stare into the participant's eyes, but controlled by the experimenter immediately avert the gaze upon eye contact.

Type 2: Scanning. The agent scans the scene, rather like a searchlight. Eye contact can not be established and the agent does not meet the eyes of the participant.

Type 3: Staring. The eyes of the agent look into the participant's eyes throughout the experiment.

Eighteen university students who major in informatics participated in this psychological experiment. The participants sat in front of three agents whose eye movement corresponded to each of the above types.

C. Indicators of Observation

The experimenter counts the frequency with which the participant looks at each type of agent as an indicator of behavioral response. Moreover, the participants' perceptions and impressions with regard to the agents' motions and intentionalities are investigated by a questionnaire after the experimental task.

Questions about the participants' perceptions and impressions were:

- Which agent were you most concerned with in the experiment?
- Where/What did each agent observe?
- Which agent's attention did you want to get?
- Which agent did you perceive had intentionality toward you?

D. Procedure

The procedure of this experiment is as follows.

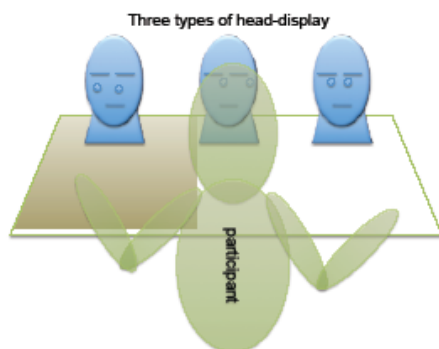


Fig. 2. Experimental settings

1. A blindfolded participant is guided to the experimental room (Fig. 2), and seated in a chair in front of the three agents.
2. The participant is given instructions by the experimenter.
3. The experimenter removes the blindfold. The experimenter keeps the participant sitting for five minutes, which is the main task of this experiment.
4. The participant answers the questionnaire.

E. Hypothesis and Predictions

To explore the following research issues, we carried out a psychological experiment:

- Does the agent averting its gaze from the human's make the human perceive the agent's attention and concern toward him/her?
- How does a human assume the intentionalities of the agent with each type of agent behavior?

In this experiment, we hypothesize that the agent's unsocial behavior of averting its gaze from the human induces attention to the agent more than the case in which the agent looks around or stares at the human.

This hypothesis will be supported by the following participant responses:

- The frequency of looking back at the agent that refuses eye contact with the participant (Type 1) is higher than the other two types of agent.
- The participants perceive more attention from the agent that refuses eye contact (Type 1) than the other two types of agent.

F. Results

Behavior and Perception

Figure 3 shows the average frequency of looking back at each type of agent. A statistical analysis indicated the main effect in the difference of agent behavior ($F(2,17)=22.32$, $p<.01$). There were also significant differences between Type 1 and 2, Type 1 and 3, and Type 2 and 3.

Figure 4 shows the participants' guess of each agent's intention of looking at them. The question was asked, "Which agent did you think would look at you?" The participants were permitted to give multiple answers. When the participant selected one of the agents, it was given a score of one. Accordingly, the participants answered most for the Type-1 agent that averts its eyes from those of the human. A statistical analysis indicates the main effect ($(F(3,17)=14.62$, $p<.01$).

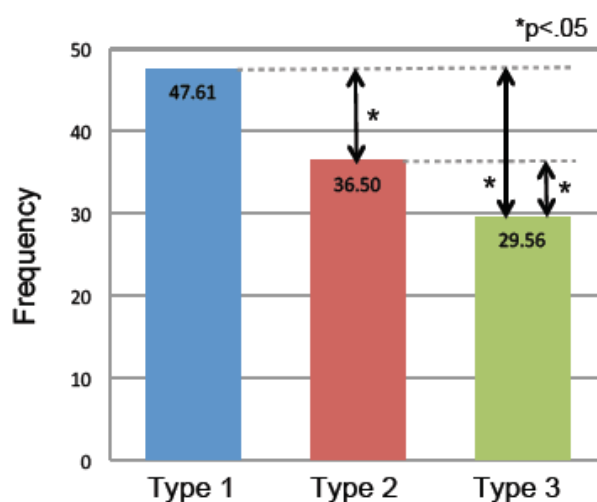


Fig.3. Average frequency of looking back at each type of agent.

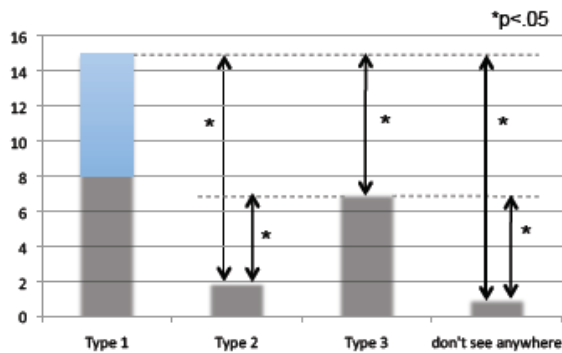


Fig.4. Participants' presumption of each agent's intention of looking them.

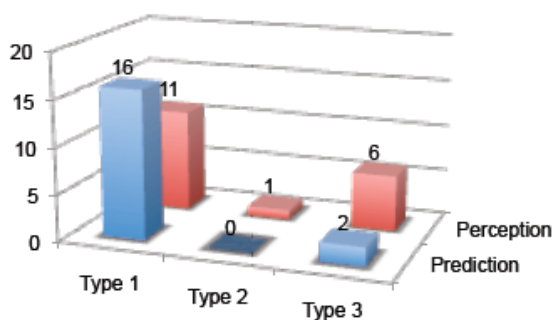


Fig. 5. Participants' perception of agent's consciousness of them.

Figure 5 shows the participants' perception of the agent's consciousness of them. The front side of the figure shows the participants' of which agent would be most concerned with them. The rear of the figure shows the participants' perception of the agent most concerned with them. It was obviously demonstrated that Type 1 was the most concerned.

Impressions

The questionnaire asked participants for their impressions based on two perspectives. One perspective was impressions of themselves from the agent's viewpoint, and the other was impressions of the agent from their original viewpoint. These are demonstrated in Figs. 6 and 7, respectively. The scores for these results are shown on a seven-degree Likert scale, which corresponded to the magnitude of agreeability for each question.

IV. CONCLUSION

The results supported the hypothesis that the agent's unsocial behavior of averting its gaze from a human

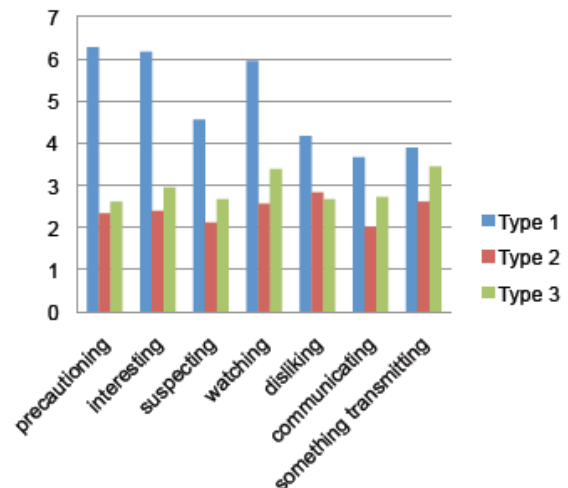


Fig. 6. Participants' impressions of themselves from the agent's viewpoint.

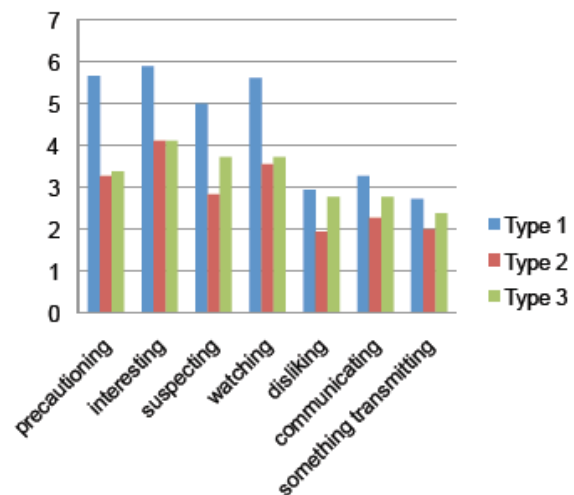


Fig.7. Impressions toward the agent from participants' original viewpoint.

induced attention to the agent more than the cases in which the agent looked around or stared at the human. These human impressions were not always positive. That the humans behavior and attitude was strongly affected by the averting of the agent's eyes provides a clue to natural human-agent interaction.

REFERENCES

- [1] Gibson, J. J. (1963), Perception of another person's looking behavior. *American Journal of Psychology* 76:386-394
- [2] Mukawa, N. (2002), Survey of Roles of Gaze in Communication: How are Intentions and Feelings Conveyed by Gaze? (in Japanese). *IEICE* 85(10):756-760

Behaviors for Getting Conscious Responses

Toshihiro Osumi*, Masato Noda*, Hirotaka Osawa**, Yuki Kuwayama*,
Kazuhiko Shinozawa*** and Michita Imai****

*Graduate School of Science and Technology, Keio University, Yokohama, Kanagawa, 223-8522, Japan
(toshihiro@ayu.ics.keio.ac.jp)

**PRESTO, Japan Science and Technology Agency, Chiyoda-ku, Tokyo, 102-0075, Japan

***ATR Intelligent Robotics and Communication Laboratories, Hikaridai, Kyoto, 619-0288, Japan

****Faculty of Science and Technology, Keio University, Yokohama, Kanagawa, 223-8522, Japan

Abstract: This paper investigates robot's behaviors to get voluntary conscious responses from users. Our final goal is to construct an asynchronous human-to-human communication mediated by a portable robot. The robot has a behavior system which makes the robot behave in response to the acquired conscious response. The system also enables the user to give the robot feedback at anytime and anywhere while the robot presents a script which an author prepared. We investigate how well the behavior system encourages the users to give the robot feedback and how much the users consider inputting the response to be meaningful. The results show that there are definite relation between response behavior and the acquisition of the conscious responses.

Keywords: Conscious response, Computer-Mediated Communication, Input and Interaction technologies

I. INTRODUCTION

In this paper, we investigate robot's behaviors to get a voluntary conscious response from users. Our final goal is to construct an asynchronous human-to-human communication mediated by a portable robot (Figure 1). The robot has an advantage over the other interface when giving user information. It can tailor the contents of the information to him/her based on his/her environment by using emotional expressions and gestures [2, 3]. In particular, the emotional and gestural expressions provide an author with the memorable way of presenting his/her view and emotion experienced at a certain place. The embodied expressions of a pointing gesture and a gaze movement also provide him/her with the exact way of presenting information related to a certain place or an object. The author-to-user communication via the robot increases the author's motivation for creating and revising the content of the interaction. In addition, the interactive presentation by the robot can prompt a user to prepare his/her response to the presented information. To substantialize the robot mediated communication, we must develop an individually-owned robot, an environment that author can create contents without an expert knowledge and a behavior system that generates robot's behaviors for presenting information and encouraging the user to give his/her response to the presentation. In this paper, we focus on the acquisition of a conscious response and investigate the effect of the robot's behaviors when getting the users responses.

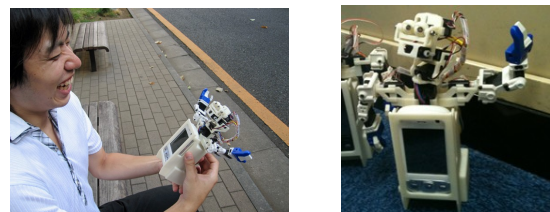


Fig. 1. Communication via the portable robot

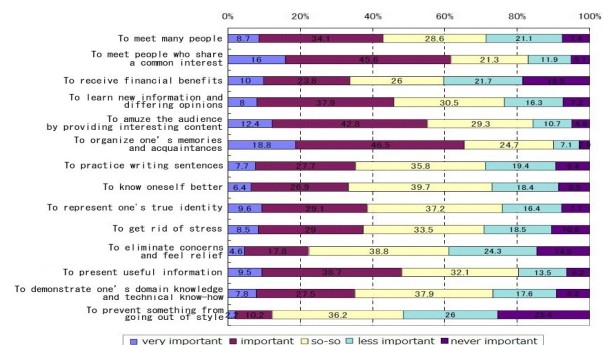


Fig. 2. Motivations for updating blogs

The style of the author-to-users communication is the common on the web. The style is that an author creates his/her original content and a PC user provides a comment after reading it. For example, blogs and social networking services have the function which is able to be posted comments about the entry as the feedbacks from users. The feedbacks are strongly linked to motivation to use the service. In Japan, more than half of users said that getting to know people who share their interests and including entries that visitors enjoyed were great motivations for them to update their blogs [5] (see Figure 2). This result suggests the significance of

feedback such as a comment, a reply and a ReTweet. Nico Nico Douga [6], a characteristic video-sharing website in Japan, has caught on with many people. In contrast to other video-sharing sites such as Youtube, Nico Nico Douga allows comments on specific time code and can superimpose the comments directly on the video when showing the commented video frames. The feedbacks on the web are posted voluntarily and consciously from users and are not the one that a system obtains by analyzing the user's behavior of browsing or access logs.

However, many communication robots acquire feedback from a user by using sensors (e.g. cameras, touch sensors, laser range finder and other devices) or the user's choices in a scenario. The feedback is the unconscious responses of the user's behaviors. It is different from the communication services on the web acquire conscious feedback which is provided voluntarily from the user. But feedbacks by using sensors and the users' choices are insufficient for the use as the author-to-user communications, because the unconscious feedbacks do not reflect the user's impression of the presented content. To communicate with other people via a robot, the robot requires the function that can acquire voluntary conscious feedbacks from users, like the services on the web.

The design which gives users a motivation for inputting conscious feedback is necessary to acquire conscious feedbacks efficiently. Kuno et al. [1] showed that museum visitors' nodded and mutually gazed more frequently when a robot turned its head at significant points than when a robot did not. This result suggests that felicitous behavior at a relevant point establishes joint attention and arouses interest in the robot. Therefore we developed a behavior system which generates a behavior for encouraging the user to feed conscious response anytime and anywhere while the robot presents the content which an author provided. The behavior is generated in response to acquired conscious responses. The reactive behavior induces natural interaction which includes the conscious responses. We installed the system into the mobile phone based robot called "TenoriAvatar". We also conducted two experiments to observe the effects of the behaviors on the frequency and range of the conscious response and on how meaningful users thought their response was. We believe that the acquisition of the conscious response from users is necessary in the author-to-user communication via a robot or an agent.

The study provides a fundamental knowledge to acquire conscious responses.

II. EXPERIMENT

1. Apparatus

In our experiments, we used a phone based portable robot called "TenoriAvatar" (Figure 1), a modified version of "BlogRobot" [4]. TenoriAvatar is HTC Corporation's mobile phone HTC P3600, upon which a robotic head and robotic arms are installed.

In the experiments, we used simple linear scenarios which were composed only of sentences for utterances and tags for gestures and images. Thus, the scenarios had no branches. When a scenario is selected, TenoriAvatar loads the scenario and utters sentences in turn. If TenoriAvatar loads a gesture tag in a sentence, TenoriAvatar does the gesture associated with the loaded tag right there. The gestures come in twelve types including happy, unhappy, bye-bye, wow, and walking. In addition, when TenoriAvatar is not doing a gesture, it blinks at fixed intervals to show the system is running.

2. Behavior system

The user feeds conscious response by pushing a feed button set up on the display of the mobile phone. Only two types of conscious response can be fed: positive and negative. The arrangement of feed buttons is shown in Figure 3. The lower left button is the positive feed button, and the lower right is the negative feed button. When the user sympathizes with the content or finds a content funny, s/he pushes the positive feed button. When the user does not sympathize with the content or finds the content anemic s/he pushes the negative feed button.

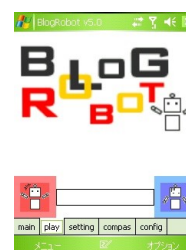


Fig.3. Arrangement of feed buttons

When the user pushes a feed button, TenoriAvatar plays the sound and stops the playback and then performs a response behavior for the fed conscious response. We believe that a break in the playback gives the user the impression that the robot responded to the

fed conscious response. The response behavior is a random combination selected from a gesture list and an utterance list that are prepared based on type of conscious response. The list consists of suitable utterances and gestures for the type of feed button. Thus, a response behavior that is suitable for the feed button that the user pushed is executed. After the response behavior, TenoriAvatar utters a sentence selected from the utterance list for restarting the playback scenario. When restarting, the scenario is played back from beginning of the line of the interrupted sentence. To prevent the same sentence from being uttered over and over, if a user already fed response at the sentence, the response behavior is not executed when s/he feeds conscious response again. Therefore, the response behavior is executed only once for each sentence. If conscious response was fed between the end of the utterance of one sentence and the start of the utterance of the next sentence, the response is contained within the sentence which was uttered at that time. In this case, response behavior is executed, but TenoriAvatar will not play back the uttered sentence and will start playing back from the next sentence.

3. Evaluation of Response Behaviors

Conscious response function attempts to help the user to feel meaningful in input conscious response. We conducted two experiments to observe the effects on the frequency and range of conscious response inputs and on how meaningful users thought their response was. The playback time for each scenario was about two minutes, and each scenario had about ten gesture tags. Each participant held TenoriAvatar in one hand at about 50-cm distance from them. Before the experiment, the participants received a briefing from an experimenter on TenoriAvatar and on the response input method. Participants did not receive an explanation about the response behavior, regardless of the function of the response behavior.

A. Evaluation of Frequency

The experiment on conscious response input frequency was conducted at our university festival. Fifty-eight Japanese people (10 - 59 years old) who came to view our booth participated. Participants played back the scenario with TenoriAvatar with or without response behavior and fed conscious response. The content of the scenario was about expressing a sentiment about the robot, the device, and TenoriAvatar, which were displayed in our booth.

An experimenter handed TenoriAvatar with or without the response behavior to a participant, and the participant played back the scenario about our booth and fed conscious response. An experimenter randomized participants to receive TenoriAvatar with or without it, and to the extent possible, kept the number of experiments with or without the response behavior the same.

B. Evaluation of Motivation

The experiment on conscious response input motivation was conducted at our university laboratory. Fourteen Japanese engineering students (20 - 29 years old) participated. Participants played back the two scenarios with and without the response behavior. We investigated the effect of the response behavior on the motivation to provide conscious response input from the questionnaires that participants filled out after the experiment.

Participants played back two scenarios that explained a college cafeteria and a local character in Japan with TenoriAvatar. One scenario was with the response behavior, and the other was with only sound. To avoid the order effect, the order of scenarios with the response behavior and with only sound was changed for every participant. The order of the scenarios remained the same. After the playbacks, the experimenter had the participants answer questionnaires about their impressions of the first and second playbacks. Evaluation items were about how meaningful they felt their input conscious response was, pleasantness of the process, and whether they would use continuously in seven levels.

III. RESULTS

Figure 4 plots the mean number of conscious responses in the experiment on the response input frequency. In the response behavior condition, the mean number of positive feedback responses was 9.19, negative feedback was 2.90, and the sum total was 12.09. In only the sound condition, the mean number of positive feedback responses was 7.50, negative feedback was 1.04 and the sum total was 8.54. There were no significant differences in mean number of positive feedback responses ($p=.44$) or in the total conscious feedback ($p=.18$). There was a significant difference in the mean number of negative feedback responses ($p=.02$).

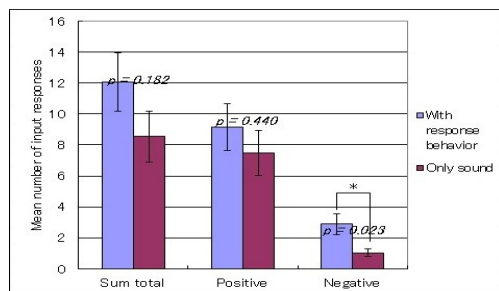


Fig.4. Mean number of input responses with SE

Figure 5 shows the mean number of sentences in which positive or negative feedback was fed. In the response behavior condition, the mean number of sentences was 7.38. In only the sound condition, the mean number of sentences was 5.29. There was a difference in the mean number of sentences in which feedback was fed ($p=.07$).

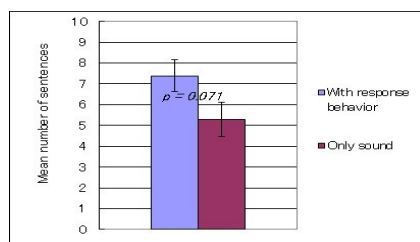


Fig.5. Mean number of sentences with SE

Figure 6 shows the questionnaire results from the experiment on conscious response input motivation. In the response behavior condition, the average mark of meaningfulness in conscious response input was 5.53, pleasantness was 6.00, and will use continuously was 5.13. In only the sound condition, the average mark of meaningful in conscious response input was 3.20, pleasantness was 4.98 and will use continuously was 4.27. There was a significant difference in meaningfulness ($p=.01$) in conscious response input and pleasantness ($p=.02$). There was no significant difference in will use continuously ($p=.14$).

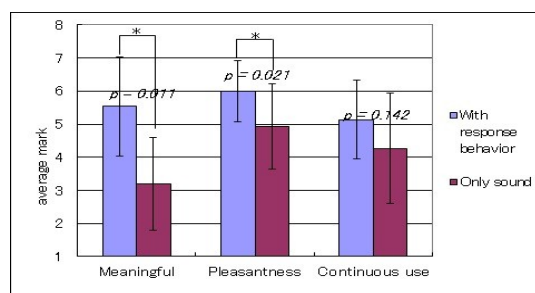


Fig.6. Questionnaire results with SD

VI. DISCUSSION AND CONCLUSION

This paper reported our investigation of the effect of response behaviors on the acquisition of the conscious responses. The results of the first experiment indicated that the existence of the response behavior enhanced the acquisition of negative feedback. These data indicate the possibility of increasing the number of fed conscious responses. Without response behavior, many users pressed the negative feedback button only once. With response behavior, the negative feedback button was pressed more than two times. The result indicates that the input of negative feedback is not done casually like positive feedback is, and response behavior makes it easier to input negative feedback. From the results of the second experiment, the existence of response behavior had an effect on significance and enjoyment. We believe that the result indicate that frequency of acquiring conscious responses motivates the scenario author.

The results indicate that there are definite relation between response behavior and the acquisition of the conscious response. In obvious, the methods using only positive and negative feedback have limitations. We must therefore think of more appropriate ways to obtain conscious responses. If the robot can obtain the rich content of the conscious response, the robot can behave in a very adaptive way.

REFERENCES

- [1] Kuno, Y., Sadazuka, K., Kawashima, M., Yamazaki, K., Yamazaki, A., and Kuzuoka, H. (2007). Museum guide robot based on sociological interaction analysis. In *Proceedings of CHI '07*, 1191-1194.
- [2] Satake, S., Kanda, T., Glas, D., Imai, M., Ishiguro, H., and Hagita, N. (2009). How to Approach Humans? - Strategies for Social Robots to Initiate Interaction. In *Proceedings of HRI '09*, 109-116.
- [3] Lee, M. K., Kiesler, S., and Forlizzi, J. (2010). Receptionist or information kiosk: how do people talk with a robot? In *Proceedings of CSCW '10*, 31-40.
- [4] Osumi, T., Fujimoto, K., Kuwayama, Y., Noda, M., Osawa, H., Imai, M., and Shinozawa, K. (2009). Blogrobot: Mobile terminal for blog browse using physical representation. In *International Conference on Social Robotics*, Vol44, 96-101.
- [5] Investigation research of realities of blogs
Institute for information and communications policy
<http://www.soumu.go.jp/iicp/chousakenkyu/data/research/survey/telecom/2009/2009-02.pdf> (in Japanese)
- [6] Nico Nico Douga. <http://www.nicovideo.jp>

Cross-modal effects between gestures and words in human robot interaction

Takamasa Iio^{1,2}, Masahiro Shiomi¹, Kazuhiko Shinozawa¹, Takaaki Akimoto¹,
Katsunori Shimohara² and Norihiro Hagita¹

¹ Advanced Telecommunications Research Institute International, Kyoto, JAPAN

² Doshisha University, Kyoto, JAPAN
(Tel : 81-774-95-1405; Fax : 81-774-95-1408)
(iio@atr.jp)

Abstract: This paper reports a new finding of a phenomenon that person's gestures or words are implicitly modified by robot's gestures or words. Previous researches focused on an implicit effect of robot's gestures on person's gestures or an implicit effect of robot's words on person's words, but they did not focused on an implicit effect of robot's gestures on person's words or an implicit effect of robot's words on person's gestures. We supposed that there was such an effect as to arise between different modalities, and we defined it as a cross-modal effect. In order to verify hypotheses about the cross-modal effect, an experiment was conducted, in which a pair of a pointing gesture and a deictic word was focused on. This result showed that participants used a pointing gesture more often when a robot used a deictic word, and participants used a deictic word more often when the robot used a pointing gesture. Therefore, person's pointing gesture was implicitly modified by robot's deictic word, and also person's deictic word was implicitly modified by robot's pointing gesture. The cross-modal effect is expected to be applied to robot's dialog design to elicit comprehensible behavior from a person.

Keywords: Entrainment, Cross-modal effects, Multi-modal interaction, Human-robot interaction.

I. INTRODUCTION

Social robots that support people in daily life are expected to communicate with them in humanlike manners such as body movements or voices. That is because even people who do not use computers well could smoothly converse with the robots as if they converse with other people. For achieving natural communications, it is important to research human robot interaction [1]. One of purposes of the research is to understand how people communicate with the robots.

When a person communicates with a robot, an interesting phenomenon called entrainment often arises. This is the phenomenon that the person's gestures are synchronized with the robot's gestures or the person's words are synchronized with the robot's words as shown in Fig.1. For example, Ono et al. reported that person's gestures became similar with robot's gestures in a route direction conversation [2]. Iio et al. showed that when a person and a robot repeatedly referred to the same objects, the person tend to use the same words as the robot used [3]. By using the entrainment, a robot could implicitly elicit a certain behavior from a person. Such elicitation would make it possible for the robot to improve its recognition capability because the robot could elicit comprehensible gestures or words from the

person. Therefore, we should understand how to modify person's behavior by robot's behavior.

The effect between each similar modality like the entrainment has been researched in human robot interaction. However, we have to consider not only the effect but also the effect between each different modality because all modalities are not independent respectively but some modalities, especially gestures and words are dependent on each other [4, 5]. If there is the effect, the robot could effectively elicit a certain gesture or a word from the person by using the effect with the entrainment.

We defined the effect between different modalities as cross-modal effect. Based on the entrainment between similar modalities and the mutual dependence of gestures and words, we supposed that there was the

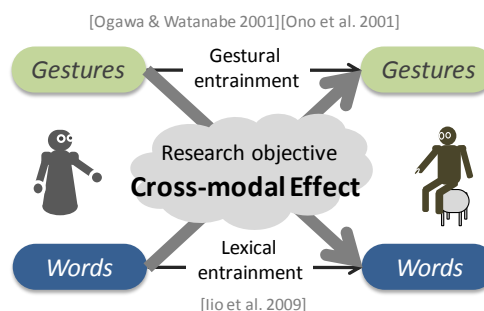


Fig.1. Entrainment and cross-modal effect.

following cross-modal effect: We assume that a gesture and a word are used together at the same time. If a robot often uses the gesture, a person would often use the similar gesture too; this phenomenon is gestural entrainment. Since the gesture tends to be used with the word, the person is also likely to use the word often. This means a cross-modal effect of the robot's gesture on the person's word. Based on the above logic, we can consider a cross-modal effect of the robot's word on the person's gestures.

In this paper, we supposed that there was the effect between different modalities. We defined it as cross-modal effect. The hypotheses about the cross-modal effect were made and verified through a laboratory experiment. Finally, a process of the cross-modal effect was discussed.

II. EXPERIMENT

1. Target gesture and word

This experiment aimed at a pair of a pointing gesture and a deictic word because they are coupled with each other. The deictic word cannot identify an object by itself; therefore they are likely to be used with a pointing gesture.

2. Experimental conversation

In order to introduce a pointing gesture and a deictic word, we employed an object reference conversation in the experiment. The conversation was as follows; the robot asked a participant to choose an object and the participant chose an object. Then, the robot confirmed the object. If the confirmation was correct, the participant indicated another object; otherwise the participant indicated the same object again.

We adopted books as the objects because books are

found in many households; moreover, books involve the various referential expressions, such as title, color, category, author and location.

3. Hypotheses

We made the following hypotheses about a cross-modal effect during the object reference conversation.

H1: When the robot uses a deictic word, the rate of his or her pointing gesture is high.

H2: When the robot uses a pointing gesture, the rate of his or her deictic word is high.

4. Conditions

We controlled robot's pointing gesture and robot's deictic word used to confirm a book. The experiment had four conditions listed in Table 1. The detail of each condition was as follows.

PD: The robot turned its face on a book and pointed at the book, saying "Sore desuka?" (In English, That one?)

P_nD : The robot only turned its face on a book but kept its arms stationary in the side of its body, saying "Sore desuka?"

PD_n : The robot turned its face on a book and pointed at the book, saying the book title.

P_nD_n : The robot only turned its face on a book but kept its arms stationary in the side of its body, saying the book title.

5. Measurement

We measured the pointing gesture rate and the deictic word rate to verify our hypotheses.

The pointing gesture rate: We counted how many times a participant did references with a pointing gesture and verified the rate is changed by the lexical factor.

The deictic words rate: We counted how many times participants did references with a deictic word and verified the rate is changed by the gestural factor.

6. Experimental environment

Fig. 2 depicts our experiment. A participant was seated in front of the robot. The robot was Robovie-R ver.2, which is a humanoid robot developed by the Intelligent Robotics and Communication Labs, ATR. There were five different books between the participant and the robot.

7. Procedure

A participant was first given a brief description of the purpose and the procedure of the experiment. We told the participant that we were developing a robot for

Table 1. The experimental conditions.

		Gestural factor	
		Pointing	No Pointing
Lexical factor	Deictic	PD	P_nD
	No deictic	PD_n	P_nD_n



Fig.2. The pictures of our experiment.

recognizing an object and would like their help in evaluating the design. Then, the participant was assigned randomly to the four conditions. A participant referred five books three times, that is to say, the participant did 15 references. Therefore, we totally obtained 90 references in each condition.

The robot was controlled remotely by an operator, that is to say, our experiment employed the Wizard of Oz method. That was because the difficulty of recognizing participant's pointing gesture and participant's voice automatically. Considering robot's recognition capability expected in the future, the operator rejected participant's references which did not pass the following rules.

- Reference by bibliographical information.
- Reference by attributions able to identify each book.
- Reference by pointing a finger at a book.

8. Participants

There were 24 participants in the experiment. They were native-Japanese-speaking university students from Kansai area. Since they were assigned randomly to the four conditions, each condition has six participants.

III RESULTS

In order to analyze main effects and interaction of the gestural factor and the lexical factor, we did the analysis of variance using chi-square distribution based on the arcsine transformation method. This analysis can test the difference between proportions of unpaired two factors.

1. Pointing gesture rate

The pointing gesture rate of each condition is shown in Fig.3. The analysis is as follows.

Main effect of the gestural factor: The pointing gesture rate of PD and P_nD was higher than that of PD_n and P_nD_n . The difference was significant ($\chi^2(1) = 11.017$, $p < 0.01$). Therefore, when the robot used a pointing gesture, participants tended to use a pointing gesture.

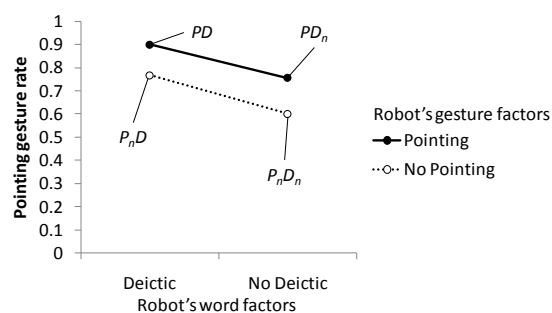


Fig.3. Pointing gesture rate of each condition.

The result says there was gestural entrainment of robot's pointing gesture on participant's pointing gesture.

Main effect of the lexical factor: The pointing gesture rate of PD and P_nD was higher than that of the PD_n and P_nD_n . The difference was significant ($\chi^2(1) = 12.719$, $p < 0.01$). Therefore, when the robot used a deictic word, participants tended to use a pointing gesture. The result says there was the cross-modal effect of robot's deictic word on participant's pointing gesture. That is to say, the result supports our hypothesis 1.

Interaction between the gestural factors and the lexical factors: There was no significant interaction between these factors.

2. Deictic word rate

The deictic word rate of each condition is shown in Fig.4. The analysis found out there was significant interaction between the gestural factor and the lexical factor ($\chi^2(1) = 7.209$, $p < 0.01$). We describe the detail of the interaction.

Simple main effect of the gestural factor: The deictic word rate of PD_n was significantly higher than that of P_nD_n ($\chi^2(1) = 12.216$, $p < 0.01$), but the deictic word rate of PD was similar with that of PD_n . Therefore, when the robot used a pointing gesture without a deictic word, participants tended to use a deictic terms. The result says there was partially the cross-modal effect of robot's deictic word on participant's pointing gesture. That is to say, the result partially supports our hypothesis 2.

Simple main effect of the lexical factor: The deictic word rate of P_nD was significantly higher than that of P_nD_n ($\chi^2(1) = 14.417$, $p < 0.01$), but the deictic word rate of PD was similar with that of P_nD . Therefore, when the robot used a deictic word without a pointing gesture, participants tended to use a deictic terms. The result says there was partially lexical entrainment of robot's deictic word on participant's deictic word.

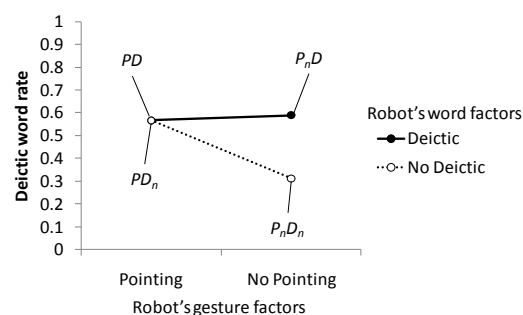


Fig.4. Deictic word rate of each condition.

IV. DISCUSSION

1. The process of the cross-modal effect

At first, we investigate whether a pointing gesture and a deictic word was used with each other. We grouped person's references into (A) a reference with both a pointing gesture and a deictic word, (B) a reference with a pointing gesture and without a deictic word and (C) a reference with a deictic word and without a pointing gesture. These rates were $A = 0.625$, $B = 0.346$ and $C = 0.029$, and they were significantly different ($\chi^2(I) = 149.621$, $p < 0.01$). According to a multiple comparison, the rate of A was higher than that of B or C. Therefore, a pointing gesture and a deictic word are more likely to be used together.

Next, we consider the process of the cross-modal effect of robot's deictic word on participant's pointing gesture. According to the results in the section 4.2, there was partially lexical entrainment of robot's deictic word on participant's deictic word. Considering that a pointing gesture and a deictic word tended to be used together, we can say that, if only partially, the cross-modal entrainment arose from the mutual dependence of the pointing gesture and the deictic word and lexical entrainment.

Finally, we consider another process of the cross-modal effect of robot's pointing gesture on participant's deictic word. According to the results in the section 4.1, there was gestural entrainment of robot's pointing gesture on participant's pointing gesture. Like the above consideration, considering that a pointing gesture and a deictic word tended to be used together, we can say that the cross-modal entrainment arose from the mutual dependence of the pointing gesture and the deictic word and gestural entrainment.

2. Application of the cross-modal effect

We can consider to applying the cross-modal effect to a design of robot's behavior. For example, a robot could raise the possibility that a person use a pointing gesture by the gestural entrainment and the cross-modal effect. This helps the robot to recognize a referred-to object correctly because there are various objects in the real environment and sometimes the robot cannot identify each object only with words.

Although the experiment aimed at a pointing gesture and a deictic word, the results suggest that the cross-modal effect would arise from the mutual dependence of a gesture and a word and the entrainment. Therefore, if

a gesture and a word are coupled, it might be possible for the cross-modal entrainment to arise in the other pair.

V. CONCLUSION

This paper defined an effect of one robot's modality on another person's modality as cross-modal effect. We supposed that if a gesture and a word are more likely to be used together, the cross-modal effect would arise through gestural entrainment or lexical entrainment, and we investigated that through a laboratory experiment.

The experiment focus on a pointing gesture and a deictic word during a conversation that a person and a robot refer to objects and investigated how the rate of person's pointing gestures and that of person's deictic words were changed by the combination of robot's pointing gestures and robot's deictic word. The experimental results were as follows; (1) a person used pointing gestures more often when the robot used deictic words; (2) a person used deictic words more often when the robot used pointing gestures.

In the cross-modal effect, a robot's modality elicits a similar person's modality by entrainment and the person's modality triggers another coupled modality. Therefore, when we design robot's behavior for maneuvering person's behavior, we should take account of not only the entrainment but also the cross-modal effect. We believe that this knowledge is useful for designing new conversational strategies for a robot.

REFERENCES

- [1] Ishiguro H, Ono T, Imai T, Maeda T, Kanda T and Nakatsu, R (2001), Robovie: An interactive humanoid robot, *International Journal Industrial Robotics*, 28(6):498-503.
- [2] Ono T, Imai M and Ishiguro H (2001), A Model of Embodied Communications with Gestures between Humans and Robots, *Proc. 23rd Annual Meeting of the Cognitive Science Society* 732-737.
- [3] Iio T, Shiomi M, Shinozawa K, Miyashita T, Akimoto T and Hagita N (2009), Lexical Entrainment in Human-Robot Interaction: - Can Robots Entrain Human Vocabulary? -, *IEEE/RSJ International Conference on Intelligent Robots and Systems*, 3727-3734.
- [4] Kita, S (1998), Expressing turns at an invisible location in route direction: the interplay of speech and body movement, *Sign-space Raum zeichen*, 160-172.
- [5] Kita, S (2000), How representational gestures help speaking, *Language and Gestures: Window into Thought and Action*, 162-185. Casti JL (1995), Bell curves and monkey languages. *Complexity* 1:12-15

Adaptive co-construction of state and action spaces in reinforcement learning

Masato Nagayoshi^a, Hajime Murao^b, and Hisashi Tamaki^c

^a Niigata College of Nursing, 240, Shinnan, Joetsu 943-0147, Japan
nagayosi@niigata-cn.ac.jp

^b Faculty of Cross-Cultural Studies, Kobe Univ. 1-2-1, Tsurukabuto, Nada-ku, Kobe 657-8501, Japan
murao@i.cla.kobe-u.ac.jp

^c Graduate School of Engineering, Kobe University, Rokko-dai, Nada-ku, Kobe 657-8501, Japan
tamaki@al.cs.kobe-u.ac.jp

Abstract

Reinforcement Learning (RL) attracts much attention as a technique of realizing computational intelligence such as adaptive and autonomous decentralized systems. In general, however, it is not easy to put RL into practical use. This difficulty includes a problem of designing suitable state and action spaces of an agent.

Until now, we have proposed an adaptive state space construction method which is called “state space filter” and an adaptive action space construction method which is called “switching RL”, after the other space has been fixed. In this paper, we reconstitute these two construction methods as one method by treating the former method and the latter method as the combined method for mimicking infants’ perceptual development in which perceptual differentiation progresses as infants become older and more experienced, and infants’ motor development in which gross motor skills develop before fine motor skills respectively. Then the proposed method is based on introducing and referring to the “entropy”. Further, a computational experiment was conducted by using a so-called “path planning problem” with continuous state and action spaces. As a result, the validity of the proposed method has been confirmed.

1 Introduction

Engineers and researchers are paying more attention to reinforcement learning (RL)[1] as a key technique of realizing autonomous systems. In general, however, it is not easy to put RL into practical use. Such issues as satisfying the requirement of learning speed, resolving the perceptual aliasing problem, and designing reasonable state and action spaces of an agent, etc. must be resolved. Our approach mainly deals with the problem of designing state and action spaces. By designing suitable state and action spaces adaptively, it can be expected that the other two problems will be resolved simultaneously. Here, the prob-

lem of designing state and action spaces involves the following two requirements: (i) to keep the characteristics (or structure) of an original search space as much as possible in order to seek strategies that lie close to the optimal, and (ii) to reduce the search space as much as possible in order to expedite the learning process. These requirements are, in general, in conflict.

Until now, we have proposed an adaptive state space construction method which is called “state space filter[2]” and an adaptive action space construction method which is called “switching learning system[3]”, after the other space has been fixed. In this paper, we reconstitute these two construction methods as one method by treating the former method and the latter method as the combined method for mimicking infants’ perceptual and motor developments respectively. The proposed method is to construct state and action spaces adaptively by introducing and referring to the “entropy” as indexes of both necessity for division of the state space in the state and sufficiency for the number of learning opportunities in the state. Further, a computational experiment was conducted by using a so-called “path planning problem” with continuous state and action spaces.

2 Typical RL Methods

2.1 Q-learning

Q-learning works by calculating the Quality of a state-action combination, namely Q-value, that gives the expected utility of performing a given action in a given state. By performing an action $a \in \mathcal{A}_Q$, where $\mathcal{A}_Q \subset \mathcal{A}$ is the set of available actions in Q-learning and \mathcal{A} is the action space of the agent, the agent can move from state to state. Each state provides the agent a reward r .

The Q-value is updated according to the following formula, when the agent is provided the reward :

$$Q(s(t-1), a(t-1)) \leftarrow Q(s(t-1), a(t-1)) + \alpha (r + \gamma \max_{a'} Q(s(t-1), a') - Q(s(t-1), a(t-1)))$$

$$+\alpha_Q \{r(t-1) + \max_{b \in \mathcal{A}_Q} Q(s(t), b) - Q(s(t-1), a(t-1))\} \quad (1)$$

where $Q(s(t-1), a(t-1))$ is the Q-value for the state and the action at the time step $t-1$, $\alpha_Q \in [0, 1]$ is the learning rate of Q-learning, $\gamma \in [0, 1]$ is the discount factor.

The agent selects an action according to the stochastic policy, $\pi(a|s)$, which based on the Q-value. $\pi(a|s)$ specifies probabilities for taking each action a in each state s . Boltzmann selection, which is one of the typical action-selection methods, is used in this research. Therefore, the policy $\pi(a|s)$ is calculated as follows:

$$\pi(a|s) = \frac{\exp(Q(s, a)/\tau)}{\sum_{b \in \mathcal{A}} \exp(Q(s, b)/\tau)} \quad (2)$$

where τ is a positive parameter.

2.2 Actor-Critic

Actor-Critic methods have a separate memory structure to explicitly represent the policy independent of the value function. The policy structure is called “Actor”, which selects actions, and the estimated value function is called “Critic”, which criticizes the actions made by the Actor. The Critic is a state-value function. After each action selection, the Critic evaluates the new state to determine whether things have gone better or worse than expected. That evaluation is TD-error:

$$\delta(t-1) = r(t-1) + V(s(t)) - V(s(t-1)) \quad (3)$$

where $V(s)$ is the state Value.

Then, $V(s(t-1))$ is updated according to Eq. (4) in the Critic, based on this $\delta(t-1)$. In parallel, it is updated for the stochastic policy, $\pi(a|s)$, in the Actor.

$$V(s(t-1)) \leftarrow V(s(t-1)) + \alpha_C \delta(t-1) \quad (4)$$

where $\alpha_C \in [0, 1]$ is the learning rate of the Critic.

It is typical for the normal distribution to be used, shown in Eq. (5), as the stochastic policy in the Actor, when Actor-Critic is applied to a continuous action space. In this case, both the mean $\mu(s)$ and the standard error of the mean $\sigma(s)$ about the normal distribution are calculated using TD-error $\delta(t-1)$ in the Actor, as Eq. (6), (7).

$$\pi(a|s) = \frac{1}{\sigma(s)\sqrt{2\pi}} \exp\left(-\frac{(a - \mu(s))^2}{2\sigma(s)^2}\right) \quad (5)$$

$$\mu(s(t-1)) \leftarrow \mu(s(t-1)) + \alpha_\mu \delta(t-1)(a(t-1) - \mu(s(t-1))) \quad (6)$$

$$\sigma(s(t-1)) \leftarrow \sigma(s(t-1)) + \alpha_\sigma \delta(t-1)((a(t-1) - \mu(s(t-1)))^2 - \sigma(s(t-1))^2) \quad (7)$$

where $\alpha_\mu \in [0, 1]$, $\alpha_\sigma \in [0, 1]$ are the learning rate of the mean and the standard error of the mean respectively. Here, if Eq. (7) is used directly, the standard

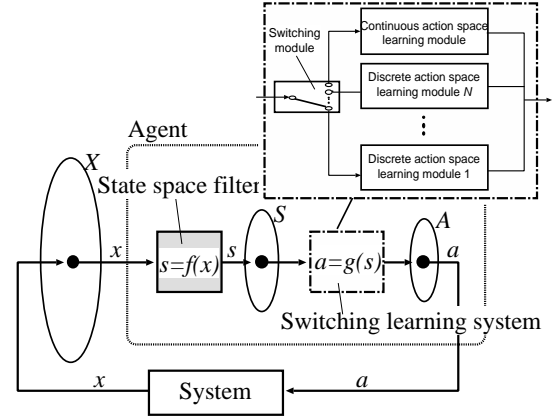


Figure 1: Proposed developing RL model.

error could be 0 or a negative value. So, it is necessary for the setting of the standard error to be creative to specify the range, etc.

3 Developing RL

3.1 Outline of a Computational Model

In this section, we propose developing RL model to mimic processes of infants’ perceptual and motor developments. The proposed model is constructed by “state space filter[2]” to mimic a process of perceptual development in which perceptual differentiation progresses as infants become older and more experienced and “switching learning system[3]” to mimic a process of motor development in which gross motor skills develop before the motor skills, as shown in Fig. 1.

This model mimics the process of perceptual development by differentiating the state space gradually from the undifferentiated state space. In parallel, this model mimics the process of motor development by switching discrete action space learning modules (hereafter called “DA module”) from more coarse-grained DA module to more fine-grained DA module, and finally switching to a continuous action space learning module (hereafter called “CA module”).

3.2 State and Action Spaces Construction Method

3.2.1 Basic Idea

A variety of methods to acquire the state space filter and to switch learning module can be considered. In this paper, we propose a method based on introducing and referring to the “entropy”, which is defined on action selection probability distributions in a state, and the number of learning opportunities in the state. It is expected that the proposed method (i) is able to learn in parallel the state space filter and the switching learning system, (ii) does not require specific RL methods for the learning module.

The entropy of action selection probability distributions using Boltzmann selection in a state, $H_D(s)$, is defined by

$$H_D(s) = -(1/\log |\mathcal{A}_D|) \sum_{a \in \mathcal{A}_D} \pi(a|s) \log \pi(a|s) \quad (8)$$

where \mathcal{A}_D is the action space and $|\mathcal{A}_D|$ is the number of available actions of the DA module.

The state space filter is adjusted and the learning module is switched by treating this entropy $H(s)$ as an index of necessity of division for an inner state s and the action space. In parallel, the learning module is switched by treating this entropy $H(s)$ as an index of sufficiency for the number of learning opportunities in the state.

If the entropy does not get smaller despite being the learning module learned a sufficient number of opportunities in the inner state, then the state space filter is adjusted by dividing the inner state and the learning module is switched to more fine-grained one. In contrast, if the entropy get small regardless of the number of learning opportunities, the learning module is switched to the CA module due to the number of learning opportunities being sufficient.

In this paper, Q-learning and Actor-Critic are applied to the DA module and the CA module respectively. The learning module is switched in the order of Q-learning with an action space divided evenly into $n, 2n, \dots, 2^{(N-1)}n$, finally ending with Actor-Critic, where N is a number of DA modules.

3.2.2 Adjustment of State Space Filter

If $L(s) > \theta_L$ and $H(s) > \theta_H$, where $L(s)$ is the number of learning opportunities in s , θ_L is a threshold value of the number of learning opportunities, θ_H is a threshold value of the entropy, and θ_L is set at a sufficiently big number, then the state space filter is adjusted by dividing a range of the input state mapped to the inner state s into 2 parts for each dimension, and mapping each part to a different inner state respectively. Simultaneously, the learning module is switched. Through this operation, a size of the inner state space after divided increases by $(2^M - 1)$, where M is a number of dimension. Also note that the values of the new 2^M inner states are the value of the inner state before divided.

In addition, after the learning module is switched to the CA module, if $L(s) > \theta_L$, then the state space filter is adjusted by dividing the inner state to be more fine-grained.

3.2.3 Switching of Learning Module

If $H(s) > \theta_H$, then the learning module is switched to the CA module due to the number of learning op-

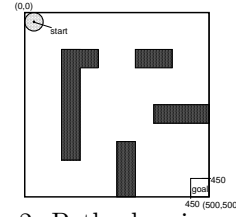


Figure 2: Path planning problem.

portunities being sufficient. In the procedure to switch controllers, the result of Q-learning is succeeded by Actor-Critic. The following procedure is conducted :
i) the state value of the Critic, $V(s)$, is initialized by

$$V(s) = \sum_{a \in \mathcal{A}_Q} \pi(a|s) Q(s, a) \quad (9)$$

ii) the normal probability distribution used by the Actor is calculated by

$$\mu(s) = \arg \max_{a \in \mathcal{A}_Q} Q(s, a), \quad (10)$$

$$\sigma(s) = |A_Q(\arg \max_{a \in \mathcal{A}_Q} Q(s, a))|/6 \quad (11)$$

where $|A_Q(i)|$ is a range of the action space which represents action i of Q-learning.

If $L(s) > \theta_L$ and $H(s) > \theta_H$, then the learning module is switched to more fine-grained DA module, and finally ending with to the CA module. Simultaneously, the state space filter is adjusted.

Q-values of actions newly added a_i at this time are set according to the following formula : $Q(s, i) = \max_{j \in i-1, i+1} Q(s, j)$ where action $i-1$ and $i+1$ are adjacent to action i . This formula is set in consideration of a more efficient search as well as the idea of the optimistic initial values.

4 Computational Example

4.1 Path Planning Problem

The proposed method is applied to a so-called “path planning problem” where an agent is navigated from a start point to a goal area in a continuous space as shown in Fig. 2. Here, the agent has a circular shape (diameter = 50[mm]), and the continuous space is 500[mm] × 500[mm] bounded by the external wall with internal walls as shown in black. The agent can observe the center position of the agent: (x_A, y_A) as the input, and move 25[mm] in a direction, i.e., decide the direction: θ_A as the output.

The positive reinforcement signal $r_t = 10$ (reward) is given to the agent only when the center of the agent arrives at the goal area and the reinforcement signal $r_t = 0$ at any other steps. The period from when the agent is located at the start point to when the agent is given a reward, labeled as 1 episode, is repeated.

4.2 Comparison to Adaptive Methods

We have confirmed that a combined method of the state space filter and the switching learning system (hereafter called method “FS”) demonstrates better performance than three Q-learning methods with the action space divided evenly into 4, 8 and 16, and two Actor-Critic methods with the state space divided evenly into 10, 10 and 40, 40 in this task.

In this section, method FS is compared with two methods using the switching learning system with the state space divided evenly into 10, 10 and 40, 40 spaces (hereafter called method “S10” and “S40” respectively), Actor-Critic using the state space filter and Q-learning with the action space divided evenly into 4 spaces using the state space filter (hereafter called method “FAC” and “FQ4” respectively). Here, the initial state space filter is designed that divides the state space evenly into 10, 10 spaces.

Then, the entropy of a continuous action space in a state for method FAS, $H_C(s)$, is defined by

$$H_C(s) = - \int_{-\infty}^{\infty} \pi(a|s) \log \pi(a|s) da. \quad (12)$$

By substituting the Eq. (5) into this formula, $H_C(s) = \log(\sqrt{2\pi e})$. In method FAS, if $H_C(s) < \theta_{HC}$, then the state space filter is adjusted.

All initial values and the range of (x) are set at π and $[0.001, 2\pi]$ respectively, all initial means are set to randomize within a range of $[-\pi, \pi]$ for Actor-Critic. Then, all initial state values and Q-values are set at 5.0 as the optimistic initial values[1] for Actor-Critic and Q-learning respectively. Here, the initial values and the maximum limit of (x) are set so that ± 1 and the maximum limit become the size of the action space: 2π . Further, the adjustment of the state space filter is assumed until the third attempt in all inner states because it is impossible to evaluate sufficiency for division of the state space.

Computer experiments have been done with parameters as shown in Table 1. Here, θ_{HD} was set referring to about 0.312 : the maximal value of the entropy when the highest selection probability for one action is 0.9, θ_{HC} was set referring to about 0.335 : the entropy when the standard error is $\pi/6$, θ_L was set in consideration of the enough big number.

The number of average steps required to accomplish the task was observed during learning over 20 simu-

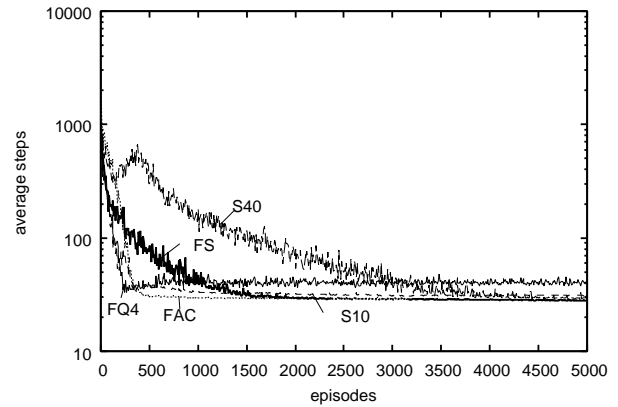


Figure 3: Required steps.

lations with various methods as described in Fig. 3. Learning speed and obtained control rule : It can be confirmed from Fig. 3 that, 1) method FS has worse performances than method FQ4, FAC and S10, but better performances than method S40 with regard to the learning speed, 2) method FS has good performance as well as method FAC and S40 with regard to the obtained control rule,

Therefore, we have confirmed that method FAC and method FS, in that order, demonstrate better performance than any other method on the path planning problem with the continuous state and action spaces.

5 Conclusion

In order to design the suitable state and action spaces adaptively, we propose, in this paper, the developing RL model, and state and action spaces construction method referring to the “entropy”. Then, through the computational experiment, we have confirmed that the combined method of the state space filter and Actor-Critic, and the combined method of the state space filter and the switching the learning system, in that order, demonstrate better performance than any other method on the path planning problem with the continuous state and action space.

Our future projects include to apply more complicated problems and real world problems, etc.

Acknowledgment

This work was supported in part by a Grant-in-Aid for Young Scientists (B), (No. 21700258), from MEXT, Japan.

References

- [1] R.S. Sutton and A.G. Barto: Reinforcement Learning, A Bradford Book, MIT Press (1998).
- [2] M. Nagayoshi, H. Murao, and H. Tamaki: A State Space Filter for Reinforcement Learning, *Proc. AROB 11th'06*, 615-618(GS1-3) (2006).
- [3] M. Nagayoshi, H. Murao and H. Tamaki: A Reinforcement Learning with Switching Controllers for Continuous Action Space, *Proc. the 15th International Symposium on Artificial Life and Robotics 2010*, 236-239 (2010).

Table 1: Parameters for experiments

Parameter	Value	Parameter	Value
$\alpha_Q, \alpha_C, \alpha_\mu, \alpha_\sigma$	0.1	τ	0.9
θ_{HD}, θ_{HC}	0.3		0.1
θ_L	1000		

Autonomous acquisition of cooperative behavior based on a theory of mind using parallel Genetic Network Programming

Kenichi Minoya¹, Takaya Arita² and Takashi Omori³

^{1, 2}*Graduate School of Information Science, Nagoya University
Furo-cho, Chikusa-ku, Nagoya 464-8601, JAPAN*

³*College of Engineering, Tamagawa University*

6-1-1 Tamagawa Gakuen, Machida, Tokyo 194-8610, JAPAN

E-mail: ¹kenichiminoya@alife.cs.is.nagoya-u.ac.jp, ²arita@nagoya-u.jp, ³omori@lab.tamagawa.ac.jp

Abstract: Understanding of others as having intentional states such as beliefs and desires is called Theory of Mind (ToM). To clarify the mechanism of the autonomous acquisition of cooperative behavior based on the ToM, we constructed a functional model of the brain based on the *Functional Parts Combination* (FPC) model. This model consists of a set of functional parts and activation signals specifying selective activated patterns, and activated modules can be executed in parallel based on the flow of control tokens. The module network and activation signals can be acquired by the evolutionary computation techniques used in the *Genetic Network Programming* and *Genetic Algorithm*, respectively. We use a hunter task as a task to be solved by the agents, and encode inherent activation signals into the genome as a first step. The result of computer simulation shows an emergence of the pattern of the functional parts for processing ToM through evolution characterized by punctuated equilibrium.

Keywords: Functional Model of the Brain, Theory of Mind, Cooperation, Evolution, Genetic Network Programming.

I. INTRODUCTION

Humans are extremely social animals. One aspect of social cognition sets us apart from other primates: *Theory of Mind* (ToM). It enables us to understand others as having intentional states such as beliefs and desires [1]. The evolutionary origins of it can be traced back in extant non-human primates; ToM probably emerged as an adaptive response to increasingly complex primate social interaction [2]. The aim of our study is to investigate how cooperative behaviors based on ToM emerge through evolutionary processes by modeling the brain at the functional level.

A *Genetic Network Programming* (GNP) is one of the evolutionary computation techniques which can autonomously generate behavior sequences by evolution. Eto et al. (2006) realized functional localization of GNP by switching the nodes depending on the situation [3]. However, their model cannot realize parallel processing because nodes activate sequentially from a start node as well as the conventional GNP. Considering the fact that the multiple areas in the brain activate simultaneously, we assumed that nodes can be executed in parallel.

A limited number of attempts have so far been made at the constructive approach to ToM characterized by the use of computational models for simulating its evolution. Among them, there are only a few studies which investigate the underlying mechanism of evolutionary acquisition of the recursion level in a ToM

[4] [5]. However, functions of ToM in these studies are procedurally defined a priori by the designers.

We focus on the emergence of a ToM without defining it a priori by modeling the brain at the functional level. Next section explains a functional model of the brain and Section 3 illustrates a task and components of the brain. Section 4 shows the experiments and Section 5 summarizes the paper.

II. FUNCTIONAL MODEL OF THE BRAIN

As the functional model of the brain, we adopted the *Functional Parts Combination (FPC) model* [6] in order to control the topology of the modules. The FPC model is based on the neuroscientific fact that each cerebral cortical area has a different role and is selectively activated depending on the task [7]. This model consists of a set of functional parts and activation signals specifying selective activated patterns. Fig. 1 shows a functional model of the brain based on the FPC model. There are modules M_i in the brain, which constitute a module network. A set of modules in the network are activated by a set of activation signals. A set of activation signals A is represented as a vector of binary values 0 and 1: $A = (a_0, \dots, a_i, \dots, a_{k-1})$, where k is the number of modules, and a_i is an activation signal for module M_i . The activation signals are searched depending on the tasks. In the module network, parallel computation is controlled based on the simple parallel control flow paradigm [8] as follows. All data are

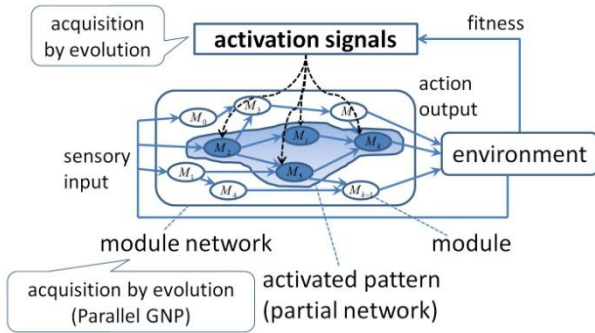


Figure 1. Functional model of the brain.

transferred indirectly between modules via updatable memory cells. The execution starts from the sensory input. In a case that all input links receive a control token the activated modules begin its computation while the non activated modules do not execute it. Then both activated and non activated modules output tokens from all output links. However, the modules whose input links are not connected do not output tokens, regardless of whether or not the modules are activated. Besides, the memory cells are initialized before each sensory input. In a case that the non-written data is attempted to load, an error occurs, the process is suspended and tokens are output from all output links.

III. MODULE NETWORK AND TASK

The module network can be acquired by the GNP, however; this paper focused on the emergence of activation signals for forming ToM sub-networks to achieve cooperative behavior in a hunter task as a first step. The discussion on the emergence of modules network is outside the scope of this paper and we assumed that they had been acquired.

1. Hunter Task

There are two hunter and two prey agents in a 20×20 a two-dimensional grid folded to a torus. Each hunter moves one cell per step to the left, right, up or down, or stays in the current cell according to its own strategy, while each prey moves one cell per step stochastically (right; 40 %, up; 20 %, or stop; 40 %).

When starting the task, all 4 agents are randomly located in the grid, and each hunter selects the closer prey as an initial target. Each episode ends when each hunter captures the different prey or the number of time steps exceeds the upper limit $step_{max}$.

2. The Function of Each Module and Its Networks

We assumed that humans estimate the intention or goal of others by simulating it based on their own

action-selection process as if they were in the same situation [9]. Action-selection process is represented by a probability of action a under the condition state s and goal G ; $P(a/s, G)$ [10]. We defined following strategies based on a Dennett's intentional stance [11]: (1) Agent at *level 0* takes action based on own goal independently of the intention of others; (2) Agent at *level 1* estimates the intention of others by assuming that others would be at level 0, and takes action based on it; (3) Agent at *level 2* estimates the intention of others by assuming that others would be at level 1, and takes action based on it. In order to realize a smooth cooperative behavior, we adopted the *mixed strategy* [10] which dynamically changes above three strategies. The module network and functions of each module we adopted in the experiments are described in Box 1.

IV. EXPERIMENTS

1. Experimental Setup

We conducted simulations in which the activation signals of agents were evolved by using a genetic algorithm. A chromosome was represented by binary encoding, which represents the activation signals $A = (a_0, \dots, a_i, \dots, a_{k-1})$. We first created N individuals whose activation signals were randomly generated, and every pair of agents solved the hunter task E times in a round robin manner. Then, time steps to solve the task were averaged over those games, and agents were evaluated as: $Fitness = 100/step$. The offspring in the next generation were selected by the linear ranking selection method by Baker [12]. Then, cross over was performed on the parents to form a new offspring (single point crossover) with a crossover probability P_c , and each activation signal of all offspring was mutated with a mutation probability P_m . We conducted evolutionary experiments 13 times using the parameters shown in the Table 1.

Table 1. Experimental setup.

length of the history: T	5	w_i ($i = 0, 1, 2$)	4
temperature parameter: β	1	episode: E	10
α_1	0.4	population size: N	20
α_2	0.6	generation	4000
threshold: θ	32	crossover probability: P_c	0.001
upper limit: $step_{max}$	500	mutation probability: P_m	0.001
b_i ($i = 0, 1, 2$)	5	Baker parameter	2

2. Results

Fig. 2 shows the transition of the ratio of the activation signals in the population (black lines) and the fitness (the gray line) on a certain trial. The bar above Fig. 2 represents the acquired activated patterns. We see

that the fitness in the early stage remained very low. This is because agents randomly selected their actions, and thus they could not solve the task within the upper limit (500 steps). The fitness slightly increased at around 450th generation with the activation of M_9 . At that time, the activation signals of the major portion of

agents were (0, 1, 1, 0, 0, 0, 1, 0, 0, 1, 1, 1, 0, 1, 1, 0, 1). This means that agents acquired the network for level 0 ToM. The fitness remained stable in the subsequent generations, and then it increased at around 1100th generation with the activation of M_5 and M_7 . By then, agents had acquired the following activation signals:

Box 1. The module network and function of each module.

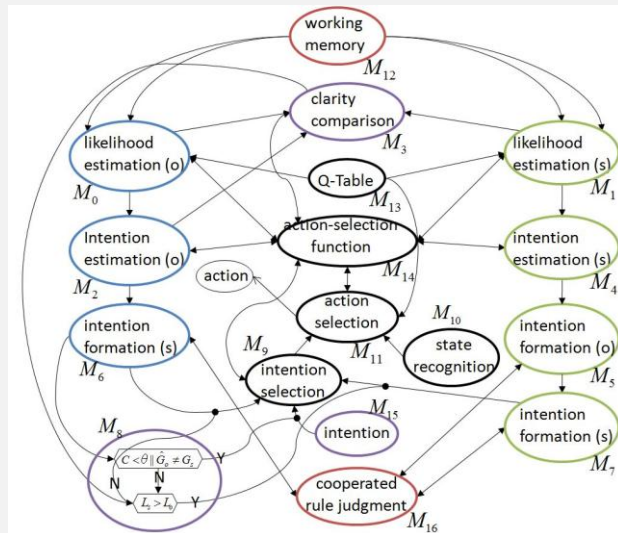


Figure 1. The module network used for the experiments.

M_{10} : state recognition

Own and other's state ($s_s(t)$ and $s_o(t)$) and action ($a_s(t)$ and $a_o(t)$) at the time t are recognized. The state is defined as relative coordinates between the hunter and two preys.

M_{12} : working memory

Own and other's state ($s_s(t-1)$ and $s_o(t-1)$) and action ($a_s(t-1)$ and $a_o(t-1)$) at the time $t-1$ are recognized.

M_0, M_1 : likelihood estimation

$a(t-1)$, $s(t-1)$ and G are substituted to own action-selection process $P(a|s, G)$ in order to calculate the likelihood that goal would be G as follows: $l(G, t) = P(a(t-1) | s(t-1), G)$. Likelihood $l(G, t)$ is calculated for all possible goals, and is stored in a likelihood history to make estimation of intention stable: $m(G, t) = \{l(G, t), \dots, l(G, t-T+1)\}$, where T is the length of the history. Then, cumulative log likelihood $L(G, t/m)$ is calculated for all possible goals: $L(G, t/m) = \sum_{l \in m(G, t)} \log l$. In particular, conviction degree C which represents the reliability that the estimated other's goal would be G is calculated in M_0 : $C = L(G_{1st}, t/m) - L(G_{2nd}, t/m)$, where $G_{1st} = \text{argmax}_G L(G, t/m)$ and $G_{2nd} = \text{argmax}_{G \neq G_{1st}} L(G, t/m)$.

M_2, M_4 : intention estimation

Others' goal G_o or own goal G_s is estimated by an action-selection function based on soft-max reinforcement learning in M_2 and M_4 , respectively: $g(G, t/m) = \frac{\exp(\beta L(G, t/m))}{\sum_{G'} \exp(\beta L(G', t/m))}$, where β is a parameter called the temperature.

1) $s_s(t)$, $s_o(t)$, $a_s(t)$, $a_o(t)$, $s_s(t-1)$, $s_o(t-1)$, $a_s(t-1)$, $a_o(t-1)$ and $a_s(t+1)$ (action output) are set randomly per step, and then those values are updated if related modules are activated. Also, cumulative log likelihood $L(G, t/m)$ and conviction C are set to -10000 per step, and then those values are updated if related modules are activated.

2) Sub networks including modules $\{M_9, M_{10}, M_{11}, M_{13} \text{ and } M_{14}\}$, $\{M_9, M_{10}, M_{11}, M_{13}, M_{14}, M_{12}, M_{16}, M_0, M_2 \text{ and } M_6\}$ and $\{M_9, M_{10}, M_{11}, M_{13}, M_{14}, M_{12}, M_{16}, M_1, M_4, M_5 \text{ and } M_7\}$ correspond to ToM 0, 1 and 2, respectively.

M_3 : clarity comparison

A hunter judges which more precise is: the clarity of the estimated other's goal ($L_l(G_o, t/m_o)$) or that of the estimated own goal ($L_l(G_s, t/m_s)$): $p_i = \frac{\alpha_i \exp(\beta L_i)}{\sum_{i=1,2} \alpha_i \exp(\beta L_i)}$ ($i = 1, 2$), where α_i is the weight to the L_i ($\alpha_1 + \alpha_2 = 1$).

M_8 : conviction and clarity judgment

In a case that conviction degree C (calculated in M_0) is less than threshold θ or there is no necessity to change own goal (i.e. the cooperated rule is already satisfied) the bias of M_{15} is set to b_0 . If this is not the case, the bias of M_6 is set to b_1 when the clarity of the estimated other's goal ($L(G_o, t/m_o)$) is higher than that of the estimated own goal ($L(G_s, t/m_s)$), otherwise; the bias of M_7 is set to b_2 .

M_{16} : intention formation

A hunter judges whether the others' goal G_o and own goal G_s satisfy a cooperated condition. For this task, $G_o \neq G_s$ (i.e. others' goal differs from own goal) is simply a condition of cooperation.

M_5, M_6, M_7 : intention formation

In M_6 , own goal G_{s1} is formed to satisfy the cooperated condition, and the weight of the connection between M_6 and M_9 is set to w_1 . In M_7 , own goal G_{s2} is also formed to satisfy the cooperated condition, and the weight of the connection between M_7 and M_9 is set to w_2 . Other's goal is also formed to satisfy the cooperated condition in M_5 .

M_{15} : intention

Own goal $G_s(t-1)$ selected in M_9 (intention selection) at the time $(t-1)$ is stored in the own goal G_{s0} , and the weight of the connection between M_{15} and M_9 is set to w_0 .

M_9 : intention selection

Own goal G_{si} is selected: $G_{si} = \frac{\exp(\beta h_i)}{\sum_{j=0,1,2} \exp(\beta h_j)}$ ($i = 0, 1, 2$, where $h_i = b_i + w_i$ ($i = 0, 1, 2$)).

M_{11} : action selection

Action a is selected by an action-selection function: $P(a|s, G) = \frac{\exp(\beta Q(a|s, G))}{\sum_{a'} \exp(\beta Q(a'|s, G))}$, where Q represents an evaluation value which is acquired by reinforcement learning.

M_{14} : action-selection function

It is the one based on soft-max reinforcement learning.

M_{13} : Q-Table

It is an evaluation value Q which is acquired by reinforcement learning [18]. Before we conducted experiments in Section 4, each agent had acquired a different Q-Table on its own by the soft-max reinforcement learning in the setting where there were a hunter and a prey (temperature parameter $\beta = 1$).

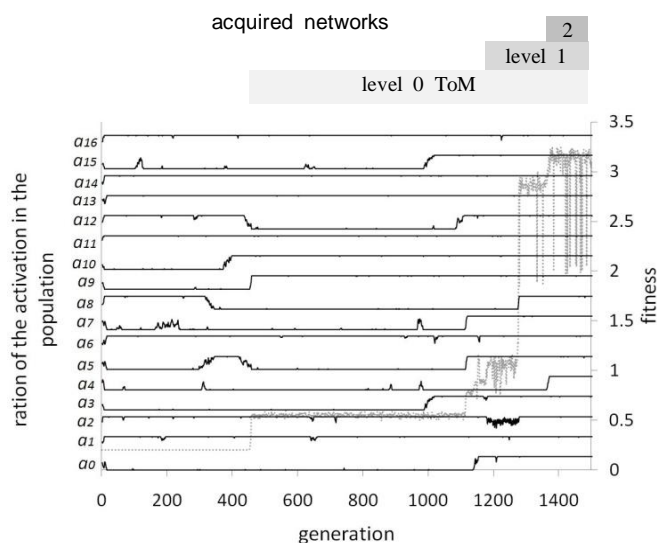


Figure 2. The transition of the ratio of the activation signals in the population and the fitness on a certain trial.

(0, 1, 1, 1, 0, 1, 1, 1, 0, 1, 1, 1, 1, 1, 1, 1, 1), in other words, all modules other than M_0 , M_4 , and M_8 were activated. This means that agents could not estimate other's and own goal correctly as M_0 and M_4 were not activated, and changed own goal randomly. Subsequently, the activated pattern for level 1 ToM was emerged with the activation of M_0 under the condition that the other prerequisites for level 1 ToM (M_{10} , M_{11} , M_{13} , M_{14} , M_2 , M_6 , and M_{12}) had been acquired. Next, there was a remarkable increase in the fitness in parallel with the activation of M_8 . By then, all modules other than M_4 were activated. This means that agents could change strategies between level 0 and level 1 ToM based on the conviction degree C representing the reliability that the estimated other's goal would be G . After that, the activated pattern for level 2 ToM was emerged with the activation of M_4 under the condition that the other prerequisites for level 2 ToM (M_{10} , M_{11} , M_{13} , M_{14} , M_1 , M_5 , M_7 , and M_{12}) had been acquired. This means that agents changed strategies between level 0, level 1, and level 2 ToM based on the conviction degree C and the comparison of the clarity of the estimated other's goal ($L(G_o, t/m_o)$) and that of the own goal ($L(G_s, t/m_s)$).

What it comes down to is that the activated pattern of the functional parts for processing ToM tended to evolve in incremental steps as: (1) an emergence of the activated pattern for level 0 ToM; (2) an emergence of that for level 1 ToM; (3) an emergence of that for level 2 ToM. Looking at other trials, the same tendency could be found.

V. CONCLUSION

In this paper, we constructed a functional model of the brain using a functional parts combination (FPC) model to clarify the mechanism of the autonomous acquisition of cooperative behavior based on the ToM. The result of computer simulation shows an emergence of the pattern of the functional parts for processing ToM through evolution characterized by punctuated equilibrium as: (1) level 0 ToM; (2) level 1 ToM; (3) level 2 ToM. The next step would be to investigate the acquisition of not only the activation signals but also the connections between modules. We believe that the proposed method would contribute to clarify the origin of ToM. It might be also interesting to discuss the feasibility of the acquisition of ToM in humanoid robots.

REFERENCES

- [1] Premack, D. and Woodruff, G., Does the chimpanzee have a theory of mind? *The Behavioral and Brain Sciences*, 1, 515–523, 1978.
- [2] Brothers, L., The social brain: A project for integrating primate behavior and neurophysiology in a new domain. *Concepts Neuroscience*, 1, 27–51, 1990.
- [3] Eto S., Hatakeyama H., Mabu S., Hirasawa K., Hu J., Realizing Functional Localization Using Genetic Network Programming with Important Index, *Journal of Advanced Computational Intelligence and Intelligent Informatics*, 10 (4), 555–566, 2006.
- [4] Takano, M. and Arita, T., Asymmetry between Even and Odd Levels of Recursion in a Theory of Mind, *Proc. of the 10th International Conference on the Simulation and Synthesis of Living Systems (ALIFE X)*, 405–411, 2006.
- [5] Noble, J., Hebborn, T., Horst, J., Mills, R., Powers, S. and Watson, R., Selection pressures for a Theory-of-Mind faculty in artificial agents. *Proc. of the 12th International Conference on the Simulation and Synthesis of Living Systems (ALIFE XII)*, 2010.
- [6] Omori, T. and Ogawa, A., Two hypothesis for realization of symbolic processing in brain. *Proc. of the 9th International Conference on Neural Information Processing*, 2001.
- [7] Liu, M. J., Fenwick, P. B. C., Lumsden, J., Lever, C., Stephan, K.-M. and Ioannides, A. A., Averaged and single-trial analysis of cortical activation sequences in movement preparation, initiation, and inhibition. *Human Brain Mapping*, 4, 254–264, 1996.
- [8] Trealeven, P. C., Hopkins, R. P., and Rautenbach, P. W., Combining data flow and control flow computing, *Computer Journal*, 25 (2), 207–217, 1982.
- [9] Gallese, V., & Goldman, A., Mirror neurons and the simulation theory of mind-reading. *Trends in Cognitive Sciences*, 2, 493–501, 1998.
- [10] Nagata, Y., Ishikawa, S., Omori, T., and Morikawa, K., Computational model of cooperative behavior based on dynamical selection of intention based action decision strategy, *Cognitive studies*, 17(2), 280–286, 2010.
- [11] Dennett, D., *The Intentional Stance*, MIT Press, Cambridge, 1987.
- [12] Baker, J. E., Reducing bias and inefficiency in the selection algorithm, *Proc. of the Second International Conference on Genetic Algorithms*, 14 - 21, 1987.

A comparison of learning performance in two-dimensional Q-learning by the difference of Q-values alignment

Kathy Thi Aung, Takayasu Fuchida

(Department of System Information Science, Graduate School of Science and Engineering, Kagoshima University,
Kagoshima, Japan)

(Tel: 81-99-285-8453; Fax: 81-99-285-8464)

(kathythiaung@gmail.com, fuchida@ibe.kagoshima-u.ac.jp)

Abstract: Q-learning is a kind of reinforcement learning where the agent solves the given task based on rewards received from the environment. In this paper, we compared the performance of the Q-learning based on the reward examined by the difference of Q-values alignment in two-dimensional (2D) state space under various conditions such as angle of VQE rotation which is arranged like a lattice and angle of the agent's action rotation to correctly evaluate the optimal Q-values for state and action pairs, in order to deal with continuous-valued inputs. We apply the proposed method with an agent that learns to reach the reward area successfully during the reward-based learning process. A reward is given to the learning agent if the agent reaches the reward area during a process of trial.

Keywords: Q-learning, Q-value, VQE

1 Introduction

Learning algorithms based on evaluative feedback signal is generally referred to as RL algorithms.[1,4] In a RL paradigm, [4] a system called agent senses the environment and produces control actions. The environment responds to these control actions. Based on these responses a reward function will evaluate the control actions. The agent tries to optimize the control policy to maximize the total expected reward over a finite time-span. Learning may occur using the prediction error of expected rewards.

Reinforcement learning (RL) methods are a powerful and useful way to control agents such as an autonomous robot. [1] Q-learning [2] is the most widely used in RL method which deals with only discrete-valued inputs (states) and outputs (actions) to represent Q-function (action value function) that evaluates state/action pairs.

The aim of this work is to significantly improve the learning performance of Q-learning between the state space and the action space. Therefore, we implement and investigate here in order to clearly show the effectiveness of proposed learning method under various problems.

In this paper, we first briefly explain our agent model in a single-agent environment. Secondly, we define VQE with radius to decide the position. Next we describe each of the simulation methods, and then the performance of each strategy is examined by computer simulations on competitive situations of several strategies. We also show that the performance of each

strategy strongly depends on the situation of our simulation methods and the simulation results are explained.

2. Q-Learning

In Q-learning, [2] the expected value of each action in each state is stored. In the other way, the Q-value is the expected value of each action in a certain state, which is the discounted sum of the rewards agent received for state and action pair. We can estimate and update the Q-value, which is denoted by $Q(s_t, a_t)$ according to the following equation by taking the one with the maximum Q-value (highest expected value) for the current state.

$$Q(s_t, a_t) = Q(s_t, a_t) + \alpha(r + \gamma \max_a Q(s_{t+1}, a) - Q(s_t, a_t)) \quad \text{Eq. (1)}$$

When the agent is in state t , the agent observes the state s_t and executes the action a_t . The agent obtains the reward r_t , and senses a new state s_{t+1} by selecting an action a_t in state s_t . In this equation, α is the learning rate and γ is the discount rate, both are between 0 and 1.

In the standard Q-learning implementation, Q-values are stored in a table, is known as Q-table. It looks like a square lattice in two dimensions and one cell is required per combination of state and action. This implementation is not amenable to continuous state and action problems. [3] As the number of state and action variables increase, the size of the table used to store Q-values grows exponentially, is called *Curse of dimensionality*. On the other hand, as the number of

dimensions increases, the state space also increases exponentially and the learning speed decreases dramatically.

2.1. Behavioral Decision

The agent selects the next action which has the highest Q-value. An action which has a large Q-value is considered to be a good way to achieve the reward. However, selecting the highest Q-value continually decreases the opportunity to find a better way. Therefore, the agent sometimes selects the next action at random. This random selection is useful for exploring the state space and finding a new better way which has not been found yet.

2.2. Voronoi Q-value Element (VQE)

VQE is a point that has Q-value but we don't know where VQEs should be placed in the states space at the initial time. If we got many rewards, we would be able to evaluate the positions of VQEs for the optimal policy of state-action pair.

By using the VQE, we can place the Q-value arbitrarily in the state space and reduce the waste of space. Therefore, as the degree of freedom to select the position of VQE is so numerous, we have to decide carefully where the VQEs are placed in the state space.

3. Experimental Model

In these experiments, we tested with one agent and one reward area. The working environment of the agent is shown in Figure1, in where, it is intended to learn efficient action of an agent which is to reach the reward area in the state space.

The agent's action of maximum Q-value is selected while observing in a certain condition and the agent is a random action with a fixed probability. The agent observes the distance (r) and the angle (θ) toward the reward area.

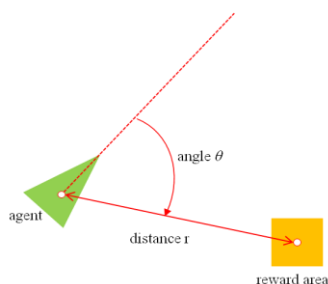


Fig.1. Working environment of an agent

There are two input variables: 1, the distance between an agent and the reward area; 2, an angle

between the direction of agent's action and the reward area. The state space is constructed with these two input values. In this model, the agent is represented by a triangular arrowhead which indicates the direction in which the agent is moving. The rectangular area represents as the reward area.

3.1. Experimental Environment

An agent moves in a closed two-dimensional state space. Figure 2 shows an image of the agent that learns to reach the reward area. A reward is given to the learning agent if the agent reaches to the reward area, in the other states the reward is always zero.

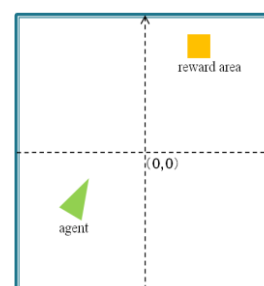


Fig.2. Agent Problem

In Figure 2, since the number of reward area is one, the agent observes two parameters. These two parameters construct the two-dimensional state space. The dimension of the state space goes up by two dimensions when one reward area is increased.

The possible actions of the agent are: 1, straight ahead; 2, turn left; 3, turn right. If the agent reaches the reward area, the position of the agent is randomly changed in this state space.

3.2. Experimental Parameters

width and height of space	-100,100
size of reward area	5
learning rate α	0.1
discount rate γ	0.9
random action rate	0.3
initial Q-value	$0 \leq Q(s_t, a_t) \leq 0.01$
travel distance of agent	2.0~5.0
Number of execution times	10 trials
One trial	20 episodes
One episode	100000 times

4. Simulation Methods and Results

We carried out three types of simulation experiment.

4.1. Square Lattice with random noise

The lattice below is a general 2-dimensional lattice on partition number 10, shown in figure 4.1.1. The idea of the lattice was proposed by VQEs and designates a 2-

dimension of 100 VQEs in lattice by symbol 10*10 grid environment. If we conduct this general 2-dimensional lattice with random noise (i.e., 0, 0.01, 0.02, 0.03, 0.04, 0.05 randomly arranged VQEs), we get the lattice like figure 4.1.2.



Fig.4.1.1 Original 2-D lattice

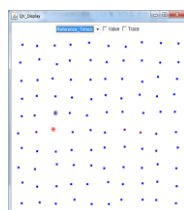


Fig.4.1.2. Random Lattice

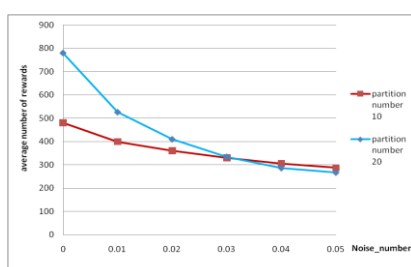


Fig.4.1.3. From regular to random VQE

As we can see from this above figure, the number of rewards is slowing down, thus its performance by this strategy depends on the arrangement of VQEs.

4.2. Lattice VQE rotation by Degrees

In this subsection, we rotated the above original 2-dimensional lattice by the angle of clockwise rotation on partition number 10 and 20. It turns for each degree of rotation by five degrees of angle intervals in the ranges from 0 to 90 degrees.

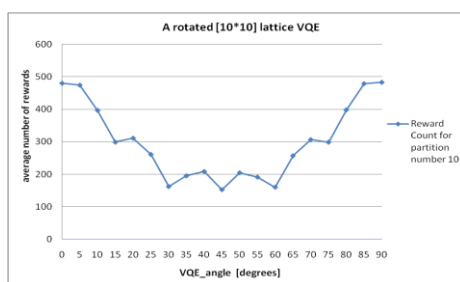


Fig.4.2.1. Reward count in a 10*10 grid environment

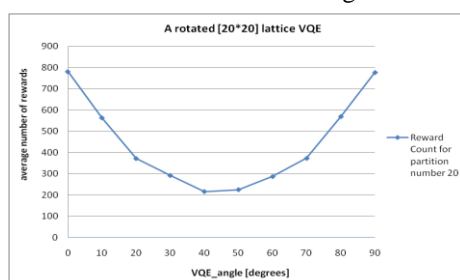


Fig.4.2.2. Reward count in a 20*20 grid environment

As in the experimental results shown in figure 4.2.1 for the 10*10 grid environment, the number of rewards clearly was slow, and a similar result also occur in a 20*20 grid environment because the reward propagation is delayed.

As the number of reward count decreases, we considered the following possible casual points.

- When the state changes, a state certainly transit to a different state if the action is different.
- But if lattice VQE rotates, also take in different action, grows the probability that the state of result go into the same state.
- Q-value decreases if the action is acting in the same area by the Q-learning method as shown in above equation (1).
- Since the angle of lattice VQE rotation for learning is enormous, we implemented the next strategy.

4.3. Rotation of Lattice VQE and agent's action

Here, we propose a new simulation experiment method in which the reward area is denoted by closed circle and the agent is denoted by open circle. The new strategy of learning for our target problem is defined as figure 4.3.1. Note that the agent takes actions with four directions: go up, go down, go left and go right.

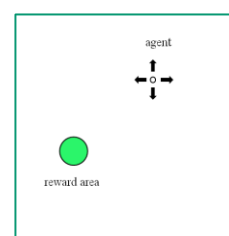


Fig.4.3.1. Structure of a new agent

In this case, we rotated the location of reward area and initial/default position of agent also. In each degree of our rotation, the action selection is simultaneously performed by the agent.

In our computer simulations, we used two elements rotations: act-angle and VQE-angle of rotations which measure between 0 degrees and 90 degrees by five degrees of angle intervals. (Figure 4.3.2)

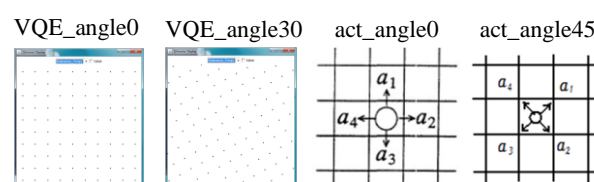


Fig.4.3.2. Rotation of VQE and agent's action

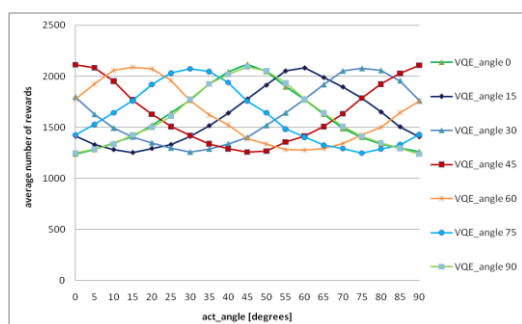


Fig.4.3.3. Reward count in a 10*10 grid environment

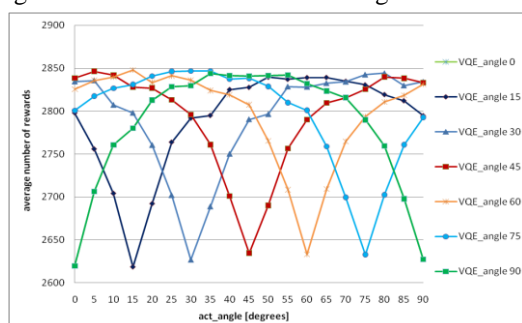


Fig.4.3.4. Reward count in a 20*20 grid environment

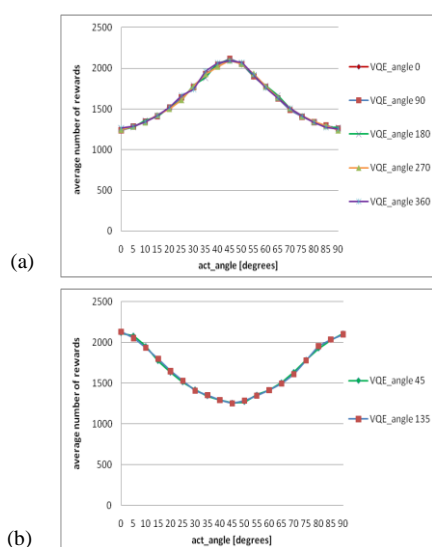


Fig.4.3.5. Angle of rotation for (a) 0,90,180,270,360 degrees and (b) 45,135 degrees

As Fig. 4.3.3 and Fig.4.3.4 reveals, when the turning angle of VQE are 0 degrees and 90 degrees, the results are entirely same at all, in fact there's no difference between them. In addition, Fig.4.3.5 also has totally same at the turning angle of 0, 90, 180, 270, 360 degrees and 45, 135 degrees. In this situation, we can see that the number of rewards increases due to the agent's optimum actions are four in this strategy.

Since Fig.4.3.6 generates the number of rewards that are put VQE randomly with noise on a number of (0,1,2,3,4,5) is relatively compared with in the Fig.4.1.3 above.

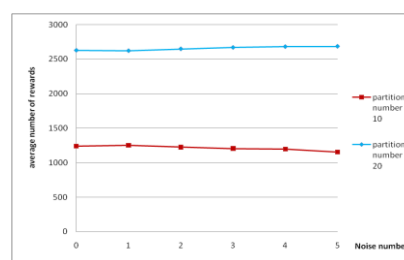


Fig.4.3.6. From regular to random VQE

5. Conclusion and Future Work

As a result, the learning performance was decrease by turning the angle of VQE only. When we turn act angle and VQE angle, it improves in performance. The difference between the number of actions 3 and 4 is according to the following reason.

The agent's action space and the state space is match or not. In the case of the agent's action space corresponds to the state space, the performance improves while shifting in the angle of rotation especially VQE angle and act angle is shifting by 45 degrees is greatly improved. Therefore, it is match of agent's action space and the state space that gives good performance.

In fact, it is different by expression of state input. It means when the number of action is 4, the agent observes by its position but in the case of action number 3, it observes the distance and the angle of agent relative to the reward area.

In the current research, we proposed learning method of Q-learning based on Voronoi Q-value element. In this paper, we examined the learning performance of various strategies in a different situation for our experimental environment. Although at the current stage, we only performed experiments in two dimensions, as future topics of research, we plan to a high-dimensional problem by generating an N-dimensional state space.

References

- [1] R.S. Sutton and A.G. Barto, "Reinforcement Learning: An Introduction", MIT Press, 1998.
- [2] C.J.C.H. Watkins and P. Dayan, "Q-learning", Machine learning, Vol8, pp.279-292, 1992.
- [3] Christopher J.C.H. Watkins. "Learning from Delayed Rewards", PhD thesis, University of Cambridge, 1989.
- [4] K.Kiguchi, T.Nanayakkara, K.Watanabe, T.Fukuda, "Multi-Dimensional Reinforcement Learning Using a Vector Q-Net - Application to Mobile Robots", Internal Journal of Control, Automation and Systems, vol.1, no.1, pp.142-148, 2003.

Robot path planning in unknown environment based on ant colony algorithm

Cu Xuan Tien, Young Sik Hong

*Department of Computer Science, Dongguk University
26 Pil-dong, 3-ga, Jung gu, Seoul, South Korea, 100 - 715
{tienbkct8@gmail.com, hongys@dgu.edu}*

Abstract: In this paper, we present Ant Colony Optimization Algorithm for path planning to a target for mobile robot in unknown environment. The proposed algorithm allows a mobile robot to navigate through static obstacles, and find the path in order to reach the target without collision. This algorithm provides the robot the possibility to move from the initial position to the final position (target). The proposed path finding strategy is designed in a grid-map form of an unknown environment with static unknown obstacles. The robot moves within the unknown environment by sensing and avoiding the obstacles coming across its way towards the target.

This work provides overviews of swarm intelligence and Ant Colony Optimization applications applied to many fields of our life particularly we will focus in mobile robot routing. Various mechanisms are presented in this paper to demonstrate the useful and wide combination of Ant Colony Optimization. Finally, enhancement to the mechanism is suggested and it is evaluated in MATLAB environment.

Keywords: Ant Colony Optimization (ACO), mobile robot, path planning

I. INTRODUCTION

Today, the robotics become favorite topics of many studies and its applications are applied in various problem of our life. There are many type of robot and they perform many functions. In the conquest of space exploration where they can be used to collect environment data such as rock, soil samples... In medical field, some specialized robots support physicians diagnose and help people with disabilities. Scientists in the world have created special type of robots replace human activities in the particularly dangerous position, for example in case of incidents at nuclear power factory or hygiene robot working in high building...

One of most important tasks in the control of mobile robot is path planning. In environment with obstacles, the role of path planning is to finding the appropriate collision – free path for mobile robot to move from start location to the destination point. There are many methods have been studied and applied in grid-based path planning such as A * (A star) algorithm [1], road map (Voronoi diagram and visibility graphs) [2], artificial potential field [3]...

In robotics field, working environment is divided into three kinds: the totally known, partly known, and total unknown. This paper will focus to total unknown environment, each robot has forage to find the way the target by co-operate with each other.

Ant colony algorithm was invented in 1992 by Marco Dorigo in his doctoral thesis. Since then this algorithm is used in many studies and achieve high performance. Multi ant system has been successfully applied in Travelling Salesman problem (TSP) [4], the Quadratic Assignment problem [5], Vehicle Routing problem [6], etc...

The paper is organized as follow: in the second section the ant colony algorithm is introduced and the next section is discussed about the path planning algorithm realization. In the last section, some result, experiment and conclusion are provided.

II. ANT COLONY ALGORITHM

Ant colony algorithm, based on behavior of real ants, is a nature approach to establish optimization path from nest to food source, it is a stochastic search algorithm and good effect has been obtained in solving combination optimization, function optimization, system identification, robot path planning, data mining, and network routing algorithm.

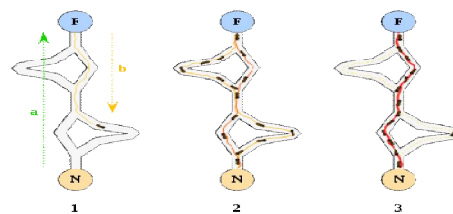


Figure 1: Ant colony foraging food

At the time of beginning, all ants move at random direction to find the way to the destination. Biologist have found by many studies and experiment that ants leave some chemical substance on the route that they have passed, which call “pheromone”. Other ants can smell this pheromone, and their path-taking decisions are depended on the amount of pheromone. When subsequent ants sense this trail of pheromone, they will follow the trail with a probability that is proportional to the concentration of pheromone – the higher the concentration, the larger the probability that subsequent ants will follow the trail. The pheromone evaporates at a

given rate which means that the strength of pheromone encountered by another ant is a function of the original pheromone strength and the time since the trail was laid.

Besides pheromones are deposited on the foraging path, ants also rely on heuristic information as well. The heuristic information is defined as the inverse of distance between the current point and the next point which ant can be go as show in below equation:

$$\mu_{ij} = \frac{1}{d_{ij}}$$

Therefore, the shorter the distance between two locations is, the better their heuristic information and vice-versa. Following with the intensity of pheromone trails and the heuristic information, the probability of the path which will be chosen by ant can be calculated. This probability is known as the transition probability:

$$P_{ij}^k(t) = \begin{cases} \frac{[\tau_{ij}(t)]^\alpha [\mu_{ij}(t)]^\beta}{\sum_{j \in Z} [\tau_{ij}(t)]^\alpha [\mu_{ij}(t)]^\beta} & \text{if } j \in Z \\ 0 & \text{if } j \notin Z \end{cases}$$

Where t is the time index, μ_{ij} is the heuristic information, τ_{ij} is the pheromone trail which has been evaporated when the ant move from point i to point j , α, β are the parameter of pheromone function and heuristic function, Z is the set of all moveable point from current point.

III. IMPLEMENTATION OF ANT COLONY ALGORITHM IN ROBOT PATH PLANNING

1. Environment initialization

We will use 20x20 grid model to present the environment of mobile robot. Assume that the space in which a robot moves is a limited region with several obstacles of different size in two – dimensional plane. Assume that the edge of each cell is 1 unit that presents the radius size of scope in which a robot could move freely. Obstacles occupy one or more grids are created by a matrix which each value is distributed from 1 to 5. The value 1 is indicated a cell of obstacles, and the values from 2 to 5 are the free cell.

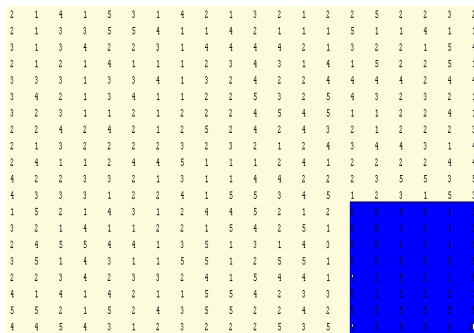


Figure 2: Robot environment matrix

As we can see in the figure 2 the zone near the destination point have high value which is the more

attractive for the ant robot. This is the parameter will be used to calculate the cost function in probability transition in next section.

From the matrix in figure 2 the environment for robot path planning will be constructed as figure 3 with the top – left are the starting cell and the bottom – right is the destination cell

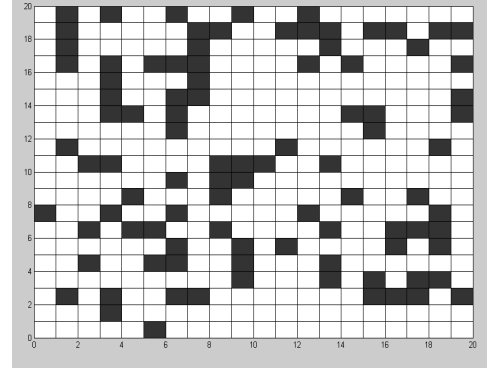


Figure 3: Robot environment

2. Coordinate and mapping

Each cell is assigned by a number from 1 to 400 as figure below which is defined by marking sequentially from left to right, top to bottom.

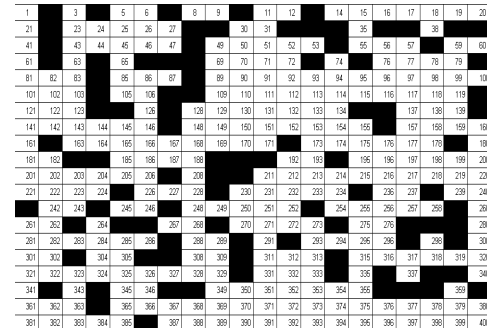


Figure 4: Environment mapping

The mapping relationship between (x_i, y_i) and node number i can be defined by formula:

$$\begin{cases} x_i = \text{mod}(i, N) - 0.5 \\ y_i = N - \text{ceil}\left(\frac{i}{N}\right) + 0.5 \end{cases}$$

If $x_i = -0.5$ then $x_i = N - 0.5$. Where N is the size of map ($N=20$), $\text{mod}(i, N)$ is function to calculate the remainder value when integral number i divide by N , $\text{ceil}(x)$ is function which return the largest integral value of x .

3. Movement Rule

Moveable area for ant robot in each step is chosen

from maximum 8 cells around the current cell without obstacles. For example, assume that the current position of robot is cell number 168 then the set of next step are 148, 149, 167, 169, 187, and 188

147	148	149
167	168	169
187	188	189

Figure 5: Moveable area

Each ant robot will chose the next cell to move accordance the visibility of the cell and pheromone intensity. In the initialization state, all ants have no information about environment so they forage to reach the destination by random step.

After that ant robot will go to the next point P_j and J given by:

$$j = \begin{cases} \text{argmax}\{[\tau_i(P_i)]^\alpha [\mu_i(P_i)]^\beta [\text{cost}(P_i)]^\gamma\}, & \text{if } q \leq q_0 \\ J, & \text{if } q > q_0 \end{cases}, i \in Z$$

Where q is the random number uniformly distributed between [0, 1], $q_0 \in [0,1]$ is the threshold value set in the initialization, $\text{cost}(P_i)$ is the value of cell P_i , γ denotes the relative significance of cost value and J is calculated by:

$$P_j^k(n) = \frac{[\tau_i(P_i)]^\alpha [\mu_i(P_i)]^\beta [\text{cost}(P_i)]^\gamma}{\sum_{j \in Z} [\tau_i(P_i)]^\alpha [\mu_i(P_i)]^\beta [\text{cost}(P_i)]^\gamma}$$

Z is the set of moveable area which is discussed above and P_j^k is the transition probability to point J. The heuristic information will be determined as equation below to improve the efficiency and getting better solution:

$$\mu_i = \frac{1}{\sqrt{(x_i - x_e)^2 + (y_i - y_e)^2}}$$

Here i is the next node and e is the destination node.

4. Pheromone Updating Rule

- Localized pheromone update

When the ant has passed the cell P_i , the pheromone will be updated by:

$$\tau_i(n+1) = (1 - \rho)\tau_i(n) + \rho\tau_0$$

- Global update:

After all ants reached the target, the pheromone will be refreshed and update by equation below:

$$\begin{aligned} \tau_i(n+1) &= (1 - \rho)\tau_i(n) + \Delta\tau_i(n) \\ \Delta\tau_i(n+1) &= (1 - \rho)\Delta\tau_i(n) + Q/\min(L_k) \end{aligned}$$

Where $0 < \rho < 1$ is the erased rate of pheromone and τ_0 is the initial value of pheromone

IV. EXPERIMENT AND RESULT

The algorithm has been simulated by MATLAB language by Intel Pentium IV with Core2Dual 1.8 GHZ, 1Gigabytes memory running in WindowXp environment. This experiment we use a map with 20x20 grid and all operations were done by 10 ant robots. All parameters have been using for simulation $\alpha = 0.5$, $\beta = 5$, $\gamma = 0.5$, $q_0 = 0.5$, $\rho = 0.1$, number iteration is 50 and initialization value of pheromone is 1. The figure below is the result when ant robot using basic algorithm, the length of minimal path is 31.5563 (28 cells)

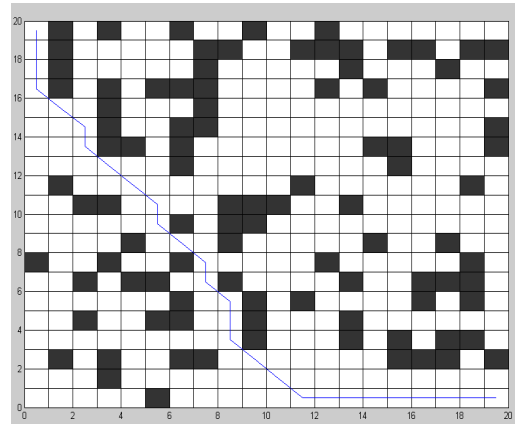


Figure 6: Basic algorithm result

And the result with improved ant colony algorithm with minimal length is 29.779 (25 cells)

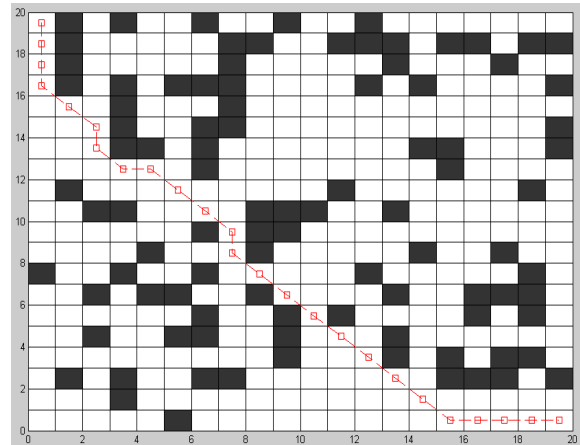


Figure 7: Improved algorithm result

V. CONCLUSION

In this paper, ant colony optimization is presented detail to provide an efficient method for solving robot path planning problem. Ant colony optimization is a meta-heuristic in which a colony of artificial ants cooperates in finding good solutions to difficult discrete optimization problems. Cooperation is a key design component of ACO algorithms: The choice is to allocate the computational resources to a set of relatively simple agents (artificial ants) that communicate indirectly, that is, by indirect communication mediated by the environment.

The application of ACO is particularly interesting for: (1) NP – hard problem, which cannot be efficiently solved by most traditional algorithms; (2) Dynamic shortest path problem in which some properties of the problem's graph representation change over time concurrently with the optimization process; and (3) problems in which the computational architecture is spatially distributed. The key elements are cost value and improved heuristic function, the robot path planning scheme has been simulated using MATLAB language to solve efficiently the Ant Colony Algorithm using two-dimension grid model with static obstacles in order to make the robot's environment.

REFERENCES

- [1] (2010) Junfeng Yao, Chao Lin, Xiaobiao Xie, Andy JuAn Wang, Chih-Cheng Hung, "Path planning for Virtual Human Motion Using Improved A* Algorithm" 2010 Seventh International Conference on Information Technology, DOI 10.1109/ITNG.2010.53
- [2] (2007), Priyadarshi Bhattacharya and Marina L. Gavrilova, "Voronoi diagram in optimal path planning", 4th International Symposium on Voronoi Diagrams in Science and Engineering (ISVD 2007)
- [3] (1991), J. Borenstein, Y. Koren, "The vector field histogram -fast obstacle avoidance for mobile robots", IEEE Journal of Robotics and Automation Vol 7, No 3, June 1991, pp. 278-288.
- [4] (1997), Marco Dorigo, Luca Maria Gambardella, "Ant colonies for the traveling salesman problem", publication in BioSystems.
- [5] (2006), Malek Mouhoub and Zhijie Wang, "Ant Colony with Stochastic Local Search for the Quadratic Assignment Problem", Proceedings of the 18th IEEE International Conference on Tools with Artificial Intelligence (ICTAI'06)
- [6] (2010), Hua Bin, Ding Huai-long, "Vehicle Routing Problem of Logistics Based on Dynamic Ant Colony Algorithm", 2010 Second International Workshop on Education Technology and Computer Science

Improved Artificial Bee Colony Algorithm for Large-Scale Optimization Problems

Ryuta Gocho[†], Akihide Utani[‡], and Hisao Yamamoto[‡]

[†]Graduate School of Engineering, Tokyo City University

[‡]Faculty of Knowledge Engineering, Tokyo City University

1-28-1, Tamazutsumi, Setagaya, Tokyo 158-8557, Japan

{autani; yamahisa}@tcu.ac.jp

Abstract: This paper proposes a new optimization algorithm based on Artificial Bee Colony (ABC) algorithm that has the good performance on large-scale optimization problems. We evaluate the proposed algorithm through numerical experiments on well-known benchmark functions, such as *Rosenbrock* function, *Rastrigin* function, *Schwefel* function, *Ackley* function and *Griewank* function, and discuss its development potential. In numerical experiments, the performance of the proposed algorithm is compared with those of the existing optimization algorithms.

Keywords: Wireless Sensor Networks, Particle Swarm Optimization, Query Dissemination, Long-Term Operation.

I. INTRODUCTION

The minimization of multimodal functions with many local and global minima is a problem that frequently arises in diverse scientific fields and numerous engineering design problems. This problem is NP-hard in the sense of its computational complexity even in simple cases. As techniques of computing a global minimum of the objective function, many meta-heuristics, which are search algorithms for optimization based on heuristic knowledge, have been proposed. Some well-known representative meta-heuristics are Simulated Annealing and Tabu Search, which are the traditional optimization algorithms, Genetic Algorithms and Immune Algorithms, which are classified as evolutionary computation techniques, and Ant Colony Optimization algorithms and Particle Swarm Optimization algorithms, which belong to the category of swarm intelligence algorithms.

In meta-heuristics, Genetic Algorithms and Immune Algorithms, classified as evolutionary computation techniques, are generally techniques for combination optimization problems. In Genetic Algorithms and Immune Algorithms, the variables of continuous type are frequently translated into those of discrete (genetic) type. If there is a dependency between variables, therefore, a promising solution may be destroyed during the solution search process (genetic operation) and the solution search performance may deteriorate. To the contrary, Particle Swarm Optimization algorithm can directly handle the variables of continuous type. Even when there is a dependency between variables, therefore, an efficient and effective solution search can be realized. Recently, Particle Swarm Optimization algorithm is intensively researched because it is superior to the other algorithms on

many difficult optimization problems. The ideas that underlie Particle Swarm Optimization algorithm are inspired not by the evolutionary mechanisms encountered in natural selection, but rather by the social behavior of flocking organisms, such as swarms of birds and fish schools. Particle Swarm Optimization algorithm is a population-based algorithm that exploits a population of individuals to probe promising regions of the search space. The algorithm is simple and allows unconditional application to various optimization problems. However, it has been confirmed that the performance of Particle Swarm Optimization algorithm on large-scale optimization problems is not always satisfactory.

This paper proposes a new optimization algorithm based on Artificial Bee Colony (ABC) algorithm that has the good performance on large-scale optimization problems. We evaluate the proposed algorithm through numerical experiments on well-known benchmark functions, such as *Rosenbrock* function, *Rastrigin* function, *Schwefel* function, *Ackley* function, and *Griewank* function, and discuss its development potential. In numerical experiments, the performance of the proposed algorithm is compared with those of the existing optimization algorithms. The rest of this paper is organized as follows. In Section II, the proposed algorithm is described. In Section III, experimental results are reported. Finally, the paper closes with conclusions and ideas for further study in Section IV.

II. PROPOSED ALGORITHM

In ABC algorithm, the colony of artificial bees contains three groups of bees: employed bees, onlookers and scouts. In the initial state of “artificial bee colony”, the colony consists of the employed bees and the onlookers.

At the initial stage of ABC algorithm, multiple solution points are randomly set in multidimensional solution search space. For every solution point, there is only one employed bee. In other words, the number of employed bees is equal to the number of solution points. The employed bee of an abandoned solution point becomes a scout. The search carried out by the artificial bees can be summarized as follows:

1. Each employed bee randomly searches a more suitable solution point within the neighborhood of the solution point in its memory.
2. Employed bees share their search information with onlookers and then onlookers select one of solution points by the following equations:

$$fit_i^k = \begin{cases} \frac{1}{1 + f(\mathbf{x}_i^k)}, & f(\mathbf{x}_i^k) \geq 0 \\ 1 + abs(f(\mathbf{x}_i^k)), & f(\mathbf{x}_i^k) < 0 \end{cases} \quad (i = 1, \dots, SN) \quad (1)$$

$$P_i^k = fit_i^k / \sum_{n=1}^{SN} fit_n^k \quad (2)$$

where $f(\mathbf{x})$ is the objective function of variables (\mathbf{x}) . The subscript $i (i = 1, \dots, SN)$ and the superscript k indicates the solution point's index and the number of search iterations, respectively. SN is the number of solution points. Onlookers select one of solution points by referring to the probability (P_i^k) of each solution point based on the search information from employed bees.

3. Each onlooker randomly searches a more suitable solution point within the neighborhood of the solution point chosen by itself.
4. The employed bee of an abandoned solution point becomes a scout and starts to search a new solution point randomly.

The proposed algorithm is an advanced ABC algorithm. For effectively searching a global optimum solution, ABC algorithm is improved as follows:

- 1) Improvement of Eq.(1) to compute fitness (fit_i^k)

For improving the adaptability to various engineering problems, in the proposed algorithm, the fitness (fit_i^k) of each solution point is computed as follows:

$$fit_i^k = \begin{cases} \frac{1}{f(\mathbf{x}_i^k) - f_{bound}}, & f(\mathbf{x}_i^k) - f_{bound} \geq f_{accuracy} \\ \frac{1}{f_{accuracy}}, & f(\mathbf{x}_i^k) - f_{bound} < f_{accuracy} \end{cases} \quad (i = 1, \dots, SN) \quad (3)$$

where f_{bound} represents the boundary value of $f(\mathbf{x}^+)$ on \mathbf{x}^+ acceptable as a solution for every engineering pro-

blem and $f_{accuracy}$ shows the exactness of convergence to f_{bound} .

- 2) Improvement of Step1 and Step3 in ABC algorithm

For improving the performance of solution search, in the proposed algorithm, a more suitable solution point is determined by roulette or elite selection based on the probability (P_i^k) of Eq.(2).

- 3) Improvement of Step4 in ABC algorithm

The search by scouts corresponds to the mutation of Genetic Algorithms. In the proposed algorithm, the search by scouts is not executed to no effect.

III. EXPERIMENTAL RESULTS

Through numerical experiments on the following D dimensional benchmark functions, the performance of the proposed algorithm is investigated to verify its effectiveness.

- Rosenbrock function

$$\begin{aligned} \min. f_1(\mathbf{x}) &= \sum_{j=1}^{D-1} \{ 100(x_{j+1} - x_j^2)^2 + (x_j - 1)^2 \} \\ \text{subj. to } &-100 \leq x_j \leq 100, \quad j = 1, \dots, D \\ \mathbf{x}^* &= (1, \dots, 1), \quad f_1(\mathbf{x}^*) = 0 \end{aligned}$$

- Rastrigin function

$$\begin{aligned} \min. f_2(\mathbf{x}) &= \sum_{j=1}^D \{ x_j^2 - 10 \cos(2\pi x_j) + 10 \} \\ \text{subj. to } &-5.12 \leq x_j \leq 5.12, \quad j = 1, \dots, D \\ \mathbf{x}^* &= (0, \dots, 0), \quad f_2(\mathbf{x}^*) = 0 \end{aligned}$$

- Schwefel function

$$\begin{aligned} \min. f_3(\mathbf{x}) &= 418.98288727 D + \sum_{j=1}^D -x_j \sin(\sqrt{|x_j|}) \\ \text{subj. to } &-512 \leq x_j \leq 512, \quad j = 1, \dots, D \\ \mathbf{x}^* &= (420.968750, \dots, 420.968750), \quad f_3(\mathbf{x}^*) = 0 \end{aligned}$$

- Ackley function

$$\begin{aligned} \min. f_4(\mathbf{x}) &= 20 + e - 20 \exp \left(-0.2 \sqrt{\frac{1}{D} \sum_{j=1}^D x_j^2} \right) \\ &\quad - \exp \left(\frac{1}{D} \sum_{j=1}^D \cos(2\pi x_j) \right) \\ \text{subj. to } &-30 \leq x_j \leq 30, \quad j = 1, \dots, D \\ \mathbf{x}^* &= (0, \dots, 0), \quad f_4(\mathbf{x}^*) = 0 \end{aligned}$$

- Griewank function

$$\begin{aligned} \min. f_5(\mathbf{x}) &= \frac{1}{4000} \sum_{j=1}^D x_j^2 - \prod_{j=1}^D \cos \left(\frac{x_j}{\sqrt{j}} \right) + 1 \\ \text{subj. to } &-600 \leq x_j \leq 600, \quad j = 1, \dots, D \\ \mathbf{x}^* &= (0, \dots, 0), \quad f_5(\mathbf{x}^*) = 0 \end{aligned}$$

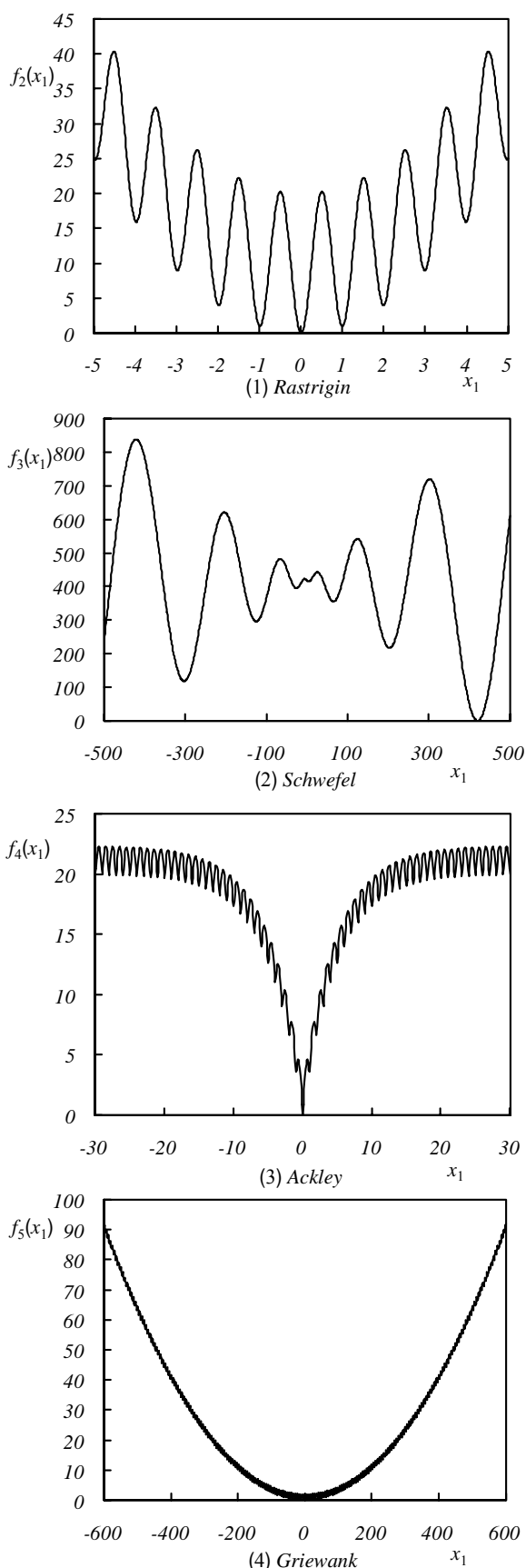


Fig.1. Landscapes of multimodal functions ($D = 1$)

\mathbf{x}^* of each benchmark function represents a global optimum solution. Fig.1 shows landscapes of multimodal functions ($D = 1$).

In experimental results reported, the proposed algorithm is evaluated through the comparison with the existing ones, which are Particle Swarm Optimization algorithm[1,2], Differential Evolution algorithm[3], and the original ABC algorithm[4]. The results of numerical experiments are shown in Tables 1, 2, 3, and 4. Experimental results indicate that the proposed algorithm is a promising one for large-scale optimization problems.

IV. CONCLUSIONS

In this paper, a new optimization algorithm based on Artificial Bee Colony (ABC) algorithm has been proposed. The proposed algorithm has been evaluated through numerical experiments on well-known benchmark functions, such as *Rosenbrock* function, *Rastrigin* function, *Schwefel* function, *Ackley* function, and *Griewank* function. From experimental results, it has been confirmed that the proposed algorithm has the development potential as an efficient one for large-scale problem.

REFERENCES

- [1] Kennedy J and Eberhart RC (1995), Particle swarm optimization. Proc. IEEE International Conference on Neural Networks, pp.1942-1948
- [2] Kennedy J and Eberhart RC (2001), Swarm intelligence. Morgan Kaufmann Publishers, San Francisco.
- [3] Storn R and Price K (1997), Differential evolution - A simple and efficient heuristic for global optimization over continuous space. J. of Global Optimization, vol.11, pp.341-359
- [4] Karaboga D and Basturk B (2007), A powerful and efficient algorithm for numerical function optimization: artificial bee colony (ABC) algorithm. J. Global Optimization, vol.39, pp.459-471.

Table 1 Experimental results on PSO algorithm

Problem	Dim.	Best	Ave.	Worst
Rosenbrock	50	4.38×10^3	7.00×10^4	2.26×10^5
	75	9.20×10^3	1.79×10^5	4.63×10^5
	100	5.08×10^4	7.28×10^5	3.18×10^6
	150	9.86×10^4	1.48×10^6	5.91×10^6
Rastrigin	50	1.05×10^2	1.81×10^3	3.14×10^3
	75	1.58×10^2	2.30×10^3	3.26×10^3
	100	2.72×10^2	3.71×10^3	6.10×10^3
	150	3.54×10^2	6.60×10^3	9.31×10^3
Schwefel	50	5.39×10^3	9.78×10^3	1.25×10^4
	75	9.20×10^3	3.48×10^4	4.52×10^4
	100	1.92×10^4	6.92×10^4	9.88×10^4
	150	3.35×10^4	4.07×10^5	5.65×10^5
Ackley	50	1.82×10^0	2.11×10^1	2.65×10^1
	75	2.54×10^0	4.05×10^1	6.02×10^1
	100	4.84×10^0	2.40×10^2	4.30×10^2
	150	5.79×10^0	2.61×10^2	8.90×10^2
Griewank	50	1.23×10^0	1.91×10^1	2.13×10^1
	75	3.89×10^0	4.93×10^1	9.83×10^1
	100	4.01×10^0	7.12×10^1	1.51×10^2
	150	5.99×10^0	7.05×10^1	1.87×10^2

Table 3 Experimental results on ABC algorithm

Problem	Dim.	Best	Ave.	Worst
Rosenbrock	50	1.36×10^0	1.25×10^2	8.80×10^2
	75	2.30×10^0	5.36×10^2	9.79×10^3
	100	9.96×10^1	9.07×10^2	9.82×10^3
	150	9.76×10^2	2.85×10^3	1.40×10^4
Rastrigin	50	4.51×10^{-4}	3.53×10^0	1.25×10^1
	75	4.93×10^0	2.42×10^1	9.82×10^1
	100	6.22×10^1	7.16×10^1	1.02×10^2
	150	1.28×10^2	2.77×10^2	3.22×10^2
Schwefel	50	8.98×10^2	1.30×10^3	1.97×10^3
	75	2.73×10^3	6.01×10^3	6.56×10^3
	100	6.02×10^3	9.31×10^3	1.00×10^4
	150	9.60×10^3	1.62×10^4	3.20×10^4
Ackley	50	4.74×10^{-4}	1.71×10^{-3}	2.24×10^{-2}
	75	1.30×10^{-1}	7.96×10^{-1}	1.58×10^0
	100	1.89×10^0	2.49×10^0	4.12×10^0
	150	4.57×10^0	5.75×10^0	6.68×10^0
Griewank	50	8.50×10^{-7}	9.21×10^{-3}	3.73×10^{-2}
	75	4.26×10^{-4}	4.57×10^{-2}	1.28×10^{-1}
	100	8.17×10^{-3}	7.94×10^{-2}	5.34×10^{-1}
	150	1.79×10^{-2}	7.17×10^{-1}	9.97×10^{-1}

Table 2 Experimental results on DE algorithm

Problem	Dim.	Best	Ave.	Worst
Rosenbrock	50	9.01×10^1	1.32×10^2	9.02×10^2
	75	7.09×10^2	1.38×10^3	1.92×10^3
	100	1.08×10^4	1.73×10^4	2.79×10^4
	150	8.45×10^5	1.97×10^6	4.12×10^6
Rastrigin	50	7.62×10^{-2}	4.55×10^0	4.23×10^1
	75	1.53×10^1	8.77×10^1	1.81×10^2
	100	1.54×10^2	2.21×10^2	3.22×10^2
	150	2.98×10^2	5.59×10^2	7.38×10^2
Schwefel	50	1.14×10^3	2.24×10^3	4.62×10^3
	75	6.27×10^3	9.87×10^3	1.11×10^4
	100	1.24×10^4	3.45×10^4	4.10×10^4
	150	5.72×10^4	6.70×10^4	7.54×10^4
Ackley	50	9.89×10^{-4}	2.44×10^{-3}	3.56×10^{-3}
	75	2.66×10^{-1}	8.52×10^{-1}	7.25×10^0
	100	5.26×10^0	7.81×10^0	8.01×10^0
	150	8.59×10^0	9.15×10^0	9.45×10^0
Griewank	50	5.42×10^{-6}	9.80×10^{-3}	7.30×10^{-2}
	75	5.72×10^{-2}	1.47×10^{-1}	3.89×10^{-1}
	100	4.19×10^{-1}	6.24×10^{-1}	3.83×10^0
	150	2.02×10^0	3.08×10^0	5.31×10^0

Table 4 Experimental results on the proposed algorithm

Problem	Dim.	Best	Ave.	Worst
Rosenbrock	50	1.39×10^{-2}	8.73×10^0	9.71×10^1
	75	7.01×10^{-1}	2.57×10^1	1.14×10^2
	100	5.75×10^0	5.34×10^1	2.10×10^2
	150	9.98×10^1	1.32×10^2	4.39×10^3
Rastrigin	50	2.08×10^{-10}	8.10×10^{-1}	2.99×10^0
	75	2.80×10^0	8.00×10^0	1.57×10^1
	100	1.21×10^1	1.39×10^1	2.92×10^1
	150	4.67×10^1	5.66×10^1	9.53×10^1
Schwefel	50	1.18×10^2	2.03×10^2	1.18×10^3
	75	1.43×10^3	2.39×10^3	3.06×10^3
	100	2.54×10^3	3.03×10^3	5.26×10^3
	150	6.78×10^3	9.02×10^3	9.91×10^3
Ackley	50	3.30×10^{-9}	5.70×10^{-5}	2.21×10^{-3}
	75	1.85×10^{-5}	2.44×10^{-4}	1.55×10^{-3}
	100	1.51×10^{-3}	7.17×10^{-2}	3.74×10^{-1}
	150	1.48×10^{-1}	1.96×10^{-1}	2.46×10^0
Griewank	50	1.14×10^{-16}	9.13×10^{-5}	4.56×10^{-3}
	75	7.92×10^{-11}	3.61×10^{-3}	6.84×10^{-2}
	100	4.00×10^{-8}	5.49×10^{-3}	3.76×10^{-2}
	150	1.74×10^{-4}	1.68×10^{-2}	2.56×10^{-1}

Simulation of self-reproduction phenomenon of cells in two-dimensional hybrid-cellular automata model

Takeshi Ishida

*Nippon Institute of Technology, 4-1, Gakuendai, Miyashiro, Minami-Saitama, Saitama, 345-8501 Japan
(Tel : 81-480-33-7719; Fax : 81-480-33-7745)
(Email ishida06@ecoinfo.jp)*

Abstract: Understanding the generalized mechanism of self-reproduction is considered to be fundamental for application in various fields such as mass-production of molecular machines of nanotechnology. We developed a model for simulating cellular self-reproduction in two-dimensional cellular automaton. We demonstrated that the following 3 functions can be realized. (1) Formation of a border similar to cell membrane. (2) Self-replication is achieved while maintaining a carrier containing information. (3) The division of the cell membrane is achieved while maintaining the total structure. Furthermore we constructed a hybrid cellular automaton model. To reduce the transition rules number, we considered not only the state transition rules but also the concentration diffusion of the Gray Scott model, which emerges self-reproduction phenomenon with certain parameters.

Keywords: self-reproduction, cellular automaton, cell division, Gray Scott model

I. INTRODUCTION

Understanding the generalized mechanism of self-reproduction is considered to be fundamental for application in various fields such as mass-production of molecular machines of nanotechnology and artificial synthetic of biology (synthetic biology). Furthermore, it is considered that large, complex machine systems of over a certain size are difficult to construct by the top-down approach. Therefore, these complex systems are required to be constructed by the bottom-up approach, by applying the phenomenon of biological self-organization. Thus we have to elucidate not only the details of the real cellular reaction network but also the necessary conditions for self-organized, self-replicating cells.

Fifty years ago, von Neumann[1] initiated the study of self-reproduction model from a mathematical view point. This study theoretically proved the possibility of constructing a self-reproducing machine by cell state and transition rules of two-dimensional square cells. On the other hand, Neumann's self-reproducing machine was large in size; therefore, it is difficult to implement this machine perfectly in a computer system [2]. Thereafter, Langton[3] developed a simple machine capable of self-reproduction abandoning the completeness of Neumann's machine. Although the shape was very simple, the rules of transition are complicated and it could reproduce specific shapes.

In our previous study[4], we developed a model for simulating cellular self-reproduction in two-dimensional cellular automaton. We demonstrated that the following 3 functions can be realized by the transition of two adjacent cells.

- (1) Formation of a border similar to a cell membrane.
- (2) Self-replication is achieved while maintaining a carrier containing information (information carrier).
- (3) The division of the cell membrane is achieved while maintaining the total structure of the cell.

This study demonstrated the self-reproducing ability of a shape that was similar to that of real living cell. Figure 1 showed the results of a cell-type self-reproducing two-dimensional cellular automaton. This is not a study to clarify all the necessary and sufficient conditions of self-reproduction. It is considered that it is

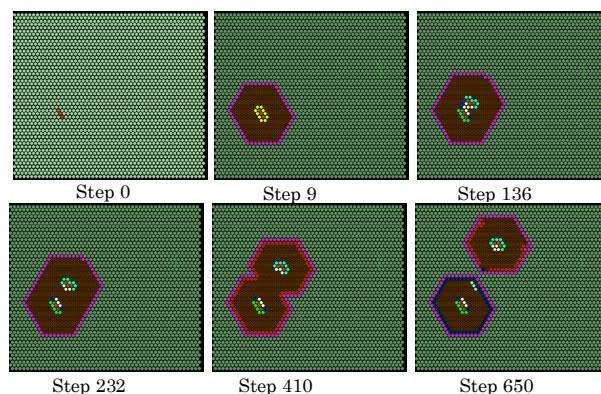


Fig.1. Results of a cell-type self-reproducing two-dimensional cellular automaton [4]

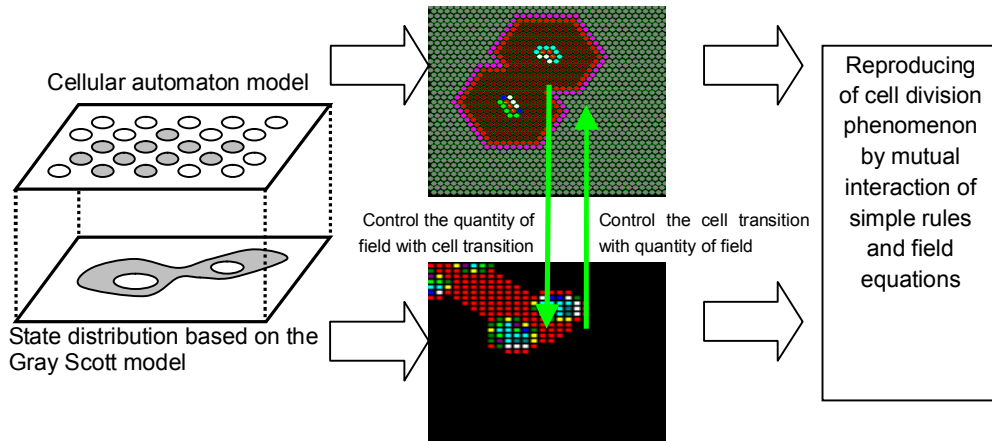


Fig.2. Outline of hybrid cellular automaton model

possible to simulate self-replication in a real dynamic chemical reaction environment by applying the transition rules determined in this study.

II. OBJECTIVE

In this study, we constructed a hybrid cellular automaton model. Figure 2 shows the outline of hybrid model. To reduce the transition rules number, we considered not only the state transition rules but also the concentration diffusion of the field. We chose the Gray Scott model, which emerges self-reproduction phenomenon with certain parameters. In this hybrid model, information carriers activate the trigger of the self-reproduction phenomenon of the Gray Scott model, and cell membrane was formed by a part of the specific concentration of Gray Scott model. Using this model, we reduced the number of transition rules.

transition rules of cell membrane formation and settled the total states in all cells. Then, we applied the transition rules for the division of information carriers, following which we applied the transition rule of movement of the information carriers and formation of the nuclear membrane.

To cause objective state transitions of the cellular automata, these rules cause unexpected side effects. We divided the transition into 4 phases and discovered the transition rules because the discovery of whole transition rules was difficult at a time.

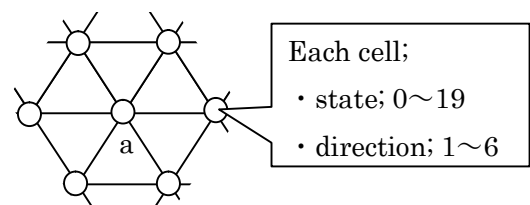


Fig.3 Triangular grid model in this study

III. RESEARCH METHOD

1. Cellular automaton model

A two-dimensional triangular grid model was used in this study (Fig.3). The cell automaton was constructed by transition rules such that the state of the next step was decided by the state of the own cell and that of 6 neighboring cells. Each cell has a state (0–19) and direction (6 directions) as an attribute. In the triangular grid, calculation starts from a certain initial condition. The transition rules were divided into the following 4 phases: 1) state transition concerning cell membrane formation, 2) division of the information carriers, 3) movement of the information carriers, and 4) formation of the nuclear membrane surrounding the information carriers. In other words, first we applied

2. Gray Scott model

Concerning this cellular automaton model, cell transitions patterns are similar to the physical phenomena. Thus we considered the possibility of substitute of transition rules to non-linear quantity model like Gray Scott model. Equations of Gray Scott model is as follow. Self-replication patterns are caused under certain conditions ($D_u = 0.04$, $D_v = 0.02$, $F = 0.02$, $k = 0.06$, in this study).

$$\frac{\partial V}{\partial t} = D_u \Delta V - U^2 V + F(1 - V) \quad (1)$$

$$\frac{\partial U}{\partial t} = D_v \Delta U + U^2 V - (F + k)U \quad (2)$$

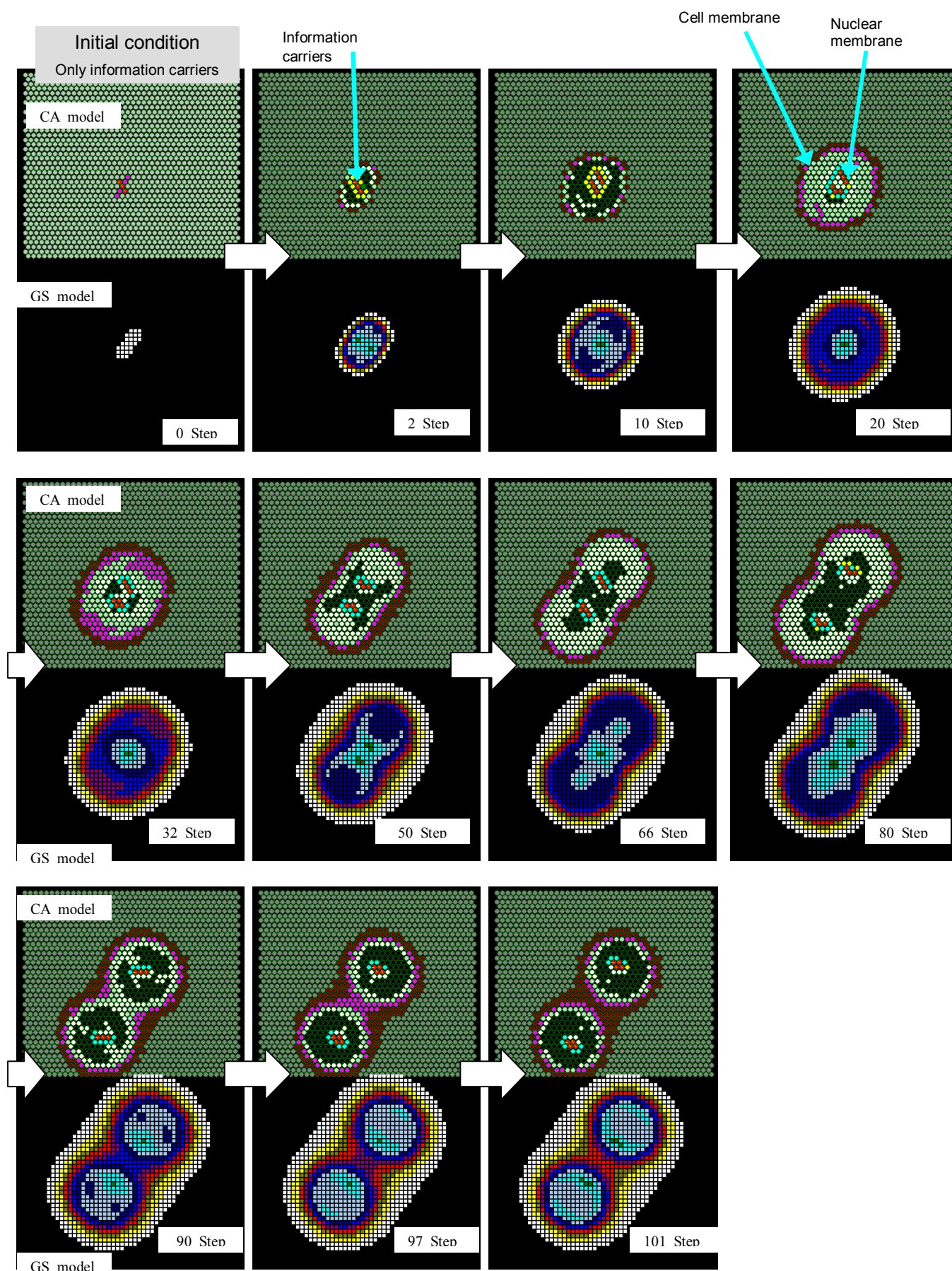


Fig.4 Results of hybrid cellular automaton model

Table.1 Number of transition rules

CA model		Hybrid model	
Process	Number of transition rules	Alternate physical phenomenon	Number of transition rules
Application of transition rules of cell membrane formation	34	Gray Scott Model	4
Application of transition rules of information carriers division	17	—	17
Application of transition rules of information carriers movement	12	—	12
Application of transition rules of nuclear membrane formation	13	—	5

3. Transition rules

Each cell was renewed by transition rules and the state of the next step was decided by the state of the cell and that of 6 neighboring sites. It is not found the method to derive transition rules according to uniformity law automatically at this time. Therefore, we constructed step-by-step transition rules according to the movement of the cell in the automaton.

In this hybrid model, firstly information carriers activate the trigger of the Gray Scott model. States of cell membrane appears under certain concentration of Gray Scott fields. The movement of nuclear membrane was controlled by concentration of Gray Scott fields.

IV. RESULTS

Figure 4 shows the process of formation of cell membrane, and the process of division of the information carriers with the cell membrane. Thus, we were able to replicate the phenomenon of cell-like division.

Table1 shows the number of transition rules of cellular automaton model and hybrid model. Using this hybrid model, we reduce the number of transition rules.

V. CONCLUSION

Our model produced a self-reproducing phenomenon in a cell shape with few state transition rules. Future directions are as follows:

- Find other transition rule sets.
- Find a way to automatically derive transition rules based on the uniformity law.
- Apply transition rules to particle collision theoretically.

We believe that transition rules of this model can be applied to simulate self-replication phenomena in a real dynamic chemical reaction environment by applying transition rules determined in this study. We plan first to achieve cell-division simulation of a discrete particle reaction. It is comparatively easy to replace state transition rules with collision / reaction rules of discrete particles.

We next plan to achieve cell-division simulation of continuous chemical reaction simulation. We can convert discrete particles rules to chemical equations.

REFERENCES

- [1] J. von Neumann; Theory of Self-replicating Automata, University of Illinois Press, 1966
- [2] D. Mange, A. Stauffer, L. Peparodo, and G. G. tempesti; A Macroscopic View of Self-Replication, Proceeding of the IEEE, vol.92, No.12, Dec. 2004
- [3] C. Langton ed, Artificial Life, 1/48, Addison-Wesley, 1989
- [4] Takeshi Ishida, Simulating self-reproduction of cells in a two-dimensional cellular automaton., Journal of Robotics and Mechatronics, Vol.22, No.5, pp.669-676, 2010

A Physics Modeling of Butterfly's Flight Control by GA and ANN and Its Over-evolution Problem

R. Ooe, I. Suzuki, M. Yamamoto and M. Furukawa

Graduate School of Information and Science, Hokkaido University, Sapporo, Hokkaido, Japan

(Tel : +81-11-706-6445; Fax : +81-11-706-6443)

{ooe, ikuo, masahito, mack}@complex.eng.hokudai.ac.jp)

Abstract: We describe a simple physics model of a butterfly and an approach to its flight control by the genetic algorithm (GA) and the artificial neural network (ANN). A physics model consists of two kinetic equations which are led by a simplification of fluid force. A butterfly's flight is controlled by an ANN. The GA optimizes weights of the ANN for the suitable flight. This approach resulted in the flight which is obtained by maximizing the prepared fitness. However, the optimized ANN did not have a generality and a butterfly fell down in changing the initial height. A transition of fitness throughout processes of evolution showed that too much optimization tends to break the generality. We call this phenomenon "over-evolution". Changing conditions of experiments prevented the over-evolution.

Keywords: Physical simulation, Drag force, Butterfly, Real-coded genetic algorithm, Artificial neural network

I. INTRODUCTION

Flights by a flap of wings are difficult actions. The motion of life existing on the ground is restricted to the two-dimensional space, that is, the ground. On the other hand, life in the air, such as the bird and the butterfly, is able to move freely in the three-dimensional space without falling down. It is very interesting to understand these flying creatures deeply. However, there are few researches on them as the artificial life because of the requirements of many computational resources.

We first overlook previous works on the three-dimensional physical simulation. Terzopoulos et al [1]. modeled the artificial fish by springs and sensors. Although it seemed to be a real fish, the calculation of the drag force was dispensed with. Usami [2] simulated the motion of a fish using the moving particle method. However, it was confined to the two-dimensional simulation. Wu et al [3]. proposed a model of bird for the computer graphics. Their bird consisted of parts connected by springs and it was taken account of the lift and drag forces. It is one of a few studies of the flying creatures.

Sims [4] showed various shapes of artificial life and behaviors, such as walking, jumping and swimming. Both shapes and behaviors had been acquired by the evolutionary algorithm (EA). This work showed that the environment gave life various shapes and behaviors, so it is very remarkable. Reil et al [5]. applied EAs to the control problem of bipedal walking.

We had studied a modeling and simulating method

for various types of artificial life using physics engines [6]. To simplify the flight mechanism and to reduce a computational amount, we modeled a butterfly's flight into two kinetic equations. In this paper, we describe the method of a model and control of butterfly. A model is described in Section Two and the control in Section Three. We also refer to the problem about an optimized controller. Section Four explains the details of this problem and a solution based on properties of actions. Finally, our work is summarized in Section Five as conclusion.

II. MODELING

1. Drag force

The external force that acts on a flying butterfly is drag force besides gravity. Simplified the drag force ΔD for each surface of an object is

$$\Delta D = \frac{1}{2} \rho \Delta A_p C_d v_p^2 \quad (1)$$

where ρ is the density of air, ΔA_p is the area of a surface, C_d is the drag coefficient and v_p is the velocity relative to air.

The drag force works at the center of gravity and it is perpendicular to a surface. In applying (1) to an object, the drag force is calculated for only the surface facing to the direction of the velocity. If the surface is relatively large, we divide it into sub-surfaces and calculate for each sub-surface for accuracy.

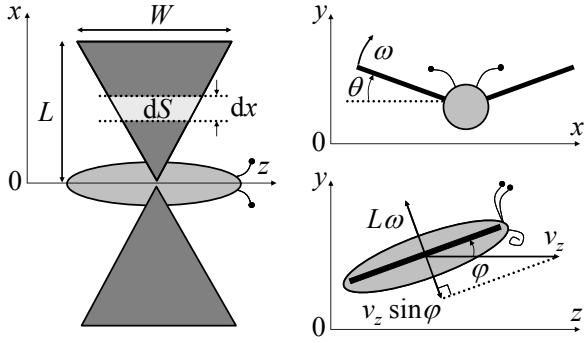


Fig.1. The shapes and parameters of the model

2. Modeling butterfly

Based on (1), two kinetic equations are formalized. For simplification, we assume that a wing of butterfly is an inverted triangle plane which is shown in Fig.1. Parameters used in the model are listed in Table 1.

A. Drag force acting on wings

Wings rotate up and down on the body. A minute area $dS(x)$ at a distance x from the body, and drag force $dF(x)$ which acts on $dS(x)$ is expressed by

$$dS(x) = \frac{W}{L} x dx \quad (2)$$

$$dF(x) = \frac{1}{2} \rho C_d (x \omega)^2 dS \quad (3)$$

(3) is integrated from $x = 0$ to $x = L$, then the total drag force F acting on two wings is given by

$$F = \frac{\alpha}{4} v_w^2 \quad (4)$$

where α is a coefficient and v_w is a velocity of the end of a wing. They are expressed by

$$\alpha = \rho C_d L W, \quad v_w = L \omega \quad (5)$$

B. Change of drag force by tilt angle

It is known that the flapping motion of a butterfly is expressed by the cosine function. In this case, the total amount of the drag force for one cycle of the flapping equals zero, then a butterfly goes down by gravity. Changing the tilt angle ϕ makes a butterfly fly up.

For simplification, we assume that the upward velocity v_y is relatively small. When a butterfly is tilted by ϕ and moving forward at speed of v_z , v_w is replaced by v_w' . It is expressed by

Table 1. The parameters of the model

Explanation	Variable
Length of wings	L
Width of wings	W
Angular velocity of wings	ω
Flapping angle of wings	θ
Representative area of a body	S_b
Mass of a butterfly	M
Tilt angle of a butterfly	ϕ
Horizontal distance	z
Forward velocity	v_z
Height	y
Upward velocity	v_y

$$v_w' = L \omega - v_z \sin \phi \quad (6)$$

Accordingly, the drag force (4) is also re-expressed. Dividing it into the forces in the direction of y and z axis and considering the flapping angle θ lead to

$$M \frac{d^2 y}{dt^2} = \frac{\alpha}{4} v_w'^2 \cos \phi \cos \theta + F_{by} \quad (7)$$

$$M \frac{d^2 z}{dt^2} = \frac{\alpha}{4} v_w'^2 \sin \phi \cos \theta + F_{bz}$$

where F_{by} and F_{bz} are the drag forces acting on a body. They are expressed by

$$F_{by} = \frac{1}{2} \rho C_d S_b v_y^2, \quad F_{bz} = \frac{1}{2} \rho C_d S_b v_z^2 \quad (8)$$

III. CONTROL

The flight of a butterfly is controlled by an evolving artificial neural network (EANN) [7]. θ is given by the cosine function of 10[Hz], while ϕ is controlled by an EANN.

1. A controller by EANN

We use a three-layered feed-forward artificial neural network (ANN) as a controller. There are six neurons in the input layer, six in the middle layer and one in the output layer. The input signals are ϕ , ω , θ , v_y , y and v_z . The output is a difference value of ϕ .

A real-coded genetic algorithm (RCGA) is used to optimize weights of ANNs. The tournament selection of size = 2, the elite selection, the BLX- α crossover of $\alpha = 0.45$ and multiplying each weight by a random value in range of $[-2, 2]$ for a mutation are used as operators of the RCGA. The group size is 40, the crossover rate is 1.0 and the mutation rate is 0.01 for each weights.

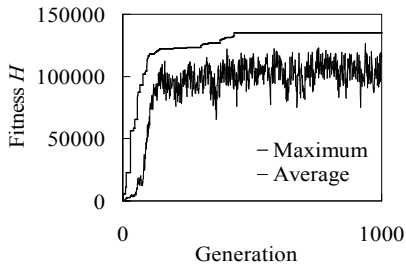


Fig.2. The fitness in evolution

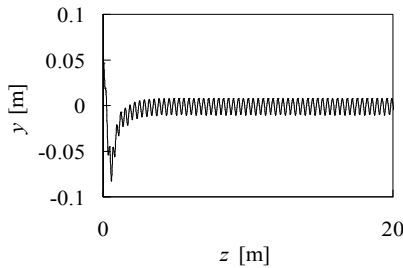


Fig.3. The track of a flight

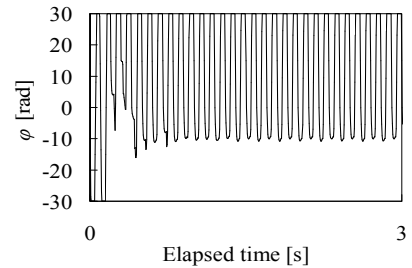


Fig.4. The optimized output φ

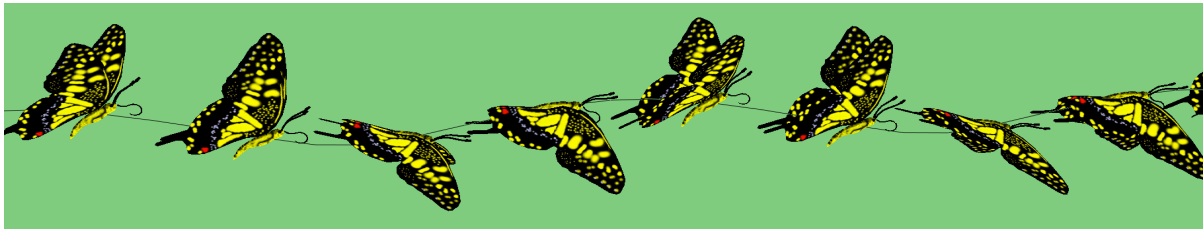


Fig.5. The snapshot of a optimized flight

2. A result of evolution

We have experimented on a simple evolution of our butterfly model. The fitness value H is given by

$$H = \sum_{t=0}^{t_{\max}} \left\{ \frac{v_z(t)}{\text{abs}(y(t)) + 0.1} \right\} \quad (9)$$

where t is a time in the simulation and t_{\max} is a terminated time of a simulation. H is very high when a butterfly goes forward rapidly and stays at height of 0[m]. In this experiment, we use $t_{\max} = 20.0[\text{s}]$, a time step in Runge-Kutta method is 1/240 and the initial height of a butterfly is 0[m].

Transitions of the fitness are shown in Fig.2. The maximum fitness hardly increase in late generations, therefore ANNs are evolved enough.

A track of the flight by the best ANN is shown in Fig.3 and a transition of φ in Fig.4. A height of a butterfly changes little in early time and finally keeps at 0[m]. φ always changes periodically like θ . However, a range of φ changes along with a change of a height. A snapshot of a flight is shown in Fig.5.

IV. OVER-EVOLUTION

It is known that an ANN has a generality. For example, an ANN learned by sample data usually recognizes other data in the pattern recognition. Therefore we have examined a generality of the evolved ANNs. Then we have discovered a problem.

1. Generality for changes of initial heights

The ANN learned by evolution in Section Three enables a butterfly to keep a height. Therefore we supposed that this ANN works well for different initial heights. When a butterfly starts at 10[m] or -10[m], however, it falls down quickly and can not keep at 0[m].

This might happen unfortunately, so we tried some times. Through some experiments, we found out that ANNs in a middle of evolution tend to be successful for different initial heights. Typical transitions of the fitness are shown in Fig.6. Fitness starting at different initial heights, that is to say, a generality, mostly increases in early generations. However, as the fitness for 0[m] that is an evolutionary guidance increases enough, a generality tends to be lost. A generality for -10[m] is easier to be lost than one for 10[m].

We call this reduction of generality “over-evolution”. It resembles the over-learning, which appears in a training of ANNs with sample data sets. An excessive learning reduces a generality in both over-learnings and over-evolutions. However, an over-evolution does not always happen, but happens by the probability.

To show a characteristic of over-evolutions numerically, we have experimented on evolution three hundred times. Each evolution is continued to the two thousandth generation. The average fitness is shown in Fig.7. The average fitness for 0[m] gradually increases, while the average fitness for 10/-10[m] decreases after a certain generation in a middle of evolution. The probabilities that the fitness for 10/-10[m] is within a range from a half times to one and a half times as many

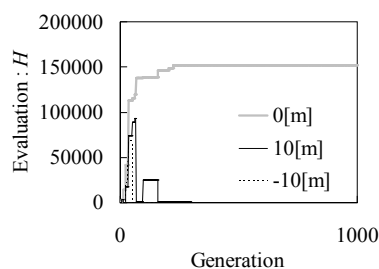


Fig.6. The typical evolution

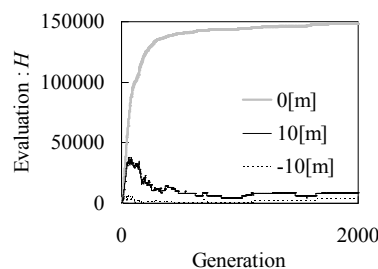


Fig.7. The average fitness of 0[m]

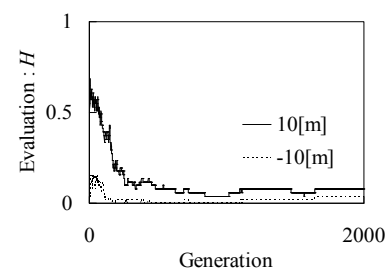


Fig.8. The probability

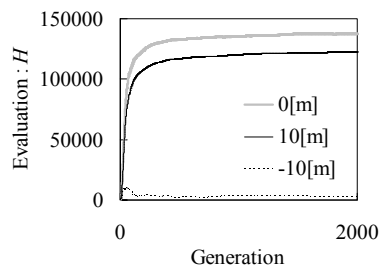


Fig.9. The average fitness of 10[m]

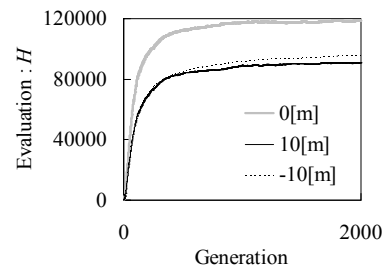


Fig.10. The average fitness of -10[m]

as the fitness for 0[m] are shown in Fig.8. As evolution progresses, the probability decreases.

2. Variation of generality by aimed tasks

Based on the results above, we set a hypothesis; the generality depends on the behavior led by given conditions. In our evolution, the best behavior is a flying forward as possible as fast at height of 0[m]. Compared with 0[m], a descending from 10[m] to 0[m] is additionally needed in starting at 10[m]. In the same as 10[m], flying up is additionally needed in starting at -10[m]. The best behavior in starting at 10[m] or -10[m] includes one in starting at 0[m], therefore we supposed that a generality of the ANN learned by the evolution in starting at 10[m] or -10[m] is higher than one at 0[m].

The average fitness in three hundred evolution started at 10[m] is shown in Fig.9 and one of -10[m] is shown in Fig.10. The ANN evolved by starting at 10[m] performs well in starting at 0[m] and 10[m] only, while the ANN evolved by starting at -10[m] is successful in all three cases. Flying up is more difficult action than flying down, therefore this result probably happened. In this simulation, the flight starting at a low height is a “critical task”, which leads to higher generality.

VI. CONCLUSION

We modeled a butterfly based on the physical law and controlled it by EANNs. By many evolutionary simulations, it is shown that an over-evolution problem

can happen in evolution of EANNs. The generality of EANNs are rarely discussed. However, if a universal method to achieve high generality is discovered, EANNs become more useful. Our research can be a key for leading to this great discovery. In the future, there will be need to examine whether an over-evolution can appear in other model or not.

REFERENCES

- [1] Terzopoulos D, Tu X, Grzeszczuk R (1994), Artificial fishes: Autonomous locomotion, perception, behavior, and learning in a simulated physical world. *Artificial Life IV*, pp.327–351
- [2] Usami Y (2007), Re-examination of swimming motion of virtually evolved creature based on fluid dynamics. *Advances in Artificial Life*, pp.183-192
- [3] Wu J, Popovic Z (2003), Realistic modeling of bird flight animations. *Proceedings of ACM SIGGRAPH 2003*, pp.888-895
- [4] Sims K (1994), Evolving virtual creatures. *Proceedings of the 21st annual conference on Computer graphics and interactive techniques*, pp.15-22
- [5] Reil T, Husbands P (2002), Evolution of central pattern generators for bipedal walking in a real-time physics environment. *IEEE Transactions on evolutionary computation* 6(2):159-168
- [6] Yamamoto M, Iwade K, Ooe R, et al (2009), Autonomous animated robots. *International Journal of CAD/CAM* 9(1):85-91
- [7] Yao X (1999), Evolving artificial neural networks. *Proceedings of the IEEE* 87(9):1423-1447

Emergence of Behavior Intelligence on Artificial Creature in Different Virtual Fluid Environments

Keita Nakamura, Ikuo Suzuki, Masahito Yamamoto, and Masashi Furukawa

*Graduate School of Information Science and Technology, Hokkaido University,
Kita 14, Nishi 9, Kita-ku, Sapporo, Hokkaido, 060-0814, Japan
(Tel: +81-11-706-6445)
({poco, ikuo, masahito, mack}@complex.eng.hokudai.ac.jp)*

Abstract: This paper presents how the differences appear when the artificial creature, which has wings in right and left sides of the body, autonomously behaves in the air environment and in the water environment. We construct approximate fluid environments with low computing costs to simulate the behavior acquisition for artificial creature. Also, we propose a simulation method for the artificial creature in two environments. As a result of simulation, we verify that it is possible for the creature to acquire behaviors in two different virtual fluid environments. After evolution, the creature behaves effectively by using leverage fluid forces in each virtual environment.

Keywords: Artificial Life, Evolutionary Computations, Control Methods

I. INTRODUCTION

Many computer simulations have been performed for studying acquiring behaviors, evolution, and learning methodologies on a virtual artificial life creature in the field of artificial life (Alife) and evolving robotics. X.Tu et al.[1] realized a behavior of an artificial fish whose controller learns swimming in the virtual water environment. C.W.Reynolds[2] proposed a flock simulation approach based on a distributed behavioral model without setting the orbit of each bird. This approach makes it easy to create flock animation. K.Sims[3][4] showed that the virtual creature can acquire its morphology and behavior by an evolutionary methodology based on the creature's competition. Many studies for behavior acquisition are based on Sims' studies. N.Chaumont et al.[5] applied Sims' model to evolution of virtual catapults. This creature could throw its parts as far as possible. There are a lot of simulations for artificial creature using physical calculating engines. They enable these creatures to obey physics law easily. I.Tanev et al.[6] simulated a side winding locomotion of a "snake-like robot". In these studies, the experimental environment is set as an ideal environment in a computer simulation space because they considered that the methodology of evolving learning behavior in an ideal environment is more important than acquisition of the similar behavior in a realistic environment. Therefore, the influenced force from the fluid environments to the artificial creature is not precisely

analyzed. Instead, the implemented force adopted the simple calculation methods for reducing the computing time. On the other hand, in a field of numerical fluid dynamics, many fluid simulations are based on a finite element method and a particle method and so on. S.Koshizuka et al.[7] suggested the moving particle semi-implicit method. It makes it easy to create animation on the water surface. Y.Usami[8] did a simulation of swimming motion on *Anomalocaris* model in the virtual two-dimensional water environment using the particle method. The finite element method and the particle method give accurate results but consume much computational time. Therefore, it is unsuitable for a real-time simulation to acquire appropriate behaviors in virtual environment. However, we consider that the virtual environment needs to obey the physical laws for the virtual creature to acquire a more natural policy of adaptive behaviors.

In this study, we construct approximate fluid environments which enable us to do the behavior acquisition simulation with low computing costs. Also, we propose a simulation method for the artificial creature in consideration of two different environments, under-water and air. The artificial creature imitating bird is modeled by connecting rigid bodies. This artificial creature can behave by flapping their wings in two environments, which are given by changing some physics parameters such as density and drag coefficients. To control wings and learn the behaviors, an artificial neural network (ANN) is implemented with the creature.

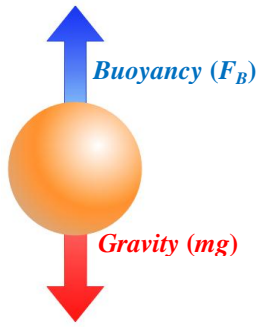


Fig.1. Buoyancy model

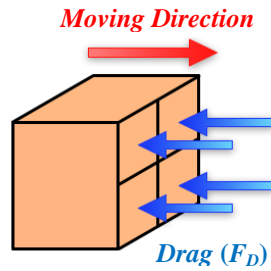


Fig.2. Drag model

Genetic algorithm (GA) is applied to ANN by its evolution. As a result of simulation, we verify that it is possible for this creature to acquire behaviors in two different virtual fluid environments. After evolution, this creature behaves effectively by using leverage fluid forces in each virtual environment. In addition, we analyze the acquired behaviors by the examining a relation between fluid environments and acquired behaviors.

II. CONSTRUCTION OF VIRTUAL FLUID ENVIRONMENTS

We assume that the buoyancy and drag act as the force that virtual objects (rectangular parallelepipeds) receive from the fluid effect. We construct a virtual fluid environment by modeling two forces acting on the object in the environment. These two forces compare to the buoyancy and drag respectively. The simulation is performed by calculating movement of the object which obeys a physics law, resulting in an animation. We use the "PhysX[11] (offered by the NVIDIA)" as a physical calculating engine. PhysX is applied to calculate a basic physical operation, for example, gravity, frictional force, collision among virtual objects, and so on. In the virtual environment, the density of the air ρ_A is $1.205[\text{kg}/\text{m}^3]$, the density of the water ρ_w is $998.203[\text{kg}/\text{m}^3]$ and acceleration of the gravity g is $9.8067[\text{m}/\text{s}^2]$. We construct two fluid environments by changing the parameter of fluid density.

1. Modeling Buoyancy

Based on Archimedes' principle, we model the buoyancy as a force whose strength F_B is equal to the weight of the fluid volume which an object occupied in the fluid. This force acts on the center of mass in the opposite direction of gravity (Fig.1). The strength of the buoyancy in the fluid environment, $F_B[\text{N}]$ is given by equation (1),

$$F_B = \rho V g \quad (1)$$

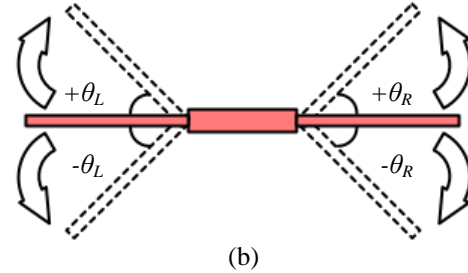
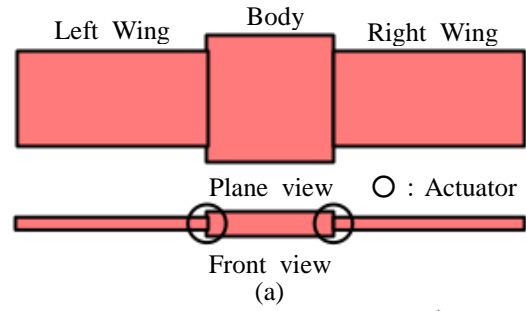


Fig.3. Artificial creature model

where $\rho[\text{kg}/\text{m}^3]$ is the density of the fluid, $V[\text{m}^3]$ is the volume of the object, and $g[\text{m}/\text{s}^2]$ is the acceleration of the gravity.

2. Modeling Drag

Based on fluid dynamics, we model the drag as uniformly distributed forces to the surface of the object in the opposite direction of moving direction (Fig.2). In the field of fluid dynamics, using the dynamic pressure of a flow $\frac{1}{2} \rho U^2 [\text{kg}/\text{m} \cdot \text{s}^2]$ derived analytically as the strength of the drag in the fluid, $F_D[\text{N}]$ is given by equation (2),

$$F_D = \frac{1}{2} C_D \rho S U^2 \quad (2)$$

where C_D is a scalar quantity called the drag coefficient, and $S[\text{m}^2]$ is the reference area of the object. The drag coefficient depends on the shape of the object. In this study, the drag coefficient of a rectangular parallelepiped C_D is 1.50. The reference area of the object is the projection area of the object to the plane which is perpendicular to a flow.

Artificial creature can generate propulsion force by moving its bodies because the modeled drag force is added to its bodies when this creature moves its bodies.

III. EXPERIMENT FOR BEHAVIOR ACQUISITION

We examine how the differences appear when the artificial creature autonomously behaves in the air environment and in the water environment. It is assumed that the model must move upward as efficiently as possible. Evolutionary computing (EC) is adopted to obtain the adaptive behavior.

Table 1. Dimensions of each part of model

Parts	Size [m]	Density [kg/m ³]
Body	4.0×4.0×0.50	100.0 (in air) 998.2030 (in water)
Right Wing	6.0×3.0×0.250	100.0 (in air) 998.2030 (in water)
Left Wing	6.0×3.0×0.250	100.0 (in air) 998.2030 (in water)

Table 2. Input and output parameters of ANN

Input	A flapping angle of a wing for a gradient of body in each time (θ_R, θ_L)
	An angular velocity of a wing for a body in each time (ω_R, ω_L)
	An inner product of vertical upward vector and cross direction vector of its body
	An inner product of vertical upward vector and forward direction vector of its body
Output	A difference flapping angle of a wing for a gradient of body in each time (θ_R, θ_L)

1. Artificial Creature Model

We create the artificial creature by connecting rigid bodies with actuators. The modeled artificial creature imitates a bird, which can behave by controlling its wings. After evaluation of the artificial creature by EC in two environments, this creature behaves effectively by using leverage fluid forces in each virtual environment. Figure 3 (a) shows an artificial creature model. This model consists of three rectangular parallelepipeds. Table 1 shows the dimensions of each part of this model. The model has two actuators with one degree of freedom (Fig.3 (b))

2. Control Method for Artificial Creature Model

ANN is introduced to control artificial creature's actuators for flapping autonomously based on its state. ANN consists of the outputs of the three-layer feed-forward ANN. Table 2 shows the input and output parameters of the ANN. The number of the neurons in the hidden layer is same number of ones in the input layer. Synaptic weights of the ANN are initialized by a random value at first. This creature enables itself to behave by optimizing the ANN synaptic weights.

3. Experiments for Behavior Acquisition

We experiment to examine how the differences appear when the artificial creature autonomously behaves in the air environment and in the water environment. The GA optimizes the synaptic weights of an ANN. Table 3 shows experimental conditions. An evaluated value for the GA as a fitness function is set so that the creature flies as high as possible. This evaluated value F_{eval} is given by equation (3).

Table 3. Experimental condition

ANN	The number of the neuron in the input layer	6
	The number of the neuron in the hidden layer	6
	The number of the neuron in the output layer	2
	A range of an object flapping angle	[-50°, 50°]
GA	Genotype	$Weight_{ij}$
	Phenotype	F_{eval}
	Population	30
	1Step	1/120 [s]
	Simulation step	1200
	Generation number	200
	Crossover probability	0.10
	Mutation probability	0.90

$$F_{eval} = \sum_{t=0}^{Step} Height(t) \quad (3)$$

where $Step$ is the number of steps used for the simulation at each generation, $Height(t)$ is the height of the artificial model at step t . We use a rank selection as a reproduction operation based on the evaluated value and an elite preserving operation in the GA. We sort the individuals in ascending order of their evaluated value and preserve the best five individuals. The others are modified by crossover and mutation operations. The artificial creatures evolve, learn, and acquire the behaviors in the two fluid environments.

4. Result and Discussion

We upload the movies to URL[12] that the artificial model acquired behaviors in two fluid environment. Figure 4 shows the angle between the body and both wings in the air environment for one second after learning. Figure 5 shows the angle for one second after learning in the water environment.

From these results, in the air environment, both wings of the model oscillate periodically. The speed to swing down the wings is faster than that to swing up the wings. Therefore, the model after leaning can move upward by rather swinging down the wings than swing up the wings to generate a drag difference (Fig.6 (a)) and needs to balance itself by generating the force larger than gravity. On the other hand, in the water environment, the angle between the body and both wings propagate from the right wing to the left wing. The angle between the body and left wing is larger than that between the body and the right wing. Therefore, the

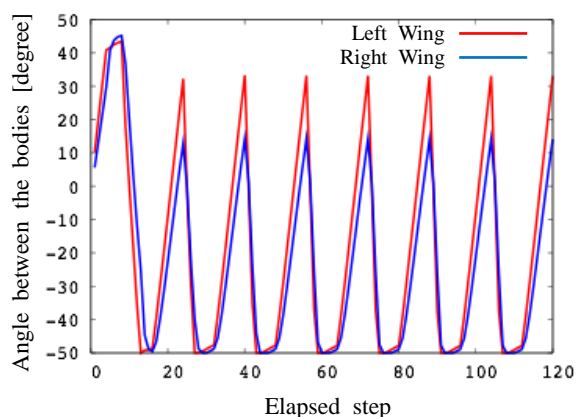


Fig.4. Angle of body and both wings in the air environment

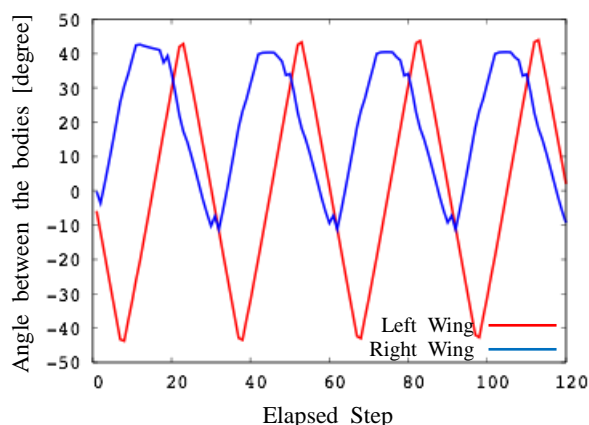
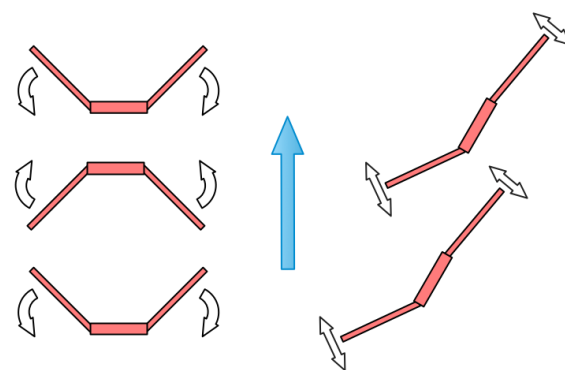


Fig.5. Angle of body and both wings in the water environment

model after leaning can move upward by oscillating periodically like a sea snake (Fig.6 (b)). The right wing plays a role of head, and the left wing plays a role of tail.

VI. CONCLUSION

In this paper, we modeled the received effect from the fluid environment by introducing two forces comparing to buoyancy and drag and constructed two fluid environments (in air environment and in water environment) by changing the parameter of fluid density. Secondly, we examine how the differences appear when the artificial creature model autonomously behaves in the air environment and in the water environment. From the result, it is possible for the model to acquire behaviors in two different virtual fluid environments by using evolutionally computations (ANN and GA). After learning, this creature behaves effectively by using leverage fluid forces in each virtual environment. In a future, we would like to experiment that the artificial creature which has wings in right and left sides of the



(a) Air environment (b) Water environment
Fig.6. The model acquired behavior

body acquires behaviors to move freely in the air environment and in the water environment by controlling flapping angles and feathering angles. Additionally, we would like to explore "life-as-it-could-be" by controlling the artificial creature which has many wings.

REFERENCES

- [1] X.Tu and D.Terzopoulos (1994), Artificial fishes: physics, locomotion, perception, behavior. In Proceedings of the 21st annual conference on Computer graphics and interactive techniques:43-50
- [2] C.W.Reynolds (1987), Flocks, herds and schools: A distributed behavioral model. In Proceedings of the 14th annual conference on Computer graphics and interactive techniques:25-34
- [3] K.Sims (1994), Evolving virtual creatures. In Proceedings of the 21st annual conference on Computer graphics and interactive techniques:15-22
- [4] K.Sims (1994), Evolving 3D morphology and behavior by competition. In Proceedings of the Fourth International Workshop on the Synthesis and Simulation of Living Systems:28-39
- [5] N.Chaumont, R.Egli, and C.Adami (2007), Evolving Virtual Creatures and Catapults. Artificial Life 13(2):139-157
- [6] I.Tanev, T.Ray, and A.Buller (2005), Automated evolutionary design, robustness, and adaptation of sidewinding locomotion of a simulated snake-like robot. IEEE Transactions On Robotics 21(4):632-645
- [7] S.Koshizuka, A.Nobe, and Y.Oka (1998), Numerical analysis of breaking waves using the moving particle semi-implicit method. International Journal for Numerical Methods in Fluids 26(7):751-769
- [8] Y.Usami (2007), Re-examination of Swimming Motion of Virtually Evolved Creature Based on Fluid Dynamics. Lecture Notes in Computer Science 4648:183-192
- [9] NVIDIA PhysX: http://www.nvidia.com/object/physx_new.html
- [10] Result Movie: <http://autonomous.complex.eng.hokudai.ac.jp/researches/physics-modeling/movies/nakamura/>

Behavior emergence of virtual creature living in complex environments

Kenji IWADATE, Ikuo SUZUKI, Masahito YAMAMOTO and Masashi FURUKAWA

Affiliation of authors, address

(Tel : 81-11-706-6445; Fax : 81-11-706-6445)

(Email address : kenji-i@complex.eng.hokudai.ac.jp)

Abstract: This study aims at establishing a new computer aided animation method using the agent-based and physics modeling based animation. The specific problem we treat in this paper is to acquire an adaptive behavior of a virtual creature placed in a complex environment and to create the animation of its behavior automatically. The virtual creature is regarded as an autonomous agent who has sensors, actuators, and controllers. For controlling the virtual creature, ANN and CPG are adopted as the controllers. Optimization algorithm is introduced for learning the controllers. Numerical experiments proved that the virtual creature acquires effective motions (walking, swimming) to pursuit the destination, and to avoid the obstacle and other creatures.

Keywords: Artificial Neural Network, Central Pattern Generator, Evolutionary Algorithm, Artificial Life

I. INTRODUCTION

Computer-aided animation using the computer graphics technology becomes more important in various fields such as physics, engineering, entertainment, and medical science. In entertainment field, physics modeling based simulation for generating the realistic object motion has attracted researchers attention, and many works have been presented in this decade[1],[2]. On the other hand, the physics modeling based animation for artificial-beings, which can autonomously behave as living organisms in the earth, is still an undergoing research matter. A motion capture method is mostly adopted to create the animation for the artificial-beings. However, this method consumes lots of time and requires an expert knowledge for creating the animation.

The agent-based approach is efficient solutions for overcoming problems that the motion capture method has. This study aims at establishing a new computer aided animation method using the agent-based and physics modeling based animation. The specific problem we treat in this paper is to acquire an adaptive behavior of a virtual creature placed in a complex environment and to create the animation of its behavior automatically. The complex environment means a dynamically changed environment caused by fluid influences, obstacles and interaction among agents.

For generating a control signal with rhythmic pattern which is observed in living organisms, we implement a controller of the virtual creature by a combination of a central pattern generator (CPG) and an artificial neural network (ANN).

Evolution of the virtual creature is realized by learning ANN and CPG. An optimization algorithm is introduced into learning for evolving the virtual creature placed in complex environments. An evaluation function to evaluate the behavior of the virtual creature for the optimization algorithm is based on radical characteristics of life such as energy conservation, target pursuit and evasion from obstacle. This evaluation function is applicable to evaluate virtual creature which has any shapes.

II. VIRTUAL ENVIRONMENT

All experiments described below are performed under virtual environment which fundamental physical law is considered. We adopt a dynamics engine for implementing the fundamental physical law with virtual environment. The adopted engine is PhysX, presented by NVIDIA[4]. PhysX allows us to simulate physical dynamics and phenomenon of a rigid object such as gravity, action-reaction, friction, restitution, and collision. Additionally, this environment is implemented influenced forces caused by fluid.

III. VIRTUAL CREATURE

1. Salamander model

A salamander is modeled as a virtual creature. The salamander can behave itself under the water and air resistances namely a complex environment. Then, we examine the salamander behavior by evolving it in the complex environment. The salamander consists of seventeen rigid objects whose geometric and physical data are shown in Table1. The salamander has two sensors and twelve actuators (see Fig.1).

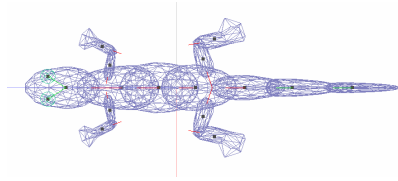


Fig.1. Salamander model

Table1. Data of components of the salamander model

Body Components	Value
Density	$\rho=1000$ [kg/m ³]
Restitution	0.2
Static friction	0.2
Dynamic friction	0.1
Limb Components	Value
Density	$\rho=1000$ [kg/m ³]
Restitution	0.2
Static friction	0.9
Dynamic friction	0.8

2. Sensors

Optical sensors can detect a light strength S_L from a light source placed in a virtual space. S_L is defined by (1), where θ_L is an angle between the light source and the sensor direction, and B_r is brightness of a light source. Inclination sensors detect a Inclination of sensors S_I according to (2), where θ_I is a inclined angle. Pressure sensors detect a environmental pressure S_P according to (3). These values turn into inputs of the salamander controller.

$$S_L = \begin{cases} -\pi/2 < \theta_L < \pi/2 : & B_r \cos \theta_L \\ \text{otherwise} & : 0 \end{cases} \quad (1)$$

$$S_I = \cos \theta_I \quad (2)$$

$$S_P = \begin{cases} P > \text{threshold} : & 1 \\ \text{otherwise} & : 0 \end{cases} \quad (3)$$

3. Actuators

Actuators have a three degree of freedom in rotation, and these are driven according to driving torques which is generated by the controller.

4. Controller

For generating a control signal with a rhythmic pattern, a controller of the virtual creature is modeled by a combination of a central pattern generator (CPG) and an artificial neural network (ANN). A structure of the controller is shown in Fig.5. ANN receives signals from sensors and actuators (see Table2), and it calculate CPG parameters. CPG converts ANN outputs into control signals which have the rhythmic pattern.

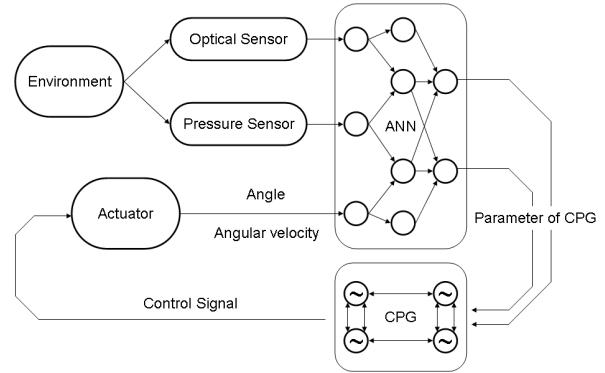


Fig.2. Controller Configuration diagram

Table2. Input signal of ANN

From each sensor	Value
Light strength	$S_L \in [-1, 1]$
Inclination of sensor	$S_I \in [-1, 1]$
Environmental pressure	$S_P \in [0, 1]$
From each actuator	Value
Angle	$\cos \theta_A \in [-1, 1]$
Normalized angular velocity	$\omega_A / \omega_{Amax} \in [-1, 1]$

ANN is a well-known brain model. It consists of a set of neurons and set of synapses. Learning of ANN is performed by adjusting a set of weights assigned to synapses. A neuron model of ANN is defined by (4) and (5), where u_i is an input of each neuron, v_i is an output of each neuron, w_{ji} is a synaptic weight, and T is a temperature coefficient. An output of ANN becomes parameters for modifying a CPG output.

$$u_i = \sum_j w_{ji} v_j \quad (4)$$

$$v_i = \frac{1}{e^{-u_i/T} + 1} \quad (5)$$

CPG is a well-known neural model for generating a rhythmic pattern which is observed in behavior of living organisms [4],[5]. A neuron model of CPG is defined by (6)-(8), where T_r and T_a are coefficients of time response, a_{ij} is a synaptic weight between CPG neurons, g_i is a parameter for modifying an amplitude of output signal, and b_i is a parameter for modifying a frequency of the output signal. CPG parameters are optimized by an optimization algorithm to acquire a periodical signal whose frequency is under 60[Hz] (see Table3). The number of CPG neurons is equals to the total number of degrees of freedom for actuators. Actuators are driven according to output signals from CPG as control torques.

$$T_r \dot{x}_i + x_i = -\sum_j a_{ij} y_j - b_i z_i + g_i \quad (6)$$

$$T_a \dot{z}_i + z_i = y_i \quad (7)$$

$$y_i = \max(0, x_i) \quad (8)$$

Table3. CPG constants

Synaptic weight	$a_{ij}=1.070772$
Rise time constant	$T_r=1.181958$
Time lag of the adaptation effect	$T_a=0.153337$

3. OPTIMIZATION OF CONTROLLER

A salamander's behavior is dominated by the controller. Therefore, adapting the salamander to an environment depends on adjustment of weights assigned to synapses in ANNs and CPGs. This adjustment is so-called learning. However, it is difficult to define learning signals to train controller when the virtual creature has complicated shapes and it virtually lives in the complex environment. For letting the controllers learn, we adopt Genetic Algorithm (GA) with real number encoding. The GA optimizes synaptic weights of ANNs and CPGs. A chromosome is represented by a set of weights. Table4 shows parameters for optimization.

Table4. Parameters for Genetic Algorithm

Number of chromosome	200
Mutation rate	$P_M=0.05$
Crossover probability	$P_C=0.1$

The optimization process consists of the following steps.

- I. Simulate each virtual creature in a constructed environment according to ANNs and CPGs generated by each chromosome.
- II. Evaluate behaviors of each creature by use of a given fitness function.
- III. Reproduce new creatures.
- IV. Perform GA operations (selection, crossover, and mutation).
- V. Return to step II and repeat until the termination condition is satisfied.

The mutation operation randomly selects a chromosome (a set of weights) and extracts a gene (a weight) from it with the mutation rate P_M and replace the gene to a random number $[-1.0, 1.0]$. The crossover operation selects a couple of chromosomes with the crossover probability P_C and selects one of the output neuron and its neighborhood synapses (which are connected to the selected neuron unit directly). Then these selected synapses of one chromosome are swapped to those of other chromosome.

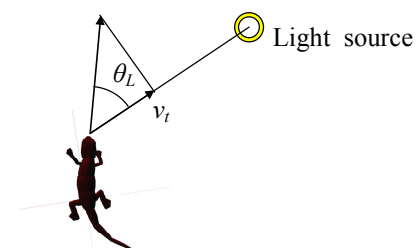


Fig.3. Evaluation values

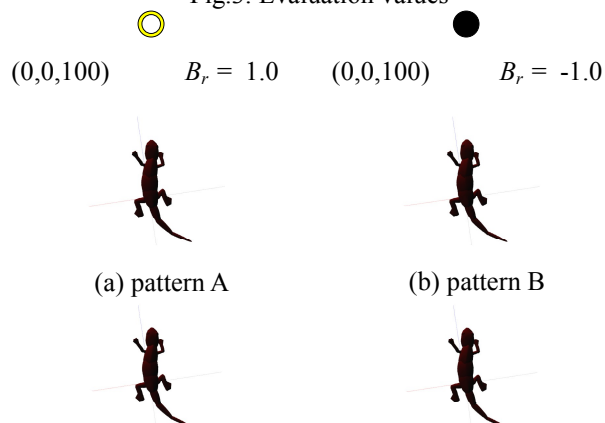


Fig.4. Settings of the Evaluation

We treat a learning problem what behavior a salamander can acquire when it moves towards a given destination and evade from obstacle. It is expected that walking, running, or swimming emerges from the acquired behavior in the given environment.

In this problem, a light source is set in the field as a pheromone (destination or obstacle). All light source can change these brightness B_r within $[-1,1]$. When the brightness has positive value, we treat it as the destination. Otherwise, we treat it as the obstacle.

A fitness function consists of two fundamental behavior evaluations. The first evaluation is formulated so as to maximize the cumulated propulsive component of velocity V during the salamander moving (see Fig.3). The second one is formulated so as to maximize the cumulated cosine value of the angle between the sensor and the light source L during the salamander moving.

These two evaluations are expressed in (11)-(12), where N_S is the number of sensors.

$$V = \sum_t \sum_i^{N_S} v_{t,i} \quad (11)$$

$$L = \sum_t \sum_i^{N_S} S_L \quad (12)$$

These values are calculated under four initial positions shown in Fig.4. Therefore, the fitness function (Eq.(13)) is expressed as a cumulated product of Eq.(11) and Eq.(12).

$$f(\vec{V}, \vec{L}) = \sum_p^{pattern} V_p L_p \quad (13)$$

4. EVOLVING SALAMANDER BEHAVIOR

Experiments are performed in the following conditions. Basic parameters of experiments are shown in Table 5.

Table5. Parameters for optimization

Time resolution	1/60 [sec]
Simulation time	3000 [step] = 50 [sec]

Each experiment is performed under the different environment described bellow.

1. Acquired behavior on the ground

In the first experiment, the salamander is placed on the ground. Also, the friction and air influence are implemented with the environment.

Fig.5 shows a snapshot of a motion that the salamander moves on the ground after the optimization. The salamander acquires effective motions to reach the goal as fast as possible. The achieved motion looks like a “walk” behavior.

2. Acquired behavior in the water

In the second experiment, the salamander is placed in the water environment.

Fig.6 shows a snapshot of a motion that the salamander moves in the water after learning. The controller acquires control signals which cause rapid propagation of vibrations for generating a thrust force by harnessing the water resistance. The achieved motion looks like a “swim” behavior.

3. Behavior emergence in complex environments

Fig.7(a)-(c) show behavior emergence of the virtual creature in the environment with an obstacle. Fig.7(d) shows emergence of a swarm behavior. Each Creature acquires the tracking behavior toward to the destination, and the avoiding behavior from obstacles and other creatures.

VI. CONCLUSION

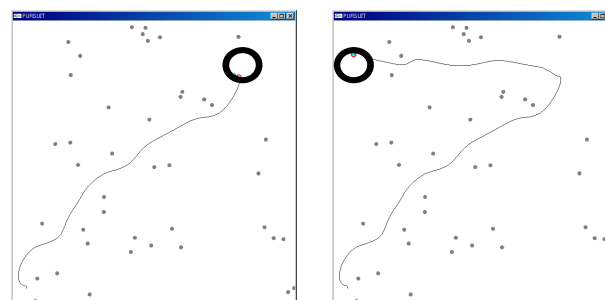
We aim at establishing a new computer aided animation method. For this purpose, the agent-based



Fig.5. An acquired behavior on the ground

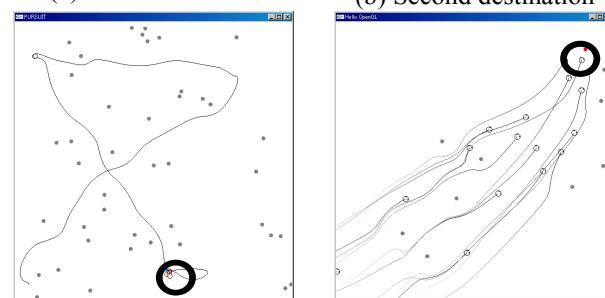


Fig.6. An acquired behavior in the water



(a) First destination

(b) Second destination



(c) Third destination

(d) Swarm behavior

Fig.7. behavior emergence in complex environments

and physics modeling-based animation method is introduced. Numerical experiments proved that the virtual creature acquires effective motions (walking, swimming) to pursuit the destination and to avoid the obstacle and other creatures.

REFERENCES

- [1] J. J. Monaghan (1992), Smoothed Particle Hydrodynamics. Annual Review of Astronomy and Astrophysics
- [2] S. Koshizuka, A. Nobe, Y. Oka (1998), Numerical Analysis of Breaking Waves Using the Moving Particle Semi-Implicit Method. Numerical Methods in Fluids 26(7):751-769
- [3] NVIDIA PhysX, http://www.nvidia.com/object/nvidia_physx.html
- [4] K Matsuoka, “Sustained oscillations generated by mutually inhibiting neurons with adaptation”, Biol Cybern 52, pp. 367-376, 1
- [5] L. N. Patel, A. Murray, J. Hallam (2005), Increased Swimming Control with Evolved Lamprey CPG Controllers. Neural Networks, IJCNN '05 4:2195-2200

Three-dimensional Morphogenesis by Cell Division and Death in Viscoelastic Amorphous Computing

Eisuke Arai, Fumiaki Tanaka and Masami Hagiya

*Department of Computer Science, Graduate School of Information Science and Technology, University of Tokyo,
7-3-1 Hongo, Bunkyo-ku, Tokyo 113-8656, JAPAN.
(Tel : +81-3-5841-4093)
(arai917@is.s.u-tokyo.ac.jp)*

Abstract: Amorphous computing is a computational paradigm for realizing global computation as a result of local communication among identical computational particles which are irregularly distributed over space. Each computational particle has a small computing power and a small amount of memory, and executes an identical program with no synchronization. In the original model of amorphous computing, particles did not have motility resulting from physical interactions and could not form any significant structures by their self-organization in three-dimensional space. In this paper, we propose a new approach to construct desired structures of programmable particles in three-dimension by extending the original model of amorphous computing. In addition to general operations in the original model, we introduce operations for generation and destruction of particles. Furthermore, we allow particles to have slight motility by viscoelasticity, because we assume physical interactions among particles. So far, we have built a simulator to observe behaviors of moving particles in three-dimensional space and control their morphogenetic process. In this simulator, the particles execute an identical program which includes the operations for generation and destruction. We have investigated and optimized parameters of the simulator so that the particles moderately cluster and form some fixed structure.

Keywords: Amorphous computing, Morphogenesis, Viscoelasticity, Three-dimension.

I. INTRODUCTION

Models of amorphous computing consist of a collection of small computational particles distributed irregularly over space where each particle has a small computing power and a small amount of memory. These individual particles are entirely identical and not synchronized. Each particle can communicate with a few nearby neighbor particles. Although all particles are programmed identically, each particle is distinguished from other particles by its local state which includes the list of neighbor particles, distance from each neighbor, and local variables. The study of amorphous computing was introduced by Abelson et al. in [1] and the computational models based on the idea of amorphous computing were summarized in [2]. Among the models, that of programming amorphous medium was established by Beal et al. [3]. Amorphous medium is the continuous limit of models of amorphous computing in which particles are infinitesimal and distributed densely over space. Proto [4] is a Lisp-like programming language which targets such amorphous medium. As an example of programming amorphous medium, a sensor network was implemented in Proto [5]. The advantage of amorphous computing is its robustness compared with other general computational paradigms because the original model of amorphous computing was inspired

by biological systems [6]. Thus there has been developed an application of amorphous computing in which cells such as E coli are targeted [7]. Needless to say, one of the goals of such applications is to construct shapes and structures composed of particles, just as biological systems realize morphogenesis.

In this paper, we present a new approach to three-dimensional morphogenesis in a model of amorphous computing. We give particles slight motility that depends on interactions among them, and implement the generation and destruction operations in addition to the operations in the original model of amorphous computing. Two-dimensional morphogenesis in a model of amorphous computing was investigated in a preliminary attempt [8]. Although a three-dimensional approach to morphogenesis in amorphous computing was also proposed [9], motility of particles was not based on their physical interactions but due to predefined background signals, and particles did not execute an identical program. In our approach, we assume that each particle executes an identical program and moves automatically by viscoelastic force. The viscoelasticity of particles is generated according to distance from the neighbors and density of the neighbors. We refer to smooth particle hydrodynamics (SPH [10]) in order to simulate the viscoelastic behaviors of particles and implement calculation of

viscoelastic force using a method established by Clavet et al. [11]. We need to update neighbors of each particle at every simulation step, because particles have motility and change their positions. Thus we have implemented efficient neighbor search strategy of particle-based fluids [12].

II. THE MODEL

Our simulation model is based on the original amorphous computing model. The originality of our work is roughly divided into four important points. In this section, we explain these points individually.

1. Motility of computational particles

We introduce motility of particles, because we assume that particles are like biological organisms or biomolecules. Thus it is natural that there are physical interactions among particles such as viscosity and elasticity. We use the well known method for particle-based viscoelastic fluid simulation in order to add viscoelastic force to particles. This force is assumed to be produced by interactions among nearby particles and affects them. For each particle, we need to calculate force by all interactions with its neighbors at every computation step. Although we introduce motility, we do not add to particles the ability to move freely because we only allow particle to be affected by external force.

2. Implementation of particle operations

To execute programs written in the style of amorphous computing in our model, it is necessary to implement several basic operations and build them into particles. We can execute complex programs by systematically combining these operations. Concretely, we implement the following operations.

A. Minimum and maximum operations

In the minimum operation, each particle obtains the minimum of the specified values owned by all neighbor particles by repetition of local communication. A particle refers to the specified values of neighbors, finds the minimal value of them and then stores this value into itself in a single communication step. Similarly, the maximum operation allows each particle to find the maximal value of those owned by all neighbors.

B. Gradient operation

The gradient operation is a way for each particle to know distance from a specified particle as the gradient value. Each particle finds the local minimal value of

neighbor gradient values and the local maximal value of ranges to its neighbors which ranges are known as a priori information. Sum of these local values is stored as new gradient value in single communication step of the operation. By repetition of the local communication, all particles know their distance values from the specified particle.

C. Generation and destruction operations

Inspired by cell division and death, we implement the generation and destruction operations which increase and decrease particles, respectively. In the generation operation, a particle reproduces itself with its own state at an adjacent point. On the other hand, in the destruction operation, a particle kills itself. In our model, we do not consider the energy consumption with reproduction of particles and the remains of particles in the destruction operation.

3. Mechanism of our simulator

We built a simulator which executes the particle operations just as we introduced above. After initialization, the simulator repeats updating states of particles and visualizing them. The single update process executes the necessary tasks as follows. At first, the simulator executes the neighbor search for all particles, calculates viscoelastic force between all particle pairs, and then moves all particles by the calculated force. Next, the simulator executes the neighbor search again because neighbor particles are changed by their movement. Finally, each particle communicates with its neighbors and updates its state which includes some values related to the operations. Only one communication step for one particle is allowed in a single update. Thus, by repetition of the update process, the value for each operation converges. In our simulation, we use modestly converged values for a cascade of operations.

4. Dynamic neighbor search in 3D space

In our system, it is necessary for each particle to always know its neighbor particles so that it can contact and interact with each other. Since we assume that particles move by some operations, we have to dynamically update neighbors at every computation step of each operation. To search for neighbors, we need not check all particles, but need to check only some particles which are included in particular divisions of space called cells. Each cell is a 3D grid with size of the neighborhood radius of a particle. We divide space into such cells and index them depending on coordinates of

their minimal corner. Furthermore we associate each particle with its corresponding cell index. For searching for neighbors of a particle, it is only necessary to check particles inside 26 cells around the cell containing the particle. In addition to this cell indexing approach, we use also subdivision of the cell in order to further reduce search space.

III. EXAMPLE

In this section, we demonstrate the process to form a tubular structure as an example of our approach. We explain an algorithm for modeling tubular structure and then show simulation results of this example using our simulator.

1. Algorithm for modeling tubular structure

We assume that there is one computational particle at the initial condition. This particle begins the generation (divide) operation and keeps on dividing until the number of particles is sufficient to form any structure. After the particles are clustered, one particle on the surface of the cluster is selected as a source. By searching for the particle which has the minimal number of neighbors in all particles, we can find the source on the surface. We then execute the gradient operation from the source and choose the destination particle which has the maximum gradient value, that is to say, the farthest particle from the source. The destination is also assumed to be on the surface of the cluster. Figure.1 shows the state of choosing the source and destination particles in the cluster.

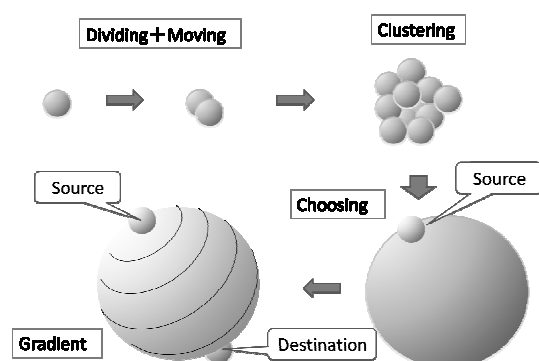


Fig.1. Choosing specific particles

After both source and destination particles are found, each particle starts the gradient operation towards the destination to determine the specific particles lying between the source and the destination. We call the line

of these particles “path”. For a particle on path, the sum of its gradient values from the source and from the destination is almost equal to distance between the source and the destination. Neighbors of particles on the path comprise a channel which connects the source and the destination with slight width. In Figure.2, it is shown how to make the path and channel in the cluster. After determination of the particles in channel, each particle in the channel executes the destruction operation and disappears from the space.

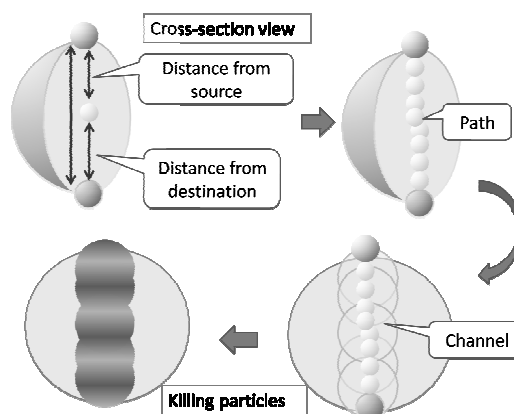


Fig.2. Creating tubular structure

An important issue in this algorithm is that each particle executes an identical program and communicates with only its neighbors. Although each particle has no a priori knowledge about other particles except for its neighbors, it is distinguished from other particles by its internal state such as the gradient value. Therefore, we can control identically programmed particles in order to model desired structures like this example.

2. Simulation results

Using our simulator we could construct a cluster of 500 particles which is shown in Figure.3. There was only one particle at the initial condition and then the number of particles started increasing by the generation operation. To cluster particles as shown in Figure.3, we investigated and optimized some parameters of the simulator by trial and error. These parameters include neighborhood radius, spring constant, density constant and other values related to calculate viscoelastic force.



Fig.3. A cluster of 500 particles

After clustering particles and finding the source, each particle executed the gradient operation from the source and then could determine the destination particle which had the maximum gradient value. Each particle also could judge whether it was on the path and furthermore in the channel. The particles in the channel executed the destruction operation and disappeared. As a result, we obtained a tubular structure like a bead (see Figure.4).



Fig.4. A tubular structure

IV. CONCLUSION

In this paper we have presented a new approach for constructing a specified structure from a cluster of computational particles which are programmed to execute an identical operations. To cluster the particles we implemented the generation operation and gave them slight motility based on viscoelasticity among particles. As an example of our approach, we demonstrated construction a tubular structure by each particle's executing an identical program. Although we do not have actual implementation of such programmable particles at present, we expect that we can possibly use living cells for our research in future, because a cell behaves according to its program, that is DNA.

V. FUTURE WORKS

Our future work can be considered in several ways as follows.

- We need to increase efficiency of each simulation step because we want to enlarge the size parameters of our model such as the simulation space and the number of particles. To this end, we will attempt to optimize the dynamic neighbor search and the calculation process of local interactions.
- Although we currently assume a spherical cluster of particles in our model, we need to consider a cluster of any shape like a distorted one.
- In this paper, we demonstrated construction of a tubular structure. We want to extend our study to establish a new method for constructing arbitrarily complex structures.

REFERENCES

- [1] H. Abelson, D. Allen and D. Coore et al. (2000), Amorphous computing. *Communications of the ACM*, 43:74-82
- [2] H. Abelson, J. Beal and G.J. Sussman (2007), Amorphous Computing. MIT Technical Report 2007-030.
- [3] J. Beal (2006), Amorphous Medium Language. MIT Technical Report 2006-040.
- [4] J. Beal and J. Bachrach (2006), Infrastructure for engineered emergence in sensor/actuator networks. *IEEE Intelligent Systems*:10-19
- [5] J. Bachrach and J. Beal (2006), Programming a Sensor Network as an Amorphous Medium. MIT Technical Report 2006-069.
- [6] J. Beal and G. Sussman (2005), Biologically-Inspired Robust Spatial Programming. MIT Technical Report AI Memo 2005-001.
- [7] J. Beal and J. Bachrach (2008), Cells Are Plausible Targets for High-Level Spatial Languages. *Self-Adaptive and Self-Organizing Systems Workshops*, 2008: 284-291
- [8] A.Kondacs (2003), Biologically-Inspired Self-Assembly of Two-Dimensional Shapes Using Global-to-Local Compilation. *IJCAI'03 Proceedings of the 18th international joint conference on Artificial intelligence*.
- [9] A. Bhattacharyya (2006), Morphogenesis as an Amorphous Computation. *Proceedings of the 3rd conference on Computing frontiers*:53-63
- [10] J.J. Monaghan (1988), An introduction to SPH. *Computer Physics Communications* 48(1):89-96
- [11] S. Clavet, P. Beaudoin, and P. Poulin (2005), Particle-based Viscoelastic Fluid Simulation. *Proceedings of the 2005 ACM SIGGRAPH/Eurographics symposium on Computer animation*:219-228
- [12] J. Onderik and R. Durikovic (2008), Efficient Neighbor Search for Particle-based Fluids. *Journal of Applied Mathematics, Statistics and Informatics* (4):29-43

Demand level investigation for future domestic system

Shuki Inoue¹, Eiji Mimura¹, Shingo Aoki² and Hiroshi Tsuji²

1) Department of Energy Use R&D Center
The Kansai Electric Power Co., Inc. Hyogo, Japan

2) Department of Computer Science and Intelligent Systems
Osaka Prefecture University, Osaka, Japan
(Tel : 81-72-254-9353; Fax : 81-72-294-9915)
([inoue.shuuki@d4.kepc.co.jp](mailto:iinoue.shuuki@d4.kepc.co.jp))

Abstract: Although the future domestic system has been visualized as smart house, it is difficult to decide if each product or service in smart house is useful or not because value senses in our daily life are diversified. To forecast the strength of demand on future domestic system, this paper describes questionnaire analysis. Creating six kinds of future domestic systems which innovate our daily life, we design questionnaire which consists of question on personal attributes, value senses and requirement on designed systems. This paper also introduces original analysis methods and illustrates findings in the responses of questionnaire.

Keywords: Future Assessment, Home Energy Consumption, Value Analysis, Market Analysis

I. INTRODUCTION

To assess the future domestic system, experts have tried to create future living environment called smart house [1]. However, experts often created their ideas not based on consumers' requirement but on technical possibilities. Therefore, some ideas may fall into fans but do not contribute to new product and service development. In fact, our daily life is diversified based on our variety of value senses: convenience, housework support, health case, security, comfort and global environment.

In this research, we will create life domain map. Introducing six daily life scenes (inventory control for household, media database, health care by an electric dietician, home security service, daily case for children and aged persons, total control for illumination and air-conditioning), we will illustrate future domestic images. Each image allows us to create future domestic items. To find out the relation among personal attributes, value senses and their items, we will design questionnaire. Then, we will demonstrate findings from the questionnaire and finally describes

future plan.

II. FUTURE DOMESTIC SYSTEM

First, in order to design questionnaire on future domestic system, let us imagine future artificial life. Referring to the conventional future assessment described in [2] [3], we have conducted brain storming. It took about three months.

Under the assumption that our daily life consists of communication, input, work, learning and entertainment,

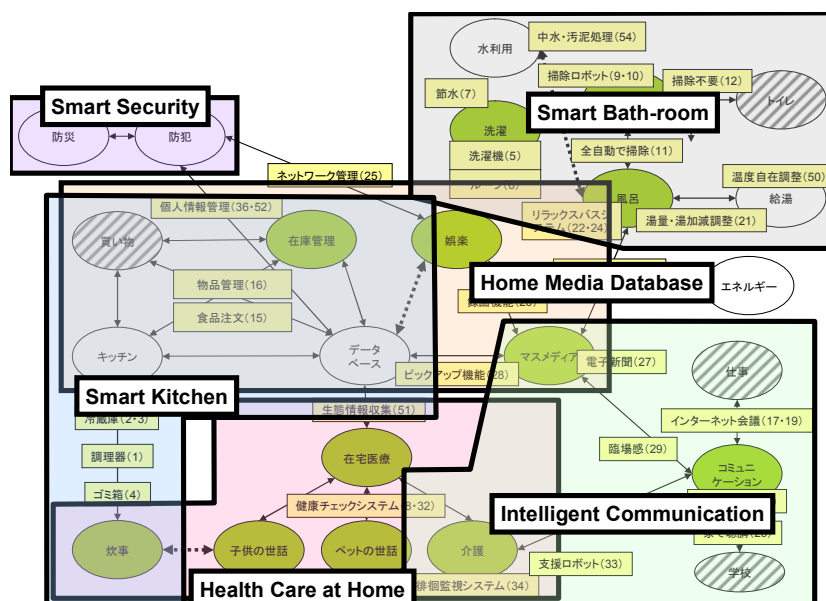


Fig. 1 Idea Map for Future Domestic System

the future domestic system shall satisfy our values such as healthy life, comfortable life, sustainable environment, and secure living space. The household support and convenience are another value senses in our life.

Based on value senses in our daily life, we depict imaginary future scenes in home security, intelligent air conditioner, smart kitchen and adaptive illumination. The idea on product domain has been induced by analyzing relation between place and action as shown in Figure 1.

While there are six categories in the product domain map, the example for home security service is shown in Figure 2. This figure implies that intelligent sensors with image recognition and voice recognition should connect with external network. We have collected a lot of suggestion from the product domain map.

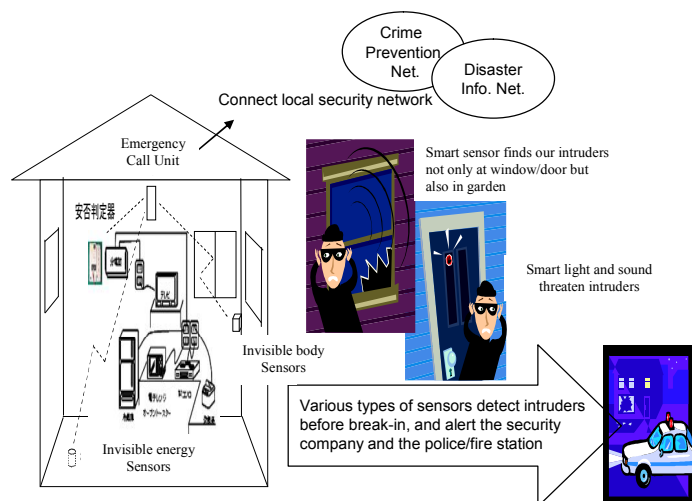


Fig. 2 Future Home Security System

III. QUESTIONNAIRE DESIGN

Paying attention on daily value senses, we should find out relation between them and future domestic items. Because we prepare six kinds of value senses, there are fifteen pair wise comparison. Because we are afraid some consumers are sensitive for questionnaire (in other words, they may not have confirmative opinion on value senses), the questionnaire asks preference among value senses twice. The overview of questionnaire is shown in Figure 3 where some items are borrowed from [4] and [5].

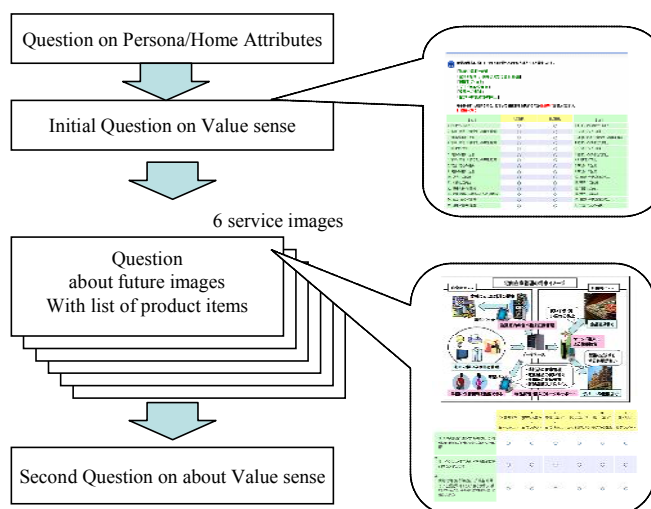


Fig. 3 Constitute of Questionnaire

1. Future domestic items

From six kinds of future life scenery, we imagine future domestic items. In principle, these future domestic items are illustrated in scenery figures as shown in Figure 2.

Our demand level investigation has two layers: whether you like to use the illustrated items or not, and whether you think if most people like to use them or not. On the other hand, it has three requirement strengths: it will be in five years, in ten-twenty years or needless.

2. Value sense and life style

As introduced in the previous chapter, we first consider on four kinds of value senses: healthy life, comfortable life, sustainable environment, and secure living space. Because cost expresses the strength of requirement, we do not consider it as value. Then based on the introduced future domestic items, two are added: housework support and convenience.

Because life style as well as personal attributes and house attributes may affect on the strength of demand level, the questionnaire includes questions on behaviour of responders and their family.

3. Response collection

We conducted strata sampling for response collection. The stratum consists of gender and age. The age strata has five segmentation: 20's, 30's, 40's, 50's and elders than 60. Each stratum includes 103 samples and then totally the sample number is one thousand and thirty.

IV. RESULT OF ASSESSMENT

1. Overview

On occupation, twenty two percent of responders are housekeepers. There are also sixteen percent for office clerks and thirteen percent for engineers/ technicians.

On the demand levels for six kinds of future life scenery, home security service is the highest: 60 percent of responders like to live in the illustrated secure home environment in five years. As another remarkable result, fifty percent of responder requests to improve weak persons (children and aged persons) support in five years. The rate of responders who like to use adaptive illumination living space is fifty three percent.

On the other hand, most responders are afraid the excessive service in another scene, especially in inventory service. The detail rate of responders is shown in Table 1.

Table 1 Future Assessment for New Home Service

#		In Five Years	In 10-20 years	Worthless	Total
S1	Inventory control for household	354 (34%)	346 (34%)	330 (32%)	1030 (100%)
S2	Media database	415 (40%)	335 (33%)	280 (27%)	1030 (100%)
S3	Health care by an electric dietician	438 (43%)	339 (33%)	253 (25%)	1030 (100%)
S4	Home security service	619 (60%)	296 (29%)	115 (11%)	1030 (100%)
S5	Daily care for children and aged persons	564 (55%)	343 (33%)	123 (12%)	1030 (100%)
S6	Total control for illumination and air-conditioning	550 (53%)	295 (29%)	185 (18%)	1030 (100%)

2. Value sense

The result is summarized in Table 2. Many responders put their importance on their health care (32%) or home security (18%). Then Table 2 also shows that there are so many responders (26.5%) who cannot put importance on the unique value sense.

Table 2 Important Value Sense by Age

Age	Convenience	Housework Support	Healthy Life	Secure Living Space	Comfort	Sustainable Environment	Unclear	Total
20	18	9	58	39	17	9	56	206
30	11	17	41	50	21	9	57	206
40	14	10	64	33	17	14	54	206
50	11	10	81	26	22	9	47	206
60-	9	7	74	29	18	18	51	206
Total	63	53	318	177	95	59	265	1,030

From the result of age strata in Table 2, importance on value sense strongly depends on the age of responders. In fact, there are clear differences as follows: For convenience, 20s is the highest. For housework support, 30s is the highest and for health care, 50s is the highest. On the other hand, 60 and more put their importance on sustainable environment.

The pair wise comparison can be described in VS-map [6] where the drawing algorithm is shown in Figure 4. The VS-map visualizes preference on value senses as bird-eye where health care and home security have large circle and housework support and sustainable environment have smaller circle totally.

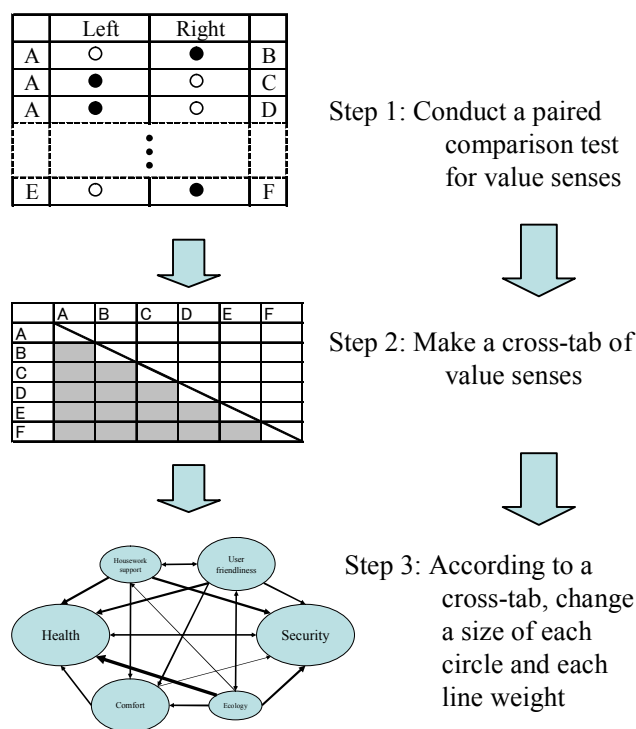


Fig. 4 Procedure for generating Value Sense Map

V. CAUSAL RELATION

As found in the previous chapter, there is different importance on value sense among ages. Then it is expected that there is causal relationship among responder's demographics (gender, age, family occupation, living environment, etc.), their value senses and demand level for future domestic items in the created scenes.

To verify the existence of causal relation, we have built three layers Bayesian network. The network structure shown in Figure 5 allows us to examine sensitivity by assigning evidence on nodes in the network. The detail discussion of BN is presented elsewhere [7].

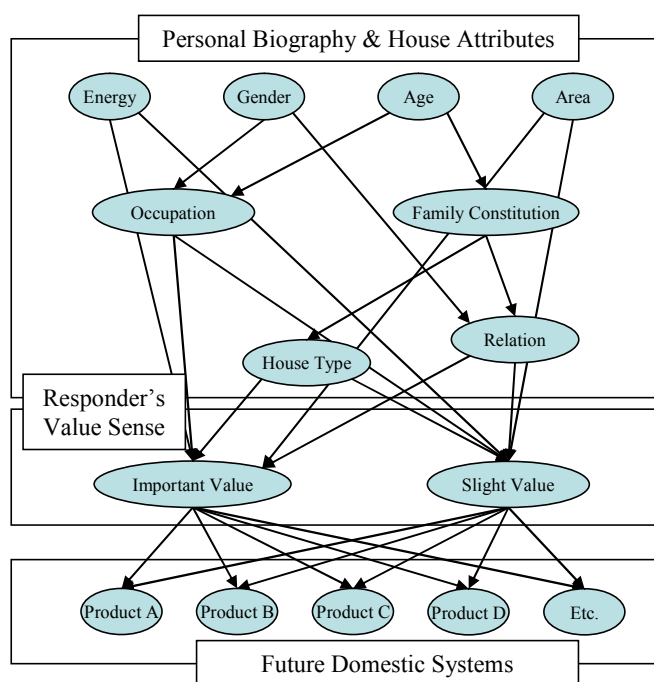


Fig. 5 Basic structure for Bayesian Network

VI. CONCLUSION

This paper has investigated the demand level for future domestic systems. Especially, this paper has contributed to find out the causal relationship between our daily life style and preference on future items generated from future life scenes. The remarks are summarized as follows:

- (1) To create life domain map, we have introduced six daily life scenes. Further, based on the scenes, we have illustrated future domestic items.

- (2) To find out the relation among personal attributes, value senses and their items, we have introduced four general values (health case, security, comfort and global environment) and two life-related values (convenience, housework support).
- (3) As a result of pair-wise comparison on value senses, there are not always ordinal preferences on value senses. Then we have proposed visualizing method called VS-map.
- (4) To analyze the causal relationship among personal biography, house attributes, responders' value senses and future domestic systems, we have constructed Bayesian network and found its possibility.

REFERENCES

- (1) R. L. Smith (1987), The Coming Revolution in Housing. Go Courseware
- (2) Yano Research Institute (2006), Digital Home Appliance Network Consumer Needs Survey (in Japanese). Yano Research Institute
- (3) NISTEP Report No.82 (2005), The 8th Science and Technology Foresight Survey (in Japanese)
- (4) NHK Broadcasting Culture Research Institute (2006), NHK Data book 2005 National Time Use Survey (in Japanese).
- (5) Architectural Institute of Japan, Energy consumption for residential buildings in Japan (in Japanese) (2006). Architectural Institute of Japan ISBN978-4-8189-4202-8
- (6) H. Tsuji, M. Kojoma, A. Takahashi, M. Nakano, S. Aoki, S. Inoue, K. Asari, E. Mimura (2008), Preference Mining on Future Home Energy Consumption, IEEE International Conference on Systems, Man & Cybernetics (IEEE/SMC 2008), pp.3697-3701
- (7) A. Takahashi, S. Aoki, H. Tsuji and S. Inoue (2008), Bayesian Network for Future Home Energy Consumption, in Lecture Notes on Artificial Intelligence (LNAI 5243: Ed by A. Dengel et al. (Eds)), Springer-Verlag Berlin Heidelberg, pp.372-379

Visualizing language evolution as an emergent phenomenon based on biological evolution and learning

Tsubasa Azumagakito, Reiji Suzuki and Takaya Arita

Graduate School of Information Science, Nagoya University

Furo-cho, Chikusa-ku, Nagoya 464-8601, Japan

Tel : +81-52-789-4266; Fax : +81-52-789-4258

E-mail : azumagakito@alife.cs.is.nagoya-u.ac.jp

Abstract: From the artificial life perspective, language can be viewed as a complex adaptive system emerging from linguistic interactions between individuals. Language and the human brain have evolved in parallel and interacting with each other. In this study, we propose a model of language evolution based on biological evolution and learning. In our model, the linguistic space is expressed in the polar coordinate system in which each possible language is expressed as a point. We conduct evolutionary experiments based on the model and visualize the results in the linguistic space. The trajectory of distribution of innate linguistic abilities shows the diversification and complexity growth of language. In the extended experiment, in which the angular coordinate represents the additional effect on cost for the plasticity, we observe a general tendency that the cost of plasticity evolves to become smaller. However, it never evolves to be zero, which might suggest that some cost of plasticity producing the Baldwin effect is adaptive in language evolution.

Keywords: language evolution, visualization, learning, artificial life.

1 Introduction

Language distinguishes humans from other animals. Language allows us to accumulate knowledge and transmit it across both space and time. This has led to a greater understanding of the world and accelerated cultural achievement. The evolution of language has been the subject of numerous debates and speculations. Nevertheless, it is difficult to study in a scientific manner and remains an open research question.

Recently, a constructive approach has been adopted to investigate language evolution [1]. It is characterized by the use of computational models from the viewpoint that language is a complex adaptive system emerging from linguistic interactions between individuals. Another viewpoint states that language and the human brain have evolved in parallel and interacting each other. In other words, they have coevolved. If we focus on the evolution of the human brain, there are two typical adaptive processes at different time scales: biological evolution and learning (phenotypic plasticity) [2].

Based on these viewpoints, in previous work [3], we investigated the coevolution between communication ability and phenotypic plasticity to clarify whether and how learning can facilitate evolution in dynamic environments arising from communicative interactions among individuals. To do this, a simple computational model was devised to do this. The levels of adaptive communication of signaling and receiving processes are determined by different sets of traits. Each level represents the expected value of fitness contribution for a successful communication. A communication is successful only when the levels of the signaler and the receiver are the same. The agents try to improve their communication levels through learning in which the values of plastic traits can be modified from their genetically determined values. The evolutionary experiments showed that the population with a learning ability successfully increased its shared level of communication while the popu-

lation with no leaning was not able to increase the level. It was also shown that the Baldwin effect (typically interpreted as a two-step evolution of the genetic acquisition of a learned trait without the Lamarckian mechanism [4]) repeatedly occurred and facilitated the evolution.

The purpose of this research is to study the general roles of biological evolution and learning in the evolution of language. For this purpose, we construct a generalized model for the coevolution between the communication ability and phenotypic plasticity. It is a generalization over the model devised in the previous work [3] in the following two aspects. 1) The linguistic space is expressed in the polar coordinate system in which each possible language is expressed as a point, and the success in the conversation is determined geometrically (instead of using a specific task as in the previous work). Therefore, we can observe the coevolution as trajectories of innate linguistic abilities of agents in the linguistic space. 2) The fitness can be defined by adjusting the benefit from the communicating agents, the benefit from the complexity of the used language, and the cost of learning, independently.

2 Model

2.1 Agent and communication

N agents in the population communicate with each other using their language capacity. The linguistic space is expressed in the polar coordinate system in which each possible language is expressed as a point (Figure 1). The distance from the origin (r) represents the complexity of the language, and the angle from the positive x-axis (θ) represents a language type. Each agent is represented as a point and a field surrounding the point in the linguistic space. The former corresponds to the agent's innate language, and the latter corresponds to linguistic plasticity as an innate attribute of the agent. The plasticity is expressed as a fan-shaped field with area determined by r_p

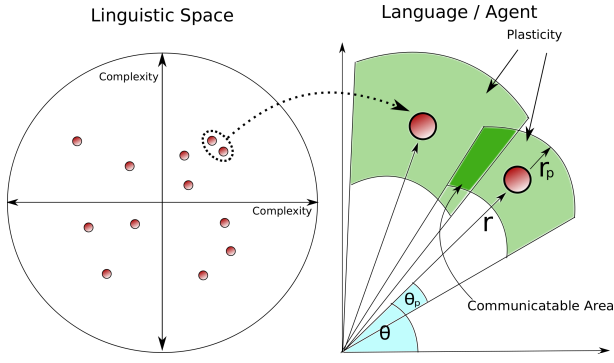


Figure 1: Linguistic space and agents.

and p as shown in Figure 1.

Overlap of two plasticity fields means that corresponding two agents can communicate with each other by learning (using their plasticity). Agents with large plasticity can communicate with many agents although they incur a large cost proportional to the area of their plasticity field. The polar coordinate system reflects the situation where the difficulty and cost of communication is proportional to the complexity of the language.

2.2 Fitness Evaluation

The fitness of each agent depends on the number of communicating agents, the complexity of the innate language, and the area of the linguistic plasticity. The fitness function is defined as:

$$Fitness = (L - \frac{L^2}{2G})^{w^1} \cdot r^{w^2} - (4 p r_p r)^{w^3}, \quad (1)$$

where w^i ($i=1, 2$ and 3) are weights for three components of the fitness function. The first term represents the benefit from the number of communicating agents. L is number of communicating agents and G is the population size. α is a parameter that determines the change in the benefit of communications with the increase in the number of communicating agents. There are three possible situations: a) a linear increase ($\alpha=0$), b) an exponential increase ($\alpha < 0$), c) the existence of an optimal number of communicating agents for the best benefit ($\alpha > 0$), as shown in Figure 2. Case b) corresponds to the situation in which there is a synergetic effect in information sharing, and c) corresponds to the situation in which the benefit of the information decreases if it is shared by too many agents due to some restrictions (e.g., the limitation of resources). The second term represents the benefit of communications depending of the complexity of the language. The more complexity will bring about the greater benefits. The third term represents the cost of learning. We assume that it is proportional to the area of plasticity ($4 p r_p r$), as it is probable that more complex and different languages are difficult be learned.

2.3 Evolution

The agents are selected using roulette wheel selection to reproduce according to their fitness to form the next generation. Mutation is performed with probability P_m . The genotypes of offspring are mutated by adding a small random value: $R(0, 12)$ for r_p , r , and $5/r \cdot R(0, 1)$ for α , p , where $R(\mu, \sigma^2)$ is a normal random number with mean

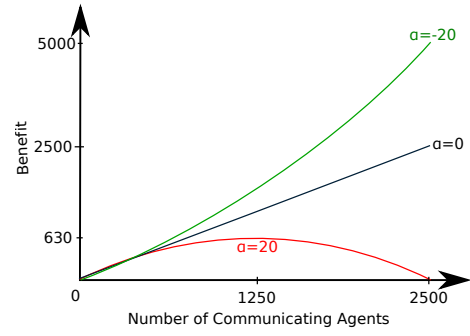


Figure 2: The effect of α on the benefit.

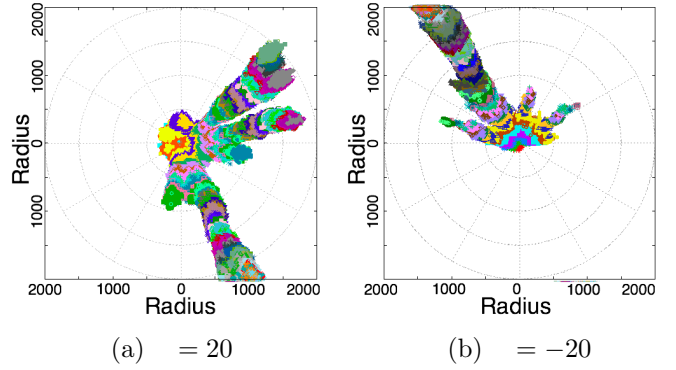


Figure 3: Results of language evolution.

and variation σ^2 . Note that the range of a random value for α , p is inversely proportional to r of the parent. This property keeps the amount of displacement of the innate language or change in its plasticity due to mutation constant independent of the location of the agent in the linguistic space.

3 Results

We conducted evolutionary experiments for 1000 generations and visualized the results in the linguistic space. The following parameters were used: $N=25000$, $w^1=1$, $w^2=1$, $w^3=1.1$, $P_m=0.8$. The initial values of the genotypes of the agents (r, r_p, α, p) were all zero.

3.1 Evolution of linguistic diversity and complexity

We conducted two experiments in which α was 20 or -20 . The results using the two-dimensional polar coordinate system are shown in Figure 3. The innate linguistic abilities of all agents were plotted with a unique color for every 10 generations. Figure 3(a) and (b) show the trajectory in the case of $\alpha=20$ and -20 respectively. Both figures indicate that the agents formed some linguistic clusters from the initial population at the origin, then they increased their complexity of language gradually. However, the clusters converged to one large cluster with high complexity by the end of experiments. It is notable that distant clusters coexisted for a longer generation when α was positive (Fig 3(a) vs. (b)). This means that the negative effect of information sharing on the fitness caused by the excess number of communicating agents contributed to the maintenance of high linguistic diversity.

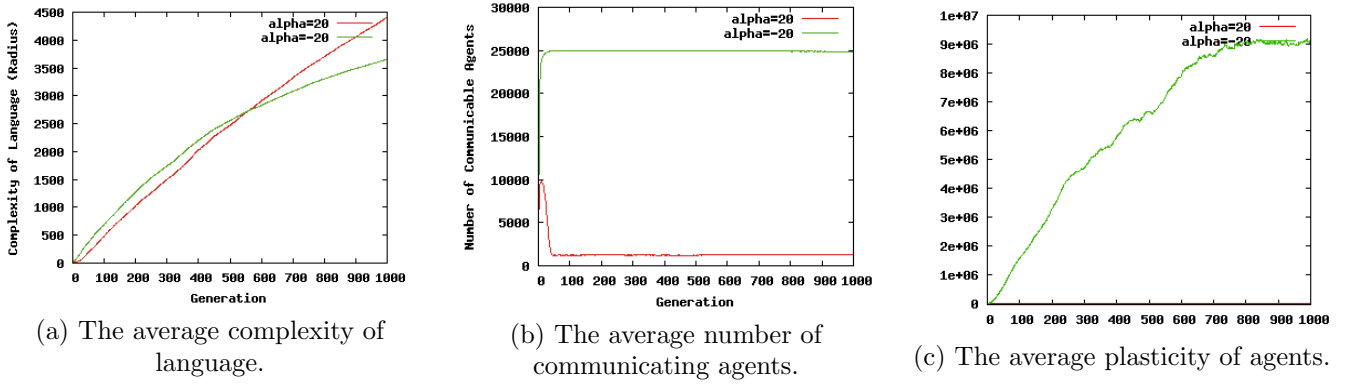


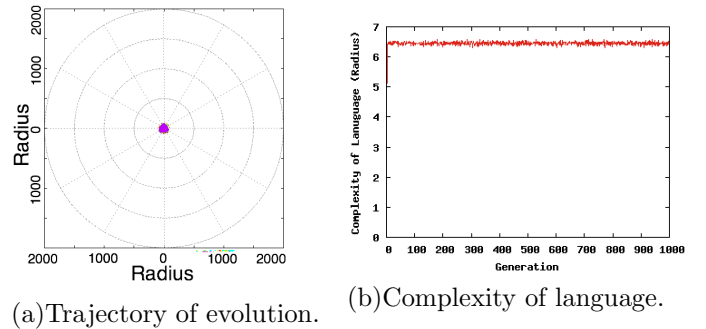
Figure 4: The comparison of agent abilities between experiments with $\alpha=20$ and $\alpha=-20$.

Figure 4 compares some properties of agents in both cases. Figure 4 (a) shows the evolution of the average innate complexity of language. The horizontal axis represents the generation. We see that the average complexity in the case with $\alpha=20$ was higher than the one in the case with $\alpha=-20$ after around the 550th generation. This implies that the negative effect of information sharing could also accelerate the later evolution of the complexity of language.

Figure 4(b) and (c) shows the evolution of (b) the average number of communicating agents and (c) the average plasticity for each agent respectively. We define the plasticity of each agent as its area ($4 \cdot r_p \cdot r_p \cdot r$). Figure 4(b) showed a sharp increase in the number of communicating agents for about 20 generations and its subsequent decrease to the small value (about 1250) in the case of $\alpha=20$. In contrast, the number of communication in the case of $\alpha=-20$ sharply increased to its maximum 25,000 (equal to the population size). Figure 4(c) shows that the sufficient amount of plasticity increased drastically from the initial generation in the case of $\alpha=-20$. In the case of $\alpha=20$, the plasticity evolved to the relatively smaller value 12694 at 1000th generation, although it is too small to see its value in Figure 4(c). This indicates that agents in the case of $\alpha=20$ formed linguistic clusters that keep the most beneficial size (about 1250) by controlling their plasticity. Note that, although Figure 3(a) shows that the linguistic clusters seem to have converged to one cluster in the last generation, that cluster is composed of small sub-clusters that kept the most beneficial size. Furthermore, the linguistic clusters that were close to each other were more robust against a mutation of α . This is an explanation of why the linguistic clusters converged to one cluster in spite of $\alpha=20$.

As a whole, the results indicate that the evolutionary scenario of linguistic diversity as follows. 1) In the early stages of evolution, there was an increase in the number of agents with more plasticity to communicate each other. 2) Then, in the case of $\alpha=20$ (means there is negative effect of information sharing), the plasticity is adjusted to small value to keep population size in optimal value.

In addition, we conducted experiments without learning in which agents have no plasticity. Specifically, a communication between two agents results in success when they share the same r and θ perfectly. The results with $\alpha=20$ are shown in Figure 5. We see that the complexity of language rapidly converged to about 6.5 in early generations.



(a)Trajectory of evolution. (b)Complexity of language.
Figure 5: Results of experiments without learning.

It shows that the evolutionary process of the complexity of language tended to constant without learning.

3.2 Effects of learning cost

We conducted further experiments to understand the effects of the leaning cost on the evolution of the population. We used various weights for learning cost (w^3) ranging from 0 to 2 at intervals of 0.05. Here we focused on the case of $\alpha=20$. Figure 6 shows four typical trajectories of the population when $w^3=0, 1.2, 1.4$ and 1.6 respectively. It shows that as the weight of learning cost increased, the increasing rate of the linguistic complexity decreased, and the linguistic clusters tended to converge around the origin.

The average plasticity and complexity of language in the last generation in these cases are shown in Figure 7.

When the weight was relatively small ($w^3 < 1.0$), the complexity of language reached a high value around 4800. The plasticity value has a wide distribution between low value and significant high value comparatively. In these cases, the increase in the complexity of language brings about the higher benefit compared with its effect on the cost. Thus, the higher complexity of language was essential for survival of agents. Besides, due to the smaller cost of learning, the plasticity often became high value. As a result, the language tended to become more complex and the plasticity often reached high values.

When $1.0 < w^3 < 1.4$, both indices tended to become smaller as w^3 increased due to the increased cost of learning. There is a possibility that the smaller plasticity retarded the evolution of the complexity because agents might not be able to communicate with their own mutants or not be able to keep the optimal number of communicating agents.

When $w^3 \geq 1.4$, the complexity converged to the small

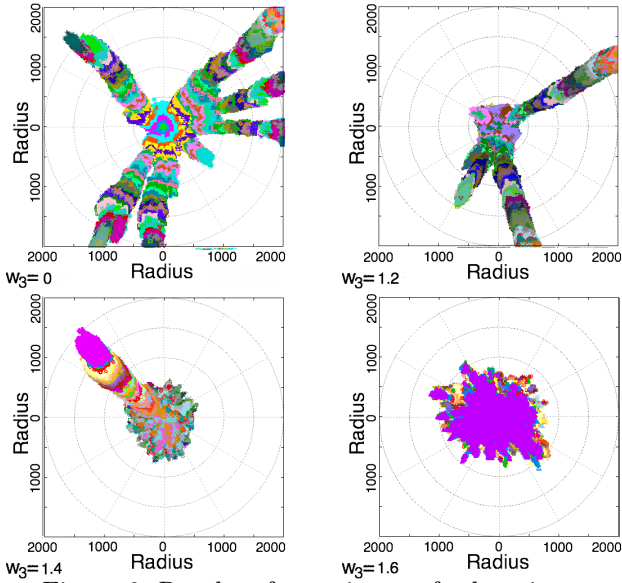


Figure 6: Results of experiments for learning cost.

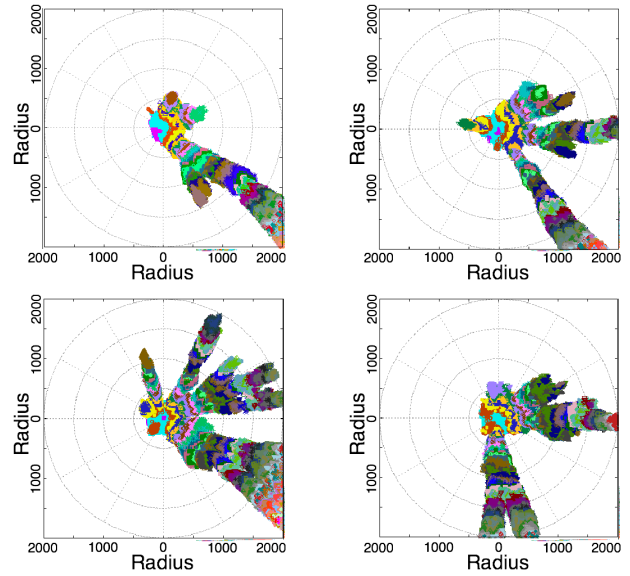
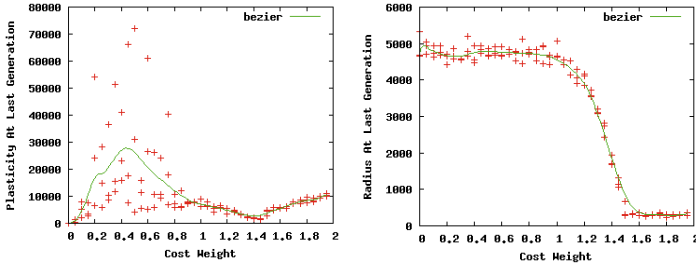


Figure 8: Results of extended experiments.



(a) The average plasticity of agents. (b) The average complexity of agents.

Figure 7: The results comparison of learning cost.

value around 200 as w^3 increased. In these conditions, the increase in the complexity of language yields much larger cost. Thus, the population was supposed to evolve to use the less complex languages. The gradual increase in the average plasticity when $w^3 \geq 1.4$ was due to the slower convergence to the small values caused by the higher cost.

As a whole, it turned out that the degree of learning cost strongly affected the diversification of languages and their properties.

3.3 Additional cost experiments

Finally, we conducted experiments to consider the evolution of learning cost. In these experiments, the angular coordinate of an agent was associated with an additional cost of learning $Cost$, which was added to the fitness value calculated as follows:

$$Cost = \begin{cases} -(|\frac{\pi}{2} - \theta| \cdot \frac{2(4\theta_p r_p r)^{w^3}}{\pi}) & \text{if } 0 < \theta < \pi/2, \\ (|\frac{\pi}{2} - \theta| \cdot \frac{2(4\theta_p r_p r)^{w^3}}{\pi}) & \text{if } \pi/2 < \theta < \pi, \\ -(|\frac{\pi}{2} - \theta| \cdot \frac{2(4\theta_p r_p r)^{w^3}}{\pi}) & \text{if } \pi < \theta < 3\pi/2, \\ -(|\frac{\pi}{2} - \theta| \cdot \frac{2(4\theta_p r_p r)^{w^3}}{\pi}) & \text{otherwise.} \end{cases}$$

When θ is 0 or 2π , there is no effect of the additional cost. As θ gets closer to $\pi/2$, the additional cost increases. We used 20 as θ_p .

The typical results are shown in Figure 8. Each figure shows the result of a trial with a different random seed. They illustrate that linguistic diversification occurred in the first or the fourth quadrant due to the higher cost

in the second and third quadrant. Thus, the language that had low cost to learn was selected in the evolution of language. The results show that excessive cost of learning prevents evolution of language.

4 Conclusion

In this paper, we conducted experiments with a comprehensive model of language evolution. The results of our experiments showed some implications for language evolution as follows. First, the linguistic complexity and diversity can emerge through interactions between evolution and learning. Second, the negative effect of information sharing on the fitness caused by the excess number of communicating agents contributed to the maintenance of high linguistic diversity. Third, agents may not be able to advance their linguistic complexity without the plasticity of linguistic abilities. Finally, the excessive cost of learning can prevent evolution of language because the plasticity is not enough to cover the mutation range. It is not necessarily the case that the low cost of learning accelerate evolution of language due to the plasticity covering the whole mutation range.

Future work includes considering geographical factors in linguistic diversification and the asymmetric aspects of benefit of communications by extending our model.

References

- [1] Luc Steels. The synthetic modeling of language origins. *Evolution of Communication*, Vol. 1, No. 1, pp. 1–34, 1997.
- [2] Yusuke Watanabe, Reiji Suzuki and Takaya Arita. Language evolution and the Baldwin effect. *Artificial Life and Robotics*, Vol. 12, pp. 65–69, 2008.
- [3] Reiji Suzuki and Takaya Arita. How learning can guide evolution of communication. *Proceedings of Artificial Life XI*, pp. 608–615, 2008.
- [4] Peter Turney, Darrell Whitley and Russell Anderson. Evolution, learning, and instinct: 100 years of the Baldwin effect. *Evolutionary Computation*, Vol. 4, No. 3, pp. 4–8, 1996.

Self-organizing stability of food web that emerges from the evolution of restrictions on speciation

Hirofumi Ochiai Reiji Suzuki Takaya Arita

Graduate School of Information Science, Nagoya University

Furo-cho, Chikusa-ku, Nagoya 464-8601, Japan

E-mail: ochiai@alife.cs.is.nagoya-u.ac.jp, reiji@is.nagoya-u.ac.jp, arita@nagoya-u.jp

Abstract

The food chain length has been considered as a key characteristic of food webs, and thus understanding its determinants is becoming increasingly important for ecosystem management and biodiversity conservation. For this purpose, we propose an evolutionary network model of food webs that captures the essential features of the ones in the real-world. The results show some universal features of food webs including the fractions of top, intermediate and basal species in the webs, which are in good agreement with empirical data. We will discuss how this structure can emerge in the simple evolutionary model of food webs.

Keywords: Ecosystem, Evolution, Extinction, Restriction, Food chain, Scale-free network.

1 introduction

A food web is a highly complex network which defines prey-predator relationships of species. Understanding the structure and functioning of ecosystems by exploring the network topology has long been a central topic of ecological research. Various modeling levels and types of models have been proposed by ecologists, mathematicians and physicists for understanding the mechanisms of ecological dynamics.

Amaral and Meyer's model [1] is a well-known example based on a dynamic growth structure to clarify universal features of food webs. They constructed a network model for large-scale extinction and evolution of species, in which there exists a strong restriction that limits the number of the species on each trophic level and the establishment of prey-predator relationship between distant trophic levels. The results showed a power-law distribution of extinction avalanche sizes, in good agreement with available data from fossil records. However, they did not discuss on the influence of such restriction on the global behavior of the network.

In the previous work, we clarified how the restriction based on the trophic level can affect the evolution and extinction of food webs [8], by expanding their model so that the strength of the trophic level restriction on evolution can be adjusted by a single parameter. We found that the network structure and the stability of the ecosystem strongly depended on

the strength of the restrictions, which implies that the evolution of restriction on speciation events itself is a key factor that can affect the self-organization of food webs.

It has been the subject of debates and speculations among ecologists why the food chain length is short [2, 6]. Some researchers argue that they are productivity, system size or their combination [11, 12]. The understanding of its determinants has recently become important for ecosystem management and biodiversity conservation [4].

In this paper, we focus on this subject and investigate it by using an evolutionary network model of food webs in which the restriction of speciation events is evolvable [9].

2 The Model

2.1 Network representation

Figure 1 shows an example of food webs in our model. There is one special node representing the sun in an abstract form, which is the permanent energy source. The other nodes represent species. The directed links represent the energy flow from one species (prey) or the sun to another species (predator). The trophic level of the sun is defined as 0, and the trophic level of each species is defined as the minimum distance from the sun. The species at the level 1 correspond to the autotrophic species, and cannot survive

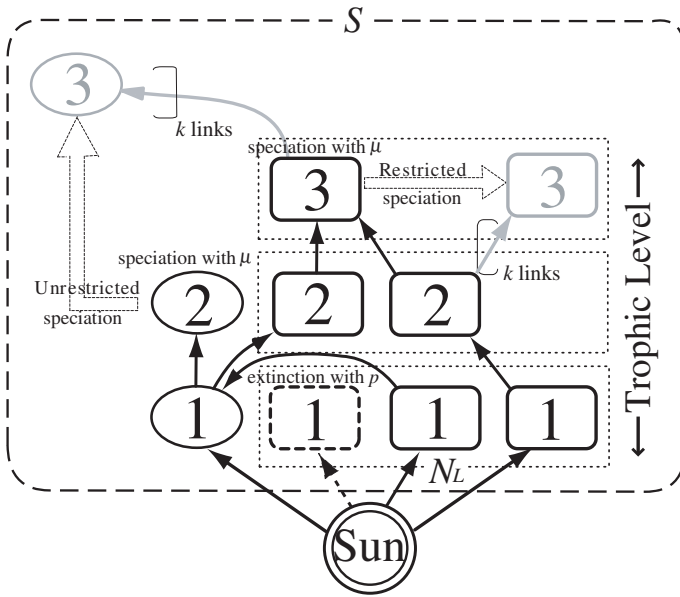


Figure 1: Schematic representation of the model. Circle and square nodes represent omnivorous species and restricted species, respectively.

without the link from the sun. The other species correspond to heterotrophic species, and cannot survive without incoming links from the other species. There are two types of species, which are determined genetically. The first type is a restricted species preying on species at lower trophic levels and speciating at a neighboring trophic level. The second is an omnivorous species preying on any species and speciating at any trophic level.

2.2 Algorithm

The dynamics of the web is driven by the speciation and extinction of species. The model starts with N_0 species at the level 1 and evolves according to the following rules:

1. Speciation.

Every existing species at the level l tries to speciate with a probability μ .

- **Restricted species:** A restricted species creates a new restricted species in an available niche at the same or neighboring levels $l-1$, l or $l+1$, and then make K_l links from species at the lower level. This event occurs only when the number of nodes at the speciating

level is smaller than the saturation point of each level N_L .

- **Omnivorous species:** An omnivorous species creates a new omnivorous in an available niche at any levels, and then make K_l links from randomly-selected species in all levels. This event occurs only when the number of nodes in the system N_S is smaller than the system size S .

The number of prey links K_l is loosely inherited from the one of the original species $K_{o,l}$. Specifically, K_l is chosen randomly from $K_{o,l-1}$, $K_{o,l}$ or $K_{o,l+1}$. However, the speciation does not happen if K_l is 0.

In addition, the type of the new species is mutated (flipped) with a probability ϕ .

2. Extinction.

Only autotrophic species can trigger an avalanche¹ as is the case with Amaral and Meyer's model. When a species goes extinct, all the links from it to other species are removed. The extinction occurs on all species which have lost all incoming links recursively.

3 Experiments

We used the system size $S = 1000$, the saturation point of each level $N_L = 100$, the extinction probability $p = 0.01$, the probability of speciation $\mu = 0.02$ and mutates $\phi = 0.01$. Those parameter values are based on the previous studies [5, 7, 10].

We adopted a food web composed of 10 restricted species and 10 omnivorous species at the level 1 that receive a link from the sun as the initial state of this simulation.

3.1 Basic Dynamics

Figure 2a shows a typical result of the experiments. The number of entire species N_S tended to fluctuate around the maximum value 1000 while it often decreased sharply. We observed the extinction of entire species as seen at the 21000th step in the figure. It is also shown that there is a strong correlation between the number of speciation and extinction, which is in good agreement with empirical data [1].

Figure 2b shows the transition of the length of the food chain of restricted and omnivorous species. The

¹The avalanche means chains of extinction.

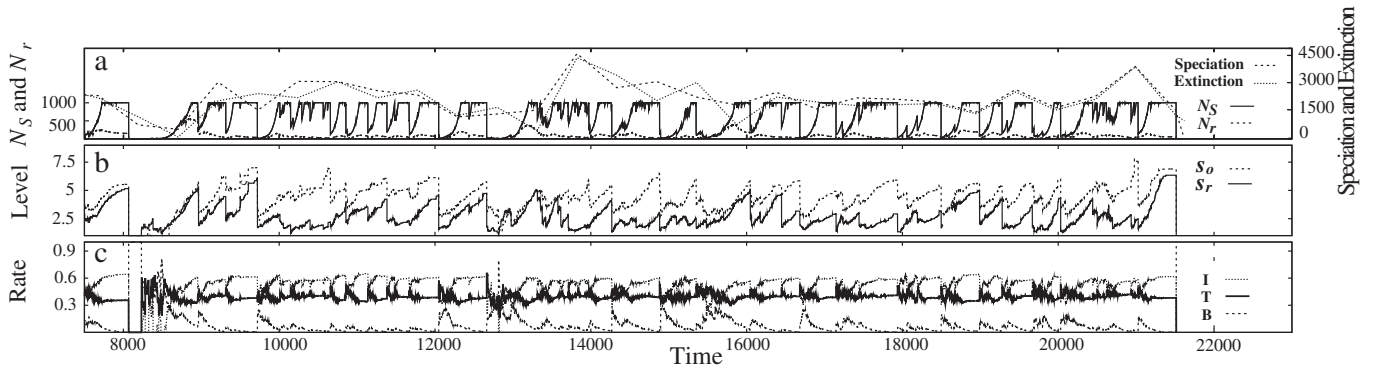


Figure 2: Time sequence of the number of species, speciation and extinctions events. The number of speciation or extinction is the total number of speciation or extinction events during consecutive non-overlapping intervals of 512 time steps.

values of the length was oscillating at around level $1 \sim 7$ with the number of species N_S , and the length of omnivorous species kept longer level than the one of restricted species. This indicates that the system was composed of two layers; lower layer: restricted species, higher layer: omnivorous species, and the food chain length was oscillating around the lower level.

Cohen and Briand [3] found a fundamental property of food webs that the ratio among basal species B (predators without predators), intermediate species I (predators and prey species) and top species T (prey species without prey) is roughly constant: $B : I : T = 0.19 : 0.52 : 0.29$. Figure 2c shows the fraction of the BIT at each step. The average of the fraction in the time sequence for 50 runs is $B : I : T = 0.104 : 0.513 : 0.383$. The fraction shows the same tendency with empirical data [3].

3.2 Effect of the system size

Table 1 summarizes the results of the simulations for 50 runs with the three different size of system $S = 500, 1000$ and 2000 . As the system size increased, the survival time² and the rate of the number of all species and restricted species decreased. On the other hand, the length of the food chain and the fraction of intermediate species increased. This means that the system has same features of partial sphere which tended to increase the ratio of volume area to surface and to be unstable in larger system.

²The elapsed time before all the species went extinct.

The results show that the length of food web does not get longer compared to the increasing of the system size. Here, we explain the reason of the relatively short length of food web.

The system has two tendencies. The length of food web tends to increase with the system size increasing. The system also tends to be unstable as the system size becomes large. This instability is supposed to derive from the inherent property concerning the ratio: $I > T > B$, which appears when the system size is large. The smaller number of basal species could be the cause of mass extinction.

For these reasons, the length of food web is oscillating around lower level without reaching a higher level.

4 Conclusion

It has long been discussed among ecologists what the determinant factors of the food web length are. Some researchers agree that they are productivity, system size or their combination [11, 12]. However, from the results of the simple constructive food web model, it is strongly suggested that the determinative factor of the short length is the general property concerning the ratio among basal species B (predators without predators), intermediate species I (predators and prey species) and top species T (prey species without prey): $I > T > B$. This tendency coupled with the basic tendency of the system to grow is supposed to control the high frequency of extinction, which leads to a limited

Table 1: Effects of system size on the behavior which was the averages taken over 50 runs.

S	Survival time	Rate of species			Average chain length			Fraction of BIT		
		s	s_r	s_o	s	s_r	s_o	s	s_r	s_o
500	5677.04	74.67 %	35.74 %	64.26 %	3.75	2.98	4.04	0.112 %	0.494 %	0.394 %
1000	4460.16	66.17 %	22.12 %	77.88 %	4.27	2.92	4.44	0.104 %	0.513 %	0.383 %
2000	3714.26	59.94 %	17.15 %	82.85 %	4.62	2.71	4.76	0.095 %	0.530 %	0.375 %

length of the food-web. It should be noted that the scenario presented in this paper is in good agreement with empirical data.

References

- [1] L. A. N. Amaral and M. Meyer. Environmental changes, coextinction, and patterns in the fossil record. *Phys. Rev. Lett.*, 82(3):652–655, Jan 1999.
- [2] M. Begon, J. L. Harper, and C. R. Townsend. *Ecology: Individuals, Populations and Communities [3rd edition]*. Blackwell Scientific Publications, Oxford, 1996.
- [3] Joel E. Cohen. *Food Webs and Niche Space*. Princeton University Press, Princeton, 1978.
- [4] Michio Kondoh and Kunihiro Ninomiya. Food-chain length and adaptive foraging. *Proceedings of the Royal Society B: Biological Sciences*, 276(1670):3113–3121, 2009.
- [5] M. Lässig, U. Bastolla, S. C. Manrubia, and A. Valleriani. Shape of ecological networks. *Phys. Rev. Lett.*, 86:4418 – 4421, 2001.
- [6] K. Matsuno and N. Ono. How many trophic levels are there? *Journal of Theoretical Biology*, 180:105 – 109, 1996.
- [7] M. E. J. Newman and P. Sibani. Extinction, diversity and survivorship of taxa in the fossil record. *Proceedings: Biological Sciences*, 266:1593 – 1599, 1999.
- [8] H. Ochiai, R. Suzuki, and T. Arita. The effects of the trophic level on the stability of food webs. *Artificial Life and Robotics*, 14(3):374 – 383, 2009.
- [9] H. Ochiai, R. Suzuki, and T. Arita. A constructive model for the evolution of food web structure based on the trophic constraint. *Japan Society for Software Science and Technology (in Japanese)*, (in press).
- [10] A. Pekalski, J. Szwabiński, I. Bena, and M. Droz. Extinction risk and structure of a food web model. *Phys. Rev. E*, 77:031917 (8 pages), 2008.
- [11] S. L. Pimm and J. H. Lawton. Number of trophic levels in ecological communities. *Nature*, 268:329 – 331, 1977.
- [12] D. M. Post, M. L. Pace, and N.G. Hairston. Ecosystem size determines food-chain length in lakes. *Nature*, 405(6790):1047–1049, 2000.

Modeling Electrosensory System of Weakly Electric Fish

Miyoung Sim and DaEun Kim

*Biological Cybernetics Lab
School of Electrical and Electronic Engineering,
Yonsei University, Schinchon, Seoul, 120-749
(Tel : 82-2-2123-5879)
(daeeun@yonsei.ac.kr)*

Abstract: Weakly electric fish have specialized sensory system to detect the electric field. They generate the electric field with the electric organ and sense the intensity change of the electric field with their electroreceptors. If there is a target object in the environment, the electric fish detect the distortion of electric field, caused by the target object. A set of sensor readings in the rostrocaudal line or the dorsoventral line provides the localization information of a target object as well as the object features such as the material and shape. We model the electrosensing mechanism of the weakly electric fish for possible application to the underwater robot. It will be shown how the electric pole distribution in electric organ affects the electrolocation mechanism. The agent can bend the tail for the body movement and a series of sensor readings in the temporal domain and spatial domain are observed. The temporal change with tail-bending movements can be used to estimate the accurate position of a target object. The relative slope with the bent tail is similar to the original relative slope when the fish body is in the neutral line. Regardless of the position, we can apply the same electrolocation rule. This study helps to develop the electrosensor system and the biomimetic sensory system can be applied to the underwater robotic fish.

Keywords: weakly electric fish, electrolocation, distance measure, tail bending, robotic fish.

I. INTRODUCTION

Weakly electric fish are very specialized to electroreception. They have three types of sensor systems, mechanosensory lateral line, ampullary electroreceptors, and tuberous electroreceptors [1-2]. Among the three types of sensors, a large number of sensors belong to tuberous electrosensors which are sensitive to the change of electric field. The tuberous system is used for active sensing and weakly electric fish can detect distortion of self-generated electric field [3-5].

The electrosensory system can be applied to the biomimetic robotic fish. Weakly electric fish can identify the location and characteristics such as size and conductivity of a target object [3-4]. When the electrosensory system is equipped in robotic fish, it is possible to localize and identify the characteristics of a target. The electrosensory system is composed of the electric organ discharge and electroreceptors along the body. In this study, two types of electric organ structure, fish-like multiple-pole distribution and a simplified two-pole model, will be tested for electrolocation.

It is shown that some species of weakly electric fish can use spatiotemporal information to localize a target object, especially with tail-bending movements [6-9]. The relative slope is known as a distance measurement regardless of the size and conductivity of a target [10-12].

Normally the electric organ is composed of many poles [5] and in this paper a simplified electric organ model will be introduced with two electric poles. The two-pole electrosensory system can be a practical model which can be easily realized in the electric fish robot. We study two different electric organ models for the electrosensory system and see how the models influence the electrosensory performance. It is useful to study the temporal sensor response with the electric organ models. The relative slope will be tested for distance estimation, and we will show the change of relative slopes with tail-bending movements. The developed electric organ structure and object localization features can be applied to the electrosensory system of a robotic fish.

II. MATERIALS AND METODS

1. Modeling of the electric field

The electric organ of weakly electric fish can be modeled as a composition of many electric poles. The electric potential at position x is calculated as the sum of potential differences generated by each electric pole [3].

$$V(x) = \sum_{i=1}^{n-1} \frac{q/(n-1)}{|x-x_p^i|} - \frac{q}{|x-x_p^n|} \quad (1)$$

where $n-1$ positive poles and one negative pole exist [3]. This electric field model is based on Gymnotiformes. In the rostrocaudal line, n positive poles are arranged in rows and one negative pole is located in the last point of the electric organ [3-5]. The electric field is the gradient of the electric potential.

$$E(x) = \sum_{i=1}^{n-1} \frac{q/(n-1)}{|x-x_p^i|^3} (x-x_p^i) - \frac{q}{|x-x_p^n|^3} (x-x_p^n) \quad (2)$$

The electric perturbation of a simple sphere object is derived as

$$\delta V(x) = \chi \frac{a^3 E(x_{obj}) \cdot (x - x_{obj})}{|x - x_{obj}|^3} \quad (3)$$

where a is the radius and x_{obj} is the center of a target and χ the electrical contrast - 1 for perfect conductor and - 0.5 for perfect insulator [5].

When we consider the component normal to the electroreceptor, the transdermal potential is

$$V_{td}(x_s) = E(x_s) \cdot \hat{n}(x_s) \frac{\rho_{skin}}{\rho_{water}} \quad (4)$$

where $\hat{n}(x_s)$ is a normal vector at the measured point x_s and ρ resistivity. *Apteronotus albifrons* belonging to Gymnotiformes bends the tail from side to side in a range from 45° to -45° [5]. The arrangement of the electric organ is transformed according to tail-bending movements.

In this study, we established two types of electric organ structures, fish-like multiple pole model and a simplified two-pole model as shown in Fig.1. The multiple pole model is based on the model for real electric fish. The simplified electric organ model has two electric poles, positive and negative. The arrangement is different from the multiple-pole model and sensor readings are affected by the electric organ structure.

The relative slope with electroreceptors along the

rostrocaudal line is known as a distance measurement [10-12] and it will be introduced in the next section.

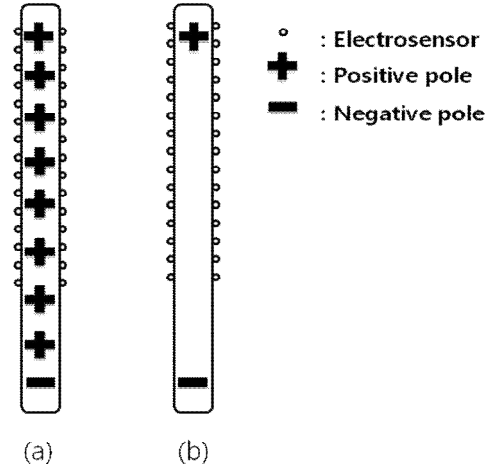


Fig.1. Electric organ models

(a) fish-like multiple pole system and (b) two-pole electric organ

2. Relative slope

The sensor readings can be represented as an electric image. The electric image has been studied to understand the electrolocation mechanism. In this study, the box model is used for electrolocation [13]. The electroreceptors are distributed along the rostrocaudal line parallel to the mid-line of the fish, which is called a box model. The normal vector of the electroreceptor, $\hat{n}(x_s)$, is vertical to the mid-line of the fish.

In three-dimensional space, weakly electric fish have to estimate the position of a target in the rostrocaudal (from head to tail), dorsoventral (from ventral to dorsal area), and lateral (from fish to side) axis with respect to the fish body. The rostrocaudal and dorsoventral position can be extracted from the maximal point of the electric image [3,5]. The lateral distance changes the intensity and width of the electric image. The relative slope is the ratio of the maximal slope to maximal slope (equation 5). It is possible to estimate the lateral distance regardless of the size and conductivity of a target object.

$$\text{Relative slope} = \frac{\max_i \{I(x_{i+1}) - I(x_i)\}}{\max_i \{I(x_i)\}} \quad (5)$$

The relative slope is a localization feature of a target object in the environment and it is one of essential properties in weakly electric fish as well as artificial robotic fish.

III. Experiments

We applied the relative slope to two electric organ models for distance estimation. Fig.2 and Fig.3 show change of relative slope when the lateral distance and rostrocaudal position of a target object change.

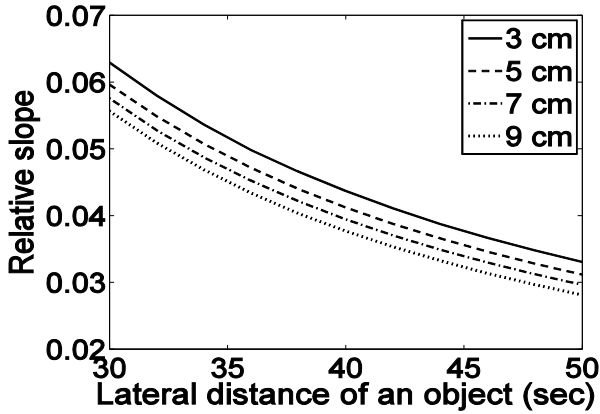


Fig.2. Relative slope for multiple-pole electric organ when the rostrocaudal position of a target changes

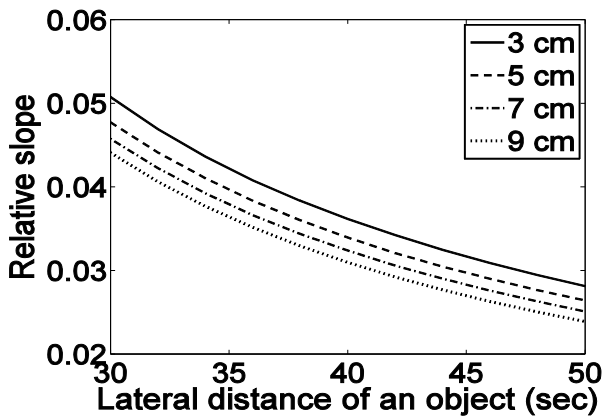


Fig.3. Relative slope for two-pole electric organ when the rostrocaudal position of a target changes

The relative slope is affected by both lateral distance and rostrocaudal position of a target object. When the rostrocaudal position changes from 3cm to 9cm, the shape of the electric image and relative slope are affected. However, the relative slopes in the two-pole system have similar patterns with those in the multiple-pole system when the rostrocaudal position changes. The rostrocaudal position of a target object can be estimated with the peak amplitude in the electric image. Then the relative slope curve can be used for the lateral distance estimation.

We also test the temporal change of electrosensor readings with tail-bending movements. The relative

slope is largely independent on the tail-bending movements [8]. The multiple-pole electric organ structure changes the arrangement of the electric poles with tail bending movements. The caudal area of weakly electric fish is approximately 65% of the body length and bends drawing circular portion around the pivot. The radius of the arc is $R=L/2\theta$ where θ is the bending angle. The simplified two-pole model has bending area, 50% of the body length, and this area is bended in a straight line. These two electric organ models have a bending-angle range from 45° to -45° .

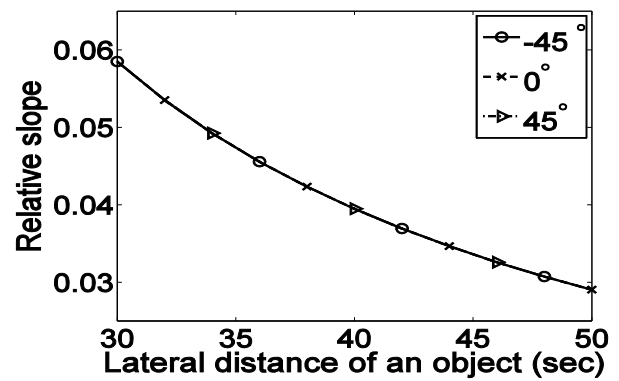


Fig.4. Change of relative slope when the weakly electric fish bend the tail with the multiple-pole model

Fig.4 shows the relative slope with tail-bending movements with the multiple-pole electric organ model. When weakly electric fish bend the tail to the left and right, the relative slope is about the same. Weakly electric fish might use relative slope with bent tail to assure the estimated distance in noisy environment [8].

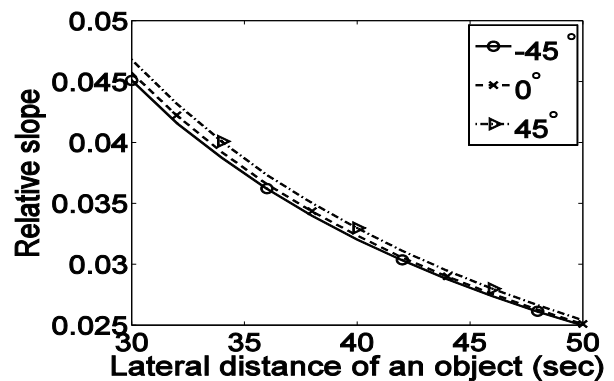


Fig.5. Change of relative slope when the weakly electric fish bend the tail with the two-pole model

Fig.5 shows change of the relative slope when the simplified two-pole model is used. The relative slopes with the two-pole model have a little change, but the patterns are quite similar. We can use relative slope to estimate the distance regardless of the bending angle.

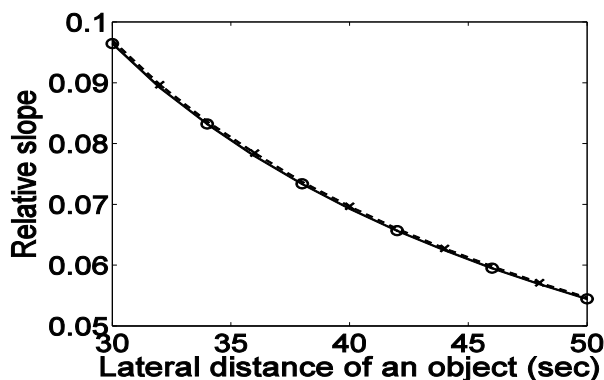


Fig.6. Relative slope with simplified electrosensory model (the marker 'o' is the original relative slope and the marker 'x' the relative slope in integrated electric image with tail-bending)

Fig.6 shows the original relative slope with the fish in a straight line and the relative slope in integrated electric image generated by tail-bending movements. The integrated image calculates the summation of the electric image for each bending phase. In the integrated electric image with the two poles, these relative slopes are about the same to original one. The integrated electric image with tail-bending can more exactly estimate the distance of a target object, which can be useful in noisy environment.

VI. CONCLUSION

In this study, we compared the fish-like multiple-pole model and a simplified electrosensory model with two poles for electrolocation. From the relative slope pattern, we can estimate the location of a target object. Interestingly, the two-pole model shows similar performance of electrolocation as the multiple-pole system, although the two-pole system has slightly more variations in electrolocation.

Weakly electric fish can use temporal structures with tail-bending movements to estimate the estimated distance. When they bend the tail, it is possible to extract relative slope from the electric image and also the temporal integration of sensor readings during the tail-bending movement can be applied to the two-pole

system for more exact estimation of target distance. This study shows that we can use a simple electrosensory model with two poles for a robotic fish instead of the complex fish-like multiple-pole model.

V. ACKNOWLEDGMENTS

This work was supported by Mid-career Researcher Program through an NRF grant funded by the MEST (No. 2010-0000460)

REFERENCES

- [1] Nelson, M. and MacIver, M. (1999), Prey capture in the weakly electric fish *Apteronotus albifrons*. *Journal of Exp. Biology* 202(10):1195-1203
- [2] Nelson, M., MacIver, M., and Coombs, S. (2000), Modeling electrosensory and mechanosensory images during the predatory behavior of weakly electric fish. *Brain, Behavior and Evolution* 59(4):199-210.
- [3] Rasnow, B. (1996), The effects of simple objects on the electric field of *Apteronotus*, *Journal of Comparative Physiology A* 178(3):397-411.
- [4] Assad, C. and Rasnow, B. (1999), Electric organ discharges and electric images during electrolocation, *Journal of Experimental Biology* 202:1185-1193.
- [5] Chen, L., House, J., Krahe, R., and Nelson, M. (2005), Modeling signal and background components of electrosensory scenes, *Journal of Comparative Physiology A* 191(4):331-345.
- [6] Sim, M. and Kim, D. (2009), Distance discrimination of weakly electric fish with a sweep of tail bending movements, 10th European Conference on Artificial Life.
- [7] Sim, M. and Kim, D. (2009), Electrolocation of weakly electric fish with differential electric image in tail-bending movement (in Korean), *Korea Robotics Society Annual Conference*, 348-350.
- [8] Sim, M. and Kim, D. (2010), Electrolocation using a relative slope with a distortion of an electric field in robotic fish (in Korean), *Korea Robotic Society Annual Conference*, 182-183.
- [9] Sim, M. and Kim, D. (2010), Estimating distance of a target object from the background objects with electric image (in Korean), *Journal of the Institute of Electronics Engineers of Korea-SC*, 56-62.
- [10] von der Emde, G. (1999), Active electrolocation of objects in weakly electric fish, *Journal of Experimental Biology*, 202(10):1205-1215.
- [11] Schwarz, S. and von der Emde, G. (2001), Distance discrimination during active electrolocation tasks in the weakly electric fish *Gnathonemus petersii*, *Journal of Comparative Physiology A* 186(12):1185-1197.
- [12] Sicardi, E., Caputi, A., and Budelli, R. (2000), Physical basis of distance discrimination in weakly electric fish, *Physica A* 283(1-2):86-93.
- [13] Babineau, D., Longtin, A. and Lewis, J. (2006), Modeling the electric field of weakly electric fish, *Journal of Experimental Biology* 209(18):3636-3651.

Simultaneous cognitive origin of life and information

Koji Ohnishi^{1,2}

¹*Institute for Theoretical and Evolutionary Sciences (ITES),
c/o Koji Ohnishi, 8712-30, Ikarashi-2, Nishi-ku, Niigata, 950-2102, Japan
(Tel : 81-25-262-5237; Fax : 81-25-262-5237)*

(ohnishi@sc.niigata-u.ac.jp, ohnishi@ma.tlp.ne.jp)

²*Department of Biology, Faculty of Science, Niigata University,
Ikarashi-2, Nishi-Ku, Niigata, 950-2181, Japan*

Abstract: Shannon's information quantity, $I(E) = \log(1/P(E))$, is defined under the assumption of the existence of "cognitive subjective entity" capable of judging yes/no or occurred/non-occurred of an event E (which occurs with a probability $P(E)$). Final acceptor/user of information is a living individual, although first and/or intermediate sender(s) and/or acceptor(s) of information may be either living individual(s) or non-living element(s) or man-made machine(s). Thus we can conclude that information is a most essential character of living individuals, and that information and life must have had simultaneously emerged as "minimum cognitive system (MCS)". Since then, living individuals/lives must have evolved as "self-improving learning neural network machine" capable of "active evolution". How MCS could have emerged was discussed. Not only cognitive origin and evolution of life, but also active evolution of cognitive organisms were concluded as basic, general evolutionary principles.

Keywords: origin of information, semio genesis, minimum cognitive system, active evolution

I. INTRODUCTION

Biotic systems are full of "information" [1][2], but the question, "what is information?" is not fully answered in biology as well as in other areas of information sciences. In this paper, the origin and evolution of information systems and semiotic systems were analyzed from evolutionary and cognitive viewpoints. The results strongly suggest that information-accepting ability is an essential character of life, and information and life seem to have simultaneously occurred by the emergence of earliest cognitive life. Semio genesis would have generated efficient biomachines which are bio-individuals.

II. ORIGIN OF INFORMATION

Shannon's "amount of information", $I(E) = \log(1/P(E))$, is defined under the assumption of the existence of "cognitive subjective entity" capable of judging yes/no or occurred/non-occurred ($= 1/0$) of an event E (which occurs with a probability $P(E)$). Final receiver/user of information is a living individual, although first and/or intermediate sender(s) (=outputter(s)) and receiver(s) of information may be either living individual(s) or non-living element(s), or man-made/organism-made machine(s).

Let us consider some examples of information systems.

Example 1. Solar light energy (photon) $h\nu$ ($\nu = \nu_0$) is received as information for driving a bioenergy-acquiring proton-pump by bacteriorhodopsin of an archaean, *Halobacterium salinarum* [1]. In this case, initial sender of $h\nu_0$ information is the sun, a non-living entity, and the information is recognized by the living archaean with using its information-receiving molecular tool or machine (receptor), bacteriorhodopsin.

The sender of the information is a non-living thing (the sun), and the last receiver (acceptor) of the information is the living individual of an archaebacterial uni-cellular organism which can use a protein-tool or protein-machine for receiving the $h\nu_0$ -information, which is further converted to bioenergy inside the uni-cell individual via proton-pump. The $h\nu_0$ energy was not "information" before the emergence of bacteriorhodopsin-possessing archaea, and the end-user of this information is the living uni-cell organic individual. Therefore the origin of the $h\nu_0$ -information occurred when archaea first possessed or made the $h\nu_0$ -utilizing bacteriorhodopsin.

Example 2: A unicellular individual of a eubacteria, *E. coli*, receives DNA codon-information from its intracellular DNA derived from the previous generation, by using intracellular information-processing molecular machines called mRNAs. The sender of codon-information is the DNA derived (via cell division) from the uni-cell individual of the previous generation, and the final user/receiver of the DNA-information is the living uni-cell organism capable of using mRNA and other RNA-machines and protein-enzymemachines.

Example 3: A multicellular human individual utilizes solar $h\nu_{00}$ light-energy ($\nu = \nu_{00}$) by using green-sensitive rhodopsin molecules embedded in the membrane of green-sensitive optic cells in human's optic organ. The final user of the $h\nu_{00}$ -energy information is the living multicellular human individual. Note that optic cells as well as green-sensitive rhodopsins are not living individuals, and do not actively use the $h\nu_{00}$ -photon information.

Example 4. In vocal conversation between two persons, both of the first sender of vocal information and the last receiver/user of the vocal information are living human individuals, who can actively use the finally

received information.

Example 5. In radio-broadcasting of various sounds, the first sender(= outputter) of the sound-information is either non-living entity/element or a living organismic individual, and inter-mediate information-receivers and intermediate information-senders are also either non-living entity or living organic individuals, as well as man-made information-processing machines which are biotic (or human) cultural products. The last information receivers/acceptors being end-users of the sound-information are living human individuals possessing acoustic organ, “ears”.

From all of these Examples 1-5, end-users of information are unexceptionally living organic individuals, every of which is the unit of Darwinian natural selection. Thus, “information” is a kind of value for the living individual in increasing Darwinian fitness. Before the emergence of life, any end-user of information did not exist, and therefore, any “information” cannot be reasonably defined for pre-biotic world. Information-using is an actively cognizing behavioral process of living organic individuals.

In conclusion, “information” first emerged simultaneously with the origin of life (= the origin of living individuals capable of evolving via Darwinian natural selection). This means that “information” is a most essential feature of life itself, and that life and information have had emerged simultaneously. A most important problem for finding the origin of life is, therefore, how to know the earliest “minimum cognitive system” which possesses information-using faculty. How “minimum cognitive machine” could have emerged is an important problem remaining to be solved.

II. ORIGIN AND HIERARCHICAL EVOLUTION OF INDIVIDUALITY

Biotic individuals such as unicell bacteria and multicellular animals are actively behaving entities which are units capable of evolving via natural selection. Throughout evolution different levels of individualities have had evolved, and every behaving individual is well-made biomachine having cognitive information-processing systems [3][4].

In modern living organic individuals, unicell bacteria and haploid uni-cell organisms are lowest levels of individuality, confirming that unicell organismic individuals having one set of DNA genes are earliest living-organisms immediately after the emergence of DNA-type genetic machinery. Any of living organic individuals before the emergence of DNA has not yet been known to date. Emergence of unicell diploid individuals is the first hierarchical evolution of individuality, as has been discussed by Maynard Smith [5] and Dan-Sohkawa [6]. Multicellularization of unicell diploid and/or haploid individuals is the next step of hierarchical evolution. The so-called super-organism of bee or other hymenopterian eusociety is the most highly evolved

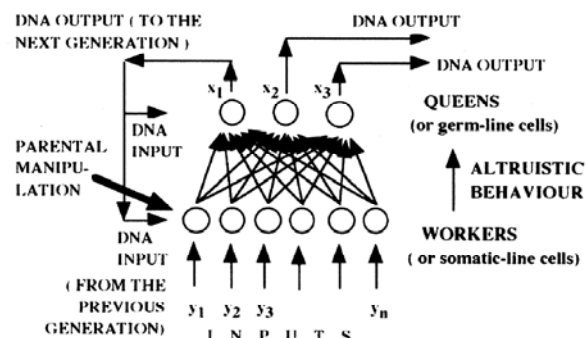


Fig. 1. Hierarchical neural network-type biomachinogenesis generating upper-leveled individuals via Altruistic sociogenesis (Modified from [3]). Bee-superorganisms and multicellular individuals are compared. DNA-flows make a hierarchical neural network machine possessing feed-back DNA flows. “Parental manipulation” such as *Polytes* maternal manipulation and *Drosophila* bicoid-mRNA seems to function as “teacher information” in man-made learning neural network machines.

level of hierarchical individuality [3].

Parallel hierarchical evolution of individuality has occurred in generating bee-super-organismic individuals and multi-cellular animal individuals, as illustrated in Fig.1. Queen-worker-type hierarchical (eu-)society such as bee society is known to have evolved by kin selection [7]. Since relatedness (r) between workers and queens(=worker’s younger sisters) is $3/4$ of DNA ($r=3/4$), such altruistic behavior is considered to be equivalent to DNA-information flow from workers to queens, as shown in Fig. 1. DNAs outputted by gametes of queens are further inputted to the workers and queens of the next generation via fertilization, which makes feedback DNA-flows from the queens of present generation to the workers and queens in the next generation.

Similar DNA-flows can be found in multicellular animals in which each animal is originally an altruistic queen-worker-type hierarchical society of uni-cell animals consisting of queen-type germ-line cells (=queen-cells) and worker-type somatic cells (=worker-cells). Hamilton considered multicellular animals have had evolved via altruistic behaviors of worker-cells (= originally, uni-cell animals) to queen-cells [7].

In animals, multicellular individuals are considered to have evolved via an early super-organismic kin society of uni-cell animals. However, the evolutionary results show that upper-leveled (multi-cellular) individuals really live and behave as active evolving organisms, and that germ-line cells and somatic cells are elements or parts of upper-leveled living individuals. This is very similar to bee-superorganisms, which strongly suggests that “worker-bees and queen-bees are not living individuals, and are elements or parts of super-organisms. The living individuals are bee-superorganisms.

Parallelisms between bee-superorganisms and multicellular animal individuals are much more striking, as shown in Fig.2, where the well-known bee-dance system for collecting pollens and honey is compared with the *Aplysia* simple neural system. Worker-bees coming back to hive and making dance (=sensory bees) well correspond to sensory neurons (= worker-cells) in *Aplysia* siphon system, and bees receiving dance-language correspond to *Aplysia* motor-neurons (worker-cells). The dance language being a semiotic signal corresponds to synaptic molecular signals evolved as semiotic signals. Thus, dancing bees and dance-recognizing bees are “sensory bees” and “motor-bees”, respectively. Semio-genesis generating bee-dance and *Aplysia* synaptic molecular signals must have had important roles for the genesis of biomachine consisting of queens(or queen-cells) and workers(or worker-cells). Neurons are not living individuals, and quite similarly, bees are not living animal individuals. Bee-superorganisms are “genuine living bee-individuals”.

In Fig. 2, *Aplysia* neural system is evidently a “cognitive system” for accepting water-flow information and making adaptive muscle-moving. Very similarly, bee-dance system is also a “cognitive system” of bee-superorganism for accepting pollen-information and making adaptive pollen-collecting movements of motor-bees. The parallelism between these two cognitive systems tells us “how biotic cognitive systems could have evolved.” Semio-genesis is very essential for making efficient biomachinogenesis.

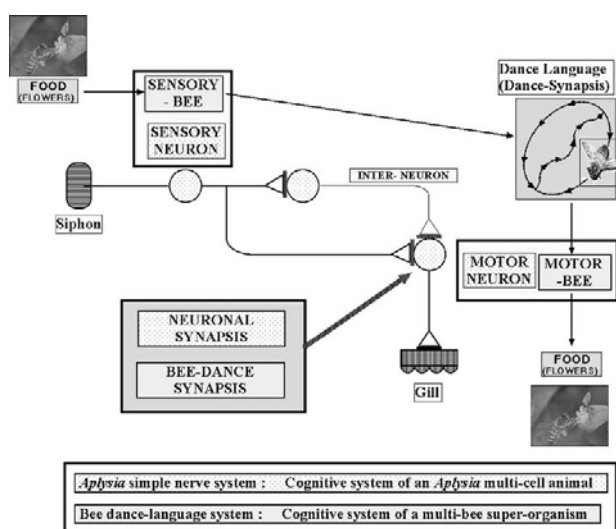


Fig.2. Close similarities between the *Aplysia* nerve system and the bee dance-language system.

II. BIOTIC INDIVIDUALS AS THINKING MACHINES

Returning to Fig.1, we can find that the DNA-information flows in the hierarchical superorganismic

biomachine suggest that biotic individuals would be a cognitive machine similar to a hierarchical neural network machine. In the case of the eusociety of *Polistes* (hymenopteran), maternal manipulation to daughter wasps makes daughters be worker-wasps. Similarly, earliest determination of embryonic cells in *Drosophila* depends on the gradient of the concentration of maternal mRNAs (such as *bicoid*-mRNA). These maternal effects are very similar to the so-called “teacher-information depending on feed-back information” in learning neural network machines, as shown in Fig. 1. Thus the scheme in Fig 1 suggests that these superorganismic biomachines would have evolved as “hierarchical learning neural network biomachines”. Such biomachines can input environmental and intra-body information, and output DNA information as schematized in Fig.1. Accordingly, repeating of generation is a “thinking process” of the individual, which is a cognitive neural network machines. Thus “thinking” of the well-made cognitive bio-machines must have improved biomachines in generating the present-day well-made bioorganisms. Repeating of generations of such learning biomachines is thinking processes of organisms. Now we have reached to a clear answer to the important question, “Who made the well-made biomachines?”, proposed by Dawkins [8]. The answer is that “Biotic individuals have had “actively” made and improved the well-made biomachines by “thinking” via repeating generations.

The essential difference between autopoietic/active bio-machines (= biotic individuals) and man-made learning neural network machines (NNwMs) are the difference of teacher-information (TI). TI is given from outside by man-made program in man-made learning NNwMs. However, as shown in Fig.1, IT is included in the biotic system, and therefore, bio-individuals can actively self-improve their own individuals (=bio-machines) by repeating generations. Thus, bio-individuals are cognitive self-improving learning NNwMs. The NNwM in Fig.1 is not a simple 2-layered NNwM capable of performing “linearly separable” cognitions, but a multi-layered complex NNwM capable of performing “non-linearly separable” cognitions, because every element of the both layers (= queen-layer and worker-layer) in Fig.1 is originally a cognitive (uni-cell or multi-cellular) living individual possessing intra-individual neural networks of information-flows. Hierarchical sociogenesis is thus considered to make an efficient multi-layered neural-network bio-machine via semiotic function.

Uni-cell organisms also have intracellular complex information networks capable of inputting environmental and intracellular information, and adaptively outputting various kinds of information. Thus unicell organisms are also considered to be cognitive machines which are complex thinking NNwMs. Accordingly we have reached a conclusion that

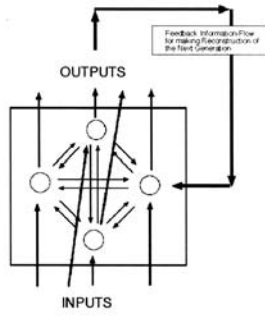


Fig. 3. Generalized model of biotic individual possessing intra-individual cognitive complex neural networks of information flows and feedback information-flows.

living individuals are cognitive NNw bio-machines which can actively think/consider and self-improving. Accordingly, evolution is “active thinking process” of living organisms, resulting in “active evolution”.

A most generalized bio-individual consisting of complex NNwM possessing feed-back information flow from present to the next generation is schematically shown in Fig. 3.

Furthermore, diploid “species” can be considered as a “hierarchical super-neural network machine” shown in Fig. 4, where multi-cellular male and female diploid individuals are input layer, and haploid gametes (ova/sperms) are output layer elements which make feedback DNA-flows to the next generation. The “species really exists as a probabilistic neural network machine, which is also a cognitive biosystem capable of thinking and improving to make more adaptive bio-systems and eco-systems.

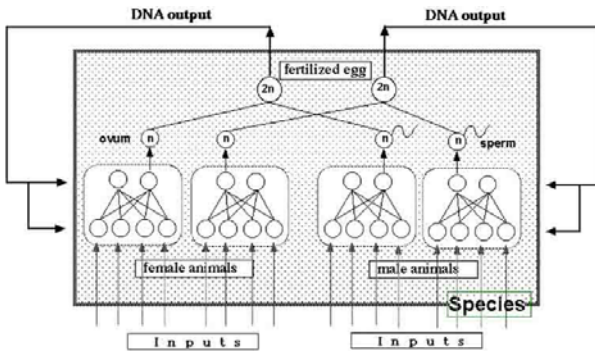


Fig.4. Hierarchical probabilistic neural network machine model of diploid species.

III. EMERGENCE OF “MINIMUM COGNITIVE SYSTEM” AS A FIRST LIFE

The question, “What is first life?”, needs to be re-considered from the aspect of above-mentioned cognitive life. “Information” emerged simultaneously with the emergence of cognitive individuals as the last receiver(or acceptor)/user of information. For efficient bio-individuals to evolve as thinking bio-

machines, semiogenesis must have been important throughout evolution.

Early evolution having generated “minimum cognitive system(MCS)” needs to be analyzed from various aspects. An interesting approach is to analyze the emergence of MCS from simple harmonic oscillator, $F^2x = -\omega^2x$, where $x = (x_1, x_2)^T$, $F = (a_{ij})_{2,2}$, in which $a_{22} = -a_{11}$, $a_{21} = -(a_{11}^2 + \omega^2) / a_{11}^2$, and where x_i and a_{ij} ($i, j = 1, 2$) are real numbers or real functions. This model gives a MCS-like oscillator, as shown in Fig.5, as has been recently discussed. See legend of Fig.5 and ref. [8] for details.

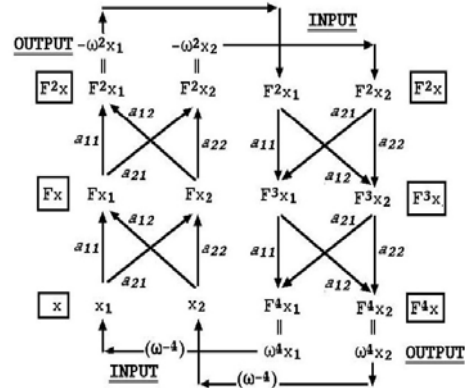


Fig. 5. Three-layered neural network-like structure of generalized harmonic oscillator system, where $F = {}^t((a_{11}, a_{12}), (a_{21}, a_{22}))$, where $a_{22} = -a_{11}$, $a_{21} = -(a_{11}^2 + \omega^2) / a_{11}^2$. By letting $Q_s = F^4$, and $w = \omega^4$, we find that Q_s and w satisfy a self-replication equation, $Q_s x = w x$. If $\omega^2 = 1$, then F^2 is a complete self-replication operator. $x = F^0x = (F^0x_1, F^0x_2)^T = (x_1, x_2)^T$; $Fx = F^1x = (F^1x_1, F^1x_2)^T = (a_{11}x_1 + a_{12}x_2, a_{21}x_1 + a_{22}x_2)^T$; $F^2x = (F^2x_1, F^2x_2)^T$, where $F^2x_1 = a_{11}F^{k-1}x_1 + a_{12}F^{k-1}x_2$, and $F^2x_2 = a_{21}F^{k-1}x_1 + a_{22}F^{k-1}x_2$.

REFERENCES

- [1] Albert B, et al.(2008) Molecular Biology of the Cell, 5th ed., Garland Science, New York, NY.
- [2] Rowe, GW(1994), Theoretical Models in Biology. Oxford Univ.Press, Oxford.
- [3] Ohnishi K, et al.(2002): Neural-network-like biogenesis via semeiogenesis : A unified theory on the origin of genetic codes and other semeiotic systems. *Viva Origino* 30(2), 63-78.
- [4] Ohnishi K., Shutou H., Sawamura H., and Goda M. (2001): Neural-Network-like machinogenesis via semeiogenesis: Origins of genetic codes and other semeiotic systems. *SIG Technical Reports* 2001(37), 3-6.
- [5] Maynard-Smith J (1989), Evolutionary Genetics, Oxford Univ. Press, Oxford.
- [6] Dan-Sohkawa M(1996), Reading the complexity of Life. Biology of hierarchy (In Japanese), Heibon-sha, Tokyo.
- [7] Hamilton WD (1964), The genetical evolution of social behaviour I, II. *J. Theor. Biol.* 7: 1-16, 17-52.
- [8] Dawkins R (1996) *The Blind Watchmaker*. Norton & Co., New York.
- [8] Ohnishi, K. (2008): A preliminary consideration on the origin of life as a cognitive system. *Proc. of the 13th Int. Conf. on Artificial Life and Robotics*, pp.686-689, Oita.

Study on Discrete Adiabatic Quantum Computation in 3-SAT Problems

Mohamed El-fiky Satoshi Ono Shigeru Nakayama

Department of Information and Computer Science,
Faculty of Engineering, Kagoshima University

1-21-40, Korimoto, Kagoshima 890-0065, Japan

TEL: +81-099-285-8453 FAX: +81-099-285-8464

E-mail: {mh_fiky77, ono, shignaka }@ibe.kagoshima-u.ac.jp

Abstract

This paper proposes a new variation method for the phase functions of the adiabatic quantum algorithm, quadric variation method. Experiments are carried out solving 3-SAT problem with discrete adiabatic quantum algorithm to compare the proposed two formulation of quadric variation method performance with the previously proposed methods linear and cubic.

Keywords:

Quantum Computation; Adiabatic Theory; Hamiltonian; k -SAT Problem.

I. INTRODUCTION

The field of quantum computation have gone through an amazing development in past decade, it has rise as one of the hot area of research after existence of many quantum algorithms showing that the quantum algorithms greatly enhance the efficiency of solving problems believed to be intractable on classical computers. as Peter Shor's polynomial time quantum algorithm for factorizing integers [1], Grover algorithm for unstructured search with quadric speed up over any classical algorithm [2] and Hogg algorithm [3].

The Model of adiabatic quantum computation is a new paradigm for designing quantum algorithms proposed by Farhi et al.[4]. The Adiabatic model is based on quantum adiabatic theorem, where the quantum computer evolves the quantum system slowly to switch gradually from an initial Hamiltonian with ground state easy to construct, to a final Hamiltonian whose ground state encodes the solution of the problem being solved.

In recently published articles, the Adiabatic quantum algorithm, was shown to give polynomial average cost growth for some NP combinatorial search problems as Satisfiability problems [5], and set partitioning problem [6].

This paper compares the adiabatic algorithm performance in solving 3-SAT problems using three different variation methods Linear, cubic, and the proposed method, as result the corresponding search costs and probability of finding the solution are shown.

II. k -SAT PROBLEMS

The k -satisfiability problem (k -SAT) is a combinatorial search problem, whose instance is a Boolean expression written using AND, OR, NOT, n variables, and m clauses. A clause is a logical OR of k variables, each of which may be negated. Given an expression, the solution is an assignment ,i.e., a value of TRUE or FALSE values for each variable that will make the entire expression true,i.e., satisfying all the clauses [7]. An example 2-SAT instance with 3 variables and 2 clauses is $(v_1 \text{ OR } (\text{NOT } v_2)) \text{ AND } (v_2 \text{ OR } v_3)$, which has 4 solutions, for example, $v_1 = v_2 = \text{false}$ and $v_3 = \text{true}$. For a given instance, the cost $c(s)$ of an assignment s is the number of clauses it does not satisfy. For $k \geq 3$, k -SAT is NP-complete, i.e., among the most difficult NP problems in the worst case [8].

III. THE QUANTUM ADIABATIC THEOREM

The adiabatic theorem states that, if the Hamiltonian of any quantum system $H(t)$ varies slowly enough, the state of the system will stay close to the instantaneous ground state of the Hamiltonian at each time t [3]. Assume we can build a Hamiltonian $H^{(c)}$ with ground state encodes the solution of the problem instance to be solved, and prepare the system in the known ground state of another Hamiltonian $H^{(0)}$. Then the adiabatic algorithm can continuously evolve the state of the quantum computer using

$$H(f) = (1 - f)H^{(0)} + fH^{(c)} \quad (1)$$

Table I
THE PARAMETERS USED IN DISCRETE AND CONTINUOUS VARIATION METHODS.

Parameters phase functions	Variation methods			
	Linear	Quadric 1	Quadric 2	Cubic
Δ	$1/\sqrt{j}$	const(=1)	const(=1)	const(=1)
Phase shift function	$\rho(f) = f$	$\rho(f) = f^2$	$\rho(f) = 2f - f^2$	$\rho(f) = 1.921f - 2.665f^2 + 1.782f^3$
Phases Mix function	$\tau(f) = 1 - f$	$\tau(f) = 1 - \rho(f)$	$\tau(f) = 1 - \rho(f)$	$\tau(f) = 1 - \rho(f)$

with f ranging from 0 to 1 [3]. Under suitable conditions, i.e., with a nonzero gap between relevant eigenvalues of $H(f)$, and with sufficiently slow changes in f , the adiabatic theorem guarantees that the evolution maps the ground state of $H^{(0)}$ into the ground state of $H^{(c)}$, so a subsequent measurement gives a solution.

IV. THE DISCRETE ADIABATIC ALGORITHM

In this paper, we use the algorithmically equivalent discrete formulation of the adiabatic algorithm acting on the amplitude state vector initially in the ground state of the Hamiltonian $H^{(0)}$, which can be represented as $|\psi_s^{(0)}\rangle = \frac{1}{\sqrt{N}}[1, 1, \dots, 1]^T$. Consider a discrete Hamiltonian $H(f)$ of the general form

$$H(f) = (f)H^{(0)} + (f)H^{(c)} \quad (2)$$

where (f) and (f) are phase mixing and phase shift function, respectively. both of them are arbitrary functions of f where $(0 \leq f \leq 1)$, see Table.1, subject to the boundary conditions

$$(0) = 1, (0) = 0 \quad (3)$$

$$(1) = 0, (1) = 1 \quad (4)$$

Although, the two functions (f) , and (f) are not necessary to be monotonic (i.e. obey the constraint $(f) + (f) = 1$), we consider only the monotonic functions [?].

In matrix form [3], the Hamiltonian $H^{(c)}$ is a diagonal matrix

$$H_{r,s}^{(c)} = c(s)\delta_{r,s}, \text{ where } \delta_{r,s} = \begin{cases} 1 & \text{if } r=s \\ 0 & \text{otherwise} \end{cases} \quad (5)$$

This Hamiltonian introduces a phase shift factor in the amplitude of assignment s depending on its associated cost $c(s)$, where the higher cost results in more phase shift. The Hamiltonian $H^{(0)}$ can be implemented with elementary quantum gates by use of the Walsh-Hadamard transform with elements $W_{r,s} = 2^{-n/2}(-1)^{r \cdot s}$ [3], where $H^{(0)} = WDW$ and D is a diagonal matrix with the value for state r given by the sum of the bits, i.e, the element $D_{r,r}$ is just a count for the number of bits equal to 1 in state r .

A single trial of the algorithm consists of j steps, parameter and can be described as

- 1) Initialize the amplitude state vector to the ground state of $H^{(0)}$ giving equal values for all states as $|\psi_s^{(0)}\rangle = \frac{1}{\sqrt{N}}[1, 1, \dots, 1]^T$

- 2) For Steps $h = 1$ through j repeat the matrix multiplication :

$$|\psi^{(h)}\rangle = U_h(f)|\psi^{(h-1)}\rangle \quad (6)$$

where $|\psi^{(h-1)}\rangle$ is the amplitude state vector at step $h - 1$, and $U_h(f)$ is unitary evolution operator for h th step which can be represented as

$$U_h(f) = e^{-i\tau(f)H^{(0)}} / 2 \cdot e^{-i(f)H^{(c)}} \cdot e^{-i\tau(f)H^{(0)}} / 2 \quad (7)$$

- 3) Measure the final system After the j steps take place, the probability to find a solution is given by $P_{soln} = \sum_s ||\psi^{(j)}||^2$ with the sum over all solutions s .

As a choice for the evolution, f is chosen to vary linearly from 0 to 1. Specifically, we take $f = h/(j + 1)$ for step h , where h is ranging from 1 to j .

V. EXPERIMENTS AND CONSIDERATIONS

A. Variation Methods and parameter

Recently several variation methods for phase shift function (f) , and phase mixing function (f) were presented as an attempts to decrease the overall search cost [3]. In this paper we present monotonic (means $+ = 1$) version of quadric variation method in two formula of quadric polynomial in f . Table .1. summaries this methods , linear , cubic and the two quadric formula we presents, and also it shows the values of the parameter as used with each method.

Figures 1, 2, 3, and 4 shows the phase fuctions for each variation method *vs.* the f value from 0 to 1, focusing in the figures we can note that the quadric variation method shown in fig. 3, has smalle diversity area than the others whcih gives a sign for expecting better results. A good performance of the discrete adiabatic algorithm requires an appropriate choice of parameter . The experiments have shown that the performance of the algorithm remains good for moderate value of j provided that is below some threshold value. The experiments for solving 3-SAT problems with $n \leq 20$ has shown this threshold to be somewhat near 1.

B. Search behavior

In this section we compare the search behavior of the discrete adiabatic algorithm using the variation methods as summarized in Table.1. First is the linear variation method

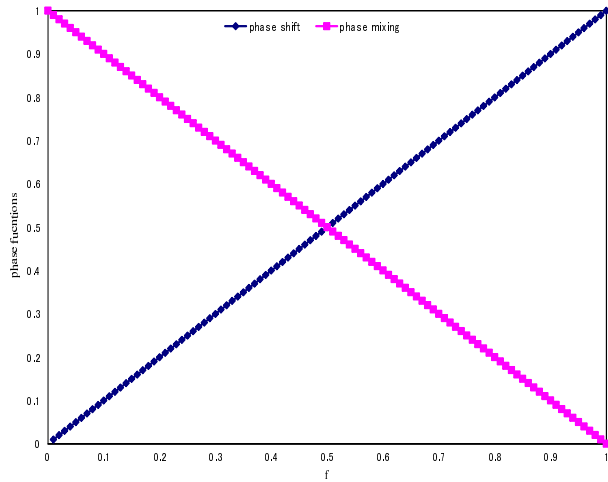


Figure 1. Phase shift and phase mix functions $Vs f$ for the linear variation method.

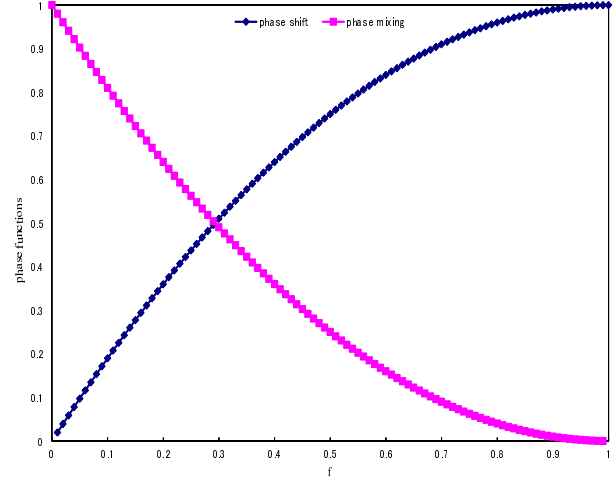


Figure 3. Phase shift and phase mix functions $Vs f$ for the quadric variation method with $\rho = 2f - f^2$ formula.

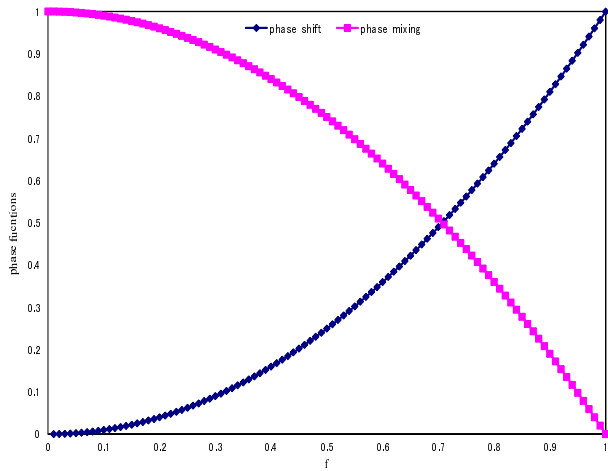


Figure 2. Phase shift and phase mix functions $Vs f$ for the quadric variation method with $\rho = f^2$ formula.

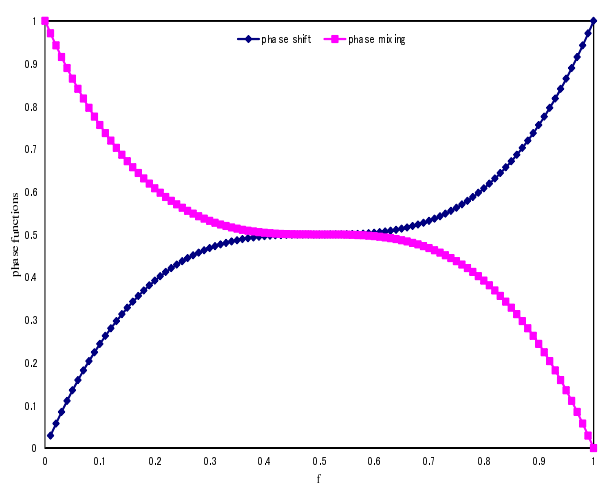


Figure 4. Phase shift and phase mix functions $Vs f$ for the Cubic variation method.

corresponds to the continuous adiabatic algorithm, this method uses $\rho = 1/\sqrt{j}$, phase shift (f) and phase mixing (f) functions varies monotonically as linear function of f , and number of steps j grows as cubic number of bits n^3 . Second method is the cubic variation [?] with (f) and (f) varies monotonically as cubic polynomial in f , constant ρ , and uses j grows as square number of bits n^2 , and finally the quadric variation method with two formula $(f) = f^2$ and $(f) = 2f - f^2$.

Figures 5, and 6 compare the search behavior of the algorithm in solving 3-SAT problem with $n = 8$, and 16, respectively. The figures show that the quadric variation method with number of steps j only as $2 * n$ can achieve P_{soln} near 0.5, which shows faster search behavior when it is compared with the algorithm behavior using cubic

variation with number of steps at least n^2 and the linear variation with $j = n^3$.

C. Search cost

The search cost is defined to be the expected number of steps required to find a solution $C = j/P_{soln}$. Fig. 7 compares the average search cost C for the Linear, cubic, and the two formulation of quadric variation methods for the adiabatic algorithm. it shows that using quadric variation with just enough number of steps $j = 2 * n$ to achieve moderate P_{soln} as shown in Figures. 5, and 6, reduces the search cost below the other methods. However the algorithm with linear variation could achieve P_{soln} near 1 in most of the trials as shown, the number of steps required j grows as n^3 giving a large search costs, far higher than those of other

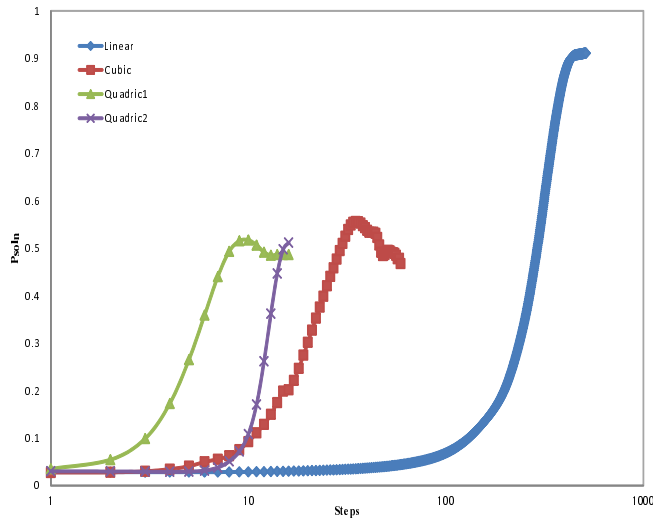


Figure 5. P_{soln} vs number of steps h for the 3 methods averaged over 10 random instances of 3-SAT problems with $n = 8$

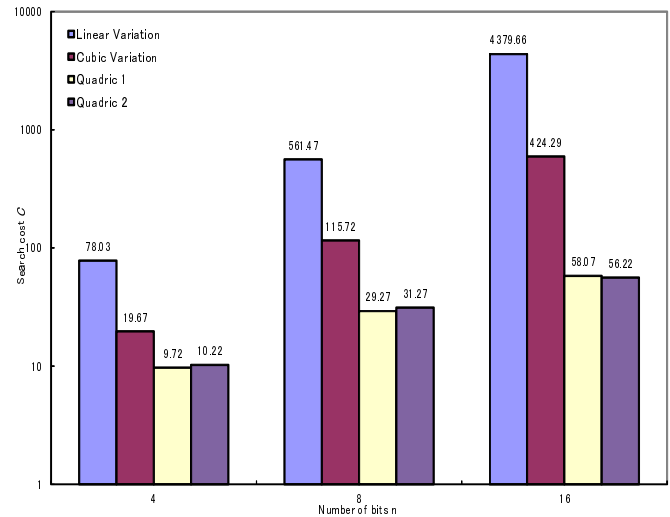


Figure 7. Log plot of the average search cost vs the number of variables n using the same instances in Figures 5 and 6.

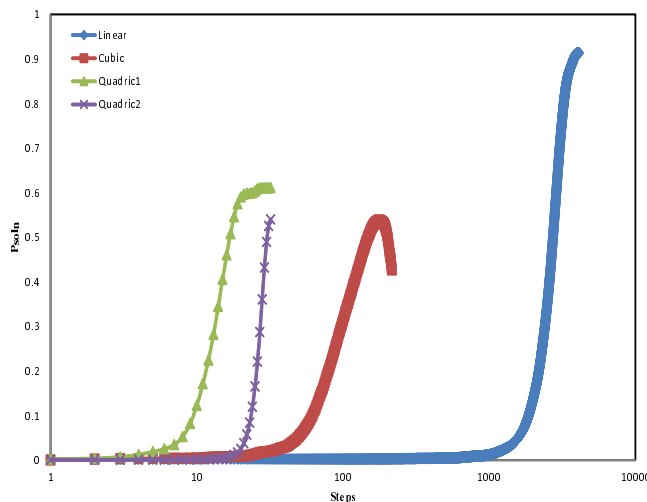


Figure 6. P_{soln} vs number of steps h for the 3 methods averaged over 10 random instances of 3-SAT problems with $n = 16$

method. For comparison the figure shows that the median search cost at $n = 16$ for the quadric1, quadric2, cubic, and linear methods to be 58.07, 56.22, 424.29 and 8749, respectively. which shows improve in the resulting cost reduction using quadric variation method, due to reduced number of steps .

VI. CONCLUSIONS

The quantum adiabatic algorithm is a remarkable discovery because it offers new insights into the usefulness of quantum resources for computational tasks. In this paper, we have presented an experimental study in solving 3-

SAT problems with the discrete the adiabatic algorithm, using a new monotonic variation method for the phase shift and phase mixing function , quadric variation with two different formula. The experiments have revealed that using the quadric variation method improves on other variation methods, in resulting Search cost and search behavior.

REFERENCES

- [1] P. Shor, "Polynomial-Time Algorithms for Prime Factorization on a Quantum Computer", SIAM J. Computing, Vol. 26, 1997.
- [2] L. Grover, " Fast Quantum Mechanical Algorithm for Database Search", ACM Symp. Theory of Computing, ACM Press, New York, 1996, pp. 212-219.
- [3] T. Hogg, Adiabatic Quantum Computing for Random Satisfiability Problems, quant-ph/0206059, 2004.
- [4] E. Farhi, J. Goldstone, S. Gutmann, and M. Sipser, Quantum Computation by Adiabatic Evolution, quantph/0001106 .
- [5] E. Farhi. A quantum adiabatic evolution algorithm applied to random instances of an NP-complete problem. Science, 292:472-476, 2001.
- [6] V. N. Smelyanskiy, and D. A. Timucin. Simulations of the adiabatic quantum optimization for the set partition problem. Los Alamos preprint quant-ph/0112143, 2002.
- [7] M. R. Garey and D. S. Johnson. Computers and Intractability: A Guide to the Theory of NP-Completeness. W. H. Freeman, San Francisco, 1979.
- [8] S. Kirkpatrick and B. Selman, Critical behavior in the satisfiability of random boolean expressions. Science, 264:1297-1301, 1994.
- [9] S. Das , R. Kobes, and G. Kunstatter Energy and Efficiency of Adiabatic Quantum Search Algorithms, quant-ph/0204044v4; Phys.Rev. A 57, (2003).
- [10] W. van Dam, M. Mosca, and U. Vazirani, How Powerful is Adiabatic Quantum Computation?, quant-ph/0206003 v1 (2002).

Fault-tolerant Image Filter Design using Particle Swarm Optimization

Zhiguo Bao, Fangfang Wang, Xiaoming Zhao and Takahiro Watanabe

Graduate School of Information Production and Systems

Waseda University

Kitakyushu-shi, Japan

Email: baozhiguo@moegi.waseda.jp

Abstract

This paper describes mixed constrained image filter design with fault tolerant using Particle Swarm Optimization (PSO) on a reconfigurable processing array. There may be some faulty Configurable Logic Blocks (CLBs) in a reconfigurable processing array. The proposed method with PSO autonomously synthesizes a filter fitted to the reconfigurable device with some faults, to optimize the complexity and power of a circuit, and signal delay in both CLBs and wires. An image filter for noise reduction is experimentally synthesized to verify the validity of our method. By evolution, the quality of the optimized image filter on a reconfigurable device with a few faults is almost same as that with no fault.

Keywords

Particle Swarm Optimization, Mixed Constrained Image Filter Design, Fault Tolerant

1 Introduction

The image filter design problem is often approached by means of evolutionary design techniques. In addition to an optimization of filter coefficients (for example, [1]), evolutionary approaches are applied to find a complete structure of image filters. In [2], Gaussian noise filters were evolved using a variant of Cartesian Genetic Programming in which target filters were composed of simple digital components, such as logic gates, adders and comparators. A few years later, image filters for other types of noise and edge detectors were evolved using the same technique [3, 4, 5]. But there were few discussions about fault-tolerance for an image filter design.

Recently chip integration is higher and higher, so that it increases the probability of faulty components and the complexity of designs increases the probability of human errors. The tolerance for faults is diminishing as the systems are demanded for high reliability. Therefore, the needs for fault-tolerant designs are stated as the long-term grand challenges in [6]. To solve this problem, we proposed a fault-tolerant image filter design using GA (Ge-

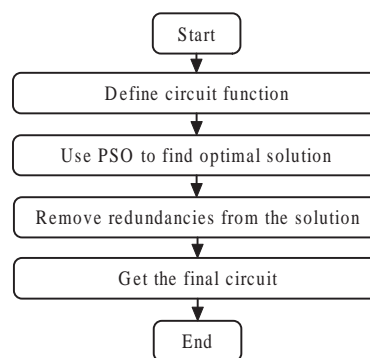


Figure 1: The overview of our method.

netic Algorithm) [8], and the experimental results showed that the resultant image filter was surely fault-tolerant. But the problems of quality and processing time still remain, and which evolutionary method (such as GA, GP (Genetic Programming), PSO (Particle Swarm Optimization) and ACO (Ant Colony Optimization)) is most suitable has not been investigated.

This paper describes an efficient image filter design for noise reduction using PSO on a reconfigurable processing array, where some faulty Configurable Logic Blocks (CLBs) may exist at random. The mixed constrained on circuit complexity, power and signal delay in both logic blocks and wires are optimized. In this design, first, the evaluating value about correctness, complexity, power and signal delay are introduced to the fitness function. Then PSO autonomously synthesizes an image filter which is simple and has better performance and fits to the reconfigurable processing array with some faults. To verify the validity of our method, an image filter for noise reduction is experimentally synthesized.

The organization of this paper is as follows: a brief overview of PSO is described in the next section. Section 3 describes fault-tolerant design optimization for an image filter using PSO. Section 4 shows the experimental results. Finally, Sect. 5 concludes this paper.

2 Particle swarm optimization

PSO is an algorithm model on swarm intelligence that finds a solution to an optimization problem in a search space.

In PSO, a particle represents a candidate solution to the problem. Each particle is treated as a point in the D -dimensional problem space. The i -th particle is represented as $X_i = (x_{i1}, x_{i2}, \dots, x_{iD})$. The best previous position (the position giving the best fitness value) of the i -th particle is recorded and represented as $P_i = (p_{i1}, p_{i2}, \dots, p_{iD})$. The index of the best particle among all the particles in the population is represented by the symbol g . The rate of the position change (velocity) for particle i is represented as $V_i = (v_{i1}, v_{i2}, \dots, v_{iD})$. The particle is updated according to the following equations:

$$v_{id}^{(t+1)} = w * v_{id}^{(t)} + c_1 * rand() * (p_{id} - x_{id}^{(t)}) + c_2 * Rand() * (p_{gd} - x_{id}^{(t)}), \quad (1)$$

$$x_{id}^{(t+1)} = x_{id}^{(t)} + v_{id}^{(t+1)}. \quad (2)$$

where,

$$0 \leq i \leq (n - 1), 1 \leq d \leq D.$$

n : number of particles in a group.

D : number of members in a particle.

t : pointer of iterations (generations).

w : inertia weight factor.

c_1, c_2 : acceleration constant.

$rand(), Rand()$: uniform random value in the range $[0, 1]$.

$v_{id}^{(t)}$: velocity of particle i at iteration t , $V_{id}^{min} \leq v_{id}^{(t)} \leq V_{id}^{max}$.

$x_i^{(t)}$: current position of particle i at iteration t .

The inertia weight factor w is employed to control the impact of the previous history of velocities on the current velocity, thereby influencing the trade-off between global (wide-ranging) and local (fine-grained) exploration abilities of the “flying points”. A larger w facilitates global exploration (searching new areas) while a smaller w tends to facilitate local exploration to fine-tune the current search area. Good values of w are usually slightly less than 1 [7].

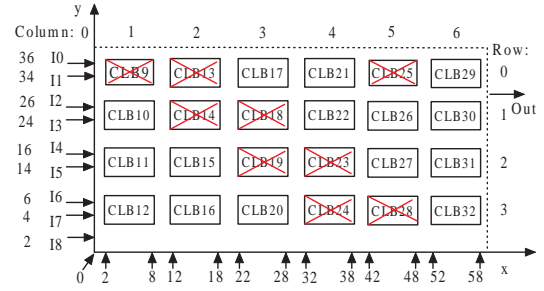


Figure 2: A reconfigurable processing array with faults.

3 Image filter design using PSO

PSO is applied to search good solutions to optimize the image filter design on a reconfigurable processing array with some faults.

The resultant image filter has an identical functional behavior with less circuit complexity, less power and less signal delay.

3.1 Image Filter

Every image operator is considered as a digital circuit with nine 8-bit inputs and a single 8-bit output, which processes gray-scaled (8-bit/pixel) images.

Every pixel value of the filtered image is calculated using a corresponding pixel and its eight neighbors in the processed image [4, 5].

3.2 Reconfigurable Processing Array for Image Filter

The reconfigurable image filter is implemented as a Virtual Reconfigurable Circuits (VRC) (Fig. 2) originally proposed in [4]. As a new pixel value is calculated using nine pixels, the VRC has got nine 8-bit inputs and a single 8-bit output. The VRC consists of two-input Configurable Logic Blocks (CLBs) placed in an array. In our proposed, a 6×4 array is needed because its size is enough for our image filter from the results in paper [8]. Any input of each CLB may be connected to either a primary circuit input or the output of a CLB in the preceding column. Any CLB can be programmed to implement one of the functions given in Table 1 [8, 9], all these functions operate with 8-bit operands and produce 8-bit results.

The CLB with different function, has different complexity, power and signal delay. We newly define the values of complexity (FC), power (FP) and signal delay (SD) for each function in a CLB, as in Table 1.

As shown in Fig. 2, the coordinates of inputs and output of each logic block are defined based on VRC, so that we

Table 1: Functions implements in a CLB.

ID	Function	Description	FC	FP	SD
0	255	Constant	8	5	1
1	x	Identity	16	10	2
2	$255 - x$	Inversion	24	15	3
3	$x \vee y$	Bitwise OR	32	20	3
4	$\bar{x} \vee y$	Bitwise \bar{x} OR y	40	25	4
5	$x \wedge y$	Bitwise AND	32	20	3
6	$\text{not}(x \wedge y)$	Bitwise NAND	40	25	4
7	$x \oplus y$	Bitwise XOR	64	38	4
8	$x \gg 1$	Right shift by 1	15	9	2
9	$x \gg 2$	Right shift by 2	14	8	2
10	$(x \ll 4) \vee (y \gg 4)$	Swap	16	10	2
11	$x + y$	+ (addition)	358	215	18
12	$x +^s y$	+ with saturation	367	220	19
13	$(x + y) \gg 1$	Average	350	210	18
14	$\max(x, y)$	Maximum	240	145	16
15	$\min(x, y)$	Minimum	240	145	16
-	(wire)	(wire)	16	10	2

FC: function complexity.

FP: function power.

SD: signal delay.

can calculate the critical length of connection wires.

There may be some faulty CLBs in a reconfigurable processing array at random. The output of a faulty CLB is a value in the range [0,255] at random.

3.3 Genetic encoding

The chromosome (particle) is a string of integers where each three continuous integers constitute a logic block. Each triplet in the chromosome encodes the two inputs and the function type of a logic block, respectively, such as:

$$(Input_1, Input_2, Function_type).$$

A typical chromosome then can be a sequence of triplets, such as:

$$X_i = ((IN_1^1, IN_2^1, F_{type}^1) \cdots (IN_1^i, IN_2^i, F_{type}^i) \cdots)$$

Here, IN_1^i and IN_2^i mean positions of the correspond input signal. F_{type}^i means function type of logic block. For primary input, $0 \leq IN^i \leq 8$. For input from output of a logic block CLB_m shown in Fig. 2, $IN^i = m$. Function in a CLB is defined as shown in Table 1.

3.4 Fitness function

The pixels of corrupted image ci are used as inputs of VRC. Pixels of filtered image fi are generated, which are compared to the pixels of original image oi .

The design objective is to minimize the difference between the filtered image and the original image. The image size is $nc*nr$ pixels, but only the area of $(nc-2)*(nr-2)$ pixels is considered, because the pixel values at the borders

are ignored, and thus remain unfiltered. The fitness value of a candidate filter is obtained as follows:

(1) the VRC is configured using a candidate chromosome,

(2) the created circuit is used to produce pixel values in the image fi , and

(3) the fitness value is calculated as

$$Fitness = (-1) * (F_1 * \beta + F_2). \quad (3)$$

where,

F_1 and F_2 are defined as follows and β is the weight on F_1 .

$$F_1 = \sum_{i=1}^{nc-2} \sum_{j=1}^{nr-2} (|fi(i, j) - oi(i, j)|). \quad (4)$$

where,

nc : the number of columns of the pixels in the image.

nr : the number of rows of the pixels in the image.

$fi(i, j)$: the pixel (i, j) in filtered image fi , the value range is [0,255].

$oi(i, j)$: the pixel (i, j) in original image oi , the value range is [0,255].

$$F_2 = SD * \alpha_{sd} + Pg * \alpha_{pg} + Cg * \alpha_{cg} + Pw * \alpha_{pw} + Cw * \alpha_{cw}. \quad (5)$$

where,

SD : signal delay of a circuit individual, determined by a critical path.

Pg : power of logic blocks in a circuit, calculated by summation of all logic block's power.

Cg : complexity of logic blocks in a circuit, calculated by summation of all logic block's complexity.

Pw : power of all wires in a circuit, calculated by summation of all wire's power.

Cw : complexity of wires in a circuit, calculated by summation of all wire's complexity.

$\alpha_{sd}, \alpha_{pg}, \alpha_{cg}, \alpha_{pw}, \alpha_{cw}$: the weights on SD, Pg, Cg, Pw, Cw , respectively.

Table 2: Conditions for evolution.

Number of Generation : 300
Population Size : 1210
Inertia weight factor $w : 0.9$.
Limit of change in velocity of each member in an individual: $V_{id}^{max} = 0.5 * p_{id}^{max}, V_{id}^{min} = -0.5 * p_{id}^{max}$.
Acceleration constant : $c1 = 2, c2 = 2$.

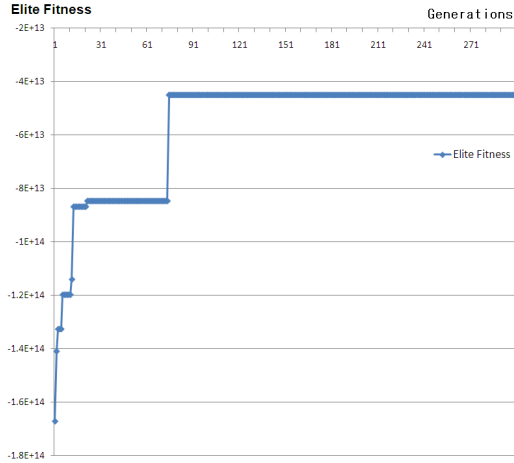


Figure 3: Elite fitness of PSO (Y-axis) vs. the number of generations (X-axis).

The priority of evaluating values in Eq. (3) is: $F_1 > F_2$. In this experiment, β is set to $0.1 * 10^9$. The priority of evaluating values in Eq. (5) is: $SD > Pg > Cg > Pw > Cw$. In this experiment, α_{sd} is set to $0.1 * 10^9$, α_{pg} is set to $0.1 * 10^6$, α_{cg} is set to $1 * 10^3$, α_{pw} is set to 100, and α_{cw} is set to 1. All α 's and β are empirically assigned in our experiment.

4 Experimental results

Table 2 shows the parameters of the evolution of PSO used in this experiment. Some preliminary experiments were performed in advance to decide parameters suitable for our experiment.

The proposed method was implemented in Eclipse SDK 3.5.1 with Java Runtime Environment(JRE) 1.6.0; and tested on a PC with Inter(R) Core(TM) i7 CPU at 3.33 GHz and 9.0 GB RAM.

The image filter is evolved for a $512 * 512$ Lena image corrupted by 5% salt-and-pepper noise, shown in Fig. 5 (a).

Fig. 3 shows the elite fitness of PSO vs. the number of generations during the image filter evolution. The elite

fitness is increasing during evaluation time.

Table 3 shows the results on a reconfigurable processing array with different faults. For each case, we execute over 10 independent trials. "Available" means the number of available CLBs. "Best one" means the best optimized image filter in terms of Mean Difference Per Pixel (MDPP) [10] among 10 trials, "Average" the average values of 10 individuals, and "Worst one" the worst optimized image filter among 10 trials. The number of used CLBs, the value of the MDPP and running time are listed. "Ratio" is the relative value of MDPP of each case compared to that of no fault $Faults(0)$. The larger the fitness is, the better the quality of image filter is. The less the MDPP value is, the better the quality is. The less the ratio is, the better the quality is.

The quality of the optimized image filter on a reconfigurable processing array with a few faults (2-4 faults) is almost same as that on a reconfigurable processing array with no fault, that is less than 12.6% in the item of different value of MDPP of the best one.

The quality of the optimized image filter of $Fault(2)$ is only 1.2% less than that of $Fault(0)$ in the item of the MDPP value of the best one.

An example of chromosome of best one of $fault(2)$ is as follows:

(0, 0, 0)(0, 0, 0)(1, 4, 15)(8, 0, 0)(0, 0, 0)(0, 0, 0)
(11, 12, 11)(11, 0, 0)(0, 0, 0)(0, 0, 0)(0, 0, 0)(15, 7, 5)
(0, 0, 0)(0, 0, 0)(0, 0, 0)(4, 20, 14)(0, 0, 0)(0, 0, 0)
(0, 0, 0)(0, 0, 0)(16, 24, 11)(0, 0, 0)(0, 0, 0)(0, 0, 0)

The graphical representation of this chromosome is shown in Fig. 4.

As the used Lena image size is relatively large, we can say that the resultant evolved filter is general purpose for the same type of noise, that is the filter is able to remove the same type of noise also from other images. Therefore, the image filter was first evolved using Lena image and then tested on other images.

Figures in Fig. 5 show the input image with 5% salt-and-pepper noise, the MDPP value of these images are 6.33, 6.39 and 6.28, respectively. Figures in Fig. 6 show the output image by the image filter of Fig. 4, the MDPP value of these images are 1.74, 1.42 and 1.76, respectively. Obviously, this image filter could reduce noise for all cases, even if there are two faulty CLBs.

5 Conclusions

This paper described mixed constrained image filter design with fault tolerance for noise reduction using PSO on a reconfigurable processing array. By evolution, the quality of the optimized image filter on a reconfigurable processing array with a few faults is almost same as that on a reconfigurable processing array with no fault. Consequently



Figure 5: The input images with noise.

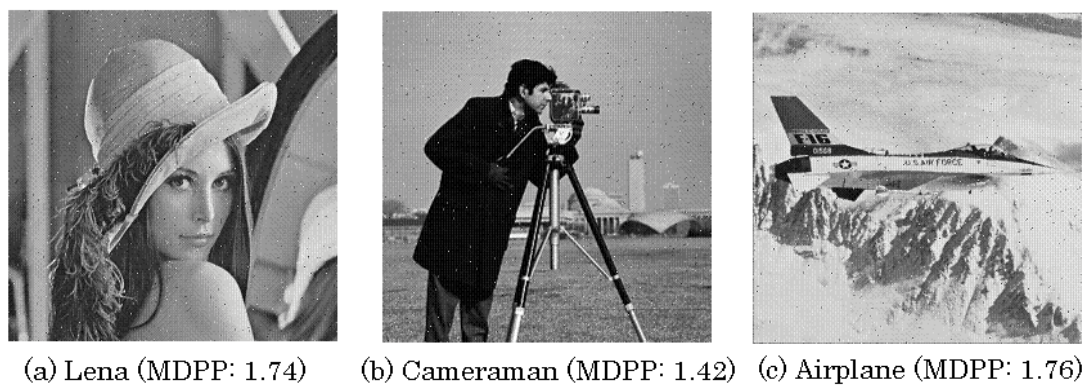


Figure 6: The output images by the evolved filter of Fig. 4.

Table 3: Results on a reconfigurable processing array with different faults.

Item	CLBs		Best one								Average				Worst one		
	Available	Used	MDPP	Ratio	SD	P_b	C_b	P_w	C_w	Used	MDPP	Ratio	Time	Used	MDPP	Ratio	
Faults(0)	21	8	1.722	1.000	71	645	1064	372	593	6.6	2.365	1.000	405.2	8	2.442	1.000	
Faults(2)	19	7	1.742	1.012	88	695	1150	263	419	5.7	2.390	1.011	411.5	7	2.537	1.039	
Faults(4)	17	12	1.939	1.126	85	1070	1774	393	625	5.6	2.955	1.249	416.7	5	3.453	1.414	
Faults(6)	15	6	2.008	1.166	50	550	910	227	362	5.4	2.965	1.254	425.2	4	3.525	1.443	
Faults(8)	13	3	3.117	1.810	48	435	720	198	316	4.8	3.624	1.533	432.0	2	3.889	1.593	

Available: In a 6*4 CLBs array, only one CLB is used in the last column, so the max number of available CLBs is 21.

Faults(x): A reconfigurable processing array with x faulty CLBs at random position, $x = 0, 2, 4, 6, 8$.

Used: the number of the used CLBs.

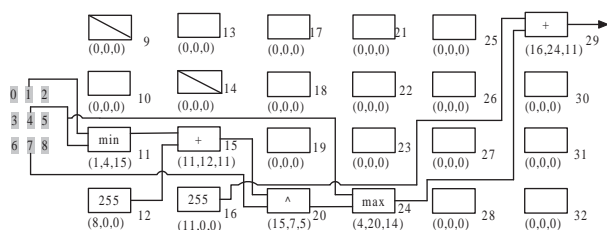


Figure 4: The optimized image filter of *Fault(2)*.

our proposed design method is effective for fault-tolerant optimization.

We will also apply PSO to autonomous design circuits for more complex functional requirements, and enhance more practical information about circuit to fitness function. Future works are to find better genetic encoding method to apply PSO to large sized circuits, and to improve PSO to reduce the processing time.

Acknowledgements

This research was supported by Waseda University Global COE Program ‘International Research and Education Center for Ambient SoC’ sponsored by the Ministry of Education, Culture, Sports, Science and Technology (MEXT), Japan, and partially by the Regional Innovation Cluster Program 2nd stage of MEXT, Japan and the Core Research for Evolutional Science and Technology (CREST) of Japan Science and Technology Agency (JST).

References

- [1] J. Dumoulin, J. Foster, J. Frenzel, et al. (2000), “Special Purpose Image Convolution with Evolvable Hardware,” Real-World Applications of Evolutionary Computing, vol. 1803 of LNCS, Springer, 2000, pp. 1-11.
- [2] L. Sekanina (2002), “Image Filter Design with Evolvable Hardware,” Applications of Evolutionary Computing, (the 4th Workshop on Evolutionary Computation in Image Analysis and Signal Processing,

EvoIASP 2002), vol. 2279 of LNCS, Springer, 2002, pp. 255-266.

- [3] L. Sekanina (2004), Evolvable components: From Theory to Hardware Implementations, Springer.
- [4] T. Martinek and L. Sekanina (2005), “An Evolvable Image Filter: Experimental Evaluation of a Complete Hardware Implementation in FPGA,” Evolvable Systems: From Biology to Hardware, vol. 3637 of LNCS, Springer, 2005, pp. 76-85.
- [5] Z. Vasicek and L. Sekanina (2007), “Evaluation of a New Platform For Image Filter Evolution,” Proc. the Second NASA/ESA Conference on Adaptive Hardware and Systems, 2007 (AHS 2007), Aug. 2007, pp. 577-586.
- [6] International Roadmap Committee (2009), “Executive Summary, International Technology Roadmap for Semiconductors,” <http://www.itrs.net/Links/2009ITRS/Home2009.htm>.
- [7] Jacob Robinson and Yahya Rahmat-Samii (2004), “Particle swarm optimization in electromagnetics,” IEEE Transactions on Antennas and Propagation, Volume 52, Issue 2, Feb. 2004, pp. 397 - 407.
- [8] Z. Bao and T. Watanabe (2009), “Evolutionary Design for Image Filter using Genetic Algorithm,” Proc. IEEE TENCON 2009, Singapore, Nov. 2009, pp. 1-6.
- [9] Z. Bao and T. Watanabe (2010), “Mixed Constrained Image Filter Design Using Particle Swarm Optimization,” Proc. The Fifteenth International Symposium on Artificial Life and Robotics 2010 (AROB 15th 2010), Beppu, Oita, Japan, pp. 230-235.
- [10] B. Rajan and S.Ravi (2006), “FPGA Based Hardware Implementation of Image Filter With Dynamic Reconfiguration Architecture,” IJCSNS International Journal of Computer Science and Network Security, Vol. 6, No. 12, pp. 121-127.

A most simple, non-computer-aided proof of the Four-Color Theorem

Koji Ohnishi^{1,2}

¹*Institute for Theoretical and Evolutionary Sciences (ITES),
c/o Koji Ohnishi, 8712-30, Ikarashi-2, Nishi-ku, Niigata, 950-2102, Japan
(Tel : 81-25-262-5237; Fax : 81-25-262-5237)*

(ohnishi@sc.niigata-u.ac.jp)

²*Department of Biology, Faculty of Science, Niigata University,
Ikarashi-2, Nishi-Ku, Niigata, 950-2181, Japan*

Abstract: An alternative brief proof of the Four Color Theorem without using a computer is described. The proof is essentially similar to the brief proof very recently described by the author as a bird's-eye view, but is much more simple than that, and more importantly, differs from that in the way of vertex-reducing of complete triangulation graph. This new, most simple proof is much shorter than the recently described one, and both of these two proofs are far more easily understood than Appel and Haken's proof in 1977. These new findings of non-computer-aided proofs clearly tell us about what the essential portion of the enormous complexity of the Four Colour Theorem is.

Keywords: Triangulation, Vertex reduction of colored triangulation graph

I. INTRODUCTION

The Four-Colour Conjecture (FCC) concerning map-coloring first proposed by Guthrie [1], had long been one of the most difficult unsolved problems in mathematics. In 1977, Appel and Haken (A&H) [2] succeeded in proving the FCC using a computer. The question whether or not the Four-Colour Theorem (FCT) could be proved without using a computer has since arisen as a most important problem remaining to be solved. Very recently, I have presented the details of a bird's-eye view of a very plausible brief proof of the FCT without using a computer [3]. In this paper, an alternative brief proof is described which is much more simple, although it is essentially similar to the brief proof described in Ohnishi (2009) [3], but considerably differs from that in the way of vertex-reducing of complete triangulation graph on sphere, S^2 .

II. PRELIMINARIES

In this section, some basic definitions useful for achieving a most simple proof of the FCT are described. "■" denotes the end of each definition or theorem, whereas "□" denotes the end of each proof.

The following terms are defined as given in the previous paper [3].

Jordan curve QQ' and its *endpoints* Q and Q' : see Definition 1 in ref. [3].

Internal and external domains ($int C$, $ext C$, $Int C$, $Ext C$, where C is a closed Jordan curve.):

see Theorem 1 in ref. [3].

Graph, vertex, spherical graph $G(S^2)$, *connected graph*: see Definitions 2 and 5 in ref. [3].

Valency (degree) of a vertex P , written as $val P$: see Definition 3 in ref. [3].

v -colorable; v -colored graph written as $col^v(G)$:

see Definitions 8 in ref. [3].

$col^v(P) = a$, (where $P \in G$), as denoting that vertex P is colored with a in $col^v(G)$: see

Definitions 8 in ref. 1.

Kempe-block, ab -Kempe-blocks written as $K_{ab}(P_i)$, $K_{ab}(P_i, P_j)$ in $col^t(G)$: see Definition 10 in ref. [3].

Definition 1: edge, adjacent: Edge is defined as a Jordan curve connecting and excluding two vertices (which are end-points) P and P' . An edge e , connecting two vertices P and P' is written as $e = [P, P']$. A vertex P is called to be *adjacent* to P' , if a graph Γ has an edge, $[P, P']$. ■

Note that **Definition 1** differs from the definition of "edge" given in the previous paper (see **Definition 2** in ref. [3]), and is identical to the definition of Berge [4]. Accordingly, some terms need to be re-defined based on Definition 1.

The next theorem is well-known as given in Ore [5].

Theorem 1: If C is a closed Jordan curve on a sphere S^2 , then we have $S^2 = int C + ext C + C = Int C + Ext C - C$. ■

Definition 3: s -cycle, s -gon, s -path: An (s)-cycle is defined by a s -vertex-graph, $C = C^s = C^s(e_{12}, e_{23}, \dots, e_{s,1}) = P_1 + e_{12} + P_2 + e_{23} + \dots + e_{s-1,s} + P_s + e_{s,1}$. An (s)-path is defined by $U(P_i, P_s) = U^s(P_i, P_s) = C^s(e_{12}, e_{23}, \dots, e_{s,1}) - e_{s,1}$. C^s is also called s -gon (= s -hedron) (e.g., poly-gon, di-gon, tri-angle, tetrahedron=quadrilateral, pentagon, etc.). ■

Definition 4: face: If $G(S^2)$ has a s -cycle (= s -gon), C^s , where $int C^s = \emptyset$, then $int C^s$ is called *face* (or s -gon *face*). ■

Thus we find $S^2 = int C^s + C^s + ext C^s$.

Definition 5: (complete) triangulation: If $G(S^2)$ is a connected graph dividing S^2 into exclusively triangular faces, G is called “complete triangulation (of S^2)”. If “ $G(S^2) = C^s$ ” satisfies $\text{ext } C^s = \emptyset$, and if G divides $\text{Int } C^s$ into exclusively triangular faces, G is called “triangulation of s -gon, C^s ”.

The next theorem is well-known [6,7,11], as described in [3].

Theorem 2: Let $T(S^2)$ be an arbitrarily selected complete triangulation of S^2 . The four-color theorem (FCT) is equivalent to the statement that “Proposition A is true”, where Proposition A is given by;

Proposition A: $T(S^2)$ is vertex four-colorable. ■

Definition 6: Two-faced quadrilateral (Fig. 1): “Two-faced quadrilateral with a diagonal edge e_{13} ” is defined as a subgraph of $G(S^2)$, and is given by $Q^{2f} = C^4_0 + e_{13} \subseteq G$, where $C^4_0 = C^4(e_{12}, e_{23}, e_{34}, e_{41})$, $e_{ij} = [P_i, P_j]$, $e_{13} \subset \text{int } C^4_0$, and e_{13} is a boundary edge dividing $\text{int } C^4_0$ into two triangular faces. Q^{2f} is written as $Q^{2f} = Q^{2f}(C^4_0; e_{13})$. If Q^{2f} in $G(S^2)$ has any edge, e'_{13} or e'_{24} , satisfying $e'_{13} = [P_1, P_3] \subset \text{ext } C^4_0$, or $e'_{24} = [P_2, P_4] \subset \text{ext } C^4_0$, then the Q^{2f} is called “incomplete quadrilateral”, whereas it is called “complete quadrilateral” if there is none of such edges. $G(S^2)$ having its sub-graph $Q^{2f}_0 = Q^{2f}(C^4_0; e_{13})$ is written as $G = G(Q^{2f}_0; C^4_0)$. ■

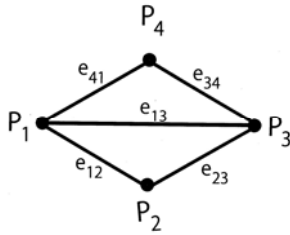


Fig.1 Two-faced quadrilateral, $Q^{2f}(C^4_0; e_{13})$, where C^4_0 is a 4-cycle (= quadrilateral) given by $C^4_0 = C^4(e_{12}, e_{23}, e_{34}, e_{41})$, $e_{ij} = [P_i, P_j]$, $e_{13} \subset \text{int } C^4_0$. $\{Q^{2f}\}$ is an unavoidable (one-element)-set of subgraphs in $T_k(S^2)$, a complete triangulation of S^2 with k vertices ($k \geq 4$). see Definition 6.

III. BASIC THEOREMS

The following basic theorems are useful for proving the FCT.

Theorem 3: For an ab -Kempe-block, $K_{ab}(P_i, P_j) \in G(S^2)$, where P_i and $P_j \in G(S^2)$, there exists a 2-coloured path $U_{ab}(P_i, P_j)$ as a subgraph of the 2-coloured graph, $K_{ab}(P_i, P_j)$. ■

[Proof] Evident from the definitions of connected graph (Definition 5 in ref.[3].) and vertex 2-colored graph (Definition 8 in ref.[3].). ■

This theorem means that P_i and P_j are connected by a 2-coloured Jordan curve, $U_{ab}(P_i, P_j)$, which is a 2-coloured path.

Theorem 4: Let $T_k(S^2)$ be a complete triangulation of S^2 , having k vertices ($k \geq 4$). Then there exists at least one quadrilateral given by $Q^{2f}_{k,0} = Q^{2f}(C^4_{k,0}; e_{13}) \subset T_k$, where $C^4_{k,0} = C^4(e_{12}, e_{23}, e_{34}, e_{41})$, $e_{13} \subset \text{int } C^4_{k,0}$, and $e_{ij} = [P_i, P_j]$. Furthermore, $Q^{2f}_{k,0}$ satisfies $\text{val } P_1 \geq 3$, $\text{val } P_3 \geq 3$, $\text{val } P_2 \geq 2$, and $\text{val } P_4 \geq 2$. ■

[Proof] Let $e_{13} (= [P_1, P_3])$ be an arbitrarily selected edge of $T_k(S^2)$, then we find two cases (i) and (ii), as below;

(i) In the case where one or more 2-cycles exist as subgraph(s) of $T_k(S^2)$ ($k \geq 4$ as shown in Fig. 2[A]. Let an arbitrarily selected 2-cycle be $C^2_k(e_{13}, e'_{31})$, where $e_{ij} = [P_i, P_j]$, then one finds that the edge e_{13} is a boundary of two 3-gon (triangular) faces, whose boundaries are 3-cycles, $C^3(e_{12}, e_{23}, e_{31})$ and $C^3(e_{13}, e_{34}, e_{41})$ (where $e_{ij} = [P_i, P_j]$), as shown in Fig.1 [A]. Thus there exist a quadrilateral, $G = G(Q^{2f}_0; C^4_0)$, where $C^4_0 = C^4(e_{12}, e_{23}, e_{34}, e_{41})$, and e_{13} is a diagonal edge. Since $C^2_k(e_{13}, e'_{31})$ is a closed Jordan curve, there does not exist $e_{34} = [P_3, P_4]$. Then it follows that $\text{val } P_1 \geq 4$, $\text{val } P_3 \geq 4$, $\text{val } P_2 \geq 2$, $\text{val } P_4 \geq 2$.

(ii) In the case where any 2-cycle does not exist as subgraph of $T_k(S^2)$. By letting an arbitrarily selected edge be denoted by $e_{13} = [P_1, P_3]$, P_2 and P_4 are found to be different two vertices (See Fig 2[B]), since an identical single vertex of P_2 and P_4 means the existence of a 2-cycle, $C^2(e_{12}, e_{21})$, which is in conflict with the case (ii), and belongs to the case (i). In case (ii), we thus find a quadrilateral, $G = G(Q^{2f}_0; C^4_0)$, where $C^4_0 = C^4(e_{12}, e_{23}, e_{34}, e_{41})$, and e_{13} is a diagonal edge, as shown in Fig. 2[B], satisfying $\text{val } P_1 \geq 3$, $\text{val } P_3 \geq 3$, $\text{val } P_2 \geq 3$, $\text{val } P_4 \geq 3$.

Thus we find that there exist a quadrilateral, $G = G(Q^{2f}_0; C^4_0)$, where $C^4_0 = C^4(e_{12}, e_{23}, e_{34}, e_{41})$, and e_{13} is a diagonal edge, and $\text{val } P_1 \geq 3$, $\text{val } P_3 \geq 3$, $\text{val } P_2 \geq 2$, $\text{val } P_4 \geq 2$. ■

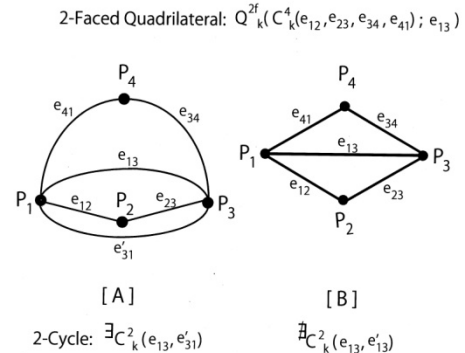


Fig. 2. Proof of Theorem 3.1 showing the existence of two-faced quadrilateral in $T_k(S^2)$ ($k \geq 4$)

[A] The case (i) where a 2-cycle, $C^2_k(e_{13}, e'_{31})$, exists as a subgraph of $T_k(S^2)$ ($k \geq 4$). ($\text{val } P_1 \geq 4$, $\text{val } P_3 \geq 4$, $\text{val } P_2 \geq 2$, $\text{val } P_4 \geq 2$). [B] The case where any 2-cycle does not exist as a subgraph of $T_k(S^2)$ ($k \geq 4$), ($\text{val } P_1 \geq 3$, $\text{val } P_3 \geq 3$, $\text{val } P_2 \geq 3$, $\text{val } P_4 \geq 3$).

Lemma 4.1: In Theorem 4, a set, $\{Q^{2f}_k\}$ is an

unavoidable set (See [6,8] for definition.) of subgraphs in $T_k(S^2)$, and consists of only one element being a quadrilateral. ■

[Proof] Evident from Theorem 4. ■

Theorem 5 : For an arbitrarily selected four-colorable complete triangulation graph with k vertices, $T_k(S^2)$ ($k \geq 4$), let $col^4_0(T_k)$ be a 4-coloured graph of T_k . Concerning an arbitrarily selected quadrilateral $Q^{2f}_{k,0} = Q^{2f}(C^4_{k,0}; e^{(k)}_{13}) \subset T_k$, where $C^4_{k,0} = C^4(P_1^{(k)}, P_2^{(k)}, P_3^{(k)}, P_4^{(k)})$ and $e^{(k)}_{13} = [P_1^{(k)}, P_3^{(k)}] \subset int C^4_{k,0}$, $col^4_0(T_k)$ belongs to either one of the two types, type I and type II, defined by:

type I: $K_{ac}(P_1^{(k)}, P_3^{(k)}) (\subset col^4_0(T_k; Q^{2f}_{k,0}))$ exists.

type II: $K_{ac}(P_1^{(k)}, P_3^{(k)}) (\subset col^4_0(T_k; Q^{2f}_{k,0}))$ does not exist. ■

[Proof] Evident. ■

Definition 6 : (case I and case II 4-colorations) Let $col^4_I(T_k; Q^{2f}_{k,0})$ and $col^4_{II}(T_k; Q^{2f}_{k,0})$ denote 4-colored complete triangulation graph of case I and that of case II (in Theorem 5), respectively. ■

III. FINAL PROOF

Definition 7 (Vertex-reducing operations f_1 and f_2): Definitions, f_1 and f_2 , (and their reverse operations f_1^{-1} and f_2^{-1}), are given by Definition 12 in ref.[3]. Suboperations f_{1a} , f_{1b} and f_{2a} , f_{2b} satisfying $f_1 = f_{1b}f_{1a}$, and $f_2 = f_{2b}f_{2a}$ are defined as schematized in Fig.3 and Fig.4 ■

Theorem 6. Let a complete triangulation $T_k(S^2)$ be four-colorable ($k \geq 4$), then $T_{k-1}(S^2)$ defined by $T_{k-1} = T_k - I(T_k; Q^{2f}_{k,0}) = f(T_k; Q^{2f}_{k,0})$ is four-colorable, where $Q^{2f}_{k,0} = Q^{2f}(C^4_{k,0}; e^{(k)}_{13}) \subset T_k$, $C^4_{k,0} = C^4(P_1^{(k)}, P_2^{(k)}, P_3^{(k)}, P_4^{(k)})$, and $e^{(k)}_{13} = [P_1^{(k)}, P_3^{(k)}] \subset int C^4_{k,0}$, and further, f denotes a operation given by $f = f_1$ or f_2 for type I or type II 4-coloration of $T_k(Q^{2f}_{k,0}, e^{(k)}_{13})$, respectively. Then $T_{k-1}(T_k; Q^{2f}_{k,0})$ is 4-colourable. ■

[Proof] Let $col^4(T_k; Q^{2f}_{k,0})$ be a 4-coloured graph of $T_k(S^2)$. Vertex-reducing operations of $col^4(T_k; Q^{2f}_{k,0})$ are as below;

Case I: If $col^4(T_k; Q^{2f}_{k,0})$ is type I in Theorem 5, then operation of graph modification $f_1(T_k; Q^{2f}_{k,0}) = f_{1b}(f_{1a}(T_k; Q^{2f}_{k,0}))$ gives a reduced triangulation graph $T_{k-1}(T_k; Q^{2f}_{k,0})$ and its 4-coloured graph, $col^4_{II}(T_{k-1}; Q^{2f}_{k,0})$, as shown in Fig.3. Note that $T_{k-1}(T_k; Q^{2f}_{k,0})$ and $col^4_{II}(T_{k-1}; Q^{2f}_{k,0})$ are defined by $T_k(S^2)$ and $col^4(T_k; Q^{2f}_{k,0})$, respectively. Thus $T_{k-1} = f_1(T_k; Q^{2f}_{k,0})$ is 4-colourable.

Case II: If $col^4(T_k; Q^{2f}_{k,0})$ is type II in Theorem 5, then operation of graph modification $f_2(T_k; Q^{2f}_{k,0}) = f_{2b}(f_{2a}(T_k; Q^{2f}_{k,0}))$ gives a reduced triangulation graph $T_{k-1}(T_k; Q^{2f}_{k,0})$ and its 4-coloured graph, $col^4_I(T_{k-1}; Q^{2f}_{k,0})$, as shown in Fig.4. Note that $T_{k-1}(T_k; Q^{2f}_{k,0})$ and $col^4_I(T_{k-1}; Q^{2f}_{k,0})$ are defined by $T_k(S^2)$ and $col^4(T_k; Q^{2f}_{k,0})$, respectively. Thus $T_{k-1} = f_2(T_k; Q^{2f}_{k,0})$ is 4-colourable.

Accordingly, $T_{k-1}(T_k; Q^{2f}_{k,0})$ is 4-colourable. ■

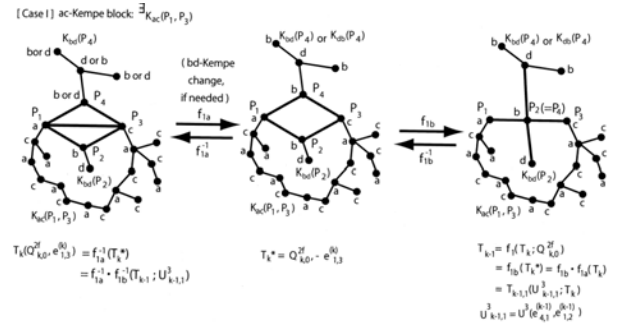


Figure 3. Reversible vertex-reduction and its reverse operation of a 4-coloured complete triangulation graph, $col^4_0(T_k; Q^{2f}_{k,0})$ in case I, where there exists an ac -Kempe block, $K_{ac}(P_1, P_3)$, in $Ext C^4_{k,0}$. The left and right schematized $col^4_{0,II}(T_k; Q^{2f}_{k,0})$ and $col^4_{0,I}(T_{k-1}; Q^{2f}_{k,0})$, respectively. (From Fig. 4 in [3])

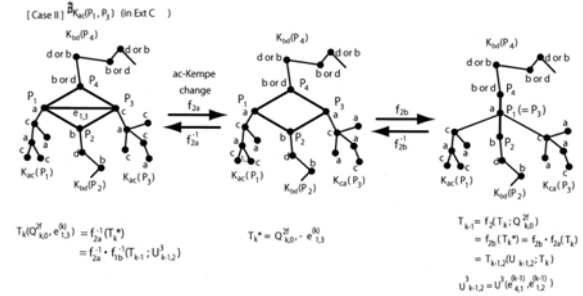


Figure 4. Reversible vertexreduction and its reverse operation of a 4coloured complete triangulation graph, $col^4_0(T_k; Q^{2f}_{k,0})$ in case II, where there does not exist any ac -Kempe block, $K_{ac}(P_1, P_3)$, in $Ext C^4_{k,0}$. The left and right schematized $col^4_{0,II}(T_k; Q^{2f}_{k,0})$ and $col^4_{0,I}(T_{k-1}; Q^{2f}_{k,0})$, respectively. (From Fig.5 in [3])

Theorem 7. Let $T_k(S^2)$ be 4-colourable, then there exists a series of 4-coloured complete triangulation graphs, $\{col^4_0(T_k; Q^{2f}_{k,0}), col^4_0(T_{k-1}; Q^{2f}_{k,0}), \dots, col^4_0(T_4; Q^{2f}_{5,0}), col^4_0(T_3; Q^{2f}_{4,0})\}$, where $col^4_0(T_{k-i}; Q^{2f}_{k-i+1,0})$ ($i=1,2, \dots, k-3$) is defined by $T_{k-i} = f(T_{k-i+1}; Q^{2f}_{k-i,0})$, where $f = f_1$ (for type I coloration of T_{k-i+1}) or f_2 (for type II coloration of T_{k-i+1}), and $Q^{2f}_{k-i+1,0}$ is an arbitrarily selected quadrilateral of T_{k-i+1} . ■

[Proof] From theorem 6, $col^4_0(T_{k-i}; Q^{2f}_{k-i+1,0}) = f(col^4_0(T_{k-i+1}; Q^{2f}_{k-i,0}))$. Repeated applications of this equation to $T_k(S^2)$, for $i = 1, 2, \dots, k-3$, we obtain a series of 4-coloured complete triangulations, $\{col^4_0(T_k; Q^{2f}_{k,0}), col^4_0(T_{k-1}; Q^{2f}_{k,0}), \dots, col^4_0(T_4; Q^{2f}_{5,0}), col^4_0(T_3; Q^{2f}_{4,0})\}$. Note that $col^4_0(T_3; Q^{2f}_{4,0})$ is a 4-coloured 3-gon graph (3-vertex complete graph) whose coloration depends on $col^4_0(T_k; Q^{2f}_{k,0})$. ■

Lemma 7.1: The necessary condition for a complete triangulation graph, $T_k(S^2)$, ($k \geq 4$), to be four colorable is the existence of $col^4_0(T_3; Q^{2f}_{4,0})$, defined in Theorem 7. ■

[Proof] Evident from theorem 7. ■

Lemma 7.2: The necessary condition for a complete triangulation graph, $T_k(S^2)$, ($k \geq 4$), to be four colorable, defined in Lemma 7.1 is satisfied. ■

[Proof] $\text{col}^4_0(T_3; Q^{2f}_{4,0})$ is a 4-coloured 3-gon graph (3-vertex complete graph) whose coloration depends on $\text{col}^4_0(T_k; Q^{2f}_{k,0})$. Therefore, $\text{col}^4_0(T_3; Q^{2f}_{4,0})$ really exists as one of the $4 \times 3 \times 2 = 24$ 4-colorations of the 3-gon graph. ■

Theorem 8. For a given coloration, $\text{col}^4_0(T_3; Q^{2f}_{4,0})$, which is one of the 24 possible coloration of trigon, $\text{col}^4_0(T_4; Q^{2f}_{5,0})$, given in Theorem 7 can be reconstructed from $\text{col}^4_0(T_3; Q^{2f}_{4,0})$. ■

[Proof] Since $\text{col}^4_0(T_3; Q^{2f}_{4,0})$ really exists from Lemma 7.1, then $\text{col}^4_0(T_4; Q^{2f}_{5,0})$ can be reconstructed by $\text{col}^4_0(T_4; Q^{2f}_{5,0}) = f^1(\text{col}^4_0(T_3; Q^{2f}_{4,0}))$, because the operation f defined in Fig. 3 is reversible graph modification. Thus, by applying $\text{col}^4_0(T_4; Q^{2f}_{5,0}) = f^1(\text{col}^4_0(T_3; Q^{2f}_{4,0}))$ for all of the possible operations of f^1 , there exists at least one operation generating $\text{col}^4_0(T_4; Q^{2f}_{5,0})$, whether or not T_4 , $Q^{2f}_{4,0}$, and $\text{col}^4_0(T_3; Q^{2f}_{4,0})$ are known. ■

Lemma 8.1. For a given coloration, $\text{col}^4_0(T_{k-i}; Q^{2f}_{k-i+1,0})$ ($i=k-3, k-4, \dots, 2, 1$), defined by Theorem 8, $\text{col}^4_0(T_{k-i+1}; Q^{2f}_{k-i+2,0})$ given in Theorem 7 can be reconstructed from $\text{col}^4_0(T_{k-i}; Q^{2f}_{k-i+1,0})$. ■

[Proof] Since $\text{col}^4_0(T_{k-i}; Q^{2f}_{k-i+1,0})$ really exists, from Lemma 7.2, for $i = k-4$, $\text{col}^4_0(T_5; Q^{2f}_{6,0})$ can be reconstructed by $\text{col}^4_0(T_5; Q^{2f}_{6,0}) = f^1(\text{col}^4_0(T_4; Q^{2f}_{5,0}))$, because the operation f defined in Fig. 3 is reversible graph modification. Thus, by applying $\text{col}^4_0(T_5; Q^{2f}_{6,0}) = f^1(\text{col}^4_0(T_4; Q^{2f}_{5,0}))$ for all of the possible operations of f^1 , there exists at least one operation generating $\text{col}^4_0(T_5; Q^{2f}_{6,0})$, even if T_5 , $Q^{2f}_{6,0}$, and $\text{col}^4_0(T_5; Q^{2f}_{6,0})$ are unknown.

Similarly, for $k-4 \leq i \leq 2$, when $\text{col}^4_0(T_{k-i}; Q^{2f}_{k-i+1,0})$ can be known to exist by $\text{col}^4_0(T_{k-i}; Q^{2f}_{k-i+1,0}) = f^1(\text{col}^4_0(T_{k-i-1}; Q^{2f}_{k-i,0}))$, $\text{col}^4_0(T_{k-i+1}; Q^{2f}_{k-i+2,0})$ can be reconstructed by $\text{col}^4_0(T_{k-i+1}; Q^{2f}_{k-i+2,0}) = f^1(\text{col}^4_0(T_{k-i}; Q^{2f}_{k-i+1,0}))$, because the operation f defined in Fig. 3 is reversible graph modification. Thus, by applying $\text{col}^4_0(T_{k-i+1}; Q^{2f}_{k-i+2,0}) = f^1(\text{col}^4_0(T_{k-i}; Q^{2f}_{k-i+1,0}))$ for all of the possible operations of f^1 , there exists at least one operation generating $\text{col}^4_0(T_{k-i+1}; Q^{2f}_{k-i+2,0})$, even if T_5 , $Q^{2f}_{6,0}$, and $\text{col}^4_0(T_5; Q^{2f}_{6,0})$ are unknown.

The final similar application of $\text{col}^4_0(T_{k-i}; Q^{2f}_{k-i+1,0}) = f^1(\text{col}^4_0(T_{k-i-1}; Q^{2f}_{k-i,0}))$, for $i = 0$, it follows that $\text{col}^4_0(T_k; Q^{2f}_{k,0}) = f^1(\text{col}^4_0(T_{k-1}; Q^{2f}_{k-1,0}))$, as shown in Fig.4 and Fig.5. Thus the initial coloration of $\text{col}^4_0(T_k; Q^{2f}_{k,0})$ has now been reconstructed. ■

Lemma 8.2. The sufficient condition for a complete triangulation graph, $T_k(S^2)$, ($k \geq 4$), to be four colorable is the existence of $\text{col}^4_0(T_3; Q^{2f}_{4,0})$, defined in Theorem 7. ■

[Proof] If there exists $\text{col}^4_0(T_3; Q^{2f}_{4,0})$, defined in Theorem 7, by applying $\text{col}^4_0(T_{k-i}; Q^{2f}_{k-i+1,0}) = f^1(\text{col}^4_0(T_{k-i-1}; Q^{2f}_{k-i,0}))$, for $i = k-4, k-5, \dots, 1$, $\text{col}^4_0(T_{k-i}; Q^{2f}_{k-i+1,0})$ can be reconstructed even if T_{k-i} , $Q^{2f}_{k-i+1,0}$, and $\text{col}^4_0(T_{k-i-1}; Q^{2f}_{k-i,0})$ are unknown. This means that The sufficient condition for for a complete triangulation

graph, $T_k(S^2)$, ($k \geq 4$), to be four colorable is the existence of $\text{col}^4_0(T_3; Q^{2f}_{4,0})$. ■

Theorem 9. The necessary and sufficient condition for a complete triangulation graph, $T_k(S^2)$, ($k \geq 4$), to be four colorable is the existence of $\text{col}^4_0(T_3; Q^{2f}_{4,0})$, defined in Theorem 7. ■

[Proof] Evident from Lemma 7.1 and Lemma 8.2. ■

Lemma 9.1. The necessary and sufficient condition (defined in Theorem 9) for a complete triangulation graph, $T_k(S^2)$, ($k \geq 4$), to be four colorable, is satisfied. ■

[Proof] In theorem 9, $\text{col}^4_0(T_3; Q^{2f}_{4,0})$ really exist as one of the $4 \times 3 \times 2 = 24$ colorations with 4 colours. Thus we have reached Lemma 9.1. ■

Theorem 10. (The Four-Colour Theorem): Every complete triangulation graph, $T_k(S^2)$ ($k \geq 3$) is four-colourable. ■

[Proof] Evident from Lemma 9.1. ■

III. REFERENCES

- [1] Guthrie F (1880), Notes on the colouring maps. Proc.R. Soc. Edinburgh 10: 727-728.
- [2] Appel K et al. (1977), Every planar map is four colorable. Parts I, II. III. J. Math. 21: 429-489, 490-597.
- [3] Ohnishi K (2009), Towards a brief proof of the Four-Color Theorem without using a computer. Artif. Life Robotics 14(4):551-556.
- [4] Berge C (1970), Graphe et hypergraphes. Dunod, Paris.
- [5] Ore O (1967), The Four-Color Problem. Academic Press, New York.
- [6] Hitotsumatsu S (1978), Yon-shoku Mondai (The Four Colour Theorem). Kodansha, Tokyo (in Japanese).
- [7] Saaty TL and Kainen PC (1977), The Four Color Problem. assaults and conquest. McGraw Hill International Company, New York.
- [8] Wilson R (2002), Four colours suffice: how the map problem was solved. Penguin Books, London.

Acknowledgements: Valuable discussions with Dr. Shigeki Akiyama (Department of Mathematics, Niigata University) are acknowledged. This study was partly funded by the financial support of the Uchida Energy Science Promotion Foundation, No. 131520.

Autonomous Decentralized Control Scheme for Large Scale and Dense Wireless Sensor Networks with Multiple Sinks

Masahito Maki[†], Akihide Utani[‡], and Hisao Yamamoto[‡]

[†]*Graduate School of Engineering, Tokyo City University*

[‡]*Faculty of Knowledge Engineering, Tokyo City University
1-28-1, Tamazutsumi, Setagaya, Tokyo 158-8557, Japan
{autani; yamahisa}@tcu.ac.jp*

Abstract: A wireless sensor network has great potential as a key network to facilitate ubiquitous environments. A wireless sensor network is generally made up of many sensor nodes limited resource. Therefore, a data gathering scheme saving and balancing energy consumption of each sensor node is needed to prolong the lifetime of a wireless sensor network. This paper proposes an autonomous decentralized control scheme for a large scale and dense wireless sensor network, which is a new data gathering scheme with transmission power control that adaptively reduces the load of load-concentrated nodes and facilitates the long-term operation of a large scale and dense wireless sensor network. The proposed scheme is evaluated by computer simulations.

Keywords: Data gathering, Autonomous load-balancing, Transmission power control, Wireless sensor networks.

I. INTRODUCTION

A wireless sensor network has great potential as a key network to facilitate ubiquitous environments [1]. In this study, a large scale and dense wireless sensor network made up of static sensor nodes with GPS is assumed. In a large scale and dense wireless sensor network, generally, hundreds or thousands of static sensor nodes limited resource are placed in an observation area and sensing data of each node is gathered to a sink node by inter-node wireless communication. Therefore, a data gathering scheme capable of meeting the following two requirements is mainly needed to prolong the network lifetime.

- 1) Efficiency of data gathering
- 2) Balance on communication load among sensor nodes

In a large scale and dense wireless sensor network, the communication load is generally concentrated on sensor nodes around a sink node during the operation process. In case sensor nodes are not placed evenly in a large scale observation area, the communication load is concentrated on sensor nodes placed in an area of low node density. As the scheme that satisfy the above two requirements, gradient-based routing protocol has attracted attention [2]. However, this does not ease the communication load concentration to sensor nodes around a sink node that is the source of problems on the long-term operation of a wireless sensor network. Intensive data transmission to specific nodes, such as sensor nodes around a sink node and sensor nodes placed in an area of low node density, brings on concentrated energy consumption of them and causes them to break away from the network early. This makes the long-term observation by a wireless sensor network difficult.

To solve this communication load concentration problem, a data gathering scheme for a wireless sensor network with multiple sinks has been proposed [3]. Each sensor node, in this scheme, sends sensing data to the nearest sink node. In comparison with the case of a one sink wireless sensor network, the communication load of sensor nodes around a sink node is reduced. In each sensor node, however, the destination (sink) node cannot be selected autonomously and adaptively. In case original data transmission rate from each sensor node is not even, therefore, the load of load-concentrated nodes is not sufficiently balanced. An autonomous load-balancing data transmission scheme is required.

This paper proposes an autonomous decentralized control scheme for a large scale and dense wireless sensor network, which is a new data gathering scheme with transmission power control that adaptively reduces the load of load-concentrated nodes and facilitates the long-term operation of a large scale and dense wireless sensor network with multiple sinks. The proposed scheme is an autonomous load-balancing data transmission one devised by considering the application environment of a wireless sensor network as a typical example of complex systems where the adaptive adjustment of the entire system is realized from the local interactions of components of the system.

II. PROPOSED SCHEME

For facilitating the long-term operation of an actual sensor network service, recently, it has been considered to introduce multiple sinks in a wireless sensor network

[3]. In a wireless sensor network with multiple sinks, sensing data of each node is generally allowed to gather at any of the available sinks. The proposed scheme is a new data gathering one based on this assumption, which can be expected to produce a remarkable effect in a multiple sink wireless sensor network. In this study, it is assumed that each sensor node can select either of high power and low power for packet transmission. In the proposed scheme, high power corresponds to normal transmission power and low power is newly introduced for moreover balancing the load of each sensor node.

1. Routing Algorithm

Each sink node has a connective value named a "value to self", which is not updated by transmitting a control packet and receiving data packets. In the initial state of a multiple sink wireless sensor network, each sink node broadcasts a control packet containing its own location information, ID, hop counts(=0), and "value to self" by high power. This control packet is rebroadcast throughout the network with hop counts updated by high power. By receiving the control packet from each sink node, each sensor node can grasp the "value to self" of each sink node, the location information and IDs on its own neighbor nodes, and the hop counts from each sink node of neighbor nodes.

Initial connective value of each sensor node, which is the connective one before starting data transmission, is generated by using the "value to self" of each sink node and the hop counts from each sink node. The procedure for computing initial connective value of a node (i) is as follows:

1. The value $[v_{ij}(0)]$ on each sink node ($j = 1, \dots, S$) of node (i) is first computed according to the following equation

$$v_{ij}(0) = v_{oj} \times dr^{hops_{ij}} \quad (j=1, \dots, S) \quad (1)$$

where $v_{oj}(j = 1, \dots, S)$ is the "value to self" of sink node (j), $hops_{ij}(j = 1, \dots, S)$ is the hop counts from sink node (j) of node (i), and dr represents the value attenuation factor accompanying hop determined within the interval $[0,1]$.

2. Then, initial connective value $[v_i(0)]$ of node (i) is generated by the following equation

$$v_i(0) = \max v_{ij}(0) \quad (j=1, \dots, S) \quad (2)$$

where this connective value $[v_i(0)]$ can be also conducted from the following equation

$$v_i(0) = vm_i(0) \times dr \quad (3)$$

In the above Eq.(3), $vm_i(0)$ represents the greatest connective value before starting data transmission in ne-

ighbor nodes of node (i).

Before data transmission is started, each sensor node computes initial connective value of each neighbor node based on Eq.(1) and Eq.(2) and stores the computed connective value, which is used as the only index to evaluate the relay destination value of each neighbor node, in each neighbor node field of its own routing table.

2. Data Transmission

For a while from starting data transmission, each sensor node selects the neighbor node with the greatest connective value from its own routing table as a relay node and transmits the data packet to this selected node by high power. In case more than one node shares the greatest connective value, however, the relay node is determined from them at random. In each sensor node, the data packet is not sent to a specified sink node. By repetitive data transmission to the neighbor node with the greatest connective value, data gathering at any of the available sinks is completed. In the proposed scheme, the connective value of each sensor node is updated by considering residual node energy. By repetitive data transmission to the neighbor node with the greatest connective value, therefore, data transmission routes are not fixed.

To realize autonomous load-balancing data transmission, in the proposed scheme, the data packet from each sensor node includes its own updated connective value. Let's assume that a node (l) receives a data packet at time (t). Before node (l) relays the data packet, it replaces the value in the connective value field of the data packet by its own renewal connective value computed according to the following connective value update equation

$$v_l(t) = vm_l(t) \times dr \times \frac{e_l(t)}{E_l} \quad (4)$$

where $vm_l(t)$ is the greatest connective value at time (t) in the routing table of node (l), and $e_l(t)$ and E_l represent the residual energy at time (t) of node (l) and the battery capacity of node (l), respectively.

In the proposed scheme, the data packet addressed to the neighbor node with the greatest connective value is intercepted by all neighbor nodes. This data packet includes the updated connective value of the source node based on the above Eq.(4). Each neighbor node that has intercepted this packet stores the updated connective value in the source node field of its own routing table. The proposed scheme requires the construction of a data gathering environment in the initial state of a wireless sensor network but needs no special communication for network control. The above simple system alone achieves autonomously adaptive load-balancing data transmissi-

on using multiple routes and sinks. The lifetime of a wireless sensor network can be extended by reducing the communication load for network control and solving the node load concentration problem.

3. Transmission Power Control

For data packet transmission, the transmission power of each sensor node is switched to low power if its own residual energy is less than the set threshold $[T_e]$. In this case, each sensor node selects the neighbor node with the greatest connective value within range of radio wave of low power as a relay node and transmits the data packet to this selected node by low power.

Fig.1 shows an example on the above transmission power control, which means that the transmission power of each sensor node is switched to low power according to the above condition. In this example, node (m) is a load concentration node. Node (m) has autonomously transmitted the data packet to node (r) with the greatest connective value within low power range by low power because its own residual energy has become less than the set threshold $[T_e]$. By switching to low power, the energy consumption of node (m) is saved, but node (k) and node (l) may continue to transmit the data packet to node (m) because they cannot grasp the updated connective value of node (m). In the proposed scheme, therefore, every tenth data packet from the node switched to low power is transmitted by high power.

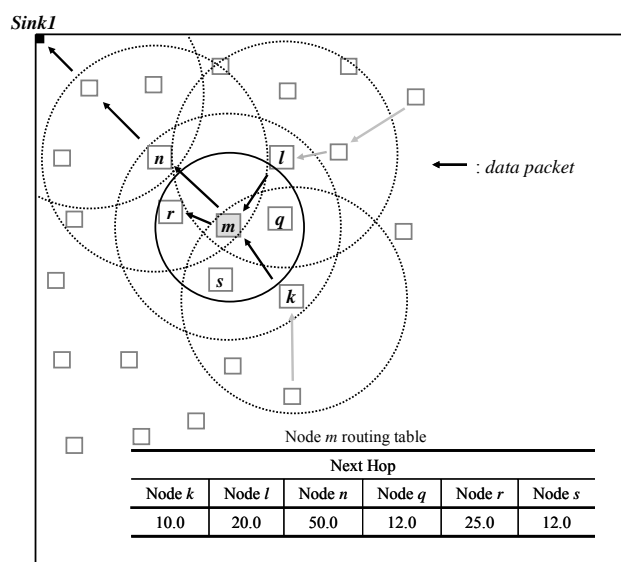


Fig.1 An example on transmission power control

III. SIMULATION EXPERIMENT

Through simulation experiments on a large scale wireless sensor network with three sinks, the performance of the proposed scheme is investigated.

1. Condition of Simulations

In a wireless sensor network with three sinks consisting of many static sensor nodes placed in a large-scale observation area, the only sensor nodes that detected abnormal data set were assumed to transmit the measurement data. The condition of simulations, which were used in the experiments performed, is shown in Table 1. In the initial state of simulation experiments, static sensor nodes are randomly arranged in the set simulation area and three sinks are placed on the three boundaries containing the two corners of this area. In Fig.2, the network configuration is illustrated.

Table 1. Condition of simulations

Simulation size	2,400m × 2,400m
The number of sensor nodes	750, 1,000, 1,250
Range of radio wave	200m(high power), 150m(low power)
The number of sinks	3

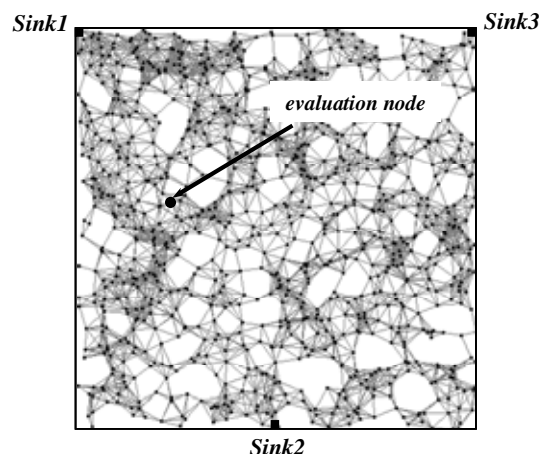
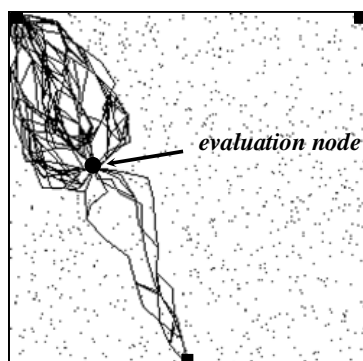


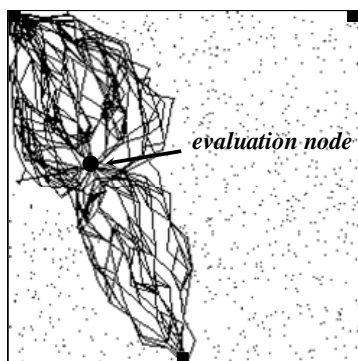
Fig.2 Wireless sensor network with three sinks

2. Experimental Results

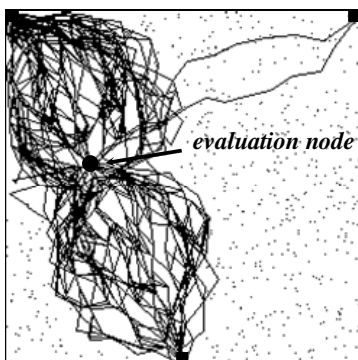
As the first experiment, it was assumed that the evaluation node marked in Fig.2 detected an abnormal value and transmitted the data packet with the detected abnormal value periodically. The routes used by applying the proposed scheme are shown in Fig.3 and Fig.4, where the number of sensor nodes is 1,000. Of the 2,000 data packets transmitted from the evaluation node, the routes used by the first 500 data packets are shown in Fig.3 and Fig.4(1), those by the first 1,000 data packets are shown in Fig.3 and Fig.4(2), and those by a total of 2,000 data packets are shown in Fig.3 and Fig.4(3). From Fig.3 and Fig.4, it can be confirmed that the proposed scheme enables autonomous load-balancing transmission of data packets to three sinks using multiple routes and its effect is extended by early switching to low power.



(1) 1 to 500 data packets



(2) 1 to 1,000 data packets

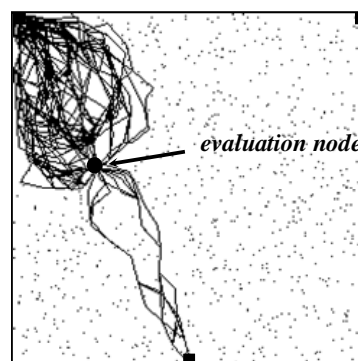


(3) 1 to 2,000 data packets

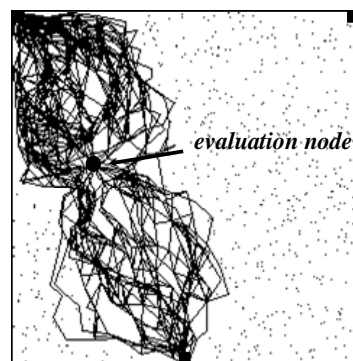
Fig.3 Routes used by applying the proposed scheme ($T_e = E \times 0.5J$)

IV. CONCLUSIONS

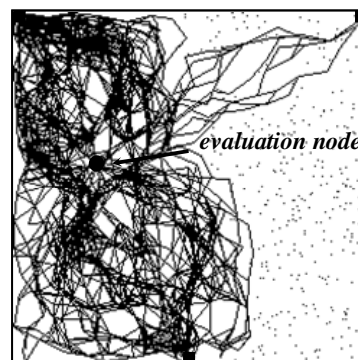
In this paper, a new data gathering scheme with transmission power control that adaptively reduces the load of load-concentrated nodes and facilitates the long-term operation of a large-scale wireless sensor network with multiple sinks, which is an autonomous load-balancing data transmission one devised by considering the application environment of a wireless sensor network to be a typical example of complex systems, has been proposed. Experimental results indicate that the proposed scheme is superior to the existing one and has the development potential as a promising one from the viewpoint of the l-



(1) 1 to 500 data packets



(2) 1 to 1,000 data packets



(3) 1 to 2,000 data packets

Fig.4 Routes used by applying the proposed scheme ($T_e = E \times 0.9J$)

ong-term operation. Future works include evaluation on parameters introduced in the proposed scheme in detail and verification of its effectiveness on various network environments.

REFERENCES

- [1]I. Akyildiz, W. Su, Y. Sankarasubramaniam and E. Cayirci, "Wireless sensor networks: A survey," Computer Networks Journal, vol.38, no.4, pp.393-422, 2002.
- [2]L. Xia, X. Chen and X. Guan, "A new gradient-based routing protocol in wireless sensor networks," Lecture Notes in Computer Science, vol.3605, 2004.
- [3]E. I. Oyman and C. Ersoy, "Multiple sink network design problem in large scale wireless sensor networks," Proc. of the International Conference on Communications, 2004.

Advanced Adaptive Communication Protocol for Ubiquitous Sensor Networks

Shuichi Osawa[†], Akihide Utani[‡], and Hisao Yamamoto[‡]

[†]*Graduate School of Engineering, Tokyo City University*

[‡]*Faculty of Knowledge Engineering, Tokyo City University*

1-28-1, Tamazutsumi, Setagaya, Tokyo 158-8557, Japan

{autani; yamahisa}@tcu.ac.jp

Abstract: There is growing expectation for a wireless sensor network as a means of realizing ubiquitous information environments. A wireless sensor network, which is a key network to facilitate ubiquitous information environments, has great potential as a means of realizing a wide range of applications, such as natural environment monitoring, environmental control in office buildings and factories, object tracking, and precision agriculture. Control mechanism for a wireless sensor network should adapt to the variety of types of communication (one-to-one, one-to-many, many-to-one, many-to-many), depending on application requirements and the context. This paper proposes a new adaptive communication protocol for the long-term operation of a wireless sensor network. We evaluate the proposed protocol using computer simulations and discuss its development potential. In the experiments performed, the performance of the proposed protocol is investigated in detail to verify its effectiveness.

Keywords: Wireless Sensor Networks, Ubiquitous Environments, Adaptive Communication Protocols.

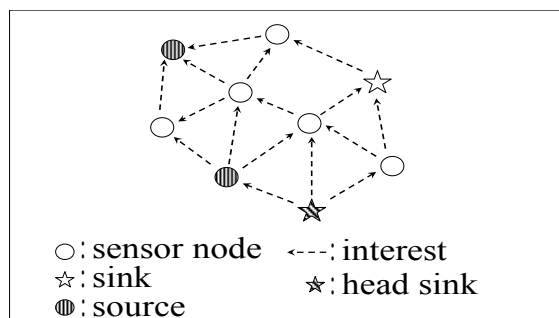
I. INTRODUCTION

Various network services have been provided. They include inter-vehicle communication, which is a network service in intelligent transport systems, natural environmental monitoring, and emergent communication between mobile nodes in such the case of emergency as disaster. As a means of realizing the above network services, autonomous decentralized networks, such as a mobile ad-hoc network and a wireless sensor network, have been intensively studied with great interests. Especially, a wireless sensor network, which is a key network to facilitate ubiquitous information environments, has great potential as a means of realizing a wide range of applications, such as natural environmental monitoring, environmental control in office buildings and factories, object tracking, and precision agriculture [1]. In a general wireless sensor network, hundreds or thousands of micro sensor nodes, which are generally compact and inexpensive, are placed in a large scale observation area and sensing data of each node is gathered to a sink node by inter-node wireless multi-hop communication. Each sensor node consists of a sensing function to measure the status (temperature, humidity, motion, etc.) of an observation point or object, a limited function on information processing, and a simplified wireless communication function, and generally operates on a resource of a limited power-supply capacity such as a battery. Therefore, in the existing studies, the efficient and load-balancing data transmission scheme to sink nodes has been proposed.

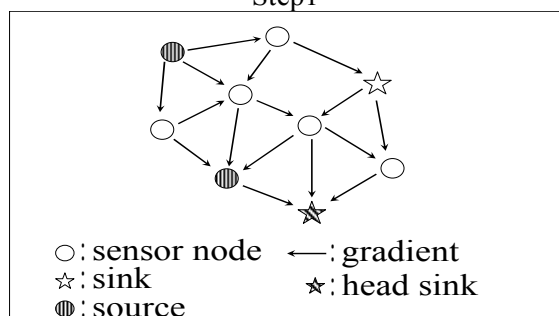
This paper proposes a new adaptive communication protocol for the long-term operation of a wireless sensor network. We evaluate the proposed protocol using computer simulations and discuss its development potential. In the experiments performed, the performance of the proposed protocol is investigated in detail to verify its effectiveness. This paper is organized as follows. In Section II, the proposed protocol is outlined. In Section III, the experimental results are reported and the effectiveness of the proposed protocol is demonstrated by comparing the performance of it with those of the existing ones. Finally, the paper closes with conclusions and ideas for further study in Section IV.

II. PROPOSED PROTOCOL OUTLINE

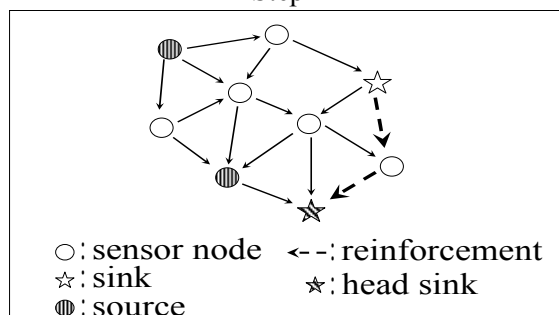
For facilitating ubiquitous information environments, control mechanism for a wireless sensor network should adapt to the variety of types of communication, i.e., one-to-one, one-to-many, many-to-one, and many-to-many, depending on application requirements and the context. Recently, many adaptive protocols for a large scale and dense wireless sensor network, which are “directed diffusion”[2,3] and “ant-based rendezvous communication protocol”[4] have been proposed. “directed diffusion”, that a representative scheme for adaptive communication consists of the following protocols: Two-Phase Pull diffusion, One-Phase Pull diffusion, Push diffusion, where “Pull” adapts itself to the case that the number of source nodes is more than the number of sink nodes. “Push” adapts itself to the case that the number of sink nodes



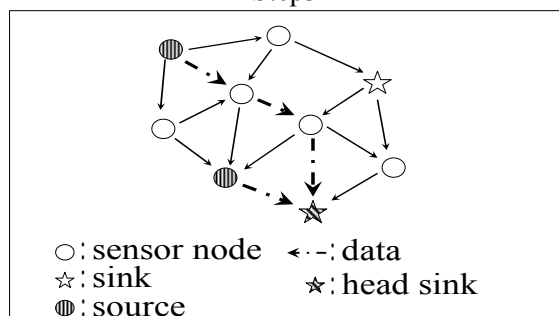
Step1



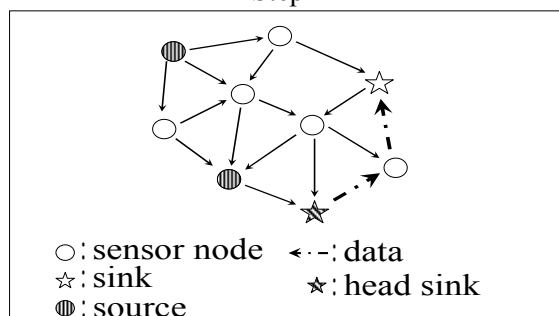
Step2



Step3

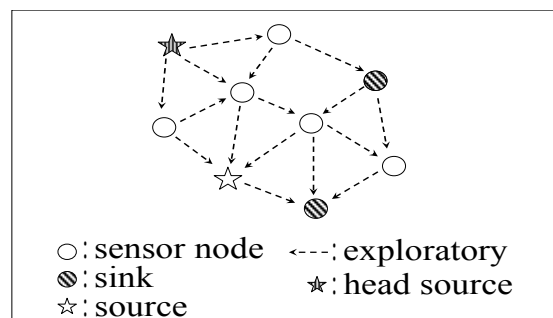


Step4

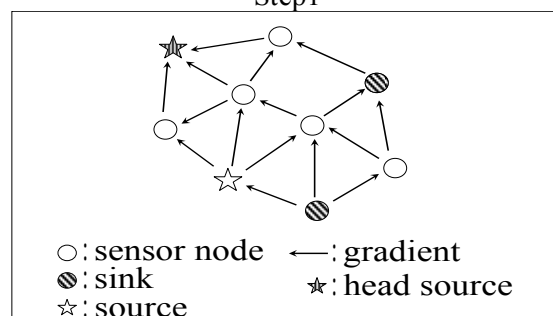


Step5

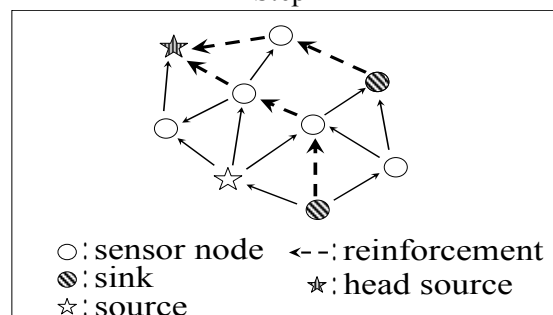
Fig.1. From sink node



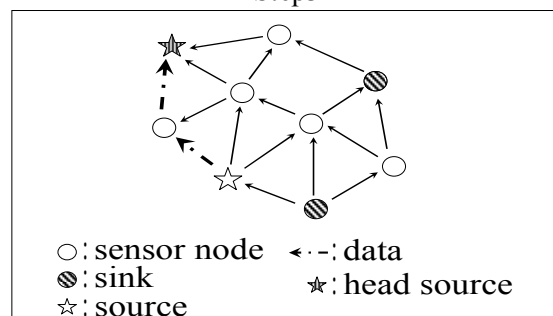
Step1



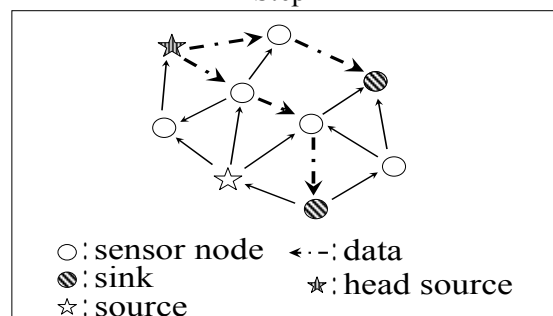
Step2



Step3



Step4



Step5

Fig.2. From source node

is more than the number of source nodes. However, the existing adaptive communication protocols cause flooding storm problems. The proposed protocol improves flooding storm problems. In Fig.1 and Fig.2, the example on the proposed protocol is shown.

IV. SIMULATION EXPERIMENT

Through simulation experiments, the performance of the proposed protocol is investigated in detail to verify its effectiveness. A wireless sensor network consisting of many sensor nodes placed in a wide range is assumed. The conditions of simulation, which were used in the experiments performed, are shown in Table1. In the simulation area, sensor nodes are randomly placed. In Fig.3, the network configuration is illustrated.

Table1. Conditions of simulation

Simulation times	1,000s
Simulation size	2,400m \times 2,400m
The number of sensor nodes	1,000
Range of radio wave	150m
Data transmission interval	10s
Model change interval	250s

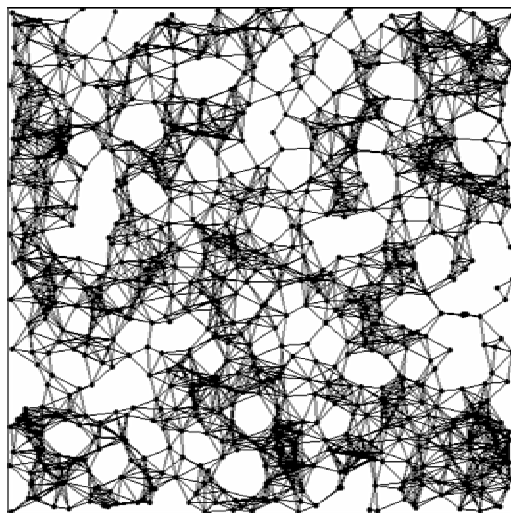


Fig.3. Network configuration

In the experiments performed, the proposed protocol is evaluated through the comparison with “Pull” or “Push” of “directed diffusion”. Figs.4 and 5 show total energy consumption of a network. Figs.6 and 7 show the transition of delivery ratio, where the battery capacity of each sensor node has been set to 0.5J. Experimental results verify that the proposed protocol is substantially advantageous for the long-term operation of a large scale and dense wireless sensor network.

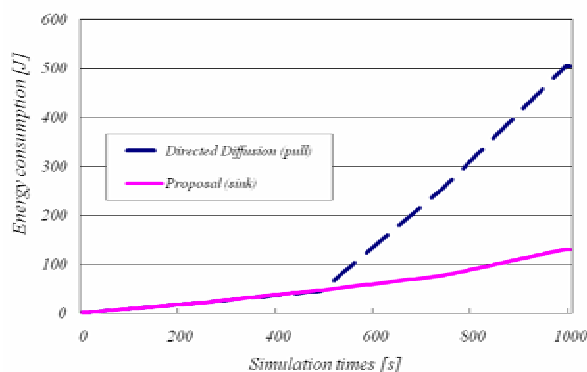


Fig.4. Total energy consumption (from sink node)

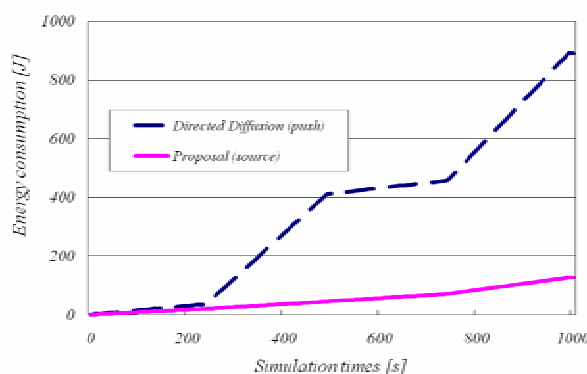


Fig.5. Total energy consumption (from source node)

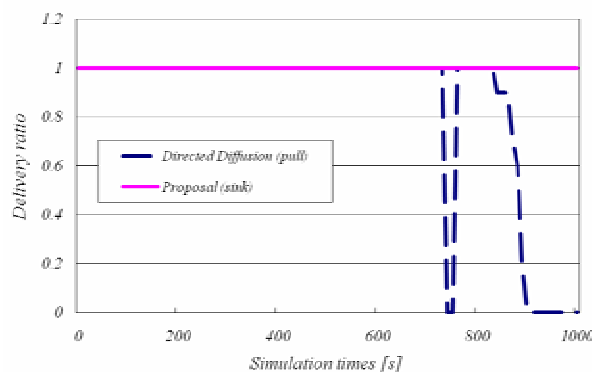


Fig.6. Transition of delivery ratio (from sink node)

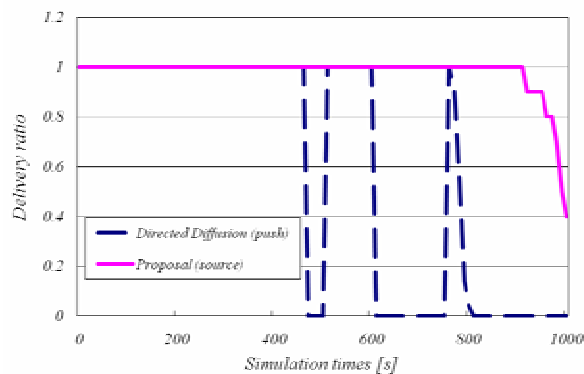


Fig.7. Transition of delivery ratio (from source node)

IV. CONCLUSIONS

In this paper, a new adaptive communication protocol, which adapts itself to the variety of types of communication, has been proposed. This protocol can improve flooding storm problems. In the experiments performed, the performance of the proposed protocol was compared with those of the existing ones. Experimental results indicate that the proposed protocol is superior to the existing ones and has the development potential as a promising one from the viewpoint of the long-term operation of a wireless sensor network. In future studies, we evaluate the performance of the proposed protocol in detail.

REFERENCES

- [1] I. Akyildiz, W. Su, Y. Sankarasubramaniam, and E. Cayirci, "Wireless sensor networks: A survey," *Computer Networks Journal*, vol.38, no.4, pp.393-422, 2002.
- [2] C. Intanagonwiwat, R. Govindan, D. Estrin, J. Heidemann, and F. Silva, "Directed diffusion for wireless sensor networking," *ACM/IEEE Trans. on Networking*, vol.11, pp.2-16, 2003.
- [3] F. Silva, J. Heidemann, R. Govindan, and D. Estrin, "Directed diffusion", *Tech. Rep.*, ISI-TR-586, 2004.
- [4] M. Wakabayashi, H. Tada, N. Wakamiya, M. Murata, and M. Imase, "Proposal and evaluation of a bio-inspired adaptive communication protocol for sensor networks", *IEICE Tech. Rep.*, vol.107, no.294, pp.89-94, 2007.

Lateral Control of Unmanned Vehicle Using PD Controller

Young Chul Cha*, Jong Il Bae**, Kil Soo Lee*, Dong Seok Lee*, Yun Ja Lee***, and Man Hyung Lee*

**School of Mechanical Engineering, Pusan National University, Busan, 609-735, Korea
(Tel : 82-51-510-1456; Fax : 82-51-512-9835)*

(mecha-cha@pusan.ac.kr, melgibsoo@pusan.ac.kr, dslee@pusan.ac.kr, mahlee@pusan.ac.kr)

***Department of Electrical Engineering, Pukyong National University, Busan, 608-739, Korea
(Tel : 82-51-629-6314;)*

(jibae@pknu.ac.kr)

****Department of Dance, Pusan National University, Busan, 609-735, Korea*

(Tel : 82-51-510-2949)

(leeyj@pusan.ac.kr)

Abstract: In order to control an unmanned vehicle, steering, acceleration, braking etc., an actuator control is required. This paper proposes a lateral control system for an unmanned vehicle to improve the responsiveness of the system with a PD control. If a PD controller is used in the system, angle errors from autonomous navigation can be stabilized and the system will improve the transient response characteristics. Generally, when calculating a mathematical model of a vehicle, 4m/s^2 the lateral acceleration in less as two degrees of freedom bicycle model also shows better performance. In this paper, a mathematical modeling of a vehicle using two degrees of freedom model was calculated with a controller designed by Matlab, and autonomous navigation simulations were carried out. Path estimation method of autonomous navigation was done with the Point to Point algorithm, current position of vehicle gained with GPS. Performance of the designed controller was verified through autonomous navigation with a real vehicle.

Key words : Lateral control, PD Controller, Unmanned Vehicle, P to P algorithm

I. INTRODUCTION

Today, society has become more convenient with the rapid development of transportation; however, as a result, traffic congestion and accidents are increasing the seriousness of the traffic problems. The cause of most accidents occurs from the carelessness of an individual. So safety-devices for preventing accidents are being developed [1, 2], and research and development of unmanned vehicles are being conducted in advanced countries as well as our country [3, 4].

Here, lateral control of unmanned vehicles and lateral control method using a PD-controller from existing P to P driving were studied. The original P to P driving is driving from the current location to the next location. The driving method calculates the angle between the current position and the next to obtain the steering value. However, in the original method, stable driving is not guaranteed due to the rapid changes of the steering value at the waypoints which are renewed along the path.

A PD controlled driving can stabilize the occurring error angles of the rapidly changing steering value which makes reliable driving possible. In the main part of this paper, 2WS modeling and PD-controller design is described and the original P to P driving is introduced. And using the PD-controller, the P to P driving and the original driving results are analyzed and compared.

II. 2WS MODEL

A 2WS(2 wheel steering) car has two front steering wheels while the rear wheels of the vehicle are fixed. Analysis of the general steering characteristics of the car when driving, that is, if the lateral acceleration is less than $0.4G$, a linear model of two degrees of freedom can be used to obtain accurate results. Degrees of freedom linear model uses lateral displacement and yaw. The purpose of this study is a 2WS vehicle steering control so the roll, pitch motions were ignored, and experiments were done assuming that the differences of the angle of yaw direction were small.

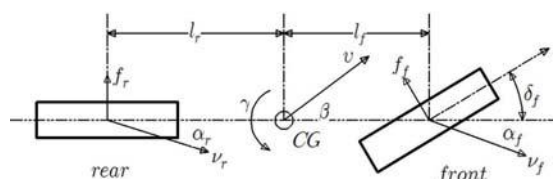


Fig. 1 2WS Bicycle Model.

Slip angle α_f, α_r can be calculated as shown below by speed of vehicle v , each distance from the center of gravity to the front-wheel and rear-wheel l_f, l_r , the center of gravity of the vehicle yaw rate $\dot{\gamma}$ and lateral velocity γ , rear-wheel steering angle δ_r , front-wheel steering angle δ_f , Fig. 1 for each of the front tire and rear tire slip angle α_f, α_r .

$$\alpha_f = \delta_f - \frac{v + \gamma l_f}{v} \quad (1)$$

$$\alpha_r = \delta_r - \frac{v + \gamma l_r}{v} \quad (2)$$

Since a linear tire model is used, the cornering force f_f and f_r acts on the front tire and rear tire so their relevancy are shown as Equation (1) and Equation (2).

$$f_f = c_f \cdot \alpha_f \quad (3)$$

$$f_r = c_r \cdot \alpha_r \quad (4)$$

c_f and c_r are the cornering stiffness. Therefore, using Equation (3) and Equation (4), as shown in Fig. 1, the equilibrium conditions of the vehicle's lateral and yaw moment are used to derive the Equations of motion.

$$m(\dot{v} + v\gamma) = c_f \cdot \alpha_f + c_r \cdot \alpha_r \quad (5)$$

$$J\dot{\gamma} = c_f \cdot l_f \cdot \alpha_f - c_r \cdot l_r \cdot \alpha_r \quad (6)$$

m is the mass of the vehicle, J is the vehicle's yaw moment of inertia. When Equations (1) and (2) are substituted in Equations (5) and (6), then linear Equations of the model are shown in the determinant (7) and then Equation (8) can be expressed in the form of a determinant as.

$$\dot{x}(t) = Ax(t) + Bu(t)$$

$$x(t) = \begin{Bmatrix} v \\ \gamma \end{Bmatrix}, \quad u(t) = \begin{Bmatrix} \delta_f \\ \delta_r \end{Bmatrix} \quad (7)$$

$$A = \begin{bmatrix} a_{11} & a_{12} \\ a_{21} & a_{22} \end{bmatrix}, \quad B = \begin{bmatrix} b_{11} & b_{12} \\ b_{21} & b_{22} \end{bmatrix}$$

$$\begin{bmatrix} \dot{v} \\ \dot{\gamma} \end{bmatrix} = \begin{bmatrix} a_{11} & a_{12} \\ a_{21} & a_{22} \end{bmatrix} \begin{bmatrix} v \\ \gamma \end{bmatrix} + \begin{bmatrix} b_{11} & b_{12} \\ b_{21} & b_{22} \end{bmatrix} \begin{bmatrix} \delta_f \\ \delta_r \end{bmatrix} \quad (8)$$

Elements of system matrix A and input matrix B are given in the below Equations (9) and (10).

$$b_{11} = -\frac{(c_r + c_f)}{mv}, \quad b_{12} = -\frac{(c_r l_f + c_f l_r)}{mv} - v$$

$$b_{21} = -\frac{(c_r l_f + c_f l_r)}{Jv}, \quad b_{22} = -\frac{(c_r l_f^2 + c_f l_r^2)}{Jv} - v \quad (9)$$

$$b_{11} = \frac{c_f}{m}, \quad b_{12} = \frac{c_r}{m}$$

$$b_{21} = \frac{c_r l_f}{J}, \quad b_{22} = -\frac{c_r l_r}{J} \quad (10)$$

In this study, the necessary parameter is steering angle θ of the unmanned vehicle. Thus, Equation (11) is added, and then Equation (12) is expressed as the Equation of state [5].

$$\dot{\theta} = \gamma \quad (11)$$

$$\begin{bmatrix} \dot{v} \\ \dot{\gamma} \\ \dot{\theta} \end{bmatrix} = \begin{bmatrix} a_{11} & a_{12} & 0 \\ a_{21} & a_{22} & 0 \\ 0 & 1 & 0 \end{bmatrix} \begin{bmatrix} v \\ \gamma \\ \theta \end{bmatrix} + \begin{bmatrix} b_{11} - b_{12} \\ b_{21} - b_{22} \\ 0 \end{bmatrix} \begin{bmatrix} \delta_f \end{bmatrix} \quad (12)$$

Table 1 Unmanned Vehicle Parameters.

Parameter	Value
$m(\text{kg})$	2,055
$v(\text{m/s})$	2.78~8.33
$J(\text{kgm}^2)$	193.25
$c_f(\text{kgf/rad})$	387.3~3690.6
$c_r(\text{kgf/rad})$	848.8~9409.1
$l_f(\text{m})$	1.158
$l_r(\text{m})$	1.737
$L(\text{m})$	2.895

III. PD-CONTROLLER DESIGN

PD-Controller reduces error signals effectively since the feedback of the control signal is proportional to the change of the differential value of the error signal, the damping ratio is increased and the overshoot is suppressed. Considering the effect of these differential controls in the controller design, the system can improve the transient response characteristics. Transfer function $K(s)$ of controller is as shown in Equation (13).

$$K(s) = K_p(1 + T_d s) \quad (13)$$

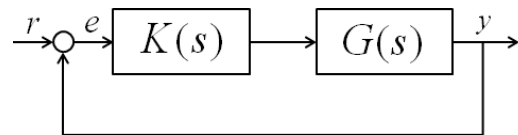


Fig. 2 Block Diagram of PD-Controller.

Fig. 2 is a block diagram of a simulation. Here, r is the control input representing the destination, e is steering angle error which is the difference between the destination and current location. $G(s)$ is represented by Equation (13) as a plant function. The maximum steering angle of the unmanned vehicle was set to ± 30 degrees, and control gain was set throughout the experiments.

Proportional gain $K_p = 0.8$ and derivative gain $K_d = 0.35$ is calculated [6].

IV. LOCATION RECOGNITION AND DRIVING

In autonomous navigation, the vehicle's current position and the heading of the vehicle have to be known. In this study, location-aware system used DGPS (Differential Global Positioning System). The DGPS reference station and rover is composed. Rover's absolute position is known, and then GPS measurements of Rover are calibrated based on this. If the destination station is located within the station's range of about 2km, the system provides a precision of 20cm CEP (95%).

Novatel's GPS receiver ProPak-V3 was used, and antenna, GPS-701-GG was used. For the unmanned vehicle experiments, the roof of the vehicle was equipped with two GPS receivers, so the azimuth of the vehicle can be obtained from two GPS coordinates.

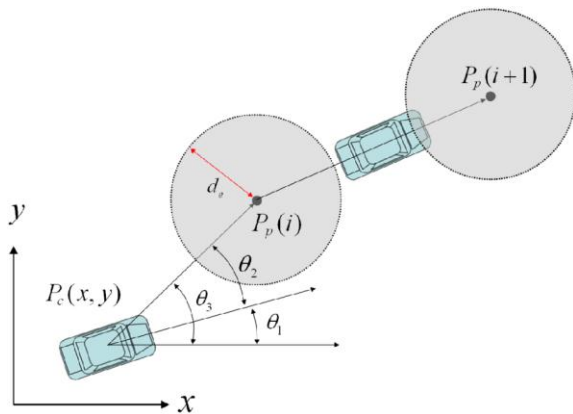


Fig. 3 Lateral Control Model.

Fig. 3 is model for lateral control of vehicle. $P_p(i)$ represents the current position of the vehicle, destination location $P_p(i+1)$, azimuth(heading) of the vehicle θ_1 , azimuth(heading) of the destination location θ_3 , θ_2 is the steering angle of the vehicle. The vehicle's current location is known by DGPS measurements, and the waypoint on the path to the destination is also known. Therefore, the vehicle's steering angle can be calculated by Equation (14).

$$\theta_2 = \theta_3 - \theta_1 \quad (14)$$

The steering angle is calculated from the difference of the destination azimuth and the current position of the vehicle. When the steering angle is 0 degrees, the vehicle is head in the destination allowing you to reach the

destination [6].

V. EXPERIMENTS

In this study, a PD-controller is applied to a two-steering unmanned vehicle, general P to P path tracking algorithm and P to P driving algorithm using a PD controller are experimentally compared. When the general vehicle's driving characteristics for analyze, in other words, when the maximum steering angle of 20 degrees at the lateral acceleration of 0.4G is less than the degrees of freedom linear model, approximately 20km/h speed is turning.

Fig. 4 is a vehicle used in the experiment, and driving speed 10km/h, 20km/h, were carried out, respectively. The experiment vehicle used was a Hyundai-Kia MOHAVE, and the experiment was carried out in the school field. GPS coordinates were obtained through P to P driving experiment while turning on an ellipse course.



Fig. 4. Equipment used in the experiment.

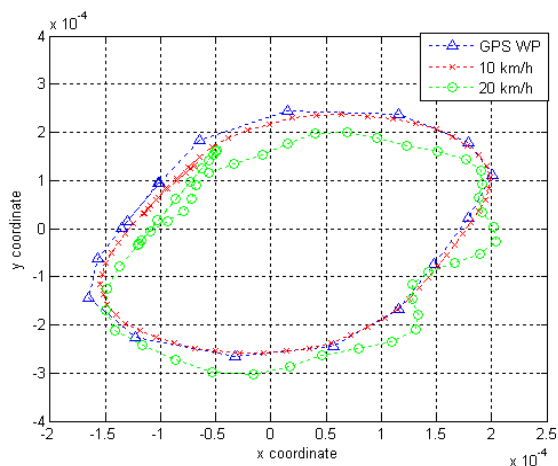


Fig. 5 P to P Driving with P controller.

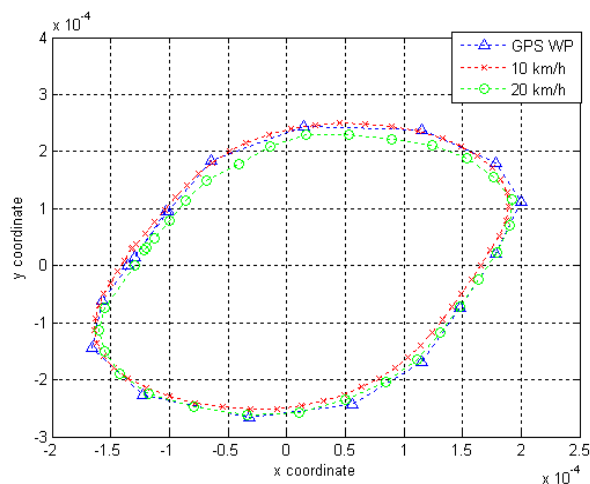


Fig. 6. Using the PD Controller Driving.

The experiment was set up in the path by using DGPS, and driving speed of 10km/h ~ 20km/h were performed while changing the driving speed, and the resulting values were compared with those of the original path.

Fig. 5 is a result of normal P to P driving. GPS path can be tracked successfully while driving at the speed of 10km/h, however, the path was not successfully tracked when at 20km/h.

In Fig. 6, using the PD-controller P to P driving, it shows reliable path tracking regardless of speed. The biggest differences in the two experiments appear when driving along the corners. When you track a straight line path from the current location of vehicle to the destination in the original P to P driving, arrival at the destination causes rapid increase in the steering angle. However, P to P driving with PD controller can reach the destination without a major change in steering angle because of stable driving. Therefore, in this study, using a PD controller P to P road driving than the original P to

P driving shows the results of smooth and stable driving.

VI. CONCLUSION

Lateral control of an unmanned vehicle using PD controller is proposed in P to P driving. To apply to the actual vehicle, DGPS was used. When using DGPS, azimuth of the vehicle can be measured more precisely. A PD controller was applied to lateral control, and results of experiments using the PD controller confirmed it to be stable than general P to P driving. However, when the original path and experiment result's GPS coordinate were compared, the turning radius was larger than that of the original path. This error occurred because the dynamic elements of the vehicle were not considered. Research design considering the dynamic elements need to be done so that reliable path tracking can be performed for variable state of velocity.

REFERENCES

- [1] Y. R. Oh, H. J. Lee, and Y. P. Park, "A Study on Validation of Braking Performance Considered ABS Friction Characteristics," *The Korean Society of Automotive Engineers*, Vol. 2, pp. 884~889, 2007.
- [2] J. H. Choi, "Wheel Slip Control of ABS Using Adaptive Control Method," *Journal of the Korean Society of Manufacturing Process Engineers*, Vol. 5, No. 3, pp. 71~79, 2006.
- [3] H. C. Moon, C. M. Kim, and S. G. Kim, "The Research for the Vision System of Tele-operated Unmanned Vehicle," *The Korean Society of Automotive Engineers*, Vol. 2, pp. 1316~1323, 2001.
- [4] J. Y. Um and I. S. Lee, "A Study for DGPS Navigation System for an Autonomous Vehicle," *The Korean Society of Automotive Engineers*, Vol. 3, pp. 1179~1188, 2004.
- [5] Y. H. Lee, S. I. Kim, M. W. Suh, H. S. Son, and S. H. Kim, "Linearized Dynamic Analysis of a Four-wheel Steering Vehicle," *The Korean Society of Automotive Engineers*, Vol. 2, No. 5, pp. 101~109, 1994.
- [6] K. S. Lee, M. K. Kim, Y. H. Koh, J. I. Bae, and M. H. Lee, "Control of Unmanned Container Transporters and Management System Development," *Korea Association of Automatic Control*, 2009.

A Control Method with Pheromone Information for Transport System

Yoshitaka Imoto ^{*1}, Yasutaka Tsuji ^{*2} and Eiji Kondo ^{*2}

^{*1} Faculty of Engineering, Kyushu University, 744 Motoooka, Nishi-ku, Fukuoka, 819-0395, Japan
(Tel: 81-92-802-3167; Fax: 81-92-802-0001; imoto@zeus.mech.kyushu-u.ac.jp)

^{*2} Faculty of Engineering, Kyushu University

ABSTRACT

Since control methods of a transport system between processing machines are specialized for each layout of the system, it is difficult to design prompt schedules and control logic for recent complicated systems, especially in case of machine troubles or restructuring of system to modify the layout. In this paper, we propose a multi-agent transport control system which utilizes pheromone information. Each element of the system acts as an agent and estimates the appropriate path and time to drive out the products with information obtained by communication with other elements and pheromone information deposited on the track of products.

Keywords : Swarm Intelligence, Pheromone Information, Transport System

I. INTRODUCTION

Since control methods of a transport system between processing machines in manufacturing systems are specialized for each layout of the system, it is difficult to design prompt schedules and control logic of recent complicated systems, especially in emergent situations such as machine troubles or restructuring of the system to modify the layout[1].

On the other hand, in recent study in Information Transport System (ITS), pheromone model for prediction of traffic congestion has been proposed[2]. In the study, the pheromone model is used to make a short term prediction of the traffic congestion for frequent change.

In this paper, we propose a multi-agent transport control system which utilizes pheromone information. In the proposed system, the transport system consists of processing machines, buffers which temporally store products and drive them out in appropriate time, belt conveyors and turntables. Each element acts as an agent and estimates the appropriate path to drive out products with information obtained by communication with other elements and

pheromone information deposited on the track of products. These two types of information are updated in different frequency. we examine validity and usefulness of the proposed method through simulation experiments.

II. RELATED STUDIES

Pheromone is a chemical material with which social insects, such as ants, communicate with each other indirectly through the environment. Ants deposit pheromones on their path when they find a food in their search. By using the pheromone information, other ants can find efficient path to the food. The deposited pheromone evaporates over time and old information loses their effect on the path selection gradually. In the engineering area, the mechanism is modeled as a “*pheromone model*” and utilized in many applications[3][4].

In the pheromone model, agents deposit the pheromone information onto the environment. The information decreases in its value gradually over time and is also updated by agents, so that the information goes along with the changes of the environment. Especially, in a recent study of the ITS (Information Transport System), pheromones are used to predict traffic congestions [2]. In the study, some information is used as the pheromone information, such as number of the braking and distance from other cars. The information enables short term prediction for frequent change of traffic congestion which can not be realized by long term prediction such as statistic.

On the other hand, there are some applications which utilize multi-agent control method for transport system. A multi-agent control method base on A*-algorithm is proposed in [4]. It considers a system in which products have priority to be transported, and reduce relocation of products in buffers. In [5], another multi-agent control method is introduced. It uses several types of virtual agent to find a path to the destination or to collect information.

In these studies, the controlled systems have only one processing machine as a destination and need

some centralized control such as a server of virtual space, so that they are not enough in the case that the system contains several processing machines and several types of products or the scale of the system becomes larger.

In this paper, we propose a decentralized multi-agent transport control method for the system which contains several types of products and processing machines.

III. PROPOSED METHOD

1. Assumption of production system

The production system addressed in this work includes several kinds of processing machine and a transfer system, which consists of belt-conveyors, turntables and buffers. A belt-conveyor can carry a product in only one direction and a turntable can change a move direction of products. Buffers, located back and forth of a processing machine, can temporarily storage products. In this work, it is assumed that each element of the production system can communicate with each other elements connected to it.

Each element of the transfer system sets the machines as candidate destinations, which perform next process to a product on it, and can obtain useful information of the candidates to transport the product through the communication between the elements. When a production system is large, amounts of information sent and stored are also huge. In this work, therefore, the each element sends only information of the next destinations, i.e. next machines in downstream, and the communication between them is executed on periodic interval.

Each element of the transport system can obtain information of candidate destinations, which may be a little past, but they do not have a current status of its neighbor element. In order to estimate the local information of neighbor element, each turntable counts number of products which have moved in each direction as trail of a product move. We call this number as “pheromone”. The pheromone is evaporated and the effect of the past information decreases gradually as the natural pheromones.

With these kinds of information, we construct the method which determines the optimal path for the situation on each element by considering the whole of the system. As the information is obtained by communication between neighbor elements or an element and a product, the control can be decentralized. Thus, it is expected that the transport changes flexibly for the change of the system.

2. Information about the path to the candidate destinations

In the communication, the following three types of parameters (estimations) are used,

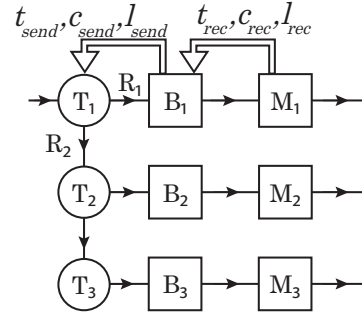


Figure 1: Flow of information

t : waiting/moving time to next element

c : vacant capability of a buffer

l : completion time of next processing

Processing machines send their own information to the elements which connected to them in the upstream side. Each element receives the information and sends the information added with its own status value to the upstream side, but the information is not sent to the processing machines in upstream side.

Each element receives three parameters t_{rec} , c_{rec} and l_{rec} from its downstream side, then sends t_{send} , c_{send} , l_{send} to its upstream side. When sending these parameters, each parameter is updated as Eqs.(1)-(3).

$$t_{send} = \max(t_{own}, t_{rec}) \quad (1)$$

$$c_{send} = \min(c_{own}, c_{rec}) \quad (2)$$

$$l_{send} = l_{own} + l_{rec} \quad (3)$$

t_{own} , c_{own} , l_{own} are parameters of the element. t_{own} is the process time in the processing the machine or time interval from input to output on the buffer. The element sends bigger one of t_{own} and t_{rec} . c_{own} is value of empty space in the buffer. The element sends smaller one of c_{own} and c_{rec} . l_{own} is the time for process completion on the destination. The element adds l_{own} to l_{rec} and sends it to the upstream side. By using these parameters, the evaluate function of the path is defined as:

$$E = c_{send}^\alpha / (a t_{send} + b l_{send})^\beta \quad (4)$$

Here α , β , a , b are weighting coefficients.

3. Pheromone information

The pheromone information is deposited when a product is transported from an element to the next element, in the direction of the next element. The large value of the information implies the congestion and the direction is avoided to transport. The pheromone increases with constant value Δ for a product. The deposited pheromone evaporates and decreases its effect on path selection. The

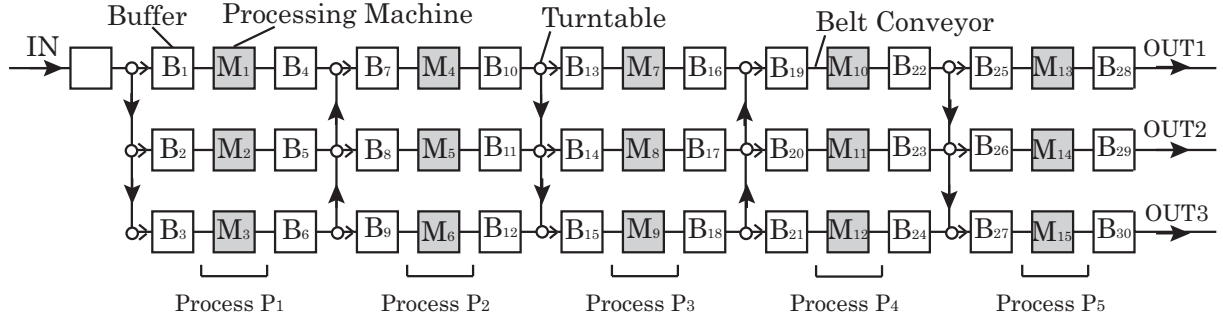


Figure 2: Layout of the production system

pheromone (s) on time s evaporates in time period Δs as given in the Eq.(5). Here, ρ is evaporative rate.

$$(s + \Delta s) = (1 - \rho) (s) \quad (5)$$

By using these two types of information, next element of the transport is selected for each product p_k . The best element $e_k^{(opt)}$ is determined, which can perform the next process to p_k and have small value of the pheromone information and large value of the evaluate function E . If the candidate elements have several destinations, they are evaluated as the weighted sum of the evaluation function E (see Eq.(7)). The optimal element to transport is determined as shown in the followings.

$$e_k^{(opt)} = e_i, i = \arg \min_{j \in D} (\gamma_j / E_{k,j}) \quad (6)$$

$$E_{k,j} = \sum_{m \in S} E_m c_m \delta_{k,m} / \sum_{m \in S} c_m \delta_{k,m} \quad (7)$$

$$\delta_{k,m} = \begin{cases} 1 & (p_k \text{ can be processed}) \\ 0 & (p_k \text{ can not be processed}) \end{cases} \quad (8)$$

D is the set of possible elements where p_k can be transported. S is the set of path including element j . $\delta_{k,m}$ is 1 when the destination element e_m of the path can process the product p_k , otherwise $\delta_{k,m}$ is 0.

In Fig.1, M_1 - M_3 represent processing machines and they are set as candidate destinations for B_1 - B_3 and T_1 - T_3 . For example, M_1 sends the information about its self such as process time t to B_1 . B_1 also sends the information updated as in Eqs.(1)-(3) to T_1 . In the same way, T_1 gets information about the path to M_2 and information about the path to M_3 . The products on T_1 are transported based on the information and pheromone. If the product p_k on T_1 can be processed on both M_2 and M_3 , the evaluation of the direction R_2 is calculated as weighted sum of evaluation of the path to M_2 and that of the path to M_3 . Finally, the product is transported to the optimal direction and the pheromone information is deposited on the direction.

4. Collision avoidance

In the system which contains some confluent point, collisions must be considered. In this study, as the considered system is constructed by belt-conveyors, it is difficult to avoid collisions by adjacent avoidance. For the problem, we put a buffer in the upstream side of each confluent point and make them communicate with each other to transport elements one by one in order of input. Therefore, the system in Fig.2 assumes that the each of buffers B_4 - B_6 , B_{10} - B_{12} , B_{16} - B_{18} and B_{22} - B_{24} can communicate and determine the time of output.

IV. SIMULATION EXPERIMENT

We examine validity and usefulness of the proposed method through simulation experiments. The parameters ρ , γ are varied to examine the effectiveness of the proposed information. ρ is fixed.

In the simulation experiments, we use the layout shown as Fig.2. $M_i (i = 1, \dots, 15)$ represent processing machines, $B_i (i = 1, \dots, 30)$ represent buffers and lines between them are belt conveyors. Products are carried into the system from IN with constant interval, performed each process $P_i (i = 1, \dots, 5)$ on processing machines M_1 - M_{15} , and finally output from $OUT1$ - $OUT3$. The system has several processing machines of same type. For example, process P_1 is processed in M_1 - M_3 , but each processing machine has difference in process time as shown in Table 1. The maximum capability of the buffers is 20. The type of products is only one type. Products are carried into the system for every 30 steps. The number of the products is 200. The time from the output of the 50th product to the output of the 150th product is measured, and the value is defined as $T_{(est)}$. The work rate w is calculated as the ratio of working time of the processing machines to the $T_{(est)}$. The results of the experiments are shown in Table 2, Table 3 and Table 4.

Table 2 shows the work rate of each processing machine in the condition of $\rho = 1.0$, $\gamma = 1.0$, $\gamma = 1.0$. Table 3 and Table 4 show $T_{(est)}$ in each condition. In each experiment, $a = 1.0$, $b = 0.01$.

Table 1: Process time t of each processing machine for a product

	M_1	M_2	M_3	M_4	M_5	M_6
P	P_1			P_2		
t	60	50	35	80	50	40
	M_7	M_8	M_9	M_{10}	M_{11}	M_{12}
P	P_3			P_4		
t	50	30	25	50	40	40
	M_{13}	M_{14}	M_{15}			
P	P_5					
t	30	25	20			

Table 2: Work rate w for each processing machine ($\beta = 1.0$, $\gamma = 1.0$, $\gamma = 1.0$)

	M_1	M_4	M_7	M_{10}	M_{13}
w	0.419	0.780	0.156	0.487	0.117
	M_2	M_5	M_8	M_{11}	M_{14}
w	0.378	0.466	0.268	0.339	0.204
	M_3	M_6	M_9	M_{12}	M_{15}
w	0.335	0.293	0.396	0.189	0.209

The transport was finished properly except in some conditions. In the case that pheromone information has no effect ($\gamma = 0.0$) or little effect ($\gamma = 0.1, 0.2$), products are transported to the buffer over its capability and the transport was not finished properly. Thus, it is considered that the pheromone information plays important role in path selection. On the other hand, the transport is also not finished properly, where the effect of the pheromone information is bigger ($\gamma = 2.0$). γ has to be adjusted to proper value. The small or the big effect of the time information also results in overflow of the buffers ($\beta = 0.1, 10.0$). As $T_{(est)}$ changes remarkably for the change of β , it is considered that the information about waiting/moving time t has a great influence on the utility.

In the experiments, the input time of products is constant, so that the work rate should be improved if the input time is controlled properly. However, considering some loss of time to transport products from the buffers to the machines, the work rate of M_4 is nearly bound to improve. Thus, the unbalance of work rates between processing machines needs to be improved. For example, the work rate of M_6 is less than that of M_4 and M_5 . It is caused by a lack of the information about products which is processed in M_1 and M_2 . Although some of the information about the products processed in M_1 and M_2 is given as waiting/processing time t and capability of the buffer c , which improve the unbalance in the condition of bigger β , additional introduction of some new information is needed.

Table 3: Process time for 100 products ($\beta = 1.0$, $\gamma = 1.0$)

β	0.1	0.5	1.0	1.5	2.0	3.0
$T_{(est)}$	—	4615	4366	4239	4208	3927
β	5.0	10.0				
$T_{(est)}$	3765	—				

Table 4: Process time for 100 products ($\beta = 1.0$, $\gamma = 1.0$)

γ	0.0	0.1	0.2	0.5	1.0	1.5	2.0
$T_{(est)}$	—	—	—	4424	4366	4351	—

V. CONCLUSIONS

In this paper, we have proposed the multi-agent transport control system which utilizes pheromone information and examined validity and usefulness of the proposed method through simulation experiments. As a result of the experiments, although there is some unbalance in work rates, the proposed method can transport products properly in some conditions. For future works, we need to improve the work rate by controlling the input time of product, adjust some parameters and introduce new information such as pheromone of distanced elements.

ACKNOWLEDGMENT

This work has been supported in part by a financial aid for Encouragement of Young Scientists of Faculty of Engineering, Kyushu University(2009).

REFERENCES

- [1] K. Uchiyama, T. Yoshikawa, K. Uchimura and Z. Hu: Construction of transport control system using congestion index, *IEICE Technical Report*, ITS 105(166), pp.23-28, (2005), (in Japanese).
- [2] Y. Ando, Y. Fukazawa, O. Masutani, H. Iwasaki and S. Honiden: Performance of pheromone model for predicting traffic congestion, *AAMAS '06 Proceedings of the fifth international joint conference on Autonomous agents and multiagent systems*, Vol.3, No.1, pp.1-16 (2006).
- [3] M. Dorigo and T. Stutzle: *Ant Colony Optimization*, The MIT Press, (2004).
- [4] T. Seidel, J. Hartwig, R.L.Sanders and D. Helbing: An Agent-Based Approach to Self-organized Production, *Swarm intelligence*, Springer, pp.219-252 (2008).
- [5] P. Valckenaers and T. Holvoet: The environment: An essential abstraction for managing complexity in MAS-based manufacturing, *In Lecture notes in computer science*, Springer Verlag, (2006).

Implementation of real-time distributed control for discrete event robotic manufacturing systems using Petri nets

G. Yasuda

Nagasaki Institute of Applied Science, Nagasaki 851-0193, JAPAN

(Tel & fax : 81-95-839-8973)

(yasuda_genichi@pilot.nias.ac.jp)

Abstract: The paper deals with a systematic method of modeling and real-time control for discrete event robotic manufacturing systems using Petri nets. Because, in the complex manufacturing systems, the controllers are distributed according to their physical structure, it is desirable to realize real-time distributed control. In this paper, the task specification of discrete event manufacturing processes is represented using a global Petri net. Then it is decomposed and distributed into the machine controllers, which are coordinated through communication between the coordinator and machine controllers. The coordination algorithm was derived using formal expressions of transition firing and state change so that the decomposed transitions fire simultaneously. Implementation of real-time distributed control using a microcomputer network is described for an example robotic manufacturing cell. The demonstrations show that the proposed method can be used as an effective tool for consistent modeling, simulation and real-time control of large and complex manufacturing systems.

Keywords: Discrete event robotic manufacturing systems, modeling, real-time control, implementation, Petri nets.

I. INTRODUCTION

As the factory automation systems have been becoming larger and more complex. The system architecture has shifted to distributed and parallel processing from centralized processing in order to reduce the development cost and to improve the reliability. In the field of factory automation systems, a demand for the automatic control has diversified and the control logic has become extremely complicated, because the combinative complexity of the control requirement, which comes from the non-deterministic features of event driven systems such as manufacturing control systems, is inevitable. To deal with the complexity, a new methodology on control system design based on the concept of event driven system is necessary. However, appropriate representation methods and analysis methods for control mechanism have not sufficiently been established.

Programming paradigm modeled by a network, such as Petri net, has been considered to be useful, because the network model can describe the execution order of parallel/sequential processes directly without ambiguity. The Petri net is excellent in expression and analysis of the dynamic behavior of event driven systems, because it can model the system that consists of simultaneous process elements that interfere to each other. The programming technique makes it possible to realize systematic and high-level description of system

specification. Therefore, it has been applied to a variety of system developments such as real-time systems, production systems, communication systems, and so on.

However, in case of factory automation systems, the network model becomes complicated and it lacks for the readability and comprehensibility. Besides, only specification analysis stage has been supported, and the support for the control software coding stage is insufficient [1]. Therefore, the flexibility and expandability are not satisfactory in order to deal with the specification change of the system.

Due to its complexity, a large and complex manufacturing system is commonly structured into a hierarchy; factory, line, station, machine, and actuators. The manufacturing system handles complicated tasks by dividing a task hierarchically in this structure, which is expected to be effective in managing cooperation tasks executed by great many machines or robots. Conventional Petri net based control systems were implemented based on an overall system model. Since in the large and complex systems, the controllers are geographically distributed according to their physical (hardware) structure, it is desirable to realize the hierarchical and distributed control. If it can be realized by Petri nets, the modeling, simulation and control of large and complex discrete event manufacturing systems can be consistently realized by Petri nets. In this paper, the author presents a methodology for hierarchical and distributed control of large and

complex robotic manufacturing systems using extended Petri nets, to construct the control system where the cooperation of each controller is implemented so that the aggregated behavior of the distributed system is the same as that of the original system and the task specification is completely satisfied.

II. MODELING OF DISCRETE EVENT SYSTEMS USING EXTENDED PETRI NETS

Discrete event systems such as robotic manufacturing systems have the properties of asynchronism, ordering, concurrency and conflict, so that deadlock will be apt to occur in the systems. The Petri net is one of the effective means to represent such systems. For applying it to the design, analysis, and control of the systems the guarantee of safeness and the notation of input/output of signals from/to machines should be required. A kind of graph deduced from the Petri net was proposed so as to satisfy the above requirements [2].

The extended Petri net consists of the following six elements: place, transition, directed arc, token, gate arc, output signal arc. A place represents a condition of a system element or action. A transition represents an event of the system. A directed arc connects a place to a transition, and its direction shows the input and output relation between them. Places and transitions are alternately connected using directed arcs. The number of directed arcs connected with places or transitions is not restricted. A token is placed in a place to indicate that the condition corresponding to the place is holding.

A gate arc connects a transition with a signal source, and depending on the signal, it either permits or inhibits the occurrence of the event which corresponds to the connected transition. Gate arcs are classified as permissive or inhibitive, and internal or external. An output signal arc sends the signal from a place to an external machine.

Formally, the firability condition and external gate condition of a transition j are described as follows:

$$t_j(k) = \bigcap_{m=1}^M p_{j,m}^I(k) \wedge \bigcap_{n=1}^N \overline{p_{j,n}^O(k)} \wedge \bigcap_{q=1}^Q g_{j,q}^{IP}(k) \wedge \bigcap_{r=1}^R \overline{g_{j,r}^{II}(k)} \quad (1)$$

$$g_j^E(k) = \bigcap_{u=1}^U g_{j,u}^{EP}(k) \wedge \bigcap_{v=1}^V \overline{g_{j,v}^{EI}(k)} \quad (2)$$

where,

M : input place set of transition j

$p_{j,m}^I(k)$: state of input place m of transition j at time sequence k

N : output place set of transition j

$p_{j,n}^O(k)$: state of output place n of transition j at time sequence k

Q : internal permissive gate signal set of transition j

$g_{j,q}^{IP}(k)$: internal permissive gate signal variable q of transition j at time sequence k

R : internal inhibitive gate signal set of transition j

$g_{j,r}^{II}(k)$: internal inhibitive gate signal variable r of transition j at time sequence k

U : external permissive gate signal set of transition j

$g_{j,u}^{EP}(k)$: external permissive gate signal variable u of transition j at time sequence k

V : external inhibitive gate signal set of transition j

$g_{j,v}^{EI}(k)$: external inhibitive gate signal variable v of transition j at time sequence k

The state (marking) change, that is, the addition or removal of a token of a place, is described as follows:

$$p_{j,m}^I(k+1) = p_{j,m}^I(k) \wedge \overline{(t_j(k) \wedge g_j^E(k))} \quad (3)$$

$$p_{j,n}^O(k+1) = p_{j,n}^O(k) \vee (t_j(k) \wedge g_j^E(k)) \quad (4)$$

An enabled transition may fire when it does not have any external permissive arc signaling 0 nor any external inhibitive arc signaling 1. The firing of a transition removes tokens from all its input places and put a token in each output place connected to it. The assignment of tokens into the places of a Petri net is called marking and it represents the system state. In any initial marking, there must not exist more than one token in a place. According to these rules, the number of tokens in a place never exceeds one, thus the Petri net is essentially a safe graph; the system is free from the bumping phenomenon. If a place has two or more input transitions or output transitions, these transitions may be in conflict for firing. When two or more transitions are firable only one transition should fire using some arbitration rule.

In the proposed procedure of modeling of robotic manufacturing systems, a global, conceptual Petri net model is first chosen which describes the aggregate manufacturing process. The places which represent the subtasks indicated as the task specification are connected by arcs via transitions in the specified order corresponding to the flow of subtasks and a workpiece.

For the example manufacturing cell with two robots,

one machining center, and two conveyors, where one is for carrying in and the other is for carrying out, the main execution of the system is indicated as the following task specification:

- (1) A workpiece is carried in by the conveyor CV1.
- (2) The workpiece is loaded to the machining center MC by the Robot R1.
- (3) The workpiece is processed by the machining center MC.
- (4) The workpiece is unloaded to the conveyor CV2 by the Robot R2.
- (5) The workpiece is carried out by the conveyor CV2.

The places representing the existence of machines are also added to connect transitions which correspond to the beginning and ending of their subtasks. Thus at the conceptual level the manufacturing process is represented as shown in Fig. 1 for the cell with two robots.

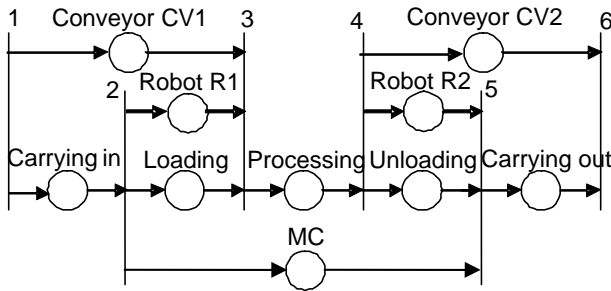


Fig.1 Petri net representation of example system with two robots at the conceptual level

Next, based on the hierarchical approach, the Petri net is translated into detailed subnets by stepwise refinements from the highest system control level to the lowest machine control level. At each step of detailed specification, a place of the Petri net is substituted by a subnet in a manner which maintains the structural properties. The detailed Petri net representation of the loading operation in the example system, which is a typical task at the subsystem coordination level in the factory automation system, is shown in Fig.2. Loading a workpiece to the machining center necessitates the cooperative or synchronized activities among the input conveyor, the machining center, and the robot. Similarly, unloading a workpiece from the machining center, necessitates the cooperative or synchronized activities among the output conveyor, the machining center, and the robot.

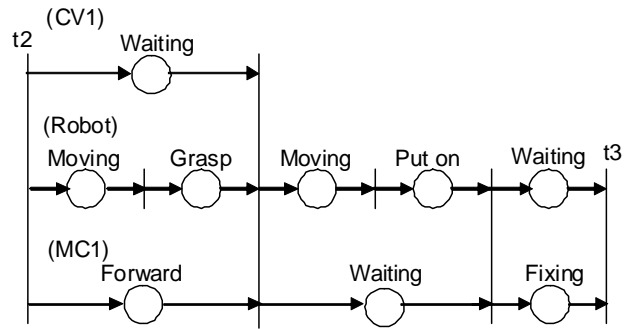


Fig.2 Detailed Petri net representation of loading operation

III. DECOMPOSITION AND COORDINATION ALGORITHM

For the manufacturing system, an example structure of hierarchical and distributed control is composed of one station controller and three machine controllers. The detailed Petri net is decomposed into subnets, which are executed by each machine controller.

In the decomposition procedure, a transition may be divided and distributed into different machine controllers as shown in Fig.3. The machine controllers should be coordinated so that these transitions fire simultaneously, that is, the aggregate behavior of decomposed subnets should be the same as that of the original Petri net. Decomposed transitions are called global transitions, and other transitions are called local transitions.

By the Petri net model, the state of the discrete event system is represented as the marking of tokens, and firing of any transition brings about change to the next state. So the firing condition and state (marking) change before decomposition should be the same as those after decomposition. If transition j is divided into s transitions $j1, j2, \dots, js$, the firability condition of a transition after decomposition is described as follows:

$$t_{jsub}(k) = \bigwedge_{m=1}^{Msub} p_{jsub,m}^I(k) \wedge \bigwedge_{n=1}^{Nsub} p_{jsub,n}^O(k) \wedge \bigwedge_{q=1}^{Qsub} g_{jsub,q}^{IP}(k) \wedge \bigwedge_{r=1}^{Rsub} g_{jsub,r}^{II}(k) \quad (5)$$

$$g_{jsub}^E(k) = \bigwedge_{u=1}^{Usub} g_{jsub,u}^{EP}(k) \wedge \bigwedge_{v=1}^{Vsub} g_{jsub,v}^{EI}(k) \quad (6)$$

From eq.(1) and eq.(5),

$$t_j(k) = \bigwedge_{sub=1}^s t_{jsub}(k) \quad (7)$$

From eq.(2) and eq.(6),

$$g_j^E(k) = \bigcap_{sub=1}^S g_{jsub}^E(k) \quad (8)$$

where,

S : total number of subnets

M_{sub} : input place set of transition j_{sub} of subnet sub

$p_{jsub,m}^I(k)$: state of input place m of transition j_{sub} of subnet sub at time sequence k

N_{sub} : output place set of transition j_{sub} of subnet sub

$p_{jsub,n}^O(k)$: state of output place n of transition j_{sub} of subnet sub at time sequence k

Q_{sub} : internal permissive gate signal set of transition j_{sub} of subnet sub

R_{sub} : internal inhibitive gate signal set of transition j_{sub} of subnet sub

U_{sub} : external permissive gate signal set of transition j_{sub} of subnet sub

V_{sub} : external permissive gate signal set of transition j_{sub} of subnet sub

The addition or removal of a token of a place connected to a decomposed transition is described as follows:

$$p_{jsub,m}^I(k+1) = p_{jsub,m}^I(k) \wedge (t_j(k) \wedge g_j^E(k)) \quad (9)$$

$$p_{jsub,n}^O(k+1) = p_{jsub,n}^O(k) \vee (t_j(k) \wedge g_j^E(k)) \quad (10)$$

From the logical formulation of firability condition and marking before and after decomposition, it is proved that the firability condition of the original transition is equal to AND operation of firability conditions of decomposed transitions. In case that a transition in conflict with other transitions is decomposed, these transitions should be coordinated by the station controller. The coordinator was introduced to execute the coordination algorithm [2].

IV. PETRI NET MODEL BASED CONTROL EXPERIMENTS

The control software is distributed into the station controller and machine controllers. The station controller is composed of the Petri net based controller and the coordinator. The conceptual Petri net model is allocated to the Petri net based controller for management of the overall system. The detailed Petri net models are allocated to the Petri net based controllers in the machine controllers. The control of the

overall system is achieved by coordinating these Petri net based controllers such that decomposed transitions fire at the same time and the task specification is completely satisfied. The overall control structure of the example manufacturing system was implemented on a local area network of computers as shown in Fig.3.

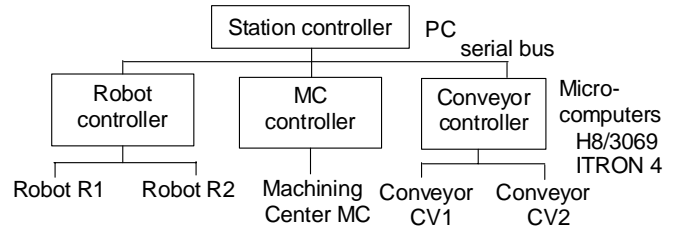


Fig.3 Implementation of real-time control system on microcomputer network

Each Petri net based machine controller on a dedicated microcomputer (Renesas H8/3069, real-time OS ITRON 4.0) executes real-time machine control, by initiating the execution of the unit actions attached to the fired transitions. The machine controller in charge of robot control executes robot motion control through the transmission of command and the reception of status report with serial interface to the real robot controller. The station controller implemented on another computer is also used to support modeling, simulation, and debugging of Petri nets and to load the Petri net based control program into the machine controllers. Communications among the controllers are performed using TCP/IP protocol. The coordinator sends the commands based on the conceptual, global Petri net model and coordinates the global transitions, which are accessed by the controllers as a shared file, such that decomposed transitions fire simultaneously.

V. CONCLUSIONS

An implementation of real-time distributed control for discrete event robotic manufacturing systems was described to realize consistent modeling, simulation and real-time control of large and complex robotic systems.

REFERENCES

- [1] Hasegawa, K., Takahashi, K., and Miyagi, P. E., (1988) Application of the Mark Flow Graph to represent discrete event production systems and system control, Trans. of SICE, 24, 69-75
- [2] Yasuda, G., (2009) Implementation of distributed cooperative control for industrial robot systems using Petri nets, Preprints of the 9th IFAC Symposium on Robot Control (SYROCO '09), 433-438

Development of Motion Analysis System using Acceleration Sensors for Tennis and its Evaluations

Takaya Maeda, Kenichirou Fuji, Hiroki Tamura, and Koichi Tanno

Dept. of Electrical & Electronic Engineering, University of Miyazaki, 1-1 Gakuen-kibanadai-nishi, Miyazaki-city, Miyazaki, 889-2192, Japan

(Tel : 81-985-58-7409; Fax : 81-985-58-7409)

(Email address: htamura@cc.miyazaki-u.ac.jp)

Abstract: The term biological motion is often used by researchers studying the patterns of movement generated by living forms and sport forms. We study the pattern recognition system of sport motion using the biological motion data. Biological motion data are acquired using 3D motion capture system. However, 3D motion capture system is too expensive. In this paper, the biological motion capture system was built using acceleration sensors. Our proposed system has the technique of Gaussian fitting and regression analysis. We tested our proposed system in the pattern recognition of the outdoor tennis and its evaluations.

Keywords: Motion Analysis System, Acceleration Sensors, Biological motion data, Gaussian fitting

1. Introduction

The motion capture system is one of the techniques to retrieve the action of the human body and the animal in the three-dimensional space in a computer as digital data. We wear a marker and a sensor on parts becoming the imperative construct of the movement such as the head or a hand foot joint and record those movements in the space. However, many cases were impossible to measure the outdoor sport. These systems were used a certain indoor. In addition, there are problems that the price of machine parts is expensive [1].

Therefore, in this paper, we built the motion capture system which used an acceleration sensor. The proposal system needs little load of the wearing, but it can acquire data fast outdoors. Because we can acquire many data by using this system, it is easy to build a database of outdoor sport. Therefore, in this paper, we build the database of the sports that individual difference is big and perform the operating analysis of data. We targeted the tennis. In this paper, we acquire the database of experienced persons and inexperienced persons form of tennis swing using the proposal system. And, we examine the point of difference of experienced person and inexperienced person for the form of tennis swing. We analyzed the data and performed the computer experiment that estimated of the tennis career. This paper used the technique of Gaussian fitting and multi regression analysis. From these experiments, we tried that find out a common knack from an experienced person.

2. Feature Extraction from Biological Motion

2.1 Procedure to obtain biological motion data

To obtain the biological motion data of subjects, we put

12 acceleration sensors (WAA-006: ATR-promotions Co.,Ltd) onto the subject's wrist / elbow / shoulder / waist / knee / ankle of both the left and the right side [2]. However, we analyzed three places of data of the wrist / elbow / shoulder of the dominant arm. These accelerations information are important place in the tennis form and the much clear than other datas changes in acceleration information. A motion sensing system is acceleration and a sampling frequency of the system is 237.5Hz. We show the photograph of Figure 1 when the player worn the acceleration sensors. The subjects are eleven male university students. The tennis experienced are five people, and the tennis inexperienced person are five people. These experimental conditions are similar to paper [3].



Figure 1. An acceleration sensor and the state that player wore the acceleration sensors.

2.2 The proposal analysis system.

In this subsection, we propose a feature extraction method for the estimates of the tennis career from the acceleration data. The proposed method is summarized in Figure 2.

As a first step, the player wears the acceleration sensor and play tennis to acquire acceleration data (X-axis, Y-axis, Z-axis). Next, one swing from acceleration data of the tennis swing were pulled out.

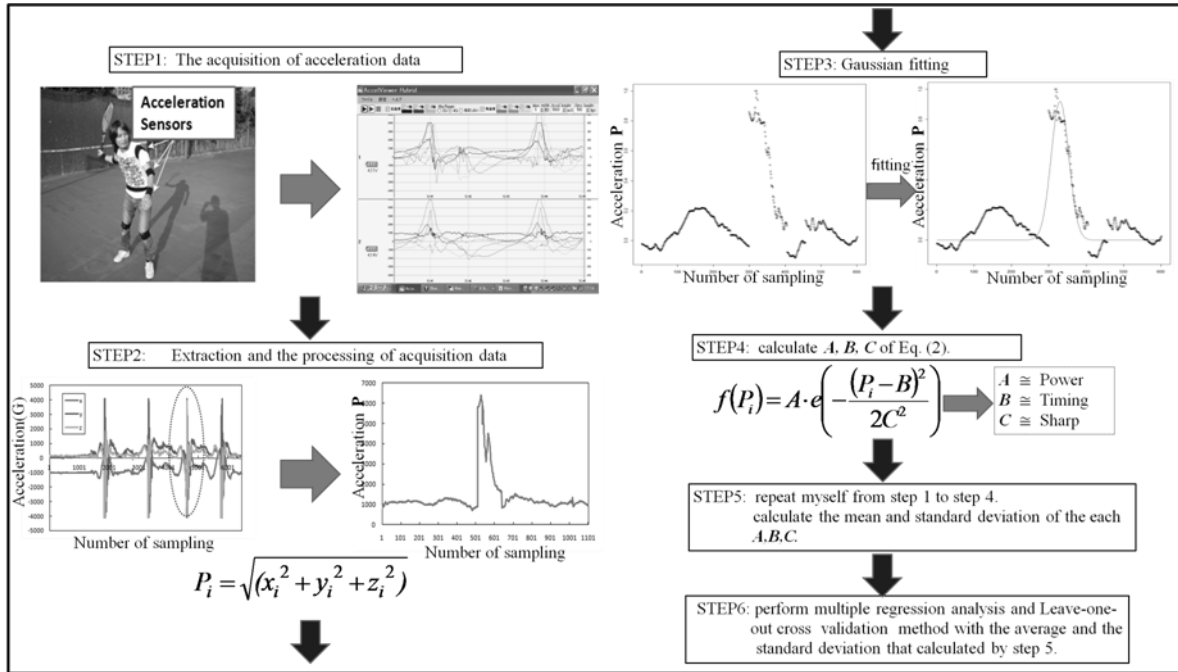


Figure 2. The summary of the proposal analysis system.

The STEP 2, P_i are computed by Eq.(1) [4]. P_i means the amount of the change of the acceleration of three axes. Next STEP3 and 4, we perform a Gaussian fitting with Eq.(2), and calculate A , B , C of Eq.(2). A means power, B is timing, and C is sharp of tennis form. The timing of B are calculated based on the shoulder. We repeat ourselves from STEP1 to STEP4. And we calculate the average and the standard deviation of the each A , B , C . Finally STEP 6, we perform multiple regression analysis and Leave-one-out cross validation method with the average and the standard deviation from computed by this analysis system.

$$P_i = \sqrt{(x_i^2 + y_i^2 + z_i^2)} \quad (1)$$

$$f(P_i) = A \cdot e^{-\frac{(P_i - B)^2}{2C^2}} \quad (2)$$

2.3 The interlocking movement characteristics of the dominant arm

We guessed that the interlocking movement of the wrist / elbow / shoulder of the dominant arm might be related to the person who experienced tennis. And, we presumed the career of tennis that uses only the interlocking movement by the previous research [3]. We show the graph of the wrist / elbow / shoulder in Figure 3 to express the interlocking movement characteristics of the dominant arm. As for the data, it normalized so that the maximum value becomes 1.0 and the average value becomes 0.0. We focus attention on the

interlocking movement characteristics of the wrist / elbow / shoulder and calculate the degree of similarity E between two joints using Eq. (3). N in Eq.(3) is the number of the samplings, P_i^k is one of the data of the wrist / elbow / shoulder. P_i^l is a non- P_i^k information. We calculate the average and the standard deviation of Eq.(3). In this paper, we added the data of the degree of similarity E to the STEP6.

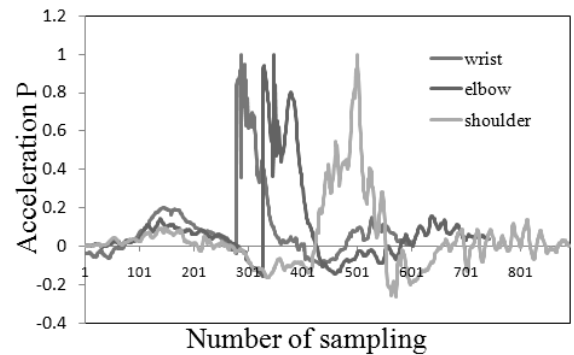


Figure 3. The interlocking movement characteristics of the dominant hand

$$E(\text{degree of similarity}) = \sqrt{\frac{1}{N} \left| \sum_i^N (P_i^k \times P_i^l) \right|} \quad (3)$$

3. Experiment Results

In order to test the effectiveness of proposal analysis system, we compared its performance with only used A ,

B , C and only used the degree of similarity E . In this paper, we perform multiple regression analysis and evaluate using Leave-one-out cross validation method.

3.1 The results of multiple regression analysis

We show the result of the multiple regression analysis how we used only the degree of similarity E in Figure 4. From t value and the P value of the analysis result, we understood that wrist / elbow (average) of Eq.(3) and wrist / shoulder (standard deviation) of Eq.(3) were meaning for tennis career. We assume these two elements E' . Next, we show the multiple regression analysis how we used the A (Power), B (Timing), C (Sharp) of Eq.(2) in Figure 5. The simulation of Figure 5 was used 8 elements. 8 elements are the average value. Finally, we show the multiple regression analysis how we used E' and the A (Power), B (Timing), C (Sharp) of Eq.(2) in Figure 6. The simulation of Figure 6 was used 9 elements. A value of R^2 (a coefficient of correlation) got results more than 0.8 from Figure 4 and Figure 5 and Figure 6. In three graphs, when a predicted value by the multiple regression analysis assumes the smallest person boundary value among the person who experienced tennis, we can pull the boundary line of an experienced person and the inexperienced person. But only one person did wrong identification among inexperienced people in Figure 4. A graph of Figure 6 was the best in these computer simulation results. Therefore, we selected the results of Figure 6, and to analyze it in detail in the next subsection.

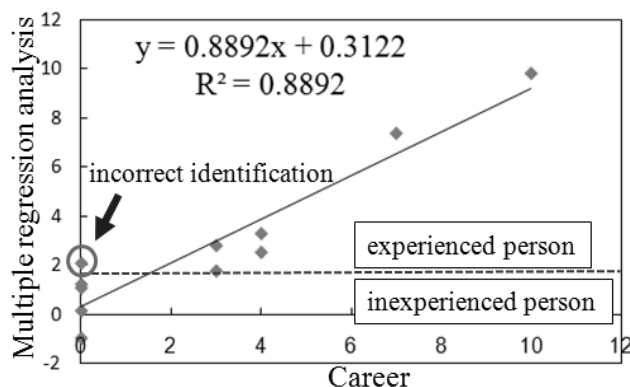


Figure 4. The result of the multiple regression analysis using the degree of similarity E .

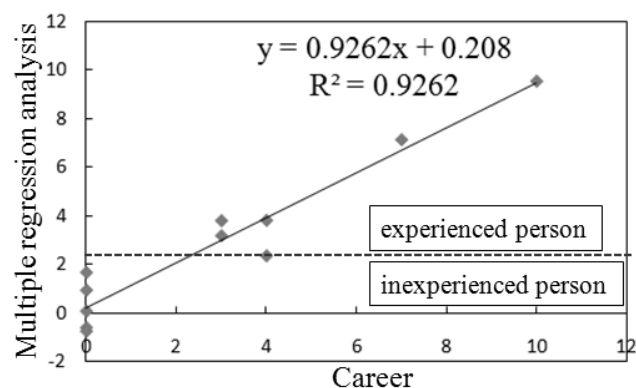


Figure 5. The result of the multiple regression analysis using the A (Power), B (Timing), C (Sharp).

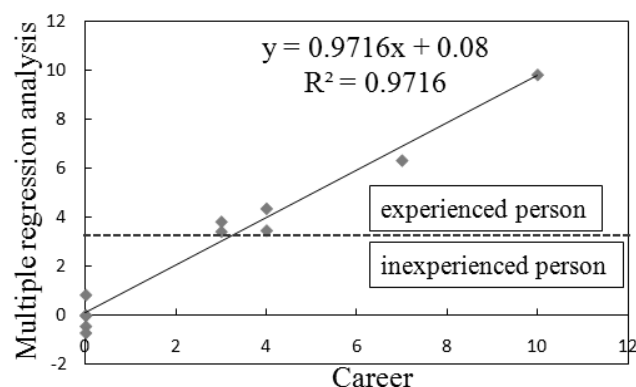


Figure 6. The result of the multiple regression analysis using the degree of similarity E' and the A (Power), B (Timing), C (Sharp).

3.2 The result of Leave-one-out cross validation method

From many analysis results, we selected the three following elements using t value and P value.

- The timing B of elbow (standard deviation)
- The degree of similarity of wrist / elbow (average)
- The degree of similarity of wrist / shoulder (standard deviation)

We show the result of the multiple regression analysis how we used three elements mentioned above in Figure 7. From Figure 7, value of R^2 got results more than 0.8.

The result of the Leave-one-out cross validation method using three elements are shown in Figure 8. When a predicted value by the multiple regression analysis assumes the smallest person boundary value among a person who experienced tennis, we can pull the boundary line of an experienced person and the inexperienced person. As a result, only one person did wrong identification among inexperienced people.

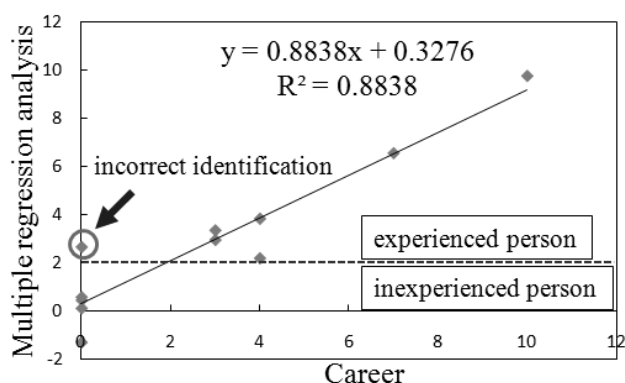


Figure 7. The result of multiple regression analysis.

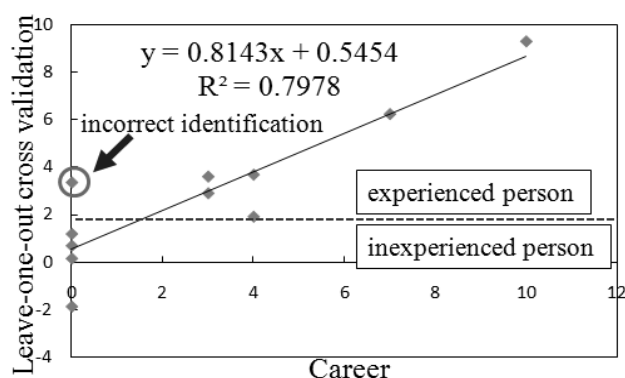


Figure 8. The result of Leave-one-out cross validation method.

4. Conclusion and Future Work

We aimed for examining the point of difference of experienced person and inexperienced person for the form of tennis swing. In this paper, we built the motion capture system which used an acceleration sensor. We acquire the database of experienced persons and inexperienced persons form of tennis swing using the proposal system. And we analyzed these data and performed the experiment that estimated of the tennis career. For sports, we were able to extract power and timing and sharpness and the interlocking movement characteristics of the joint from acceleration information. As a result, we could discriminate the inexperienced person from an experienced person from tennis swing with an acceleration sensor and was able to find out a thing such as a common knack from an experienced person. It is thought that three points of the following are common to an experienced person in conclusion.

- 1) The movement of the shoulder and the elbow is stable.
- 2) The interlocking movement characteristic of the elbow and the wrist is strong.
- 3) The interlocking movement characteristic of the wrist and the shoulder is stable.

In future work, we must increase the number of subjects. We think that it raises the reliability of this study.

References

- [1] Hiroki Tamura, Daisuke Sasajima, Koichi Tanno, Takako Toyama (2008), "Human Motion Recognition System using Nintendo wii Remote Controller", in Japanese, Memoirs of the Faculty of Engineering, Miyazaki University, 37:PP141-146
- [2] Hidenori Maruta, Masahiro Ishii (2007), "Feature extraction from Biological motion of human gait patterns for emotion discrimination", IAPR Conference on Machine Vision Application, 13-15, pp492-495
- [3] Kenichirou Fuji, Takaya Maeda, Hiroki Tamura, Takako Toyama, Kouichi Tanno (2010), "Development of Motion Analysis System using Acceleration Sensors for Outdoor Sports and its Applications (in Japanese)", HINOKUNI information symposium
- [4] Takaya Maeda, Hiroki Tamura, Takako Toyama, Kouichi Tanno, Masahiro Ishii (2009), "A study about the feelings estimate from ambulation movement (in Japanese)", Student Activity Committee, Kyusyu Section IEICE

Discriminate approach for data selection in data envelopment analysis

Akio Naito and Shingo Aoki

*Osaka Prefecture University, 1-1 Gakuencho Naka-ku Sakai Osaka
(Tel : 81-72-254-9353; Fax : 81-72-254-9915)
(naitou@mis., aoki@cs.osakafu-u.ac.jp)*

Abstract: DEA (Data Envelopment Analysis) is a well-known method for evaluating management efficiency of DMUs (Decision Making Units). To calculate efficiency of DMUs, analytical data are necessary. However, there are not clear criteria for data selection so that analysts have to choose the data on their own. Therefore, it is important to support data selection by reasonable ways to let analysis be informative and beneficial. In order to deal with this matter, new methods are proposed based on traditional ones. Support for data selection is realized by considering analyst's intention. Analytical data for making some specific DMUs efficient are obtained by reflecting knowledge or experience analysts have. TDS-DEA (Tight Data Selection based DEA) reflects the analyst's intention strongly and tries to make only intended DMUs efficient. On the other hand, LDS-DEA (Loose Data Selection based DEA) reflects it loosely and at least intended DMUs can be efficient. Then both methods should be examined more detail and how data selection is carried out effectively. On this point, this study prepares the experimental data to clarify the effectiveness and drawback of the methods. According to the experimental result, additional ideas such as discriminate approach or assurance region method are considered to improve the quality of data selection.

Keywords: Data Envelopment Analysis, Linear Programming, Decision Making Support, Data Selection

I. INTRODUCTION

DEA (Data Envelopment Analysis) is a method for measuring efficiency of DMUs (Decision Making Units) like company, hospital, municipal government or so. DMUs are evaluated by index called "efficiency score". Each DMU is classified as the state of efficient or that of inefficient based on the score [1]. DEA calculates efficiency score of each DMU based on Pareto optimal line which is called efficiency frontier consists of efficient DMUs. Then DEA shows a plan for improvement to inefficient DMUs.

DEA assumes activity of DMUs that produce output from input. This mechanism is interpreted as production function. DEA is a data-oriented method so that efficiency score depends on analytical data. Then all data related to DMUs can be possible to be selected for analysis. Therefore, data selection is really important. It is not easy to prove whether selected data correspond to purpose of analysis or not. Criteria of data selection are unclear practically. Hence, some methods were proposed to support data selection. The basic idea of the traditional methods is to utilize analyst's intention such as experience or knowledge regarding evaluated DMUs.

Though numerical experiment is carried out, but still need more trial to clarify the power and effectiveness.

Therefore, the purpose of this study is to examine the traditional method in detail and find benefit and drawback to improve the approach.

II. DATA ENVELOPMENT ANALYSIS

1. Outline

DEA was proposed by A. Charnes et al. in 1978 as a method for management analysis [2]. DEA has room to treat a lot of data related to DMUs. Then necessary elements (capital, employee, etc) for operation are generally recognized as input and yielded elements (sales, profit rate, etc) are recognized as output. DEA calculates efficiency by input and output so that less input and larger output is more preferable. And the efficiency of each DMU is evaluated relatively among analyzed DMUs.

Efficient DMUs are regarded as best practice among DMUs and they get efficiency score as "one". Inefficient DMUs have that score less than one. Efficiency score is denoted as θ and calculated by dividing virtual output by virtual input. Virtual input and output are the useful for dealing with multi elements. DEA puts weight to each element and it is not fixed but variable. Therefore, it is possible to evaluate advantages of DMUs as much as possible [1].

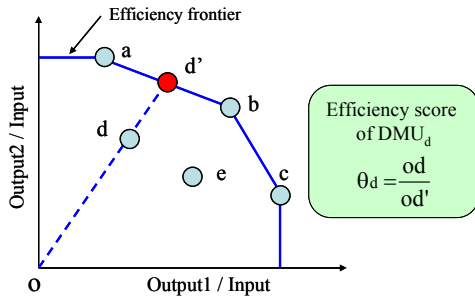


Fig.1. Efficiency frontier and efficiency score

Fig. 1 demonstrates efficiency frontier and efficiency score. There are five DMUs (a~e) with one input and two outputs. Each DMU is dotted based on score that output is divided by input. Hence, DMU located far from origin is more efficient. Here three DMUs are the state of efficient and they form efficiency frontier. DMU_c has largest output1 and DMU_a has largest output2. In addition, DMU_b has larger output1 and output2 with well-balanced. Characteristics of these three DMUs are evaluated well respectively. Thus DEA is able to reflect strength of DMUs for evaluation. Therefore, analytic data play an important role to extract characteristic of each DMU.

Efficiency score of inefficient DMU is calculated by distance to efficiency frontier that expresses ideal state. In case of DMU_d, ideal state of management is d'. Then efficiency score θ_d is calculated by the ratio of distance from origin to d and d'. In other words, efficiency score is calculated based on efficient DMUs among analytical objects.

2. Formulation

When analysis is carried out, linear programming is utilized. Here formulation of CCR model is shown. Assuming that there are n DMUs (DMU₁, DMU₂, ..., DMU_n) with m inputs and s outputs. DMU_k is characterized by inputs ($x_{1k}, x_{2k}, \dots, x_{mk}$) and outputs ($y_{1k}, y_{2k}, \dots, y_{sk}$). Then efficiency score of DMU_k is calculated by following formula.

$$\begin{aligned} & \text{Max } \sum_{r=1}^s u_r y_{rk} \\ & \text{s.t. } -\sum_{i=1}^m v_i x_{ij} + \sum_{r=1}^s u_r y_{rj} \leq 0 \quad (j=1,2,\dots,n) \\ & \quad \sum_{i=1}^m v_i x_{ik} = 1 \\ & \quad v_i \geq 0 \quad (i=1,2,\dots,m), \quad u_r \geq 0 \quad (r=1,2,\dots,s) \end{aligned} \quad (1)$$

Inputs and outputs are denoted as x_{ij}, y_{rk} while v_i, u_r are weights for input and output elements.

Hence, $v_i x_{ij}$ and $u_r y_{rj}$ represent virtual input and output. One of the constraints works for virtual input of DMU_k to be "one". Then virtual output is maximized on condition that virtual input exceeds that of output for each DMUs. If virtual output is equal to one, DMU_k is the state of efficient. On the other hand, DMU_k is the state of inefficient if virtual output is less than one. Thus objective function, namely, virtual output signifies efficiency score directly.

As a result, efficiency score and weight value are shown by solving linear programming. Then weight that has value means corresponding input and output elements are employed in analysis. That is why DEA enables analyst to know strength of each DMU.

III. TRADITIONAL METHOD

1. Outline

The previous study focused on data selection for making intended DMUs efficient [3]. That is because some of the analysts are quite familiar with analyzed DMUs and they can predict result roughly. For beginners, deciding efficient DMUs they want is helpful to have reasonability of analytic data elements. Of course, it is possible to incorporate external information to the data selection.

Traditional methods need to take inverse procedure compared with fundamental DEA. It means result that some DMUs are efficient is assumed first and then used data are calculated based on the assumption. Fig. 2 shows stream of traditional method. Dotted line is route concerning fundamental DEA and procedure consists of data collection, analysis and result. However, traditional method assumes the result in advance and then data elements are calculated in order to guarantee assumed result (analyst's intention).

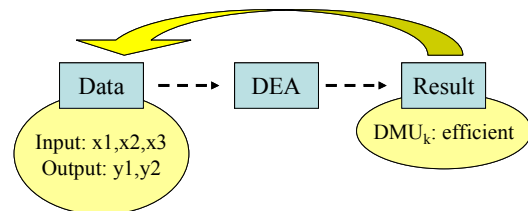


Fig.2. Procedure of the method

While idea of traditional method is formed, we consider possible users, namely, analysts who utilize the methods. There are mainly three types of users. Expert who has knowledge to DMUs, decision maker who

belongs to analyzed DMU, and beginners. The merits of the methods are mentioned for every type of user.

For experts, they have forecast for result based on their deep knowledge. That is why they can know effective data elements to realize their intentional analysis thanks to traditional methods. So it is effective for analyzing DMUs. For decision makers, they can find strengths of their company and competitive one by assuming those two DMUs as efficient. That is to say, management strategy can be planned by DEA since they know characteristic in detail for themselves and rival. For beginners, they are often confused when they decide data. Then traditional methods can show necessary data elements for them and support smooth analysis. Thus various analysts are able to get benefit by utilizing the method.

2. TDS-DEA

TDS-DEA (Tight Data Selection based on DEA) calculates data elements that make only intended DMUs efficient. Hence, it is possible to decrease the number of elements in analysis. TDS-DEA introduces condition for slack variable that treat surplus of input and lack of output. If slack variable has value, the DMU is the state of inefficient. On the other hand, the DMU is the ideal state if slack variable is zero. Thus only specific DMUs can be efficient and others can be inefficient. Here analyst would like to make DMU_k efficient. Then slack variable should be satisfied with following conditions;

$$\begin{aligned} s_j &= 0 \quad (j=k) \\ s_j &> 0 \quad (j=1,2,\dots,n:j \neq k) \end{aligned} \quad (2)$$

Only slack variable of DMU_k is zero and others have value. Traditional method enables analyst's intention to be reflected strongly with these conditions. And the used elements are found by the weights v_i, u_r . If weight has value, corresponding element is used for analysis. Therefore, weight is a key to know which elements should be selected. Formula (3) is a linear programming regarding TDS-DEA. Assume that there are n DMUs with m inputs and s outputs. $\{J-k\}$ signifies set including DMUs except for DMU_k . In order to realize concept of TDS-DEA, objective function are maximized. It means TDS-DEA tries to decrease efficiency of DMUs except for intended one as much as possible with keeping intended DMU efficient. When multi DMUs are assumed as efficient, elements are calculated by repeating analysis for each DMU.

$$\begin{aligned} \text{Max} \quad & \sum_{j \in \{J-k\}} s_j \\ \text{s.t.} \quad & -\sum_{i=1}^m v_i x_{ik} + \sum_{r=1}^s u_r y_{rk} = 0 \\ & -\sum_{i=1}^m v_i x_{ij} + \sum_{r=1}^s u_r y_{rj} + s_j = 0 \quad (j=1,2,\dots,n:j \neq k) \\ & \sum_{i=1}^m v_i x_{ik} = 1 \\ & v_i \geq 0 \quad (i=1,2,\dots,m), \quad u_r \geq 0 \quad (r=1,2,\dots,s) \end{aligned} \quad (3)$$

3. LDS-DEA

As long as data selection relies on TDS-DEA, we need to care the accuracy of analyst's intention. That is because intended DMU surely get the state of efficient after calculation. At the same time extension of the method was necessary. It is to analyze DMUs by employing common elements for intended DMUs.

- The number of DMUs : n
- The number of intended DMUs : α
- Combination for choosing two DMUs from intended DMUs : $h(1, 2, \dots, \alpha C_2)$
- DMU No. of t -th DMU among intended ones : q_t ($t=1,2,\dots,\alpha$)

$$\begin{aligned} \text{Min} \quad & \sum_{h=1}^{\alpha C_2} \left\{ \sum_{i=1}^m (d_{ih}^{x+} + d_{ih}^{x-}) + \sum_{r=1}^s (d_{rh}^{y+} + d_{rh}^{y-}) \right\} \\ \text{s.t.} \quad & -\sum_{i=1}^m v_i^t x_{iq_t} + \sum_{r=1}^s u_r^t y_{rq_t} = 0 \quad (t=1,2,\dots,\alpha) \\ & -\sum_{i=1}^m v_i^t x_{ij} + \sum_{r=1}^s u_r^t y_{rj} + s_j^t = 0 \quad (j=1,2,\dots,n:j \neq q_t) \quad (t=1,2,\dots,\alpha) \\ & \sum_{i=1}^m v_i^t x_{iq_t} = 1 \quad (t=1,2,\dots,\alpha) \\ & v_i^k x_{ik} - v_i^l x_{il} + d_{ih}^{x+} - d_{ih}^{x-} = 0 \\ & u_r^k y_{rk} - u_r^l y_{rl} + d_{rh}^{y+} - d_{rh}^{y-} = 0 \\ & (i=1,2,\dots,m), (r=1,2,\dots,s), (k,l \in t: k < l), (h=1,2,\dots,\alpha C_2) \\ & v_i^t \geq 0, \quad v_i^l \geq 0 \quad (i=1,2,\dots,m) \\ & u_r^t \geq 0, \quad u_r^l \geq 0 \quad (r=1,2,\dots,s) \end{aligned} \quad (4)$$

IV. NUMERICAL EXPERIMENT

To confirm the effectiveness, experimental data that has some features is prepared. There are twenty DMUs with six inputs and six outputs. The feature is that DMU_1 to DMU_6 have strong points in input1, input2, output1, and output2. DMU_7 to DMU_{12} have strength in input5, input6, output5, and output6. DMU_{15} to DMU_{20} has strength in input3, input4, output3, and output4. Then TDS-DEA is applied and calculates the data element to realize analyst's intention. Table. 1 shows the experimental data in this study.

Table 1. Experimental data

Element		DMU									
		DMU ₁	DMU ₂	DMU ₃	...	DMU ₁₀	DMU ₁₁	...	DMU ₁₈	DMU ₁₉	DMU ₂₀
Input	x1	0.111	0.222	0.444	...	0.444	0.556	...	0.556	0.667	0.444
	x2	0.778	0.667	0.444	...	0.778	0.333	...	0.778	0.556	1
	x3	0.897	0.691	0.918	...	0.804	0.763	...	0.433	1	0.351
	x4	0.545	0.364	0.852	...	0.523	0.511	...	1	0.477	0.273
	x5	0.311	0.378	0.333	...	0.200	0.244	...	0.622	0.711	0.422
	x6	0.317	0.293	0.610	...	0.244	0.512	...	0.976	0.512	0.659
Output	y1	0.778	1	0.889	...	0.556	0.222	...	0.243	0.220	0.060
	y2	0.625	0.500	0.875	...	0.500	0.375	...	0.875	0.500	0.250
	y3	1	0.188	0.800	...	0.350	0.800	...	0.753	0.753	0.494
	y4	0.351	0.485	0.897	...	0.472	0.485	...	1	0.763	0.371
	y5	0.899	0.528	0.876	...	0.270	0.506	...	0.461	0.360	0.247
	y6	0.214	0.827	0.459	...	0.663	0.867	...	0.337	0.306	0.112

Table 2. Result

Weight	DMU											
	DMU ₁	DMU ₂	DMU ₃	DMU ₄	DMU ₉	DMU ₁₀	DMU ₁₁	DMU ₁₂	DMU ₁₅	DMU ₁₆	DMU ₁₇	DMU ₁₈
v1	9.000	4.500	0	1.446	0	0	0	0	0	0	0	0
v2	0	0	0	0.804	0	0	0	0	0	3.000	0	0
v3	0	0	0	0	2.243	0	0	0	4.042	0	0	2.310
v4	0	0	0	0	0	0	0	0	0	0	6.286	0
v5	0	0	3.000	0	0	5.000	4.091	0.285	0	0	0	0
v6	0	0	0	0	0.626	0	0	2.854	0	0	0	0
u1	0	0.464	0	0	0	1.800	0	0	0	0	0	0
u2	0	0	0	1.143	0	0	0	0	0	0	0.766	0
u3	1.000	0	0	0	0	0	1.250	0	0	1.149	1.542	0
u4	0	0	1.115	0	0	0	0	0	1.738	0	0	1.000
u5	0	0	0	0	1.000	0	0	0	0.027	0	0	0
u6	0	0.648	0	0	0	0	0	1.000	0	0	0	0

Table. 2 shows the result for the input and output should be chosen. Shaded area is that each DMU's strong elements. According to the result, we find some knowledge through experimentation.

Let us focus on DMU₁ to DMU₄. They originally have strong input1, input2 and then TDS-DEA actually calculates those elements. The method signifies input5 is strong for DMU₃. That is because DMU₃ has larger input compared with other DMUs and choosing input5 is inevitable for individual efficiency. However, data selection for output is not enough since obtained result does not reflect the actual strength DMUs have. This is the drawback of the traditional method. That is to say, it is possible to get necessary data roughly but sometimes it is not reliable and accuracy. In this point, introducing assurance region method is helpful to improve the method. Also discriminate approach will have influence to data selection better.

The traditional method calculates some unsuitable element for other DMUs though they get desirable result. Analyst is able to set the analytical data based on certain reasonability and confidence thanks to the method. And it is beneficial for not only analysts who are expert but also analysts who don't have enough

knowledge regarding evaluated DMUs. if analyst have problem for data selection, they just utilize the method and get the direction for their analytical procedure.

V. CONCLUSION

This paper examines the power of traditional method for data selection. The result shows how the method calculates necessary data. However, it is important to improve quality of the approach since some of the data are not calculated well based on analyst's intention. Then we consider introducing assurance region method or discriminate way in order to complement current method.

REFERENCES

- [1] W. W. Cooper, L. M. Seiford and K. Tone (2007), Data Envelopment Analysis A comprehensive Text with Models, Applications, References and DEA-Solver Software Second Edition. Springer
- [2] A. Charnes, W. W. Cooper and E. L. Rhodes (1978), Measuring the Efficiency of Decision Making Units. European Journal of Operational Research, vol. 2, pp. 429-444
- [3] A. Naito and S. Aoki (2010), Support for Awareness of Data Selection in Data Envelopment Analysis. The 2nd International Symposium on Aware Computing (ISAC 2010)

Proposal of recommender system simulator based on small-world model

Ryosuke Saga*, Kouki Okamoto*, Hiroshi Tsuji**, and Kazunori Matsumoto*

**Kanagawa Institute of Technology, 1030 Shimo-ogino, Atsugi, Kanagawa, Japan*

***Osaka Prefecture University, 1-1 Gakuen-cho, Nakaku, Sakai, Osaka, Japan*

(Tel : +81-46-291-3235; Fax : + 81-46-242-8490)

(saga@ic.kanagawa-it.ac.jp)

Abstract: This paper proposes the development of a software simulator that allows a simulator's users to evaluate algorithms for recommender systems. This simulator consists of agents, items, Recommender, Controller, and Recorder, and it locates the agents and allocates the items based on a small-world network. The agent plays a role in a user in the recommender system and the recommender plays a role in the recommender system. Controller handles the simulation flow that (1) Recommender recommends items to agents based on the recommendation algorithm, (2) each agent evaluates the items based on agents' rating algorithm using each item's and agent's attribute, and (3) Recorder obtains the results of the rating and the evaluation measurement for the recommendation pertaining to such information as precision and recall. This paper discusses the background of proposal and the architecture of this simulator.

Keywords: Recommender System, Multi-agent simulation, evaluation, small-world model.

I. INTRODUCTION

Recommender systems have been used for several applications and systems such as news sites, information sharing system, e-commerce and so on [1][2][3]. The systems offer benefits to consumer and item providers. These recommender systems help consumers in particular acquire new as well as preferable items and users can expect effective acquisition of the information. Therefore, an appropriate algorithm is needed for the recommender system.

Several researchers have proposed and developed many algorithms since collaborative filtering, one of the most successful technologies for recommender systems, was introduced and attracted many attentions [4][5][6][7]. However, developing and applying the algorithm of collaborative filtering are difficult. One reason is based on the difficulty of evaluating these algorithms. For example, the algorithms were developed for any purposes and have validated specified and limited datasets in many cases. Therefore, the generality of the algorithms is not clear. Another reason for the difficulty is that the validation of the algorithm needs massive dataset.

Therefore, we developed a multi-agent-like simulator for evaluating the collaborative filtering and it is described in this paper.

II. Motivation

Recommender systems aim to recommend preferable items to users from user profile [1][2][3]. The profile is constructed by analyzing the content, user's

voting and rating, and access logs, etc. Two types of filtering algorithms are used for dynamic recommendation: content-based filtering and collaborative filtering [6]. Especially, collaborative filtering is the most successful algorithms, and its profile is based on relationships among users or items [7]. It has an advantage wherein collaborative filtering is applicable for any items because the algorithm does not need to analyze the content itself. Also, the hybrid algorithm combining collaborative filtering and content-based filtering [8] has also been developed.

Generally, the recommender system algorithms work better as the dataset that includes the user's rating and item information becomes more massive. However, the algorithms do not work for a small dataset because the dataset is insufficient for calculating similarity and predicting items (called cold-start problems).

Therefore, developing the algorithms has various problems associated with it. The first problem is a limited dataset. To evaluate the algorithms, we need to use various environments by collecting various datasets. However, collecting the various datasets is difficult because we generally do not make use of recommender systems and do not have the data source. Therefore, many researchers have utilized limited dataset such as MovieLens Dataset and EachMovie Dataset. the evaluation measurement may change according to the goals of the algorithm. The algorithm is developed for specified goals, and in order to evaluate the algorithm, the proper evaluation measurements and data set are needed [3]. Also, each method has strong/weak points,

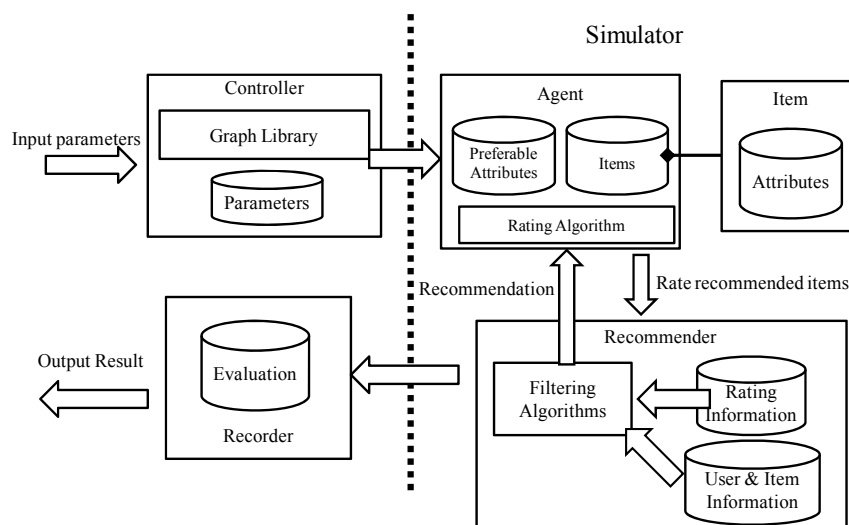


Fig.1. Simulator architecture

and if we apply the algorithms for other goal, we cannot easily judge whether any of the algorithms are suitable. In order to identify the suitable algorithm, to compare the algorithms is useful; however, an experiment with a limited dataset and with different goals is difficult.

Therefore, we build the simulator to enable the comparison of the algorithms. The requirements/goals of simulator are defined as the followings.

1. The simulator can build the evaluation environment for the recommender system.
2. The simulator can compare the filtering algorithms of collaborative filtering and content-based filtering.
3. The simulator can output the results of evaluations to compare the filtering algorithms.

III. OVERVIEW OF RECOMMENDER SYSTEM SIMULATOR

This simulator consists of agents, items, Recommender, Controller, and Recorder as shown in Fig. 1. In this simulator, a simulator user gives the number of agents, items, thresholds, and algorithms as parameters. Agent acts as the user of recommender systems, and the algorithm of collaborative filtering is modeled into Recommender. Recommender has information on agents and items' ratings for each user. Controller receives parameters from the simulator user and handles the simulator such as initialization, progression, and suspension. Controller accepts not only the number of agents and items, but also thresholds for the simulator environment, preference, and agent status.

The simulation steps are as follows:

1. The simulator user inputs parameters.

2. Controller initializes the status of the agents and items and configures the simulator based on the parameters.
3. Recommender calculates the user similarity and recommends items to agents.
4. The agents vote on the rating of recommended items and update the status.
5. Recorder compiles the result of recommendation and evaluates the recommendation using several measurements such as MAE, recall, precision, novelty, diversity, and discovery [9][10].
6. Controller updates agent status and preference.

The simulator regards step 3 to step 6 as one turn, and it goes through the steps and iterates the turns.

IV. ARCHITECTURE OF SIMULATOR

1. Agents, Items, and Ratings

A. Definition of attributes

The key point of modeling recommender systems is the preferences of agents for items. This paper assumes that the agents and items have many attributes. Here, we assume that the agents have specified preferable genres and domain, and in order to express the assumption, the simulator lets agents have a positive real number for all attributes for their degree of preference. The simulator also defines the attributes whose degree of preference is over the *preference threshold* as preferable attributes. In contrast, an item has the 0/1 flags for each attribute.

B. Rating items

In this simulator, the agents and Recommender evaluate each item. For the agents, the rating r_{ij} of an

item j for an agent i is generally evaluated by the formulation,

$$r_{ij} = A(U_i, I_j, u_i)$$

Here U_i is the preferable attribute set of agent i . Also, I_j is the attribute set of Item j whose value is 1. u_i is the information about agent. Also, we call the function an rating algorithm. For an example of rating algorithm, we can configure it as follows

$$r_{ij} = \frac{\sum_u \frac{u}{\max(U_i)}}{|U_i \cap I_j|}$$

where $|E|$ indicates the number of the elements of set E , u is the elements of attributes of U_i corresponding to the index of $U_i \cap I$ and $\max(U_i)$ indicates the maximum of U_i , which is given by users as one of parameters.

On the other hand, Recommender, which is the implementation of the filtering algorithm, predicts the ratings of the items and recommends high-rated items to the agents. For example, the predicted rating of an item for the agent is generally shown in the following formulation on collaborative filtering:

$$r_{ij} = R(\text{sim}(i, u), R)$$

,where r_{ij} is the rating of item j for user i , $\text{sim}(u, v)$ indicates the similarity between user/item u and user/item v among a set of user U who evaluate the item j , and R shows the rating information. For example, GroupLens[4], which is a representative system using collaborative filtering, has the following formula.

$$r_{ij} = \bar{r}_i + \frac{\sum_{u \in U} (\text{sim}(u, i)(r_{uj} - \bar{r}_u))}{\sum_{u \in U} |\text{sim}(u, i)|}$$

In this formula, \bar{r}_i is the average rating when a user i has already voted.

C. Status of Agents

One of the problems that requires attention is the *tiresome status*. This simulator allows agents to change the status in order to express the degree to which an agent is tiresome. In this simulator, agents have two statuses, *normal* and *tiresome*, and the trigger of changing status occurs in recommendation. The measurement for tiresome is calculated concretely by the evaluation formula, and when the measurement is less than the *tiresome threshold*, the agent changes the status to *tiresome*, otherwise it remains *normal*. The simulator implements the following formula, which is an example of the evaluation formula;

$$t = \sum_{i \in I} \frac{n_i r_{aj}}{\text{rank}_i}$$

Here, I is the set of recommended items from Recommender, r_{ij} is the rating of item j by agent i which is used for rating algorithm, rank_i is the rank of the item i , and n_i is 0 if i has already been recommended; otherwise it is 1.

2. Building Simulator environment

The configuration of the simulator environment is one of the most important steps in the simulation process because an inappropriate environment leads to inappropriate and wasteful result.

The simulator environment is built during initialization and is updated after the recommendation is done. In order to configure the proper simulator environment, we utilize the structural (topological) features of the recommender system.

A. Initialize simulator environment from small world network.

Generally, communities tend to follow complex networks and, according to several references, they find that the networks tend to be small-world networks. Here, a small world is a phenomenon in a real world network, and the model has several features such as stability and compression of network. The structure was first formulated by Watts and Strogatz [10]. The structure appears in several networks, and the trend also appears in recommender system. Therefore, we create the environment based on the small-world network.

If we restrict the community to the recommender system, the network of the recommender system is scale-free network like it is in References [11][12][13]. Therefore, we regard an agent as a node and initialize agents and items according to generating a scale-free network. The algorithm in detail is as follows, given n agents and m items as simulation parameters from the user,

1. Create the k -core clique in order to generate the scale-free network, and allocate the C_0 common items among k nodes.
2. Add an agent (a_i ($i=1, 2, \dots, n$)) to the network according to the algorithm of BA(Barabasi-Albert) model which is a scale-free network, and allocate the C_j common items to the clique including a_i . Note that $\sum C_j = m$.
3. Iterate step 2 by allocating a_n .
4. Allocate the attributes of items to agents who have items in common.
5. Let Recommender calculate the similarity between the agents for recommendation.

B. Update simulator environment

The simulator needs to be update because the agents may have new interests and because Recommender identifies the new relationships between agents because of the rating of recommended items by agents. In this simulator, the agent's preferences are updated by a simple approach. When an agent regards an item as the preferable items, then we can assume naturally that the impression for the item is good. Therefore, when r_{ij} , which is the rating of item j by agent i , is over the *preferable item threshold*, then agent regards the item as the preferable item and the simulator adds a constant value to the attribute of agents that corresponds to those of the item.

On the other hand, Recommender has trouble indentifying new relationships between agents because the cost of calculation of similarity is normally very high. In order to constrict the complexity of calculating similarity, SketchSort, which is software for all pairs similarity search, is useful [14]. The basic idea of SketchSort is to combine Locality Sensitive Hashing (LSH) and Multiple Sorting Method (MSM). SketchSort takes as an input data points and outputs approximate neighbor pairs within a distance. SketchSort is so quick that the cost of calculating the similarity can be lower. Here, In order to uses the SketchSort, the rating data of agent is recorded by the matrix where the row indicates items and column indicates the agents. However, most agents have not evaluated many items yet so that the simulator cannot build the matrix. Therefore, using default voting [15] and filling the ratings of items which a agent has not evaluated yet, we build the matrix and utilize SketchSort for similarity calculation.

V. CONCLUSION

This paper has proposed a simulator to allow a user to evaluate the algorithms for recommender systems. In order to evaluate the algorithms, the simulator builds an environment of a virtual recommender system based on a complex network model from parameters; Recommender makes recommendations to agents, and the simulator evaluates and outputs the results though Recorder. In future work, we will validate the simulator by gaining a resurgence of the phenomenon of collaborative filtering, and we will test the usability.

REFERENCES

[1] Resnick, P. and Varian, H.R., (1997). Recommender systems. *Commun. ACM*, 40(3), 56-58.

[2] Adomavicius, G. and Tuzhilin, A., (2005). Toward the Next Generation of Recommender Systems: A Survey of the State-of-the-Art and Possible Extensions. *IEEE Transactions on Knowledge and Data Engineering*, 17(6), 734-749.

[3] Saga. R., Tsuji, H. and Onoda, J., 2005. Agent System for Notifying Hotel Room Reservation Alternatives, *Proc. of 11th International Conference on Human Computer Interaction (HCII2005)*, Vol. 5, pp. 1-10, July 2005

[4] Resnick, P. et al., (1994). GroupLens: an open architecture for collaborative filtering of netnews. In *Proceedings of the 1994 ACM conference on Computer supported cooperative work*. Chapel Hill, North Carolina, United States: ACM, pp. 175-186.

[5] Sarwar, B. et al., (2001). Item-based Collaborative Filtering Recommendation Algorithms. *Proc. 10th International Conference on the World Wide Web*, 285-295.

[6] Pazzani, M. (1999). A Framework for Collaborative, Content-Based and Demographic Filtering. *Artificial Intelligence Review*. 13(5-6) 393-408.

[7] Linden, G., Smith, B. and York, J., (2003). Amazon.com recommendations: item-to-item collaborative filtering. *Internet Computing, IEEE*, 7(1), 76-80.

[8] Claypool, M., Gokhale, A., and Miranda, T. (1999). Combining content-based and collaborative filters in an online newspaper. In *Proceedings of the SIGIR-99 workshop on recommender systems: algorithms and evaluation*.

[9] Herlocker, J.L. et al., (2004). Evaluating collaborative filtering recommender systems. *ACM TRANSACTIONS ON INFORMATION SYSTEMS*, 22(1), 5--53.

[10] Watts, D.J. and Strogatz, S.H. (1998). Collective dynamics of 'small-world' networks. *Nature* 393 (6684): 409-410.

[11] Albert, R. and Barabasi, A., (2002). Statistical mechanics of complex networks. *Reviews of Modern Physics*, 74, 47-97.

[12] Martin-Buldú, J., Cano, P., Koppenberger, M., Almendral, J., Boccaletti, S. (2007). The complex network of musical tastes. *New Journal of Physics*. 9,

[13] Cano, P., Celma, O., Koppenberger, M., Martin-Buldú, J. (2006). The Topology of music recommendation networks. *Chaos An Interdisciplinary Journal of Nonlinear Science*. 16,

[14] Tabei, Y., Uno, T., Sugiyama, M., and Tsuda, K., (2010). Single versus Multiple Sorting in All Pairs Similarity Search, *The 2nd Asian Conference on Machine Learning (ACML)*

[15] Breese, J. S., Heckerman, D., and Kadie, C., (1998). Empirical analysis of predictive algorithms for collaborative filtering. In *Proceedings of the fourteenth conference on uncertainty in artificial intelligence*, Madison, Wisconsin.

Construction and analysis of purchase factor model by using creativity method

Kodai Kitami, Ryosuke Saga, Kazunori Matsumoto

*Kanagawa Institute of Technology, 1030 Shimoogino, Atsugi, Kanagawa, Japan
(Tel : +81-46-291-3235 ; Fax : +81-46-242-8490)
(saga@ic.kanagawa-it.ac.jp)*

Abstract: This paper describes a purchase factor analysis for best-selling software games. Japanese game industry has grown remarkably since 1983. Developers have to produce best sellers in order to get a profit. However, the concrete factors for a best-selling game have not yet been qualified. Structural equation modeling (SEM) seems to have the beneficial effect on causality analysis. However, the SEM results may lack the reliability because the model is constructed based on the analyzers' subjective assumptions. We need to construct a factor model for solving this problem by extracting the purchase factor from diverse viewpoints. Consequently, we use the KJ method, which is one of the creativity methods, to do just that. There are four steps in the process for analyzing the factor model from the results of KJ method: (1) extract the factors from the KJ method results, (2) refine the model by integrating conceptualistic meanings, (3) assign the collected data to the model, and (4) construct and analyze the model by indentifying the variables. From the result of our analysis of the model, we could qualify the factors of best-selling games by using an objective purchase factor model that was mainly constructed of the "Contents", "Advertisement", and "Brand".

Keywords: creativity method, KJ method, Structural Equation Modeling, marketing, purchase factor analysis.

I. INTRODUCTION

The Japanese game industry has grown remarkably since 1983 beginning with the "Family Computer" product released by Nintendo Co. The size of the market in 2007 was twice as large as that in 1987, and now software games play a central role in the industry^[1]. However, the running costs of the developers have become compressed, and there is more absorbability between the makers as a result of the ever-increasing appreciation for the development of new and better software games. Therefore, the developers are forced to produce best sellers in order to make a profit. However, the concrete factors surrounding the development of a best seller and the latent factors have yet to be qualified. There are many analysis methods for estimating the consumers' purchase factor, such as Factor Analysis^[2-3], Regression^[4], and Baysian Modeling^[5]. In particular, Structural Equation Modeling (SEM)^[6] has a more beneficial effect on a causality analysis because this method can express the complex causal relationship between the observational and latent factors.

We have analyzed the factors by using SEM in order to qualify the factors surrounding best-selling software games. As a result of our analysis, we found that a model constructed by Kitami^[7] proved that the consumers' purchasing factor was affected by the basic

information about the games and the consumers' expectation. However, this result may not be able to extract substantial paths or latent factors, and thus, the reliability and relevance of this model may be insufficient. The reason for this is derived from the subjective assumptions of the analyzers.

To solve this problem, we propose a process for constructing a SEM model from the results when using the creativity method and that analyzes the consumers' purchasing factor. In this paper, we use a bottom-up type KJ method. We outline the investigative items and apply them to a factor model composed of the factors when using the KJ method.

The rest of this paper is presented as follows. We describe the problem with the approach when using SEM in Chapter 2. Chapter 3 explains the process of constructing a model from the KJ method. Chapter 4 explains a model constructed according to the process and the result of our analysis. The results are the considered and discussed in Chapter 5. Finally, Chapter 6 concludes with a summary of the key points.

II. PROBLEM WITH SEM AND SOLUTION

1. Structural Equation Modeling

SEM is an analysis method that quantitatively evaluates the causality relationship between the more

remarkable variables in statistic data and causality information, and has been used in causality analysis since the 1950's in many domains, such as economics and social science [8]. SEM can visualize and quantify the complex causality relationships between variables. The formula for SEM is as follows.

$$x_i = \sum_{x_k \in pa_i} a_{ik} x_k + u_i, \quad i = 1, \dots, n \quad (1)$$

x_i is a set of variables are considered direct factors. pa_i corresponds to the variables that have coefficients that are not 0 on the right side. Also, u_i shows the error that is not expressed. SEM presents the strength of the correlation and the covariance as the path coefficient. Also, if the path coefficient between variables is large, we assume the relationship between the variables is strong.

2. Problem of approach by SEM

SEM has some advantages as stated above, and is an effective method in causality analysis. However SEM has the following problems.

- (1) Experience needed: The analyzer in a targeted analysis when using SEM needs a lot of prior knowledge, because the construction of the model is only exploratory if the analyzer lacks sufficient knowledge, which may lead to bad results and contradictions.
- (2) The construction of model is subjective: Even though the analyzer has sufficient knowledge about the target of analysis, there is the possibility that the objectivity of model is lacking.
- (3) The accuracy is more weighted than the explanatory power when constructing the model: As previously noted, the accuracy is exploratory when the analysis model is not clarified. Therefore, there is a possibility that the model which has low explanatory power is constructed because the analyzer too achieves the accuracy.

In order to solve these problems, we need to construct a SEM model that is objective and has a broad range of explanatory power. Therefore, we constructed a purchase factor model and clarified the factors for a best

seller by using the KJ method, which is one of the creativity methods.

3. Suggestion of model construction by using creativity method

The creativity method is a systematic method that thinks out and arranges many ideas in order to creatively solve a technical problem. In this paper, we systematized the consumers' opinions by using the KJ method. The KJ method is a method used for information integration and can effectively organize innovative ideas by arranging and refining segmented ideas [9]. This method appropriates a causality analysis because it can express the causal relationship between the factors by using arrows. We expect the following merits from using the KJ method.

- (1) A subjective model constructed of diverse opinions.
- (2) We can construct a model that has explanation power.
- (3) A causal relationship model is expressed.

In this paper, we construct the SEM model based on the completed chart of the KJ method.

However, problems arise when constructing a factor model from the KJ method results. The first problem is the way the factors are decided. If we assume all the groups to be factors, there is a possibility that a massive latent factor will be embedded in the model. So, there are problems with the goodness of fit and the relevance of model. The second problem is the difference of expression. There is a possibility that constructing a model is difficult because the cards are written in a free-form language so that cards with similar meanings are found throughout the model. Therefore, it is necessary to construct a model while solving these problems.

III. MODELING PROCESS FROM KJ METHOD

After experimenting with the KJ method, we construct a SEM model that contains the four following processes (Fig. 1).

- (1) Extract factors from the KJ method results.
- (2) Refine graph by integrating expressions.

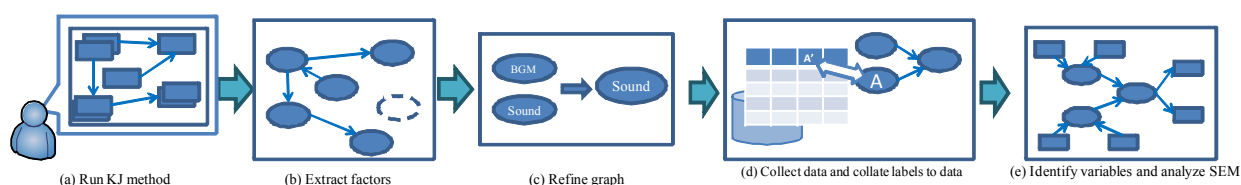


Fig.1 The flow of construction of purchase factor model

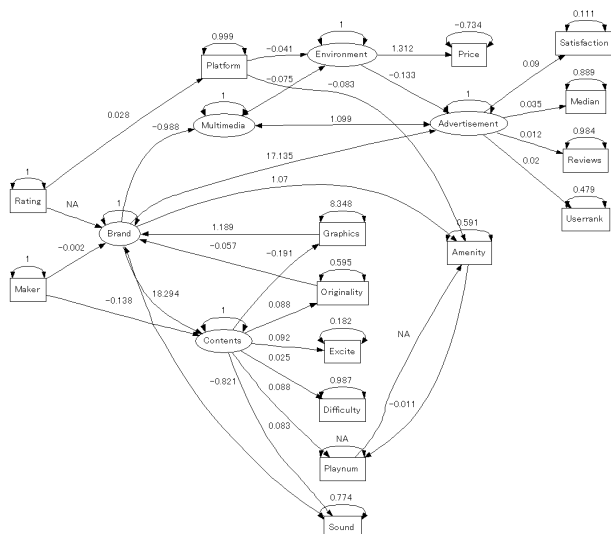


Fig.2 Completed SEM model

Table.1 Fit indices of model

Goodness-of-fit index	0.858
Adjusted goodness-of-fit index	0.784
RMSEA index	0.118
SRMR	0.100
BIC	2061.4

- (3) Collate labels to data.
- (4) Identify variables and analyze SEM.

The processes for each of the above listed step are as follows.

- (1) Extract factors: First, we identify the factor settings for the threshold of the degree and exclude the cards and arrows that adjoin the factors. By using process, we can compress the model excluding the cards and arrows that barely relate to the final factor model.
- (2) Refine graph: Second, we refine the model conceptually by integrating the expressions among the cards. In this step, we integrate cards that mutually look alike and exclude cards and arrows that barely relate to the final model.
- (3) Collate labels to data: After the above processes, it is necessary to collate the labels to the analysis data. In addition, as much of the data in which the conceptual meanings are approximated with the cards and factors is as collected as possible regardless if its structured or semi-structured data.
- (4) Identify variables and analyze SEM: Finally, we identify the variables and analyze the factors for a best seller based on the graph completed by using the above mentioned processes.

When constructing the model, we have to identify the latent and observational variables. In this paper, we assume the factors that cannot collate with the observational data to be latently variable. In addition, we assume the factors and the cards that can collate with the observational data to be observational variables, and we construct the model excluding cards that cannot collate with the observational data.

IV. CASE STUDY

1. Target of experiment

We constructed a purchase factor model from the consumers' opinions by using the process proposed in Chapter 3. In this paper, we ran the KJ method targeting five university students as our case study. In this experiment, the theme was set to "the factors for best-selling software games".

The target data for software games included 2381 products that were evaluated by consumers in PlayStation mk2 [10]. There were 17 data attributes (maker name, platform, genre, price, rating of target age, publish date, the number of players, game rank, the game criterion (difficulty, originality, graphic, sound, excitement and amenity), the number of reviews, the degree of satisfaction, and comprehensive evaluation). We also used R 2.10 [11] when analyzing the factors in SEM.

2. Experiment results

The KJ method results showed that the model consisted of 63 cards and 73 arrows. According to the process proposed in Chapter 3, we set threshold to four and constructed a SEM model consisting of five latent and 15 observational variables using this process.

The results from analyzing the completed model are shown in Fig. 2. The fit indices of the model are listed in Table. 1. The Goodness-of-fit index (GFI) of this model was calculated to be 0.858 and was unable to achieve a rough standard of 0.9. However, we could express part of the consumers' purchase factor [12].

This factor model was assumed to consist of the contents of the games, the maker brand, and advertisement because their degrees were the largest. Next, in the calculated path coefficients, the contents more relatively strongly influenced the "Sound", "Excite", and "Originality" than "Graphics", "Difficulty", and "Playnum" (the number of players). "Brand" had the high influence on the "Advertisement" (17.135) and "Contents" (18.294). In addition, "Brand"

was strongly affected by the “Graphics” (1.189). “Advertisement” showed a strong relationship with Multimedia (1.099).

V. CONSIDERATION

We understood that the consumers’ purchase factor mainly depends on the contents of games, maker brand and advertisement from the results of our analysis. “Contents” positively influenced “Sound”, “Graphics”, and “Originality”. The reason for this is that the consumers want novel games that can be played for longer periods of time, and they want an aural allurements that is yielded by next-generation hardware. Next, “Brand” highly influenced “Advertisement” and “Contents”. Therefore, the maker brand for consumers consists of the degree of advertisement and quality of the contents. We also found that “Advertisement” was affected by “Environment” and has a strong relationship with “Multimedia”. So, we learned that the amount and quality of current information greatly influences the consumers’ purchase factor.

Five male university students ran the KJ method for this research paper. They had a lot of experience playing games, so the KJ method results highly relevant and the “Brand” and “Advertisement” were taken into consideration. However, the KJ method has a problem in that the level of objectivity may be lacking due to the age-bracket of the test subjects, their gender, and the degree of knowledge for the set theme. Therefore, it would be more effective for us to run multiple KJ methods targeting different test subjects and combine these results to construct a more objective factor model that contained broader view points.

Next, we look into consideration the model construction process. First, for the extraction method of the factors, we set threshold for the degree and assumed the cards that were over the threshold to be a factor. In addition, we excluded 14 cards and 14 arrows that did not adjoin the factor. If we extract too many factors, there is a possibility that a model identification problem may occur because a lot of latent factors are set in the model. Therefore, when we set the threshold, it is important to have the cogitate attributes of the data and the extracted factors. In integrating the expressions between cards, we integrated the cards by confirming their meanings one by one in order to avoid wrongly classifying them during the automated process.

VI. CONCLUSION

We propose a construction process of a consumers’ purchase factor model using a creativity method, and clarified the factors surrounding the best seller of software games. We constructed a model by using the KJ method, which is one of the creativity methods, to solve the problems with SEM concerning the objectivity of the model and the construal difficulty caused by individual differences.

The results from constructing a model and analyzing the factors concerning the best seller when using the KJ method when the theme was set to “the factor of the best-selling software games” showed a consumers’ purchase factor that mainly consisted of the contents of the games and the brands of the makers.

However, the KJ method has some problems in that a difference in the height of an interest for a theme and the degree of knowledge bias are caused by individual differences. Therefore, some issues with the overall reliability and adequacy of the factor model may remain if we construct a factor model based on only one experiment. Therefore, we will construct a factor model by integrating multiple results from our experiments. We can construct a factor model that has a higher level of objectivity by improving this process.

REFERENCES

- [1] Famitsu.com, <http://www.famitsu.com/>
- [2] H.Yanai, K.Shigemasu and S.Maekawa et al (1990), Factor analysis –theory and process (in Japanese), Asakura Publishing Co
- [3] S.Muto (1995), Handbook of statistics analysis (in Japanese), Asakura Publishing Co
- [4] D. Freedman, R. Pisani and R. Purves (2007), Statistics, W. W. Norton & Company
- [5] N.Terui (2008), Marketing analysis by Bayesian modeling (in Japanese), Tokyo Denki University Press
- [6] H.Toyoda (1998), Structural Equation Modeling [Beginner ver.] (in Japanese), Asakura Publishing Co
- [7] K. Kitami and R. Saga (2010), Causality Analysis for Best Seller of Software Game by Regression and Structural Equation Modeling, 2010 IEEE International Conference on Systems, Man, and Cybernetics
- [8] J. Pearl: Causality (2000), Models, Reasoning, and Inference, Cambridge University press
- [9] D. Silverstein, P. Samuel and N. Decarlo (2009), The innovator’s toolkit, Breakthrough Management Group International
- [10] PlayStation mk2, <http://www.psmk2.net/>
- [11] The R project for Statistical Computing, <http://cran.r-project.org/>
- [12] H.Toyoda (2007), Structural Equation Modeling [Amos ver.] (in Japanese), TokyoTosho Co

Developing a monitoring psychological stress Index system via photoplethysmography

Jiann-Shing Shieh¹, Yu-Ren Chiou¹, Shou-Zen Fan²

¹*Department of Mechanical Engineering, Yuan Ze University, Taiwan*

²*Department of Anesthesiology, College of Medicine, National Taiwan University, Taiwan
(Tel :886-3-463-8800 ext. 2470; Fax : 886-3-455-8013)
(jsshieh@saturn.yzu.edu.tw)*

Abstract: The purpose of this paper is to assess the psychological stress index (PSI) by using oxyhemoglobin saturation by SpO₂ (i.e., plethysmograph (PPG) signal), which is measured easily and conveniently. We use plethysmograph amplitude (PPGA) and heart beat interval (HBI) extracted from SpO₂ waveform to obtain the stress index and quantify it from 0 to 100. Also, the respiration rate can be extracted from heart rate interval according to our previous research. Therefore, the PPG signal can display heart rate, SpO₂ waveform, SpO₂ concentration, respiration rate and psychological stress index. This methodology has been tested in 9 volunteers under English presentation stress for Taiwanese students. The experiment in 30 min for each student was separated into three stages: preparation, presentation & discussion, and relaxation. The PSI values of these three stages are 49±10, 60±11, and 56±10, respectively. The results have been shown very successful for PSI value changing from low, high, and low during these three stages. In the near future, we try to implement this system into robotic wheelchair in order to monitor this PSI of elderly at nursing home to evaluate their psychological condition based on this method.

Keywords: Photoplethysmograph, pulse oximeter, plethysmograph amplitude (PPGA), heart beat interval (HBI), psychological stress index (PSI).

I. INTRODUCTION

In society, there are more and more factors that affect people's health. Recently, a lot of people have excessive stress, which leads to physical disease [1]. There are many diseases that occur due to excessive stress. Psychological stress leads to physiological changes that help people cope with unexpected situations and critical incidents. But frequent, strong, and sustained stress will create an adverse impact on the body. In the past, there are several famous scholars who research stress. One is Walter Cannon, who proposed "Homeostasis"[2]. He thought stress affects an individual's balance. If the body's system cannot keep balance, the person will "flight or fight". This response from epinephrine is trying to restore a stable body. The other is Hans Selye, who found that stress response is a "General Adaptation Syndrome" [3]. When feeling stress, the body will go through alarm, resistance and exhaustion where Glucocorticoid is playing a vital role in this part. Both stress responses were similar no matter where the stressors come. When people suddenly have a threatening situation or emotional stimuli, there is an increase in heartbeat, blood pressure, adrenaline etc. [4,5]. Hence, a lot of researchers try to measure physiological signals to represent the stress.

In order to monitor physical condition continuously, people usually need to wear a lot of equipment. Based on the patient's condition, they may have many physiological signals that need to be monitored, like electrocardiography (ECG), pulse oximeter (SpO₂), respiration, etc. When people have many signals that need to measure, they wear multiple devices. Considering patients only have limited ability, complicated physiological monitoring systems are inconvenient to them. If people only wear one device to capture one signal, with other signals derived by this, it can get comprehensive physiological information easily.

In 2007, Huiku et al. [6] developed a method to assess stress index during surgical operations. The experiment in the paper is to observe the effect of various physiological signals such as plethysmograph amplitude (PPGA), heart beat interval (HBI), pulse transit time (PTT), response entropy (RE) when a patient suffers two opposite stimulus, incision and anesthetic drugs. They point out PPGA and HBI have the most remarkable correlation with stress and establish an equation to calculate surgical stress index (SSI). We analyzed the psychological condition based on this method.

Hence, the purpose of this paper is to assess the psychological stress index (PSI) by using oxyhemoglobin saturation by SpO2, which is measured easily and conveniently. We use PPGA and HBI extracted from SpO2 to obtain the stress index and quantify it from 0 to 100. Also, the respiration rate can be extracted from heart rate interval according to our previous research. Therefore, the PPG signal can display heart rate, SpO2 waveform, SpO2 concentration, respiration rate and psychological stress index.

II. METHODOLOGY

1. Photoplethysmography

A plethysmograph sensor is a medical instrument used mainly to determine variations in oxygen saturation. PPG [7] selects a skin area and measures the optical characteristics of that region. Usually we send red and infrared light through the skin and blood vessels. The components of blood Hb (reduced hemoglobin) and HbO (oxygenated hemoglobin) [8] will have different degrees of absorption. Therefore, the amount of oxygen in the blood can be measured due to the different absorption of red and infrared light through the skin and blood vessels.

2. Calculating heart rate from PPG

We mainly used maximum gradient to detect the peak point of SpO2 signal that is similar to the R-R interval in ECG signals as shown in Fig. 1. The first derivative was calculated at each point of SpO2 in the following equation (1):

$$Y(n)=X(n+1)-X(n) \quad (1)$$

If the gradient was larger than 60, we marked the X (n) point. Then, we found the local initial climbing point. According to this point, we took the front and back 30 points as a domain and found the maximum and minimum points. Then, PPGA is the amplitude between adjacent peak point and foot point (Fig. 2). And, HBI is the time interval between adjacent peak points (Fig. 2) that is similar to the R-R interval in ECG signals so the heart rate is easily obtained from this P-P interval.

3. Calculating respiration rate from PPG

The calculation of HBI from SpO2 signal in previous section can be applied to calculate the

respiration rate. More details can be seen in our previous study [9].

4. Psychological stress index

Surgical stress index (SSI) [10, 11] has been used in surgery. It can be used to determine a patient's pain during surgery. SSI values near 100 corresponding to a high stress level, and values near zero corresponding to a low stress level. Firstly, we need to get PPG amplitude and the heartbeat intervals. Secondly, the standard deviations of PPG amplitude and heart rate variability are needed to calculate for normalization as shown in Fig. 3 (a). Finally, we can calculate the PSI value according to the following equation (2) as shown in Fig. 3 (b).

$$PSI=100-(0.7 \times PPGAnorm - 0.3 \times HBInorm) \dots (2)$$

where PPGAnorm is normalized continuous blood oxygen pulse amplitude and HBInorm is normalized heart beat interval.

We tried to use this algorithm to calculate psychological stress index (PSI), but the volunteer did not lay on an operating table during surgery. We designed a pressure environment and measured the physiological signals during this period. We can measure the signal and used the equation (2) to calculate PSI.

III. RESULTS

This study has been tested in 9 volunteers under English presentation stress for Taiwanese students. They are not use English as their mother language and asked to discuss their research with two professors in English. The experiment in 30 min for each student was separated into three stages: preparation, presentation & discussion, and relaxation as shown in Fig. 4. Therefore, the PPG signal can display heart rate, SpO2 waveform, SpO2 concentration, respiration rate and psychological stress index as shown in Fig. 5. The PSI values from 9 volunteers of these three stages are 49 ± 10 , 60 ± 11 , and 56 ± 10 , respectively as shown in Table 1. The results have been shown very successful for PSI value changing from low, high, and low during these three stages.

IV. CONCLUSION

In conclusion, we confirm a new method to assess the psychological stress index by using SpO2 signals. At the moment, the method is limited to normal people and short-term condition. The method is particularly useful in situation where the SpO2 is the only available information source. Using a pulse oximeter, the user can obtain both psychological and physiological information at the same time.

REFERENCES

- [1] Agid O, Kohn Y, Lerer B (2000), Environmental stress and psychiatric illness. *Biomedicine & Pharmacotherapy* 54:135-141.
- [2] Cannon W (1935), Stresses and strains of homeostasis. *The American Journal of the Medical Sciences* 189(1):1-25.
- [3] Wortsman J, Frank S, Cryer PE (1984), Adrenomedullary response to maximal stress in humans. *The American journal of medicine* 77:779-784.
- [4] Crye PE (1980), Physiology and pathophysiology of the human sympathoadrenal neuroendocrine system. *The New England journal of medicine* 303:436-444.
- [5] Munck A, Guyer PM, Holbrook NJ (1984), Physiological functions of glucocorticoids in stress and their relation to pharmacological actions. *The Endocrine Society* 5:25-44.
- [6] Huiku M, Uutela K, van Gils M, Korhonen I, Kymäläinen M, Meriläinen P, Paloheimo M, Rantanen M, Takala P, Viertiö-Oja H, Yli-Hankala A (2007), Assessment of surgical stress during general anaesthesia. *Br J Anaesth* 98: 447-55.
- [7] Allen J (2007), Photoplethysmography and its application in clinical physiological measurement, *Physiol Meas* 28:1-39.
- [8] Sinex J (1999), Pulse oximetry: Principles and limitations, *The American Journal of Emergency Medicine*, vol. 17, 1:59-66.
- [9] Singhathip R, Si-Hui Yang SH, Abbod M, Yeh RG, Jiann-Shing Shieh JS (2010), Extracting Respiration Rate from Raw ECG Signals. *Biomedical Engineering – Applications, Basis & Communications* 22(4): 307-314.
- [10] Wennervirta J, Hynynen M, Koivusalo A.M, Uutela K, Huiku M. and Vakkuri A (2008), Surgical stress index as a measure of nociception/antinociception balance during general anesthesia, *Acta Anaesthesiologica Scandinavica* 52(8):1038-1045.
- [11] Ahonen J, Jokela R, Uutela K, Huiku M (2007), Surgical stress index reflects surgical stress in gynaecological laparoscopic day-case surgery *Br J Anaesth.* 98(4):456-61.

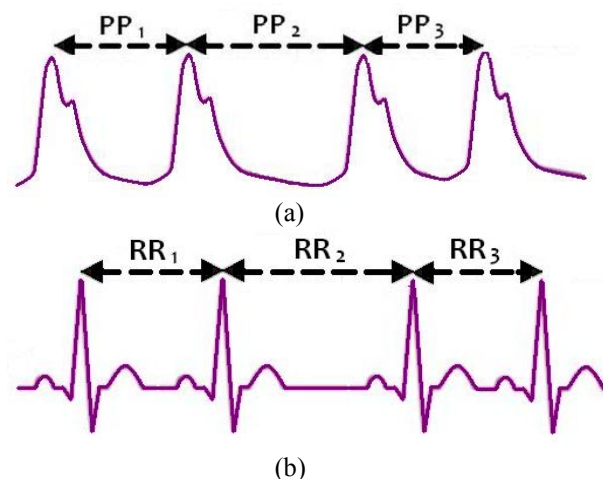


Fig. 1. Definition of peak to peak signals (a) from PPG signal (b) from ECG signal

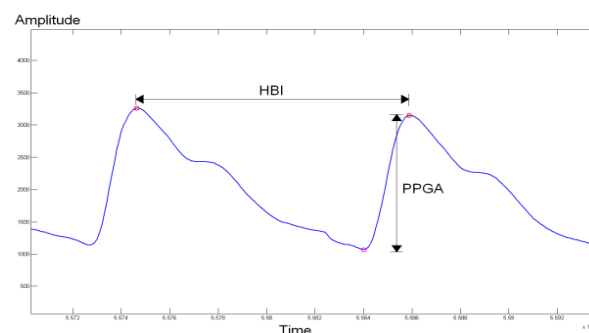


Fig. 2. Definition of PPGA and HBI

Table 1. The PSI in the experiment during skype meeting

	Before	During	After
Case	Presentation	Presentation	Presentation
A	46 ±13	57±11	56 ±20
B	33 ±10	52 ±17	62 ±12
C	59 ±10	68 ±10	57 ±9
D	60 ±12	57 ±16	57 ±14
E	45±12	57±11	51±2
F	60±10	60±10	64±10
G	34±10	62±11	53±8
H	N/A	62±12	61±6
I	59±12	65±9	48±10
Average ±SD	49±10	60±11	56±10

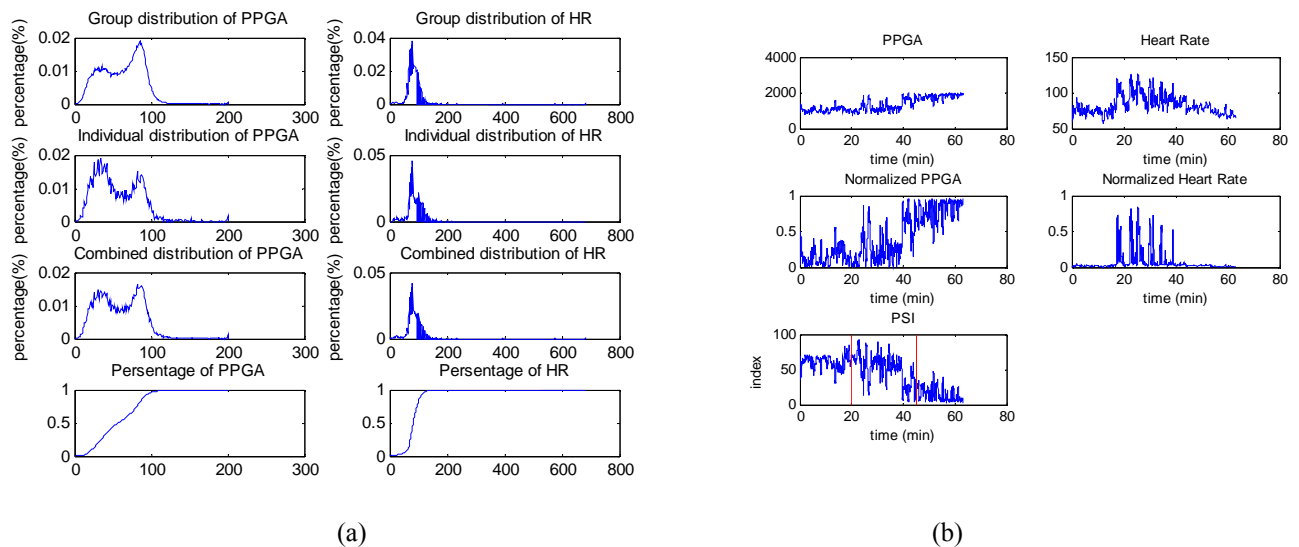


Fig. 3 An example of (a) the process of normalization and (b) the variety of PSI in experiment

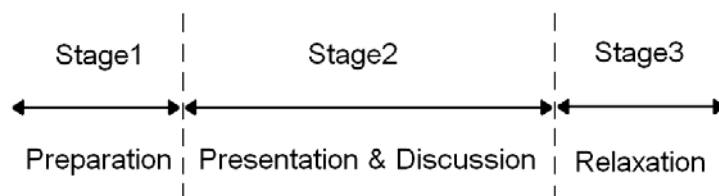


Fig. 4. The procedure of experiment

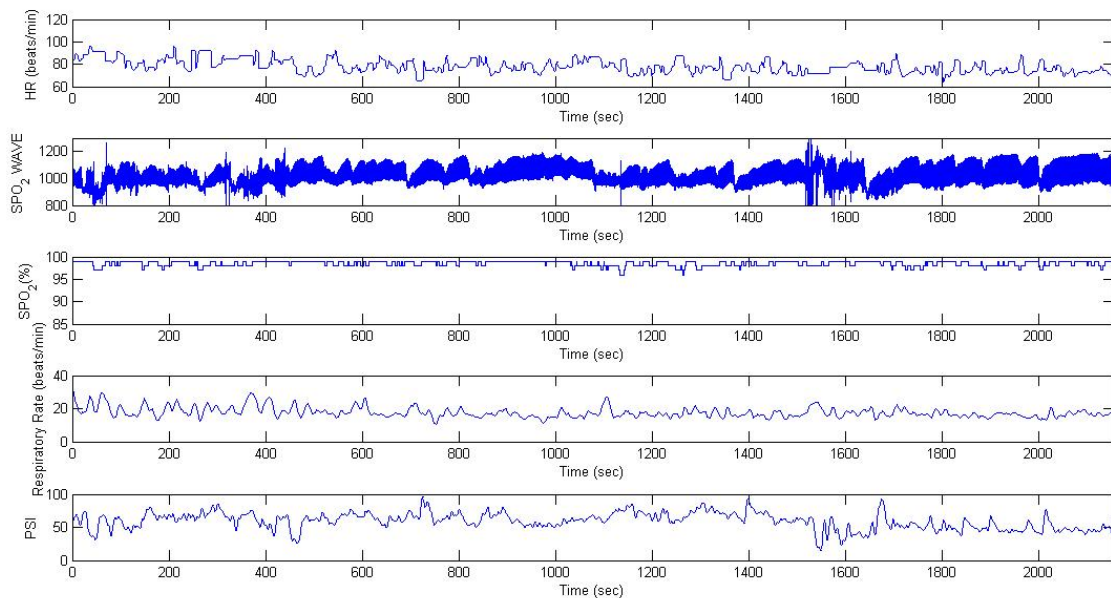


Fig. 5. An example of volunteer's heart rate, SpO₂ waveform, SpO₂ concentration, respiration rate and psychological stress index during skype meeting

A Study on Efficient Query Dissemination in Distributed Sensor Networks -Forwarding Power Adjustment of Each Sensor Node Using Particle Swarm Optimization-

Junya Nagashima[†], Akihito Utani[‡], and Hisao Yamamoto[‡]

[†]*Graduate School of Engineering, Tokyo City University*

[‡]*Faculty of Knowledge Engineering, Tokyo City University*

1-28-1, Tamazutsumi, Setagaya, Tokyo 158-8557, Japan

{autani; yamahisa}@tcu.ac.jp

Abstract: In a wireless sensor network, flooding is required for the dissemination of queries or event announcements. The original flooding causes the overlap problems. In the original flooding, generally, all sensor nodes receiving a broadcast message forward it to its neighbors by full forwarding power, resulting in a lot of collisions and duplicate messages. For a dense wireless sensor network, the impact caused by the original flooding may be overwhelming. The original flooding may result in the reduced network lifetime. Therefore, an efficient query dissemination method is needed to prolong the lifetime of a wireless sensor network. This paper proposes a new query dissemination method based on the particle swarm optimization method for the long-term operation of a wireless sensor network. We evaluate the proposed method using computer simulations. In simulation experiments, the performance of the proposed method is compared with those of the existing ones to verify its effectiveness.

Keywords: Wireless Sensor Networks, Particle Swarm Optimization, Query Dissemination, Long-Term Operation.

I. INTRODUCTION

A wireless sensor network, which is a key network to realize ubiquitous information environments, has attracted a significant amount of interest from many researchers. In a wireless sensor network, hundreds or thousands of micro sensor nodes, which are compact and inexpensive, are placed in a large scale observation area and sensing data of each node is gathered to a sink node by inter-node wireless multi-hop communication. Each sensor node consists of a sensing function to measure the status (temperature, humidity, motion, etc.) of an observation point or object, a limited function on information processing, and a simplified wireless communication function, and generally operates on a resource of a limited power-supply capacity such as a battery. Therefore, the suppression of communication load is generally required for the long-term operation of a wireless sensor network.

In a wireless sensor network, flooding is required for the dissemination of queries or event announcements. The original flooding causes the overlap problems. In the original flooding, generally, all sensor nodes receiving a broadcast message forward it to its neighbors by full forwarding power, resulting in a lot of collisions and duplicate messages. For a dense wireless sensor network, the impact caused by the original flooding may be overwhelming. The original flooding may result in the reduced network lifetime. Therefore, the selecting method of for-

warding nodes for the dissemination of queries or event announcements has been studied to prolong the lifetime of a wireless sensor network. The existing methods of [1-4] have been proposed to resolve or improve the overlap problems of the original flooding in disseminating queries or event announcements in a wireless sensor network. However, the gossiping of [1] may result in some nodes not receiving queries. The existing methods of [2,3] can disseminate queries to the whole nodes construct a wireless sensor network, but can not select a most efficient and optimum forwarding nodes set. The method of [4] can compute an optimum forwarding nodes set, but a more efficient query dissemination method is needed to prolong the network lifetime.

This paper proposes a new query dissemination method based on the particle swarm optimization method for the long-term operation of a wireless sensor network. The rest of this paper is organized as follows. In Section II, the proposed method is described. In Section III, experimental results are reported, and the effectiveness of the proposed method is demonstrated by comparing the performance of it with those of the existing ones. Finally, the paper closes with conclusions and ideas for further study in Section IV.

II. PROPOSED METHOD

In this paper, an efficient query dissemination method based on the Particle Swarm Optimization (PSO) method, which adjusts the forwarding power of each node

that constructs a wireless sensor network, is proposed. In this section, the PSO method is first outlined. Then, the proposed method based on the PSO method is described.

1. Particle Swarm Optimization

The PSO method belongs to the category of swarm intelligence methods. It was developed and first introduced as a stochastic optimization algorithm [5]. Currently, the PSO method is intensively researched because it is superior to the other algorithms on many difficult optimization problems. The ideas that underlie the PSO method are inspired not by the evolutionary mechanisms encountered in natural selection, but rather by the social behavior of flocking organisms, such as swarms of birds and fish schools. The PSO method is a population-based algorithm that exploits a population of individuals to probe promising regions of the search space. In this context, the population is called a *swarm* and the individuals are called *particles*. In the PSO method, a multidimensional solution space by sharing information between a swarm of particles is efficiently searched. The algorithm is simple and allows unconditional application to various optimization problems.

Assume an n -dimensional search space S , and a swarm consisting of N particles. Each particle (The i th particle) has a position vector

$$\mathbf{x}_i = (x_{i1}, x_{i2}, \dots, x_{in})^T \in S,$$

and the velocity vector

$$\mathbf{v}_i = (v_{i1}, v_{i2}, \dots, v_{in})^T \in S,$$

where the subscript i ($i=1, \dots, N$) represents the particle's index. In addition, each particle retains the position vector \mathbf{pbest}_i of the best evaluation value found by the particle in the search process and the position vector \mathbf{gbest} of the best evaluation value among all particles as information shared in the swarm in the search process.

In the PSO method, each particle produces a new velocity vector \mathbf{v}_i^{k+1} by linearly coupling the best solution $[\mathbf{pbest}_i^k]$ found by the particle in the past, the best solution $[\mathbf{gbest}^k]$ shared in the swarm, and the previous velocity vector \mathbf{v}_i^k and moves to the next position \mathbf{x}_i^{k+1} , where the superscript k indicates the number of search iterations. At the $k+1$ search, the velocity vector \mathbf{v}_i^{k+1} and the position vector \mathbf{x}_i^{k+1} of the i th particle is updated as follows (Fig.1):

$$\begin{aligned} \mathbf{v}_i^{k+1} &= \omega \cdot \mathbf{v}_i^k + c_1 \cdot r_1 \cdot (\mathbf{pbest}_i^k - \mathbf{x}_i^k) \\ &\quad + c_2 \cdot r_2 \cdot (\mathbf{gbest}^k - \mathbf{x}_i^k) \\ \mathbf{x}_i^{k+1} &= \mathbf{x}_i^k + \mathbf{v}_i^{k+1} \end{aligned} \quad (1)$$

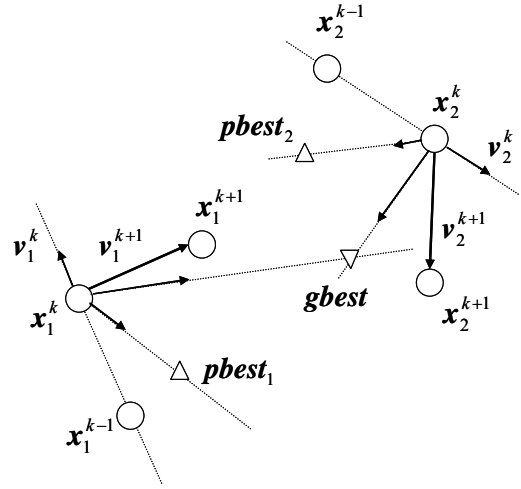


Fig.1. The movement of particles

where r_1 and r_2 are random numbers, uniformly distributed within the interval $[0,1]$. ω is a parameter called the *inertia weight*, and c_1, c_2 are positive constants, referred to as *cognitive* and *social* parameters, respectively.

2. Proposed Method

In this study, a general wireless sensor network consisting of static sensor nodes with Global Positioning System (GPS) placed in an observation area is assumed. At the initial stage of the network, the sink node set requests the location information from every sensor node by broadcasting a Location Discovery Message. Each sensor node receiving this Location Discovery Message sends a Location Response Message to the sink node. The sink node can grasp the location information of each sensor node from the gathered Location Response Messages.

By applying the PSO method, this study detects an adjustment solution on the forwarding power of each sensor node that constructs a wireless sensor network based on the location information gathered by the sink node. In this study, variables are the forwarding power of each sensor node as follows:

$$\mathbf{x} = (E_T(1), E_T(2), \dots, E_T(n_{total}))^T \quad (2)$$

where $E_T(i)$ is the forwarding power of sensor node (i), and n_{total} represents the number of all sensor nodes that constructs a wireless sensor network.

To compute an adjustment solution on the forwarding power of each sensor node for disseminating queries or event announcements to all sensor nodes in a wireless sensor network and minimizing total energy consumption on forwarding of queries or event announcements, the objective function is set as follows:

$$f(\mathbf{x}) = \frac{S^{-(n_{\text{total}} - n_{\text{receive}})}}{\sum_{i=1}^n E_T(i)} \quad (3)$$

where n_{receive} represents the number of sensor nodes that received queries or event announcements.

III. EXPERIMENTAL RESULTS

Through simulation experiments, the performance of the proposed method is investigated to verify its effectiveness. The conditions of simulation and the values on PSO parameters, which were used in the experiments performed, are shown in Table 1, where the selected values on PSO parameters are considered proper default values and they are used in the relevant literature on the PSO method. In Fig.2, an optimum forwarding nodes set is shown when range of radio wave of each sensor node is set to 25m, where static sensor nodes are randomly arranged in the set experimental area.

Table1. Condition of simulations and settings on PSO parameters

Simulation size	100(m) × 100(m)
The number of sensor nodes	73
Range of radio wave	0 ~ 25(m)
The number of particle	30
Cognitive parameter c_1	2.1
Social parameter c_2	0.8
Inertia weight ω	1.0

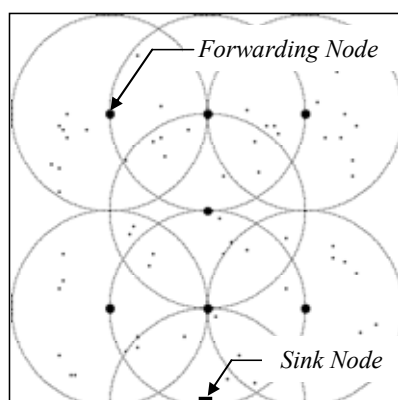
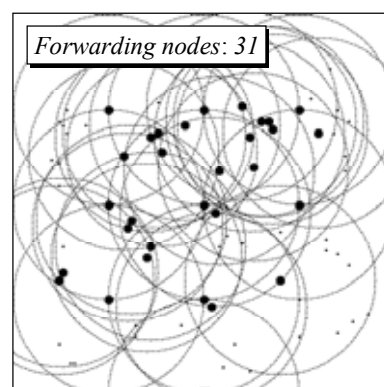


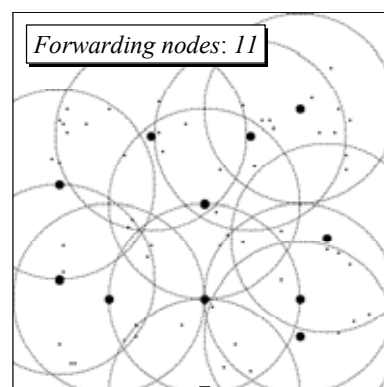
Fig.2. Simulation model

In experimental results reported, the proposed method is evaluated through the comparison with the existing ones of [2-4]. On the existing methods, range of radio wave of each sensor node was set to 25m, and the parameter settings that were used in [4] and produced good

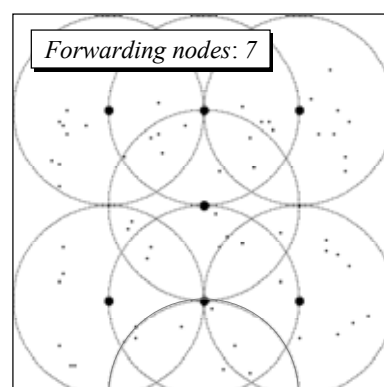
results in a preliminary investigation were adopted for the comparison with the proposed method. In Fig.3, a forwarding nodes set and the number of forwarding nodes selected by using the existing methods of [2-4] are shown. From the results of Fig.3, it is confirmed that the existing methods of [2,3] can not detect an optimum forwarding nodes set. The method of [4] computes an optimum forwarding nodes set, but a more efficient query dissemination method is required to prolong the lifetime of a wireless sensor network.



(a) Results by the method of [2]

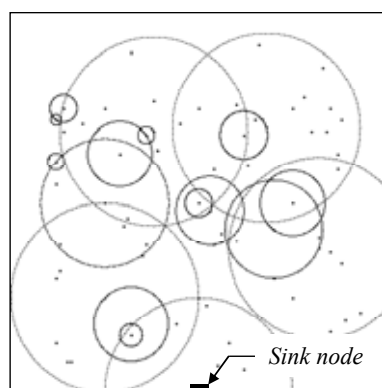


(b) Results by the method of [3]

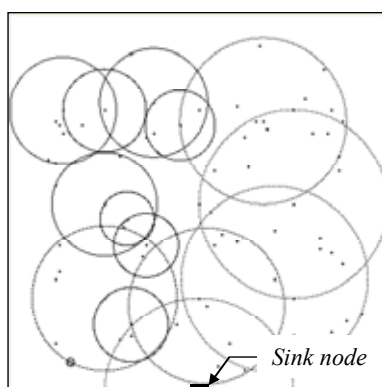


(c) Results by the method of [4]

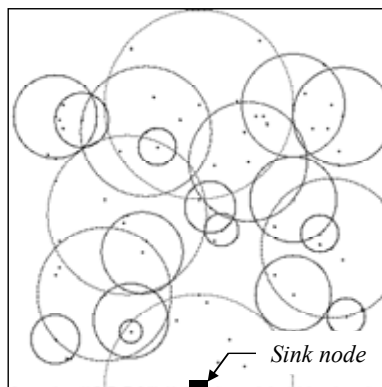
Fig.3. Forwarding nodes set computed by using the existing methods of [2-4]



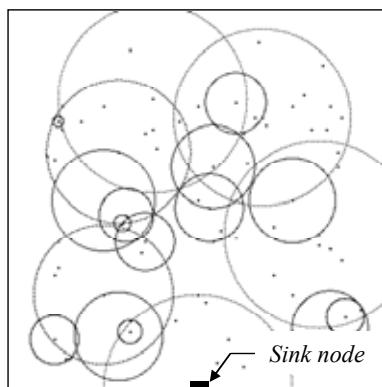
(a) The first search



(b) The second search



(c) The third search



(d) The fourth search

Fig.4. Results obtained by using the proposed method

Table2. Total energy consumption

		Total energy consumption
The method of [2]		100.6 μ J
The method of [3]		78.1 μ J
The method of [4]		73.6 μ J
Proposal	Best value	71.7 μ J
(4searches)	Mean value	72.2 μ J

Ranges of radio waves of all sensor nodes computed by using the proposed method are illustrated in Fig.4. In Table 2, total energy consumption on query dissemination of all sensor nodes that construct a network is shown. From Fig.4 and Table 2, it can be confirmed that the proposed method is a promising query dissemination one for the long-term operation of wireless sensor networks.

IV. CONCLUSIONS

In this paper, an efficient query dissemination method based on the PSO method for the long-term operation of a wireless sensor network, which adjusts the forwarding power of each sensor node for disseminating queries or event announcements to the whole nodes in a wireless sensor network, has been proposed. Experimental results indicate that the proposed method has the development potential as an efficient query dissemination one. In an actual sensor node, however, detailed adjustment of the forwarding power is difficult. In future studies, we want to improve the proposed method by considering actual sensor nodes.

REFERENCES

- [1] Lin MJ, Marzullo K, and Masini S (2000), Gossip versus deterministic flooding: Low message overhead and high reliability for broadcasting on small networks. DISC, pp.253-267
- [2] Adjih C, Jacquet P, and Viennot L (2002), Computing connected dominated sets with multipoint relays. Technical Report 4597, INRIA:1-16
- [3] Nagashima J, Utani A, and Yamamoto H (2009), A study on efficient flooding in wireless sensor networks. IEICE Technical Report 108(443):49-52
- [4] Nagashima J, Utani A, and Yamamoto H (2010), Efficient flooding method for wireless sensor networks based on discrete particle swarm optimization computing multiple forwarding node sets. Proc. Fifteenth International Symposium on Artificial Life and Robotics, pp.244-248
- [5] Kennedy J and Eberhart RC (1995), Particle swarm optimization. Proc. IEEE International Conference on Neural Networks, pp.1942-1948

Evaluation of a competitive particle swarm optimizer in multimodal functions with complexity

Yu Taguchi[†], Hidehiro Nakano[†], Akihito Utani[†], Arata Miyauchi[†]
and Hisao Yamamoto[†]

[†]*Tokyo City University*
1-28-1, Tamazutsumi, Setagaya-ku, Tokyo, 158-8557 Japan
(taguchi@ic.cs.tcu.ac.jp)

Abstract: In this paper, we present a simple competitive particle swarm optimizer (CPSO) for finding plural solutions. In the CPSO, particles are divided into groups corresponding to the required number of solutions. Each group simultaneously searches solutions having a priority search region. This region affects to prohibit that different groups search the same solutions. The CPSO can effectively find desired plural acceptable solutions with a high accuracy and with a low computation cost, and can easily control combinations of these solutions by adjusting a parameter. This paper evaluates the CPSO in complex global optimization benchmarks. Through the numerical experiments, searching performances of the CPSO are clarified.

Keywords: Particle Swarm Optimization, Optimization Problems, Plural Solutions.

I. INTRODUCTION

Particle Swarm Optimizers (PSOs) are known as a kind of metaheuristic algorithms [1]-[4]. Swarms such as birds and fishes decide actions to consider not only status information of each individual but also status information as whole of their swarms. The PSO expresses such actions by simple arithmetic operations. In the PSO, particles search solutions in an objective problem. Each particle has velocity and position information, and moves in a multidimensional search space considering a personal best solution which each particle memorizes and a global best solution which all particles share. The PSO can fast solve various optimization problems with a low computation cost.

On the other hand, in the actual engineering optimization problems, there exist a lot of design variables and constrained conditions to be considered. Then, the exact modeling for these problems can be hard. Also, solutions obtained from approximated models are not always available in the actual problems. Therefore, it is needed that plural acceptable solutions as design candidates can be provided in reasonable computation time. Many methods along this line have been proposed [5]-[9]. These methods can sequentially find plural acceptable solutions by behaving like general tabu search. However, by the effect of competitive search, the quality of each solution obtained from these methods is often lower than that obtained from the original PSO. In addition, these methods have many parameters; it is hard to control them.

In our previous works, a simple Competitive PSO (CPSO) for finding plural solutions has been proposed [10]. In the CPSO, particles are divided into groups corresponding to the required number of solutions. Each group simultaneously searches solutions having a priority search region. This region affects to prohibit that different groups search the same solution. The CPSO can effectively find desired plural acceptable solutions and can easily control combinations of these solutions by adjusting a parameter. Also, quality of some solutions obtained from the CPSO are almost the same as or better than that obtained from the original PSO. This means that the competitive search in the CPSO does not suppress the searching performances of the original PSO, and realize to effectively search plural acceptable solutions. In addition, the CPSO can fast find plural solutions without repeating many trials.

The CPSO has been evaluated for basic global optimization benchmarks and has been applied to a problem in sensor networks [10]. However, in practical problems such as the sensor networks, objective functions can be complex shapes and can include complex dependencies between design variables. The detailed evaluations of the CPSO in such functions have not been sufficient so far. This paper evaluates the CPSO in complex global optimization benchmarks. Through the numerical experiments, searching performances of the CPSO are clarified.

II. PARTICLE SWARM OPTIMIZERS

Swarms such as birds and fishes decide actions depending on not only status information of each individual but also status information as whole of their swarms. PSO is an optimization method that imitates behavior of the swarms. In PSO, particles efficiently search solutions in a target problem, by updating their positions and velocities based on personal best solutions which each particle has and a global best solution which all the particles have. Basic algorithm of PSO is described as follows (see Fig.1).

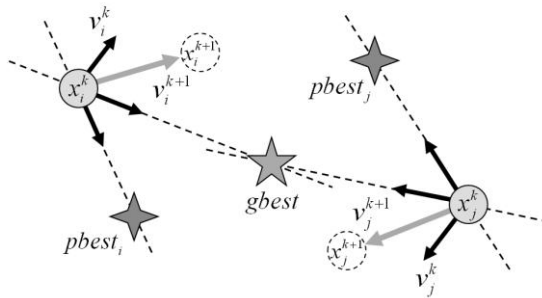


Fig.1. Movements of particles

(step1) Set positions and velocities of each particle at random.

(step2) Update the positions of each particle by Equation (1).

$$x_i^{k+1} = x_i^k + v_i^k \quad (1)$$

where x_i^k and v_i^k are position and velocity of the i -th particle at the k -th iteration, respectively.

(step3) Calculate evaluation values of each particle and update each personal best solution ($pbest_i$).

(step4) Update global best solution ($gbest$).

(step5) Update the velocities of each particle by Equation (2).

$$v_i^{k+1} = w \cdot v_i^k + c_1 \cdot r_1 \cdot (pbest_i - x_i^k) + c_2 \cdot r_2 \cdot (gbest - x_i^k) \quad (2)$$

where w is an inertia coefficient for the previous velocity vector. c_1 is a weight coefficient for the personal best position vector. c_2 is a weight coefficient for the global best position vector. r_1 and r_2 are uniform random numbers from 0 to 1.

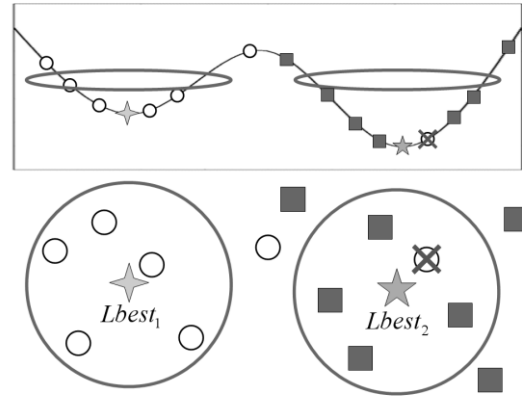


Fig.2. Groups of particles with priority search regions

(step6) Repeat from step2 to step5 until the number of iterations or an evaluation value of a solution reaches a predetermined value.

III. COMPETITIVE PSO

In general, it will be difficult to model design variables and constraint conditions exactly when optimization algorithms are applied to real problems. Then, it is more practical to obtain plural acceptable solutions as design candidates and to select the best solution from them rather than to obtain a single exact optimum solution. This paper presents a competitive PSO (CPSO) that can efficiently find the plural different acceptable solutions by dividing particles into plural groups. In the original PSO, it is difficult to find plural solutions because all the particles converge to a single solution by moving toward a global best solution. In the CPSO, it is considered that particles are divided into arbitrary m groups. In addition, these groups have own local best solution instead of global best solution as shown in Fig.2. As a result, plural solutions can be found because particles move toward each own local best solution. But, only dividing into plural groups, they may converge to the same solution. Therefore, priority search regions from each local best solution are introduced. In the region, the particles of a group can search more preferential than other groups. If a particle moves into the regions of the other groups, the CPSO excepts for the particle from the candidate in updating own local best solution. Then, it is possible to search the plural different solutions efficiently because each group does not approach to the regions of the other

groups to each other. The algorithm of the CPSO is described as follows.

(step1) Set positions and velocities of each particle at random and set the parameter r corresponding to priority search region.

(step2) Divide p particles into arbitrary m groups.

(step3) Update positions of all the particles regardless of groups by Equation (1).

(step4) Calculate evaluation values of each particle and update each personal best solution ($pbest_i$).

(step5) Let $lbest_j$ be the local best solution which particles in the j -th group have. Calculate Euclidean distances between positions of each particle in the j -th group and positions of $lbest_j$ in the j -th group ($j' \neq j$).

(1)Euclidean distance is shorter than the range r :

The particle is excepted from a candidate of $lbest_j$.

(2)Euclidean distance is longer than the range r :

The particle is included as a candidate of $lbest_j$ in the same way as $gbest$ in the original PSO.

(step6) Update each $lbest_j$ that are chosen from the particles of each group.

(step7) If each position of $lbest_j$ and $lbest_{j'}$ ($j' \neq j$) overlaps to each other for the priority search regions, values of $lbest_j$ and $lbest_{j'}$ are compared. If $lbest_j$ is better, the positions of the particles in the j -th group are left. Otherwise, their positions and $lbest_j$ are reset at random.

(step8) Update the velocities of each particle by Equation (3).

$$v_i^{k+1} = w \cdot v_i^k + c_1 \cdot r_1 \cdot (pbest_i - x_i^k) + c_2 \cdot r_2 \cdot (lbest_j - x_i^k) \quad (3)$$

(step9) Repeat from step3 to step8 until the number of iterations or an evaluation value of a solution reaches a predetermined value.

When a group always overlaps priority search regions of other groups, this group can obtain no solution because local best solution of the group is reset every time.

IV. SIMULATION RESULTS

The CPSO is applied to some benchmark problems and the performances are confirmed. In all the experiments, some parameter values are fixed as follows: $p = 500$, $w = 0.9$, $c_1 = c_2 = 1.0$, $m = 5$.

Varying the parameter of range r and the number of dimensions n , typical results are presented.

The CPSO is applied to Modified Rastrigin function defined by Equation (4).

$$F(x) = \sum_{i=1}^n (z_i^2 - 10 \cos(2\pi z_i) + 10) \quad (4)$$

$$z_i = R(\alpha)(x_i - x_i^*)$$

$$x_i^* = U(-4.0, 4.0), \alpha = \pi/4, -5.0 < x_i < 5.0$$

x^* is a random optimal solution and $U(a, b)$ denotes uniform random numbers from a to b . And rotation matrix R is given by Equations (5a) and (5b).

$$R = T^{12} \times T^{13} \times \dots \times T^{1n} \times T^{23} \times \dots \times T^{(n-1)n} \quad (5a)$$

$$T_{kl}^{ij} = \begin{cases} \cos \alpha & k = i, l = i \\ -\sin \alpha & k = i, l = j \\ \sin \alpha & k = j, l = i \\ \cos \alpha & k = j, l = j \\ 1 & k = l \neq i, j \\ 0 & \text{not above} \end{cases} \quad (5b)$$

This function has a complex shape. This function gives minimum value 0 when design variables are x^* . It has many suboptimum solutions in arrangement like a lattice around the optimum solution.

First, we show the simulation results for $n = 2$. As $r = 0.8$, the CPSO can find the optimum and better suboptimum solutions as shown in Fig.3. Therefore, when the range is set appropriately, it is possible to find desired plural acceptable solutions. As $r = 1.3$, the CPSO can find optimum and better suboptimum solutions as shown in Fig.4. In addition, the discovered suboptimum solutions are more distant from the optimum solution than those obtained in $r = 0.8$. This reason is that the suboptimum solutions obtained in $r = 0.8$ are contained in priority search region of the group at the optimum solution as $r = 1.3$. As a result, the CPSO can accurately search for better solutions outside the range r . This means that the CPSO can easily control the distance of each solution by adjusting the range r .

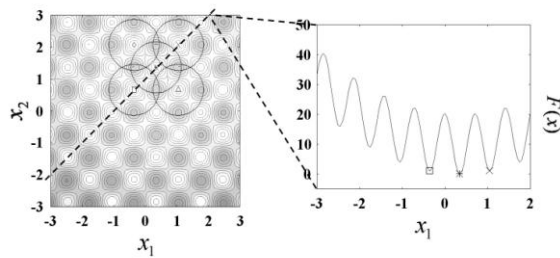


Fig.3. Simulation results ($n = 2$, $r = 0.8$)

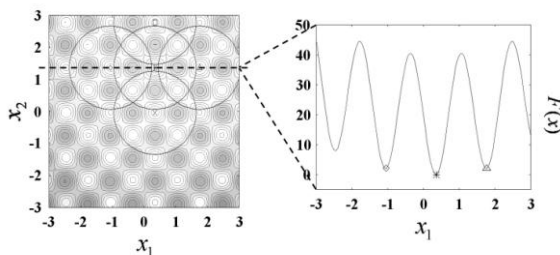


Fig.4. Simulation results ($n = 2$, $r = 1.3$)

Next, simulation results for higher dimensional Modified Rastrigin function ($n = 20$) are shown. The trials are repeated 100 times and the average values are presented. Table 1 shows the results for $r = 0.8$. Although the optimum solution cannot be found, plural acceptable suboptimum solutions can be found as shown in Table 1. Therefore, the CPSO can obtain plural solutions easily also in high dimensional and complex problems. In addition, quality of some solutions obtained from the CPSO are almost the same as or better than that obtained from the original PSO.

V. CONCLUSION

This paper has been evaluated a simple competitive PSO for multimodal functions with complexity. Adjusting a parameter of a priority search range, desired plural acceptable solutions can be effectively found and can be easily controlled. In the practical engineering optimization problems, not only a single exact optimum solution for the problems but also plural acceptable solutions for them are often required. The CPSO will be a simple and powerful tool to effectively solve these problems. Future problems include (1) adaptive control of parameters in the CPSO, (2) investigations of performances for various higher-dimension problems, and (3) applications to various engineering optimization problems.

Table 1. Evaluation values ($n = 20$, $r = 0.8$)

Group	F_2		
	average	best	worst
1	23.10	9.95	38.80
2	29.42	17.91	50.74
3	34.96	22.88	60.69
4	40.49	26.86	61.69
5	51.63	28.85	95.52
Original PSO	37.08	13.93	71.58

REFERENCES

- [1] J. Kennedy and R. C. Eberhart, "Particle Swarm Optimization," Proc. of IEEE Int. Conf. on Neural Networks, pp.1942-1948, 1995.
- [2] R. C. Eberhart and J. Kennedy, "A New Optimizer Using Particle Swarm Theory," Proc. of the Sixth International Symposium on Micromachine and Human Science, pp.39-43, 1995.
- [3] R. C. Eberhart and Y. Shi, "Comparing Inertia Weights and Constrictions Factors in Particle Swarm Optimization," Proc. of IEEE Congress on Evolutionary Computation, pp.84-88, 2000.
- [4] J. Kennedy and R. C. Eberhart, "Swarm Intelligence," Morgan Kaufmann Publishers, 2001.
- [5] A.Kumamoto, A.Utani and H.Yamamoto, "Advanced Particle Swarm Optimization for Computing Plural Acceptable Solutions," Int. J. Innovative Computing, Information and Control, vol.5, no.11, pp.4383-4392, 2009.
- [6] Y.Yoshimura, H.Nakano, A.Utani, A.Miyauchi and H.Yamamoto, "An Effective Allocation Scheme for Sink Nodes in Wireless Sensor Networks Using Suppression PSO," ICIC Express Letters, vol.3, no.3 (A), pp.519-524, 2009.
- [7] G.G.Yen and M.Daneshyari, "Diversity-based Information Exchange among Multiple Swarms in Particle Swarm Optimization," Proc. IEEE Congress on Evolutionary Computation, pp. 6150-6157, 2006.
- [8] S.Janson and M.Middendorf, "A Hierarchical Particle Swarm Optimizer and Its Adaptive Variant," IEEE Trans.Systems, Man, and Cybernetics, Part B, vol.35, No.6, pp.1272-1282, 2005.
- [9] S.Nakano, A.Ishigami and K.Yasuda, "Particle Swarm Optimization Based on the Concept of Tabu Search," Proc. IEEE Congress on Evolutionary Computation, pp.3258-3263, 2007.
- [10] Y.Taguchi, Y.Kanamori, H.Nakano, A.Utani and A.Miyauchi, "A Competitive PSO Based on Evaluation with Priority for Finding Plural Solutions" Proc. IEEE Congress on Evolutionary Computation, pp.102-107, 2010.

An effective allocation method of ZigBee sensor nodes using a discrete particle swarm optimizer

Ryota Saito, Hidehiro Nakano, Akihito Utani, Arata Miyauchi

and Hisao Yamamoto

Tokyo City University

1-28-1, Tamazutsumi, Setagaya-ku, Tokyo, 158-8557 Japan

(saito@ic.cs.tcu.ac.jp)

Abstract: This paper proposes a method to find effective allocations of ZigBee coordinators using the Discrete Particle Swarm Optimizer (DPSO). In the proposed method, an observation area is represented as a grid space. For a given ZigBee end device location, it is decided whether each ZigBee coordinator is allocated or not on each intersection of the grid. Such binary state variables are optimized by the DPSO. In the simulation experiments, the proposed method is evaluated to some of given ZigBee end device locations. It is shown that the proposed method can provide effective allocations of ZigBee coordinators.

Keywords: ZigBee sensor networks, Coordinator, Discrete Particle Swarm Optimization

I. INTRODUCTION

ZigBee sensor networks are known as a wireless technology of an open global standard [1] [2]. The ZigBee sensor networks have a wide range of applications, such as voice services [3] and vehicular environments [4]. Also, many protocols for ZigBee sensor networks have been proposed. ZigBee sensor nodes are classified into a Full-Function Device (FFD) and a Reduced-Function Device (RFD). The RFD is a low-cost device and can be a ZigBee end device which monitors status information around it, such as temperature, light intensity, and moving objects. The FFD can be not only a ZigBee end device but also a ZigBee coordinator or a ZigBee router which gathers sensing information transmitted from RFDs via wireless communication.

The basic network topologies of the ZigBee sensor networks are star networks, cluster tree networks, mesh networks, and so on. This paper focuses on the star networks. In the networks, one coordinator and end devices exist; routers do not exist. Each end device does not have routing functions; it only transmits its own sensing information directly to a coordinator and does not relay sensing information from the other devices. Since multi-hop wireless communication is not required to the end devices, energy consumption of each end device can be saved. Hence, long-term observation is possible. In addition, constructing cluster tree networks of plural coordinators, large scale observation is also possible. However, it is needed that all end devices can communicate directly to one of coordinators via

wireless communication, since each end device does not have routing functions. Therefore, effective allocations of coordinators in an observation area should be considered. That is, the number of coordinators and their locations should be optimized. This is also regarded as a problem to design a kind of cluster tree networks.

This paper proposes a method to find effective allocations of coordinators using a discrete particle swarm optimizer (DPSO) [5]. In the DPSO, each particle having binary state variables represents a solution of an objective function, and moves in a multidimensional search space based on its own and other particles' experiences. As each particle effectively interacts to each other, an optimum solution for the objective function can be found. The DPSO can fast solve various optimization problems although the algorithm uses only simple and fundamental operations. In the proposed method, an observation area is represented as a grid space. For a given end device location, it is decided whether each coordinator is allocated or not on each intersection of the grid. Such binary state variables are optimized by the DPSO. Desired allocations of coordinators are defined as follows: all end devices can communicate directly to one of coordinators with the minimum number of coordinators. The objective function is designed by considering them. In the simulation experiments, the proposed method is evaluated to some of given end device locations. It is shown that the proposed method can provide effective allocations of coordinators.

II. ZIGBEE SENSOR NETWORKS

ZigBee is one of the world standards on a short distance wireless sensor network [1]. The ZigBee belong to the WPAN (Wireless Personal Area network), and can construct low-cost and low-power networks. Specification of the ZigBee in a basic part is standardized as IEEE 802.15.4 [2]. The typical data-transfer speed is from 20kbps to 250kbps. Each ZigBee sensor nodes can operate during several years by batteries. ZigBee sensor nodes are classified into a Full-function Device (FFD) and a Reduced-function Device (RFD). The RFD is a low-cost device and can be a ZigBee end device which monitors status information around it, such as temperature, light intensity, and moving objects. The FFD can be not only a ZigBee end device but also a ZigBee coordinator or a ZigBee router which gathers sensing information transmitted from RFDs via wireless communication.

The basic network topologies of the ZigBee sensor networks are star networks, cluster tree networks, mesh networks, and so on (see Fig.1). In all the networks, one coordinator controls whole of their networks. In the star networks, a root node becomes a coordinator and leaf nodes become end devices; routers do not exist in the networks. In the cluster networks, a root node becomes a coordinator, leaf nodes become end devices, and the other nodes become routers. In the mesh networks, one node becomes a coordinator and all the other nodes become routers.

This paper focuses on the star networks. In the networks, each end device does not have routing functions; it only transmits its own sensing information directly to a coordinator and does not relay sensing information from the other nodes. Since multi-hop wireless communication is not required to end devices, energy consumption of each end device can be saved. Hence, long-term observation is possible. In addition, constructing cluster tree networks of plural coordinators, large scale observation is also possible as shown in Fig.2. However, it is needed that all end devices can communicate directly to one of coordinators via wireless communication, since each end device does not have routing functions. Therefore, effective allocations of coordinators in an observation area should be considered. That is, the number of coordinators and their locations should be optimized. This is also regarded as a problem to design a kind of cluster tree networks.

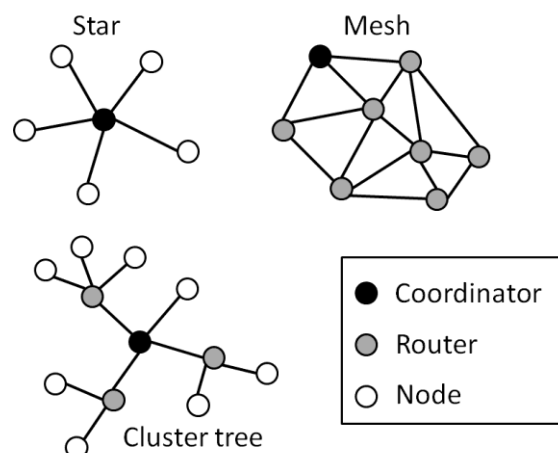


Fig.1. Basic topologies of ZigBee sensor networks.

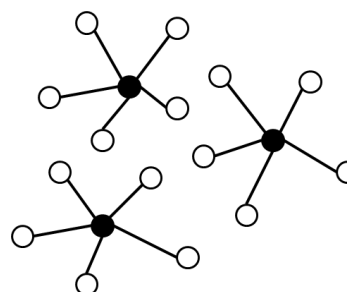


Fig.2. Effective allocations of plural coordinators.

III. DISCRETE PARTICLE SWARM OPTIMIZER

The Particle Swarm Optimizer (PSO) is known as a kind of metaheuristic algorithms, and can fast solve solutions in various optimization problems, compared with the other optimization methods [6]. The PSO is modeled by particles with positions and velocities in multidimensional search space. Each particle has a personal best solution as a search history of its particle and shares a global best solution as a search history of all particles. The Discrete Particle Swarm Optimizer (DPSO) is a discrete binary version of the PSO [5]. The DPSO can be applied to various combinational optimization problems. Basic algorithm of the DPSO is described as follows.

(step1) Set positions and velocities of each particle at random.

(step2) Update the positions of each particle by Equation (1). They are decided as binary values by substituting the current velocities to the sigmoid function (2), and comparing them with uniform random numbers.

$$\text{if } \rho < \text{sig}(v_i^{k+1}) \text{ then } x_i^{k+1} = 1 \quad (1)$$

$$\text{else } x_i^{k+1} = 0$$

$$\text{sig}(v_i^{k+1}) = \frac{1}{1 + \exp(-v_i^{k+1})} \quad (2)$$

where x_i^k and v_i^k are the position and velocity of the i -th particle at the k -th iteration, respectively. $\text{sig}(\cdot)$ is the sigmoid function, and ρ is a uniform random number from 0 to 1.

(step3) Calculate evaluation values of each particle.

(step4) Update each personal best solution ($pbest_i$).

(step5) Update global best solution ($gbest$).

(step6) Update the velocities of each particle by Equation (3).

$$v_i^{k+1} = w \cdot v_i^k + c_1 \cdot r_1 \cdot (pbest_i - x_i^k) + c_2 \cdot r_2 \cdot (gbest - x_i^k) \quad (3)$$

where w is an inertia coefficient for the current velocity vector. c_1 is a weight coefficient for personal best position vector. c_2 is a weight coefficient for global best position vector. r_1 and r_2 are uniform random numbers from 0 to 1.

(step7) Repeat from step2 to step6 until the number of iterations or evaluation value of a solution reaches a predetermined value.

IV. PROPOSED METHOD

In this section, the proposed method is explained and typical simulation results are shown. We apply the DPSO to the ZigBee coordinator allocation problem as follows. The observation area is delimited as the grid space. Each intersection of the grid represents a candidate location of coordinators, and the combination whether coordinators are allocated is optimized by the DPSO. The purpose of this problem is that all end devices are connected directly by one hop with one of coordinators via wireless communication. In such a constraint condition, the number of coordinators is minimized. The evaluation function is given by Equation (4).

$$F = \frac{1}{f_1} + Wf_2 \quad (4)$$

where F is an evaluation value. f_1 is the number of coordinators, f_2 is the number of end devices which can directly connect with one of coordinators, and W is a weight parameter.

End devices (nodes) are allocated in the observation area at random. The size of the observation space is 20×20 . The radio range of nodes is 5. The number of particles in the DPSO is 10. The number of cycles for a single trial is 100. In all the experiments, the DPSO uses the fixed parameter values:

$$w = 1.0, c_1 = c_2 = 1.0, W = 1.0.$$

First, we show the simulation results for 10 nodes. Fig.3 shows the example allocation of coordinators obtained by the DPSO when the grid is 5×5 . In the figure, obtained minimum number of coordinators is 5. Fig.4 shows the results when the grid is 9×9 . In the figure, obtained minimum number of coordinators is 4. As compared with the case of 5×5 , the number of candidate locations of coordinators increases. Then, the obtained minimum number of coordinators decreases. Table 1 shows the number of allocation patterns and their obtained times for 100 trials.

Next, we show the simulation results for 20 nodes. Figs.5 and 6 show the example allocations when the grid is 5×5 and 9×9 , respectively. Table 2 shows the number of allocation patterns and their obtained times for 100 trials.

Depending on the number of nodes and their locations, total number of effective allocation patterns of coordinators change. However, it should be noted that the proposed method based on the DPSO can find acceptable solutions for all trials.

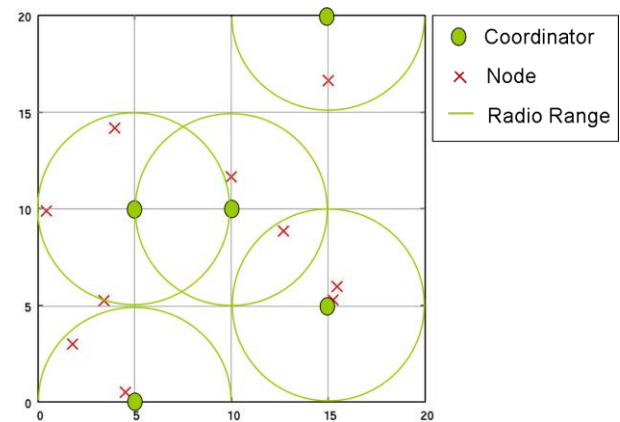


Fig.3. Allocation result (10 nodes, 5×5 grid).

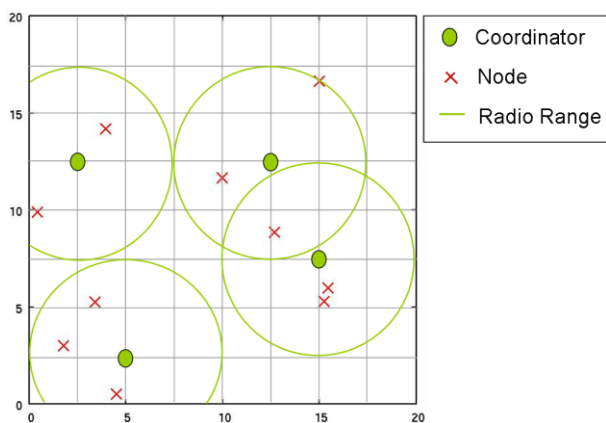


Fig.4. Allocation result (10 nodes, 9×9 grid).

Table 1. Number of allocation patterns (10 nodes).

Grid	Number of coordinators	Obtained frequency	Number of patterns
5×5	5	79	28
	6	21	20
9×9	4	35	35
	5	57	57
	6	8	8

VI. CONCLUSION

This paper has proposed an application of the DPSO to ZigBee sensor networks. The proposed method can provide effective allocations of ZigBee coordinators such that all ZigBee end devices can connect directly with one of coordinators via wireless communication, as minimizing the number of coordinators. Also, the proposed method can provide various allocation patterns by changing initial values. If the grid becomes finer, the problem becomes more difficult. However, the possibility that a better solution can be discovered increases. This means that allocations of the coordinators can be effectively optimized by the DPSO by appropriately setting the grid considering the radio range and the scale of problems.

Future problems include (1) more detailed analysis of searching performances, (2) application of the method for finding plural acceptable solutions.

REFERENCES

- [1] ZigBee Alliance, <http://www.zigbee.org>, 2007.
- [2] 802.15.4-2003 IEEE Standard for Information Technology-Part 15.4, 2003.
- [3] C.Wang, K.Sohraby, R.Jana, L.Ji, and M.Deneshmand, "Voice communications over ZigBee

networks," IEEE Commun. Mag., vol.46, no. 1, pp.121-127, 2008.

[4] H.M.Tsai, O.K.Tonguz, C.Saraydar, T.Talty, M.Ames, and A.Macdonald, "ZigBee-based inter-car wireless sensor networks: A case study," IEEE Wireless Commun., vol.14, no.6, pp.68-77, 2007.

[5] J.Kennedy & R.Eberhart, "A discrete binary version of the particle swarm optimization algorithm," Proc. SMC '97, pp.4104-4109, 1997.

[6] J. Kennedy and R. C. Eberhart, "Particle Swarm Optimization," Proc. ICNN, pp.1942-1948, 1995.

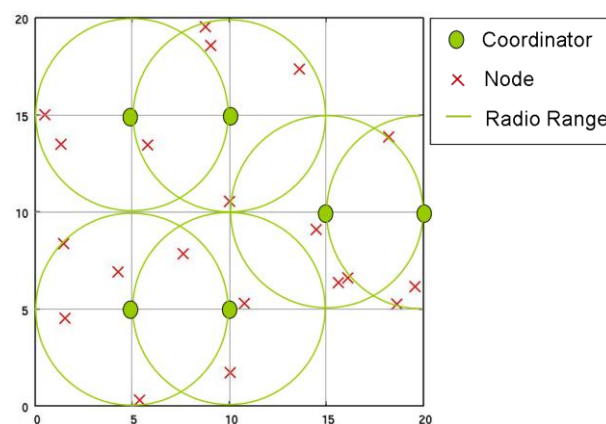


Fig.5. Allocation result (20 nodes, 5×5 grid).

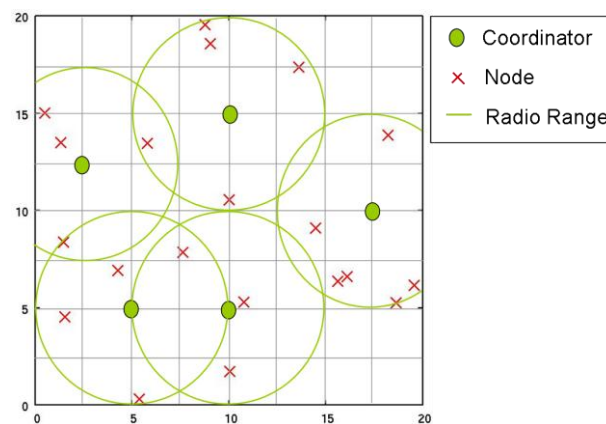


Fig.6. Allocation result (20 nodes, 9×9 grid).

Table 2. Number of allocation patterns (20 nodes).

Grid	Number of coordinators	Obtained frequency	Number of patterns
5×5	6	55	14
	7	39	28
	8	6	6
9×9	5	3	3
	6	26	26
	7	50	50
	8	21	21

An Implementation of Probabilistic Model-Building Coevolutionary Algorithm

Takahiro OTANI and Takaya ARITA

Graduate School of Information Science, Nagoya University
Furo-cho, Chikusa-ku, Nagoya 464-8601, Japan
(Email: t-otani@alife.cs.is.nagoya-u.ac.jp, arita@nagoya-u.jp)

Abstract: We propose an extended coevolutionary algorithm (CA) with probabilistic model-building (CA-PMB) in order to improve search performance of CA. This paper specifically describes an implementation of CA-PMB called coevolutionary algorithm with population-based incremental learning (CA-PBIL), and analyzes behavior of the algorithm through computational experiments using intransitive numbers game as a benchmark problem. The experimental results show that desirable coevolution may be inhibited by the *over-specialization* effect, and that the algorithm shows complex dynamics caused by the game's *intransitivity*. However, further experiments show that the intransitivity encourages desirable coevolution when a different learning rate is set for each population.

Keywords: Coevolutionary algorithm, Probabilistic model-building genetic algorithm, Intransitive numbers game.

I. INTRODUCTION

Competitive coevolutionary algorithm is an extension of standard evolutionary algorithms in which each solution is not evaluated by a fixed objective function (or fitness function), but is evaluated based on interactions between other solutions.

The first application of the algorithm is design of a sorting network proposed by Hillis [1]. He showed CA can design a feasible network structure which has fewer comparators than a network designed by a standard genetic algorithm. CA has also been successfully applied to various problems including evolution of artificial neural network for classification problems, function approximation, evolving strategies of game players, coevolving predator-prey robots, and so on.

In this study, we propose an extended CA called coevolutionary algorithms with probabilistic model-building (CA-PMB) in which probabilistic model-building genetic algorithm (PMBGA) [2] is used as a search heuristics, and analyzes behavior of the algorithm through computational experiments.

Standard CA uses the search mechanism of the genetic algorithm to evolve candidate solutions. CA-PMB adopts PMBGA as a search heuristics in order to improve search performance of standard CA. PMBGA (also called estimation of distribution algorithm) is a generic name given to a class of evolutionary algorithms in which genetic operators, crossover and mutation, are replaced by building a probabilistic model which represents the distribution of promising solutions and generating new solutions based on the model.

PMBGA can explicitly deal with dependence of variables in a problem, and therefore it shows better search performance on various optimization problems than standard GAs. This paper shows an implementation of CA-PMB called coevolutionary algorithm with population-based incremental learning (CA-PBIL).

This paper analyzes behavior of CA-PBIL through computational experiments using intransitive numbers game as a benchmark problem. Intransitive numbers game is an abstract model devised by Watson and Pollack [3] to study *intransitivity* which refers to cyclic dominance such as the Rock-Paper-Scissors game, and has been seen as a substantial obstacle to progress in competitive coevolutionary algorithms. Experimental results show that desirable coevolution may be inhibited by the *over-specialization* effect, and that the algorithm shows complex dynamics caused by the game's *intransitivity*. However, further experiments show that the intransitivity encourages desirable coevolution when a different learning rate is set for each population.

II. COEVOLUTIONARY ALGORITHM

CA is an extension of standard evolutionary algorithms. An important difference between (competitive) CA and standard evolutionary algorithms is how to define an evaluation function. In CA, each solution is not evaluated by a fixed objective function as in the standard evolutionary computations, but is evaluated based on interactions between other solutions. A model of CA dealt in this paper uses two solution sets S^1 and S^2 . A solution s in a solution set is evaluated based on interactions with all of solutions in the other

solution set. An evaluation function $F(s)$ is defined as follows,

$$F(s) = \begin{cases} \sum_{t \in S^2} E(s, t) & \text{if } s \in S^1 \\ \sum_{t \in S^1} E(s, t) & \text{if } s \in S^2 \end{cases}, \quad (1)$$

where $E(s, t)$ denotes a payoff of solution s depending on an interaction with solution t , which is defined based on a targeted problem.

III. COEVOLUTIONARY ALGORITHM WITH PROBABILISTIC MODEL-BUILDING

1. Scheme of Proposed Algorithm

PMBGA (also called estimation of distribution algorithm) is a generic name given to a class of evolutionary algorithms in which genetic operators, crossover and mutation, are replaced by building a probabilistic model which represents distribution of promising solutions and generating new solutions based on the model.

In this study, we propose coevolutionary algorithms with probabilistic model-building (CA-PMB) in which PMBGA is used as a search heuristics. A scheme of the algorithm is described in Fig. 1. This algorithm generates each solution set using probabilistic model which represents the distribution of promising solutions, and evaluates each generated solution according to the equation (1). Then, the model is updated based on good solutions.

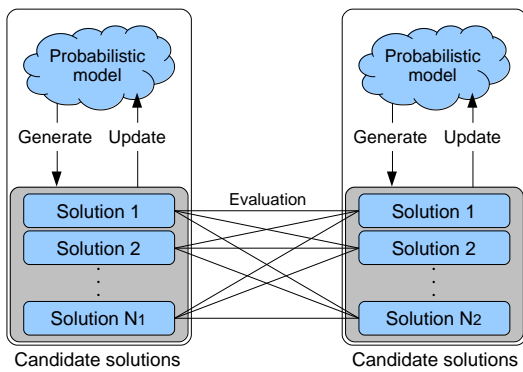


Fig. 1. Scheme of CA-PMB.

2. CA-PBIL: An Implementation of CA-PMB

This paper shows an implementation of CA-PMB called coevolutionary algorithm with population-based incremental learning (CA-PBIL). A pseudocode of the algorithm is described in Fig. 2. CA-PBIL uses PBIL algorithm [4] as a search heuristics. PBIL is a simple variation of PMBGA. This algorithm deals with candidate solutions as bit-strings, and uses and updates

probability vector as a probabilistic model which represents the probability of assigning value “1” to the corresponding bit for a new candidate solution.

```

 $p_i^1 \leftarrow 0.5, i = 1, \dots, L_1$ 
 $p_i^2 \leftarrow 0.5, i = 1, \dots, L_2$ 
while Termination condition not met do
   $S^1 \leftarrow N_1$  solutions generated by  $\mathbf{p}^1$ 
   $S^2 \leftarrow N_2$  solutions generated by  $\mathbf{p}^2$ 
   $best^1 \leftarrow \operatorname{argmax}_{s \in S^1} F(s)$ 
   $best^2 \leftarrow \operatorname{argmax}_{s \in S^2} F(s)$ 
   $p_i^1 \leftarrow p_i^1 \cdot (1.0 - LR_1) + best_i^1 \cdot LR_1, i = 1, \dots, L_1$ 
   $p_i^2 \leftarrow p_i^2 \cdot (1.0 - LR_2) + best_i^2 \cdot LR_2, i = 1, \dots, L_2$ 
  for  $i = 1, \dots, L_1$  do
    if  $\text{rand} < MP_1$  then
       $p_i^1 \leftarrow p_i^1 \cdot (1.0 - MS_1) + \text{rand}(0, 1) \cdot MS_1$ 
    end if
  end for
  for  $i = 1, \dots, L_2$  do
    if  $\text{rand} < MP_2$  then
       $p_i^2 \leftarrow p_i^2 \cdot (1.0 - MS_2) + \text{rand}(0, 1) \cdot MS_2$ 
    end if
  end for
end while

```

Fig. 2. Pseudocode of CA-PBIL.

IV. INTRANSITIVE NUMBERS GAME

This paper analyzes the behavior of CA-PBIL through computational experiments using intransitive numbers game (ING) [3] as a benchmark problem. ING is an abstract model to study *intransitivity* (as in the well-known Rock-Paper-Scissors game) which has been seen as a substantial obstacle to progress in competitive coevolutionary algorithms, and is usually used to compare the performance of coevolutionary algorithms.

1. Problem Definition

A solution of ING is a n -dimensional vector, and a range of each dimension's value is $[0, k]$. The payoff function $E(s, t)$ is defined as follows,

$$E(s, t) = \operatorname{sign} \left(\sum_{i=1}^n g_i \right), \quad (2)$$

where

$$g_i = \begin{cases} s_i - t_i & \text{if } h_i = \min_j h_j \\ 0 & \text{otherwise} \end{cases}$$

$$h_i = |s_i - t_i|.$$

The function *sign* returns 1 when an input value is positive value, returns -1 when an input value is negative value, and returns 0 when an input value is 0. Therefore, the winning solution is the one with higher magnitude in the dimension of least difference between the two solutions.

Furthermore, a modified ING is also used for experimental analysis of the algorithm. In this problem, the function *sign* in equation (2) is modified as follows. The function returns 1 when an input value is positive value, otherwise returns 0. These settings cause algorithm's complex dynamics more frequently.

2. Bit-strings Solution Representation

A bit-string b is converted to a vector solution s as follows. The length of the bit-string is set to $L_1 = L_2 = nk$, and i -th dimension's value of a vector solution is calculated as follows,

$$s_i = \sum_{j=1}^k b_{(i-1)k+j},$$

where b_i denotes i -th bit value of the bit-string.

V. COMPUTATIONAL EXPERIMENTS

In this section, we analyze the behavior of CA-PBIL using ING. The number of dimension and the maximum value of each dimension were set to $n = 2$ and $k = 100$ respectively. Optimal solution is $(100, 100)$. The length of a bit-string was set to $L_1 = L_2 = 200$.

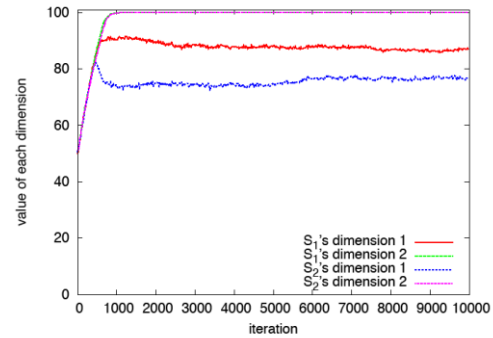
1. Dynamics on the Standard ING

First of all, we carried out following experiments using the standard ING to study how the average evaluated value of generated solution progresses. Algorithm's parameters were set as follows, the learning rates: $LR_1 = LR_2 = 0.01$, the numbers of solutions generated every iteration: $N_1 = N_2 = 100$, and the mutation probabilities: $MP_1 = MP_2 = 0.0$. This means mutation procedure was not executed. The number of iteration was set at 10000, and the experiment was trialed 100 times.

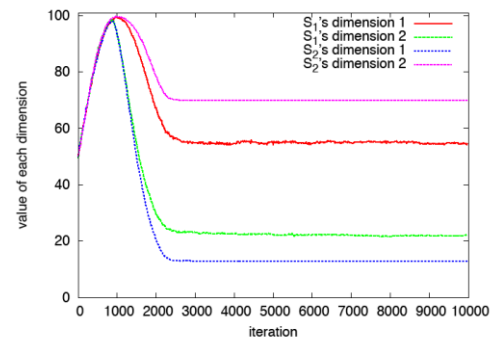
The experimental results show that a *stagnation* pattern occurred in almost all trials while a *convergence to a low value* pattern rarely occurred. Typical examples of each occurred pattern are described in Fig. 3. Fig. 3(a) describes the stagnation pattern which is called the *over-specialization* effect [3]. If two values in one dimension become closer to each other than in the other dimension enough, the other dimension does not play a role in decision of payoffs. Therefore, the former will evolve desirably, however the latter will stagnate.

Fig. 3(b) shows a rare case in which the convergence to a low value pattern occurred. This pattern is caused by the intransitivity of the game, and is called *relativism* effect in the literature [3]. For example, consider $a = (4, 7)$ and $b = (5, 5)$. The dimension of least

difference is the first, and b gets positive payoff. Now, $a' = (3, 6)$ is a small variation from a . The dimension of least difference when a' and b is the second dimension and a' gets a positive payoff. Therefore, a should be replaced by a' . Then, $b' = (4, 4)$ gets a positive payoff depending on the interaction with a' , and b should be replaced by b' . These solutions evolve to low values in this manner repeatedly.



(a) Stagnation (99 times).



(b) Convergence to a low value (1 time).

Fig. 3. Typical examples of progress patterns on the standard intransitive numbers game.

2. Dynamics on the Modified ING

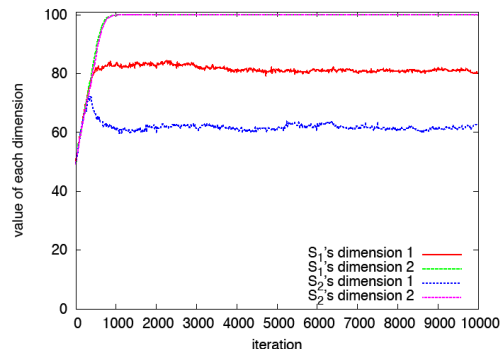
We carried out the same experiments using the modified ING. Algorithm's parameters were set to same as previous experiments. In this experiments, four types of patterns occurred. Typical examples of each pattern are described in Fig. 4. Dynamic patterns described in Fig. 4(b)(c)(d) were caused by the intransitivity of the game.

3. Coevolution under a Different Learning Rate

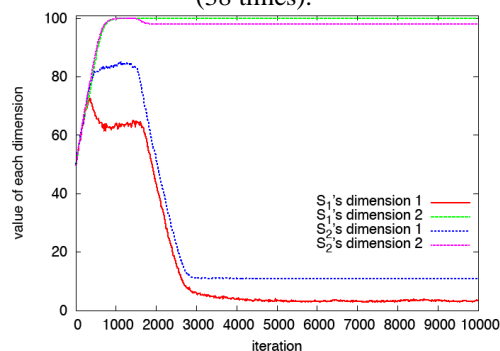
Finally, we carried out experiments to analyze the behavior of the algorithm when a different learning rate was set for each solution set. We examined the number of reached optimal solutions varying S^2 's learning rate LR_2 from 0.01 to 0.03. And other parameters were set to same as the previous experiments.

Fig. 5 shows the experimental results. According to these results, the search performance was increased

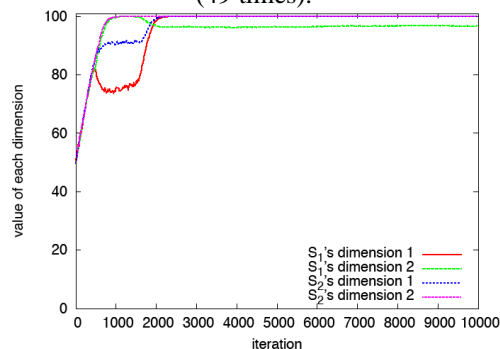
when a different learning rate was set for each population on the modified ING. The reason is supposed to be that these settings could encourage convergence to high values as shown in Fig. 4(c).



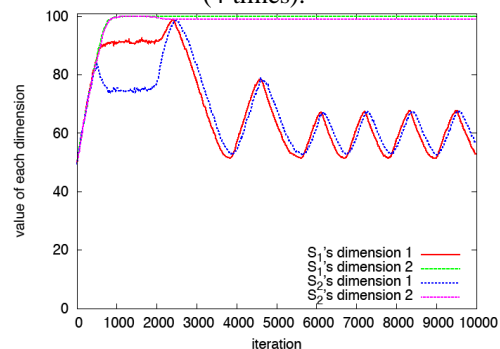
(a) Stagnation caused by the over-specialization (38 times).



(b) Converges to a low value in one dimension (49 times).



(c) Convergence to high values in both dimensions (4 times).



(d) Oscillation starting in one dimension (9 times).

Fig. 4. Typical examples of progress patterns on the modified intransitive numbers game.

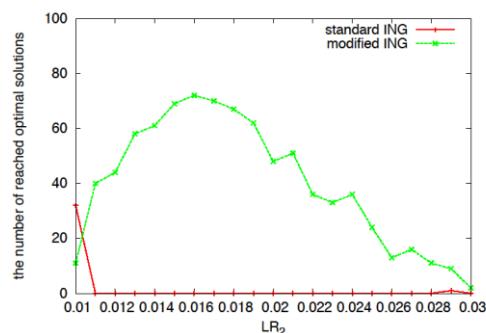


Fig. 5. The number of reached optimal solutions.

VI. CONCLUSION

In this paper, we proposed an extended CA called CA-PMB, showed CA-PBIL as an initial implementation, and examined the algorithm's behavior through experiments using ING. Experimental results showed that desirable coevolution may be inhibited by over-specialization effect. We also observed an interesting coevolutionary behavior caused by the game's intransitivity especially on the modified ING. Further experiments showed that the intransitivity encourages desirable coevolution when a different learning rate is set for each population. This feature has a possibility to provide new ways to solve various problems in coevolutionary domain more effectively and efficiently.

Future work includes the analysis of the proposed algorithm by conducting further experiments. In particular, the effectiveness of a different learning rate should be evaluated in more detail. Another direction would be to compare the performance with other algorithms and to evaluate using other more practical problems. It might be also interesting to implement CA combined with other PMBGA.

REFERENCES

- [1] W. D. Hillis (1990), Co-evolving parasites improve simulated evolution as an optimization procedure. *Physica D: Nonlinear Phenomena* 42:228-234
- [2] M. Pelikan, D. E. Goldberg, and F. G. Lobo (2002), A survey of optimization by building and using probabilistic models. *Computational Optimization and Applications* 21:5-20
- [3] R.A. Watson and J.B. Pollack (2001), Coevolutionary dynamics in a minimal substrate. *Proc. of the Genetic and Evolutionary Computation Conference*:702-709
- [4] S. Baluja (1994), Population-based incremental learning: A method for integrating genetic search based function optimization and competitive learning. *Technical Report CMU-CS-94-163*, Computer Science Department, Carnegie Mellon University, Pittsburgh, PA

Modeling and solution for optimization problems with incomplete information

– A general framework and an application to cruising taxi problems –

Makoto OHARA and Hisashi TAMAKI
Kobe University, 1-1 Rokkodai-cho, Nada-ku, Kobe
(Tel: +81-78-803-6102; Fax: +81-78-803-6102)
(ohara@al.cs.kobe-u.ac.jp)

Abstract: The purpose of this study is to construct a general model for optimization problems with incomplete information, and to assist designing solutions. The term “incomplete information” means that information of target system, e.g. the dynamics and the status variables, is not obtained enough to optimize. Before description of proposed model with incomplete information, an optimization model with “complete” information is structured. The occasions with “incompleteness” of information are explained on this optimization model, and approaches to resolving them are described. Then, the optimization model with incomplete information is defined. Moreover, in order to investigate the validity of the proposed framework, it is applied to cab-dispatching (of cruising taxis) problems, where the objective is to distribute a set of cabs efficiently by indicating the adequate location to each taxi driver. Through some computational examples, the effectiveness and the potential of the proposed approach is confirmed.

Keywords: Uncertainty, Optimization Model, Distributing Taxi Problem

1. INTRODUCTION

This research deals with a class of optimization problems with incomplete information, in which the information about the structure as well as the dynamics of the target system is not sufficient. To this class of the problems, in this paper, a general framework for both modeling the problem formally and designing a solution structure systematically is newly proposed. This class includes such types of optimization problems as containing some uncertainty in systems, e.g. due to the spatially partial or temporarily late observability, and/or some unobservability in decision-making.

So far, lots of researches have been presented on several types of optimization problems with uncertainty, from the viewpoints of the description of the problem as well as the design of solutions [1~3]. However, there have been few studies on general frameworks of both optimization models and their solutions. By introducing informational viewpoints, a variety of uncertain aspects may be dealt with in a uniform way, which is the keynote point of our research.

For confirming validity of the proposal approach, it is applied distributed cruising taxi problems. In these cab-dispatching problems, there are many unobservable state variables, e.g., the occurrence of passengers and the positions of the cabs of competitive companies. It is difficult or it might be impossible to optimize the dispatching beforehand due to incompleteness. In designing the solution, a set of rules (rule-set) for indicating the priority areas in the information layer, and a genetics-based machine learning (GBML) method is adopted to adjust a rule-set in the supervisor layer. As a result of the computational examples, the effectiveness and the potential of the proposed approach is confirmed.

2. OPTIMIZATION PROBLEMS

2.1 Optimization Model with Complete Information

Optimization problems are defined as problems to maxi-

mize/minimize evaluation values about behaviors of systems. Components of the optimization problems are referred as; “Target System” is the target of evaluation for optimization, and is controlled directly, “Relevant System” interacts with Target System, in other words, Relevant System may be possible to be controlled indirectly, “Environment” acts Target System, and can’t be controlled, “Controller” decides a direction of Target System’s behaviors, “Supervisor” affects the decision-making of Controller.

In order to optimize, these components have to convey decisions for others, i.e., “Control”: Controller sends operations, which indicate what to do, to Target System, “Supervision”: Supervisor sends orders for decision-making to Controller.

For making decisions, the components know about others, i.e., “Observation”: The states of Target System, Relevant System and Environment are sensed by Controller, “Evaluation”: Controller sends results, which are clues to judge the effectiveness of decision-making, to Supervisor. These components and information-exchanges are collectively called “Optimization Model” in this paper.

To understand easily, Optimization Model is identified as a hierarchical manner; “Physical Layer” shows the physical side of the problems, and includes continuous-time systems, i.e. Target System, Relevant System and Environment, “Information Layer” shows the information side of the problems, and includes short-rate discrete-time system, i.e. Controller, “Supervisor Layer” shows an optimizer for the problems, and includes long-rate discrete-time system, i.e. Supervisor.

Definition of Time Constant: Target System is optimized during \mathcal{T} ($= [0, T)$). Controller evaluates behaviors of Target System every time interval τ^E , and Physical Layer is observed each sampling cycle τ^O . The time horizon \mathcal{T} is discretized to n^E terms by the interval τ^E , and each k -th term $\mathcal{T}^{(k)}$ is discretized to n^O periods by the cycle τ^O . Then, $\mathcal{T}^{(k)}$ corresponds the time interval $[k\tau^E, (k+1)\tau^E)$, and $m^{(k)}$ th period corresponds $[k\tau^E + m\tau, k\tau^E + (m+1)\tau)$. The set of periods \mathcal{T}^D is

defined as below;

$$\mathcal{T}^{O(k)} = \{0, \dots, n^O\} \quad (n^O = (\tau^E / \tau^O) - 1). \quad (1)$$

If notation “(k)” isn’t be needed, it is omitted in following. The information-exchanges on the time axis are illustrated in Fig. 1.

Elements: The elements of the optimization model (and correspondent elements of Dispatching Cruising Taxi Problems which are described later) are shown in Table 1.

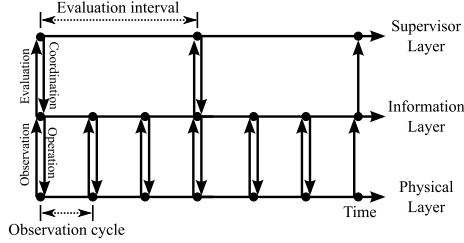


Fig. 1 Information-exchanges between each layer.

Input/Output: Each component’s inputs/outputs with complete information is defined as below;

$$\begin{aligned} a^S(t) &= o^R(t), & e^S(t) &= o^V(t), & a^R(t) &= o^S(t), \\ e^R(t) &= o^V(t), & u(t) &= v[\lfloor t/\tau \rfloor], \\ y[m] &= (x^S(m\tau), x^R(m\tau), x^V(m\tau)), \\ p[o^{(k)}] &= c[o^{(k)}], & r[n^{E(k)}] &= Z[n^{E(k)}]. \end{aligned}$$

Optimization Problems: The objective function and the restriction is formulated as;

$$\begin{aligned} \min Z &= F\{y[0], \dots, y[n^O]\} + P(G)\{y[0], \dots, y[n^O]\} \\ \text{s.t. } v[m] &\in H[m] \quad (\forall m \in \mathcal{T}^O) \end{aligned}$$

Controller obtains the states of Target System by observations. Then, the state restriction is used in a penalty P .

2.2 Incompleteness

2.2.1 Classification

A variable y is observation quantities of a status variable x . The relation of y and x with complete information is as follow;

$$y[m] = x(m\tau^O). \quad (2)$$

The classes of incompleteness in the observations are;

(i) Accuracy (error): An observed value includes an error $\sigma(t)$ [%].

$$y[m] = x(m\tau^O) + \sigma(m\tau^O). \quad (3)$$

(ii) Time delay: A status value of time $\tau(t)$ ago is observed.

$$y[m] = x(m\tau^O - \tau). \quad (4)$$

(iii) Unobservable: A status value is unobservable.

$$y[m] = *. \quad (5)$$

The symbol $*$ means uncertain value.

The observations are classified completeness, incompleteness (i), (ii), (iii), or combination of theirs.

2.2.2 Completion

Completion functions are required for each incompleteness;

• for incompleteness (i) : f^C

$$y[m] = f^C(x(m\tau^O) + \sigma(m\tau^O)) = x(m\tau^O), \quad (6)$$

• for incompleteness (ii) : f^E

$$y[m] = f^E(x(m\tau^O - \tau)) = x[m], \quad (7)$$

• for incompleteness (iii) : f^P

$$y[m] = f^P(*) = x[m]. \quad (8)$$

The functions f^C , f^E and f^P each are called “Correction”, “Estimation” and “Prediction”.

In order to implement completion of incompleteness, information as follows are needed. “History”: an history about a status variable to observe is effective for Correction and Prediction. “Same kind of a status variable”: if a system is consists of subsystems, e.g. multi-agent, status variables of each subsystem, which are same kind of a state to observe, help Estimation. “Other kind of a status variable”: if a status variable can’t be observed, other state values of a same system might be valid for Estimation. “Knowledge”: knowledge about a system or dynamics assist all completions.

2.3 Optimization Model with Incomplete Information

Optimization Model with incomplete information has completion functions defined in Section 2.2.2. Completion Module converts observed values, and sends complementary values to Controller. An overview of Optimization Model with incomplete information and an inside of Completion Module are illustrated in Fig. 2.

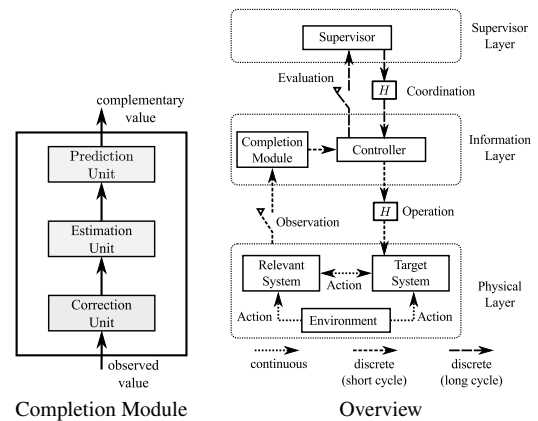


Fig. 2 Hierarchical model of optimization problem with incomplete information

3. DISPATCHING CRUISING TAXI PROBLEMS

For confirming validity of the proposal optimization model, the model applies Dispatching Cruising Taxi Problem.

3.1 Outline

Since the revision of Road Transportation Law in Japan, the taxi business is becoming saturated by new entries. In particular, rookie drivers have a lot of trouble finding passengers,

Table 1 Elements of optimization problems and corresponding with Dispatching Cruising Taxi Problems

Layer	Component/System [†]	Symbol [‡]	Element [†]
Physical	Target System (Cooperative Company)	• x^S	state (position, assigned passenger and number of assignment)
		+ u	control input (dispatching area)
		+ a^S	relevant action (position, destination and assigned cab)
		+ e^S	environment action (traffic jam)
		* T^S	transition function (move rule)
		- o^S	output action (position and assigned passenger)
		* U^S	output function (take rule)
	Relevant System (1) (Passengers)	• x^R	state (position, destination, appearance time and assigned cab)
		+ a^R	relevant action (position and assigned passenger)
		+ e^R	environment action (weather)
		* T^R	transition function (appear rule)
		- o^R	output action (position, destination and assigned cab)
		* U^R	output function (ride rule)
	Relevant System (2) (Competitive Company)	• x^R	state (position and assigned passenger)
		+ a^R	relevant action ([Not Available])
		+ e^R	environment action (traffic jam)
		* T^R	transition function (move rule)
		- o^R	output action (position and assigned passenger)
		* U^R	output function (take rule)
	Environment (Environment)	• x^V	state (states about weather and traffic jam)
		* T^V	transition function (weather and traffic translation)
		- o^V	output action (weather and traffic jam)
		* U^V	output function (weather and traffic action rule)
Information	Controller (Dispatch Controller)	+ y	observed value (cabs states, passengers actions and environment actions)
		• \mathcal{M}	observed record (observed record)
		- v	operation (dispatching area)
		+ p	operation parameter (weight coefficients)
		* G	state restriction ([Not Available])
		* H	operation restriction (area permitted business)
		* C	operation function (priority calculation)
		- Z	evaluated value (total of assignment)
		* F	evaluation function (sum of assignment)
Supervisor	Supervisor (Supervisor)	+ r	result (total of assignment)
		• \mathcal{R}	result record (assignment record)
		- c	order (weight coefficients)
		* o	order function (GBML)
		• \mathcal{O}	order record (weight coefficient record)

[†] Words in parentheses are corresponding components or elements of Dispatching Cruising Taxi Problems.

[‡] Header symbols mean +:input, -:output, •:state, and *:other, e.g. dynamics.

because taxi business has relied on individual experience of drivers. The taxi companies need systems which assist less-experienced drivers for finding passengers. There have been studies based on statistical models [4], [5], in contrast, few studies have been carried out to analyze Dispatching Cruising Taxi Problem agent-models.

3.2 Approach

Positions of passengers, targets of taxis, are unobservable in these problems. Thus, taxis are dispatched regions. This paper suggests an optimization framework for taxi dispatching by the rule-set which calculates target areas with observable state variables. The corresponds of the proposed model and Dispatching Cruising Taxi Problems have been described in Table 1.

Definition of Space: A region \mathcal{A} is intended in a problem, and a cooperative company is permitted business in a region \mathcal{A}^B . The region \mathcal{A} is divided to regions \mathcal{A}_a ($a = 1, \dots, n^A$), and each cab of the cooperative company is distributed to any region \mathcal{A}_a . The region \mathcal{A}_a is called "Area a " below.

Priority Rule: A priority rule calculates priorities of each area for every cab. Each cab is dispatched to the area which is highest priority for the cab. The rule calculates priority which is a weighted summation of preparing equations.

Learning Method: In this paper, condition is defined as partially feature quantity space of whole areas, and action is defined as weight coefficients in the priority rule [6].

Elements: The elements of dispatched cruising taxi problems have been shown in Table 1.

4. COMPUTATIONAL EXAMPLE

Simulations which learn the rules and evaluate them are performed to verify the validity of proposed approach for distribution cruising taxi problems. The Rules learned by GBML are compared with a heuristic rule by evaluated values.

4.1 Setting

Simulator: The cooperative company's cabs go to its own dispatching area by the shortest distance, and move randomly

in the dispatching areas after arrival. The competitive company uses a proportion rule, this rule dispatches proportional number cabs to the ratio of estimated number of passengers in each area to whole areas. The passengers appear only in permitted business region \mathcal{A}^B . The number of emerging passengers in whole areas is 3 per a time unit on average. The number of the areas is 100, and the number of the permitted business areas is 64.

Priority Rule: The priorities are calculated by weighted equations with properties as below. The areas have more priority, in which more passengers appear probably and more nearly. The areas have more priority, in which less cabs of the cooperative company, The areas have more priority, in which more passengers appear probably, The prior areas are decided at random. The weight of equations have been normalized in refer to results of preliminary experiment.

GBML: The number of individuals is 30, and the number of generations is 100. Each individual is simulated 2 times in each condition (I) ~ (III), about random variables for passengers, weather and traffic jam, and the average of evaluated value are treated as a fitness of the individual. The conditions of passenger appearance are combination of 4 patterns. The patterns are illustrated in Fig. 3, and the combinations are (I): pattern 1 in the noon and pattern 2 in the night, (II): 3 and 3, (iii) 4 and 4 which are made by different seeds. GBML searches the weight coefficients from 0, ± 0.25 , ± 0.5 , ± 0.75 or ± 1 . The feature quantity space is composed of variables defined as, deviation of the number of cabs in each area, estimated number of appearing passengers in whole areas, ratio of cabs carrying no passengers, time slot. The space is divided by small or large of each variable.

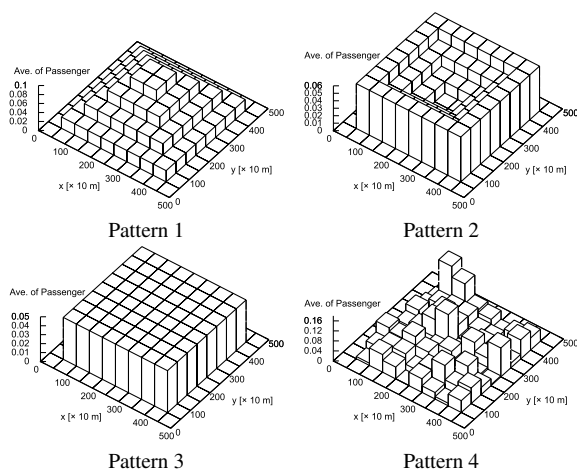


Fig. 3 Examples of appearance patterns of the passengers

Example Problem

The simulations for learning are performed in 2 cases; (a) the cooperative company has 10 cabs, and the competitive company has 20 cabs, (b) the cooperative company has 80 cabs, and the competitive company has 160 cabs, and each case are learned 3 trials. Moreover, the best solutions of each trail and the proportion rule are evaluated 4 times in each condition (I) ~ (III) and all conditions.

4.2 Result

The learning process of the best solution in every trial are

plotted in Fig. 4. The result for evaluation the acquired rule and the proportion rule is plotted in Fig. 5.

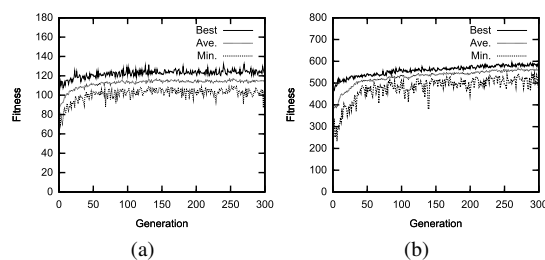


Fig. 4 Learning processes of GBML

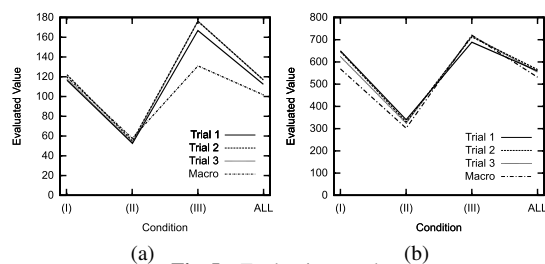


Fig. 5 Evaluation results

From the figures, the acquired rules are valid as well as the proportion rule in all conditions, and better than substantially in particular situations.

5. CONCLUSION

The optimization problems and incompleteness on observation are described. By using them, the optimization model with incomplete information is defined. In addition, in order to confirm utility of the proposed model, it applies Dispatching Cruising Taxi Problems. As the result, the proposed model has potential to express the taxi problems, and to acquire the good solutions. The following are left for future study: to improve the optimization model focused on incompleteness of information, and to apply the proposed model to other problems for future works.

REFERENCES

- [1] Ian Jordaen: Decisions under Uncertainty, Cambridge University Press (2005).
- [2] Zhiang Lin: Environmental determination or organizational design: An exploration of organizational decision making under environmental uncertainty, Simulation Modeling Practice and Theory, 14, 438–453 (2006).
- [3] Enrique Alba, Christian Blum, Pedro Asasi et al.: Optimization Techniques for Solving Complex Problems, Wiley (2009).
- [4] Wong K.I., Wong S.C. and Yang H.: Modeling urban taxi services in congested road networks with elastic demand, Transportaion Research Part B, 35, 819–842 (2001).
- [5] Yu Jianxin, Zhou Xiaomin and Zhao Hongyu: Design and Implementation of Taxi Calling and Dispatching System based on GPS Mobile Phone A Research for LBS Application Teaching Case, Proceedings of 2009 4th International Conference on Computer Science & Education, 1163–1169 (2009).
- [6] Sakakibara K., Tamaki H., Murao H. et al.: Genetics-Based Machine Learning Approach for Flexible Shop Scheduling Problems : Rule Acquisition for Real-time Scheduling (in Japanese), Journal of Information Processing Society of Japan, 45, 2, 91–98 (2004).

Prime Number Generation Using Memetic Programming

Emad Mabrouk¹, Julio César Hernández Castro² and Masao Fukushima³

¹*Dept. of Applied Mathematics and Physics, Graduate School of Informatics, Kyoto University, Kyoto 606-8501, JAPAN.*

Dept. of Mathematics, Faculty of Science, Assiut University, Assiut, EGYPT.

(hamdy@amp.i.kyoto-u.ac.jp)

²*School of Computing, University of Portsmouth, Buckingham Building, Lion Terrace, Portsmouth PO1 3HE, UK.*

(Julio.Hernandez-Castro@port.ac.uk)

³*Dept. of Applied Mathematics and Physics, Graduate School of Informatics, Kyoto University, Kyoto 606-8501, JAPAN.*

(Tel: +81-75-753-5591; Fax: +81-75-753-4756)

(fuku@i.kyoto-u.ac.jp)

Abstract: For centuries, the study of prime numbers has been regarded as a subject of pure mathematics in number theory. Recently, this vision has changed and the importance of prime numbers increased rapidly especially in information technology, e.g., public key cryptography algorithms, hash tables, and pseudorandom number generators. One of the most popular topics that attract attention is to find a formula that maps the set of integers into the set of prime numbers. However, up to now there is no known formula that produces all primes. In this paper, we use a hybrid evolutionary algorithm, called the Memetic Programming (MP) algorithm, to generate mathematical formulas that produce distinct primes. Using the MP algorithm, we succeeded to discover an interesting set of formulas that produce sets of distinct primes.

Keywords: Hybrid Evolutionary Algorithm, Iterated Local Search, Memetic Programming, Prime Number

I. INTRODUCTION

A natural number greater than 1 is called a prime if it is only divisible by 1 and itself. The study of prime numbers and their properties have attracted mathematicians for several centuries. Questions related to prime numbers have puzzled mathematicians for many years, e.g., “is there a formula that maps the set of integers into the set of primes?” Recently, several applications in the field of information technology have increased the importance of prime numbers, and changed the vision that classifies the study of primes as pure mathematics.

The Memetic Programming (MP) algorithm is a new evolutionary algorithm that hybridizes the well-known Genetic Programming (GP) algorithm, Koza [1], with some local search procedures over a tree space to intensify promising programs generated by the GP algorithm. The aim of this paper is to use the MP algorithm to generate some mathematical formulas which produce distinct primes for a set of consecutive integers.

The paper is organized as follows. In the next section, we introduce the MP algorithm briefly. In Section III, we report the results of three experiments for generating formulas which produce distinct primes. Finally, conclusions make up Section IV.

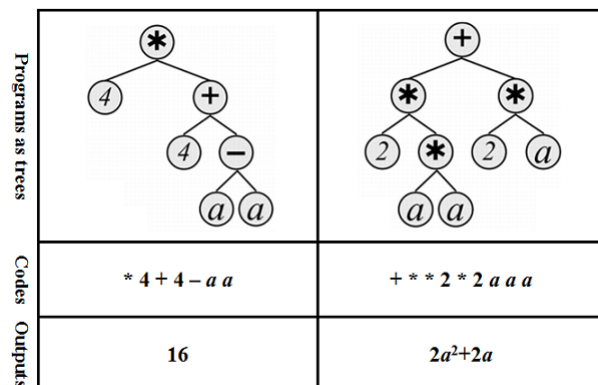


Figure 1: Examples of MP representation

II. MEMETIC PROGRAMMING

The Memetic Programming algorithm is a hybrid evolutionary algorithm that searches for desirable computer programs as outputs. Computer programs treated in the MP algorithm are represented as trees in which leaf nodes are called terminals and internal nodes are called functions. Depending on the problem at hand, the user defines the domains of terminals and functions. In the coding process, the tree structure of a solution should be transformed to an executable code. Fig. 1 shows two examples of MP programs represented as trees, along with their executable codes.

The main loop of the MP algorithm consists of two phases; diversification phase and intensification phase.

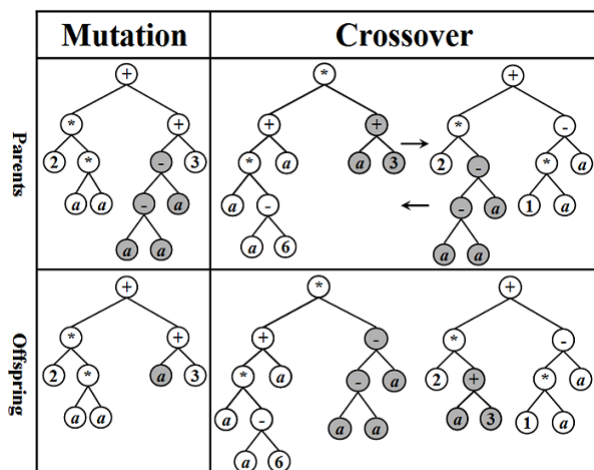


Figure 2: Generating a new offspring using mutation and crossover

In the diversification phase, the MP algorithm guarantees the diversity in the current population by using the GP strategy. Specifically, the MP algorithm selects some programs using a suitable selection strategy, and generates a new population from the current one by using crossover and mutation operators.

Fig. 2 illustrates an example of applying the crossover and mutation operators for some trees. In the intensification phase, the MP algorithm uses a set of local search procedures to intensify elite programs of the current population. These local search procedures will be described in the following subsection. Using these procedures, the Local Search Programming (LSP) algorithm will be introduced in Subsection 2, which is used in the intensification phase of the MP algorithm. Finally, the whole picture of the MP algorithm will be sketched in Subsection 3.

1. Local Searches over Tree Space

The local search procedures aim to generate new trees in a neighborhood of a given tree X . In this subsection, we discuss two types of local searches; static structure search and dynamic structure search, Mabrouk et al [2, 3]. Static structure search explores the neighborhood of a tree by altering its nodes without changing its structure. On the other hand, dynamic structure search changes the structure of a tree by expanding its terminal nodes or cutting its subtrees. Shaking operator is used as a static structure search procedure, while Grafting and Pruning operators are introduced as dynamic structure search procedures.

Shaking search generates a new tree \tilde{X} from the current one X , by altering some nodes of X without

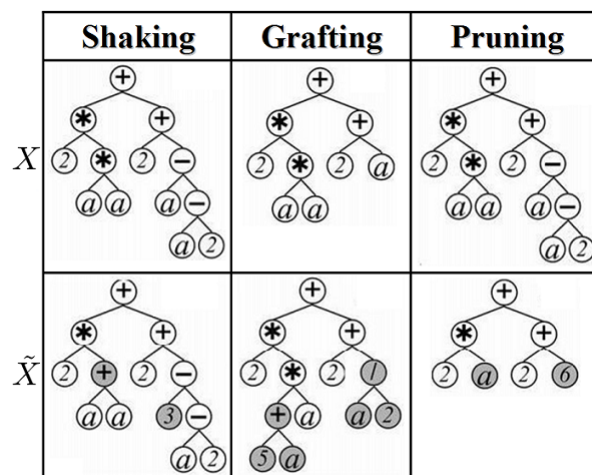


Figure 3: Generating new trees using shaking, grafting and pruning procedures

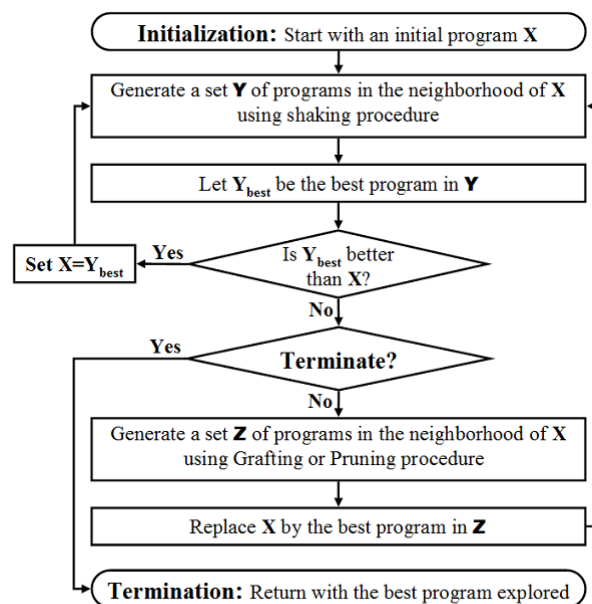


Figure 4: The flowchart of the LSP algorithm

changing its structure. The altered nodes are chosen randomly and replaced by alternative ones, i.e., a terminal node is replaced by a new terminal value and a function node is replaced by a new function of the same number of arguments as the original one. Grafting search generates a new tree \tilde{X} from a tree X by replacing some of its terminals, chosen randomly, by branches of depth $\zeta \geq 1$, where these branches are generated randomly. In contrast to grafting search, pruning search generates an altered tree \tilde{X} from a tree X by cutting some of its branches of depth $\zeta \geq 1$ and replacing them by new terminals, where these branches and terminals are chosen randomly. One may note that X and \tilde{X} have different tree structures in case of applying the grafting or pruning procedures. Fig. 3 shows examples of generating a new tree \tilde{X} from a tree X by applying

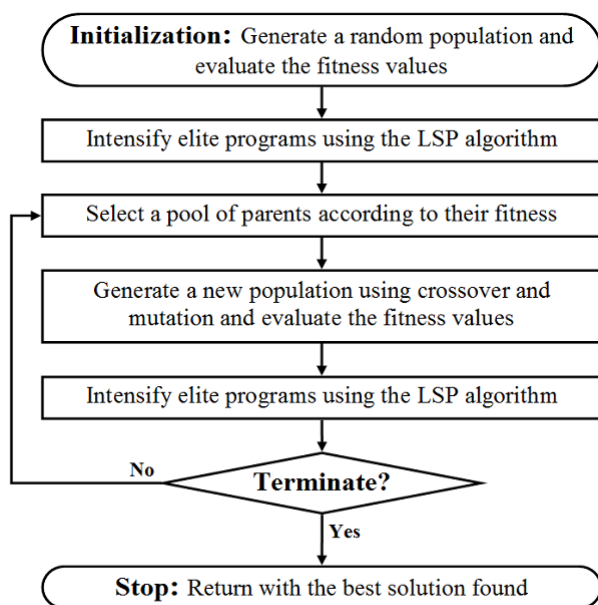


Figure 5: The flowchart of the MP algorithm

shaking, grafting and pruning procedures. For more details see Mabrouk et al [2, 3].

2. LSP Algorithm

In this subsection, we introduce the LSP algorithm to discover the best program in the neighborhood of the current program X . This algorithm uses the local search procedures described in the previous subsection to generate trial programs in the neighborhood of the current one. This process iterates until the termination condition is satisfied, and then the algorithm returns the best program found. Fig. 4 shows the flowchart of the LSP algorithm, where it returns the original program X in case of no improvement.

3. MP Algorithm

The main target of the MP algorithm is to improve the results of the GP algorithm by performing a local search for some promising programs. If the search process succeeds to reach the area near an optimal solution, then a simple local search algorithm can capture that optimal solution easily. Fig. 5 shows the flowchart of the MP algorithm that behaves like the GP algorithm if the LSP algorithm fails to improve the selected programs. However, in this case the MP algorithm will be more costly than the GP algorithm, because of the computational effort spent through the intensification phase.

Each program treated in the MP algorithm consists of one or more gene(s), where a gene represents a sub-tree consisting of terminal and function nodes. Genes in a program are linked together by using a suitable linking

function. The addition function “+” is used as the linking function in this paper. To generate a gene in the initial population, we generate a temporary random gene consisting of two parts, head (functions and terminals) and tail (terminals only). Then, we adjust the final form of the gene by deleting unnecessary elements, based on the functions and terminals that are generated randomly within the gene. For more details see Mabrouk et al [2, 3].

Once the initial population is generated, it will be evolved and improved using the MP operations; i.e., crossover, mutation, shaking, grafting and pruning. For each problem to solve, the function set, the terminal set, the set of representation parameters, the set of search parameters, and the fitness function must be determined before calling the algorithm. The set of representation parameters contains the head length $hLen$ of an initial gene, the maximum length $MaxLen$ of a gene, the number of genes $nGenes$ of each program. On the other hand, the set of search parameters, which guide the algorithm during the search process, consists of the population size $nPop$, the number of generations $nGnrs$, the number of programs nLs that are selected to apply local search procedures, the number of trial programs $nTrs$ that are generated in the neighborhood of a program using a local search procedure, and the maximum number of non-improvements $nFails$. In particular, $nFails$ is used to terminate the LSP algorithm. For more details about these parameters see Mabrouk et al [2, 3].

III. NUMERICAL EXPERIMENTS

In this section we report the results of three different experiments for the MP algorithm to generate formulas that produce primes. The parameter values for the MP algorithm during all experiments are $hLen = 3$, $MaxLen = 40$, $nGenes = 3$, $nLs = 4$, $nTrs = 4$, $nFails = 1$, $nPop = 100$ and $nGnrs = 100$. In addition, the selection strategy for the diversification phase is the tournament selection of size 4. The fitness value for each program is computed as the maximum number of consecutive integers in the interval $[-100, 100]$ for which the program produced distinct primes.

1. Polynomials

In this experiment, we used the set of binary functions $\{+, -, *\}$ as the function set, i.e., each program generated by the MP algorithm represents a polynomial. In addition, we used $\{x, 2, 3, 5, 7, 9\}$ as the

terminal set, where x is an integer. We performed 1000 independent runs for the MP algorithm, and we got a number of polynomials with the fitness values up to 40.

Table 1 shows some of polynomials which generated by the MP algorithm. The first three polynomials in Table 1 have already been found in the literature. Specifically, the first two polynomials are the Euler and Legendre polynomials, and the third one is the polynomial generated by the CGP algorithm, Walker [4]. During our experiments, these three polynomials were found frequently. To the best of the authors' knowledge, the other polynomials seem to be new polynomials.

Table 1. Polynomials generated by the MP algorithm to produce distinct primes

	Polynomial	Fitness	x
1	$x^2 - x + 41$	40	$\{1, \dots, 40\}$
2	$x^2 + x + 41$	40	$\{0, \dots, 39\}$
3	$x^2 - 3x + 43$	40	$\{2, \dots, 41\}$
4	$9x^2 + 33x + 71$	40	$\{-28, \dots, 11\}$
5	$4x^2 - 50x + 197$	40	$\{-13, \dots, 26\}$
6	$8x^2 - 22x - 647$	40	$\{-19, \dots, 20\}$

In the literature, researchers consider the first three polynomials in Table 1 to be different polynomials. However, all of these polynomials produce the same set of primes for different values of the independent variable x . Specifically, one can generate those entire polynomials one after another by using $x := x - \lambda$ for some integers λ . On the other hand, the last three polynomials in Table 1 produce different sets of distinct primes for different sets of consecutive integers. Therefore, we consider these three polynomials to be the best results for the current experiment since all of them are different and independent.

2. Rational Functions

We performed another experiment to find formulas that produce primes with fitness values greater than 40. In this experiment, we modified the function set in the previous experiment to include the protected division operator $\%$, where $x \% y = 1$ if $y = 0$, and $x \% y = x / y$ otherwise. In this case, programs of the MP algorithm will produce real values. Therefore, we let the nearest integer less than or equal to the produced real value be the output of the program. Using the new function set, we got several new formulas that produce up to 42 distinct primes for a set of consecutive integers, for

example, $\lfloor \lfloor (-8x^3 + 69x^2 - 461x - 176) / (8x + 3) \rfloor \rfloor$, with the fitness value 42.

3. Composition Functions

Since we have already got new independent polynomials that can generate different sets of distinct primes, we can use these polynomials to composite new formulas. In this experiment, the output of a program evolved by the MP algorithm is expressed as a linear composition of its genes with some independent polynomials that produce distinct primes. Suppose that G_1 , G_2 and G_3 are the genes of a program evolved by the MP algorithm. Then, the output formula of this program is composed as $f(x) = \lfloor G_1 \rfloor * P_1 + \lfloor G_2 \rfloor * P_2 + \lfloor G_3 \rfloor * P_3$, where P_1 , P_2 and P_3 are independent polynomials. Using this strategy, we got new formulas that produce distinct primes up to 59, for example, $\lfloor \lfloor 7 / (81x + 27) \rfloor (x^2 + x + 41) + \lfloor 9 / (5 - 45x) \rfloor (8x^2 - 22x - 647) \rfloor$, with the fitness value 59.

IV. CONCLUSION

The MP algorithm has succeeded to generate several new formulas that produce sets of distinct primes. Some of the new formulas are polynomials that are able to produce up to 40 distinct primes for a set of consecutive integers. Other rational functions are also generated and they are able to produce up to 59 distinct primes for a set of consecutive integers.

REFERENCES

- [1] Koza JR (1992) Genetic programming: On the programming of computers by means of natural selection. MIT Press, Cambridge
- [2] Mabrouk E, Hedar A, Fukushima M (2008) Memetic programming with adaptive local search using tree data structures. In: Chbeir R et al (eds.), Proceedings of the 5th International Conference on Soft Computing as Transdisciplinary Science and Technology (CSTST08), Cergy-Pontoise, Paris, France, October 27–31, 2008, pp. 258–264
- [3] Mabrouk E, Hedar A, Fukushima M (2010) Memetic programming algorithm with automatically defined functions. Technical Report 2010-015, Department of Applied Mathematics and Physics, Kyoto University, Japan
- [4] Walker JA, Miller JF (2007) Predicting prime numbers using Cartesian genetic programming. In: Ebner M et al. (eds.), Proceedings of the 10th European Conference on Genetic Programming (EuroGP), Valencia, Spain, April 11–13, 2007, pp. 205–216

EMG control of a pneumatic 5-fingered hand using a Petri net

Osamu FUKUDA*, Jonghwan KIM*, Isao NAKAI**, and Yasunori ICHIKAWA**

**National Institute of Advanced Industrial Science and Technology,
Measurement Solution Research Center, 807-1 Shuku-machi, Tosu, Japan*

***SQUSE Inc., 67-21 Nishinokyouyokushi-chou, Nakagyou-ku, Kyoto
(Tel : 81-942-81-3633; Fax : 81-942-81-3698)
(fukuda.o@aist.go.jp)*

Abstract: This paper presents a control method of a 5-fingered artificial hand using EMG signals. Our targeted artificial hand is driven by pneumatic actuators to reduce its weight. Also we do not use electro pneumatic regulators but use ON/OFF solenoid valves to simplify the control system. The pneumatic hand has 15 degrees of freedom, and it seems difficult to discriminate all finger motions only from the EMG signals. Therefore, in this paper, we describe typical hand motions using a Petri net, and efficiently control the finger motions based on this model. Each state of the Petri net indicates a step of the hand posture to complete the intended motion. Simultaneously, this state corresponds to the ON/OFF pattern of the 15 solenoid valves. This enables the operator to control the 5-fingered dexterous hand smoothly, transiting the state in the Petri net according to the EMG motion discrimination. We conducted experiment to verify validity of the proposed method. In the experiment, the typical 5 motions (Spherical grasp, Power grip, Hook grip, Key grip, Precision grip) were successfully performed using the 6-channel EMG signals measured from the operator's forearm.

Keywords: EMG, pneumatic hand, Petri net, motion discrimination, neural network

I. INTRODUCTION

Until now, many researchers have designed EMG-controlled artificial hands for amputees. Its motion was previously limited only the opening and closing hand, but novel 5-fingered dexterous hands have been emerged, due to the progress in robotics and mechatronics fields [1]-[3]. For example, Otto Bock Inc. [1] and TOUCH BIONICS Inc. [2] have launched Michelangelo Hand and i-LIMB Hand, respectively. These hands are controlled by EMG signals and realize human-like finger movements.

However, a servo motor is used as the actuator of each finger joint, it is inevitable that its weight raises a physical burden of the operator during a long time of operation, with increasing number of degrees of freedom. Accordingly, a pneumatic actuator was tried to use as the substitute for the servo motor, and several researchers developed the robotic hands driven by the pneumatic actuator [4], [5]. The pneumatic actuator has a great advantage because it has a very light weight so that it can be expected to reduce the hand weight significantly. For example, Tsujiuchi et al. and SQUSE Inc. [6] newly designed the small pneumatic actuator, which can be installed into finger joints, and developed 5-fingered artificial hand [4], [5]. This pneumatic

actuator can be driven by a lower air pressure than the previous one. Also, the system becomes compact using a small compressor. But, it is considerably difficult to control the multi-channel finger joints precisely, because non-linear relationship exists between the input air pressure and the output tension.

This paper proposes a novel control method for a 5-fingered prosthetic hand using EMG signals. We adopt pneumatic actuators to control the multiple joints to reduce the hand weight. Also, we use ON/OFF solenoid valves instead of electro pneumatic regulators to simplify the control system. The pneumatic hand has 15 degrees of freedom, so that it appears to be difficult to discriminate the motion of all joints. Therefore, we design the state transition model for the typical hand motions using a Petri net. This model enables the operator to control dexterous finger motions based on the simple discrimination of the discrete hand motions, such as hand opening, hand closing, and so on. Each state of the state transition model corresponds to the hand posture completing to the intended motion, and the ON/OFF pattern of the 15 solenoid valves are changed according to this state. Transiting the state in the Petri net, the operator can skillfully control the 5-fingered dexterous hand smoothly.

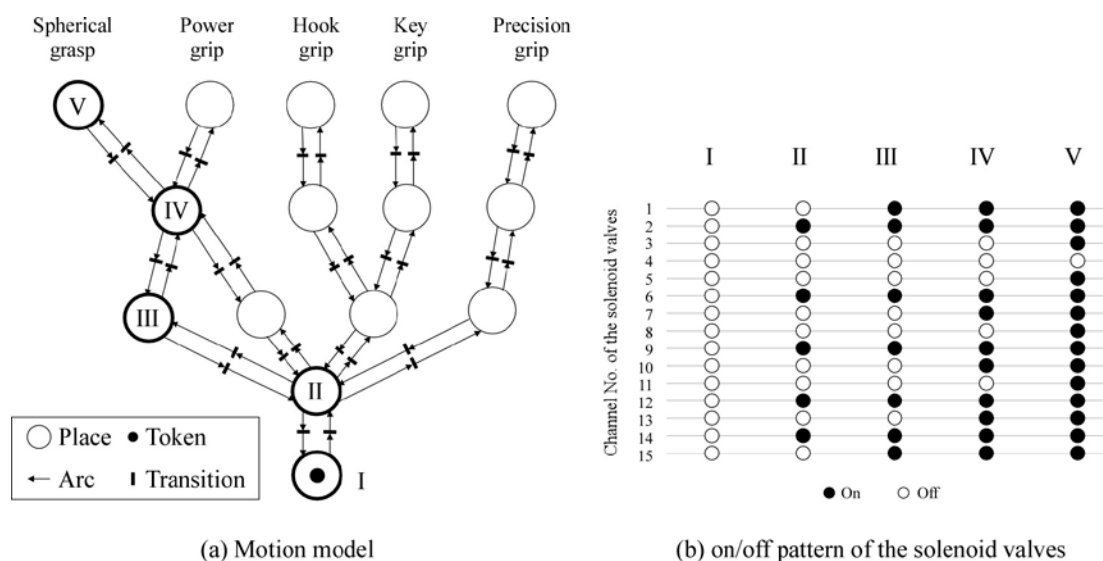


Fig. 1 Control strategy

This paper is organized as follows. The control strategy of the 5-fingered pneumatic hand is introduced in Section II, the structure of the developed system is explained in Section III, the experiment is reported in Section IV, and Section V concludes the paper.

II. Control strategy

This paper proposed a novel control strategy of the 5-fingered pneumatic hand. The pneumatic hand used in this study has the 15 pneumatic actuators, and each actuator is controlled by the ON/OFF solenoid valve. Therefore, we have to consider how ON/OFF patterns are designed using 15 solenoid valves, and when these patterns are changed. Fig. 1 explains the control strategy of the hand motion based on the proposed method. (a) expresses the state transition model described by the Petri net, and (b) depicts the ON/OFF pattern of the 15-channel solenoid valves. The Petri net is composed of some places, transitions and arcs, that denote the states of the hand postures, the conditions based on the EMG discrimination, and the flows of the hand postures, respectively. At the start of the operation, a token is set on the initial place. The transition means that the duration time of a discriminated motion exceeds the prespecified threshold. For example, the token is moved from I to V, if Spherical grasp is discriminated in the system and its duration time exceeds the prespecified thresholds. Conversely, if No motion is discriminated and its duration time exceeds the threshold, the token is moved from V to I and the hand is opened. According to

the places where the token exists, 15 solenoid valves are controlled depicted in (b).

In this paper, we select 5 motions for the discrimination targets: 1. Spherical grasp, 2. Power grip, 3. Hook grip, 4. Key grip, 5. Precision grip. These motions were frequently used in the previous research, and have possibility to discriminate with high accuracy using the EMG signals. It is noted that the proposed control method is not restricted within these 5 motions. We can choose appropriate motions according to operator's operability.

III. Components of the system

Fig. 2 indicates the components of the system. The EMG signals are measured by the EMG amplifier system (DELSYS Inc., BAGNOLI EMG SYSTEM), and are transferred to the personal computer (Hewlett-Packard Inc., HP Pavilion, Intel(R)Core(TM)2 Duo CPU 2.27GHz) via the multi function DAQ (National Instruments Inc., NI USB-6229).

The signal processing, which is conducted in the personal computer, is composed of 3 parts: 1. Feature extraction, 2. Motion discrimination, 3. pattern generation of the solenoid valves. Each process is explained in the following sections.

1. Feature extraction

First, the measured EMG signals are rectified and filtered out through the 4th order Butterworth filter (cut-off frequency: 1.0[Hz]) to extract the amplitude information. The filtered signals are resampled with a sampling frequency of 50.0[Hz], and defined as $E_l(n)$.

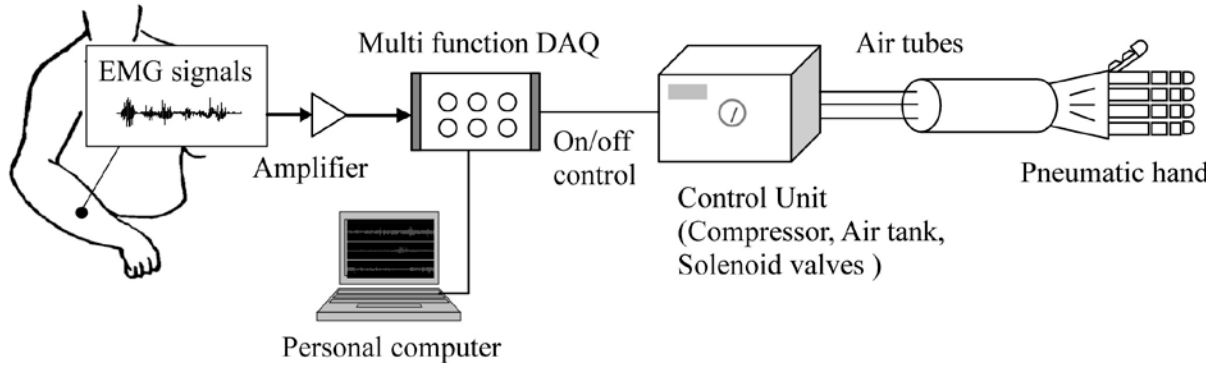


Fig. 2 Components of the system

Then, the pattern vector $x_l(n)$ for the motion discrimination is calculated as

$$x_l(n) = \frac{E_l(n)/E_l^{max}}{\sum_{l=1}^L E_l(n)/E_l^{max}}$$

where E_l^{max} is the maximum value of $E_l(n)$ while the operator executes the maximum voluntary contraction. Also, the muscular contraction level $F(n)$ is calculated to recognize the motion.

$$F(n) = \frac{1}{L} \sum_{l=1}^L \frac{E_l(n)}{E_l^{max}}$$

If $F(n)$ exceeds the prespecified threshold α , the system considers motion has occurred.

2. Motion discrimination

In the proposed method, we use a neural network to discriminate the operator's intended motion. The neural network can learn feature patterns and adapt the system to the differences due to the individuality, the electrode locations, and so on. Before the motion discrimination, the neural network has to be trained using learning samples. The initial value of the weight coefficient is a random number from 0 to 1. The mean square error is used as the energy function, and the learning is carried out to minimize this function. The back propagation method is adopted for the learning algorithm.

3. Pattern generation of the solenoid valves

Finally, the ON/OFF patterns of the solenoid valves are generated. In this process, we use the state transition model which describes typical grasp motions using a Petri net. The control signal for the ON/OFF solenoid valves is generated, transitioning the state in the Petri net according to the EMG motion discrimination. These

signals are returned to the control unit through the Multi function DAQ. The compact compressor (SQUSE Inc., MP-2-C) is installed in the control unit, and it drives the pneumatic actuators in the finger joints.

IV. Experiment

We conducted experiment to verify the validity of the proposed method. Subject controlled the 5-fingered pneumatic hand using his EMG signals. Before the experiments, we explained the purpose of the experiments and obtained informed consents from the subject. Subject was briefly trained for about 30 minutes before the measurements. The EMG signals were measured from 6 electrodes, and the number of the discrimination target were 5 motions: 1. Spherical grasp, 2. Power grip, 3. Hook grip, 4. Key grip, 5. Precision grip, which frequently arise in daily activities. The 6 electrodes were placed on the right forearm surrounding regular intervals. The operator does not have to set the electrodes on the associated muscles strictly, due to the learning ability of the neural network. The neural network can learn the pre-extracted EMG patterns to adapt the system to individualities, electrode locations, and so on. The parameters in the signal processing were set as follows: the number of the learning data was 50 samples for each motion. The threshold of the duration time of the transitions was 0.5[sec].

Fig. 3 shows examples of the motion control using the developed system. Subject performed the 5 motions. The figure indicates the 6-channel of EMG signals, the muscular contraction information, the changes of the place in the Petri net, and the discrimination results. During the operation, no discrimination error was observed and the token in the Petri net appropriately transited based on the discrimination result. We

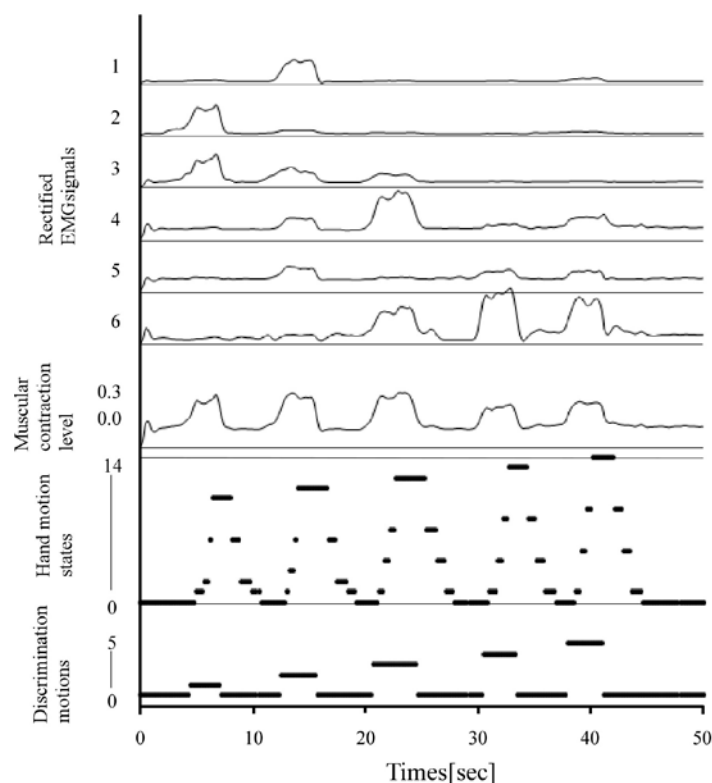


Fig. 3 Control example

confirmed that all 5 motions were successfully carried out in regular order.

V. CONCLUSION

This paper proposed the novel EMG control method for 5-fingered pneumatic hand. We introduced the typical hand motion model described by a Petri net into the control system, because it was difficult to control 15 degree-of-freedom hand precisely using only the EMG signals. Each place in the Petri net corresponds to the ON/OFF pattern of the solenoid valves, and the token is moved based on the result of the motion discrimination. The pneumatic actuators installed in the finger joints are controlled according to places where the token exist. Consequently, the operator can control 5 finger motions smoothly and naturally discriminating only the discrete motions, e. g. hand grasping, hand opening, and so. on. To verify the validity of the proposed method, the experiment was conducted. In the experiment, we examined the control performance of 5 typical grasping motions: 1. Spherical grasp, 2. Power grip, 3. Hook grip, 4. Key grip, 5. Precision grip. The experimental result confirmed the validity of the proposed method.

In future study, we would like to re-design discrimination algorithm to improve the discrimination

performance. Also, we will optimize the mechanism of the pneumatic hand for amputee's daily activities. A part of this work was supported by Adaptable and Seamless Technology Transfer Program through Target-Driven R & D of Japan Science and Technology Agency.

REFERENCES

- [1] <http://www.ottobock.com>
- [2] <http://www.touchbionics.com>
- [3] M. C. Carroza, G. Cappiello, S. Micera, B. B. Edin, L. Beccai, C. Cipriani: Design of a cybernetic hand for perception and action, *Biological Cybernetics*, Vol. 95, No. 6, pp. 629-644, 2006.
- [4] Nobutaka TSUJIUCHI, Takayuki KOIZUMI, Shinya NISHINO, Hiroyuki KOMATSUBARA, Tatsuwo KUDAWARA, Masanori HIRANO: Development of Pneumatic Master-Slave Hand and Joint Control, *The Japan Society of Mechanical Engineers*, Vol. 74, No. 741, pp. 223-228, 2008.
- [5] Hiroyuki Takeda, Nobutaka Tsujiuchi, Takayuki Koizumi, Hiroto Kan, Masanori Hirano, Yoichiro Nakamura: Development of Prosthetic Arm with Pneumatic Hand and Tendon-Driven Wrist, *Proceedings of the 31st Annual International Conference of the IEEE Engineering in Medicine and Biology Society*, pp. 5048-5051, 2009.
- [6] <http://www.squse.co.jp/index.html>

Depth Calculation by using Face Detection ASIC

Seung Min Choi, *Jae-chan Jeong, Jaeil Cho

Electronics and Telecommunications Research Institute
*University of Science and Technology

{ccsmm, jicho}@etri.re.kr
*channij@ust.ac.kr

Abstract - Real-time processing at mobile devices is always a hot issue. Although face detection and stereo matching, specially, are core elements for HRI application, they are one of the processes with heaviest loads at real-time processing. In this paper, we present novel methods of calculating disparity and detecting face with one chip, named Altair, which can detect 32 frontal faces/frame at 30 fps. Stereo image can be inputted into Altair, because it is designed to detect face on frame by frame and has two input ports. If the left image is inputted on N-th frame time and then the right image is inputted on (N+1)-th frame time, we can get face information of left and right images with one frame delay. Then we can calculate the disparity of face with this information and we can easily estimate distance from robot to human with it. When one or more faces are detected, we classify various cases to identify correspondent faces. We can detect faces and calculate the distances of them at 15 fps and can adjust the frame rate.

Keywords: HRI, HCI, face detection, stereo vision, disparity, real-time

I. INTRODUCTION

We introduce a novel method of calculating disparity of stereo camera with face detection chip. Because, real-time processing at mobile devices has been always a hot issue, many researchers have studied about speedy and light image processing algorithms for years. Although, face detection and stereo matching, specially, are core elements for HRI application, they are one of the applications with heaviest loads at processing.

In this paper, we present novel methods of calculating disparity and detecting face with one chip, named Altair, which can detect 32 frontal faces/frame at 30 fps. Stereo image can be inputted into Altair, because it is designed to detect face on frame by frame and has two input ports. If left image is inputted on N-th frame time and then the right image is inputted on (N+1)-th frame time, we can get face information of left and right images with one frame delay. Then we can calculate the disparity of face with this information and we can easily estimate distance from robot to human with it. When one or more faces are detected, we classify various cases to identify correspondent faces.

II. Stereo Camera and face detector

Disparity can be calculated by finding correspondence of stereo cameras. Fig.1 shows geometry of stereo camera system which consists of two camera and field of object models. Because in fig.1 there are 4 triangles which have properties of triangle similarity, depth of disparity equations can be derived from them like table 1.

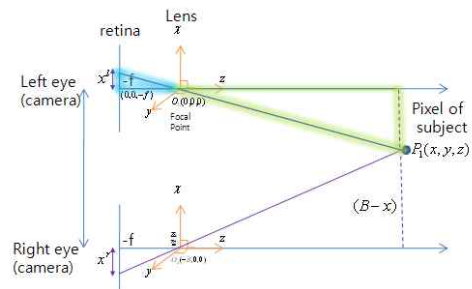


Fig.1. Geometry of Stereo Camera Model

Table 1. Equation of Stereo Camera Model

By triangle similarity of Left Camera System,
$x^l : x = f : z \rightarrow xf = zx^l \rightarrow x^l = \frac{xf}{z}$
By triangle similarity of Right Camera System,
$x^r : B - x = f : z \rightarrow (B - x)f = zx^r$
$\rightarrow x^r = \frac{Bf - xf}{z} \rightarrow x^r = \frac{Bf}{z} - \frac{xf}{z} = \frac{Bf}{z} - x^l$
$\therefore d = \frac{Bf}{z}, \text{ or } z = \frac{Bf}{d}$
$\text{, where } d = x^l + x^r \text{ (absolute value)}$

In generally finding correct disparity of stereo images is key point of stereo correspondence problem. So, many stereo vision algorithms are suggested over the years. According to [1], however, there are few real-time algorithms (over 30 fps) as shown in taxonomy.

Because of difficulty of real-time processing and huge power consumption for stereo matching, in some application where disparity of whole image pixel are not need, only disparity or depth of ROI(Region Of Interest) is important value in the camera image. For example, when a service robot has to keep a distance and serves some convenience to human, it only needs to know the distance from human to it. If it has a face detection function with its platform, it's easy to know the distance from human.

We present the way that calculates the distance with face detection chip. Fig.2 shows the outline of the novel method of calculating disparity of stereo camera with face detection chip. Two of camera image enters face detection unit in time division manner. Then face detector finds face and calculate the difference of center of face in left and right images.

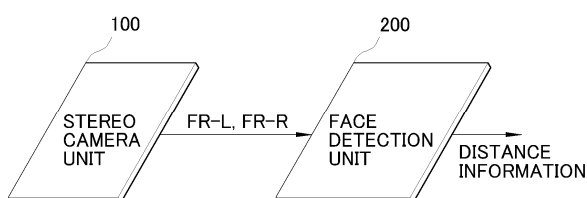


Fig.2. Outline of novel method.

We use the Altair as a face detection unit in fig. 3. Altair is the ASIC chip(1.2×1.2cm²) for face detection that can detect 32 person per frame at 30 fps of QVGA(320x240) image[3]. It covers frontal and ±15° slant face. The chosen method of face detection is the AdaBoost algorithm, which consist of MCT (Modified Census Transform) confidence

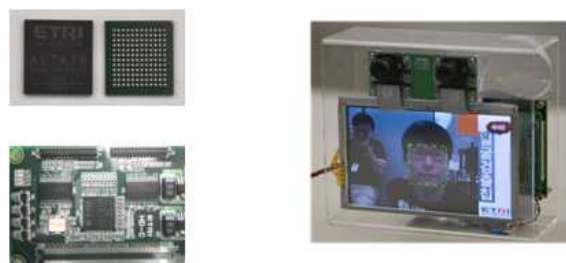


Fig.3. Altair (Frontal face detect ASIC)

III. Disparity Calculation with Face Detector

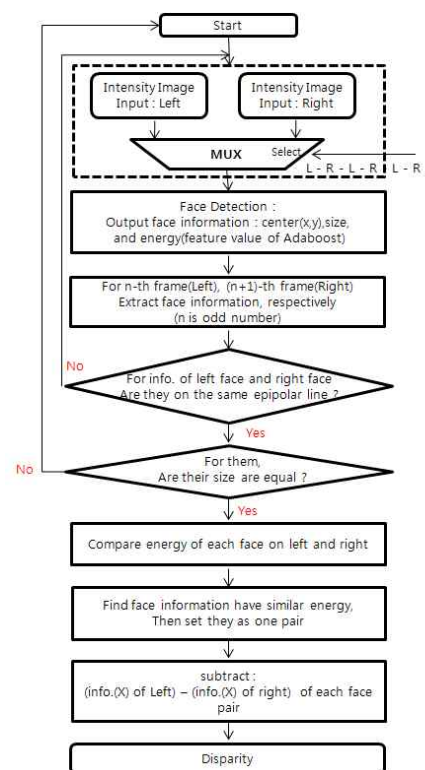


Fig.4. Flow Chart of our new method.

Fig.4 shows the flow chart of our novel method for calculating disparity of stereo camera with face detection chip. After start left and right camera images input into the multiplexer (MUX), then left or right image outputs from MUX in regular sequence by 'Select' signal. Then this interlaced image with frame order enters face detection block whose output is information of faces that consists of following table 2.

Table 2. Face information register of Altair

Mem(0x0c)	7 6 5 4 3 2 1 0	<table><tr><td>y/r</td><td>pos0</td><td>pos1</td><td>pos2</td><td>pos3</td><td>pos4</td><td>pos5</td><td>pos6</td></tr><tr><td>x/r</td><td>x/8</td><td>y/8</td><td>S4</td><td>S5</td><td>S2</td><td>S1</td><td>S0</td></tr></table>	y/r	pos0	pos1	pos2	pos3	pos4	pos5	pos6	x/r	x/8	y/8	S4	S5	S2	S1	S0	fd_count(6 bits)
y/r	pos0	pos1	pos2	pos3	pos4	pos5	pos6												
x/r	x/8	y/8	S4	S5	S2	S1	S0												
Mem(0x0f)	7 6 5 4 3 2 1 0	<table><tr><td>x/y</td><td>x/8</td><td>y/8</td><td>S4</td><td>S5</td><td>S2</td><td>S1</td><td>S0</td></tr></table>	x/y	x/8	y/8	S4	S5	S2	S1	S0	step								
x/y	x/8	y/8	S4	S5	S2	S1	S0												
Mem(0x10)	7 6 5 4 3 2 1 0	<table><tr><td>x/r</td><td>x/6</td><td>x/5</td><td>x/4</td><td>x/3</td><td>x/2</td><td>x/1</td><td>x/0</td></tr></table>	x/r	x/6	x/5	x/4	x/3	x/2	x/1	x/0	x_pos_LSB_n								
x/r	x/6	x/5	x/4	x/3	x/2	x/1	x/0												
Mem(0x11)	7 6 5 4 3 2 1 0	<table><tr><td>y/r</td><td>y/8</td><td>y/5</td><td>y/4</td><td>y/3</td><td>y/2</td><td>y/1</td><td>y/0</td></tr></table>	y/r	y/8	y/5	y/4	y/3	y/2	y/1	y/0	y_pos_LSB_n								
y/r	y/8	y/5	y/4	y/3	y/2	y/1	y/0												
Mem(0x12)	7 6 5 4 3 2 1 0	<table><tr><td>x/y</td><td>x/10</td><td>x/9</td><td>x/8</td><td>y/11</td><td>y/10</td><td>y/9</td><td>y/8</td></tr></table>	x/y	x/10	x/9	x/8	y/11	y/10	y/9	y/8	x_y_MSB_n								
x/y	x/10	x/9	x/8	y/11	y/10	y/9	y/8												

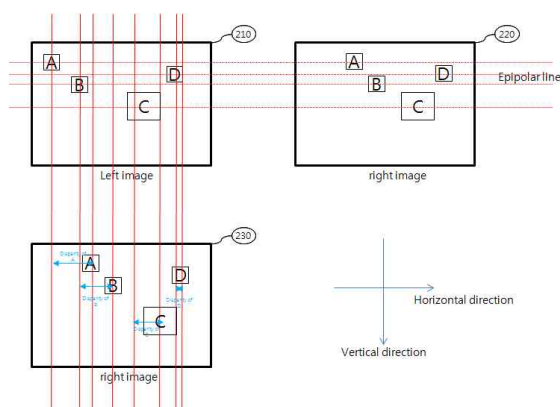
Register	range	Bitwidth	Bit
FD_count	0~31	5+1(L/R)	Fd_count(50)
Bits/frame		6	

Register	range	Bitwidth	Bit
STEP_n	0~20	5	step(40)
X_POS_n	0~639	10	step(76) & x_pos_LSB(7:0) or x_y_MSB(7:4) & x_pos_LSB(7:0)
Y_POS_n	0~479	9	step(5) & y_pos_LSB(7:0) or x_y_MSB(3:0) & x_pos_LSB(7:0)
Bits/person		24	

After getting face information from Altair, next step is to compare information of faces on left frame and on right frame as shown in table 3.

Table 3. Comparing face and Calculating disparity

item	Information	note
On the same epipolar line ?	'x' coordinate of center point	Vertical direction
Has the same size of face	Size of face	
Has the similar energy value?	Sum of Confidence	Sum of feature of Adaboost algorithm (1/probability)
Calculate Disparity	'x' coordinate of center point	Horizontal direction



VI. Experiment

We capture two sets of stereo image with system in fig. 4. One is the continuous image set where a human moves around camera as shown in fig. 5

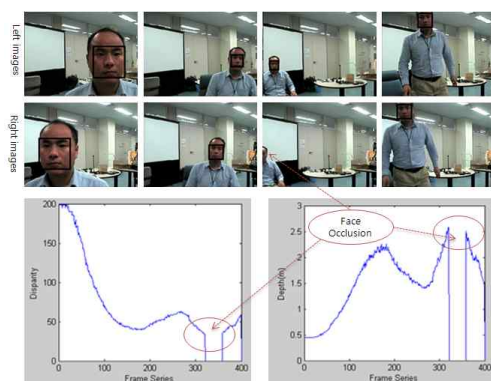


Fig.5. depth calculation for moving human

A human is near camera at first and move far from it then comes to near again. Because face was not detected for a while at around about 350-th frame, face occlusion occurred and disparity and depth could not be estimated. Depth can be converted from disparity by using following equation which is modified version of table 1.

We multiply the constant 'k' to depth, because B(baseline),f(focal length) and wpp(width per pixel) may have measurement error, and it's hard to know correct parameters for the combination of lens and CMOS sensor used in this experiment('k' is a experience value).

$$Depth = \frac{B \times f}{d} = k \times \frac{B \times f}{disparity \times wpp}$$

where, our system has

$$B = 0.24m$$

$$f = 0.0045m$$

$$wpp = 0.0000123m$$

$$k = 0.85$$

Another test set consists of 7 frames where a human has a paper written the real measured distance from camera to him as shown in fig.6. The distances are 0.5m ~ 3.5m with step of 0.5m. After gaining disparity with this second test set by our new method, we compared it to real measured distance as shown fig. 7. and table 4. We can detect faces and calculate the distances for human in range of 0.5m ~ 3.5m with 0.5~ 8.9% error



Fig.6. test image set with real distance value (0.5~3.5m)

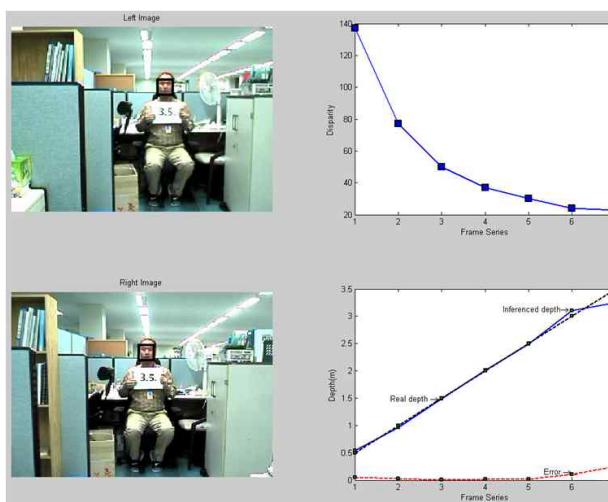


Fig.7. our method's accuracy of depth calculation

Table 4. Result of Depth calculation
(average of tests in 5 times)

Frame	Depth(m) (Inference)	Depth(m) (Real Measurement)	Error(m) (Difference of two)
1	0.5448	0.5	0.0448(8.9%)
2	0.9693	1.0	0.0307(3.1%)
3	0.1497	1.5	0.0073(0.5%)
4	2.0171	2.0	0.0171(0.9%)
5	2.4878	2.5	0.0122(0.5%)
6	3.1098	3.0	0.1098(3.7%)
7	3.2450	3.5	0.2550(7.0%)

Because Altair has two ports for input image and stereo camera inputs are multiplexed with time division manner, frame rate for depth result is half (15 fps) of Altair's that. By configuring Altair chip, we can adjust the frame rate of face detection and depth calculation.

V. CONCLUSION

We can calculate the disparity of face with this information and we can easily estimate distance from robot to human with it. When one or more faces are detected, we classify various cases to identify correspondent faces. We can detect faces and calculate the distances for human in range of 0.5m ~ 3.5m with 0.5~ 8.9% error

We are planning to do experiment for the case where there are many people a frame

Acknowledgement

This work was supported by the R&D program of the Korea Ministry of Knowledge and Economy (MKE) and the Korea Evaluation Institute of Industrial Technology (KEIT). [Project KI001813, Development of HRI Solutions and Core Chipsets for u-Robot].

REFERENCES

- [1] Scharstein, Daniel and Richard Szeliski., "A taxonomy and evaluation of dense two-frame stereo correspondence algorithms", International Journal of Computer Vision. 2002
- [2] Jiho Chang, Seung Min Choi, et al, " Design and Implementation of Real-Time stereo vision ASIC and embedded system", IEEK 2010 Summer Conference, CFP-326, June, 2010.
- [3] Seung Min Choi, et al, " Implementation of Robust Real-time Slant Face Detection ASIC", IEEK 2010 Summer Conference, CFP-326, June, 2010.

An experimental study on interactive reinforcement learning

Tomoharu Nakashima, Yosuke Nakamura, Takesuke Uenishi and Yosuke Narimoto

Osaka Prefecture University, 1-1 Gakuen-cho, Nakaku, Sakai, Osaka
(Tel : 81-72-254-9351; Fax : 81-72-254-9351)
(*nakashi@cs.osakafu-u.ac.jp*)

Abstract: Q-Learning is a popular non-supervised reinforcement learning (RL) technique that learns an optimal action-value function characteristic of a learning problem. Due to the complexity of some problems, the number of training episodes to reach the convergence of the learning problem can increase drastically. In order to fasten the learning speed of an agent on a particular problem, researchers have been exploring interactive reinforcement learning (IRL), i.e. a way to interact with an agent so that it does not learn to solve a problem only by itself. This paper proposes an interactive reinforcement learning to try to fasten the learning speed of an agent. Especially, the combination of an agent asking for advice and getting advice from supervisors was explored. A simple way to experiment this combination is an agent evolving on a maze (a gridworld problem) trying to find its path to a fixed goal point. Experiments show how an interactive learning agent solve the problem compared to a classical learning agent.

Keywords: Q-Learning, interactive reinforcement learning, human machine cooperative systems

I. INTRODUCTION

Reinforcement learning methods [1] are quite popular in the robotic field but classical reinforcement learning does not work so good in many cases on real environment. In order to overcome this fact, new reinforcement learning algorithms, such as policy gradient [2], have been developed. Another idea was to transform classical reinforcement learning into interactive reinforcement learning to speed up the learning of behaviors. Interactions have been stated in many terms like interactions with a human teacher [3], [4], or incorporation of advice [5].

There are of several kinds of interactive learning. The interactions can come from an agent asking for advice [6] — When it does not know what to do — to an advisor that completely knows the environment. Another one is a human advisor or a computed advisor that gives advice to a learning agent to correct its behavior while learning by giving variable amount of reward/penalty or directly the action to perform [7], [8]. In multi-agent systems, advice can come from the other agents as a way of sharing experience by observing their actions [9], by being able to evaluate the weight of the other agents advice [10], by requesting episodic advice to other agents solving the same kind of problems [11], or by getting information from other agents about the environment that the learning agent is not (yet) aware of [12]. On the other hand, advice can be seen as a way of transferring information from previous experience to a new similar situation [13], [14], [15].

In all of those explorations in IRL, the learning was fastened by the interactions between the learning agent and the outside world.

In the following chapters, an overview of reinforcement learning will be shown, followed by the presentation of the interactive reinforcement learning method,

which is the proposed method in this paper. After presenting the results of the experiments and their results, we give the conclusions and future works.

II. OVERVIEW OF TRADITIONAL REINFORCEMENT LEARNING

1. Traditional reinforcement learning

A. Definition

Traditional reinforcement learning is the third mode of learning where an agent learns to act by itself in an environment by interacting with this environment and getting feedback from it. The agent can choose to explore its environment by acting randomly or to exploit its knowledge of the environment it got from previous experiences through trial and error. In addition, the learning agent reinforces the knowledge it gets from experiences by getting a numerical reward when doing a good action or a penalty when doing wrong or forbidden actions. The learning agent, by iterating experiences, aims at taking actions that maximize the sum of the rewards over the time to find an optimal policy.

B. Algorithm

There exists many kind of reinforcement learning algorithms such as Temporal Difference (TD) learning, actor-critic learning, *Q*-Learning.

The basic reinforcement learning model is the following one:

- A set of possible states of the environment
- A set of possible actions
- Transition rules to go from the current state to the next state

- Rules to determine when an agent receives a reward or a penalty

Algorithm 1 shows a basic reinforcement learning algorithm.

Algorithm 1 Basic RL algorithm

```

Initialize the value function arbitrarily
Initialize the policy to evaluate
repeat
  Initialize  $x$  randomly
  repeat
    Choose action  $a$  from  $S$  given by the policy for  $x$ 
    Take action  $a$  and observe  $r$  and  $x'$  (the next state)
    Update algorithm's value function
     $x \leftarrow x'$ 
  until  $x$  is terminal
until
```

2. Q -Learning

A. Principle

Q -Learning is an online reinforcement learning technique where the agent evolve in a completely unknown environment. In Q -Learning, the agent approximates the policy function directly. Q -Learning algorithm is guaranteed to converge under some circumstances.

For this paper, the Boltzman distribution probability was used for action selection. The Boltzman temperature factor T included in this distribution is used for the trade-off of the exploration/exploitation rate.

B. Detailed algorithm

The value function of a state and an action is calculated by the following equation:

$$Q(x, a) \leftarrow (1 - \alpha)Q(x, a) + \alpha(r + \gamma \max_{b \in A} Q(x, b)) \quad (1)$$

when x is the state of the agent, A the set of possible actions, $a, b \in A$ an action, r the reward, α the learning rate, and γ the discount rate. The probability of taking an action is calculated by the Boltzman distribution as follows:

$$p_x(a) = \frac{\exp \frac{Q(x,a)}{T}}{\sum_{b \in A} \exp \frac{Q(x,b)}{T}} \quad (2)$$

At the end of each episode, the Boltzman temperature factor T is divided by a fixed step, to decrease the exploration rate. The algorithm is run in the following way:

Algorithm 2 Q -Learning

```

Initialize  $Q(x, a)$  arbitrarily
Initialize  $T$  at 0
repeat
  Initialize  $x$  randomly
  repeat
    Choose action  $a$  from  $S$  using policy derived from  $Q$  (here the probability action selection)
    Take action  $a$  and observe  $r$  and  $x'$  (the next state)
    Update  $Q$ 
     $x \leftarrow x'$ 
  until  $x$  is terminal
  Decrease  $T$ 
until
```

III. INTERACTIVE REINFORCEMENT LEARNING

1. Proposed interactive reinforcement learning method

In this research, two types of interactive reinforcement learning were combined: asking for advice mode and getting advice mode.

A. Asking for advice

When the probability for a learning agent to take an action is almost the same for all the possible actions, an agent can ask for advice to an advisor. This advisor is completely aware of the environment of the agent and is considered to know the action that can lead to a maximum reward. When receiving an answer from the supervisor on what action to perform, the agent does the advised action and updates its state-action value as if it was its own decision.

B. Getting advice

While learning, an agent can receive advice from an advisor agent that is resolving the same problem. The supervisor agent can have different level of expertness: *BEGINNER*, *INTER.*, and *EXPERT*. The learning agent acts differently in function of the expertness level of its advisor.

C. Constraints

As being in possession of advice from several sources at the same time may be confusing, to simplify the algorithm it has been decided that an agent cannot ask for advice and get advice at the same time, with the following priority: asking advice is predominant over getting advice. Moreover, in one episode, only one advisor can observe an agent to avoid confusing advice.

2. Overview of the framework

At each step the learning agent calculates the probability of taking an action. When the agent does not know what to do, it asks for advice to an advisor, in this case the A* algorithm, then the learning agent takes the advised action and updates its map of the state-action values. After calculating the probability of taking an action, if the learning agent does not ask for advice, the learning agent chooses the action it performs. The advisor is notified of the chosen action the learning agent wants to perform, and from time to time decides to give an advice knowing this action and the state of the learning agent. Finally, when getting an advice, the learning agent acts and updates its map of the state-action value in function of the expertness level of the advisor giving the advice.

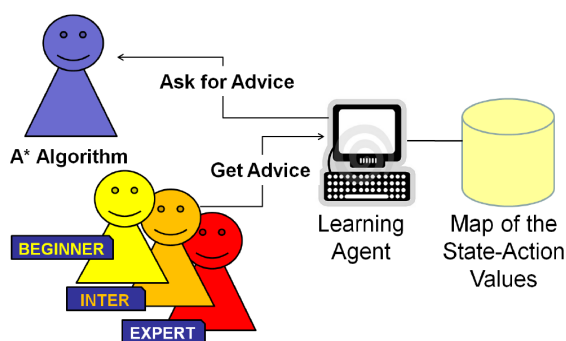


Fig. 1. System components

3. Details on the framework

To take into account the advice in its policy, a learning agent gets a variable reward from its advisor every time it receives an advice. The advisor agent that gives advice to the learning agent is chosen at the beginning of each episode randomly. An agent can receive advice only from advisor agent whose level of expertness is equal or superior to its own. An agent's expertness level is defined the following way:

- **BEGINNER:** success to resolve the problem < 33%
- **INTER.:** 33% success to resolve the problem < 67%
- **EXPERT:** success to resolve the problem $\geq 67\%$

Knowing the expertness level of an advisor agent, the learning agent acts the following way when getting an advice:

- **BEGINNER:** the learning agent take the advised action but does not update its state-action value.

- **INTER.:** the learning agent update the state-value related to the advisor advice, but take its own decided action.
- **EXPERT:** the learning agent take the advisor action and update its state-action value as if it was its own decision.

IV. EXPERIMENT

1. Maze problem

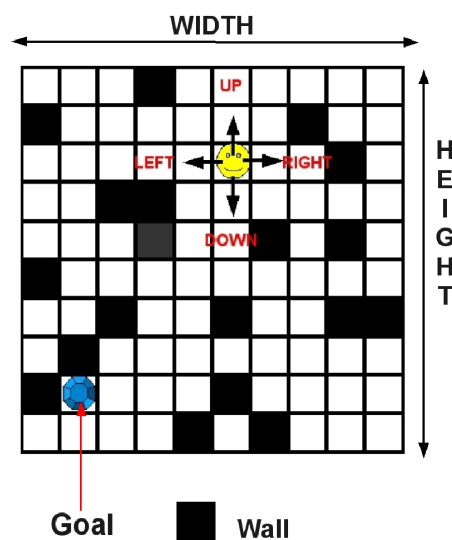


Fig. 2. Maze problem

A. Principle

For this research, IRL was applied to the grid world problem. In the case of this research, the grid world is a simple maze made of impassable walls. The principle of this problem is the following one: an agent is positioned on a randomly chosen starting point on a maze, and tries to find its path into the grid world to reach the goal. The agent can perform four possible actions: **Direction**={UP, DOWN, LEFT, RIGHT}. The following rules are applied: the agent receives a reward when reaching the goal and a penalty when trying to go on a wall or outside of the maze, otherwise nothing. If the selected action is a valid action (not a wall, or not the outside of the maze), the agent performs the selected action, otherwise it remains at the same place. The agent updates its action-state values after each move. When the agent reaches the goal the episode is interrupted and the agent is ready to begin a new episode. During an episode the maximum number of move is limited to the number of squares of the maze, that is to say, the maze width multiplied by the maze length.

B. Parameters details

A transition is a pair of (agent-state, direction). An advice consists of a reward or penalty and a transition. To determine when an agent can ask for advice, instead of asking randomly, it calls the advisor only when the difference between the highest and the lowest probability of taking a direction is lower than threshold δ . A agent gives to a learning agent an advice the following way: If the learning agent selected action correspond to the agent highest state-action value, then it gives an extra reward to the learning agent for this action. If the selected action correspond to the lowest state-action value, it gives an extra penalty to the learning agent. Otherwise, the agent gives the learning agent the next action to perform with an extra reward. The framework has been tested on different sizes of maze: 10x10, 15x15, 20x20, 25x25. The numbers of walls and their place in the maze are set randomly. Three difficulty types of maze were created. The simplest type of maze is covered by 0 to 25% of wall squares, the normal type by 25 to 50% of wall squares, and the most difficult one by 50 to 75% of wall squares.

The exploration rate was also tested by using different coefficient steps to decrease the exploration rate during the learning (step = 2, 5, 10).

Each mode has been run separately before being combined as a base of comparison.

2. Evaluation index

The success rate of an agent to resolve the gridworld problem is evaluated as the number of time an agent succeed in reaching the goal from each possible starting points divided by the number of possible starting points. At the end of each episode, the success rate of the agent is calculated by proceeding to an offline turn where the action decision is greedy and where there is no update of the state-action values. The evaluation index is defined as the number of episodes it takes to reach a high success rate. When the learning speed is high then the number of required episode to reach the convergence point is low. On the contrary, with a low learning speed, the number of required episodes is high.

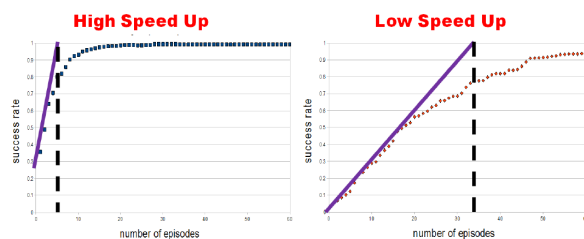


Fig. 3. Illustration of evaluation index

3. Case study

The performance of the proposed method is compared with traditional *Q*-Learning method. The interactive reinforcement learning with asking for advice method and getting advice method was employed for the performance evaluation.

A. Influence of size

The influence of the size was evaluated by increasing the size of the maze. The results show that the proposed method as well as the other type of interactive reinforcement learning increases the learning speed of the agent and that the success rate converge quicker than with traditional *Q*-Learning.

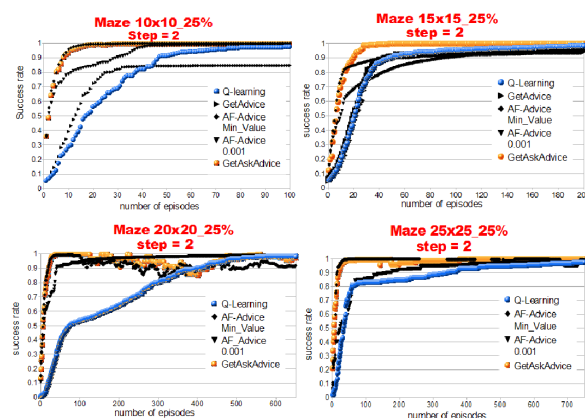


Fig. 4. Influence of the size on the success rate

B. Influence of difficulty

The influence of the difficulty of the maze was tested by increasing the number of walls in the maze. The results show that by increasing the number of walls, the traditional *Q*-Learning agent needs more episodes to converge to a 100% success rate, but with the proposed IRL the learning speed remains higher than with classical *Q*-learning, at least at the beginning for the most difficult mazes.

C. Size evaluation

We can observe that for the most difficult and biggest maze after showing good results at the beginning of the learning there is a decreasing peak in the success rate for the proposed method and the ask for advice mode after around a hundred of episodes. This phenomenon can be considered as a loss of memory since the agent forgets what he learned with its advisor.

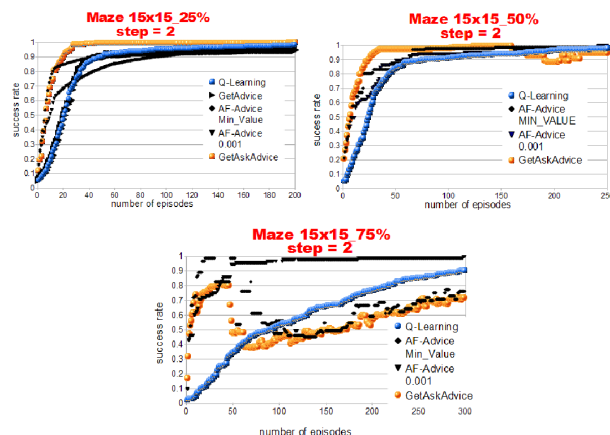


Fig. 5. Influence of the difficulty on the success rate

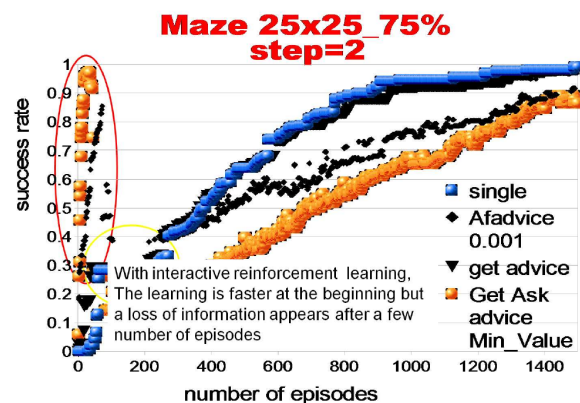


Fig. 7. Size evaluation for a big and difficult maze

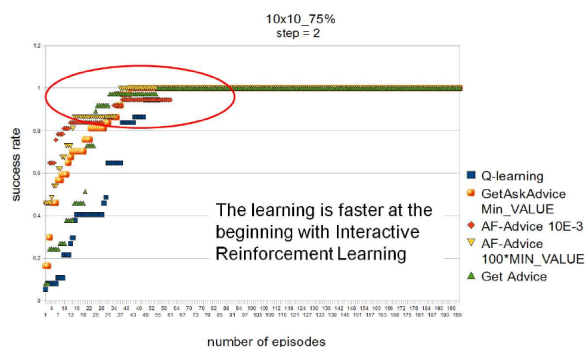


Fig. 6. Size evaluation for a small and difficult maze

V. CONCLUSION

A method combining two types of interactive reinforcement learning to speed up behavior learning was proposed. The first one is an agent asking for advice and the second one an agent getting advice from other agent. According to the numerical experiments, the proposed method showed good result at the beginning of the learning but still has rooms to improve performance. In future work, the following actions should be done:

- To have stable performance which does not depend on the number of episodes, the proposed method should be combined with other methods.
- The candidate complementary methods are collaborative reinforcement learning where several agents on the same maze can spy on each other actions

REFERENCES

- [1] R. S. Sutton and A. G. Barto. *Reinforcement learning : An Introduction*, The MIT Press Cambridge, Massachusetts London, 1998.
- [2] S. Vijayakumar, T. Shibata, and S. Schaal. Reinforcement learning for humanoid robotics, *Proceedings of the Third IEEE-RAS International Conference on Humanoid Robots (Humanoids2003)*, pp.1-20, 2003
- [3] A. L. Thomaz, G. Hoffman, and C. Breazeal. Reinforcement learning with human teachers: Understanding how people want to teach robots, *Proceedings of the 15th IEEE International Symposium on Robot and Human Interactive Communication*, pp. 352-357, 2006.
- [4] A. L. Thomaz and C. Breazeal. Learning from human teachers with socially guided exploration, *Proceedings of the 2008 IEEE International Conference on Robotics and Automatio*, pp.3539-3544, 2008.
- [5] R. Maclin and J. W. Shavlik. Incorporating advice into agents that learn from reinforcements, *Proceedings of the 12th National Conference on Artificial Intelligence*, pp. 694-699, 1994.
- [6] J. A. Clouse. *An introspection approach to querying a trainer*, University of Massachusetts, 1996.
- [7] A. L. Thomaz and C. Breazeal. Reinforcement learning with human teachers: evidence of feedback and guidance with implications for learning performance, *Proceedings of the 21st national conference on Artificial intelligence*, Vol.1, pp.1000-1005, 2006.
- [8] V. N. Papudesi and M. Huber. Learning from reinforcement and advice using composite reward func-

tions, *Proceedings of the 16th International FLAIRS Conference*, pp.361-365, 2003.

- [9] W. J. Gutjahr. Interaction dynamics of two reinforcement learners, *Central European Journal of Operations Research*, Vol.14, pp.59-86, 2006.
- [10] M. N. Ahmadabadi, M. Asadpour, and E. Nakano. Cooperative Q -learning: the knowledge sharing issue, *Advanced Robotics*, Vol.15, pp.815-832, 2001.
- [11] L. Nunes and E. Oliveira. Advice-Exchange Between Evolutionary Algorithms and Reinforcement Learning Agents: Experiments in the Pursuit Domain, *Lecture Notes in Computer Science*, Vol.3394, pp.185-204, 2005.
- [12] S. Kalyanakrishnan, Y. Liu, and P. Stone. Half field offense in robocup soccer: A multiagent reinforcement learning case study, *RoboCup 2006: Robot Soccer World Cup X*, pp. 72-85, 2007.
- [13] L. Torrey, T. Walker, R. Maclin, and J. Shavlik. Advice taking and transfer learning: Naturally inspired extensions to reinforcement learning. *AAAI Fall Symposium on Naturally Inspired AI*, 2008.
- [14] L. Torrey, T. Walker, and R. Maclin. Skill acquisition via transfer learning and advice taking. *Proceedings of the 17th European Conference on Machine Learning*, pp.425-436, 2006.
- [15] L. Torrey, J. Shavlik, T. Walker, and R. Maclin. Advice-based transfer in reinforcement learning, *University of wisconsin machine learning group working paper 06-2*, 2006.

Crutch Gait Pattern for Robotic Orthosis by the Feature Extraction

I.H. Jang, J.Y. Jung, D.Y. Lee, D.W. Lee, H.G. Lee, H.S. Park*

*Korea Institute of Industrial Technology, Republic of Korea
(Tel : 82-31-8040-6292; Fax : 82-31-8040-6370)
hsubpark@kitech.re.kr*

Abstract: In this paper, we present the method to generate crutch gait pattern for robotic orthosis to walk using motor. In first we define the features to characterize gait pattern and extract features from the normal gait pattern, which is experimental encoder data of hip and knee being taken from motion capture device. We also present the selected features containing physical meaning in gait pattern enable us to vary speed, step size and foot clearance easily. Finally, we make crutch gait patterns using these features and apply them to our exoskeleton robot ROBIN-P1 to verify our method.

Keywords: Exoskeleton, Robotic Orthosis, Gait Pattern, Feature Extraction.

I. INTRODUCTION

The exoskeleton type of wearable robots can be divided into power suits for enhancement of a healthy person's activities and rehabilitation robots for support of a physically challenged person.

Of two categories, rehabilitation robots are noted more and more recently as the Aging Society is going on quickly. Robotic orthosis draws special attention recently because the application of rehabilitation robot is extended to a development of rehabilitation robot assisting gait for spinal cord injury patients and their clinic.

In view of control aspects, the movement of wearable robot should be synchronized with a user for safety and natural movement. Therefore we assumed and defined role sharing as follows.

- Assumption 1: user has to play a role in the awareness of environment and the decision of movements.
- Assumption 2: robot has to control its motion according to user intention.
- Assumption 3: user has to play a role in shifting their weight and balancing for robot movements.

Suzuki et al. [1] have applied HAL-3 for paraplegia patients to walk again. This paper describes how to detect user intention by robot for solving the problem concerning assumption 2. For the gait pattern, they use the one extracted from a healthy person's walking. However it can be applied only to a hemiplegia patient and the gait parameters such as walking speed and step

size cannot be changed in real time, once it has been determined. ReWalk[2] is a robot for Spinal Cord Injury(SCI) patients but there is no paper or patents describing their control technology. However the analysis of the various video clips on internet showed that ReWalk has several gait patterns depending patient's condition but it also seems not to change its walking speed and step size once the gait pattern is selected. I.H. Jang et al. [3] also have made wearable robotic orthosis ROBIN-P1 for assisting gait of SCI patients. ROBIN-P1 also memorize reference gait pattern in the form of lookup table and use the corresponding gait pattern to control motors according to user intention.

It is not proper for those kinds of methods shown in the case of HAL, ReWalk, ROBIN-P1 to be used in dynamic environments of day life. Therefore this paper describes how to generate gait pattern from the several features and shows that we can change the gait pattern online with the several features.

The rest of this paper is structured as follows. Section II defines features from normal gait pattern and describes the algorithm to generate gait pattern for our exoskeleton robot platform ROBIN-P1. Experimental results are provided in Section III, and finally, Section VI concludes the paper and suggests future research.

II. DESCRIPTIN OF THE ALGORITHM FOR GENERATING GAIT PATTERN

1. Definition of the feature for gait pattern

Previous works for gait pattern say that normal people has a gait pattern like Fig.1. The (a) (b) and (c)

represent the range of Ankle, Hip and Knee motion respectively. We can find several peaks and both end points from the gait patterns. Meanwhile, if we can know those points, we may be able to recover whole gait pattern by connecting those points with spline method. Therefore we can select those points as the features for gait pattern.

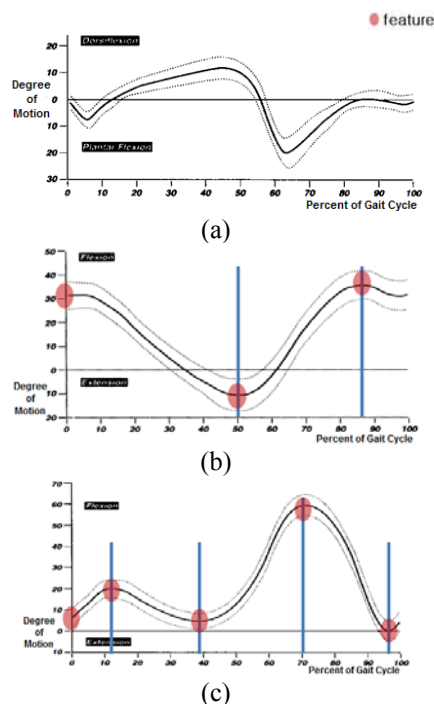


Fig.1. (a) Ankle Range of Motion (b) Hip range of motion and (c) Knee range of motion

2. Algorithm for generating gait pattern

In order to get the crutch gait pattern of normal people, we have designed encoder system that is the exoskeleton type of dummy robot having encoders at hip and knee joint replacing DC motor of ROBIN-P1. The encoder system has same constraint as our platform ROBIN-P1.

ROBIN-P1 actually has DC motors at hip and knee joints and each joint has full range of motion as shown in Table 1.

Table 1. The range of motion at each joint for the ROBIN-P1

Joint	Range (degree)
Hip	-10 ~ 125
Knee	0 ~ 115
Ankle	Fixed

In order to generate a gait pattern for ROBIN-P1, we have edit normal people's gait pattern being acquired

using this encoder system. In previous case, we have to renew the whole gait pattern and restore that in a lookup table whenever the gait speed or step size changes. Therefore, ROBIN-P1 cannot change its gait pattern by online manner and then it is very difficult for robot to adapt itself in dynamic environment of day life. In order to solve this problem, we have developed new algorithm to generate gait pattern and this new algorithm use the features which is defined at previous chapter.

Our new algorithm consists of totally 6 steps as follows:

Step1: sample one period of gait pattern, heel strike to heel strike, from the encoder data on Fig.2.

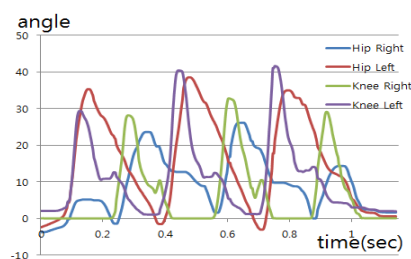


Fig.2. The raw data being acquired from the encoder system in the case of healthy person

Step2: Make the time-axis of sampled gait pattern to normalize with the range of 0 to 100.

Step3: Select peaks, both end points and points being changed rapidly on a gait pattern as the features.

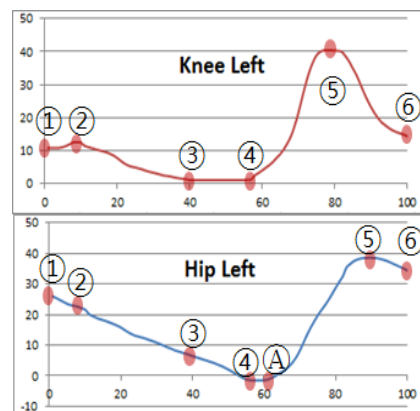


Fig.3. Feature extraction from hip and knee encoder data

Step4: Repeat step1~3 and make an average of each feature point over the sets of feature point.

Step5: Connect each averaged feature point by using spline method and prune graph out of joint movement range as shown in Fig.4

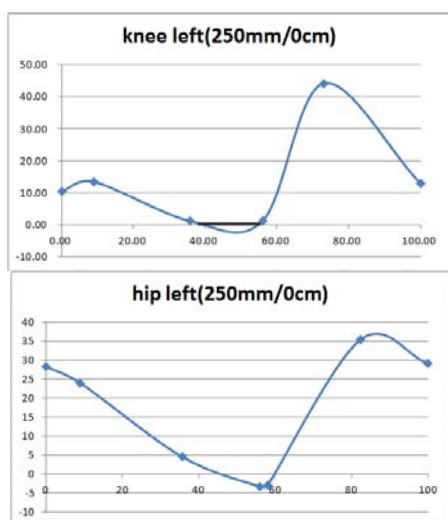


Fig.4. Gait pattern made by connection of feature points through cubic spline and correction

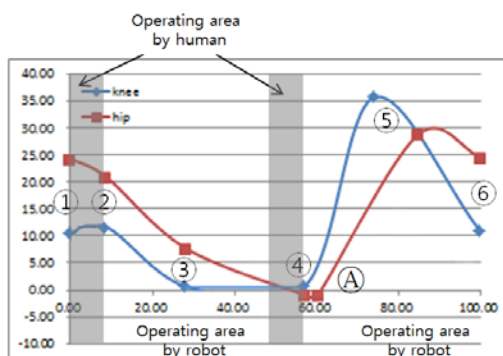


Fig.5. The gait pattern can be divided two parts: operating area by human and that by robot.

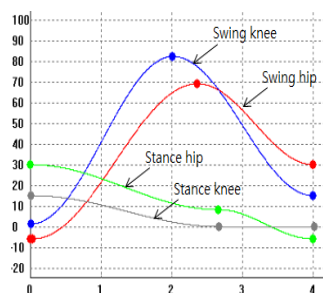


Fig.6. The DC motor input data at hip and knee joint for a stance and a swing phase respectively.

From the assumption being described at introduction, one period of gait pattern has to be divided into two parts for controlling DC motor: Fig. 5 shows these two parts that are *operating area by human* and *operating area by robot*. The operating area by human indicates the area that users shift their weight and balance themselves for next step. The operating area by robot indicates the area that all motors at joints are actually operated. The first operating area by robot in Fig.5 means the phase of stance for gait and the second

operating area by robot means the phase of swing for gait. One leg is always at stance phase whenever the other is at swing phase, so the robot motions on these two phases occur at the same time for the different two legs alternately. Therefore we can capture these two phases of operating are by robot from a period of gait pattern and make them overlap as shown in Fig.6.

Step6: Finally, Correct the gait pattern for use them as DC motor input values. In other words, we need to adjust the starting point of the stance and the end point of the swing at hip and knee joint respectively for recurring use.

III. EXPERIMENTAL RESULTS

The gait pattern was generated from only 8 features if we count both end points as one because both end points are same on Fig.5. And then the speed can be varied according to the desired time value being converted from the normalized time value.

Fig.6 represents that it takes 4seconds in a swing/stance phase time while the step size is fixed at 250mm. We have experimented with our exoskeleton platform ROBIN-P1 varying its swing/stance time from 2seconds to 5seconds. We also changed the step size by varying the *step size in angle domain* that is defined as the difference between the starting angle of *swing hip* and the starting angle of *stance hip* on Fig.6. However there are more things we have to take into account because the peak angle values at hip and knee on swing phase may also have some correlation with the step size. In our experiments, ROBIN-P1 did not show natural gait pattern when we varied the *step size in angle domain* beyond 5 degree.

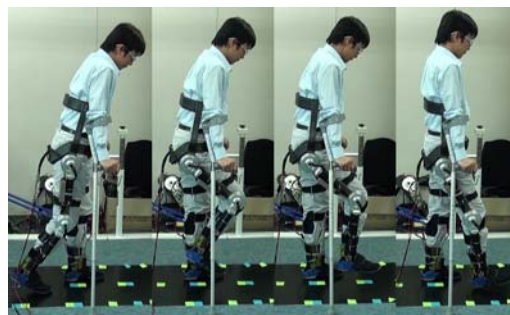


Fig.7. Results of experiment assisting gait using ROBIN-P1 with a gait pattern which is generated through feature extraction.

VI. CONCLUSION

We defined the feature in a gait pattern and described our algorithm to regenerate gait pattern using several features in Section II. Our experimental results in Section III also showed that it is possible for the ROBIN-P1 to walk not by lookup table type of control data but by a gait pattern being generated from several features in real time. This means that it is possible to change the gait parameters (speed, step size) in online manner. However, we find it necessary to analyze the correlation the features and the step size in order not to lose natural of original reference gait pattern. What gait pattern do we select as a reference gait pattern? These are for our future work.

REFERENCES

- [1] Suzuki K, Kawamura Y, Hayashi T, et al. (2005), Intention-based walking support for paraplegia patient. IEEE International Conf. on Systems, Man and Cybernetics; 2005: 2707–2713.
- [2] [Online] Available: <http://www.argomedtec.com/>
- [3] I.H. Jang et al.(2010), Development of the rehabilitation robot assisting gait for spinal cord injury patients (in Korean). J. Institute of Control, Robotics and System 16(9): 860-865

Design of Personal Support System in Telephone Correspondence using Smart Phone

Hiroyuki Nishiyama and Fumio Mizoguchi
Faculty of Sci. and Tech. Tokyo University of Science
Yamazaki 2641, Noda-shi, CHIBA, 278-8510, Japan
(Tel: +81-47122-1106; Fax: +81-47122-1106)

Abstract: In this paper, we design a personal support system in telephone correspondence using smart phone. This system consists of a phone-monitor tool that checks the use state of the smart phone, and a personal support tool that gives the user advice on the personal computer. The phone-monitor tool recognizes and manages the state of the smart phone, including outgoing and incoming calls, and sends information via wireless communications to the personal support tool. These tools can select the suitable type of wireless communication (Wi-Fi or Bluetooth), depending on the situation. Our system determines the user's state by using the sensor system on a smart phone and achieves secretarial personal support, including advice on the response confirmation, for telephone correspondence using smart phone.

Keywords: Smart Phone, Personal Support System, Telephone Correspondence, Bluetooth

1 INTRODUCTION

Recently, many multifunctional cellular phone terminals, such as the smart phone (e.g., Android cellular phone and iPhone), have been developed as a result of the evolution of the computer, network infrastructure, and lightweight technology of the battery; thus, the number of users is rapidly increasing [7]. Many use the smart phone as a daily support tool by taking advantage of various services (e.g., downloading free or paid applications), in addition to talking on the telephone through the Internet connection. However, these applications are limited to the functions of one smart phone, and few applications cooperate with other terminals (e.g., smart phones or laptop computers). Those that do exist temporarily enable intelligence sharing through a connection between the smart phone and the computer terminal, using the USB. Additionally, general research on user support intended for the cellular phone specializes in the function of the portable terminal that can connect with the Internet [1, 2, 4, 5]. In such studies, when the portable terminal is used by the office and the home in a private network, an external server machine is needed [2, 5].

Considering this background, we have designed a system for wide user support by enabling cooperation between a smart phone and other computer terminals (e.g., the laptop personal computer that the user carries, and desktop personal computers that the user uses in the home or the office). This system automatically selects the communication facility that is appropriate for the situation when cooperating with the various communication facilities of a smart phone (e.g., wireless LAN, Bluetooth, and 3G), and dynamically monitors the use state of the smart phone. By using these functions, we have designed a system to enable casual support without disturbing the use of the smart phone. For example, we achieve a secretarial personal support system that manages the sending and receiving of calls on a smart phone (Android phone).

Our design enables user support by cooperation between a smart phone and other computer terminals (e.g., laptop personal computer and desktop personal computer). Cooperation includes dynamically gathering information on a smart phone and transmitting the information to a computer terminal, depending on the situation. The telephone call situation and sensor information can be collected from the smart phone. This system recognizes the user's situation and the state of the smart phone from obtained sensor information, and decides the content that should support the user.

Our support system dynamically manages outgoing and incoming calls on a smart phone, and enables management by wireless communications on a specific desktop or laptop personal computer. Thus, this system achieves user support for the response confirmation through the telephone correspondence in a smart phone.

2 PERFORMANCE OF THE SMART PHONE

In our study, we use HTC Desire SoftBank X06HT as a smart phone (Android phone). The smart phone is similar to a small laptop personal computer. However, a smart phone has a telephone call function, and it is easy to carry because it is small and light. Its display is rather small, and it does not have a keyboard. Moreover, the development of an Android smart phone is comparatively easy because the development language basically conforms to Java in the Android application. In our research, we regard a smart phone as a general portable computer terminal that has a telephone call function, and enable cooperation with the various personal computer terminals that the user uses.

2.1 Communication Facility of the Smart Phone

Three kinds of communication facilities can be used with the smart phone. The wireless LAN is a wireless communications function that can communicate at a maximum

speed of 54Mbps, which the computer terminal uses. Its use requires a connection to a wireless LAN router. Bluetooth is a wireless communications function that connects to a computer terminal by a PtoP connection and can communicate at a maximum speed of 2.1Mbps. Connection requires paired setting with a connected terminal (only once). 3G high speed is basically a communication facility intended for the cellular phone, and the wireless communications function can communicate at a speed of 7.2Mbps or less. Its use requires a contract with the communication enterprise, and the cost corresponds to the wire traffic.

The use of a wireless LAN is considered suitable, considering the transmission rate and the cost, based on the performance comparison above. However, the use of a wireless LAN is difficult because the connected access point changes when the smart phone is used at many bases.

2.2 API for Telephone Use

By using API [8], the Android application can call another phone and recognize the use state of its own phone. Additionally, API (android.telephony.TelephonyManager) dynamically identifies calling and receiving, and the following information can be collected.

- Ringing State (CALL_STATE_RINGING):
The ringing state is the state by which a telephone call is received. The calling person's telephone number can be identified.
- Off-hook State (CALL_STATE_OFFHOOK):
When the telephone receiver is raised in response to a received call, the ringing state changes to the off-hook state. It can be assumed that the smart phone is calling another phone when the idle state changes to the off-hook state.
- Idle State (CALL_STATE_IDLE) :
A change from the ringing state to the idle state of the standby mode means no response to a call. A change from the off-hook state to the idle state means the telephone call ended.

The API is a function basically intended for receiving; when sending, not much information can be obtained. The obtained information involves calling and ending only, and the telephone number and whether it was possible to talk over the telephone cannot be confirmed. Therefore, it is necessary to acquire information about the calling telephone number and the calling person's response after the end of telephone call by using the API (android.provider.CallLog.Calls) to acquire the vital information prepared for the Android phone.

2.3 Sensor System and API of the Android Phone

The Android phone has a variety of sensor systems (e.g., acceleration sensor, brightness sensor, and temperature

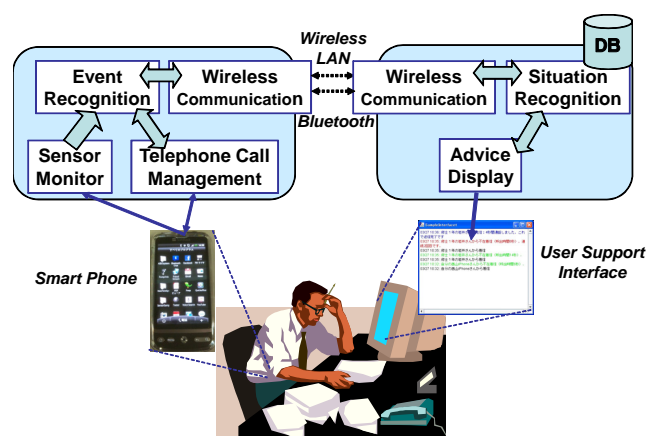


Figure 1: System configuration

sensor), besides the GPS function. Each sensor can confirm a change of sensor value by using the sensor manager API (android.hardware.SensorManager). For example, the acceleration sensor can measure acceleration in three directions (X axis, Y axis, and Z axis).

When a user is carrying an Android phone, the user's behavior can be detected with the use of the acceleration information [1, 3]. Moreover, a brightness sensor can detect whether the smart phone is put away in the bag at the office. Additionally, the API (android.media.AudioManager) of the phone's manner mode and silent mode sets and confirms it exists, too.

3 SYSTEM ARCHITECTURE

In our study, we have designed a system that enables user support through cooperation between a smart phone (Android phone) and computer terminals (e.g., laptop personal computer and desktop personal computer). We achieve user support as cooperation by dynamically gathering information on the smart phone and sending the information to the computer terminal, depending on the situation. Information collected on a smart phone includes the telephone call situation and sensor information described in the preceding section 2. This system decides what content should be supported by recognizing the user's situation and the state of the smart phone, based on the sensor information.

The system configuration is depicted in Fig. 1. The smart phone consists of four modules that monitor the state of the phone. The user-support interface consists of three modules that support the user with a GUI that displays advice.

In the smart phone, each module monitors the telephone call situation and the sensor situation. When a change is recognized, information is sent to the event recognition module. This module requests the transmission of information from the wireless communications module when it judges that the recognized change should be transmit-

ted to the user-support interface. The wireless communications module sends information to and receives information from the personal computer that is operating the user-support interface by wireless LAN or Bluetooth.

In the user-support interface of the personal computer, when event information is received through the wireless communications module, the situation recognition module recognizes a change in the situation. When it is judged that the change requires user support, information is transmitted to the display module, and advice is displayed on the GUI.

3.1 Information Sharing by Wireless Communications

Communication between a smart phone and a personal computer is executed by the correspondence procedures of wireless LAN and Bluetooth. To give priority to the use of wireless LAN for the reasons described in section 2, we have established the following correspondence procedure.

- Step 0: Wait until entering the range of communication by Bluetooth.
- Step 1: To Step 2 if both terminals can use wireless LAN and to Step 5 if otherwise.
- Step 2: Share IP address with wireless LAN according to Bluetooth communication.
- Step 3: Send and receive information by wireless LAN.
- Step 4: Repeat Step 3 as long as it is in the range of Bluetooth communication.
- Step 5: Send and receive information by Bluetooth.

In a range where Bluetooth can be used for communication, this system usually uses wireless LAN; Bluetooth communication is used only when wireless LAN is not possible.

4 SYSTEM IMPLEMENTATION

In order to achieve the system depicted in Fig. 1, we implemented each module on the smart phone (Android phone) and a personal computer. Each module in the Android phone can be implemented using Android SDK [8] via a computer terminal. Since the programming language is basically similar to Java, we used Java language for the implementation of all modules.

4.1 Monitor Tool on the Android Phone

The content of the processing of the modules in the monitor tool on the Android phone is as follows.

The telephone call management module dynamically monitors the telephone call situation of the smart phone using the function of the Android telephone API described

in section 2.2. When a change in the situation is recognized, this module sends information to the event recognition module with additional information (e.g., telephone number). Moreover, this module can call the other phone using the given number.

The sensor monitor module dynamically monitors information, such as the acceleration sensors using the function of the Android sensor API described in section 2.3. The user's state can be recognized from the information of each sensor by registering the user's behavior beforehand with the SVM [3]. When a change is recognized in the registered state of behavior, this module sends the information to the event recognition module. This module monitors mainly the acceleration sensor and the brightness sensor, as well as the state of the smart phone's speaker (e.g., manner mode and silent mode).

The event recognition module recognizes information from the telephone call management module and the sensor monitor module as an event, and sends information to the user-support interface, according to the content of the event, through the wireless communications module. This module recognizes the state by which the smart phone receives or sends calls as the main event, and sends the state of the user and the cellular phone as additional information.

The wireless communications module sends to and receives from the personal computer according to the procedure of section 3.1. This module regularly confirms the range of Bluetooth communication and confirms whether the personal computer with which the user-support interface is operating is in useful range. When it is outside the effective range, this module postpones the transmission of information until entering a useful range.

4.2 User Support Interface on a Personal Computer

The processing content of the modules in the user-support interface on the personal computer is as follows.

The wireless communications module for the personal computer sends to and receives from the Android phone according to the procedure described in section 3.1.

The situation recognition module recognizes the receiving and sending situation of the phone through the wireless communications module, and records this information in the data base (DB). Next, this module transmits advice to the user by collating new information with the vita information in the DB and sends the advice to the display module. For example, a smart phone receives a call; the smart phone is in manner mode, and the brightness of the smart phone is low (e.g., put away in the bag). This module considers the possibility that the user does not notice the call and sends advice (an alert) on the user-support interface.

The advice display module displays the advice information received from the situation recognition module on the user-support interface. Several display methods of advice exist. For example, this module generates a new supplementary window and displays important advice in large

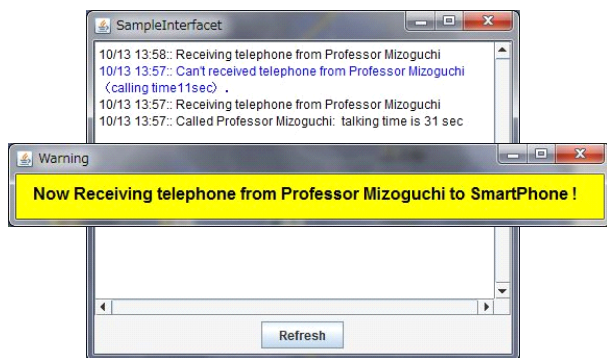


Figure 2: An alert display that presents a strong warning that the user is receiving a call

characters.

With these modules, the user can dynamically confirm the receipt of a call even when the phone's sound is off and the phone is in a bag. Moreover, the user can confirm the history of the smart phone while the user is moving, after the user arrives at the office or arrives home.

5 SYSTEM EXECUTION

When the user arrives at the office, it is possible to connect the monitor tool on a smart phone with the user-support interface on the office personal computer. As a precondition, the smart phone is assumed to connect with the Wi-Fi router in the office and to acquire the IP address. First, the monitor tool on the smart phone connects to the user-support interface on the personal computer using Bluetooth communication. The tool sends the IP address of Wi-Fi of the smart phone to the user-support interface, and the interface sends the IP address of the personal computer (private IP address in the office) to the tool. Next, the smart phone's monitor tool tries the socket connection to the IP address of the personal computer that receives it. If successful, information is sent and received via Wi-Fi communication. If not, Bluetooth communication is used. Supplementary communication is executed by automatically using Bluetooth when the communication fails with Wi-Fi use. In addition, the monitor tool accumulates information and, after reconnection, retransmits the accumulated data when the Bluetooth communication fails.

5.1 Processing When Receives a Call

When a smart phone receives a call with the phone put away in a bag while the user is working in the office, the warning advice (Fig. 2) is displayed on the user-support interface. Figure 2 is an alert display with a strong warning that the user is receiving a call. This alert display assumes that the user does not notice the call because the smart phone is in manner mode or silent mode. When the smart phone is placed on a desk or the ring tone is the pronounced normal mode, the vita information is displayed on the GUI.

6 CONCLUSIONS

We designed a personal support system in telephone correspondence using smart phone. This system consists of a phone-monitor tool that checks the use state on a smart phone, and a personal support tool that gives the user advice on the personal computer. The phone-monitor tool recognizes and manages the state of the smart phone, including outgoing and incoming calls, via the smart phone, and sends information via wireless communications for the personal support tool, which is operating on a desktop or a laptop personal computer. These tools can select the suitable type of wireless communication, depending on the situation. Our system determines the user's state using the smart phone's sensor system and achieves secretarial user support, including the advice of the response confirmation for telephone correspondence by cooperation between these two tools.

References

- [1] T. Brezmes, J. Cotrina, J. Gorricho, M. Rersa: User activity monitoring using conventional cell phones for IMCIC 2010 *The International Multi-Conference on Complexity, Informatics and Cybernetics: IMCIC 2010*, 2010.
- [2] S. Fujino, G. Motoyoshi and H. Tani: Personal Network Accommodation System by a Mobile Network, *The transactions of the Institute of Electronics, Information and Communication Engineers. B*, J92-B(10), pp. 1669-1676, 2009. [in Japanese]
- [3] H. Nishiyama and F. Mizoguchi: Design and Implementation of Personal Service System based on Human's Motion Recognition with Sensor Device, 27st Conference Proceedings Japan Society for Software Science and Technology, 2B-3, 2009. [in Japanese]
- [4] K. Tajima, K. Ando, K. Ohshima and M. Terada: Automatic Information Display System: Design and Implementation, *The transactions of the Institute of Electronics, Information and Communication Engineers. B*, J92-B(7), pp. 1084-1097, 2009. [in Japanese]
- [5] K. Takasugi, M. Nakamura, S. Tanaka, M. Kubota and K. Koyanagi: Technology for Service Continuity Adapting to Dynamic Environment Seamlessly(Mobile Computing) , *Transactions of Information Processing Society of Japan*, 46(2), pp. 608-623, 2005. [in Japanese]
- [6] V. Vapnik: *The Nature of Statistical Learning Theory*, Springer-Verlag, 1995.
- [7] Mobile Content Forum: *K-tai white paper 2010*, Impress R&D, 2009. [in Japanese]
- [8] Android API Guide, <http://www.android.com/>

Advanced Networking and Robotics for Societal Engagement and Support of Elders

Peter Sapaty

Institute of Mathematical Machines and Systems, National Academy of Sciences
Glushkova Ave 42, 03187 Kiev, Ukraine, sapaty@imm.kiev.ua

Masanori Sugisaka

Department of Mechanical and Electrical Engineering, Nippon Bunri University
1727 Oaza Itiki, Oita, 870-0397, Japan, ms@alife-robotics.co.jp

Abstract

The percentage of older population is growing quickly, especially in developed countries, where the retired elders have to be paid by the expense of people who are working, often remaining, however, the most experienced, knowledgeable, and skilful part of the society, also accumulating considerable material wealth. Elders also have specific requirements to be satisfied to ensure their prolonged decent and independent life. The paper considers the use of an advanced distributed knowledge processing and control technology capable of solving broad and complex tasks in modern societies, including continuing involvement of elders in their development.

The approach integrates distributed physical and networked virtual worlds, which can cover from smart home to smart city to smart nation, being coordinated and processed altogether by a powerful spatial engine capable of solving any knowledge processing, control, and coordination tasks in parallel and distributed manner. The key element of the approach, Distributed Scenario Language, is briefed, along with practical examples of elderly population support in it. Having been prototyped in different countries and tested on various network-related problems, the technology can be easily put on any software or hardware platform, with massive cooperative use in mobile phones and mobile robots.

Keywords: Ageing population, decent life, elderly support, knowledge processing, distributed scenario language, mobile phones, mobile robots.

1 Introduction

The world is facing a rapid growth of elderly population, which causes serious social and economic problems. To satisfy specific needs and ensure prolonged decent and independent life of elders, advanced information and networking technologies are considered at the forefront of possible solutions.

European Union (EU) has created a special Ambient Assisted Living (AAL) Joint Program and initiated a number of big research projects to tackle such problems, with considerable funds being invested [1, 2, 3]. EU made thorough analyses of the potential for developing Information and Communication Technologies (ICT) for the elderly and summarized them:

- Europeans over 65 possess wealth and revenues of over 3000 Billion € (Euro).

- The market for smart home applications (age-related assistance in shopping, dressing, moving independently) will triple between 2005 and 2020, from 13 million people up to 37 million.
- 68 million people in 2005 had several forms of age-related impairment. This will grow to 84 million in 2020.
- Early patient discharge from hospital due to the introduction of mobile health monitoring would save € 1.5 billion per year in Germany alone.
- EU research projects have developed technologies for personalized route guidance; home care and remote health monitoring and advice; intelligent alarms; natural interfaces for accessible ICT.

A related project in Japan [4, 5, 6] addresses technological aspects of the AAL and employs innovative methods and facilities for ambient information control based on attaching spatial connotation to surfaces that surround elderly people. In this way, semantic surfaces for direct ambient interactions can be created and invisible intuitive support to the elders can be provided.

Semantic surfaces could make a difference in the lifestyle of the aging population and ensure the much needed self-confidence and dignity of the elders, also continue keeping them as an integral and productive part of the society. These works are also in line with known broader concepts of seamless interfaces “between people, bits and atoms” [7].

The current work represents a further development of these and related projects in Europe and Japan towards practical implementation in distributed networked environments. The approach offered allows us to solve various non-local problems for the elderly support, especially those in need of involvement and joint use of distributed resources (manned as well as unmanned) and smart networking in dynamic situations. The paper also inherits the semantic web concept [8], offering for the latter its possible solution for a specific domain.

2 Using Spatial Grasp Technology

The developed Spatial Grasp Technology [9, 10, 11] has been successfully prototyped in different countries and studied for most diverse networked applications – from classical graph and network problems to distributed knowledge bases to intelligent network management to

distributed interactive simulation of dynamic systems to road traffic management to collective robotics to security and defense [12-34]. Many of these applications (if not all) can be useful in some or other form for the alleviation of demographic problems linked with ageing population.

For the current application, the semantic surfaces, assisting the elderly, can be represented altogether within a heterogeneous semantic network describing the whole domain in an integral form, with certain nodes having double digital-physical representation. This network can be arbitrarily and seamlessly distributed throughout any territory (including smart home, smart city, "smart" country, or even worldwide) using computers or other commonly used electronic devices (like mobile phones, smart sensors, or mobile robots).

High-level operational scenarios in a special Distributed Scenario Language (DSL) can start from any point (node), runtime covering this semantic world (with it, the physical one too) in a spatial pattern-matching mode, bringing operations to data, data to operations, and control to both, organizing overall goal-driven behavior in the way required.

Complex network-related problems can be expressed in DSL in a compact and simple form (often up to a hundred times shorter and proportionally simpler than, say, in Java). And the language interpretation can be organized in a parallel and fully distributed mode, without central resources, thus increasing robustness of the whole system and capability of self-recovery from damages.

The use of SGT can be purely user-centric, when the injected system scenario serves exclusive interests of a single person (possibly, subsequently involving other people and distributed resources for this). It is also possible to create any active distributed system and organize collective behavior of many individuals in it (humans or robots) pursuing together a common goal, with global control of this distributed activity.

SGT also directly works within the same formalism with distributed physical world, or any combination of the semantic (virtual, digital) and physical worlds, with (parallel) operations in the former capable of guiding the ones in the latter in a look-ahead distributed simulation manner.

3 The Distributed Scenario Language (DSL)

DSL is quite different from traditional programming languages. Rather than describing data processing in a computer memory, as usual, it allows us to directly move through, observe, and make any actions in fully distributed environments (whether physical or virtual), seeing and treating them as an organized whole rather than collection of parts. DSL operates with:

- *Virtual World* (VW), which is finite and discrete, consisting of nodes and semantic links between them.
- *Physical World* (PW), an infinite and continuous, where each point can be identified with physical coordinates (with a certain precision).
- *Virtual-Physical World* (VPW), being finite and discrete similar to VW, but associating some or all virtual nodes with PW coordinates.

DSL also has the following features:

- A scenario expressed in it develops as a transition between sets of progress points (or *props*) in the form of parallel waves.

- Starting from a prop, an action may result in one or more new props.
- Each prop has a resulting value (which can be multiple) and resulting state, being one of the four: *thru* (full success allowing us to proceed further from this point), *done* (success with termination of the activity in this point), *fail* (regular failure with local termination), and *abort* (emergency failure, terminating the whole distributed process, associated with other points too).
- Different actions may evolve independently or interdependently from the same prop, contributing to (and forming altogether) the resultant set of props.
- Actions may also spatially succeed each other, with new ones applied in parallel from props reached by the preceding actions.
- Elementary operations can directly use local or remote values of props obtained from other actions (the whole scenarios including), resulting in value(s) of prop(s) produced by these operations.
- These resultant values can be used as operands by other operations in an expression or by the next operations in a sequence (the latter can be multiple, if processes split). These values can also be directly assigned to local or remote variables (for the latter case, an access to these variables may invoke scenarios of any complexity).
- Any prop can associate with a node in VW or a position in PW, or both (when dealing with VPW); it can also refer to both worlds separately and independently.
- Any number of props can be simultaneously associated with the same points of the worlds (physical, virtual, or combined).
- Staying with the world points, it is possible to directly access and update local data in them.
- Moving in physical, virtual or combined worlds, with their possible modification or even creation from scratch, are as routine operations as, say, arithmetic, logical, or control flow of traditional programming languages.
- DSL can also be used as a universal programming language (similar to C, Java or FORTRAN), thus serving as a single language for expressing knowledge processing, intelligent communication protocols, and overall control in distributed systems.

DSL has recursive syntax, represented on top level as follows (programs called *grasps*, reflecting their main semantics as gasping and integrating distributed resources into goal-driven systems).

```

grasp      → phenomenon | rule ( { grasp , } )
phenomenon → constant | variable | special
constant   → information | matter | combined
variable   → heritable | frontal | environmental |
            nodal
rule       → movement | creation | elimination |
            echoing | fusion | verification |
            assignment | advancing |
            branching | transference |
            timing | granting

```

The basic construct, *rule*, can represent any definition, action or decision, for example:

- elementary arithmetic, string or logic operation;

- hop in a physical, virtual, or combined space;
- hierarchical fusion and return of (remote) data;
- distributed control, both sequential and parallel;
- a variety of special contexts for navigation in space, influencing operations and decisions;
- type or sense of a value, or its chosen usage, guiding automatic interpretation.

There are different types of variables in DSL:

- *Heritable variables* – these are starting in a prop and serving all subsequent props, which can share them in both read & write operations.
- *Frontal variables* – are an individual and exclusive prop's property (not shared with other props), being transferred between the consecutive props, and replicated if from a single prop a number of props emerge.
- *Environmental variables* – are accessing different elements of physical and virtual words when navigating them, also a variety of parameters of the internal world of DSL interpreter.
- *Nodal variables* – allow us to attach an individual temporary property to VW and VPW nodes, accessed and shared by props associated with these nodes.

These variables, especially when used together, allow us to create efficient spatial algorithms not associated with particular processing resources, working in between components of distributed systems rather than in them. These algorithms can also freely move in distributed processing environment (partially or as a whole), always preserving integrity and overall control.

DSL also permits the use of traditional operational symbols and delimiters, to simplify and shorten programs, if this proves useful.

4 Exemplary Solutions in DSL

We will consider here some elementary solutions in DSL for the support of elderly population, which show compactness and simplicity of the higher-level code. All these can work in fully distributed environments, with casual channels and casual computing devices appeared available in different places and time (like individually kept by elderly persons, embedded in wheelchairs, mobile robots, smart sensors, or accessed via the internet).

4.1 Assisted Search for Forgotten or Lost Things

The part of a semantic network, oriented on guiding the search for regularly used items (like door keys, glasses, or wallet, for example), setting up an optimized movement between places in the house where such things may happen to be, is shown in Fig. 1. Different DSL solutions based on this network (from purely manual to fully robotic) may be as follows.

Assisted manual solution: advised manual movement and manual items recognition. The elderly person, informing the system about her current location by a physical contact with the semantic surfaces, is then advised to go to the nearest location where the item of interest can be found. This is followed by a further stepwise guidance to move to other such places via the optimum path between them (fixed in advance by the semantic network of Fig. 1), unless the item is found, about which the person informs the system. The DSL solution may be as follows:

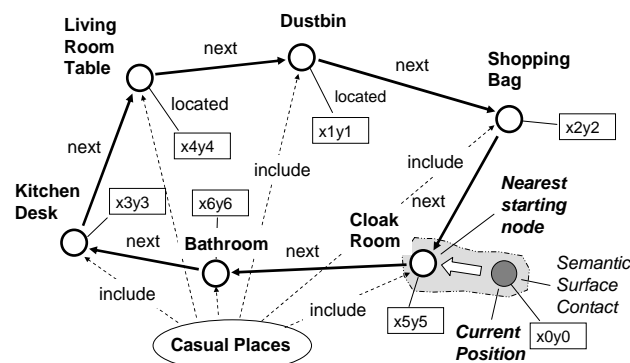


Figure 1. Networked search for a lost item.

```
heritable (Initial) = WHERE;
minimum destination (
  hop (direct, Casual Places);
  hop (include, all);
  distance (hop (located), Initial));
repeat (
  output ('go to', NAME, 'try finding');
  if (input == 'ok', done);
  hop (first come, + next))
```

Assisted automated wheelchair movement with manual items recognition. This case differs from the previous one in that the movement between Casual Places of Fig. 1 is performed automatically by a robotized wheelchair using given physical coordinates of the places, with visual search and recognition of the item by the elderly person herself. The latter terminating the automated movement if she finds the item. The DSL solution:

```
heritable (Initial) = WHERE;
minimum destination (
  hop (direct, Casual Places);
  hop (include, all);
  distance (hop (located), Initial));
repeat (WHERE = hop (located);
  output ('try finding');
  if (input == 'ok', done);
  hop (first come, + next))
```

Fully robotic solution: automatic movement and image recognition. This may all be accomplished by an intelligent robot, if employed in the house. It receives the name of the item to be found (supposedly having video camera and automatic items recognition software, as well as matching templates for different items), and starts from the nearest Casual Place to its current physical position. In DSL this may be as:

```
heritable (Initial = WHERE;
  Item = door keys);
minimum destination (
  hop (direct, Casual Places);
  hop (include, all);
  distance (hop (located), Initial));
repeat (WHERE = hop (located);
  if (discover (Item), done);
  hop (first come, + next))
```

In a similar way, more complex cases of navigation and movement throughout distributed territory by “dismounted” (albeit computer-assisted) individuals or with the help of robotic wheelchairs (and in the ultimate case—by single or multiple robots) can be organized in DSL with distributed maps coded as semantic networks, as, for example, in [33].

4.2 Finding Shortest Paths

The shortest path found to a certain destination may be a good guide to move through a building, region, or city, say, between nodes a and e as in the following DSL scenario (corresponding to Fig. 2). It is being found by navigating the network of weighed links in parallel and fully distributed mode, without any central resources, where the digital networked map can be arbitrarily distributed between any electronic devices having processing capabilities.

```
frontal (Remoteness, Path);
sequence (
  (hop (direct, a); Distance = 0;
    repeat (hop (all links);
      Remoteness += LINK;
      or (Distance == nil,
        Distance > Remoteness);
      Distance = Remoteness;
      Predecessor = BACK)),
  (hop (direct, e);
    repeat (Path = NAME & Path;
      hop(Predecessor));
    output (Path)))
```

The result gradually accumulated and returned to node a will be (a, b, d, e).

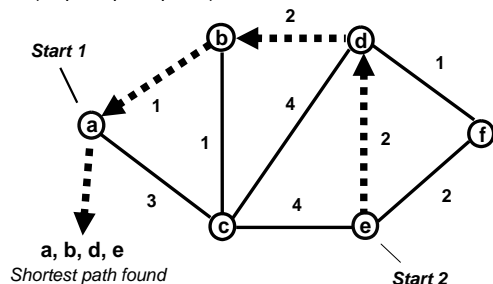


Figure 2. Finding shortest path between nodes a and e.

Many important problems of optimization and control can be expressed as finding shortest paths in distributed spaces. The solution shown (already tested on different distributed network applications) may also be useful for tasks related to the elderly and handicapped, like, for example, finding ways to shops, hospitals, friends, even their own homes (in case of being lost in a forgotten place). This may be possible in full, however, if advanced integration between distributed physical and virtual worlds exists in the society, which may be achieved with the technology discussed.

4.3 Tracking Physical Movement of Individuals by Mobile Intelligence

As in recent known cases in Japan, the elderly people and traces of them can be lost in the society. The DSL scenario in this section shows how whereabouts of the elderly can be regularly checked and traced by a mobile spatial intelligence propagating in a virtual world while following the movements in physical world, as in Fig. 3.

Current positions of certain individuals can be fixed by their physical contacts with semantic surfaces or by networked video cameras (to which key pictures of the persons can be delivered by mobile intelligence accompanying them, for automatic recognition). The tracking intelligence can analyze and accumulate behavior of the moving person, demand checking her current physical condition (e.g. heartbeat, blood pressure, body temperature, etc.). It can also alarm the nearest medical facilities in case

of irregular situations. Many moving persons can be simultaneously and individually checked and nursed by the DSL scenario shown below.

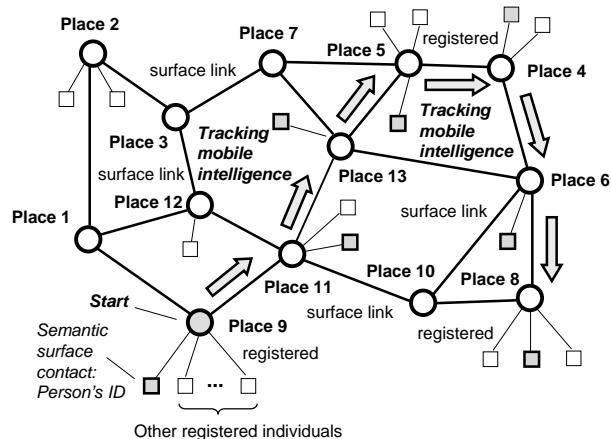


Figure 3. Networked tracking of individuals.

```
frontal (ID = individual; History);
repeat (loop (
  belong (ID, hop (registered, all));
  update (History, check condition);
  if (problems (History),
    alarm (nearest medical staff));
  delay (delay));
  hop (surface link, all);
  belong (ID, hop (registered, all)))
```

4.4 Collective Evacuation from a Disaster Zone

In case of major disasters (earthquakes, hurricanes, flooding, landslides, forest fires, etc.) the elderly and handicapped may appear to be the least protected and most vulnerable ones, thus needing particular help, possibly, even to survive. A related DSL scenario may be activated by any person caught in such an event, or by a special emergency organization setting up coordinated massive evacuation from the disaster zone, regularly issuing instructions to individuals (say, via mobile phones, hopefully still working) on where and how to move.

A chained collective movement in this respect through a safe narrow passage in the disaster zone is shown by the program below and in Fig. 4, where individuals move in a coordinated (with each other and with the waypoints supplied externally) way. Only the first individual in this emergency chain is a pure leader (directly following the waypoints), and the last one is a pure follower, while the others combine both functionalities (thus moving right after the previous person, and being directly followed by the same next person).

```
cycle (if (exist (unmarked individuals),
  (N += 1; assign (next individual,
    create (node (N))));
  (NAME == 1; Waypoints= (w1, w2, w3, ...);
  loop (output ('move to',
    withdraw (Waypoints, 1));
    wait (input == 'ok'))),
  (NAME != 1; sling (
    Leader coordinates =
      (hop (direct, NAME - 1); WHERE);
    output ('move by', direction
      (WHERE, Leader coordinates))))
```

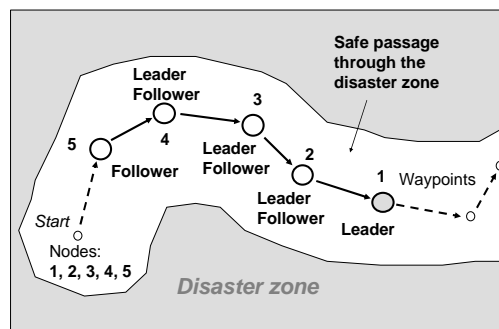


Figure 4. Chained evacuation from a disaster zone.

4.5 Using Service Robots

This example shows how home cleaning robots (on a demand of an elderly person) can process the area needed. Let us consider DSL scenarios for a single cleaning robot, and also for their swarm operating in parallel.

Sequential cleaning. The sequential coverage of a territory (assumed here to be rectangular, for simplicity) by a single robot can be organized in a variety of ways, including the one with minimum waypoints to pass, in a zigzag fashion, as shown in Fig. 5. For this latter option, the DSL program may be as simple as follows (the movement between adjacent waypoints is supposed to be accompanied by the cleaning process).

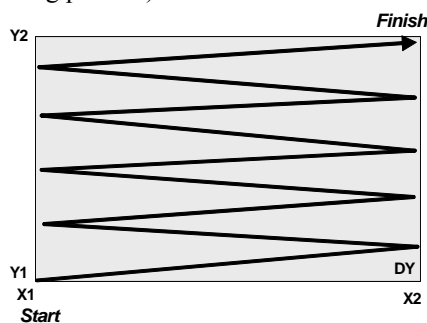


Figure 5. Sequential cleaning by a single robot.

```
X1 =...; X2 =...; Y = Y1 =...; Y2 =...; DY =...;
loop (move_clean (X1, Y); (Y += DY) < Y2;
      move_clean (X2, Y); (Y += DY) < Y2)
```

Parallel cleaning. Parallel cleaning of a territory (assumed here to be of arbitrary shape) by a cooperative robotic swarm can also be organized in different ways, for example, *randomly*, as in Fig. 6. For this, each cleaning device finds its next possible position independently by a random choice, checking if the new destination is not occupied by other robot to avoid collision, and also has not been visited (cleaned) before (using visual sensors).

Such parallel random navigation may have advantages before any predetermined search as can eventually cover the whole area with at least a single robot operable. Such a search, where physical processes start from a number of initial points (named *c1* to *c5*), which can be chosen randomly too, and keep a threshold distance from each other, may be expressed by this program:

```
move (c1, c2, c3, c4, c5);
Range = range;
Polygon = (x1y1, x2y2, x3y3, x4y4,
           x5y5, x6y6); D = shift;
loop (New = WHERE +
      twice (random (-D, D)));
```

```
inside (New, Polygon);
and (empty (hop (New, Range)),
    non_cleaned (New),
    move_check_clean (New));
```

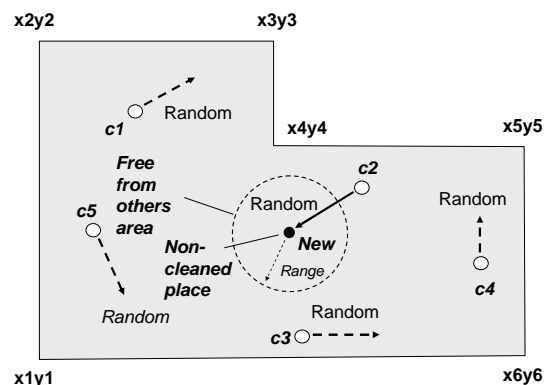


Figure 6. Parallel random cleaning by a robotic swarm.

Many such scenarios, due to high level and simplicity of DSL, may be created by the users (elders) themselves, or may just be activated by names, being prepared in advance and regularly updated by special social services, as a library of recommended reactions on different events (accessible from laptops or mobile phones).

5 Conclusions

The described approach, effectively integrating physical and virtual worlds, with individuals comfortably living in both under the guidance of a powerful spatial engine, can allow us to effectively formulate and solve complex non-local problems in human societies, demographic ones including.

High level but fully formal societal scenarios in DSL may contain a good deal of flexibility for their implementation: a) by younger people, who may be following them creatively, as general recommendations; b) by elders, with possibly weakened decision-making, to follow them closely, and if needed, directly; and c) by mobile robots and their swarms—just executing them strictly as formal programs.

The scenarios may provide any combination of and shifts between these options, with unified goal-driven control allowing for gradual transition to fully unmanned systems effectively solving urgent problems, including special support of elderly and handicapped people and their further active engagement for the benefit of the whole society.

The approach offered can be easily implemented on any platform, say, as a special intelligent module in laptops, mobile phones (the number of which is approaching 3bn worldwide), smart sensors or mobile robots, and this work can be effectively carried out by both professionals and university students (as for the previous versions of the technology [10, 11]).

References

- [1] European Commission, Ageing well in the Information society, An i2010 Initiative, 2007, <http://eur-lex.europa.eu/LexUriServ/LexUriServ.do?uri=COM:2007:0332:FIN:EN:HTML>.
- [2] European Commission, Ageing well in the Information society, An i2010 Initiative, 2007, <http://eur-lex.europa.eu/LexUriServ/LexUriServ.do?uri=COM:2007:0332:FIN:EN:HTML>.

- lex.europa.eu/LexUriServ/LexUriServ.do?uri=COM:2007:0332:FIN:EN:HTML.
- [3] AAL, Ambient assisted living, Case studies, 2004., <http://www.aal169.org/Published/casestud.pdf>.
- [4] Kanev, K., Mirenkov, N., Pervasive carpet encoding for active knowledge semantic surfaces, Book chapter in Ubiquitous multimedia computing, Qing Li and Timothy K. Shih (Eds), Chapman & Hall/CRC Press, 2010.
- [5] Kanev, K., Mirenkov, N., Brimkov, B., Dimitrov, K., 2009. Semantic surfaces for business applications, In Proceedings of the Int. Conf. on Software, Services and Semantic Technologies, Sofia, Bulgaria.
- [6] Kanev, K., Morishima, Y., Watanabe, K., Surface code readers for image based human-computer interfaces, In Proceedings of the Eleventh Int. Conf. on Humans and Computers HC'08, Nagaoka, Japan, 2008.
- [7] Ishii, H., Tangible bits: towards seamless interfaces between people, bits and atoms, Proceedings of the 2nd Int. Conf. on Tangible and Embedded Interaction, Bonn, Germany, 2008.
- [8] Berners-Lee, T., Hendler, J., and Lassila, O., The semantic web, Scientific American Magazine, May 2001.
- [9] Sapaty, P., Distributed technology for global control, Book chapter, Lecture Notes in Electrical Engineering, Vol. 37, Springer-Verlag, 2009.
- [10] Sapaty, P., Ruling distributed dynamic worlds, John Wiley & Sons, New York, 2005.
- [11] Sapaty, P., Mobile processing in distributed and open environments, John Wiley & Sons, New York, 1999.
- [12] P. Sapaty, and M. Sugisaka, "Distributed Artificial Brain for Collectively Behaving Mobile Robots," In Proc. Symposium & Exhibition Unmanned Systems 2001, Jul. 31-Aug. 2, Baltimore, MD, 2001.
- [13] P. Sapaty, and M. Sugisaka, "Towards the Distributed Brain for Collectively Behaving Robots", In Proc. International Conference on Control, Automation and Systems, ICCAS 2001, October 17-21, 2001, Cheju National University, Jeju Island, Korea, 2001.
- [14] P.S. Sapaty, M. Sugisaka, "A Language for Programming Distributed Multi-Robot Systems", Proc. of The Seventh International Symposium on Artificial Life and Robotics (AROB 7th '02), January 16-18, 2002, B-Con Plaza, Beppu, Oita, Japan.
- [15] P. Sapaty, M. Sugisaka, "Universal Distributed Brain for Mobile Multi-robot Systems", in the book "Distributed Autonomous Robotic Systems", H. Asama, T. Arai, T. Fukuda, and T. Hasegava (Eds.), Springer-Verlag Tokyo 2002, SPIN: 10869189. Also reported at the International Symposium on Distributed Autonomous Robotic Systems DARS'02, June 25-27, 2002, Fukuoka, Japan.
- [16] P. Sapaty, M. Sugisaka, "Optimized Space Search by Distributed Robotic Teams", Proc. International Symposium on Artificial Life and Robotics (AROB 8th), January 24-26, 2003, Beppu, Japan.
- [17] P. Sapaty, M. Sugisaka, "Optimized Space Search by Distributed Robotic Teams", Proc. World Symposium Unmanned Systems 2003, Jul. 15-17, 2003, Baltimore Convention Center, USA.
- [18] M. Sugisaka, P. Sapaty, K. Imamura, K. Tokuda, N. Masuda, R. Finkelstein, J. Albus, "Research on Biologically Inspired Bipedal Dynamic Humanoid Robots", Proc. World Symposium Unmanned Systems 2003, Jul. 15-17, 2003, Baltimore Convention Center, USA.
- [19] P. Sapaty, M. Sugisaka, "Towards a Universal Distributed Brain for Mobile Multi-Robot Systems", Mathematical Machines and Systems, ISSN: 1028-9763, No. 3-4, 2003.
- [20] P. Sapaty, K. Kawamura, M. Sugisaka, R. Finkelstein, "Towards Fully Distributed Cognitive Systems", Proc. Ninth International Symposium on Artificial life and Robotics (AROB 9th), Beppu, Japan, January 2004.
- [21] P. Sapaty, K. Kawamura, M. Sugisaka, R. Finkelstein, "Towards Fully Distributed Cognitive Systems", Mathematical Machines and Systems, ISSN: 1028-9763, No. 1, 2004.
- [22] Sapaty, P., M. Sugisaka, "WAVE-WP (World Processing) Technology", Proc. First International Conference on Informatics in Control, Automation and Robotics, Setubal, Portugal, Vol.1, August 25-28, 2004.
- [23] Sapaty, P., N. Mirenkov, M. Sugisaka, and M. Osano, "Distributed Artificial Life Using World Processing Technology", Proc. of the Fifth Int. Conference on Human and Computer (HC-2004), September 1-3, 2004, The University of Aizu, Japan, 2004.
- [24] P. Sapaty, M. Sugisaka, N. Mirenkov, M. Osano, R. Finkelstein, "Grasping the Distributed Entirety", Proc. Tenth International Symposium on Artificial Life and Robotics (AROB 10th), Beppu, Japan, February 4-6, 2005.
- [25] P. Sapaty, M. Sugisaka, R. Finkelstein, J. Delgado-Frias, N. Mirenkov, "Emergent Societies: An Advanced IT Support of Crisis Relief Missions", Proc. Eleventh International Symposium on Artificial Life and Robotics (AROB 11th'06), Beppu, Japan, Jan 23-26, 2006, ISBN 4-9902880-0-9.
- [26] P. Sapaty, M. Sugisaka, R. Finkelstein, J. Delgado-Frias, N. Mirenkov, "Advanced IT Support of Crisis Relief Missions", Journal of Emergency Management, Vol.4, No.4, ISSN 1543-5865, July/August 2006.
- [27] P. Sapaty, M. Sugisaka, R. Finkelstein, J. Delgado-Frias, N. Mirenkov, "Emergent Societies: An Advanced IT Support of Crisis Relief Missions", Artificial Life and Robotics, Vol. 11, No. 1, 2007, ISSN 1433-5298.
- [28] P. Sapaty, M. Sugisaka, J. Delgado-Frias, J. Filipe, N. Mirenkov, "Intelligent Management of Distributed Dynamic Sensor Networks", Proc. Twelfth International Symposium on Artificial Life and Robotics (AROB 12th'07), Beppu, Japan, Jan 25-27, 2007.
- [29] P. Sapaty, M. Sugisaka, J. Filipe, "Making Sensor Networks Intelligent", Proc. of the 4th International Conference on Informatics in Control, Automation and Robotics, ICINCO-2007, Angers, France, 9-12 May 2007.
- [30] P. Sapaty, A. Morozov, R. Finkelstein, M. Sugisaka, D. Lambert, "A new concept of flexible organization for distributed robotized systems", Artificial Life and Robotics, Volume 12, Numbers 1-2 / March, 2008, ISSN: 1433-5298 (Print) 1614-7456 (Online), Springer Japan.
- [31] P. Sapaty, M. Sugisaka, J. Delgado-Frias, J. Filipe, N. Mirenkov, "Intelligent management of distributed dynamic sensor networks", Artificial Life and Robotics, Volume 12, Numbers 1-2 / March, 2008, ISSN: 1433-5298 (Print) 1614-7456 (Online), Springer Japan.
- [32] P. Sapaty, K.-D. Kuhnert, M. Sugisaka, R. Finkelstein, "Developing High-Level Management Facilities for Distributed Unmanned Systems", Proc. Fourteenth International Symposium on Artificial Life and Robotics (AROB 14th'09), B-Con Plaza, Beppu, Oita, Japan, Feb. 5-7, 2009.
- [33] Sapaty, P., Sugisaka, M., Kuhnert, K.-D. "Spatial scenarios for distributed unmanned systems", Proc. AUVSI's Unmanned Systems North America 2009, Washington, DC, USA, 2009.
- [34] P. Sapaty, M. Sugisaka, "Countering Asymmetric Situations with Distributed Artificial Life and Robotics Approach", Proc. Fifteenth International Symposium on Artificial Life and Robotics (AROB 15th'10), B-Con Plaza, Beppu, Oita, Japan, Feb. 5-7, 2010.

Construction of the Muscle Fatigue Evaluation Model based on Accuracy of Power

Akihiro Suzuki, Norihiko Kato, Yoshihiko Nomura, Hirokazu Matsui

*Mie University, Kurimamachiya 1577, Tsu Mie Japan
(Tel : 81-59-231-9473; Fax : 81-59-231-9663)
(suzuki@robot.mach.mie-u.ac.jp)*

Abstract: We develop a rehabilitation support system that assists the exercise training to reduce the physical load of therapists. In this study, we propose a muscle fatigue evaluation method to decide appropriate momentum for patients. Lots of studies of the muscle fatigue by EMG have been reported. However, muscle fatigue evaluation by EMG has disadvantages of complexity of preparation and gives patients mental stress. To solve this problem, in this study, we propose the muscle fatigue evaluation by the accuracy of muscle power. We verify proposed method on abduction/adduction of shoulders. We investigate how the accuracy of the muscle power changes under abduction/adduction repeatedly maintaining constant power of tangential direction. From the experimental results, we confirm correlation increase of amplitude of EMG and increase of power in direction of normal by power direction shift from tangential direction that is direction of target as the muscle fatigue increase.

Keywords: Rehabilitation, Robotics, Shoulder, Muscle, Fatigue, Motor Unit

I. INTRODUCTION

Recent years, the load of therapists and caregivers increases with the declining birthrate and a growing proportion of elderly people of the society. We aim to assist and reduce the load of the physical therapists who train rehabilitation, especially the exercise therapy training (maintenance and increase training for joint's range of motion, muscle-strengthening exercise, endurance training, and cooperated movement training, etc.), and then, we develop and the program of easy-to-use robot arms which assists these training operation and evaluate them.

We propose the muscle fatigue evaluation method to decide appropriate momentum for patients. Lots of studies of the muscle fatigue by EMG have been reported. In the muscle fatigue evaluation by EMG, as the muscle fatigue increases, amplitude of EMG increases. Generally speaking, it is said that is because of the increase of the amplitude by the collection of muscle fibers to keep its power, shifting from large and faster motor unit to a small and low one, and also shifting of the frequency element to the low-frequency area by the synchronizing ignition which ignites all motor units at the same time. However, muscle fatigue evaluation by EMG has the disadvantage of complexity of preparation and making the patients mentally stressful. To solve this problem, in this study, we propose the muscle fatigue evaluation by accuracy

of muscle power. We investigate correlation of the muscle fatigue evaluation by the EMG and accuracy of the muscle power, and propose muscle fatigue evaluation model.

II. REHABILITATION SUPPORT SYSTEM

As shown in Figure 1, robot arm with 7 degrees of freedom is used, and the force-torque sensor is installed in the tip of the arm. We control the motion by operating robotic arm based on the information of power and the torque measured by the sensor.

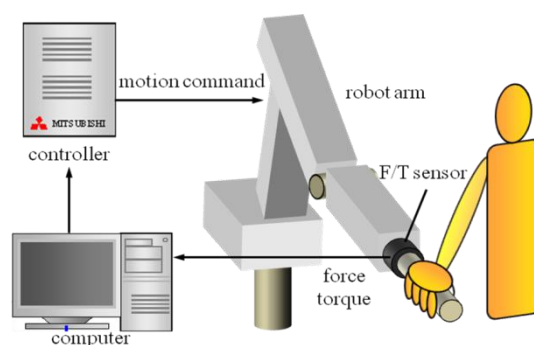


Fig.1. Rehabilitation Support System

III. MUSCLE FATIGUE EVALUATION

In this study, we propose the muscle fatigue evaluation based on the accuracy of the power. We

verify the accuracy of the power according to the muscle fatigue from two viewpoints such as amount and the direction. As shown in Fig.2, we divide the power in Fr of subject into normal direction element F_n and tangential direction element F_t centers on the shoulder joint, and evaluate them respectively. As shown with F_g in Fig.2, it aims at the movement which only the value is specified only for a tangential direction works effectively. We verify the accuracy of amount of power by the increase and the decrease of the difference from the targeted value $|F_g - F_t|$. And about, we verify direction of power because of the increase and decrease of the normal direction element of power $|F_n|$ by power direction shifted from tangential direction that is the direction of target. We calculated BIN average of the measuring data every one degree in the movement angle and compared with the total values of every one round trip.

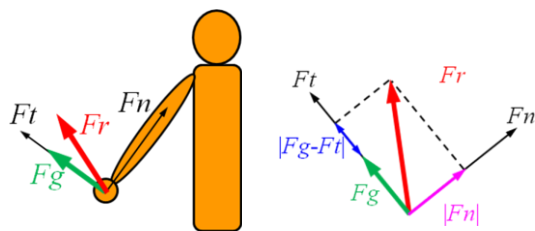


Fig.2. Evaluation of Muscle Fatigue

IV. EXPERIMENT

4.1. Method

The subjects are nine healthy persons. We had them move their arms within the angle of 30 to 90°. Load was set to be 30% of maximum isometric contraction for three seconds in 60°. We had them keep working until they become less than set amount with the constant movement angular speed (8deg/sec). To understand the muscle activity under the movement, we measured EMG of Deltoid (middle, anterior, posterior), Cowl muscle that relates to the abduction and Pectoral major muscle relates to the adduction.

We had the subjects exercise to follow the targeted value of the power and the target orbit displayed in the monitor as much as possible.

4.2. Result

4.2.1. Change in Accuracy of Power of Each Movement Frequency

We show the normal direction element $|F_n|$ of each movement frequency by abduction/adduction in Fig.3 (a) and the difference of the targeted value of the tangential direction element $|F_g - F_t|$ in Fig.3 (b) by average moving deviations of every round trip of five. We confirmed that the normal direction element $|F_n|$ increased every time the movement frequency was piled up. The similar tendency was not shown on the tangential direction element $|F_g - F_t|$.

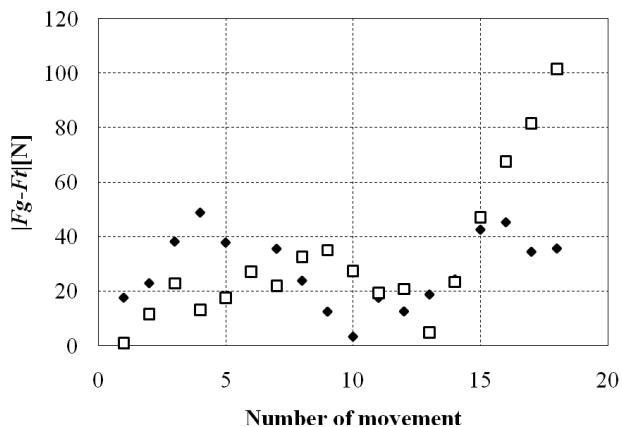
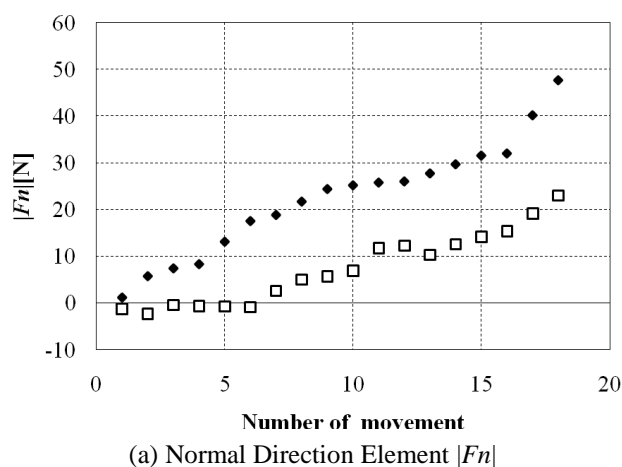


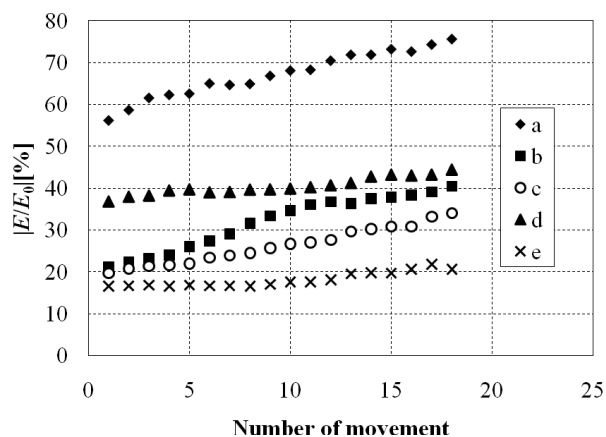
Fig.3. Accuracy of Power of each Movement Frequency

4.2.2. Amplitude of EMG of Each Movement Frequency

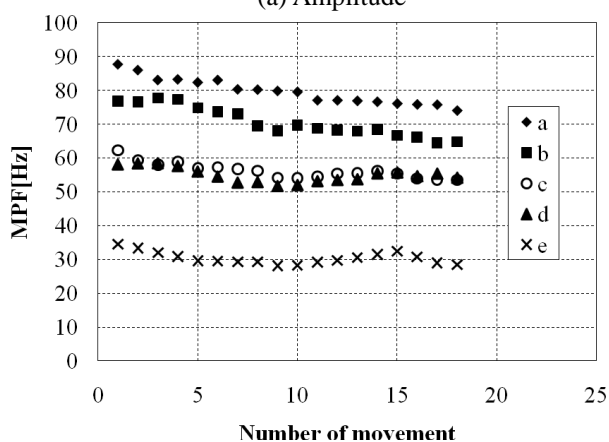
In Fig. 4(a), a relative value which was taking at the maximum isometric contraction of 100% in 60° is shown. As the movement frequency is piled up, we confirmed the increase in the level of each muscle activity level.

We show the mean power frequency (MPF) of each movement in Fig.4 (b). We confirmed the muscle

fatigue from the increase of the amplitude of EMG and the shift of the frequency element to the low frequency region.



(a) Amplitude



(b) Mean Power Frequency

Fig.4. EMG

a: Deltoid Middle

b: Deltoid Anterior

c: Deltoid Posterior

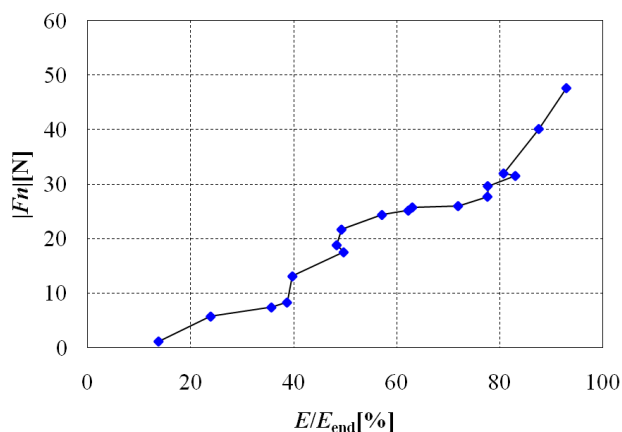
d: Cowl Muscle

e: Pectoral Major Muscle

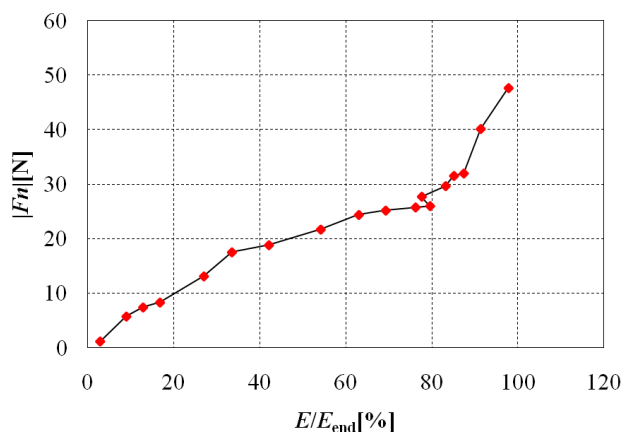
4.2.3. Correlation of Amplitude of EMG and Accuracy of Power

We show the correlation for the amplitude of EMG in each muscle and normal direction element of power $|Fn|$ in Fig.5. The horizontal axis in the graph shows is the value in which measured amplitude of EMG assuming the first mean value of three round trips to be standard value of 0, and makes the last mean value of three round trips a relative value as 100. The vertical axis in the graph shows the normal direction element of power in difference by the first mean value of three round trips. As the amplitude of EMG increases, we confirmed the increase of the normal direction element

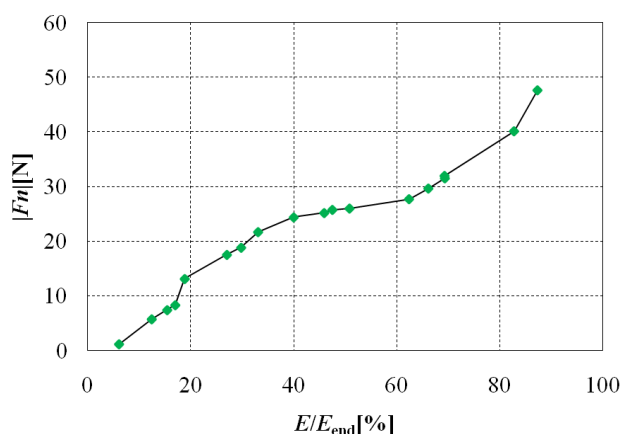
of power $|Fn|$. We show the correlation coefficient of the amplitude of EMG of each muscle and normal direction element of power in Table 1. We confirmed that there was a strong correlation between muscle fatigue and the accuracy in direction of power.



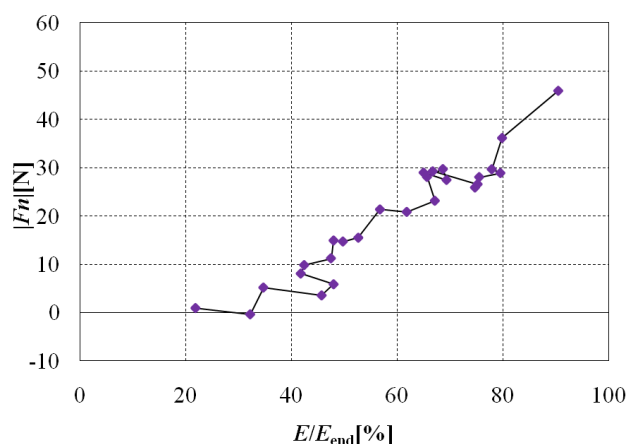
(a) Deltoid Middle



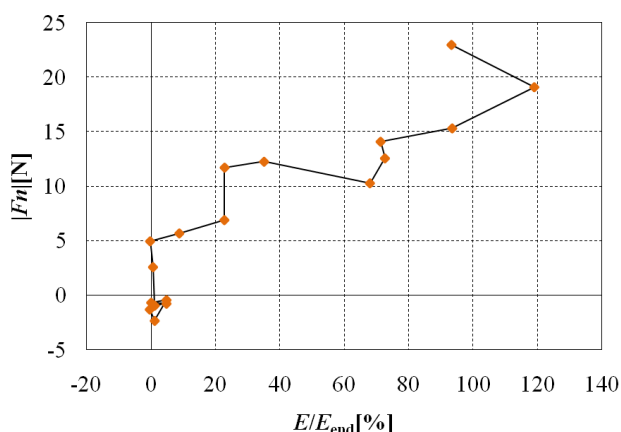
(b) Deltoid Anterior



(c) Deltoid Posterior



(d) Cowl Muscle



(e) Pectoral Major Muscle

Fig.4. Correlation of Amplitude of EMG and $|F_n|$

Table 1 Correlation Coefficient

	Coefficient Correlation
Deltoid Middle	0.964
Deltoid Anterior	0.958
Deltoid Posterior	0.971
Cowl Muscle	0.950
Pectoral Major Muscle	0.903

V. CONSIDERATION

We had subject isotonic movement under low load, and confirmed that the normal direction element of power increases by the decline of the accuracy in direction of power with increase of the muscle fatigue.

Immediately after the movement begins, the power is maintained by the muscle which is comparatively small (ST-MU) because of the load was set low. When the tension of ST-MU decreases, the power is made up by restarting of stopping muscle that motor unit is

comparatively large. It is thought that the control of power roughens, and the decrease of accuracy of power was caused by this. In addition, the smoothness of muscle contraction is ruined by the synchronization phenomena of motor unit that all motor units is mobilized, and it becomes an explosive activity style in the vicinity of the movement limit. Therefore, we think that accuracy of power decreased more

VI. CONCLUSION

In this study, we proposed muscle fatigue evaluation based on accuracy of power under a low load, and confirmed that there was a strong correlation in the relation between increase of normal direction element of power caused by the decrease of accuracy in direction of power and muscle fatigue.

The comparative study of a load and the movement speed that differs and depends is necessary as future tasks. Moreover, we should consider the individual variation depends on the subjects by constructing the model type because there is a difference in the value of $|F_n|$ when muscle fatigue reaches to the critical limit.

Also, we should verify whether our proposal technique is useful for actual rehabilitation patients who are waiting for.

REFERENCES

- [1] Jyunichirou Aoki, Yuu Satou, Isao Muraoka (2005), sports physiology
- [2] Syuu Yatojima, Asahiro Kiduka, Hioroshi Yajima (2003) Influence that movement leg position and angle variation when shoulder abduction on activity aspect of surroundings muscle of shoulder
- [3] Syuu Yatojima, Asahiro Kiduka, Naoki Mukai, Jin Siragi, Yutaka Miyana, Muscle activity characteristic when shoulder abduction on different movement condition
- [4] Sinichi Huruya, Fatigue
- [5] Haruo Sugi (2003), The muscle is mysterious, Shown mechanism that gives birth to power
- [6] Noriyuki Hayami, Eiishi Tanaka, Souta Yamamoto, Hiorki Takeuchi, Modeling of muscle fatigue that considers difference of fatigue tolerance of motor unit type
- [7] Yasushi Itoh, Kumi Akataki, Katsumi Mita, Watakabe Makoto, Kunihiro Itoh (2003), Time of Mechanomyogram of continuation contraction with muscle fatigue- Frequency analysis

Anomalous Situations Detection Based on Confluence

Tatsuya Gibo[†] Shigeki Aoki[‡] Takao Miyamoto Motoi Iwata Akira Shiozaki
Osaka Prefecture University
1-1 Gakuen-cho, Naka-ku, Sakai-shi, Osaka, JAPAN, 599-8531
gibo_t@ch.cs.osakafu-u.ac.jp[†] aoki@las.osakafu-u.ac.jp[‡]

Abstract: Recently, surveillance cameras have been set up everywhere such as streets and public places in order to detect anomalous situations. In the existing surveillance systems, since only a handful of surveillance agents watch a lot of images from surveillance cameras, there may be some possibilities that they miss the important scenes such as accidents or abnormal incidents. So, we propose a method of the sequential learning and recognition of comprehensive behavioral patterns in the crowded places. Firstly, we extract the comprehensive confluence from an input image using optical flows. Secondly, we extract the behavioral patterns based on change-point detection of the confluence. Finally, we recognize the behavioral pattern by comparing the previous behavioral pattern in the database with a newly observed one. We carried out experiments to verify the effectiveness of our approach by placing a surveillance camera on our campus.

Keywords: Behavioral pattern recognition, Optical flow, Dynamic programming.

1 Introduction

Recently, surveillance cameras have been set up everywhere such as streets and public places in order to detect anomalous situations. In the existing surveillance systems, since only a handful of surveillance agents watch a lot of images from surveillance cameras, there may be some possibilities that they miss the important scenes such as accidents or abnormal incidents. In order to solve this problem, there have been the considerable researches on the system which automatically recognizes human behavior in a surveillance footage. It warns security guards when it detects anomalous situations.

Several methods[1, 2, 3] for recognizing human behavior focus on a few people in a room, and it is difficult to apply the methods to more people in crowded places.

The methods for recognizing crowd behavior using a range scanner or a 3D point measurement device[4, 5] have been proposed. These researches, they can make confluence analysis of dense crowd possible. However, it is not easy to apply these methods because most of the existing surveillance systems use only a monocular surveillance camera.

So, we propose a method for detecting an anomalous situation in crowded places using a monocular surveillance camera.

2 Learning and Recognition of Comprehensive Behavioral Patterns

In this section, we describe a method for recognizing the behavioral patterns of people in such places as multiple people keep moving. In the public places, occlusion occurs frequently, hence it is difficult to

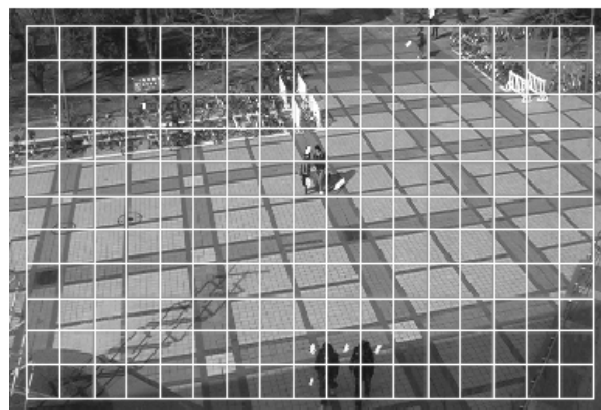


Figure 1: A mode values of optical flows and a divided image into 20×20 [pixels] segments. A mode value was drawn on center of each segment.

keep track of people individually. Because there is an enormous types of motions of people, it is not easy to recognize every behavioral pattern. So, in order to learn the comprehensive behavioral patterns of multiple people and to recognize them, we regard the motions of people as one comprehensive confluence based on the moving direction of people.

2.1 Extraction of Feature Vector of Confluence

In this subsection, we explain a technique for extracting a feature vector of motions.

Firstly, to extract a feature vector of the motions, we compute an optical flow of each pixel in an input image. Secondly, a mode value $v_n = \{du, dv\} (n = 1, 2, \dots, N)$ are computed by dividing an input image into 20×20 [pixels] segments and in each segment,

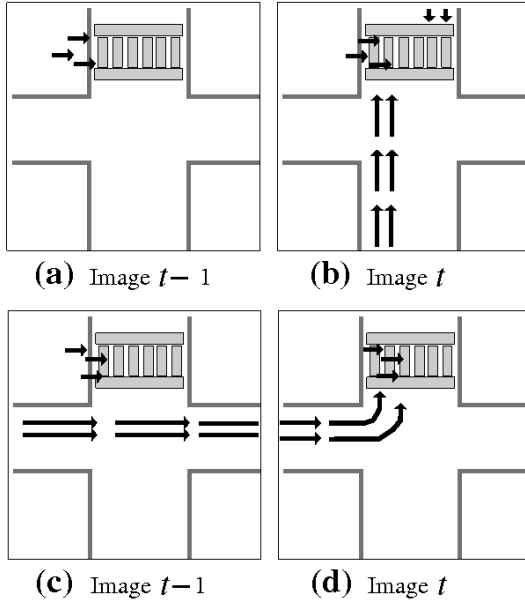


Figure 2: Example of change-point detection by degree of congestion and confluence.

we compute a mode value of optical flows. Where N is the number of segments. Fig.1 shows an example of the mode values. Finally, a feature vector of confluence $\mathbf{V}_t = \{v_1, v_2, \dots, v_N\}$ is created by raster-scanning the mode value of the optical flows v_n in each segment.

2.2 Extraction of Behavioral Patterns

Generally, the following behavioral patterns are observed in crowded places.

- I. People appear in sight of a camera \rightarrow people go out of sight of a camera
- II. As shown Fig.2 (a) people walk on a pedestrian crossing \rightarrow (b) when they are walking, vehicles go toward the people
- III. As shown Fig.2 (c) people and vehicles go straight \rightarrow (d) they turn to the left

We regard the time when people appear in sight of surveillance camera, the time when degree of congestion changes (Fig. 2(b)) and the time when confluence changes (Fig. 2(d)) as new behavioral pattern starts and we called it division point. We set the division points to the sequence of feature vectors $\{\dots, \mathbf{V}_{16}, \mathbf{V}_{17}, \dots, \mathbf{V}_{21}, \mathbf{V}_{22}, \dots\}$ to extract the behavioral patterns. We define the feature vectors of confluence between division point as a behavioral pattern. We describe it the extracted p -th behavioral pattern $\mathbf{I}_p = \{\mathbf{V}_1^p, \mathbf{V}_2^p, \dots, \mathbf{V}_{T_p}^p\}$. Where T_p is length of the sequence \mathbf{I}_p . Fig.3 shows, an example of \mathbf{I}_p and \mathbf{I}_{p+1} extracted from a sequence of feature vectors.

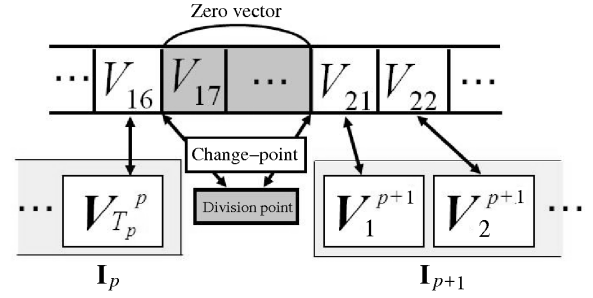


Figure 3: The behavioral pattern extraction by checking the existence of motion.

2.2.1 Division Point Setting Method by Checking Motion Existence

We regard the time when $\mathbf{V}_t = \mathbf{0}$ were observed for the fourth time in a row afterward \mathbf{V}_t returned to non 0 as division point for the start of the behavioral pattern.

2.2.2 Division Point Setting Method by Detecting Congestion Changes

Firstly, we calculate the number of the non $\mathbf{0}$ mode values $v_n (n = 1, 2, \dots, N)$ in the \mathbf{V}_t . We defined it as h_t . h_t express a degree of congestion. Secondly, when h_t meets the following requirement, we consider the time t to be a division point on a sequence of the feature vectors, where θ is a threshold value.

$$|h_t - \frac{1}{5} \sum_{m=1}^5 h_{t-m}| > \theta \quad (1)$$

2.2.3 Division Point Setting Method by Detecting Confluence Changes

In this method, in order to survey the similarity between the confluence at time t (\mathbf{V}_t) and the confluence at time $t-1$ (\mathbf{V}_{t-1}), we use Wilk's Λ and M-BOX. Significant level is 5%. The null hypothesis is "distribution of \mathbf{V}_t and \mathbf{V}_{t-1} is identical", and the alternate hypothesis is "distribution of \mathbf{V}_t and \mathbf{V}_{t-1} is different". When the null hypothesis is rejected, the alternate hypothesis is adopted. We set division point when the alternate hypothesis is adopted.

2.3 Learning and Recognition Method

The procedure of sequential learning and recognition of behavioral patterns and detection of anomalous situations was composed the three general phases. Firstly, when behavioral pattern \mathbf{I}_p is observed, we perform the comparison process (Fig. 4 Comparison) to confirm the existence of the same patterns in the database. Secondly, we carry out the recognition (Fig. 4 Recognition) of \mathbf{I}_p . When \mathbf{I}_p is

Table 1: Experimental results of sequential learning, recognizing and anomalous situation detection.

Date	Number of patterns	Behavioral		anomalous		Number of Cumulative patterns
		recognition	misclassification	recognition	misclassification	
2 – 8	12,993	11,920 (94.9%)	635 (5.1%)	420 (95.9%)	18 (4.1%)	793
9 – 15	11,749	-	18	415	-	950
Total	24,742	-	658	835	-	-

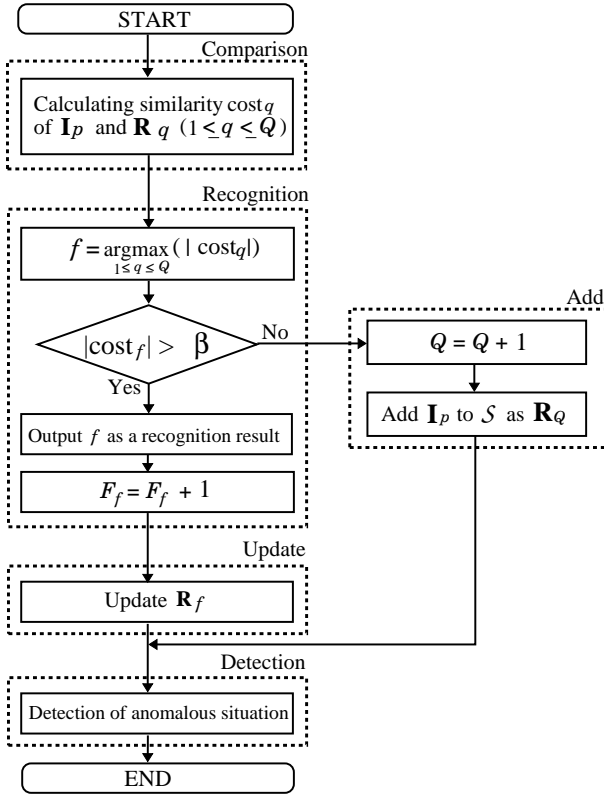


Figure 4: The procedure of sequential learning and recognition behavioral patterns and constructing reference patterns and detecting anomalous situations.

extracted, we compare \mathbf{I}_p with the fore-past behavioral patterns \mathbf{R}_q in the database by computing the similarities $|\text{cost}_q| (q = 1, 2, \dots, Q)$ using the dynamic programming. After that, \mathbf{R}_f that has the highest similarity is chosen from the database. If the $|\text{cost}_f|$ is higher than β , we recognize \mathbf{I}_p as \mathbf{R}_f , and we perform updating process (Fig. 4 Update). Where β is a threshold value for recognition. If the $|\text{cost}_q|$ is lower than β , we add (Fig. 4 Add) \mathbf{I}_p to the database as a new behavioral pattern \mathbf{I}_{Q+1} . Finally, we perform detection process (Fig. 4 Detection) of anomalous situations.

2.3.1 Method of Anomalous Situations Detection

If \mathbf{I}_p which was observed is daily behavior, the frequency of observation F_f of \mathbf{R}_f is greater than that of other reference pattern $\mathbf{R}_q (q = 1, 2, \dots, Q)$ in the database. If \mathbf{I}_p is anomalous behavior, F_f is lower than that of other $\mathbf{R}_q (q = 1, 2, \dots, Q)$. So, we calculate the observation probability $\text{Pr}(f)$ to detect anomalous situation. If the value is lower than the threshold γ , we detect \mathbf{I}_p as an anomalous situation.

$$\text{Pr}(f) = \frac{F_f - 1}{\sum_{q=1}^Q F_q} \quad (2)$$

3 Experiments and Discussions

In order to verify the effectiveness of the proposed method, we performed an experiment. We evaluated the recognition success rate and the misclassification rate of the behavioral patterns and the recognition success rate and the misclassification rate of the anomalous situations. Data set were observed between Dec.2, 2008 and Dec.15, 2008 using a surveillance camera placed on Osaka-Prefecture University. The image size is 360×240 [pixels]. The thresholds are $\beta = 2.0$, $\alpha = 0.05$ and $\gamma = 0.01$.

3.1 Experimental Results

The second column of Table 1 shows the number of observed patterns in several days. The third and fourth columns show the number of recognition success and misclassification of the behavioral patterns. The recognition success of the behavioral patterns is that the classifier correctly recognizes behavioral pattern as behavioral pattern. The misclassification of behavioral patterns is that the classifier falsely recognizes behavioral pattern as anomalous situation. The fifth and sixth columns show the number of recognition success and misclassification of the anomalous situations. The recognition success of anomalous situations is that the classifier correctly recognizes anomalous situation as anomalous situation. The misclassification of the anomalous situations is that the classifier falsely recognizes anomalous situation as behavioral pattern. The last column shows

the number of patterns that were registered in the database.

In terms of experiments during Dec.2–Dec.8, in order to verify recognition accuracy of our method, we survey observed all patterns. In Table 1, 12,993 observed patterns during Dec.2–Dec.8 were recognized by 793 different reference patterns. We had 94.9% recognition success rate of the behavioral patterns and 95.9% recognition success rate of anomalous situations. In Dec.5, misclassification of the behavioral patterns occurs because it is rainy. In the case that we omit the data of Dec.5 from the data sets, we had 99.8% recognition success rate of behavioral patterns and 95.6% recognition success rate of anomalous situations, during Dec.2–Dec.8.

In terms of during Dec.9–Dec.11, in order to verify detection accuracy of anomalous situations of our method, we survey the objects which the classifier recognizes as anomalous situations. During Dec.9–Dec.11, 749 different reference patterns were registered in the database, and 11,749 observed patterns were recognized by 950 different reference patterns. Therefore, we confirmed a satisfaction of our method.

3.2 Discussions

In this paper, we have proposed a novel method for detecting the anomalous situations in crowded places using a monocular surveillance camera. We describe below outline of the proposed method.

Extraction of feature vector of confluence

In this method, we divided an input image and we compute the mode values of optical flows to extract comprehensive confluence. We could extract confluence in crowded places by this approach.

However, we could not extract the feature of quiescent people using optical flows. To tackle the problem, we will use optical flows and background-subtraction.

Extraction of behavioral patterns

We extract of behavioral patterns by using the three rules combination. These are people motion existence, congestion changing points and confluence changing points. We could extract the behavioral patterns correctly using the rules. If we use only the first rule, we do not extract behavioral patterns under the situation that constant flow of confluence is observed always. However, we could extract behavioral pattern under such a situation by using second and third rules.

Learning, recognition and detection

From the results, The increase in the number of patterns in the database is reductive as day goes on. From this reason, we could see that the classifier

learns many behavioral patterns on earlier stage, and the classifier learns the behavioral patterns which are not existent in the database.

In order to detect anomalous situation, we use the observation probability. Detected anomalous situations are throwing the ball back and forth, lingering around. These behaviors were too observed. Therefore, we confirmed that the proposed method can recognize behavioral patterns and can detect anomalous situations.

4 Conclusion

We presented a novel method for detecting the anomalous situation in crowded places using a monocular surveillance camera. To learn and to recognize behavior of the multiple people and to recognize them, we regard the motions of people as one comprehensive confluence with a focus on the moving direction of people. Besides, in order to detect anomalous situations, we calculated the observation probability based on the frequency of observation. In the results, we confirm the effectiveness of the proposed method in crowded places.

References

- [1] B. Scholkopf, J.C. Platt, J. Shawe-Taylor, A.J. Smola, R.C. Williamson (2001), Estimating the Support of a High-Dimensional distribution, *Neural Comput*, Vol.13, No.7, pp.1443–1471
- [2] H. Zhong, J. Shi, M. Visontai (2004), Detecting Unusual Activity in Video, *Proc. IEEE Conf. on CVPR*, Vol.2, pp.819–826
- [3] S. Aoki, Y. Iwai, M. Onishi, A. Kojima, K. Fukunaga (2005), Learning and Recognizing Behavioral Patterns Using Position and Posture of Human Body and Its Application to Detection of Irregular States, *System and Computers in Japan(SCJ)*, Vol.36, No.13, pp.45–56
- [4] K. Nakamura, H. Zhao, R. Shibasaki, K. Sakamoto, T. Ooga, N. Suzukawa (2005), Tracking Pedestrians Using Multiple Single-Row Laser Range Scanners and Its Reliability Evaluation (in Japanese), *IEICE Trans. D-II*, Vol.J88–D–I I, No.7, pp.1143–1152
- [5] M. Onishi, I. Yoda (2010), Comparison and Visualization Method of Pedestrian Trajectories in a Complex Office for a Long Period (in Japanese), *IEICE Trans. D*, Vol.J93–D, No.4, pp.486–493

Automatic Segmentation of Liver Region from Non-contrast and Contrast CT images Employing Tree-structural Image Transformations

Masafumi Komatsu¹⁾, Guangxu Li¹⁾, Hyounseop Kim¹⁾,
Joo Kooi Tan¹⁾, Seiji Ishikawa¹⁾, Akiyoshi Yamamoto^{1), 2)}

1) Kyushu Institute of Technology, 1-1, Sensui, Tobata, Kitakyushu, Japan

2) Kyoaikai Tobata Kyoritsu Hospital, Japan

(Tel: +81-93-884-3185; Fax: +81-93-861-1159)

(komatsu@kimlab.cntl.kyutech.ac.jp)

Abstract: In the medical image processing field, segmentation from the CT image is one of the most important problems for analyzing the abnormalities and diagnosis on visual screening. Many related segmentation techniques have been developed for automatic extraction of ROI. It is however, there are still no fully automatic segmentation methods that are generally applicable to ROI based on CT image set. In this paper, we present a technique for automatic extraction of liver region on the MDCT images employing automatic construction of tree-structural image transformation (ACTIT). We propose a new technique for extraction of organs employing ACTIT with non-contrast and contrast image set in order to introduce temporal change information. We apply the proposed technique to three abdominal image set and satisfactory segmentation results are achieved.

Keywords: Segmentation, Liver region, MDCT, Tree-structural filter, ACTIT, Temporal change.

I. INTRODUCTION

In recent years, various imaging equipments have been introduced into medical fields. Especially, high resolution helical computed tomography (HRCT) is one of the most useful diagnosis systems because it provides a high resolution image to medical doctors as clear image. Radiologist can easily detect abnormalities by use of the image with high resolutions. Accordingly, many related image processing techniques are proposed into medical fields for extraction of abnormal area. Automatic extraction of the region of the interest (ROI) is an important theme of medical imaging and computer vision technologies.

In the medical image processing field, segmentation from the CT image is one of the most important problems for analyzing the abnormalities and diagnosis on visual screening. Many related segmentation techniques have been developed for automatic extraction of ROI before analyzing the abnormalities. Especially, in order to extract multi organs and to understand the structure of internal organ, several approaches have been developed in the past. Ney *et al.* [1] proposed a technique based on tracing the liver boundary section with a mouse. Gao *et al.* [2] applied a method of automatic segmentation of the liver region employing knowledge based and a model based boundary finding scheme. Bae *et al.* [3] devised a segmentation method of liver structures employing Gaussian smoothing and eight-point connectivity

tracking. Shimizu *et al.* [4] proposed the simultaneous methods that are generally applicable to regions of interest based on CT image sets. We also have developed the segmentation technique of spleen and gallbladder region employing rib information and region growing technique [5]. Many other techniques are proposed for segmenting the organs. It is however, there are still no fully automatic and satisfactory segmentation methods that are generally applicable to ROI based on CT image set.

On the other hand, in the image analyzing fields, automatic construction of tree-structural image transformations (ACTIT) is used for constructing the filtering tree [6]. The ACTIT is the method that automatically generates image transformation process from several given examples by use of genetic algorithm. By use of the ACTIT, we can get the image transformation filtering tree as a combination of known filters, which is able to be applied to unknown image.

In this paper, we present a technique for automatic extraction of liver region on the MDCT images employing ACTIT. In our study, we propose a new technique for extraction of organs employing the ACTIT with non-contrast and contrast image set. In the past, ACTIT used only one image as tree-nodes. In this paper, we set the non-contrast image and the contrast one as tree-nodes of filtering tree. By using this method, we can introduce temporal change information between non-contrast and contrast images.

The organization of this article is as following. Firstly, we present a method for segmentation of CT image by use of ACTIT in section 2. Then we give some experimental results in section 3. Finally, in section 4, we give conclusions along with discussion of the problems obtained from experimental results.

II. METHODS

Figure 1 shows the flow of the proposed method. In the first step, we input non-contrast images, contrast images and reference images which are made manually. Non-contrast and contrast images are used as the nodes of tree-structural filter. In the second step, we apply ACTIT in order to generate tree-structural filter. Finally, we apply generated filter to unknown images.

1. ACTIT

ACTIT is the method which generates the structural filter as the combination of known filters. In order to optimize the filters, the genetic algorithm is used. Fig. 2 shows the overall scheme of the ACTIT. First, we make a lot of tree-structural filters as initial genes. Next, we calculate fitness by the following equation.

$$fitness = \frac{1}{K} \sum_{i=1}^K \left\{ 1 - \frac{\sum_{x=1}^{W_x} \sum_{y=1}^{W_y} w_i(x, y) |O_i(x, y) - T_i(x, y)|}{\sum_{x=1}^{W_x} \sum_{y=1}^{W_y} w_i(x, y) \cdot V_{max}} \right\} \quad (1)$$

Here, O_i , T_i , and K shows output image, reference image, and the number of slices respectively. W_x , W_y , V_{max} shows image width, image height, and the maximum value of image density respectively. w_i shows the weight.

Furthermore, we optimize the tree filters by genetic algorithm (elitist selection, crossover, and mutation (1%)). In the crossover step, we apply crossover between branches.

If the fitness is over 99% or does not change for 30 loops, we stop the examination and get optimized filters.

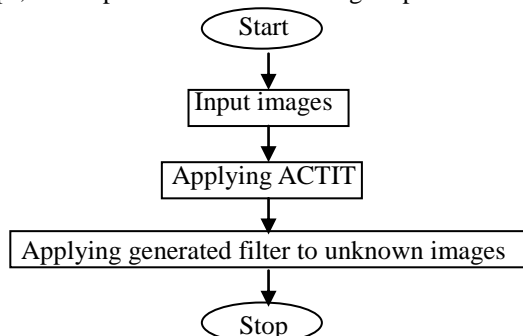


Fig.1 The flow of procedure.

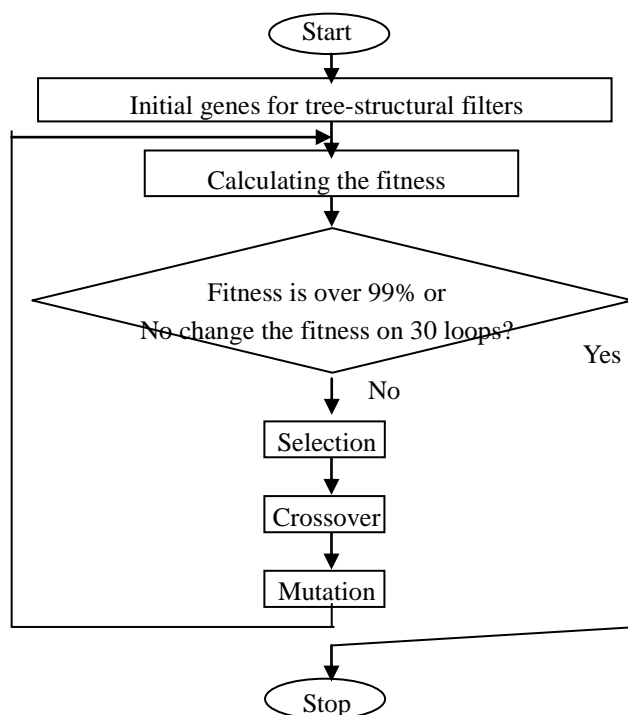


Fig.2 Overall scheme of ACTIT

2. ACTIT with temporal information

In general, ACTIT used one image as the nodes of tree. However, when we applied the ACTIT to non-contrast CT images, we could not achieve satisfactory results (Fig.3), because there are a lot of noises on the result image.

In the abdominal CT images, soft tissues such as liver, kidney and spleen are shown as 50~60[H.U.]. And the pixel value of muscles indicates 30~60[H.U.]. It is a difficult problem to separate between soft tissues and muscles.

To overcome this problem, we propose ACTIT with temporal subtraction information between the non-

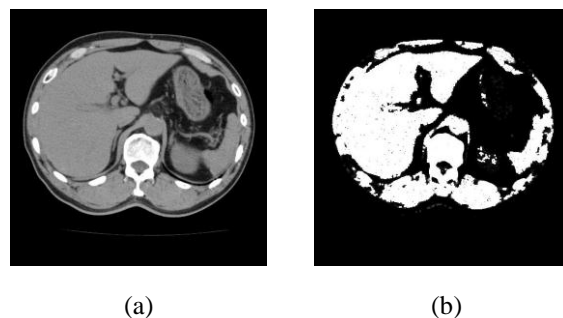


Fig. 3 Experimental results of ACTIT with only one image as nodes of tree filter. (a) shows original image, (b) shows the experimental result.

contrast images and the contrast one. We can introduce contrast medium information by exchanging a part of non-contrast image to the contrast one randomly. Contrast medium changes image contrast and appears around soft tissue or blood vessels with high CT values. So we can get contrast medium information by subtraction of images. Each features which is adopted are shown in Table.2

III. RESULTS

1. Experimental environments

We apply the proposed technique to three real CT cases in order to extract the liver region. The acquisition parameters and experimental environments are shown in Table 1. The images are 512×512 pixels in size with a pixel spacing of 0.616 to 0.744 mm. And we use 5 slices per case in order to construct tree filter and calculate fitness. Table 2 shows the list of filters which we used for constructing tree-structural filters. In Table 2, V_1 and V_2 show the pixel value of image 1 and image 2, respectively. Furthermore V_{max} shows the maximum pixel value of the image.

2. Results

Figure 4 shows the experimental result for extraction of liver regions by use of proposed algorithm. In Fig. 4, (a) shows the non-contrast original image, (b) shows the contrast image, (c) shows the reference image, (d) shows the experimental result which is achieved by applying generated filter to (a) and (b). (e) and (f) show other non-contrast image and the image obtained by applying tree-constructed filter generated from (a) and (b) to (e), respectively.

Table 1 Experimental environments

OS	Microsoft Windows XP
Development environment	Microsoft Visual C++
CPU	Intel Pentium 4 3[GHz]
Memory	1[GB]
CT scanner	Toshiba Aquilion 16
Image size	512×512 [pixels]
Pixel spacing	0.616~0.744[mm]
Image resolution	16[bits]
Slice thickness	2[mm]

Table 2 Filters for constructing tree-structural filter

Filter	Effect
Average	3-neighbors average filter
Minimum	3-neighbors minimum filter
Maximum	3-neighbors maximum filter
Inverse	Inversion of pixel value
Erosion	Erosion
Dilation	Dilation
Binarization (discriminant analysis)	Binarization using discriminant analysis
Binarization (average)	Binarization using the average value of image
Laplacian	Laplacian filter
Laplacian + V_{max}	Laplacian + the maximum value of image
Sobel	Sobel filter
Segmentation of Maximum area with binarization (discriminant analysis)	Segmentation of maximum area with binarization using discriminant analysis
Segmentation of Maximum area with binarization (average)	Segmentation of Maximum area with binarization using the average value of image
Elimination of symmetrical area	Elimination of symmetrical area
Elimination of non- symmetrical area	Elimination of non- symmetrical area
Subtraction	The absolute value of subtraction
Logical summation	The larger value between V_1 and V_2
Logical product	The smaller value between V_1 and V_2
Algebraic summation	$V_1 + V_2 - (V_1 \times V_2) / V_{max}$
Algebraic product	$(V_1 \times V_2) / V_{max}$
Bounded summation	$V_1 + V_2$
Bounded product	$V_1 + V_2 - V_{max}$
Drastic summation	If V_1 and V_2 are not 0, it returns V_{max} . Else if only V_1 is 0, it returns V_2 . Else if only V_2 is 0, it returns V_1 .
Drastic product	If V_1 and V_2 are not V_{max} , it returns 0. Else if only V_1 is V_{max} , it returns V_2 . Else if only V_2 is V_{max} , it returns V_1 .

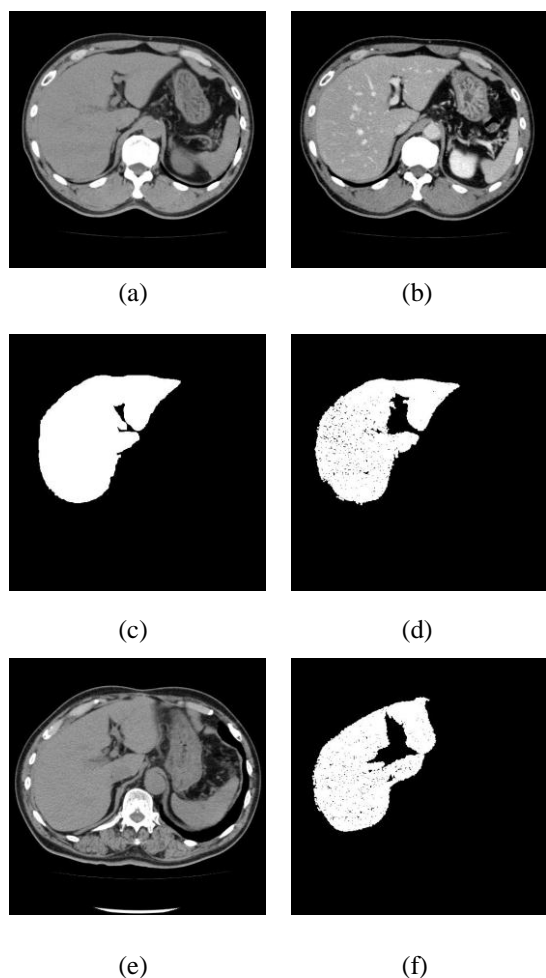


Fig. 4 Experimental results : (a) shows non-contrast image, (b) shows the contrast image, (c) shows the reference image, (d) shows extracted region by applying tree-constructed filter generated from (a) and (b). (e) and (f) show other non-contrast image and the result obtained by applying filter used for generating (d) to (e) image.

Table 3 Fitness of experimental results

Reference	Case 1	Case 2	Case 3
Case 1	(97.95)[%]	97.36[%]	97.56[%]
Case 2	97.42[%]	(97.86) [%]	97.38[%]
Case 3	97.58[%]	97.25[%]	(97.59) [%]

The fitness of experimental results by calculating equation (1) is shown in Table 3.

VI. CONCLUSION

In this paper, we proposed a segmentation technique for liver region employing ACTIT. In the experimental results, satisfactory segmentation performances are

achieved. We can check that the proposed technique is useful for extraction of liver regions.

We proposed the new method for ACTIT in order to introduce temporal change information by use of non-contrast and contrast images as nodes of tree-structural filter. We can check that it is useful for eliminating the noises caused by similarity of pixel values between muscle and other soft tissues.

The proposed technique is useful for extraction of the liver regions. But it still remains miss-segmentation errors. We use the reference image including blood vessels nearby liver regions, but when we apply the obtained tree filters to other CT cases, blood vessel regions do not remain on the experimental result. It is because the fitness did not exceed 99%. We think that the combination between proposed technique as coarse segmentation and level set method [7] as fine segmentation is useful in order to improve segmentation accuracy. Furthermore improvement of algorithm is now in progress. We believe this segmentation method makes possible to improve the segmentation accuracy for analyzing the internal structure of human body before the operation.

REFERENCES

- [1] D. R. Ney, R. A. Drebin, E. K. Fishman, D. Magid, "Volumetric rendering of computed tomography data : Principles and techniques", *IEEE Comput. Graph. Appl.*, Vol.10, pp.24-32, 1990.
- [2] L. Gao, D. G. Heath, B. S. Kuszyk, E. K. Fishman, "Automatic liver segmentation technique for three-dimensional visualization of CT data", *Radiology*, Vol.201, No.2, pp.359-364, 1996.
- [3] K. T. Bae, M. L. Giger, C. T. Chen, C. E. Kahn Jr., "Automatic segmentation of liver structure in CT images", *Med. Phy.*, Vol.20, No.1, pp.71-78, 1999.
- [4] A. Shimizu, R. Ohno, T. Ikegami et al. "Simultaneous extraction of multiple rgans from abdominal CT", *Proc. of CARS*. P.1275, 2005.
- [5] S. Toyota, H. Kim, S. Ishikawa et al., "Automatic detection of spleen and gallbladder region employing rib information", *IEICE*, MI2006-97, pp.53-54, 2007.
- [6] T. Nagao, S. Masunaga, "Automatic construction of image transformation processes using genetic algorithm", *Proceedings of the ICIP' 96*, vol. 3, pp. 731-734, 1996.
- [7] T. Hitosugi, A. Shimizu, M. Tamura et al., "Development of a liver extraction method using a level set method and its performance evaluation", *Journal of Computer Aided Diagnosis of Medical Images*, Vol. 7, No. 4-2, pp.1-8, 2003.

Obstacle Detection Using a Moving Camera

Shao Hua Qian¹, Joo Kooi Tan¹, Seiji Ishikawa¹, Takashi Morie²

¹Department of Mechanical & Control Engineering, ²School of Brain Science & Engineering
Kyushu Institute of Technology

Sensuicho 1-1, Tobata, Kitakyushu, 804-8550, Japan

E-mail: {qian, etheltan, ishikawa}@ss10.cntl.kyutech.ac.jp, morie@brain.kyutech.ac.jp

Abstract: This paper proposes a method of detecting obstacles from a video taken by a moving camera mounted on a vehicle by background subtraction. The background subtraction is often used to detect moving objects when camera is static. But according to the characteristics of a road, we can also employ Gaussian mixture model to detect all objects (either static or moving objects) on the road in the case of moving camera. Then we use two consecutive image frames, and warps the first image according to the geometrical relationship between these two images. The road area is then extracted by comparing the warped image with the second image. Using this road area, we can delete all things which are not obstacles. In the performed experiments, it is shown that the proposed method is able to detect obstacles such as vehicles and pedestrians on a road.

Keywords: Obstacle detection, moving camera, monocular vision, Gaussian mixture model, road area detection.

I. INTRODUCTION

Thousands of people die by car accidents year by year. Many of those accidents could be avoided or alleviated by vision-based driving assistance systems. These systems cause drivers to respond more quickly in the face of danger. In these systems, the ability to detect obstacles from a vehicle moving on a planar road surface is essential. In recent years, many obstacles detection approaches have been developed. There are mainly three popular methods, based on a-priori knowledge, based on optical flow, and based on stereo vision. The method based on a-priori knowledge is often used to detect specific objects or limited objects classes, such as vehicles or pedestrians. We often call this method pattern recognition. Optical flow and stereo vision methods can detect arbitrary objects which pose a threat to safe driving. But these two methods are sensitive to vehicle motion, and when obstacles have small or null speed, optical flow techniques fail.

In this paper, we propose a method of estimating a road area in general road environments. This method uses two consecutive image frames, and warps the first image according to the geometrical relationship between these two images. The road area is then extracted by comparing the warped image with the second image.

II. OUTLINE OF THE PROPOSED METHOD

The process flow of the proposed method is shown in Fig. 1.

In the first place, we employ a Gaussian mixture model [1,2] in reconstructing the background from a video image sequence taken by a moving camera. According to road characteristics, we can assume camera and road are static, and then we can get an imaginary scene. In this scene, the background is a road area; objects and pedestrians on the road, buildings, road marks and zebra crossings are foreground objects. Because foreground image includes everything on the road, buildings, shadows and road marks (such as zebra crossing, lane lines). Our goal is to extract obstacles on the road, so we need to delete other things in the foreground image.

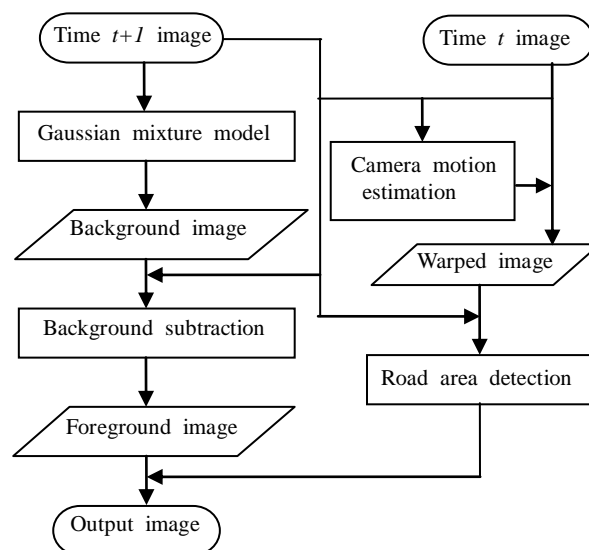


Fig. 1. Overview of the proposed method.

In the second place, we estimate the camera motion parameters from the correspondences of feature points between two successive images [3]. The camera motion parameters consist of 3D rotation and 3D translation parameters. In this method, it is assumed that the camera is calibrated, i.e. the internal parameters of the camera are known. Two consecutive images are used at any time, i.e. the image taken at time t and that taken at time $t+1$ are used at time $t+1$. In the third place, we warp time t image using camera motion parameters [4,5,6]. Comparing the warped image with time $t+1$ image, we can get the road area at time $t+1$. Finally, delete other things in the foreground image using this road area, and then we can get the obstacles on the road.

III. GAUSSIAN MIXTURE MODEL

The values of a particular pixel over time are a time series of pixel values. At any time t ($t=1,2,\dots,T$), a particular pixel (x_0, y_0) has X_t pixel values:

$$\{X_1, \dots, X_T\} = \{I(x_0, y_0, t) : 1 \leq t \leq T\} \quad (1)$$

where I is the image sequence. GMM method models each pixel by a mixture of K Gaussian distributions. The probability to observe the current pixel value X is

$$P(X_t) = \sum_{k=1}^K \omega_{k,t} * \eta(X_t, \mu_{k,t}, \sigma_{k,t}^2) \quad (2)$$

where K is the number of distributions (currently, from 3 to 5 are used); $\omega_{k,t}$ is an estimate of the weight of the i^{th} Gaussian in the mixture at time t ; $\mu_{k,t}$ is the mean value of the i^{th} Gaussian in the mixture at time t ; $\sigma_{k,t}^2$ is the covariance matrix of the i^{th} Gaussian in the mixture at time t ; η is a Gaussian probability density function defined by

$$\eta(X_t, \mu_{k,t}, \sigma_{k,t}^2) = \frac{1}{\sqrt{2\pi}\sigma} \exp\left\{-\frac{1}{2} \frac{(X_t - \mu_{k,t})^2}{\sigma_{k,t}^2}\right\} \quad (3)$$

IV. CAMERA MOTION ESTIMATION

1. Feature point detection

In the image at time t , we detect feature points using Harris corner detector [7], then, using Lucas-Kanade method [8], we detect the corresponding points of the Harris feature points in the image at time $t+1$, and by using RANSAC [9] we delete outliers. The camera motion parameters are then estimated from the correspondence of the feature points.

2. Fundamental matrix

The fundamental matrix F is the algebraic representation of epipolar geometry. And F is the unique 3×3 rank 2 homogeneous matrix which satisfies

$$m_{t+1}^T F m_t = 0 \quad (4)$$

for all corresponding points $m_t \leftrightarrow m_{t+1}$.

$$\text{Here, } F = \begin{bmatrix} f_{11} & f_{12} & f_{13} \\ f_{21} & f_{22} & f_{23} \\ f_{31} & f_{32} & f_{33} \end{bmatrix}$$

$$m_t = \begin{bmatrix} x_t \\ y_t \\ 1 \end{bmatrix} \quad m_{t+1} = \begin{bmatrix} x_{t+1} \\ y_{t+1} \\ 1 \end{bmatrix}$$

In this paper, we use the 8-point algorithm [10] to compute the fundamental matrix. The key to success with the 8-point algorithm is proper careful normalization of the input data before constructing the equations to solve. In the case of the 8-point algorithm, the suggested normalization is a translation and scaling of each image so that the centroid of the reference points is at the origin of the coordinates and the RMS distance of the points from the origin is equal to $\sqrt{2}$.

Algorithm:

Step_1: Normalization: Transform the image coordinates according to $\hat{m}_t = T_t m_t$ and $\hat{m}_{t+1} = T_{t+1} m_{t+1}$, where T_t and T_{t+1} are normalizing transformations consisting of a translation and scaling.

Step_2: Finding the fundamental matrix \hat{F} corresponding to the matches $\hat{m}_t \leftrightarrow \hat{m}_{t+1}$.

Step_3: Denormalization: Set $F = T_{t+1}^T \hat{F} T_t$. Matrix F is the fundamental matrix corresponding to the original data $m_t \leftrightarrow m_{t+1}$.

3. Camera motion parameters

The relationship between the fundamental and essential matrices is

$$E = K^T F K \quad (5)$$

Where, K is a camera calibration matrix.

The essential matrix can be represented by motion parameters of a camera between two images, i.e., the rotation matrix R and the translation T .

$$E = [T]_x R \quad (6)$$

Here, $[T]_x = \begin{bmatrix} 0 & -t_z & t_y \\ t_z & 0 & -t_x \\ -t_y & t_x & 0 \end{bmatrix}$ is the

corresponding skew-symmetric matrix of the translation T .

By applying the singular value decomposition to the matrix E , we have

$$E = U\Sigma V^T \quad (7)$$

Using the results of the singular value decomposition (Eq.(7)), we calculate the rotation matrix R and the translation T as follows;

$$R = UWV^T \text{ or } R = UW^TV^T \quad (8)$$

$$[T]_x = U\Sigma WU^T \text{ or } [T]_x = U\Sigma W^TU^T \quad (9)$$

Here, $W = \begin{bmatrix} 0 & 1 & 0 \\ -1 & 0 & 0 \\ 0 & 0 & 1 \end{bmatrix}$

There are four possible choices of the camera motion parameters, based on the two possible choices of R and two possible choices of T .

The selection of the camera motion parameters is done by using the four combinations to do the motion compensation then check which combination's compensation image is correct.

V. ROAD AREA ESTIMATION

1. Motion compensation

The location of the camera at time t and $t+1$ is shown in **Fig. 2**. Suppose the world coordinate system coincides with the camera coordinate system at time t . Then the projection equation at time t and time $t+1$ are given by

$$sm_t = K[I \ 0]M \quad (10)$$

$$sm_{t+1} = K[R \ T]M \quad (11)$$

where m_t and m_{t+1} are the 2-D points on the image plane at time t and time $t+1$; M is the 3-D point in the world coordinate system; K is the camera calibration matrix; R and T are the camera motion parameters; I is the unit matrix; s is a scalar.

Eq.(10) and Eq.(11) are easily written in terms of the known coordinates m_t and m_{t+1} as follows;

$$s \begin{bmatrix} x_t \\ y_t \\ 1 \end{bmatrix} = \begin{bmatrix} 1 & 0 & 0 & 0 \\ 0 & 1 & 0 & 0 \\ 0 & 0 & 1 & 0 \end{bmatrix} \begin{bmatrix} X \\ Y \\ Z \\ 1 \end{bmatrix} \quad (12)$$

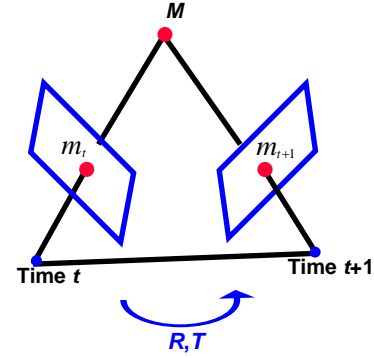


Fig.2. The location of the camera at time t and $t+1$

$$s \begin{bmatrix} x'_{t+1} \\ y'_{t+1} \\ 1 \end{bmatrix} = \begin{bmatrix} r_{11} & r_{12} & r_{13} & t_x \\ r_{21} & r_{22} & r_{23} & t_y \\ r_{31} & r_{32} & r_{33} & t_z \end{bmatrix} \begin{bmatrix} X \\ Y \\ Z \\ 1 \end{bmatrix} \quad (13)$$

First, for each pixel in the image at time t , we calculate the corresponding coordinate of 3-D point M based on Eq. (12). Here, we assume all 3-D points M are on the road plane, so Y is equal to the height of a camera above the ground.

Then we use X , Y and Z obtained from the above procedure and we calculate x'_{t+1} and y'_{t+1} based on Eq. (13). We create a new image, in which the pixel value at (x'_{t+1}, y'_{t+1}) is the pixel value at (x_t, y_t) in the image at time t . This new image is the warped image.

2. Road area

In order to detect the road area at time $t+1$, we calculate NCC (Normalized Cross-Correlation) between the warped image and the image at time $t+1$. In the experiment, we use a 7×7 window for calculating NCC. The road area can be obtained by extracting those pixels that have a NCC value below a specified threshold.

VI. EXPERIMENTAL RESULTS

Experiments have been done on a video under the existence of a person passing in front of a camera. The video is taken by a camera mounted at the front seat of a car, and includes image sequences of frontal road environments while the car is driving in the town. **Fig. 3** shows the result of the detection of a pedestrian crossing the road. (a) are the input images; (b) are the foreground images obtained from GMM; (c) are road area detection results; and (d) are the results of obstacles detection.

VII. DISCUSSION AND CONCLUSIONS

This paper proposes a method of detecting obstacles on a video taken by a vehicle-mounted monocular camera. As shown in the experimental results, performance of the proposed method is reasonable. This method has some advantages over other existing methods. This method can detect arbitrary objects which may pose a threat to safe driving on the road, not only a specific object or limited object classes, but it can also detect both static and moving objects. Moreover it can be employed in both static and moving camera cases.

ACKNOWLEDGEMENT

This work was partly supported by a grant of Knowledge Cluster Initiative implemented by MEXT.

REFERENCES

[1] C. Stauffer and W.E.L. Grimson(1995), Adaptive back-ground mixture models for real-time tracking. Proc. Conference on Computer Vision and Pattern Recognition, Vol.2, 246-252.
[2] P. KaewTraKulPong and R. Bowden(2001), An improved adaptive background mixture model for real-time tracking with shadow detection. Proc. 2nd European Workshop on Advanced Video Based Surveillance Systems, Computer Vision and Distributed Processing.

[3] R. Hartley and A. Zisserman(2004), Multiple View Geometry in Computer vision. Cambridge University Press, 2nd edition.
[4] K.Yamaguchi, A. Watanabe and T. Naito(2008), Road region estimation using a sequence of monocular images, Proc. the 20th International Conference on Pattern Recognition.
[5] K.Yamaguchi, T. Kato and Y. Ninomiya(2006), Vehicle ego-motion estimation and moving object detection using a monocular camera. Proc. the 18th International Conference on Pattern Recognition.
[6] K.Yamaguchi, T. Kato and Y. Ninomiya(2005), Obstacle detection in road scene using monocular camera. Proc. Information Processing Society of Japan, 69-76. (in Japanese)
[7] C. Harris and M. Stephens(1988), A combined corner and edge detector. Proc. Alvey Vision Conference, 147-151.
[8] B. Lucas and T. Kanade(1981), An iterative image registration technique with an application to stereo vision. Proc. International Joint Conference on Artificial Intelligence, 674-679.
[9] M. Fischler and R. Bolles(1981), Random sample consensus: A paradigm for model fitting with applications to image analysis and automated cartography. Proc. Communications of the ACM, 24(6): 381-395.
[10] R. Hartley(1977), In defence of the eight-point algorithm. Proc. IEEE Transactions on Pattern Analysis and Machine Intelligence, 19(6):580-493.

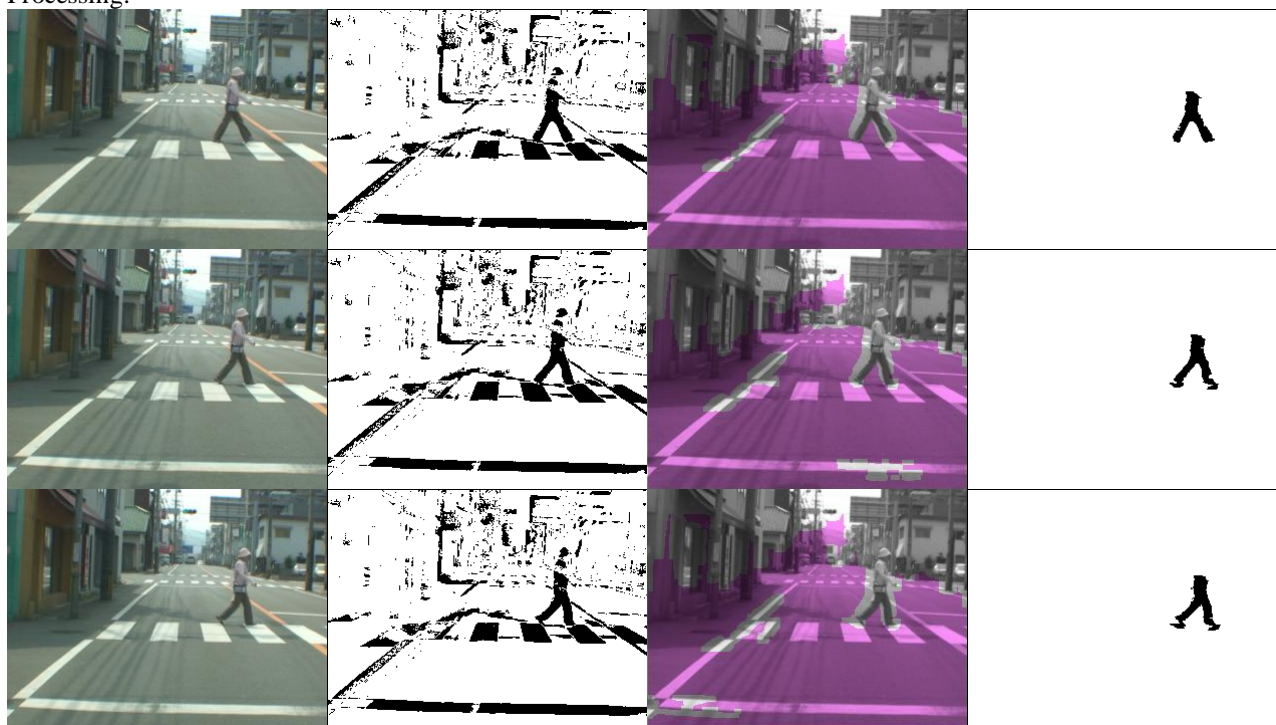


Fig.3.Experimental result: (a) Original video image frames; (b) foreground images; (c) road areas; (d) obstacle.

Hardware implementation of a census-based stereo matching using FPGA

Jiho Chang, Seung Min Choi, Eul-Gyoon Lim, Jae-il Cho

Electronics and Telecommunication Research Institute, Korea
(Tel : 82-42-860-6131; Fax : 82-42-860-6796)
{changjh, ccsmm, eglim, jicho}@etri.re.kr

Abstract: The real-time stereo vision is becoming important increasingly in the field of Robotics. It is very difficult to implement the real-time stereo vision system, because it requires very powerful processors. For solving this problem, we present the real-time hardware architecture of the census-based stereo matching IP (Intellectual Property) comprising support-weight and trellis dynamic programming structure. We use census-based cost that is robust for difference in brightness. Using Cost aggregation with support-weight window, our stereo vision system has more robustness for real environment. The stereo matching processor is implemented on a FPGA with the pre-processing part for the rectification and post-processing for reduction of noise. This stereo vision IP is implemented with HDL language and performed up to 30 FPS.

Keywords: Stereo matching, Dynamic programming, Census transform

I. INTRODUCTION

The stereo vision is becoming important increasingly in the field of virtual interface, gesture recognition, robot navigation, depth measurements and environment reconstruction as well as in many other aspects of security, robotics, and entertainment[1, 7]. In order to adapt 3D depth on these various applications, many different algorithms have been developed and materialized in various systems.

Especially in robots, the real time is a very important issue since the circumstances are changing continuously and many of studies have been progressed in various ways to indicate the stereo vision in real time base[7]. However, due to the complexity of matching algorithm, it is very difficult to materialize in real time base and this may require very powerful processors.

Normally, many real time systems use the local method. Although it has low complexity, there are some local problems where it fails to match due to occlusion, uniform texture, ambiguity of low texture etc. Also, in the popular local matching method, the block matching skill blurs disparity data in the object boundary[3, 8]. Through these results, though it is practically usable in simple applications, they bring many restrictions on the applications which require more accurate data. Recently, a few real-time global matching methods have been implemented through GPU in the graphic card or MMX of CPU[6, 9]. But, in the mobile robot which was composed with the small embedded system, since the size and power usage is the important issue, it is

difficult to materialize using the PC or GPU. If there were cases of materialization using high efficiency embedded processors, but, the real time performance (30fps) cannot be guaranteed as well, since it is the use of the resources of main processor, other applications in embedded system cannot be performed.

In our previous work, census-based stereo matching IP which is based on trellis dynamic programming[2]. For the case of previous work, since it uses census transform, is robust for difference in brightness. But there are some steak noises, because it is based on dynamic programming and there are some calibration errors.

In this paper, our stereo matching algorithm has support-weighted cost aggregation and census-based stereo matching IP. For the case of Trellis DP algorithm, since it is strong for the occlusion by generating center referenced disparity, it is very effective under the practical circumference[4, 5]. And cost function of the Stereo matching IP use census transform, so that is robust for difference in brightness. Also we aggregate the matching cost by adaptive Support weight that is used for decreasing steak noise.

The stereo matching IP has three parts. First, Pre-processing part is composed with the Rectification, Calibration and controlling the brightness which affect to the result a lot in stereo matching. A second part is main-processing which is consisted of census transform, support weight and trellis DP algorithm. At last, post-processing which reduces the noise that is being generated in Dynamic programming.

In this paper, we described for the total block diagram and the performance and conclusion through the result gained from this system.

II. Stereo matching IP

In this paragraph, we described the stereo matching IP which has three part - pre-processing, main-processing, post-processing.

1. Pre-processing part

Pre-processing part can improve the performance of stereo matching by minimizing the distortion of camera using the functions of individual brightness control and rectification of left and right images. The constraint of one point in one side image in stereo image geometry corresponds on epipolar line in other image. Therefore, due to the constraint of this epipolar line, the more epipolar line of the two left and right images matches each other accurately, the more the accuracy is increased. Since the stereo vision processing technology in this paper composed the algorithm subject to this epipolar line constraint, input after matching the left and right image accurately before it is input on the stereo matching part affects on the performance a lot.

In order to match this epipolar line, extract the rectification parameter in various ways. Thus save the pre computed parameters in the pre-processing register files and rectify the images by paralyzing the epipolar line using the above parameters. Also, in order to control the difference of physical characteristics of left and right camera or brightness of left and right images occurred by the strong light input in one camera only, the brightness control function is applied. Above functions are set to input the revised information continuously matching to the characteristic and circumstances through the host interface.

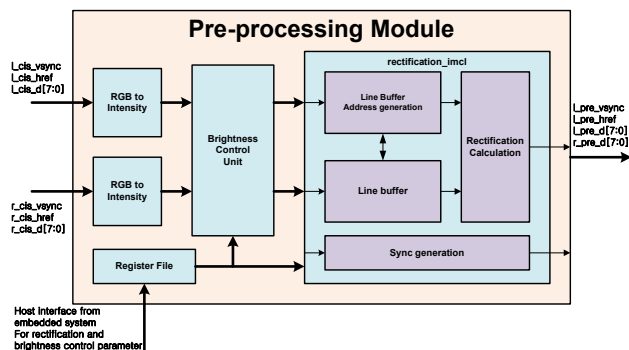


Fig.1. Block diagram of pre-processing part.

Figure 1. shows pre-processing block diagram. There are n-lines buffer memory, rectification parameter register and Calculation unit. This line buffer size depends on user requirement and mechanical structure of stereo camera. Calculation unit computes using a rectification formula described on Luping An et al.'s paper[12].

2. Main processing part

Main-processing part calculates the disparity from the rectified left and right input image which was processed at pre-processing module and makes disparity information as the intensity data. Following is the algorithm for practical performance at stereo matching module.

One of the deciding methods of the standard image of the 3 dimensional images in stereo vision is to select one of the left or right images and the other case is to define a virtual one(center reference disparity) in between those two. When express the depth map of image, there is a balance of these expressions if use the center referenced disparity while there are much of image loss for discontinuity of the other side if show the information using one of the images only. Also, it has many good points in interpreting the discontinuous space and finding the solution.

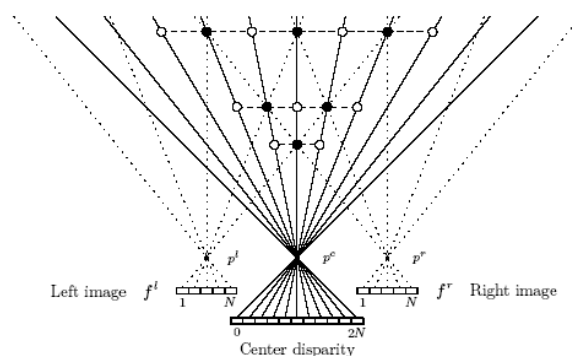


Fig. 2. Center referenced coordinate systems.

Figure 2. shows how the center referenced disparity which became the base of the used algorithm in stereo matching module can be formed. The coordinates of center referenced disparity includes the territories that can be generated by both of the left and right images and if it is composed with each of image N columns, it is verified that the center disparity image has $2N + 1$ indexes.

In Figure 2., white/black dots represent stereo matching element that is consisted of cost computation

and cost aggregation. Also, the trellis structure is connected to those dots, has optimal path minimized energy. And we find the optimized route in the space using Dynamic Programming.

The block dots combines matching cost computation and cost aggregation. We use Census transform as matching cost computation and fixed weight window for cost aggregation. The Census Transform(CT) is a stereo matching cost algorithm with high robustness to illumination variations and exposure difference. The CT transforms the intensity data into feature data, before the matching costs of each disparity level are calculated. For a higher accuracy of the algorithm, the calculation of the matching costs can be followed by a further aggregation

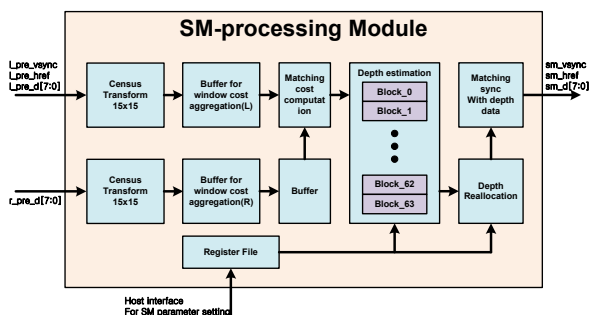


Fig. 3. Block diagram of main-processing method A.

Figure 3. is one method of stereo matching processing module which calculates disparity. Main-processing part is consist of census transform module to create raw costs, cost aggregating for support weight window computation and depth estimation module with trellis DP. But, this structure of block diagram use lots of Flip-Flops and memory for saving census data.

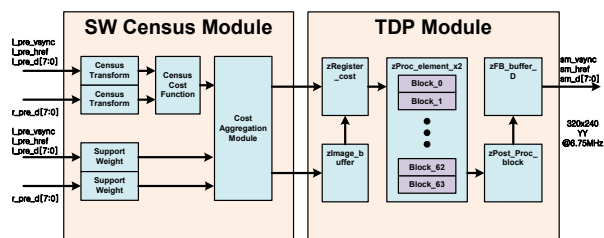


Fig. 4. Block diagram of main-processing method B.

Figure 4. is another method for SW census-based trellis dynamic programming. This method is used more memory than method A for saving Census raw cost. But this structure uses less Flip-Flops than method A, So

this method is efficient for implementing hardware IP. Even if a larger size of the window



Fig. 6. Result images from main-processing part.

Figure 6. are sample results by using Normal Dynamic programming(left) and SW Census DP(right). This results represents that SW census cost function make robust system in real world.

3. Post-processing part

Post-processing part is designed to remove the noise from the disparity map which was acquired from Stereo matching part and distinguish the objects and output each of them. Especially, in the stereo matching using Dynamic programming technology, the steak noise in horizontal direction will be generated. For this kind of noise that is generated to outside of object cases, they can be treated at backward application step. However, for the case it is generated to inside of the object, it makes the object to be shown as disconnected. In order to prevent these phenomena, it tried to reduce with 3 steps of filtering on the result from the Main-processing part.



Fig. 7. Results of post-processing part.

III. Testing FPGA

Following picture shows the Test board set for verification. This test board set operates itself without connection between any computer. Stereo vision system is implemented with HDL using Xilinx virtex-5 XC5VLX330 FPGA. The performance of system is 30

FPS(dependent on a CMOS camera) when size of images is 320x240(when census size is 15x15, support weight window size is 5x5 and maximum disparity range is 128), which is enough performance for autonomous robots and the other applications.

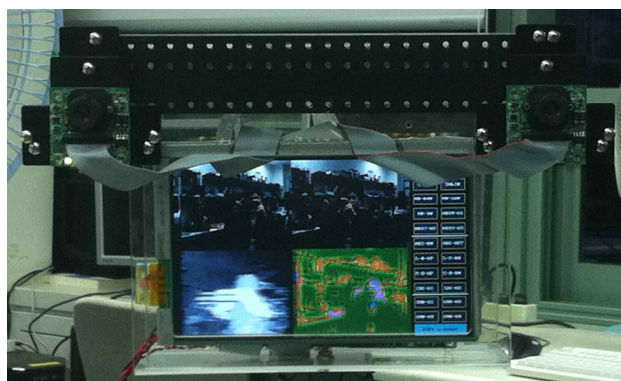


Figure 8: Example of the stereo vision system which is presented in this paper

Slice Logic Utilization	Used	Available	Usage
Number of Slice Registers	52,804	207,360	25%
Number of Slice LUTs	171,836	207,360	82%
Number used as logic	152,121	207,360	73%
Number used as Memory	12,507	54,720	22%
Number of route-thrus	15,953		
Slice Logic Distribution			
Number of occupied Slices	49,571	51,840	95%
Number of LUT Flip Flop pairs used	178,718		
Number with an unused Flip Flop	125,914	178,718	70%
Number with an unused LUT	6,882	178,718	3%
Number of fully used LUT-FF pairs	45,922	178,718	25%
Number of unique control sets	1,222		
Number of slice register sites lost to control set restrictions	1,510	207,360	1%
Specific Feature Utilization			
Number of Block RAM/FIFO	281	288	97%

Table 1. Device utilization summary on XC5VLS330

Table 1. shows the results reported by Xilinx ISE tool after synthesis and place-and-route.

IV. CONCLUSION

We developed the adaptive support-weighted census-based stereo matching IP using trellis dynamic programming structure and this includes the pre-processing part for the rectification and post-processing for reduction of noise. Also, in order to use this Stereo vision IP on various applications, we developed the test

system and this makes stereo matching result as images(left, right, disparity map and others), they can be used in embedded system itself.

Acknowledgement

This work was supported by the R&D program of the Korea Ministry of Knowledge and Economy (MKE) and the Korea Evaluation Institute of Industrial Technology (KEIT). [Project KI001813, Development of HRI Solutions and Core Chipsets for u-Robot].

REFERENCES

- [1] Scharstein, Daniel and Richard Szeliski. A taxonomy and evaluation of dense two-frame stereo correspondence algorithms. *International Journal of Computer Vision*. 2002
- [2] Jiho Chang, Sung-Min Choi, Eul-Gyoon Lim, Jaeil Cho, Dae-Hwan Hwang. Hardware implementation of a census-based stereo vision for real environment. *The 7th International Conference on Ubiquitous Robots and Ambient Intelligence*. 2010
- [3] Murray, Don and James J. Little, Using real-time stereo vision for mobile robot navigation. *Autonomous Robots*. 2000
- [4] Jeong, H. and S. Park. Generalized Trellis Stereo Matching with Systolic Array. In *Parallel and Distributed Processing and Applications*, Berlin-Heidelberg: Springer Verlag. 2004.
- [5] Park, Sungchan and Hong Jeong. Real-time stereo vision FPGA chip with low error rate. *Proceedings of International Conference on Multimedia and Ubiquitous Engineering*. 2007.
- [6] Wang, Liang, Miao Liao, Minglun Gong, Ruigang Yang, and David Nister. High-quality real-time stereo using adaptive cost aggregation and dynamic programming. *Proceedings of Third International Symposium on 3D Data Processing, Visualization, and Transmission*. 2006.
- [7] Nalpantidis Lazaros, Georgios Christou Sirakoulis, and Antonios Gasteratos. REVIEW OF STEREO VISION ALGORITHMS: FROM SOFTWARE TO HARDWARE. *International Journal of Optomechatronics*. 2008
- [8] Chris Murphy, Daniel Lindquist, Ann Marie Rynning, Thomas Cecil, Sarah Leavitt, Mark L. Chang. Low-cost stereo vision on an FPGA, *International Symposium on Field-Programmable Custom Computing Machines*. 2007
- [9] Gong, Minglun and Yee-Hong Yang. Near real-time reliable stereo matching using programmable graphics hardware. *Proceedings of IEEE Computer Society Conference on Computer Vision and Pattern Recognition*. 2005

Hand Detection using AdaBoost

Jae-chan Jeong^{1,2}, Seung-min-Choi¹, Ho-chul Shin^{1,2}, Jae-il Cho¹

Electronics and Telecommunication Research Institute¹
University of Science and Technology²
(Tel : 82-42-860-6116; Fax : 82-42-860-6796)
(channij@ust.ac.kr)

Abstract: In this paper, we present hand database automatic generator and hand detection logic using AdaBoost. To generate hand database, we acquire videos using webcam on restrict conditions: posture, background, number of human and so on. After the video acquired, face is detected frame by frame on the videos. On the face region, color of face is analyzed to generate skin color model. Based on skin color model, hand candidate regions are detected. Only one region may exist except face region because of restricted condition. The region of hand is clipped and is saved. By this method, hand database is generated automatically. Once hand database is generated, none-hand database is also generated by randomly clipping the region. Using hand and none-hand database, First Look Up Table (FLUT) is generated by using AdaBoost training algorithm. Detecting hand is similar to the method of hand database generation.

Keywords: Hand Detection, AdaBoost, HRI

I. INTRODUCTION

Interacting human and robot is one of the active research topic. Keyboard, mouse, and joystick classically are used for Human Robot Interaction (HRI)[1]. In these methods, users need to carry external interface devices to control robots. So nowadays, many researchers try to do HRI using vision or voice[2]. In case of vision, to recognize human gestures is most important part. And most of gestures are made by hand and arm. Therefore, detecting hand is necessary for HRI. To detecting hand, there are two main methods: marker based and marker-less. Without marker, skin detection or pattern analysis are used. However, detecting hand is difficult and its detection ratio low because of various shapes of hand and illumination changes. We detect only fist to avoid difficulty of hand detection. In this paper, we propose fist detection system using AdaBoost. First of all, we made fist database and trained it by AdaBoost. FLUT is made by the result of training. Using FLUT, we should rapidly detect hand with high detection ratio.

II. AdaBoost

AdaBoost[3] is an aggressive mechanism for selecting a small set of good classification functions which nevertheless have significant variety. Drawing an analogy between weak classifiers and features, AdaBoost is an effective procedure for searching out a small number of good "features". A weak classifier ($h_j(x)$) consists of a feature ($f_j(x)$), a threshold (θ_j), and parity (P_j) indicating the directions of the inequality sign:

$$h_j(x) = \begin{cases} 1, & \text{if } P_j f_j(x) < p_j \theta_j \\ 0, & \text{otherwise} \end{cases}$$

In Table 1 shows the AdaBoost training procedure and right side value of the final strong classifier $\frac{1}{2} \sum_{t=1}^T \alpha_t$ is the threshold for detecting objects.

Table1. The AdaBoost Algorithm

- Given example images $(x_1, y_1), \dots, (x_n, y_n)$ where $y_i = 0, 1$ for negative and positive examples respectively.
- Initialize weights $w_{1,i} = \frac{1}{2m}, \frac{1}{2l}$ for $y_i = 0, 1$ respectively, where m and l are the number of negatives and positives respectively.
- For $t = 1, \dots, T$:
 1. Normalize the weights,

$$w_{t,i} \leftarrow \frac{w_{t,i}}{\sum_{j=1}^n w_{t,j}}$$
 so that w_t is a probability distribution.
 2. For each feature, j , train a classifier h_j which is restricted to using a single feature. The error is evaluated with respect to w_t , $\epsilon_j = \sum_i w_i |h_j(x_i) - y_i|$.
 3. Choose the classifier, h_t , with the lowest error ϵ_t .
 4. Update the weights:

$$w_{t+1,i} = w_{t,i} \beta_t^{1-e_i}$$
 where $e_i = 0$ if example x_i is classified correctly, $e_i = 1$ otherwise, and $\beta_t = \frac{\epsilon_t}{1-\epsilon_t}$.
- The final strong classifier is:

$$h(x) = \begin{cases} 1 & \sum_{t=1}^T \alpha_t h_t(x) \geq \frac{1}{2} \sum_{t=1}^T \alpha_t \\ 0 & \text{otherwise} \end{cases}$$
 where $\alpha_t = \log \frac{1}{\beta_t}$

IV. Hand DataBase

We generate a hand database automatically. Before generating the hand database, we record a video clip with only one person who is forwarding a hand. And then, we execute our automatic hand database algorithm on this video clip. Fig1 shows a algorithm of automatic hand database generation. We detect a face on the gray image by MCT based face detector[4]. Skin color model based on YCbCr is generated by analyzing pixel of the face location. Using the skin color model, we detect hand candidate regions except face region. When we make video, we restrict the posture of the human and

background. Only one hand candidate region exists. To find boundary of the hand candidate region, we use corner detector. We extract hand image by boundary of the hand. The extracted images are resized to 20x20. The hands are stored to video clip. Non-hand DB is generated randomly.

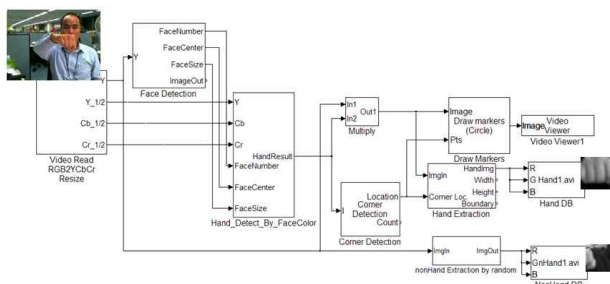


Fig.1 Automatic Hand Database Generation

V. Hand Detection

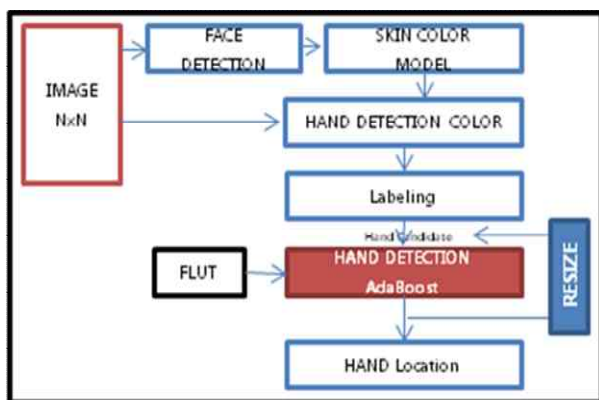


Fig.2 Hand Detection Method

Fig.2 describes hand detection method. Before detecting hand, we find face location to make skin color model. The skin color model is used to generate hand candidate regions. Among the hand candidate regions, face location is eliminated and hand is detected by AdaBoost. To detect various size of hand, hand candidate region is resized repeatedly until the size of image become 40x40 which is image resolution of hand data base.

VI. Experimental Result

To detect hand, we made hand train DB which is capture with 2 people by Microsoft VX-500. The training DB consists of 2427 hand image and 3450 non-hand. Fig.3 shows the train database. The size of image is 20x20. After making database, we trained hand DB by AdaBoost. Consequently, we generated FLUT. Fig.4 describes the result of hand detection.

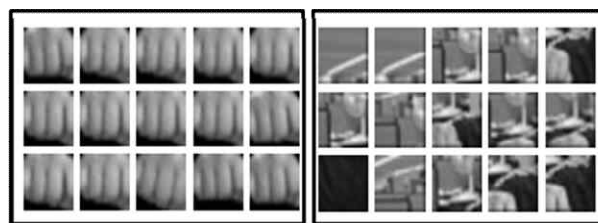


Fig.3 Hand and Non-Hand Data Base



Fig.4 Hand detection Result

VII. CONCLUSION

We presented hand detection by AdaBoost and generated hand database automatically. After that hand db was trained by AdaBoost with six haar features. The train result is FLUT which is used to detect hand. To increase detection ratio, regions of hand candidates are generated by face detector and skin color model. In the future, we'll collect more hand and non-hand images, and apply the hand detection result to human computer interaction or human robot interaction.

Acknowledgement

This work was supported by the R&D program of the Korea Ministry of Knowledge and Economy (MKE) and the Korea Evaluation Institute of Industrial Technology (KEIT). [Project KI001813, Development of HRI Solutions and Core Chipsets for u-Robot].

REFERENCES

- [1] Fong, T., Nourbakhsh, I., Dautenhahn, K., "A survey of socially interactive robots" *Robotics and Autonomous Systems*, 42 (3-4), pp. 143-166, 2003
- [2] Ude, A., Shibata, T., Atkeson, C.G., "Real-time visual system for interaction with a humanoid robot" *Robotics and Autonomous Systems*, 37 (2-3), pp. 115-125, 2001
- [3] Paul Viola and Michael J. Jones, "Robust real-time face detection" In *International Journal of Computer Vision*, pp. 137-154, 2004.
- [4] Fröba, B., Ernst, A., "Face detection with the modified census transform", 6th IEEE International Conference on Automatic Face and Gesture Recognition, pp. 91-96., 2004

Improvement of Early Recognition of Gesture Patterns based on Self-Organizing Map

Atsushi Shimada, Manabu Kawashima and Rin-ichiro Taniguchi

Department of Advanced Information Technology, Kyushu University

744 Motoooka, Nishi-ku Fukuoka 819-0395 Japan

(Tel : +81-92-802-3580; Fax : +81-92-802-3579)

(Email: {atsushi, kawashima, rin}@limu.ait.kyushu-u.ac.jp)

Abstract: We propose an approach to achieve early recognition of gesture patterns. Early recognition is a method to recognize sequential patterns at their beginning parts. Therefore, in the case of gesture recognition, we can get a recognition result of human gestures before the gestures have finished. The most difficult problem of early recognition is that when the system determines the recognition result. Most traditional approaches suffer from this problem since the gestures comprehend ambiguity. Especially at the beginning part of them, it is very difficult to determinate the recognition result since enough input data has not been observed yet. Therefore, we have improved traditional approach by using Self-Organizing Map.

Keywords: Gesture Recognition, Early Recognition, Self-Organizing Map

I. INTRODUCTION

A man-machine seamless interaction is an important tool for various interactive systems such as virtual reality systems, video game consoles, human-robot communication, and so on[5,6]. To realize such an interaction, the system has to estimate human gestures in real-time. Generally, a gesture recognition result is acquired after the gesture has finished. Therefore, if a long gesture is observed, we have to wait for the response until the recognition result is determined. This is a problem to realize a “real-time” man-machine interaction.

Recent years, a new approach called “early recognition” has been proposed for gesture recognition[4,8,1]. The early recognition means that a system outputs a recognition result before a gesture has finished. It is a very useful technique to realize a real-time interaction. The most difficult problem of early recognition is that when the system determines the recognition result. In other words, the system has to ensure the recognition result before the observing gesture has finished. Most traditional approaches suffer from this problem since the gestures comprehend ambiguity. Especially at the beginning part of them, it is very difficult to determinate the recognition result since enough input data has not been observed yet.

In this paper, we propose a new strategy to achieve early recognition of gesture patterns. In the training phase, Self-Organizing Map (SOM)[2,3] is used to learn

postures, which are elements of all gestures. The advantages of using SOM are 1) to reduce dimensionality of gesture patterns, 2) to reduce some redundant postures, 3) to represent a gesture pattern by a combination (set) of smaller number of neurons; we call it “Sparse Code”. In the test phase, we introduce the Hausdorff distance to measure the similarity to measure the similarity between sparse code of unknown input pattern and sparse code of training patterns. The Hausdorff distance is more effective criterion for judgment than Euclidean distance or so on, since it can measure the distance between not two elements but sets of pattern.

II. DEFINITION OF EARLY RECOGNITION

1. Typical Gesture Recognition

Let $\mathbf{C}^i = \{c_1^i, \dots, c_n^i\}$ be a training gesture pattern which belongs to gesture class $i \in L$. The L is a set of class labels. A gesture can be represented in a sequential n -long posture patterns. Therefore, c_n^i means the n -th posture of the gesture. When an unknown gesture $\mathbf{X} = \{x_1, \dots, x_l\}$ is observed, the typical gesture recognition problem is to find the most similar gesture from training patterns by

$$p = \underset{i}{\operatorname{argmin}} \{f(\mathbf{X}, \mathbf{C}^i)\}$$

where p is the class label and $f()$ is a distance function which evaluates the similarity between gesture pattern \mathbf{X} and \mathbf{C}^i .

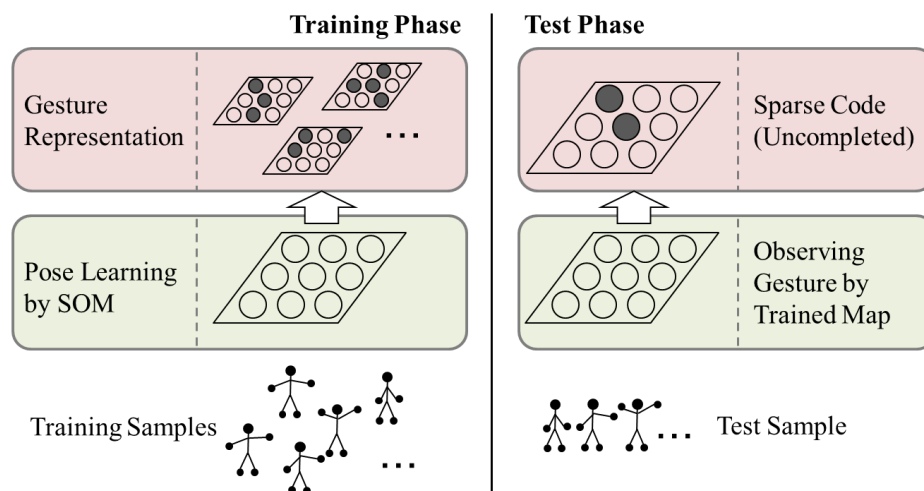


Fig. 1 Processing flow of training/recognition

2. Early Recognition of Gesture Patterns

The key issue of early recognition is to output a recognition result before acquiring complete input pattern. In the case of gesture recognition, it corresponds to the following problem. When a part of gesture pattern (unfinished gesture) $\mathbf{X}' = \{x_1, \dots, x_k\}$, ($k < l$) is observed, the recognition result is determined by

$$p = \underset{i}{\operatorname{argmin}} \{f(\mathbf{X}', \mathbf{C}^i) < TH\}$$

where TH is a threshold of distance which adjusts the timing of recognition result. If the threshold is not introduced, a recognition result will be output without concrete proof. Therefore, we set a threshold to ensure reliability for the recognition result.

III. STRATEGY OF EARLY RECOGNITION

1. System Overview

First of all, we show the system overview in Fig. 1. The process can be divided into two phases; training phase and test phase. In the training phase, Self-Organizing Map (SOM) is used to learn postures, which are elements of all gestures. The advantages of using SOM are 1) to reduce dimensionality of gesture patterns, 2) to reduce some redundant postures, 3) to represent a gesture pattern by combination of smaller number of neurons and so on. Due to space limitation, we skip the detailed explanation about SOM and how to learn the postures (refer to the literature [7]). After the training of all postures, element postures of each gesture are input

to the map again. And then, we can get a “Sparse Code” which represents a gesture pattern on the SOM.

In the test phase, the system observes person’s gesture. Then, a parse code corresponding to the observing gesture is generated/updated immediately whenever a new observation is acquired. Finally, the sparse code is examined whether or not the system outputs the recognition result. Actually, the examination is achieved by measuring the distance between sparse codes based on Hausdorff distance.

1. Sparse Coding

When a posture x_k is input to the SOM, one neuron will be selected as winner. When a set of postures which consist of a gesture is sequentially input to the SOM, some neurons will be activated. We regard such an activation pattern as “Sparse Code”, which represents an input gesture. Here, we define the notation of a sparse code. In the training phase, all training gestures are represented by using sparse code. For simplicity, we use the same notation \mathbf{C}^i , which was used for representation of training samples in section II, as the sparse code of them. Meanwhile, in the test phase, a sparse code of observing gesture is represented by \mathbf{X}' .

Note that the sparse code described here has not an ability to distinguish the gesture patterns whose elements are the same but the sequences are different. However, we can easily improve introduce temporal information into the system by our previous study[7].

2. Similarity Evaluation with Hausdorff distance

The number of elements in sparse code is different from each other since the number of activated neurons

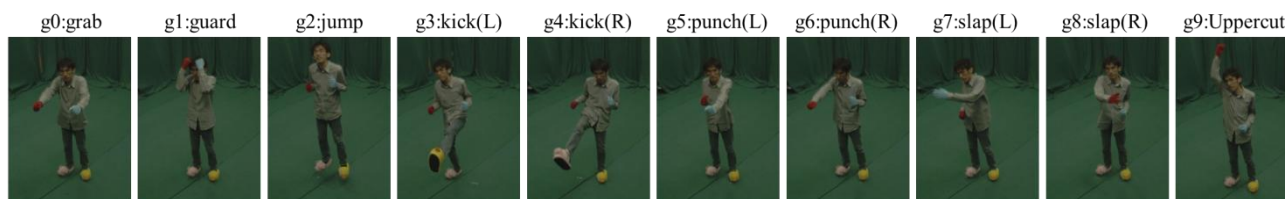


Fig. 2 10 kinds of gesture patterns

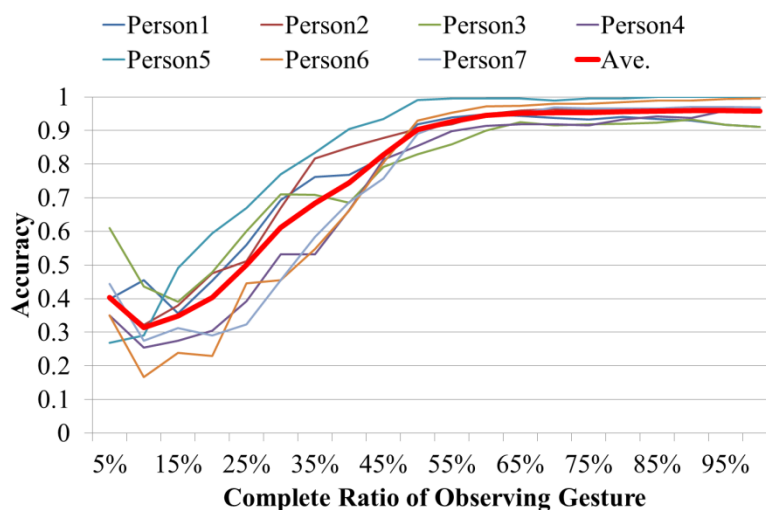


Fig. 3 Early Recognition Accuracy vs. Complete Ratilof Observing Gesture

depends on the gesture length and the gesture pattern. Therefore, we introduce the Hausdorff distance to measure the similarity between two sets of sparse code.

Let X and Y be two non-empty subsets of a metric space. The Hausdorff distance $f(X, Y)$, which corresponds to the distance function explained in section II, is defined by

$$f(X, Y) = \max\{\sup_i \inf_{x \in X} d(x, y_i), \inf_{y \in Y} \sup_{x \in X} d(x, y)\}$$

where $d(x, y)$ is the distance function. In our research, we use L2-distance between the coordinates of activated neurons.

IV. EXPERIMENTAL RESULT

1. Preparation

We demonstrate proposed early recognition of gesture patterns using motion data prepared by ourselves. Each gesture consists of a sequence of postures, and each posture is represented by 5 measured markers. Each marker is composed of data of (x, y, z)-axis. We prepared 10 kinds of gesture patterns ($L = 10$, see Fig. 2) from 7 examinees. Each person did each gesture 40 times. We used 20 patterns for training and

other 20 patterns for test. We conducted the experiment through cross-validation among examinees.

2. Recognition Result

Fig. 3 shows the result of early recognition. The horizontal axis denotes the complete ratio of observing gesture pattern, and the vertical axis denotes the recognition accuracy. The bold curve indicates the average ratio of accuracy. For example, the recognition ratio exceeded 90% when more than 50% long gestures had been observed on average.

Fig. 4 shows the recognition accuracy of each gesture class. And the detailed analysis results are shown in Table 1. Totally, we got good results for whole gesture classes. However, some cells in Table 1 have lower values. We investigated the matter why such results came out. There are some similar gesture patterns between gesture classes. For example, in the case of gesture class 5 and 7, the person moves his/her right hand forward from in front of his/her body. The difference between these gestures is the trajectory of the hand. However, the trajectory depended on examinee's habit. As the result, some trajectory was very similar

Table 1 Recognition Accuracy of Each Gesture Class and Each Person

	g0	g1	g2	g3	g4	g5	g6	g7	g8	g9
Person1	0.84	0.83	1.00	0.82	0.53	0.75	0.85	0.70	0.81	1.00
Person2	0.85	0.70	1.00	0.83	1.00	0.95	0.75	0.54	1.00	0.70
Person3	0.50	0.91	0.85	0.77	0.99	0.71	0.63	0.89	0.65	0.95
Person4	0.84	0.89	0.72	0.85	0.63	0.89	0.83	0.53	0.68	0.74
Person5	1.00	0.82	1.00	0.90	0.67	0.83	0.75	1.00	0.62	0.93
Person6	0.86	1.00	1.00	0.61	0.75	0.89	0.74	0.73	0.53	0.61
Person7	0.74	0.79	0.79	0.72	0.61	0.64	1.00	0.74	0.55	0.83
Average	0.81	0.85	0.91	0.79	0.74	0.81	0.79	0.73	0.69	0.82

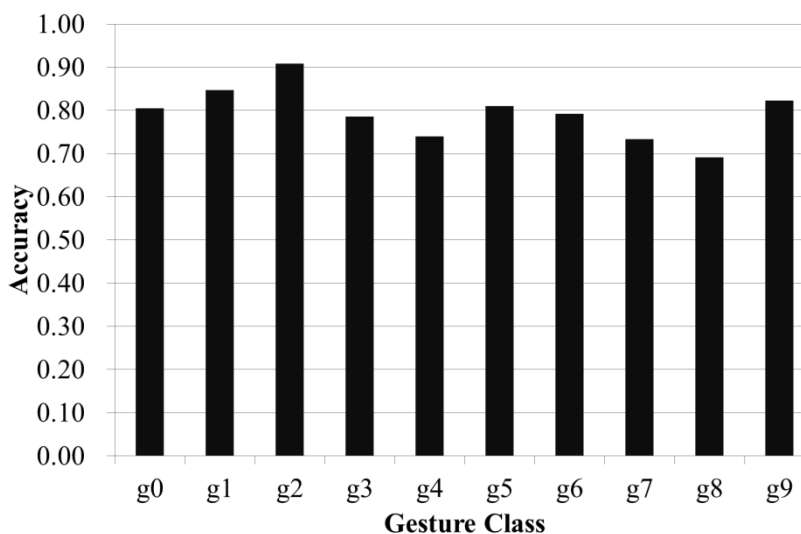


Fig. 4 Recognition Accuracy of Each Gesture Class

with the trajectory of the other gesture class. This is one of the factors which brought not good results.

V. CONCLUSION

We have proposed a new framework of early recognition of human gestures. We have used Self-Organizing Map (SOM) to learn human gestures. The SOM outputs sparse codes for each gesture. We estimated a human gesture based on Bayesian estimation using the sparse code. We got positive results of early recognition in the experiment. We are now researching to tackle the problem of common postures which are included in some gestures.

REFERENCES

[1] M. Kawashima, A. Shimada, and R. Taniguchi. Early recognition of gesture patterns using sparse code of self-organizing map. In 7th International Workshop On Self-Organizing Maps, pages 116–123, 06 2009.

[2] T. Kohonen. “Self-Organization and Associative Memory”. Springer-Verlag, 1989.

[3] T. Kohonen. “Self-Organizing Maps”. Springer Series in Information Science, 1995.

[4] A. Mori, S. Uchida, R. Kurazume, R. Taniguchi, T. Hasegawa, and H. Sakoe. Early recognition and prediction of gestures. In Proc. of International Conference on Pattern Recognition, volume 3, pages 560–563, 2006.

[5] H. S. Park, D. J. Jung, and H. J. Kim. Vision-based game interface using human gesture. In Advances in Image and Video Technology, volume 4319, pages 662–671, 2006.

[6] J. Park and J. Yi. Gesture recognition based interactive boxing game. In International Journal of Information Technology, volume 12, pages 36–44, 2006.

[7] A. Shimada and R. Taniguchi. Gesture recognition using sparse code of hierarchical som. In Proc. of International Conference on Pattern Recognition, 2008.

[8] S. Uchida and K. Amamoto. Early recognition of sequential patterns by classifier combination. In Proc. of International Conference on Pattern Recognition, 2008.

Detection of a Bicycle and Its Driving Directions Using HOG Feature

Heewook Jung, Joo Kooi Tan, Hyoungeop Kim, Seiji Ishikawa

Department of Mechanical & Control Engineering, Kyushu Institute of Technology, Kitakyushu, Japan

(Tel: 81-93-884-3183; Fax: 81-93-884-3183)

{jung, etheltan, ishikawa}@ss10.cntl.kyutech.ac.jp, kim@cntl.kyutech.ac.jp

Abstract: Studies on car vision have currently been practiced around recognizing a human enthusiastically. The Histograms of Oriented Gradients (HOG) feature has been proposed as useful feature for recognizing a human standing in various kinds of background. On the other hand, although a bicycle is important transportation vehicle in urban environment, its automatic recognition or detection is not an easy task for a computer vision system, because bicycle's appearance can change dramatically according to viewpoints and a person riding on the bicycle is a non-rigid object. Thus, automatic bicycle detection is an important research subject in an intelligent perception system using car vision. In this paper, we propose a method of detecting a bicycle and its driving direction using the HOG feature and RealAdaboost algorithm. Experimental results show satisfactory performance of the proposed method.

Keywords: Bicycle detection, car vision, HOG feature, RealAdaboost.

I. INTRODUCTION

An automated perception system with a car is currently very helpful in preventing traffic accidents and contributes to decreasing traffic accidents. But it is difficult to prevent traffic accidents perfectly. Factors that endanger traffic safety still remain around a moving car. If the detection of the risk of traffic accidents (a human, a bicycle, a car, a bicyclist, etc.) is employed in automated perception system, the number of traffic accidents will further decrease.

The Histograms of Oriented Gradients (HOG) feature has been proposed by Dalal and Triggs [1] as useful feature for recognizing a human standing in various kinds of background. The HOG feature proposed by them seems an effective feature for representing and recognizing a human image. But, in their paper, it includes an unnecessary part of the image such as the background. It is not conceivable that the background feature contributes to high recognition rate of a human image. Zhu et al. [2] employ the HOG feature based on variable block size, but they also include the background in the feature. In this paper, we propose an object detection method employing an improved HOG feature.

The research on car vision is currently practiced around recognizing a human and not a bicycle which is important transportation in urban environment. Although the number of whole traffic accidents is decreasing, the rate of bicycles' accidents to the whole traffic accidents

is increasing. Detection of a bicycle by a computer vision system is, however, not an easy task, because bicycle's appearance can change dramatically among viewpoints and a person riding on a bicycle is a non-rigid object.

In this paper, we propose a method of detecting a bicycle and its driving direction using improved HOG feature and RealAdaboost algorithm.

II. LEARNING ALGORITHM

A learning algorithm is used to HOG feature and RealAdaboost. The proposed method can detect bicycle's driving direction, because we make a bicycle model using HOG feature. The algorithm of learning is given in Fig 1.

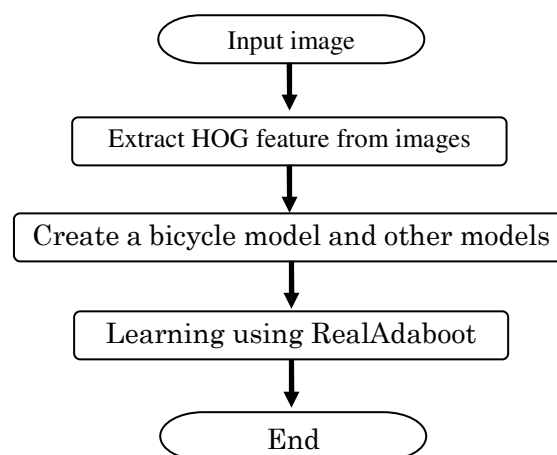


Fig. 1 Overview of the learning algorithm.

1. HOG feature

The HOG feature [1] is a method that extracts feature of outlines in images. Because gradients of adjacent pixels receive histogramization and normalization at each area, it is robust to illumination change and to geometric change.

The HOG feature is extracted in the following way.

Step1: Compute the magnitude $m(x, y)$ and orientation $\theta(x, y)$ of images using equation (1). Given coordinates of images $I(x, y)$,

$$\begin{aligned} m(x, y) &= \sqrt{f_x(x, y)^2 + f_y(x, y)^2} \\ \theta(x, y) &= \tan^{-1} \frac{f_x(x, y)}{f_y(x, y)} \end{aligned} \quad (1)$$

Here,

$$\begin{aligned} f_x(x, y) &= I(x+1, y) - I(x-1, y) \\ f_y(x, y) &= I(x, y+1) - I(x, y-1) \end{aligned}$$

The result of the oriented gradients image is shown in Fig. 2.

Step2: Derive the orientation histogram from the orientations and magnitudes.

Oriented gradients image has a large amount of information. But if there is such an amount of information, it needs more time to classify and to learn in the procedure of pattern recognition. Deriving the orientation histogram from the orientations and magnitudes has an effect of making the amount of information decrease.

Here each cell size is 5×5 pixels and the orientation histogram has 9 bins with each cell.

Step3: Perform histogram's normalization using an overlapping block.

Here, each block size is 3×3 cells. Each block contains $9 \times 9 = 81$ features and each 30×60 sub-image contains $4 \times 10 \times 81 = 3240$ features.

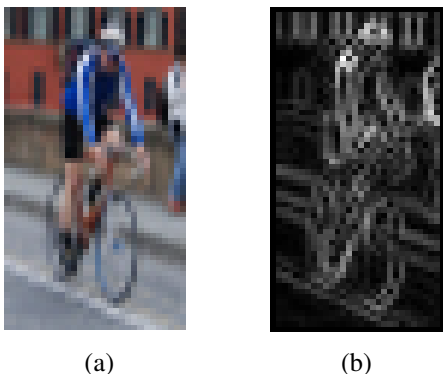


Fig. 2 A processed bicycle image: (a) An input image, and (b) its oriented gradients image.

2. A bicycle model

Many researchers calculate the HOG feature from an entire image irrespective of the foreground or the background. We have proposed an improved HOG feature calculation by the employment of a bicyclist mask and a bicycle mask. This employment shows better performance in the bicycle detection/recognition. This improved HOG feature is employed in the proposed method of this paper.

The main idea of the proposed method is to calculate the HOG feature on a bicyclist and a bicycle mask instead of calculating it on the whole image. A bicyclist and a bicycle mask are created in the following way.

Step1: The intensity of gradient is calculated of all the images in an image database.

Step2: The average values of the intensity of the gradient are calculated at every pixel on the images and a normalized average gradient intensity image is produced.

Step3: An edge image is produced from the average gradient intensity image.

Step4: A silhouette image is created from the average gradient intensity image and a skeleton image is made from the silhouette image.

Step5: Finally a bicyclist and a bicycle mask are yielded by performing logical OR operation between the edge image obtained at step 3 and the skeleton image obtained at step 4.

3. RealAdaboost

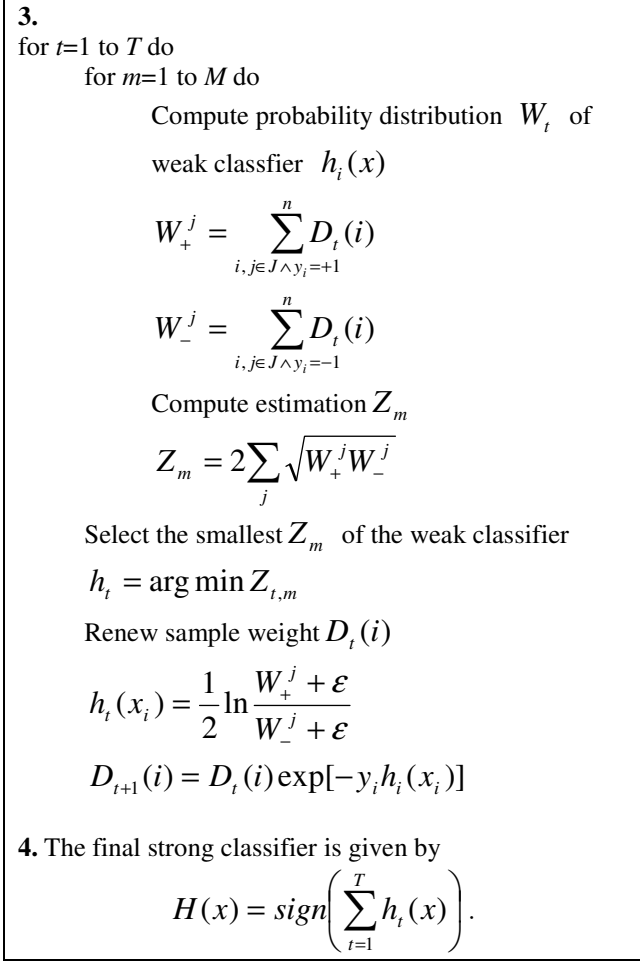
The adaboost algorithm is a method of uniting weak classifier of a simple hypothesis and generating a strong classifier. A bicyclist and a bicycle model are defined and trained via a RealAdaboost to detect bicycles under various circumstances. In training using RealAdaboost, we use 1000 positive training samples and 2000 negative samples and we train a two-component (a bicyclist and a bicycle) model. Effectiveness of the proposed method is shown by experiment. The algorithm of RealAdaboost is given in Table 1.

Table.1 RealAdaboost algorithm.

1. Suppose $S = \{(x_1, y_1), (x_2, y_2), \dots, (x_N, y_N)\}$ as a sample space, where $x \in X$ are feature vectors and $y \in \{-1, +1\}$ are labels.

2. D_i is the initial distribution

$$D_1(n) = \frac{1}{N}$$



III. DETECTION ALGORITHM

A detection algorithm is used to a bicycle model using HOG feature. And we use five mask models for detecting driving directions. The algorithm of detection is given in Fig 3.

1. Merge processing

When detection of a bicycle is performed using HOG feature, many windows containing a single common bicycle are obtained in an image. They are then merged into a single window using mean shift clustering and the nearest neighbor algorithm.

A. Mean shift clustering

The first step of mean shift clustering is assumption of density using kernel function. Here we use a kernel function represented by

$$k(x) = \begin{cases} c(1 - \|x\|) & \|x\| < 1 \\ 0 & \text{otherwise} \end{cases} \quad (2)$$

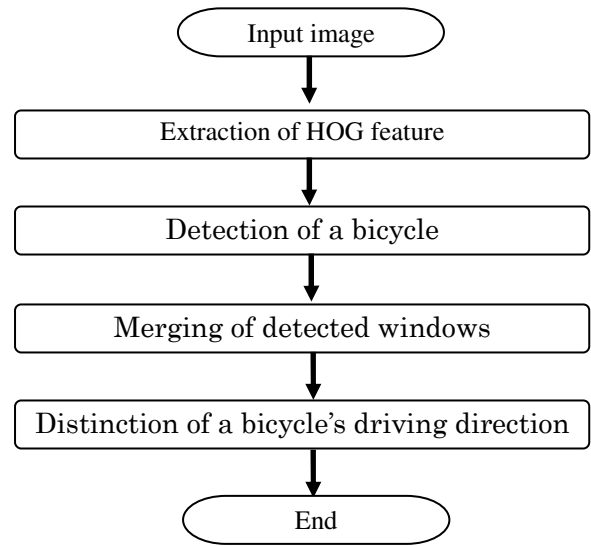


Fig. 3 Overview of the detection algorithm.

The second step is shifting the mean to high density employing a mean shift vector. A mean shift vector is given as follows;

$$m(x) = \frac{\sum_{i=1}^n x_i k\left(\left\|\frac{x - x_i}{h}\right\|^2\right)}{\sum_{i=1}^n k\left(\left\|\frac{x - x_i}{h}\right\|^2\right)} - x \quad (3)$$

Here, the first term of the mean shift vector assumes density and the second term shifted mean. When the mean shift vector is 0, the density is the highest.

B. Nearest neighbor

Euclid distance d is computed from the point of the highest density to each sample point.

$$d = \sqrt{(x - x_i)^2 + (y - y_i)^2} \quad (4)$$

Merging is executed, if d is smaller than a predefined threshold. The result of the merging processing is shown in Fig. 4.



Fig. 4 Merge processing: (a) Before merging, and (b) after merging.



Fig. 5 Bicycle's five driving direction.

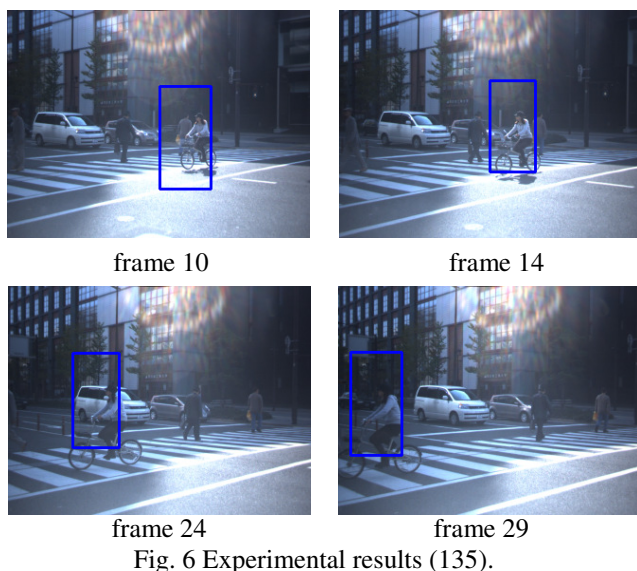


Fig. 6 Experimental results (135).

2. Detection of driving direction

We use five mask models (See **Fig. 5**) for detecting driving directions. They are 0, 45, 90, 135 and 180 degrees.

IV. EXPERIMENTAL RESULTS

Experiments have been done on a video containing a bicyclist and a human passing in front of a camera. **Fig. 6** and **Fig. 7** show successful cases, but a human itself is not detected. Because learning data of the positive class is a bicycle and a bicyclist.

V. CONCLUSIONS

In this paper, we propose a method of detecting a bicycle and its driving direction using improved HOG feature and RealAdaboost algorithm. This method has several advantages over existing methods. This method

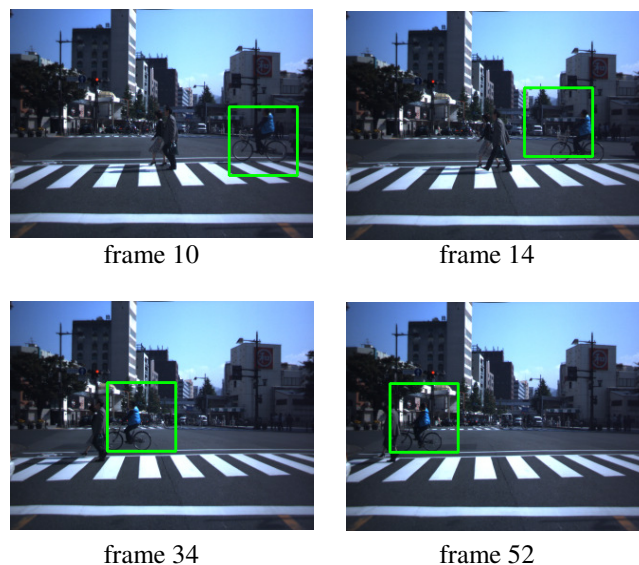


Fig. 7 Experimental results (180).

calculates the HOG feature on a bicyclist mask and on a bicycle mask instead of calculating it on the whole image. Therefore, the computation time of this method is fast. Moreover, this method is applicable to the detection of various objects. In future, we plan to enhance the performance of the detection and to detect various objects.

ACKNOWLEDGEMENT

This work was supported by JSPS Grant-in-Aid for Scientific Research (C) 22510177

REFERENCES

- [1] N. Dalal, B. Triggs, "Histograms of oriented gradients for human detection", Proc. IEEE Conf. on Computer Vision & Pattern Recognition, 886-893, 2005.
- [2] Q. Zhu, et al, "Fast human detection using a cascade of histograms of oriented gradients", Proc. IEEE Conf. on Computer Vision & Pattern Recognition, 2006.
- [3] K. Khattab, J. Dubois, and J. Miteran, "Cascade boosting-based object detection from high-level description to hardware implementation", EURASIP Journal on Embedded Systems, 2009.
- [4] Y. Nakashima, J. K. Tan, S. Ishikawa, T. Morie, "On the detection of a human and its body direction from a video", Proc. of 15th Int. Symposium on Artificial Life and Robotics, 294-297, 2010.
- [5] R. E. Schapire and Y. Singer, "Improved boosting algorithms using confidence-rated predictions", Machine Learning, **37**, 3, 97-336, 1999.

Simple Analog-Digital Circuit for Motion Detection and Its Application to Target Tracking System

Takuya Yamamoto and Kimihiro Nishio

Tsuyama National College of Technology, 624-1, Numa, Tsuyama, Okayama, 708-8509, Japan.

(Tel : 81-868-24-8266; Fax : 81-868-24-8219)

(nishio@tsuyama-ct.ac.jp)

Abstract: We proposed in this study an analog-digital circuit for detecting the motion of the object. The proposed unit circuit is simple structure since the digital part of the proposed circuit is only constructed with one NOT circuit and one NOR circuit. The proposed circuit was simulated with the simulation program with integrated circuit emphasis (SPICE). The simulation results showed that the proposed circuit can operate normally. The test circuit was fabricated on the breadboard. The measured results of the fabricated test circuit showed that the proposed circuit can output the pulsed voltage (motion signal) when the object moves on the circuit. We proposed in this study the system for tracking the target. Since the array of the proposed analog-digital circuit was introduced at the first stage of the system, the circuit for tracking the target became simple structure. It was clarified from the measured results of the fabricated test system and the simulation results that the proposed system and the simulation results can track the target and capture the target on the center of the input part.

Keywords: analog circuit, digital circuit, motion detection, target tracking, vision chip

I. INTRODUCTION

It is necessary for the monitoring system, robotics vision and other systems to perform the high speed image processing. However, it is difficult for typical image processing system using Neumann-type computer to realize the high speed image processing. On the other hand, the biological vision system can perform the high speed processing since the nerve cells in the vision system perform information processing in parallel.

Analog complementary metal oxide semiconductor (CMOS) circuits for motion detection were proposed based on the biological vision system [1]-[8]. These circuits are characterized by the high speed processing, low power consumption and simple structure. Researchers tried to use these circuits as the input part of the target tracking system [6]-[8]. However, these circuits have a problem of incorrect operation by device mismatches due to use the analog technology. Thus, it is difficult to use these analog circuits to the application systems such as the target tracking system.

Digital circuits for motion detection were proposed based on the biological vision system [2]. These circuits do not have a problem of incorrect operation. However, the circuit by using digital technology has the problem of the complex structure. If the simple digital circuit for motion detection is proposed, it is able to use it to various application systems.

In this study, we tried to propose the simple analog-digital circuits for motion detection by mimicking the information processing of the vertebrate retina. Particularly, we tried to realize the simple digital circuit.

The simulation results of the proposed circuit with the simulation program with integrated circuit emphasis (SPICE) showed that the proposed circuit can operate normally. The test circuit is fabricated on the breadboard. The measured results of the test circuit showed that the proposed simple circuit can generate the motion signal. The target tracking system was proposed by applying the simple analog-digital circuits. The measured results of the fabricated test system for tracking the target and the simulation results showed that the proposed system can operate normally.

II. MOTION DETECTION CIRCUIT

The proposed unit circuit for motion detection based on the vertebrate retina in this study is shown in Fig. 1. By arranging the circuits in one- or two-dimensionally, it is able to detect the motion velocity and direction of the object. The circuit is constructed with the analog part and the digital part. The analog circuit detects the object (light) or the edge of the object. The digital circuit generates the motion signal when the object moves on the photodiode PD.

When the object is projected on PD, the current I_p which is proportional to light intensity is generated. The voltage $V_{DD}-V_p$ is proportional to I_p , where V_{DD} is the supply voltage. The constant voltage V_{con1} is set to the circuit. The voltages V_a and V_b are given by the following equation.

$$V_a = V_b \cong \frac{V_{DD} - V_p}{(V_{DD} - V_p) + V_{con1}} V_{DD} \quad (1)$$

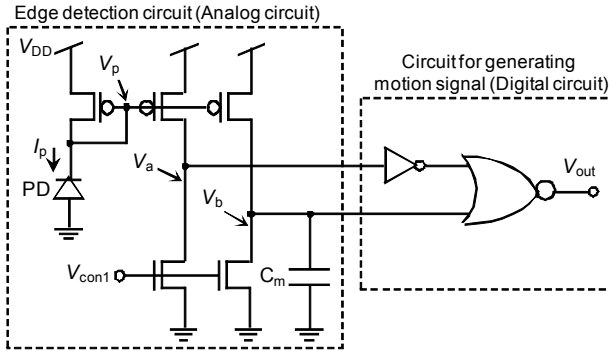


Fig. 1. Unit circuit for motion detection.

Table 1. A Truth table of proposed digital circuit.

V_a	V_b	V_{out}
0	0	0
0	1	0
1	0	1
1	1	0

At first, the object is not projected on PD. In this case, V_a is equal to about 0 since $V_{DD}-V_p$ is smaller than V_{con1} . When the object is projected on PD, V_a becomes about V_{DD} because $V_{DD}-V_p$ is larger than V_{con1} . At the moment that V_a becomes V_{DD} , V_b is 0. After time t_d , V_b becomes V_{DD} since the capacitor C_m is connected at the terminal of V_b .

A truth table of the proposed digital circuit is shown in table 1. When V_a is 0 and V_b is V_{DD} , V_{out} becomes V_{DD} . Therefore, the circuit outputs the pulsed voltage when the object moves on PD. The width of the pulsed voltage is t_d . The pulsed voltage is the motion signal since the voltage is generated when the object moves on PD.

The proposed digital circuit is constructed with a NOT circuit and a NOR circuit. The NOT circuit consists of two metal oxide semiconductor (MOS) transistors. The NOR circuit consists of four MOS transistors. The proposed circuit is simple structure since the circuit consists of only six MOS transistors.

III. Target Tracking System

In this study, we tried to apply the proposed motion detection circuits to the target tracking system. The model for tracking the target is shown in Fig. 2.

At the first stage, the one-dimensional array of the proposed circuits is introduced. When the target moves on the array, the circuits output the motion signals. The output signals input to the integrator.

The integrator of the right side outputs the signal I_{right} . I_{right} becomes large when the target moves to the

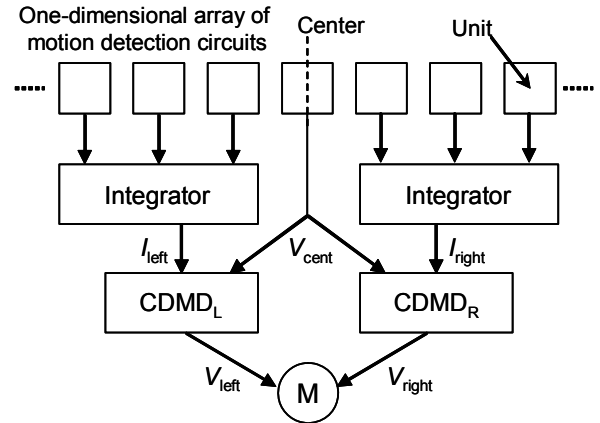


Fig. 2. The model for tracking the target.

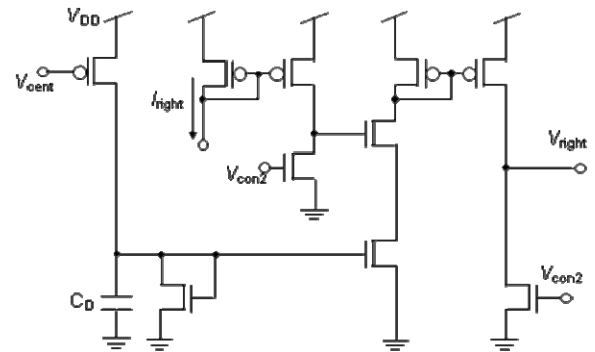


Fig. 3. Circuit for detecting the motion direction (CDMDR).

right side. The integrator of the left side outputs the signal I_{left} . I_{left} becomes large when the target moves to the left side. The circuit in the center generates the signal V_{cent} . V_{cent} is large when the target located on the center of the array.

I_{left} and V_{cent} are input to the circuit for detecting the motion direction (CDMDL). I_{right} and V_{cent} are input to CDMDR. The output signals V_{left} and V_{right} become 0 when the target does not move on the input array. V_{left} becomes about V_{DD} when the target moves toward the left side. V_{right} becomes about V_{DD} when the target moves toward the right side.

The motor M rotates when V_{right} is V_{DD} and V_{left} is 0. Then, the system can track the target toward the right side. The motor rotates inversely when V_{right} is 0 and V_{left} is V_{DD} . Then, the system can track the target toward the left side.

After tracking the target, V_{cent} becomes large when the target is captured on the center of the input array. Then, V_{left} and V_{right} become 0 (reset) by using V_{cent} . When both V_{left} and V_{right} are 0 or V_{DD} , the motor is stopped. Thus, using the model and system, it is able to track the target and capture the target

Figure 3 shows the proposed CDMDR. The circuit is proposed based on the correlation model [9]. The circuit is constructed with nine MOS transistors and 1

capacitor. Thus, the proposed circuit is simple structure.

IV. EXPERIMENTAL RESULTS

1. Motion detection circuit

The proposed circuit for motion detection circuit was simulated with SPICE. Input current I_p was set to 100 nA when the object was projected on PD. C_m was set to 100 nF. The supply voltage V_{DD} was set to 5 V. Figure 4 shows the simulation result of the proposed circuit. I_p was shown in Fig. 4(a). Figure 4(b) shows the transient response of V_{out} . At the moment that the light was projected on PD, V_{out} become 5 V. The circuit output the pulsed voltage. Thus, it was clarified from the simulation results that the proposed circuit can generate the motion signal.

The test circuit of the unit circuit was fabricated on the breadboard. The analog part in Fig. 1 was fabricated by using discrete MOS transistors (nMOS:2SK1398, pMOS:2SJ184). The digital part in Fig. 1 was fabricated by the field programmable gate array (FPGA) (Xilinx, Spartan III). V_{DD} was set to 5 V. V_{con1} was set to 1.6 V. C_m was set to 4.7 μ F. Thus, it was clarified that the proposed circuit can generate the signal for rotating the motor of the tracking system.

Figure 5 shows the transient response of V_{out} . At the moment that the light was projected on PD, V_{out} became 5 V. The circuit output the pulsed voltage. Thus, it was clarified from the measured results that the fabricated test circuit can generate the motion signal.

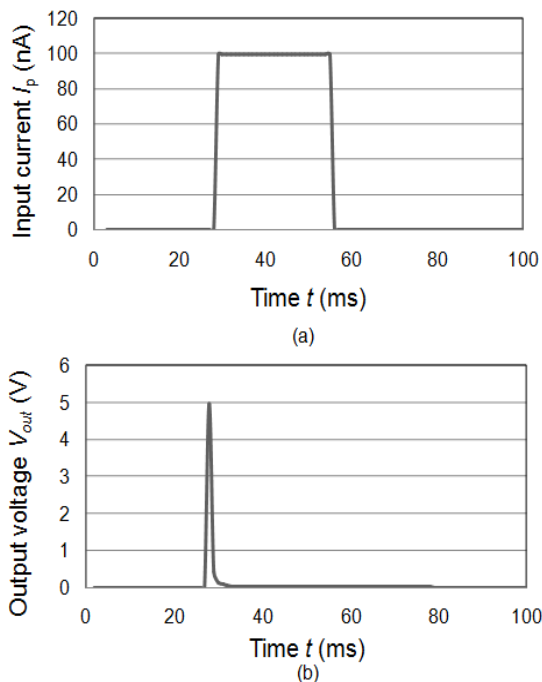


Fig. 4. Simulated results of the proposed circuit. (a) Input current I_p . (b) Transient response of V_{out} .

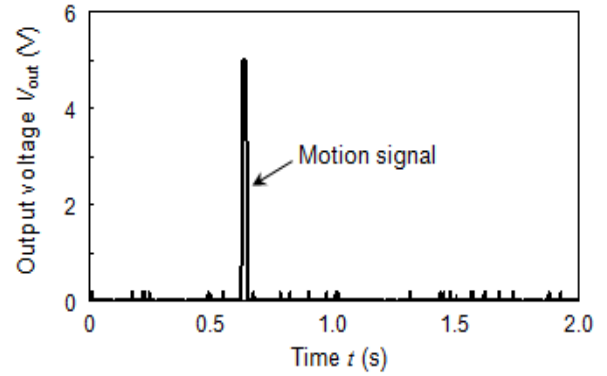


Fig. 5. Measured results of the test circuit.

2. Target tracking system

The proposed circuit for tracking the target based on the model in Fig. 2 was simulated with SPICE. Five unit circuits were utilized to each input part.

C_m was set to 300 nF. V_{DD} was set to 5 V. V_{con1} was set to 3.5 V. V_{con2} was set to 0.5 V. V_{th} was set to 1.58 V. Figure 6 shows the transient response of V_{right} obtained by SPICE. In this simulation, the object moved toward the right side. V_{right} showed about 4 V when the object moved.

The test system for tracking the target was fabricated based on the model in Fig. 2. The photograph of the fabricated tracking system is shown in Fig. 7. The current I_{left} was generated by PD_L . The current I_{right} was generated by PD_R . The voltage V_{cent} was generated by PD_C .

V_{DD} was set to 5 V. V_{con2} was set to 1.27 V. C_D was set to 100 μ F. The light was provided as the object. The motor was controlled by the motor driver (TA7257P, TOSHIBA).

Figure 7 shows the measured results. The light moved toward the right side from $t=0$ to $t=1.2$ s. At $t=1.2$ s, the light was stopped. To $t=2$ s, the system tracked the target. At $t=2$ s, the system captured the target on the center of the input array.

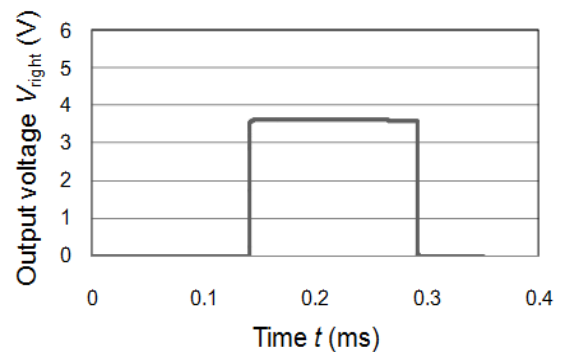


Fig. 6. Simulated results of the proposed circuit transient response of output voltage V_{right} .

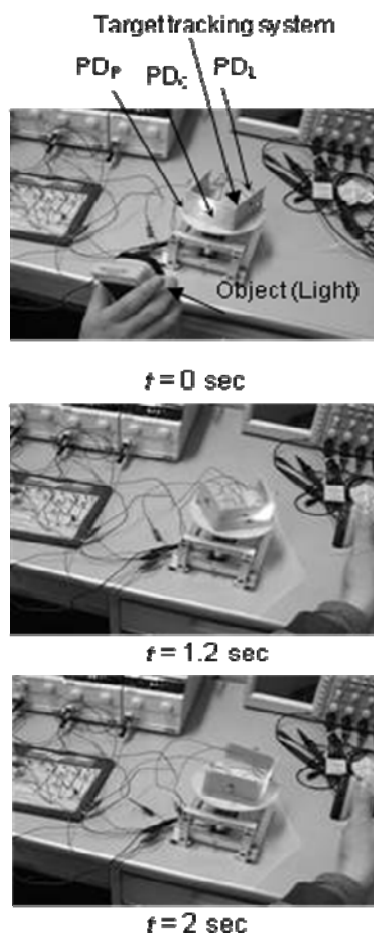


Fig. 7. Measured results of the target tracking system.

V. CONCLUSION

The simple analog-digital circuit for generating the motion signal was proposed in this study. Particularly, the digital part for motion detection is constructed with a NOT circuit and a NOR circuit. The test circuit is fabricated based on simulated results. The measured results and the simulation results showed that the proposed circuit can generate the motion signal. The target tracking system was proposed by using the array of the proposed analog-digital circuit for motion detection. The circuit for tracking the target is simple structure. It was clear from the measured results and the simulation results that the proposed system can track the target and capture the target on the center of the input array. The realization of the advanced image processing system for the robotics vision, the security system and other systems can be expected by applying the proposed circuit and system.

ACKNOWLEDGMENT

This research was partially supported by Artificial Intelligence Research Promotion Foundation.

REFERENCES

- [1]C. A. Mead, Analog VLSI and Neural Systems, Addison Wesley, Reading, MA, 1989.
- [2]A. Moini, Vision Chips, Kluwer Academic, Norwell, MA, 1999.
- [3]K. Nishio, K. Matsuzaka and H. Yonezu, "Simple Analog Complementary Metal Oxide Semiconductor Circuit for Generating Motion Signal", *Optical Review*, vol. 14, pp. 282-289, 2007.
- [4]H. Yamada, T. Miyashita, M. Ohtani, K. Nishio, H. Yonezu and Y. Furukawa, "Signal Formation of Image-Edge Motion Based on Biological Retinal Networks and Implementation into an Analog Metal-Oxide-Silicon Circuit", *Optical Review*, vol. 8, pp. 336-342, 2001.
- [5]W. N. Dalila, S. N. Ain and K. Nishio, "Analog Motion Detection Circuits Using Simple Edge Detection Circuits Based on the Vertebrate Retina", *The 9th Int. IFAC Symp. on Robot Control (SYROCO 2009)*, pp. 159-164, 2009.
- [6]K. Nishio and K. Matsuzaka, "Target Tracking System Using Analog Circuit for Motion Detection", *Proc. of 2008 IEEE Int. Conf. on Mechatronics and Automation (ICMA 2008)*, TC3-5, 2008.
- [7]K. Nishio and K. Matsuzaka, "Target Tracking System Using Analog Motion Detection Circuit Based on Biological Vision System", *Far East Journal of Electronics and Communications*, vol. 3, pp. 111-124, 2009.
- [8]S. C. Liu and A. U. Viretta, "Fly-Like Visuomotor Responses of a Robot Using a VLSI Motion-Sensitive Chips", *Biological Cybernetics*, vol. 85, pp. 449-457, 2001.
- [9]W. Reichardt, *Principles of Sensory Communication*, Wiley, New York, 1961.

Analog Motion Detection Circuit Using CCD Camera Based on the Biological Vision System and Its Application to Mobile Robot

Yasuyuki Kondo*, Takumi Yamasaki*, Kimihiro Nishio* and Toshinori Furukawa**

*Tsuyama National College of Technology, 624-1, Numa, Tsuyama, Okayama, 708-8509, Japan

**Kurashiki University of Science and the Arts, 2640 Nishinoura, Tsurashima, Kurashiki, 712-8505, Japan

(Tel : 81-868-24-8266; Fax : 81-868-24-8219)

(nishio@tsuyama-ct.ac.jp)

Abstract: We proposed an analog motion detection circuit based on the biological vision system. The charge coupled device (CCD) camera was used as the input part which obtains the input image. By using the CCD camera, it is immediately able to detect the motion of the high resolution images. The unit motion detection circuit is constructed with 8 metal oxide semiconductor (MOS) transistors and 1 capacitor. The unit circuit becomes simple structure. The test circuit was fabricated on the breadboard by using discrete MOS transistors. The measured results of the test circuit showed that the proposed circuit can detect the motion direction. The fabricated test circuit was connected with the microcomputer introduced in the mobile robot. It was clarified from the measured results that the motion detection circuit can control the mobile robot.

Keywords: analog circuit, motion detection, image processing, vision chip.

I. INTRODUCTION

It is necessary for robotics vision, monitoring system and other systems to achieve the high speed image processing. However, it is difficult to process the image information for the typical image processing system using Neumann-type computer because the information is processed in time sequential way. In the biological vision system constructed with the retina and the brain, it is able to accomplish the high speed image processing. The processing is performed in massively parallel nerve networks.

The integrated circuits (chip) were proposed based on the biological vision system [1]-[6]. The circuit can detect the edge and motion of the object in real time. However, there is a problem of the low resolution in the case to add many functions.

In this study, we proposed an analog motion detection circuit based on the biological vision system. The charge coupled device (CCD) camera was used as the input part which obtains the input image. By using the CCD camera, it is immediately able to detect the motion of the high resolution images. The unit motion detection circuit becomes simple structure. The measured results of the test circuit showed that the proposed circuit can detect the motion direction. The fabricated test circuit was connected with the mobile robot. The robot could operate by using the motion signal.

II. MOTION DETECTION MODEL

Figure 1(a) shows the motion detection model based on the biological vision system. We call the model the correlation model. The model is constructed with the photoreceptors P, delay neurons D and correlators C. The arrows show the flow of the signals. The solid line shows the model for detecting the right motion. The dashed line shows the model for detecting the left motion. In this paper, the model for detecting the right motion is described.

Figure 1(b) shows the signals of the motion

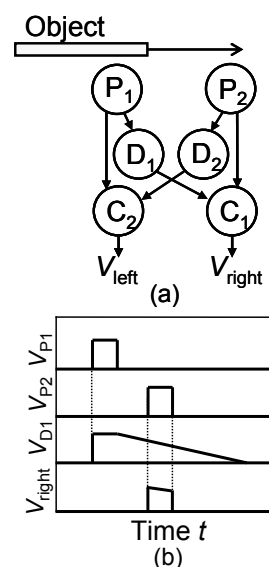


Fig.1. Motion detection model. (a)Model. (b)Transient response of each cell.

detection model when the object moves toward the right side. Firstly, the object is projected on P_1 . P_1 generates the signal which is proportional to light intensity. The signal of P_1 is input to D_1 . The signal of D_1 decreases. When the object is projected on P_2 , P_2 generates the signal. The signal of P_2 is input to C_1 . Since the output signal V_{right} of C_1 is proportional to D_1 , V_{right} becomes large when the object moves toward the right side. Then, the output signal V_{left} of C_2 is 0.

When the object moves toward the left side, V_{left} becomes large and V_{right} is 0. Thus, the model can detect the motion direction.

III. MOTION DETECTION CIRCUIT

1. Input part

Figure 2(a) shows the relationship between the object and CCD camera. The object is projected on the CCD through the lens.

Figure 2(b) shows the projected image. In this study, it is necessary to generate the signals of P_1 and P_2 , as shown in Fig. 1. As shown in Fig. 2(b), the image is segmented. The signals of the segmented image are

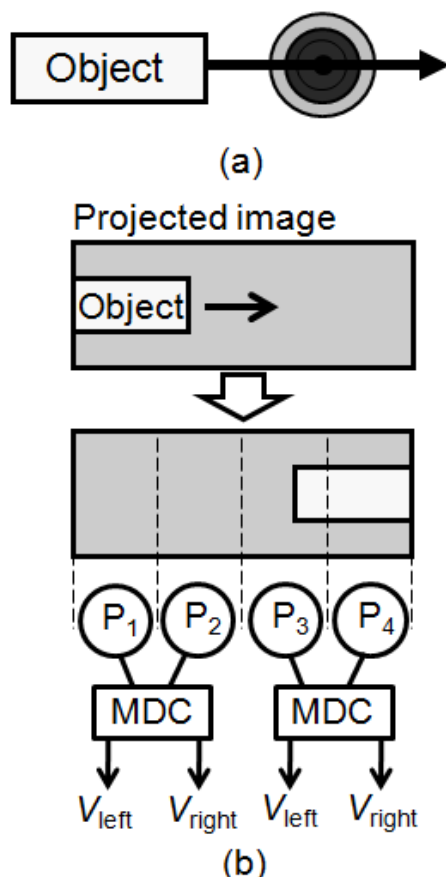


Fig.2. Relationship between the object and CCD camera.

utilized as those of photoreceptors.

2. Unit circuit

Figure 3 shows the unit motion detection circuit. V_{P1} and V_{P2} are input voltages. V_{P1} corresponds to the signal of P_1 in Fig. 1. V_{P2} corresponds to the signal of P_2 . V_{right} is the output voltage. In this circuit, the constant currents V_{th1} , V_{th2} and V_{th3} are set.

The delay neuron D in Fig.1 is realized by 1 metal oxide semiconductor (MOS) transistor and 1 capacitor. The correlator is constructed with 5 MOS transistors. The unit circuit is constructed with 8 MOS transistors and 1 capacitor. The circuit is simple structure.

In the case of the circuit for detecting the left motion, the output voltage becomes V_{left} . Thus, the motion direction can be detected by using 2 unit circuits.

IV. MEASURED RESULTS OF CIRCUIT

The test circuit was fabricated with discrete MOS transistors on the breadboard. C was set to 100 nF. V_{th1} , V_{th2} and V_{th3} were set to 2.18 V, 1.2 V and 1.36 V, respectively. The supply voltage V_{DD} was set to 5 V.

Figure 4 shows the measured results of the test circuit when the object moved toward the right side. V_{right} became 5 V. Then, V_{left} became 0.

Figure 5 shows the measured results of the test circuit when the object moved toward the left side. V_{left} became 5 V. Then, V_{right} became 0.

Thus, the test circuit can detect the motion direction.

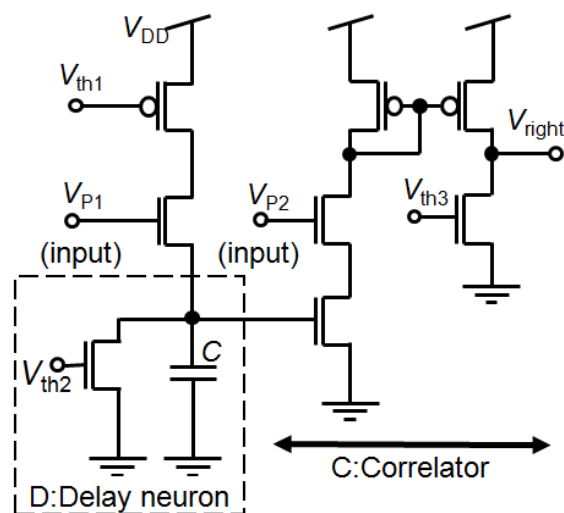


Fig.3. Unit motion detection circuit.

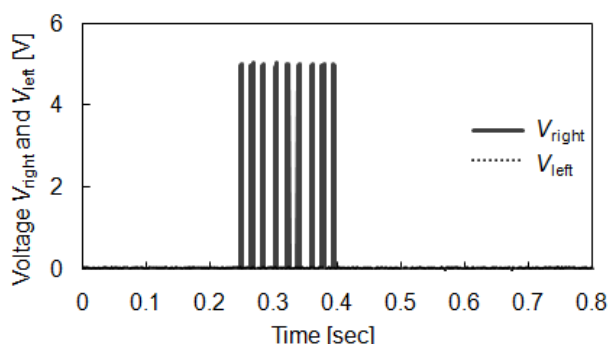


Fig.4. Measured result of test circuit (right side).

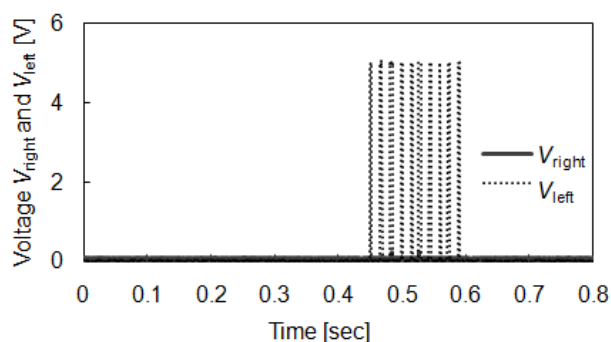


Fig.5. Measured result of test circuit (left side).

V. APPLICATION TO MOBILE ROBOT

We tried to control the mobile robot by using our motion detection circuits. The fabricated test system is shown in Fig. 6. In the robot (ROBONOVA-I, Hitec Multiplex Japan), the microcomputer (MR-C3024) is introduced. The output terminals of the test circuits, i.e., V_{right} and V_{left} were connected with input terminals of the microcomputer.

In this study, we programmed that the robot hands up the right arm when the object moves toward the right side, i.e., when V_{right} becomes V_{DD} . We programmed that the robot hands up the left arm when the object moves toward the left side, i.e., when V_{left} becomes V_{DD} .

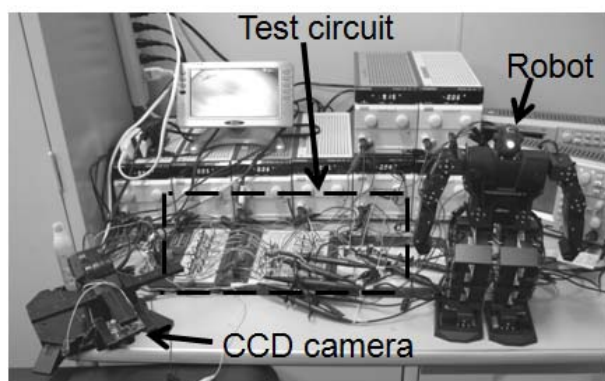


Fig.6. Photograph of the fabricated test system.

Figure 7 shows the measured results of the test system when the object moved toward the right side. The robot handed up the right arm.

Figure 8 shows the measured results of the test system when the object moved toward the left side. The robot handed up the left arm.

Thus, it is able to control to the robot by using our proposed circuit.

VI. CONCLUSION

An analog motion detection circuit was proposed based on the biological vision system. By using the CCD camera as the input part, it is able to detect the motion of the high resolution images. The unit circuit becomes simple structure since the unit circuit is constructed with 8 MOS transistors and 1 capacitor. The measured results of the test circuit showed that the proposed circuit can detect the motion direction. The

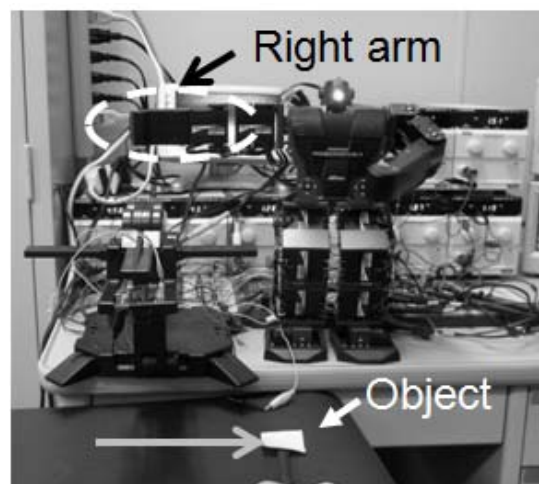


Fig.7. Measured result of test system (right side).

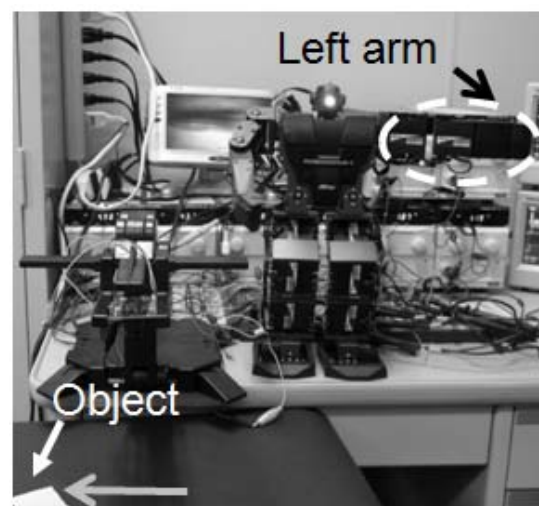


Fig.8. Measured result of test system (left side).

test circuit was connected with the mobile robot. It was clarified from the measured results that our proposed circuit can control the robot. In the future, by applying the proposed motion detection circuit, it is able to use as the motion sensor such as the robotics vision.

ACKNOWLEDGMENT

This research was partially supported by strategic support project for university collaboration, science triangle in Okayama sponsored by the education and science ministry of Japan.

REFERENCES

- [1] C. A. Mead (1989), Analog VLSI and neural systems, Addison Wesley, Reading, MA
- [2] A. Moini (1999), Vision chips, Kluwer Academic, Norwell, MA
- [3] K. Nishio and K. Matsuzaka (2009), Target tracking system using analog motion detection circuit based on biological vision system, Far East Journal of Electronics and Communications 3 : 111-124
- [4] K. Nishio, H. Yonezu, A. B. Kariyawasam, Y. Yoshikawa, S. Sawa and Y. Furukawa (2004), Analog integrated circuit for motion detection against moving background based on the insect visual system, Optical Review, 11 : 24-33
- [5] K. Nishio, H. Yonezu, and Y. Furukawa (2006), Analog integrated circuit for detection of an approaching object with simple-shape recognition based on lower animal vision, IEICE Transactions on Fundamentals of Electronics, Communications and Computer Sciences E89-A : 416-427
- [6] K. Nishio, H. Yonezu and Y. Furukawa (2007), Analog vision chip for motion detection of approaching object against moving background based on insect visual system", Optical Review 14 : 111-119

Detecting Human Flows on a Road Different from Main Flows

Mison Park, Joo Kooi Tan, Yuuki Nakashima, Hyungseop Kim and Seiji Ishikawa

*Department of Mechanical and Control Engineering
Kyushu Institute of Technology*

Sensuicho 1-1, Tobata, Kitakyushu 804-8550, Japan

E-mail: {park, etheltan, ishikawa}@ss10.cntl.kyutech.ac.jp, kim@cntl.kyutech.ac.jp

Abstract: Automatic detection of human flows on a road by a computer vision system is of great importance mainly in surveillance systems, where human flows are observed by a camera and a computer analyzes the videos that the camera provides to detect a person having a different flow of movement, such as a person walking toward a certain direction while most of the people walk in the opposite direction, or a person running in a group of walking people. This paper describes a technique for finding a person having a different behavior or motion from others. The idea of the paper is to classify motion flows (or optical flows) extracted from a video into respective groups having respective directions of the motion by analyzing the motion flows. Experimental results show effectiveness of the proposed technique.

Keywords: Motion detection, abnormal motion, Harris corner detector, L-K tracker, clustering, feature space.

I. INTRODUCTION

In recent years, along with the unceasing intellectualization of video image monitoring technology, the intelligent monitoring technology has gained more and more domestic and foreign merchants' and scholars' recognition and has conducted a series of researches. One of the most challenging tasks in intelligent monitoring technology is the analysis of human motion in crowded scenes and detecting the people who have a different motion from others. The detection of an abnormal motion can trigger video transmission and recording, and can be used to attract the attention of a human observer to a particular video channel.

This paper describes a novel technique for finding a person having a different motion from others. The idea of the paper is to classify motion flows (or optical flows) extracted from a video into respective groups having respective directions of the motion by analyzing the motion flows. In order to realize this, the Harris corner detector is applied to an initial image frame to extract feature points on the image: The Lucas-Kanade tracker is then applied to the successive frames to detect motion flows on the video: Pyramidal search is considered, if necessary, to detect the motion flows having different flow lengths indicating difference of the motion speed. The obtained motion flows are finally classified into some groups which have respective motion directions or speed.

II. OVERVIEW OF THE ABNORMAL MOTION DETECTION SYSTEM

The process of detecting abnormal motion involves two primary contents: 1) tracking feature points. First,

extract feature points from the initial image frame. Then, track the feature points in the next frame to find the motion vector. However, it is impossible to determine whether the motion is normal or abnormal only by the motion vector of the two successive frames.

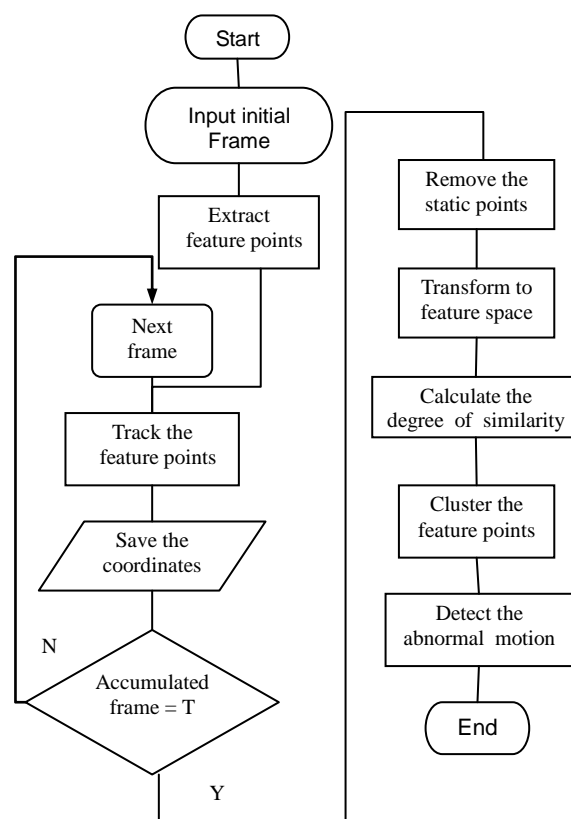


Fig.1. Overview of the proposed abnormal motion detecting method

Therefore, we need to accumulate some image frames from the first frame and store the location of the feature points that are tracked over the entire frames into the coordinate space. 2) Clustering. Remove stationary points from the coordinate space and convert the coordinate space into a feature space. Finally, cluster the feature points to detect abnormal motions. **Fig. 1** shows the overview of the abnormal motion detecting method.

III. METHOD

1. Extracting feature points

Generally, motion vectors are calculated by using the pixel values in the local region around the attracted point. We cannot obtain the right motion vector if texture conditions are poor in this local region. Therefore we need to find an adaptive feature point. In this paper, Harris corner detector, a popular feature point detector, is applied to extract the feature points.

The Harris corner detector is based on the local auto-correlation function of a signal, where the local auto-correlation function measures the local changes of the signal with patches shifted by a small amount in different directions.

For a small shift $[u, v]$, we have bilinear approximation as follows;

$$E(u, v) \cong [u, v] M \begin{bmatrix} u \\ v \end{bmatrix} \quad (1)$$

where M is a 2×2 matrix of the following form computed from image derivatives;

$$M = \sum_{x,y} w(x, y) \begin{bmatrix} I_x^2 & I_x I_y \\ I_x I_y & I_y^2 \end{bmatrix} \quad (2)$$

The Harris measure of a corner is defined by

$$R = \det M - k (\text{trace } M)^2 \quad (3)$$

where

$$\begin{aligned} \det M &= \lambda_1 \lambda_2 \\ \text{trace } M &= \lambda_1 + \lambda_2 \end{aligned} \quad (4)$$

where λ_1 and λ_2 are the eigenvalues of the matrix M .

Find the points with large corner response function R ($R > \text{threshold}$), and take the points of local maxima of R . **Fig. 2** shows the image of extracted feature points.

2. Tracking feature points

The Lucas-Kanade tracker, one of the most well-known feature points tracking algorithms is employed in the proposed method.

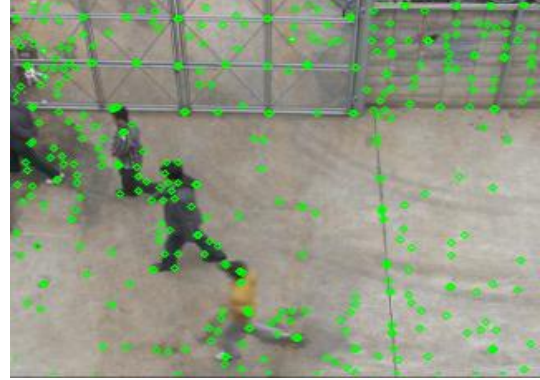


Fig.2. Feature points extraction

The L-K algorithm relies only on local information that is derived from some small windows surrounding each of the points of interest. Based on the condition, we can get the final expression in the form of

$$d = (A^T A)^{-1} A^T b \quad (5)$$

where

$$A = \begin{bmatrix} I_x(x_1, t) & \cdots & I_x(x_n, t) \\ I_y(x_1, t) & \cdots & I_y(x_n, t) \end{bmatrix}^T \quad (6)$$

The disadvantage of using small local windows in Lucas-Kanade algorithm is that large motions can move points outside of the local window and thus become impossible for the algorithm to find them. This problem led to the development of the pyramidal L-K algorithm, which starts tracking from the highest level of an image pyramid and working down to lower levels. Tracking over image pyramids allows large motion to be caught by local windows. **Fig. 3** shows the image of motion vectors.



Fig.3. Motion vectors

3. Creating the feature space

Since it is difficult to detect an abnormal motion only by the motion vectors between successive frames, we need to accumulate some frames from the first frame.

The feature points are tracked over the entire frames and their location information is stored into a coordinate space. Suppose that a feature point n ($n=0,1,2,\dots,N-1$) is tracked through T image frames and its position on the frame t ($t=0,1,2,\dots,T-1$) is denoted by $(x_t^{(n)}, y_t^{(n)})$. We then define a sequence of T coordinates of the feature point by the following form;

$$\begin{aligned} X_0 &= [x_0^{(0)}, y_0^{(0)}, x_1^{(0)}, y_1^{(0)}, \dots, x_{T-1}^{(0)}, y_{T-1}^{(0)}] \\ X_1 &= [x_0^{(1)}, y_0^{(1)}, x_1^{(1)}, y_1^{(1)}, \dots, x_{T-1}^{(1)}, y_{T-1}^{(1)}] \\ &\vdots \\ X_{N-1} &= [x_0^{(N-1)}, y_0^{(N-1)}, x_1^{(N-1)}, y_1^{(N-1)}, \dots, x_{T-1}^{(N-1)}, y_{T-1}^{(N-1)}] \end{aligned} \quad (7)$$

Fig. 4 shows the tracking result throughout the T frames.

However, the movement cannot be known only by the position information of points in the coordinate space. Therefore the coordinate space is converted to three kinds of feature space such as velocity (8), velocity magnitude (9), and velocity orientation (10).

$$\begin{aligned} V_0 &= [v_x^{(0)}, v_y^{(0)}] = [x_{T-1}^{(0)} - x_0^{(0)}, y_{T-1}^{(0)} - y_0^{(0)}] \\ V_1 &= [v_x^{(1)}, v_y^{(1)}] = [x_{T-1}^{(1)} - x_0^{(1)}, y_{T-1}^{(1)} - y_0^{(1)}] \\ &\vdots \\ V_N &= [v_x^{(N)}, v_y^{(N)}] = [x_{T-1}^{(N)} - x_0^{(N)}, y_{T-1}^{(N)} - y_0^{(N)}] \end{aligned} \quad (8)$$

$$\begin{aligned} |V_0| &= \sqrt{(x_{T-1}^{(0)} - x_0^{(0)})^2 + (y_{T-1}^{(0)} - y_0^{(0)})^2} \\ |V_1| &= \sqrt{(x_{T-1}^{(1)} - x_0^{(1)})^2 + (y_{T-1}^{(1)} - y_0^{(1)})^2} \\ &\vdots \\ |V_N| &= \sqrt{(x_{T-1}^{(N)} - x_0^{(N)})^2 + (y_{T-1}^{(N)} - y_0^{(N)})^2} \end{aligned} \quad (9)$$

$$\begin{aligned} \theta_0 &= \arctan\left(\frac{y_{T-1}^{(0)} - y_0^{(0)}}{x_{T-1}^{(0)} - x_0^{(0)}}\right) \\ \theta_1 &= \arctan\left(\frac{y_{T-1}^{(1)} - y_0^{(1)}}{x_{T-1}^{(1)} - x_0^{(1)}}\right) \\ &\vdots \\ \theta_N &= \arctan\left(\frac{y_{T-1}^{(N)} - y_0^{(N)}}{x_{T-1}^{(N)} - x_0^{(N)}}\right) \end{aligned} \quad (10)$$

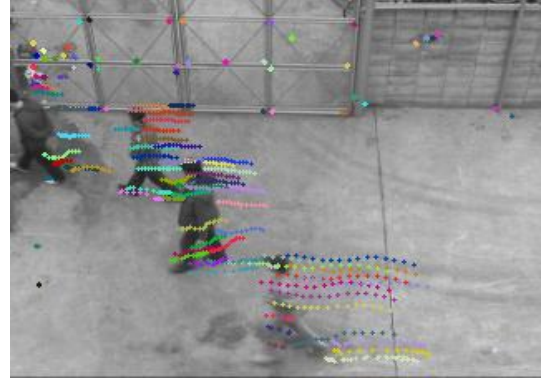


Fig.4. Tracking result throughout T frames

3. Detecting an abnormal motion

The flow chart of clustering is shown in Fig. 5, where d_{ij} and Th are defined as follows;

$$d_{ij} = \text{SSD}(s_j, s_i) \quad (11)$$

$$\begin{aligned} Th &= \alpha(\max - \min) + \min \equiv \gamma \\ \alpha &= 0.001 \end{aligned} \quad (12)$$

The similarity of the features with respect to the feature points are calculated among them. This

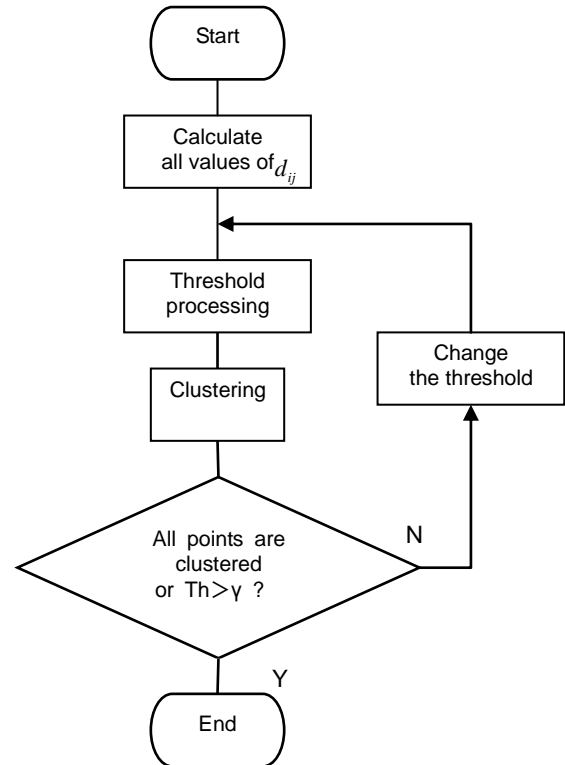


Fig.5. Flow chart of clustering

similarity is clustered by threshold processing. At first, the threshold is set strictly. The threshold is adjusted so as to cluster all the points or larger than γ . Look-up table is used in the clustering process. After clustering, count the number (n) of feature points clustered in each class. The class that satisfies the following condition, $n \leq \text{total number of points} \times R\%$, is defined as an abnormal motion.

IV. EXPERIMENTS AND CONCLUSIONS

The abnormal motion detection algorithm proposed here was successfully tested on various outdoor scenes. Fig. 6 shows the final result.

In this paper, we propose a novel technique of abnormal motion detection from the images obtained from a surveillance camera. The Harris corner detector and the pyramidal Lucas-Kanane algorithm are applied to feature tracking and calculation of motion vectors. Then a coordinate space and a feature space are

created based on the tracked points coordinates. The feature points are clustered by a Look-up table. Finally abnormal motions are detected based on the clustered points. The future work is to integrate the multiple features in order to improve the accuracy.

REFERENCES

- [1] C. Harris, M. Stephens (1988), A combined corner and edge detector, Proc. of the 4th Alvey Vision Conference, pp.147-151.
- [2] B. D. Lucas, T. Kanade (1981), An iterative image registration technique with an application to stereo vision", Proc. of the 7th International Joint Conference on Artificial Intelligence, pp.674-679.
- [3] M. A. Fischler, R. C. Bolles (1981), Random sample consensus: a paradigm for model fitting with applications to image analysis and automated cartography, Communications of the ACM, vol.6, no.24, pp.381-395.

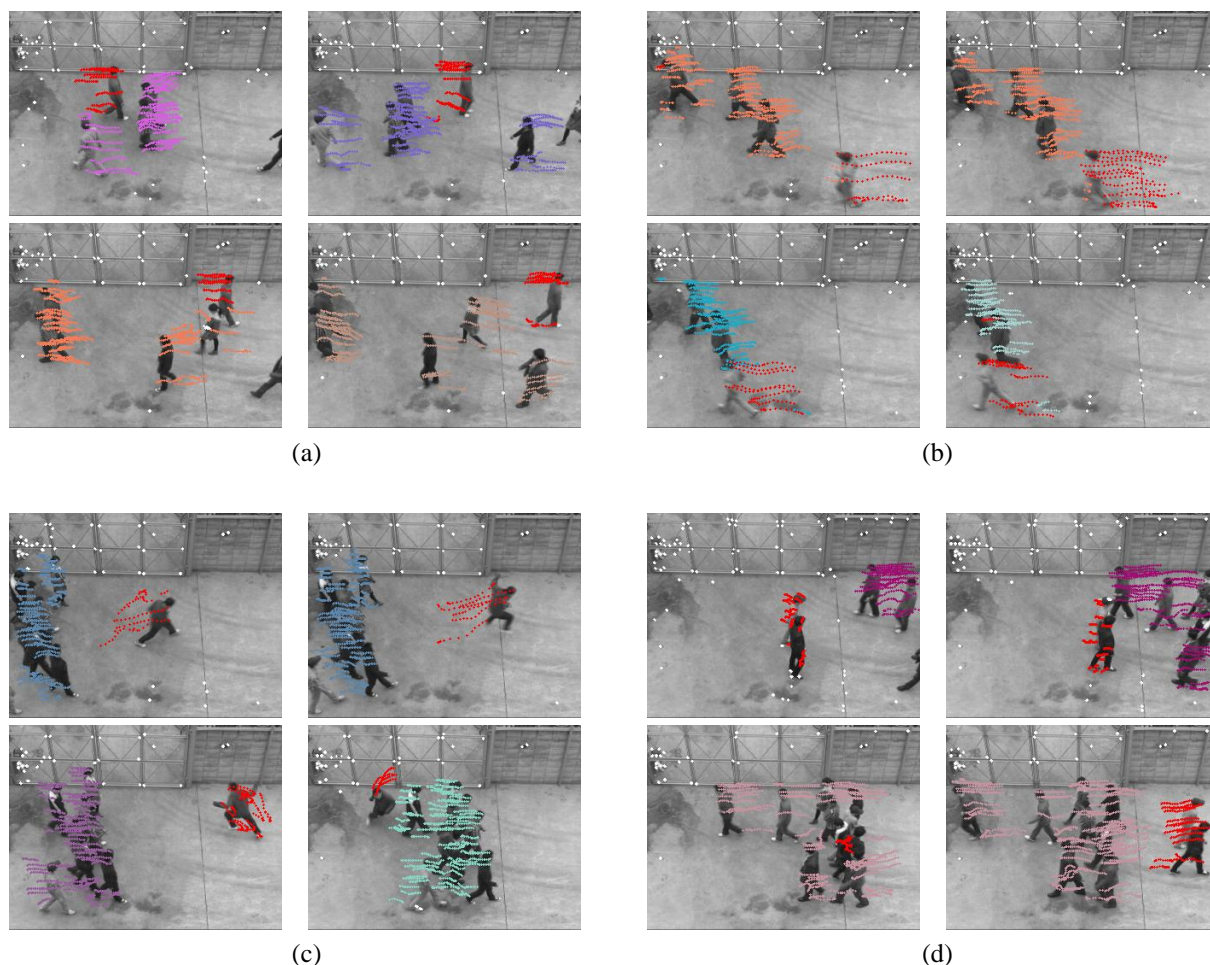


Fig.6. Performance of abnormal motion detection from various scenes. The red line in the frames shows the abnormal notion of a person having a different motion from others. Time elapses in the order of upper left, upper right, lower left and lower right image.

Study on the height measurement based on the image processing technique

Jiwu Wang¹ Weijie Gao¹ Yisong Wang¹

*Department of Mechanical and Electrical Engineering, Beijing Jiaotong University,
Beijing, China, 100044¹*

*Sugisaka Masanori²
Nippon Bunli University, Oita, Japan²*

Abstract: It is difficult to realize the height measurement based on the image processing technique. In this paper, we study how to carry on the height measurement with one CCD camera. In order to reduce the influence of the lighting conditions in the environment, the near-infrared laser and filter were used. We tested our method with various materials. The experiments show we can get reliable results in our laboratory conditions. The further research and some verifications of our algorithms will do later.

Keywords: Image processing, Height measurement, Near-infrared laser

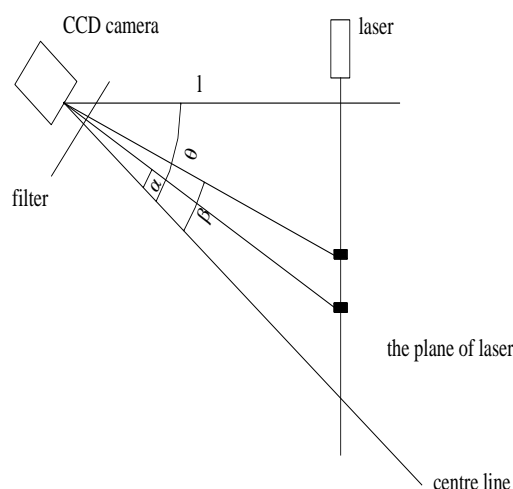
I. INTRODUCTION

Height measurement problem has a long history, and there are variety of measurement, some of these measurement also use the technology of image processing. It mostly use of mathematical computation with extra scale and multifarious algorithm of image processing, not only compute complexly but also is influenced easily, so influence the precision of measure. The following text will introduce how to carry on the height measurement with one CCD camera

II. The mechanism of measurement

As illustrated, we make CCD camera and laser fixed, then we can get the length between camera and laser through precision measuring instrument. We also can get the value of angle between the centre line of camera and horizontal plane by measuring instrument. In the picture two black piece represent the reaction of height when the light emitted by laser fired the measured object. The angle of α and β can be got through image processing, based on geometrical relationship we can calculate the h as the next formula.

$$h = l \times \tan(\theta - \alpha) - l \times \tan(\theta - \beta)$$



The picture depicts the situation that the CCD camera's center line and the measured pixel of the luminous beam are in the same plane. We call this plane the vertical center plane. There is another situation where the camera's center line and the measured pixel of the luminous beam are not in the same plane. We mark the angle between the center line and the measured pixel as γ , which we can get through image processing. We found a parameter L , make $L = l / \cos \gamma$, and then instead of h . Now we can continue using this formula.

III. The principle of measurement

The light emitted by laser fired on the profile of a workpiece,forming a bright curve that is the profile of the workpiece.The bright points do not in a straight line because of curve profile of workpiece.Through the camera we can get the picture and then we process the picture.

In image processing,we use the algorithm of model conversion,edge detection,binaryzation and so on,above all we use of filter.This can greatly reduce the difficulty of image processing,simple the algorithm,shorten the computation time,improve the detection efficiency,and can obtain accurate and stable results.We already know the wide angle of camera,through image processing,we can get position relation of bright pixel and centr pixel,then find out the angle of α and β .According to formula (1) ,we can figure out height difference,and then get the profile.

IV. Experiment research

In the laboratory we build a simple platform,with a screwdriver handle to be tested.First we show the picture without filter;And then put the filter in front of the lens,the picture we get is as 2; The third picture is after processing.The effect of image processin as flows:

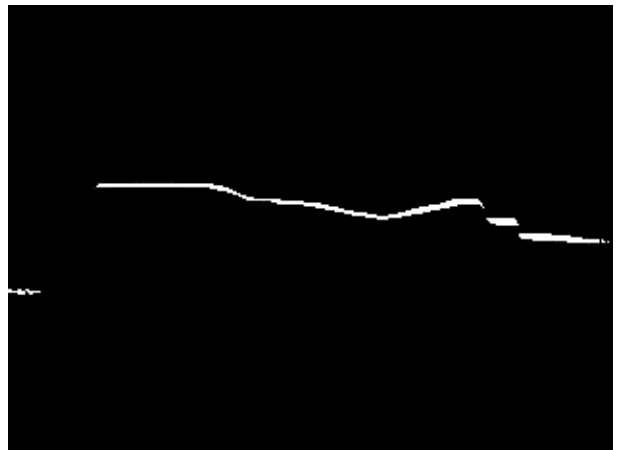


Without filter



Filter

After using filter,we will amazed:how a perfect picture.However this is not the final result we want,we must extract a line,a centre line of the luminous beam.Then we can get the position of every pixel in the line.In order to get α , β and γ ,we must calculate the distance between measured pixel and centre line of the picture,which is not difficult. We can use this equation which is shown by matrix.We can achieve this equation in programming way,then we process these data that we have get about height.With these data we can get the profile easily.



After processing

$$\begin{bmatrix} h_1 \\ h_2 \\ \bullet \\ \bullet \\ \bullet \\ h_n \end{bmatrix} = \begin{bmatrix} l / \cos \gamma_1 & l / \cos \gamma_2 & \bullet & \bullet & l / \cos \gamma_n \end{bmatrix}$$

$$\times \begin{bmatrix} \tan(\theta - \alpha_1) \\ \tan(\theta - \alpha_2) \\ \vdots \\ \tan(\theta - \alpha_n) \end{bmatrix} + \begin{bmatrix} \tan(\theta - \beta_1) \\ \tan(\theta - \beta_2) \\ \vdots \\ \tan(\theta - \beta_n) \end{bmatrix}$$

V. CONCLUSION

Image processing method to measure the height mainly includes two parts: hardware component and software component. It will increase the costs and working environment if we make hardware better only. And it will increase the processing time if use complicated algorithms. Now we use cheap equipment to meet the requirements of precision, and greatly reduce the equipment cost. However if we want to improve measurement accuracy, better camera will be used.

REFERENCES

- [1] Luping Xu. Digital Image Processing. Science press, 2007.
- [2] Guan Xin, Luo Zhi sheng, Wu Jianle, Gao Xiaorong. Locomotive wheel 3d reconstruction, IPPRIE, 2010
- [3] Lin Yuping, Medioni G. Mutual information computation and maximization using GPU[C]. In : IEEE Computer Society Conference on Computer Vision and Pattern Recognition Workshops. Alaska, USA, 2008. 1-6.

Reinforcement learning with the mechanism of short-term depression for learning rate

S. Kubota

*Department of Biomedical Information Engineering, Yamagata University
4-3-16 Jonan, Yonezawa, Yamagata, 992-8510, Japan
(Tel : 81-238-26-3356; Fax : 81-238-26-3299)
(kubota@yz.yamagata-u.ac.jp)*

Abstract: The temporal-difference (TD) reinforcement learning (RL), typically formulated in discrete state space, is frequently applied to the control problems represented by continuous state variables. The use of a coarse space discretization to describe the RL algorithm may degrade the control performance, whereas a fine discretization requires a large number of iteration steps to complete learning. In this study, I examine a novel RL algorithm by which the learning rate is dynamically and spatially modulated to improve the learning performance even when a relatively coarse space discretization is employed. This method is inspired by physiological phenomenon of short-term depression observed in biological synapses, and aims to produce a bias in the TD learning toward the states that have not been recently visited. The proposed algorithm is incorporated with Sarsa-lambda and tested in a nonlinear control task of swinging up a pendulum using limited torque. The simulation results show that the proposed dynamic learning rate can robustly reduce the number of trials required before accomplishing the task by facilitating efficient exploration in the RL process.

Keywords: Temporal difference, Reinforcement learning, Dynamic learning rate, Synapse.

I. INTRODUCTION

The temporal-difference-(TD)-based reinforcement learning (RL) not only provides an efficient approach to control and decision problems, but also can be considered as an attractive model for studying the brain [1]. In fact, a broad range of experimental evidence suggests the involvement of neural activities occurring at a variety of brain areas in the mediation of reward processing as well as the TD error signal [1-3]. A close connection between the RL theory and the relevant physiological data implies that the theoretical scheme of RL could provide a quantitative framework for future studies in the related area of neuroscience [2]. Furthermore, it also appears possible to improve the RL algorithm by incorporating neurobiological mechanisms underlying adaptive behavior of animals, as this study aims to do.

An important application of RL technique is to control a strong nonlinear dynamical system, which would be difficult to be solved by a conventional engineering approach. In many interesting real-world control tasks, the state variables evolve with time in continuous space, although the progress of RL theory has been mainly restricted to the problems described by the Markov decision process (MDP) formulated in discrete state space [4]. Therefore, in the application studies of RL, the most common approach is first to discretize the state space and then to apply the learning algorithm described

in a discrete stochastic system. In this approach, a fine discretization of state space necessarily requires a large number of memory storage as well as many iteration steps to complete learning the value functions. In contrast, a coarse space discretization leads to a situation where, when the state variables evolve slowly with time, an update of value functions takes place many times repeatedly at identical states; in such a case, it is likely that wrong actions repetitively taken at the same state are excessively reinforced, particularly during early learning phases.

Ideally, one would like to develop an algorithm that can improve the RL performance even when a relatively coarse space discretization is employed. In this study, I propose a novel method, which incorporates spatiotemporal modulation of learning rate to enhance the learning efficiency in such coarse discretized space. This method is inspired by physiological phenomenon of short-term depression (STD) observed in central synapses, i.e., a transient decrease in the strength of synaptic inputs following their repetitive activation. The proposed algorithm is introduced in Sarsa (λ) [5] and applied to a nonlinear control task of swinging up a pendulum with limited torque. I show in simulations that the task can be accomplished by employing the proposed dynamic learning-rate modulation in a number of trials less than by employing a conventional static learning rate. Further, I demonstrate that the proposed

method can decrease the sensitivity of the task performance to the scaling of learning rate, implying that this method can make the tuning of the learning parameter easier.

II. METHODS

1. Sarsa (λ)

As a basic RL algorithm to which the proposed method is to be incorporated, the author used Sarsa (λ) [5]. In this algorithm, the action-value function $Q(s, a)$, for each state s and action a , is updated as follows:

$$Q(s, a) \leftarrow Q(s, a) + \alpha e(s, a) \delta. \quad (1)$$

Here, α (>0) denotes the learning rate. δ represents the TD error described as

$$\delta = r + \gamma Q(s(t+1), a(t+1)) - Q(s(t), a(t)), \quad (2)$$

where r is the reward obtained by the state transition from $s(t)$ to $s(t+1)$ through action $a(t)$. γ is a discount rate satisfying $0 \leq \gamma \leq 1$. Each action is assumed to be decided from the ϵ -greedy policy with respect to $Q(s, a)$. The eligibility trace $e(s, a)$ for all the state-action pairs, s, a , is updated by the following equation:

$$e(s, a) \leftarrow \begin{cases} \gamma \lambda e(s, a) + 1, & (s = s(t) \text{ and } a = a(t)) \\ \gamma \lambda e(s, a), & (\text{otherwise}) \end{cases} \quad (3)$$

2. STD mechanism for controlling learning rate

The author designed an algorithm for spatiotemporal control of learning rate, which models short-term activity-dependent modification of synapses. In the central nervous system, the synaptic inputs that are activated with higher frequency are rapidly and temporarily depressed so that the input-output gain for high-rate inputs decreases [6]. This phenomenon, called STD, occurs through the transmitter vesicle depletion at the pre-synaptic terminals, and can be modeled by the following equation [6,7]:

$$dD(t)/dt = -\rho_v D(t) \sum_j \delta(t - t_j) + [1 - D(t)]/\tau_r, \quad (4)$$

where $D(t)$ ($0 \leq D(t) \leq 1$) represents the synaptic strength normalized by its maximum value, and t_j is the j th activation time of the synapse. Equation 4 indicates that the synaptic strength is weakened just following activation such that $D(t_j^+) = (1 - \rho_v)D(t_j^-)$ ($0 \leq \rho_v \leq 1$), whereas it recovers toward 1 with the time constant τ_r in the absence of activation [7]. If

time is discretized by using Euler's method, Eq. 4 can be written, by defining parameters $\rho \equiv 1 - \rho_v$ and $\mu \equiv \Delta t / \tau_r$ ($0 \leq \rho, \mu \leq 1$), as follows:

$$D(t+1) = \begin{cases} \rho D(t) + \mu[1 - D(t)], & (\text{following synaptic activation}) \\ D(t) + \mu[1 - D(t)], & (\text{otherwise}) \end{cases} \quad (5)$$

Assume that, based on the classical cell assembly hypothesis [8], firing activity of a group of interconnected neurons encodes a specific information regarding environment. Then, the repetition of the same state in MDP could be represented in the brain by the repetitive spiking of the same cell group, which will weaken input activity for such group of neurons through STD [9]. Further, experimental evidence suggests that the resultant weakened activation of NMDA receptors (NMDARs), one of major receptor subtypes for glutamatergic synapses, may cause the suppression of long-term plasticity underlying learning in the brain [10]. This may correspond, in the terminology of RL, to the decreased value of learning rate.

Therefore, to incorporate the mechanism resembling STD to an RL algorithm, the author introduces a function $d(s)$ ($0 \leq d(s) \leq 1$) and considers that $d(s)$ for all the states s are updated, similar to Eq. 5, as follows:

$$d(s) \leftarrow \begin{cases} \rho d(s) + \mu[1 - d(s)], & (\text{for } s = s(t)) \\ d(s) + \mu[1 - d(s)], & (\text{otherwise}) \end{cases} \quad (6)$$

The value of α (Eq. 1) is multiplied by $d(s)$ so that the function Q is updated, instead of Eq. 1, as

$$Q(s, a) \leftarrow Q(s, a) + \alpha d(s) e(s, a) \delta. \quad (7)$$

According to Eq. 6, $d(s)$ for a given state s will decrease each time the state s is visited, whereas it gradually recovers to 1 in the absence of visiting s . Therefore, it can be expected that $d(s)$ acts to decrease the change in the action-value function $Q(s, a)$

Table 1. The learning parameters

Parameter	Value
Parameter to decide the level of STD ρ	0.6
Rate of recovery from STD μ	0.04
Scale of learning rate α	0.8
Discount rate γ	0.98
Decay rate of eligibility trace λ	0.8
Randomness of policy ϵ	0.1

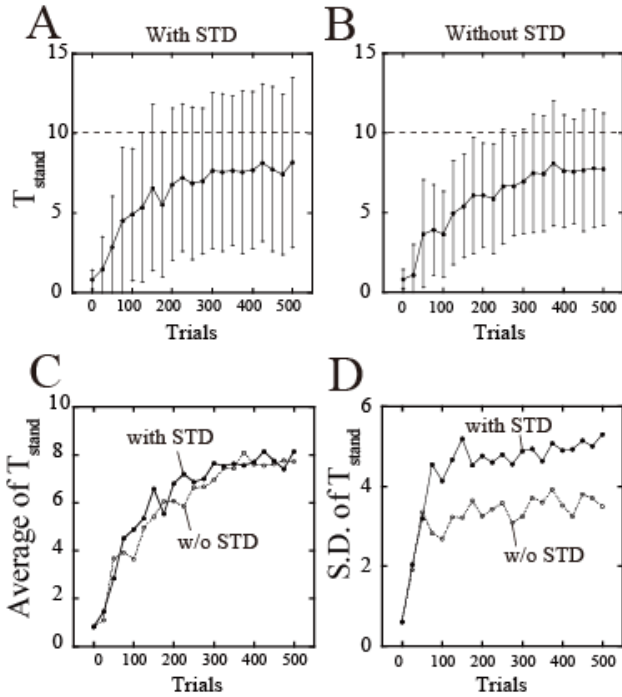


Fig.1. (A and B) The change in the average and standard deviation (error bar) of T_{stand} as a function of the number of trials in the presence (A; $\rho = 0.6$) and absence (B; $\rho = 1$) of the STD mechanism. The dashed lines show the level of T_{stand} above which a trial is considered successful ($T_{\text{stand}} > 10$). (C and D) The average (C) and standard deviation (D) of T_{stand} are plotted for both the cases with (solid) and without (dashed) STD in the same graph. The parameters for the system dynamics are as follows: $m = l = 1$, $g = 9.8$, $c = 0.01$, and $u_{\text{max}} = 5$ [4].

for the states that have been visited in the near past. This also implies that by the inclusion of the STD mechanism, the TD learning tends to proceed with a bias that assigns a higher weight to the states that have not been recently visited. The learning parameters in Table 1 are used unless otherwise stated.

III. RESULTS

To test the proposed algorithm, the author performed simulations for the control task of swinging up a pendulum with limited torque [4]. The dynamics of the pendulum are described as $d\theta/dt = \omega$ and $d\omega/dt = (-c\omega + mgl \sin \theta + u)/ml^2$ with the external torque $u = \pm u_{\text{max}}$, implying that only its direction can be controlled. The physical parameters used are summarized in the Fig. 1 caption. For numerical integration,

the Euler's method was used with the time step size $\Delta t = 0.02$. The reward given was set to be $r = 1$ for $|\theta| < \pi/4$, $r = -75/\Delta t$ for $|\theta| > 4\pi$, and $r = 0$ otherwise, where the negative reward for large θ is to prevent the over rotation. The state space $\{(\theta, \omega) | -4\pi < \theta, \omega < 4\pi\}$ was digitized into subspaces with the length of $\Delta\theta = \Delta\omega = \pi/3$. A trial ended at $t = 20$ or when the pendulum became over-rotated ($|\theta| > 4\pi$). To quantify the task performance, the total length of time at which the pendulum stands up ($|\theta| < \pi/4$) was defined as T_{stand} . The trial was considered to be successful when $T_{\text{stand}} > 10$, and the learning speed was measured by using the number of trials, N_{success} , required before achieving 10 successful trials.

Figure 1 shows the comparison of the time course of T_{stand} obtained by using and not using the STD mechanism of learning rate (Figs. 1A and 1B, respectively). Note that although the mean value of T_{stand} is largely the same regardless of the inclusion of STD (Fig. 1C), the temporal variation of T_{stand} becomes significantly increased by the STD function (Fig. 1D). This would be attributed to the fact that STD will contribute to assigning higher weight to the learning of 'novel' states that have not been recently visited, as mentioned above. The result here shows that the STD function will be effective to facilitate the exploration in RL almost without changing the average task performance.

When similar simulations were performed by using various values of ρ and α , the value of N_{success} was found to take a minimum at an intermediate value of α for all ρ (Fig. 2A). Importantly, the minimum N_{success} value for each ρ with $\rho < 1$ is considerably smaller than that for $\rho = 1$ (i.e., the case of no STD) (Fig. 2B), suggesting that the inclusion of STD can robustly improve the learning performance. To further explore the robustness of the outcome, the upper and lower limits of the α range, where the value of N_{success} is less than a threshold ($= 250$), were defined as α_U and α_L , respectively, and the α_U/α_L ratio was plotted as a function of ρ (Fig. 2C). The figure shows that this ratio becomes greater than that obtained without STD when ρ is relatively large ($0.7 \leq \rho \leq 0.9$). This implies that in this range of ρ , STD can decrease the sensitivity of the task performance to the scale of

learning rate, which will make the tuning of the learning parameter easier. Note that around similar values of ρ ($0.5 \leq \rho \leq 0.9$), the minimum N_{success} becomes quite small (Fig. 2B), indicating that this range of ρ will be near-optimal in that the task performance is both robustly and significantly enhanced.

IV. CONCLUSION

In this study, I have proposed an STD mechanism for TD-based RL, where the learning rate is spatiotemporally modulated, and have shown that this method can reduce the number of trials required before accomplishing the control task. This method is motivated by the physiological experimental findings on synapses that their activation are rapidly followed by depression [6]. The proposed learning rate modulation (represented by the change in $d(s)$) tends to assign a greater weight to the learning of value functions for the states that have not been recently visited. This appears to be similar to the observed response of dopamine neurons, which can reflect the novelty of the presented stimuli [11]. Therefore, given that the TD error δ closely resembles the dopamine cell response representing the unpredictability of reward [11], the term $d(s)\delta$ (Eq. 7) may correspond to the dopamine signal that encodes both the novelty and unpredictability of the reward. The present study may suggest a new framework of RL research in which the functional significance of a biological mechanism can be examined by constructing an RL algorithm that incorporates the mechanism and testing it through the application to control problems.

REFERENCES

- [1] Doya K (2008), Modulators of decision making. *Nature Neuroscience* 11:410-416.
- [2] Schultz W, Dayan P, Montague R (1997), A neural substrate of prediction and reward. *Science* 275:1593-1599.
- [3] Schultz W, Apicella P, Ljungberg T (1993), Responses of monkey dopamine neurons to reward and conditioned stimuli during successive steps of learning a delayed response task. *Journal of Neuroscience* 13: 900-913.
- [4] Doya K (2000), Reinforcement learning in continuous time and space. *Neural Computation* 12:219-245.
- [5] Sutton R. S., Barto A. G. (1998) Reinforcement learning: An introduction. The MIT Press, Cambridge.

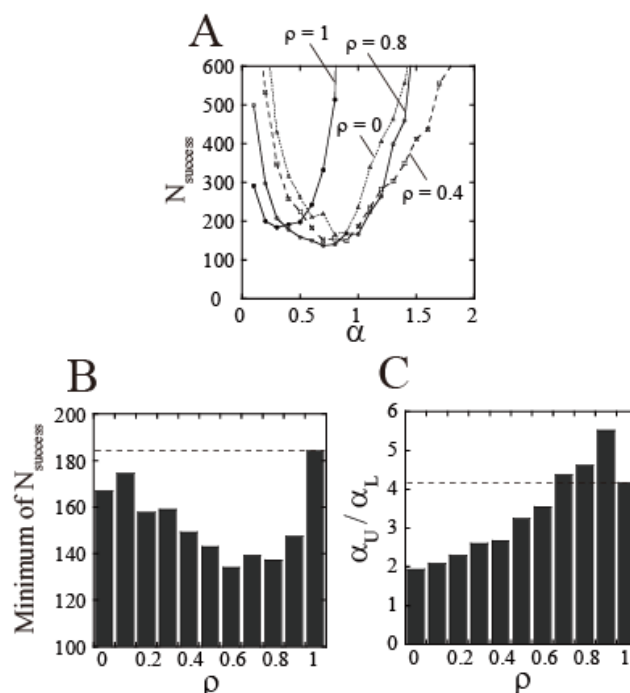


Fig.2. The comparison of task performance for various values of α and ρ . (A) The change in the value of N_{success} , which is averaged over 32 cases, as a function of α and ρ . (B and C) The minimum N_{success} value (B) and the α_U/α_L ratio (C), which are obtained by using various values of α , are plotted for each ρ . The cases of $\rho = 1$ (denoted by the horizontal dashed lines) correspond to those without the STD mechanism.

- [6] Abbott L. F., Varela J. A., Sen K., et al. (1997) Synaptic depression and cortical gain control. *Science* 275: 220-224.
- [7] Wang X.J. (1999) Synaptic basis of cortical persistent activity: the importance of NMDA receptors to working memory. *Journal of Neuroscience* 19: 9587-9603.
- [8] Lansner A. (2009) Associative memory models: from the cell-assembly theory to biophysically detailed cortex simulations. *Trends in Neuroscience* 32:178-186.
- [9] Zucker R. S. (1999) Calcium- and activity-dependent synaptic plasticity. *Current Opinion in Neurobiology* 9:305-313.
- [10] Bear M. F. (1996) A synaptic basis for memory storage in the cerebral cortex. *Proceedings of the National Academy of Sciences of the United States of America*, 93:13453-13459.
- [11] Shultz W. (1998) Predictive reward signal of dopamine neurons. *Journal of Neurophysiology*, 80: 1-27.

A Method for Finding Multiple Subgoals for Reinforcement Learning

Fuminori Ogihara and Junichi Murata

*Kyushu University, 744, Motoooka, Nishi-ku, Fukuoka, Fukuoka, Japan
(Tel : 092-802-3675; Fax : 092-802-3692)
(ogihara@cig.ees.kyushu-u.ac.jp)*

Abstract: This paper proposes a new method for discovering multiple subgoals automatically to accelerate reinforcement learning. There have been proposed several methods for discovery of subgoals. Some use state visiting frequencies in the trajectories that reach the goal state. When a state visiting frequency is very high, this state is regarded as the subgoal. Because this kind of methods need that the goal state is reached many times to collect trajectories, they take a long time for discovering subgoals. In addition, they cannot discover the potential subgoals that will become appropriate subgoals when the goal state changes. On the other hand, some methods identify subgoals by partitioning local state transition graphs. But this kind of methods require large calculation amounts. We propose a new method that solves the above drawbacks. The new method utilizes state visiting frequencies. But we collect trajectories that go through particular non-goal states selected at random. For each particular state, trajectories are collected. Most of the trajectories reach the particular state more easily than the goal state. Therefore, it is expected that we can discover subgoals quickly and discover multiple subgoals together.

Keywords: reinforcement learning, subgoal discovery, the state visiting frequency, the particular state

I. Introduction

Reinforcement Learning is the method that decides proper actions at each state by trial and error. The trial and error method is effective when the environment is complicated or unknown. But learning by trial and error takes a long time. So it is important to accelerate the learning. There have been proposed several methods that accelerate reinforcement learning. Symmetrical-Actions [1] utilizes symmetry of the environment, and Macro-Actions [2] and Options [3] divide the environment to reduce the learning problem size.

Dividing environment by subgoals is one of the methods that speed up the learning, since the number of selections of states or actions reduces. To use this method, it is necessary to discover subgoals.

There have been proposed several methods for finding subgoals. These methods utilize the feature of subgoals [4]. Some utilize the feature that the trajectories that reach the goal state always go through subgoals. In this kind of methods, we collect only positive trajectories (the trajectories that reach the goal state) and ignore negative ones (the trajectories that do not reach the goal state). When the state visiting frequency, which is the value given by dividing the number of positive trajectories into the visiting counts of the state, is very high, it is judged that the state is the subgoal. However, it takes a long time to collect a

number of positive trajectories. On the other hand, some methods utilize the transitions between states [5]. If the number of transition paths between two states is small, the learning environment can be cut between those states and they are judged as subgoals. However, this kind of methods must count the transitions for all neighboring pairs of states, and judge if each count of transitions is lower than the threshold. So they require large calculation amounts.

In this paper, we propose a new method for finding multiple subgoals. The purpose of this paper is discovery of multiple subgoals. In addition, we solve the drawbacks of the existing methods. The new method utilizes the state visiting frequencies. However, we collect not only positive trajectories but also negative ones that go through particular non-goal states chosen at random. These trajectories can be collected faster and thus the subgoals can be found more quickly.

The structure of this paper is as follows. In Section 2 we explain subgoals. In Section 3 we introduce a new method for finding multiple subgoals. Experiment of the use of the new method and the results are written in Section 4. And Section 5 gives conclusions.

II. Subgoal Overview

Subgoals are the states that the agent must go through before the task goal is reached. In

reinforcement learning, if the environment is large and many states or actions are involved, learning tends to be slow owing to trial and error. So it is very effective for reduction of the number of states or actions taken to divide the task environment at subgoals. For example, when an agent goes from one room to another room by way of the doorway, it is very difficult that the agent goes to another room with random actions. But it is easier that the agent goes to the doorway. In this case, the agent must go through the doorway to reach another room. So the doorway becomes a subgoal, which divides the whole task into two smaller tasks.

The methods of Macro-Actions and of Options also divide the environment for speeding up learning. They can be readily constructed once subgoals have been discovered. So finding subgoals is very useful.

III. A new method for finding multiple subgoals

The conventional methods that utilize the state visiting frequency for finding subgoals have several drawbacks [4]. The goal state must be reached many times to count the visiting frequencies, and finding subgoals takes a long time in large or complicated environments. Besides, if the goal state changes, subgoals that were found are not effective for the new situation. In addition, because the trajectories go through the states near the start state very often, the visiting frequencies of these states may be high and these states are judged as subgoals by mistake.

We propose a new method for finding multiple subgoals that solves the above drawbacks. The new method utilizes the state visiting frequencies. But in this method, the definition of the state visiting frequency is different from the past definition in terms of the two points.

First, the way of collecting trajectories is different. The agent takes random actions for several episodes and then selects several particular states among the states that have already been visited. We collect the trajectories that go through the particular state regardless of whether the task goal is reached or not. The state visiting counts are counted up for the states between the start state and the particular state. Figure 1 shows the way of collecting trajectories. Here is one positive trajectory, so we can collect only one trajectory for the existing method. But if we use the new method,

we can collect three trajectories including two negative ones. Therefore, we can obtain enough data to accurately calculate the visiting frequencies and the doorway between two rooms will be selected as the subgoal more quickly. Besides for each particular state, trajectories are collected. So it is expected that multiple subgoals are found.

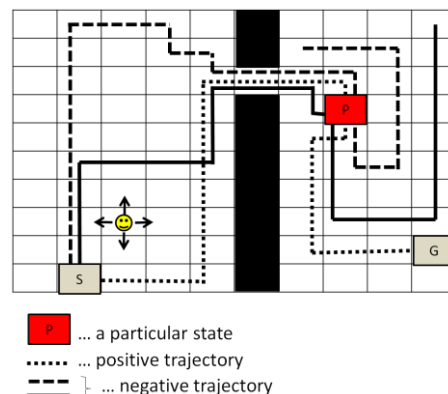


Fig.1 The trajectories that go through a particular state.

Second, in this method, the visiting counts are divided by the average state visiting frequency. The average state visiting frequency is the expected frequency that the trajectory goes through the state when the agent selects an action with equal probability at any state. Figure 2 shows the average state visiting frequency of each state around the start state. The average visiting frequencies of the states around the start state tend to be high. On the other hand, as the state becomes far from the start states, the average state visiting frequency becomes low. So dividing the observed visiting frequency by the average state visiting frequency reduces the seemingly high visiting counts of the states around the start state, and prevents that these states from being judged as subgoals by mistake

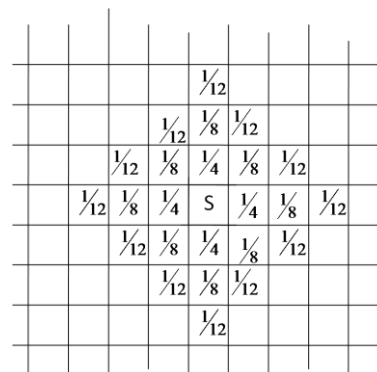


Fig.2 The average state frequency of each state in a gridworld environment.

The visiting frequency F_i of state i for the particular state p is defined by

$$F_i = \frac{\frac{\text{the visiting count of state } i}{\text{\# of trajectories that go through the particular state } p}}{\text{the average visiting frequency of state } i}$$

The Algorithm of the new method is sketched below:

1. At the first several episodes, the agent selects random actions at any states.
2. The agent selects several particular non-goal states at random among the states it has already visited. In addition, if the goal state has been reached during these episodes, the states belonging to a positive trajectory and the goal state are selected as the particular states, because this leads to easy finding of the effective subgoals.
3. The agent collects trajectories that go through the particular state while it learns the policy and selects actions with Q-learning.
4. For each particular state, the state visiting frequencies are calculated.
5. For each particular state, if the state visiting frequency of a state is the maximum over all the states on the way to the particular state and higher than the threshold, the state is judged as the subgoal.

IV. Experiment

We test the new method for finding multiple subgoals. Figure3 shows the environment used in the experiment. It consists of three rooms. The start state and the goal state are indicated by S and G, respectively, in Fig.3. Besides, the horizontal axis and the vertical axis are indicated by x and y , respectively, and the state is represented by (x,y) . The location of the upper doorway is $(3,10)$ and the right doorway is $(10,5)$. The agent can select from four actions: going up, down, right, and left. It uses Q-learning with ϵ -greedy with ϵ that is 0.3 at the first episode and is reduced by 0.001 at every episode down to 0.1. The learning rate α in Q-learning is 0.1, and the discount rate γ is 0.9.

The agent takes random actions for the first 25 episodes. Then the agent uses Q-learning, and collects

the trajectories that go through the particular non-goal states for 300 episodes. The fixed threshold 36 is used.

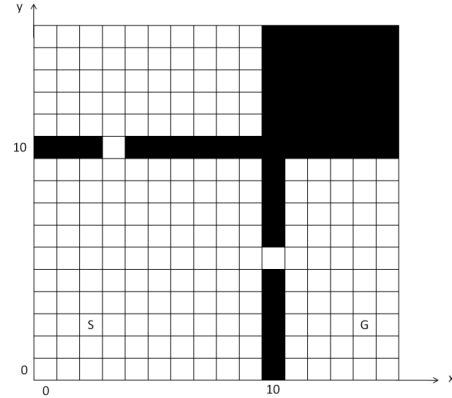


Fig.3 The environment.

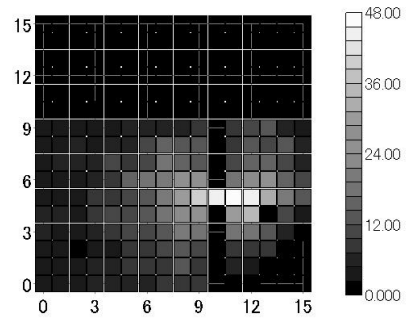


Fig.4 State visiting frequencies for the particular state (13,4).

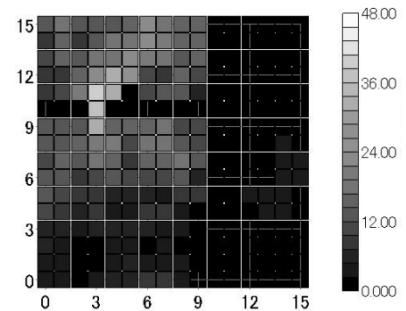


Fig.5 State visiting frequencies for the particular state (5,11).

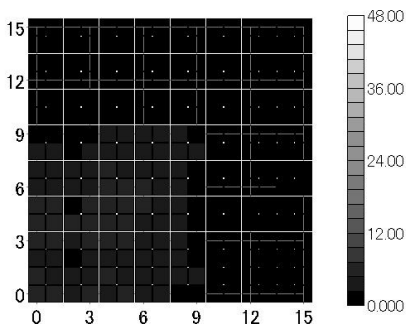


Fig.6 State visiting frequencies for the particular state (2,5).

Figure 4 through Fig.6 show the state visiting frequencies. The lighter the state's color is, the higher the state visiting frequency is. In Fig.4 the particular state is located in the right room where the goal state locates. This particular state is situated near the right doorway, so collecting the trajectories that go through the particular state is easier than collecting the trajectories that reach the goal state. In fact, the number of the trajectories that go through the state (13,4) is 24, which is higher than the number of positive trajectories that is 15. Figure 4 shows that the visiting frequencies of the states around the right doorway are high. The maximum visiting frequency is the visiting frequency of the state (11,5) that is 48 and higher than the threshold. So the state (11,5) is selected as the subgoal.

In Fig.5 the particular state is located in the upper room and near the upper doorway. For this particular state, the visiting frequencies of the states around the upper doorway are high. It is not useful to select one of these states as the subgoal in this environment. But for example, when the goal state moves to the upper room, the upper doorway will become the good subgoal. In other words, even if the goal state moves to the upper room, the agent will not need to repeat the discovery of subgoals. The maximum visiting frequency is the visiting frequency of the state (3,11) that is 40 and higher than the threshold. So the state (3,11) is selected as the subgoal. Again, the number of the trajectories that go through the state (5,11) is 20, which is higher than the number of positive trajectories that is 15.

In Fig.6 the particular state is located in the start room. Because the trajectories often go through this particular state before the agent gets out the start room, the visiting frequency of the doorway state is very low, and the visiting frequency of one of the states in the start room is the maximum. But the visiting frequencies overall are generally low. The maximum visiting frequency is the visiting frequency of the state (3,4) that is about 6.8 and lower than the threshold. So no state is selected as the subgoal from the trajectories passing through this particular state.

VI. Conclusions

In this paper we propose a new method for finding multiple subgoals that solves the existing drawbacks. We tested it in the three-room gridworld environment.

The experiment shows that our new method can solve the conventional methods' drawbacks. First, the

method can collect the trajectories that go through the particular state more than the positive trajectories. So, it can find subgoals more quickly. Second, it can find the state that may become an effective subgoal when the goal state changes. Third, the use of the average state visiting frequencies suppresses the erroneous selection of the states around the start state as the subgoals.

But our method has a drawback. The particular non-goal states are selected at random. If all the particular states happen to be located in the start room, any doorways will not be selected as the subgoals. To solve the drawback, there need some devises, for example, increasing the number of the particular states, or selecting each particular state to be distant from other particular states.

References

- [1] M.A.S.Kamal and J.Murata (2004), Reinforcement Learning for High Dimensional Problem with Symmetrical Actions. Proc. of 2004 IEEE Int. on Systems, Man, and Cybernetic: 6192-6197.
- [2] T. Tateyama, S. Kawata, T. Oguchi (2002), Automatic Generation of Macro-Actions using Genetic Algorithm for Reinforcement Learning, SICE2002 AUG5-7, Osaka.
- [3] Martin Stolle and Doina Precup (2002), Learning Options in Reinforcement Learning, SARA 2002, LNAI 2371, 213-223.
- [4] R. Matthew Kretchmar, Todd Feli, Rohit Bansal (2003), Improved Automatic Discovery of Subgoals for Options in Hierarchical Reinforcement Learning, Journal of Computer Science & Technology, Vol.3-No.2.
- [5] Özgür Şimşek, Alicia P. Wolfe, Andrew G. Barto (2005), Identifying Useful Subgoals in Reinforcement Learning by Local Graph Partitioning, the Twenty-second International Conference on Machine Learning, 816-823.
- [6] Shie Mannor, Ishai Menache, Amit Hoze, Uri Klein (2004), Dynamic Abstraction in Reinforcement Learning via Clustering, twenty-first International Conference on Machine Learning, 71-77.

Temporal difference approach in linearly-solvable Markov decision problems

Burdellis, M.A.P. and Ikeda, K.

*Nara Institute of Science and Technology, Grad. School of Information Science,
A606, 8916-5 Takayama, Ikoma, NARA, 630-0192, Japan
(Tel : 81-743-72-5984; Fax : 81-743-72-5989)
(mauricio-b@is.naist.jp)*

Abstract: Todorov has recently introduced a class of linearly-solvable MDPs (LSMDPs) which greatly simplifies reinforcement learning. By attending some specific conditions, the problem of choosing optimal actions (sequential decision making) can become linear, and then be solved in closed-form. A similar method to temporal difference learning (TD learning) for this class of MDPs has also been introduced, and is called Z-learning. In this work we present the results of simulations using Z-learning to solve a navigation problem of a virtual agent in a grid world, in which physical properties of the system (Newtonian mechanics) were introduced in the MDP model in the definition of the passive dynamics probability distribution, which is crucial in the theory. Those MDPs were solved both in closed-form and using Z-learning. In all experiments, the approximation errors of Z-learning consistently decreased with the increase in the number of simulation steps.

Keywords: Linear Bellman Equation; Reinforcement Learning.

I. INTRODUCTION

The Reinforcement learning (RL) approach to Machine Learning is a technique to learn how to make decisions in order to achieve a desired goal. In RL, the model does not include the presence of a supervisor, and the agent must learn by trial and error, interacting with the environment and observing a reward (or cost) signal [1]. Examples of possible applications of RL include: playing board games like chess, checkers or “tic-tac-toe”; and a nervous system generating muscle activations to maximize movement performance [2].

RL problems are usually defined on a discrete-time Markov decision process (MDP) with stochastic dynamics. Recent work [3] has presented a class of linearly-solvable MDPs, which greatly simplify the solution of reinforcement learning problems. Z-learning is a temporal-difference approach to the RL problem, which takes advantage of this class of MDPs, and presents faster convergence than traditional RL methods (e.g. Q-learning) [3] [2]. The present work has the motivation of including Newtonian mechanics effects (inertia and collisions) in the passive dynamics probability distribution of the linearly-solvable MDP used for Z-learning.

II. LINEARLY-SOLVABLE MARKOV DECISION PROCESSES (LSMDP)

Let us denote the state of the environment in a discrete time instant t as x_t . If this state signal retains all relevant information for the decision, it is said to have the “Markov property”, and

$$\Pr(x_{t+1} | x_t) = \Pr(x_{t+1} | x_t, x_{t-1} \dots). \quad (1)$$

This means that the history of past states has no influence on the probability of the next state. A reinforcement learning task that satisfies the Markov property is called a Markov decision process (MDP) [1] [4].

A particular finite MDP is defined by: a set of possible states X , a set of possible actions U , state transition probabilities $p(x_{t+1}|x_t, u_t)$ (which mean the probability that the next state is state x_{t+1} when the current state is state x_t and action u_t is taken), and immediate cost $l(x_{t+1}|x_t, u_t)$ for being at state x_t , taking action u_t and having a transition to state x_{t+1} .

The reinforcement learning agent’s sole objective is to minimize the total accumulated cost it receives in the long run [1] [2]. The “cost-to-go” function (or “value” function) of a state (denoted $v(x)$) is defined as the expected total cost the agent accumulates starting from that state, and following the optimal policy thereafter.

The cost-to-go (or “value”) function is the only solution to its Bellman equation [1] (refer to section III for details). This solution can be obtained by using Dynamic Programming (DP), but this can be time-consuming due to the explosion of unknown variables.

Recent work [3] has introduced a class of MDPs which greatly simplifies reinforcement learning. By attending some specific conditions, the Bellman equation of the MDP becomes linear, and its solution can be obtained in closed-form. The conditions are as follows [2]:

In the original MDP framework, the agent specifies discrete actions $u \in U$. The probabilities of state transitions starting from the current state $x \in X$ depend on the action u taken at that state. In other words, the probability of transition from a state $x \in X$ to a state $x' \in X$ is given by $p(x'|x, u)$.

In LSMDPs, however, the agent can specify the transition probabilities directly. In other words, there are no discrete actions u nor the set of actions U . Instead, the agent can directly specify the probability of transition from the current state $x \in X$ to any possible future state $x' \in X$, without the existence of discrete actions. These probabilities will be represented by using the letter u and therefore $p(x'|x, u)$ becomes $u(x'|x)$ [2].

Another necessary condition is the definition of a probability distribution called “passive dynamics”, denoted $p_d(x'|x)$, which corresponds to the behavior of the system in the absence of controls [2].

The total cost incurred in a state transition will be defined as follows [2]:

$$l(x, u) = q(x) + KL(u(\cdot|x) \| p_d(\cdot|x)) \quad (2)$$

Where $q(x)$ is called “state-cost” (which depends only on the state, therefore representing how undesirable a state is) and

$$KL(u(\cdot|x) \| p(\cdot|x)) \equiv E_{x' \sim u(\cdot|x)} \left[\log \frac{u(x'|x)}{p_d(x'|x)} \right] \quad (3)$$

is the Kullback–Leibler (KL) divergence between the controlled state transition distribution and the passive dynamics. This measures how “different” these distributions are from one another, and is called “action cost” [2].

The last condition is that $u(x'|x)=0$ when $p_d(x'|x)=0$, in order to keep the KL divergence well-defined and avoid impossible state transitions [2].

III. Z-LEARNING

When the passive dynamics distribution is known, as well as all the states and their respective state costs, then the problem of obtaining the cost-to-go function $v(x)$ can be solved using dynamic programming and the Bellman equation. The Bellman equation expresses the relationship between the cost-to-go of state and the expected cost-to-go of the next state:

$$v(x) = \min_u \{ l(x, u) + E_{x' \sim p(\cdot|x, u)} [v(x')] \} \quad (4)$$

where

$$E_{x' \sim p(\cdot|x, u)} [v(x')] \equiv \sum_{x'} p(x'|x, u) v(x') \quad (5)$$

In LSMDPs, the Bellman equation can be expressed as [2]:

$$z(x) = e^{(-q(x))} \sum_{x'} p(x'|x) z(x'), \quad (6)$$

where

$$z(x) \equiv e^{(-v(x))} \quad (7)$$

is called the “desirability function” of a state. This Bellman equation (6) is linear in z .

Equation (6) can be written in vector notation, by enumerating the states from 1 to n , representing $z(x)$ and $q(x)$ as column vectors \mathbf{z} and \mathbf{q} , and representing $p(x'|x)$ as a matrix \mathbf{P} (where the row-index corresponds to x and the column-index corresponds to x') [2]. By partitioning \mathbf{z} , \mathbf{q} and \mathbf{P} according to terminal and non-terminal states (using index N for non-terminal and T for terminal), equation (6) becomes [2]:

$$(\text{diag}(\exp(q_N)) - \mathbf{P}_{NN}) \mathbf{z}_N = \mathbf{P}_{NT} \exp(-q_T) \quad (8)$$

where “diag” transforms vectors into diagonal matrices. By acknowledging that $v(x) = q(x)$ at terminal states, the unknown \mathbf{z}_N (vector of desirabilities at the non-terminal states) can be calculated by using matrix factorization or an iterative linear solver [2].

When the state costs and passive dynamics are not known, then simulations must be made in order to solve the problem of estimating the cost-to-go function by using reinforcement learning.

Z-learning is a temporal-difference-like method which takes advantage of the linear class of MDPs to

achieve faster convergence than traditional reinforcement learning methods [2].

As in traditional TD learning methods, initial estimates are constantly updated until convergence is obtained. The Z-learning update formula is as follows [2]:

$$z_{upd}(x_t) \leftarrow (1 - \eta_t) z_{cur}(x_t) + \eta_t \exp(-q_t) z_{cur}(x_{t+1}) \quad (9)$$

Where $z_{upd}(x_t)$ is the updated estimate of $z(x_t)$, $z_{cur}(x_t)$ is the current estimate of $z(x_t)$, $z_{cur}(x_{t+1})$ is the current estimate of $z(x_{t+1})$, q_t is the state cost of state x_t , and η_t is a learning rate which decreases over time.

IV. MODELING NEWTONIAN MECHANICS EFFECTS

In the present work two Newtonian mechanics effects were modeled in the passive dynamics probability distribution (which is usually defined simply as “random walk”): inertia and collisions. These Newtonian mechanics effects were modeled and simulated in a 2-dimensional “grid-world” (10x10 size, with obstacles - Fig.1). The goal of the agent is to find the goal position, while avoiding the obstacles on the path.

Initially, a few difficulties have emerged from modeling the state signal in the grid world as the position of the learning agent. In order to model inertia, it is necessary to know the current and the previous position of the agent. If the state signal contains only the information on the current position, then it is necessary to know the current and the previous state in order to model the passive dynamics, and this would violate the “Markov property” (1).

Also, in order to model collisions with obstacles and walls, the agent would originally need to be able to take discrete actions of movement in the direction of the wall or obstacle, and this would violate one of the necessary conditions to have a LSMDP.

In order to overcome these two difficulties, the state signal was modeled to include information of position pairs: the current and the previous position.

A simple model of inertia was created by assigning a pre-defined “highest probability” value (denoted hp) to the passive dynamics probability of the next position in the current trajectory of the agent. The remaining adjacent non-obstacle positions equally share the probability $(1-hp)$ (Fig. 2).

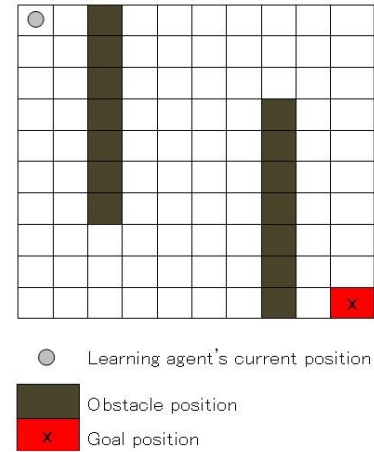


Fig.1. A two-dimensional “grid world” (size 10x10)

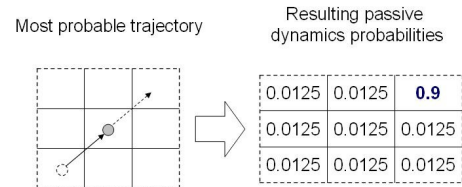


Fig.2. Modeling inertia (with $hp = 0.9$)

Two types of walls and obstacles were considered in order to model collisions: reflexive walls and obstacles (which reflect the normal components of impacts); and absorptive walls and obstacles (which absorb the normal components of impacts). The passive dynamics probability distribution is updated based on the current position and the previous position of the agent. When the agent's position is adjacent to a wall or obstacle, and the most probable trajectory (driven by inertia) is in the direction of the wall or obstacle, then the position that receives the highest probability value hp is the most likely position after a collision with this wall or obstacle, and the remaining possible positions share the remaining $(1-hp)$, as shown in Fig.3

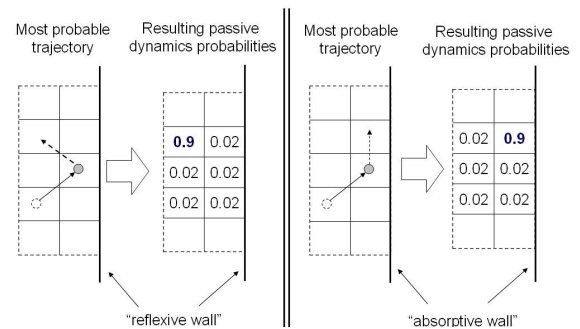


Fig.3. Collisions with a reflexive and an absorptive wall (with $hp = 0.9$)

V. COMPUTATIONAL EXPERIMENTS

The grid world shown in Fig.1 was solved analytically (using equation (8) [2]) and also using Z-learning. The state cost of every state (except for the goal state) is 1 (in order to penalize the agent for producing long trajectories) and 0 only at the goal state. Both reflexive and absorptive walls and obstacles were considered. In Z-learning, three different policies were used: policy equal to the passive dynamics; random walk policy; and ϵ -greedy policy (with $\epsilon=0.2$). When the applied policy differs from the passive dynamics distribution, importance sampling is required [2]: the last term in equation (9) needs to be multiplied by $p_d(x_{t+1}|x_t)/\hat{u}(x_{t+1}|x_t)$, where \hat{u} is the applied policy – in this case it is necessary to know the passive dynamics distribution p_d .

In order to measure the quality of the approximation of the cost-to-go function estimates produced by Z-learning, the approximation error (comparing the estimates with the correct values obtained in closed-form) was calculated using the formula:

$$Error = \frac{\sum_{i=1}^N |v(x_i) - v^*(x_i)|}{\sum_{i=1}^N v^*(x_i)} \quad (10)$$

where x_i represents the i^{th} state; N is the total number of states; $v(x)$ is the current approximation of the cost-to-go function (obtained by Z-learning) and $v^*(x)$ is the optimal cost-to-go function obtained analytically.

The results of the simulations can be seen in Fig.5 and Fig.6. In all experiments the learning rate η_t decays obeying the formula $\eta_t = c/(c+t)$ where t is the time step and c is a constant which was different for each case. The results for both models (the model with absorptive walls and obstacles; and the model with reflexive walls and obstacles) are very similar, indicating that the framework is considerably robust. When sampling from the passive dynamics, the error takes more steps to converge, because the inclusion of inertia in the passive dynamics makes this distribution less exploratory than random walk. The other two policies (random walk and ϵ -greedy) presented faster convergence, but their use requires access to p_d . In all cases the Z-learning approximation errors consistently decrease as the number of simulation steps increases.

Absorptive walls and obstacles

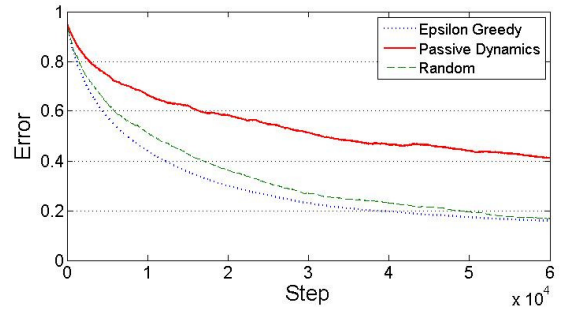


Fig.5. Z-learning approximation errors (absorptive walls and obstacles)

Reflexive walls and obstacles

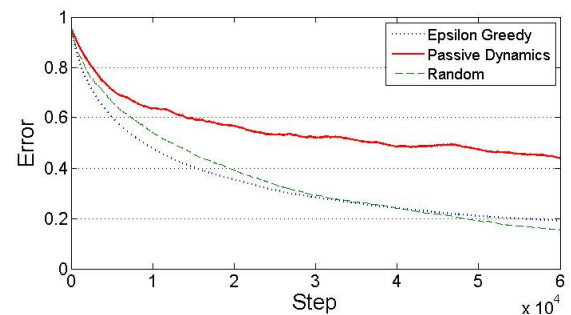


Fig.6. Z-learning approximation errors (reflexive walls and obstacles)

VI. CONCLUSION

The flexible framework of linearly-solvable MDPs allowed for simple models of Newtonian mechanics effects to be simulated in the passive dynamics probability distribution. The cost-to-go function of the resulting model was obtained both in closed-form and using Z-learning. The Z-learning algorithm was able to approximate the correct cost-to-go function, presenting errors which consistently decreased with the increase in the number of simulation steps.

REFERENCES

- [1] Sutton R S, Barto A G (1998). Reinforcement learning: An introduction. MIT Press.
- [2] Todorov E. (2009) Efficient computation of optimal actions. Proc Natl Acad Sci USA 106:11478–11483.
- [3] Todorov E (2006) Linearly-solvable Markov decision problems. Adv Neural Informatin Proc Syst 19:1369–1376.
- [4] Iwata K, Ikeda K, Sakai H (2006). The asymptotic equipartition property in reinforcement learning and its relation to return maximization. Neural Networks 19(1), 62–75.

Mutual learning of multi consciousness agent including the ego for autonomous vehicle

Mori Atsunori, Matsui Hirokazu

*Faculty of Engineering Mie Univ., Kurimamachiya1577,Z-city,Mie-pref,Japan
(Tel : 81-59-231-9802)
(mori@robot.mach.mie-u.ac.jp)*

Abstract: In this report, we propose a multi agent learning system for an intelligent robot control, based on the model of the human consciousnesses with including the ego. We pay attention to an intelligent learning process of human beings. We try to give high ability of learning to a robot by modeling roles of the human consciousnesses with including the ego. In almost ordinary methods, the instructions for learning are given only from outside of system. In the proposed method, the instructions are given not only from outside but also inside (from other agents in the system). Therefore, a robot can learn efficiently, since it uses more instructions than the ordinaries. The learning is more flexible, since agents learn while a learning agent and instructing agents exchange the roles by changing of environment. We verify experimentally that the proposed method is efficient by using an actual robot.

Keywords: Machine learning, Autonomous mobile robot, Multi-Agent system, Ego, Consciousness

I. Introduction

Autonomous robots are increasing such as cleaning robots and guard robots. It is requested that robots has more intelligence. Even if a human encounters a complex situation, he or she can adjust to the situation by learning. We pay attention to an intelligent learning process of human beings. Human beings has a feature that he/she can learn an environment while evaluating his/her decision by the ego. We try to give high ability of learning to robots by modeling the feature.

We think about the consciousness and the ego. But, none knows the mechanism of the consciousnesses and the ego yet. Moreover, the words are defined variously in various fields. For example, the words Consciousness and Unconsciousness are defined in each field as followings.

1. Psychology: Plural consciousness exists in a body. Unconsciousness is consciousness without the ego.
2. Philosophy: Consciousness is an ability to recognize. Unconsciousness is an ability to recognize oneself objectively.
3. Medicine: Consciousness is state that can feel stimulation to senses by activate working of a brain. Unconsciousness is state that cannot do them.
4. Upanishad philosophy: Consciousness are classified into 4 states. One is Unconsciousness.

In another field, they are defined as another. We take the idea of German psychologist Wundt. He analyzed human consciousness by internal perception, and

thought that the ego is the subject of consciousness. We model them for engineering based on the above psychological definition.

There are ordinary researches for the model of the consciousness. Minsky describes that a human intelligent behavior has been achieved by the interaction of hierarchized mind agents. Maeno proposed consciousness model that controlled by the ego for episode memory.

However, there is no general model for the consciousness including the ego. There are a few researches about above-mentioned. In less cases, human consciousnesses were actually applied to robot control. We define the consciousness including the ego as multi-agent system, and try to apply to mechanical learning.

There are the following as a research of multi-agent reinforcement learning. Wiering[1], Osada[2] improved the learning efficiency by hierarchically arranging an agents and setting an sub-goal in each hierarchy. Ono[3], Fujita[4] learns efficiently by limiting the range of a state in Q-learning used the partial state composed of an agent and another agent. In this report, we proposed a method that is modeled as multi-agent system based on the consciousness including the ego without the hierarchy, and verify that the proposed method is efficient for an actual robot by experiment.

II. Proposed Model

1. A definition of the consciousness and an ego

We define and model the human consciousness and the ego as follows. The model is regarded by the internal perception, and does not contradict the anatomy.

- (1) Number of consciousness is more than two in a body.
- (2) The human operation is caused by cooperating and competing of some consciousness.
- (3) The ego is only one.
- (4) The ego exists on the consciousness with the highest priority.
- (5) When the consciousness with the ego competes against another in resources, it uses the resources by priority, the another is stopped.
- (6) Only the consciousness with the ego can learn.
- (7) The consciousness with the ego learns with using results of other consciousnesses recognition.

2. Modeling of a consciousness and an ego

We treat the above-mentioned consciousnesses rules as multi agent system (Fig.1).

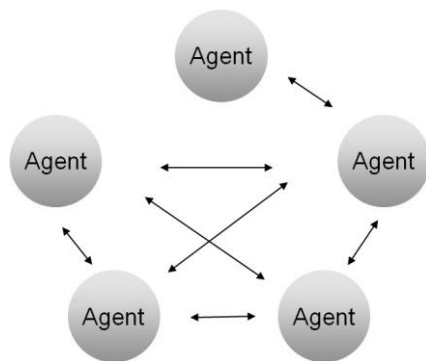


Fig.1 Proposed model

- (1) Each consciousness is treated as agent.
- (2) An agent is a data processor or a sensor with a priority and a condition for the running.
- (3) If an environment satisfies a condition for the running, an agent executes processing.
- (4) An agent has higher priority, if the agent is satisfied with the condition.
- (5) An agent receives instructions and the priority from other agents.
- (6) An agent uses only the instruction with the highest priority, when the instructions from other agents compete with each other.
- (7) Only an agent with high priority can learn.

- (8) When an agent learns, it uses recognition results of other agent.

III. Experiment

We verify experimentally that the proposed method is efficient. We select an image sensing and a body sensing for a mobile robot as agents that instruct and learn each other. Each agent estimates the current pose of the robot from each sensing data.

We use an actual mobile robot (MieC) for the experiment (Fig2).



Fig.2 Autonomous mobile robot MieC

The robot MieC has a camera as vision sensor, 4 touch switches as touch sensor and two crawlers as movable device.

The robot MieC is on a horizontal plane enclosed by vertical planes. Borders are between the horizontal plane and the vertical planes. Image sensing agent and body sensing agent find the distance from the robot to a border, respectively. Image sensing agent finds a border on an image by an appropriate threshold, and estimates 3-D pose of a border in the environment by transformation from image coordinate to robot coordinate. Body sensing agent finds the border under a vertical plane, if the robot MieC touches the plane. Otherwise, body sensing agent estimates the 3-D pose of a border by dead-reckoning with appropriate parameters.

In the future, each agent will be full built by the proposed framework, but currently, the Image sensing agent adjusts only the threshold, the body sensing agent adjusts only the dead-reckoning parameters.

The less accurately each agent recognizes the pose of a border, the higher priority it gets. For actual experiment, moving agent is added to the other agents image sensing and body sensing, but the agent doesn't learn nor instruct.

1. Learning in a case of clear recognition for image sensing agent

The image sensing agent could recognize a border in a situation (Fig.3 (b)). In other words, the image sensing

agent usually has lower priority than the body sensing agent. In the initial state, moving agent has higher priority than image sensing agent and body sensing agent. The body sensing agent doesn't know the pose of a border. The robot MieC might touch a vertical plane according to moving agent (Fig.3 (c)). And then the body sensing agent has higher priority than the others. The moving agent is stopped, and the body sensing agent is waked up and learns appropriate parameters from information of the image sensing agent (Fig.3 (d)). Concretely, the body sensing agent adjusts the dead-reckoning parameters while it is estimating the robot MieC self pose from the border pose found by the image sensing agent.

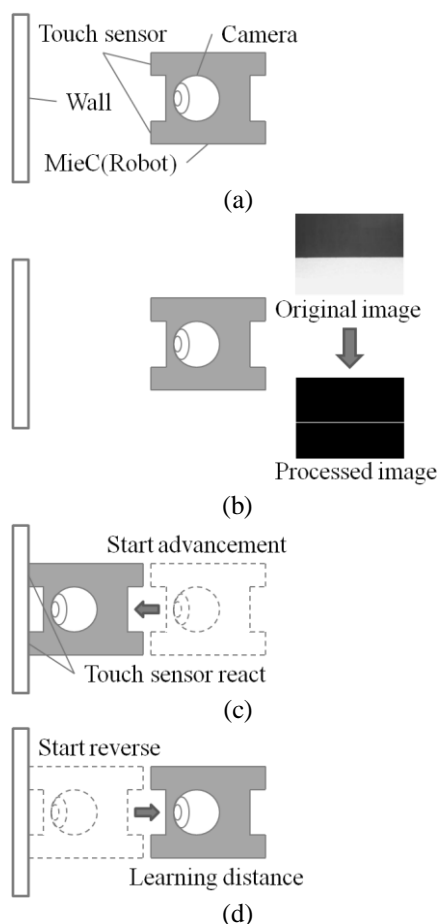


Fig.3 Learning of the body sensing agent

2. Learning in a case of hardly recognition for image sensing agent

The image sensing agent could not recognize a border in another situation (Fig.4 (e)). In other words, the image sensing agent usually has higher priority than the body sensing agent. The robot MieC might touch again a vertical plane according to moving agent (Fig.4 (f)).

And then the image sensing agent has higher priority than the others. The moving agent is stopped, and the image sensing agent is waked up and learns appropriate threshold from information of the body sensing agent with already adjusted dead-reckoning parameters. Concretely, the image sensing agent adjusts the threshold so that it can find the border at the border pose estimated by the body sensing agent (Fig.4 (g) (h)).

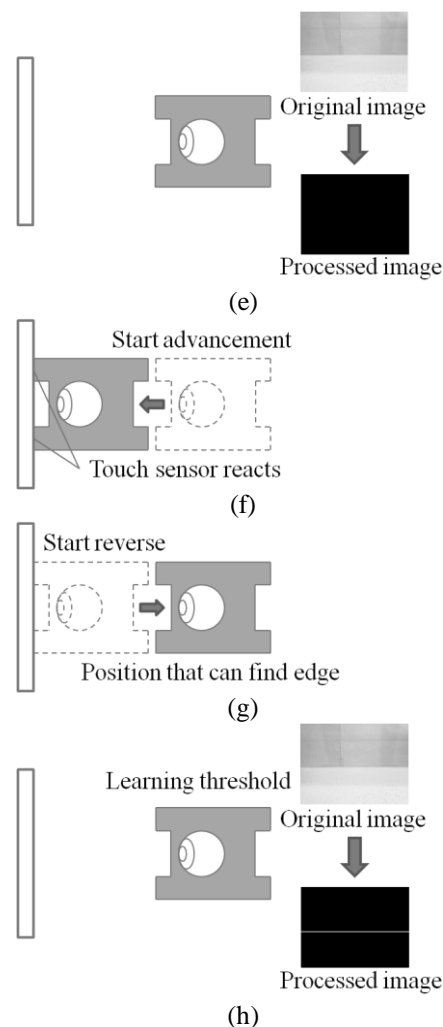


Fig.4 Learning of the image sensing agent

We experimented in the environment such as (Fig.5). In the left side (Fig.5), the image sensing agent can recognize the border easily, since the colors of the vertical and the horizontal planes are different clearly. In the upper side (Fig.5), it can hardly recognize the border, since the colors are similar. The robot MieC learned in the sequence of two above-mentioned environments.

By the above-mentions, we confirmed that two agents could learn cooperatively by the environment, and the proposed method was effective. (Fig.6) shows the pose of the robot MieC in 2-D coordinate system. (Fig.7)

shows learning and instructing state of the body sensing and the image sensing agents. We can confirm the following from (Fig.6) and (Fig.7). In the beginning, the body sensing agent was a learning agent, and learned from the image sensing agent as instructing agent. And then, the image sensing agent was a learning agent, and learned from the body sensing agent as instructing agent.

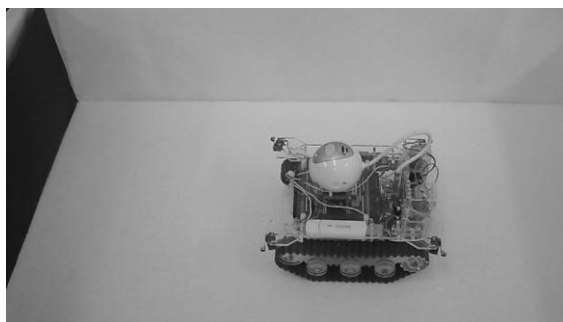


Fig.5 Environment of experiment

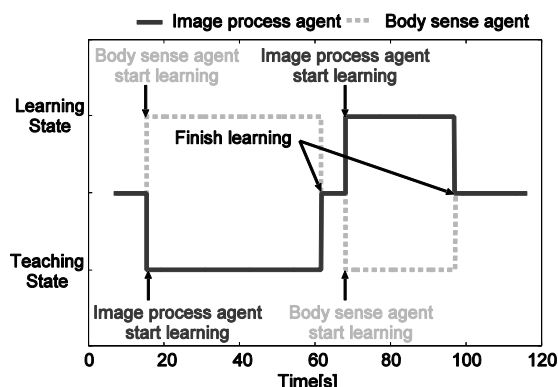


Fig.6 Result of agent's state

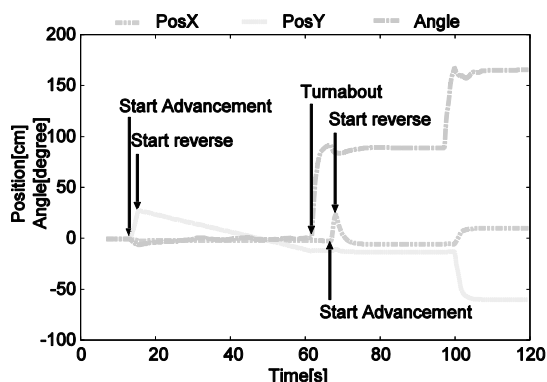


Fig.7 Result of robot's pose

IV. Conclusion

We proposed a learning model based on a mechanism of human learning that consists of consciousnesses including the ego defined by the psychology. We applied the proposed model to the actual robot MieC

developed in our lab.. Concretely, in the experiment, we selected two agents, the image sensing agent and the body sensing agent, and confirmed that the agents exchanged the roles of learner and instructor each other to change the environment by MieC's movement.

We expect that the proposed method can learn by less trial frequency than ordinary reinforcement learning, since the proposed method uses instruction not only from the outside but also from the inside. But currently, the proposed method has been programmed for only a part of environment. In the future, the proposed method is applied to larger environment to increase agent types, and to select an agent by environment, automatically.

Concretely, we prepare some templates of an agent. When a robot cannot adjust an environment, an agent is generated by selecting a template automatically. In the initial state, the agent's parameter is given at random. The agent adjusts parameter by learning. If it's cannot learning, a new agent is made by selecting another template. An agent is automatically generated by environment like the above-mentioned, and robot may be able to adjust to a complex situation.

REFERENCES

- [1] M.Wiering and J.Schmidhuver (1997), HQ-learning. Adaptive Behavior 6(2):219-246
- [2] H.Osada and S.Fujita (2005), CHQ:A Multi-Agent Reinforcement Learning Scheme for Partially Observable Markov Decision Processes. IEICE Trans. Inf. & Syst., Vol. e88-D No. 5:1004-1011
- [3] N.Ono O.Okeda (1996), Synthesis of Herding and Specialized Behavior by Modular Q-learning Animats. ALIFE V Poster Presentations:26-30
- [4] K.Fujita and H.Matsuno (2005), Multi-Agent Reinforcement with the Partly High-Dimensional State Space (in Japanese). IEICE D-I Vol. j88-D-I No. 4:864-872

Reinforced learning by using a learned results of a different form robot

Nobuo Shibata, Hirokazu Matsui

Kurimamachiya 1577 Tsu Mie
(Tel : 81-59-231-9802)
(shibata@eds.elec.mie-u.ac.jp)

Abstract: The reduction on the trial frequency is important for reinforcement learning under an actual environment. In this report, we propose a method that can learn an unknown environment efficiently by applying an already learned Q-table to another new learning. Concretely, an agent (Target agent) learns efficiently by using Q-table that a different from agent (Source agent) has learned at the same environment. The proposed method uses the two Q-tables of Source agent and Target agent and an action-translation-table (AT-table). The Q-table of Source agent has already been learned at the same environment. The AT-table is learned for the suitable mapping of actions between Source and Target agents by information of the stored state transition probabilities when Source agent learned. Concretely, when Target agent takes an action at a situation, the AT-table is learned so which action of Source agent is similar to the action of Target agent. We think that Target agent can learn the suitable action efficiently by using the previous proposed method (for learning efficiently by using dual Q-tables) with Target Q-table and the set of Source Q-table and the AT-table instead of dual Q-tables. We verify that the proposed method is effective in a simulation.

Keywords: Reinforcement learning

I. INTRODUCTION

The reduction on the trial frequency is important for reinforcement learning. We propose an efficient learning method for robots by using knowledge.

When human being walks, he stores them as knowledge, the relations between moving and change of viewing. When he drives a car, he learns efficiently the steering operation by using the stored knowledge in walking. But, he cannot drive a car by only using the knowledge, he must learn new change of viewing, that never happens in walking. We apply an efficient learning method of human being to the proposed learning method for robots. In ordinary research, to reuse the knowledge, a learning task is separated into the smaller tasks[1], or using multi-layered reinforcement learning system[2]. In this report, we propose an efficient learning method that reuses the knowledge learned by another robot without transformation of learning modules. The proposed method is an extended method from our previous proposed method "Reinforcement Learning with Self-Instruction by using dual Q-tables"[3]. We verify that the proposed method is effective in a simulation.

II. LEARNING WITH DUAL Q-TABLES

Here, we describe that the previous proposed method(the dual learning method)[3] can learn the environment, earlier and in more detail by using the dual Q-tables.

1. Algorithm

The dual learning method uses two Q-tables (Fig.1),

for experience storing and for knowledge storing. We thought experience and knowledge as followings. An experience is a collection of instances in an environment, so we use the whole space of the environment for the Q-table of experience. A knowledge is a compression of instances in an environment, so we use a compressed space (partial space) of the environment for the Q-table of knowledge. The smaller Q-table (for the knowledge storing) makes the learning finish earlier. The larger Q-table (for the experience storing) makes the learning be in more detail.

The dual learning method consists of repeated steps, the first step is that the action is selected by using the Q-table with lower information entropy, the second is that the two Q-tables are updated at the same time by the action. This research aims at the method that learns an environment earlier and in more detail with using dual Q-tables.

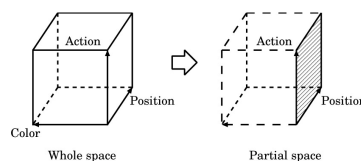


Fig.1. Q-tables for the partial space and the whole space

2. Materialization

Here, we materialize the above-mentioned concept to the procedures, as shown in Fig.2.

(1) Init dual Q-tables

The agent initializes the two Q-tables for the partial and for the whole Q-table.

(2) Select Q-table

The agent selects the Q-table with lower information entropy $H(s)$, out of the partial and the whole Q-table, that is driven by Eq.1.

$$H(s) = \sum_{a \in A} p(a|s) \log_2 \frac{1}{p(a|s)} \quad (1)$$

where $p(a|s)$ is a probability of selecting action a at state s , that is defined by Eq.2. We consider that the Q-table to be so effective, that the information entropy of Q-table is lower.

(3) Select Action (for both Q-tables)

The agent selects an action by the Boltzmann selection used generally in Q-learning. The selection probability of the action a is shown by Eq.2.

$$p(a|s_k) = \exp\left(\frac{Q(s_k, a)}{T}\right) / \sum \exp\left(\frac{Q(s_k, a')}{T}\right) \quad (2)$$

where $p(a|s_k)$ is probability of selecting action a on state s_k , k is times, T is temperature.

(4) Update Q-table (for both Q-tables)

Each Q-value is updated by Eq.3. The equation is used generally when updating Q-value.

$$Q(s_k, a_k) \leftarrow (Q(s_k, a_k) + \alpha(r + \gamma \max_a Q(s_{k+1}, a) - Q(s_k, a_k))) \quad (3)$$

where, k is time, s_k is state at time k . $Q(s, a)$ is Q-value at state s and action a . $r(s, a)$ is reward decided by each pair of s and a . α is learning rate and γ is discount rate.

3. Result of simulation

We show results of average of the 1000 trials simulation in Fig.3. Fig.3(a) is a result in the case that partial Q-table is 100% effective, In other words, the states component of partial Q-table can distinguish the needed states by 100%. The case of Fig.3(b) and the (c) are 50% and 0% effective, respectively. The ordinary method uses only the partial Q-table or only the whole Q-table. As the results of (a)(b)(c) three cases, the dual learning method is not less effective than the ordinaries in any case.

III. PROPOSED METHOD

We propose a learning method that reuses the already stored Q-table and stored Environment table for another agent with different structure by extending the dual learning method. We call the previous learning

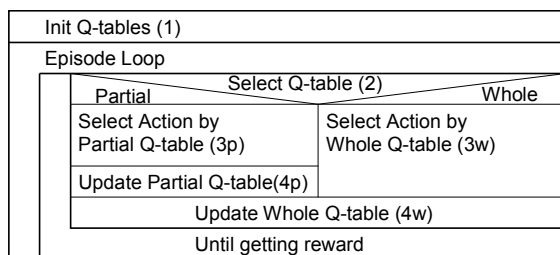


Fig.2. NS chart of the previous proposed method

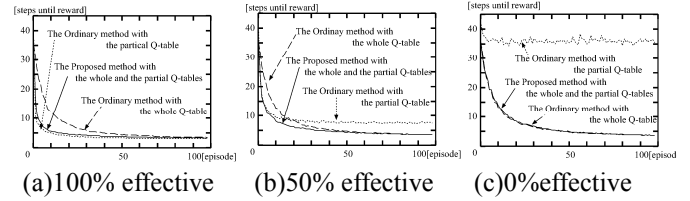


Fig.3. Results of computer simulation

agent, Source agent, and the current learning agent, Target agent. For the proposed method, we assume that the agent(Target) can access a result, that another agent(Source) with a different structure, learned in the same environment for the same goal.

1. Algorithm

In the proposed method, Target agent has four tables, two information tables and two learning tables. One information table is the already stored Q-table for Source agent. The other is the already stored Environment table(Env-table), that is the probability table of state transition by the state-action of Source agent. One learning table is an action-translation-table(AT-Table) for associating the actions of Source agent with the actions of Target agent. The other is a new Q-table for state and action of Target agent.

In the proposed method, the action of Target agent by a state is selected in two ways. In one way, the action for Source by the state is selected by using already stored Q-table for Source agent, and then the action for Source is translated to the action for Target by using AT-Table. By these steps, the action for Target agent by the state is selected. In this way, the learning space cannot be expressed perfectly for Target, but it is small. In the other way, the action by the state is selected directly by using a Q-table only for Target agent.

We apply the dual learning method mathematically to the learning of the AT-table and Target Q-table as smaller Q-table and larger Q-table. We expect as similar to the dual learning, that only by the first way Target agent learn more roughly and earlier, only by the second way it learn later and in more detail. But applying the previous, Target agent can learn earlier in more detail. In the proposed method, in order to learn more earlier, the agent can be evaluated by each action step, adding an evaluation by the Env-table to the first way.

2. Materialization

Here, we materialize the concept in the above-mentioned to the procedures of the proposed method, as shown in Fig.5.

(a) Learning of the Source Agent (the previous learning)

Source agent learns a suitable action at the environment and stores the state transition probabilities to Env-

table at each combination of action, current state and next state. The Env-table is shown in Fig.6(a).

(b) Learning of the Target Agent(the main learning)

(1) Init Target Q-table and Load Source Q-table and Env-table

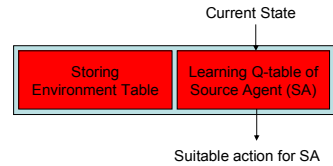
Target agent initializes the Q-table of Target agent to set each Q-value to an init value and load the AT-table and the Env-table from the previous learned data. The values of the AT-table and the Env-table are fixed (shown by the hatching areas in Fig.4(b)).

(2) Select way

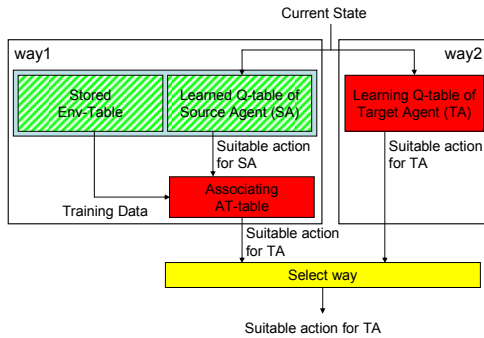
Target agent selects the way with lower information entropy H_{way1} or H_{way2} , out of the two ways, that are driven by Eq.4, Eq.5, Eq.6, Eq.7 and Eq.8.

$$H_{target-Q}(s) = \sum_{a_t \in A_t} p(a_t | s) \log_2 \frac{1}{p(a_t | s)} \quad (4)$$

$$H_{source-Q}(s) = \sum_{a_s \in A_s} p(a_s | s) \log_2 \frac{1}{p(a_s | s)} \quad (5)$$

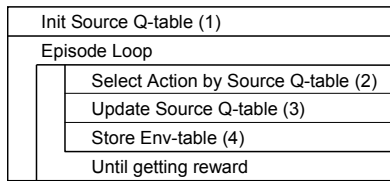


(a) Learning of the Source Agent

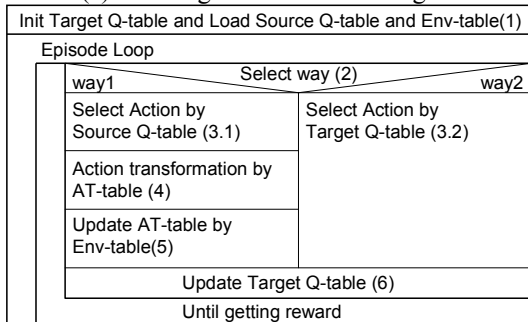


(b) Learning of the Target Agent

Fig.4. Block diagram of the proposed method



(a) Learning of the Source Agent



(b) Learning of the Target Agent

Fig.5. NS chart of the proposed method

$$H_{AT-table}(a_s) = \sum_{a_t \in A_t} p(a_t | a_s) \log_2 \frac{1}{p(a_t | a_s)} \quad (6)$$

$$H_{way1}(s) = H_{source-Q}(s) + H_{AT-table}(a_s(s)) \quad (7)$$

$$H_{way2}(s) = H_{target-Q}(s) \quad (8)$$

where a_t is an action of Target agent, a_s is action of Source agent, $p(a | s)$ is probability of selecting action a at state s , that is defined by Eq.2. $p(a_t | a_s)$ is probability of selecting action a_t at already selected action a_s , that is stored in the AT-table. We consider that the way to be so effective, that the information entropy of the way is lower. Function $a_s(s)$ in Eq.7 is represented for that a_s is decided by s (selected by using Boltzmann selection with Source Q-table).

(3) Select Action (for both Q-tables)

Target agent selects an action by the Boltzmann selection. The selection probability of action a is shown by Eq.3.

(4) Action Translation by AT-table

Action a_s selected by Source agent Q-table is translated to action a_t by using the AT-table. Action a_t corresponding to action a_s is selected by the Boltzmann selection with AT-table. The selection probability of action a_t is driven by Eq.9.

$$p(a_t | a_s) = \exp\left(\frac{AT(a_s, a_t)}{T_{AT}}\right) / \sum \exp\left(\frac{AT(a_s, a_t)}{T_{AT}}\right) \quad (9)$$

where $p(a_t | a_s)$ is probability of selecting action a_t at already selected action a_s , k is times, T_{AT} is temperature.

(5) Update AT-table

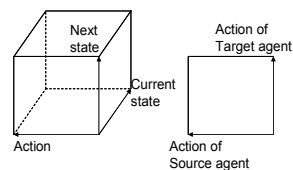
The AT-table is learned for the associating of actions between Source and Target agents by Env-table. AT-table is updated by Eq.10.

$$AT(a_{s_k}, a_{t_k}) \leftarrow (\alpha_{AT} AT(a_{s_k}, a_{t_k}) + \gamma_{AT} p(s_{k+1} | s_k, a_{s_k})) \quad (10)$$

where $p(s_{k+1} | s_k, a_{s_k})$ is state transition probability to state s_{k+1} by pair of action a_{s_k} and state s_k , α_{AT} and γ_{AT} are such that $0 \leq \alpha_{AT} < 1$ and $0 \leq \gamma_{AT} < 1$.

(6) Update Q-table

Each Q-value is updated by Eq.3.



(a) Env-table (b) AT-table
Fig.6. Env-table and AT-table

IV. SIMULATION

In this chapter, we verify that the proposed method is effective in a simulation.

1. Environment

Experiment environment is shown in Fig.7. It consists of an agent, a goal and an object in a field(100[cm]x50[cm]). In the experiment, the agent learns the task to carry the object to the goal area, given reward at the case that the object carried into the goal. We define an episode to be time until getting reward. The initial pose of the agent, the object and the goal are shown in Fig.7. An initial pose of agent is selected randomly from two pose shown in Fig.7 at each episode. The pose of agent is changed 0.5[cm] and 0.1[deg] per move respectively. We define one step to be time until the current state is changed to next state. The agent keeps taking the same action until the current state is changed.

2. Action set and State set

Action set: The actions of Source and Target agents are shown in Fig.8. Source agent has 4 actions “go forward”, “go backward”, “pivot turn right” and “pivot turn left” and Target agent has 6 actions “go forward”, “go backward”, “turn right (forward)”, “turn left (forward)”, “turn right (backward)” and “turn right (backward)”.

State set: A state set consists of the position states of goal and object. The state set has 160 states that are each position and size of the object and the goal. The object state has 6 states, combinations of positions(left, center, or right) and sizes(large or small). The goal state has 18 states, combination of positions(left, center, or right), sizes(large or small) and directions(left, front, right). In addition to these 78 states, we add states that only the object or only the goal view or lose.

3. Result

The results of the simulation are shown in Table.1 and Fig.9. Each graph is the average of 1000 trials. In these results, all the values of Q-tables, AT-table and Env-table are initialized to 0.0 and the parameters for Q-learning and AT-table mapping are set to following.

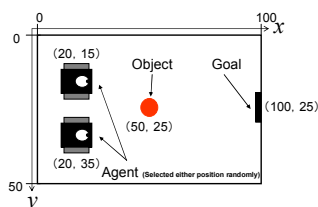
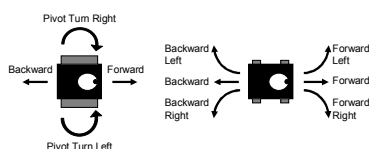


Fig.7. Experiment environment



(a) Source agent (b) Target agent
Fig.8. Actions of the Source and Target agents

The reward r is set to 1.0, the learning rate α is set to 0.4, and the discount rate γ is set to 0.9, the temperature T of Boltzmann selection is set to 0.05, α_{AT} is set to 0.9, γ_{AT} is set to 0.35, T_{AT} is set to 0.5.

In Table.1, high value is represented for correct mapping between Source and Target action pair. For example, “Forward Right” of Target agent allocated to “Pivot turn Right” of Source agent. So in Fig.9, the method with Source agent Q-table and AT-table (way1) can learn earlier than the method with Target agent Q-table (way2). But way1 cannot learn in detail since the pair of Q-table of Source agent and AT-table cannot express all the corresponding action to Target agent. Way2 can learn in detail but needs a lot of time. However, the proposed method (way1 and way2) can learn the environment earlier and in more detail by using Source and Target Q-table and AT-table.

Table 1. Result of AT-table

Source \ Target	Forward	Backward	Pivot turn Right	Pivot turn Left
Forward	2.573	0.172	0.517	0.150
Backward	0.175	1.761	0.469	0.405
F Right	0.874	0.405	1.758	0.002
F Left	0.652	0.339	0.028	1.292
B Right	0.451	0.645	0.002	1.189
B Left	0.687	0.711	1.848	0.003

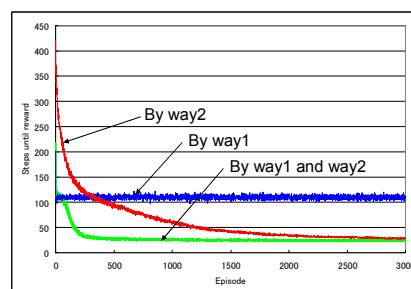


Fig.9. Results of computer simulation

V. CONCLUSION

We verified that the proposed method can learn more efficient than the MTQ and MSQAT in simulation.

In the future, we will apply the proposed method to an actual environment and verify that the proposed method can learn efficiently in an actual environment.

REFERENCES

- [1] Akihiko Yamaguchi, Norikazu Sugimoto, Mitsuo Kawato (2009): Reinforcement Learning with Reusing Mechanism of Avoidance Actions and its Application to Learning Whole-Body Motions of Multi-Link Robot (in Japanese), Journal of the Robotics Society of Japan Vol.27 No.2, pp.209-220
- [2] Yasutake Takahashi, Minoru Asada (2003): State-Action Space Construction for Multi-Layered Learning System (in Japanese), Journal of the Robotics Society of Japan Vol.21 No.2, pp.164-171
- [3] Osamu NISHIMURA, Hirokazu MATSUI, Chieko HIOKI, et al (2006): Reinforcement Learning with Self-Instruction by using dual Q-tables, AROB 11th

The acquisition of sociality by using Q-learning in a multi-agent environment

Yasuo Nagayuki

*Department of Social and Management Studies, Otemae University
2-2-2 Inano, Itami, Hyogo 664-0861, Japan
nagayuki@otemae.ac.jp*

Abstract: In multi-agent environments, it is important that the agents have the "sociality". In this article, I propose a reinforcement learning framework, which is based on Q-learning, that the agent is able to learn the "sociality" in a multi-agent environment. In this framework, the agent learns to ignore the near goal, which is left for the other agent, and go toward the farther goal, if the agent judges that the decision is effective from the social viewpoint, but not from the agent's greedy viewpoint.

Keywords: multi-agent environment, reinforcement learning, acquisition of sociality, Q-learning

1. INTRODUCTION

It is hard that the agent, which learns by using a reinforcement learning [1] algorithm, learns to go toward the farther goal rather than the near goal. If the values of the reward obtained by reaching each goal are not different, it is all the more.

In the case that the environment the agent faces is a single-agent environment, the agent should not ignore the near goal because the agent should be greedy for the environment, that is, the near goal. If the agent learns to go toward the farther goal rather than the near goal in this case, the reinforcement learning algorithm must have some defect.

In the case that the environment the agent faces is a multi-agent environment [2], on the other hand, there are the situations that the agent should ignore the near goal, which is left for the other agent, and go toward the farther goal. If the agent's decision is not effective from the agent's greedy (selfish) viewpoint, but effective from the social (global) viewpoint, it is called that the agent has the "sociality". In multi-agent environments, it is important that the agents have the "sociality".

However, it is difficult that the agent applied the reinforcement learning algorithms proposed so far learn the "sociality" in multi-agent environments, because the reinforcement learning algorithms are designed that the agent learns greedy policies for the environment.

In this article, I propose a reinforcement learning framework, which is based on Q-learning [3], that the agents learn the "sociality" in a multi-agent environment. In this framework, the agents learn to ignore the near goal and go toward the farther goal, if the agent judges that the decision is effective from the social viewpoint.

2. LEARNING TASK

In this study, I prepared a two-agents problem as a task. This task is designed that one agent should learn to ignore the near goal and go toward the farther goal from the social viewpoint, and the other agent should learn to go toward the near goal from the social and greedy viewpoint.

- In a 4×7 grid space, two agents exist and there are two goal positions as shown in Fig.1.
- At each episode, the initial positions of the agents are the positions shown in Fig.1.
- At a discrete time step in an episode, the agents synchronously execute one out of five actions: moving up, down, left, or right from the current position, or staying in the current position. But, the agents are not able to execute the actions that the agents go out of the grid space. For example, in Fig.1, the agent A1 is not able to execute the two actions: moving down and right.
- The agents are able to look over the whole grid space.

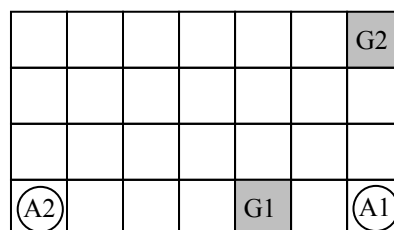
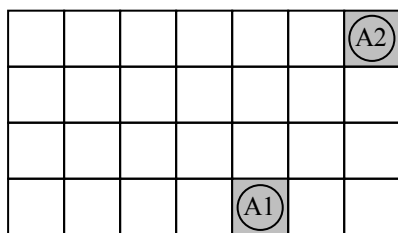
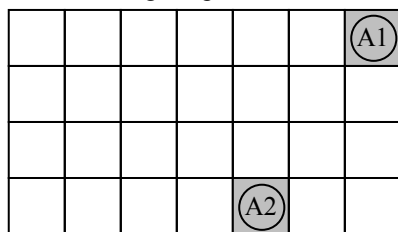


Fig.1. Grid space of learning task: A1 and A2 are the agents, and G1 and G2 are the goal positions for the agents.



(a) Goal situation-1: the agent A1 reaches the goal position G1 and the agent A2 reaches the goal position G2.

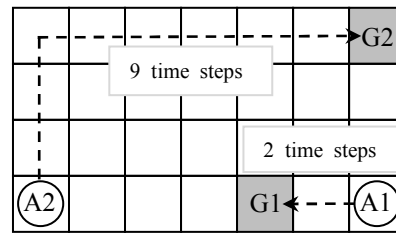


(b) Goal situation-2: the agent A1 reaches the goal position G2 and the agent A2 reaches the goal position G1.

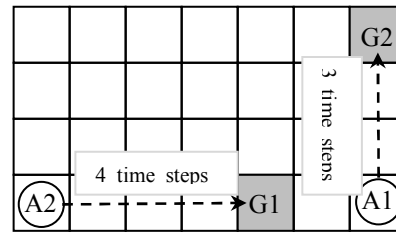
Fig.2. Goal situations of this learning task

- When an agent reaches a goal position (G1 or G2), the agent obtains a positive reward. The value of the reward is 1.0 regardless of G1 or G2.
- The reward of each goal position disappears when an agent arrives at the goal position. Therefore, in each goal position, the reward is given for only one agent.
- The global goal as this task is that each of two agents reaches either of the two goal positions. But, the goal positions two agents reach must be different. That is, there are two goal situations in this task as shown in Fig.2 (a) or Fig.2 (b). When a goal situation is achieved, the episode ends.

Here, I consider which goal situations are more effective if each agent goes toward its goal position from its initial position with the shortest pass in this task. In the case of the goal situation-1 shown in Fig.2 (a), the agent A1 is able to reach the goal position G1 with 2 time steps, and the agent A2 is able to reach the goal position G2 with 9 time steps as shown in Fig.3 (a). Therefore, the number of the shortest time step that the goal situation-1 is achieved is 9. It is remarked that the agent A1 is waited until the agent A2 reaches the goal position G2. In the case of the goal situation-2 shown in



(a) An example of shortest passes for the agents until achieving the goal situation-1.



(b) An example of shortest passes for the agents until achieving the goal situation-2.

Fig.3. Shortest passes until achieving each goal situation for each agent from the initial positions.

Fig.2 (b), on the other hand, the agent A1 is able to reach the goal position G2 with 3 time steps, and the agent A2 is able to reach the goal position G1 with 4 time steps as shown in Fig.3 (b). Therefore, the number of the shortest time step that the goal situation-2 is achieved is 4.

As above-mentioned, if each agent goes toward its goal position with shortest pass, the goal situation-2 is more effective than the goal situation-1 because the number of the time step until achieving the goal situation is shorter. However, in order to achieve the goal situation-2, the agent A1 must give up going toward the near goal position G1, which is left for the agent A2.

3. MDP AND Q-LEARNING

The reinforcement learning framework proposed in this article is based on Q-learning [3]. Q-learning was originally defined to deal with Markov decision processes (MDPs) [4].

3.1. MDP

An MDP is defined by a set of finite states of the environment, S , and a set of finite actions, A . At each time step, an agent observes a state $s (\in S)$, executes an action $a (\in A)$ and receives a reward r from the

environment. The state transition of the environment is defined by a transition probability function:

$$P_{s'}^a = \Pr(s'|s, a) \quad (1),$$

which is the probability that the environment changes to a new state $s' (\in S)$ when the agent executes the action a in the state s . The reward r is a variable, possibly probabilistic, which depends only upon the current state s and action a .

3.2. Q-learning

Q-learning [3] is an incremental reinforcement learning method. According to Q-learning, the agent selects an action based on an action-value function (called the Q-function), $Q(s, a)$, which is a scalar function and represents the value that the agent executes the action a at the state s . The Q-function is updated using the agent's experiences. The learning flow is as follows:

1. For the current state s , the agent executes an action $a_i (\in A)$ with the probability:

$$\pi(a_i | s) = \begin{cases} \frac{1-\epsilon}{h} + \frac{\epsilon}{|A|} & (a_i = \operatorname{argmax}_b Q(s, b)) \\ \frac{\epsilon}{|A|} & (\text{otherwise}) \end{cases} \quad (2),$$

where $\pi(a_i | s)$ represents the probability that the agent executes the action a_i in the state s , and $|A|$ is the number of the element of the action set A , and $\epsilon (\in [0, 1])$ is a parameter for determining the randomness of the action selection, and h is the number of the action $b (\in A)$, with which the value of the Q-function $Q(s, b)$ is max.

2. The agent executes the action a selected in step 1. The environment changes to a new state s' according to $P_{s'}^a$, and a reward r is given from the environment. The Q-function $Q(s, a)$ is updated as follows:

$$Q(s, a) \leftarrow (1-\alpha)Q(s, a) + \alpha(r + \gamma \max_{a' \in A} Q(s', a')) \quad (3),$$

where $\alpha (0 \leq \alpha < 1)$ is a parameter called the learning rate, and $\gamma (0 \leq \gamma \leq 1)$ is a parameter called the discount factor.

3. If the new state s' satisfies a terminal condition, then the episode ends. Otherwise, let $s' \rightarrow s$ and go back to step 1.

4. MULTI-AGENT REINFORCEMENT LEARNING

4.1. Point of problem

Here, I consider that each agent in the task shown in section 2 learns its policies by using reinforcement learning. It is remarked that the goal situation-2 (shown in Fig.2 (b) or Fig.3 (b)) is more effective than the goal situation-1 (shown in Fig.2 (a) or Fig.3 (a)) from the global (social) view point.

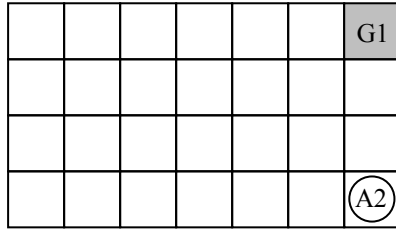
If the agents learn its policy by using the general reinforcement learning algorithms proposed so far (like Q-learning), it is unfortunately expected that the learning converges to the goal situation-1. The reason is that the agent applied the reinforcement learning algorithms proposed so far is greedy for the nearer goal. Therefore, it is expected that the agent A1 does not give up going toward the near goal position G1. Even if the agent A2 aims at reaching the nearer goal position G1 with shortest time step (4 time steps), the agent A1 reaches the goal position G1 (with 2 time steps) earlier than the agent A2. Furthermore, because the positive reward of the goal position G1 disappears after the agent A2 reaches the goal position G1, the agent A2 inevitably goes toward another goal position G2. That is, it is difficult that the agent applied the reinforcement learning algorithms proposed so far learns the "sociality" in a multi-agent environment as shown in section 2.

In this article, I propose a reinforcement learning framework, which is based on Q-learning [3], that the agents are able to learn the "sociality" in a multi-agent environment as shown in section 2.

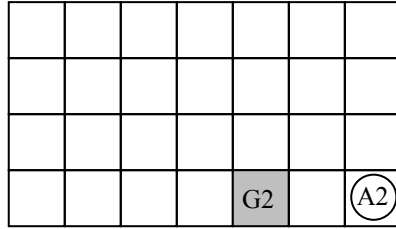
4.2. Learning framework

First, the grid space shown in Fig.1 is divided into two virtual task spaces from each agent's view point. In each virtual task space, there is only one goal position. For example, the two virtual task spaces from the agent A2's view point are as shown in Fig.4 (a) and (b).

Each agent has two Q-functions $Q^1(c_1, a)$, $Q^2(c_2, a)$ corresponding to the two virtual task spaces c_1 , c_2 , respectively. Here, c_1 , c_2 are the virtual task spaces corresponding to the goal positions G1, G2, respectively. Each agent does Q-learning with each virtual task space (that is, each Q-function), separately and simultaneously. At the beginning of each learning episode, the agent decides which of Q-function should be used by using the value of w_j^i . Here, w_j^i , which is a variable, is updated



(a) Task space-1.



(b) Task space-2.

Fig.4. Virtual task spaces from the agent A2's viewpoint.

when either of the goal situations is satisfied. The update rule is as follows:

$$w_j^i \leftarrow \theta w_j^i + (1-\theta)y_j^i \quad (4),$$

where $\theta (\in [0,1])$ is a parameter, and y_j^i is the number of the time steps from the initial state (as shown in Fig.1) until a goal situation, in which the agent A_i reaches the goal position G_j , is satisfied. The measure of choosing the Q-function, which is used when the agent selects the action during the episode, is as follows. If $w_1^i > w_2^i$, then $Q^2(c_2, a)$ is chosen with probability ω ($0 \leq \omega \leq 1$), or $Q^1(c_1, a)$ is chosen with probability $1-\omega$. If $w_1^i \leq w_2^i$, then $Q^1(c_1, a)$ is chosen with probability ω ($0 \leq \omega \leq 1$), or $Q^2(c_2, a)$ is chosen with probability $1-\omega$.

The learning flow is as follows:

1. At the beginning of each episode, the agent decides which of Q-function should be used during the episode based on the value of w_j^i as above mentioned. Here, it assumes that $Q^1(c_1, a)$ was chosen.
2. For the current state s (the virtual task spaces c_1, c_2), the agent executes an action $a_i (\in A)$ with the probability:

$$\pi(a_i | s) = \begin{cases} \frac{1-\varepsilon}{h} + \frac{\varepsilon}{|A|} & (a_i = \operatorname{argmax}_b Q^1(c_1, b)) \\ \frac{\varepsilon}{|A|} & (\text{otherwise}) \end{cases} \quad (5).$$

3. The agent executes the action a selected in step 2.

The environment changes to a new state s' (the virtual task spaces c_1', c_2') and a reward r is given from the environment. The two Q-function is updated as follows:

$$Q^1(c_1, a) \leftarrow (1-\alpha)Q^1(c_1, a) + \alpha(r + \gamma \max_{a' \in A} Q(c_1', a')) \quad (6),$$

$$Q^2(c_2, a) \leftarrow (1-\alpha)Q^2(c_2, a) + \alpha(r + \gamma \max_{a' \in A} Q(c_2', a')) \quad (7).$$

4. If the new state s' satisfies a terminal condition, then the episode ends. Otherwise, let $s' \rightarrow s$ and go back to step 2.

5. EXPERIMENT AND RESULTS

Here, I did two experiments for the task shown in section 2. One is the experiment that the usual Q-learning (as shown in subsection 3.2) is applied to the agents, the other is the experiment that proposed reinforcement learning framework (as shown in subsection 4.2) is applied to the agents. The parameters are: $\alpha=0.3$, $\gamma=0.9$, $\varepsilon=0.3 \times 0.9977^{\text{num_ep}}$, $\theta=0.3 \times 0.9977^{\text{num_ep}}$, $\omega=0.5 \times 0.9977^{\text{num_ep}}$, where num_ep is the number of the learning episodes.

In the case that the usual Q-learning is applied, the learning converges to the goal situation-1 at the 1000 learning episodes. In the case that the proposed learning framework is applied, on the other hand, the learning converges to the goal situation-2 at the 1000 learning episodes.

6. CONCLUSION

In this article, I propose a reinforcement learning framework, which is based on Q-learning, that the agent is able to learn "sociality" in a multi-agent environment. In this framework, the agent learned to ignore the near goal, which is left for the other agent, and go toward the farther goal.

REFERENCES

- [1] Sutton RS, and Barto AG (1998), Reinforcement Learning: An Introduction, MIT Press
- [2] Wooldridge M (2009), An Introduction to Multi Agent Systems, John Wiley & Sons
- [3] Watkin CJCH, and Dayan P (1992), Technical note Q-learning. Machine Learning 8(3):279-292
- [4] Puterman ML(1994), Markov Decision Processes. Wiley Interscience

Effect of interaction between rules on rule dynamics in a multi-group minority game

Takashi Sato

*Okinawa National College of Technology
905 Henoko, Nago, Okinawa 905-2192, JAPAN
(Tel : +81-980-55-4179; Fax : +81-980-55-4012)
(stakashi@okinawa-ct.ac.jp)*

Abstract: Rules, such as laws, institutions, and norms, are shaped by interaction among social members, which are affected by the rules. Since they have such mutually regulating relationship, the rules can be changed dynamically. This paper discusses how interaction between rules shaped in different groups has an influence on the rule dynamics. In order to investigate it, we propose a multi-group minority game model in which each agent plays it in different groups independently with contact to other group's members through the game. Our simulation showed that the frequency of synchronization in the rule dynamics is more than a model without interaction. Further, we found that, in a model with interaction by exchanging agents in different groups, the frequency is increased till the exchange number of agents between different groups is increased to half of the members, but this effect is lost by decreasing the interaction opportunity and increasing the exchange number from more than half of the members.

Keywords: Rule Dynamics, Multi-Group Minority Game, Multi-Agent System, Internal Dynamics, Micro-Macro Loop, Simple Recurrent Network with Self-Influential Connection

I. INTRODUCTION

In our society, there are many rules such as laws, institutions, and norms. Such rules shown in a macro level are shaped by interaction among social members at a micro level from bottom up. The rules have an influence on the members. The members affected by the rules might change their ways of thinking and understanding about the world. Consequently, the rules might also be changed, and totally-new rules might emerge. This mutually regulating relationship between a micro and a macro levels can be referred to as the micro-macro loop [1]. In this paper, we describe such dynamical change of rule as rule dynamics.

For example, the institutions have been discussed among many economists. Veblen [2] defines an institution as "settled habits of thought common to the generality of men." According to North [3], institutions can be defined as "the formal rules (common law, etc), the informal constraints (norms, etc), and the enforcement characteristics of each." Both of Veblen and North emphasize an importance of interaction between institutions and individuals (or organizations consisted of individuals) in their discussions on the institutional change.

Based on these arguments, in our previous works [4-5], we investigated about relationship among the micro-macro loop, internal dynamics, and changes of macro structures like the rules by using our proposed multi-agent system. This system is consisted of many agents with the internal dynamics. An autonomous change of internal state, on which the agent's

action depends, refers to as the internal dynamics. As the results in our previous work, we found that internal dynamics and micro-macro loop are necessary to form and maintain an endogenous dynamics of social structure. Further, our simulation showed that the macro structure shaped by all agents' actions is internalized in the agents through the learning process.

In the previous simulation system, only one group was used, and coexistence and competition of many macro structures could not be observed simultaneously in the one group. However, there are many groups, many rules, and interaction among them in actual world. Moreover, there are hardly researches which take internal dynamics, micro-macro loop and interaction between different rules into consideration.

The purpose of this study is to investigate how interaction between rules shaped in different groups has an influence on the rule dynamics. In order to discuss it, we propose a multi-group minority game in which many agents in different groups play the minority game independently and interact with other members.

II. MULTI-GROUP MINORITY GAME

The minority game (MG) [6] is a simple game which can be regarded as a simple stock market model. In this game, n (odds)-players must select one out of two hands (e.g., -1 or 1) independently. And then, those who are in the minority side win. Here, the MG is employed as social interaction. The

schematic view of the basic MG in our simulation is illustrated in Fig.1.

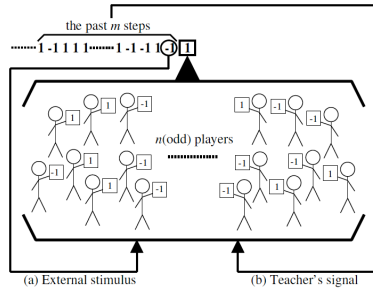


Fig.1. The schematic view of the basic MG in our simulation. (a) Each agent receives past minority hand shaped by all agents' actions. (b) All agents learn a time series of the minority hands for past m steps.

We propose a multi-group minority game (MGMG), where there are many groups playing the MG independently, and at the same time interacting with other members of different groups. There are three types of interacting ways as follows:

1. All agents in each group play the MGMG independently. That is to say, they have no interaction (Fig.2a).
2. Each agent receives not only own past minority hand but also other group's past minority hand at each step (Fig.2b).
3. The agents in different groups play together with other group's members by periodically exchanging agents between groups (Fig.2c).

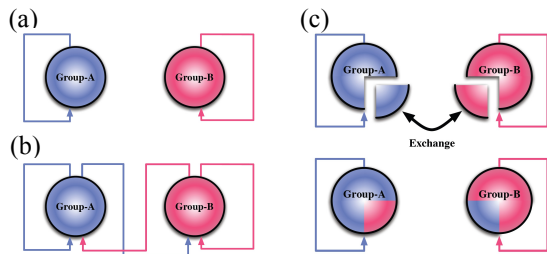


Fig.2. Three types of interactions in our proposed MGMG. (a) No interaction. (b) Each agent receives not only their group's past minority hand but also other group's past minority hand at each step. (c) Each agent interacts with other group's members by exchanging agents at fixed intervals.

We adopt a model of dynamical cognitive agent with internal dynamics represented by a simple recurrent network with self-influential connection (SRN-SIC) proposed in our

previous work [4] as illustrated in Fig.3. The SRN-SIC is an Elman-type network [7] modified by adding recurrent connections between the output and the input layers so that the agent can determine his/her own action based on its past action.

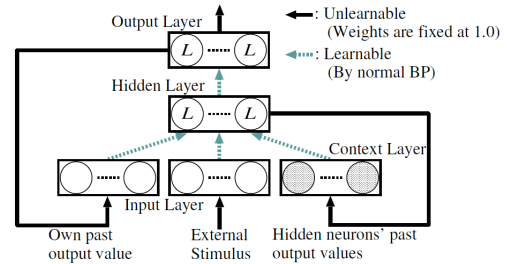


Fig.3. The SRN-SIC proposed in our previous work as an architecture of agent with internal dynamics. This is a particular Elman-type network with additional recurrent connections between the output and the input layers. The symbol L indicates a differentiable nonlinear function to output a real number between -1.0 and 1.0. Not all connections are shown.

In our previous work, we observed various ordered patterns such as fixed point and periodic motions at macro level. These ordered patterns can be generated by some rules of dynamical systems. Therefore, when an ordered pattern is shown in a time series of minority hands, we can interpret that a rule emerges through interaction among the agents. Besides, we confirmed that the agents can internalize the rules in their SRN-SIC and act based on the internalized rule. That is to say, by using the MGMG and the SRN-SIC, we can observe dynamics of interaction between certain rules shaped in different groups.

III. SIMULATION RESULTS

The basic parameters of our simulation are set up as follows:

The population size of a group is set to 101. The number of group is set to 2. The settings of the SRN-SIC are omitted for space constraint (For more details refer to [4]). The simulation is conducted for 1,000 turns, where 10,000 steps are referred to as 1 turn, namely, for 10,000,000 steps. The learning of each agent is processed by using the error-backpropagation every 1 turn.

1. Interaction by receiving another group's minority hand on rule dynamics

First, we compare the results of the simulation without interaction to that of the simulation with interaction in which

all agents receive not only their minority hand but also the one shaped by another group.

Figure 4a shows the difference of the number of all rule dynamics that the period number is the same at the identical turn. However, all rule dynamics with more than 3,500 periods are regarded as the same aperiodic dynamics, since last 7,000 steps of 1 turn are used to analyze the period number of the dynamics. As can be seen from Fig.4a, the number of the rule dynamics with the same period in the simulation having interaction is more than that of the dynamics in the simulation without interaction.

Figure 4b depicts the difference of the number of times that both of different groups' rule dynamics in each simulation become only aperiodic at the same turn. As shown in Fig.4a, there is a major difference between the result of the simulation without interaction and the simulation with interaction.

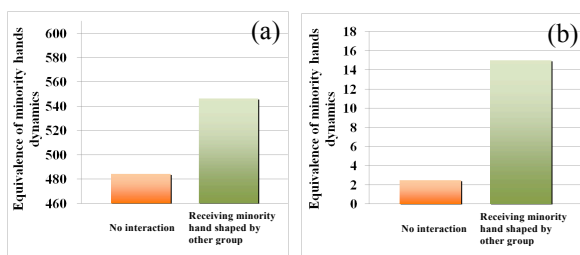


Fig.4. Comparison between the results of our simulation without interaction and with interaction in number of the rule dynamics with the same period between different groups. (a) The difference of the number of all rule dynamics that the period number is the same at the identical turn. (b) The difference of the number of times that both of different groups' rule dynamics in each simulation become only aperiodic at the same turn.

Next, we confirm whether the patterns of the rule dynamics shaped by different groups in the simulation with interaction are completely the same or not. Analysis reveals that most patterns of rule dynamics except for period-2 dynamics are different, although the period number of the dynamics is the same. Even if the patterns between the rule dynamics are the same, most of them are out of phase. It is rarely seen the cases that the dynamics shaped in different groups are completely the same. These rule dynamics are exemplified in Fig.5¹.

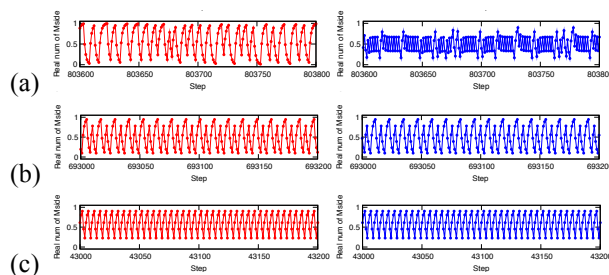


Fig.5. Three examples of the rule dynamics with the same period numbers. (a) Both period numbers are 610 but the patterns are absolutely different. (b) Both period numbers are 12 with the same patterns but out of phase. (c) This is a rare case that the dynamics are exactly the same. Each period number in this case is 5.

2. Interaction by exchanging the agents between different groups

As the other simulation with interaction, we conduct the MGMG in which some agents exchange between different groups in order to investigate what kind of effect it has on the rule dynamics and what type of change it produces in the one.

Figure 6 shows how the equivalence of minority hands dynamics is affected by changing the number of exchanging the agents between different groups and its interval.

As the number of agents exchanged between different groups is increased, it increases the number of times that each period number of the rule dynamics shaped in different groups is the same at the identical turn is increased. When the exchange number is 50, the number of times peaks and is more than the one shown in the simulation with the interaction receiving another group's minority hand, as can be seen from comparison between Fig. 4a and 6.

As the exchange number is increased from greater than half of the members, and as the exchange interval is extended from 10,000 to 1,000,000 steps, however, when the number of times that the rule dynamics shaped in different groups are synchronized, the number of times is decreased. On the surface, it also seems that extending the exchange interval has an effect of decreasing the synchronization of the rule dynamics. But in fact, by changing the length of steps and making the number of interacting opportunity the same, we found there is not a dime's worth of difference between the equivalence observed in our simulations using different exchange intervals. Therefore, it suggests that learning the rule dynamics at different group emphasizes synchronization of the rule dynamics.

¹ The graphs in Fig.5 are drawn after converted the time series of the minority hands to the real number between 0.0 and 1.0.

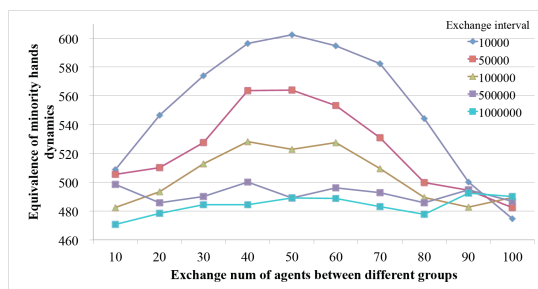


Fig.6. Effect of exchange number of agents and exchange interval on equivalence of minority hands dynamics. As the exchange number is increased, the equivalence of minority hands dynamics is also increased til the exchange number is 50. However, this effect is lost by increasing the exchange number from more than half the members.

IV. DISCUSSION

Let us consider the difference causes of results shown in three types of simulations.

In the simulation in which agents receive other group's minority hand, the agents can know not only the rule dynamics formed by themselves but also the one shaped by different group. Therefore, both of rules are internalized in their SRN-SIC through the learning process, and synchronization between the rule dynamics is induced by all agents' behaviors based on their internalized rules. However, the agents cannot learn the other's rule dynamics appropriately, because teacher's signal using the learning is only their own minority hand. Thus, unstable states expressed as complex aperiodic dynamics in different groups would emerge.

Why is the equivalence shown in the simulation with interaction exchanging the agents in different groups higher than the one observed in the simulation with interaction receiving the another group's minority hand? In the simulation having the replacement, the agents can learn both of different rule dynamics shaped in each group by alternating between the groups and form such dynamics as the members of the same group temporarily. That is to say, it would appear that both rules are internalized and commoditized in the agents at the mutual groups. Therefore, it is important that the exchanged agents learn the opponent's rule dynamics to improve the equivalence of rule dynamics shaped in different groups.

V. CONCLUSION

In order to investigate how interaction between rules shaped in different groups has an influence on rule dynamics, we have proposed a multi-group minority game (MGMG) and conducted three types of the MGMG simulation without

interaction, with interaction by receiving other's minority hand, and by exchanging the agents in different groups.

The simulation results showed that the frequency of synchronization of the rule dynamics shaped in different groups is increased by interaction that the agents receive not only their own minority hand but also other's minority hand. Further, we have found that, as the exchange number of the agents is increased to about half of the group member, the equivalence of rule dynamics is also improved.

Our simulation results suggested that internalizing and commoditizing several different rules in the individuals through direct learning of the rules shaped by others play an important role to emerge stable societies and rule dynamics.

ACKNOWLEDGEMENT

The author thanks Takashi Hashimoto and Zacharie Mbaitiga for their important discussions. This work was supported by the Grant-in-Aid for Young Scientists (B) No.22700242 from the Japan Society for Promotion of Science (JSPS).

REFERENCES

- [1] Shiozawa Y (1997), Consequences of Complexity (in Japanese), NTT Shuppan
- [2] Veblen T (1919), The Place of Science in Modern Civilization and Other Essays. Huebsch, New York
- [3] North D (1994), Economic performance through time, American Economic Review, 84(3):359-368
- [4] Sato T, Hashimoto T (2007), Dynamic social simulation with multi-agents having internal dynamics. In: Sakurai A (ed), New Frontiers in Artificial Intelligence: Joint Proceeding of the 17th and 18th Annual Conferences of the Japanese Society for Artificial Intelligence. Springer, Berlin, pp. 237-251
- [5] Sato T, Hashimoto T (2005), Effect of internal dynamics and micro-macro loop on dynamics of social structures (in Japanese), Transactions on Mathematical Modeling and its Applications (TOM), 46:81-92
- [6] Challet D, Zhang YC (1997), Emergence of cooperation and organization in an evolutionary game, Physica A, 246: 407-418
- [7] Elman JL (1990), Finding structure in time, Cognitive Science, 14(2):179-211

Geometrical analysis and design of motion transmitting element for mobile vehicles

Masaharu Komori, Fumi Takeoka, Jungchul Kang and Yukihiro Kimura

*Department of Mechanical Engineering and Science, Kyoto University
Yoshidahonmachi Sakyo Kyoto 606-8501 Japan
(Tel : 81-75-753-5858; Fax : 81-75-753-5858)
(komorim@me.kyoto-u.ac.jp)*

Abstract: The range of speed or torque of motors is limited to some degree. Industrial vehicles working in factories are required to realize both outputting a large force when they carry loads and moving with high velocity when they move to the destination. However, it is impossible to realize those requirements if the conventional reduction devices is used. Velocity variation devices using gears are widely used to change the velocity ratio between input and output shafts. However, the motion transmission from the input shaft to the output shaft is interrupted during the velocity ratio variation process. In order to solve this problem, velocity variation method that can transmit motion precisely is proposed, in which a motion transmitting element is used. In this report, the geometrical analysis method of the motion transmitting element is proposed, and the expressing method of the curve using dispersed points is proposed and the calculation method of the inclination and the distance concerning the curve is developed. Based on the proposed method, the geometrical form of the transmitting element is analyzed.

Keywords: ratio variation

I. INTRODUCTION

The range of speed or torque of motors is limited to some degree considering the size, weight and cost of the motors. Industrial vehicles are required to realize both outputting a large force when they carry loads and moving with high velocity when they move to the destination in order to shorten the moving period. If the velocity ratio between input and output shafts is changed, a wide range of speed or torque can be realized even if the ability of the motor is limited in speed or torque. Velocity variation devices using gears are widely used in the industrial fields. In a geared transmission, it is needed to change the working gear pairs to vary the velocity of the transmission. However, the motion transmission from the input shaft to the output shaft is interrupted during changing process. Therefore it is impossible to change the velocity while transmitting rotation between the input and output shafts. In order to solve this problem, velocity variation method that can transmit motion precisely is proposed in our research, in which a motion transmitting element is used. In this report, the geometrical analysis method of the motion transmitting element is proposed. A variety of motion characteristics of the motion transmitting element are possible but it is necessary to obtain the inclination of each point on the curve and the distance between the points on the curve in order to calculate the geometrical form of the motion transmitting element. The expressing method of the curve using dispersed

points is proposed and the calculation method of the inclination and the distance concerning the curve is developed. Base on the proposed method, the geometrical form of the transmitting element is analyzed.

II. VELOCITY VARIATION METHOD

In the proposed velocity variation method, as shown in Fig.1, there are two shafts, i.e. input shaft and output shaft, and three gear pairs A, B and C, and three clutches T_A , T_B and T_C . When the clutches T_A is engaged, the gear pair A works and the velocity ratio of gear pair A is realized. When the clutches T_B is engaged, the gear pair B works and the velocity ratio of gear pair B is realized. In the change of the working gear pair from gear pair A to gear pair B, the clutches T_C is engaged, and gear pair C works.

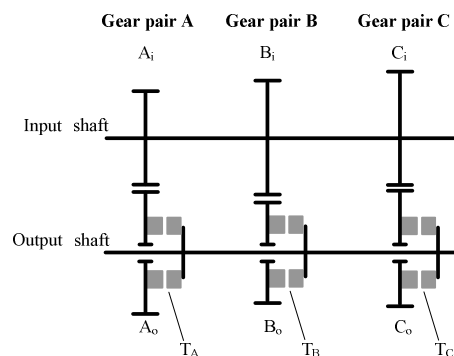


Fig.1. Structure of the Velocity Ratio Variation Device

In the pitch curve of noncircular gear pair C, there are four sections. The pitch curve of the noncircular gear pair C is partly same as that of gear pair A, and partly same as that of gear pair B. Those parts of pitch curve are smoothly connected. Therefore, the velocity ratio can be changed from that of gear pair A to that of gear pair B while gear pair C works. Therefore, the rotational motion is precisely transmitted from the input shaft to the output shaft.

III. ANALYZING METHOD OF GEOMETRICAL PROPERTY

The noncircular gear has such a complex profile form that it is difficult to analyze its geometrical form. An analyzing method of geometrical property of noncircular gear is developed. The profile of a gear is generated by the relative motion between the tool and the work material along the pitch curve of the gear. Therefore, the profile of the gear can be calculated by investigating the locus of the profile of the tool. If the pitch curve of the gear is expressed by a mathematical function, the length of the pitch curve of the gear L and the angle ϕ of the normal direction of the pitch curve can be obtained, which are essential to calculate the locus of the profile of the tool. However, it is impossible to express any pitch curve by the mathematical function. Therefore, to deal with various forms of noncircular gears, a method to express the pitch curve by the set of the discrete points is proposed. In this method, the pitch curve of a gear is composed of the set of the discrete points, and corresponding profile is calculated based on the points. The length L and the angle ϕ are calculated using approximation. Figure 2 shows the concept of the approximation. The length L is approximated by the sum of the distances between the discrete points on the pitch curve as shown in Fig. 2(a). The angle ϕ of the normal direction on point P_n is approximated by that of the bisector of the angle between the line passing through points P_{n-1} and P_n , and that through points P_n and P_{n+1} . Suppose that the coordinate for the discrete points on the pitch curve are (x_i, y_i) ($i=0, 1, 2, \dots$). The length L and the angle ϕ corresponding to the pitch point (x_n, y_n) are approximated as follows.

$$L = \sum_{i=1}^n \sqrt{(x_i - x_{i-1})^2 + (y_i - y_{i-1})^2} \quad (1)$$

$$\phi = \frac{\tan^{-1} \frac{y_{n+1} - y_n}{x_{n+1} - x_n} + \tan^{-1} \frac{y_n - y_{n-1}}{x_n - x_{n-1}}}{2} - \frac{\pi}{2} \quad (2)$$

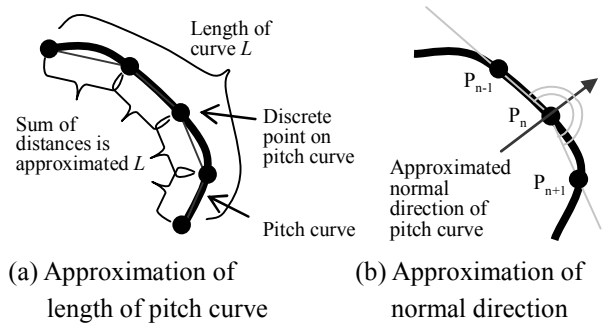


Fig. 2 Approximation in the proposed method

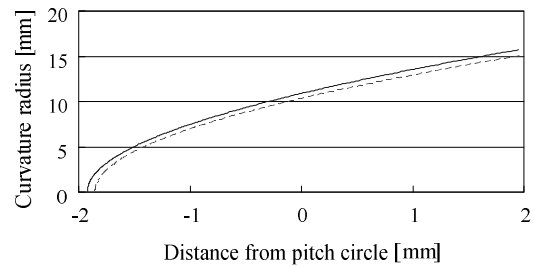


Fig. 3 Curvature radius of profile of gear C

Based on the above discrete point method, the numerical analysis program to calculate the profile of the noncircular gear is developed. Figure 3 shows curvature radius of two different teeth of a noncircular gear. The profile of the noncircular gear is calculated without any problem by using the developed program. Figure 3 shows that there is a different of form between two teeth.

VI. CONCLUSION

In this research, the velocity ratio variation device that can realize precise transmission of the rotation from the input shaft to output shaft is treated. The expressing method of the curve of the motion transmitting element using dispersed points is proposed and the calculation method of the inclination and the distance concerning the curve is developed.

ACKNOWLEDGEMENT

This study was supported by Industrial Technology Research Grant Program in 2009 from New Energy and Industrial Technology Development Organization (NEDO) of Japan.

Underwater unknown acoustic source localization based on Sound Propagation Loss : theory analysis and simulation results

Han Zhang, Bin Fu , Chunhu Liu, Lian Lian

Shanghai Jiaotong University

* Email: bfu@sjtu.edu.cn; Fax: 021-54361833; TEL: 021-34202134

Abstract: A new method based on SPL to estimate the position of unknown acoustic source was put up forward. And theoretical analysis and computer simulation has been used to analyze the accuracy of underwater sound source localization which is interfered by water background noise and multipath reflection. Using simulated data of two different real marine sound sources, we show that when the sound source is far from hydrophone array (greater than 200 meters), the accuracy of this method is high, up to 1 meter. However, with the distance decreasing, the intense reflection of offing brings multipath reflection interference and a correction based on decline analysis of multi-centre frequency of sound source was proposed which can increase localization accuracy by 10%-30%. Therefore, for short-range localization, use of a combination of passive sonar and this method can achieve a good accuracy. The research results verify the effectiveness of the function relationship between acoustic attenuation and the propagation distance in underwater unknown sound source localization. Especially it is advantageous on the remote positioning and can be combined with high accuracy passive positioning to realize great-range and high-accuracy location search.

Keywords: Unknown Sound Source; Sound Propagation Loss (SPL); Sound Pressure; Characteristic Frequency

1. INTRODUCTION

Acoustic positioning technology concerns the safety and efficiency of underwater operation. Previous acoustic positioning cannot satisfy the needs in scientific research, marine exploration, underwater operation and biological targets monitoring. The primary and new demand is how to locate the unknown acoustic source.

The aim of sound source localization is to estimate the Cartesian coordinates of the source or the speed of the moving source. Many algorithms have been put up forward for sound source localization. Approaches using distributed microphone network are presented. In addition, approaches based on energy Measurements have also been studied in recent years. But in the ocean, there is still no appropriate sound source localization algorithm. Now the time-difference-of-arrival estimation methods, such as Super Short Base Line system (SSBL) and Lone Base Line system (LBL) are widely accepted, but these methods have large errors in noisy and multipath reflections condition. In recent years, wireless sensor networks and Sound Propagation Loss (SPL) has been studied. However, due to the complicated data processing and the limitations of localization algorithm, the accurate position of unknown source cannot be

achieved.

In this paper, we put up forward a new method based on SPL to estimate the position of unknown acoustic source, and we carry on the research, using theoretical analysis and computer simulation, to analyze the acoustic pressure of underwater sound signal which is interfered by water background noise and multipath reflection. According to the results, we got functional relation between acoustic pressure attenuation of the unknown source and the propagation distance. Then we have done preliminary calculation and analysis in the accuracy of the unknown acoustic source localization, which provides theoretical basis for large scale and low cost acoustic positioning technology and offers a new approach for tracking the movement of complicated underwater source, such as the unknown sailing noise, underwater construction noise, biological noise, natural disasters noise.

The waveform and frequency spectrum of echo signal of each node are analyzed and when we use the single center frequency of acoustic pressure information in short range, the accuracy of localization is not high. To solve this problem, we extract multiple center frequency of acoustic pressure information, optimize the information and eliminate the incorrect acoustic source

information. Then we can obtain the position of unknown acoustic source with the SPL algorithm. The computer simulation results also show that extracting single center frequency of acoustic pressure information has enough precision in the long distance. But when the distance between acoustic source and hydrophone array becomes short, owing to the powerful interference of reflection wave and the phase difference between directed wave and reflected wave, extracting one center frequency of acoustic pressure information cannot meet the accuracy needs. Then we extract multiple center frequency and optimize the results, which greatly reduces the errors.

2. PRINCIPLE

2.1. Sound Propagation Loss

SPL mainly includes two sections: Extended Loss and Absorption Loss, show as (1).

$$PL = 20\log 10(r) + \alpha r + \Delta \quad (1)$$

$$\text{Extended Loss: } PL = 20\log 10(r) \quad (2)$$

Absorption Loss: based on experimental formula, determined by α .

When sound transmits with electrical signal, following equation (2) can be obtained.

$$PL = 20\log 10(Tv / Rv) + Rx + Rg \quad (3)$$

Where, Tv [V] is Transmission voltage, Rv [V] is Reception voltage, Rx [dB]: Reception sensitivity, Rg [dB] is Reception gain. Rv is measured data and other 4 are all constants.

By solving the equations (1) and (3) simultaneously, (4) can be obtained.

$$20\log 10(Tv / Rv) + Rx + Rg = 20\log 10(r) \quad (4)$$

We got the relations between propagation distance r and Tv , Rv . By measuring Rv at different distances and through the following mathematical model, source coordinates was got.

2.2 Mathematical Model

Set the surface nodes as $N_i (x_i, y_i, z_i)$ ($i=1,2,3,4$), and sound source as $P(x, y, z)$, build the equation (5) and (6), By measuring Rv at N_i and through equations (5) and (6), source coordinates was got.

$$\begin{cases} (x-x_1)^2 + (y-y_1)^2 + (z-z_1)^2 = r_1^2 \\ (x-x_2)^2 + (y-y_2)^2 + (z-z_2)^2 = r_2^2 \\ (x-x_3)^2 + (y-y_3)^2 + (z-z_3)^2 = r_3^2 \\ (x-x_4)^2 + (y-y_4)^2 + (z-z_4)^2 = r_4^2 \end{cases} \quad (5)$$

$$\begin{cases} 20\log 10(Tv / Rv_1) + Rx + Rg = 20\log 10(r_1) \\ 20\log 10(Tv / Rv_2) + Rx + Rg = 20\log 10(r_2) \\ 20\log 10(Tv / Rv_3) + Rx + Rg = 20\log 10(r_3) \\ 20\log 10(Tv / Rv_4) + Rx + Rg = 20\log 10(r_4) \end{cases} \quad (6)$$

3. NUMERICAL SIMULATION

3.1. Simulation Conditions

3.1.1 Sound source

Use two different signals : submarine propeller noise and marine life sound.

3.2 Simulation Contents

3.2.1 Layout of hydrophone array.

Four hydrophones can be set up in Figure 1. We can establish OXY coordinate system, as shown in Figure 1. Then nodes coordinate: Node1 (-30,0,0), Node2(-10,0,10)、Node3(10,0,0)、Node(30,0,0).

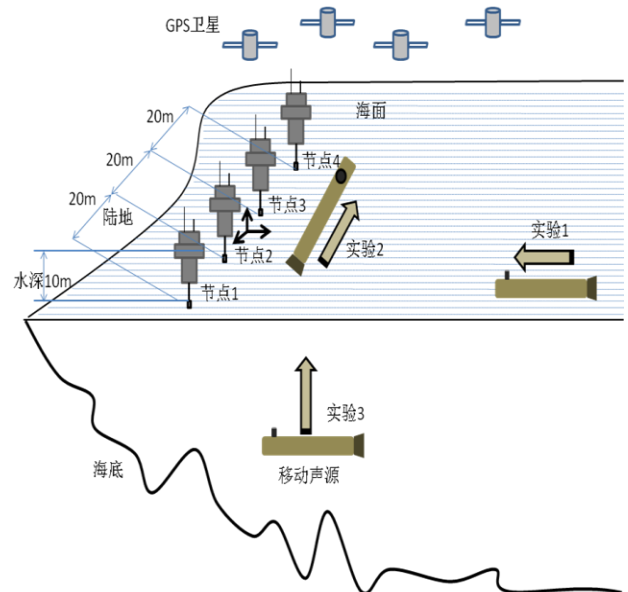


Figure 1 Layout of hydrophone array and simulation contents

3.2.2 Contents

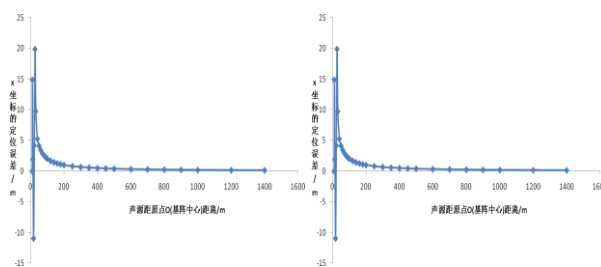
- (1) Sound source moves from far and near in XOY plane, the vertical distance of 10 meters to the X axis, along negative direction on X axis, verifying the influence of directivity of hydrophone on positioning accuracy.
- (2) Sound source moves from far and near in XOY plane, along Y axis, verifying the influence of distance between sound source and array on positioning accuracy.
- (3) Sound source moves from far and near in YOZ plane, the vertical distance of 10 meters to the Z axis, along negative direction on Z axis, verifying the influence of reflected wave on positioning accuracy.

3.3 Simulation results

(1) Simulation content (1) results are shown in Figure 2, when the distance between hydrophone array and sound source is greater than 200 meters, error in X axis is less than 1 meter; However, when the distance is less than 200 meter, the directivity of hydrophone array changes , which results in error in X axis increases sharply, up to 20 meters, about one-tenth of slope distance. Error in Y and Z axis is so small that related error figures is not given.

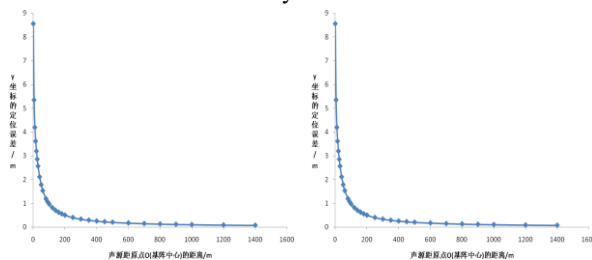
(2) Simulation content (2) results are shown in figure 3, when the distance between hydrophone array and sound source is greater than 200 meters, error in Y axis is less than 1 meter.; However, when the distance is less than 200 meter, error increases gradually, up to 8.5 meter. Error in X and Z axis is so small that related error figures is not given.

(3) Simulation content (3) results are shown in Figure 4, when the distance between hydrophone array and sound source increases , the phase difference of direct wave and reflected wave fluctuates among “greater than one times wave length----- half-wavelength---less than one times wave length”, which results in error in Z axis fluctuates among “large ---small---large”; when the distance is greater than 200 meters, the phase difference goes towards zero, error goes towards 10 meters. Error in X and Y axis is so small that related error figures is not given.



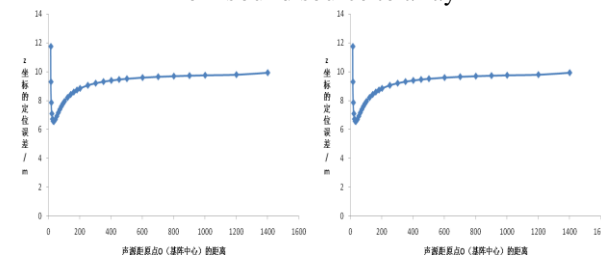
(a) Submarine propeller noise (b) Marine life sound.

Figure 2 x-coordinate positioning error with distance from sound source to array



(a) Submarine propeller noise (b) Marine life sound.

Figure 3 y-coordinate positioning error with distance from sound source to array



(a) Submarine propeller noise (b) Marine life sound

Figure 4 z-coordinate positioning error with distance from sound source to array

4. ERROE CORRECTION

4.1 Correction Method

when the distance between hydrophone array and sound source is less than 200 meters, by using positioning method based on single characteristic frequency , significant error may occur, even cannot solve position equation .Due to the intereference in close enviroment, t he phase difference of direct wave and reflected wave fluctuates among “greater than one times wave length----- half-wavelength---less than one times wave length” that results in R_v cannot be calculated easily. To solve this problem, we selected more characteristic frequency, and analyzed sound pressure loss in different characteristic frequency. As shown in Figure 5, In the received signal spectrum, more characteristic frequency

has been selected and sound pressure can be calculated, then according to Section 2.2 mathematical model, the sound source coordinate can be got, at last weighted average.

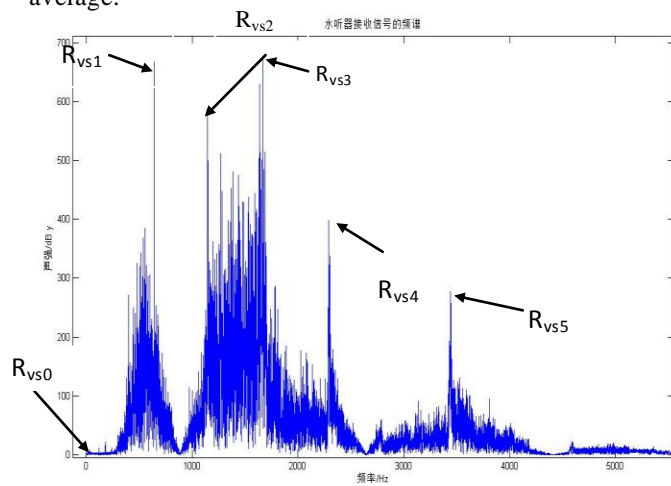


Figure 5 Collection of multi-centre frequency

4.2 Corrected Results

Corrected results of simulation content (2) are shown in Figure 6, compare using single characteristic frequency (R_{v0}), three characteristic frequency (R_{v0}, R_{v1}, R_{v3}) and five characteristic frequency ($R_{vs0}, R_{vs1}, R_{vs2}, R_{vs3}, R_{vs4}, R_{vs5}$). The results show that using more characteristic frequency can effectively eliminate impractical position equation, the positioning accuracy at close ranges has been improved.

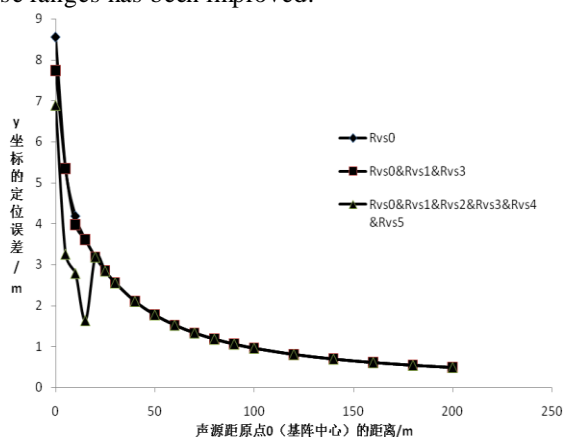


Figure 6 Corrected results of multi-centre frequency

5. CONCLUSION

In a previous work basis of underwater positioning method based on wireless sensor networks, A mathematical model of Underwater unknown acoustic source localization was put forward. And by using two

different types of measured sound, By means of computer simulation, analyzed the positioning accuracy influenced by background noise and multipath reflection. The simulation results show that when the distance between the hydrophone array and sound source is so long, the accuracy of the method based on SPL is high, However, when the distance is short, the accuracy is very poor. On this basis, localization model based on multiple characteristic frequency was put forward and unanswered questions of positioning equation can be effectively solved, moreover this method has a certain correction effect to locating at a close range.

In future work, we will further discuss correction method to reduce the influence by phase difference and improve positioning accuracy. Topological structure of hydrophone array has an important effect on improving positioning accuracy and we prepare some relevant experiments to verify it.

The author would like to express their sincere gratitude to Bin Fu, School of Naval Architecture and Ocean Civil Engineering, Shanghai Jiaotong University, The work of this study was Granted supported by the National Science Foundation for Young Scientists of China

REFERENCE

- [1] Milne, P.H. Milne, Underwater Acoustic Positioning Systems, Gulf Pub. Co., Huston, 1983.
- [2] I.F. Akyildiz, W. Su, Y. Sankarasubramaniam and E. Cayirci, A survey on sensor networks, IEEE Communications Magazine 40 (8) (2002), pp. 104–112.
- [3] 2010 B. Fu, F. Zhang, M. Ito, Y. Watanabe, T. Aoki, L. Lian, Sea trials of new underwater positioning system Based on Sensor networks I. Experiments of underwater ranging method of Sound Propagation Loss, Proceeding of Oceans 2010.
- [4] Christos I. Papadopoulos, 2003, Development of an optimized, standard compliant procedure to calculate sound transmission loss: numerical measurements, Applied Acoustic(64), 1069-1085.
- [5] X. Chen, U. Tureli, Underwater source localization based on energy measurement with randomly distributed sensor array, in: E.M. Carapezza, Unattended Ground, Sea, and Air Sensor Technologies and Applications IX, Proceedings of the SPIE, vol. 6562, 2007.

Position Recognition System of Autonomous Vehicle via Kalman Filtering

Dong Jin Kim^{*}, Jong Il Bae^{**}, Kil Soo Lee^{*}, Dong Seok Lee^{*}, Yun Ja Lee^{***}, and Man Hyung Lee^{*}

^{*}*School of Mechanical Engineering, Pusan National University, Busan, 609-735, Korea.
(Tel : 82-51-510-1456; Fax : 82-51-512-9835)*

(dong7@pusan.ac.kr, melgibsoo@pusan.ac.kr, dslee@pusan.ac.kr, mahlee@pusan.ac.kr)
^{**}*Department of Electrical Engineering, Pukyong National University, Busan, 608-739, Korea
(Tel : 82-51-629-6314)
(jibae@pknu.ac.kr)*

^{***}*Department. of Dance, Pusan National University, Busan, 609-735, Korea.
(Tel : 82-51-510-2949)
(E-mail: leeyj@pusan.ac.kr)*

Abstract: This paper proposes a position recognition system for autonomous vehicle via Kalman filtering. Absolute positioning is required to obtain successful operation of an autonomous vehicle's process. To get reliable positions, there are two ways, either using a GPS or dead reckoning from velocity and steering angle of the vehicle. Error elements exist in both the uses of GPS and dead reckoning. Stable position data of the autonomous vehicle is necessary for a successful operation even with the error elements. Kalman filter is suggested between the GPS and dead reckoning to get stable position data. Correction is performed during the localization of the processing position by using Kalman filter between GPS and dead reckoning.

Keywords: Navigation System, Autonomous Vehicle, GPS, Dead Reckoning, Kalman Filter, Position Location

I. INTRODUCTION

With the continued development of the auto industry, vehicle parts have changed from the mechanical linkage device to the electronic device to the computing system. Also, the vehicle has been changed from a simple transport device to one of the most advanced technology integrations. This development also has the potential to save lives and make lives more convenient based on the ITS(Intelligent Transport System).

The ITS is intended to solve real-world problems, such as reducing the number of motor vehicle accidents. An autonomous system which studies the intelligent system for the vehicle to assist operators or control whole system of the vehicle by itself is part of the ITS. Its aim is to prevent motor vehicle accidents[1]. The autonomous system is the most important part in the future auto industry. In Korea as well as advanced countries, research and development of an autonomous vehicle is actively being conducted.

For successful operation of an autonomous vehicle, stable positioning is required. GPS(Global Positioning System) is widely used for absolute positioning but it requires at least 4 satellites to get the position data. The obtained position data is determined with about 1m errors by GPS receiver. There is no accumulation of error. Dead reckoning is another method to get the

positioning of the vehicle. It calculates the vehicle's position from the velocity and steering angle. However, this method accumulates errors [2, 3]. Since GPS does not operate well in places such as cities with skyscrapers, tunnels, and forests, the method using only the GPS does not guarantee successful positioning performance. Also the method relying only on the dead reckoning is not reliable due to the accumulation of the errors with wheel sliding, mechanical errors, and surface roughness.

In order to improve the positioning performance, this paper proposes a position recognition system for an autonomous vehicle via Kalman filtering. The Kalman filter algorithm is designed for the integration of GPS and dead reckoning. The positioning performances of the proposed Kalman filtering algorithms are verified and evaluated by experiments.

II. DEAD RECKONING FOR VEHICLE

When considering a car-like vehicle, the mobile frame is chosen with its origin P attached to the center of the rear axle. The x-axis is aligned with the longitudinal axis of the car. At time t_k , the vehicle position is represented by the (x_k, y_k) Cartesian

coordinates of in a world frame. The heading angle is denoted θ_k .

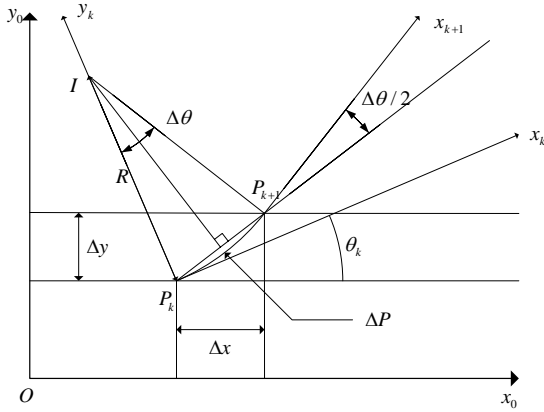


Fig. 1 Elementary Displacement between Two Samples

Let P_k and P_{k+1} be two successive positions. Supposing the road is perfectly planar and horizontal, as the motion is locally circular as shown in Fig.1.

$$\Delta P = R \cdot \Delta \theta \quad (1)$$

Here ΔP is the length of the circular arc followed by P , θ , R (the radius of curvature), I (the instantaneous center of rotation).

Supposing the car is moving forward, the variation on the position is expressed as:

$$\begin{aligned} \Delta x &= |P_k P_{k+1}| \cdot \cos(\theta_k + \Delta \theta / 2) \\ \Delta y &= |P_k P_{k+1}| \cdot \sin(\theta_k + \Delta \theta / 2) \end{aligned} \quad (2)$$

In general, the sampling rate of state is very small compared to their rate of change, so we can approximate $\Delta P \approx |P_k P_{k+1}|$. The integration process is then:

$$\begin{aligned} x_{k+1} &= x_k + \Delta P \cdot \cos(\theta_k + \Delta \theta / 2) \\ y_{k+1} &= y_k + \Delta P \cdot \sin(\theta_k + \Delta \theta / 2) \\ \theta_{k+1} &= \theta_k + \Delta \theta \end{aligned} \quad (3)$$

In Fig.1, the distance traveled ΔP , and the angle changed $\Delta \theta$, resulting from the movement P_{k+1} from P_k can be calculated in terms of the incremental changes of the dead reckoning measurements of the right and left wheel motions[4,5].

The dead reckoning state equation of the vehicle can be described as follows :

$$\begin{aligned} \mathbf{x}_{k+1} &= f(\mathbf{x}_k, \mathbf{u}_k, \omega_k) \\ &= \begin{bmatrix} x_k + \Delta P \cos(\theta_k + \Delta \theta / 2) + \omega_{1,k} \\ y_k + \Delta P \sin(\theta_k + \Delta \theta / 2) + \omega_{2,k} \\ \theta_k + \Delta \theta + \omega_{3,k} \end{bmatrix} \end{aligned} \quad (4)$$

Here the state vector $\mathbf{x} = [x_D \ y_D \ \theta_D]^T$ is composed of the position measured at the dead reckoning. The system noise ω is regarded as the White Gaussian noise.

III. POSITION RECOGNITION SYSTEM VIA KALMAN FILTERING

In the proposed position recognition system, the GPS and the dead reckoning calculate the position independently and then Kalman Filter estimates the position using the position data.

The measurement equation of the GPS can be described as follows:

$$\mathbf{z}_k = H_k \mathbf{x}_k + \mathbf{v}_k \quad (5)$$

$$H_k = \begin{bmatrix} 1 & 0 & 0 \\ 0 & 1 & 0 \\ 0 & 0 & 1 \end{bmatrix} \quad (6)$$

Here the measurement vector $\mathbf{z} = [x_G \ y_G \ \theta_G]^T$ is composed of the position measured with the GPS. The measurement noise \mathbf{v} is regarded as the White Gaussian noise.

In order to estimate the position of the vehicle, the proposed Kalman Filtering was applied from state equation (4) and measurement equation (5):

$$\begin{aligned} \bar{\mathbf{x}}_{k+1} &= f(\mathbf{x}_k, \mathbf{u}_k, 0) \\ P_{k+1}^- &= \Phi_k P_k \Phi_k^T + Q \\ K_k &= P_k^- H_k^T (H_k P_k^- H_k^T + R)^{-1} \\ \mathbf{x}_k &= \bar{\mathbf{x}}_k + K_k (\mathbf{z}_k - H_k \bar{\mathbf{x}}_k) \\ P_k &= (I - K_k H_k) P_k^- \end{aligned} \quad (7)$$

Here P is the error covariance matrix, K is the Kalman gain, and the Jacobian matrix Φ_k is given as follows:

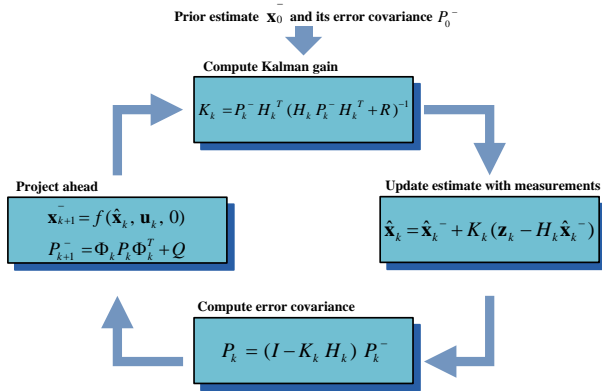


Fig. 2 Kalman filter loop.

$$\Phi_k = \begin{bmatrix} 1 & 0 & -\Delta P \sin(\theta_k + \Delta\theta/2) \\ 0 & 1 & -\Delta P \cos(\theta_k + \Delta\theta/2) \\ 0 & 0 & 1 \end{bmatrix} \quad (8)$$

Equation (7) comprises the Kalman filter recursive equations. It should be clear that once the loop is entered, it can be continued infinitum. The pertinent equations and the sequence of computational steps are shown pictorially in Fig. 2[6].

IV. EXPERIMENT

Fig.4 is a vehicle (MOHAVE of KIA motors) used for experiments. A control PC acquires velocity and steering angle data from vehicle through the CAN Communication. Fig. 4 is PCI 7841 by ADLINK which transmit CAN data from the Local CAN Network to a control PC. For autonomous driving, it requires current vehicle position and heading angle. In this paper, ProPak-V3 of Novatel's GPS receiver is used as the localization system. And two antennas, GPS-701-GG are installed on the autonomous vehicle's roof in a row for getting heading angle.



Fig. 3 Autonomous Vehicle.

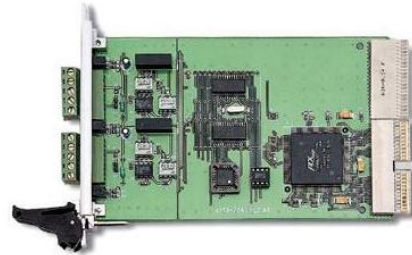


Fig. 4 PCI 7841.

Experiment was done with path set on the ground as 10km/h.

Fig. 5 shows the test area. The result of position location does not follow the reference path because velocity data consists of constant value. So its reliability is less than other external sensors. However, autonomous driving was done without additional external sensors.

GPS also does not follow the reference path. Since the experiment was done in an open area, the error element is bias error.



Fig. 5 Test Area.

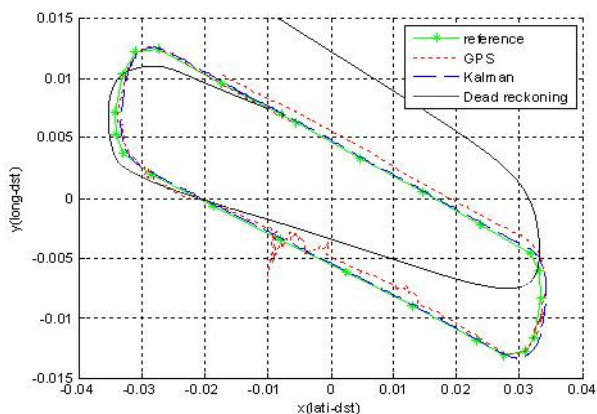


Fig. 6 Experiment Result.

V. CONCLUSION

In this paper, we suggest an autonomous vehicle's position location for navigation system. To get successful operation, absolute position and heading angle are required. GPS and dead reckoning used separately to get the current position of the vehicle does not warranty successful operation. GPS and dead reckoning both have error elements. Dead reckoning has constant velocity data and accumulation of the error element. So it needs to be compensated with algorithm.

For successful operation of navigation system, the Kalman filter is suggested in this paper. The trace of wheels is stable with Kalman filter than using GPS and dead reckoning separately. GPS can compensate the error accumulation of dead reckoning. Results indicate good performance with GPS and the internal system of dead reckoning through the Kalman filter.

REFERENCES

- [1] Keiichi Yamada, Tomoaki Nakano, and Shin Yamamoto, "A Vision Sensor Having an Expanded Dynamic Range for Autonomous Vehicles," *IEEE transactions on vehicular technology*, Vol. 47, No 1, pp. 332-341, 2007.
- [2] Philip G Mattos, "Integrated GPS and Dead Reckoning for Low-cost Vehicle Navigation and tracking," *Vehicle Navigation and Information Systems Conference Proceedings of IEEE*. pp. 569-574, 1994.
- [3] J. Y. Park, D. S. Kang, and J. H Lee, "Kernel RLS Aided Kalman Filtering for Integrated GPS/INS," *KIIS Spring Conference 2009*. Vol. 19, No. 1, 2009.
- [4] K. S. Lee, M. K. Kim, and M. H. Lee, "Control of Unmanned Container Transporters and Management System Development," *Korea Association of Automatic Control 2009*.
- [5] C. S. Kim, J. H. Park, and M. H. Lee, "Improving odometry accuracy for car-like vehicles by using tire radii measurements," *Industrial Electronics Society, 2004. IECON 2004. 30th Annual Conference of IEEE* Vol. 3 pp.2546-2551, 2004.
- [6] Robert G. B and Patric Y. C. Hwang, *Introduction to Random Signals and Applied Kalman Filtering: with MATLAB exercises and solutions*, Wiley & Sons, 1997.

Motion Analysis of Towed Vehicle on Survey System for Deep Sea

Kohei Oshima, Etsuro Shimizu, Masanori Ito
Tokyo University of Marine Science and Technology

Abstract: The aim of this paper is to develop a survey system for deep sea with high accuracy and speed. The proposed survey system consists of tow ship and towed underwater vehicle equipped with sensors. A towed underwater vehicle is thought of as an effective method to survey the bottom of the seabed at large depths. In order to develop the system, motion analysis of towed vehicle for survey system is carried out in this paper.

Keywords: Underwater vehicle, BELUGADEEP

I. Introduction

It is necessary to survey an exact depth when land reclamation works are carried out in the ocean. The sonar equipped on the ship is used in ordinary survey. However, reclamation area has been expanded and deeply in recent years. The ordinary survey method cannot provide the required accuracy. Therefore, a new survey method that using an underwater robot equipped with sensor is proposed. Underwater robots are divided into Autonomous Underwater Vehicles (AUVs), Remotely Operated Vehicles (ROVs) and Towed Vehicles. When underwater towed vehicle compared to other underwater robots can obtain advantages such as:

- (I) Vehicle position can be obtained easily.
- (II) Vehicle can operate for a long time, because power can be transmitted through the cable.
- (III) The data can be transmitted in real time.
- (IV) High accurate data can be obtained because

there is no screw-noise.

In the use of the towed vehicle, keeping position and stable movement are required. The shape of towed vehicle is important for keeping position and stable movement.

In this study, fluid analysis of the towed vehicle is carried out. The effect of the change of body shapes and the effect of the change of attachment position are analyzed. Solidworks and Flowworks including Solidworks are used for analysis.

Fig. 1 shows survey method using underwater towed vehicle.

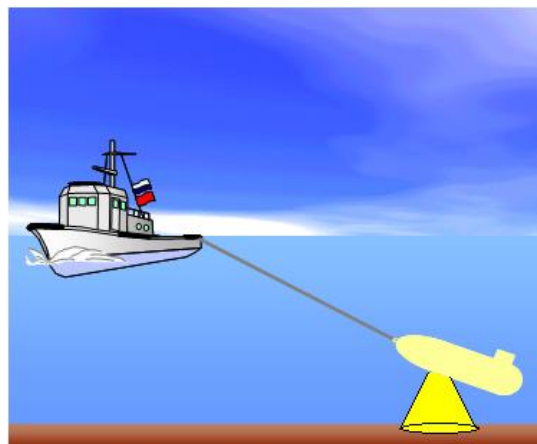


Fig. 1 Survey method

II. Analysis model

1. Body

The model created in Solidworks is shown in Fig.

2. The origin of the analyzed model is BELUGA DEEP shown in Fig. 3, which is developed by TOA-CORPOLATION. Table. 1 shows summary of the vehicle.

Table. 1 Summary of the BELUGADEEP

Size	1.45[m]*0.74[m]*0.84[m] (L*W*H)
Mass	140[kg]
Depth rating	150[m]
Towed Speed	3[knot]
Multibeam Echosounder	Seabat 8101(RESON) 1~400[m],0.01[m]
Attitude and Heading	AHRS440(Crossbow) ± 0.1 [deg]
Depth Navigation	Micro P(Applied Microsystems) 0.05% of depth 6000[m]



Fig. 2 BELUGADEEP

2. Rear attachment

Fig. 4 shows a rear attachment for vehicle. Attachment is set up in rear of BELUGA DEEP. Rear attachment can change each angle in a perpendicular plane or horizontal plane. The effect of attachment is to stabilize posture of vehicle and the effect like rudder. And them, the attachment changes each angle, a flexible action can be done in a changeable real sea area. And, when the ship turns, it is possible to follow quickly.

In this time, the angle changes in only a perpendicular plane. The role like rudder is given to attachment.

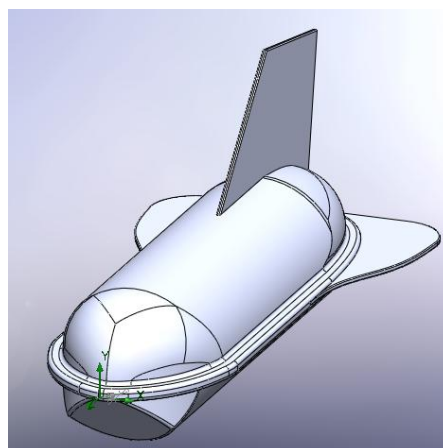


Fig. 3 analyzed model

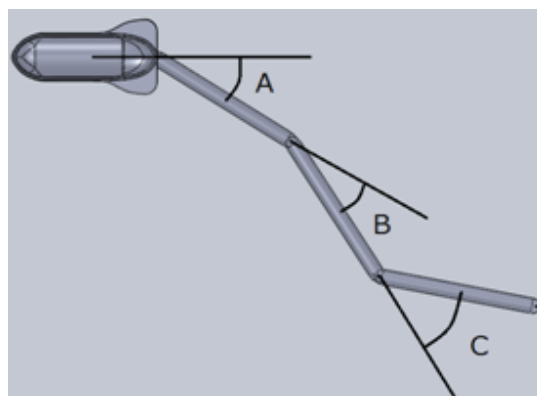


Fig. 4 Vehicle and attachment

III. Fluid analysis

1. Analysis condition

The model is analyzed on the condition that Table.

2. Condition other than Table. 2 are defaults condition. When analyzing it, A, B, C in Fig. 4 is changed, and each result is considered.

Table. 2 Analysis condition

The fluid liquid	Water
Temperature of liquid	280[K]
Water pressure	1114.575[kPa]
Type of analysis	External flow
The velocity of a moving fluid	2[knot],5[knot]
Resolution level of the result	level 3 of 8 level
The degree of A,B,C in Fig .4	each angle is 10[deg] or 20[deg] or 30[deg]

2. Simulation result

The angle and the speed are changed, 24 patterns in total are simulated. Distribution of the pressure and path of particle are calculated.

The sub title (a), (b) of Fig. 5 and Fig. 6 mean “velocity [degree of A/ degree of B/ degree of C]”.

A. Distribution of the pressure

The distribution of the pressure that hangs to the vehicle and the attachment is displayed in Fig. 5.

From the pressure that hangs to the tow body and the pressure that hangs to the attachment, it is possible that the attachment functions enough as a

rudder. Because, the pressure that hangs to the attachment is larger than the pressure that hangs to the tow body. This is the same also in the simulation by 2[knot] and 5[knot].

If the angle of 20[deg] attaches to the flow in the speed of 2[knot], forecasting the behavior is difficult because the pressure in front of the stick distributes like spots. If the angle of 30[deg] attaches to the flow, because the differential pressure on the front side and the back of the stick, stability will be ruined.

When the angle of 10[deg] attaches to the flow. There is no large difference in the pressure distribution that hangs to the stick. From this, the attachment will be not likely to ruin stability though keeps the function of the rudder.

It is preferred that the applied angle of the attachment is about between from 10[deg] to 20[deg] to the flow.

For the simulation by 5[knot], it is roughly consideration similar to the case of simulating it by 2[knot]. However, the influence with the attachment grows because the difference of the pressure distribution is large for simulating it by 2[knot].

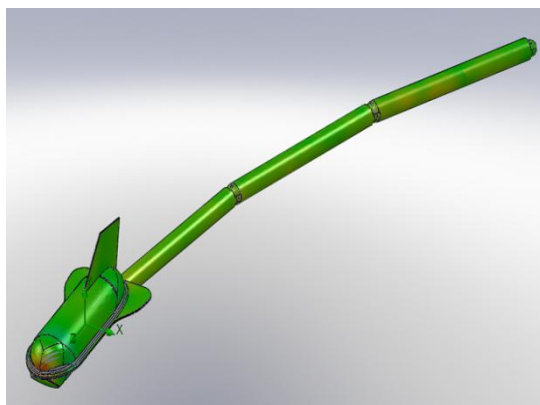
B. Path of particle

The path of particle around the vehicle and attachment is displayed in Fig. 6.

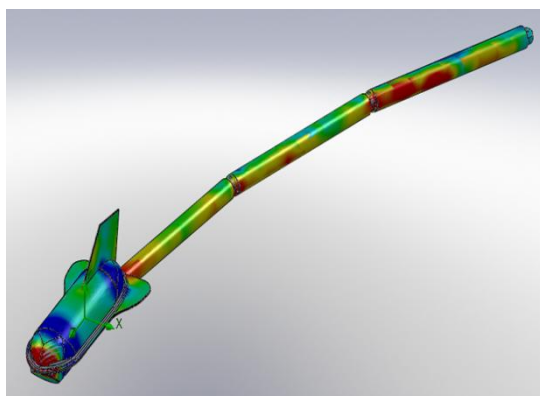
There is no difference in the shape of the path of particle when 2[knot] and 5[knot] are compared. It is thought that tracks of the fluid do not change depending on the speed. The path of particle changes greatly by angle about the attachment large to the flow. Stability will be ruined by the large change of the path of particle. Therefore, it

is necessary not to change the angle of the attachment too much greatly.

Moreover, when the angle of A of fig. 4 changes. The fluid flows into the joining section of the tow body and the attachment. The whirlpool occurs if the fluid flows in the small place. The existence of the whirlpool will ruin the stability of the tow body. Therefore, A of Fig. 4 should be 0[deg]. It is necessary to get the effect as rudder by changing B and C.



(a)2knot[-10/-10/-10]



(b)5knot[-10/-10/-10]

Fig. 5 Distribution of the pressure



(a)

(b)

Fig. 6 Path of particle

((a)5knot[-30/0/0],(b)5knot[-10/0/0])

IV. Conclusion

In this paper, the survey system for deep sea with high accuracy and speed was developed. The proposed survey system consists of tow ship and towed underwater vehicle.

The following results were obtained.

The attachment is effective, and carries out the function as the rudder. However, ruining the stability of the vehicle is predictable under a specific situation.

Reference

- [1] 3DCAD system practical guide Solidworks (In Japanese)
- [2] Solidworks simulation Tutorial (in Japanese)
- [3] <http://www.toa-const.co.jp/>

Path planning of an autonomous mobile robot considering region with velocity constraint in real environment

Tae Hyon Kim*, Kiyohiro Goto[†], Hiroki Igarashi*, Kazuyuki Kon*,
Noritaka Sato* and Fumitoshi Matsuno*

* Kyoto University, Yoshida Honmachi, Sakyo-ku, Kyoto, 606-8501, Japan

[†]The University of Electro-Communications, 1-5-1 Chofugaoka, Chofu-shi, Tokyo, 182-8585, Japan.

(Tel : +81-75-753-5235; Fax : +81-97-594-5235)

(t.kim@ky2.ecs.kyoto-u.ac.jp)

Abstract: Recently, various autonomous mobile robots are tried to drive in the real world in many researches or competitions. In this case, it is very important for the robot to identify the self-position and orientation in real time. Therefore, we apply a localization method based on particle filter to the autonomous robot. Moreover, in order to improve the safety of autonomous locomotion, we improve the algorithm for path planning and trajectory generation so that it can consider the regions with the limitations of maximum velocity. In order to demonstrate the validity of the proposed methods, we will participate in the Real World Robot Challenge 2010.

Keywords: Autonomous robot, trajectory generation, localization

1 Introduction

Recently, many researches related to the autonomous mobile robot have been reported. Various competitions for autonomous robots have also been held to validate the autonomous locomotion functions in the public environment (see e.g [1, 2, 3, 4]).

We have participated in RWRC since 2007 (see [5, 6, 7]), to validate our autonomous robot system in the real environment. In RWRC, the robot has to move within the general pedestrian paths including general people, unicycle and etc. Therefore, unlike the other competitions, the robot is required not only the autonomous locomotion functions but also the safety of the autonomous locomotion. In [7, 8], we proposed a trajectory generation method considering “The Region with Velocity Constraint” (RVC) to improve the safety of the autonomous locomotion. The RVCs are the region where the velocity of the robot is restricted to the predefined velocity, and introduced to around the hazardous regions by the operator. The trajectory generation method in [7, 8] generates the trajectory avoiding the hazardous regions or reducing the risk in the hazardous region by constraining the velocity according to RVCs. However, there is a limitation that the method cannot consider the unknown or dynamic obstacles (e.g. humans and unicycles), because it generates the trajectory based on the predefined map.

Moreover, in [6], we estimate the position of the robot from the odometry data and GPS data by using the extended kalman filter. In general, if the satellite condition is good, we can obtain the accurate position data from GPS by using differential GPS or Real time kinematic GPS. However, since there are many obstacle (e.g. trees, buildings) within the course of RWRC, we could not obtain the GPS data with enough accuracy for correcting the position of the robot at many

locations. Therefore the localization method fully depends on GPS is not suitable for such environment.

In this study, we improve the trajectory generation method so that it can consider not only the registered obstacles but also the unknown or dynamic obstacles, while considering the RVCs as in [7, 8]. Moreover, we improve the accuracy of the localization by combining gyroodometry and particle filter based localization method. We validate the improved system in RWRC2010. The contents of this paper are as follows. In Section 2, we improve the trajectory generation method, and in Section 3, describe localization method used in this paper. In Section 4, we show the developed robot system and show some experimental results. We conclude this paper in Section 5.

2 Trajectory generation with RVCs

As mentioned before, the trajectory generation method[8] considers RVCs. The RVCs are the region where the velocity of the robot is restricted to the predefined velocity, and introduced to around the hazardous regions by the operator in advance. For example, the hazard areas where the robot is not allowed to enter (e.g steps, neighborhood of the pond) are registered as the regions with velocity constraint $v_{max} = 0$, and the area where the robot should reduce the velocity (e.g rough road, narrow street) are registered as the regions with the velocity constraint $v_{max} < 1.0$ (see Fig. 1). Since the robot plans the trajectory according to the registered information, it is expected that the predicted hazard can be avoided. (e.g. reduction of the shock if the robot collides an obstacle, passing smoothly at the complicated narrow road)

In [8], the grid map including the RVCs, the known obstacles and waypoints information is given in advance, and is used for trajectory generation. There-

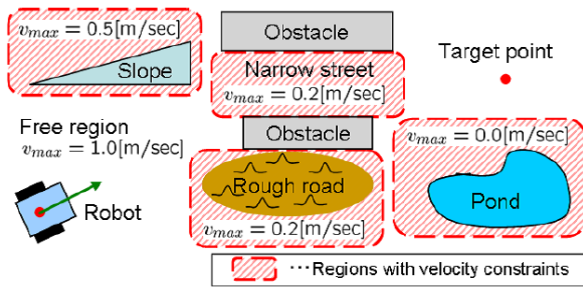


Fig.1 The concept of RVCs

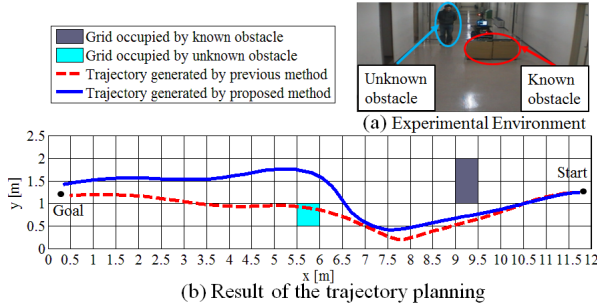


Fig.2 Example of generated trajectory

fore, the generated trajectory avoids only the registered obstacles. However, since there are unregistered obstacles (e.g. humans and bicycles) in the real world, the robot also has to avoid such dynamic obstacles. To this end, we modify the grid map used in trajectory generation so that it can take into account unknown and dynamic obstacles. More precisely, we generate a new map in each sampling time by combining the priori grid map and current obstacle information obtained from sensor. Then the trajectory is generated based on this map in each sampling period.

Fig. 2 shows an example of the trajectory generated by two methods. Fig. 2(a) shows the experimental settings. In Fig. 2(b), a red line shows a trajectory generated by the past work and a blue line shows one by the method described in this section. From this figure, we can see that the trajectory, generated by past work, collides with the unknown obstacle (i.e. an unregistered obstacle). Therefore, since we have to use external obstacle avoidance function to apply this trajectory to the real robot, the optimality of the trajectory might be reduced. On the other hand, the proposed method generates the optimal trajectory while avoiding every obstacles.

3 Localization method

The localization method used in this study can be divided into two part: gyroodometry and particle filter based localization. First the accuracy of the odometry is improved by using gyroodometry[10] based on the fiber optic gyro (Sec. 3-1). Second, the gyroodometry data is corrected by the particle filter based localization method using the priori map and current obstacle information obtained from a laser range scanner (Sec. 3-2).

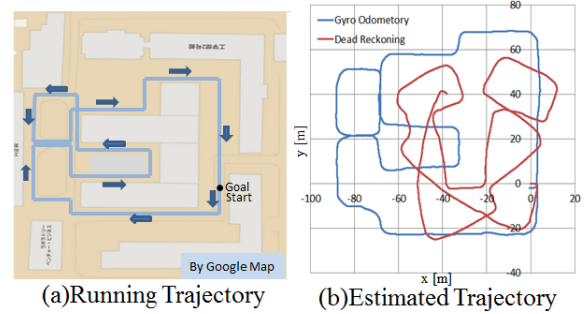


Fig.3 Example of raw odometry and gyroodometry

3-1 Gyroodometry using optic fiber gyro

The gyroodometry is a method estimating a pose of the robot from the odometry and gyro sensor data. In this study, we use the 1-axis optic fiber gyro, and gyro sensor data is used for yaw rate.

Fig. 3 shows one of our experimental results. In this example, the robot is operated by manually on the campus road at Kyoto University from start position to goal position according to the direction of arrows (about 500[m]) as shown in Fig. 3(a). Fig. 3(b) shows the trajectory of the robot estimated by raw odometry and gyroodometry. Note that, the start position and goal position on the map were set at $(x, y) = (0, 0)$. From Fig. 3(b), it can be seen that the gyroodometry shows much better result compared with the raw odometry. In fact, the error between start and goal position is bounded less than 2[m].

3-2 Pose correction by using particle filter

In order to correct the gyroodometry data, we use a Monte Carlo Localization (MCL) method[9]. MCL is a method for estimating the pose of the robot based on Particle Filter (PF). In this study, we use a priori 2D grid map and range data from a laser range scanner for MCL. The outline of our localization method is as follows: First, the pose of the robot in each particle are calculated based on gyroodometry. Next, the range data obtained from LRF is converted into global map based on the pose of the robot in each particle. Then the weight of each particles are calculated by comparing the priori grid map and the converted obstacle map in each particle. Finally, resample the particles according to their weight. By iterating above procedure in each sampling period, the pose of the robot is estimated.

The priori map used in MCL is generated according to the following procedure. First, we obtain 3D range data from the 2D laser range finder mounted on a pitch rotating platform. In RWRC, since many dynamic obstacles (e.g. humans, unicycles) are exist, much noise is included in the lower parts of 3D range data. In order to reduce affection by noise, we use only the 3D range data in the part higher than 2[m] height. The partial 3D range data is converted into global map according to gyroodometry and converted

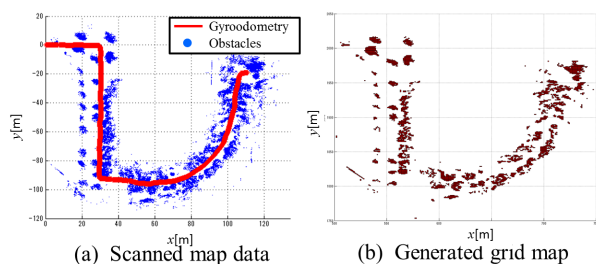


Fig.4 Example of the priori map

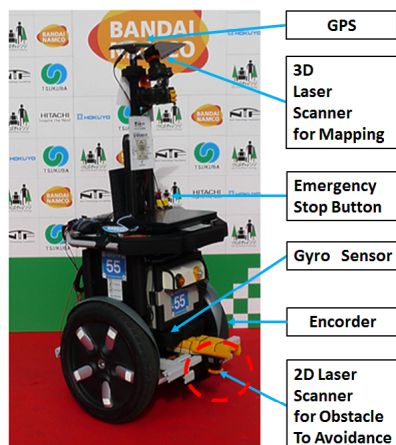


Fig.5 System configuration of the developed robot

into 2D map with orthogonal projection to ground plane(e.g. Fig. 4(a)). Then, the map is saved as the grid map to reduce the memory (e.g. Fig. 4(b)). In the case of Fig. 4, Fig. 4(b) is used as a priori map in PF based localization.

Note that, as mentioned in Sec. 2, this priori map is used for trajectory generation as well. For trajectory generation, waypoints, RVCs and current obstacle information are included to this grid map in each iteration,

4 Experiments

The trajectory generation method in Sec. 2 and the localization method in Sec. 3 are applied to the developed robot as shown in Fig. 5. The developed robot equips a GPS, a fiber optic gyro, a 3D laser scanner, encoders, an emergency stop buttons and a 2D laser scanner to detect obstacles. Note that the software is implemented by using RT-Middleware[11].

In order to verify the developed system, we execute the following three experiments in RWRC2010.

Experiment 1 Verification of the performance with the fiber optic gyroodometry described in Sec. 3-1

Experiment 2 Validation of trajectory generation method described in Sec. 2

Experiment 3 Verification of particle filter based localization method described in Sec. 3-2

In RWRC2010, as shown in Fig. 6, the course is divided into to two parts: the trail course (about



Fig.6 The full course of the RWRC2010

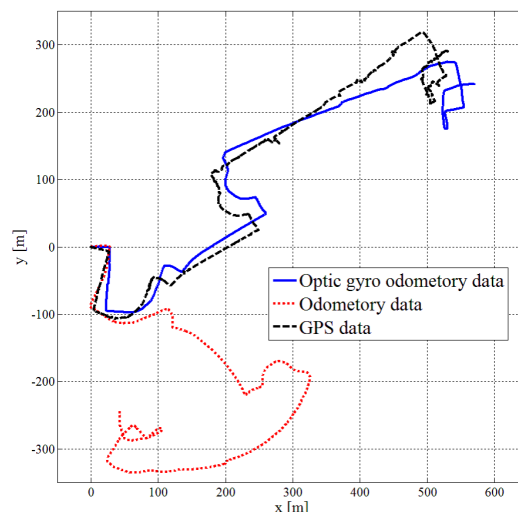


Fig.7 The estimated trajectory in Experiment 1

240[m]) and full course (about 1100[m]). Experiment 1 is done in the full course, and Experiment 2 and 3 are done in the trial course, because of the restriction of time in RWRC2010.

4.1 Experiment 1

Fig. 7 shows the experimental result of Experiment 1. In this experiment, the robot is operated manually. From Fig. 7, it can be seen that the gyroodometry reduces the estimation error compared with the raw odometry data. However, compared with the course in Fig. 6, the estimated trajectory differs from the global map as the robot moves long distance. Especially, we can see that the trajectory curves slightly even in the straight line course. This is mainly because the drift of the gyro sensor. Therefore, although the gyroodometry is enough accurate for a short course, the correction by PF is necessary to run the long course.

4.2 Experiment 2

In Experiment 2, the RVCs are set as shown in Fig. 8(b). The robot moves autonomously according to the trajectory generation method described in Sec. 2. The gyroodometry data is used for localization (i.e. PF is not used in this case).

Fig. 9 shows the translational velocity of the robot

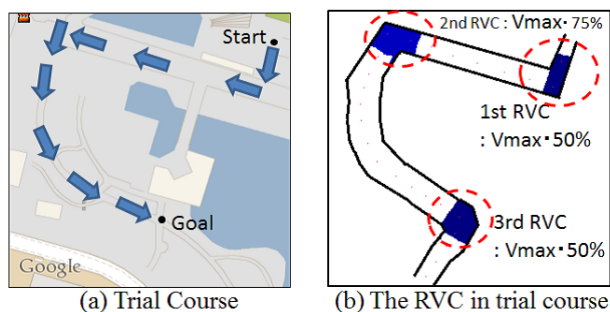


Fig.8 RVCs for the trial course

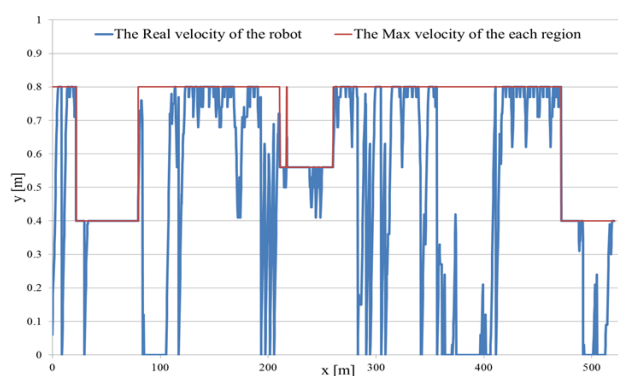


Fig.9 Translational velocity profile in Experiment 2

in Experiment 2. In Fig. 9, a red line shows a admissible maximum velocity of the robot according to the registered RVCs information. From Fig. 9, we can see that the robot reduces the velocity before moving into the each RVC enough, and satisfies the velocity constraint of each RVC. Moreover, the robot could reach goal position of the trial course without colliding any obstacle, even though there were many unknown and dynamic obstacles. Therefore, it can be said that the improvement of the method works correctly.

4.3 Experiment 3

Fig. 10 shows the experimental result of the Experiment 3. In Fig. 10, a green line shows a trajectory when the priori grid map is generated, a red line shows a trajectory estimated by the gyroodometry, and a blue line is a trajectory estimated by the particle filter. In other word, a green line is a "true" trajectory in this case. From Fig. 10, we can see that the trajectory estimated by gyroodometry differs from the one in the priori map (i.e. a green line). On the other hand, the trajectory estimated by PF agrees well with the green line. Therefore our particle filter based localization method estimates the position correctly.

5 Conclusions

In this study, we improved the trajectory generation method proposed in [8] and the localization method for an autonomous robot in the real environment. We participated in RWRC2010 to validate the developed system, and some experimental results showed that

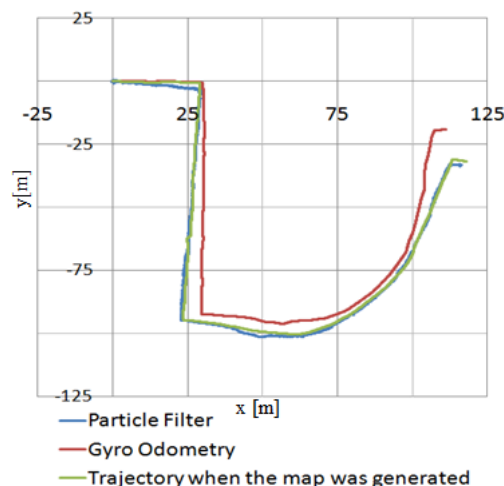


Fig.10 The estimated trajectory in Experiment 3

the validity of our system. One of the future works is to predict motion of the dynamic obstacles, and improve the safety of the autonomous locomotion by considering their information.

Acknowledgements

This work was supported by commissioned business of New Energy and Industrial Technology Development Organization (NEDO).

References

- [1] Urban Challenge, <http://www.darpa.mil/grandchallenge/index.asp>
- [2] Intelligent Ground Vehicle Competition, <http://www.igvc.org/>
- [3] Thailand Intelligent Vehicle Challenge, <http://www.ise.ait.ac.th/TIVChallenge/index.htm>
- [4] Real world robot challenge, <http://www.ntf.or.jp/challenge/challenge10/index.html>
- [5] K. Miyazawa, et al., Development of an autonomous mobile robot in outdoor environment based on Sensor Fusion For RWRC, Proceeding of SICE System Integration, pp.965-966, 2007 (in Japanese)
- [6] K. Kon, et al., Development of RTCs for mobile robots with autonomy and operability Report 7, Proceeding of SICE System Integration, pp.381-382, 2008 (in Japanese)
- [7] K. Goto, et al., Development of RTCs for mobile robots with autonomy and operability Report 13, Proceeding of SICE System Integration, 2B1-1, 2009 (in Japanese)
- [8] K. Goto, K. Kon and F. Matsuno, Motion planning of an autonomous mobile robot considering regions with velocity constraint, IEEE, Int. Conf. on Intelligent Robot and Systems, pp.3269-3274, 2010
- [9] S. Thrun, W. Burgard and D. Fox, Probabilistic Robotics, The MIT Press, 2006
- [10] J. Borenstein and L. Feng, Gyroodometry: A new method for combining data from gyros and odometry in mobile robots, Proc. of IEEE Int. Conf. on robotics and automation, pp.423-428, 1996
- [11] RT-Middleware, <http://www.is.aist.go.jp/rt/>

A Study of SVM using the Combination with Online Learning Method and Midpoint-Validation Method

Shingo Yamashita, Takeshi Yoshimatsu, Hiroki Tamura and Koichi Tanno

*Dept. of Electrical & Electronic Engineering, University of Miyazaki, 1-1 Gakuen-kibanadai-nishi, Miyazaki-city,
Miyazaki, 889-2192 Japan
(Tel : +81-985-58-7409; Fax : +81-985-58-7409)
(htamura@cc.miyazaki-u.ac.jp)*

Abstract: The support vector machine (SVM) is known as one of the most influential and powerful tools for solving classification and regression problems, but the original SVM does not have an online learning technique. Therefore, many researchers have introduced online learning techniques to the SVM. In our former paper, we proposed an unsupervised online learning method using the technique of the self-organized map for SVM. In other paper, we proposed the midpoint-validation method for the improvement of SVM. Therefore, we test the performance of SVM using the combining of two techniques in this paper. Moreover, we compare its performance with the original hard-margin SVM, soft-margin SVM and k -NN method, and also experiment our proposal method on surface electromyogram recognition problems with changes in the electrode position. From these experiments, our proposal method has the best performance in the technique of other SVM and corresponds to the changing data.

Keywords: Support vector machine, Online learning, Midpoint-validation, Pattern classification problem, Surface-electromyogram.

I. INTRODUCTION

The SVM proposed by Cortes and Vapnik [1] is one of the most influential and powerful tools for solving classification problems [2][3][4][5].

We are studying the surface-electromyogram (s-EMG) recognition of using SVM. The purpose is development of the human interface of using s-EMG. In this study, we pay attention to problems such as the change of the s-EMG pattern by the muscle fatigue and the position gap of the sensor to measure. And in our former paper [6], we proposed the online unsupervised learning method using a technique of self-organized map for a SVM. Furthermore, the proposed method has a technique for the reconstruction of a SVM.

In addition, we are studying SVM which is not limited to recognition of s-EMG. In this study, we pay attention to a problem of the deflection of the separating hyperplane in the input space of non-linear SVM and proposed the improvement method [7][8]. We call this method Midpoint-Validation Method. This Method assumes a Midpoint between the classes of training data an index of the deflection and moves the separating hyperplane according to the index. This method also has a technique for the reconstruction of a SVM.

These two studies achieve good result each. However, we have not combined two methods so far. Therefore, we test the performance of SVM using the combining of

two techniques in this paper. Moreover, we compare its performance with the original hard-margin SVM, soft-margin SVM and k -NN method, and also experiment our proposal method on s-EMG recognition problems with changes in the electrode position.

II. PROPOSED METHOD

In this section, we introduce SVM, our Online Learning Method and Midpoint-Validation Method. And we propose the method that combined Online Learning Method with Midpoint-Validation Method.

1. SVM

The SVM is a mechanical learning system that uses a hypothetical space of linear functions in a high-dimensional feature space.

Nonlinear SVM is expressed by the three equations (Eq. (1), Eq. (2) and Eq. (3)). Here, we used the Gaussian kernel given in Eq. (1) as the kernel function, while the SVM decision function $g(\mathbf{x})$ and the output of the SVM are as given in Eqs. (2) and (3).

$$K(\mathbf{x}, \mathbf{x}_i) = \exp\left(\frac{-\|\mathbf{x} - \mathbf{x}_i\|^2}{2\delta^2}\right) \quad (1)$$

$$g(\mathbf{x}) = \sum_{i=1}^N w_i K(\mathbf{x}, \mathbf{x}_i) + b \quad (2)$$

$$O = \text{sign}(g(\mathbf{x})) \quad (3)$$

2. Online Learning Method [6]

In this subsection, we introduce unsupervised online learning method using SOM algorithm for SVM and restructure technique.

Let the input space be denoted by $\mathbf{x}_{in} \in \mathbb{R}$. \mathbf{x}_{in} ($i \in \{1, \dots, N\}$) is the input vector without the label. The training vectors are included in kernel function, \mathbf{x}_i with $i = 1, \dots, N$, belongs to either of the two classes. Thus these are given a label $y_i \in \{-1, 1\}$. Each training vector has the same dimension of input space.

Next, the flows of our online learning method are shown in Fig.1.

- Step 1:** To find the smallest distance of input vector \mathbf{x}_{in} with the training vectors \mathbf{x}_i , the Euclidean distance between \mathbf{x}_{in} and each \mathbf{x}_i is compute (Fig.2.a).
- Step 2:** The following processing (Step 3-4) are not done to \mathbf{x}_{in} when the label of \mathbf{x}_{win} is not the same as the label of the output result of SVM of \mathbf{x}_{in} .
- Step 3:** To find the smallest distance of the \mathbf{x}_{win} with the training vectors \mathbf{x}_j , the Euclidean distance \mathbf{x}_{win} and each \mathbf{x}_j is computed (Fig.2.b).
- Step 4:** If d_w is condition of rule of Eq. (4), \mathbf{x}_{win} is update according to the learning rule of Eq. (5) (Fig.2.c and Fig.2.d).
- Step 5:** Step1-4 are done to all input vector.
- Step 6:** Proposed method repeats *Num* cycles these processing (Step1-5) using same inputs vector \mathbf{x}_{in} .

$$d_w \leq d_o \quad (4)$$

$$\mathbf{x}_{win}^{new} = \mathbf{x}_{win}^{old} + \eta(\mathbf{x}_{in} - \mathbf{x}_{win}^{old}) \quad (5)$$

Fig.1 Flow of the Online Learning Method

Parameter η is update parameter. The idea of this rule is an idea near the adaptive resonance theory-like.

If SV changed after the update, SVM is restructured using the updated training vectors. Even if training vectors changes using the Step 1-5, maximizing the margin of SVM is kept from this restructuring processing.

3. Midpoint-Validation Method [7][8]

In this subsection, we introduce Midpoint-Validation Method. Midpoint-Validation Method adjusts the SVM output with Midpoint data. Here, Midpoint is a point to be located on midway between two classes on input space. In Fig.3, we showed a change of the improvement rate when Midpoint-Validation Method

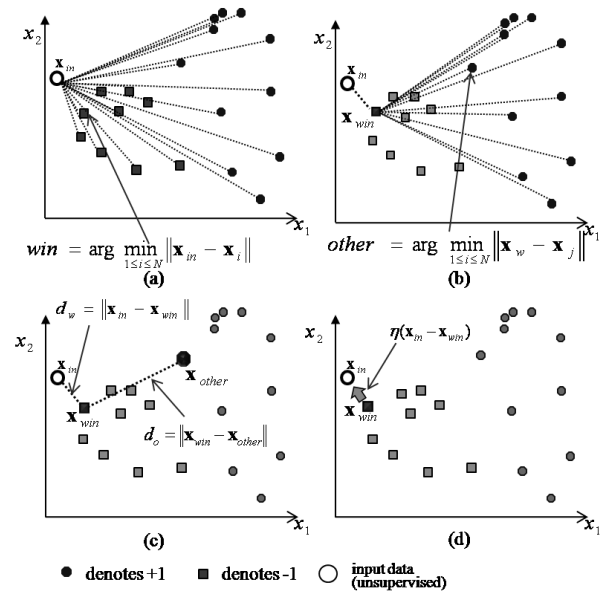


Fig.2. The flow of Online Learning Method

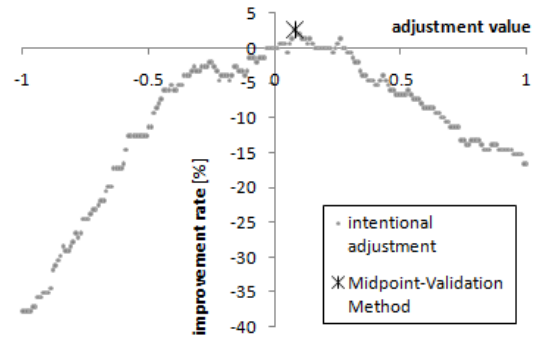


Fig.3 Adjustment value and improvement rate (Pima-indians-diabetes data)

- Step 1:** SVM is created by the known training data.
- Step 2:** Create the midpoint data.
- Step 3:** The output value of SVM of the midpoint data and training data computed.
- Step 4:** The value of B is computed according to Eq. (8).
- Step 5:** The output of the proposed SVM is also computed according to Eq.(6) and Eq.(7).

$$h(\mathbf{x}) = g(\mathbf{x}) + B \quad (6)$$

$$O = \text{sign}(h(\mathbf{x})) \quad (7)$$

$$B = -\frac{1}{M} \sum_{m=1}^M g(\mathbf{x}_m) \quad (8)$$

Fig.4 Flow of the Midpoint-Validation Method

added adjustment value B to the SVM output. We showed a procedure of Midpoint-Validation Method in Fig.4.

By past study, we know that this method improve success rate with high probability when satisfies condition $|B| \geq 0.50$. And we know that the classifier is a high tendency when the value of $|B|$ is small [8].

4. Combination with Online Learning Method and Midpoint-Validation Method

In this subsection, we propose combination method using above-mentioned 2 methods. The procedure at first, we perform Online Learning Method. Next, we create SVM by the updated training data. Finally, we perform Midpoint-Validation Method. By this procedure, we can complete the proposed method.

III. EXPERIMENTS

In this section, the system configuration for recognition experiments of forearm motions using s-EMG is explained. Next, the result of computer simulations is described.

1. Experimental Condition

S-EMG of each movement pattern is measured with electrode sensors, and the feature quantity is extracted from the s-EMG. The feature quantity is given to the recognition machine as an input and each movement pattern that generates s-EMG is presumed. The feature quantity uses minimum-maximum (abbr. min-max) values and integration values [9]. Paper [9] showed that technique of min-max values and integration values are more easy and superior to FFT processing. The sampling frequency of the measurement data is 1 KHz. And the band is from 0 Hz to 500 Hz.

2. Experiments of Forearm Muscles

We experimented on the effectiveness of the proposed method by the s-EMG recognition problem that the feature quantity changes by the electrode position. We compared proposed method performance with Online Learning Method, Midpoint-Validation Method, the original hard-margin SVM, soft-margin SVM (C-SVC) and k -NN method. Proposed method and Midpoint-Validation Method have two results.

The experimental subjects are 4 healthy men (T.Y, K.F, S.Y, T.M). The subjects sit on a chair. The recognition experiment of the 6 motions pattern is conducted by using s-EMG obtained from four sensors set in the arm of the right hand (Fig.5). Moreover, the input given to the identification machine is eight inputs. The experiments are conducted for one day.

The experiment method, first acquires the training data from s-EMG concerning the movement of forearm. Next, SVM and C-SVC learn the relation between s-EMG and motion from the training data (the training vectors). And, each motion is identified 60 times. Next, the object moves the electrode position (sensor 1) by 2mm. And, additional unsupervised learning data (the input vector: each motion is 40 times) is obtained from each motion. Afterwards, test data for recognition rate calculation is identified 20 times of each motions. The experiments tested the measurement four times in total by moving the electrode position of 2mm, 5mm, 7mm and 10mm (Fig.6).

The base of proposed method is hard-margin SVM using Eq. (1). Gaussian kernel parameters of SVM were decided from the evaluation that used training data. Subject T.Y was 0.7, K.Y was 2.0, S.Y was 0.9, and T.M was 0.3. In these experiments, the value of parameter η was 0.1. And the value of Num was 15.

3. Experimental Result

We performed with each method and the simulation results are table 1. In table 1, we showed the average of success rate. Here, “ k -NN with Online Learning” is k -NN method using training data updated by Online Learning Method. From the table 1, proposed methods are the highest value and the second highest value.

In Fig.7, we showed the success rate by 3 methods, Proposed Method ($|B| \geq 0.25$), SVM, k -NN with Online Learning. The horizontal axis expresses the sensor position. Proposed method has improved SVM at 14

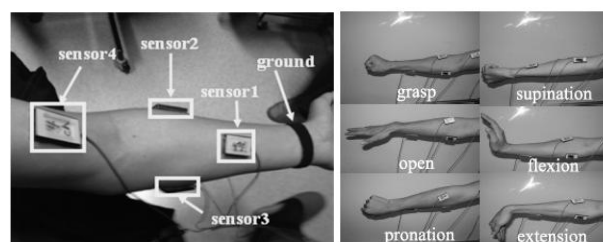


Fig.5. Image figure of forearm motion

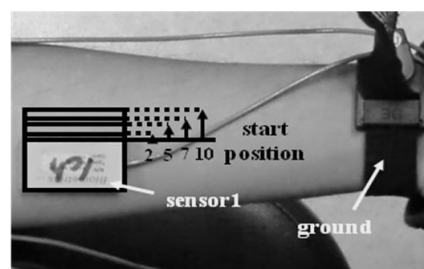


Fig.6. S-EMG recognition problems with changes in the electrode position (2mm, 5mm, 7mm and 10mm)

Table 1. Success rate average [%]

Proposed Method ($ B \geq 0.25$)	Proposed Method ($ B \geq 0.50$)	Midpoint Validation ($ B \geq 0.25$)	Midpoint Validation ($ B \geq 0.50$)	SVM with Online Learning	SVM	C-SVC	k -NN with Online Learning	k -NN
82.8	82.7	78.8	79.9	80.7	77.8	76.1	80.8	79.8

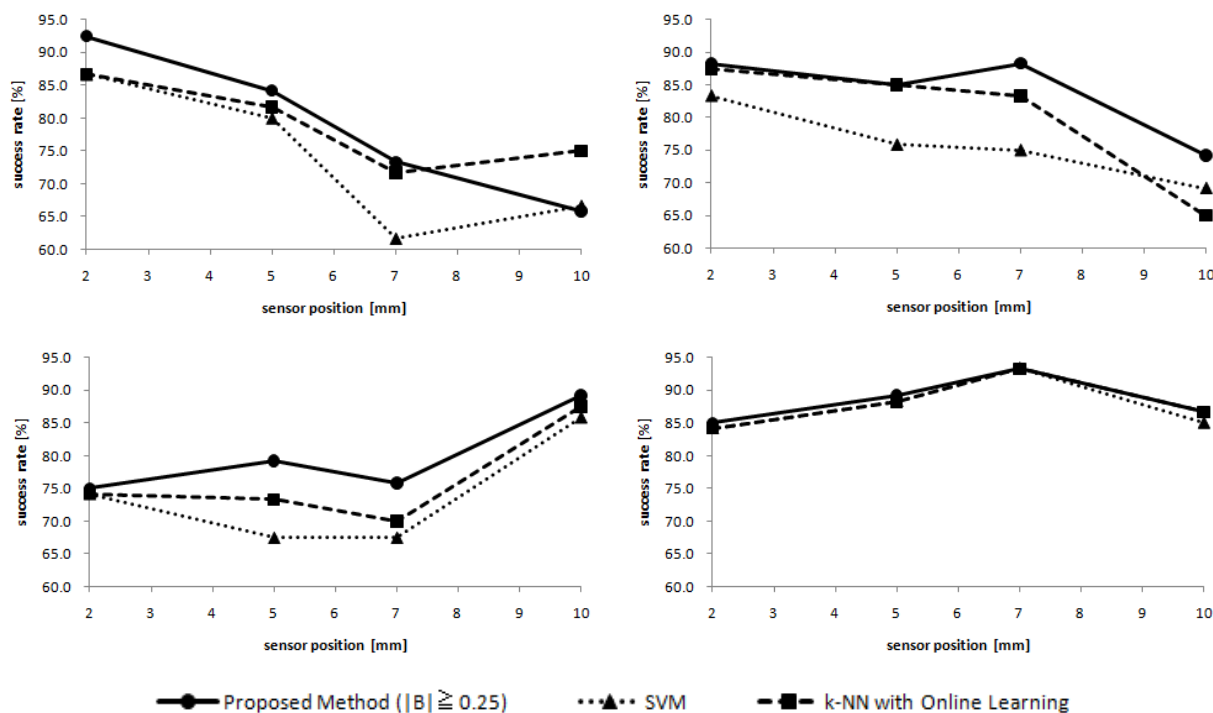


Fig.7 Experimental results of four subjects

items among 16 items. In comparison with k -NN with Online Learning, Proposed method gets high success rate generally. From these simulation results, it is shown that the combination of proposed method is effective.

VI. CONCLUSION

In this paper, we proposed the improvement method for SVM that is the combination with Online Learning Method and Midpoint-Validation Method. The experiment results showed that the proposed method was effective to s-EMG recognition problem with changes in the electrode position. SVM had improved by using our proposed method. In future work, we will experiment on the effectiveness of the proposed method by the other recognition problems.

REFERENCES

- [1] Cotes C, Vapnik V.N (1995) Support Vector Networks. Machine Learning, 20(3), pp. 273-297
- [2] Burges CJC (1998) A tutorial on support vector machines for pattern recognition. Data Mining and Knowledge Discovery, vol 2, no 2

- [3] Joachims T (1999) Making large-scale support vector machine learning practical. In: Sholkopf B, Burges C, Smola A (eds) Advances in kernel methods: support vector learning. pp 169-184
- [4] Mangasarian OL, Musicant DR (2000) Active support vector machines. Technical Report 00-04, Data Mining Institute, Computer Sciences Department, University of Wisconsin, Madison, WI, April
- [5] Mangasarian OL, Musicant DR (2001) Lagrange support vector machines. J Mach Learn Res 1:161-177
- [6] Tamura H, Yoshimatu T, Tanno K (2010) Support Vector Machines with Online Unsupervised Learning Method and its Application to s-EMG Recognition Problems. NOLTA 2010
- [7] Tamura H, Tanno K (2008) Midpoint-validation method for support vector machine classification. IEICE Trans Inform Syst, vol E91-D, No. 7, pp 2095-2098
- [8] Yamashita S, Tamura H, Toyama T, et al (2010) The Effectiveness of Midpoint-Validation Method for Support Vector Machines (in Japanese). Proceedings of Electronics, Information and Systems Conference ; IEEJ, CD:GS12-5
- [9] Tamura H, Gotoh T, Okumura D, et al (2009) A Study on the s-EMG Pattern Recognition using Neural Network. International Journal of Innovative Computing, Information and Control, Vol.5, No.12(B) pp.4877-4884

Video Object Segmentation Using Color-Component-Selectable Learning for Self-Organizing Maps

Shin-ya Umata, Naotake Kamiura, Ayumu Saitoh, Tejiro Isokawa and Nobuyuki Matsui
Division of Computer Engineering, Graduate School of Engineering,
University of Hyogo, 2167 Shosha, Himeji, 671-2280, Japan

Abstract: In this paper, self-organizing-map-based video object segmentation is proposed, assuming that either Y-quantification or HSV-quantification can be systematically selected. Given a video sequence, the value of probability density function is calculated for each component value according to kernel estimation at the first frame. Some areas randomly chosen from the background are then examined, using each component value, whether it is misjudged that they include the target object. The quantification is determined so that occurrence frequency of the above false extraction can be reduced. The data presented to maps are generated, based on the selected quantification. Experimental results show that the proposed method well recognizes the target object.

Keywords: self-organizing maps, block-matching-based learning, video object segmentation

I. INTRODUCTION

A number of video object segmentation algorithms [1]-[4] have been developed, based on soft computing. In [3] and [4], fast block-matching-based self-organizing maps (SOM's) referred to as T-BMSOM's are employed. In them, a rectangular area covering a target object in a frame of a given video sequence is split into units with some pixels. The area is referred to as a window. A unit has a vector with element values associated with Y color component. The color attribute of the window is therefore quantified by the above vectors of all units in it. The map for segmentation is constructed by using such vectors as training data. The vectors corresponding to units in the subsequent frame under segmentation are also presented to the map. The map then judges whether the unit corresponding to the presented vector belongs to the target object. The adequacy in quantifying color attributes is thus strongly related to segmentation capability of the map. It is clear that the above Y-quantification does not always fit to arbitrary video sequences.

This paper proposes map-based video object segmentation, assuming that the quantification is selectable. The HSV-quantification is prepared in addition to Y-quantification. The quantification selection is made with the first frame in a given video sequence. The value of probability density function is calculated for each component value according to kernel estimation[5], using the area with the target object. The function value associated with some component value determines the label to be assigned to that component value. The label specifies whether the component value

with it is relevant to the target object. Some rectangles are next randomly clipped from the background. They are examined, using labeled component values, whether units in them are accurately classified as part of the background. The quantification selection depends on the number of units accurately classified in such manner. The training data are generated according to the selected quantification, and a map for segmentation is constructed by T-BMSOM learning using them. Experimental results reveal that the quantification selection works well for the segmentation without excessive overextraction.

II. PRELIMINARIES

In this paper, T-BMSOM learning[3] is adopted. A block is defined as shown in Fig. 1. The average of neuron reference vectors in it is given as its reference vector. The Euclidean distance between a block reference vector and the presented data is calculated to find a winner. For the $N \times N$ -sized map, the maximum (or minimum) block size is $(N-1) \times (N-1)$ (or 2×2).

Straightforwardly adopting the concept of blocks brings about increase in computational time complexity for learning. In [3], the decision-tree-like search of winner and batch learning process are employed to overcome this issue. The former chooses $(N-2)$ candidates for winner, each time a member of the training data set is presented to the $N \times N$ -sized map. The first candidate is one of the four $(N-1) \times (N-1)$ -sized blocks. The $(N+1-s)$ -th candidate is chosen out of the four $(s-1) \times (s-1)$ -sized blocks included in the same $s \times s$ -sized block, which has been most recently determined as the $(N-s)$ -th candidate. The candidate

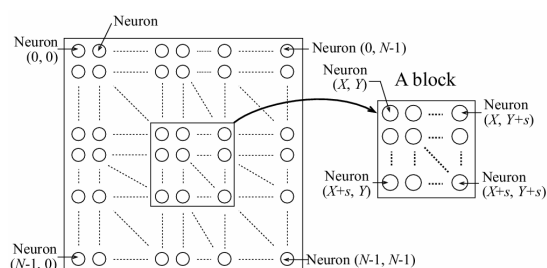


Fig. 1. An $N \times N$ -sized map and a block it

with the shortest distance to the presented data is formally determined as winner block for it. The vectors to be updated are those of neurons in the winner.

The batch learning process is summarized as follows. The values associated with modifications on each neuron reference vector are stored for every member in the training data set. Once an epoch is complete, all of the neuron reference vectors are simultaneously updated. The learning termination condition is specified by the number of epochs. Detailed steps of T-BMSOM learning are described in [3].

III. MAP-BASED VIDEO OBJECT SEGMENTATION

The proposed extraction quantifies the first frame in a given video sequence by vectors employed as members of a training data set. T-BMSOM learning is then applied. In the resultant map, the following two clusters are formed: the cluster with neurons mainly firing for the data generated from the moving object and that mainly firing for the data generated from the background. The moving object in each subsequent frame is extracted using the constructed map, and an extraction result appears on the computer screen in the form of a window-like area including the target object.

A. Generation of training data

In the first frame, a rectangular window including a target object is defined as shown in Fig. 2. T-BMSOM learning uses only the data generated from this window for map training. The first window (i.e., the window in the first frame) is formed as follows. In the following, an $n \times n$ -sized set of pixels is considered to be a unit. The background difference is applied to the first frame, and units belonging to the target object are systematically extracted. The minimum rectangle with which all units of the extracted target object can be covered is then specified, provided that its center equals the center of gravity of the extracted object. Let $leng_B$

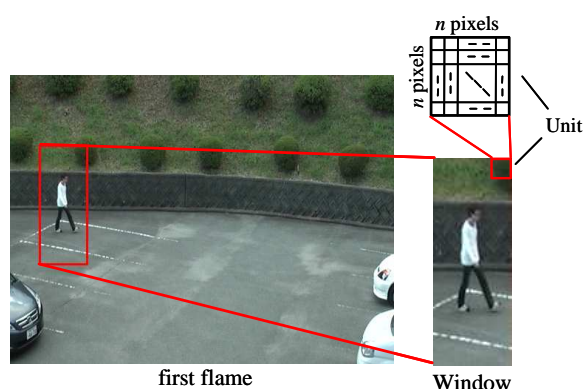


Fig. 2. Window with a target object

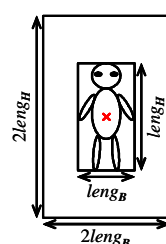


Fig. 3. Window with center of gravity of extracted object as its center

(or $leng_H$) denote the base (or height) length associated with the minimum rectangle. Fig. 3 depicts a schematic representation of the window. The window has the center of gravity of the extracted object as its center.

In [3], the unit has a vector with two element values. Y values of YUV color components of all n^2 pixels in the unit are averaged, and the resultant value is given as one element value. The other equals the standard deviation for the Y component associated with pixels in the unit. The training data associated with the above unit corresponds to the above vector with average and standard deviation. Y-quantification hereinafter denotes the above approach quantifying color attributes based on Y component colors.

If some quantification scheme is unsuitable for a given video sequence, it is highly likely that the target object is lost at some point in time when object segmentation is in progress. To overcome this issue, data are generated on condition that HSV-quantification is also available. When HSV-quantification is adopted, the average and the standard deviation are calculated for each component as well as when Y-quantification is adopted. The number of elements is six for each of the data generated from the units.

A method for determining the quantification scheme is described as follows. It is solely applied to the first frame. The value of probability density function is

calculated for every component value, according to the kernel estimation[5]. Let the l -th window denote the window with the target object in the l -th frame. The calculation is executed by using units belonging to the target object in the first window. Let t_u^q denote the average of q -component values in the s -th unit belonging to the target object, where $q \in \{Y, H, S, V\}$, $1 \leq u \leq W$ and W is the number of units in the target object. The density function is given as follows:

$$\hat{p}^q(t) = (1/Wh^q) \sum_{s=1}^W K((t-t_u^q)/h^q), \quad (1)$$

where $K(t)$ and h^q are kernel function[5] and bandwidth, respectively. They are as follows:

$$K(t) = e^{(-t^2/2)} / \sqrt{2\pi}, \quad (2)$$

$$h^q = 0.9\sigma^q / W^{1/5}, \quad (3)$$

where $\sigma = \min(SD, IQR/1.349)$, SD is the sample standard deviation and IQR is the inter-quartile range. A label is next assigned to each q -component value. The label implies whether the q -component value is relevant to the target object. Let LB_i^q denote the label assigned to some q -component value, t^q . It is determined according to the following equation:

$$LB_i^q = \begin{cases} TO & \text{if } \hat{p}(t^q) > th^q, \\ BG & \text{if } \hat{p}(t^q) \leq th^q, \end{cases} \quad (4)$$

where th^q equals the average of values of $\hat{p}^q(t)$ calculated for the first window. If $LB_i^q = TO$ (or BG), it is considered that the value t^q strongly characterizes the color attribute of the target object (or the background).

Next, WN rectangles are randomly clipped from the background area excluding the first window, provided that the size of each rectangle is equal to the size of the first window. The average of the q -component values associated with pixels is calculated for any unit in each chosen rectangle, and the label that Eq. (4) assigned to the value equal to the average is checked. If the label is TO (or BG), the unit with this average has high probability of being incorrectly (or correctly) judged as the target-object part (or the background part). This scheme is similarly applied to any unit in the clipped WN rectangles. Let N_{BG}^q denote the number units with high probability of being correctly judged as the background part, where $q \in \{Y, H, S, V\}$. For N_{BG}^H , N_{BG}^S and N_{BG}^V , if at least two values are larger than N_{BG}^Y , the data based on HSV-quantification are employed for training a map; otherwise, the data based on Y-quantification are employed. For example, HSV-quantification is chosen if $N_{BG}^Y < N_{BG}^H$ and $N_{BG}^Y < N_{BG}^S$.

B. Construction of maps and object extraction processing

Once T-BMSOM learning is complete, neurons are labeled as follows. All of the members in the training data set are presented again to the just trained map. Each of the members has either 'target object (TO)' or 'background (BG)' as its label. Let NL_{TO}^i (or NL_{BG}^i) denote the firing frequency for the i -th neuron while all of the members with label TO 's (or BG 's) are presented. Let BN^i denote the label to be assigned to the i -th neuron. It is given as follows:

$$LBN^i = \begin{cases} TO & \text{if } NL_{TO}^i > NL_{BG}^i, \\ BG & \text{if } NL_{TO}^i \leq NL_{BG}^i, \end{cases} \quad (5)$$

The map is unavailable to extract the target object until all of the neurons are labeled in the above way.

Let us briefly explain object extraction processing. Once the segmentation is complete for the $(l-1)$ -th frame, the data to be presented is generated from each of the units in the l -th window, on condition that coordinates of four vertexes of the l -th window are equal to those of the $(l-1)$ -th window. This l -th window is said to be nonconclusive. The data is generated according to the quantification determined in the first frame. If a winner for the data associated with some unit is a neuron labeled TO (or BG), it is judged that the corresponding unit belongs to the target object (or background). After arbitrary units are similarly examined, the nonconclusive l -th window area is updated using the extracted object as shown in Fig. 3. The updated area is fixed as the conclusive l -th window. Extracting the target object is similarly conducted for each of the subsequent frames.

IV. EXPERIMENTAL RESULTS

T-BMSOM learning produces well-trained maps [3], [4] on condition that training data sets are updated during learning, compared to conventional SOM learning. The method based on T-BMSOM learning is therefore applicable as follows.

- 1) The l -th map is constructed, using the training data set generated from the l -th window.
- 2) The l -th map classifies units in the $(l+1)$ -th window.
- 3) The training data set is updated according to the classification result associated with the $(l+1)$ -th window. The $(l+1)$ -th map is constructed, using the updated training data set.

If the map constructed with the training data set generated from some window has enough capability of appropriately extracting the units in several of its

subsequent windows, incremental learning conducted in the above manner can be skipped for such windows. This capability is clearly useful in reducing the loads imposed on the computer. The proposed segmentation is therefore evaluated on condition that only the training data set generated from the first window is available. Experimental conditions are as follows: the frame with 640×480 pixels, the unit with 8×8 pixels, 5×5-sized map and learning termination condition is 20 epochs. These are similarly employed in [4]. WN is set to 100. The proposed segmentation is compared with the segmentation in [4]. They are implemented on computer (CPU: Athlon 2.0GHz, Memory: 1.0GB).

The proposed segmentation and the segmentation in [4] are applied to sequences referred to as Video 1, Video 2 and Video 3. Figure 4 depicts some frame in each sequence and extraction results. Recall that the method in [4] is solely based on Y-quantification, whereas the proposed scheme uses HSV-quantification in addition to Y-quantification. The proposed method generates data based on Y-quantification for Video 1, and data based on HSV-quantification for Video 2 and Video 3. Note that the extraction results obtained by the method in [4] correspond to the cases of data generation solely based on Y-quantification.

In Figs.4 (a)-(c), units, each of which is judged as part of the target object (pedestrian), are marked by dots. For the results achieved by the proposed method, the pedestrian appropriately appears in the rectangular window. On the other hand, the method in [4] judges a number of units to be actually included in the background as those of the pedestrian, as shown in Figs.4 (b) and (c). It is thus revealed that the quantification selection works well for generating data presented to maps.

V. CONCLUSIONS

This paper proposed video object segmentation, using a map constructed on condition that training data were generated in accordance either with Y-quantification or with HSV-quantification. The quantification selection is made with the first frame in a given video segmentation. Each component value is labeled either as TO or as BG , and N_{BG}^q 's are calculated, using labeled component values, as measures correlating with probability that units in the background are rightly classified. The quantification selection depends on N_{BG}^q 's. Experimental results established that the

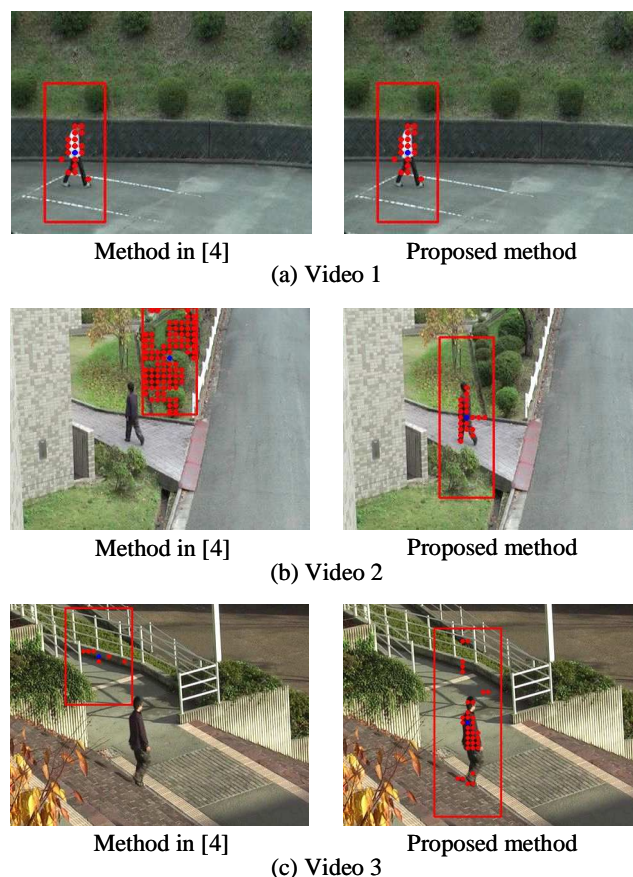


Fig. 4. Object segmentation results for each quantification

selection is useful in generating data tolerant to the overextraction that occurs in the background.

In future, the proposed method will be modified so that extraction accuracy can be improved.

REFERENCES

- [1] H.Mochamad, H.C.Loy and T.Aoki, "Semi-Automatic Video object Segmentation Using LVQ with Color and Spatial Features," IEICE Trans. INF. & SYST., vol. E88-D, no. 7, pp. 1553-1560, 2005.
- [2] H.Grabner and H.Bischof, "On-line Boosting and Vision," In Proc. IEEE Conf. on Computer Vision and Pattern Recognition, vol. 1, pp. 260-267, 2006.
- [3] T.Isokawa, K.Iwatani and A.Ohtsuka et al., "On Self-Organizing Maps Learning with High Adaptability under Non-Stationary Environments," Proceeding of SICE-ICASE International Joint Conference 2006, pp.4575-4580, 2006.
- [4] N.Kamiura, Y.Ohki and A.Saitoh et al., "On Video Object Segmentation Using Fast Block-Matching-Based Self-Organizing Maps," Proc. Of IEEE TENCON 2008, Hyderabad (CDROM), 2008.
- [5] B.W.Silverman, "Density Estimation for Statistics and Data Analysis," London: Chapman and Hall, 1986.

Properties of Localized Oscillatory Excitation on the Non-Linear Oscillatory Field

Ryota Miyata* and Koji Kurata**

*Graduate School of Engineering and Science, University of the Ryukyus

**Faculty of Engineering, University of the Ryukyus

*,**1 Senbaru, Nishihara, Okinawa JAPAN 903-0213

miyata@mibai.tec.u-ryukyu.ac.jp

Abstract: We analyze the dynamics of the non-linear oscillatory field composed of Radial Isochron Clocks (RICs) or Stuart-Landau (SL) oscillators, which are the simplest dynamical systems that have one stable limit cycle around one unstable equilibrium. According to our computer simulation, the non-linear oscillatory field with two kinds of Mexican-hat-type connection had the function of several peak detection of an external input by the localized oscillatory excitation areas. Moreover, this non-linear oscillatory field could also realize in-phase phase-locking within each localized oscillatory excitation area, but maximize the phase difference between different localized oscillatory excitation areas. As Amari (1977) model of the nerve field provided mathematical base for the self-organizing map (SOM) algorithm, the non-linear oscillatory field is expected to provide theoretical base for the oscillatory SOM algorithm.

Keyword: non-linear oscillatory field, localized oscillatory excitation, RIC, SL oscillator, phase-locking, Mexican-hat-type connection

1 Introduction

Many 1970's experimental results suggested that feature-extracting cells are self-organized in visual cortex through postnatal sensory experience [1, 2]. Hirsch and Spinelli (1970), for example, observed such self-organization in the visual cortical cells of young kitten [1].

In response to this, a lot of neural network models were proposed at the time to describe this phenomenon. Malsburg (1973) proposed the earliest model which explained the mechanism of self-organization of the visual cortex [3]. Amari and Takeuchi (1978) formulated the Malsburg model in the mathematically simple form [4]. In this model, they adopted Amari (1977) model of the nerve field, which had been shown to allow stable localized excitation areas [5]. This stable excitation pattern in the nerve field provides base for neighborhood learning used in Malsburg model and Kohonen's Self-Organizing Map (SOM) algorithm [6]. SOM is one of the simplest learning model of the cerebral cortex. Amari expressed the property of peak detection of the function through the dynamics of the nerve field with the Mexican-hat-type connection pattern, while Kohonen built that of peak detection to the algorithm directly in the SOM.

Meanwhile, recent studies found that the sign and magnitude of synaptic plasticity depend critically on the precise timing of pre- and postsynaptic firing. This phenomenon is called spike timing dependent plasticity (STDP) [7]. Moreover, there is

a hypothesis that the property binding should be represented by phase-locking among neuronal oscillatory firing, called synchronous firing hypothesis. Eckhorn et al. (1988) and Gray et al. (1989) discovered synchronous periodic firing of neurons in the visual cortex of the monkey and that of the cat [8, 9].

Regarding periodic neuronal firing as oscillation, and synchronous firing as in-phase phase-locked oscillation, we extend Amari model of the nerve field to the oscillatory field. Kuramoto (1982) first proposed the oscillatory field [10]. The difference of our model from the preceding models such as Kuramoto model is that oscillation occurs in local area in the oscillatory field. We call this excitation pattern *localized oscillatory excitation* [13]. In this paper, we study the mechanism of formation of localized oscillatory excitation areas in the oscillatory field. To this end, we consider a non-linear oscillatory field composed of Radial Isochron Clocks (RIC) or Stuart-Landau (SL) oscillators, which are the simplest dynamical systems that have one stable limit cycle around one unstable equilibrium [11, 12].

Our computer simulation showed that the non-linear oscillatory field with two kinds of Mexican-hat-type connection had the function of several peak detection of an external input by the localized oscillatory excitation areas, and could also realize in-phase phase-locking within each localized oscillatory excitation area, but maximize the phase difference between different localized oscillatory excitation areas.

This non-linear oscillatory field is expected to provide theoretical base for the oscillatory SOM algorithm, as Amari (1977) model of the nerve field provided mathematical base for the SOM algorithm [14].

2 Model

2.1 RIC (SL Oscillator)

RICs (SL oscillators) are known to be one of the simplest dynamical systems which have one stable limit cycle around one unstable equilibrium [11, 12]. The dynamics of RICs are written in polar form as below.

$$\frac{dr}{dt} = r(1 - r^2) \quad (1)$$

$$\frac{d\theta}{dt} = 1 \quad (2)$$

As shown in Fig.1, any orbit beginning with $r > 0$ approaches the stable limit cycle ($r = 1$) as t increases. According to the equation (2), the behavior of the phase θ does not depend on the amplitude r .

2.2 Non-Linear Oscillatory Field

Let us consider a non-linear oscillatory field consisting of RICs (SL oscillators) as shown in the following equations.

$$\frac{dr(x)}{dt} = r(x)(I_1(x) - r(x)^2) + \delta \quad (3)$$

$$\frac{d\theta(x)}{dt} = 1 + I_2(x) \quad (4)$$

$$I_1(x) = \sum_{\xi} w_1(\xi - x)r(\xi) \quad (5)$$

$$I_2(x) = \sum_{\xi} w_2(\xi - x)r(\xi) \sin(\theta(\xi) - \theta(x)) \quad (6)$$

$$w_1(x) = (1 - 2(\frac{x}{\sigma_1})^2) \exp\{-(\frac{x}{\sigma_1})^2\} \quad (7)$$

$$w_2(x) = \exp\{-(\frac{x}{\sigma_2})^2\} - C \quad (8)$$

Fig.2 illustrates our model of the non-linear oscillatory field. One oscillator is connected with all the other oscillators through two kinds of Mexican-hat-type connection, w_1 and w_2 . To facilitate visualization, we assume in this section that the oscillators

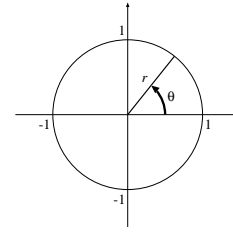


Fig. 1: The structure of a RIC (SL oscillator).

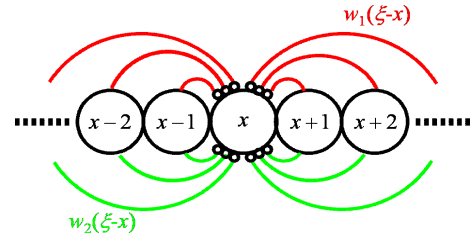


Fig. 2: Our model of the non-linear oscillatory field.

are arranged in one dimension. Moreover, only the connections from the oscillator in the center to the others is described in Fig.2, but actually, the other oscillators also have similar connection.

The oscillator located at place x has information of the amplitude $r(x)$ and the phase $\theta(x)$. the positive value of the amplitude $r(x) > 0$ represents neuronal firing, and $r(x) = 0$ represents that the neuron is not firing. The small positive constant δ deviate the amplitude $r(x)$ from an unstable equilibrium ($r(x) = 0$).

The input $I_1(x)$ effects on the amplitude $r(x)$ of the oscillator. One localized oscillatory excitation area exists over a range of the positive value of $I_1(x) > 0$. On the other hand, the input $I_2(x)$ effects the phase $\theta(x)$. The positive value of $I_2(x) > 0$ increases the phase velocity.

As shown in Fig.3, two kinds of Mexican-hat-type connection $w_1(\xi - x)$ and $w_2(\xi - x)$ depend on the distance from one oscillator at place x to another oscillator at place ξ . Although both w_1 and w_2 are Mexican-hat-type connection, these two types of effect on the distant unit are different. While w_1 has no effect on the distant unit as $w_1(\infty) = 0$, w_2 has the negative effect on the distant unit as $w_2(\infty) = -C$, in order to maximize the phase difference between the distant units. For in-phase phase-locking within one localized oscillatory excitation area, the range of positive effect of $w_2(\xi - x) > 0$ must be wider than that of the localized oscillatory excitation area, $I_1(x) > 0$, namely, $\sigma_1 < \sigma_2$.

This non-linear oscillatory field allows one or several localized oscillatory excitation areas, as described in the next chapter.

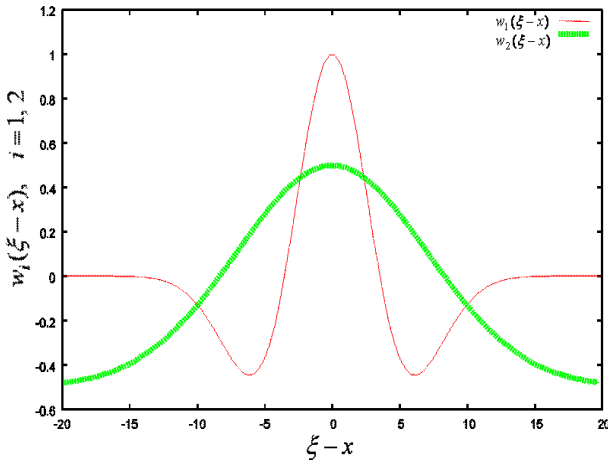


Fig. 3: Two kinds of Mexican-hat-type connection.

3 Computer Simulation

3.1 Settings

In this chapter, we assume two-dimensional field $\mathbf{x} = (x, y)$, $\mathbf{x}' = (\xi, \eta)$. Hence, the mathematical expression $\mathbf{x}' - \mathbf{x}$ represents $\|\mathbf{x}' - \mathbf{x}\|$. The non-linear oscillatory field consists of 40×50 oscillators, and the distance between one oscillator and the neighboring oscillator is defined as 0.05.

The winner of the ordinary dot-product SOM has the weight vectors which maximize the dot-product between the input [6]. In other words, the ordinary SOM algorithm has the ability of the peak detection. Amari (1977) model justifies the ability of the SOM algorithm by the dynamics of the nerve field [5].

Recently, oscillatory SOMs, the extended version of the SOMs by the oscillators, have been proposed [14]. The oscillatory SOMs allow the several winners in the output layer. In other words, the oscillatory SOMs detect the several maximal points of the function, or the dot-product between the input vectors and the weight vectors. The ability of the oscillatory SOMs to detect the several peaks of function is also required to be justified by the dynamics of the oscillatory field.

Therefore, we carried out the computer simulation of peak detection of function, using our model of the non-linear oscillatory field.

As shown in Fig.4, the constant extranal input $I_{\text{ex}}(\mathbf{x})$ which had three maximal points was added to $I_1(\mathbf{x})$ in the following equation (9). The external input was given by the equation (10), and the three maximal points were located at place $\mathbf{x}_1 = (7, 20)$, $\mathbf{x}_2 = (20, 40)$, $\mathbf{x}_3 = (30, 10)$.

$$I_1(\mathbf{x}) = \sum_{\mathbf{x}'} w_1(\mathbf{x}' - \mathbf{x})r(\mathbf{x}') + I_{\text{ex}}(\mathbf{x}) \quad (9)$$

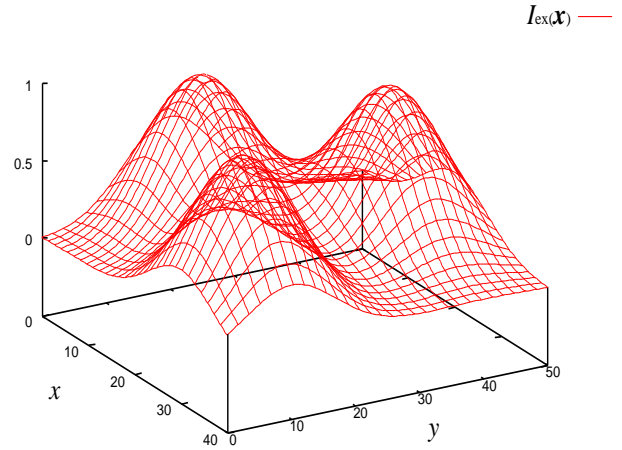


Fig. 4: The external input $I_{\text{ex}}(\mathbf{x})$ on the computer simulation.

Table 1: Parameters on the computer simulation

δ	σ_1	σ_2	C	σ
0.001	0.25	0.5	0.5	0.5

$$I_{\text{ex}}(\mathbf{x}) = \exp\left(-\frac{\|\mathbf{x} - \mathbf{x}_1\|^2}{\sigma^2}\right) + \exp\left(-\frac{\|\mathbf{x} - \mathbf{x}_2\|^2}{\sigma^2}\right) + \exp\left(-\frac{\|\mathbf{x} - \mathbf{x}_3\|^2}{\sigma^2}\right) \quad (10)$$

The simulation was carried out by using the Runge-Kutta method of which the size of time step was 0.005. Each oscillator was set the initial value of the amplitude to 0, and set that of the phase to the uniform pseudorandom number from 0 to 1. Each parameter was given as Table 1.

3.2 Results

Fig.5 illustrates the non-linear oscillatory field when the external input which has the three local maximal points is given. The circle represents the activated oscillator $r(\mathbf{x}) > 0$. The direction of the radius represents the phase $\theta(\mathbf{x})$ of the oscillator, or the timig of neuronal firing. Three framed rectangles denote the maximal points of the external input.

As shown in Fig.5, the non-linear oscillatory field kept stably three localized oscillatory excitation areas around the same number of maximal points of the external input. Therefore, the non-linear oscillatory field had the ability of detection of several

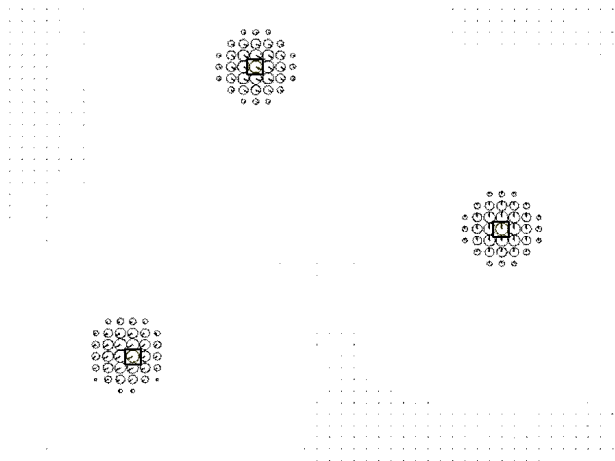


Fig. 5: The non-linear oscillatory field given the external input which had three maximal points. Three localized oscillatory excitation areas were kept stably around the same number of maximal points.

peaks from the external input by the localized oscillatory areas.

In this case, the oscillatory field entrained in-phase within each localized oscillatory excitation area, and entrained the phase difference $2\pi/3$ between the different localized oscillatory excitation areas.

4 Conclusion

We analyzed the dynamics of the non-linear oscillatory field consisting of RICs, or SL oscillators.

Our computer simulation showed that the non-linear oscillatory field with two kinds of Mexican-hat-type connection could keep three localized oscillatory excitation areas stably around the same number of maximal points of the external input. Thus, our model has the ability of peak detection of the function, which Amari model also has. Moreover, the non-linear oscillator field could also realize in-phase phase-locking within each localized oscillatory excitation area, but maximize the phase difference between different localized oscillatory excitation areas.

This non-linear oscillatory field provides theoretical base for the oscillatory SOM algorithm, as Amari (1977) model of the nerve field provided mathematical base for the SOM algorithm [14].

References

[1] H. V. B. Hirsch and D. N. Spinelli, "Visual experience modifies distribution of horizontally

and vertically oriented receptive fields in cats." *Science*, Vol.168, pp.869-871, 1970.

- [2] C. Blackmore and G. F. Cooper, "Development of the brain depends on the visual environment", *Nature*, Vol.228, pp.477-478, 1977.
- [3] C. von der Malsburg, "Self-organization of orientation sensitive cells in the striate cortex", *Kybernetik*, Vol.14, pp.85-100, 1973.
- [4] S. Amari and A. Takeuchi, "Mathematical theory on formation of category detecting nerve cells", *Biological Cybernetics*, Vol. 29, PP.127-136, 1978.
- [5] S. Amari, "Dynamics of pattern formation in lateral-inhibition type neural fields", *Biological Cybernetics*, Vol. 27, PP.77-87, 1977.
- [6] T. Kohonen, "Self-Organizing Maps" *Springer-Verlag*, 1995.
- [7] L. F. Abbott and S. B. Nelson, "Synaptic plasticity: taming the beast", *Nature*, Vol.3, pp.1178-1183, 2000.
- [8] R. Eckhorn, R. Bauer, W. Jordan, M. Brosch, W. Kruse, M. Munk, and H. J. Reiboeck, "Coherent oscillations: a mechanism of feature linking in the visual cortex?", *Biological Cybernetics*, Vol. 60, pp.121-130, 1988.
- [9] C. M. Gray, P. Konig, A. K. Engel, and W. Singer, "Oscillatory responses in cat visual cortex exhibit intercolumnar synchronisation which reflects global stimulus properties", *Nature*, 388, pp.334-337, 1989.
- [10] Y. Kuramoto, "Chemical oscillations, waves, and turbulence", *Springer Verlag*, 1982.
- [11] F.C. Hoppensteadt, and J.P. Keener, "Phase-locking of biological clocks", *Journal of Mathematical Biology*, Vol.15, No.3, pp.339-349, 1982.
- [12] T. Aonishi, "Macroscopic asymptotic property from Stuart-Landau oscillator to phase oscillator -A case of the third order Stuart-Landau equation- (in Japanese)", *IEICE Technical Report*, Vol.101, No.238, pp.17-24, 2001.
- [13] R. Miyata, A. Date and K. Kurata, "Phase-locking in localized oscillatory excitation on neural oscillatory fields (in Japanese)", *SOFT*, in press, 2010.
- [14] R. Miyata, and K. Kurata, "Solving the binding problem with separated extraction of information by Oscillatory self-organizing maps", *SCIS & ISIS*, in press, 2010.

Multiple Granger causality tests for network structure estimation from time-series data

Hikaru Harima¹, Shigeyuki Oba^{1,2}, and Shin Ishii¹

¹*Graduate School of Informatics, Kyoto University*

²*PRESTO, Japan Science and Technology Agency*

(harima-h@sys.i.kyoto-u.ac.jp, oba@i.kyoto-u.ac.jp, ishii@i.kyoto-u.ac.jp)

Abstract: To identify network structures is a key for elucidating functions of various kinds of networks such as cortical local circuits. Granger causality (GC) test has been used for estimating directed network structure from time-course of neuronal activities. Although GC statistic for a pair of nodes can be substantially influenced by other nodes, ignoring such influence can degrade detection performance of multiple GC tests. To improve the multiple GC tests, and hence the estimation of large network structures, therefore, we propose an extension of GC by introducing optimal discovery procedure (ODP) that shows the best detection power in general multiple testing problems. Applying our proposed method to a benchmark dataset, we show the performance of estimating the network structure is improved over those by the existing methods.

Keywords: Granger causality, network structure, time-series analysis, optimal discovery procedure

I. INTRODUCTION

To identify network structures is a key for elucidating functions of various kinds of networks; for example, a cortical local circuit would have its own function in the brain information processing, which is basically defined by the connectivity between constituent neurons. Since it is often difficult to directly observe anatomical structures especially in vivo, there have been numerous attempts to estimate network structures based on electrophysiological activities of neurons. For examples, multiple-electrode arrays [1] have been widely used, and recently, functional multi-neuron calcium imaging (fMRI) [2] comes to be available for observing neural activities with both temporally and spatially high resolutions.

Causal structure of a directed network can be uniquely represented by the set of directed causal links between pairs of network nodes; then testing whether a directed link exists or not between a single pair of nodes is the basis for estimating the whole network's causal structure. Granger causality (GC) [3] has become popularly used for estimating existence of each link; a directed causal influence from a node A to a node B is detected if time-series prediction accuracy for node B by means of an autoregressive (AR) model is significantly improved by incorporating time-series observation for node A into its explanatory variable. Although GC provides a useful tool for estimating network structure, there still remains the problem of 'multiplicity'. As the number of elements (e.g., neurons)

becomes large, the number of possible links grows huge, which makes the estimation of false positives and false negatives in the results obtained by GC tests quite difficult. A solid treatment of such multiplicity was previously proposed by Storey [4,5]; his optimal discovery procedure (ODP) is known to be the most powerful test in multiple simultaneous statistical hypothesis testing (MSHT), like the detection problem of causality links from huge number of possible links in neuronal networks.

In this study, we propose a new method to determine directed network structure based on application of ODP to GC tests. We demonstrate the performance of causal link detection of the proposed method is better than those by the existing method when applied to a benchmark datasets.

II. METHODS

1. Granger Causality

A GC test tries to identify causal relationship between two nodes by assuming an autoregressive (AR) model between them. Consider a test of a causal link from an input node I_i to an output node O_i based on their observations $\mathbf{x}^{(I_i)}$ and $\mathbf{x}^{(O_i)}$, where $\mathbf{x}^* = (x_1^*, \dots, x_T^*)$ denotes a time-course observed at a node *. The null hypothesis assumes the output node admits an individual AR process: then, if the null hypothesis holds, $x_t^{(O_i)}$ is predicted by

$$\hat{x}_t^{(Oi)}(\mathbf{x}^{(Oi)}) = \sum_{j=1}^p w_j^{(Oi:null)} x_{t-j}^{(Oi)},$$

where p is the order of the AR process. On the other hand, the alternative hypothesis assumes causal influence from Ii to Oi . In this case, $x_t^{(Oi)}$ is predicted by a vector autoregressive (VAR) model which employs not only the past observations of Oi but also those of Ii as its explanatory variable:

$$\hat{x}_t^{(Oi)}(\mathbf{x}^{(Oi)}, \mathbf{x}^{(Ii)}) = \sum_{j=1}^p (w_j^{(Oi:alta)} x_{t-j}^{(Oi)} + w_j^{(Ii:alta)} x_{t-j}^{(Ii)}), \quad (1)$$

where $w_j^{(Oi:null)}$, $w_j^{(Oi:alta)}$, and $w_j^{(Ii:alta)}$ are regression parameters. By simply assuming the prediction errors obey Gaussian distribution, the null and alternative likelihoods are given by

$$f_i(\mathbf{x}^{(Oi)}, \mathbf{x}^{(Ii)}) = \prod_{t=p+1}^T N(x_t^{(Oi)}; \hat{x}_t^{(Oi)}(\mathbf{x}^{(Oi)}), \mu, \sigma_{i:null}^2),$$

$$g_i(\mathbf{x}^{(Oi)}, \mathbf{x}^{(Ii)}) = \prod_{t=p+1}^T N(x_t^{(Oi)}; \hat{x}_t^{(Oi)}(\mathbf{x}^{(Oi)}, \mathbf{x}^{(Ii)}), \mu, \sigma_{i:alta}^2),$$

where $N(x; \mu, \sigma^2)$ denotes Gaussian probability density function of mean μ and variance σ^2 . The regression parameters in these likelihood functions, $\hat{f}_i(\mathbf{x}^{(Oi)}, \mathbf{x}^{(Ii)})$ and $\hat{g}_i(\mathbf{x}^{(Oi)}, \mathbf{x}^{(Ii)})$, can be determined by maximum likelihood (ML) estimation, based on the observations. The variances in the null and alternative likelihood functions can also be determined by ML estimations, as:

$$\hat{\sigma}_{i:null}^2 = \frac{\sum_{t=p+1}^T (x_t^{(Oi)} - \hat{x}_t^{(Oi)}(\mathbf{x}^{(Oi)}))^2}{T-p},$$

$$\hat{\sigma}_{i:alta}^2 = \frac{\sum_{t=p+1}^T (x_t^{(Oi)} - \hat{x}_t^{(Oi)}(\mathbf{x}^{(Oi)}, \mathbf{x}^{(Ii)}))^2}{T-p}.$$

After obtaining the null and alternative likelihood functions, we have the log-likelihood ratio as

$$LLR_i = \frac{T-p}{2} \log \left(\frac{\hat{\sigma}_{i:null}^2}{\hat{\sigma}_{i:alta}^2} \right).$$

Since we have assumed the two likelihood functions both obey Gaussian, we can apply the standard F-test to the likelihood ratio; thus, the GC test can be used for identifying the causal relationship.

2. Optimal Discovery Procedure

The ODP defines the most powerful test in MSHT situations [4]. According to the theory of ODP, expected number of true positives (ETP) and expected number of false positives (EFP) in MSHT are considered, and a statistical test is said most powerful if any other test with smaller EFP cannot have larger ETP. Storey showed that such an ideal statistic, ODP, exists that

setting any threshold on the ODP statistic becomes the most powerful test. More concretely, in MSHT, we consider m hypothesis tests at the same time, in each of which it is tested whether the null or alternative hypothesis is plausible after given observations of a single variable: $X_i, i=1, \dots, m$, based on the null and likelihood functions: $f_i(X_i)$ and $g_i(X_i)$. In this situation, the true ODP statistic (TODP) is defined by

$$S^{\text{TODP}}(X_i) = \frac{\sum_{j=1}^m (1-w_j) g_j(X_i)}{\sum_{j=1}^m w_j f_j(X_i)},$$

where $w_i=1$ (or $w_i=0$) holds if the null (or alternative) hypothesis is true for the i -th test. Since $f_i(X_i)$, $g_i(X_i)$ and w_i are unknown in actual situations, however, the ODP statistic should be estimated based on observed data. Then, instead, we use estimated ODP (EODP):

$$S^{\text{EODP}}(X_i) = \frac{\sum_{j=1}^m (1-\hat{w}_j) \hat{g}_j(X_i)}{\sum_{j=1}^m \hat{w}_j \hat{f}_j(X_i)},$$

where \hat{w}_i is estimated by a conventional statistical test, and $\hat{f}_i(X_j)$ and $\hat{g}_i(X_j)$ are null and alternative likelihoods, respectively, estimated based on available observations. Let $\hat{F}_{ij} \equiv \hat{f}_i(X_j)$ and $\hat{G}_{ij} \equiv \hat{g}_i(X_j)$; we call these terms self-likelihood terms if $i=j$ and mutual-likelihood terms otherwise. The ODP statistic involves mutual-likelihood terms, and then, the detection power is improved over ordinary likelihood ratio tests which employ only the self-likelihood terms.

3. ODP for GC

Here, we apply the idea of ODP to multiple GC tests. When a directed network consists of N nodes, the number of its possible connections is as many as $M = N(N-1)$. Although the conventional application of GC tests to network structure estimation has been ignored this multiplicity, introduction of the idea of ODP would improve the detection power, because of possible correlations between constituent nodes in the network. In multiple GC test situations, the i -th test would be performed based on a set of observations of the corresponding pair of nodes. Then, the mutual-likelihood functions of null and alternative hypotheses in ODP employ observations of the two nodes as:

$$\hat{F}_{ji} = f_j(\mathbf{x}^{(Oi)}, \mathbf{x}^{(Ii)}),$$

$$\hat{G}_{ji} = g_j(\mathbf{x}^{(Oi)}, \mathbf{x}^{(Ii)}).$$

To obtain the estimate EODP statistic, the weight parameters w_i in equation (1) is necessary; in this case, we set $\hat{w}_i=1$ (or $\hat{w}_i=0$) if the null (or alternative) hypothesis is accepted in the individual i -th GC test. It should be noted that this individual test is just for

defining EODP statistic, and actual MSHT is performed based on the EODP statistic, not by the individual GC test. Consequently, we obtain ODPGC (EODPGC) statistic as:

$$EODPGC_i(\mathbf{x}^{(Oi)}, \mathbf{x}^{(Ii)}) = \frac{\sum_j (1 - \hat{w}_j) \hat{G}_{ji}}{\sum_j \hat{w}_j \hat{F}_{ji}}.$$

III. SIMULATION

1. Setting

Computer simulation was performed to examine the proposal method. By assuming that true network structure consists of 5 nodes and 5 directed causal links (Fig. 1), simulated time-series were obtained by means of a VAR model of the true order being $p = 3$; this benchmark setting was also used in a previous study [6].

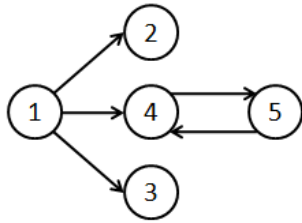


Fig.1. A five node network

In addition, we prepared larger but redundant networks which were constructed by copying the 5-node graph (Fig. 1) $m = 1, 2, \dots, 14$ times; then we have in total 14 networks with $M = 5, 10, \dots, 70$ nodes. For example, the network with 15 nodes has three identical sub-networks of five nodes and no causal link between the sub-networks. For each of the 14 networks, time-series of length $T = 50$ was for every node generated. This length $T = 50$ was set to examine the applicability of statistical tests to short time-series.

Detection accuracy of causal links was examined for the proposed method (EODPGC), ODP with true weights (TODPGC), and simple individual GC tests. The general performance of statistics was examined in terms of ROC curves. Since an ROC curve represents the behavior of the statistic within a two-dimensional plane of the false positive rate (horizontal axis) and the true positive rate (vertical axis), for each threshold setting. Because detection accuracy of the statistic depends on this threshold setting, we also examined area under the ROC curve (AUC) as a general criterion; a larger AUC means higher detection accuracy regardless of the threshold setting.

2. Result

Figure 2 shows ROC curves for the three methods in the case of $p = 3$ and $M = 50$.

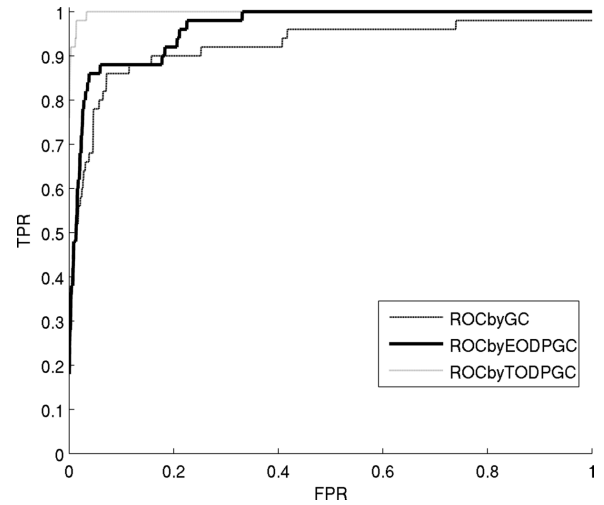


Fig.2. ROC curves of EODPGC (black), TODPGC (light gray) and GC test (gray): $(p, T, M) = (3, 50, 50)$

In this case, ODPGC with the true weight values (w) (TODPGC) achieved almost 100% accuracy with appropriate thresholds, though the true weight parameter is not available in actual applications. EODPGC, which employs the estimated weight values performed better than the GC tests; this is also confirmed by AUC scores (EODPGC: ODPGC with the estimated weight values (\hat{w}), GC: Granger causality).

Next, the performances were compared by varying the order of AR model p . The number of nodes M was set at 50. Both GC and EODPGC performed the best when $p = 3$. This result is reasonable because we used a VAR-model of the order of 3 to generate the simulation time-series data.

Next, we examined how the AUC behaves as the network size increased: $M = 5, 10, \dots, 70$ (Fig. 3). The order of AR model p was fixed at 3.

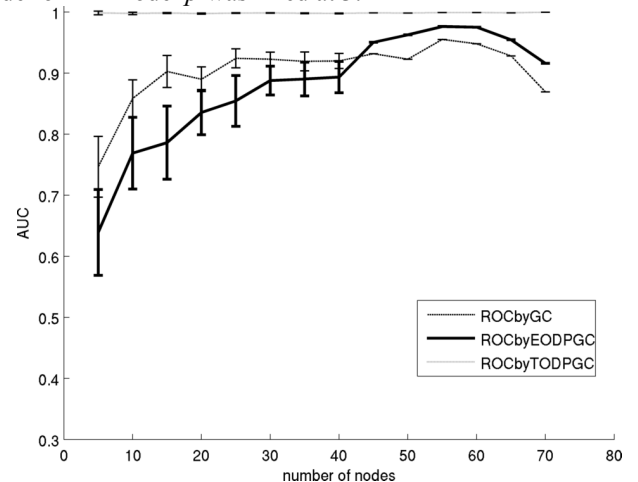


Fig.3. AUC for a various numbers of network nodes, where $(p, T) = (3, 50)$

In this figure, the mean AUC value and half of standard deviation over 20 trials are shown for $M = 5, \dots, 40$,

and a single AUC value for $M = 45, \dots, 70$. As the multiplicity became large due to the increase in the number of network nodes, such as $M > 40$, the performance of EODPGC was likely better than that of GC. Although individual GC tests do not consider the correlation between the tests, the correlation does exist effectively, because the connectivity between a pair of nodes is not independent of that of another pair, due to the eventual effective correlation between the nodes in the network. The statistics based on ODP show good performance especially when such effective correlation exists between the multiple tests to be performed at the same time.

IV. CONCLUSION

We proposed a powerful method to identify a large causal network structure. This method is an application of the ODP theory to multiple GC tests. Comparing our method with the standard GC tests, we showed a good performance for identifying the network structure especially when the network size is large. There would be some remaining issues; comparison with recent methods, for example, conditional granger causality (CGC) [7] and partial granger causality (PGC) [6] should be done in the near future. Application to electrophysiological data from real neuronal networks is also an important future work.

REFERENCES

- [1] R. Q. Quiroga, S. Panzeri (2009), "Extracting information from neuronal populations: information theory and decoding approaches", *Nature Reviews Neuroscience*, 10:173-185.
- [2] T. Sasaki, N. Matsuki, Y. Ikegaya (2007), "Metastability of active CA3 networks", *The Journal of Neuroscience*, 27:517-528.
- [3] C. Granger (1969), "Investigating causal relations by econometric models and cross-spectral methods", *Econometrica*, 37:424-438.
- [4] J. D. Storey (2007), "The optimal discovery procedure: a new approach to simultaneous significance testing", *Journal of the Royal Statistical Society. Series B, Statistical methodology*, 69: 347-368.
- [5] J. D. Storey (2006), "The optimal discovery procedure for large-scale significance testing, with applications to comparative microarray experiments", *Biostatistics (Oxford, England)*, 8: 414-439.
- [6] S. Guo (2008), A. K. Seth, K. M. Kendrick, C. Zhou, J. Feng, "Partial Granger causality-Eliminating exogenous inputs and latent variables", *Journal of Neuroscience Methods*, 172: 79-93.
- [7] J. Geweke (1982), "Measurement of linear dependence and feedback between multiple time series",

Journal of the American Statistical Association, 77: 304-313.

A Simulation Study of Visual Perceptual Learning with Attentional Signals

Satoshi Naito¹, Naoto Yukinawa¹ and Shin Ishii^{1,2}

¹*Graduate School of Informatics, Kyoto University
Gokasho, Uji, Kyoto, Japan*

Tel : 0774-81-3938; Fax :0774-38-3941

²*RIKEN, Computational Science Research Program*

naito-s@sys.i.kyoto-u.ac.jp, naoto-yu@sys.i.kyoto-u.ac.jp, ishii@i.kyoto-u.ac.jp

Abstract: Repeated exposure to a specific stimulus can enhance animal's sensitivity to it so that the perceptual capability is improved. This experience-induced perceptual improvement is referred to as perceptual learning. However, the neural system has some robustness and is not necessarily modified by its any input. In the case of visual perceptual learning (VPL), perceptual performance for a task-relevant stimulus can be selectively improved without any sensitivity change to task-irrelevant stimuli which are presented even simultaneously with the task-relevant one. In this study, we propose a feed-forward spiking neural network model consisting of a primary visual cortex (V1) layer and a higher visual area (V4) layer; their inter-layer feed-forward connections are modified by synaptic learning in a particular interest in how VPL can be affected by neural activities in the higher area due to attentional signals. Through simulations, we show attentional inputs are needed to facilitate inter-layer synaptic learning which yields improved sensitivity to the task-relevant stimulus, and thus to increase the task performance.

Keywords: Perceptual learning, Visual attention, Spiking neural network, Spike-timing dependent plasticity

I. INTRODUCTION

Animal's brain continues to modify the structures of its neural networks to adapt to environmental changes even after its maturation. Repeated exposure to a specific stimulus can enhance animal's sensitivity to it so that the perceptual capability is consequently improved. This experience-induced perceptual improvement is referred to as perceptual learning. However, the neural system has some robustness and is not necessarily modified by its any input. In the case of visual perceptual learning (VPL), perceptual performance for a task-relevant stimulus can be selectively improved without any sensitivity change to task-irrelevant stimuli which are presented even simultaneously with the task-relevant one. These observations raise the following questions: what is the computational basis of VPL and how does the brain accomplish VPL in such a noisy environment with appropriately detecting relevant information?

There is a hypothesis that VPL is due to changes in synaptic connections between neurons of the primary visual cortex which acts as feature extractors of visual elements and those of the higher visual cortical areas which are involved in decision making functions [1]. A preceding study reported that the bell-shaped tuning curve for the task-relevant stimulus gets sharpened in V4 neurons which receive inputs from V1 neuronal population, but not in V1 neurons [2], supporting this

hypothesis. In terms of Fisher information, sharpening of a tuning curve leads to increase in information, suggesting the improvement of representation of sensory information encoded by neuronal population [3]. In addition, it has been suggested that active and persistent attention to a feature to be learned is also needed for VPL [4]; one of the previous studies reported that when two different stimuli were presented simultaneously but the subject was required to pay attention to one of them, no VPL occurred for the stimulus to which the subject did not pay attention [5]. Another existing study reported that responses of V4 neurons to a particular stimulus with paying attention were significantly higher than those without paying attention [6], which also suggested the existence of attentional control on VPL.

Nevertheless, there is still a missing link; no previous study has clarified the direct relationship between sharpening of tuning curves of V4 neurons and connection changes between V1 and V2 which is affected by the attentional control during VPL. For unified explanation of attentional effects on V4 neurons and sharpening of their tuning curves induced by VPL, we propose in this study a feed-forward spiking neural network model which includes a V1 layer and a V4 layer; neurons in the V4 layer receive inputs from neurons in the V1 layer and also top-down attentional excitatory signals. Performing a learning simulation of this network, we show that the task performance is

improved due to changes in neuronal connections, and is more facilitated by V4's activities enhanced by the attentional signals.

II. MODEL

In this study, we used a grating task [7] for simulating a VPL situation. In a single trial of the real grating task, two grating images are sequentially presented to a subject; the second grating image is rotated from the first one. Then a subject is required to answer whether the tilt orientation of the second image has changed from that of the first one in a clockwise manner or in a counterclockwise manner. A previous experimental study observed that repeated exposure to such grating stimuli induces changes in tuning curves of V4 neurons [2]. According to the hypothesis that VPL is due to connectional changes between neurons of the primary visual cortex and those of the higher visual cortical areas [1], it is thought that changes in V4 responses are mainly due to connectional changes between V4 and V1 neurons; the former corresponds to the higher visual cortical area and is projected by the foveal region of V1 directly [8], and the latter codes tilt orientation of presented grating stimuli by means of its orientation selectivity. Based on these assumptions, in this study, we propose a hierarchical and feed-forward neural network model which consists of two neuronal layers of V1 and V4 where connections between the layers can be modified by a spike-timing dependent plasticity (STDP) rule (Fig. 1). In the actual experimental setting, a subject would be exposed not only to the target stimuli but also to many distracters; however, in this study we assume that the model neurons respond only to grating image stimuli for simplicity. We present the details of the model in the following sections.

1. V1 layer

The V1 layer consists of 80 model neurons each of which was implemented as a Poisson spike generator with frequency $r(\theta_{\text{input}})$; the frequency was given by a Gaussian-like neuronal response function with a preferred orientation θ_{PD} , to the tilt orientation of an input grating stimulus θ_{input} :

$$r(\theta_{\text{input}}) = a \exp\left(-\frac{|\theta_{\text{input}} - \theta_{\text{PD}}|}{2\sigma_r^2}\right) + R, \quad (1)$$

$$\theta_{\text{PD}} = \bar{\theta}_{\text{PD}} + \Delta\theta_{\text{PD}},$$

$$\bar{\theta}_{\text{PD}} \in \{n\pi/8\} (n=0, \dots, 7), \quad \Delta\theta_{\text{PD}} \sim N(0, \sigma_{\text{PD}}^2),$$

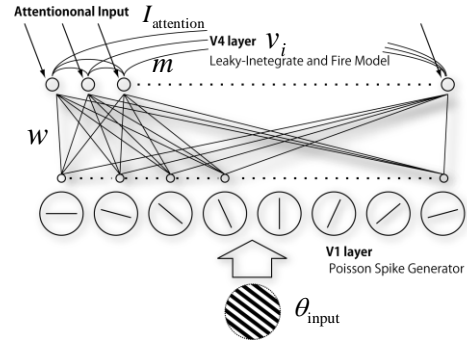


Fig.1. The architecture of network model

where a , σ_r and R are constants; we set $a=0.02$, $\sigma_r=0.5$ and $R=0.002$ in the simulation. Each V1 neuron has own orientation selectivity to gratings (σ_r) and the preferred tilt orientation (θ_{PD}). The V1 layer consists of 8 groups of 10 neurons which have different orientation preference (Fig. 1); the preferred orientations of the 10 neurons in each group do not vary so much around its average $\bar{\theta}_{\text{PD}}$, but they have different means between the 8 groups.

2. V4 layer

The V4 layer consists of 100 neurons each of which was implemented as a leaky-integrate and fire neuron model:

$$\tau_v \frac{dv_i}{dt} = -(v_i - V_{\text{rest}}) + I_i + I_{\text{attention}}, \quad (2)$$

$$v_i \leftarrow V_{\text{rest}} \text{ if } v_i \geq V_{\text{threshold}},$$

where τ_v is a membrane time constant. v_i , V_{rest} , and $V_{\text{threshold}}$ are membrane potential, resting potential, and firing threshold, respectively. In this study, we set $\tau_v = 1$, $V_{\text{rest}} = -64$ and $V_{\text{threshold}} = 30$. I_i and $I_{\text{attention}}$ represent input current and attentional input current, respectively. A V4 neuron i receives synaptic currents I_i from V1 and V4 neurons:

$$I_i = \int_0^t f(t-t') \left\{ \sum_j w_{ij} u_j^{v1}(t') + \sum_k m_{ik} u_k^{v4}(t') \right\} dt', \quad (3)$$

$$f(t) = \frac{t}{\tau_u} e^{1-t/\tau_u},$$

where $u_j^{v1}(t)$ and $u_i^{v4}(t)$ represent indicator functions of spike occurrences at V1 neuron j and V4 neuron i , respectively. When a spike occurs in V1 (V4) neuron $j(i)$ at t , $u_{j(i)}^{v1(v4)}(t) = 1$ and otherwise $u_{j(i)}^{v1(v4)}(t) = 0$. w_{ij} is synaptic strength of feed-forward connection from V1 neuron j to V4 neuron i , and m_{ik} is synaptic strength of recurrent connection from V4 neuron k to V4 neuron i . In this study, we set $m_{ik} = 0.1(i=k)$ or $-0.04(i \neq k)$. $f(t)$ is a spike response function with the time constant of $\tau_u (=1.5)$.

3. Spike-timing dependent plasticity

During VPL, synaptic strength w_{ij} between a V1 neuron j and a V4 neuron i was updated by an additive STDP rule [9] as follows:

$$w_{ij} \leftarrow w_{ij} + \Delta w,$$

$$\Delta w = \begin{cases} \alpha_+ \exp\left(-\frac{|\Delta t|}{\tau_+}\right) & \text{if } \Delta t \geq 0, \\ -\alpha_- \exp\left(-\frac{|\Delta t|}{\tau_-}\right) & \text{if } \Delta t < 0, \end{cases}$$

$$\Delta t = t_i - t_j, \quad (4)$$

where t_i and t_j are spike timing of neuron i (post) and j (pre), respectively. α_+ (α_-) > 0 and τ_+ (τ_-) define the maximum amount of synaptic change and the time constant of long-term potentiation (depression). We used $\alpha_+ = 0.0103$, $\alpha_- = 0.0051$, $\tau_+ = 13.3$ and $\tau_- = 34.5$ in this study. On the other hand, we assumed that the connections within the V4 layer did not change, so they were fixed during VPL.

III. SIMULATION EXPERIMENTS

1. Simulation procedures

To examine the effects of top-down attentional inputs on VPL, we conducted a network simulation assuming the grating task. First, we initialized the synaptic connections between V1 and V4 neurons w_{ij} by presenting 20,000 uniformly random stimuli θ_{input} to the model network. This initial phase encouraged each V4 neuron to form a sparse receptive field for input stimuli, which is similar to the result by the sparse coding scheme [10]. An example of the resultant tuning curves which correspond to responses of V4 neurons to orientation of input grating stimuli are presented in Fig.2.

We then trained our model network by simulating the grating task. In a single simulation trial of the grating task, two grating stimuli were successively presented to the model network for 300 ms each. Tilt of the first grating was fixed to the base orientation $\theta_{\text{input}} = \theta_o$, and that of the second one was $\theta_{\text{input}} = \theta_o + \theta_d$ in each trial. In this simulation, we set $\theta_o = 24^\circ$ and θ_d was randomly drawn from a uniform distribution of $U(-10, 10)$.

2. Evaluation of attentional effects

To evaluate how the VPL proceeds in the model network, we calculated normalized tuning curves of V4 neurons, each of which was the connection-weighted summation of tuning curves of V1 neurons and normalized to make its maximum response a fixed value.

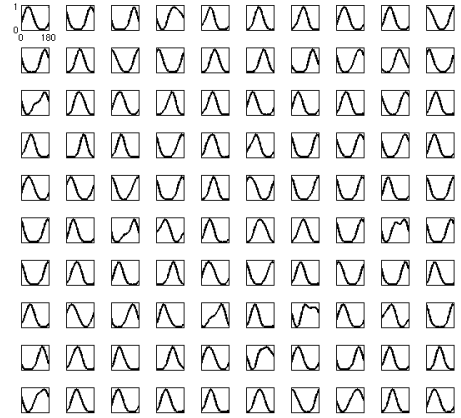


Fig.2. Orientation selectivity of V4 neurons before VPL. Each tuning curve was calculated based on tuning curves of V1 cells weighted by the connection values from the V1 cells to the corresponding V4 cell. The horizontal axis represents tilt of input grating stimuli and the vertical axis represents the normalized response. It is assumed that the V4 network can decode the orientation of input grating by integrating the patterns of V4 responses.

We then estimated “sharpness” of each V4 neuron to measure the degree of sensitivity to input stimuli by fitting its normalized tuning curve to a Gaussian function and then obtaining its variance. Finally, we tested how the sharpness of the neuronal population changed between before and after the VPL phase based on one-sided t-test [2]. Since we are also interested in the dependence of VPL on the top-down attentional signals, we conducted the simulation above by changing the level of attentional inputs.

IV. RESULTS

After simulating the model network in the grating task by setting various levels of attentional signals, $I_{\text{attention}} = \{0, \dots, 30\}$, we obtained tuning curves after learning (Fig. 3). This figure shows that the turning curves of some V4 neurons got sharpened significantly after VPL with a relatively large level of attentional signals ($I_{\text{attention}} = 22$), which is consistent with the existing experimental result in which tuning curves of V4 neurons became sharpened after VPL [2]. Fig. 4 shows histograms of sharpness of tuning curves of V4 neurons, before learning (upper panel) and after learning with no attentional inputs (middle panel) and relatively large attentional inputs (lower panel). The sharpening of tuning curves after VPL occurred in the population-wide manner in the V4 layer regardless of

the level of attentional inputs, whereas the stronger attentional signals likely induced sharper tuning curves ($I_{\text{attention}} = 0, p = 0.065$ and $I_{\text{attention}} = 22, p = 0.0011$). In addition, the minimum value of the sharpness with $I_{\text{attention}} = 22$ (18.8°) was smaller than that with $I_{\text{attention}} = 0$ (23.1°). On the other hand, too large attentional inputs induced broader tuning curves; indeed, mean sharpness after VPL with $I_{\text{attention}} = 30$ was $39.9^\circ \pm 0.00^\circ$ (the initial mean sharpness was $30.0^\circ \pm 8.7^\circ$). These results imply that appropriate level of attentional control to V4 neurons would work for promoting perceptual sensitivity.

V. DISCUSSION AND CONCLUSION

In this study, we simulated network learning in which synaptic connections between V1 and V4 neurons were modified by STDP during the grating task, and showed that our network model well reproduced sharpening of tuning curves of the V4 neurons. We also found that moderate attentional inputs yield sharpen tuning curves of the V4 neurons. These results imply that appropriate level of attention contributes to facilitating VPL while VPL occurs even without paying attention. In our network model, reductions in connectional strength between V1 and V4 neurons were often observed in V4 neurons which acquired sharpened tuning curves (result not shown). These synaptic reductions can depress responses of V4 neurons to input stimuli, while a previous study reported increase in spike frequency after VPL [2]. This inconsistency may be resolved by introducing backward attentional control from V4 to V1, as suggested in a previous study [11]. Backward attentional pathway would increase spike frequency of V1 neurons such to facilitate activities of the projected V4 neurons. In future work, therefore, we will examine attentional effects in VPL by cortical model networks including mutually-connected V1 and V4 layers.

REFERENCES

- [1] Doshier BA and Lu ZL (1998), Perceptual learning reflects external noise filtering and internal noise reduction through channel reweighting. *Proc. Natl. Acad. Sci. U.S.A.* 95(23): 13988-13993.
- [2] Yang TM and Maunsell JHR (2004), The effect of perceptual learning on neuronal responses in monkey visual area V4. *J Neurosci.* 24(7): 1617-1626.
- [3] Seung HS and Sompolinsky H (1993), Simple Models for Reading Neuronal Population Codes. *Proc. Natl. Acad. Sci. U.S.A.* 90(22): 10749-10753.

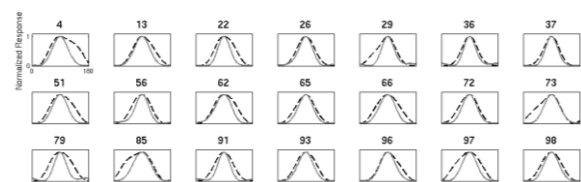


Fig.3. Tuning curves of V4 neurons before (dashed line) and after (solid line) 5,000 gating task trials with attentional input of $I_{\text{attention}} = 22$. Each tuning curve was rescaled and shifted to adjust the peak to the center of the horizontal axis.

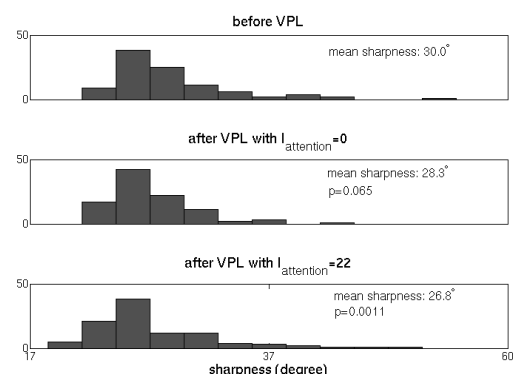


Fig.4. Histogram of sharpness of tuning curves of V4 neurons. Upper: before learning. Middle: after learning with no attentional inputs ($I_{\text{attention}} = 0$). Lower: after learning with a relatively strong attentional inputs ($I_{\text{attention}} = 22$).

- [4] Ahissar M and Hochstein S (1993), Attentional Control of Early Perceptual-Learning. *Proc. Natl. Acad. Sci. U.S.A.* 90(12): 5718-5722.
- [5] Schoups A, Vogels R et al. (2001), Practising orientation identification improves orientation coding in V1 neurons. *Nature* 412(6846): 549-553.
- [6] Luck SJ, Chelazzi L et al. (1997), Neural mechanisms of spatial selective attention in areas V1, V2, and V4 of macaque visual cortex. *J Neurophysiol* 77(1): 24-42.
- [7] Orban GA, Dupont P et al. (1997), Human brain activity related to orientation discrimination tasks. *Eur J Neurosci* 9(2): 246-259.
- [8] Zeki SM (1978), The cortical projections of foveal striate cortex in the rhesus monkey. *J Physiol* 277:227-244.
- [9] Bi GQ and Poo MM (1998), Synaptic modifications in cultured hippocampal neurons: Dependence on spike timing, synaptic strength, and postsynaptic cell type. *J Neurosci* 18(24): 10464-10472.
- [10] Olshausen BA and Field DJ (1996), Natural image statistics and efficient coding. *Network* 7(2): 33-339.
- [11] Buffalo EA et al. (2010), A backward progression of attentional effects in the ventral stream. *Proc. Natl. Acad. Sci. U.S.A.* 107(1): 361-365.

Medical Image Diagnosis of Lung Cancer by Revised GMDH-type Neural Network using Various Kinds of Neurons

Tadashi Kondo¹⁾ and Junji Ueno²⁾

^{1),2)} School of Health Sciences, The University of Tokushima, 3-18-15 Kuramoto-cho Tokushima 770-8509, Japan

¹⁾kondo@medsci.tokushima-u.ac.jp

Abstract: A revised Group Method of Data Handling (GMDH)-type neural network algorithm using various kinds of neurons is applied to the medical image diagnosis of lung cancer. The optimum neural network architecture for the medical image diagnosis is automatically organized using revised GMDH-type neural network algorithm and the regions of lung cancer are recognized and extracted accurately.

Keywords: Neural network, GMDH, Medical image diagnosis

I. INTRODUCTION

The conventional GMDH-type neural networks [1]-[3] are automatically organized using the heuristic self-organization method [4],[5] and the structural parameters such as the number of layers, the number of neurons in each layer, useful input variables and optimum neuron architectures are automatically determined so as to minimize the prediction error criterion Akaike's Information Criterion (AIC) [6] or Prediction Sum of Squares (PSS) [7]. In this paper, a revised GMDH-type neural network algorithm is developed. In this algorithm, the polynomial type and the radial basis function (RBF) type neurons are used for organizing the neural network architecture. A lot of complex nonlinear combinations of the input variables fitting the complexity of the nonlinear system are generated using the polynomial type neurons and only useful combinations of the input variables are selected for organizing the neural network architecture. In the output layer, the RBF type neuron is used for organizing the neural network and the output value of the neural network becomes between zero and one. The revised GMDH-type neural network is applied to the medical image diagnosis of lung cancer and it is shown that the revised GMDH-type neural network is accurate and useful method for the medical image diagnosis of lung cancer.

II. HEURISTIC SELF-ORGANIZATION

The GMDH-type neural network algorithm can automatically develop the optimum neural network architectures by the heuristic self-organization. The heuristic self-organization in the GMDH-type neural network is implemented through the following five procedures:

1) Separating the original data into training and test sets.

The original data are separated into training and test sets. The training data are used for the estimation of the weights of the neural network. The test data are used for organizing neural network architectures.

2) Generating the combinations of the input variables in each layer.

All combinations of r input variables are generated in each layer. The number of combinations is $\frac{p!}{(p-r)!r!}$. Here, p is the number of input variables and

the number of r is usually set to two.

3) Selecting the optimum neuron architectures

For each combination, the optimum neuron architectures which describe the partial characteristics of the nonlinear system can be calculated by applying the regression analysis [8] to the training data. The output variables y_k of the optimum neurons are called intermediate variables. In the GMDH-type neural network, the optimum neurons are selected from different neuron architectures.

4) Selecting the intermediate variables.

The L intermediate variables which give the L smallest test errors calculated using the test data are selected from the generated intermediate variables y_k . Selected L intermediate variables are set to the input variables of the next layer and calculations from procedure 2 to 4 are iterated.

5) Stopping the multilayered iterative computation.

When the errors for the test data in each layer stop decreasing, the iterative computation is terminated. The complete neural network which describes the characteristics of the nonlinear system can be constructed using the optimum neurons which are generated in each layer.

III. REVISED GMDH-TYPE NEURAL NETWORK USING VARIOUS KINDS OF NEURONS

The revised GMDH-type neural network architecture is shown in Fig.1. Here, nonlinear function g_i is described by the following Kolmogorov-Gabor polynomial:

$$g_i(x_1, x_2, \dots, x_p) = a_0 + \sum_i a_i x_i + \sum_i \sum_j a_{ij} x_i x_j + \dots \quad (1)$$

This nonlinear function is automatically organized by using the polynomial neurons. The architecture of the revised GMDH-type neural network is automatically organized using the heuristic self-organization and is produced as follows:

In the revised GMDH-type neural network, the original data are not separated into training and test sets

because PSS can be used as the test errors.

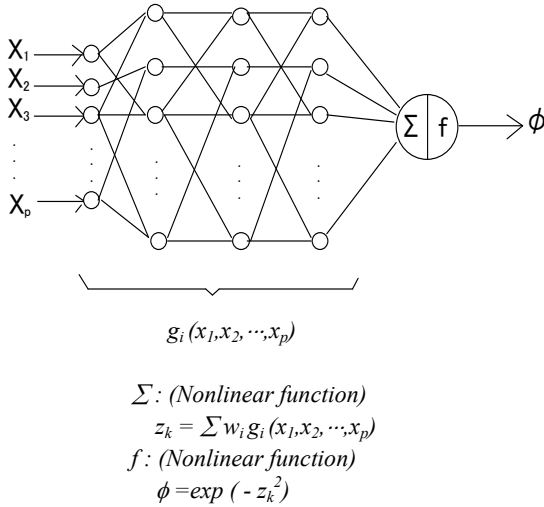


Fig.1 Architecture of revised GMDH-type neural network

1. The first layer

$$u_j = x_j \quad (j=1, 2, \dots, p) \quad (2)$$

where x_j ($j=1, 2, \dots, p$) are the input variables of the system, and p is the number of input variables. In the first layer, input variables are set to the output variables.

2. The second layer

Many combinations of two variables (u_i, u_j) are generated. For each combination, the neuron architecture is described by the following equations:

Σ : (Nonlinear function)

$$z_k = w_1 u_i + w_2 u_j + w_3 u_i u_j + w_4 u_i^2 + w_5 u_j^2 + w_6 u_i^3 + w_7 u_i^2 u_j + w_8 u_i u_j^2 + w_9 u_j^3 - w_0 \theta_l \quad (3)$$

f : (Linear function)

$$y_k = z_k \quad (4)$$

where $\theta_l = 1$ and w_i ($i=0, 1, 2, \dots, 9$) are weights between the first and second layer. The weights w_i ($i=0, 1, 2, \dots, 9$) are estimated by using the multiple regression analysis. This procedure is as follows:

First, the values of z_k are calculated using the following equation:

$$z_k = (-\log_e \phi')^{1/2} \quad (5)$$

where ϕ' is the normalized output variable. Then the weights w_i ($i=0, 1, 2, \dots, 9$) are estimated by using the stepwise regression analysis which selects useful input variables using the PSS. Therefore, only useful variables in (3) are selected and neuron architecture can be organized by these selected useful variables.

From these generated neurons, L neurons which minimize PSS values are selected. The output values (y_k) of L selected neurons are set to the input values of the neurons in the third layer.

3. The third and succeeding layers

In the third and succeeding layers, the same computation of the second layer is continued until PSS values of L neurons are not decreased. When the iterative computation is terminated, the following calculation of the output layer is carried out.

4. The output layer

In the output layer, the output values of the neural network are calculated from z_k as follows:

$$y_k = \exp(-z_k^2) \quad (6)$$

So, in the output layer, the neuron architecture becomes as follows:

Σ : (Nonlinear function)

$$z_k = \sum w_i g_i(x_1, x_2, \dots, x_p) \quad (7)$$

f : (Nonlinear function)

$$\phi = \exp(-z_k^2) \quad (8)$$

At last, the complete neural network architecture is produced by selected neurons in each layer.

Figure 2 shows the flowchart of the revised GMDH-type neural network.

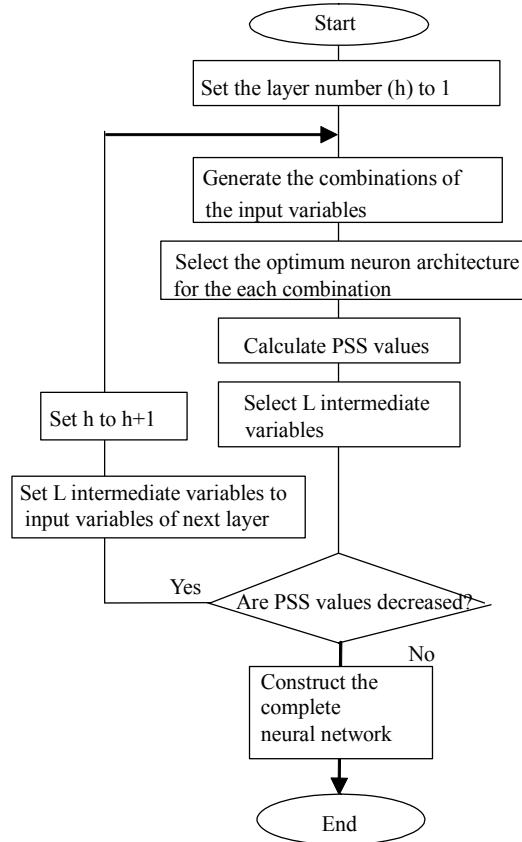


Fig. 2 Flowchart of the revised GMDH-type neural network

IV. APPLICATION TO THE MEDICAL IMAGE DIAGNOSIS OF LUNG CANCER

In this study, the regions of lung cancer were recognized and extracted automatically by using the revised GMDH-type neural network. Multi-detector row CT (MDCT) images of the lungs are used in this study. In the recognition procedure, the revised GMDH-type neural network is organized to recognize the lung regions and then the regions of lung cancer are extracted.

1. Extraction of the candidate image regions of lung cancer

A lung image shown in Fig. 3 was used for organizing the revised GMDH-type neural network. The statistics of the image densities and x and y coordinates in the neighboring regions, the $N \times N$ pixel regions, were used as the image features. Only five parameters namely, mean, standard deviation, variance and x and y coordinates were selected as the useful input variables. The output value of the neural network was zero or one. When $N \times N$ pixel region was contained in the lung regions, the neural network set the pixel value at the center of the $N \times N$ pixel region to one and this pixel was shown as the white point. The neural networks were organized when the values of N were from 3 to 15. It was determined that when N was equal to 4, the neural network architecture had the smallest recognition error. Five useful neurons were selected in each hidden layer. Figure 4 shows the variation of PSS values in the layers. The calculation of the revised GMDH-type neural network was terminated in the sixth layer. The PSS value in the second layer was not small but the PSS value was decreased gradually through the layers and the small PSS value was obtained in the sixth layer. The revised GMDH-type neural network outputs the lung image (Fig.5) and the first post-processing analysis of the lung image was carried out. In the first post-processing of the output image, image processing such as closing, opening and so on were carried out and the small isolated regions were eliminated and the outlines of the lung regions were expanded outside by $N/2$ pixels. Figure 6 shows the output image after the first post-processing and the lung regions that contains the abnormal regions were extracted. The output image after the first post-processing was overlapped to the original image (Fig.3) in order to check the accuracy of the image recognition as shown in Fig.7. The recognized lung regions are accurate. The lung regions were extracted from the original image using the output image. Figure 8 shows the extracted image of the lungs. The second post-processing such as closing, opening and so on was carried out and the lung regions which did not contain the abnormal regions was obtained as shown in Fig.9. Figure 10 shows the extracted image of the lungs. The candidate image region of lung cancer were extracted from Fig.8 using Fig.10 and shown in Fig.11. The recognition results were compared with those of the conventional sigmoid function neural network trained using the back propagation method.

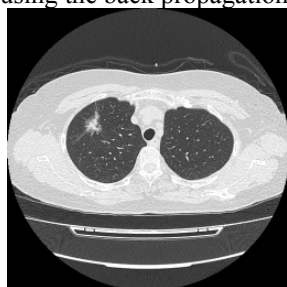


Fig.3 Original image

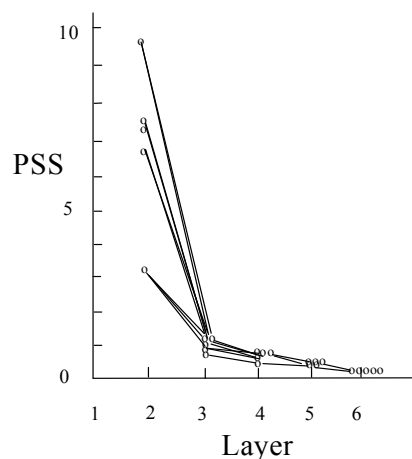


Fig.4 Variation of PSS in the revised GMDH-type neural network



Fig.5 Output image of the neural network

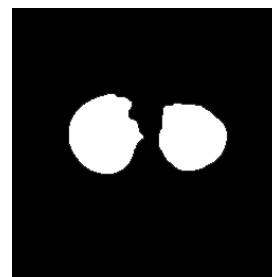


Fig.6 Output image after the first post-processing

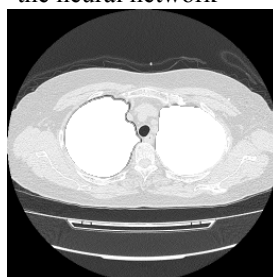


Fig.7 Overlapped image

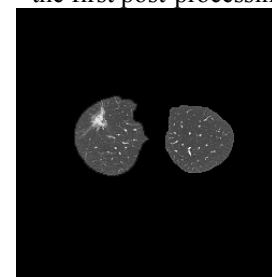


Fig.8 Extracted image (1)

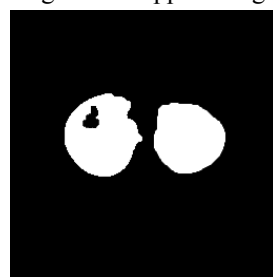


Fig.9 Output image after the second post-processing

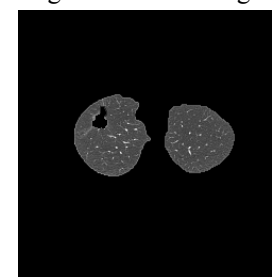


Fig.10 Extracted image (2)

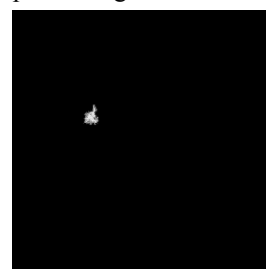


Fig.11 The candidate image region of lung cancer

2. Recognition results of the conventional neural network trained using the back propagation algorithm

A conventional neural network trained using the back propagation algorithm was applied to the same diagnosis problem and the results were compared with the results obtained using the revised GMDH-type algorithm. The conventional neural network had a three layered architecture, which was constructed using the input, hidden and output layers, and the same five input variables, which were mean, standard deviation, variance, x and y coordinates, were used in the input layer. Weights of the neural network were estimated using the back propagation algorithm and initial values of the weights were set to random values. The learning calculations of the weights were iterated changing structural parameters such as the number of neurons in the hidden layer and the initial values of the weights. The output images, when the numbers of neurons in the hidden layer (m) are 3, 5 and 7, are shown in Fig.12. These images contain more regions which are not part of the lungs and the outlines of the lungs are not extracted with required clarity compared with the output images obtained using the GMDH-type neural network algorithm, which is shown in Fig.5. Note that, in case of the conventional neural network, we obtain many different output images for various structural parameters of the neural network and many iterative calculations of the back propagation are needed for various structural parameters in order to find more accurate neural network architecture. In case of the revised GMDH-type neural network, the optimum neural network architecture is automatically organized so as to minimize prediction error criterion PSS using heuristic self-organization method [4],[5] and many iterative calculations for various structural parameters are not needed because all structural parameters are automatically determined.

V. CONCLUSION

In this paper, the revised GMDH-type neural network algorithm was applied to the medical image diagnosis of lung cancer and the results of the revised GMDH-type neural network were compared with those of the conventional sigmoid function neural network trained using the back propagation algorithm. Structural parameters such as the number of layers, the number of neurons in hidden layers and useful input variables are automatically selected to minimize prediction error criterion defined as PSS. In the case of the conventional neural network, we obtain many different output images for various structural parameters of the neural network and many iterative calculations of the back propagation are needed for various structural parameters in order to find more accurate neural network architecture.

In this paper, the revised GMDH-type neural network algorithm was applied to the medical image diagnosis of lung cancer and it was shown that the revised GMDH-type neural network algorithm was a

useful method for the medical image diagnosis of lung cancer because the neural network architecture is automatically organized so as to minimize the prediction error criterion defined as PSS.

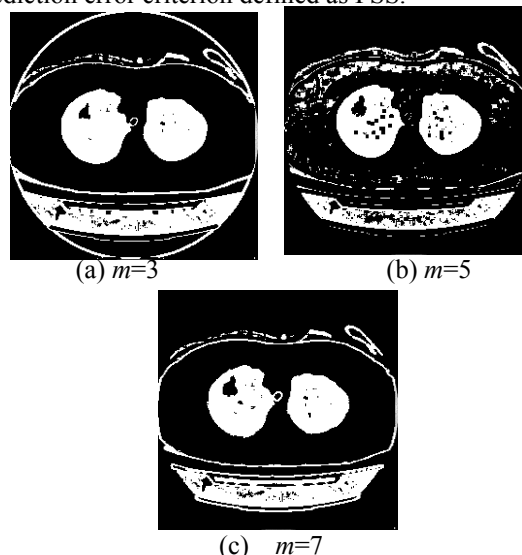


Fig.12 Output images of the conventional sigmoid function neural network

Acknowledgment This work was supported by (JSPS) KAKENHI 22560403.

REFERENCES

- [1] Kondo T. and J.Ueno (2008), Multi-layered GMDH-type neural network self-selecting optimum neural network architecture and its application to 3-dimensional medical image recognition of blood vessels, *International Journal of innovative computing, information and control*, Vo.4, No.1, pp.175-187.
- [2]. Kondo T.(1998), GMDH neural network algorithm using the heuristic self-organization method and its application to the pattern identification problem, *Proc. of the 37th SICE Annual Conference*, pp.1143-1148.
- [3] Tamura H. and T.Kondo (1980), Heuristics free group method of data handling algorithm of generating optimum partial polynomials with application to air pollution prediction, *Int. J. System Sci.*, Vol.11, No.9, pp.1095-1111.
- [4] Farlow S.J. ed. (1984), *Self-organizing methods in modeling, GMDH-type algorithm*, Marcel Dekker, Inc., New York.
- [5] Ivakhnenko A.G. (1970), Heuristic self-organization in problems of engineering cybernetics, *Automatica*, Vol.6, No.2, pp.207-219.
- [6] H. Akaike (1974), A new look at the statistical model identification, *IEEE Trans. Automatic Control*, vol.AC-19, no.6, pp.716-723.
- [7] H. Tamura, T. Kondo (1980), Heuristics free group method of data handling algorithm of generating optimum partial polynomials with application to air pollution prediction, *Int. J. System Sci.*, vol.11, no.9, pp.1095-1111.
- [8] Draper N.R. and Smith H. (1981), *Applied Regression Analysis*, John Wiley and Sons, New York.

Neural network application using GPGPU

Y. Tsuchida and M. Yoshioka

Osaka Pref. Univ., Sakai, Osaka 599-8531 Japan

tsuchida@sig.cs.osakafu-u.ac.jp

Abstract

In this paper, we have proposed the speed up method of neural network's running especially in learning time using GPU resource. Implementation of the General-Purpose computing on GPU- GPGPU became easier by the integrated development environment, CUDA distributed by NVIDIA. GPU has dozens or a hundred arithmetic circuit, whose allocations are controlled by CUDA. We propose the neural network implementation using GPGPU. Local minimum, one of the limitation of neural network, is conquered by using some networks with different initial weight coefficient in parallel. On the other hand, the neural network structure was discussed to adapt to parallel processing. One of this implementation is applied to the remote sensing. As a result, this implementation is 20 times faster than CPU.

keywords GPGPU ,CUDA, Neural Network

1 Introduction

Recently, graphic boards have higher performance with development of 3DCG and movie processing than CPU, and widely used with progress of computer entertainment. In this paper, we have proposed that the neural network's running time become speed up especially in learning time using GPU resource. Implementation of the General-Purpose computing on GPU- GPGPU became easier by the integrated development environment, CUDA distributed by NVIDIA. GPU has dozens or a hundred arithmetic circuit, whose allocations are controlled by CUDA. We propose the neural network implementation using GPGPU. Local minimum, one of the limitation of neural network, is conquered by using some networks with different initial weight coefficient in parallel. The performance depends on the allocation of threads, because the CUDA has hierarchical framework to treat many threads. Second, CUDA has many types of memories too, especially, how to treat the shared memory, one of the on-chip memory, influences performances. Therefore

the neural network structure was discussed to adapt to parallel processing.

2 CUDA

CUDA, Compute Unified Device Architecture, is a software development kit distributed free by NVIDIA. By employing a supported graphics board, the parallel computing architecture is used easily. In computing using CUDA, the threads are stored in hierarchy structure. The grid exist as highest hierarchy in GPU, in the grid there are $65,535 \times 65,532$ blocks, and the threads are managed by three dimensions in the block. Some types of memories are implemented in CUDA, and, among them, the shared memory exists in each blocks. This memory is implemented as on-chip memory, therefore the access to the memory is faster than any other memories. However this memory is used in threads only. This memory is "shared" among threads existing in a block.

3 The parallelization for the whole neural network

At first, one neural network is implemented as one computational thread of parallel computing, and these threads have each different initial weight coefficients.

In the CUDA, it must be configured which hierarchy the threads are assigned to. Therefore, when N networks are executed, the number of thread in block is expressed by m and the number of blocks in grid is N/m , which m and N are integer. The relationship between m and processing time are evaluated firstly.

Table 1 shows the specification of GeForce GTX480 which is used in this research. Test network has 2 neurons in input layer, 3 neurons in hidden layer, and the 1 neuron in output layer. There are 4 learning patterns, and the learning is repeated by 2200 steps at each pattern. This routine is employed as one thread, and the time of processing for N threads are measured

Table 1: GeForce GTX480

Number of cores	480
Global Memory	1.5GB
Constant Memory	64KB
Shared Memory	48KB/block
Clock rate	1.40GHz
Maximum threads	1024/block

by changing N and m . Figure refmap shows the measuring result, where $m = N$ represents all threads are assigned in one block. Because of the limited number of arithmetic units, the process time is proportional to N upward $N = 40$ in $m = 1$, and because of the time of memory access, the performance is down in $m = N$ too.

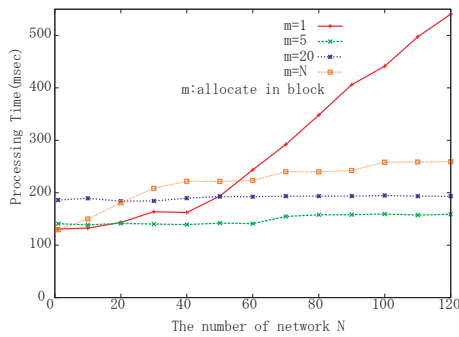


Figure 1: Processing time for whole network thread

One of the goal of the parallelization, the calculation time became flat independent of N , is achieved rid of $m = 1$. From this result, the time is depend on m , however the influence is small.

The problem of m is influenced to the shared memory on implementation, because this memory size uses m times, and this is allocated fixed size in each block. Because shared memory is less than global memory, m must be decided by the scale of the network.

4 Parallelization of the inner structure of network

In previous section, one entire network is implemented as one thread, therefore we propose that the network structure is broken up and scattered on GPU. Figure 2 shows the model of the neural network. In the network, some neurons exist in a layer, these neurons can be evaluated in same time.

However, the inputs of the neurons are previous layer's results, therefore the momentary pause is

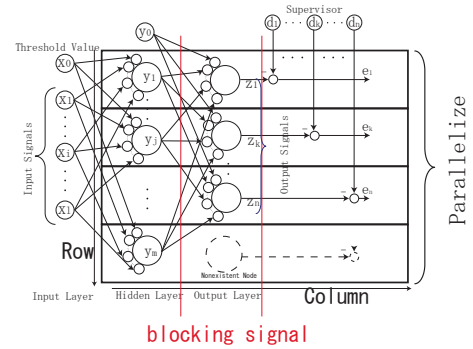


Figure 2: The neural network model

needed until the output from the previous layer become complete. The block signals are employed in front of each layers, which show 'stop' until the all neurons have been calculated completely. It is necessary to calculate one network, The number of threads which is necessary to calculate one network is maximum numbers of neurons per layers, n_{max} . Note that the processing waits for the other when it comes in the layer where the neuron is nonexistent.

The phase of foreword propagation is independent in calculating other patterns too, so p patterns loop can be calculated in parallel. In the phase of the back propagation, more flags are needed to calculate in parallel, these are hoisted to protect the one neuron from other propagation.

The sizes of grids and blocks are expressed by three dimensions, where z -direction of grid is 1. In the experiment, the grid allocate $(N/m, p, 1)$ blocks, and the block allocate $(m, n_{max}, 1)$, and the processing time was measured. The sample network is same as previous section, therefore the $p = 4, n_{max} = 3$. Figure 3 shows the result.

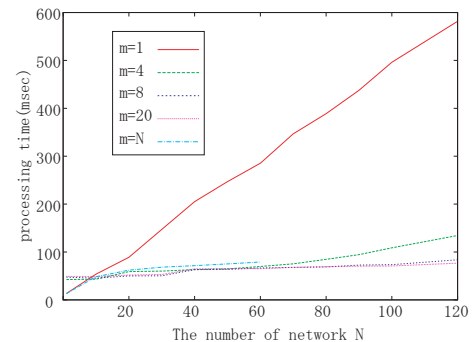


Figure 3: Processing time for scattered network

Table 2: CPU(host machine specification)

CPU	AMD Phenom 9600
Frequency	2.31GHz
Memory	3.8GByte
Operating System	Windows XP sp2

As a result, the time is proportional to N in early stage when $m = 1$. The tendency of the total plot resembles a previous section, then the influence of an calculation cost by m on hardware is small. The result was speed-up only 2.4 times in comparison with the foregoing chapter. So, the further improvement of the block signal and flags is necessary.

5 Comparison with the CPU

This suggestion was compared with a CPU. Table 2 shows the specification of a comparison CPU.

The experiment is evaluated in processing time by changing the number of hidden layer and pattern.

Test network of this section has 3 neurons in input layer and the 3 neuron in output layer. The learning is repeated by 2200 steps at each pattern. The number of network $N = 40$ and the network in block $m = 4$ is assigned. The number of hidden layer is selected from 3, 6, 9 and the pattern is chosen from 5, 10, 15, 20.

Table 3 shows the processing time of the GPU, and table 4 show the ratio of CPU to GPU. The columns is the number of pattern, and the row is the number of hidden layer.

Table 3: Processing time for patterns and hidden layers by GPU

		The number of pattern			
		5	10	15	20
The number of hidden layer	3	65.34	107.92	161.19	246.22
	6	69.47	110.72	159.07	249.67
	9	111.75	218.38	326.04	436.61
	12	112.53	214.67	318.54	436.96

Compared with the CPU, 22.4 times in average is faster. When the number of hidden layer is 3 and 6, the time of the same number of pattern is equivalent. And when the number of hidden layer is 9 and 12, the time is equivalent too.

This result shows that the usage of the block influences the performance.

Table 4: The ratio of CPU to GPU (CPU/GPU)

		The number of pattern			
		5	10	15	20
The number of hidden layer	3	15.33	17.53	17.16	14.79
	6	21.57	26.19	27.73	23.39
	9	18.06	18.08	18.01	18.14
	12	22.37	23.11	23.20	22.43

6 Conclusion

We proposed the speed-up method of neural network learning by using GPGPU. The GPGPU has the hierarchical structure to store the threads, the performance is influenced by assigning hierarchy. At first, the learning time of some networks in parallel was measured to show the effect of the hierarchy.

The neurons of each layer in network are processed in parallel, and patterns are processed in parallel too. This method shows the 2.4 times faster than the first method, and compared with CPU, the processing time is 22.4 times faster.

This method will be applied for home use. The method is applied with the graphics or motion pattern recognition easily, because GPU is the hardware for graphic processing. This goal of this method application is sign for the speech recognition.

In the other hand, this method is used in remote sensing field. The goal in the future is that the new learning algorithm adopted on GPGPU is created.

Evaluation of an optimal design method for multilayer perceptron by using the Design of Experiments

E. Inohira and H. Yokoi

*Kyushu Institute of Technology, 2-4 Hibikino, Kitakyushu, Fukuoka, Japan
(Tel: 81-93-695-6050; Fax: 81-93-695-6050)
({inohira,yokoi}@life.kyutech.ac.jp)*

Abstract: We evaluate performance of an optimal design method for multilayer perceptron (MLP) by using the Design of Experiments (DOE). In our previous work, we have proposed the optimal design method for MLPs in order to determine optimal values of such parameters as number of neurons in hidden layers and learning rates. In this paper, we evaluate performance of the proposed design method through a comparison with a genetic algorithm (GA) based design method. We target at optimal design of MLPs with six layers. Moreover, we evaluate the proposed designed method in terms of calculation amount of optimization. Through the above-mentioned evaluation and analysis, we aim at improving of the proposed design method in order to obtain the optimal MLP with less effort.

Keywords: Multilayer perceptron, Neural network, Optimal design, Design of Experiments, Genetic algorithm

I. INTRODUCTION

A multilayer perceptron (MLP) can approximate an arbitrary nonlinear mapping at an arbitrary accuracy [1]. Accuracy of a trained MLP depends on two factors. The first factor is learning algorithm. Connection weights and biases of the neurons are adjusted according to the learning algorithm. Typical learning algorithm is error back-propagation (EBP) algorithm [2]. There are many learning algorithms other than EBP algorithm. It is clear that accuracy of a trained MLP depends on it learning algorithm. However, the learning algorithm is the unique factor. Another factor is design of the MLP. Before training, number of layers, numbers of neurons in hidden layers and training conditions such as learning rates are determined. Trial-and-error, brute-force approaches, network construction and pruning are used as conventional design methods. It is difficult to apply these methods to MLPs with many layers because their design parameter space becomes huge. Another problem is that the approximation accuracy of MLPs with the same design parameters has variation due to use of random number to initial values of connection weights. We need a design method with statistical analysis for MLP.

In our previous work [3,4], we proposed design method using the Design of Experiments (DOE) [5], which features efficient experiments with an orthogonal array and quantitative analysis with analysis of variance (ANOVA). We demonstrated that optimal design of five-layer MLPs could be obtained using our design

method. However, we have a problem of evaluation of the proposed design method. The problem is quantitative comparison between the proposed design method and other design methods. It is clear that the proposed designed method is better than trial-and-error, brute-force approaches. We focused on a genetic algorithm based design method, which is a nonlinear optimization technique and expected to be as efficient method as the proposed method.

In this paper, we evaluate performance of the proposed design method through a comparison with a genetic algorithm based design method. We target at optimal design of MLPs with six layers. When we deal with few design parameters, a difference between the proposed design method and other method is small. Our previous work implied that accuracy of MLPs with more layers would become high for the same training data. Therefore, we should focus on MLPs with six layers. Moreover, we evaluate the proposed designed method in terms of calculation amount of optimization. We use various types of training data because performance of a trained MLP depends on training data. We refer to UCI machine learning repository [6] for the evaluation. Through the above-mentioned evaluation and analysis, we aim at improving of the proposed design method in order to obtain the optimal MLP with less effort.

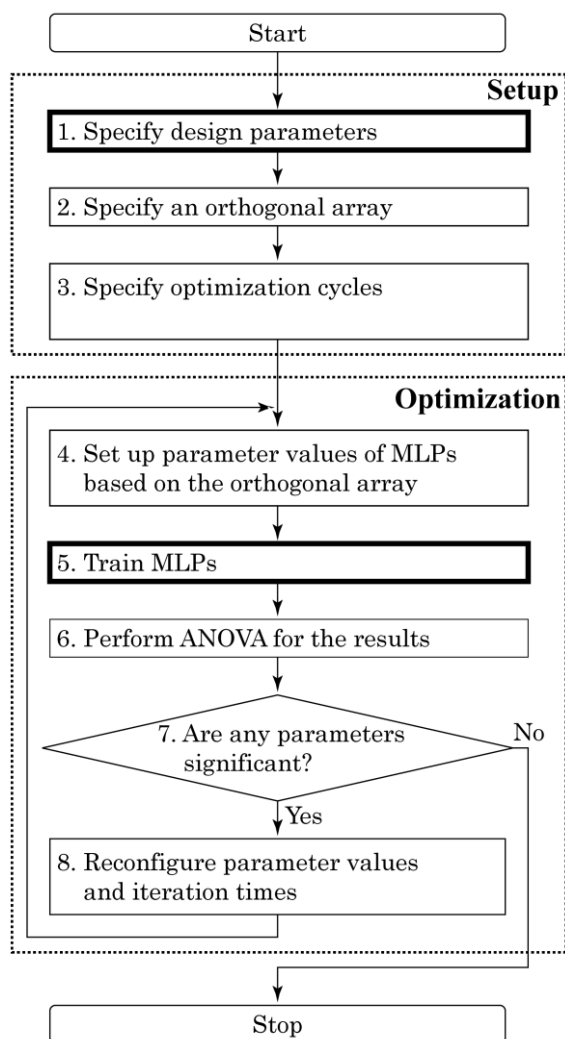


Fig.1. A flow chart of DOE-based optimal design method

II. OPTIMAL DESIGN OF MLP

1. DOE-based optimal design method

We have proposed an optimal design method using DOE in our previous work [3,4]. Our basic idea is that DOE is applied to an optimal design problem of MLP. We show a flow chart of our proposed method using DOE in Fig.1. Detailed explanation has been described in [4]. Training of MLPs corresponds to experiments in DOE. For example, we used the number of hidden nodes, learning rates, momentum coefficients and range parameters of initial connection weights as the design parameters in [4]. And we used squared sum of training errors after specific learning cycles as the performance index. The used training dataset is common in all experiments.

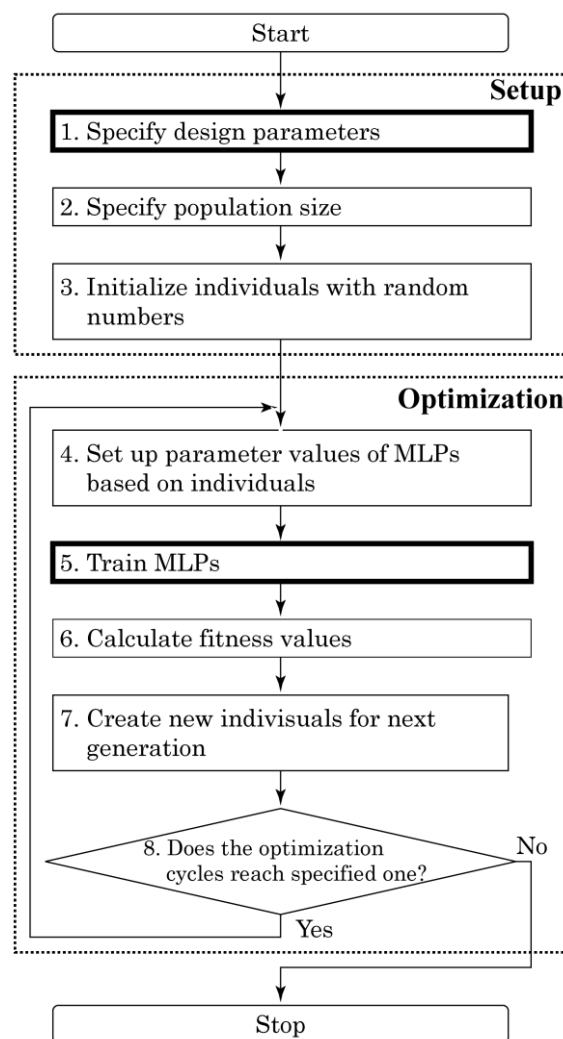


Fig.2. A flow chart of GA-based optimal design method

We implemented our optimal design process on MATLAB programs except training of MLP. In [4], Step 8 needed manual operation. On the other hand, in [5] and this paper, Step 8 is programmed with predefined rules.

2. GA-based optimal design method

We have proposed the optimal design method using DOE and evaluated it on three-layer MLPs and five-layer MLPs. We have demonstrated our method and not compared with other methods. We focused on genetic algorithm (GA). GA-based approaches [7,8] have already been proposed. However, our proposed method and GA-based approaches cannot be compared directly because selected design parameters are different.

In order to compare our proposed method and a GA-based approach, we prepared GA-based optimization programs using Global Optimization Toolbox on MATLAB. We show a flow chart of optimal design method using GA in Fig.2. We programmed GA-based optimization programs as similar to our proposed method using DOE as possible. Step 1 to specify design parameters and Step 5 to train MLPs are common in both optimization programs. The remaining part of the optimization depends on the optimization algorithms, that is, DOE or GA. Our GA-based optimization program can deal with the same design parameters and training data set as the DOE-based program.

We used a simple GA-based optimization algorithm. An individual consists of design parameter values in real numbers. A value of the used fitness function is a training error of a MLP. The default crossover function of the Global Optimization Toolbox is used.

III. Experiments

1. Training dataset

We used concrete compressive strength data [9,10] in UCI machine learning repository as the training dataset. The training dataset has 8 input variables and 1 output variable. Therefore, input and output of a MLP are determined by specifying the training dataset. The number of instances is 1030. Ranges of the variables are largely different in this dataset. We normalized each variable to be range -1 from +1 for input and -0.99 and +0.99 for output. We used a sigmoid function ranging from -1 to +1. When an input of the sigmoid function is infinity, its output becomes +1. This takes very long learning time. To avoid this situation, we set range of output variable to be from -0.99 to +0.99.

2. Targeted MLP and design parameters

We used six-layer MLPs for the target system. Their design parameters are as follows: the number of nodes in hidden layers (4 parameters) and learning rate in each layer (5 parameters). Range of the number of nodes in hidden layers is from 1 to 50 in order to limit the parameter space. Range of the learning rate in each layer is from 0 to 1. On the optimization program, the design parameters are normalized in range from 0 to 1. When MLPs is set up before training, the design parameter values are restored. In DOE, we used an orthogonal array with 27 combinations and 3 levels.

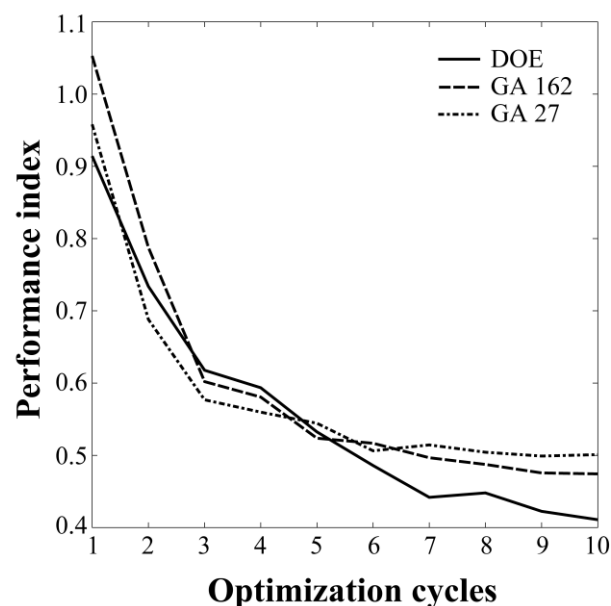


Fig.3. A comparison between DOE-based method and GA-based method in median of performance indices

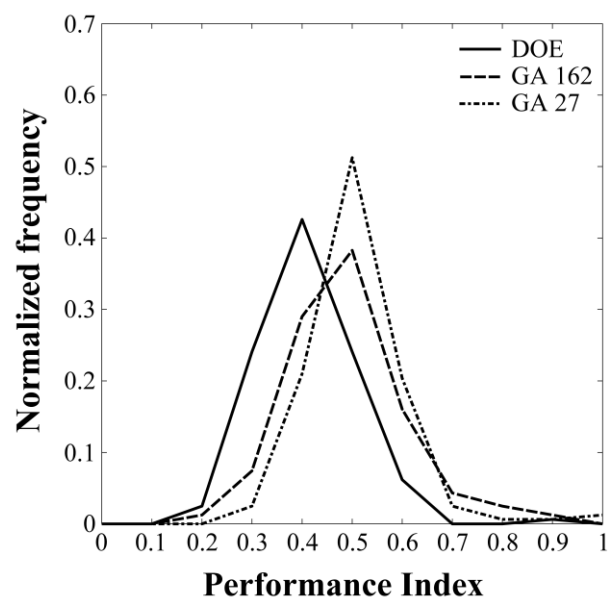


Fig.4. A comparison between the two methods in distribution of performance indices at the tenth cycle

Therefore, $27N$ MLPs are trained each optimization cycle. Here N denotes trial iteration counts and is adjusted automatically in the optimization. In GA, number of individuals is set to 27 or the maximum number of $27N$ because of comparison with the DOE-based optimization. This means that calculation amount is the same in both methods. When number of individuals is 27, training of MLPs is performed N times under different initial connection weights. In this case, value of fitness function is average of those results.

3. Training algorithm and performance index

We used a back-propagation algorithm to training MLPs. In this paper, the learning rates are prepared every layer. This approach has an effect to reduce the training error as shown in our previous work [4]. We used common logarithm of squared sum of error for all instances as the performance index. Small performance index is better because small error is good. We also evaluated distribution of performance indices at specific optimization cycles instead of best performance index. The reason is that the best performance index has large variance. We used median of the performance indices as representative value.

IV. EXPERIMENTAL RESULTS

We show experimental results in Figs. 3 and 4. Fig.3 shows a comparison between DOE-based optimization method and GA-based method in median of performance indices at each optimization cycle. In both methods, median of performance indices decreases when optimization proceeds. After the sixth cycle, the DOE-base method is better than the other. Fig.4 shows distributions of performance indices of the two methods at the tenth cycle. The distribution in the DOE-based method is on the left of the distribution in the GA-based method. This means a set of combinations of parameter values in the DOE-based method is better than the GA-based method. In other words, probability of getting the best performance index in the DOE-based methods is higher than the GA-based method.

V. DISCUSSION

We showed that the DOE-based method is better than the simple GA-based method in optimal design of MLP. The problem of the simple GA-based method is to ignore variance of performance indices. In Fig.4, the result of GA 27, which means number of individuals is 27, is worst. The reason is that mean of N times results is used in GA 27. Calculation amount is wasted by using mean because variance is ignored. GA 162 is worse than the DOE-based method under the same calculation amount. The reason is that the GA-based method has no statistical analysis. In the GA-based method, children of a good individual are not always better because performance indices have variance. On the other hand, the DOE-based method can adjust parameter values properly without misleading due to ANOVA.

In this paper, a kind of MLP and training dataset was used. It is necessary to apply the optimal design methods to many types of problems in order to clarify their limitation

VI. CONCLUSION

We evaluated performance of an optimal design method for MLP by using DOE through a comparison with a GA-based design method. We demonstrated optimal design of MLP with six layers by using DOE-base method is better than GA-based method under the same calculation amount.

In the future work, our proposed optimal design method will be applied to other types of problem such as classification and control in order to investigate applicable scope of our method.

REFERENCES

- [1] Tikk D, Koczy T and Gedeon TD (2003), A survey on universal approximation and its limits in soft computing techniques, *Intl J of Approximate Reasoning* 185-202
- [2] Rumelhart D, Hinton G and Williams R (1986), *Parallel Distributed Processing*, MIT Press.
- [3] Inohira E and Yokoi H (2007), An optimal design method for artificial neural networks by using the design of experiments, *J of Advanced Computational Intelligence and Informatics*. 11(6):593-599.
- [4] Inohira E and Yokoi H (2010), Development of an optimal design method for multilayer perceptrons by using the design of experiments (in Japanese), *Proc of the 2010 IEICE general conference*. D-2-1.
- [5] Dean A and Voss D (1999), *Design and analysis of experiments*.
- [6] Frank A and Asuncion A (2010), *UCI Machine Learning Repository* [<http://archive.ics.uci.edu/ml/>], Irvine, CA: University of California, School of Information and Computer Science.
- [7] Castullo PA, Merelo JJ, Prieto A, Rivas V and Romero G (2000), G-Prop: global optimization of multilayer perceptrons using Gas, *Neurocomputing*, 35:149-163
- [8] Leung FHF, Lam HK, Ling SH and Tam PKS (2003), Tuning of the structure and parameters of a neural network using an improved genetic algorithm, *IEEE Trans Neural Networks* 4(1):79-88
- [9] Yeh IC (2007), Modeling slump flow of concrete using second-order regressions and artificial neural networks, *Cement and Concrete Composites* 29(6):474-480.
- [10] Yeh IC (1998), Modeling of strength of high performance concrete using artificial neural networks, *Cement and Concrete Research* 28(12):1797-1808

A Learning Method for Dynamic Bayesian Network Structures Using a Multi-Objective Particle Swarm Optimizer

Kousuke Shibata, Hidehiro nakano, Arata, Miyauti

*Tokyo City University
1-28-1, Tamadutsumi, Setagay-ku, Tokyo, 158-8557 Japan
(Shibata@ic.cs.tcu.ac.jp)*

Abstract: In this paper, we present a multi-objective Discrete Particle Optimizer (DPSO) for the learning of Dynamic Bayesian Network (DBN) structures. The proposed method introduces a hierarchical structure consisting of DPSOs and a Multi-Objective Genetic Algorithm (MOGA). Groups of DPSOs find effective DBN sub-network structures and a group of MOGA finds whole of the DBN network structure. Through numerical simulations, the proposed method can find more effective DBN structures and can obtain them faster than the conventional method.

Keywords: Dynamic Bayesian Networks, Structure Learning, Multi-Objective Optimization, Discrete Particle Swarm Optimization

I. INTRODUCTION

The Dynamic Bayesian Network (DBN) describes causal relations in various systems by using stochastic network structures, and represents them as directed acyclic graphs and conditional probabilities for transitions of each observed state variable [1]-[3]. The DBN is an extended model of the Bayesian Network (BN). As compared with the BN, the DBN can describe temporal causal relations of state variables. The DBN has been applied to speech recognition, genetic networks and so on. When the structural topology of a DBN is unknown, the learning of the DBN structure is needed [2][3]. In the learning, two trade-off characteristics must be considered. One is a characteristic which indicates how well the network fits the observed data. Another is structural complexity of the network. A fully-connected network can represent all relationships between each state variable. However, such a redundant network cannot adapt target model well, and the network size becomes extremely large. Therefore, it is preferred that networks should be constructed as simple as possible. That is, the degree of connectivity in the networks must be controlled in learning methods. Many learning methods introduce criteria which evaluate networks in terms of both probabilistic likelihood and structural complexity. However, they generally use a single evaluation function to combine these factors by a weight parameter. Since appropriate weight parameters depend on target models, it is difficult to determine a unique parameter value. The learning methods based on Multi-Objective GA (MOGA) [4] or Immune Algorithm (IA) can

overcome this problem. However, in these algorithms, the learning for large scale DBN structure requires significantly long computation time.

In this paper, we present a multi-objective Discrete Particle Optimizer (DPSO) for the learning of DBN structures. The proposed method introduces a hierarchical structure. First, the objective DBN is divided into plural sub-networks depending on observed state variables. The lower layer consists of groups of DPSO. The DPSO is well-known as one of the fast solvers for various optimization problems [5]. In the proposed method, each particle has binary states corresponding to causal relations between state variables in each sub-network. Each group of particles in the lower layer finds each effective sub-network structure. The higher layer consists of MOGA [4]. A group of individuals in the higher layer finds the whole of the DBN structure sharing information from the lower layer by migration. Evaluation values of each particle or individual are given as Pareto solutions for likelihood and complexity to obtained DBN structures. The hierarchical structure in the proposed method can reduce computation time for the learning of larger scale DBN structures. We evaluate both likelihood and complexity to obtained DBN structures, and compare with the conventional learning method based on MOGA [3]. Through numerical simulations, the proposed method can find more effective DBN structures and can obtain them faster than the conventional method. Generally, there exist trade-off relations between likelihood and complexity to DBN structures in various actual applications. The proposed method can also provide many candidate structures of DBNs.

II. BACK GROUND

A Dynamic Bayesian Network (DBN) is a kind of probabilistic networks which represent temporal relationships between observed state variables. A DBN has three elements represented by (i) Node: observed state variables, (ii) Edge: dependencies between each node, (iii) Conditional Probability Table (CPT): degree of dependencies. An end point node and an origin node of an edge are a child node and a parent node, respectively. Let $X_1[t], \dots, X_N[t]$ be N discrete state variables at time t . A DBN consists of (i) a prior network DBN_0 that specifies prior probabilities $\Pr(X[0])$ and (ii) a transition network DBN_T that specifies transition probabilities $\Pr(X[t+1] | [X[t])$. The Joint probabilities over all the variables for time $t = 0, 1, 2, \dots, T$ is

$$DBN_0(X[0]) \cdot \prod_{t=0}^{T-1} DBN_T(X[t+1] | X[t]) \quad (1)$$

For simplicity, this paper considers on the transition network only.

If a DBN structure is unknown, some learning methods by using search algorithms and evaluation criteria are necessary. Evolutionary computation and Bayesian Information Criterion (BIC) [3] have been widely used to the learning of DBN structures. BIC has two terms that indicate likelihood and complexity of networks. BIC is represented by the following formula.

$$BIC = \text{Likelihood} - \omega \cdot \text{Complexity} \quad (2)$$

where ω is the weight parameter which balances between Likelihood and Complexity. The Likelihood term signifies the plausibility of the network. It is calculated by counting occurrences within sequences. The likelihood is then defined as:

$$\text{Likelihood} = \sum_i \sum_{j_i} \sum_{k_i} N_{i,j_i,k_i} \cdot \log \left(\frac{N_{i,j_i,k_i}}{\sum_{k_i} N_{i,j_i,k_i}} \right) \quad (3)$$

where N_{i,j_i,k_i} denotes the number of occurrences in observation data sequences such that a child node i has a value k_i and its parent node has a value j_i . The Complexity term signifies the structural complexity of the network which is defined as:

$$\text{Complexity} = \sum_i |\text{parent}(X_i)| \quad (4)$$

where $\text{parent}(\cdot)$ is the number of parent nodes.

In case of using BIC, we must determine an optimum weight parameter between two terms. If setting of this parameter is improper, the resulting graph is too complex or sparse. However, it is difficult to determine a unique optimum weight beforehand, because it depends on target models and training data sets. To solve this problem, the learning method by using a Multi-Objective Genetic Algorithm (MOGA) has been proposed [3]. The method applies a Pareto ranking scheme to the MOGA [4]. In the Pareto ranking scheme, each vector is evaluated by the number of the other vectors which have better values about all objectives. Using this method, a variety of solutions about likelihood and complexity can be obtained.

However, multi-objective methods tend to need much iteration to convergence, compared with single-objective methods. Since these methods acquire solutions for a variety of likelihood and complexity, the solutions are dispersed in search space. Typically, evaluation of the network requires enormous computation time which is proportional to complexity and amount of data. Therefore, it is desirable to reduce computation time to the learning convergence.

III. PROPOSED METHOD

In this paper, we use Discrete Particle Swarm Optimizers (DPSOs) [5] as a search algorithm to reduce computation cost to structure learning of DBNs. The DPSO is an optimization method that is a kind of swarm intelligence. In DPSO, particles efficiently search solutions in target problems, by updating their positions and velocities based on personal best solutions which each particle has and a global best solution which all the particles have. The DPSO is known as simple and fast algorithm. In the proposed method, a structure of a DBN is represented by binary variables in the DPSO. Particles have binary variables which denote existence of connections in the DBN. If a connection exists between a child node and a parent node, the value of the binary variable is 1. Otherwise, it is 0 (see Fig 1). If N variables can be observed, $N \times N$ strings are required.

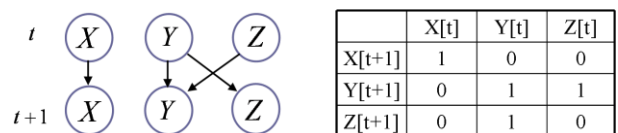


Fig.1 A DBN structure and binary variables in DPSO.

In order to solve multi-objective problems by the DPSO, some schemes are needed. In this paper, we use the existing method. We apply a multi-objective optimization scheme by using the Archive scheme [6]. The Archive has two features that are the Archive controller and the Grid. The Archive controller determines whether to save solutions into Pareto solutions. If the Archive has no solution with better evaluation values about all objectives compared with a selected solution, the Archive controller saves the selected solution into the Archive. The Grid produces well-distributed Pareto front. The function-space is divided into grids. If particles are dense in a grid, one of solutions in the grid is eliminated. With these features, a variety of solutions can be obtained.

In addition, we apply a hierarchical structure to DPSOs in order to reduce computation cost. In formulas (3) and (4), BIC can be divided into computations for each child node i . This means that the learning of DBN structures can be split for each child node. In this paper, we propose a learning method by two layers. In the lower layer, each group of Multi-objective DPSOs finds each sub-network structure divided for each child node. That is, in the lower layer, the number of groups corresponds to the number of child nodes. In the higher layer, a group of MOGA finds the whole of the DBN structure. For every iteration, the lower and higher layers exchange respective solutions by migration. The overview of this hierarchical structure is shown in Fig 2.

The proposed algorithm is described by the following steps:

- (step1) In the each layer, initialize particles and individuals.
- (step2) Evaluate particles and individuals.
- (step3) Update the positions of each particle in the lower layer by equation (5).

$$\begin{aligned} & \text{if}(\text{rand}() < \text{sig}(v_{id})) \text{ then } x_{id} = 1 \\ & \quad \text{else } x_{id} = 0 \\ & \text{sig}(v_{id}) = \frac{1}{1 + e^{-v_{di}}} \end{aligned} \quad (5)$$

- (step4) Update the each Archive.
- (step5) Update the velocities of each particle in the lower layer by equation (6).

$$\begin{aligned} v_{id}^{k+1} = & w \cdot v_{id}^k + c_1 \cdot r_1 \cdot (P_{id} - x_{id}^k) \\ & + c_2 \cdot r_2 \cdot (G_d - x_{id}^k) \end{aligned} \quad (6)$$

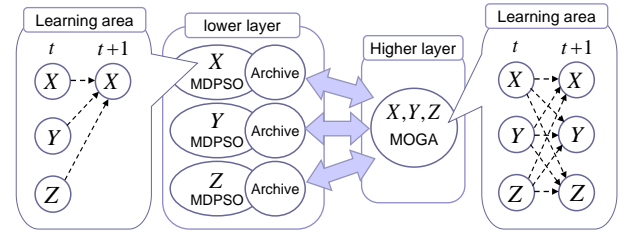


Fig.2 Overview of a hierarchical learning method.

- (step6) Manipulate individuals in the higher layer.
- (step7) Migrate between each layer.
- (step8) Repeat from (step2) to (step7).

In migration steps, a particle which is chosen randomly overwrites a part of individual whose rank is not 1.

VI. SIMULATION RESULT

The proposed method is applied to several benchmarks which have a variety of complexities and performances. In order to compare the proposed method with the conventional method, we use some benchmarks which were tested by the conventional method. Target networks (a) and (b) are shown in Fig 3. Table 1 shows training data sets. These nodes in the networks generate discrete probabilistic values according to dependencies. If nodes have no parents, they generate random values. Parameters used for the simulation are shown in Table 2.

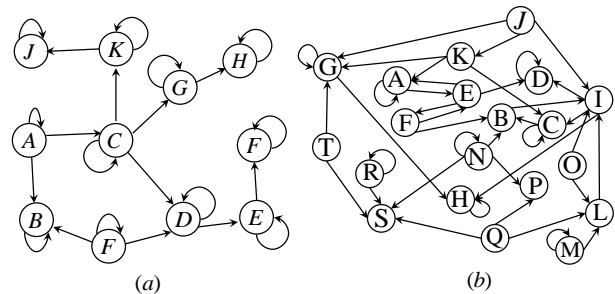


Fig.3 Target networks.

Table 1 Training data sets.

Network	Variables	Links	Examples	Parent Links
(a)	10	20	100	0-3
(b)	20	40	200	0-4

Table 2 Simulation parameters.

Parameter	Conventional Method	Proposed Method
iteration	50	50
population	200,500	100,250
particles	-	100,250
GA operation	tournament	tournament

Figs. 4 and 5 show the simulation results for the networks (a) and (b). It can be found that the proposed method obtains a variety of solutions which have better values with less iteration than the conventional method. A structure which has high complexity and good likelihood becomes complex and has extra edges. On the other hand, a structure which has low complexity and bad likelihood has many missing edges. Generally, there exist trade-off relations between likelihood and complexity to DBN structures in various actual applications. The proposed method can also provide many candidate structures of DBNs.

V. CONCLUSION

In this paper, we have proposed a hierarchical multi-objective DPSO for the structure learning of DBNs. Dividing computations, the proposed method requires less iteration to learning convergence than the conventional. In addition, diversity and accuracy of solutions are equal or higher than the conventional method. Since the hierarchical structure can reduce the computation cost for the learning, the proposed method is effective in high-dimensional problems.

Future problems include (1) application to other benchmarks, (2) evaluation for learning speed, and (3) consideration of appropriate group size of particles or individuals.

REFERENCES

- [1] K.Murphy, "Dynamic Bayesian Networks: Representation, Inference and Learning," PhD thesis, Computer Science Division, UC Berkeley, 2002
- [2] W.Guo, X.Gao & Q.Xiao, "Bayesian Optimization Algorithm for Learning Structure of Dynamic Bayesian Networks from Incomplete Data," Proc. CCDC 2008, pp. 2088-2093, 2008.
- [3] B.J.Ross & E.Zuvria, "Evolving dynamic Bayesian networks with Multi-objective genetic algorithms," Applied Intelligence, vol. 26, no. 1, pp. 13-23, 2007.
- [4] R.E.Steuer, *Multiple Criteria Optimization: Theory, Computations, and Application*. New York: John Wiley & Sons, Inc., ISBN 047188846X, 1986.
- [5] J.Kennedy & R.Eberhart, "A discrete binary version of the particle swarm optimization algorithm," Proc. SMC '97, pp.4104-4109, 1997.
- [6] C.A.C.Coello, G.T.Pulido & M.S.Lechuga, "Handling Multiple Objectives with Particle Swarm Optimization," IEEE Transactions on Evolutionary Computation, vol. 8, no. 3, pp. 256-279, 2004.

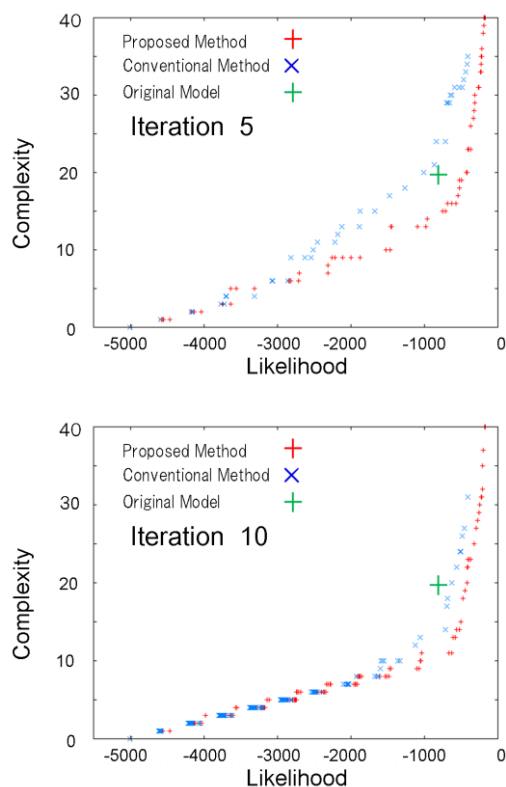


Fig.4 Pareto solutions for the network (a).
Upper: iteration=5. Lower: iteration=10.

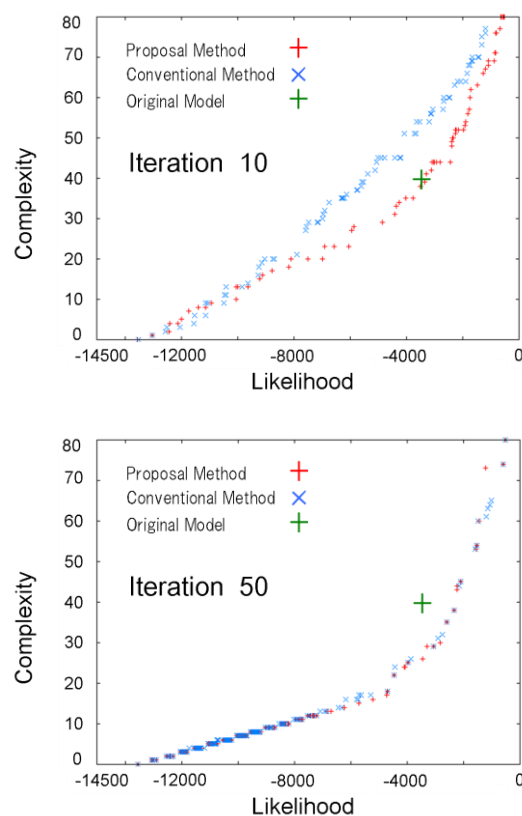


Fig.5 Pareto solutions for the network (b).
Upper: iteration=10. Lower: iteration=50.

Remarks on Folding Behavior of Mapping Capability of Neural Network Direct Controller for Many-to-one Plant

Takayuki Yamada

Department of Computer and Information Sciences

Faculty of Engineering

Ibaraki University

4-12-1 Nakanarusawa, Hitachi, Ibaraki, 316-8511, Japan

Abstract: We believe that a neural network learns an inverse dynamic of a target plant in a servo level neural network controller application. However, a practical plant generally has a nonlinear dynamics and there is no inverse dynamics of it usually. This paper studied this problem through the use of the neural network direct controller. Simulation results confirmed that the neural network learned the branch of the inverse characteristics (; a part of the inverse characteristics and it can be expressed as a one-to-one function mathematically) and if the neural network learned only one branch, the plant output matched with the desired value in whole region. Through the simulation, the whole inverse characteristics of the plant seems to be folded into one branch when the neural network learns this branch. This behavior is called the neural network folding behavior in this paper.

Keywords: Neural network, Controller, Learning, Adaptive

I. INTRODUCTION

Many studies have been undertaken in order to apply both the flexibility and the learning capability of neural networks to control systems. We are believing that a neural network learns an inverse dynamic of a target plant in a servo level neural network controller application.[1][2] This is because the target plant dynamics can be cancelled by this learned inverse dynamics if the neural network can learn it. That is, this cancellation means that a plant output completely matches with a desired value and we can realize an ideal control system. On the other hand, a practical plant generally has a nonlinear dynamics and it is mathematically expressed as a many-to-one function whose more than one input values which correspond to one output value. It is well known that there is no inverse function of such many-to-one function. However, many practical neural network controller applications have been successfully reported. Does the neural network learn the inverse dynamics of the plant on the practical applications? For this question, we studied that the neural network obtains the branch of the inverse characteristics of the plant (; a part of the inverse characteristics and it can be expressed as a one-to-one function mathematically) if the learned region is restricted to the one-to-one region.[3] If the learned region is not restricted, what happen? When we apply the neural network to the practical applications, the plant characteristics are unknown usually. Such restriction is impossible. For this question, we studied that the neural network learned the mean characteristics of the several plant inverse branches for off-line learning neural network

controller.[3] However we did not study the detail of the on-line neural network controller for this problem yet.

Thus, this paper studies the above question through the use of a neural network direct controller with online learning. The reason to use this type controller is that it is simplest among the servo level neural network controllers. The sine function is selected as a target plant. This plant is static, but it is suitable for a basic study. Simulation results confirm folding behavior of the neural network mapping capability. This behavior is that the neural network learns only one branch of the inverse characteristics of the target plant in order to obtain whole plant output. This fact means that we can realize an ideal control system if the neural network can learn only one inverse branch of the plant. This is because the plant output can match with the desired value. When the neural network realizes such input-output mapping, the whole inverse characteristics of the target plant seem to be folded into one branch of the inverse characteristics.

II. NEURAL NETWORK STRUCTURE FOR TEST OF FOLDING BEHAVIOR

This section explains a neural network structure for the test of folding behavior. For this test, a following sine function is selected as a target plant.

$$Y(k) = \sin(U(k)) \quad (1)$$

where Y is the plant output, U is the plant input and k is the sampling number. The reason of this selection is that the sine function has smooth feature and it is easily

mapped by a neural network. The reason of the discrete time system selection is to examine the discrete time control system as a future study. Since this paper selects the direct controller, the plant input U is composed of the following equation.

$$U(k) = \sum_{i=1}^n [\omega_i(p) f\{W_i(p)Y_d(k) + T_i(k)\}] \quad (2)$$

where ω_i is the i th element of the weight vector between the hidden layer and the output layer, W_i is the i th element of the weight vector between the input layer and the hidden layer, T_i is the i th element of the offset values added to the hidden layer neuron, n is the neuron number of the hidden layer, p is the learning number and f is the sigmoid function expressed by the following equation.

$$f(x) = \frac{X_g \{1 - \exp(-4x/X_g)\}}{2 \{1 + \exp(-4x/X_g)\}} \quad (3)$$

where x is the input of the sigmoid function and X_g is the parameter which defines the sigmoid function shape. The scheme of the neural network direct controller and the structure of above neural network are shown in Fig.1 and Fig.2 respectively.

The output error ε and the cost function J are defined as follows:

$$\varepsilon(k) = Y_d(k) - Y(k) \quad (4)$$

$$J(p) = \frac{1}{2} \sum_{k=1}^p \varepsilon^2(k) \quad (5)$$

where Y_d is the desired value for the control system and p is the sampling number within one learning period. The learning rule of this neural network controller is designed so as to minimize the cost function J . When we apply the δ rule to this learning rule, it is expressed as

$$\omega_i(p) = \omega_i(p+1) - \eta \frac{\partial J(p)}{\partial \omega_i(p)} \quad (6)$$

$$W_i(p) = W_i(p+1) - \eta \frac{\partial J(p)}{\partial W_i(p)} \quad (7)$$

$$T_i(p) = T_i(p+1) - \eta \frac{\partial J(p)}{\partial T_i(p)} \quad (8)$$

$$\frac{\partial J(p)}{\partial \omega_i(p)} = - \sum_{k=0}^p \{(\varepsilon(k) f(W_i(p)Y_d(k) + T_i(p)) \cos(U_k))\} \quad (9)$$

$$\frac{\partial J(p)}{\partial W_i(p)} = - \sum_{k=0}^p \{(\varepsilon(k) \omega_i(p) f'(W_i(p)Y_d(k) + T_i(p))Y_d(k) \cos(U_k))\} \quad (10)$$

$$\frac{\partial J(p)}{\partial T_i(p)} = - \sum_{k=0}^p \{(\varepsilon(k) \omega_i(p) f'(W_i(p)Y_d(k) + T_i(p)) \cos(U_k))\} \quad (11)$$

where f' is the derivative of the sigmoid function and η is the parameter to determine the neural network learning speed.

III. SIMULATION

This paper selects the following sine wave as a desired value for control.

$$Y_d(k) = \sin(X_t(k)) \quad (12)$$



Fig.1 Scheme of neural network direct controller.

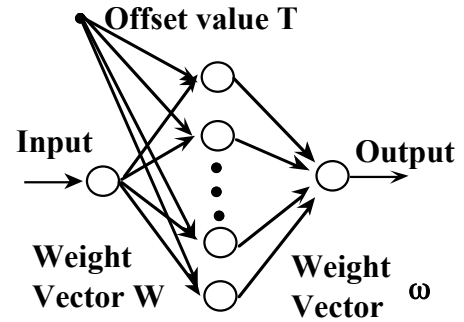


Fig.2 Structure of neural network.

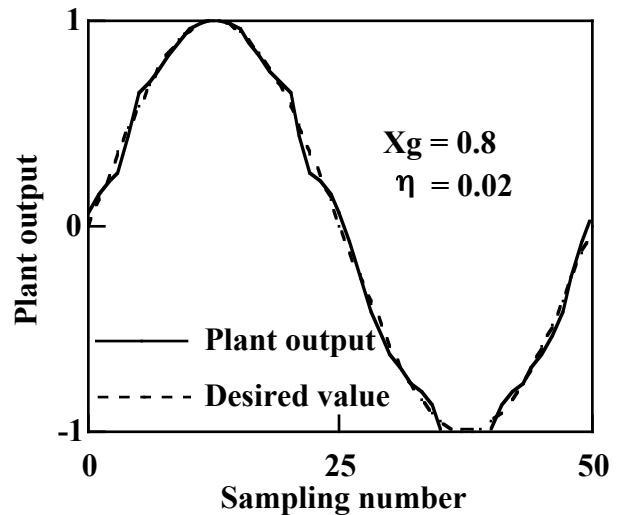


Fig.3 Learning result of example 1.

where X_t is the signal for the generation of the desired value. The sampling number within one learning period $\rho = 50$ is also selected.

Figure 3 shows the learning result of the example 1. The solid line in this figure is the plant output and the broken line is the desired value. As shown here, the output error remains between the plant output and the desired value, but it is small and the plant output well match with the desired value. This fact means that the neural network learning well performs and our neural network can map the sine wave. Figure 4 shows the neural network output (equals the plant input). The solid line shows the neural network output. As shown in this figure, it is restricted from $\pi/2$ to $3\pi/2$ although the plant output matches with the sine wave in one cycle as shown in fig.3. If the neural network can map the inverse characteristic of the sine wave from 0 to 2π , the neural network output should be 0 to 2π as shown in the broken line in fig.4. Fig.5 shows the neural network input-output relation of the example 1. The solid line is the learned neural network input-output relation. The broken line is the inverse characteristics of the plant from 0 to 2π . As shown in this figure, the neural network learns a part of the whole inverse characteristics and the learned part is restricted from $\pi/2$ to $3\pi/2$. In this restricted region, the inverse characteristics is expressed as the one-to-one function. Such region is called the branch of the inverse characteristics in this paper. In other word, if the neural network learns only one branch, the plant output matches with the desired value in whole region. This feature of the neural network is called the folding behavior in this paper. This is because the whole inverse characteristics seems to be fold into one branch.

Figure 6 shows the learning result of the example 2. The solid line and the broken line are the plant output and the desired value respectively. As shown here, the neural network learning also performs well. Figure 7 shows the neural network output. The solid line is the neural network output and the broken line is the ideal characteristics if the neural network can map the whole inverse characteristics of the plant. As shown here, the neural network output is restricted from $3\pi/2$ to $5\pi/2$ although the plant output is similar to that of the example 1. Figure 8 shows the neural network input-output relation of the example 2. The solid line is the neural network input-output relation and the broken line is the ideal characteristics if the neural network can map the whole inverse characteristics of the plant. As shown here, the neural network input-output relation is restricted from $3\pi/2$ to $5\pi/2$. This fact means that the neural network learns the different branch from that of fig.5 of the example 1. The difference between the examples 1 and 2 is only initial neural network weight. That is, the initial neural network weight determines which branch is learned by the neural network and if the neural network learns any branches, the plant output can be matched with the desired value.

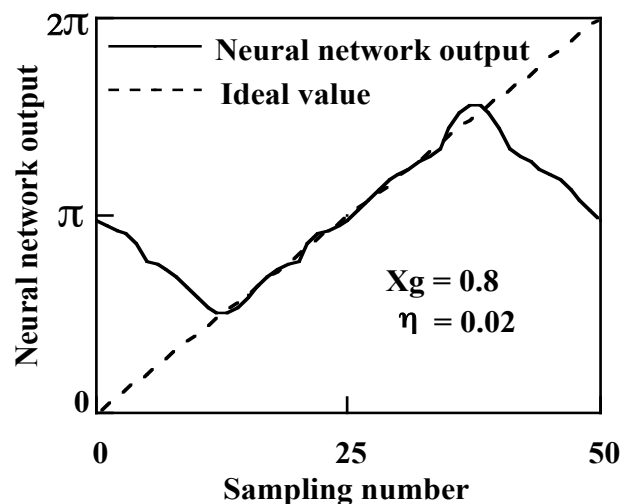


Fig.4 Neural network output of example 1.

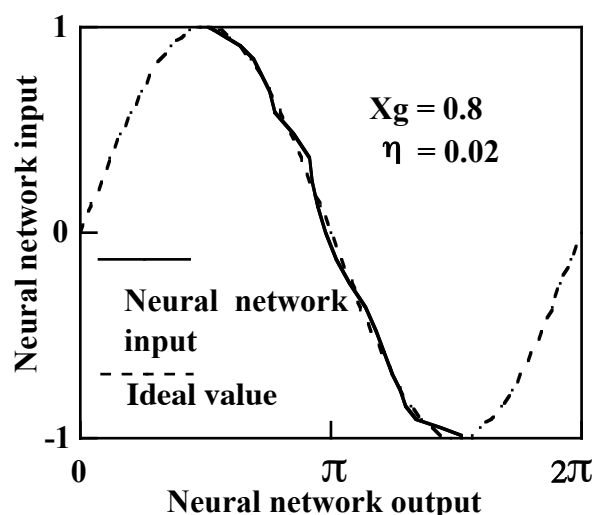


Fig.5 Neural network input-output relation of example 1.

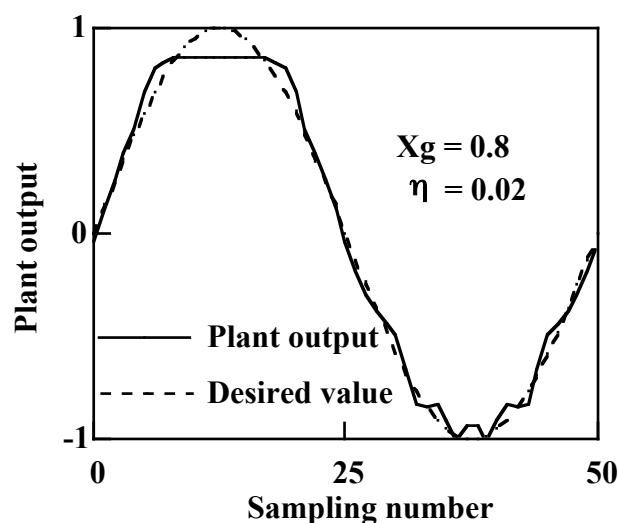


Fig.6 Learning result of example 2.

With regard to other remarkable feature of the neural network, the branches monotonously increase or decrease. This fact means that the derivative of the plant characteristics learned by the neural network also monotonously increases or decreases. As shown in eqs.(9)-(11), the leaning rules in this paper use the derivative of the plant characteristics. However, it may not be necessary. The reason of the requirement of the plant derivative is that we believe the neural network should converge to the whole plant inverse characteristics and its derivative changes in whole region usually. The value of this derivative is the petty problem. This is because it relates to the convergence speed and we can compensate through the use of the parameter η tuning in the learning rules. The sign of its derivative is the serious problem. This is because this relates to which the neural network converges or not. However, the above simulation results confirm that the sign of the slope of the plant inverse characteristics learned by the neural network is constant. This is because the signs of the branch derivatives are constant. That is, if the parameter η in eqs.(6)-(8) has the constant sign (plus or minus) and the small value, we can expect that the neural network converge to either branch although the derivatives of the plant inverse characteristics are removed in the learning rule. As shown in above simulation results, if the neural network converges to either branch, the plant output matches with the desired value and we can obtain the ideal control characteristics in whole region. This expectation will be shown in my future work.

IV. CONCLUSION

This paper studied what characteristics did the neural network learn through the use of the neural network direct controller. This is because we expect that the neural network learns the inverse dynamics of the object plant, but such inverse dynamics does not exist for the usual nonlinear plant. Simulation results confirmed that the neural network learned the branch of the inverse characteristics (; a part of the inverse characteristics and it can be expressed as a one-to-one function mathematically) and if the neural network learned only one branch, the plant output matched with the desired value. Through the simulation, the whole inverse characteristics of the plant seems to be folded into one branch when the neural network learns this branch. This behavior is called the neural network folding behavior in this paper.

ACKNOWLEDGMENT

The author wishes to express his thanks to Mr. Junpei Oota, graduated student, Ibaraki University, for his programming and simulation.

REFERENCES

[1]K.S.Narendra and K.Parthitsarathy, "Identification and

Control of Dynamics Systems Using Neural Networks", IEEE Transactions on Neural Networks, 1-1, pp.4-27(1990)

[2]M.Kawato, "Computational Schemes and Neural Network Models for Formation and Control of Multijoint Arm Trajectory", Neural Networks for Control (W.T.Miller, R.S.Sutton, P.J.Werbos ed.), MIT Press, pp.197-228(1990)

[3]T.Yamada, "Remarks on Neural Network Controller for Inverse Dynamics of Many-to-One Plant", IAS'95 (1995 International IEEE/IAS Conference on Industrial Automation and Control; Emerging Technologies), Taipei, Taiwan, R.O.C., May 22-27,(1995)

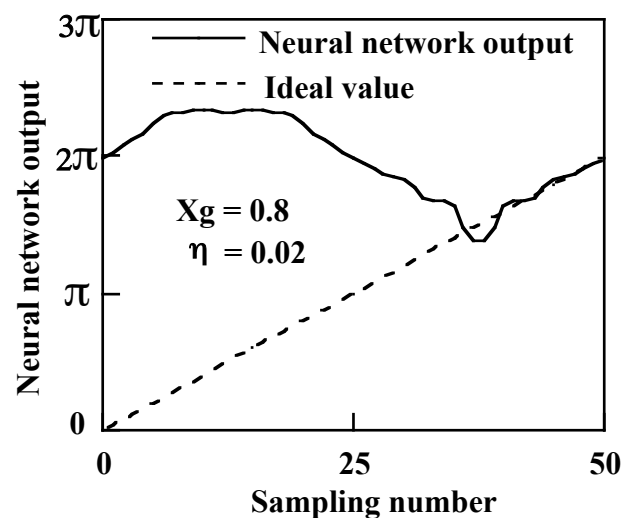


Fig.7 Neural network output of example 2.

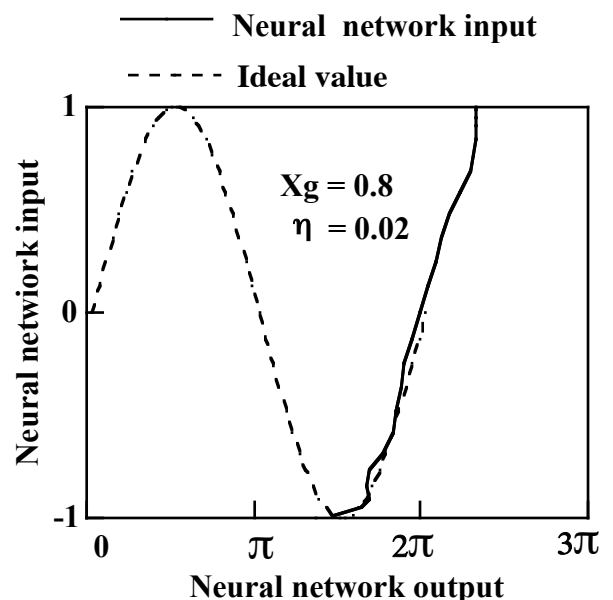


Fig.8 Neural network input-output relation of example 2

Parts Layout Decision of Cell Production Assembly Line using Genetic Algorithm and Virtual System

Hidehiko Yamamoto¹, Tomokazu Watanabe², Takayoshi Yamada³, Masahiro Nakamura⁴, Raafat H. Elshaer⁵

^{1,3}Department of Human and Information Systems, Gifu University, Japan

¹(yam-h@gifu-u.ac.jp), ³(yamato@gifu-u.ac.jp)

²Graduate School of Engineering, Gifu University, Japan, (o3128038@edu.gifu-u.ac.jp)

⁴Lexar Research Inc., Japan

⁵Zagazig University, Egypt, (r_h_elshaer@zu.edu.eg)

Abstract: One of the problems of cell production system is how to decide the parts layout locations. Traditionally, the problem is solved using trial and error method which takes a lot of efforts and time. In this paper, we propose a Virtual Assembly Cell-production system (VACS) for the cell production assembly line. The VACS use a genetic algorithm (GA) system to find a reasonable solution and a virtual production (VP) simulator for giving us a visibility of that solution in the production system. The validation and the efficiency of the proposed VACS system are tested on ten varieties of a product. The simulator results show that the VACS system is capable of getting good solution in a reasonable computational time when compared to the traditional one.

Keywords: Genetic algorithm, Parts layout locations, Cell production, Virtual production.

I. INTRODUCTION

Recently, the production system has changed from mass production of a limited variety of products to low volume production of a wide variety of products, mass customization^[1,2]. It is because the consumers' individual needs are diversified. Therefore, it is important to produce products of a wide variety efficiently. One of the needs for modern production methods is the cell production system^[3]. A cell production system is a production system in which a single worker or small team of production workers perform multiple production jobs in short segment lines. The cell design places a wide range of tools and equipment in close proximity to workers, enabling them not only to perform a wide range of production tasks, but to customize the products as well. One of the problems of cell production system is the parts layout locations. The current state of this problem is to be solved empirically using a trial and error method which takes a lot of effort and time. In addition, the improvement in production efficiency is going up gradually during the assembling process where there is no opportunity to make the production efficiency a peak from the beginning.

In this research, we propose a Virtual Assembly Cell-production System (VACS), a cell production simulation system, for solving the problem. The VACS integrates a Parts Layout Decision system (PLD system) and a Virtual Production simulator (VP simulator). To carry out the PLD system, we adopt a genetic algorithm

(GA) system whose crossover method is the original called TTC.

The paper is further organized as follows. Section 2 introduces the VACS system and its two functions, PLD and VP systems. In section 3, the test problem and the computational results are presented. Finally, section 4 concludes the paper.

II. VACS

The VACS system consists of two collaborating functions, the PLD System including GA system and the VP simulator, as shown in Figure 1. The steps of the VACS system are described in Table 1.

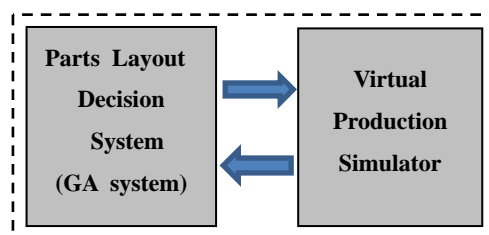


Fig.1 VACS system

Table 1. Steps of the VACS system.

Step 1.	VP simulator draws the workshop floor, and sends the coordinated data of the locations, such as shelves and worktables, to the PLD system.
Step 2.	In the PLD system, the parts layout locations are decided using the GA system and are sent back to the VP simulator.
Step 3.	VP simulator draws the parts layout and animately visualizes the working environment.

1. VP simulator

The VP simulator arranges the parts inside the shelves in workshop floor according to the received information from PLD system showing that in three dimensions. In addition, it visualizes the working environment in which an animation of the assembling process is shown (see section III.3).

2. PLD system

The PLD system uses a GA system to decide the better parts layout locations in terms of minimum total moving distances. In the GA system^[4], the information of the parts layout locations encodes into feasible chromosome. In the searching process for finding a better parts layout locations, genetic operators, such as crossover and mutation ...etc., are repeated, until a predefined stop criteria is verified. More details about the proposed GA in the following paragraphs.

1. Chromosome representation

To treat the information of the parts layout locations, we use a direct representation in which a part number is expressed as a gene, and the part position in the chromosome is expressed as the part location in the layout. For instance, Figure 2 is expressed with the following chromosome: <DFABEC>.

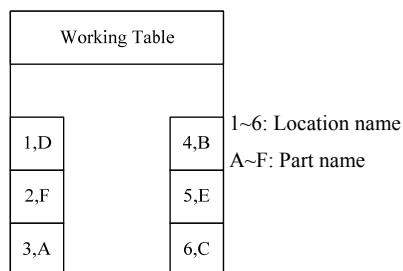


Fig.2. An example of chromosome representation

2. Initial population and fitness function

Initial population is randomly generated and the fitness function is expressed as the reciprocal of the total moved distances to achieve a certain amount of production.

3. Selection, crossover and mutation methods

In selection for crossover^[4], in this paper, Roulette-wheel selection method is used. Applying conventional crossover methods in our proposed chromosome may generate a lethal chromosome. To solve this problem, we develop what we call Twice Transformation Crossover (TTC). By this method, the chromosome is

transformed into the shape that can be cross over, and it is reversely transformed after crossover to its former shape. One point crossover is applied with probability CP. The TTC is as shown in Table 2. As an example, from Figure 2, consider Ch1<CEDFAB> and Ch2<AFBCDE> be two selected chromosomes for crossover. The steps of TTC for generating two offsprings, Off1 and Off2, from the two chromosomes, Ch1 and Ch2, are explained in Table 3.

Each gene in the chromosome may be mutated with probability MP. Mutation method is to swap the selected gene with randomly selected one.

Table 2: Twice transformation crossover method

- 1 In non-decreasing order the parts are arranged in list L
- 2 Take the first gene, i , in the current chromosome
- 3 While L is non-empty, Do:
 - 3.1 Replace gene i with its order in list L .
 - 3.2 Remove part i and update list L
 - 3.3 i equals next gene
- 4 Apply Steps from 1 to 3 to transform two selected chromosomes.
- 5 Apply one point crossover to generate two offsprings
- 6 Use the reverse method of steps 1 to 3 to transform the two offsprings into the original shape

Table 3. An example for the TTC method

First Chromosome: Ch1< CEDFAB >
 $L = \{A, B, C, D, E, F\}$, and $i = C$
 Ch1<3EDFAB>, Update L
 $L = \{A, B, D, E, F\}$, and $i = E$
 Ch1<34DFAB>, Update L
 $L = \{A, B, D, F\}$, and $i = D$
 Ch1<343FAB>, Update L
 ...
 Ch1<343311>
 By the same method Ch2<151111>
 Assume that a one point crossover is randomly chosen between position 3 and 4 to generate Off1 and Off2.
 Off1<151311> and Off2<343111>
 Decode Off1 to original shape:
 $L = \{A, B, C, D, E, F\}$
 Off1<A51311>, Update L
 $L = \{B, C, D, E, F\}$
 Off1<AF1311>, Update L
 ...
 Off1<AFBECD>
 By the same method Off2<CEDABF>

4. Stop criteria and GA parameters

The control parameter values and terminating condition used in our GA was selected based on several preliminary runs with alternate control parameters and terminating conditions on different instances of the problem. These values were then used for the test problem reported in the computational results. The final parameter values are summarized in Table 4.

Table 4. Parameter values for the proposed GA

Description	Values
● Pop. Size	100
● Crossover rate	0.9
● Mutation rate	0.05
● % of solutions replaced by new gen.	0.95
● Stop criteria	100*

*Stop after 100 generations without improvement

III. COMPUTATIONAL RESULTS

1. Test problem

The developed VACS system is tested on a cell-production assembly line of a personal computer. The workplace design and the required parts are as shown in Figure 3. The workshop shelves layout and the final product are as shown in Figures 4 and 5 using VP simulator. There are ten varieties of the product in which each one contains at most 18 parts. The assembly process sequence of each product type is known. The parts of the same type are arranged in one shelf. The workplace contains one worker, and the movement between the shelf and the worktable is in a straight line.

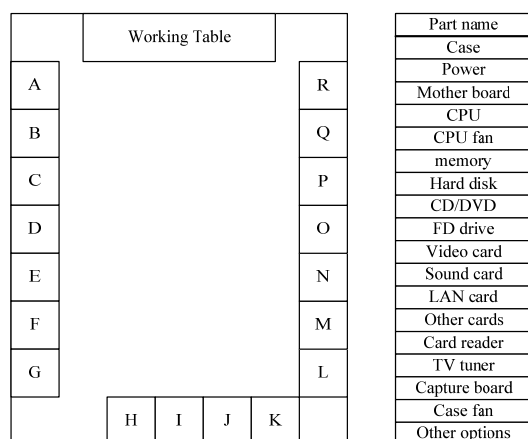


Fig.3. Test problem information

2. Results

Table 5 shows the computational results of 10 runs for the PLD system with the proposed genetic algorithm and with the random method. Columns 2 and 3 show the

best total moving distances of the both methods. The percentage improvement of the GA and the computational CPU time are shown in columns 4 and 5 respectively. Using T-test at 99% confidence level, we find that our developed algorithm makes a statistically significant improvement over the random one.

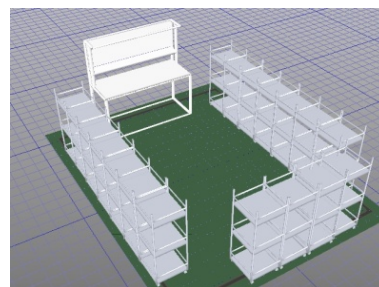


Fig.4. workshop floor shown the worktable and shelves

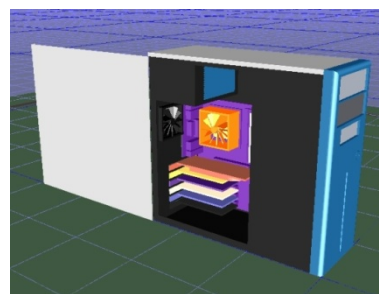


Fig.5. 3D configuration of the final product

Table 5. Comparison between PLD with GA and without GA (units in meter)

Simulation No.	Random Method	GA Method	% of Imp.	GA's CPU time (msec)
1	5087	5003	1.65	718
2	5238	5053	3.53	795
3	5251	5053	3.77	780
4	5226	5011	4.11	920
5	5179	5092	1.68	468
6	5150	5027	2.39	843
7	5157	5025	2.56	921
8	5099	4975	2.42	1104
9	5210	5190	0.39	717
10	5227	5021	3.95	655

A comparison between the fitness curve and the distance reciprocal curve of the random method for getting a best layout in the first simulation is as shown in Figure 6. It is clear from the figure that the random method makes a dramatically improvement in the beginning after that it continues without gaining any improvement. In the other side, the fitness curve is getting better. This difference between the two methods is because the GA exploits the historical information to make improvement, but the random method is not. Figure 7 shows the best parts layout location obtain using the GA from the first simulation.

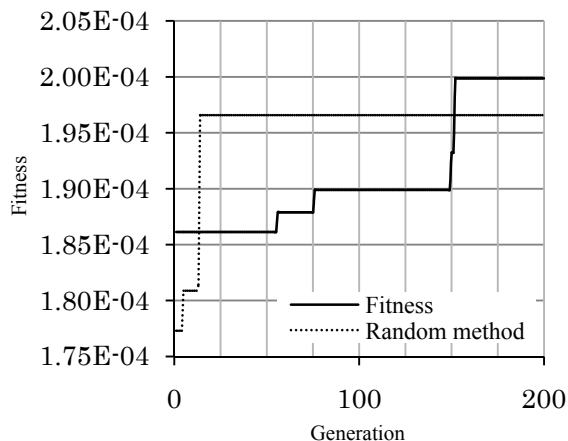


Fig.6. Best fitness curve

Working Table					Location	Part name
A				R	A	Sound card
B				Q	B	Case
C				P	C	Video card
D				O	D	Capture board
E				N	E	FD drive
F				M	F	CPU fan
G				L	G	Other options
	H	I	J	K	H	Case fan
					I	LAN card
					J	Card reader
					K	Other cards
					L	CD/DVD
					M	Mother board
					N	Hard disk
					O	Power
					P	memory
					Q	CPU
					R	TV tuner

Fig.7. Best parts layout using GA from first simulation

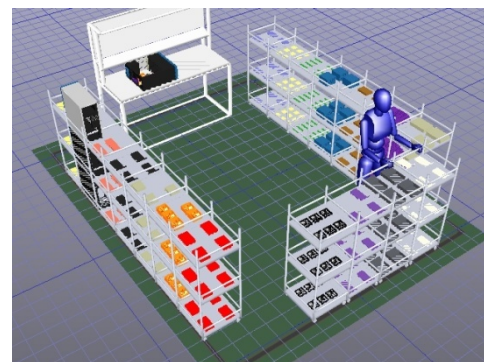
3. Visualization by VP simulator

VP simulator receives the output results from PLD system and visualizes the working environment. Figure 8(a and b) shows snapshots from the virtual production of our test problem for the best parts layout locations shown in Figure 7.

VI. CONCLUSIONS

In this paper, we developed VACS system that integrated PLD system and VP simulator. The PLD system used our developed GA system whose crossover method used the original TTC. The PLD system obtained a good layout for the parts locations in a reasonable computational time. The VP received the layout from the PLD system and visualized the working environment.

From the computational results, we found that the PLD system with the proposed GA was statistically significant impact on the results than the PLD without the GA. Moreover, the VP simulator can be used for educational purposes where the steps of assembling process are visualized with animation.



(a)



(b)

Fig.8. Virtual production for the layout shown in Fig.7.

REFERENCES

- [1] Juan Diego Frutos, Denis Borenstein(2004), A framework to support customer-company interaction in mass customization environments, Computers in Industry 54 (2):115-135
- [2] Suresh Kotha (1996), From mass production to mass customization: The case of the National Industrial Bicycle Company of Japan, European Management Journal 14(5):442-450
- [3] Katsuhide Isa, Tsuyoshi Tsuru (2002), Cell production and workplace innovation in Japan: Toward a new model for Japanese manufacturing?, Industrial Relations: A Journal of Economy and Society 41(4):548-578.
- [4] D.E. Goldberg, Genetic algorithms in search (1989), optimization, and machine learning, Addison-Wesley

Parallelizing Fuzzy Rule Generation using GPGPU

T. Uenishi, T. Nakashima and N. Fujimoto
Osaka Prefecture University, 1-1 Gakuen-cho, Nakaku, Sakai, Osaka
(Tel : 81-72-254-9351; Fax : 81-72-254-9915)
(nakashi@cs.osakafu-u.ac.jp)

Abstract: This paper proposes a method to parallelize the process of generating fuzzy if-then rules for pattern classification problems in order to reduce computational time. The proposed method makes use of GPGPUs' parallel implementation with CUDA, a development environment. CUDA contains a library to perform matrix operations in parallel. In the proposed method, published source codes of matrix multiplication are modified so that the membership values of given training patterns with antecedent fuzzy sets are calculated. In a series of computational experiments, it is shown that the computational time is reduced for those problems that require high computational efforts.

Keywords: fuzzy if-then rule, parallel computation, GPGPU, pattern classification

I. INTRODUCTION

It is known that fuzzy systems based on fuzzy if-then rules perform well for pattern classification problems [1]. However, the computational cost of a fuzzy system is often huge when it is applied to high-dimensional problems with a large amount of training patterns. This is mainly due to explosive increase in the number of fuzzy if-then rules that are generated to construct a classification system. One solution to this problem is to reduce the number of rules. For example, the number of rules to be generated can be restricted, or a small number of fuzzy if-then rules can be selected by using genetic algorithms [2].

This paper proposes a method for speeding up the process of generating fuzzy if-then rules for pattern classification problems without reducing the number of rules. The proposed method is to implement the fuzzy-rule generation process on GPGPU (General Purpose computation on Graphics Processing Units) in order to reduce the computational time.

GPUs, which were originally developed for graphics processing, have a lot of multiprocessors and have potential for high-speed parallel computation. Implementation of GPUs is usually done in C programming language using CUDA (Compute Unified Device Architecture) [3]. To implement with CUDA, it should be considered that a GPU has its own memories which are only accessible from the GPU. GPU's memories are composed of several types of devices with different access speeds and capacities. Thus the efficiency of parallel computing with GPUs depends on the optimality of the memory access. However, it is difficult to design the memory access optimally without understanding the details of the hardware architecture of GPUs. In this paper, we adapt existing implementation to fuzzy classification system.

A library, called CUBLAS, is included in the CUDA package [4]. CUBLAS is an implementation of BLAS (Basic Linear Algebra Subprograms) computation for GPGPU. It allows us to develop parallel computing programs more easily without heavily modifying source codes. While all algorithms in CUBLAS are published

as binary files, some source codes of SGEMM (Single precision General Matrix Multiply) algorithms have been published by the developer.

In the proposed method, calculation of the membership values is parallelized by viewing them as matrix calculation, using two matrices which represent antecedent fuzzy sets and training patterns. The published source codes of the matrix multiplication in SGEMM are modified so that the membership values of given training patterns with antecedent fuzzy sets are calculated in parallel. In a series of computational experiments, the computational time of the proposed method is compared with that of the traditional method that only uses a CPU. It is shown that the proposed method reduces the computational time for pattern classification problems that have high dimensionality and/or a large number of training patterns.

II. FUZZY RULE GENERATION

In this paper, we propose a method to parallelize fuzzy-rule generation that is formulated in the fuzzy system by Ishibuchi et al [1]. It should be noted that the method can be applied to any forms of fuzzy if-then rules because it parallelizes only membership calculation. An overview of the system in [1] is shown below.

In a pattern classification problem with n dimensionality and M classes, we suppose that m training patterns, $\mathbf{x}_p = \{x_{p1}, x_{p2}, \dots, x_{pn}\}$, $p = 1, 2, \dots, m$, are given and each attribute of \mathbf{x}_p is normalized to a unit interval $[0, 1]$. From training patterns we generate fuzzy if-then rules of the following type:

$$R_q : \text{If } x_1 \text{ is } F_{q1} \text{ and } \dots \text{ and } x_n \text{ is } F_{qn} \\ \text{then Class } C_q \text{ with } CF_q, \quad (1) \\ q = 1, 2, \dots, N,$$

where R_q is the label of the q -th rule, $\mathbf{F}_q = (F_{q1}, \dots, F_{qn})$ represents a set of antecedent fuzzy sets, C_q a the consequent class, CF_q is the confidence of the rule R_q , and N is the number of rules. We use triangular membership functions as antecedent fuzzy sets. Figure 1

shows triangular membership functions which divide the attribute axis into five fuzzy sets. Suppose that an attribute axis is divided into L fuzzy sets. The membership function of the k -th fuzzy set is defined as follows:

$$\mu_k(x) = \max \left\{ 1 - \frac{|x - x_k|}{v}, 0 \right\}, k = 1, \dots, L, \quad (2)$$

$$x_k = \frac{k-1}{L-1}, k = 1, \dots, L, \quad (3)$$

$$v = \frac{1}{L-1}. \quad (4)$$

Compatibility of a training pattern x_p with a fuzzy if-then rule R_q is denoted by $\mu_{F_q}(x_p)$ and is calculated as follows:

$$\mu_{F_q}(x_p) = \prod_{i=1}^n \mu_{F_{qi}}(x_{pi}), q = 1, 2, \dots, N, \quad (5)$$

where $\mu_{F_{qi}}(x_{pi})$ is the compatibility of x_{pi} with the fuzzy set F_{qi} and x_{pi} is the i -th attribute value of x_p . $\mu_{F_{qi}}(x_{pi})$ is calculated by equation (2).

Equation (5) implies that the same procedure is iterated for calculating the compatibility of a training pattern with each fuzzy if-then rule: First calculating the compatibility for each attribute, and then multiplying them. Therefore, we can view this process as a function of two matrices. One matrix represents a set of fuzzy if-then rules. The size of this matrix is $N \times n$ and is composed of N row vectors whose lengths are n and elements are antecedent fuzzy sets F_{qi} . The other matrix represents a set of training patterns. This matrix is $n \times m$ and is composed of m column vectors whose lengths are n and each column is a training pattern x_p . In the conventional matrix multiplication for two matrices, the (q, p) element of the product, r_{qp} , is represented as:

$$r_{qp} = \sum_{i=1}^n F_{qi} \cdot x_{pi}. \quad (6)$$

We adapt the above calculation to the calculation of membership value $\mu_{F_{qi}}(x_{pi})$ with the same access order as matrix multiplication. Thus the (q, p) element of the result, r'_{qp} , is represented as:

$$r'_{qp} = \prod_{i=1}^n F_{qi} \odot x_{pi}, \quad (7)$$

where \odot denotes the membership calculation, i.e., equation (2). That is, the membership calculation (i.e., equation (7)) can be regarded as a matrix operation where product operation is replaced with a membership function and sum operation is replaced with a product operation.

The number of fuzzy rules to be generated is L^n . That is, the number of rules increases exponentially for the division number and the dimensionality.

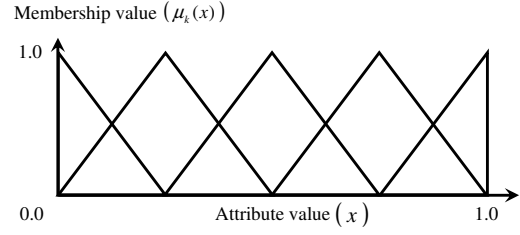


Fig. 1. Triangular fuzzy sets

III. GPGPU

GPUs have a lot of multiprocessors and thus have high potential for parallel computation. The performance of GPUs have been improved tremendously. NVIDIA have released CUDA, a development environment of GPGPU.

In CUDA, functions which are executed on a CPU are compiled with a c-compiler (we used GCC in this paper). While functions which are executed on a GPU are compiled with NVCC (NVIDIA CUDA Compiler). Data and control structures available for GPUs are the same as that of CPUs. However, a GPU has its own memories which are only accessible from it. Thus data transportation between a CPU and a GPU is required before the actual computation. The basic procedure of GPU computing is composed of four steps: A CPU transports data to a GPU, the CPU instructs the GPU to calculate, the GPU executes the calculation, and the GPU transports result to the CPU. Instructions for a GPU are composed of threads, blocks, and grids depending on the level of parallelization. A thread is an atomic execution of the instructions. A blocks is a set of threads, and a grid is a set of blocks. CPUs can only send instructions to grids. Upon receiving the instructions, threads in a block execute the calculations parallelly depending on instructions, and instructions of blocks in a grid are also executed parallelly. During the calculations, threads which belong to the same block can be synchronized and make use of shared memory whose access speed is higher than the global memory. The number of thread per block and the number of blocks per grid need to be determined. Thus the efficiency of parallel computing with GPUs depends on the memory access and the composition of threads, blocks, and grids. However, it is difficult to design the optimal memory access without understanding the details of the hardware architecture of GPUs. As an optimized library of BLAS(Basic Linear Algebra Subprograms) for CUDA, CUBLAS is published together with CUDA. In CUBLAS, SGEMM(Single precision General Matrix Multiply) and DGEMM(Double precision GEMM) are implemented by Volkov et al [5]. Some source codes of SGEMM are published by them. Since the memory access of CUBLAS is designed efficiently, user can implement their algorithms without any concern about memory access diverting the memory access of it. In this paper, we modify the source code of SGEMM so that the calculation of membership values

are parallelized in order to reduce the computational time. Representation and processing of floating point on GPUs follows IEEE754, and we suppose that real numbers on CPUs and GPUs are both single precision in this paper.

IV. IMPLEMENTATION

As mentioned in Section II, the formulation of membership values for fuzzy-rule generation is similar to that of matrix multiplication. We modify the SGEMM algorithm introduced in section III, to be the algorithm to generate fuzzy if-then rules. Volkov et al [5] published the SGEMM algorithm that calculates the following equation:

$$\mathbf{C}^{\text{new}} = \alpha \mathbf{A} \mathbf{B}^T + \beta \mathbf{C}^{\text{old}}, \quad (8)$$

where \mathbf{A} is a $x \times y$ matrix, \mathbf{B}^T is a $y \times z$ matrix, and \mathbf{C} is a $x \times z$ matrix. α and β are scalar values. Equation (8) is calculated parallelly by a GPU after initialization by a CPU. In this paper we specify that $\alpha = 1$ and $\beta = 0$ to consider only the matrix multiplication. By representing elements of the matrices as $\mathbf{A} = (a_{ij})$, $\mathbf{B}^T = (b_{ij})$, and $\mathbf{C} = (c_{ij})$ and a temporal variable as t , the procedure to calculate an element of \mathbf{C}^{new} , c_{ij} , can be shown as the pseudocode in Fig. 2(a). The parallel procedure to calculate compatibility is shown in Fig. 2(b), where a_{ik} is the label of the antecedent fuzzy set, and b_{kj} is the input value and $\mu(a_{ik}, b_{kj})$ is the membership function of the input value b_{kj} for the fuzzy set a_{ik} . Thus the order to access the elements of each matrices is the same as that of the original matrix multiplication. Therefore, the consistency of the parallel computation holds by replacing addition and multiplication of the elements in matrix multiplication to multiplication and membership calculation respectively. In addition, Volkov et al [5] employs 16 threads per block and $(x/64) \times (y/16)$ blocks per grid to make the memory access efficient. However, this limitation has no effect on the calculation of the equation. Now we can parallelize the membership calculation on GPUs by applying the above procedure to matrices which represent antecedent fuzzy sets and training pattern sets.

We suppose that $x_{F_{qi}}$ is an element of \mathbf{A} , where $x_{F_{qi}}$ is the mode of the fuzzy set F_{qi} computed by equation (3):

$$\mathbf{A} = \begin{bmatrix} x_{F_{11}} & \cdots & x_{F_{1n}} \\ \vdots & \ddots & \vdots \\ x_{F_{N1}} & \cdots & x_{F_{Nn}} \end{bmatrix}. \quad (9)$$

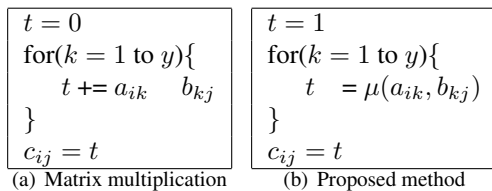


Fig. 2. Pseudocodes of the matrix multiplication and the proposed method

And for a set of training patterns, we set a transposed matrix \mathbf{B}^T as follows:

$$\mathbf{B}^T = \begin{bmatrix} x_{11} & \cdots & x_{m1} \\ \vdots & \ddots & \vdots \\ x_{1n} & \cdots & x_{mn} \end{bmatrix}. \quad (10)$$

By applying the calculation of compatibility modified from matrix multiplication to the above two matrices, a $N \times m$ matrix \mathbf{C} is computed as:

$$\mathbf{C} = \begin{bmatrix} \mu_{F_1}(\mathbf{x}_1) & \cdots & \mu_{F_1}(\mathbf{x}_m) \\ \vdots & \ddots & \vdots \\ \mu_{F_N}(\mathbf{x}_1) & \cdots & \mu_{F_N}(\mathbf{x}_m) \end{bmatrix}, \quad (11)$$

where a row vector of \mathbf{C} corresponds to the compatibility of rules for each patterns, i.e., equation (5). The procedure to parallelize fuzzy-rule generation with a GPU takes the following steps. First, by a CPU, \mathbf{A} and \mathbf{B}^T are made, and transported to a GPU. Second, the GPU calculates \mathbf{C} using the matrix operation for \mathbf{A} , \mathbf{B}^T . Finally, \mathbf{C} is transported to the CPU, and then it determines the consequents.

V. COMPUTATIONAL EXPERIMENTS

To verify the effect of parallelization with GPUs, the computational time to generate fuzzy rules with a GPU is compared to that of a CPU. Table 1 shows the environment of the experiments. Although GeForce GTX 295 has a dual-chip structure, we use only one chip. In the experiments, the computational time for solving a two-class problem is compared. 100 classification problems with different number of training patterns and dimensionalities were used to evaluate the computational time. The number of fuzzy sets for each axis is fixed to two. The results were averaged to compare the efficiency of the parallelization. The results of the experiments are shown in Figs. 3-6. Figure 3 shows how dimensionality of the problem has an effect on the computational time when the number of training patterns is 64. Figure 4 shows how dimensionality of the problem has an effect on the computational time when the number of training patterns is 816. In Fig. 3, the computational time with a CPU is shorter than that with a GPU when the dimensionality is small. As the dimensionality increased, the computational time with a CPU increased drastically while that with a GPU keeps short. In Fig. 4, the computational time with a GPU is shorter than that with a CPU constantly. Figures 5 and 6 show that the number of patterns has an effect on the computational time when the dimensionality of the problem is 12 or 18 respectively. In Fig. 5, the computational time with a CPU is shorter than that with a GPU when the number of patterns is small. However, when the number of training patterns is large, the computational time with a GPU is shorter than that with a CPU. In Fig. 6, the computational time with a GPU is shorter than that

with a CPU constantly. Thus the parallel computation for generating fuzzy rules with a GPU has the effect of reducing the computational time except in the case of low-dimensionality problems with small amount of training patterns.

Table 1. Environment of the experiments

CPU	Intel Core i7 Extreme 945
Clock Frequency	3.20 GHz
Memory Size	5.8 GB
Memory Clock	667 MHz
GPU	NVIDIA GeForce GTX 295
Processor Core	240
Processor Clock	1242 MHz
Memory Size	896 MB
Memory Clock	999 MHz
OS	Linux x86_64
Development Environment	CUDA(NVCC)2.2, GCC4.3

VI. CONCLUSIONS

In this paper, we proposed a method to parallelize fuzzy-rule generation with a GPU using matrix multiplication that is optimized for CUDA. Computational experiments showed that the method reduced the computational time when the dimensionality of the problem and/or the number of training patterns were large. For future works, we will try to parallelize fuzzy inference with GPU, or resolve lack of memory on GPU when the method is applied to problems with further dimensionality and/or the number of training patterns.

REFERENCES

- [1] Ishibuchi H, Nakashima T and Nii M (2003), Classification and Modeling with Linguistic Information Granules. Springer
- [2] Ishibuchi H, Nozaki K, Yamamoto N, and Tanaka H (1993), Selection of Fuzzy If-Then Rules by a Genetic Method(in Japanese). The Transactions of the Institute of Electronics, Information and Communication Engineers Vol.J76-A No.10:1465-1473
- [3] NVIDIA CUDA, http://www.nvidia.com/object/cuda_home.html
- [4] NVIDIA CUBLAS Library, http://developer.download.nvidia.com/compute/cuda/2_1/toolkit/docs/CUBLAS_Library_2.1.pdf
- [5] Volkov V and Demmel JW (2008), LU, QR and Cholesky factorizations using vector capabilities of GPUs. Technical Report No.UCB/EECS-2008-49

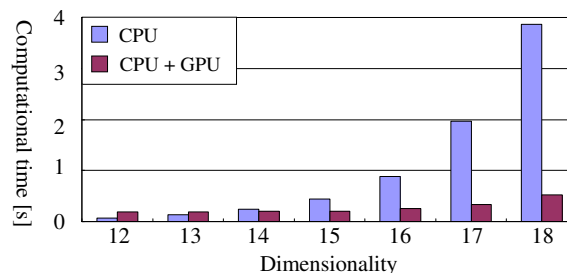


Fig. 3. Computational time for dimensions (64 training patterns)

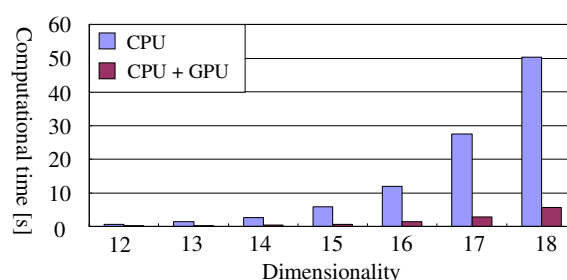


Fig. 4. Computational time for dimensions (816 training patterns)

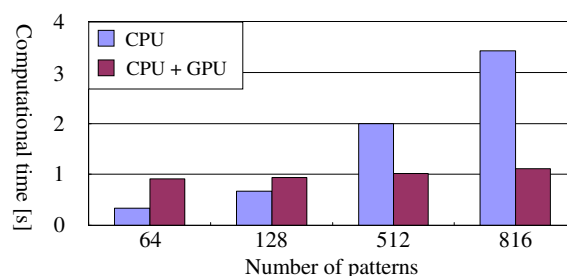


Fig. 5. Computational time for number of patterns (12 dimensionality)

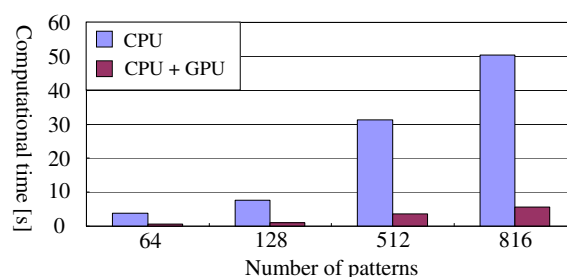


Fig. 6. Computational time for number of patterns (18 dimensionality)

Interactive musical editing system to support human errors and offer personal preferences for an automatic piano

- A method for searching for similar phrases using DP matching -

Kenichi Koga and Kentaro Minowa and Eiji Hayashi

*Department of Mechanical Information Science and Technology
Faculty of Computer Science and Systems Engineering, Kyushu Institute of Technology
680-4, Kawazu, Iizuka-City, Fukuoka Prefecture, Japan*

Abstract: We have developed a system that allows a piano to perform automatically. In order to play music in the manner of a live pianist, we must add expression to the piano's performance. In the case of piano music, there are often 1000 or more notes in the score of even a short piece of music, requiring that an editor spend a huge amount of time to accurately simulate the emotionally expressive performance of a highly skilled pianist. Therefore, we have developed an interactive musical editing system that utilizes a database to edit music more efficiently. We have analyzed MIDI data regarding the performances of highly skilled pianists in order to observe the stylistic tendencies of their performances. Our result showed that phrases having similar patterns in the same composition were performed in similar styles. Therefore, we developed a system that searches for similar phrases throughout a musical score and evaluates the style of their performance. The method of searching for similar phrases uses DP (Dynamic Programming) matching. Using the method of searching, we developed a phrase and music search engine. We thought that as long as it is able to search for similar phrases, it would be able to search for a tune including the phrase from among various tunes.

Keywords: automatic piano, knowledge database, computer music, DP matching

I. INTRODUCTION

We have developed a performance system for an automatic piano. In this system, 90 actuators are installed on the 88 keys and the 2 pedals of a grand piano. These actuators operate key strokes and execute pedaling on the piano. (See Figure 1.1)

Reproducing music with the piano is similar in some ways to reproducing music on the computer. Essentially, variations in tempo, dynamics, and so on are needed to arrange the respective tones in the desired way. However, in the case of piano music, there are 1000 or more notes in a score of even a short piece of music, and for this reason an editor must spend an enormous amount of time working with an arrangement in order to simulate the expressions of an actual performance. Therefore, in this research, we have developed an interactive musical editing system to edit music more efficiently^[1].

We have analyzed MIDI data from the performances of highly skilled pianists in order to observe the stylistic tendencies of their performances. Our results showed that phrases having similar patterns in the same composition were performed in similar styles. Moreover, we found that the pattern of notes in a score sometimes influences the expression of a piece of music.

In this research we developed a system that searches for similar phrases throughout a musical score and

evaluates the style of their performance. We propose a method that uses DP matching as a way to search for similar phrases. This system converts notes into character strings. In addition, the system runs DP matching using character strings and calculates the degree of disagreement between these strings. We use these calculations as an index to determine whether the strings resemble each other. At the end, we introduce a phrase and music search engine using the method of searching.

In this paper, we describe the results of searching for similar phrases using DP matching.



Figure 1.1: View of the automatic piano

II. Musical Editing Support System

2.1 System Architecture

The structure of the system is shown in Figure 2.1. The user edits music via the user's interface on a computer display. The user can also access a database that has musical grammar, the user's preferences, and so on. As a result, editorial work is reduced and efficient editing becomes possible.

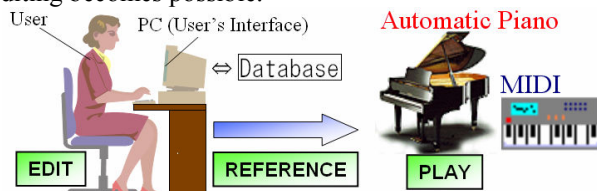


Figure 2.1: Structure of the editing system

2.2 Format of Performance Information

The parameters of performance information are shown in Tables 1 and 2. The automatic piano that we have developed uses a music data structure that is similar to MIDI. We defined performance information, dividing it into two categories: the notes and the pedals. The note information is comprised of the six parameters involved in producing a tone: "Key" (note), "Velo" (velocity), "Gate", "Step", "Bar", and "Time". "Velo" is the dynamics, given by the value of 1–127. "Gate" is the duration of the note in milliseconds. "Step" is the interval of time between notes, and it also exhibits tempo. "Bar" is the vertical line placed on the staff to divide the music into measures.

The pedal information is comprised of four parameters: "Key" (indicating the kind of pedal: "Damper" or "Shifting"), "Velo" (the pedaling quantity), "Time" (the duration for which the pedal is applied)", and "Bar".

2.3 Editing Support Process with Database

Our system can automatically apply a rough performance expression using a Musical Rules Database and Score Database. (See Figure 2.2)

In addition, the system has Preference Database, which stores the editing characteristic of the user.

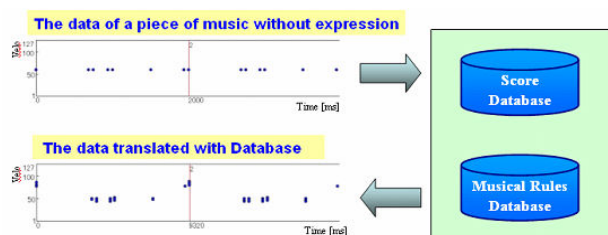


Figure 2.2: Automatic translation with database

2.3.1 Musical Rules Database

This database contains the architecture of musical grammar necessary to interpret symbols in musical notation. It is composed of five tables containing "Dynamics marks", "Articulation marks", "Symbol of Changing Dynamics or Changing Tempo" (symbol that affects the speed of a note or the increase or decrease of the volume), "Time signature", and "Tempo marks".

Analyzing a music symbol according to its usage allows efficient information processing by the system.

2.3.2 Score Database

This database has symbols including time signatures, notes, rests and so on in standard musical notation. Symbols were pulled together in order of bars, and bar symbols were arranged in a time series. Performance expression in itself is only information such as pitch, strength, and length and concerns only the enumeration of a sound. Because the identification of each sound is difficult, editing of the performance expression is difficult. By adding the Score Database's information to performance expression, we can connect each note to its enumeration. In doing so, it becomes easy to edit each phrase.

This database consists of three tables, the "Element table" (showing the position of the note and the composition of the chord), the "Symbol table" (showing the position of the music symbol) and the "Same table" (showing the position of the repetition of the phrase).

The Element table contains the field "Note Value". Data in this field indicates the type of note, e.g., a quarter note, a triplet, and so on. "Note Value" is expressed by three hexadecimal numbers, which are shown in Figure 2.3.

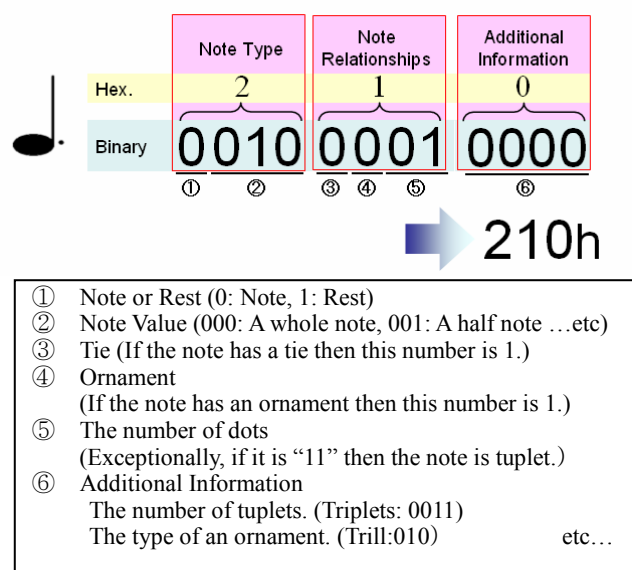


Figure 2.3: Note Value

III. Searching for Similar Phrases

As a result of the analysis, it was found that phrases of the same pattern existing in the same tune are performed in a similar expression. This time, we used DP matching to search for similar phrases.

3.1 DP matching

DP matching is a technique used widely in the field of speech recognition, bioinformatics and so on. It has a feature that can calculate the similarity between two words that are different in a number of characters from each other.

In Figure 3.1, the route of minimum cost in each point is taken, and the route with the lowest cost is assumed finally to be the optimal path. The cost at that time is defined as the distance between patterns. In this system, this distance is handled as a threshold to judge whether the phrases are similar to each other.

For example, if the cost moves up or to the right, then it is increased by 1. If it moves to the upper right, then it does not increase. Also, if the characters do not correspond in each point, then the cost is increased by 5.

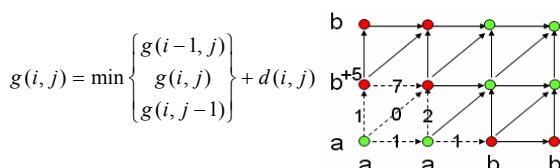


Figure 3.1: DP matching

3.2 Searching with DP matching

In this passage, we describe a method of searching with DP matching. We had to convert a musical score into character strings (a Note Pattern) before searching for similar phrases. This process is explained below.

3.2.1 Note Pattern

Our system converted a score into a Note Pattern using Note Values (See Passage 2.3) in order to perform DP matching. Of the three columns of Note Values, we used the two columns on the left. The system replaces numbers in the second column with letters of the alphabet (from G) because a letter, being a different notation than that used in the first column, allows the expression of one note with two columns. An example of a Note Pattern conversion is shown in Figure 3.2.

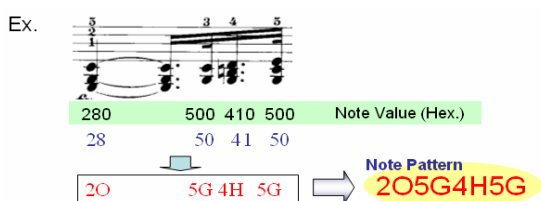


Figure 3.2: Example of Note Pattern

3.2.2 The Method of Searching

The flow of the similar phrase search is shown in Figure 3.3.

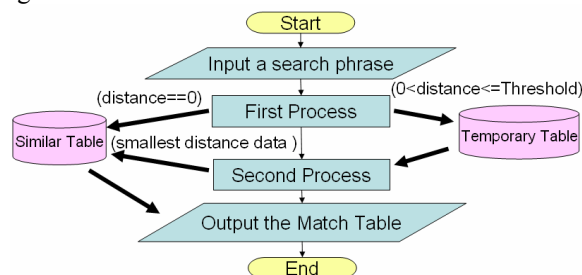


Figure 3.3 The flow of the similar phrase search

Essentially, three rounds of search processing are performed. The first processing round narrows down the points to those having a resemblance in all search ranges. A pattern with the same number as the search phrase is pulled out, and the distance between the two patterns is calculated using DP matching. If they are in complete accord (distance = 0), then the phrase is stored in the Similar Table. If the distance is lower than the threshold, then the phrase is stored in the Temporary Table. (See Figure 3.4)

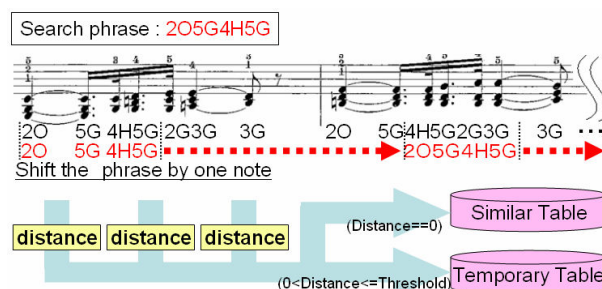


Figure 3.4: The first process

In the second round of processing, DP matching is performed again using the phrases in the Temporary Table while increasing the number of characters. In other words, the system looks for the most similar phrases in the surrounding phrases. The threshold of this system is decided by trial and error. (See Figure 3.5)

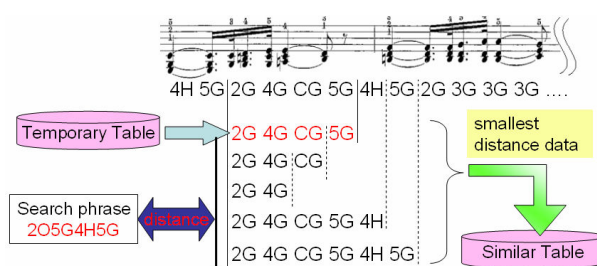


Figure 3.5: The second process

VI. Phrase and music search engine

We can use this system to search for similar phrases in a piece of music. Thereupon, we thought that as long as it is able to search for similar phrases, it would be able to search for a tune including the phrase from among various tunes.

Therefore, we developed a phrase and music search engine. It searches a tune from various tunes with one phrase of voice data. The voice is first inputted; then the interval between the sounds of the inputted voice data is converted back to notes according to the tempo of music. As a result, we thought would be able to search for sequence similarity to the phrase rhythm and notes. The search strategy uses 3.2.2 The Method of Searching.

4.1 Processing that inputs voice

It is shown that voice is input in the shape of waves as shown in Fig. 1. The vertical axis of Fig. 4.1 shows loudness (mdB), and the horizontal axis shows time. By setting a threshold on the vertical axis, the presence of voice can be recognized. The interval of this sound is measured as the time. In other words, as shown in Fig. 1, the interval of sound is the period between the initial iterative peak and the next time the sound iterative peak. The shapes of the waves tell us the note values (See section 2.3) of the phrase.

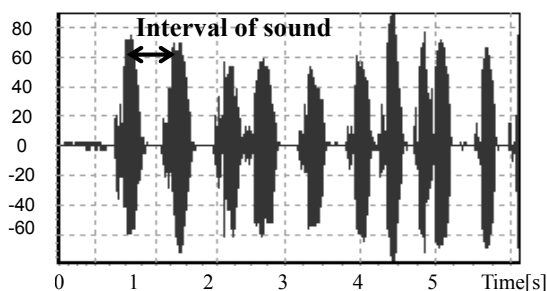


Figure 4.1: Result of sound input

4.2 Search Experiments and Discussion

We searched for music using the phrase and music search engine. The search phrase was the phrase from fourth sound of bar 24 to first sound of bar 27 of “asita ga arusa” ULFULS. Results were set to output phrases with a distance of 20 or less. Table 4.1 summarizes the results. Looking at the results, “asita ga arusa” has the smallest average distance. Thus, the system can find “asita ga arusa” to select smallest average distance sound.

Table 4.1: Search results

Name of sound	Number of searches for phrases	The average distance between the phrase
Sekai ni hitotu dake no hana	46	17.20
Asita ga arusa	128	16.98
Agehatyou	9	18.33
Asuhe no tobira	26	18.42
Can you keep a secret	135	17.12
Haruka	83	17.01
Pieces of a dream	47	17.91
Tenntai kannsoku	13	19.62
sakura	1	20.00

V. CONCLUSION

We designed methods of searching for similar phrases using DP matching and combined these functions into a single system.

In a similar phrase search, the system was able to find similar phrases using DP matching in a short time, and it was even possible to find phrases whose resemblance might not be immediately apparent.

In the phrase and music search engine, we develop a system to search for tune by inputting the data of a voice performing the tune. The interval between the sounds of the inputted voice data is converted it into a note according to the tempo of music. By this, we can search for sequence similarity to the phrase rhythm and notes.

In this study, we were able to perform similar phrase searches and searching for tune by voice. In our future research we will perform evaluations with different pieces of music and will evaluate the existing system. In addition, we will develop the voice-input search system to perform a search for changes in pitch.

REFERENCES

- [1] Hayashi, E. et al, “Behavior of piano-action in a grand piano.I”, Journal of acoustical Society of America, Vol.105, pp.3534-3544, 1999.
- [2] Hayashi, E et al, “Interactive musical editing system for supporting human errors and offering personal preferences for an automatic piano”, Proc. of the 7th International Symposium on Artificial Life and Robotics, Vol.2, pp 513-516, 2002.
- [3] Hikisaka, Y., Hayashi, E., et al, “Interactive musical editing system for supporting human error and offering personal preferences for an automatic piano –Method of searching for similar phrases with DP matching and inferring performance expression-”, Proc. of the 12th International Symposium on Artificial Life and Robotics, GS4-3, 2007.

Subsurface imaging for anti-personal mine detection by Bayesian super-resolution with Smooth-gap prior

Satoshi Kozawa, Takashi Takenouchi and Kazushi Ikeda

Nara Institute of Science and Technology
8916-5 Takayama, Ikoma, Nara, Japan

Phone: +81-0743-72-5986, E-mail: {satoshi-ko,ttakashi,kazushi}@is.naist.jp

Abstract: Ground penetrating radars (GPRs) have been studied to reconstruct a subsurface image. Signal observed by the GPRs typically includes very strong noise and reconstruction of the image is a difficult task. We propose a new subsurface imaging method based on the framework of the Bayesian super-resolution. In the framework, we can incorporate additional information into the reconstructed image by considering a smooth-gap prior, which can represent smoothness of the subsurface image and gaps between materials, and improves the quality of the reconstructed image. We investigated performance of the proposed method with a synthetic GPR dataset, and confirmed the validity of the proposed method.

Keywords: Subsurface Imaging, Inverse problems, Smooth-gap prior

1. Introduction

In the past, anti-personnel mines were mainly made from metals and hence metal detectors were typical tools for detecting buried anti-personnel mines. However, recent plastic mines are difficult to detect because they include few metal parts. Highly sensitive metal detectors may enable us to find plastic mines, but they also induce high false detection error caused by small metallic pieces such as nails or cans. To overcome this difficulty, ground penetrating radars (GPRs) have been studied. A GPR transmits electromagnetic waves into a ground surface, observes the reflected waves, and reconstructs an image that represents the condition of the ground subsurface. An observed signal includes very strong noise that degrades the quality of the reconstructed image and the performance of detection. To improve the image quality, some methods for subsurface imaging with GPRs have been proposed.

Feng and Sato [1] tried to reconstruct the subsurface image by applying the pre-stack migration (which is a subsurface imaging method) for synthetic aperture radars (SARs). A SAR has two or more antennas that transmit or receive electromagnetic waves. The method improves the image quality and shows clear shapes of objects, however, still has noise in the reconstructed image, and the resultant image causes high false positive error for mine detection. Gurbuz *et al.* [2] formulated the imaging problem as an inverse problem based on the model used in [1], and applied the Dantzig selector, which assumes sparseness with respect to the existing probability of buried objects. The assumption of the sparseness is a kind of regularization for the inverse

problem, and the method for reconstructing images is more informative for specification of the location of subsurface objects. However, the reconstructed images lose information on the shapes of objects, which makes it difficult to distinguish mines from other objects.

We propose a new subsurface imaging method based on the Bayesian inference. In the Bayesian framework, we can incorporate additional information into the reconstructed image by considering a smooth-gap prior. The prior can describe smoothness of the subsurface image as well as gaps between materials, by introducing binary latent variables representing whether there is a gap or not between two points. However calculation of the posterior distribution using the prior is not computationally feasible because marginalization of latent variables for all pair of points requires exponential computation time. To overcome the difficulty, we employ the Variational-Bayes (VB) method, in which the posterior is assumed to be written in a factorized form. We investigated performance of the proposed method with a synthetic GPRs datasets, and confirmed the validity of the proposed method.

2. Bayesian Framework

The GPRs use electromagnetic waves to explore the subsurface of the target. In this paper, we consider a bistatic GPR, which has two antennas, one of which transmits electromagnetic waves and the other receives the reflected waves. For subsurface imaging, the GPRs observe the reflected signals $\mathbf{y}_k \in \mathbb{R}^{N_t}$ at k -th scan points and are moved to the next scan point; and as a whole, a dataset $\{\mathbf{y}_k\}_{k=1}^K$

is observed. We assume that the transmitted waves are reflected at only the boundary of two materials with different dielectric constants and then the received signals include information on the boundary in the subsurface. Additionally, we assume that the observed signals at the scan point are represented as a linear superposition of reflected signals from points over the boundary at a scan point. In a practical sense, there are interactions among the reflected signals from points in the subsurface and then the assumption of linear superposition cannot be appropriate; however, we use the model for simplicity.

Let us consider a physical model that represents a relationship between the received signal reflected from a point p and the transmitted signal $s(t)$ as

$$\zeta_{k,p}(t) = \frac{p s(t - \tau_k(p))}{A_{k,p}} \quad (1)$$

where $\zeta_{k,p}(t)$ is the received signal reflected from the point p in the subsurface at the k -th scan point, $\tau_k(p)$ is the total round-trip delay between the antennas and the target point p at the k -th scan point, p is the reflection coefficient of the target point and $A_{k,p}$ is a scaling factor accounting for loss of the signal. Note that the reflection coefficient is positive when the target point p is on the boundary of two materials with different dielectric constants, and otherwise is zero. A whole model of the observed signal $d_k(t)$ at k -th scan point is the superposition of reflected signals and then is written as

$$d_k(t) = \iiint_{\Omega} \zeta_k(x, y, z, t) dx dy dz \quad (2)$$

where Ω is a target region of interest. This is called the point-target model [1][2].

To calculate the right hand side of (2), we discretize the integration in (2) as follows:

$$d_k(t_i) = \sum_{j=1}^N s(t_i - \tau_k(j)) \frac{(j)}{A(k, j)} \quad (3)$$

where j is an index of a discretized point in the target region Ω , $t_i = t_0 + i/Fs$, t_0 is an initial time of measurement and Fs is a sampling frequency. We observe that a vector $\mathbf{d}_k = (d_k(t_0), \dots, d_k(t_{N_t-1}))^t$ of $d_k(t)$ is written as

$$\mathbf{d}_k = \mathbf{W}_k \mathbf{x} \quad (4)$$

where \mathbf{x} is an N -dimensional vector whose n -th element is $(n)/A(k, n)$ and \mathbf{W}_k is a matrix whose (i, j) component is

$$\mathbf{W}_k(i, j) = s(t_i - \tau_k(j)) \quad (5)$$

Here we assume that the GPRs measurement data at k -th scan point is represented as

$$\mathbf{y}_k = \mathbf{W}_k \mathbf{x} + \boldsymbol{\epsilon} \quad (6)$$

where $\boldsymbol{\epsilon}$ is measurement noise. Note that the n -th element of \mathbf{x} represents a reflectivity profile corresponding to the n -th point in the target subsurface space. In other words, \mathbf{x} corresponds to the subsurface image itself of the target space and then our goal is to estimate \mathbf{x} using the observed dataset $\{\mathbf{y}_k\}_{k=1}^K$.

2.1. Probabilistic formulation

We assume that a probability distribution of the measurement noise $\boldsymbol{\epsilon}$ is given by an isotropic Gaussian with a mean vector $\mathbf{0}$. Then a conditional distribution of \mathbf{y}_k given \mathbf{x} is written as

$$p(\mathbf{y}_k | \mathbf{x}) = \mathcal{N}(\mathbf{y}_k | \mathbf{W}_k \mathbf{x}, \beta^{-1} \mathbf{I}), \quad (7)$$

$$= \frac{1}{Z} \exp \left(-\frac{\beta}{2} \|\mathbf{y}_k - \mathbf{W}_k \mathbf{x}\|^2 \right) \quad (8)$$

where β is a prediction parameter and Z is a normalization constant. As a prior distribution of \mathbf{x} , we employ the following smooth-gap prior distribution [3]

$$p(\mathbf{x}) = \sum_{\boldsymbol{\eta}} p(\mathbf{x}, \boldsymbol{\eta}), \quad (9)$$

$$p(\mathbf{x}, \boldsymbol{\eta}) = \frac{1}{Z} \exp \left(-\frac{\rho}{2} E(\mathbf{x}, \boldsymbol{\eta}) \right) \quad (10)$$

where $\boldsymbol{\eta}$ is a vector of binary latent variables, each of which represents the gap between two materials, ρ is a hyper parameter that controls the strength of the effect of the prior distribution, and E is an energy function defined as follows:

$$E(\mathbf{x}, \boldsymbol{\eta}) = \sum_{i \sim j} (\eta_{ij} (x_i - x_j)^2 + (1 - \eta_{ij}) \lambda). \quad (11)$$

The summation $\sum_{i \sim j}$ is taken over all pairs of neighboring pixels. The latent variable η_{ij} represents the local characteristics of the prior and indicates whether a pair of pixels take similar values or not. When $\eta_{ij} = 1$, the pixels i and j are smoothed due to the quadratic penalty, and there is no effect for the smoothing when $\eta_{ij} = 0$. Thus, this prior controls

whether there is a gap or not between two materials by the latent variable $\boldsymbol{\eta}$.

We can rewrite the joint distribution (10) as

$$p(\mathbf{x}, \boldsymbol{\eta}) = p(\mathbf{x} | \boldsymbol{\eta}) p(\boldsymbol{\eta}) \quad (12)$$

where,

$$p(\boldsymbol{\eta}) = \text{Ber}(\boldsymbol{\eta} | \nu), \quad (13)$$

$$p(\mathbf{x} | \boldsymbol{\eta}) = \mathcal{N}(\mathbf{x} | \mathbf{0}, \rho^{-1} A_{\boldsymbol{\eta}}^{-1}). \quad (14)$$

Here, $\nu = 1/(1 + \exp(-\lambda\rho/2))$ is a parameter for the Bernoulli distribution $\text{Ber}(\eta|\nu) = \prod_{i \sim j} \nu^{\eta_{ij}} (1 - \nu)^{1 - \eta_{ij}}$, and (i, j) component of a matrix A_η is defined by

$$[A_\eta]_{ij} = \begin{cases} \sum_{k \in N(i)} \eta_{ik}, & i = j, \\ \eta_{ij}, & i \sim j, \\ 0, & \text{otherwise,} \end{cases} \quad (15)$$

where $N(i)$ is the set of neighboring pixels of the pixel i . Then the posterior can be strictly calculated as follows:

$$\begin{aligned} p(\mathbf{x}|\{\mathbf{y}_k\}_{k=1}^K) &= \frac{p(\mathbf{x}) \prod_{k=1}^K p(\mathbf{y}_k|\mathbf{x})}{p(\{\mathbf{y}_k\})} \quad (16) \\ &= \sum_{\eta} p(\eta|\{\mathbf{y}_k\}) \mathcal{N}(\mu_\eta, \Sigma_\eta), \quad (17) \end{aligned}$$

where

$$\Sigma_\eta = \left[\rho A_\eta + \beta \left(\sum_{k=1}^K \mathbf{W}_k^t \mathbf{W}_k \right) \right]^{-1}, \quad (18)$$

$$\mu_\eta = \beta \Sigma_\eta \left(\sum_{k=1}^K \mathbf{W}_k^t \mathbf{y}_k \right). \quad (19)$$

We employ the maximum *a posteriori* (MAP) estimate $\sum_{\eta} p(\eta|\{\mathbf{y}_k\}) \mu_\eta$ of (16) for the estimated of subsurface image $\hat{\mathbf{x}}$. However, since this estimate has the summation over all pairs of neighboring pixels, it requires exponential order of computational complexity and hence it is impossible to explicitly compute the estimate. To cope with this problem, we employ Variational-Bayes (VB) method to approximate the posterior in this study.

2.2. Variational-Bayes method

For the VB approximation, we introduce a trial distribution $q(\mathbf{x}, \eta)$ which maximizes the variational-energy function

$$F(q) = \sum_{\eta} \int q(\mathbf{x}, \eta) \ln \frac{p(\mathbf{x}, \eta, \{\mathbf{y}_k\})}{q(\mathbf{x}, \eta)} d\mathbf{x}. \quad (20)$$

The trial distribution can approximate $p(\mathbf{x}, \eta|\{\mathbf{y}_k\})$ since maximization of the variational-energy function with respect to q is equivalent to minimization of Kullback-Leibler divergence between $p(\mathbf{x}, \eta|\{\mathbf{y}_k\})$ and $q(\mathbf{x}, \eta)$. Although the trial distribution can be an arbitrary probability distribution for the unknown variables \mathbf{x} and η in principle, for the sake of tractability, we assume that it can be factorized as:

$$q(\mathbf{x}, \eta) = q_{\mathbf{x}}(\mathbf{x}) \prod_{i \sim j} q_{\eta_{ij}}(\eta_{ij}). \quad (21)$$

Under the assumption, the optimal trial distribution maximizing (20) is analytically given as

$$q_{\mathbf{x}}(\mathbf{x}) = \mathcal{N}(\mathbf{x}|\mu, \Sigma) \quad (22)$$

where

$$\Sigma = \left(\rho \mathbb{E}_\eta[A_\eta] + \beta \sum_{k=1}^K \mathbf{W}_k^t \mathbf{W}_k \right)^{-1}, \quad (23)$$

$$\mu = \Sigma \left(\beta \sum_{k=1}^K \mathbf{W}_k^t \mathbf{y}_k \right), \quad (24)$$

and,

$$q_{\eta_{ij}}(\eta_{ij}) = \text{Ber}(\eta_{ij}|\nu_{ij}) \quad (25)$$

where

$$\nu_{ij} = \frac{1}{1 + \exp(-\frac{\rho}{2}(\lambda - \mathbb{E}_{\mathbf{x}}[(x_i - x_j)^2]))}. \quad (26)$$

We employ μ in (22) as the approximated variable of the estimated subsurface image \mathbf{x} .

3. Experiments

In this section, we examined performance of the proposed methods by comparing with the existing methods (Feng and Sato [1] and Gurbuz [2]) using a synthetic GPR dataset. We created a target space as shown in Fig. 1(a): three objects (rectangle, diamond shape, “O”) are buried in the target space. The GPR space-time observation $\{\mathbf{y}_k\}_{k=1}^K$ is generated by (6), in which the SNR is 15 dB. In this experiment, the transmitter-receiver distance is 10 cm and both antennae are a height of 10 cm. The number K of GPR scan points is 400 and an interval of each scan point is uniform.

Results by the Feng and Sato method, and the Gurbuz method are shown in Fig. 1(b) and (c), respectively. In our Bayesian approach, we applied three kinds of prior distributions, the non-informative prior, the smooth prior [4] and the smooth-gap prior defined by (9). The non-informative prior is given by $p(\mathbf{x}) = \mathcal{N}(\mathbf{x}|\mathbf{0}, Z^{-1})$ with a precision matrix $Z^{-1} = \mathbf{0}$, whose posterior mean is written as $\hat{\mathbf{x}} = (\sum_{k=1}^K \mathbf{W}_k^t \mathbf{W}_k)^{-1} \sum_{k=1}^K \mathbf{W}_k^t \mathbf{y}_k$. The smooth prior is a special case of (9) and is given by setting $\eta_{ij} = 1(\forall i, j)$, which results in $\hat{\mathbf{x}} = (\rho A_\eta|_{\eta=1} + \beta \sum_{k=1}^K \mathbf{W}_k^t \mathbf{W}_k)^{-1} \beta \sum_{k=1}^K \mathbf{W}_k^t \mathbf{y}_k$. Figure 1(d), (e) and (f) respectively show the reconstructed subsurface images with the non-informative prior, the smooth prior ($\beta = 0.1$, $\rho = 1.0$) and the smooth-gap prior ($\lambda = 0.04$, $\beta = 0.1$, $\rho = 1$). While the proposed method with the non-informative prior (Fig. 1(d)) failed to reconstruct the subsurface image, the proposed method with the smooth prior (Fig. 1(e)) and the smooth-gap prior (Fig. 1(f)) could reconstruct the subsurface image by which we can recognize shapes of three buried objects. Also, Fengs method (Fig. 1(b)) could reconstruct the image; however, boundaries of target objects

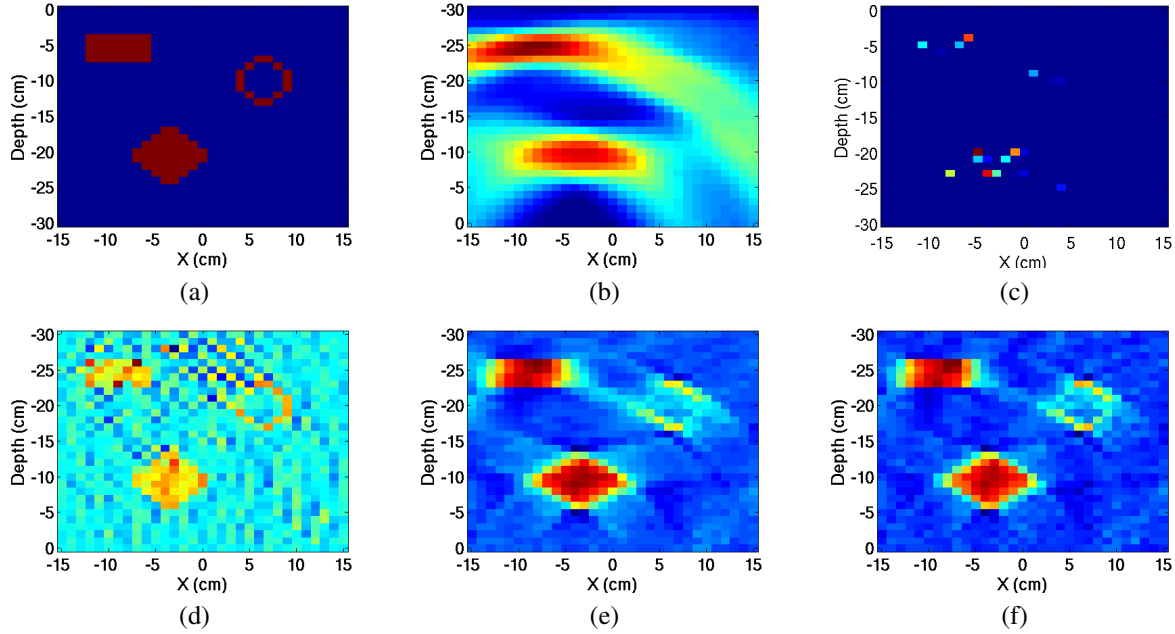


Figure 1: (a) Target space in which three objects are buried: Horizontal axis represents a spatial position in a lateral direction and vertical axis represents the depth. (b) Feng and Sato method, (c) Gurbuz method, (d) Proposed method with the non-informative prior, (e) Proposed method with the smooth prior, (f) Proposed method with the smooth-gap prior

were obscure compared with Fig. 1(e), (f), and we cannot find the object shaped like a “O”. The resultant image by the Gurbuz method in Fig. 1(c) distinctly indicated points of existing objects because of the assumption of the sparseness with respect to the existing probability of buried objects. However, information on shapes of buried objects was lost and it is difficult to determine whether the detected object is a landmine or not.

To investigate the quality of the reconstructed subsurface image, we calculate a normalized SNR of the image reconstructed by the proposed method, with the smooth prior and the smooth-gap prior, and the method of Feng and Sato, respectively. We define a normalized SNR between the true subsurface image and the reconstructed image as

$$10 \log_{10} \frac{\|\mathbf{x}_{true} / \max \mathbf{x}_{true}\|^2}{\|\hat{\mathbf{x}} / \max \hat{\mathbf{x}} - \mathbf{x}_{true} / \max \mathbf{x}_{true}\|^2} \text{ [dB]} \quad (27)$$

where \mathbf{x}_{true} is a vector associated with Fig. 1(a) and $\hat{\mathbf{x}}$ is an estimated vector. The result of Feng and Sato method is -1.96 dB, Gurbuz method -0.119 dB, and the results of the proposed method with the smooth prior and the smooth-gap prior are 5.96 dB and 6.176 dB, respectively. Then we observe that the proposed method significantly outperformed the method of Feng and Sato, and also, the smooth-gap prior which can represent gap information, improved performance compared to the smooth prior.

4. Conclusion

In this paper, we proposed a new subsurface imaging method based on Bayesian framework which enables us to use prior knowledge such that represents the smoothness of the subsurface and the gap between two materials. We observed that the proposed method attained better performance compared with conventional methods for the synthetic dataset. Application of the proposed method for real datasets will be a future work.

References

- [1] X. Feng and M. Sato: Pre-stack migration applied to GPR for landmine detection, *Inverse Problems*, Vol. 20, pp. 99-115, 2004.
- [2] A.C. Gurbuz, J.H. McClellan and W.R. Scott Jr: Compressive sensing for subsurface imaging using ground penetrating radar, *Signal Processing*, Vol. 89, pp. 1959-1972, 2009.
- [3] A. Kanemura, S. Maeda and S. Ishii: Super-resolution with smooth-gap prior, *IEICE Technical Report. (NC)*, Vol. 105, No. 130, pp. 31-36, 2005.
- [4] S. Kozawa, T. Takenouchi, I. Kazushi: Subsurface imaging by Bayesian super-resolution for anti-personal mine detection using ground penetrating radar, *Journal of Signal Processing*, Vol. 14, No. 4, 2010.

Construction of a sense of force feedback and vision for micro-objects: Development the Haptic Device's controlling

J. Noda

*Graduate School of Computer Science
and System Engineering
Kyushu Institute of Technology
680-4, Iizuka City, Fukuoka, Japan, 820-8502
noda415@mmcs.mse.kyutech.ac.jp*

E. Hayashi

*Department of Mechanical Information
Science and Technology
Kyushu Institute of Technology
680-4, Iizuka City, Fukuoka, Japan, 820-8502
haya@mse.kyutech.ac.jp*

Abstract. The purpose of this research was to develop a combined sense system that uses both force feedback and visual feedback to determine the shape of the microscopic features of a microsample. Efficiency in performing minute procedures should be improved if the operator can have a sense of force while using a manipulator. We used a cantilever to touch a minute object and obtain a reaction force from the degree of bending. We constructed a haptic device that gives a sense of that force to the operator when touching the sample with a cantilever. When the haptic device was used in simulations, the user could feel a force as if he had touched the sample.

Key words: force feedback, haptic interface, simulation.

1. Introduction

Technologies that can accurately perform minute work are now being sought for both medical treatment and in the field of manufacturing semiconductors. Such minute work is improved by using micromanipulators, but their operation is difficult because the operator has no sense of force; he or she relies only on sight through a microscope. As a result, a person skilled in the use of this technology is needed for all minute work. The efficiency of minute work would be improved if the operator were able to have a sense of force while using a manipulator.

Here we describe the development of a more efficient system for minute operations. Our aim was to develop a system using not only the sense of sight through a microscope but also a sense of force from the manipulator. For this fundamental research, a system was created to assess the reaction force when a minute sample was touched. A cantilever was used to touch the sample, and the reaction force was obtained from the degree to which the sample bent. In addition, we used a haptic device and amplified the force feedback from a minute sample of a virtual object.

2. System Structure

2-1. System summary

The structure of the system is shown in Fig. 1a, and a schematic view is shown in Fig. 1b. This system consists of a microscope with an automatic x-y stage, a piezo stage, a feedback stage controller to control the x-y stage, a piezo stage controller, a haptic device for transmitting force feedback (Fig. 2), a cantilever (Fig. 3), and a PC

via which the user can control and operate these components. The sample was fixed on the x-y stage by an injector (Fig. 4) and a holding pipette (Fig. 5). When the cantilever, which was fixed to the piezo stage, touched the sample, the operator could maintain the cantilever's position by obtaining the value of the reaction force through the interface. The resolution of the piezo stage is 1 nm. Table 1 gives the specifications of the injector, and Table 2 gives the specifications of the holding pipette.

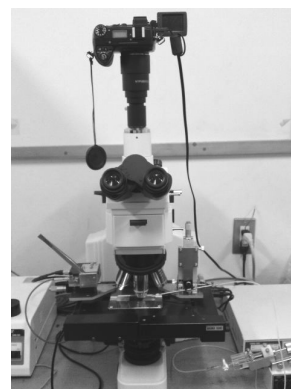


Fig. 1a. Photograph of the structure of the system.

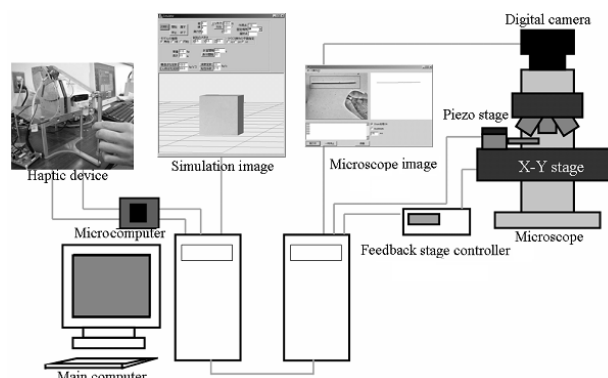


Fig. 1b. A schematic view of the system's structure.



Fig. 2. Haptic device.

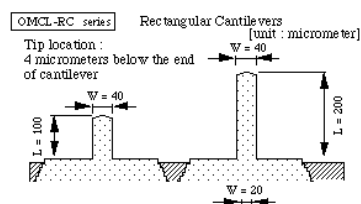


Fig. 3. Cantilever.



Fig. 4. Injector.

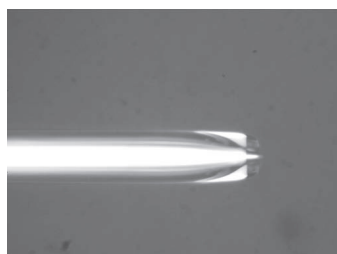


Fig. 5. Tip of holding pipette.

Table 1. Specifics of the injector.

Drive distance	40 mm
Braking distance	800 μ
Size	200 \times 80 \times 30 mm
Weight	2 kg

Table 2. Specifics of the holding pipette.

Length	60 mm
Inside diameter	13 μ m

2-2. Haptic device

Figure 6 is a diagram of the haptic device. It consists primarily of a rotor, a laser, and a position-sensitive device (PSD). We installed a coil on the rotor with a polarity magnet, which generated electromagnetic induction by an electric current and a magnetic force. The angle of the rotor can be measured by the laser and the PSD. The rotor was able to follow any input waveform.

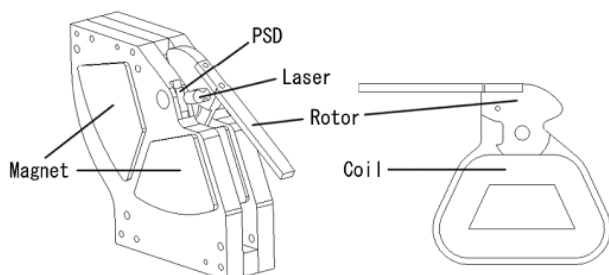


Fig. 6. Diagram of the haptic device.

The actuator is controlled by a servomechanism on the actuator. Therefore, the system driving the actuator consisted of four actuators: a microcomputer, an inputting AD/DA port, an outputting microcomputer, and a PC outputting order value. The system controls the actuator during each part of the process. Figure 7 shows the structure of the haptic device.

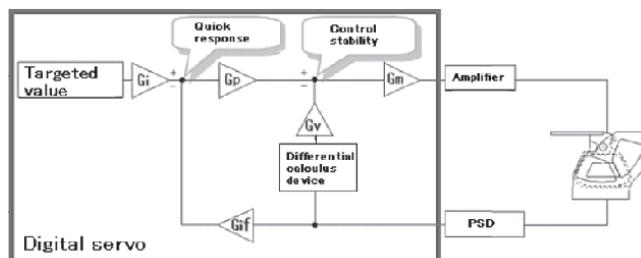


Fig. 7. Structure of the haptic device.

The actuator, whose actions are governed by the PD control, is operated through a digital differential calculus device. A transfer function for the quadratic function system shown in Fig. 8 is provided for the actuator servo system. The role of each parameter of the control system is to adjust the total offset to a master in G_i/G_{if} , to regulate the item viscosity/resonance point in G_p/G_v , and to regulate the total gain in G_m . Table 3 is a list of the control parameters of the servomechanism system.

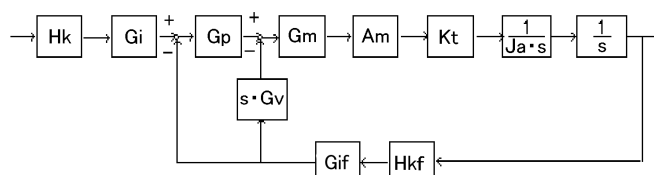


Fig. 8. Block diagram of the servomechanism system.

Table 3 Control parameters of the servomechanism system

Parameter	Reference	Unit
G_i	Controller Input Gain	1.0
G_{if}	Position Feedback Gain	1.0
G_p	Position Gain	1.0
G_v	Velocity Gain	0.0015
G_m	Manipulation Gain	1.0
H_k	Position Voltage Constant	18.531 V/rad
H_{kf}	Position Voltage Feedback Constant	18.531 V/rad
A_m	Amplifier Constant	1.0 A/V
K_t	Torque Constant	2.768 Nm/A
J_a	Moment of Inertia	0.0002147 kg \cdot m ²

3. Measuring the reaction force

The reaction force is used to calculate the force that is applied by the minute object. In this experiment, we touched the minute object with the cantilever shown in Fig. 3, and the reaction force was obtained from the degree of bend of the cantilever. The layout of the experiment is shown in Figs. 7 and 8, and the environment of the experiment is shown in

Figs. 9 and 10. As a result of this experiment, we obtained the reaction force applied by the minute object.

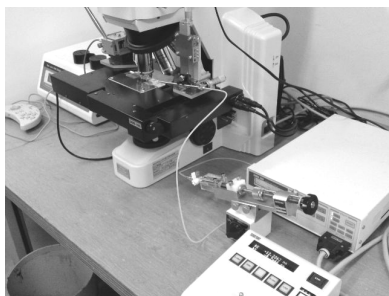


Fig. 9. Environment of the experiment.



Fig. 10. Close-up of the environment of the experiment.

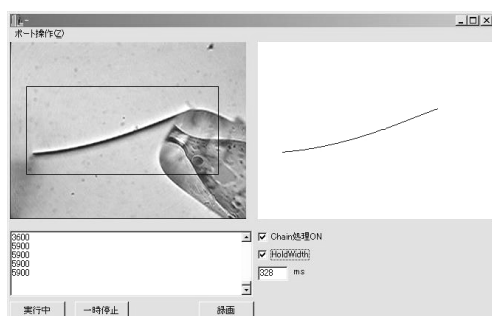


Fig. 11. Cantilever touching the tip of the holding pipette.

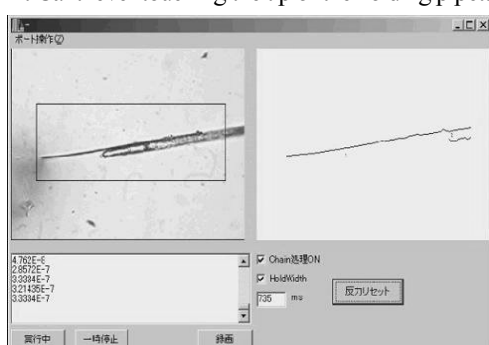


Fig. 12. The cantilever detection program.

Figure 11 shows the cantilever touching the tip of the holding pipette. Figure 12 shows the experiment that measures the reaction force of the downy hair. The image processing speed of the cantilever was improved by the tracking process. The bend of the cantilever is assumed to be linear-elastic so that Hooke's law may be applied. The restoring force, F , of the bend of the cantilever is given by

$$F = kx \quad (1)$$

where x is the compression distance from the equilibrium position, and k is the spring constant.

4. Deforming the sample in simulation

In this study, we aimed to build a working system using a microscope, a haptic device, and a simulation. A fundamental element was the simulation of the deformation of a minute object. Figure 13 shows the graphical user interface (GUI) of the simulator. A graphic tool is created using OpenGL to draw the object and to choose the shape of the sample, for instance, a cube or sphere. A dynamic model of the sample consists of a spring-mass array of mass points in both the vertical and horizontal directions. An example of the arrangement of mass points is shown in Fig. 14. When a force was applied at a mass point, the simulation calculated the speed of all mass points that had been affected. The image is renewed after every ten calculations.

We defined a spring as having a size but no weight, and a mass point as having a size, a weight, and a rigid body. An arbitrary mass object can be placed on a spring on a bitmap (Fig. 15). In addition, a sample can be seen from various viewpoints, and the deformation of the sample, which is impossible to observe by microscope, can be checked. The shape of this object can be either a cube or a sphere, and any point may be selected as a fixed point or an operating point.

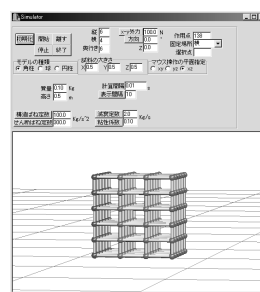


Fig. 13. Simulator.

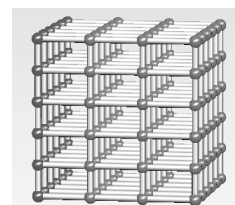


Fig. 14. Arrangement of mass points

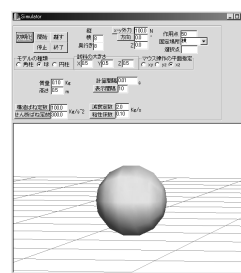


Fig. 15. Placing an arbitrary object on a bitmap.

The calculation method for the displacement of each mass point is based on Newton's equation of motion (Eq. 1) using

the Euler method. A mass point is linked to an adjacent mass point at both ends of a spring. When the spring between the mass points is in the equilibrium position, the restoring force, F , is the sum of the elastic force of the construction spring and the shear spring, and the viscous force is given by

$$ma = \sum F \quad (2)$$

where m is mass and a is acceleration.

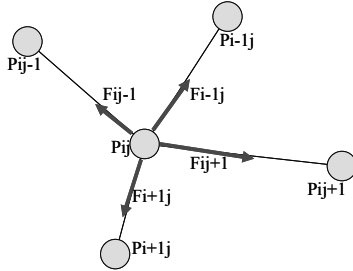


Fig. 16. Elasticity.

$\sum F$ is the sum of the elastic force of the construction spring and shear spring, the viscous force, and the damping force. To obtain F , we divided the restoring force into $F_{damping}$, F_{spring} , and $F_{viscous}$. Equation 2 gives the following equations using the model shown in Fig. 16:

$$F_{spring} = \sum F_{ij} \quad (3)$$

$$F_{damping} = -C_d v_i \quad (4)$$

$$F_{viscous} = -C_v (v_i - v_j) \quad (5)$$

$$\sum F = F_{spring} + F_{damping} + F_{viscous} \quad (6)$$

where C_d is the damping factor, C_v is viscosity, and v_i and v_j are the velocities.

5. Conclusion

In the present study we evaluated whether the force feedback could be amplified by touching a virtual object with a haptic device in a PC. We found that it is possible to amplify the reaction force, but we were unable to create a large enough reaction force for a worker to feel its elasticity.

Future research should focus on building a system that allows a reaction force to be detected and shown more precisely. Such a system would make it possible to test smaller samples.

6. Acknowledgement

This research was partially supported by the Ministry of Education, Science, Sports and Culture, Grant-in-Aid for Scientific Research, 2010.

References

1. Li X, Zhang Z (2008) Probe-type microforce sensor for micro/nano experimental mechanics. Trans Tech Publications, Stafa-Zurich, Switzerland
2. Zhang J, Xi N, Li G, et al. (2006) Atomic force microscopy sensing using multiple modes. 2006 IEEE/RSJ International Conference on Intelligent Robots and Systems, Beijing, China, 9-15 October. IEEE, Piscataway, NJ
3. Hrouzek M (2005) Feedback control in an atomic force microscope used as a nano-manipulator. Acta Polytech Czech Tech Univ Prague 45(4):65-69
4. Ujihara R (2004) Developing the haptic device. Kyushu Institute of Technology
5. Yaacoub F, Hamam Y, Abche A (2008) Computer-based training system for simulating wrist arthroscopy. Université Paris-Est, ESIEE, Laboratoire A²SI, Cité Descartes, 93162 Noisy Le Grand, France. University of Balamand, Department of Electrical Engineering, P.O.Box 100, Tripoli Lebanon F'Satie – TUT, Private Bag X680, Pretoria 0001, South Africa. Proceedings of the 21st IEEE International Symposium on Computer-Based Medical Systems (CBMS 2008)
6. Tahmasebi AM, Taati B, Mobasser F, et al. (2005) Dynamic parameter identification and analysis of a PHANToM trade haptic device. School of Computing, Queen's University, Kingston, ON, Canada. Department of Electrical and Computer Engineering, Queen's University, Kingston, ON, Canada. 2005 IEEE International Conference on Control Applications (CCA) (IEEE Cat. No. 05CH37713)
7. Sonoda T (2006) Construction of super-micro sense of force feedback and visual for an elastic body. Kyushu Institute of Technology. Proceedings of the 12th International Symposium on Artificial Life and Robotics, Beppu, Oita, Japan, 2006
8. Miyamoto K (2007) Construction of super-micro sense of force feedback and visual for micro objects. Kyushu Institute of Technology. Proceedings of the 12th International Symposium on Artificial Life and Robotics, Beppu, Oita, Japan, 2007
9. Uehara R (2010) Construction of super-micro sense of force feedback and visual for micro objects. Kyushu Institute of Technology. Proceedings of the 15th International Symposium on Artificial Life and Robotics, Beppu, Oita, Japan, 2010

Trajectory Control of Biomimetic Robots for Demonstrating Human Arm Movements

T. Kashima and M. Iwaseya

*Tomakomai National College of Technology, Aza Nishikioka 443, Tomakomai, 059-1275, Japan
(Tel/Fax : 81-144-67-8013)
(kashima@me.tomakomai-ct.ac.jp)*

Abstract: This study presents the trajectory control of biomimetic robots by developing human arm trajectory planning. First, the minimum jerk trajectory of joint angles is analytically produced, and the trajectory of elbow joint angle is modified by time adjustment of joint motion of the elbow relative to the shoulder. Next, experiments in which gyro sensors are utilized have been conducted, and produced trajectories are compared with observed ones. According to the results, the validity of this proposed trajectory control for demonstrating human arm movements has been evaluated.

Keywords: biomimetic robot, human arm movement, trajectory planning, gyro sensor

I. INTRODUCTION

It is an important issue for biomimetic robots not only to design appearance resembling a human arm but also to move its arm along humanlike trajectories. An effective method for controlling biomimetic robots along such trajectories is to apply human arm trajectory planning. Here, the criteria such as joint torque change[1] and consumed energy[2] are proposed for characterizing human arm trajectory. The optimal trajectories minimizing these criteria have good agreements with human arm trajectories if movement duration and arm parameters are properly set up. This optimal trajectory is sensitively influenced by the change of movement duration or external load. In contrast, the hand path and velocity profile of human arm trajectory is kept invariant when the movement duration or the external load is changed[1]. In addition, numerical calculations for producing optimal trajectories become extremely difficult to converge under specific movement conditions. Consequently, such criteria have difficulty with these problems for the trajectory planning of biomimetic robots.

Meanwhile, it is possible to formulate humanlike trajectories which satisfy with the invariant property, if we assume the trajectory planning geometrically determined. Here, the criteria defined by derivative of the hand position including jerk in Cartesian coordinates have been proposed[4]. The produced hand velocity profile is always bell-shaped and shows property of human arm trajectory. However, curved hand paths occasionally observed in human arm movements can not be demonstrated, since the produced path is consistently straight. Such curved paths can be represented by supposing a linear relationship between the shoulder and the elbow angles in joint angle coordinates. Furthermore, this idea leads to an important fact that most of human hand paths can be duplicated by adequately setting a time delay of joint motion onset of the elbow relative to the shoulder[5]. However, there

remains a crucial problem that a hand trajectory can not be produced unless the human trajectory to be duplicated is given.

This study presents the trajectory control of biomimetic robots. At the beginning, the minimum jerk trajectory of joint angles is analytically produced, and the trajectory of elbow joint angle is modified by time adjustment of joint motion of the elbow relative to the shoulder. As regards time adjustment, a newly provided case in addition to a case reported in a past literature[5] is taken into account. This time of elbow joint motion to be adjusted is numerically determined so as to reach the maximum hand velocity at the midpoint of movement. Consequently, the hand trajectory derived from the joint angle trajectories can be uniquely produced once the initial and target positions and movement duration are given. Subsequently, experiments have been conducted in which gyro sensors are utilized for measuring angular velocities with high accuracy and high resolution. Then, trajectories are numerically produced by use of the movement condition observed by experiments, and they are compared with observed ones in joint angle coordinates and Cartesian coordinates. Finally, it is shown that the proposed trajectory control is reasonable for biomimetic robots to demonstrating human arm trajectories.

II. METHODS

A. Trajectory formation

Human trajectories sometimes show a linear relationship between a shoulder and an elbow angles in joint angle coordinates[3],[5]. With respect to this relationship, the trajectory planning, so called "staggered interpolation" has been proposed. According to this method, most of hand paths can be reproduced if a linear relationship between these two angles is initially supposed, and a time delay of joint motion onset of the elbow relative to the shoulder is appropriately provided. However, this time delay can

not be determined unless the human trajectory to be duplicated is given. Besides, the hand velocity profile, in some movement conditions, becomes distorted bell-shape. In our study, these problems are overcome by newly developed trajectory planning which reflects properties of human arm trajectory in Cartesian coordinates.

At the beginning, the performance criterion of a minimum jerk in a joint angle space is defined as

$$J = \frac{1}{2} \int_0^{t_f} (\ddot{\theta}_1(t)^2 + \ddot{\theta}_2(t)^2) dt, \quad (1)$$

where $\theta_1(t)$ and $\theta_2(t)$ are shoulder and elbow angles, and t_f is a movement duration. When the initial condition of movement is given by

$$\begin{cases} \theta_i(0) = \theta_{is}, \dot{\theta}_i(0) = 0, \ddot{\theta}_i(0) = 0 \\ \theta_i(t_f) = \theta_{if}, \dot{\theta}_i(t_f) = 0, \ddot{\theta}_i(t_f) = 0 \end{cases} \quad i=1,2, \quad (2)$$

the optimal trajectory becomes

$$\theta_i(s) = \theta_{is} + (\theta_{if} - \theta_{is})(15s^4 - 6s^5 - 10s^3), \quad i=1,2, \quad (3)$$

where $s = t/t_f$ is a normalized time. The trajectory given by Eq. (3) shows a perfect linear relationship between two angles. However, the hand velocity profile in Cartesian coordinates does not necessarily show the maximum velocity at the midpoint of movement. In other words, it does not, in a precise sense, implement the property of human trajectory. Therefore, we need to provide time adjustment which makes the hand velocity profile reach the maximum at the halfway point.

A robot arm model is shown in Fig. 1. Here, the hand position is described by

$$\begin{cases} x = l_1 \cos \theta_1 + l_2 \cos(\theta_1 + \theta_2) \\ y = l_1 \sin \theta_1 + l_2 \sin(\theta_1 + \theta_2) \end{cases} \quad (4)$$

By differentiating Eq. (4), the relationship of velocity between Cartesian and joint angle coordinates becomes

$$\begin{cases} \dot{x} = -l_1 \dot{\theta}_1 \sin \theta_1 - l_2 (\dot{\theta}_1 + \dot{\theta}_2) \sin(\theta_1 + \theta_2) \\ \dot{y} = l_1 \dot{\theta}_1 \cos \theta_1 + l_2 (\dot{\theta}_1 + \dot{\theta}_2) \cos(\theta_1 + \theta_2) \end{cases} \quad (5)$$

Accordingly, the tangential velocity of hand is

$$v = \sqrt{\dot{x}^2 + \dot{y}^2}. \quad (6)$$

In general, this velocity does not reach the maximum at the halfway point. Hence, a time adjustment of elbow has to be taken into account. The first is the case that

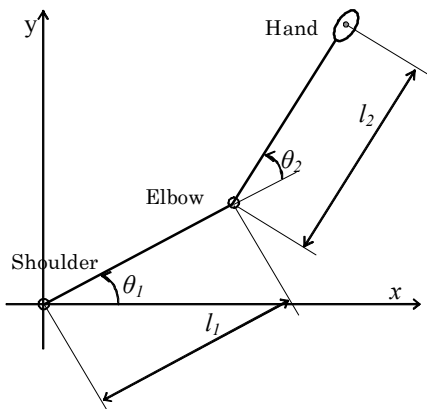


Fig. 1. Robot arm model

joint motion onset of the elbow relative to the shoulder is delayed, and only this case is considered in a past study[5]. We newly set the second case that the elbow joint motion stops before the shoulder joint motion does. In the first case, we suppose the elbow joint motion delayed time d with respect to normalized time s . Then, the elbow joint angle using Eq. (4) can be described by

$$\theta_2(s) = \theta_{2s} + (\theta_{2s} - \theta_{2f})(15p^4 - 6p^5 - 10p^3) \quad (7)$$

where

$$p = \begin{cases} 0, & 0 \leq s < d \\ (s-d)/(1-d), & d \leq s \leq 1 \end{cases} \quad (8)$$

In the second case, when the elbow joint stops time d early before the shoulder joint does, p in Eq. (7) is

$$P = \begin{cases} s/(1-d), & 0 \leq s < 1-d \\ 0, & 1-d \leq s \leq 1 \end{cases} \quad (9)$$

When the shoulder joint angle of Eq. (3) and the elbow joint angle of Eq. (7) are substituted into Eq. (5), the hand velocity becomes function of s and d . Then, by differentiating it, we have

$$\frac{dv}{ds} = \frac{1}{2\sqrt{\dot{x}^2 + \dot{y}^2}} \frac{d(\dot{x}^2 + \dot{y}^2)}{ds} \quad (10)$$

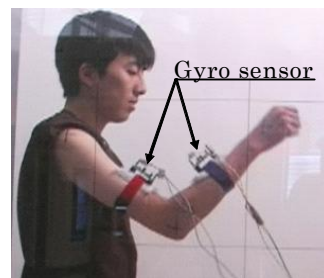
Accordingly, a condition that the maximum velocity exists at the midpoint of movement can be written as

$$\begin{aligned} \left. \frac{d(\dot{x}^2 + \dot{y}^2)}{ds} \right|_{s=0.5} &= [2l_1^2 \dot{\theta}_1 \ddot{\theta}_1 + 2l_2^2 (\dot{\theta}_1 + \dot{\theta}_2) (\ddot{\theta}_1 + \ddot{\theta}_2) \\ &+ 2l_1 l_2 [(2\dot{\theta}_1 \ddot{\theta}_1 + \ddot{\theta}_1 \dot{\theta}_2 + \dot{\theta}_1 \ddot{\theta}_2) \cos \theta_2 \\ &- \dot{\theta}_1 \dot{\theta}_2 (\dot{\theta}_1 + \dot{\theta}_2) \sin \theta_2]]_{s=0.5} = 0 \end{aligned} \quad (11)$$

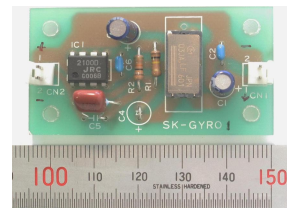
Since the time difference is uniquely decided by Eq. (11), the arm trajectory is perfectly determined once initial and target positions are given. In this study, we initially set as $d=0$, and time d satisfying with Eq. (11) has been searched by Newton-Raphson method.

B. Experiment

The important feature of human arm trajectory is the dynamic behavior of joint angular velocity as well as the hand trajectory in Cartesian coordinates. Therefore, the joint angular velocity has to be measured with a high degree of accuracy since a time difference of joint motion of the elbow relative to the shoulder is essential. One of the most effective methods for measuring angular velocity is to utilize gyro sensors[6]. In this study, two gyro sensors are used on the upper arm and



(a) Arrangement



(b) Circuit board

Fig. 2 Gyro sensor

the forearm of a subject, and this gyro sensor is mounted in a circuit board as shown in Fig. 2. As regards movement conditions, several sets of initial and target hand positions are provided for observing basic properties of human arm trajectories. The trajectory is measured for movements in which a subject moves a hand from the initial to the target hand positions, and this is named direct movement. Then, the initial and target hand positions are exchanged, and the trajectory is also observed for movements which is called inverse movement. Besides, the detail of experimental procedure and data processing is described in a literature[7]

III. RESULTS AND DISCUSSION

The hand path in human arm movements is either almost straight or simply curved[1]-[3]. So, these typical trajectories of direct movement are shown in Figs. 3 and 4. Results of inverse movement to each direct movement are also shown in Figs. 5 and 6. In the experiment, a subject is instructed to move his hand without concerning himself fine accuracy of the target point. As a result, a pair of hand positions of direct movement is not, in a precise sense, the same as a pair of hand positions of inverse movement.

As regards angular velocity, the observed trajectory basically shows bell-shaped profile on motion in both direct and inverse movements. Besides, most of the angular velocities overshoot near the termination time. This phenomenon is called “zero velocity crossing” as introduced in Ref. [8]. The angular velocity profile of produced trajectory well agrees with that of observed one in all movements except oscillation of angular

velocity in some movements and the phenomenon of zero velocity crossing. However, these dissimilarities are not serious drawbacks for representing human arm trajectory because fluctuation within a small range of angular velocity does not seriously influence the velocity profile and the hand path.

With respect to an angular velocity, the elbow joint motion in direct and inverse movements for a pair of hand positions exhibits an interesting feature. Fig.3 indicates that the elbow joint motion starts after the shoulder joint motion does. Conversely, Fig. 5 for in inverse movement shows an opposite result that the elbow joint motion stops before the shoulder joint motion does. The same phenomenon can be seen in direct and inverse movements of condition2. This time difference between the elbow and the shoulder joint motions takes an important role of human arm trajectory planning.

The hand trajectory is one of the most important issues for biomimetic robots demonstrating human arm movements. Besides, it can be represented by the path and the velocity profile of a hand. As can be seen from Fig. 3 to Fig. 6, observed trajectories show such typical properties that the hand path is either straight or simply curved, and the hand velocity profile is bell-shaped with the maximum value in the vicinity of the halfway point. As for produced trajectories, the hand path of direct movement of condition 1 is slightly different from the path of observed trajectory. However, judging from the experimental results conducted under plural subjects[9], a variation of this degree can be considered within a range of individual difference. In all movements other than that, the hand path nearly overlapped in the

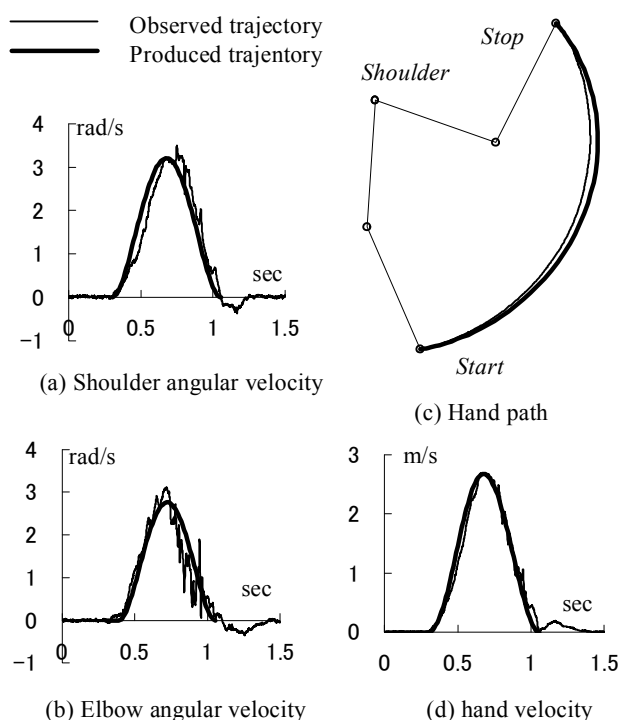


Fig. 3 Direct movement of condition 1

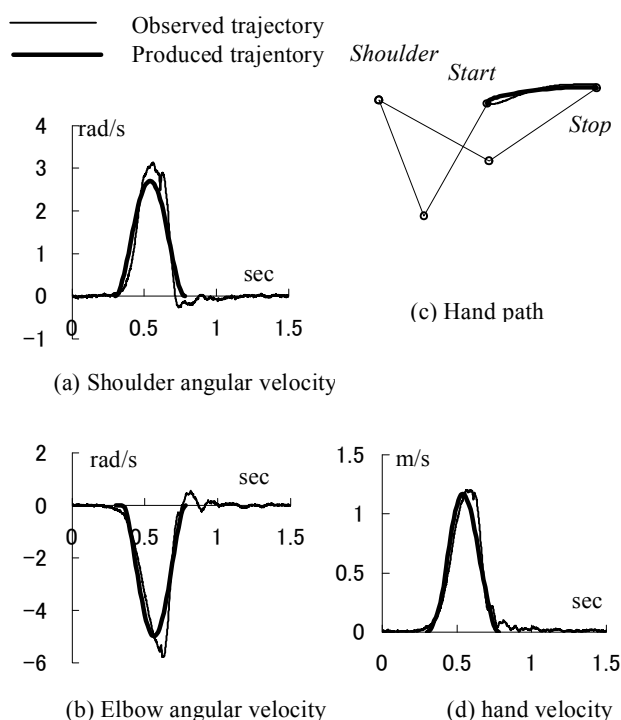


Fig. 4 Direct movement of condition 2

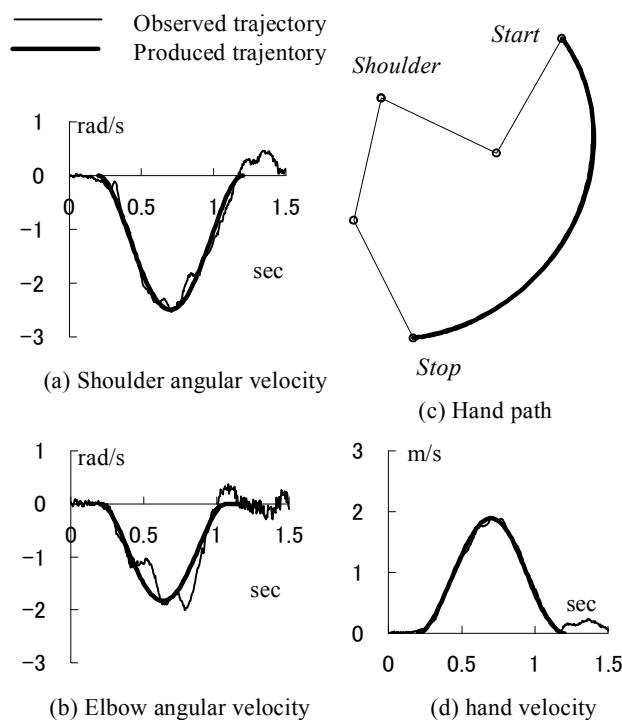


Fig. 5 Inverse movement of condition 1

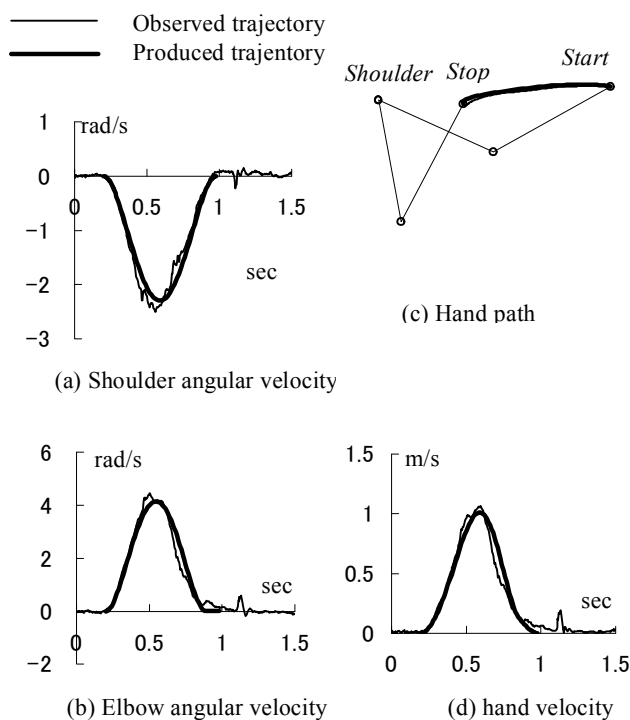


Fig. 6 Inverse movement of condition 2

produced and the observed trajectories. In addition to this consistency of the hand path, the hand velocity profile of produced trajectories is identical to that of observed trajectories in all movements. These results lead to the conclusion that trajectories produced according to the proposed trajectory planning well demonstrate human arm property.

IV. CONCLUSION

In this study, the trajectory planning for biomimetic robot has been conducted in kinematic coordinates, and produced trajectories have been compared with experimental results. Consequently, it is confirmed that the produced trajectories well demonstrate the properties of human arm trajectories. According to this trajectory planning, the trajectory can be uniquely produced if initial and target positions and movement duration are given. Furthermore, it always represents the properties of human arm trajectory even though movement duration or external load is changed. In addition to these advantages, the numerical calculation for producing trajectories is relatively simple. These features show that the proposed trajectory planning is effective for controlling biomimetic robots along humanlike trajectories.

There are, however, some problems which remain to be solved. The angular velocity of human arm trajectory fluctuates near the end of movement, and zero velocity crossing occurs especially when high angular velocity is required. This phenomenon can not be covered by our trajectory planning. Further development of trajectory planning reflecting such detail property of human trajectories is the issue to be solved in the future.

REFERENCES

- [1] Uno Y, Kawato M, Suzuki R (1989), Formation and Control of Optimal Trajectory in Human Multi-Joint Arm Movement. *Biol.Cybern.*, 61:89-101
- [2] Alexander R (1997), A minimum energy cost hypothesis for human arm Trajectories. *Biol. Cybern.* 76:97-105
- [3] Atkeson C and Hollerbach J (1985), Kinematic Features of Unrestrained Vertical Arm Movements. *J. of Neurosci.*, 5-9: 2318-2330
- [4] Richardson M and Flash T (2002), Comparing Smooth Arm Movements with the Two-Thirds Power Law and the Related Segmented-Control Hypothesis. *J. of Neurosci.*, 22-18: 8201-8211
- [5] Hollerbach J and Atkeson C (1987), Deducing Planning Variables from Experimental Arm Trajectories : Pitfalls and Possibilities. *Biol. Cybern.*, 56: 279-292
- [6] Zhou H and Hu H (2007), Internal sensors for motion detection of human upper limbs. *Sensor review*, 27-2: 151-158
- [7] Sasada D, Kashima T, Iwaseya M (2008), Analysis of Arm Trajectory Based on Measurements Utilizing Inertial Sensors, *Third Asia Inter. Sympo. on Mechatronics*, 399-402
- [8] Plamondon R, Feng C and Woch A (2003), A kinematic theory of rapid human movement, Part IV: a formal mathematical proof and new insights. *Biol. Cybern.*, 89: 126-138
- [9] Kashima T, Isurugi Y (1998), Trajectory formation based on physiological characteristics of skeletal muscle, *Biol Cybern.*, 78: 413-422

A Study on Reinforcement Learning Scheme in Cooperative Network-Systems of Sensor Nodes and Mobile Robots

Koichi Hirayama[†], Akihide Utani[‡], and Hisao Yamamoto[‡]

[†]*Graduate School of Engineering, Tokyo City University*

[‡]*Faculty of Knowledge Engineering, Tokyo City University*

1-28-1, Tamazutsumi, Setagaya, Tokyo 158-8557, Japan

{autani; yamahisa}@tcu.ac.jp

Abstract: Recently, there is growing expectation for a new network service by a wireless sensor network consisting of many sensor nodes placed in an object area and not a few mobile robots as a result of the strong desire for the development of systems that function flexibly in dramatically changing environments. This study proposes a reinforcement learning scheme in a cooperative network-system of many static sensor nodes and not a few mobile robots, named the Network-Robot System (N-R System) for adaptive cooperation of many static sensor nodes and not a few mobile robots. We evaluate the proposed reinforcement learning scheme by computer simulations on a benchmark problem. In the experiments performed, the performance of the proposed scheme is investigated to verify its effectiveness.

Keywords: Reinforcement Learning, Cooperative Systems, Static Sensor Nodes, Mobile Robots.

I. INTRODUCTION

Various network services have been provided. They include inter-vehicle communication, which is a network service in intelligent transport systems, natural environmental monitoring, and emergent communication between mobile nodes in such the case of emergency as disaster. As a means of realizing the above network services, autonomous decentralized networks, such as a mobile ad-hoc network and a wireless sensor network, have been intensively studied with great interests. Especially, a wireless sensor network, which is a key network to facilitate ubiquitous information environments, has great potential as a means of realizing a wide range of applications, such as natural environmental monitoring, environmental control in office buildings and factories, object tracking, and precision agriculture [1]. Recently, there is growing expectation for a new network service by a wireless sensor network consisting of many sensor nodes placed in an object area and not a few mobile robots as a result of the strong desire for the development of systems that function flexibly in dramatically changing environments.

This study proposes a reinforcement learning scheme in a cooperative network-system of many static sensor nodes and not a few mobile robots, named the Network-Robot System (N-R System) for adaptive cooperation of many static sensor nodes and not a few mobile robots. We evaluate the proposed reinforcement learning scheme by computer simulations on a benchmark problem. In the experiments performed, the performance of t-

he proposed scheme is investigated to verify its effectiveness. This paper is organized as follows. In Section II, the proposed scheme is outlined and the experimental results on a benchmark problem are reported. Finally, the paper closes with conclusions and ideas for further study in Section III.

II. PROPOSAL AND RESULTS

In the existing studies, many reinforcement learning algorithms have been proposed as agent-adaptive algorithms. In the existing reinforcement learning algorithms, the agent is reinforced (trained) using only rewards from the environment. Reinforcement learning algorithms can be classified into two approaches. One is “exploitation-oriented” approach, and the other is “exploration-oriented” approach. This study uses the “exploitation-oriented” approach. In the proposed N-R System, many static sensor nodes limited resource, which are compact and inexpensive, are placed in an object area. Each sensor node consists of a sensing function to measure the status of an object, a limited function on information processing, and a simplified wireless communication function, and operates on a resource of a limited power-supply capacity such as a battery. Not a few mobile robots have learning function and learn adaptive actions based on information obtained from static sensor nodes placed in an object area.

The proposed N-R System, which is a cooperative network-system of many static sensor nodes and not a few mobile robots, consists of the following main modules: Perception Module, Learning Module.

1. Perception Module

In the perception module, the sensor node perceives the task (request) and disseminates the task (request) information and the route information to the task point to all nodes that include mobile robots.

2. Learning Module

In the learning module, each mobile robot learns adaptive actions based on information obtained from static sensor nodes placed in an object area. As the learning scheme, the profit sharing plan is used [2,3].

Through simulation experiments on the delivery problem by mobile robots in the plant shown in Fig.1, the performance of the proposed N-R System is investigated to verify its effectiveness. The N-R System consisting of twenty-five static sensor nodes arranged in the object plant and two mobile robots is assumed. The conditions of simulation, which were used in the experiments performed, are shown in Table1. In the initial stage, each mobile robot has fifty requirements.

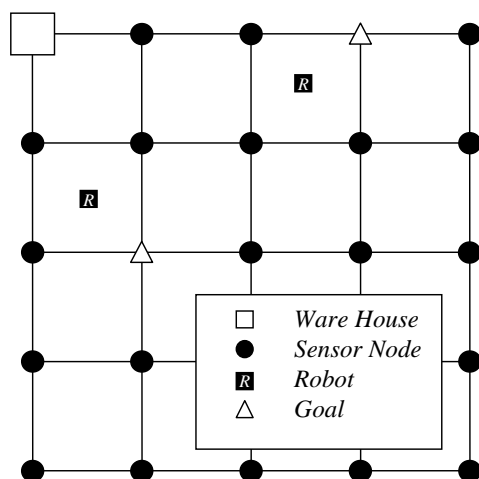


Fig.1. Simulation model

Table1. Conditions of simulation

Simulation size	50m × 50m
The number of sensor nodes	5 × 5
The number of mobile robot	2
The number of warehouses	1
The number of requirement points	2
The number of episodes	500
Reward	6.0×10^5

Experimental results on each pattern shown in Table2 are illustrated in Fig.2 and Fig.3. Fig.3 shows the learning curves of the case that the warehouse functions as

a subgoal. In case that the warehouse functions as a subgoal, the profit is shared with each mobile robot by the profit sharing plan [2,3] when it reaches the warehouse. Fig.4 and Fig.5 show the experimental results on Pattern 4 and Pattern 5. From these results, it can be confirmed that the subgoal effectively functions.

Table2. Experimental patterns

	The total number of requirements	Direct
Pattern1	0 ~ 50	2
Pattern2	51 ~ 100	2
Pattern3	51 ~ 100	1
Pattern4	101 ~ 150	1
Pattern5	101 ~ 150	0
Pattern6	151 ~	0

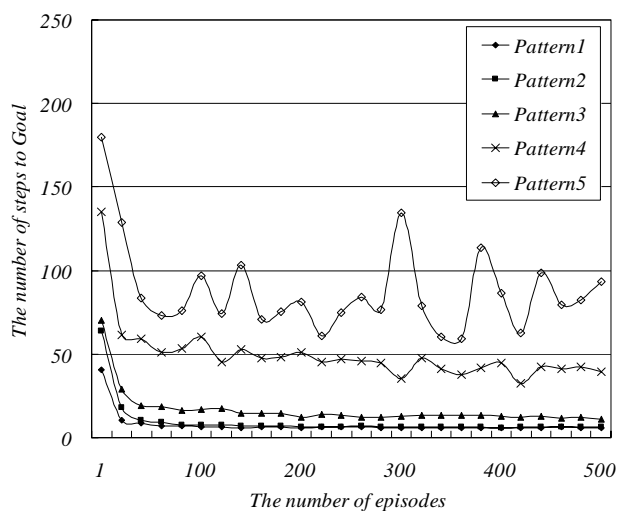


Fig.2. Learning curves

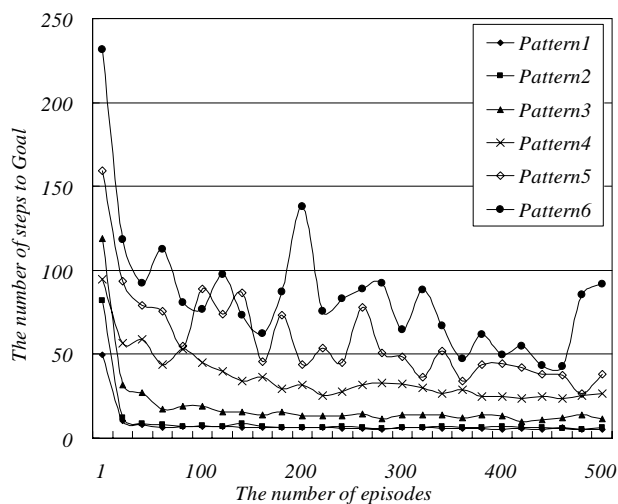


Fig.3. Learning curves (Subgoal is used)

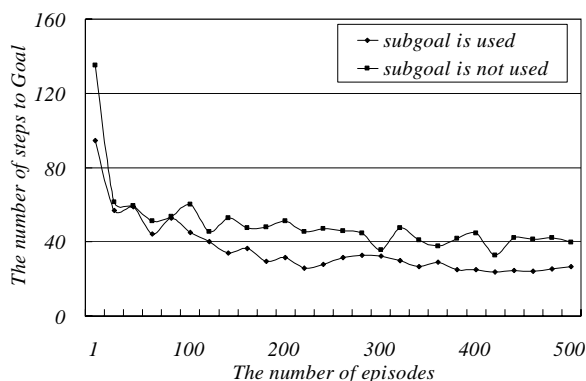


Fig.4. Learning curves on Pattern 4

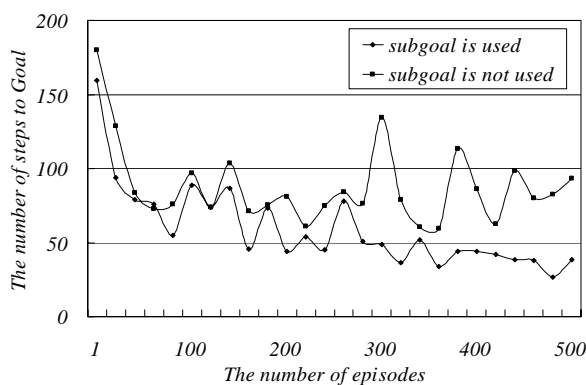


Fig.5. Learning curves on Pattern 5

III. CONCLUSIONS

In this paper, a reinforcement learning scheme in a cooperative network-system of static sensor nodes and mobile robots, named the Network-Robot System for adaptive cooperation of static sensor nodes and mobile robots, has been proposed. In simulation experiments on the delivery problem by mobile robots in the plant, the performance of the proposed system was investigated to verify its effectiveness. Experimental results indicate that the proposed system has the development potential to facilitate ubiquitous information environments. In future studies, we evaluate the performance of the proposed system in detail.

REFERENCES

- [1]I. Akyildiz, W. Su, Y. Sankarasubramaniam, and E. Cayirci, "Wireless sensor networks: A survey," *Computer Networks Journal*, vol.38, no.4, pp.393-422, 2002.
- [2]K. Miyazaki, M. Yamamoto, and S. Kobayashi, "A theory of profit sharing in reinforcement learning," *Trans. of the Japanese Society for Artificial Intelligence*, vol.9, no.1, pp.104-111, 1994.
- [3]K. Miyazaki, H. Kimura, and S. Kobayashi, "Theory and applications of reinforcement learning based on profit sharing," *Trans. of the Japanese Society for Artificial Intelligence*, vol.14, no.5, pp.800-807, 1999.

Towards the automation of cashew shelling operation

Son Doan Tran¹, Naoki Uchiyama², Suguru Kirita², Norifumi Yamanaka², Phat Minh Ho¹

¹*Ho Chi Minh University of Technology; 268 Ly Thuong Kiet Street, Dis. 10 HoChiMinhCity Vietnam
(Tel : 84-90-382-5695; Fax : 84-83-866-0244 ;Email: Tdsonbk@yahoo.com)*

²*Toyohashi University of Technology; 1-1 Hibarigaoka, Tempaku, Toyohashi, Aichi 441-8580, Japan*

Abstract: Vietnam is one of the world's largest countries in terms of exporting cashew nuts in kernel form. Gross export value in this field was \$750 million in 2009. Domestic production of raw cashews is about 400,000 tons and they are also imported from abroad about 100,000 tons. Hence, a large number of labors work for cashew processing industry. Although most cashew processing operations have been automated, the shelling operation is still conducted manually. Hence, not only shelling rate is very low compared to other operations, but also labor conditions are strenuous and unsafe. Currently, more than 200,000 labors engage in cashew shelling operations in Vietnam. This paper presents a robotic system design for cashew shelling operation to improve working conditions and production efficiency. The proposed design includes the milling operation of cashew shell and splitting process of the milled shell by wedge. In addition, the conveyer system to transport cashews is also designed for increasing the production efficiency. For designing the system, we consider the following three criteria to evaluate the efficiency [1]: (1) shelling rate (kg/h): weight of cashew kernels obtained per unit time, (2) shelling efficiency (%): ratio of shelled cashews over total cashews handled, and (3) whole-kernel recovery (%): ratio of whole kernels obtained over whole and broken kernels. The proposed system achieves 300kg/h, 95% and 80 %, respectively.

Keywords: cashew shelling; milling operation; splitting process; wedge; plate disk

I. INTRODUCTION

Vietnam is one of the world's largest countries in terms of exporting cashew nuts in kernel form. Although most cashew processing operations have been automated, the shelling operation is still manually conducted. Hence, not only shelling rate is very low compared to other operations, but also labor conditions are strenuous and unsafe. Currently, more than 200,000 labors engage in cashew shelling operations in Vietnam.

There are mainly two methods for shelling cashews as follows:

- Cut the shell using form-milling cutter
- Break the shell using hammer-like tool or split it by wedge-type tool

The first method is applied in countries such as Vietnam, Indonesia, Thailand, India and some African countries. Cutters with two thin blades whose profile is based on the cashew shape are used for shelling the cashew (Fig. 1 and 2). Cashews have to be previously classified by size in this approach. Cashew nuts are manually placed between two blades. These blades are connected with two foot pedals by links. Workers pedal them to operate the blades. They use one pedal to cut the cashew and the other pedal to rotate one blade by 90 degree to remove the shell from the cashew kernel.



Fig. 1 Cashew shell cutter



Fig.2 Manual cashew shelling

After this operation, workers also use a small knife to take the kernel out of the shell. This method has advantages and disadvantages as follows:

Advantages:

- Simple and inexpensive equipment
- Easy operation

Disadvantages:

- Low shelling rate (approximately 40-60 kg / shift)
- Hard and unsafe working conditions
- The whole-kernel recovery depends on worker's skill

Some countries employ hammer-like tools for breaking the cashew shell. Workers break the cashew shell and take the kernel out of the shell manually. Although this method is simpler than the previous method, the whole-kernel recovery is very low and it largely depends on the worker's ability.

Although wedge-like tools are also used for automatic split of the cashew shell, shelling efficiency and whole-kernel recovery are not sufficient.

This paper presents a robotic system design for cashew shelling operation to improve working conditions and production efficiency. The proposed design includes the milling operation of cashew shell and splitting process of the milled shell by wedge. In addition, the conveyer system to transport cashews is also designed for increasing the production efficiency.

II. SHELLING MACHINE DESIGN

1. Specifications and machine structure

The following specifications are required for automatic shelling machine:

- shelling rate (kg/h): 2000 kg / shift for each system.
- shelling efficiency (%): > 70%
- whole-kernel recovery (%) > 90%

Figure 3 shows a schematic of the designed cashew shelling machine. This machine consists of the following five parts: (1) vibratory cashew feeder, (2) conveyer belt for transporting the cashew, (3) rollers to clamp the cashew tightly, (4) cashew milling cutter, and (5) cashew shell splitter.

The vibratory cashew feeder provides cashews between the pair of conveyor belts continuously. The conveyor belts transport cashews into a position between a pair of disk cutters. After cutting, cashews are put into a splitter that removes shells from kernels.

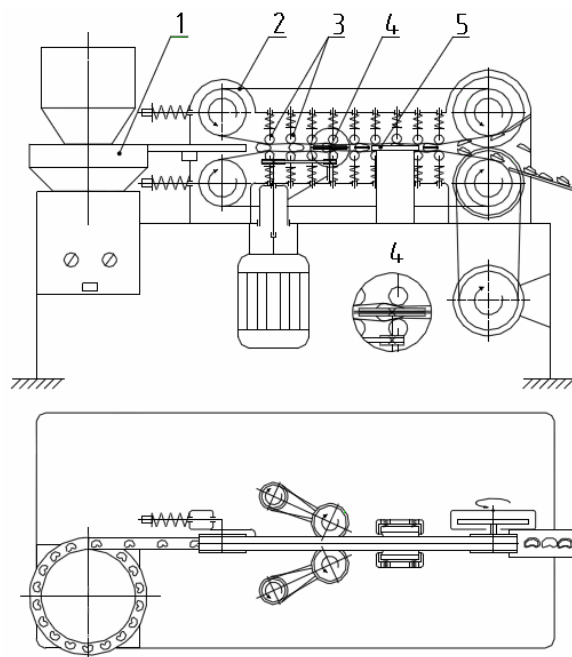


Fig.3 Cashew shelling machine structure

2. Shell cutting system

Figure 4 shows a schematic of the cashew shell cutting system, which includes disc milling cutters rotating with an appropriate speed.

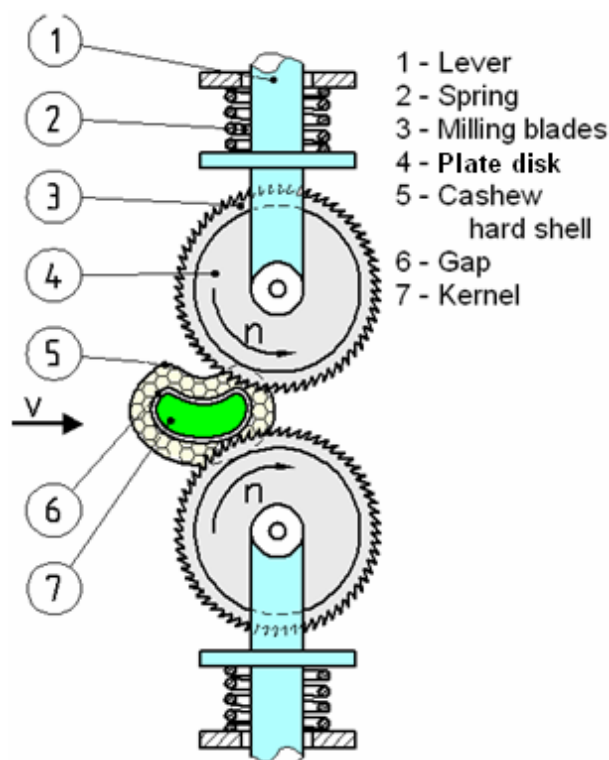


Fig.4 Cashew shell cutting system

The cutters are supported by springs. Cashews are transferred into a position between two milling cutter blades by conveyers.

3. Clamping system

Cashew nut is positioned between two V-shaped conveyor belts (No. 2 in Fig. 5) and tightly clamped by springs (No. 4) and pins. Rollers (No. 3) are employed to reduce friction. Cashew nuts are transferred by the conveyor belt to the cutter (No. 1) position. Clamping force of the spring must be large enough so that pins penetrate the cashew shell and the belt settles the cashew position. Cashew nut is kept fixed against the cutting force.

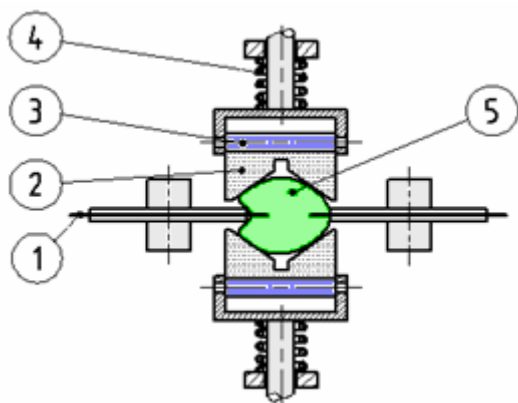


Fig. 5 Cashew clamping system

4. Design calculations

A. Force magnitudes

The cashew cutting force was measured by experiment. The force is less than 5N for a 100 mm diameter blade. The clamping force for cutting is calculated theoretically based on the cutting force, and is estimated approximately as 60 N. The separating force of the shell from the kernel is calculated theoretically, and is estimated approximately as 9 N. The clamping force for the separation is calculated theoretically based on cutting force, and is estimated approximately as 18N for each side.

B. Cutting tool parameters

A cashew shell is a type of wood composed of natural organic compounds, plastic outer shell, spongy middle layer, and hard and brittle inner layer. We have the following parameter values: Number of teeth of the disc cutter is $z = 64$, the cutter width is $W = 2$ mm (This cutter width has a larger value than that in [2] to create a

larger groove for the separation of the shell from the kernel by wedges.) Because the shell has a wood-like material, we employ 9XC alloy steel for the cutter whose hardness is 39-40 HRC, and the cutting speed is $v = 10.5$ m / s.

C. Cutting conditions

Figure 6 shows forces in the cashew and cutters at the beginning of cutting process. The following notations are used.

R : thrust force

F_c : cutting force

F_{lx1} , F_{lx2} : spring force acting in the direction perpendicular to lines AO_1 and CO_2 , respectively.

N_{11} , N_{21} : forces acting from the cashew to plate disks

N_{12} , N_{22} : forces acting from plate disks to the cashew

F_{ms1} , F_{ms2} : frictions between plate disks and the cashew (They have the same direction with F_c).

α_1 : Angle between N_{11} and the vertical line.

α_2 : Angle between N_{21} and the vertical line.

f' : Friction coefficient between the cashew and plate disks.

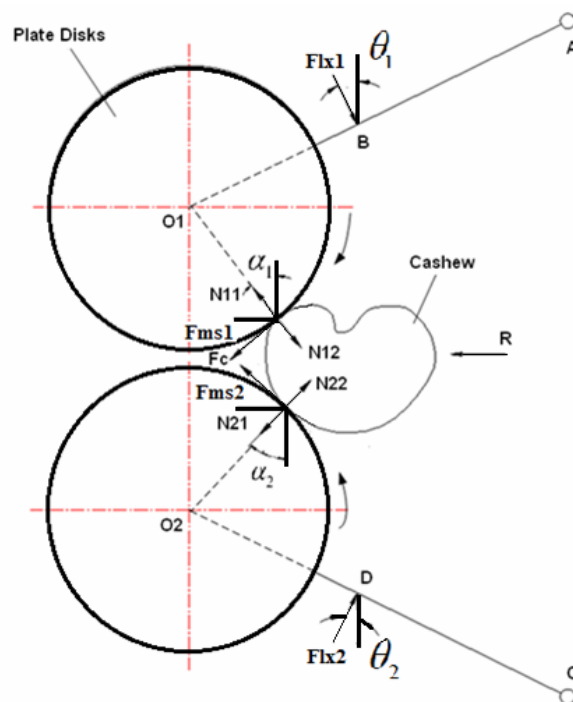


Fig. 6 Forces in cashew and cutter

We have the following conditions for cutting the cashew shell:

$$\begin{cases} N_{11} \cdot \cos \alpha_1 - F_{ms1} \cdot \sin \alpha_1 \geq F_{ht1} \cdot \cos \theta_1 \\ N_{11} \cdot \sin \alpha_1 \geq -F_{ms1} \cdot \cos \alpha_1 + F_{ht1} \cdot \sin \theta_1 \end{cases} \Leftrightarrow \begin{cases} N_{11} \cdot \cos \alpha_1 - f' \cdot N_{11} \cdot \sin \alpha_1 \geq F_{ht1} \cdot \cos \theta_1 \\ N_{11} \cdot \sin \alpha_1 \geq -f' \cdot N_{11} \cdot \cos \alpha_1 + F_{ht1} \cdot \sin \theta_1 \end{cases} \quad (1)$$

$$\begin{cases} N_{21} \cdot \cos \alpha_2 - F_{ms2} \cdot \sin \alpha_2 \geq F_{ht2} \cdot \cos \theta_2 \\ N_{21} \cdot \sin \alpha_2 \geq -F_{ms2} \cdot \cos \alpha_2 + F_{ht2} \cdot \sin \theta_2 \end{cases} \Leftrightarrow \begin{cases} N_{21} \cdot \cos \alpha_2 - f' \cdot N_{21} \cdot \sin \alpha_2 \geq F_{ht2} \cdot \cos \theta_2 \\ N_{21} \cdot \sin \alpha_2 \geq -f' \cdot N_{21} \cdot \cos \alpha_2 + F_{ht2} \cdot \sin \theta_2 \end{cases} \quad (2)$$

Consider the force balance in the horizontal direction, we have

$$\begin{aligned} R + F_c \cdot (\cos \alpha_1 + \cos \alpha_2) + F_{ms1} \cdot \cos \alpha_1 + F_{ms2} \cdot \cos \alpha_2 &= N_{12} \cdot \sin \alpha_2 + N_{22} \cdot \sin \alpha_2 \\ \Leftrightarrow R + F_c \cdot (\cos \alpha_1 + \cos \alpha_2) &= N_{12} (\sin \alpha_1 - f' \cdot \cos \alpha_1) + N_{22} (\sin \alpha_2 - f' \cdot \cos \alpha_2) \end{aligned} \quad (3)$$

and for vertical direction,

$$\begin{aligned} F_c \cdot (\sin \alpha_1 - \sin \alpha_2) + F_{ms1} \cdot \sin \alpha_1 - F_{ms2} \cdot \sin \alpha_2 &= -N_{12} \cdot \cos \alpha_1 + N_{22} \cdot \cos \alpha_2 \\ \Leftrightarrow F_c \cdot (\sin \alpha_1 - \sin \alpha_2) &= -N_{12} \cdot (\cos \alpha_1 + f' \cdot \sin \alpha_1) + N_{22} (\cos \alpha_2 + f' \cdot \sin \alpha_2) \end{aligned} \quad (4)$$

Letting

$$x = \sin \alpha_1 - f' \cdot \cos \alpha_1$$

$$y = \sin \alpha_2 - f' \cdot \cos \alpha_2$$

$$z = \cos \alpha_1 + f' \cdot \sin \alpha_1$$

$$\text{and } u = \cos \alpha_2 + f' \cdot \sin \alpha_2,$$

and considering $N_{11} = N_{12}$ and $N_{21} = N_{22}$, we obtain

$$N_{11} = [u \cdot [R + F_c \cdot (\cos \alpha_1 + \cos \alpha_2)] - y \cdot F_c \cdot (\sin \alpha_1 - \sin \alpha_2)] / (y \cdot z + x \cdot u) \quad (5)$$

$$N_{21} = [z \cdot [R + F_c \cdot (\cos \alpha_1 + \cos \alpha_2)] + x \cdot F_c \cdot (\sin \alpha_1 - \sin \alpha_2)] / (y \cdot z + x \cdot u) \quad (6)$$

Substituting N_{11} and N_{21} in (5) and (6) into (1) and (2), we have

$$\begin{cases} \frac{[u \cdot [R + F_c \cdot (\cos \alpha_1 + \cos \alpha_2)] - y \cdot F_c \cdot (\sin \alpha_1 - \sin \alpha_2)]}{(y \cdot z + x \cdot u)} (\cos \alpha_1 - f' \cdot \sin \alpha_1) \geq F_{ht1} \cdot \cos \theta_1 \\ \frac{[u \cdot [R + F_c \cdot (\cos \alpha_1 + \cos \alpha_2)] - y \cdot F_c \cdot (\sin \alpha_1 - \sin \alpha_2)]}{(y \cdot z + x \cdot u)} (\sin \alpha_1 + f' \cdot \cos \alpha_1) \geq F_{ht1} \cdot \sin \theta_1 \end{cases} \quad (7)$$

$$\begin{cases} \frac{[z \cdot [R + F_c \cdot (\cos \alpha_1 + \cos \alpha_2)] + x \cdot F_c \cdot (\sin \alpha_1 - \sin \alpha_2)]}{(y \cdot z + x \cdot u)} (\cos \alpha_2 - f' \cdot \sin \alpha_2) \geq F_{ht2} \cdot \cos \theta_2 \\ \frac{[z \cdot [R + F_c \cdot (\cos \alpha_1 + \cos \alpha_2)] + x \cdot F_c \cdot (\sin \alpha_1 - \sin \alpha_2)]}{(y \cdot z + x \cdot u)} (\sin \alpha_2 + f' \cdot \cos \alpha_2) \geq F_{ht2} \cdot \sin \theta_2 \end{cases} \quad (8)$$

Applying experimental parameters $\alpha_1 = 21^\circ$, $\alpha_2 = 28^\circ$, $f' = 0.25$ and $\theta_1 = \theta_2 = 26/28^\circ$, we confirm that conditions (7) and (8) are satisfied as follows:

For (7), we have

$$311 \text{ (N)} > 23.7 \text{ (N)} \text{ and } 218.05 \text{ (N)} > 11.55 \text{ (N)} \quad (9)$$

For (8), we have

$$285.98 \text{ (N)} > 23.7 \text{ (N)} \text{ and } 257.82 \text{ (N)} > 11.55 \text{ (N)} \quad (10)$$

5. Summary of experiment

The first prototype achieves the following performance experimentally: (Test with 1 ton raw cashew and 5 trials, 200Kg for each trial.)

- Shelling rate (kg/h): 2200 kg / shift for each system.
- Shelling efficiency (%): larger than 72%
- Whole-kernel recovery (%): larger than 95%

III. CONCLUSION

Automatic cashew shelling equipments are required in many countries that produce cashews in kernel form, because shelling rate is not sufficient and labor conditions are strenuous and unsafe in manual shelling operations. This paper presents a shelling machine design based on the milling of cashew shell and the conveyer system. A prototype system was developed to verify the performance of the proposed machine design. This research has opened a new direction for the automation of Vietnam's cashew industry.

ACNOWLEDGEMENTS

This work has been supported by the SUPREM-HCMUT (Strengthening University Project for Research-Based Education Model in Ho Chi Minh University of Technology) with assistance provided by the Japan International Cooperation Agency (JICA).

REFERENCES

- [1] T. Thivavarnvongs et al. (1995) Development of compact sized cashew nut shelling machinery (Part 1). Synthesis of effective manual and semi-automatic shelling methods. *Journal of the Japanese Society of Agricultural Machinery* 57(2) 57-65.
- [2] Đặng Đình Bôi (2005) Machine and equipment processing wood, printed in Nong Lam University, Vietnam.

Research on the velocity variation method for precise motion transmission

Masaharu Komori, Jungchul Kang, Yukihiro Kimura and Fumi Takeoka

*Department of Mechanical Engineering and Science, Kyoto University
Yoshidahonmachi Sakyo Kyoto 606-8501 Japan
(Tel : 81-75-753-5858; Fax : 81-75-753-5858)
(komorim@me.kyoto-u.ac.jp)*

Abstract: A wide range of speed or torque is required for some types of robots. It is possible for the motors to realize some range of speed or torque but the range is limited to some degree considering the size, weight and cost of the motors. Therefore it is impossible to realize those requirements if a reduction device with a ratio is used. Velocity variation devices using gears are widely used in the industrial fields. However, the motion transmission from the input shaft to the output shaft is interrupted during the velocity ratio variation process. In order to solve this problem, velocity ratio variation method that can transmit motion precisely in the changing process of velocity ratio is proposed in this report. The process of changing the velocity ratio in the proposed method is developed and the experimental device that can change the velocity ratio is constructed. The experimental results show that the proposed device can transmit motion precisely between the input shaft and the output shaft while changing velocity ratio and it is confirmed that the proposed method is effective to realize the precise motion transmission.

Keywords: ratio variation

I. INTRODUCTION

A variety of robots usually use some reduction devices with high ratio because they must support the high load in their motion and they require high torque to accomplish it. The reduction devices decrease the velocity and therefore the velocities of the robots are limited to some extent. However, a wide range of speed or torque is required for some types of robots. Moving robots used in the industrial fields are required to realize both outputting a large force when they carry loads and moving with high velocity when they move to the destination in order to shorten the moving period. It is possible for the motors to realize some range of speed or torque but the range is limited to some degree considering the size, weight and cost of the motors. Therefore it is impossible to realize those requirements if the reduction device with high ratio is used. If the velocity ratio between input and output shafts is changed, a wide range of speed or torque can be realized even if the ability of the motor is limited in speed or torque. Velocity variation devices using gears are widely used in the industrial fields and there are many research reports in terms of device control and mechanisms. Cylindrical gears such as spur gears have advantages in high torque capacity, precise rotation transmission and high efficiency and that is the reason why cylindrical gears such as spur gears are used in a variety of devices. In a geared transmission, it is needed to change the working gear pairs to vary the velocity ratio of the transmission. However, the motion

transmission from the input shaft to the output shaft is interrupted during this process. Therefore it is impossible to change the velocity ratio while transmitting rotation between the input shaft and the output shaft. In order to solve this problem, velocity ratio variation method that can transmit motion precisely in the changing process of velocity ratio is proposed in this report. Design of the experimental device of the proposed velocity variation method is carried out. The process of changing the velocity ratio in the proposed method is developed and the experimental device that can change the velocity ratio is constructed. The experimental results show that the proposed device can transmit motion precisely between the input shaft and the output shaft while changing velocity ratio and it is confirmed that the proposed method is effective to realize the precise motion transmission.

II. VELOCITY VARIATION METHOD

Figure 1 shows the schematic model of the basic structure of the velocity variation device. This device accommodates two shafts, i.e. input shaft and output shaft, and three gear pairs A, B and C, and three clutches T_A , T_B and T_C . The gear pairs A and B are composed of typical circular gears, and gear pair C is composed of noncircular gears. Gears A_o , B_o and C_o can be connected to the output shaft by engaging the clutches T_A , T_B and T_C , and then they rotate together with the output shaft. In contrast, gears A_i , B_i and C_i are

fixed to the input shaft, which rotate at the same speed as the input shaft.

Suppose that the velocity ratio of the gear pair A is r_A , and that of the gear pair B is r_B . In the pitch curve of noncircular gear pair C, there are four sections as shown in Fig.2. The pitch curve of the noncircular gear pair C is partly same as that of gear pair A, and partly same as that of gear pair B. Those parts of pitch curve are smoothly connected. In the four sections, the velocity ratio is constant at r_A , it changes to r_B , it is constant at r_B , and it changes to r_A respectively.

The proposed velocity ratio variation process from r_A to r_B is explained. Under the condition that the clutch T_A is engaged, and the other clutches are disengaged, the velocity ratio is r_A . When the meshing of gear pair C comes into the section corresponding to r_A , the clutch T_C is engaged, and, after the engagement of clutch T_C , the clutch T_A is disengaged. Then the meshing of gear pair C transits to the section corresponding to r_B . In the section corresponding to r_B , the clutch T_B is engaged, and, after the engagement of clutch T_B , the clutch T_C is disengaged. Through this process, the transition from r_A to r_B is completed. At all steps in this process, at least one of the clutches is engaged. Therefore, the rotational motion is precisely transmitted from the input shaft to the output shaft.

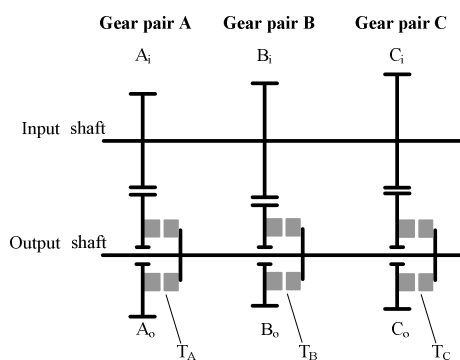


Fig.1. Structure of the Velocity Ratio Variation Device

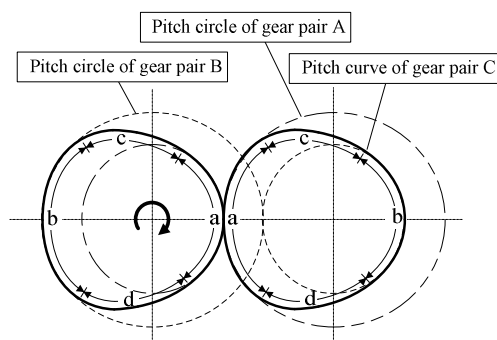


Fig.2. Pitch curve of gear pair C

III. EXPERIMENT

The experimental device based on the proposed ratio variation method is designed and constructed. Experiment of the velocity ratio variation from r_A to r_B is carried out. The experimental result is shown in Fig.3. The velocity ratio is calculated from the rotary encoder attached to the input and output shafts. The designed value of r_A is 0.8, and that of r_B is 1.25. Figure 3 shows that the velocity ratio is smoothly changed during the varying process. In the conventional geared transmission, it is impossible to transmit the rotation during the velocity ratio varying process. Thus, the velocity ratio might become zero or negative in the conventional transmission. In contrast, the velocity ratio in Fig.3 does not become zero or negative. This result indicates that the proposed system solves this problem.

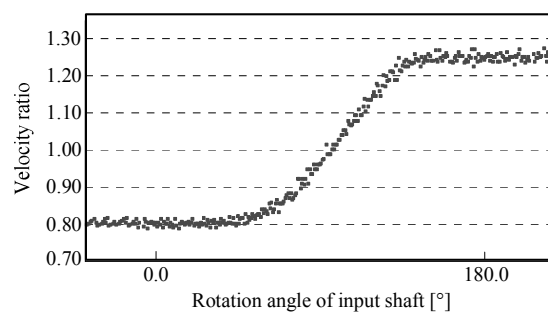


Fig.3. Experimental result when the ratio is changed

VI. CONCLUSION

In this research, the velocity variation method that realizes precise transmission of the rotation from the input shaft to output shaft, is proposed. The experimental device based on the proposed method is constructed, and the fundamental experiment is carried out. The result shows that the proposed device is capable to transmit rotation during the velocity ratio varying process.

ACKNOWLEDGEMENT

This study was supported by Industrial Technology Research Grant Program in 2009 from New Energy and Industrial Technology Development Organization (NEDO) of Japan.

Towards the Enhancement of Biped Locomotion and Control Techniques - Walking Pattern Classification

Basak Yuksel^{(1) (2)} and Kemal Leblebicioğlu⁽²⁾

⁽¹⁾ *Mitsubishi Electric Corporation, Advanced Technology R&D Center, Japan*
(Tel : 81-80-3595-0395)
(basak@ieee.org)

⁽²⁾ *Department of Electrical & Electronics Engineering*
Middle East Technical University, Ankara, Turkey
(Tel : 90-312-210-2358)
(kleb@metu.edu.tr)

Abstract: A new walking pattern classification method is proposed for uneven floor walking of 5-link 7 DOF biped robot. This method extracts the patterns as per the stance foot's current floor position and swing foot's transitioning floor conditions during locomotion. When a global path composed of stairs, obstacles, etc. and certain walking parameters, such as the speed of walking and total walking time, are given to the system, the guidance controller unit determines footstep trajectory in terms of step patterns by using a genetic algorithm based optimization technique while ensuring biped's stability criterion. The demonstration of biped for different pattern classes is realized by a dynamic simulator.

Keywords: Walking pattern classification, biped locomotion, uneven floor walking.

I. INTRODUCTION

Reference gait trajectory generation is one of the critical issues and another challenging problem in the biped locomotion and control study. The biped reference trajectory synthesis is hard due to the fact that it necessitates a complete comprehension and analysis of the system characteristics. In the past 40 years, considerable improvement has been realized in the biped reference trajectory generation and in the literature, many methods have been proposed. Most common ones used are gait generation by analytical [1], [2], [3], center of gravity (COG) based [4], [5], [6], Zero Moment Point (ZMP) based [7], [8], [9], computational intelligence based [10], [11], [12], measured human walking data based [13], [14] and optimality based [15], [16] methods.

In this paper, full kinematical and dynamical model for 5-link 7 degrees of freedom (DOF) 3D biped robot, derived by analytical calculations and Lagrangian method, respectively, is used to implement and test the proposed method. The overall system is composed of a guidance unit (high level controller), trajectory planner unit (reference trajectory generator), supervisory control unit (low level controller) and biped model [17].

When a global path is given to the system, guidance unit plans the footstep trajectory by using genetic algorithm based optimization technique, while ensuring

the stability of the system by using ZMP as a stability measure. The generation of footstep trajectory is realized by finding energy optimal foot step parameters of each walking step, such as step length, step speed, etc. for a given desired global path as per the different environmental conditions.

Implementation of optimal footstep planner is realized by using the classified walking patterns identified for the motion in uneven surface, as explained in this paper in detail. Note that the biped motion in this context is not necessarily periodic motion. The footstep planning is realized to ensure that dynamic stability measure (ZMP) is satisfied for non-periodic locomotion on uneven surfaces, such as walking on an environment with obstacles or stairs. After designing the optimized footstep trajectory formed by the sequence of walking patterns, the hip point and swing foot ankle point reference trajectories in sagittal and frontal planes of biped robot are obtained by using 3rd order (cubic) spline interpolation and then, the reference joint angle trajectory is calculated by inverse kinematics, for each sequential step's pattern class. In the supervisory control unit level, PID and Computed Torque Control methods are implemented successfully. The overall system, including the forward dynamics integrator, high level controller, trajectory planner, low level controller and 3D biped dynamic animator is implemented in MATLAB.

II. WALKING PATTERN CLASSIFICATION

The aim of the reference trajectory generation in this paper is to generate walking pattern classes so that the desired gait trajectory of the biped system can be generated similar to natural human locomotion. For this purpose, a systematical method to generate reference gait trajectory for a 5-link 7 DOF biped robot on different floor conditions such as walking on even surface, stepping over obstacles, stepping up and stepping down motions which results in a natural human-like walking is generated. The proposed method is a pattern classification method for the biped locomotion, whereas these patterns are chosen so that they cover stepping motions on different floor conditions, such as even floor walking, stepping over obstacles, stepping up and stepping down motions including staircase walking.

The pattern classes are extracted as per the biped's current and next steps' floor conditions in sagittal plane. In other words, the patterns are designed depending on the stance foot's current floor position and swing foot's transitioning floor conditions. The pattern classification composes of 9 patterns as shown from Fig. 1 to Fig. 9 in detail. Note that stepping over an obstacle directly corresponds to Pattern 1 with proper step height adjustment.

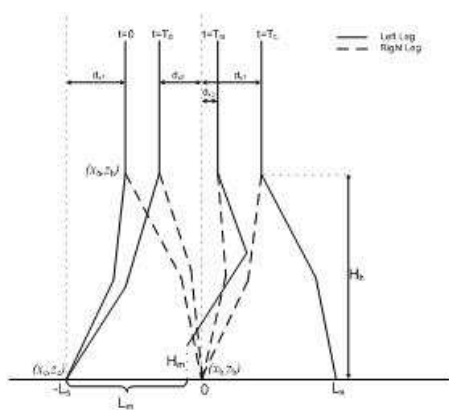


Fig. 1. Pattern 1: Walking on Even Floor

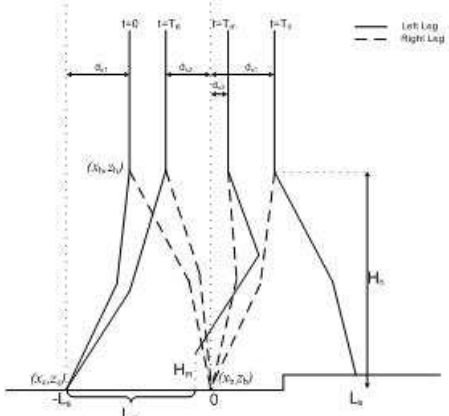


Fig. 2. Pattern 2: Stair Up - First Step

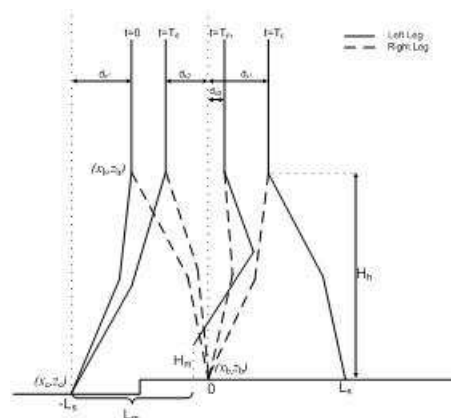


Fig. 3. Pattern 3: Stair Up - Second Step

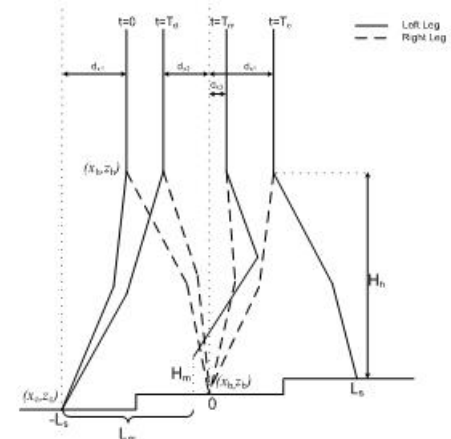


Fig. 4. Pattern 4: Stair Up - Second Periodic Step

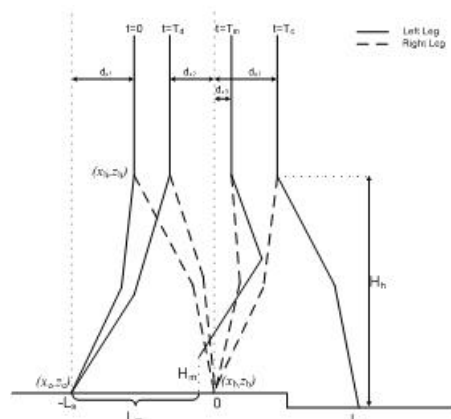


Fig. 5. Pattern 5: Stair Down - First Step

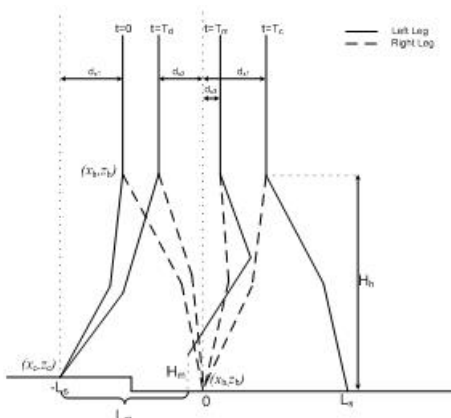


Fig. 6. Pattern 6: Stair Down - Second Step

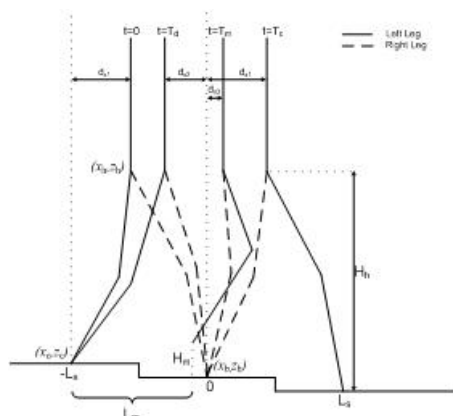


Fig. 7. Pattern 7: Stair Down - Second Periodic Step

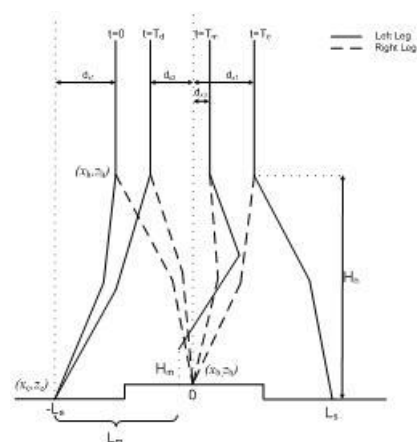


Fig. 8. Pattern 8: Stepping on Up

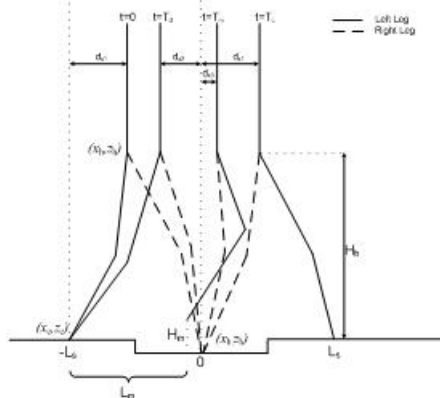


Fig. 9. Pattern 9: Stepping on Down

III. SIMULATION RESULTS

The walking is classified into 9 patterns, as per the environmental conditions that robot interacts taken into account. The simulation results of the biped walking for Pattern 2 are presented in Fig. 10 to Fig. 12. In Fig. 10, the joint angle trajectories are given; in Fig. 11, the joint angular velocity trajectories are depicted and in Fig. 12, the simulation snapshots of the biped walking are shown for Pattern 2. To further elaborate the walking patterns, the periodic staircase motion is also investigated and the results for the periodic stair up case are presented in Fig. 13 to Fig. 15 by means of joint angle trajectory, joint angular velocity trajectory and simulation snapshot of the biped walking.

IV. CONCLUSION

In this study, we developed a systematical method that classifies the biped walking patterns into 9 classes for a 5-link 7 DOF 3D biped robot. It covers the walking of biped on uneven surfaces composed of rectangular shape obstacles and stairs. The ultimate purpose is to generate enough walking patterns so that the walking steps of biped can be designed systematically by only using the sequences of these patterns for any given environment to achieve a successful biped walking. To achieve a complete pattern classification, this work will be extended to cover the inclined surfaces so that design of biped reference trajectories for any given environment will be achieved.

VI. ACKNOWLEDGEMENT

This research work presented in this paper is conducted in Middle East Technical University with Prof. Dr. Kemal Leblebicioglu.

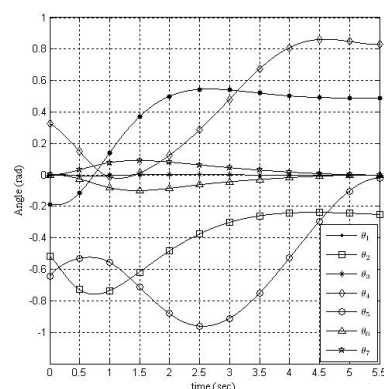


Fig. 10. Simulated trajectory joint angle profile for Pattern 2

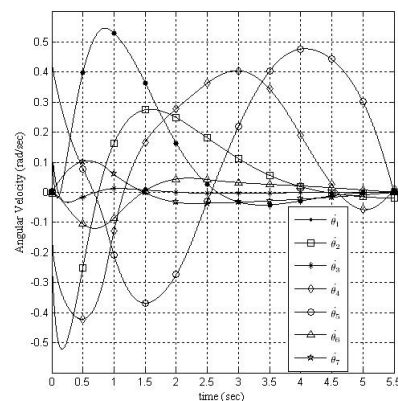


Fig. 11. Simulated trajectory joint angular velocity profile for Pattern 2

REFERENCES

- [1] Hurmuzlu Y (1988), Dynamics of bipedal gait part I: objective functions and the contact event of a planar five-link biped
- [2] Huang Q, Yokoi K, Kajita S, et. al. (2001), Planning walking patterns for a biped robot, IEEE trans. on robotics and automation 17(3):280-289

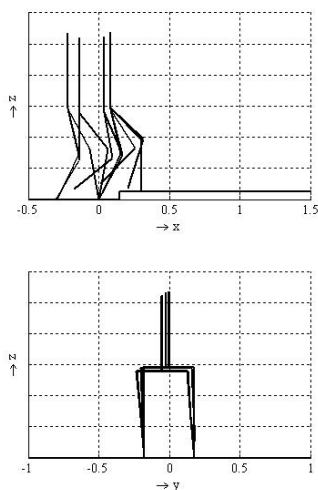


Fig. 12. Simulated trajectory walking snapshot - sagittal (top) and frontal (bottom) plane views - for Pattern 2

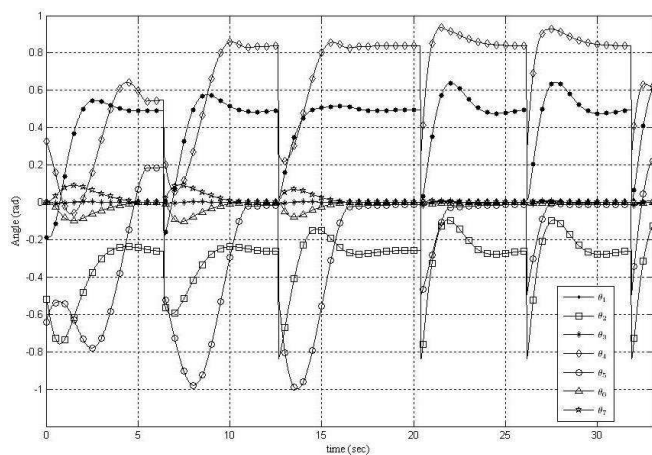


Fig. 13. Simulated trajectory joint angle profile for periodic stair up walking

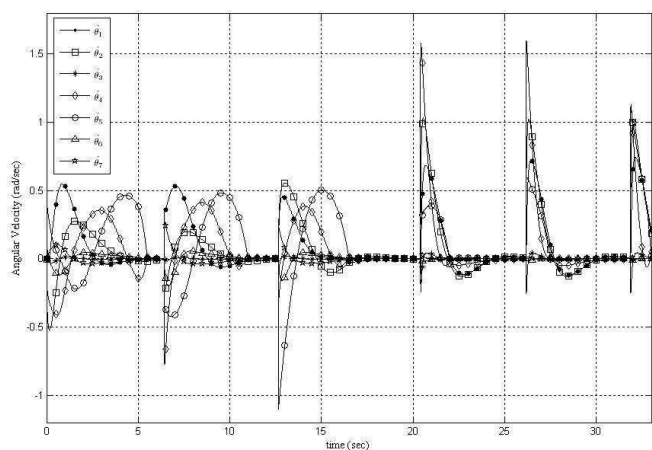


Fig. 14. Simulated trajectory joint angular velocity profile for periodic stair up walking

[3] Shih CL(1997), Gait Synthesis for a Biped Robot, *Robotica*, 15:599-607

[4] Kurematsu Y, Kitamura S, Kondo Y (1988), Trajectory planning and control of a biped locomotive robot - simulation and experiment, *Robotics & manufacturing, recent trends in research, education & applications*, 65-72

[5] Zielinska T (1996) Coupled oscillators utilized as gait rhythm generators of two legged walking machine, *Biological cybernetics*, 4(3):263-273

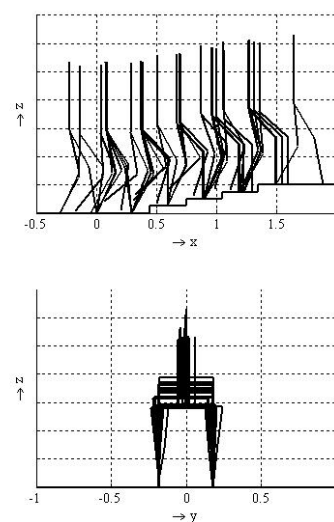


Fig. 15. Simulated trajectory walking snapshot - sagittal (top) and frontal (bottom) plane views - for periodic stair up walking

[6] Kajita S, Tani K (1991) Study of dynamic biped locomotion on rugged terrain-derivation and application of the linear inverted pendulum mode, *Proceedings of the IEEE international conference on robotics and automation*, 2:1405-1411

[7] Zheng YF, Shen J (1990), Gait synthesis for the SD-2 biped robot to climb sloping surface, *IEEE transactions on robotics and automation*, 6(1):86-96

[8] Hirai K, Hirose M, Takenaka T (1998) The development of Honda humanoid robot, *Proc. of the IEEE int. conf. on robotics & automation*

[9] Kun AL, Miller WT(1999), Control of variable-speed gaits for a biped robot, *IEEE robotics & automation magazine*

[10] Zheng YF (1990), A Neural gait synthesizer for autonomous biped robots, *proceedings of the IEEE international workshop on intelligent robots and systems: towards a new frontier of applications*, 2:601-608

[11] Arakawa T, Fukuda T (1996) Natural motion trajectory generation of biped locomotion robot using genetic algorithm through energy optimization, *IEEE international conference on systems, man, and cybernetics*, 2:1495-1500

[12] Cheng MY, Lin CS (1998) Genetic algorithm for control design of biped locomotion, *Journal of robotic systems*, 14(5):365-373

[13] Hemami H, Farnsworth RL (1977) Postural and gait stability of a planar five link biped by simulation, *IEEE transactions on automatic control*, 22(6):452-458

[14] Dasgupta A, Nakamura Y (1999) Making feasible walking motion of humanoid robots from human motion capture data, *Proceedings of the IEEE international conference on robotics and automation*, 2:1044 -1049

[15] Chevallereau C, Aoustin Y (2001) Optimal reference trajectories for walking and running of a biped robot, *Robotica*, 19:557-569

[16] Channon PH, Hopkins SH, Pham DT (1992) Derivation of optimal walking motions for a bipedal walking robot, *Robotica*, 10(2):165-172

[17] Yuksel B (2008), Towards the enhancement of biped locomotion and control, *Dissertation, Middle East Technical University*

DEA various method used Restricted Multiplier DEA

Shingo Aoki, Ryota Gejima, and Tomoharu Nakashima

Osaka Prefecture University, 1-1 Gakuencho Naka-ku, Sakai, Osaka 599-8531, Japan

Tel : 81-72-254-9353; Fax : 81-72-254-9915

{aoki@, gejima@mis., nakashi@}cs.oskafu-u.ac.jp

Abstract: Data Enveloped Analysis (DEA) is used for evaluating management efficiency of Decision Making Units (DMUs). The traditional DEA has restrictions on weight for multiple objectives. This paper proposes a DEA method that puts restrictions on not the weight but the multi-input and multi-output items in order to incorporate decision makers' subjective viewpoint. More DEA variant models can be derived from its basic model. Therefore, the proposed method allows to use evaluation criteria that cannot be used in the traditional method. Thus, the proposed method is able to widely analyze for various efficiency of DMU. The numerical experiments show the performance of the proposed method where teams that participated in the RoboCup 2010 Soccer Simulation 2D are evaluated.

Keywords: Data Envelopment Analysis, Linear Programming, Decision Making Support, RoboCup

I. INTRODUCTION

Data Envelopment Analysis (DEA) is a method for evaluating management efficiency of entities. DEA evaluates entities called DMUs (Decision Making Units). DMUs evaluated by comparing with their competitors. The main characteristics of DEA are the following:

- DEA evaluates DMUs that are characterized by multi-input and multi-output elements.
- The efficiency factors are calculated from multi-input and multi-output elements.

Therefore, DEA can perform evaluation from a lot of aspects and also can be used in various problems such as evaluation of universities, baseball players.

DEA calculates the weights for each of multi input and output elements. Different DMUs have different weights. The weights show the advantages of DMUs. However, the more input and output elements DMU has, the more weights become zero. In this case, it is difficult to clarify the difference between DMUs. Moreover, some elements that do not have a clear meaning for business judgment might cause a significant difference between DMUs.

Restricted Multiplier DEA (RM-DEA) was proposed to solve the above problem by including a priori knowledge in DEA. In this method, all weights are able to have nonzero value. However, it is difficult to apply DEA because RM-DEA is infeasible when the restrictions of weights are too severe.

To remedy the disadvantage of RM-DEA, this paper suggests a method that puts restrictions on not the weight but the multi input and output elements in order

to incorporate a priori knowledge. The utility and effectiveness of the proposed method are shown through a series of numerical experiments.

II. DATA ENVELOPMENT ANALYSIS

1. Outline of DEA

DEA was proposed by Charnes et al. in 1978 as a method for management analysis [1]. The applicable field of DEA is widely used in data mining such as the prediction of bankruptcy.

DEA regards each DMU as a production function that produces outputs from inputs. Then the efficiency of a DMU is calculated by comparing with other DMUs. There are two characteristics in DEA; (1) Weights are assigned to each input and output data and virtual input and output are generated. These weights are not fixed but variable so that each DMU can employ suitable weights to be evaluated better. (2) Common index for evaluation is shown as efficiency value. The value of the most efficient DMU is one. On the other hand, the efficiency value is less than one if a DMU is not efficient compared with the others.

2. Formulation of DEA

While DEA has various models, this paper employs efficiency model and inefficiency model [2]. The former model evaluates the relative efficiency by the advantage points. On the other hand, the latter model evaluates the relative inefficiency by the disadvantage points.

Let us assume that there are n DMUs and each DMU is characterized by m input and s output. That is, the input for DMU _{k} has input expressed as x_{1k}, \dots, x_{mk}

and the output expressed as y_{1k}, \dots, y_{sk} . Here the efficiency value is calculated by solving the following linear programming:

$$\begin{aligned} \text{Max} \quad & \sum_{r=1}^s u_r y_{rk} \\ \text{s.t.} \quad & \sum_{i=1}^m v_i x_{ik} = 1 \\ & -\sum_{i=1}^r v_i x_j + \sum_{r=1}^s u_r y_{rj} \leq 0 \quad (j=1, \dots, n) \\ & u_r \geq 0 \quad (r=1, \dots, s), \quad v_i \geq 0 \quad (i=1, \dots, m) \end{aligned} \quad (1)$$

The above equation signifies that weights are assigned to the input elements of DMU_k so that the weighted sum of the input elements equals to one. This guarantees that the efficiency value of other DMUs does not exceed one. The objective function has the role for maximizing the output of remarkable DMU. Moreover, it is possible to analyze the advantage points of each DMU by the assigned weights. This is because these input and output elements that have nonzero weight are considered in evaluation. In other words, those elements that have nonzero weight are considered advantage points.

The inefficiency value is calculated by solving the following linear programming:

$$\begin{aligned} \text{Min} \quad & \sum_{r=1}^s u_r y_{rk} \\ \text{s.t.} \quad & \sum_{i=1}^m v_i x_{ik} = 1 \\ & -\sum_{i=1}^r v_i x_j + \sum_{r=1}^s u_r y_{rj} \geq 0 \quad (j=1, \dots, n) \\ & u_r \geq 0 \quad (r=1, \dots, s), \quad v_i \geq 0 \quad (i=1, \dots, m) \end{aligned} \quad (2)$$

The above equation allows to analyze the disadvantage point of each DMU by weights. Therefore, these input and output elements that have nonzero weight are considered disadvantage points.

3. Problem of DEA

In DEA, the number of evaluation criteria is increased if the number of input and output elements is increased. Therefore, even if the input or output elements have only one advantage point, DMU is evaluated efficient. In this case, other elements becomes weaker. Thus, the elements that are not advantageous are not emphasized as more zero weights are assigned to more input and output. Thus excessive number of input and output lead the following two problems: (1) Many DMUs are evaluated as efficient, which makes the evaluation meaningless. (2) Some advantages of input

or output elements that make DMU efficient are not concerned in the standard business judgment. To deal with these problems, RM-DEA was proposed. In the RM-DEA, maximum and minimum of weights are restricted using a priori knowledge. However, the RM-DEA is infeasible when the restrictions of weights are too severe. Due to the above problems, it is difficult for decision makers to adjust the restriction using RM-DEA.

III. PROPOSED METHOD

This section shows the proposed model that unifies the efficiency model and the inefficiency model to solve the problem that is described in the previous section. By controlling the process of transformation from the efficiency model to the inefficiency model, the method is considered so that a priori knowledge can be incorporated.

1. Reformulation of the efficiency model

The dual problem of Equation (1) is written as follows:

$$\begin{aligned} \text{Min} \quad & \theta_k \\ \text{s.t.} \quad & -\sum_{j=1}^n x_{ij} \lambda_j + \theta_k x_{ik} \geq 0 \\ & \sum_{j=1}^n y_{rj} \lambda_j \geq y_{rk} \\ & \lambda_j \geq 0, \theta_k : \text{free} \end{aligned} \quad (3)$$

Where, θ and λ are variables for the dual problem. Equation (2) which $(d_{x_i}^+, d_{x_i}^-)$, $(d_{y_i}^+, d_{y_i}^-)$ are added as constraints for x and y respectively can be transformed as follows:

$$\begin{aligned} \text{Min} \quad & \sum_{i=1}^m d_{x_i}^- + \sum_{r=1}^s d_{y_r}^- + M \left(\sum_{i=1}^m d_{x_i}^+ + \sum_{r=1}^s d_{y_r}^+ \right) \\ \text{s.t.} \quad & -\sum_{j=1}^n x_{ij} \lambda_j + x_{ik} + d_{x_i}^+ - d_{x_i}^- = 0 \\ & \sum_{j=1}^n y_{rj} \lambda_j + d_{y_r}^+ - d_{y_r}^- = y_{rk} \end{aligned} \quad (4)$$

where M is a very big number, $(d_{x_i}^-, d_{y_r}^-)$ are slack vectors to hold the equality, and $(d_{x_i}^+, d_{y_r}^+)$ are artificial vectors to unify the model. This equation regards the efficiency value as the distance from efficiency frontier. Thus, if a DMU is efficient, its efficiency value is zero. If a DMU is not efficient, the efficiency value is greater than zero.

2. Reformulation of the inefficiency model

The inefficiency model is reformulated in a similar way to the efficiency model. Reformulation of the inefficiency model is shown in the following:

$$\begin{aligned} \text{Max} \quad & \sum_{i=1}^m d_{x_i}^+ + \sum_{r=1}^s d_{y_r}^+ - M \left(\sum_{i=1}^m d_{x_i}^- + \sum_{r=1}^s d_{y_r}^- \right) \\ \text{s.t.} \quad & - \sum_{j=1}^n x_{ij} \lambda_j + x_{ik} + d_{x_i}^+ - d_{x_i}^- = 0 \\ & \sum_{j=1}^n y_{rj} \lambda_j + d_{y_r}^+ - d_{y_r}^- = y_{rk} \end{aligned} \quad (5)$$

where $(d_{x_i}^+, d_{y_r}^+)$ are slack vectors to hold the equality, and $(d_{x_i}^-, d_{y_r}^-)$ are artificial vectors to unify the model.

3. Unification of two models

Both the reformulated models have the same constraint. Thus, it is possible to unify the efficiency model and the inefficiency model by transforming the objective function. In order to unify the models, we define the objective function as follows:

$$\begin{aligned} \text{Min} \quad & \sum_{i=1}^m (d_{x_i}^+ \sin \varphi_{x_i} - d_{x_i}^- \sin \varphi_{x_i}) \\ & + \sum_{r=1}^s (d_{y_r}^+ \sin \varphi_{y_r} - d_{y_r}^- \sin \varphi_{y_r}), \quad -\frac{\pi}{2} \leq \varphi \leq \frac{\pi}{2} \end{aligned} \quad (6)$$

where φ is the Value of Deciding Evaluation Criteria (VDEC). VDEC is used to control the degree of the transformation between the efficiency and the inefficiency models. Thus, the proposed method is shown by calculating the following linear programming:

$$\begin{aligned} \text{Min} \quad & \sum_{i=1}^m (-d_{x_i}^+ \sin \varphi_{x_i} + d_{x_i}^- \sin \varphi_{x_i}) \\ & + \sum_{r=1}^s (-d_{y_r}^+ \sin \varphi_{y_r} + d_{y_r}^- \sin \varphi_{y_r}) \\ \text{s.t.} \quad & - \sum_{j=1}^n x_{ij} \lambda_j + x_{ik} + d_{x_i}^+ - d_{x_i}^- = 0 \quad (i=1,2,\dots,m) \\ & \sum_{j=1}^n y_{rj} \lambda_j + d_{y_r}^+ - d_{y_r}^- = y_{rk} \quad (r=1,2,\dots,s) \end{aligned} \quad (7)$$

$$\lambda \geq 0, d_{x_i}^+ \geq 0, d_{x_i}^- \geq 0, d_{y_r}^+ \geq 0, d_{y_r}^- \geq 0, -\frac{\pi}{2} \leq \varphi \leq \frac{\pi}{2}$$

In this equation, optimal DMUs are evaluated with the efficient value of zero. On the other hand, the values for non-optimal DMUs are greater than zero.

Equation (7) is the efficiency model when φ_{x_i} and φ_{y_r} are equal to $\pi/2$ for all i and r . Equation (7) is the inefficiency model when φ_{x_i} and φ_{y_r} are equal to $-\pi/2$ for all i and r . Moreover, Equation (7) is regarded as the

mixture of efficiency and inefficiency models when given φ_{x_i} are distinct primes for each input elements. In addition, when φ_{x_i} is less than $\pi/2$ and φ_{x_i} is greater than 0, the value of $d_{x_i}^-$ is not likely to increase compared to the case when φ_{x_i} is $\pi/2$. Then, input element of i -th number is unlikely to search for an advantage as compared with other input elements. Therefore, the proposed method is able to calculate difference of value for each element.

From the above discussion, we can see that the proposed method is able to show the various models such as the mixture of the efficiency and the inefficiency models. Moreover, it is able to incorporate a priori knowledge by VDEC.

IV. NUMERICAL EXPERIMENTS

1. Experimental conditions and data

In order to show the effectiveness of proposed method (Equation (7)) visually, we apply it to an artificial data set. The data set consists of 16 input-output DMUs that are characterized by one input and two output elements (Table 1). We conducted four experiments using VDEC as follows:

- (1) φ are $\pi/2$ for all elements
- (2) φ are $-\pi/2$ for all elements
- (3) φ_{x1} is $-\pi/2$ for input1, φ_{x2} is $\pi/2$ for input2.
- (4) φ_{x1} is $\pi/2$ for input1, φ_{x2} is $-\pi/2$ for input2.

In the numerical experiments in this section, characteristics of the method clarify to look at differences of efficiency value. Experiments using data of RoboCup will be shown in the presentation at the symposium.

Table 1. Artificial data set

DMU	input1	input2	output
1	1	1	1
2	1	2	1
3	1	3	1
4	1	4	1
5	2	1	1
6	2	2	1
7	2	3	1
8	2	4	1
9	3	1	1
10	3	2	1
11	3	3	1
12	3	4	1
13	4	1	1
14	4	2	1
15	4	3	1
16	4	4	1

2. Experimental Results

The results are shown in Table 2. For instance, the value of the DMU_2 is evaluated value as zero in the case (1), and as six in the case (2).

Table 2. Distance from optimal DMU

DMU	(1)	(2)	(3)	(4)
1	0	6	3	3
2	1	5	4	2
3	2	4	5	1
4	3	3	6	0
5	1	5	2	4
6	2	4	3	3
7	3	3	4	2
8	4	2	5	1
9	2	4	1	5
10	3	3	2	4
11	4	2	3	3
12	5	1	4	2
13	3	3	0	6
14	4	2	1	5
15	5	1	2	4
16	6	0	3	3

3. Discussion

The numerical experiments of case (1), (2), and (3) are shown in the Fig. 1, Fig 2, and Fig. 3 in order to examine the effectiveness of the proposed method viscerally. All X-axes are input1 over output and all Y-axes are input2 over output. The grid points show DMUs and the lines connecting them show DMUs which have the same evaluated value.

A. Case (1)

DMU_1 is the optimal DMU in this case, and its evaluated value is "0". The DMUs which are equidistance from DMU_1 have the same evaluated value. Moreover, as the distance from DMU_1 becomes farther, the evaluated value also become large. This shows that DMU with smaller input and larger output is able to become optimal. Thus, given that ϕ is $\pi/2$ for all elements, the proposed method is able to be regarded as efficiency model.

B. Case (2)

DMU_{16} is the optimal DMU in this case, and its evaluated value is "0". All evaluated values are inverted in comparison with case (1). Thus, given that ϕ is $-\pi/2$ for all elements, the proposed method is able to be regarded as inefficiency model.

C. Case (3)

DMU_4 is the optimal DMU in this case, and its evaluated value is "0". DMU_4 is efficient when DEA calculates it for input1 and output. On the other hand,

DMU_4 is inefficient for input2/output. Thus, the proposed method is able to evaluate DMUs by mixing the of efficiency and inefficiency.

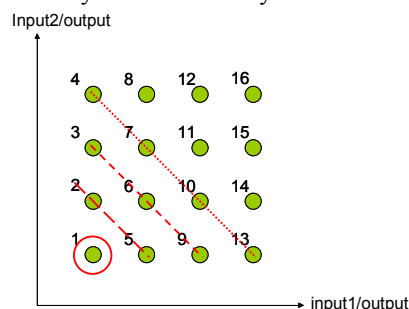


Fig. 1. Visualization of case (1)

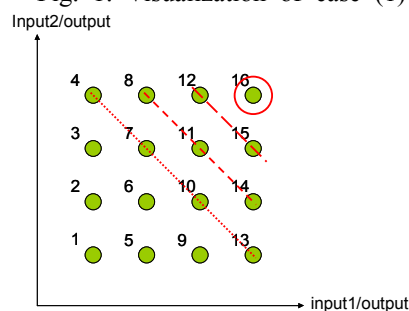


Fig. 2. Visualization of case (2)

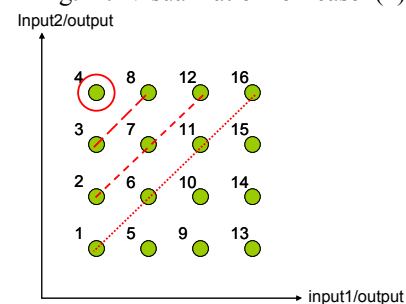


Fig. 3. Visualization of case (3)

V. CONCLUSION

This study proposed a DEA model which unifies the efficiency model and the inefficiency model. The proposed model is able to evaluate various criteria which the traditional model can not evaluate. Moreover, VDEC helps incorporating a priori knowledge. The effectiveness of the proposed method was illustrated in the numerical experiments.

REFERENCES

- [1] Charnes, A., Cooper, W. W. and Rhodes, E. L. (1978), Measuring the Efficiency of Decision Making Units. European Journal of Operational Research, Vol. 2, pp. 429-444.
- [2] Yamada Y., Matsui T. and Sugiyama M. (1994), An Inefficiency Measurement Method for Management Systems (in Japanese). Journal of the Operations Research Society of Japan, Vol. 37, No.2, pp.158-168.

Efficient Distributed Ontology Management Scheme for Inference in Surveillance Networks

S. Yang

*Department of Information Engineering,
The University of Suwon, 445-743, KOREA
(Tel : 82-31-229-8138; Fax : 82-31-229-8284)
(Smyang@suwon.ac.kr)*

Abstract: In this paper, we propose an efficient and scalable surveillance network providing better context inference based on distributed ontology framework. Upon our distributed ontology management system, each agent can build and process ontology cooperatively. They share context ontology for cooperative combined inference. Data source servers not only can get services from a region server, but also they can form and generate a P2P(peer-to-peer) network to provide services to each other. For an efficient and scalable cooperation we adopt a P2P communication through common API and adaptive caching.

Keywords: Surveillance network, Agent, Context ontology, Peer to peer network.

I. INTRODUCTION

In our network surveillance environment, each surveillance devices is equipped with a customized agent. The distribution of demands for multimedia data items is often skewed, and the surveillance devices have different capabilities and data formats. These can lead to poor data communication and dropped messages resulting in narrow reasoning and decision. Therefore for more easy and efficient cooperation between the agents, we propose a more efficient and scalable communication framework utilizing P2P computing and an adaptive cache scheme based on heterogeneous devices and data network.

Context is any information that can be used to characterize the situation of environment entities. To overcome the variety of data source servers, we build agent for each and interface through common APIs. Our network surveillance application can be thought of semantic web. Each agent tries to be context-aware through integration, analysis and inference of data and information. For better inference, they need not only data of their own but also data of other neighbor agents. P2P computing utilizing common API provides flexible, scalable and efficient ontology sharing method.

In this paper, we also propose a distributed adaptive cache scheme based on heterogeneous device and data network. Our scheme uses caching and conformity to update and share data in a cooperative way. Experiments and implementation are conducted to evaluate the effectiveness of our flexible cache scheme.

The rest of the paper is organized as follows, Section 2 we suggest a distributed inference framework for surveillance networks. Experiments and implementation is explained in Section 3. Section 4 reviews the related work on distributed inference based on ontology, particularly focusing on the user interface and the adaptive caching technique. Section 5 concludes this paper with a short summary.

II. DISTRIBUTED INFERENCE FRAMEWORK

Our surveillance network constructs a web of inference systems. Each data source server is equipped with an independent agent having local context ontology and inference engine. Cooperative inference such as object tracking requires the cooperation among local data source servers. Data associations between data sources are required to cover larger areas and solve occlusion problems. Our distributed inference framework manages ontology processing, ontology location and ontology connection on behalf of each agent.

Data source servers form a graph structure. For the high level inference, regional hierarchies are included in it. Each data source server can communicate each other freely within access control permission forming P2P computing networks. Equipped with agents, they perform their own intelligent distributed inference based on their own ontology knowledge base. In the case of multi-agent systems, association of data across the data

source servers is indispensable for context awareness and decision making for the integration of ontologies and prevention of the narrow decision.

For each data request, data source server n_i first tries to find the required data item from its local cache. If it encounters a local cache miss, it broadcasts a request message to its neighbor peers via P2P broadcast communication. Our ontology framework includes common APIs for the operations. If a neighbor peer does not have the needed data item, the agent will send the request to the higher region server instead to obtain the needed data. The representative common APIs are `getVideoSource()`, `getVideoSourceConfiguration()`, `getVideo()`, `setVideo()`, `getVideoStatistics()`, `getVideoCaptureSize()`, `getUsers()`, `getVideoResolution()`, `requestSignal()`, `sendSignal()`, `getBitrateControlMode()`, etc.

For the broadcasting, the latency is defined as the sum of the request and reply packets divided by network bandwidth through the hops the data gets transmitted. As peers can exchange such information as the cache sizes of their neighbors and the transmission ranges, they can negotiate and come up with a cache strategy based on the messages exchanged. As a result, better usage of their limited cache space and higher system performance can be obtained

The multimedia data and biometric feature information caching will be distributed over the region servers and data source servers. The data source servers need to carry out the indexing and retrieval of the information distributed across the servers in an efficient manner. To maintain the freshness and effectiveness of the data, we should cache data adaptively. We measure the weight of cached data to describe its relative importance as compared to the other data as proposed in [4]. The higher the weight, the lower is the probability of the data being replaced. We also use a policy based on the size of the objects, in which the weight is proportional to the size of the data. Therefore the weight is computed as the product of the access frequency, size of the data and the data recency:

$$Weight = Frequency^f DataSize^s Recency^r$$

The exponents are weighting factors. As a result, we can expect the packet traffic would be proportional to the probability of cache miss, latency, the probability of

packet loss, the weight of data and the inverse of the number of hops.

III. EXPERIMENTS AND IMPLEMENTATION

In a distributed surveillance environment, multimedia data and biometric feature information are produced continuously. Furthermore the multimedia data transmission consumes large network bandwidth. When the adaptive caching technique is applied, experiments show better performance as shown in Figure 1. The data source servers might be grouped by region. The caching skewed by region could be reflected through the variance in caching ratio.

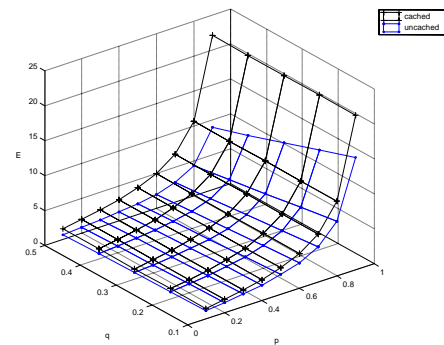


Fig.1. The expected packet transmission comparison

For the integration of ontologies between data source servers, we developed common APIs according to the standard [7]. The pseudo code for the representative common APIs is as the following:

```
function grcc(key){
    this.name = 'grcc';
    this.key = key;
    this.XmlHttpRequest = function() { //abridged
    }
    this.validChk = function(){
        var add;
        add = location.href;
        add = add.split("/");
        add = "http://" +
        add[1].substr(0, add[1].indexOf("/")) + "/";
        host = 'http://localhost/grcc/';
        URL = host + 'validChk.php?key=' + this.key
        + '&add=' + add;
        xmlhttptr = new XMLHttpRequest();
        xmlhttptr.open('GET', URL, true);
        xmlhttptr.send(null);
    }
}
```

```

xmlhttp.onreadystatechange();//abridged
}
this.GetUsers = function(){
    this.validChk();
    host = 'http://localhost/grrc/';
    URL = host + 'getUsers.php';
    location.href = URL;
}
this.GetVideoSource = function(){
    this.validChk();
    host = 'http://localhost/grrc/';
    URL = host + 'getVideoList.php';
    location.href = URL;
}
this.GetVideoSourceConfiguration =
function(){
    this.validChk();
    host = 'http://localhost/grrc/';
    URL = host + 'getAllVideoList.php';
    location.href = URL;
}
this.GetVideoCaptureSize = function(){
    CaptureSize = new Array(1);
    CaptureSize[0] = new Array(2);
    this.validChk();
    host = 'http://localhost/grrc/';
    URL = host + 'VideoInfo.php';
    xmlhttp = this.XmlHttpRequestObject();
    xmlhttp.open('GET', URL, true);
    xmlhttp.send(null);
    xmlhttp.onreadystatechange = function();
    //abridged
    return CaptureSize[arrWidth][arrHeight];
}
this.GetVideoResolution = function(){
    Resolution = new Array(1);
    Resolution[0] = new Array(2);
    this.validChk();
    host = 'http://localhost/grrc/';
    URL = host + 'VideoInfoResolution.php';

    xmlhttp = this.XmlHttpRequestObject();
    xmlhttp.open('GET', URL, true);
    xmlhttp.send(null);
    xmlhttp.onreadystatechange =
function();//abridged
    return Resolution[arrResolutionWidth]
[arrResolutionHeight];
}
this.getVideo = function(num){
    this.validChk();
    host = 'http://localhost/grrc/';
    URL = host + 'getVideo.php';
    xmlhttp = this.XmlHttpRequestObject();
    xmlhttp.open('GET', URL, true);
    xmlhttp.send(null);
    xmlhttp.onreadystatechange =
function();//abridged
}
}

```

Our work is aimed at designing and deploying a system for the surveillance and monitoring of province area containing about 15 cities. Final product is to be included in the construction of the ubiquitous city. The agent platform should be distributed across various data acquisition systems such as CCTV, RFID sensors, sound monitors, etc. We show the live video and the stored video to monitoring clients and devices are controlled via a remote GUI even from a smart phone. Figure 2 shows screenshot of map interface. It shows the stored event data. On the left frame we can see the google map. On the right frame, alarming events are listed first with features. When we select the CCTV, we can see the specific videos on the bottom side.

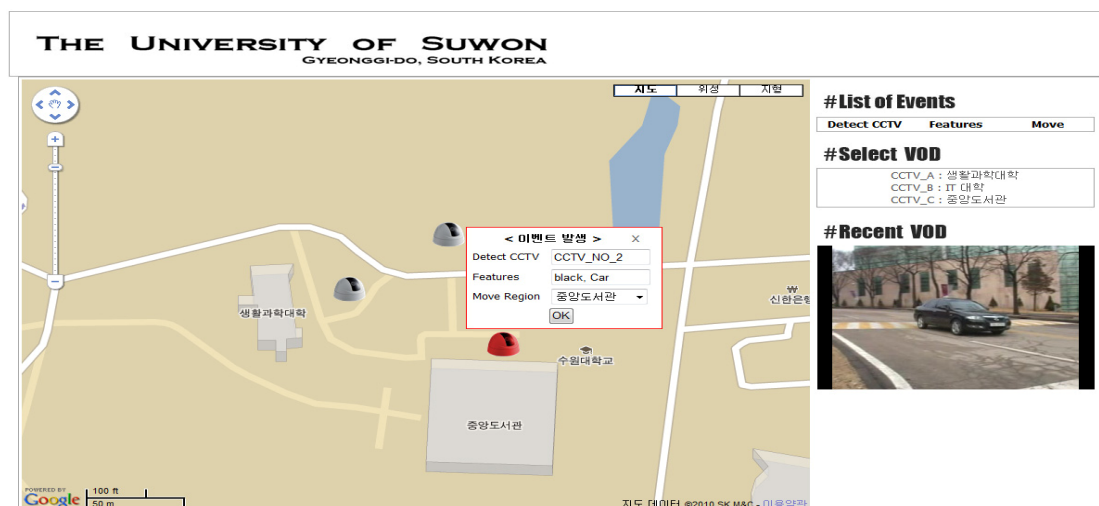


Fig.2. The sample user interface with google map

IV. RELATED WORK

Several ontology reasoning systems have been developed for reasoning and querying the semantic web and they show good performance as seen in [1,2,3]. We want to adopt, customize and improve them adequate for our surveillance system. Especially all of them do not use common API for communication. In [4], a cooperative caching framework is introduced and claimed to be effective to data availability. In [5], a replica allocation method and clustering in distributed networks are introduced to improve data accessibility in a mobile communication environment. Another cooperative cache scheme for similar peers is described in [6], which combines the P2P communication technology with a conventional mobile system. However they do not apply their technique to the distributed surveillance system.

V. CONCLUSION

We describe an efficient ontology management scheme for better context inference based on distributed ontology framework. Data acquisition servers communicate each other freely within access control permission to perform their own intelligent distributed inference based on integrated ontology knowledge base utilizing common APIs. Our scheme uses P2P computing using common APIs and data conformity to update and share data in a cooperative way. For such a P2P network, an effective cache framework that can handle heterogeneous devices is required. We also present a flexible cache scheme which is adaptive to the actual device demands and that of its neighbors. We analyzed our distributed ontology management scheme through experiments and implementation.

VI. ACKNOWLEDGMENTS

This work was supported by the GRRC program of Gyeonggi province. [GGA0801-45700, Center for U-city Security and Surveillance Technology]

REFERENCES

[1] A. Flahive, W. Rahayu and D. Taniar, (2005), A Distributed Ontology Framework in the Semantic Grid Environment, 19th International Conference on Advanced Information Networking and Applications (AINA'05)

[2] J. Z. Pan, (2007), A Flexible Ontology Reasoning Architecture for the Semantic Web, IEEE Transactions on Knowledge and Data Engineering archive Volume 19, Issue 2, 246-260
[3] Anne Schlicht, Heiner Stuckenschmidt, (2008), Towards Distributed Ontology Reasoning for the Web, IEEE/WIC/ACM International Conference on Web Intelligence and Intelligent Agent Technology
[4] L.Yin, G. Cao, (2006), Supporting Cooperative Caching in Ad Hoc Networks. IEEE Tr. On mobile computing, Vol. 5, No. 1.
[5] Zheng, J., Su, J., and Lu, X. (2005), A Clustering based Data Replication Algorithm in Mobile Ad Hoc Networks for Improving Data Availability, Lecture Notes in Computer Science 3358
[6] Chow, C., Leong, H., and Chan, A. (2005), Distributed Group-based Cooperative Caching in a Mobile Broadcast Environment, MDM 2005
[7] ONVIF, 2009, Open Network Video Interface Forum Core Specification version 1.01

Recovery Technique from Classified Errors in Adjustment Tasks of Domestic Appliances

Akira Nakamura and Yoshihiro Kawai

*Intelligent Systems Research Institute
National Institute of Advanced Industrial Science and Technology (AIST)
Central 2, 1-1-1 Umezono, Tsukuba, Ibaraki, 305-8568 Japan
a-nakamura@aist.go.jp, y.kawai@aist.go.jp*

Abstract: Dexterous manipulation is an important function for working maintenance robots. Manipulator tasks such as disassembly and reassembly can generally be divided into several motion primitives. The authors call such motion primitives “skills” and explain how most manipulator tasks can be composed of sequences of these skills. In their planning to construct a maintenance robot for domestic appliances, the authors considered hierarchizing the manipulation tasks since the maintenance of such appliances has become increasingly complex. Additionally, they considered grouping errors into several classes according to their possible causes. The reliability of the task achievement was found to increase with the classification of errors. There are various kinds of tasks for maintenance robots besides disassembly and reassembly, and adjustment tasks, which are often executed in the final stage of maintenance, are also important. This paper presents a proposal for error recovery during adjustment tasks performed by a robot in the maintenance of domestic appliances.

Keywords: manipulation skill, maintenance task, error recovery.

1. Introduction

Manipulation robots need to achieve various tasks using special techniques to be useful in wide-ranging fields. By analyzing the motions of human hands in tasks such as disassembly and reassembly, we found that the movements consisted of several significant motion primitives. We call these motion primitives “skills” and have shown that most of the tasks of a manipulator can be composed of sequences of such skills [1]–[3].

We have already researched maintenance robots working in various factories and power plants. In our future research, we will consider manipulation robots working closer to people and used for the maintenance of household appliances and consumer electronics. At present, we are working toward producing a prototype of a maintenance robot for home audio-visual system components and personal computers (Fig. 1). The principle tasks of such maintenance robots will be not only disassembly and reassembly as considered in [3]–[5] but also adjustment tasks. Such adjustment tasks might involve rotating thumbscrews to tune various settings such as frequency, amplitude and brightness. Maintenance requires the use of many manipulation skills, and the nature and range of the tasks may be complex. However, stratification of the tasks makes development more manageable.

Manipulation tasks using skills are performed in theory by sequences of visual sensing, geometric modeling, planning and execution. In an ideal environment, the tasks are achieved without any errors

occurring. During actual manipulation, however, errors often occur for various reasons. Various approaches for error recovery have been reported [6]–[9]. However, few methods for realistic error recovery have been proposed for the various errors that could actually occur during maintenance tasks. We have previously described our concept of error classification and process flow using error recovery in the task hierarchy [4], [5]. Errors are grouped into several classes according to their possible causes. In this present paper, we describe a method of error recovery during adjustment tasks such as rotating knobs when maintaining domestic appliances. The reliability of the task achievement increased with the stratification of tasks and classification of errors.

The next section explains manipulation skills and skills used in adjustment tasks. The stratification of manipulation tasks is shown in section 3. Our classification of errors and error recovery in the task hierarchy intended for adjustment tasks are shown in section 4.

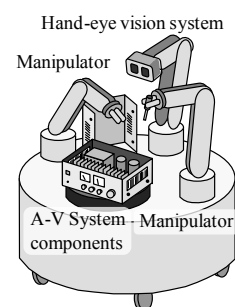


Fig. 1 Maintenance robot for audio-visual system components

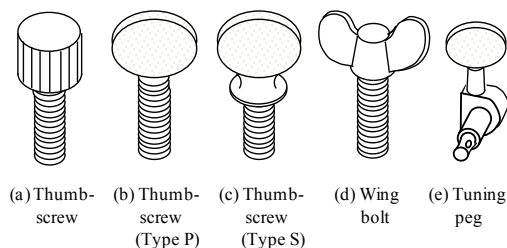


Fig. 2 Thumbscrews and similar fasteners

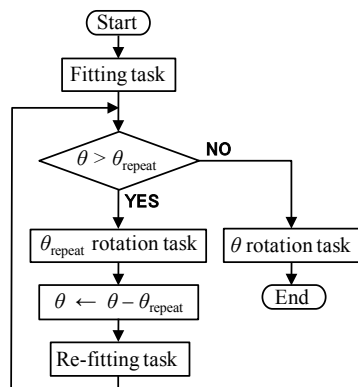


Fig. 3 Process flow of adjustment task using a thumbscrew

2. Manipulation Skills

This section explains our concept of skills and examples of the skills used in adjustment tasks. See References [1], [2] for more details.

2.1. Concept of Skills

We analyzed human motions in such tasks as disassembly and reassembly and found that the movements consisted of several significant motion primitives. We call such motion primitives “skills” [1], [2]. We considered three fundamental skills: move-to-touch, rotate-to-level and rotate-to-insert, all of which play an important part in such tasks. A specific task is composed of sequences of skill primitives such as these three skills. Moreover, many related skills such as the rotate-to-bite and rotate-to-loosen skills in tasks using screwdrivers can be defined based on slightly modified versions of these three fundamental skills. These skills are frequently used for component replacement during the repair of household appliances [3]–[5].

2.2. Skills in Adjustment Tasks

In the maintenance of household electrical appliances and home audio-visual equipment, a parts adjustment step is often needed in addition to the main tasks of disassembly and reassembly such as component replacement [3]–[5].

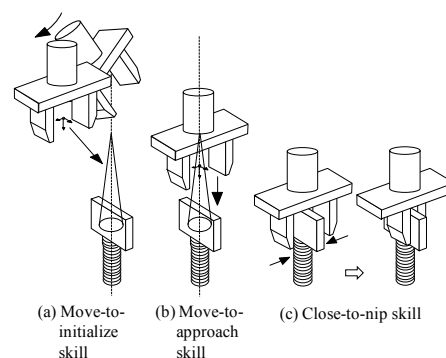


Fig. 4 Task of fitting a gripper on a thumbscrew

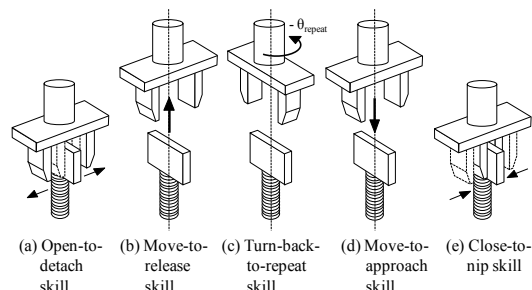


Fig. 5 Task of re-fitting a gripper on a thumbscrew

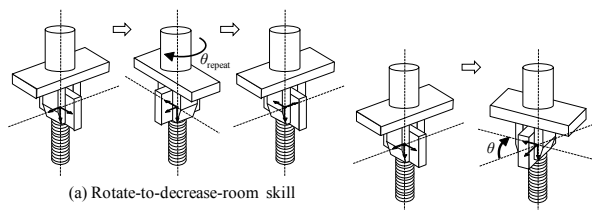


Fig. 6 Task of θ_{repeat} rotation

(a) Rotate-to-adjust skill

Fig. 7 Task of θ rotation

The knobs of adjustment screws used in maintenance tasks come in various head shapes. Figures 2(a), 2(b) and 2(c) show various types of thumbscrews including cylindrical type, “P” (plain) type, and “S” (shoulder) type. There are also wing bolts (Fig. 2(d)) and tuning pegs on string instruments (Fig. 2(e)). For simplicity, in this paper we focus on screws with flat head projections (Fig. 2(b), 2(c), 2(d), 2(e)) that can be nipped by parallel grippers.

Figure 3 shows the process flow for an adjustment task using a thumbscrew. First, a fitting task using a parallel gripper on a plain knob is performed (Fig. 4). Rotation tasks of the same angle θ_{repeat} such as π , 2π (rad) are iterated (Fig. 6), while the re-fitting tasks of the gripper are performed between successive rotation tasks (Fig. 5). Finally an adjustment task comprising rotation at a small angle θ ($\leq \theta_{repeat}$) is performed (Fig. 7). However, the value of angle θ is hardly a suitable reference value. In most cases, the values of angles θ are adjusted so that settings such as frequency, amplitude

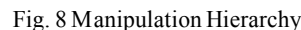
Figure 8 shows a hierarchy of manipulation tasks during maintenance [4]. If we ignore the servo layer, the skill layer, which consists of elements such as the move-to-approach and close-to-nip skills, is located in the lowest layer called the $task^{(0)}$ layer. Each skill is performed by the processes of visual sensing, geometric modeling, planning and execution. One tier above the $task^{(0)}$ layer is the $task^{(1)}$ layer. Similarly, $task^{(i+1)}$ is composed of sequences of $task^{(i)}$ elements. The top layer, where the error recovery loop is closed, is called $task^{(max)}$ and one tier above $task^{(max)}$ is called the project layer. The project layer might also be hierarchized, but we will not discuss it in this paper.

4. Error Recovery in Stratified Tasks

In an ideal environment, tasks are achieved without any errors occurring. In actual manipulation, however, errors often do occur from various causes. Our concept of error classification and process flow with error recovery in the task hierarchy are described in this section. See References [4] for more details with respect to component replacement tasks. In this present paper, errors occurring in adjustment tasks during maintenance of domestic appliances and electronic equipment are explained and error recovery techniques in the adjustment tasks are shown.

The causes of failures can be attributable to several kinds of errors. We group error states into several classes according to their possible causes as follows. The classes of errors are described in detail in Reference [4].

- ## 4.2. Error Recovery based on Classification in Adjustment Tasks



Class 1: When the error is judged to be an execution error, $\text{task}_{(i1)}^{(1)}$ is executed again without a correction in the parameters.

Class 2: When the error is judged to be a planning error, $\text{task}_{(i1)}^{(1)}$ is executed again with a change in the planning parameters.

Class 3: When the error is judged to be a modeling error, $\text{task}_{(i1)}^{(1)}$ is executed again with a change in the modeling parameters.

Class 4 (= Class $T^{(1)}$): When the error is judged to be a sensing error, $\text{task}_{(i1)}^{(1)}$ is executed again with a change in the sensing parameters.

Class $T^{(2)}$: $\text{task}_{(i2)}^{(2)}$ is executed again after the execution of the necessary changes and returns to the start of one tier above the layer $\text{task}_{(i1)}^{(1)}$.

:

Class $T^{(\max)}$: $\text{task}_{(\max)}^{(\max)}$ is executed again after the execution of the necessary changes and returns to the start of $(\max - 1)$ tier above the layer $\text{task}_{(i1)}^{(1)}$.

Class $T^{(\max+1)}$: When it is judged that too many changes will be required, the process being executed is interrupted and the process returns to the start of the overall task.

Parameters judged in any given Class are revised and error recovery is performed according to a flowchart. In most adjustment tasks, the target angle θ is decided so that another setting value such as frequency or brightness becomes the most suitable value as shown in section 2.2. Therefore, it is often necessary to rotate the thumbscrew in the opposite direction because of excess rotation. In such cases, the required change in skill sequence is performed through Class $T^{(2)}$. This means re-planning in one tier above the lowest task layer. In general, the adjustment task converges while the required rotation and the opposite rotation are being repeated. On the other hand, it may be necessary to return to a smaller angle due to excess rotation, for instance when adjustment is possible only in processes in which the frequency varies from low to high as in the adjustment of a musical instrument.

5. Conclusions

In recent years, dependability has been a frequent topic in robotics research. It is necessary to increase the reliability of the maintenance tasks performed by robots working on household appliances. Since error recovery is important, we considered a method that uses the concepts of both task stratification and error classification. In this paper, we have described our error recovery technique for adjustment tasks performed by maintenance robots. The capability to recover from errors during such tasks is improved by stratification of tasks and classification of errors.

In the future, we will further research the optimum adjustment methods for the various parameters used in error recovery and a fully automatic method to confirm task achievement composed of skills. We will attempt to apply our technique to actual maintenance robots.

References

- [1] Hasegawa T, Suehiro T, Takase K (1992), A model-based manipulation system with skill-based execution. *IEEE Trans Robotics Autom* 8(5):535-544
- [2] Nakamura A, Ogasawara T, Suehiro T, Tsukune H (1996), Skill-based backprojection for fine motion planning, *Proceedings of the IEEE/RSJ International Conference on Intelligent Robots and Systems (IROS '96)*, Osaka, Japan, Nov 4-8, 1996, pp.526-533
- [3] Nakamura A, Ogasawara T, Kitagaki K, Suehiro T (2001), Using robust and simplified geometric models in skill-based manipulation, *Proceedings of the IEEE/RSJ International Conference on Intelligent Robots and Systems (IROS 2001)*, Hawaii, USA, Oct 29-Nov 3, 2001, pp.138-145
- [4] Nakamura A, Kotoku T (2009), Systematization of Error Recovery in Skill-Based Manipulation, *Proceedings of the 14th International Symposium on Artificial Life and Robotics (AROB 14th '09)*, Oita, Japan, Feb 5-7, 2009, pp.610-613
- [5] Nakamura A, Kawai Y (2010), Recovery Technique from Classified Errors in Skill-Based Manipulation, *Proceedings of the 15th International Symposium on Artificial Life and Robotics (AROB 15th '10)*, Oita, Japan, Feb 4-6, 2010, pp.1010-1013
- [6] Donald BR (1989), *Error detection and recovery in robotics*. Springer-Verlag, Berlin Heidelberg New York, pp.1-256
- [7] Seabra Lopes L, Camarinha-Matos LM (1995), A machine learning approach to error detection and recovery in assembly, *Proceedings of the IEEE/RSJ International Conference on Intelligent Robots and Systems (IROS '95)*, Pennsylvania, USA, Aug 5-9, 1995, vol.3, pp.197-203
- [8] Yamazaki K, Tomono M, Tsubouchi T, Yuta S (2006), Motion planning for a mobile manipulator based on joint motions for error recovery, *Proceedings of the IEEE/RSJ International Conference on Intelligent Robots and Systems (IROS 2006)*, Beijing, China, Oct 9-15, 2006, pp.7-12
- [9] Scheutz M, Kramer J (2007), Reflection and Reasoning Mechanisms for Failure Detection and Recovery in a Distributed Robotic Architecture for Complex Robots, *Proceedings of the IEEE International Conference on Robotics and Automation (ICRA 2007)*, Roma, Italy, Apr 10-14, 2007, pp.3699-3704

A Visual Debugger for Developing RoboCup Soccer 3D Agents

Yosuke Nakamura and Tomoharu Nakashima

Osaka Prefecture University, 1-1 Gakuen-cho, Nakaku, Sakai, Osaka
(Tel : 81-72-254-9351; Fax : 81-72-254-9351)
(*nakashi@cs.osakafu-u.ac.jp*)

Abstract: In this paper, we introduce a visual debugger that helps us develop soccer agents for RoboCup Soccer 3D Simulation. The visual debugger enables us to graphically monitor the internal state of a soccer agent and the soccer field such as joint angles, the position of objects, and text messages. We employ a server/client framework where the debugger acts as a server while the agent acts as a client. A soccer agent connects to the debugger using TCP/IP and sends the information about the field and the internal status. The information that is sent from the soccer agent to the visual debugger consists of three parts: visible objects of the soccer field, the joint angles of the soccer agents, and text messages from the agents. These are shown in separate components on the screen of the debugger. The debugger draws the current pose of the soccer agent from the information on the joint angles that is sent from the soccer server. Text messages are used as a debugging message. The developer of soccer agents are allowed to check if the developed agent works properly through the screen of the visual debugger. A soccer agent that is manually controlled using a game-pad is also included as a part of the debugger. Each of the above features is explained in detail.

Keywords: RoboCup, soccer robot, multi-agent system

I. INTRODUCTION

Soccer simulation league is one of the oldest leagues in the RoboCup competitions. The main aim of the soccer simulation league is to develop decision making systems that achieve intelligent behavior in both high and low levels. It is expected that successful decision making systems are translated to that of real robots. The developers of soccer agents in the simulation league have proposed various techniques from both top-down and bottom-up manners. For example, Stone[1] proposed a layered approach to achieve a complex decision system. FC Portugal proposed a flexible formation model that is based on the ball position[2]. These are categorized as top-down approaches. On the other hand, Stone et al.[3] proposed a neural network-based approach for learning low-level skills. Sean et al.[4] also showed that the team formation is successfully evolved by a genetic programming. A fuzzy reinforcement learning method is proposed for a ball intercept task by Nakashima et al.[5].

In the early years of the RoboCup soccer simulation league, soccer matches were played on a virtual two-dimensional field. The first prototype of 3D simulation was proposed by Oliver[6] in 2003. The community of the 3D simulation has rapidly grown up since then. In 2005 the first competition of 3D simulation was held in Osaka, Japan. The soccer agents were modeled as a sphere object with a kick device. In 2007 bipedal humanoid robot model was employed for soccer agents. This made the development of soccer agents very challenging because not only intelligent decision making but also the movement of joints have to be considered when implementing even lower level skills. The standard way to check the behavior of developed agents is to use the

soccer monitor, which is included in the package of the soccer server[7]. Although the soccer monitor is useful to check the movement of joints of soccer agents, it is not possible to check the internal status of the soccer agents such as vision, ground force, body rotation, and their decision making process. Furthermore the soccer monitor does not record the movement of soccer agents during the course of the game. Thus it is not possible to play back the match even if we want to retrospectively watch the behavior of the soccer agents. These things make the development of 3D soccer agent very difficult. Even if we use files to replay a match, the internal status of agents such as sensory information and the intention of agents cannot be shown and we only have to guess them from the behavior of the agents.

In the 2D simulation league, several high functional debuggers have been proposed. For example, soccerwindow2[8] has useful features such as monitoring internal status, modeling team formation based on the ball position. The developer of soccer agents can also check the decision making process inside the soccer agents through the messages that are sent from the soccer agents to soccerwindow2. Furthermore, soccerwindow2 has a play-back function where the developer can check the behavior of the soccer agents at the past time steps. SoccerScope[9] has similar useful features as soccerwindow2, though SoccerScope can analyze the game logs and give statistics of the game such as the number of successful pass, ball possession rate, and the total number of pass, dribble or shoot. In contrast, in 3D simulation league, there are no such tools available in public. Therefore, we have developed a visual debugger as a development support tool that connects to an agent, displays sensor information and checks the agent's behavior.

II. ROBOCUP SOCCER 3D SIMULATION LEAGUE

RoboCup Soccer 3D simulation league is the project where autonomous agents play soccer in a virtual 3D soccer field. The first prototype of 3D simulation was proposed in 2003. In 2005 the first competition of 3D simulation was held in Osaka, Japan. In this competition, the soccer agents were modeled as a sphere object with a kick device. In 2007, a bipedal humanoid robot model was employed for soccer agents. This made the development of soccer agents very challenging because not only intelligent decision making but also the movement of joints has to be considered when implementing even lower-level skills. The humanoid robot which was used in the RoboCup world competition 2008 is given in Fig. 1. This robot model is based on the Nao[10] which is used in the standard platform league. In the RoboCup world competition 2009, one team consisted of three robots. Six-vs-six games were played in RoboCup 2010.

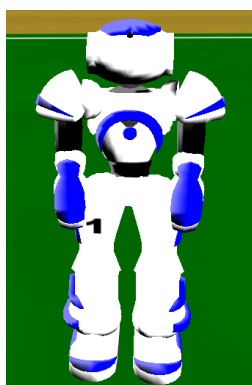


Fig. 1. Humanoid robot

Each soccer agent is autonomously controlled in the 3D simulation league. A game is divided into two halves and each half has 300 seconds according to the official rule. Since one time step is 20 ms, a half consists of 15000 steps. During the simulation, the soccer server sends a message to agents every time step. The message includes joint angles, the value of gyro sensor, the value of foot force resistance sensor, the position of visible objects, and say-messages from other agents. The gyro sensor is equipped in torso. It senses the orientation of the torso in the global coordinates. The foot force resistance sensor informs about the force that acts on a foot. This sensor is equipped in the bottom of feet. A soccer agent can also receive the position of visible objects (the ball, other agents, goal posts, and landmark flags) from the soccer server. An agent is equipped with the camera on its head and the server sends the position of objects which are in the sight of the camera. The angle of sight had been 360 degrees until the world competition 2008 and agents could see all objects from everywhere. However, in the 2009 competition, the angle of the sight was changed to limit to 120 degrees and thus agents have to turn neck and search for objects to receive

the position of objects from as broader area as possible. An aural sensor gets one message from both teams every 3 time steps. Agents make a decision based on the above information. Furthermore, the decision made by an agent must be converted to the necessary changes to the joint angles by the agents themselves. Agents send joint change rates to the server. There are 22 joints in a Nao robot. To control this robot perfectly, an agent program is required to control 22 joint angles every time step.

The RoboCup Soccer 3D Simulation Server is available in a Sourceforge project[7]. The package includes the soccer server, the sample agent, and the soccer monitor. The soccer monitor is the standard way to check a behavior of agents. But the monitor shows the soccer field in the third person viewpoint and we can only check the state of joints from their pose. Therefore, a software tool that shows the internal state of agent is required. In this paper, we develop a visual debugger as a development support tool that connects with an agent, displays the value of sensors and checks the agent's behavior. We also develop a soccer agent that can be controlled by a game-pad as a part of the debugger. In the next section, we introduce the visual debugger in detail.

III. VISUAL DEBUGGER

1. Overview

The visual debugger is connected to a soccer agent via TCP/IP and receives information on the field and the agent's internal status every cycle. The functions that the visual debugger provides make it easier for us to develop agents. A screen shot of the visual debugger is shown in Fig. 2. The soccer agent can send a one-line message to the debugger at each time step. The message contains the information on the state of the field and the agent graphically. The visual debugger graphically shows the information on the display.

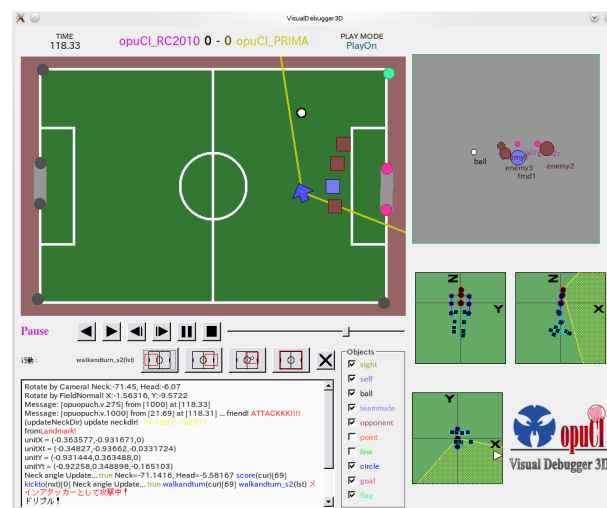


Fig. 2. The visual debugger

2. Debug Message

The one-line message from the soccer agent includes four pieces of information, that is, game state, visual information, joint angles, and gyro information. We explain each of the above information in detail.

- **Game State**

The game state information consists of the game time, the playmode, each team's name, and each team's score.

- **Visual Information**

The agent receives the visual information from the soccer server in three dimensional polar coordinates. The visual information is then sent to the visual debugger as a three dimensional vector in Cartesian coordinates. This information provides the position of visible objects.

- **Joint Angles**

Joint angle includes the joint angles of the agent at the current time step. One message format corresponds to one joint angle.

- **Gyro Information**

Gyro information includes the value of the gyro sensor. The gyro sensor shows the angular velocity of agent's torso.

3. Visible Objects in the Soccer Field

The debugger shows visible objects in the soccer field within the agent's view cone as explained in subsection 3.2. The agent sends the debugger a message that contains field information about whether each object is in the eyesight of the agent or not and if it is visible, its position is also included in the message. The position of visible objects is given in the local coordinates of the agent. The debugger converts it into the absolute coordinates (i.e., the origin is set to the center of the field) and draws it in the overhead view of the soccer field. Figure 3 shows an example of the overhead view of the soccer field. In Fig. 3, the arrow in the rightside of the field indicates the position and direction of the agent's torso, two lines from an arrow to rightside and to top of the figure shows the eyesight of the agent, the white circle indicates the ball, the light gray square indicates a teammate player, and the dark gray square indicates an opponent player. The debugger draws each of the above objects when it is in the agent's eyesight. The position of landmarks such as flags and goal posts are described by gray circles or black circles. The positional relation among landmarks are pre-specified by the soccer server according to the official rule of the league. Therefore, if at least two landmarks are visible to the agent, the position of landmarks which are out of sight can be identified. Lighter circles in Fig. 3 are visible, while black circles are out of sight.

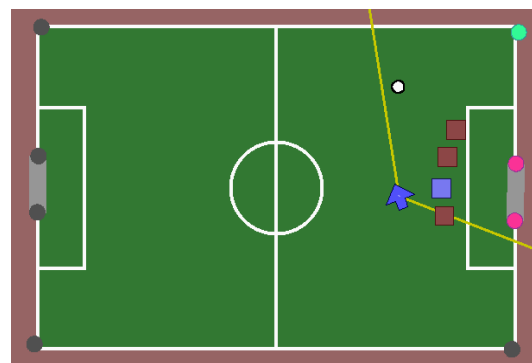


Fig. 3. Visible object in the soccer field

4. Pose of the Agent

The debugger can also draw the pose of the agent and the positional relation between agent's feet and the ball as shown in Figs. 4 and 5. In Fig. 4, the left image shows each joint position from the frontal view and the right sagittal view. In both images the pose of the agent is shown by nodes and edges. The top circle indicates the head, the under circles indicate neck joint and torso. Square nodes indicate leg, heel, and toe joints. In the left images, the right and left circles means arm joints. These figures are drawn based on the message from the agent that contains the joint angles of each time step. Shaded area is the eyesight of the agent. In the left image of Fig. 4, the horizontal axis and the soccer field are assumed parallel, and in the right image of Fig. 4, the vertical axis and the soccer field are orthogonal. The developer of the agent checks the pose of the agent from the two images in Fig. 4.

The positional relation between agent's feet and the ball is shown in Fig. 5. Figure 5 is the mapping of each joint position to the horizontal plane. The white circle indicates the ball, the black circles indicate the nodes of the agent; in this figure they represent the upper body of the agent, and the black squares indicate the lower body of the agent. When the ball is in the eyesight of the agent but is too far to draw in the display, a white triangle locator appears to indicate the direction toward the ball.

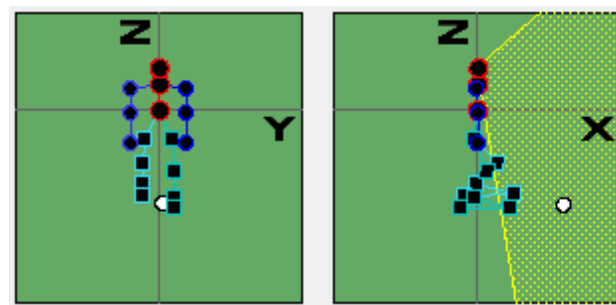


Fig. 4. Pose of the agent

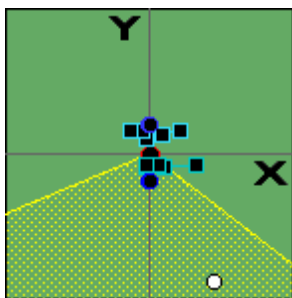


Fig. 5. Position of feet and ball

5. Replay Function

The debugger can replay the game without running the soccer server by loading a text file which includes all debug messages sent by the agent during a game. We call this text file “debug message file” in this paper. The main difference between a debug message file and a log file is that the debug message file contains the internal information from the viewpoint of an agent while a log file just records the joint angles each time step. While replaying a game from a debug message file, extra operations such as pause, go-to-next-step, or go-to-previous-step are available. By using these functions, we can examine an agent’s behavior in detail during a game. These functions are also available while a soccer match is played.

6. Manually-Operable Agent

The behavior of an agent sometimes requires the interaction with other agents. Passing the ball to a teammate and avoiding opponent agents that are approaching the agent are examples of such behaviors. Even though there are released binaries of those teams who participated in previous competitions, it is hard to examine those behavior using the released binaries because soccer agents are autonomously moving and never manually controlled. To overcome this problem, it is helpful to prepare an agent that can be manually controlled. For this purpose, we have developed a manually-operable soccer agent. To control the agent, we use a USB Gamepad with 12 buttons and 2 sticks. Figure 6 shows the game-pad for manually operating the agent.



Fig. 6. Game-pad

IV. CONCLUSION

In this paper, we introduced a visual debugger that helps develop a soccer agent of the RoboCup soccer 3D simulation league. We also showed a manually-operable agent by game-pad for debugging. Using the debugger, the visible object on the soccer field and agent’s internal state are graphically shown. The debugger can also replay the game on itself by loading a debug message file so that we can check agent’s behavior in detail. The source code of the visual debugger will be available in the near future. We hope the debugger makes the agent development more efficient for all teams of soccer simulation 3D league.

REFERENCES

- [1] Stone P (2000), Layered learning in Multiagent Systems: A Winning Approach to Robotic Soccer. MIT Press
- [2] Reis L P, Lau N, Oliveira E C (2001), Situation Based Strategic Positioning for Coordinating a Team of Homogeneous Agents. Balancing Reactivity and Social Deliberation in Multi-Agent Systems, LNCS 2103:175–197
- [3] Grasemann U, Stronger D, Stone P (2007), A Neural Network-Based Approach to Robot Motion Control. RoboCup 2007: Robot Soccer World Cup XI:480–487
- [4] Luke S, Hohn C, Farris J, et al. (1997), Co-Evolving Soccer Softbot Team Coordination with Genetic Programming. RoboCup 1997: Robot Soccer World Cup I:398–411
- [5] Nakashima T, Udo M, Ishibuchi H (2003), A Fuzzy Reinforcement Learning for a Ball Interception Problem. RoboCup 2003: Robot Soccer World Cup VII:559–567
- [6] Kogler M, Obst O (2003), Simulation League: The Next Generation. RoboCup 2003: Robot Soccer World Cup VII: 458–469
- [7] Spark - A generic physical simulator, Sourceforge project, <http://sourceforge.net/projects/simspark/files>
- [8] rc-tools, released web page, <http://rctools.sourceforge.jp/pukiwiki/>
- [9] SoccerScope2003, released web page, <http://ne.cs.uec.ac.jp/~newone/SoccerScope2003>
- [10] Nao, Aldebaran web page, <http://www.aldebaran-robotics.com>

Development of Pulse Control Type MEMS Micro Robot with Hardware Neural Network

Kazuto Okazaki[†], Tatsuya Ogiwara[†], Dongshin Yang[†], Kentaro Sakata[†], Ken Saito^{†1}, Yoshifumi Sekine^{††2}
and Fumio Uchikoba^{†3}

[†]*Department of Precision Machinery Engineering, College of Science & Technology, Nihon University*

^{††}*Department of Electronics & Science, College of Science & Technology, Nihon University
7-24-1, Narashinodai, Funabashi-shi, Chiba, Japan
(Tel. +81-47-469-5343)*

¹*Email:kensaito@eme.cst.nihon-u.ac.jp*

²*Email:ysekine@ecs.cst.nihon-u.ac.jp*

³*Email:uchikoba@eme.cst.nihon-u.ac.jp*

Abstract: This paper presents the MEMS (Micro Electro Mechanical Systems) micro robot which demonstrates the locomotion, controlled by the HNN (Hardware Neural Network). The size of the micro robot fabricated by the MEMS technology was 4×4×3.5 mm. The frame of the robot was made of silicon wafer, equipped with the rotary type actuator, the link mechanism and 6 legs. The rotary type actuator generated the rotational movement by applying the electrical current to artificial muscle wires. The locomotion of the micro robot was obtained by the rotation of the rotary type actuator. Same as the living organisms HNN realized the robot control without using any software programs, A/D converters, nor additional driving circuits. CPG (Central Pattern Generator) model was implemented as a HNN system in this micro robot to emulate the locomotion pattern. The MEMS micro robot emulated the locomotion method and the neural network of the insect by the rotary type actuator, link mechanism and HNN. The micro robot performed forward and backward locomotion, and also switched the direction by inputting the external trigger pulse. The locomotion speed was 19.5 mm/min and the step width was 1.3 mm.

Keywords: Micro Robot, MEMS, Hardware Neural Network, Pulse-Type Hardware Neuron Pair Model, CPG model

I. INTRODUCTION

Many studies have intensively been done on micro robots for several applications such as medical field, precise manipulations, and so on. Although the miniaturization of the robot has conventionally been progressed by mechanical machining and assemblies, some difficulty has appeared in order to achieve further miniaturizations. Instead of the conventional mechanical machining, MEMS technology based on the IC production lines has been studied for making the components of the micro robot [1],[2].

Programmed control by a microprocessor has been the dominant system among the robot control. However, some advanced studies of artificial neural network have been paid attention for applying to robots. A lot of studies have reported both on software models and hardware models [3]-[6]. It is difficult to implement the complicate neural network such as higher animal to artificial neural network systems. In contrast, the neural networks of lower organisms realize the excellent sensory information processing and locomotion control by simple neural networks. Therefore, we are studying

about implement the neural networks of lower organisms to HNN for the purpose to construct the flexible micro robot system.

In this paper, the millimeter size micro robot is proposed. The fabrication process is based on MEMS technology. Also, the locomotion system is controlled by HNN which is composed of CPG model. We will explain about the micro robot system from the view point of the mechanical system, the fabrication process by MEMS technology, the HNN system, and the evaluation of the action of the robot.

II. MECHANISM OF MEMS MICRO ROBOT

The design of the fabricated MEMS micro robot is shown in Fig.1. The number of the legs of the micro robot is 6. The structure and the step pattern of the robot is emulated those of the insect. The micro robot consists of frame parts, rotary type actuators and link mechanisms. The rotary type actuator generates the locomotion of the robot by applying the electrical current to the artificial muscle wires [4]. The size of the

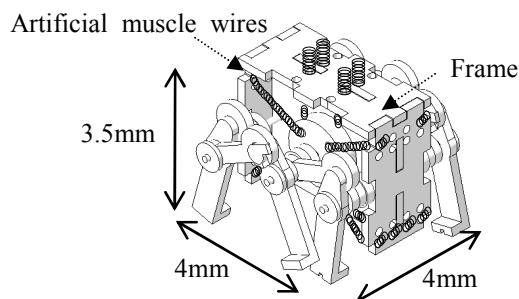


Fig.1 Design of the fabricated MEMS micro robot.

robot fabricated by the MEMS technology is designed as $4 \times 4 \times 3.5$ mm.

The rotary type actuator is shown in Fig.2. The rotary type actuator is composed of the rotor and 4 piece of artificial muscle wire. The frame is assembled from the front frame, rear frame, center frame, and top frame. The both ends of artificial muscle wires are fixed to the frame. The wire shrinks at high temperature and extends at low temperature. In this study, the wire is heated by electrical current flowing, and cooled by stopping the flowing. The rotational movement of the each actuator is obtained by changing the flowing sequence.

The link mechanism is shown in Fig.3. The front leg and the rear leg are connected to the center leg by link bars, respectively. The center leg is connected to the rotor by the shaft. Therefore, the rotational phase is same as the rotor. On the contrary, the other two legs are connected by the link bar that generates 180 degree phase shift. Also, backward step is obtained by the counter rotation of the actuator.

Figure 4 shows the schematic diagram of locomotion method. In the case of heating the artificial

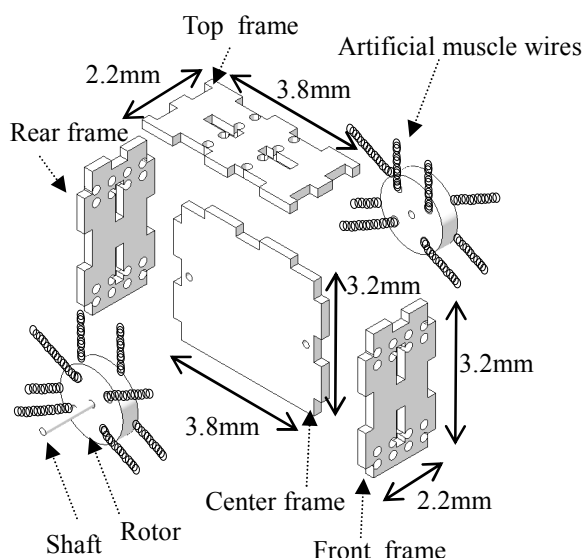


Fig.2 Design of the rotary type actuator.

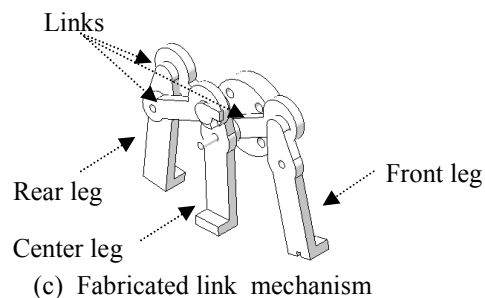
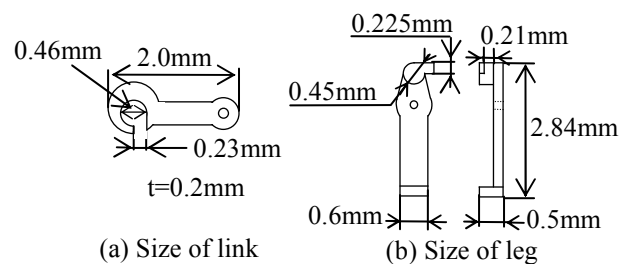


Fig.3 Design of the link mechanism.

muscle wire from EI_1 to EI_4 , the micro robot moves forward. In contrast, heating the artificial muscle wire from EI_4 to EI_1 , the robot moves backward. The locomotion pattern is 180 degree phase shift on each side to represent the locomotion of insect.

III. COMPONENT FABRICATION BY MEMS TECHNOLOGY

The fabrication process of the component of micro robot was based on MEMS technology. The designed shape was formed by the photolithographic process. ICP dry etching process realized high aspect ratio machining.

The components of the MEMS micro robot are shown in Fig.5. The starting material was silicon wafer with various thickness (100, 200, 385, 500 μm) which was used depending on the shape.

The size of the fabricated component is shown in Fig.6. The designed diameter of the joint was 450 μm . The designed diameter of the receptacle was 460 μm . The error of the joint was 0.23 %, and the error of receptacle was 1.38 %. Therefore, the link mechanism was made within the error of $\pm 2\%$. The link bars and

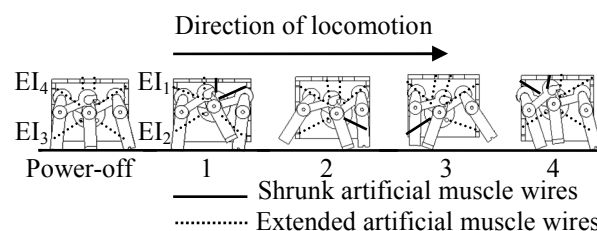


Fig.4 Schematic diagram of locomotion method.

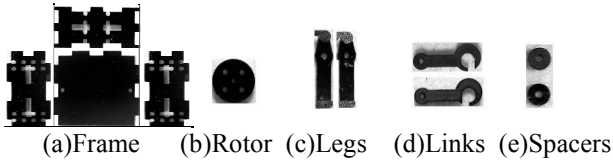
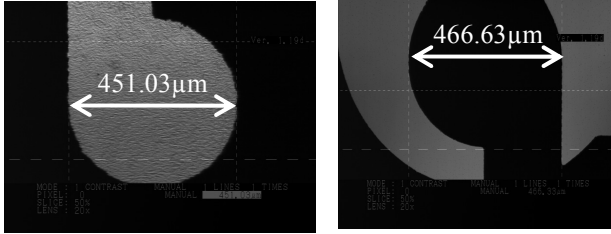


Fig.5 Components of the MEMS micro robot.



(a) Joint of the leg (b) Receptacle of the link
Fig.6 Size of the fabricated component.

the legs were assembled in the gap between $15.6 \mu\text{m}$.

Figure 7 shows the fabricated MEMS micro robot. The size of our MEMS micro robot was $4 \times 4 \times 3.5 \text{ mm}$, same as designed size as shown in Fig.1. The wire from the micro robot was connected to the HNN.

IV. HARDWARE NEURAL NETWORK FOR MOTION CONTROL

The HNN generates driving pulse of the rotary type actuator without using software programs, A/D converters, nor additional driving circuits. The pulse-type hardware neuron pair model compose of the neuron pair of excitatory and inhibitory and each neuron compose of the synaptic circuit and the cell body circuit.

Figure 8 shows the circuit diagram of the pulse-type hardware neuron pair model. The synaptic circuit has the spatio-temporal summation characteristics similar to those of living organisms. The spatial summation characteristics are realized by the adder. Moreover, the

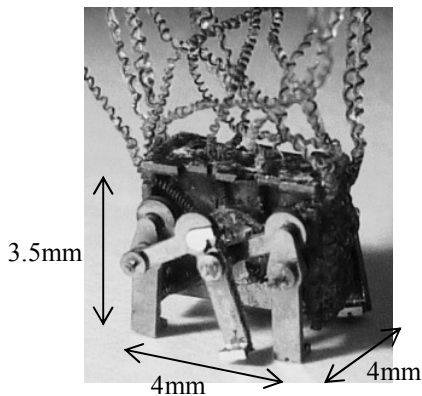


Fig.7 Fabricated MEMS micro robot.

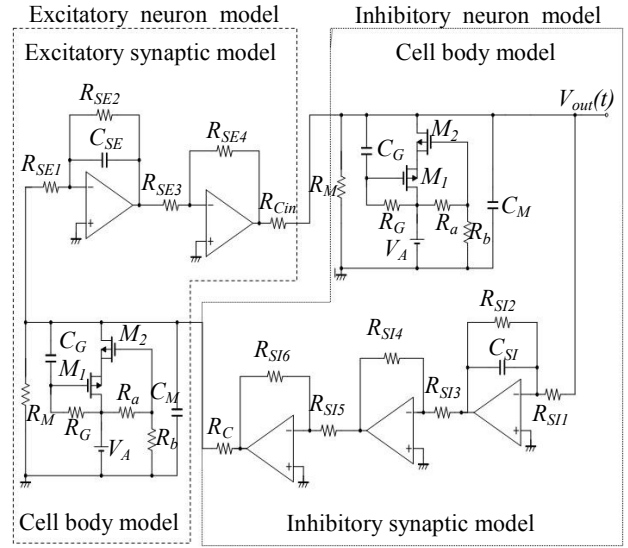


Fig.8 Circuit diagram of pulse-type hardware neuron pair model.

adder includes an inverting amplifier using an operational amplifier (Op-amp), the amplification factor of the inverting amplifier varies according to synaptic weight. The temporal summation characteristics are realized by the Op-amp RC integrator. The circuit parameters of the excitatory synaptic circuit were as follows: $R_{SE1}=R_{SE2}=R_{SE3}=R_{SE4}=1 \text{ M}\Omega$, $C_{SE}=1 \text{ pF}$. The inhibitory synaptic circuit is obtained by reversing the output of the excitatory synaptic circuit. The excitatory synaptic circuit and the inhibitory synaptic circuit are single input but in the CPG model we use multi-inputs including excitatory inputs and the inhibitory inputs. The circuit parameters of the inhibitory synaptic circuit were as follows: $R_{SI1}=R_{SI2}=R_{SI3}=R_{SI4}=R_{SI5}=R_{SI6}=1 \text{ M}\Omega$, $C_{SI}=1\text{pF}$. The cell body circuit consists of a voltage control type negative resistance and an equivalent inductance, a membrane capacitor C_M . The voltage control type negative resistance circuit with the equivalent inductance consists of a n-channel enhancement-mode MOSFET, a p-channel enhancement-mode MOSFET, a voltage source V_A , resistors R_M , R_G , and a capacitor C_G . The cell body circuit has the negative resistance property which changes with time like a biological neuron, and enables the generation of a continuous action potential by a self-excited oscillation and a separately-excited oscillation. Moreover, the cell body circuit can switch between both oscillations by changing V_A . The separately-excited oscillation occurs by the direct-current voltage stimulus or the pulse train stimulus. The circuit parameters of the cell body circuit were as follows: $C_M=470 \text{ nF}$, $C_G=4.7$

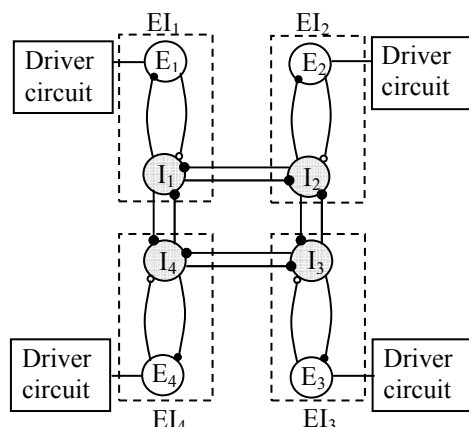


Fig.9 Schematic diagram of the CPG model.

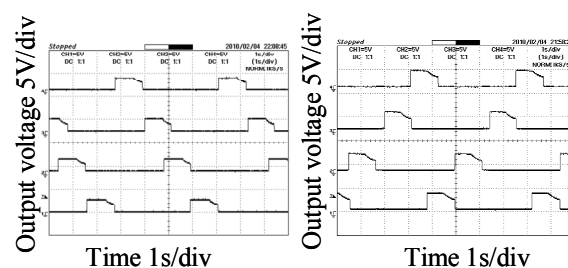
μF , $R_M=10\text{ k}\Omega$, $R_G=680\text{ k}\Omega$, $R_a=20\text{ k}\Omega$, $R_b=15\text{ k}\Omega$. The voltage source $V_A=3.5\text{ V}$.

Figure 9 shows the schematic diagram of CPG model. In this study, four sets of the neuron pair were connected inhibitory then the four output ports were extracted. The CPG model consists of four pulse-type hardware neuron pair models (EI₁, EI₂, EI₃, and EI₄). E and I represent an excitatory neuron circuit and an inhibitory neuron circuit, respectively. The solid circle indicates an inhibitory connection. We denote the pulse-type hardware neuron pair model by EI. The hardware neuron pair model was mounted on a print circuit board and source power was supplied externally.

Figure 10 shows the output waveform of the generated locomotion pattern. It is shown that our constructed CPG model can output the waveform of the forward locomotion and the backward locomotion corresponding to Fig.4. Thus, the constructed CPG model is effective to generate the locomotion of the MEMS micro robot. As a result, our fabricated robot performed forward and backward locomotion, and also the locomotion switched by inputting the external trigger pulse. The locomotion speed was 19.5 mm/min and the step width was 1.3 mm.

V. CONCLUSIONS

In this paper, we fabricated the 4×4×3.5 mm size micro robot by MEMS technology. The locomotion of micro robot was controlled by the HNN. The CPG model was implemented as a HNN system in this micro robot to emulate the locomotion pattern. The MEMS micro robot emulated the locomotion method and the neural network of the insect by the rotary type actuator, link mechanism and CPG model. As a result, the output



(a) Forward locomotion (b) Backward locomotion

Fig.10 Output waveform of the generated locomotion pattern

waveform of the locomotion pattern was generated by the CPG model without using any software programs. The fabricated micro robot was performed forward and backward locomotion, and also the locomotion switched by inputting the external trigger pulse. The locomotion speed was 19.5 mm/min and the step width was 1.3 mm.

ACKNOWLEDGMENTS

The fabrication of the MEMS micro robot was supported by Research Center for Micro Functional Devices, Nihon University. We appreciate the support.

REFERENCES

- [1] E. Edqvist, N. Snis, R. C. Mohr et al (2009), Evaluation of building technology for mass producible millimeter-sized robots using flexible printed circuit boards. *J. Micromech. Microeng* 19:11
- [2] H. Suematsu, K. Kobayashi, R. Ishii et al (2009), MEMS Type Micro Robot with Artificial Intelligence System. *Proceedings of International Conference on Electronics Packaging*:975-978
- [3] Ken Saito, Kazuto Okazaki, Tomonari Kawakami et al (2010), Pulse-Type Hardware CPG Model for MEMS Type Micro Robot. *AVLSIWS 2010*:201
- [4] K. Matsuoka (1987), Mechanism of Frequency and Pattern Control in the Neural Rhythm Generators. *Biological Cybernetics* 56:345-353
- [5] T. Ikemoto, H. Nagashino, Y. Kinouchi, T. Yoshinaga (1997), Oscillatory Mode Transitions in a Four Coupled Neural Oscillator Model (in Japanese). *International Symposium on Nonlinear Theory and its Applications*:561-564
- [6] K. Nakada, T. Asai, Y. Amemiya (2003), An Analog CMOS Central Pattern Generator for Interlimb Coordination in Quadruped Locomotion. *IEEE Transaction on Neural Networks* 14:1356-1365
- [7] Dai Homma (2003), "Metal Artificial Muscle 'BioMetal Fiber' (in Japanese). *RSJ Vol.* 21:22-24

Design of the transmitting device for motion control of robots

Masaharu Komori, Jungchul Kang, Fumi Takeoka and Yukihiro Kimura

*Department of Mechanical Engineering and Science, Kyoto University
Yoshidahonmachi Sakyo Kyoto 606-8501 Japan
(Tel : 81-75-753-5858; Fax : 81-75-753-5858)
(komorim@me.kyoto-u.ac.jp)*

Abstract: It is possible for the motors to realize some range of speed or torque but the range is limited to some degree considering the size, weight and cost of the motors. Moving robots used in the industrial fields are required to realize outputting a large force in some cases, and moving with high velocity in other cases. Therefore a velocity variation system is an ideal method in which the velocity ratio between input and output shafts is changed. However, the motion transmission from the input shaft to the output shaft is interrupted during the velocity ratio variation process in the conventional velocity variation system. In order to solve this problem, velocity variation method that can transmit motion precisely is proposed. The principle of this velocity ratio variation method is explained and its components are considered. The required conditions to the design of the transmitting element of this variation device are clarified in order to realize transmitting motion precisely. By this analysis, it is confirmed that the proposed ratio variation method can change the velocity ratio while transmitting the motion precisely between the input shaft and the output shaft.

Keywords: ratio variation

I. INTRODUCTION

It is possible for the motors to realize some range of speed or torque but the range is limited to some degree considering the size, weight and cost of the motors. Moving robots used in the industrial fields are required to realize both outputting a large force when they carry loads and moving with high velocity when they move to the destination in order to shorten the moving period. Therefore a velocity variation system is an ideal method in this point. Velocity variation devices using gears are widely used in the industrial fields. Cylindrical gears such as spur gear have advantages in high torque capacity, precise rotation transmission and high efficiency and that is the reason why cylindrical gears such as spur gears are used in a variety of devices. In a geared transmission, it is needed to change the working gear pairs to vary the velocity of the transmission. However, the motion transmission from the input shaft to the output shaft is interrupted during this process. This leads to an important problem in the field of robots. In order to solve this problem, velocity variation method that can transmit motion precisely is proposed in our research. In this method, each transmitting element must satisfy each condition, which is different among each element. The required conditions to the design of the transmitting element are clarified in order to realize transmitting motion precisely. By this analysis, it is confirmed that the proposed ratio variation method can change the velocity ratio while transmitting the motion precisely between the input shaft and the output shaft.

II. VELOCITY VARIATION METHOD

In the proposed velocity ratio variation method, there are two shafts, i.e. input shaft and output shaft, three gear pairs A, B and C, and three tooth clutches T_A , T_B and T_C as shown in Fig.1. The gear pairs A and B are composed of typical circular gears, and gear pair C is composed of noncircular gears. Gears A_o , B_o and C_o can be connected to the output shaft by engaging the clutches T_A , T_B and T_C . In contrast, gears A_i , B_i and C_i are fixed to the input shaft. Suppose that the velocity ratio of the gear pair A is r_A , and that of the gear pair B is r_B . In the pitch curve of noncircular gear pair C, there are four sections. The pitch curve of the noncircular gear pair C is partly same as that of gear pair A, and partly same as that of gear pair B. Those parts of pitch curve are smoothly connected. In the four sections, the velocity ratio is constant at r_A , it changes to r_B , it is constant at r_B , and it changes to r_A respectively.

The proposed velocity ratio variation process from r_A to r_B is explained. Under the condition that the clutch T_A is engaged, and the other clutches are disengaged, the velocity ratio is r_A . When the meshing of gear pair C comes into the section corresponding to r_A , the clutch T_C is engaged, and, after the engagement of clutch T_C , the clutch T_A is disengaged. Then the meshing of gear pair C transits to the section corresponding to r_B . In the section corresponding to r_B , the clutch T_B is engaged, and, after the engagement of clutch T_B , the clutch T_C is disengaged. Through this process, the transition from r_A

to r_B is completed. At all steps in this process, at least one of the clutches is engaged. Therefore, the rotational motion is precisely transmitted from the input shaft to the output shaft.

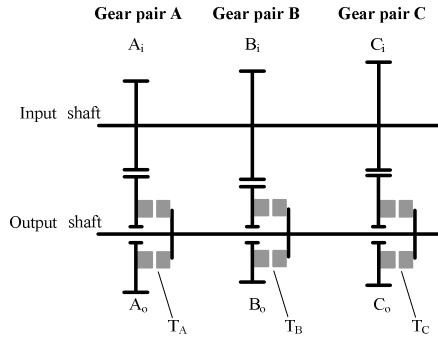


Fig.1. Structure of the Velocity Ratio Variation Device

III. CONDITIONS OF TRANSMITTING ELEMENTS

In the proposed velocity ratio variation method, tooth clutch is used to transmit the motion precisely. However, to use the tooth clutch, it is required that the dog teeth on the output shaft side and that on the gear side are in appropriate condition so that they can be meshed. Suppose the numbers of the dog teeth of tooth clutches T_A , T_B and T_C are n_d . The case that the velocity ratio is changed from r_A to r_B , and returned from r_B to r_A is considered. At the initial state, all of tooth clutches T_A , T_B and T_C can be engaged. In addition, gear pair C meshes in the middle of the section corresponding to velocity ratio of gear pair A.

First, suppose that the input shaft is rotated N_A times, and then the velocity ratio variation process starts, in other words, clutch T_C is engaged, where N_A is natural number. After the rotation of N_A , the difference between the rotational angle of the output shaft and that of gear C_o is $2\pi N_A(r_A - 1)$. To engage clutch T_C , this value must be integral multiple of pitch between the teeth of the clutch. This condition is expressed as follows, where J_1 is arbitrary integer.

$$2\pi N_A(r_A - 1) = \frac{2\pi J_1}{n_d} \quad (1)$$

Secondary, the output shaft is rotated by π , and then clutch T_B is engaged. To engage clutch T_B , considering the difference between the rotational angle of the output shaft and that of gear B_o , following condition must be satisfied, where J_2 is arbitrary integer.

$$2\pi N_A(r_A - r_B) + \pi(1 - r_B) = \frac{2\pi J_2}{n_d} \quad (2)$$

Thirdly, the output shaft is rotated N_B times, and then clutch T_C is engaged. To engage clutch T_C , considering the difference between the rotational angle of the output shaft and that of gear C_o , following condition must be satisfied, where J_3 is arbitrary integer.

$$2\pi N_B(r_B - 1) = \frac{2\pi J_3}{n_d} \quad (3)$$

Finally, the output shaft is rotated by π , and then clutch T_A is engaged. To engage clutch T_A , considering the difference between the rotational angle of the output shaft and that of gear A_o , following condition must be satisfied, where J_4 is arbitrary integer.

$$2\pi N_B(r_B - r_A) + \pi(1 - r_A) = \frac{2\pi J_4}{n_d} \quad (4)$$

These equations are organized, and the following conditions to the design of the transmitting element are clarified, where Z is set of integer.

$$\left. \begin{aligned} n_d(r_A - r_B) &\in Z \\ \frac{n_d(1 - r_A)}{2} &\in Z \\ \frac{n_d(1 - r_B)}{2} &\in Z \end{aligned} \right\} \quad (5)$$

VI. CONCLUSION

In the system proposed in our research, precise transmission of the rotation from the input shaft to output shaft is realized. The required conditions to the design of the transmitting element are clarified. It is confirmed that the proposed ratio variation method can change the velocity ratio while transmitting the motion precisely between the input shaft and the output shaft.

ACKNOWLEDGEMENT

This study was supported by Industrial Technology Research Grant Program in 2009 from New Energy and Industrial Technology Development Organization (NEDO) of Japan.

Construction and basic performance tests of underwater monitoring network

Chunhu Liu, *Bin Fu, Han Zhang, Lian Lian

Shanghai Jiao Tong University

* *b_fu@sjtu.edu.cn*, +(86)-21-34207293

Abstract:

With the rapid development of economy, environmental pollution has become one of the major problems in coastal areas and cities along the river. Real-time observation of the water quality along the river has been considered as an efficient way to control wastewater emission and manage environment of water quality. Traditional ways to observe ocean environment, including satellite telemetry, radar, investigation ship, ocean observation station and etc, are not applicable for water quality observation along river because of their high cost, Poor real-time, low accuracy and so on. Based on Wireless Sensor Networks, the study discussed in this paper proposes a new observation system using under-water multisensory information. After processing multisensory data of each sensor the system transmits it to hub node through wireless sensor networks, and then transmits it to land data center through GPRS wireless network. In order to check the basic performance of this system, the authors have completed the node positioning experiment based on GPS module and the communication experiment based on ZigBee. This paper reports the hardware design and the experimental results.

Keywords: Wireless Sensor Networks(WSN), Underwater, ZigBee, Communication

1. Introduction

With the rapid development of economy in these years, environmental pollution has become a major fact of invading people's life and influencing global climate change. Especially, wastewater emission and leakage from the cities along the river and ocean lead to pollution of water quality, and it could bring global environmental deterioration impact. Nowadays, the major ways to observe ocean environment, mainly depends on satellite telemetry, radar, investigation ship, stationery ocean observation station and etc, which are not applicable for water quality observation along river because of their high cost, poor real timeness, low accuracy and so on. The study introduces WSN technology of land field to observation system of water quality. By setting continuous underwater sensor nodes, the water quality environment in a large area can be real-time observed. By setting up wireless communication network among multinode networks, physical information, including water temperature, PH value, oil leakage, noise and etc, can be converted to electrical signal, and then transmitted to surface unit. In this system, each unit is not only a node, but also a data transmission relay of other nodes. Node's information can be exchanged and transmitted to land data management center through wireless communication in order to assure that observed data is real-time, actual, universal and continuous. However, the biggest technology difficulty of gathering and sending underwater information is to overcome

the influence of antenna swaying on communication performance and organize a network in a hundred-meter range area between several hundred meters. In addition, the properties of network organization mode, communication protocol, optimum topology structure and etc, are not clear yet when the height between antenna and water surface is low. Therefore, based on theoretical calculation and analysis on extreme conditions mentioned above, the paper proposes a design scheme of system network organization, and reports the test of basic performances of the system by installing it in the water area of Shanghai, China.

2. wireless sensor network design

2.1 system summary

As shown in figure 1, the system is composed of some surface nodes, hub nodes, and land data terminal. The carrier of each sensor node is buoy. The buoy carries surface wireless communication unit, data processing unit and many underwater sensors. The nodes communicate with each other by wireless communication, and they are composed of wireless sensor network with node topology structure. The network converges information at hub node. The hub node is located along river shore. First, it transmits information by GPRS network of cell phone, and then transmits the information to land data terminal through remote wireless communication.

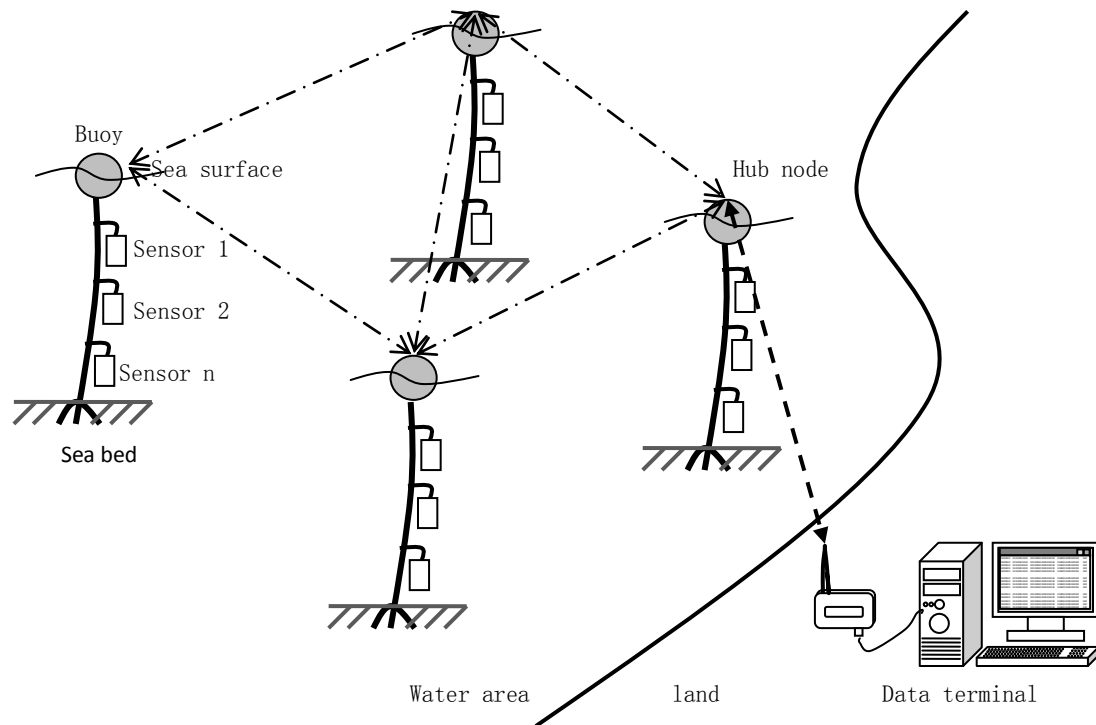


Fig. 1 System Composition

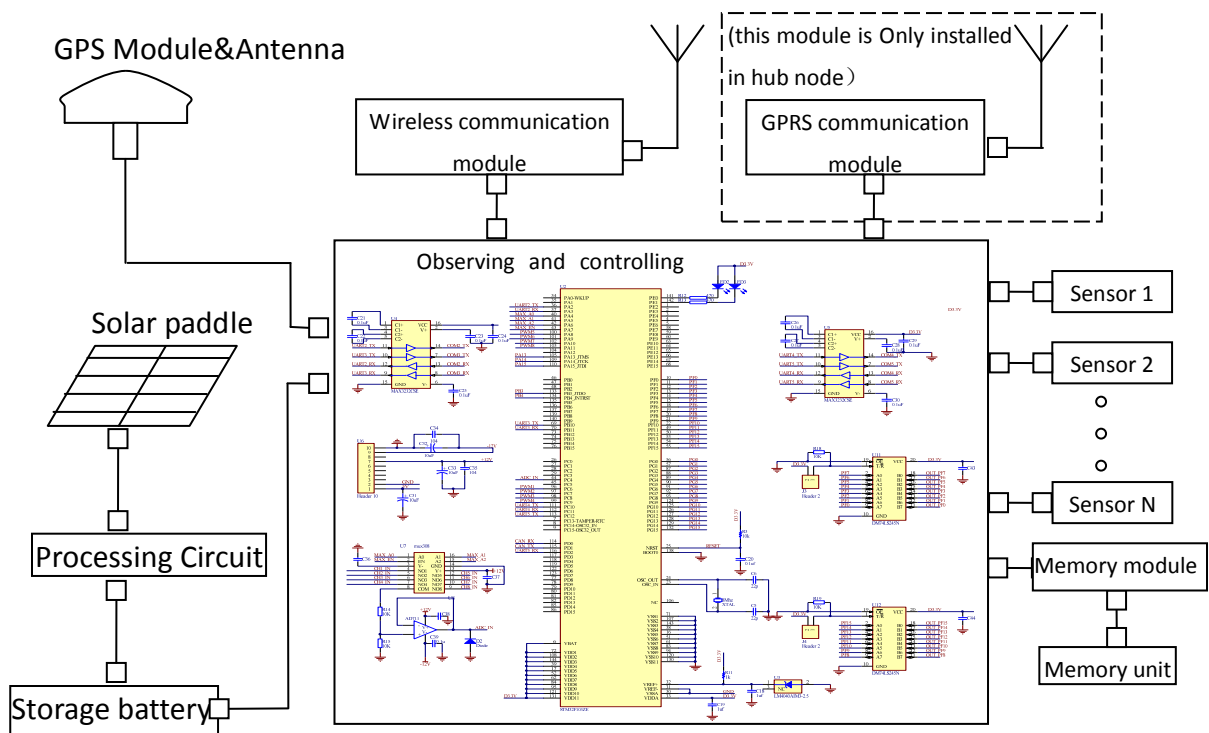


Fig. 2 Schematic Diagram of Surface node

2.2 sensor node design

As shown in figure 2, in our design, each node in the sensor network has an observing and controlling unit, memory unit, battery unit cell of solar energy, GPS

positioning unit, wireless communication unit and some sensor interfaces. Observing and controlling unit is capable of data collecting, digital control, data transmission and so on. Hub node includes remote

wireless communication unit which communicates with land data terminal. Micro embedded GPS module with Patch Antenna is used in Node positioning in the study; Zigbee is used in wireless communication among nodes because it is highly reliable, free and network organizable; Because GPRS mode is low cost and has a wide coverage of network, it is used in a long-distance wireless communication between nodes and land data terminal. Power supply of nodes takes form of combination of solar energy and storage battery; in order to assure the integrity of collected data, each node is self containing. Which in other words, the collected data is saved before it is retransmitted. In order to collect data from different underwater sensors, observing and controlling unit contains modulation function of analog signals and serial port communication function; the collected data need to be preliminarily processed to reduce redundancy node.

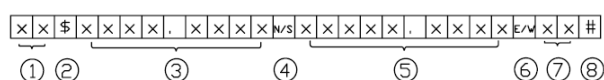
2.3 Deign of data transmission rule

ZigBee module itself doesn't support error correction and automatic repetition mechanism, so in order to increase success rate of data transmission, the system need the following functions:

- a) short frame transmission rule
- b) automatic error correction and repetition function

For example, transmitting end transmits data to designated node, and then receiving end responds after receiving data; if latency is overtime, transmitting end will retransmit the data. If it doesn't receive any response from receiving end after 3-time retransmitting, the system will consider it a data-link failure between the transmitting end and receiving end and abort current data transmission; at the same time, the system saves all data for the subsequent data analysis and processing.

Data of each node are composed of node position information and sensor information. Each node is equipped with GPS positioning module, and can position each node itself. Positioning information is transmitted in a format as shown in figure 3(a), and the transmission time interval of this format is longer than the format shown in figure 3(b). If position of the node changes a lot, the position information will be transmitted to control center where staff can timely process it. Comparatively, data information of each sensor is transmitted in a data format as shown in format 3(b.)

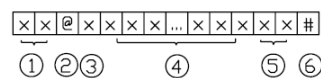


- ①Address; ②Flag of GPS data; ③Latitude;
- ④N:North latitude, S:South Latitude; ⑤Longitude;

⑥E: East Longitude, W: West Longitude;

⑦CRC16 Verification; ⑧End of Frame.

(a) Format of Position Information



①Address; ②Sensor Data Flag; ③Frame Info.;

④ Sensor data; ⑤ CRC16 Verification; ⑥ End of Frame.

(b) Data Information of Sensor Information

Fig.3 Data Format

3. Performance Experiment

3.1 Objective

Node positioning, efficient working distance and communication between nodes are key technologies in this system. The following questions remain to be validated in this experiment:

- a) Communication performance of wireless sensor network in a open water area.
- b) Positioning accuracy of the node drifting within a small area

3.2 Contents

a) The neighboring water area in shanghai is taken to be the subject in this experiment. An experiment point is respectively chosen from Huangpu River, East China Sea and Qiantang River to test positioning accuracy of sensor node.

b) Take offshore area of East China Sea for an example, actual efficient communication distance of ZigBee is measured and compared with theoretical distance value. Also, the effect of antenna's oscillation angle change on communication distance is tested.

c) The relation between transmission bit error rate and transmission distance of ZigBee mode is tested. Short-frame and long-frame transmission error rate are also reported.

3.3 Results

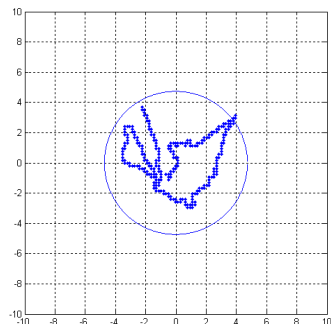
a) Positioning Accuracy of Node

The theoretical positioning accuracy of GPS module used in this experiment is 3[m], and actual positioning accuracy of the 3 tested point are respectively 9.47[m], 4.77[m], and 3.86[m]. The positioning accuracy of horizontal direction is shown as figure 4. The node positioning error is within 10[m], which is good enough to meet the need of the system.

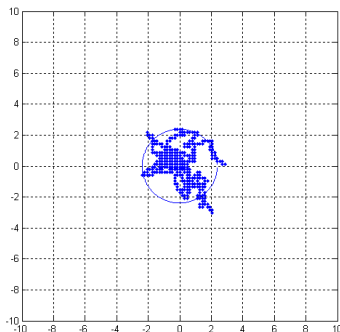
b) Error Rate

Table 1 shows comparison of error rate between long-frame and short-frame communication when 10K -byte date is transmitted. The data length of long frame is more than 30 bytes, while the data length of

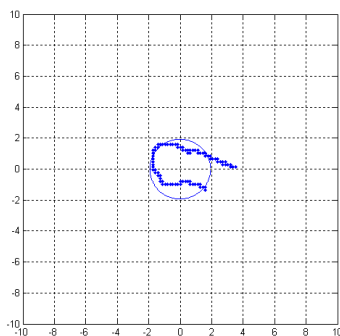
short frame is no more than 10 bytes. Apparently, error rate of short frame communication is much lower than that of long frame's communication. Efficient communication distance is about 600[m] when error rate is less than 4‰.



(a) Qiantang River (2DRM=9.47[m])



(b) Huangpu River (2DRM=4.77[m])



(c) East China SEA (2DRM=3.86[m])

Fig.4 Positioning accuracy of sensor node

Table 1 Comparison on bit error rate between long frame and short frame communication

Distance	Long frame	Short frame
300	0	0
400	2.4e-4	1.8e-4
500	1.3e-3	8.4e-4
600	2.4e-2	3.6e-3
700	6.3e-2	4.3e-3
800	2.4e-1	6.2e-3

c) Efficient Communication Distance

Theoretically, P_R , the free-space power received by receiving unit is determined by equation(1)^[1,2]

$$P_R(d) = \frac{P_T G_T G_R \lambda^2}{(4\pi)^2 d^2} \quad \dots(1)$$

Where, P_T [dB] is transmitting power, P_R [dB] is receiving power, G_T [dB] and G_R [dB] are respectively antenna gain of transmitting and receiving, d [m] is the transmission distance, λ [m] is wavelength. Then transmission loss P_L [dB] can be obtained by the following equation^[2].

$$P_L(d) = 20 \log_{10}(f_{MHz}) + 20 \log_{10}(d) - 28 \dots(2)$$

In this experiment, $P_T=10$ [dBm], sensitivity of receiver is -94[dBm], $P_L=104$ [dB]. Then theoretical value of transmission distance is 1658[m]. Not only a certain margin is allowed, coefficient of transmission attenuation is bigger due to big air humidity around sea. Besides, energy loss is caused by imperfect transmitting circuit and receiving circuit. As revealed by actual measurement, when bit error rate is less than 4‰, efficient communication distance is about 600[m] which is only 36% of theoretical transmission distance. However, we can increase efficient communication distance by boosting antenna gain or transmitting power.

In addition, because of the antenna directivity of ZigBee module, antenna mounting height have to be increased to raise communication efficiency in a rough wave environment

4. Summary

The key technologies, which are used for data collecting, data processing, node positioning, communication among nodes and etc, are proposed in this study and have been validated through experiments. And we are trying to go on with a long-term observation test about water quality. In addition, the technologies mentioned are expected to be used in intelligent observation with large information transmission such as underwater acoustics, video and etc.

ACKNOWLEDGMENTS: The study is supported by Public Welfare Project of Science and Technological Department, Zhejiang Province, China. Contract No. 2010C33183.

References

1. Rappaport, Theodore S, Wireless Communications Principles and Practice, Prentice Hall, 2001, P70-74.
2. Shreharsha Rao, Estimating the ZigBee transmission-range ISM band, EDN, May 2007, P67-72

On the Use of Human Instruction for Improving the Behavior of RoboCup Soccer Agents

Yosuke Nakamura and Tomoharu Nakashima

Osaka Prefecture University, 1-1 Gakuen-cho, Nakaku, Sakai, Osaka
(Tel : 81-72-254-9351; Fax : 81-72-254-9915)
(nakashi@cs.osakafu-u.ac.jp)

Abstract: In this paper, we propose a behavior generation approach from human instruction to improve the strategy of RoboCup soccer 3D simulation team. Many teams implement their strategies based on the programmers' own knowledge about soccer. That is, the programmers have to write action rules that cover any situations of the soccer field. Although it is clear that this is not the best approach, there are only a few research works that tackle this problem. In this paper, we solve this problem using human instruction to improve the manually implemented behavior of soccer robots. It is shown that the team performance is improved by the generated rules by this approach.

Keywords: RoboCup, soccer robot, learning, multi-agent system

I. INTRODUCTION

RoboCup is an international project which aims at building autonomous soccer robots. RoboCup has some main leagues such as Soccer, Rescue, @Home and Junior. We focus on the soccer simulation league, which is a subleagues of the RoboCup Soccer League. The soccer simulation league is one of the oldest leagues in the RoboCup competitions.



Fig. 1. 2D Simulation

There are two categories in the soccer simulation league. One is 2D league where all objects such as the ball, players, flags, and goal posts are modeled as a circle. The other is 3D league where humanoid robots with 22 degrees of freedom are autonomously controlled in a three-dimensional field. Figure 1 shows the snapshot of the 2D simulation game. In the 2D simulation league, all objects are realized in a two-dimensional space. This league is valuable as a test bed for high level decision making systems. There are many famous papers about 2D league. Gabel et al.[1] considered a defense scenario of crucial importance and employed a reinforcement learning methodology to autonomously acquire an aggressive duel behavior. Kyrylov and Hou [2] treated

optimal defensive positioning as a multi-criteria assignment problem and demonstrated that pareto-optimal collaborative positioning yields good results. Kalyanakrishnan and Stone [3] introduced a policy search method for a keepaway task, which is a popular benchmark for multiagent reinforcement learning from the simulation soccer domain.



Fig. 2. 3D Simulation

On the other hand, the 3D simulation league includes the concept of height and can simulate the real world better than the 2D league. Figure 2 shows a game of the 3D simulation league. We can watch the game of the 3D soccer simulation league through the soccer monitor, which is included in the package of the soccer server [4]. The first prototype of the 3D soccer agent was proposed in 2003 [5]. In the early stage of the 3D simulation league, the soccer agents were modeled as a sphere object with a kick device. In 2007, a bipedal humanoid robot model was employed for soccer agents for the first time in the league. This made the development of soccer agents quite challenging because not only intelligent decision making but also low level skills such as the movement of joints have to be considered when devel-

oping the controller of the robot. Shafii et al.[6] employed a truncated fourier series approach for a stable biped walking of a humanoid robot and optimized it by using particle swarm optimization. Warden et al.[7] proposed a framework for spatio-temporal real-time analysis of dynamic scenes to improve the grounding situation of autonomous agents in physical domains. Recently low level skills have been significantly improved by top teams in the world. In addition, the number of agents in one team is increasing: one team had three agents in RoboCup 2009, and it was increased to six in RoboCup 2010. It will finally become 11 in the near future. Therefore, it is getting more important to implement team strategy to win a game. In this paper, we propose a method that generates action rules automatically from human instruction. A human instructor is expected to give more appropriate actions to the soccer agents. In the proposed method, the instructions are recorded and converted to action rules after selecting any useful instructions.

II. BEHAVIOR GENERATION USING HUMAN INSTRUCTION

1. Overview

Many teams implement their strategies based on the programmers' own knowledge about soccer. That is, the programmers have to write action rules that cover any situations of the soccer field. Although it is clear that this is not the best approach, there are only a few research works that tackle this problem. In this paper, we solve this problem using human instruction to improve the already implemented behavior of soccer robots. For this purpose, we developed a human-agent interface. In this system, a gamepad is used to send human instructions to agents. The human instructions are then converted to a set of action rules that are used to modify the behavior of the soccer robots. The process of our approach is the following:

- i. Recording instructions.
- ii. Reducing and clustering instructions.
- iii. Generating action rules.

In the following subsection, we explain our approach in detail.

2. Recording instructions

The action of the soccer agent is semi-automatically determined. That is, the soccer agent has its own decision based on the sensory information. However, if the human instructor thinks that the action currently taken by the soccer agent is not appropriate, the action of the soccer agent is overruled by the instruction from the human instructor. Each time a human sends an instruction to the soccer agent, the instruction is recorded along

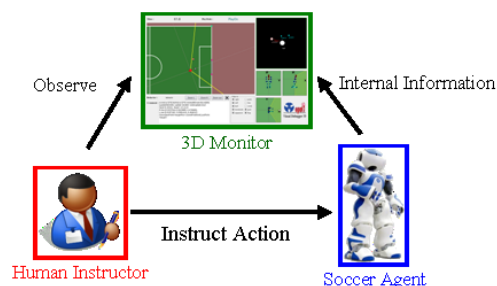


Fig. 3. Human instruction



Fig. 4. 3D Monitor for instruction

with sensory information that the soccer agent receives at that time. A user interface is used to monitor the sensory information that the soccer agent is currently receiving. The above process is graphically shown in Fig. 3. The 3D monitor in Fig. 3 is developed for the purpose of this paper. The snapshot of the 3D monitor is shown in Fig. 4. The 3D monitor allows human instructors to check the internal status of the soccer agents since the sensory information sent to the soccer agent is limited to the front area of its head.

When the human instructor sends an instruction to the soccer agent, the 3D monitor records it along with the internal status of the soccer agent. The internal status recorded with the action instruction consists of the positions of the ball and five soccer agents (three opponents, the other mate attacker, and itself). There are three actions available for the human instructors: kick, dribble, and wait. For the kick and the dribble actions, the human instructors also have to send the action direction. Although the human instructor can specify any direction for the two actions, the 3D monitor quantizes it into one of the eight directions such as up, down, right, left, up-right, up-left, down-right, down-left, and toward-opponent-goal. The nearest direction out of the nine to the specified one is selected and recorded in the 3D monitor.

3. Reducing and clustering instructions

Since a huge number of instructions are sent from humans during a match, it is not practical to use all the instructions. Also, some instructions are useful while others are not helpful for better strategies (e.g., scoring a goal). In this paper, we only use the recorded instructions that led to a goal while discarding the other instructions. Thus only helpful action rules are generated to improve the behavior of the soccer agent.

Since there are still a large number of instructions after removing not successful instructions, we apply a clustering method to compress the information contained in the instructions. We apply an incremental clustering method to the field status for each action. In the incremental clustering method, a pair of two instructions with the minimum distance in the field status space is combined and the average is used as the representative of the pair. This process is iterated until the number of clusters becomes a pre-specified number. In the computational experiments of this paper, we applied the clustering method to obtain 100 clusters (i.e., 100 representatives of the cluster) for each action. During the paring process, the distance between two clusters is measured as the minimum distance among all possible combinations of the elements within the clusters.

4. Generating action rules

The representatives of each cluster obtained in the previous subsection are converted into a set of action rules. As described in the previous subsection, only successful instructions leading to a score are converted to action rules after clustering. For each cluster center, an action rule of the following form is generated:

R: If the current status is P then the action is A ,

$$P: (x_{\text{self}}, y_{\text{self}}, x_{\text{ball}}, y_{\text{ball}}, x_{\text{opp1}}, y_{\text{opp1}}, x_{\text{opp2}}, y_{\text{opp2}}, x_{\text{opp3}}, y_{\text{opp3}}, x_{\text{mate}}, y_{\text{mate}}) \quad (1)$$

A: Instructed action,

where P is the status of the field. The status of the field contains the positions of the opponent agents, the other mate agent, and the ball. The action in the consequent part of the action rule is the instruction that was specified by the human instructor.

III. PERFORMANCE EVALUATION

1. Experimental settings

In the computational experiments in this paper, a set of action rules are generated from human instructions in 3-on-3 soccer matches. That is, a team consists of three soccer agents (two attackers and a goal keeper). The strategy of the team is manually written beforehand. While the soccer agents autonomously play according to the written strategy, a human instructor can overrule the

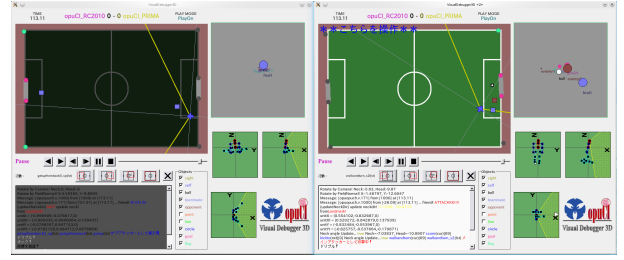


Fig. 5. Instructing scene

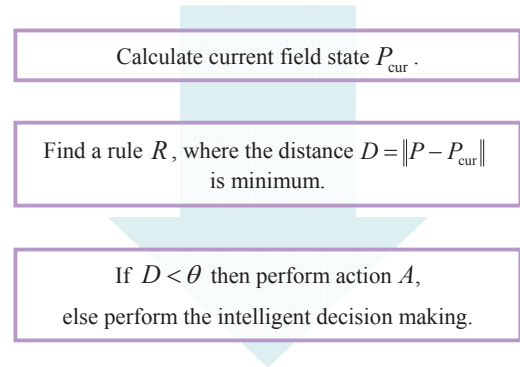


Fig. 6. Decision making process

agent's action if the action is thought to be not appropriate for the instructor. In this paper, the action taken by the main attacker (i.e., the player nearest to the ball) is the focus of the overrule by the human instructor.

Figure 5 shows a snapshot of the interface for the human instructor. This interface is used to send instructions that overrule the currently executed actions of the main attacker. The instructions are then converted to action rules as described Section II. The generated action rules are added to our team, opuCI_3D_2010, which participated in RoboCup 2010 Singapore. The agent first looks at the rules that are manually written. Then the fittest rule with the current field status is chosen to select an action. The rule R which has the nearest P to the current field status is selected and the distance D between P and the current field status is calculated as follows:

$$D = \|P - P_{\text{cur}}\| \quad (2)$$

$$= \left[\sum_{i \in Obj} \{(x_i - x_i^{\text{cur}})^2 + (y_i - y_i^{\text{cur}})^2\} \right]^{\frac{1}{2}} \quad (3)$$

where P_{cur} is the current state vector and Obj includes self, ball, opp1, opp2, opp3, and mate. The distance D is calculated in Euclidean distance. If D is smaller than a certain threshold value θ , the behavior A is executed. Otherwise, an agent makes a decision according to manually written action rules. Figure 6 shows the decision making process of an agent using action rules.

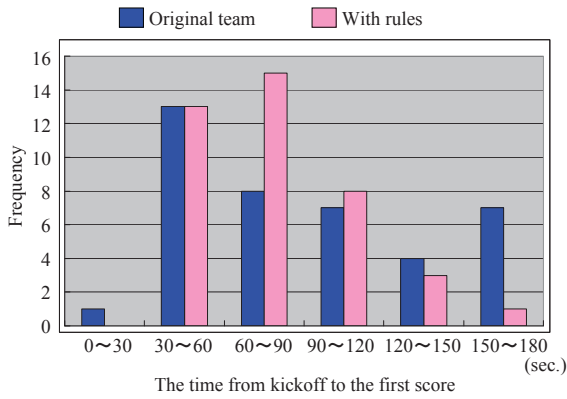


Fig. 7. Performance comparison between the original team and the experimental team

Table 1. Mean and variance of the time necessary for scoring

	Original team	With rules
Mean	90.20	75.04
Variance	2333.1	946.92

In the performance evaluation, the team with the action rules generated by the proposed method played against team opuCI_3D_2010. A game starts by the experimental team's kickoff and the time from kickoff to the first score by the experimental team is measured. 40 games are played for the performance evaluation.

2. Results

The results of the performance evaluation are shown in Fig. 7. In Fig. 7, the vertical axis means the frequency and the horizontal axis means the time necessary to get a score. Table 1 shows the mean and the variance of the time necessary for scoring a goal. From Fig. 7 and Table 1, we can find that the generated rules, that is generated behaviors, lead to the decrease in the time from kickoff to a goal. In order to show the statistical significance of our method, we performed a one sided t-test in order to show that there is a significant difference between these two means. The null hypothesis H_o and the alternative hypothesis H_a are the following:

$$H_o : u_t = u_r \quad (4)$$

$$H_a : u_t > u_r \quad (5)$$

where u_t is the mean of the original team's first score time and u_r is the mean of the rule experimental team's first score time. The result of the t-test is shown in Table 2. We can find the fact that the p-value $P(T \leq t)$ associated with the t-test is smaller than α from Table 2 and there is evidence to reject the null hypothesis H_o in favor of the alternative hypothesis H_a . Therefore we can

Table 2. The result of t-test

α	0.05
t-value	1.674
$P(T \leq t)$	0.0494

say that the proposed method effectively decreased the time necessary to score a goal.

IV. CONCLUSIONS

In this paper, we introduced the behavior generation approach from human instruction. The proposed method enables us to improve the behavior of autonomous soccer agents through human instructions. The results of computational experiments showed that the agents with human instructions are superior to the original ones in terms of time from kickoff to the first score. Now top level teams which participate in the world competition have developed highly sophisticated skills, and it becomes more important to improve the team strategy. Our method can be expanded to apply to defender's behavior to improve the defense ability.

REFERENCES

- [1] Gabel T, Riedmiller M, Trost F (2008), A Case Study on Improving Defense Behavior in Soccer Simulation 2D: The NeuroHassle Approach. RoboCup 2008: Robot Soccer World Cup XII:61–72
- [2] Kyrylov V, Hou E (2009), Pareto-Optimal Collaborative Defensive Player Positioning in Simulated Soccer. RoboCup 2009: Robt Soccer World Cup XIII:179–191
- [3] Kalyanakrishnan S, Stone P (2009), Learning Complementary Multiagent Behaviors: A Case Study. RoboCup 2009: Robt Soccer World Cup XIII:153–165
- [4] Spark - A generic physical simulator, Sourceforge project, <http://sourceforge.net/projects/simspark/files>
- [5] Kogler M and Obst O (2003), Simulation League: The Next Generation, RoboCup 2003: Robot Soccer World Cup VII:458–469
- [6] Shafii N, Nezami O M, Aslani S et al. (2009), Evolution of Biped Walking using Truncated Fourier Series and Particle Swarm Optimization. RoboCup 2009: Robot Soccer World Cup XIII:344–354
- [7] Warden T, Lattner A, Visser U (2008), Real-Time Spatio-Temporal Analysis of Dynamic Scenes in 3D Soccer Simulation. RoboCup 2008: Robot Soccer World Cup XII:366–378

Development of an autonomous-drive personal robot “An environment recognition system using image processing and an LRS”

Yasushi Kibe and Hideki Ishimaru and Eiji Hayashi

*Department of Mechanical Information Science and Technology
Faculty of Computer Science and Systems Engineering, Kyushu Institute of Technology
680-4, Kawazu, Iizuka-City, Fukuoka Prefecture, Japan*

Abstract: We are developing an autonomous personal robot able to perform practical tasks in a human environment based on information derived from camera images and an LRS (a laser range sensor). It is very important that the robot be able to move autonomously in a human environment, and to select a specific target object from among many objects. For this reason, we developed a system by which these functions would become possible. This environmental recognition system is composed of an autonomous driving system and an object recognition system. First, the autonomous driving system calculates the driving route from the visual information provided by the CCD camera. The robot is driven by this system. The object recognition system proceeds by identifying the specified object using image processing and an LRS. The robot can grasp the object using this system. An environment recognition system is essential to both of these functions. Here we explain the algorithm by which the robot recognizes the surrounding environment. In addition, we apply this system to the robot, evaluate its performance and discuss our experimental results.

Keywords: Personal robot, monocular camera, Image processing, LRS, Autonomous driving, Object recognition

1. Introduction

In the near future, autonomous self-driving robots are expected to provide various services in human living environments. For this to occur, the robots will need to gain a grasp of the human environment. Therefore, systems to provide environmental recognition based on image information are being widely studied. However, it is very difficult to recognize all driving environments from image information only; so far, no prospects for such a system have emerged. Here, we report on the development of an autonomous personal robot able to perform practical tasks in a human environment based on information derived from camera images and an LRS (a laser range sensor), which is used to acquire two-dimensional distance information.

The system for this robot is composed of an autonomous run system for movement and an object recognition system for the recognition and grasping of an object. First, the autonomous run system decides upon a robot driving command based on information in the limited space map. Information such as walls and barricades are set to the map, and the data obtained from the CCD camera are compared against the map data. The route is decided, and the robot drives. The object recognition system is composed an object-recognition processing part and a location-information acquisition processing part, both of which use the monocular camera and the LRS. An object is recognized and identified using range information obtained from LRS in addition to the processed image data provided by the

camera. The robot performs a grasping operation for the object according to this system.

2. System for robot

Our robot has a drive mechanism consisting of two front and two back wheels. The front wheels are attached to a motor that operates the wheels on either side independently, while the back wheels function as castor wheels. This method has the advantage of allowing a small turning radius. In addition, to acquire image information, both a single CCD camera with approximately 2,000,000 pixels and an LRS are installed on the head of the robot and can be rotated to all sides by two motors. DC servo motors are used for the robot's drive mechanism, and position and speed control are achieved by the control system of the drive mechanism. The robot also has two arms and hands equipped with sensors, which enable it to respond to the various demands of humans. Finally, an installed wireless LAN can provide remote control for humans. All devices are controlled by a PC, and lead batteries supply the robot's electric power.

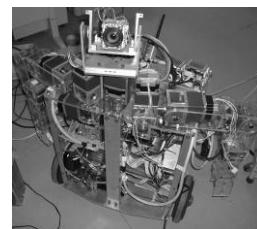


Fig. 1 Our developed robot

3. Specification of the LRS

LRS is a noncontact laser measurement system; our LRS is made by HOKUYO AUTOMATIC CO., Ltd.,. The maximum detection distance of this LRS is 4m. Moreover, the horizontal plane space is scanned by 270° at intervals of about 0.36° ($360^\circ/1024$) to detect both the distance and the direction of the target body. This LRS requires a time of only 100 msec for a single scan. Therefore, a reduction in the distance acquisition time was enabled by using LRS to gain details about the target object recognized with the monocular camera. Fig. 2 shows the externals of the LRS.



Fig. 2 Scanning laser range sensor

4. Autonomous driving system

4.1 Outline of the system

We developed an autonomous driving system for robots that can move with image information captured by monocular CCD camera. It has two subsystems: a route searching system, which decides the course of the robot, and a course correction system, which traces a safe course during the actual run.

4.2 Method for autonomous driving

In this section, we explain the method for autonomous driving. The flow for the autonomous driving is shown in Fig. 3.

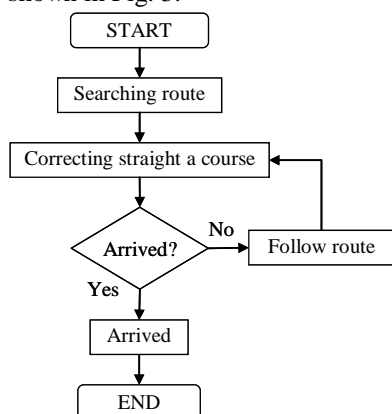


Fig. 3 Autonomous driving system flow

I. Route searching system

In this system, the robot searches for routes based on a limited space map. This map includes information such as the start position of the robot, the goal, walls,

and danger zones. When there is a wall and an obstacle on the course to a goal, the robot travels along the middle point between them. The robot always takes the shortest route and removes other routes. The system is shown in Figs. 4 and 5.

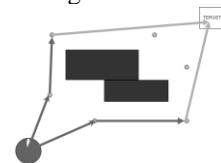


Fig. 4 Removed route

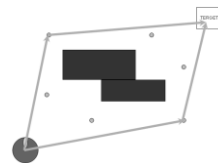


Fig. 5 Correct route

II. Course correction system

Using this system the robot corrects its path by measuring and equalizing the distance on the right and left to prevent it from crashing into a wall.

(i) The data are stored in a database.

The data are the pattern of the slope of the line on the image, and they are made and stored in database. The data are calculated from the width of the course and the CCD camera angle. The width of the course, direction of the robot, slope of the line and the distance from the center of the course are stored in the database.

(ii) Image processing

The robot acquires the image, and it is processed by edge-based binarization and noise removal. After that, straight lines are extracted, and the image is processed by the Hough transform into straight lines. This process is shown in Fig. 6.

(iii) Correcting self-position

The robot estimates its position and direction and corrects the latter by a straight line matched with the data from the database.



Original image



Noise remove



Hough transform

Fig. 6 Image processing

4.3 Experiment of system evaluation

I. Method of experiment

In order to evaluate this system, we experimented at Research building 3F of Kyushu Institute of Technology. The total distance that the robot ran was about 35m, and we verified that its systems worked successfully.

The images used in the experiment were acquired from a camera mounted on the robot. This camera was at a height of 875mm from the floor and its depression angle was 20 degrees.

II. Results of the experiment

The robot could reach the goal thanks to the successful operation of the systems. The course correction system was at work during the run. A picture of the course that the robot followed is shown in Fig. 7. This shown that robot ran in a crooked diagonal line, but the course correction system worked, so that the robot corrected the gap.

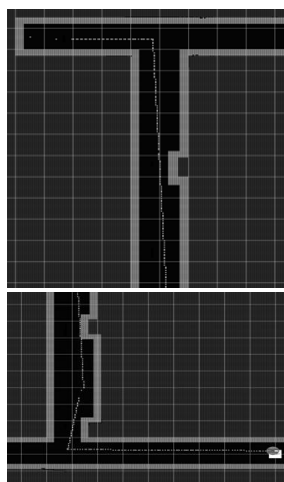


Fig. 7 Results of experiment

5. Object recognition system

5.1 Outline of the system

We developed an object recognition system for robots that can acquire the target object position with image information captured by monocular CCD camera and range information obtained by LRS. This system can acquire the object position on the assumption, for example, that the object is placed on a desk. The system then acquires the location information of the object by using LRS with the recognized object. Afterwards, the arm is driven based on the location information, and the object can be grasped and held.

5.2 Method for object recognition

In this section, we explain the method for object recognition. The flow for the object recognition is shown in Fig. 8.

I. Object recognition processing part

This processing part can search for objects with image information captured by a monocular CCD camera. The system then searches for the object with the shape and color of the object registered in the database. This processing part notes the shape and color of the object and then step by step narrows down the objects it

“sees”. Fig. 9 shows an example of the results of the object recognition processing.

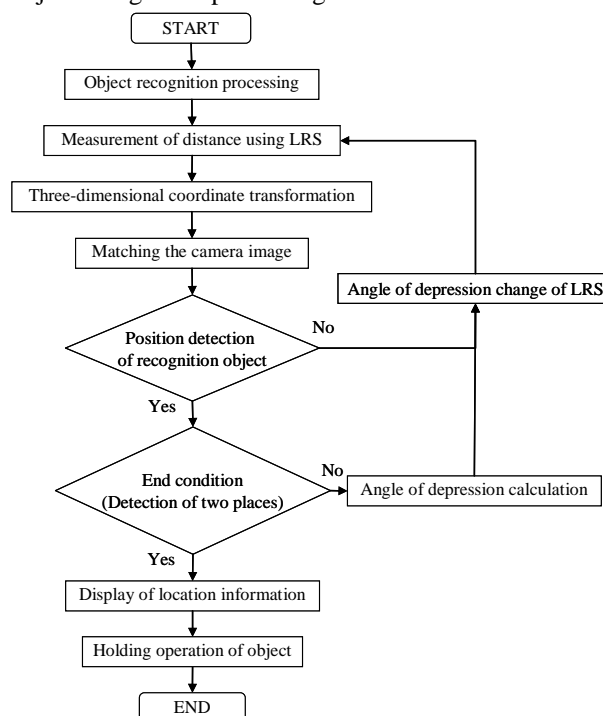


Fig. 8 Object recognition system flow



Fig. 9 Object recognition processing

II. Measurement of distance using an LRS

The LRS then acquires range information on the object recognized in the object recognition processing. The LRS is fixed to the robot head, and moves with the camera. Fig. 10 shows the situation in which the range information is acquired.

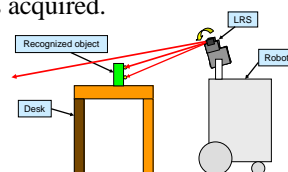


Fig. 10 Position information acquisition situation

III. Three-dimensional coordinate transformation

The range data of LRS is range information from the irradiation point to the measurement point of the LRS. Therefore, this range data is converted into three-dimensional coordinates. This conversion is derived in the provided data based on the distance data and the horizontal and perpendicular angles.

IV. Matching the camera image

The system successfully matched the LRS data to the camera image by integrating the camera image with the LRS data.

V. Position detection of recognized object

Whether the LRS data accurately describes the location information of the object was judged. This involved determining which position of the camera image provides the best measurement point for LRS to detect the object. If the object area recognized in the object recognition processing corresponds to the image coordinates of the LRS measurement point, the measurement can be considered successful. This system acquires three-dimensional coordinates in the vicinity of the center of the object as the location information, provided that the LRS measurement point is at the 60% height level, from the bottom of the object. In addition, to prevent false detection and to provide good, accurate detection, data acquisition is done in a second place in the area (below the 60% mark).

VI. Angle of depression calculation method

The system acquires location information on the object at two places (an upper part and a lower part). After the first location information is acquired in the upper part, the angle of depression of LRS is calculated according to this information. If the distance of the object and the robot can be found, the angle of depression can be calculated from the image information by a geometrical calculation.

VII. Display of location information

When the location information of the recognition object in two places can be acquired, final location information on the object is displayed in two places. Because it is preferable that the acquired positional data reflect the exact position of the object, a part in the center of the two examined places is acquired as the object location information.

VIII. Grasping operation of object

The target object is located within a certain distance (2 feet) of the robot. Target coordinates are first set in front of the object, based on the acquired object position, and the arm is driven to the coordinates. An image is acquired after the arm arrives, and the remaining drive distance of the arm is calculated from the position of the

object and the distance of the hand to the object. The arm is driven again based on the calculated driving amount, and the grasping operation of the object is performed.

5.3 Experiment of system evaluation

I. Method of experiment

We performed the following experiment to evaluate the performance of this system in the grasping operation of an object, in which it searches by object recognition processing. The angle of depression of the camera was set at 10°. Fig. 11 shows the experimental environment when the object is a PET bottle. Its location was on a single-color desk in the laboratory.

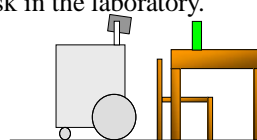


Fig. 11 Experiment environment of the target PET bottle

II. Results of experiment

Fig. 12 shows the result of the robot's actually performing the grasping operation of the target object. The target object was a PET bottle.



Fig. 12 Result of arm drive experiment

The arm was able to be driven to the location coordinates of the object, and the grasping operation by the hand was able to be performed. However, the location of the hand varied a little in relation to the location of the object. Therefore, it is necessary to improve the accuracy by which the arm is driven.

6. Conclusions

We propose a system that recognizes the driving environment of a robot using image processing and an LRS. This environmental recognition system is composed of an autonomous driving system and an object recognition system. The driving environment of the robot can be processed by these systems, and the behavior pattern of the robot can expand. At present, it is possible to move in a preselected area, and to locate and grasp a target object. Expansion of the action area and the transportation operation of the robot with the object are in our sights and will be developed in the future.

Design of robotic behavior that imitates animal consciousness — Emotion expression of robotic arm based on eyeball movement —

Kouichirou Kurogi Kei Ueyama Eiji Hayashi

*Department of Mechanical Information Science and Technology
Faculty of Computer Science and Systems Engineering, Kyushu Institute of Technology
680-4, Kawazu, Iizuka-City, Fukuoka Prefecture, Japan*

Abstract: In this research, with the aim of “user affinity”, a trial which gives a robot “consciousness” like people or an animal is performed. Here, the goal of user affinity suggests the capability for a robot to inspire a sense of closeness in the user, such that the user is not bored with its use. Our laboratory previously conceived a model of the mechanism of consciousness and action and a software architecture by which this model can be used to control the action of an artificial animal based, called the Consciousness-based Architecture (CBA). Here, we newly built a “motivation model” which assumes that certain motives inhere in the actions of an animal, and therefore ascribes to the robot the motive of action. In this motivation model, the dopamine-generating mechanism of an animal is modeled. Moreover, an eye display for the robot to simulate the expression of feelings was developed. As a first step to coherent, “conscious” expression, the speed of the blink was changed according to the motivation model.

Keywords: CBA, consciousness of the robot, Motivation of the robot

I. INTRODUCTION

In recent years, the development of non-industrial robots in such fields as medical care and welfare and for life in general has flourished. The operation of these robots requires not only the basic functions of robots, such as a high level of intellectual activity, but also the function of user compatibility or affinity so that a user can feel close to the robot as a result of its appearance and behavior. User compatibility implies that the user is easily able to operate the given robot, without getting bored with its use, and can easily develop a sense of closeness with it; ultimately, the user can receive the healing benefits experienced in relationships with other conscious beings.

Although a robot may gain in user compatibility by being genuinely modeled after a face, it is far more difficult to achieve user compatibility through its behavior and actions, including human-like “capricious behavior”. The attempt to give robots “consciousness” such as that identified in humans and animals is a part of these requirements.

Our laboratory has studied animals’ adjustments to their environments in an attempt to emulate animal behavior. We constructed a hierarchic structural model in which consciousness and behavior were hierarchically related. In regard to this, we developed a software architecture we call Consciousness-based Architecture (CBA). CBA introduces an evaluation

function for behavior selection, and controls the robot’s behavior.

In the present study, we developed a robotic arm that has six degrees of freedom, with the aim of providing the robot with the ability to autonomously adjust to a target position. Fig. 1 shows an overview of the robotic arm. The robotic arm that we used has a hand consisting of three fingers in which a small monocular WEB camera is installed. The landmark object is detected in the image acquired by the WEB camera, enabling it to perform grasping and carrying tasks. As an autonomy action experiment, CBA was applied to the robot arm and the behavior then inspected.

This research was intended to develop the “emotional” display of a robot. Thus, it paid attention to eyes, where feelings appear most easily in the expressions.



Fig.1. Overview of Robotics arm

II. SYSTEM STRUCTURE

Fig. 2 shows the appearance of the robot arm, and Fig. 3 shows its degrees of freedom. The robot arm has 7 levels of flexibility {shoulder (Joint1, Joint2), elbow (Joint3, Joint4), wrist (Joint5, Joint6), and finger (Joint7)} at its full length of 450 [mm]. The hand part has 3 fingers with one flexibility; the weight of the main part is about 0.8 kg. A small Web camera, equipped at the tip of a robot arm, can recognize the external situation. The web camera and the robot arm's actuator are controlled by USB communication.

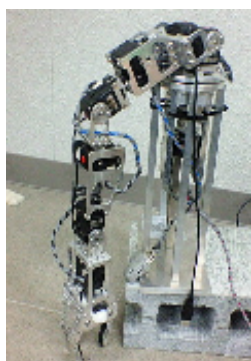


Fig. 2 robot arm

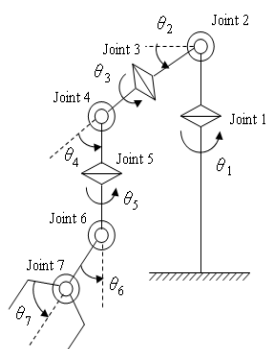


Fig. 3 degree of robot arm

III. AUTONOMOUS BEHAVIOR

1. The motivation of the robot

Most robots are pleasing to people because of their unique movements. However, the action choices of robots are too mechanical. Action choices that resemble those of human beings and animals are needed to actualize user compatibility. Therefore, we at first thought about a human action.

When an animal, including a human being, takes some action, it can be represented by a flow chart such as "Recognition → Comprehension → Motivation → Action".

On the other hand, the action of the robot repeats a simple flow such as "Recognition (Comprehension) → Action".

The flowchart of this system is shown in Fig. 4, and the details of each item are given below.

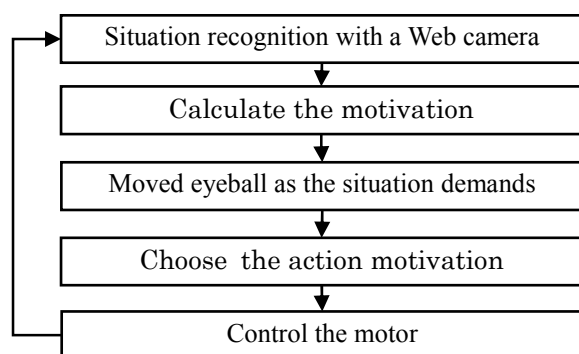


Fig. 4 Flowchart of this system

2. Situation recognition with a Web camera

The first step of the "humanized" robot's system is to recognize a situation. For this purpose we devised a labeling image which we divided into green, blue, and flesh color parts from an image of web camera installed on the robot hand. Then we divided the green, blue, and flesh color into separate blobs and extracted the shape, size, and center of gravity position. From this information and the posture of the robot arm, the robot could recognize the position and the distance of the target colored object. Furthermore, the system memorized the central point for three frames.

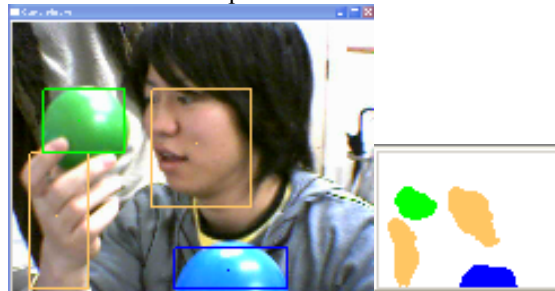


Fig.5 A Web camera image and a labeling image

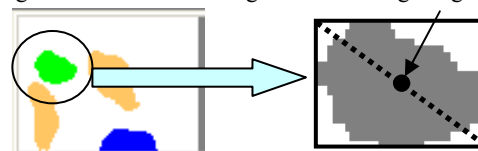


Fig.6 Central point

2-1. The objective move direction prediction

A picture is divided into eight domains in order to predict the movement direction. The movement direction is predicted only when an object is missed at the time of situation recognition. The prediction direction corresponding to the eight domains and the area as a whole is shown in Fig. 9.

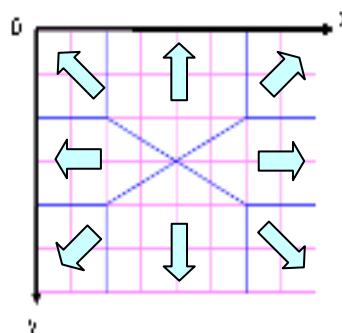


Fig.7. A division domain and the prediction direction

2-2. Virtual object creation

The virtual object corresponding to the predicted movement direction of the object is created in the visual angle. Since it is possible to pursue the object within the visual angle, a virtual object is created, and the robot runs after a real object by running after the virtual object.

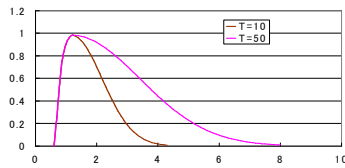
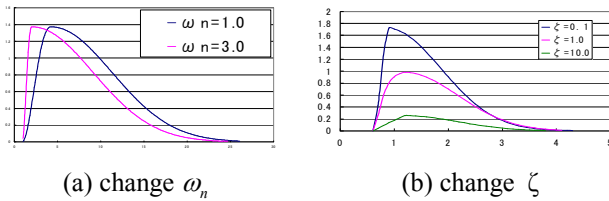
3. Calculation of dopamine and motivation based on the situation

When a man and an animal interact, changes occur in the dopamine level in the brain. The dopamine-generating locus is regarded as the robot's motivation model, and the generating locus was copied using the control model. A control model is shown below. In the graph, sample changes in ω_n, ζ and T are shown.

$$\text{Rising } y'' + 2\omega_n \zeta y' + \omega_n^2 y - \omega_n^2 u_{(t)} = 0 \cdots (1)$$

$$\text{Decaying } y = e^{-\frac{t}{T}} \cdots (2)$$

ω_n : natural angular frequency : earliness of a rising
 ζ : braking rate : height of the peak of a rising
 T : time constant : attenuation performance



(c) change T

Fig.8 Motivation model

In this study, we captured the trace of this dopamine as the motivation of the robots and termed this function the "Motivation model". Fig.9 shows this Motivation model.

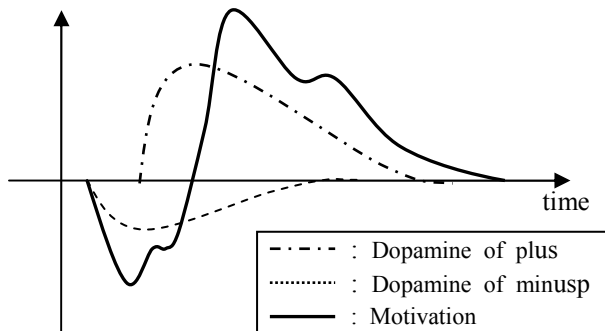


Fig.9 Motivation model

4. Choice of the action that accepted motivation

The action level was set up by dividing a robot's motivation by a fixed value. In this way, the action which can be chosen according to an action level was limited.

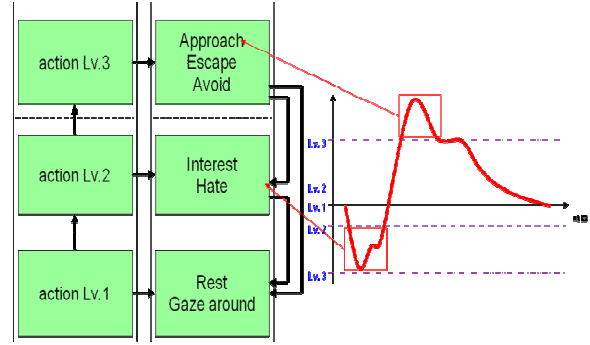


Fig. 10 Choice of the action based on motivation

5. Consciousness architecture (CBA)

Fig. 11 shows a diagram of a hierarchical structure model called CBA (Consciousness-based Architecture) which relates consciousness to behavior hierarchically. The characteristic of this model is that the consciousness field and behavior field are built separately. In a dynamic environment, this model determines the consciousness level to the environment that a robot most strongly consider, and the robot then selects the behavior corresponding to that consciousness level and performs the behavior. This model is characterized in that the consciousness level approaches an upper level so robot can select advanced behavior when certain behavior corresponding to the consciousness level is discouraged by some external environmental factor.

Additionally, an upper-level consciousness can make a choice of low-level behavior. The mechanism of this model is that it selects the optimum behavior within the low-level behaviors, so the robot aims for goals.

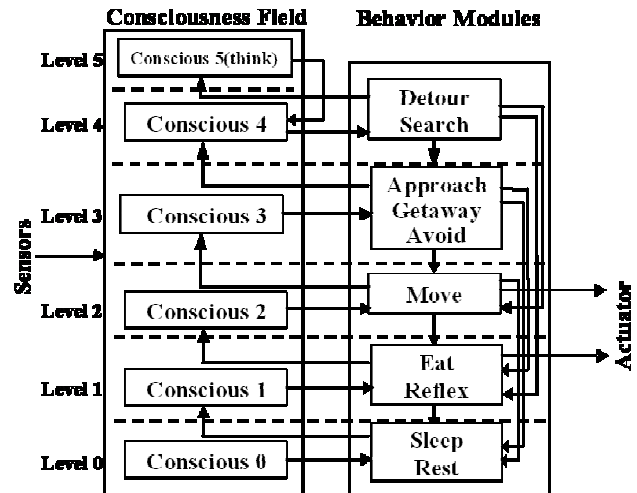


Fig.11 Consciousness-based Architecture (CBA)

IV. The eyeball system which operate in response to external conditions

Facial expression is an important factor in the role of conveying feelings. This study focuses on the eyes, which greatly influence emotional expression. A pair of eyes was made in 3-D graphics using the Open GL (Open Graphics Library). Fig. 12 shows the eye display we created.

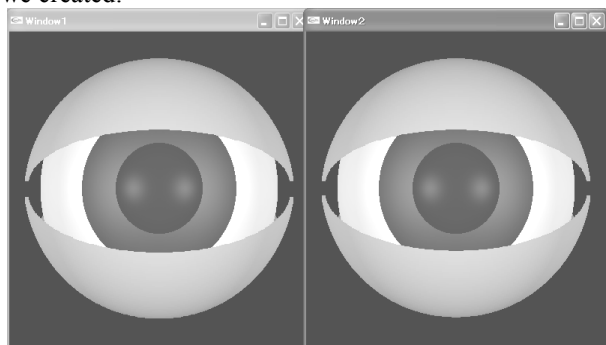


Fig.12 The eyeball created

1. The eyewink system

The study implemented the eye-blinking system found in the human eye. Blinking is among the most important expressive human eye movements. In order to imitate the actual state of mind, we measured the timing of blinks of humans in different psychological states. Fig. 13 shows the measurement result of blinking in a human.

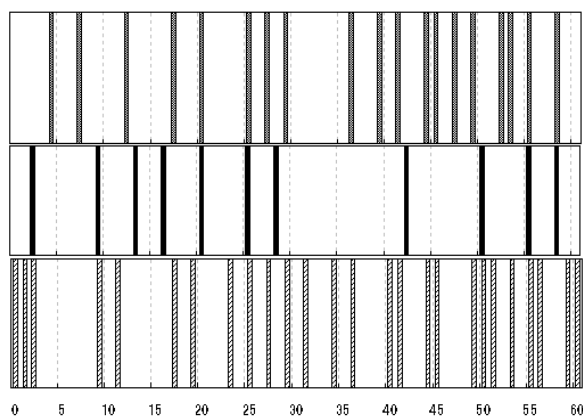


Fig.13 Measured result of the wink of human

In this figure, the horizontal axis represents one minute of time and the three timelines show the timing of blinks in different psychological states. The upper graph of Fig.13 shows the usual state. The second graph shows a state of concentration and the third graph shows a state of agitation. This result can be confirmed that eye-blinking rate is suppressed with concentration and is increased with excitation. This provides clues to a person's psychological state. Based on this result, an eye-blinking system was developed to synchronize with the robot's assigned "motivation"...

V. INSPECTION OF AUTONOMOUS BEHAVIOR

1. Validation experiment

We conducted a validation experiment to synchronize the robot arms with the eye system. The experiment confirmed whether the eye would follow a green ball when someone moved the green ball before the camera on the robot arm. Another experiment confirmed whether the number of blinks changed in response to the robot arm's motivation.

Fig. 14 shows validation results. It demonstrates that the eye operates in response to external conditions.

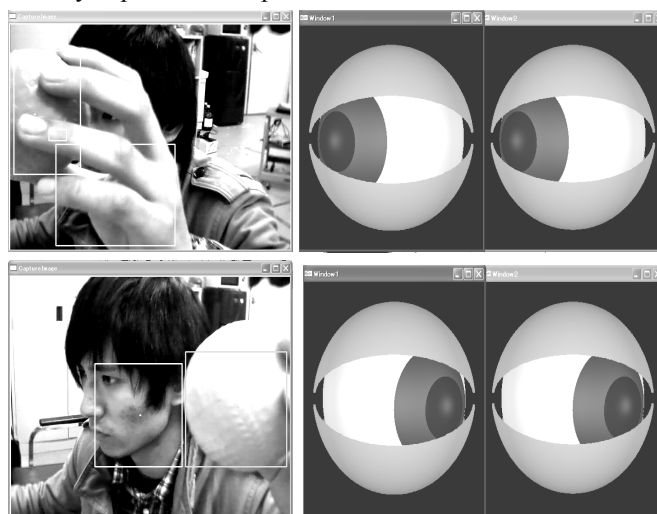


Fig.14 Validation results of the eye display system

VI. CONCLUSION

In this paper, we created the eye display of a robot arm using Open GL. It became possible to synchronize the expression depending on the situation outside.

In the future, we will try to improve the eye display system because the eyeball's movement was delayed. Although we focused on only one color of ball at present, we will expand the robot's repertoire to respond to another color in a different way; i.e., a system which performs eye movement that refuses to follow a blue ball's motion.

VIII. Acknowledgement

This research was partially supported by the Ministry of Education and Science,

Sports and Culture, Grant-in-Aid for Scientific Research, 2010.

IX. References

- [1] Motoki Shimono, Eiji Hayashi, Design of robotic behavior that imitates animal consciousness (AROB 13th ' 2008), Bepu, Oita, Japan, 2008
- [2] Takahiro Yamasaki, Eiji Hayashi, Design of robotic arm's action to imitate -the mechanism of an animal's consciousness-, (AROB 15th ' 2010), Beppu, Oita, Japan, 2010

Development and Experimental Study of a Novel Pruning Robot

S. Ueki¹⁾, H. Kawasaki²⁾, Y. Ishigure³⁾, K. Koganemaru²⁾, and Y. Mori⁴⁾

1)Toyota National Colleges of Technology, 2-1 Eiseicho, Toyota, Aichi, 471-8525

2)Gifu University, 1-1 Yanagito, Gifu, Gifu, 501-1193

3)Marutomi Seikou Co., Ltd., 3147-7 aza ikuda, kurachi, Seki, 501-3936

4)Hashima karyuu kougyou Ltd., Hashima, Gifu

Abstract: This paper presents the development progress of a timberjack-like pruning robot. The climbing principal is an imitation of the climbing approach of timberjacks in Japan. The robot's main features include having the center of its mass outside of the tree and an innovative climbing strategy fusing straight and spiral climbs. This novel design brings both lightweight and high climbing speed features to the pruning robot. We report our progress in developing the robot, focusing on straight climbing, the behavior for uneven surface, and pruning.

Keywords: Pruning Robot, Climbing Robot,

I. INTRODUCTION

The timber industry in Japan has gone into a decline because the price of timber is falling and forestry workers are rapidly aging. This has caused the dilapidation of forests, resulting in landslides following heavy rainfall and the dissolution of mountain village society. However, a pruned tree in a suitably trimmed state is worthwhile because its lumber has a beautiful surface with well-formed annual growth rings. The development of a pruning robot is important for the creation of sustainable forest management. The research and development of a pruning robot [1,2,3,4,5] has been scarce and only one commercial product was available in Japan [6]. The machine climbs a tree spirally and cuts branches using a chainsaw. This machine's weight (25 kg) and slow speed hinder it from being an optimal solution to resolve the forest crisis. A lightweight platform is required, because most of the mountains in Japan have high slopes, and transportation of a pruning robot is a demanding task. To advance the state of the art of pruning robots, we present an innovative pruning robot that locates the center of its mass outside of a tree. The wheel mechanism is designed for a hybrid climbing method, i.e., the robot is able to switch between straight and spiral climbs. This method ensures both lightweight and high climbing speed features of the robot.

In earlier paper [7], we introduced the basic design concept and described experiments with the prototype robots in detail. Moreover, hybrid climbing method have proven that the proposed pruning robot can climb up and down at high speed [8]. Here, we report our progress in developing the robot, focusing on straight climbing, the behavior for uneven surface, and pruning.

II. DEVELOPED PRUNING ROBOT

With the ultimate goal of building a lightweight pruning robot, we have developed a novel climbing method that uses no pressing or grasping mechanism but relies on the weight of the robot itself, like a Japanese traditional timberjack does when climbing a tree (Fig. 1). The timberjack uses a set of rods and ropes, which is called "Burinawa," and does not hold or grasp the tree strongly while his center of mass is located outside of the tree. That is, the timberjack can stay on the tree using own weight.



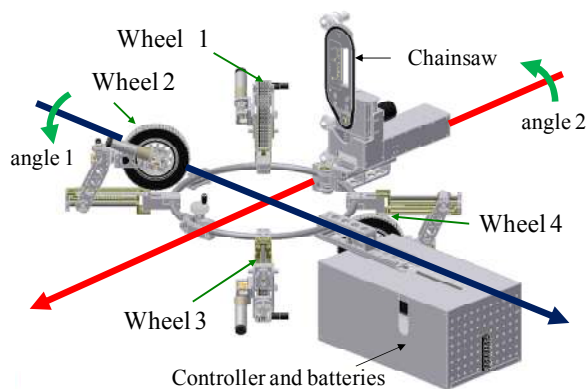
Fig. 1 Tree climbing method using "BURINAWA"

Based on this new design concept and the requirements from the forestry industry, the pruning robot has been developed. As shown in Fig. 2, the robot is equipped with four active wheels. Wheel 1 and wheel 2 are located on the upper side, and wheel 3 and wheel 4 are located on the lower side. Each wheel is driven by a DC servomotor and a worm wheel reduction mechanism which has non-back-drivability. The steering angle of

each wheel is also driven by the DC servomotor and worm wheel reduction mechanism. Based on the analysis[7,8,9], the center of mass was located outside of the tree with the help of weight of controller and batteries. The center of mass was located with margin, because the friction coefficient is unclear and the position of center of mass may be moved by disturbance. For example, the robot will be tilted when the robot climb up on uneven surface. In the Fig. 2 (a), the center of mass was located with parameter as follows: H is 0.3[m], W is 0.22[m]. As shown in Fig. 3, where, H is distance between upper side wheel and lower side wheel, W is distance between trunk surface and center of mass. The robot is robustness from the analysis when D is 0.25[m], even if the robot is tilted about 0.1[rad].



(a) Photo image



(b) CAD image

Fig. 2 3rd prototype of pruning robot

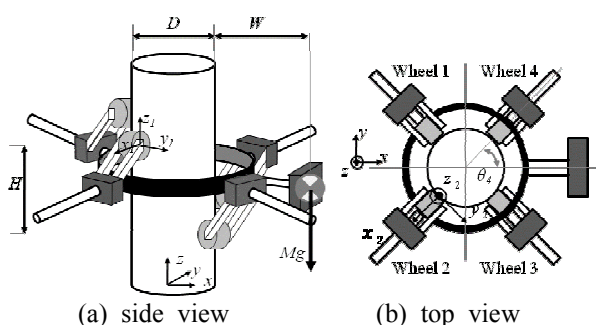


Fig. 3 3D figure of pruning robot on a tree

The controller is constructed using CPU board, which is equipped with wireless LAN. The controller is able to communicate data/command with personal computer via wireless LAN. Each wheel is controlled by velocity PI control. Feedback input, velocity through high-pass filter, is appended.

By comparison with 2nd prototype[8], 3rd prototype is lightweight expect controller and batteries. Also, controller and electrical source were located outside when the 2nd prototype. Also, the 3rd prototype is equipped with wireless LAN and a chainsaw. Although detail of the chainsaw is omitted in this paper, an experiment will be performed to show an ability of cutting branch using the 3rd prototype.

III. EXPERIMENTS

Three experiment were performed to evaluate the 3rd prototype. The 1st experiment was performed to evaluate basic performance of the 3rd prototype. The 2nd experiment was performed to evaluate the robustness for uneven surface. The 3rd experiment was performed to show whether the robot can prune a branch. All experiment were performed using substitute tree in doors. The diameter of substitute tree was 0.25[m]. The frictional coefficient of the substitute tree was about 0.4, which was smaller than natural tree. To collect the experimental data, motor current, position of the robot, and orientation of the robot were measured. The motor current was measured using shunt resistance. The position were measured by a 3-D position measurement device (OPTOTRAK, Northern Digital Co.). The orientation were measured by a 3-D orientation sensor (InertiaCube2, InterSense Inc.).

3.1 Basic performance

Straight climbing experiment was performed to evaluate basic performance. The desired speed of four wheels was given by trapezoidal profile. A acceleration was 0.2[m/s²], a speed was 0.2[m/s] as 0.075[m] of wheel radius.

The experiment result is shown in Figs. 4, 5, and 6. Fig. 4 shows the speed of the robot. The speed of each wheels was calculated from values of rotary encoder. The robot was able to be climbed up at 0.2[m/s]. Although the delay of start was about 0.5[sec] owing to control law, it was not a problem. Fig. 5 shows the movement distance. "3D" is measured value by a 3D position measurement device, and movement distance

of each wheel was calculated from value of rotary encoder. In the Fig. 5, we found three kind of error as follows: (E1) errors of movement distance between each wheel and 3D position measurement device, (E2) error between wheel 1 (or 3) and wheel 2 (or 4), (E3) error between wheel 1 and wheel 3 (and error between wheel 2 and wheel 4). We considered two reasons. The 1st reason is difference of deformation of each wheel. The movement distance of each wheel was calculated as 0.075[m] of wheel radius. The wheel was composed of urethane and inner tube, which was deformed by acting force. The deformation volume is depend on the force magnitude. From the theoretical analysis[7,8,9], the force magnitude of 3rd prototype tends toward as follows: the normal force at nearer the center of mass becomes bigger than it of opposite side. Hence, $F_{n4} = F_{n2} > F_{n3} = F_{n1}$ was considered, where F_{ni} is magnitude of normal force of wheel i . (E1) and (E2) can be explained by 1st reason. Also, we considered that reason of (E3) was slippage of wheel on the trunk. Fig. 6 shows the electric current of wheel motors that were measured by shunt resistance. The theoretical analysis[7,8,9] also has shown that the tangential force at lower side become bigger than it of upper side. Fig. 6 tends toward the theoretical analysis.

3.2 Behavior for uneven surface

To use the robot safely, the robot must be robustness for uneven trunk. The bump is caused by the growth of remnant of pruned branch. Therefore, straight climbing

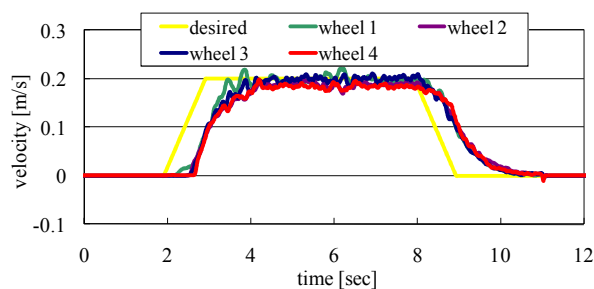


Fig. 4 Climbing speed

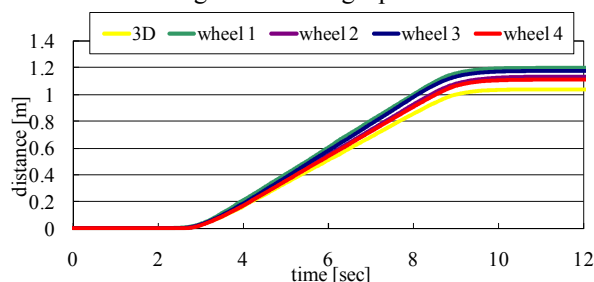


Fig. 5 Climbing distance

experiment were performed to evaluate the robustness of the developed pruning robot for bump on trunk. This experiment was performed substitute bump. The bump was made of ABS plastics, which was bigger size than natural bump. Also, the desired speed of four wheels was given by trapezoidal profile. A acceleration was 0.2[m/s²], a speed was 0.2[m/s] as 0.075[m] of wheel radius.

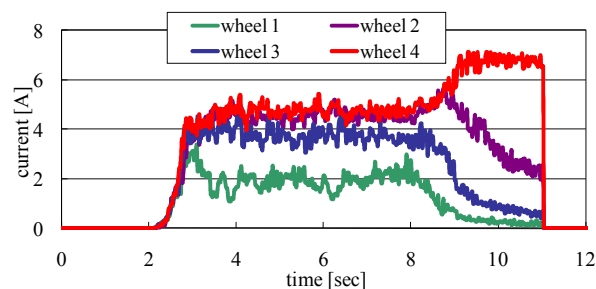
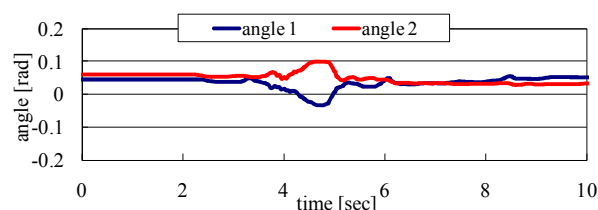
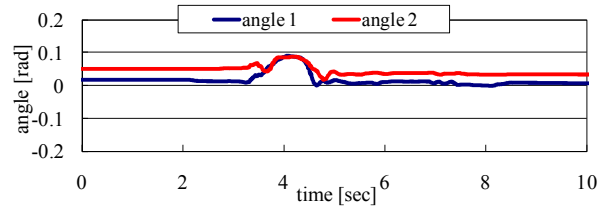


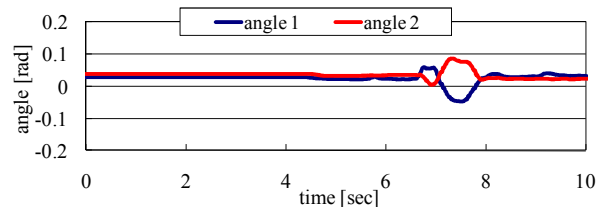
Fig. 6 Electric current of each wheel



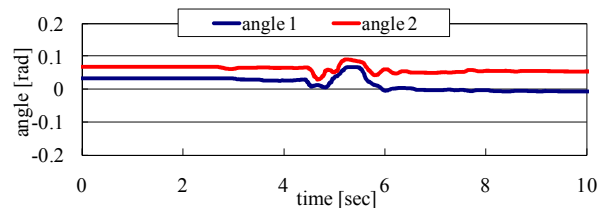
(a) Wheel 1 goes over the bump



(b) Wheel 2 goes over the bump



(c) Wheel 3 goes over the bump



(d) Wheel 4 goes over the bump

Fig. 7 Roll angle and pitch angle each case

The experimental results are shown in Figs. 7. Figs. 7 shows the trajectories of angle 1 and angle 2 (About angle 1 and 2, see in Fig. 2(b)). The angle 2 rotated toward the plus direction in all cases, that is the controller box was uplifted. This means that the center of mass moved toward the tree. Equally, the center of mass moved toward the tree when angle 1 rotates toward the plus direction. It means decreasing of the friction force to stay the robot on the tree. However, the electric currents of wheel 2 and 4 were bigger than continuous current in the experiment. Therefore, there were no danger of falling down. On the other hand, those angles were returned back to former angles, although both angle 1 and angle 2 were changed when the each wheel get over the bump. This results shows the good robustness.

3.3 Pruning Experiment

An experiment was performed to show whether the 3rd prototype can prune a branch. An attached chainsaw was driven by DC motor with 24[V] battery. The robot climbed up spirally at 0.03[m/s] speed. The diameter of target branch was 0.01[m].

The experimental scene is shown in Fig. 8. As the result, the branch was cut with short remnant, which was less than 0.005[m]. Also, the trunk was not injured.



Fig. 8 Pruning experiment with pruning robot

VI. CONCLUSION

The development progress of a timberjack-like pruning robot is presented, focusing on straight climbing, behavior for uneven surface, and pruning. The straight climbing experiment has proven enough basic performance of 3rd prototype. The experimental result of climbing up on the uneven surface has proven the good robustness for the bump, because most bumps on

the tree of afforested area is smaller than it in general. Moreover, pruning experiment has proven that the 3rd prototype can prune a branch.

In the future work, we would like to test in the real environment, and improve the robot more.

V. ACKNOWLEDGMENTS

The authors' thanks are addressed to the members of the pruning robot research project of Gifu University. This research is supported by NEDO (The New Energy and Industrial Technology Development Organization) in Japan.

REFERENCES

- [1] M. Takeuchi et al., Development of Street Tree Climbing Robot WOODY-2, Proc. of Robomec 2009, 1A2-D07, 2009 (In Japanese)
- [2] Y. Kushihashi et al., "Development of Structure of Measuring Grasping Power to Control Simplification of Tree, Climbing and Pruning Robot, Woody-1", Proc. of the 2006 JSME Conference on Robotics and Mechatronics, 2006 (in Japanese).
- [3] Y. Suga et al., "Development of Tree-climbing and Pruning Robot .WOODY- Actuator Arrangement on the End of Arms for Revolving Motion", Proc. of SI2006, p. 1267-1268, 2006 (in Japanese).
- [4] T. Yokoyama, K. Kumagai, Y. Arai, and M. Soga, "Performance Evaluation of Branches Map Building System for Pruning Robot", Proc. of the 2006 JSME Conference on Robotics and Mechatronics, 2006 (in Japanese).
- [5] T. Yamada, K. Maeda, Y. Sakaida, and T. Tamaru, "Study on a Pruning System Using Robots - Development of Prototype Units for Robots - ", Proc. of the 2005 JSME Conference on Robotics and Mechatronics, 2005 (in Japanese).
- [6] S. I. Co., <http://www.seirei.com/products/fore/b232r/ab232r.html>.
- [7] H. Kawasaki, S. Murakami, H. Kachi, and S. Ueki, "Analysis and Experiment of Novel Climbing Method", Proc. of SICE Annual Conference 2008, pp. 160-163, 2008.
- [8] H. Kawasaki, S. Murakami, K. Koganemaru, W. Chonnaramutt, Y. Ishigure, and S. Ueki, "Development of A Pruning Robot with the Use of Its Own Weight", Proc. of Clwar 2010, pp.455-463, 2010.
- [9] T. Kato, K. Koganemaru, A. Tanaka, S. Ueki, Y. Ishigure, Y. Mori, H. Kawasaki, Development of a Pruning Robot with the Use of Its Own Weight, Proc. of RSJ2010, Nagoya, 2010(in Japanese).

Design of the android robot head for stage performances

Dongwoon Choi, Dong-Wook Lee, Duk Yeon Lee, Jun Young Jung and Hogil Lee
Department of Applied Robot Technology, Korea Institute of Industrial Technology
(Tel: 81-031-8040-6317; Fax: 81-031-8040-6370)
(cdw / dwlee / proldy / paran1 / leehg@kitech.re.kr)

Abstract: In this paper, we propose an android robot head for stage performances. As you know, an android robot is one of humanoid robots but more like human. It has human like joint structures and artificial skin, so the android robot is the nearest creature to human appearance. To date, there are several android robots are developed but most of them are made for research purpose or exhibitions. We had our attention to commercial values of android robot, especially in the acting field. EveR-3, our android robot, already had commercial plays in the theater and through these; we could learn what requisite points for robot as an actor are. The new 9 D.O.F head is developed for stage performances. The D.O.F is reduced for using larger motors can make exaggerated expressions, because exaggerated expressions are more important than detail, complex expression on the stages. L.E.D lights are installed in the both cheeks to emphasize emotion expression by color exchanging like make-up. From these trials, new head is more suitable for stage performances.

Keywords: Android, robot, head, emotion, stage, performance

I. INTRODUCTION

For a long time, the main issues of robotic researches have been applications in the industrial fields, but now, the advancement of robot technology can expand applying of robots to variable fields. One of new field what we focus is the arts, in detail, area of the stage performances. Though the applications of robots to arts have been nonmainstream, some attempts have been trying continuously. TAREK M. SOBH made robot musicians to play real instruments [1]. It is very realizable application of robot on the stage, but it was more likely to automation. Some researches tried to investigate relationship between autonomous robots and intelligent environment [2] [3]. The main concerns of these researches are about interaction with human, environment and robots. Cynthia Breazeal made cyber flower and intelligent theater to study interactive effects between robot performer and audiences [4]. These works are very meaningful to know interaction of human with robots in the arts, but our interest is more likely to the commercial performances. We made Android robot EveR-3 for stage performances which has silicon skin covered face, humanoid body and movable lower body. Our first android robot EveR-1 was made for exhibitions [5] as a secretary but we find other possibility as an actor, so our recent hardware EveR-3 was made for stage performances. We already had several commercial performances and through these, we could find what requisite points for robot as an actor

were. The first point is beauty, the second is durability and the third is exaggerated expressions. Finally, we make new 9 D.O.F head which has reduced but large motors, L.E.D lights beneath the skin. This head has less expression but it can express more clearly and with L.E.D lights, it can emphasize expressions.

II. Hardware design

1. Design of the android face

In the part of making face, our goal is to make beautiful face but “beautiful” is very subjective. To solve this problem, we survey many comments of audiences who enjoyed our performances and find some important factors of beautiful face. One is the size of face. Most people consider small face as beautiful face than large one, so we should reduce the size of head. The other factor is age. The young face seems to be more beautiful than old face. From these considerations, we try to make smaller, younger face than exist one.

There are no models to our face. We designed our model by 3-D program (Cinema 4D) (Fig.1), because it is easier to make beautiful character by imagination than using a real model and our goal is commercial performance, so portrait right is very important problem. With 3-D design, we can have beautiful face freely and no problem of portrait right even if it is unreal character. After design, we made mold for real skin. The mold is made by RP (RAPID PROTOTYPING). The silicon

complex is used as skin because it is the nearest material to human skin. With 3D design and mold, we can duplicate and modification our face easily.



Fig.1 Face and 3D image

2. Mechanical part

The mechanical parts are divided an inner frame and a motor frame. The inner frame is designed by 3D CAD program (3D MAX) and its shape is based on face image (Fig.2). We use strings to pull and push the skin to make emotions. The routes of strings guided by Kevlar tubes and they are located at inner frame and the inner frame roles as connector between skin and motor frame. The inner frame is made of urethane to have strength of structure. The motor frame has 9 RC servo motors (Hs85mg, HiTec). It is bigger size than our existing hardware EveR-1's, so it can make bigger movement of skin to express exaggerated expressions. The locations of motors are decided by FACS [6] [7], but we should reduce the number of motors, because small size head, large motors and simplifying structure for durability. The D.O.F is one of important factors for durability. If there are many motors in the head, it's hard to maintain and the possibility of disorder is becoming highly. From these reasons, we choose 9 essential points and they are shown in table 1. These purposes of design brought less number of expressions, so we used L.E.D lights to emphasize the expressions to solve this problem.

Action	D.O.F
Eyelid open-close	2
Eye raise-down	1
Eye rotation	2
Chin open-close	1
Lip corner stretch-press	2
Lip stretch-press	1

Table.1 D.O.F for actions

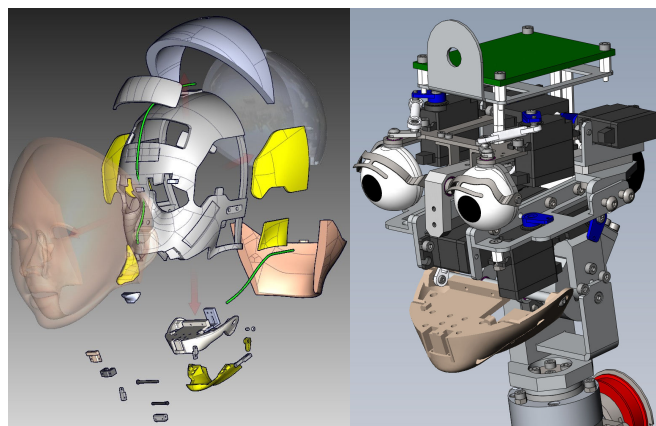


Fig. 2 Inner frame and motor frame

3. L.E.D lights

The L.E.D lights are used to emphasize emotion expression (fig.3). People often use color of skin to emphasize emotions unconsciously. When people feel shame their face become red, for example, and fear make the color of skin white. To change all colors of skin is not easy, so we choose both cheeks as the L.E.D point, because cheeks are highlight points of the face. The L.E.D lights are designed which can express all colors by combing three basic colors (red, blue, green). These L.E.D lights are made as panels and they are attached under the silicon skin. These are connected to main controller to synchronize with emotions. Though we made our efforts to use effectively, we faced one big problem. The L.E.D modules works well without skin, but when it is attached beneath the skin, it can make only red color. We can find the color of skin and penetration ratio disturbs the color of L.E.Ds. As a result, we can express only red color and our next goal is to solve this problem.

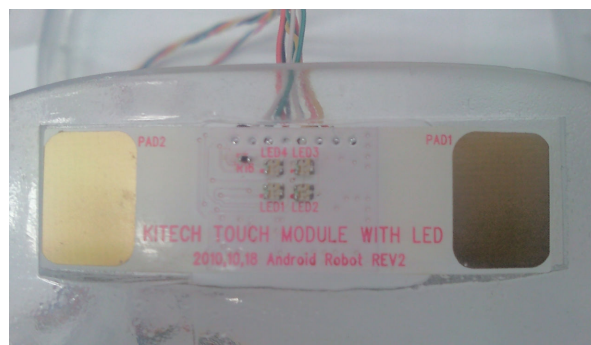


Fig. 3 L.E.D light module

III. Experiment and result

The experiment took to check 3 aims. The first is whether it can make 7 expressions (pleasure, smile, surprise, fear, pain, wink, and sorrow) or not, the second is the comparison with exaggerated expression and existing expression and the third is how L.E.D effects when it is used with expression. We attached new head to our hardware, android robot EveR-3, and make mentioned expressions. Suggested seven expressions are working well. We can also the exaggerated expressions are more clear and easy to recognize than existing ones. Of course, it is very subjective to judge the mount how much exaggerated, so we need to make kinds of standards of judgment. The comparison of two models is shown fig. 4. We also compared same expression with L.E.D and without L.E.D. All seven expressions are tested and we can verify that L.E.D lights can emphasize the emotion expression (fig. 5).



Fig. 4 The effect of exaggerated expression (surprise)



Fig.5 The L.E.D effect in same expression (smile)

IV. CONCLUSION

The 9 D.O.F android head which is made for stage performances is presented. In the stage, important factors are beauty, durability and exaggerated expressions. To satisfy these factors, we reduce D.O.F of head to make small head, use large motors and raise durability by simplifying. The problem of less expression is caused, by reducing D.O.F, so we use bigger motors to make exaggerated expression and L.E.D lights to emphasize expressions. After several experiments, we can confirm our goals and find our future works which are L.E.D problems with skin and some kinds of expression standard to judge.

Acknowledgement

This research is supported by Ministry of Culture, Sports and Tourism(MCST) and Korea Creative Content Agency(KOCCA) in the Culture Technology(CT) Research & Development Program 2010

References

- [1] TAREX M. SOBH and BEI WANG (2003), Experimental Robot Musicians. *Journal of Intelligent and Robotic Systems* 38: 197-212
- [2] Mari Velonaki and David Rye (2010), Human-Robot Interaction in a Media Art Environment. *HRI Workshop* 16-20
- [3] Kwang-Hyun Park, Kyoung Jin Kim, Sang-Rok Oh and Il Hong Suh A Miniature Robot Musical Using Roboid Studio. *HRI Workshop* 47-48
- [4] Cynthia Breazeal, Andrew Brooks, Jesse Gray, Matt Hancher, Cory Kidd, John McBean, Dan Stiehl, Joshua Strickon (2003), Interactive Robot Theater. *IROS2003*.
- [5] Taegeun Lee, Moosung Choi, Taeju Kim, Kwangung Yang (2006), Development of an Android Robot: K-1004, *CASS2006*.
- [6] P. Ekman and W. Friesen (1978), "Facial Action Coding System (FACS). A technique for the measurement of facial action," Palo Alto, CA: Consulting.
- [7] Tingfan Wu, Nicholas J. Butko, Paul Ruvulo, Marian S. Bartlett, Javier R. Movellan (2009), Learning to Make Facial Expressions. *IEEE 8TH international conference on development and learning*.

Implementation of IMU using wavelet transform and variable IIR filter

Woojin Seo¹, Bongsu Cho¹, Jaehong Lee², and Kwang Ryul Baek¹

¹*Department of Electrical Engineering, Pusan National University, Busan, Korea*

²*Hyosung Industrial Machinery, Anyang, KyeongGiDo, Korea*

(Tel : +82-51-510-1697)

(E-mail: seowoojin@gmail.com)

Abstract: Preprocessing to original signal of IMU is used for getting more reliable information. Generally, LPF(Low-Pass Filter) which has low cut-off frequency is designed to reduce noise of inertial sensors. However, in the case that an object travels with acceleration, IMU cannot determine motion of the object due to this LPF. Therefore, LPF with low phase delay has to be designed.

In this paper, suggest following algorithm to solve this problem. Design two LPF with 1Hz and 4Hz cut-off frequency. Then apply 1Hz cut-off frequency LPF at a constant velocity or stationary and 4Hz cut-off frequency LPF at acceleration. It is possible to implement IMU which has suitable response by selecting suitable filters to the conditions. Wavelet transform to angular velocities from gyroscopes can be applied to measure the characteristic of the motion. Wavelet transform suggests the way to observe the area of interest at frequency domain through multi-level decompositions. The changes of motion characteristics are measured by the detail coefficients. Detail coefficients of gyroscopes can be used to find out start and finish points of motions. Threshold value is needed to determine which characteristic the system has. This threshold value can be used to divide condition of acceleration and a constant velocity or stationary condition. The aim of this algorithm is to get reliable control information and quick response.

In this paper, used Stewart platform in order to simulate movement of an object. We compared traditional IMU and IMU applied suggested algorithm for an acceleration condition and a constant velocity or stationary condition. Suggested algorithm shows better result in acceleration. Because LPF with 4Hz cut-off frequency shows faster response due to lower phase delay at acceleration.

Keywords: IMU, robotics, artificial life, wavelet, variable filter.

I. INTRODUCTION

Today, as the advancement of MEMS (MicroElectroMechanical Systems) technology, research into systems using SDINS(Strap Down Inertial Navigation Systems) is being developed. An IMU(Inertial Measurement Units) consists of tri-axial accelerometers and tri-axial gyroscopes. The IMU is used for determination of velocity, position and attitude by integration of acceleration and angular velocity of an object. Since it relies on Newton's law of motion, sensor biases and noise are unbounded due to the integral windup. Noise from IMU affects velocity, position and attitude information. Therefore, the object has unbounded velocity, position and attitude errors.

Preprocessing to original signal is needed for reducing noise and bias to estimate position and attitude. This is for providing more reliable information. LPF(Low-Pass Filter) is generally used for preprocessing. Low cut-off frequency or high order LPF causes high phase delay. And high cut-off frequency or low order LPF causes bad frequency response. Therefore, suitable order and cut-off frequency have to be chosen.

In this paper, suggest an algorithm switching two LPF according to condition of an object. One has noise

resistance response but high phase delay. Another has quick response but sensitive response about noise. Each one is applied at stationary or constant velocity condition and acceleration condition. Wavelet transform is used for dividing motion of an object into stationary or constant velocity condition and acceleration condition.

II. ALGORITHM

It is applied to switch two LPF which have different cut-off frequency by using wavelet transform. Then, LPF which has noise resistance at stationary or constant velocity and quick response at acceleration can be designed.

1. LPF(Low Pass Filter)

IIR LPF which has 6th order and 1Hz cut-off frequency is designed to apply at stationary or constant velocity. This filter has noise resistance. IIR LPF which has 6th order and 4Hz cut-off frequency is designed to apply at acceleration. This filter has quick response.

2. Wavelet transform

Wavelet transform represents original signal by using basis function which has finite length. Basis

functions of wavelet transform are scale function called ϕ and detail function called ψ .

$$\phi_{j,k}(x) = 2^{j/2} \phi(2^j x - k) \quad (1)$$

$$\psi_{j,k}(x) = 2^{j/2} \psi(2^j x - k) \quad (2)$$

$$\int \phi(x) dx = 1$$

$$\int \psi(x) dx = 0$$

Scaling parameter is j and translation index is k . If j increases then width and height of basis function is going to be narrow and high. If k increases then basis function is going to be translated to right side.

Original function is represented by linear combination of basis function.

$$f(x) = \sum_k c_{j,k} \phi_{j,k}(x) + \sum_j \sum_k d_{j,k} \psi_{j,k}(x) \quad (3)$$

Scale coefficients are $c_{j,k}$ and detail coefficients are. They are calculated by following pyramid algorithm.

$$c_{j,k} = \langle f(x), \phi_{j,k}(x) \rangle = \sum_n h_{n-2k} c_{j+1,n} \quad (4)$$

$$d_{j,k} = \langle f(x), \psi_{j,k}(x) \rangle = \sum_n (-1)^n h_{-n+2k+1} c_{j+1,n}$$

' h ' is a transform coefficient of basis function and ' n ' is a time index of a coefficient. Original signal is scale coefficient of the highest level. And calculate scale and detail coefficient of lower level by using equation (4). Decomposition of wavelet transform is same at every level.

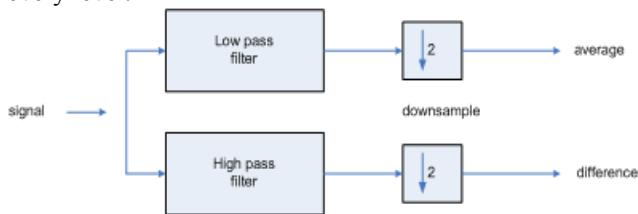


Fig.1. Decomposition of wavelet

3. Haar wavelet transform

In this paper use basis functions of Haar wavelet transform. Haar wavelet transform is easy to implement and fast to calculate. Following functions are basis functions of Haar wavelet transform.

$$\phi(x) = \begin{cases} 1, & (0 \leq x < 1) \\ 0, & (otherwise) \end{cases}$$

$$\psi(x) = \begin{cases} 1, & (0 \leq x < \frac{1}{2}) \\ -1, & (\frac{1}{2} \leq x < 1) \\ 0, & (otherwise) \end{cases} \quad (5)$$

4. Recognition of acceleration condition

Sampled data with 50 Hz frequency are applied wavelet transform. Wavelet transform of 6th level gives information that shows changes of low frequency data from gyroscope. Detail coefficient of 6th level is used for information that shows which condition the system is in. Two LPF are changed according to the condition of a system from detail coefficient of 6th level. Threshold value of detail coefficient is determined experimentally.

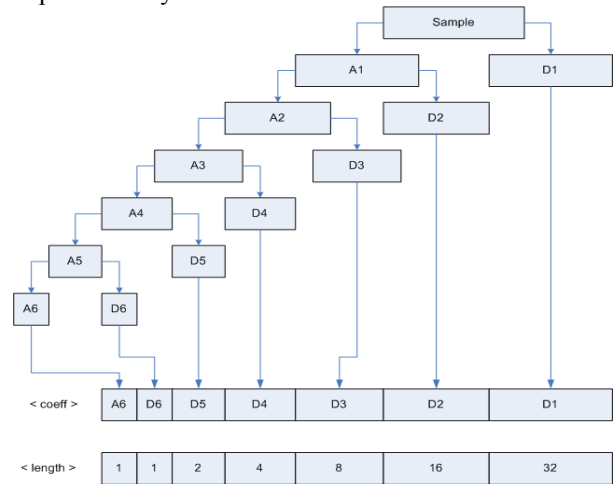


Fig.2. Decomposition of multi-level 6.

III. EXPERIMENT

A system has gyroscope, accelerometer and compass sensor. Stewart platform is used for measuring performance of suggested algorithm. In this paper use IMU made by Crista to compare with suggested system. The IMU has at most 200 Hz data output rate and 1 kHz internal A/D rate. It consists of 300 degree/s gyroscopes and 10g accelerometers at 3-axis. Stewart platform for HILS(Hardware In the Loop Simulation) is used for modeling movement of the system. Stewart platform has resolution of 0.1 degree and was proved its accuracy.

1. Component of system

A. Gyroscope

ADIS16100 gyroscope is used for measuring condition of an object. The gyroscope can measure angular velocity at most ± 300 degree/s. SPI interface is used for accessing gyroscope. Each 3 gyroscope consist of 3-axis.

B. Accelerometer

SCA3000-D01 accelerometer is used for measuring acceleration. An accelerometer can measure acceleration

of 3-axis. Maximum measurable acceleration is $\pm 2g$. SPI interface is used for accessing accelerometer.

C. Compass sensor

CMPS03 compass sensor module is used for implementation of IMU. The compass sensor is not important in this paper. This is a component of IMU.

D. Controller

TMS320F2812 32bit DPS made by Texas Instrument is used for IMU. It operates at 150 MHz frequency.

2. Result of experiment

A. External noise

In this paper supposed two situations. One is normal situation with no vibration. Another is special situation with vibration when Stewart platform moves as fast as possible. Vibration occurs at start and stop point of moving.

Table 1. Setting of situation

	Velocity [mm/s]	Acceleration [mm/s ²]	Movement (angle of roll)
Normal	48.6	50	0→30→0→30
Special	48.6	1504	Degree

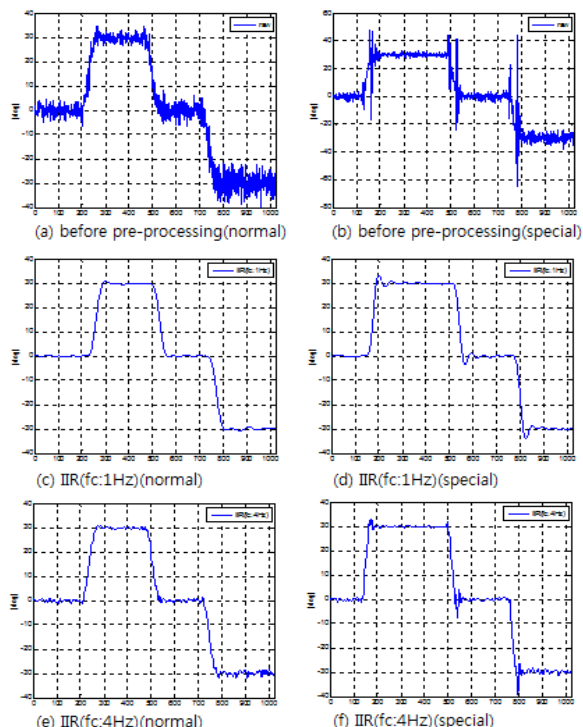


Fig.3. Comparison of 1Hz and 4Hz LPF

B. Transient section of the two conditions

Define transient section of the two conditions by applying suggested algorithm. The lowest detail

coefficient of raw data is -0.026 at a normal situation and -0.068 at a special situation. Therefore, -0.025 is applied as suitable threshold value. If IMU switches their LPF, hold for 1500 cycle of their control period.

(a) and (b) in Fig.4. show raw data from gyroscope at each situation. (c) and (d) are detail coefficient from gyroscope. Flat section appears because detail coefficient is not necessary when IMU holds their acceleration condition.

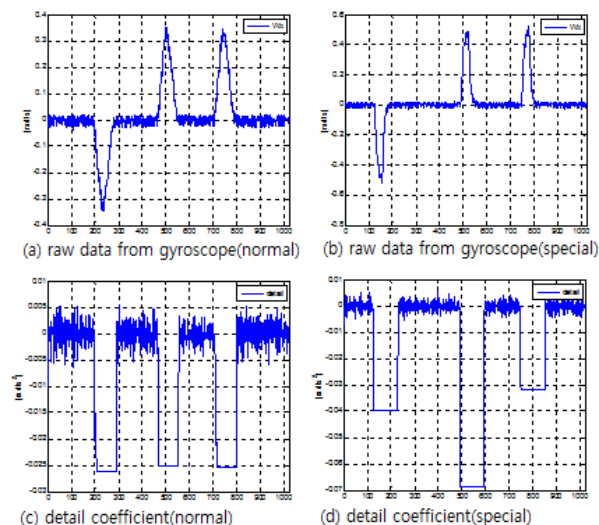


Fig.4. Transient section of the two conditions

C. Result of experiment

Fig.5. shows difference between Traditional IMU and IMU with suggested algorithm. Two IMU are almost same at normal situation. However, IMU with suggested algorithm is better at special situation. (b) shows a lot of noise at transient section. (d) shows vibration with reduced noise.

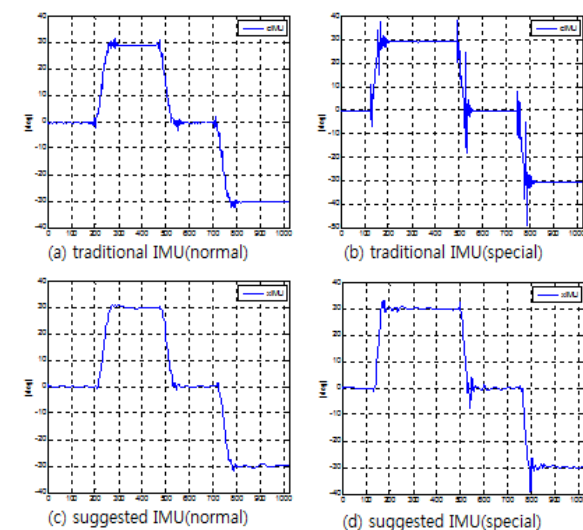


Fig.5. Comparison of the two IMU

V. CONCLUSION

In this paper, suggested IMU switching two LPF. We used data from gyroscope to improve performance of accelerometers. Detail coefficient is used for estimating condition of a system from angular velocity. The detail coefficient was calculated by using wavelet transform. Suitable LPF was chosen according to condition of a system. Then, noise of accelerometer was reduced and vibration was remained. Since inertial sensor is very sensitive to noise, reducing noise is very important at preprocessing. Furthermore, vibration has to be remained because it is very important to estimate attitude.

Stewart platform is used to estimate performance of IMU with suggested algorithm. We made static condition like stationary or constant velocity and dynamic condition like acceleration. In addition to this, vibration was added at each condition. Then, we compared traditional IMU and IMU with suggested algorithm. The result shows two IMU are almost same at stationary or constant velocity. However, IMU with suggested algorithm shows better performance at acceleration. Noise has to be removed. However, vibration doesn't have to be removed. Actually, it is very difficult to distinguish noise and vibration. Noise and vibration are high frequency area at frequency domain. Therefore, noise can be reduced by low cut-off frequency LPF at stationary or constant velocity condition because there is only noise at high frequency area. However, in acceleration condition high frequency data must be remained because vibration is important information to estimate attitude of a system.

The result of experiment shows IMU with suggested algorithm has low noise at stationary or constant velocity. It is better result than IMU with 4Hz LPF. In addition to this, IMU with suggested algorithm has quick response in acceleration. Therefore, attitude can be estimated from vibration. It is better result that IMU with 1Hz LPF. As a result IMU with suggested algorithm has low noise like 1Hz LPF and quick response like 4Hz LPF. This satisfies the aim of this paper.

This work was supported by the Grant of the Korean Ministry of Education, Science and Technology" (The Regional Core Research Program/Institute of Logistics Information Technology)

REFERENCES

- [1] Jeong Hwan Lee(2005), Chungnam National University, Design and Implementation of GPS/INS Navigation System of UAVs"
- [2] Lee Ki Seong, Chungnam National University, "The Operation System Design for Unmanned Aerial Vehicle"
- [3] D.H Titterton, J.L. Weston, American Institute of Aeronautics and Astronautics. "Strapdown Inertial Navigation Technology - Second Edition"
- [4] <http://www.koreauav.com>, "Korea Robot Aircraft Competition"
- [5] <http://www.uavcenter.com>, "UAV Center"
- [6] <http://www.cloudcaptech.com>, "Variety information of IMU"
- [7] JaeHyun Lee, Jijyun Kim, JiBin Hwang, Sung-Shick Kim(2007), Korea University, "A Study on Fault Detection of Cycle-based Signals using Wavelet Transform"
- [8] Jun-Seok Yoon(2010), Pusan National University, "Development of 6 Degree-of-Freedom Motion Table for Performance Verification of Unmanned Helicopter Flight Control Computer"
- [9] Seongmin Baek(2001), Postech, "Posture-based Motion Conversion, Evaluation and Advice System"
- [10] N.El Sheimy and S.Nassar and Aboelmagd Noureldin(2004 October) "Wavelet De-Noising for IMU Alignment" IEEE A&E SYSTEMS MAGAZINE,
- [11] Seong-Baek Kim, Seung-Yong Lee, Ji-Hun Choi, Kyong-Ho Choi, Byung-Tae Jang(2003), Tangible GIS Research Team, Spatial Information Technology center, ETRI, "Low cost IMU/DGPS Integration using Wavelet"

Development of Crawler type Rescue Robot with Slide Mechanism

Go Hirano

*Dep. of Electrical and Communication Eng.
Kinki University
11-6 Kayanomori, Iizuka, Fukuoka 820-8555
Japan
(Tel:81-948-22-5655; Fax:81-948-29-8936)
(hira@fuk.kindai.ac.jp)*

Seiji Furuno

*Dep. of Control and Information Systems Eng.
Kitakyushu National College of Technology
5-20-1 Shii, Kokuraminami-ku, Kitakyushu, Fukuoka, 802-0985
Japan
(Tel:81-93-964-7261; Fax:81-93-964-7236)
(furuno@kct.ac.jp)*

Abstract: In this paper, we develop a rescue robot that searches for the victim in the disaster scene. To go in to a narrow space in such a scene, size of the robot should be small. But the ability to pass over the trench and the rubble is important. We propose the crawler type robot which has the expandable side crawler. This mechanism can enlarge mobility of the robot by expanding the side crawler when it is necessary. And this rescue robot pass the rubble by using the side crawler as the arm. So that the swing mechanism for the side crawler is also installed. Details of the developed robot and several experiments are denoted in this paper.

Keywords: Rescue Robot, Expandable Side Crawler, Narrow Environment

I. INTRODUCTION

When the disaster such as earthquakes occurs, there might be the survivors left in collapsed buildings. The life rescue in the disaster scene has hope for 72 hours, then the survival rate after that decreases remarkably. Therefore, quick and safe rescue operation for the survivors are important. But the rescue team can not go into the rubble immediately, because there is danger of the second disaster. Moreover, it takes much time for the rescue in a narrow space where is difficult for human to enter. In such a situation, it is important to know whether the survivor is trapped in the rubble.

To search for the survivors in a narrow space in the rubble, snake-like or multi-connected robots are developed by many researchers. Mori et al developed the snake-like robot "ACM-R3" [1]. They proposed three-dimensional serpentine motion to realize omni-directional locomotion. The multi-vehicle connected crawler type rescue robot are developed [2],[3],[4]. These robots connect several units in serial so that total length of the robot is long. A turning motion in the narrow environment might become difficult for the robot with long length. The size of the robot should be small to go into a narrow space in such a scene. But the ability to pass over the trench and the rubble is important.

In this paper, we develop the rescue robot with compact body to search for the survivors trapped in a narrow space. This robot is composing four crawlers

and transformed corresponding to the environment in the rubble. We propose a novel slide mechanism. This mechanism can enlarge mobility of the robot by expanding some crawlers when it is necessary. And the swing mechanism is also installed. The robot can pass the rubble by using expandable crawlers as the arm. This paper organized into four sections. In section 2, we describe concept of the rescue robot and details of proposed mechanisms for the side crawler. The experimental results are shown in section 3. Finally, the conclusion is given in section 4.

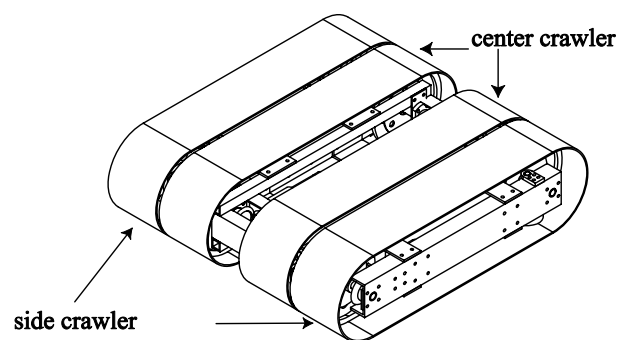


Fig.1. Rescue robot with Expandable Side Crawler

II. CONCEPT OF PROPOSED ROBOT

We consider the searching task in the narrow space of the rubble. We propose the crawler type rescue robot which has the expandable side crawlers shown in Fig.1.

Four crawlers are arranged in parallel, two crawlers fixed to the main body are called the center crawler. Other two crawlers installed in both sides are named the side crawler. Each crawler can be controlled independently. The robot moves by these driving forces in searching filed. Position of the side crawler is Fig.2 (a) usually. Under such a condition, the robot goes into the inside of the rubble and can change the direction of move on. When the robot can not move because of stack or the existence of high obstacle, the side crawler is expanded as shown in Fig.2 (b). Then the side crawler can rotate as shown in Fig.3. As a result, the side crawler can be used like the arm to improve the performance of the robot temporarily. The side crawler of the robots developed by other researchers doesn't have the slide mechanism and only have rotate one. Therefore, the space in the direction of height to rotate is necessary. Our robot expands the side crawler in parallel to the robot body direction even in a low ceiling. The total length can be freely adjusted without changing the total height of the robot.

It is possible to transform the configurations of the robot even in the narrow and tight space. The degree of freedom of the robot is eight, four degree of freedom for each crawler drive, two degree of freedom for slide mechanism and two degree of freedom for swing mechanism. The DC motors that installed in the robot drive these mechanisms. However, it is necessary to think about the center of gravity of the robot when expanding the side crawler. So as not to influence even if the position of the crawlers are change, the positions of the DC motors are arranged in symmetry as shown in Fig.4. As a result, it doesn't depend on the position of the side crawler, and the center of gravity of the robot can be located at the center of the total length at any time. We explain the mechanism, the design, and the hardware organization of the proposed rescue robot as follows.

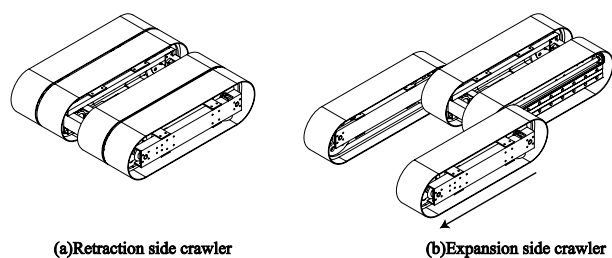


Fig.2. Slide motion of side crawler

1. Swing mechanism

The side crawler and the main body are united only with the rotation shaft. This shaft is also united with the slide mechanism. Then, the side crawler will rotate around this shaft. In this robot, two DC motors are used for crawler drive and for swing motion. And each driven mechanism is built into the inside of the side crawler. As a result, the side crawler becomes heavy. Because the robot passes over the obstacles and the rubbles, the side crawler must be maintained in arbitrary posture. Sometimes a big impact and the reaction force act on the side crawler while moving. It is necessary to consider the breakage prevention of the motor and the gear. Then, a worm gear is adopted in the swing mechanism so as not to rotate reversibly mechanically by a high reduction ratio.

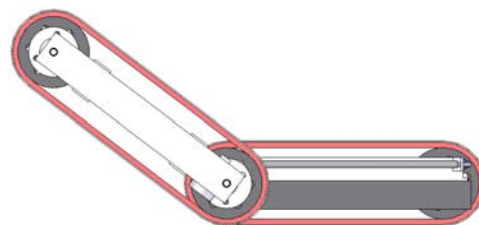


Fig.3. Swing motion of side crawler

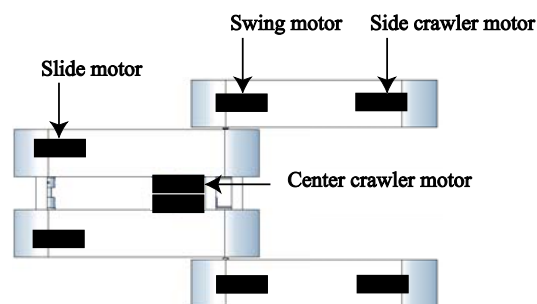


Fig.4. Installed location of DC motors

2. Slide mechanism

The side crawler moves in parallel along the center crawler. The range of movement is from the position in Fig.2 (a) to the position in Fig.2 (b). In a word, it is possible to slide only in the wheelbase length of this robot. The slide mechanism and its actuators are installed in the main body of the robot. The rotation shaft of the swing mechanism is connected with the slide mechanism. Therefore, the impact forces are applied to the slide mechanism when the robot is moving on the rubble. A linear guide is used as a slide

mechanism in consideration of these forces and moments. Weight of the side crawler, resultant force and moment that act on the rotation shaft are estimated. The trapezoid screw is used for the drive of the slide mechanism, and installed it inside of the center crawler as shown in Fig.5.

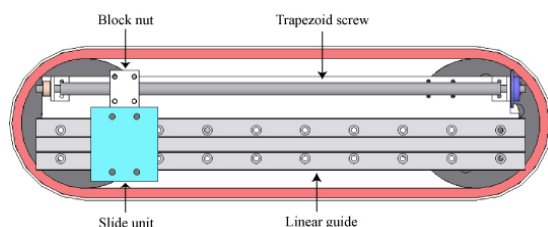


Fig.5. Arrangement of slide mechanism

3. Crawler mechanism

The crawler driven mechanism is composed of the sprocket with the chain. Two sprockets are used for each crawler, and the DC motor is installed and driven it. The aluminum boards are installed in the chain with the attachment that transmits the driven power to the ground. In addition, rubber is disregarded on the aluminum board to improve the frictional force with the field.

4. Developed Rescue Robot

The rescue robot that we developed here is shown in Fig.8 and Fig.9. Figure 8 shows the normal configuration of the robot, and Fig.9 denotes the configuration of expanded in the maximum position. This robot has eight degree of freedom and use eight DC motors. Details of the DC motor and the reduction ratio, etc. used are shown in Table 1. All the same motors are used for four crawlers. The rotary encoder is equipped in all DC motors, so that rotational speed can be measured. The turning angle speed of each crawler, the amount of the slide length and the swing angle of the side crawler can be calculated. The space is open between center crawlers of the main body, the battery, the power supply circuit, sensors and CCD camera, etc. can be built in.

Table 1. Specifications of selected DC motors

	DC motor	Gear head	encoder
swing	Amax26,12V	GP32A,66:1	MR-500
slide	RE13,12V	GP13A,17:1	MR-256
crawler	Amax26,12V	GP32A,86:1	MR-500



Fig.6. Overview of rescue robot in initial position



Fig.7. Overview of expanding side crawler

Table 2. Specifications of rescue robot

Length[mm]	444
Max. length[mm]	763
Width[mm]	408
Height[mm]	125
Weight[kg]	16

III. EXPERIMENTS

We show some experiments to confirm the mobility of the proposed rescue robot. The specifications of the developed robot are shown in Table 2.

1. Basic motions

At first, we demonstrate straight and turning motion of the robot. The straightforward motion is able to drive with stability regardless of the expansion of the side crawler. The maximum speed of the robot is 581[mm/sec], the time that finishes sliding is 24[sec] and the time to swing the side crawler up to 90[degree] is 24[sec]. However, the turning motion is unstable operation according to the condition. It is thought that friction to the road of four crawlers is large. But the

robot turns as the crawler slipping. This friction forces change depending on the contact state of the crawler and ground. The center of rotation is depending on the amount of the slide of the side crawler and the speed of each crawler. Therefore it is necessary to derive those relational expressions of the motion to do the turn operation with stability.

2. Step climbing

Next, we try to confirm the ability of the step climbing of the robot. The procedure is shown below. Here, the step height is 170[mm], and the side crawlers are shrinks at initial position.

- Step1. Move just before the step (Fig.8 (a)).
- Step2. Expand the side crawlers to the maximum position (Fig.8 (b)).
- Step3. Rotate the side crawlers until it exceeds the step, then move forward the robot and contact the side crawlers with the edge of the step (Fig.8(c)).
- Step4. Rotate the side crawlers in the opposite direction to Step2 to lifts the main body and center crawlers (Fig.8 (d)).
- Step5. Move ahead until the whole of the side crawlers get on the top of the step (Fig.8 (e)).
- Step6. Rotate the center crawler body by swing mechanism until the main body and the side crawlers become straight. Then shrink the center crawlers by expand mechanism (Fig.8 (f)).

This robot can also climb the continuous stairs as same procedure.

IV. CONCLUSION

In this paper, we develop crawler type rescue robot that has the expandable side crawlers. The main aim of this robot is to search survivors trapped in the rubble made by an earthquake or a disaster. Proposed rescue robot is designed to go into a narrow space in such a scene. Then, the side crawlers are expanded when it is necessary to enhance the mobility of the robot. Some experiments are performed, and effectiveness and the problem of this mechanism are shown. As future works, we will improve the stability at the turn running, derive the control method based on kinematics, and construct the remote control systems.

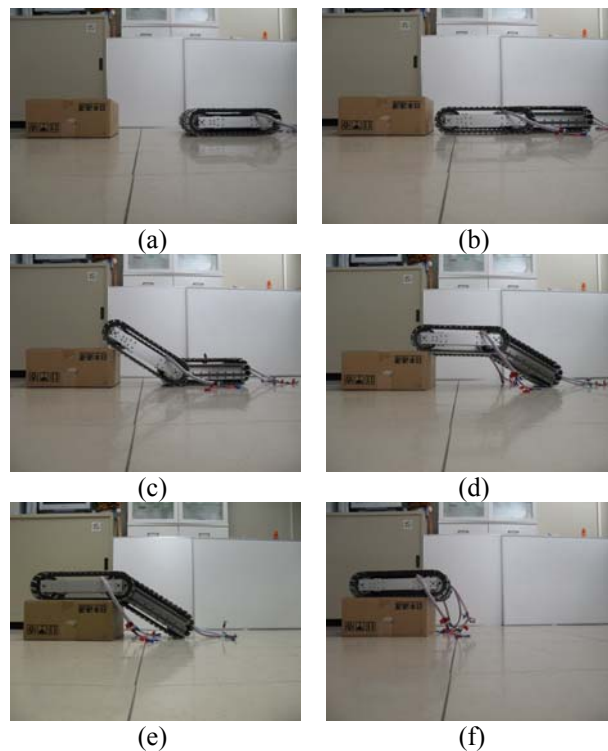


Fig.8. Experiment of step climbing motion

REFERENCES

- [1] M. Mori and S. Hirose (2002), Three-dimensional serpentine motion and lateral rolling by Active Cord Mechanism ACM-R3. Proc. of IEEE/RSJ International Conference on Intelligent Robots and Systems: 829-834
- [2] A. Masayuki, T. Takayama and S. Hirose (2004), Development of "Souryu-III":Connected Crawler Vehicle for Inspection inside Narrow and Winding Spaces. Proc. of IEEE/RSJ International Conference on Intelligent Robots and Systems: 52-57
- [3] H. Miyanaka, N. Wada, T. Kamegawa et al (2007), Development of an unit type robot "KOHGA2" with stuck avoidance ability. Proc. of IEEE International Conference on Robotics and Automation: 3877-3882
- [4] K. Osuka and H. Kitajima (2003), Development of Mobile Inspection Robot for Rescue Activities: MOIRA. Proc. of IEEE/RSJ International Conference on Intelligent Robots and Systems: 3373-3377

Proposal of Intelligence Module Type Robot that can Exchange It in Seamless

Shunta Takahashi, Kohei Miyata, Yuhki Kitazono, Lifeng Zhang, Seiichi Serikawa

Kyushu Institute of Technology, 1-1 Sensui-cho Tobata-ku Kitakyushu-shi Fukuoka 804-8550, Japan

(Tel : 090-6278-9441)

(Email takahashi@boss.ecs.kyutech.ac.jp)

Abstract: Although industrial robot has been developed well from the end of the last century, and has been well used in various fields, robotics is still being actively researched in Japan now. Chasing after national research institute, the educational institution and robot manufacturer also cost a lot of resource to develop a new generation robot. Moreover, the society gives a high expectation to robot. To provide a low price robot that can be widely used in home, in medical treatment, in welfare, and in disaster relief, etc., a high function, low cost module that can be easily exchanged for maintenance is very necessary. To achieve this aim, it is undesirable to develop the robot based on an original standard in the research institute, in the educational institution, and in the robot manufacturer, etc. separately. Therefore, a common standard in the robotic development needs to be established, and develop the robot based on the common standard. In this research, a new concept for next generation robot development is proposed. This concept contributes a higher intelligence to module, a lower manufacture cost and an easy exchange operation.

Keywords: Robot, Module, Concept, Command, Communication, Intelligence.

I. INTRODUCTION

Japan is leading the world as a country where robot is actively researched now. Robot is researched and developed in various fields such as national research institute, the educational institution and robot manufacturer now. Many of robots that has been researched and developed in Japan are industrial robots. These are still active around the manufacturing industry now^[1]. Moreover, the society gives a high expectation to robot day by day, that the robot should active in these fields which are close to our daily life such as home help, medical treatment, welfare, and disaster relief, etc, in the future. It is required that the robot composition module should be a high function, low cost, and be easily exchanged for a good maintenance ability so that it can expand the application field with a low restriction. And, to realize this aim, it is undesirable to develop the robot based on an original standard in the research institute, in the educational institution, and in the robot manufacturer, etc. separately. Therefore, a common standard in the robotic development needs to be established, and develop the robot based on the common standard^[2].

Then, as a typical research example concerning sharing the standard in the robotic development, New Energy and Industrial Technology Development Organization (NEDO)^[3] executed the project of next generation's robotic development aiming at sharing the

standard in the robotic development in 2005. The specification of the project is shown as follows.

- Robot is equipped high functional Central Processing Unit (CPU) in it and works with depending on Operating System (OS) such as Windows and Linux, etc.
- The command of the communication between robot body and module is made at the level of signal.
- Module need to be installed the middleware for the module when module is exchanged.
- Module need to be wire physically between robot body and module when module is connected.
- Module works with depending on the command of robot body.

Here, a signal-level command indicates the physical values of the distance, the speed, and weight, etc.

In this research, a new concept for next generation robot development is proposed. This concept contributes a higher intelligence to module, a lower manufacture cost and an easy exchange operation. The specification of the concept is shown as follows.

1. The robot works without depending on Operating System (OS).
2. The command of the communication between robot body and module is made at the level that human perceives and works.
3. Module has its own intelligence by equipping the microcomputer in it.

4. The communication between the robot body and the module is made wireless.
5. The module works by the unit even if it separates from the robot body.
6. The brain of the robot can be dispersed from the robot body to each module^{[4]~[6]}.

Moreover we produced a prototype robot that works simply based on the concept of 2, 3, 4, 5. As a verification experiment result, the robot worked correctly. Therefore, validity and the effectiveness of this concept were confirmed, then we described the detail following.

II. OUTLINE OF CONCEPT

This section explains the specification of the proposal concept.

A. Proposal concept 1

Because of robot body is not depending on Operating System (OS), it is possible to make the robot work even if a high-end Central Processing Unit (CPU) is not installed in the robot body. According to circumstances, it is possible to make the robot work with the one-chip microcomputer.

B. Proposal concept 2

The human perceive/act-level command is a command that uses the language, which just shows recognition and action by the robot and the module. In the communication between the robot body and the module, it is possible to correspond to a different module that has the same function by sending and receiving the human perceive-level command. Moreover, because the command is easy, the driver software need not be installed in the module.

C. Proposal concept 3

It is possible to convert the human perceive/act-level command into the signal level command by installing the microcomputer in the module.

D. Proposal concept 4

By using the wireless communication between robot body and module, it is possible to connect easily the module to the robot body by putting and changing it only.

E. Proposal concept 5

It is possible to use the module individually by separating the module from the robot body. Moreover, if necessarily, it is possible to use the module that is connected to the robot body as robot.

F. Proposal concept 6

Because the communication between the robot body

and the module is at human perceive/act-level command, the program of robot body is simple. Therefore, even if the robot body break down, it is possible to take a backup operation by using the module.

III. INTELLIGENCE MODULE TYPE ROBOT THAT CAN EXCHANGE IT IN SEAMLESS

1. Outline of intelligence module type robot that can exchange it in seamless

To be realized the concept of 2, 3, 4, 5, we produced a prototype robot that move on the line, and recognizing the object that is on the line experimentally. This robot can work correctly with depending on the same command even when we put and change the different module that has the same function on the robot body.

2. Composition of intelligence module type robot that can exchange it in seamless

The prototype robot that we produced experimentally this time is composed of the robot body, distance measurement module and movement module. As the robot body, we used small note computer. As distance measurement module, we used PSD module that is composed of infrared LED and Position Sensitive Detector (PSD) and ultrasonic module that is used ultrasonic sensor. As movement module, we used tire type line tracer and caterpillar type line tracer. The composition of the robot is shown as Fig.1. The robot body (Refer to Fig.2 (a)), distance measurement module (Refer to Fig.2 (b), (c)) and movement module (Refer to Fig.2 (d), (e)) is shown as Fig.2.

3. Communication between robot body and module

The state of the communication between robot body and module is shown as Fig.3. The communication is serial communication. The command that is the level that human perceives and works is send and received periodically. About the communication between the robot body and the distance measurement module, when robot body send the command "Measure the distance between the robot and the object" to the module, the module understand the command and measure the distance with the microcomputer that is installed in the module. After the module measure the distance, it recognizes the distance as "Near" or "Far". The result of the recognition is send to the robot body as character string. About the communication between the robot body and movement module, when the robot body send

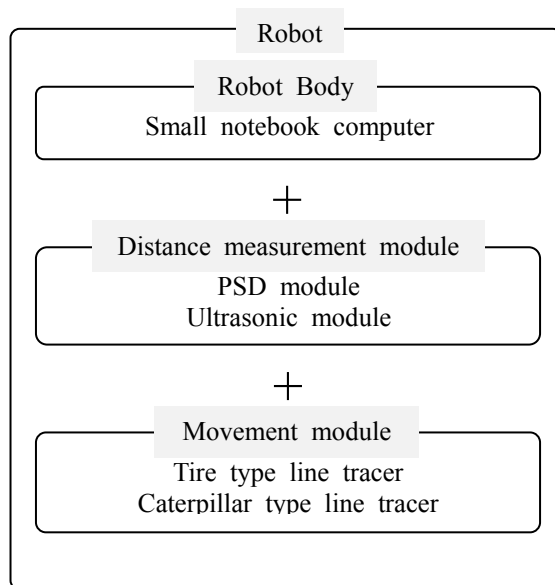


Fig.1. Composition of robot

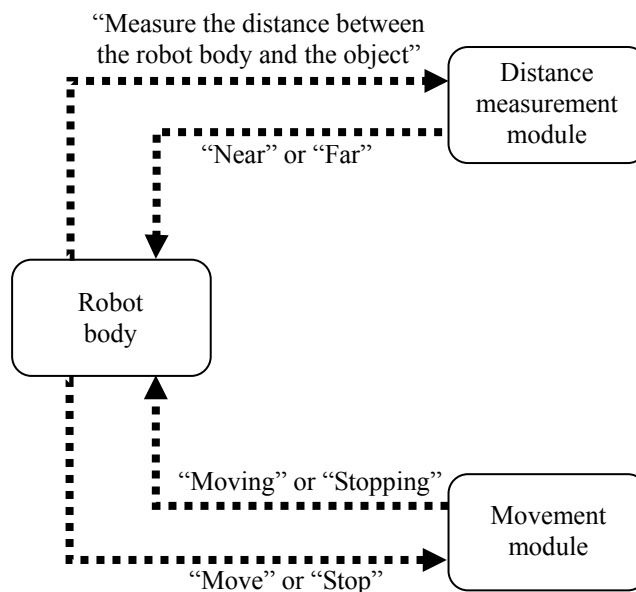


Fig.3. Communication between robot body and module



(a)Robot body



(b)PSD module



(c)Ultrasonic module



(d)Tire type line tracer



(e)Caterpillar type line tracer

Fig.2. Picture of Robot body and module

the command “Move” to the module, the module understand the command as well as distance measurement module and move on the line by the microcomputer that is installed in the module. Moreover, the module sends the state of working of the module to the robot body at the same time.

IV. EXPERIMENTS

For verification of working for the robot, a small notebook computer was equipped on the robot body to control the robot and to send the human perceive/act-level command to each module. Moreover, distance measurement module and movement module was docked to the robot body separately for the robot moving on the line.

First, the line was drawn like circle on the floor and the object was put on the line. The robot move on the line while measuring the distance with the object. After it approaches the object, it recognized the distance as “Near” and stopped on the line.

Second, the object was removed on the line. The robot recognized the distance as “Far” and moved on the line again.

Four kinds of module groups that change combination of modules (Refer to Fig.4 (A), (B), (C), (D)) are shown as Fig.4. About validation methodology of robot, the robot was worked by putting and changing the robot body into four kinds of module groups that is change combination of the distance measurement module and the movement module. Putting and changing four kinds of module groups on the robot body (Refer to Fig.4 (A), (B), (C), (D)), using the exactly same human perceive/act-level command, the robot worked correctly.



(a)PSD module and
Tire type line tracer (A)



(b)Ultrasonic module and
Tire type line tracer (B)



(c)PSD module and
Caterpillar type line tracer (C)



(d)Ultrasonic module and
Caterpillar type line tracer (D)

Fig.4. Four kinds of module groups

As a result, the robot worked correctly according to the same human perceive/act-level command even use the different module group.

V. CONCLUSIONS

In this research, a new concept for next generation

robot development is proposed. Moreover, we could experimentally produce robot that works easily based on the concept of 2, 3, 4, 5. And we could confirm that the concept of 2, 3, 4, 5 was effective.

In the future, we are going to produce robot that works easily based on the concept of 1, 2, 3, 4, 5, 6 experimentally and confirm that the concept of 1, 2, 3, 4, 5, 6 was effective.

REFERENCES

- [1] H. Asoh, et al: "Jijo-2:"An office robot that communicates and learns", IEEE Intelligent System, Vol.16, No.5, pp.46-55, SEPTEMBER/OCTOBER (2001)
- [2] Fumio Kanehiro, Kiyoshi Fujiwara, Shuuji Kajita, Kazuhito Yokoi, Kenji Kaneko, Hirohisa Hirukawa, Yoshihiko Nakamura and Katsu Yamane: "Open Architecture Humanoid Robotics Platform: OpenHRP" Journal of the Robotics Society of Japan, vol.21, No.7, pp.785-793, (2003)
- [3] NEDO, <http://www.nedo.go.jp/english/index.html>
- [4] Kenji Kaneko, Fumio Kanehiro, Shuuji Kajita, Kazuhiko Yokoyama, Kazuhiko Akachi, Toshikazu Kawasaki, Shigehiko Ota, and Takakatsu Isozumi: "Design of Prototype Humanoid Robotics Platform for HRP", In IEEE/RSJ International Conference on Intelligent Robots and Systems, pp. 2431-2436, (2002)
- [5] R. Bischoff and V. Graefe: "Integrating, Vision, Touch and Natural Language in the Control of a Situation-Oriented Behavior-Based Humanoid Robot", In IEEE International Conference on Systems, Man, and Cybernetics, pp. 999- 1004, (1999)
- [6] Fumio Kanehiro, Ikuo Mizuuchi, Kotaro Koyasako, Youhei Kakiuchi, Masayuki Inaba, and Hirochika Inoue: "Development of a Remote-Brained Humanoid for Research on Whole Body Action" In IEEE International Conference on Robotics and Automation, pp. 1302-1307, (1998)

Designing Practical Omni-directional Mobile Module in the Robot Hardware Platform for Common Use

Moosung Choi, Sulhee Lee, Byungkyu Ahn, Euncheul Shin, Kwangyoong Yang, Hongseuk Kim

Korea Institute of Industrial Technology, Ansan Korea

(Tel : 82-31-8040-6332; Fax : 82-31-8040-6399)

(moosung, leesury, bk.ahn, unchol, page365, hskim}@kitech.re.kr)

Abstract: As a holonomic omni-directional mobile robot is useful with its high mobility in a narrow or crowded area, it has been studied for a long time. But until now most of the omni-directional mobile robot developed in the laboratory level, universities and research institutes for study. Commercially available omni-directional mobile robots are mostly educational robots, toy robots, and omni-directional forklift. This study looks forward to presents commercialization of omni-directional mobile robot with many advantages and developed prototype. In this paper, we introduce the details of this progression and use it throughout the experiment and practical application proved.

Keywords: Omni-directional, Mobile robot, Practical design, Modularization

I. INTRODUCTION

Differential drive, most mobile robots are used in, have benefits such as rotation in place and simple structure, but cannot move laterally and have restrictions on the movement. Omni-directional steering mechanism can be applied to perform tasks in a small, complex environment due to the ability of 3DoF movement(front and back, left and right, rotated), which makes possible to travel in any direction from the position, in two-dimensional planar.

Omni-directional mechanism is largely divided into using a structure without omni-directional wheels and using omni-directional wheels. There are several types of omni-directional wheels like universal wheel, mecanum wheel, double wheel, alternate wheel, half wheel, orthogonal wheel, ball wheel, etc[1][2][3].

In Synchro-drive mechanism, the representatives of the structural omni-directional implementation, each wheel drives and steers at the same time. In other words, a driving motor drives all wheels and a steering motor steers all wheel-assemblies. The advantage of this structure, all wheel driving force is equal which allows excellent friction and odometry performance. Little couple relation between the driving and steering can minimize the heading error and make easier to control. And because there is no turning radius, learn to operability. Less destructive force against the floor lets high-efficient and also reduces power consumption[4][5].

The concept of the omni-directional movement, which has already been established long ago, has many

advantages, but it is a matter of practicality and there are not commercially available. In this paper, the structural simplicity, usability, scalability and modular design to move forward by suggesting consideration commonization robot platform can be used as the possibility of getting the look. In Chapter 2, design direction, simulation processes are described to explain the overall concept. The component selection process, mechanical designing are depicted in Chapter 3. In Chapter 4, the performance and specifications are verified through the experiment with a prototype.

II. CONCEPTUAL DESIGN

1. Point of Design

Products to be used can be applied to a variety of forms, and compact size, reliability, scalability and direction were the main design.

First, moving from general indoor environment, there is no problem, because you should not bad-efficient to forward the implementation of structural and slip ring in order to simplify the structure was used actively. Most existing methods of synchro-drive mobile robot with a driving axis to synchronize steer axis and the axis between the two couple to resolve the problem requires a complex mechanical mechanism[4]. Due to its complexity, this approach reduces efficiency and reliability were also problems. Low contact resistance was used as a communication line, even when there are no problems using the slip ring to allow rotation of each

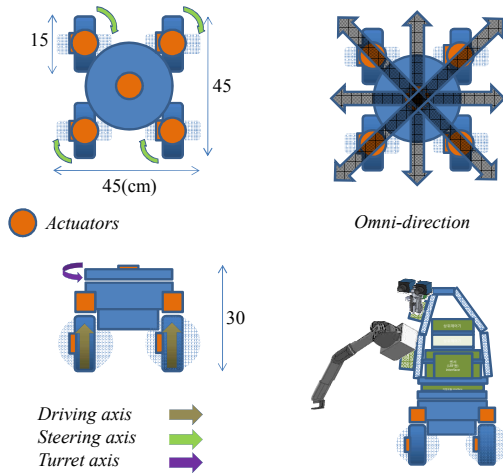


Fig.1. Conceptual Design of Omni-directional Mobile Module

axis, the infinite couple minor fixes and simplification of power delivery for each axis are available.

In addition to the scalability of the main drive sub-module a variety of sizes to accommodate the demand was for. Payload, even if a similar application area of robots to the base part may differ. In such a case the size of the base plate needed to produce the driving axis sub-module by attaching the desired shape of the omni-directional mobile base can be built.

Payload of a human scale dual arm, head, battery, 2~3kg lightweight enough to mount around the body is 65cm wide and narrow areas of the body moves without change of direction is possible, the size of a person's normal walking speed (3km/h) was faster than the speed targets. Wheel configuration hill driving or high speed and cause to stability in the face of slowing excellent 4-wheel synchronous structure was adopted as shown in Fig.1.

Homing direction for reducing time-axis turret axis absolute encoder is used. If you use the proximity sensor and because there is no absolute position in your robot, the robot may move up to 180 degrees and homing time can take a very long time.

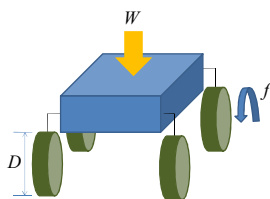


Fig.2. Basic Structure of Omni-directional Mobile Module

2. Specifications of Joints

Specifications for a driving axis are obtained as following.

$$\begin{aligned}\tau &= \tau_a + \tau_m \\ \tau_a &= \frac{J}{g} \times \pi \times \frac{f}{t} \\ &= \frac{3000kg \cdot cm}{980cm/sec^2} \cdot \frac{\pi \times 1.59rev/sec}{0.5sec} \\ &= 30.5kg \cdot cm \\ \tau_m &= \mu WD / 8 \\ &= (0.1 \times 60kg \times 20cm) / 8 = 15kg \cdot cm \\ \tau &= 45.5kg \cdot cm = 4.46N \cdot m\end{aligned}$$

,where τ_a is acceleration torque, τ_m is friction torque, moment of inertia $J = WD^2 / 8 = 60kg \times (20cm)^2 / 8 = 3000kg \cdot cm^2$, desired angular velocity $f = 1.59rev/sec$ (linear velocity 1m/sec), desired acceleration time $t = 0.5sec$, W is weight of load and D is diameter of a wheel.(Fig.2)

Joint specifications are calculated from the upper formulas like 4.46N·m, 128rpm for a driving axis, 3.5N·m, 120rpm for a steering axis, and 7.96N·m, 60rpm for a turret axis.

3. Simulation

As shown in Fig.3, a commercial simulator (RecurDyn V7R1) was used to validate the joint specification calculated from the formula in Chapter II-2. The results derive the required joint torque and the current is consumed.

Fig.4 shows the result of simulation. Besides the result of steering axis, which might be caused by the friction condition, we got the similar values to one of the formula.

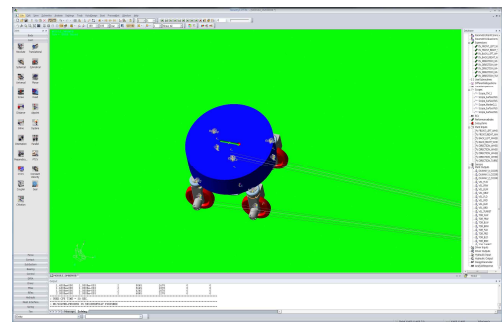


Fig.3. Simulation with RecurDyn

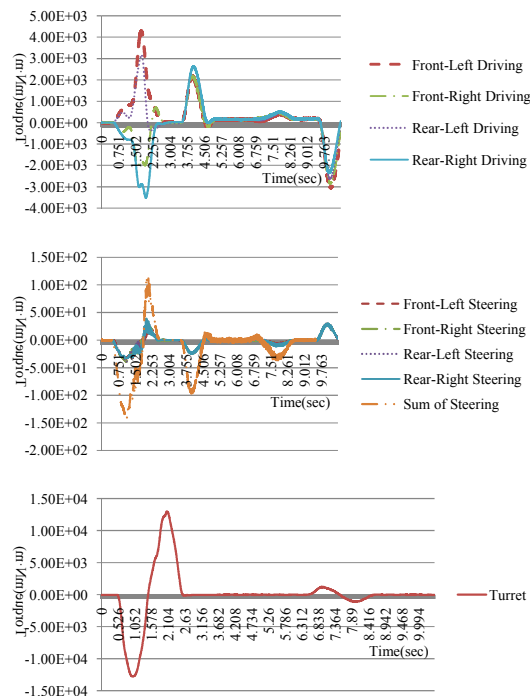


Fig.4. Results of Simulation

III. DETAILED DESIGN

1. Mechanical Design

The selection of each component was carried out on the basis of joint specification obtained from the simulation and the formula. Motors of *maxon motor Co., Ltd.* are used for the purpose of the small volume over power. For the driving axis, *EC-powermax*, which has small diameter and is BLDC-typed, is used to be mounted inside the wheel and for compact design. For the reduction gear of steering axis, a *SHD* model of *Harmonic Drive Systems Inc.* is selected, because it has lower overall height, but a little defect on the precision. For the slip ring, one of the important elements for the simplification of the structure, *630K* model of *Mercotac Inc.* is used due to relatively small contact resistance. However, for the steering axis, *SRS* model of *Rotac Inc.* is selected, because there is not enough space. The wheel made from the material of thermoplastic rubber elastomer tread is used, because there should be small friction with ground in steering, and small reaction force. The details are shown in Table 1.

CAD image of three kinds of sub-modules are shown in Fig.5. The used tool is *Solid Edge ST2*.

Table 1. Specifications of Parts

Items		Manu- facturer	Model
Actuation	Driving axis	Maxon motor, HDS	EC-powermax 30 (200W) + GP32C(66:1)
	Directing axis		EC-powermax 30 (200W) + SHD 14(50:1) + pulley(1.5:1)
	Turret axis		EC-powermax 30 (200W) + SHD 17(100:1) + pulley(1.2:1)
Slip ring	Directing axis	Rotac	SRS1802-12 (12 conductors)
	Turret axis	Mercotac	630K (6 conductors)
Wheel		Blickle	TPA 150/12K (Dia. 150mm)
Abs. encoder	For origin	US Digital	MAE3 (12bit/turn)
Motor controller		Solubot Co. Ltd.	BLDC 10A 1-axis controller (CAN interface)

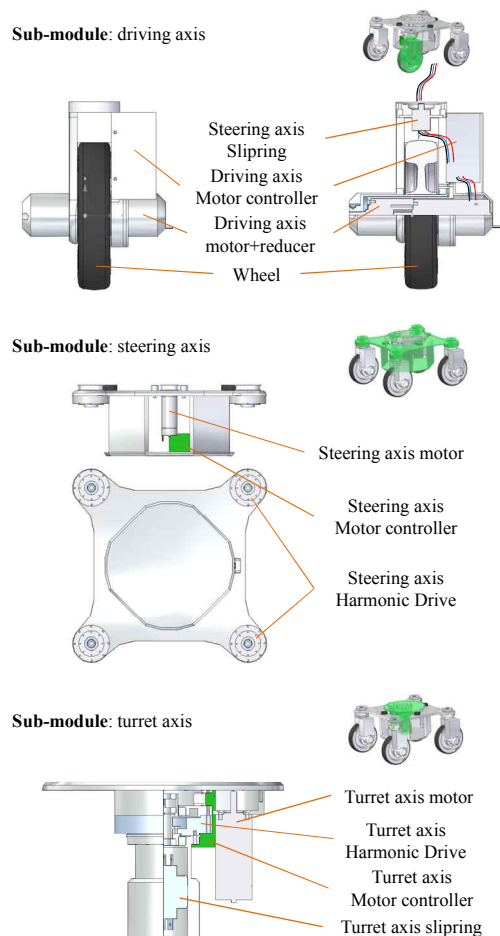


Fig.5. Sub-modules and Detailed Structure

2. Electrical Design

Components of this mobile module are divided by their functions like motion controllers, absolute encoders, IMU sensors, and so on. CAN interface and CANopen communication protocol are used for connecting with one another as shown in Fig. 6.

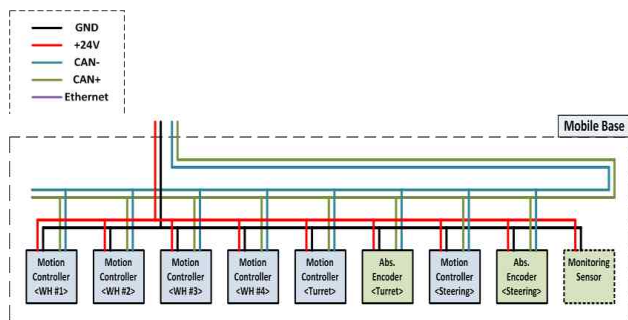


Fig.6. Electrical structure

IV. EXPERIMENT

The experiment is carried out to verify the achievement of the desired specifications in payload and velocity, which are main indicator. For the experiment of payload, the frame is mounted on the mobile module and the load, including the battery, of 50kg is added as shown in Fig.8. In this state, round trip moving test is progressed in the velocity of 1m/sec in three meters intervals like Fig.8.



Fig.7. Prototype of Omni-directional Mobile Module

Table 2. Specifications of Module

	Specifications
wheel config.	omni-directional
Max. velocity(m/sec)	1
Payload(kg)	50
Weight(kg)	16.2
Dimension(cm)	45×45×23.5
Communication	CAN

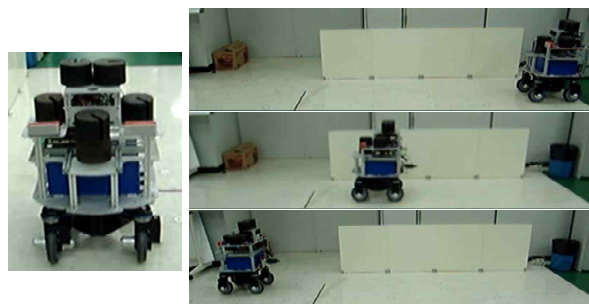


Fig.8. Payload Test of the Mobile Module

V. CONCLUSION

In this paper, a practical form of omni-directional mobile module is described in the design and prototype. It is true that the omni-directional mobile module is useful, but complex and expensive relatively to the differential drive mobile robot. However, as proposed in this paper, if the structure is simplified by using the parts helpful for simplifying aggressively and the modularization is considered for the scalability, it is possible to produce on a large scale by being able to respond to the various demands, to decrease the cost of manufacturing, and to be used widely in the end.

In the near future, the mobile module designed in this study will be used for research of robot hardware platform in common use, and should be improved for the reliability by the more experiment and complements.

REFERENCES

- [1] Kenjiro Tadakuma, Riichiro Tadakuma, Jose Berengeres (2007), Development of Holonomic Omnidirectional Vehicle with "Omni-Ball": Spherical Wheels. Proceedings of the 2007 IEEE/RSJ International Conference on Intelligent Robots and Systems:33-39
- [2] I.E. Paromtchik, H. Asama, T. Fujii, L. Endo (1999), A control system for an omnidirectional mobile robot. Proceedings of the 1999 IEEE International Conference on Control Applications:1123-1128
- [3] Giovanni Indiveri (2009), Swedish Wheeled Omnidirectional Mobile Robots: Kinematics Analysis and Control. IEEE Transactions on Robotics 25(1):164-171
- [4] Suk Hyung Jung, O Sang Kwon, Byung Soo Kim, Seung Hong Hong (1999), Local obstacle avoidance for synchro-drive mobile robot. Proceedings of the IEEE Region 10 Conference TENCN 99:1524-1527
- [5] M. Wada (2000), A synchro-caster drive system for holonomic and omnidirectional mobile robots. Industrial Electronics Society 2000:1937-1942

New Acoustic Positioning System for Under Water Robot Using Multiple Frequencies

XiuJing Gao , Feifei Zhang , Masanori Ito

(Tokyo University of Marine Science and Technology, Japan)

Abstract: Recently, positioning system for under water robot becomes a very important subject. The conventional positioning system is based on the time difference or phase lag. However, the systems are expensive and complex, and we proposed a new system using sound propagation loss. In this system, we separated the direct wave from received wave, and measure the amplitude or power of it. Using this data we calculated the distance. However, the signal accepted the influence of reflected waves, and it couldn't obtain correct distance for long distance where the direct wave can't be separated from reflected waves. In this study, we propose a new analysis method based on multiple frequencies. This method uses several different frequency sounds, and sends them sequentially. The distance can be calculated from taking the average power of received signals. The advantage of this method is not necessary of separating process, and can measure longer distance.

Keywords: Underwater Positioning, Propagation Loss, Multiple Frequencies, Direct Waves, Mixture waves

I. INTRODUCTION

In recent years, the research for the oceanic survey or development of oceanic natural resource is actively advanced. The needs of the underwater robots used for those purpose have been becoming higher and higher. For the autonomous underwater robot, positioning system is one of the important subjects to exercise their full performance. The conventional positioning system in the water is based on the time difference or phase lag of transferred sound from source to receiver. It measures the distance between moving object and station where the position has already fixed. When 3 stations are prepared, we can fix 3 dimensional coordinate of object.

However, the systems are expensive and complex. Then it is difficult to measure the position in real time and expand work area of the robot. From 2006, we are proposing a new system using sound propagation loss. In this system, the distance can be calculated using the relation between the propagation distance and sound propagation loss. In the former study, we separated the direct wave from received wave, and measured the amplitude or power of it. Using this data we calculated the distance. However, we cannot separate direct wave and reflected waves from the received signal in usual case and it couldn't obtain correct distance. Figure 1 is the simulation result with this method for 5m and 50m distance of 1m depth. Top graph shows the received waves without reflected wave. Second graph shows the received waves of 5m distance and third graph is the result of 50m. It shows that the part of direct wave is clear in case of short distance, but in case of long

distance, the reflected wave appears at the first stage of received wave.

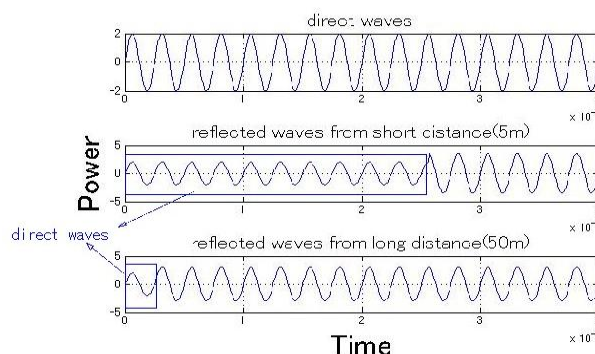


Fig.1 Simulation Results for Propagation of Sound Wave

In that case, the distinction and the separation of the direct wave from the received wave are impossible. So, in this study, we paid attention to the reflected waves, and used them actively in the data analysis. In this system, instead of the single-frequency sound, we use several different frequency sounds, and send them sequentially. In the step of data-analysis, we use mixed wave which contains direct wave and reflected wave, and take the average power of received wave. This signal is used to calculating the distance. The performance of this method was proved with simulation and experiment. The advantage of this method is that it can measure longer distance.

II. Experimental system

It is called propagation loss that the sound pressure level damps depending on a distance when a sound

propagates in the water/air. The relations of the propagation loss PL[dB] and propagation distance R[m] can be presented as follows.

$$PL = 20 \times \log_{10}(R) + \alpha \times R \quad (1)$$

Here, loss coefficient α [dB/m] is calculated with SOAP equation as follows

$$\alpha = \frac{0.11 \times f^2}{1 + f^2} + \frac{44 \times f^2}{4100 + f^2} + 3 \times 10^{-4} \times f^2 \quad (2)$$

On the other hand, in this system, PL can be calculated with

$$PL = 20 \log_{10}(T_v R_v) + T_g + T_s + R_s + R_g \quad (3)$$

The parameters are defined as follows:

T_v [V] : Transmitted signal voltage

R_v [V] : Received signal voltage

T_g [dB] : Transmission gain

R_g [dB] : Reception gain

T_s [dB] : Transmission sensitivity

R_s [dB] : Reception sensitivity

It is clear that the propagation distance R can be calculated from the transmitted and received signal (T_v and R_v).

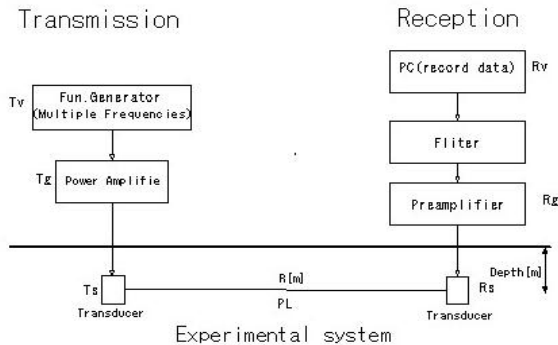


Fig.2 Experimental System

Figure 2 shows the experimental system. The transmitting unit consists of a function generator to generate the multiple frequencies sounds with same voltage of T_v , a power amp to amplify the level of the signal with gain T_g and transducer to transmit the signal into the water with the sensitivity of T_s . The receiving unit consists of a transducer to catch the signal with receiving sensitivity of R_s , a pre-amplifier to amplify the received signal to a necessary level, a band-pass filter to clearing the noises and a computer to record the data.

III. Simulation and Experiment

1. Simulation

Before experiments, we made simulation study for the decision of sound frequency.

At the condition of constant depth and propagation distance, we suppose the amplitude of each transmitting wave is 3[v], the amplitude of the direct waves at the receiver is 2[v] and the amplitude of the delayed and reflected waves is setting by random, and we examined about each received signal.

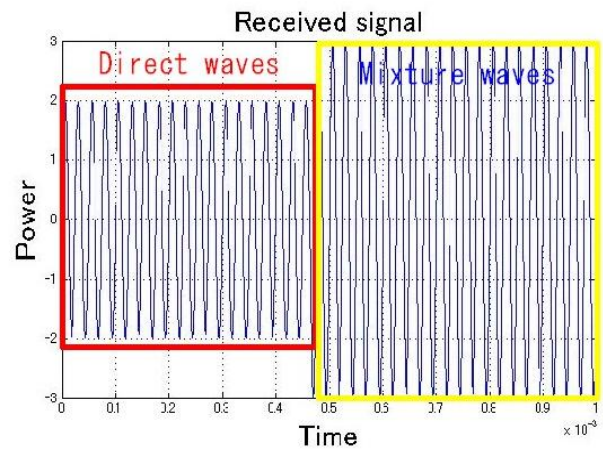


Fig.3 Received Signal (40 kHz)

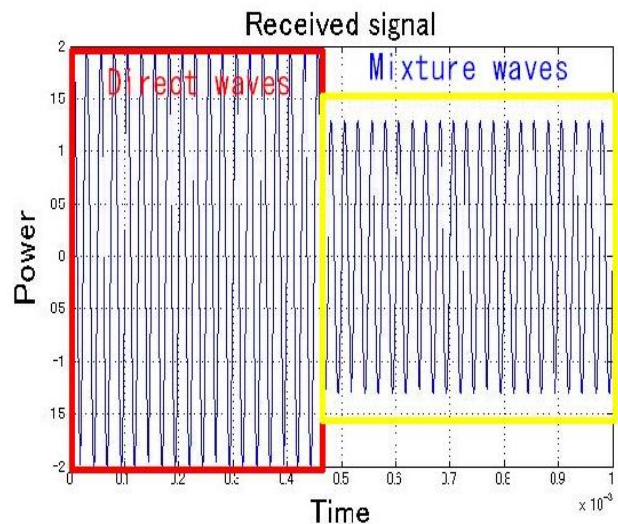


Fig.4 Received Signal (38 kHz)

Figure 3 and figure 4 show the received signals when the depth is 1[m] and the propagation distance is 3[m].

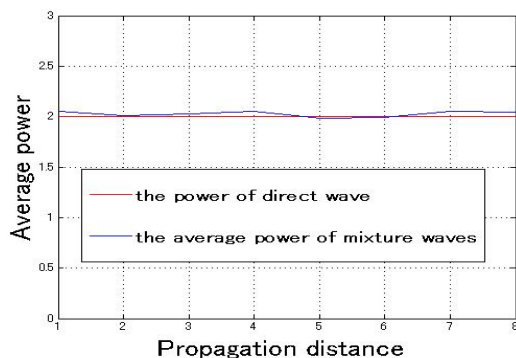


Fig.5 Comparison of Powers (1)

Figure 5 is the results of simulation with changing the propagation distance at same depth. It shows that the power of direct waves and average power of the mixed waves are nearly equal on every propagation distance.

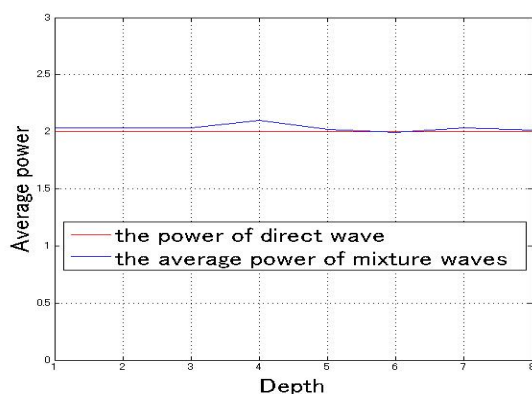


Fig.6 Comparison of Powers (2)

Figure 6 is the results of simulation with changing the depth of transmitter and receiver at same depth under same propagation distance. It shows that, at the same propagation distance, the power of the direct waves and average power of the mixed waves are also nearly equal with changing the depth of the transmitter and receiver who are at the same depth.

The results say that the level of received wave changes because of the change of phase lag depending on the frequency of transmitted wave. However, when we used multiple frequencies of 40kHz, 39kHz, 38kHz, 37kHz, 36kHz, 35kHz, 34kHz, 33kHz and 32kHz as transmission signals, the average level of their received signal is corresponding to the level of received signal of the direct waves. And there exist many groups of frequency that shows such kind of characteristics. So, we can decide the useful combination of frequency with the simulation.

IV. Experiment and Results

2.1 Experiment



Fig.7 Water Tank in TUMSAT

We made the experiments in the water tank in TUMSAT which has the size of 10m(W)×50m(L)×2m(D) as showed in Fig. 7.

All instruments are put on the moving train. We put down the transducer for transmitting sound into the water at depth of 1m and fixed it at center axis of the water tank (Equidistance from both side wall: 5m) with a crane. The transducer for reception is put into the water at depth of 1m and fixed on moving train. We moved the train with every 1m to change the distance between transmitter and receiver.

2.2 Results

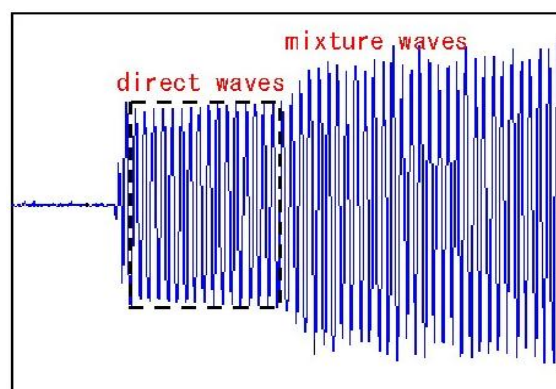


Fig.8 Example of Received Wave

Figure 8 shows a example of received wave. The first part of this wave is direct wave which is arrived firstly. The following part is mixed wave that contains direct wave and reflected wave. In this study, the received

signal is measured with taking the average of power gained through FFT to mixed signal.

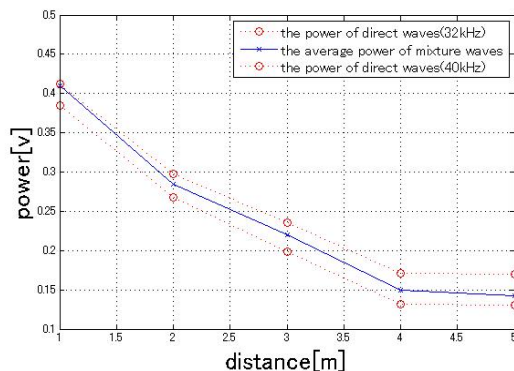


Fig.9 Comparison of Power for Received Waves

Figure 9 shows the results measured the power of received wave from direct wave of single frequency (32 kHz and 40 kHz) and average of the mixed wave of multiple frequencies for 1 to 5m distances. There exists no clear difference.

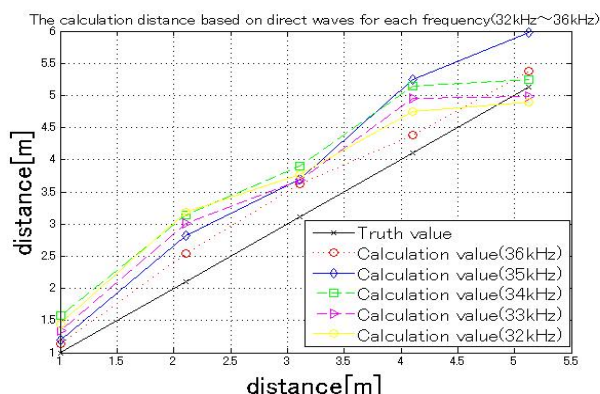


Fig.10 Calculated Distance Based on Direct Waves of Each Frequency (32kHz~36kHz)

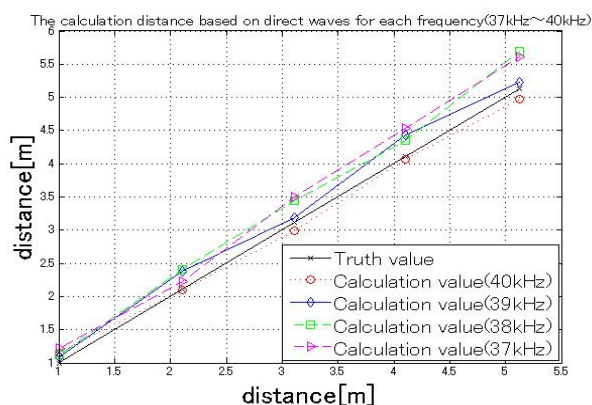


Fig.11 Calculated Distance Based on Direct Waves of Each Frequency (37kHz~40kHz)

Figure 10 and 11 show the distance calculated by the conventional method that uses the power of the direct wave from received signal. In these results, the influence of reflected waves appears clearly and the accuracy becomes not stable.

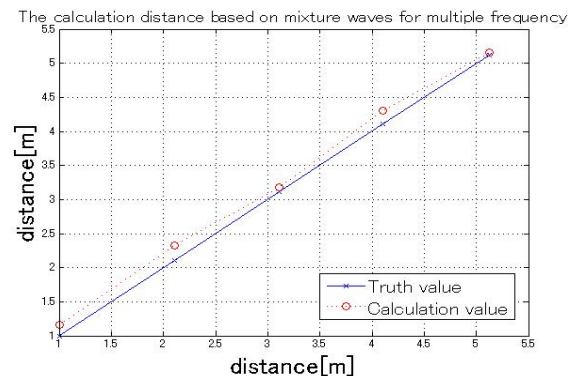


Fig.12 Calculated Distance Based On Mixed Waves of Multiple Frequency

On the other hand, we show the distance calculated from average power of the mixed wave that contains the direct wave and the reflected wave in Fig. 12. Comparing those results, we can say that new method has higher accuracy than conventional method.

V. Conclusion

- (1) In this study, we propose a new method to get the collect distance that is transmitting several frequency wave and taking average of power including direct and reflected wave from received signal. We confirmed the availability and performance of this method with experiment and simulation.
- (2) As the next tasks, we will make a experiment in the real sea area for long distance and prove the practicality of this method.
- (3) On the basis of this method, we will construct a sensor network system and establish real time positioning system for underwater robot.

References

- [1] The Marine Acoustics Society of Japan, Fundamentals and Applications of Marine Acoustics, Seizando 2004
- [2] Yosikawa, Fluid Acoustics of Sound Source, Tokyo: korona, 2007
- [3] FuBin, A New Positioning System for Under Water Based on Sound Propagation Loss and Sensor Network, 2008

Development of under water use humanoid robot

Yunyi Li, Eturo Shimizu, Masanori Ito

Tokyo University of Marine Science and Technology

2-1-6, Ecchujima, Koto-ku, Tokyo, Japan

(Tele: 03-5245-7300-8756 Fax: 03-5245-7300-8756)

(iamliyunyi2000@yahoo.co.jp, shimizu@e.kaiyodai.ac.jp, itom@kaiyodai.ac.jp,)

Abstract: In this research, we have developed a swimming robot with flutter kick of two legs, which can swim freely both on the surface of water and in the water, and established the control method for all kinds of motion of this robot, we considered a dynamic model of undulatory fins and it has been used to construct the dynamic model of propulsion and control system and analyze its motion velocity, and propulsion efficiency. We proposed and designed the corresponding control algorithms to generate appropriate thrust force and to decrease disadvantageous influences of the interference of flutter kick. We can realize free posture control and get various motion forms.

Keywords: Humanoid, Underwater Robot

I. INTRODUCTION

With the great development of science, the robot technology has been experiencing rapid advancement. As the intercrossed subject of under water engineering and robot technology, under water robots are among current interest all over the world. However the research on underwater humanoid robot has not been particularly investigated. The authors think that the humanoid type underwater robot is convenient for underwater works as on the ground. The underwater environment is so dangerous for human, that many kinds of robot have been extensively used for underwater work, such as underwater resources exploration, oceanographic mapping, undersea wreckage salvage, ocean engineering survey, dam security inspection, and so on. However, there has been no underwater robot, which can take the place of the diver by now. Considering those situations, the authors are putting the focus on developing Underwater Humanoid Robot.

II. DESIGN OF ROBOT

In this section, we briefly present a design of underwater humanoid robot prototype, describing its propulsive mechanism and mechatronics design.

As illustrated in Fig.1, the propulsive structure treated here is a free-swimming humanoid robot. It is composed of three parts: a body with two arms and two legs. Each of the legs is composed of two links and one

oscillating fin. The robot is wearing a waterproof suit on the body. And it is designed to get neutral buoyancy also. The neutral buoyancy is the condition that the gravity equal to buoyancy. And the center of buoyancy and gravity are arranged to be collinear along the body z-axis.

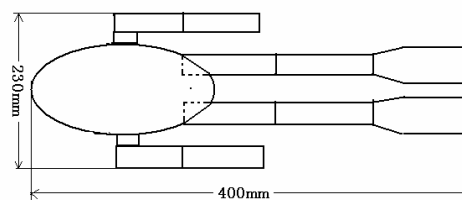


Fig.1 Image of Underwater Humanoid Robot



Fig.2 Underwater Humanoid Robot

Fig. 2 shows prototype of radio-controlled underwater humanoid robot. The body of the robot is wrapped with gum. In the body, following devices are installed in a water shielded package. 1)Microcontroller board: Motion Greater for TTL and PS/2 Bluetooth controller, 2)Communication devices: Parani ESD-200 Bluetooth Serial Adapter, 3)Arm servo motors,

4)Batteries and 5)Underwater camera. The total weight is approximately 1.5 kg. And the length is 400mm. We can control the swim of robot with wireless communication. Its speed is adjusted with frequency and amplitude of oscillating signal, and its turning motion is controlled with arm motion.

III.MOTION ANALYSIS

In this section, the authors built the dynamic model on the basis of undulated fins and the drag model in fluid mechanics. The dynamic model of undulated fins can make clear the relation between the forces/moments and propulsive wave parameters, geometric parameters as well as swimming velocity. We can study about the motion of the robot, control method and efficiency of propulsion. This dynamic model for undulated fin has been validated with experimental tests in thrust, and propulsive velocity of the underwater robot.

1. Forces on the system

Given the composition of this robot, the set of external forces on this robot is lift and drag from the legs, lift and drag from the body, lift and drag from the arms, the force of buoyancy, the force of gravity, and the moments resulting from these forces. These forces are shown in Fig.3.

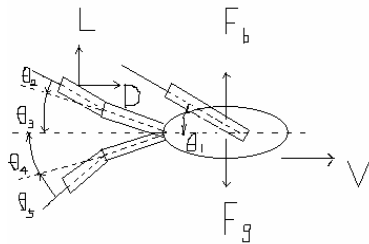


Fig.3 modeled forces

2. Unforced equations of motion

The position and orientation of the body segment of the robot are denote by g which can be written in homogeneous matrix notation as

$$g = \begin{bmatrix} R & x \\ 0 & 1 \end{bmatrix} \quad (1)$$

Where R is the orientation of the body, and x is the position of center of mass of the body, both relative to a fixed inertial reference frame .the longitudinal axis of

the body is taken to be x axis, the lateral axis is to be y axis, and z axis to be positive upward. The body-fixed translational and angular velocities are denoted by the vectors V and Ω . The velocity of the body is given by

$$\begin{aligned} \dot{R} &= R\hat{\Omega} \\ \dot{x} &= RV \end{aligned}$$

$$\hat{\Omega} = \begin{bmatrix} 0 & -\omega_3 & -\omega_2 \\ \omega_3 & 0 & -\omega_1 \\ -\omega_2 & \omega_1 & 0 \end{bmatrix} \quad (2)$$

where ω_i is the joint angular rotation rate.

In order to calculate the moment of inertia and added mass simplicity, we approximating the body as an ellipsoid, the arms and legs as columns.

3. Potential forces

The robot is assumed to be neutral buoyancy with centers of buoyancy and gravity that are noncoincident but are collocates along an axis parallel to the z axis. By the effect of gravity and buoyancy we can get a torque.

$$\begin{aligned} T &= -\frac{1}{2}m\gamma R^T k \times r_b \\ k &= [0 \quad 0 \quad -1]^T \\ r_b &= [0 \quad 0 \quad h]^T \end{aligned} \quad (3)$$

here γ is the magnitude of the gravitational force, h is length from the center of mass to the center of buoyancy.

4. Forces on legs

To simulate the dynamics of the swimming, we simply considered an equation of force with flutter kick. It includes the lift and drag on the legs.

$$\begin{aligned} L &= \frac{1}{2} \rho c_l A (v_1^2 + v_2^2) \cos\left(\frac{\pi}{2} - \psi\right) \\ D &= \frac{1}{2} \rho c_d A (v_1^2 + v_2^2) \sin\left(\frac{\pi}{2} - \psi\right) \end{aligned} \quad (4)$$

where L is Lift force, D is Drag force, ρ is density of fluid, c_l and c_d are the lift and drag coefficients, A is the planform area of the leg in the x - y plane, v_1 is tangential velocity, v_2 is normal velocity, ψ is the angle between leg and body. As the influences of the interference of flutter kick is very complex, we use the approximation and calculate under ideal condition in this paper.

5. Forces on the body and arms

We assume the shape of body is not plate but a n ellipsoid, and then the resistance force on the body is assumed to be generated in the usual steady flow. Under this assumption, the drag and lift force becomes as follows

$$\begin{aligned} D_b &= \frac{1}{2} c_{db} \alpha \rho S v^2 \\ D_a &= \frac{1}{2} c_{da} (\alpha + \theta) \rho S v^2 \\ L_b &= \frac{1}{2} c_{lb} \alpha \rho S v^2 \\ L_a &= \frac{1}{2} c_{la} (\alpha + \theta) \rho S v^2 \end{aligned} \quad (5)$$

where v is velocity of the body, c_{Db} and c_{Da} are the drag coefficients of the body and arms, c_{lb} and c_{la} are the lift coefficients of the body arms, α is attack angle, s is projected area of body in the y - z plane, θ is the angle between body and arms.

6. Force Equations of motion

For systems such as this one where forces on the system are independent of the body position and orientation, Lagrange equation can be used to describe the system dynamics. A mechanical system of the type considered here can be described by the states of the body g , termed group states, in combination with the values of the states that describe the relative placement of moving components to the body, denoted R and termed the shape states. The shape state states R are the joint angles of legs and arms.

The Lagrangian for this robot with states r, g, \dot{r}, \dot{g} can be written as

$$\begin{aligned} L(r, g, \dot{r}, \dot{g}) &= \frac{1}{2} \begin{bmatrix} \dot{r} & \dot{g} \end{bmatrix} M(r, g) \begin{bmatrix} \dot{r} \\ \dot{g} \end{bmatrix} - U(r, g) \\ r &= \begin{bmatrix} \theta_1 \\ \theta_2 \\ \theta_3 \end{bmatrix} \end{aligned} \quad (6)$$

Where $U(r, g)$ is potential energy, and V and M correspond to the body-fixed velocity and mass matrix in the robot system. r is the matrix of the joint angles of arms and legs.

IV. CONTROL

In order to evaluate the validity of the model in the previous section to actual robot, we must determine

the control method that will generate desired motion primitives.

1. Forward locomotion

Since the robot moving in straight course is described as a posteriorly propagating wave, the desired motion for the robot links is expected to approximate the wave to generate forward thrust, the desired motion can be expressed as

$$f(x, t) = \left(c_1 \frac{x}{l} + c_2 \left(\frac{x}{l} \right)^2 \right) \sin \left(k \frac{x}{l} + \omega t \right) l \quad (7)$$

where f is transverse displacement of the body, x is displacement along the main axis. t is time, k is body wave number, ω is body wave frequency, l is length of the robot. In order to generate the body wave, we set the joint angles as follows

$$\begin{aligned} \theta_1 &= 0, \theta_2 = \theta_0 \sin(\omega t), \\ \theta_3 &= \theta_0 \sin(\omega t - \varphi) \end{aligned} \quad (8)$$

We can achieved the forward locomotion, here θ_0 is amplitude. φ is the phase difference. Using the analysis results, we can get the relationship between velocity and frequency of flutter kick. Then with changing fluttering frequency, we can get a desired swimming speed.

2. Turning

When the robot is required to turn uniformly with given angular velocity w and turning diameter D , a centripetal force F should be offered as

$$F = \frac{1}{2} m \omega^2 D \quad (9)$$

If we set the robot arms making angle between body as θ , we can get the centripetal force from thrust force and resistance force. Using the analysis results we can get the relationship between θ and w .

V. SIMULATION

In order to evaluate the applicability and capabilities of humanoid robot, we made simulations study with using developed model. The results of simulation for forward swimming and turning are shown in Fig.4 and Fig.5. The condition for simulation is shown in Table 1.

Table 1 Condition of Simulation

Dimension of Robot:

Body Width: 23cm, Body Length:40cm

Body Depth; 11cm, Leg Length;20cm

Fin Size; 10cm*6cm

Weight; 1.5kg

Frequency of Leg Motion; 2Hz

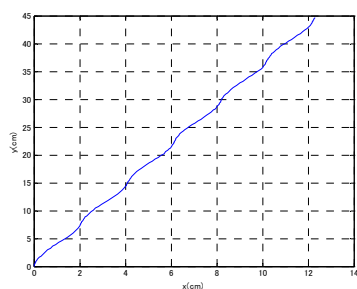


Fig.4 simulation result for forward swimming

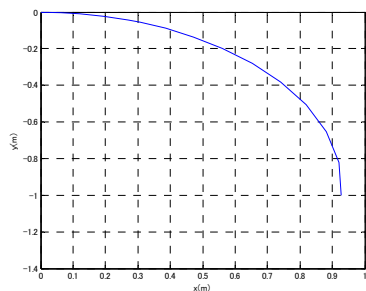


Fig.5 simulation result for turning

VI. EXPERIMENT

For the confirmation of the simulation results and further study, we made experiments with actual robot.

1. Experiment system

In this experiment, we used a high performance humanoid robot as a base machine and covered it with waterproof suit. It can be controlled with game controller remotely or with program autonomously. The photograph of is shown in Fig.6. This robot was tested in the water tank in our laboratory.

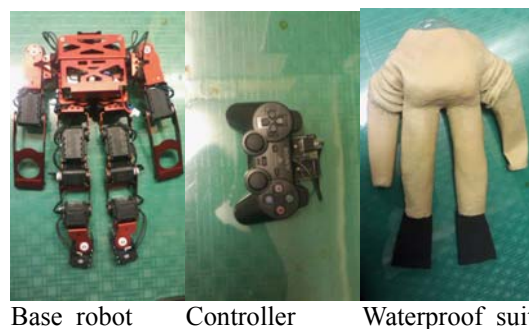


Fig. 6 Robot System for Experiment

2. Experiment Results

We would like to report those results on the symposium as much as possible.

VI. CONCLUSION

In this paper, we considered a dynamics model and control method. Concretely, we introduced mainly the propulsion system, such as principal, the structural design or control algorithms to generate appropriate thrust force. This mechanism has a disadvantage that the flutter kick of both leg interfere each other. This propulsion system can also generate turning moment, upward going moment or downward going moment adding thrust force with selecting angular velocity of fluttering and center angle of fluttering. And with integrating basic control to cooperated control, we can realize free posture control and get various kind of motion. Of course, more accurate parameters remains to be seen, and we would like to develop the system to higher level.

REFERENCES

- [1] YAMAMOTO I, TERADA Y (1995) Propulsion system with flexible / rigid oscillating fin [J]. IEEE Journal of Ocean Engineering 20 (1): 23-30.
- [2] Colgate J E, Lynch KM(2004), Mechanics and Control of Swimming .A Review [J] . IEEE J . Oceanic Eng,29 (3) :660 - 673.
- [3] J.Yu, Wang, and M. Tan, (2007), Geometric optimization of relative link lengths for biomimetic robotic fish, IEEE Trans.Robot 23(2): pp.382-386.

Linear Estimation Method for Position and Heading with RDOA Measurements

G. H. Choi*, H. S. Cheon**, J. B. Park*, and T. S. Yoon**

**Department of Electrical and Electronic Engineering, Yonsei University, Seoul, Korea
(Tel: 82-2-2123-2773)*

(E-mail: {choigh99 & jbpark}@yonsei.ac.kr)

***Department of Electrical Engineering, Changwon National University, Changwon, Korea
(Tel: +82-55-213-3633)*

(E-mail: {starchon & tsyoon}@changwon.ac.kr)

Abstract: Passive localization in the sensor network has been studied in many areas. Especially, the estimation of the position and heading for the target is an important subject in the navigation problems. We estimate the position and the heading information only with range difference of arrival measurements. The proposed algorithms are based on the pseudo linear measurement equation transformed from the nonlinear one and uses the instrumental variable method to remove estimation errors. It does not need additional computational burden so that it will be advantageous to real time applications. To show the usefulness of the proposition, we simulate it in the various positions and headings comparing with a nominal least squares method and the robust least squares method.

Keywords: RDOA, Localization, Heading estimation, Least squares, Instrumental Variable.

I. INTRODUCTION

Passive localization in sensor network has been studied in many areas such as control, communication, signal processing and etc. For the localization, the utilized measurements of sensor network are such as TOA (time of arrival), TDOA (time difference of arrival), RDOA (range difference of arrival), or RSS (received signal strength). TDOA or RDOA-based localization methodologies have been applied for finding target's position because it does not need synchronization between the target and the network. Additionally, if one can get two different positions concerned on-board of the target, heading estimation is possible. This method has been used in a navigation problem [1]. In this paper, we are focusing on the heading and position estimation with RDOA measurements.

In a plane, the localization problem with RDOA measurements is regarded as an MLE (maximum likelihood estimation) problem which decides a crossing point between two parabolic functions [2]. However, there is always a possibility that the MLE method is not converged to the global minimum but converged to a local minimum depending on the initial point. Additionally, its solution is often derived with numerical analysis methods which can be a burden for computation.

To convert nonlinear estimation problem to linear one, an intermediate variable method has been proposed with adding a new state variable [3]. This transformed linear equation is called as a pseudo linear equation. With this equation, it can be relaxed for the initial guess problem. However, there are still two problems for the linear equation. The one is that there is an uncertainty in the

measurement matrix which causes an estimation error by correlation with itself or with measurement noise [5-7]. The other problem is a bias of the measurement noise. These problems are concerned with the RDOA measurement noise and they may be neglected under the assumption that the variance of the noise is small [2-5]. However, if the condition of SNR is not good, the estimation error can be increased rapidly.

The IV (instrument variable) method can be a proper solution, because the method uses an instrumental variable in the measurement matrix for fleeing from the correlation [8]. It does not require additional computational burden so that it will be advantageous to real time applications.

Therefore, we propose the position and heading estimators based on the IV method and assume the stochastic information is unknown. To treat the bias of measurement noise of the pseudo linear equation, we estimate the bias by augmenting to the state variables based on the bias common model [9]. The useful aspects of the proposition are shown by simulation in the various positions and headings and by comparison with a nominal least squares method and the robust least squares method in [6] which can be adapted to this linear uncertain problem.

II. POSITION AND HEADING ESTIMATION MODEL WITH RDOA MEASUREMENTS

1. Position Estimation Model

We assume the target has two transmitters. The transmitters generate some signals which the sensor nodes of a network can realize the target. The network does not know the burst time of the signal but it can

measure the arrival time. In this case, one can use a time difference to localize the target's position and the time difference can be transformed to the RDOA by multiplying a propagation velocity.

$$r_{1,2} = v_p(t_1 - t_2) \quad (1)$$

where v_p is the propagation velocity, t_1 and t_2 are arrival time at each sensor node, and $r_{1,2}$ is the RDOA.

To make this problem simple, we derive it in the 2-D case as Fig. 1.

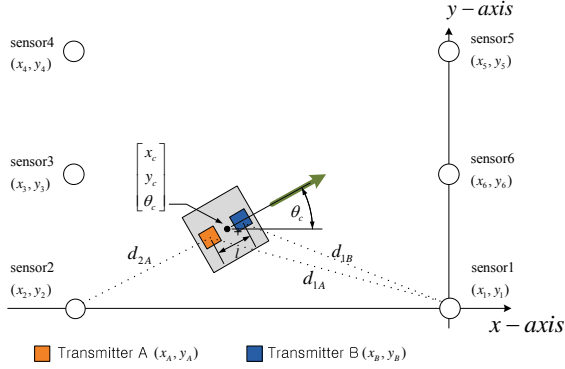


Fig. 1. Positions of the sensor nodes and the target in the 2-D plane

By using the intermediate variable method [4], the measurement model is given by

$$\underbrace{(\tilde{r}_{1,2}^A)^2 - d_{02}^2 + d_{01}^2}_{y_1^A} = -2 \underbrace{\begin{bmatrix} (x_2 - x_1) \\ (y_2 - y_1) \\ -\tilde{r}_{1,2}^A + \delta r_{1,2}^A \end{bmatrix}}_{H_1^A} \underbrace{\begin{bmatrix} x_A \\ y_A \\ d_{1A} \end{bmatrix}}_{x^A} + \underbrace{2\tilde{r}_{1,2}^A \delta r_{1,2}^A - (\delta r_{1,2}^A)^2}_{v_1^A} \quad (2)$$

where

$$d_{1A} = \sqrt{(x_A - x_1)^2 + (y_A - y_1)^2}, \quad d_{01} = \sqrt{(x_1 - 0)^2 + (y_1 - 0)^2} \quad (3)$$

, and $\delta r_{1,2}^A$ is the RDOA measurement noise and its stochastic property is a white and zero mean. The measurement noise of (2), v_1^A can be assumed to be a white noise but it cannot be assumed zero mean.

$$E[v_1^A] = (\sigma^2)_1^A \quad (4)$$

where $(\sigma^2)_1^A$ is the variance of the RDOA measurement noise, $\delta r_{1,2}^A$. In a low SNR condition, this factor can cause an estimation error, so that it needs to be removed from the measurements y_1^A or to be estimated by setting it as a new state variable.

For the other transmitter, B, the measurement equation can be derived likewise.

2. Position and Heading Estimation Model

The intermediate variable method makes the nonlinear localization problem to the linear problem so that a

linear estimator can be applied to find the transmitters' positions. If one can obtain two positions for the target, its center position and heading can be derived by using the positions. The center position is

$$x_c = \frac{x_A + x_B}{2}, \quad y_c = \frac{y_A + y_B}{2} \quad (5)$$

, and the heading is

$$\theta_c = \cos^{-1}\left(\frac{x_B - x_A}{l}\right) = \sin^{-1}\left(\frac{y_B - y_A}{l}\right) \quad (6)$$

By using this idea, we can build a linear model for the position and heading. Using (5) and (6), the linear equation is given by

$$\underbrace{\begin{bmatrix} y_1^B + y_1^A \\ y_1^B - y_1^A \end{bmatrix}}_{z_1} = -2 \underbrace{\begin{bmatrix} 2(x_2 - x_1) & 0 \\ 2(y_2 - y_1) & 0 \\ 0 & l(x_2 - x_1) \\ 0 & l(y_2 - y_1) \\ -\tilde{r}_{1,2}^A + \delta r_{1,2}^A & \tilde{r}_{1,2}^A - \delta r_{1,2}^A \\ -\tilde{r}_{1,2}^B + \delta r_{1,2}^B & \tilde{r}_{1,2}^B - \delta r_{1,2}^B \end{bmatrix}}_{H_1} \underbrace{\begin{bmatrix} x_c \\ y_c \\ d_{1A} \\ d_{1B} \end{bmatrix}}_{x} + \underbrace{\begin{bmatrix} v_1^B + v_1^A \\ v_1^B - v_1^A \end{bmatrix}}_{n_1} \quad (7)$$

, and its generalized form when there are n+1 sensors is

$$\underbrace{\begin{bmatrix} z_1 \\ z_2 \\ \vdots \\ z_n \end{bmatrix}}_z = \underbrace{\begin{bmatrix} \tilde{\Pi}_1 \\ \tilde{\Pi}_2 \\ \vdots \\ \tilde{\Pi}_n \end{bmatrix}}_{\tilde{\Pi}} - \underbrace{\begin{bmatrix} \Delta\Pi_1 \\ \Delta\Pi_2 \\ \vdots \\ \Delta\Pi_n \end{bmatrix}}_{\Delta\Pi} \underbrace{\begin{bmatrix} n_1 \\ n_2 \\ \vdots \\ n_n \end{bmatrix}}_n + X \quad (8)$$

where

$$\tilde{\Pi}_j = -2 \begin{bmatrix} 2(x_j - x_1) & 0 \\ 2(y_j - y_1) & 0 \\ 0 & l(x_j - x_1) \\ 0 & l(y_j - y_1) \\ -\tilde{r}_{1,j}^A & \tilde{r}_{1,j}^A \\ -\tilde{r}_{1,j}^B & \tilde{r}_{1,j}^B \end{bmatrix}^T, \quad \Delta\Pi_j = -2 \begin{bmatrix} 0 & 0 \\ 0 & 0 \\ 0 & 0 \\ 0 & 0 \\ -\delta r_{1,j}^A & \delta r_{1,j}^A \\ -\delta r_{1,j}^B & \delta r_{1,j}^B \end{bmatrix}^T \quad (9)$$

III. LINEAR ESTIMATION METHODS FOR POSITION AND HEADING

1. Instrumental Variable Algorithm

The stochastic compensation solution, the RoLS (robust least squares) in [6] is an useful method because its formulation resembles with the general least squares method and computational burden is low. However, if the sensor network has a characteristic of stochastic information being varying, the estimation results may be incorrect. To overcome this problem when the stochastic properties are unknown, the IV method can be an alternative solution. The IV method uses instrument variable for avoiding the correlations which are between the measurement matrix uncertainties,

$cor(\Delta\Pi, \Delta\Pi)$ or between the measurement matrix uncertainties and the measurement noise, $cor(\Delta\Pi, n)$ [8]. This method is unlike the RoLS algorithm which removes the correlations by using the scale-factor error compensation term, W and the biased error compensation term, V but flees from the correlations by replacing the measurement matrix with an IV matrix. The IV matrix can be built simply with one-step delayed measurement matrix because we assume the measurement noise is white.

$$\begin{aligned} cor[\Delta\Pi(k-1), \Delta\Pi(k)] &= 0_{2n \times 2n} \\ cor[\Delta\Pi(k-1), n(k)] &= 0_{2n \times 1} \end{aligned} \quad (10)$$

Therefore, the position and heading estimator with the IV algorithm is

$$\hat{X}^{IV}(k) = \{(\tilde{\Pi}^{k-1})^T \tilde{\Pi}^k\}^{-1} \{(\tilde{\Pi}^{k-1})^T z^k\} \quad (11)$$

However, an error still exists in the estimation result by the measurement noise bias in (4). Because we assumed the stochastic properties of the RDOA measurement are not available, the bias which is the variance of the RDOA noise cannot be removed from the measurements. If the sensor network is able to assume that the RDOA noise variances are identical for all measurements as the bias common model in [9], it is possible to estimate the common bias. To estimate the bias, we set the bias as a new state variable and derive the measurement equation as follows:

$$z(k) = \begin{bmatrix} \tilde{\Pi}(k) & I \end{bmatrix} - \begin{bmatrix} \Delta\Pi(k) & 0 \end{bmatrix} \begin{bmatrix} X(k) \\ b(k) \end{bmatrix} + \bar{n}(k) \quad (12)$$

$\tilde{\Pi}_{Aug}(k)$ $X_{Aug}(k)$

where I is a $2(n-1)$ dimensional vector which is

$$I_{2(n-1) \times 1} = \begin{bmatrix} [1 & 0] & [1 & 0] & \cdots & [1 & 0] \end{bmatrix}^T \quad (13)$$

and $\bar{n}(k)$ is the zero mean and white noise which eliminates the bias from n in (8). With (12), the augmented position and heading estimator is

$$\hat{X}_{Aug}^{IV}(k) = \{(\tilde{\Pi}_{Aug}^{k-1})^T \tilde{\Pi}_{Aug}^k\}^{-1} \{(\tilde{\Pi}_{Aug}^{k-1})^T z^k\} \quad (14)$$

Theorem 1. (Convergence to true position and heading of the proposed algorithm) If there are enough sensors to observe the position, heading and the biases, and the noises of sensor network are i.i.d. (independent and identically distributed), then the estimation results of the proposed method converge to true position and heading in probability.

$$\text{plim}_{k \rightarrow \infty} \hat{X}_{Aug}^{IV}(k) = X_{Aug} \quad (15)$$

□

Proof:

Since the measurement noises are i.i.d., the auto-correlation of the measurement matrix uncertainties and the cross-correlation between the measurement matrix uncertainties and the measurement are derived as follows:

$$E\{\tilde{\Pi}_{Aug}(k-1)\}^T \{\tilde{\Pi}_{Aug}(k)\} = \Pi_{Aug}^T \Pi_{Aug} \quad (16)$$

$$E\{\tilde{\Pi}_{Aug}(k-1)\}^T \{z(k)\} = \Pi_{Aug}^T \Pi_{Aug} X \quad (17)$$

Therefore, each correlation can be rewritten as convergence in probability.

$$\text{plim}_{k \rightarrow \infty} \frac{1}{k} (\tilde{\Pi}_{Aug}^{k-1})^T (\tilde{\Pi}_{Aug}^k) = \Pi_{Aug}^T \Pi_{Aug} \quad (18)$$

$$\text{plim}_{k \rightarrow \infty} \frac{1}{k} (\tilde{\Pi}_{Aug}^{k-1})^T (z^k) = \Pi_{Aug}^T \Pi_{Aug} X_{Aug} \quad (19)$$

With these convergences, (18) and (19), the estimation result, (14) is also able to converge to true position and heading by Slutsky's theorem [8].

$$\begin{aligned} \text{plim}_{k \rightarrow \infty} \hat{X}_{Aug}^{IV}(k) &= \text{plim}_{k \rightarrow \infty} \left[\{(\tilde{\Pi}_{Aug}^{k-1})^T \tilde{\Pi}_{Aug}^k\}^{-1} \{(\tilde{\Pi}_{Aug}^{k-1})^T z^k\} \right] \\ &= \text{plim}_{k \rightarrow \infty} \left\{ \frac{1}{k} (\tilde{\Pi}_{Aug}^{k-1})^T \tilde{\Pi}_{Aug}^k \right\}^{-1} \times \text{plim}_{k \rightarrow \infty} \left\{ \frac{1}{k} (\tilde{\Pi}_{Aug}^{k-1})^T z^k \right\} \\ &= \{(\Pi_{Aug})^T \Pi_{Aug}\}^{-1} \{(\Pi_{Aug})^T X_{Aug}\} = X_{Aug} \end{aligned} \quad (20)$$

■

IV. SIMULATION RESULTS

To show the performances of the position and heading estimators, we compare them with the nominal least squares method through simulations. The sensor network contains 6 fixed sensor nodes at (0, 0), (-1.015, 0), (-1.015, 1.015), (-1.015, 2.03), (0, 2.03), and (0, 1.015) [m]. The variances of the RDOA measurements are all set to $0.02[m^2]$. For batch type comparison, we accumulate 5000 measurements and calculate the error performance by using 100 iterations. In this simulation, we fix the transmitter A and rotate the transmitter B every 10 degree to check the estimation performances at different target's center position and heading.

The mean error (ME) for the position is shown in Fig. 2 and its RMSE is shown in Fig. 3. As referred in [6], the NLS (nominal least squares) method has a large estimation error by the measurement matrix uncertainty and the bias of the measurement noise. On the contrary, the RoLS, IV and augmented IV methods have low estimation error within $0.02[m]$. The bias of the IV method caused by non-zero mean of the measurements noise is not relatively serious. However, the augmented IV method compensates properly the error by estimating it.

The estimation results for the heading are shown in Fig. 4 and Fig. 5. The trend of heading results of the NLS resembles with the position results. The heading error from the cosine is bigger than the one from the sine like the position error. The reason for this is that the heading from the cosine depends on the x-position of the target and the other is vice versa as shown in (6). The heading estimation by the augmented IV method also shows good performance as the RoLS estimator. Therefore, the augmented IV method can be a practical method because it does not need any stochastic

information and additional computational burden.

V. CONCLUSION

The target's position and heading can be estimated in the RDOA measured sensor network with linear estimator. However, since a nominal least squares estimator causes estimation error by the measurement matrix uncertainty and the bias of the measurement noise, there needs a proper compensation algorithm. We propose the position and heading estimator and it does not need an additional compensation procedure and the stochastic information of the RDOA measurement noise. The proposition is based on the instrumental variable method and estimates the bias of the measurement noise under the bias common model assumption. The estimator works well in noisy environment like the robust least squares method and shows better performance than the nominal least squares estimator. The useful aspects that it has low computational burden and does not need any stochastic information make it utilized for the practical applications.

ACKNOWLEDGMENT

This research was supported by Basic Science Research Program through the National Research Foundation of Korea (NRF) funded by the Ministry of Education, Science and Technology (2010-0005318).

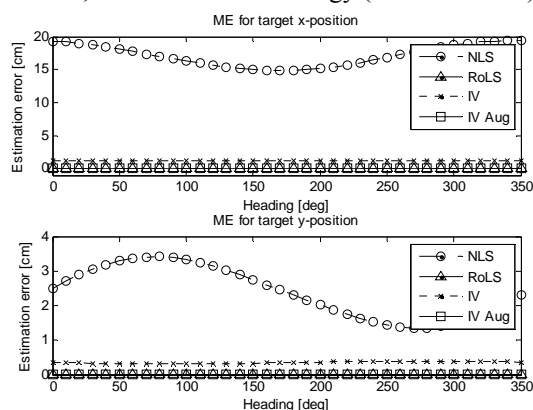


Fig. 2. Mean error for the target's center position

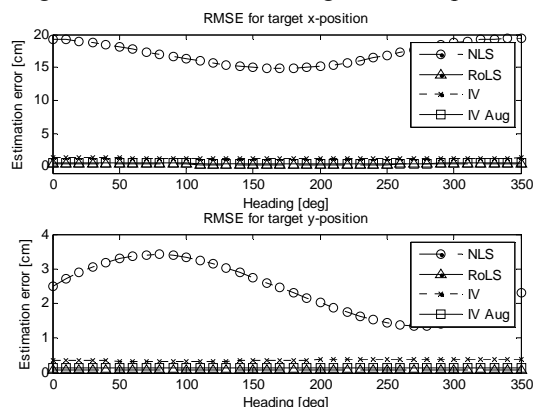


Fig. 3. RMSE for the target's center position

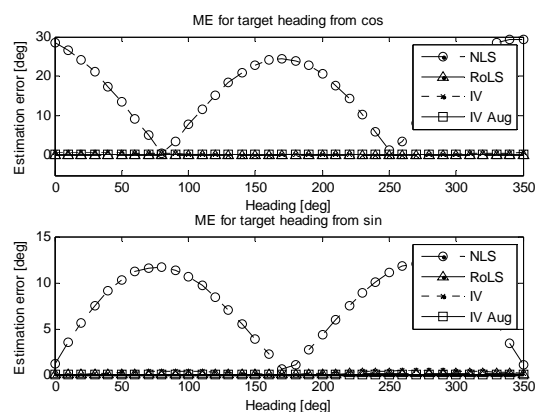


Fig. 4. Mean error for the target's heading

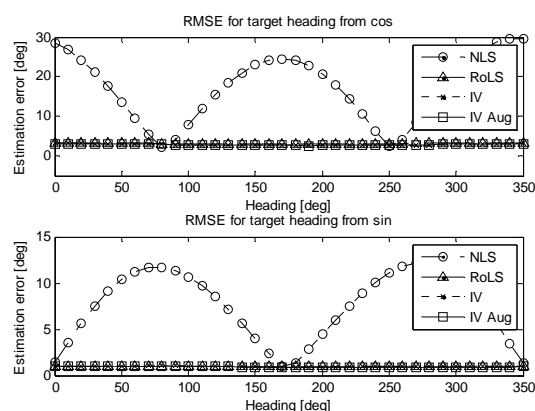


Fig. 5. RMSE for the target's heading

REFERENCES

- [1] Agihili, F., and Salerno, A. (2009), Attitude determination and localization of mobile robots using two RTK GPSs and IMU, *IEEE/RSJ Int. Conf. Intelligent Robots and Systems*, 1:2045-2052.
- [2] Abel, J. S., and Smith, J. O. (1989), Source range and depth estimation from multipath range difference measurements, *IEEE Trans. Acoustics, Speech, and Processing*, 37(8):1157-1165.
- [3] Chan, Y. T., and Ho, K. C. (1994), A simple and efficient estimator for hyperbolic location, *IEEE Trans. Signal Processing*, 42(8): 1905-1915.
- [4] Cheung, K. W. et al. (2006), A constrained squares approach to mobile positioning: algorithms and optimality, *EURASIP J. Appl. Signal Process.*, 2006: 1-23.
- [5] Huang, Y. et al. (2001), Real-time passive source localization: a practical linear-correction least squares approach, *IEEE Trans. Speech and Audio Processing*, 9(8):943-956.
- [6] Ra, W. S., et al. (2007), Recursive robust least squares estimator for time-varying linear systems with a noise corrupted measurement matrix, *IET. Control Theory & Applications*, 1(1):104-112.
- [7] Ra, W. S., Whang, I. H., and Yoon, T. S. (2009), Constrained robust Kalman filtering for passive localization, *ICROS-SICE Int. Joint Conf.*, 1: 4516-4521.
- [8] Dogancay, K. (2006), Bias compensation for the bearing-only pseudo-linear target track estimator, *IEEE Trans. Signal Processing*, 54(1): 59-68.
- [9] Picard, J. S., and Weiss, A. J. (2008), Localization of networks using various ranging bias models, *Wirel. Commun. Mob. Comput.*, 9(1): 553-562.

Omnidirectional State-Changing Gripper Mechanism for Various Objects

Kenjiro Tadakuma¹, Riichiro Tadakuma², Hiroki Tanaka¹, Takuto Fukuda¹, Mitsuru Higashimori¹, Makoto Kaneko¹, 1.(Osaka University, Japan), 2(Yamagata University, Japan)

This paper describes the morphing omnidirectional gripper which is able to grasp various objects with low melting point alloy, functional fluid, dilatancy fluid, and so on. The deformable part of the gripper changes its shape by covering all direction of objects and makes the contacting area higher. This time, we especially focus on the "Hot Ice" phenomena to realize higher grasping motion. The basic performance of fluid of CH₃COONa has been observed.

Key Words: Mechanism, Deformable, Hot-Ice Phenomenon, Omni-Gripper, Conformable

1. Introduction

1.1: Mechanism of the former morphing omnidirectional gripper

The former morphing omnidirectional gripper had a mechanical problem of poor response when the low melting point alloy, enclosed substance, changed its phase from liquid to solid. In this paper, we propose a method to improve gripping response making use of the phenomenon of supercooling.

As the enclosed substance, functional fluids like magneto rheological and electro rheological fluids, dilatant fluid, mixture of particulate and its solvent, and mixture/composite of all these substances, we speculate, may be possible candidates.

In our former prototype, we used a low melting point alloy which solidifies at room temperatures. Though that exhibits relatively high rigidity when it grasps objects compared to the candidates listed above, it has a problem of poor response caused by rather long time required to the phase change from liquid to solid which needs to occur after conforming to objects. Thus, in this report, we propose two alternatives for applications which impose higher importance on quick response than on high rigidity when gripping objects.

1.2: A proposal to improve response

One is a mixture of gas and particulate substance (glass beads) and another saturated water solution of sodium acetate CH₃COONa which exhibits supercooling known as "Hot Ice" phenomenon.

When trihydrate of sodium acetate is cooled below 58 degree Celsius, the melting point, it solidifies suddenly in response to added nucleus or to stimulation done by metal fragment, for example. This is the Hot Ice phenomenon we refer to. The triggering for solidification may be replaced by electric stimulation, like application of voltage and we are examining this method. In addition to that, mixture of water solution of sodium acetate and other enclosed substances such as functional fluids described in Chap. 2 are being studied as well.

In this report, the two items regarding to the basic characteristics of our morphing omnidirectional gripper will be examined. One is the basic gripping performance when angle offsets are given to gripped objects and another how to use the supercooling of water solution of sodium acetate which is aimed at improvement of gripping response.

Just only the jamming phenomena have already proposed in the 1982[12]. In recently(in 2010), Cornell University, University of Chicago, and iRobot reported the jamming gripper, but the configuration is almost the same of that work by G. Bancon et al. It can grasp various kinds of object, but it needs the pushing force to deform. It means, the grasped object should take the same force

from the gripper. Our proposed configuration (in 2008) can grasp soft objects effectively without any large damages, and configuration of the gripper itself is totally different from the previous any researches. And we already proposed the mixtures of the plural numbers of the particles and air or liquid as the contents of the grippers sack in that paper.

2. Morphing omnidirectional gripper

Quick response does not seem, in our experience, to be compatible with high rigidity at solid- or almost solid state.

Here, we examine the adaptability of the morphing gripper with bag-shaped structure continuously extending from inner- to external parts to longitudinal and angular offsets. High degree of tolerance to offsets may be favorable when objects to be grasped are vibrating, objects set on moving bed are vibrating and gripper itself is vibrating. In addition to the present gripper with bag-shaped structure continuously extending from inner- to external parts, we are developing a double-layered structure that may be folded.

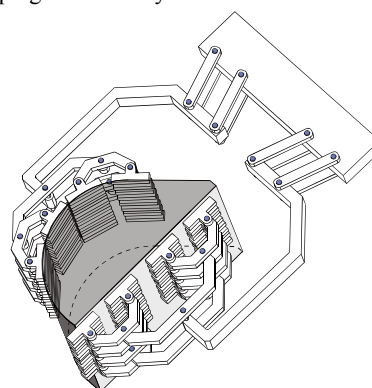


Fig. 1: Example of Previous Mechanical Gripper

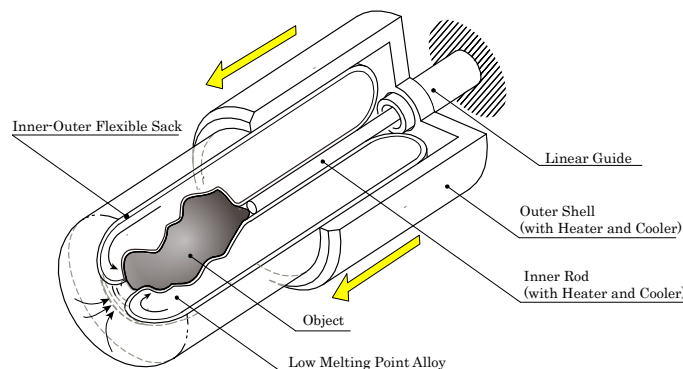


Fig. 2: Basic Concept of the Morphing Omni-Gripper

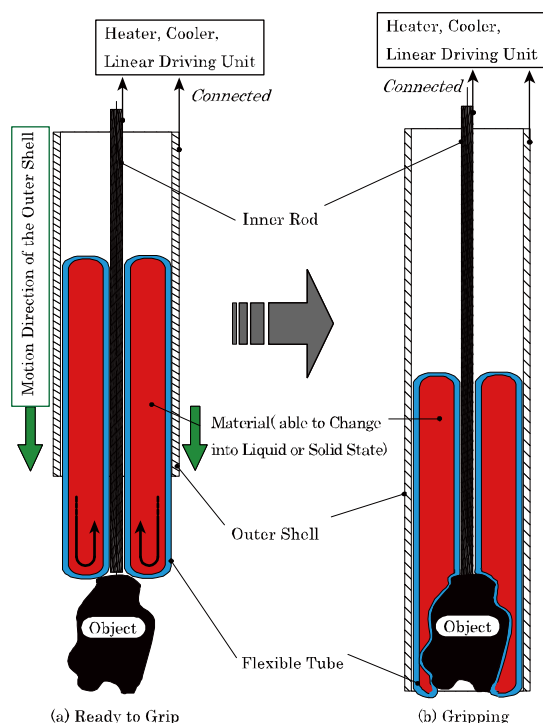


Fig. 3: Grasping Motion of the Morphing Omni-Gripper

Figure 2 depicts the basic sequence of conforming gripping. By direct displacement of only outer shell (an element of gripper) toward the grasped object, gripper may catch it eliminating the displacement of the object. It may be possible, conversely, to grasp object drawing it toward gripper.

3. Gripping characteristics when offset exists

We have measured the gripping characteristic for tilted objects. Kamakura et al. [2] coated paint on objects and observed the location of paint attached in the hand of person who grasped it. While in our experiment, we coated paint on gripper taking consideration on large contact area of grasped object.

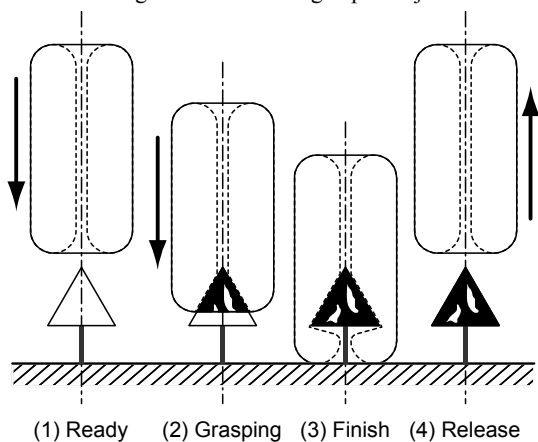


Fig. 4 Gripping Experiments

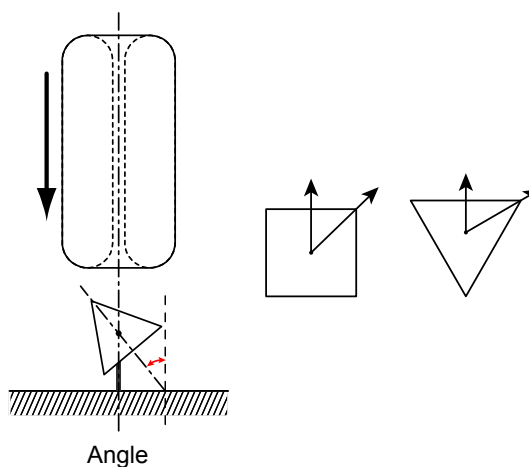
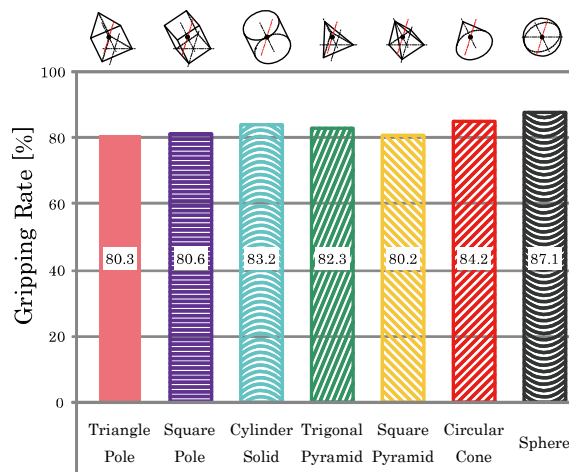


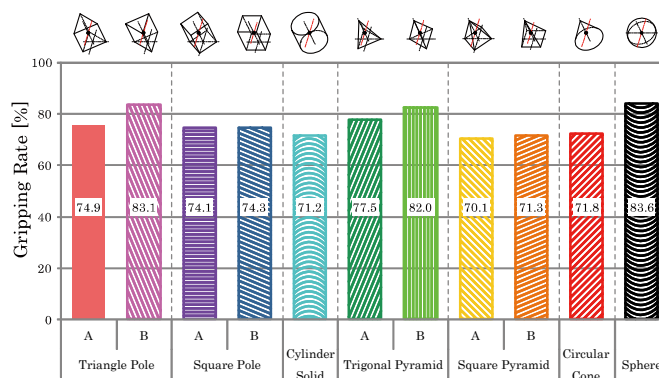
Fig. 5 Gripping Experiments with Offset

Results obtained by analyzing the amount of paint are shown in Figs. from 4 through 8. These figures demonstrate high conforming of the gripper we proposed.



Gripping Rate (No offset)

Fig. 6 Experimental Result without offset



Gripping Rate (5mm)

Fig. 7 Experimental Result with offset

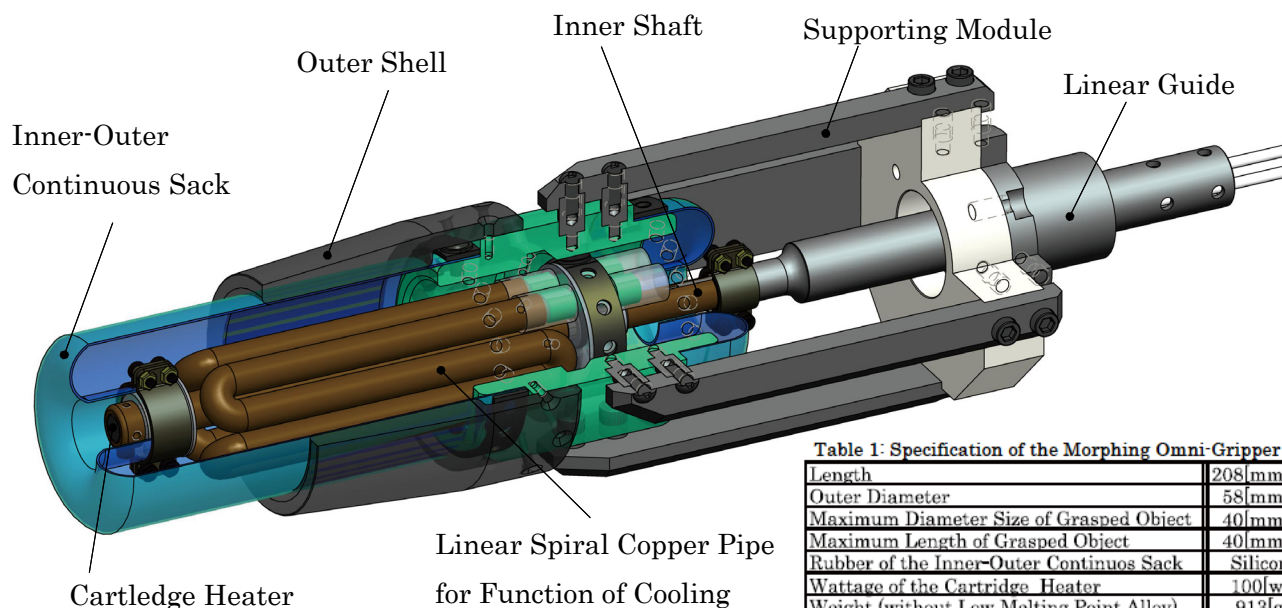


Fig. 8 Prototype Mechanical Design of the Omni-Gripper



Fig. 9 Overview of the Omni-Gripper

4. Taking advantage of Hot-Ice phenomenon

Here, we discuss how to improve the response performance of solution (exhibits supercooling described above) as the enclosed substance in gripper with bag-shaped structure continuously extending from inner- to external parts. Triggering to solidification may be done by:

- 1) mechanical stimulation
- 2) introduction of nucleus
- 3) electric stimulation

In our experiment this time, we took the third of electric stimulation in view of simple implementation. The result of our preliminary experiment is shown in Fig. 9. Solution of 200ml volume solidified in some four seconds. This speed depends on the method of introducing electric stimulation. We are examining response performance and rigidity of solidified substance varying concentration of sodium acetate. Thus, we are working to improve the performance of enclosed substance in gripper which is conforming to grasped object and grips it firmly at the same time.

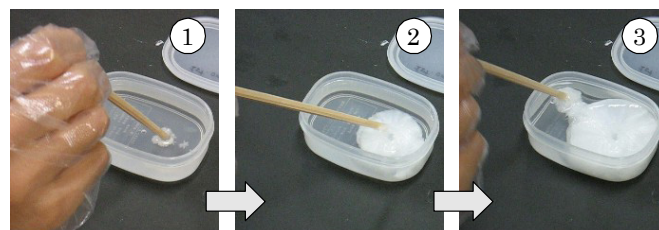


Fig. 10 Phenomenon of "Hot-Ice"

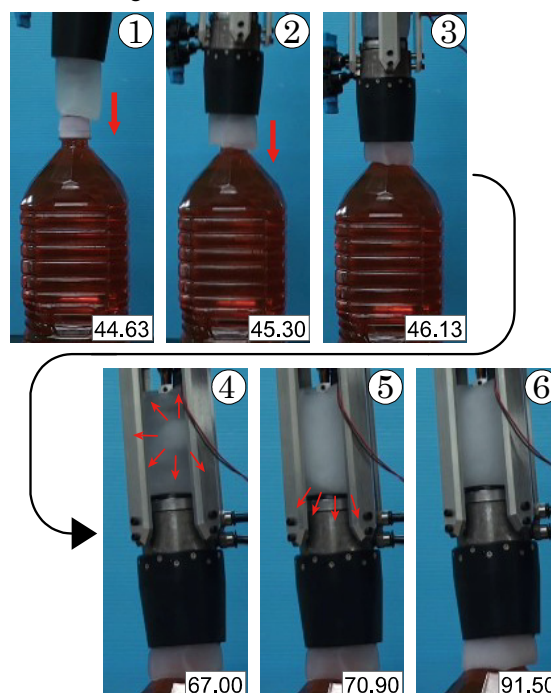


Fig. 11 Grasping Motion of the Omni-Gripper

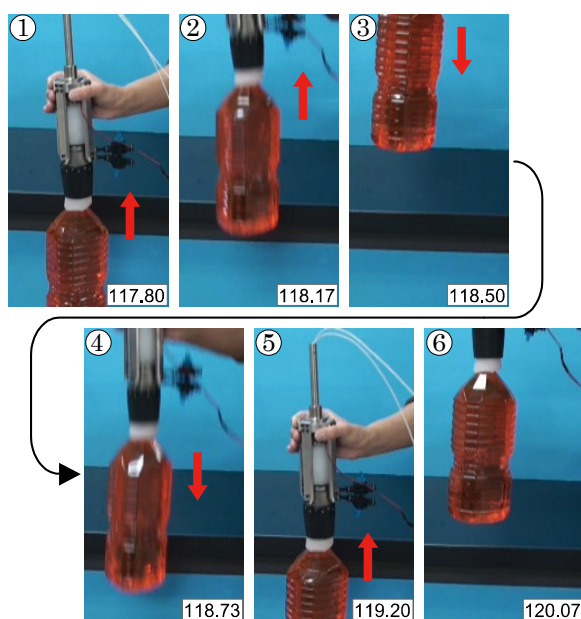


Fig. 12 Grasping Power of the Gripping in Solid State

5. Summary

We have carried out an experiment on angular offset of grasped objects to examine the basic performance of our morphing omnidirectional gripper. It proved the good conforming performance of the gripper. And some description was made on application of supercooled sodium acetate to improve the grasping performance of the gripper.

References

- [1] Name of invention: Device to grasp objects, Number of application: Applied patent 1995-306353, Date of application: November 1, 1995, Publication number: Publicized patent 1997-123082, Date of publication: May 13, 1997, Applicant: Kao Corporation, Inventor: K. Uehara and another
- [2] N. Kamakura, M. Ohmura, H. Ishii, F. Mitsuboshi, and Y. Miura ,Gripping pattern of healthy hands - An approach to their categorization-, Japanese Journal of Rehabilitation Medicine, vol.15, no.2, June, 1978
- [3] N. Kamakura, F. Mitsuboshi, N. Asami, and M. Nakata, Moving pattern of healthy hands when they manipulate object, Japanese Journal of Rehabilitation Medicine, vol. 23, no.2, March, 1986
- [4] K. Harada and M. Kaneko, Conforming gripping of objects more than one – Kinetics and conforming grasp , J. Japan Robotics Society, Vol.16, No.6, pp.860-867, 1998
- [5] T. Yoshitomi, Story of fish squama, editorial supervisor, Japanese Society of Fisheries Science, ISBN978-4-425-85261-1
- [6] S. Hirose, Biomechanical Engineering, Kogyo Chosakai Publishing, 1987
- [7] N. Yamano, S. Takamuku, and K. Hosoda, Development of underactuated humanoid robot hand with conforming grip, 1A1-A11, Robotics-Mechatronics Conference, 2008
- [8] H. Iwata, T. Hayashi, H. Shiozawa, K. Kimura, S. Ishii, K. Sakagami, T. Ohta, K. Iwamoto, and S. Kanno, Structural design of high skill and multi-fingers equipped with passive flexibility on finger and palm, 1A1-A01, Robotics-Mechatronics Conference, 2008
- [9] K. Takagi and T. Omata, Electric artificial hand with augmentation mechanism of gripping force, 12th Robotics Symposium, 2B4
- [10] K. Tadakuma, R. Tadakuma, S. Teshigawara, Y. Mizoguchi, H. Hasegawa, K. Terada, T. Takayama, T. Omata, A. Ming, and M. Shimojo, Morphing omnidirectional gripper-Proposal of basic concept and first prototype of mechanical structure, 1E1-01 , 26th Conference of Japan Robotics Society, 2008
- [11] M. Wakabayashi, T. Mitsuda, and S. Kawamura, Development of a force display for leg motions using adhesive particles with variable constraints, 1P1-F06, Robotics- Mechatronics Conference, 2002.
- [12] G. Bancon and B. Huber: Depression and Grippers with Their Possible Applications, 12th ISIR, Paris (1982) pp. 321-329.

Object Co-occurrence Graph for Object Search in 3D Environment

Puwanan Chumtong, Yasushi Mae, Kenichi Ohara, Tomohito Takubo, Tatsuo Arai

*Graduate School of Engineering Science, Osaka University
1-3, Machikaneyama-cho, Toyonaka, Osaka, Japan 560-8531
(Tel: 81-66-850-6365)*

*{c_puwanan, k-ohara, takubo}@arai-lab.sys.es.osaka-u.ac.jp
{mae, aria}@sys.es.osaka-u.ac.jp*

Abstract: We propose a method of using object co-occurrence graph for mobile service robots to search for small-scale objects in 3D environments without pre-defined map. Object co-occurrence graph describes co-occurrence relations between objects in scenes. The presence of other large objects in the environment, which are easier to be found, provides cues to search for a small object related to the large object. If the target object is often near to a large object, robot firstly finds the large object, and then searches around the large object for the target object. Thus, using object co-occurrence graph makes object searching task easier and more efficient. The object co-occurrence graph is automatically constructed by many tagged images from the WWW. Our experiment shows a robot searching for a target object using object co-occurrence graph.

Keywords: Object Co-occurrence Graph, Object searching, Mobile robot.

I. INTRODUCTION

The object search is an essential task for mobile robot which helps human in everyday environment. Many methods for object search in 3D environment have been proposed. For example, David et al. [1], Masuzawa et al. [2] and Jeremy et al. [3] use color information to verify the candidate of target object in the scene. However robot may face some difficulties to find the small target object in the case of occlusion problem and insufficient current image's resolution.

On the contrary, some methods focus on existing cues in the observing environment for object search. Dominik et al. [4] proposed the usage of object's relationship to search for target objects in unknown environment. Cipriano et al. [5] use the position probability of the observing map and found objects in their searching task. Ksenia et al. [6] utilize position probabilistic with the given hint in motion planning for searching task. Importantly, the utilizing of cues can decrease the difficulty of searching task when target object, especially small object, cannot be observed in the current robot's view.

In our approach, we focus on employing object's co-occurring relation as our cues because this relation is represented for the frequency for how often object A and object B co-occur together. Thus we propose the Object Co-occurrence Graph (OCG) describing the co-occurring property between objects. That is, we utilize the existing of cue objects to search for target object in unknown environment. This idea can be illustrated in Fig. 1. The benefit of using object co-occurring cues among previous mentioned researches is that our approach can be easily constructed and applied as robot's knowledge.

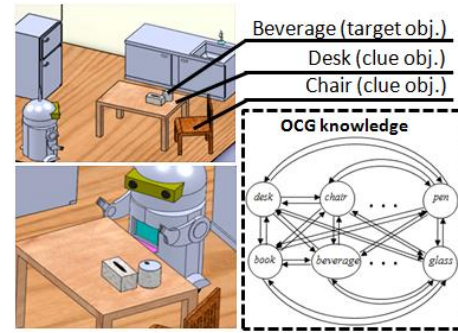


Fig. 1: The utilizing of cues in observing environment for robot's searching task

II. OBJECT CO-OCCURRENCE GRAPH

In our approach, the concept of Object Co-occurrence Graph for robot's searching task can be illustrated in Fig. 2. One arbitrary object o_i (e.g., desk, chair, etc) may have many related objects according to its reference database. Moreover, in term of co-occurring relation, each related objects of o_i may have some relationship with any objects in OCG database. For each couple of objects o_i and o_k , we will obtain 2 values; $p(o_i | o_k)$ and $p(o_k | o_i)$. At here, $p(o_i | o_k)$ is the probability to find target object o_i when cue object o_k is found and vice versa.

In order to utilize these probability values, we select the next visiting object candidate based on the priority ranking among others in database. That is, if our target object, o_i , is not observed while cue objects are found, robot then can determine next visiting object o_j by using the following concept:

$$\hat{o}_j = \underset{o_j \in Obj}{\operatorname{argmax}} p(o_i | o_j) \quad (1)$$

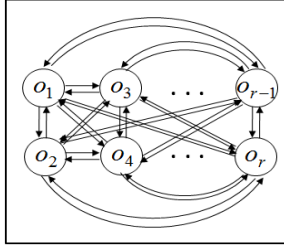


Fig. 2: The main concept of OCG structure

We know that $Obj = \{o_1, \dots, o_r\}$ where r is number of objects. It is assumed that the higher possibility value, the higher chance to find target object nearby that cue.

III. INTERNET-BASED OCG CONSTRUCTION

The OCG can be constructed by manually learning from observing actual situation. However this learning method is not appropriate since it is time consuming. As a learning method, one interesting research [7] uses the object co-occurrence gathering from many internet images as prior knowledge for robot. As a result of this, the expected length of the path to the object is minimized. Due to benefits of internet data, the similar concept was also applied in our work. The different point of our approach from others is that our approach does not require pre-defined map for robot's searching.

To construct OCG, we employ image hosting website that contains a form of metadata as our reference database. Instead of employing well-known web search engine such as Google, the related work [8] describes the difficulty of using images from Google search as training data because most of returned images may be visually unrelated to the intended keyword. Moreover Google's images do not contain tagged information. Thus we use website such as Flickr that gives us word-tagging images provided by millions of internet users. Most of those provided images are related to searching keyword since its image searching process is based on word-tagging of each image.

The concept of OCG construction is shown in Fig. 3. The name of o_i is used as keyword to search for relevant images within main page, $W(o_i)$. Based on tags of these images in sub-webpage, $w_{k,i} \in W(o_i)$, the standalone object occurrence and object co-occurrence will be obtained. In this work, we have proposed 2 methods; dependent and independent co-occurring method, for OCG construction. For dependent co-occurring method, possibility values depend on tagged information in all searching images but the adding of new item or the deleting of existing item can affect the changing of possibility values of all object couple in database. Thus the recalculation of all values is needed. On the other hand, for independent co-occurring method, it is assumed that probability values between couples are independent. Thus probability values of new adding items with others can be separately calculated. The

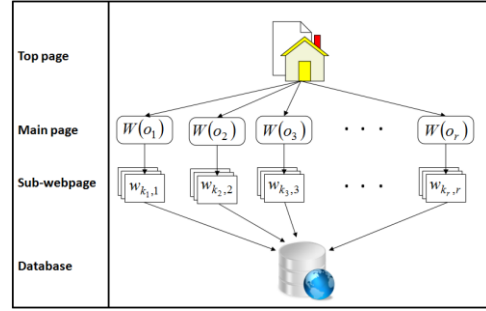


Fig. 3: Proposed method for OCG construction

computation of these 2 construction methods are based on different searching concept as follow.

1. Dependent Co-occurring based Construction

This method constructs database based on the relationship of all objects. By using name of o_i as searching keyword, we will obtain $w_{k,i} \in W(o_i)$. The standalone occurrence $n(o_i)$ and co-occurrence $n(o_i \cap o_j)$ are counted from all images, $\forall w_{k,i} \in W(o_i) : i = \{1, \dots, r\}$. In order to gain the co-occurrence possibility value, we employ the definition of conditional probability:

$$p(o_i | o_j) = \frac{p(o_i \cap o_j)}{p(o_j)} \quad (2)$$

We employ the following definition:

$${}_nC_k = \binom{n}{k} \quad (3)$$

Thus, we will have ${}_rC_2$ pairs of object co-occurring couple. We will finally have $2 \cdot ({}_rC_2)$ possibility values for OCG database.

2. Independent Co-occurring based Construction

In the case of considering relationship of ρ -th pair between o_i and o_j , the standalone occurrence $n_\rho(o_i)$ and $n_\rho(o_j)$ are calculated from images $w_{k,i} \in W(o_i)$ and $w_{k,j} \in W(o_j)$. At here, we define that $\rho \in \{1, \dots, C_2\}$ because we will obtain ${}_rC_2$ pairs of object co-occurring couple. We also can obtain $n_\rho(o_i \cap o_j)$ from those images. When the relationship between o_i and o_c is needed, we just focus on the information in $w_{k,i}$ and $w_{k,c}$. Unlike previous mentioned method, recalculation of entire values is not necessary.

IV. TRAINING RESULTS AND DISCUSSION

We design the training set based on images in Flickr website. The word "period" defines the image-searching of $\forall o_i \in Obj : i = \{1, \dots, r\}$ within M images. We define that:

$$M = \sum_{i=1}^r m_i \quad (4)$$

At here, m_i can be varied according to the number of returned images in 1 webpage when name of o_i is used as searching keyword. Thus the searching of M

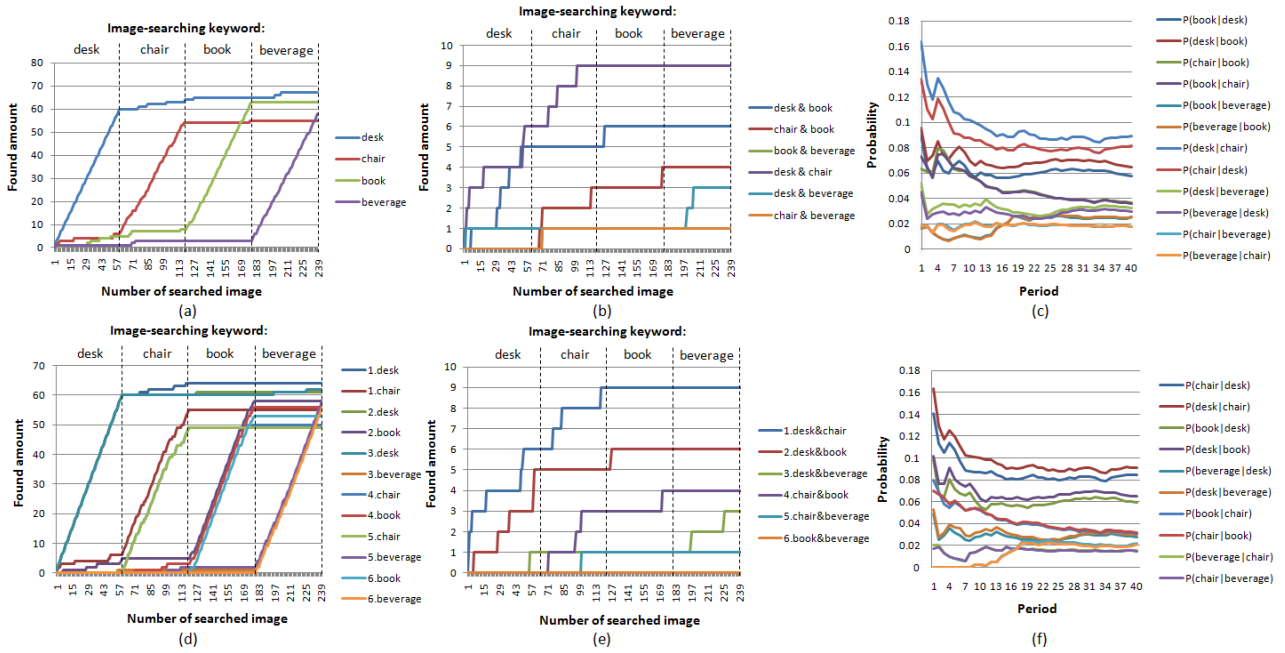


Fig. 4: Training results for OCG construction. Training results of dependent co-occurring method are shown in (a), (b), and (c) while training results of independent co-occurring method are shown in (d), (e), and (f).

images is so called one period. In our experiment, we take a consideration to 4 sample objects which are *desk*, *chair*, *book*, and *beverage*; that is, we will have $r = 4$.

For our OCG construction, we train data up to 40 periods and examine how possibility values change as the number of searching images increases. As can be seen in Fig. 4, we also provide the following definition:

- 1st phase: searching keyword of *desk* (o_1)
- 2nd phase: searching keyword of *chair* (o_2)
- 3rd phase: searching keyword of *book* (o_3)
- 4th phase: searching keyword of *beverage* (o_4)

1. Experimental Results of Dependent Co-occurring-based Construction

According to the method in section III-1, During 1st phase of Fig. 4(a), it can be noticed that $n(o_1)$ rapidly increases until the number of searching images reaches m_1 images because the name of o_1 is used. During 2nd phase, $n(o_1)$ slowly increases although name of o_2 is used. This shows that there are some co-occurrences of o_1 and o_2 during 2nd phase. The co-occurrence of *desk* (o_1) & *chair* (o_2) can be easily observed in Fig. 4(b). On the contrary, $n(o_2)$ does not change during the 4th phase of Fig. 4(a). This shows that there is no co-occurrence of o_2 and o_4 during this phase. We can also see the co-occurrence of *chair* (o_2) & *beverage* (o_4) in Fig. 4(b) whose data-line remains constant during 4th phase.

For 40 period-results in Fig. 4(c), data-lines of probability values, $p(o_i | o_j)$ where $o_i, o_j \in Obj : i \neq j$, provide less fluctuation as the number of searching period increases. In our experiment, the data training of

40 searching periods returns us 9,571 related images. It can also be noticed that data-lines provide less fluctuation when number of searching images is more than 4560 images (after 19th period).

2. Experimental Results of Independent Co-occurring-based Construction

According to the method in section III-2, we obtain 6 pairs of co-occurring relationship as can be seen in Fig. 4(d). Their change is based on the appearance of o_i in related images. For the 1st pair ($\rho = 1$) whose members are *desk* and *chair*, $n_1(o_1)$ changes during the 1st and 2nd phase where we use searching keywords of *desk* and *chair*, respectively. From Fig. 4(e), $n_1(o_1 \cap o_2)$ increases during 1st and 2nd phase and remains constant in other phases because this method concerns only images of $w_{k,i} \in W(o_1)$ and $w_{k,j} \in W(o_2)$.

According to Fig. 4(f), the training process of 40 periods returns us 9,578 searching images. It can be noticed that data-lines in Fig. 4(f) have similar characteristic as data-lines in Fig. 4(c).

3. Comparison Between 2 Construction Methods

The probability results of each couple of objects after 40-period training are shown in Table 1. Although the numerical results of probability values between 2 proposed methods are different, their ranking order of hypothesis cue objects convey the same ranking order and they indeed accord to the fact of object's relationship in realistic environment. From Table 1, it can be noticed that this knowledge lets robot know visiting location for object search. That is, if robot is assigned to search for *book* but it cannot be found in the

Target Object	Cue Object	Dependent Co-occurring	Independent Co-occurring
desk	chair	0.0890	0.0910
	book	0.0643	0.0649
	beverage	0.0325	0.0298
chair	desk	0.0815	0.0846
	book	0.0364	0.0320
	beverage	0.0176	0.0149
book	desk	0.0575	0.0598
	chair	0.0355	0.0309
	beverage	0.0250	0.0208
beverage	desk	0.0296	0.0279
	book	0.0255	0.0219
	chair	0.0175	0.0151

Table 1: The comparison of experimental results between 2 proposed methods

1st scene, robot then has to determine where it has to go next to search for it. In case that *desk* and *chair* are observed in the 1st scene, robot will know that *desk* is 1st place to be visited while *chair* is the 2nd place to be visited. This robot's knowledge is obtained from OCG.

Although both construction methods provide us the same meaningful results, the usage of independent will be more appropriate for real experiment because it can be easily adjusted when new object is added or existing object is removed from current database.

V. OBJECT SEARCH USING OCG

We show a simulation of object search using OCG and example of object recognition. In our object recognition method, range data and color image gathering from single stereo camera are employed as our input data for robot's exploration. The experimental set up can be viewed in Fig. 5(a). In this test, *book* is assigned as target object for robot's searching task. The robot employs well-known SIFT [9] for target object's detector. As can be seen in Fig. 5(b), robot cannot observe *book* in the 1st scene due to low image's resolution and occlusion from other objects. However robot found some cues; *desk* and *chair*, labeling with red ellipse and green ellipse, respectively. Cue objects, considered as large objects, are detected based on range data and color segmentation result [10]. Consequently robot obtains cue objects in the observing environment. Thus, robot can determine the sub-goal's location based on OCG knowledge. As a result of this, robot chooses to visit the desk's location and continue searching for *book* as can be seen in Fig. 5(c). From Fig. 5(d), it can be noticed that robot can finally verify the existing of *book* which is placed on *desk* (cue object).

VI. CONCLUSION

This paper has described the usage of OCG as robot's knowledge for searching task in unknown

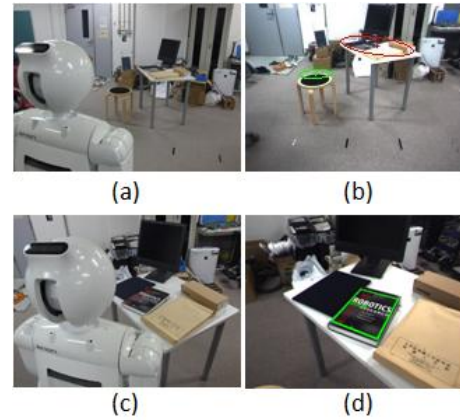


Fig. 5: Simulation of object search using OCG. (a) shows initial robot's position. (c) shows robot's positions after approaching to *desk*. (b) and (d) show robot's views with recognition results.

environment. The OCG is automatically constructed based on searching images within Flickr website. Two proposed methods for OCG construction; dependent and independent co-occurring methods are also presented. In this paper, we also show the successive result of robot's simulation of object search using OCG without pre-defined map.

REFERENCES

- [1] David Meger, Per-Erik Forssén, Kevin Lai, Scott Helmer, Sancho McCann, Tristram Southey, Matthew Baumann, James J. Little, David G. Lowe, and Bruce Dow, "Curious George: An Attentive Semantic Robot", in *Robotics and Autonomous Systems*, 2008
- [2] Hiroaki Masuzawa and Jun Miura, "Observation Planning for Efficient Environment Information Summarization", in *International Conference on Intelligent Robots and Systems (IROS)*, Louis, USA, 2009
- [3] Jeremy Ma and Joel W. Burdick, "A Probabilistic Framework for Stereo-Vision Based 3D Object Search with 6D Pose Estimation", in *IEEE International Conference on Robotics and Automation (ICRA)*, Alaska, USA, 2010
- [4] Dominik Joho and Wolfram Burgard, "Searching for Objects: Combining Multiple Cues to Object Locations Using a Maximum Entropy Model", in *IEEE International Conference on Robotics and Automation (ICRA)*, Alaska, USA, 2010
- [5] Cipriano Galindo, Juan-Antonio Fernández-Madrigal, Javier González, and Alessandro Saffiotti, "Robot task planning using semantic maps", in *Robotics and Autonomous Systems*, Volume 56, 2008, pp.955-966
- [6] Ksenia Shubina and John K. Tsotsos, "Visual search for an object in a 3D environment using a mobile robot", in *Computer Vision and Image Understanding*, Volume 114, 2010, pp.535-547
- [7] T. Kollar and N. Roy, "Utilize object-object and object-scene context when planning to find things", in *IEEE International Conference on Robotics and Automation (ICRA)*, Kobe, Japan, 2009
- [8] R. Fergus, L. Fei-Fei, P. Perona, A. Zisserman, "Learning Object Categories from Google's Image Search", in *International Conference on Computer Vision (ICCV)*, Beijing, China, 2005
- [9] David G. Lowe, "Local Feature View Clustering for 3D Object Recognition", in *Computer Vision and Pattern Recognition (CVPR)*, Hawaii, USA, 2001:2-15
- [10] Pedro F. Felzenszwalb and Daniel P. Huttenlocher, "Efficient Graph-Based Image Segmentation", in *International Journal of Computer Vision*, Volume 59, 2004, pp.167-181

Study on the wall climbing robot driven by the caterpillar tracks

Jiwu Wang¹ Yisong Wang¹ Weijie Gao¹

Department of Mechanical and Electrical Engineering, Beijing Jiaotong University, Beijing, China, 100044¹

Sugisaka Masanori²

Nippon Bunri University, Oita, Japan²

(jwwang@bjtu.edu.cn)

Abstract: With the development of economy and various techniques, the development of the wall climbing robot is getting more and more attention. This is because various jobs are not appropriate for human beings, such as some tasks in some special or dangerous environments, wall cleaning of high building, etc. In view of such problems, it is necessary to develop a wall climbing robot moving in various working conditions. In this paper, we developed a wall climbing robot driven by the caterpillar tracks. It can pass some simple obstacles. At the same time it can capture the environment pictures with a CCD camera and send the image data directly to the server. Moreover, we analysis its structures and some functions.

Keywords: Wall climbing robot, caterpillar track.

I. INTRODUCTION

Climbing robots can attach to the wall and move with carrying capacity of the working tool. And work in some special or dangerous circumstances to substitute humans to complete the relevant tasks. Xiaodong Chen et al [1]. shows that they are used primarily for wall cleaning, maintenance of nuclear power stations, hull painting, sand blasting, anti-terrorism and testing of petrochemical oil tank. In recent years, with the developing of the railway, bridge inspection becomes a new direction of climbing robots.

They can be classified by the type of moving. There are wheel-type, crawler-type and sucker-type.

Robots with sucker-type can go across small obstacles, but slowly. And they have lest two suckers and legs for movement. Then not only the weight will increase by setting more legs and suckers, but the system of control maybe more complex. It is bad for stability.

Wheel-type provides a faster, flexibility-control means. But it is difficult to holding a continued adsorptive power. And robots need a big sucker to provide absorptive power. When robots are working on some bumpy plane, it is a little trouble of control. We can't ensure the wheels have rolled the same distant. If we add some system to correct routes, the energy consumption will be raised.

Caterpillar haves strong adaptability to wall and its landing area is large, but not easily turn. To work on the wall or under bridges, sucker devices are necessary. The caterpillar is heavier than wheel-type structure. It is mean that caterpillar expends more energy. But it can

work on different planes.

Compared with these three types, we find they use the same way to against the gravity—some mechanical devices. Consequently, a big part of energy was used by these devices.

Because of the technology development, people have higher requirements of climbing robots. Small size, mobility, environmental adaptability, low noise, low energy consumption and long cruising time become the further goals.

Because of the traditional climbing robot has many shortcomings, therefore the future climbing robot structure should towards practical direction.

Xuming Cui, Yingfei Sun, Fujun He [2]. shows that in this few years, scientists discovered the secret of how does gecko walk on the wall. The secret is the Van der Waals force. It is weak electromagnetic attraction produced by neutral molecules, when they are extremely close. This means can be used into developing a new kind of adsorption device. And the energy problem has been considered. We need a battery with high-capacity and light, or by remote control approach for robots to provide energy and signal control.

To solve the problems above, we discovered a easy means of using helium balloon. We can use the buoyancy of the helium balloon to against the gravity. Then we can save a lot of energy to lengthen the robots working time. And it is safe for robot, because we don't need worry about it drop from the wall or the bottom of bridges when it power off suddenly.

Helium is one of the six inert gasses. When some helium leak from balloon and mixed with air, it results in blast or fire. So helium is very safe for practical using.

II. ELEMENTS AND FUNCTIONS

Most of climbing robots must be working with some mechanical parts to provide the power to against the gravity. But when we are designing a climbing robot, decreasing the weight is an important qualification. As we know that more weight consumes more energy. So we have to balance the two aspects---using more mechanical parts to provide more power and diminishing more structure to lengthen the working time.

Now we present a new means to against the gravity. It is the helium.

Helium is a very light colorless gas that is one of the six inert gasses; the most difficult gas to liquefy; occurs in economically extractable amounts in certain natural gases. And the helium balloon was used for aviation in the primary period. Now it can play the same role in climbing robot field to provide buoyancy.

We use the buoyancy in two ways, some part of buoyancy to counteract the weight of the robot. And the other part is used to create enough pressure for friction. Then the friction can transform into the impetus of plane motion under the bridge.

Here are some basic equations.

$$F_b = M \times g + F_p \quad (1)$$

F_b ——the buoyancy;

M ——the weight of whole robot;

F_p ——the pressure;

g ——the gravity acceleration;

$$F_m = F_f = \mu \times F_p \quad (2)$$

F_m ——the impetus of plane motion;

μ ——the coefficient of friction;

F_f ——the friction between the travelling mechanism and the bottom of bridge;

Here are some figures to show the structure.

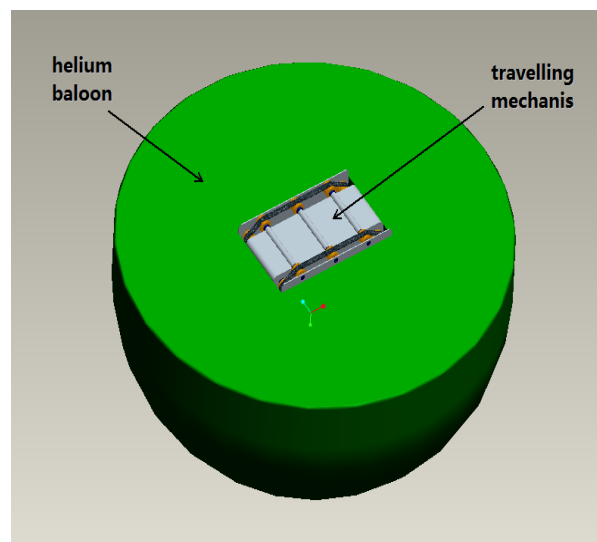


Fig.1. The illustration of the structure

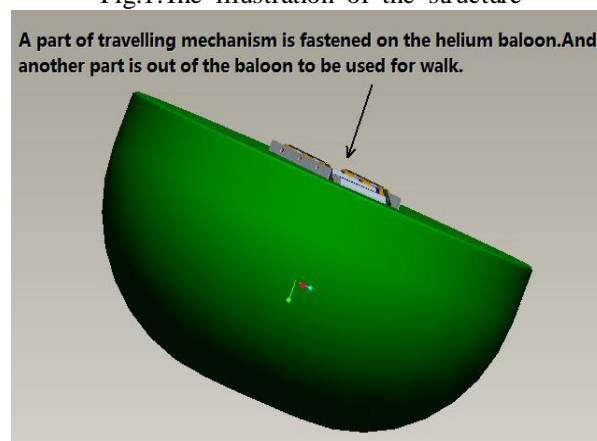


Fig.2. The detail of the structure

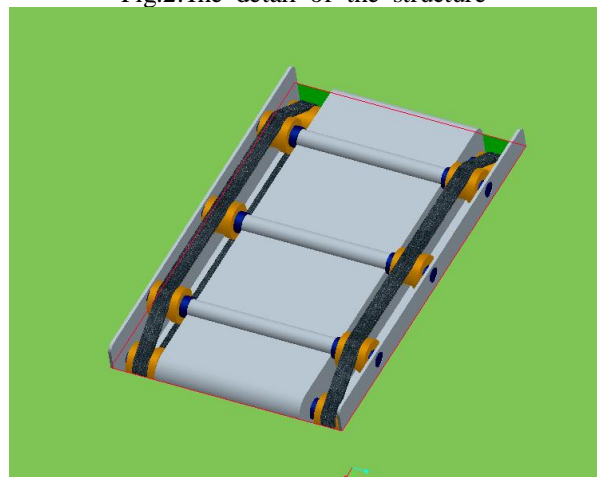


Fig.3. The walking structure

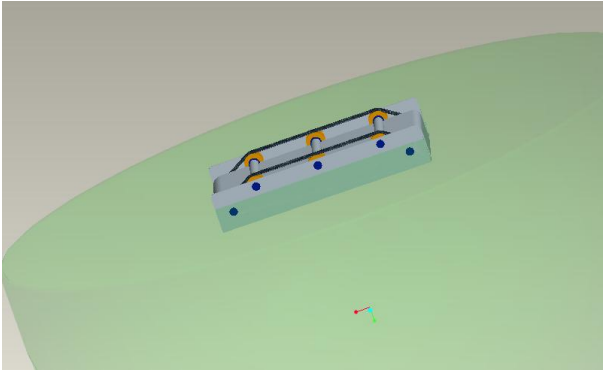


Fig.4. Inset a part of walk structure in balloon

III. ANALYSIS AND EXPERIENCES

For proving the means can be used into reality, we made some analysis about it.

According to the equations below, we drew the curves to describe the relation between volume of helium and buoyancy.

The density of helium is 0.1786g/L (0℃, 1atm).

1. Equations

We assumed the shape of balloon is cube. Then we set three thickness of balloon. They were 0.0005m, 0.0007m and 0.001m.

$$F_b = (\rho_a \times V_a - \rho_h \times V_h - \rho_b \times (V_a - V_h)) \quad (3)$$

F_b — the buoyancy (kg);

ρ_a — the density of air (kg/m^3);

ρ_h — the density of helium (kg/m^3);

V_a — the volume of helium (m^3);

ρ_b — the density of balloon (kg/m^3);

V_b — the volume of balloon (m^3);

$$V_a - V_h = (r_a^3 - r_h^3) \quad (4)$$

r_a — the radius of the volume of balloon replaced air (m);

r_h — the radius of the volume of helium (m);

$$r_a - r_h = h_b \quad (5)$$

h_b — the thickness of balloon (m);

2. Figures

After we did some calculation, we draw the curves between volume and the buoyancy.

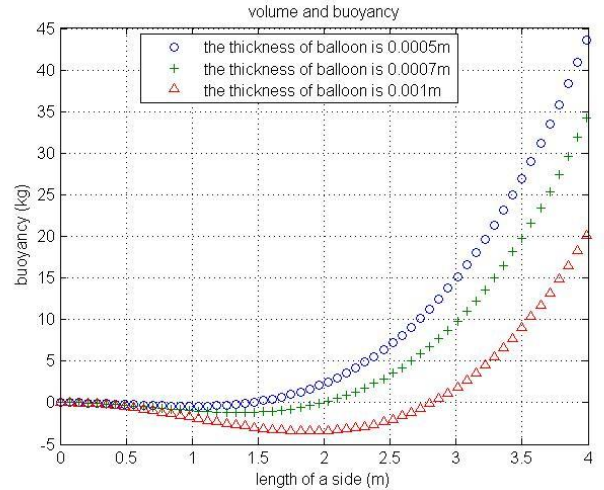


Fig.3. The relation between volume and buoyancy

IV. CONCLUSION

After analysis, we can see that this means can be used in some robots which have a big body type. And when the length of a side is above 3m, the helium balloon can provide appreciable buoyancy. And the power is clear, without any energy consumption. What's more, this means can avoid some accident. Such as, when the robot shut down suddenly or power off in working time, the helium balloon can protect the robot from crashed. Consequently, this means is safety and energy-saving. But we find that wind bring a bad effect on the big balloon. Now we are working on finding a way to decrease the bad effect.

REFERENCES

- [1] Xiaodong Chen et al.(2007) , Police robot. Science press, Beijing.134-135
- [2] Xuming Cui, Yingfei Sun, Fujun He.(2010), Research and Development of Wall-climbing Robot , Science Technology and Engineering. China academic journal electronic publishing house, P.R.China.2672-2677

Authentication of the reconstructed image from Computer Generated Hologram: To use the digital watermark.

Norihiro Fujii, Ken-ichi Tanaka

School of Science and Technology, Meiji University
1-1-1 Higasi-Mita, Tama, Kawasaki-City, Kanagawa 214-8571, Japan
E-mail: ce91055@isc.meiji.ac.jp, tanaken@isc.meiji.ac.jp

Abstract: Computer Generated Hologram has been targeting the application areas such as a reconstruction three dimensional image, project the image of virtual object, optical information processing and optical memory. Laser beam is not required when synthesis and reconstruct CGH. In addition, it is expected to function as a digital watermarking. Digital watermarking is a technology to embed data into digital content. Digital content needs information security. Digital watermarking is used for information security. In this paper, the correlation between original image and watermark image are taken. Watermark image is made from CGH. Phase Only Correlation is adopted as a correlation method. As a result, have expanded the size of the image, little negative impact did not appear on the correlation value. It is possible to identify self and others using the image correlation value a state of the image of expanded size. These results suggest that the using of this proposal can be considered easier to identify the state between the auto correlation and cross correlation. In addition, we found that even large images are identified. Therefore, this proposal will be able to increase the possibility of adaptation to the authentication of the reconstructed image calculated by CGH.

Keywords: Computer Generated Hologram (CGH), Complex Hadamard Transform (CHT), authentication

I. INTRODUCTION

Computer Generated Hologram has been targeting the application areas such as a reconstruction three dimensional image, project the image of virtual object, optical information processing and optical memory.[1] Laser beam is not required when synthesis and reconstruct CGH. In addition, it is expected to function as a digital watermarking. Digital watermarking is a technology to embed data into digital content. Digital content needs information security. Digital watermarking is used for information security.[2] CGH is considered to be the practical application of information security as a first purpose. Therefore, authentication of the reconstructed image from CGH is necessary for digital watermarking. In this paper, the correlation between original image and watermark image are taken. Watermark image is made from CGH. Phase Only Correlation is adopted as a correlation method.

II. EXPERIMENT

1. Complex Hadamard Transform

Hadamard transform is the orthogonal transformation. Processing can be performed by the sum of the product of Hadamard matrix and the input data.[3] The basis of Hadamard transformation is a Hadamard matrix. Hadamard matrix is described as follows.

$$H(0) = [1] \quad (1)$$

$$H(n) = \begin{bmatrix} H(n-1) & H(n-1) \\ H(n-1) & -H(n-1) \end{bmatrix} \quad (2)$$

At this time, the size of the input image should be the same as that of Hadamard matrix. Two dimensional Hadamard Transform is described as Eq.(3) of follows.

$$F = (1/n)HfH^T \quad (3)$$

$$HH^T = I \quad (4)$$

f : input	H : Hadamard matrix
F : output	H^T : transposed Hadamard matrix

Inverse Hadamard Transform is Eq.(5).

$$f = nHfH^T \quad (5)$$

Complex Hadamard transform is used to complex Hadamard matrix. Complex Hadamard matrix is using the real and imaginary parts. Complex Hadamard matrix is described as follows.

$$H(0) = [1] \quad (6)$$

$$H(n) = \begin{bmatrix} H(n-1) & iH(n-1) \\ iH(n-1) & H(n-1) \end{bmatrix} \quad (7)$$

Complex Hadamard Transform is as similar processing as Eq.(3), and use complex conjugate of transposed matrix. The character similar to Eq.(4) is approved to Complex Hadamard Transform because complex conjugate matrix is similar to inverse matrix.

$$F = (1/n)HfH^* \quad (8)$$

$$f = nHfH^* \quad (9)$$

H^* : complex conjugate Hadamard matrix

2. Sample images

512 × 512 pixels on the image of the black, starting at the top left of the image of the alphabet A ~ Z of the one which created the characters are written in white letters. Image files are created with 256 colors bitmap format. This image as original image, used to convert those who applied.

Under the same conditions, 256 × 256 pixels images are made.

Each images shown in Fig.1, Fig.2 and Fig.3.

3. Experiment

Correlation values of images are measured in the following combination of image groups. Correlation values in type 1 and type 2 are measured with a combination of brute force. FT is Fourier Transform

Table 1. Combination of image groups

N	Type 1	Type 2
1	Original image	Reconstructed image from CGH made by FT
2	Original image	Reconstructed image from CGH made by CHT
3	Reconstructed image from CGH made by FT	Reconstructed image from CGH made by FT
4	Reconstructed image from CGH made by CHT	Reconstructed image from CGH made by CHT
5	Original image	Original image



Fig.1. Original image (A)

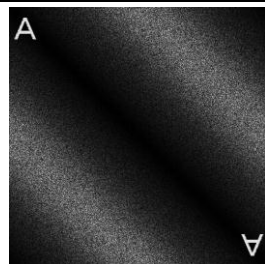


Fig.2. Reconstructed image from CGH made by FT (A)

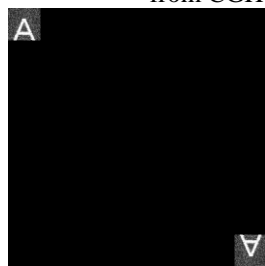


Fig.3. Reconstructed image from CGH made by CHT (A)

III. RESULTS AND CONSIDERATION

The threshold is set to identify “self” and “other”. Threshold is set as the value shall be uniform in each of the correlation. Threshold is set between “autocorrelation” (maximum) value and the second highest correlation value. The width between maximum value and the second highest correlation value should be broad as possible. The second highest correlation values were as follows.

In the experiment No.1 and No.2, maximum values which a state of “autocorrelation” are not in 1.0. Therefore, in the process of dividing the value of each element in that series the maximum value of the series (normalization process) are done.

Table 2. Combination of image groups and correlation value: The second highest correlation value

	a. 512×512	b. 256×256	a - b
1	0.89104747	0.80709695	0.08395052
2	0.91058764	0.83366690	0.07692074
3	0.03422546	0.03426302	-0.00003756
4	0.16488647	0.14813232	0.01675415
5	0.69196076	0.56340830	0.12855246

In the experiment No.2, the width between maximum value and the second highest correlation value is about 0.08941236. Set of threshold is difficult.

Meanwhile, result of experiment No.3 is the best value. And, result of experiment No.4 is the second best value.

In the experiment No.4, the width has been reduced to 86% of the width of experiment No.3. This result is better than the result of experiment No.5. Threshold setting is easily if the width of this level can be secured.

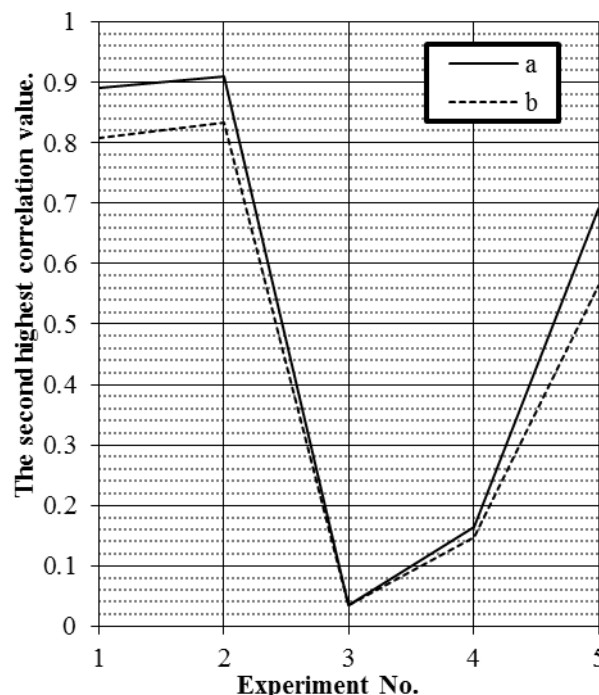


Fig.4. Combination of image groups and correlation value

VI. CONCLUSION

Reconstructed image from CGH made by CHT is compared with reconstructed image from CGH made by FT at the points of the detection accuracy with correlation value. And this study, to expand the size of the original image and the watermark image are tried.

Using a combination of autocorrelation can be obtained. It is possible to identify self and others using the image correlation value. These results suggest that the using of this proposal can be considered easier to identify the state between the auto correlation and cross correlation.

Therefore, there is a good possibility that the adaptation to authentication, in the case of this proposal using for calculation method.

REFERENCES

- [1]T.Yatagai, (2004), Optical Computing, Kyoritu Shuppan Ltd (in Japanese).
- [2]N.Komatsu, K.Tanaka (2004), Digital-watermarking technology, The Institute of Image Electronics Engineers of JAPAN (in Japanese).
- [3]Z.Kiyasu (1983), The Hadamard matrix and its application, IEICE (in Japanese).

An aerial handwritten character recognition based on motion direction and ratio of stroke length

Y. Nishida¹, K. Ogura², H. Miura², N. Matsuda², H. Taki² and N. Abe³

¹*Fukui University of Technology, Japan (nishida@fukui-ut.ac.jp)*

²*Wakayama University, Japan*

³*Kyushu Institute of Technology, Japan*

Abstract: This paper describes a method to recognize a character handwritten in the air. This recognition method evaluates the motion direction instead of positions of the device. It also doesn't evaluate the motion direction of pen's up-down, so it is one-stroke cursive character recognition. It selects character candidates with dynamic programming (DP) matching algorithm. We made one-stroke cursive character recognition software prototype based on mouse pointer trajectory. We adopted Genetic Algorithm in order to define matching parameters. We improved recognition rates by comparing "motion direction and ratio of stroke length" of detected data with dictionary. As a result, we achieved correct recognition rate about 90% for categories of Hiragana characters and numeral characters.

Keywords: on-line character recognition, one-stroke cursive character

I. INTRODUCTION

Recently, we have a lot of opportunity to use Cloud services. However, it is necessary to input text data in order to use many Cloud services. It is difficult for us to input text or character without the desk. If we can use a new device which provides the input function by handwriting in the air at anytime and anywhere, it is more convenient for us to use Cloud services. So, we study on-line aerial handwritten character recognition system. There are many problems to realize such recognition system. Our issues are "detection of pen's up-down in the air" and "limitation of handwriting area, character size and writing speed".

We proposed an on-line one-stroke cursive character recognition method based on motion direction. This recognition method regards a character as one-stroke and evaluates the motion direction instead of position information. The recognition system obtains the direction data (called "direction code") when a user moves an input device. And it selects character candidates with DP matching algorithm. One of the advantages of using DP matching algorithm is that the recognition system obtains the pattern of the inputted character and avoids individual differences.

We made one-stroke cursive character recognition software prototype based on mouse pointer trajectory. In this paper, we present an improvement of an aerial handwritten character recognition based on both motion direction and ratio of stroke length.

II. RELATED WORK

In the preceding researches, these character recognition systems use the pen lifting information (pen's up-down information) [1] [2]. The pen's up-down is natural operation to write the character on the paper. But when we write the character in the mobile environment in which there is neither tablet nor paper, the system should be designed so that the pen's up-down operation is omitted from the user job. Therefore, we adopted one-stroke cursive character recognition.

III. CODING METHOD

In our previous work [3], we adopted the series of the stroke direction code "a"- "h" and "S" code which means the start point, the end point and slight movements, to find the characteristic of the Hiragana pattern (as shown in Fig. 1). In this case, the sample code of Hiragana character "し" shown in Fig.2. was "SdcbaS".

And we applied Genetic Algorithm in order to define penalty codes and dictionary parameters for DP matching algorithm. As a result, we got general penalty codes which don't depend on users' habit of writing and the dictionary. The system's correct recognition rate has come to 85% for categories of Hiragana characters. But there are some recognition errors in similar shape characters, for example "う", "ら" and "ろ". This is because our previous system is not based on the information of stroke length.

Our new method accumulates same direction code based on proportion of stroke length.

For example, if Hiragana character "し" consists of 50% code "d", 10% code "c", 10% code "b" and 30% code "a" and if total number of coding data size is 30, the sample code of Hiragana character is "ddddddddddccccbbbaaaaaaa".

Table1 shows dictionary examples of new method (total number of coding data size is 50).

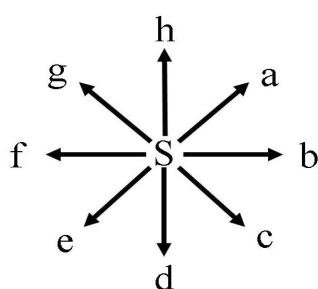


Fig.1. Direction code data

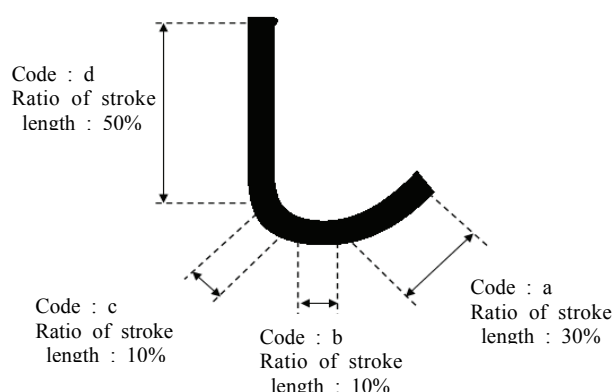


Fig.2. The shape of Hiragana character "し"

Table1. A part of dictionary code

Char.	Code
あ	bbbbbbbbbgggeedddccaaeeefhaaabbccdde
い	ddddddcccccaaaaaaaaaaaaaaacccddddd
う	ccccccfffeeeaaabbbbbbcccddeeeeee

IV. EVALUATION

We made one-stroke cursive character recognition prototype system based on mouse pointer trajectory and evaluated correct recognition rate by comparing our new method to our previous method.

Fig.3 shows a dialog of the prototype system's GUI view and Table2 shows comparison between the previous method and the new method with correct recognition rates and recognition failure characters.

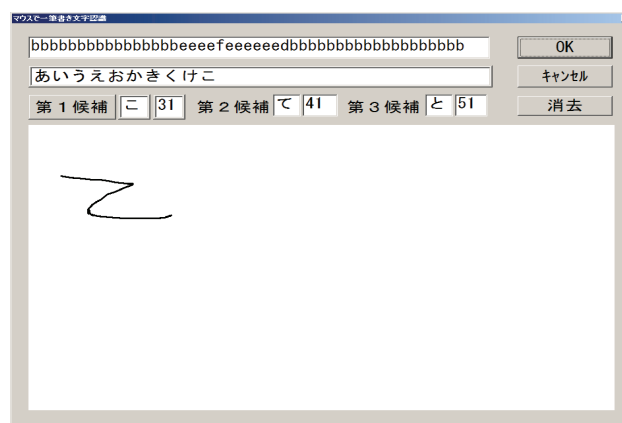


Fig.3. A screen-print of the prototype system's GUI

Table2. Improvement of ratio of stroke length

	Previous method		New method	
	Rec. rate	Error	Rec. rate	Error
い	8/10	り, し	10/10	-
う	8/10	ら	9/10	ら
こ	9/10	て	10/10	-
ら	6/10	う	9/10	す
ろ	6/10	ら, う	10/10	-
Total	400/470 (85.1%)		436/470 (92.8%)	

V. CONCLUSION

This paper has shown the on-line one-stroke cursive character recognition and its improvement method of the aerial handwritten character recognition based on both motion direction and ratio of stroke length. Not only characters "う", "ら", and "ろ", the correct recognition rate grow up as a whole. The system's correct recognition rate has come to about 90% for categories of Hiragana characters and numeral characters. The new method can ignore the detection noise caused by the slight movement code "S". This method is more robust and effective for addition of new characters than the previous system.

REFERENCES

- [1] Sudou T, Nakai M, Shimodaira H et al (2002), On-line Overlapped Handwriting Recognition Based on Substroke HMM (in Japanese). IEICE PRMU2001-65, pp.163-170
- [2] Oki T, Nakagawa M (2003), Implementation and Evaluation of a Combined Recognition System using Normalization of Likelihood Values (in Japanese). IEICE PRMU2002-196, pp.43-48
- [3] Nishida Y, Ogura K, Miura H et al (2010), An Aerial Handwritten Character Recognition Using Moving Direction Only (in Japanese). HIS Vol.12 No.3:91-98

Gamer robot for the rock-paper-scissors game by hand motion recognition

Ho Seok Ahn, Dong-wook Lee, and Hogil Lee

*Korea Institute of Industrial Technology (KITECH), Republic of Korea
(Tel : 82-31-8040-6318; Fax : 82-31-8040-6330)
(hoseoka@gmail.com, dwlee@kitech.re.kr, hglee@kitech.re.kr)*

Abstract: This paper presents a gamer robot system for the rock-paper-scissors game by hand motion recognition without any additional units. The proposed system consists of three parts: game management part, hand motion recognition part, and robot hand control part. 1) The game management part decides a motion of robot hand among rock, paper, and scissors. After gaming, it makes a reaction about the result of the game using speech or facial expression. 2) The hand motion recognition part realizes the hand motion of the opponent. It does not use any additional unit on body, and only uses a camera on a robot. 3) The robot hand control part shows the decided motion of robot hand. A robot hand has four fingers which are controlled independently.

Keywords: Hand motion recognition, gamer robot, rock-paper-scissors game, finger design & control.

I. INTRODUCTION

Humans usually communicate with computer or robot using additional input devices, such as keyboard, touch screen. To make simple communication environment, many researchers have studied about Human Computer Interaction (HCI) and Human Robot Interaction (HRI) [1-3]. Especially, communication using hand motion, which is the most definite expression in human body, is studied for interaction with robot systems. Moreover, the speech-impaired and the hearing-impaired are able to communicate with robots using sign language [4, 5].

There are various researches about hand motion recognition, for example, motion detecting by wearing glove with sensors, vision processing of hand motion, etc. In the motion detecting by wearing glove with sensors, although it is easy to detect and recognize hand motion in real time, additional input device is needed [6]. On the other hand, in the vision processing of hand motion, although additional input device is not needed, recognition rate is dependent on environment, such as shadow, illumination.

In this paper, we present a gamer robot system for the rock-paper-scissors game by hand motion recognition using vision processing. The gamer robot system consists of three parts; game management part, hand motion recognition part, and robot hand control part. In Section 2, we introduce a hand motion recognition system. In Section 3, we explain a four-fingered robot hand system. In Section 4, we show the experimental results. Finally, we conclude this paper in Section 5.

II. Hand Motion Recognition System

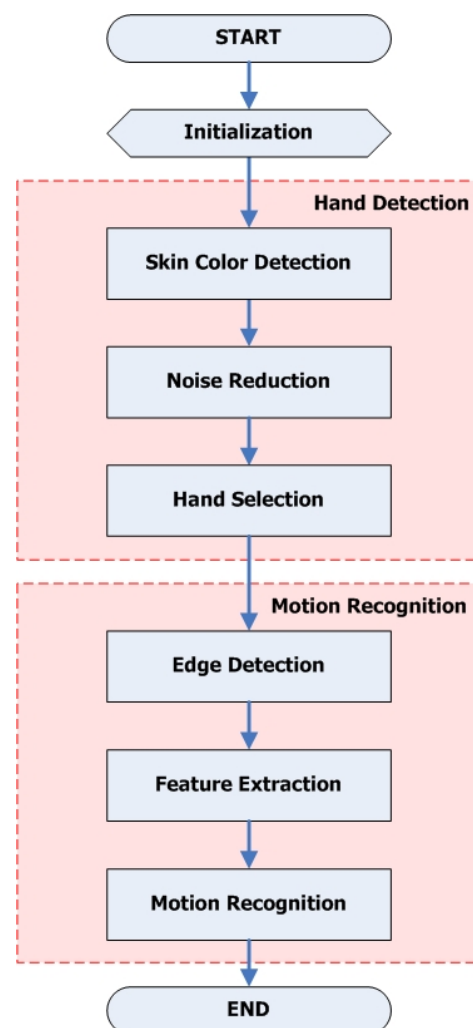


Fig. 1. The diagram of the proposed hand motion recognition system

As humans make various hand motions, it is difficult to understand all hand motions. The hand motion recognition system by vision processing, we introduce in this paper, understands only three hand motions; rock, paper, and scissors. Fig. 1 shows the diagram of the proposed hand motion recognition system. There are two steps; the first step is hand detection and the second step is motion recognition. In the hand detection, we get the biggest hand image from the camera of robot system. In the motion recognition, we classify hand motion among rock, paper, and scissors. We use HSV color space for the hand motion recognition system, because it is conceptualized in human vision in terms of other color-making attributes, such as hue, lightness, and chroma [7].

2.1. Hand Detection

We extract candidate pixels of hand using skin color



Fig. 2. The input image from camera



Fig. 3. The hue image of skin color (white)



Fig. 4. The saturation image of skin color (black)

detection. From Fig. 2 to Fig. 5 shows the results of skin color detection process. 1) We get the input image from the camera of robot as shown in Fig. 2. 2) We set the threshold range for skin color. 3) We get the image shown in Fig. 3 from the hue image of Fig. 2 using threshold range. The white colored pixels are detected pixels as skin color. 4) We get the image shown in Fig. 4 from the saturation image of Fig. 2 using threshold range. The black colored pixels are detected pixels as skin color. 5) We get the skin colored image shown in Fig. 5 by logical operator conjunction between Fig. 3 and Fig. 4. The white colored pixels are detected pixels as skin color. As skin color detection extracts similar colored pixels with skin color, noise is mixed in Fig. 5. Therefore, we reduce noise of Fig. 5 by Morphology algorithm [8]. Then, we classify the candidate pixels of hand by well-known Labeling algorithm. We assume that the biggest lump of pixels is the hand.



Fig. 5. The candidate pixels of hand (white)



Fig. 6. The edge image of hand (white)



Fig. 7. The significant features of hand

2.2. Motion Recognition

We detect the edge of the hand to recognize hand motion as shown in Fig. 6. Then, we extract significant features such as convex points for the end points of fingers and concave points for the interdigital points of fingers as shown in Fig. 7. We calculate the length of fingers using convex points and concave points of fingers. We classify the hand motion using the calculated result among three candidate hand motions; rock, paper, and scissors.

III. Four-Fingered Robot Hand System

We design the four-fingered robot hand system for playing the rock-paper-scissors game. The robot fingers are designed using small gears instead of wires to accurate control without compensation. Each finger is able to control independently to express scissors. Fig. 8 shows the designed four-fingered robot hand system. Fig. 9 shows the 3 DOF (Degree Of Freedom) designed robot finger with three knuckles and three robot fingers are designed identically. Fig. 10 shows the 4 DOF designed thumb with three knuckles. Thumb has one more DOF due to the saddle joint to lift some objects.

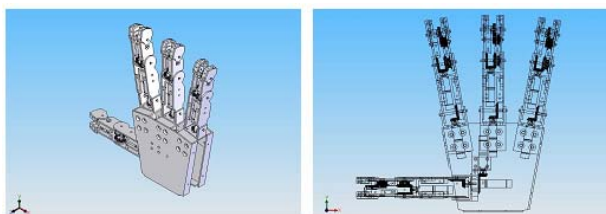


Fig. 8. The four-fingered robot hand system

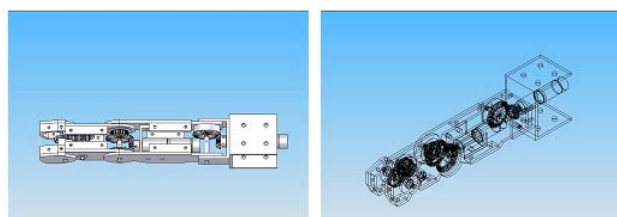


Fig. 9. The designed robot finger

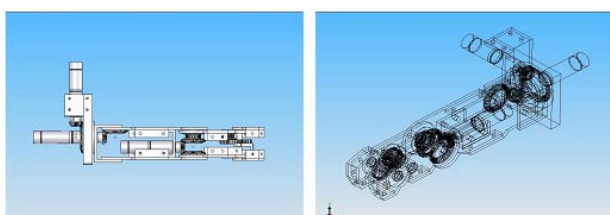


Fig. 10. The designed thumb

VI. EXPERIMENTS

We tested the explained hand motion recognition system. Fig. 11 shows the recognition result about rock. Fig. 12 shows the recognition result about scissors. Fig. 13 shows the recognition result about paper. Although background is disordered, the explained hand motion recognition system recognized correctly.



Fig. 11. The recognition result about rock



Fig. 12. The recognition result about scissors



Fig. 13. The recognition result about paper

We implemented the designed four-fingered robot hand system based on the heterogeneous reconfigurable modular architecture [9]. Fig. 14 shows the expression of rock. Fig. 15 shows the expression of scissors. Fig. 16 shows the expression of paper.



Fig. 14. The expression of rock



Fig. 15. The expression of scissors



Fig. 16. The expression of paper

V. CONCLUSION

As hand of human is the most definite expression part in human body, it can be useful way for the interaction between human and robot. In this paper, we proposed the hand motion recognition system and introduced the four-fingered robot hand system. In the hand motion recognition system, we found hand by skin color detection and then, recognized the hand motion by edge detection and analysis. As the proposed hand motion recognition system classified hand motion into three categories, it had high recognition rates in our experiments.

In the four-fingered robot hand system, we designed palm, thumb, and finger using small gears instead of wires to accurate control without compensation. Then, we implemented the designed robot hand system of their fingers are controlled independently. Two systems are integrated based on the heterogeneous reconfigurable modular architecture for playing the rock-paper-scissors game. In the future, we will research about recognition of sign language.

REFERENCES

- [1] Bronstein, A.M., Bronstein, M.M., and Kimmel, R., "Rock, Paper, and Scissors: extrinsic vs. intrinsic similarity of non-rigid shapes," *In Proceedings of the 11th IEEE International Conference on Computer Vision*, pp. 1-6, 2007.
- [2] Hasuda, Y., Tshibashi, S., Kozuka, H., Okano, H., and Ishikawa, J., "A robot designed to play the game "Rock, Paper, Scissors"", *In Proceedings of the IEEE International Symposium on Industrial Electronics*, pp. 2065-2070, 2007.
- [3] Lae Kyoung Lee, Sungshin Kim, Young-Kiu Choi, and Man Hyung Lee, "Recognition of hand gesture to human-computer interaction," *In Proceedings of the 26th Annual Conference of the IEEE Industrial Electronics Society*, vol. 3, pp. 2117-2122, 2000.
- [4] Maebatake, M., Suzuki, I., Nishida, M., Horiuchi, Y., and Kuroiwa, S., "Sign Language Recognition Based on Position and Movement Using Multi-Stream HMM," *In Proceedings of the Second International Symposium on Universal Communication*, pp. 478-481, 2008.
- [5] Bauer, B., and Hienz, H., "Relevant features for video-based continuous sign language recognition," *In Proceedings of the IEEE International Conference on Automatic Face and Gesture Recognition*, pp. 440-445, 2000.
- [6] Heumer, G., Amor, H.B., Weber, M., and Jung, B., "Grasp Recognition with Uncalibrated Data Gloves - A Comparison of Classification Methods," *In Proceedings of the IEEE Virtual Reality Conference 2007*, pp. 19-26, 2007.
- [7] Michael W. Schwarz, William B. Cowan, and John C. Beatty, "An experimental comparison of RGB, YIQ, LAB, HSV, and opponent color models," *ACM Transactions on Graphics*, vol. 6, no. 2, pp. 123-158, 1987.
- [8] Peters, R.A., "A new algorithm for image noise reduction using mathematical morphology," *IEEE Transactions on Image Processing*, vol. 4, no. 5, pp. 554-568, 1995.
- [9] Ho Seok Ahn, Young Min Beak, In-Kyu Sa, Woo Sung Kang, Jin Hee Na, and Jin Young Choi, "Design of Reconfigurable Heterogeneous Modular Architecture for Service Robots," *In Proceedings of the 2008 IEEE/RSJ International Conference on Intelligent Robots and Systems (IROS 2008)*, pp.1313-1318, 2008.

Analysis method of tooth meshing condition and motion of gears

Edzrol Niza Mohamad^{*1}, Masaharu Komori^{*1}, Hiroaki Murakami^{*1} and Aizoh Kubo^{*1}

^{*1}

Department of Mechanical Engineering and Science, Kyoto University
Yoshidahonmachi, Sakyo-ku, Kyoto-shi, Kyoto, 606-8501 JAPAN
komorim@me.kyoto-u.ac.jp

1. Introduction

The fluctuation in rotational motion of gears is a critical issue for gear designers. Effective methods of analyzing motion error are needed. Based on the author's developed method [1], this study proposes a new function of stiffness considering actual contact ratio (c.f. Fig. 1). By comparing the obtained results of motion error from the new method and the previous method, the effectiveness is validated.

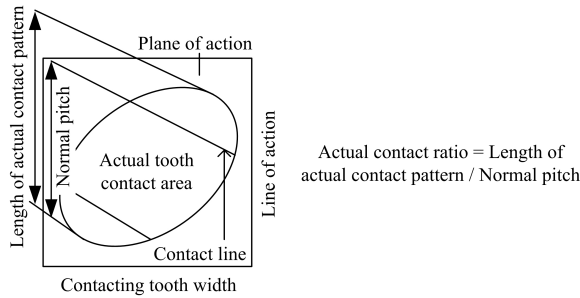


Fig. 1 Definition of actual contact ratio

2. Novel general model of tooth meshing condition

2.1 Tooth flank form deviation

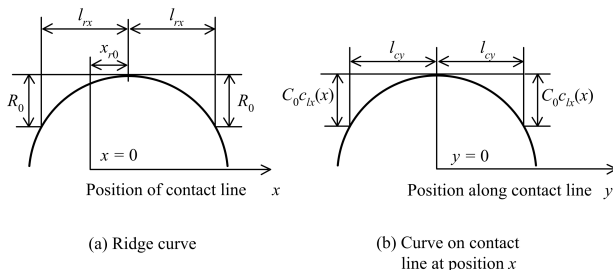


Fig. 2 Definition of ridge curve of tooth flank form and its curve on contact line

Figure 2(a) shows a schematic diagram of the infinitely expanded ridge curve on tooth flank [1]. The ridge curve $R(x)$ is represented as:

$$R(x) = R_0 \left(\frac{|x - x_{r0}|}{l_{rx}} \right)^s \quad (1)$$

Figure 2(b) shows a schematic diagram of the deviation form on the contact line at position x . The form of the curve on the contact line is expressed:

$$C(x, y) = C_0 c_{lx}(x) c_{ly}(y) \quad (2)$$

$$c_{lx}(x) = 1 + (c_x - 1) \left(\frac{|x - x_{c0}|}{l_{cx}} \right)^u \quad (3)$$

$$c_{ly}(y) = \left(\frac{|y|}{l_{cy}} \right)^v \quad (4)$$

2.2 Tooth meshing stiffness

The non-linear change of stiffness against the variations in the actual contact ratio is represented as follows:

$$K(x, h_1, \varepsilon) = K_0 s_{tx}(x) s_{tc2}(x, h_1, \varepsilon) \quad (5)$$

$$s_{tx}(x) = 1 - (1 - k_x) \left(\frac{|x - x_{k0}|}{l_{kx}} \right)^i \quad (6)$$

$$s_{tc2}(x, h_1, \varepsilon) = 1 - (1 - k_2) \left(\frac{\left| x - \frac{2h_1 - \varepsilon}{2} \right|}{\frac{\varepsilon}{2}} \right)^{ii} \quad (7)$$

where K_0 controls the magnitude of the unit stiffness and ε is actual contact ratio. Figure 3 shows the definitions of the proposed function of unit stiffness.

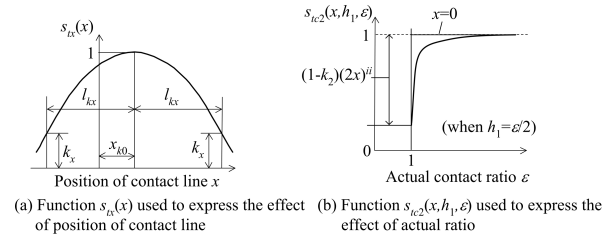


Fig. 3 Functions to define stiffness

2.3 Formulation of motion error

From the expressions mentioned, the absolute amount of motion error T_e is represented as:

$$T_e = R_0 \left\{ r_{id}(x) + \zeta \left(\frac{r}{s_{tx}(x) s_{tc2}(x, h_1, \varepsilon) t_r(x)^2} \right)^{\frac{v}{v+1}} c_{lx}(x)^{\frac{1}{v+1}} \right\} \quad (8)$$

$$\zeta = \frac{C_0}{R_0} \left(\frac{l_{cl}}{2l_{cy}} \right)^v \left(\frac{c_{lx}(x) s_{tx}(x) s_{tc2}(x, h_1, \varepsilon) t_r(x)^2}{r} \right)^{\frac{v}{v+1}} \quad (9)$$

The normalized motion error T_{e0} is defined:

$$T_e = R_0 T_{e0} \quad (10)$$

3. Effect of changes of parameters in distribution function of unit stiffness

Figure 4 shows the distribution function of unit stiffness on x -direction under each value of parameter k_x . The conditions that, compared with the stiffest contact

line (at the center of tooth flank), the stiffness of other contact lines are lower can be expressed by parameter k_x .

The changes of the actual contact ratio at peak and valley and also the amplitude of motion error at peak against parameter k_x is shown in Fig. 5. It can be concluded that parameter k_x has an influence on the actual contact ratio at peak and valley and also the amplitude of motion error at peak position. Figure 6 shows the distribution function of unit stiffness on x -direction under each value of parameter i .

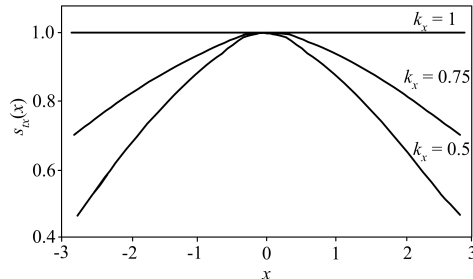


Fig. 4 Relationship between parameter k_x and position of contact line, x

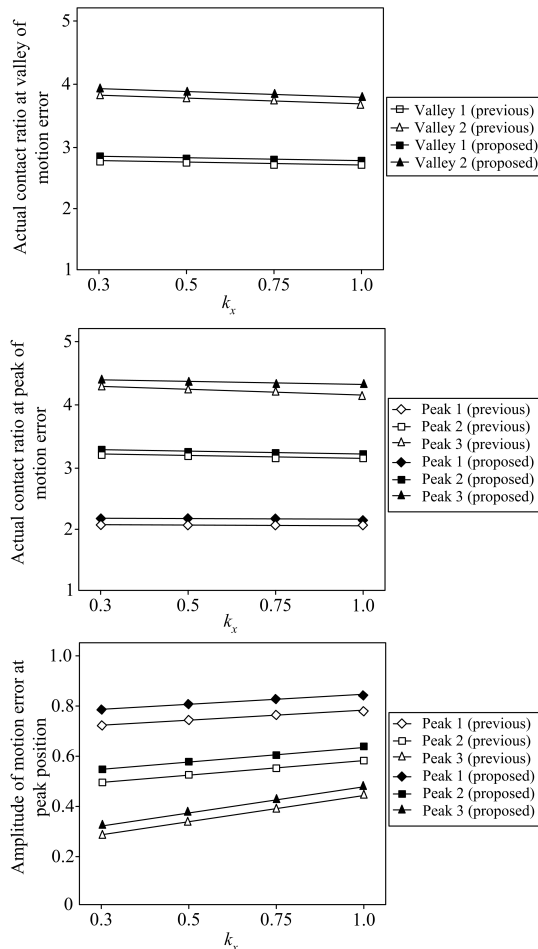


Fig. 5 Relationship between parameter k_x and motion error at peak and valley positions

Figure 7 shows the changes of against the amplitude of motion error at peak position against parameter i . Overall, the effect of parameter i is very small. Based on these results, previous method and the newly proposed method show the identical trend.

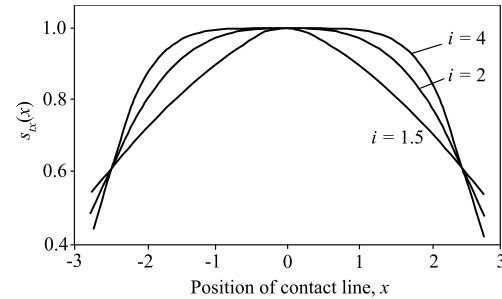


Fig. 6 Relationship between parameter i and position of contact line, x

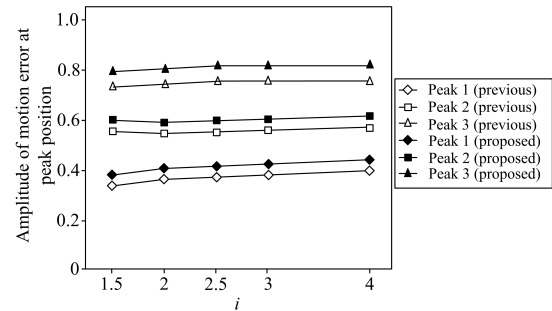


Fig. 7 Relationship between parameter i and motion error at peak and valley positions

4. Conclusions

In this report, by using a formulation for gear motion error based on a general model for meshing condition, the effectiveness of the newly proposed method to represent the stiffness was analyzed. The results obtained by both methods show that the analyzed characteristic of the motion error were in a good correspondence between the proposed method and the previous one.

Acknowledgment

This study was supported by Industrial Technology Research Grant Program in 2009 from New Energy and Industrial Technology Development Organization (NEDO) of Japan.

References

- [1] E. Niza Mohamad, M. Komori, Hiroaki Murakami, A. Kubo, and Suping Fang (2009), Analysis of General Characteristics of Transmission Error of Gears With Convex Modification of Tooth Flank Form Considering Elastic Deformation Under Load, Journal of Mechanical Design, Vol. 131, No. 6

Research for an Adaptive User's Intent-Detection Method for the Use in Rehabilitation Robots

J. Y. Jung, D. Y. Lee, D. W. Choi, I. H. Jang, H. G. Lee, H. S. Park and D. W. Lee

Department of Intelligent Robotics, University of Science and Technology, Daejeon, Korea

(Tel : 82-31-8040-6314; Fax : 82-31-8040-6370)

(paran1@kitech.re.kr)

Division of Applied Robot Technology, Korea Institute of Industrial Technology, Ansan, Korea

(Tel : 82-31-8040-6292; Fax : 82-31-8040-6370)

(hsubpark @kitech.re.kr)

Abstract: In this paper, research on how to make an adaptive algorithm for user's walking intent detection is presented. User's intent detection is the most critical problem in rehabilitation robots designed to help paraplegic patients. It is very difficult to overcome this problem in the dynamic environments. The idea of adaptive method is the combination of machine learning technics. Grammatical evolution is used to evolve C++ codes related user's intent detection. Dynamic time wrapping is used in appraiser which is in charge of a fitness function for the evolutionary process.

Keywords: Rehabilitation Robot, User's Intent Detection, Adaptation, Genetic Algorithm, Symbolic Regression, Dynamic time wrapping

I. INTRODUCTION

Recently, many researches related to helping the disabled and elderly are conducted. Most popular is the area of wearable robots. A wearable or exoskeleton robot is a robot which one can wear like a second skeleton. Representative researches are HAL[1], and ReWalk[2]. HAL was initially designed to augment muscle power of the elderlies but its abilities were extended to walking assistance for paraplegia patients. Another well-known robot is ReWalk, developed by Argomedtec, Israel. ReWalk uses tilt sensors, attached to the torso, and force sensors, located in the robot's soles, to detect the user's intent. The robots mentioned above succeeded in detecting the user's intent, but they have their limitations. The reason for this is that the robots have only been applied to experimental scenarios. Daily life or dynamic environments are much more difficult since several unexpected situations can arise.

In this paper, we propose an adaptive method to detect user's intent in dynamic and daily environments. In order to acquire a proper method, we combined two methods, symbolic regression and dynamic time wrapping.

II. DEFINITION OF USER'S INTENT DETECTION

Before developing a method for adaptive user's intent detection, intent detection for both robot and human has to be defined. In the case of wearable robots,

'the decision at what time which action should be performed is dependent on the users and the actions selected by the user are simply conducted by robot'. In other words, the robot's role can be limited to detecting signals WHAT and WHEN from users and then executing the according behavior. The problem of detecting behavior intention could thus be regarded as a user's intent detection problem. It can be defined mathematically as follows:

$$f(x_t, s_t) \rightarrow x_{t+1} \quad (1)$$

$$x_t \in \{state_1, state_2, state_3, \dots, state_n\} \quad (2)$$

$$s_t = [fl_1 fl_2 \dots ms] \quad (3)$$

In equation (1), function f is the function of user's intent detection. This function computes the state x at time $t+1$ using the current state x_t and the sensor values s_t as input. The new state x_{t+1} can be the same or different to the previous state. Using the new state, the robot determines and conducts its next behavior.

III. RESEARCH FOR AN ADAPTIVE USER'S INTENT METHOD

Two phases are introduced, one which is a training phase and the other which is an adaptation phase for the proposed method.

Furthermore, the system is organized as shown in Fig. 1. In the training phase, an intention estimator, detecting the user's intent, is developed by grammatical evolution (GE)[3] with off-line sensor data. After development,

this block detects the user's intent from the inputs of the robot's current state and the sensor data at time t . The intention estimator is continuously adapted by GE throughout the robot's task. This phase is called the adaptation phase. In the adaptation phase, a dynamic time wrapping algorithm is used as a fitness function of the intention estimator in an intention estimator appraiser block.

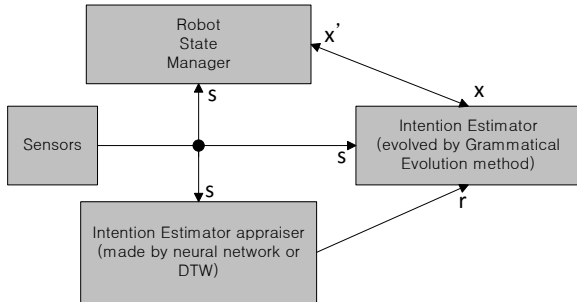


Fig. 1. The block diagram of proposed method

1. Grammatical Evolution

Grammatical evolution (GE) is a sort of symbolic regression method evolving the program code using a genetic algorithm and a Backus-Naur form (BNF). A BNF is a meta language to describe the syntax of programming languages. BNF grammars are defined and binary chromosomes evolved to make the program code of the intention estimator.

2. Dynamic Time Wrapping

Dynamic time wrapping is used to make the fitness functions for the genetic algorithm described above in the adaptation phase. This algorithm has the specialty of measuring similarities between two sequences which may vary in time or speed. In this paper, the similarities between previous and current foot sensor patterns would be detected by this algorithm.

IV. EXPERIMENTS PLAN

To verify our proposed method, experiments are planned using 16 force sensing register (FSR) sensors, located in foot part of rehabilitation robots. Two different experiments will be conducted.

In the training phase experiment, off-line sensor data is used to make the intention estimator function. This data includes 16 FSR values and the result of user's intent detection. A grammar that generates programs for an intention estimator is given below.

```

<code> ::= <line><code> | <line>
<line> ::= <lhs>=<rhs>; \n
<lhs> ::= <var> | <state>
<state> ::= state
<var> ::= r[0]|r[1]...|r[13]
<rhs> ::= <arg1> <op> <arg2>
<arg1> ::= <var> | <sensor>
<sensor> ::= s[0]|s[1]...|s[15]
<arg2> ::= <const> | <var> | <sensor>
<const> ::= <pm>0x<hex><hex><hex>
<pm> ::= +|-
<hex> ::= 0|1...|f
<op> ::= + | - | * | & | BITOR | ^ | << | >>

```

The genetic algorithm setting to be used in the training phase is as follows.

- The generation size is 5000.
- Single-point crossover with probability 0.9
- Bitwise mutation with probability 0.01
- The population size is 500.

In the adaptation phase experiment, we decrease the generation size to 20 and the population size to 3 in order to get the fast evolution. The intention estimator appraiser is used as fitness function of the grammatical evolution.

VI. CONCLUSION

An adaptive user's intent detection method is proposed in this paper. By combining two machine learning method and dividing the process of evolution into two phases, we expect to acquire an adaptive method to detect user's intent. In the future, we will apply this method to our robot and verify its effectiveness.

REFERENCES

- [1] Suzuki K, Mito G, Kawamoto M and et al. (2007), Intention-Based walking Support for paraplegia patients with robot suit HAL. *Advanced Robotics* 21(12):1441-1469
- [2] Goffer A, and Tivon K (2002), Gait-locomotor apparatus. European Patent 1 260 201 A1
- [3] O'Neill M, and Ryan C (2003), *Grammatical Evolution*. Kluwer Academic Publishers.

Development of touch sensor system of silicone-type artificial skin for an interactive android robot

Duk-Yeon Lee, Dong-Wook Lee, Dongwoon Che, Hyun-Sub Park, Ho-Gil Lee and Jun-Young Jung

*Korea Institute of Industrial Technology (KITECH), Republic of Korea
(Tel : 82-31-8040-6315; Fax : 82-31-8040-6330)*

*(proldy@kitech.re.kr, dwlee@kitech.re.kr, cdw@kitech.re.kr, hsubpark@kitech.re.kr, leehg@kitech.re.kr,
paran1@kitech.re.kr)*

Abstract: This paper presents a touch sensor system of an android robot developed by authors. In our android, touch sensors are embedded under artificial skin which is composed of special silicone. Also the thickness of the skin is about 5 to 20 mm in the face and hands. In general, as the skin is thicker, the recognition rate of conventional resistive touch sensor is worse. In addition, irregular artificial skin surface does not guarantee the recognition of various touching movements. To improve the recognition rate of touch sensor, we developed capacitive touch sensors with touch controller module. In order to verify the effectiveness of our touch sensor system, we test it in various conditions of thickness and touching movements. Also we show some applications of interactive communication using our touch sensor system between human and android robot.

Keywords: Android robot, Capacitive sensor, Touch sensor, Flexible Tactile sensor.

I. INTRODUCTION

Using the touch-sensor technology is contacted by the human often has been applied to many mobile devices. This technology is shown in Figure 1 applied to the Android robot or Humanoid robot was also used.

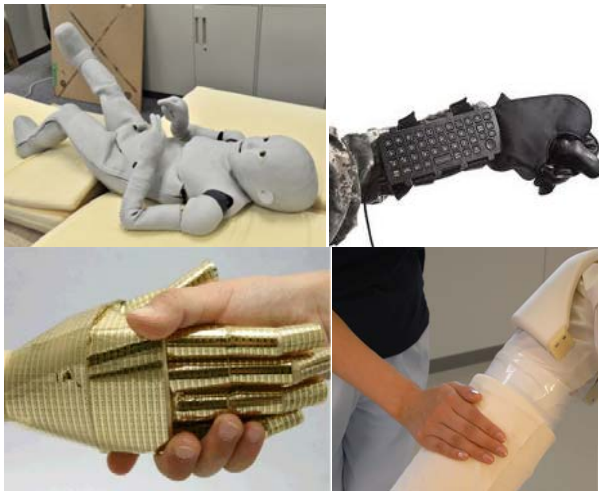


Fig. 1 Robots using tactile sensors

However, the general robot used touch-sensor technology in the purpose for which power was measured. Touch-sensor technology in the android robot, rather than for the purpose of measuring the force for the purpose is to interact with human. In the case of android robots are composed of thick artificial skin. The force exerted from the outside is difficult to be passed inside the touch sensor pad. In addition, the android robot out of the artificial skin should not be exposed to the touch sensor pad. Also more than 10mm in thickness artificial skin was used in the general robotics and force-based touch technology is difficult to apply. The outer surface of the android-robot is complex as Figure 2 shows the typical force-based touch sensor using a



Fig. 2 Ever-2 Head : inner structure and face
variety of movements can not be guaranteed. Therefore, various facial expressions are critical problems in the android robot.

In this paper, a touch sensor system for android robot interaction is about the development. Change in capacitance value due to contact with the human body to detect and obtain data from each of the touch sensor pad for the touch sensor module; Touch sensor module to collect the data obtained by the various touch-operation results can be transferred to the host device, the touch module controller; Analysis of the data received from the touch module controller for the robot to determine whether any act came in, the robot is to do as a result of behavioral patterns were selected to generate a corresponding control command signal sent to control the target controller, the host processor(PC: personal computer) unit program Includes.

II. OPERATING PRINCIPLE OF CAPACITIVE TOUCH SENSORS

Capacitive touch sensors that measure the variation in capacitance of the touch sensor pad and the humidity,

pressure, location, etc. can be measured. Pressure sensors, touch sensors, accelerometer sensors, etc. are typical.

Common measurement for capacitance sensor can range from the tens of pF to pF. In this paper, we apply the touch sensor SoC(System On Chip) is used to model the NTS1006 product by NextChip Ltd. Chip capacitance measurement precision and resolution has 0.1pF capacitance also has six input channels. In this paper, in an SoC was used the two capacitive input channels.

General formula of capacitance relationship between PAD size and relative permittivity are as follows.

$$C = \frac{\epsilon S}{d} = C = \frac{\epsilon_0 \epsilon_r S}{d} \quad (1)$$

ϵ_0 : Vacuum Permittivity, ϵ_r : Relative Permittivity, S : Size, d : Distance

Touch sensor pad occurs in the size of the capacitance in the above formula (1) and the same, the touch is inversely proportional to the distance and is proportional to the pad size. In addition, the touch pad and the contacts between the relative permittivity capacitance can be a significant change in capacity.

Typical relative permittivity of the acrylic 2.5 ~ 3, FR4 PCB 4.3 ~ 4.6, 2.0 to 3.5 rubber, air 1, the water has 80 properties. Silicone artificial skin on the android-robot picks up the attributes on the relative permittivity constant of 2 to 3.5 typically rubber like material properties and the mixing ratio varies depending on the value. Low relative permittivity and complex face various forms of internal structure of the metal frame is mounted. Thus, the capacitive touch pads are difficult to operate reliably in the android robot. Between touch pad and is particularly close to a thick artificial silicone skin, due to the low relative permittivity constant is difficult to obtain sufficient capacitance. To overcome these problems, this paper has developed a touch sensor pad size of 10X12mm. Also, SoC RF Noise in a number of input channels to prevent the incoming input channels were mounted in front of the LPF(Low pass filter). As a result, a touch sensor operates from a variety of RF Noise was an error does not happen. The SoC delta detection algorithm based on the threshold algorithm is applied to a variety of changes in capacitance values could be obtained quickly.

III. DESIGN OF TOUCH SENSOR SYSTEM

The authors have developed a touch sensor system is shown in Figure 3. Two touch pad with a touch module, comparative data for each touch pad may be sensing the moving action. Touch module was applied to a high-performance SoC(NTS1006), and I2C communication with the touch module controller is connected. 400KHz and 100KHz to 100KHz of the speed of I2C communication used.

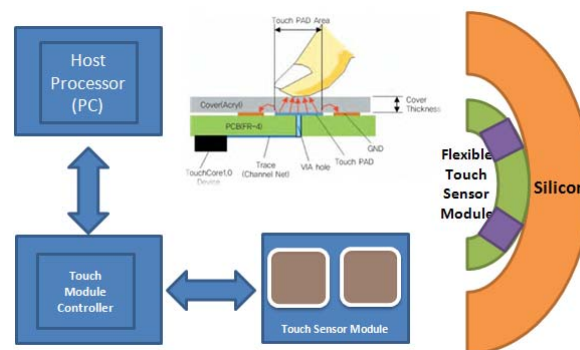


Fig. 3 Touch Sensor System

Communication speed is too high for the sampling period is short, touch-sensing value is acquired abnormal value by experimental and applied to the communication speed of 100KHz. Calibration of touch module, initialization, and communications functions are programmed in the touch module controller. Contact with touch sensor pad have a relative permittivity capacitance occurs as should perform calibration. The reference value is set to occur as the capacitance and capacitive touch operation changes the value of accurate sensor reference value must be deducted from the acquisition can be.

Communication mode UART / USB / CAN approach can be used, but in this paper for easy multiple access CAN2.0A version was used.

Host device (PC: personal computer) 25ms intervals from the touch module controller touch sensor pad for each data value is obtained within the sensing. Obtained touch data based on the behavior patterns which determine whether the touch and judge the results shown in the touch module was mounted on the LED.

In this paper, the behavior patterns of touch PAD1, PAD2 a 25ms cycle Data obtained from the touch-verify the data obtained were analyzed based on the behavioral patterns of touch. In the developed touch sensor system can distinguish between various touch behavior patterns that looked out through the following experiment.

IV. EXPERIMENT



Fig. 4 Touch operation on the touch sensor pad

Exposed as shown in Figure 4 on the touch sensor pad touch action was tried. Touch sensor pad exposed in the middle do not have a relative permittivity capacitance value could be obtained as the results shown in Figure 5.

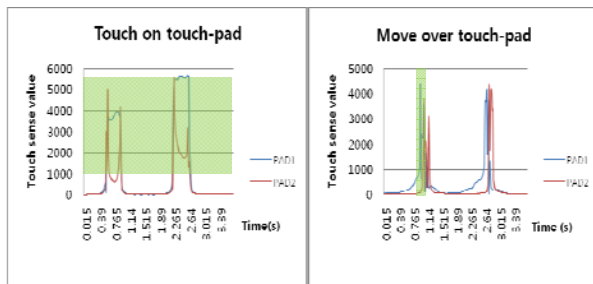


Fig. 5 Touch operation on the results of the touch sensor pad

Touch sense value, as shown in Figure 5, the sensing range is 1000-5500, and after a touch more than 100ms in case of move has a time-shift operations, sensing that a well could be confirmed by experiments.

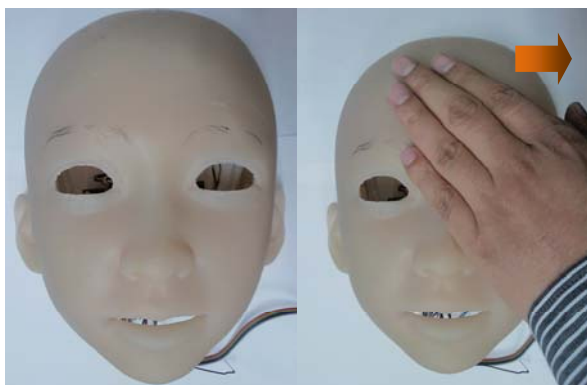


Fig. 6 Touch operation on the artificial silicon skin

Figure 6 shows a touch sensor and a relative permittivity between the chains in the presence of artificial silicon skin the experimental data shown in Figure 7. Android robots face a common area of artificial silicon skin thickness has a thickness of about 0.5cm ~ 1.4cm.

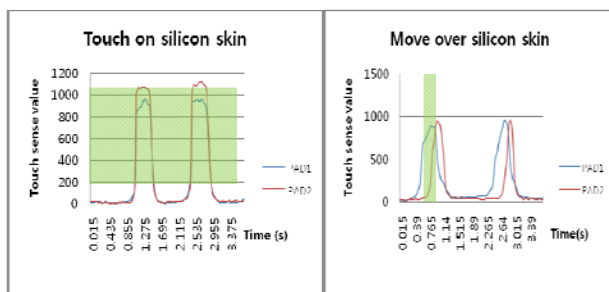


Fig. 7 Touch operation on the results of the artificial silicon skin

As shown in Figure 7 500-1000 range between the sensor data and experimental results in Figure 5 confirmed that more data can be reduced in scope. Distance increases and the relative permittivity as described in Formula 1 is the reason. However, as shown in Figure 7 from the touch sensor operates

sufficient change in capacitance could be confirmed. Figure 7 is stable to have been confirmed by comparison with Figure 5.

V. CONCLUSION

In this paper, for Android Robot capacitive touch sensor system was developed. Android robots applied to the face above the thick artificial silicon skin that stable operation is performed through the previous experiments could be confirmed. Android robots through experiments and a variety of human interaction can be sure that it could be seen. In this paper, the perfect interaction with the robot did not perform. If further studies continue to design the entire touch sensor will be mounted on the robot. Through this pattern, corresponding to various natural touch interaction research is carried out is expected to continue.

REFERENCES

- [1] Dong-Wook Lee, Development of an Android for Emotional Expression and Human Interaction, The International Federation of Automatic Control Seoul, Korea, July 6-11, 2008
- [2] Kwang-Su, Mu-jin Lee, "A Design of capacitive Sensing Touch Sensor Using RC Delay with Calibration", Journal of Korea Institute of Illuminating and Electrical Installation Engineers Vol23, No.8, pp.80~85 August 2009
- [3] Takashi Minato, et, al., "CB2: A child robot with biomimetic body for cognitive developmental robotics", Humanoid Robots, 2007 7th IEEE-RAS International Conference on, Nov. 29 2007-Dec. 1 2007
- [4]"Capacitive Sensors," Larry K. Baxter, IEEE Press, 1997.
- [5] Thorsten P. Spexard, et, al., "Human-Oriented Interaction With an Anthropomorphic Robot", IEEE TRANSACTIONS ON ROBOTICS, VOL. 23, NO. 5, OCTOBER 2007
- [6] NEXTCHIP Co, Ltd
ULR : <http://www.nextchip.com/>

Remote Control and Conversation System between Human and Android Robot via Internet

Dong-Wook Lee, Dongwoon Choi, Jun-Young Joung, Hoseok Ahn, Hyunsub Park, and Ho-Gil Lee

Korea Institute of Industrial Technology, 426-791 Ansan, Republic of Korea

Tel : 81-31-8040-6312; Fax : 81-31-8040-6370

Email {dwlee, cdw, paran1, hoseoka, hsubpark, leehg}@kitech.re.kr

Abstract: In this paper, we propose remote control and conversation system between human and android via internet. Android is a robot resembles human being not only its appearance but also behaviors. The android EveR-3 which was developed by authors can express facial expressions and lip synchronizations. Also it can talk with a human, because it has voice recognition/synthesis engine and conversation database. To control the android in remote place, we develop an online chatting program with webcam and connect it to the program of the android. At this time, the Android's side becomes a server and user side is a client. Then, user can order the operation commands to the android using this system or talk with it by voice and text messages. In this paper, we will show some examples to verify the effectiveness of our system.

Keywords: Remote control, Remote conversation, android robot

I. INTRODUCTION

Remote control in robotics, have been developed in the field of dangerous environments such as nuclear power plant, deep sea, and space. In recent years, as intelligent service robots in our home or life have been developed, the application of remote control is wider. The home service robots, such as pet robot, home guard robot, education robot, are produced as commercial goods. In this paper, we proposed remote control and conversation system for applying to a personal service robot. Proposed system is verified by applying to the android robot developed by authors.

II. ANDROID ROBOT

Android robot resembles human being not only the appearance but also its behaviors. We have developed android robot for researching the emotional interaction between human and robot.

Our first android, EveR¹-1 is capable of motion from her torso up because her lower body is a dummy. She has 35 D.O.F (degree of freedom) with 15 D.O.F in head [1]. She can do facial expressions of four emotions. EveR-1 is applied to guidance service of an exhibition, oral narration of fairy tales. EveR-2 is bipedal type [2]. So she can sing a song in standing. EveR-2 has the lower body with 12 D.O.F. She has the function of EveR-1 and is added the function of whole body coordination and dialogue engine. Her gesture, facial

expression, lip synchronization, and vision recognition are upgraded. EveR-3 is the latest version of our android [3]. She can move the ground because she has wheel based lower body. So she could be debuted as a robot actress in Korean musical performance, "EveR comes to Earth" at Feb. 18, 2009. Also the design of facial muscles in head (23 D.O.F) is based on anatomical structure of human face. So the expression ability of emotions is more abundant. Fig. 1 shows some examples of facial expressions of EveR-3.

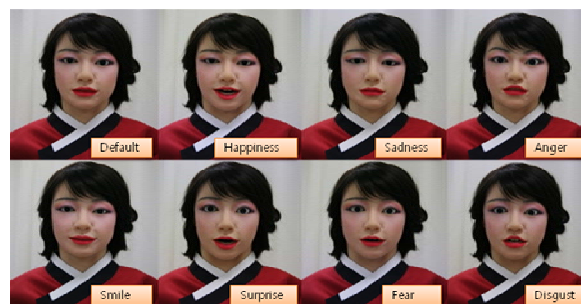


Fig.1. Facial Expressions of EveR-3

III. REMOTE CONTROL SYSTEM

1. Remote control and conversation

To control and have a conversation with robot in remote site via internet, we use one of internet messaging software which has the function of video conferencing; Skype (www.skype.com) is used in this experiment. Fig. 2 shows the proposed system that is composed of three parts; one is user (or client), the second is a server with webcam, the other is android robot, EveR-3. Internet messaging software must be

¹ The name EveR derives from the Biblical 'Eve', plus the letter 'R' for robot.

installed in user computer and the server. After a user and server are connected each other in online, the user can type or tell a message. Server interprets the message is a command or a conversation.

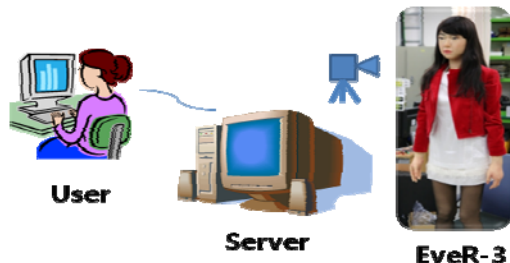


Fig.2. Components of remote system

The difference between a command and a conversation is whether input message (by typing or voice) is same with one of reserved scenario files or not. Scenario files will be explained in sec. III-2. For example, if 'right hand up.txt' is one of scenario files, also if an input message is 'right hand up', and then EveR-3 plays the scenario files. If the input message is not matched with reserved scenario files, then the robot responds the answer as the input message is a question. At this time, dialogue engine of EveR-3 is used.

Fig. 3 shows the internet messaging software used in this paper. We can see the robot and can type a message. Also we can say using microphone which is connected in PC. The internet messaging software transmits the message and voice to the server in remote site.

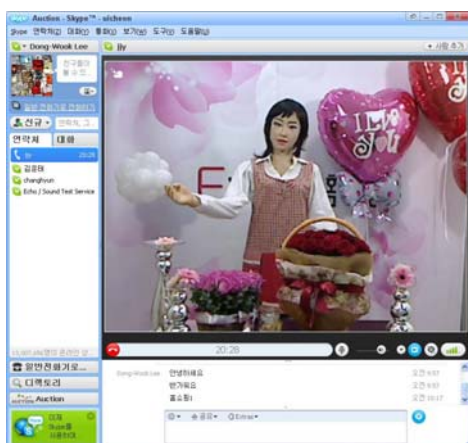


Fig.3. Remote control and conversation tool based on video conference using Skype

2. Scenario editing tool

EveR-3 has dialogue engine with conversation pairs that has 5,000 Q&A pairs which is used in ordinary life. So if one asks a question to the robot, it answers the question using dialogue engine.

Another working mode of EveR-3 is scenario mode. In scenario mode, a robot plays the scenario files. A scenario file has composed of voice, facial expression, and gesture with the start time of each. As times goes, the voice, facial expression, or gesture is played. User can create and edit the scenario files using the tool in Fig. 4.

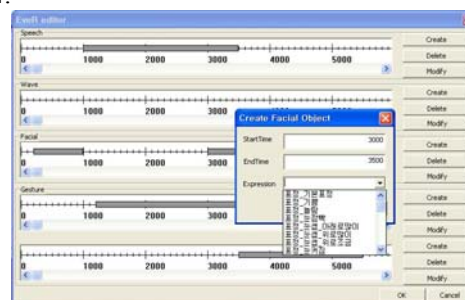


Fig.4. Scenario editing tool

VI. CONCLUSION

In this paper, we developed remote control and conversation system. Using video conference software, user can see the moving images of a robot in remote site, and can control or talk with the robot by text messages or voice commands. If user types or orders the commands through the software, then the robot can do some actions according to the command. If user talks about something, the robot responds. We think that the proposed system will be applied to remote medical examination, remote education, and so on.

ACKNOWLEDGEMENT

This research is supported by Ministry of Culture, Sports and Tourism(MCST) and Korea Creative Content Agency(KOCCA) in the Culture Technology(CT) Research & Development Program 2010

REFERENCES

- [1] H.G.Lee, M.H. Baeg, D.W.Lee *et al.* "Development of an Android for Emotional Communication between Human and Machine," *Proc. of Int. Symp. on Advanced Robotics and Machine Intelligence*, pp.41-47, 2006.
- [2] D.W.Lee, T.G.Lee, B.R.So *et al.* "Development of an Android for Emotional Expression and Human Interaction, *Proc. of World congress on International Federation of Automatic Control (IFAC 2008)*, pp. 4336-4337, 2008.
- [3] D.W.Lee, D.W.Che, D.Y. Lee *et al.* "Development of an Android for a Performance," *Proc. of Int. Conf on Ubiquitous Robot and Ambient Intelligence (URAI 2010)*, p. 664, 2010.

THE OPTIMAL METHOD OF SEARCHING THE EFFECTIVE COMBINATION OF DITHER MATRIX

Tsune yasu Kato and Ken-ichi Tanaka

School of Science and Technology, Meiji University

1-1-1, Higashi-Mita, Tama, Kawasaki, Kanagawa 214-8571 Japan

E-mail: tanaken@isc.meiji.ac.jp | ce91022@isc.meiji.ac.jp

Abstract: In this study, three methods are compared for checking the most effective method of searching the optimal combination of dither matrix. Three methods are Genetic Algorithm (GA), Simulated Annealing (SA) and Taboo Searching. The images that are used in this study are Human, Human rotating 180 degrees and Swiss. As a result, the method of GA is the most excellent in these methods.

Keywords: Dither matrix, Bayer method, GA, SA, taboo searching, optimal combination.

I. INTRODUCTION

Nowadays, there are some popularly methods of dither matrix. These methods are good on a viewpoint of image quality. However, the study that is searching effective dither matrix viewpoint of optimization combination without method of GA is not able to be found. Then, the best effective method for searching better dither matrix is checked. Searching methods are three, GA, SA and Taboo Searching. The comparing candidate is Bayer method. Algorithm of GA, evaluating method and the exposition of dither matrix are shown by Tsune yasu[1].

II. ALGORITHM OF SA

The algorithm of SA is as below.

- (1) An individual that have matrices which is set elements in at random is prepared.
- (2) New individual is made by changing element of the individual which is made at operation (1).
- (3) Comparing two individuals
- (4) New individual is made by exchanging element of the individual getting better evaluated value
- (5) Running over from (3) to (4) until the satisfaction of the conditions.

In this study, the conditions are that temperature is under number which is set at hand or evaluated value of SA is better than Bayer method.

III. ALGORITHM OF TABOO SEARCHING

The method of Taboo Searching is as below.

- (1) The matrices which have elements set in at random are prepared (it is named individual A)
- (2) Making some individuals based the individual A
- (3) Evaluating and comparing these individuals
- (4) The best evaluated value individual (it is named individual B) is selected by these individuals
- (5) If combination of individual A and B has been selected before, return to operation (2)
- (6) Comparing individual A and individual B
- (7) If individual A is better than individual B, return to operation (2)
- (8) If individual B is better than individual A, making some individuals based the individual B
- (9) Running over from (3) to (8) until numbers of repeat time surpass numbers of generations

IV. RESULT

The evaluated value of four methods changing each images are as below.

- (1) The image of human
Bayer: E=102.846, GA: E=102.785
SA: E=102.823, Taboo searching: E=102.836
- (2) The image of human rotating 180 degrees
Bayer: E=102.848, GA: E=102.817

SA: E=102.813, Taboo searching: E=102.929

(3) The image of Swiss

Bayer: E=101.544, GA: E=101.484

SA: E=101.526, Taboo searching: E=101.532

Then, the best evaluated value of Human rotating 180 degrees is SA. However, the best evaluated value of all patterns is GA. In addition, evaluated values of each image by using GA are averagely good. Then, as this result, the optimal method of searching the effective combination of dither matrix is thought that is GA.

VI. FIGURES/TABLES



Fig1. The image of human by using Bayer method



Fig2. The image of human by using GA



Fig3. The image of human by using SA



Fig4. The image of human by using Taboo Searching

2. Table

Table1. The matrix of using GA to human

7	11	0	8
3	13	6	15
9	2	10	4
12	5	14	1

Table2. The matrix of using SA to human

5	2	11	12
13	14	6	0
10	3	8	4
1	15	7	9

Table3. The matrix of using Taboo Searching to human

15	8	7	4
6	14	1	12
2	3	13	10
11	5	9	0

V. CONCLUSION

Unless using same image, the results of GA for human and human rotating 180 degree are not point symmetry. This reason will be that these results of GA are convergent local solution. Then, the problem is accuracy enhancement of GA by making change factors.

REFERENCES

- 1) Tsuneyasu Kato, "The optimal combination of dither matrix by using genetic algorithm" Artificial Life and Robotics. 15, pp137
- 2) Ken-ichi Tanaka. "Color Images Halftoning Using Simulated Annealing" The Journal of The Institute of Image Information and Television Engineers. 61.6, pp828-837
- 3) Toshiharu Nagao. "evolutionary image processing" Publication Shoukoudou Inc. Year 2002.

AUTHOR INDEX

**Notation of session name: PT: Plenary Talk, IT: Invited Talk,
OS: Organized Session, GS: General Session, PS: Poster Session**

Note: **P-44** / 359 = (page no. in Technical Paper Index) / (page no. in Papers)

[A]				Chang	C.Y.	OS11-1	P-32/269
Abdul-Rahman	O.	OS15-2	P-44/359	Chang	J.	GS10-4	P-25/771
Abe	N.	PS1-2	P-29/1008	Che	D.W.	PS1-6	P-29/1018
Abe	T.	OS13-3	P-35/322			PS1-7	P-29/1021
Adachi	R.	OS14-4	P-40/346	Chen	C.A.	OS11-1	P-32/269
Ahn	B.	GS21-1	P-27/979	Chen	T.H.	OS10-5	P-32/261
Ahn	H.S.	PS1-3	P-29/1010	Cheng	Y.	OS21-2	P-43/499
		PS1-7	P-29/1021	Cheon	H.S.	GS21-4	P-27/991
Aibe	N.	OS15-6	P-45/375	Chiang	F.C.	OS10-1	P-32/245
		OS15-7	P-45/379	Chiang	H.K.	OS11-1	P-32/269
Aihara	K.	OS14-1	P-39/334	Chien	T.L.	OS10-6	P-32/265
		OS14-2	P-39/338	Chiou	Y.R.	GS6-5	P-42/699
		OS14-3	P-39/342	Cho	B.	GS20-2	P-46/967
		OS14-4	P-40/346	Cho	J.I.	GS8-3	P-34/731
		OS14-5	P-40/350			GS10-4	P-25/771
Aikawa	C.	OS3-2	P-24/91			GS10-5	P-25/775
Aikawa	M.	OS15-4	P-45/367	Cho	Y.I.	OS23-1	P-43/549
Akama	K.	OS15-2	P-44/359			OS23-5	P-44/565
Akimoto	T.	OS24-4	P-28/585	Choi	D.W.	GS20-1	P-45/964
Akita	S.	OS15-6	P-45/375			PS1-5	P-29/1016
		OS15-7	P-45/379	Choi	G.H.	GS21-4	P-27/991
Aoki	Shigeki	GS10-1	P-25/759	Choi	M.	GS21-1	P-27/979
Aoki	Shingo	GS3-1	P-28/629	Choi	S.M.	GS8-3	P-34/731
		GS6-2	P-42/687			GS10-4	P-25/771
		GS18-1	P-37/922			GS10-5	P-25/775
Arai	E.	GS2-6	P-34/625	Chumtong	P.	GS21-6	P-27/999
Arai	T.	IT2	P-22/23	Chung	C.Y.	OS10-2	P-32/249
		GS21-6	P-27/999			OS10-4	P-32/257
Arita	T.	GS1-2	P-47/593	Cui	C.Y.	OS21-3	P-43/503
		GS3-2	P-28/633				
		GS3-3	P-28/637	[D]			
		GS7-4	P-35/715	Dai	F.	OS22-1	P-41/519
Asada	T.	OS9-2	P-36/219	Do	J.	OS12-5	P-38/310
		OS9-3	P-36/225	Dong	H.	OS22-2	P-41/523
		OS9-4	P-36/231				
Aung	K.T.	GS1-3	P-47/597	[E]			
Azumagakito	T.	GS3-2	P-28/633	E	M.	OS22-7	P-42/545
				El-fiky	M.	GS4-1	P-28/649
				Elshaer	R.H.E.	GS16-1	P-25/885
[B]				[F]			
Bae	J.I.	GS5-3	P-31/671	Fan	S.Z.	GS6-5	P-42/699
		GS13-3	P-39/834	Fu	B.	GS13-2	P-39/830
Baek	G.	OS12-5	P-38/310			GS19-2	P-30/944
Baek	K.R.	GS20-2	P-46/967	Fu	Y.Y.	OS11-5	P-33/285
Bao	Z.	GS4-2	P-28/653	Fu	T.	GS1-3	P-47/597
Beak	J.	OS12-4	P-38/306	Fuchida	K.	GS6-1	P-42/683
Bhattacharya	B.	OS21-6	P-43/515	Fuji	N.	PS1-1	P-29/1006
Burdellis	M.A.P.	GS12-3	P-45/808	Fujii	N.	GS16-2	P-25/889
				Fujimoto	T.	OS9-2	P-36/219
[C]				Fujimura	T.	OS17-3	P-29/419
Cai	G.	OS22-7	P-42/545	Fujiwara		OS17-4	P-30/423
Castro	J.C.H.	GS7-6	P-35/723				
Cha	Y.C.	GS5-3	P-31/671				

Fukuda	O.	GS8-1	P-34/727	Horiike	K.	OS9-5	P-36/237
Fukuda	T.	GS21-5	P-27/995	Hosokawa	S.	OS1-5	P-23/66
Fukumura	Y.	OS6-2	P-40/150	Hsia	K.H.	OS11-3	P-32/277
Fukushima	M.	GS7-6	P-35/723	Hsu	T.Y.	OS10-2	P-32/249
Funahashi	K.	OS3-4	P-24/99	Hu	J.	OS21-2	P-43/499
Furukawa	M.	GS2-3	P-34/613	Hwang	Y.	OS12-2	P-38/297
		GS2-4	P-34/617				
		GS2-5	P-34/621				
Furukawa	T.	GS11-2	P-42/789	[I] Ichikawa	Y.	GS8-1	P-34/727
Furuno	S.	GS20-3	P-46/971	Ide	T.	OS7-4	P-31/187
Furutani	H.	OS7-4	P-31/187			OS7-5	P-31/191
		OS7-5	P-31/191	Igarashi	H.	GS13-6	P-39/842
		OS15-1	P-44/354	Iio	T.	OS24-4	P-28/585
				Ikeda	A.	OS22-6	P-42/541
				Ikeda	K.	GS12-3	P-45/808
[G] Gao	W.	GS11-5	P-43/797			GS16-4	P-26/897
		GS21-7	P-27/1003	Ikeda	M.	OS16-4	P-47/395
Gao	X.J.	GS21-2	P-27/983	Ikeda	S.	OS7-4	P-31/187
Gejima	R.	GS18-1	P-37/922	Imai	C.	OS14-5	P-40/350
Gibo	T.	GS10-1	P-25/759	Imai	M.	IT1	P-22/21
Gocho	R.	GS2-1	P-34/605			OS24-3	P-28/581
Goto	K.	GS13-6	P-39/842	Imoto	Y.	GS5-4	P-31/675
Guo	J.H.	OS10-4	P-32/257	Inenaga	S.	OS13-5	P-36/330
		OS11-6	P-33/289	Inohira	E.	GS15-3	P-37/873
Guo	W.	OS22-7	P-42/545	Inoue	H.	OS17-1	P-29/411
				Inoue	S.	GS3-1	P-28/629
				Ishida	T.	GS2-2	P-34/609
[H] Habib	M.K.	OS23-2	P-43/533	Ishida	Y.	OS7-1	P-31/174
Hagita	N.	OS24-4	P-28/585			OS19-1	P-46/447
Hagiya	M.	GS2-6	P-34/625			OS19-2	P-46/451
Han	J.	OS12-1	P-38/293			OS19-3	P-46/455
Han	K.Y.	OS21-1	P-43/495			OS19-4	P-46/459
Harada	K.	OS19-4	P-46/459			OS19-6	P-46/467
Harima	H.	GS14-4	P-44/858			OS20-2	P-41/475
Hasama	H.	OS7-2	P-31/178			OS20-3	P-41/479
Hashimoto	K.	OS17-1	P-29/411			OS20-4	P-41/483
Hashimoto	Kiyota	OS6-1	P-40/146			OS20-5	P-41/487
		OS6-3	P-40/154			OS20-6	P-41/491
		OS6-5	P-40/162	Ishigure	Y.	GS19-6	P-30/960
Hata	Y.	OS20-6	P-41/491	Ishiguro	M.	OS15-6	P-45/375
Hattori	T.	OS8-1	P-33/195			OS15-7	P-45/379
		OS8-2	P-33/199	Ishii	S.	GS14-4	P-44/858
		OS8-3	P-33/203			GS14-5	P-44/862
		OS8-4	P-33/207	Ishikawa	S.	GS10-2	P-25/763
		OS8-5	P-33/211			GS10-3	P-25/767
Hayashi	E.	GS16-3	P-26/893			GS10-7	P-25/781
		GS16-5	P-26/901			GS11-4	P-43/793
		GS19-4	P-30/952	Ishimaru	H.	GS19-4	P-30/952
		GS19-5	P-30/956	Ishitobi	M.	OS3-1	P-24/87
Hayashi	T.	OS20-6	P-41/491	Isokawa	T.	GS14-2	P-44/850
He	P.	OS22-5	P-41/537	Ito	M.	OS3-4	P-24/99
Heo	J.	OS12-3	P-38/301			GS13-5	P-39/838
Higashimori	M.	GS21-5	P-27/995			GS21-2	P-27/983
Higuchi	K.	OS1-4	P-23/62			GS21-3	P-27/987
Hirano	G.	GS20-3	P-46/971	Ito	T.	OS7-1	P-31/174
Hirayama	K.	GS17-2	P-38/909			OS7-2	P-31/178
Hirokawa	S.	OS6-7	P-40/170			OS7-3	P-31/183
Hitaka	Y.	OS3-5	P-24/103			OS7-4	P-31/187
Ho	P.M.	GS17-3	P-38/912			OS7-5	P-31/191
Hong	Y.S.	GS1-4	P-47/601	Iwadata	K.	GS2-5	P-34/621

Iwaseya	M.	GS17-1	P-38/905	Kibayashi	R.	OS13-4	P-35/326
Iwata	M.	GS10-1	P-25/759	Kibe	Y.	GS19-4	P-30/952
Izumi	K.	OS16-4	P-47/395	Kim	C.	OS12-4	P-38/306
		OS16-7	P-47/407	Kim	D.E.	GS3-4	P-28/641
Izumi	T.	OS8-1	P-33/195	Kim	D.J.	GS13-3	P-39/834
		OS8-2	P-33/199	Kim	Hongseuk	GS21-1	P-27/979
		OS8-3	P-33/203	Kim	Hyoungseop	GS10-2	P-25/763
		OS8-4	P-33/207			GS10-7	P-25/781
		OS8-5	P-33/211			GS11-4	P-43/793
				Kim	J.	GS8-1	P-34/727
				Kim	K.	OS23-3	P-43/557
[J]				Kim	S.	OS12-5	P-38/310
Jang	I.H.	GS9-1	P-36/741	Kim	T.	OS12-5	P-38/310
		PS1-5	P-29/1016	Kim	T.H.	GS13-6	P-39/842
Jeong	J.C.	GS8-3	P-34/731	Kim	Y.J.	OS23-4	P-43/561
		GS10-5	P-25/775	Kimura	Y.	GS13-1	P-39/828
Jia	C.	OS4-1	P-26/107			GS17-4	P-38/916
Jia	X.	OS22-4	P-41/533			GS19-1	P-30/942
Jia	Y.M.	OS4-2	P-26/110			GS17-3	P-38/912
		OS4-3	P-26/114	Kirita	S.	GS6-4	P-42/695
		OS4-5	P-26/122	Kitami	K.	OS20-5	P-41/487
Jo	J.	OS12-2	P-38/297	Kitamura	K.	OS9-1	P-36/215
Joung	J.Y.	PS1-7	P-29/1021	Kitaoka	T.	GS20-4	P-46/975
Jung	E.	OS12-5	P-38/310	Kitazono	Y.	OS11-5	P-33/285
Jung	H.	GS10-7	P-25/781	Ko	C.N.	OS14-1	P-39/334
Jung	J.Y.	GS9-1	P-36/741	Kobayashi	W.	OS6-6	P-40/166
		GS20-1	P-45/964	Kodama	S.	GS16-3	P-26/893
		PS1-5	P-29/1016	Koga	K.	GS19-6	P-30/960
		PS1-6	P-29/1018	Koganemaru	K.	OS14-2	P-39/338
				Kohno	T.	OS14-3	P-39/342
[K]						GS10-2	P-25/763
Kakudou	T.	OS16-3	P-47/391	Komatsu	M.	GS13-1	P-39/828
Kamisato	S.	OS20-4	P-41/483	Komori	M.	GS17-4	P-38/916
Kamitomo	H.	OS13-2	P-35/318			GS19-1	P-30/942
Kamiura	N.	GS14-2	P-44/850			PS1-4	P-29/1014
Kanda	M.	OS17-5	P-30/427			GS13-6	P-39/842
Kaneke	M.	GS21-5	P-27/995	Kon	K.	GS5-4	P-31/675
Kanematsu	H.	OS6-2	P-40/150	Kondo	E.	OS15-3	P-44/363
Kang	J.	GS13-1	P-39/828	Kondo	K.	GS15-1	P-37/866
		GS17-4	P-38/916	Kondo	T.	GS11-2	P-42/789
		GS19-1	P-30/942	Kondo	Y.	OS9-6	P-37/241
Kashima	T.	GS17-1	P-38/905	Konishi	H.	OS18-1	P-24/431
Katamune	R.	OS7-4	P-31/187	Konishi	O.	OS3-2	P-24/91
		OS7-5	P-31/191	Kono	M.	OS7-4	P-31/187
Katayama	F.	OS18-2	P-24/435			OS7-5	P-31/191
Kato	J.	OS1-5	P-23/66			GS16-4	P-26/897
Kato	N.	GS9-4	P-36/755	Kozawa	S.	PS1-4	P-29/1014
Kato	Tatsuya	OS16-6	P-47/403	Kubo	A.	GS12-1	P-45/800
Kato	Tomonori	OS3-5	P-24/103	Kubota	S.	OS1-2	P-23/54
Kato	Tsuneyasu	PS1-8	P-29/1023	Kume	Y.	OS3-1	P-24/87
Katsumata	Y.	OS19-2	P-46/451	Kunimatsu	S.	GS14-3	P-44/854
Kawai	Y.	GS18-3	P-37/930	Kurata	K.	GS19-5	P-30/956
Kawano	H.	OS8-1	P-33/195	Kurogi	K.	OS15-4	P-45/367
		OS8-2	P-33/199	Kurose	S.	OS22-1	P-41/491
		OS8-3	P-33/203	Kushida	N.	OS24-3	P-28/581
		OS8-4	P-33/207	Kuwayama	Y.	OS12-1	P-38/293
		OS8-5	P-33/211	Kwon	Y.		
Kawano	K.	OS5-5	P-24/142				
Kawanobe	H.	OS17-2	P-29/415	[L]			
Kawasaki	H.	GS19-6	P-30/960	Leblebicioğlu	K.	GS17-5	P-38/918
Kawashima	M.	GS10-6	P-25/777	Lee	C.M.	OS11-5	P-33/285

Lee	D.S.	GS5-3	P-31/671	Lund	H.H.	IT5	P-22/43
		GS13-3	P-39/834				
Lee	D.W.	GS9-1	P-36/741	[M]			
		GS20-1	P-45/964	Ma	Q.L.	OS15-1	P-44/354
		PS1-3	P-29/1010	Mabrouk	E.	GS7-6	P-35/723
		PS1-5	P-29/1016	Mackin	K.J.	OS18-3	P-24/439
		PS1-6	P-29/1018			OS18-4	P-24/443
		PS1-7	P-29/1021	Mae	Y.	GS21-6	P-27/999
Lee	D.Y.	GS9-1	P-36/741	Maeda	T.	GS6-1	P-42/683
		GS20-1	P-45/964	Maeyama	S.	OS16-5	P-47/399
		PS1-5	P-29/1016			OS16-6	P-47/403
		PS1-6	P-29/1018	Maki	M.	GS5-1	P-30/663
Lee	H.G.	GS9-1	P-36/741	Masuda	S.	OS8-3	P-33/203
		GS20-1	P-45/964	Matsuda	N.	PS1-2	P-29/1008
		PS1-3	P-29/1010	Matsui	H.	GS9-4	P-36/755
		PS1-5	P-29/1016			GS12-4	P-45/812
		PS1-6	P-29/1018			GS12-5	P-45/816
		PS1-7	P-29/1021	Matsui	N.	GS14-2	P-44/850
Lee	H.H.	OS21-1	P-43/495	Matsumoto	H.	OS13-4	P-35/326
		OS21-3	P-43/503	Matsumoto	K.	GS6-3	P-42/691
		OS21-5	P-43/511			GS6-4	P-42/695
Lee	J.E.	OS21-5	P-43/511	Matsuno	F.	GS13-6	P-39/842
Lee	J.J.	OS23-4	P-43/561	Matsuno	S.	OS7-1	P-31/174
		OS23-6	P-44/569	Matsuo	F.	PT3	P-22/15
Lee	J.M.	OS12-1	P-38/293	Matsuo	T.	OS17-5	P-30/427
		OS12-2	P-38/297	Matsushita	K.	OS18-3	P-24/439
Lee	Jaehong	GS20-2	P-46/967	Mehta	R.	OS7-2	P-31/178
Lee	Jaeoh	OS12-1	P-38/293			OS7-3	P-31/183
Lee	Jungju	OS23-3	P-43/557	Meng	D.	OS4-2	P-26/110
Lee	Junseok	OS12-2	P-38/297	Mikami	Y.	OS6-6	P-40/166
Lee	K.S.	GS5-3	P-31/671	Mimura	E.	GS3-1	P-28/629
		GS13-3	P-39/834	Minowa	K.	GS16-3	P-26/893
Lee	M.	OS12-3	P-38/301	Minoya	K.	GS1-2	P-47/593
		OS12-4	P-38/306	Miura	H.	PS1-2	P-29/1008
Lee	M.H.	GS5-3	P-31/671	Miyamoto	T.	GS10-1	P-25/759
		GS13-3	P-39/834	Miyata	K.	GS20-4	P-46/975
Lee	S.	GS21-1	P-27/979	Miyata	R.	GS14-3	P-44/854
Lee	Y.J.	GS5-3	P-31/671	Miyauchi	A.	GS7-2	P-35/707
		GS13-3	P-39/834			GS7-3	P-35/711
Li	G.	GS10-2	P-25/763			GS15-4	P-37/877
Li	X.	OS22-3	P-41/529	Mizoguchi	F.	GS9-2	P-36/745
Li	Y.	GS21-3	P-27/987	Mizoguchi	N.	OS14-2	P-39/338
Lian	L.	GS13-2	P-39/830	Mizuno	T.	OS1-2	P-23/54
		GS19-2	P-30/944	Mogi	K.	OS2-1	P-26/70
Liao	Y.L.	OS10-3	P-32/253	Mohamad	E.N.	PS1-4	P-29/1014
Lien	S.F.	OS11-3	P-32/277	Moon	Y.	OS12-3	P-38/301
Lim	E.G.	GS10-4	P-25/771	Mori	A.	GS12-4	P-45/812
Lin	C.L.	OS11-2	P-32/273	Mori	K.	OS18-4	P-24/443
Lin	W.B.	OS11-1	P-32/269	Mori	Y.	GS19-6	P-30/960
Lin	W.C.	OS10-5	P-32/261	Mori	Yukihiro	OS20-4	P-41/483
Lin	Yung-Chien	OS10-5	P-32/261	Morie	T.	GS10-3	P-25/767
Lin	Yung-Chin	OS10-5	P-32/261	Munetomo	M.	OS15-2	P-44/359
Liu	C.	GS13-2	P-39/830	Murakami	H.	PS1-4	P-29/1014
		GS19-2	P-30/944	Murao	H.	GS1-1	P-47/589
Liu	G.Y.	OS11-5	P-33/285	Murata	J.	GS12-2	P-45/804
Liu	Y.	OS4-3	P-26/114				
		OS4-4	P-26/118	[N]			
Lu	C.	OS13-1	P-35/314	Nagai	I.	OS16-3	P-47/391
		OS13-2	P-35/318			OS16-7	P-47/407
Lund	H.H.	IT4	P-22/36	Nagamatsu	Y.	OS14-2	P-39/338

Nagamine	T.	OS22-6	P-42/541	[O]			
Nagashima	J.	GS7-1	P-35/703	Oba	S.	GS14-4	P-44/858
Nagata	F.	OS16-1	P-46/383	Ochiai	H.	GS3-3	P-28/637
		OS16-2	P-46/387	Ogai	H.	OS21-4	P-43/507
Nagayoshi	M.	GS1-1	P-47/589			OS21-6	P-43/515
Nagayuki	Y.	GS12-6	P-45/820	Ogihara	F.	GS12-2	P-45/804
Naito	A.	GS6-2	P-42/687	Ogiwara	K.	OS16-1	P-46/383
Naito	S.	GS14-5	P-44/862	Ogiwara	T.	GS18-5	P-37/938
Naitoh	K.	OS17-1	P-29/411	Ogura	K.	PS1-2	P-29/1008
		OS17-2	P-29/415	Oh	J.H.	PT1	P-22/1
Nakahira	K.T.	OS6-2	P-40/150	Ohara	K.	GS21-6	P-27/999
		OS6-6	P-40/166	Ohara	M.	GS7-5	P-35/719
Nakai	D.	OS9-1	P-36/215	Ohnishi	K.	GS3-5	P-28/645
Nakai	I.	GS8-1	P-34/727			GS4-4	P-28/659
Nakamura	Akihiro	OS18-3	P-24/439	Ohta	N.	OS1-1	P-23/50
Nakamura	Akira	GS18-3	P-37/930	Ohta	Y.	OS17-5	P-30/427
Nakamura	K.	GS2-4	P-34/617	Ohta	Yoshihiro	OS1-4	P-23/62
Nakamura	Masahiro	GS16-1	P-25/885	Oka	T.	OS13-3	P-35/322
Nakamura	Masatoshi	OS22-3	P-41/529			OS13-4	P-35/326
		OS22-6	P-42/541			OS13-5	P-36/330
Nakamura	Yohei	OS14-3	P-39/342	Okamoto	K.	GS6-3	P-42/691
Nakamura	Yosuke	GS8-4	P-34/735	Okamoto	T.	OS19-5	P-46/463
		GS18-4	P-37/934			OS20-2	P-41/475
		GS19-3	P-30/948	Okazaki	K.	GS18-5	P-37/938
Nakamura	Yusuke	OS20-5	P-41/487	Oku	M.	OS14-1	P-39/334
Nakano	H.	GS7-2	P-35/707	Okumura	K.	OS5-1	P-23/126
		GS7-3	P-35/711	Omichi	S.	GS13-5	P-39/838
		GS15-4	P-37/877	Omori	T.	GS1-2	P-47/593
Nakano	K.	OS1-4	P-23/62	Ono	S.	GS4-1	P-28/649
		OS1-5	P-23/66	Ooe	R.	GS2-3	P-34/613
Nakashima	T.	GS8-4	P-34/735	Osawa	H.	OS24-1	P-27/573
		GS16-2	P-25/889			OS24-3	P-28/581
		GS18-1	P-37/922	Osawa	S.	GS5-2	P-31/667
		GS18-4	P-37/934	Oshima	K.	GS13-5	P-39/838
		GS19-3	P-30/948	Osumi	T.	OS24-3	P-28/581
Nakashima	Y.	GS11-4	P-43/793	Otani	T.	GS7-4	P-35/715
Nakategawa	N.	OS1-2	P-23/54	Oya	M.	OS5-1	P-23/126
Nakato	T.	OS6-7	P-40/170			OS5-2	P-23/130
Nakayama	S.	GS4-1	P-28/649			OS5-3	P-23/134
Namba	H.	OS6-6	P-40/166	Oyabu	R.	OS21-6	P-43/515
Narimoto	Y.	GS8-4	P-34/735				
NG	L. P.	OS7-3	P-31/183	[P]			
Niimi	A.	OS18-1	P-24/431	Pagliarini	L.	IT5	P-22/43
		OS18-2	P-24/435	Park	H.J.	OS21-1	P-43/495
Niki	E.	OS7-3	P-31/183	Park	H.S.	GS9-1	P-36/741
Nishida	Y.	PS1-2	P-29/1008			PS1-5	P-29/1016
Nishijima	K.	OS21-6	P-43/515			PS1-6	P-29/1018
Nishimuta	K.	OS15-5	P-45/371			PS1-7	P-29/1021
Nishio	K.	GS11-1	P-42/785	Park	J.B.	GS21-4	P-27/991
		GS11-2	P-42/789	Park	J.G.	OS18-3	P-24/439
Nishiyama	H.	GS9-2	P-36/745			OS18-4	P-24/443
Noda	J.	GS16-5	P-26/901	Park	Minho	OS23-4	P-43/561
Noda	M.	OS24-3	P-28/581			OS23-6	P-44/569
Noguchi	K.	OS20-4	P-41/483	Park	Mison	GS11-4	P-43/793
Noh	C.	OS12-4	P-38/306				
Nomura	Y.	GS9-4	P-36/755	[Q]			
Nozawa	A.	OS1-1	P-23/50	Qian	S.H.	GS10-3	P-25/767
		OS2-3	P-26/79				
		OS2-4	P-26/83	[R]			
Nunohiro	E.	OS18-3	P-24/439	Razali	S.	OS16-5	P-47/399

Ryu	S.	OS23-6	P-44/569	Son	J.	OS12-1	P-38/293
[S]	S.	GS6-3	P-42/691	Song	H.	OS23-3	P-43/557
				Song	J.	OS22-3	P-41/529
Saga	R.	GS6-4	P-42/695	Sorimachi	M.	OS17-5	P-30/427
Sagara	S.	OS5-4	P-23/138	Su	H.	OS4-5	P-26/122
		OS5-5	P-24/142	Su	H.S.	OS11-6	P-33/289
		GS18-5	P-37/938	Su	J.P.	OS11-3	P-32/277
Saito	K.	GS7-3	P-35/711	Su	K.L.	OS10-2	P-32/249
Saito	R.	OS1-4	P-23/62			OS10-3	P-32/253
Saitoh	Atsushi	GS14-2	P-44/850			OS10-4	P-32/257
Saitoh	Ayumu	OS7-1	P-31/174			OS10-5	P-32/261
Sakamoto	M.	OS7-2	P-31/178			OS11-2	P-32/273
		OS7-3	P-31/183	Sugino	J.	OS11-6	P-33/289
		OS7-4	P-31/187	Sugisaka	M.	OS5-3	P-23/134
		OS7-5	P-31/191			OS22-1	P-41/519
		OS15-1	P-44/354			OS22-4	P-41/533
Sakata	K.	GS18-5	P-37/938			OS22-7	P-42/545
Sakata	M.	IT3	P-22/32			GS9-3	P-36/749
Sakurai	N.	OS17-3	P-29/419			GS11-5	P-43/797
		OS17-4	P-30/423	Sugita	K.	GS21-7	P-27/1003
Sakurama	K.	OS1-5	P-23/66			OS13-3	P-35/322
Samura	T.	OS20-3	P-41/479	Suh	J.	OS13-5	P-36/330
Sapaty	P.	GS9-3	P-36/749	Sun	K.	OS23-3	P-43/557
Sato	A.	OS3-3	P-24/95	Susanto	E.	OS13-1	P-35/314
Sato	K.	OS1-3	P-23/58	Suzuki	A.	OS3-1	P-24/87
Sato	N.	GS13-6	P-39/842	Suzuki	H.	GS9-4	P-36/755
Sato	O.	OS3-2	P-24/91	Suzuki	I.	OS14-5	P-40/350
		OS3-3	P-24/95			GS2-3	P-34/613
Sato	T.	GS12-7	P-45/824			GS2-4	P-34/617
Sato	Y.	OS2-2	P-26/74	Suzuki	M.	GS2-5	P-34/621
Sekine	Y.	GS18-5	P-37/938	Suzuki	R.	OS24-2	P-27/577
Seo	W.	GS20-2	P-46/967			GS3-2	P-28/633
Serikawa	S.	GS20-4	P-46/975			GS3-3	P-28/637
Seta	K.	OS6-1	P-40/146	[T]			
		OS6-4	P-40/158				
Shang	L.	OS22-1	P-41/519	Tabata	Y.	OS6-7	P-40/170
Shiao	S.W.	OS11-6	P-33/289	Tabuse	M.	OS9-1	P-36/215
Shibasaki	H.	OS22-6	P-42/541			OS9-2	P-36/219
Shibata	K.	GS15-4	P-37/877			OS9-3	P-36/225
Shibata	N.	GS12-5	P-45/816			OS9-5	P-36/237
Shida	H.	OS20-2	P-41/475	Tachikawa	Y.	OS2-4	P-26/83
Shieh	J.S.	GS6-5	P-42/699	Tadakuma	K.	GS21-5	P-27/995
Shimada	A.	GS10-6	P-25/777	Tadakuma	R.	GS21-5	P-27/995
Shimada	H.	OS15-6	P-45/375	Tagawa	S.	OS7-2	P-31/178
		OS15-7	P-45/379	Taguchi	R.	OS6-2	P-40/150
		OS9-3	P-36/225	Taguchi	Y.	GS7-2	P-35/707
Shimada	K.	OS6-3	P-40/154	Taira	Y.	OS5-1	P-23/126
Shimamura	K.	GS13-5	P-39/838			OS5-3	P-23/134
Shimizu	E.	GS21-3	P-27/987	Tajima	S.	OS14-5	P-40/350
		OS24-4	P-28/585	Takagi	N.	OS5-3	P-23/134
Shimohara	K.	OS5-4	P-23/138	Takahashi	M.	OS18-2	P-24/435
Shimozawa	T.	OS5-5	P-24/142	Takahashi	N.	OS3-2	P-24/91
		GS21-1	P-27/979			OS3-3	P-24/95
		GS10-5	P-25/775	Takahashi	S.	GS20-4	P-46/975
Shin	E.C.	OS24-3	P-28/581	Takashi	T.	OS17-5	P-30/427
Shin	H.C.	OS24-4	P-28/585	Takamura	R.	OS21-4	P-43/507
Shinozawa	K.	OS24-4	P-28/585	Takeda	M.	OS21-3	P-43/503
Shiomi	M.	OS24-4	P-28/585		K.	OS8-1	P-33/195
Shiozaki	A.	GS10-1	P-25/759			OS8-2	P-33/199
Sim	M.	GS3-4	P-28/641			OS8-3	P-33/203

Takeda	K.	OS8-4	P-33/207	Uchikoba	F.	GS18-5	P-37/938
		OS8-5	P-33/211	Uchiyama	N.	GS17-3	P-38/912
Takei	Y.	OS2-3	P-26/79	Ueda	T.	OS19-3	P-46/455
Takenouchi	T.	GS16-4	P-26/897	Ueki	S.	GS19-6	P-30/960
Takeoka	F.	GS13-1	P-39/828	Uenishi	T.	GS8-4	P-34/735
		GS17-4	P-38/916			GS16-2	P-25/889
		GS19-1	P-30/942	Ueno	J.	GS15-1	P-37/866
Takeshita	M.	OS6-6	P-40/166	Ueyama	K.	GS19-5	P-30/956
Takeuchi	K.	OS6-1	P-40/146	Umata	S.	GS14-2	P-44/850
		OS6-3	P-40/154	Utani	A.	GS2-1	P-34/605
		OS6-5	P-40/162			GS5-1	P-30/663
Takeuchi	Y.	OS24-2	P-27/577			GS5-2	P-31/667
Taki	H.	PS1-2	P-29/1008			GS7-1	P-35/703
Takida	R.	OS7-1	P-31/174			GS7-2	P-35/707
		OS7-2	P-31/178			GS7-3	P-35/711
		OS7-3	P-31/183			GS17-2	P-38/909
Takubo	T.	GS21-6	P-27/999				
Tamaki	H.	GS1-1	P-47/589	[V]			
		GS7-5	P-35/719	Voges	K.	OS7-1	P-31/174
Tamaru	S.	OS5-2	P-23/130				
Tamura	H.	GS6-1	P-42/683	[W]			
		GS14-1	P-44/846	Wada	H.	OS5-1	P-23/126
Tan	J.K.	GS10-2	P-25/763	Wang	B.	OS22-6	P-42/541
		GS10-3	P-25/767	Wang	C.C.	OS10-4	P-32/257
		GS10-7	P-25/781			OS11-2	P-32/273
		GS11-4	P-43/793			OS11-4	P-33/281
Tanaka	F.	GS2-6	P-34/625	Wang	F.	GS4-2	P-28/653
Tanaka	Hiroki	GS21-5	P-27/995	Wang	Jiwoo	OS22-7	P-42/545
Tanaka	Hisaya	OS2-2	P-26/74			GS11-5	P-43/797
Tanaka	K.	PS1-1	P-29/1006			GS21-7	P-27/1003
		PS1-8	P-29/1023	Wang	Lan	OS21-2	P-43/499
Tanaka	Yoshito	OS3-5	P-24/103	Wang	Lei	OS4-4	P-26/118
Tanaka	Yutaka	OS3-5	P-24/103	Wang	Q.	OS5-2	P-23/130
Tani	K.	OS20-3	P-41/479	Wang	X.	OS22-6	P-42/541
Taniguchi	R.	GS10-6	P-25/777	Wang	Y.	GS11-5	P-43/797
Tanno	K.	GS6-1	P-42/683			GS21-7	P-27/1003
		GS14-1	P-44/846	Wang	Z.	OS21-6	P-43/515
Tarn	T.J.	PT2	P-22/4	Watanabe	K.	OS16-1	P-46/383
Thorsteinsson	T.	IT4	P-22/36			OS16-2	P-46/387
Tien	C.X.	GS1-4	P-47/601			OS16-3	P-47/391
Tokumitsu	M.	OS19-1	P-46/447			OS16-4	P-47/395
		OS20-5	P-41/487			OS16-5	P-47/399
Tokuyama	T.	OS9-5	P-36/237			OS16-6	P-47/403
Tran	S.D.	GS17-3	P-38/912			OS16-7	P-47/407
Tsuchida	Y.	GS15-2	P-37/870	Watanabe	S.	OS17-5	P-30/427
Tsuji	H.	OS6-1	P-40/146	Watanabe	Takahiro	GS4-2	P-28/653
		GS3-1	P-28/629	Watanabe	Tomokazu	GS16-1	P-25/885
		GS6-3	P-42/691	Watanabe	Y.	OS20-1	P-40/471
Tsuji	Y.	GS5-4	P-31/675	Watari	S.	OS20-5	P-41/487
Tsuruhori	Y.	OS1-4	P-23/62	Wu	X.	OS6-7	P-40/170
Tsuzuki	Y.	OS19-6	P-46/467				
Tzou	J.H.	OS10-2	P-32/249	[X]			
				Xu	Y.	OS13-2	P-35/318
[U]				[Y]			
Uchida	K.	OS7-4	P-31/187	Yamada	S.	OS24-1	P-27/573
		OS7-5	P-31/191	Yamada	Takayoshi	GS16-1	P-25/885
Uchida	M.	OS1-3	P-23/58	Yamada	Takayuki	GS15-5	P-37/881
		OS2-1	P-26/70	Yamaguchi	D.	OS18-2	P-24/435
Uchida	Y.	OS7-4	P-31/187	Yamaguchi	Takashi	OS18-4	P-24/443
		OS7-5	P-31/191				

Yamaguchi	Takehiro	OS18-1	P-24/431	[Z]			
Yamamori	K.	OS15-3	P-44/363		Zain	Z-Md.	OS16-7 P-47/407
		OS15-4	P-45/367		Zhang	C.	OS22-5 P-41/537
		OS15-5	P-45/371		Zhang	F.	OS3-4 P-24/99
Yamamoto	A.	GS10-2	P-25/763				GS21-2 P-27/983
Yamamoto	Hidehiko	GS16-1	P-25/885	Zhang	H.		GS13-2 P-39/830
Yamamoto	Hisao	GS2-1	P-34/605				GS19-2 P-30/944
		GS5-1	P-30/663	Zhang	L.		GS20-4 P-46/975
		GS5-2	P-31/667	Zhang	M.	PT2	P-22/4
		GS7-1	P-35/703	Zhang	N.	OS22-2	P-41/523
		GS7-2	P-35/707	Zhang	Q.Y.	OS4-4	P-26/118
		GS7-3	P-35/711	Zhang	T.	OS22-3	P-41/529
		GS17-2	P-38/909			OS22-5	P-41/537
Yamamoto	M.	GS2-3	P-34/613	Zhang	Y.A.	OS15-1	P-44/354
		GS2-4	P-34/617	Zhao	H.	OS22-4	P-41/533
		GS2-5	P-34/621	Zhao	M.	OS22-2	P-41/523
Yamamoto	T.	GS11-1	P-42/785	Zhao	Xiaoming	GS4-2	P-28/653
Yamanaka	N.	GS17-3	P-38/912	Zhao	Xin	OS21-4	P-43/507
Yamasaki	K.	OS17-3	P-29/419	Zheng	Z.	OS17-3	P-29/419
		OS17-4	P-30/423			OS17-4	P-30/423
Yamasaki	T.	GS11-2	P-42/789	Zhou	H.	OS22-5	P-41/537
Yamashiro	N.	OS20-4	P-41/483	Zhu	Y.	OS22-3	P-41/529
Yamashiro	T.	OS16-2	P-46/387	Zhuo	J.	OS5-2	P-23/130
Yamashita	S.	GS14-1	P-44/846	Zou	J.T.	OS10-1	P-32/245
Yang	D.	GS18-5	P-37/938				
Yang	K.	GS21-1	P-27/979				
Yang	R.	PT2	P-22/4				
Yang	S.	GS18-2	P-37/926				
Yao	Y.	OS13-1	P-35/314				
Yasuda	G.	GS5-5	P-31/679				
Yasunaga	M.	OS15-5	P-45/371				
		OS15-6	P-45/375				
		OS15-7	P-45/379				
Yin	C.	OS6-7	P-40/170				
Yokoi	H.	GS15-3	P-37/873				
Yokomichi	M.	OS3-3	P-24/95				
Yokota	M.	OS13-3	P-35/322				
		OS13-5	P-36/330				
Yoon	T.S.	GS21-4	P-27/991				
Yoshihara	I.	OS15-3	P-44/363				
		OS15-4	P-45/367				
		OS15-5	P-45/371				
		OS15-6	P-45/375				
		OS15-7	P-45/379				
Yoshimatsu	T.	GS14-1	P-44/846				
Yoshinaga	T.	OS7-4	P-31/187				
		OS7-5	P-31/191				
Yoshioka	M.	GS15-2	P-37/870				
Yoshitomi	Y.	OS9-2	P-36/219				
		OS9-3	P-36/225				
		OS9-4	P-36/231				
		OS9-5	P-36/237				
		OS9-6	P-37/241				
Yoshizawa	K.	OS17-3	P-29/419				
		OS17-4	P-30/423				
Yu	K.	OS12-3	P-38/301				
Yu	M.	OS21-2	P-43/499				
Yukinawa	N.	GS14-5	P-44/862				
Yuksel	B.	GS17-5	P-38/918				



まろやかな夜、始まる。

ふくらむ香り。まろやかな深み。「iichiko SPECIAL」は、この香りと味わいのために、新しい酵母によるつくりと、永い熟成の時を重ねて醸した、長期貯蔵の本格焼酎です。香りきわだつオンザロック。伸びのある味わいの水割り。そして、個性ゆたかなストレートで、ひめられた深いうまさの世界を、お楽しみください。

[iichiko いいちこスペシャル]

三和酒類株式会社 TEL:0978-6499 大分県中津市山本道空蔵子 TEL:0978-321431(代) FAX:0978-331658 <http://www.iichiko.co.jp>

飲酒は20歳を過ぎてから。お酒はおいしく適量を。
妊娠中や授乳期の飲酒は、胎児・乳児の発育に影響するおそれがありますので、気をつけましょう。飲酒運転は絶対にやめましょう。

エム・イーシステム株式会社			〒 879-1506 大分県速見郡日出町971-5
TEL	0977-72-7716	URL	http://www.me-system.co.jp
FAX	0977-72-8771	E-mail	info@me-system.co.jp

自動組立機・自動検査装置・画像処理装置の設計製作

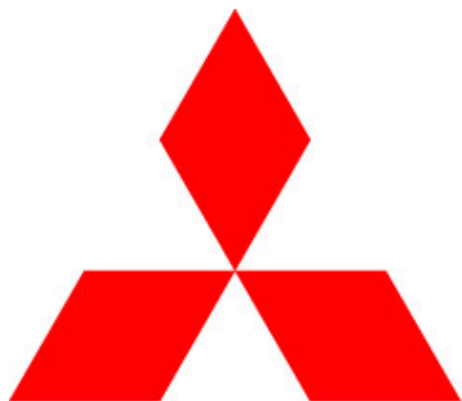


E&C
ENERGY & COMMUNICATION

 **OITA GAS**

5-25 KITA-MATOGAHAMA
BEPPU-CITY OITA
JAPAN 874-0928

PHONE 0977-24-2111



MITSUBISHI ELECTRIC



Taylor & Francis
Taylor & Francis Group

Computer Science Journals from Taylor & Francis

Applied Artificial Intelligence
www.tandf.co.uk/journals/uai

Argument & Computation
www.tandf.co.uk/journals/tarc

Behaviour & Information Technology
www.tandf.co.uk/journals/tbit

Connection Science
www.tandf.co.uk/journals/ccos

Cybernetics and Systems
www.tandf.co.uk/journals/ucbs

Human-Computer Interaction
www.tandf.co.uk/journals/hhci

**International Journal of
Human-Computer Interaction**
www.tandf.co.uk/journals/hihc

**International Journal of Parallel,
Emergent and Distributed Systems**
www.tandf.co.uk/journals/gpaa

**International Journal of Systems
Science**
www.tandf.co.uk/journals/tsys

**Journal of Experimental &
Theoretical Artificial Intelligence**
www.tandf.co.uk/journals/teta

Spatial Cognition & Computation
www.tandf.co.uk/journals/hssc



Taylor & Francis publishes a wide variety of journals in the field of **Artificial Intelligence**.

Visit the journal homepages to:

- Register for table of contents alerts
- Order back issues
- Submit your research
- Find out about special and themed issues
- Recommend the journals to your library
- Read an online sample copy
- Discover free articles

www.tandf.co.uk/journals